Quelques contributions en mécanique de milieux poreux déformables, mélanges solides et fluides : Fractures, liquéfaction, avalanches et déformations lentes.

Renaud Toussaint

Mémoire présenté en vue de l'obtention du diplôme

d'**Habilitation à Diriger des Recherches**

de l' **Université de Strasbourg.**

Discipline : géophysique

Quelques contributions en mécanique de milieux poreux déformables, mélanges solides et fluides : Fractures, liquéfaction, avalanches et déformations lentes.

Présenté par Renaud Toussaint

Chargé de Recherches CNRS,

Institut de Physique du Globe de Strasbourg

Soutenue publiquement

le 19 mars 2013

à l'Ecole et Observatoire des Sciences de la Terre

devant le jury suivant :

Harold Auradou, Rapporteur, Directeur de Recherches CNRS au FAST, Orsay – Université de Paris Sud

Frédérick Delay, Rapporteur, LHYGES, Professeur de l'Université de Strasbourg

Jean-Christophe Géminard, Rapporteur, Directeur de recherches CNRS au Laboratoire de Physique LP - ENS Lyon.

Eirik Grude Flekkøy, Examinateur, Advanced Materials and Complex Systems, Professeur au Département de Physique de l'Université d'Oslo

Knut Jørgen Måløy, Examinateur, Advanced Materials and Complex Systems, Professeur au Département de Physique de l'Université d'Oslo

Gerhard Schäfer, Examinateur, LHYGES, Professeur de l'Université de Strasbourg

Laurence Jouniaux, Directrice de recherches CNRS, Examinatrice, Garante, Institut de Physique du Globe de Strasbourg

Préambule

Attiré par la physique, les mathématiques et les milieux naturels, j'ai parcouru des branches différentes de ces sciences durant mes études et mes recherches. Commençant par des études de mathématiques, j'ai assez vite recherché des formes dans le monde physique. Ceci m'a amené à bifurquer vers la physique théorique, notamment attiré par la cosmologie et les applications énergétiques en fusion contrôlée. Recherchant des formes plus palpables, j'ai ensuite bifurqué vers la géophysique, avec toujours une prédilection pour la physique statistique et la physique de la matière condensée.

Travaillant à la frontière de la géophysique, la physique et la mécanique, les problèmes sur lesquels je me suis penché me définissent petit à petit en physicien mécanicien des mélanges solides et fluides, réactifs ou non, en milieu naturels qu'on peut définir comme multiphasiques et désordonnés, en un mot « malpropres » : mécanique des granulaires saturés ou des écoulements multiphasiques en milieu poreux ou fracturés, instabilités, fracturation, formation d'interfaces réactives naturelles par couplage entre chimie et mécanique. Ces processus complexes présentent de nombreuses applications en science de la terre : soit dans les systèmes naturels présentant des situations de risques potentiels, avec la compréhension du fonctionnement des failles ou des avalanches saturées, soit dans les systèmes que les humains exploitent pour développer ou améliorer le contrôle des processus : exploitation de l'eau, des puits de gaz ou d'hydrocarbures, gestion des déchets, leur stockage et leur migrations, ou la dépollution des sols par remédiation durant des écoulements forcés.

Ma démarche est donc celle d'un géo-physicien, soit un physicien des systèmes terrestres. Mon métier quotidien est fait d'aller-retour entre beaucoup de théorie et simulations, des développements expérimentaux en laboratoire, et un soupçon d'observation d'objets naturels sur le terrain ou à grande échelle – dont je m'inspire pour tenter des descriptions simplifiées des phénomènes. Je suis principalement intéressé par les processus à l'œuvre dans les systèmes géologiques, et leur fonctionnement complexe.

Dans la mesure où ce document est un mémoire d'Habilitation à Diriger des Recherches, il a pour intention de décrire les recherches que j'ai menées jusqu'ici et les problèmes que j'esquisse pour la suite, mais également de montrer ma capacité à fonctionner dans le milieu de la recherche académique, mes talents en jonglerie entre ses différents volets, et mes capacités de conseil pour mener les étudiants qui mèneraient leurs recherches doctorales sous ma houlette à bon port – raison pour laquelle je sollicite de l'Université de Strasbourg cette Habilitation, plutôt que de diriger des recherches non habilitées. La structure de ce document reflète donc cette forme imposée et cette double ambition: je présenterai tout d'abord des éléments sur ma carrière de chercheur et ses divers aspects, mon expérience d'encadrement, d'animation locale de la recherche, d'animation internationale des thèmes que j'ai à cœur, de valorisation, de vulgarisation, de recherche de fonds …

La seconde partie de ce document tentera de présenter un peu plus le fond de ma recherche de façon succincte et synthétique, et d'introduire les publications auxquelles ces recherches ont donné lieu, ainsi que d'esquisser le programme des questions ouvertes qui me guident pour ces prochaines années.

Je profite enfin de ce manuscrit pour remercier les nombreux collaborateurs avec lesquels s'est réalisé ce travail de recherche, principalement en Norvège, en France, en Allemagne et à Glasgow, en Israël, aux Etats-Unis, en Chine et à Cuba. Je remercie également avec grand plaisir les nombreux étudiants, master, doctorants et les jeunes collègues postdoctorants avec lesquels j'ai eu le plaisir d'interagir, et qui ont dans la plupart des cas approfondi et mené à bien des études sur des questions dont je ne maîtrisais que des éléments initiaux.

Résumé : Fractures, liquéfaction et avalanches :mécanique de mélanges solides et fluides

La géophysique, au sens de la physique d'objets et processus géologiques, est une formidable source de problèmes complexes, au sens de la physique de la matière complexe. Par exemple, des problèmes essentiels ont trait à la mécanique des failles, les avalanches, chargées de fluides ou non, de matière en grain ou plus pâteuse, les phases dynamiques de la sédimentation et les instabilités pendant celle-ci, la fracturation, sèche ou déclenchée par le transport des fluides parcourant les pores de la roche ou du sol, la liquéfaction durant les tremblements de terre, les écoulements d'une ou plusieurs phases fluides non miscibles dans des roches poreuses de géométrie irrégulière, la morphogénèse durant l'évolution des roches sédimentaires où évoluent composition chimique et équilibre mécanique entre les composants des roches, l'évolution dynamique de colloïdes aux interactions variables, les échanges de chaleur dans des écoulements chenalisés, l'évolution de la température et son effet sur la mécanique du système en évolution… .
Ces systèmes présentent des interactions qui relèvent de la physique et la mécanique classique, mais avec la présence d'un désordre dans la structure, ou des non-linéarités dans les interactions fondamentales, qui peuvent générer à grande échelle un comportement complexe : notamment, ils peuvent fonctionner sur des échelles de temps et d'espace très étendus, avec coexistence de phases rapides et de phases extrêmement lente, ou avec des déformations diffuses alternant avec des fonctionnements où la déformation est très localisée.
L'aspect polyphasique ou polydisperse de ces systèmes peut générer une telle complexité, sans que celle-ci reflète nécessairement la multiplicité des échelles déjà présentes dans la composition du système : dans des systèmes au fonctionnement critique, ou au voisinage de transitions de phases dites du second ordre, de nombreux systèmes dynamiques sont connus pour faire émerger, à partir de désordre présent à petite échelle et d'interaction simples, des organisations à grande échelle du processus en jeu.
On aborde dans ce mémoire des modèles analytiques, numériques et des expériences ayant trait à la mécanique de tels systèmes naturels : écoulements mono- ou multiphasiques en milieux poreux ou fracturés, déformables ou non, fractures, avalanches, fonctionnement mécanique des failles, déformation lente des roches avec couplage entre chimie et mécanique.

Résumé du cadre de mon parcours de chercheur

Je suis chargé de recherches CNRS à l'Institut de Physique du Globe de Strasbourg depuis 2004. Entré alors comme Chargé de Recherches 2eme classe, j'ai été promu chargé de recherches 1ère classe en 2008 – en tant qu'agent 21727.

Auparavant, j'ai poursuivi des études de mathématiques (licence, maîtrise, agrégation, option mécanique), puis de physique théorique (licence, maîtrise, magistère, DEA) à l'ENS Lyon, comme élève normalien de 1991 à 1995, faisant suite à des études secondaires à Troyes, et une prépa maths à Louis le Grand, Paris. J'ai d'abord en parallèle à mes études et recherches, enseigné les mathématiques après 1994 comme professeurs agrégé, moniteur et ATER, à divers niveaux du collège à la licence. En 2005, on m'a annoncé par écrit que j'avais été extrait de mon corps, désagrégé des mathématiques, mais fort heureusement immédiatement réintégré dans un corps de chargé de recherches du CNRS.

Après avoir évolué des mathématiques vers la physique, intéressé par la jonction entre théories et monde naturel environnant, je me suis finalement tourné en dernière année d'ENS vers des applications naturelles plus proches que l'astrophysique, la cosmologie et les particules : ceci m'a mené au DEA de géophysique interne de l'Institut de Physique du Globe de Paris, en 1995.

J'ai ensuite enseigné de 1995 à 1997 dans le cadre de son service civil, comme professeur de mathématiques agrégé à l'étranger, en Bulgarie. Une fois ce service effectué, j'ai mené à bien ma thèse sur des modèles théoriques de fracturation en milieux hétérogènes avec Steve Pride, géophysicien théoricien enthousiaste rencontré à Paris. Cette thèse mêlait des aspects théoriques et les applications vers l'objet étudié, à savoir la compréhension de la génèse de la localisation dans la fracture. Dans l'espoir de poursuivre une carrière de recherche académique, j'ai ensuite effectué un ATER à Géosciences Rennes, puis 3 ans de postdoctorat de 2001 à 2004, à travers quatre contrats successifs, dans le groupe matière complexe des Universités d'Oslo et de Trondheim (NTNU), en Norvège. J'ai alors pu développer des techniques numériques de mécanique des fluides et des solides, en sus des approches analytiques que j'avais développées auparavant. J'ai également alors initié une activité expérimentale sur des problèmes d'écoulements multiphasiques en milieux poreux, et sur des problèmes de fracturation générée par des surpressions de fluides.

Par la suite, rejoignant l'Institut de Physique du Globe de Strasbourg en 2004 en tant que chargé de recherches CNRS, j'ai poursuivi ces activités, en étroite collaboration avec mes collaborateurs précédents, Steve Pride au Lawrence National Berkeley Laboratory, et le groupe Complex, d'Eirik G Flekkoy et KJ Maloy à Oslo. J'ai rejoint les études sur l'eau faites en collaboration avec le LHyGeS et REALISE, et les études sur les migrations d'hydrocarbones sous diverses sollicitations mécaniques, avec les projets appliqués au département de physique d'Oslo. J'ai également étendu des collaborations avec des groupes de physique (ESPCI) et géophysique (Grenoble, IsTerre), et avec des groupes étrangers, principalement en travaillant sur des couplages entre mécanique et chimie avec le groupe de tectonophysics de l'Université de Mainz (D Koehn), et avec le département de sciences de la Terre de l'Université de Jérusalem (Einat Aharonov), sur des problèmes de liquéfaction et de modélisation de mécanique des failles. J'ai in fine développé des méthodes et modèles permettant de déterminer les paléocontraintes de formation de stylolites dans des roches, et d'estimer l'impact de la dissolution sur la génèse de contraintes dans les carbonates, permettant d'aborder par de nouveaux outils mélangeant physique, mécanique et chimie, la rhéologie à grande échelle de temps et d'espace des bassins sédimentaires – problèmes cruciaux pour les problématiques de stockage.

Depuis 2002, où j'ai débuté ma carrière de chercheur docteur, j'ai coencadré 18 thèses entre 50% et 5% (dont plusieurs comme codirecteur à l'étranger). Chacune des 14 thèses soutenues a fait l'objet de 2 à 6 publications cosignées. Les thésards ont tous trouvé un travail comme postdoctorants ou dans l'industrie. J'ai également accompagné les recherches de 5 postdoctorants à Strasbourg. Ces études ont fait l'objet de 54 publications de rang A, et 18 proceedings, plus 11 publications actuellement en cours de révision.
Ces travaux sont dans une certaine mesure reconnus par la communauté de géophysique et par celle de physique des milieux granulaires, comme en atteste des citations (~7/article sur ces 10 dernières années), des invitations à présenter mes travaux dans une trentaine de conférences internationales ou laboratoires, et de très régulières présentations sur une base volontaire (environ 250 présentations ou posters). Le CNRS m'a également attribué une « prime d'excellence scientifique » pour la période 2010-2013.

Sur les aspects pédagogiques, j'ai enseigné à de nombreux niveaux, à partir du secondaire lors de ses débuts comme agrégé de mathématiques, jusqu'au niveau doctoral. Ces dernières années, j'ai enseigné régulièrement en école d'ingénieurs, en université ou en classe préparatoire aux grandes écoles (entre 50 et 200 heures par an d'équivalent TD au total selon les années depuis 2005).
Je participe actuellement au montage de la « Maison des sciences en Alsace au service des professeurs », projet de formation continue des enseignants du primaire et du collège portée par l'université de Strasbourg, l'académie de Strasbourg, l'académie des sciences et la fondation « la main à la pâte » - en temps que coordinateur responsable des géosciences.

J'ai également à l'IPGS encadré, principalement ou comme encadrant secondaire, 9 stages de M2 ou DEA, 23 stages de M1, et de nombreux projets de courte durée (quelques dizaines de stages courts d'élèves ingénieurs en informatique, de travaux d'intérêt personnel encadrés d'élèves de prépa.)

In fine, je participe activement à la vie du laboratoire, à travers la définition et animation du projet comme responsable d'équipe géophysique expérimentale à partir de janvier 2013, ma participation au conseil d'institut (EOST) comme membre élu depuis 2006, membre élu du conseil scientifique de l'ULP avant la fusion dans l'Université de Strasbourg, et comme responsable des séminaires du laboratoire, du web de l'équipe, et des membre des commissions de définitions de moyens de calcul parallèle du laboratoire. J'ai participé à trois jurys de thèses et d'assez nombreux jurys de Master.

Je participe également aux tâches d'organisation et animation de la recherche au niveau international, avec l'organisation de session (5 dans les dernières rencontres européennes de géophysique, l'EGU) ou l'organisation du workshop international « FlowTrap » en Octobre 2011, l'édition d'un volume spécial de Journal of Structural Geology sur la Mécanique des Failles, et la participation comme expert et reviewer de nombreux articles et projets, en national et en international, en géophysique et en physique.

Pour la période 2013-2016, je participe comme chercheur principal à Strasbourg, et co-coordinateur du réseau avec Daniel Koehn, Glasgow, au projet européen « FlowTrans », Flow and Transformation in Porous Media, Initial Training Network du programme Marie Curie. Deux étudiants thésards seront recrutés sur cette thématique, sur des écoulements réactifs, et des simulations de fracturation et écoulements fluides. Ce projet regroupe huit universités, et six partenaires privés en Europe.

J’ai également régulièrement monté des projets et obtenus des contrats auprès du CNRS, de l’Université, de l’ANR, de l’ANDRA, ou de partenaires internationaux. J’ai ainsi obtenu dans une dizaine de projets que j’ai monté et mené, près de 400 kEuros de financement sous forme de contrats et projets depuis 2004, dont une moitié sous forme de salaires de jeunes chercheurs postdocs. J’ai aussi participé à quelques autres projets comme partenaire.

Bref Curriculum Vitae

Renaud TOUSSAINT, Chargé de Recherches CNRS (Agent 21727), Université de Strasbourg, Institut de Physique du Globe de Strasbourg. Born 9.30.1971.

Education

2001-2004 Postdoc in the Complex group, University of Oslo and NTNU. Funding from EU, NFR, UiO and NTNU.

1997-2001 Ph.D. (Fracture) in Géosciences Rennes, University of Rennes I

1991-1995 Normalien at ENS Lyon: M2 (DEA) in Geophysics, University Paris VI, M2 (DEA) in Theoretical Physics, ENS Lyon, Magistère in Physics, M1 in Physics and M1 in Mathematics, ENS Lyon. Agregation de Mathématiques, Option Mécanique analytique.

Appointments

2004-present CR CNRS, (1st class since 2008), Experimental Geophysics, IPGS, Univ Strasbourg

2004-2010 Regularly invited professor for short stays at the University of Oslo.

2001-2004 Postdoc at the University of Oslo and University of Trondheim Physics Depts.

Awards: 2010: PES (CNRS recognition for « Scientific Excellence »).

Synergetic activities since 2000

Co-coordination of ITN "FlowTrans", 2013-2016, 8 Universities & 2 companies, 2 PhD in Strasbourg. French-norwegian PICS project "Mechanical instabilities and geophysical hazards", (8000 euros / year) 2006-2008, DyeTI (INSU) project ``fluid-rock interactions'', (12000 euros) 2006, and of the 3F project (INSU) ''Rheology of fault asperities", (10000 euros), 2007. Project "stylolites and paleostresses in Bure", CNRS/ANDRA FORPRO (25000 euros, 2009), and "stylolites and transport (45000 euros, 2010). Participation to 17 french or international research programs since 2001. (ANR, Mi Lourds, European TMR network, NFR, Norway, Max Planck Gesellschaft). Participation to GdR MeGe and TransNat.

Cosupervisor of 17 PhD students (between 10 and 50 %) having defended their PhD (from 2 to 6 publications / PhD), and 2 students currently carrying their PhD.

Cosupervision of 10 Master 2 and 23 Master 1 students. Cosupervisor of 4*1 year of postdoc students. Elected member of the board of the institute EOST (2006-), and of the Scientific Council of the University (2006-2008). Convener at EGU (4 sessions), Reviewer for ANR projects, Norwegian, German projects, Universities of Grenoble and Orsay projects, JGR, Phys Rev Lett, Phys Rev E, TIPM, J Struct Geol, Water Resource Res..... (~15 projects and 100 articles).

5 selected recent publications

81 publications, peer reviewed journals (55+9 submitted) and proceedings (17) (*h*=14, 521 citations, Scholar Google),

- Niebling, M.J., R. Toussaint, E.G. Flekkøy and K.J. Måløy, Dynamic aerofracture of dense granular packings, Phys. Rev. E, accepted, 2012.
- Niebling, M.J., E.G. Flekkøy, K.J. Måløy, R. Toussaint, 2010. Sedimentation instabilities: impact of the fluid compressibility and viscosity, ***Phys. Rev. E*** 82, 051302.
- Neuville, A., R. Toussaint and J. Schmittbuhl, 2010. Hydrothermal flows in a rough fracture, ***Phys. Rev. E***, 82, 3, doi: 10.1103/PhysRevE.82.036317
- Toussaint, R., G. Løvoll, Y. Méheust, K.J. Måløy and J. Schmittbuhl, Influence of pore-scale disorder on viscous fingering during drainage, ***Europhys. Lett.***, 71, 583 (2005).
- Toussaint R. and S.R. Pride, Statistical mechanics of quasistatic interacting damage models, ***Phys. Rev. E***, 71, 046127 (2005).

Publications accessibles sur ftp://ftp-eost.u-strasbg.fr/renaud/HDR/ ou généralement sur http://eost.unistra.fr/renaud/

Activités d'enseignement et de formation :
Responsable à l'EOST de la « Maison pour la science », organisme de formation continue de professeurs des écoles et professeurs du secondaire, 2012-… (72 heures eq. TD).
Automates cellulaires et méthodes numériques discrètes en géophysique : CM et TD, M2, 3A, 24h (2011-…)
Mécanique des granulaires et des mélanges: CM et TD, 6 à 10 h/an (2005-2012) M2, 3A ingenieurs EOST
Mécanique des fluides, CM et TD, 24 h/an (2007-2012), 1ere annee (1A) ingenieurs EOST
Mathématiques pour économistes, CM et conception/organisation des TD (2008-2009), 72 h eq. TD, L2 (280 étudiants), PEGE (Pole Européen de Gestion et d.Economie), UdS (Université de Strasbourg)
Colles de Physique en maths spé, 35 à 60h / an, et rédaction de sujet de physique aux concours CCP
Encadrement de stages, M2 (8), 2A ingénieurs ou M1 (20), 1A ingénieurs (16), TIPE (15).
Formation continue de professeurs de physique: Ecole d'été E2Phy.
avant 2001, monitorat, ATER, CM et TD (300 h eq TD) de physique et mathématiques de DEUG à L1
2 ans enseignant du secondaire à plein temps, professeur agrégé de mathématiques (1995-1997, service civil, lycée français en Bulgarie)

Contrats avec des entreprises ou des organismes publics ou privés – levée de fonds de recherche auprès d'agences de recherche ou troisièmes partenaires.
Contrat européen ITN (Initial Training Network) « Flowtrans », 2013-2016. (4.5 Meuros, dont 517 kEuros à Strasbourg).
Contrat ANR Blanc « Landquake », 2012-2014. (60kEuros, dont 40 kEuros de salaire de doctorant)
Contrat ANR Blanc « Airflow », en liste complémentaire en 2012.
Contrat avec l'Ambassade de France à Cuba « Physique des catastrophes naturelles », 2 kEuros.
Contrat FORPRO (CNRS/ANDRA) "Stylolites, rhéologie et transport dans les roches carbonatées", 55 kEuros (28 kEuros à Strasbourg), 2010-2012, et "Histoire des contraintes et cinematique dans les formations calcaires du site de Bure", 25 kEuros, 2008-2009.
Participation au PPF REALISE : 50 kEuros d'équipements de 2008 à 2012,
Participation au CPER REALISE : Caméra rapide, 69 kEuros, 2012.
Contrats ANR mentionnés dans la partie "animation", ci-dessus, équipements et salaires de jeunes chercheurs (participant à l'élaboration de projet et co-encadrement pour 5 ans de postdoc sur 4 ANR).
Elaboration et Gestion du contrat d'accueil de jeune chercheur (postdoctorat "morphogénèse durant l'aérofracture") UDS, 45 kEuros.

Valorisation économique, sociale, culturelle de vos activités de recherche :
Participation chaque année à la science en fête sous forme de visite lors de journées portes ouvertes de laboratoire, ou à la nuit des chercheurs.
Environ une conférence annuelle de vulgarisation en milieu scolaire (lycée).
Quelques animations lors de rencontres de professeurs de physique.
Participation en 2010 à la nuit des chercheurs, rencontre table ronde, projection et débat public.

Contacts avec élèves de lycée et prépa par encadrement de leurs TIP et TIPE (3 à 8 par an).
Accueil de collégiens en stage d'observation.
Quelques interviews lors d'émissions de télévision et radio locale.
Contacts avec des industriels lors de conférences ou sollicitations, occasionnant parfois un contrat ultérieur.

Management de la recherche :
Responsabilité du groupe « Géophysique expérimentale », IPGS, Janvier 2013-…
Responsabilité du thème transverse « Eau », IPGS, 2013-…
Co-encadrement de 5 postdoctorants, 18 thésards (10 à 50%) et 5 M2 depuis 2002.
Responsable de l'équipe Géophysique expérimentale à partir de 2013 (préparation du quinquennal).
Responsable des séminaires du laboratoire (2005-), du web de l'équipe et membre du groupe moyens de calcul
Membre du conseil de l'Institut EOST (2005-)
Membre du Conseil scientifique de l'université Louis Pasteur (2007-2008. Fusion des trois universités strasbourgeoise à l'issue de cette période)
membre du comité d'évaluation de l'AERES pour l'UMR 7516, 2008: représentant du CS de l'UdS
participation aux commissions de spécialiste et commissions mixtes de recrutement de l'EOST
Participation à 4 jurys de thèse, 4 jurys de master 2 et 10 jurys de master 1

Informations complémentaires :
Collaborations actives régulières avec des groupes internationaux: norvégiens, allemands, israeliens, UK, chinois, états-unis.
Collaboration en France avec des collègues de Paris (ESPCI, IPGP), Grenoble (LGIT), Montpellier.

Animation scientifique / Scientific coordination :
Responsabilité de l'équipe Géophysique Expérimentale, IPGS (quinquennal 2013-2017),
Animation du thème transverse « Eau » de l'IPGS,
Participation à deux projets de quadriennaux (2005-2008 et 2009-2012) de l'IPGS.
Participation comme "PI" ou responsable de "WP" à l'élaboration des projets de recherche: responsable du PICS France Norvege, "instabilites mecaniques et aleas geophysiques" 2006-2008, du
WP Strasbourg de l'ANR Triggerland (1 an de postoctorat), 2006-2008, du postdoc UDS d'accueil de jeune chercheur "morphogénèse et aérofracture", 2010, coresponsable de postdoc dans l'ANR MODALSIS et SUPNAF (2006-2008 et 2009-2011), et dans l'ANR SISCA (2010-2012), responsable de 4 projets INSU et 2 projets FORPRO (2004-2010).
Convener de 5 sessions à l'EGU (2009 à 2013), Rapporteur de projets (~25, ANR, Universités, NFR) et d'environ 130 articles (Phys Rev, JGR, J surf and colloids) depuis 2000.

Changements thématiques / Thematic mobility :
Débuts de mathématicien et mécanicien (ENS Lyon, parcours maths/physique et agrégation de mathématiques), poursuite en
physique théorique (DEA) et géophysique (DEA, thèse), applications théoriques de mécanique statistique la fracturation en
géophysique (thèse), couplages mécanique des solides / fluides lors de 3 ans de postdoc en physique: développement de techniques

numériques (granulaires / fluides). Depuis le recrutement comme CR, en sus des approches théoriques et numériques,
développement d'expériences, suivi optique, acoustique et contrôles.
Thématiquement, après fracturation, ajout des thématiques: fluides, mono ou multiphasiques, fluidisation, écoulements de surface, couplages chimique (stylolites) et thermique, mécanique des failles.

Parcours professionnel au sein d'entreprises ou d'organismes publics ou privés / Professional experience in the private sector, or with public or private research organizations :
Mobilité sur 2004-2010:
2011-2012 : membre participant du Center for Advanced Studies « Complex Flows » à l'Académie des Sciences de Norvège. (1 mois)
2004-2010 : courts séjours de professeur invité (~ 1 mois par an) à l'université d'Oslo, université d'Hawaii et université de Jérusalem.
2003-2004: chercheur (financement: Norsk Forsknings Radet), université d'Oslo, groupe "Complex"
2002-2003: Postdoc, université de Trondheim (NTNU), groupe "advanced materials and complex systems"
2001-2002: Postdoc, groupe matière condensée, université d'Oslo, "European research program - Training and mobility network - Fractals".
2000-2001: ATER agrégé, Géosciences Rennes. 1 an. Chargé de cours, TD et TP en licence et DEUG
1997-2000: Moniteur agrégé à l'université de Rennes. Chargé de cours et TD en licence, 64h/an, 1997-2000
1995-1997: Enseignant agrégé à plein temps, 1995-1997 (Coopérant Service National, Lycée Français de Sofia, Bulgarie)
1991-1995: Elève Normalien ENS Lyon (professeur stagiaire, agrégé de mathématiques/mécanique en 1994)
1989-1991 : Elève (M2,M'1) de prépa au lycée Louis le Grand, Paris.

Distinctions :
Prime d'Excellence Scientifique du CNRS 2010,
publication du CV dans diverses bases bibliographiques type who's who.

CV détaillé

Etat Civil :

Nom :Toussaint
Prénom : Renaud
Date de naissance : 30/09/1971
Marié, deux enfants.

Affectation :
Corps-grade : CR1 CNRS (depuis 2008, CR2 CNRS de 2004 à 2008)
Professeur agrégé de mathématiques, option mécanique analytique.(1994)

Établissement public d'affectation:
Université de Strasbourg
Unité de recherche d'appartenance : IPGS, UMR 7516, Institut de Physique du Globe de Strasbourg, Université de Strasbourg, 5 rue Descartes, F-67000 Strasbourg
Nom du responsable de l'unité : Jacques HINDERER
Groupe de géophysique expérimentale
Institut du CNRS : INSU
Délégation du CNRS : Alsace
Section du Comité National : 18

Contact/pages

N° de téléphone : 0673142994
e-mail : Renaud.Toussaint@unistra.fr
Pages personnelles :
http : //eost.u-strasbg.fr/renaud/
Pages du laboratoire :
http://eost.unistra.fr/

Diplômes et experiences professionnelles de recherche :

2008-11 :
CR1 CNRS à l'IPG Strasbourg. PES 2010.
2004-08 :
CR2 CNRS à l'IPG Strasbourg
2004 :
Recrutement au CNRS en tant que CR2 : 1er Octobre 2004
2003-04
PostDoc à l'Université d'Oslo (UiO), ``Complex Systems" group, avec les Pr.. Eirik Flekkøy and Knut Jørgen Måløy, salaire du Norwegian Research Council (NFR) / UiO.
2002-03
PostDoc à l'Université de Trondheim (NTNU), groupe ``Complex Systems" avec les Pr. Alex Hansen and Jon Otto Fossum, salaire du NTNU Trondheim.
2001-02
PostDoc à l'Université d'Oslo (UiO), avec le Pr. Jens Feder, dans le cadre du "Training and Mobility of Researchers (TMR) program" de l'UE - contract number FMRXCT980183 , "Fractal Structures and Self-Organization" -
2000-01
A.T.E.R. à Rennes I (98 heures de cours).
1997-01
* Doctorat de sciences de la Terre à ``Géosciences Rennes", Université de Rennes I, sous la direction du Pr. Steven R. Pride, titre:
``Fracturation des Roches en Compression: le Processus de Localisation en tant que Phénomène Critique" soutenue le 23 Mars 2001, avec la plus haute distinction - ``très honorable".
* Moniteur à Géosciences Rennes.
* Bourse de thèse et monitorat obtenu sur contingent ENS Lyon.
1995-97
Service National – cooperation,
Professeur de mathématiques agrégé au lycée francais de Sofia, Bulgarie.
1991-95
Élève normalien de l'E.N.S. Lyon. Recu sur le concours de mathématiques en 91. (48 eme / 1200 candidats)
1994-95
D.E.A de Géophysique Interne, Institut de Physique du Globe de Paris, Paris - VII (2eme/30).
1993-94
* D.E.A. en Physique Theorique, Theorie des Champs, Université Claude Bernard / ENS Lyon.
* Agrégation de Mathématiques , option mécanique analytique.
* Magistère de Sciences de la matière, E.N.S. Lyon / Université Claude Bernard.
1992-93
Maîtrise de Physique, E.N.S. Lyon / Université Claude Bernard.
1991-92
Licence de Physique, Licence de Mathématiques, E.N.S. Lyon / Université Claude Bernard.

1989-91

Classes Préparatoires: Mathématiques Supérieures and Mathématiques Spéciales M' au Lycée Louis-le-Grand, Paris

1989

Baccalauréat, série C, Mention TB. Lycée Chrestien de Troyes, Troyes.

1974-1989

Scolarité primaire et secondaire dans les établissements publics des villes de Aix-en-Othe et Troyes, Aube.

Expérience de recherche durant la scolarité à l’ENS, la thèse et la période postdoctorale

1992

L.A.P.P. (Particle Physics Laboratory of Annecy) and C.E.R.N. (European Center on Nuclear Physics, Geneva), 2 Months. Numerical analysis of experimental data on the determination of the W boson, under the direction of Dr. D. Perret-Gallix (C.N.R.S.).

1993

Physics Laboratory of the E.N.S. Lyon, Astrophysics Group, 2 Months. Numerical modelization on phase transitions between ionized states of Helium and Iron in Brown Dwarves, under direction of M. G. Chabrier (C.N.R.S.).

1994

C.E.A. (Atomic Energy Center), D.R.F.C (Controlled Fusion Research Department) in Cadarache, France, 3 months. Theoretical work on noncollisional thermalization of electrons and protons in the plasmas generated in tokamaks, under direction of Pr. D. Escande.

1995

I.P.G.P. (Institute of Globe Physics, Paris), Geomagnetism Department, 3 months. Theoretical work and numerical modelization on the physico-chemical processes at the electrolyte/oxyde interfaces in porous rocks, under direction of Pr. Steven R. Pride.

1997-01

University of Rennes I, Geology Institute ``Géosciences Rennes", Geophysics group: PhD, under direction of Pr. Steven R. Pride, defended on March the 23rd, 2001: ``Rock Fracturation in Compression: Localization Process as a Critical Phenomenon". Interdisplinary theoretical subject, development of a general framework to use statistical mechanics techniques in rock mechanics problems.

2001-04

PostDoc in the ``Complex Systems" groups of the Departments of Physics of the University of Oslo (2003-2004) and University of Trondheim (NTNU) (2002-2003), and in the center of excellence ``Physics of Geological Processes" at the Department of Physics of the University of Oslo (2001-2002):

In collaboration with Prs E. Flekkøy, K.J. Måløy and J.O. Fossum, simulation and experimental work on confined coupled fluid granular flows and hydrofracture, and on biphasic flows in random porous media.

In collaboration with Pr. Eirik G. Flekkøy (University of Oslo, UiO), Pr. Arne Skjeltorp (I.F.E., Kjeller and UiO), Dr. Geir Helgesen (I.F.E., Kjeller, Norway) and M. J. Akselvoll (I.F.E. and UiO): theoretical, analytical and numerical work on the self-organization of non-magnetic microspheres in ferrofluid layers, interacting with each other under the effect of a magnetic field.

In collaboration with Pr. Alex Hansen (NTNU), analytical study of fuse models and fracture networks. In collaboration with Pr. Jens Feder (UiO) and Mrs L. Uri (PhD student, UiO), modelization of the dynamics of granular flows with elastoplastically deformable grains, analog system to describe the phenomenon of primary migration and compaction.

Supervision de jeunes chercheurs et d'étudiants

(Mentoring junior researchers and student supervision)

Encadrement et coencadrement de jeunes chercheurs postdoctorants :

(Collaboration with and « mentoring of» postdoc researchers)

Georg Koval, 2008, postdoc in the framework of the ANR ``TRIGGERLAND", 9 months, fluidization experiments and numerical simulations, with J. Schmittbuhl. Georg found a position as Maitre de conferences at INSA Strasbourg.

Guillaume Daniel, 2008, postdoc in the framework of the ANR ``MODALSIS", 9 months, development of microseismology techniques applied to laboratory acoustic emissions during interfacial fracture, and to large scale seismic monitoring data from the Marmara sea, with J. Schmittbuhl. Guillaume found a position as Maitre de Conférences at the Université de Franche Comté, and moved to a private seismology company , Magnitude, with whom we collaborate via the ITN FlowTrans

Olivier Lengliné, 2009-2012, postdoc in the framework of the ANR ``SUPNAF", and of the CAS "Complex Flows", Oslo: development of localization techniques and characterization of acoustic emissions during interfacial fracture experiments, and thermal effects in fracture, with J. Schmittbuhl and K.J. Maloy. Olivier pursued as a postdoc in Oslo, another one in Caltech, and found a position as Maitre de Conférences at IPGS.

Anke Spickermann, 2009-2012, postdoc (ANR SISCA, European project SAFELAND), with J.P. Malet and J.Schmittbuhl. Anke went on maternity leave.

Michael Niebling, 2010, postdoc (University of Strasbourg) on ``Study of morphogenesis during hydrofracture". Michael pursued as a postdoc in UiO.

Co-encadrement d'etudiants de thèse (10 à 50%):

(co-Supervision of PhD students)

* Grunde Løvoll, UiO, Norway, 2001-2003, with Pr. K.J. Måløy: analysis of experimental viscous fingering in porous Hele-Shaw cells. Grunde did a postdoc at UiO, and continued a career at Veritas, Oslo. 5 joint publications.
* Jan-Ludvig Vinningland, UiO, Norway, 2002-2006, with Pr. E.G. Flekkøy: simulations of coupled granular flow in fluidized beds. Jan-Ludvig did a postdoc at ETH Zurich, and found a position as permanent researcher at IRIS, Oslo. 6 joint publications.
* Jørgen Akselvoll, UiO-IFE, Norway, 2001-2005, with Pr. A.T. Skjeltorp and Dr. G. Helgesen: experimental work on the equilibrium properties and dynamics of magnetic colloids. Jørgen found a position at the national patent office. 3 joint publications.
* Lina Uri, UiO-PGP, Norway, 2001-2004, with Pr. J. Feder and Dr. D.K. Dysthe: experimental work on the gravitational compaction of populations of viscoelastoplastic grains. Lina pursued a career at EMGS, an exploration company dedicated to electropagnetic techniques.

* Øistein Johnssen, UiO, Norway, 2004-2007, Petromax NFR funding, with Prs. K.J. Måløy and E.G. Flekkøy, experimental work on sand production trigerred by fluid flow. Oistein did a postdoc at ESPCI, Paris, and found a stable researcher position at the Norsk Geoteknisk Institutt, Oslo. 5 joint publications.
* Michael Niebling, UiO, Norway, 2006-2009, Petromax NFR funding, with Prs. E.G. Flekkøy and K.J. Måløy, numerical work about hydrofracture. Michael did a postdoc in Strasbourg, and a later postdoc in UiO. 4 joint publications.
* Mikhailo Jankov, UiO, Norway, 2006-2010, Petromax NFR funding, with Prs. E.G. Flekkøy, K.J. Måløy and Steve Pride, experimental work about seismic stimulation of hydrocarbon production, multiphasic flow in oscillatory pressure gradients. Mihailo found a permanent engineering position at UiO. 3 joint publications.
* Olav Aursjø, UiO, Norway, 2006-2010, Petromax NFR funding, with Prs. E.G. Flekkøy, K.J. Måløy and Steve Pride, numerical work about seismic stimulation, multiphasic flow in oscillatory pressure gradients (few interactions during his thesis). Olav did a postdoc at Lawrence Berkeley national lab.
* Mélanie Grob, IPG Strasbourg, 2006-2009, University of Strasbourg, with Jean Schmittbuhl, Stéphane Santucci, Knut Jørgen Måløy, Alain Cochard and Luis Rivera, experimental work on laboratory sismogenesis. Mélanie pursued an academic career as a postdoc at the University of Calgary. 3 joint publications.
* Liran Goren, Weizmann Institute, Israel, 2006-2010, with Einat Aharonov, numerical and experimental work about fluidization of granular material during EQ due to intersticial fluid. Liran pursued as a postdoc at ETH Zurich, and found a permanent researcher position in Israel. 4 joint publications.
* Amélie Neuville, IPG Strasbourg, 2007-2010, University of Strasbourg, with Jean Schmittbuhl and Eirik G. Flekkøy, ``Comportement hydro-thermique d'un écoulement de fluide dans une fracture rugueuse: Modélisation et application à des massifs fracturés.''. Theoretical and numerical work on thermo-mechanical coupling between fluids and rocks during flow in fractures. Amélie pursued her academic career through several postdocs at the University of Oslo. 6 joint publications.
* Marcus Ebner, University of Mainz, 2007-2009, DFG (German Research Fundation) funding, with Daniel Koehn, experimental, numerical and field work on patterns resulting from stress induced dissolution, and the link between the morphology and the applied stress. Marcus found a permanent position at the Austrian Geological Survey. 3 joint publications.
* Julien Travelletti, University of Strasbourg, ITN Mountain risk funding, 2008-..., with J.P. Malet and J. Schmittbuhl, development of 3-dimensional multiscale CIV techniques to monitor the variations of the velocity field of SuperSauze landslide. Julien found a stable position as a researcher in a geotechnical private company in Switzerland. 2 joint publications.
* Leehee Laronne-Ben-Itzhak, Weizmann Institute, Israel, 2009-2012, with Einat Aharonov, work on modeling stylolite genesis and analyzing stylolite characteristics as strain markers. Leehee became a physics teacher. 2 joint publications.
* Alexandra Rolland, University of Strasbourg / ANDRA funding, 2010-..., Rheology of calcite and use of stylolites as paleostress gauges: stress history of the Bure massif, with P. Baud, F. Cornet and J. Schmittbuhl. 2 joint publications.
* Irfan Ghani, University of Mainz, FRACS Consortium funding, 2009-..., with D Koehn, numerical work on the role of fluid on the morphogenesis of rock joints. 1 joint publication. * Maxime Farin, University of Paris VII, 2011-..., ANR LANDQUAKE funding, with A. Mangeney, avalanches and microseismicity, experimental approach

Direction de thèses

(Supervision of PhD student as primary advisor)

* Cécile Clément, University of Strasbourg, with T. Reuschlé, 2012-..., Work on two-phase flow in deformable soils, and applications in air sparging remediation methods - ``Remédiation des sols pollués par liquéfaction par injection d'air : Modèles numériques d'écoulements triphasiques air/eau/granulaires."
* Gustavo Sanchez-Colina, University of Havana, research stay financed by the french Embassy in Cuba, with E. Altshuler, 2012-…, Instrumental developments and experiments on ``Physics of natural catastrophes"
* available position to EU students outside France, Sept 2013-2016, Marie Curie ITN Transflow thesis on Flow in chemically evolving fractures
* available position to EU students outside France, Sept 2013-2016, Marie Curie ITN Transflow thesis on Evolution of tight rocks during fluid injection

Encadrement de stages de Master et d'élèves ingenieurs:

Supervision d'étudiants de M2

(Master students: Master 2 research projects or year long Master programs):

*Øistein Johnssen, UiO, 2002-2004, with Prs. K.J. Måløy and E.G. Flekkøy, experimental work on flow and hydrofracture of confined granular medium by air injection in Hele-Shaw cells.
* Herbert Yanksson, NTNU, 2002, with Pr. J.O. Fossum: tribology of the laponite/glass contact, experimental work.
* Morten Gunnufsen, UiO-NTNU, 2003-2004, with Prs. E.G. Flekkøy and A. Hansen: simulations on gravitational settling of dipole populations.
* Melanie Grob, IPG Strasbourg, 2005, Master 2 Research, , with Jean Schmittbuhl and Alain Cochard: Simulations of supershear fracture propagation.
* Emilie Walker, IPG Strasbourg, 2006, Master 2 Research, with Patrick Baud and Jean Schmittbuhl: Experiments on pressure solution and stylolite formation in calcite rocks.
* Amelie Neuville, IPG Strasbourg, 2006, Master 2 research, with Jean Schmittbuhl: Simulations of thermo-hydraulic properties of rough fractures.
* Berthilde-Maud Schelstraete, Master 2, EOST / Master university of Nancy, 2009, with J. Schmittbuhl, seismic stimulation at lab scale.
* Toufik Bencharif, Master 2, EOST, 2010, with J. Schmittbuhl and O. Lengliné, Caractérisation de la fracturation et de l'endommagement par des mesures acoustiques: applications aux ouvrages souterrains.
* Mickael Bastard, Master 2, EOST, 2010, with J. Schmittbuhl, Analyse de la déformation d'interfaces tridimensionnelles par corrélation d'images jointe à des techniques de stéréophotogrammétrie.
* Menka Stojanova, Master 2, University of Lyon, 2012, Numerical study of liquefaction: ``Etude numérique de la liquéfaction du sol".
* Eve Agnès Fiorentino, Master 2, EOST, 2013, with L. Jouniaux, Modélisation des couplages entre flux hydriques et flux électriques dans les roches par méthode Lattice-Boltzmann

M1
Supervision of Master students: Master 1 research projects or Engineering school 2nd year research projects:

* Pierre Knobel, IPG Strasbourg, 2006, Master 1, with Jean Schmittbuhl and Patrick Baud: Simulations of discrete element modeling on compaction band and stylolite formation.
* Malgven Roudot, IPG Strasbourg, 2006, Master 1, with Jerome Van der Woerd and Jean Schmittbuhl,: Characterization of coseismic slip power spectrum for major earthquakes.
* Gwendal Fily, IPG Strasbourg, 2006, Master 1, with Jean Schmittbuhl: Coupling chemical erosion and flow fluctuations in rough fractures - simulations.
* Samuel Maucourant, IPG Strasbourg, 2006, Master 1, with Jean Schmittbuhl and Laurence Jouniaux: Coupling chemical erosion and flow fluctuations in rough fractures - experiments.
* Alice Pussacq, IPG Strasbourg, 2007, Master 1, with Alain Steyer and Jean Schmittbuhl: Analog modelization of underwater avalanches.
* Aude Cesbron, EOST, 2008, 2nd year, with J Schmittbuhl and A Cochard, Shear fracture experiment
* Guillaume Reichart, EOST, 2008, 2ndyear, with J Schmittbuhl and A Cochard, Shear Fracture Experiment.
* Nelly Lagrima-Azul, EOST, 2009, 2nd year, with JP Malet and J Schmittbuhl, avalanches triggered by fluid overpressure
* Olivier Vidal, EOST, 2009, 2nd year, with J.P. Malet, A. Remaitre and J. Schmittbuhl, avalanches triggered by fluid overpressures.
* Mickael Bastard, EOST, 2009, 2nd year, with J.P. Malet, G Koval and J. Schmittbuhl, CIV determination of velocity map of Super Sauze landslide.
* G. Musnier, EOST 2nd year (Master 1), 2010, Mechanical impact of a gouge on a fault rheology: a numerical study, supervision: A. Cochard, R. Toussaint
* H. Baier, EOST 2nd year (Master 1), 2010, Imaging an open fracture by echography, supervision: J. Schmittbuhl, R. Toussaint, A. Neuville, A. Steyer
* Cheik Koutam, M1, 2011 EOST, with G Schäfer and K Nsir, acoustic tomography of biphasic flow.
* Madeleine Drubigny, M1, 2011 EOST, CIV techniques for the determination of density evolution during aerofracture experiments.
* Cecile Clement. M1, 2011 EOST, Landquakes in the lab: a preliminary study.
* Thomas Dupont, Master 1, 2nd year engineer ENSPS, 2011, with Alain Cochard: coupling granular mechanics and elastodynamics.
* Delphine Léobal, M1, 2012 EOST, with C. Doubre: Etude des lois d'échelle spatio-temporelles des glissements de failles normales à partir de donnés INSAR.
* Arthur Thénon, M1, 2012 EOST; Réactivation de chemins de transport fluide - détermination du squelette de percolation d'une structure de transport connecté dans un écoulement biphasique
* Camille Rénat, M1, 2012 EOST, with G. Schäfer: Tomographie acoustique d'un écoulement biphasique en milieu poreux
* Muriel Thomas, M1, 2012 EOST: Essais expérimentaux de liquéfaction de granulaires partiellement saturés
* Eve-Agnès Fiorentino, M1, 2012 EOST, with K.J. Maloy: Relations

pression/saturation d'un écoulement biphasique en milieu poreux: influence des conditions aux frontières
* Romaric Macault, M1, 2012 EOST, with T. Reuschlé: Ondes de gravité dans un fluide non-Newtonien durcissant - aspect expérimental
* Pierre Douchin, M1, 2012 EOST, with M. Cara: Ondes de gravité dans un fluide non-Newtonien durcissant - aspect caractérisation de structures de terrain
* Aubery Wissocq, M1, 2013 EOST : Liquéfaction de sols – une étude expérimentale
* Jeanne Mercier de Lépinay, M1, 2013 EOST, with T. Reuschlé : Formation de cratères et rides de fond de lac
* Marc-Antoine Brossault, M1, 2013 EOST, with C. Clément : Etude expérimentale d'air sparging
* Paul Milan, M1, 2013 EOST, with A. Cochard : Impact mécanique d'une gouge sur la rhéologie d'une faille
* Joffrey Rozman, M1, 2013 EOST, with N. Gourmelen : Modélisation inverse et suivi de séquestration de CO2 à partir de données brutes INSAR

Supervision de stages d'etudiants ingenieurs:
Supervision of Engineer student:
* Frederic Lorion, EOST, 2005, 1st year, engineering school: Simulations on morphology of rough fractures.
* Nicolas Zerr, EOST, 2006, 1st year, engineering school: Simulations of 2 dimensional Wolfram cellular automata.
* Alexandra Guy, EOST, 2006, 1st year, engineering school: Simulations of 1 dimensional Wolfram cellular automata.
* Marion Bourdet, EOST, 2007, 1st year, engineering school, with MO Boulanger, JM Brendle and X Rose, : php/MySQL base to generate scientific image viewer.
* Matthieu Derunes, EOST, 2007, 1st year, engineering school, with MO Boulanger, JM Brendle and X Rose,php / MySQL application to present and sort laboratory scientific production
* Corysande Prié, EOST, 2007, 1st year, with J Schmittbuhl, implementation of PIV technique
* Basile Hector, EOST, 2007-2008, 1st year, with J Schmittbuhl, avalanche model (cellular automaton)
* Guillaume Reichart, EOST, 2007-2008, 1st year, with J Schmittbuhl, avalanche model (Slider Block model)
* Sandra Liaigre, EOST, 2008-2009, 1st year, Julia ensembles
* Florent Robin, EOST, 2008-2009, 1st year, Transition towards chaos by period doubling in a simple discrete dynamic model
* A. Deloche, EOST, 2008-2009, 1st year, Julia fractals and Mandelbrot set
* M. Lapotre, EOST, 2008-2009, 1st year, Lotka-Volterra model
* Jean-Baptiste Simmarano, EOST, 2008-2009, particle image velocimetry
* Guillaume Dumont, EOST, 2008-09, image reconstruction by hierarchical methods using maximum correlations in multiscale techniques
* Fanny Leyrat, EOST, 2008-09, cluster identification and image analysis in multiphasic flow in a Hele-Shaw cell
* Louis Hecker, EOST, 2008-09, Invasion percolation: model for multiphasic flow under gravity in a disordered porous medium.
* Emilie Cazes, EOST, 2009-10, Arnold's cat: squeeze it yourself.
* Jan-Stanislas Cornet, EOST, 2009-10, Percolation models.

* Tsang Hin Sun, EOST, 2009-10, Lorentz attractor.
* Tom Vincent-Dospital, EOST, 2010-11, heat dissipation during fracture propagation.

Supervision de TIPE d'étudiants de Maths Spé:
Supervision of younger (preparatory classes) students:

* TIPE, 2006-2007: Josselyn Bernadoff and Francois Parcy, students of M. D. Meier, highschool Kleber, Strasbourg: TIPE (50 hours), laboratory study of seismic wave propagation and simple tomography. TPE: supervision of two highschool students (highschool of Walbourg, Alsace) about avalanches.
* TIPE, 2007-2008: 4 students of M. D. Meier, highschool Kleber, Strasbourg: TIPE (50 hours), laboratory study of wave propagation and fracture.F Ok, L Schneider, C Gauthier, A.Christophe. three students of biology/geology preparatory classes in E. Rostand, Strasbourg, about friction. Laure Quentin, student of Versailles about liquefaction and avalanches.
* TIPE, 2008-2009: 1 student of maths spe, highschool Kleber, AS Schell, about treatment of seismic signals. 1 student of math spe Kleber, N. Lack, about topography measurements.
* TIPE, 2009-2010: 1 student of maths spe, highschool Kleber, Pierre Thiriet, about the microscopic morphology analysis of laser cutting surfaces in metals and 2 students of maths spe, Kleber, Aline Marguet and Marie-Flore Iltis, about the experimental determination of Lamb modes in various shaped filled fractures.
* TIPE, 2010-2011: 4 students (Maths spé Kleber): Lucille Schillinger, fault mechanics. Franck Pipart, sedimentation model. Yannick Hamida et Stanislas, avalanche studies in granular media
* TIPE, 2011-2012: 1 student (Maths spé Kleber): Carl Tourkis, Experimental tests of acoustic resonance modes of solid plates.

Supervision de lycéens et collégiens
Supervision of teenagers during internships/ lab visits

A few teenagers visiting the lab per year. (projects: Kids University, or personal project of professional environment discovery from french education program) (example: 3 15 years all pupils, one day to week training period, 2012-2013)

Administration de la recherche et fonctions d'intérêt collectif

(Research Administration)

Responsabilités scientifico-administratives (Administrative responsibilities):

2006-2009, 2010-… : Elected member of the EOST council, ``Ecole et Observatoire des Sciences de la Terre'' Institute in Strasbourg.
2009,2012: Member of the thesis follow-up committee for the Doctoral School in Strasbourg (membre du comité de suivi des thèses de l'Ecole Doctorale).
2008: member of the AERES visiting committee at IPGS, representative of the scientific concil of University Louis Pasteur.
2008: Member of the Conseil d'administration du CURRI (service for software administration, university of Strasbourg)
2006: Member of the mixed earth science specialists' committee of the university Louis Pasteur, participating in the recruitment procedure of new professors and Maitre de Conference at the UMR7516 laboratory.
2007: Elected member of the commission of the earth science specialists' committee of the university Louis Pasteur, participating in the recruitment procedure of new professors and Maitre de Conference at the UMR7516 laboratory.
2006-2008 : Elected member of the scientific council of the University Louis Pasteur of Strasbourg.

Animation scientifique et administration de: (Scientific animation and web administration:)

2013- : Responsible of the "Experimental Geophysics" team at IPGS (11 permanent researchers, 4 engineers, ~ 10 PhD students and 1 postdoc) (http://eost.unistra.fr/recherche/ipgs/ge/)
2003- : Responsible for the "Water" transverse research theme at IPGS.
2008- : Responsible for the web section of the Experimental Geophysics team at IPGS.
2006-2008 : Responsible for the web section of the Rock Physics team at IPGS
2002-2004: Administrator of the news section of the complex web page (http://www.phys.ntnu.no/complex): advertising at the local group, national group and faculty level of the group seminars and visitors, and of the papers and conferences activity of the group members.

Participation à des jurys académiques (Participation to academic jurys):

2007 : Examiner for 20 geophysics Master students at EOST
2008: Rapporteur and scientific opponent for 3 MSc. students at Physics of Geological Processes, University of Oslo.
2009, 2012: Representative of IPGS at Doctoral school STUE, University of Strasbourg, 1st year thesis committee jury for 30 PhD students.
2009: Examiner of the PhD (Doctorat) of M. Khalifa Nsir, ``Etude expérimentale et numérique de la migration de polluants non miscibles dans un milieu poreux saturé à

l'échelle de Darcy", at LhyGeS, Strasbourg.
2010 : Participation to the PhD jury of Amélie Neuville, IPGS, Strasbourg.
2012 : Participation (rapporteur) to the PhD jury of Damien Habouzit, ``Rheophysique du beurre de cacao et stabilite du materiau heterogene solide / liquide soumis a une perturbation thermique", Physico Chimie, University of Bordeaux I.
2012: Examiner and opponent for the MSc. "Characterization of Two-phase flow in non-deformable and deformable porous media", by M. F.K. Eriksen, University of Oslo
2013 : Participation to the PhD jury of Alexandra Rolland, IPGS, Strasbourg
2013: Examiner and referee of the PhD of Michlmayr Gernot, ETH Zurich
2013: Examiner and referee of the PhD of Franziska Möbius, ETH Zürich

Positions académiques invitées (Academic invited positions)

Invited professor at the university of Oslo, Complex, and University of Hawaii: October 2004.
Invited professor at the University of Oslo, Complex: October 2009.
Invited professor at the University of Oslo, Complex: August 2010.
Invited professor at the Center for Advanced Study on ``Complex Flow", Norwegian Academy of Sciences, 2011-2012.
Invited professor at the University of Oslo, Complex: November 2012.
Enseignement (intervenant) à l'Université Louis Pasteur, puis à l'Université de Strasbourg (certains rémunérés, d'autres non), 2004-2013.
Invited position as Reference for Earth Sciences, Maison des Sciences en Alsace au service des professeurs, 2012-2013

Invitation de professeurs étrangers à l'IPGS (Invitation of foreign professors at IPGS):

Dragos V. Anghel, Institute of Physics, Bucarest. (1 month, 2005-2006)
Ernesto Altshuler, Dept of Physics, University of Havana, Cuba (1 month/year, 2005-2006, 2011-2012)
Eirik G Flekkoy, Dept of Physics, University of Oslo, Norway (1 month, 2007-2008)
Knut Jorgen Maloy, Dept of Physics, University of Oslo, Norway (1 month/year, 2007-2013)
Oistein Johnsen, NGI, Oslo, Norway (1 month, 2008-2009)
Jianzhao Yan, Geoscience Dept, Beijing, Chinese Academy of Science (1 month/year, 2009-2011)
Jan Ludvig Vinningland, IRIS, Oslo, Norway (1 month, 2011-2012)

Organisation de conferences et workshop (Conference and Workshop organization):

2013: Convener of the session TS2.4/EMRP4.5, ``Flow in transforming porous media (co-organized)", at EGU 2013, Vienna
(25 presentations, http://meetingorganizer.copernicus.org/EGU2013/session/12068)
2012: Convener of the session TS2.3/EMRP2.8/HS8.1.7, ``Flow properties of transforming porous media (co-organized)", at EGU 2012, Vienna
(23 presentations, http://meetingorganizer.copernicus.org/EGU2012/session/9412)
2011: Organization of the international workshop ``Flow and Transformations of Porous Media", University of Strasbourg. (http://eost.unistra.fr/flowtrap/ , 60 participants)
2011: Co-convener of the session TS2.1, ``Fault zone structure, mechanics and evolution in the laboratory" at EGU 2011, Vienna

(44 presentations, http://meetingorganizer.copernicus.org/EGU2011/session/6803)
2010: Convener of the session SM2.1, ``Mechanics and structure of seismic fault zones'' at EGU 2010, Vienna
(67 presentations, http://meetingorganizer.copernicus.org/EGU2010/session/2166)
2009: Convener of the session SM2.1, ``Mechanics and structure of seismic fault zones'' at EGU 2009, Vienna
(30 presentations, http://meetingorganizer.copernicus.org/EGU2009/session/838)
2009: Co-convener of the session MPRG4, ``Heterogeneity and anisotropy in geomaterials: a scaling issue?'' at EGU 2009, Vienna
(20 presentations,http://meetingorganizer.copernicus.org/EGU2009/session/660)
2004: Organization and animation of the scientific program of the workshop: Lillehammer 2004 meeting of the national ``Complex Systems and Soft Materials'' group (40 participants),

Organisation de seminaires (Seminar organization):

2005-....: Responsible of the seminars of the Institut de Physique du Globe, Strasbourg. (cf http://eost.u-strasbg.fr/semipgs for planning and archives, and http://audiovideocast.unistra.fr/avc/search?search=true&fullname=Toussaint%20Renaud for the video & slides presentations)
2002-2004: Responsible of the seminars and of the student seminars of the Advanced Materials and Complex Systems group in University of Oslo (UiO).

Responsabilités editoriales:

Editeur invité du volume special "fault zone structure, mechanics and evolution in nature and laboratory", Journal of Structural Geology. (2012, 13 articles, editors: F. Agosta, S. Smith, R. Toussaint and R. Holdsworth)

Relecture pour journaux (Reviewer for scientific journals): (~250 articles)

for Physical Review Letters, Physical Review E, Journal of Geophysical Research - Solid Earth (JGR B), Transport in Porous Media (T.I.P.M.), eEarth, Colloids and Surface A, Water Resource Research, Journal of Structural Geology, Computers and Fluids, Geoscientific Instrumentation, Methods and Data Systems, Earth Science Reviews, Journal of Geophysical Engineering, International Journal for Numerical and Analytical Methods in Geomechanics, Geophysical Research Letters, Journal of Colloid and Interface Science, Pure and Applied Geophysics, Tectonophysics, Journal or Petroleum and Gas Engineering, …

Expertise pour agences nationales et universities (Reviewer for funding agencies and research programs):

for the ANR (french national research funding agency), program "Catastrophes Telluriques et Tsunamis", program ``Blanc'', program ``Jeunes chercheurs'' and program "Concept, Systemes et Outils pour la Securite Globale". For the CIFRE program, for the University of Grenoble, University of Orsay, and University of Strasbourg. for the Israeli National Research fundation, for the German National Research agency.

Affiliations à des sociétés savantes :

membre de EGU (European Geophysics Union), AGU (American Geophysics Union), APS (American Physics Society), SFP (Societe Francaise de Physique), NFS

(Norwegian Fysisk Selskapp), Société des Anciens Eleves de Normale Sup Lyon, Fontenay et Saint Cloud.
Participation aux GDR PHENIX, TRANSNAT, MEPHY, MEGE

Animation et administration de projets de recherche

Administration of Research projects

Responsibility of research projects and third-party fund raising:

Marie Curie Initial Training Network ``FlowTrans'', Flow in Transforming Porous Media, 2013-2016. Coordinator in Strasbourg (2 PhD positions, 517 kE at IPGS, incl 387 kE in salary, mobility and overheads.),
Marie Curie ITN ``FlowTrans'', Co-coordination of the network with D. Koehn, Glasgow. (4.1 ME budget in the whole EU network)
ANR Blanc project “AIRFLOW”, resp.: R. Toussaint (IPGS) and J.F. Géminard (ENS Lyon), project on environemtal remediation using air injection in saturated soils, complementary list (2012), resubmitted (2013)
Monitoring fast flow and capillary instabilities - CPER REALISE, 69 kE (fast camera, 2012) + 22.5 kE (fast acquisition central unit, 2010-2011).
"Transformations des milieux poreux par injection ou extraction rapide de fluides (CO2 supercritique, eau ou air), INSU CESSUR program, 2012. (9,2 kE)
ANR Blanc project ``Landquake'' , resp: F Bouchut, (R Toussaint in Strasbourg). 2012-2014. (23 kE at IPGS)
FORPRO program, ``Stylolites, rhéologie et transport dans les roches carbonatées - 2'', 2011. (2 kE at IPGS)
"Accueil de jeune chercheur étranger", Postdoc program of the scientific council of the university of Strasbourg, M. Niebling project, ``Morphogenesis during hydrofracture'', 2010. (43 kE at IPGS)
FORPRO program, ``Stylolites, rhéologie et transport dans les roches carbonatées'', 2010. (22 kE)
FluidoFracFlow, INSU CESSUR program, 2010. (12 kE)
FORPRO program ``Histoire des contraintes et cinématique dans les formations calcaires du site de Bure : utilisation des stylolites comme jauges de mesures de contraintes passées et actuelles. Etude de faisabilité de la méthode'', 2008-2009. (25 kE)
french-chinese CNRS collaboration program ``Studies on Mechanism of lateral migration in porous medium carriers'', with Pr. X. Luo, Chinese Academy of Sciences, 2008. (2,5 kE)
french-norwegian PICS, with Knut Jørgen Måløy, University of Oslo: ``Mechanical instabilities and geophysical hazards'', 2006-2008. (7,5 kE / year)
3F program (INSU) "Rheology of fault asperities: role of the fluids - integration at the seismic cycle scale", 2007. administrator: R. Toussaint. (8 kEuros)
DyeTI (INSU) program ``fluid-rock interactions: impacts on the localization of lithospheric deformation'', 2006. (12 kEuros)
REALISE PPF and Action Structurante, participation in GE: 20 kE of experimental material and functioning costs over 2004-2012
recurrent funding from the University of Strasbourg and the CNRS: 15 kE over 2004-2012

Participation à projets de recherche

Participation to Research projects

« Evolution de porosité par dissolution cristallisation sous contrainte
et effet thermique : expérimentation, caractérisation, modélisation », NEEDS-Milieux poreux program, 2013-2014. resp : JP Gratier (R Toussaint in Strasbourg)
ANR MNN DIM, « Data mining-based model Inversion for gravitational Mass flow monitoring » resp : N. Méger (JP Malet in Strasbourg)
"Transformations des milieux poreux par injection ou extraction rapide de fluides (CO2 supercritique, eau ou air), INSU CESSUR program, 2012. (PI, RT)
ANR Blanc project ``Landquake" , resp: F Bouchut, (R Toussaint in Strasbourg). 2012-2014.
REALISE, 2010-..., Action structurante de l'Université de Strasbourg, administrator: F. Chabaux., L Jouniaux at IPGS
REALISE, CPER, 2007-..., administrator: F. Chabaux, L Jouniaux at IPGS
KLIMIT project, N.F.R., resp: J.O. Fossum, Norway, 2010-2013
Petromax project, N.F.R., resp: K.J. Måløy and E.G. Flekkøy, 2011-2014
FRACS network, resp: D. Koehn, University of Mainz, 2010-2012, 2013-2015
INSU CTT program, "Experimental and numerical analysis of the fluidization in gravitational processes", resp: J.P. Malet, 2011
European program ``SAFELAND", experiments on fluid dependent gravitational instabilities, cosupervision of the postdoc of Anke Spickermann. administrator in Strasbourg: J.P. Malet. 2010-2011.
"Accueil de jeune chercheur étranger", Postdoc program of the scientific council of the university of Strasbourg, M. Niebling project, ``Morphogenesis during hydrofracture", 2010. (PI, RT)
FORPRO program, ``Stylolites, rhéologie et transport dans les roches carbonatées", 2010,2011. (PI, RT)
FluidoFracFlow, INSU CESSUR program, 2010. (PI, RT)
ANR Jeune Chercheur "DoRA (Dynamics of Rifting in Afar)", 2009-2011, administrator in Strasbourg: C. Doubre
ANR RiskNat "Système Intégré de Surveillance de Crises (SISCA) de glissements de terrain argileux), 2009-2011, administrator in Strasbourg: J.P. Malet
PICS program between Norway and France, 2009-2011, "The Physics of Geological Complex Systems", coordinators: Y. Méheust (France), A. Hansen (Norway)
3F program (INSU) "Modélisation analogique de la rupture dans une structure de faillle complexe en présence de fluide", 2009. administrator: A. Corfdir
ANR CTT SUPNAF, 2009-2011, administrator: J. Schmittbuhl.
FORPRO program ``Histoire des contraintes et cinématique dans les formations calcaires du site de Bure : utilisation des stylolites comme jauges de mesures de contraintes passées et actuelles. Etude de faisabilité de la méthode", 2008-2009.
3F program (INSU) "Rheology of fault asperities: role of the fluids - integration at the seismic cycle scale", 2007. administrator: R. Toussaint.
ANR CTT TRIGGERLAND, 2007-2009, administrator: D. Amitrano.
INSU program ``Mi lourds" SIMULATERRE, about parallel computing in IPG Strasbourg, administrator: E. Debayle.
PNTS program (INSU) about inversion of deformation field from optical satellite images. administrator: D. Fitzenz.
french-norwegian PICS(CNRS, DREI), with Knut Jorgen Maloy, in the University of Oslo: ``Mechanical instabilities and geophysical hazards", 2006-2008. administrator: R. Toussaint.
DyeTI (INSU) program ``fluid-rock interactions: impacts on the localization of

lithospheric deformation", 2006. administrator: R. Toussaint.
ECCO PNRH (INSU/ANR) ECOU-PREF, 2006-2008, administrators: J. Schmittbuhl, O. Maquaire.
ANR CTT MODALSIS, 2006-2008, administrator: J. Schmittbuhl.
REALISE, PPF, 2005-20010, administrator: F. Chabaux.
EHDRA (EU), 2005-2006, administrator: J. Schmittbuhl.
Aurora (french Ministry of foreign affairs) France-Norway, 2004-2006, administrators: A. Lindner and E.G. Flekkoy.
Petromax, 2004-2006, NFR, Norway, ``hydrofracture", administrator: Knut Jorgen Maloy
Petromax, 2005-2007, NFR, Norway, ``seismically stimulated production", administrator: Eirik G. Flekkoy.
German proposal "The development of stylolites, from small-scale heterogeneities to multi-scale roughness", administrator: D. Koehn.
NFR project on hydrofracture, 2003-2004, administrator: Eirik G. Flekkoy.
NTNU project on complex systems and advanced materials, 2002-2003, administrator: Jon O. Fossum.
EU TMR network "Fractal Structures and Self-Organization", 2001-2002, administrator: J. Feder.

Distinctions variées

(various distinctions)

Prime d’excellence scientifique du CNRS, 2010-2013.
Prix de recherche collaborative, Ecole de Physique de Geilo, 2012
Publication de CV dans bases bibliographiques de type Who’s who, 2007-…

ENSEIGNEMENT:
(TEACHING)

2012-13

Course on cellular automata and computational fluid mechanics in geophysics, M2/engineering school, EOST, University of Strasbourg, Strasbourg. (24 hours)

2011-12

Course on cellular automata and computational fluid mechanics in geophysics, M2/engineering school, EOST, University of Strasbourg, Strasbourg. (12 hours)

2009-12

Course on fluid mechanics (25 hours/year), Engineering Geophysics School, University of Strasbourg, Strasbourg.

2010-13

Participation to the organization of national recruitment concourses for physics engineers (Physique aux concours d'ecoles d'ingénieurs. Participation à la conception de sujets nationaux, Correction de 200-250 copies/an, participation à jury de concours de l'EOST, jury de passage d'oraux. à l'EOST)

2010-13

"Physique des materiaux et des ecoulements ": Course on granular and granular fluid dynamics, (6 hours), Master of Geophysics, University of Strasbourg.

2012-13

Preparatory classes ``Mathématiques Spéciales" in secondary school Ort, Strasbourg: weekly oral examinations in physics. (2 hours per week, 40 hours/year).

2010-12

Preparatory classes ``Mathématiques Spéciales" in secondary schools Kléber, Strasbourg, and Ort, Strasbourg: weekly oral examinations in physics. (2 hours per week, 50 hours/year).

2007-10

Preparatory classes ``Mathématiques Spéciales" in secondary schools Kléber, Strasbourg: weekly oral examinations in physics. (2 hours per week, 35 hours/year).

2009-10

Course on granular and granular fluid dynamics, (10 hours), Master of Geophysics, University of Strasbourg.

2008-09

Course on flows in porous media, granular media, friction and fracture (12 hours), Master of Geophysics, University Louis Pasteur, Strasbourg.

2008-09

Course on hydrodynamics (16 hours/year), Engineering Geophysics School, University of Strasbourg, Strasbourg.

2008-09

Course on Mathematics for economists, (48 hours, 72 h Eq TD, plus organization of the 7 associated exercise groups), batchelor 2nd year, PEGE, University of Strasbourg.

2007-08

Course on flows in porous media, granular media, friction and fracture (20 hours), Master of Geophysics, University Louis Pasteur, Strasbourg.

2007-08

Course on hydrodynamics (16 hours/year), Engineering Geophysics School, University Louis Pasteur, Strasbourg.

2006-07

Course on flows in porous media (8 hours), Master of Geophysics, University Louis Pasteur, Strasbourg.

2005-06

Course on rock physics, poroelasticity and granular/fluid flows (8 hours), Master of Geophysics, University Louis Pasteur, Strasbourg.

1993-95

Preparatory classes ``Mathématiques Supérieures'' in secondary schools Fauriel, Saint-Étienne and Pascal, Orsay: weekly oral examinations in mathematics and physics. (3 hours per week).

2000-01

University of Rennes I: ``A.T.E.R.'' position, i.e. teaching and research associate: 98 hours teaching. Courses in Oceanophysics (``D.E.U.G.'') and Statistical Physics (``Licence'' in Geophysics: Courses and exercises) - courses and exercises developed from scratch, teaching, conception and correction of the examinations.

1997-00

University of Rennes I: ``Moniteur'' position, i.e. professor assistant: 64 hours teaching / year. Courses in Partial Differential Equations (``Licence'' in Geophysics: Course, Bachelor's degree level.), and in Oceanophysics (``D.E.U.G.'', first year of University: Laboratory and Exercises) - courses and exercises developed from scratch, teaching, conception and correction of the examinations.

1995-97

Secondary french school Victor Hugo, Sofia, Bulgary: full teaching position in Mathematics.

Formation pour adultes, diffusion des sciences vers les professeurs du secondaire:

2012 - … Responsabilité des formations de géosciences pour la «Maison des sciences en Alsace au service des professeurs », (MSA) organisme de formation continue de professeurs des écoles et des collèges, partenariat Université de Strasbourg, Rectorat académique, Académie des Sciences, Fondation la Main à la Pate.
Montage de l'offre de formation pour les géosciences, avec collègues EC de l'EOST, et équipe de la MSA.
http://www.maisons-pour-la-science.org/fr/alsace

2013 : Participation à la formation « Risques et sismologie », 2 jours, 25 participants, secondaire.

2013 : Responsabilité de la formation « Quand la Terre gronde », 3*1 jour, primaire.

2013 : Encadrement / animation d'ateliers au stage de formation de professeurs du secondaire et inspecteurs de l'education nationale « E2Phys », Strasbourg, été 2007.

Diffusion d'information scientifique vers des publics non spécialistes :

Rencontres, conférences grands publics, interviews, vidéo :

2013 : Interview, la Radio en construction, « *Comment enregistrer les sons transmis à l'intérieur de la Terre ? Quel est le son d'une éruption volcanique ? Comment construire et préparer un sol qui résiste à la pluie, aux tremblements de terre et aux avalanches ?...* »
http://www.radioenconstruction.com/index.php?post%2F2012%2F10%2F25%2FInterviews-aux-chercheurs-de-l-Universit%C3%A9-de-Strasbourg-%2F%2F-Rencontre-avec-Renaud-Touissant

2013 : Participation au comité scientifique de l'exposition « Energies », Jardin des Sciences de l'Université de Strasbourg. (http://jardin-sciences.unistra.fr/expositions/ , http://jardin-sciences.unistra.fr/uploads/media/flyer-energie_web_.pdf)

2010, 2012 : Participation à « La nuit des chercheurs ». Rencontre avec le public, une soirée, Stammtisch. (http://eost.unistra.fr/uploads/media/programmeNDC_web_2012_01.pdf)

2012 : Conférence de vulgarisation invitée au Jardin des Sciences de l'Université de Strasbourg « Pourquoi changer de modèle énergétique », cycle « Quelles énergies pour demain » (http://audiovideocours.unistra.fr/avc/courseaccess;jsessionid=590C2C692A25D1D84B84EEC208814CE6.stream8?id=8132&type=flash).

2012 : Film réalisé par F. Mauviard, « Gestes de recherches : sols et liquides», sur un projet de liquéfaction de sols
http://www.youtube.com/watch?v=B5cgroBHktA&feature=player_embedded

2008-2010: Visite de laboratoire pour grand public: 1 journée de demonstrations d'expériences de laboratoire à l'IPGS auprès du grand public lors des fêtes de la science.

Participation a la fete de la science 2005-2013 : conferences dans des lycées organisées par le rectorat d'Alsace et la mission communication scientifique de l'université Louis Pasteur :
2005, dans le cadre de « World year of physics » :``Aleas geophysiques: seismes, tsunamis et avalanches - Ecoulements fluides et solides'', R. Toussaint, lycee Mermoz, St Louis
2006, « Aleas geophysiques : Tremblements de Terre et avalanches '', R. Toussaint, lycee de Walbourg
2007, « formes emergentes dans les poudres, sables et grains », lycee Jean Monnet, Strasbourg
2012, « Avalanches », école primaire de Mutzig
2013, « Energie », lycée Saint Etienne, Strabsbourg, 2 conférences

Conference de vulgarisation grand public invitee par la Société Française de Physique, section d'Alsace, 2007, « Fluides et Grains »

Participation/encadrement (une semaine) lors un stage de formation à la vulgarisation scientifique aupres de professeurs et animateurs socio culturels, dans le cadre d'un projet d'échanges de pratiques pedagogiques, CNRS/Petits debrouillards/Mairies de Varna et Strasbourg, été 2006.

Participation au programme TV « Cyclope TV » , emission locale sur des anecdotes dans la pratique scientifique.des chercheurs, 2007.

Communiqués de presse et communication :
Actualités web INSU,

> "Dans les systèmes géothermiques, la complexité des fractures pourrait expliquer des rendements moindres que prévus.", INSU actualités, 19.01.2011, Page INSU-CNRS

(http://www.insu.cnrs.fr/a3680,systemes-geothermiques-complexite-fractures-pourrait-expliquer-rendements-moindres-que-prevus.html)

Kaleidoscope, pages de popularisation de Phys Rev E, Novembre 2012

Selection of Image from "Dynamic aerofracture of dense granular packings."[Michael J. Niebling, Renaud Toussaint, Eirik G. Flekkøy, and Knut Jørgen Måløy, Phys. Rev. E **86**, 061315 (2012)] http://pre.aps.org/kaleidoscope/December2012

Kaleidoscope, pages de popularisation de Phys Rev E, Novembre 2010

Selection of Image from "Sedimentation instabilities: Impact of the fluid compressibility and viscosity" [Michael J. Niebling, Eirik G. Flekkøy, Knut Jørgen Måløy, and Renaud Toussaint, Phys. Rev. E 82, 051302 (2010)] http://pre.aps.org/kaleidoscope/pre/82/5/051302

PRE Kaleidoscope Images: September 2010

Selection of Image from "Hydrothermal coupling in a self-affine rough fracture" [A. Neuville, R. Toussaint, and J. Schmittbuhl, Phys. Rev. E 82, 036317 (2010)] http://pre.aps.org/kaleidoscope/pre/82/3/036317

PRE Kaleidoscope Images: July 2010

Selection of Image from "Mixing of a granular layer falling through a fluid" [Michael J. Niebling, Eirik G. Flekkøy, Knut Jørgen Måløy, and Renaud Toussaint, Phys. Rev. E 82, 011301 (2010)] http://pre.aps.org/kaleidoscope/pre/82/1/011301

Brèves régulières sur le site de l'Université de Strasbourg :
http://eost.unistra.fr/actualites/actualite/article/leost-partenaire-de-la-maison-pour-la-science-en-alsace/

http://eost.unistra.fr/actualites/actualite/article/radio-en-construction-sinteresse-a-la-recherche-en-sciences-de-la-terre/

http://eost.unistra.fr/actualites/actualite/article/la-geophysique-experimentale-en-train-de-se-faire/

http://eost.unistra.fr/actualites/actualite/article/nuit-europeenne-des-chercheurs/
http://eost.unistra.fr/actualites/actualite/article/leost-partenaire-de-deux-nouveaux-reseaux-europeens/

Renaud Toussaint : Liste de publications.

(cf http://eost.unistra.fr/renaud pour détails)

Bibliométrie: depuis 2002, 68 articles répertoriés (dont 10 soumis et en révision,) 17 proceedings et chapitres d'ouvrages, 1 ouvrage (deux formats), 651 citations, h=16 d'après Google scholar, 14 d'après Scopus ou 13 sur ISI, en Janvier 2013.

Articles soumis, en révision :

85. Neuville, A., E.G. Flekkøy, and R. Toussaint,
    Influence of asperities on fluid and thermal flow in a fracture: a coupled Lattice Boltzmann study, submitted to JGR B, 2013.
84. A. Spickermann, R. Toussaint, J. Travelletti, J.-P. Malet, Th.W.J. van Asch,
    A grain-fluid mixture model to characterize the dynamics of active landslides in fine-grained soils, submitted to J.G.R. E, 2013.
83. Tallakstad, K.T., R. Toussaint, S. Santucci, and K. J. Måløy,
    The non-Gaussian nature of fracture and the survival of fat-tail exponents, submitted to Phys. Rev. Lett., 2013.
82. Allègre, V., F. Lehmann, L. Jouniaux, P. Sailhac, and R. Toussaint
    Modelling the streaming potential dependence on water-content during drainage: Influence of pressure dynamics and fluid flow, submitted to T.I.P.M., 2013.
81. Aochi, H., B. Poisson, R. Toussaint, X. Rachez and J. Schmittbuhl,
    The impact of spatial and temporal changes in fault characteristics on induced seismicity due to fluid circulation, submitted to Geoph. J. Int., 2013.
80. Laronne Ben-Itzhak, L., E. Aharonov, Z. Karcz, M. Kaduri and R. Toussaint,
    Sedimentary stylolite populations in Limestone: Large-scale field observations and implications for structure evolution, submitted to Journal of Structural Geology, 2013.
79. Rolland, A., R. Toussaint, P. Baud, N. Conil and P. Landrein,
    Morphological analysis of stylolites for paleostress estimation in limestones surrounding the Andra Underground Research Laboratory site, submitted to Int. J. Rock Mech. Min. Sci., 2013.
78. Lengliné, O., J. Schmittbuhl, K.J. Måløy, A. Cochard and R. Toussaint,
    A brittle creep model of interfacial crack propagation, submitted to Physical Review Letters, 2013.
77. Vasseur, G., Luo, X., Yan, J., Loggia, D., Schmittbuhl, J. and Toussaint, R.
    Flow regime associated with secondary migration, submitted to Journal of Marine and Petroleum Geology, 2013.

Articles Publiés ou sous presse :

76. Ghani, I., D. Koehn, R. Toussaint, C. W. Passchier,
    Dynamic development of hydrofracture - 2d hybrid numerical modeling of brittle deformation coupled with fluid pressure diffusion, Pure and Applied Geophysics, accepted, 2012.
    P228
75. Niebling, M.J., R. Toussaint, E.G. Flekkøy and K.J. Måløy,
    Dynamic aerofracture of dense granular packings, Phys. Rev. E, **86**, 061315, 2012.
    P45
74. Tallakstad, K.T., R. Toussaint, S. Santucci, and K. J. Måløy,

Non Gaussian fluctuations of crack front velocity, Proc. of Soft Matter & Complex Flow congress, Lofoten, Norway, accepted, 2012.
P612

73. Smith, S.A.F., F. Agosta, R. Toussaint, and R.E. Holdsworth,
Foreword to Special Issue: "Fault Zone Structure, Mechanics and Evolution in Nature and Experiment", Journal of Structural Geology, 45, 1-2, 2012.
P226

72. Laronne Ben-Itzhak, L., E. Aharonov, R. Toussaint and A. Sagy,
Upper bound on stylolite roughness as indicator for the duration and amount of dissolution, Earth and Planetary Science Letters, 337-338, 186-196, 2012. doi: 10.1016/j.epsl.2012.05.026
P738

71. Rolland, A., R. Toussaint, P. Baud, J. Schmittbuhl, N. Conil, D. Koehn, F. Renard and J.P. Gratier,
Modeling the growth of stylolites in sedimentary rocks, J. Geoph. Res., 117(6), B06403, 2012. doi: 10.1029/2011JB009065
P670

70. Koehn, D., Ebner, M., Renard, F., Toussaint, R., Passchier, C.W.,
Modelling of stylolite geometries and stress scaling, Earth and Planetary Science Letters, 341-343, 104-113, 2012. doi: 10.1016/j.epsl.2012.04.046
P660

69. Toussaint, R., K.J. Måløy, Y. Méheust, G. Løvoll, M. Jankov, G. Schäfer and J. Schmittbuhl,
Two-phase flow: structure and upscaling, consequences on macroscopic transport properties, Vadose Zone Journal, 11, vzj2011.0123, 2012. doi:10.2136/vzj2011.0123 HAL
P271

68. Niebling, M., R. Toussaint, E.G. Flekkøy and K.J. Måløy,
Estudios numéricos de Aerofractures en medios poros / Numerical Studies of Aerofractures in Porous Media, Revista Cubana de Fisica, 29, 1E, 1E66, 2012. Open Access
P40

67. Neuville, A., R. Toussaint, J. Schmittbuhl, D. Koehn and J.O. Schwarz,
Characterization of major discontinuities from borehole cores of located in the black consolidated marl formation of Draix, Hydrological Processes, 26, 14, 2085-2094, 2012. doi: 10.1002/hyp.7984 pdf
P381

66. Neuville, A., R. Toussaint, J. Schmittbuhl,
Fracture aperture reconstruction and determination of hydrological properties: a case study at Draix (French Alps), Hydrological Processes, 26, 14, 2095-2105, 2012. doi: 10.1002/hyp.7985 pdf
P391

65. Vinningland, J.L., R. Toussaint, M. Niebling, E.G. Flekkøy and K.J. Måløy,
Family-Vicsek scaling of detachment fronts in Granular Rayleigh Taylor Instabilities during sedimenting granular/fluid flows, European Physics Journal Special Topics, 204(1):27-40, 2012. doi: 10.1140/epjst/e2012-01550-2
P117

64. Travelletti, J., C. Delacourt, P. Allemand, J.-P. Malet, J. Schmittbuhl, R. Toussaint, M. Bastard,

Correlation of multi-temporal ground-based images for landslide monitoring: application, potential and limitations. ISPRS Journal of Photogrammetry and Remote Sensing 70, 39-55, 2012. doi: 10.1016/j.isprsjprs.2012.03.007
P192
63. Nsir, K., G. Schäfer, R. Di Chiara Roupert, O. Razakarisoa, R. Toussaint,
Laboratory experiments on DNAPL gravity fingering in water-saturated porous media, Internat. J. of Multiphase Flow, 40, 83-92, 2012. doi: 10.1016/j.ijmultiphaseflow.2011.12.003
P365
62. Yan, J., X. Luo, W. Wang, R. Toussaint, J. Schmittbuhl, G. Vasseur, A. Yu, Z. Likuan,
An experimental study of oil secondary migration in a three dimensional tilted porous medium, A.A.P.G. Bulletin, 96(5), 773-788 , 2012. doi: 10.1306/09091110140
P340
61. Lengline, O., J. Elkhoury, G. Daniel, J. Schmittbuhl, R. Toussaint, J.-P. Ampuero, M. Bouchon
Interplay of seismic and aseismic deformations during earthquake swarms: an experimental approach, Earth and Planetary Science Letters, 331-332, 215-223, 2012. doi: 10.1016/j.epsl.2012.03.022
P618
60. Yan, J., X. Luo, W. Wang, F. Chen, R. Toussaint, J. Schmittbuhl, G. Vasseur, Z. Likuan
Testing oil saturation distribution in migration paths using NMRI, Journal of Petroleum Science and Petroleum Engineering, 86-87, 237-245, 2012. doi: 10.1016/j.petrol.2012.03.027
P356
59. Lengliné, O., R. Toussaint, J. Schmittbuhl, J. Elkhoury, J.P. Ampuero, K.T. Tallakstad, S. Santucci and K.J. Måløy,
Average crack front velocity during subcritical fracture propagation in a heterogeneous medium, Phys. Rev. E, 84, 6104, 2011. doi: 10.1103/PhysRevE.84.036104
P647
58. Goren, L., E. Aharonov, D. Sparks and R. Toussaint,
The mechanical coupling of fluid-filled granular material under shear, P.A.Geoph., 168, 12, 2011. doi: 10.1007/s00024-011-0320-4
P138
57. Tallakstad, K.T., R. Toussaint, S. Santucci, J. Schmittbuhl, K.J. Måløy,
Local dynamics of a randomly pinned crack front during creep and forced propagation: an experimental study, Phys. Rev. E, 83, 046108, 2011. doi: 10.1103/PhysRevE.83.046108
P597
56. Lengliné O., J. Schmittbuhl, J. Elkhoury, J.P. Ampuero, R. Toussaint and K.J. Måløy,
Down-scaling of the fracture energy during brittle creep experiments, J. Geoph. Res. B, 116, B0815, 2011. doi: 10.1029/2010JB008059
P627
55. Neuville, A., R. Toussaint and J. Schmittbuhl,
Hydraulic transmissivity and heat exchange efficiency of rough fractures: a spectral approach , Geoph. J. Int., 186, 1064, 2011. doi: 10.1111/j.1365-246X.2011.05126.x
P416
54. Neuville, A., R. Toussaint and J. Schmittbuhl,
Hydrothermal flows in a rough fracture, Phys. Rev. E, 82, 3, 2010. doi: 10.1103/PhysRevE.82.036317 pdf

P402
53. Niebling, M.J., E.G. Flekkøy, K.J. Måløy, R. Toussaint,
Sedimentation instabilities: impact of the fluid compressibility and viscosity, Phys. Rev. E 82, 051302, 2010. doi: 10.1103/PhysRevE.82.051302 pdf
P95
52. Santucci, S., M. Grob, R. Toussaint, J. Schmittbuhl, A. Hansen and K.J. Måløy,
Fracture roughness scaling: A case study on planar cracks, Europhys. Lett., 92, 4, 44001, 2010. DOI: 10.1209/0295-5075/92/44001 pdf
P592
51. Løvoll, G., M. Jankov, K.J. Måløy, R. Toussaint, J. Schmittbuhl, G. Schaefer and Y. Méheust,
Influence of viscous fingering on dynamic saturation-pressure curves in porous media, Transport in Porous Media, 86, 1, 305-324, 2010 DOI: 10.1007/s11242-010-9622-8 pdf
P299
50. Niebling, M.J., E.G. Flekkøy, K.J. Måløy, R. Toussaint,
Mixing of a granular layer falling through a fluid, Phys. Rev. E 82, 011301 (2010) doi: 10.1103/PhysRevE.82.011301 pdf
P79
49. Goren, L., E. Aharonov, D. Sparks and R. Toussaint,
Pore pressure evolution in deforming granular material: A general formulation and the infinitely stiff approximation, J. Geophys. Res., 115, B09216, (2010). doi:10.1029/2009JB007191 pdf
P173
48. Vinningland, J.L., Ø. Johnsen, E.G. Flekkøy, R. Toussaint and K.J. Måløy,
Influence of particle size in Rayleigh Taylor granular flow instability, Phys. Rev. E 81, 041308 (2010). doi: 10.1103/PhysRevE.81.041308 pdf
P71
47. Jankov, M., G. Løvoll, H.A. Knudsen, K.J. Måløy, R. Planet, R. Toussaint and E.G. Flekkøy,
Effects of pressure perturbations on drainage in an elastic porous medium, Tr. in Porous Media, 84, 3, 569 (2010). doi: 10.1007/s11242-009-9521-z pdf
P319
46. Ebner, M., R. Toussaint, J. Schmittbuhl, D. Koehn and P. Bons,
Anisotropic scaling of tectonic stylolites: a fossilized signature of the stress field? , J. Geophys. Res., 115, B06403, (2010). doi:10.1029/2009JB006649 pdf
P722
45. Neuville, A., R. Toussaint and J. Schmittbuhl,
Fracture roughness and thermal exchange: a case study at Soultz-sous-Forets, C.R.A.S. Geoscience, 342, 616 (2009). doi:10.1016/j.crte.2009.03.006 pdf
P425
44. Grob, M., J. Schmittbuhl, R. Toussaint, L. Rivera, S. Santucci and K.J. Måløy,
Quake catalogs from an optical monitoring of an interfacial crack propagation, P.A.Geoph., 166, 777 (2009).doi:10.1007/s00024-004-0496-z pdf
P569
43. Tallakstad, K.T., H.A. Knudsen, T. Ramstad, G. Løvoll, K.J. Måløy, R. Toussaint and E.G. Flekkøy
Steady-state two-phase flow in porous media: statistics and transport properties, Phys. Rev. Lett. 102, 074502 (2009). doi:10.1103/PhysRevLett.102.074502 pdf
P336

42. Ebner, M., D. Koehn, R. Toussaint, F. Renard and J. Schmittbuhl,
Stress sensitivity of stylolite morphology, EPSL, 277, 394 (2009).
doi:10.1016/j.epsl.2008.11.001 pdf
P706
41. Bonnetier, E., C. Misbah, F. Renard, R. Toussaint and J.P. Gratier,
Does roughening of rock-fluid-rock interfaces emerge from a stress-induced instability? European Phys. J. B., 67, 121 (2009). doi:10.1140/epjb/e2009-00002-2 pdf
P749
40. Ebner, M., D. Koehn, R. Toussaint and F. Renard,
The influence of rock heterogeneity on the scaling properties of simulated and natural stylolites, J. Struct. Geol., 31, 72 (2009). doi:10.1016/j.jsg.2008.10.004 pdf
P711
39. Johnsen, Ø., C. Chevalier, A. Lindner, R. Toussaint, E. Clément, K.J. Måløy, E.G. Flekkøy and J. Schmittbuhl,
Decompaction and fluidization of a saturated and confined granular medium by injection of a viscous liquid or a gas, Phys. Rev. E, 78, 051302 (2008).
doi:10.1103/PhysRevE.78.051302 pdf
P28
38. Altshuler, E., R. Toussaint, E. Martinez, O. Sotolongo-Costa, K.J. Måløy and J. Schmittbuhl,
Revolving rivers in sandpiles: from continuous to intermittent flows, Phys Rev E, 77, 031305 (2008). doi:org/10.1103/PhysRevE.77.031305 pdf
P131
37. Johnsen, Ø., R. Toussaint, K.J. Måløy, E.G. Flekkøy and J. Schmittbuhl,
Coupled air/granular flow in a linear Hele-Shaw cell, Phys Rev E, 77, 011301 (2008).
doi:10.1103/PhysRevE.77.011301 pdf
P15
36. Vinningland, J.L., Ø. Johnsen, E.G. Flekkoy, R. Toussaint and K.J. Måløy,
Experiments and Simulations of a gravitational granular flow instability, Phys. Rev. E, 76, 051306 (2007). pdfdoi:10.1103/PhysRevE.76.051306
P58
35. Schmittbuhl, J., A. Steyer, L. Jouniaux and R. Toussaint,
Fracture morphology and viscous transport, Int. J. Rock Mech. Min. Sci., 45, 422 (2007). pdf doi:10.1016/j.ijrmms.2007.07.007
P444
34. Vinningland, J.L., Ø Johnsen, E.G. Flekkøy, R. Toussaint and K.J. Måløy,
A granular Rayleigh-Taylor instability: experiments and simulations, Phys. Rev. Lett., 99, 048001, (2007). pdf doi:10.1103/PhysRevLett.99.048001
P54
33. Koehn, D., F. Renard, R. Toussaint, C. Passchier
Growth of stylolite teeth patterns depending on normal stress and finite compaction, EPSL, 257, 582 (2007). pdf doi:10.1016/j.epsl.2007.03.015
P688
32. Toussaint, R., E.G. Flekkøy, and G. Helgesen,
The memory of fluctuating brownian dipolar chains, Phys. Rev. E, 74, 051405 (2006).
pdf doi:10.1103/PhysRevE.74.051405
P764
31. Johnsen, Ø., R. Toussaint, K.J. Måløy and E.G. Flekkøy,

Pattern formation during central air injection into granular materials confined in a circular Hele-Shaw cell, Phys. Rev. E, 74, 011301 (2006). pdf doi:10.1103/PhysRevE.74.011301
P1.

30. Toussaint R. and A. Hansen
Mean field theory of damage nucleation in the fuse model, Phys. Rev. E, 73, 046103 (2006). (condmat/0403217) pdf, ps doi:10.1103/PhysRevE.73.046103
P520

29. Måløy, K.J., S. Santucci, J. Schmittbuhl and R. Toussaint
Local waiting time fluctuations along a randomly pinned crack front, Phys. Rev. Lett., 96, 045501 (2006). pdf, ps doi:10.1103/PhysRevLett.96.045501
P535

28. Toussaint, R., G. Løvoll, Y. Méheust, K.J. Måløy and J. Schmittbuhl
Influence of pore-scale disorder on viscous fingering during drainage, Europhys. Lett., 71, 583 (2005). pdf, ps doi:10.1209/epl/i2005-10136-9
P292

27. Toussaint R. and S.R. Pride
Interacting damage models mapped onto Ising and percolation models, Phys. Rev. E, 71, 046127 (2005). (condmat/0403412) pdf doi:10.1103/PhysRevE.71.046127
P499

26. Schmittbuhl, J., F. Renard, J.P. Gratier and R. Toussaint
Roughness of stylolites: Implications of 3D high resolution topography measurements , Phys. Rev. Lett., 93, 238501 (2004). pdf doi:10.1103/PhysRevLett.93.238501
P702

25. Toussaint, R., G. Helgesen and E.G. Flekkøy
Dynamic roughening and fluctuations of dipolar chains, Phys. Rev. Lett., 93, 108304 (2004). (cond-mat/0311340) pdf doi:10.1103/PhysRevLett.93.108304
P760

24. Løvoll, G., Y. Méheust, R. Toussaint, J. Schmittbuhl and K.J. Måløy,
Growth activity during fingering in a porous Hele Shaw cell, Phys. Rev. E., 70, 026301 (2004). (cond-mat/0310204) pdf doi:10.1103/PhysRevE.70.026301
P280

23. Toussaint, R., J. Akselvoll, G. Helgesen, E.G. Flekkøy and A.T. Skjeltorp,
Interactions of magnetic holes in ferrofluid layers, Progress in Colloid and Polymer Science, 128, 151 (2004). pdf link doi:10.1007/b12355
P792

22. Toussaint, R., J. Akselvoll, E.G. Flekkøy, G. Helgesen and A.T. Skjeltorp,
Interaction model for nonmagnetic holes in a ferrofluid layer, 2004, Phys. Rev. E 69, 011407 (2004). (cond-mat/0304683). pdf doi:10.1103/PhysRevE.69.011407
P777

21. Pride, S.R. and R. Toussaint,
Statistical mechanics of fiber bundles, Physica A, 312, 159 (2002). (condmat/0209131) pdf doi:10.1016/S0378-4371(02)00816-6
P486

20. Toussaint, R. and S.R. Pride,
Fracture localization of disordered solids in compression as a critical phenomenon: III: Analysis of the localization transition, Phys. Rev. E, 66, 036137 (2002). (cond-mat/0209129). pdf doi:10.1103/PhysRevE.66.036137
P475

19. Toussaint, R. and S.R. Pride,

Fracture localization of disordered solids in compression as a critical phenomenon: II: Model hamiltonian for a population of interacting cracks., Phys. Rev. E, 66, 036136 (2002). (cond-mat/0209127). pdf doi:10.1103/PhysRevE.66.036136
P466

18. Toussaint, R. and S.R. Pride,
Fracture localization of disordered solids in compression as a critical phenomenon: I. Statistical Mechanics Formalism., Phys. Rev. E, 66, 036135 (2002). (cond-mat/0209124). pdf doi:10.1103/PhysRevE.66.036135
P456

Proceedings avec comité de lecture :

17. Neuville, A., Flekkoy, E.G., Maloy, K.J., Toussaint, R., Schmittbuhl, J.,
Hydrothermal exchange in an open, rough fracture, Proceedings from Kickoff, Complex Matter Physics, Center for Advanced Study, eds: Jon Otto Fossum, Tom Henning Johansen and Pavlo Mikheenko, September 26, 2011, CAS, Oslo, Norway
16. Travelletti, J., C. Delacourt, J.P. Malet, P. Allemand, J. Schmittbuhl, R. Toussaint,
Performance of image correlation techniques for landslide displacement monitoring, Proc. of the 2nd world landslide forum, Rome, 2011. pdf
P218
15. Travelletti, J., J.P. Malet, J. Schmittbuhl, R. Toussaint, C. Delacourt, P. Allemand,,
Performance of image correlation techniques for landslide displacement monitoring, Proc. des Journées Aléas Gravitaires 2011, Strasbourg, A. Remaitre et J.P. Malet, eds.
14. Renaud Toussaint, Liran Goren, Einat Aharonov ,David Sparks, Michael Niebling, Eirik Flekkoy, KJ Maloy.,
Role des fluides dans les glissements de terrain, la liquefaction et la lubrification des failles: importance des forces de filtration en conditions drainees. Proceedings des Journees Aleas Gravitaires 2011, Strasbourg, A. Remaitre et J.P. Malet, eds.
13. Travelletti, J., Malet, J.P., Schmittbuhl, J., Toussaint, R., Bastard, M., Delacourt, C., Allemand, P. and van Dam, D.B.,
Multi-temporal terrestrial photogrammetry for landslide monitoring, Proc. of the Florence conference Mountain Risks: Bringing Science to Society, 2010. pdf
P209
12. Vinningland, J.L., Ø. Johnsen, E.G. Flekkøy, R. Toussaint and K.J. Måløy,
Granular Rayleigh Taylor instability, Proc. of the 6th international conference on micromechanics of granular media, Powder and grains 2009, M. Nakagawa and S. Luding, eds, 2009. pdf
P103
11. K. Nsir, G. Schaefer, O. Razakarisoa, R. Toussaint, J. Schmittbuhl,
Approche expérimentale et numérique des instabilités de déplacement d'un DNAPL en milieu poreux saturé à l'échelle de Darcy, Actes du 19ème Congrès Franc ais de mécanique, Marseille, 2009. pdf
P375
10. K.Nsir, G. Schäfer, O. Razakarisoa, R. D. Roupert, R. Toussaint,
Etude expérimentale et simulation numérique à l'échelle de pore des instabilités de déplacement d'un DNAPL en milieu poreux saturé à l'échelle de Darcy. Acte de la 10ième Journée d'Etude sur les Milieux Poreux. 2010. (Conférence, session Suivi de front-Instabilités de 10ième Journées d'Etude sur les Milieux Poreux, Nancy, 20 -21 Octobre 2010.)

9. Santucci, S., M. Grob, R. Toussaint, K.J. Måløy, A. Hansen, and J. Schmittbuhl,
Crackling dynamics during the failure of heterogeneous material: Optical and acoustic tracking of slow interfacial crack growth, Proc. of the ICF12, 12th International Conference on Fracture, Ottawa, 2009. pdf
P559
8. Pindra, N., V. Lazarus , J.B. Leblond, J. Schmittbuhl and R. Toussaint,
Deformation of the crack front during propagation in some disordered medium: theoretical and experimental studies, Proc. of the ICF12, 12th International Conference on Fracture, Ottawa, 2009. pdf
P550
7. Neuville, A., R. Toussaint and J. Schmittbuhl,
Effects of the roughness of a fracture on thermal exchange, Proc. of the EDHRA (European Hot Dry Rock Association) scientific conference, Soultz-sous-Forêts, 2008. pdf
P436
6. Vinningland, J.L., Ø. Johnsen, E.G. Flekkøy, R. Toussaint and K.J. Måløy,
Granular Rayleigh Taylor instability, Proc. of the Trffic and Granular Flow conference, 2007, Orsay, 2009. pdf
P107
5. Neuville, A., R. Toussaint and J. Schmittbuhl,
Hydrothermal flow in a rough fracture, Proc. of the EDHRA (European Hot Dry Rock Association) scientific conference, Soultz-sous-Forêts, 2006. pdf
P453
4. Måløy, K.J., R. Toussaint and J. Schmittbuhl
Dynamics and structure of interfacial crack fronts, Proc. of the ICF11, 11th International Conference on Fracture, Torino, 2005. pdf proceedings
P641
3. Toussaint, R.
Statistical mechanics of interacting fiber bundles, Proc. of the ICF11, 11th International Conference on Fracture, Torino, 2005. pdf proceedings
P514

Chapitres d'ouvrage :

2. Santucci, S., K.J. Måløy, R. Toussaint, and J. Schmittbuhl, "Self affine scaling during interfacial crack front propagation", in ``Dynamics of Complex Interconnected Systems: Networks and Bioprocesses", NATO ASI series, edited by A.T. Skjeltorp , Kluwer, Dordrecht, 2006. pdf, ps
P539

1. Skjeltorp, A.T., J. Akselvoll, K.d.L. Kristiansen, G. Helgesen, R. Toussaint, E.G. Flekkøy, and J. Cernak; ``Self-assembly and dynamics of magnetic holes", in ``Forces, growth and form in soft condensed matter: at the interface between physics and biology", NATO ASI series, edited by A.T. Skjeltorp and A.V. Belushkin; Kluwer, Dordrecht, 2004. pdf
P797

Ouvrages:

2. Manuscrit de thèse de doctorat
    "Rock fracture during compression: the localization process as a critical phenomenon". site

1. Manuscrit de thèse, format livre
    Fracturation des roches: la localisation comme phénomène critique. Editions Universitaires Européennes, 2012. ISBN-13 978-3-8417-9391-1, ISBN-10:3841793916 http://www.morebooks.fr

Conférences invitées dans des congrès:

Havana, Cuba, MarchCoMeeting, 2012, International conference on complex flows
Liquefaction and seepage forces during fracture".

Chennai, India, 2012
Workshop on fractures and flow, University of Chennai, India. Invited talk on "Fractures: I role of fluid flow, II competition between quenched and thermal disorder during fracture".

FAST, Orsay, 2012
Séminaire de laboratoire invite, hudrofracturation et aérofracturation: contrôle de la morphogénèse avec la vitesse d'injection

ESPCI, PMMH, 2011
Séminaire de laboratoire invité, "Liquéfaction et influence du fluide dans les granulaires cisaillés

Interpore 2011, Bordeaux
Flow and channel formation in deforming porous media. R. Toussaint et al., Invited talk.

April 2011:
EGU 2011.
Influence of stylolite networks on transport properties in carbonates
R. Toussaint et al. Invited talk.

Feb 2011
MUSIS conference, Lauterbad, Germany.
Channel formation during biphasic flow in porous media, or during fast monophasic flow and matrix hydrofracture: Consequences on the dynamic pressure-saturation and relative permeability relations.
R. Toussaint et al. , invited talk

Dec 2010
Inernational conference on Complex physical phenomena in materials, Recife,
Role of the intersticial fluid in channel formation during piping erosion or liquefaction, R. Toussaint, M. Niebling,E.G. Flekkøy, J.L. Vinningland, K.J. Måløy, B.−M. Schelstraete, J. Schmittbuhl, Ø. Johnsen, A. Lindner, L. Goren, E. Aharonov, D. Sparks, E. Clément. Invited talk.

Dec 2010
International Conférence "CO2 and other fluids in porous media", Brasilia
Channel formation and dynamic effects during CO2/water and other multiphasic flows in fractures and porous media, or during hydrofracture. par Renaud Toussaint, Michael Niebling, Amelie Neuville, Jean Schmittbuhl, Knut Jorgen Maloy, Eirik G Flekkoy, Keynote lecture.

May 2010
EGU 2010, Vienna, Modeling coupled fluid-grain deformation within fault zones.
Liran Goren, Einat Aharonov, Renaud Toussaint, and David W. Sparks (invited)

November 2009

5th International Symposium on Hydrocarbon Accumulation Mechanisms and Petroleum Resource Evaluation, Beijing, invited communication, Flow regime associated with secondary migration, G. Vasseur, X. Luo, D. Loggia, R. Toussaint and J. Schmittbuhl.

April 2008

EGU 2008, Vienna, hydromechanical coupling in hydrofracture, sedimentation and friction weakened by fluid flow: application of hybrid granular / continuous fluid flow modeling. Toussaint, R.; Johnsen, O.; Flekkoy, E.G.; Vinningland, J.L.; Niebling, M.; Schmittbuhl, J.; Maloy, K.J.; Goren, L.; Aharonov, E.; Sparks, D. (solicited)

June 2008

CMG 2008, Svalbard, Norway, Velocity fluctuations of a slow crack front during slow propagation: experimental approach, generation of microquake catalogs and comparison to large scale spatio temporal scaling law in fault slip dynamics, Toussaint, R.; Schmittbuhl, J.; Maloy, K.J.; Santucci, S.; Grob, M.; Doubre, C. ; Van der Woerd, J.; Peltzer, G., Rivera L.; invited talk

October 2008

ESF-FWF Conference on New Challenges in Earthquake Dynamics: Observing And Modelling A Multi-scale System. Variability of fault slip distribution: an experimental approach, J. Schmittbuhl et al. (invited)

Spring 2005

Turin, Italy, 11th Congress on Fracture (ICF11), ``Statistical mechanics of interacting damage", Renaud Toussaint, solicited talk.

June 2006

Sea of Galilee, Israel, 26th IUGG Conference on Mathematical Geophysics on "Solids, Fluids and Life", "Modeling stylolite formation: control of quenched disorder, elastic forces and surface tension over the morphology", R. Toussaint, D. Koehn, J. Schmittbuhl, F. Renard and J.P. Gratier, solicited talk.

June 2007

Bergen, Norway, "Complex conference", "Saffman Taylor instabilities and underwater avalanches in coupled granular / fluid flows", R. Toussaint, O. Johnsen, E.G. Flekkoy, K.J. Maloy and J. Schmittbuhl, invited talk.

April 2003

Nice (France), EGS-AGU-EUG Joint Assembly, ``Statistical physics of damage in fiber bundles and sheared disordered brittle rocks", Toussaint, R. and S.R. Pride (solicited)

December 2002

San Francisco (USA), AGU Fall meeting, ``Statistical theory of shear localization in brittle rock", Pride, S.R. and R. Toussaint (solicited)

Participations à congrès, seminaires de laboratoire, conférences internationales (~250): voir liste sur http://eost.u-strasbg.fr/renaud/cv-current/node15.html et http://eost.u-strasbg.fr/renaud/cv-current/node20.html

Fractures, liquéfaction et avalanches :mécanique de mélanges solides et fluides

La géophysique, au sens de la physique d'objets et processus géologiques, est une formidable source de problèmes complexes, au sens de la physique de la matière complexe. Par exemple, les problèmes que j'étudie ont trait à la mécanique des failles, les avalanches, chargées de fluides ou non, de matière en grain ou plus pâteuse, les phases dynamiques de la sédimentation et les instabilités pendant celle-ci, la fracturation, sèche ou déclenchée par le transport des fluides parcourant les pores de la roche ou du sol, la liquéfaction durant les tremblements de terre, les écoulements d'une ou plusieurs phases fluides non miscibles dans des roches poreuses de géométrie irrégulière, la morphogénèse durant l'évolution des roches sédimentaires où évoluent composition chimique et équilibre mécanique entre les composants des roches, l'évolution dynamique de colloïdes aux interactions variables, les échanges de chaleur dans des écoulements chenalisés, l'évolution de la température et son effet sur la mécanique du système en évolution… .
Ces systèmes présentent des interactions qui relèvent de la physique et la mécanique classique, mais avec la présence d'un désordre dans la structure, ou des non-linéarités dans les interactions fondamentales, qui peuvent générer à grande échelle un comportement complexe : notamment, on ils peuvent fonctionner sur des échelles de temps et d'espace très étendus, avec coexistence de phases rapides et de phases extêmement lente, ou avec des déformations diffuses alternant avec des fonctionnements où la déformation est très localisée.
L'aspect polyphasique ou polydisperse de ces systèmes peut générer une telle complexité, sans que celle-ci reflète nécessairement la multiplicité des échelles déjà présentes dans la composition du système : dans des systèmes au fonctionnement critique, ou au voisinage de transitions de phases dites du second ordre, de nombreux systèmes dynamiques sont connus pour faire émerger, à partir de désordre présent à petite échelle et d'interaction simples, des organisations à grande échelle du processus en jeu.

La démarche que j'adopte en général pour décrire les systèmes que j'étudie est propre à la physique des systèmes complexes : à partir de l'observation du système étudié et sa caractérisation et quantification expérimentale, on cherche à établir un modèle conceptuel réductionniste, avec le plus petit nombre possible de constituants – (« *A scientific theory should be as simple as possible, but no simpler », suivant à mon petit niveau les préceptes du plus célèbre physicien du 20ème siècle au nom à consonance géologique, A. Einstein)* – mais qui reproduise les éléments essentiels du phénomène. La complexité du phénomène tient au fait qu'une théorie avec un petit nombre de constituants, grâce aux non linéarités des interactions, et/ou au caractère désordonné de certains ingrédients, peut mener à des structures présentant une complexité fondamentale : des structures par exemple ne présentant pas d'échelle de temps ou d'espace privilégiées, i.e. par exemple au fonctionnement intermittent, présentant un aspect fractal ou auto-affine,…
On a alors à faire à des systèmes mécaniques qui peuvent présenter un désordre dans les propriétés matérielles, liées à ses constituants – comme le caractère plus ou moins déformable ou soluble des minéraux d'une roche, ou la variété des formes des pores d'une roche, ou la taille diverses des grains dans un tas de sable ou un dépôt sédimentaire, ou encore le caractère rugueux des parois d'une fracture –. On parle alors de désordre gelé. On peut aussi avoir à faire à des systèmes où les interactions microscopiques désordonnées qui trouvent leur origine

dans l'agitation thermique excitent des degrés de liberté de systèmes mécaniquement couplés à diverses échelles, ce qui mène à une réponse occupant un large spectre en temps, avec des temps de réponse beaucoup plus grands que ceux des chocs individuels pour les modes spatialement les plus étendus.

Finalement, mon travail met en jeu des aller-retour réguliers entre théorie et observation expérimentale: esthétiquement, un modèle non confronté à des données expérimentales reste quelque peu stérile, tout comme un bloc de données sans approche interprétative permettant une quantification, et dans de bonnes circonstances de caractérisation, une prédiction. Par goût pour cette confrontation, j'ai progressivement élargi le champ de mes approches : parti d'une thèse en très grande partie analytique, j'ai développé des modèles numériques lorsque j'ai notamment voulu enrichir les problèmes de fracturation de la mécanique du fluide en écoulement rapide dans les roches. Je me suis ensuite rapproché de démarches expérimentales, notamment par la confrontation de modèles théoriques avec les expériences conduites par mes collaborateurs d'Oslo, et le montage ou la participation à quelques expériences conduites à Strasbourg. Ma participation à des activités de terrain, jusqu'ici, a été limitée à quelques sorties et observations de terrain, à la caractérisation d'objets échantillonnés ou à l'analyse quantitative de données acquises par des collaborateurs.

Thèmes de recherche développés :

1 Ecoulements mixtes, grains et fluides : rôle du fluide dans la mécanique d'interfaces pressurisées, cisaillées dans les failles et instabilités gravitaires :
1.1 Hydrofracturation et aérofracturation
1.2 Instabilités de sédimentations et Rayleigh Taylor granulaire dans les mélanges eau/grains et air/grain
1.3 Mécanique d'interfaces cisaillées et avalanches

Projets :
exploration des paramètres d'aerofracturation par extraction,
monitoring des processus de fluidofracturation par les activités microsismiques,
instabilités de pentes et processus de liquéfaction.

2 Ecoulements en milieux poreux et fracturés :
2.1 Ecoulements multiphasiques dans les milieux poreux,
2.2 Ecoulements en fractures rugueuses (transferts de masse et transferts d'énergie),

Projets :
. intégration des grandes déformations de milieux poreux et de plusieurs phases fluides immiscibles dans les modèles numériques
. fracturation thermique générée par les écoulements,

3 Fracturation des milieux hétérogènes fragiles,
3.1 Modèles sur réseau, mécanique de la fracture et désordre gelé
3.2 Fracturation interfaciale, quantification des régimes intermittents et de la dynamique, influence des effets thermiques

Projet : mélange de désordre thermique et de désordre gelé dans la mécanique de la fracture en propagation, ainsi que dans la dynamique d'interface cisaillée. Influence du transport de chaleur sur la dynamique de la fracture.

4 Interactions entre mécanique et chimie dans les systèmes fluides/roches (stylolites),
4.1 Modèles de formation de stylolites
4.2 Interprétations comme marqueurs de contraintes et marqueurs de déformation

Projet : couplage de dissolution/précipitation et évolution des contraintes durant la diagénèse en massif fracturé. Incorporation des effets thermiques.

5 Développement de techniques d'imagerie

Projet : coupler stéréophotogrammétrie et déformation par corrélation d'image

6Mélanges granulaires fluides aux interactions controlables : modèles de colloides et fluides magnétorhéologiques

Projet : utilisation comme création de fluide en volume comme modèle analogique de fluidofrature

1 Ecoulements mixtes, grains et fluides : rôle du fluide dans la mécanique d'interfaces cisaillées, les failles et instabilités gravitaires.

Les milieux granulaires ont été étudiés intensivement depuis l'avènement d'ordinateurs de calcul permettant la prise en compte d'un grand nombre de composants discrets, dans les années 1980. Ils constituent un paradigme mécanique d'éléments aux interactions simples et dissipatives. On les utilise couramment pour simuler la mécanique de sédiments, ou de roches poreuses en prenant en compte la cohésion entre les grains. Ces études permettent ainsi l'émergence d'une rhéologie macroscopique non triviale, à partir d'interactions individuelles simples. Ils présentent des caractéristiques macroscopiques intéressantes : par exemple, des phases dilatantes, ou de la ségrégation spontanée par taille, propriétés de friction, … et pas uniquement par densité.

Dans la mesure où la rhéologie des milieux granulaires est l'objet de recherches actives, les instabilités mécaniques dans leurs écoulements, et la façon dont ils s'organisent en fonction des conditions aux frontières, peuvent être utilement explorés par la simulation.
Lorsque les grains sont suffisamment petits, ou le fluide intersticiel entre les grains suffisamment visqueux, l'écoulement ne dépend par uniquement des interactions entre grains, mais également des forces de friction entre grains et fluide, ou des forces d'Archimède.

Prendre en compte ces forces d'interaction avec les fluides, dans des situations de milieux granulaires denses et confiés, comme c'est le cas pour les roches, est souvent pertinent pour des écoulements naturels ou forcés. Ces forces sont notamment importantes pour comprendre la déformation des roches autour d'un puits lors d'une injection ou une extraction, l'érosion par les forces de filtration dans des levées, digues naturelles ou artificielles, ou dans des processus d'avalanches sous marines ou chargées en eau.

La prise en compte de ces interactions peut se faire à l'aide de modèles hybrides granulaires / fluides, où deux descriptions couplées occupent la totalité de l'espace, permettent de suivre les grains individuellement, comme modèle discret, alors que le fluide est décrit à l'aide d'équations continues. L'écoulement du fluide est décrit en moyenne sur quelques grains, à l'échelle dite de Darcy. Les forces d'interaction entre grains et fluide sont calculées à l'aide de la force de Darcy, et interviennent dans les équations dynamiques de la partie granulaire, et la partie fluide du modèle. Celles-ci sont résolues alternativement en temps. Les opérateurs qui permettent de calculer la force de friction fluide sont extrapolés par un opérateur de projection entre l'espace discret, porté par les grains individuels, et l'espace continu du fluide, représenté sur une grille fixe de maille faisant quelques grains. Par exemple, l'opérateur permettant de distribuer une fraction solide ou toute quantité attachée au modèle continu, depuis un nœud vers les grains voisins, est une convolution par la fonction de projection représentée par le niveau de gris ci-dessous (Vinningland et al., Phys Rev E 051306, 2007).

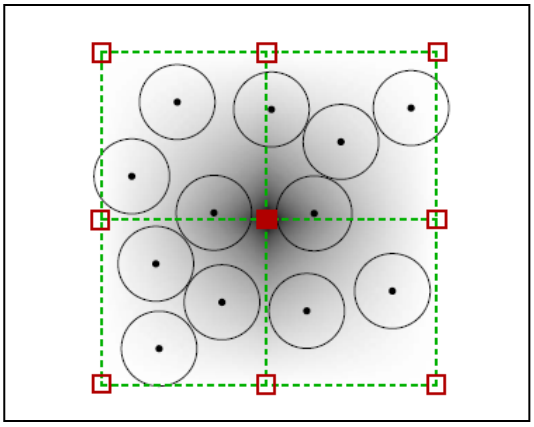

L’avantage essentiel de cette technique est le fait que le milieu granulaire, poreux, et le fluide, n’ont pas besoin d’être séparés sur deux domaines spatiaux distincts. Une autre approche, courante, consiste à traiter des modèles en éléments finis avec couplage de la contrainte par conditions aux frontières communes, avec une résolution de l’équation de Navier Stokes dans la partie fluide, et une résolution de l’équation de l’élastodynamique dans la partie solide. Cette approche classique à deux domaines spatiaux, dans les problèmes en grande déformation, nécessite toutefois un traitement explicite de l’interface, et pour les traitements d’équations sur des mailles, nécessite en général des remaillages fréquents quand la frontière évolue. La méthode hybride granulaire / fluide permet d’éviter ce problème.

1.1 Hydrofracturation et aérofracturation

Cette méthode hybride est particulièrement bien adaptée à décrire des problèmes d’injection ou extraction de fluides dans des milieux poreux.

1.1.1 *Article [Johnsen et al., Phys Rev E, 2006]: Pattern formation during air injection into granular materials confined in a circular Hele-Shaw cell, Ø. Johnsen, R. Toussaint, K. J. Måløy, and E. G. Flekkøy,* PHYSICAL REVIEW E **74**, 011301, 2006

En particulier, dans [Johnsen et al., Phys Rev E, 2006], on a décrit le problème d’une injection contrale dans un milieu granulaire faiblement consolidé, représentatif de situation de fracturation par injection de fluide dans un milieu poreux. Dans un milieu circulaire, entre deux plaques de verres (dites cellule de Hele-Shaw) à bords ouvert initialement remplies de granulaire compact, on fait monter la pression centrale et on maintient cette surpression. Du à la compressibilité du milieu, la perturbation de pression met un certain temps à se propager. Pour des surpressions suffisantes, des gradients de pression s’établissent dans le système, et les grains se déplacent.

Code de couleur : surpression évoluant au cours du temps. En noir : les grains se déplacent, successivement en (a), (b), (c). A droite, champ de perméabilité correspondant.

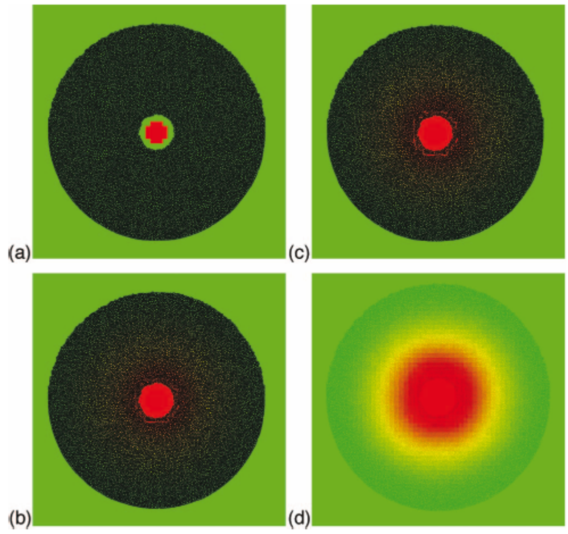

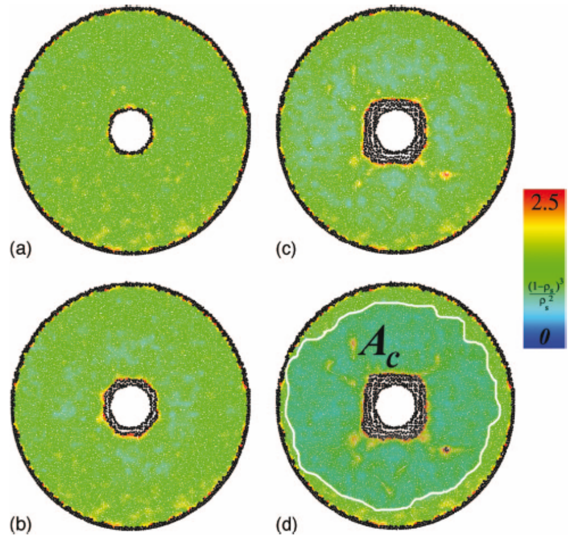

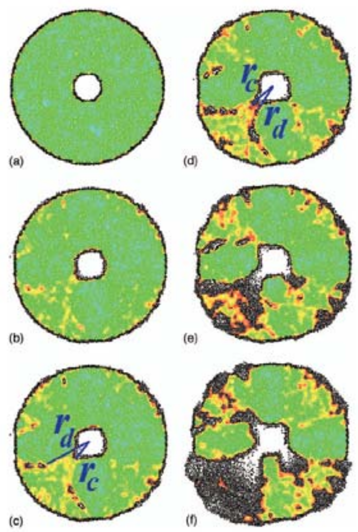

Formation de bulles et de doigts lors de la fracturation.

On a pu comparer ces simulations à des expériences réalisées dans les mêmes conditions, et suivies par une caméra rapide. L'étude des déplacements des grains , par des traitements optiques de différence de niveaux de gris, a mis en évidence que les grains étaient compactés autour d'une bulle vide de grains : voir ci-dessous.

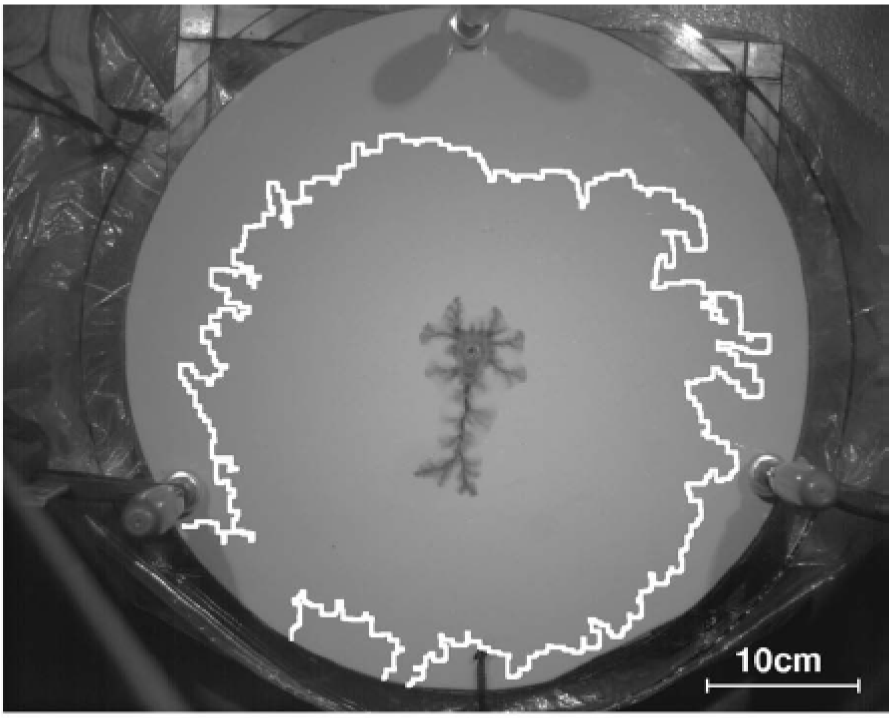

La zone à l'intérieur du liséré blanc a été compactée.

A partir d'une certaine surpression, on a observé une instabilité et une brisure de la symétrie circulaire de la zone vide de grains : on a formation de digitations fines et ramifiées. Analysant les forces en jeu, on a mis en évidence dans ce système la présence d'un mécanisme déstabilisateur sismilaire à celui présent lors de l'injection d'un fluide peu visqueux dans un fluide plus visqueux : les gradients de pression sont supérieurs à l'avant des doigts les plus avancés, ce qui les accélère et les détache du reste. Par contre, le mécanisme de stabilisation est différent du cas de Saffman Taylor de deux fluides newtoniens : ici, aucune tension de surface n'est présente à l'interface entre pâte de grains et d'air, et zones contenant uniquement de l'air. Par contre, l'extension d'une zone compactée lorsque les grains se poussent les uns les autres autour de la zone dégagée mobilise la friction solide contre l'enceinte de confinement, et tend à stabiliser les zones les plus avancées.

Cette étude a permis d'établir la validité du modèle numérique, dans la mesure où une comparaison quantitative des vitesses de propagation des doigts en fonction des conditions de surpression a été établie. D'autre part, on a pu établir les différents régimes possibles pour la propagation de ces fractures, ou doigts, par injection de fluide central dans des milieux poreux hautement déformables (granulaires peu consolidés en empilements denses).

1.1.2 *Article [Johnsen et al., Phys Rev E, 2008a]: Coupled air/granular flow in a linear Hele-Shaw cell, Ø. Johnsen, R. Toussaint, K. J. Måløy, E. G. Flekkøy and J. Schmittbuhl.* PHYSICAL REVIEW E **77**, 011301, 2008

Dans [Johnsen et al. 2008a], "Coupled air/granular flow in a linear Hele-Shaw cell", on a poursuivi l'étude des instabilités lors d'injection d'air dans un granulaire confiné. Le premier article traitait des instabilités dynamiques en configuration radiale. Dans cet article, on s'est intéressé aux brisures de symétrie en configuration linéaire. Cette étude est essentiellement expérimentale.

La configuration explorée correspond à un granulaire confiné initialement sous son propre poids en cellule de Hele Shaw. La cellule est alors placée horizontalement, les bords sont imperméables, et l'on fait monter la surpression d'air à un bord jusqu'à un niveau où on le maintient. L'autre bord est libre. Voir la figure suivante pour la configuration du montage expérimental.

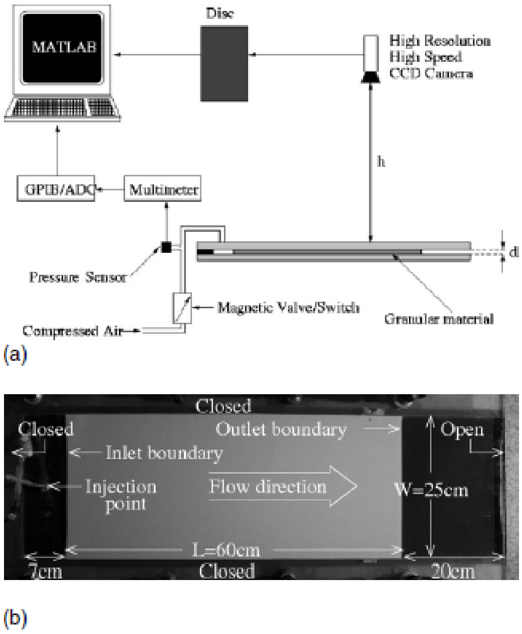

Dans cette configuration, on a étudié les différents régimes possibles : pour des graidents de pression imposés suffisamment faibles, on n'a que perméation du fluide sans déformation notable du milieu oeruex. Au-delà d'une certaine surpression critique, une compaction était observée dans la chambre d'entrée (régime II). Le régime suivant correspondait à une compaction initiale, suivi d'une propagation de la surpression à l'intérieur du milieu granulaire, d'une érosion du milieu avec démobilisation de la friction avec les parois, à partir de la croissance de la frontière extérieure, puis la propagation d'un doigt vide de grains dans le milieu fragilisé.
Le dernier régime, IV, où « régime piston », correspond à la propagation du doigt vide de grains sans arrêt. La figure ci-dessous illustre ces différents régimes en fonction de la séparation entre les plaques et la surpression imposée.

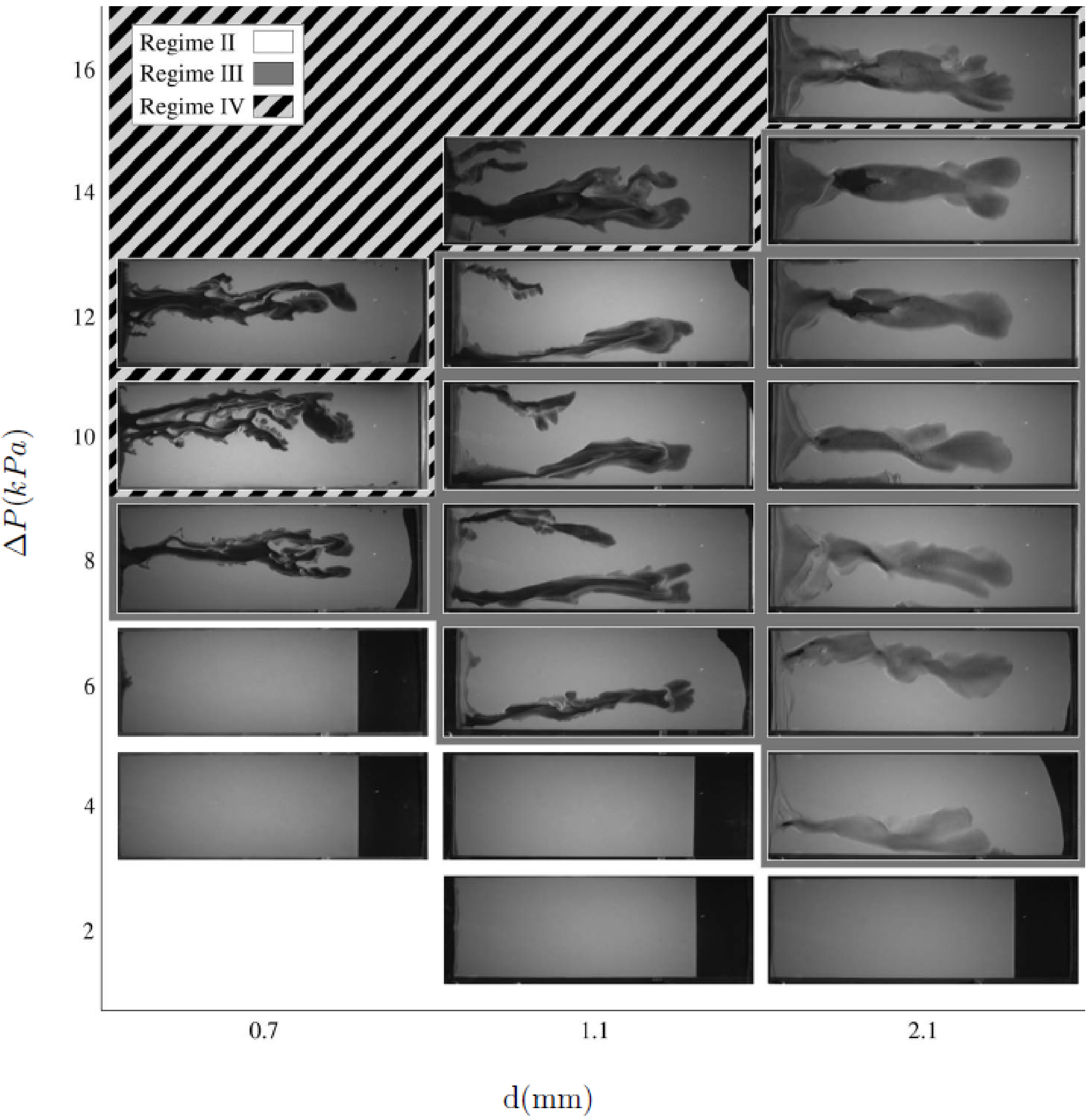

On a pu mettre en évidence la dynamique de la surpression lors de la phase d'attente entre compaction initiale et propagation d'un doigt vide de grains. Celle-ci est décrite à partir d'approximations simples de propagation diffusive de surpression, obtenue par la combinaison de la loi de Darcy et de l'équation d'état du fluide intersticiel de compressibilité finie.

L'analyse des forces de friction et des parties de la contrainte portées par le fluide et le solide, ainsi que l'analyse de la propagation de la surpression, permettent de calculer les séparations entre les différents régimes observés, ainsi que le temps d'attente dans le troisième régime. Pour la comparaison entre théorie et expériences, à partir d'analyses par différence d'images sur des séries acquises par caméra rapide, on a étudié la propagation du mouvement en avant de la zone d'injection, et la propagation du front de diffusion de pression.

On a ensuite mis en évidence les caractéristiques de propagation du doigt vide de grain dans la phase dynamique : largeur du doigt en fonction de la position et de la pression d'injection. Le matériau étant de plus en plus mobile au fur et à mesure de l'injection, les doigts s'élargissent dans la phase initiale, jusqu'à occuper autour de la moitié du chenal.

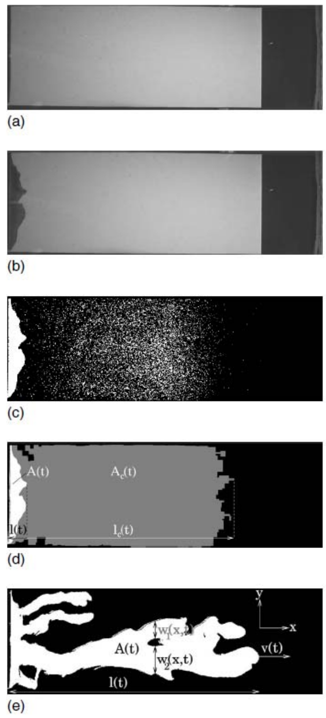

Succession d'images : (a) état initial, (b) après compaction, (c) différence de niveau de gris, (d) traitement et extraction de partie mobile, € doigt vide de grain extrait des images

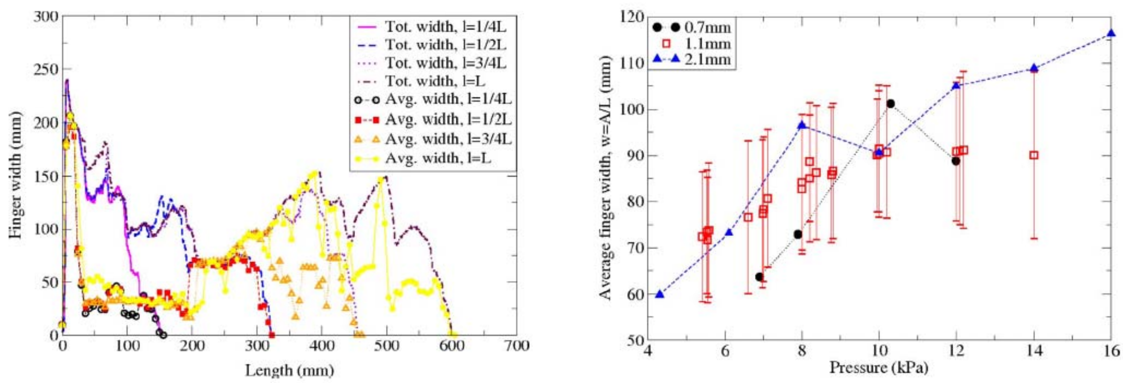

Largeur du doigt à différentes étapes.

1.1.3 *Article [Johnsen et al., Phys Rev E, 2008b]: Decompaction and fluidization of a saturated and confined granular medium by injection of a viscous liquid or gas*
Ø. Johnsen, C. Chevalier, A. Lindner, R. Toussaint, E. Clément, K. J. Måløy, E. G. Flekkøy, and J. Schmittbuhl PHYSICAL REVIEW E **78**, 051302, 2008

Cette étude a été conduite en collaboration avec l'équipe granulaire et suspension de l'ESPCI. En utilisant les mêmes sphères de Ugelstad, de diamètre très calibré, on a effectué une étude comparative de l'instabilité de Saffman-Taylor dans un granulaire soumis à surpression du fluide intersticiel, avec deux fluides très différents par leurs propriétés de viscosité et compressibilité, notamment : l'air à pression atmosphérique, et une huile (isodense avec les particules). Des états typiques de propagation dans les deux systèmes sont représentés ci-dessous :

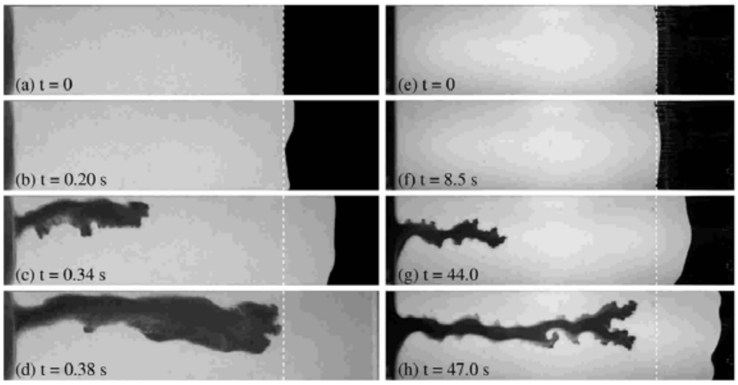

FIG. 2. Typical experiments. The left column shows an air-grain experiment at $\Delta P_{air}=93$ mbar and $b=1.15$ mm. In the right column an oil-grain experiment at $\Delta P_{oil}=85$ mbar and with $b=1.15$ mm is displayed. (a) and (e) shows the sample before fluid injection. The dashed lines indicate the initial position of the outer boundary, L_0. Before a finger empty of grains starts developing the granular packing has been dilated, indicated by an increase of length beyond L_0 seen in (b) and (f). In (c) and (g) typical finger patterns are shown, after propagating for $L_0/2$, and in (d) and (h) the fingers have propagated a distance L_0.

On a pu mettre en évidence le fait qu'en première approximation, les deux systèmes sont très proches, en travaillant en temps réduit, normalisé par la viscosité du fluide intersticiel. La forme exacte des doigts n''est pas exactement identique, avec notamment une mobilité qui augmente plus lors de l'avancée des digitations dans de l'air que dans de l'huile : il est plus facile de décompacter le milieu poreux dans un fluide compressible, et les doigts augmentent un peu plus en largeur lors de leur avancée dans un canal granulaire/air que dans un canal granulaire/huile.

On a également observé un seuil de différence de pression à imposer pour avoir une digitation dans le système air/grains, alors que ce seuil est quasi nul pour le système huile grains (voir ci-dessous). Ceci a pu être expliqué par une friction coulombienne et une contrainte venant du poids des grains dans ce cas, alors que cet effet disparaît dans l'huile isodense où les forces d'Archimède compensent le poids des grains.

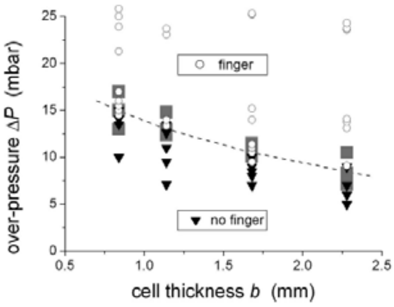

FIG. 3. Threshold pressure for the onset of grain mobilization and finger formation in the air-grain system. The gray squares correspond to the ΔP at which fingering occurs for experiments where the injection pressure is gradually increased from zero. For the oil-grains system finger formation is observed for all tested ΔP.

Le rapport entre largeur du doigt vide de grains se propageant et la largeur du canal grandit lors de la progression du doigt dans les deux systèmes. Elle est typiquement plus petite, entre 0.1 et 0.2, dans le système huile/grains, et légèrement plus grande, de 0.1 à 0.3 vers la sortie du canal, dans le système air/grains. (voir figure ci-dessous).

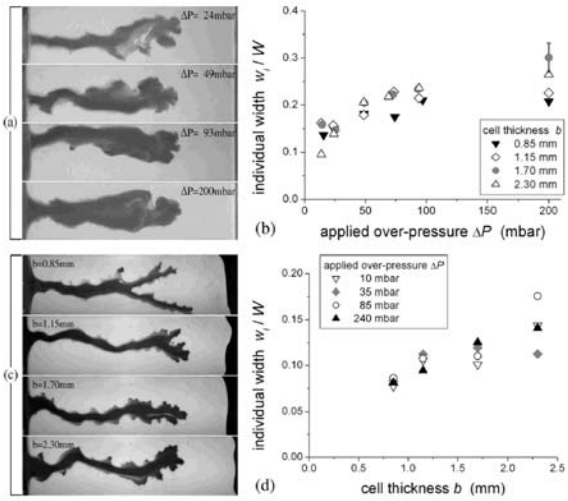

FIG. 11. (a), (c). Typical Patterns, respectively, for air-grain and oil-grain systems: for the presentation of air-grain results $b=1.15$ mm and ΔP is varied. For oil-grain systems the experiments are presented at a fixed $\Delta P \sim 55$ mbars but at different b. Right panels: Averaged individual finger width w_i, scaled on the cell width W for (b) air-grain and (d) oil-grain systems. For the air-grain system, w_i/W is a function of ΔP. Each point represents an average over roughly 27 experiments. For the oil-grain system, w_i/W is a function of b.

L'autre différence remarquée est un temps de retard entre le début de l'injection et la déformation de la surface libre externe, mesurée dans le cas de l'air et calculée à l'aide de la compressibilité de l'air, alors qu'elle est infime dans la suspension d'huile – de compressibilité quasi nulle.

Dans les deux systèmes, on a observé un temps de retard entre l'injection et la pénétration d'un doigt vide de grains. Ce temps d'érosion de la pâte initialement présente est un processus analogue aux formations de renards et d'érosion internes observés dans les digues ou les sols naturels lors d'écoulements internes : un écoulement peut lentement réarranger le milieu, en particulier à partir du bord libre, et mener finalement à l'ouverture d'un canal, drain principal, et à une rupture catastrophique. Le temps d'érosion a pu être modélisé à l'aide d'un écoulement visques nécessaire pour amener du fluide dans la zone à décompacter : voir ci-dessous.

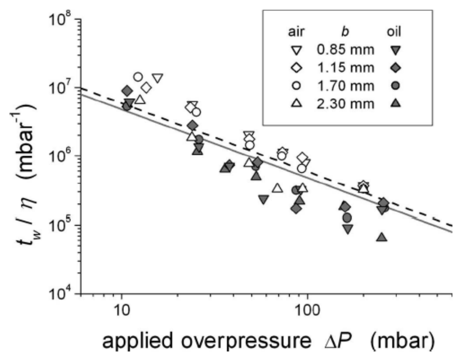

FIG. 5. Log-log representation of the waiting time t_w scaled with the fluid viscosity, as a function of the applied ΔP. The dashed line is the modeled waiting time for the air-grain system, and the solid line is the modeled waiting time for the oil-grain case.

.

Dans les deux cas, air et huile, le mécanisme de décompaction et d'érosion du pack initialement compact, qui prépare l'intrusion des digitations vide de grains, est en lui-même un mécanisme instable qui forme des canaux décompactés croissant de manière rétrograde à l'écoulement : voir les résultats par soustraction d'image ci-dessous.

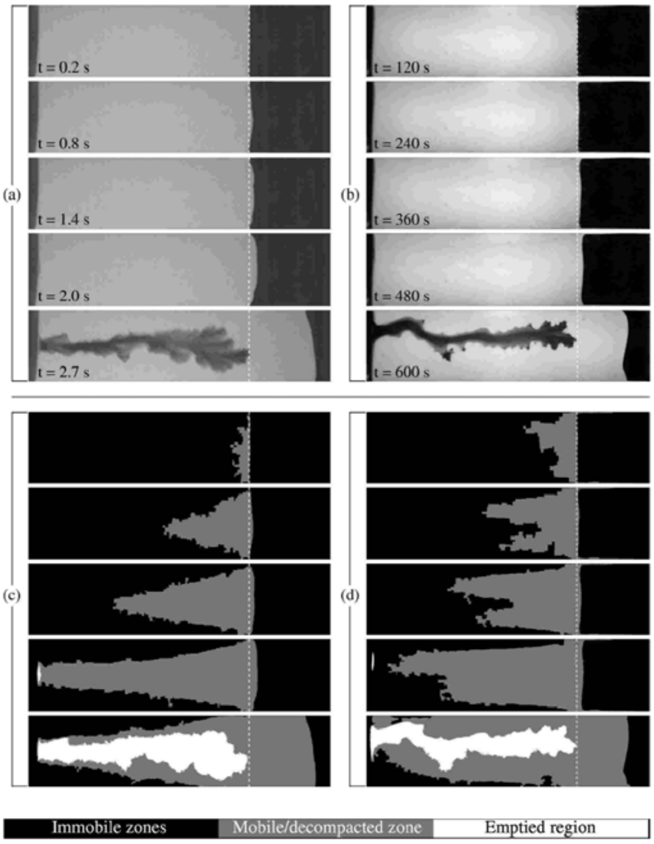

FIG. 4. Typical experiments. Images in (a) and (b) show the raw images for, respectively, air-grain and oil-grain mixtures, while in (c) and (d) the corresponding subtracted and filtered images show the mobile zones. Air-grain system: $b=1.15$ mm, $\Delta P=13$ mbars. Oil-grain system: $b=1.15$ mm, $\Delta P=11$ mbars. The dashed vertical lines indicate the initial position of the outer grain boundary. The bar on the bottom displays the color code representing immobile zones with solid fraction ρ_0, mobile or decompacted zone with solid fraction $\rho_{dec}<\rho_0$, and the finger virtually emptied of grains where $\rho\sim 0$.

Dans les deux systèmes, la mobilité, définie comme la vitesse du doigt vide de grains divisée par le gradient de pression macroscopique imposé, est fonction essectiellement de la position du doigt dans la cellule , mais dépend peu de la différence de pression imposée ou la largeur de la cellule. Lorsque cette mobilité est exprimée de manière adimensionnelle, en la normalisant par la viscosité du fluide porteur diviser par le carré de l'épaisseur de la cellule, on obteint des mobilités réduites très proches pour les deux systèmes : ils peuvent effectivement être comparés directement en unités réduites – voir figure ci-dessous.

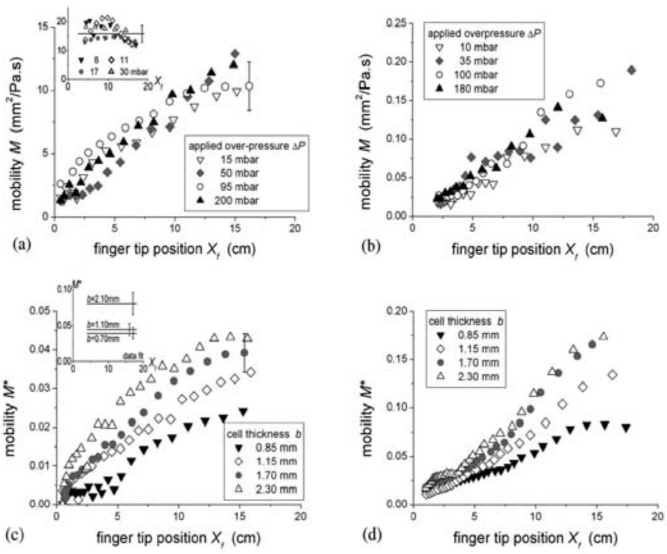

FIG. 9. Mobility M as a function of finger tip position X_f for (a) air-grain and (b) oil-grain systems. The cell thickness $b=1.15$ mm. (c) and (d) show the rescaled mobility $M^*=M/(d^2/\eta)$ as a function of finger tip position for air-grain and oil-grain systems, respectively. The rescaled mobility is averaged over all ΔP for each given b. Approximately 27 trials are used for the air-grain experiments and seven for the oil-grain case. The insets similarly show M and M^* obtained for the experiments involving an initially loosely packed granular matrix.

1.1.4 Article [Niebling 2012a] Niebling, M., R. Toussaint, E.G. Flekkøy and K.J. Måløy, Estudios numéricos de Aerofractures en medios poros / Numerical Studies of Aerofractures in Porous Media, Revista Cubana de Fisica, 29, 1E, 1E66, 2012

Dans la situation où un fluide est rapidement injecté dans un milieu confiné, comme une roche poreuse ou une fracture remplie d'un milieu légèrement perméable et fragile, on a régulièrement une injection loin de toute surface libre – via par exemple un puits de forage, ou lors d'une surpression dans une chambre magmatique, ou la rupture d'une paroi peu perméable en bord de réservoir souterrain avec mise en place d'injectites.
Comme observé dans les expériences décrites ci-dessus, lorsque le gradient de pression de pore atteint un bord libre, un processus de décompaction a lieu à partir de ce bord, lors duquel la friction solide est démobilisée, ce qui mène finalement à une rupture catastrophique par progression de grandes digitations.
Pour explorer la situation où ce processus de décompaction n'est pas à l'œuvre, on doit donc soit utiliser un système très grand, où les bords libres n'aient pas le temps d'être atteints, ou alors où le gradient de pression y soit nettement inférieur à celui du niveau de l'injection (pas exemple, dans une géométrie circulaire étendue).
L'alternative est d'empêcher le processus de décompaction par le bord en empêchant les grains de passer par le bord libre, mais en les retenant par un filtre qui laisse passer le fluide. Ceci permet de simuler un milieu plus étendu, mais aussi de se mettre en situation connue des géotechniciens pour empêcher la rupture des digues : en effet, des méthodes connues pour prévenie la formation de renards et la rupture par « piping erosion » consistent à poser une membrane sur la sortie de l'écoulement, et ainsi faire un filtre similaire.

Numériquement, on étudie une telle situation avec le modèle décrit ci-dessus :

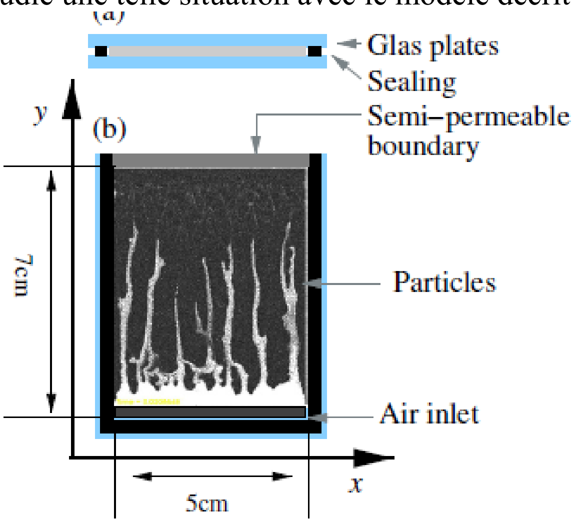

Figure 1: Numerical setup of the system.

On impose une surpression d'air en bord du système, puis on la maintient. La surpression se propage dans le système qui se compacte alors que les grains sont déplacés. Les équations résolues correspondent à la conservation de masse du gaz, avec une loi de Darcy et une équation d'état de gaz parfait, ce qui se ramène à l'équation non linéaire de diffusion advection

$$\phi\left[\frac{\partial P}{\partial t}+\boldsymbol{u}\cdot\nabla P\right]=\nabla\cdot\left[P\frac{\kappa}{\mu_f}\nabla P\right]-P\nabla\cdot\boldsymbol{u}$$

avec u la vitesse des grains, P la pression, Φ la porosité, κ la perméabilité, et μ_f la viscosité du fluide.

Ceci est résolu par une méthode « ADI » (Alternate Direction Implicit Method).
Pour la partie granulaire, l'équation de Newton pour chaque particule prend en compte des répulsions élastiques et frictions avec les grains voisins $\boldsymbol{F_I}$, forces visqueuses durant les chocs $\boldsymbol{F_d}$ et interaction élastiques avec parois de confinement $\boldsymbol{F_a}$, ainsi qu'une friction fluide linéaire en gradient de pression (régime de Darcy) :

$$m\frac{dv_p}{dt} = \boldsymbol{F_I} + \boldsymbol{F_d} + \boldsymbol{F_a} - \frac{\nabla P}{\rho_n}$$

où ρ_n est le nombre de grains par unité de volume.
On observe qu'à pression imposée suffisante, des doigts fins et ramifiés se propagent dans la zone compactée. Des simulations faites dans des cellules de quelques centimètres montrent le phénomène ci-dessous. La pression imposée augmente de bas en haut, le temps de gauche à droite. Sur la figure de droite, on observe la pression de pore. Elle se propage par advection avec les grains, et par diffusion autour des doigts. La compressibilité effective est plus grande à pression plus petite, ainsi que la diffusivité de la surpression, en conséquence. En effet, celle-ci est de

$$D = \frac{\kappa_T \kappa}{(1-\rho_s)\mu_f}$$

où κ_T est la compressibilité – égale à 1/P pour un gaz parfait, et ρ_s = 1- Φ est la fraction solide. Le résultat est que les gradients sont plus localisés dans les expériences à plus grande pression imposée, ce qui amène une plus grande pénétration des fractures induites par l'injection d'air – alors qu'a plus faible pression et plus grande diffusivité, la surpression diffuse rapidement et le phénomène s'arrête faute de gradient de pression pour déplacer les grains.
On observe ci-dessous que le nombre de ces doigts diminue lorsque la surpression imposée augmente, en même temps que leur profondeur augmente. La diffusion de la surpression est plus rapide à faible pression.

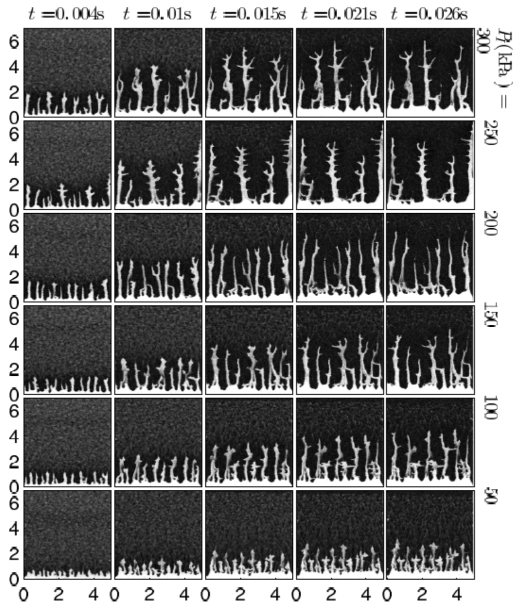

Figure 2: Snapshots during the simulations of the particle density in the Hele-Shaw cell, displayed for decreasing injection pressure P_I from top to bottom and as a function of time (left to right). Low particle density appears brighter in the snapshots. Under air injection, fractures, fingers and dispersed bubbles of low particle density emerge and propagate. x- and y-axis units are given in cm. The y-axis specifies the distance from the inlet.

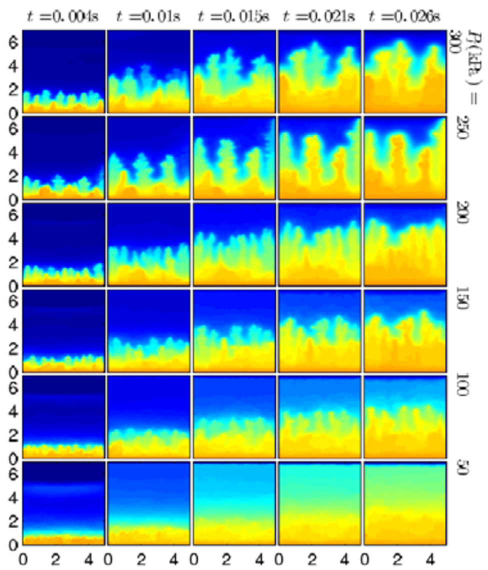

Figure 3: The pressure evolution for decreasing injection pressure P_I (top to bottom) and as a function of time (left to right). High pressure appears yellow (brighter) in the snapshots. x- and y-axis units are given in cm.

On a pu mettre en évidence que la dynamique de pénétration des doigts suit une courbe maitresse, à partir du moment où des doigts pénètrent, avec une longueur proportionnelle à la racine de la surpression imposée : voir ci-dessous.

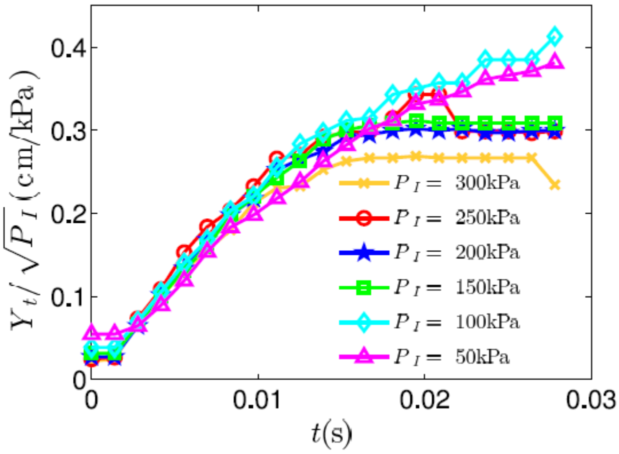

Figure 5: The position of the most advanced finger/fracture rescaled by the square root of the injection pressure $\sqrt{P_I}$. As a function of time the graphs at different injection pressure P_I collapse onto a single graph.

La distance caractéristique entre les aérofractures a été caractérisée par une analyse de Fourier de la densité de grains, permettant d'extraire le nombre d'onde dominant en utilisant le spectre de Fourier comme poids dans une moyenne sur les nombres d'ondes: ci-dessous, on montre une tendance à la décroissance du nombre de doigts en fonction de la pression imposée.

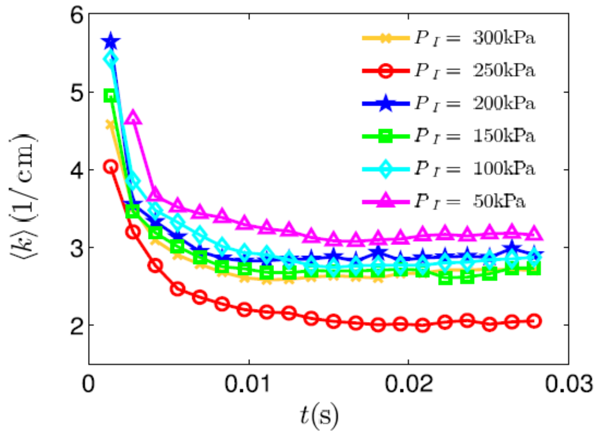

Figure 6: The average of the spatial finger wavenumber in x direction.

1.1.5. *Article [Niebling 2012b] Niebling, M.J., R. Toussaint, E.G. Flekkøy and K.J. Måløy, Dynamic aerofracture of dense granular packings, Phys. Rev. E, 2012.*

Le but de cet étude est de pouvoir explorer des régimes un peu plus vastes de viscosité ou taille du système, les deux problèmes étant intimement liés. Pour pouvoir le faire numériquement tout en gardant un nombre de particules limité – quelques centaines de milliers de particules sont simulées - on a choisi de faire varier systématiquement la viscosité dans ce type de simulations.
On a ainsi pu mettre en évidence deux types de régimes, pour les mêmes paramètres de surpressions imposées (à quelques pressions atmosphériques) : un régime où on voit apparaître des bulles vides de grains de façon transitoire, suivi d'une compaction contre le filtre de sortie. Ou, pour des surpressions supérieures, des digitations assez larges suivies de

ramifications. La figure ci-dessous illustre ces deux régimes, dans les configurations de grains et la pression de pore.

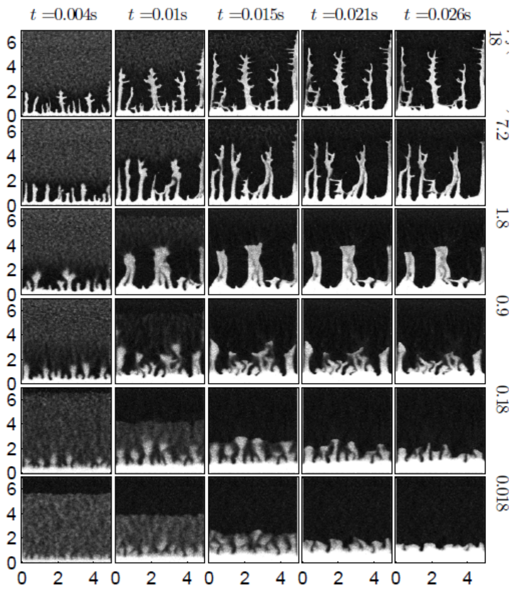

FIG. 3: Particle density for decreasing gas viscosity from top to bottom and as a function of time (left to right). Low particle density appears brighter in the snapshots. Under air injection fractures, fingers and bubbles of low particle density emerge and propagate.

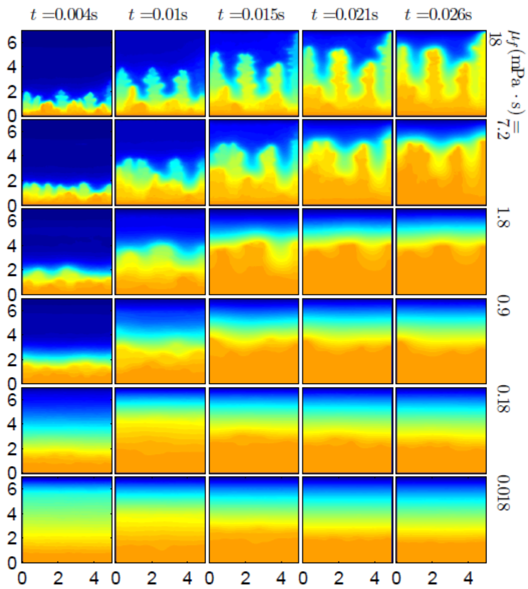

FIG. 4: (Color online) The pressure evolution for decreasing gas viscosity (top to bottom) and as a function of time (left to right). High pressure appears yellow (brighter) in the snapshots.

L'origine de cette différence s'explique par la vitesse de propagation de la diffusion de la surpression, par rapport à la vitesse d'un front de compaction qui amène les grains en contact compressif : Tant que ce front est en avance sur un front de diffusion, une dynamique où la surpression dans des doigts pousse des grains avec une transmission de contrainte par phase solide mène à des instabilités similaires à celles observées dans la fracturation/digitation de fluides viscoélastiques. Si par contre la diffusion est suffisamment rapide, les grains sont poussés en profondeur, loin de l'interface fluide clair / milieu granulaire, par la friction fluide (le gradient de pression), sans contacts. On n'observe alors qu'une insabilité transitoire, avec bulles similaires à celles obtenues dans des situations de lits fluidisés, après quoi l'ensemble des grains se retrouve compactés contre le filtre de sortie. Le code de couleur, représentant la trace de la contrainte solide ci-dessous, illustre cette différence fondamentale entre les deux mécanismes.

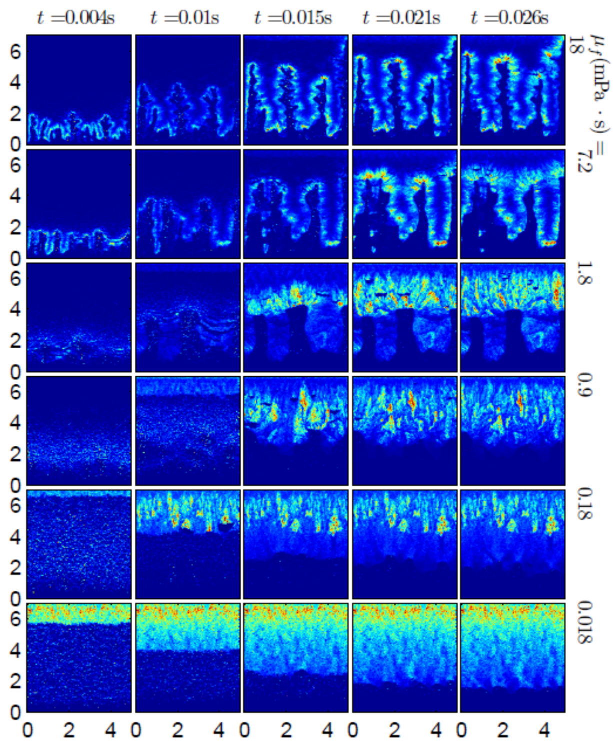

FIG. 6: (Color online) The inplane pressure on the particles for decreasing gas viscosity (top to bottom) and as a function of time (left to right). High stress appears yellow (brighter) in the snapshots.

1.2 Instabilités de sédimentations et Rayleigh Taylor granulaire dans les mélanges eau/grains et air/grain

On s'intéresse à l'influence du fluide intersticiel sur les écoulements de matière divisée, granulaires plus ou moins fins. On modélise ainsi les instabilités génériques ayant lieu dans de tels écoulements : lors de sédimentations (sedimentation, avalanches, Rayleigh Taylor), ou celles dues à des surpressions (Saffman Taylor, hydrofracture) .
On étudie comment la viscosité et la compressibilité du fluide intersticiel affecte les écoulements de milieux granulaires dans la déposition de sediments étudiés en cellules fermées, aussi nommées les instabilities granulaires de Rayleigh Taylor. On a comparé le cas de mixtures air/grains et eau/grains [Niebling et al. 2010, Vinningland et al. 2010]. Ceci a permis de calibrer les codes en les comparant à des expériences. Ensuite, on a étudié les effets de viscosité variable [Niebling et al., 2010b], ou l'effet de la taille des rains sur les processus de sédimentation.

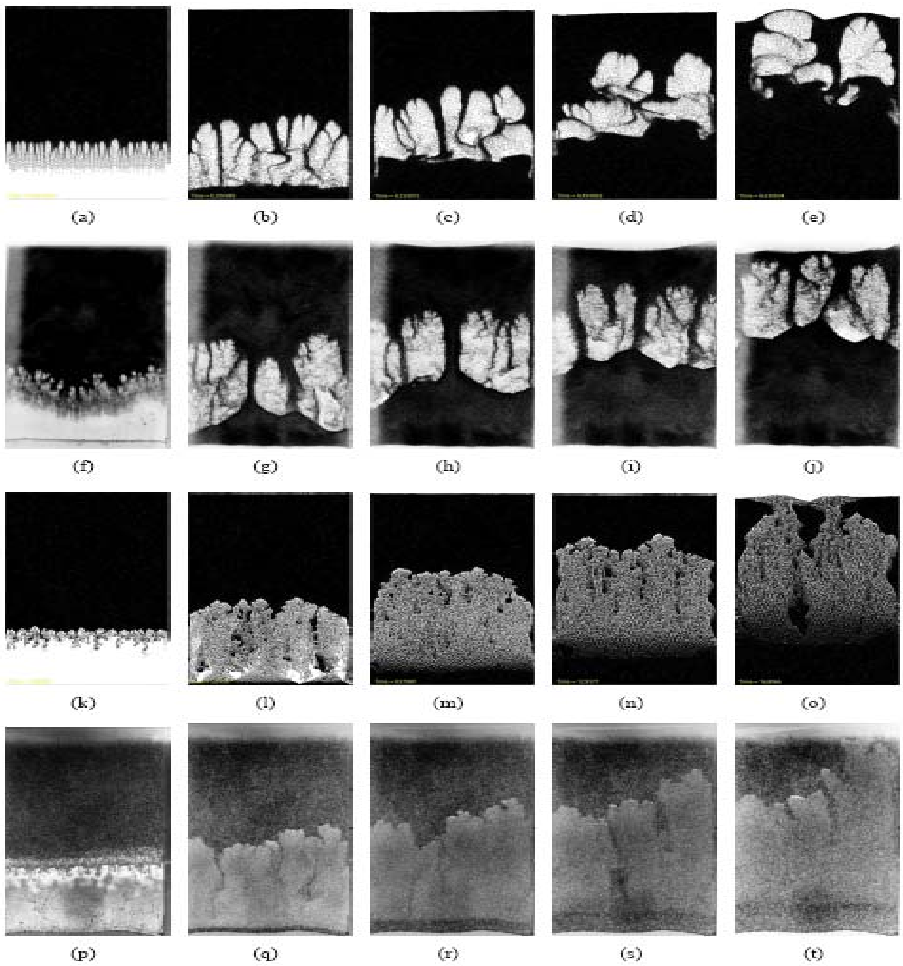

Figure 5.1: Simulation in comparison to experiments of the granular Rayleigh-Taylor instability. The first sequence shows simulations and the second sequence shows corresponding experiments with air. In third sequence simulations and the forth sequence corresponding experiments with water/glycerol are shown.

Ces expériences de sédimentation, dans des systèmes de granulométrie contrôlée, dans de l'eau, de l'air et des mélanges eau glycérol, ont permis de valider les modèles numériques développés.

1.3 Mécanique d’interfaces cisaillées et avalanches

On étudie à l’aide de ces codes comment la presence du fluide intersticiel affecte la friction macroscopique de granulaires cisaillés, comme des gouges de failles saturées, avec un encaissant imperméable [Goren et al., JGR B, 2010, Goren et al., PAGeoph, 2011]. On a ainsi mis en évidence, dans des phénomènes de cisaillement rapide, que la pression de pore est inhomogène, et que même dans un système à bords perméables, la présence d’eau permet de liquéfier les gouges et leur faire perdre la résistance au cisaillement.
On a également mis en œuvre des versions quasi bidimensionnels de tels modèles en surface libre, pour pouvoir modéliser l’avalanche de systèmes marneux de grande échelle, contenant argiles et fines partiellement saturées et pouvant se liquéfier lors de précipitations (Spickermann et al. 2012) .

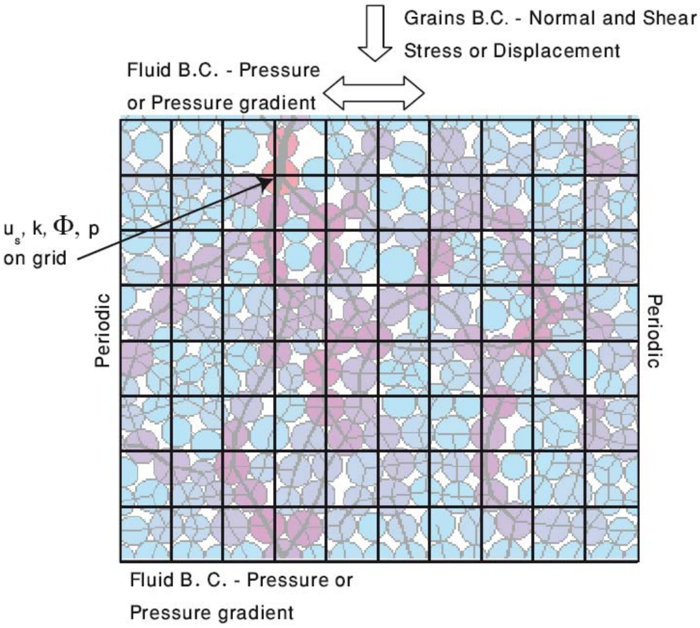

Figure 1: A schematic representation of our 2D coupled grain-fluid model. The grain level, depicted by shaded spherical discs, is solved by a granular dynamics algorithm. The color-scale represents the total forces acting on each particle, where red corresponds to the maximal force and light blue to minimal forces. The width of lines connecting pairs of particles, correlates to the magnitude of the normal force between pairs, and allow visualization of stress chains. Fluid equation (6) is solved on a super imposed grid, with grid spacing larger than the largest grain diameter. The porosity, Φ, permeability, k, and granular velocity, $\boldsymbol{u_s}$, are calculated along each grid point by interpolating from neighboring grains. The calculated pressure is interpolated back from each grid point to the surrounding grains.

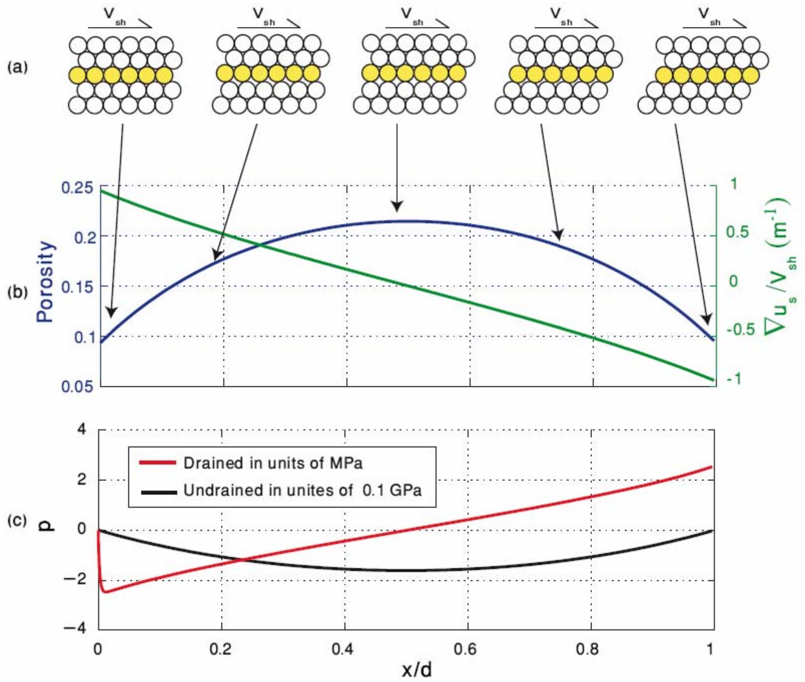

Figure 5: Results from shearing of hexagonal grain pack subjected to a constant shear velocity, V_{sh}, at its top. (a) Shear is accommodated in a localized manner along a single sliding row, depicted by yellow filled discs. The system first dilates and then compacts. Dilation and compaction induce time and space dependent porosity, permeability and granular velocity. (b) Evolution of porosity and $\nabla \cdot u_s$ along the sliding row as a function of the horizontal displacement, x, scaled by grain diameter, d. (c) The maximum value of PP during sliding. The temporal evolution of PP suggests that under drained conditions, large values of PP may be generated during shearing, even when the initial configuration is very dense (red). This is in contrast to the negative PP generated under undrained conditions due to the lack of fluid influx through the boundary that would have compensated for the dilation (black).

Résumé des activités de recherche : autres thématiques :

2 Ecoulements multiphasiques dans les milieux poreux, et Ecoulements en fractures rugueuses (transferts de masse et transferts d'énergie),
3 Fracturation des milieux hétérogènes fragiles, et hydro et aérofracturation
4 Interactions entre mécanique et chimie dans les systèmes fluides/roches (stylolites),
5 Développement de techniques d'imagerie

2 Transport dans les milieux poreux et fracturés

2.1 Transport multiphasique en milieux poreux

On étudie l'effet de la vitesse d'invasion, de la gravité et de possibles sollicitations oscillatoires en pression sur les caractéristiques des écoulements durant des écoulements biphasiques en milieux poreux transparents. Ces écoulements impliquent des fluides non miscibles, de viscosité et densité différentes. Les processus et structures de déplacement sont étudiées par suivi optique dans leur complexité spatio temporelle.
On se concentre sur les aspects suivants:

2.1.1. Dans des écoulements biphasiques stationnaires, on étudie la relation entre chute de pression macroscopique et flux macroscopique, i.e. la perméabilité relative, et on étudie comment ce rapport dépend de la distribution des taille amas du fluide peu visqueux [Tallakstad et al. 2009].

Ecoulements biphasique permanents en milieux poreux: statistiques et propriétés de transport [Tallakstad et al, 2009]

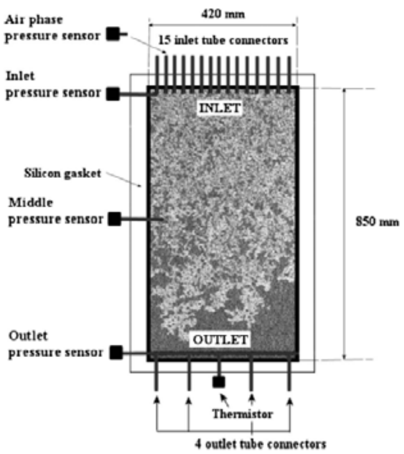

Chute de pression dans la cellule en function de la vitesse d'écoulement:

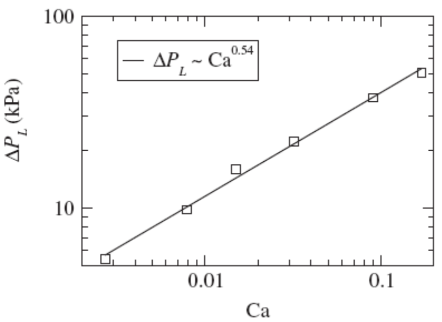

FIG. 2. Mean pressure difference ΔP_L during steady state as a function of Ca. The fluctuations in ΔP_L are of the order of 1 kPa, i.e., very small compared to the mean values. A power law dependence is found, with exponent $\beta = 0.54 \pm 0.08$.

2.1.2. Dans des situations de drainage, on étudie comment la géométrie d'invasion peut être expliquée à partir d'effets visqueux et capillaires, avec une dépendance des propriétés par rapport au désordre dans la distribution des seuils d'invasion. On montre comment ceci peut mener à des lois dits d'effets capillaires dynamiques [Løvoll et al. 2010].

Expériences de drainage rapide à flux imposé: les courbes de retention, pression-saturation, dépendent de la vitesse d'écoulement, ainsi que la saturation résiduelle : effets dynamiques. (Lovoll et al., 2011)

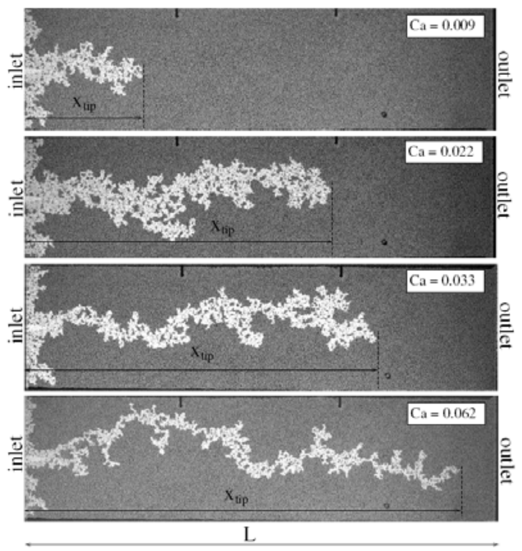

Figure 5. Images of experiments done at different withdrawal rates (capillary numbers) at the point in time where they have the same (viscous) pressure difference from the front of the invader to the outlet channel. The viscous pressure difference is $\Delta P_v \sim 490$ Pa in all the pictures.

Chute de pression à travers le système:

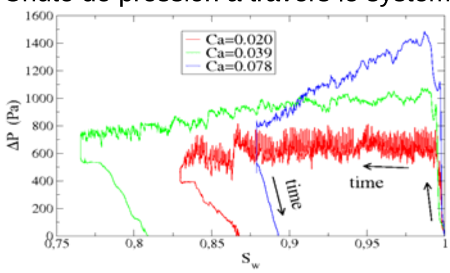

Collapse de la pression dynamique en fonction de la saturation en fluide mouillant

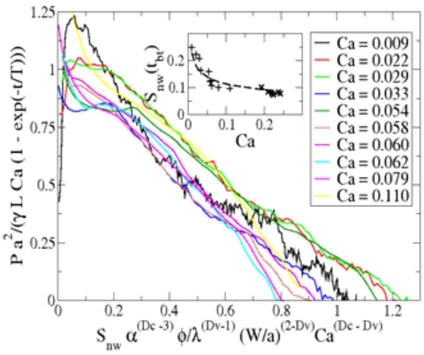

2.1.3. On s'intéresse également à l'impact de champs de pressions oscillants superposés à une vitesse d'écoulement constante, et à leur influence sur la structuration de l'écoulement [Jankov et al. 2010] : les effets de stimulation sismique sur l'écoulement de deux fluides immiscibles dans des milieux poreux synthéiques permettent de classifier les structures en fonction de la fréquence et l'amplitude de l'oscillation, caractérisées par un nombre de fragmentation. Les effets de compressibilité des fluides apparaissent primordiaux dans la compréhension de la mécanique de ces structures.

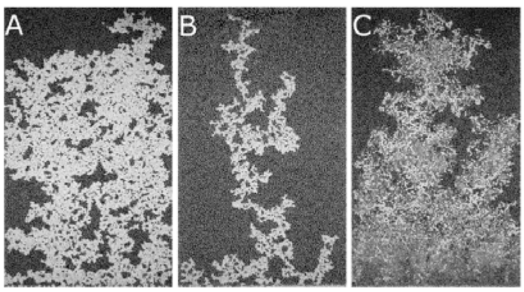

Figure 3. Examples of breakthrough images of the invading cluster created in a drainage process stimulated with the oscillating pressure. The applied frequency is 0.2 Hz and the amplitudes of the oscillating component vary. The structures shown on the images A, B and C are created at 20, 560 and 3700 Pa, respectively. The outflow rate of the wetting fluid is Q=0.022 ml/min. The dark area on the images represents the wetting fluid while the white area is the invading air cluster.

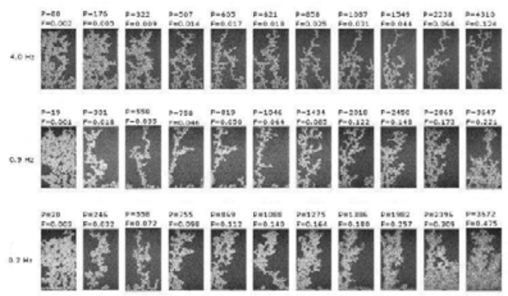

Figure 6. Breakthrough images of all experiments. The numbers above individual images indicate the amplitude of the pressure oscillations given in Pa (top row) and the fragmentation number (F) in the bottom row. The numbers 0.2, 0.9 and 4.0 refer to the frequency of the oscillations (Hz) at which the experiments are carried out. The flow direction is from the bottom of each individual image and up.

2.1.4. In fine, on travaille sur les conséquences pour les écoulements en hydrologie de ces relations. Notamment, en collaboration avec le LHyGeS, on étudie la migration de polluants denses et non aqueux dans des sols initialement saturés, et les digitations résultant de l'instabilité de Rayleigh Taylor dans de tels écoulements [Nsir et al., 2009].
Ces développement servent également dans le suivi de migration d'hydrocarbures dans des réservoirs [Jianzhao et al. , 2012a, 2012b].

2.2 Ecoulements dans des fractures naturelles et couplage thermique entre le fluide et la roche environnante

Ces études portent sur la simulation de l'écoulement d'un fluide dans une roche plus chaude, et comment cet écoulement permet d'extraire la chaleur de la roche et transporter efficacement cette énergie. Il s'agit d'étude fondamentale liée à l'efficacité des processus géothermiques. On se concentre à incorporer la complexité des fractures naturelles, pour évaluer l'effet de ceci sur l'efficacité du couplage. On a étudié la morphologie des fractures naturelles, d'une part dans le réservoir d'échange de Soultze-sous-Forets [Neuville et al., CRAS 2009], d'autre part dans les joints présents dans le bassin de Draix, dont la susceptibilité aux avalanches dépend du tranport par de tels joints [Neuville et al., Hydrological processes, 2010, a and b

Le transport et le couplage dans ces fractures est effectué à l'aide d'approches en differences finies [Neuville et al, 2011]. On développe actuellement des approches par modèles de Lattice Boltzmann couplés pour pouvoir s'affranchir des hypothèses de lubrication, et monter en nombre de Reynolds et en complexité des écoulements considérés.

Modèles de difference finie:

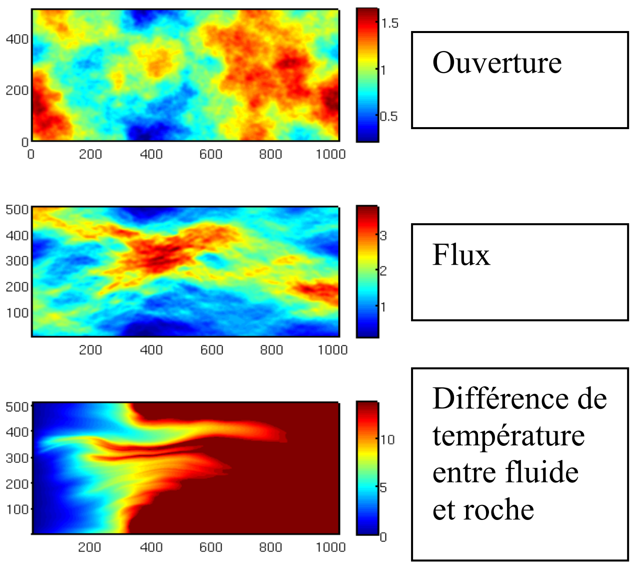

Modèle de Lattice Boltzmann:

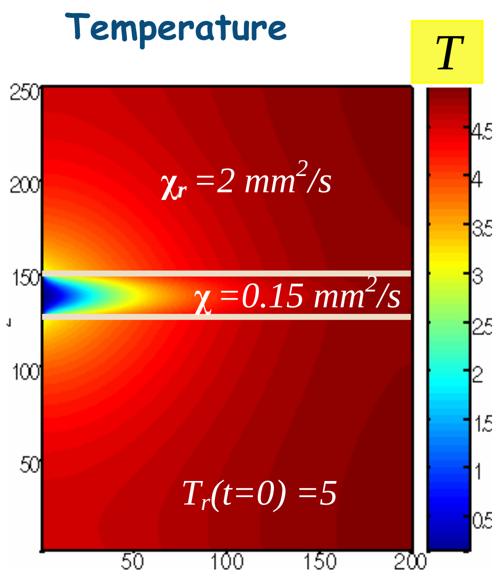

3 Processus de Fracturation

3.1 Propagation de fracture en milieux hétérogènes

On étudie nucléation et la propagation de fracture en milieu hétérogène. Ceci a permis de mettre en évidence l'influence des interactions et de la nature du désordre gelé dans le type de localisation du dommage [Toussaint et Pride, 2005, Toussaint et Hansen, 2005], et dernièrement, dans la propagation de fractures et les avalanches durant celles-ci. On étudie en particulier comment la présence à la fois de désordre gelé de bruit thermique permet de faire coexister un caractère intermittent à petit échelle, avec des lois de Gutenberg Richter et des corrélations à longues portées entre évènements [Grob et al., 2009, Santucci et al., 2009a,b, Pindra et al. 2009], et un comportement macroscopique de creep, fortement affecté par les effets thermiques [Tallakstad et al, 2011, Lengliné et al, 2011].

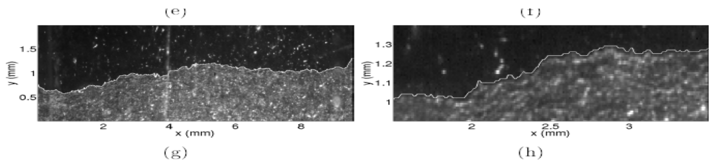

FIG. 4.9 – (a) Example of raw image taken with the high speed camera. (b) Example of the resulting picture of a subtraction between two raw images. (c) Gray level histogram of the preceding picture. (d) Image after thresholding. (e) Gradient of the clipped image. (f) Extraction of the percolating cluster from the gradient picture. (g) Extracted front (white line) superimposed on its corresponding raw image. (h) Zoom on the extracted front.

4. Interaction entre mécanique et chimie: formation de stylolites, analyse de paléocontraintes et generation de contraintes en milieu sédimentaire.

On développe des modèles de génération de stylolites par pression solution dans des milieux désordonnés. Ceci a permis de mettre en évidence que la morphologie des stylolites garde la trace des contraintes sous lesquelles elles ont été formées.[Rolland et al. 2012, Ebner et al. , 2009a,b, Ebner et al.,, 2010, Koehn et al 2007, 2012]. Cette théorie, testée avec succès sur des stylolites échantillonnées au cirque de Navacelles, est actuellement mise en application sur les stylolites de Bure, en collaboration avec l'ANDRA (thèse d'A Rolland).
Ces travaux permettent également d'explorer la génèse de contraintes actuelles par dissolution de fractures anisotropes héritées d'évènements tectoniques. L'anisotropie de ces structures est à l'origine d'anisotropie de contraintes mesurables, obtenues par un processus intrinsèque de déformation du au couplage chimique entre fluide et solide dans les calcaires du assin de Paris. Les contraintes résultantes sont compatibles avec celles actuellement observées (collaboration avec F Cornet).
In fine, on s'intéresse à l'impact de ces structures, stylolites et joints, sur les propriétés de transport dans les carbonates (projet FORPRO II, collaboration avec Jerusalem et Londres). Ceci est important pour de nombreux réservoirs.

Stylolite, analyse de lois d'échelle et cross over permettant de déterminer la paléocontrainte de formation

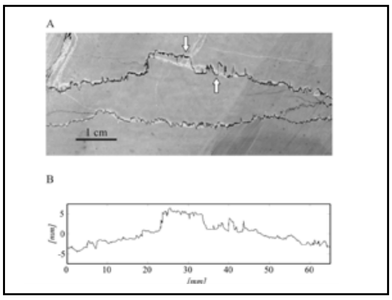

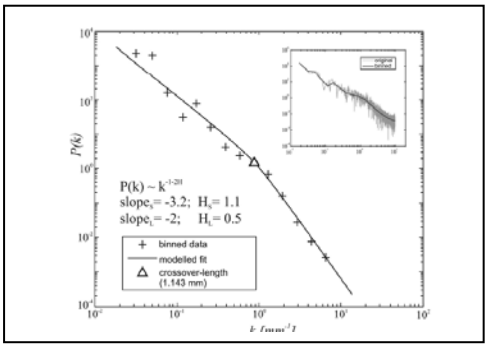

4.1/ Impact de la dissolution sur l'évolution des contraintes régionales – modélisation d'une source intrinsèque de contraintes et pression.

Objectifs et état de l'art.

Les campagnes de mesure de contraintes réalisées par l'ANDRA sur le site de Bure suggèrent une origine actuelle pour les contraintes observées (Wilevau and Cornet, 2007). En effet, ces contraintes semblent trop importantes pour être maintenues depuis des épisodes tectoniques anciens, à travers Lors de l'étude théorique de la dissolution le long de stylolites (Koehn et al., 2007, Schmittbuhl et al, 2004), ou du processus de transport dans des fractures, les mécanismes d'un transport de masse le long d'interfaces, fractures ou intérieurs de stylolites, ont été explorés théoriquement.
Ces mécanismes ayant lieu sur des interfaces anisotropes et localisées peuvent transporter de la matière sous forme dissoute vers la porosité environnante, la source étant spécifiquement le long de fractures ou stylolites préexistantes. On a cherché à étudier l'impact de ce processus sur l'évolution des contraintes à grande échelle dans un bassin sédimentaire.

Méthodes choisies : Les fractures présentes dans les puits de l'ANDRA ont été cartographiées pour accéder à leurs caractéristiques géométriques et leur densité. Un modèle analytique couplé chemico-mécanique a été développé pour relier la composition du fluide intersticiel, la dissolution, la déformation liée à cette dissolution et l'évolution de contrainte dans l'encaissant calcaire.

Résultats récents:
On a mis en évidence qu'avec des concentrations raisonnables et avec la densité orientée de fractures observées, la dissolution permet d'expliquer à la fois l'orientation du tenseur des contraintes actuelles, avec un déviateur non compatible avec les directions tectoniques alpines, et son ordre de grandeur. Les contraintes expliquées sont compatibles avec la synthèse des contraintes mesurées dans le bassin de Paris a été publiée dans un article de tectonophysics, sous presse (Cornet et al. 2011).
De plus, ce modèle implique une cinétique toujours active de dissolution dans les formations calcaires entourant la formation du COX. En prenant en compte la cinétique ainsi déterminée et en la traduisant en déformation des frontières du COX, on a mis en évidence un mécanisme de pressurisation de l'eau porale de cette couche, qui mène à un profil parabolique de surpression en fonction de la profondeur. Le profil et l'ordre de grandeur de cette surpression prédite est de l'ordre de celle observée par l'ANDRA dans la formation du COX. Ces résultats ont été présentés en conférences en 2011 (Mont St Odile), un article est en préparation.

Les perspectives pour cette thématique sont notamment de définir un modèle de transport macroscopique couplant dissolution et transport de masse, avec effets poroélastiques induits pour étudier l'influence de la chimie et des orientations de surfaces réactives sur l'évolution du tenseur des contraintes et de la pression de pore dans un bassin sédimentaire comme le bassin de Paris.
Ceci devrait permettre de prendre en compte l'ensemble du cycle du CO_2 et de son transport dans ces réactions de pression/solution, à partir des compositions atmosphériques historiques et des précipitations. Il est en effet intéressant de noter qu'une modification durable de la teneur en CO_2 peut affecter cette cinétique de réaction dans les carbonates, et le mécanisme d'évolution des contraintes associé.

4.2/ Estimation de paléocontraintes à l'aide de la morphologie de stylolites :

Objectifs et état de l'art.

En 2009, le programme FORPRO a permis d'échantillonner des stylolites dans les compartiments de calcaire du site de Bure, et d'étudier la faisabilité d'une méthode récente d'analyse de la morphologie des stylolites, pour estimer les contraintes anciennes et actuelles dans les calcaires sur le site de Bure. Ceci a permis d'établir sur quelques échantillons, la présence des marqueurs de contrainte nécessaire.
Actuellement, nous sommes en phase dans la thèse d'A. Rolland, de généraliser ces prélèvements et les techniques d'analyse pour obtenir une détermination des paléocontraintes à partir de cette morphologie, dans les compartiments du Dogger et de l'Oxfordien. On a également pu étendre les techniques analytiques et numériques de modélisation sous-jacente à la théorie à la base de cette méthode, et leur validation par comparaison avec des données de terrain.
L'objectif général de ces études est d'obtenir une information historique sur la direction et l'amplitude de ces contraintes, pouvant donner des informations sur la cinématique du site. Ceci est effectué par prélèvement d'échantillons de stylolites et analyse rugosimétrique haute définition de leur morphologie, et applications de liens récemment testés entre morphologie et contrainte de formation.

Méthodes choisies : On a travaillé en parallèle sur des modèles analytiques, des modèles numériques et le développement de techniques d'analyse de forme à partir d'imagerie à haute résolution de stylolites prélevées dans les carottes de Bure.

Résultats :
Théorie : On a validé de plusieurs manières la théorie reliant la morphologie des stylolites à leur contrainte de formation. La durée de formation de stylolites étant trop longue pour être possible en

laboratoire à des échelles compatibles avec celles du terrain, celle-ci s'est faite de plusieurs manières :
Dérivation analytique détaillée de la variation de potentiel chimique le long d'une interface rugueuse en fonction de sa forme, et développement d'un modèle analytique destiné à analyser les lois d'échelles des surfaces développées, et leur lien avec la contrainte appliquée. Le détails de cette analyse ont été soumis à Journal of Geophysical Research B (Rolland et al. 2011).
Développement de codes de dynamique moléculaire couplée à un schéma de dissolution, et analyse quantitative de la morphologie des surfaces de stylolites obtenues. Ces simulations numériques, conduites à grandes déformations, ont permis de confirmer indpendamment le lien entre contrainte appliquée et crossover entre deux lois d'échelles Cette aalyse a été soumise à Earth and Planetary Science Letters (Koehn et al. 2011).
Validation de la dépendance du cross-over par rapport à la contrainte sur une série de stylolites, dans un site où les paléocontraintes peuvent être estimées par la profondeur et une histoire connue. Cette analyse a confirmé la théorie (Ebner et al. 2009).
Validation du modèle de développement de morphologie lors de la stylolitisation à l'aide de séries de stylolites où on peut estimer le racourcissement par le dépôt dans la porosité initiale (bilans de masse). Ceci a permis de vérifier la validité des morphollogies prédites à grande échelle par le modèle physique. L'amplitude des stylolites observées à grande échelle était compatible avec celle estimée par la théorie et les bilans de masse (Laronne et al. 2011, soumis à EPSL).

Méthodologie pratique :
On a choisi d'analyser la morphologie des stylolites échantillonnées à Bure de plusieurs manières : par photographie haute résolution de profils plans, de profils pris sur le tour extérieur des carottes, et par profilométrie optique de surfaces ouvertes. L'ouverture dans ces carottes posant problème, la reconstitution des fonctions à analyser à partir du profil observé en pourtour de carotte a fait l'objet de la mise au point d'une procédure automatique de traitement d'image et de signal. La technique d'analyse et l'estimation des barres d'erreur de la technique sur ce type de données fait l'objet d'un article en préparation.
L'application systématique de cette technique sur des familles de stylolites est en cours dans le cadre de la thèse d'Alexandra Rolland. Un article a été soumis, et un publié dans JGR B. Cette thèse devrait être soutenue début 2013.

4.3/ Impact des stylolites sur le transport dans les calcaires et leur rhéologie:

Le but de ce volet était d'étudier l'impact des stylolites sur les propriétés de transport et de perméabilité des roches.

En effet, les stylolites sont régulièrement rapportées comme des barrières de perméabilité (Baron et al 2007), et elles sont potentiellement un contrôle important des propriétés de transport des bassins sédimentaires.
On a proposé dans les récents projets :
1. D'une part, de déterminer par imagerie par micro-tomographie par scanner X (Louis et al., 2006 et 2007, Ebner et al. 2010) la morphologie in situ des couches transportant le fluide dans ces stylolites. En effet, ces couches sont déterminantes pour les propriétés de transport et pour la formation de ces stylolites , et leur compréhension est primordiale pour interpréter la morphologie de ces stylolites, et les propriétés de transport fluide de ces calcaires.
2. In fine, on veut pouvoir faire des tests de comportement rhéologique de roches stylolitisées : on veut pouvoir étudier l'évolution de celles-ci lors de leur mise sous contrainte, et l'évolution de la perméabilité de ces roches. On effectue pour ceci des tests mécaniques, avec mesure des propriétés élastiques et mesure de perméabilité sous contrainte, d'échantillons de roches stylolitisées, comparées aux échantillons de roches saines.
3. On a voulu caractériser les propriétés statistiques de connectivité des stylolites dans des réseaux naturels, pour interpoler à plus grande échelle les propriétés de transport individuelles.

L’analyse microstructurale d’échantillons stylolitisés a permis de mettre en évidence une multiplicité de cas dans cette microstructure : Il a été observé dans plusieurs cas une disparition de la macroporosité autour des stylolites, tout en maintenant la microporosité a une valeur élevée dans les roches stylolitisées par rapport à la porosité de carbonates typiques. La dissolution, plus facile dans les macropores où la tension de surface ne contribue pas à l’énergie libre du calcium sous forme solide, peut expliquer cette disparition sélective de la macroporosité.

Deuxièmement, on a observé dans certains échantillons la présence de structures connectées de plusieurs dizaines de microns de taille, relativement linéaires. Ces structures semblent localisées autour de la stylolite, et forment une microfracturation potentiellement générées par les concentrations de contraintes sur les dents des stylolites – comme suggéré par des essais triaxiaux dont on a mesuré les champs de déformation de surface. Sur les essais en laboratoire associés à ces échantillons, la perméabilité transverse à la stylolite était significativement augmentée, alors que la perméabilité perpendiculaire semblait très proche de celle de la roche intacte. D’autres essais on montré, sur certains échantillons de stylolites peu développées, une insensibilité de la perméabilité à la présence des stylolites.

Enfin, on a observé la présence, dans certaines stylolites où une quantité significative d’argile s’est accumulée, d’une microfissuration à l’intérieur de l’argile dans la stylolite. Cette structure a été analysée en détail en microtomographie X. Il a été calculé qu’elle pouvait rendre compte d’une importante augmentation de la perméabilité longitudinale dans la stylolite.
Ces résultats ont faire l’objet de plusieurs présentations invitées en congrès internationaux, et sont l’objet d’une publication en préparation.

Enfin, en plus des propriétés de transport de stylolites individuelles, on a étudié un réseau de stylolites plurimétrique, accessible dans une carrière à ciel ouvert. L’analyse des intersects de stylolites avec des plans de coupes perpendiculaires entre eux, sur plusieurs mètres carrés, a été faite à l’aide de photographies à haute résolution (pixels autour d’une centaine de microns), où le réseau stylolitique a été digitalisé. Les statistiques de taille et d’angle de branchement du réseau stylolitique ont été faites sur les segments de stylolites, et sur les volumes interstylolitiques. L’angle de branchement a également été analysé entre stylolites, et on a montré qu’il se regroupait sur de petits angles, ou des angles droits. Ces informations, avec le modèle morphologique de stylolites individuelles, permettent de générer des modèles
synthétiques de réseaux de stylolites. Nous avons développé un tel modèle numérique. Actuellement, en attribuant des valeurs de perméabilité au éléments individuels, on débute l’étude numérique de la perméabilité associée à ces réseaux au niveau macroscopique. Ce travail s’effectue dans le cadre de la collaboration avec l’université de Jérusalem (M Kaduri, Master).

Des tests de perméabilités ont été conduits avec Mike Heap, Patrick Baud et Phil Meredith, sur des échantillons de calcaires stylolitisés issus des puits de forage de l’URL de Bure :

Limestones surrounding the Bure URL

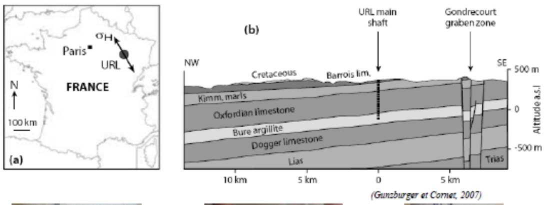

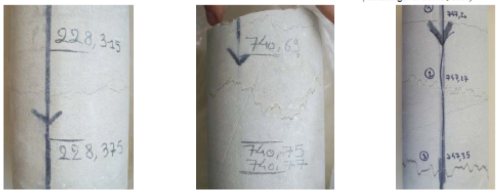

	Oxfordian	Dogger
Depth (m)	159 - 310	719 - 748
Composition	>95% calcite	
Porosity (%)	7 - 18	2 - 6
Vp (km/s)	4 - 6	6 - 7
BET (m^2/g)	0.8 – 1.15	X
E (GPa)	17 - 36	36 - 70
ν	0.35	0.37

Les propriétés mécaniques de ces calcaires ont été déterminées, et résumées dans la table ci-dessus. On a également mené des études microstructurales, à l'aide de tomographie par rayon X et au Microscope Electronique à Balayage.

•Microstructure

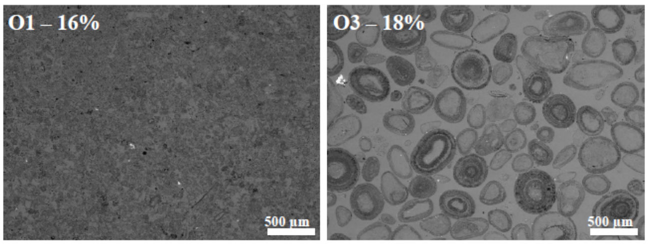

- Allochemical limestones with a wide range of grain size
- No crack porosity

Les tests de perméabilité sous contrainte isotrope, sur des échantillons intacts et stylolitisés, on été conduits sur des échantillons représentés ci-dessous

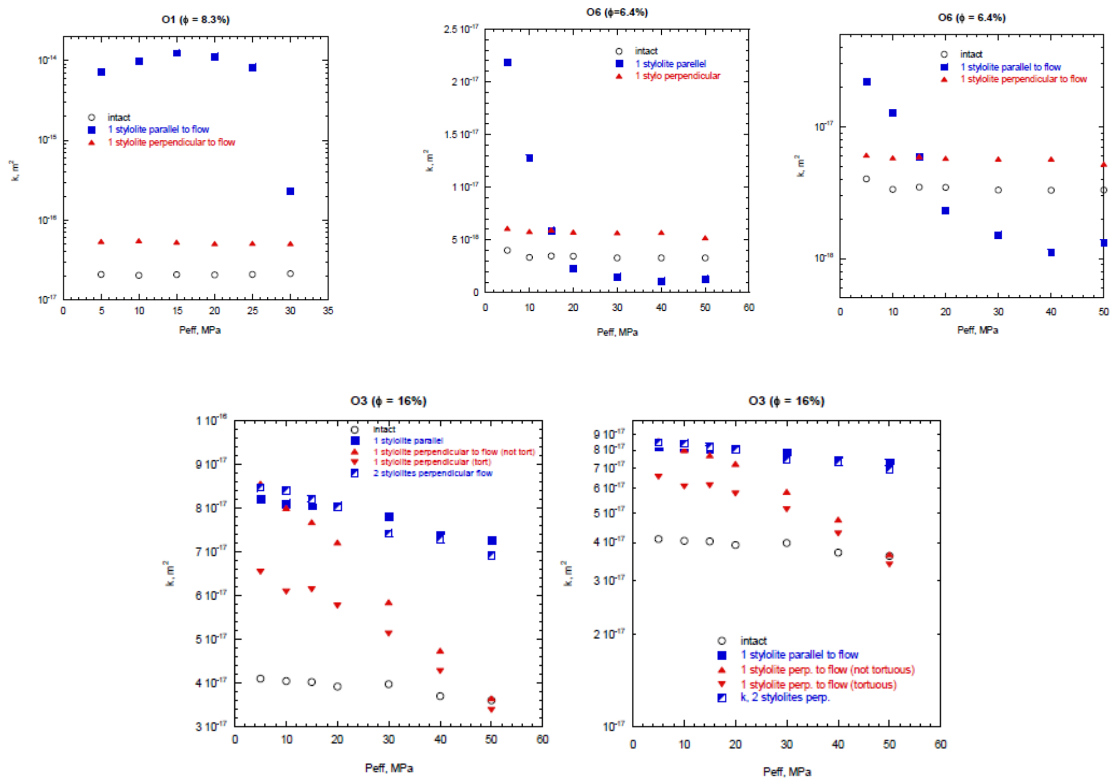

Pour ce type de stylolites, assez fines (pour permettre le carottage et le test) et remplies principalement d'argiles, on a mis en évidence un faible effet des stylolites sur la perméabilité, qui tendent à l'augmenter, en particulier dans la direction principale de la stylolite. L'effet reste toutefois assez modéré, avec une augmentation inférieure à un facteur 20 dans la plupart des cas à faibles pressions de confinement.

5 Developpement de techniques d'imagerie

On travaille, pour analyser experiences de laboratoire et écoulements de terrain, à développer des techniques d'analyse d'émissions acoustiques, des techniques de vélocimétrie par suivi de particule ou par corrélation d'image [Niebling et al 2010, Travelletti et al 2011, Travelletti et al. 2012], et des techniques de stéréophotogrammétrie permettant de reconstituer le volume des surfaces observées dans des paires d'images [Bastard 2010]. Exemple : détermination de champo de vitesse pendant une expérience de sédimentation (instabilité de Rayleigh Taylor granulaire) :

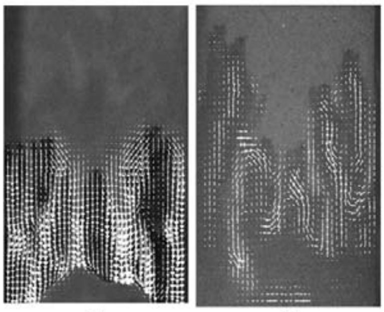

(a) (b)

Figure 3.3: The velocity field visualized with white arrows in experiments with air 3.3(a) and with water/glycerol 3.3(b) extracted with the CIV technique.

Collaborations :

Externes à l'IPGS :
Internationales (non exhaustif):
Complex group, Norway, Advanced Materials and Complex Systems,, University of Oslo, Norway, Physics Department, K.J. Måløy, E.G. Flekkøy, O Johnsen, G Lovoll, S. Santucci, H. Knudsen, M. Jankov, O. Aursjoe, M. Niebling.
Complex Materials, NTNU Trondheim, Norway, Physics Department, A. Hansen, J.O. Fossum.
Institute for Energy Technology, Kjeller, Norway G. Helgesen, A.T. Skeltorp.
University of Jerusalem, and Weizmann Institute, E. Aharonov
Earth Sciences Division, Lawrence Berkeley national laboratory, California, USA, S.R. Pride,
Institut fur Geowissenschaften, Tektonophysik, University of Mainz, Daniel Koehn, Marcus Ebner, Cees Paschier.
ETH Zurich: Jan Ludvig Vinningland
Department of theoretical Physics, Institute of Physics and Nuclear Engineering, Bucharest, Romania: Dragos V. Anghel
Department of Physics, University of Havana, Cuba, Ernesto Altshuler
Chinese Academy of Sciences, Earth sciences, Beijing, China, Xiarong Luo.

Francaises:
ISTERRE Grenoble, J.P. Gratier , Francois Renard
ENS Lyon, S. Santucci, J.C. Géminard, V. Vidal
ESPCI / PMMH: granular group, A. Lindner, C. Chevalier, E. Clement
Geosciences Rennes, Y. Meheust
IPGP, Anne Mangeney et Maxime Farin
REALISE, reseau d'hydrologie en Alsace, IPGS/CGS/IMFS
Réseau d'ANR LANDQUAKE, Réseau d'ANR AIRFLOW

Cadre et objectifs au laboratoire

Les objectifs développés ci après correspondent aux objectifs communs auxquels je participe pour le projet du quinquennal 20013-2017 de l'IPGS, dans l'équipe « Geophysique expérimentale », dont je suis actuellement responsable.
Elles s'inscrivent également dans le thème transverse « Eau », que j'anime à l'IPGS, en collaboration avec le projet CPER, inter UMR, REALISE.

Cette équipe de géophysique expérimentale se structure sur troix pôles : mécanique des roches, mécanique des fluides, imagerie de subsurface. Les objets d'études sont les suivants :

- **Suivi des mouvements de fluides:** modélisation des écoulements
- **Formation et déformation des structures géologiques dans les réservoirs:** localisation, fractures, bandes de compaction, endommagement, stylolites, imagerie des microstructures et de leur déformation
- **Rhéologie des failles:** source sismique, séismes lents, loi de frottement, physique des multiplets, nucléation, cycle sismique, sismicité induite
- **Instabilités de pente:** avalanches humides, rôle des fluides, modélisation analogique, écoulements couplés.

Les techniques développées dans ces travaux permettent de mieux comprendre les couplages entre mécanique, physique et chimie dans les systèmes naturels. Ceci devrait me permettre de poursuivre l'étude du processus de fracture de systèmes désordonné, et d'approfondir mes recherches sur les interactions fluides roches: d'une part, en régime de déformation lente, où le couplage mécanico chimique est primordial pour comprendre la déformation, et d'autre part dans les régimes rapides où les variations de pression fluide sont à l'origine d'aléas gravitaires et d'instabilités de pentes.

Projet de recherches

Mécanique de milieux poreux déformables, mélanges solides et fluides :
Fractures, liquéfaction, avalanches et déformations lentes.

Renaud Toussaint

Thèmes de recherche développés :

1 Ecoulements mixtes, grains et fluides : rôle du fluide dans la mécanique ddes sols, d'interfaces pressurisées, cisaillées dans les failles et instabilités gravitaires :
1.1 Hydrofracturation et aérofracturation
1.2 Instabilités de sédimentations et Rayleigh Taylor granulaire dans les mélanges eau/grains et air/grain
1.3 Mécanique d'interfaces cisaillées et avalanches

Projets :
exploration des paramètres d'aerofracturation par extraction,
monitoring des processus de fluidofracturation par les activités microsismiques,
instabilités de pentes et processus de liquéfaction.

2 Ecoulements en milieux poreux et fracturés :
2.1 Ecoulements multiphasiques dans les milieux poreux,
2.2 Ecoulements en fractures rugueuses (transferts de masse et transferts d'énergie),

Projets :
. intégration des grandes déformations de milieux poreux et de plusieurs phases fluides immiscibles dans les modèles numériques
. fracturation thermique générée par les écoulements,

3 Fracturation des milieux hétérogènes fragiles,
3.1 Modèles sur réseau, mécanique de la fracture et désordre gelé
3.2 Fracturation interfaciale, quantification des régimes intermittents et de la dynamique, influence des effets thermiques

Projet : mélange de désordre thermique et de désordre gelé dans la mécanique de la fracture en propagation, ainsi que dans la dynamique d'interface cisaillée. Influence du transport de chaleur sur la dynamique de la fracture.

4 Interactions entre mécanique et chimie dans les systèmes fluides/roches (stylolites),
4.1 Modèles de formation de stylolites
4.2 Interprétations comme marqueurs de contraintes et marqueurs de déformation

Projet : couplage de dissolution/précipitation et évolution des contraintes durant la diagénèse en massif fracturé.

5 Développement de techniques d'imagerie

Projet : coupler stéréophotogrammétrie et déformation par corrélation d'image

6 Mélanges granulaires fluides aux interactions contrôlables : modèles de colloides et fluides magnétorhéologiques

Projet : utilisation de ces matériaux modèles comme analogues aux interactions finement contrôlées pour fracturation de pâtes solides fluides

Dans les pages suivantes, je vais développer succintement dans une première partie quelques projets en cours, choisis parmi ceux mentionnés dans le cadre global ci dessus. Ces thématiques sont en général liées à des projets nationaux, ANR ou européens.

Dans une deuxième partie de ce programme de recherche, je développe plus en détail un de ces projets, sur la fracturation par transport fluide, et la liquéfaction.

Projets liés aux thématiques :

1 Ecoulements mixtes, grains et fluides : rôle du fluide dans la mécanique des sols, d'interfaces pressurisées, cisaillées dans les failles et instabilités gravitaires, et

2 Ecoulements en milieux poreux et fracturés :

La thématique sur la fracturation de milieux poreux due à l'injection de fluide est à la croisée d'une approche fondamentale, et de développements applicatifs.

On songe notamment à la

Remédiation environnementale :

Dans les problèmes d'injection en subsurface, on souhaite d'une part développer les situations d'injection forcée de fluides dans un sol. Ceci devrait permettre de développer, notamment, des techniques de dépollution des sols, par l'étude fondamentale de processus d'air sparging, où de l'air est injecté dans des sols saturés. Cette technique permet de mobiliser des polluants piégés dans la phase aqueuse dans la zone vadose, où les gouttes d'eau restent piégées par capillarité. De telles applications requièrent le développement de modèles où l'on prenne compte les équations du mouvement des deux fluides immiscibles, air et eau, et la déformation du sol envisagé comme milieu granulaire peu cohésif. Ceci nécessitera un modèle qui prenne en compte à la fois le coulage entre fluides et grains, et la prise en compte de la tension interfaciale entre les deux fluides.
On envisage un tel développement dans le cadre de la thèse de Cécile Clément, financée par l'école doctorale STUE à Strasbourg, qui débute en Décembre 2012.
Ce sujet est également le cœur d'une ANR blanche, « AirFlow », dont je suis porteur, qui a été classée en liste complémentaire en 2012 et sera resoumise cette année. Cette ANR implique notre équipe de géophysique expérimentale, avec la participation de Laurence Jouniaux, Alain Steyer et moi-même, et une équipe d'expérimentateurs physiciens de l'ENS Lyon, J.C. Géminard, V. Vidal et S. Santucci.
Cette thématique se fait également dans le cadre du réseau régional « REALISE », RÉseau Alsace de Laboratoires en Ingénierie et Sciences pour l'Environnement (http://realise.unistra.fr/), et du thème transverse « Eau » de l'UMR, inscrit dans le quinquennal 2013-2017, dont je suis animateur.

Elle se concrétise également dans le projet « AirFlow ». Résumé :
AIRFLOW : Nettoyage du Sol par injection d'air: techniques de remédiation environnementale

Nous proposons d'étudier les processus relies au transport d'air dans des milieux poreux saturés en eau et déformables, comme des sols ou des milieux granulaires denses. La connaissance de ces processus fondamentaux est essentielle pour comprendre les processus naturels largement rencontrés dans les sédiments, comme la déstabilisation de sol ou la liquéfaction. Ceci est également en jeu durant la libération de gaz piégés dans les sédiments, tels que du méthane ou des hydrates de gaz, qui peuvent être libérés volontairement pour être exploités, ou naturellement. Ce relâchement peut se faire de manière régulière, ou avoir lieu par instabilités, conduisant à des libérations de gaz potentiellement catastrophiques. La connaissance de ces processus fondamentaux est en particulier essentielle pour : . Les situations expérimentales d'écoulements multiphasiques dans des milieux poreux modèles (eau / air et polluant, miscibles ou non) . Les situations expérimentales de migration de bulles dans des milieux poreux déformables et saturés . Le développement d'outils d'imagerie adaptés : techniques optiques en laboratoire, techniques électriques et acoustiques (passives et actives) pour adaptation sur le terrain . Le développement de modèles mécaniques et numériques pour les écoulements généraux triphasiques air / eau / milieu solide divisé. Le projet proposé a pour but de caractériser expérimentalement les fondamentaux du transport dans de tels systèmes, développer de nouveau modèles numériques capables de reproduire ces expériences , et développer des techniques d'imagerie électriques adaptées pour la transposition de ces situations pour suivre les situations de terrain : par exemple, durant la remédiation environnementale selon des techniques d' injection et mobilisation de sols par air (« air sparging »), de l'exploitation de réservoir ou de l'injection de CO_2.

Avalanches et Liquéfaction des sols

On s'intéresse également à la liquéfaction des sols lors de tremblements de Terre.

On développe des modèles hybrides granulaires / fluides, avec plusieurs phases fluides dans le granulaire. Ces éléments sont soumis à des sollicitations de type décharge hydrique et augmentation de la pluviométrie, ou au contraire à des évènements de type passage d'onde sismique. On s'intéresse alors au déclenchement et à la propagation d'instabilités gravitationnelles, ou simplement à la liquéfaction, c'est-à-dire à la résistance du matériau par rapport au cisaillement, avec indenteur de surface (une fondation de bâtiment ou de structure), .et niveau d'eau libre à l'intérieur du milieu poreux déformable.

On développe également un projet sur la mécanique des avalanches, couplée à la mécanique de la propagation d'ondes sismiques dans le substrat. Un projet de master et une collaboration avec Jérusalem et Oslo ont lieu actuellement sur ce sujet. Le Master de Menka Stojanova, sur des modélisation bidimensionnelles de liquéfaction, devrait être poursuivi en trois dimensions, via la thèse de Cécile Clément et une collaboration avec Dion Weatherley, Australie.

Suivi sismique d'avalanches

Cette propagation des ondes sismiques générées par une avalanche peut être utilisée pour imager les caractéristiques de ces avalanches.

Actuellement, en collaboration avec l'IPGP et le laboratoire Langevin, la thèse de Maxime Farin a lieu dans l'ANR Landquake sur cette thématique. Elle permet de conduire des séries d'expériences sur le sujet

ANR Landquake :Résumé :

Les instabilités gravitaires jouent un rôle clé dans les processus d'érosion à la surface de la Terre et représentent un des risques naturels majeurs pour les populations et les infrastructures en zone montagneuse, sismique, volcanique et côtière. Malgré les nombreux travaux dédiés à ce problème, les mécanismes gouvernant la dynamique des écoulements et leur dépôt dans le milieu naturel restent très mal compris. Il existe deux points de blocage importants empêchant d'appréhender ces processus. D'abord, les modèles numériques ne prennent pas en compte la transition statique/mobile dans les milieux granulaires et les interactions des phases fluides (eau) et solides dans la masse en écoulement, ces deux processus jouant un rôle clé dans les instabilités gravitaires. De plus, les mesures de terrain sur la dynamique des écoulements sont très rares, rendant impossible la validation des modèles. Des études récentes ont montré que l'analyse des signaux sismiques générés par les instabilités gravitaires fournit un diagnostique unique sur ces écoulements et donc un nouveau moyen de discriminer entre les processus physiques impliqués. En effet, la contrainte appliquée par le glissement sur la topographie, qui génère des ondes sismiques, est très sensible à l'histoire de l'écoulement et donc aux paramètres rhéologiques et aux propriétés physiques mis en jeu. En se basant sur de nouveaux résultats obtenus par notre groupe, nous proposons de faire un pas en avant significatif dans la compréhension et la détection des instabilités naturelles en développant simultanément des modèles d'écoulement prenant en compte des processus physiques plus réalistes, et en simulant, analysant et inversant le signal sismique généré par ces évènements. Dans ce but, nous développerons une approche interdisciplinaire ambitieuse, impliquant modélisation mathématique, méthodes numériques, expériences de laboratoire, sismologie et géomorphologie, indispensables à la réalisation d'un tel projet. Pour diminuer le coût numérique lié à la description précise de la topographie, essentielle pour les applications naturelles, des modèles de couche mince seront développés. La transition statique/mobile et les interactions solide/fluide seront décrits de manière appropriée pour l'écoulement d'un milieu granulaire sur une topographie 3D, à partir de modèles 3D relativement bien établis (modèles de fluidisation partielle, visco-plastique, éléments discrets) pour lesquels nous développerons des méthodes numériques pertinentes. Le principal défi sera d'établir, à partir d'analyses asymptotiques, des formulations mathématiques et des solutions numériques dans de nouveaux modèles à surface libre, déduits de la dynamique non-newtonienne de matériaux granulaires visco-plastiques. Les ondes sismiques générées par l'écoulement sur le terrain seront simulées en couplant ces modèles avec des modèles de pointe de propagation d'ondes. Un des objectifs ambitieux est de développer des méthodes de couplage efficaces sur la base de formulations variationnelles. Les ondes sismiques simulées seront comparées aux émissions acoustiques générées par des écoulements granulaires dans des expériences de laboratoire. Les écoulements géophysiques et les signaux sismiques associés seront alors simulés, en utilisant des données sismiques et morphologiques largement sous-exploitées. La sensibilité du signal sismique aux caractéristiques des glissements et à la topographie sera étudiée et l'inversion des signaux sismiques sera réalisée en utilisant des techniques de renversement temporel. Un des objectifs ultimes est de développer et de diffuser des codes opérationnels d'écoulement sur une topographie 3D, intégrant des processus physiques réalistes. Nous espérons établir de nouvelles méthodes pour la détection des instabilités et pour l'interprétation des données sismiques, avec des retombées en recherche fondamentale et pour la surveillance et le suivi de l'activité gravitaire.

Maîtrise géotechnique des forces de filtration pour contrôler la fracture ou l’érosion interne par injection de fluide :

On poursuit actuellement le travail sur l’érosion d’un granulaire par un écoulement à travers celui-ci. Notamment, lors de l’extraction d’un fluide à travers un bord libre, la décompaction semble s’effectuer de manière instable, avec croissance de doigts de zones décompactées qui prépare la formation des chenaux.
Cette étude, en collaboration avec des partenaires norvégiens (JL Vinningland, O Johnsen) et des physiciens parisiens de l’ESPCI (A Lindner et E Clément), se focalise sur une étude expérimentale, numérique et théorique de cette instabilité.
Il s’agit à la fois d’un projet de comprendre les mécanismes fondamentaux de la propagation de l’érosion, et d’explorer un phénomène de grande importance pratique (cf effondrements de digues et levées, accidents par formation de renards).

Contrôle et suivi des chemins de fracturation fluide :
Sur ce sujet, en collaboration étroite avec l’université d’Oslo et l’ESPCI, on s’intéresse à la façon dont une surpression, au-delà d’une certaine valeur critique, peut modifier la géométrie de l’espace poral d’un milieu solide. [Niebling et al, 2011, Schelstraete, 2009, Johnsen et al, 2007]. A l’aide de simulations hybrides granulaires fluides, et d’expériences, on montre comment le fluide intersticiel peut soit élargir des fluidofractures locales, nucleer un dommage distribué, ou faire apparaître des arbres et chenaux. La maitrise et la compréhension de ces structures est fondamentale, et pour pouvoir éviter la formation involontaire de chenaux et renards menant à des ruptures catastrophiques de digues, barrages ou flancs de puits, mais aussi pour contrôler les processus de fracture générés par surpressions de fluides. Ceci sert dans l’industrie gazière, mais aussi dans les techniques de remédiation de pollution en subsurface.

Dans le cadre d’un postdoc de l’ITN Flowtrans en collaboration avec Baker Hugues, et d’une thèse de l’université d’Oslo, on compte développer ce sujet d’un point de vue mécanique expérimentale, et développer le suivi microsismique des évènements associés.

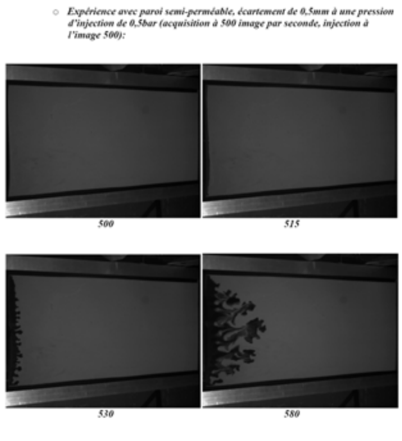

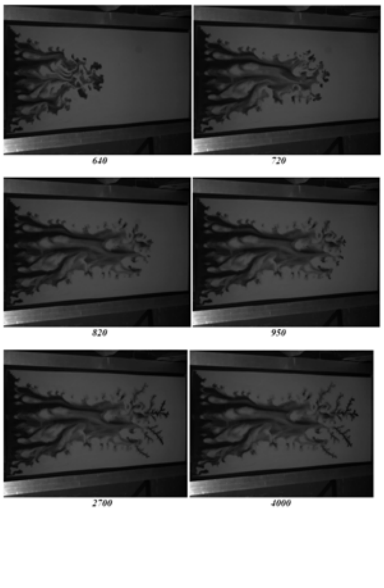

Aerofracture rapide d’un milieu poreux faiblement consolidé. Le temps indiqué est en ms.

Projets lié au thème

3 Fracturation des milieux hétérogènes fragiles :

Fracture : influence de la température et du désordre

On travaille à développer, à partie de principe élémentaires de physique statistique (lois d'Arrhenius, taille des sites actifs, distribution désordonnée et granulaire des propriétés matérielles), des modèles de propagation de fracture en milieu désordonner, et de nucléation de fracture en mode I ou II (cisaillement, friction).
Ces modèles amènent à se pencher sur la dissipation locale, et le transport de chaleur, ainsi que le rôle que celui-ci joue dans la phase dynamique de la fracture.
Ce projet se fait en étroite collaboration avec l'Université d'Oslo.

Fracturation en milieu dense déformable, écoulements triphasiques eau/air/grains

Après avoir exploré la fracturation par injection d'un fluide dans des milieux poreux denses saturés du même fluide, on commence maintenant, dans le cadre de l'ITN FlowTrans (PhD 1, Strasbourg) et de la thèse de Jon Alm Eriksen, à Oslo, à explorer la fracturation d'un milieu déformable saturé par injection d'un fluide immiscible avec le saturant (e.g., air dans une roche déformable saturée d'eau).
Cette étude permet de rejoindre les études faites jusqu'ici, de fluide injectés dans un milieu déformable saturé du même fluide, et les cas de fluides injectés dans un fluide non miscible et milieux indéformables.
Elle devrait permettree d'aborder des situations génériques classiques dans l'industrie (gestion d'eau, de gaz, d'hydrocarbures dans les réservoirs).

Projet lié au thème

4 Interactions entre mécanique et chimie dans les systèmes fluides/roches (stylolites),

Fracture et stylolites : influence de la chimie sur la mécanique, et réciproquement, dans des systèmes de fractures, chenaux et stylolites.

(Projet MC Network «FlowTrans », PhD Strasbourg sur les écoulements réactifs,
Projet NEEDS 2013, collaboration avec JP Gratier et F Renard)

L'objectif est de comprendre comment la porosité d'une roche peut évoluer sous contrainte, effets thermiques et flux de fluides sur de très longues durées (milliers d'années) en identifiant les forces motrices et la cinétique des processus de dissolution et re-cristallisation avec transferts de matière à diverses échelles depuis la taille d'un pore (diffusion) jusqu'à l'épaisseur des séries sédimentaires (diffusion puis advection). Dans le premier cas les forces motrices sont pour l'essentiel liées aux contraintes, dans le deuxième cas, il s'agit d'un couplage entre effets de contrainte et de température. La méthode d'étude est une approche pluridisciplinaire intégrant expérimentation (poinçonnement, écoulement réactif et mesure de contrainte), caractérisation (MEB, FIB-MET et micro-tomographie à rayons X) et modélisation (transferts réactifs et construction d'un réseau poreux analogue par imagerie 3D).

Une part importante de l'évolution de porosité des roches, tant dans la nature que par des effets anthropiques, est liée à des processus de transfert de matière par dissolution cristallisation sous contrainte. Ce mécanisme implique une dissolution au niveau des zones soumises aux plus fortes contraintes (contact entre grains), un transfert par diffusion le long de chemins jalonnés de phase fluides piégées sous contrainte et une possible re-cristallisation de ces phases dissoutes dans le réseau poreux, à des distances qui sont fonction des propriétés de transfert du milieu, par diffusion ou advection. C'est à la fois un mécanisme de fluage *(Weyl, J.G.R., 1959)* et un mécanisme de réduction de porosité (*Lehner, Tectonophysics, 1995)*. Les paramètres les plus difficiles à acquérir en vue d'une modélisation de ce mécanisme sont ceux qui concernent ses forces motrices et surtout sa cinétique. En effet, la diffusion le long de chemins comportant des phases fluides piégées sous contrainte est toujours extrêmement lente, clairement suffisante dans la nature mais très difficile à reproduire au laboratoire sur des durées inférieures à quelques mois voire quelques années.
Cela explique que ce mécanisme reste encore très mal connu.
Ce phénomène est pourtant particulièrement important pour des roches comme les argilites Callovo-Oxfordiennes de Bure (pressenties comme lieu de stockage souterrain de déchets nucléaires) qui, sur une centaine de mètres d'épaisseur, présentent des teneurs en minéraux potentiellement solubles sous contrainte (calcite, quartz, feldspath, dolomite...) qui varient de 50 à 80% (Fig. 1a). Même dans la zone la plus riche en argiles, le total des minéraux potentiellement solubles sous contrainte reste supérieur à 50%. La solubilité sous contrainte de ces minéraux est diversement activée en fonction de la température. Ainsi, la solubilité de la calcite est inversement proportionnelle à la température et celle du quartz au contraire augmente avec la température. Dans un site où les températures sont susceptibles de fluctuer ces comportements contrastés sont importants à prendre en compte.
La conductivité hydraulique des formations du Callovo-Oxfordien dépend de la géométrie à la fois de la porosité interconnectée et de la fracturation. Les propriétés de diffusion sont également influencées par la répartition spatiale des minéraux (*Robinet et al., WRR, 2012*). La géométrie actuelle du réseau poreux est en relation avec la composition de la roche avec deux types de porosité : (i) porosité à l'interface entre la matrice argileuse et les autres minéraux plus rigides (et solubles) : quartz, calcite, feldspaths... correspondant à des pores de taille submicrométrique (macroporosité); (ii) porosité de la matrice argileuse ellemême, avec des tailles de pores de quelques dizaines de nanomètres à quelques micromètres surtout connectée par le biais de la mésoporosité (2-50 nm). La part relative de la macroporosité par rapport à la mésoporosité dépend de la teneur en minéraux rigides et varie donc à travers la formation (Fig. 1a). Le réseau de fractures rencontrées dans la formation n'affecte actuellement que très peu la conductivité hydraulique parce que ces fractures ont été colmatées naturellement par des carbonates probablement par des mécanismes de dissolution - cristallisation. Il faut donc comprendre et modéliser comment porosité et fracturation sont susceptibles d'évoluer dans le temps et dans l'espace face aux sollicitations induites par le stockage : modification de contraintes, températures, fluides interstitiels. L'analyse de l'évolution de la porosité et la fracturation dans le passé aide à cette compréhension. Mais elle doit être complétée par des expérimentions pour évaluer la force motrice et la cinétique des processus.

Même si a priori on peut penser que les minéraux les plus susceptibles de réaction sous contrainte en présence de fluides sont la calcite le quartz, le feldspath et la dolomie, on sera très attentif à étudier les interactions entre ces minéraux et les argiles. On sait en effet que la présence d'argile est un activateur fondamental des processus de dissolution sous contrainte. Dans les mêmes conditions thermodynamiques, un matériau comportant à la fois des minéraux solubles et des argiles se déforme toujours beaucoup plus facilement par dissolution cristallisation qu'un matériau composé exclusivement de minéraux solubles. Par ailleurs, certains minéraux argileux du site gonflent de manière très importante en présence de fluides non à l'équilibre. Un tel comportement est susceptible de transformer grandement les propriétés rhéologiques et de transfert des argilites.

Ce projet vise, par une approche pluridisciplinaire, à résoudre un certain nombre de problèmes non résolus actuellement et indispensables à la modélisation du comportement du stockage sur les grandes durées de temps requises en système ouvert. On soulignera notamment l'importance d'une meilleure connaissance des forces motrices des transferts. Il s'agit d'estimer la part respective (i) des effets de la contrainte normale sur les surfaces sous contrainte (Fig.1c-1), et (ii) des effets d'énergie élastique, plastique, de surface ou de sur- ou sous-saturation des fluides sur les surfaces libres (Fig.1c-2) et pour les deux des effets de température. Il est aussi crucial d'identifier la cinétique des processus limitants dans de tels systèmes en série, processus qui peuvent être la vitesse de dissolution, la vitesse de diffusion ou d'advection, la vitesse de cristallisation, dans des systèmes où la distance entre zones de dissolution et de re-cristallisation peut varier depuis la taille d'un pore (transfert par diffusion jusqu'à la taille des séries sédimentaires (transfert entre séries calcaires et séries argilitiques ou au sein des séries argilitiques et ceci sur des durées de plusieurs milliers d'années. Des gradients de transfert inverses entre quartz et calcite sont notamment attendus compte tenu de la dépendance inverse de la solubilité de ces minéraux avec température, qui est importante à prendre en compte. On cherchera également à étudier les changements de contrainte reliés à ces transferts réactifs, notamment à comprendre comment ces processus affectent l'évolution possible des contraintes dans le bassin de Paris, et la genèse possible de surpressions de pore similaires à celles observées dans le Callovo-Oxfordien.

Expérimentation sous contrainte et température

Une technique particulièrement bien adaptée à l'étude de la dissolution cristallisation sous contrainte est le poinçonnement sous contrainte en présence de fluides solvants du minéral (Fig. 2a). Cette technique, à contrainte imposée, permet de focaliser la contrainte, et donc la dissolution, sur de très petites zones qui peuvent être analysées ensuite au MEB, au METFIB ou en micro-tomographie et comparées à l'état initial préservé autour du poinçon. Elle a déjà été utilisée sur des argilites de Bure pour en étudier les mécanismes de fluage *(Gratier et al, Appl. Clay Sci. 2004)*. La dissolution ne s'est pas dévelopée de manière localisée (schistosité de dissolution). En revanche, les observations n'excluaient pas la possibilité d'un fluage en masse par glissement entre les grains accommodée à la fois (i) par la dissolution cristallisation des minéraux "rigides-solubles" et (ii) le cisaillement des argiles. Mais le gonflement d'argiles et le développement de fractures n'ont pas permis d'évaluer la part de chacun de ces mécanismes de fluage. Il reste possible de travailler sur les échantillons disponibles pour caractériser l'évolution de porosité associée au fluage de ces roches, en comparant la porosité sous le poinçon avec celle (initiale) loin de son emprise, mais la taille des pores risque de rendre très compliquée une telle étude qui sera néanmoins tentée. Pour mieux comprendre les mécanismes fondamentaux à l'échelle des pores il apparaît plus pertinent de travailler sur un analogue. En effet, pour obtenir assez rapidement au laboratoire des changements significatifs de porosité (en fait au mieux en quelques mois...) par dissolution cristallisation sous contrainte il faut se mettre dans des conditions particulières. Il faut que la solubilité des minéraux soit la plus importante possible et il faut que la porosité initiale soit aussi la plus élevée possible. Si on veut rester sur les minéraux naturels susceptibles d'être affectés par une compaction par dissolution sous contrainte que

l’on rencontre dans les sites de stockage, les meilleurs matériaux sont la diatomite et la craie.
Ces roches sont composées de tests siliceux ou carbonatés de microfossiles avec des porosités initiales très élevées qui peuvent dépasser 40%. La silice présente cependant l’intérêt d’avoir une solubilité qui peut être grandement activée en utilisant des solutions basiques (à 350°C la solubilité de la silice peut dépasser 50 g/l, un ordre de grandeur de plus que ce qu’il est possible d’obtenir au mieux pour la calcite dans les meilleures conditions de solubilité c’est à dire en conditions hydrothermales en présence de NH_4Cl). Des essais préliminaires d’une durée de quelques mois démontrent la faisabilité du projets. Des essais sur ces matériaux seront conduits à Grenoble, en faisant aussi varier la température entre 40 et 350°C.

De plus, à Strasbourg, afin d’évaluer l’évolution des contraintes lors de transformations chimiques dues à des écoulements lents, on propose d’effectuer des tests mécaniques réactifs au cours desquels on enregistre les contraintes extérieures sur les minéraux réactifs et les argilites, lors d’écoulements dans l’espace poral par des fluides de saturation contrôlée. De telles évolutions d’espace poral ont été observées par (*Detwiler GRL 2003*) dans des écoulements réactifs en fracture. Un tel dispositif peut être couplé à une mesure de contrainte aux frontières de l’échantillon, avec bords immobiles.

Caractérisation

Cette partie, conduite en collaboration avec F Renard et JP Gratier, devra permettre de caractériser l’évolution de la géométrie du réseau poreux en comparant l’état déformé (sous le poinçon) dans diverses conditions thermodynamiques et de durées des essais avec l’état initial préservé hors de l’emprise du poinçon. Ces observations seront effectuées par diverses méthodes : MEB (résolution moyenne et très haute résolution), MET-FIB (reconstruction 3D à partir de coupes avec une résolution ~10 nm), analyses à la microsonde, microtomographie RX *(Renard, Eu.Phy.J.Ap.Phy. 2012, Renard et al. Ear.Pl.Sci.Let. 2009)*. Ainsi, des images 3D de la structure du milieu poreux sous le poinçon seront acquises sur la ligne ID19 à l’ESRF (Grenoble), où une résolution de 0.7 micron peut être atteinte. Un essai préliminaire d’imagerie 3D de la zone déformée sous un poinçon dans un échantillon de diatomite (Figure 2d) montre clairement le développement de zones de compaction sous le poinçon. Ces zones correspondent à une localisation de la déformation, qui provoque une densification locale du matériau. Identifier si cette densification est d’origine chimique (dissolution sous contrainte) ou simplement mécanique (bande de compaction) reste une question ouverte.

Modélisation

Dans les processus diagénétiques, les transferts de masse via l’eau dans les pores font évoluer l’espace poral, et peuvent également influer sur les contraintes. Il a été notamment observé, lors de campagnes de mesures de contrainte réalisées par l’Andra *(Wileveau et al., 2007)* sur le site de Bure, l’existence d’un déviateur de contrainte dans les argilites du Callovo-Oxfordien ainsi qu’une très faible variation de la contrainte principale minimum horizontale dans les bancs calcaires sus- et sous-jacents. *Gunzburger et Cornet (2007)* ont proposé d’expliquer ce champ de contrainte par des phénomènes de dissolutioncristallisation sous contrainte encore actifs actuellement. En effet, la présence des fluides dans la croûte terrestre affecte significativement la rhéologie de celle-ci, sa cinématique, l’évolution des contraintes et les modes de localisation de la déformation. Dans ce projet, on s'intéresse à l'influence mécanique de deux processus majeurs ayant pour origine la présence de fluides au sein des roches: la dissolution cristallisation et le transport de fluide.
Les processus de dissolution cristallisation ainsi que le transport sous forme dissoute dans le fluide interstitiel sont des phénomènes à l'origine d'une redistribution de masse des zones sous forte contrainte mécanique vers les zones sous faible contrainte mécanique. Le fluide interstitiel peut également avoir un rôle mécanique important sur l’évolution des contraintes locales, et sur la façon dont celles-ci s’équilibrent ou non avec les contraintes régionales. Les contraintes déviatoriques observées dans les couches de calcaire au-dessus des argilites de Bure semblent être largement supérieures à celles transmises à travers la couche d’argilite.

En effet, la contrainte tectonique lointaine est appliquée aux couches profondes, les couches supérieures au-dessus de l'argilite étant à bords libres avec la courbure du bassin parisien, et la fin de ces strates à l'Est, avant les Vosges. On cherche à comprendre une origine actuelle des contraintes du bassin parisien, et de bons candidats pour de grandes déformations sont les processus réactifs dans les calcites, et dans les argilites, et entre les deux séries. Ces processus dépendent en grande partie de la possibilité de redistribuer de la calcite sous forme dissoute, et donc des propriétés de transport des couches de calcaire où elles se forment. De plus, ces propriétés de transport sont également capitales pour comprendre la migration à long terme des fluides à travers ces grandes formations calcaires autour de la couche d'argilite. On cherchera à modéliser un transfert réactif lors d'un écoulement en fracture et d'un écoulement dans l'espace poral déterminé lors des phases de caractérisation.
La cinétique mise en évidence lors des expériences servira à faire les choix de la condition aux frontières implémentées pour l'échange chimique entre phases dissoutes et phases précipitées. En contrôlant la composition et la vitesse du flux d'injection, et en modélisant la déformation élastique du solide, le transport du fluide et l'échange de masse lors des réactions de dissolution cristallisation, on cherchera à modéliser le transport, l'évolution de la porosité et l'évolution des contraintes associées, dans des milieux typiques des calcaires ou des argilites du bassin de Paris, avec ou sans fractures. On s'attachera en particulier à prendre en compte l'anisotropie possible des orientations des surfaces libres, avec des conditions de bord correspondant à des déplacements latéraux négligeables, pour étudier la possible genèse de contraintes déviatoriques associée à l'écoulement.

In fine, on propose ci après un projet de recherche détaillé sur deux des volets ci-dessus :

Liquides et Grains, Fractures et Avalanches

(Liquids and Grains, Fractures and Avalanches)

Context of the proposed research program

We propose to develop and implement simulations to study the impact of interstitial fluids over the mechanics of dense solid mass flows, in two contexts :
. Fracture mechanics in saturated media, and mechanisms of microseismicity migration associated to this fracture mechanics in fault gouges
. Impact of the interstitial fluids on the liquefaction of mass flow during avalanches.
Indeed, interstitial fluids can play an important lubrication role over granular flows, debris flows or saturated fault slips, modifying notably the flow regime with respect to dry cases.

The **applications** are of two types:
1 In natural systems:
1A **Modelisation of earthquake sources:**
Earthquakes have a major impact in terms of risk, and economic cost. The role of fluids in the fault mechanics is often evocated, and notably appears in situations of slow migration of microseismicity.
For saturated fault gouges, pore pressurization effects are studied lately. Effective friction laws for granular gouges are affected by the presence of fluids and lubrication forces. This is notably important for all models of seismicity migration, and for models needing to understand the fluid transport inside fault gouges, as models of thermo hydro mechanical couplings.

1B **Gravitational flows of saturated debris, such as** underwater avalanches, mudslides and debris flows. These type of flows creates major damage and a large number of victims every year, and is one of the main natural risks in Europe.
To understand the role of interstitial fluids in the liquefaction of initially coherent materials is a key challenge to which we intend to apply these methods.

2 In the industry: **Hydrofracture**
The structure resulting from injection of a fluid into a granular layer has two main applications in industries involving drills and pumps, as geothermy and oil production. Namely, the effect in intentional fractures created to enhance near-well permeability, and the effect in unintentional fractures created down-hole in depleted reservoirs.

Fundamental studies of well intervention by hydrofracturing and sand injection is of central importance to improve the permeability near the drilling well. The fracture is formed by water that is injected under high pressure, and it is maintained by sand that remains in the fracture as the water pressure is released. The resulting, increased permeability gives more cost effective drilling and production. We will, by use of model experiments and simulations, study the transport properties of this sand layer. In particular, we will consider the effect of channeling trough the sand packing as a method to increase the local permeability. We will also study the shape and pressure threshold of the created fractures, since hydrofracture is the main in situ technique of stress determination.

In depleted reservoirs, the fluid pore pressure falls and the solid stress increases. In these reservoirs fractures form more readily during drilling and the loss of drilling mud into the fractures creates a problem of significant economic and practical importance. In these reservoirs injection of a granular material is used to remedy the mud-loss problem significantly. In both cases the resulting transport properties in the granular packing is a key factor that needs to be understood.

General context in the team and laboratory:

A number of experiments have been initiated in our team (experimental geophysics) on the role of fluids in simple experimental situations: hydrofracture, injection of fluids in fractures, gravitational instabilities. This research thematic, developed by the team of young researchers collaborating with myself of is project, is so far essentially experimental. In parallel, a number of theories and simulations on the effect of fluids on the mechanics of a solid phase have been developed by the PI, in collaboration with the university of Oslo and the university of Jerusalem, and calibrated on experiments carried in Oslo and Strasbourg. The project proposes a significant step forward to develop these models further, and apply them to the experimental cases developed in our laboratory. This project will give the opportunity to develop the models further, notably by integrating the elastic response of the boundaries of the deforming systems, and to reinforce in our laboratory the pole on jammed solids / fluid couplings. We propose in funding agencies and doctoral schools the recruitment of a PhD on this subject, dedicated mostly to these simulations, which will allow to reach a critical mass of work on the theoretical/numerical studies dedicated to the experimental situations studied in the laboratory. The collaborators mentioned in this project are a team of researchers arrived in the IPGS laboratory progressively over the last 5 years, and of postdocs and PhDs working mostly on experimental problems.

In terms of developments for the laboratory, this project will significantly use a material recently acquired in the laboratory:

Experimentally, a fast streaming machine (50 MHz, 32 channels, 12 TB) was acquired in 2011, as well as a fast camera, thanks to regional and ANR programs, and the CPER REALISE.

Several projects (ANR, CPER REALISE) have led to the acquisition in 2008 of a parallel computer of 256 nodes in our laboratory. The two main projects that were carried on this machine are continuing in other laboratories. The present proposal will allow to develop on much larger systems, on parallel machines, codes whose preliminary versions are on single machine. This project will represent a significant advance for the use of the calculation tools of our laboratory, and will allow the continuation and expansion of the numerical computation pole of the lab.

French, european and international context:

The current project aims at applying and developing numerical techniques to understand these granular/fluid flows, and validate these techniques by comparison with simple experiments. We are in the process of developing numerical models to understand such hybrid liquid/solid flows, with a high solid content, when friction is mediated both by fluid viscous deformations and solid contacts.

We have already started to develop theoretical and numerical understanding of such coupled flows in other contexts, and compared them to laboratory experiments, through different stages.

Recent numerical and theoretical developments:
Collaborations with Norway (PICS and projects of the Norwegian Science Foundation), where we have developed in the framework of “Petromaks” projects models to render for Air/granular flows applied to
. aerofracture of granular materials (PhD of O Johnsen, 2004-2008), with coupled flows of air and fluids
. The study of instabilities during sedimentation of grains in compressible fluids: PhD of Jan Ludvig Vinningland (2003-2007),
. Variations of the compressibility of the interstitial fluid, up to incompressible ones:
PhD of Michael Niebling (2007-2009)

In collaboration with the Earth Department of the university of Jerusalem (PhD of Liran Goren, 2007-2010), we have simulated saturated gouges with stiff confining rock, sheared at constant speed.

Related experimental and numerical projects.
Some projects have allowed to start experiments to which the proposed simulations can be applied:
In the framework of the ANR Triggerland project (2007-2009), of the ANR SISCA project (2009-2011) and of the European SAFELAND project, experiments of liquefaction of saturated granular materials are being carried under various conditions (current postdoc of Anke Spickermann). The determination of the associated microseismicity is planned in the postdoc project associated with SAFELAND and in the PhD (Alice Tonnellier) associated to SISCA.

In the framework of the ANR MODALSIS project (postdoc of Olivier Lengliné, 2009-2011), acoustic emission and localization techniques in fractures are being developed, and simulations of deformed confining elastic media during these processes are carried out. In the the postdoc of Michael Niebling in the university of Strasbourg (2010-2011), experiments of flow in confined porous media deformed by the overpressurization of the interstitial fluid are planned.

Scientific description

Background, state of art

The focus of this project is a fundamental research about the mechanics of highly heterogeneous media, namely geological interfaces. Some of them play a particular role, as central objects in mechanical instabilities responsible for important natural risks: seisms, slope instabilities. The natural media involved in them have often a long story and a structure implying a very wide range of timescales, from seconds during a rupture event to millions of years for the accumulated deformations.
They are also structurally complex: arising through multiple processes of deformation localization, they develop a morphology over spatial scales ranging from micrometer to a thousand kilometers, and their functioning often implys a very large number of degrees of freedom. Eventually, the complexity of these natural media results of the strong heterogeneity of the involved materials (e.g., from very homogeneous calcareous micrites to porphyritic

granites, whose mineral structure is very coarse and heterogeneous, with inbetween marns constituted of mixtures of calcite and clay), and of the rheological contrasts: elastic solid, plasticity, presence of interstitial fluid, fault gouge, dense suspension, etc, and of the permanent rehandling of structures.

This project aims more specifically at studying the genesis of the structural complexity of the involved mechanical interfaces, and the influence thereof on their mechanical behavior. We will analyze the formation and role of the asperities, granular gouges and fluids in the processes of fracture and hydrofracture, in the mechanical response of sheared interfaces (as e.g., localized deformation zones where landslides initiate, or faults). For the analysis of the mechanical behavior, we propose a general simplified framework which consists in the study of a geometrically complex sheared interface in an elastic medium, with potentially fluid and grains embedded in the interface. The response of these systems to mechanical loading (static or dynamic tectonic loading, fluid injection or loading due to gravity) leads to instabilities which can dissipate in a few seconds the energy which was accumulated over long periods, sometimes thousands of years. The spatiotemporal complexity of this dissipation is intimately related to the multiscale aspect of the problem, both in space and time, and to the small scale heterogeneities which can lead to the emergence of a complex collective behavior at large scale.

Various mechanical processes are at play in these systems : elastic stress is transmitted through the surrounding rock, solid friction between the asperities and the grains inside the interface, interstitial fluid pressure, fluid flow through a porous medium whose permeability is evolving during the process due to its deformation.

The goal is to link the elementary mechanical processes between these constitutive elements, starting from first principles of physics, including notably the disorder present at small scale, and to study the emerging spatio temporal complexity at large scale. The center of this project is to quantify the impact on the macroscopic behavior of these parameters: presence of granular media and fluids in friction and fracture processes, presence of disorder in the geometry or material properties, noise in the external loading.

For this purpose, we propose to combine interdisciplinary techniques of numerical modeling on the topics of granular/fluid hybrid flows, and of seismic sources, of statistical physics and experiments on contact mechanics and disordered systems, and of comparison to large scale data in geomorphology.

Topic 1 (experimental) and 2 (modelling): Mechanisms of hydrofracture and friction implying saturated gouges

Context : Structures formed by hydrofracture resulting from the injection of a fluid into a porous medium or a granular material have numerous applications in natural systems and in the oil industry. They are also used to analyze the stress orientation in the vicinity of oil wells.

Simulations of fluid injection (air) in a deformable porous medium (dense and fine granular packing, 80 microns particles, 200 000 particles): Time is from left to right.
From top to bottom: particle density, solid stress, pore pressure and particle velocity along the flow (vertical flow on the picture). Simulations by M Niebling, R Toussaint, EG Flekkoy

t =0.004s t =0.01s t =0.015s t =0.021s t =0.026s

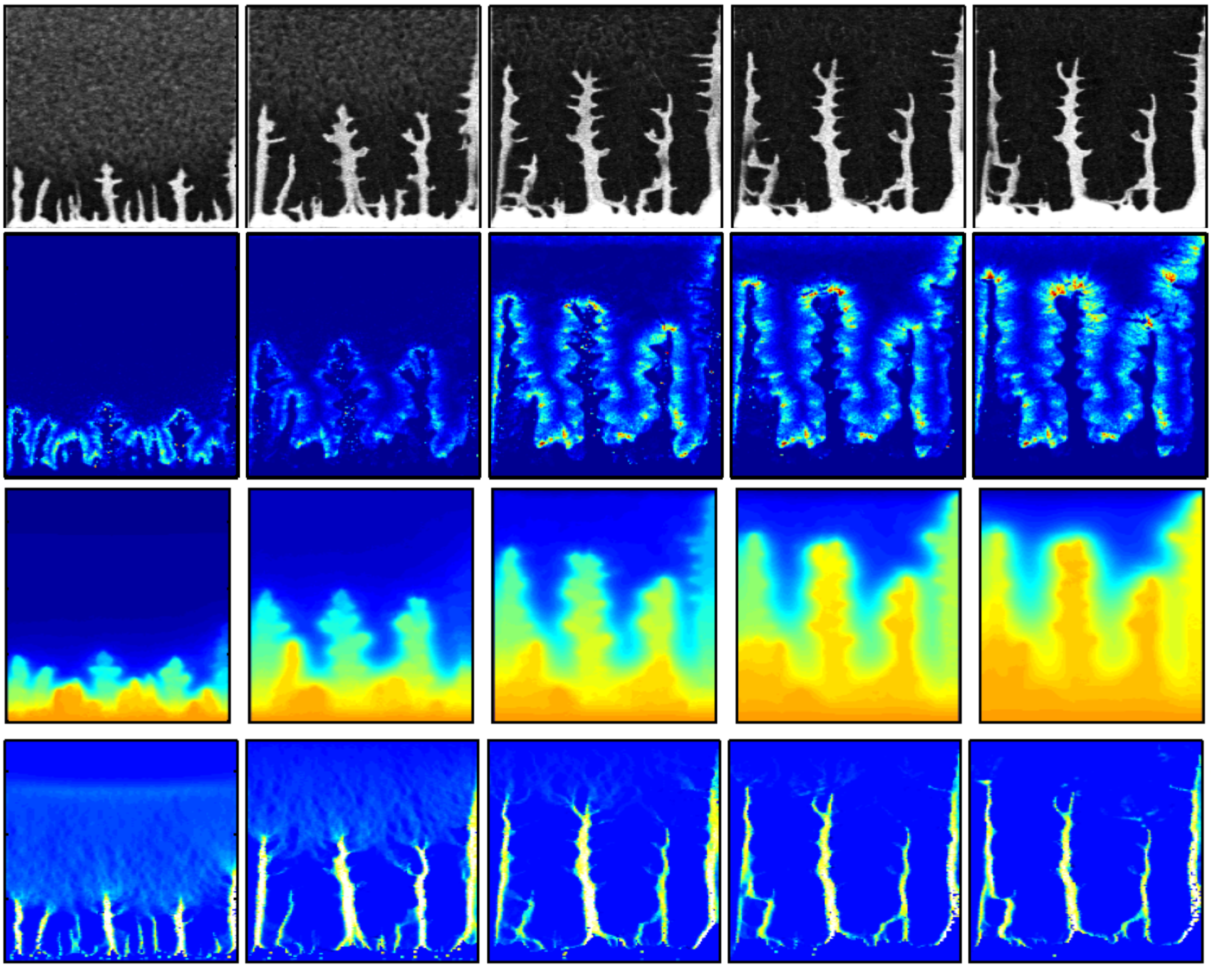

Experimental picture of a dense and frictional porous packing of 80 microns beads deformed by fast air injection at the bottom of the picture. Experiments by M Schelstraete, R Toussaint, KJ Maloy:

In natural systems, local overpressures can lead to the formation of hydrofractures in granular materials, like gouges or injectites. They thus strongly modify the permeability and the transport properties of the material. In industrial applications they are mostly used to stimulate reservoirs (like water, natural gas or oil reservoirs) by improving the permeability of the surroundings of a drilling. On the contrary, for other cases, the formation of these fractures has to be avoided, in particular to prevent loss of drilling fluids in wells, or worse, the mobilization of sediments under pressure, that can lead to massive mud eruptions.

Fundamental studies on hydrofracture, its application to wells and sand injection are important to improve the control of the permeability in the surroundings of extraction wells. In the case of a reservoir stimulation, hydrofractures are formed by water injected under high pressure, and are kept open by sand that is maintained in the fractures once the water pressure is decreased. The resulting increased permeability thus allows an easier exploitation of the drilling. The precise control of this technique has significant economical impact.

In natural systems, as fault gouges during earthquakes, the presence of fluids in the fault can, under the effect of fluid flow due to the high pressure gradients, lead to a hydrofracture and finally to the formation of channels of high permeability. This high permeability modifies the transport properties of fluid and heat in the confined granular material and can thus have an important impact on the energy dissipation by friction and the processes of weakening by thermo-pressurization. It is also important to characterize the seismic signal associated to seismic sources linked to hydrofracture with the aim to understand and perhaps detect seismically, the slow modifications of strain (and migration of microseismicity) associated with these fluid motions.

For all the cases mentioned above, it is essential to understand the mechanism of hydrofracture from a fundamental point of view, especially in the case of a strongly heterogeneous material. The modifications of the transport properties result from both the geometry of the hydrofractures itself and the evolution of permeability within these hydrofractures.

Eventually, independently from the industrial and geological applications of these structures, the pattern formation during injection of a pure fluid into a fluid/grains mixture formed by the same fluid is a model system for two mobile systems without surface tension. It is thus from a fundamental point of view a paradigm to resolve an essential fluid dynamics problem, namely the formation of finite time singularities in this type of systems [see review of the articles of Johnsen et al 2006 and Cheng et al, 2008 in Nature, News and Views, 28 January 2008, by R. Courtland]

State of the art :
These problems are well known in the petrol industry and intensively studied in geological literature [Gordeyez 1993, Valko et al 1995]. However the study of formation of complex patterns of hydrofracture and the modelization of coupled fluid grain flows, beyond the limit of poro elastic models, is still in its infancy [Tzschichholz 1994, Flekkoy 1993].

Over the recent years, we have developed experiments [Johnsen et al 2008, 2006, Chevalier et al, 2008] and numerical models [Niebling et al 2010a,b, Johnsen et al 2006, Vinningland et al 2007a,b,c, 2010] in order to study the fracturation of granular systems in transparent Hele Shaw cells, with a focus on the pattern formation during this process. We have studied these instabilities in systems where the interstitial fluid was air [Johnsen et al, 2006, 2008 a] or oil [Johnsen et al, 2008b, Chevalier et al 2008]. Insodoing, we have shown the existence of nontrivial compaction / decompaction patterns arising during these processes (see figures).

The existence of such finger like patterns in simple and complex fluids is a well developed scientific field [Taylor and Saffman 1958, Lindner et al 2002, Bonn et al 1995]. On the contrary, the study of pattern formation during hydrofracture, or the dynamic of coupled fluid/grains systems, is much less well establishes, and is a quickly developing field [Vinningland et al 2007, a,b,c,2010, Johnsen et al 2006, 2008, Chevalier et al, 2007, 2008, Xu et al 2008, Flekkoy et al 2001, Gendron et al 2001, Jaeger et al 1996, Yop et al 2006, Malloggi et al 2006, Pinto et al 2007, Aranson et al 2006, Baxter et al 1989, Lemaire et al 1993, Mills et al 1995]. We have actively participated to this field over the last year, both on the experimental and on the theoretical side. [Vinningland et al 2007, a,b,c, Johnsen et al 2006, 2008a,b, Chevalier et al, 2007, 2008]. The detailed mechanical basis of the mathematical model used for these problems are described in the “Research program” section.

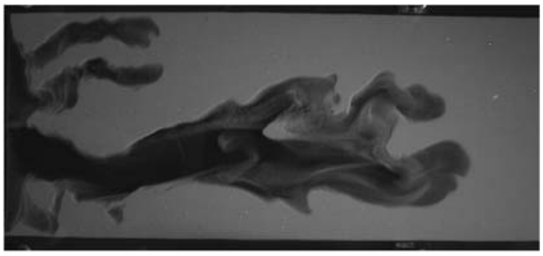

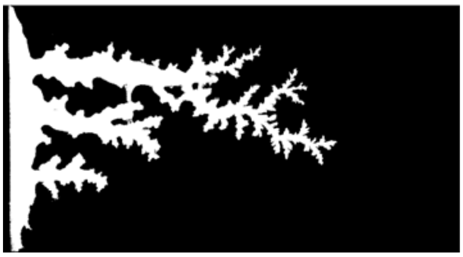

Displacement figures in a rectangular Hele Shaw cell, where air is injected through a granular medium, from a compression chamber on the left of these pictures. The upper and lower boundaries are impermeable. In the left picture, where the grains are gray/white, the right boundary is open. In the right picture, where the grains are represented in black, and the zones empty of grains in white, this boundary is semi permeable, blocking the particles, and open to air.

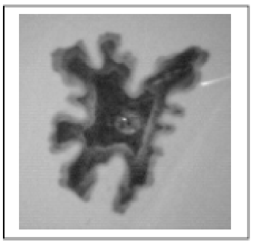

Figure: coupled model for a granular medium confined in a Hele-Shaw cell during a central fluid injection: left, experiment, 10 cm large view [Johnsen, Toussaint, Maloy and Flekkoy]. Right, corresponding simulation where the color code represents the local permeability [Toussaint and Flekkoy]. In these codes, the modeled fluid flows through the grains according to the local permeability, and at the same time pushes over the grains, which are modeled individually.

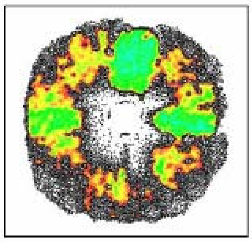

Topic 1 (experimental) and 3 (modeling): Role of lubrication in liquefaction during gravitational instabilities

The role of fluids in liquefying landslides has been the subject of numerous research. The state of the art in the geotechnical approach can be described as follows:
In order to explain and specify how slow-moving landslide transforms into debris flow, scientists and engineers have elaborated comprehensive theories using well-established results from soil mechanics. In this view, the transformation from a landslide into a debris flow is depicted in three stages as underlined by Ancey (2001): (a) failure localized along a surface within a soil, generally described by the Mohr-Coulomb failure criterion, (b) partial or complete liquefaction of the material as a result of high pore-fluid pressure, (c) initiation and acceleration of the liquefied material. Although great effort has been devoted to the study of pore pressure generation and dissipation within a rigid landslide block, the understanding of fluidization of landslides due to differential movement and hence local compression in the moving body is as yet limited.

Here, liquefaction is defined as the process destroying the solid framework of a water-saturated sediment and creating a mixture with the behaviour of a liquid. From a mechanical view point, it represents the conditions where excess pore-fluid pressure in a soil mass is equal to the initial effective overburden.

There are several processes, which may generate liquefaction in coarse-grained or fine-grained sediments (Wang and Sassa, 2003). For coarse-grained, loosely-packed low density soils (typically sands or volcanic ashes), the most well known liquefaction mechanism is the collapse of the soil structure due to the rapid generation of large plastic strains by applying a given stress or load (Casagrande, 1971; Yoshimi et al, 1989; Harp et al 1990, Sasitharan et al, 1993; Anderson and Riemer, 1995). Several flume experiments have confirmed this mechanism of contraction of the soil structure for saturated materials in poorly drained conditions. For instance, the experiments of Iverson et al (1997) in a 95 m-long channel, performed on coarse-grained loose soils consisting of poorly sorted sands and fine gravels, showed dramatic increase in pore water pressure until liquefaction at all depths throughout the sliding block. Laboratory experiments carried out by Fuchu et al (1999), Eckersley (2000) and Chu et al (2003) on loose soils in essentially drained conditions showed the same mechanisms.

Mode of failure and initial bulk density seem to be first order factors controlling liquefaction failure according to Wang and Sassa (2003). They carried out a number of laboratory flume tests on fine silica sand textures mixed with silts at different densities. The authors showed the influence of grain size on the optimal density for which there is contraction of the materials and a maximum pore pressure build-up during and after failure. In addition, they clearly showed that pore pressures within saturated loose sandy textures increased with increasing velocities of the sliding block. Contracting behaviours related to changes in stresses has been observed also at the field scale for saturated materials (Olson et al, 2000). Contraction may also occur in case of unsaturated materials. Olivares at al. (2003) did several triaxial tests and laboratory flume experiments on loosely packed volcanic ashes, which failed by increase in saturation caused by rainfall infiltration, and consequently reduction in suction strength. During wetting the pyroclastic material showed failure at rather low suction stresses but not complete saturation. However drastic volume decrease occurs during failure, leading to saturation.

Apart from liquefaction induced by a contracting behaviour of the soil masses, the possibility of dilating behaviour prior to failure might also occur for dilative loose sands that lie below the critical-state line such as observed by Been et al (1988), Fleming et al (1989) and Harp et al (1990).

Another mechanism causing liquefaction is related to the direction of the seepage forces of the groundwater flow. For instance, in infinite slope stability analyses it is commonly assumed that the groundwater flow and hence the seepage force vector is parallel to the topographical surface. Common theory in soil mechanics will show however that when the seepage force turns more and more in a direction opposite to gravity, effective stress progressively decreases, may become null and causes liquefaction of the sliding block (Nieuwenhuis, 1989; Iverson at al, 1997).

Another theory is related to the complex moving patterns of landslides. These landslides may have a net excess force down-slope generating acceleration of the moving block and hence an increase in translational kinetic energy. A part of this energy may be conversed to kinetic vibration energy of agitated soil particles. According to Iverson et al (1997), this energy can have a positive feedback on the liquefaction process in the landslide block. In flume experiments, it became clear that complete liquefaction occurred during runout of the material through agitation of the particles caused by the vibration energy and the development of intergranular pore pressures.

Finally, Sassa (1998) proposed another theory of landslide liquefaction. He hypothesized that shearing may break the soil particles near the slip surfaces causing a reduction of void ratio and possibly liquefaction.

Among these theories, less attention was given in the literature to the effects of landslide geometry and kinematic deformation in possible liquefaction of the sliding block. The hypothesis, on the basis of field evidence and literature review, is that excess pore pressures develop because compression zones and extension zones may arise in a moving body due to changes in slope gradient along the slip surface or by thrusts of newly failing slumping blocks in the upstream source area of the landslide. For instance, Okura et al (2002) showed in a 9 m-length flume associating a steeper slope and a flatter slope, how the collapse of the soil on the steeper upslope part induced compression, liquefaction and a new slide in the lower less steep part. Savage and Smith (1986), Baum and Fleming (1991), Picarelli et al (1995) and Giusti et al (1996) showed that internal deformation of slow-moving landslides results in positive or negative volumetric strain and hence the generation of negative or positive excess pore pressure under initially undrained conditions.

In addition to such theories, that treat in general the flowing medium as a fluid with a complex evolving rheology, other approaches allow the differential motion of the fluid and the solid phase [Iverson, 1997]. These approaches, termed mixture theories, describe the rheology of the interstitial fluid, the one of the solid, considered as a non Newtonian fluid characterized by a certain granular temperature (describing the amount of kinetic energy for the incoherent part of the grain velocities), and the momentum exchange between the two phases.

These models allow to explain grain size segregation, thickening and thinning of flow as function of the drainage properties, and the difference between the pore pressure and the average stress in the medium. They are thus among the most advanced models used to describe debris flow. However, they suffer from the fact that there is no known general constitutive equation of granular materials, i.e. their rheology is only precised in some limited regime. To overcome this difficulty, we propose to keep the mixture character of the simulations, but to add up the fact that we treat the grains as an assembly of discrete elements which was done recently with success to model many dry granular media [Forterre]. Insodoing, we will expand the models that we have used to describe gravitational instabilities in sedimentary situations, where slabs of grains fall in compressible [Vinningland et al] or incompressible [Niebling et al] fluids.

This model has also been used in situations of sheared layer, to capture the behavior of interstitial fluids during shear between granular layers in a granular material. It was shown to be equivalent to the computations of Biot [Biot] and Wang [Wang] for poroelasticity and poroplasticity. Its granular feature, nonetheless, can go beyond these particular cases in terms of rheology.

These models will be used on generic situations of gravitational instability:
tilted free slopes of granular materials with 1/ accumulation of material, 2/ water infiltration and modication of pore pressure, or 3/ shaking of a free slope close to critical angle.

Rationale of the proposal

The scientific objective of this project is a better understanding of the mechanical behavior of geological interfaces under shear. Indeed, their behavior controls mechanical instabilities responsible for important natural hazards and risks. We will mainly focus on interfaces implied in seismic risk (faults) and in risks associated to slope instabilities (detachment zones). Indeed, the response of these systems to mechanical loading (static or dynamic tectonic loading, loading by gravity) leads to instabilities that can dissipate in a few seconds the energy accumulated over long timespans, sometimes thousands of years. Our framework is that of a fundamental research on physical and mechanical processes in order to be able to propose to the operational instances some observables physically and mechanically argumented, which, we hope, can allow advances in the understanding of the concerned hazards, natural prerequisite to any possible quantitative hazard assessment.

In all the implied phenomena, we have mainly selected two families of problems. In general, we expect advances on the mechanics of highly deformable media saturated in fluids. Important works have already been carried out on the deformation of granular media, and on the hydrodynamics in porous media. The challenge that we propose to tackle is to couple these two domains of study, where the mechanics of the solid matrix and the fluid hydrodynamics strongly interact.

The first topic will provide us an experimental database to benchmark our models. This will concern hydrofracture problems, sheared saturated interfaces, and liquefaction of saturated granular media.
From the second topic, we expect a better understanding of the evolution of the transport properties, and of the evolution of the friction and dynamics of sheared interfaces. We also expect a better understanding of the migration of microseismicity during shearing of a fluid-filled gouge, or during fluid migration in interfaces.
The third topic will provide clues on the role of fluids on the catastrophic liquefaction during mudslides and debris flows.

For the outcome of these second and third topics, there is a link between formation, structuration and deformation of geological interfaces. The goal is to analyze how the interface formation, i.e. its morphogenesis, controls its mechanical response during an external loading (in particular, a shear). We think that this approach is original and absolutely necessary to study geological media, whose mechanical history is long, and thus composed of a neverending rehandling of their structure.

The main scientific difficulty to solve is the great complexity of natural media. The difficulty is to succeed in the identification of the dominant processes, in particular in the question of the mechanical instability. Indeed, these media have a long story (up to millions of years) but can react in a few seconds during seisms, for example. In space, the systems are also strongly multi-scale: from a few micrometer-sized grains to structures of several thousands of kilometers. The materials can be very diverse, with very different rheologies (solid, fluid, granular, elastic continua, etc). To address these key difficulties, the basis will be our experience in this domain, and the pluridisciplinary character of the collaborating team.

We expect that the effort to improve our models by comparison with experiments will provide versatile numerical tools for further mechanical studies of instabilities in natural media.

Scientific programme

Scientific programme, specific aims

We will develop models of mixed granular/fluid flows, in situations where lubrication is important, where the exchange of momentum between the granular and the fluid phase leads to the creation of channels modifying the permeability, or where it modifys the effective friction properties of a sheared interface (confined sheared saturated gouge) or of a flowing surface layer (liquefaction).
For this purpose, we will develop simple laboratory experiments with realizations corresponding to these situations, and we will implement numerically the hybrid models to reproduce the experimental observations.
The experiments, in Topic 1, will benefit of already existing setups. The analysis of the experimental data should be well advanced in the first years, so that the results will be available for the detailed tuning of the parameters of the simulations.

Topics 2 and 3 correspond to the numerical simulations aiming at reproducing the observed mechanical functioning in the experiments (topic 1).
Topic 2 concerns the simulations of confined granular interfaces, submitted to overpressure (hydrofractures) or shear (gouges).
Topic 3 concerns the study of liquefaction of a saturated granular layer with a free drained boundary on top.

The general idea of the structuration of this project is to preserve an articulation between laboratory experiments and simulations (articulation between Topic 1 and 2 others)
This project will allow the development of simulations to understand new problems, and hopefully will eventually offer a versatile tool: a general parallelized tool for the simulation of momentum exchange between fluid and solid phase.
The choice of applications we did for this project was to apply these techniques to natural instabilities and hazard analysis.
This led to the following choice of simple scenario studied:
Topic 2: fluid injection and seismicity migration in confined interfaces, or role of interstitial fluid in buried sheared interfaces.
Topic 3: Other type of sheared interface: gravitational loading and liquefaction.

Detailed description of the work organised by topic

Topic 1

Experimental study of hydrofracture and friction of interfaces implying saturated gouges.
International collaborators: Eirik G Flekkøy, Knut Jorgen Maloy, Oslo

1A/ In order to create and study morphogenesis during hydrofracture or aerofracture, we propose to develop an experimental approach where water under pressure is injected in a water-saturated sand layer (or the same with air under pressure in air-saturated sand). This layer will be placed in a transparent Hele Shaw cell. The experiment will be equipped with pressure sensors and fluxmeters, and an optical tracking will be performed by the use of a fast camera (1000 frames per second). We will also equip the experiments with piezoelectric acoustic sensors in order to analyze the microseismicity associated to this fracturation mode.

We will so study experimentally the hydrofracture process, and will aim at classifying and quantify the fracture / channelization process, the pattern growth, and the resulting permeability. We will specially focus on the influence of:

- the geometry of the system and injection mode (circular, linear)
- the influence of the boundary conditions (permeable, semi permeable: preliminary studies show the importance of these in the process)
- The influence of the grain and cell size, injection conditions (imposed flux or pressure, time of rise of the injection)
- The influence of gravity, inclining the cell in various positions – indeed, gravity is a key parameter for hydrofracture in wells.
- The characterization of the observed seismic sources.

1B/ Influence of the morphology of a fault containing grains and fluids and of an applied shear stress: experiments of gouge hydrofracture.

As previously suggested, we will carry new experiments in Hele Shaw cells where a lowly cohesive granular medium will be perturbed by the injection of a viscous fluid, and extended to the problem of the injection in a granular medium confined in an open fracture. This will be realized through the replacement of the two parallel glass plates by two transparent and rigid epoxy casts of two surfaces of fault mirror. Insodoing, we will be able to measure the influence of spatial correlations between asperities (and thus fluctuations of the local thickness for the confined granular medium) on the shapes arising for the permeability field in the fault gouge. This description is a key parameter for many models of the effect of the thermopressurisation effects – the effect of the temperature rise induced by friction over the fault rheology. Indeed, in most models, the hypothesis of the flow in a classical rigid porous medium is done. This hypothesis might turn out to be far from reality in situations where the interstitial fluid is submitted to large flow. We will also systematically study the influence of prestressing the confining plates under shear over the structures arising.

The experiments carried out will allow a/ to record the microseismic signals associated to these processes, b/ to run these experiments under a shear loading using uniaxial loading machines around the setup, and c/ to run hydrofracture experiments in fracture geometries (transparent molds).

Michael Niebling participates in these experiments. The help of Olivier Lengliné will allowed to set up the machine to record the microseismic emissions during these processes.

1C Experiments on liquefaction of saturated granular slopes:
Landslides and avalanche triggering due to fluid overpressures
Collaborators: Jean-Philippe Malet, Alexandre Remaitre, Anke Spickermann, IPGS, Eirik G Flekkøy, Knut Jorgen Maloy, Oslo, Einat Aharonov, Jerusalem

Landslides happening after heavy rainfalls represent an important geophysical hazard, with associated risks on human life and equipment costs. In the triggering process of such events, the rise of interstitial fluid pressure plays a major role to allow such fluidization transition. In a poorly consolidated material of granular nature, the fluids brought by preferential paths of high permeability can accumulate over permeability barriers in the close subsurface, leading to the local rise of interstitial fluid pressure. The fluid pressure gradients resulting of such fluid accumulation can mobilize the surrounding grains, and lead to the destabilization of the granular material, which was otherwise mechanically stable. We are interested in such coupled granular fluid flows, and more specifically, in the triggering of avalanches due to fluid overpressures, in the framework of gravitational hazards. We propose to study the destabilization of granular piles with an inclined free surface experiencing shear of gravitational origin, under the effect of the flow of interstitial fluid, at low Reynolds number. This study will combine laboratory studies of hybrid granular/fluid flow followed optically in transparent setups (topic 1), and numerical approaches (topic 3).

In general, for materials whose solid elements are of millimetric size or above, their granular character has an important impact on avalanche triggering: the stability of such systems, when their free surface is inclined on the horizontal at an angle close to the critical rest one, is strongly sensitive to small fluctuations of the stress field, and to slight changes of the contact network. For systems composed of grains and blocks, the stress heterogeneities arise naturally from the presence of force arches exerted through the contact network between the grains, which leads to stress heterogeneities at a scale significantly larger than the scale of the grains themselves. This feature results in a spurious avalanche precursor activity for such systems on the verge of mechanical instability. To capture this effect, we propose to model the solid part of such system by a discrete granular model.

We will build granular slopes close to critical angles, and sollicite them by three different mechanisms:
Localized injection of interstitial fluid,
Adding of grains on top of the slope,
And shaking at various frequencies and amplitudes.
The role of the boundary conditions (drained, impermeable), will be studied, as well as the one of initial solid fraction, which reveals to be very important for the value of overpressured reached and for the existence of lubrication [Goren et al , 2009].

Example of liquefied granular media during sedimentation:

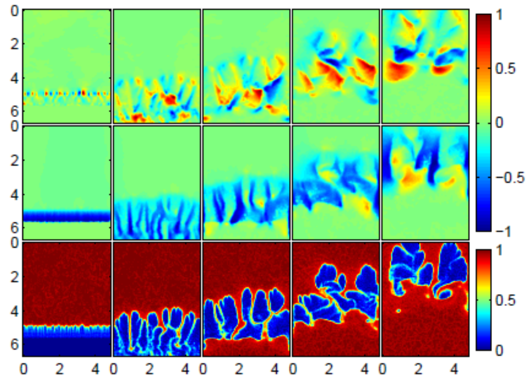

(a)Simulation with air. Axis units given in (cm).

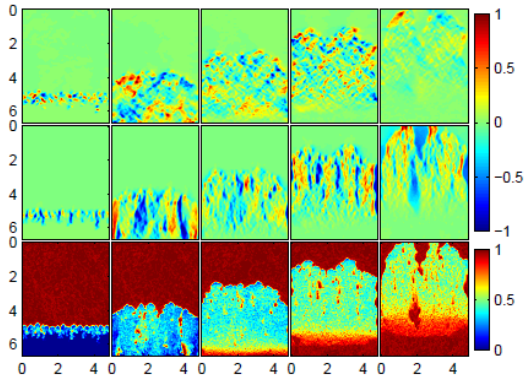

(a)Simulation with water/glycerol. Axis units given in (cm).

Simulations of injection of air or water at the bottom of a granular medium saturated with the same fluid. Top panels: color scale corresponds to lateral and vertical velocities. Bottom: Density. [Niebling et al 2010a].

Topic 2

Development of numerical simulations of hybrid flows of confined flows in hydrofracture or fractured gouge to reproduce the experimental results.

Collaborations at IPGS : Alain Cochard,
International: Eirik G Flekkøy, Knut Jorgen Maloy, Michael Niebling , Oslo, Einat Aharonov, Jerusalem

Development of numerical simulations of hybrid flows of confined flows in hydrofracture or fractured gouge to reproduce the experimental results.

The numerical simulations in the configurations corresponding to these experiments will be carried out, according to a numerical scheme detailed hereafter :

Theoretical principles of the coupled granular/fluid dynamic model
This model is based on a discrete representation of the solid matrix in solid elastic particles, initially cohesive. The transport of insterstician fluid is described by continuum mechanics, the relative displacement of the fluid with respect to the solid matrix being ruled by a Darcy law, where the local permeability evolves according to the solid fraction. As long as the pressure variations are small at the scale of the constitutive particles, in comparison to the variations of stress in the solid elements (which can be singular close to fracture tips), the pressure field can be described by a discretized version on a lattice whose step is a few particle diameter large. The relationship between the solid fraction and the local permeability is given by the Carman Kozeny relationship [Carman, 1937] when the simulated particles correspond indeed to a population of spherical grains, or a variant of this relation reflecting the tortuosity of the permeability channels at scales smaller than the elementary particle scale. The particles representing the solid matrix are subject to elastic repulsive contact forces with their neighbors, to elastic cohesive forces acting as long as random rupture thresholds are not overcomed, and sustain moreover the local fluid pressure gradient. This is implemented using a molecular dynamic scheme. The resolution algorithm is based at each time step on a velocity Verlet scheme for the evolution of the speeds and position of the particles, alternated

with a time step based on a Cranck Nicholson algorithm for the advection/diffusion equation ruling the local pressure evolution [Tildesley and Allen 1989, Press et al 1992].

In the figure below, we have represented a state corresponding to a central injection of air (0.1 bar) in a bidimensional cell of 10000 noncohesive elastic particles, of granulometry raging from 70 to 150 microns (the initial texture is a random loose pile, the simulation represents the situation after 0.5 s of injection).

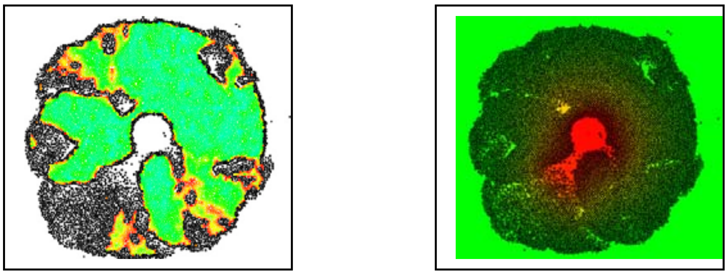

Simulation of quasitwodimensional non cohesive particles, expelled by a central injection of air (0.1 bar), confined between two planes with open boundaries (R. Toussaint and E.G. Flekkoy]. The particles are submitted to fluid pressure gradients, and to friction with the confining plates. The color code represents on the left, the permeability and on the right, the interstitial fluid pressure. This situations corresponds to 0.5 s of flow in a 20 cm large cell. The deformation quickly localizes in paths of high permeability, analog to viscous fingers in nonNewtonian fluids, or ahead of these to fractures with a high aspect ratio. Further ahead, bubbles empty of grains nucleate, as in the corresponding experiments.

We will replace, in these simulations, the highly compressible fluid by a fluid of lower compressibility, in order to simulate water flowing in a lowly cohesive granular medium. We will try to reproduce the morphological characteristics and the transport properties of the granular/fluid mixture observed in the corresponding experiments of injection in a confined granular layer (imposed local rise of overpressure) – similarly to the work done so far on air/grains mixtures [Johnsen et al 2006, Vinningland et al 2007a,b,c, Niebling 2010a].

In parallel, the simulation of acoustic emissions related to the observed displacements will be carried out by using the Green function of elastodynamics to propagate the wave generated by stress changes due to the forces exerted by the granular layer over the confining plates. We will thus model the microseismicity associated to the deformation of this layer.

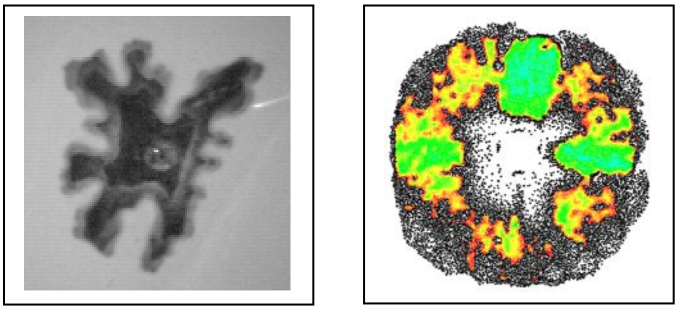

Left: experiment, 10 cm large. The light and dark tones are respectively populated with or empty of grains. Right: corresponding simulation. The color code carried by the grains represents the local permeability.

Next numerical step : integration of rheological laws of contact in rupture models – coupling with hydrodynamic models - -Darcy)

With a rheological description for the coupled flow of a granular gouge and a fluid, it is natural to integrate them in a large scale fault model, in order to apprehend the influence of these laws (mechanics of saturated gouge) on the behavior of a fault filled with a granular gouge and a fluid.
We will then couple the hybrid granular fluid models described above, to codes describing the elastic or poroelastic deformation of the embedding medium: boundary element models, (or alternatively, spring chains or molecular dynamics of cohesive particles).
The question raised is: is the macroscopic behavior of the fault different from the one at micro scale? Under the light of our previous results, in particular on the critical displacement involved in the slip weakening law and the fracture energy, we plan to study the role of fluids, as allowed by our numerical tools with the experimental results, depending on whether the poroelastic zone evolves with the displacement, or not. Can the fluid accelerate (or delay) the nucleation of rupture, or in extreme cases stop it?

This will be performed by the development of a coupling between boundary integral element model, describing the propagation of elastic waves in the confining medium, with the hybrid grain/fluid models.

We will propose a PhD subject on the numerical part to work about the development and interfacing of these codes, and to the analysis of seismic signals recorded during the experiments, in order to be able to compare them to numerical models of microseismic sources.

Details on the Numerical modeling of the shearing of rough fractures-- poro-elasticity of rough fractures.

The objective is to extend the model of normal elastic indentation of a rough fault to shear loading. We will use a boundary element code (BIEM) [Hansen et al, 2002; Cochard and Madariaga, 2000; Aochi et al,, 2000]. The difficulty with the shearing mode consists of the treatment of local instabilities related to the unlocking of asperities. We will tackle this aspect by first neglecting rock inertia, i.e., by studying the quasistatic limit of this model during instability.

Another aspect is to couple the model with a model of fluid flow, and/or grains (gouge) in the fractured domain (the fault). This coupling will be done in four stages. The first will consist in assuming the porous space entirely open or filled with a rigid porous medium hence obeying Darcy's law.

The second stage will be to consider a deformable porous medium, but remaining in the elastic regime. The surrounding medium will then impose the boundary conditions on the porous medium, filled with fluid and gouge. If the gouge remains cohesive and elastic, it will be described by Biot's equations.

In a third stage, we will consider changes in the porous medium due to his weak cohesion, in a surrounding non-altered non-deformable solid rock. We will use algorithms developed for hybrid models applied for air/grains situations [Johnsen et al, 2006, 2008; Vinningland et al, 2007abc]. These models have been validated by direct comparison with Hele Shaw cell experiments, so far without macroscopic shearing.

The fourth stage will be to also take into account the deformation of the porous medium, not only because of the weak cohesion but also because of the deformation of surfaces of the fracture enclosing this porous medium.

The response of the medium surrounding the fault will be considered as quasi-elastic. We will use our BIEM (Boundary Integral Element Model) codes by simply introducing the forces resulting from the dynamics of the fluid/grains mixture as as force boundary condition. With staggered time steps, the resulting deformation of the edge of the solid described by the BIEM formulation will provide the boundary conditions for the hybrid fluid/grains code.

Topic 3 :

Numerical modelisation of liquefaction using hybrid fluid/granular mixed code

collaboration: IPGS : Alain Cochard, Anke Spickermann, Alexandre Remaitre
International: Eirik G Flekkøy, Knut Jorgen Maloy, Oslo, Einat Aharonov, Jerusalem

For the liquefaction problem, we will implement the same type of numerical code, and add gravity and tilted boundaries.
The proper boundary conditions will be considered for Debris flows or underwater avalanches: free top layer, drained or undrained bottom.
Several initial solid fractions will be considered, since preliminary results on sheared interfaces show that this is a major control parameter for the arising of lubrication.

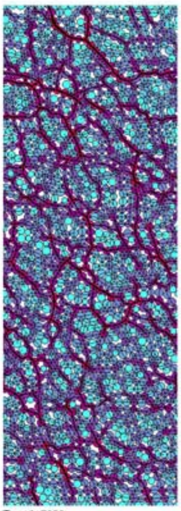
T = 1217053.

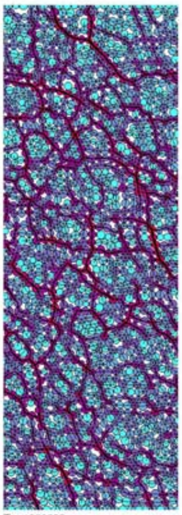
T = 1220633.

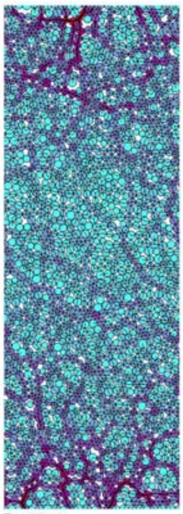
T = 1224212.

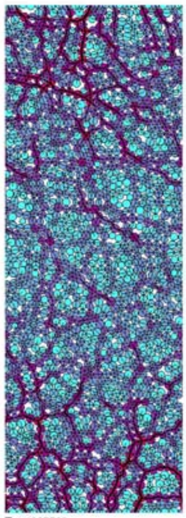
T = 1227792.

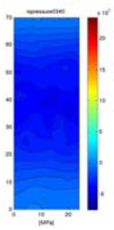

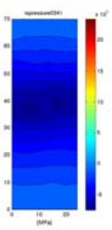

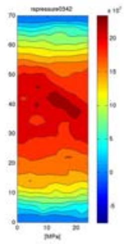

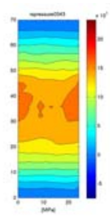

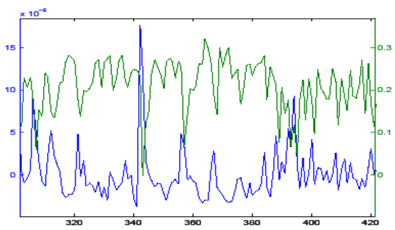

Figure above: simulation by Goren, Toussaint et al of a sheared layer with drained boundary conditions. [Goren et al, 2010b, 2011]
Top: the color code represents the contact forces between the grains (time goes from left to right).
Middle: Pore Pressure during the same 4 times.
Bottom: Apparent shear force (green) and average pore pressure (blue) as function of time. After the pressure rise, overpressures diffuse away, and break the solid contacts, reducing the shear (friction) in this simulation at imposed shear velocity. The snapshots correspond to the largest peak in these curves.
During the stage where the pore pressure became higher, the contact forces between grains diminished, and the shear stress dropped (with a constant normal stress).

We will implement a code of hybrid granular fluid flow, in the situation of saturated debris flow and underwater avalanches.
The goal is to understand the impact of the fluid on the liquefaction.
According to preliminary results (see figure above), the compressibility of the fluid, although very small, might be an important parameter to explain a sudden apparent friction decrease (the fluid goes out as the grains are expelled, which could not happen simultaneously with an incompressible fluid). We will thus consider situations at various permeabilities. The first codes, developed during the few months of postdoc of G Koval in incompressible fluids, will be extended (see Fig below for a snapshot of such code: the color code represents the pressure).

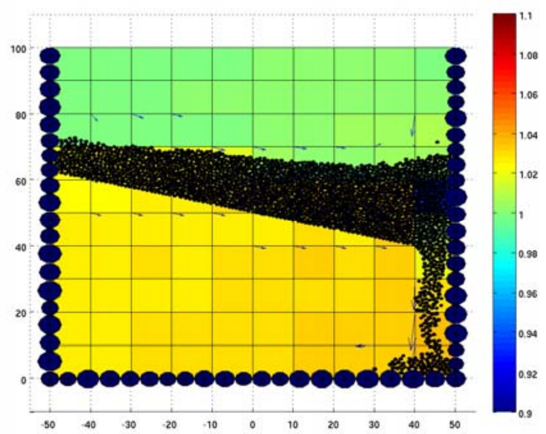

The triggers considered will be: accumulation of sediments or Tilt of slope, Rain and bottom fluid injection; Seismic trigger.
These four cases will be investigated to classify the behavior of the slope as function of its intial angle and compaction, and the characteristics of the loading mode.
If large granular and fluid Reynolds numbers are required to describe the liquefaction, we think of the possibility of extending the fluid part to a new Lattice Gas type of models based on current liquefied beds models [El Shamy].

We will also establish the exact connection between these granular/fluid models and the mixture theory used in mass flow community, as e.g. described by RM Iverson, notably by putting an effort into the translation of the ensemble of contact forces and computed overpressures, into total stresses, effective stresses and pore pressure. The relationship between the values of overpressure, and the drag force reated to pressure gradients, will b studied.

Eventually, these results will be compared to results of simulations of classical models in the geomechanics community: simulations using ABACUS or COMSOL (available at the laboratory) by A. Spikermann.

valorisation des résultats et exploitation des résultats / Data management, sharing and results exploitation

The results expected for this research program are :

A better understanding of the role of fluids, grains and heterogeneities in the dynamics of faults, and the formation of hydrofractures during fluid overpressures.

Topic 1 : we expect a numerical and experimental study of the hydrofracture process in a confined granular medium. The classification of hydrofracture regimes, as function of the control parameters (flux, applied fluid overpressure, shear, grain size, geometry of the embedding rock), and the study of the dynamics and resulting hydrofracture shape, should allow to better control this process and the resulting permeability channels. This is of primary importance, both for the technology associated to the stability of well boreholes, the use of hydrofractures to measure in situ stresses, and the industrial use of these techniques. This is also very important to understand the functioning of faults, which are commonly filled with gouges, and saturated in fluids.

The recording of microseismic data during these experiments will allow to establish a catalog to that can be usefully compared to those of field data.

Topic 2: we expect to develop and adapt a model of mixed flow for the hydrofracture and sheared saturated fault cases.

The confrontation of these models to experimental data will allow to adapt them gradually, in order to keep only the leading terms in the dynamic equations for the fluid and the solid part. The goal is to eventually validate the simplest models that can reproduce properly the patterns observed, and the pressures and rates of deformation observed.

The models developed, coupling fluid flow, solid frictional flow and elastic propagation in the boundaries, will be a quite versatile tool to apply it on many situations.

Concerning the comparison to large scale data, we expect to be able to estimate the impact of the complex geometry of natural faults and fractures on spatio-temporal scaling laws during the fracturing and friction processes. Experiments and numerical modelings of increasing complexity will be compared, and will also be compared to large scale INSAR data [Doubre and Peltzer 2007] that give information on the slow dynamics of active faults (The INSAR data provides a spatio-temporal observation of normal slip at the earth surface, displaying long range correlations both in time and space, that can be compared to the slip correlations in models at imposed shear rate via an elastic interface). This should make it possible to test these models, and in particular to test the influence of cohesion disorder asperities' geometry on the behavior of a fault. We then hope to be able to detect, in the seismic signal or the history of surface deformations, a quantifiable change in the state of stress on natural faults, which in turn can be translated into a quantitative evolution of earthquake hazard.

Topic 3: we expect to be able to investigate in some details the liquefaction process of a saturated debris flow, and thus to predict some characteristic observable, as an acceleration shape, pressure variation, microseismic acceleration or other observables than can be used in the geomorphology community to mitigate the risk of catastrophic liquefied mudslide.

Progress will be reported in peer-review international journals, such as Physical Review, Geophysical Review Letters, Journal of Geophysical Research; participation to conferences will be ensured.

Available equipment

Experimental platform of the experimental geophysics team at IPGS, with in particular a 32 channel full waveform, 50 MHz sampling rate, acoustic central machine (NI PXI streaming machine). A set of 8 piezoelectric sensors sensitive u the range 100 kHz-5 MHz is available.

Fast camera (1000 frames/second at 1.5 Mpixels)

Optical microscope

A computational cluster, 38 quadricore nodes with 8Go RAM per node, connected through Gigabit Ethernet network, is currently acquired and being installed at IPGS. A complementary demand (Mi Lourds INSU) to raise its RAM and connexion speed is under study.

Software for the analysis and representation of three dimensional structures, both for experimental data and numerical data, and Xray micro CT facility::
For the representation of three dimensional data issued from CT scans of the experiments, a visualization software is used. The CT scans will be performed at running cost in collaboration with Pr D. Koehn, from the University of Mainz. The vizualisation software, AMIRA, allows to represent accurately the density of localized density structures appearing during the experiments, when the cells are scanned after shearing.
It also allows to represent the three dimensional results of simulations in an efficient way.

Other developed research themes

Without developing the details of these research themes here, I plan to go on working on the following themes, on which I will present a few tracks in the following lines:

Multiphasic flow in deforming porous media: this theme, of utter importance in soil science and oil-related one, will be brought closer to the granular/fluid flow theme. Together the collaborators in LHYGES, with Laurence Jouniaux at IPGS, with collaborators in Lyon and Orsay and with the Oslo group, we plan to develop approaches allowing both the granular matrix to break irreversibly, i.e. the grains to move, and several fluids with interfacial tension to be present in the system. This should give rise to a whole new family of complex surface and crustal flows. This is important for applied environmental problems, as those to understand the efficiency of air sparging and soil cleaning by bubble injection. This is also essential to understand the release of CO2 , methane or trapped gas hydrates. This can happen both naturally, as in lakes, sediments or leaking reservoirs, or in exploitation, around boreholes. This can have both catastrophic consequences during instabilities (floodings, liquefaction, dam rupture…) or important costs-reduction consequences during exploitation.

Mechanico chemical couplings and stylolite formation and evolution:
We plan to pursue the modeling of the stylolite interface evolution, the associated deformation (compaction) and the associated modification of the transport paths (appearance of long range correlated stylolitic networks, playing both a role as longitudinal drains and transverse barriers). We plane to simulate numerically the solute transport in these systems to advance on this fascinating problem, and we also plan to use these systems to try to advance on the questions of the long time evolution of a reservoir during exploitation (heat, or other) or sequestration. This work will be performed in collaboration with the university of Mainz and with the university of Grenoble.

Fracture propagation: role of thermal versus quenched disorder
I will go on studying theoretically and numerically how finite temperature modifys fracture propagation in disordered media.

Heat exchange and flow in rough fractures – collaboration with Amélie Neuville, Oslo.

Avalanches and related seismic activity – experimental project, collaboration on the modeling with IPG Paris, Anne Mangeney.

Development of experimental deformation measurement techniques, CIV (correlation image velocimetry), PIV (particle image velocimetry), stereophotogrammetry (3D reconstruction of surfaces from sets of pictures).

Annexes

References of the proponent mentioned in this project

L. Goren, E. Aharonov, D. Sparks and R. Toussaint; ``Pore pressure evolution in deforming granular material: A general formulation and the infinitely stiff approximation, J. Geophys. Res., 115, B09216, 2010.

L. Goren, E. Aharonov, D. Sparks and R. Toussaint; ``The mechanical coupling of fluid-filled granular material under shear'', P.A.Geoph., 2011.

Ø. Johnsen, R. Toussaint, K.J. Måløy, E.G. Flekkøy and J. Schmittbuhl; ``Coupled air/granular flow in a linear Hele-Shaw cell'', Phys Rev E, 77,011301, 2008.

Ø. Johnsen, R. Toussaint, K.J. Måløy and E.G. Flekkøy; ``Pattern formation during central air injection into granular materials confined in a circular Hele-Shaw cell'', Phys. Rev. E, 74, 011301, 2006.

Ø. Johnsen, Christophe Chevalier, Renaud Toussaint, Anke Lindner, Knut Jørgen Måløy, Eric Clément, Eirik Grude Flekkøy, and Jean Schmittbuhl: "Fluidization of granular medium confined in a Hele –Shaw cell by injection of the interstitial fluid: oil or air." Phys.Rev.E, 2008

D. Koehn, F. Renard, R. Toussaint, C. Passchier, The development of stylolite teeth and their relation to stress and finite compaction, EPSL, 2007.

K.J. Måløy, S. Santucci, J, Schmittbuhl and R. Toussaint, Local Waiting Time Fluctuations along a Randomly Pinned Crack Front, Phys. Rev.Lett. **96**,045501 (2006).

M.J. Niebling, E.G. Flekkøy, K.J. Måløy, R. Toussaint; ``Mixing of a granular layer falling through a fluid'', Phys. Rev. E 82, 011301 (2010) doi: 10.1103/PhysRevE.82.011301

M.J. Niebling, E.G. Flekkøy, K.J. Måløy, R. Toussaint; ``Sedimentation instabilities: impact of the fluid compressibility and viscosity'', Phys. Rev. E 82, 051302, 2010. doi: 10.1103/PhysRevE.82.051302

S.R. Pride and R. Toussaint; ``Statistical mechanics of fiber bundles'', 2002, Physica A, 312, p 159-171, 2002.

S. Santucci, K.-J. Maloy, R. Toussaint & J. Schmittbuhl, in Dynamics of Complex Interconnected Biosensor Systems: Networks and Bioprocesses, edited by A. T. Skjeltorp (Kluwer, Amsterdam, 2006).

J. Schmittbuhl, A. Steyer, L. Jouniaux and R. Toussaint; ``Fracture morphology and viscous transport'', Int. J. Rock Mech. Min. Sci., 2007.

R. Toussaint and A. Hansen , ``Mean field theory of damage nucleation in the fuse model'', Phys. Rev. E, 73, 046103, 2006.

R. Toussaint and S.R. Pride, ``Statistical mechanics of quasistatic interacting damage models'', 2005, Phys. Rev. E, 71, 046127, 2005.

R. Toussaint and S.R. Pride; ``Fracture localization of disordered solids in compression as a critical phenomenon: III: Analysis of the localization transition'', Phys. Rev. E, 66, 036137, 2002.

R. Toussaint and S.R. Pride; ``Fracture localization of disordered solids in compression as a critical phenomenon: II: Model hamiltonian for a population of interacting cracks.'', Phys. Rev. E, 66, 036136, 2002.

R. Toussaint and S.R. Pride; ``Fracture localization of disordered solids in compression as a critical phenomenon: I. Statistical Mechanics Formalism.'', 2002, Phys. Rev. E, 66, 036135, 2002.

J.L. Vinningland, Ø. Johnsen, E.G. Flekkoy, R. Toussaint and K.J. Måløy; Experiments and Simulations of a gravitational granular flow instability, Phys. Rev. E, 76, 051306, 2007.

J.L. Vinningland, Ø Johnsen, E.G. Flekkøy, R. Toussaint and K.J. Måløy; ``A granular Rayleigh-Taylor instability: experiments and simulations'', Phys. Rev. Lett., 99, 048001, 2007.

J.L. Vinningland, Ø. Johnsen, E.G. Flekkøy, R. Toussaint and K.J. Måløy; ``Granular Rayleigh Taylor instability'', Proc. of the Traffic and Granular Flow conference, Orsay, 2007.

J.L. Vinningland, Ø. Johnsen, E.G. Flekkøy, R. Toussaint and K.J. Måløy; Influence of particle size in Rayleigh Taylor granular flow instability, , Phys. Rev. E 81, 041308 (2010). doi: 10.1103/PhysRevE.81.041308

References of other investigators, mentioned in this project :

D. Amitrano and J. Schmittbuhl. Fracture roughness and gouge distribution of a granite shear band. J. Geophys. Res., 107(B12):2375, doi:10.1029/2002JB001761, 2002.

Ancey, C., 2001. Debris flows and related phenomena. In Balmforth, N.J., Provenzale, A. (Eds): Geomorphological Fluid Mechanics, Springer-Verlag, Heidelberg, 528-547.

Anderson, S.A., Riemer, M.F., 1995. Collapse of saturated soil due to reduction in confinement. Journal of Geotechnical Engineering, American Society of Civil Engineers, 121(2), 216-220.

Aochi, H. and S. Ide, Importance of scale-dependent parameter on rupture dynamics and seismicity evolution during seismic cycle, submitted to Geophys. Res. Lett (2008).

Aranson, I. S. & Tsimring, L. S. *Patterns and collective behavior in granular media: Theoretical concepts* .Rev. Mod. Phys. **78**, 641-692 (2006).

Baum, R., Fleming, R.W., 1991. Use of longitudinal strain in identifying driving and resisting elements in landslides. Geological Society American Bulletin, 103, 1121-1131.

G. G. Batrouni, Alex Hansen, and J. Schmittbuhl. Heterogeneous interfacial failure between two elastic blocks. Phys. Rev. E, 65(03):61261-61267, 2002.

G.G. Batrouni, A. Hansen, and J. Schmittbuhl. In-plane roughness of brittle cracks. Int. J. Mod. Phys. B, 17(29):5631-5644, 2003. Phys. Rev. E, 68:011304, 2003.

Baxter, G.W., R. P. Behringer, T. Fagert and G. A. Johnson, *Pattern formation in flowing sand,* Phys. Rev. Lett. **62** 2825 (1989)

Been, K., Conlin, B.H., Crooks, J.H.A., Fitzpatrick, S.W., Jefferies, M.G., Rogers, B.T., Shinde, S., 1987. Back analysis of the Nerlerk berm liquefactions slides: discussion. Canadian Geotechnical Journal, 24, 170-179.

Ben-Zion Y, Rice JR, Earthquake failure sequences along a cellular fault zone in a 3-dimensional elastic solid containing asperity and nonasperity regions, *J. Geophys. Res.* 98 (B8): 14109-14131, 1993

Biot, M. A., Theory of propagation of elastic waves in a fluid-saturated porous solid, part I: low frequency range, *J. Acoust. Soc. Am.*, **28**, p. 168, and part II: higher frequency range, *ibidem,* p. 179, (1956).

R. Burridge et L. Knopoff, Model and theoretical seismicity, Bull. Seism. Soc. Am. 57, 341, 1967.

D. Bonn, H. Kellay, M. Ben Amar, and J. Meunier, *Viscous Finger widening with Surfactants and Polymers,* Phys. Rev. Lett.**75**, 2132 (1995).

J. M. Carlson and J. S. Langer, Properties of earthquakes generated by fault dynamics, Phys. Rev. Lett. 62, 2632, 1989

Carman, P., Fluid flow through granular beds, *Trans. Inst. Chem. Eng. Lond.*, **15**, p. 150 (1937).

Casagrande, A., 1971. On liquefaction phenomena, Report of Lecture to British Geotechnical Society, Geotechnique, 21(3), 197-202.

G. Chambon, J. Schmittbuhl, A. Corfdir, J.P. Vilotte, and S. Roux. Shear with comminution of a granular material: Microscopic deformations outside the shear band, Phys. Rev. E, 68, 011304, (2003).

G. Chambon, J. Schmittbuhl, and A. Corfdir. Frictional response of a thick gouge core: 1. mechanical measurements and microstructures. J. Geophys. Res., 111:10.1029/2003JB002731, (2006).

G. Chambon, J. Schmittbuhl, and A. Corfdir. Frictional response of a thick gouge core: 2. friction laws and implications for faults. J. Geophys. Res., 111:10.1029/2004JB003339, (2006).

Cheng, X. Xu, L., Patterson, A. Jaeger, H.M. & Nagel, S.R., *Towards the zero-surface tension limit in granular fingering instability,* Nature Physics, Letters (28 Jan 2008)

C. Chevalier, A. Lindner, and E. Clément, Destabilization of a Saffman-Taylor Fingerlike Pattern in a Granular Suspension, Phys. Rev. Lett. 99, 174501 (2007).

C. Chevalier, E. Clément et A. Lindner, Mobilization of a fully immersed dense granular matrix, to be submitted to Phys. Fluids (2008).

Chu, J., Leroueil, S., Leong, W.K., 2003. Unstable behaviour of sand and its implication for slope stability. Canadian Geotechnical Journal, 40, 873-885.

Dieterich J.H. and B.D. Kilgore, Imaging surface contacts: power law contact distributions and contact stresses in quartz, calcite, glass ad acrylic plastic, Tectonophysics, 256, 219-239, 1996.

Dieterich J.H., Modeling of Rock friction. 1. Experimental Results and Constitutive Equations. J. Geophys. Res. 84, 2161, 1979.

Doubre C., and Peltzer G (2007), Fluid-controlled faulting process in the Asal Rift, Djibouti, from 8 yr of radar interferometry observatiobs. Geology, 35, 69-72.

Eckersley, J.D., 1990. Instrumented laboratory flowslides. Geotechnique, 40, 489-502.

U. El Shamy and M. Zeghal. A micro-mechanical investigation of the dynamic response and liquefaction of saturated granular soils. Soil Dynamics and Earthquake Engineering, 27(8):712{729, 2007.

E. G. Flekkøy, K. J. Måløy, S. McNamara, and D. Gendron, *Structure formation and instability in bubbling granular tube-flow,* Phys. Rev.Lett. **87** p.134302 (2001).

E. G. Flekkøy, A. Malthe-Sørensen, and B. Jamtveit,, *Modeling Hydrofracture* 10.1029/2000JB000132 J. Geophys. Res. (2002).

Fleming, R.W., Ellen, S.D., Algus, M.A., 1989. Transformation of dilative and contractive landslide debris into debris flows: an example from Marin County, California. Engineering Geology, 27, 201-223.

Fletcher, J. B., and A. McGarr, Distribution of stress drop, stiffness, and fracture energy over earthquake rupture zones, J. Geophys. Res., 111, B03312, doi:10.1029/2004JB003396, 2006

Fuchu, D., Lee, C.F., Sijing, W., Yuong, F., 1999. Stress-strain behaviour of loosely compacted volcanic-derived soil and its significance to rainfall-induced fill slope failures. Engineering Geology, 53(3-4), 359-370.

G. Friesecke et J.A Wattis. Existence theorem for solitary waves on lattices, Commun. Math. Phys. 161, 391-418 (1994).

G. Friesecke et R.L. Pego. Solitary waves on FPU lattices : I. Qualitative properties, renormalization and continuum limit, Nonlinearity 12, 1601-1627 (1999).

G. Friesecke et K. Matthies. Atomic-scale localization of high-energy solitary waves on lattices. Physica D 171, 211-220 (2002).

G. Friesecke et R.L. Pego. Solitary waves on FPU lattices: II. Linear implies nonlinear stability, Nonlinearity 15, 1343-1359 (2002).

G. Friesecke et R.L. Pego. {Solitary waves on FPU lattices : III. Howland-type Floquet theory, Nonlinearity 17, 207-227 (2004).

G. Friesecke et R.L. Pego. Solitary waves on FPU lattices : IV. Proof of stability at low energy, Nonlinearity 17, 229-251 (2004).

J. Garnier et F.Kh. Abdullaev. Soliton dynamics in a random Toda chain, Phys. Rev. E 67, 026609 (2003).

D. Gendron, H. Troadec, K. J. Måløy and E. G. Flekkøy, *Bubbles in granular tube-flow*, Phys. Rev. E **64** 021509 (2001).

J. Giannoulis et A. Mielke. The nonlinear Schrödinger equation as a macroscopic limit for an oscillator chain with cubic nonlinearities, Nonlinearity 17, 551-565 (2004).

J. Giannoulis et A. Mielke. Dispersive evolution of pulses in oscillator chains with general interaction potentials, Discrete and Continuous Dynamical Systems B 6, 493-523 (2006).

Giusti, G. Iacarino, G., Pellegrino, A., Russo, C., Urcioli, G., Picarelli, L. 1996. Kinematic features of earthflows in Southern Apennines, Italy. Proceedings of the 7th International Symposium on Landslides, Trondheim, Balkema, 1, 457-462.

Y. N. Gordeyev, *Growth of crack by hydraulic fracture in a poroelastic medium,* Int. J. Rock Mech. Min. Sci. **30**, 233 (1993).

A. Hansen, G.G. Batrouni, T. Ramstad, and J. Schmittbuhl. Self-affinity in the gradient percolation problem. Phys. Rev. E, 75:030102, 2007.

A. Hansen, J. Schmittbuhl, G.G. Batrouni, , and F.A. De Oliveira. Normal stress distribution of rough surfaces in contact. Geophys. Res. Lett., 27:3639-3643, 2000.

A. Hansen and J. Schmittbuhl. Origin of the universal roughness exponent of brittle fracture surfaces: Stress-weighted percolation in the damage zone. Phys. Rev. Lett., 90:045505, 2003

Harp, E.W., Weels, W.G., Sarmiento, J.G., 1990. Pore pressure response during failure in soils. Geological Society of America Bulletin, 102(4), 428-438.

G. Iooss. Travelling waves in the Fermi-Pasta-Ulam lattice, Nonlinearity 13, 849-866 (2000).

G. Iooss et K. Kirchgässner. Travelling waves in a chain of coupled nonlinear oscillators, Commun. Math. Phys. 211, 439-464 (2000).

G.Iooss, D.Pelinovsky. Normal form for travelling kinks in discrete Klein-Gordon lattices. Physica D 216 (2006) 327-345.

Iverson, R.M., Reid, M.E., LaHusen, R.G., 1997. Debris flow mobilization from landslides. Annual Review of Earth and Planetary Sciences 25, 85-138.

Iverson, R.M., The Physics of Debris Flow, Reviews of Geophysics, 35, 3, 245, 1997

Jaeger, H. M., Nagel, S. R. & Behringer, *Granular solids, liquids, and gases,* .R. P. Rev. Mod. Phys. **68**, 1259-1273 (1996).

Johnson, A. M., 1970. Physical Processes in Geology. Freeman, New York, 577pp.

Johnson LR, Nadeau RM, Asperity model of an earthquake: Dynamic problem, BSSA 95 (1): 75, 2005.

L.A. Kalyakin. Long wave asymptotics. Integrable equations as asymptotic limits of non-linear systems., Russian Math. Surveys 44, n.1, 3-42 (1989).

E. Lemaire, Y. O. M. Abdelhaye, J. Larue, R. Benoit, P. Levitz and H. van Damme, *Pattern Formation in Noncohesive and Cohesive Granular Media* Fractals, Vol. **1**, No.4, 968-976 (1993).
Lee W.L., H. Kanomori, P. Jennings, and C. Kisslinger, International Handbook of Earthquake and Engineering Seismology, Academic Press, 2002
Linker, M.F. and J.H. Dieterich, Effects of variable normal stress on rock friction – observations and constitutive equations, J. Geophys. Res. B 97, 4923, 1992.
Lindner, A., Bonn, D., Poiré, E.C., Amer, M.B. & Meunier, *Viscous fingering in non-Newtonian fluids,* J. Fluid Mech. **469**, 237-256 (2002).
Malloggi, F., Lanuza, J., Andreotti, B. & Clement, E. *Erosion waves: transverse instabilities and fingering.* Europhys. Lett. 75 825-831
K.J. Måløy, J. Schmittbuhl, A. Hansen, and G.G. Batrouni. Scaling and dynamics of an interfacial crack front. Int. J. Fract., 121:9-22, 2003.
K.J. Måløy, J. Schmittbuhl, Phys. Rev. Lett. 87, 105502 (2001).
S. Mc Namara and E. G. Flekkøy and K.J. Måløy, *Grains and Gas flow: Molecular dynamics with hydrodynamic interactions*, Phys. Rev. E **61**, 4054 (2000).
Matsu'ura, M, Kataoka, H and B. Shibazaki, Slip-dependent friction law and nucleation process in earthquake rupture, *Tectonophysics*, 211, 135-148, 1992.
Miller, S. A., Y. Ben-Zion, and J.P. Burg (1999), A three-dimensional fluid-controlled earthquake model: Behavior and implications, *J. Geophys. Res.*, 104(B5), 10,621–10,638, 1999.
Mills, P. Cerasi and S. Fautrat, *Erosion Instability in a Non-consolidated porous Medium* P. Europhys. Lett. **29**, 215-220 (1995).
O'Hara K, Evaluation of asperity-scale temperature effects during seismic slip, J. Struct. Geol. 27 (10): 1892-1898 2005
Okura, Y., Kithahara, H., Ochiai, H., Sammori, T., Kawanami, A., 2002. Landslide fluidisation process by flume experiments. Engineering Geology, 66, 65-78.
Olivares, L., Damiano, E., Picarelli, L., 2003. Wetting and flume tests on volcanic ash. Proceedings of the International Conference on Fast Slope Movements, Prediction and Prevention for Risk Mitigation, Naples, Pàtron Editore, 399-404.
Olson, S.M., Starck, T.D., Walton, W.H., Castro, G., 2000. 1907 static liquefaction flow failure of the north dike of Wachusett dam. Journal of Geotechnical and Geoenvironmental Engineering, American Society of Civil Engineers, 126(12), 1184-1193.
Page, M. T., E. M. Dunham, and J. M. Carlson (2005), Distinguishing barriers and asperities in near-source ground motion, J. Geophys. Res., 110, B11302, doi:10.1029/2005JB003736.
Picarelli, L., Russo, C., Urcioli, G., 1995. Modelling earthflow movement based on experiences. Proceedings of the 11th European Conference on Soil Mechanics and Foundation Engineering, Copenhagen, Balkema, 6, 157-162.
Press, W. H., S. A. Teukolsky, W. T. Vetterling, and B. P. Flannery, *Numerical Recipes,* Cambridge Univ. Press, New York (1992).
Pyrak-Nolte L.J., The seismic response of fractures and the interrelations among fracture properties, Int. J. Rock Mech. Mining Sci., 33:8, 785-802, 1996.
Pyrak-Nolte, L.J., L. Myer and N.G.W. Cook, Transmission of seismic waves accross single natural fractures, J. Geophys. Res, 95(B6) 8617-8638, 1990.
Pinto, S. F., Couto, M. S. Atman, A. P. F. et al *Granular Fingers on Jammed Systems: New Fluidlike Patterns Arising in Grain-Grain Invasion Experiments.* Phys. Rev. Lett. **99**, 068001 (2007).
A. Ponno, D. Bambusi, Korteweg-de Vries equation and energy sharing in Fermi-Pasta-Ulam
Chaos 15 , 015107/1-5 (2005).
Ramanathan S and D. Fisher, Quasistatic crack propagation in heterogeneous media, Phys. Rev. Lett., 79, 873-876, 1997
Ramanathan S and D. Fisher, Onset of propagation of planar cracks in heterogeneous media, Phys. Rev. B, 58, 6026-6046, 1998
Rice, J. R., Heating and weakening of faults during earthquake slip, J. Geophys. Res., 111, B05311, doi:10.1029/2005JB004006 (2006).
Rice, J.R. and Ruina, A.L., Stability of Steady frictional slipping, J. Appl. Mech. 50, 343 (1983).
Ruina A., Slip instability and state variable friction law, J. Geophys. Res. 88,359 (1983).
Sasitharan, S., Robertson, P.K., Sego, D.C., Morgenstern, N.R., 1993. Collapse behaviour of sand. Canadian Geotechnical Journal, 30, 569-577.
Sassa, K., 1998. Mechanisms of landslide triggered debris flow. In Sassa, K. (ed.), Environmental Forest Science. Kluwer, Dordrecht, 471-490.

Savage, W.Z., Smith, W.K., 1986. A model for the plastic flow of landslides. US Geological Survey, Professional Paper, 1385, 32pp.
J. Schmittbuhl, A. Delaplace, K.J. Må lø y, H. Perfettini, and J.P. Vilotte. Slow crack propagation and slip correlations. PAGEOPH, 160(5-6):961-976, 2003.
J. Schmittbuhl, J.P. Vilotte, and S. Roux. Propagative macrodislocation modes in an earthquake fault model. Europhys. Lett., 21:375-380, 1993.
J. Schmittbuhl, S. Roux, J.P. Vilotte, and K.J. Måløy. Interfacial crack pinning: effect of non local interactions. Phys. Rev. Lett., 74:1787-1790, 1995.
J. Schmittbuhl, J.P. Vilotte, and S. Roux. Velocity weakening friction: A renormalisation approach. J. Geophys. Res., 101:13911-13917, 1996
J. Schmittbuhl, J.P. Vilotte, and S. Roux. A dissipation based analysis of an earthquake fault model. J. Geophys. Res., 101:27741-27764, 1996
J. Schmittbuhl and J.P. Vilotte. Interfacial crack front wandering: influence of correlated quenched noise. Physica A, 270:42-56, 1999.
J. Schmittbuhl, A. Hansen, and G.G. Batrouni. Roughness of interfacial crack front: Stress-weighted percolation in the damage zone. Phys. Rev. Lett., 90:045504, 2003.
Scholz, C. H. (2002), The Mechanics of Earthquake and Faulting, Cambridge Univ. Press, New York.
Schaff, D. P., G. H. R. Bokelmann, G. C. Beroza, F. Waldhauser, and W. L.Ellsworth (2002), High-resolution image of Calaveras Fault seismicity, J. Geophys. Res., 107(B9), 2186, doi:10.1029/2001JB000633.
G. Schneider et C.E. Wayne. Counter-propagating waves on fluid surfaces and the continuum limit of the Fermi-Pasta-Ulam model. Dans : B. Fiedler, K. Gröger et J. Sprekels, éditeurs, International Conference on Differential Equations Appl. 5, n.1, p.69-82 (1998).
Segall, P., and J. R. Rice (2006), Does shear heating of pore fluid contribute to earthquake nucleation?, J. Geophys. Res.,111, B09316, doi:10.1029/2005JB004129.
Sleep NH, Physical basis of evolution laws for rate and state friction, GEOCHEMISTRY GEOPHYSICS GEOSYSTEMS 6: Art. No. Q11008 NOV 15 2005
Sleep N.H., Frictional dilatancy, GEOCHEMISTRY GEOPHYSICS GEOSYSTEMS 7: Art. No. Q10008 OCT 11 2006 a
Sleep N.H., Real contacts and evolution laws for rate and state friction, GEOCHEMISTRY GEOPHYSICS GEOSYSTEMS 7: Art. No. Q08012 AUG 22 2006b
Smith, G.N., Smith, I.G.N., 1998. Elements of Soil Mechanics. Blackwell Science, Oxford, 494pp.
U.S. National Research Council, 1985. Liquefaction of soils during earthquakes. Committee on Earthquake Engineering, National Academy Press, Washington, 240p
Tanguy A, M. Gounelle and S. Roux, From individual to collective pinning : Effect of long-range elastic interactions, Phys. Rev. E, 58, 1577-1590, 1998.
Taylor, G. I. & Saffman, P. G.*The penetration of a fluid into a porous medium or Hele-Shaw cell containing a more viscous fluid.* Proc. R. Soc. A **245**, 312-329 (1958).
F. Tzschichholz, H.J. Herrmann, H.E. Roman and M. Pfuff, *Beam model for hydraulic fracturing*, Phys. Rev. B **49**, 7056--7059 (1994).
P. Valko and M. J. Econimedes, *Hydraulic Fracture Mechanics* John Wiley, New York (1995).
Van Damme, H., Lemaire, E., Abdelhaye, Y. O. M., Mourchid, A. & Levitz, P. *Pattern formation in particulate complex fluids: A guided tour. In Non-linearity and breakdown in soft condensed matter* (eds Bardhan, K. K., Chakrabarti, B. K. & Hansen, A.) (Springer, Berlin, 1993).
Wang, W.F., Sassa, K., 2003. Pore pressure generation and movement of rainfall induced landslides: effect of grain size and fine particle content. Engineering Geology, 69, 109-125.
Yoshimini, Y., Tanaka, K., Tokimatsu, K., 1989. Liquefaction resistance of partially saturated sand. Journal of Soil and Foundation Engineering, 29(3), 157-162.
K. Yoshimura et K. Arai, Phase reduction of stochastic limit cycle oscillators (2007), arXiv:0711.4653v1 [nlin.AO]
Yop, P., Forterre, Y. & Pouliquen, O., *A constitutive law for dense granular flows.* Nature **441**, 727-730 (2006).
A Ziv and J Schmittbuhl. Seismic cycle and the difference between foreshocks and aftershocks in a mechanical fault model. Geophys. Res. Lett., 30(24):2237, 2003.

Annexe : publications

11. Niebling, M.J., E.G. Flekkøy, K.J. Måløy, R. Toussaint,
Sedimentation instabilities: impact of the fluid compressibility and viscosity, Phys. Rev. E 82, 051302, 2010. doi: 10.1103/PhysRevE.82.051302 pdf P264

12. Vinningland, J.L., Ø. Johnsen, E.G. Flekkøy, R. Toussaint and K.J. Måløy,
Granular Rayleigh Taylor instability, Proc. of the 6th international conference on micromechanics of granular media, Powder and grains 2009, M. Nakagawa and S. Luding, eds, 2009. pdf P272

13. Vinningland, J.L., Ø. Johnsen, E.G. Flekkøy, R. Toussaint and K.J. Måløy,
Granular Rayleigh Taylor instability, Proc. of the Traffic and Granular Flow conference, 2007, Orsay, 2009. pdf P276

14. Vinningland, J.L., R. Toussaint, M. Niebling, E.G. Flekkøy and K.J. Måløy,
Family-Vicsek scaling of detachment fronts in Granular Rayleigh Taylor Instabilities during sedimenting granular/fluid flows, European Physics Journal Special Topics, 204(1):27-40, 2012. doi: 10.1140/epjst/e2012-01550-2 P286

I.iii Mécanique d'interfaces cisaillées et avalanches *300*

15. Altshuler, E., R. Toussaint, E. Martinez, O. Sotolongo-Costa, K.J. Måløy and J. Schmittbuhl,
Revolving rivers in sandpiles: from continuous to intermittent flows, Phys Rev E, 77, 031305 (2008). doi:org/10.1103/PhysRevE.77.031305 pdf P300

16. Goren, L., E. Aharonov, D. Sparks and R. Toussaint,
The mechanical coupling of fluid-filled granular material under shear, P.A.Geoph., 168, 12, 2011. doi: 10.1007/s00024-011-0320-4 P307

17. Goren, L., E. Aharonov, D. Sparks and R. Toussaint,
Pore pressure evolution in deforming granular material: A general formulation and the infinitely stiff approximation, J. Geophys. Res., 115, B09216, (2010).
doi:10.1029/2009JB007191 pdf P342

18. Travelletti, J., C. Delacourt, P. Allemand, J.-P. Malet, J. Schmittbuhl, R. Toussaint, M. Bastard,
Correlation of multi-temporal ground-based images for landslide monitoring: application, potential and limitations. ISPRS Journal of Photogrammetry and Remote Sensing 70, 39-55, 2012. doi: 10.1016/j.isprsjprs.2012.03.007 P361

19. Travelletti, J., Malet, J.P., Schmittbuhl, J., Toussaint, R., Bastard, M., Delacourt, C., Allemand, P. and van Dam, D.B.,
Multi-temporal terrestrial photogrammetry for landslide monitoring, Proc. of the Florence conference Mountain Risks: Bringing Science to Society, 2010. pdf P378

20. Travelletti, J., C. Delacourt, J.P. Malet, P. Allemand, J. Schmittbuhl, R. Toussaint,
Performance of image correlation techniques for landslide displacement monitoring, Proc. of the 2nd world landslide forum, Rome, 2011. pdf P387

21. Smith, S.A.F., F. Agosta, R. Toussaint, and R.E. Holdsworth,
Foreword to Special Issue: "Fault Zone Structure, Mechanics and Evolution in Nature and Experiment", Journal of Structural Geology, 45, 1-2, 2012. P395

22. Travelletti, J., J.P. Malet, J. Schmittbuhl, R. Toussaint, C. Delacourt, P. Allemand,,

Performance of image correlation techniques for landslide displacement monitoring, Proc. des Journées Aléas Gravitaires 2011, Strasbourg, A. Remaitre et J.P. Malet, eds.

23. Renaud Toussaint, Liran Goren, Einat Aharonov ,David Sparks, Michael Niebling, Eirik Flekkoy, KJ Maloy.,
Role des fluides dans les glissements de terrain, la liquefaction et la lubrification des failles: importance des forces de filtration en conditions drainees. Proceedings des Journees Aleas Gravitaires 2011, Strasbourg, A. Remaitre et J.P. Malet, eds.

24. Toussaint, R., K.J. Måløy, Y. Méheust, G. Løvoll, M. Jankov, G. Schäfer and J. Schmittbuhl,
Two-phase flow: structure and upscaling, consequences on macroscopic transport properties, Vadose Zone Journal, 11, vzj2011.0123, 2012. doi:10.2136/vzj2011.0123 HAL P397

25. Løvoll, G., Y. Méheust, R. Toussaint, J. Schmittbuhl and K.J. Måløy,
Growth activity during fingering in a porous Hele Shaw cell, Phys. Rev. E., 70, 026301 (2004). (cond-mat/0310204) pdf doi:10.1103/PhysRevE.70.026301 P406

26. Toussaint, R., G. Løvoll, Y. Méheust, K.J. Måløy and J. Schmittbuhl
Influence of pore-scale disorder on viscous fingering during drainage, Europhys. Lett., 71, 583 (2005). pdf, ps doi:10.1209/epl/i2005-10136-9 P418

27. Løvoll, G., M. Jankov, K.J. Måløy, R. Toussaint, J. Schmittbuhl, G. Schaefer and Y. Méheust,
Influence of viscous fingering on dynamic saturation-pressure curves in porous media, Transport in Porous Media, 86, 1, 305-324, 2010 DOI: 10.1007/s11242-010-9622-8 pdf P425

28. Jankov, M., G. Løvoll, H.A. Knudsen, K.J. Måløy, R. Planet, R. Toussaint and E.G. Flekkøy,
Effects of pressure perturbations on drainage in an elastic porous medium, Tr. in Porous Media, 84, 3, 569 (2010). doi: 10.1007/s11242-009-9521-z pdf P445

29. Tallakstad, K.T., H.A. Knudsen, T. Ramstad, G. Løvoll, K.J. Måløy, R. Toussaint and E.G. Flekkøy
Steady-state two-phase flow in porous media: statistics and transport properties, Phys. Rev. Lett. 102, 074502 (2009). doi:10.1103/PhysRevLett.102.074502 pdf P462

30. Yan, J., X. Luo, W. Wang, R. Toussaint, J. Schmittbuhl, G. Vasseur, A. Yu, Z. Likuan,
An experimental study of oil secondary migration in a three dimensional tilted porous medium, A.A.P.G. Bulletin, 96(5), 773-788 , 2012. doi: 10.1306/09091110140 P466

31. Yan, J., X. Luo, W. Wang, F. Chen, R. Toussaint, J. Schmittbuhl, G. Vasseur, Z. Likuan
Testing oil saturation distribution in migration paths using NMRI, Journal of Petroleum Science and Petroleum Engineering, 86-87, 237-245, 2012. doi: 10.1016/j.petrol.2012.03.027 P482

32. Nsir, K., G. Schäfer, R. Di Chiara Roupert, O. Razakarisoa, R. Toussaint,
Laboratory experiments on DNAPL gravity fingering in water-saturated porous media, Internat. J. of Multiphase Flow, 40, 83-92, 2012. doi: 10.1016/j.ijmultiphaseflow.2011.12.003 P491

33. K. Nsir, G. Schaefer, O. Razakarisoa, R. Toussaint, J. Schmittbuhl,

Approche expérimentale et numérique des instabilités de déplacement d'un DNAPL en milieu poreux saturé à l'échelle de Darcy, Actes du 19ème Congrès Franc ais de mécanique, Marseille, 2009. pdf P501

34. K.Nsir, G. Schäfer, O. Razakarisoa, R. D. Roupert, R. Toussaint,
Etude expérimentale et simulation numérique à l'échelle de pore des instabilités de déplacement d'un DNAPL en milieu poreux saturé à l'échelle de Darcy. Acte de la 10ième Journée d'Etude sur les Milieux Poreux. 2010. (Conférence, session Suivi de front-Instabilités de 10ième Journées d'Etude sur les Milieux Poreux, Nancy, 20 -21 Octobre 2010.)

35. Neuville, A., R. Toussaint, J. Schmittbuhl, D. Koehn and J.O. Schwarz,
Characterization of major discontinuities from borehole cores of located in the black consolidated marl formation of Draix, Hydrological Processes, 26, 14, 2085-2094, 2012. doi: 10.1002/hyp.7984 pdf P507

36. Neuville, A., R. Toussaint, J. Schmittbuhl,
Fracture aperture reconstruction and determination of hydrological properties: a case study at Draix (French Alps), Hydrological Processes, 26, 14, 2095-2105, 2012. doi: 10.1002/hyp.7985 pdf P519

37. Neuville, A., R. Toussaint and J. Schmittbuhl,
Hydrothermal flows in a rough fracture, Phys. Rev. E, 82, 3, 2010. doi: 10.1103/PhysRevE.82.036317 pdf P528

38. Neuville, A., R. Toussaint and J. Schmittbuhl,
Hydraulic transmissivity and heat exchange efficiency of rough fractures: a spectral approach , Geoph. J. Int., 186, 1064, 2011. doi: 10.1111/j.1365-246X.2011.05126.x
P542

39. Neuville, A., R. Toussaint and J. Schmittbuhl,
Fracture roughness and thermal exchange: a case study at Soultz-sous-Forets, C.R.A.S. Geoscience, 342, 616 (2009). doi:10.1016/j.crte.2009.03.006 pdf P551

40. Neuville, A., R. Toussaint and J. Schmittbuhl,
Effects of the roughness of a fracture on thermal exchange, Proc. of the EDHRA (European Hot Dry Rock Association) scientific conference, Soultz-sous-Forêts, 2008. pdf P562

41. Schmittbuhl, J., A. Steyer, L. Jouniaux and R. Toussaint,
Fracture morphology and viscous transport, Int. J. Rock Mech. Min. Sci., 45, 422 (2007). pdf doi:10.1016/j.ijrmms.2007.07.007 P570

42. Neuville, A., R. Toussaint and J. Schmittbuhl,
Hydrothermal flow in a rough fracture, Proc. of the EDHRA (European Hot Dry Rock Association) scientific conference, Soultz-sous-Forêts, 2006. pdf P579

43. Neuville, A., Flekkoy, E.G., Maloy, K.J., Toussaint, R., Schmittbuhl, J.,
Hydrothermal exchange in an open, rough fracture, Proceedings from Kickoff, Complex Matter Physics, Center for Advanced Study, eds: Jon Otto Fossum, Tom Henning Johansen and Pavlo Mikheenko, September 26, 2011, CAS, Oslo, Norway

44. Toussaint, R. and S.R. Pride,
Fracture localization of disordered solids in compression as a critical phenomenon: I. Statistical Mechanics Formalism., Phys. Rev. E, 66, 036135 (2002). (cond-mat/0209124). pdf doi:10.1103/PhysRevE.66.036135 P582

45. Toussaint, R. and S.R. Pride,
Fracture localization of disordered solids in compression as a critical phenomenon: II: Model hamiltonian for a population of interacting cracks., Phys. Rev. E, 66, 036136 (2002). (cond-mat/0209127). pdf doi:10.1103/PhysRevE.66.036136 P592

46. Toussaint, R. and S.R. Pride,
Fracture localization of disordered solids in compression as a critical phenomenon: III: Analysis of the localization transition, Phys. Rev. E, 66, 036137 (2002). (cond-mat/0209129). pdf doi:10.1103/PhysRevE.66.036137 P601

47. Pride, S.R. and R. Toussaint,
Statistical mechanics of fiber bundles, Physica A, 312, 159 (2002). (condmat/0209131) pdf doi:10.1016/S0378-4371(02)00816-6 P612

48. Toussaint R. and S.R. Pride
Interacting damage models mapped onto Ising and percolation models, Phys. Rev. E, 71, 046127 (2005). (condmat/0403412) pdf doi:10.1103/PhysRevE.71.046127 P625

49. Toussaint, R.
Statistical mechanics of interacting fiber bundles, Proc. of the ICF11, 11th International Conference on Fracture, Torino, 2005. pdf proceedings P640

50. Toussaint R. and A. Hansen
Mean field theory of damage nucleation in the fuse model, Phys. Rev. E, 73, 046103 (2006). (condmat/0403217) pdf, ps doi:10.1103/PhysRevE.73.046103 P646

51. Måløy, K.J., S. Santucci, J. Schmittbuhl and R. Toussaint
Local waiting time fluctuations along a randomly pinned crack front, Phys. Rev. Lett., 96, 045501 (2006). pdf, ps doi:10.1103/PhysRevLett.96.045501 P661

52. Santucci, S., K.J. Måløy, R. Toussaint, and J. Schmittbuhl,
"Self affine scaling during interfacial crack front propagation", in ``Dynamics of Complex Interconnected Systems: Networks and Bioprocesses", NATO ASI series, edited by A.T. Skjeltorp , Kluwer, Dordrecht, 2006. pdf, ps P665

53. Pindra, N., V. Lazarus , J.B. Leblond, J. Schmittbuhl and R. Toussaint,
Deformation of the crack front during propagation in some disordered medium: theoretical and experimental studies, Proc. of the ICF12, 12th International Conference on Fracture, Ottawa, 2009. pdf P676

54. Santucci, S., M. Grob, R. Toussaint, K.J. Måløy, A. Hansen, and J. Schmittbuhl,
Crackling dynamics during the failure of heterogeneous material: Optical and acoustic tracking of slow interfacial crack growth, Proc. of the ICF12, 12th International Conference on Fracture, Ottawa, 2009. pdf P685

55. Grob, M., J. Schmittbuhl, R. Toussaint, L. Rivera, S. Santucci and K.J. Måløy,

Quake catalogs from an optical monitoring of an interfacial crack propagation, P.A.Geoph., 166, 777 (2009).doi:10.1007/s00024-004-0496-z pdf P695

56. Santucci, S., M. Grob, R. Toussaint, J. Schmittbuhl, A. Hansen and K.J. Måløy,
Fracture roughness scaling: A case study on planar cracks, Europhys. Lett., 92, 4, 44001, 2010. DOI: 10.1209/0295-5075/92/44001 pdf P718

57. Tallakstad, K.T., R. Toussaint, S. Santucci, J. Schmittbuhl, K.J. Måløy,
Local dynamics of a randomly pinned crack front during creep and forced propagation: an experimental study, Phys. Rev. E, 83, 046108, 2011. doi: 10.1103/PhysRevE.83.046108 P723

58. Tallakstad, K.T., R. Toussaint, S. Santucci, and K. J. Måløy,
Non Gaussian fluctuations of crack front velocity, Proc. of Soft Matter & Complex Flow congress, Lofoten, Norway, accepted, 2012. P738

59. Tallakstad, K.T., R. Toussaint, S. Santucci, and K. J. Måløy,
The non-Gaussian nature of fracture and the survival of fat-tail exponents, Phys. Rev. Lett., 2013. P744

60. Lengline, O., J. Elkhoury, G. Daniel, J. Schmittbuhl, R. Toussaint, J.-P. Ampuero, M. Bouchon
Interplay of seismic and aseismic deformations during earthquake swarms: an experimental approach, Earth and Planetary Science Letters, 331-332, 215-223, 2012. doi: 10.1016/j.epsl.2012.03.022 P752

61. Lengliné O., J. Schmittbuhl, J. Elkhoury, J.P. Ampuero, R. Toussaint and K.J. Måløy,
Down-scaling of the fracture energy during brittle creep experiments, J. Geoph. Res. B, 116, B0815, 2011. doi: 10.1029/2010JB008059 P760

62. Måløy, K.J., R. Toussaint and J. Schmittbuhl
Dynamics and structure of interfacial crack fronts, Proc. of the ICF11, 11th International Conference on Fracture, Torino, 2005. pdf proceedings P774

63. Lengliné, O., R. Toussaint, J. Schmittbuhl, J. Elkhoury, J.P. Ampuero, K.T. Tallakstad, S. Santucci and K.J. Måløy,
Average crack front velocity during subcritical fracture propagation in a heterogeneous medium, Phys. Rev. E, 84, 6104, 2011. doi: 10.1103/PhysRevE.84.036104 P780

64. Koehn, D., Ebner, M., Renard, F., Toussaint, R., Passchier, C.W.,
Modelling of stylolite geometries and stress scaling, Earth and Planetary Science Letters, 341-343, 104-113, 2012. doi: 10.1016/j.epsl.2012.04.046 P793

65. Rolland, A., R. Toussaint, P. Baud, J. Schmittbuhl, N. Conil, D. Koehn, F. Renard and J.P. Gratier,
Modeling the growth of stylolites in sedimentary rocks, J. Geoph. Res., 117(6), B06403, 2012. doi: 10.1029/2011JB009065 P803

66. Koehn, D., F. Renard, R. Toussaint, C. Passchier
Growth of stylolite teeth patterns depending on normal stress and finite compaction, EPSL, 257, 582 (2007). pdf doi:10.1016/j.epsl.2007.03.015 P821

67. Schmittbuhl, J., F. Renard, J.P. Gratier and R. Toussaint

Roughness of stylolites: Implications of 3D high resolution topography measurements , Phys. Rev. Lett., 93, 238501 (2004). pdf doi:10.1103/PhysRevLett.93.238501 P835

68. Ebner, M., D. Koehn, R. Toussaint, F. Renard and J. Schmittbuhl,
Stress sensitivity of stylolite morphology, EPSL, 277, 394 (2009).
doi:10.1016/j.epsl.2008.11.001 pdf P839

69. Ebner, M., D. Koehn, R. Toussaint and F. Renard,
The influence of rock heterogeneity on the scaling properties of simulated and natural stylolites, J. Struct. Geol., 31, 72 (2009). doi:10.1016/j.jsg.2008.10.004 pdf P844

70. Ebner, M., R. Toussaint, J. Schmittbuhl, D. Koehn and P. Bons,
Anisotropic scaling of tectonic stylolites: a fossilized signature of the stress field? , J. Geophys. Res., 115, B06403, (2010). doi:10.1029/2009JB006649 pdf P855

71. Laronne Ben-Itzhak, L., E. Aharonov, R. Toussaint and A. Sagy,
Upper bound on stylolite roughness as indicator for the duration and amount of dissolution, Earth and Planetary Science Letters, 337-338, 186-196, 2012. doi: 10.1016/j.epsl.2012.05.026
P871

72. Bonnetier, E., C. Misbah, F. Renard, R. Toussaint and J.P. Gratier,
Does roughening of rock-fluid-rock interfaces emerge from a stress-induced instability? European Phys. J. B., 67, 121 (2009). doi:10.1140/epjb/e2009-00002-2 pdf P882

73. Toussaint, R., G. Helgesen and E.G. Flekkøy
Dynamic roughening and fluctuations of dipolar chains, Phys. Rev. Lett., 93, 108304 (2004). (cond-mat/0311340) pdf doi:10.1103/PhysRevLett.93.108304 P893

74. Toussaint, R., E.G. Flekkøy, and G. Helgesen,
The memory of fluctuating brownian dipolar chains, Phys. Rev. E, 74, 051405 (2006). pdf doi:10.1103/PhysRevE.74.051405 P897

75. Toussaint, R., J. Akselvoll, E.G. Flekkøy, G. Helgesen and A.T. Skjeltorp,
Interaction model for nonmagnetic holes in a ferrofluid layer, 2004, Phys. Rev. E 69, 011407 (2004). (cond-mat/0304683). pdf doi:10.1103/PhysRevE.69.011407 P910

76. Toussaint, R., J. Akselvoll, G. Helgesen, E.G. Flekkøy and A.T. Skjeltorp,
Interactions of magnetic holes in ferrofluid layers, Progress in Colloid and Polymer Science, 128, 151 (2004). pdf link doi:10.1007/b12355 P925

77. Skjeltorp, A.T., J. Akselvoll, K.d.L. Kristiansen, G. Helgesen, R. Toussaint, E.G. Flekkøy, and J. Cernak; ``Self-assembly and dynamics of magnetic holes'', in ``Forces, growth and form in soft condensed matter: at the interface between physics and biology'', NATO ASI series, edited by A.T. Skjeltorp and A.V. Belushkin; Kluwer, Dordrecht, 2004. pdf P930

Ouvrages:

78. Manuscrit de thèse de doctorat
"Rock fracture during compression: the localization process as a critical phenomenon". site

79. Manuscrit de thèse, format livre

Fracturation des roches: la localisation comme phénomène critique. Editions Universitaires Européennes, 2012. ISBN-13 978-3-8417-9391-1, ISBN-10:3841793916
http://www.morebooks.fr

Articles soumis, en révision :

80. Neuville, A., E.G. Flekkøy, and R. Toussaint,
Influence of asperities on fluid and thermal flow in a fracture: a coupled Lattice Boltzmann study, submitted to JGR B, 2013.

81. A. Spickermann, R. Toussaint, J. Travelletti, J.-P. Malet, Th.W.J. van Asch,
A grain-fluid mixture model to characterize the dynamics of active landslides in fine-grained soils, submitted to J.G.R. E, 2013.

82. Allègre, V., F. Lehmann, L. Jouniaux, P. Sailhac, and R. Toussaint
Modelling the streaming potential dependence on water-content during drainage: Influence of pressure dynamics and fluid flow, submitted to T.I.P.M., 2013.

83. Aochi, H., B. Poisson, R. Toussaint, X. Rachez and J. Schmittbuhl,
The impact of spatial and temporal changes in fault characteristics on induced seismicity due to fluid circulation, submitted to Geoph. J. Int., 2013.

84. Laronne Ben-Itzhak, L., E. Aharonov, Z. Karcz, M. Kaduri and R. Toussaint,
Sedimentary stylolite populations in Limestone: Large-scale field observations and implications for structure evolution, submitted to Journal of Structural Geology, 2013.

85. Rolland, A., R. Toussaint, P. Baud, N. Conil and P. Landrein,
Morphological analysis of stylolites for paleostress estimation in limestones surrounding the Andra Underground Research Laboratory site, submitted to Int. J. Rock Mech. Min. Sci., 2013.

86. Lengliné, O., J. Schmittbuhl, K.J. Måløy, A. Cochard and R. Toussaint,
A brittle creep model of interfacial crack propagation, submitted to Physical Review Letters, 2013.

87. Vasseur, G., Luo, X., Yan, J., Loggia, D., Schmittbuhl, J. and Toussaint, R.
Flow regime associated with secondary migration, submitted to Journal of Marine and Petroleum Geology, 2013.

Pattern formation during air injection into granular materials confined in a circular Hele-Shaw cell

Ø. Johnsen,[1] R. Toussaint,[1,2] K. J. Måløy,[1] and E. G. Flekkøy[1]
[1]*Department of Physics, University of Oslo, P.O. Box 1048 Blindern, 0316 Oslo, Norway*
[2]*IPGS University Louis Pasteur of Strasbourg, France*
(Received 23 October 2005; published 11 July 2006)

We investigate the dynamics of granular materials confined in a radial Hele-Shaw cell, during central air injection. The behavior of this granular system, driven by its interstitial fluid, is studied both experimentally and numerically. This allows us to explore the associated pattern formation process, characterize its features and dynamics. We classify different hydrodynamic regimes as function of the injection pressure. The numerical model takes into account the interactions between the granular material and the interstitial fluid, as well as the solid-solid interactions between the grains and the confining plates. Numerical and experimental results are comparable, both to reproduce the hydrodynamical regimes experimentally observed, as well as the dynamical features associated to fingering and compacting.

DOI: 10.1103/PhysRevE.74.011301 PACS number(s): 81.05.Rm, 47.11.−j, 83.50.−v

I. INTRODUCTION

We have studied pattern formations during air injection in a granular material confined in a radial Hele-Shaw cell [1] and have characterized and quantified the features of the granular pattern formations and the associated dynamic processes.

The dry porous matrix is loosely packed inside the cell, and the particles are able to move together with the fluid phase. The origin of the instability is similar to what was described by Saffmann and Taylor [2]. The pressure gradient in the fluid is the driving force of the granular motion. The pressure is more or less constant within a central grainless region, and the driving pressure gradient is largest at the tip of the longest finger of this structure. According to Darcy's law [3], the fluid flow and the fluid drag is highest at the tips, so that the growth of the most advanced finger is favored at the expense of the rest of the structure. The stabilizing mechanism, on the other hand, is *not* surface tension as in the classical Saffmann-Taylor system, but friction mobilized between the granular material and the confining plates. The resulting patterns observed are either uniform, almost circularly shaped patterns or branched finger patterns, depending on the injection pressure.

We are dealing with a coupled fluid-grain flow where the grains are small and gas-grain interactions are of central importance. Such interactions play a key role in a wide range of systems from fluidized beds [4–7] to flow in tubes [8–13], and ticking hour glasses [14,15].

A system similar to ours, wherein a fluid invades a confined granular material, was studied experimentally by van Damme *et al.* [16] in 1993. In contrast to that study, ours involves quantitative measurements and comparison with simulations. In the situation wherein a fluid is retracted from a confined nonconsolidated porous medium, several hydrodynamic regimes have also been reported [17,18].

Other systems with general similarities and important geological aspects to it include those of multiphase flow in porous media [19–39]. The pattern formations and instabilities that we observe in our system bear resemblance to those seen in Hele-Shaw cell experiments using both Newtonian [2,40–42] and non-Newtonian fluids [43–46]. In the non-Newtonian case a transition from a viscous fingering regime to a viscoelastic fracturing regime [47,48] has been observed. The difference between these studies and the present one is that our structures depend entirely on the existence of static and sliding friction.

Like the viscoelastic fracture experiments our system can provide insight into the underlying physics of geological hydrofracture processes [49–53]. However, while fracture in viscoelastic media involves separated fluids, the experiment involve interpenetrating phases, and there is an effect of pressure diffusion of the air through the grain packing that has no analog in the viscoelastic systems. Unlike our system of nonconsolidated grains, viscoelastic fracturing and hydraulic fracturing of solids have been previously studied by numerical simulations [54–57].

This article is organized as follows: in Sec. II, the experimental model, setup, and sample preparation are described. In Sec. III, we give a classification of the observed pressure regimes and discuss the underlying physics. In Sec. IV, we present our simulation model and basic equations used in the algorithm. In Sec. V, the classification of the different regimes is recovered in the simulations. We then turn to quantitative measures on our system in Sec. VI before concluding and summarizing in Sec. VII.

II. SYSTEM DESCRIPTION

The system consists of a horizontally fixed circular Hele-Shaw cell [1] 0.45 m in diameter, separated with 1 mm ball bearing beads, and then clamped together at three points. The injection hole is 6 mm in diameter. The granular material, consists of polydisperse spherical glass beads, with diameters between 75–150 μm. Beads of this size are sensitive to the humidity of the ambient air; excessive humidity creates capillary bridges between the particles making the material more cohesive, while at a too low humidity the electrostatic forces make them stick together. The relative humidity in the

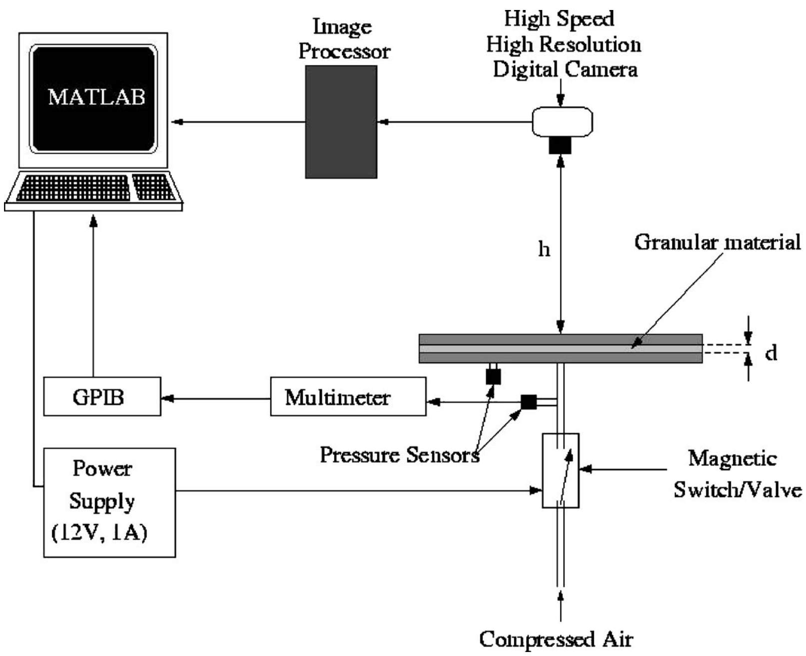

FIG. 1. Experimental setup: The horizontally fixed Hele-Shaw cell is connected to a pressure source. A high-speed, high-resolution CCD camera is used to follow the development of the displacement pattern and the pressure is read at the inlet and in the middle of the sample. Air is injected at constant overpressure in the center of the cell when the magnetic valve is triggered to open, and a displacement pattern appears.

room is therefore controlled at approximately 30% using a humidifier/dehumidifier.

Filling the Hele-Shaw cell homogeneously with powder is not an easy and straightforward task, and might be realized in many different ways. In order to have a loosely packed granular layer as homogeneous as possible, and to optimize the reproducibility of the initial state, we have developed the following filling procedure: We keep the cell in an upright position, close the bottom boundary, and let the particles rain down continuously over the system width using a guide, instead of filling from a point, which gives texture of different density due to avalanches around the angle of repose. The particles are packed under gravity when held vertically and the Janssen effect contributes to making the granular packing density homogeneous [58].

The cell is placed in a horizontal position after it is filled, the side boundary is opened, and the air inlet is connected to a gravitationally driven pressure control device. Two Honeywell 26PCAFA6G pressure sensors records the pressure at the inlet and in the middle of the cell. At the same time as the pressure recording is started, images are taken every 1/250 s using a Redlake MotionPro high-speed CCD camera with spatial resolution of 1280×1280. Central injection of air into the model is triggered by switching a magnetic valve open, 1 s after the image and the pressure recording is initiated. Figure 1 shows a simple sketch of the experimental setup.

III. CLASSIFICATION OF OBSERVED REGIMES

A. Phenomenology

The characteristics of the pattern formation changes with the injection pressure. At threshold values for the injection pressure there are sharp transitions from one situation to the other. By tuning the injection pressure in small steps, we find pressure thresholds that separate four pressure regimes.

1. The first pressure regime: $\Delta P < P_1$

When the injection pressure ΔP is smaller than P_1 no pattern will form in the granular material. The pressure is not high enough to displace particles, so that the injected air just permeates through the pores of the granular layer. Below this threshold we define *the first pressure regime*. Given the conditions for our experimental configuration, $P_1\approx 0.20$ kPa will be the lower threshold for pattern formation.

Note that although the granular velocity is zero in this situation, the fluid velocity is finite. As can be established by flux measurements or by pressure measurements and by use of the Darcy law, the typical air velocity decays radially from around 30 mm s^{-1} along the injection zone to 0.4 mm s^{-1} close to the outer boundary, for $\Delta P \sim P_1$.

2. The second pressure regime: $P_1 < \Delta P < P_2$

For injection pressures $P_1 < \Delta P < P_2$, defined as the *second pressure regime*, the particles are pushed outwards, leaving a relatively small and quite circular pattern with no grains, as shown in Fig. 2. Experimentally, we find the lower threshold for pattern formation to be $P_1 \approx 0.20$ kPa and the upper threshold for this regime $P_2 = 1.90 \pm 0.1$ kPa. The emptied structure is typically stabilized after $\sim$0.1 s. The size of the structure increases with increasing pressure.

As the emptied structure grows, the material ahead of the structure compactifies over a depth dependent on the size of the structure. With sufficiently high spatial resolution, this zone can be found using image analysis. By subtracting, pixel by pixel, the image at a given time from an image taken before gas injection, we can detect minute motions of grains. By thresholding this subtraction image, there is a well-defined densely speckled region, like a halo, around the emptied zone. By performing noise averaging on the difference image, we can detect the front of the compacted region. An example of this front is inserted onto the image from the experiment in Fig. 2.

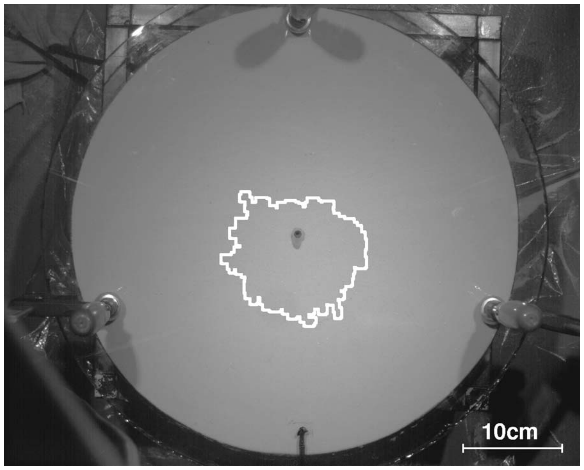

FIG. 2. A picture of a fully developed structure within the second pressure regime at injection pressure $\Delta P = 1.26$ kPa. Ahead of the emptied region there is a zone where the material is compacted, shown by the white line.

The more or less circular uniform structures, which are empty of grains in the second regime, are observed up to $\Delta P \approx 2.00$ kPa, at which point the structure becomes unstable.

This circular symmetry breaking is quantitatively identified as follows: The boundary of the final empty region has radial coordinates bounded by $r_{\min}$ and $r_{\max}$. When $r_{\max}/r_{\min} > 2$, the pattern is classified as characteristic of the third pressure regime.

3. The third pressure regime: $P_2 < \Delta P < P_3$

Between P_2 and P_3, an instability in the displacement process becomes significant, and a finger pattern very similar to those seen for invasion in non-Newtonian fluids starts developing (cf. Fig. 3). We find $P_2 = 1.90 \pm 0.1$ kPa and $P_3 = 2.40 \pm 0.1$ kPa. The structure typically ceases to grow and stabilizes by ~ 0.1 s after initiation. The instability over the front appears as branched fingers. The number of fingers at a given pressure is variable among different experiments. This can be attributed to a strong sensitivity to the details of the initial state. However, a noticeable trend is that the structure develops more in the direction along which the particles were poured into the cell.

During filling, the cell is held vertically and the particles are packed under gravity, which results in the friction between the granular layer and the confining plates being polarized in the opposite direction of the gravity field [58]. Correspondingly, there will be an anisotropy in the granular stress, which may explain the direction of the displacement pattern.

As the cell is filled the weight on the bottom particles also becomes slightly higher than the case is at the top, resulting in a slightly higher density and higher normal stress acting on the confining plates. Particles in the upper part of the cell may therefore be pushed and compacted more easily. This might also contribute to a preferred directionality opposite to gravity during filling, though the Janssen effect [58] will restrict the influence of this feature.

(a)

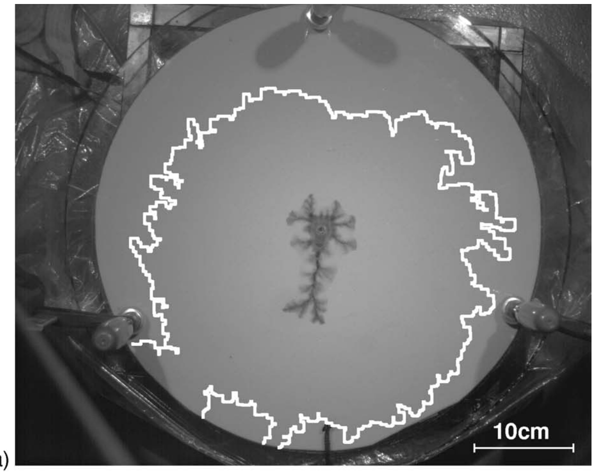

(b)

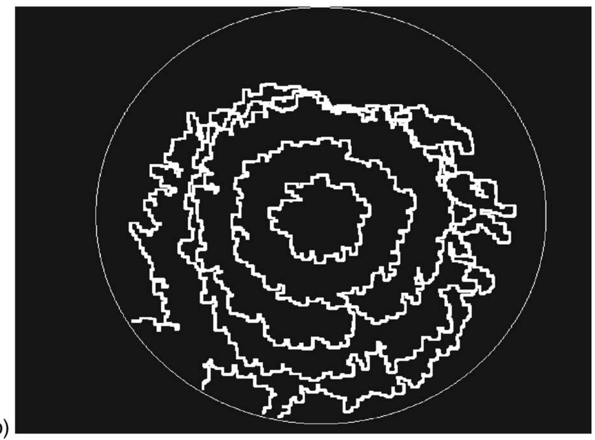

FIG. 3. (a) Displacement pattern at $\Delta P = 2.34$ kPa, in the third pressure regime. The front of the compacted region is indicated with a white colored line. The short black line at the bottom of the image shows the direction of the particle motion during filling of the cell. (b) The front of the compacted region at $t = 0.008$ s, $t = 0.020$ s, $t = 0.080$ s, $t = 0.480$ s, and $t = 0.800$ s after injection.

When increasing the pressure, the empty and compacted structures get bigger. We follow the development of the compacted front in Fig. 3(b). The radial velocity of the front is large immediately after injection starts, but the growth rate of the emptied structure decreases due to the increasing in-plane friction.

There is a crossover between regimes 2 and 3 for pressures 1.80 kPa $< \Delta P <$ 2.00 kPa. In this pressure interval one usually obtain a circular structure, but sometimes a branched structure. For pressures above 2.00 kPa, on the other hand, unstable structures are always observed, and we therefore use this value to define the crossover. We believe that this crossover has to do with the sample preparations where the granular packing cannot be duplicated from experiment to experiment.

Ahead of the longest finger, the compacted region may reach all the way up to the open boundary before it stops evolving. When this is the case, we are close to the border between the third and the fourth pressure regime.

4. The fourth pressure regime: $\Delta P > P_3$

If we exceed P_3, which in our case is $P_3 = 2.40 \pm 0.1$ kPa, the empty finger formation breaks through the granular packing, creating an eroded channel from the inlet to the external boundary.

A finger structure similar to those seen for the higher pressures in the third regime forms in the order of a tenth of a second. The front slows down a little before the most advanced finger accelerates toward breakthrough of the external boundary. As it accelerates, the air flow erodes the interior of the advancing finger. When we have a finger leading from the injection point to the open boundary, the pressure within the emptied region cannot be maintained with this pressure source, and then the rest of the structure will not be able to grow any further. The breakthrough finger "chooses" the direction where the particles were poured into the cell. At very high pressures, typically ~4.00 kPa and higher, it is not unusual to have more than one finger breaking through the granular material.

Between pressure regimes 3 and 4, in the interval 2.30 kPa $< \Delta P <$ 2.50 kPa, we occasionally have a finger breaking through, but this is not systematic.

B. Physical discussion

The origin of the instability is similar to what was described by Saffmann and Taylor [2]. The pressure gradient, ∇P is the driving force of the granular motion and the pressure field in the system is described by Darcy's law [3]. Within the fingers, the permeability is huge compared to the one in the pore space of the granular material, which will favor air flow in the emptied region. The pressure is more or less constant within the emptied structure and the driving pressure gradient $\nabla P = \Delta P / l$ is largest at the tip of the longest finger since here the distance l from the tip to the open boundary is the smallest. Growth of the most advanced finger is therefore favored at the expense of the rest of the structure.

As the granular bulk is pushed upon, particles are displaced and rearranged in such a way that the granular material is compacted in a zone around the emptied structure, as indicated in Figs. 2–4. When granular motion is induced, the in-plane forces on the grains will cause a granular pressure to act in the transverse directions as well, as is illustrated in Fig. 5. The "induced" granular force acting perpendicular on the upper plate will be denoted as $P_g^{\perp}$. On the bottom plate there will also be a rather small contribution from gravity, $\rho g d$, where g is gravity, d the plate spacing, and ρ is the mass density of the porous medium, i.e., $\rho = \rho_s \rho_g$ with ρ_g the mass density of the particles themselves, and ρ_s the local solid fraction.

The mobilized friction force per unit surface is described by a Coulomb friction model, i.e., it opposes the granular motion, and it is bounded by a Coulomb friction coefficient γ, times the normal pressure exerted by the grains. The friction force exerted by the top and bottom plate are respectively denoted F_γ^1 and F_γ^2, and the total friction force exerted by both plates over the local granular column is $F_\gamma = F_\gamma^1 + F_\gamma^2$. The normal pressure exerted against the top plate is $P_g^{\perp}$,

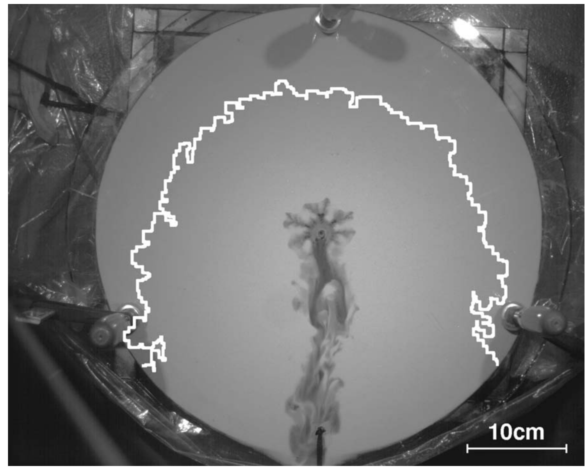

FIG. 4. Injection pressure $\Delta P = 2.58$ kPa is within the fourth pressure regime where the structure breaks through the model. In this frame the finger has reached the outer boundary. The front of the compacted region is indicated with the white line.

and the one exerted against the bottom plate also accounts for the weight of the local granular column, i.e., $(P_g^{\perp} + \rho g d)$. The normal pressure $P_g^{\perp}$ itself arises from the compression of the granular matrix. It is considered to be proportional to the in-plane pressure acting on the grains from the surrounding grains in contact, $P_g^{\parallel}$, with a proportionality constant $\lambda/2$: this amounts to assume locally a Janssen [58] hypothesis for the grains between the confining plates, as illustrated in Fig. 5. Thus, we assume that $P_g^{\perp} = \lambda P_g^{\parallel}/2$, and that the friction exerted by the top and bottom plates are, respectively, $F_\gamma^1 \leqslant \gamma \lambda P_g^{\parallel}/2$ and $F_\gamma^2 \leqslant \gamma[\lambda P_g^{\parallel}/2 + \rho g d]$, so that the total friction exerted by the confining plates per unit area is

$$F \leqslant \gamma P_g^{\perp} = \gamma(\lambda P_g^{\parallel} + \rho g d). \tag{1}$$

In other words, we assume that much of the stress acting upon the area of the displacement front is transmitted to the glass plates through particle contacts, in a way similar to Janssen's silo experiments [58]. Friction is the stabilizing phenomenon in our system.

As the injected air flows through the granular material, the pressure gradient will smoothen out and be reduced over the front. When the friction force is large enough to balance the

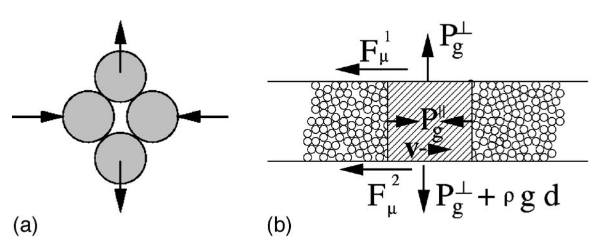

FIG. 5. (a) A sketch of the principle of how a vertical force is induced when applying a horizontal force on particles in contact. In our case the granular layer is about ten particle diameters. (b) The forces in action, where F_γ is the friction force exerted by the plates on the material, $\rho g d$ the column weight, and $P_g^{\perp}$ and $P_g^{\parallel}$ a normal and in-plane stress, respectively.

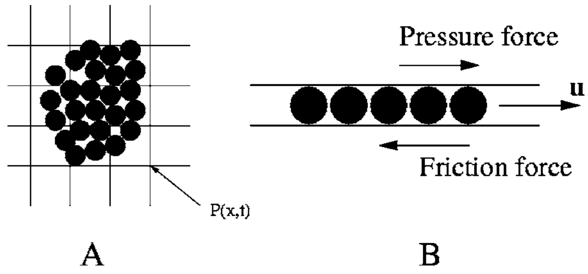

FIG. 6. A conceptual picture of the model. (A) The top view shows the particles and the grid onto which the pressure equation is discretized. (B) The side view shows how the granular layer in the experiment is represented by a single layer in the simulations, and it shows the action of the friction forces and the pressure forces.

hydrodynamic drag on the particles, the emptied structure will stop developing. How these processes are cast in a mathematical description is the subject of the next section.

IV. SIMULATION MODEL

A. Principles

Figure 6 illustrates conceptually the basis for the model. The gas flow takes place between grains that define a local permeability κ.

The details of the model are presented in Ref. [7]. In the following, we sketch its main features and the particular adaptation to the present application. The main assumption of the model is that the fluid dynamics may be described on a spatial scale above the grain scale, and that the fluid may then be described adequately in terms of the local pressure only. The solid phase, which is simulated in terms of individual particles, defines a deformable porous medium through which the gas flows.

The fluid pressure satisfies the equation

$$\phi\left(\frac{\partial P}{\partial t} + \mathbf{u}\cdot\boldsymbol{\nabla}P\right) = \boldsymbol{\nabla}\cdot\left(P\frac{\kappa}{\mu}\boldsymbol{\nabla}P\right) - P\boldsymbol{\nabla}\cdot\mathbf{u}, \tag{2}$$

where ϕ is the local porosity, $\mathbf{u}$ the local granular velocity, μ the viscosity of air, and κ the permeability.

In all the experiments, the flow velocity of the air is below 5 cm/s, so that the Reynolds number based on particle diameter is less than 0.2. In this flow regime, we are justified in using the Carman-Kozeny relation for the permeability as long as the porosity is smaller than roughly 0.7. See Ref. [59] for a more elaborate discussion of continuum equations such as Eq. (2).

Writing the permeability in terms of the local solid volume fraction ($\rho_s = 1-\phi$), the Carman-Kozeny relation [60] takes the form

$$\kappa(\rho_s) = \frac{a^2}{45}\frac{(1-\rho_s)^3}{\rho_s^2}, \tag{3}$$

where a is the particle radius.

The particles evolve according to Newton's second law:

$$m\frac{d\mathbf{v}}{dt} = m\mathbf{g} + \mathbf{F}_I - \frac{\boldsymbol{\nabla}P}{\rho_n} + \mathbf{F}_\gamma \tag{4}$$

where $\mathbf{g}$ is the gravity, m the particle mass, $\mathbf{F}_I$ the interparticle force, $\mathbf{F}_\gamma$ is the friction force of Eq. (1), and $\rho_n = \rho_s\rho_g/m$ is the number density, with ρ_g the mass density of the material composing the particles.

The repulsive interaction force F_I between two particles in contacts is modeled as a frictionless linear elastic contact, i.e., its direction lies along the separation vector between the particle centers, and its magnitude is proportional to the overlap distance between the particles. The linear repulsion model used here is meant to be a numerical approximation of a hard-sphere model. The proportionality factor between force and overlap, or repulsive spring constant, is set such as the characteristic overlap between the particles is a negligible fraction of their distance in the simulations. In other terms, the characteristic time associated with a particle-particle collision is much smaller than any other elementary characteristic times in this model (which are a particle advection time due to the applied overpressure, another one due to gravity, and a characteristic time of diffusion of the pressure field at particle scale). We have checked numerically that changing this proportionality constant by a factor of 5 did not affect the simulation results; i.e., that we indeed effectively model a hard-sphere situation.

In order to model systems of size comparable to the experimental ones, we need to use grains of effective size larger than the experimental ones; i.e., numerical grains representing clusters of real grains. Indeed, the experiments performed involve flows of roughly 10^8 grains, which is beyond numerical capacities for the model described here. Thus, we chose to model numerical particles of diameter equal to the plate separation. The simulations are thus performed using a quasi-two-dimensional (2D) granular code, in order to model a situation whereing typically 10–15 grains lie in the thickness of the system. This is justified *a priori* by the fact that when motion happens in the experiments, the full granular layer is displaced. Note, however, that in order to evaluate the granular/fluid interactions, the permeability evaluation is based on the real size of the pores; i.e., on the diameter of the real grains. In addition, an important three-dimensional feature of the granular population is incorporated in the numerical model, by evaluating a three-dimensional Cauchy stress tensor in order to incorporate friction with the confining plates, as we will detail hereafter.

To compute the friction force F_γ exerted by the plates via a Janssen hypothesis from Eq. (1), the average in-plane stress exerted over a particle of index a, in contact with a set of particles $b \in C_a$, is obtained after [61–63], as

$$\bar{\sigma}^{\parallel}_{ij} = (1/V_a)\int_{V_a}\sigma_{ij}dV \tag{5}$$

$$= (1/V_a)\sum_{b\in C_a} x_i^b f_j^b \tag{6}$$

where x^b is the position of the contact with the grain b, f^b the contact force exerted by the grain b over the grain of index a,

V_a is the grain volume, and the magnitude of the in-plane stress is $P_a^{\parallel} = -(\bar{\sigma}_{11} + \bar{\sigma}_{22})/2$.

In this application, we carry out the simulations in 2D and use molecular dynamics integrated with the velocity Verlet scheme to solve Eq. (4) [64]. Soft-sphere molecular dynamics [65] and contact dynamics [66] could be used instead.

For the model to work in practice, it is necessary to introduce a cutoff ρ_{min} on the density. This has to do with limitations both of the Carman-Kozeny relation and the present numerics (see [7] for a more detailed discussion of this point). This cutoff is implemented as follows: Whenever the measured solid fraction ρ_s is lower than $\rho_{\text{min}} = 0.25$, it is replaced by the cutoff $\rho_s = \rho_{\text{min}}$ in the evaluation of the permeability by Carman-Kozeny [Eq. (3)].

Although the practical implementation of the present model in three dimensions is not significantly harder than in two dimensions, we wish to simulate a two-dimensional system because it is numerically less expensive. However, the Carman-Kozeny equation (3) is a three-dimensional relation as it gives the permeability in terms of the volume fraction of spheres ρ_s, and we wish in the end to compare our results to real three-dimensional experiments. Consequently, we need to transform the area fraction of grains in the simulations $\rho_s^{(2D)}$, to the volume fraction ρ_s in such a way that the close packed value of $\rho_s^{(2D)}$ corresponds to the close packed value of ρ_s. Such linear transform of ρ_s, mapping 0 onto 0, and the close packed value of $\rho_s^{(2D)}$ onto its counterpart for the three-dimensional problem, is approximately achieved by the transformation $\rho_s = (2/3)\rho_s^{(2D)}$, which we use in the following [7,67,68].

B. Preparation of the initial stage

Since the behavior of a granular material is strongly dependent on its history of deformation [69], and since the dynamical behavior of our system, and the initial stress state over the system, is sensitive on the initial preparation procedure [70], special attention is devoted to this initial state in order to match as closely as possible the experimental situation. As in the experiments, particles are initially stacked under gravity in a vertical cell. Particles are launched one by one from random positions over a flat bottom surface, they fall vertically and topple off already formed piles until they reach a geometrically stable position [cf. Fig. 7(a)]. Particles are considered as hard spheres without friction in the contact in this stage, and the collisions are totally inelastic; i.e., the particle velocity is set to zero after each contact. This entirely determines the geometrical stacking rule. Since friction is neglected in this preparation stage, this procedure builds a classical isostatic packing of polydisperse hard spheres. This defines a geometrical rule to stack the particles. In order to avoid the formation of hexagonally ordered crystallites of large extent arising from an artificially monodisperse particle size distribution in a two-dimensional packing, we use polydisperse particles. The granulometry used corresponds to a flat distribution of diameters, chosen such as the relative dispersion of the diameters of the numerical particles matches the one of the experiments; i.e., with a factor of 2 between the upper and lower cutoff of the granulometry.

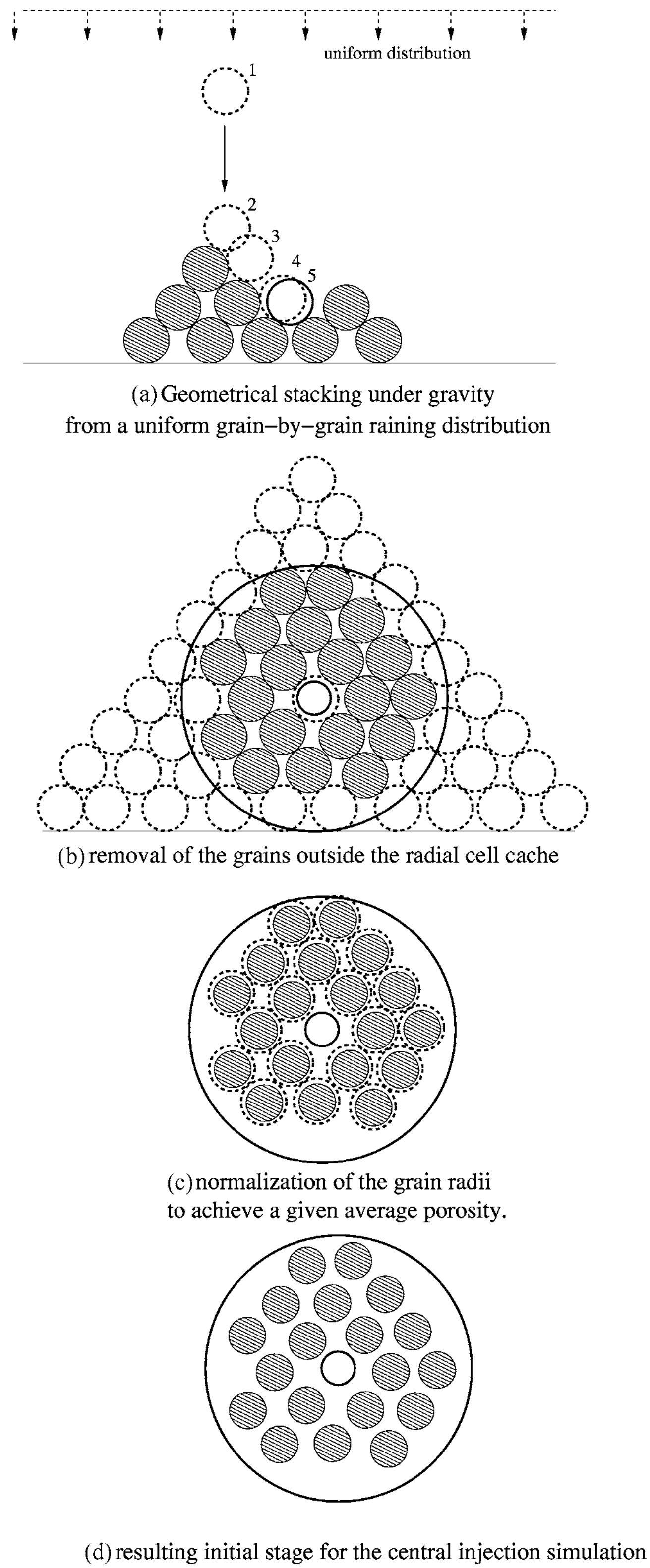

FIG. 7. The preparation stage. (a) The grains are stacked one by one over a basic plane, as hard spheres piling up under gravity, with purely inelastic collisions and no friction between them. (b) Grains outside a circular cell with a central hole are removed from the ensemble. (c) The diameter of the grains is reduced by an overall factor to produce a prescribed initial average density. (d) Initial state for the injection stage.

In a second stage, once a pile is built, we remove the particles that are not entirely in the radial cell, which has a crown shape limited by a central hole and an external circular boundary [cf. Fig. 7(b)]. This mimics the second step of the experimental preparation procedure: in experiments, particles were first stacked under gravity with the help of a guiding channel leading to the vertically placed cell, closed at the bottom, up to complete filling of the system. Next, the cell was placed horizontally, and the guides and plug of the central hole were removed, leading to the removal of the particles outside the outer radius.

Eventually, a third numerical preparation stage is added to fine tune the initial porosity so that the deviation in solid fraction from the random close packed value is the same in simulations and experiments. More precisely, if $\rho_0^{\exp}$ and $\rho_c^{\exp}$ are the initial and closed packed densities in the experiments, respectively, and $\rho_0^{(2D)}$ and $\rho_c^{(2D)}$ are the initial and close packed densities in the simulations, respectively, we impose the equality

$$\frac{\rho_c^{(2D)}-\rho_0^{(2D)}}{\rho_c^{(2D)}}=\frac{\rho_c^{\exp}-\rho_0^{\exp}}{\rho_c^{\exp}}. \tag{7}$$

This is achieved by slightly reducing the particle radii in the simulations prior to air injection [see Fig. 7(c)]. Initially, the 2D packing fraction is $\simeq 0.75$, which is slightly below the known 2D random close packing fraction value of 0.84 [67]. The measured deviation is $(\rho_c^{\exp}-\rho_0^{\exp})/\rho_c^{\exp}\approx 0.032$, as will be detailed in Sec. VI.

Alternatively, simulations can be performed without the last shrinking stage in the packing preparation. Such packing preparation only utilizes gravity, as in the experiments. However, since the model is two dimensional, the resulting packing fraction is different from the experimental one. Notably, the two-dimensional state resulting from the sole gravitational stacking is closer to a limiting close packing fraction than the three-dimensional experimental one. As a result, simulations carried from such alternative initial state leads to a smaller ratio of the central empty zone size over the compact zone size, i.e., without this fine-tuning stage, the simulated central empty zones are smaller, all other things kept equal. The other structural features described in Sec. VI and hydrodynamic regimes as a function of pressure, are otherwise unaffected by this last preparation stage. The only reason to include this optional third shrinking stage is to fine tune the size of the central empty fingers in order to better match the experiments.

There are eventually two remaining free parameters in such models, corresponding in Eq. (1) to λ, the Janssen proportionality parameter between in plane and normal stress, and γ, the Coulomb friction coefficient between the particles and the confining plates. These have been chosen to match as closely as possible:

1. The classification of regimes as function of the applied overpressure, i.e., the fact that four pressure regimes are observed, with transition pressures P_1, P_2, and P_3, corresponding to the experimental ones, up to roughly 30%.

2. The time to breakthrough, where a given internal finger reaches the outer boundary, which was required to lie within 30% of the experimental one in the simulations carried out.

Exploring the parameter space of these two remaining parameters, to satisfy such constraints, led to the use of parameters $\lambda=1$ and $\gamma=0.25$ in the simulations.

V. NUMERICAL ASPECTS: OBSERVED REGIMES AS FUNCTION OF THE PRESSURE

We will here show how the numerical simulations render for the observed phenomenology in the experiments.

A. Low injection pressure

As in the experiments, there is a lower threshold for the imposed central pressure below which no granular motion takes place, and for which there is only air permeation through the material, held in place by friction exerted by the confining plates. For imposed pressures sufficient to exit this trivial regime, the same mechanism is observed for moderate imposed central pressures: In Fig. 8, we display the pressure field and the grain positions for a simulation carried out with an overpressure of 2 kPa. The color code ranges from green for atmospheric pressure, to red for overpressures exceeding 1 kPa (half of the imposed central one). First, the pressure field diffuses through the granular material, and quickly adapts to the initial configuration of the granular packing [cf. Fig. 8(b), 15 ms after initial time]. The drag created by the pressure gradient is sufficient to overcome friction, and the fluid flow evacuates the granular material from the center, forming an empty central zone. This central motion compacts the material over a growing depth ahead of the central decompacted zone (cf. Fig. 9). In this figure, the color code represents the local permeability of the granular packing, which is evaluated from the Carman Kozeny expression [Eq. (3)]. The permeability gives the diffusion constant $D=P\kappa/\mu$ in the fluid flow equations.

As the material is compacted ahead of the emptied zone, the friction against the plates is mobilized increasingly, and this leads to the stabilization of the granular motion. In this simulation, the granular motion is stabilized in Figs. 8 and 9(d), after 60 ms. In this stationary state, the mobilized friction forces exerted by the side plates, balances exactly the fluid drag exerted by the air that flows permanently between the grains, driven by the pressure gradient shown in Fig. 8(d).

To make a quantitative comparison with the experiments, we have adopted in these simulations, measures of a central emptied area A_i, and of the compacted area A_c, that were inspired by the experimental image analysis techniques: A_i is the area that is left in the center after the grains have moved, which is connected to the central hole, after subtraction of the area of the initial central hole. A_c is the area of the zones where the solid fraction has increased by more than 2% relatively to the initial solid fraction. Both definitions are illustrated on Fig. 10, 15 ms after the start of the injection. These areas will be used in Sec. VI to compare the dynamics of the simulations and experiments.

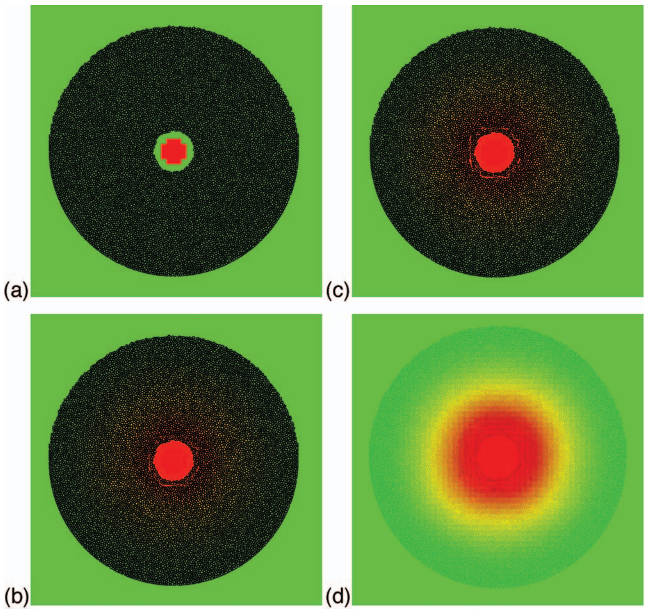

FIG. 8. (Color) Low injection pressure regime. The grains are represented in black, the color code of the background represents the overpressure: from green at zero overpressure, to red for overpressures reaching or exceeding half of the central one. (a)–(d) correspond, respectively, to times 0, 15, 45, and 60 ms after the central overpressure is imposed. The decompaction of a central zone is observed, similarly to the experiments. The system stabilizes in state (d). Note that air still flows in this stable stationary state, as shows the nonhomogeneous pressure field displayed through transparent grains in (d).

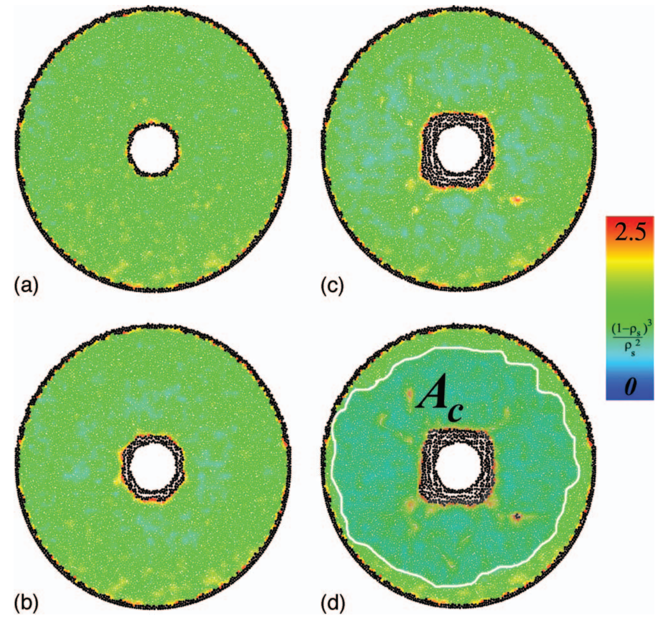

FIG. 9. (Color) Permeability representation of Fig. 8. The color code represents the local permeability, and thereby the solid fraction. Blue corresponds to $\kappa=0$, red to a two-dimensional solid fraction of 0.5. Larger local permeabilities are represented with black grains. The color bar represents $\rho_s^3/(1-\rho_s)^2$, which is proportional to the permeability κ. This quantity goes from 0 (blue) to 2.5 (red). In (d), the limit of the compacted region in the ultimate stationary state is displayed by a white line.

B. Higher injection pressure: breakthrough regime

As in the experiments, the increase of the injection pressure leads to other type of flow behaviors. As the pressure is increased, two characteristic features are observed: the roughly circular symmetry of the patterns observed at lower pressures breaks down, and the finger formation is observed. The next characteristic feature is the formation of a large empty finger breaking through the compacted granular material. These features are illustrated in Figs. 11 and 12, which correspond to snapshots of the pressure field and permeability field in a simulation carried at an imposed central overpressure of 3 kPa.

The preparation procedure, Coulomb friction parameter γ and Janssen proportionality parameter λ are identical to those of the previous simulations.

Figure 11 illustrates that the pressure field mainly adapts to the shape of the granular material, in a system of such dimensions: As shown in Fig. 11(b), the characteristic response time of the pressure field to the shape of the overall granular material is initially much shorter than the response time of the granular material itself to the imposed global pressure difference across the system. However, both times become comparable in the latest stages of the simulation, where a large empty finger breaks through.

Another interesting feature of these simulations is that in addition to the central empty zones, the compacted area ahead, and the finger formation, another type of structure arises: Close to the external boundary in Figs. 12(c) and 12(d), bubbles start to form. The formation of these isolated empty zones is reminiscent of the granular bubble formation in some fluidized beds [11,13], and it is fundamentally linked to the granular nature of our system; i.e., similar patterns are never formed by immiscible fluids that do not interpenetrate. The bubbles progress outwards towards the external open boundary of the system. The nucleation zone where such bubbles appear, grows during time, and its internal boundary progresses inwards, as is indicated in Figs. 12(b)–12(e). This illustrates a decompaction mechanism starting from the outer boundary, and allows the system to unjam. Note that contrary to the compaction mechanism starting from the center, which is mediated by solid contacts between grains, this decompaction mechanism is mediated essentially by the fluid-solid coupling.

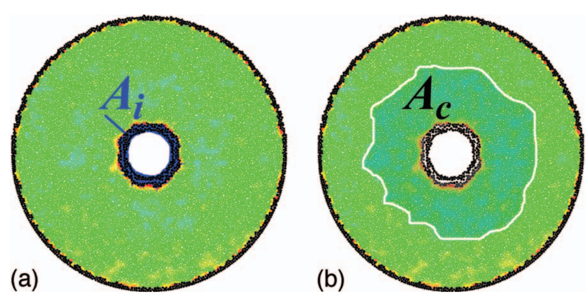

FIG. 10. (Color) (a) Central emptied area A_i, in blue, versus (b) compacted area A_c, after 15 ms of injection in the same low-pressure simulation

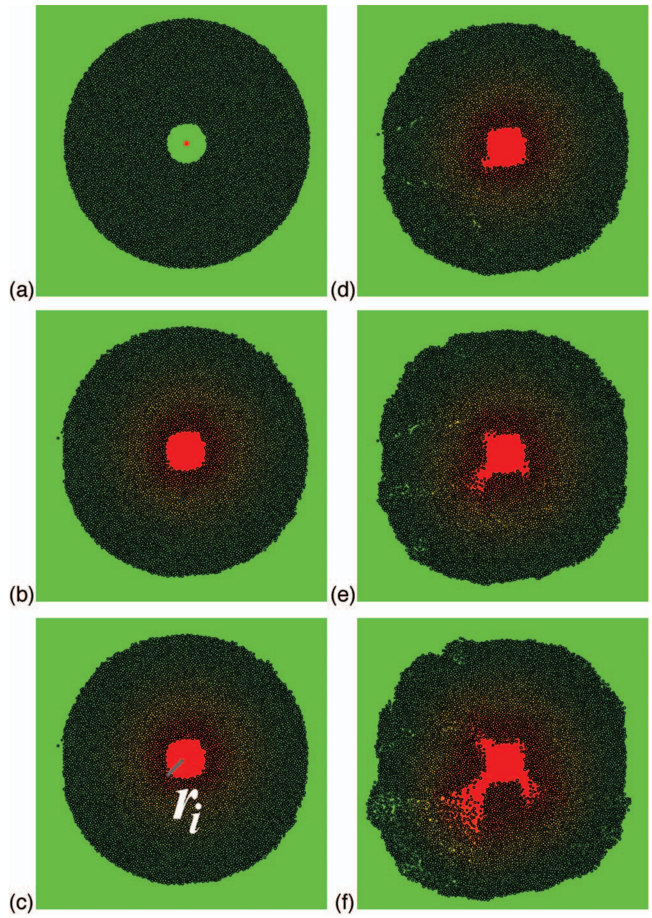

FIG. 11. (Color) Simulation snapshots at an imposed overpressure of 3 kPa. The color code in the background of the grains represents the pressure field and is the same as in Fig. 8. Times are (a) 0 s, (b) 40 ms, (c) 80 ms, (d) 120 ms, (e) 200 ms, and (f) 280 ms.

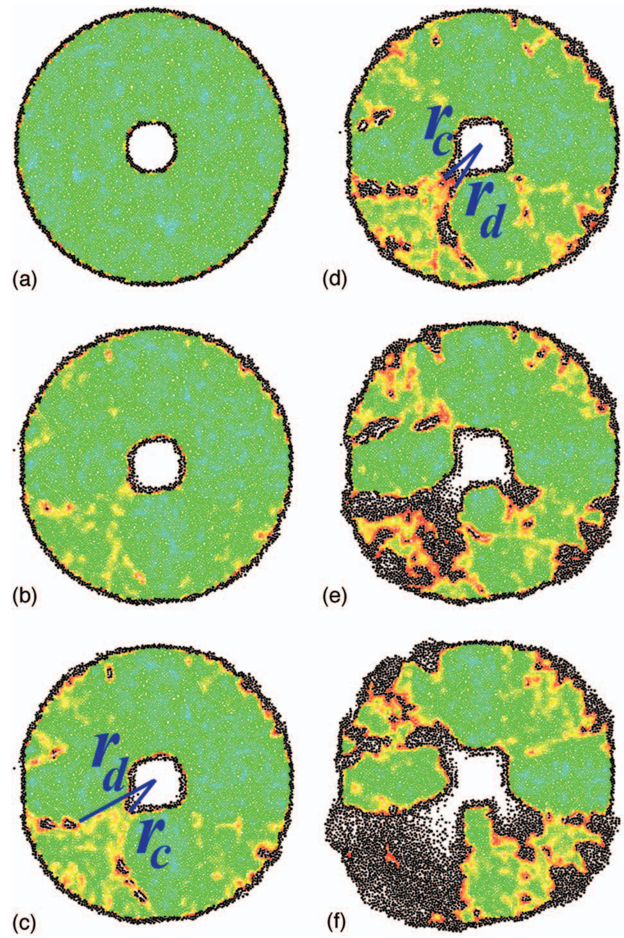

FIG. 12. (Color) Permeability map associated with the same snapshots as in Fig. 11. The radii r_i, r_c and r_d refer to the radii of the central empty zone, the zone ahead with a large enough motion so that $\phi > 0.5$, and the decompactification zone progressing inwards from the external boundary.

To establish a quantitative comparison with the experiments in Sec. VI (cf. Fig. 14), we define measures of the radii of three types of structures, inspired by the experimental techniques: r_i, shown in Fig. 11(c), is the maximum radial coordinate of the geometrically connected central zone empty of grains. The radius r_c, shown in Figs. 12(c) and 12(d), is the maximum radial coordinate of the zone geometrically connected to the center, by regions where the locally averaged two-dimensional porosity exceeds 0.49; i.e., the zone that includes grains represented in black in Figs. 11 and 12. Eventually, r_d, shown in Figs. 12(c) and 12(d), represents the minimum radial coordinate of the bubble zone, or, to be more precise, the decompaction area, where the solid fraction is lower than 0.5 (black color code) and still unconnected to the central zone. Note in Figs. 11(c) and 11(d) that while r_i and r_c are growing functions of time, r_d decreases.

Although such definitions and choice of threshold for the solid fraction are necessarily subjective, they have the advantage of allowing a quantitative comparison. However, some unavoidable discrepancies are naturally expected between numerical and experimental measures of the areas of these three types of zones (central finger, compacted zone, decompacted zone).

VI. DYNAMICAL ASPECTS

In Fig. 13, r_i is followed in time for three experiments. We see that for the case of injection pressures within pressure regimes 2 and 3, in this case $\Delta P = 1.78$ kPa and $\Delta P = 2.20$ kPa, the pattern grows rapidly in the beginning up to ~ 0.1 s From ~ 0.1 s the growth rate is reduced due to mobilization of friction. The structures fully saturates after ~ 0.4 s. In this particular example, the pattern formations reaches final radial size ~ 1.7 cm after 0.44 s for the system in pressure regime 2, and ~ 4.9 cm after 0.43 s for the system in pressure regime 3.

The growth characteristics is similar for the compacted region in Fig. 13(b). After an initial stage where the zone is established it grows to a plateau within ~ 0.1 s. There is some small expansion of the compacted region within this plateau matching the motion of the emptied structure.

At higher pressures, $\Delta P = 2.58$ kPa, belonging to the fourth pressure regime the mobilized friction slows down the development and speed of the growing structure. As the emptied structure continues to develop, the material ahead of this structure compacts over a larger area. This is a manifes-

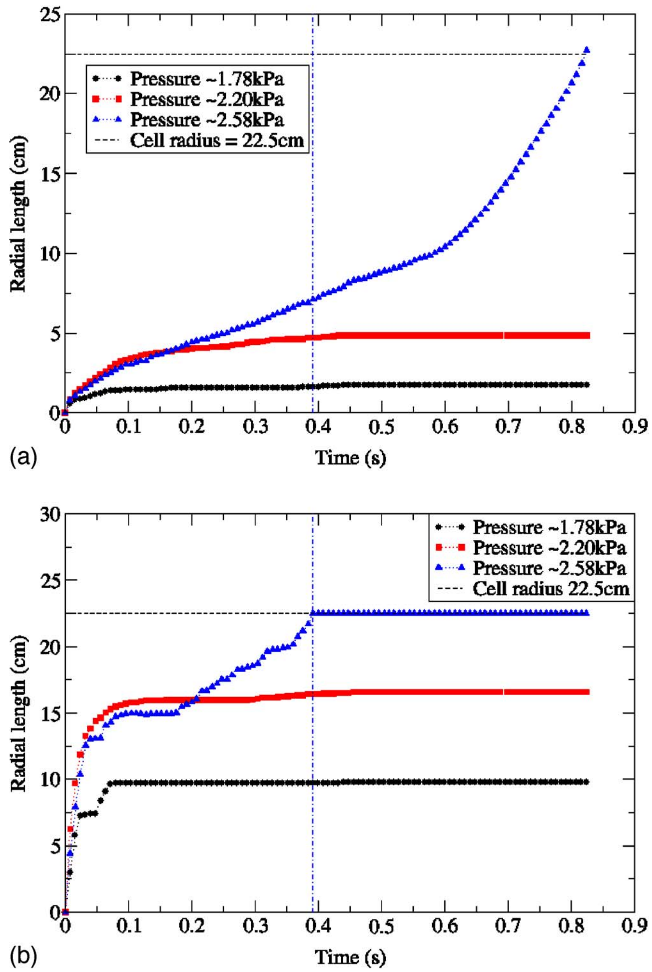

FIG. 13. (Color online) Experimental measurements of r_i (a) and the maximum radial extent of the compacted region (b) for three different values of the injection pressures. The vertical line indicates the time when the compacted zone reaches the open boundary.

tation of an upper limit to the possible compaction in the already compacted zone (solid fractions are always below unity).

When the region where the packing can be compacted no further has reached the open boundary, the particles will be pushed out of the system. The (in-plane) friction is then reduced due to the smaller contact area with the confining walls. This situation is unstable and the propagating finger(s) accelerates. This is seen in Figs. 13(a) and 13(b): When the compacted zone reaches the outer boundary the most advanced finger, which is measured by r_i, accelerates. This is evident by the fact that the figure shows $d^2r_i(t)/dt^2>0$. Figure 14, which displays a comparison between an experiment and simulation at $\Delta P=3.00$ kPa, shows the same effect. At the time $\sim$0.15 s, indicated with a vertical blue line, the compacted zone reaches the boundary. From this moment the advancing finger starts to accelerate and the finger finally breaks through the model at the end of the measurement.

Another interesting feature is the decompaction zone, measured by r_d, near the boundary in the preferred growth direction. As the particles near the boundary start to feel the

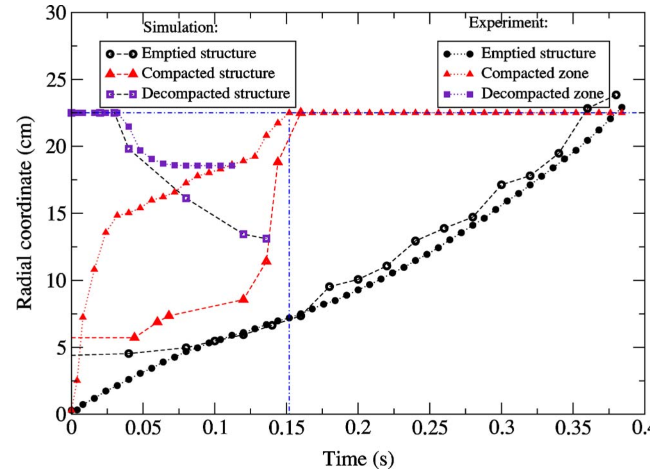

FIG. 14. (Color online) Experimental and simulation measurements of r_i, r_c, and r_d at a pressure of approximately 3.00 kPa. The dashed vertical line at $\sim$0.15 s indicates the time for which the compacted zone reaches the open boundary.

pressure gradient, they are displaced and some of the outermost particles are pushed out of the cell. As can be seen from Fig. 14, the decompacted zone grows deeper into the material towards the center, in the opposite direction of air flow. While the decompacted zone saturates, the compacted region still grows along with the developing emptied structure. The compacted region eventually catches up with the decompacted zone, and starts to compact this region as well. Bubbles are observed near the external boundary in some experiments and appear to be coupled to this decompaction zone. The reduction of the granular density there will allow bubbles to form, as was observed in the simulations. In Fig. 14 there is good agreement between experiments and simulations for r_i measurements, and qualitative agreement for the extension of the compacted regions and r_d.

Figure 15 shows a compacted structure after injection: The compacted (region 2) solid fraction is ρ_c while the unperturbed zone (region 3) has kept the initial solid fraction ρ_0. By conservation of grain mass, we may write

$$\rho_0(A_1+A_2)=\rho_c A_2, \tag{8}$$

where the areas A_1 and A_2 are shown in Fig. 15, and define

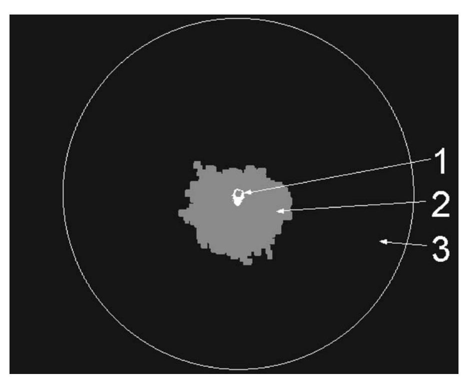

FIG. 15. Empty (1), compacted (2), and unperturbed regions (3) after air injection.

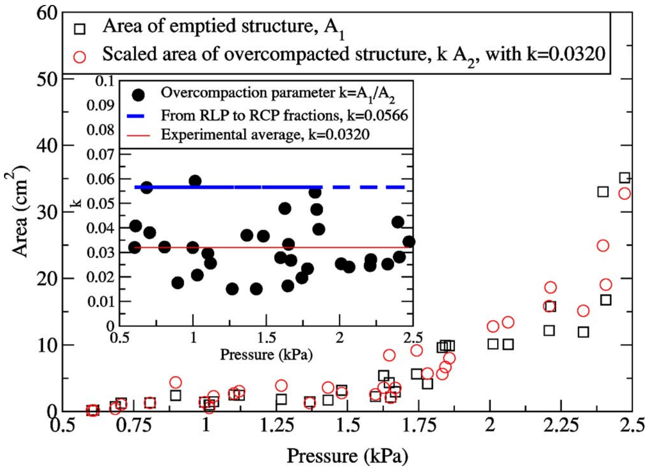

FIG. 16. (Color online) The estimated and experimentally measured area of the empty region as a function of pressure. The inset shows the compaction parameter k for our data set. The blue line shows an upper bound for k.

$$k \equiv \frac{A_1}{A_2} = \frac{\Delta\rho_s}{\rho_0}, \tag{9}$$

where $\Delta\rho_s=\rho_c-\rho_0$. For a number of experiments performed at different injection pressures we have measured A_1 and A_2 by image analysis. The area of the injection hole is not included in the measured A_1 and A_2. In the inset of Fig. 16, $k=A_1/A_2$ is plotted as function of the pressure. The mean value of these fractions is found to be $\bar{k}=0.032\pm0.015$. An upper bound to this compaction parameter k can in principle be estimated as follows: Studying the random loose packing (RLP) and random close packing (RCP) of spheres, Scott found $\rho_{\mathrm{RCP}}=0.635\pm0.005$ and $\rho_{\mathrm{RLP}}=0.601\pm0.005$ [68]. These are the lowest and highest densities for random packings of spheres—called, respectively, loose packed and close packed fractions. A transition between these two extreme random packing fractions would lead to the compaction parameter $k_{max}=\Delta\rho_s/\rho_0=(0.635-0.601)/0.601\approx0.056$. This value should correspond to the maximum k obtained for a variation from the loosest to the most compact random packing. This upper bound is shown in the inset of Fig. 16.

By weighing the granular material, and measuring the area it covers in the cell, knowing the glass density, 2.6 g cm^{-3}, we obtain the solid fraction 0.44 before air injection. Using Eq. (9) and the mean fraction $A_1/A_2=0.032$ found from experiments, the solid fraction is calculated to be $\rho_c=0.46$, which is 27% lower than the random close packed fraction $\rho_{\mathrm{RCP}}=0.635\pm0.005$. The solid fraction of the initial state is 26% lower than the random loose packed fraction $\rho_{\mathrm{RLP}}=0.601\pm0.005$. These low solid fractions are consistent with the presence of the walls. The particles within the packing, which is only ten particle diameters thick, will feel the walls which cause a frustrated system with higher porosity for both the initial and the compacted state [71].

Given the average value of k we can work backwards and calculate the area A_1 of the empty region from the area of the compacted region using as $A_1=kA_2$. Comparing this estimate of A_1 with measurements gives another way of viewing the fluctuations in k. Figure 16 shows this comparison using $k=\Delta\rho_s/\rho_0=0.032$, which gives a good fit to the experimental results.

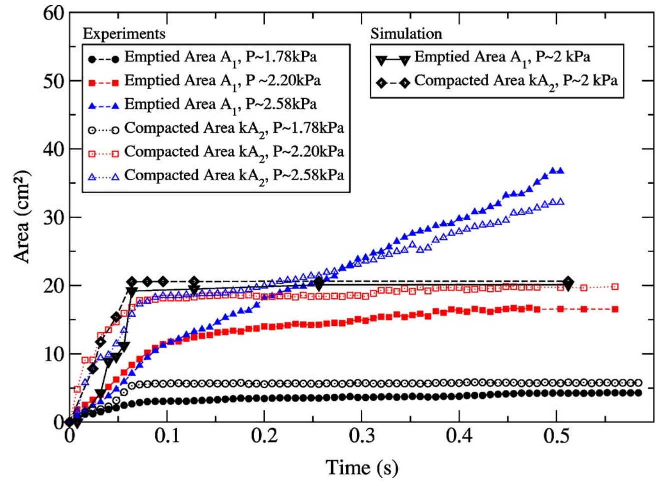

FIG. 17. (Color online) Area of the central emptied region and scaled compacted region for different injection pressures, in three experiments and one simulation.

Figure 17 shows the measured area A_1 from three experiments (one for each of pressure regime 2, 3, and 4) and one simulation (regime two) as function of time. In this figure we have also plotted kA_2 where the A_2 are measured in the same experiments.

The first pressure regime structure is typically established after ~0.1 s and can either stop evolving completely or grow slightly more in a slow fashion for a couple of tenths of seconds. In the second pressure regime, A_1 saturates after 0.45 s. In the third regime we have the onset of instability. The measured area of both the branched empty region and the compacted region is larger. The outer perimeter of the compacted region stays uniform but asymmetric around the center, in accordance with the asymmetric shape of the emptied structure. The time for which the patterns are established and the final size and shape obtained are more or less the same as in the second regime; i.e., ~1 s. There might also here be some relatively slow "creeping" motion a couple of tenths of seconds after the structure is established. The compacted zone can reach all the way up to the open boundary, but with only a tiny amount of particles being pushed out of the cell and without the breakthrough instability setting in.

From the moment at which the flux of particles leaving the cell becomes continuous, the empty region expands rapidly. We see that the breakpoint where the structure growth slows down or reaches a plateau coincides for all three experimental cases and the simulation at about $t\approx0.1$ s. The ripples in the experimental plots in Fig. 17 reflect the uncertainty related to the method of identifying and finding the areas.

Simulations and experiments reflect the same physical behavior in the sense that the different regimes as function of pressure are observed and that their evolution happens over the same times. The linear extent of the compacted or decompacted zones coincide reasonably well, as well as the area of the emptied and compacted zone. Some discrepancies for the magnitude of the area are present between numerics and experiments. These discrepancies are believed to arise from the subjective choice of threshold values used to define compaction: In the experimental measures, this threshold is hardly quantifiable, being related to the sensitivity of the camera used—since the compaction area is extracted by image treatment from subtraction images, as is illustrated in Fig. 3. In the numerical case, the value of the compacted area is rather sensitive to the adopted value for the threshold.

There are also discrepancies between the experimental emptied area and the calculated rescaled compacted area, which might be associated with the fact that an average k-value is used when estimating the area. From the inset in Fig. 16, we see that the k-values are spread quite wide around the average, and therefore might not always fit a specific set of data perfectly.

VII. SUMMARY AND CONCLUSIONS

Studying the system experimentally and numerically, we have described the displacement behavior and patterns in granular materials confined in circular Hele-Shaw cells—qualitatively as well as quantitatively. Simulations have been a central tool to understand the system.

The driving force of this system is the pressure gradient over the material between the front of the pattern and the open boundary. The friction between the granular material and the confining plates act as the stabilizing mechanism. These two competing mechanisms may be controlled to produce a range of patterns resulting from air injection. Four well-defined pressure regimes giving different patterns have been found. In the first regime, no displacement of grains is recorded, so that the injected air just permeates through the pores of the granular material. In the second regime, particles are displaced and a roughly circular pattern appears. The structures become larger as the injection pressure is increased. The third regime is entered with the onset of instability as the shape of the displacement front loses its circular symmetry. This happens as the front starts to bulge and to form branches. The length of the branches increases with increasing injection pressure. As in the Saffmann-Taylor instability, the driving pressure gradient is larger ahead of the most developed finger. Hence, the most developed finger grows at the expense of the others.

For both the second and third pressure regimes, image analysis reveals a zone ahead of the emptied formation where the granular material becomes more dense. By grain conservation, we relate the area of the structure empty of grains (A_1) and the area of the compacted region (A_2). At pressures at which the compacted region reaches the boundary and particles are expelled, the in-plane friction will decrease. When a sufficient amount of particles is pushed out, such that the friction no longer can balance the hydrodynamic drag, the material will fluidize locally ahead of the most advanced finger, which eventually leads to breakthrough. At this point we find ourselves in the fourth pressure regime.

As an extension, system size and boundary condition dependences should be subject to both experimental and numerical investigations. It would also be interesting to examine the displacement field of the bulk zone using correlation imaging velocimetry technique.

ACKNOWLEDGMENTS

The work was supported by NFR, the Norwegian Research Council through a Petromax, and a SUP grant. We thank Ernesto Altshuler, Alex Hansen, Jean Schmittbuhl, Anke Lindner, and Christophe Chevalier for many interesting and helpful discussions.

[1] H. S. Hele-Shaw, Nature (London) **58**, 34 (1898).
[2] P. G. Saffman and G. I. Taylor, in Proc. R. Soc. London, Ser. A **245**, 312 (1958).
[3] H. Darcy, *Les Fontaines Publiques de la Ville de Dijon* (Dalmont, Paris, 1856).
[4] J. F. Davidson and D. Harrison, *Fluidization* (Academic, New York, 1971).
[5] J. F. Davidson, *Bubbles in Fluidized Beds* (Kluwer Academic, New York, 1995), p. 197.
[6] K. Lim, J. Zhu, and J. Grace, Int. J. Multiphase Flow **21**, 141 (1995).
[7] S. McNamara, E. G. Flekkøy, and K. J. Måløy, Phys. Rev. E **61**, 4054 (2000).
[8] G. W. Baxter, R. P. Behringer, T. Fagert, and G. A. Johnson, Phys. Rev. Lett. **62**, 2825 (1989).
[9] K. J. Måløy, T. L. Pennec, E. G. Flekkøy, D. Bideau, M. Ammi, J. C. Messager, X. L. Wu, and A. Hansen, *Physics of Dry Granular Media*, NATO Advanced Studies Instituto, Series E: Applied Sciences, 350 (Kluwer Academic, Dordrecht, Boston, London, 1998).
[10] T. L. Pennec, K. J. Måløy, E. G. Flekkøy, J. C. Messager, and M. Ammi, Phys. Fluids **10**, 3072 (1998).
[11] E. G. Flekkøy and K. J. Måløy, Phys. Rev. E **57**, 6962 (1998).
[12] D. Gendron, H. Troadec, K. J. Måløy, and E. G. Flekkøy, Phys. Rev. E **64**, 021509 (2001).
[13] E. G. Flekkøy, S. McNamara, K. J. Måløy, and D. Gendron, Phys. Rev. Lett. **87**, 134302 (2001).
[14] X. I. Wu, K. J. Måløy, A. Hansen, M. Ammi, and D. Bideau, Phys. Rev. Lett. **71**, 1363 (1993).
[15] T. L. Pennec, K. J. Måløy, A. Hansen, M. Ammi, D. Bideau, and X. I. Wu, Phys. Rev. E **53**, 2257 (1996).
[16] E. Lemaire, Y. O. M. Abdelhaye, J. Larue, R. Benoit, P. Levitz, and H. van Damme, Fractals **1**, 968 (1993).
[17] P. Mills, P. Cerasi, and S. Fautrat, Europhys. Lett. **29**, 215 (1995).
[18] P. Cerasi and P. Mills, Phys. Rev. E **58**, 6051 (1998).
[19] R. Chandler, J. Koplik, K. Lerman, and J. F. Willemsen, J. Fluid Mech. **119**, 249 (1982).
[20] R. Lenormand and C. Zarcone, Phys. Rev. Lett. **54**, 2226 (1985).

[21] R. Lenormand and C. Zarcone, Transp. Porous Media **4**, 599 (1989).
[22] G. M. Homsy, Annu. Rev. Fluid Mech. **19**, 271 (1987).
[23] K. J. Måløy, J. Feder, and T. Jøssang, Phys. Rev. Lett. **55**, 2688 (1985).
[24] O. I. Frette, K. J. Måløy, J. Schmittbuhl, and A. Hansen, Phys. Rev. E **55**, 2969 (1997).
[25] E. Aker, K. J. Måløy, and A. Hansen, Phys. Rev. Lett. **84**, 4589 (2000).
[26] G. Lovoll, Y. Meheust, R. Toussaint, J. Schmittbuhl, and K. J. Måløy, Phys. Rev. E **70**, 026301 (2004).
[27] R. Toussaint, G. Lovoll, Y. Meheust, K. J. Måløy, and J. Schmittbuhl, Europhys. Lett. **71**, 583 (2005).
[28] T. A. Witten and L. M. Sander, Phys. Rev. Lett. **47**, 1400 (1981).
[29] T. A. Witten and L. M. Sander, Phys. Rev. B **27**, 5686 (1983).
[30] P. Meakin, Phys. Rev. A **27**, 1495 (1983).
[31] L. Paterson, Phys. Rev. Lett. **52**, 1621 (1984).
[32] E. L. Hinrichsen, K. J. Måløy, J. Feder, and T. Jossang, J. Phys. A **22**, L271 (1989).
[33] F. A. L. Dullien, Chem. Eng. Technol. **11**, 407 (1988).
[34] J. Bear, *Dynamics of Fluids in Porous Media* (American Elsevier, New York, 1972).
[35] M. Sahimi, Rev. Mod. Phys. **65**, 1393 (1993).
[36] P. van Meurs, Trans. Am. Inst. Min., Metall. Pet. Eng. **210**, 295 (1957).
[37] A. K. Gustensen and D. H. Rothman, J. Geophys. Res. **98**, 6431 (1993).
[38] H. Tchelepi and F. Orr, SPE Reservoir Eng. **9**, 266 (1994).
[39] I. Ginzburg and P. Adler, Transp. Porous Media **20**, 37 (1995).
[40] D. Bensimon, L. P. Kadanoff, S. Liang, B. I. Shraiman, and C. Tang, Rev. Mod. Phys. **58**, 977 (1986).
[41] R. L. Chuoke, P. van Meurs, and C. van der Poel, Trans. Am. Inst. Min., Metall. Pet. Eng. **216**, 188 (1959).
[42] J. V. Maher, Phys. Rev. Lett. **54**, 1498 (1985).
[43] D. Bonn, H. Kellay, M. Ben Amar, and J. Meunier, Phys. Rev. Lett. **75**, 2132 (1995).
[44] A. Lindner, D. Bonn, E. Poiré, M. B. Amar, and J. Meunier, J. Fluid Mech. **462**, 237 (2002).
[45] G. Daccord, J. Nittmann, and H. E. Stanley, Phys. Rev. Lett. **56**, 336 (1986).
[46] J. Nittman, G. Daccord, and H. E. Stanley, Nature (London) **314**, 141 (1985).
[47] E. Lemaire, P. Levitz, G. Daccord, and H. van Damme, Phys. Rev. Lett. **67**, 2009 (1991).
[48] H. Zhao and J. V. Maher, Phys. Rev. E **47**, 4278 (1993).
[49] D. Mader, *Hydraulic Proppant Fracturing and Gravel Packing* (Elsevier, Amsterdam, 1989).
[50] Y. Gordeyev, Int. J. Rock Mech. Min. Sci. **30**, 233 (1993).
[51] P. Valkø and M. J. Econimedes, *Hydraulic Fracture Mechanics* (John Wiley, New York, 1995).
[52] E. Fjaer, R. M. Holt, P. Horsrud, A. M. Raaen, and R. Risnes, *Petroleum Related Rock Mechanics* (Elsevier Science, New York, 1992).
[53] W. Fyfe, N. Price, and A. Thompson, *Fluids in the Earth's Crust* (Elsevier, Amsterdam, 1978).
[54] A. Levermann and I. Procaccia, Phys. Rev. Lett. **89**, 234501 (2002).
[55] E. G. Flekkøy, A. Malthe-Sorenssen, and B. Jamtveit, J. Geophys. Res. **107**, 2115 (2002).
[56] F. Tzschichholz, H. J. Herrmann, H. Roman, and M. Pfuff, Phys. Rev. B **49**, 7056 (1994).
[57] F. Tzschichholz and H. Herrmann, Phys. Rev. E **51**, 1961 (1995).
[58] H. A. Janssen, Zeitschrift des Vereines Deutscher Ingenieure **39**, 1045 (1892).
[59] D. Gidaspau, *Multiphase Flow and Fluidization* (Academic, San Diego, 1994).
[60] P. Carman, Trans. Inst. Chem. Eng. **15**, 150 (1937).
[61] J. P. Bardet, *Introduction to Computational Granular Mechanic* (Springer, Berlin, 1998), pp. 99–169.
[62] J. Christoffersen, M. Mehrabadi, and S. Nemat-Nasser, ASME J. Appl. Mech. **48**, 339 (1981).
[63] J. D. Goddard, J. Non-Newtonian Fluid Mech. **2**, 169 (1977).
[64] M. Allen and D. Tildesley, *Computer Simulation of Liquids* (Clarendon Press, Oxford, 1987).
[65] L. Brendel and S. Dippel, *Physics of Dry Granular Media* (Kluwer Academic, Dordrecht, 1998), p. 313.
[66] F. Radjai and D. Wolf, Granular Matter **1**, 3 (1998).
[67] C. S. O'Hern, S. A. Langer, A. J. Liu, and S. R. Nagel, Phys. Rev. Lett. **88**, 075507 (2002).
[68] G. D. Scott, Nature (London) **188**, 908 (1960).
[69] J. Duran, *Sands, Powders and Grains: An Introduction to the Physics of Granular Materials* (Springer, Berlin, 2000).
[70] A. Atman, P. Brunet, J. Geng, G. Reydellet, G. Combe, P. Claudin, R. Behringer, and E. Clement, J. Phys.: Condens. Matter **17**, S2391 (2005).
[71] D. R. Nelson, in *Topological Disorder in Condensed Matter: Proceedings of the Fifth Taniguchi International Symposium*, edited by F. Yonesawa and T. Ninomiya (Springer, Berlin, 1983), pp. 164–180.

[11] X.-l. Wu, K. J. Måløy, A. Hansen, M. Ammi, and D. Bideau, Phys. Rev. Lett. **71**, 1363 (1993).
[12] T. LePennec, K. J. Måløy, A. Hansen, M. Ammi, D. Bideau, and X. L. Wu, Phys. Rev. E **53**, 2257 (1996).
[13] E. Lemaire, Y. O. M. Abdelhaye, J. Larue, R. Benoit, P. Levitz, and H. VanDamme, Fractals **1**, 968 (1993).
[14] Ø. Johnsen, R. Toussaint, K. J. Måløy, and E. G. Flekkøy, Phys. Rev. E **74**, 011301 (2006).
[15] P. Mills, P. Cerasi, and S. Fautrat, Europhys. Lett. **29**, 215 (1995).
[16] P. Cerasi and P. Mills, Phys. Rev. E **58**, 6051 (1998).
[17] H. S. Hele-Shaw, Nature (London) **58**, 34 (1898).
[18] P. G. Saffman and G. I. Taylor, Proc. R. Soc. London, Ser. A **245**, 312 (1958).
[19] D. Bensimon, L. P. Kadanoff, S. Liang, B. I. Shraiman, and C. Tang, Rev. Mod. Phys. **58**, 977 (1986).
[20] R. L. Chuoke, P. van Meurs, and C. van der Poel, Trans. AIME **216**, 188 (1959).
[21] J. V. Maher, Phys. Rev. Lett. **54**, 1498 (1985).
[22] A. Lindner, D. Bonn, E. C. Poiré, M. B. Amar, and J. Meunier, J. Fluid Mech. **469**, 237 (2002).
[23] D. Bonn, H. Kellay, M. Ben Amar, and J. Meunier, Phys. Rev. Lett. **75**, 2132 (1995).
[24] G. Daccord, J. Nittmann, and H. E. Stanley, Phys. Rev. Lett. **56**, 336 (1986).
[25] J. Nittmann, G. Daccord, and H. E. Stanley, Nature (London) **314**, 141 (1985).
[26] E. Lemaire, P. Levitz, G. Daccord, and H. Van Damme, Phys. Rev. Lett. **67**, 2009 (1991).
[27] H. Zhao and J. V. Maher, Phys. Rev. E **47**, 4278 (1993).
[28] T. Hirata, Phys. Rev. E **57**, 1772 (1998).
[29] R. Chandler, J. Koplik, K. Lerman, and J. F. Willemsen, J. Fluid Mech. **119**, 249 (1982).
[30] R. Lenormand and C. Zarcone, Phys. Rev. Lett. **54**, 2226 (1985).
[31] R. Lenormand and C. Zarcone, Transp. Porous Media **4**, 599 (1989).
[32] G. M. Homsy, Annu. Rev. Fluid Mech. **19**, 271 (1987).
[33] K. J. Måløy, J. Feder, F. Boger, and T. Jøssang, Phys. Rev. Lett. **61**, 2925 (1988).
[34] O. I. Frette, K. J. Maløy, J. Schmittbuhl, and A. Hansen, Phys. Rev. E **55**, 2969 (1997).
[35] E. Aker, K. J. Måløy, and A. Hansen, Phys. Rev. Lett. **84**, 4589 (2000).
[36] G. Løvoll, Y. Méheust, R. Toussaint, J. Schmittbuhl, and K. J. Måløy, Phys. Rev. E **70**, 026301 (2004).
[37] R. Toussaint, G. Løvoll, Y. Méheust, K. J. Måløy, and J. Schmittbuhl, Europhys. Lett. **71**, 583 (2005).
[38] T. A. Witten and L. M. Sander, Phys. Rev. Lett. **47**, 1400 (1981).
[39] T. A. Witten and L. M. Sander, Phys. Rev. B **27**, 5686 (1983).
[40] P. Meakin, Phys. Rev. A **27**, 1495 (1983).
[41] L. Paterson, Phys. Rev. Lett. **52**, 1621 (1984).
[42] E. L. Hinrichsen, K. J. Måløy, J. Feder, and T. Jøssang, J. Phys. A **22**, L271 (1989).
[43] F. A. L. Dullien, Chem. Eng. Technol. **11**, 407 (1988).
[44] J. Bear, *Dynamics of Fluids in Porous Media* (Elsevier, New York, 1972).
[45] M. Sahimi, Rev. Mod. Phys. **65**, 1393 (1993).
[46] P. van Meurs, Trans. AIME **210**, 295 (1957).
[47] A. K. Gustensen and D. H. Rothman, J. Geophys. Res. **98**, 6431 (1993).
[48] H. A. Tchelepi and F. M. Orr, SPE Reservoir Eng. **9**, 266 (1994).
[49] I. Ginzbourg and P. M. Adler, Transp. Porous Media **20**, 37 (1995).
[50] D. Mader, *Hydraulic Proppant Fracturing and Gravel Packing* (Elsevier, Amsterdam, 1989).
[51] Y. Gordeyev, Int. J. Rock Mech. Min. Sci. **30**, 233 (1993).
[52] P. Valkø and M. J. Econimedes, *Hydraulic Fracture Mechanics* (Wiley, New York, 1995).
[53] E. Fjaer, R. M. Holt, P. Horsrud, A. M. Raaen, and R. Risnes, *Petroleum Related Rock Mechanics* (Elsevier, Amsterdam, 1992).
[54] W. S. Fyfe, N. Price, and A. B. Thompson, *Fluids in the Earth's Crust* (Elsevier, Amsterdam, 1978).
[55] A. Levermann and I. Procaccia, Phys. Rev. Lett. **89**, 234501 (2002).
[56] E. G. Flekkøy, A. Malthe-Sørenssen, and B. Jamtveit, J. Geophys. Res. **107**, 2151 (2002).
[57] F. Tzschichholz, H. J. Herrmann, H. E. Roman, and M. Pfuff, Phys. Rev. B **49**, 7056 (1994).
[58] F. Tzschichholz and H. J. Herrmann, Phys. Rev. E **51**, 1961 (1995).
[59] H. Darcy, *Les Fontaines Publiques de la Ville de Dijon* (Dalmont, Paris, 1856).
[60] H. A. Janssen, Z. Vereines Deutscher Ingenieure **39**, 1045 (1892).
[61] D.-V. Anghel, M. Strauss, S. McNamara, E. G. Flekkøy, and K. J. Måløy, Phys. Rev. E **74**, 029906(E) (2006).
[62] P. Carman, Trans. Inst. Chem. Eng. **15**, 150 (1937).

Coupled air/granular flow in a linear Hele-Shaw cell

Ø. Johnsen,[1] R. Toussaint,[2] K. J. Måløy,[1] E. G. Flekkøy,[1] and J. Schmittbuhl[2]
[1]*Department of Physics, University of Oslo, P.O. Box 1048, Blindern, 0316 Oslo, Norway*
[2]*IPGS, Université Louis Pasteur, 5 rue René Descartes, 67084 Strasbourg Cedex, France*
(Received 16 April 2007; published 7 January 2008)

We investigate experimentally the pattern formation process during injection of air in a noncohesive granular material confined in a linear Hele-Shaw cell. We characterize the features and dynamics of this pattern formation on the basis of fast image analysis and sensitive pressure measurements. Behaviors are classified using two parameters—injection pressure and plate opening—and four hydrodynamic regimes are defined. For some regions of the parameter space, flows of air and grains are shown to be strongly coupled and instable, and lead to channelization within the granular material with obvious large-scale permeability variations.

DOI: 10.1103/PhysRevE.77.011301 PACS number(s): 45.70.−n, 83.50.−v, 47.15.gp

I. INTRODUCTION

During air injection into noncohesive and weakly confined granular materials where particles are able to move together with the fluid phase, a variety of patterns are formed. In particular when the particles are small, the gas-grain interactions are of central importance. Such interactions are host to a wide range of fascinating physical phenomena and play a vital role in a variety of systems from fluidized beds [1–4] to flow in tubes [5–10] and ticking hour glasses [11,12].

Instabilities during air injection into confined nonconsolidated granular materials has previously been studied for a radial geometry [13,14]. It is found that the obtained patterns can be classified into different hydrodynamical regimes depending on the injection pressure. Similarly characteristic flow regimes are studied when a fluid is retracted from a nonconsolidated porous medium [15,16].

The patterns and instabilities observed in such experiments bear resemblance to Hele-Shaw [17] experiments where viscous fluid invades a more viscous one, either using Newtonian [18–21] or non-Newtonian fluids [22–25]. For the non-Newtonian case a transition from a viscous fingering regime to a viscoelastic fracturing regime is observed [26–28]. Multiphase flows in immobile porous media are other systems with general similarities [29–49].

Studies of coupled fluid/granular flow can be of great geological interest and provide insight into underlying physical processes taking place in, for instance, fluid intrusions into sediment rocks and hydrofracture [50–54]. Viscoelastic fracturing and hydrofracture have also been subject to several numerical studies [55–58].

Similarly to the Saffman-Taylor instability [18] observed in nonmiscible biphasic flows, the driving force of the granular motion is the fluid pressure gradient. Given the fact that the pressure is more or less constant inside the grainless region, the pressure gradient being the largest at the tip [59], the particles near the finger tip experience a higher drag force in the flow direction. This favors the growth of the most advanced finger while the growth of shorter fingers is suppressed. On the other hand, an important difference from the classical Saffman-Taylor problem is that in the granular case surface tension is absent. The stabilizing mechanisms are a matter of friction mobilization between the granular matrix and the confining plates rather than surface tension as in the classical two-fluid system. The structures studied in the dry granular case do, in other words, depend on the existence of friction.

Phase mixing is also an essential difference between the coupled fluid/granular system and nonmiscible biphasic flows, such as, e.g., the viscoelastic biphasic flow and the Saffman-Taylor instability between two fluids. In many systems the phases are separate, i.e., nonmiscible, while for our granular configuration the phases are interpenetrating. The phases can be defined from a mesoscopic point of view by their particle density: distinguishing between a fluid phase where this density is low and a powder phase where it is higher. Both states exchange fluid, i.e., interpenetrate (even though at smaller scales, one solid grain does not exchange mass with the surrounding fluid). Since the phases are able to mix, the driving force—i.e., the pressure gradient acting upon the displacement front—will dissipate in time. This mechanism also contributes to stabilization of the pattern formation.

In this study, we characterize and quantify the global features of pattern formations and their associated dynamic processes during injection of air in a noncohesive granular material confined in a linear Hele-Shaw cell. This geometry is complementary to the circular cell used in Refs. [13,14], and these two represent the standard geometries for studying flow problems such as, e.g., the two-fluid Saffman-Taylor instability or multiphase flows in porous media. The linear cell geometry allows us to study the translation symmetry breaking during destabilization since it is spatially invariant along the flow direction, while the rotational symmetry breaking has previously been investigated in the radially invariant circular cell [13,14]. Using a fast digital camera, we obtain a quantitative description of the patterns and their evolution. We explore the parameter space using three different openings and a large range of injection pressure.

The article is organized as follows: In Sec. II the experimental setup, sample preparations, and imaging methods are described. In Sec. III we present our experimental results: we describe the observed hydrodynamical regimes and classify the different pattern formed into a phase diagram as function of the pressure and plate separation. Section IV is dedicated to characterizing the geometrical and dynamical features of

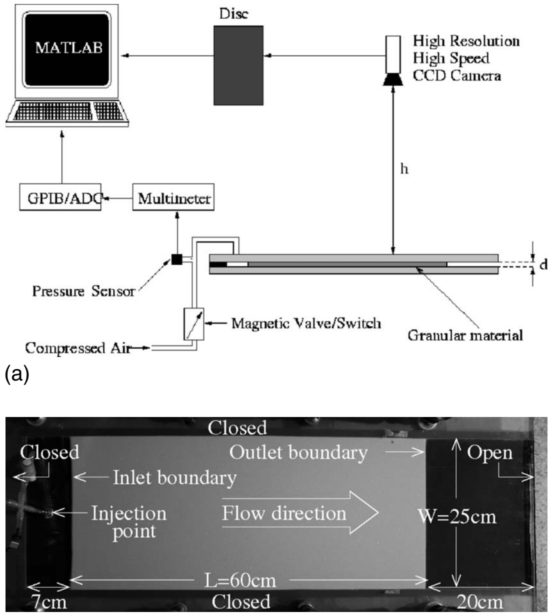

FIG. 1. (a) Experimental setup. The horizontally fixed Hele-Shaw cell is connected to a pressure-control unit and air is injected at constant overpressure when the magnetic valve is triggered to open. A high-speed, high-resolution charge-coupled-device (CCD) camera is used to follow the development of the displacement pattern and pressure is read at the inlet. (b) Image of the 25 cm $\times 87$ cm channel before the experiment begins. The cell is open in the direction of the indicated flow direction and closed elsewhere. During the experiment, air is injected through the tube near the closed boundary on the left opposite to the outlet. The cell is filled with approximately 25 cm$\times$60 cm$\times d$ of loosely packed material, consisting of polydisperse spherical glass particles, with mass density $\rho=2.6$ g cm^{-3} and diameters distributed between 75 and 150 μm. d is the plate separations used: 0.7 mm, 1.1 mm, or 2.1 mm. In order to apply the injected pressure, hence the pressure gradient, over the whole straight front and not only at a point just immediately near the injection hole, there is a $\sim$5 cm$\times$25 cm inlet chamber free of particles on the left around the injection point.

the system. In Sec. V we present a theoretical model and compare its predictions to experiments before concluding and summarizing in Sec. VI.

II. SYSTEM DESCRIPTION

A. Experimental setup

Figure 1(a) shows a simple sketch of the experimental setup, and Fig. 1(b) shows the sample before air injection. A Hele-Shaw cell [17] is built from two 1-cm-thick glass plates with dimensions 40 cm$\times$90 cm. One of the short boundaries and both of the long ones are sealed with a silicon rubber band and double-sided tape and then clamped together. These are labeled "Closed" in Fig. 1(b). The other short boundary, on the right-hand side in Fig. 1(b), is open. This gives a 25 cm$\times$87 cm$\times d$ channel. The injection hole is 4 mm in diameter and is situated 3 cm from the sealed short boundary along the longitudinal center. The system is studied for three different separations between the plates; $d=0.7$ mm, $d=1.1$ mm, and $d=2.1$ mm. Measuring the thickness of the glass plates individually and in the cell configuration at several locations, the plates are ensured to be parallel prior to performing the experiments.

The cell with a ready made sample is placed horizontally and connected to a gravitationally driven pressure source. At the inlet a pressure sensor is mounted in order to record the injection pressure. Images are acquired at a frame rate of 250 frames per second using a Redlake MotionPro high-speed charge-coupled-device (CCD) camera with spatial resolution of 1024$\times$1280 pixels. Pixels have a size of 0.6 mm, which corresponds to 4–8 particle diameters. The pressure injection is described by a step function in time: In the "low state," before air injection, the pressure recorded at the inlet equals the atmospheric pressure P_0. In the "high state," during air injection, the inlet pressure is maintained within a few percent at $P_0+\Delta P$, where ΔP is the imposed overpressure. The pressure step and image acquisition are synchronized. Injection of air into the model is triggered by switching on a magnetic valve 1 s after the beginning of the image sampling and the pressure recording.

B. Sample preparations

The granular material consists of polydisperse spherical glass beads, with diameters between 75 and 150 μm. Cohesion of a material consisting of beads of such small sizes is very sensitive to the humidity of the ambient air. To ensure the reproducibility of the experiment, it is important to control the humidity at a suitable level. The relative humidity in the room is therefore kept around 35% using a humidifier/dehumidifier.

During sample preparations the cell is filled from the open cell boundary when held upright with loosely packed granular material. For each experiment the volume of the cell that is filled is approximately 25 cm (width)$\times$60 cm (length) $\times d$ (thickness). The outlet is then temporarily sealed with a metal plate, which is slid roughly 20 cm deep into the open end of the channel. With the plate preventing particles from falling out, the cell is turned upside down a couple of times to produce a homogeneous and loose packing. The measured initial solid fractions for the three plate separations is $\rho_s^{init} \approx 0.55\pm0.03$. The presented method of sample preparation is chosen out of reproducibility purposes: We consider it to be more easily controllable than producing a more densely packed initial state by, e.g., gently tapping or vibrating the filled cell.

To position the granular packing inside the cell with a reproducible solid fraction and obtain straight boundaries at a reproducible distance from the inlet and outlet, the final rotation is done such that the particles fall inside the vertically positioned cell—from the inlet side toward the outlet blocked by the metal plate. The friction acting on the particles from the confining plates is then polarized [60] in the opposite direction of fluid/particle flow indicated in Fig. 1(b). The cell is then finally put in a horizontal position and the metal plate is removed. The position of the 60-cm-long granular packing inside the cell is such that ahead of the grains, a region of 20 cm between the grain packing and the cell opening is free of particles. The grain/air boundary facing the outlet is denoted the *outlet boundary*. Behind the packing, far to the left in the figure, a $\sim$7 cm (length) $\times$25 cm (width)$\times d$ (thickness) grain-free zone is acting as a "pressure-leveling" chamber. This large inlet chamber will ensure that the granular material feels the pressure gradient over the whole width of the cell rather than in a localized point around the injection point as would be the case if we were to inject directly into the granular matrix. This will allow us to study the translation symmetry breaking during the destabilization of initially straight fronts. The rotational symmetry breaking in the case of point injection has been previously studied [14]. The grain/air boundary facing the inlet is called the *inlet boundary*.

C. Image analysis

Image analysis provides several pieces of quantitative information on the ongoing processes like boundary motions or compaction processes. Indeed, when air is injected at sufficient overpressure, a zone free of grains develops around the inlet. As this emptied structure grows, the material ahead of it is compacted over a depth dependent on the size of the structure. With sufficiently high spatial resolution, as provided by our recording equipment, the compacted zone can be determined by image analysis.

We load two images of interest, such as, for instance, Figs. 2(a) and 2(b), into two matrices in our MATLAB image-processing program. Subtracting the gray levels between these images, pixel by pixel, and thresholding the resulting subtraction image at a suitable gray level, we can both extract the emptied displacement pattern and detect the motion of grains ahead of the emptied zone. After subtraction and thresholding, we obtain the result shown in Fig. 2(c), where the emptied pattern appears as a solid white region, while the particle displacements within the packing itself appear as white speckles on a black background. For presentation purposes the speckles are dilated such that they are visible in an image of such small scale. The well-defined densely speckled region ahead of the emptied zone is the compacted region where particles have been rearranged internally in the packing. There may be some isolated speckles both outside the defined compacted region and outside the cell. These are not due to particle motion, but are regarded as noise due to light flickering and reflection over single glass beads. In order to have a well-defined way of recognizing the compacted zone, we separate the densely speckled zone from the isolated speckles by performing a coarse-graining spatial filter as follows: We find a suitable box size, typically 1 cm, to check for speckle density. We move the box over the subtraction image and box-sized regions containing two or more speckles are regarded as belonging to the compaction region and tagged in gray. If there is only one or zero speckles within the reach of one box, the zone is regarded as immobile and tagged in black. The compaction region is found as the largest cluster and is shown in gray in Fig. 2(d), while the unperturbed region ahead appears all black. The vertical white line indicates the position of the outlet grain boundary.

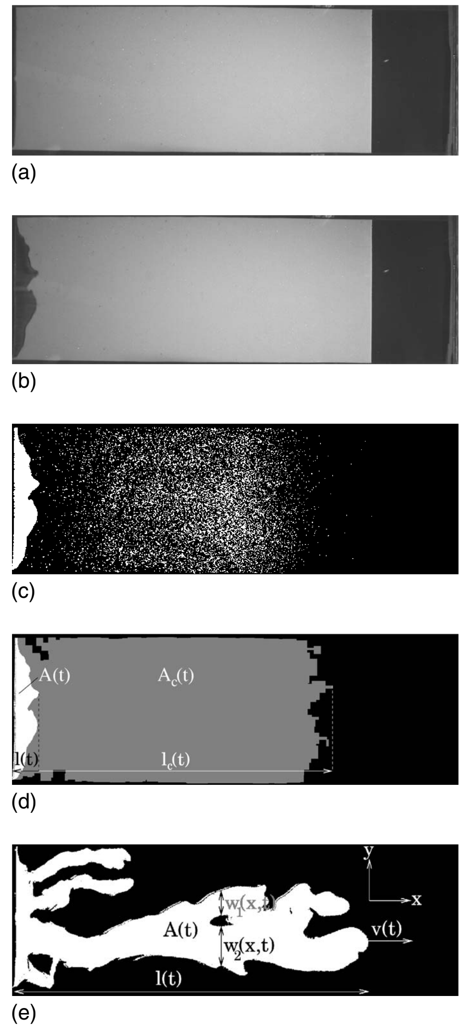

FIG. 2. Treating two images, one before injection (a) and one during and after (b), one can extract both the displacement structure and identify a speckled region ahead of it, representing a region where the granular material is compacted (c). Further image treatment allows us to extract the well-defined compacted region (d). (e) gives an example of the fingering growth phase and of the geometrical quantities that are typically measured.

This image treatment allows us to easily measure geometrical quantities for the emptied region, like, e.g., the emptied area $A(t)$, finger tip positions $l(t)$, and finger tip velocity $v(t)$ as indicated in Fig. 2(e). The finger width is defined as the total of the widths over all n individual fingers crossing position x at time t: $w(x,t)=\sum_{i=1}^{n} w_i(x,t)$, as shown in Fig. 2(e). For the compacted region, the area $A_c(t)$ and the linear extent $l_c(t)$ are also measured, as indicated in Fig. 2(d).

III. FOUR PRESSURE REGIMES

A. Phenomenology

In Fig. 3 we show and compare some of the experiments that we have conducted for the three different plate spacings at a range of injection pressures. The patterns and their dy-

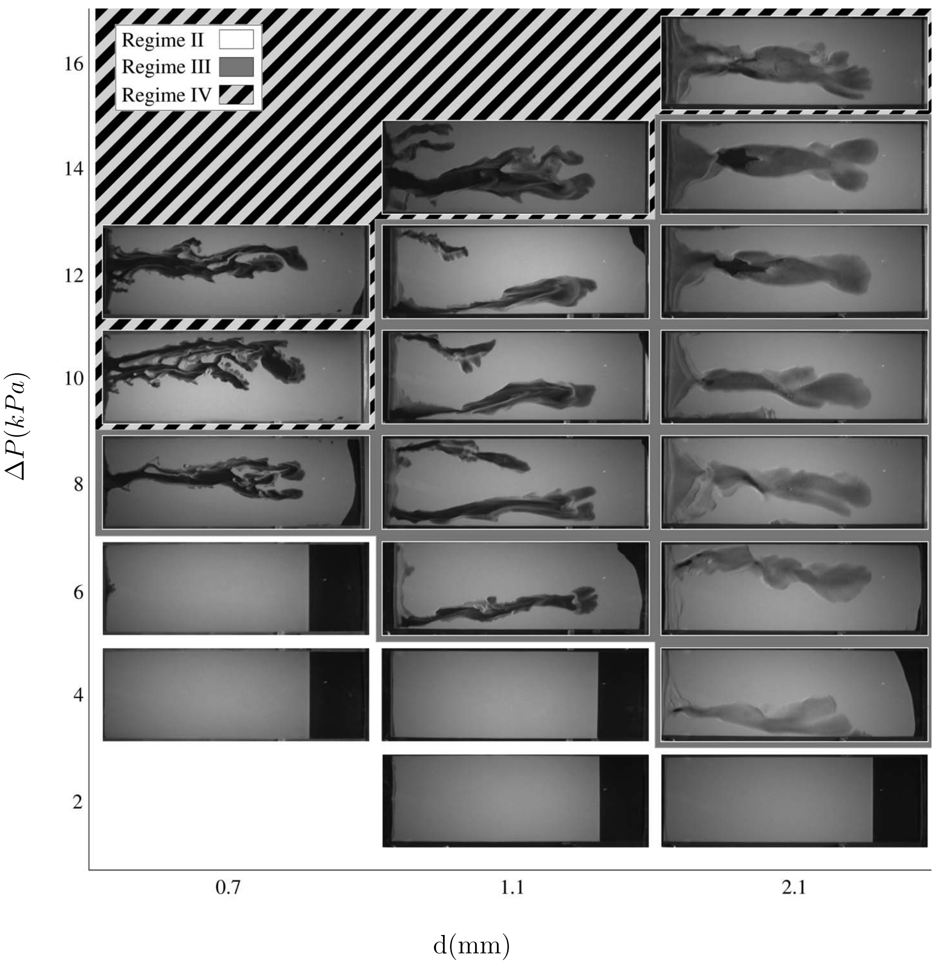

FIG. 3. Pattern formations for different pressures and plate separations. Apart from the experiment at 6 kPa for the 0.7-mm cell spacing, the experiments presented for regime II are attributed with displacements of short extent, and some particles are left inside the otherwise emptied structures. In these small-scale images this makes the displacements of these particular experiments not so easily visible.

namic properties are largely dependent on the pressure of the injected air, and the patterns formed can be classified into four different regimes as a function of this parameter.

1. Regime I: $\Delta P < P_1$

For injection pressures ΔP below some threshold pressure P_1 the hydrodynamic drag on the particles is not large enough to produce any detectable particle motion. The granular packing remains rigid while the air just permeates through the pore space, leaving no displacement pattern.

2. Regime II: $P_1 < \Delta P < P_2$

For injection pressures $\Delta P > P_1$, small displacement patterns develop and stabilize after a time t_1 [see Fig. 4(a)]. Typically, $t_1 \sim 0.1$ s and $l(t_1) \sim 2$ cm. Figure 4(b) shows the temporal development of the most advanced point of the emptied structure for $\Delta P = 4.4$ kPa and 1.1-mm plate separation. Both t_1 and $l(t_1)$ are increasing with injection pressure. The front of the patterns appears as relatively smooth with only some smaller bulges along it. Typically the pattern is not completely emptied of grains, but a layer a couple of grain diameters deep remains, lying on the bottom plate, inside the otherwise emptied structure. The depth of this sedimentary layer decreases with the injection pressure and increases with the plate separation. For large pressures and especially for 0.7-mm plate separation, the bottom plate is swept clean of grains inside the emptied zones.

As the emptied structure grows, the material ahead of it is compacted over a depth dependent on the extent of the size of this emptied zone. The compacted region is represented in gray in Fig. 4(a), and the temporal evolution is shown in Fig. 4(b). The size of both the empty zone and their associated compacted region increases with increasing pressure. By conservation of grain mass we may write

$$\rho_s^{init}(A + A_c) = \rho_s^{comp} A_c, \tag{1}$$

where ρ_s^{init} is the initial solid fraction, ρ_s^{comp} the solid fraction of the compacted area, and A and A_c are, respectively, the area of the emptied structure and the compacted zone as defined in Fig. 2(d). Equation (1) gives the solid fraction of the compacted region, $\rho_s^{comp} \approx 0.58 \pm 0.03$, which is $\sim 5\%$ denser than the initial solid fraction ρ_s^{init}.

Close to the upper transition pressure P_2, stick-slip motion of the front ahead of the empty structure is observed. The front advances one step and then stops again—often repeatedly. The outlet boundary is not observed to move except close to P_2, where it bulges slightly. For the 1.1-mm cell, deformation occurs for injection pressures above 5 kPa. From image subtraction it is seen that the deformation is localized in a zone smaller than the cell width and connected to the outer boundary, but disconnected from the inlet and

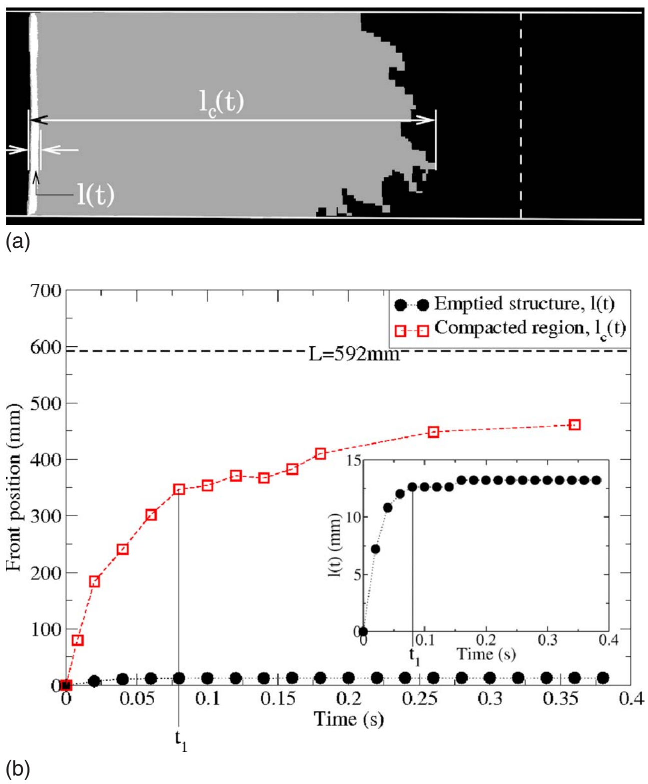

FIG. 4. (Color online) (a) Image subtraction between an image in the final state and a picture before injection of air reveals both the emptied structure (white) and compacted region (gray) for an experiment performed at injection pressure $\Delta P=4.4$ kPa (second pressure regime) and with 1.1-mm plate separation. $l(t)$ and $l_c(t)$ are the most advanced points of, respectively, the emptied and compacted zones. The vertical white dashed line indicates the position of the granular packing's outlet grain boundary. (b) Temporal evolution of the most advanced point of the emptied structure $l(t)$, and the associated compacted region $l_c(t)$, in correspondence with (a). The inset in (b) shows the most advanced point of the emptied structure at a finer length scale. At time t_1, the empty structure stops evolving.

the compacted region ahead of it. Thus, we interpret this grain motion at the outlet as a result of the hydrodynamic drag felt by the outermost particles when the pressure gradient reaches a significant level. An alternative cause for this motion at the outer boundary would be a force resulting from the motion of the grains at the inner boundary, being transmitted through solid contacts from grain to grain through the whole packing. That would, however, result in a granular motion all along the grains, transmitting the force, which does not correspond to the observation of two disconnected regions where grains move, around the inlet and around the outlet. As indicated by the fact that the region of the mobile grains around the outlet expands in volume, the material is being locally decompacted starting at the outlet boundary. The boundary of this mobile region is a decompaction front which progresses in the direction opposite of the air and grain flow direction. In this second pressure regime, this motion is transient, and this front stops at a few centimeters from the outlet. While it is a transient feature in this regime, the decompaction starting at the outlet and propagating backward is a characteristic and well-marked feature of the third pressure regime, where it is easier to visualize (see Fig. 5).

We define the *second pressure regime* by the fact that the inlet boundary eventually stops completely and never reaches the system outlet. In terms of applied overpressure, the pressure limits of this regime are denoted $P_1<\Delta P<P_2$.

3. Regime III: $P_2<\Delta P<P_3$

Above P_2, a structure similar to those seen in the second regime forms and stabilizes after t_1 seconds at a length $l(t_1)$. As in the second pressure regime, both t_1 and $l(t_1)$ are increasing with pressure. After t_1 the growth of the emptied structure stops, and the velocity of the front is zero apart from some occasional stick-slip movement. However, contrarily to the second regime, after this transient rest period, the empty zone starts growing again and eventually breaks through the entire cell. This feature defines the third pressure regime.

The time interval of no growth is seen as a plateau in Fig. 5(d). Figure 5(b) shows the early stages of growth of the emptied structure and the compacted region at $\Delta P=5.6$ kPa and $d=1.1$ mm [see Fig. 5(a) for color code]. Just as $l(t_1)$ is larger in the third regime than in the second, so is the extent of its associated compacted region. The solid fraction of the compacted region, ρ_s^{comp}, is $\sim 5\%$ higher than the initial ρ_s^{init}.

In Fig. 3 the emptied structure is observed to have some small branches, with radii of curvature comparable to the cell thickness, for the cell with 0.7-mm plate separation, while for 1.1 mm and 2.1 mm the front is increasingly bulged, but not ramified; i.e., its local radius of curvature is of the order of the cell width, or larger.

After some time t_2 the outlet grain boundary is observed to deform due to local decompaction. Figures 5(b) and 5(d) show that the decompacted region extends farther and farther into the packing, its rear front propagating backward, opposite to the flow direction. When the decompacted and compacted regions merge, we are no longer able to distinguish them with image subtraction, but by eye we observe that the decompacted region grows farther into the packing (bubbles empty of grains sometimes nucleate in the mobile region in a zone initially around the outlet and expanding backward toward the inlet). As the material is further decompacted, the in-plane friction decreases. The fluid drag is able to overcome the mobilized friction that initially stabilized the growth of the emptied structure. The granular material becomes locally fluidized and a "river" of grain flow connecting the decompacted and emptied structure is observed, while the propagation of the empty structure front resumes. Following the track of the granular river where bubbles have sometimes appeared, the emptied zone becomes a propagating finger, which eventually breaks through the entire packing. Such a typical finger structure is shown in Fig. 5(c) and is formed after a characteristic time t_3 indicated in Fig. 5(d). During the propagation of the empty finger, the air flow erodes the surrounding grains and carries them along, eroding its side boundaries. Ahead of the growing finger the granular material is mobilized over the whole cell width. We

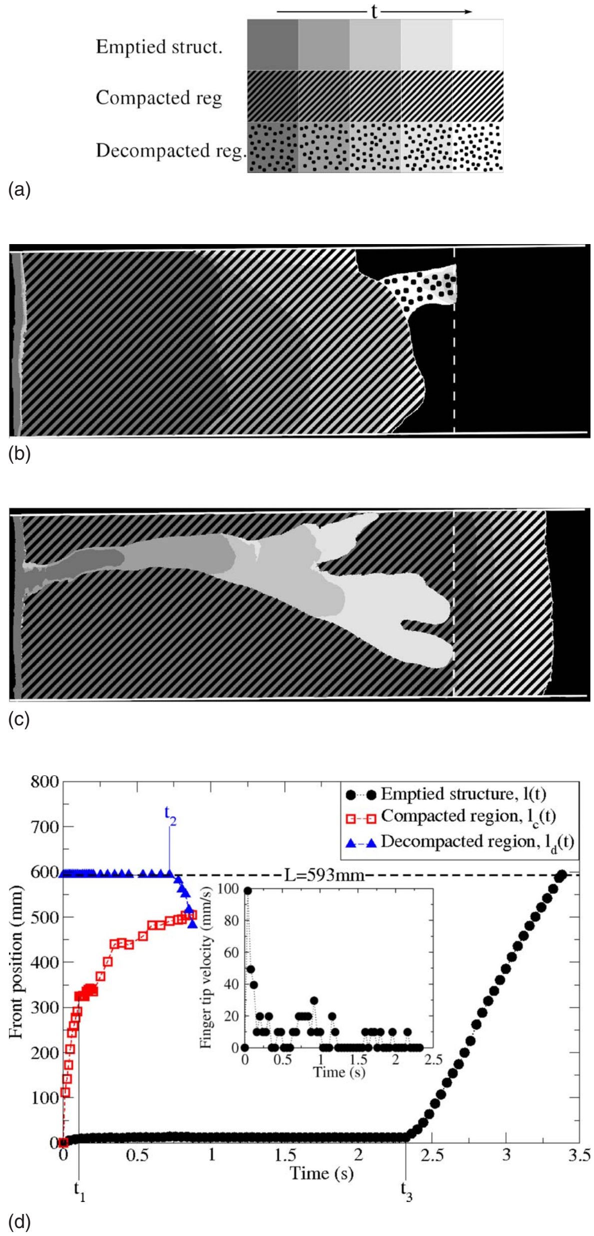

FIG. 5. (Color online) (a) Color coding of the emptied structure, compacted region, and decompacted region as function of time in (b) or emptied structure and mobile region in (c). (b) Early stages of the evolution of emptied, compacted and decompacted region ($t=0.01$ s, $t=0.60$ s, $t=0.78$ s, $t=0.84$ s, and $t=0.90$ s) at pressure $\Delta P=5.6$ kPa (the third pressure regime) and plate separation $d=1.1$ mm. The vertical dashed line indicates the initial position of the outlet grain boundary of the granular packing. (c) Fingering stage of the structure growth. The position of the finger tip is $l=L/4$ ($t=2.60$ s), $l=L/2$ ($t=2.86$ s), $l=3L/4$ ($t=3.09$ s), and $l=L$ ($t=3.37$ s), where $L=593$ mm is the initial length of the packing indicated with a dashed line. The shaded zones correspond here to mobile grain regions. (d) Position of the most advanced point of the emptied structure $l(t)$, compacted zone $l_c(t)$, and decompacted zone $l_d(t)$ as a function of time. Onset of growth events t_1, t_2, and t_3 is indicated. The dashed line indicates the initial position of the outlet boundary. The inset shows the velocity profile of the early growth stage and the rest period. The small peaks indicates stick-slip motion of the structure front.

are not able to distinguish this zone of granular flow as being compacted or decompacted. Hence the hatched marked region in Fig. 5(c) refers to the zone where grains have moved during a time t.

When the finger has penetrated the granular packing, forming a wide open channel linking the injection point to the open boundary, the flow accelerates suddenly, and due to the limitations of the source pump, the overpressure within the emptied region can no longer be sustained. The drag is consequently reduced, and the rest of the structure will not be able to grow any further. When the monitored overpressure in the inlet chamber decreases more than a few percent, the subsequent stages are not taken into account in the analysis, since this last stage is device dependent, being associated with the limitations of the source pump.

For injection pressures close to the upper threshold of the third regime, the deformation of the outlet boundary is observed to be a result of the compacted region extending over the length of the packing, rather than the result of a fluid drag becoming significant at the outlet. This transition will be characterized more quantitatively in Sec. IV.

During the resting time t_3-t_1, from the moment when the empty zone stops growing until it starts again to develop toward breakthrough, the front of the emptied structure typically undergoes some stick-slip motion—growing an increment and stopping again, repeatedly. This is indicated in the inset plot of the velocity as a function of time for the early stage of growth and the rest state in Fig. 5(d).

t_3-t_1 is decreasing with increasing pressure and approaches zero near the transition pressure P_3. Injection pressures where no transient rest of the growth of the empty zone is observed mark the transition to the fourth pressure regime.

4. Regime IV: $\Delta P > P_3$

Exceeding P_3 the transient stage of no growth of the empty zone does not exist, and the finger formation will grow continuously to breakthrough, a feature defining the *fourth pressure regime*. Figures 6(a) and 6(b) display the temporal evolution for the emptied pattern formation and its associated compacted region for an experiment at 14 kPa in a 1.1-mm-thick cell, respectively, at an early stage and during the fingering stage. Figure 6(c) shows the position of the emptied and compacted fronts. Within this pressure regime, the deformation of the outlet grain boundary is not due to decompaction, as will be shown in Sec. IV. The injection pressure is high enough to overcome jamming effects and pushes the granular material like a piston. In such a process the compacted region reaches and deforms the outlet boundary in $t_2 \sim 0.2$ s. During compaction, the solid fraction increases by $\sim 5\%-6\%$ with respect to the initial one.

The advancing fingers, as shown in Fig. 6(b), is different from those in the third pressure regime in the sense that they are wider and more eroded. From Fig. 3 we also see that the influence of a reduction of the plate separations leads to more numerous and more complex fingers.

B. Phase diagram

The transition pressures between the regimes used for classifying the displacement patterns change with the plate

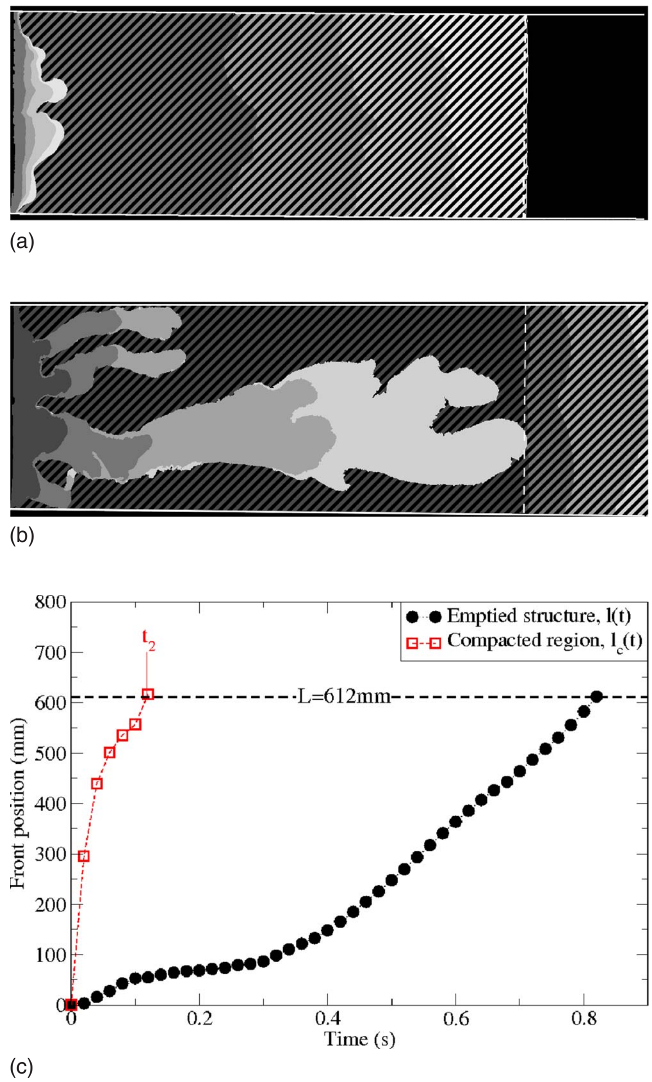

FIG. 6. (Color online) (a) Early stages of emptied and compacted regions with $\Delta P = 14$ kPa and plate separation $d = 1.1$ mm (fourth pressure regime). The positions of the respective fronts are shown for 0.02 s, 0.04 s, 0.08 s, 0.16 s, and 0.20 s following the same color code as Fig. 5(a). The vertical white line to the right indicates the outlet boundary of the granular packing $t = 0$. (b) shows the pattern formation at a later stage; $t = 0.2$ s, 0.4 s, 0.6 s, and 0.8 s. In (c) the position of the most advanced point of the emptied zone, $l(t)$, and the compacted region, $l_c(t)$, is plotted versus time.

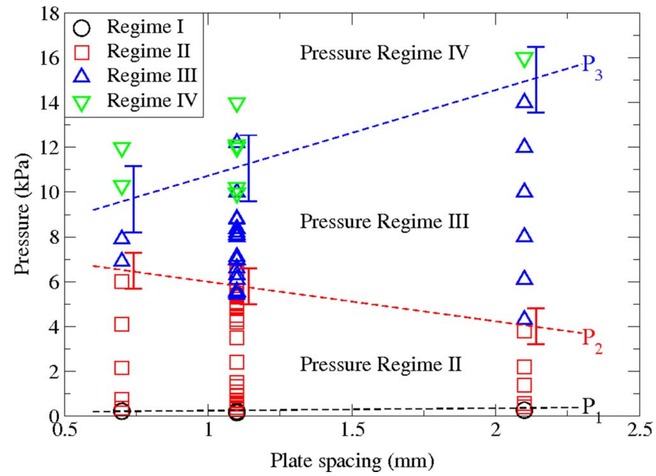

FIG. 7. (Color online) Phase diagram where we have classified and separated the patterns into pressure regimes. The patterns and into which regime they belong is a function of pressure and cell spacing. The dashed lines indicate the transition pressures P_1, P_2, and P_3 between the flow regimes.

separation. In Fig. 3 experiments for plate spacings 0.7 mm, 1.1 mm, and 2.1 mm are displayed and compared for a range of injection pressures. This information can be condensed into and visualized in form of a phase diagram as in Fig. 7.

The minimum pressure required to mobilize particles defines the transition pressure P_1 between the first pressure regime and the second. Depending on the plate separation, we measure $P_1(0.7\ \text{mm}) \simeq 0.20 \pm 0.05$ kPa, $P_1(1.1\ \text{mm}) \simeq 0.25 \pm 0.05$ kPa, and $P_1(2.1\ \text{mm}) \simeq 0.35 \pm 0.1$ kPa. The transition from the second pressure regime to the third is taking place at a lower pressure as the plate separation is increased; i.e., P_2 is a decreasing function of the plate separation: $P_2(0.7\ \text{mm}) \simeq 6.3 \pm 0.5$ kPa, $P_2(1.1\ \text{mm}) \simeq 5.9 \pm 0.5$ kPa, and $P_2(2.1\ \text{mm}) \simeq 4.0 \pm 0.5$ kPa. However, the trend is the opposite for the transition between the third and fourth regime, where P_3 is an increasing function of the plate separation: $P_3(0.7\ \text{mm}) \simeq 9.0 \pm 1.0$ kPa, $P_3(1.1\ \text{mm}) \simeq 11.0 \pm 1.0$ kPa, and $P_3(2.1\ \text{mm}) \simeq 14.0 \pm 1.0$ kPa.

The transition pressures are represented by a pressure interval rather than a uniquely defined value, which is due to the fact that identical realization of the initial conditions of the granular packing from one experiment to the other is not possible. For each trial the granular packing will always present small variations in, e.g., solid fraction and disorder associated to their internal configuration.

The error bars are based on the scattering of data points from the experiments of the $d = 1.1$ mm configuration, for which the number of experiments conducted is far more significant than the other two configurations. The length of the bars is determined by the overlap of data points between successive regimes. We assume that the uncertainty is of the same order for all plate separations. For P_1 the error bars are smaller than the symbol size and therefore omitted in Fig. 7 due to presentation considerations.

A character of the flow is worth noticing in these experiments: The flow is mainly oriented along the plates, and the velocity and density seem mainly invariant along the vertical axis in the two thinnest cells. The system exhibits a "quasi-two-dimensional" (quasi-2D) character. We see, for instance, from Fig. 3 that in the 0.7- and 1.1-mm cells, the bottom plate in the emptied zone is swept clean of grains. However, in the largest (2.1-mm-thick) cell, 14–28 grain diameters gather between the plates and the "quasi-2D" aspect starts to lose its validity. The blurred appearance for these experiments (see Fig. 3) is coupled with a more "3D-like" behavior where the edges of the finger formations have a slope at a low angle of repose, and also layers of grains are deposited on the bottom plate within the finger formation during propagation. The injected air moves the upper particles more easily. This might be due to the fact that the gas phase travels

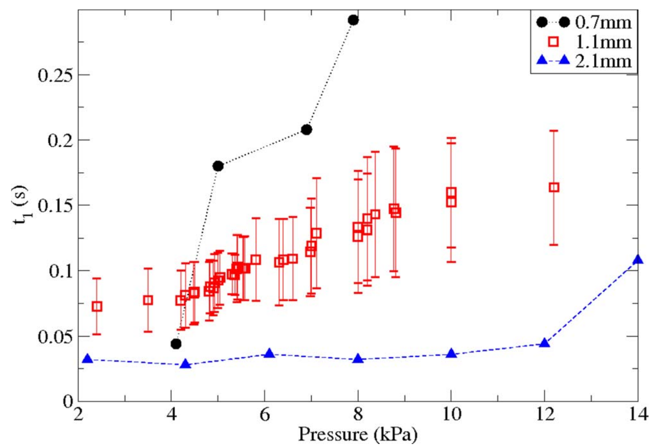

FIG. 8. (Color online) The time t_1 a as function of injection pressure for the three different plate separations. t_1 is the time between the injection start and the first stop of the growth of the emptied structure.

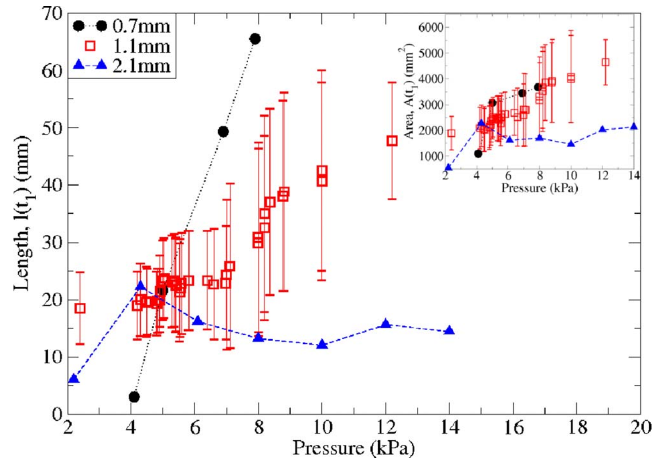

FIG. 9. (Color online) The length $l(t_1)$, penetration depth of the emptied structure after its initial growth, as function of pressure and plate separation.

more favorably along the upper plate, combined with the friction between the granular material and the bottom plate being higher than along the upper plate due to the gravity acting locally on the granular column.

IV. FINGER DYNAMICS

Properties of the pattern formations emerging during air injection, such as the characteristic times (t_1, t_2, and t_3), position of the structure front, its width, and finger velocity, are all sensitive to changing the injection pressure and/or plate separation. These are measurements that we will now compare for different ΔP and d.

The fact that an identical realization of a packing from one experiment to another is impossible due to a high level of randomness and heterogeneity in the granular packing leaves us with significant scattering of data points acquired through the experiments. To determine the mean value and standard deviation and interpret the data in a conclusive and statistically reliable manner, we perform running averages on the experimental set. The mean value is obtained independently for each plate separation and gives an indication of the variations of the observables expected as a function of this parameter. The standard deviations of the observables, which are used to define the error bars, are obtained from the scattering of the data points within the interval used by the running average. The averaging is applied over the set of experiments carried out in the 1.1-mm-thick system, which is the most significant one statistically speaking. We do not expect the standard deviation of the observed quantities to vary significantly with the plate separation.

The time to form a stable structure (in pressure regime 2) or a temporarily stable structure (in pressure regime 3), t_1, and the length of the structure at this moment, $l(t_1)$, is increasing with the injection pressure, as shown, respectively, in Figs. 8 and 9. Changing the plate separation also seems to affect t_1 and $l(t_1)$. They both become more sensitive to variations in the injection pressure as the plate separation decreases. We cannot see the systems behaving very differently at low and moderate injection pressures. For the area at time t_1, $A(t_1)$ (inset in Fig. 9), only the 2.1-mm case differs, while the 0.7-mm and 1.1-mm cases are quite comparable.

Depending on the injection pressure and the pressure regime we are in, the deformation of the outlet boundary can either be due to decompaction or compaction. The time t_2, which is the time it takes for the outlet boundary to start deforming, is seen to decrease with increasing pressure for all plate separations in Fig. 10. From Fig. 10 we conclude that varying the plate separation does not significantly influence t_2.

The time before the inner boundary starts moving again, t_3, is also not sensitive to the plate separation either, as observed from Fig. 11. t_3 is decreasing as a function of the injection pressure within the third pressure regime, from an infinite value in the first or second regime, toward zero entering the fourth pressure regime.

The velocity of the front of the emptied structure as a function of time is displayed in Fig. 12 and changes characteristics from one pressure regime to the other. Generally, the velocity v increases with injection pressure. In the first pres-

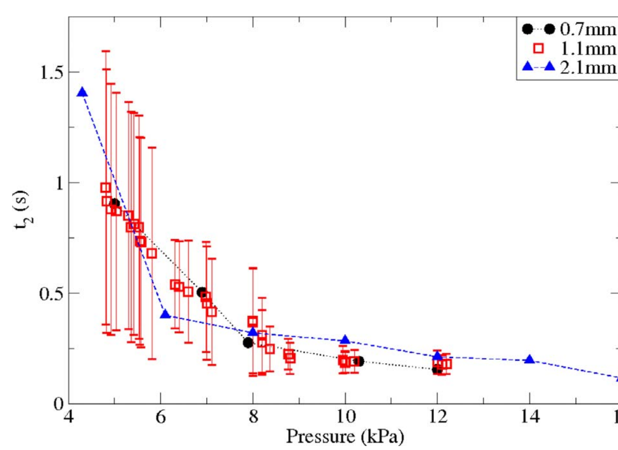

FIG. 10. (Color online) Time before deformation of the outlet grain boundary t_2.

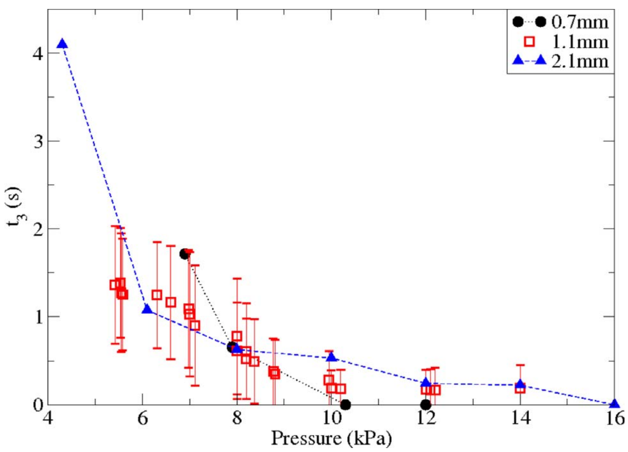

FIG. 11. (Color online) The time t_3 as a function of injection pressure for the three different plate separations. t_3 is the time elapsed between the start of the experiment and the start of the second period of motion of the inner boundary.

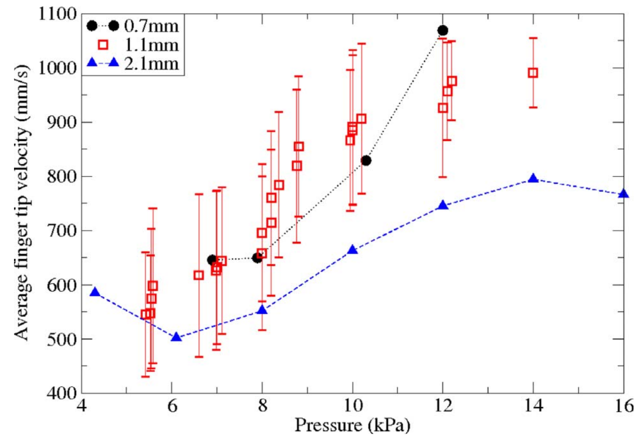

FIG. 13. (Color online) Average velocity of the most advanced finger as a function of pressure for the three different plate separations. The velocity is measured and averaged over a window at distances of the inlet from $L/4$ to $3L/4$, where $L \approx 60$ cm is the length of the granular packing before injection is initiated.

sure regime, $v=0$ all over. The velocity peaks during formation of an emptied structure within the second pressure regime, before the structure is stabilized after t_1 and the velocity falls to zero. For experiments within the third pressure regime, it is worth noticing that in the time interval from t_1 to t_3 where the front is more or less inactive, there are occasional stick-slip motions before a finger accelerates toward breakthrough after t_3. In practice, to discriminate this fast stick-slip motion from the more global rest period, t_3 is measured as the last moment where a zero velocity of the finger tip is observed. In the continuous-flow regime, the fourth pressure regime, the finger does not go into a rest state on its way to breakthrough, but is certainly slowed down when friction is mobilized.

To obtain a characteristic value for the velocity as function of ΔP and d, the average velocity of the tip of the most advanced finger is found within a central window extending over distances from the inlet going from $L/4$ to $3L/4$ as presented in Fig. 13. Here $L \approx 60$ cm is the length of the granular packing before the air injection is initiated. Since we are interested in the average speed of the progressing finger formation, it is reasonable to neglect the first stages, which include rapid growth and a transient rest stage with sporadic stick-slip motion, and consider only the continually advancing finger. When particles start to be pushed out of the cell, friction decreases, which in turn results in an acceleration of the finger—which may cause an undesirable effect on our velocity calculations also. So choosing a window from $L/4$ to $3L/4$ ensures that we are averaging over a zone where the velocity is almost constant and restricted to little randomness. We can conclude that there is an obvious increase of the finger velocity as the pressure is increasing. Changing the plate separation does not seem to affect the average finger velocities significantly. The finger velocities of the 0.7-mm cell fall within the error bars of the 1.1-mm configuration and likewise for the 2.1-mm case at low pressures. At higher pressures, the 2.1-mm case differs slightly from the other data, but falls within two standard deviations, regarded to be within the natural scattering of data points within our system. We conclude that the plate separation chosen for these experiments does not influence significantly the finger tip velocity.

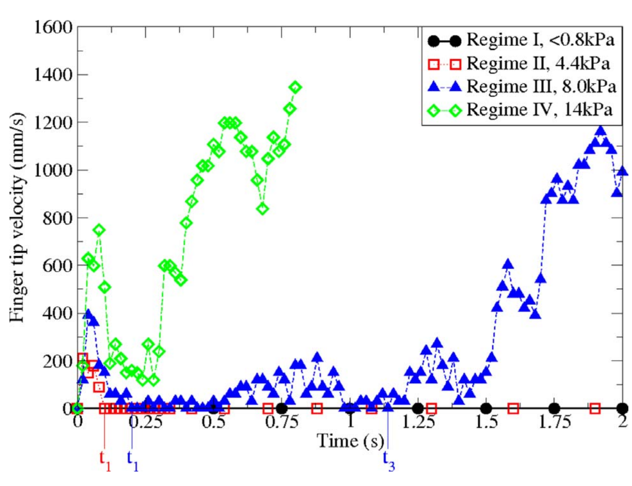

FIG. 12. (Color online) Velocity as a function of time for different injection pressures within the four defined pressure regimes.

As the fingers advance toward breakthrough, the interior of the structure is slightly eroded. This can be seen as discrepancies between subsequent graphs both for the total and averaged finger width as function of position in Fig. 14. Here the average finger width is the total width of the intersection between the empty zone and cuts perpendicular to the flow direction, divided by number of fingers. For comparison and justification of the differences between the total and averaged finger width an image of the finger having developed $1L$ is inserted into the plot.

It is also possible to measure alternatively a characteristic finger width for a structure that has advanced over a distance L through the entire cell, as $\hat{w}(\Delta P, d) = A/L$, where A is the area of the emptied zone. The number of fingers does not affect $\hat{w}$. This alternative measure is shown in Fig. 15. We

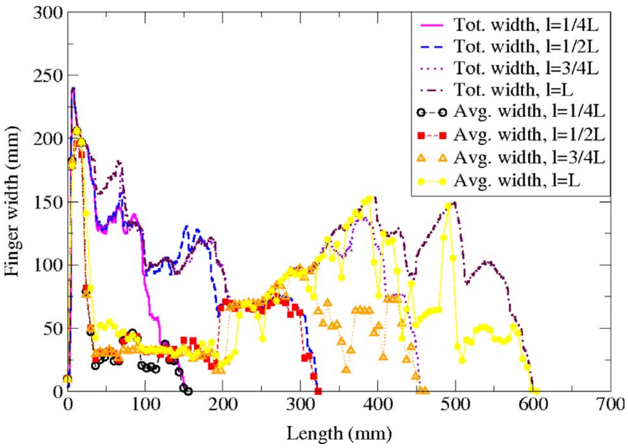

(a)

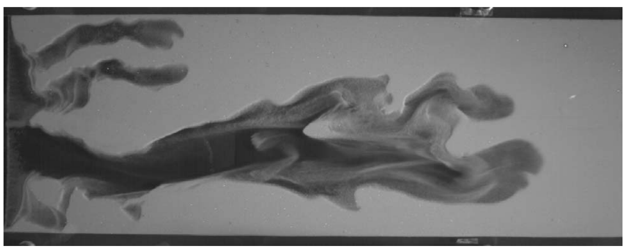

(b)

FIG. 14. (Color online) Total and average finger widths as function of time when the finger has advanced a distance $L/4$, $L/2$, $3L/4$, and L, where $L \approx 60$ cm is the initial length of the granular packing. The experiment is performed with 1.1-mm plate spacing at 14 kPa overpressure. Below the graph a picture of a finger that has advanced a distance $l=L$ is inserted to illustrate and help the comparison between total and averaged finger widths.

notice a trend of fingers widening with respect to increasing pressure, while the plate separation does not seem to be of any influence.

V. DISCUSSION

The origin of the instability is similar to the mechanism first described by Saffman and Taylor [18], in nonmiscible fluid flow where a low-viscous fluid displaces a more viscous one. The pressure gradient $\vec{\nabla} P$ is the driving force of the granular motion: the fluid drag over the grains is a growing function of the local velocity of the air through the grains, which is obtained by dividing the Darcy velocity [59] by the local porosity Φ, giving [61]

$$\vec{u}_a = -\frac{\kappa(\Phi)}{\eta\Phi}\vec{\nabla} P, \tag{2}$$

where η is the air viscosity and $\kappa(\Phi)$ the local porosity-dependent permeability of the granular assembly. Within the fingers the permeability is huge compared to the one in the pore space of the granular material, which will favor air flow in the emptied region. Consequently, the pressure is more or less constant within the emptied structure, and at the tip of the longest finger, the distance l from the tip to the open boundary is the smallest, so that the driving pressure gradient $\vec{\nabla} P \simeq \Delta P / l$ is largest here. Growth of the most advanced finger is therefore favored at the expense of the rest of the structure. This is the origin of the observed instability, which gives rise to fingering and destabilizes the initially straight interfaces. In contrast with the Saffman-Taylor instability observed in nonmiscible fluid flow, the pure air and the granular/gaseous fluid mixture exchange mass, i.e., interpenetrate without any surface tension effect. The stabilizing phenomenon is not surface tension here, but the friction mobilized between the granular matrix and the confining plates.

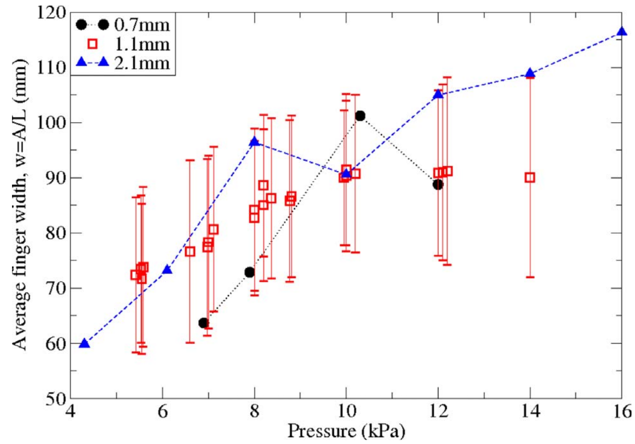

FIG. 15. (Color online) Average finger widths $w=A/L$, as a function of pressure when a finger has advanced a distance equal to the initial length $L \approx 60$ cm.

Another mechanism that contributes to the stabilization of the structure front is a result of another important difference between the system described here and Saffman and Taylor's system: in the present case, the granular material and the fluid are interpenetrating. As the air flows through the granular material, the pressure field diffuses and the gradient will smoothen out and be reduced over the front. If the growing friction becomes large enough to balance the decreasing hydrodynamic drag on the particles, the emptied structure stops growing.

In the formation of the emptied structure and the associated compacted region the initial solid fraction may be of great importance. For an initially loose realization of the granular packing, as presented in this study, the material must compact before "jamming" through the mobilized friction and balance with the hydrodynamic drag force can occur. Before the onset of jamming particles may be displaced over a large extent, leaving what is defined as an emptied structure. For higher initial packing fraction obtained by, e.g., tapping the cell, the material is precompacted and the friction acting between the granular material and the plates is higher due to stronger arching effects. Further compaction and particle displacement become more difficult, and emptied structures of smaller extent are expected. No systematic experimental studies have been conducted regarding the effect of initial packing fraction variations on the extension of the emptied and compacted region for this system, but it is evident in numerical simulations performed in relation with

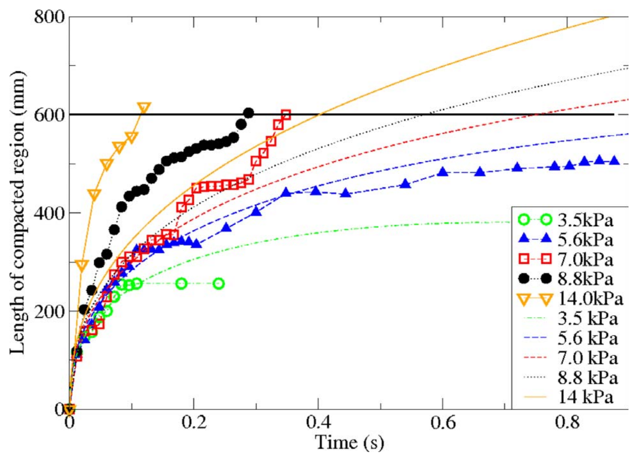

FIG. 16. (Color online) Position of the compacted zone's most advanced point as a function of time at different injection pressures. The plate separation is 1.1 mm. The analytical solution in Eq. (12) gives a good fit for low injection pressures. Friction coefficient $\mu=0.20$ is used for this particular fit.

the studies on granular flow in the circular cell geometry in Ref. [14].

As the emptied structure grows, the material ahead of this structure compacts over a depth dependent on the size of the structure. Information on the size of the compacted region is extracted using image subtraction techniques. In Fig. 16, the position x of the most advanced point of the compacted zone is plotted as function of time t, $x(P_i,t)$, for five experiments at different injection pressures P_i, in the 1.1-mm-thick cell: one within the second pressure regime, three within the third, and one from the fourth. For the lowest injection pressures, the empty structure and its associated compacted structure reach saturation after ~ 0.1 s and no deformation of the outlet boundary is seen. For larger injection pressures P_i, the growth of this compacted zone eventually reaches the outer boundary at a time previously defined as $t_2(P_i)$.

We propose below a simple model which in the lowest-pressure regimes successfully renders for these two observables the extent of the compacted zone as function of time, $x(P_i,t)$, and the time to deform the outer boundary, $t_2(P_i)$.

Following from the mass conservation of air,

$$\frac{\partial \rho_a}{\partial t} + \vec{\nabla}\cdot[\rho_a \vec{u}_a] = 0, \tag{3}$$

where ρ_a is the mass of air per unit of total volume (including grains and pores) and $\vec{u}_a$ is the interstitial gas velocity.

Considering air as an isothermal ideal gas,

$$\rho_a = \frac{\Phi P}{k_B T} M, \tag{4}$$

where M is the mean mass of the gas molecules, $k_B T$ is Boltzmann's constant times the temperature, $P=P(x,t)$ is the position- and time-dependent pressure within the granular material, and Φ is the porosity of the granular matrix.

During the initial compaction stage, the velocity of the granular medium is negligible compared to the gas velocity, so that the velocity of the interstitial gas is directly obtained from Eq. (2). Neglecting the small initial variations of porosity, Φ is constant and homogeneous so that

$$\Phi \frac{\partial P}{\partial t} = \vec{\nabla}\cdot\left[\frac{\kappa}{\eta} P \vec{\nabla} P\right] = 0. \tag{5}$$

Writing $P=P_0+\Delta P$, with P_0 the atmospheric pressure at the outlet, the imposed overpressure is only a few percent of the atmospheric pressure, so that $\Delta P \ll P_0$, and Eq. (5) can be approximated as a simple diffusion law

$$\frac{\partial P}{\partial t} = D\nabla^2 P, \tag{6}$$

with a diffusion constant $D=\kappa P_0/\eta\Phi$. The atmospheric pressure is $P_0=10^5$ Pa, and the viscosity of air $\eta=1.8\times10^{-5}$ Pa s. With the porosity $\Phi=1-\rho_s\approx 0.45$ for the loose-packed granular "plug," the permeability can be estimated using the density dependent Carman-Kozeny relation [62], so that for particles of mean radius $a\approx 50$ μm,

$$\kappa = \frac{a^2}{45}\frac{\phi^3}{(1-\phi)^2} = 1.67\times10^{-11}\ \mathrm{m}^2. \tag{7}$$

The diffusion constant can then be estimated as $D\approx \kappa P_0/\eta\Phi = 0.207\ \mathrm{m}^2\,\mathrm{s}^{-1}$. A characteristic time for the overpressure to diffuse through the length of the granular plug $L=0.60$ m is

$$\tau = \frac{L^2}{2D} \simeq 0.9\ \mathrm{s}, \tag{8}$$

which is a rough estimate, but in agreement with what is observed for low pressures in Figs. 10 and 17.

We impose a constant overpressure at the inlet at positive times and a null one at negative ones, i.e., $\Delta P(x=0,t)=P_i\Theta(t)$ where Θ is a Heaviside function, while the overpressure is maintained at zero at the outlet. As long as the packing stays essentially immobile, the pressure source is obtained by solving this diffusion equation with these boundary conditions, with initial condition $P(x\geq 0,\ t=0)=0$. A last approximation can be done by considering a long packing, i.e., by considering that the outlet condition is imposed at infinite distances: $P(x=\infty,t)=0$. This leads to a simple analytical solution of the diffusion equation,

$$\Delta P(x,t) = P_i \frac{2}{\sqrt{\pi}}\int_{x/\sqrt{2Dt}}^{\infty} e^{-y^2} dy. \tag{9}$$

The pressure gradient $\vec{\nabla}P=\partial P/\partial x$ gives the fluid velocity $\vec{u}_a = -(\kappa/\eta\Phi)\vec{\nabla}P$ which we use to estimate the Reynolds number $\mathrm{Re}=\rho_{air}u_a a/\eta$. The mass density of air is $\rho_{air}=1.1\ \mathrm{kg\,m}^{-3}$. The pressure gradient and hence the velocity are at their highest at the inlet boundary $x=0$, which gives

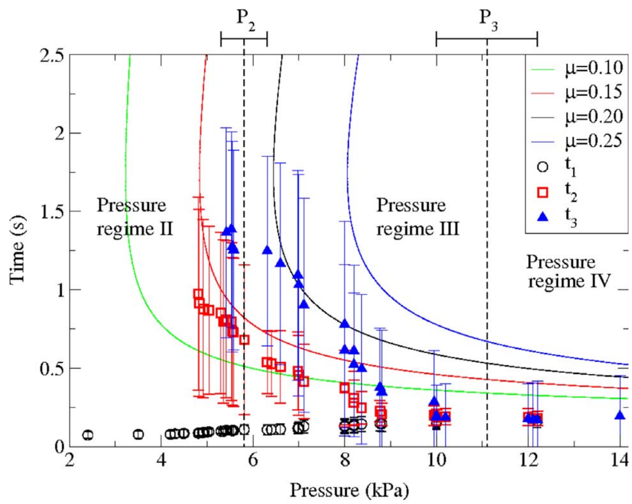

FIG. 17. (Color online) Time to form an initial emptied structure, t_1; time before deformation of the boundary, t_2; and time before breakthrough, t_3, as a function of injection pressure. t_2 is compared with the analytical solution for different friction coefficients μ. Pressure regimes and their associated thresholds with estimated error bars are indicated.

$$\mathrm{Re}_{\max} \approx 1.1 \times 10^{-5}\ \mathrm{s}^{1/2}\ \mathrm{Pa}^{-1}\frac{P_i}{\sqrt{t}}. \tag{10}$$

Such a small Reynolds number confirms that we are operating within the laminar flow regime for our experiments and justifies the use of the Darcy law in our theoretical model.

One can exploit the diffusion equation (9) to estimate the extent of the compacted zone: At the front of the mobile zone, the initial in-plane forces are presumably negligible, and we can assume that the motion of the grains is caused by the fact that the fluid drag exceeds the friction threshold exerted by the plates over the grains, at the tip of the mobile zone. For a layer of thickness Δz the fluid drag per unit area of the plates is $-\vec{\nabla}P\,\Delta z$. The friction can be modeled as a Coulomb friction, with a pressure over the bottom plate obtained from the weight of the grain column and forces neglected along the top plate, so that the friction force per unit area is $f=\mu(1-\Phi)\rho g\,\Delta z$, where μ is a Coulomb friction coefficient and $\rho=2.6\ \mathrm{g\,cm^{-3}}$ is the density of the glass beads. Using the pressure profile, Eq. (9), this leads to the following for the position of the tip of the mobile zone:

$$\mu(1-\Phi)\rho g = \sqrt{\frac{2}{\pi D t}}P_i e^{-x^2/2Dt}. \tag{11}$$

Solving this equation for $x=x(t)$ gives the position beyond which grains will not have moved:

$$x(t) = \sqrt{2Dt}\sqrt{-\min\left[\ln\left(\sqrt{\frac{\pi D t}{2}}\frac{\mu(1-\Phi)\rho g}{P_i}\right),0\right]}. \tag{12}$$

Note that for small times the logarithm function is negative so that the square root is a real number. The function $x(t)$ is positive and increasing up to a maximum value

$$x_m = \frac{P_i}{\mu(1-\Phi)\rho g\sqrt{\pi e/2}}, \tag{13}$$

which occurs at a time

$$t_m = \frac{2P_i^2}{\pi\, eD[\mu(1-\Phi)\rho g]^2}. \tag{14}$$

When $t>t_m$ the coordinate $x(t)$ decreases through positions where displacement has already occurred and where nothing more will happen. Eventually $x(t)=0$ and for larger times, the pressure force is smaller than the friction threshold everywhere.

Using $\mu=0.20$, close to what was estimated in simulations of a similar system [14], the analytical solution, Eq. (12), gives a good approximation for the position of the tip of the mobile zone at low and moderate injection pressures (within the second pressure regime and beginning of the third), as seen when comparing with experimental data in Fig. 16. This is valid up to the moment when it reaches the outer boundary.

This solution fails, however, to give a description at higher injection pressures where the material is observed to compact all the way up to the outlet boundary in roughly $\sim$0.1–0.3 s (see Fig. 16). The growth process of the compacted region is much quicker than the time it takes the air flow to travel the linear distance of the system size. In this case, the assumption that contact forces between the particles at the tip of the compacted zone are negligible probably fails, and presumably the compaction is carried through particle contact rather than through hydrodynamic drag.

Eventually, this solution can be considered to derive the time the moment when the fluid drag is sufficient to deform the outer boundary, which defined the time t_2. Specifying $x(t_2,P_i)=L$ in Eq. (12), we obtain an implicit equation for $t_2(P_i)$. In Fig. 17 all the pressure-dependent time measurements t_1, t_2, and t_3 for the experimental sets of the 1.1-mm configuration are compiled together for comparison. The pressure regimes and their associated transition pressures with estimated error bars are also indicated. The analytical solution for t_2 is plotted for different friction coefficients μ, where $\mu=0.15$ fit the experiments very closely. This value of μ deviates slightly from the one used to model the compacted region—Eq. (12)—in Fig. 16. The foundation of the model of both the compacted region and the time before deformation of the outlet boundary is the solution in Eq. (9) for an infinite length of the conducting medium, while in the real world the packing is indeed of finite extension. This, together with the fact that porosity variations are neglected, might be a significant source of error. In conclusion, we estimate roughly $\mu\sim0.15$–0.20.

Local porosity variations may modify this simplified model. Its influence can be estimated through comparing the pressure gradients $\vec{\nabla}P_{\Phi}(x,t)$ and $\vec{\nabla}P_{\Phi_c}(x,t)$, found by $\vec{\nabla}P(x,t)=\partial P/\partial x$ of Eq. (9), respectively, for the initial solid fraction $\Phi=1-\rho_s^{init}=0.45$ and the compacted state represented by $\Phi_c=1-\rho_s^{comp}=0.42$. By division

$\vec{\nabla} P_{\Phi_c}(x,t)/\vec{\nabla} P_{\Phi}(x,t)$ in the limit of small x and t—i.e., near the inlet air/grain interface during the first stage of displacement and compaction—we find that $\vec{\nabla} P_{\Phi_c}$ may be $\sim 16\%$ higher than $\vec{\nabla} P_{\Phi}$. Local porosity variations may indeed induce large pressure variations and significantly influence the grain dynamics.

VI. SUMMARY AND CONCLUSIONS

Through our study we have given a qualitative and quantitative description of displacement patterns in granular materials confined in a rectangular Hele-Shaw cell.

The driving force in this system is the pressure gradient acting between the front of the pattern formation and the outlet grain boundary. The competing stabilizing mechanisms are friction mobilized between the granular material and the confining plates. These two mechanisms can be controlled by tuning the injection pressure and separation between the glass plates, giving a wide range of patterns. Given the different pattern formations and their dynamic behavior, four pressure regimes are defined into which the patterns are categorized.

In the first pressure regime there is no grain motion and the air simply permeates through the pores of the granular packing.

In the second pressure regime, particles are being displaced, forming a stable formation after t_1 seconds. The patterns appear with a relatively flat interface for large plate separation and become increasingly bulged when the plate separation is decreased. Deformation of the pattern front is more noticeable when a higher injection pressure is applied. The time to form a pattern, t_1, is increasing with the injection pressure ΔP and smaller plate spacing, which is also the case of the pattern size $l(t_1)$. The extent of the compacted zone is also increasing with ΔP. This feature is also captured in our theoretical model based on balance of the hydrodynamic forces acting on the particles (governed by the diffusion equation) and Coulomb friction between the particle matrix and confining plates.

The instability becomes more pronounced when entering the third pressure regime—especially for narrow plate separation. An empty structure is established in t_1 seconds before a transient stabilization. Deformation of the outlet boundary is observed after a t_2 seconds. The material near the boundary is locally decompacted after the propagation of a diffusive pressure front, which decreases friction with the confining plates and the ability to balance the hydrodynamic forces. The granular material is locally fluidized during this decompaction, eventually resulting in a finger breaking through the sample. A secondary motion of the inner boundary happens after t_3 seconds. t_3 is pressure dependent, but not sensitive to plate separation. The duration of the rest-state, t_3-t_1, becomes shorter with higher injection pressure and approaches zero. $t_3-t_1=0$ marks the transition to the fourth pressure regime. Close to this transition, but still in the third regime, deformation of the outlet boundary after t_2 seconds is due to the compacted zone reaching the boundary carried through particle contacts, rather than being local decompaction as a result of hydrodynamic forces acting on the outermost particles. Our prediction of the length of the compacted zone fails in this case, since it is based on hydrodynamical considerations.

When a continually advancing finger is observed from beginning until the end, the system is classified in a fourth pressure regime. The fluid and grain flow are strongly coupled and instable.

Generally for the pressure regimes the characteristic times t_1, t_2, and t_3, when defined within the regime, are all pressure dependent. While t_2 and t_3 are decreasing with ΔP and do not show a dependence on plate separation, t_1 is increasing with both ΔP and plate spacing d. Our theoretical model gives a good fit for t_2 in the range of pressures where the advancement of the compacted region is not dominated by solid contacts.

Features of the propagating finger, such as the tip velocity and width, are increasing with higher injection pressure, but are not sensitive to plate separation.

Although no systematic studies on the influence of varying the initial solid fraction have been conducted, it might be of central importance to the grain dynamics both locally and globally.

ACKNOWLEDGMENTS

This work was supported by NFR, the Norwegian Research Council, through a Petromax and a SUP grant, and by CNRS through a PICS grant. We thank Anke Lindner, Christophe Chevalier, and Ernesto Altshuler for many interesting and helpful discussions.

[1] J. F. Davidson and D. Harrison, *Fluidization* (Academic Press, New York, 1971).
[2] J. F. Davidson, *Bubbles in Fluidized Beds* (Kluwer Academic, New York, 1995), p. 197.
[3] K. S. Lim, J. X. Zhu, and J. R. Grace, Int. J. Multiphase Flow **21**, 141 (1995).
[4] S. McNamara, E. G. Flekkøy, and K. J. Måløy, Phys. Rev. E **61**, 4054 (2000).
[5] G. W. Baxter, R. P. Behringer, T. Fagert, and G. A. Johnson, Phys. Rev. Lett. **62**, 2825 (1989).
[6] K. J. Måløy, T. L. Pennec, E. G. Flekkøy, D. Bideau, M. Ammi, J. C. Messager, X. L. Wu, and A. Hansen (unpublished).
[7] T. Le Pennec, K. J. Måløy, E. G. Flekkøy, J. C. Messager, and M. Ammi, Phys. Fluids **10**, 3072 (1998).
[8] E. G. Flekkøy and K. J. Måløy, Phys. Rev. E **57**, 6962 (1998).
[9] D. Gendron, H. Troadec, K. J. Måløy, and E. G. Flekkøy, Phys. Rev. E **64**, 021509 (2001).
[10] E. G. Flekkøy, S. McNamara, K. J. Måløy, and D. Gendron, Phys. Rev. Lett. **87**, 134302 (2001).

Decompaction and fluidization of a saturated and confined granular medium by injection of a viscous liquid or gas

Ø. Johnsen,[1,2,3] C. Chevalier,[1,4] A. Lindner,[1] R. Toussaint,[3] E. Clément,[1] K. J. Måløy,[2] E. G. Flekkøy,[2] and J. Schmittbuhl[3]
[1]Laboratoire de Physique et Mécanique des Milieux Hétégogènes (PMMH), UMR 7636 CNRS, ESPCI, Universités Paris 6 et 7, 10, rue Vauquelin, 75231 Paris Cedex 05, France
[2]Advanced Materials and Complex Systems (AMCS), Department of Physics, University of Oslo, P. O. Box 1048 Blindern, 0316 Oslo, Norway
[3]Institute of Globe Physics in Strasbourg (IPGS), UMR 7516 CNRS, Université Louis Pasteur, 5 rue Descartes, F-67084 Strasbourg Cedex, France
[4]Université Paris Est, LCPC, MSRGI, 58 boulevard Lefebvre, 75015 Paris, France
(Received 19 June 2008; published 6 November 2008)

We compare quantitatively two experimental situations concerning injection of a miscible fluid into an initially jammed granular medium saturated with the same fluid, confined in a Hele-Shaw cell. The two experiments are identical, apart from the interstitial and injected fluid, which is in one case air injected into a dry granular packing, and in the other case silicone oil injected into a dense suspension. In spite of the strong differences regarding the nature of the two fluids, strikingly similar dynamical and geometrical features are identified as functions of the control parameters: cell thickness and applied fluid injection pressure. In both cases an initial hydrodynamically driven decompaction process controls the unjamming and prepares the final displacement process characterized by fingerlike patterns empty of grains. The pattern shapes are comparable. In addition, the mobilities of the coupled fluid-grain flow, rescaled by the interstitial fluid viscosity and grain diameter squared, are of the same range and behave comparably. The mobility proves to depend on the initial solid fraction of the medium. Subtle differences are observed in geometrical aspects like the finger width with respect to the control parameters.

DOI: 10.1103/PhysRevE.78.051302 PACS number(s): 45.70.Qj, 47.15.gp, 47.55.Kf

I. INTRODUCTION

The hydrodynamic instabilities and fingerlike patterns emerging as a less viscous fluid displaces a more viscous fluid in Hele-Shaw cell configurations [1] have been extensively studied and vastly documented for both Newtonian [2–5] and non-Newtonian fluids [6–11]. Another flow situation with a well-established physical description of its own is that of a fluid flow through a fixed porous medium [12]. However, where these two systems merge, the miscible case of fluid injection into a deformable porous phase close to the jamming transition [13–18], the solid grains can behave as a conducting porous matrix, or can be suspended, forming an effective fluid. The transition between the two flow types has been studied during fluid injection into a loosely packed granular medium [19,20] or a dense granular suspension [21], and is similarly observed when a fluid is retracted through a granular matrix [22,23]. The fluid displacement of grains by injection is an unstable process leading to the formation of fingerlike patterns [19,20,24,25], visually quite similar to those found for non-Newtonian fluids. Coupled fluid-grain flows and fluid-grain interactions, on which these processes rely, are rather poorly understood and their study is in its infancy. The case of bubbling instability in fluidized beds under gravity is perhaps the most studied issue related to this case [26–37]. Nevertheless, for a very dense granular medium the situation is quite complex, essentially due to the nature of a granular material: it may act as a complex fluid and can jam at higher concentrations and become a solid porous matrix.

In practice, the problem addressed is an important issue since many industrial or geophysical applications rely on such an elementary process. Internal piping erosion due to flow concentration into tubular macropores during runoff may ultimately cause failure of soils in, e.g., dikes, embankments, and dams [38]. In nature, this type of erosion may also trigger hill-slope instabilities [39,40], as well as sudden and potentially catastrophic drainage of the water contained in calderas [41], or in natural lakes formed after earthquakes.

In the present paper we present two experiments developed in parallel due to common interest in the following situation: injection of a fluid into a loosely consolidated granular packing with a solid fraction brought close to the random close packed (RCP) limit [42]. We study the fluidization process of an initially jammed granular medium.

Two simple model realizations of the miscible injection problem are considered: the granular material, consisting of monodisperse polystyrene spheres, is confined in a horizontal Hele-Shaw cell, ensuring identical situations as far as geometry is concerned. The injection is made with either air into the initially densely packed and dry assembly of spheres, or by a silicone oil invading a dense suspension made with the same granular material and the same silicone oil as injected. At sufficiently high overpressures, the drag exerted by the permeating fluid over the weakly consolidated granular medium mobilizes the grains. The goal of this study is to classify and describe quantitatively the mobilization of the initially jammed granular medium and the patterns emerging during this fluidization process, and comparatively reveal similarities and differences due to the nature of the surrounding and injected fluid.

The paper is organized as follows. First, in Sec. II the experimental setup and the principle of the injection experi-

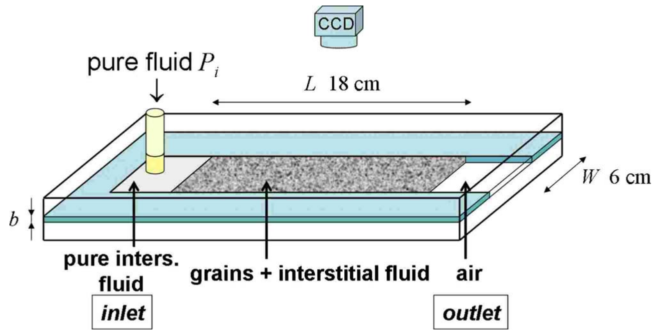

FIG. 1. (Color online) Experimental setup. A closed channel is made between two glass plates with three impermeable side boundaries and one open (right). Either air or silicone oil is injected at pressure P_i into, respectively, a dry assembly of grains, or grains saturated with the same type of silicone oil. Around the inlet (left part of the cell) there is a grain-free zone occupied by pure fluid. The region ahead of the grain and fluid and up to the outlet (far right) is occupied by air at atmospheric pressure for both cases.

ments are described. Then in Sec. III the aim is to characterize the evolution of the unjamming process of typical experiments: decompaction dynamics and its role on the subsequent selection of the pure fluid fingerlike patterns emerging in the dense matrix. The flow properties and geometrical features of these fingerlike patterns are discussed in Sec. IV, before we summarize and address final conclusions in Sec. V.

II. EXPERIMENTAL SETUP

The experiments are performed in a linear Hele-Shaw cell [1] as illustrated in Fig. 1. A straight channel of rectangular section with a width $W=6$ cm and a length of $L=30$ cm is cut out of a Mylar sheet of calibrated thickness. The cell thickness is $b=0.85$, 1.15, 1.70, or 2.30 mm. The Mylar sheet is sandwiched between two thick glass plates acting as spacers and ensuring that three of the sides of the channel are impermeable. The end of the channel is left open and will be referred to as the *outlet*. Opposite to the outlet there is an injection point ($\varnothing=7$ mm) in the upper plate positioned 1 cm from the impermeable boundary, referred to as the *inlet*.

The granular medium in the cell is saturated with a given interstitial fluid as described in Secs. II A and II B. In this work, we consider two cases with clearly distinct fluids: air (compressible, viscosity $\eta_{\text{air}}=1.8\times10^{-5}$ Pa s), and silicone oil (incompressible, viscosity $\eta_{\text{oil}}=5.0\times10^{-3}$ Pa s). The space around the inlet is initially filled with the same fluid as the interstitial one. This space acts as a pressure chamber. At the beginning of the experiment, the fluid injection starts at a given injection pressure $P_i=\Delta P+P_{\text{atm}}$. ΔP is the fluid overpressure with respect to atmospheric pressure P_{atm}, at the outlet. ΔP is applied by manually opening a valve. Opening the valve fully takes $\sim$0.02 s. Thus, the pressure profile of the injection is close to a step function: after the onset, ΔP is maintained constant throughout the experiment. The probed range of the applied ΔP is between $\sim$10 and $\sim$200 mbars for the dense packing prepared by tapping.

Complementary to the comparative study involving two distinct fluids for otherwise similar conditions, we have performed experiments with an initially less dense packing of the granular material. In this case, the cell thickness is $b=0.70$, 1.10, and 2.1 mm, and ΔP is in the range $\sim$2 to $\sim$30 mbars.

To record the motion of the grains, images are obtained by reflection, with the use of a dark background to increase the contrast between the zones free of grains and the granular regions. The setup is illuminated from above using two 800 W halogen projectors, and images of 400×1600 pixels are acquired at a frequency of 500 images per second, using a Phantom V9 high-speed camera for the air-grain experiments, and for the oil-grain system a Prosilca EC1280 charge-coupled device (CCD) camera is used at a sample frequency of ten images per second, at a resolution of 1280×400 pixels.

A. Sample preparations: Air-grain system

The granular medium consists of spherical monodisperse polystyrene beads (Dynoseeds) with a diameter $d=80\pm3$ μm, and density $\rho_{\text{grain}}=1.05\pm0.01$ g cm^{-3}. To ensure a good reproducibility of the experiments, the following preparation stages were adopted to put the granular medium into place: the cell is placed vertically and the grains are introduced via the outlet. Once the proper quantity is introduced, a Mylar plate matching the width and height of the channel is inserted $\sim$6 cm into the channel. This will prevent the grains from moving through the outlet during the sample preparation. The cell is then tilted upside down, which brings the granular medium against the Mylar plate, and frees space around the inlet. The granular material is further compacted by tapping the filled cell in a defined manner, which ultimately brings the packing into a dense initial state with solid fraction $\rho_0=(62\pm1)\%$, found by weighing the grains and measuring the volume they occupy in the cell. This is close to the random close packed limit [42].

For the complementary experiments the procedure is the same, except that in this case the particles are simply assembled in the cell under gravity without mechanically imposing any further compaction. The solid fraction is $\rho_0=(56\pm1)\%$.

During the sample preparation solid contacts between the grains are established and friction forces from the walls on the grains are mobilized, pointing toward the inlet. The preparation stages produce a granular sample with a length $L_0=18$ cm. The grain-free zone around the inlet is about $\sim$6 cm and the air-grain boundary facing the inlet is reasonably straight. This interface is referred to as the *inner boundary*. The cell is then brought into a horizontal position and the Mylar plate used during the preparation is removed, leaving a straight grain-air boundary facing the outlet. We refer to this boundary as the *outer boundary*.

For the experiments performed with air as the interstitial fluid, control of the humidity of the experimental environment during sample preparations is important. The interactions between $\sim$80-μm-sized beads are sensitive to the humidity of the surroundings: in very dry conditions,

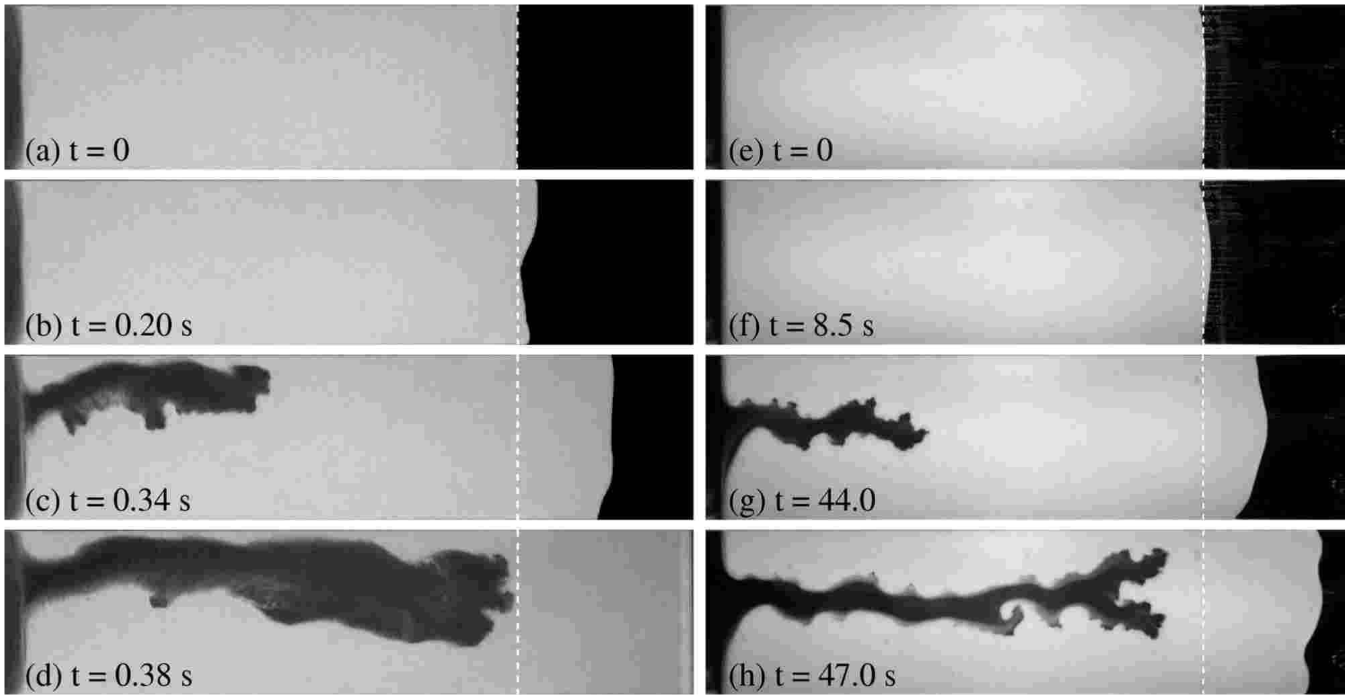

FIG. 2. Typical experiments. The left column shows an air-grain experiment at $\Delta P_{air}=93$ mbar and $b=1.15$ mm. In the right column an oil-grain experiment at $\Delta P_{oil}=85$ mbar and with $b=1.15$ mm is displayed. (a) and (e) shows the sample before fluid injection. The dashed lines indicate the initial position of the outer boundary, L_0. Before a finger empty of grains starts developing the granular packing has been dilated, indicated by an increase of length beyond L_0 seen in (b) and (f). In (c) and (g) typical finger patterns are shown, after propagating for $L_0/2$, and in (d) and (h) the fingers have propagated a distance L_0.

electrostatic forces play a role, while under excessively humid conditions, capillary bridges form between neighboring beads, resulting in small but significant cohesive forces. To ensure the reproducibility of these individual interactions, the relative humidity of the air was kept between 30% and 40%.

B. Oil-grain system

For the oil-grain system the same beads and cells are used. An identical sample preparation procedure to obtain the dense packing for the air-grain is applied. But before removing the Mylar plate that blocks the outlet a different final step is performed: imbibition of the granular medium with the silicone oil. Note that, in order to imbibe the medium successfully without trapping air bubbles and to avoid rearrangement of grains leading to large density heterogeneities within the granular matrix, the packing fraction must be near the close packed limit. Hence, only the dense initial packing is obtainable for the oil-grain case.

The granular medium is imbibed with a silicone oil Rhodorsil 47V05 from Rhodia Silicones with a viscosity $\eta_{oil}=5.0\times10^{-3}$ Pa s, as given by the supplier and measured with a Thermo-Haake rheometer. The oil is introduced via the inlet from an oil reservoir at constant overpressure. During imbibition of oil into the granular medium one can observe a propagating imbibition front. (Note that the Mylar plug prevents the grains from moving and oil from escaping but is permeable to air.) The imbibition front is a straight line, indicating a homogeneous porosity of the dry jammed grains and validating our preparation step. When measuring the velocity of the imbibition front as a function of the applied pressure gradient, one can deduce the permeability of the porous medium [12]. Applying the Carman-Kozeny relation [43] the solid fraction estimation is $\rho_0\sim60\%$, which agrees with the solid fraction obtained by weighing the grains and measuring the occupied volume of the granular medium. Once the porous medium is completely immersed the pressure is reduced to atmospheric pressure (corresponding to a zero pressure gradient) and the Mylar plug is removed. The initial state consists then of a zone of grains fully immersed in a silicone oil and limited by two well-defined interfaces. The interface between the pure oil and the immersed granular medium facing the inlet is referred to as the inner boundary and the interface between the granular medium and air, facing the outlet, is referred to as the outer boundary. Note that an oil-grain-air interface at the outer boundary is chosen out of reproducibility considerations. This leads to a difference in the boundary conditions by the presence of interfacial surface tension. The oil and the grains are close to density matched; thus, sedimentation can be neglected.

III. EMERGING PATTERNS

A. Typical experiments

Figures 2(a) and 2(e) show images respectively of the air-grain and the oil-grain systems just before injection (at t_0) for cell thickness $b=1.15$ mm, at a comparable $\sim60\%$ initial solid fraction. When a ΔP within the given pressure range is applied at the inlet, no grain motion is detected along the inner boundary at the onset of the fluid flow. Moving grains are first observed on the outer boundary that starts to deform, typically appearing slightly bulged. This decompaction stage is visible in Figs. 2(b) and 2(f). The decompaction process deserves more attention and will be described in depth in the next section. While the outer boundary progresses the total grain-fluid area increases, indicating an average decrease of solid fraction, i.e., the medium is decompacted. During such a process, the friction forces between the grains and the confining plates are decreased, and the grains start to move with the interstitial fluid. After a characteristic time, the grains are mobilized over the entire length of the packing and the inner boundary starts to move. The inner boundary rapidly deforms and departs from the initial straight shape. A finger empty of grains forms in the center of the cell, signaling an unstable penetration mechanism. The shape of this finger is illustrated in Figs. 2(c) and 2(d) for the air-grain system, and in Figs. 2(g) and 2(h) for the oil-grain case. In Figs. 2(c) and 2(g) the finger tip has propagated a distance $L_0/2$, and in Figs. 2(d) and 2(h) a distance L_0, respectively the half and the full extent of the initial system length. The similar aspect of this finger between the air-grain and the oil-grain systems is visible qualitatively on these images. They are also reminiscent of fingerlike structures observed in many non-Newtonian fluids [6–11].

This behavior is systematically observed in the oil-grain system, for the probed range of ΔP (from 10 up to 200 mbars). On the other hand, for the air-grain system, there is a threshold to exceed for the applied ΔP in order to set the grains into motion from the jammed state. For ΔP below this threshold there is no observed deformation of the outer grain-air boundary and no finger propagation: the air permeates through the grains without demobilizing the friction forces. The threshold is dependent on cell thickness b, as shown in Fig. 3. The threshold is also probed by gradually increasing the fluid overpressure from zero: the gray square markers indicate at which ΔP the fluidization and the finger patterns first take place during this pressure ramp. A threshold for the oil-grain case is likely, but might be located at a lower ΔP than our pressure control device allows. A contingent absence is another possibility, and might in that case rely on several factors which are difficult to assess, given the sample preparation procedure. Hypothetically, the presence of an interface with surface tension might pull particles along when the fluid flow is initiated; in addition, lubrication forces and the low level of buoyancy forces might alter the friction conditions between the granular matrix and the confining walls.

Eventually, we notice that the deformation of the outer boundary starts after a short delay after the injection for the air-grain system, whereas no delay is observed for the oil-grain system. This delay has also been observed in experiments performed in larger cells with a similar air-grain system [20] and has been shown to originate from the finite compressibility of the interstitial fluid. It corresponds to a diffusive propagation of the overpressure through the packing. The characteristic time for this diffusion is L_0^2/D, where the diffusivity constant is $D=\kappa_0/(\eta_{air}C)$. $\kappa_0=5.1\times10^{-12}$ m^2

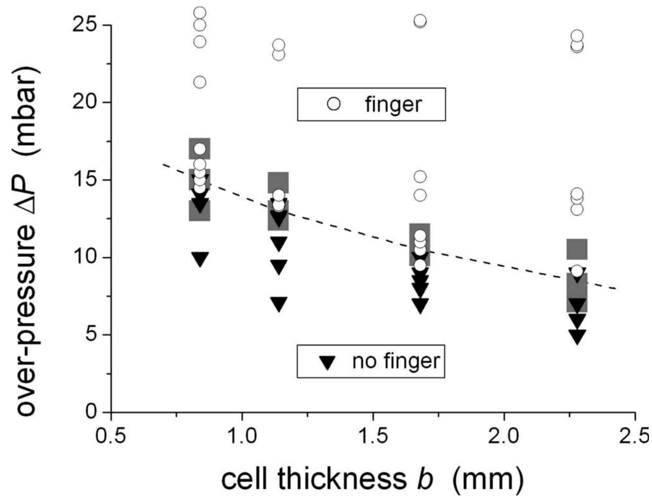

FIG. 3. Threshold pressure for the onset of grain mobilization and finger formation in the air-grain system. The gray squares correspond to the ΔP at which fingering occurs for experiments where the injection pressure is gradually increased from zero. For the oil-grains system finger formation is observed for all tested ΔP.

is the permeability of the granular packing at the initial solid fraction $\rho_0\sim62\%$, and is estimated by the Carman-Kozeny relation [43]. η_{air} is the viscosity of the interstitial fluid, and C is the compressibility of the fluid [20,26]. The pressure diffusivity for air is found to be $D\simeq0.04$ m^2/s, so that for the small cells considered here with $L_0\simeq0.18$ m, the characteristic time is around 1 s. This delay is observable in the experiments, but is very short with respect to the total duration of the experiment. For the system with grains and oil, the oil's vanishing compressibility makes this time much too small to be observable.

The global dynamic behavior of the dense air-grain and oil-grain systems is significantly different from that of the complementary air-grain experiments with a lower initial solid fraction. No contraction of the granular matrix leading to a compaction front traveling in the fluid flow direction starting from the inner boundary is observed, as in the case of an initially loose packed granular material [20].

B. Decompaction

During the initial stage, while the outer boundary moves and the inner one stays fixed, we analyze the internal decompaction by applying an image subtraction treatment. This post-treatment will allow us to resolve spatially the structural features of the decompaction process. An image shot before applying the overpressure ΔP serves as a reference frame. Its pixel gray-level map (numbers between 1 and 256, from dark to bright) is subtracted from the pixel gray-level values of an image at time t during the fluid injection. The absolute values of these differences form a gray-level map which reflects the particle mobilization relative to the reference image: the mobile zones appear bright, while the immobile zones appear dark. To further increase the contrast between the mobile and immobile zones the resulting image difference is filtered by applying a threshold determined by a local minimum between the two main peaks in the gray-level histogram of individual images. The image is then binarized by putting all pixels with a value below this threshold to 1 and all pixels with a value exceeding the threshold to 256. The finger structures appear as solid white, but also very small particle displacements can be detected and recognized as white speckles. The decompacted region is identified as a clearly defined zone of high speckle density. To separate the densely speckled region from speckles that originate from, e.g., noise due to small light intensity variations, we check for each speckle the nearest neighbors within a range of $\sim 4\times 4$ mm^2. If two or more speckles are contained within this range, the grain area within a spanned rectangle defined with the speckles as the vertices is tagged in gray. Figures 4(c) and 4(d) show the treated images for the two sets of experiments shown in Figs. 4(a) and 4(b).

The decompaction process does not correspond to a homogeneous decrease of the solid fraction over the whole granular material, but to a localized decompaction zone starting from the outer boundary. The decompacted zone is a region of mobile grains carried with the flowing fluid in an area $A_{\mathrm{dec}}(t)$ determined by analysis of the treated images. When the initial packing fraction ρ_0 is known *a priori*, we estimate the average solid fraction $\rho_{\mathrm{dec}}\sim 59\%$ for both of the systems. Hence, the relative decompaction of the air-grain system is slightly larger than for the oil-grain system, with their respective initial packing fractions of $\rho_0\sim 62\%$ and $\sim 60\%$ (evident in Fig. 7). As a contrast, in the immobile zone the fluid permeates through grains that stay fixed. A boundary between the immobile and the decompacted zone can thus be distinguished as a *decompaction front*. The solid friction between the grains and the wall gets demobilized, and the granular medium gets unjammed when the front passes. The decompaction front moves backward, opposite to the average fluid flow, toward the inlet of the channel.

In both the oil-grain and air-grain systems, the mobile zone growing from the outer boundary evolves into finger-like structures. It is worth noticing that several fingers may form and progress in parallel (see Fig. 4). In the air-grain system, as many as four decompaction fingers were observed during the initial stage of injection. The decompaction fingers observed in the oil-grain system are typically wider.

C. Waiting time

The waiting time denoted t_w is defined as the time elapsed from the moment when grain motion is first observed at the outer boundary until a propagating finger structure is initiated at the inner boundary. It is the typical time for the decompaction front to move over the whole system length L_0. Since the decompaction process is a direct result of the drag force exerted on the particles, the fluidization process is expected to occur after shorter t_w with increasing ΔP. This is indeed confirmed in Fig. 5. On the other hand, there is no clear dependence on the cell thickness b, except for the air-grain system where the experiments performed with $b=2.3$ mm distinguish themselves. In this case, the difference might be attributed to the role of gravity and decreased role of friction as one crosses over to a more three-dimensional packing ($b=2.3$ mm ~ 29 particle diameters). This is not an issue in the oil-grain system since we have an isodense suspension.

By recognizing two zones with distinguishable solid fractions, we construct a simple analytical model for the waiting time, mainly based on mass conservation. For simplicity, we consider a one-dimensional model in the sense that the decompaction front is flat and uniform over the cell width, and perpendicular to the sidewalls (see Fig. 6). With the inner boundary defined as $X=0$, the initial condition is $X_g(t=0)=X_{\mathrm{dec}}(t=0)=L_0$. Here X_g is the position of the outer boundary, X_{dec} is the position of the decompaction front, and L_0 is the initial length of the packing. The length of the decompaction zone at a time t is $l_{\mathrm{dec}}(t)=X_g(t)-X_{\mathrm{dec}}(t)$. At an arbitrary time t, conservation of mass and grains gives

$$\rho_0 X_{\mathrm{dec}}+\rho_{\mathrm{dec}} l_{\mathrm{dec}}=\rho_0 L_0. \tag{1}$$

Conservation of grain flux links the velocity of the outer boundary $V_g=dX_g/dt$, and the velocity of the decompaction front $V_{\mathrm{dec}}=dX_{\mathrm{dec}}/dt$, through

$$V_g=\left(1-\frac{\rho_0}{\rho_{\mathrm{dec}}}\right)V_{\mathrm{dec}}. \tag{2}$$

For the oil-grain case, the fluid velocity into the decompacted region equals the velocity of the outer boundary, and the Darcy law gives

$$\frac{P_i-P_{\mathrm{dec}}}{X_{\mathrm{dec}}}=\frac{\eta_0}{\kappa_0(\rho_0)}V_g. \tag{3}$$

P_i-P_{dec} is the pressure drop over the nondecompacted material, which acts as a fixed porous material with a Carman-Kozeny permeability $\kappa_0(\rho_0)$. P_i is the injection pressure, and P_{dec} is the pressure at the front positioned at X_{dec}. Similarly, over the decompacted region Darcy's relation gives

$$\frac{P_{\mathrm{dec}}-P_{\mathrm{atm}}}{l_{\mathrm{dec}}}=\frac{\eta_{\mathrm{paste}}}{\kappa_{\mathrm{HS}}(b)}V_g. \tag{4}$$

Here the grains and the fluid are considered as an effective fluid with a viscosity η_{paste}, and the permeability is given by the confining space of the Hele-Shaw cell as $\kappa_{\mathrm{HS}}(b)=b^2/12$. We introduce "paste" as a common nomenclature for both the air-grain and the oil-grain systems, referring to the granular material and the fluid flowing together.

The above flux conservation consideration is valid only if the fluid velocity is comparable to the velocity of the outer boundary. For the oil-grain system the fluid-air interface adjacent to the outlet is visually accessible, and the fluid flux is measurable. The velocity of the outer grain boundary, V_g, is the same as the oil velocity V_{oil}. Since the fluid is not visually traceable and flux measurements not made available for the air-grain case, we estimate the fluid seepage velocity relative to the grains, V_{flux}, using the Darcy relation. At the instant just before forming a finger, the granular medium is decompacted over the whole system length. The Carman-Kozeny permeability is $\kappa(\rho_{\mathrm{dec}}=59\%)=7.0\times 10^{-12}$ m^2, and V_g is typically from 0.5 to 20 cm s^{-1} for the corresponding ΔP from 10 to 200 mbars. With the fraction

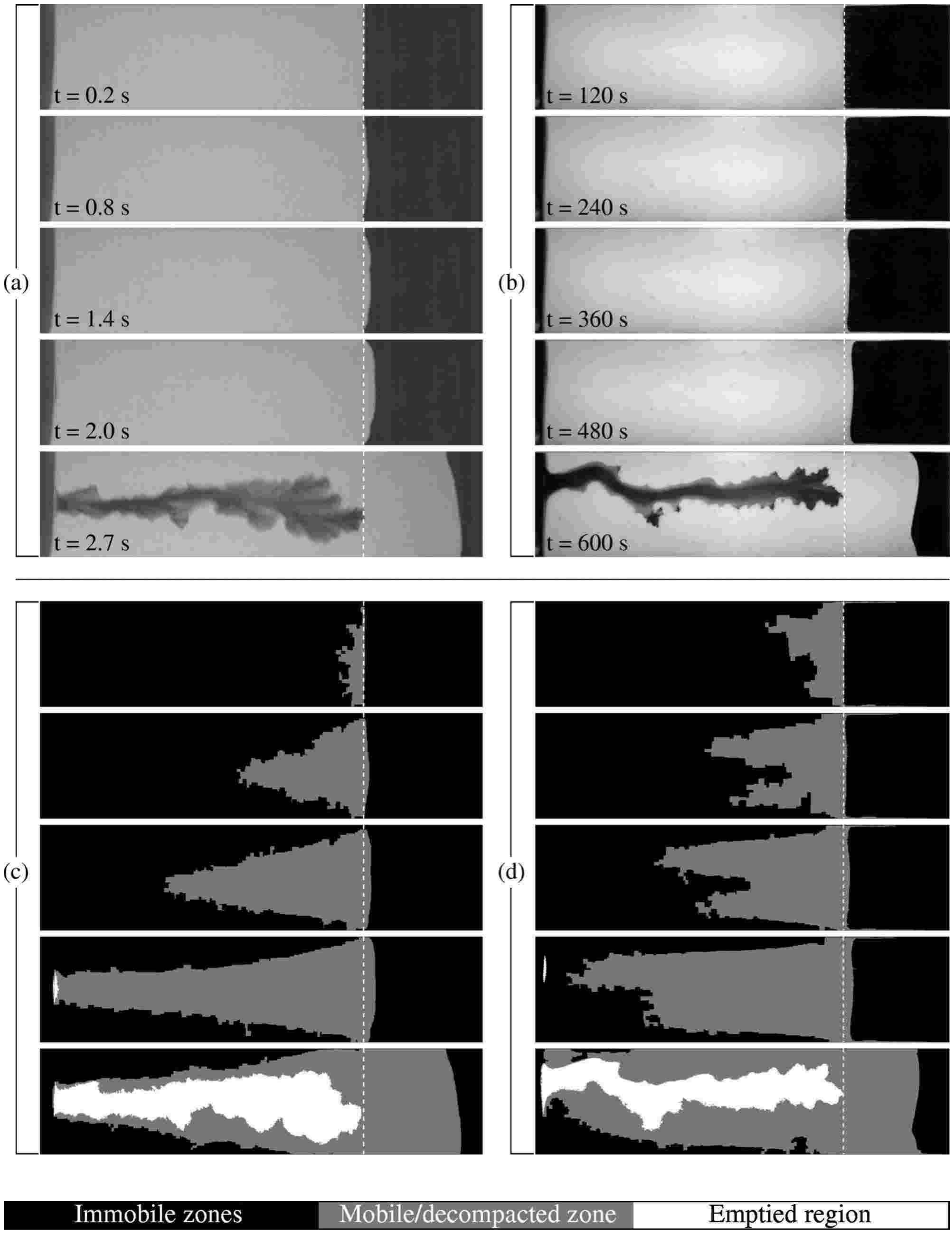

FIG. 4. Typical experiments. Images in (a) and (b) show the raw images for, respectively, air-grain and oil-grain mixtures, while in (c) and (d) the corresponding subtracted and filtered images show the mobile zones. Air-grain system: $b=1.15$ mm, $\Delta P=13$ mbars. Oil-grain system: $b=1.15$ mm, $\Delta P=11$ mbars. The dashed vertical lines indicate the initial position of the outer grain boundary. The bar on the bottom displays the color code representing immobile zones with solid fraction ρ_0, mobile or decompacted zone with solid fraction $\rho_{\mathrm{dec}}<\rho_0$, and the finger virtually emptied of grains where $\rho \sim 0$.

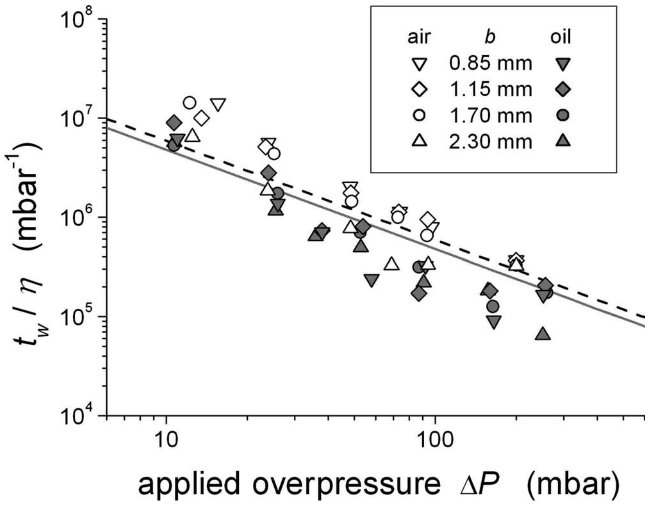

FIG. 5. Log-log representation of the waiting time t_w scaled with the fluid viscosity, as a function of the applied ΔP. The dashed line is the modeled waiting time for the air-grain system, and the solid line is the modeled waiting time for the oil-grain case.

$$\frac{V_{\text{flux}}}{V_g} = \frac{(\kappa/\eta_{\text{air}})\,\nabla P}{V_g} \sim 0.43, \tag{5}$$

the proposed model seems reasonable to use also for the air-grain system.

Combining Eqs. (3) and (4), we obtain

$$\frac{P_i - P_0}{V_g} = \frac{\eta_0}{\kappa_0} X_{\text{dec}} + \frac{\eta_{\text{paste}}}{\kappa_{\text{HS}}} l_{\text{dec}}. \tag{6}$$

From Eq. (1) we have $l_{\text{dec}} = \rho_0/\rho_{\text{dec}}(L_0 - X_{\text{dec}})$, and by performing a substitution of V_g using Eq. (2), Eq. (6) yields

$$\frac{\Delta P}{V_{\text{dec}}} = \left(1 - \frac{1}{c}\right)\left[\frac{\eta_{\text{paste}}}{\kappa_{\text{HS}}}\frac{1}{c} L_0 + \left(\frac{\eta_0}{\kappa_0} - \frac{\eta_{\text{paste}}}{\kappa_{\text{HS}}}\frac{1}{c}\right) X_{\text{dec}}\right], \tag{7}$$

where $c = \rho_{\text{dec}}/\rho_0$. By using $V_{\text{dec}} = dX_{\text{dec}}/dt$ and integrating with the boundary conditions $t=0$, $X_d = L_0$, and $t = t_w$, $X_{\text{dec}} = 0$, we obtain the time t_w for the decompaction front to travel the length of the granular packing. In the framework of this model, the waiting time becomes

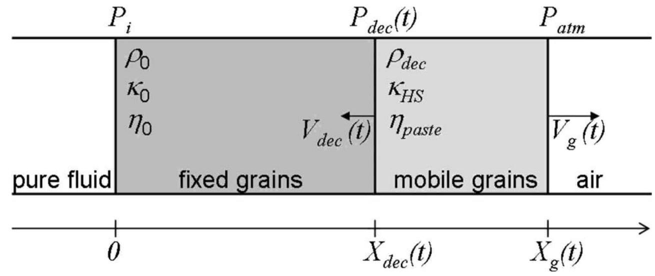

FIG. 6. Scheme and quantities involved in the modeling of the decompaction process.

$$t_w = \frac{(1/c - 1)L_0^2}{2\Delta P}\left(\frac{\eta_{\text{paste}}}{\kappa_{\text{HS}}}\frac{1}{c} + \frac{\eta_0}{\kappa_0}\right). \tag{8}$$

We now determine the quantities of the model: c is measured experimentally as $A_0/A(t)$, and gets its value from Fig. 7 at the instant $t = t_w$: $c_{\text{air}} \sim 0.985$ and $c_{\text{oil}} \sim 0.987$. The viscosity of the pure fluid η_0 is 1.8×10^{-5} Pa s for air and 5.0×10^{-3} Pa s for the silicone oil. The initial permeability is estimated using the Carman-Kozeny relation giving $\kappa_0 = 5.1 \times 10^{-12}$ m^2 at $\rho_0 \sim 62\%$ for the air-grain system, and for the oil-grain system $\kappa_0 = 6.6 \times 10^{-12}$ m^2 at $\rho_0 \sim 60\%$. Analogously to flow of a simple fluid in a Hele-Shaw cell, Darcy's law is used in order to link $\eta_{\text{paste}}/\kappa_{\text{HS}}$ to the applied pressure gradient and the flow velocity, via the mobility $M^{\text{dec}}_{\text{paste}}$:

$$M^{\text{dec}}_{\text{paste}} = \frac{\kappa_{\text{HS}}}{\eta_{\text{paste}}} = \frac{V_g}{|\nabla P|}, \tag{9}$$

where $\nabla P = \Delta P / X_g(t)$ is the pressure gradient over the length of the granular packing $X_g(t = t_w)$. V_g and ∇P are measured independently for each experiment at the instant $t = t_w$, which is just on the verge of finger propagation, when the packing has been decompacted over the whole length L_0. The paste mobility at t_w is roughly 1.3×10^{-6} m^2 Pa^{-1} s^{-1} for the air-

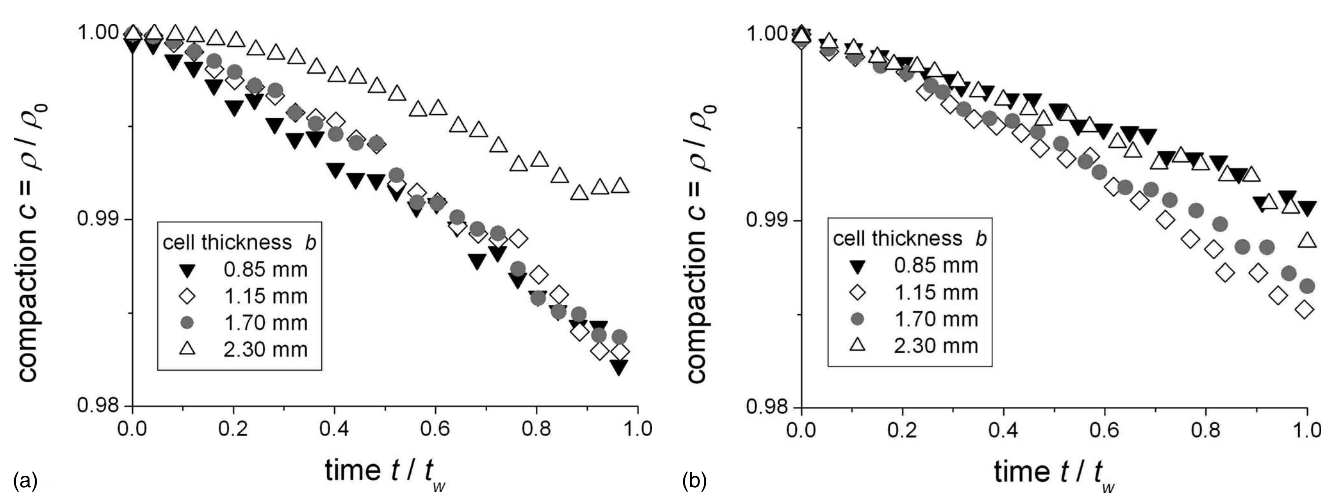

FIG. 7. Temporal evolution of the average global solid fractions $\rho(t)/\rho_0$ for (a) air-grain and (b) oil-grains systems. Along the x axis the time t is scaled with respect to the waiting time t_w.

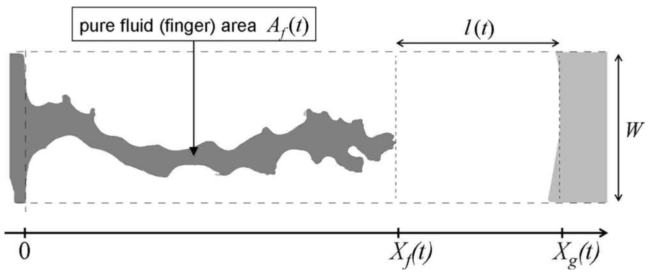

FIG. 8. Quantities measured during image analysis of the propagating fingers empty of grains.

grain system, and 2.8×10^{-9} m^2 Pa^{-1} s^{-1} for the oil-grain system.

The modeled waiting time scaled by the respective fluid viscosity is given in Fig. 5. Given the one-dimensional model, which represents a significant simplification of the observed decompaction front, and other simplifications like the assumed Darcy law for the mobile paste across the cell, the model compares favorably with the experiments. The $1/\Delta P$ relation of modeled waiting time fits with the experimental data for the higher applied overpressures, while slightly deviating at lower pressures.

IV. "EMPTY" FINGER PROPAGATION

It is evident that the decompaction process prepares the medium for further channeling. The subsequent fingerlike structure empty of grains progresses preferentially in the zone that has been decompacted during the passage of the decompaction front. In this section we focus on the flow properties of the granular material and the finger structures developing after the unjamming process.

A. Image analysis and definition of the measured quantities

In order to quantitatively compare the two systems we identify the measurements of interest, as given in Fig. 8. Great effort has been put into numerically processing the subsequent images as closely as possible, so as to extract time-dependent quantities that can be compared.

The driving force of the grain motion is the pressure gradient $|\nabla P|$. It can be estimated as the pressure difference over the extent of the paste, $\Delta P/l(t)$, where $l(t)=X_g(t)-X_f(t)$ is the length of the paste ahead of the most advanced point of the finger. X_f is the linear extent of the finger, and X_g is the position of the outer air-grain boundary. ΔP is considered constant within the finger empty of grains. Due to a very high permeability contrast with that of the confined paste, the entire pressure drop is over the paste.

We take advantage of the mobility to characterize and quantify the coupled fluid-grain flow. In the same spirit as the definition of the paste mobility during the decompaction stage given in Eq. (9), the mobility during finger propagation is

$$M = \frac{V_{\text{paste}}}{|\nabla P|}. \tag{10}$$

We adapt a common practice among similar studies and determine the mobility by measuring the velocity of the paste pushed ahead of the propagating finger as

$$V_{\text{paste}} = \frac{1}{W}\frac{dA_f(t)}{dt}, \tag{11}$$

where $A_f(t)$ is the area of the finger structure, and W is the cell width. This definition of V_{paste} comes from mass conservation and is effectively the same as λV_f, where V_f is the finger tip velocity, and $\lambda = w_f/W$ with w_f as the average finger width. Note that, even though we are dealing with a miscible two-phase system, Eqs. (10) and (11) assume that ∇P is entirely driving the finger propagation, and seepage is negligible during this stage. We compare the typical velocities of the fluid flux into the pore space of the granular matrix V_{flux}, and the finger tip velocity V_f. The permeability κ is between 5.1 and 7.0×10^{-12} m^2, and V_f is typically 20–50 cm s^{-1} for the air-grain and 0.1–2 cm s^{-1} for the oil-grain system. Within the probed range of pressures, we find the fraction

$$\frac{V_{\text{flux}}}{V_f} = \frac{(\kappa/\eta_0)\,\nabla P}{V_f} \tag{12}$$

to be less than 10% for the air-grain and less than 1% for the oil-grain system. This suggests that the velocity of the fluid flow on the pore scale is negligible compared to the finger velocity, but comparable to the grain velocity during finger propagation. ∇P is thus mainly driving the finger and thus the paste, rather than contributing to seepage. This validates the use of Eqs. (10) and (11).

As the patterns are relatively complex, we choose the definition for the individual finger width $w_i = 2A/s$, where A is the area occupied by the finger empty of grains divided by half of the perimeter s. We always consider the finger only over a distance of 6 cm (corresponding to the cell width W) measured from the finger tip. This approach of measuring the finger width corresponds to considering a single branched structure.

B. Flow properties

When the emptied finger propagates through the higher-permeability path prepared during the decompaction stage, the granular material is pushed in front of the finger tip. We use the mobility to characterize the flow properties and show to what extent the material is mobilized as a function of the applied overpressure ΔP and the cell thickness b.

Surprisingly, we find that, unlike flow of viscous fluids in Hele-Shaw cells and flow in porous media, the mobility is observed to be increasing during finger propagation, for a given experiment at constant ΔP. The mobility is thus represented as a function of this finger tip position X_f, for a given b, and varying ΔP, as in Figs. 9(a) and 9(b).

The almost linearly increasing mobility observed for the air-grain system as well as for the oil-grain system, implies that the granular material is increasingly fluidized and flows more easily during the course of the experiment. We cannot at the moment precisely account for the evolution of the mobility, and despite the strong similarities observed in the two systems, this phenomenon might originate from different mechanisms.

For the air-grain case, the evolving mobility might be attributed to the continuous decompaction of the granular ma-

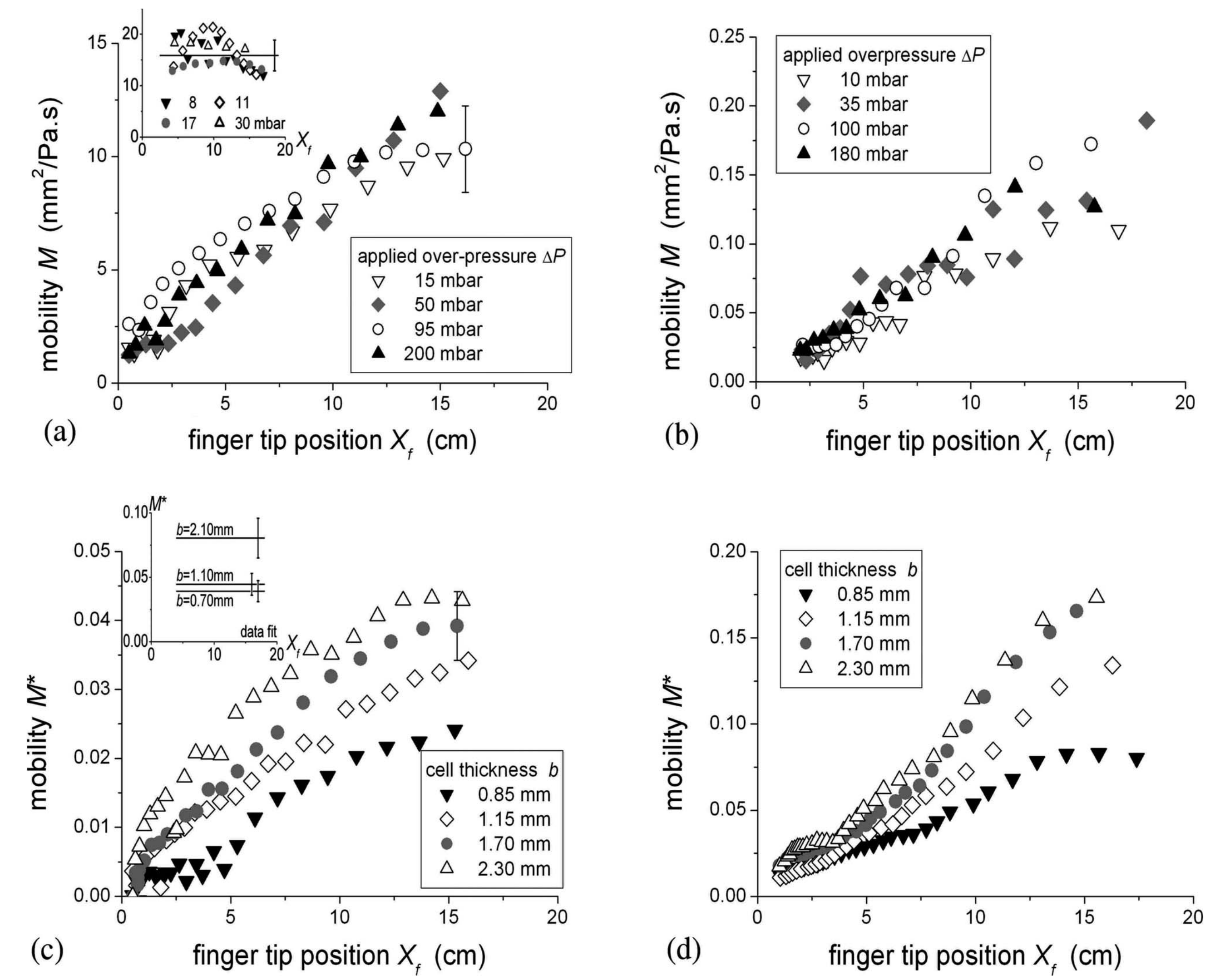

FIG. 9. Mobility M as a function of finger tip position X_f for (a) air-grain and (b) oil-grain systems. The cell thickness $b=1.15$ mm. (c) and (d) show the rescaled mobility $M^*=M/(d^2/\eta)$ as a function of finger tip position for air-grain and oil-grain systems, respectively. The rescaled mobility is averaged over all ΔP for each given b. Approximately 27 trials are used for the air-grain experiments and seven for the oil-grain case. The insets similarly show M and M^* obtained for the experiments involving an initially loosely packed granular matrix.

terial during finger propagation, as shown in Fig. 10. The solid fraction of decompacted material versus the initial fraction seems to be independent of the applied ΔP. Note that in some cases it is not possible to reliably estimate the compaction index during finger propagation for the air-grain system. For experiments performed with a large cell thickness b and a low ΔP, particles tend not to be as effectively transported along with the air flow within the finger. In this case, grains sediment on the bottom plate inside the finger in layers a few particle diameters deep. The depth of these layers is expected to be some function of ΔP, but this piece of information is not accessible for these experiments. For the results shown in Fig. 10 for $b=1.15$ mm, only experiments where the fingers are completely empty of grains are included. For the oil-grain case, since it is an isodense suspension, such gravity effects are not an issue.

The fact that change in the initial packing density strongly alters the behavior of the mobility is a piece of evidence supporting a relation between the increasing mobility and an overall decreasing compaction by fluidization during the finger growth. At ~62% initial packing fraction, the granular material is far beyond the jamming transition. It takes time to reach a completely unjammed state. If, however, the granular material is already initially close to the jamming transition, as for the samples produced for the air-grain case with a packing fraction ~56%, the paste flows readily as an effective fluid. The mobility is roughly constant during the progression of the finger [see insets in Figs. 9(a) and 9(c)].

The decompaction during finger propagation is rather modest for the oil-grain experiments, and mainly localized around finger tip positions $X_f<1$ cm [see Fig. 10(a)]. This suggests that the decompaction alone cannot explain the increasing mobility. In this case, lubrication effects due to restructuring in terms of particle migration [44] toward the center of the cell gap might be an important factor.

For both systems, the mobilities are found to be independent of the applied ΔP. Hence, we average over all the experimental runs with variable ΔP, for the various cell thick-

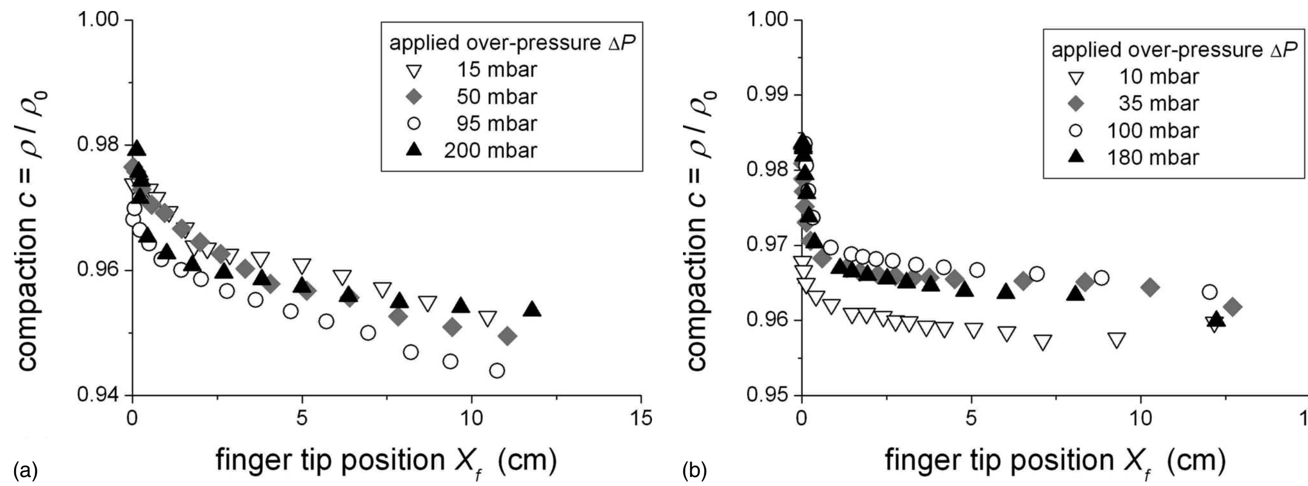

FIG. 10. Evolution of the compaction index [comparing average solid fractions, $\rho(t)/\rho_0 = A_0/A(t)$] during finger propagation for (a) air-grain and (b) oil-grain systems.

nesses b. To be able to compare the magnitude of these averaged mobilities between the two systems, we scale M with d^2/η, which is the typical mobility for flow of a fluid of viscosity η through a pore of size d. This defines $M^* = M/(d^2/\eta)$, where d is the diameter of the grains, and η the viscosity of the pure fluid (oil or air). M^* is plotted as function of the finger tip position in Figs. 9(c) and 9(d), displaying, respectively, the air-grain and oil-grain experiments. We find that the mobilities compare favorably—they are roughly of the same order of magnitude for the two systems. For both air-grain and oil-grain experiments, there is a noticeable effect on the mobility from varying b. There is a tendency of a higher mobilization rate for larger b, given the increasing slopes from small to large b. During finger propagation the mobilities seem to saturate, indicating that there might be a transition to a steady state of the paste flow, characterized by a constant mobility at a given b. The experiments performed at an initially lower packing fraction and close to the jamming transition indeed show the existence of such a state [see inset in Fig. 9(c)]. To further investigate the transition from a regime where the mobility is evolving with the finger tip position to a stationary flow regime, a longer sample would be required.

For the air-grain system, the overall higher mobility for increasing cell thickness b might be attributed to less effective friction between the fluidized granular material and its confining walls as b is made larger, by considering friction mobilization in terms of a Janssen type of stress distribution [45]. If indeed lubrication is a key component in explaining the positively evolving mobility, the friction argument fails for the oil-grain situation.

We know from other Hele-Shaw types of studies involving viscous fluids that the mobility behaves as a quadratic function of the cell thickness b. For flow through a porous medium the mobility is independent of b. Given the geometry and aspect ratio of our experiments, we are not able to distinguish a coherent relation with respect to this parameter.

C. Finger widths

By direct visual comparison, the propagating fingers are found to appear wider for the air-grain system. Tip splitting is more evident for the oil-grain experiments, and common for smaller cell thickness. Typical finger structures are shown in the left column in Fig. 11.

We characterize the observed patterns in terms of the individual finger width w_i as defined in Sec. IV A. For all the probed ΔP and cell thicknesses b, there is a weak linear increase of the individual finger width as function of the finger tip position, for both the air-grain and the oil-grain systems. We use this feature to obtain an average individual finger width. For a given ΔP and b, the averaging is performed for finger widths corresponding to finger tip positions within the interval $8 < X_f < 17$ cm.

A striking difference is observed when applying the two different fluids: for the air-grain case the finger width is a slightly increasing function of ΔP, as shown in Fig. 11(b). In this case, the width is nonsensitive to variation of the cell thickness b. On the contrary, for the oil-grain system, the finger width is observed to be independent of ΔP and thus independent of the finger velocity. However, for the oil-grain system the finger width is a function of b [see Fig. 11(d)]. Thus, the main parameter defining the finger width is the applied overpressure ΔP for the air-grain case, whereas for the oil-grain situation the cell thickness b selects the finger width.

V. CONCLUSION

We have presented an experimental study of two cases concerning fluid injection into a granular medium saturated by the same fluid as the injected phase. The two systems have been described phenomenologically and quantitatively within the parameter space of the applied fluid overpressure ΔP and the thickness of the granular phase b.

The basic mechanism of fluidization is the same for the two cases. Since the granular packing is in a dense initial state, close to the random close packed configuration, the system is completely jammed. In order to transport grains, the packing must first dilate. Dilation is observed starting at the outer boundary facing the outlet. This dilation is referred to in terms of decompaction in the sense that we are able to

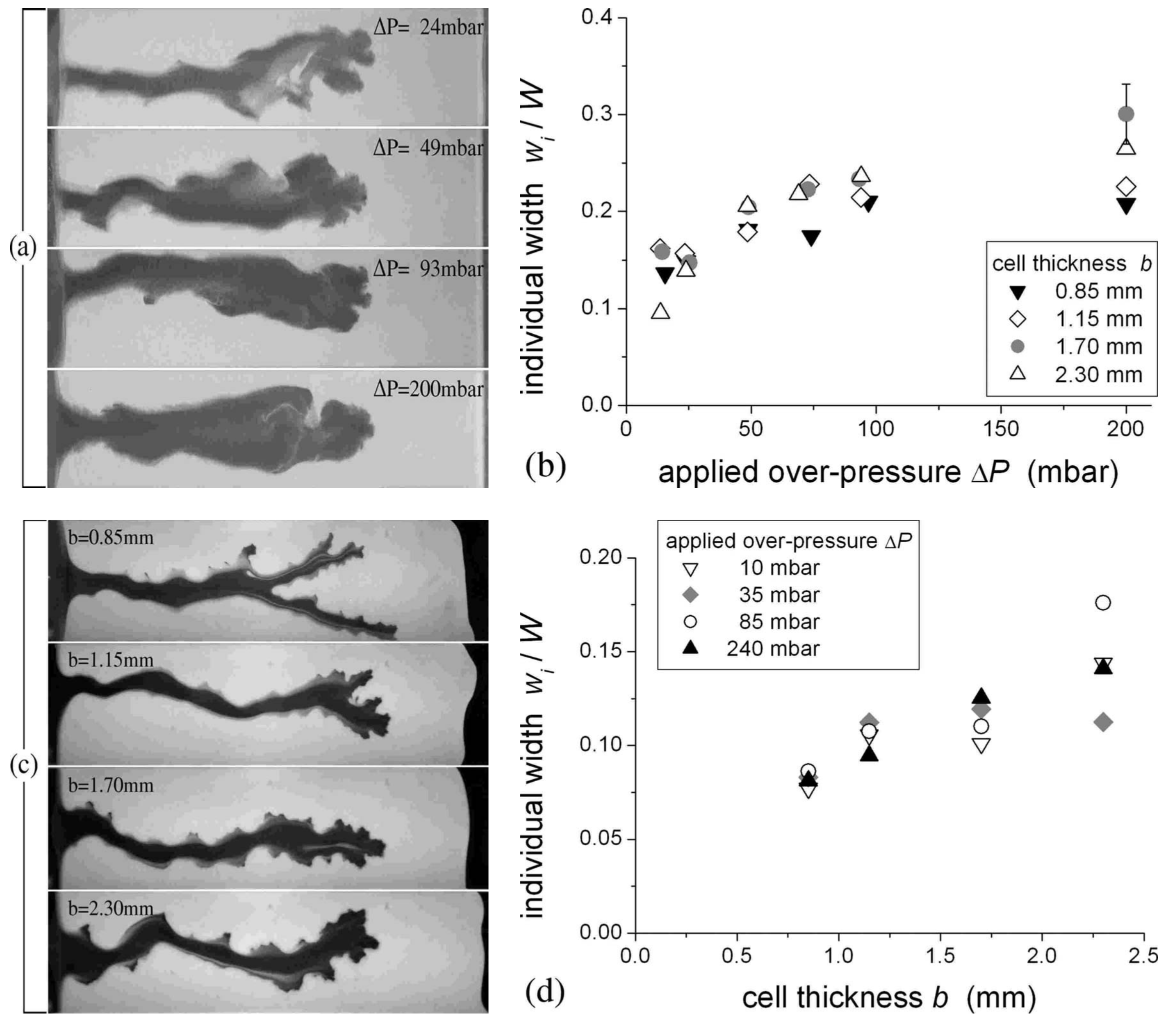

FIG. 11. (a), (c). Typical Patterns, respectively, for air-grain and oil-grain systems: for the presentation of air-grain results $b=1.15$ mm and ΔP is varied. For oil-grain systems the experiments are presented at a fixed $\Delta P \sim 55$ mbars but at different b. Right panels: Averaged individual finger width w_i, scaled on the cell width W for (b) air-grain and (d) oil-grain systems. For the air-grain system, w_i/W is a function of ΔP. Each point represents an average over roughly 27 experiments. For the oil-grain system, w_i/W is a function of b.

distinguish a zone with $\sim$3% decrease in solid fraction compared to the initial one. This decompaction zone evolves in time, propagating in the opposite direction of the effective fluid flow. During the passing of the decompaction front the granular packing is successively unjammed. In this way, the decompaction prepares the system for a very effective fluid and grain transport. When the decompaction front has reached the inner boundary, a localized zone characterized by a higher permeability connects the inlet side directly to the outlet side of the packing. Within this zone the particles are effectively transported along with the fluid, giving room for a fingerlike pattern emptied of grains to propagate through the decompacted medium.

Information on the unjamming decompaction process is retrieved by using an image subtraction technique, from which the temporal evolution of the decompaction area is found. The area measurements provide information on the average solid fraction of the decompacted region, which can be exploited to model the observed waiting time. The waiting time is the time it takes for the decompaction front to travel over the whole system length—hence representing the duration for localized unjamming to occur over the entire length of the granular packing. The modeled waiting time compares favorably to both the respective experimental data sets. The waiting time found experimentally for the two systems compares very well when scaled with their fluid viscosity.

The emerging fingerlike patterns following the unjamming process of the granular phase are quite similar between the two systems. Geometrically, these fingers are quantified through their width. In both systems a slight widening of the fingers is observed during finger propagation. A striking difference on the finger width is observed as a result of injection of two different fluids. When the injection is made with air, the finger width is increasing as a function of ΔP, but does not respond to varying the cell thickness b. However, when oil is injected into the oil-grain system the finger width is no longer a function of ΔP but increases instead with b. Furthermore, the fingers are typically wider in the air-grain case.

The fluidization process during finger propagation is described in terms of the mobility. Contrary to the constant mobilities measured in Hele-Shaw systems with strong analogies with the present study, i.e., two-fluid viscous fingering or fluid flow in fixed porous media, the mobility is increasing during finger propagation. This is the signature of a continuously more effective particle transport that might be attributed to a decreasing solid fraction during finger propagation, and perhaps also migration of the suspended particles toward the center of the cell gap in the oil-grain case. The mobilities of the two systems are of the same magnitude when scaled with respect to the fluid viscosity. For both systems the mobility of the flowing fluid-grain mixture is an increasing function of the cell thickness.

Evidently, experiments performed (air-grain system) at different initial packing fractions manifests the initial packing fraction as a crucial parameter for the overall dynamic behavior of the system. An initially loose granular matrix flows more like an effective fluid through the entire course of the experiment, recognized by a constant mobility during finger propagation. Prospected studies with a longer linear cell might reveal a transition from a regime characterized by an evolving mobility to such a stationary regime for the initially denser system.

ACKNOWLEDGMENTS

This work was supported by the Norwegian Research Council (NFR), CNRS through a PICS grant, and ANR through the ECOUPREF and TRIGGERLAND grants.

[1] H. S. Hele-Shaw, Nature (London) **58**, 34 (1898).
[2] P. G. Saffman and G. I. Taylor, in Proc. R. Soc. London, Ser. A **245**, 312 (1958).
[3] D. Bensimon, L. P. Kadanoff, S. Liang, B. I. Shraiman, and C. Tang, Rev. Mod. Phys. **58**, 977 (1986).
[4] R. L. Chuoke, P. van Meurs, and C. van der Poel, Trans. Metall. Soc. AIME **216**, 188 (1959).
[5] J. V. Maher, Phys. Rev. Lett. **54**, 1498 (1985).
[6] D. Bonn, H. Kellay, M. Ben Amar, and J. Meunier, Phys. Rev. Lett. **75**, 2132 (1995).
[7] G. Daccord, J. Nittmann, and H. E. Stanley, Phys. Rev. Lett. **56**, 336 (1986).
[8] J. Nittman, G. Daccord, and H. E. Stanley, Nature (London) **314**, 141 (1985).
[9] A. Lindner, P. Coussot, and D. Bonn, Phys. Rev. Lett. **85**, 314 (2000).
[10] A. Lindner, D. Bonn, E. C. Poiré, M. Ben Amar, and J. Meunier, J. Fluid Mech. **462**, 237 (2002).
[11] C. Chevalier, A. Lindner, and E. Clement, Phys. Rev. Lett. **99**, 174501 (2007).
[12] H. Darcy, *Les Fontaines Publiques de la Ville de Dijon* (Dalmont, Paris, 1856).
[13] M. E. Cates, J. P. Wittmer, J.-P. Bouchaud, and P. Claudin, Phys. Rev. Lett. **81**, 1841 (1998).
[14] A. L. Liu and S. Nagel, Nature (London) **396**, 21 (1998).
[15] C. S. O'Hern, L. E. Silbert, A. J. Liu, and S. R. Nagel, Phys. Rev. E **68**, 011306 (2003).
[16] T. S. Majmudar, M. Sperl, S. Luding, and R. P. Behringer, Phys. Rev. Lett. **98**, 058001 (2007).
[17] S. F. Pinto, M. S. Couto, A. P. F. Atman, S. G. Alves, A. T. Bernardes, H. F. V. de Resende, and E. C. Souza, Phys. Rev. Lett. **99**, 068001 (2007).
[18] K. Lu, E. E. Brodsky, and H. P. Kavehpour, Nat. Phys. **4**, 404 (2008).
[19] Ø. Johnsen, R. Toussaint, K. J. Måløy, and E. G. Flekkøy, Phys. Rev. E **74**, 011301 (2006).
[20] Ø. Johnsen, R. Toussaint, K. J. Måløy, E. G. Flekkøy, and J. Schmittbuhl, Phys. Rev. E **77**, 011301 (2008).
[21] C. Chevalier, A. Lindner, M. Leroux, and E. Clément, J. Non-Newtonian Fluid Mech. (2008) doi: 10.1016/j.jnnfm.2008.07.007 (to be published).
[22] P. Mills, P. Cerasi, and S. Fautrat, Europhys. Lett. **29**, 215 (1995).
[23] P. Cerasi and P. Mills, Phys. Rev. E **58**, 6051 (1998).
[24] E. Lemaire, Y. O. M. Abdelhaye, J. Larue, R. Benoit, P. Levitz, and H. V. Damme, Fractals **1**, 968 (1993).
[25] X. Cheng, L. Xu, A. Patterson, H. M. Jaeger, and S. R. Nagel, Nat. Phys. **4**, 234 (2008).
[26] J. L. Vinningland, Ø. Johnsen, E. G. Flekkøy, R. Toussaint, and K. J. Måløy, Phys. Rev. E **76**, 051306 (2007).
[27] J. L. Vinningland, Ø. Johnsen, E. G. Flekkøy, R. Toussaint, and K. J. Måløy, Phys. Rev. Lett. **99**, 048001 (2007).
[28] E. G. Flekkøy, S. McNamara, K. J. Måløy, and D. Gendron, Phys. Rev. Lett. **87**, 134302 (2001).
[29] D.-V. Anghel, M. Strauss, E. G. Flekkøy, S. McNamara, and K. J. Måløy, Phys. Rev. Lett. **97**, 059902(E) (2006).
[30] X.-l. Wu, K. J. Måløy, A. Hansen, M. Ammi, and D. Bideau, Phys. Rev. Lett. **71**, 1363 (1993).
[31] D. Gidaspow, *Multiphase Flow and Fluidization* (Academic Press, San Diego, CA, 1994).
[32] J. F. Davidson, *Bubbles in Fluidized Beds* (Kluwer Academic, New York, 1995), p. 197.
[33] J. F. Davidson and D. Harrison, *Fluidization* (Academic Press, New York, 1971).
[34] K. S. Lim, J. X. Zhu, and J. R. Grace, Int. J. Multiphase Flow **21**, 141 (1995).
[35] C. Zeilstra, M. A. van der Hoef, and J. A. M. Kuipers, Phys. Rev. E **74**, 010302(R) (2006).
[36] D. Lohse, R. Bergmann, R. Mikkelsen, C. Zeilstra, D. van der Meer, M. Versluis, K. van der Weele, M. van der Hoef, and H. Kuipers, Phys. Rev. Lett. **93**, 198003 (2004).
[37] D. Lohse, R. Rauhé, R. Bergmann, and D. van der Meer, Nature (London) **432**, 689 (2004).
[38] C. F. Wan and R. Fell, J. Geotech. Geoenviron. Eng. **130**, 373 (2004).
[39] T. W. J. V. Asch, J. Buma, and L. P. H. V. Beek, Geomorphology **30**, 25 (1999).
[40] T. Uchida, K. Kosugi, and T. Mizuyama, Hydrolog. Process. **15**, 2151 (2001), and references therein.
[41] D. Karátson, J.-C. Thouret, I. Moriya, and A. Lomoschitz, Bull. Volcanol. (Heidelberg) **61**, 174 (1999).
[42] G. D. Scott, Nature (London) **188**, 908 (1960).
[43] P. C. Carman, Trans. Inst. Chem. Eng. **15**, 150 (1937).
[44] D. Leighton and A. Acrivos, J. Fluid Mech. **181**, 415 (1987).
[45] H. A. Janssen, Z. Ver. Dtsch. Ing. **39**, 1045 (1892).

NUMERICAL STUDIES OF AEROFRACTURES IN POROUS MEDIA

ESTUDIOS NUMÉRICOS DE AEROFRACTURAS EN MEDIOS POROSOS

M. J. Niebling[a,b,c †], R. Toussaint[b,c,d], E. G. Flekkøy[a,d] and K. J. Måløy[a,d]

a) Department of Physics, University of Oslo, P.O. Box 1048, 0316 Oslo, Norway, Michael.Niebling@fys.uio.no[†]
b) Institut de Physique du Globe de Strasbourg, CNRS
c) University of Strasbourg, 5 rue Descartes, 67084 Strasbourg Cedex, France
d) Centre for Advanced Study at the Norwegian Academy of Science and Letters, Drammensveien 78, 0271 Oslo, Norway
† corresponding author

During the hydraulically induced compaction of a granular layer fracture patterns arise. In numerical simulations we study how these patterns depend on the gas properties as well as on the properties of the porous medium. In particular the relation between the speed of fracture propagation and injection pressure is here studied in detail.

Durante la compactación hidráulicamente inducida de una capa granular surgen patrones de fractura. En éste artículo estudiamos cómo éstos patrones dependen tanto de las propiedades del gas como de las del medio, utilizando simulaciones numéricas. En particular, estudiamos en detalle la relación entre la presión de inyección y la velocidad de propagación de la fractura.

PACS: Pattern formation in complex systems, 89.75.Kd; flow through porous materials, 47.56.+r; compressible flows, 47.40.-x

INTRODUCTION

Stress induced by fluid or gases can cause diverse materials to break and fracture. Such hydraulic fractures are a natural and common phenomenon in the field of volcanism and are artificially initiated to enhance the recovery of natural gas and mineral oil by fracturing the reservoir rock with pressurized fluids. Recently a new perspective on hydrofractures was added with the storage of supercritical CO_2 attracting the interest of an increasing number of researchers. In this respect two scenarios are considered. First it is one option to inject CO_2 into existing hydrofractures, and second the injection of the CO_2 can create additional fractures [1, 2]. The typical components for such fractures are a porous material and a compressible gas. Injection of pressurized fluids in a porous material, deforming beyond the elastic limit, has been studied in granular materials in Hele-Shaw cells, [3–8], with the injection of air or oil in systems with open boundary conditions, and during cyclic loading [9]. It was also studied in systems with a confinement for the grains, prevented from getting out of the cell, which allowed to observe the formation of thin fractures [10]. In this paper [10] it was found and discussed a criterion that the porous media and the fluid need to fulfill to allow the formation of fractures. For this purpose the gas' viscosity was varied. It was further discussed how the shape of the fractures depend on the properties of the porous material and of the injected gas in simple 2 dimensional (2D) numerical simulations.

In contrast to the previous article we will not change the properties of the injected gas or the porous material in this present article. Here we explore in particular the effect of the amplitude of the gas pressure imposed in the source on the fracture morphology. Furthermore, all simulations here will be ran in a regime where fractures are created.

SIMULATION SETUP

As shown in Fig. 1 the setup consists of a cell with two glass plates separated by 1 *mm*. The gap between the plates is filled with particles. The empty space between the grains is saturated with a fluid that has the same properties as the fluid that is injected. Consequently, the only two media involved in the dynamics are the grains and the fluid. At the start of the simulations the average solid volume fraction of the grains is $\rho_s^{(0)} = 0.42$. This starting solid volume fraction is homogeneous with negligible density fluctuations although the particles are at random positions. The value of $\rho_s^{(0)} = 0.42$ is chosen to be less than the possible maximum of $\rho_s^{(\max)} = 0.60$ to allow compaction of the grains. On the inlet side of the cell the pressure is increased gradually in a set of six different simulations from a value of $P_I = 0.5 \times 10^5$ *Pa* to a value of $P_I = 2.5 \times 10^5$ *Pa* above the atmospheric pressure of $P_0 = 1.0 \times 10$ *Pa*. On the opposing side to the inlet the cell has an open boundary for the fluid but particles are not able to leave the cell here. In a real experiment, this could be achieved by using a net with a mesh smaller than the particles. The remaining boundaries are completely sealed for both media. In the simulation around 200 000 grains of diameter 140 ± 10% *μm* are involved. Finally, the pressure at the inlet is increased and maintained as a step function in time, at a steep ramp, and particles hardly move before the maximum injection pressure P_I is reached.

THEORY AND MODEL

Using a well tested numerical model we have the freedom to explore the parameter space independently. The details of the method can be found in [6, 11-17], and alternative models can be found in [18-22]. The model describes the fluid in terms of a pressure field while the porous medium is modeled by simulating discrete particles.

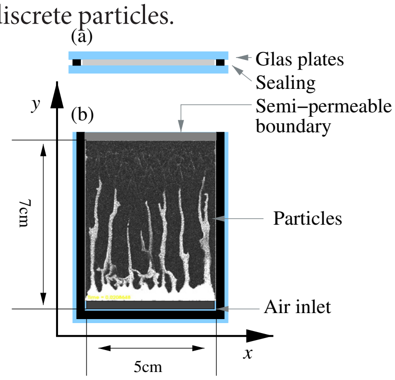

Figure 1: Numerical setup of the system.

THEORY AND SIMULATIONS

Dynamics of the gas phase. The equation for the evolution of the pressure $P = \tilde{P} + P_0$, where P_0 is the atmospheric pressure and $\tilde{P}$ the local pressure fluctuations is given by

$$\phi\left[\frac{\partial P}{\partial t} + \boldsymbol{u}\cdot\nabla P\right] = \nabla\cdot\left[P\frac{\kappa}{\mu_f}\nabla P\right] - P\nabla\cdot\boldsymbol{u} \tag{1}$$

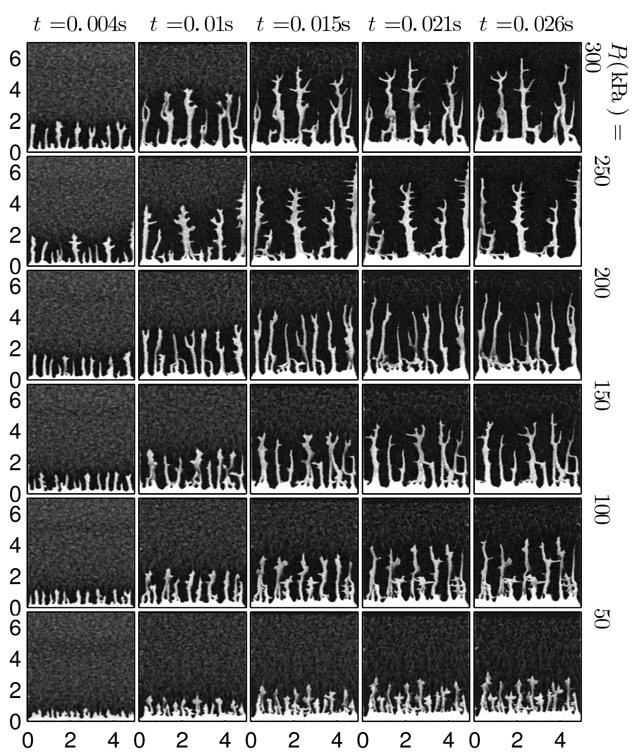

Figure 2: Snapshots during the simulations of the particle density in the Hele-Shaw cell, displayed for decreasing injection pressure P_I from top to bottom and as a function of time (left to right). Low particle density appears brighter in the snapshots. Under air injection, fractures, fingers and dispersed bubbles of low particle density emerge and propagate. x- and y-axis units are given in cm. The y-axis specifies the distance from the inlet.

In this equation, the pressure is described in terms of the local granular velocity $\boldsymbol{u}$, the viscosity μ_f of the gas, the local porosity $\phi = 1 - \rho_s$ and the local permeability κ. Eq. (1) is derived from mass conservation of the gas and the granular medium and by assuming a local Darcy law.

Dynamics of the particles. For the particles we basically use Newton's second law

$$m\frac{dv_p}{dt} = \boldsymbol{F_I} + \boldsymbol{F_d} + \boldsymbol{F}_a - \frac{\nabla P}{\rho_n}, \tag{2}$$

with particle velocity v_p, particle mass m, particle mass density ρ_m, cell spacing h and the number density $\rho_n = \rho_s\rho_m/m$. $\boldsymbol{F_I}$ are linear inter-particle solid contact forces. $\boldsymbol{F_d}$ is a viscous damping force during particle collisions. For F_a, the interaction with the side plates we assume that the normal stress $P_g^{\perp}$ in the granular packing is proportional to the in-plane stress $P_g^{\parallel}$ by a factor λ (Janssen hypothesis). Using further a Coulomb friction model we state that the frictional force F_a per particle with the glass plates is proportional to the normal stress by a friction coefficient γ. With these two assumptions we find an expression for the friction force with the side plates.

$$F_a \leq \gamma S_a(2P_g^{\perp} + \rho_m gh) = \gamma S_a(2\lambda P_g^{\parallel} + \rho_m gh). \tag{3}$$

$S_a = \pi a^2$ is the contact area of the particles with the plates.

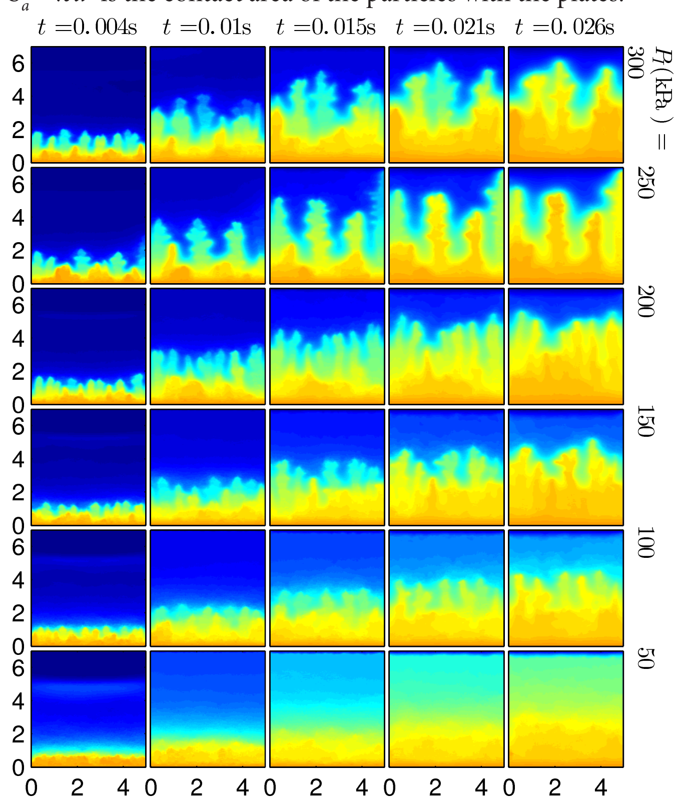

Figure 3: The pressure evolution for decreasing injection pressure P_I (top to bottom) and as a function of time (left to right). High pressure appears yellow (brighter) in the snapshots. x- and y-axis units are given in cm.

RESULTS

We ran a set of six simulations for injection pressures of P_I = (0.5, 1.0, 1.5, 2.0, 2.5, 3.0) × 10^5 Pa above atmospheric pressure P_0, a fluid viscosity of μ_f = 18.0 $mPa{\cdot}s$ and a friction coefficient with the side plates of $\gamma\lambda = 4.0$. The injected gas is considered as an ideal gas and has the compressibility of air $\beta_T = 1/P_0$ at P_0. The value of P_I at the inlet is reached very fast and particles start to move shortly after. During this compression of the particles fractures emerge in the granular packing. In Fig. 2 a set of snapshots of the particle density is shown. The snapshots are taken at increasing time from left to right. Each horizontal row of pictures corresponds to one of the six simulations at a different injection pressures. In Fig. 3 snapshots of the corresponding pressure field in the cell are displayed. The pressure field is normalized to one to allow a qualitative comparison.

In these plots an apparent feature is the different propagation speed and position of the emerging fractures. A high injection pressure causes the fractures to propagate faster. To quantify this observation we can plot the position of the most advanced finger tip as a function in time. This is done in Fig. 4. The plot clearly proves the previous observation. Furthermore it turns out that the systematic increase of the propagation speed is also proportional to the square root of the injection pressure. This is checked in Fig. 5. Here the rescaling of the fracture tip position by the square root of the injection pressure $\sqrt{P_I}$ results in a collapse of the graphs. The disagreement at the later stages of the simulations in this plot results from the finite size of the system, which allows fractures to grow only up to a certain size. Finally we can state that the fingers grow according to

$$Y_t = \sqrt{P_I}\, f(t), \tag{4}$$

where *f(t)* is a function which appears in the plots to be almost linear at early stages of the finger growth for $t < 0.01$ *s*.

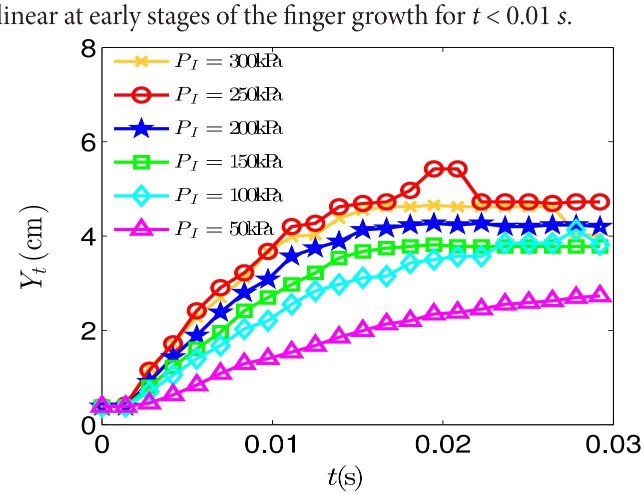

Figure 4: The position of the most advanced finger/fracture as a function of time at different injection pressure P_I. The higher the injection pressure P_I the further fingers grow.

In Fig. 2 we also observe that the fingers at high injection pressure propagate further into the packing before complete compaction of the grains takes place. This can be also seen in Fig. 4 where the finger position stops growing at longer distances from the inlet the higher the injection pressure is.

Apart from the finger position, the increase of the injection pressure also affects the shape of the fingers. In Fig. 2 it can be seen that the fingers get more branched and fracture-like at higher injection pressure. At low injection pressure fingers appear to be straighter while increasing the injection pressure, fingers develop more and more branches. At the highest injection pressure of $P_I = 3.0 \times 10^5$ *Pa* the fingers clearly show characteristics of fractures.

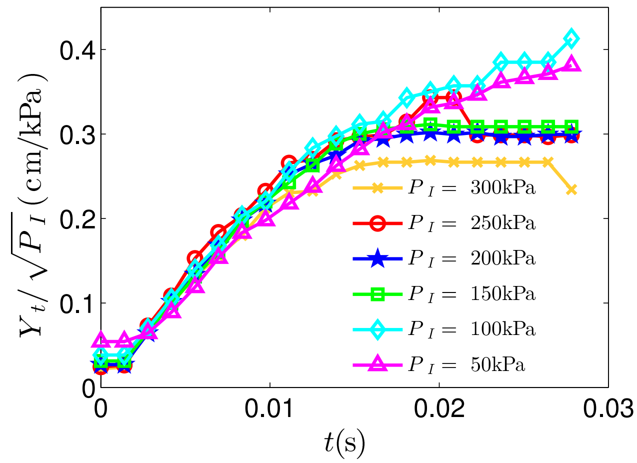

Figure 5: The position of the most advanced finger/fracture rescaled by the square root of the injection pressure $\sqrt{P_I}$. As a function of time the graphs at different injection pressure P_I collapse onto a single graph.

At high injection pressure P_I the pressure gradients are the largest. When the boundary is deformed the expected changes of the pressure gradients are therefore also higher at high injection pressure than at low injection pressure. At low P_I, one expects a lower pressure gradient everywhere, and thus a low effect of seepage forces and a slower deformation. Leading to overall smoother pressure gradients and a more stable front deformation. We thus expect faster finger propagation, and more branching at a higher injection pressure.

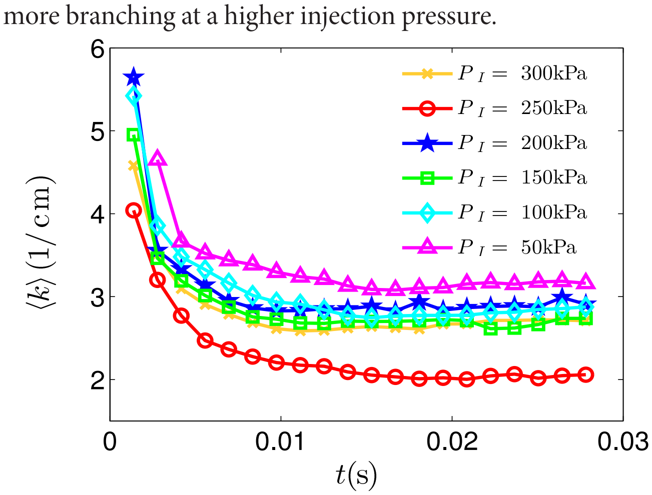

Figure 6: The average of the spatial finger wavenumber in x direction.

Finally also the spatial distance between the fingers depends on the injection pressure (see Fig. 6). At low injection pressure the number of fingers is higher than at high injection pressure, as can be also seen in Fig. 2. In general the finger spatial frequency decreases in time after injection has started and fingers propagate through the cell. This can be shown by calculating the average of the characteristic spatial finger wavenumber in x direction. First the power spectrum S_j of each horizontal line j of the particle density is calculated. Taking the average of these power spectra results in a single power spectrum $\overline{S}$. From this average distribution of wave numbers the characteristic wave number $\langle k \rangle$ in the *x*-direction is defined and calculated in the following way, using an average of *k* with the power spectrum as a weight

$$\langle k \rangle = \frac{\sum_k k\bar{S}(k)}{\sum_k \bar{S}(k)}. \tag{5}$$

The results in Fig. 6 show a decrease of finger frequency in time. As a trend we notice that at higher injection pressure the finger frequency decreases faster than at low injection pressure. However the simulation at $P_I = 250\ kPa$ differs from the other simulations. In this simulation we also observe a finger propagating directly along the right boundary in Fig. 2. Close to the wall this finger appears to propagate faster than the other fingers in this simulation. Because the simulation at $P_I = 250\ kPa$ is the only simulation where this appears it also stands out in the plots for the average wave number Fig. 6. This is presumably due to a finite size effect, and such outlier is frequently met in granular systems, which are known to present a large variability and sensitivity on details of the initial state. (see e.g. [17]). Otherwise for higher injection pressure, the finger frequency not only decreases faster but also drops to a lower value before the grains get compacted.

This coarsening of the finger frequency is the result of two mechanisms. First the pressure gradient between the finger tip and the outlet gets higher the closer the finger tip moves to the outlet. Assuming a linear pressure profile though the porous media the pressure would drop to zero on a shorter and shorter distance the closer the finger advances to the outlet. At the same time the gas also leaks into the side walls of the finger. This increases the pressure in the porous material around a finger. In the areas where this pressure increase takes place less advanced neighboring fingers would thus experience a lower pressure gradient. The speed of these fingers is thus reduced. This means the more a finger advances to the outlet the faster it moves. At the same time the pressure increase in the area around an advanced finger decreases the pressure gradient in front of less advanced fingers. This causes the less advanced fingers to propagate slower or to stop completely. This mechanism will result in a coarsening of the finger frequency. Further more we expect this mechanism to be active on a typical length scale which is comparable to the skin depth of the pressure profile. In the limit of a infinite pressure skin depth this mechanism is similar to the basic Saffman Taylor instability [23].

A second mechanism that will account for a coarsening of the finger frequency is the compaction of the grains on the sides of a finger. During the propagation the finger width increases and branches at a 90 degree angle arise on the sides of fingers. This compacts the granular material on the sides of an advancing finger. How far this compaction propagates on the sides depends on the properties of the granular material and also on the finger width and how the side branches develop. Where this compaction has occurred preceding fingers are slowed down or stopped. The size of the compaction front around the fingers sets a second length scale for the coarsening of the finger frequency.

CONCLUSIONS

The increase of the injection pressure primarily causes fingers to propagate faster through the granular packing. Fingers at high injection pressure also tend to be more branched and fracture-like than the fingers at low injection pressure. It was shown that the position of the fracture propagation in time increases with the square root of the injection pressure $\sqrt{P_I}$. Furthermore we discussed the observed coarsening of the characteristic spatial finger wavenumbers in terms of two mechanisms. A first mechanism that controls the coarsening arises from the fluid seepage into the granular media. Where the length scaled for this mechanism was argued to be of the size of the pressure skin depth. To further explain the coarsening a second mechanism causing the coarsening of the finger wavenumber was highlighted. This second mechanism introduces a length scale for the coarsening with the size of the compaction front in the granular material around a finger.

ACKNOWLEDGMENTS

We thank Gustavo Sánchez-Colina for help in the Spanish grammar.

[1] M. Bickle, A. Chadwick, H. E. Huppert, M. Hallworth and S. Lyle, Earth Planet. Sci. Lett. **255**, 164 (2007).
[2] F. C. Boait, N. J. White, M. J. Bickle, R. A Chadwick, J. A. Neufeld and H. E. Huppert, J. Geophys. Res. B: Solid Earth **117**, B03309 (2012).
[3] E. Lemaire, Y. O. M. Abdelhaye, J. Larue, R. Benoit, P. Levitz and H. Van Damme, Fractals **1**, 968 (1993).
[4] X. Cheng, L. Xu, A. Patterson, H. M. Jaeger and S. R. Nagel, Nat. Phys. **4**, 234 (2008).
[5] H. Huang, F. Zhang, P. Callahan and J. Ayoub, Phys. Rev. Lett. **108**, 258001 (2012).
[6] Ø. Johnsen, R. Toussaint, K. J. Måløy and E. G. Flekkøy, Phys. Rev. E **74**, 011301 (2006).
[7] Ø. Johnsen, C. Chevalier, A. Lindner, R. Toussaint, E. Clément, K. J. Måløy, E. G. Flekkøy and J. Schmittbuhl, Phys. Rev. E **78**, 051302 (2008).
[8] Ø. Johnsen, R. Toussaint, K. J. Måløy, E. G. Flekkøy and J. Schmittbuhl, Phys. Rev. E **77**, 011301 (2008).
[9] A. Nermoen, C. Raufaste, S. D. de Villiers, E. Jettestuen, P. Meakin and D. K. Dysthe. Phys. Rev. E **81**, 061305 (2010).
[10] M. J. Niebling, R. Toussaint, E. G. Flekkøy and K. J. Måløy, Phys. Rev. E (submitted).
[11] M. J. Niebling, E. G. Flekkøy, K. J. Måløy and R. Toussaint, Phys. Rev. E **82**, 011301 (2010).
[12] M. J. Niebling, E. G. Flekkøy, K. J. Måløy and R. Toussaint, Phys. Rev. E **82**, 051302 (2010).
[13] J. L. Vinningland, R. Toussaint, M. J. Niebling,

E. G. Flekkøy and K. J. Måløy, European Phys. J. Special Topics **204**, 27 (2012)
[14] S. McNamara, E. G. Flekkøy and K. J. Måløy, Phys. Rev. E **61**, 4054 (2000).
[15] J. L. Vinningland, Ø. Johnsen, E. G. Flekkøy, R. Toussaint and K. J. Måløy, Phys. Rev. Lett. **99**, 048001 (2007).
[16] J. L. Vinningland, Ø. Johnsen, E. G. Flekkøy, R. Toussaint and K. J. Måløy, Phys. Rev. E **76**, 051306 (2007).
[17] J. L. Vinningland, E. G. Flekkøy, R. Toussaint and K. J. Måløy, Phys. Rev. E **81**, 041308 (2010).
[18] M. A. van der Hoef, M. van Sint Annaland and J. A. M. Kuipers, Chem. Eng. Sci. **59**, 5157 (2004).
[19] N. G. Deen, M. van Sint Annaland, M. A. van der Hoef and J. A. M. Kuipers, Chem. Eng. Sci. **62**, 28 (2007).
[20] N. G. Deen, M. van Sint Annaland, M. A. van der Hoef and J. A. M. Kuipers, Prog. Comput. Fluid Dyn. **7**, 152 (2007).
[21] M. A. van der Hoef, M. van Sint Annaland, N. G. Deen and J. A. M. Kuipers, Ann. Rev. Fluid Mech. **40**, 47 (2008).
[22] C. Zeilstra, J. G. Collignon, M. A. van der Hoef and J. A. M. Kuipers, Powder Tech. **184**, 166 (2008).
[23] P. G. Saffman, G. Taylor, Proc. R. Soc. Lond. A **245**, 312 (1958).

Dynamic aerofracture of dense granular packings

Michael J. Niebling,[1,2] Renaud Toussaint,[2,3] Eirik G. Flekkøy,[1,3] and Knut Jørgen Måløy[1,3]
[1]*Department of Physics, University of Oslo, P.O. Box 1048, 0316 Oslo, Norway*
[2]*Institut de Physique du Globe de Strasbourg, Ecole et Observatoire des Sciences de la Terre, Université de Strasbourg, CNRS, 5 rue Descartes, F-67000 Strasbourg, France*
[3]*Centre for Advanced Study at the Norwegian Academy of Science and Letters, Drammensveien 78, 0271 Oslo, Norway*
(Received 12 October 2011; revised manuscript received 28 September 2012; published 26 December 2012)

A transition in hydraulically induced granular displacement patterns is studied by means of discrete numerical molecular dynamics simulations. During this transition the patterns change from fractures and fingers to finely dispersed bubbles. The dynamics of the displacement patterns are studied in a rectangular Hele-Shaw cell filled with a dense but permeable two-dimensional granular layer. At one side of the cell the pressure of the compressible interstitial gas is increased. At the opposite side from the inlet of the cell a semipermeable boundary is located. This boundary is only permeable towards the gas phase while preventing grains from leaving the cell. The imposed pressure gradient compacts the grains. In the process we can identify and describe a mechanism that controls the transition of the emerging displacement patterns from fractures and fingers to finely dispersed bubbles as a function of the interstitial gas's properties and the characteristics of the granular phase.

DOI: 10.1103/PhysRevE.86.061315 PACS number(s): 81.05.Rm, 47.54.−r, 62.25.Mn

I. INTRODUCTION

Hydraulic fractures occur when diverse materials break under the stress induced by fluids or gases. Understanding how hydraulic fracturing is initiated and progresses is of fundamental importance whenever safe dams are constructed, supercritical CO_2 is stored, or sustainable wells are drilled. Volcanic dikes and sills arise naturally by hydraulic fracturing processes. Just as we learn to protect ourselves from the unwanted effects of hydraulic fractures, it has been proven to be a useful technology to fracture the reservoir rock formations around a well bore to enhance the recovery of mineral oil and natural gas.

In previous studies [1–17] experiments have been conducted in circular and rectangular Hele-Shaw cells filled with small grains. Under air injection in the center of the circular cell, multiple fingers of low particle density emerged from the inlet [1,2].

For the rectangular cell it was observed that a decompaction front travels first from the outlet to the inlet before a few fingers of low particle density grow from the air inlet [3,4]. Furthermore, in a recent work, the coarsening of such fingers was studied [5]. In Ref. [6] loosely compacted grains were exposed to a pressure gradient. In the process of these simulations and experiments a spinodal-like instability was observed that displayed emerging and growing dispersed bubbles of low particle density.

Considering this background various dynamics and structures have been observed and described. However, a theory accounting for the transition from dynamics that display dispersed bubbles to dynamics that display fractures and fingerlike patterns has not been presented. In this article we will study and explain the mechanism that controls the transition between these two types of emerging structures during the compaction of a granular layer.

After a number of experiments have been performed in a rectangular cell [18], we chose to perform a numerical simulation. Using a discrete numerical molecular dynamic model, we have thereby the possibility to systematically and independently vary the viscosity of the interstitial fluid. Effectively this corresponds to changing the size of the system, as we will discuss in the following. This approach allows us to study system sizes that experimentally would be extremely complicated and dangerous to achieve. In the following section we will briefly discuss the parameters and the setup used for the numerical model.

II. SETUP OF THE NUMERICAL MODEL

The setup is illustrated in Fig. 1. Two glass plates are separated by 1 mm. The space in between the glass plates is filled with dense grains. The gas phase injected at the inlet following the increase of pressure is identical to the gas saturating initially the porous packing. The solid volume fraction of the grains is $\rho_s^{(0)} = 0.42$, which is less than the maximum of $\rho_s^{(\max)} = 0.60$ to allow compaction of the grains. The pressure at the inlet is set to a constant value of $P_I = 2.5 \times 10^5$ Pa. The outlet is located on the opposite side of the cell. Here a semipermeable boundary stops the grains from leaving the cell but is open towards the gas phase. Apart from the semipermeable boundary at the outlet, all three other boundaries are fully sealed. There gas or particle exchange is impossible. Around 200 000 grains of $140 \pm 10\%$ μm in diameter are simulated. The size distribution of 10% is artificially set to suppress the formation of a triangular grain packing. Initially the particles are inserted into the cell, each with a random velocity. Shortly after the friction between particles and the plates and energy dissipation during particles collisions is activated and the particles build up a fixed random packing after they lost their kinetic energy. At the start of the simulations the pressure at the inlet is increased; just after the pressure was increased a pressure front starts to propagate through the cell and compacts the particles. The length of the pressure front skin depth is adjusted and varied by changing the gas viscosity.

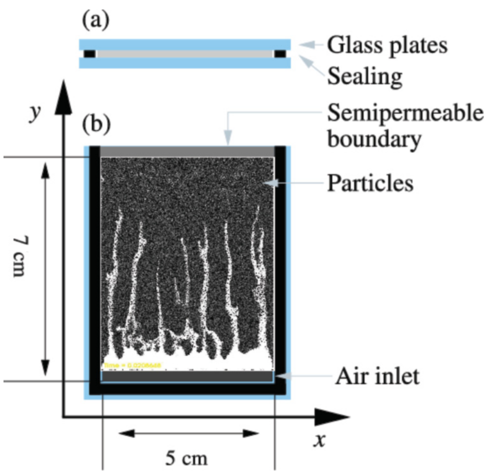

FIG. 1. (Color online) Setup of the system: (a) cross section and (b) top view. Compressed air is injected at the inlet. The outlet is semipermeable: open towards the gas phase and closed for the granular phase.

III. THEORY AND SIMULATIONS

The numerical model employed is a two-dimensional hybrid model. It uses a continuum description for the gas phase and a discrete description of the granular phase. Friction between particles and the top and bottom plates is included. It was compared to well matched experiments and shown to reproduce closely the dynamics of granular flows at low Reynolds numbers [19–21] and under conditions similar to those assumed in the present article [1].

IV. DYNAMICS OF THE GAS PHASE:

The equations ruling the evolution of the pressure $P = \tilde{P} + P_0$, where P_0 is the atmospheric pressure and $\tilde{P}$ is the local pressure fluctuation, are derived in detail in Refs. [1,19,20,22–26]. We calculate P according to

$$\phi\left[\frac{\partial P}{\partial t} + \mathbf{u}\cdot\nabla P\right] = \nabla\cdot\left[P\frac{\kappa}{\mu_f}\nabla P\right] - P\nabla\cdot\mathbf{u}. \quad (1)$$

This equation basically describes how the divergence of the local granular velocity $\mathbf{u}$ leads to local pressure changes according to the gas displacement by the grains and between them. The viscosity μ_f of the gas determines how fast the gas diffuses through the permeable grains to equalize the pressure fluctuations. The local porosity is $\phi = 1 - \rho_s$ and the local permeability κ is calculated by the Carman-Kozeny relation [22,27]. Equation (1) is derived from mass conservation of the gas, mass conservation of the granular medium, and by assuming a local Darcy law.

V. DYNAMICS OF THE PARTICLES

The dynamics of each individual particle with the velocity v_p, particle mass $m = \rho_m \pi a^2 h$, particle mass density ρ_m, volume $V_a = \pi a^2 h$ in a cell with a plate spacing of h, and the number density defined as $\rho_n = \rho_s \rho_m / m$ is described by

$$m\frac{dv_p}{dt} = \mathbf{F_I} + \mathbf{F_d} + \mathbf{F_a} - \frac{\nabla P}{\rho_n}, \quad (2)$$

where $\mathbf{F_I}$ is the linear interparticle solid contact force. The third term on the right-hand side of Eq. (2) arises from the momentum exchange between the gas and granular phase. Here $\mathbf{F_d}$ is a viscous force accounting for energy dissipation during particle collisions. More details are given in Refs. [19,20].

In the granular packing we assume that the normal stress $P_g^{\perp}$ is proportional to the in-plane stress $P_g^{||}$ by a factor λ. This relation is known as the Janssen hypothesis [1,19]. Considering also a Coulomb friction model, we get that the frictional force F_a per particle with the glass plates is proportional to the normal stress by a friction coefficient γ:

$$F_a \leqslant \gamma S_a(2P_g^{\perp} + \rho_m g h) = \gamma S_a(2\lambda P_g^{||} + \rho_m g h). \quad (3)$$

The factor 2 in the first term accounts for the two glass plates on each side of the particle. Here $S_a = \pi a^2$ is the contact area of the particles with the plates. The second term is a contribution due to the gravitational acceleration g on the grains, which leads to additional friction between the bottom plate and the particles. This term is included for completeness, but has a negligible effect on the following results. Finally, the particle propagation is modeled by the velocity Verlet scheme [28,29].

VI. RESULTS

The coefficients that determine the friction with the glass plates are set to $\gamma\lambda = 4.0$, a rather high value. Lower values have also been tested and resulted in less branched fractures. The pressure at the inlet is increased as a steep ramp, fast enough that the maximum pressure at the inlet of $P_I = 2.5 \times 10^5$ Pa is reached before particles significantly start to move. The injected gas is considered as an ideal gas and has the compressibility of air $\beta_T = 1/P_0$. The compressibility is kept constant. The gas viscosity, however, is increased gradually in different simulations, from the value for air $\mu_f^{(\mathrm{air})} = 0.018$ mPa s by a factor of 1000 up to $\mu_f = 18.0$ mPa s. The results of the simulations for the particle density are shown in Fig. 2 (see also Ref. [30]). Dark regions correspond to a high particle density while brighter areas represent low particle density. The gas viscosity decreases from top to bottom while time progresses from left to right. In the time sequences the emerging structures change drastically as a function of the gas viscosity. In the simulation with the lowest gas viscosity dispersed bubbles of reduced particle density appear in the whole cell apart from a darker region at the outlet, where particles get compacted at the semipermeable boundary [see Fig. 2 for $\mu_f = 0.18$–0.018 mPa s and $t = 0.004$–0.01 s or Fig. 3(b) for a close-up]. Increasing the viscosity, structures change from dispersed bubbles to fractures. Furthermore, compaction of the grains occurs here at the inlet and in front of the fingers instead of at the outlet. Taking a close look at the simulations at high viscosity in Fig. 2, this is indicated by a dark region in front of the fractures and fingers that was absent for low viscosity gas [see also Fig. 3(a) for a close-up].

For a better quantification, we represent in Fig. 4 the dependence of three quantities as a function of y across the cell, at different times. The choice of parameters represented allows us to understand whether grains close to the boundary are pushed through solid stress or fluid drag: The solid volume

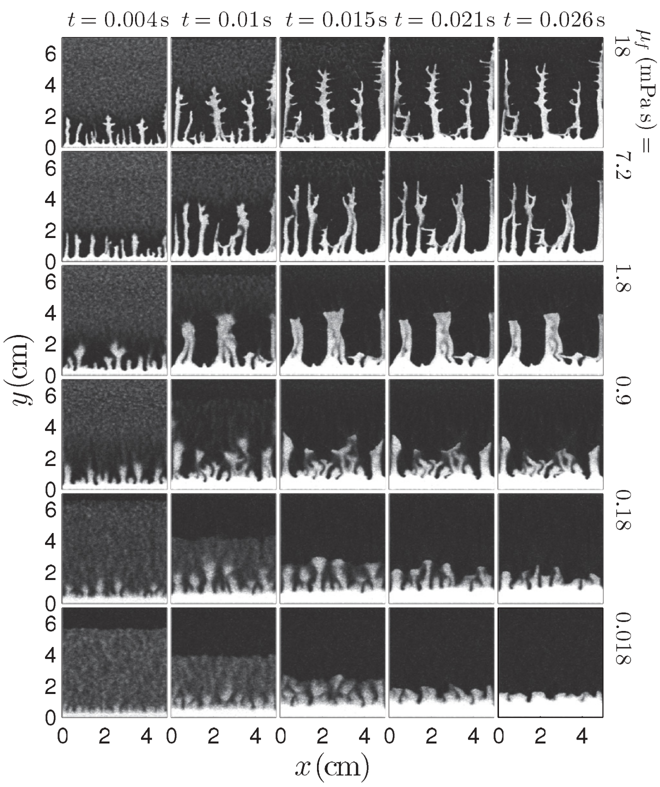

FIG. 2. Snapshots during the simulations of the particle density in the Hele-Shaw cell, displayed for decreasing gas viscosity from top to bottom and for increasing time (left to right). Low particle density appears brighter in the snapshots. Under air injection, fractures, fingers, and dispersed bubbles of low particle density emerge and propagate in time towards the outlet of the cell. The y axis specifies the distance from the air inlet in cm. The maximal density is normalized to one.

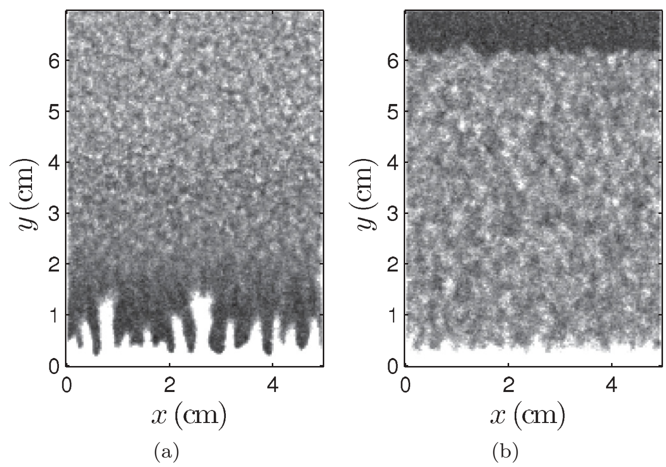

FIG. 3. Close-up of snapshots of the particle density in the Hele-Shaw cell during the simulations at $t = 0.003$ s. The snapshots correspond to the plots in Figs. 4(a), 4(d), and 4(g). In 3(a) $\mu_f = 1.8$ mPa s and in (b) $\mu_f = 0.018$ mPa s. The density is normalized to one and the color bar range is chosen from 0 to 0.5 to enhance the density contrast. In the plots the darker areas represent higher grain density. In (a) a compaction front at the inlet around the finger tips has emerged. In (b) grains get compacted at the outlet of the cell, which corresponds to a darker stripe at the outlet (for $y > 6$ cm).

fraction corresponds to the grain density and allows us to clarify the formation of compacted zone in different regions, which play an important role in the system dynamics. The grain velocity allows us to image where and when the packing deforms, and the pressure gradient is directly related to the fluid drag force.

The solid volume fraction is averaged along the x direction and plotted as a function of the y direction for three time steps in Figs. 4(a)–4(c). In these figures zones of compacted grains correspond to solid volume fraction values larger than 0.45. The inlet side of the cell is just like before located at a y position close to zero. The outlet is located at $y = 6.9$ cm. At the first time step in Fig. 4(a) we notice that compaction fronts arise at the inlet side for viscosity values of $\mu_f < 0.018$ mPa s and at the outlet side of the cell for the lowest gas viscosity of $\mu_f = 0.018$ mPa s. During the next time steps in Figs. 4(b) and 4(c) the compaction fronts at the inlet progress towards the outlet. At the outlet compaction of grains now also appears for simulations with gas viscosity values up to $\mu_f = 0.9$ mPa s. The zone of particle compaction at the outlet grows and expands in time towards the inlet.

To understand how the grain compaction depends on the gas viscosity we will have to take the pressure evolution in the cell into account. In Fig. 5 the gas pressure in the cell is displayed for time steps and gas viscosity values corresponding to Fig. 2. The bottom row, where the gas viscosity has the smallest value in this figure, shows that the pressure decays continuously towards the outlet. Alternatively we can look at Fig. 4(d), where the pressure average in the x direction is plotted as a function of the y direction. Confirming our observation from above, Fig. 4(d) shows a linear pressure profile in the y direction for the lowest viscosity right at the start of the simulation. In this regime the pressure gradient acts as a body force displacing all particles in the cell simultaneously and homogeneously and therefore preventing particles from jamming. Furthermore, the homogeneous grain motion is also confirmed for the low viscosity value in Fig. 4(g). Here u_y, the y component of the particle velocity averaged along the x direction, is constant as a function of y.

The appearance of low particle density bubbles under these conditions has previously been reported and described in Ref. [6]. However, in the present setup the semipermeable boundary at the outlet interferes with the otherwise uniform particle motion. This results in the previously mentioned compaction layer at the outlet.

The pressure decay in Fig. 5 becomes more localized if the viscosity is increased. Now the pressure drops rapidly at the interface between the granular phase and the growing particle free region at the inlet side of the cell. Alternatively we can confirm this localized pressure decay in Figs. 4(d)–4(f), where the pressure is averaged along the x direction and plotted as a function of y. This time sequence of plots shows that increasing the viscosity results in an increasingly steep pressure decay at the interface. Further inside the granular packing towards the outlet the pressure remains initially unchanged. In this regime the pressure gradient acts as a surface force on the particles at the interface between granular and gas phase. Due to the localized pressure gradient, particles at the interface close to the pressure inlet are initially accelerated more quickly than

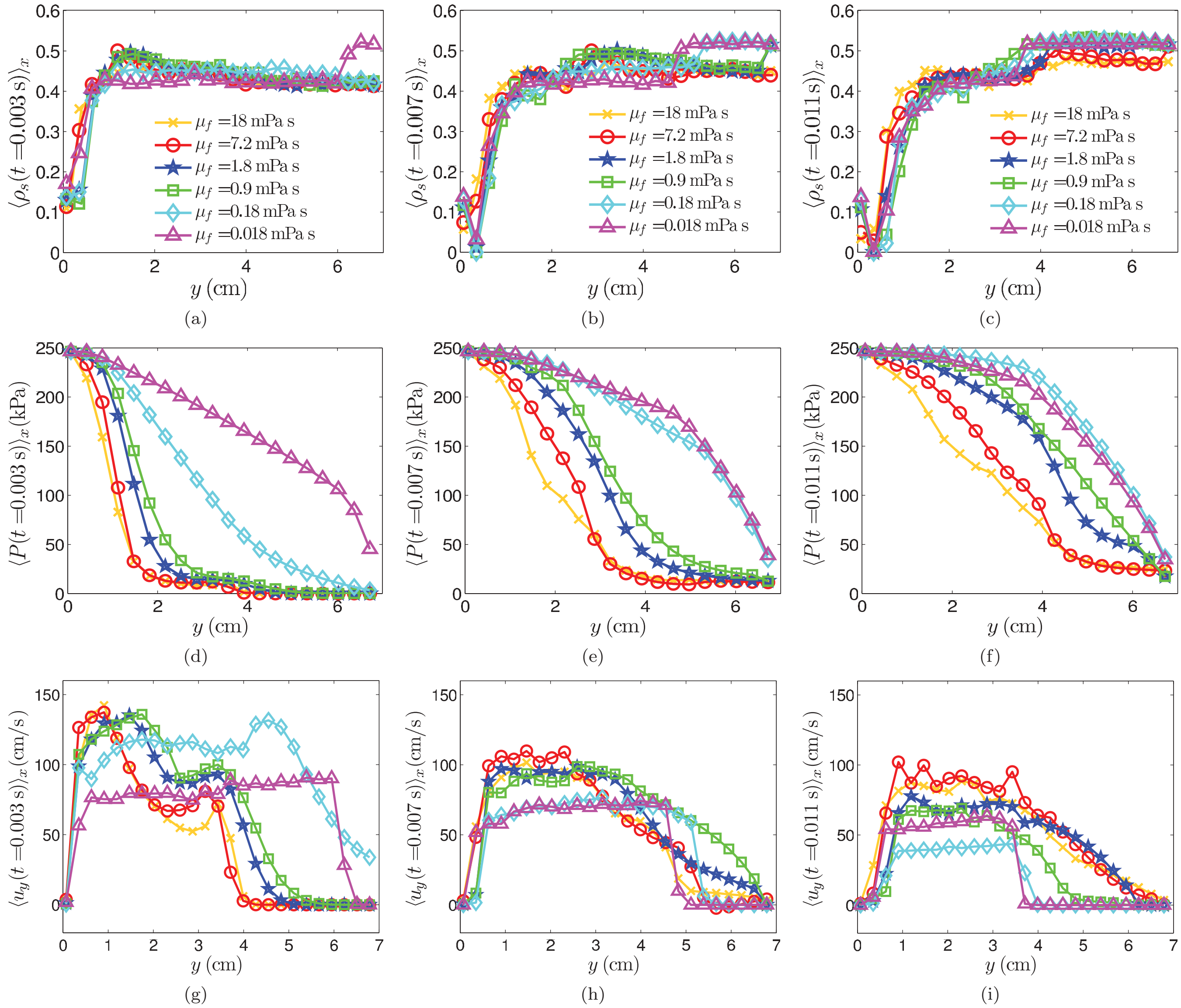

FIG. 4. (Color online) Several quantities have been averaged along the x direction and are plotted in rows from top to bottom: (a)–(c) solid volume fraction ρ_s, (d)–(f) pressure P, and (g)–(i) y component of the grain velocity u_y. From left to right the three figures in each row correspond to the times $t = 0.003$, 0.007, and 0.011 s after the start of the injection. The legend is consistent in all plots and is displayed only in the first row.

the particles close to the outlet. This leads to particle collisions and jamming in the granular packing at the interface where a compaction front builds up.

Where the grains are compacted the solid stress increases as displayed in Fig. 6. The solid stress is shown to increase first at the outlet for the least viscous gas. For higher viscosity values the solid stress is localized around the finger tips. Here the solid stress decays inside the granular packing over a certain distance, which is the same size as the compaction front. This distance can be larger than the distance over which the pressure gradient decays from the interface into the granular packing. In this regime the particles further inside the packing are accelerated through solid contacts rather than by the pressure gradient of the fluid. Such solid contacts in a compacted granular medium transmit the stress localized along distinct force chains. This causes a heterogeneous acceleration of the particles and the particle velocity in the y direction is increased along certain localized paths, as shown in Fig. 7. Local noise and disturbance are now affecting the evolution of the interface directly and fractures appear.

In this situation local particle rearrangement and jamming results in the observed fracture pattern. To quantify the transition between the two regimes we will briefly define the characteristics of the pressure diffusion, as done in detail in Ref. [20]. We neglect the motion of the granular phase and consider a standard diffusion equation for the pressure evolution within the granular phase. This approach allows us to define a diffusion constant for the pressure

$$D = \frac{\kappa}{(1 - \rho_s)\beta_T \mu_f}. \tag{4}$$

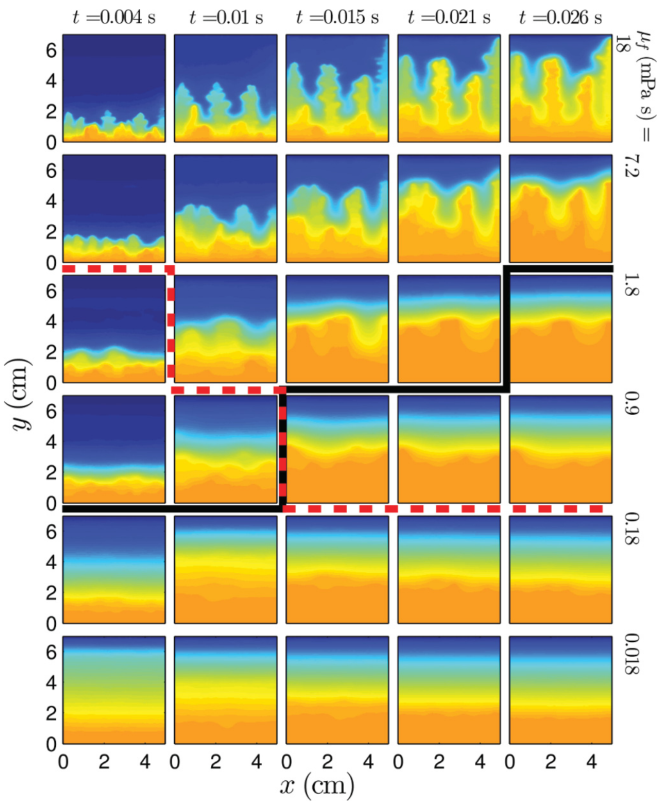

FIG. 5. (Color online) Snapshots show the pressure evolution for decreasing gas viscosity (top to bottom) and as a function of time (left to right). High pressure appears yellow (brighter) in the snapshots. The dashed (red) line between the snapshots shows the time t_f [see Eq. (7)]. In the snapshots above this dashed (red) line the compaction front thickness is greater than the skin depth of the pressure s defined in Eq. (5). Below the black line the skin depth s has reached half of the system size in a theoretical system where particles do not move. The maximal pressure is normalized to one.

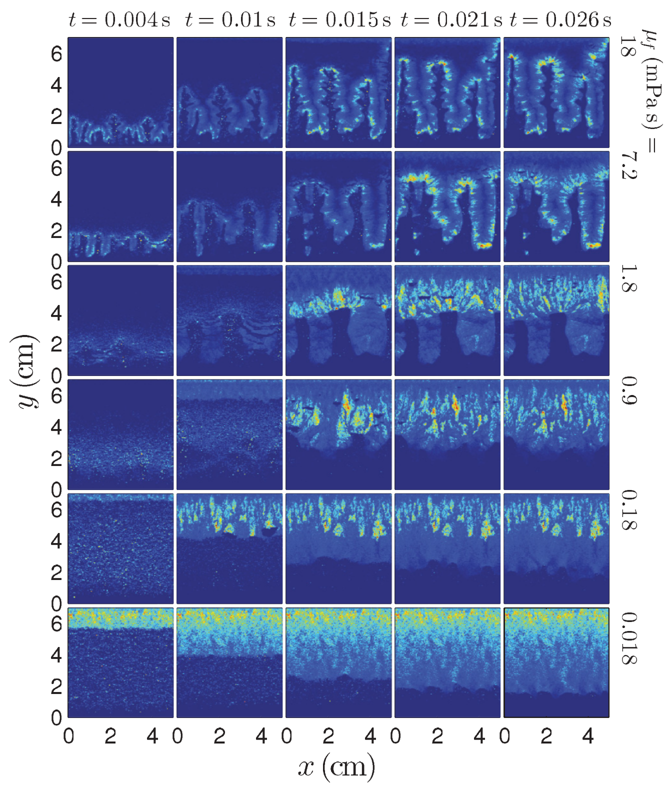

FIG. 6. (Color online) Snapshots of the normal solid in-plane stress between the particles for decreasing gas viscosity (top to bottom) and as a function of time (left to right). High stress appears yellow (brighter) in the snapshots. The maximal normal solid in-plane stress is normalized to one.

Furthermore, we define a skin depth

$$s = \sqrt{4Dt}, \tag{5}$$

where s is the distance from the gas-particle interface over which the pressure has decayed by $P(s) = \frac{1}{e}P_I$ [31]. The diffusion constant in Eq. (4) specifies how fast the fluid flow can equalize pressure changes at given gas properties and characteristics of the porous medium.

We can compare how well this assumed pressure evolution fits to the simulations. For this purpose we average the pressure in the x direction and calculate the maximum gradient in the y direction of this pressure average: $\max(\partial_y \langle P \rangle_x)$ as a function of time [see Fig. 8(b) for all viscosity values]. The y position of $\max(\partial_y \langle P \rangle_x)$ propagates from the inlet towards the outlet as time passes as shown in Fig. 8(a). At low viscosity the position of the maximum gradient reaches the outlet almost immediately after the simulation has started while at high viscosity values this maximum gradient never reaches the outlet during the simulated time.

In Fig. 8(a) the y position of $\max(\partial_y \langle P \rangle_x)$ depends on the combined position of the skin depth and the position of the gas-particle interface. To study the pressure evolution relative to the gas-particle interface at the finger tip in a Lagrangian reference frame it is more useful to calculate $\max(\partial_y \langle P \rangle_x)$ as a function of time. If the assumed propagation of the skin depth for the pressure as a square root in time relative to the interface is correct we should be able to rescale $\max(\partial_y \langle P \rangle_x)$ by multiplication with the skin depth $s(t)$ defined in Eq. (5). The rescaling is done in Fig. 8(c) and Fig. 9 shows a close-up of the graphs with the four highest viscosity values tested. The rescaled graphs are constant in time. This supports the proposed diffusive pressure behavior relative to the particle motion. For low viscosity values the rescaling does not result in a constant behavior because of the limiting finite size of the cell. Furthermore, we observe that the plots do not fall directly above each other. For increasing viscosity values the graphs are shifted downwards by a constant. This effect is not captured in our explanation and is most likely due to rearrangements and motion of the particles. In the following the skin depth is used as a measure of how steep and how far the pressure decays into the granular phase in the cell.

We notice in Eqs. (4) and (5) that increasing the viscosity reduces the skin depth. Using Eq. (5), the calculated time for the skin depth to propagate through the cell in the y direction is 0.0009 s at the lowest viscosity value. This is faster than the time needed to notice a significant movement of the grains. For the highest viscosity value in the simulations the calculated time is 0.9 s until the skin depth has grown to the size of the cell assuming a fixed granular packing.

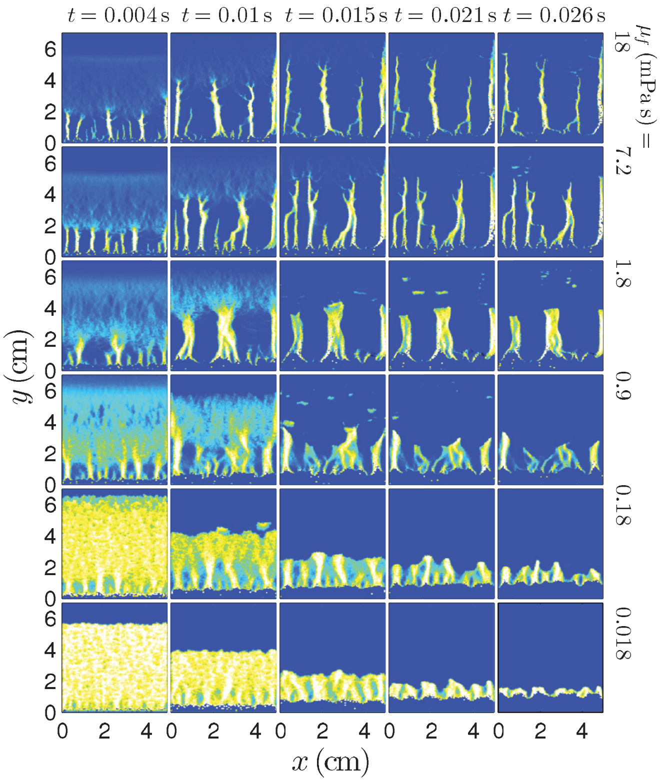

FIG. 7. (Color online) Snapshots of u_y, the y component of the particle velocity, for decreasing gas viscosity (top to bottom) and as a function of time (left to right). High velocity appears yellow (brighter) in the snapshots. Here u_y is normalized to one.

At the very start of the simulations the evolution of the system is controlled by two length scales. The first length scale is the length of the skin depth. The second length scale is the thickness of the compaction front at the gas-particle interface at the inlet. Before fractures appear the thickness of this compaction front is related to the growth of the particle free zone at the inlet. When the particle free zone at the inlet of the cell grows to a certain length of Y_t in the y direction from the inlet the displacement of the particles leads to a compaction

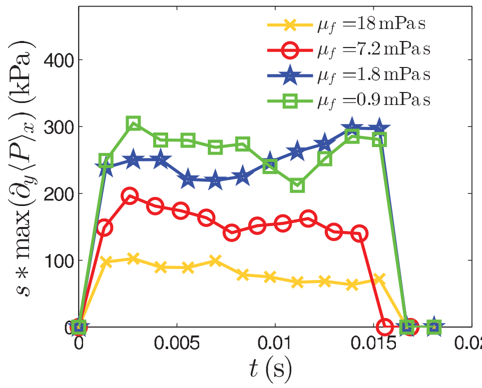

FIG. 9. (Color online) Close-up of Fig. 8(c) for the four highest viscosity values tested.

front with a minimal thickness of

$$d_c = \frac{Y_t \rho_s^{(0)}}{\rho_s^{\max} - \rho_s^{(0)}}, \tag{6}$$

where d_c depends on the initial solid volume $\rho_s^{(0)}$ fraction and the possible maximal volume fraction $\rho_s^{\max}$ of the grains. Before fractures appear Y_t is equivalent to the position of the most advanced finger tip, which is plotted in Fig. 10. The figure shows that the particle free zone at the inlet progresses linearly in time for all viscosity values with constant velocity $\dot{Y}_t$ until complete particle compaction occurs at $t > 0.01$ s. For the viscosity value of $\mu_f = 0.18$ mPa s distinct fingers and fractures are yet not formed. Nevertheless, the figure shows that the growing particle free zone at the pressure inlet already progresses linearly in time before fingers form. According to Eq. (6) this also implies a linear growth in time for the thickness of the compaction front. However, the pressure skin depth increases proportionally to the square root in time as shown in Eq. (5). At a certain transition time

$$t_f = \frac{4D}{\dot{d}_c^2} \tag{7}$$

the thickness of the compaction front d_c will therefore overtake the skin depth s.

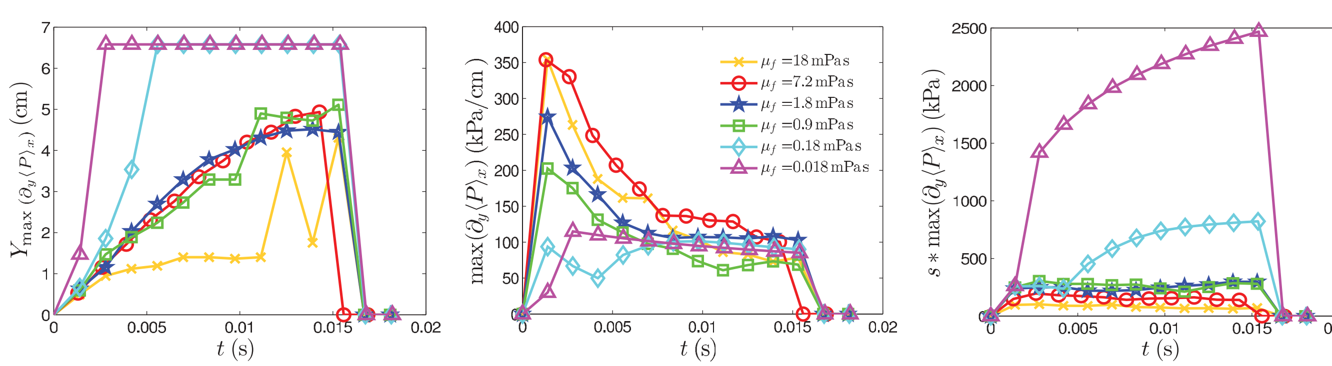

(a) (b) (c)

FIG. 8. (Color online) (a) The y position of the maximum gradient in the y direction of the average $\langle P \rangle_x$ of the pressure in the x direction as a function in time. (b) Maximal gradient in the y direction of the in x direction averaged pressure: $\partial_y \langle P \rangle_x$ as a function in time. (c) This maximum derivative is rescaled by the skin depth $s = \sqrt{4Dt}$. The legends is consistent in all plots and is displayed only in (b).

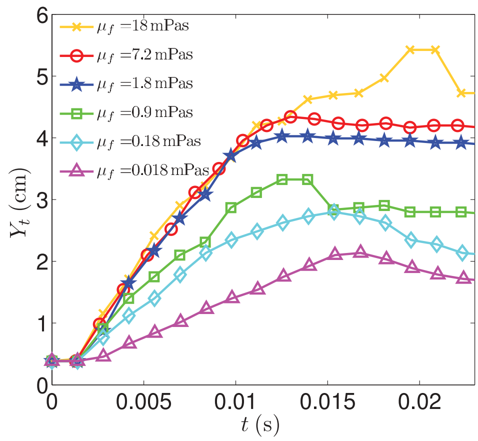

FIG. 10. (Color online) Position of the most advanced finger tip Y_t as a function of time and for different viscosity values. The position of the most advanced finger was found by normalizing the particle density by its maximum value and averaging in the x direction. If this averaged particle density drops to a value of 0.85, approaching from the outlet side of the cell, we define the corresponding y position Y_t as the position of the most advanced finger tip.

At time t_f we expect the transition from a body force to a surface force and the appearance of fractures instead of dispersed bubbles. For a direct comparison we visualized the transition time t_f in Fig. 5 by a dashed (red) line. Above this line the thickness of the compaction front is larger than the skin depth. When the compaction front is ahead of the skin depth fractures were predicted in the previous discussion. The fractures in Figs. 2 and 5 emerge at the predicted time and thus demonstrate good agreement between the analytical prediction and the simulations.

After fingers emerge in the regime of high gas viscosity ($\mu_f > 0.9$ mPa s) the compaction front propagates at a constant speed through the cell. This is shown in Fig. 11(a), where the y position of the maximum solid volume fraction averaged in the x direction $\max(\langle\rho_s\rangle_x)$ is plotted in time. For a gas viscosity of $\mu_f < 0.9$ mPa s the compaction front manifests first at the outlet side of the cell, in good agreement with that previously discussed Fig. 3.

In Fig. 11(b) we plotted the thickness of the particle compaction front in time. Although the data are very noisy, it can be seen that the thickness of the compaction front for all tested viscosity values initially grows in time. The compaction front for a gas viscosity $\mu_f < 0.9$ mPa s is located at the outlet of the cell and the thickness grows until complete compaction of the grains. The more interesting values are found for a gas viscosity of $\mu_f > 1.8$ mPa s because here the compaction front is located at the gas-particle interface and the thickness is measured during the fracturing of the granular packing is taking place. In this regime for the two highest viscosity values an initial increase of the compaction front thickness occurs. After a time of approximately $t = 0.002$ s the growth of the compaction front thickness slows down and appears to stay rather constant during the further propagation of the fractures until boundary effects start to play a role and the grains get completely compacted. This happens at $t \approx 0.01$ s for the gas of highest viscosity and at $t \approx 0.007$ s for the gas with a viscosity of $\mu_f = 1.8$ mPa s.

Reducing the skin depth by increasing the viscosity has the same effect on the pressure evolution as increasing the system size instead. We can demonstrate this in the following discussion by nondimensionalizing Eq. (1). We have previously shown that when the gas viscosity is increased the pressure drop gets more and more localized along the interface between the gas and the grains. Thus a limit is approached continuously where only the outermost particles at the interface are accelerated by the pressure gradient. The presented simulations approach this limit of a pure surface force. As a consequence, the velocity of the finger tip in Fig. 10 reaches a maximum for gas viscosity values above $\mu_f \geqslant 0.9$ mPa s. By calculating the slope of the graphs in Fig. 10, this maximal characteristic velocity for the finger tips in the plots is measured to be around $U_0 = 470$ cm/s and stays constant for $t < 0.01$ s. A further increase of the gas viscosity will not significantly increase the maximal velocity of the finger tips. In the limit of a pure surface force this maximal velocity is now primarily dependent on the injection pressure and on the properties of the granular phase. To nondimensionalize Eq. (1) we use this characteristic velocity U_0 to define a dimensionless velocity $u = U_0 u'$ and

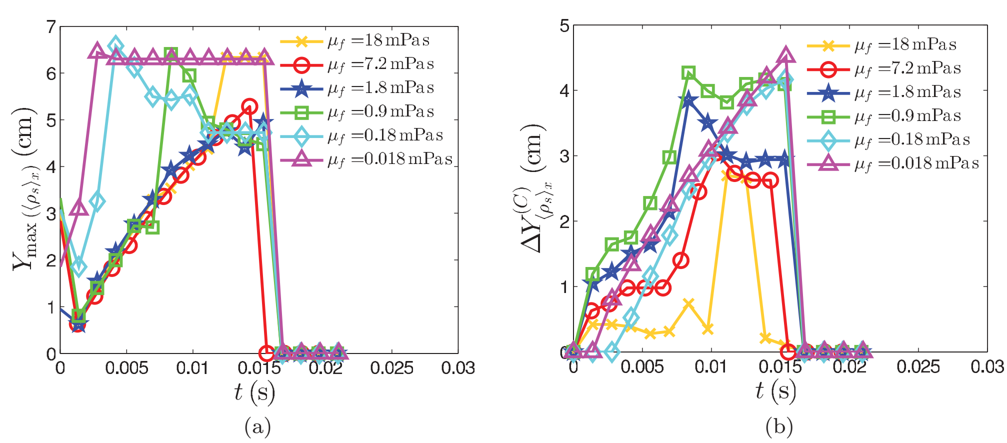

FIG. 11. (Color online) (a) The y position of the maximum solid volume fraction $\max(\langle\rho_s\rangle_x)$ as a function of time. Before the position of the maximum is calculated the solid volume fraction in the cell was averaged along the x direction. (b) A measure of the compaction front thickness $\Delta Y^{(C)}_{\langle\rho_s\rangle_x}$. It is the distance in the y direction over which the $\langle\rho_s\rangle_x$ value lies above a threshold of 0.47 as a function of time.

introduce $\kappa_0 = a^2/9K$ as the characteristic magnitude of the permeability. To define further dimensionless variables we use the unit length l as a characteristic length scale with $x = lx'$ and $y = ly'$. Scaling the system size by l keeps the ratio between the x and y dimensions of the cell constant. When scaling the system size l the rheology of the granular phase and the particle size remains unchanged. The atmospheric pressure P_0 is used as the characteristic pressure to define $P = P_0 P'$. From these quantities follows a characteristic time scale $\tau = l/U_0$ and $t = \tau t'$ [22]. The resulting nondimensionalized equation is

$$\phi\left[\frac{\partial P'}{\partial t'} + \mathbf{u}' \cdot \nabla' P'\right] = \frac{1}{\mathrm{Pe}} \nabla' \cdot \left[P' \frac{(1-\rho_s)^3}{\rho_s^2} \nabla' P'\right] - P' \nabla' \cdot \mathbf{u}'. \tag{8}$$

In this equation the Péclet number was defined as

$$\mathrm{Pe} = \frac{U_0 \mu_f l}{P_0 \kappa_0}. \tag{9}$$

This analysis shows that alternatively changing the viscosity, the length scale, or the inverse permeability has the same effect on Eq. (8), which describes the pressure evolution. Increasing the gas viscosity is equivalent to using a larger system or reducing the permeability. In our simulations it leads to extremely time consuming calculations to decrease the particle size in order to reduce the permeability of the granular phase. Instead we chose to increase the viscosity to study the system dynamics at a small pressure skin depth. In contrast, in experiments it might be much easier to reduce the pressure skin depth by using smaller particles instead of increasing the cell size by a factor of 1000.

VII. CONCLUSION

The emerging structures sensitively depend on whether the particles are accelerated primarily by solid contacts or by the imposed pressure gradient. We could show that the evolving structures depend on a characteristic length scale that is given by the skin depth s. For a skin depth larger than the system size, large scale homogeneous motion and the formations of dispersed bubbles are the results. For a short skin depth compared to the system size a compaction front builds up that allows fracturing. Hence, controlling the time dependence of the injection pressure should in principle allow one to control the pressure response in the packing and transit from fracturing to diffusely compacting regimes. It should also in principle enable fracturing of a porous rock at adjustable distances from the inlet.

ACKNOWLEDGMENTS

We acknowledge the support from the Centre for Advanced Study at the Norwegian Academy of Science and Letters, the NFR, the University of Strasbourg, the CNRS-INSU, and the Alsace region through the REALISE network. We thank Joachim Mathiesen, Luiza Angelutha, Maud Schelstraete, Øistein Johnsen, Jan Ludvig Vinningland, Paul Meakin, Einat Aharonov, and Dion Weatherley for fruitful discussions.

[1] Ø. Johnsen, R. Toussaint, K. J. Måløy, and E. G. Flekkøy, Phys. Rev. E **74**, 011301 (2006).
[2] X. Cheng, L. Xu, A. Patterson, H. M. Jaeger, and S. R. Nagel, Nat. Phys. **4**, 234 (2008).
[3] Ø. Johnsen, C. Chevalier, A. Lindner, R. Toussaint, E. Clément, K. J. Måløy, E. G. Flekkøy, and J. Schmittbuhl, Phys. Rev. E **78**, 051302 (2008).
[4] Ø. Johnsen, R. Toussaint, K. J. Måløy, E. G. Flekkøy, and J. Schmittbuhl, Phys. Rev. E **77**, 011301 (2008).
[5] M. J. Niebling, R. Toussaint, E. G. Flekkøy, and K. J. Måløy, Rev. Cub. Fis. **29** (1E), 66 (2012).
[6] J. L. Vinningland, R. Toussaint, E. G. Flekkøy, and K. J. Måløy, in Complex Activity Report 2009, edited by E. G. Flekkøy and K. J. Måløy [http://www.complexphysics.org/Projects/PDF/ComplexActivityReport2009.pdf], p. 108.
[7] A. Nermoen, C. Raufaste, S. D. de Villiers, E. Jettestuen, P. Meakin, and D. K. Dysthe, Phys. Rev. E **81**, 061305 (2010).
[8] B. Sandnes, E. G. Flekkøy, H. A. Knudsen, K. J. Måløy, and H. See, Nat. Commun. **2**, 288 (2011).
[9] R. Holtzman, M. L. Szulczewski, and R. Juanes, Phys. Rev. Lett. **108**, 264504 (2012).
[10] H. Huang, F. Zhang, P. Callahan, and J. Ayoub, Phys. Rev. Lett. **108**, 258001 (2012).
[11] S. D. de Villiers, A. Nermoen, B. Jamtveit, J. Mathiesen, P. Meakin, and S. C. Werner, Geophys. Res. Lett. **39**, L13204 (2012).
[12] M. A. van der Hoef, M. van Sint Annaland, and J. A. M. Kuipers, Chem. Eng. Sci. **59**, 5157 (2004).
[13] N. G. Deen, M. van Sint Annaland, M. A. van der Hoef, and J. A. M. Kuipers, Chem. Eng. Sci. **62**, 28 (2007).
[14] N. G. Deen, M. van Sint Annaland, M. A. van der Hoef, and J. A. M. Kuipers, Prog. Comput. Fluid Dyn. **7**, 152 (2007).
[15] M. A. van der Hoef, M. van Sint Annaland, N. G. Deen, and J. A. M. Kuipers, Annu. Rev. Fluid Mech. **40**, 47 (2008).
[16] C. Zeilstra, J. G. Collignon, M. A. van der Hoef, and J. A. M. Kuipers, Powder Technol. **184**, 166 (2008).
[17] T. Börzsönyi, R. E. Ecke, and J. N. McElwaine, Phys. Rev. Lett. **103**, 178302 (2009).
[18] M. Schelstraete, Master's thesis, University of Strasbourg, 2009.
[19] M. J. Niebling, E. G. Flekkøy, K. J. Måløy, and R. Toussaint, Phys. Rev. E **82**, 011301 (2010).
[20] M. J. Niebling, E. G. Flekkøy, K. J. Måløy, and R. Toussaint, Phys. Rev. E **82**, 051302 (2010).
[21] J. L. Vinningland, R. Toussaint, M. Niebling, E. G. Flekkøy, and K. J. Måløy, Europhys. Lett. **204**, 27 (2012).
[22] S. McNamara, E. G. Flekkøy, and K. J. Måløy, Phys. Rev. E **61**, 4054 (2000).
[23] J. L. Vinningland, Ø. Johnsen, E. G. Flekkøy, R. Toussaint, and K. J. Måløy, Phys. Rev. Lett. **99**, 048001 (2007).
[24] J. L. Vinningland, Ø. Johnsen, E. G. Flekkøy, R. Toussaint, and K. J. Måløy, Phys. Rev. E **76**, 051306 (2007).

[25] J. L. Vinningland, Ø. Johnsen, E. G. Flekkøy, R. Toussaint, and K. J. Måløy, Phys. Rev. E **81**, 041308 (2010).
[26] D. V. Anghel, M. Strauss, S. McNamara, E. G. Flekkøy, and K. J. Måløy, Phys. Rev. E **74**, 029906(E) (2006).
[27] P. C. Carman, Trans. Inst. Chem. Eng. **15**, 150 (1937).
[28] E. G. Flekkøy, R. Delgado-Buscalioni, and P. V. Coveney, Phys. Rev. E **72**, 026703 (2005).
[29] W. H. Press and W. T. Vetterling, *Numerical Recipes* (Cambridge University Press, Cambridge, 2002).
[30] See Supplemental Material at http://link.aps.org/supplemental/10.1103/PhysRevE.86.061315 for high-resolution movies of the particle density evolution during the compaction.
[31] E. Butkov, *Mathematical Physics* (Addison-Wesley, Reading, MA, 1968).

Granular Rayleigh-Taylor Instability: Experiments and Simulations

Jan Ludvig Vinningland,[1,*] Øistein Johnsen,[1] Eirik G. Flekkøy,[1] Renaud Toussaint,[2] and Knut Jørgen Måløy[1]

[1]*Department of Physics, University of Oslo, P.O. Box 1048, N-0316 Oslo, Norway*

[2]*Institut de Physique du Globe de Strasbourg, CNRS, Université Louis Pasteur, 5 rue Descartes, 67084 Strasbourg Cedex, France*

(Received 13 October 2006; published 24 July 2007)

A granular instability driven by gravity is studied experimentally and numerically. The instability arises as grains fall in a closed Hele-Shaw cell where a layer of dense granular material is positioned above a layer of air. The initially flat front defined by the grains subsequently develops into a pattern of falling granular fingers separated by rising bubbles of air. A transient coarsening of the front is observed right from the start by a finger merging process. The coarsening is later stabilized by new fingers growing from the center of the rising bubbles. The structures are quantified by means of Fourier analysis and quantitative agreement between experiment and computation is shown. This analysis also reveals scale invariance of the flow structures under overall change of spatial scale.

DOI: 10.1103/PhysRevLett.99.048001 PACS numbers: 45.70.Qj, 47.11.−j, 47.20.Ma, 89.75.Da

Improved understanding of granular flows would be of essential importance to a range of industrial applications, to the study of geological pattern forming processes, and, in general, to the theoretical description of disordered media.

As grains become smaller the effect of the interstitial fluid becomes more important. The result is a combination of dry granular dynamics and the hydrodynamics of the fluid. These systems give rise to a variety of exotic and most often poorly understood phenomena such as fluidization [1] and bubble instabilities [2], quicksand and jet formation [3], and sandwich structures in systems where different particle types segregate [4]. While the study of dry granular media has been extensive over the past decades, the exploration of fluid-granular systems has been of more limited scope.

In this Letter we study a granular analog of the Rayleigh-Taylor instability [5] in the sense that an interface instability arises as a heavier phase (the grains) displaces a lighter phase (the air). The experimental setup consists of a closed Hele-Shaw cell that confines air and fine grains. When the cell is turned upside down we observe the evolution of an initially sharp front formed by the falling grains. This evolution has three stages: (1) An initial decompaction phase is followed by (2) the formation of vertical falling fingers (the dark filaments in Fig. 1) organizing into cusp-shaped structures that subsequently develop into (3) coarser finger-bubble structures. The last structures, seen in Fig. 1, represent a quasisteady state where two competing mechanisms produce a characteristic wavelength. The mechanism producing coarser scales originates as smaller bubbles lag behind bigger bubbles, giving rise to a finger merging process shaped like an inverted Y (see Fig. 1). This process resembles the coarsening seen in crystal growth [6]. The other mechanism, that produces finer scales and is active right from the start, is reminiscent of the tip splitting process seen in viscous fingering. It is manifested as thin filaments forming in the center of the rising bubbles.

Over the past few years a wide range of granular instabilities where various structures form along fluid-grain interfaces have been reported [2,7]. Notably, the patterns formed by grains falling in a highly viscous liquid were investigated experimentally and theoretically by Völtz *et al.* [8]. However, while the instability reported by Völtz shares its main qualitative characteristics with the classical Rayleigh-Taylor instability, i.e., a single dominating wavelength growing right from the start, our gas-grain instability grows through coarsening cusp structures.

The evolving structures further exhibit scale invariance under change of particle size, a feature which is supported both by observations and theoretical considerations. The simulations and experiments that are employed to shed light on the phenomenon at hand agree qualitatively, and

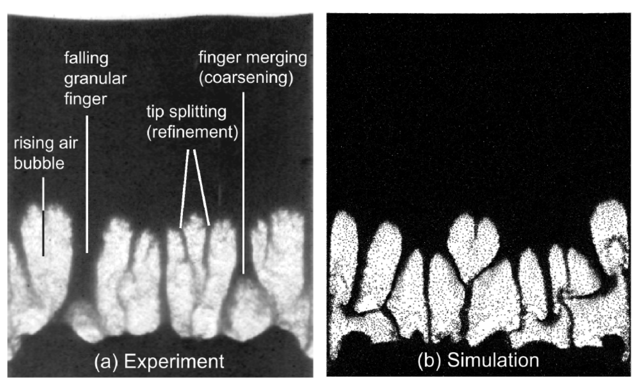

FIG. 1. (a) Experimental image and (b) numerical snapshot of a vertical Hele-Shaw cell where polystyrene beads (in black) of 140 μm in diameter displace air (in white). The cells are 56 mm wide and were rotated 0.2 s ago.

to a significant extent, quantitatively, even though the model neglects both granular friction and the spatial direction normal to the Hele-Shaw cell.

In the experiment a Hele-Shaw cell of inner dimensions 56 mm × 86 mm × 1 mm is partially filled with air and monodisperse beads (mass density 1.05 g/cm^3, diameter 140 μm) at atmospheric pressure. The cell is rotated manually in about 0.2 s from a lower to an upper vertical position to rapidly bring the layer of beads above the layer of air. Images of the evolving instability are recorded at a rate of 500 frames per second by a high speed digital camera with a resolution of 512 × 512 pixels; see Fig 1(a). A simultaneous numerical snapshot is given in Fig. 1(b).

The numerical model combines a continuum description of the air with a discrete description of the granular phase [9]. The effect of the granular phase on the air pressure is that of a deformable porous medium locally defined by the granular packing. The granular phase is modeled as discrete particles from which coarse grained solid fraction $\rho(x, y)$ and velocity fields $\mathbf{u}(x, y)$ are obtained by means of a linear smoothing function [9]. This function distributes the mass and velocity of a particle among its four neighboring grid nodes (2.5 grain diameters apart). The continuum gas phase is described solely by its pressure $P(x, y)$. The inertia of the gas, and hence its velocity field, is not considered. This is justified for small particle Reynolds numbers which is the case for our system.

The pressure is governed by the equation [9]

$$\phi\left(\frac{\partial P}{\partial t} + \mathbf{u}\cdot\nabla P\right) = \nabla\cdot\left(P\frac{\kappa(\phi)}{\mu}\nabla P\right) - P\nabla\cdot\mathbf{u}, \quad (1)$$

where $\phi = 1 - \rho$ is the porosity, κ the permeability, $\mathbf{u}$ the granular velocity field, and μ the gas viscosity. This equation is derived from the continuity of air and grain mass, and Darcy's law with permeability κ. The Carman-Kozeny relation is assumed for the permeability, and the isothermal ideal gas law for the air.

The grains are governed by Newton's second law:

$$m\frac{d\mathbf{v}}{dt} = m\mathbf{g} + \mathbf{F}_I - \frac{V\nabla P}{\rho}, \quad (2)$$

where m, $\mathbf{v}$, and V are, respectively, the mass, velocity, and volume of the grain. Contact dynamics [10] is used to calculate the interparticle force $\mathbf{F}_I$ which keeps the grains from overlapping. The dynamics of the grains are simplified by neglecting particle-particle and particle-wall friction. A lower cutoff is imposed on the solid fraction because the Carman-Kozeny relation is not valid as the solid fraction drops below 0.25 [11]. This cutoff causes the permeability of the most dilute regions of the system to be slightly lower than the true permeability. The effect is a slight overestimation of the pressure forces acting on the grains in the dilute regions.

The spatiotemporal evolution of the air-grain interface in the experiment and simulation is presented in Figs. 2(b) and 2(e), respectively. For every horizontal position x the interface height $y(x)$ is defined in the following way: Moving down from the top, $y(x)$ is the height where $\rho(x, y)$ drops below a given threshold value [see Figs. 2(a) and 2(d)]. Because of the large density contrasts in the system the interface position is rather insensitive to the exact value of this threshold. For the experimental data the threshold is set on the gray levels in the images.

The shape of the initial interfaces in Figs. 2(b) and 2(e) is quite different. The initial experimental interface has noise on all wavelengths, whereas the initial numerical interface is virtually flat with noise dominantly at smaller wavelengths. Perturbations introduced in the cell by the rotation and sudden stop disturb the initial experimental interface. However, as the instability evolves the discrepancy between experiment and simulation reduces and the later interfaces are in better agreement.

In order to give a more quantitative comparison of the interfaces, the discrete Fourier transform with a Hamming window is applied on every second interface in Figs. 2(b) and 2(e) to produce the power spectra presented in Figs. 2(c) and 2(f). The power spectra are colored as their corresponding interfaces, and the location of the maximum wave number for each power spectrum is indicated by a circle. While the maximum wave number of the numerical interfaces moves from high values to low values, the maximum wave number of the experimental interfaces hardly moves at all, most likely because the experiment does not evolve from an initially flat interface. However, the experimental and numerical power spectra converge to approximately the same form when normalized.

To study the coarsening of the observed structures quantitatively we perform an average over the solid fraction for the entire system: The discrete Fourier transform and the power spectrum of each horizontal line of $\rho(x, y)$ are calculated. The averaged power spectrum $\bar{S}(k)$ is then obtained by averaging over all these horizontal power spectra. An average wave number is defined as $\langle k\rangle = \sum_k \bar{S}(k)k/\sum_k \bar{S}(k)$, where $1/k$ is the wavelength. Likewise, we define the squared standard deviation $\sigma_k^2 = \sum_k \bar{S}(k)k^2/\sum_k \bar{S}(k) - \langle k\rangle^2$. For the experimental data the image pixel values are used to estimate the solid fraction.

Figure 3 shows the temporal evolution of $\langle k\rangle$ and σ_k (inset) for one simulation and two experiments. The numerical curve starts out with a significantly higher wave number than the experimental curves. However, the numerical data decrease monotonically until they coincide with the experimental data at about 0.2 s, after which the simulation and experiments show a similar coarsening behavior. Fingers are not observed in the experiment until 0.06 s have elapsed. During this time the grains merely form a dilute sheet that appears homogeneous on the experimental images. This particular experimental initial state is caused by the sudden stop of the cell and is the most probable reason for the initial discrepancy between simulation and experiment in Fig. 3. The fluctuations of $\langle k\rangle$ and

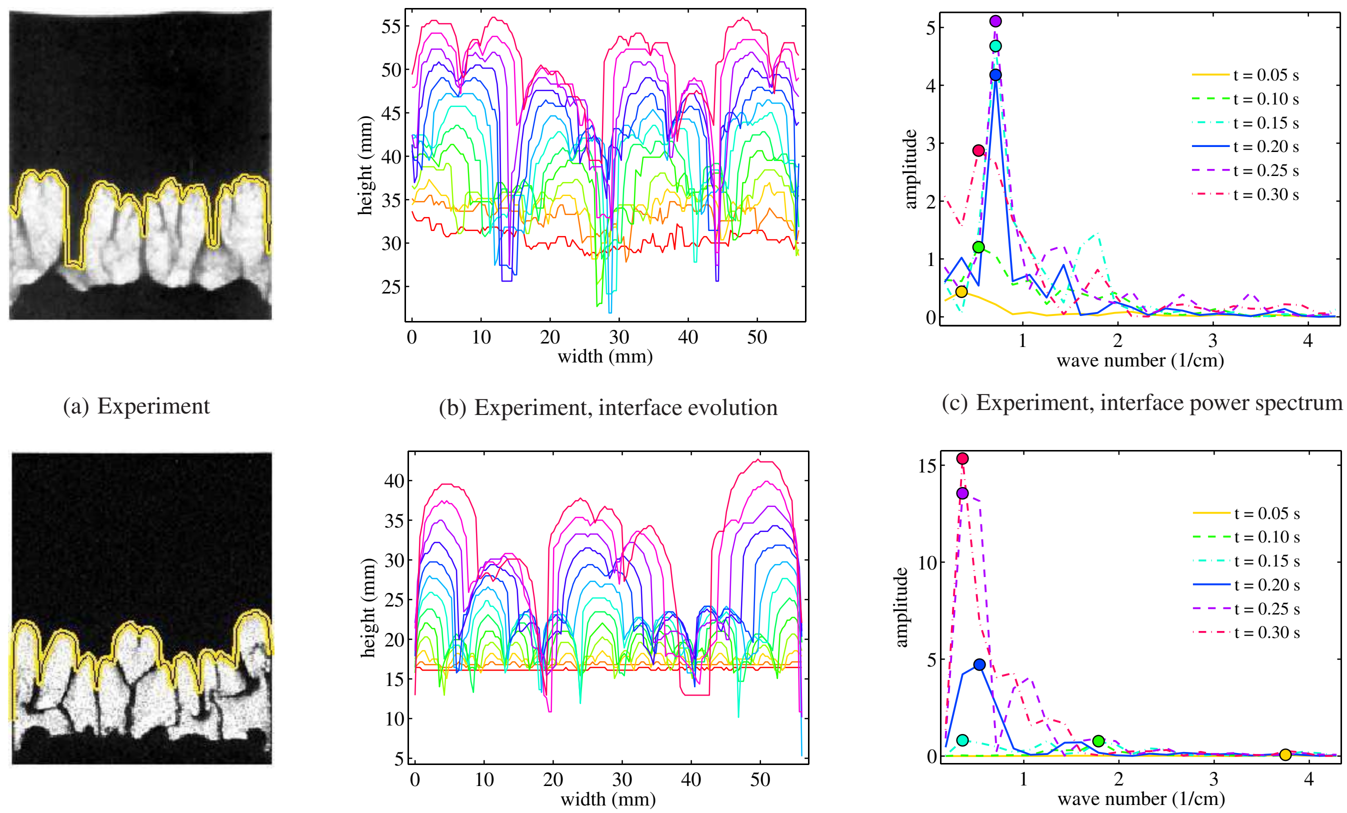

(a) Experiment (b) Experiment, interface evolution (c) Experiment, interface power spectrum

(d) Simulation (e) Simulation, interface evolution (f) Simulation, interface power spectrum

FIG. 2 (color online). (a),(d) Interfaces superposed on the snapshots ($t = 0.20$ s) from Fig. 1. (b),(e) Spatiotemporal evolution of the air-grain interface from $t = 0.00$ s (bottom) to $t = 0.29$ s (top). (c),(f) Temporal evolution of the power spectrum of the interfaces. The circles indicate the location of the maximum wave number.

σ_k are associated with the continuous nucleation and merging of fingers.

We further investigate the behavior of the system as the overall spatial scale is changed: Keeping all length ratios and the particle number fixed, the size of the system will scale according to the diameter d of the grains. We measure the characteristic inverse length scale $\langle k\rangle$ as d is changed and observe a scale invariance of the evolution. A series of seven simulations is performed where d varies from 70 to 490 μm in steps of 70 μm. The dimension of the numerical cell confining grains of 70 μm in diameter is 28 mm $\times$ 34 mm. In these simulations we have introduced the larger density of glass, rather than polystyrene, in order to minimize the numerical artifacts associated with the solid fraction cutoff in the permeability. To compare, a series of experiments using polystyrene beads of 80, 140, 230, and 570 μm in diameter, confined in Hele-Shaw cells that scale proportionally with d in all directions, is performed.

Data-collapse plots of the rescaled mean wave number $d\langle k\rangle$ are shown in Figs. 4(a) (simulation) and 4(b) (experiment). These plots indicate that the characteristic size of the structures is invariant when size is measured in units of d; the number of grains that spans the width of the bubbles is the same for a wide range of grain sizes.

Theoretically, the scale invariance of the product $d\langle k\rangle$ may be interpreted as follows: Compared with the other terms of Eqs. (1) and (2), the $m d\mathbf{v}/dt$, F_I, and $P\nabla\cdot\mathbf{u}$ terms may be shown to be small [12]. For that reason, these equations exhibit an approximate invariance under system size scaling. If we take δP to be the pressure deviation from the background pressure, express the velocity of grain i as $\mathbf{v}_i = \delta\mathbf{v}_i + \mathbf{u}_0$ and the locally averaged granular velocity as $\mathbf{u} = \delta\mathbf{u} + \mathbf{u}_0$, where $\mathbf{u}_0$ is the constant sedimenta-

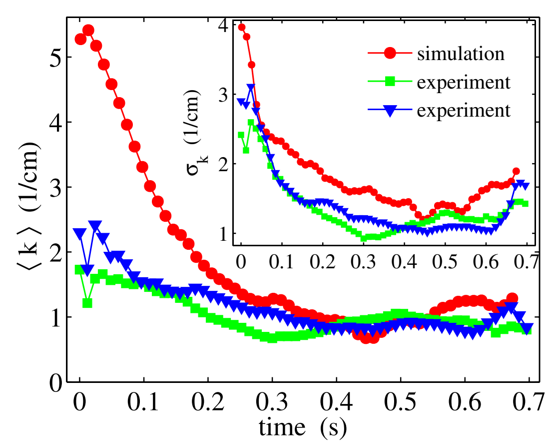

FIG. 3 (color online). Mean wave number $\langle k\rangle$ and standard deviation σ_k (inset) for two experiments and one simulation, all using polystyrene beads of 140 μm in diameter.

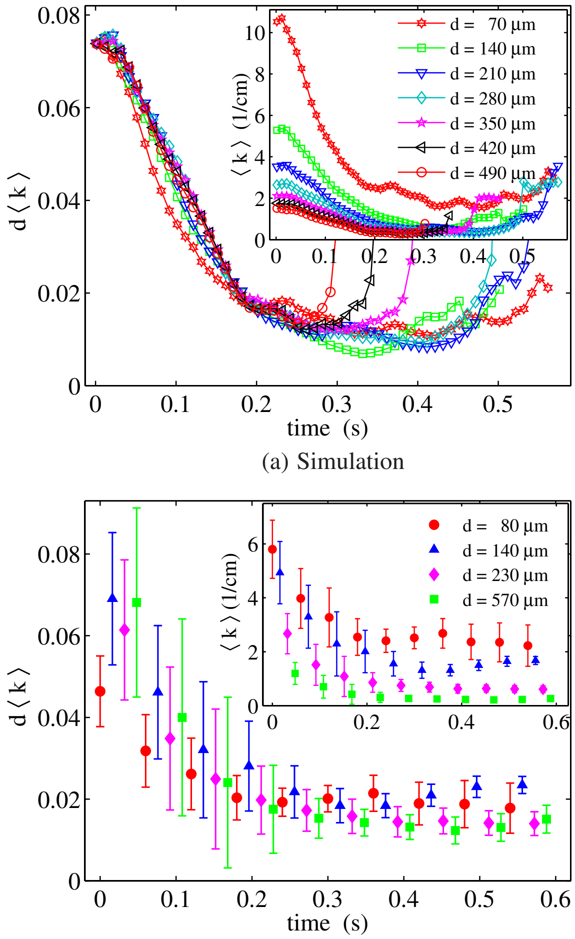

(a) Simulation

(b) Experiment

FIG. 4 (color online). Data-collapse plot of $d\langle k\rangle$ for a series of (a) simulations using glass beads and (b) experiments using polystyrene beads. The grain diameters d are given in the legend box. The inset shows the evolution of $\langle k\rangle$.

tion velocity of a close packed system, this scaling may be expressed as $\mathbf{x}\rightarrow\lambda\mathbf{x}$, $\delta P\rightarrow\lambda\delta P$, $\mathbf{u}_0\rightarrow\lambda^2\mathbf{u}_0$, $\delta\mathbf{u}\rightarrow\lambda\delta\mathbf{u}$, and $\kappa\rightarrow\lambda^2\kappa$, where λ is a scale factor. The structure formation of the system is governed by $\delta\mathbf{u}$ and, since this velocity scales the same way with λ as the length scales themselves, the evolution of any structure measured in units of d will be scale invariant. In particular, this is true for the structures measured by the length $1/\langle k\rangle$, and so $d\langle k\rangle$ is scale invariant. However, the invariance deteriorates both when particle size is increased and when it is decreased. In the first case, the relative effect of granular inertia is increased, in the second, the relative effect of the $P\nabla\cdot\mathbf{u}$ term is increased.

The convergence of the numerical data collapse in Fig. 4(a) is quite good. The deviation of the 70 μm curve for small t is probably explained by the increase in the relative importance of the $P\nabla\cdot\mathbf{u}$ term. The divergences of the 350, 420, and 490 μm curves for greater t in the same plot arise because the bubbles in the coarser packings disappear before they reach the surface due to the increase of $\mathbf{u}_0$ with λ^2 [12]. The experimental data in Fig. 4(b) have a wider distribution but collapse satisfactorily given the standard deviation error bars. The experimental data are obtained by averaging over three experiments for each diameter d. The standard deviation is calculated over a time window of 0.3 s. The accuracy of the experiments is at its lowest during the initial coarsening of the structures, but as the mean wave number stabilizes around 0.2 s the accuracy improves. Nevertheless, the data points are, with a few exceptions, within a distance of 1 standard deviation from one another. The loss of precision for small times is most likely caused by the inaccuracy involved with the manual rotation.

In conclusion, we have presented experimental and numerical results of a gravity-driven granular flow instability which is significantly different from its classical hydrodynamic analog. The simulations reproduce the characteristic shape and size of the experimentally observed structures and provide fine patterns in the early phase of the process that are not resolved experimentally. Data-collapse plots of the mean wave number $\langle k\rangle$ indicate that the flow and the resulting structures are invariant when measured on a scale proportional to the grain diameter d for a range of diameters that spans from 70 to 570 μm.

*janlv@fys.uio.no

[1] *Physics of Dry Granular Media*, edited by H. J. Herrmann, J.-P. Hovi, and S. Luding (Kluwer Academic, Dordrecht, 1998); D. Gidaspow, *Multiphase Flow and Fluidization* (Academic, San Diego, 1994).
[2] D. Gendron, H. Troadec, K. J. Måløy, and E. G. Flekkøy, Phys. Rev. E **64**, 021509 (2001); E. G. Flekkøy, S. McNamara, K. J. Måløy, and D. Gendron, Phys. Rev. Lett. **87**, 134302 (2001).
[3] D. Lohse, R. Rauhé, R. Bergmann, and D. van der Meer, Nature (London) **432**, 689 (2004).
[4] C. Zeilstra, M. A. van der Hoef, and J. A. M. Kuipers, Phys. Rev. E **74**, 010302 (2006).
[5] Lord Rayleigh, Proc. London Math. Soc. **s1-14**, 170 (1883); G. Taylor, Proc. R. Soc. A **201**, 192 (1950).
[6] J. S. Langer, Rev. Mod. Phys. **52**, 1 (1980).
[7] C. Chevalier, M. B. Amar, D. Bonn, and A. Lindner, J. Fluid Mech. **552**, 83 (2006); Ø. Johnsen, R. Toussaint, K. J. Måløy, and E. G. Flekkøy, Phys. Rev. E **74**, 011301 (2006); F. Malloggi, J. Lanuza, B. Andreotti, and E. Clement, Europhys. Lett. **75**, 825 (2006).
[8] C. Völtz, W. Pesch, and I. Rehberg, Phys. Rev. E **65**, 011404 (2001).
[9] S. McNamara, E. G. Flekkøy, and K. J. Måløy, Phys. Rev. E **61**, 4054 (2000); D.-V. Anghel, M. Strauss, S. McNamara, E. G. Flekkøy, and K. J. Måløy, Phys. Rev. E **74**, 029906(E) (2006).
[10] F. Radjai, M. Jean, J.-J. Moreau, and S. Roux, Phys. Rev. Lett. **77**, 274 (1996).
[11] A. A. Zick and G. M. Homsy, J. Fluid Mech. **115**, 13 (1982).
[12] J. L. Vinningland, Ø. Johnsen, E. G. Flekkøy, R. Toussaint, and K. J. Måløy (unpublished).

Experiments and simulations of a gravitational granular flow instability

Jan Ludvig Vinningland,[1,*] Øistein Johnsen,[1] Eirik G. Flekkøy,[1] Renaud Toussaint,[2] and Knut Jørgen Måløy[1]
[1]*Department of Physics, University of Oslo, P.0. Box 1048, 0316 Oslo, Norway*
[2]*Institut de Physique du Globe de Strasbourg, CNRS, Université Louis Pasteur, 5 rue Descartes, 67084 Strasbourg Cedex, France*
(Received 1 November 2006; revised manuscript received 28 September 2007; published 27 November 2007)

An instability is observed as a layer of dense granular material positioned above a layer of air falls in a gravitational field [Phys. Rev. Lett. **99**, 048001 (2007)]. A characteristic pattern of fingers emerges along the interface defined by the grains, and a transient coarsening of the structure is caused by a coalescence of neighboring fingers. The coarsening is limited by the production of new fingers as the separation of the existing fingers reaches a certain distance. The experiments and simulations presented are shown to be comparable both qualitatively and quantitatively. The characteristic inverse length scale of the structures, obtained as the mean of the solid fraction power spectrum, relaxes toward a stable value shared by the numerical and experimental data. Further, the response of the numerical model to changes in various model parameters is investigated. These parameters include the density of the grains, the shape of the initial air-grain interface, and the dissipation of the granular phase. Also, the growth rates of the bulk solid fraction and the air-grain interface are obtained from Fourier power spectra of the numerical data. This analysis reveals that the instability is never in a linear regime, not even initially.

DOI: 10.1103/PhysRevE.76.051306 PACS number(s): 81.05.Rm, 47.20.Ma, 47.11.−j, 45.70.Qj

I. INTRODUCTION

Sands and powders are indispensable materials in our modern society. Nevertheless, a complete theoretical description of granular materials and their dynamical properties are still not available, despite their widespread use. An improved understanding of granular flows would provide valuable contributions to many industrial applications such as pneumatic transport, fluidized beds, and catalytic cracking [1–3]. Granular materials are also involved in a host of natural and geological phenomena, most of which are still in need of a proper understanding. Such phenomena include sedimentation [4,5], erosion and river evolution [6], underwater avalanches and turbidities [7], and soil fluidization during earthquakes [8].

The relatively complete description of classical fluid dynamics is also useful in the interpretation of granular flows. Instability is a central problem in fluid dynamics [9,10], and over the past few years some classical hydrodynamic instabilities have also been reported in granular systems. Examples of such are the Saffman-Taylor instability [11] in a granular suspension [12] or in gas-grain mixtures [13], the Kelvin-Helmholtz instability [14] in a vibrated granular mixture [15], the Richtmyer-Meshkov instability in a shock propagating at the interface between two types of grains [16], as well as some novel instabilities in submarine avalanches [17] and in a tube of sand [18,19]. The granular Rayleigh-Taylor instability discussed here was first reported by the same authors in Ref. [20]. The present paper provides a more elaborate and complete discussion of the instability in addition to further results and analyses.

While we study a gas-grain system, the liquid-grain interface in a Hele-Shaw cell was investigated experimentally and theoretically by Völtz *et al.* [21]. Sieved glass beads of 80 μm in diameter was used in their experiments, and a behavior very similar to the classical Rayleigh-Taylor instability [10,22] was observed. In contrast, the instability discussed in this paper arises in a liquid-free granular material and displays processes of tip splitting and finger renucleation. Our experimental and numerical data compare favorably both qualitatively and quantitatively, despite the two-dimensionality of the model and the neglect of interparticle friction and gas inertia. Linear stability analysis is not adequate to predict the final dominating wavelength because nonlinear effects govern the selection of the final wavelength. This is demonstrated explicitly in the numerical data as the growth rates of the solid fraction wave numbers are shown not to follow an exponential growth of any significant duration. The parameter space of the model is explored by changing the density of the grains, the shape of the initial granular interface, and the granular dissipation.

The motivation for the simulations and experiments presented in this paper is to study a granular version of the Rayleigh-Taylor instability [22] known from hydrodynamics, where a dense Newtonian liquid is positioned on top of a less dense liquid in a gravitational field. In our case the dense fluid is replaced by a granular material which, in contrast to the liquid, is not subject to surface tension.

The simulation of two-phase flow is particularly interesting for many engineering purposes, and historically most simulations of two-phase flows have treated the solid phase as a continuum, which allowed numerical techniques known from fluid dynamics to be applied. A continuum approach to granular media (see, e.g., Ref. [23]) is, however, only approximate, and will in cases of discontinuous density variations break down completely. Moreover, many interesting phenomena in granular media are closely related to its particularity. A complete description of the interactions between a continuum fluid phase and a discrete solid phase would require the full Navier-Stokes equation for the fluid, coupled with moving boundary conditions given by the surfaces of the grains and the geometry of the container, together with differential equations for the grains. Such a detailed scheme would consume prohibitive computational resources, and a

*janlv@fys.uio.no

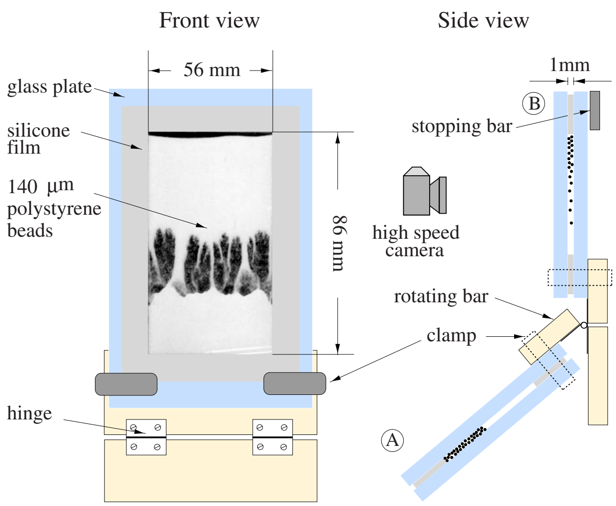

FIG. 1. (Color online) Illustration of the experimental setup viewed from the front and the side. Two cell positions are superimposed in the side view to demonstrate the manual rotation from position *A* to *B*.

number of techniques (see Ref. [24] for a brief summary) have been developed in order to reduce the computational efforts while preserving the physics. In contrast, we use a hybrid technique that affords a continuum description of the gas phase and a particulate description of the granular phase. Our model neglects friction, the spatial direction normal to the cell, and the inertia of the air. Yet, this computationally agile model yields results in good agreement with experimental observations.

The paper is organized as follows. Section II presents the setup and execution of the experiment, followed by an outline of the numerical model and its implementation in Sec. III. The numerical and experimental results are presented and analyzed in Sec. IV, which is split into four subsections devoted to qualitative descriptions of the instability (Sec. IV A), numerical solid fraction and pressure profiles (Sec. IV B), Fourier power spectra and growth rate analysis (Sec. IV C), and the variation of the model parameters (Sec. IV D). The paper is completed with a short conclusion in Sec. V.

II. EXPERIMENT

The experimental setup, illustrated in Fig. 1, consists of a closed Hele-Shaw cell mounted on a hinged bar which enables the cell to rotate 130° from a lower to an upper vertical position (from *A* to *B* in Fig. 1). The Hele-Shaw cell is made of two 8-mm-thick glass plates clamped onto a 1-mm-thick silicone frame. The internal dimensions of the cell are $56 \times 86 \times 1$ mm^3, and it is filled with polystyrene beads and air at atmospheric pressure. The cell is rotated manually and it takes about 0.2 s to bring the cell to an upright, vertical position. The off-center pivot of the cell cause the rotation to slow down the falling motion of the grains due to centrifugal forces. A bar is mounted at position *B* in order to control the final vertical position of the cell. However, this bar has some undesirable side effects, causing nonpersistent perturbations of the initial stages of the instability (see Sec. IV A). The full development of the instability is recorded by a high-speed digital camera (Photron Fastcam-APX 120K) taking images with a resolution of 512×512 pixels at a rate of 500 frames per second.

Monodisperse polystyrene beads of 140 μm in diameter from Microbeads® (Dynoseeds TS 140-51) are used in the experiments. The filling of the cell is performed with one glass plate lying down horizontally and the silicone frame adhered on top. Small portions of beads are carefully deposited on the plate and leveled with the silicone frame before the upper plate is attached and fastened with clamps. The cell is flipped a few times after closure to allow the grains to form a random loose-packed configuration.

The humidity in the laboratory is important in order to keep the electrostatic and cohesive properties of the grains at a suitable level to prevent the grains from clustering or sticking to the glass plates. During the filling of the cell and the execution of the experiment the humidity was kept constant at about 30%.

The experimental results are presented and discussed together with the numerical results in Sec. IV.

III. SIMULATION

A. Model

The numerical model is a hybrid model that combines a discrete description of the grains with a continuum description of the gas. The foundation and derivation of the model are presented in detail in Refs. [25,26]; only an outline of the model is given here.

The granular phase is considered as an agglomeration of spheres that makes up a deformable porous medium which in our model is described by coarse-grained solid fraction $\rho(x,y)$ and velocity fields $\mathbf{u}(x,y)$, where (x,y) are the two-dimensional space coordinates. The continuum gas phase is solely described by its pressure field $P(x,y)$; hence the inertia and velocity field of the gas are not considered in this model. The focus of the model is to describe the granular flow on a scale of a few grain diameters, not the fluid flow field on a subgranular level. It is justified to neglect the inertia of the fluid as long as the Reynolds number is small, which is the case for particles on a micrometer scale sedimenting in air.

The pressure is governed by the equation [25,26]

$$\phi\left(\frac{\partial P}{\partial t} + \mathbf{u} \cdot \boldsymbol{\nabla} P\right) = \boldsymbol{\nabla} \cdot \left(P \frac{\kappa}{\mu} \boldsymbol{\nabla} P\right) - P \boldsymbol{\nabla} \cdot \mathbf{u}, \qquad (1)$$

where $\phi = 1 - \rho$ is the porosity, ρ is the solid fraction, κ is the permeability, and $\mathbf{u}$ is the velocity field of the granular phase. P is the gas pressure, and μ is the gas viscosity. This equation is derived from the conservation of air and grain mass, using Darcy's law [27] to obtain the pressure drop over a given volume described by a permeability κ. The Carman-Kozeny relation [28] is assumed for the permeability, and the isothermal ideal gas law is assumed for the compressible gas. The empirical Carman-Kozeny relation is given as

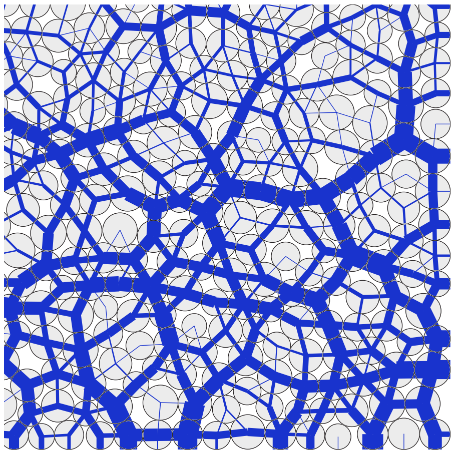

FIG. 2. (Color online) Network of interparticle forces $\mathbf{F}_\mathrm{I}$ calculated by contact dynamics. This image shows the lower right corner of a frictionless packing of 1200 grains relaxed under gravity.

$$\kappa(\rho,d) = \frac{d^2}{180}\frac{(1-\rho)^3}{\rho^2}, \tag{2}$$

where ρ is the local solid fraction, d is the diameter of the grains, and $1/180$ is an empirical constant valid for a packing of beads.

The dynamics of the grains are governed by Newton's second law

$$m\frac{d\mathbf{v}}{dt} = m\mathbf{g} + \mathbf{F}_\mathrm{I} - \frac{\nabla P}{\rho_n}, \tag{3}$$

where m is the grain mass, $\mathbf{v}$ is the grain velocity, $\mathbf{F}_\mathrm{I}$ is the interparticle force which keeps the grains from overlapping, $\rho_n = \rho\rho_g/m$ is the number density, and ρ_g is the mass density of the material the grains are made of. Contact dynamics [29] is used to calculate the interparticle force $\mathbf{F}_\mathrm{I}$ but molecular dynamics techniques [30,31] could have been used instead. Contact dynamics is an iterative scheme that calculates the interparticle distribution of normal forces consistent with the kinematic constraints imposed by the impenetrable beads. The solution yields a force network that satisfy volume exclusion at every contact. The relative force change from one iterative step to the next is used as a convergence criterion: If the change at every contact is less than a given threshold the solution has converged. The resulting force network shows how the weight of the grains, and possible external forces such as the gas pressure, are transmitted and carried by the grains and the container. More detailed descriptions of contact dynamics are found in Refs. [32–34]. Figure 2 gives an example a force network obtained in a frictionless packing of 1200 grains relaxed under gravity. The direction and magnitude of the forces are respectively given by the direction and the thickness of the lines. Typical features of a force network are the heterogeneous distribution of forces and the existence of force chains that transmit a major fraction of the load.

The interparticle and wall-particle friction are not taken into account in this model. The dissipation of the granular phase is controlled by a coefficient of normal restitution, ε, that determines the loss of kinetic energy associated with each collision.

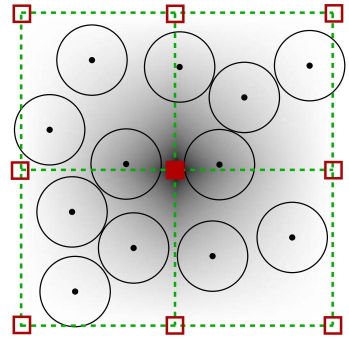

FIG. 3. (Color online) Illustration of the linear smoothing function used to calculate the continuous fields from the discrete positions and velocities of the grains. The red squares are nodes on the grid, and the gray-level background illustrates the weight map of the central node; black is 1, white is zero.

B. Implementation

A smoothing function is necessary to translate the mass m_i and velocity $\mathbf{v}_i$ of the individual grains (indexed by i) into continuous solid fraction $\rho(x,y)$ and velocity fields $\mathbf{u}(x,y)$ on the grid. A fractional value of m_i or $\mathbf{v}_i$ is assigned to each of the four neighboring grid nodes and the value is determined by the positional weight of the grain through a linear smoothing function $s(\mathbf{r}-\mathbf{r}_0)$ expressed mathematically as [25]

$$s(\mathbf{r}-\mathbf{r}_0) = \begin{cases} \left(1-\dfrac{\Delta x}{l}\right)\left(1-\dfrac{\Delta y}{l}\right) & \text{if } \Delta x, \Delta y < l, \\ 0 & \text{otherwise,} \end{cases} \tag{4}$$

where $\mathbf{r}(x,y)$ is the position of the grain, $\mathbf{r}_0(x_0,y_0)$ is the position of the grid node, $\Delta x = |x-x_0|$ and $\Delta y = |y-y_0|$ are the relative distances, l is the lattice constant, and $\Sigma_k s(\mathbf{r}-\mathbf{r}_k) = 1$ with k indexing the four sites. The smoothing of the grains is illustrated in Fig. 3 where nine grid nodes are depicted as red squares on a gradient background. This background is the positional weight map of the central node which is shown as a solid square. From this illustration we observe that all the grains in Fig. 3 make contributions to the field values of the central node: A grain positioned at the central node is assigned a weight of 1 (black background), while a grain positioned along the dotted outline in Fig. 3 is assigned a weight of zero (white background). The weight map, or smoothing function, may also be considered as a collection of equidistant tent functions, distributed over the area in Fig. 3, with maxima rising linearly from zero to 1 and then back to zero. More explicitly, the number density ρ_n and average velocity $\mathbf{u}$ associated with a node at position $\mathbf{r}_0$ are, respectively, $\rho_n(\mathbf{r}_0) = \Sigma_i s(\mathbf{r}_i - \mathbf{r}_0)$, and $\mathbf{u}(\mathbf{r}_0) = \Sigma_i \mathbf{v}_i s(\mathbf{r}_i - \mathbf{r}_0)$, where i runs over the number of particles [25].

The positional weight used to obtain the continuous fields is also used to obtain the pressure forces, $\mathbf{F}_P = -\nabla P/\rho_n$,

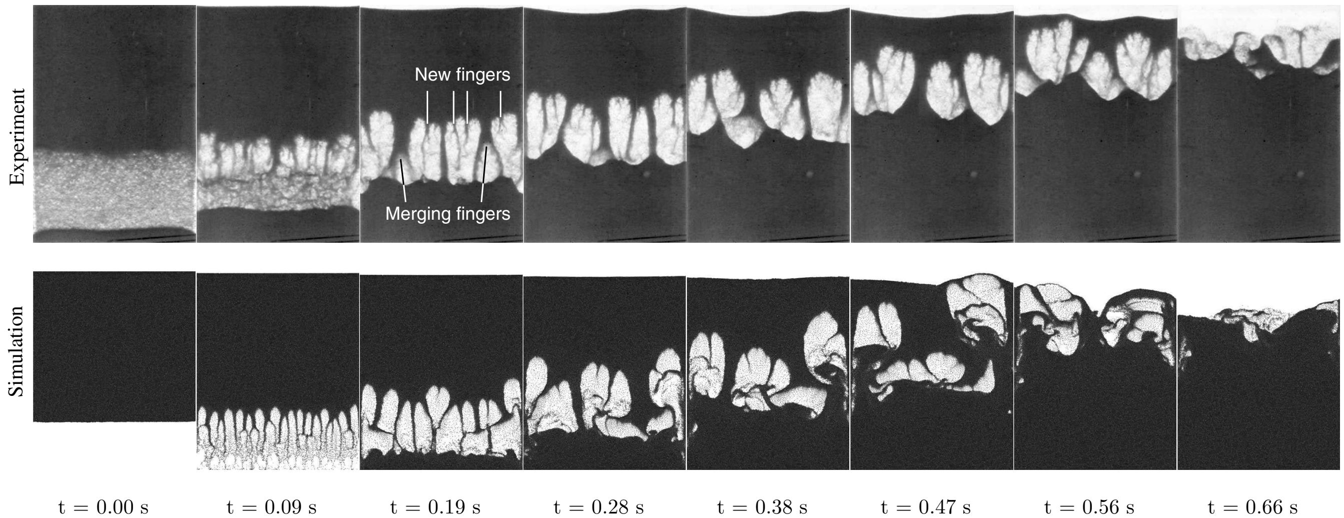

FIG. 4. Images from the experiment (top row) and simulation (bottom row) with polystyrene beads of 140 μm in diameter in a closed Hele-Shaw cell that is 56 mm wide. The experimental cell is 86 mm high and 1 mm thick, while the numerical cell is 68 mm high. The time of the snapshots is the time evolved since the cell reached the upright position. A restitution coefficient of 0.5 is used in the simulations.

acting on the grains. Explicitly for a grain at $\mathbf{r}_i$, $\mathbf{F}_P = -\Sigma_k(\boldsymbol{\nabla}P/\rho_n)_k s(\mathbf{r}_i - \mathbf{r}_k)$ with a k index running over the four nodes. In other words, the share of $\mathbf{F}_P$ assigned to the grain from the node is equal to the share of m_i or $\mathbf{v}_i$ assigned to the node from the grain.

A few approximations are made in the implementation of the model. The two-dimensional (2D) solid fraction of disks is translated into a 3D solid fraction of spheres by multiplying the 2D solid fraction with 2/3, which is the ratio of the 3D to the 2D random-close-packed solid fractions. Further, the Carman-Kozeny relation is not valid as the solid fraction approaches zero, and a lower cutoff on the 2D solid fraction, $\rho_{min}=0.25$, is introduced. These matters are elaborated in Sec. II C of Ref. [25].

The packing of grains used in the simulations is made of 160 000 grains with a mean diameter of 140 μm. This high number of grains is selected to allow a match with the spatial dimensions of the experimental cell. The simulation shown in Fig. 4 took roughly 12 days to complete on a standard PC. Note, however, that the instability emerges as well in simulations with a much more reduced number of grains (e.g., a few thousand). The size distribution adopted for the granular packing is flat and has a ±10% variation in the diameter. This minor polydispersity is necessary to avoid a hexagonal stacking of the grains.

The granular packing is generated by raining grains from a given height, with random horizontal positions, in a cell without air. After all the grains have settled the packing is allowed to further compactify and relax before the air is introduced. This is to prevent the source term of Eq. (1), $-P\boldsymbol{\nabla}\cdot\mathbf{u}$, to introduce local pockets of overpressure, due to moving grains, that otherwise could perturb the numerical results.

IV. RESULTS

The rich behavior of the instability provides a number of interesting results which is presented as follows. A qualitative discussion and comparison of the experimental and numerical images are given first, followed by solid fraction and pressure profiles from the numerical data in Sec. IV B. A series of investigations, spawned by the Fourier power spectrum of the solid fraction, is presented in Sec. IV C. These results include a quantitative comparison of the experimental and numerical data, in addition to the temporal evolution of the wave numbers obtained from the solid fraction power spectra. Section IV D investigates the response of the instability to changes in the granular dissipation, the initial air-grain interface, and the grain density.

A. Experimental and numerical images

Figure 4 shows experimental and numerical images of the granular Rayleigh-Taylor instability: A layer of grains displacing a layer of air in a gravitational field. The width of both the experimental and numerical system is 56 mm, while the height of the experimental cell is 86 mm, and the height of the numerical cell is 68 mm. The experimental images are color-inverted and contrast-enhanced versions of the original images; the grains are black and the air is white. The time is set to zero when the cell reaches the vertical position. In the experiment some grains start to fall during the rotation of the cell and a small pile of grains has already formed at the bottom of the first frame.

An air-grain interface, initially flat in the simulation but slightly perturbed in the experiment, is defined by the falling grains. When the cell is flipped a pattern of fine fingers emerges along the interface (see Fig. 5) which subsequently develop into coarser bubble-finger structures that propagate through the packing. A more detailed analysis of the evolution introduces three stages of development: The first stage is the *nucleation stage* characterized by a transition from a homogeneous decompaction to the appearance of the first finger seeds. This stage is only observed in the numerical snapshots because of the reduced initial resolution of the experimental setup: Transient perturbations disturb the initial

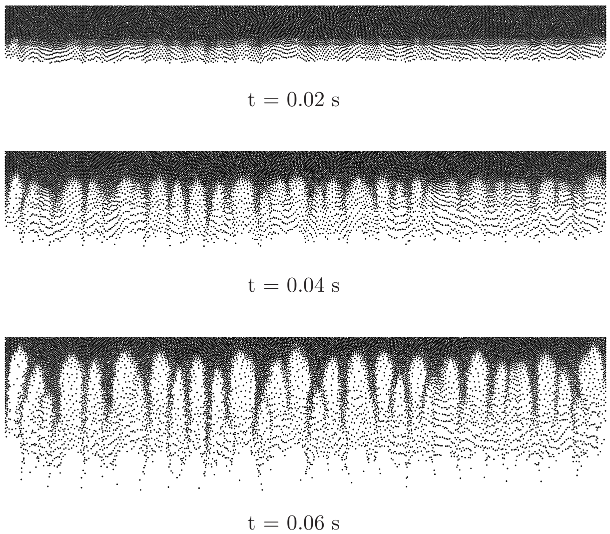

FIG. 5. A closer look at the initial formation of fingers in the simulation. Before the fingers appear there is a transient phase of homogeneous decompaction. Notice the cusp-shaped geometry of the air-grain interface.

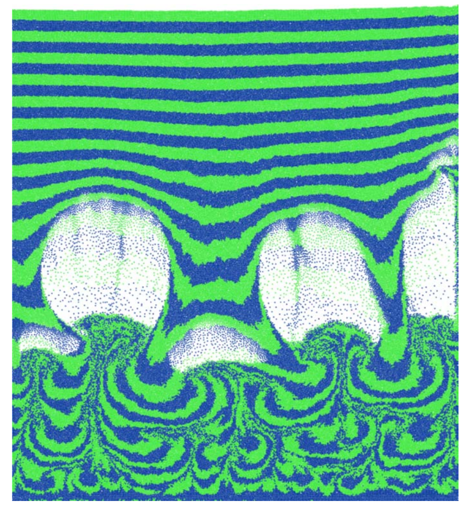

FIG. 6. (Color online) A snapshot from a simulation using glass beads of 210 μm in diameter where the initial configuration is colored in horizontal bands to bring out the dynamics of the structures as the instability evolves.

air-grain interface as the rotating cell suddenly stops. The second stage is the *growing stage* where the nucleated fingers grow in size and start to coalesce with their neighboring fingers. The third and final stage is the *propagation stage*, which is recognized by the aggregation of grains at the bottom of the cell and the formation of bubbles that propagate through the packing. Two competing mechanisms are at play here, one producing finer structures, the other producing coarser structures. The coarsening mechanism causes fingers to merge as two fingers form an inverted Y (see the experimental image at $t=0.19$ in Fig. 4). The smaller bubble trapped beneath the wedge of the inverted Y continuously lags behind the bigger bubbles until the small bubble disappears. Thus, two fingers have been reduced to one. The other mechanism, giving rise to finer structures, is manifested as thin filaments forming inside the rising bubbles. These new fingers split the bubbles and prevent them from growing indefinitely.

Figure 5 shows a more detailed series of numerical snapshots of the early evolution of the instability: In the top frame the initial homogeneous decompaction of the air-grain interface is visible. By close comparison of the frames it is possible to discern tiny finger seeds in the top frame that has developed into well-defined fingers in the second and third frames. From the second to the third frame the fingers mainly grow in size and only a few new fingers are nucleated. The first and second frame belongs to the nucleation stage, while the third frame is taken from the growing stage.

Figure 6 shows a snapshot from a simulation where glass beads of 210 μm are used. The beads are colored in bands in their initial configuration to illustrate the dynamics of the mixing and the patterns created by the propagating bubbles. The pattern that emerges is reminiscent of geological patterns observed when, e.g., water is forced through sediments of sand [35].

A qualitative comparison of the image series in Fig. 4 renders the simulation and experiment consistent in many respects. The sizes of the bubbles and the fingers are comparable, and the dynamical processes of finger merging and finger nucleation are observed in both cases. Nevertheless, some discrepancies are observed, particularly at the start and towards the end of the instability: The initial decompaction, followed by the emergence of the first fine fingers, is only observed numerically. Towards the end of the process a horizontal destabilization of the air-grain interface is visible, i.e., some bubbles reach the surface before others.

The initial discrepancies can to a large extent be explained by three experimental features: The increased thickness of the cell allowing up to seven layers of grains between the plates, the rotation of the cell, and the abrupt stop of the cell as it reaches the vertical. Ideally the rotation would be so fast that the grains did not move at all during the rotation. In the experiment this is, however, not the case and the grains will slide and roll down the inclined plate during the rotation while the air passes in a channel above the grains (known as the granular Boycott effect [19]). Only when the cell is almost vertical is the sliding layer of grains able to form an interface that fills the whole cross section of the cell so that fingers may start to form. However, a mechanical shock is created in the cell as it hits the bar. The effect is a transverse oscillation that causes the grains to be tossed back and forth between the plates. Any fingers formed prior to the shock will be strongly perturbed and even erased. The result is visible in the first experimental image of Fig. 4 where the falling grains form an almost homogeneous sheet of grains rather than well-defined fingers.

Some differences are also found in the shape of the fingers: In the numerical images the fingers appear somewhat buckled and bended compared to the experimental fingers. We believe this is an artifact caused by the cutoff imposed on the solid fraction. Since the solid fraction is not allowed to be less than 0.25, the empty space porosity, i.e., the porosity in a region with no or very few grains, will be different from 1. This again leads to overestimated pressure gradients in the most dilute regions of the system, and forces are exerted on the fingers traversing the gap of air. Nevertheless, the shape of the interface is very well reproduced by the simulations despite the buckling of the fingers.

The experimental instability seems to be more stabilized horizontally than the numerical instability. By comparing images in Fig. 4 for $t > 0.4$ s it is evident that on a detailed level the numerical images are quite different from the corresponding experimental images. It seems that the most advanced bubble in the numerical images departs from the other bubbles at an increasing rate, causing a horizontal destabilization of the interface. We believe that the reason for this is found in the zero particle-particle friction and, more importantly, the zero particle-wall friction of the numerical model. The friction between the glass plates and the grains in the experiment is probably important in the dense part of the packing, due to the Janssen effect [36]. This has most likely a stabilizing effect on the propagation of the interface. However, apart from this small difference in the propagation of the bubbles, the other quantitative features of the instability are well reproduced by our friction-free simulations. Thus, for the sake of simplicity, we have chosen to discard friction in the model. Indeed, taking friction into account would imply important numerical costs: The addition of two degrees of freedom to account for the rotation of the grains, and a new fitting parameter for the friction coefficient.

Another effect of zero friction in the simulations is observed as the rightmost bubble in the latter numerical images of Fig. 4 reaches the upper surface at about $t = 0.45$ s and leaves behind an open air-filled void. As grains rush in to fill this void convection rolls are set up that will distort and perturb the present fingers. Such convection rolls would to a large extent be dissipated away if interparticle friction were present in the simulations.

B. Pressure and solid fraction in the simulation

The temporal evolution of the pressure P and the solid fraction ρ in the simulation are respectively shown in Figs. 7 and 8. The vertical profiles $P(y)$ and $\rho(y)$ shown for different times are calculated by averaging $P(x,y)$ and $\rho(x,y)$ over the horizontal component x. Figure 7(a) provides a detailed temporal description of $P(y)$ immediately after the rotation of the cell: The initially flat profile is, within a few milliseconds, transformed into a linearly decreasing function while an overpressure builds up at the bottom of the cell. This corresponds to a fast diffusion of the pressure field [cf. Eq. (1)], and shows the transient curvature of the pressure profile relaxing towards a linear function. This happens at a time scale $\ell^2/(P\ell\kappa/\mu) \simeq 0.1$ ms, smaller than the time scale associated with grain motion due to gravity, $\sqrt{d/g} \simeq 3$ ms, where ℓ is the system size, and d the grain diameter. Figure 7(b) shows $P(y)$ for later times, and the linearity of the pressure in the upper part of the packing, above the air-grain interface, is almost unchanged. Figure 8 shows $\rho(y)$ for the same times as in Fig. 7(b). The initially sharp air-grain interface is smeared out as the grains fall and subsequently fill up the bottom of the cell.

Figure 9(a) shows the temporal evolution of the pressure at the bottom of the cell, i.e., $P(y=0,t)$. Figure 9(b) shows

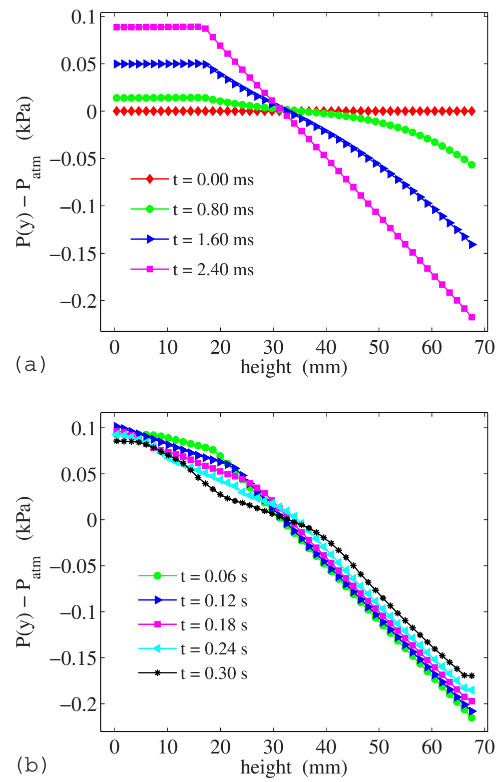

FIG. 7. (Color online) Plots of vertical pressure profiles averaged over the system width. (a) Evolution of the pressure immediately after the cell is rotated. (b) The pressure profiles at later times. The pressure is given as the deviation from 1 atm.

the averaged vertical velocity of the whole packing, $\langle v_y(t)\rangle$ (average of v_y for all the grains). Due to the compressibility of the air the pressure is observed to undergo a transient damped oscillation immediately after the cell is rotated. The rotation of the numerical cell is instantaneous, in contrast to the rotation of the experimental cell, and the sudden acceleration of the grains generates a pressure shock front that propagates into the gap of air. The oscillating pressure causes the averaged vertical velocity of the grains to display a similar oscillation as shown in Fig. 9(b).

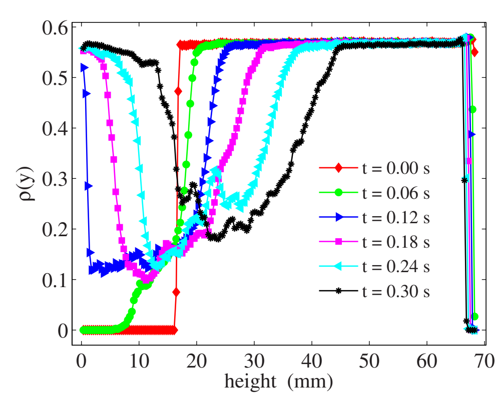

FIG. 8. (Color online) Plot of vertical solid fraction profiles averaged over the system width. The times of the profiles, except for the first profile, coincide with the times in Fig. 7(b).

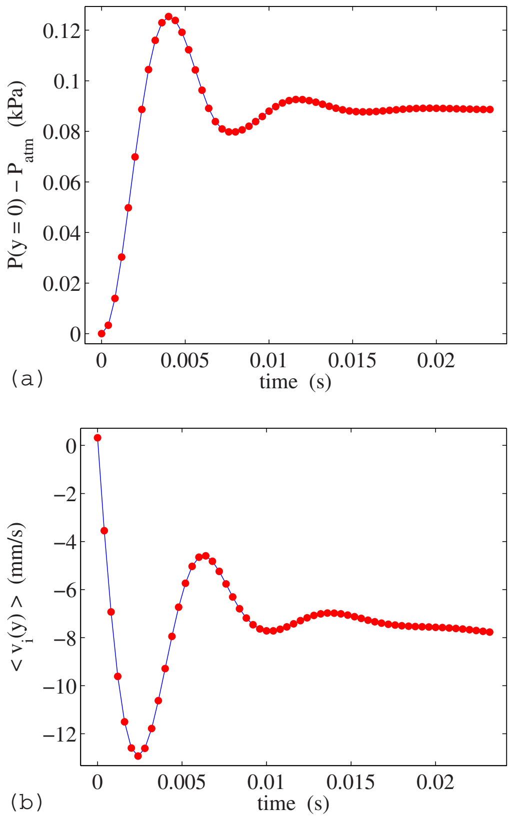

FIG. 9. (Color online) (a) Temporal evolution of the pressure at the bottom of the cell. (b) Vertical velocity of the packing calculated by averaging over all the grains. Immediately after the cell is flipped a damped oscillation is observed in both pressure and velocity, which is a signature of the compressibility of the air.

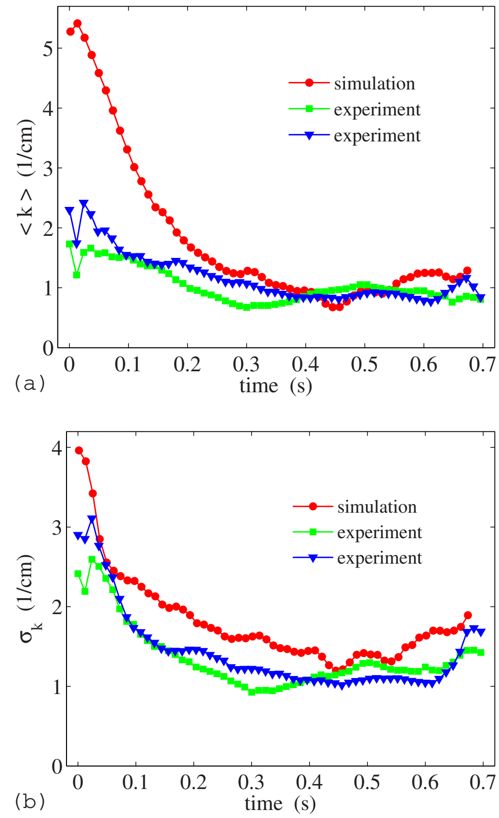

FIG. 10. (Color online) (a) Mean wave number $\langle k \rangle$ of $\bar{S}(k)$ as function of time. (b) Standard deviation σ_k of $\bar{S}(k)$ as function of time. The results are obtained for two experiments and one simulation, all using polystyrene beads of 140 μm in diameter.

C. Fourier analysis

1. Solid fraction

In addition to the qualitative comparison of the numerical and experimental data, a quantitative validification is performed by means of spatial Fourier power spectra of the solid fraction. By this analysis an average wave number $\langle k \rangle$ is obtained which measures the characteristic inverse size of the observed structures.

The average wave number $\langle k \rangle$ is calculated as follows. The power spectrum $S(k;j)$ of the solid fraction is calculated by applying the discrete Fourier transform [37] on the horizontal lines j of the solid fraction field $\rho(x,y)$. Here k denotes the wave numbers of $\rho(x;j)$, and j is an index running over the horizontal lines of the solid fraction grid. The power spectra $S(k;j)$ are further averaged over j to produce a single power spectrum $\bar{S}(k)$, representing the state of the system at a given time. The mean $\langle k \rangle$ of the averaged power spectrum $\bar{S}(k)$ is then finally obtained by the common definition of the nth moment

$$\langle k^n \rangle = \frac{\sum k^n \bar{S}(k)}{\sum \bar{S}(k)} \tag{5}$$

with $n=1$. The standard deviation

$$\sigma_k = \sqrt{\langle k^2 \rangle - \langle k \rangle^2} \tag{6}$$

is also calculated. The unit of $\langle k \rangle$ is cm^{-1}, and it is the characteristic inverse length scale of the observed structures.

The same analysis is used to extract information about the characteristic size of the experimental structures. The solid fraction is however not directly accessible in the experimental data, and the values of the image pixels, spanning from 0 (black) to 255 (white), are instead used as an estimate of the real solid fraction. The solid fraction and the pixel value are inverse quantities, i.e., dilute regions have low solid fractions but high pixel values since they appear as white in the images.

The experimental images are 322 pixels in width, whereas the numerical solid fraction grid is only 160 nodes in width. If the mean values of the two power spectra are to be comparable, the width of the two distributions must be equal. Hence, the experimental power spectrum has an upper cutoff given by the largest wave number in the numerical power spectrum.

The mean, $\langle k \rangle$, and standard deviation, σ_k, of the power spectrum are plotted as functions of time in Figs. 10(a) and 10(b), respectively. The data used here are the same as in Fig. 4, with an additional data-set from a similar experiment. As the instability evolves the initial discrepancy is reduced, and the consistency of the data for later times is quite good.

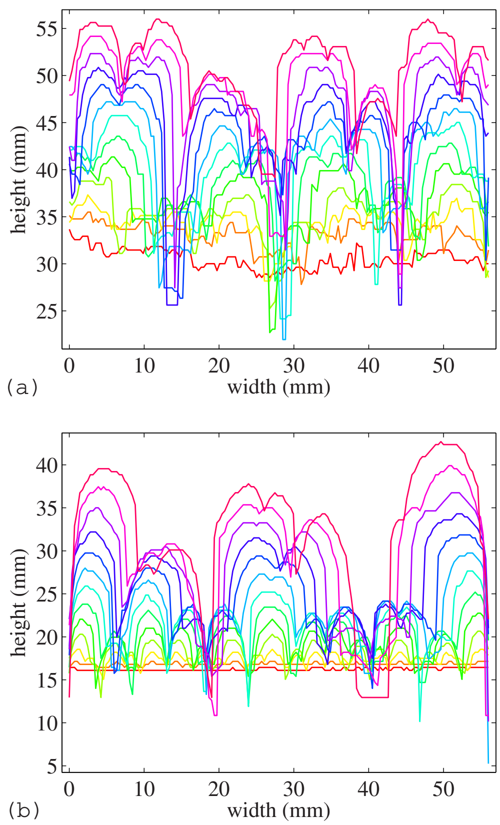

FIG. 11. (Color online) Temporal evolution of (a) the experimental air-grain interface and (b) the numerical air-grain interface. The interfaces move upward with a temporal separation of 0.024 s. The times of the first and last interface are, respectively, 0.002 and 0.29 s.

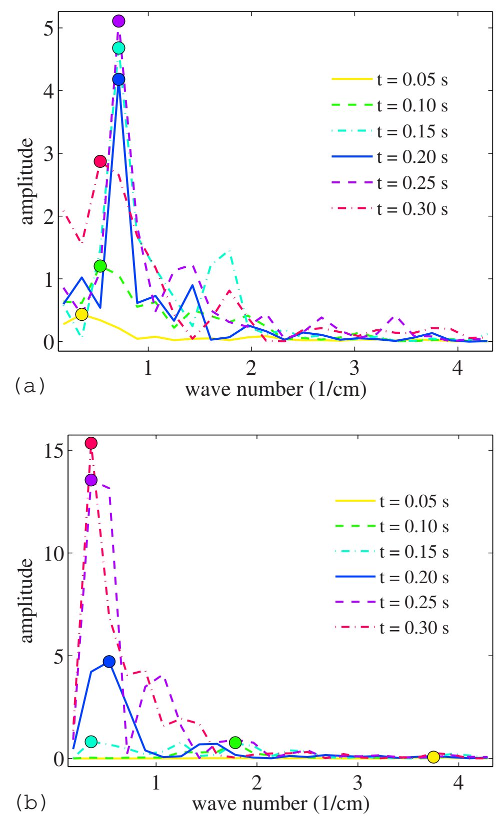

FIG. 12. (Color online) Temporal evolution of (a) the experimental power spectrum and (b) the numerical power spectrum. The power spectrum of every second interface in Fig. 11 is plotted here. The times of the power spectra are given in the legend box, and the colored circles indicate the location of the maximum wave number for every time.

The decrease of σ_k in Fig. 10(b) is caused by the increasing length of the fingers: As the fingers grow the amplitude of the wave number associated with the finger separation increases, thus reducing the width of the power spectrum distribution.

These results show that our gas-grain system is clearly different from the liquid-grain system discussed by Völtz *et al.* [21]. Their liquid-grain system did not display a wave number shift with time, nor the cusp-shaped geometry of the fingers.

2. The interface

Instead of analyzing the full solid fraction field $\rho(x,y)$ for the whole system as in the previous section, the focus is now on the dynamics of the air-grain interface itself.

The function describing the interface is determined by the following procedure. Each vertical line of the solid fraction grid is scanned from top to bottom, and the first node on the line with a solid fraction less than a given threshold is defined to be a point on the interface. Together these points define the interface. The value of the threshold is determined by plotting the calculated interfaces on top of the numerical snapshots and visually confirm that they correspond well (see Fig. 2 of Ref. [20]). The overall shape of the interface is not very sensitive to a fine-tuning of the threshold. The experimental interface is obtained by the same procedure, only with the solid fraction replaced by the image pixel values. The experimental images are rescaled to the size of the numerical solid fraction grid before the experimental interface is obtained. The resulting single-valued functions describing the interface at different times are shown in Figs. 11(a) and 11(b) for the experiment and simulation, respectively. The two series of interfaces have the same temporal separation of 24 ms, and they both start (bottom) at t=0.002 s and stop (top) at t=0.29 s. Salient features of these front evolution plots are the expansion of the bubbles and the appearance of new fingers (shaped like wedges in these plots) at the top of the latter interfaces. Comparing Figs. 11(a) and 11(b), the final shape of the interfaces is in good agreement. The initial shape of the interfaces do not coincide equally well due to the external disturbances introduced in the experimental cell.

Figures 12(a) and 12(b) show (in the same colors as in Fig. 11) the power spectrum of every second interface in Figs. 11(a) and 11(b), respectively. The location of the maximum wave number for each individual power spectrum is indicated by circles. The numerical power spectra in Fig. 12(b) starts out with a maximum wave number to the far right, whereas the experimental power spectra in Fig. 12(a) starts out with a maximum wave number to the far left. The reason for this discrepant behavior is the very different shape of the initial experimental and numerical interfaces: The nu-

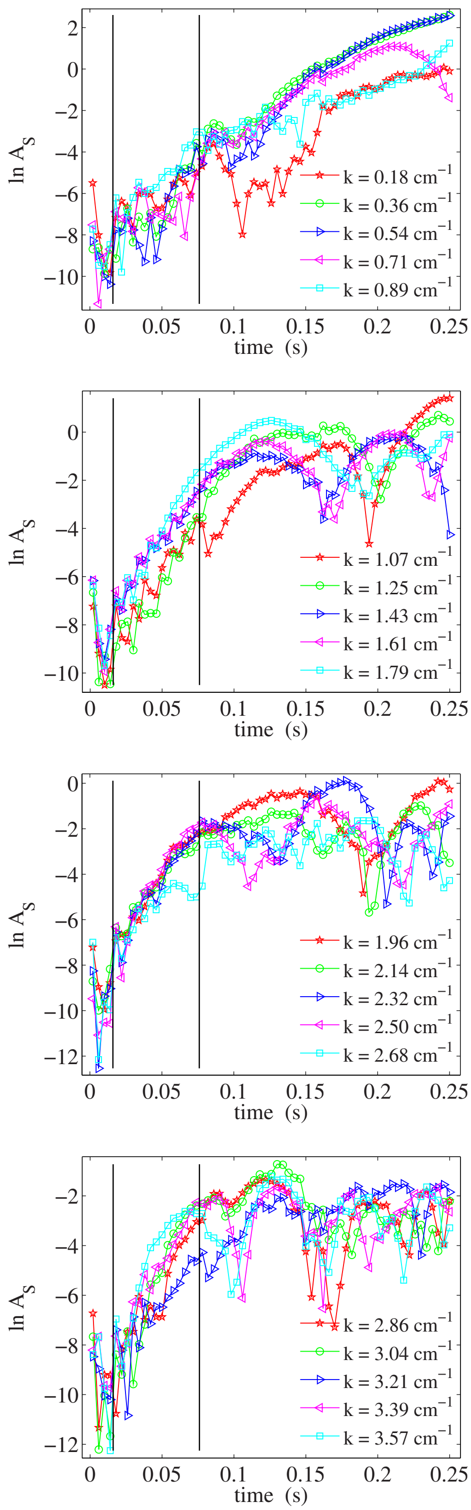

FIG. 13. (Color online) Growth rates of the air-grain interface. The wave numbers are given in the legend boxes, and the vertical lines indicate the time window where the dispersion relation in Fig. 15(a) is calculated.

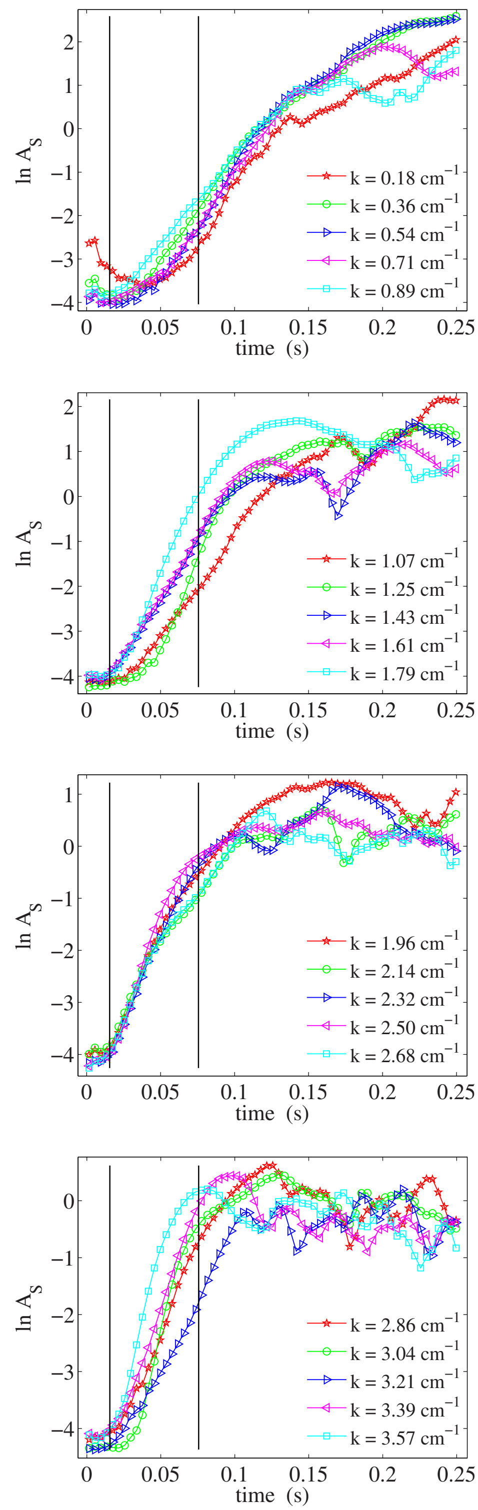

FIG. 14. (Color online) Growth rates of the bulk solid fraction. The wave numbers are given in the legend boxes, and the vertical lines indicate the time window where the dispersion relation in Fig. 15(b) is calculated.

merical interface is virtually flat, whereas the experimental interface has noise on all wavelengths. The dominating wave numbers of the latter power spectra in Figs. 12(a) and 12(b) are only slightly shifted with respect to each other, and converge to approximately the same form.

3. Growth rates

We now move on to analyze the growth rates of the wave numbers as they appear in the power spectra of the numerical data. Following the lines of a linear stability analysis we look

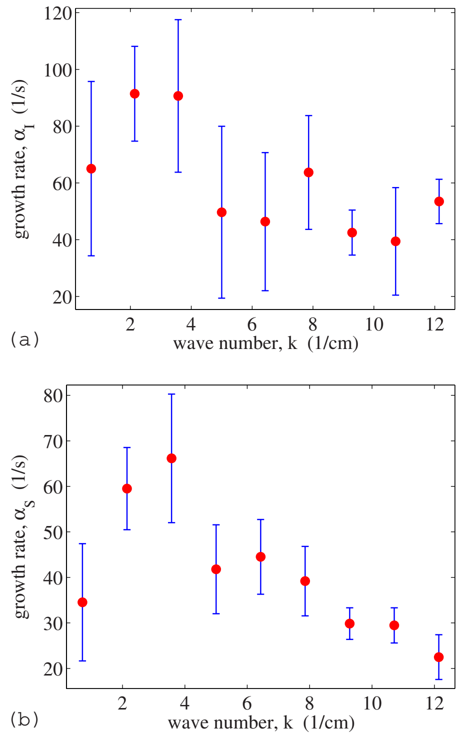

FIG. 15. (Color online) Dispersion relation (a) of the air-grain interface and (b) for the bulk solid fraction. The relations are obtained by linear fits over the approximate linear parts of the growth rate plots in Figs. 13 (interface) and 15 (bulk solid fraction). The error bars are the standard deviations within the boxes.

for possible early exponential growth of the wave numbers in the power spectrum of both the air-grain interface profile and the full solid fraction field.

The temporal evolution of the 20 smallest wave numbers in the power spectrum (or equivalently the 20 longest wavelengths) of the interface profile are plotted semilogarithmically in Fig. 13. The corresponding plots for the average power spectrum of the solid fraction field, $\bar{S}(k)$, are shown in Fig. 14. Exponentially growing wave numbers will appear as linear in these plots. The growth of the solid fraction wave numbers in Fig. 14 is less noisy compared to the growth of the interface wave numbers in Fig. 13 due to the averaging of the solid fraction power spectrum $\bar{S}(k)$ (see IV C 1).

Judging by the growth rates shown in Figs. 13 and 14 it seems fair to conclude that none of the wave numbers follow an exponential growth (at least not of any significant duration). Hence, the granular Rayleigh-Taylor instability is inherently nonlinear, in contrast to the classical Rayleigh-Taylor instability. Nevertheless, a linear least squares fit is obtained for all the wave numbers of the power spectrum, including those not displayed in Figs. 13 and 14. The fit is performed over a time window of 0.6 s as indicated in the plots. The resulting growth rates α_I (interface) and α_S (solid fraction) as functions of wave number k are shown in Figs. 15(a) and 15(b), respectively. In these figures each data point is a box average over eight wave numbers. The standard deviation is indicated by the error bars. Given the approximate linearity of the wave number growth, vigorous conclusions cannot be drawn from these plots. However, while our measurements do not serve to identify a well defined window of linear growth, the growth rates nevertheless exhibit the dominating, time dependent wave number: The maxima at $\sim 4\ \text{cm}^{-1}$ in Figs. 15(a) and 15(b) coincide with the $t = 0.05$ s maximum of the power spectrum in Fig. 12(b). However, it is clear that nonlinear mechanisms govern the selection of the final dominating wavelength.

In a well-controlled experiment of the classical Rayleigh-Taylor instability it is possible to observe exponential growth over a time sufficiently long to erase the influence of the initial noise. This is not the case, however, for the granular Rayleigh-Taylor instability since the exponential domain of the wave number growth is too short to cancel the initial noise. Hence, the structures that develop early, i.e., on a time scale of about 0.1 s, are sensitive to the initial structure of the system. Note that this initial structure is not an experimental imperfection but an intrinsic, unavoidable feature of granular packings.

D. Changing simulation parameters

A number of simulations are performed to probe the response of the instability as the input parameters are changed, i.e., the density of the grains, the roughness of the initial interface, and the dissipation of the granular phase.

1. Grain density

A comparison of simulations performed using grains of different densities, but with identical start configurations, is presented. The density of the grains is $1.05\ \text{g/cm}^3$ (polystyrene) or $2.5\ \text{g/cm}^3$ (glass), and the diameter is 140 μm. Figures 16(a) and 16(b) show plots of the mean wave number $\langle k \rangle$ and the standard deviation σ_k of the power spectrum $\bar{S}(k)$ as functions of time. From these plots it is observed that the time of breakthrough, i.e., when the bubbles reach the upper surface, is dependent on the density of the grains. The separation in time between the last data points of each curve in Fig. 16(a) shows that the instability develops faster if heavier beads are used. However, the initial decrease (i.e., from $t = 0$ to 0.1 s) of $\langle k \rangle$ and σ_k are roughly the same for the two densities.

2. Initial interface

The response of the instability to different initial air-grain interfaces is investigated by three simulations using interfaces with a variation in the roughness.

The three interfaces, shown in Fig. 18 where they are denoted A, B, and C in increasing order of roughness, are prepared as follows. Starting from a configuration where the packing rests on the bottom plate, interface A is created by displacing the packing vertically upward to fill the top half of the cell. In this case the cell is not rotated. A perfectly flat air-grain interface is now defined by the grains originally positioned on the bottom plate, prior to the vertical displacement. Interface B is created by first removing all grains with their centers above a given height just below the upper surface of the packing (again positioned on the bottom plate).

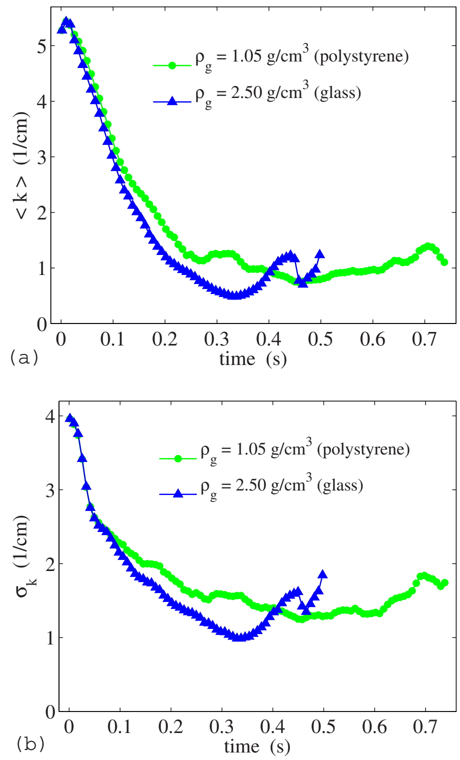

FIG. 16. (Color online) (a) Mean wave number $\langle k \rangle$ as a function of time for different grain densities. (b) Standard deviation σ_k as a function of time for different grain densities. The grain densities ρ_g used in the simulations are given in the legend box.

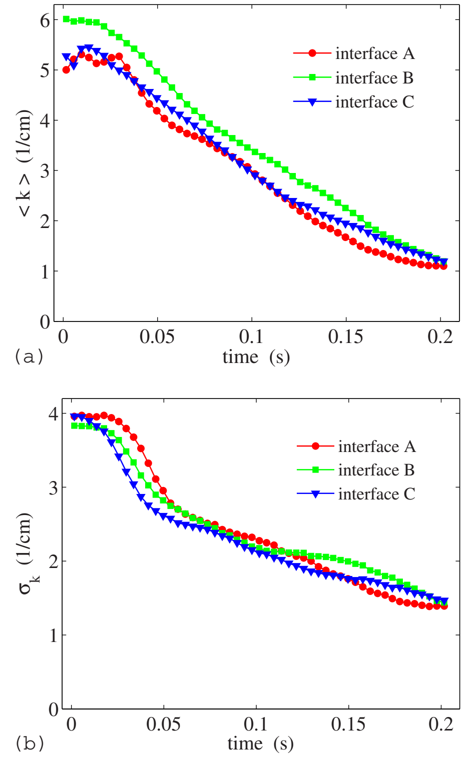

FIG. 17. (Color online) (a) Mean wave number $\langle k \rangle$ as function of time for different initial interfaces. (b) Standard deviation σ_k as function of time for different initial interfaces. The interfaces used in the simulations are labeled A, B, and C and are shown in Fig. 18.

The cell is then rotated to bring the slightly rough surface above the layer of air. Interface C is the rotated original packing with a surface determined by the local equilibrium of the grains.

The temporal evolution of $\langle k \rangle$ and σ_k for packings with their initial interfaces as shown in Fig. 18 are plotted in Figs. 17(a) and 17(b), respectively. These plots lead to the conclusion that the shape of the initial interface has an effect only during the earliest stages of the instability. It appears that the slowest evolving interface is B, and that B, not A, is the interface with the smallest initial noise. This may correspond to the fact that the porosity above interface A has larger fluctuations than in B because of the constraint imposed by the flat wall. After about 0.2 s the difference in $\langle k \rangle$ is negligible. The increased standard deviation of interface A indicates a slightly slower and delayed generation of fingers in this case. However, the effect is only temporary and the initial difference is canceled out. Note that this observation is consistent with the conclusion at the end of Sec. IV C 3: The exponential domain is too short to cancel the initial noise during the incipient evolution of the instability. However, as nonlinear effects take over, the system nevertheless evolves toward structures that are insensitive to the initial noise.

3. Dissipation

A series of simulations are performed where the coefficient of normal restitution, ε, is changed. The motivation is to investigate the effect on the fingering process and its dynamics. Figure 19 shows two snapshots for each of the six different restitution coefficient used in these simulations. The two leftmost snapshots in Fig. 19, with $\varepsilon = 1.0$ and 0.95, distinguish themselves by a diffuse outline of the interface, fewer fingers, and a general lack of detail compared to the other snapshots. To differentiate between the remaining pairs of snapshots, obtained with $\varepsilon = 0.8$, 0.5, 0.2, and 0.05, is not as evident because it is difficult to identify significant differences in these images: The number of fingers is about the same, as well as the size and shape of the bubbles. It is possible to identify minor deviations in, e.g., the number and shape of the renucleated fingers, but no significant influence of dissipation is observed on the formation of new fingers. The conclusion must be that the system is invariant under changes in the dissipation as long as the restitution coefficient is below a certain threshold. However, above this threshold the instability is sensitive to variations in the restitution, in particular the size and shape of the fingers are affected. The curvature of the bubbles is only moderately affected by the variation in ε.

The value of the threshold, above which the instability is virtually insensitive to variations in ε, is likely to depend on

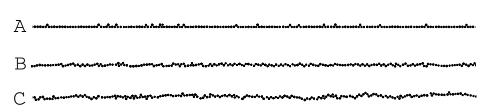

FIG. 18. Different initial air-grain interfaces used in the simulations. The interfaces are labeled A, B, and C in increasing order of roughness.

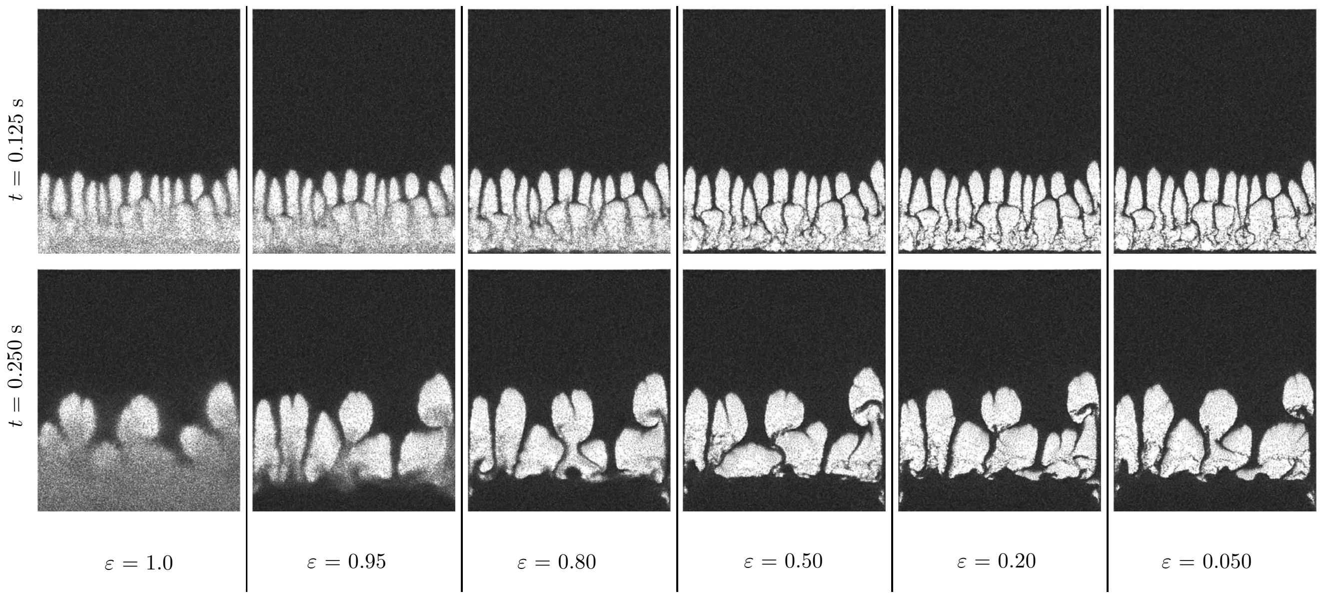

FIG. 19. Snapshots of simulations with different coefficients of restitution ε, given below the snapshots. The times of the simultaneous snapshots are given to the left of each row.

the average number of collisions the grains participate in. The number of collisions n required to reduce the kinetic energy by a given fraction F is inversely proportional to the logarithm of the restitution coefficient ε. In mathematical terms $n(\varepsilon)=\ln(1-F)/\ln(\varepsilon)$ which follows from the relation $\varepsilon^n=1-F$. A semilogarithmic plot of $n(\varepsilon)$ for three different values of F is shown in Fig. 20. Lets assume a grain has lost 90% of its kinetic energy by interacting in n' collisions with restitution coefficient ε'. If the restitution coefficient is reduced beyond ε' it will make only a negligible difference because the energy was already very small at ε'. Figure 20 demonstrates that the number of collisions needed to reduce the energy by, e.g., 90% changes significantly as the restitution coefficient changes from 0.99 (229 collisions) to 0.8 (ten collisions). Below this interval the change in the number of collisions is marginal: At $\varepsilon=0.6$ it takes five collisions to reduce the energy by 90%, compared to ten collisions at $\varepsilon=0.8$. If we assume that a grain on average is involved in ten collisions, over a time scale that is small compared to the dynamical time scale of the structures, 90% of its energy is lost if $\varepsilon=0.8$, and 99% is lost if $\varepsilon=0.6$. Since most of the energy is already dissipated at $\varepsilon=0.8$, this might explain why the simulations are virtually invariant if the restitution coefficient is reduced beyond $\varepsilon=0.8$.

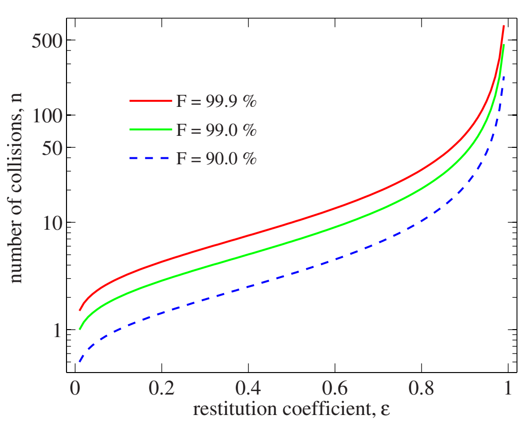

FIG. 20. (Color online) Number of collisions n as a function of restitution coefficient ε (normal). The three different curves show how many collisions it takes to reduce the kinetic energy of a grain by a fraction F (given in the legend box) for different ε.

V. CONCLUSION

A gravitational instability, observed as a layer of dense granular material is positioned above a layer of air in a closed Hele-Shaw cell, is reported both experimentally and numerically. Qualitative and quantitative comparisons of numerical and experimental data are presented with the conclusion that the simulations reproduce the essential experimental features. The growth rates of the numerical solid fraction field are obtained by Fourier analysis to look for exponential time dependence. Both the bulk solid fraction and the air-grain interface have been investigated by this analysis. Our conclusion is that granular Rayleigh-Taylor instability is inherently nonlinear since exponential dependence of significant duration is not observed in the data. Further, the response to changes in different simulation parameters was probed: The density of the grains, the initial air-grain interface, and the granular dissipation. Increasing the density leads to an earlier breakthrough of the air bubbles, without any significant change in the coarsening time of the structures. Changing the roughness of the initial interface has an effect only early in the instability; the difference is canceled after about 0.2 s. Dissipation affects only the formation of fingers above a certain threshold of the restitution coefficient.

This behavior is supported by a simple model for the loss of granular kinetic energy.

The unique behavior of the gas-grain system as compared to the liquid-grain system investigated by Völtz *et al.* might be caused by the compressibility and low inertia of the air.

As for the experimental work, some refinements of the experiment is necessary if the complete evolution of the instability, including the initial fingers, is to be probed.

ACKNOWLEDGMENTS

The work was supported by NFR, the Norwegian Research Council. A special thanks to Sean McNamara for useful comments, and for making the original F90 implementation of the gas-grain model available during the C++ reimplementation.

[1] *Physics of Dry Granular Media*, edited by H. J. Herrmann J.-P. Hovi, and S. Luding, NATO Advanced Study Institute, Series E: Applied Sciences (Kluwer Academic Publishers, Dordrecht, 1998), Vol. 350.
[2] J. F. Davidson and D. Harrison, *Fluidization* (Academic Press, New York, 1971).
[3] D. Gidaspow, *Multiphase Flow and Fluidization* (Academic Press, San Diego, 1994).
[4] G. K. Batchelor, J. Fluid Mech. **52**, 245 (1972).
[5] J. F. Richardson and W. N. Zaki, Trans. Inst. Chem. Eng. **3**, 65 (1954).
[6] P. Y. Julien, *River Mechanics* (Cambridge University Press, Cambridge, U.K., 2002).
[7] D. H. Rothman, J. P. Grotzinger, and P. B. Flemings, J. Sediment Res. **64**, 59 (1994).
[8] R. Bachrach, A. Nur, and A. Agnon, J. Geophys. Res. **106**, 13515 (2001).
[9] P. G. Drazin and W. H. Reid, *Hydrodynamic Stability* (Cambridge University Press, Cambridge, U.K., 1981).
[10] S. Chandrasekhar, *Hydrodynamic and Hydromagnetic Stability* (Dover Publications, New York, 1981).
[11] P. G. Saffman and G. Taylor, Proc. R. Soc. London, Ser. A **245**, 312 (1958).
[12] C. Chevalier, M. B. Amar, D. Bonn, and A. Lindner, J. Fluid Mech. **552**, 83 (2006).
[13] Ø. Johnsen, R. Toussaint, K. J. Måløy, and E. G. Flekkøy, Phys. Rev. E **74**, 011301 (2006).
[14] G. I. Taylor, Proc. R. Soc. London, Ser. A **132**, 499 (1931).
[15] M. P. Ciamarra, A. Coniglio, and M. Nicodemi, J. Phys.: Condens. Matter **17**, 2549 (2005).
[16] J. J. Wylie, Q. Zhang, and X. Sun, Phys. Rev. Lett. **97**, 104501 (2006).
[17] F. Malloggi, J. Lanuza, B. Andreotti, and E. Clement, Europhys. Lett. **75**, 825 (2006).
[18] D. Gendron, H. Troadec, K. J. Måløy, and E. G. Flekkøy, Phys. Rev. E **64**, 021509 (2001).
[19] E. G. Flekkøy, S. McNamara, K. J. Måløy, and D. Gendron, Phys. Rev. Lett. **87**, 134302 (2001).
[20] J. L. Vinningland, Ø. Johnsen, E. G. Flekkøy, R. Toussaint, and K. J. Måløy, Phys. Rev. Lett. **99**, 048001 (2007).
[21] C. Völtz, W. Pesch, and I. Rehberg, Phys. Rev. E **65**, 011404 (2001).
[22] G. Taylor, Proc. R. Soc. London, Ser. A **201**, 192 (1950).
[23] R. Jackson, *The Dynamics of Fluidized Particles* (Cambridge University Press, Cambridge, U.K., 2000).
[24] S. Schwarzer, Phys. Rev. E **52**, 6461 (1995).
[25] S. McNamara, E. G. Flekkøy, and K. J. Måløy, Phys. Rev. E **61**, 4054 (2000).
[26] D.-V. Anghel, M. Strauss, S. McNamara, E. G. Flekkøy, and K. J. Måløy, Phys. Rev. E **74**, 029906(E) (2006).
[27] H. Darcy, *Les Fontaines Publiques de la Ville de Dijon* (Dalmont, Paris, 1856).
[28] P. C. Carman, Trans. Inst. Chem. Eng. **15**, 150 (1937).
[29] F. Radjai, M. Jean, J.-J. Moreau, and S. Roux, Phys. Rev. Lett. **77**, 274 (1996).
[30] L. Brendel and S. Dippel, *Physics of Dry Granular Media* (Kluwer Academic, Dordrecht, 1998).
[31] M. P. Allen and D. J. Tildesley, *Computer Simulation of Liquids* (Clarendon Press, Oxford, 1989).
[32] J. J. Moreau, Eur. J. Mech. A/Solids **13**, 93 (1994).
[33] M. Jean, in *Mechanics of Geometrical Interfaces*, edited by A. P. S. Selvadurai and M. J. Boulon (Elsevier Sciencs, Amsterdam, 1995), pp. 463–486.
[34] F. Radjai and S. Roux, Phys. Rev. E **51**, 6177 (1995).
[35] A. Hurst, J. Cartwright, M. Huuse, R. Jonk, A. Schwab, D. Duranti, and B. Cronin, Geofluids **3**, 263 (2003).
[36] H. A. Janssen, Z. Vereines Deutsch. Ingenieure **39**, 1045 (1895).
[37] W. H. Press, S. A. Teukolsky, W. T. Vetterling, and B. P. Flannery, *Numerical Recipes in C++* (Cambridge University Press, Cambridge, U.K., 2002), Chap. 12, p. 505.

Size invariance of the granular Rayleigh-Taylor instability

Jan Ludvig Vinningland,[1,2,*] Øistein Johnsen,[1] Eirik G. Flekkøy,[1] Renaud Toussaint,[3] and Knut Jørgen Måløy[1]
[1]*Advanced Materials and Complex Systems, Department of Physics, University of Oslo, P.0. Box 1048, 0316 Oslo, Norway*
[2]*Physics of Geological Processes, Department of Physics, University of Oslo, P.0. Box 1048, 0316 Oslo, Norway*
[3]*Institut de Physique du Globe de Strasbourg, CNRS, Université Louis Pasteur, 5 rue Descartes, 67084 Strasbourg Cedex, France*
(Received 3 September 2008; revised manuscript received 18 February 2010; published 29 April 2010)

The size scaling behavior of the granular Rayleigh-Taylor instability [J. L. Vinningland *et al.*, Phys. Rev. Lett. **99**, 048001 (2007)] is investigated experimentally, numerically, and theoretically. An upper layer of grains displaces a lower gap of air by organizing into dense fingers of falling grains separated by rising bubbles of air. The dependence of these structures on the system and grain sizes is investigated. A spatial measurement of the finger structures is obtained by the Fourier power spectrum of the wave number k. As the size of the grains increases the wave number decreases accordingly which leaves the dimensionless product of wave number and grain diameter, dk, invariant. A theoretical interpretation of the invariance, based on the scaling properties of the model equations, suggests a gradual breakdown of the invariance for grains smaller than ~ 70 μm or greater than ~ 570 μm in diameter.

DOI: 10.1103/PhysRevE.81.041308 PACS number(s): 81.05.Rm, 47.20.Ma, 47.11.−j, 45.70.Qj

I. INTRODUCTION

Granular materials are the basis of abundant industrial and natural processes and an integral part of our everyday life. Dry granular flows have been widely studied over the past twenty years [1], but the study of granular flows where the interstitial fluid plays an important role is still in its infancy. Many natural phenomena pertaining to such granular/fluid flows are active topics of current research, e.g., sedimentation [2,3], erosion and river evolution [4], underwater avalanches and turbidites [5], and soil fluidization during earthquakes [6]. Industrial processes, such as pneumatic transport, fluidized beds, catalytic cracking [1,7,8] would also benefit from advances in granular/fluid flow research.

The granular Rayleigh-Taylor instability arises when a closed, vertical Hele-Shaw cell, partially filled with fine grains and air at atmospheric pressure, is rapidly rotated to bring the dense packing of grains above a layer of air. Shortly after the rotation fine fingers of falling grains emerge from the initially flat grain-air interface. These fine fingers subsequently develop into coarser finger structures separated by bubbles of air. In contrast to the classical Rayleigh-Taylor instability [9] the coarsening process observed in the granular case will right from the start bring about a reduction in the number of fingers and a corresponding increase in the size of the bubbles. New fingers will form in the center of the rising bubbles as they reach a certain width, and the characteristic size of the structures is thus maintained at a stable value.

This granular instability is previously studied both numerically and experimentally [10,11], using the same model and setup as in the present paper, with the conclusion that the two competing mechanisms, one producing finer scales, the other producing coarser scales, are well reproduced by the numerical model.

In contrast to the gas-grain instability reported here, Völtz *et al.* studied a liquid-grain instability experimentally and theoretically [12]. The liquid-grain instability bears a strong resemblance to the classical instability for two liquids with almost overlapping dispersion relations. The gas-grain instability, however, displays a quite different behavior with a coarsening process active from the beginning and a counteracting refinement process that stabilizes the average size of the bubbles.

The purpose of the present investigation is to study the variations in the flow structures under change of spatial scale of both the grains and the Hele-Shaw cell. Size invariance is not commonly studied for granular materials. Indeed, granular flows are quite sensitive to initial preparation and external perturbations, so that systematic grain and system size changes are delicate studies. In the present paper, using the complementarity of experimental and numerical techniques, we perform a systematic study of how the structures formed by the granular Rayleigh-Taylor instability responds to a rescaling of the system and grain sizes.

The experimental, numerical, and theoretical results presented all indicate a size invariance of the finger-bubble structures. However, the theoretical analysis predicts a breaking of the invariance if the grains are too small or too large. The simulations use grains ranging from 70 to 490 μm in diameter, and the experiments use grains ranging from 80 to 570 μm in diameter. Consistent data collapses are obtained from these results and demonstrate a fairly robust invariance within the given limits.

The simulations and experiments presented in Ref. [11] were performed with identical parameters to provide an assessment of the numerical model. In the present paper we present experimental and numerical results obtained in a new parameter regime not explored in previous publications. However, in this paper the parameters of the experiments and simulations are no longer identical, due to less emphasis on model assessment. In particular, the simulations and experiments are carried out using slightly different grain densities. The scale invariance of the granular Rayleigh-Taylor invariance was first acknowledged in Ref. [10]. The current paper provides a more elaborate discussion of this invariance in-

*janlv@fys.uio.no

TABLE I. Listing of the diameters of the grains and the dimensions of the Hele-Shaw cells used in the experiments.

Diameter (μm)	80	140	230	570
Width (mm)	31	56	91	200
Height (mm)	61	86	141	305
Depth (mm)	1.0	1.7	2.3	5.4

cluding results from experiment, simulation and theory not presented in [10].

The paper is organized as follows. A presentation of the experimental setup and implementation is given in the next section. The numerical model is briefly presented in Sec. III, and the results, together with the data analysis, are presented and discussed in Sec. IV. The theoretical basis of the size invariance, based on the scaling properties of the model equations, is presented in Sec. V. Section VI presents numerical data obtained to check for possible container size effects. Finally, a conclusion and summary are given in Sec. VII.

II. EXPERIMENT

The experimental setup is the same as was used in Refs. [10,11] and will only be presented briefly here. Four Hele-Shaw cells of different sizes are partially filled with monodisperse polystyrene beads and air at atmospheric pressure. The sizes of the cells scale proportionally with the diameter of the grains they contain, see Table I. The cells are filled with Dynoseeds polystyrene spheres of density $\rho_g = 1.05\ \mathrm{g/cm^3}$ (manufactured by Microbeads [13]). The cells are individually mounted on a hinged bar and rapidly rotated to an upright position, see Fig. 1. Images of the falling grains are recorded by a high speed digital camera (Photron Fastcam-APX 120K) at a rate of 500 frames per second.

The humidity in the laboratory was kept at about 30% during the assembling of the cells, and the grains were exposed to the air in the laboratory for some time before the filling. This is to prevent clustering of the grains due to cohesion, arising from capillary bridges, or electrostatic forces.

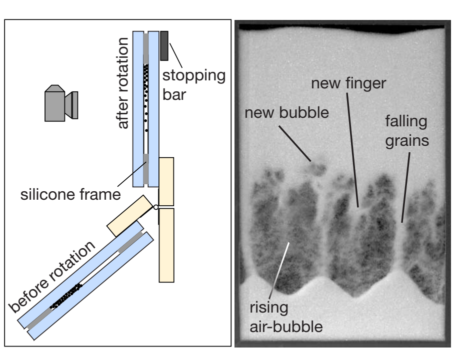

FIG. 1. (Color online) (left) Side view of the experimental setup with the initial and final cell positions superimposed. (right) Typical snapshot from an experiment using grains of 230 μm in diameter in a cell that is $91 \times 141 \times 2.3$ mm.

The experimental cells are somewhat taller than the numerical cells to account for the grains that settle during the rotation. The horizontal filling procedure of the cells makes it difficult to control the filling fraction, and it may vary slightly between the four cells. During the assembling of the cells the TS 500–53 beads was presumed to have a diameter of 500 μm. However, an analysis performed by Microbeads shows that the mean diameter of these grains is in fact 570 μm. This explains the slight discrepancy between the width of the cell and the diameter of the grains in this case.

III. SIMULATION

The numerical model has proved to be very consistent in reproducing experimentally observed structures in granular flows and instabilities in the regime of low Reynolds numbers [14–17]. The theoretical basis and derivation of the model are given in Refs. [14,15] and a description of the current implementation is given in Ref. [11]. However, a brief outline of the model will be presented here for completeness.

The granular phase is modeled as discrete, rigid spheres that collectively constitute a deformable porous medium. The pressure drop associated with the air flowing through the granular medium is given by a local Darcy's law [18] with the Carman-Kozeny relation for the permeability κ [19]. The continuum gas phase is described solely by its pressure P. The velocity field of the gas may be obtained from the pressure gradient via Darcy's law. In order to provide a continuum description of the pressure $P(x,y)$ on a grid (x,y), the continuum variables, solid fraction $\rho(x,y)$, and granular velocity $\mathbf{u}(x,y)$ need to be calculated. This is done by a linear smoothing function $s(\mathbf{r}-\mathbf{r}_0)$ expressed mathematically as [14]

$$s(\mathbf{r}-\mathbf{r}_0) = \begin{cases} \left(1-\dfrac{\Delta x}{l}\right)\left(1-\dfrac{\Delta y}{l}\right) & \text{if } \Delta x, \Delta y < l \\ 0 & \text{otherwise,} \end{cases} \tag{1}$$

where $\mathbf{r}(x,y)$ is the position of the grain, $\mathbf{r}_0(x_0,y_0)$ is the position of the grid node, $\Delta x = |x-x_0|$ and $\Delta y = |y-y_0|$ are the relative distances, l is the lattice constant, and $\Sigma_k s(\mathbf{r}-\mathbf{r}_k) = 1$ with k indexing the four neighboring sites of a grain positioned at $\mathbf{r}$.

From the continuity equations of air mass and grain mass, using the average velocity of the air in the porous matrix (i.e., $\mathbf{u}_{\mathrm{Darcy}}/\phi$), a pressure equation is derived, see [14,15],

$$\phi\left(\frac{\partial P}{\partial t} + \mathbf{u}\cdot\boldsymbol{\nabla}P\right) = \boldsymbol{\nabla}\cdot\left(P\frac{\kappa(\phi)}{\mu}\boldsymbol{\nabla}P\right) - P\boldsymbol{\nabla}\cdot\mathbf{u}, \tag{2}$$

where $\phi = 1-\rho$ is the porosity, and μ is the viscosity of air. This equation is valid for compressible flows since it assumes $\rho_a \propto \phi P$ (isothermal ideal gas law) for the air density, ρ_a. If instead an incompressible liquid is considered this assumption becomes $\rho_l \propto \phi$ for the liquid density ρ_l. The pressure Eq. (2) then simplifies to a Poisson equation for the pressure given by $\boldsymbol{\nabla}\cdot[\kappa(\phi)/\mu\boldsymbol{\nabla}P] = \boldsymbol{\nabla}\cdot\mathbf{u}$.

TABLE II. Listing of the diameters of the grains and the dimensions of the cells used in the simulations.

Diameter (μm)	70	140	210	280	350	420	490
Width (mm)	28	56	84	112	140	168	196
Height (mm)	34	68	102	136	170	204	238

The grains are governed by Newton's second law

$$m\frac{d\mathbf{v}}{dt} = mg + \mathbf{F}_\mathrm{I} - \frac{V\boldsymbol{\nabla} P}{\rho}, \tag{3}$$

where m, $\mathbf{v}$, and V are, respectively, the mass, velocity, and volume of a grain. The interparticle normal force $\mathbf{F}_\mathrm{I}$ acting between grains in contact is calculated iteratively using contact dynamics [20] (but a Hookean or Hertzian contact law may be used instead). The dynamics of the grains are simplified by neglecting particle-particle and particle-wall friction. A lower cutoff is imposed on the solid fraction because the Carman-Kozeny relation is not valid for a solid fraction less than 0.25 [21]. This cutoff causes the permeability in the most dilute regions of the system to be slightly underestimated. This leads to a slight overestimation of the pressure forces acting on grains in dilute regions. The effect of this artifact is however decreasing with increasing granular inertia.

A series of seven simulations are performed and each simulation uses monodisperse grains of different diameters, see Table II. The same relative start configuration of 160 000 grains is used in all the simulations and the size of the system, given in Table II, scales proportionally to the diameters of the grains. The mass density of the grains is 2.5 $\mathrm{g/cm^3}$, a common value for glass beads. In the simulations we have introduced a larger density than in the experiments in order to minimize the numerical artifacts caused by the solid fraction cutoff. These artifacts are manifested as slightly curved and buckled fingers that become visible as the inertia of the grains decreases.

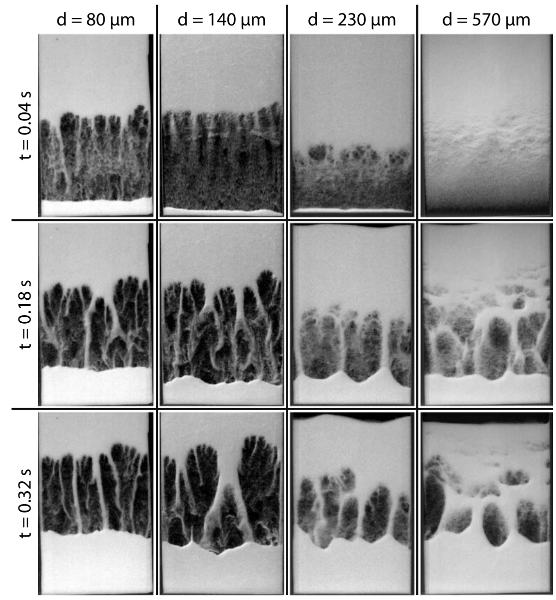

FIG. 3. Experimental snapshots. Each column represents a different experiment characterized by the diameter d of the grains used, and each row represents a different time t.

IV. RESULTS AND ANALYSIS

Images from each of the seven simulations and four experiments are, respectively, shown in Figs. 2 and 3. The corresponding spatial dimensions of the cells are given in Tables I and II. Each row of images in Figs. 2 and 3 represents a given time t, and each column of images represents a given grain-diameter d. From the snapshots in Figs. 2 and 3 it is evident that the finger-bubble structures depend strongly on grain size. For cells with grains of diameters smaller than

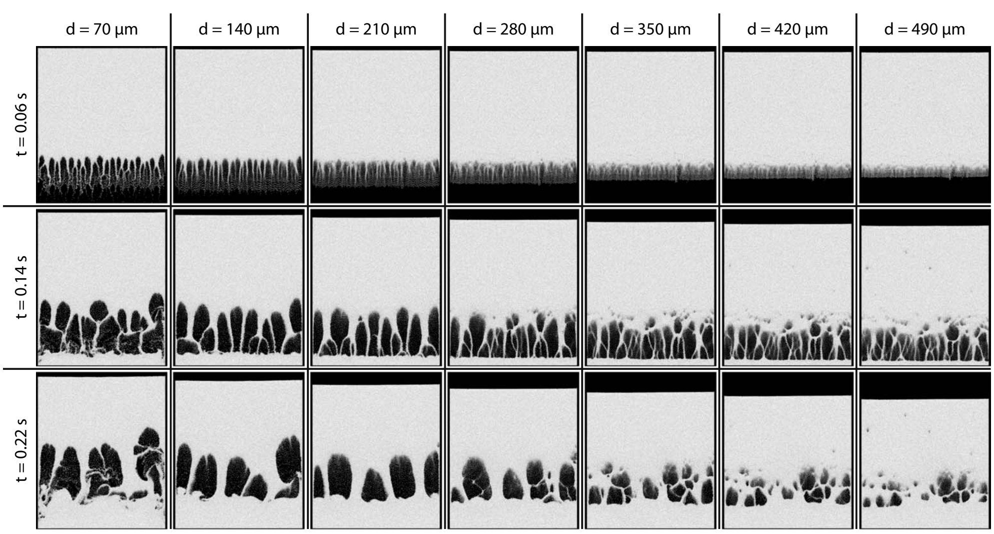

FIG. 2. Numerical snapshots. Each column represents different simulations using grains of diameter d, and each row represents snapshots at different times t.

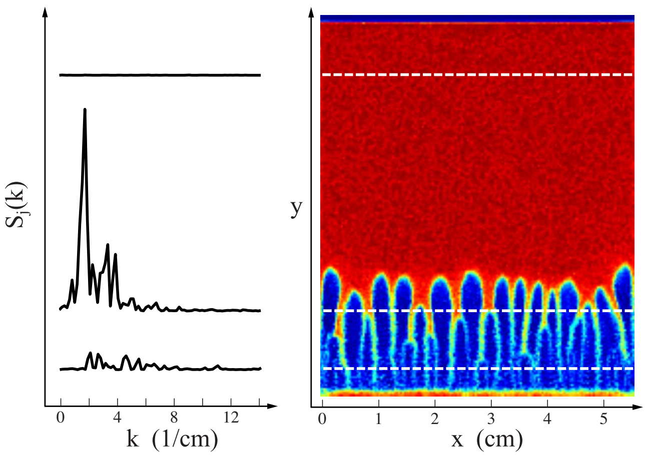

FIG. 4. (Color online) Plots of Fourier power spectra $S_j(k)$ (left) obtained at three different heights of the solid fraction field $\rho(x,y)$ (right) shown as a color coded data image [red (gray) is high ρ, blue (dark gray) is low ρ]. The stapled white lines indicate at which y position the power spectra are obtained.

200 μm it is relatively easy to identify a unique interface that separates an upper, dense granular packing from the air below. For grain diameters greater than 200 μm, however, small air-bubbles appear in the bulk of the packing above the grain-air interface. These precursory bubbles are separated by horizontal filaments of grains which form in addition to the vertical fingers. The number of precursory bubbles increases as the grain diameter increases. These structures are analogous to the bubbles observed in the ripple instability arising in a tilted tube of sand [16,22].

Scale invariance

A size measurement of the finger structures is obtained by making a Fourier transform of the solid fraction field $\rho(x,y)$. The resulting Fourier spectrum $\bar{S}(k,t)$, i.e., the wave number distribution for a given time t, enables a quantitative comparison of finger structures for different grain and system sizes.

The distribution $\bar{S}(k,t)$ is calculated as follows. The power spectrum $S_j(k)$ of each horizontal line j of the solid fraction field is obtained by the discrete Fourier transform [23], using Hamming data windows to avoid frequency leakage due to the nonperiodic character of the system. By averaging over the individual power spectra $S_j(k)$ the final average distribution $\bar{S}(k,t)$ is obtained. This procedure is illustrated in Fig. 4: the left plot shows power spectra $S_j(k)$ obtained at three given positions y_j of horizontal cuts of the density function $\rho(x,y)$ shown in the right plot of the same figure. Large ρ values appear in red (gray) and small ρ values appear in blue (dark gray).

As Fig. 4 illustrates it is not necessary to reduce the Fourier analysis to a spatial window centered around the interface. The power spectra obtained in the bulk above the interface are anyway flat and make no contributions to the final averaged power spectrum.

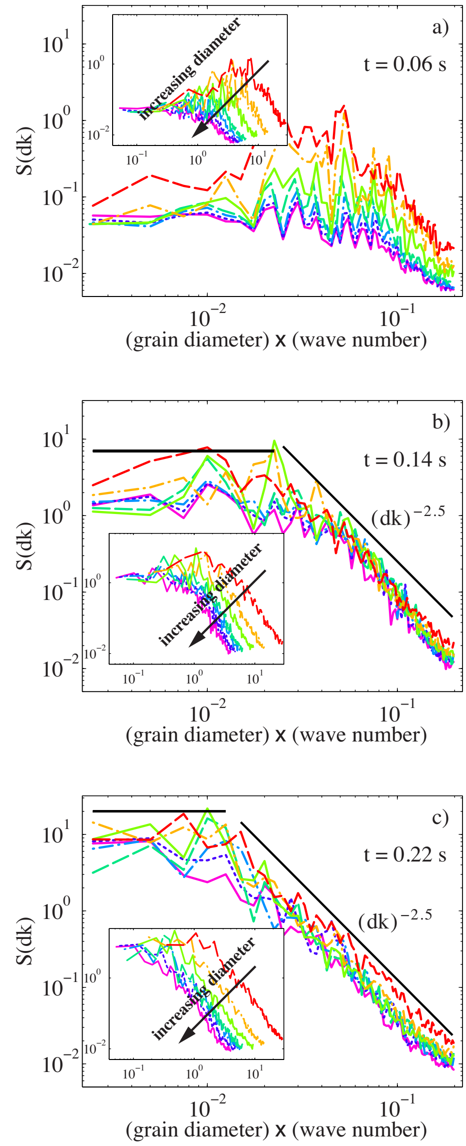

FIG. 5. (Color online) Plots of $\bar{S}(dk)$ [$\bar{S}(k)$ in inset plots] obtained from numerical data. Each plot is a data collapse of $\bar{S}(dk)$ for all grain-diameters d at three different times t (the same times as in Fig. 2). The different colors represent different grain diameters ranging from 70 to 490 μm as indicated in the inset plots. The straight black lines are power laws obeyed by $\bar{S}(dk)$ at large and small scales: $\bar{S}(dk) \sim$ constant at large scales (growing white noise), and $\bar{S}(dk) \sim (dk)^{-2.5}$ at small scales.

The experimental data are treated similarly to the numerical data. However, the solid fraction field is not directly available in the experimental data and it is therefore estimated by the gray level values of the image pixels. The pixel value is assumed to be linearly related to the solid fraction. The inaccuracy of this assumption is not likely to have a large effect on the measurements.

Figure 5 shows log-log plots of $\bar{S}(dk)$, i.e., the power spectra $\bar{S}(k)$ rescaled by the grain-diameter d, for the numerical data. The inset plots show the unscaled spectra $\bar{S}(k)$ as function of k in cm^{-1}. Notice that the power spectra in Fig. 5

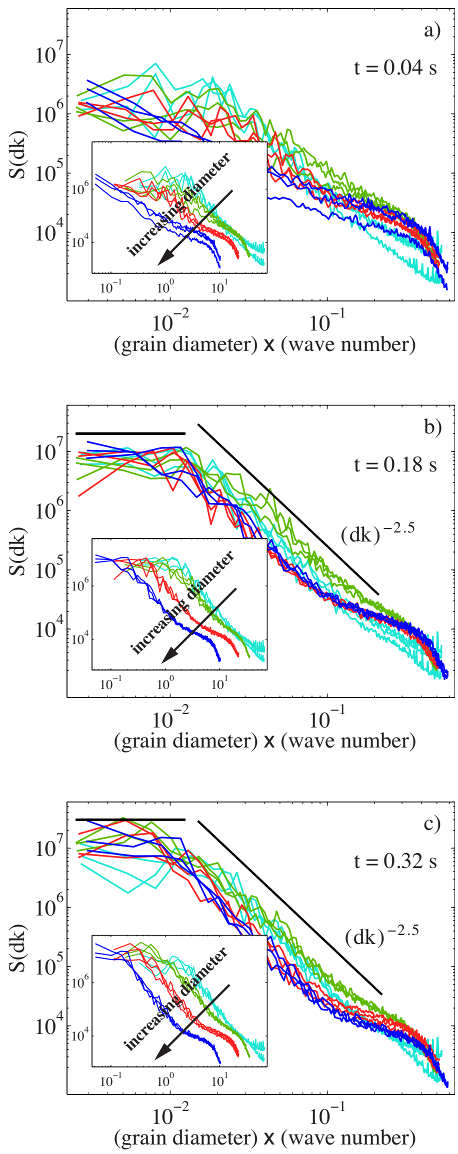

FIG. 6. (Color online) Plots of $\bar{S}(dk)$ [$\bar{S}(k)$ in inset plots] obtained from experimental data. Each plot is a data collapse of $\bar{S}(dk)$ for all grain-diameters d at three different times t (the same times as in Fig. 3). The different colors represent different grain diameters ranging from 80 μm to 570 μm as indicated in the inset plots. The straight black lines are power laws obeyed by $\bar{S}(dk)$ at large and small scales, as in the numerical case: $\bar{S}(dk) \sim$ constant at large scales, and $\bar{S}(dk) \sim (dk)^{-2.5}$ at small scales.

are calculated from the numerical data shown in Fig. 2. Figure 6 similarly shows log-log plots of $\bar{S}(dk)$ obtained from the experimental data presented in Fig. 3. The inset plots show the unscaled spectra $\bar{S}(k)$.

The plot in Fig. 5(a) hardly qualifies as a data collapse, in contrast to the other plots in Figs. 5 and 6. This is due to the fact that initially the falling grains are constantly expanding which increases the divergence of the velocity field, $\nabla \cdot \mathbf{u}$. As is shown in Eq. (8) the source term, $P \nabla \cdot \mathbf{u}$, of the pressure equation Eq. (2) will break the invariance. Hence, the invariance observed for larger times is only possible due to the smallness of the source term for larger times.

The characteristic wave number (where the power spectra start to decrease) seen in Fig. 5 gradually shifts from higher to lower values as time evolves. This corresponds well with the observed coarsening with time of the finger structures both in the numerical and the experimental data. However, compared to the numerical data, the shift from higher to lower wave numbers is less evident in the experimental data since the initially very fine fingers is not observed in the experiments.

After the very initial period, the (collapsed) power spectra plotted in Figs. 5 and 6 can be shown to be consistent with two power laws: $\bar{S}(dk) \sim$ constant for large scales (growing white noise), and $\bar{S}(dk) \sim (dk)^{-2.5}$ at small scales (straight black lines in Figs. 5 and 6). These exponents can be obtained from linear fits of the bilogarithmic plots, and are determined with a precision of order 0.5. These power laws are valid both for the numerical (Fig. 5) and experimental (Fig. 6) results. In the experiments, however, there is also an additional bump of the power spectra for the smallest scales (largest wave numbers) departing from the $\bar{S}(dk) \sim (dk)^{-2.5}$ scaling behavior. This behavior may be attributed to the fact that these largest k values are at the limit of the spatial resolution in the experiments.

The early-time power spectra displayed in Figs. 5(a) and 6(a) are quite scattered around the power laws. This might be related to the fact that at early times the size scaling is also not satisfied due to accelerating grains, as previously discussed.

V. THEORETICAL INTERPRETATION

Let us assume that we have a solution of our gas and grain equations. Now, if we magnify all physical scales, the velocities and the pressure variations by a constant factor λ, how close will we come to a solution of our equations?

In mathematical terms, let P, $\rho(\mathbf{x},t) = m\rho_n(\mathbf{x},t)$, and $\mathbf{v}_i$ be the pressure field, the mass density field, and particle velocities that solve the equations

$$\phi \frac{dP}{dt} = \nabla \cdot \left(\frac{\kappa P \nabla P}{\mu} \right) - P \nabla \cdot \mathbf{u},$$

$$m \frac{d\mathbf{v}}{dt} = mg + F_I - \frac{m \nabla P}{\rho}, \qquad (4)$$

where as before $\mathbf{u}$ is the local average of the $\mathbf{v}_i$'s. We split the velocity as follows: $\mathbf{v}_i = \delta \mathbf{v}_i + \mathbf{u}_0$ and $\mathbf{u} = \delta \mathbf{u} + \mathbf{u}_0$, where $\mathbf{u}_0$ is the constant sedimentation velocity of a close packed system. We substitute $P = P_0 + \delta P$ and $F_I = ma_I$ and make the observation that $\delta P \ll P_0$, which leads to the justified approximation

$$\phi \frac{\partial \delta P}{\partial t} = \nabla \cdot \left(\frac{\kappa P_0 \nabla \delta P}{\mu} \right) - P_0 \nabla \cdot \delta \mathbf{u},$$

$$\frac{d\mathbf{v}}{dt} = g + a_I - \frac{\nabla P}{\rho}. \qquad (5)$$

Here the substantial derivative has been replaced by the partial derivative because $\mathbf{u} \cdot \nabla \delta P \ll P_0 \nabla \cdot \delta \mathbf{u}$. A rough estimate using $u \sim 10^{-2}$ m/s, $\nabla \delta P \sim 10^{-3}$ Pa/m, $P_0 = 10^5$ Pa, and $\nabla \cdot \delta \mathbf{u} \sim 10$ s^{-1} justifies this assumption. As in a hydrostatic system we assume that the pressure field of the magnified system is $\delta P'(\mathbf{x}', t) = \lambda \delta P(\mathbf{x}, t) = \lambda \delta P(\mathbf{x}'/\lambda, t)$, where $\mathbf{x}' = \lambda \mathbf{x}$. We make the following scaling ansatz, expressing the solutions of Eqs. (5) in terms of the scaled fields as

$$\delta P(\mathbf{x}, t) = \frac{1}{\lambda} \delta P'(\mathbf{x}', t),$$

$$\mathbf{u}_0 = \frac{1}{\lambda^2} \mathbf{u}'_0,$$

$$\delta \mathbf{u}(\mathbf{x}, t) = \frac{1}{\lambda} \delta \mathbf{u}'(\mathbf{x}', t),$$

$$\rho(\mathbf{x}, t) = \rho'(\mathbf{x}', t), \tag{6}$$

where the sedimentation velocity $\mathbf{u}'_0$ scales as λ^2 because the local density is λ-invariant and permeability goes as length squared and scales as λ^2, i.e.,

$$\kappa' = \lambda^2 \kappa. \tag{7}$$

Note that Eqs. (5) are unaffected by the scaling of $\mathbf{u}_0$. Using the new length scale in the derivative ∇' we get $\nabla = \lambda \nabla'$. The pressure gradient $\nabla \delta P$, ρ, ϕ, and t are all invariant. By substitution we obtain

$$\phi \frac{\partial \delta P'}{\partial t} = \nabla' \cdot \left(\frac{\kappa' P_0 \nabla' \delta P'}{\mu} \right) - \lambda P_0 \nabla' \cdot \delta \mathbf{u}',$$

$$\frac{1}{\lambda} \left(\frac{d\mathbf{v}'}{dt} - a'_I \right) = g - \frac{\nabla' P'}{\rho'}, \tag{8}$$

as the equations satisfied by the scaled fields. Note that by mass conservation of the granular phase, i.e., $d\rho/dt = -\rho \nabla \cdot \delta \mathbf{u}$, the last term of the pressure equation may be written $-P_0 \nabla \cdot \delta \mathbf{u} = (P_0/\rho) d\rho/dt$, and this term thus gives the effect of density changes in a frame of reference moving with the grains. This implies that the term vanishes for a flow field without internal compression or expansion. If such a flow field is also steady, like that of a slab of connected particles moving at a constant velocity, the acceleration terms vanish along with the $-P_0 \nabla \cdot \delta \mathbf{u}$ term, i.e., all the λ-dependent terms vanish in Eq. (8). This invariance means that the scaled fields are solutions of the same equations as the original fields.

The terms that are multiplied by a λ-factor break the invariance. To get an estimate of their relative magnitude we introduce dimensionless numbers. Taking the characteristic length scale of the flow to be l and the time scale to be l/u we may write

$$\mathrm{Fr} = \frac{u^2}{gl} \sim \frac{d\mathbf{v}/dt}{g},$$

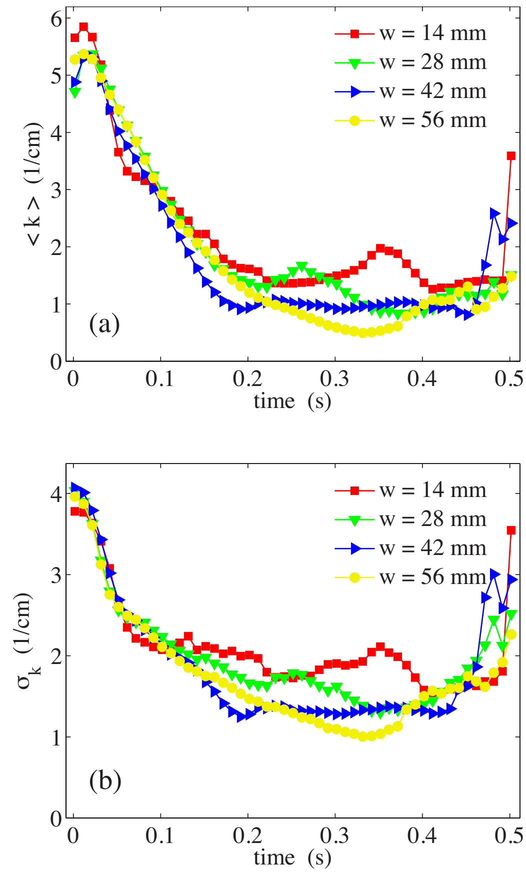

FIG. 7. (Color online) (a) Plot of the mean wave number $\langle k \rangle$ obtained from four different simulations with grains of diameter $d = 140$ μm but with four different cell widths w. (b) Same plot for the standard deviation σ.

$$A = \frac{180\ \mu u l}{\delta P d^2} \sim \frac{P_0 \nabla \cdot \delta \mathbf{u}}{\nabla \cdot \left(\frac{\kappa P_0 \nabla \delta P}{\mu} \right)}, \tag{9}$$

where Fr is known as the Froude number. Taking $d = 140$ μm, $l = \langle k \rangle^{-1} = 0.01$ m at $t = 0.5$ s and $u = l/t = 0.02$ m/s we get $\mathrm{Fr} = 0.004$. With $\delta P = 0.01$ atm. and the same values for the length scale l we get $A = 0.04$.

Since A and Fr measure the relative magnitude of the invariance-breaking terms, the smallness of A and Fr indicate that the scaled fields are close to satisfying the physical Eqs. (5). For this reason we may expect all lengths in the simulations to scale the same way, and $\bar{S}(dk)$ will be invariant under scaling by λ. However, since $\mathrm{Fr} \propto \lambda$, increasing the magnification will increase the relative effect of granular inertia, and, we expect, the deviations from this scaling property. On the other hand, $A \propto 1/\lambda$ so decreasing the particle size will cause the compression term in the pressure equation to grow in relative magnitude. It is therefore only in a certain window of particle sizes around $d = 140$ μm that we may expect the scale invariance. In particular, for the $d = 70$ μm simulations it is likely that deviations from the scaling behavior arise due to the relatively large A value.

The above scaling invariance is somewhat analogous to the scale invariance of low Reynolds number flows, where the inertial term may be neglected since it is small compared to the viscous term, and symmetries of the flow solutions emerge because the Navier-Stokes equations are replaced by the Stokes equation.

VI. CONTAINER SIZE EFFECTS

In the experiments and simulations presented so far the size of the grains and the size of the container are changed proportionally to each other such that every container confines approximately the same number of grains. To address the question of possible container size effects a series of simulations is performed where the size of the grains and the size of the container are changed independently. Four different simulation geometries are used while the grain diameter is kept fixed at 140 μm. The four numerical cells all have the same height of 68 mm but different widths of 14, 28, 42, and 56 mm. To compare the different results the power spectrum $\bar{S}(k,t)$ for each of the four simulations is obtained as explained in Sec. IV. In order to represent the temporal evolution of $\bar{S}(k,t)$ the mean and standard deviation of $\bar{S}(k,t)$ are calculated by the usual definitions

$$\langle k\rangle(t) = \frac{\sum k\bar{S}(k,t)}{\sum \bar{S}(k,t)}, \tag{10}$$

$$\sigma(t) = \sqrt{\frac{\sum k^2\bar{S}(k,t)}{\sum \bar{S}(k,t)} - \langle k\rangle(t)^2}, \tag{11}$$

where the summation is over all k values.

Figure 7 shows the mean wave number $\langle k\rangle$ and standard deviation σ for the four different geometries. During the coarsening stage, i.e., from $t=0$ s until $t=0.2$ s, the four curves overlap quite well. For $t>0.2$ s the curves are more spread due to two peaks in the $w=14$ and 28 mm data. These peaks are most likely caused by fluctuations in the evolving structures which are not averaged out due to less statistics for the narrow geometries. In addition, the different granular configurations used in the four runs also account for some variations in the data. For cell widths less than roughly 14 mm container size effects will be present since this width is smaller than the maximum width a bubble may reach in a wide cell. However, the data in Fig. 7 shows no systematic dependence on the container size.

In [10] it was shown that plots of $\langle k\rangle$ for different grain sizes will overlap only if $\langle k\rangle$ is rescaled by the grain-diameter d. In Fig. 7 the plots overlap although no rescaling of $\langle k\rangle$ by, e.g., the container width w is applied. Hence, the observed pattern scales with grain size and not container size.

VII. CONCLUSION AND SUMMARY

In summary we have uncovered an approximate scale invariance in a granular Rayleigh-Taylor instability [10,11] through experimental measurements and complementary simulations. In addition, a theoretical interpretation is provided with the conclusion that the validity of the scale invariance is limited to a window of grain diameters from roughly 70 μm to about 570 μm. The scale invariance may be interpreted as the existence of a Stokes-like regime for the investigated systems. Terms arising from grain inertia for large grains, or from pressure sources (i.e., $P\boldsymbol{\nabla}\cdot\mathbf{u}$) for small grains, will gradually break the invariance. A separate series of simulations with constant grain sizes but different geometries was performed with the conclusion that the observed scale invariance is not affected by container size effects. The deviations observed in this invariance has been given interpretations both in terms of theoretical arguments and in terms of numerical and experimental imperfections.

[1] *Physics of Dry Granular Media*, edited by H. J. Herrmann, J.-P. Hovi, and S. Luding, NATO ASI Series E: Applied Sciences Vol. 350 (Kluwer Academic Publishers, Dordrecht, 1998).

[2] G. K. Batchelor, J. Fluid Mech. **52**, 245 (1972).

[3] J. F. Richardson and W. N. Zaki, Trans. Inst. Chem. Eng. **3**, 65 (1954).

[4] P. Y. Julien, *River Mechanics* (Cambridge University Press, Cambridge, 2002).

[5] D. H. Rothman, J. P. Grotzinger, and P. B. Flemings, J. Sediment Res. **64**, 59 (1994).

[6] R. Bachrach, A. Nur, and A. Agnon, J. Geophys. Res. **106**, 13515 (2001).

[7] J. F. Davidson and D. Harrison, *Fluidization* (Academic Press, New York, 1971).

[8] D. Gidaspow, *Multiphase Flow and Fluidization* (Academic Press, San Diego, 1994).

[9] G. Taylor, Proc. R. Soc. London, Ser. A **201**, 192 (1950).

[10] J. L. Vinningland, Ø. Johnsen, E. G. Flekkøy, R. Toussaint, and K. J. Måløy, Phys. Rev. Lett. **99**, 048001 (2007).

[11] J. L. Vinningland, Ø. Johnsen, E. G. Flekkøy, R. Toussaint, and K. J. Måløy, Phys. Rev. E **76**, 051306 (2007).

[12] C. Völtz, W. Pesch, and I. Rehberg, Phys. Rev. E **65**, 011404 (2001).

[13] Microbeads AS, P. O. Box 265, N-2021 Skedsmokorset, NORWAY, Tel: +47 64 83 53 00, Fax: +47 64 83 53 01, email: support@micro-beads.com.

[14] S. McNamara, E. G. Flekkøy, and K. J. Måløy, Phys. Rev. E **61**, 4054 (2000).

[15] D.-V. Anghel, M. Strauss, S. McNamara, E. G. Flekkøy, and K. J. Måløy, Phys. Rev. E **74**, 029906(E) (2006).

[16] E. G. Flekkøy, S. McNamara, K. J. Måløy, and D. Gendron, Phys. Rev. Lett. **87**, 134302 (2001).

[17] Ø. Johnsen, R. Toussaint, K. J. Måløy, and E. G. Flekkøy, Phys. Rev. E **74**, 011301 (2006).

[18] H. Darcy, *Les Fontaines Publiques de la Ville de Dijon* (Dalmont, Paris, 1856).

[19] P. C. Carman, Trans. Inst. Chem. Eng. **15**, 150 (1937).

[20] F. Radjai, M. Jean, J.-J. Moreau, and S. Roux, Phys. Rev. Lett. **77**, 274 (1996).
[21] A. A. Zick and G. M. Homsy, J. Fluid Mech. **115**, 13 (1982).
[22] D. Gendron, H. Troadec, K. J. Måløy, and E. G. Flekkøy, Phys. Rev. E **64**, 021509 (2001).
[23] W. H. Press, S. A. Teukolsky, W. T. Vetterling, and B. P. Flannery, *Numerical Recipes in C++: The Art of Scientific Computing* (Cambridge University Press, Cambridge, 2002), p. 505, Chap. 12.

Mixing of a granular layer falling through a fluid

Michael J. Niebling,[1] Eirik G. Flekkøy,[1] Knut Jørgen Måløy,[1] and Renaud Toussaint[2,3]
[1]*Department of Physics, University of Oslo, P.O. Box 1048, 0316 Oslo, Norway*
[2]*Institut de Physique du Globe de Strasbourg, CNRS, 5 rue Descartes, 67084 Strasbourg Cedex, France*
[3]*University of Strasbourg, 5 rue Descartes, 67084 Strasbourg Cedex, France*
(Received 13 March 2009; revised manuscript received 18 May 2010; published 7 July 2010)

We analyze the granular Rayleigh-Taylor instability of densely packed grains immersed in a compressible or an incompressible fluid using numerical simulations and two types of experiments. The simulations are based on a two-dimensional (2D) molecular dynamics model and the experiments have been carried out in systems of grains immersed in water/glycerol (incompressible fluid) and in air (compressible fluid). The variation of the interstitial fluid is shown to generate different dynamical patterns and mixing properties of the granular systems. The results have been quantified using 2D autocorrelation functions, the power spectrum of the velocity field and velocity field histograms. Excellent agreement is found between the numerical simulations and the experiments.

DOI: 10.1103/PhysRevE.82.011301 PACS number(s): 81.05.Rm, 47.20.Ma, 47.11.−j, 45.70.Qj

I. INTRODUCTION

The dynamics of particles immersed in fluids has been studied in a wide range of systems such as fluidized beds [1], sedimentation [2–4], mixing problems and granular flows. Many of the studied systems have important industrial applications as well as natural equivalents in a wide range of geological systems such as land slide, erosion, hydrofracturing [5], and avalanches [6].

The granular Rayleigh-Taylor instability has been studied recently using numerical as well as experimental methods for the case of air [7,8] and for the case of grains falling in a highly viscous fluid [9–11]. Typically, experiments are conducted in closed rectangular Hele-Shaw cells where a dense granular layer falls through a gap filled with a fluid. In general, the falling layer separates into three different zones, in the top and bottom part of the cell sit compacted particles that barely move and in the space between these two zones, we have a region of moving particles of lower density perturbed by the spontaneous formation of fingerlike regions of higher particle density.

In contradistinction to previous works [7–11] where the focus has been on the evolution of the interface between the moving particle-zone and the compacted particles at the top of the cell, we shall here analyze in detail the bulk dynamics. In [7,8] the granular Rayleigh-Taylor instability in air filled systems was studied and it was found that the finger formation differed qualitatively from systems filled with highly viscous fluids [9–11] and liquid-liquid systems. In the former case the finger formation was shown to coarsen in time, in contrast to observations in classical liquid-liquid systems and systems of grains immersed in highly viscous fluids, in these latter cases a single wavelength turned out to be dominating at all times.

Previously, the numerical modeling of the granular Rayleigh Taylor instability has been limited to systems with compressible interstitial fluids [7,8]. In the present work we extend the model to account for incompressible fluids. In addition we analyze the mixing dynamics over the whole cell and the sedimentation.

We compare the sedimentation and the particle dynamics for the case of air with the case of an incompressible liquid by means of experiments and simulations. The particle dynamics are analyzed by velocity field histograms, two-dimensional (2D) autocorrelation functions and the power spectrum of the velocity and density fields. Combining these methods we find excellent agreement between our numerical model and the experiments.

The velocity field of the experiments is extracted by the use of a correlation image velocimetry (CIV) technique. A similar technique was applied in studies of sedimentation of beads in silicone oil after the suspension was mixed with a small propeller [3,4,12–15]. In this paper we present a CIV method that reduces the noise of the displacement field by use of gray-level cross correlations as weights while averaging over several pixels. Our technique significantly improves the results obtained by standard procedures. The analysis of the velocity field gives quantitative interpretation of the different sedimentation patterns in the case of air compared to the case of the water/glycerol solution.

The paper is divided as follows. In the next section the experimental setup and experimental image analysis are described, followed in Sec. III by a description on the implementation of the numerical model. The results and the analysis are presented in Sec. IV. Physical interpretations and explanations of the mixing behavior are presented in Sec. V and the concluding remarks are given in Sec. VI.

II. EXPERIMENTAL SETUP

The experimental setup is shown in Fig. 1. We use a rectangular Hele-Shaw glass cell with the dimensions 5 cm in width by 8 cm in height and a plate spacing of 1 mm. The plate spacing h is achieved by a 1mm thick silicone frame that ensures the cell to be tight toward three sides. Through the fourth side the beads, and when needed the beads in suspension with the fluid, are inserted. After the cell has been filled to the designated height of approximately 3/4 with particles the fourth side is sealed with silicone paste leaving no air bubbles in the case of a fluid. In the case of air Dynoseed polystyrene beads with a mass density of $\rho_{m_p}=1.05\ \mathrm{g/cm^3}$ and for water/glycerol glass beads with a mass density of $\rho_{m_g}=2.5\ \mathrm{g/cm^3}$ are used. In both cases we sieved particles

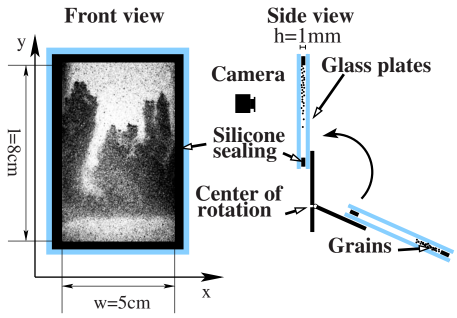

FIG. 1. (Color online) The experimental setup. The cell consists of two rectangular glass plates. Silicone sealing assures the cell to be leak proof. The front view shows a picture taken during an experiment with water/glycerol.

with an average diameter of $140\pm10\%$ μm. This corresponds to a number of 180 000 particles in the simulations.

After the preparation the cell is mounted by the use of clamps on a rotating bar. To ensure reproducibility, the sample was always prepared in the same way, flipping the cell a couple of times created a loose packing with an initially flat surface at the start of each experiment. Once the camera is running the cell is flipped upside down in about 0.2 s and pictures are taken at a rate of 1000 fps (frames per second) in the case of air and 50 fps in the case of water/glycerol. For this purpose we use a high speed digital camera (Photron Fastcam-APX 120K) to record pictures with a resolution of 512×1024 pixels.

The rotation is stopped by a stopping bar that is softened by a piece of expending rubber. Despite the damping of the cell, the initial patterns are perturbated by the impact. In the analysis, we therefore disregard the early stage of the experiments.

The experiments with air are done under room conditions of 22° in temperature and a relative humidity close to 30%. Under this conditions the viscosity of air is $\mu_a=0.000\,018$ Pa s. The water/glycerol solution has a mass concentration of 30% glycerol. At room conditions the viscosity was measured to be $\mu_f=0.002\,26$ Pa s and the mass density of the solution was measured to be $\rho_f=1.065\ \text{g/cm}^3$. It should be mentioned that a small amount of liquid soap was added to the water/glycerol solution in order to extract the small air bubbles sticking to the beads. However, it turned out that the soap lowered the interparticle friction as well as the friction between particles and the walls. Indeed, the soap approximately doubled the overall propagation speed of the unstable interface.

In all experiments, an amount of 10% of colored particles was randomly dispersed in the packing to increase the contrast for the numerical extraction of the velocity by the CIV technique. The colored particles were of the same density as the uncolored particles in the case of air and in the case of water/glycerol.

Experimental picture analysis

The subject of the analysis in this paper is the whole dynamic region of the granular Rayleigh-Taylor instability. A valuable quantity to study the dynamic region is the velocity field of the particles. In case of the simulations the velocities are computed at every time step and are directly accessible. For the experiments the velocity fields had to be extracted numerically from the pictures of the high speed camera by the means of a correlation image velocimetry (CIV) technique. For the CIV technique we use pictures of 255 gray-levels with a resolution of 512×1024 pixels. The CIV technique is implemented in real space, according to classical techniques [16]. The displacement dx, dy between two successive images at each point x, y is determined by the maximization of the cross correlation of the gray map of squared zones centered at x, y in the first image, and $x+dx$, $y+dy$ in the second one (Fig. 2). In addition to the classical treatment, we have developed an additional filtering method for the resulting velocity field, utilizing the fact that the obtained maximum cross correlation is a measure of the resemblance between the zones, and thus of the suitability of the CIV technique for the zone under consideration. To minimize the impact of artifacts due to aberrant zones where no resemblance is found with the following pictures, we convolve the velocity field obtained by a weight, that increases the better the cross correlation between the zones is. More specifically, for zones of interest of the size $2i+1$ centered at x_0,y_0 and x_1,y_1, the cross correlation between gray-map A and B is defined as

$$\langle A(x_0,y_0)B(x_1,y_1)\rangle_i \equiv \sum_{m=-i}^{i}\sum_{n=-i}^{i} A(x_0+m,y_0+n)B(x_1+m,y_1+n) \qquad (1)$$

and

$$\langle A(x_0,y_0)\rangle_i \equiv \sum_{m=-i}^{i}\sum_{n=-i}^{i} A(x_0+m,y_0+n). \qquad (2)$$

For $s_1(x,y)$ and $s_2(x,y)$ the two gray-maps of two successive images, the normalized gray maps are defined as

$$s_1'(x,y)=s_1(x,y)/\sqrt{\langle s_1(x,y)s_1(x,y)\rangle_i},$$

$$s_2'(x,y)=s_2(x,y)/\sqrt{\langle s_2(x,y)s_2(x,y)\rangle_i} \qquad (3)$$

and the cross-correlation between the two pictures as

$$C(x,y,\Delta x,\Delta y)=\langle s_1'(x,y)s_2'(x+\Delta x,y+\Delta y)\rangle_i. \qquad (4)$$

The displacement $dx(x,y),dy(x,y)$ between two successive pictures for zones centered on (x,y) is determined from maximizing $C(x,y,\Delta x,\Delta y)$ over $\Delta x,\Delta y$, i.e., such as:

$$C(x,y,dx,dy)=\max_{\Delta x,\Delta y\le l}[C(x,y,\Delta x,\Delta y)]=C_{max}(x,y). \qquad (5)$$

For this maximization, we used search values of $l=6$ pixels maximum displacement for Δx, Δy, and sample squares of 7×7 with $i=3$ pixels. Next, the resulting displacement is convolved on running square windows of linear size l, with a weight, $w(x,y)=1/[3-2C_{max}(x,y)]$ on each pixel, i.e., we determine a final average displacement

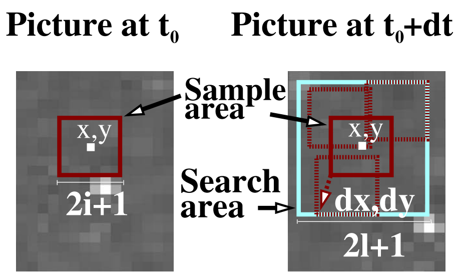

FIG. 2. (Color online) For the CIV technique the gray-level of two pictures in a time sequence is compared. In red (dark gray) a sample area is defined in the first picture. In the following picture it is then tried to find a similar area with the same gray-level distribution within the search area shown in blue (light gray).

$$dx_{fa}(x,y) = \frac{\langle w(x,y)dx(x,y)\rangle_i}{\langle w(x,y)\rangle_i}, \quad (6)$$

$$dy_{fa}(x,y) = \frac{\langle w(x,y)dy(x,y)\rangle_i}{\langle w(x,y)\rangle_i}. \quad (7)$$

The resulting procedure is tested on simulated images, by comparing directly the resulting determined velocity field with the one calculated for the particles in the corresponding simulation .

We divide the average displacement by the time step between two pictures to get the averaged particle velocity components in x and y direction u_x and u_y.

As stated before it is essential to have a good time resolution in the sequence of pictures. The size of the sample and search area has carefully been chosen according to the achieved resolution in our pictures. One pixel corresponds to 100 μm. To estimate how well our CIV technique is actually working we calculate the velocity field histogram from two pictures of the simulations one time with the CIV (left picture in Fig. 3) and another time by using the simulation data directly (right picture in Fig. 3). To make the direct simulation data comparable to the CIV data of the experiments we average the velocity of the single particles in the simulation with an equivalent procedure as in the experiments. In both pictures the velocity field is visualized on a square grid by vectors. The arrows represent the average of the velocity of the particles averaged over an area around the position of the arrow. To clarify the plot the size of the sample area was chosen to be $i=6$, $(l=6)$ and was larger than the usual $i=3$ pixels that we chose later for the analysis. In the plot the size of a vector represents the absolute value of the averaged velocity and the arrow points in direction of the averaged velocity vector. The velocity field in these two pictures only shows slight variations and the CIV technique reproduces the velocities well. For example we notice easily where fingers are falling down, the velocity is increased.

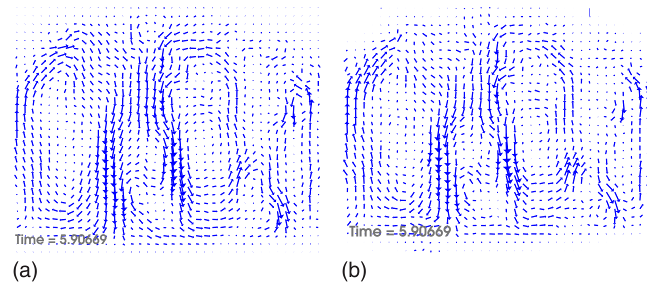

FIG. 3. (Color online) Test of the CIV technique: the left picture shows the velocity field derived directly from the simulation data in comparison with the right picture where the velocity field is obtained by the CIV technique from two pictures of the simulation. Both pictures show a section from the middle of the cell where most particles are moving.

However when we analyze the experiments and simulations we will look at the velocity field histograms in x and y direction. Therefore it is necessary that the velocity field derived with the CIV technique leads to the same histograms as the one derived from the simulation data provided that we analyze the same picture. For this reason we compare the histograms derived by the CIV technique with the histograms derived from the simulations for the x-direction in graph 4(a) and for the y-direction in graph 4(b) in Fig. 4. In the histograms we divide u_x and u_y by the average absolute value of the velocity u_a. This compensates, that later the camera in the experiments records better the beads close to the glass plates which typically move slower. The velocity u_a is defined as follows:

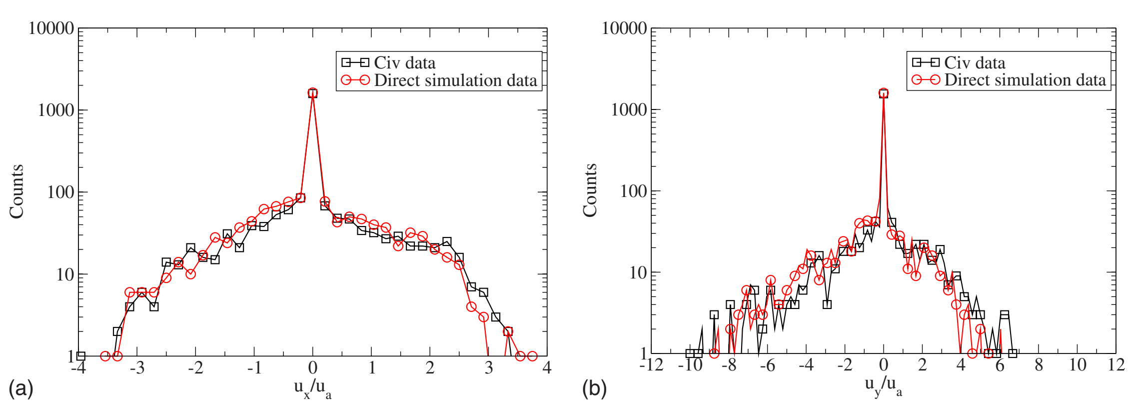

FIG. 4. (Color online) Histograms of the velocity field derived by the CIV technique and the velocity field derived directly from the simulation data.

$$u_a = \frac{1}{XY}\sum_i^X \sum_j^Y \sqrt{u_x^2(i,j) + u_y^2(i,j)}, \qquad (8)$$

where X and Y is the extend of the velocity field in x and y direction. In both figures good agreement between the two graphs is found showing that the velocity field extracted with the CIV analysis corresponds very well to the velocity field using the data directly from the simulations. By computing the deviation σ_u between the velocity fields in Fig. 3 for areas where particles travel in distance between 0.9 and 3.2 of their diameter between two pictures, we found: $\sigma_u = \langle |\mathbf{u_{civ}} - \mathbf{u_{sim}}| / u_{sim} \rangle = 0.19$. The average angle between these vectors of the two velocity fields is $\alpha = \langle | \arccos[(\mathbf{u_{civ}} \cdot \mathbf{u_{sim}})/(u_{civ} u_{sim})] | \rangle = 6.07°$.

III. THEORY AND SIMULATIONS

The numerical model consists of two parts. One part is for the fluid using a continuum description derived from mass conservation and Darcy's law. The second part is for the particle motion using Newton's second law where the net force on a volume element balances its acceleration.

The model has been applied successfully in studies of instabilities of granular flows at low fluid Reynolds numbers $\mathrm{Re} = 2\rho_f u a/\mu$. Here a is the particle radius, μ the viscosity and ρ_f the fluid mass density. The theoretical derivation of the model is given in detail in [7,17–19]. Similar models were developed in [20–22] with a more detailed description of the fluid component.

In the following we will present the main features of the model and explain how to include incompressible fluids. We shall not consider the friction between the particles and restrict the model to two dimensions to keep the model computationally simple. However the friction of the granular flow with the glass plates was found to be essential and had to be included as will be shown in Sec. III D.

A. Dynamics of the fluid-conservation of mass

The fluid description for a compressible and an incompressible fluid is derived from mass conservation and Darcy's law for the fluid velocity through the porous media. A different point of view, starting from the Navier-Stokes equation at small term, and progressively averaging over volumes of various sizes, allows to obtain the same equations. For the sake of completion, this will be developed in the Appendix. It will also allow to obtain the form of various additional terms of small magnitude in the fluid stress, notably those related to the large scale velocity curvature. This approach shows the connection between the current model with the mixture theories sometimes used for fluidized beds or debris flows [23–26].

Here, we will directly use the Darcy law to express the seepage velocity of the fluid through the grains. The local permeability κ is chosen by the Carman-Kozeny relation in the case of air and in the case of water/glycerol and can be written in terms of the local porosity ϕ and the local solid volume fraction $\rho_s = 1 - \phi$,

$$\kappa = \frac{a^2}{9K}\frac{(1-\rho_s)^3}{\rho_s^2} \qquad (9)$$

with a the particle radius and $K=5$ an empirical constant valid for a packing of spherical beads [27].

For the mass conservation of the fluid we can write:

$$\partial_t(\rho_f \phi) + \nabla \cdot (\rho_f \phi \mathbf{v_f}) = 0 \qquad (10)$$

where $\mathbf{v_f}$ is the velocity of the fluid. Similarly for the grains we get

$$\partial_t(1-\phi) + \nabla \cdot [(1-\phi)\mathbf{u}] = 0 \qquad (11)$$

where $\mathbf{u}$ is the velocity of the grains. The velocity of the fluid $\mathbf{v_f}$ has an advective term and a diffusive term. The advective term is caused by the motion of the grains and is equal to the velocity of the grains $\mathbf{u}$. The diffusive term is due to the gradient of the nonhydrostatic part of the pressure P that results in a relative velocity of the fluid to the particles. P corresponds to $P = P' - \rho_f g y'$, where P' is the pressure, g the gravity constant, and y' the depth. With air as an interstitial fluid this diffusive term is described by a local Darcy flow [28,29]. The total velocity $\mathbf{v_f}$ of the fluid is thus the sum of these two terms,

$$\mathbf{v_f} = \mathbf{u} - \frac{\kappa}{\phi\mu}\nabla P, \qquad (12)$$

where μ is the fluid viscosity. Inserting Eq. (12) in Eq. (10) and assuming that the fluid mass density ρ_f is related to the pressure by the ideal gas equation $\rho_f \propto P$ we can write

$$\partial_t(\phi P) + \nabla \cdot \left(\phi P\left[\mathbf{u} - \frac{\kappa}{\phi\mu}\nabla P\right]\right) = 0. \qquad (13)$$

$\partial_t \phi$ is eliminated in Eq. (13) by using Eq. (11) and by a few manipulations a diffusion equation is established for the nonhydrostatic part of the pressure P, the hydraulic head. This equation for the case of air includes fluid compressibility [18,19],

$$\phi\left(\frac{\partial P}{\partial t} + \mathbf{u}\cdot\nabla P\right) = \nabla \cdot \left(P\frac{\kappa}{\mu}\nabla P\right) - P\nabla \cdot \mathbf{u}. \qquad (14)$$

In the case of a viscous incompressible fluid as water/glycerol. The fluid mass density ρ_f is not dependent on the pressure and the hydraulic head can be calculated by a Poisson equation, which we will derive briefly. By adding Eqs. (10) and (11) we get:

$$\nabla \cdot (\phi \mathbf{v_f}) + \nabla \cdot [(1-\phi)\mathbf{u}] = 0. \qquad (15)$$

A fluid flow between two plates results in a tangential stress σ_t between the plates and the liquid. The origin of this stress term is discussed in more detail in the Appendix, Sec. VII.

The tangential stress between the plates and the fluid depends on the fluid viscosity. The increased viscosity in the case of the incompressible fluid makes this tangential stress potentially important. For this reason we will estimate the influence of this tangential stress with the side plates. If we solve Eq. (12) for the pressure gradient we add a contribution

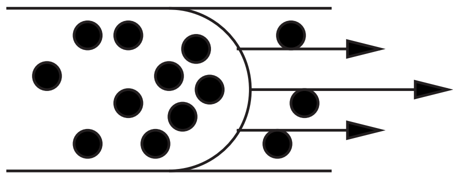

FIG. 5. Assuming a Poiseuille flow, a tangential stress between the plates and the particle fluid flow is deduced. This is a fluid-mediated friction, present even without any interparticle contact or particle-plate contact.

to the pressure gradient due to the tangential stress σ_t between the plates with plate spacing h and the fluid, Eq. (12) gives

$$\nabla P = \frac{\sigma_t}{h} + \frac{\phi\mu}{\kappa}[\mathbf{u} - \mathbf{v_f}]. \tag{16}$$

The stress σ_t between the fluid grain suspension and the glass plates depends on the fluid velocity v_f. The viscosity of this suspension $\mu_{gs}=\mu\phi^{-2.5}$ is obtained by the Einstein approximation [30] for spherical beads [31,32] where the viscosity of the fluid μ is multiplied by $\phi^{-2.5}$. Based on an assumed parabolic flow profile as shown in Fig. 5 the tangential stress on the flow can be calculated,

$$\sigma_t = -\frac{12\mu\phi^{-2.5}\mathbf{v_f}}{h}. \tag{17}$$

Defining $\frac{1}{\kappa_p}=\frac{12\phi^{-2.5}}{h^2}$ we can rewrite Eq. (16),

$$\nabla P = \frac{\phi\mu}{\kappa}\mathbf{u} - \left[\frac{\phi\mu}{\kappa} + \frac{\mu}{\kappa_p}\right]\mathbf{v_f} \tag{18}$$

we define $\frac{1}{\kappa'}=\frac{1}{\kappa}+\frac{1}{\phi\kappa_p}$ and solve for the fluid velocity,

$$\mathbf{v_f} = \frac{\kappa'}{\kappa}\mathbf{u} - \frac{\kappa'}{\phi\mu}\nabla P. \tag{19}$$

With Eq. (15) this results in a Poisson equation for the hydraulic head P,

$$\nabla \cdot \left(\frac{\kappa'}{\mu}\nabla P\right) = \nabla \cdot \left[\mathbf{u}\left(1 - \phi + \frac{\kappa'}{\kappa}\phi\right)\right], \tag{20}$$

If we compare $f=\frac{\kappa}{\phi\kappa_p}$ we find for the maximum solid fraction $\rho_s=0.6$ $f=0.0057$ for the minimum solid fraction of $\rho_s=0.15$ we find $f=0.063$. Under this conditions we can neglect the effect of the plates on the mass conservation part of the model and Eq. (18) reduces to Darcy's law, Eq. (12). For air, this reasoning leads to even smaller values of f, i.e., the correction due to the fluid coupling to the plates is even smaller, which justifies the use of Darcy's law. With incompressible fluid, Eq. (20) thus reduces to

$$\nabla \cdot \left(\frac{\kappa}{\mu}\nabla P\right) = \nabla \cdot \mathbf{u} \tag{21}$$

for water/glycerol.

Although we can neglect the stress σ_t in this part in Sec. III B σ_t contributes to the net force in Newton's second law. It has to be mentioned that the Carman-Kozeny relation is a relation where the solid volume fraction is considered as the volume fraction of a three-dimensional (3D) packing of spheres. In our simulation we consider the particles as cylinders with the base area $S_a=\pi a^2$ given by the particle radius and the height of the plate spacing h. The plate spacing of 1mm allows approximately ten particles to be placed along the normal direction, i.e., our cylinder represents ten particles in height. For this reason we multiply the solid fraction of the cylinders by a factor of 2/3 which is the solid fraction ratio between a randomly close packing of spheres to a randomly close packing of cylinders. The effect of this is to have the close packed solid fraction in 2D represent the close packed solid fraction in 3D.

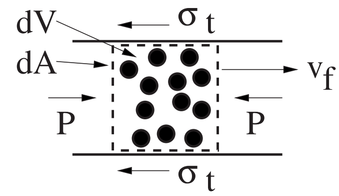

FIG. 6. Stress and pressure acting on the surface dA of a unit volume dV.

Furthermore the Carman-Kozeny relation is not valid for solid fractions below 0.15, therefore we use 0.15 as a cutoff in Eq. (9), any zone less dense is represented with a permeability corresponding to $\rho_s=0.15$. Such cutoff is also required numerically to avoid singularities during the solution of the differential Eq. (14) and (21) for the hydraulic head [18]. It effectively results in a code that rapidly homogenizes the pressure over zones with small solid fractions, which is physically sound.

B. Dynamics of the particles—Newton's second law

The movement of the particles under the effect of a fluid is subjected to buoyancy forces due to the mass density of the fluid ρ_f. To calculate the gravitational force we replace the mass density of the particles ρ_m with the effective mass density $\rho_{eff}=\rho_m-\rho_f$.

In a unit volume dV with surface dA the particle mass accounts to $\rho_m\rho_s dV$ and the fluid mass to $\rho_f\phi dV$ and we can write down the force equation in the following way:

$$\rho_m\rho_s dV\frac{d\mathbf{u}}{dt} + \rho_f\phi dV\frac{d\mathbf{v_f}}{dt} = \rho_{eff}\rho_s dV\mathbf{g} + \sum \mathbf{F_I} - \int P d\mathbf{A} + \int \sigma_t dA + \mathbf{F}_\gamma. \tag{22}$$

using $\mathbf{F_I}$ as the interparticle force, $\mathbf{g}$ is the acceleration of the gravitation and $\mathbf{F}_\gamma$ accounts for the frictional forces and energy dissipation as will be specified further in Sec. III D. We also have to integrate the pressure and stress that is acting on the surface of this unit volume as shown in Fig. 6.

To simplify Eq. (22) we will justify in Sec. III C that the particles are small enough to move approximately with the fluid in a Lagrangian way. Under this conditions we can approximate the fluid velocity acceleration by the particle acceleration for the inertial term in the left hand side of Eq. (22),

$$\frac{d\mathbf{u}}{dt} \approx \frac{d\mathbf{v_f}}{dt} \tag{23}$$

and Eq. (22) results in

$$[\rho_m\rho_s dV + \rho_f \phi dV]\frac{d\mathbf{u}}{dt} = \rho_{eff}\rho_s dV\mathbf{g} + \sum \mathbf{F_I} - \int \nabla P dV + \int \sigma_t dA + \mathbf{F}_\gamma. \tag{24}$$

Note that this approximation only affects the description of the fluid inertia, and not the drag force from the fluid on the particles. For a single particle of mass $m=\rho_m \pi a^2 h$, volume $V_a = \pi a^2 h$ and plate spacing h we can define the number density $\rho_n = \rho_s \rho_m / m$ and use in Eq. (24) the unit volume $dV = 1/\rho_n$,

$$\left[m + \rho_f \frac{\phi}{\rho_n}\right]\frac{dv_p}{dt} = \rho_{eff} V_a \mathbf{g} + \mathbf{F_I} - \frac{\nabla P}{\rho_n} + \frac{\sigma_t S_a}{\rho_s} + \mathbf{F}_{\gamma_\mathbf{p}}. \tag{25}$$

This is the force equation for each single particle with the velocity v_p. The mass of the fluid appears in the first term of this equation and is simply added to the mass of a particle. The amount of mass from the fluid that we add to the mass of each particle depends on the local porosity divided by the number density. This allows to incorporate the fluid inertia to the model, by changing the particle mass into a fluid-coated particle mass.

The interparticle force $\mathbf{F_I}$ is set to be a linear force with a spring constant k. The strength of this force is proportional to the overlap of the particles d and the direction of this force is given by the unit vector $\mathbf{n_d}$ which points from the center of the respective bead to the contact point. We choose the spring constant k strong enough, so that our particles are approximately hard spheres. That means that the overlap of the particles that occur during the simulations are a negligible fraction of their distance.

$$\mathbf{F_I}(d) = -kd\mathbf{n_d}. \tag{26}$$

The particle propagation is modeled by the velocity verlet scheme [33].

C. Fluid velocity relative to the particles

To justify our simplification in Eq. (22) we compare the relative velocity between the grains and the fluid $v_d = \frac{\kappa}{\phi\mu}\nabla P$ with the absolute velocity of the grains $\mathbf{u}$. Moreover, the acceleration of the fluid relative to the particles is compared to the absolute acceleration of the particles. For this test we study two systems. First is the system that we use for the comparison with the experiments. In this system the fluid mass is added to the grains and the friction with the plates due to the tangential stress σ_t is taken into account. Furthermore we test a second system where the fluid mass density ρ_f in Eq. (22) is set to zero and the friction due to the tangential stress σ_t is not taken into account. Such a system has a larger mass density contrast between the fluid and the particles. Consequently the difference between the accelera-

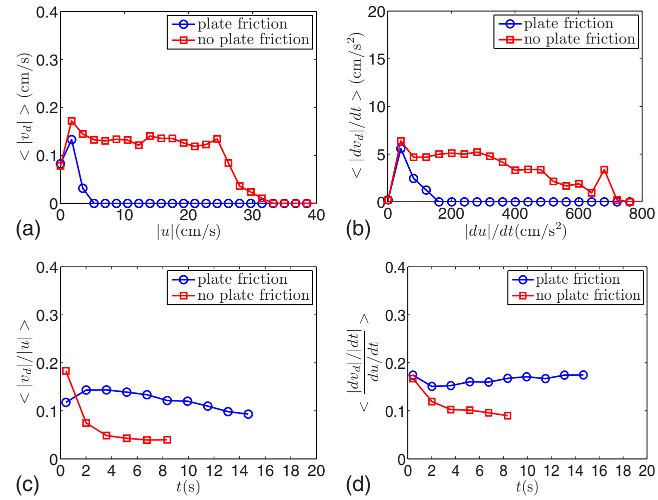

FIG. 7. (Color online) Comparison of the relative to the grains acceleration and relative to the grains velocity of the fluid to the absolute acceleration and absolute velocity of the grains. A system with plate friction due to a Poiseuille flow and added fluid mass to the particles (blue curves with circles) is compared to a system without friction due to a Poiseuille flow and without added fluid mass (red curves with squares).

tion of the grains and the fluid must be larger than in our case with $\rho_f = 1.065$ g/cm^3 where the mass density of the fluid is closer to the mass density of the grains. Obviously, for smaller mass densities of the particles relative to the fluid density, the particles are dragged more easily along with the fluid. The results of this comparison are shown in Fig. 7 in the blue curves (marked with circles) for the first system and for the red curves (marked with squares) for the second system. In Figs. 7(a) and 7(b) the plots are averaged in time over the whole simulations. These plots show for the two tested systems that the relative fluid acceleration is small compared to the total fluid acceleration and also that the relative fluid velocity is small compared to the absolute fluid velocity. It should be emphasized that the relative fluid velocity becomes a smaller and smaller fraction of the absolute fluid velocity the higher the absolute fluid velocity gets in Fig. 7(a). This also holds for the acceleration as shown in Fig. 7(b). This means that the more inertia is connected to the grains and fluid flow, the better our approximation in Eq. (23) holds. At low accelerations and granular velocities this approximation becomes less accurate but at the same time the contribution in Eq. (24) due to the acceleration: $[\rho_m\rho_s dV + \rho_f \phi V]\frac{d\mathbf{u}}{dt}$ and due to the velocity: σ_t are getting less important.

The evolution in time of the fraction between the relative fluid velocity and the absolute grain velocity is shown in Fig. 7(c) and between the relative fluid acceleration and the absolute grain acceleration is shown in Fig. 7(d). The fraction of the acceleration was averaged over all absolute grain accelerations larger than $\frac{d\mathbf{u}}{dt} \geq 20$ cm/s^2 as a cutoff which is 2% of the gravitational acceleration.

For the velocity we only averaged over values where the absolute grain velocity was larger than $\mathbf{u} \geq 1$ cm/s, at this velocity the tangential stress arising from coupling with the plates σ_t has a significant contribution of 18% of the gravi-

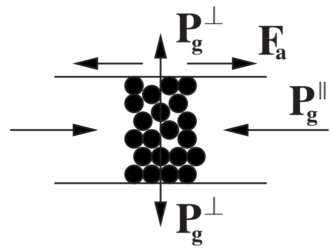

FIG. 8. The Janssen effect: the in-plane $P_g^{\parallel}$ stress is being deflected by the particles resulting in a normal stress $P_g^{\perp}$ on the plates.

tational acceleration. The check of the velocity and the acceleration differences between the grains and the fluid reveals that the fluid is largely accelerated in the same way as the grains and the difference in acceleration is less than 20% even though we examined a system with a larger density contrast between the grain and the fluid mass density than what we have in our water/glycerol solution. In the plots 8(a) and 8(b) we notice that the plate friction reduces the absolute grain velocity significantly. In the blue graph (marked with circles) in Fig. 7(a), maximum grain velocities are 5 cm/s which makes inertia effects less important than in the system without plate friction.

D. Solid friction forces

In addition to the friction between the fluid and the plates we also consider the friction between the glass plates and the particles according to the normal stress $P_g^{\perp}$ in form of a Coulomb friction model into account. It is most active in the top section and the sediments where we find not moving compacted particles. This mechanism prevents the top section of compacted particles from getting unstable and falling toward one side of the cell as a whole due to a small initial perturbation in the thickness of this layer of beads that inflates rapidly without the friction between the grains and the plates as a opposing force. Here the normal stress of the particles onto the plates is derived by assuming a local Janssen hypothesis (see Fig. 8). The average in-plane stress tensor $\langle\sigma_{ij}^{\parallel}\rangle$ exerted over a particle with index a in contact with a set C_a of particles b is obtained as [17,34]

$$\langle\sigma_{ij}^{\parallel}\rangle = \frac{1}{V_a}\sum_{b\in C_a} x_i^b f_j^b \tag{27}$$

x^b is the position of the contact with grain b, f^b the contact force between the particle a and b and i,j are Cartesian indices. $V_a=\pi a^2 h$ is the particles volume which is described by a cylinder for a plate spacing h. Equation (27) can be proven in the following way. Using the integral theorem of Gauss and replacing the sum over the surface of one particle in Eq. (27) by the surface integral over the surface of the particle and applying the Einstein sum convention we get

$$\oint x_i\sigma_{kj}^{\parallel}n_k dA = \int_{V_a}\nabla_k(x_i\sigma_{kj}^{\parallel})dV = \int_{V_a}[(\nabla_k x_i)\sigma_{kj}^{\parallel} + (\nabla_k\sigma_{kj}^{\parallel})x_i]dV. \tag{28}$$

In the top section and the sediments where particles are compressed and the Janssen effect is primarily active particles are in a quasistatic state. In this case inertial terms are negligible in front of contact forces, so that internal force balance holds: $\nabla_k\sigma_{kj}^{\parallel}=0$ [35]. In Eq. (28) we can write

$$\oint x_i\sigma_{kj}^{\parallel}n_k dA = \int_{V_a}\delta_{ki}\sigma_{kj}^{\parallel}dV = V_a\langle\sigma_{ij}^{\parallel}\rangle \tag{29}$$

and proof Eq. (27). Taking the trace of the stress tensor in Eq. (27) we get the magnitude of the in-plane stress as: $P_a^{\parallel}=-(\langle\sigma_{11}^{\parallel}\rangle+\langle\sigma_{22}^{\parallel}\rangle)/2$. According to the Janssen hypothesis the normal stress is proportional to the in-plane stress by a factor λ. With a Coulomb friction model we get that the frictional force F_a per particle is proportional to the normal stress by a friction coefficient γ. The factor 2 accounts for the glass plates on each side of the particle.

$$F_a \leq 2\gamma S_a P_g^{\perp} = 2\gamma\lambda S_a P_g^{\parallel} \tag{30}$$

This results in finding a value for $\gamma\cdot\lambda$. To get an estimate of γ we performed some basic experiments. In these experiments a layer of beads was glued to the underpart of a weight, which is placed on a glass plate. Lifting one side of the glass plate we increase the angle of inclination α gradually and measure the maximum angle α_s before the weight with the beads underneath starts to slide. We repeated this experiment under water and got in both cases for the constant $\gamma=\tan(\alpha_s)\approx 0.22$. For λ we know that it has to be smaller than 1 since the normal stress resulting from the Janssen effect can only be as large as the in-plane stress. With this idea for the range of the values we chose the constant $\gamma\lambda=0.07$ for the case of water/glycerol and $\gamma\lambda=0.042$ in the case of air. These values were fine tuned by fitting the propagation speed of the interface between the top layer and the dynamic zone in the simulation to the experimental results. We also tried $\gamma\lambda=0.07$ for the case of air with the result, that the simulations differed slightly more from the experiments. However the characteristics of the velocity field distributions remained unchanged.

We also include energy dissipation if particles collide [8]. This is done by introducing a viscous force negative proportional to the relative velocity of the particles $\mathbf{v_r}$ projected on the unit vector $\mathbf{n_d}$, which points from the center of one particle to the contact point. The direction of this force is given by the unit vector $\mathbf{n_d}$:

$$\mathbf{F_d} = -\gamma_d(\mathbf{v_r}\cdot\mathbf{n_d})\mathbf{n_d}. \tag{31}$$

For the simulations it is important to have energy dissipation of more than 20% for each collision. From energy dissipation of 20% upward the evolution of the simulations does not change noticeable. For energy dissipation under 20% and less, increasing perturbations are observed as shown in [8]. The factor γ_d was chosen to simulate a energy dissipation of more than 20% of the energy for each collision with a restitution coefficient of 0.55. These two mechanisms result in the force F_γ in Eq. (25).

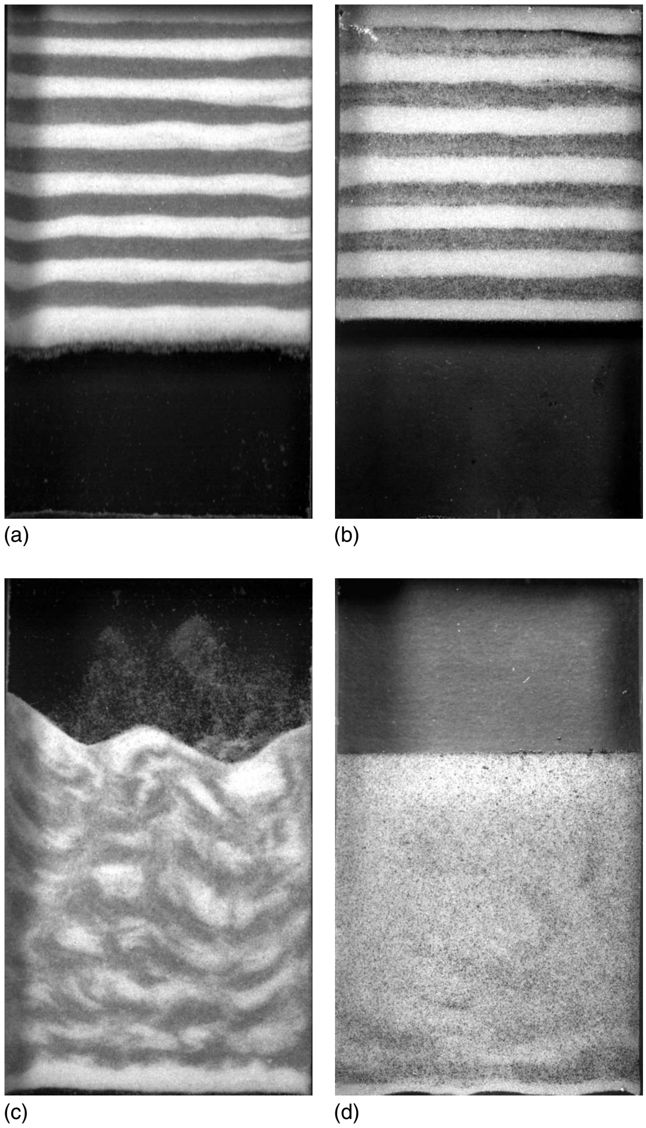

FIG. 9. Experiments showing different sedimentation patterns for the cases of air and water/glycerol.

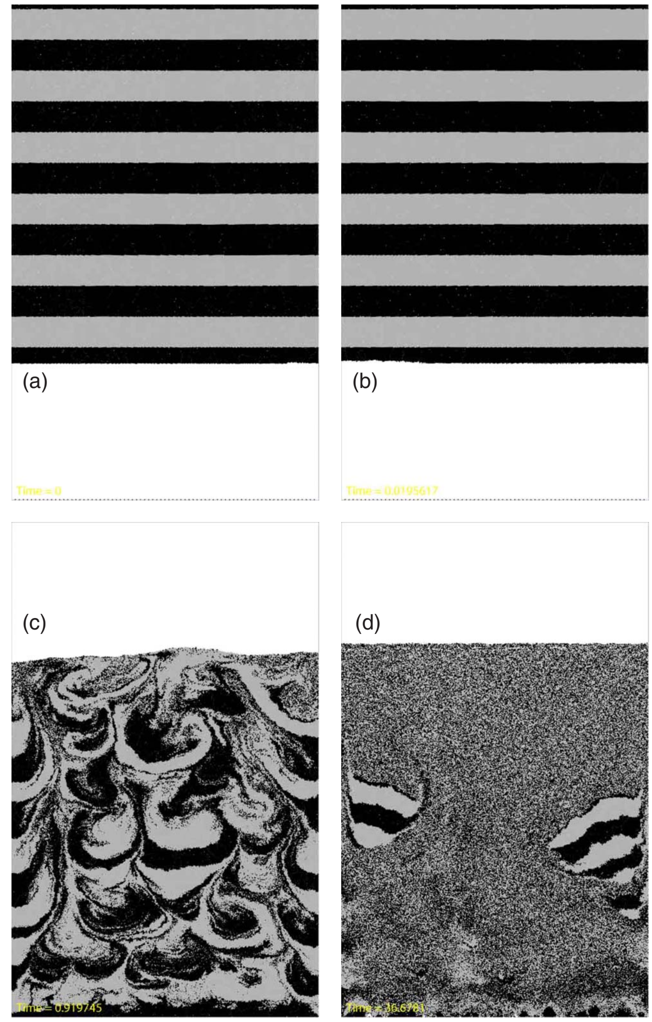

FIG. 10. (Color online) Simulations showing different sedimentation patterns for the cases of air and water/glycerol.

IV. RESULTS AND COMPARISON BETWEEN EXPERIMENTS AND SIMULATIONS

To illustrate the difference between experiments with water/glycerol and experiments with air we performed two experiments shown in Fig. 9 and two simulations shown in Fig. 10, for the two studied cases of grains with air and grains with water/glycerol.

At the start of the experiments and simulations [pictures (a) and (b) of Figs. 9 and 10] we have aligned particles with different colors at the top of a cell.

By comparison of the resulting sedimentation patterns after the experiments and simulations [pictures (c) and (d) in Figs. 9 and 10] are finished we already get a clear distinction between the two cases of air and water/glycerol. While in the case of air the structure of the initial layers of colored particles survives, we observe a complete mixing in the case of water/glycerol, apart from two chunks remaining lowly perturbed, in the case of the simulations. Such chunks have also been observed in following experiments. The reason why none of these lowly perturbated areas occurred in the samples confining particles deposited in layers, lies to some extent in the preparation procedure of these samples, which always were the first in a series of experiments. Creating a sample with layers meant to move the cell from where it was filled to the mounting where it was exposed to additional stress from clamps. This resulted in a slightly higher compaction of the cell which increased the normal stress on the particles that resulted in a higher friction of the particles with the glass plates. For analyzing purpose only following experiments were used where the sample remained in the mounting under constant stress from the clamps.

Analysis

In our experiments we chose the viscosity of the water/glycerol mixture in a way that the Reynolds number with respect to the plate spacing Re_h during the experiments was sufficient small to assume laminar flow. Typically the Reynolds number was less than $\mathrm{Re}_h \leq 5$ during the experiments with water/glycerol, and less than $\mathrm{Re}_h \leq 10$ in the case of air.

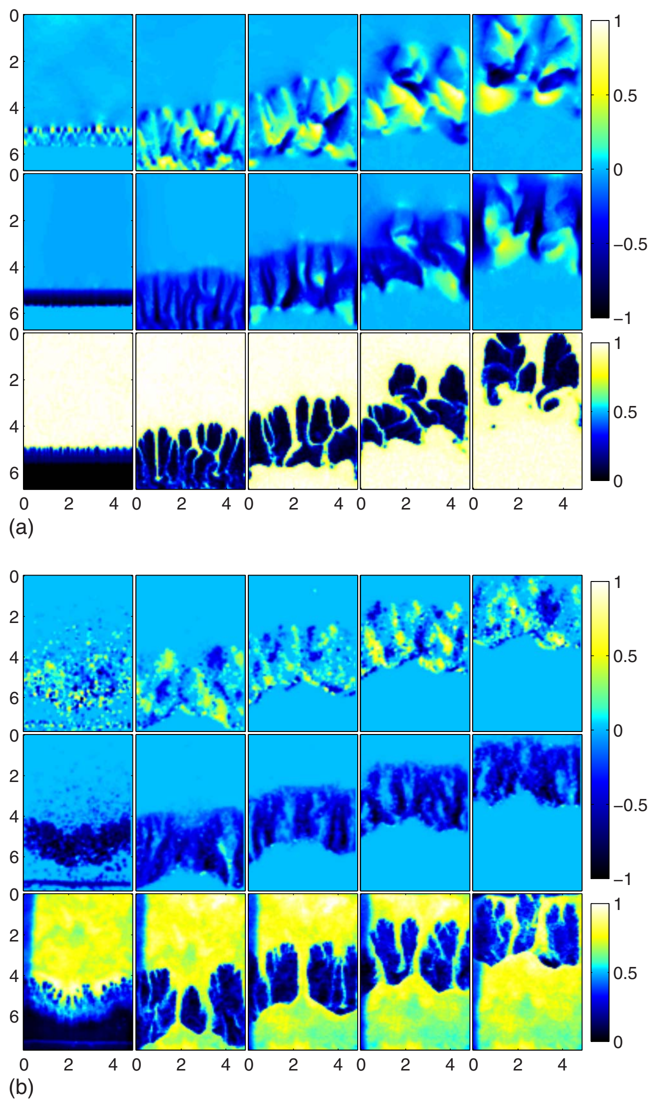

FIG. 11. (Color online) The three rows in figure (a) and (b) show the time evolution of the simulations (a) and experiments (b) with air from left to right at times $t=0.05$ s, $t=0.19$ s, $t=0.36$ s, $t=0.46$ s, and $t=0.6$ s. From top to bottom the rows illustrate the $u_x/\max(|u_x|)$ component and the $u_y/\max(|u_y|)$ component of the grain velocity vector field and the bottom row shows the density field $\rho_d/\max(\rho_d)$. All quantities have been normalized by its maximum absolute value.

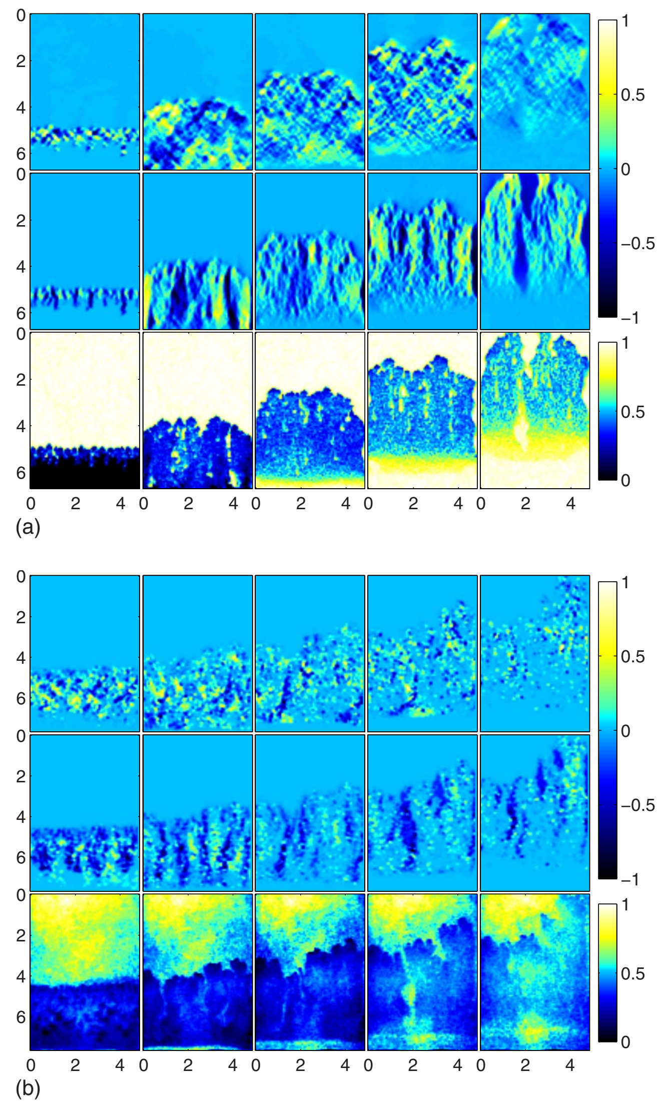

FIG. 12. (Color online) The three rows in figure (a) and (b) show the time evolution of the simulations (a) and experiments (b) with water/glycerol from left to right at times $t=0.8$ s, $t=4.6$ s, $t=8.4$ s, $t=12.2$ s, and $t=16.0$ s. From top to bottom the rows illustrate the $u_x/\max(|u_x|)$ component and the $u_y/\max(|u_y|)$ component of the grain velocity vector field and the bottom row shows the density field $\rho_d/\max(\rho_d)$. All quantities have been normalized by its maximum absolute value.

In the sequence of pictures in Fig. 11 simulations are compared with experiments and the evolution of the granular velocity field **u** and the density field ρ_d is shown for the case of air. From left to right time is progressing in equal steps from 0.05 to 0.6 s after the cell has been flipped. In the sequence of pictures in Fig. 12 the evolution of the simulations and experiments for water/glycerol is shown in the same way, except that here the time runs from 0.8 to 16.8 s after the cell has been flipped.

In this Figs. 11 and 12 we show color maps in the three rows from top to bottom of the x component, the y component of the velocity field **u** and the particle density field ρ_d. The velocity fields are calculated after the procedure described in Sec. II. The density field is in the case of the simulation directly accessible whereas for the experiments we estimated the density field from the pixel gray values in the pictures. This provides a good estimate for air where a large contrast between bubbles of low particle density and fingers of high particle density exists. However, for water/glycerol the particle density is more smeared out and the gray value of the pixels is a less good estimate of the density. In this case of the experiment of water/glycerol we will focus on the velocity data. All the quantities in the Figs. 11 and 12 have been normalized to one simply by dividing by the maximum absolute value. For air as well as for water/glycerol the lower part of the cell is filled with sediments. On top of the sediments appears a second zone with moving particles. In this zone fingers of high particle density are falling down. Even further toward the top of the cell particles are still compacted and hardly moving. But in these two sequences a major difference can also be observed. In the case of air it appears that most of the downward-falling particles are part of fingers moving from the top to the bottom of the cell. In this case of air we have clearly defined bubbles of low particle density, that have a large density contrast to the fingers of high particle density. For water/glycerol this is not the case and this strong contrast does not appear. Here the density is more smeared out and the areas between the downward-falling fingers are filled with particles moving upward together with the fluid making the downward-falling fingers less visible.

Velocity field histograms

To compare the experiments with the simulations and to quantify our observations we calculate the velocity field histograms of the x and y component of the velocity field u_x and u_y divided by the average absolute value of the velocity u_a as defined in Eq. (8). This compensates, that the camera records better the particles close to the glass walls. The result of the corresponding histograms for the sequence of pictures in the air case displayed in Fig. 11 are shown in Fig. 13 and for the water/glycerol case from Fig. 12 the corresponding histograms are shown in Fig. 14. In the histograms it was averaged over three experiments and three simulations resulting in the error bars.

We plotted all the graphs in a semi log plot and good agreement between the simulations and the experiments can be observed. Looking first at the similarities between the case of water/glycerol and air, we find that the histograms for the y component of the velocity field u_y are not symmetric showing that there are more areas where particles are moving down than up. In the contrast to the histograms of the y component the histograms of the x component of the velocity field u_x are symmetric and following an exponential distribution.

Apart from the similarities in the histograms two differences of the histograms in the case of air and water/glycerol give reason why the observed mixing behavior is so different as shown in Figs. 9 and 10. First the x- and y-velocity component histograms for the case of water/glycerol are more wide distributed compared to the case of air. Second if we compare the positive branch of the y-velocity component histograms we can see that in the case of air we have much less particles moving upward than in the case of water/glycerol. All these points show that a better mixing of the beads in the case of water/glycerol is observed.

In Fig. 13 where the cell is filled with air the positive branch of the y component of the velocity field shows a wider distribution in the case of simulations than in the case of the experiments. A possible reason for this is that we do not take friction between the particles into account. This causes in the simulations that sediments in some regions were moving upward while for the experiments the sediments were less mobile due to the friction between the particles. It is also possible to see, that the difference between the simulations and the experiments of this positive branch of the y component of the velocity field is getting larger with time, as more sediments have accumulated.

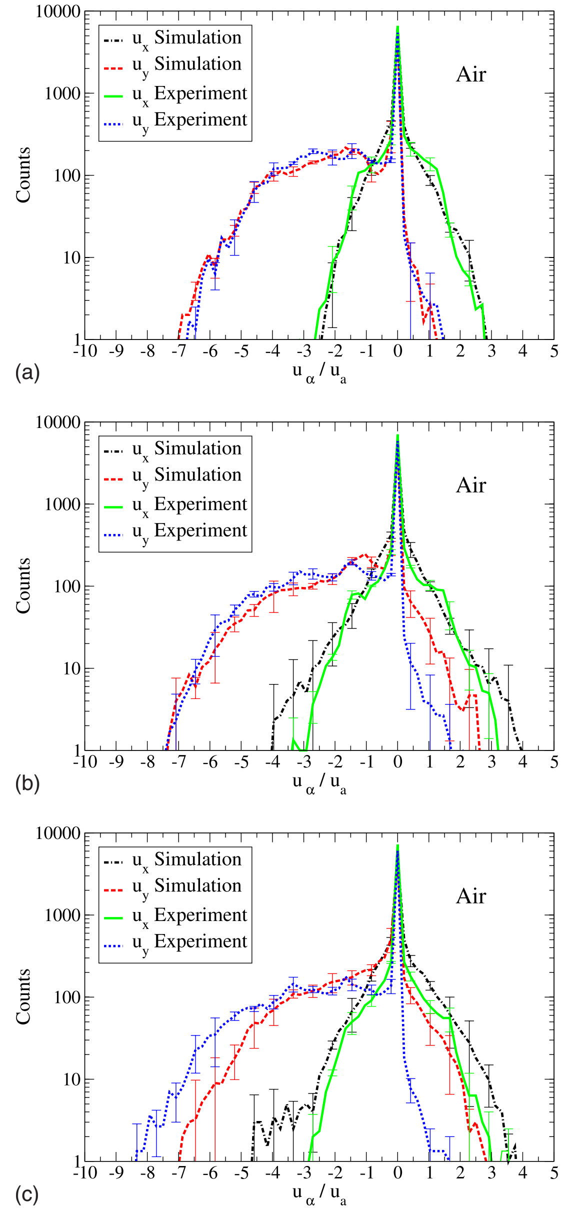

FIG. 13. (Color online) Histograms of the x and y component α of the velocity field after 0.2, 0.3, and 0.5 s from top to bottom in the case of air. The histograms show good agreement between simulations and experiments.

Autocorrelations

A way to quantify the size of the dynamic patterns is to calculate the autocorrelation function in 2D $C_\alpha(\mathbf{d})$ where $\alpha = x$, or y the x, or y component of the velocity field $\mathbf{u}(i,j)$,

$$C_\alpha(\mathbf{d}) = \frac{\sum_{\mathbf{r}} \{[u_\alpha(\mathbf{r}) - \langle u_\alpha\rangle][u_\alpha(\mathbf{r}+\mathbf{d}) - \langle u_\alpha\rangle]\}}{\sum_{\mathbf{r}} [u_\alpha(\mathbf{r}) - \langle u_\alpha\rangle]^2}. \quad (32)$$

In this equation the autocorrelation function is normalized by the standard deviation.

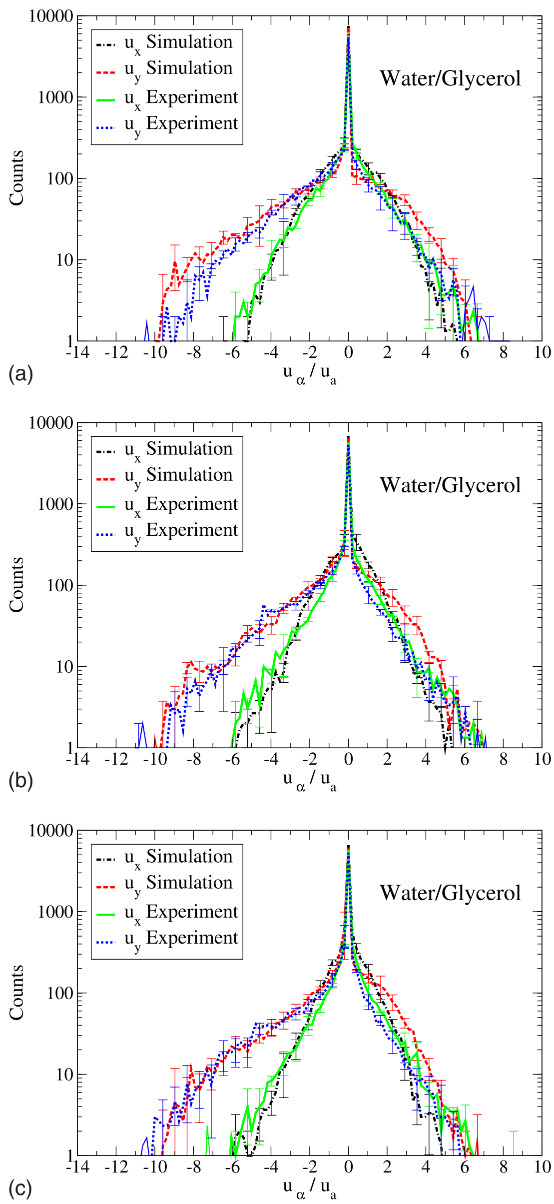

FIG. 14. (Color online) Histograms of the x and y component α of the velocity field after 6, 10, and 15 s from top to bottom in the case of water/glycerol. The histograms show good agreement between simulations and experiments.

The autocorrelation in 2D is shown in Fig. 15 for air and water/glycerol for corresponding time steps to Figs. 11 and 12. The figures in Fig. 15 demonstrate 2D autocorrelation functions of simulations in part (a) and (c) and of experiments in part (b) (d). The first row of these plots is the 2D autocorrelation function of the u_x component of the velocity field and the second row the u_y component of the velocity field with time progressing in equal steps from left to right.

In both cases the autocorrelation of the u_y component shows periodic vertical lines of stronger correlation directed along the y axis in contrast to the autocorrelation of the u_x component of the velocity field which shows equal distribution along the x and the y axis.

The difference between the example of air as a compressible and water/glycerol as an incompressible fluid are more pronounced in the figures for the u_y component of the velocity field. In these figures we can observe, that in the case of water/glycerol the periodic vertical lines of stronger correlation are thinner in x direction than in the case of air where these lines take an elliptical shape to the end of the experiments and the simulations.

With time progressing we observe that the frequency of these lines decreases in both cases. This reflects the coarsening process of the structures which we further investigate in Sec. IV. The plots show, that the simulations and the experiments lead to very similar behavior in terms of the autocorrelation field.

Mean wave number

The temporal evolution of the periodic structures can be measured by performing a Fourier analysis of both components of the velocity field $\mathbf{u}$ and the density field ρ_d. Since the density field is not accessible directly in the experiments we will use the pixel gray values instead. This approximation is a good estimate in the case of air where we have a large density contrast between the empty bubbles and the downward-falling fingers. However this approximation is a less good estimate in the case of the experiment with water/glycerol in Fig. 16(d), where the density of the particles is more smeared out and the pixel gray value does not correspond well to the density of the particles.

In this case we are forced to resort to the velocity data only and display the average wave number of the density field for completeness. The average wave number is calculated in the following procedure. For each horizontal line j of the velocity field components $u_{\alpha_j}-\langle u_{\alpha_j}\rangle$ or the density field minus the average $\rho_{d_j}-\langle \rho_{d_j}\rangle$ the power spectra $S_j(k)$ is calculated using a Hamming data window. Taking the average of these power spectra results in a single power spectrum $\bar{S}(k)$ as a function of the Fourier modes k. From this distribution the average wave number $\langle k\rangle$ and the standard deviation σ_k can be calculated by

$$\langle k\rangle = \frac{\sum k\bar{S}(k)}{\sum \bar{S}(k)}, \tag{33}$$

$$\sigma_k = \sqrt{\frac{\sum k^2\bar{S}(k)}{\sum \bar{S}(k)} - \langle k\rangle^2}. \tag{34}$$

The two measures are evaluated for the whole cell below the upper surface to avoid contributions apart from the sediments and the bulk. Figure 16 shows $\langle k\rangle$ as a function of time for the x- and y-velocity field component and the density field for air and water/glycerol. The error bars are the result from averaging over three different experiments and simulations. In the simulations for air and water/glycerol we observe that the wave number decreases during the first quarter of the total time. This coarsening is less pronounced in the experiments because the initial patterns are strongly perturbated by the rotation of the cell and the initial front contained some minor perturbations. After the first quarter a stable average wave number is achieved with air and with water/

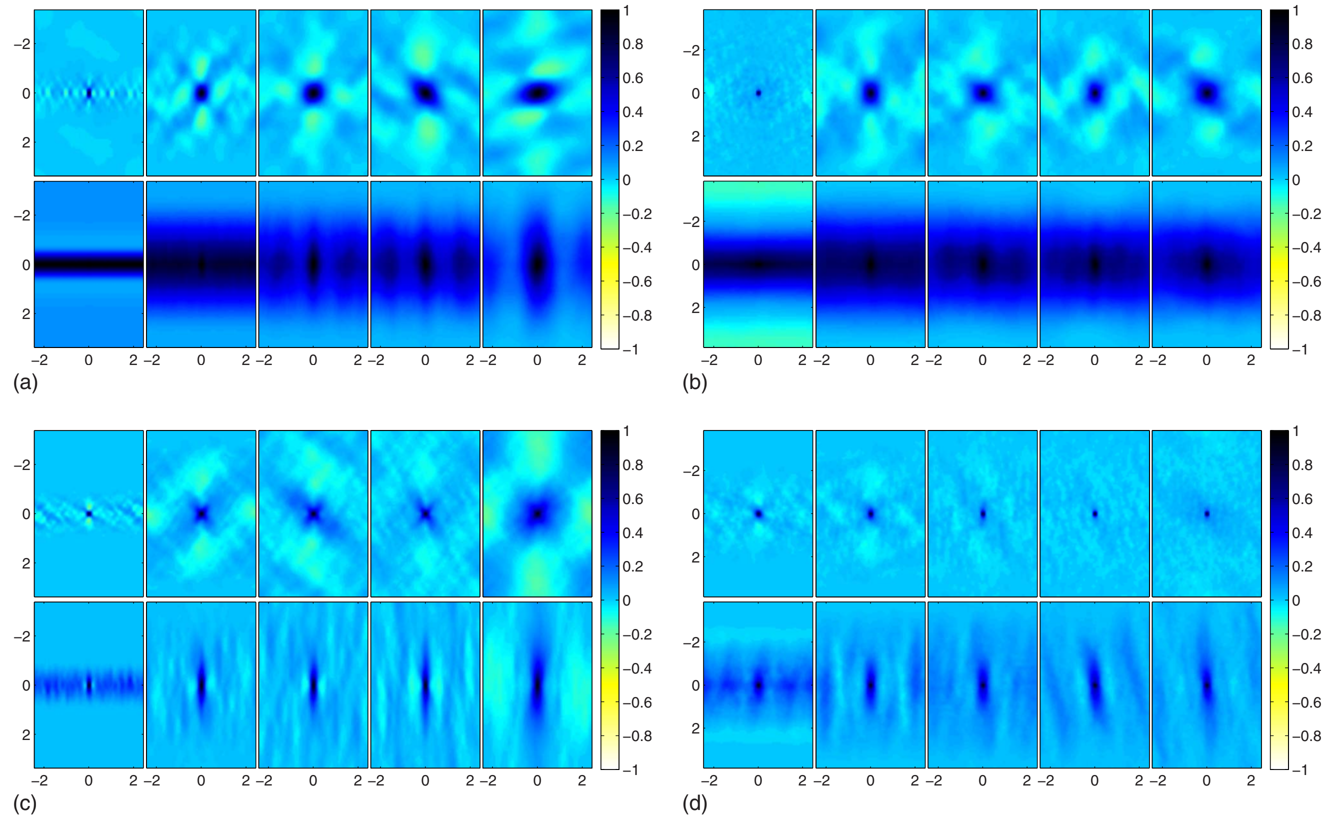

FIG. 15. (Color online) In the first rows a time sequence of the normalized autocorrelation of the x component of the velocity field $C_x(\mathbf{d})$ is shown with $\mathbf{d}=\binom{x}{y}$. The second rows show a time sequence of the normalized autocorrelation of the y component of the velocity field $C_y(\mathbf{d})$. In figure (a) and (b) simulations and experiments with grains and air are presented. Simulations and experiments with grains and water/glycerol are shown in the figures (c) and (d). The time steps from left to right correspond to Figs. 11 and 12.

glycerol. Simulations and experiments result in similar stable average wave number. This average wave number lies around two times higher in the case of water/glycerol than in the case of air.

The figures for the standard deviation of air and water/glycerol in Fig. 17 show after the first quarter of total time, that the values for water/glycerol are roughly 1.5 times higher than for air. This is the case for both simulations and experiments. The higher values for the standard deviation indicate a wider distribution of the modes in the experiments and simulation with water/glycerol.

V. PHYSICAL INTERPRETATION OF THE MIXING BEHAVIOR AS FUNCTION OF THE NATURE OF THE INTERSTITIAL FLUID

To understand the different mixing behavior of the particles in air and water/glycerol we will compare the strength of the particle interaction force through the fluid to the gravitational force. As a first measure we determine if the particles reach terminal velocity. At terminal velocity the force on the particles by the fluid balances the gravitation.

In Fig. 18 the averaged velocity y component multiplied by the fluid viscosity is plotted for the first ten lowest particles until the first particles collide with the base of the cell. Figure 18 shows that the particles in air accelerate continuously and do not reach terminal velocity before collision with the base of the cell. On contrary, in water/glycerol the particle reach a characteristic terminal velocity in a very short distance compared to the cell size. In the progress some of the particles in water/glycerol begin to move upward and the average particle velocity in water/glycerol decreases.

The acceleration related to the fluid drag can be calculated in the simulations from the pressure field: $\mathbf{a_f}=\nabla P/(\rho_s\rho_m)$. Plotting $\mathbf{a_f}$ in Fig. 19 shows that in water/glycerol the fluid acceleration is comparable and balances the gravitational acceleration of $a_g=9.81\ \mathrm{m/s^2}$. In air the fluid forces are increasing as the velocity of the particles increase but never reach the strength of the gravitational acceleration. This also shows that the particles in air collide with the base of the cell before reaching terminal velocity.

As an explanation for the different mixing behavior we shall analyze the fluid velocity field $v_f(r,\theta)$ around a falling particle of radius a and velocity v_p at position (r,θ) in polar coordinates in 2D (because of the plates). Typical solutions of the Stokes equation for a falling sphere or cylinder show that the fluid velocity induced by the motion of this single particle in an otherwise open environment is proportional to the velocity of the particle

$$v_f(r,\theta)=v_p f(r,\theta), \tag{35}$$

where f is a function independent of the viscosity that accounts for the given geometry. In this case the drag force on

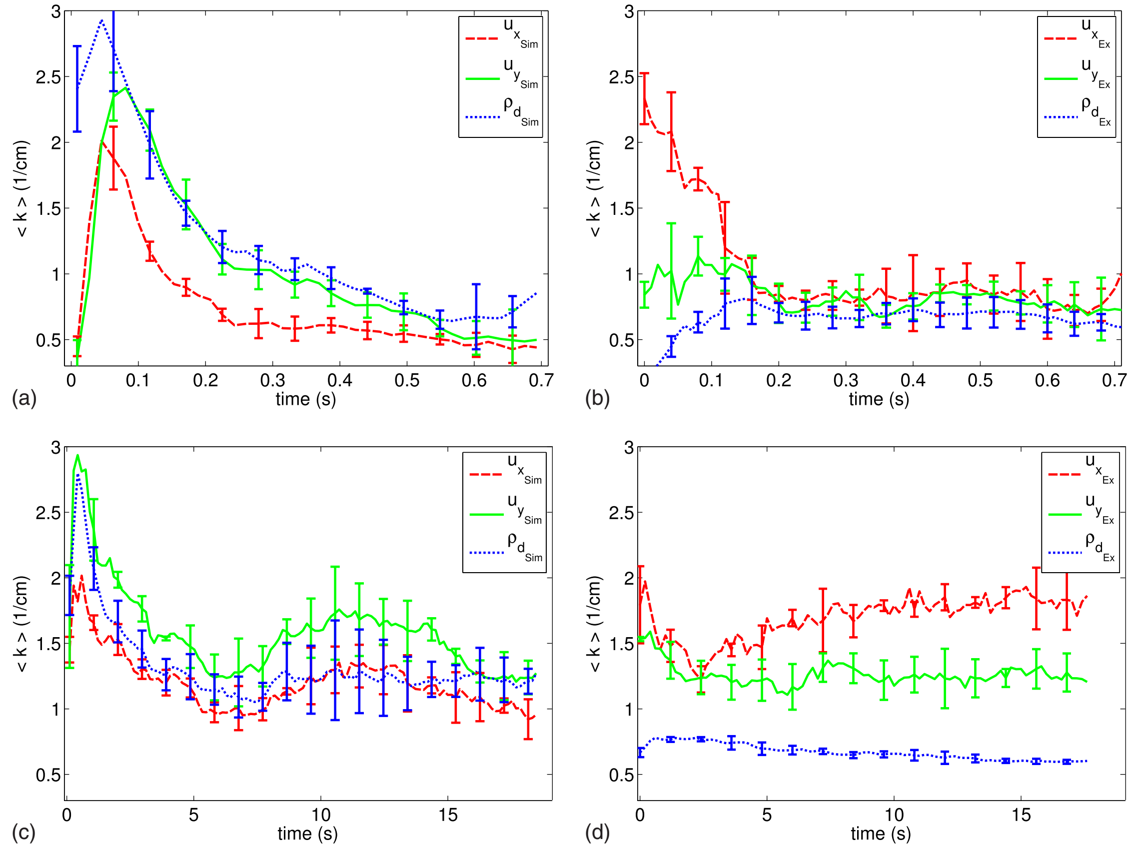

FIG. 16. (Color online) The average wave number $\langle k \rangle$ as a function of time for air and water/glycerol for the velocity field **u** and the density field ρ_d.

the particle is proportional to the viscosity and has the form,

$$F_d = \alpha \mu v_p, \tag{36}$$

where α is a constant of the magnitude of the particle size. Given such a drag force the particle will reach a characteristic terminal velocity of

$$v_t = mg/(\alpha\mu). \tag{37}$$

This follows through Newton's second law. The flow field of the falling particle exerts a force on neighboring particles. Using the hydrodynamic doublet approximation [36], this force on a second particle at rest and at position (r,θ) can be calculated by using Eq. (35) in Eq. (36),

$$F_h = \alpha\mu v_f = \alpha\mu v_p f(r,\theta) = mg\frac{v_p}{v_t} f(r,\theta). \tag{38}$$

At terminal velocity $v_p/v_t=1$ and the viscosity dependence cancels out. Once this is reached, the interaction force between the particles has a typical strength independent of the viscosity μ as shown in Eq. (38). However the particles in air do not reach terminal velocity $v_p/v_t<1$ and the fluid interaction strength between the particles is weaker than in water/glycerol. This means that in the dilute region in air the dynamics of the particles are primarily governed by the gravitation force and less by the fluid force. The gravitation is invariant in time and invariant at each position in the cell, which has the effect that the mixing of the particles in air is small. The direction and strength of the fluid force on the other hand depends on time and on the constellation and the velocities of all particles. For each particle trajectory in the cell the fluid force is therefore different. In contrast to the system with air, the fluid force in water/glycerol is larger and comparable to the gravitation because the particles in water/glycerol reach terminal velocity. The contribution of the fluid force to the total force on the particles in water/glycerol becomes significantly stronger. Hence the direction of the total force in water/glycerol becomes random and can even cause particles to move upward. This causes a better mixing of the particles.

Summarizing, the mixing of the particles is strongly dependent whether terminal velocity is reached or not. At terminal velocity the interaction strength between the particles due to the fluid has the same strength independent of the fluid viscosity. And finally, after terminal velocity is reached the time during the particles are exposed to the fluid interaction forces governs the degree of the mixing.

VI. CONCLUSION

We have developed a numerical model that describes the granular Rayleigh-Taylor instability for grains mixed either with compressible or incompressible fluids at low Reynolds numbers. In this model we adjusted the fluid compressibility from ideal gas to incompressible behavior. We incorporated

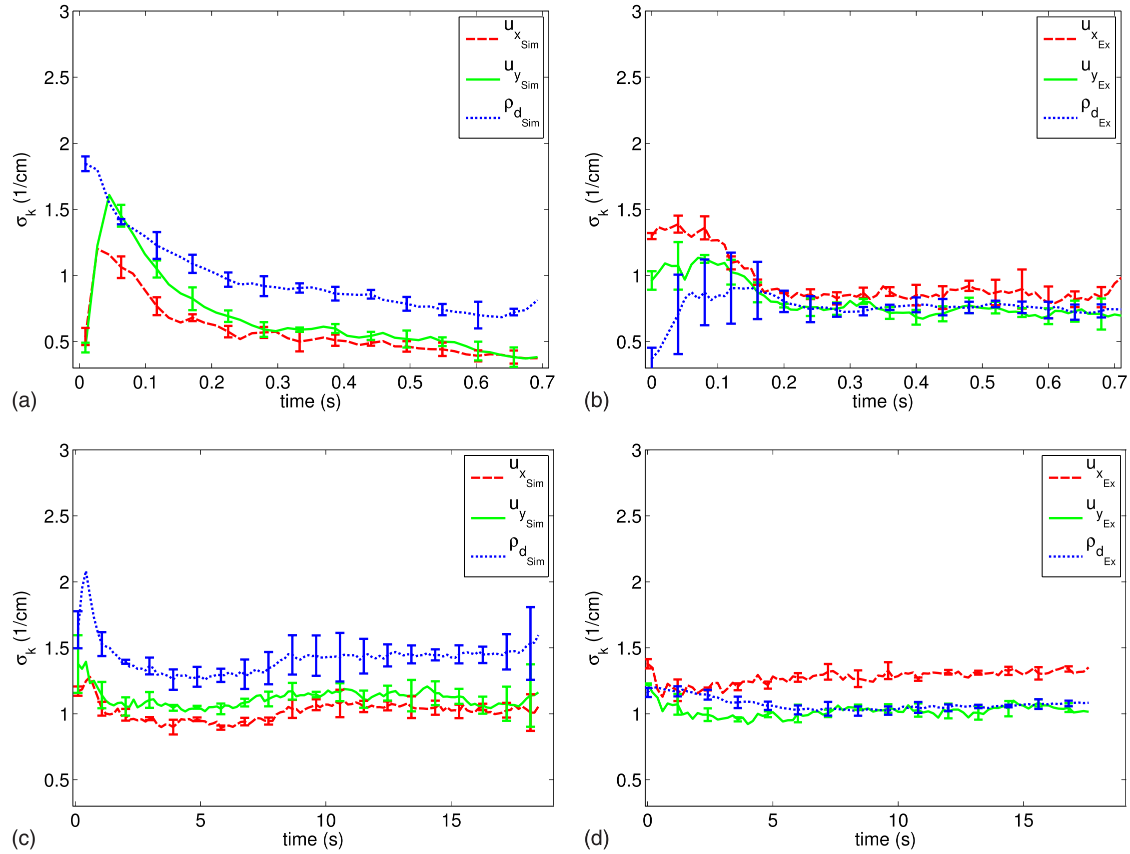

FIG. 17. (Color online) The standard deviation σ_k as a function of time for air and water/glycerol for the velocity field $\mathbf{u}$ and the density field ρ_d.

fluid inertia and viscous forces which lead to a hydrodynamic particle-particle coupling and a coupling between the fluid and the confining plates. In addition the model also includes solid friction between the particles and the confining plates. The physical effect of these various terms, their relative importance and the strategies to approximate in simple and computationally efficient ways, have been discussed and evaluated numerically by switching some of these terms on or off and evaluating the effect of the resulting flow. We designed and conducted experiments with compressible and incompressible fluids that where well matched quantitatively with our model. From these experiments the velocity field of the particles was extracted by a CIV technique that we improved relative to standard procedures by introducing an additional filtering technique.

The forming patterns and their dynamics were analyzed and compared between the experiments and the simulations. Evaluation of the pictures of the simulation and the pictures of the experiments, velocity field histograms, 2D autocorrelation and the power spectrum of the velocity field showed that our model reproduces well the dynamics of the experiments in both studied cases of water/glycerol and air. Furthermore the analysis of the velocity field and density field resulted in a better understanding of the different mixing

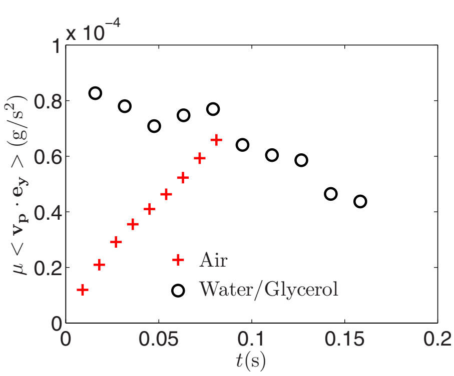

FIG. 18. (Color online) The velocity y component multiplied by the fluid viscosity averaged over the first ten lowest particles in time.

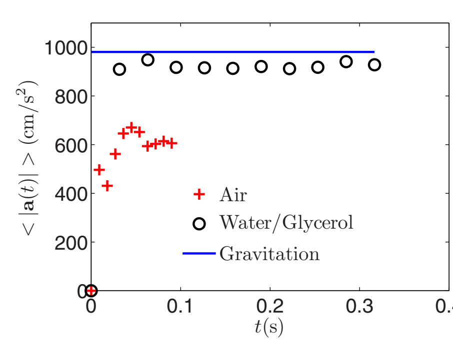

FIG. 19. (Color online) $\mathbf{a_f}=\nabla P/(\rho_m\rho_s)$ is the acceleration on the particles due to the fluid in time compared to the gravitational acceleration $\mathbf{a_g}$. The average runs over the first ten lowest particles.

behavior in the two studied cases as described in chapter I. Two main differences in the histograms and different correlation of the u_y component of the velocity field could be identified, which verifies the complete mixing in the case of water/glycerol and the observation of sedimentation patterns in the case of air. Finally in Sec. V we discussed the physical mechanism causing the different mixing behavior as function of the nature of the interstitial fluid

APPENDIX

In this appendix our model shall be compared to the work of [23,24] where the Navier-Stokes equation is solved directly. In contrast to the work on fluidized beds of [23,24] in our model we will only consider the dominating terms of the Navier-Stokes Eq. (A1) as demonstrated in the following. We will show that this approach also leads to the fluid Eqs. (14) and (21) derived in Sec. III A.

The Navier-Stokes equation for incompressible or lowly compressible fluids in the regime of low Reynolds numbers states,

$$\partial_t(\rho_f \mathbf{v_f}) = -\nabla P + \nabla \cdot T. \tag{A1}$$

In Eq. (A1) the term $\nabla \cdot T = \mu \nabla^2 \mathbf{v_f}$ accounts for the stress induced by the curvature of the fluid flow profile. It can be separated into a contribution from the fluid flow curvature at small scales, between the particles: $(\nabla \cdot T)_s = \mu \nabla_s^2 \mathbf{v_f}$ and a contribution from the fluid flow curvature on a scale larger than the particles: $(\nabla \cdot T)_l = \mu \nabla_l^2 \mathbf{v_f}$. The high wave number curvatures $(\nabla \cdot T)_s$ of the fluid flow profile between the particles are defined to be separated by a cutoff wave number K from the low wave number curvatures $(\nabla \cdot T)_l$. The cutoff wave number K represents the inverse size of the representative volume elements of the Darcy law. With a Fourier decomposition the stress term T can easily be divided into high and low wave number contributions [37],

$$\begin{aligned}\mu \nabla^2 \mathbf{v_f} &= (\nabla \cdot T)_s + (\nabla \cdot T)_l \\ &= \sum_{k>K} (\nabla \cdot T)_k e^{i\mathbf{kr}} + \sum_{k \le K} (\nabla \cdot T)_k e^{i\mathbf{kr}}.\end{aligned} \tag{A2}$$

To solve Eq. (A1) we consider a discrete square grid of 2.5 particle diameters on which we average the particle velocity and the density. Integrating the force $(\nabla \cdot T)_s$ up to this grid scale in the reference frame of the particles leads to Darcy's law in Eq. (12): $\langle(\nabla \cdot T)_s\rangle = \frac{\phi\mu}{\kappa}(\mathbf{u} - \mathbf{v_f})$. Thus Eq. (A1) can be rewritten after averaging for small volumes (see [23–26] for details),

$$\partial_t(\rho_f \phi \mathbf{v_f}) = -\phi \nabla P + \frac{\phi^2 \mu}{\kappa}(\mathbf{u} - \mathbf{v_f}) + [\nabla \cdot (\phi T)]_l. \tag{A3}$$

In this equation the second term on the right-hand side is related to Darcy's law. It is the dominating term together with the gradient of the pressure in the situations we consider. The third term on the right hand side is derived from $(\nabla \cdot T)_l$ and accounts for the curvature of the fluid velocity field in a global reference frame. It can be divided into an in-plane and an out of plane contribution,

$$\begin{aligned}[\nabla \cdot (\phi T)]_l &= (\nabla \cdot \{\mu \phi[(\nabla \mathbf{v_f}) + (\nabla \mathbf{v_f})^T]\})_l \\ &= ((\nabla_\perp + \nabla_\parallel) \cdot \{\mu \phi[(\nabla \mathbf{v_f}) + (\nabla \mathbf{v_f})^T]\})_l.\end{aligned} \tag{A4}$$

The analysis done in Sec. III C and the measured autocorrelation functions in Sec. IV show that the inertia term $\partial_t(\rho_f \phi \mathbf{v_f})$ in Eq. (A3) is negligible compared to Darcy's law. Furthermore this analysis also shows that the out of plane contribution of the term $[\nabla_\perp(\phi T)]_l$ is dominating over the in-plane one. The reason for this is that the fluid flow is correlated in average for 5 mm in the in-plane direction but only 1 mm out of plane. Integrating

$$-\phi \nabla P + \frac{\phi^2 \mu}{\kappa}(\mathbf{u} - \mathbf{v_f}) + (\nabla_\perp \phi T)]_l = 0 \tag{A5}$$

over the thickness h of the cell we get a shear stress contribution σ_t from the term $(\nabla_\perp \phi T)]_l$. With this shear stress Eq. (A5) is equivalent to Eq. (16).

A comparison of this out of plane contribution to the Darcy term was done in Eq. (17)–(20) in Sec. III A. This analysis showed that the out of plane contribution was small compared to the Darcy term. Finally only Darcy's law remains in Eq. (A3) which brings us back to the derivation of the fluid equation in Sec. III A from Eq. (12).

[1] D. Gidaspau, *Multiphase Flow and Fluidization* (Academic Press, San Diego, 1994).
[2] J. F. Davidson and D. Harrison, *Fluidization* (Academic Press, New York, 1971).
[3] D. Chehata Gómez, L. Bergougnoux, E. Guazzelli, and J. E. Hinch, Phys. Fluids **20**, 023302 (2008).
[4] D. Chehata Gómez, L. Bergougnoux, J. E. Hinch, and E. Guazzelli, Phys. Fluids **19**, 098102 (2007).
[5] O. Galland *et al.*, Earth Planet. Sci. Lett. **243**, 786 (2006).
[6] D. H. Rothman, J. P. Grotzinger, and P. B. Flemings, J. Sediment Res. **64**, 59 (1994).
[7] J. L. Vinningland, Ø. Johnsen, E. G. Flekkøy, R. Toussaint, and K. J. Måløy, Phys. Rev. Lett. **99**, 048001 (2007).
[8] J. L. Vinningland, Ø. Johnsen, E. G. Flekkøy, R. Toussaint, and K. J. Måløy, Phys. Rev. E **76**, 051306 (2007).
[9] C. Völtz, W. Pesch, and I. Rehberg, Phys. Rev. E **65**, 011404 (2001).
[10] C. Völtz, M. Schröter, G. Iori, A. Betat, A. Lange, A. Engel, and I. Rehberg, Phys. Rep. **337**, 117 (2000).
[11] A. Lange, M. Schröter, M. A. Scherer, A. Engel, and I. Rehberg, Eur. Phys. J. B **4**, 475 (1998).
[12] L. Bergougnoux, S. Ghicini, E. Guazzelli, and J. E. Hinch, Phys. Fluids **15**, 1875 (2003).
[13] E. Guazzelli, Phys. Fluids **13**, 1537 (2001).
[14] H. Nicolai, B. Herzhaft, E. J. Hinch, L. Oger, and E. Guazzelli, Phys. Fluids **7**, 12 (1995).

[15] H. Nicolai and E. Guazzelli, Phys. Fluids **7**, 3 (1995).
[16] *Advanced Optical Methods and Applications in Solid Mechanics*, edited by A. Lagarde (Kluwer, Dordrecht, The Netherlands, 2000).
[17] Ø. Johnsen, R. Toussaint, K. J. Måløy, and E. G. Flekkøy, Phys. Rev. E **74**, 011301 (2006).
[18] S. McNamara, E. G. Flekkøy, and K. J. Måløy, Phys. Rev. E **61**, 4054 (2000).
[19] D.-V. Anghel, M. Strauss, S. McNamara, E. G. Flekkøy and K. J. Måløy, Phys. Rev. E **74**, 029906(E) (2006).
[20] M. J. V. Goldschmidt, R. Beetstra, and J. A. M. Kuipers, Powder Technol. **142**, 23 (2004).
[21] R. Beetstra, M. A. van der Hoef, and J. A. M. Kuipers, Chem. Eng. Sci. **62**, 246 (2007).
[22] M. A. van der Hoef, D. Frenkel, and A. J. C. Ladd, Phys. Rev. Lett. **67**, 3459 (1991).
[23] M. A. van der Hoef, M. Ye, M. van Sint Annaland, A. T. Andrews IV, S. Sundaresan, and J. A. M. Kuipers, Adv. Chem. Eng. **31**, 65 (2006).
[24] N. G. Deen, M. van Sint Annaland, M. A. van der Hoef, and J. A. M. Kuipers, Chem. Eng. Sci. **62**, 28 (2007).
[25] R. M. Iverson, Rev. Geophys. **35**, 245 (1997).
[26] R. Jackson, *The Dynamics of Fluidized Particles* (Cambridge University Press, Cambridge, England, 2000).
[27] P. C. Carman, Trans. Inst. Chem. Engrs. **15**, 150 (1937).
[28] H. Darcy, *Les Fontaines Publiques de la ville de Dijon* (Dalmont, Paris, 1856).
[29] E. Guyon, J. P. Hulin, L. Petit, and C. D. Mitescu, *Physical Hydrodynamics* (Oxford University Press, Oxford, 2001).
[30] A. Einstein, Ann. Phys. **324**, 289 (1906).
[31] H. C. Brinkman, J. Chem. Phys. **20**, 571 (1952).
[32] R. Roscoe, Br. J. Appl. Phys. **3**, 267 (1952).
[33] E. G. Flekkøy, R. Delgado-Buscalioni, and P. V. Coveney, Phys. Rev. E **72**, 026703 (2005).
[34] *Behaviour of Granular Materials*, edited by B. Cambou (Springer Verlag, Wien, NY, 1998).
[35] L. D. Landau and E. M. Lifshitz, *Theory of Elasticity* (Elsevier Butterworth-Heinemann, Oxford, 2001).
[36] A. Y. Grosberg and A. R. Khokhlov, *Statistical Physics of Macromolecules* (American Institute of Physics, New York, 1994).
[37] U. Frisch, *Turbulence* (Cambridge University Press, Cambridge, England, 1995).

Sedimentation instabilities: Impact of the fluid compressibility and viscosity

Michael J. Niebling,[1] Eirik G. Flekkøy,[1] Knut Jørgen Måløy,[1] and Renaud Toussaint[2]
[1]*Department of Physics, University of Oslo, P.O. Box 1048, 0316 Oslo, Norway*
[2]*Institut de Physique du Globe de Strasbourg, CNRS, and University of Strasbourg(EOST), 5 rue Descartes, 67084 Strasbourg Cedex, France*

(Received 18 May 2010; published 11 November 2010)

The effect of an interstitial fluid on the mixing of sedimenting grains is studied numerically in a closed rectangular Hele-Shaw cell. We investigate the impact of the fluid compressibility and fluid viscosity on the dynamics and structures of the granular Rayleigh-Taylor instability. First we discuss the effect of the fluid compressibility on the initial fluid pressure evolution and on the dynamics of the particles. Here, the emerging patterns do not seem highly affected by the compressibility change studied. To characterize the patterns and motion the combined length of the particle trajectories in relation to the movement of the center of mass is analyzed, and the separation of particle pairs is measured as a function of the fluid viscosity.

DOI: 10.1103/PhysRevE.82.051302 PACS number(s): 45.70.−n, 45.50.−j, 47.11.−j

I. INTRODUCTION

Granular materials play an important role in geological processes, for example, in erosion or avalanche processes [1–3]. Handling granular materials is in addition the daily basis of many of our industries, such as mining, agriculture, civil engineering, and pharmaceutical manufacturing. The field of dry granular materials and the enormous richness and complexity of granular motion and granular flows have provided the research of the last 20 years with numerous questions. In granular flows the presence of an interstitial fluid has been shown to strongly affect the dynamics of the grains [4–8]. The fluid compressibility and the fluid viscosity may well have an effect on the dynamics of the grains, for example, in fluidized bed reactors, but have not been in much focus.

The Rayleigh-Taylor instability in granular fluid mixtures has been studied with different types of fluids. With air the influence of the grain size was systematically investigated [9–11], and the behavior of this instability was compared between the cases where the interstitial fluid was air or water-glycerol [12]. In a comparable study of the Saffman-Taylor instabilities for granular-fluid mixtures oil or air was utilized as the interstitial fluid [13,14]. In our previous work [12] we have found in experiments and simulations that the mixing of the grains with the fluid during the granular Rayleigh-Taylor instability was very different whether we used air or a water-glycerol solution as the interstitial fluid. In pursuit to study this influence we further developed a numerical model [9,10,13,15] that was proven [12] to reproduce well the experimentally measured dynamics of the grains in the presence of a fluid. Even though we could give a quantitative explanation with the characterization of the correlation lengths and velocity field histograms, it is still an open question if the mixing behavior is a result of the fluid grain coupling to a compressible or incompressible fluid and how big is the influence of the fluid viscosity. To further answer this question we will perform numerical simulations with the goal to study the effect of the fluid viscosity and fluid compressibility on the mixing behavior during sedimentation. For this purpose the fluid viscosity and fluid compressibility are systematically and independently varied. These simulations show that the fluid compressibility has a small effect on the mixing except in extreme cases. The change in the fluid viscosity leads to an increase in the averaged particle trajectory length as a function of the displacement of the center of mass of the particles. With respect to the separation of particle pairs, the change in the viscosity displays initially two regimes: a nonhydrodynamic or ballistic regime at low fluid viscosities and a hydrodynamic regime at high fluid viscosities, with a crossover from diffusive to turbulent-dispersive behavior. This distinction however does not hold for the later stages of the simulations.

The paper is organized as follows. In the next section the implementation of the numerical model is briefly discussed. For more details and explanations see [9,10,12,13,15]. The results of the simulations with varied fluid compressibility and viscosity are presented in Sec. III. In Secs. III A and III B the effect of the fluid compressibility is studied. The effect of the fluid viscosity is studied and discussed in Sec. III C followed by the conclusions in Sec. IV.

II. THEORY AND SIMULATIONS

The numerical model is a two-dimensional hybrid model that uses a continuum description for the fluid and a discrete description of the granular phase. Friction between particles or the particles and the side plates is neglected. Further we neglect the friction between the fluid and the side plates. The model is derived in detail in [9,10,12,13,15]. It was tested and shown to reproduce the dynamics of granular flows at low Reynolds numbers, and we will only present the main equations for the evolution of the nonhydrostatic part of the pressure field P and the dynamics of the particles briefly.

A. Dynamics of the fluid

The equations ruling the evolution of the nonhydrostatic part of the pressure, also termed the hydraulic head P, are derived in detail in Ref. [15]. The nonhydrostatic part of the pressure, P, corresponds to $P=P'-\rho_f g y'$, where P' is the pressure, g is the gravity constant, ρ_f is the fluid density, and

y' is the depth. In the following we will only present and discuss the main equations briefly. We start with mass conservation of the fluid:

$$\partial_t[\rho_f(P)\phi] + \nabla \cdot [\rho_f(P)\phi\mathbf{v_f}] = 0, \tag{1}$$

where $\mathbf{v_f}$ is the velocity of the fluid and ϕ is the local porosity: for the mass conservation of the grains we get

$$\partial_t(1-\phi) + \nabla \cdot [(1-\phi)\mathbf{u}] = 0, \tag{2}$$

where $\mathbf{u}$ is the velocity of the grains. The velocity $\mathbf{v_f}$ of the fluid is the sum of the local velocity relative to the grains, derived from Darcy's law, plus the velocity of the grains:

$$\mathbf{v_f} = \mathbf{u} - \frac{\kappa}{\phi\mu}\nabla P, \tag{3}$$

where μ is the fluid viscosity and κ is the local permeability. Using Eq. (3) in Eq. (1) we get:

$$\partial_t[\phi\rho_f(P)] + \nabla \cdot \left[\phi\rho_f(P)\left(\mathbf{u} - \frac{\kappa}{\phi\mu}\nabla P\right)\right] = 0. \tag{4}$$

Eliminating $\partial_t\phi$ between Eqs. (2) and (4) and taking the fluid mass density $\rho_f(P)$ to be related to the pressure by the compressibility $\beta_T = -(1/V)\partial V/\partial P$ through an equation of state that we linearize around the background pressure P_0 with ρ_f^0 as the fluid mass density at P_0,

$$\rho_f(P) \approx \beta_T\rho_f^0(P-P_0) + \rho_f^0, \tag{5}$$

we get after a short calculation a diffusion equation for the nonhydrostatic part of the pressure P. This equation in general implies the fluid compressibility [15,16]:

$$\phi\left[\frac{\partial P}{\partial t} + \mathbf{u}\cdot\nabla P\right] = \nabla \cdot \left[\hat{P}(\beta_T)\frac{\kappa}{\mu}\nabla P\right] - \hat{P}(\beta_T)\nabla\cdot\mathbf{u}, \tag{6}$$

where we have defined $\hat{P}(\beta_T) = \rho_f/(\rho_f^0\beta_T) = P - P_0 + 1/\beta_T$.

Since in this work we only simulate fluids with the mass density of air as the interstitial fluid, we can neglect the inertia and the weight of the fluid, and the hydraulic head correspond to the local pressure: $P' \approx P$. In the case of air, considered as an ideal gas we get $\beta_T = 1/P_0$ at P_0 and Eq. (6) results in

$$\phi\left[\frac{\partial P}{\partial t} + \mathbf{u}\cdot\nabla P\right] = \nabla \cdot \left(P\frac{\kappa}{\mu}\nabla P\right) - P\nabla\cdot\mathbf{u}. \tag{7}$$

At the other end of fluid compressibility types, the incompressible limit where $\beta_T \to 0$, Eq. (6) results in a Poisson equation:

$$\nabla \cdot \left(\frac{\kappa}{\mu}\nabla P\right) = \nabla\cdot\mathbf{u}. \tag{8}$$

In both cases we calculate the local permeability κ by the Carman-Kozeny relation [17]

$$\kappa = \frac{a^2}{9K}\frac{(1-\rho_s)^3}{\rho_s^2}, \tag{9}$$

where $\rho_s = 1-\phi$ is the solid volume fraction, a is the particle radius, and $K=5$ is an empirical constant valid for a packing of beads [15].

B. Dynamics of the particles

The force equation for a single particle with the velocity v_p, particle mass $m = \rho_m\pi a^2 h$, particle mass density ρ_m, volume $V_a = \pi a^2 h$ in a cell with a plate spacing of h, and the number density defined as $\rho_n = \rho_s\rho_m/m$ is given by

$$m\frac{dv_p}{dt} = \rho_{\text{eff}}V_a\mathbf{g} + \mathbf{F_I} - \frac{\nabla P}{\rho_n} + \mathbf{F_d}, \tag{10}$$

where $\rho_{\text{eff}} = \rho_m - \rho_f$ enters in the buoyancy forces in the first term of the left-hand side, $\mathbf{F_I}$ is the interparticle solid contact force, the third term arises from the momentum exchange between the fluid and solid, and $\mathbf{F_d}$ is a viscous force accounting for energy dissipation. To approximate a situation of hard spheres we choose the interparticle force $\mathbf{F_I}$ be a linear force with a spring constant k high enough to make the overlap of particles during collision a negligible fraction of their diameters.

If particles collide we include energy dissipation with a restitution coefficient of $r_s = 0.13$ [10]. This is modeled by a viscous force, active only during particle contact. This force is proportional to the relative velocity of the particles $\mathbf{v_r}$ and oriented along the unit vector $\mathbf{n_d}$, which points from the center of one particle to the contact point:

$$\mathbf{F_d} = -\gamma_d(\mathbf{v_r}\cdot\mathbf{n_d})\mathbf{n_d}. \tag{11}$$

The particle propagation is modeled by the velocity Verlet scheme [18,19].

III. RESULTS

For the simulations presented in this paper we used a Hele-Shaw cell in the x direction of $\Delta x = 5$ cm in width and in the y direction $\Delta y = 7$ cm in height. The cell is entirely closed on all sides, both for the fluid and for the grains. The mass density of the fluid was constant, set to the mass density of air $\rho_f = 1.29$ kg/m^3, and we considered particles of a mass density of $\rho_m = 2500$ kg/m^3. The initial pressure considered corresponds to atmospheric pressure, $P_0 = 100$ kPa at the top of the cell. The average size of the particles is 140 μm and to avoid the formation of a triangular lattice the particle diameter was defined to have a flat size distribution with a range of $\pm 10\%$ variation about the mean. In total approximately 140 000 particles are considered in the simulations. The only variables that we vary in the following are the viscosity of the fluid μ_f and the compressibility of the fluid β_T. The initial state is prepared in the following way: particles are first let to rest on the bottom up to when a fraction of 2/3 of the cell volume is filled. The interparticle space is filled with the interstitial fluid considered. Then, gravity is instantaneously reverted, corresponding to a sudden upside down flipping of the cell, and particles start to fall

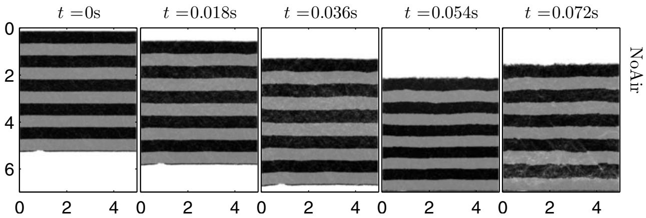

FIG. 1. A layer of beads falls through a gap in vacuum. Time progresses from left to right. White areas represent areas where the particle density is zero. The gray and black areas represent areas filled with particles, and the stripes are added artificially to better demonstrate the dynamics. From left to right time progresses in equal time steps.

from their initial configuration and initial zero velocity. In all the simulations the cell could be divided into three zones independent of the type of fluid. In the base of the cell, where particles have sedimented, and in the top section we find a bulk of compacted particles. In these two sections particles are hardly moving relative to each other. In between these two sections, we find a dynamic section with mobile dispersed particles. The particles in this section move while forming fingers of higher particle density and bubbles of lower particle density.

A. Effect of the compressibility on the granular Rayleigh-Taylor instability

The dynamics of the particles in the Hele-Shaw cell significantly depends on the interstitial fluid. In vacuum we do not see any evolution of patterns in the density field as shown in Fig. 1. Since all particles start at zero velocity, indeed, they simply all homogeneously fall in free fall, up to the moment when they contact the lower boundary and bounce back. In Fig. 2 an interstitial fluid however is present. While falling through the gap of fluid, here the particles develop downward falling fingers of high particle density and rising bubbles of low particle density. In this section we are going to investigate the effect of the fluid compressibility on the dynamics of the particles. In Fig. 2 we therefore vary and compare the dynamics for different fluid compressibilities. While the fluid viscosity is kept fixed and set to $\mu_f(\text{air})=0.018$ mPa s, which corresponds to air at room conditions of 25 °C and atmospheric pressure, the bulk modulus varied from $\kappa_T=1/\beta_T=1$ kPa to incompressible behavior.

From the plots of the density field in Fig. 2 we can identify two main differences due to the change in compressibility. First we find for the high compressible cases with a bulk modulus of $\kappa_T \leq 5$ kPa that at times $t \leq 0.12$ s bubbles of low particle density appear at the upper end of top section and right above the fingers in Fig. 2 in the picture at $t=0.126$ s in the top row. For a higher bulk modulus these bubbles are not present, and the top section stays uniformly compacted. Second we notice that in the beginning the center of mass of the whole top section moves further down the more compressible is the fluid. This movement of the top section stops when the weight of the packing is balanced by the overpressure of the compressed air in the base and the underpressure in the upper part of the cell. In Fig. 3 we

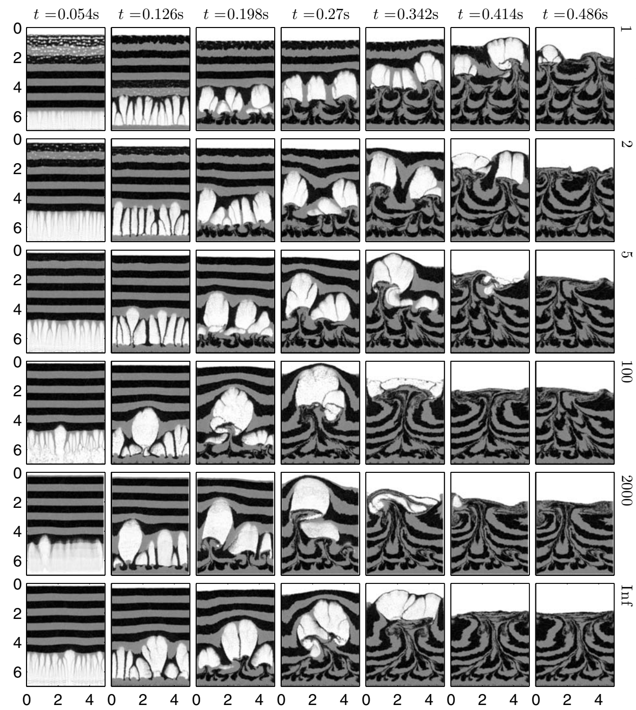

FIG. 2. Comparison of simulations with different fluid compressibilities at a fluid viscosity of air: $\mu_f(\text{air})=0.0182$ mPa s. Gray and black areas represent areas filled with particles. The stripes are added artificially to better demonstrate the dynamics. From left to right time progresses in equal time steps and from top to bottom the bulk modulus is increased.

plotted the movement of the center of mass of all particles $\Delta R_c(t)=R_c(t)-R_c(0)$ in time. In the plots we observe oscillations of the top section for all the bulk moduli below $\kappa_T \leq 5$ kPa. Above this limiting bulk modulus, the movement of the center of mass does not seem to be influenced by the compressibility of the fluid. The oscillations are governed by the inertia of the mass of the grains in the top section and the elasticity of the fluid given by the bulk modulus. After the pressure rises in the bottom part of the cell fluid seeps through the porous media, exchanging momentum between the particles and the fluid and damping the oscillations. The system can show transient oscillations, which we observe for $\kappa_T \leq 5$ kPa or be in an overdamped regime for $\kappa_T > 5$ kPa.

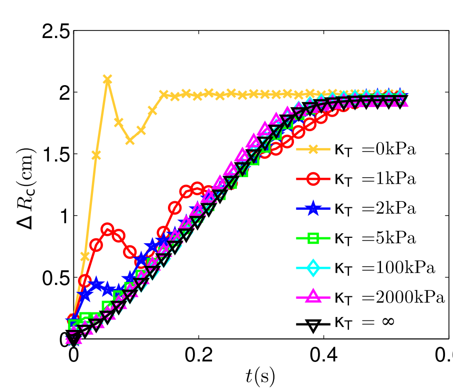

FIG. 3. (Color online) The y position of the center of mass of all particles is plotted in time for different bulk moduli.

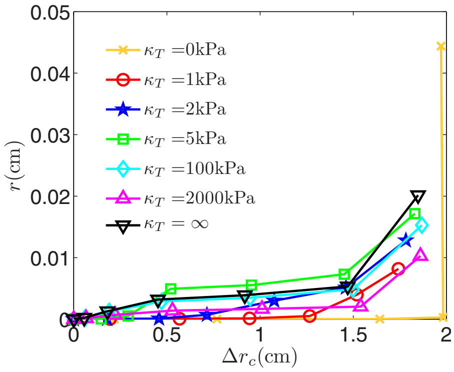

FIG. 4. (Color online) The excess path length $r(t)$ in Eq. (12) is plotted in time. Particles are falling mostly straight downward, and the bulk modulus hardly affects the excess path length.

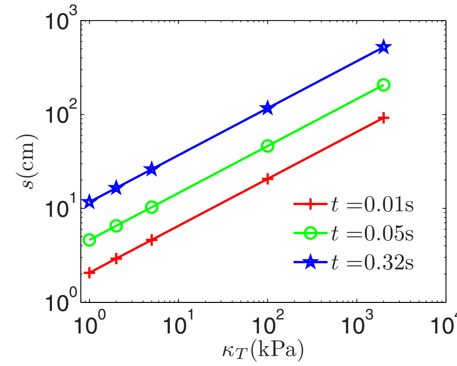

FIG. 5. (Color online) The skin depth for different bulk moduli at time steps connected with the oscillations: $t=0.01$ s and $t=0.05$ s. At the time that the top layer takes to fall through the fluid $t=0.32$ s, the skin depth is much larger than the system size.

In Fig. 4 we analyzed the excess path length $r(t)$ of the lowest layer of $N=8000$ particles at $t=0$ s, where the position of the ith particle is given by $\mathbf{r}_i(t)$. The displacement of the center of mass of the lowest layer of $N=8000$ particles is $\Delta r_c(t)=r_c(t)-r_c(0)$, and we define the excess path length $r(t)$ as

$$r(t_s) = \frac{\sum_i^N \sum_{j=1}^s |\mathbf{r}_i(t_j) - \mathbf{r}_i(t_{j-1})|}{N} - [r_c(t_s) - r_c(0)], \quad (12)$$

with the first sum over the particles and the second sum over the time steps j. If particles are falling straight with this definition in Eq. (12), the excess path length is zero. The excess path length is a measure of the complexity of the particle trajectories. The time resolution is small enough that no significant deviation was found when we only used every second time step instead of every time step.

In Fig. 4 we plotted the average excess particle trajectory $r(t)$ in relation to the movement in the y direction of the center of mass Δr_c. We notice that the excess trajectory is almost zero until the particles hit the bottom of the cell at $r_c=1.6$ cm. This shows that the particles of this lower layer are falling mostly straight through the gap, independent of the compressibility of the fluid.

B. When does compressibility become important?

To estimate when compressibility becomes an important factor and affects the dynamics, we have to check two conditions: first if the weight of the packing of grains is enough to significantly compress the fluid in the base. In Eq. (5) this means that the pressure difference is comparable to the background pressure $P_0=\kappa_T$ for an ideal gas. In this case we experience oscillations of the top section if friction is neglected like in our case for a bulk modulus $\kappa_T \leq 5$ kPa. Second we can define a skin depth for the pressure drop inside the porous matrix. For this simplified analysis we start with Eq. (6) and work in a reference frame moving with the particles. We assume small deformations of this falling particle plug, hereby neglecting the relative motion between the particles. We further take the solid fraction to be homogeneous $\nabla \frac{\kappa}{\mu}=0$ and that the pressure difference in the cell is small compared to the background pressure P_0. This gives $\hat{P} \approx \kappa_T$ and Eq. (6) simplifies to a diffusion equation:

$$\frac{\partial P}{\partial t} = \frac{\kappa_T \kappa}{\phi \mu} \Delta P. \quad (13)$$

The fundamental solution to this equation is

$$P(x) = \frac{1}{\sqrt{4\pi D t}} e^{-x^2/4Dt}, \quad (14)$$

where $D=\kappa_T \kappa / \phi \mu$. In Eq. (14) we can define a skin depth s where the pressure has decayed by $P(s)=\frac{1}{e}$. This skin depth is given by $s=\sqrt{4Dt}$. We can now compare this skin depth with the size of the Hele-Shaw cell. For typical values of $\rho_s=0.6$, $\mu_f(\text{air})=0.018$ mPa s, and $t=0.01$ s, $t=0.05$ s, and $t=0.32$ s, we find a skin depth as shown in Fig. 5. The first two time steps correspond to the time steps that are in the range of the observed pressure oscillation period. The last is the time that the top layer takes theoretically to fall through the fluid gap, when the velocity of the top layer is given by the Darcy velocity $v_d=(\kappa/\mu_f)\nabla P$, and the pressure force balances the weight of the grains $\nabla P=\rho_s \rho_m \mathbf{g}$ for a solid fraction of $\rho_s=0.6$. In this Fig. 5 we have calculated the skin depth s for different bulk moduli. At the time that the top layer takes to fall through the fluid $t=0.32$ s the skin depth is much larger than the system size for all κ_T. At the times connected with the oscillations the figure shows that the skin depth is in the range of the system size for all $\kappa_T \leq 5$ kPa. For $\kappa_T > 5$ kPa the skin depth gets much larger than the system size of 7 cm. If we compare now the plot of the density field in Fig. 2, we can see that the lower compressibility affects rather the system when the skin depth is smaller than the size of the Hele-Shaw cell. When the packing of beads starts to fall downward, the pressure in the bottom of the cell will increase while in the top of the cell the pressure decreases. In the highly compressible case and for a homogeneous layer of beads the solution of the simple diffusion equation (14) has a curved profile and a skin depth smaller than the system size as shown in Fig. 6. Since the volume of fluid in the bottom of the cell is much larger than

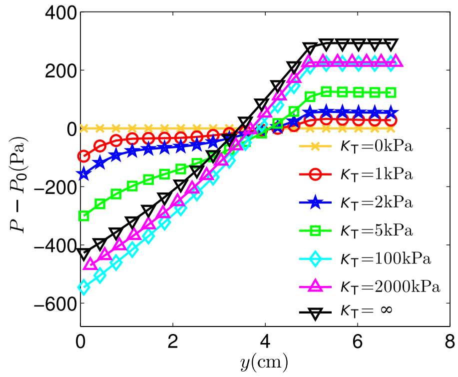

FIG. 6. (Color online) The averaged pressure profile as a function of the depth at t=0.02 s.

in the top, the movement of the particles will cause the pressure to drop faster in the top of the cell than the pressure increases in the bottom of the cell. This underpressure in the top part of the cell will strongly slow down the falling of the uppermost particles where the pressure gradient is the strongest. Inside the packing, away from the upper layer, the pressure gradient decreases and so does the upward force on the particles. Due to this decrease in the acceleration on the particles, the layer expands in the top part, creating the bubbles of low particle density. If on the contrary the skin depth is larger than the system size, the pressure profile becomes linear and the pressure gradient the acceleration of the beads is constant. The packing shows no noticeable expansion apart from its decompaction happening at its lower boundary, which is a different effect. The oscillations of the top layer can be described in a simplified way through a differential equation equivalent to a damped harmonic oscillator. The particles in the top layer shall be considered as a piston with a constant permeability and no relative movement of the particles. The initial empty volume in the bottom part is given by $V_b(0)$ and the top part by $V_t(0)$. The thickness in the y direction of the top layer is L and the cross-section area is $A=\Delta xh$. Defining $Y(t)\approx\Delta R_c(t)$ as the change in the position of the center of mass of all particles and M as their total mass, we can state

$$M\ddot{Y} - Mg = -A(P_b - P_t). \tag{15}$$

In this simplified picture the cell consists of two compartments separated by a porous piston. The pressure gradient inside the piston is assumed to be constant and equal to the overall pressure gradient between the two compartments corresponding to the long-term limit of the pressure profile if the fluid is compressible. The change in the fluid volume in the bottom compartment $V_b(t)-V_b(0)$ is negative to the change in fluid volume in the top compartment $V_b(t)-V_b(0)=-[V_t(t)-V_t(0)]$. There are two possible mechanisms affecting the fluid volumes. First is the compression or expansion of the fluid due to the movement of the piston, and second is the flow through the porous piston. This leads to the following expression for the fluid volume in the bottom compartment:

$$V_b(t) - V_b(0) = \left[-AY + \frac{A\kappa}{\mu}\int_0^t \frac{P_b - P_t}{L}dt\right]. \tag{16}$$

With the definition of the bulk modulus $\kappa_T=-V\frac{\partial P}{\partial V}$, the pressure difference between top and bottom parts can be calculated as

$$\begin{aligned} P_b - P_t = &-\frac{\kappa_T}{V_b(0)}\left[-AY + \frac{A\kappa}{\mu}\int_0^t \frac{P_b - P_t}{L}dt\right] \\ &-\frac{\kappa_T}{V_t(0)}\left[-AY + \frac{A\kappa}{\mu}\int_0^t \frac{P_b - P_t}{L}dt\right]. \end{aligned} \tag{17}$$

Using now Eq. (15) in Eq. (17) and integration results in the differential equation of a damped harmonic oscillator:

$$\ddot{Y} + \alpha\dot{Y} + \beta Y = \gamma t + g, \tag{18}$$

where the constants are defined by

$$\alpha = \frac{\kappa\kappa_T A}{\mu L}\left(\frac{1}{V_b(0)} + \frac{1}{V_t(0)}\right),$$

$$\beta = \frac{\kappa_T A^2}{M}\left(\frac{1}{V_b(0)} + \frac{1}{V_t(0)}\right),$$

$$\gamma = \frac{\kappa\kappa_T A g}{\mu L}\left(\frac{1}{V_b(0)} + \frac{1}{V_t(0)}\right). \tag{19}$$

With a standard ansatz $Y(t)=e^{\lambda t}$ in Eq. (18) two solutions of the homogeneous equation are found:

$$\lambda_{1,2} = -\frac{\alpha}{2} \pm \sqrt{\frac{\alpha^2}{4} - \beta}. \tag{20}$$

The system will be overdamped if the square root of Eq. (20) is positive, and oscillations only occur if the square root is negative. This is the case if

$$\frac{\kappa^2\kappa_T M}{4\mu^2 L^2}\left(\frac{1}{V_b(0)} + \frac{1}{V_t(0)}\right) < 1. \tag{21}$$

Assuming a system with the constants used in the simulations Eq. (21) predicts a critical bulk modulus of κ_T =589.3 kPa for the transition from an overdamped to a damped system. Here, we furthermore assumed that $V_b(0)$ $=V_t(0)=Ah(1.0\text{ cm})$ and a solid fraction of ρ_s=0.6. If the initial volume is $V_t(0)=Ah(0.1\text{ cm})$ and $V_b(0)$ $=Ah(1.9\text{ cm})$ the critical bulk modulus is κ_T=111.9 kPa. Recalling Fig. 3 it can be seen that the transition occurs at comparable values in the simulations.

C. Effect of the viscosity on the granular Rayleigh-Taylor instability

In Fig. 7 the influence of the fluid viscosity μ_f is demonstrated in plots of the density field in black and white, where black stands for high particle density. Stripes in gray were added to emphasize the particle dynamics. The viscosity is changed from a value close to the viscosity of air μ_f(air)

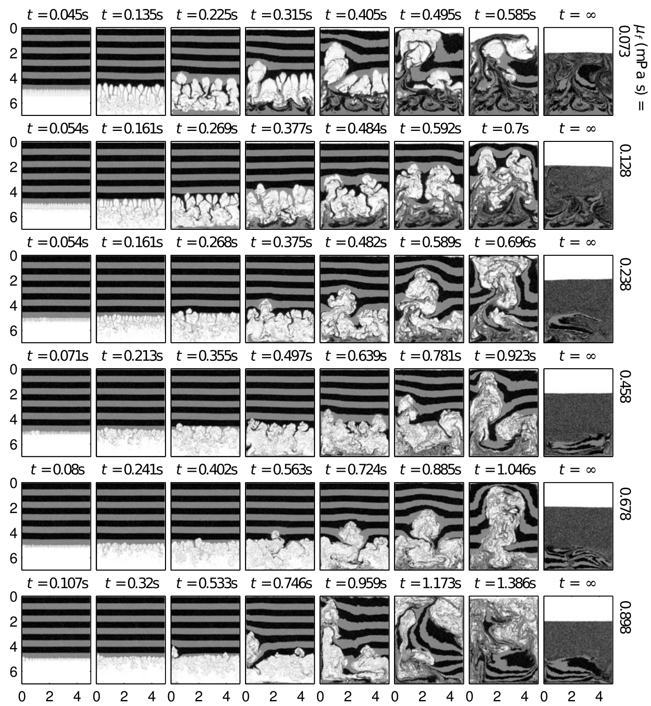

FIG. 7. The particle density field of simulations with different viscosities. From left to right time is progressing, and from top to bottom the viscosity is increased. If not specified the axis units are given in centimeters. White areas represent particle-free areas. Bubbles of low particle density can be observed.

$=0.018$ mPa s and increased in steps with increasing step size. When the viscosity is increased a clear difference in the dynamics in the cell can be observed. The structures get smaller and the evolution of the dynamics is slowed down. When the viscosity is increased, the fingers finally disperse before they have reached the base of the cell. In the further progress the most advanced bubble of low particle density accelerates until the top section of compacted grains has been broken through. After this breakthrough the top section gets unstable, and the remaining blocks of compacted grains remain compacted while falling downward. This is a rather different dynamics, where we have already observed that the friction with the side plates is an important parameter [12].

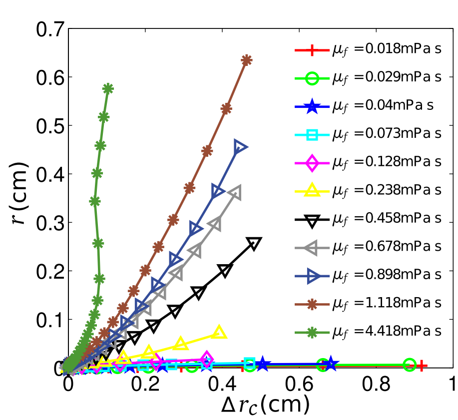

FIG. 8. (Color online) The average excess particle trajectory in relation to the displacement of the center of mass.

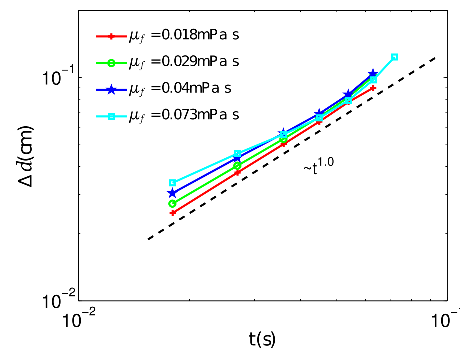

FIG. 9. (Color online) Δd the average distance of particle pairs in time for low-viscosity fluids in bilogarithmic representation. The power-law fit with an exponent $b=1.0$ shows ballistic behavior.

The focus of this paper shall be kept on the start of the Rayleigh-Taylor instability, which is less sensitive to boundary conditions, and allows us to concentrate on the parametric study of the viscosity and compressibility effects. Thus, we have chosen not to study in detail this final stage of the dynamics, and we concentrate on the beginning of the simulations when the top layer is still intact.

The analysis of the excess path length of Sec. III A in Eq. (12) performed on the simulations with different viscosities leads to the plot in Fig. 8. Here, we can see that the first 8000 particles follow a longer trajectory in relation to the movement of their centers of mass the more viscous is the fluid. There is no simple way to rescale all the plots and collapse them for all viscosities. This shows that the characteristics of the patterns in the density field and the dynamics of the particles are changed due to the viscosity.

To further analyze this change in the mixing dynamics, we define Δd as the average relative distance of particles pairs. These pairs were at time $t=0$ s separated by a distance $\Delta d_s < 0.028$ cm, which corresponds to two particle diameters. In this average only the first 600 particles are considered corresponding to the first two layers. The reason for this is that the front where particles disperse from the top section travels slower for higher viscosity, and the amount of par-

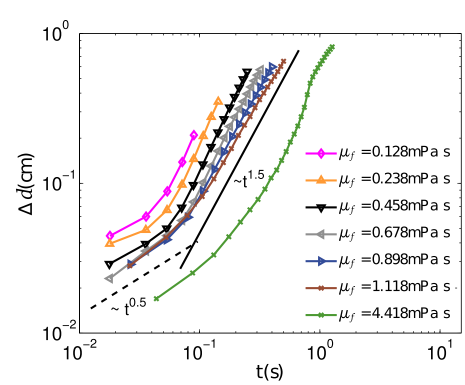

FIG. 10. (Color online) Δd the average distance of particle pairs in time for high-viscosity fluids in bilogarithmic representation. The initial separation of the pairs has a diffusive behavior with an exponent close to $b=0.5$ in the dashed line. In the progress a crossover to a turbulent-dispersive behavior is observed with a slope close to $b=1.5$ in the solid line.

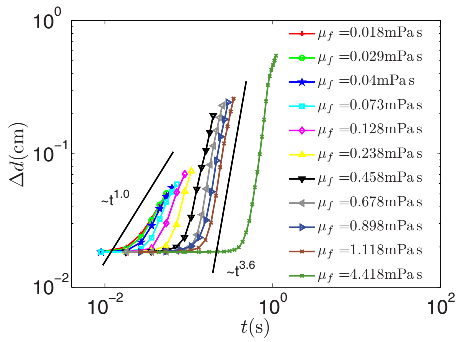

FIG. 11. (Color online) Bilogarithmic representation of Δd, the average distance of particle pairs in time, for a layer of 600 particles at a height of 2000 particles up in the packing. The slopes increase systematically with the fluid viscosity.

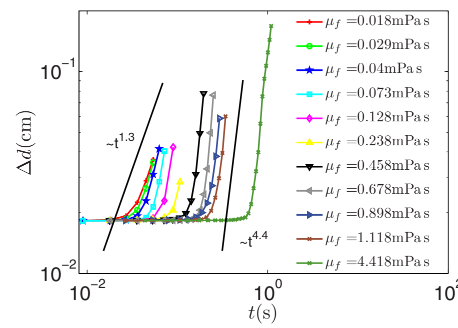

FIG. 12. (Color online) Bilogarithmic representation of Δd, the average distance of particle pairs in time, for a layer of 600 particles at a height of 4000 particles up in the packing.

ticles that contribute to the averaged particle pair distance would depend on the speed the front travels with. Furthermore the dynamic patterns in the cell also depend on the height from the bottom of the cell and coarsen in time. By taking the average over the first 600 particles, it can be ensured that all the particles almost start moving instantaneously. The analysis stops when the first particle has reached a distance of 0.14 cm to the base of the cell corresponding to ten particle diameters. The average distance between the particle pairs grows in time while the particles are falling through the fluid as shown in the bilogarithmic representations in Figs. 9 and 10. The pair separation can be classified into two regimes. The first regime for lowly viscous fluids with $0.018 \leq \mu_f \leq 0.073$ kPa s shows a nonhydrodynamic or ballistic behavior where the exponent is close to $b=1.0$ in a power-law fit of $\Delta d = at^b$. The particles in this regime fall with a constant relative velocity. In the second regime for highly viscous fluids with $0.128 \leq \mu_f \leq 4.418$ kPa s the particle pairs follow an initial diffusive separation with an exponent close to $b=0.5$ before they enter the turbulent-dispersive behavior with an exponent close to $b=1.5$. Interestingly the latter exponent of $b=1.5$ corresponds to the Richardson law that predicts an exponent of $b=1.5$ for particle pair separation in fully developed turbulence [20–24]. For later stages this observation however changes. Looking at a layer of 600 particles at a height of 2000 particles up in the packing, the pair separation displays a slope of around $b=3.6$ for particles emerged in high-viscosity fluids (see Fig. 11). The ballistic behavior for particles emerged in low-viscosity fluids is slightly more stable and holds for a layer of 600 particles until a height of 4000 particles up in the packing (see Fig. 12). In both plots the slopes increase systematically with the fluid viscosity. In addition to the coarsening of the dynamic pattern the more rugged interface at later stages can cause this behavior. The more rugged interface at later stages causes the particles to disperse from the compacted layer at different times and can also contribute to a higher slope of the pair separation in the bilogarithmic representation.

IV. CONCLUSION

As a conclusion we can state that the compressibility of the interstitial fluid affects the dynamical patterns much less than the viscosity. Under the conditions discussed in Sec. III B that the skin depth of the pressure is larger than the system size and that the weight of the grains does not lead to a significant compression of the fluid in the empty zone of the cell, the compressibility can be neglected. This results in an increase in the computational speed by a factor of around 20 for the present model from 480 to 24 h on a cluster with eight nodes. In the second part of this paper the viscosity was proven to have a strong effect on the dynamics of the particles. In terms of the mixing behavior the increase in the additional path length due to the increase in the fluid viscosity will result in a better mixing of the particles the more viscous the fluid is if internal friction is negligible. For some regions in the flow next to the initial fluid-grain pack boundary, a transient power-law behavior is observed for the dependence on time of particle pair separation. The exponent characterizing these power laws is observed to increase as a function of the fluid viscosity.

[1] P. Tegzes, T. Vicsek, and P. Schiffer, Phys. Rev. Lett. **89**, 094301 (2002).
[2] R. M. Iverson, M. Logan, and R. P. Denlinger, J. Geophys. Res. **109**, F01015 (2004).
[3] R. P. Denlinger and R. M. Iverson, J. Geophys. Res. **109**, F01014 (2004).
[4] J. Duran and A. Reisinger, *Sands, Powders, and Grains: An Introduction to the Physics of Granular Materials* (Springer-Verlag, New York, 1999).
[5] L. Bergougnoux, S. Ghicini, E. Guazzelli, and J. E. Hinch, Phys. Fluids **15**, 1875 (2003).
[6] E. Guazzelli, Phys. Fluids **13**, 1537 (2001).
[7] H. Nicolai, B. Herzhaft, E. J. Hinch, L. Oger, and E. Guazzelli, Phys. Fluids **7**, 12 (1995).

[8] H. Nicolai and E. Guazzelli, Phys. Fluids **7**, 3 (1995).
[9] J. L. Vinningland, Ø. Johnsen, E. G. Flekkøy, R. Toussaint, and K. J. Måløy, Phys. Rev. Lett. **99**, 048001 (2007).
[10] J. L. Vinningland, Ø. Johnsen, E. G. Flekkøy, R. Toussaint, and K. J. Måløy, Phys. Rev. E **76**, 051306 (2007).
[11] J. L. Vinningland, Ø. Johnsen, E. G. Flekkøy, R. Toussaint, and K. J. Måløy, Phys. Rev. E **81**, 041308 (2010).
[12] M. J. Niebling, E. G. Flekkøy, K. J. Måløy, and R. Toussaint, Phys. Rev. E **82**, 011301 (2010).
[13] Ø. Johnsen, R. Toussaint, K. J. Måløy, and E. G. Flekkøy, Phys. Rev. E **74**, 011301 (2006).
[14] Ø. Johnsen, C. Chevalier, A. Lindner, R. Toussaint, E. Clément, K. J. Måløy, E. G. Flekkøy, and J. Schmittbuhl, Phys. Rev. E **78**, 051302 (2008).
[15] S. McNamara, E. G. Flekkøy, and K. J. Måløy, Phys. Rev. E **61**, 4054 (2000).
[16] D.-V. Anghel, M. Strauss, S. McNamara, E. G. Flekkøy, and K. J. Måløy, Phys. Rev. E **74**, 029906(E) (2006).
[17] P. C. Carman, Chem. Eng. Res. Des. **75**, S32 (1997).
[18] E. G. Flekkøy, R. Delgado-Buscalioni, and P. V. Coveney, Phys. Rev. E **72**, 026703 (2005).
[19] W. H. Press and W. T. Vetterling, *Numerical Recipes* (Cambridge University Press, Cambridge, England, 2002).
[20] L. F. Richardson, Proc. R. Soc. London, Ser. A **110**, 709 (1926).
[21] T. H. Dupree, Phys. Fluids **9**, 1773 (1966).
[22] T. H. Dupree, Phys. Fluids **15**, 334 (1972).
[23] G. Boffetta, A. Celani, A. Crisanti, and A. Vulpiani, EPL **46**, 177 (1999).
[24] J. H. Misguich and R. Balescu, Plasma Phys. **24**, 289 (1982).

Granular Rayleigh-Taylor instability

Jan Ludvig Vinningland*, Øistein Johnsen*, Eirik G. Flekkøy*, Renaud Toussaint† and Knut Jørgen Måløy*

*Department of Physics, University of Oslo, P.0.Box 1048, N-0316 Oslo, Norway
†Institut de Physique du Globe de Strasbourg, CNRS, Université Louis Pasteur, 5 rue Descartes, 67084 Strasbourg Cedex, France

Abstract. A granular instability driven by gravity is studied experimentally and numerically. The instability arises as grains fall in a closed Hele-Shaw cell where a layer of dense granular material is positioned above a layer of air. The initially flat front defined by the grains subsequently develops into a pattern of falling granular fingers separated by rising bubbles of air. A transient coarsening of the front is observed right from the start by a finger merging process. The coarsening is later stabilized by new fingers growing from the center of the rising bubbles. The structures are quantified by means of Fourier analysis and quantitative agreement between experiment and computation is shown. This analysis also reveals scale invariance of the flow structures under overall change of spatial scale.

Keywords: granular flow, Rayleigh-Taylor instability, pattern formation, size invariance, simulation

INTRODUCTION

As grains become smaller the effect of the interstitial fluid becomes more important. The result is a combination of dry granular dynamics and the hydrodynamics of the fluid. These systems give rise to a variety of exotic and most often poorly understood phenomena such as fluidization [1] and bubble instabilities [2], quicksand and jet formation [3], and sandwich structures in systems where different particle types segregate [4]. While the study of dry granular media has been extensive over the past decades, the exploration of fluid-granular systems has been of more limited scope.

A wide range of granular instabilities where various structures form along fluid-grain interfaces have been reported the last few years [2, 5, 6, 7, 8] The instability discussed here arises when a closed, vertical Hele-Shaw cell, partially filled with fine grains and air at atmospheric pressure, is rapidly rotated to bring the dense packing of grains above a layer of air [9, 10]. Along the initially flat air-grain interface fine fingers emerge that subsequently develop into coarser finger-bubble structures. In contrast to the classical Rayleigh-Taylor instability [11] the coarsening process observed in the granular case will right from the start bring about a reduction in the number of fingers and a corresponding increase in the size of the bubbles. New fingers will form in the centre of the rising bubbles as they reach a certain width, thus keeping the characteristic size of the bubbles at a stable value.

Our experimental and numerical data compare favorably both qualitatively and quantitatively, despite the simplifications of the numerical model: Only two spatial dimensions, zero inter-particle friction, no gas inertia, and a grid resolution of 2.5 grain diameters. The finger-bubble structures further exhibit scale invariance under change of particle size, a feature which is supported both by observations and theoretical considerations.

EXPERIMENT

The experimental setup consists of a Hele-Shaw cell that can rotate vertically about its base, see Fig. 1(a). The Hele-Shaw cell is made of two 8-mm-thick glass plates separated by a silicone frame which defines the internal dimension of the cell. Before the second plate is attached,

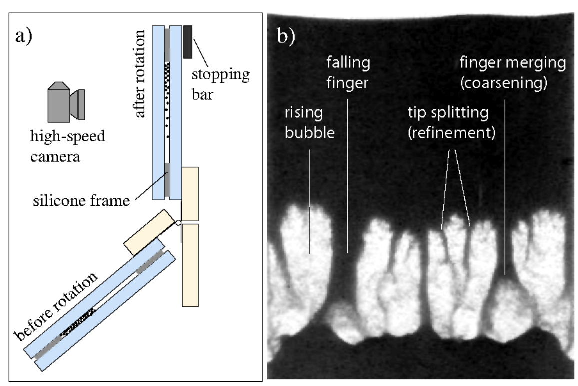

Figure 1. (a) Side view of the experimental setup. (b) Experimental image of the granular Rayleigh-Taylor instability where a layer of monodisperse polystyrene beads of 140 μm in diameter (black) displaces air (white) in a Hele-Shaw cell of dimensions 56 mm × 86 mm × 1 mm.

CP1145, *Powders and Grains 2009, Proceedings of the 6th International Conference on Micromechanics of Granular Media* edited by M. Nakagawa and S. Luding

the cell is filled with monodisperse polystyrene beads (Microbeads® from Dynoseeds) while in a horizontal position. To avoid electrostatic effects the humidity was kept constant at about 30% during the filling of the cells and throughout the experiment. Great care is taken to ensure an air tight cell by using clamps and applying a layer of silicone paste along the outer edge. The cell is flipped and tilted a few times to obtain a random loose packing of the grains and a presumably flat air-grain interface. The experiment starts by rotating the cell manually to an upright vertical position where a high speed digital camera (Photron Fastcam-APX 120K) records images (512x1024 pixels) of the advancing instability at a rate of 500 frames per second.

Four cells were assembled and filled with polystyrene beads of respectively 80, 140, 230 and 570 μm in diameter. The dimensions of the cells scale proportionally to the diameters of the grains they contain. Hence, the number of grains in the different cells is approximately constant. The experimental cells are somewhat taller than the numerical cells to account for the grains that settle during the rotation. The horizontal filling procedure makes it difficult to control the filling fraction and it may vary slightly among the four cells.

SIMULATION

The numerical model, first introduced by McNamara *et al.* [12, 13], combines a continuum description of the air with a discrete description of the granular phase. The granular phase is modeled as discrete, rigid spheres that collectively constitute a deformable porous medium. The pressure drop associated with the air flowing through the granular medium is given by a local Darcy's law with the Carman-Kozeny relation for the permeability κ [14]. The continuum gas phase is described solely by its pressure P. However, the velocity field of the gas may be obtained from the pressure gradient via Darcy's law. In order to provide a continuum description of the pressure $P(x,y)$ on a grid (x,y), the continuum variables solid fraction $\rho(x,y)$ and granular velocity $\vec{u}(x,y)$ need to be calculated. This is done by a linear smoothing function which is illustrated in Fig.2.

From the continuity equations of air mass and grain mass, using the seepage velocity of the air (i.e $\vec{u}_{Darcy}/\phi$), a pressure equation is derived, see [12, 13],

$$\phi\left(\frac{\partial P}{\partial t}+\vec{u}\cdot\vec{\nabla}P\right)=\vec{\nabla}\cdot\left(P\frac{\kappa(\phi)}{\mu}\vec{\nabla}P\right)-P\vec{\nabla}\cdot\vec{u}, \qquad (1)$$

where $\phi=1-\rho$ is the porosity. This equation is valid for compressible flow since it assumes $\rho_a \propto \phi P$ (isothermal ideal gas law) for the air-density, ρ_a. If instead an incompressible liquid is considered this assumption becomes

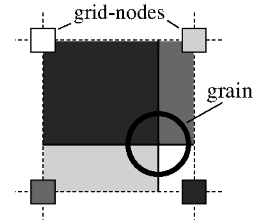

Figure 2. Illustrating the smoothing function: $\rho(x,y)$ ($\vec{u}(x,y)$) is calculated by adding a fraction of the grain's mass (velocity) to each of the four grid-nodes according to the relative position of the grain. The area of the four subdivisions corresponds to the fraction of mass (velocity) added to the node with a matching color.

$\rho_l \propto \phi$ for the liquid density ρ_l. The pressure equation (1) then simplifies to a Poisson equation for the pressure given by $\partial P/\partial t = \nabla\cdot(\kappa(\phi)/\mu\ \nabla P)-\nabla\cdot\vec{u}$.

The grains are governed by Newton's second law

$$m\frac{d\vec{v}}{dt}=m\vec{g}+\tilde{\mathrm{F}}_{\mathrm{I}}-\frac{V\vec{\nabla}P}{\rho}, \qquad (2)$$

where m, $\vec{v}$, and V are respectively the mass, velocity, and volume of a grain. The inter-particle normal force $\tilde{\mathrm{F}}_{\mathrm{I}}$ acting between grains in contact is calculated iteratively using contact dynamics [15] (but a Hookean or Hertzian contact law could also have been used). The dynamics of the grains are simplified by neglecting particle-particle and particle-wall friction. A lower cutoff is imposed on the solid fraction because the Carman-Kozeny relation is not valid for a solid fraction less than 0.25 [16]. This cutoff causes the permeability of the most dilute regions of the system to be slightly underestimated. The effect is a slight overestimation of the pressure forces acting on grains in dilute regions.

RESULTS

Comparing simulation and experiment

To study the coarsening of the finger-bubble structures quantitatively, we use the Fourier spectrum of the solid fraction to obtain a characteristic average wave number $\langle k\rangle$. An average Fourier power spectrum, $\bar{S}(k)$, is obtained from the individual power spectra calculated along each row of $\rho(x,y)$. A mean wave number is then defined as $\langle k\rangle=\sum_k\bar{S}(k)\cdot k/\sum_k\bar{S}(k)$, where $1/k$ is the wavelength. Likewise, the squared standard deviation is given by ${\sigma_k}^2=\sum_k\bar{S}(k)\cdot k^2/\sum_k\bar{S}(k)-\langle k\rangle^2$. For the experimental data the image pixel values are used to estimate the solid fraction.

Figure 3 shows the temporal evolution of $\langle k\rangle$ and σ_k (inset plot) for one simulation and two experiments. The

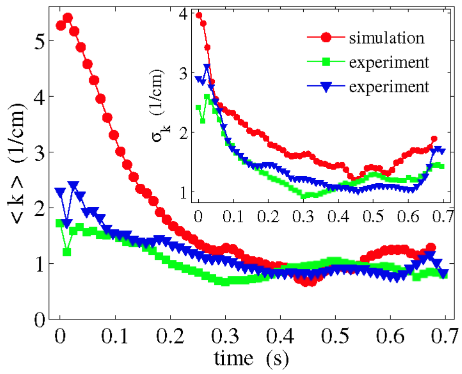

Figure 3. Mean wave number $\langle k\rangle$ and standard deviation σ_k (inset plot) for two experiments and one simulation, all using polystyrene beads of 140 µm in diameter.

initial discrepancy between the numerical and experimental data can be explained by difficulties in controlling the start conditions of the experiment, mainly caused by the manual rotation of the cell. After about 0.2 seconds the experimental and numerical data coincide and continue to show a similar coarsening behavior. The fluctuations of $\langle k\rangle$ and σ_k are associated with the continuous nucleation of new fingers and merging of existing fingers.

Scale invariance

We further investigate the behavior of the system as the overall spatial scale is changed. A series of seven simulations are performed using monodisperse packings with the grain diameter d ranging from 70 µm to 490 µm in steps of 70 µm. Each simulation starts with the same initial configuration of 160000 grains, but with a system size that scale proportionally to d.

In these simulations we have introduced the larger density of glass (2.5 g/cm^3), rather than polystyrene, in order to minimize the numerical artifacts associated with the solid fraction cutoff in the permeability. As the inertia of the grains decreases the overestimated pressure forces in the dilute regions of the system will act even stronger on the falling granular fingers.

Data-collapse plots of the rescaled mean wave number $d\langle k\rangle$ are shown in Figs. 4(a) (simulation) and 4(b) (experiment). These plots indicate that the characteristic size of the structures is invariant for a wide range of grain sizes when measured in units of d.

The convergence of the numerical data-collapse in Fig. 4(a) is quite good. The deviation of the 70 µm curve for small t is probably explained by the increase in the relative importance of the $P\vec{\nabla}\cdot\vec{u}$-term (see Ref. [9] for a theoretical interpretation of the scale invariance). The di-

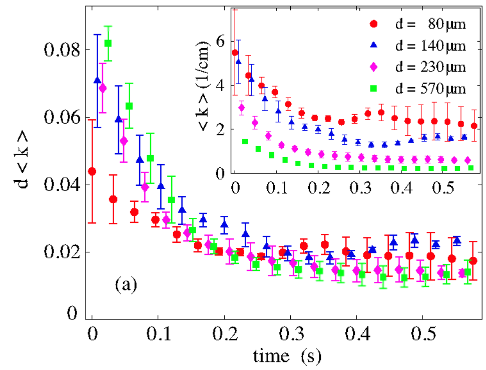

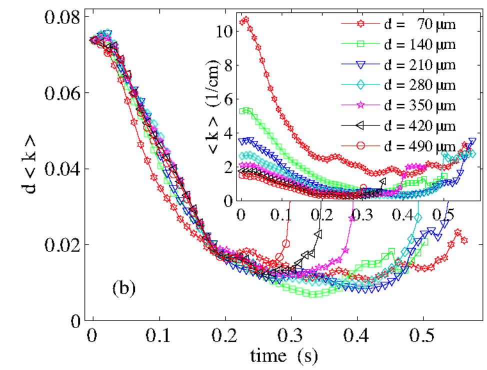

Figure 4. (a) Data-collapse plot of $d\langle k\rangle$ for experiments were the cell-size scales with the grain diameter d. (b) Data-collapse plot of $d\langle k\rangle$ for the numerical data. The inset plots show the evolution of the unscaled $\langle k\rangle$.

vergences of the 350, 420, and 490 µm curves for greater t in the same plot arise because the bubbles in the coarser packings disappear before they reach the surface since the permeability increases as grain diameter squared. The experimental data in Fig. 4(b) have a wider distribution but collapses satisfactorily given the standard deviation error bars. The experimental data are obtained by averaging over three experiments for each diameter d. The standard deviation is calculated over a time window of 0.025 seconds. The accuracy of the experiments is at its lowest during the initial coarsening of the structures, but as the mean wave number stabilizes around 0.2 seconds the accuracy improves. Nevertheless, the data points are, with a few exceptions, within a distance of one standard deviation from one another. The loss of precision for small times is most likely caused by the inaccuracy involved with the manual rotation.

Container size effects

In the experiments and simulations presented so far the size of the grains and the size of the container are

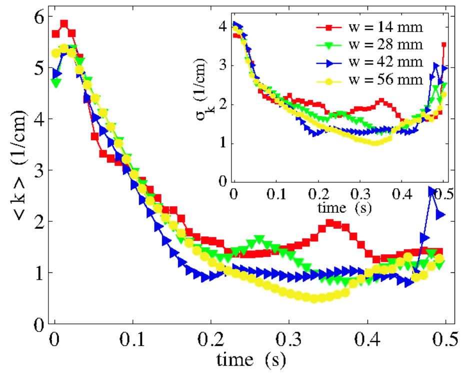

Figure 5. Plot of the mean wave number $\langle k\rangle$ and standard deviation σ_k (inset plot) obtained from simulations with grains of diameter d = 140 μm in four containers of different width w.

changed proportionally. Hence, the scale invariance can in principle depend both on the scaling of the grains and on the scaling of the container. To address this question, four simulations are performed using a fixed grain size but different container widths. Figure 5 shows $\langle k\rangle(t)$ and $\sigma_k(t)$ for four different simulations identified by the width of the packing w. During the coarsening stage, i.e. from t = 0 s until t = 0.2 s, the four curves overlap quite well. For t > 0.2 s the curves are more spread due to two peaks in the w = 14 mm and 28 mm data. These peaks are most likely caused by fluctuations in the evolving structures which are not averaged out due to less statistics for the narrow geometries. However, the data in Fig. 5 shows no systematic dependence on container size. As a consequence, the scale invariance only depends on the grain diameter d and is not sensitive to the scaling of the container.

CONCLUSION

The granular Rayleigh-Taylor instability is presented experimentally and numerically. The simulations reproduce the characteristic shape and size of the experimentally observed structures and provide fine patterns in the early phase of the process that are not resolved experimentally. Data-collapse plots of the mean wave number $\langle k\rangle$ indicate that the flow and the resulting structures are invariant when measured on a scale proportional to the grain diameter d for a range of diameters that spans from 70 μm to 570 μm.

REFERENCES

1. Hans J. Herrmann, J.-P. Hovi, and Stefan Luding, editors. *Physics of Dry Granular Media*, volume 350 of *NATO ASI Series E: Applied Sciences*, Dordrecht, 1998. Kluwer Academic Publishers.
2. D. Gendron, H. Troadec, K. J. Måløy, and E. G. Flekkøy. Bubble propagation in a pipe filled with sand. *Phys. Rev. E*, 64:021509, 2001.
3. D. Lohse, R. Rauhé, R. Bergmann, and D. van der Meer. Creating a dry variety of quicksand. *Nature*, 432(7018):689–690, December 2004.
4. C. Zeilstra, M. A. van der Hoef, and J. A. M. Kuipers. Simulation study of air-induced segregation of equal-sized bronze and glass particles. *Phys. Rev. E*, 74(1):010302(R), 2006.
5. Ø. Johnsen, R. Toussaint, K. J. Måløy, and E. G. Flekkøy. Pattern formation during air injection into granular materials confined in a circular hele-shaw cell. *Phys. Rev. E*, 74(1):011301, 2006.
6. C. Völtz, W. Pesch, and I. Rehberg. Rayleigh-taylor instability in a sedimenting suspension. *Phys. Rev. E*, 65:011404, December 2001.
7. A. Wysocki, C. P. Royall, R. G. Winkler, G. Gompper, H. Tanaka, A. van Blaaderen, and H. Löwen. Direct observation of hydrodynamic instabilities in driven non-uniform colloidal dispersions. arXiv:0810.1258v1 [cond-mat.soft], 2008.
8. Ø . Johnsen, C. Chevalier, A. Lindner, R. Toussaint, E. Clément, K. J. Måløy, E. G. Flekkøy, and J. Schmittbuhl. Decompaction and fluidization of a saturated and confined granular medium by injection of a viscous liquid or gas. *Phys. Rev. E*, 78(5):051302, 2008.
9. J. L. Vinningland, Ø. Johnsen, E. G. Flekkøy, R. Toussaint, and K. J. Måløy. Granular rayleigh-taylor instability: Experiments and simulations. *Phys. Rev. Lett.*, 99(4):048001, 2007.
10. J. L. Vinningland, Ø. Johnsen, E. G. Flekkøy, R. Toussaint, and K. J. Måløy. Experiments and simulations of a gravitational granular flow instability. *Phys. Rev. E*, 76(5):051306, 2007.
11. G. Taylor. The instability of liquid surfaces when accelerated in a direction perpendicular to their planes. I. *Proc. Roy. Soc. A*, 201(1065):192–196, March 1950.
12. S. McNamara, E. G. Flekkøy, and K. J. Måløy. Grains and gas flow: Molecular dynamics with hydrodynamic interactions. *Phys. Rev. E*, 61(4):4054–4059, 2000.
13. D.-V. Anghel, M. Strauß, S. McNamara, E. G. Flekkøy, and K. J. Måløy. Erratum: Grains and gas flow: Molecular dynamics with hydrodynamic interactions. *Phys. Rev. E*, 74(2):029906(E), 2006.
14. P. C. Carman. Fluid flow through granular beds. *Trans. Inst. Chem. Eng.*, 15:150–66, 1937.
15. F. Radjai, M. Jean, J.-J. Moreau, and S. Roux. Force distributions in dense two-dimensional granular systems. *Phys. Rev. Lett.*, 77(2):274–277, 1996.
16. A. A. Zick and G. M. Homsy. Stokes-flow through periodic arrays of spheres. *J. Fluid Mech.*, 115:13–26, 1982.

Granular Rayleigh-Taylor instability

Jan Ludvig Vinningland[1], Øistein Johnsen[1], Eirik G. Flekkøy[1], Renaud Toussaint[2], and Knut Jørgen Måløy[1]

[1] Department of Physics, University of Oslo, P.0.Box 1048, N-0316 Oslo, Norway
[2] Institut de Physique du Globe de Strasbourg, CNRS, Université Louis Pasteur, 5 rue Descartes, 67084 Strasbourg Cedex, France

Summary. A granular instability driven by gravity is studied experimentally and numerically. The instability arises as grains fall in a closed Hele-Shaw cell where a layer of dense granular material is positioned above a layer of air. The initially flat front defined by the grains subsequently develops into a pattern of falling granular fingers separated by rising bubbles of air. A transient coarsening of the front is observed right from the start by a finger merging process. The coarsening is later stabilized by new fingers growing from the center of the rising bubbles. The structures are quantified by means of Fourier analysis and quantitative agreement between experiment and computation is shown. This analysis also reveals scale invariance of the flow structures under overall change of spatial scale.

1 Introduction

Improved understanding of granular flows would be of essential importance to a range of industrial applications, to the study of geological pattern forming processes, and, in general, to the theoretical description of disordered media.

As grains become smaller the effect of the interstitial fluid becomes more important. The result is a combination of dry granular dynamics and the hydrodynamics of the fluid. These systems give rise to a variety of exotic and most often poorly understood phenomena such as fluidization [1] and bubble instabilities [2], quicksand and jet formation [3], and sandwich structures in systems where different particle types segregate [4]. While the study of dry granular media has been extensive over the past decades, the exploration of fluid-granular systems has been of more limited scope.

A wide range of granular instabilities where various structures form along fluid-grain interfaces have been reported the last few years [7, 2]. Notably, the patterns formed by grains falling in a highly viscous liquid were investigated experimentally and theoretically by Völtz et al. [8]. The instability reported by Völtz shares its main qualitative characteristics with the classical Rayleigh-Taylor instability, i.e. a single dominating wavelength growing right from the

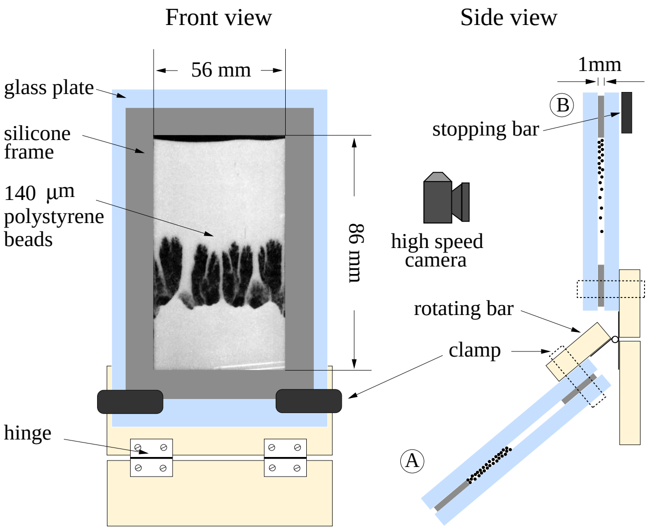

Fig. 1. Front and side view of the experimental setup. Two cell positions are superimposed in the side view to illustrate the manual rotation from position A to B.

start. In contrast, the instability discussed here arises along an air-grain interface where falling granular fingers and rising air-bubbles form [9, 10]. A coarsening of the finger-bubble pattern is observed right from the start of the instability. The coarsening subsequently stabilizes due to the continuous formation of new fingers at the centers of the rising and growing bubbles. Our experimental and numerical data compare favorably both qualitatively and quantitatively, despite the simplifications of the numerical model: Only two spatial dimensions, zero interparticle friction, no gas inertia, and a resolution of the gas-grid of 2.5 grain diameters. The finger-bubble structures further exhibit scale invariance under change of particle size, a feature which is supported both by observations and theoretical considerations.

The experiment is presented in Sec. 2, and the numerical model is outlined in Sec. 3. The analysis and the consistency check are presented in Section 4, together with the scale invariance observed when the grain diameter increases. The conclusion is given in Section 5.

2 Experiment

The experimental setup, illustrated in Fig. 1, consists of a closed Hele-Shaw cell mounted on a hinged bar which enables the cell to rotate approximately 130 degrees from a lower to an upper vertical position (from A to B in Fig. 1). The Hele-Shaw cell is made of a 1 mm thick silicone frame sandwiched between two 8 mm thick glass plates. The internal dimensions of the cell are 56 mm ×

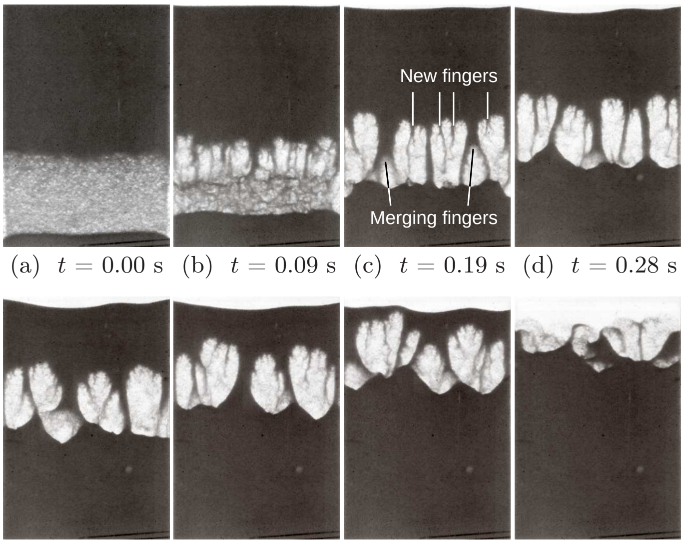

(a) $t = 0.00$ s (b) $t = 0.09$ s (c) $t = 0.19$ s (d) $t = 0.28$ s

(e) $t = 0.38$ s (f) $t = 0.47$ s (g) $t = 0.56$ s (h) $t = 0.66$ s

Fig. 2. Experimental images of the granular Rayleigh-Taylor instability where a layer of monodisperse polystyrene beads of 140 µm in diameter (black) displaces air (white) in a Hele-Shaw cell of dimensions 56 mm × 86 mm × 1 mm.

86 mm × 1 mm, and it is filled with polystyrene beads and air at atmospheric pressure. The cell is rotated manually and it takes about 0.2 seconds to bring the cell to an upright, vertical position. The off-center pivot of the cell causes the rotation to slow down the falling motion of the grains due to centrifugal forces. A bar is mounted at position B in order to have some control of the final vertical position of the cell. The evolution of the instability is recorded by a high speed digital camera (Photron Fastcam-APX 120K) taking images with a resolution of 512x512 pixels at a rate of 500 frames per second.

Monodisperse polystyrene beads of 140 µm in diameter (Microbeads® Dynoseeds TS 140-51) are used in the experiments. The filling of the cell is performed with one glass plate lying down horizontally with the silicone frame adhered on top. Small portions of beads are carefully deposited on the plate and leveled with the frame before the upper plate is attached and fasted with clamps. The cell is flipped a few times after closure to allow the grains to form a random loose packed configuration before the cell is rotated.

The humidity in the lab is important in order to keep the electrostatic and cohesive properties of the grains at a suitable level to prevent the grains from clustering or sticking to the glass plates. During the filling of the cell and throughout the experiment the humidity was kept constant at about 30%.

A series of images from the experiment is shown in Fig. 2. Due to experimental imperfections the initial air-grain interface in Fig. 2(a) is not a well-defined, horizontal front. This is mainly caused by three factors: (1) Os-

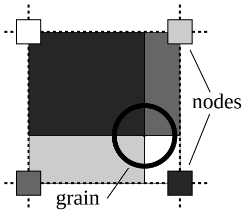

Fig. 3. Illustrating the smoothing function: A single grain i and its four neighbouring grid-nodes are shown. The four subdivisions of the cell-volume (i.e. the area between the stapled lines) correspond to the fraction of $\mathbf{v}_i$ (or m_i) that contributes to the continuous $\mathbf{u}(x, y)$ (or $\rho(x, y)$) fields at the *opposite* nodes. The gray-scale of the subdivisions indicates which node they belong to.

cillations in the cell caused by the abrupt stop as it reaches the vertical (and hits the bar), (2) the falling of grains during the rotation, and (3) the granular Boycott effect during rotation (i.e. grains and air pass each others in layers parallel to the plates) caused by the fact that up to 7 layers of beads may fit between the plates. However, all these experimental effects are non-persistent and in Fig. 2(b) the first finger-bubble structures are clearly visible. As the instability evolves a coarsening of the structures is observed. However, new fingers emerging from the center of the rising bubbles (see Fig. 2(c)) prevent the size of the structures to grow indefinitely and gives rise to a characteristic bubble-size. The coarsening is driven by fingers merging and forming an inverted Y as is indicated in Fig. 2(c).

3 Simulation

The numerical model, first introduced by McNamara *et al.* [11, 12], combines a continuum description of the air with a discrete description of the granular phase. The granular phase is a collection of rigid spheres that constitute a deformable porous media described by coarse grained solid fraction $\rho(x, y)$ and granular velocity $\mathbf{u}(x, y)$ fields on the grid where (x, y) are the two dimensional space coordinates. The continuous fields $\rho(x, y)$ and $\mathbf{u}(x, y)$ are obtained from the positions and velocities of the individual grains by means of a linear smoothing function: To calculate $\mathbf{u}(x, y)$ a fraction of $\mathbf{v}_i$ is distributed to each of the four neighbouring grid-nodes of grain i. This is illustrated in Fig. 3.

The continuum gas phase is described solely by its pressure $P(x, y)$. The inertia of the gas, and hence its velocity field, is not considered. This is justified for small particle Reynolds numbers as is the case for our system. The pressure is governed by the equation [11, 12]

$$\phi\Big(\frac{\partial P}{\partial t} + \mathbf{u}\cdot\boldsymbol{\nabla}P\Big) = \boldsymbol{\nabla}\cdot\Big(P\frac{\kappa(\phi)}{\mu}\boldsymbol{\nabla}P\Big) - P\boldsymbol{\nabla}\cdot\mathbf{u}\,, \tag{1}$$

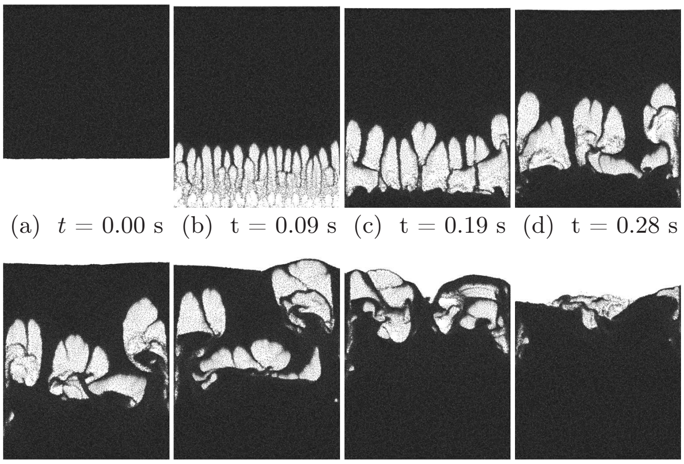

(a) $t = 0.00$ s (b) t = 0.09 s (c) t = 0.19 s (d) t = 0.28 s

(e) t = 0.38 s (f) t = 0.47 s (g) t = 0.56 s (h) t = 0.66 s

Fig. 4. Snapshots from a simulation where the input parameters are determined by the experiment in Fig. 2. The grain density is 1.05 g/cm^3, grain diameter is 140 µm, and the cell dimensions are 56 mm × 68 mm.

where $\phi(x, y) = 1 - \rho(x, y)$ is the porosity, $\kappa(x, y)$ the permeability, $\mathbf{u}(x, y)$ the granular velocity field, and μ the gas viscosity. This equation is derived from the conservation of air and grain mass, using Darcy's law [16] to obtain the pressure drop over a volume with permeability κ. The Carman-Kozeny relation [17] is assumed for the permeability, and the isothermal ideal gas law is assumed for the compressible gas. See Refs. [11, 12] for a detailed derivation. The empirical Carman-Kozeny relation is given by

$$\kappa(\rho, d) = \frac{d^2}{180} \frac{(1-\rho)^3}{\rho^2}\,, \tag{2}$$

where ρ is the local solid fraction, and d is the diameter of the grains, and 1/180 is an empirical constant valid for a packing of beads.

The grains are governed by Newton's second law

$$m\frac{d\mathbf{v}}{dt} = m\mathbf{g} + \mathbf{F}_\mathrm{I} - \frac{V\boldsymbol{\nabla}P}{\rho}\,, \tag{3}$$

where m, $\mathbf{v}$, and V are respectively the mass, velocity, and volume of the grain. Contact dynamics [18] is used to calculate the interparticle force $\mathbf{F}_\mathrm{I}$ which keeps the grains from overlapping. The dynamics of the grains are simplified by neglecting particle-particle and particle-wall friction. A lower cutoff is imposed on the solid fraction because the Carman-Kozeny relation is not valid as the solid fraction drops below 0.25 [19]. This cutoff causes the permeability of the most dilute regions of the system to be slightly lower than the true permeability. The effect is a slight overestimation of the pressure forces acting on the grains in the dilute regions.

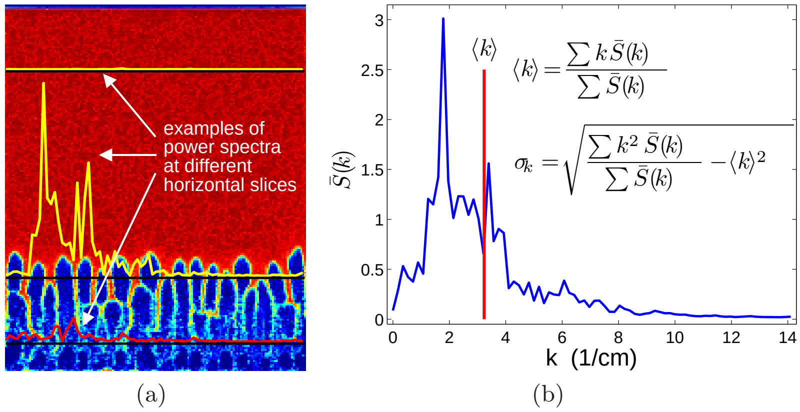

Fig. 5. (a) Power spectra superposed on the solid fraction field from which they are obtained. (b) The averaged power spectrum of the solid fraction field shown in (a) with the mean wave number $\langle k \rangle$ indicated.

Figure 4 shows a series of snapshots from a simulation with the same grain diameter, grain density, and cell dimensions (except for the cell thickness since the simulation is 2D) as in the experiment shown in Fig. 2. A qualitative comparison of the image-series in Figs. 2 and 4 renders the simulation and experiment consistent in many respects: The sizes of the bubbles and the fingers are comparable, and the dynamical processes of finger merging and finger nucleation are observed in both cases. Nevertheless, some discrepancies are observed, particularly at the start and toward the end of the instability. The initial differences are mainly attributed to imperfections of the experimental setup: In the experiments the instability start from a homogeneous sheet of grains rather than from a sharp air-grain interface as in the simulations. Further differences are observed toward the end of the instability: In the numerical snapshots bigger bubbles reach the upper surface before the smaller bubbles (see e.g. Fig. 4(f)). In the experiment, however, the row of bubbles stays more or less horizontally aligned from start to finish. We believe this is an effect of the zero grain-wall and grain-grain friction used in the simulation.

4 Results

To study the coarsening of the observed structures quantitatively we use the Fourier spectrum of the solid fraction field to obtain a characteristic average wave number $\langle k \rangle$ by the following procedure. The discrete Fourier transform and the power spectrum of each horizontal line of $\rho(x, y)$ is calculated. The averaged power spectrum, $\bar{S}(k)$, is then obtained by averaging over all these horizontal power spectra. An average wave number is defined

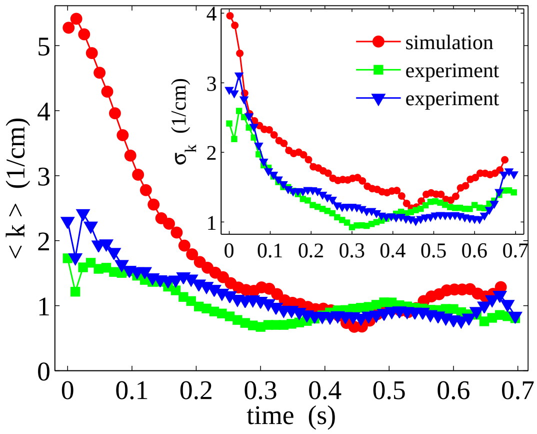

Fig. 6. Mean wave number $\langle k \rangle$ and standard deviation σ_k (inset) for two experiments and one simulation, all using polystyrene beads of 140 µm in diameter.

as $\langle k \rangle = \sum_k \bar{S}(k) \cdot k / \sum_k \bar{S}(k)$, where $1/k$ is the wavelength. Likewise, we define the squared standard deviation ${\sigma_k}^2 = \sum_k \bar{S}(k) \cdot k^2 / \sum_k \bar{S}(k) - \langle k \rangle^2$. For the experimental data the image pixel values are used to estimate the solid fraction. Figure 5(a) shows $\rho(x, y)$ for $t = 0.09$ s and three power spectra obtained at different vertical positions (indicated by black lines). Figure 5(b) shows the averaged power spectrum $\bar{S}(k)$ and mean wave number $\langle k \rangle$ of the solid fraction field in Fig. 5(a).

Figure 6 shows the temporal evolution of $\langle k \rangle$ and σ_k (inset) for the numerical and experimental data. An additional set of experimental data is added to the plot. The numerical curve starts out with a significantly higher wave number than the experimental curves. This behaviour is however expected given the difference in initial conditions. After about 0.2 seconds the experimental and numerical data coincide and continue to show a similar coarsening behavior. The fluctuations of $\langle k \rangle$ and σ_k are associated with the continuous nucleation of new fingers and merging of existing fingers.

We further investigate the behavior of the system as the overall spatial scale is changed: Keeping all length ratios and the particle number fixed, the size of the system will scale according to the diameter d of the grains. We measure the characteristic inverse length scale $\langle k \rangle$ as d is changed and observe a scale invariance of the evolution. A series of seven simulations are performed where d varies from 70 µm to 490 µm in steps of 70 µm. The dimension of the numerical cell confining grains of 70 µm in diameter is 28 mm x 34 mm. To compare, a series of experiments using polystyrene beads of 80, 140, 230, and 570 µm in diameter, confined in Hele-Shaw cells that scale proportionally with d in all directions, are performed.

In these simulations we have introduced the larger density of glass, rather than polystyrene in order to minimize the numerical artifacts associated with

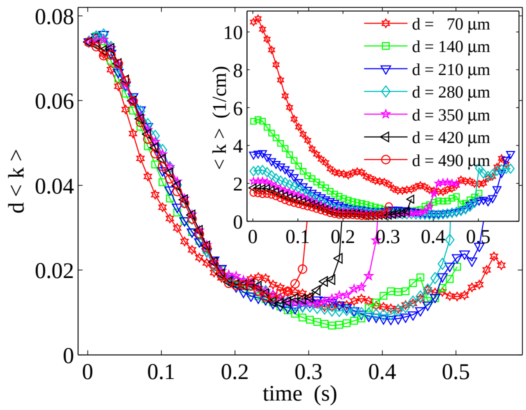

(a) Simulation

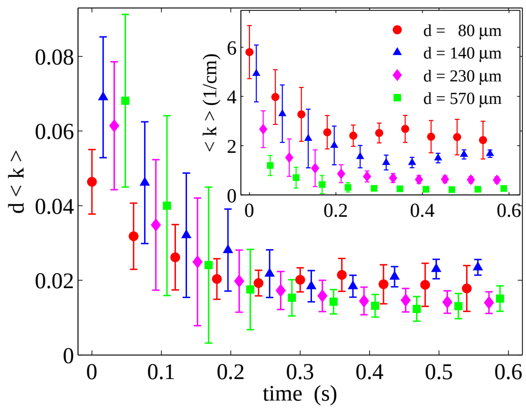

(b) Experiment

Fig. 7. Data-collapse plot of $d\langle k\rangle$ for a series of (a) simulations using glass beads, and (b) experiments using polystyrene beads. The grain diameters d are given in the legend box. The inset shows the evolution of the unscaled $\langle k\rangle$.

the solid fraction cutoff in the permeability. As the inertia of the grains decreases the overestimated pressure forces in the dilute regions of the system will act even stronger on the falling granular fingers.

Data-collapse plots of the rescaled mean wave number $d\langle k\rangle$ are shown in Figs. 7(a) (simulation) and 7(b) (experiment). These plots indicate that the characteristic size of the structures is invariant when size is measured in units of d; the number of grains that spans the width of the bubbles is the same for a wide range of grain sizes.

Theoretically, the scale invariance of the product $d\langle k\rangle$ may be interpreted as follows: Compared to the other terms of Eqs. (1) and (3) the $m\,d\mathbf{v}/dt$,

F_{I} and $P\boldsymbol{\nabla}\cdot\mathbf{u}$ terms may be shown to be small [20]. For that reason, these equations exhibit an approximate invariance under system size scaling. If we take δP to be the pressure deviation from the background pressure, express the velocity of grain i as $\mathbf{v}_i = \delta\mathbf{v}_i + \mathbf{u}_0$ and the locally averaged granular velocity as $\mathbf{u} = \delta\mathbf{u} + \mathbf{u}_0$, where $\mathbf{u}_0$ is the constant sedimentation velocity of a close packed system, this scaling may be expressed as $\mathbf{x} \to \lambda\mathbf{x}$, $\delta P \to \lambda\delta P$, $\mathbf{u}_0 \to \lambda^2\mathbf{u}_0$, $\delta\mathbf{u} \to \lambda\delta\mathbf{u}$ and $\kappa \to \lambda^2\kappa$, where λ is a scale factor. The structure formation of the system is governed by $\delta\mathbf{u}$ and, since this velocity scales the same way with λ as the length scales themselves, the evolution of any structure measured in units of d will be scale invariant. In particular this is true for the structures measured by the length $1/\langle k\rangle$, and so $d\langle k\rangle$ is scale invariant. However, the invariance deteriorates both when particle size is increased, and when it is decreased. In the first case, the relative effect of granular inertia is increased, in the second, the relative effect of the $P\boldsymbol{\nabla}\cdot\mathbf{u}$ term is increased.

The convergence of the numerical data-collapse in Fig. 7(a) is quite good. The deviation of the 70 µm curve for small t is probably explained by the increase in the relative importance of the $P\boldsymbol{\nabla}\cdot\mathbf{u}$-term. The divergences of the 350, 420, and 490 µm curves for greater t in the same plot arise because the bubbles in the coarser packings disappear before they reach the surface due to the increase of $\mathbf{u}_0$ with λ^2 [20]. The experimental data in Fig. 7(b) have a wider distribution but collapses satisfactorily given the standard deviation error bars. The experimental data are obtained by averaging over three experiments for each diameter d. The standard deviation is calculated over a time window of 0.3 seconds. The accuracy of the experiments is at its lowest during the initial coarsening of the structures, but as the mean wave number stabilizes around 0.2 seconds the accuracy improves. Nevertheless, the data points are, with a few exceptions, within a distance of one standard deviation from one another. The loss of precision for small times is most likely caused by the inaccuracy involved with the manual rotation.

5 Conclusion

In conclusion, we have presented experimental and numerical results of a gravity-driven granular flow instability which is significantly different from its classical hydrodynamic analog. The simulations reproduce the characteristic shape and size of the experimentally observed structures and provide fine patterns in the early phase of the process that are not resolved experimentally. Data-collapse plots of the mean wave number $\langle k\rangle$ indicate that the flow and the resulting structures are invariant when measured on a scale proportional to the grain diameter d for a range of diameters that spans from 70 µm to 570 µm.

References

1. H. J. Herrmann, J.-P. Hovi, and S. Luding, editors. *Physics of Dry Granular Media*, volume 350 of *NATO ASI Series E: Applied Sciences*, Dordrecht, 1998. Kluwer Academic Publishers.
2. D. Gendron, H. Troadec, K. J. Måløy, and E. G. Flekkøy. Bubble propagation in a pipe filled with sand. *Phys. Rev. E*, 64:021509, 2001.
3. D. Lohse, R. Rauhé, R. Bergmann, and D. van der Meer. Creating a dry variety of quicksand. *Nature*, 432(7018):689–690, December 2004.
4. C. Zeilstra, M. A. van der Hoef, and J. A. M. Kuipers. Simulation study of air-induced segregation of equal-sized bronze and glass particles. *Phys. Rev. E*, 74(1):010302(R), 2006.
5. G. Taylor. The instability of liquid surfaces when accelerated in a direction perpendicular to their planes. i. *Proc. Roy. Soc. A*, 201(1065):192–196, March 1950.
6. J. S. Langer. Instabilities and pattern formation in crystal growth. *Rev. Mod. Phys.*, 52(1):1–28, Jan 1980.
7. Ø. Johnsen, R. Toussaint, K. J. Måløy, and E. G. Flekkøy. Pattern formation during air injection into granular materials confined in a circular hele-shaw cell. *Phys. Rev. E*, 74(1):011301, 2006.
8. C. Völtz, W. Pesch, and I. Rehberg. Rayleigh-taylor instability in a sedimenting suspension. *Phys. Rev. E*, 65:011404, December 2001.
9. J. L. Vinningland, Ø Johnsen, E. G. Flekkøy, R. Toussaint, and K. J. Måløy. Granular rayleigh-taylor instability: Experiments and simulations. *Phys. Rev. Lett.*, 99(4):048001, 2007.
10. J. L. Vinningland, Ø. Johnsen, E. G. Flekkøy, R. Toussaint, and K. J. Måløy. Experiments and simulations of a gravitational granular flow instability. *Phys. Rev. E*, to appear.
11. S. McNamara, E. G. Flekkøy, and K. J. Måløy. Grains and gas flow: Molecular dynamics with hydrodynamic interactions. *Phys. Rev. E*, 61(4):4054–4059, 2000.
12. D.-V. Anghel, M. Strauß, S. McNamara, E. G. Flekkøy, and K. J. Måløy. Erratum: Grains and gas flow: Molecular dynamics with hydrodynamic interactions. *Phys. Rev. E*, 74(2):029906(E), 2006.
13. E. G. Flekkøy, S. McNamara, K. J. Måløy, and D. Gendron. Structure formation and instability in a tube of sand. *Phys. Rev. Lett.*, 87(13):134302, 2001.
14. M. Strauß, S. McNamara, H. J. Herrmann, G. Niederreiter, and K. Sommer. Plug conveying in a vertical tube. *Powder Tech.*, 162:16, 2006.
15. E. G. Flekkøy, A. Malthe-Sørenssen, and B. Jamtveit. Modeling hydrofracture. *J. Geophys. Res.*, 107 (B8)(2151), 2002.
16. H. Darcy. *Les Fontaines Publiques de la Ville de Dijon.* Dalmont and Paris, 1856.
17. P. C. Carman. Fluid flow through granular beds. *Trans. Inst. Chem. Eng.*, 15:150–66, 1937.
18. F. Radjai, M. Jean, J.-J. Moreau, and S. Roux. Force distributions in dense two-dimensional granular systems. *Phys. Rev. Lett.*, 77(2):274–277, 1996.
19. A. A. Zick and G. M. Homsy. Stokes-flow through periodic arrays of spheres. *J. Fluid Mech.*, 115:13–26, 1982.
20. J. L. Vinningland, Ø. Johnsen, E. G. Flekkøy, R. Toussaint, and K. J. Måløy. Size invariance in granular flows: simulation and experiment. unpublished.

Eur. Phys. J. Special Topics **204**, 27–40 (2012)

DOI: 10.1140/epjst/e2012-01550-2

THE EUROPEAN PHYSICAL JOURNAL SPECIAL TOPICS

Regular Article

Family-Vicsek scaling of detachment fronts in Granular Rayleigh-Taylor instabilities during sedimentating granular/fluid flows

J.L. Vinningland[1,2], R. Toussaint[3,a], M. Niebling[1,3], E.G. Flekkøy[1], and K.J. Måløy[1]

[1] Department of Physics, University of Oslo, PO Box 1048, 0316 Oslo, Norway
[2] International Research Institute of Stavanger, IRIS, PO Box 8046, 4068 Stavanger, Norway
[3] IPGS, University of Strasbourg, CNRS, 5 rue Descartes, 67000 Strasbourg, France

Received 23 December 2011 / Received in final form 22 February 2012
Published online 17 April 2012

Abstract. When submillimetric particles are confined in a fluid such that a compact cluster of particles lie above the clear fluid, particles will detach from the lower boundary of the cluster and form an unstable separation front giving rise to growing fingers of falling particles. We study this problem using both experiments and hybrid granular/fluid mechanics models. In the case of particles from 50 to 500 microns in diameter falling in air, we study the horizontal density fluctuations at early times: the amplitude of the density difference between two points at a certain horizontal distance grows as a power law of time. This happens up to a saturation corresponding to a power law of the distance. The way in which the correlation length builds up to this saturation also follows a power law of time. We show that these decompaction fronts in sedimentation problems follow a Family-Vicsek scaling, characterize the dynamic and Hurst exponent of the lateral density fluctuations, respectively $z \sim 1$ and $\zeta \sim 0.75$, and show how the prefactors depend on the grain diameter. We also show from similar simulations with a more viscous and incompressible fluid, that this feature is independent of the fluid compressibility or viscosity, ranging from air to water/glycerol mixtures.

1 Introduction

In many natural and industrial situations, mixtures of granular materials and fluids are deformed. Physicists have intensively studied granular mechanics using discrete methods over the last 30 years [1,2] since the rise of powerful computers, to investigate various types of avalanche dynamics [3], the dynamics of sheared layers [4,5] and the stress distribution in sandpiles [6], to mention but a few. For sufficiently small grains,

[a] e-mail: renaud.toussaint@unistra.fr

when the fluid seeps through the granular assembly, the resulting drag is sufficient to rearrange the grains, and it is necessary to take into account the momentum exchange between the granular and the fluid phase to understand the dynamics.

Such hybrid granular/fluid flows are manifested in many natural flows at the surface of the earth: e.g. in liquefaction [7], mudflows [8–10], or sand volcanoes. They also play a role in underwater avalanches and turbidites, or in sedimentation processes when large amounts of sediments are released and deposited. Eventually, their understanding are crucial for the mechanical stability in borehole exploration operations, during pumping in to or out of man-made wells, in hydrofracture [11], or for the understanding of reservoir stability and fault lubrication [12].

Elementary situations of sedimenting grains in a fluid and their stability have been recently studied in generic situations where a dense granular packing saturated with a fluid is subjected to a flow of the same fluid, as in the propagation of rising bubbles in air-grain flows in tubes, or the intermittency of flows in ticking hourglasses [13–15]. Experiments with dense granular packings displaced by pressurized air have been followed optically in Hele-Shaw cells [16–20], and studied numerically using models where the momentum exchange is based on a Darcy description of the flow with a grid resolution of a few grain diameters [21,22].

For example, when a granular packing in a circular cell where gravity acts perpendicularly to the cell walls starts to flow due to a sufficient air-overpressure in the centre, an instability corresponding to a granular Saffman-Taylor analog was observed [16,23]. Such analog behavior was also observed in linear cells, either with a free boundary at the outlet leading to decompaction [17,18], or with a confined flow for the particles leading to compaction [24,25]. Changing the properties of the interstitial fluid with orders of magnitudes in viscosity and compressibility (between oil and air) was shown to affect the dynamics of this process, but to lead to the formation of similar patterns [18].

When gravity is acting along the flow, a granular analog of the Rayleigh-Taylor instability has been studied: situations where initially a pack of dense grains are released into a zone of lighter fluid. The same fluid is also present in the interstitial space between the packed grains. This situation would naturally arise during sedimentation flows, e.g. when a sudden amount of compact material is released in open water. This instability has been studied with mixtures of grains (typically $100\,\mu$m in diameter) and air [19,26,27], and with less compressible and more viscous fluids such as water glycerol or oil [20,28,29].

The release of such dense packs of grains in a clear fluid contained in a closed cell, leads to the formation of a detachment front at the bottom of the pack. The particles fall faster from the bottom part than from the upper part of the pack, and fingers form in the previously clear fluid region. This front is unstable, grows fast in amplitude, and leads to coarsening bubbles empty of grains rising through the grain pack. The dynamics of this front has been studied using Fourier analysis by investigating the growth of each mode [19,26,30,31]. In this system, the change of the particle size, for sizes ranging from roughly 50 to $500\,\mu$m in diameter, was shown to leave the system dynamics invariant, using the grain diameter as the characteristic length scale.

We will show in this manuscript that the horizontal density profiles, as function of time and space, for different particle sizes, can be entirely collapsed and shown to follow a Family-Vicsek scaling. Such scaling, introduced by Family and Vicsek [32], was found to be obeyed by many surface growth processes. It relates the anomalous diffusion of a quantity, the growth of correlations, and the self affine geometry of the developed interface - or of the quantity characterized by this scaling [33]. For example, such a collapse was observed for the thermal fluctuations of magnetic hole assemblies, which are dipolar chains in thin fluid cells [34–36]. It is also obeyed by natural patterns slowly growing in rocks, as pressure solution seams evolve into stylolites [37–40].

This implies that a correlation length grows in this system, as a power law of time, $\xi \sim t^{1/z}$, with a dynamic exponent around $z \sim 1$. For scales above ξ, the root mean square of the lateral density fluctuations grows in a super diffusive way, as $\sigma \sim t^{\beta}$ with a growth exponent around $\beta \sim 0.75$. Below the correlation length, the density profiles are shown to be self-affine, with a Hurst exponent around $\zeta \sim 0.75$.

The Family-Vicsek scaling satisfied by the density fluctuations with these growth, Hurst and dynamic exponents is found to be universal for the granular Rayleigh-Taylor instability, in the sense that it is satisfied independently of the nature of the fluid over a rather large range of viscosities and compressibilities: we show here simulations performed both in lowly viscous and highly compressible air-granular mixtures, and in viscous and incompressible water/granular mixtures. They will be shown to follow the same Family Vicsek scaling, with the same exponents: they belong to the same universality class. Note, however, that other surface growth processes follow Family Vicsek scalings, but with different exponents (see [41] for many examples), and other growth processes do not display any such scaling. In particular cases, similar power laws are found between the fluctuation of the root mean square width as function of time and space, and the correlation length as function of time, but without the scaling relation between growth, Hurst and dynamic exponents $\beta = H/z$ obeyed in a Family Vicsek scaling form. In this case, one has a reduced form of scaling, called anomalous scaling [42].

In the next section, we will summarize the methodologies used to study the granular Rayleigh-Taylor instability, from an experimental and from a numerical perspective. Next, we will describe the types of patterns obtained at different particle sizes. Eventually, we will perform the Fourier analysis of the density fluctuations, and show that they can be collapsed at different times, for different wave numbers and for all investigated particle sizes on a master curve, displaying the fact that they follow a Family-Vicsek scaling.

2 Rayleigh-Taylor instability: Definition and methods

2.1 Experimental setup

Historically, the Rayleigh-Taylor instability arises from a flat interface when a dense fluid is initially situated above a lighter one: in a closed container, the two fluids interchange positions while forming a fingering pattern. This instability, and the selection of a preferred wavelength due to the interplay between gravitational, capillary and viscous forces was first studied by Lord Rayleigh and I. G. Taylor [43,44]. The granular analog of this instability has been studied recently with air or more viscous fluids: it arises when initially a pack of dense grains is released on top of clear fluid in a closed vessel. There is no surface tension in this problem since the fluid is also initially present in the porous space between the grains in the upper pack.

The experiments are performed in a closed impermeable Hele-Shaw cell, which is initially prepared by letting grains accumulate at the bottom. The cell is then suddenly rotated to be brought upside down, and a damping bar stops the cell in a vertical direction, attenuating vibrations as much as possible. The setup is illustrated in Fig. 1(a). Several system sizes have been used for the air-grain experiments, ranging from 80 μm diameter beads to 570 μm diameter beads. The system sizes are proportional to the bead diameters, with system widths spanning from 30 to 200 mm, see Fig. 1(c). The grains used in the experiments where polystyrene spheres (Ugelstad spheres from Microbeads), with a density of 1.05 g/cm^3.

Early stages of the experimental pictures are shown on Fig. 1(b) and Fig. 2.

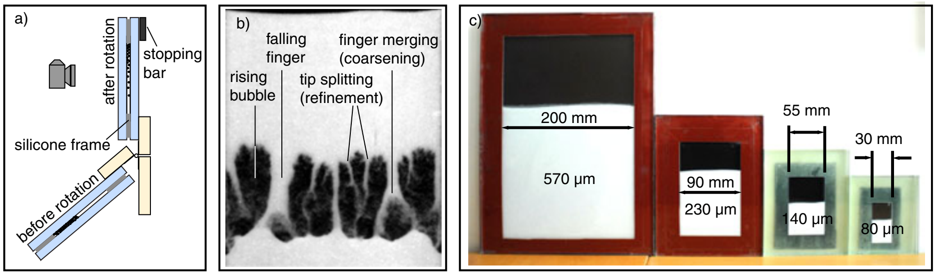

Fig. 1. (a) Experimental setup and principle, (b) typical granular Rayleigh-Taylor flow, where fingers of falling grains (white) form in the previously air-filled region (black) during an experiment, and (c) the experimental cells of different sizes with grains of proportional diameters.

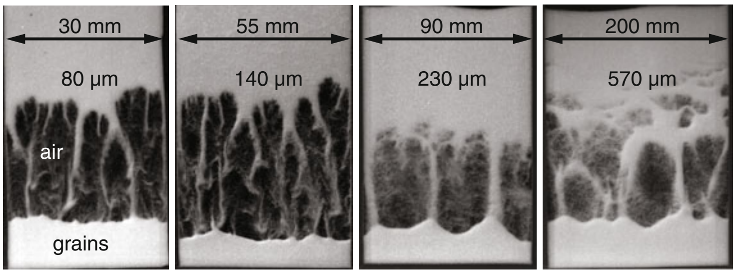

Fig. 2. Experimental snapshots of the granular Rayleigh-Taylor instability in air where the four cells shown in Fig. 1(c) are used.

2.2 Simulation technique

The simulation techniques are described in details in [19] for the flow of grains and compressible air, or [20] for the flow of grains and incompressible viscous fluid.

In summary, the principle is as follows: the grains interact via repelling contact forces and via a drag force due to the flow of the interstitial fluid. This can be expressed as Newton's second law for each grain, as

$$ma = F_I + (\rho_g - \rho_f)g - \nabla P/\rho \tag{1}$$

where m and a are the grain mass and acceleration; F_I corresponds to the solid interaction forces with neighboring grains; the third term corresponds to buoyancy forces; the last term to seepage forces; g is the gravity; ρ_f and ρ_g are the fluid and solid bulk mass densities; ρ is the number density of the grains: $\rho = V_g/(1-\Phi)$ with V_g the grain volume; Φ is the porosity. $P = P_T - \rho_f gz$ is the fluid pressure deviating from the hydrostatic profile – where P_T is the total fluid pressure and z the depth. This pressure is evaluated over a grid discretized at the representative elementary volume scale (the Darcy scale, a few grains large).

This equation is being solved at each time step, using a Verlet algorithm in molecular dynamic codes. The forces F_I are determined from elastic contact model [16,20], or from a contact dynamics scheme [19].

The dynamic equation solved for the fluid results from the following principles: mass conservation for the grains, mass conservation for the fluid, equation of state for the fluid, and Darcy's law to get the relative velocity between the fluid and the solid. Calling u the grain velocity, v the fluid velocity, and ρ_f the fluid density, this can be expressed at the Darcy scale as

$$\partial_t(1-\Phi)+\nabla\cdot((1-\Phi)\,u)=0 \tag{2}$$

$$\partial_t(\rho_f\Phi)+\nabla\cdot(\Phi\rho_f v)=0 \tag{3}$$

$$v-u=-\frac{\kappa\nabla P}{\mu\Phi} \tag{4}$$

where μ is the fluid viscosity, κ is the local permeability of the packing, evaluated from the Carman-Kozeny equation

$$\kappa=\frac{d^2}{180}\frac{\Phi^3}{(1-\Phi)^2}$$

and the fluid mass conservation is expressed as one of the two alternatives: in general, linearizing this equation of state, one gets

$$\rho_f(P)=\rho_0\,(1+\beta\,(P-P_0))$$

where β is the fluid compressibility, P_0 an initial (reference) pressure, and ρ_0 the fluid density at that pressure.

This set of equations leads to the following reduced form:

$$\Phi\,(\partial_t P+u\cdot\nabla P)=\nabla\cdot\left(\hat{P}\frac{\kappa}{\mu}\nabla P\right)-\hat{P}\nabla\cdot u \tag{5}$$

where $\hat{P}=\rho_f/(\rho_0\beta)=P-P_0+1/\beta$.

Considering air as a perfect gas, this reduces to $\rho_f=\rho_0 P/P_0$, $\beta=1/P_0$ and $\hat{P}=P$, so that

$$\Phi\,(\partial_t P+u\cdot\nabla P)=\nabla\cdot\left(P\frac{\kappa}{\mu}\nabla P\right)-P\nabla\cdot u \tag{6}$$

which is solved alternately with the molecular dynamic time steps, using a Cranck-Nicholson algorithm [45].

For a viscous fluid considered as incompressible, we have $\beta=0$, $\rho_f=\rho_0$ and the Eq. (5) in the limit $\hat{P}\to\infty$, reduces to

$$\nabla\cdot\left(\frac{\kappa}{\mu}\nabla P\right)=\nabla\cdot u$$

which is solved at each time step using a multigrid algorithm [45].

2.3 Dynamics of the granular Rayleigh-Taylor instability

In both experiments and simulations, for grains falling in air or in water/glycerol, the dynamics can be qualitatively described as follows: From the initial configuration where grains are packed above the clear fluid region, the dense grains start to flow downward, i.e. sediment, while the fluid passes through the grains. This situation leads to the formation of fingers of particles detaching from the lower boundary of the upper compact pack. These fingers of particles regroup, and bubbles of low particle

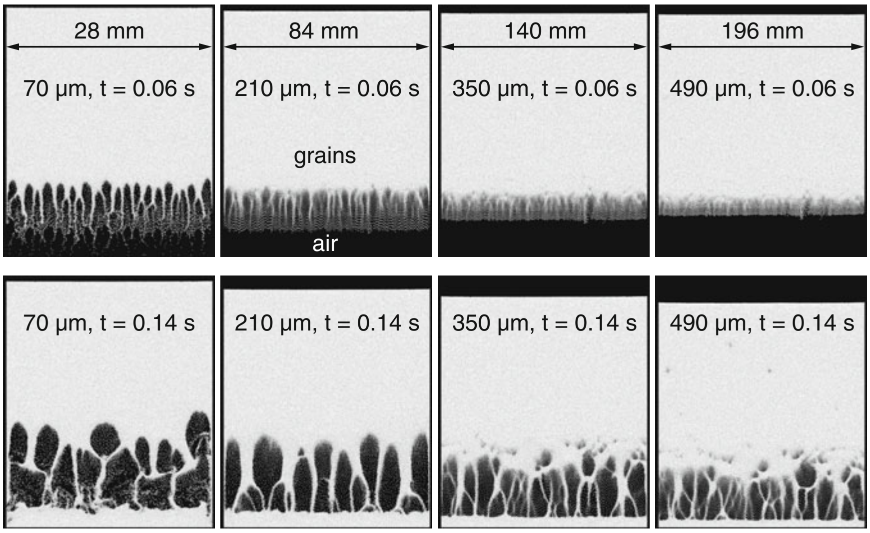

Fig. 3. Simulation at four different grain/system sizes (horizontal axis) at two different times (vertical axis) showing the development of the instability with the initial front destabilization in the top row.

density form in the pack, rise and coalesce. This dynamics is illustrated in Fig. 2 (experimentally) and Fig. 3 (numerically), for the air/grain case, and in Fig. 4 for the incompressible fluid/grain case.

We notice that at low viscosities, simulations with incompressible fluids are reminiscent of the dynamics obtained with compressible air. As the viscosity is increased (from top to bottom in Fig. 4), the fingers get mixed more rapidly as they detach from the lower front of the compact pack. The grains have here a size of 140 microns in diameter, and a density of 2.5 g/cm^3, the fluid has the density of water.

One way to analyze the instability of the detachment front, at the bottom of the compact pack, is to compute horizontal density profiles. In this way, it is possible to measure the lateral growth of density fluctuations, while the fingers form and regroup. This can be done at each horizontal level at vertical coordinate y and time t, extracting density fronts as function of the horizontal variable x, $\rho(x, y, t)$. This is illustrated in Fig. 5.

The most variable profiles as function of x are just below the detachment front: the particle density is roughly constant (at a scale above a few grains) in the compact packing above the detachment front, and constant and low in the empty region below. Hence, to increase the statistical quality of the quantity we analyze, we perform the average over all horizontal profiles at a given time, and obtain in this way horizontal density profiles $\rho(x, t) = \langle\rho(x, y, t)\rangle_y$. For the experiments, the density is not known directly, but the same procedure is performed on the basis of light intensity (pixel gray value) recorded with a fast camera.

These horizontal density functions are then spatially Fourier transformed, and their Fourier power-spectra are represented at various times and for various grain sizes using a bi-logarithmic scale, as is shown in Fig. 6 for the simulations, and in Fig. 7 for the experiments. The inset plots represent the raw power spectra for all sizes, and the full figures indicate the power spectra using the grain diameters as a unit size. The comparison between inset and main plot shows the size collapse.

The experiments and simulations with compressible air have been analyzed as function of the particle size. Snapshots of the early times of these simulations with variable particle sizes are shown in Fig. 2. A spatial rescaling using the grain diameter

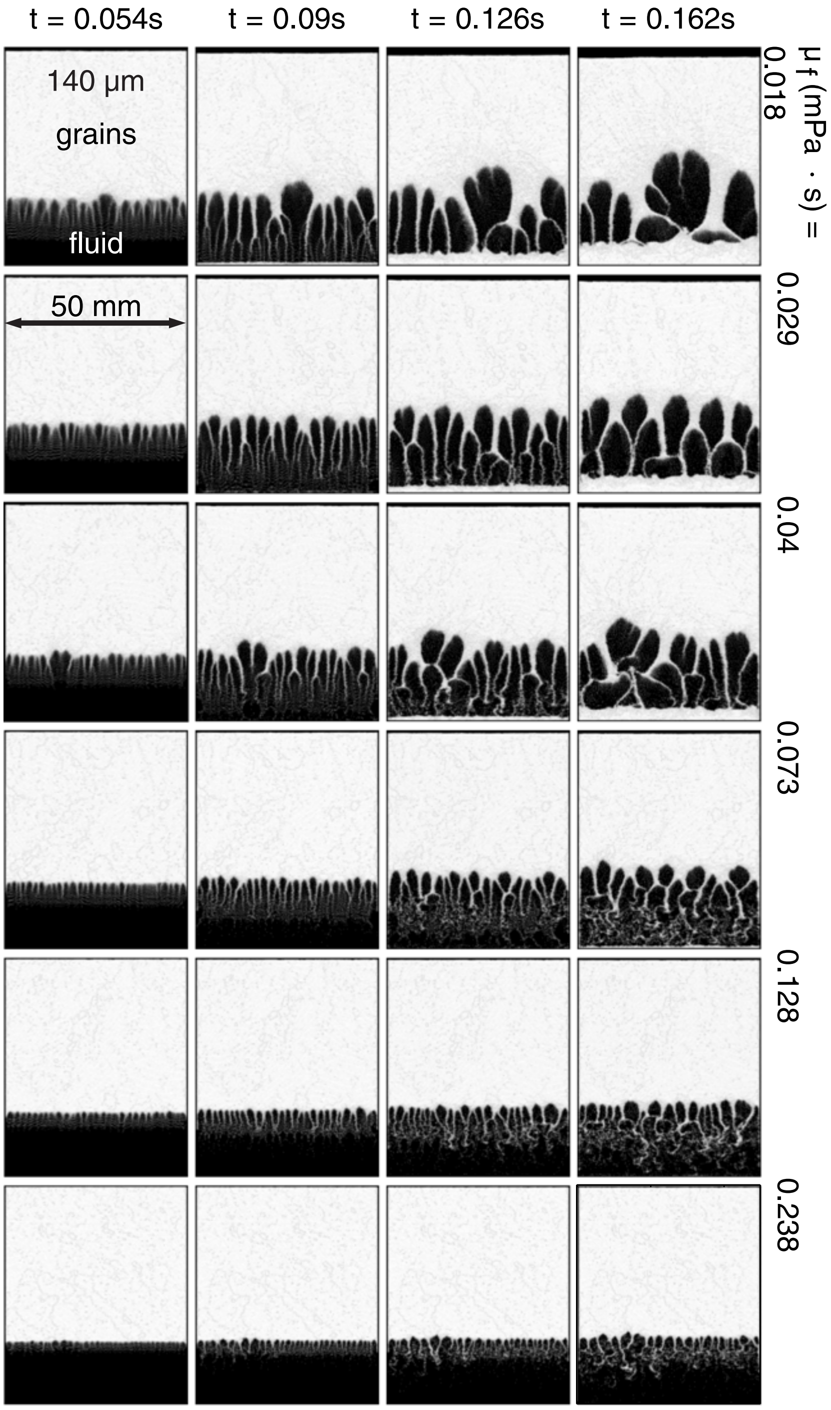

Fig. 4. Numerical simulations of grains sedimenting in an incompressible fluid of variable viscosities μ_f (increasing from top to bottom). Time runs from left to right.

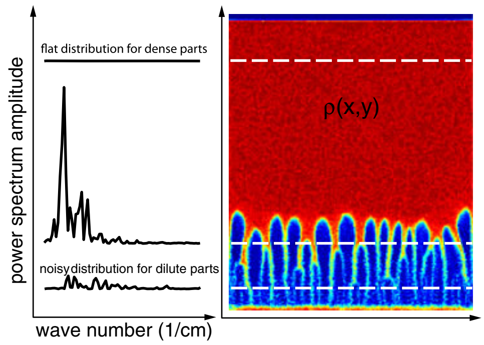

Fig. 5. Extraction of a density function under the dense plug (middle dashed line in the right figure), and computation of its Fourier power spectrum (left).

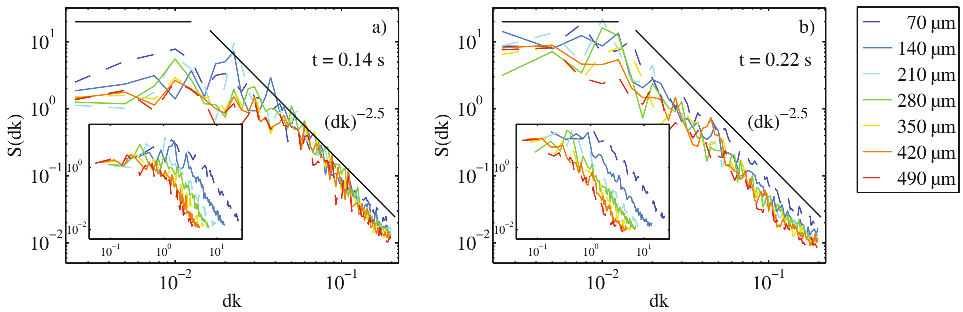

Fig. 6. Power spectrum collapse at two different times for air-grain simulations with grains of different diameters d. The inset plot shows the unscaled power spectra, $S(k)$, whereas a spatial scaling by the grain diameter yields collapsing $S(dk)$ in the main plot.

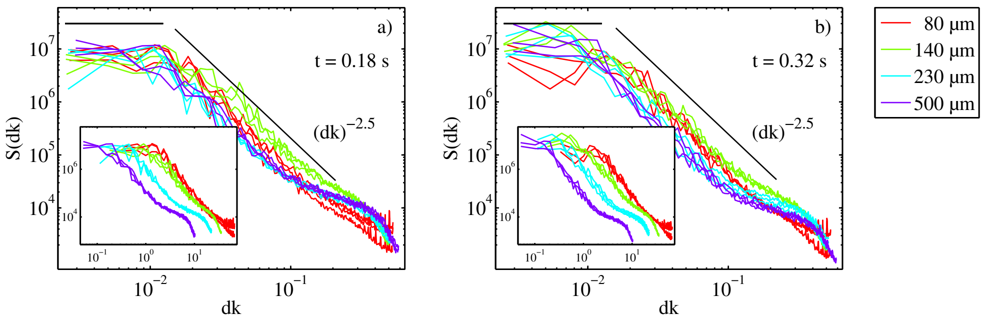

Fig. 7. Power spectrum collapse at two different times for air-grain experiments with grains of different diameters d. The inset plot shows the unscaled power spectra, $S(k)$, whereas a spatial scaling by the grain diameter yields collapsing $S(dk)$ in the main plot, apart from deviations at the smallest scales.

rendered the pattern formation mechanism similar for the range of diameters investigated. This was studied in details in [27]. The rescaling is illustrated by the collapse of the structures analyzed in Fig. 6 (for simulations) and Fig. 7 (for experiments), obtained after rescaling the spatial units with the grain diameter, d. The insets in these figures show the density profiles prior to rescaling.

3 Family-Vicsek scaling of the lower decompaction front

In the plots of the Fourier transformed density profiles in Figs. 6 and 7, one notes that, both for the experiments and for the simulations, the low wavenumber part of the spectra is flat. This corresponds to spatially uncorrelated density fluctuations for large scales (with a white noise character), whereas the power spectrum decreases as a power-law for small scales (high wavenumber). A behavior

$$S(k,t) \sim k^{-2.5}$$

is observed on this part, both for experiments and for simulations. The cutoff k_c corresponds to the maximum size of the density fluctuations, $\xi = 2\pi/k_c$, called the correlation length. The power-law behavior for scales smaller than the correlation length corresponds to the self-affine character of these density fluctuations. The power spectrum distribution of a self-affine quantity may be expressed as

$$S(k,t) \sim k^{-(1+2\zeta)},$$

which in our case yields a Hurst exponent $\zeta \sim 0.75$.

Deviations are observed for the experiments in Fig. 7 on the smallest scales, which can be attributed to a different dynamics at scales of the order of the plate separation.

Interestingly, when the case of incompressible fluids is compared, a similar behavior is observed as for the compressible case, see Fig. 8. This behavior extends to the whole range of viscosities probed, from 0.018 to 0.9 mPa·s, almost three orders of magnitude. This is the case despite the obvious difference between the developed stages of the instability, as is seen by comparing Figs. 3 and 4. The early stages, however, seem to follow the same type of behavior with respect to the lateral spreading of the density fluctuations.

The Family-Vicsek scaling behavior is summarized in the plots in Fig. 9 for the compressible case, and in Fig. 10 for the incompressible case. For the compressible case, the transformed density functions $S(k,t,d)$ for all the probed grain sizes d and for times $t \leq 0.23$ s all fall on a single master curve shown in Fig. 9(a). For the incompressible case there is, however, a deviation from the Family-Vicsek scaling for the early times and largest viscosities probed, as seen in the incomplete collapse for the first times in Fig. 10(c).

The observed Family-Vicsek scaling merely reflects the following about the power spectrum $S(k,t)$:

$$S(k,t) = Ck^{-1-2\zeta} g(dk(t/\tau)^{1/z}) \tag{7}$$

$$g(x) \sim C_1 x^{1+2\zeta} \quad \text{for } x \ll 1, \text{ i.e. } 1/k \gg \xi \text{ with } \xi \sim t^{1/z} \tag{8}$$

$$g(x) = C_2 \quad \text{for } x \gg 1, \text{ i.e. } 1/k \ll \xi\,, \tag{9}$$

where τ is a time-constant and C, C_1 and C_2 are constants. So that $S(k,t)$ is independent of k for scales above the correlation length ξ, and independent of t when the mode k has saturated, with a wavelength $1/k$ exceeding the correlation length. This leads to a generalized diffusion behavior

$$S(k,t) \sim t^{(1+2\zeta)/z} \tag{10}$$

when $1/k > \xi$, and

$$S(k,t) \sim k^{-(1+2\zeta)} \tag{11}$$

when $1/k < \xi$.

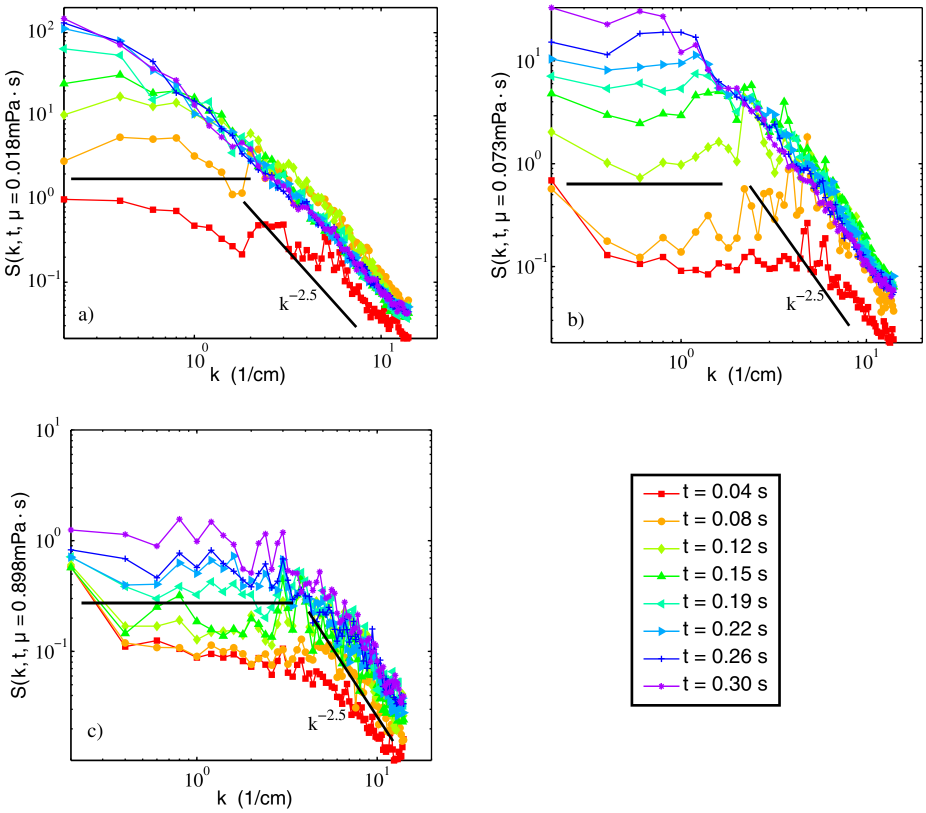

Fig. 8. Power spectra of the horizontal density profile for different times: results of simulations in an incompressible fluid. The viscosities of the fluids are respectively (a) 0.018, (b) 0.073 and (c) 0.9 mPa·s. The different curves correspond to different times after the start of the instability.

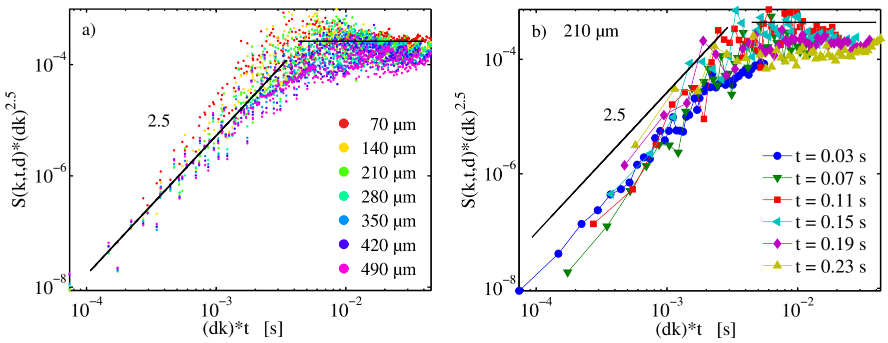

Fig. 9. Family-Vicsek scaling obtained from numerical data. (a) shows the scaling for all grain sizes and for $t \leq 0.23$ s, while (b) is the same plot as (a) but only showing the $210\,\mu$m data and where the colors indicate the time from blue (early times) to red (late times).

This corresponds, in real space, to a behavior for the root mean square of the solid density

$$\sigma_\rho = \langle \rho^2 - \langle \rho \rangle^2 \rangle^{1/2}$$

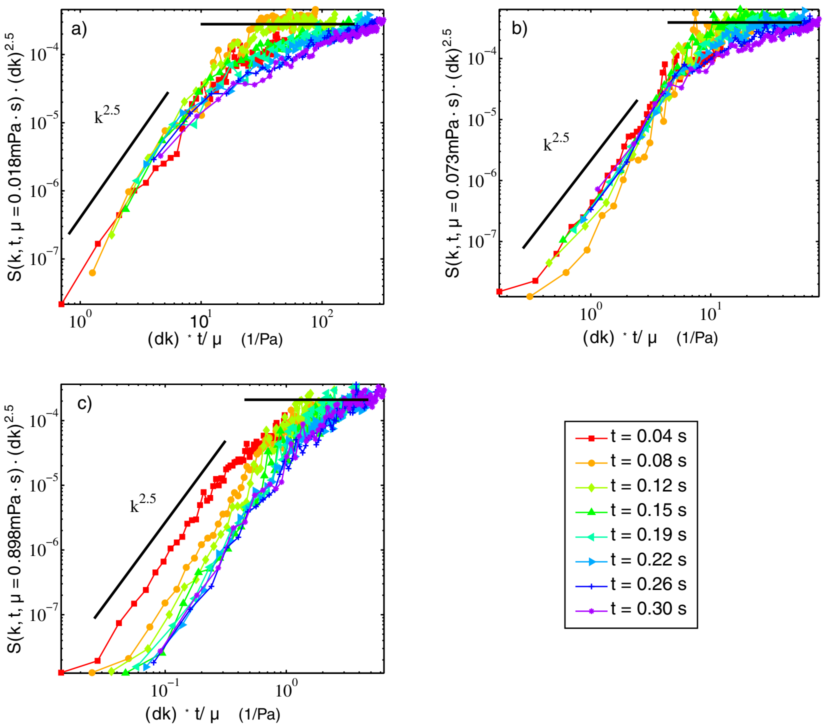

Fig. 10. Master function intervening in the Family-Vicsek scaling for the Rayleigh-Taylor instability in incompressible fluids: Scaled power spectra $S(k,t)*(d*k)^{2.5}$, which are functions g of $d*k*t/\tau$, with a behavior $g(x) \sim C_1 x^{2.5}$ at small arguments, and $g(x) \sim C_2$ at large ones. The Hurst exponent used for the scaling is 0.75, and the dynamic exponent is 1. The viscosities of the fluids are respectively (a): 0.018, (b): 0.073 and (c): 0.9 mPa·s.

following a Family-Vicsek scaling that can be obtained form Parseval's theorem, as

$$\sigma^2(L,t) = (1/L)\int_{k=2\pi/L}^{\infty} S(k,t)dk \tag{12}$$

$$= (1/L)\int_{k=2\pi/L}^{\infty} Ck^{-1-2\zeta} g(dk(t/\tau)^{1/z})dk \tag{13}$$

$$= (t/\tau)^{(2\zeta)/z}(1/L)\int_{2\pi(t/\tau)^{1/z}/L}^{\infty} k' g(k')dk' \,, \tag{14}$$

i.e.

$$\sigma(L,t) = (t/\tau)^{\beta} F(L/t^{1/z})$$

with

$$\beta = \zeta/z \,.$$

where L is the width of the system. Hence, the density profile under the detachment front saturates as a self-affine function [33] with a Hurst exponent $\zeta \simeq 0.75$ for scales below ξ, and displays a superdiffusive behavior with an exponent $\beta \simeq 0.75$. The root mean square of the solid density, $\sigma_\rho = \langle \rho^2 - \langle\rho\rangle^2\rangle^{1/2}$ displays a behavior corresponding to

$$\sigma_\rho \sim t^{\beta}.$$

Conversely, for scales l above ξ, one has a self-affine behavior,

$$\langle(\rho(x+l)-\rho(x)\rangle^2 \sim l^{2\zeta}\,.$$

The correlation length ξ is increasing as a power law with time, as $\xi \sim t^{1/z}$. The density in the detachment front exhibits these behaviors with respectively dynamic, Hurst and growth exponents

$$z = 1 \tag{15}$$

$$\zeta = 0.75 \tag{16}$$

$$\beta = \zeta/z = 0.75. \tag{17}$$

One can also equivalently express the Family-Vicsek scaling with a scaling function g, such as:

$$S(k,t) = C(dk)^{-2.5} g(dk(t/\tau)) \tag{18}$$

$$g(x) \sim C_1 x^{2.5} \quad \text{for}\, x \ll 1,\ \text{i.e. } 1/k \gg \xi \text{ with } \xi \sim t \tag{19}$$

$$g(x) = C_2 \quad \text{for}\, x \gg 1,\ \text{i.e. } 1/k \ll \xi\,. \tag{20}$$

Indeed, $S(k,t)*(d*k)^{2.5} = Cg(d*k*t/\tau)$ is represented for air/grain simulations in Fig. 9, and this scaling function master curve displays these two expected behaviors for the granular-gas flow.

This is also the case for the granular-incompressible fluid flows, as shown in Fig. 10 for the three viscosities. As observed in the previous representation, the collapse is rather followed, apart from the earliest times at larger viscosities.

4 Conclusion

We have studied situations where well packed cohesionless grain assemblies, heavier than the fluid between them, are released in a clear fluid. This gives rise to the so-called granular Rayleigh-Taylor instability, where bubbles empty of grains rise, while granular fingers form in the clear fluid region.

The principles of hybrid simulations starting from basic physical equations was established, for both cases where the carrier fluid is a perfect gas or an incompressible viscous fluid. The experimental setup and results are also shown to be consistent with the simulations in the air/grain case.

Grains are mixed during this process, and one can follow the evolution of spatial correlations in lateral density fluctuations, with vertically averaged horizontal grain density profiles $\rho(x)$. These density fluctuations are shown to follow an anomalous diffusion behavior with a growth exponent $\beta \sim 0.75$. Hence, for two points at a large horizontal distance x from each other, a difference in density will grow as $\delta\rho(x,t) \sim t^{\beta}$. The density fluctuations will follow this behavior up to a saturation when the correlation length ξ reaches x. ξ is growing as a power-law of time, with a dynamic exponent around 1. Eventually, for scales larger than ξ, the density profile displays a self-affine behavior, with a Hurst exponent around 0.75. This is seen in the spatial Fourier domain, both for experiments and simulations for air-grain systems, and for simulations for mixtures of grains and incompressible viscous fluid.

Eventually, we have shown that the power-spectra of the density at all times can be collapsed according to a Family-Vicsek scaling.

References

1. H.J. Herrmann, J.-P. Hovi, S. Luding (eds.), *Physics of Dry Granular Media*, vol. 350, NATO ASI Series E: Applied Sciences (Kluwer Academic Publishers, Dordrecht/Boston/London, 1998)
2. J. Duran, *Sands, Powders and Grains* (Springer, New York, 2000)
3. E. Altshuler, R. Toussaint, E. Martinez, O. Sotolongo-Costa, K.J. Måløy, J. Schmittbuhl, Phys. Rev. E **77**, 031305 (2008)
4. E. Aharonov, D. Sparks, Phys. Rev. E **65**, 051302 (2002)
5. E. Aharonov, D. Sparks, J. Geophys. Res. **109**, B09306 (2004)
6. G. Reydellet, E. Clement, Phys. Rev. Lett. **86**, 3308 (2001)
7. L. Goren, E. Aharonov, D. Sparks, R. Toussaint, J. Geophys. Res. **115**, B09216 (2010)
8. J. Travelletti, C. Delacourt, P. Allemand, J.-P. Malet, J. Schmittbuhl, R. Toussaint, M. Bastard, ISRPS J. Photogramm. Remote Sensing (2011) (revised)
9. J.-P. Malet, D. Laigle, A. Rematre, O. Maquaire, Geomorphology **66**, 215 (2005)
10. W.J. van Asch, Th. Malet J.-P., Natur. Hazards Earth Syst. Sci. **9**, 1897 (2009)
11. E.G. Flekkøy, A. Malthe-Sørenssen, B. Jamtveit, J. Geophys. Res. **107 (B8)**, 2151 (2002)
12. L. Goren, E. Aharonov, D. Sparks, R. Toussaint, P.A. Geoph. **168**, 12 (2011) (in press) doi: 10.1007/s00024-011-0320-4
13. T. Le Pennec, K.J. Maloy, E.G. Flekkoy, J.C. Messager, M. Ammi, Phys. Fluids **10**, 3072 (2008)
14. E.G. Flekkøy, S. McNamara, K.J. Måløy, D. Gendron, Phys. Rev. Lett. **87**, 134302 (2001)
15. D. Gendron, H. Troadec, K.J. Måløy, E.G. Flekkøy, Phys. Rev. E **64**, 021509 (2001)
16. Ø. Johnsen, R. Toussaint, K.J. Måløy, E.G. Flekkøy, Phys. Rev. E **74**, 011301 (2006)
17. Ø. Johnsen, R. Toussaint, K.J. Måløy, E.G. Flekkøy, J. Schmittbuhl, Phys. Rev. E **77**, 011301 (2007)
18. Ø. Johnsen, C. Chevalier, A. Lindner, R. Toussaint, E. Clément, K.J. Måløy, E.G. Flekkøy J. Schmittbuhl, Phys. Rev. E **78**, 051302 (2008)
19. J.L. Vinningland, Ø Johnsen, E.G. Flekkøy, R. Toussaint, K.J. Måløy, Phys. Rev. Lett. **99**, 048001 (2007)
20. M.J. Niebling, E.G. Flekkøy, K.J. Måløy, R. Toussaint, Phys. Rev. E **82**, 011301 (2010)
21. S. McNamara, E.G. Flekkøy, K.J. Måløy, Phys. Rev. E **61**, 4054 (2000)
22. D.V. Anghel, M. Strauß, S. McNamara, E.G. Flekkøy, K.J. Måløy, Phys. Rev. E **74**, 029906(E) (2006)
23. X. Cheng, L. Xu, A. Patterson, H.M. Jaeger, S.R. Nagel, Nat. Phys. **4**, 234 (2008)
24. M.J. Niebling, R. Toussaint, E.G. Flekkøy K.J. Måløy, Phys. Rev. Lett. (2011) (submitted)
25. M. Schelstraete, Master thesis, University of Strasbourg, 2009
26. J.L. Vinningland, Ø. Johnsen, E.G. Flekkoy, R. Toussaint, K.J. Måløy, Phys. Rev. E **76**, 051306 (2007)
27. J.L. Vinningland, Ø. Johnsen, E.G. Flekkøy, R. Toussaint, K.J. Måløy, Phys. Rev. E **81**, 041308 (2010)
28. M.J. Niebling, E.G. Flekkøy, K.J. Måløy, R. Toussaint, Phys. Rev. E **82**, 051302 (2010)
29. C. Völtz, W. Pesch, I. Rehberg, Phys. Rev. E **65**, 011404 (2001)
30. J.L. Vinningland, Ø. Johnsen, E.G. Flekkøy, R. Toussaint, K.J. Måløy, in *Proc. of the 6th international conference on micromechanics of granular media, Powder and grains 2009*, edited by M. Nakagawa, S. Luding
31. J.L. Vinningland, Ø. Johnsen, E.G. Flekkøy, R. Toussaint, K.J. Måløy, *Proc. of the Traffic and Granular Flow conference*, 2007 (Orsay, 2009)
32. F. Family, T. Vicsek, J. Phys. A **18**, L75 (1985)
33. A.-L. Barabasi, H.E. Stanley, *Fractal Concepts in Surface Growth* (Cambridge University Press, Cambridge, 1995)
34. R. Toussaint, G. Helgesen, E.G. Flekkøy, Phys. Rev. Lett. **93**, 108304 (2004)

35. R. Toussaint, J. Akselvoll, G. Helgesen, E.G. Flekkøy, A.T. Skjeltorp, Prog. Coll. Polymer Sci. **128**, 151 (2004)
36. R. Toussaint, E.G. Flekkøy, G. Helgesen, Phys. Rev. E **74**, 051405 (2006)
37. J. Schmittbuhl, F. Renard, J.P. Gratier, R. Toussaint, Phys. Rev. Lett. **93**, 238501 (2004)
38. D. Koehn, F. Renard, R. Toussaint, C. Passchier, EPSL **257**, 582 (2007)
39. A. Rolland, R. Toussaint, P. Baud, J. Schmittbuhl, N. Conil, D. Koehn, F. Renard, J. P. Gratier, JGR B (2011) (submitted)
40. L.L. Ben-Itzhak, E. Aharonov, A. Sagy, R. Toussaint, EPSL (2011) (submitted)
41. Fereydoon Family, T. Vicsek (eds.), *Dynamics of Fractal Surfaces* (World Scientific, Singapore, New Jersey, London Hong Kong, 1991)
42. M.L. Juan, Phys. Rev. Lett. **83**, 4594 (1999)
43. Rayleigh, Lord, Proc. London Math. Soc. **14**, 170 (1883)
44. P.G. Drazin, W.H. Reid, *Hydrodynamic Stability*, 2nd edn. (Cambridge University Press, Cambridge, 2004)
45. Press, et al., *Numerical Recipes* (Cambridge University Press, 1992)

Revolving rivers in sandpiles: From continuous to intermittent flows

E. Altshuler,[1,2] R. Toussaint,[2] E. Martínez,[1] O. Sotolongo-Costa,[1] J. Schmittbuhl,[2] and K. J. Måløy[3]
[1]*"Henri Poincaré" Group of Complex Systems, Physics Faculty, University of Havana, 10400 Havana, Cuba*
[2]*Institute of Globe Physics in Strasbourg, UMR 7516 CNRS, Université Louis Pasteur, 5 rue Descartes, F-67084 Strasbourg Cedex, France*
[3]*Department of Physics, University of Oslo, P.O. Box 1048 Blindern, 0316 Oslo, Norway*

(Received 6 November 2007; published 17 March 2008)

In a previous paper [E. Altshuler *et al.*, Phys. Rev. Lett. **91**, 014501 (2003)], the mechanism of "revolving rivers" for sandpile formation is reported: As a steady stream of dry sand is poured onto a horizontal surface, a pile forms which has a river of sand on one side flowing from the apex of the pile to the edge of the base. For small piles the river is steady, or continuous. For larger piles, it becomes intermittent. In this paper we establish experimentally the "dynamical phase diagram" of the continuous and intermittent regimes, and give further details of the piles' "topography," improving the previous kinematic model to describe it and shedding further light on the mechanisms of river formation. Based on experiments in Hele-Shaw cells, we also propose that a simple dimensionality reduction argument can explain the transition between the continuous and intermittent dynamics.

DOI: 10.1103/PhysRevE.77.031305 PACS number(s): 45.70.Mg, 45.70.Qj, 83.80.Fg

I. INTRODUCTION

When most granular materials are poured onto a horizontal surface, a conical pile builds up through an avalanche mechanism involving all the surface of the pile that "tunes" the angle of repose about a certain critical value. In a previous paper, however, we reported a different mechanism of sandpile formation [1]. In those experiments, as the pile grows, a river of sand spontaneously builds up, flowing down one side of the pile from the apex to the base. The river then begins to revolve around the pile, depositing an helical layer of material with each revolution, causing the pile to grow. Below a certain pile size and input flux, the rivers are continuous, and the surface of the pile is smooth (see upper inset in Fig. 1). The revolving direction can be either clockwise or counterclockwise, only depending on random fluctuations in the first stage of the experiment. For bigger piles, the rivers are intermittent, and the surface of the pile become undulated (see lower inset in Fig. 1). Kong and co-workers [2] reported a detailed computational model for the revolving rivers which manages to reproduce many of their features in the continuous regime, but the intermittent regime was not accounted for. They also noticed that the details of the grain-grain interactions must be tuned in order to get the revolving rivers, which matches the experimental fact that not all sands display such behavior. In this paper, we explore experimentally the "dynamic phase diagram" of the different regimes in our sandpiles (i.e., the regions of experimental parameters where they appear). We report the details of the "topography" of the sandpiles in the continuous and intermittent regimes, and present a refined "kinetic" description of the observed phenomena. We then propose an explanation for the existence of two types of revolving rivers based on an analogy with measurements performed in a simpler geometry (i.e., the Hele-Shaw cell).

II. "DYNAMIC PHASE DIAGRAM" OF THE REVOLVING RIVERS

We used sand with a high content of silicon oxide from Santa Teresa (Pinar del Río, Cuba) [1,3]. The grain size distribution is basically a Gaussian distribution centered at 200 μm, with a half-width slightly smaller than 200 μm. From now on, we will adopt the labeling of Ref. [1] for the boundary conditions used in each experiment: BCI stands for a pile grown on a closed cylindrical container with a flat, horizontal bottom, and BCII corresponds to a pile formed on an open, flat horizontal surface. To obtain the dynamic phase diagram, we grew piles in boundary condition BCII. We used glass funnels of various diameters to obtain different values of the input flux. It was determined in each experiment by measuring the volume of the conical pile, and dividing it by the time elapsed since the first grains were dropped on the table. For a given input flux, three different pile base radii were identified by simple observation as the pile grew. Below $r1$, continuous rivers appeared and disappeared (as eventually happens in common sands), so we will refer to them as *unstable*. Above $r1$ and below $r2$, a *stable* continuous river revolved around the pile in a given direction, without any

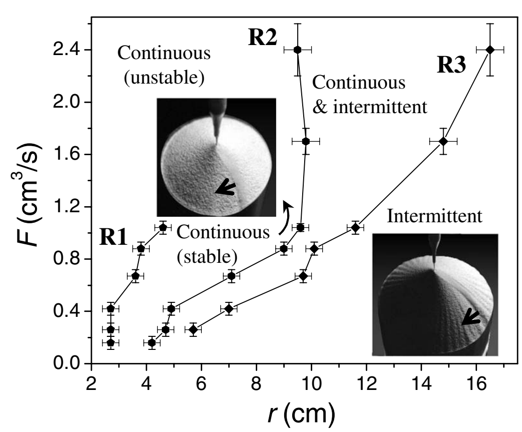

FIG. 1. Occurrence of continuous and intermittent rivers as functions of the pile radius r and the input flux F. The upper and lower insets show snapshots of the pile during the (stable) continuous and the intermittent regimes, respectively. The arrows indicate the direction of revolution around the pile.

major changes in its shape. After $r2$, the continuous river could eventually become intermittent: The downhill flow would suddenly stop at the edge of the pile, and a "finger" of sand would escalate from bottom to top, like a "stop-up" front [4]. All in all, the continuous or intermittent rivers would keep revolving around the pile with the frequency described in [1] (see also Fig. 7). However, at some point this process transformed again into a continuous, revolving river. As the radius of the pile grew from $r2$ to $r3$, the intermittent mechanism took place within larger and larger time intervals, while the continuous mechanism slowly disappeared. At $r3$, intermittent rivers were established as the only dynamical phase in the pile. As $r1$, $r2$, and $r3$ were determined for various input fluxes, three boundaries $R1$, $R2$, and $R3$ were established to separate the different dynamical phases, as shown in Fig. 1. We have observed that the positions of these lines are influenced by the distance between the funnel that delivers the sand and the tip of the pile, but we kept this distance fixed at approximately 2 cm during the experiments. It should be noticed that, for input fluxes larger than approximately 1 cm^3/s, stable continuum rivers are never established, and a direct transition from unstable continuous to intermittent rivers takes place through $R2$.

III. REFINED KINEMATIC MODEL

Figure 2 shows images taken from top of "frozen" piles in the stable continuous (upper panel) and intermittent (lower panel) regimes obtained for boundary condition BCII. Piles were formed using a steady input flux, which was just switched off to take the pictures. In both images, the river can be identified as a curved groove from the apex to the base of the pile, in a general vertical direction, below the apex. In order to quantify the topography of the piles (at least for one size), we measured its slope angle (polar angle) versus the angle around the pile (azimuthal angle). The measurement was performed by carefully setting a ruler tangential to the slope of the pile at different azimuthal angles, taking a lateral picture of the system, and calculating the angles between the ruler and the horizontal from the resulting images. This ruler was set along the section of the slope where the angle is essentially constant (this angle becomes smaller at a few cm from the top of the piles). Figure 3 shows how the slope angle depends on the azimuthal angle for the case of the continuous rivers. Contrary to the first impression when the picture of the upper panel of Fig. 2 is examined, there is a wide angular zone of variation of the slope angle, quantified in Fig. 3. This suggests that, while most of the downhill flow is concentrated into the relatively narrow river clearly visible below the apex of the pile (upper panel of Fig. 2), there is a wider area of grains rolling downhill. The slope angle is typically around 36.5° far from the river. It significantly decreases to 33° within the river. The width of the low slope angle region extends over 150° along the azimuthal direction. This corresponds to a length of around 28 cm along the circumference of the pile, which is much larger than the river (which is a few cm wide). To illustrate this, Fig. 4 shows the difference between two images of a sandpile grown in BCI in the continuous regime,

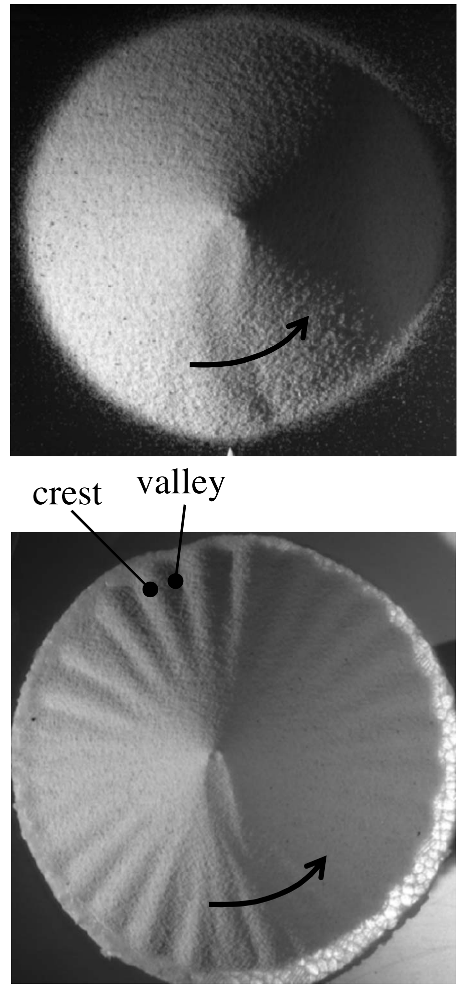

FIG. 2. Topography of the continuous and intermittent regimes. Upper panel: Top view showing a pile "frozen" during a continuous river experiment. The diameter of the pile is 11 cm. Lower panel: Top view of a pile "frozen" during an intermittent river experiment. The diameter of the pile is 17 cm—surface undulations extend approximately 6 cm from the edge of the pile in the radial direction. Black arrows on top of the flowing river indicate the direction of revolution of the rivers as sand is added from above.

separated by a lapse of 0.15 s (the video was taken by a *Photon Fastcam Ultima-ADX model 120K*, and the image was obtained using the "difference" option of *ImageJ*). Besides the fast flow along the main stream of the river, whiter and darker spots indicate the downhill movement of sand at a smaller speed behind the main stream area.

The situation is quite different in the case of the intermittent regime. The measurement of the angles of repose of several "valleys" and "crests" corresponding to the picture in the lower panel of Fig. 2 does not indicate a wide transition in the angle of repose, as in the case of the continuous rivers, but suggests two basic polar angles: $37.1° \pm 0.16°$, for the valleys, and $36.1° \pm 0.20°$ for the crests. It should be noticed, however, that the pile in the intermittent regime contains an inner circle where the surface is smooth, and an outer ring of undulating surface, as seen in Fig. 2 (lower panel). The values we have reported here for the slope angles at the valleys and crests correspond to this ring of approxi-

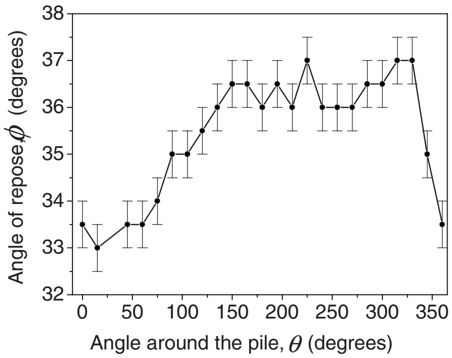

FIG. 3. Dependence of the angle of repose on the azimuthal angle for the picture of the upper panel of Fig. 2 (continuous river). The “0” of the azimuthal angle has been taken along the vertical diameter under the apex, and it increases clockwise. The error bars correspond to the largest variation of the measured angles of repose in three different attempts on the same pile.

mately 6 cm width in the radial direction, while the average slope of the pile in the inner circle is harder to measure due to rounding near the apex of the pile.

The phenomenological model for the revolving rivers presented in Ref. [1] is able to predict the radius and time dependence of the frequency of revolution of the piles, but oversimplifies the geometry of the sandpile in such a way that the angle of repose is constant around the pile, in contradiction with the real topography shown in Fig. 2 and quantified in Fig. 3. We present here a more realistic model, which is schematized in Fig. 5 for BCII. This model has a number of advantages relative to the one presented in Ref. [1]. First, it takes into account that the apex of the pile is not sharp, but presents a small “crater” (very exaggerated in the schematics shown in Fig. 5). Second, the river, located in the section on the cone on which the sand flows, has a nonzero width. Third, the angle of repose is not constant around the pile, but can be shaped as depicted in Fig. 5, where the width of the downhill flowing area has been tuned to 150° in the azimuthal direction (the figure displays a smaller angle). We add two further constraints, which roughly match experimental observations: The characteristic length δr is constant, and so is the radius of the crater.

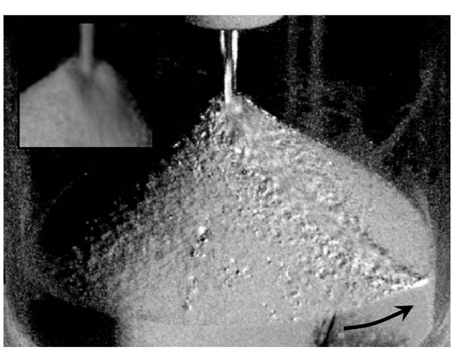

FIG. 4. Moving grains in the continuous river regime. The figure is the difference between two pictures of a continuous river separated by 0.15 s (the river was revolving around the pile at approximately 0.1 turns/s). This difference is superimposed with the first of these two pictures. The arrow indicates the direction of the revolution of the river around the pile. The inset shows a raw picture of the crater, at the upper end of the pile.

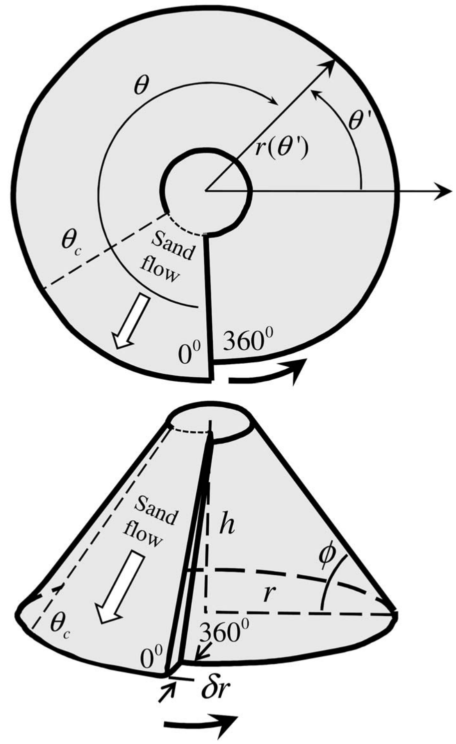

FIG. 5. Diagram of the model used to estimate the revolving speed of the rivers, and the polar bottom angle versus the azimuthal angle. Upper panel: Top view of the pile model. Lower panel: Spatial view of the pile model (notice that the angle of the flowing zone has been decreased in this representation relative to the top view, to improve drawing clarity). The black arrows indicate the direction of revolution around the pile.

The geometry of the pile, in the continuous regime, can be schematized as follows:

We define an azimuthal coordinate θ around the pile in a frame co-moving with the revolving river, so that $\theta=0$ corresponds to the position of the flowing river, where most of the flow is located. In the reference frame of the laboratory, the azimuthal coordinate θ' is $\theta'=\theta_0(t)-\theta$, where $\theta_0(t)=\theta_0(0)+\int_0^t\omega(t')dt'$ is the azimuthal angle of the river, and $\omega(t)=\dot{\theta}_0(t)$ is the instantaneous angular velocity of the revolving river.

The radius of the bottom of the pile is fixed after the river has added a layer of thickness δr: This radius is denoted $r(\theta')$. There is no evolution of this radius apart from the outlet of the concentrated river, i.e., any other surface flow than the river on the sides of the pile does not reach the bottom. This radius jumps by a characteristic length $\delta r = r(\theta'+360°)-r(\theta')$ at each passing of the river, which adds a new layer of grains to the pile. This jump corresponds to the distance over which grains flowing down the pile at a characteristic speed, dissipate entirely their kinetic energy over the flat bottom. This jump has a characteristic value around 4 mm.

Calling $h(t)$ the height of the center of the pile, there is a small crater forming around this tip. The crater corresponds

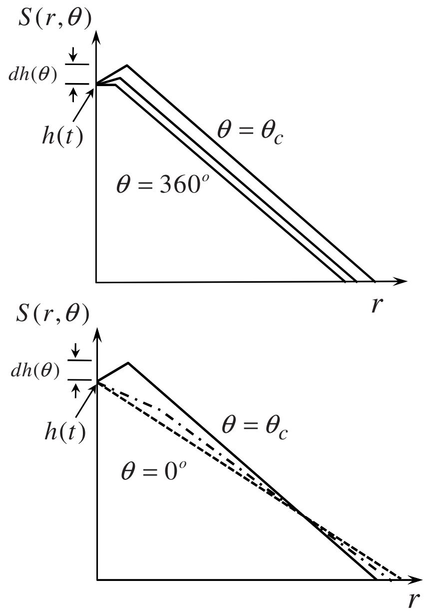

FIG. 6. Cuts of the pile side at constant azimuth θ in the continuous regime. Upper panel: Frozen side of the pile, below a crater crest. Lower panel: Part where the revolving river passes, and where the surface flow takes place behind it.

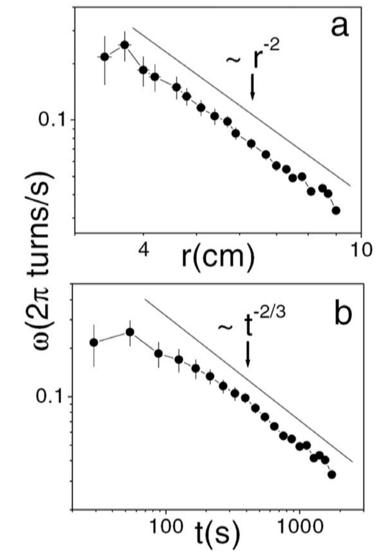

FIG. 7. Radius (a) and time (b) dependencies of the frequency of revolution of the rivers (taken from [1]). The points correspond to experimental values.

then to a sharp crest around the center of the pile, slightly higher than the central point, and exists for azimuthal angles θ between θ_c and 360°. A characteristic value observed for θ_c is around 150°, as pointed out before. There is no observed surface flow on the sides of the pile below this crater crest, i.e., the surface of the pile corresponding to $\theta_c < \theta < 360°$ is frozen. The crater crest lies at a height $\delta h(\theta)$ above the center, i.e., at an altitude $h(t)+\delta h(\theta)$: The crater shape revolves at the same speed as the flowing river. In the reference frame of the bottom plate, a point of the crest is also fixed, i.e., $h(t)+\delta h[\theta_0(t)-\theta']$ is constant, so its time derivative is $\dot{h}+(d\delta h/d\theta)\omega=0$: The crater has a screwlike shape, with an azimuthal slope of the crest $(d\delta h/d\theta)=-\dot{h}/\omega$ set by the ratio between the pile rising speed and the revolving angular velocity.

After the passing of the river, there is a small surface flux, visible as a few whiter and darker dots on Fig. 4, increasing the effective angle of the slope, as seen in Fig. 3. This surface flow happens for azimuthal angles between 0° (the river) and θ_c. The tip of the pile, for these angles, presents no change of sign of the radial slope (no crater crest). For θ larger than θ_c, the crest of the crater at the tip of the pile is formed around the central point, i.e., noting $S(r,\theta)$ the coordinates of the surface of the pile, the radial slope of $\partial S/\partial r$ is positive for low radii r, and negative for larger ones, after the crest. At these angles, this crest prevents further surface flow on the sides of the pile, so that the rest (polar) angle $\Phi_0(\theta)$ is frozen at a roughly constant value between θ_c (the beginning of the crest) and $\theta=360°$. To illustrate this organization, a collection of schematic cuts of the pile side at various azimuth θ is shown in Fig. 6.

The role of this crater on the organization of the flow in revolving rivers seems thus very important. For example, when the incoming sand flux presents too many lateral oscillations or is too wide, the crater and revolving river formation are prevented. Similarly, when the pile has not grown enough to reach a diameter beyond the distance of saltation from the impact point, the crater formation is prevented, and unstable rivers are observed, i.e., beyond the line $R1$ in Fig. 1. The fact that grains do not bounce too far when they arrive on the pile, i.e., a moderate restitution coefficient, is certainly an important ingredient to allow for the crater formation.

From this geometry, one can also infer a relationship between the pile radius and the angular velocity, as reported in [1]: During a time dt, a volume of sand Fdt is deposited over a layer of size $\delta r\tan(\Phi_0)\omega r^2 dt/2$, where Φ_0 is the repose angle along most of the pile (for azimuth θ between θ_c and 360°). Consequently, mass conservation of the grains imposes that $\omega=2F/[r^2\delta r\tan(\Phi_0)]$. This power-law dependence of the angular velocity over the pile radius is verified experimentally, as shown in Fig. 7. Since the pile radius increases from flux conservation so that $\pi r(t)^3\tan(\Phi_0)/3=Ft$, i.e., as $r(t)=[3Ft/\pi\tan(\Phi_0)]^{1/3}$, the angular velocity goes as

$$\omega=(\pi/3)^{2/3}\frac{2F^{1/3}}{\delta r(\tan\Phi_0)^{1/3}}\frac{1}{t^{2/3}}. \qquad (1)$$

This power law decrease of the angular velocity with time is also verified experimentally (Fig. 7).

At a certain critical size of the pile radius r_{ci}, the flow becomes intermittent and exhibits avalanches, while still being concentrated along a river. These avalanches extend over a basis δr from the pile bottom, comparable to the horizontal extent of layers added by the flowing river in the continuous regime. These avalanches form delta-shaped piles on the side of the main cone, with a slightly carved river penetrating above the apex of the delta (as seen below the pile's apex, lower panel of Fig. 2) which is "smoothed out" as the river

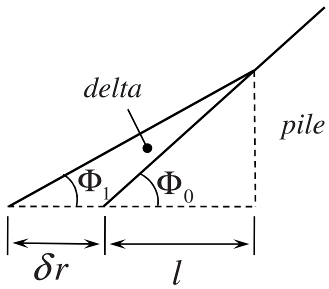

FIG. 8. Cuts of the pile near the lower boundary in the intermittent regime.

moves on laterally. The slope angle of these deltas is lower than the average angle around the pile, with typically a stop angle $\Phi_1=33°$, as on the flowing part of the continuous regimes, whereas the rest angle for the average slope of the pile is around $\Phi_0=36°$—see Fig. 3. The radial extent l of these deltas from the bottom of the pile is set by the geometrical condition $(l+\delta r)\tan(\Phi_1)=l\tan(\Phi_0)$ (see Fig. 8), which corresponds to a constant value $l\sim 6$ cm, as observed in Fig. 2. Once these deltas are filled to the top, as well as the slightly carved zone above, the river feeding this delta revolves and a new delta is formed by an avalanche developing next to the previous one.

IV. CONTINUOUS VERSUS INTERMITTENT REGIMES: COMPARISON WITH HELE-SHAW EXPERIMENTS

The transition from continuous to intermittent granular flows has been extensively studied using two basic geometries: The rotating drum [5] and the Hele-Shaw cell [6]. Typically, the intermittent (or "avalanche") flow is transformed into continuous flow by increasing the rotation speed of the drum or the input flux, respectively. In the case of the Hele-Shaw cell arrangement, a transition from continuous to intermittent flow (start down and stop up fronts [4]) takes place when the heap reaches a critical size, even if the input flux and channel width are kept constant. Here we explore such transition in our sand in order to establish an analogy with the sandpile scenario. The cell consisted in a horizontal base and a vertical side wall, sandwiched between two square glass plates with inner surfaces separated by a distance w in the range from 0.4 cm to 1.2 cm. The lengths of the base and the vertical wall were approximately $d\approx 22$ cm. The sand was poured near the vertical wall using a sliding window of width w and variable aperture along the horizontal direction. Although in most of the results we report below the distance between the funnel and the upper side of the heap varied from 10 cm to 1 cm during a typical experiment, we performed some tests keeping the distance fixed at 2 cm, getting similar results. The input volume per unit time, F, was calibrated by calculating the volume of sand deposited in the cell in a given time interval.

Figure 9 shows a spatiotemporal diagram of evolution of one heap formed into a cell with $w=4$ mm using an input flux of 0.25 cm^3/s. It is based on a digital video acquired with an *Optronics Camrecord 600*, some of which snapshots are shown as insets. A 15-cm-long horizontal line of pixels was taken 0.5 cm from the bottom of the Hele-Shaw cell every 1/10 of a second. The spatiotemporal diagram was constructed as a stack of such lines (the darker zones correspond to the air, while the clearer ones correspond to the sand). The position of the row of pixels was taken in such a way, that the interface between dark and clear zones follows the displacements at the lower end of the growing heap. As can be seen at low times, the end of the heap near the bottom of the cell grows smoothly. However, approximately when the horizontal size of the heap reaches a length of 7 cm (see arrow in Fig. 9), the spatiotemporal is no longer smooth, but resembles a ladder: We define in this way the transition between the continuous and the intermittent (or avalanche) regimes. In the latter (well described in Refs. [4,7,8]), sudden avalanches roll downhill (corresponding to the high velocity, almost horizontal segments in the spatiotemporal diagram), and then a front climbs the hill as a new layer of sand is added from bottom to top (corresponding to the zero-velocity, vertical segments in the spatiotemporal diagram). The general shape of this diagram resembles Fig. 2 in [7], where the authors use two equations for thick flows proposed in [9] to model the heap formation in Hele-Shaw geometry. However, they do not report a continuous-intermittent transition—only the intermittent regime is described. We observe, though, other predictions reported in [7], such as the "segmented" profiles of the heaps (see the two upper insets in our Fig. 9) and stratification lines parallel to the free surface of the heaps. However, stratification is only visible in our case after the heap has reached the intermittent regime,

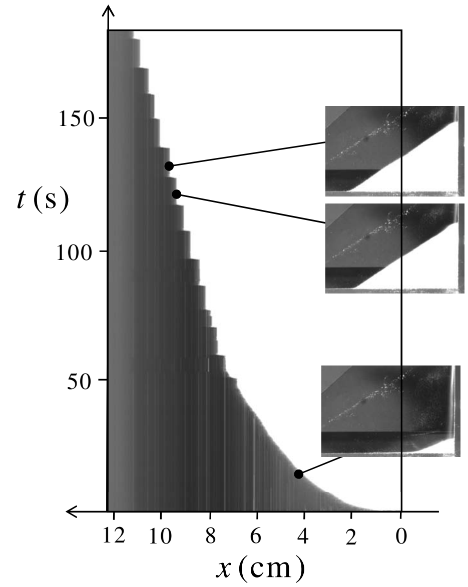

FIG. 9. Spatiotemporal diagram of the growing heap. The diagram was made for a sequence of images taken at every 0.1 s to a heap growing in a Hele-Shaw cell with $w=4$ mm and $F=0.125$ cm^3/s. The cuts were taken along an approximately 12-cm-long horizontal line near the bottom of the cell. As the time goes by, the heap grows continuously, corresponding to a smooth increase of the white area in the diagram. At a critical distance of 7 cm, avalanches start, and the diagram shows a steplike behavior. The insets on the right-hand side contain real pictures of the heap illustrating different moments of the spatiotemporal diagram.

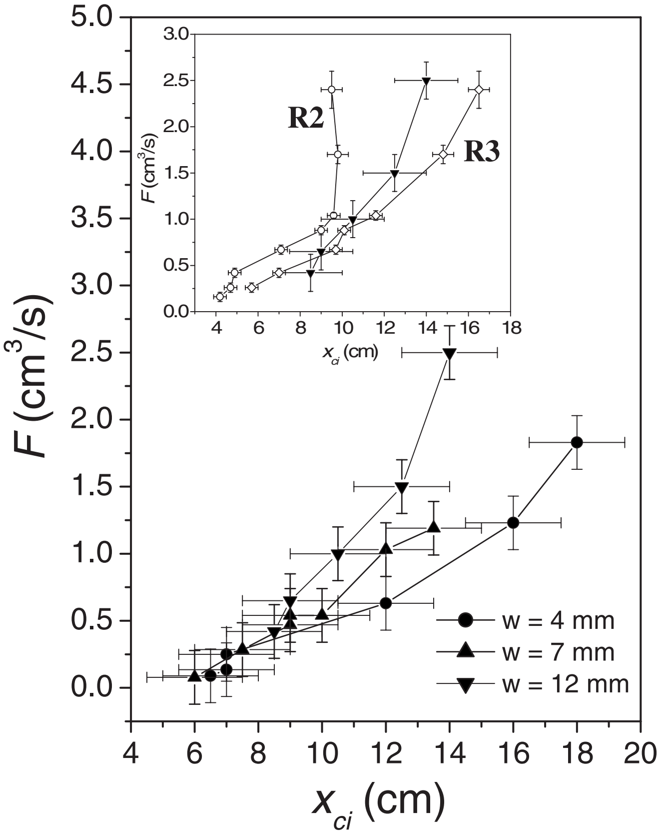

FIG. 10. Transition from the continuous to the intermittent regimes in Hele-Shaw and revolving rivers configurations. The vertical axis corresponds to input volume of sand per unit time, and the horizontal axis is the length of the base of the heap at the transition. The inset shows a comparison between the line of a 12-mm-width cell and the lines $R1$ and $R2$ taken from Fig. 1.

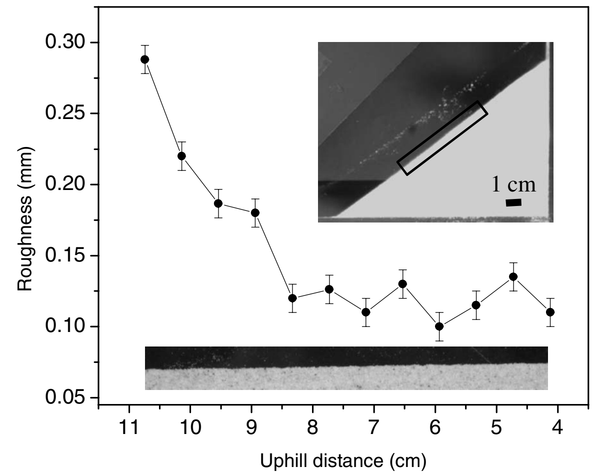

FIG. 11. Spontaneous segregation. The graph indicates the decrease in the roughness amplitude of the pile as we move uphill, suggesting segregation of bigger particles near the lower edge of the heap. The roughness amplitude has been measured as the root mean square of the elevation across 12-mm-long running windows on the free surface seen in the 7-cm-long picture of the lower inset, corresponding to the boxed region indicated in the upper inset. We define the uphill distance as the distance from a point on the surface to the top of the pile.

i.e., where the model proposed in [7] fully applies.

By quantifying the critical length, x_{ci}, at which the transition between continuous and intermittent flow happens, for different input fluxes, we construct the “phase diagram” presented in Fig. 10. There, the vertical axis represents the input flux as the volume per unit time of sand added to the cell. As the width of the cell is increased, the transition line increases its slope, indicating that, for a given F, the intermittent flow is reached for smaller piles. The inset of Fig. 10 shows a superposition of the transition line for the case of a Hele-Shaw cell of $w=12$ mm and the two lines $R2$ and $R3$ corresponding to the *wide* transition to the intermittent regime in the sandpile geometry. The relative position of the lines suggests that the revolving rivers can be taken, to a first approximation, as a 12-mm-wide “revolving Hele-Shaw” cell that performs a revolution around the pile at the same frequency of the rivers [1]. Within this picture, the role of the river is just to reduce the dimensionality of the flow in the pile.

The specific mechanism that triggers the transition from the continuous to intermittent regimes as the size of the system grows is still unclear for our sandpiles, and also probably for the Hele-Shaw configuration (we underline that a qualitative explanation is given in [4] for a heap of fixed length). Here we propose an explanation based on segregation. As well known in the case of debris flows in mountains, bigger rocks tend to accumulate in the flow front as it slides down. This is clearly illustrated, for example, in Fig. 1.4 of Ref. [10]. Careful inspection of the free surface of our heaps in the Hele-Shaw configuration also hints at segregation of big grains as we move down the slope, even when our grains are not significantly bidisperse. In fact, the roughness amplitude of the surface varies from approximately 0.1 mm to 0.3 mm as we move down the hill (see Fig. 11). If one assumes that a slope of bigger grains provides the necessary effective friction to start the growth of a “stop up” front, we speculate that, when the heap, growing to a size large enough for the segregation of big grains near the base, reaches a certain threshold, the intermittent regime is triggered. In analogy, the increase in the radius of the pile is a necessary condition to reach the intermittent regime in the revolving rivers.

V. CONCLUSIONS

We have established experimentally the “dynamical phase diagram” of the continuous and intermittent regimes for revolving rivers in sandpiles. One somewhat unexpected feature of the diagram is that *stable* continuous rivers can only exist below a certain input flux threshold: The intermittent regime is the most robust dynamics in the system. The details of the pile shape and of the movement of grains on its surface indicate that, while most of the downhill flow in the continuous regime takes place within the “river itself,” there is a wide area behind it that contributes with much smaller flow. This fact, however, plays a relevant role in the slow change in the slope as one moves around the pile. We have also improved the kinematic model presented in [1] in order to mimic in detail the measured topography of the piles in the continuous regime. The model also allows us to estimate the extension of the undulating pattern in the intermittent regime based on other experimental parameters. By performing a series of experiments with Hele-Shaw cells, we conclude that, due to the reduced dimensionality of the granular flow along the rivers, we can describe them as "revolving" Hele-Shaw cells of 12 mm width—the analogy accounts both for the continuous and the intermittent regimes. Finally, we propose that the segregation of big grains after the pile has reached a critical size is responsible for the appearance of "stop-up" fronts and, consequently, for the transition to the intermittent regime.

ACKNOWLEDGMENTS

We thank H. Herrmann for inspiration in the exploration of new sandpile models, O. Ramos, A. Stayer, and K. Robbie for experimental support, and E. Clément and S. Douady for advice and useful discussions. We acknowledge support from the French Norwegian PICS project, the INSU DYETI program, the ANR CTT ECOUPREF program, the REALISE program, the Alsace region, and the Cuban PCNT Grant entitled "Avalanche Dynamics in Physical and Biological Systems."

[1] E. Altshuler, O. Ramos, E. Martínez, A. J. Batista-Leyva, A. Rivera, and K. E. Bassler, Phys. Rev. Lett. **91**, 014501 (2003).
[2] X.-Z. Kong, M.-B. Hu, Q.-S. Wu, and Y.-H. Wu, Phys. Lett. A **348**, 77 (2006).
[3] E. Martínez, C. Pérez-Penichet, O. Sotolongo-Costa, O. Ramos, K. J. Måløy, S. Douady, and E. Altshuler, Phys. Rev. E **75**, 031303 (2007).
[4] S. Douady, B. Andreotti, and A. Daerr, Adv. Complex Syst. **4**, 509 (2001).
[5] J. Rajchenbach, Phys. Rev. Lett. **65**, 2221 (1990).
[6] P.-A. Lemieux and D. J. Durian, Phys. Rev. Lett. **85**, 4273 (2000).
[7] S. N. Dorogovtsev and J. F. F. Mendes, Phys. Rev. Lett. **83**, 2946 (1999).
[8] S. N. Dorogovtsev and J. F. F. Mendes, Phys. Rev. E **61**, 2909 (2000).
[9] Th. Boutreux, E. Raphaël, and P.-G. de Gennes, Phys. Rev. E **58**, 4692 (1998).
[10] T. Takahashi, *Debris Flow* (A. A. Balkema, Rotterdam, 1991).

Pure Appl. Geophys. 168 (2011), 2289–2323

DOI 10.1007/s00024-011-0320-4

Pure and Applied Geophysics

The Mechanical Coupling of Fluid-Filled Granular Material Under Shear

L. Goren,[1,2] E. Aharonov,[1] D. Sparks,[3] and R. Toussaint[4]

Abstract—The coupled mechanics of fluid-filled granular media controls the physics of many Earth systems, for example saturated soils, fault gouge, and landslide shear zones. It is well established that when the pore fluid pressure rises, the shear resistance of fluid-filled granular systems decreases, and, as a result, catastrophic events such as soil liquefaction, earthquakes, and accelerating landslides may be triggered. Alternatively, when the pore pressure drops, the shear resistance of these geosystems increases. Despite the great importance of the coupled mechanics of grain–fluid systems, the basic physics that controls this coupling is far from understood. Fundamental questions that must be addressed include: what are the processes that control pore fluid pressurization and depressurization in response to deformation of the granular skeleton? and how do variations of pore pressure affect the mechanical strength of the grains skeleton? To answer these questions, a formulation for the pore fluid pressure and flow has been developed from mass and momentum conservation, and is coupled with a granular dynamics algorithm that solves the grain dynamics, to form a fully coupled model. The pore fluid formulation reveals that the evolution of pore pressure obeys viscoelastic rheology in response to pore space variations. Under undrained conditions elastic-like behavior dominates and leads to a linear relationship between pore pressure and overall volumetric strain. Viscous-like behavior dominates under well-drained conditions and leads to a linear relationship between pore pressure and volumetric strain rate. Numerical simulations reveal the possibility of liquefaction under drained and initially over-compacted conditions, which were often believed to be resistant to liquefaction. Under such conditions liquefaction occurs during short compactive phases that punctuate the overall dilative trend. In addition, the previously recognized generation of elevated pore pressure under undrained compactive conditions is observed. Simulations also show that during liquefaction events stress chains are detached, the external load becomes completely supported by the pressurized pore fluid, and shear resistance vanishes.

[1] Institute of Earth Sciences, Hebrew University, Givat Ram, Jerusalem, Israel. E-mail: liran.goren@erdw.ethz.ch
[2] *Present Address*: Department of Earth Sciences, ETH, Zurich, Switzerland.
[3] Department of Geology and Geophysics, Texas A&M University, College Station, TX, USA.
[4] Institut de Physique du Globe de Strasbourg (IPGS), CNRS and University of Strasbourg (EOST), Strasbourg, France.

List of symbols

A	Area of a grid cell
A_i	Area of grain i
A_s	Weighted area of grains along a grid point
D	Diffusion coefficient
D_i	Internal diffusion coefficient (accounting only for k_i)
De	Dimensionless Deborah number
d	Characteristic grain diameter
E	Grains bulk modulus
$\mathbf{F_{ij}}$	Interaction force at the contact between grain i and grain j
$\mathbf{F_{ij}^n}$	Normal component of the interaction force
$\mathbf{F_{ij}^s}$	Shear component of the interaction force
I_i	Moment of inertia of grains i
k_b	Boundary permeability
k_c	Permeability prefactor
k_i	Internal permeability
k_0	Permeability scale factor
$\tilde{k}_n$	Nonlinear normal stiffness
$\tilde{k}_s$	Nonlinear tangential stiffness
LP	Dimensionless liquefaction potential
l	Length scale
l_x	Horizontal grid spacing
l_y	Vertical grid spacing
m_i	Mass of grain i
m_{ij}	Harmonic mean of the masses of grains i and j
$\hat{\mathbf{n}}_{\mathbf{ij}}$	Unit vector normal to the contact between grains i and j
P	Pore fluid pressure
R_i	Radius of grain i
R_{ij}	Harmonic mean of the radii of grains i and j
r_{ij}	Distance between the centers of grains i and j

$\mathbf{r_{ij}}$	Vector connecting the centers of grains i and j
$\dot{\mathbf{r}}_{\mathbf{ij}}$	Relative velocity between grains i and j
$\hat{\mathbf{s}}_{\mathbf{ij}}$	Unit vector tangent to a contact between grains i and j
s	Interpolation (weighting) function
Δs	Shear displacement since the formation of a contact between grains
t	Time
t_0	Time-scale of deformation
t_d	Time-scale of diffusion
$\mathbf{u}_i$	Translational velocity vector of grain i
$\mathbf{u_f}$	Velocity field of the pore fluid
$\mathbf{u_s}$	Smoothed velocity field of the granular phase
u_{sz}	Horizontally averaged z component of the solid velocity
u_0	Velocity scale factor
V_i	Volume of grain i
V_{sh}	Applied shear velocity
$\mathbf{w}_i$	Rotational velocity vector of grain i
$\mathbf{x}$	Coordinate of a grid point
$\mathbf{x_i}$	Coordinate of the center of grain i
z	Vertical distance from the center of a granular layer
α	Effective stress coefficient
β	Adiabatic fluid compressibility
γ	Damping coefficient
δ	Thickness of a thin boundary layer (where k_b is the permeability)
ϵ	Strain
ζ	Half thickness of a granular layer
η	Fluid viscosity
λ	Statistical factor for liquefaction potential
μ	Surface friction coefficient
μ_a	Apparent friction, τ/σ_n
v	Grains Poisson's ratio
ξ_{ij}	Overlap between grains i and j
ρ_f	Density of the pore fluid
ρ_s	Density of the bulk material of the grains
ρ_0	Fluid density at hydrostatic pressure level
σ_{ij}	Stress tensor
${\sigma_{ij}}'$	Effective stress tensor
σ_n	Normal stress to a shear surface
τ	Shear stress
Φ	Porosity
$\langle\Phi(z,t)\rangle$	Average porosity between the center of the grains layer and distance z from it

1. Introduction

Fluid-filled granular media are ubiquitous in the Earth, mostly in the upper crust. Soils, fault gouge, and landslide shear zones located below the water table are geosystems that are best described as fluid-filled granular media. Geometrically, such materials are composed of a 3D skeleton built out of contacting grains, whose exact configuration defines pore space where fluid may reside. The mechanical strength of such systems is a function of both phases: the pore fluid and the grains. Already at the beginning of the twentieth century, Terzaghi (1943) understood that it is not the stress that controls the solid–fluid system strength, but instead a quantity termed the "effective stress":

$$\sigma'_{ij} = \sigma_{ij} - \delta_{ij} P, \tag{1}$$

where σ_{ij} is the applied stress tensor, P is the pressure experienced by the fluid within the pores of a granular or porous material, δ_{ij} is Kronecker's delta, and σ'_{ij} is the effective stress tensor. Later, the effective stress was found to depend also on the properties of the bulk material composing the grains, the properties of the granular skeleton, and the properties of the pore fluid. These dependencies were formulated using an effective stress coefficient, $0 < \alpha \leq 1$, that multiplies P, where α was found to be different for different physical quantities (Wang, 2000; Pride, 2005). Still, it was shown that generally α is very close to unity and when the material composing the solid matrix is incompressible relative to the pore fluid, $\alpha = 1$, and Terzaghi's formulation is valid (Nur and Byerlee, 1971; Robin, 1973; Wang, 2000; Pride, 2005).

The most important consequence of the law of effective stress, Eq. 1, is that the shear stress, τ, required to shear the system is not a function of the normal stress as in Coulomb's law, but a function of the effective stress instead:

$$\tau = \mu(\sigma_n - P), \tag{2}$$

where σ_n is the total applied stress normal to a shear surface, μ is the surface friction coefficient, and the cohesion is neglected. It is immediately observed that if P increases to be equal to σ_n then the system completely loses its shear strength, whereas if P decreases the system has higher resistance to shear. Therefore, the pore fluid pressure is of critical importance in the mechanics of fluid-filled granular (and porous) systems undergoing shear. What is less clear is:

1. what is the physics behind the pore pressure control over the shear strength (Eqs. 1 and 2)? and
2. what are the mechanical processes that control the evolution of pore pressure?

These two questions are at the heart of this work, and their answer lays the foundations for predicting the coupled mechanics of grains and pore fluid.

Characterization and understanding of shear deformation is of particular importance in geosystems because any differential forcing or gradients in material properties may lead to shear deformation. Examples include:

– the passage of seismic shear waves through a soil column induces shear deformation of the soil;
– tectonic loading accumulated in a fault zone will eventually lead to shear sliding of the fault; and
– gravitational forces may lead to landslides that shear along a confined zone at their base.

In these examples, the presence of pore fluid changes the onset and dynamics of shear deformation in response to forcing, because the fluid pressure affects the resistance to shear, in accordance with Eq. 2. Next, we review in detail the role of pore pressure in soil liquefaction and in motion along fault zones and landslide shear zones.

Soil liquefaction. In the process of earthquake-induced soil liquefaction, the passage of seismic waves deforms the granular matrix and the fluid in such a way as to lead to pore pressure rise (Das, 1993; Kramer, 1996). The consequent reduction of shear resistance causes the granular system, which under normal conditions behaves like a solid that resists shear, to flow as a fluid. Once liquefied, soils can no longer support the infrastructure and a catastrophic collapse of buildings, roads, bridges, and other structures may take place (e.g., damage during earthquakes at Niigata, 1964 (Kawakami and Asada, 1966), or Izmit, 1999 (Cetin *et al.*, 2004)).

The coupled physics controlling soil liquefaction is not completely understood. The classical approach suggests that cyclic loading (for example the passage of shear waves during an earthquake) leads to irreversible collapse of initially under-consolidated pore volume. When drainage is poor, "the tendency for volume reduction" of the loose granular skeleton may lead to pore fluid pressurization and to liquefaction (Sawicki and Mierczynski, 2006). This basic understanding guides most engineering practices, yet the classical approach still leaves open questions:

– What is the role of fluid compressibility in the pressurization process (Garga and Zhang, 1997)?
– What are the relevant drainage conditions—can liquefaction also occur when fluid inflow and outflow to and from the system are allowed (Seed *et al.*, 1976; El Shamy and Zeghal, 2007)? and
– What is the role of the initial packing—can densely packed layers still liquefy (Soga, 1998; Gabet and Mudd, 2006)?

The importance of these questions is demonstrated when comparing two numerical models of grain–fluid systems that study soil liquefaction. Okada and Ochiai (2007) model an undrained system (with impermeable boundaries) with a highly compressible pore fluid, forced by a compressive constant strain rate. The results of Okada and Ochiai (2007) may be interpreted as an example of the conventional understanding of liquefaction, as they observe pore fluid pressurization when compacting an initially loosely packed layer subjected to undrained conditions, a situation that was observed also experimentally to lead to pore pressure rise and liquefaction (Seed and Lee, 1966; Peacock and Seed, 1968; Seed, 1979). Unlike this classical approach, El Shamy and Zeghal (2007) model a drained system (where the fluid is allowed to flow freely across the top boundary), with completely incompressible pore fluid, an assumption that follows many engineering interpretations of experiments (Garga and Zhang, 1997; Kozlov *et al.*, 1998). El Shamy and Zeghal

(2007) report on significant pore fluid pressurization and liquefaction when forcing their system with periodic shear acceleration at its base. These results are somewhat unexpected, because the drained boundary conditions contradict the classical view of liquefaction, which requires poor drainage.

Fault zones and landslides. In fault zones, deformation often localizes along a fault plane filled with fault-gouge. Fault-gouge is a granular layer formed from fragments that are the product of wear during shear between the fault-walls. In gouge layers and in similarly-formed landslide's shear zones, pressurization and depressurization may occur as a result of irreversible rearrangement of the granular skeleton during continuous shearing. In these cases, drainage conditions and porosity evolution have been shown to affect the evolution of pore pressure and the strength of the shear zone. Porosity within gouge and shear zones is a function of shearing velocity (Marone *et al*., 1990) and stress conditions (Aharonov and Sparks, 1999; Iverson *et al*., 2000). When the fault is sealed, porosity increase (i.e. dilation) during shear is often believed to prohibit unstable sliding via pore pressure reduction leading to strain hardening following Eq. 2 (Scholz *et al*., 1973; Scholz, 1978, 2002; Rudnicki and Chen, 1988; Segall and Rice, 1995; Moore and Iverson, 2002; Samuelson *et al*., 2009), while compaction of under-compacted gouge has been shown experimentally to lead to extreme weakening and unstable sliding (Blanpied *et al*., 1992).

However, similarly to soil liquefaction, the mechanisms that are responsible for pore-pressure evolution in shear zones and the effect of pore pressure variation on the mechanics of fluid-filled granular shear zones are not completely clear. A basic question that is still debated is whether significant pressurization, and, as a consequence, reduction of shear strength, can occur in an initially densely packed shear zone. This is an important question because, despite our knowledge that natural shear zones are in most cases initially over-consolidated, and thus, according to conventional thought, resistant to liquefaction (Iverson *et al*., 2000), ample observations point to significant pore fluid pressurization during earthquake and landslides: hydrofractures and liquefied injection are reported in seismically active fault zones (Boullier *et al*., 2009; Sagy and Brodsky, 2009) and along landslide shear zones (Anders *et al*., 2000), and transient liquefaction has been observed in experimental landslides constructed with initially densely packed grain and rod layers (Iverson and LaHusen, 1989).

1.1. Overview of Existing Research Approaches

To study the mechanics of pore-pressure evolution while the granular skeleton deforms, and its implications for shear strength, there is a need for a fully coupled theory for the mechanics of fluid-filled granular systems. Such full coupling should include two-directional mechanics:

1. the effect of granular matrix deformation on the pore fluid pressure and flow, and
2. the effect of fluid flow and pressure gradients on the deformation of the granular matrix.

A continuum theory for the first direction (the solid effect on the pore fluid) is available, and is reviewed below. However, the second direction requires a continuum description for the general dynamics of a collection of grains. Despite a recent advance in this field in the form of constitutive relations for the flow of dry granular material (Pouliquen *et al*., 2006; Jop *et al*., 2006), it is not clear if these relations also apply to a friction-dominated dense suspension of grains in fluid (Rondon *et al*., 2011), which is the system that we study here. Therefore a well-founded continuum theory for the second direction of our system (the fluid effect on the grains and the resulting grain dynamics) is probably still missing. In the absence of such a theory, alternative approaches are used. One approach that is adopted in many engineering applications for the study of the coupled mechanics of grains and pore fluid is the use of phenomenological models that are based on continuum mixture theory formulations (Zienkiewicz *et al*., 1999), and include many terms that require calibration.

A second approach combines the continuum theory for the fluid with a discrete elements numerical method for the dynamics of the solid grains. Indeed, a common physical method, developed over the last 30 years for dry granular systems, is to use simple interaction laws between individual grains, with few terms to characterize their interactions (Cundall and Strack, 1979). The granular rheology then arises from their collective behavior. The combination of the continuum and discrete component enables solving the first direction of the solid effects on the fluid with the continuum component, and the second direction of the fluid effect on the grain dynamics with the discrete component. Such an approach was used in the modeling of instabilities in the flow of granular media and gas fluids (McNamara *et al*., 2000; Vinningland *et al*., 2007a; Vinningland *et al*., 2007b; Johnsen *et al*., 2006; Johnsen *et al*., 2007; Johnsen *et al*., 2008; Vinningland *et al*., 2010) and liquids of various compressibilities and viscosities (Niebling *et al*., 2010), for modeling hydrofractures (Flekkøy *et al*., 2002), and for study of soil liquefaction (El Shamy and Zeghal, 2007; Okada and Ochiai, 2007). Such an approach is adopted in this work.

The continuum component is developed in Goren *et al*. (2010) for compressible pore fluid pressurization and flow in response to general (reversible and irreversible) granular matrix deformation (the first direction of the full coupling). This paper couples this continuum component for the fluid with a discrete element granular dynamics algorithm following the scheme presented in McNamara *et al*. (2000), to form a fully coupled model that may be used for study of any general granular matrix deformation, and any form of drainage boundary conditions.

The analysis of the continuum component by itself already supplies interesting results. The equation describing the evolution of pore pressure in response to grain matrix deformation is shown here to lead to a viscoelastic type of behavior in which the pore pressure (stress) depends on both the pore volume change (overall volumetric strain) and the rate of porosity change (volumetric strain rate). Two types of end-member behavior for the evolution of pore pressure emerge from the pore-pressure equation. Viscous-like response, in which the pore pressure is linearly dependent on the volumetric strain rate, dominates when the shear zone is well-drained. Elastic-like response, in which the change of pore pressure is proportional to the volumetric strain and is inversely proportional to the fluid compressibility, dominates when the shear zone is effectively undrained. This basic recognition of viscoelastic behavior of the pore pressure was predicted by Goren *et al*. (2010), who assumed the pore fluid responds to grain rearrangement, but deformation of grains is not affected by the fluid (infinitely stiff approximation). An important objective of this current work is to check whether the two types of end-member behavior also characterize the fully coupled two-way model.

1.2. *Overview of Current Research*

The first objective of this current paper is to develop the full coupling between the pore pressure model of Goren *et al*. (2010) and a granular dynamics model, and to validate it. Such a coupled model is presented in the section "Coupled Grains and Fluid Model", and its validation is presented in the section "Model Validation". Because pore-pressure evolution and its two types of end-member behavior were predicted to control the coupled grain–fluid response, the section "Pore-Pressure Evolution Mechanisms" is dedicated to reviewing in detail the pore-pressure evolution that emerges from the formulation of the pore fluid, and the conditions that control the pore pressure response to granular deformation.

The rest of the paper is dedicated to simulations with the fully coupled model, their analysis, and comparison with theoretical prediction: The simulations (presented in the section "Simulations of Shearing Granular Layers") investigate deformation of a closely-packed fluid-filled granular layers, under constant shear velocity and normal stress. During the simulations we monitor the evolution of pore pressure, porosity, and apparent friction, μ_a, (the shear stress that is required for shearing the layer at a constant velocity divided by the applied normal stress). The importance of the apparent friction is a result of our inability to define a single value of pore pressure that may be assigned in Eq. 2. Thus, Eq. 2 may be substituted by:

$$\tau = \mu_a \sigma_n. \tag{3}$$

We have performed two types of simulation using the fully coupled grains and pore fluid model that differ in their boundary conditions: undrained and drained. Simulation results agree with the two types of end-member behavior predicted by the simple pore pressure model in the section "Pore-Pressure Evolution Mechanisms" and in Goren *et al.* (2010): when the boundaries are undrained, the pore pressure response is elastic-like. Dilation with regard to the initial configuration causes pore pressure reduction and system hardening (increase of μ_a). Conversely, when shear leads to compaction, the elastic-like behavior causes rapid liquefaction with pore pressure that becomes equal to the applied normal stress throughout the system, and to a steady-state loss of shear resistance. This behavior corresponds to the classical mechanism of liquefaction.

Less intuitive results arise when simulations are conducted with well-drained boundary conditions. Here, viscous-like evolution of pore pressure may lead to high pore pressure values even if the granular system is undergoing long term dilation. The pressurization occurs during short compactive phases that always punctuate the dilative trend. In some cases, instantaneous events of localized high pore pressure may overcome the applied normal stress and lead to transient liquefaction with complete loss of shear resistance, ($\mu_a \leq 0$). Thus, we predict here that liquefaction in an initially densely packed system is possible if drainage is good. This surprising result agrees with the simplified model of Goren *et al.* (2010), and suggests a new look at liquefaction potential of natural systems. The section "Discussion" discusses the implications of our model and simulations for natural systems of grains and fluids. We show that the two types of end-member behavior we observe are consistent with previous simulations, laboratory experiments, and natural systems; however, the significance of this range of behavior was not previously fully recognized. In the "Discussion" section we also introduce a new measurable property, the liquefaction potential, that is derived from our model and may be used for evaluating the probability of liquefaction occurring in natural systems with different scales and boundary conditions.

2. Coupled Grains and Fluid Model

The numerical model for the coupled dynamics of grains and pore fluid is constructed as a two-phase two-scale model. The granular phase makes up the finer scale where each grain is modeled as a discrete lagrangian element. The fluid phase forms the coarser scale and is modeled on an eulerian grid that is superimposed on the granular level. The fluid grid spacing is approximately the size of two grain diameters. This choice of grid spacing ensures that each cell is larger than a Darcy representative volume element. Similar models reported in Johnsen *et al.* (2006) and Vinningland *et al.* (2007a) have shown that simulation results are mostly insensitive to the exact choice of grid spacing when it is between 2 and 10 grain diameters. The fluid does not see the detailed pore space geometry imposed by the grains, but instead an average field of porosity and permeability as explained below. Furthermore, although the current model is 2D, the porosity is assumed to be always connected via the third dimension to enable simultaneous percolation of both the grains and the fluid.

2.1. Granular Phase

To simulate the mechanics of a collection of grains we use a two-dimensional discrete elements granular dynamics algorithm (Cundall and Strack, 1979). Each individual grain is treated as an inelastic soft disc. Grain interactions, body forces and the force induced by the interstitial fluid lead to linear and rotational acceleration of the grains. Interaction force between two grains i and j is resolved when the distance between the centers of the two grains, r_{ij}, is less than the sum of their radii, $R_i + R_j$. The grain overlap is expressed as $\xi_{ij} = R_i + R_j - r_{ij}$. Interaction force on a contact has a normal component, $\mathbf{F^n}$, and a shear component, $\mathbf{F^s}$, that are resolved with Hertz–Mindlin contact model (Fig. 1):

$$\mathbf{F^n_{ij}}(t) = \left[\tilde{k}_n \xi_{ij} - \gamma m_{ij}(\mathbf{\dot{r}_{ij}} \cdot \mathbf{\hat{n}_{ij}})\right]\mathbf{\hat{n}_{ij}}, \quad (4)$$

where the first term on the right hand side of Eq. 4 is a nonlinear repulsive force and the second term is a damping force that depends on the damping coefficient, γ, the harmonic mean of the grains mass, m_{ij}, and the relative velocity between the grains along the direction of the contact $\mathbf{\dot{r}_{ij}} \cdot \mathbf{\hat{n}_{ij}}$, where $\mathbf{r_{ij}}$ is a vector connecting the grains centers and $\mathbf{\dot{r}_{ij}}$ is the relative grain velocity. $\mathbf{\hat{n}_{ij}} = (\mathbf{r_{ij}} \cdot \mathbf{\hat{x}}, \mathbf{r_{ij}} \cdot \mathbf{\hat{y}})/r_{ij}$ is a unit vector normal to the contact. The coefficient of the normal repulsive force is the nonlinear normal stiffness (Schäfer *et al.*, 1996):

$$\tilde{k}_n = \frac{\sqrt{2}E}{3(1-\nu^2)}(R_{ij}\xi_{ij})^{1/2} \tag{5}$$

where E and ν are the grains bulk modulus and Poisson's ratio, respectively, and R_{ij} is the harmonic mean of the grains radii. The shear force is determine using an elastic/friction law:

$$\mathbf{F}^{\mathbf{s}}_{\mathbf{ij}}(t) = -\left[\min(\tilde{k}_s\Delta s, \mu\mathbf{F}^{\mathbf{n}}_{\mathbf{ij}})\right]\hat{\mathbf{s}}_{ij}, \tag{6}$$

where Δs is the shear displacement since formation of the contact, μ is the surface friction coefficient, and $\hat{\mathbf{s}}_{\mathbf{ij}} = (\mathbf{r}_{\mathbf{ij}}\cdot\hat{\mathbf{y}}, -\mathbf{r}_{\mathbf{ij}}\cdot\hat{\mathbf{x}})/r_{ij}$ is a unit vector tangent to the contact. The coefficient of the tangent repulsive force is the nonlinear tangent stiffness:

$$\tilde{k}_s = \frac{2\sqrt{2}E}{(2-\nu)(1+\nu)}(R_{ij}\xi)^{1/2}. \tag{7}$$

Equation 6 implies that the shear force opposes the sense of the relative tangential motion between the grains. It is important to note that as long as $\mathbf{F}^{\mathbf{s}}_{\mathbf{ij}} < \mu\mathbf{F}^{\mathbf{n}}_{\mathbf{ij}}$ no sliding occurs along the contact, but there might still be relative tangential displacement between the centers of grains i and j. When Coulomb failure criterion along the contact is met, i.e. $\tilde{k}_s\Delta s \geq \mu\mathbf{F}^{\mathbf{n}}_{\mathbf{ij}}$, the contact slides with a constant shear force, $\mu\mathbf{F}^{\mathbf{n}}_{\mathbf{ij}}$, (Fig. 1).

The motion of each particle is determined by monitoring collisions between grains, resolving the

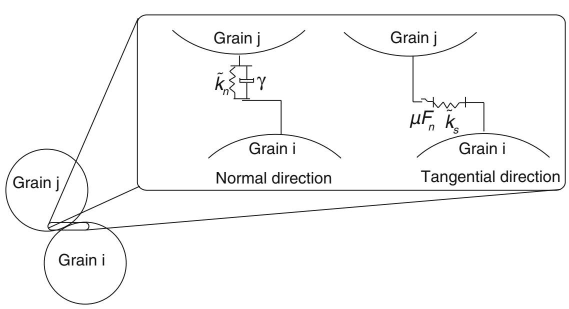

Figure 1
When two grains come into contact, a repulsive force arises. The normal component (*left*) is a function of an elastic normal spring with constant $\tilde{k}_n$, and damping that depends on the relative velocity of the grains. The tangential component (*right*) is a function of a tangential spring with constant $\tilde{k}_s$. When the tangential spring is stressed beyond Coulomb friction criterion, the contact starts sliding with a constant shear force, $\mu\mathbf{F}^{\mathbf{n}}$. Figure adapted from El Shamy and Zeghal (2007)

induced contact forces and torques, and using them in the momentum equations:

$$m_i\dot{\mathbf{u}}_i = m_i\mathbf{g} + \sum_j \mathbf{F}_{ij} - \frac{\nabla P \cdot V_i}{1-\Phi}, \tag{8}$$

$$I_i\dot{\mathbf{w}}_i = \sum_j R_i\hat{\mathbf{n}}_{ij} \times \mathbf{F}_{ij}, \tag{9}$$

where $\mathbf{u}_i$ and $\mathbf{w}_i$ are the translational and rotational velocity vectors of grain i (a superposed dot indicates time derivative). m_i is the grain mass, $\mathbf{g}$ is the gravitational acceleration, I_i is the grain moment of inertia, and $\mathbf{F}_{ij}$ refers to inter-grain force at the contact between grain i and grain j. The arm of the force in the torque balance, Eq. 9, is expressed as $R_i\hat{\mathbf{n}}_{ij}$ because all grains are perfect discs. The last term on the right-hand side of Eq. 8 refers to the force exerted on grain *if* by the pressure gradient, ∇P, of the fluid surrounding it, normalized by the solid fraction, $(1-\Phi)$, in its vicinity, where Φ is the porosity and V_i is the volume of grain i (McNamara *et al.*, 2000).

2.2. Fluid Phase

The formulation for the physics of the pore fluid is developed in Goren *et al.* (2010). For clarity, we briefly review it here. First, mass-conservation equations are written for the grains and for the fluid:

$$\frac{\partial[(1-\Phi)\rho_s]}{\partial t} + \nabla\cdot[(1-\Phi)\rho_s\mathbf{u}_\mathbf{s}] = 0, \tag{10}$$

$$\frac{\partial[\Phi\rho_f]}{\partial t} + \nabla\cdot[\Phi\rho_f\mathbf{u}_\mathbf{f}] = 0, \tag{11}$$

where t is time, ρ_s and ρ_f are the densities of the solid grains and fluid, respectively, and $\mathbf{u}_\mathbf{s}$ and $\mathbf{u}_\mathbf{f}$ are the solid and fluid velocity fields, respectively. These velocities are defined for mesoscopic volumes containing at least a few grains, where Darcy's law is applicable. In that sense $\mathbf{u}_\mathbf{s}$ is an average of $\mathbf{u}_\mathbf{i}$ over spatially close grains.

The full fluid momentum equation includes inertial terms and forcing terms of pressure gradient and viscous drag. Here we choose to neglect fluid inertia to enable theoretical analysis of the pore fluid equation. Goren *et al.* (2010) show that for the deformation field and parameter range that are used here, fluid inertia is mostly negligible, but it is important to note that such an approximation is more suitable when the permeability and grain size are relatively small. The full fluid momentum equation is treated by El Shamy and Zeghal (2007), for example, and although it is hard to compare the two models, the overall observed behavior when drainage is good (the scenario treated in El Shamy and Zeghal (2007)) is similar. When neglecting inertial terms the fluid momentum equation is approximated by Darcy's law:

$$\Phi(\mathbf{u_f} - \mathbf{u_s}) = -\frac{k}{\eta}\nabla P, \tag{12}$$

where k is the permeability, η is the fluid viscosity, and P is the excess (over hydrostatic) fluid pressure. In the small system we will consider, we take the hydrostatic pressure to be uniform throughout the system. The fluid density is given by the fluid state equation:

$$\rho_f = \rho_0(1 + \beta P), \tag{13}$$

where ρ_0 is the fluid density at hydrostatic pressure level, and β is the adiabatic fluid compressibility. We assume that the compressibility of a grain is negligible relative to the fluid compressibility, so that ρ_s can be approximated as constant. We also assume that $\beta P \ll 1$ (Goren *et al.*, 2010). Equations 10 to 13 then lead to:

$$\beta\Phi\frac{\partial P}{\partial t} - \nabla \cdot \left[\frac{k}{\eta}\nabla P\right] + \nabla \cdot \mathbf{u_s} + \beta\Phi\mathbf{u_s} \cdot \nabla P = 0. \tag{14}$$

By further assuming that the length scale of pore pressure diffusion is always larger than the diameter of a single grain (Goren *et al.*, 2010), the last term of Eq. 14 may be neglected. This assumption is revisited in the section "Pore-Pressure Evolution Mechanisms" in which non-dimensional analysis of Eq. 14 is presented. As a result, the pore-pressure evolution equation becomes a three-term equation:

$$\frac{\partial P}{\partial t} - \frac{1}{\beta\Phi\eta}\nabla \cdot [k\nabla P] + \frac{1}{\beta\Phi}\nabla \cdot \mathbf{u_s} = 0. \tag{15}$$

The first term of Eq. 15 expresses the temporal evolution of pore pressure, the second term expresses pore pressure diffusion, and the third term is the forcing to the pore pressure, which arises because of divergence in the solid velocity. When this divergence is negative, the pore volume collapses, and the fluid pressurizes and flows away from the collapsing pores. When the divergence is positive, the pore volume expands, and the pore fluid depressurizes and flows into the expanding pore volume.

It is sometimes convenient to express the forcing term as a function of porosity evolution rather than as a function of the divergence of the solid velocity. From the grains mass conservation, Eq. 10, it can be shown that:

$$(1 - \Phi)\nabla \cdot \mathbf{u_s} - \frac{\partial \Phi}{\partial t} - \mathbf{u_s} \cdot \nabla\Phi = 0. \tag{16}$$

The solid velocity divergence term scales with local compaction and dilation (local grains rearrangement), whereas the porosity gradient term describes the advection of porosity that scales with the imposed shear velocity over the whole layer thickness. Because the length scale associated with the former term is expected to be much smaller than the whole layer thickness (which is associated with the latter term), the advection of porosity is neglected, so that:

$$(1 - \Phi)\nabla \cdot \mathbf{u_s} \approx \partial\Phi/\partial t. \tag{17}$$

(A similar conclusion is reached by Walder and Nur (1984) and Snieder and van der Beukel (2004)). Under this approximation, Eq. 15 may be rewritten as:

$$\frac{\partial P}{\partial t} - \frac{1}{\beta\Phi\eta}\nabla \cdot [k\nabla P] + \frac{1}{\beta\Phi(1 - \Phi)}\frac{\partial \Phi}{\partial t} = 0. \tag{18}$$

Equations 15 and 18 were shown in Goren *et al.* (2010) to be a general form of previous formulations by Biot (1941); Wang (2000), and Bachrach *et al.* (2001) that assume only elastic deformation of the grains skeleton, and Walder and Nur (1984) that assume a specific law for the evolution of porosity. Similar formulations also appear in Iverson (1993), Rudnicki and Chen (1988), Miller and Nur (2000), Snieder and van der Beukel (2004), and Samuelson *et al.* (2009).

2.3. *Coupling Between the Grains and the Fluid Phases*

In the current model, we couple a 2D granular dynamics algorithm with a continuous solver of the pore fluid pressure and flow. To allow the coupling, information must be transferred between the two phases of the model. Fluid pressure gradients are needed in order to solve the grain force balance, Eq. 8, and the divergence of solid velocity and the porosity are required for solution of the fluid pressure, Eq. 15. To achieve this full coupling we use a 2D linear interpolation scheme between the two scales of the model. For a grain whose center is located at position $\mathbf{x_i}$ and for a fluid grid point located at position $\mathbf{x}$ the interpolation scheme is represented by the function s:

$$s(\mathbf{x_i}-\mathbf{x}) = \begin{cases} \left(1-\frac{|x_i-x|}{l_x}\right)\left(1-\frac{|y_i-y|}{l_y}\right), & |x_i-x|<l_x, |y_i-y|<l_y \\ 0 & \text{otherwise} \end{cases} \tag{19}$$

where l_x and l_y are the horizontal and vertical grid spacing. Each grain contributes its s-weighted area and momentum to the grid points surrounding it. The porosity at a grid point is calculated as:

$$\Phi(\mathbf{x}) = 1 - \frac{A_s(\mathbf{x})}{A}, \tag{20}$$

where A is the area of a grid cell, and

$$A_s(\mathbf{x}) = \sum_{i=1}^{N} s(\mathbf{x_i}-\mathbf{x})A_i, \tag{21}$$

where A_i is the area of grain i, and N is the number of grains. The solid velocity field is defined as the ratio of granular momentum to granular mass. For equal density grains the mass dependency is reduced to an area dependency, and the solid velocity field may be evaluated as:

$$\mathbf{u_s}(\mathbf{x}) = \frac{\sum_{i=1}^{N} s(\mathbf{x_i}-\mathbf{x})A_i\mathbf{u_i}}{\sum_{i=1}^{N} s(\mathbf{x_i}-\mathbf{x})A_i}. \tag{22}$$

In the simulations presented here, the grain size distribution is close to being monodispersed and Eq. 22 is reduced to:

$$\mathbf{u_s}(\mathbf{x}) = \frac{\sum_{i=1}^{N} s(\mathbf{x_i}-\mathbf{x})\mathbf{u_i}}{\sum_{i=1}^{N} s(\mathbf{x_i}-\mathbf{x})}, \tag{23}$$

where $\sum_{i=1}^{N} s(\mathbf{x_i}-\mathbf{x})$ is the on-site mass density (McNamara *et al.*, 2000). Interpolated granular velocities are calculated on a staggered grid with regard to the porosity, so that the velocity divergence is defined exactly on the porosity grid.

The ratio of pressure gradient to the solid fraction, $\nabla P/(1-\Phi)$, that is calculated on the fluid grid by solving Eq. 15, is interpolated back from the fluid grid to the grains surrounding this grid by using the same interpolation function s, Eq. 19.

The permeability is calculated with a Carman–Kozeny-like relationship. However, the Carman–Kozeny relationship gives the permeability as a function of the volume fraction of spheres, whereas the porosity in our model is computed with the area fraction of discs. Consequently, we transform the area fraction in the simulations $(1-\Phi)^{(2D)}$ to an equivalent volume fraction in 3D. The simplest map of 2D to 3D solid fraction, which ensures that the pure fluid state and the random close-packing state correspond between the two dimensionalities, is $(1-\Phi)^{(3D)} = (2/3)(1-\Phi)^{(2D)}$ (McNamara *et al.*, 2000). This mapping results in the following relationship between porosity and permeability:

$$k = \frac{k_c(1+2\Phi)^3}{(1-\Phi)^2}. \tag{24}$$

where k_c is a prefactor (units m^2) and Φ is the 2D porosity.

Stability and accuracy requirements force us to take a time-step small enough to resolve the evolution of forces during collision of the grains. In each time step, Eqs. 8 and 9 are solved to find the new location, velocity, and acceleration of each grain. The granular velocity and the porosity are then interpolated from the granular level to the fluid grid. In the next stage, an alternating-direction-implicit (ADI) algorithm is used in the solution of the fluid pressure, Eq. 15, and the pressure gradients are interpolated back to the granular level and assigned in the last term of Eq. 8 at the next time step.

3. Model Validation

To validate the coupled grains-fluid model, we perform three tests in which we compare simulation results with analytical predictions.

Effective stress validation test. The first test verifies that the model reproduces correctly the law of effective stress. Nur and Byerlee (1971) develop an effective stress law for volumetric strain of fluid-filled porous material: $\sigma'_{ij} = \sigma_{ij} - \alpha\delta_{ij}P$, where α, the effective stress coefficient, is a function of the compressibility of the solid grains and of the matrix. For the case of incompressible grains $\alpha = 1$. Nur and Byerlee (1971) support their law by means of a series of experiments showing that there is no correlation between the applied stress and the resulting measured volumetric strain, and they find a linear relationship between the effective stress and the measured volumetric strain, with a stress–strain curve similar to dry samples (Nur and Byerlee, 1971, their Figure 2). In our test we reproduce numerically the experimental series of Nur and Byerlee (1971). We perform a series of numerical simulations in which, in each simulation, a system of grains of variable size is packed under confining stress. The systems are periodic in direction x so that a normal stress, σ_n, applied to the top and bottom walls corresponds to a uniform confining stress. The upper and lower boundaries are composed of half grains that are glued together to form rough walls. In each simulation, a fluid pressure, P, is introduced and maintained constant and uniform during the simulation as if the pore fluid in the granular system is connected to a big reservoir. For that reason, in this test we do not solve Eq. 15 for the pore-pressure evolution within the layer. Simultaneously with the introduction of pressure, the applied unidirectional stress is increased by $\Delta\sigma_n$. Thus, each experiment is characterized by a couple, $\Delta\sigma_n$ and P. We measure the volumetric (vertical, because of periodicity) strain, $\Delta\epsilon$, that results from the extra loading, $\Delta\sigma_n$, under constant pore pressure, P. The setup of the numerical simulations is depicted in Fig. 2.

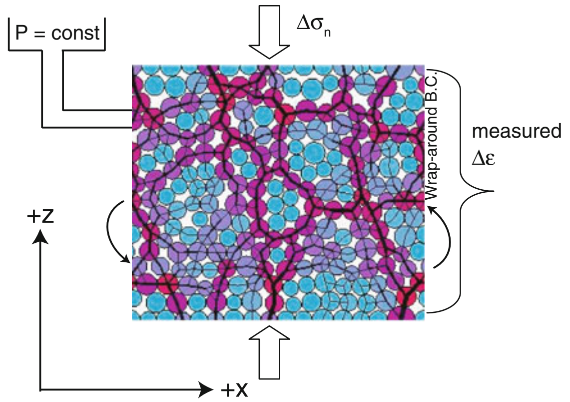

Figure 2
Setup of a numerical experiment designed to verify that the grains–fluid model reproduces correctly the law of effective stress. In each experiment, a unidirectional stress, $\Delta\sigma_n$, is applied, and a constant pore pressure, P, is maintained. The vertical strain, $\Delta\epsilon$, is measured. The white pore area between the grains is filled with fluid

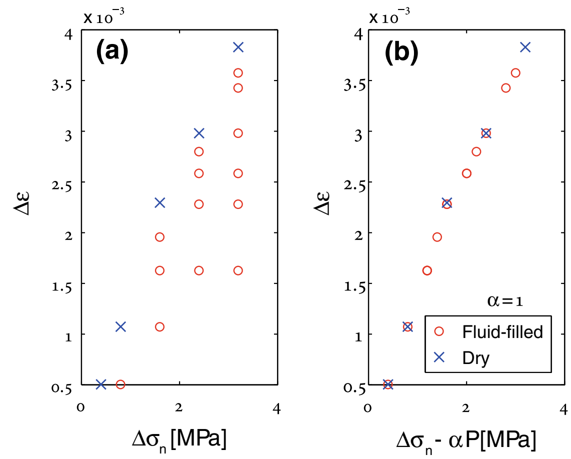

Figure 3
Effective stress validation test. **a** Volumetric strain, $\Delta\epsilon$, is plotted against the change of confining stress, $\Delta\sigma_n$, and shows no correlation for the wet simulations. **b** Volumetric strain is plotted against the effective stress and show linear relationship with the same slope as for dry simulations

Figure 3a, b shows $\Delta\epsilon$, the volumetric strain, as a function of $\Delta\sigma_n$ and $\Delta\sigma_n - \alpha P$, respectively, similarly to Nur and Byerlee (1971, Figure 2). A set of dry simulations, with no pore fluid, serves as a reference and is depicted by "x". Wet simulations are depicted by "o". Figure 3a shows that $\Delta\epsilon$ and $\Delta\sigma_n$ in the wet simulations are poorly correlated. In contrast, Fig. 3b shows a linear relationship between $\Delta\epsilon$ and $\Delta\sigma_n - \alpha P$, for $\alpha = 1$ (as expected for incompressible solid grains), with the same slope as the dry simulations. Simulation results show that the model successfully reproduces the effective stress behavior that is observed experimentally in fluid-filled porous and granular material.

Because pore pressure is maintained constant within the system, $\nabla P = 0$. Therefore, the fluid does not exert a force on internal grains, and the last term of Eq. 8 vanishes. However, because the pore pressure outside the system is assumed to be zero, boundary grains do feel the effect of fluid pressure because it is exerted on them only from one side (from the bottom on the top boundary and from the top on the bottom boundary). Thus, a pressure gradient force acts on the boundary grains in the outward normal direction to the boundaries, and opposes the external force induced by σ_n. We note here an important insight regarding the effective stress: in models, one could be tempted to apply the effective stress law at each grain contact, but that would lead to incorrect formulation of the forces, because only pressure gradients exert a net force on grains. The effective stress law may therefore be viewed as the macroscopic manifestation of microscopic gradients of pore pressure.

Sedimentation validation test. The second test compares the sedimentation velocity under gravity of grains through fluid, with the theoretical prediction that assumes that particles fall without acceleration (following McNamara *et al*. (2000)). The volume of grains transported downward must be compensated by an equal volume of fluid upflow. Thus $(1-\Phi)\mathbf{u_s} = -\Phi\mathbf{u_f}$. Combining this equation with Darcy law, Eq. 12, results in $\mathbf{u_s} = k(\Phi)\nabla P/\eta$. The pressure force must balance the weight of the grains, so that $\nabla P = \rho_s \mathbf{g}(1-\Phi)$. Assigning Eq. 24 for $k(\Phi)$, with $k_c = r^2/540$ (McNamara et al., 2000), r being the average grain radius, leads to:

$$\frac{\mathbf{u_s}}{u_{\mathrm{sed}}} = -\frac{\left[1-\frac{2}{3}(1-\Phi)\right]^3}{(1-\Phi)}\hat{\mathbf{z}}, \qquad (25)$$

where $u_{\mathrm{sed}} = r^2\rho_s g/20\eta$, and $\hat{\mathbf{z}}$ is a unit vector in the direction opposite to gravity. Each sedimentation simulation starts with a different uniform porosity. Then, every 50,000 time steps we average the porosity and the granular velocity over the grid points. To exclude material that has already settled on the bottom, and the clear region above the settling grains, we do not include in the average grid points with granular velocity smaller than $0.5\max(\mathbf{u_s})$, and grid points with $(1-\Phi) < 0.25$. Finally, each simulation is temporally averaged to obtain a space and time average of $\mathbf{u_s}$ and $(1-\Phi)$ for the simulation. These couples are depicted by "o" in Fig. 4 and show good fit to the theoretical prediction of Eq. 25.

Fluidization validation test. The third test is of fluidization of a granular layer. Initially the grains rest at the bottom of the system after sedimentation. A constant fluid pressure gradient is then applied between the top and the bottom of the system. It is predicted that when $\nabla P = -(\rho_s - \rho_f)(1-\Phi)\mathbf{g}$, the force exerted by ∇P will exactly balance the weight of the grains that rest at the base of the system (Richardson, 1971). For larger ∇P the grains will be lifted whereas for smaller ∇P the grains will not move. Figure 5 shows the granular velocity averaged in space over the grains and in time over the first million time steps, $\bar{\mathbf{u}}_\mathbf{s}$, plotted versus ∇P for several simulations. The grains move only when ∇P is larger than the predicted critical value whereas for smaller values of $\nabla P, \bar{\mathbf{u}}_\mathbf{s} = 0$.

4. *Pore-Pressure Evolution Mechanisms*

After presenting the fully coupled model and verifying it, we address the two mechanisms responsible for the evolution of pore pressure, and that arise from the pore fluid formulation presented in the section "Fluid Phase". These mechanisms, which are generic and independent of the specific deformation of grain dynamics, are discussed at length in Goren *et al*. (2010). The two mechanisms depend on the system

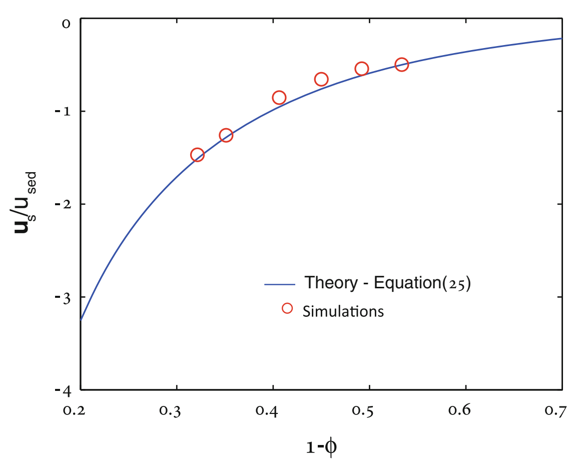

Figure 4
Sedimentation validation test. Comparison between theory, Eq. 25, and simulations of the relationship between solid fraction, $1-\Phi$, and sedimentation velocity, $\mathbf{u_s}/u_{\mathrm{sed}}$

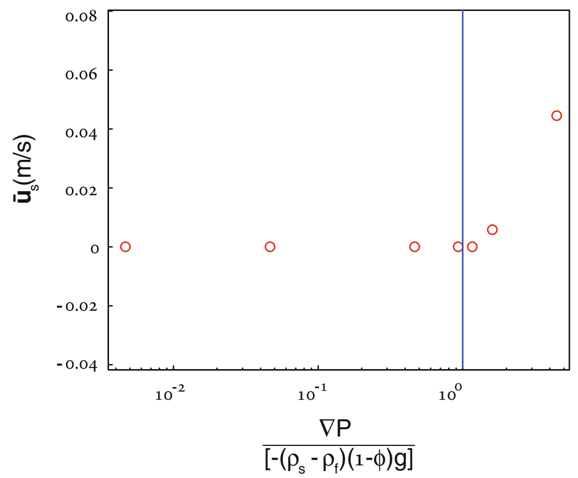

Figure 5
Fluidization validation test. Comparison between theory and simulations for the minimum pressure gradient, ∇P, required to fluidize a layer of grains with porosity Φ under gravity $\mathbf{g}$. $\bar{\mathbf{u}}_\mathbf{s}$ is the average solid velocity. ρ_s and ρ_f are the densities of the solid grains and of the fluid, respectively

boundary conditions, and on the relative magnitude of the different terms in Eqs. 15 and 18. In order to estimate the magnitude of these terms we perform a non-dimensional analysis of Eq. 14. The characteristic scales of the variables in the system are defined as: $P = \hat{P}/\beta, \mathbf{u_s} = \hat{\mathbf{u}}_s u_0, k = \hat{k}k_0$, and $t = \hat{t}t_0$, where the $\hat{}$ notation denotes non-dimensional variables, and u_0, k_0, and t_0 are the velocity, permeability, and time-scale factors, respectively. The divergence operators resulting from grain mass conservation, Eq. 10, represent grain-scale rearrangements, and are therefore scaled by d^{-1}, where d is a characteristic grain diameter. The gradient operators that result from Darcy law, Eq. 12, and act on the pressure, P, are scaled by l^{-1}, where $l = \min(\zeta, D_i/u_0)$ is a larger length scale that corresponds to the distance that is reached by the pore pressure signal. ζ is the system half thickness or the maximum distance to a boundary. $D_i = k_i/\beta\eta\Phi$ is the internal diffusion coefficient of the system that depends on the internal permeability, k_i, in accordance with Eq. 24 (while ignoring the boundary permeability), and D_i/u_0 is the internal diffusion length. D_i/u_0 may be cast as a (more common) diffusion length scale of the form $\sqrt{D_i t_1}$, with $t_1 = D_i/u_0^2$. To understand the meaning of t_1 note that when grains move at velocity u_0, the pressure next to where the motion takes place changes first because of diffusion and later because of advection. t_1 is the time at which the diffusive and advective effects balance.

According to the definition of l, if the system is relatively small or the internal permeability is relatively large, then $\zeta < D_i/u_0$ and a pore pressure signal will interact with the boundaries because the system is well connected with diffusion, leading to $l = \zeta$. If however $\zeta > D_i/u_0$, then diffusion does not have the necessary time to level out the pressure changes advected with the matrix at velocity u_0 during shear, and $l = D_i/u_0$. The time-scale factor, t_0, is defined as the time-scale of deformation:

$$t_0 = \frac{d}{u_0}. \tag{26}$$

The permeability scale factor, k_0, requires further discussion. When $\zeta > D_i/u_0$ and $l = D_i/u_0$ the boundaries are not expected to interact with a pore pressure signal originating at the system interior, and therefore, $k_0 = k_i$. However, when $\zeta < D_i/u_0$ and $l = \zeta, k_0$ should represent the effective permeability that accounts both for the value of the internal permeability, k_i, over a layer of thickness ζ, and for the value of the boundary permeability, k_b, over a thin (but finite) boundary layer of thickness δ. As the permeability is proportional to the Darcy velocity, k_0 is estimated as harmonic mean:

$$k_0 = \zeta k_i k_b/(\delta k_i + \zeta k_b), \tag{27}$$

where $\zeta + \delta \approx \zeta$. The harmonic mean is for permeabilities transverse to the boundaries and so it gives greater weight to the smaller permeability. As a result

$$k_0 = \begin{cases} k_i & \text{for well-drained systems with } k_i \ll k_b \\ \zeta k_b/\delta & \text{for poorly-drained systems with } k_i \gg k_b \\ 0 & \text{for completely undrained systems with } k_b = 0. \end{cases} \tag{28}$$

Assigning the non-dimensional variables in Eq. 14 results in:

$$\frac{\partial \hat{P}}{\partial \hat{t}} - \mathrm{De}^{-1}\hat{\nabla}\cdot(\hat{k}\hat{\nabla}\hat{P}) + \frac{1}{\Phi}\hat{\nabla}\cdot\hat{\mathbf{u}}_s + \frac{d}{l}\hat{\mathbf{u}}_s\cdot\hat{\nabla}\hat{P} = 0. \tag{29}$$

The last term of Eq. 29 is negligible compared with the first and third terms because, for any natural system, and in particular for our choice of parameters, the diffusion length is significantly larger than the diameter of a single grain, i.e. $d \ll l$ (Goren *et al.*, 2010). Equation 29 then becomes:

$$\frac{\partial \hat{P}}{\partial \hat{t}} - \mathrm{De}^{-1}\hat{\nabla}\cdot(\hat{k}\hat{\nabla}\hat{P}) + \frac{1}{\Phi}\hat{\nabla}\cdot\hat{\mathbf{u}}_s = 0, \tag{30}$$

which is the non-dimensional form of Eq. 15.

The coefficient of the second term in Eq. 30 is a function of the Deborah number,

$$\mathrm{De} = \frac{t_d}{t_0}, \tag{31}$$

which is defined as the ratio of relaxation time-scale to a characteristic process time-scale (Osswald, 1998, p. 54). Here, the relaxation time-scale, $t_d = l\ d/D$, is the time-scale for pore pressure diffusion, where $D = k_0/\beta\eta\Phi$ is the system diffusion coefficient (note that $D \le D_i$). The characteristic process time-scale, t_0, is simply the time-scale of deformation (Eq. 26). In terms of the system parameters, De may be expressed as:

$$\mathrm{De} = \frac{lu_0}{D} = \frac{lu_0\beta\eta\Phi}{k_0}. \tag{32}$$

Deborah numbers are normally used in the characterization of viscoelastic materials for estimating the relative importance of the viscous and elastic rheologies. In the following discussion we show that viscoelasticity is a good analog for description of the pore fluid pressure evolution.

4.1. Small System ($\zeta < D_i/u_0$)

When the system is relatively small compared with the diffusion length, then we take $l = \zeta$ in the definition of De, Eq. 32. If the boundaries are undrained, k_0 is zero and $\mathrm{De}^{-1} = 0$. As a result, the diffusion term in Eqs. 15 and 18 should be ignored. The non-dimensional Eq. 30 then becomes

$$\frac{\partial \hat{P}}{\partial \hat{t}} + \frac{1}{\Phi}\hat{\nabla}\cdot\hat{\mathbf{u}}_s = 0. \tag{33}$$

Under such conditions, the dimensional Eq. 18 can be solved for small changes of Φ, and for the spatially averaged pore pressure $\bar{P}$:

$$\Delta\bar{P} = -\frac{\Delta\Phi}{\beta\Phi(1-\Phi)}, \tag{34}$$

where $\Delta\bar{P} = \bar{P}(t'') - \bar{P}(t')$, for any $t'' > t'$, and $\Delta\Phi$ is defined in a similar manner. Here, changes of average pore pressure, $\Delta\bar{P}$, are linearly related to the overall change of porosity, $\Delta\Phi$, with a proportionality factor that depends on the fluid bulk modulus, β^{-1}, so that pore pressure responds "elastically" to pore strain. Pore fluid that is trapped within a shrinking pore volume ($\Delta\Phi < 0$) is pressurized, whereas pore fluid trapped in expanding pore volume ($\Delta\Phi > 0$) is depressurized.

When the boundaries are well-drained (k_0 is approximated as k_i), then always (from the definition of De and from the condition $\zeta < D_i/u_0$) De < 1. If De $\ll 1$, for example when ζ is small or k_0 is large, then the non-dimensional Eq. 30 reveals that the first time-dependent term is negligible relative to the second diffusion term. The reason the forcing term is not negligible compared with the diffusion term is that the forcing is the source of pore pressure variations and is, therefore, regarded as the pivot of the equation (Goren *et al.*, 2010). The non-dimensional pore fluid Eq. 30, then takes the form:

$$\mathrm{De}^{-1}\hat{\nabla}\cdot(\hat{k}\hat{\nabla}\hat{P}) = \frac{1}{\Phi}\hat{\nabla}\cdot\hat{\mathbf{u}}_s. \tag{35}$$

Appendix 1 presents the solution of the dimensional Eq. 18 for the pore pressure, while neglecting the time dependent term. Appendix 1 shows that the pore pressure within a system that is characterized by De $\ll 1$ may be approximated as:

$$P(z,t) = -\frac{\eta}{2k_0}\frac{\mathrm{d}\langle\Phi(\zeta,\mathrm{t})\rangle}{\mathrm{d}t}\left(\zeta^2 - z^2\right), \tag{36}$$

where $\langle\Phi(\zeta,t)\rangle$ is the average porosity in the zone between the center of the system and its boundary, that is located at distance ζ from the center (Fig. 7).

In the derivation of Eq. 36 it was assumed that the top and bottom boundaries are completely drained, i.e. $P(\zeta,t) = P(-\zeta,t) = 0$, and that the rate of change of the average porosity is uniform in space. Note that because $(\zeta^2 - z^2) \geq 0$, compaction with $\mathrm{d}\langle\Phi(\zeta,t)\rangle/\mathrm{d}t < 0$ leads to pressurization, whereas dilation with $\mathrm{d}\langle\Phi(\zeta,t)\rangle/\mathrm{d}t > 0$ leads to depressurization. Here, the evolution of pore pressure is controlled by the strain rate of porosity $\mathrm{d}\langle\Phi(\zeta,t)\rangle/\mathrm{d}t$, with a coefficient that depends on the fluid viscosity, η, and is inversely proportional to the permeability. Therefore, the pore pressure responds "viscously" to the deformation of the matrix.

When $\mathrm{De} \lesssim 1$, which may occur for larger ζ or smaller k_0, the diffusion term is not strictly larger than the time-dependent term, and both terms are expected to contribute to the evolution of pore pressure. Still, Eq. 36 should enable approximate estimation of the pore-pressure evolution.

4.2. *Large System ($\zeta > D_i/u_0$)*

When the system is large compared with the diffusion length, then we take $l = D_i/u_0$ and $k_0 = k_i$ in Eq. 32, which always results in $\mathrm{De} = 1$ (and $t_d = t_0$). In this case, the diffusion and time-dependent terms are of the same order. The non-dimensional Eq. 30 then becomes:

$$\frac{\partial \hat{P}}{\partial \hat{t}} - \hat{\nabla} \cdot (\hat{k}\, \hat{\nabla} \hat{P}) + \frac{1}{\Phi}\, \hat{\nabla} \cdot \hat{\mathbf{u}}_s = 0, \qquad (37)$$

and the dimensional evolution of the pore pressure is governed by the three terms of Eqs. 15 or 18.

4.3. *The Behavior of the Pore-Pressure Evolution*

The above analysis shows that the pore pressure Eqs. 15 or 18 express a viscoelastic-like rheology. The two end-members of this rheology, elastic and viscous, lead to two mechanisms that control the evolution of pore pressure, and operate under different drainage conditions. A schematic representation of the two mechanisms is depicted in Fig. 6. Elastic-like pore-pressure evolution dominates when the system is effectively undrained ($\mathrm{De} \gg 1$). Under such conditions, pore fluid that cannot escape and is trapped within a shrinking pore volume is pressurized (Fig. 6a) whereas pore fluid that is trapped in an expanding pore volume is depressurized. The evolution of the average pore pressure will follow Eq. 34, and the magnitude of pressurization and depressurization depends on the inverse of the fluid compressibility, β^{-1}, and is controlled by the overall change of porosity, $\Delta\Phi$. In that sense, the elastic end-member holds memory of the initial state of porosity.

Viscous-like pore-pressure evolution dominates when the system is effectively drained ($\mathrm{De} \ll 1$), and is a less intuitive mechanism. Here, because of mass conservation, convergence (or divergence) of grains causes the pore fluid that resides between the grains to flow out of (or into) this region (Fig. 6b). Because of fluid momentum conservation (Darcy law in this formulation), pressure gradients must arise between the location of converging (or diverging) grains and the surrounding region, to generate these flows. Pore pressure is governed by Eq. 36, and depends linearly on the fluid viscosity, η, and inversely on the permeability, k_0. The magnitude of pore pressure is controlled by the instantaneous strain rate of porosity, $\mathrm{d}\langle\Phi(\zeta,t)\rangle/\mathrm{d}t$. Therefore, this mechanism holds no memory of previous states of porosity. Note that when $\mathrm{De} \approx 1$, intermediate behavior is expected with some short-term memory.

The viscous end-member has normally not been offered as a mechanism for liquefaction, although it may lead to significant pressurization. Moreover, because of its "lack of memory", this mechanism may lead to generation of high pore pressure even when an initially dense granular matrix is sheared. Indeed, upon shearing an over-compacted layer, it will first dilate (Fig. 6b, left to center), and then oscillate around its critical porosity (Aharonov and Sparks, 2002; Gabet and Mudd, 2006). In the oscillatory stage, any local period of compaction, with $\mathrm{d}\langle\Phi(\zeta,t)\rangle/\mathrm{d}t < 0$, will lead to pressurization despite the fact that the instantaneous porosity may be significantly larger than the initial porosity (Fig. 6b, center to right).

It is of interest to note that the viscous-like rheology arises when $\mathrm{De} \ll 1$, and the elastic-like rheology arises when $\mathrm{De} \gg 1$. Indeed, a Deborah number of zero represents a viscous fluid and an infinite Deborah number represents an elastic solid (Osswald, 1998). In the following section, we present

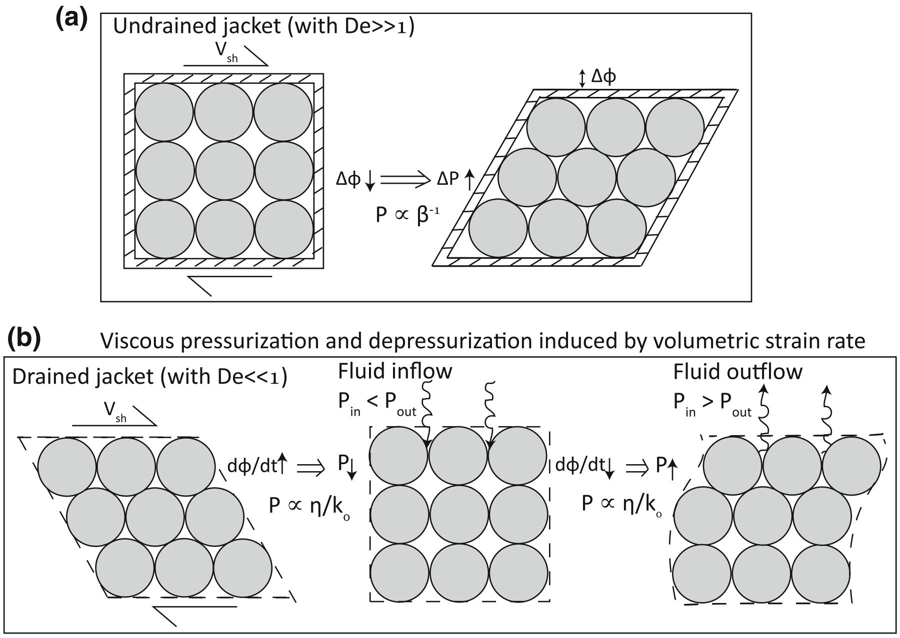

Figure 6
Two mechanisms control the evolution of pore pressure in Eq. 18. **a** When the boundaries are undrained (*marked by double solid lines*) leading to De $\gg$ 1, pore pressure responds elastically to any strain of pore volume. Compaction will lead to pressurization and dilation will lead to depressurization. The magnitude of pore pressure change depends on the overall porosity change, $\Delta\Phi$, and on the inverse of fluid compressibility, β^{-1}. **b** When the boundaries are drained (*marked by dashed lines*) and De $\ll$ 1, pore pressure evolves viscously in response to instantaneous strain rate of porosity, $\mathrm{d}\Phi/\mathrm{d}t$. Upon dilation (left to center) fluid will flow into the system. To facilitate this flow, pressure gradient must arise with low pressure within the system interior. Upon compaction (center to right), fluid escapes from the system, and an opposite pore-pressure gradient arises with higher pore pressure in the system interior. In this mechanism the evolving pore pressure depends linearly on fluid viscosity, η, and inversely on the permeability, k_0

our simulation results in light of the pressurization mechanisms that are reviewed here.

5. *Simulations of Shearing Granular Layers*

To study the coupled mechanics of granular matrix deformation and pore fluid pressurization and flow we perform simulations of a fluid-filled granular layer sheared at a constant shear velocity. The simulations are performed in a rectangular system with approximately 1680 (24 $\times$ 70) or 864 (24 $\times$ 36) grains. Grain diameters are drawn randomly from a Gaussian distribution with an average d, and a standard deviation d, clipped at plus/minus 0.2d. Although there is no gravity in the simulations, we define the vertical and horizontal directions for convenience. The top and bottom walls are composed of half grains of variable size that are glued together along their center lines to form rigid rough walls. In the horizontal direction the system is periodic, and thus analogous to a rotary shear apparatus. Each simulation is initiated by compacting a system of loosely packed grains under some normal stress, σ_n, until the porosity equilibrates. We then assume the pore space is filled with fluid at zero excess fluid pressure. Variations of pore pressure are measured relative to the initial zero value that corresponds to hydrostatic conditions. For this reason, σ_n is interpreted as the applied external stress minus hydrostatic pore pressure, i.e. the initial effective stress. Finally, a constant shear velocity, V_{sh}, is applied to the top wall. During a simulation, σ_n and V_{sh} are maintained constant, and we follow the systems' compaction and dilation, the shear stress required to shear the top wall at constant velocity, and the evolution of pore pressure. Dividing the shear stress by σ_n results in the apparent friction coefficient, μ_a, Eq. 3. Because the grains themselves are regarded as incompressible, compaction and dilation are accommodated by a

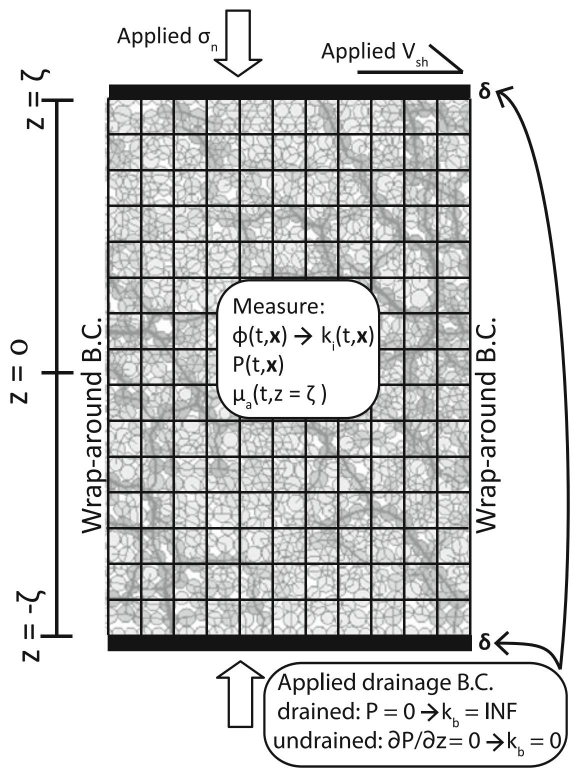

Figure 7
Grains–fluid simulations setup. In each simulation a collection of grains is packed within a rectangular box with wrap-around boundary conditions along the horizontal direction. The equation for the pore pressure, Eq. 15, is solved on a superimposed grid. Normal stress, σ_n, and shear velocity, V_{sh}, are applied and maintained constant. The spatial and temporal evolution of porosity, Φ, and of pore pressure, P, and the temporal evolution of the apparent friction μ_a are measured. k_i is the internal permeability that is set by the local porosity in accordance with Eq. 24. k_b is the boundary permeability that expresses the drainage boundary conditions. When the top and bottom boundaries are drained, $P = 0$ on the boundaries as if $k_b = \mathrm{INF}$. When the top and bottom boundaries are undrained, no pressure flux arises across the boundaries as if $k_b = 0$

change in pore volume. Figure 7 summarizes the settings of the simulations.

In the simulations, we take the pore fluid to be water, with fluid compressibility and viscosity $\beta = 4.5 \times 10^{-10}$ Pa^{-1} and $\eta = 10^{-3}$ Pa s, respectively. The granular phase is assumed to be quartz grains with a bulk modulus, $E = 8 \times 10^{10}$ Pa, Poisson's ratio, $\nu = 0.25$, density of 2640 kg/m^3, surface friction coefficient $\mu = 0.5$, and damping coefficient (in Eq. 4), $\gamma = 0.8$. We further assume that the grains have an average diameter $d = 10^{-3}$ m. Because we are interested in studying the role of permeability in the evolution of pore pressure, and because the permeability varies by orders of magnitude between different natural terrains (Saar and Manga, 2004), we vary k_c in our simulations, where k_c is the permeability prefactor that appears in Eq. 24. For the original 2D Carman–Kozeny relationship with average grain diameter of $d = 10^{-3}$ m, $k_c = 4.6 \times 10^{-10}$ m^2, but in these simulations we use a range of k_c from 4.6×10^{-10} to 4.6×10^{-15}m^2. The lower value of k_c may, alternatively, be obtained by choosing a smaller grain diameter of $d \approx 10^{-6}$ m, or by taking a heterogeneous grain size distribution. We choose to work with relatively large grains in order to enable simulations of long temporal duration (0.5 s) of thick layers (up to $\sim$0.07 m), in a reasonable computation time, but we still desire to study the role of permeability. The applied shear velocity, V_{sh}, is either 0.76 m/s or 7.6 m/s. We use applied normal stresses of $\sigma_n = 24$ or 2.4 MPa, corresponding to depths of approximately 2 km and 200 m, respectively. Two types of simulation are performed that differ in their drainage boundary conditions: drained and undrained. Table 1 summarizes the system variables used in the simulations: normal stress, σ_n, half thickness, ζ, permeability scale factor, k_0, and shear velocity, V_{sh}. The dimensionless Deborah number, De, whose significance is explained is the section "Pore-Pressure Evolution Mechanisms", and the dimensionless liquefaction potential, LP, that is based on the section "Estimating Liquefaction Potential", are also presented in Table 1.

5.1. *Drained Systems*

Completely drained systems are simulated by setting the pore pressure to be zero along the top and bottom walls. All drained simulations start with a well compacted system that dilates in the initial stages of shear deformation. After the dilation stage, the porosity oscillates around some mean critical value. Figure 8 compares the temporal evolution of three system-averaged quantities (porosity, average pore pressure, and apparent friction, μ_a) between simulations D3 and D9 that differ only in their permeability. Two differences are observed for the average pore pressure in these simulations: first, the peaks of the

Table 1

Numerical simulations

No.[a]	σ_n (MPa)	ζ (m)[b]	k_0 (m^2)[c]	V_{sh} (m/s)	De[d]	LP[e]
D1	24	0.035	1.97×10^{-10}	0.76	1.21×10^{-5}	2.8×10^{-5}
D2	24	0.035	1.97×10^{-10}	7.6	1.21×10^{-4}	2.8×10^{-4}
D3	24	0.035	1.97×10^{-11}	0.76	1.21×10^{-4}	2.8×10^{-4}
D4	24	0.035	1.97×10^{-11}	7.6	1.21×10^{-3}	2.8×10^{-3}
D5	24	0.035	1.97×10^{-12}	0.76	1.21×10^{-3}	2.8×10^{-3}
D6	24	0.035	1.97×10^{-12}	7.6	1.21×10^{-2}	2.8×10^{-2}
D7	24	0.035	1.97×10^{-13}	0.76	1.21×10^{-2}	2.8×10^{-2}
D8	24	0.035	1.97×10^{-13}	7.6	1.21×10^{-1}	2.8×10^{-1}
D9	24	0.035	1.97×10^{-14}	0.76	1.21×10^{-1}	2.8×10^{-1}
D10	24	0.035	1.97×10^{-14}	7.6	1	9.7×10^{-2}
D11	2.4	0.035	1.97×10^{-14}	0.76	1.21×10^{-1}	2.8
D12	2.4	0.018	1.97×10^{-14}	0.76	6.41×10^{-2}	1.4
U13	2.4	0.035	0 (1.97×10^{-9})	0.76	INF	–
U14[f]	2.4	0.035	0 (1.97×10^{-9})	0.76	INF	1.7

[a] In the numbering of the simulations, D stands for drained and U stands for undrained

[b] We report here the maximum vertical half thickness of the system during a simulation. ζ fluctuates by as much as 3%

[c] k_0 is defined in Eq. 28. When $k_0 = k_i$, Eq. 24 is used with $\Phi = 0.2$. When $k_0 = k_b = 0$, the value of k_i is reported in parentheses

[d] In the calculation of the Deborah number, $\Phi = 0.2$, and the velocity scale factor, u_0, is estimated as V_{sh}. In simulations D10, $l = D_i/u_0$, for the rest of the simulations $l = \zeta$

[e] Liquefaction potential. For simulations D1–D9 and D11–D12 Eq. 40 is used. For simulation D10 Eq. 43 is used. For simulation D14 Eq. 41 is used

[f] Simulations U13 and U14 differ in their initial porosity

average pore pressure are smaller by an order of magnitude in the high-permeability simulation D3 (Fig. 8c) than the peaks in the low-permeability simulation D9 (Fig. 8d). This results from the dependency of the pore pressure on the inverse of the permeability for drained systems with De $\ll$ 1. Indeed, Eq. 36 predicts that when the permeability is smaller, as is the case for simulation D9, the pore pressure will be higher. Second, the average pore pressure is negative during the first half of the low-permeability simulation D9, whereas for the high-permeability simulation D3, the average pore pressure oscillates around zero from the onset of the simulation. This is because of the competition between the rate of deformation and the rate of pore fluid flow, and will be discussed further in the section "The Evolution of Pore Pressure with Drained Conditions".

The different evolution of pore pressure between simulations D3 and D9 causes their apparent frictions to differ. The apparent friction starts with a larger value and has larger peaks in the low-permeability simulation D9 (Fig. 8f). The higher initial value results from the initially negative pore pressure that increases the effective normal stress and the shear resistance, in accordance with Eq. 2. Similarly, the larger peaks in the apparent friction result from the larger magnitudes of the negative values of the pore pressure.

In the drained simulations D1–D7 (with De $\ll$ 1) the average pore pressure, $\bar{P}$, is well correlated with the temporal derivative of the porosity, $\mathrm{d}\Phi/\mathrm{d}t$, but is not correlated with the actual value of the porosity, Φ. An example of these relationships is depicted in Fig. 9 for drained simulation D7. Indeed, Eq. 36 predicts that when the boundaries are well-drained and De $\ll$ 1, the evolution of the pore pressure is determined by the temporal derivative of the porosity. Although Eq. 36 was developed solely on the basis of the pore pressure formulation, the good correlation depicted in Fig. 9a indicates that viscous-like evolution of pore pressure also occurs when the grain and pore fluid are fully coupled.

In the drained simulations D8, D9, and D11 (with De$\lesssim$1) and in simulation D10 (with De $= 1$), it is less clear which of the two correlations ($\bar{P}$ versus $\mathrm{d}\Phi/\mathrm{d}t$ and $\bar{P}$ versus Φ) is more dominant. In fact, the

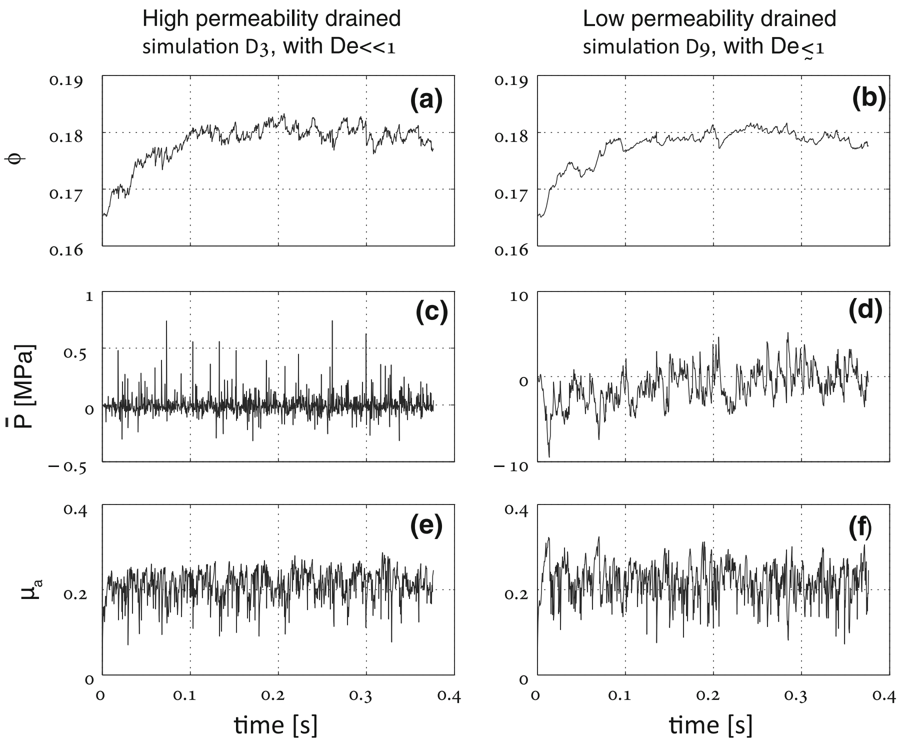

Figure 8
Time evolution of space-averaged quantities for drained simulations D3 and D9 that differ in their assigned permeability. Evolution of porosity (**a**, **b**), average pore pressure (**c**, **d**), and apparent friction (**e**, **f**). The simulation parameters are given in Table 1

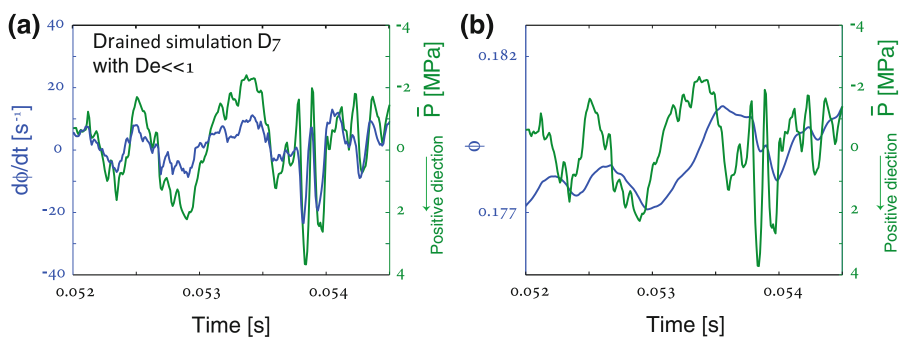

Figure 9
Results from drained simulation D7. **a** $\mathrm{d}\Phi/\mathrm{d}t$ (*blue*) and average pore pressure (*green*) for simulation D7 are plotted as a function of time and show good correlation, as predicted by Eq. 36. **b** Φ (*blue*) and average pore pressure (*green*) show no correlation. Note that $\bar{P}$ increases downwards

average pore pressure seems to be affected both by the temporal derivative of the porosity, $\mathrm{d}\Phi/\mathrm{d}t$, and by the actual value of the porosity, Φ, as can be seen in Fig. 10 for simulation D9. Indeed, according to the mechanistic analysis presented in the section "Pore-Pressure Evolution Mechanisms", when $\mathrm{De} \lesssim 1$ or $\mathrm{De} = 1$ both dependencies are expected. The drained simulation D12 (with $\mathrm{De} = 6.41 \times 10^{-2}$) shows a fairly good correlation between $\bar{P}$ and $\mathrm{d}\Phi/\mathrm{d}t$ (which is slightly less distinct than this correlation for simulations D1–D7), and also a minor effect of Φ on the evolution of $\bar{P}$.

Simulations D1–D10 are conducted under normal stress of $\sigma_n = 24$ MPa. The average pore pressure in

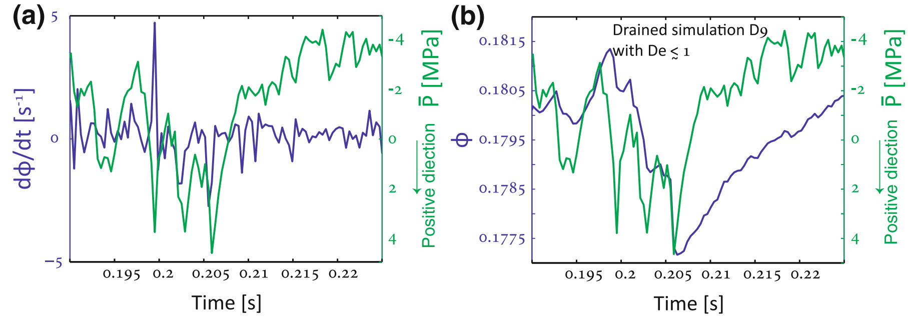

Figure 10
Results from drained simulation D9. **a** $d\Phi/dt$ (*blue*) and average pore pressure (*green*). **b** Φ (*blue*) and average pore pressure (*green*). Both $d\Phi/dt$ and Φ show some correlation with the average pore pressure, as expected for De$\lesssim$1. Note that $\bar{P}$ increases downwards

these simulations is significantly lower than the applied normal stress, with peaks that are one or two orders of magnitude smaller than σ_n. Still, in runs D8–D10 that are characterized by small permeabilities and De$\lesssim$1 or De $= 1$, there were short events in which $P > \sigma_n$. These events, being also very localized in space, did not seem to affect the system's strength. For that reason, we next consider simulations in which the applied normal stress is reduced to $\sigma_n = 2.4$ MPa. It is observed that although σ_n does not enter the formulation of the pore fluid, its reduction leads to decrease of pore pressure. However, an order of magnitude reduction in σ_n did not cause the pore pressure peaks to decrease by an order of magnitude, but only by a factor of 2–3. Therefore, the average pore pressure peaks may become of the order of the applied stress and lead to a significant reduction of the system strength. Here, the system strength is expressed as the apparent friction coefficient, μ_a, where small μ_a results from small shear resistance. If the apparent friction becomes zero or even negative, then the shear resistance of the system is completely lost, and it is liquefied.

Figure 11 shows the evolution of μ_a and of the average pore pressure for drained simulation D11. A brief liquefaction event with a reduction of the apparent friction below zero (circled) is observed. This short event is correlated with system average pore pressure of $\bar{P} = 1.9$ MPa. Although $\bar{P} < \sigma_n$, this liquefaction event is characterized by horizontal layers that experience high pore pressure of $P \simeq \sigma_n$, and a few localized zones with $P > 4$ MPa (Fig. 12e).

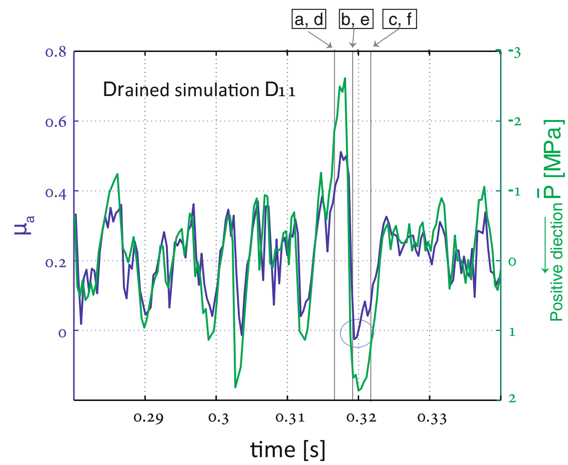

Figure 11
Apparent friction (*blue*) and average pore pressure (*green*) for drained simulation D11 are plotted as functions of time, and show good correlation. Note that the pore pressure axis increases downwards. The apparent friction becomes negative (*circled*) at time 0.32 s, when the average pore pressure becomes high, $\bar{P} \sim 1.9$ MPa, and of the order of magnitude of the applied normal stress, $\sigma_n = 2.4$ MPa. Negative apparent friction is defined here as liquefaction. *Framed letters* mark the times when the snapshots in Fig. 12 are taken

Figure 12 shows three snapshots of the grain system configuration and the corresponding pore pressure map, before, during, and after the liquefaction event circled in Fig. 11. In frames 12a–12c the thickness of the lines connecting grain centers indicates force on grain contacts. Stress chains are observed as connected force lines that percolate from the top of the system to its base. The color code of the grains corresponds to the overall normal stress that a grain sustains as a result of contact forces, with warmer colors for higher stress. In each of frames

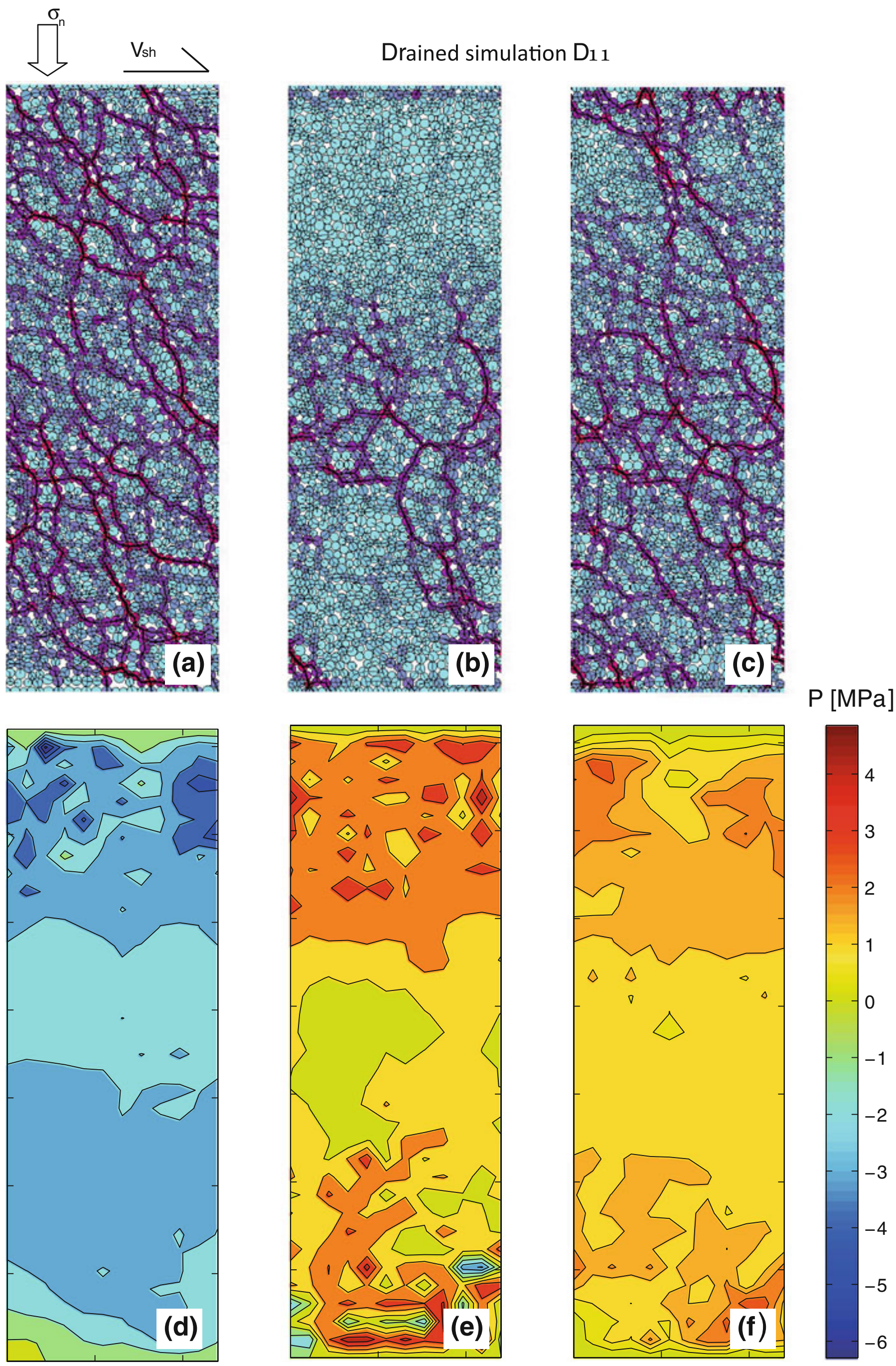

Figure 12

Snapshots of the granular configuration (*top*) and corresponding pore fluid pressure maps (*bottom*) for drained simulation D11, before, during, and after the liquefaction event shown in Fig. 11. The times when the snapshots are taken are indicated by the framed letters in Fig. 11. *Grains color code* corresponds to the overall contact-induced compressive force they sustain. *Warm colors* indicate high force and *cold colors* low force. Contact forces are depicted by lines that connect contacting grains. The width of a line correlates to the magnitude of the normal force along the contact

12a–12c, the grain color code is relative to the frame itself, where the grain that supports the maximum load is red and the grains with minimum load are light blue. Therefore, grains that are connected by thick lines and participate in the major stress chains that support the external loading are more reddish. It is clearly observed that the stress chains that support the external load before the liquefaction event (Fig. 12a) disappear during the liquefaction event (Fig. 12b) and the grains at the top and bottom of the system become light blue, indicative of minimum compressive stress on them arising from granular contacts. Percolating stress chains reappear after the event (Fig. 12c). The pore pressure before the liquefaction event in Fig. 12d is mostly negative (lower than hydrostatic). During the event the pore pressure at the top and bottom of the system becomes highly positive (Fig. 12e), and exceeds σ_n. Zones of very high pore pressure in Fig. 12e correlate with zones with no stress chains in Fig. 12b, which indicates that the high pore pressure replaces the stress chains in supporting the external load. This high pore pressure also enables the apparent friction to become negative. Shear localization is observed along the highly pressurized layers, but it is not clear if the localization preceded (and triggered) pressurization or vice versa. Simultaneously with the reappearance of stress chains in Fig. 12c, the pore pressure reduces (Fig. 12f), and the system strengthens.

To study the effect of system size, simulation D12 is conducted with the same values as simulation D11, but with a layer half as thick. Figure 13 shows a liquefaction event (circled) during simulation D12 that occurs simultaneously with an increase of average pore pressure, $\bar{P}$. The average pore pressure during this event, $\bar{P} \simeq 2.4$ MPa, is very close to the applied normal stress. Figure 14 shows snapshots of the granular configuration and the corresponding pore pressure map before, during, and after this liquefaction event. Whereas in simulation D11, high pore pressure is localized close to the top and bottom boundaries (Fig. 12e), here, when the layer is thinner, stress chains disappear and pore pressure rises throughout the whole system interior, as seen in Fig. 14b, e. It should be noted that several such

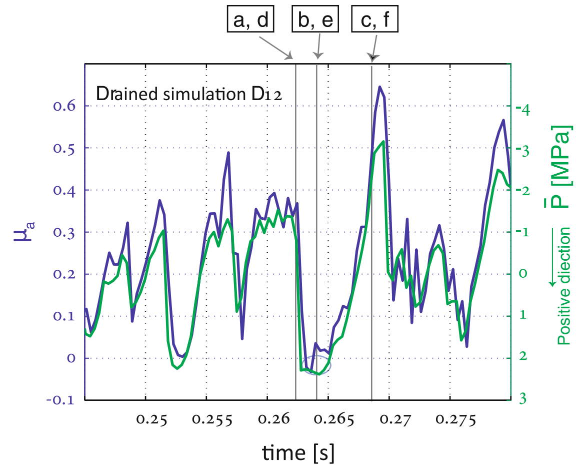

Figure 13
Apparent friction (*blue*) and average pore pressure (*green*) for the small drained simulation D12 are plotted as functions of time. Note that the pore pressure axis increases downwards. A reduction in the apparent friction below zero is observed (*circled*), and is correlated with high average pore pressure, $P \simeq 2.4$ MPa, which is almost equal to the applied normal stress, $\sigma_n = 2.4$ MPa. *Framed letters* mark the times when the snapshots in Fig. 14 are taken

liquefaction events occurred during simulations D11 and D12.

5.2. Undrained Systems

Undrained systems are simulated by assigning zero fluid flux across the top and bottom boundaries; as a result, fluid mass is conserved within the grains layer. In the undrained simulations we assign large internal permeability that enables rapid fluid flow within the system interior, and, as a consequence, rapid homogenization of pore pressure. Two simulations are performed, both with $\sigma_n = 2.4$ MPa and $V_{sh} = 0.76$ m/s, but with different initial porosities. Simulation U13 starts with the same initial configuration as the drained simulation D11, with an initial 2D porosity of 0.1719. This simulation is referred to as "dense". In simulation U14, before the onset of shear, all grains that have no contacting neighbors, and thus are not participating in stress chains, are removed, resulting in a high initial 2D porosity of 0.2385. Simulation U14 is referred to as "loose".

Dense simulation, U13, dilates when sheared and the pore pressure decreases and becomes negative (i.e., smaller than hydrostatic). Because of the large

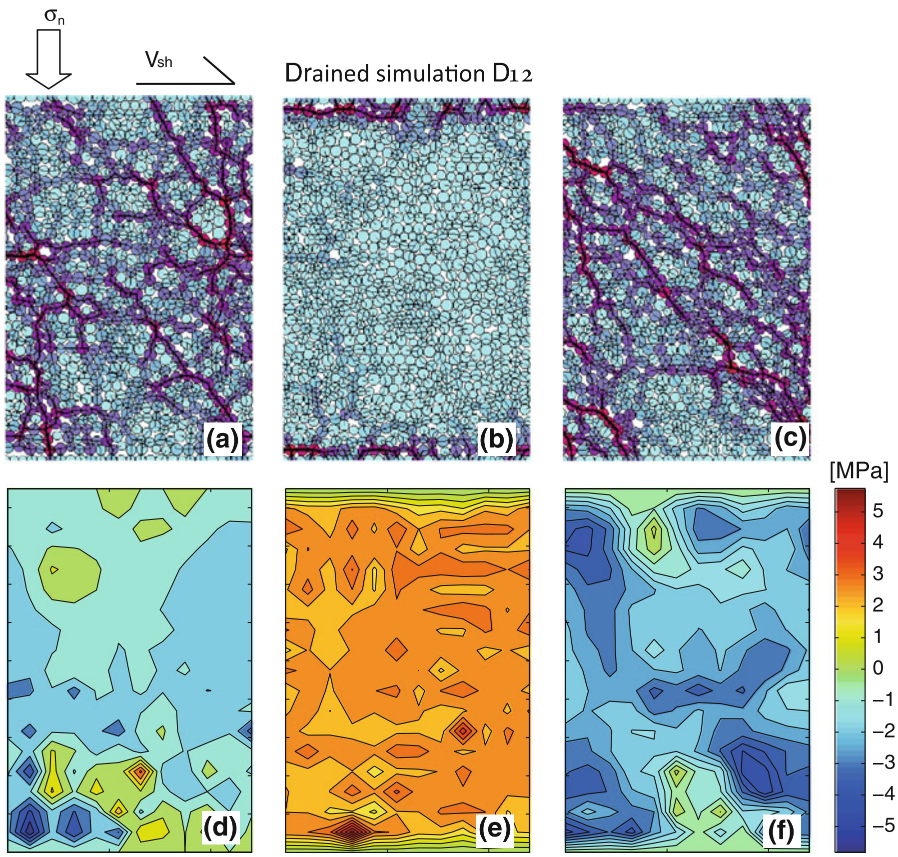

Figure 14
Snapshots of the granular configuration (*top*) and corresponding pore fluid pressure maps (*bottom*) for drained simulation D12, before, during, and after the liquefaction event shown by the circle in Fig. 13. The times when the snapshots are taken are indicated by the framed letters in Fig. 13. For the color code of the grains see the caption of Fig. 12

internal permeability, the pore pressure is uniform throughout the system, so the average pore pressure is very close to the pore pressure at any point within the system. Unlike the drained simulations, here the evolution of pore pressure is correlated with the evolution of porosity, Φ, (Fig. 15b), and not with the temporal derivative of the porosity, $d\Phi/dt$, (Fig. 15a). The dependency between average pore pressure and porosity when the boundaries are completely undrained and De = INF is predicted by Eq. 34. Therefore, although Eq. 34 is developed solely on the basis of the fluid formulation, simulation results indicate that an elastic-like evolution of the pore pressure is observed also when the two phases of the system, pore fluid and grains, are fully coupled. The apparent friction coefficient, depicted in Fig. 15c, increases with decreasing pore pressure. High apparent friction results from high shear resistance because of increasing effective normal stress, in accordance with Eqs. 1 and 2. An alternative view might be that the reduced pore pressure within the system interior exerts a suction force that hardens the system. Simulation U13 thus exhibits "dilatancy hardening".

In loose simulation U14 a short transient dilation phase with pore pressure decrease is observed on onset of shear, but then compaction occurs very quickly. Upon compaction, pore pressure increases to the value of the normal stress, $P = 2.4$ MPa, and the system liquefies (Fig. 16a). Here, the liquefaction event is a steady state and the pore pressure remains equal to σ_n until the end of the simulation. During this long liquefaction event, grains detach, stress chains disappear, and the external load is completely

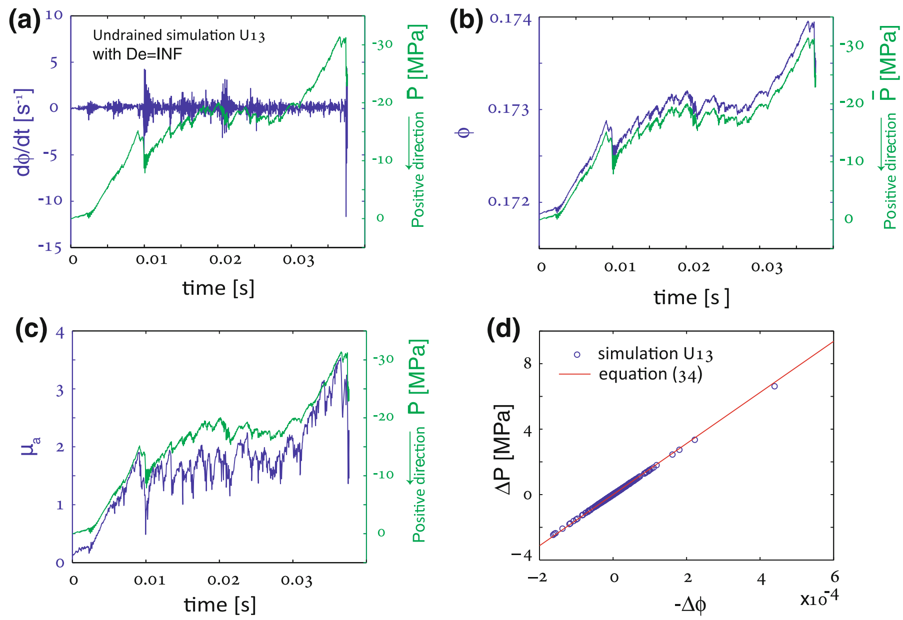

Figure 15

Results from undrained initially dense simulation U13. **a** No correlation is found between $\mathrm{d}\Phi/\mathrm{d}t$ (*blue*) and average pore pressure (*green*). **b** Good correlation is found between porosity (*blue*) and average pore pressure (*green*). **c** Correlation is shown between apparent friction (*blue*) and average pore pressure (*green*). **d** Correlation between $-\Delta\Phi$ and ΔP in the simulation (*circles*) is well matched by the linear relationship predicted by Eq. 34 (*red line*). Note that in **a**, **b**, and **c** the average pore pressure increases downwards

balanced by the pore pressure (Fig. 17). With the exception of very few contacts arising because of small collisions, the force balance on the grains is zero and they do not touch. Because grains do not slide past each other (and because viscous resistance to sliding is not accounted for in our model), there is no resistance to shear and the apparent friction drops to zero, as depicted in Fig. 16b.

6. *Discussion*

This paper uses a continuum approach, Eqs. 15 or 18, to describe the pore pressure response to granular media deformation, coupled with a discrete description of the grain dynamics. First in the discussion we address the pore pressure behavior under any general deformation of the granular skeleton, because it turns out that this behavior by itself is very rich (as already suggested by a simplified model, Goren *et al.*, 2010). The section "Pore-Pressure Evolution Mechanisms" reveals that evolution of the pore pressure in response to granular skeleton deformation obeys viscoelastic-like rheology. Indeed, Eq. 18 resembles the Maxwell model of viscoelasticity: $\mathrm{d}\epsilon/\mathrm{d}t = \eta^{-1}\sigma + \beta\mathrm{d}\sigma/\mathrm{d}t$, where the strain rate, $\mathrm{d}\epsilon/\mathrm{d}t$, is a linear combination of the stress, σ, and of the time derivative of the stress, $\mathrm{d}\sigma/\mathrm{d}t$. In Eq. 18, the time derivative of the porosity, $\mathrm{d}\Phi/\mathrm{d}t$, stands for the strain rate, and the pore pressure, P, stands for the stress. The pore pressure diffusion term in Eq. 18 acts as the term $\eta^{-1}\sigma$ in the Maxwell model (in which the spatial derivative can be approximated as $P/l\ d$). The section "Pore-Pressure Evolution Mechanisms" also shows that the system parameters, as expressed by the Deborah number, De, lead to the emergence of two end-member mechanisms for the evolution of pore pressure that are encapsulated in this rheology—elastic and viscous.

Goren *et al.* (2010) showed that these two end-member mechanisms describe well the evolution of pore pressure when the loading is assumed to be infinitely stiff, i.e., when granular deformation is externally prescribed and pore-pressure gradients do not enter the grains momentum balance. Here, our simulation results show that the two end-member

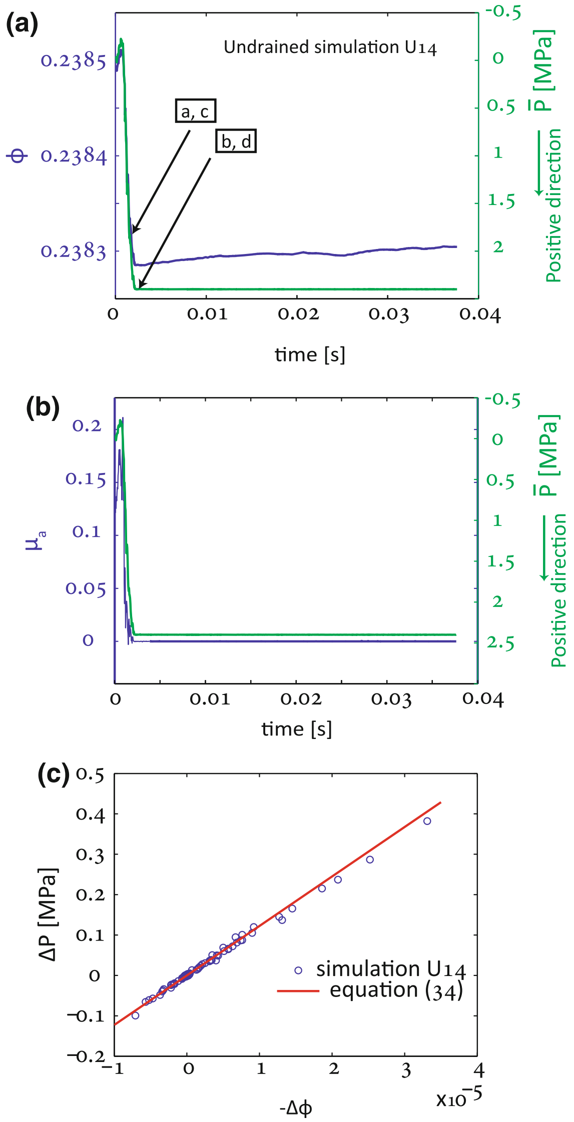

Figure 16
Results from undrained initially loose simulation U14. **a** Good correlation is found between porosity (*blue*) and the average pore pressure (*green*). *Framed letters* corresponds to the times when the snapshots in Fig. 17 are taken. **b** Correlation is shown between apparent friction (*blue*) and average pore pressure (*green*). **c** Correlation between $-\Delta\Phi$ and ΔP in the simulation (*circles*) are well matched by the linear relationship predicted by Eq. 34 (*red line*). Note that in **a** and **b** the pore pressure increases downwards

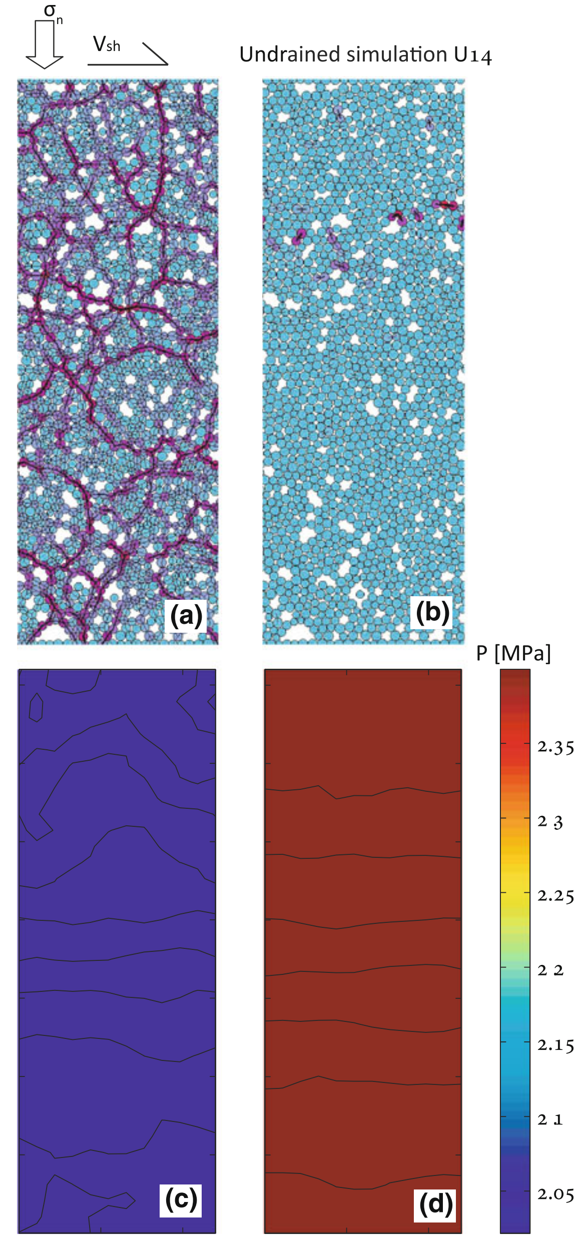

Figure 17
Snapshots of the granular configuration (*top*) and corresponding pore fluid pressure maps (*bottom*) for undrained initially loose simulation U14, before and during the liquefaction event depicted in Fig. 16. The times when the snapshots are taken are indicated by the framed letters in Fig. 16. For the color code of the grains see the caption of Fig. 12

mechanisms also apply for the fully coupled system, i.e., when the skeleton deformation affects the evolution of pore pressure, and pore-pressure gradients add up to the force balance on the grains and contribute to the deformation of the skeleton. Therefore, we claim that a viscoelastic analog for describing the evolution of pore pressure applies generally to fluid-filled granular (and porous) systems, and is independent of the exact details of grain dynamics.

Following these insights, one would like to understand how to estimate De, because it plays a crucial role in determining the pore-pressure behavior in real systems. Some parameter groups are of particular importance in the estimation of De. For example, when the system is large relative to the internal diffusion length, i.e. $\zeta > D_i/u_0$, (where ζ is the system half thickness, D_i is the internal diffusion coefficient in the system that ignores the drainage boundary conditions, and u_0 is the rate of deformation), then pore-pressure signals originating close to the layer center are unaffected by the boundaries. This situation leads to De $= 1$, which means that the pore pressure responds both to volumetric strain rate and to overall volumetric strain, resulting in combined viscoelastic-like behavior. When the layer is relatively thin, as is often the case for experimental and natural granular systems (see for example the cases discussed in the section "Field and Experimental Evidence of Liquefaction Events with Drained Conditions"), then $\zeta < D_i/u_0$, De $\neq 1$, and the drainage boundary conditions play an important role in the evolution of pore pressure. These drainage conditions are accounted for in the permeability scale factor, k_0. Here, we have considered only completely drained and completely undrained systems. However, our choice to express k_0 as the harmonic mean of interior and boundary permeabilities is general: it may be used to evaluate De for relatively complex systems, composed of several layers with different permeability, and to evaluate the expected effect of more complex drainage boundary conditions such as a linear combination of pressure and pressure gradient leading to an intermediate situation of partial drainage.

Although the pore-pressure equations, Eqs. 15 and 18, are rich and highly predictive of the classes of behavior observed in the simulations, there are some non-linear effects that arise because of the coupled response with the grain dynamics, which cannot be predicted analytically. Such an effect is the relationship between the pore pressure and the applied normal stress, σ_n. The pore fluid pressure formulation, Eq. 15 and 18, predicts that the evolution of pore pressure is independent of σ_n. Yet, it is observed that when σ_n decreases, the pore pressure is generally smaller. This indirect relationship between the applied stress and the pore pressure arises because of coupling with grain contact forces that transmit stresses of the order of σ_n. In response to grains convergence, pore fluid pressurization resists the converging grains by exerting pressure gradients across them. Grains then rearrange so that the skeleton forcing on the fluid is relaxed and so is the pore pressure. If σ_n is large, large pressure gradients (and large pressures) are needed to push the grains aside and overcome the contact forces. If σ_n is smaller, then smaller pressure gradients are sufficient to overcome the granular contact forces, push aside converging grains, and relax the skeleton forcing.

6.1. The Evolution of Pore Pressure with Drained Conditions

Next, we analyze the behavior of the pore fluid pressure in simulations with drained boundary conditions. Figure 9a shows the good correlation between the spatially averaged pore pressure and the temporal derivative of the porosity for a representative drained simulation with De $\ll 1$, following the prediction of Eq. 36. In order to further validate this correlation, we compare the slopes of the graphs of P versus $-\mathrm{d}\Phi/\mathrm{d}t$ between the drained simulations D1–D10 and Eq. 36. For each time step in a

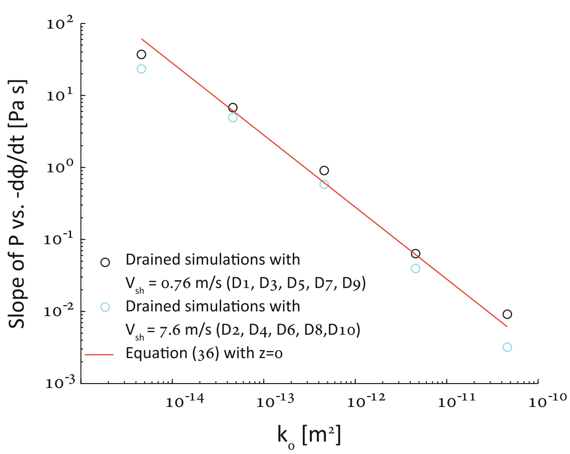

Figure 18

Log–log plot of the slope of the relationship P versus $-\mathrm{d}\Phi/\mathrm{d}t$ as a function of the permeability scale factor, k_0, for drained simulations. Theoretical prediction according to Eq. 36 appears as a *solid line* and simulations as *circles* simulation, we plotted the global extremum of the pore pressure and the instantaneous $-\mathrm{d}\Phi/\mathrm{d}t$. We then take the slope of the linear regression line of P versus $-\mathrm{d}\Phi/\mathrm{d}t$ and plot it as a function of the permeability, k_0, in Fig. 18, as "o". In the figure, the slope predicted by Eq. 36, $\eta(\zeta^2 - z^2)/2k_0$, is depicted by a solid line, where the center of the grains layer is assigned for z, i.e. $z = 0$. A good fit is found between simulation results and the analytical prediction. It is of interest to note that simulations D8 and D9 that have De$\lesssim$1, and simulation D10 with De $=1$ also show a good fit to the analytical prediction of Eq. 36 that is developed under the assumption of De $\ll 1$.

Although the overall behavior of pore pressure with drained conditions follows Eq. 36, there are some differences between the drained simulations that arise from the different parameters that are used. To study these differences we again use the value of the Deborah number. The definition of De in Eq. 32 may also be viewed as a velocity ratio between the velocity of deformation, u_0, and the velocity of diffusion D/l (Samuelson *et al.*, 2009). When De $\ll 1$ (e.g. simulation D2), the deformation is slow enough to allow for a pore pressure front originating at any depth in the layer to reach the drained boundaries in the time-scale of deformation. As a result, the pore pressure everywhere in the system is expected to follow Eq. 36, resulting in a parabolic profile, as

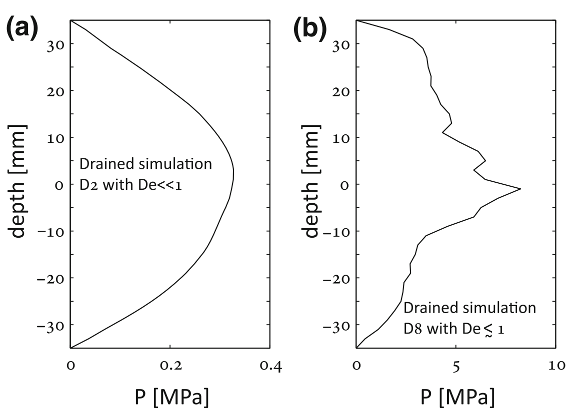

Figure 19

Snapshots of horizontally averaged pore pressure as a function of depth within the grains layer. **a** Drained simulation D2 with De $\ll$ 1 showing a parabolic pore pressure profile in accordance with Eq. 36. **b** Drained simulation D8 with De$\lesssim$1 showing a non-regular pore pressure profile along the center of the grains layer because of elastic-like transient effects

depicted in Fig. 19a. In contrast, when De approaches 1 (e.g. simulation D8), the deformation is more rapid, or further away from the boundary, and pore pressure cannot always diffuse across the whole system during the time-scale of deformation. For this reason, a non-parabolic profile is observed along the center of the layer (far from the boundaries), as depicted in Fig. 19b. Deviation from the parabolic profile is probably the result of transient elastic effects arising from the relationship between P and Φ when De ≈ 1.

The Deborah number may also be used to explain the different evolution of the average pore pressure between the high-permeability simulation D3 (with De $\ll 1$) and the low-permeability simulation D9 (with De$\lesssim$1), which are observed in Fig. 8. At the onset of the simulations, dilation occurs that increases pore space. In simulation D3, the small Deborah number enables immediate compensation of the newly generated pore space by fluid inflow from the drained boundaries, because the rate of pore pressure diffusion across the system is fast relative to the rate at which pore volume expansion occurs, because of the high permeability. For this reason, a transient effect of pore pressure reduction is not observed (Fig. 8c). In simulation D9, the larger Deborah number causes a delay in fluid inflow that compensates for the expanding pore space, leading to a transient negative pore pressure (Fig. 8d).

An additional result of the drained simulations is the observed correlation between the average pore pressure and the apparent friction, as depicted in Figs. 11 and 13. Such correlation is predicted by Eq. 2. However, it is important to note that the law of effective stress, Eq. 1, and the relationship between pore pressure and shear resistance that appears in Eq. 2, apply either only locally, or when the pore pressure is uniform within a granular or porous layer. Therefore, application of Eqs. 1 and 2 to the meso-scale implicitly assumes uniform pore pressure, a situation that only arises under quasi-static and undrained conditions. In the drained simulations, the pore pressure is not uniform within the layer, but it varies dynamically in space and time during shear. Still, the correlations between the average pore pressure and the shear resistance in Figs. 11 and 13 are good, indicating that although Eq. 2 may not be valid quantitatively for drained conditions, the concept of meso-scale effective stress is still useful when the boundaries are drained, although it merits further investigation.

6.1.1 *Simulations of Liquefaction Events with Drained Conditions*

After studying the general evolution of pore pressure and shear resistance in the drained simulations, we discuss special events that are characterized by high pore pressure and low shear resistance. In the drained simulations D11 and D12 the average pore pressure has peaks that are of the order of magnitude of σ_n, with zones that experience pore pressure that significantly exceeds σ_n. During such events the effective stress vanishes, and the shear resistance becomes negative (Figs. 11 and 13). We define these events of $\mu_a \leq 0$ as liquefaction. As long as $P < \sigma_n$ throughout most of the grains layer, granular stress chains support the external normal load by transmitting stress from top to bottom (Figs. 12a and 14a). During liquefaction events, stress chains disappear in zones that have $P > \sigma_n$ (Figs. 12b and 14b), and the external load can no longer be transmitted through the granular phase. Instead, it is supported by the highly pressurized pore fluid (Figs. 12e and 14e).

The localization of high pore pressure close to the drained boundaries during the liquefaction event in simulation D11, (Fig. 12b, e), may be explained by the near-unity De. In this simulation, high pore pressure is not generated within the center of the layer, because the De$\lesssim$1 limits the distance of pore fluid flow during the time-scale of deformation. As a result, communication by pore pressure diffusion between the drained boundaries and the layer's center is uncommon. In simulation D12, the system half size, ζ, is smaller, and, as a result, the Deborah number is smaller. For this reason the pore pressure is high throughout the whole layer during the liquefaction event, and is not localized close to the boundaries (Fig. 14b, e).

Such transient liquefaction events may have significant implications for natural systems that are driven by dynamic forcing, for example tectonic loading. The simulations presented here are driven kinematically, i.e. a constant shear velocity is imposed on the top wall, and the systems cannot accelerate. It is speculated that if the systems had been driven dynamically, by shear stress boundary conditions, then the short liquefaction events would have generated instabilities leading to acceleration. Following this initial acceleration, the absolute value of the porosity strain rate is expected to increase, potentially leading to even larger pressurization and further acceleration.

Previously, the only mechanism that was suggested to induce liquefaction was compaction of loosely packed grains under undrained conditions (Sawicki and Mierczynski, 2006), leading to elastic-like pore-pressure evolution, (as modeled in our undrained loose simulation, U14). Therefore, the occurrence of liquefaction events with densely packed drained conditions, leading to viscous-like evolution of pore pressure, is a surprising result of our model (that was also obtained in our approximate model (Goren *et al*., 2010)). Such conditions are traditionally believed to be unfavorable for liquefaction (Seed *et al*., 1976) despite field and experimental evidence that suggests otherwise. Such evidence is reviewed next.

6.1.2 *Field and Experimental Evidence of Liquefaction Events with Drained Conditions*

Field evidence for liquefaction of initially dense but well-drained layers comes from the report of Gabet and Mudd (2006) on debris flow mobilization from dense soils. Gabet and Mudd (2006) find correlation between mobilization and fines/sand ratio, where soils with a small ratio are mobilized. Assuming that a small ratio of fines contributes to good drainage, then the emergence of debris flows may be attributed to viscous-like pressurization during shear deformation induced by gravity. In such a case, the short compactive stages that followed the initial dilative phase, a scenario that is reviewed in Gabet and Mudd (2006), may have led to pore pressure rise, liquefaction, and mobilization of debris flow. A second example comes from the famous liquefaction event in Kobe, Japan, that followed the 1995 Great Hanshin Earthquake ($M = 6.9$). Soga (1998) reviewed the damage in the port facilities that were built on reclaimed islands. It was found that soils that were vibro-compacted were still liquefied, although they sustained less deformation. Such soils are expected to be highly dilative and, according to previous conventional wisdom, liquefaction resistant. We suggest that the moderate liquefaction observed may be attributed to viscous-like pore pressure rise during instantaneous and short compactive phases that punctuated the overall dilative path of the vibro-compacted fill material.

More evidence for liquefaction with drained boundary conditions comes from two sets of experiments conducted by Iverson and LaHusen (1989). In the first set, a layer of initially compacted uniform rods immersed in water was sheared at a constant shear velocity, while fluid was allowed to drain out of the top boundary. During a significant portion of the experiment, the "rods above the slip surface lost contact with the underlying rods and glided on a cushion of water", i.e. "the pressure gradients between the shearing layer and the top boundaries were high enough to support the rods weight" (Iverson and LaHusen, 1989). In the second set of experiments, natural fluid-filled sand was laid on a tilted table and slid under gravity. At the onset of sliding, the pore pressure declined, presumably because of dilation, but then, when motion became steady, pore pressure rose and started fluctuating, with pressure gradients transiently supporting the grains layer overburden. This description is very similar to our observation of pore-pressure evolution during drained simulations D11 and D12 that showed transient liquefaction events.

6.2. *The Evolution of Pore Pressure with Undrained Conditions*

Here we discuss the pore pressure response to granular skeleton deformation with undrained boundary conditions. Figures 15b and 16a show good correlations between the evolution of pore pressure and the evolution of porosity for our undrained simulations. Indeed, Eq. 34 predicts that with undrained conditions (when $\mathrm{De}^{-1} = 0$) pore-pressure evolution should be elastic-like, with ΔP that depends on $\Delta\Phi$. To further validate this relation, Figs. 15d and 16c compare undrained simulation (U13 and U14) results and the analytical prediction of Eq. 34, for the relationship between ΔP and $-\Delta\Phi$, and show good fit when assigning the initial porosity for Φ in Eq. 34.

6.2.1 *Simulations of Liquefaction and Hardening Events with Undrained Conditions*

Our simulations show that when the boundaries are undrained, the response of shear resistance to shear deformation depends on the initial packing. When the system is initially densely packed, dilative shear causes pore pressure to decrease relative to its initial value (Fig. 15b). Momentary compaction events will only slightly increase the pore pressure, but if the porosity remains higher than its initial value, the pore pressure cannot increase above its initial value. The decreasing pore pressure causes the effective normal stress and shear resistance to rise. Such "dilatancy hardening" may have important implications for nucleation of earthquakes along fault gouge (Scholz *et al.*, 1973; Scholz, 1978, 2002; Lockner and Byerlee, 1994; Samuelson *et al.*, 2009), possibly retarding the onset of earthquake instability. However, when the accumulating tectonic load eventually reaches the system shear resistivity, the slip may potentially be more rapid. This may occur, for example, when the initial slip damages the sealed boundaries, which enables fluid flow into the gouge layer. As a result, the effective stress will decrease abruptly, the tectonic shear stress will be far greater than the system shear resistivity, and runaway accelerating slip may develop. This is a plausible mechanism for dynamic weakening by fluid inflow.

When the layer is initially loosely packed, compaction occurs with shear, and pore pressure quickly rises. Equation 34 predicts that for the pore pressure to increase to the value of the normal stress, a relatively small change of porosity of $\Delta\Phi = -2 \times 10^{-4}$ is required (for pore water). The volumetric strain in simulation U14 that results from such a small reduction of porosity is 0.027%. Such a small strain may not be measurable in the laboratory, and it may seem that liquefaction occurs without any volumetric strain. Simulation U14 shows that from the onset of liquefaction and onward, the pore pressure remains at a constant value that exactly balances the external load, $P = \sigma_n$. This steady state is achieved because a normal force balance on the top and bottom walls is achieved, and further volumetric strain is prevented. In simulation U14, the stress chains that detach at the onset of liquefaction (Fig. 17b) do not rejoin. As a result, shear deformation is completely accommodated within the fluid phase, and the system loses its shear resistance as depicted by the zero apparent friction in Fig. 16b.

6.2.2 *Experiments on Liquefaction and Hardening with Undrained Conditions*

According to conventional understanding, poor drainage is believed to be a favorable condition for liquefaction. For that reason most engineering studies of the process of soil liquefaction used undrained boundary conditions. Empirical studies of both cyclic loading (simulating the passage of shear waves during earthquakes) (Seed and Lee, 1966; Peacock and Seed, 1968; Finn *et al.*, 1971), and continuous loading (simulating mass sliding under gravity) (Castro, 1975) have confirmed that loosely packed systems are more prone to liquefaction under undrained conditions. Furthermore, when cyclic loading was stress-controlled, sand layers showed an abrupt increase in their strain amplitude at the point of liquefaction. According to simulation U14, the increase of strain amplitude may be attributed to detachment of stress chains during liquefaction, which transfers support of the external load from the grains to the pore fluid, which has significantly smaller resistance to shear.

The mechanism of liquefaction was attributed to the tendency of loose soil to compact under drained conditions (Sawicki and Mierczynski, 2006), a tendency that was observed in dry and completely drained experiments (Youd, 1972). However, to the best of our knowledge, volume reduction has never been reported during undrained experiments, and the relationship between pore volume reduction and pore fluid pressurization was not acknowledged. The reason is probably limitations in measuring the tiny strains associated with compaction under undrained conditions, which may be as small as one hundredth of a percent. Unlike experiments, even very small pore volume change may be easily measured during simulations. Indeed, pore volume reduction is measured in our loose undrained simulation U14, and was shown to lead to liquefaction in accordance with Eq. 34.

Although undrained conditions have been shown to cause liquefaction when loading a loose specimen, they are also believed to cause hardening by pore volume increase (dilation) and pore pressure decrease when loading a densely packed layer (Rudnicki and Chen, 1988; Scholz, 2002). Moore and Iverson (2002) performed stress-controlled shear experiments on dilative saturated granular layers and reported that shearing of fine-grained sediments produced smaller deformation velocity than shearing of coarse-grained sediments, presumably because the fine sediments contributed to poor drainage leading to pore pressure reduction and hardening (higher shear resistance) upon dilation. When Samuelson *et al.* (2009) performed a double direct shear experiment on well-drained grain layers they observed no hardening upon dilation, because the good drainage enabled immediate pore fluid inflow into the newly generated pore volume, which prevented pore pressure reduction and layer strengthening. Indeed, simulation U13 confirms that when an undrained, initially dense system is sheared, dilation will cause pore pressure reduction and layer hardening (with increased apparent friction, Fig. 15c). When an initially dense but drained system is sheared, hardening may occur transiently (as in the onset of simulation D9, Fig. 8d, f) if the internal permeability is relatively low (leading to De$\lesssim$1). If the internal permeability is high and De $\ll$ 1, no hardening will be observed (Fig. 8c, e).

6.3. *Estimating Liquefaction Potential*

Following the analysis presented so far we may attempt to estimate the potential for liquefaction with various boundary conditions and different parameters. A precondition for liquefaction is the occurrence of compaction. When drainage is poor the overall compaction matters, and when drainage is good the rate of compaction matters. Indeed, many engineering analyses of liquefaction focus on the compaction potential as a function of the initial packing (Castro, 1975) and of the applied cyclic strain (Vucetic, 1994), where the applied cyclic loading presumably induces progressive compaction of a loosely or unevenly packed systems (Youd, 1972). In the current analysis of pore-pressure evolution mechanisms, variables such as compaction potential or number of loading cycles are not accounted for explicitly. For that reason, when we estimate the liquefaction potential in the following discussion we do not account explicitly for the initial packing and for the amount of imposed shear strain. We do, however, introduce a statistical factor that takes into account the chances of high enough pore pressure occurring in a large enough zone to completely detach a layer of stress chains during an applied shear strain. This statistical factor may be thought of as the statistical equivalent to empirical measurements such as the number of shear cycles needed for liquefaction.

When estimating the potential for liquefaction, one should first calculate the system Deborah number in order to decide which of the pore-pressure evolution regimes is dominant. Figure 20 summarizes the various options. If $\mathrm{De} \ll 1$ and viscous-like evolution of pore pressure is expected to dominate, a first-order approximation of the liquefaction potential is possible by use of Eq. 36. Equation 36 gives the expected pore pressure as a function of the temporal derivative of the porosity and the system variables. Approximating $\mathrm{d}\langle\Phi(\zeta,t)\rangle/\mathrm{d}t$ during compaction as $-V_{\mathrm{sh}}/\zeta$, and accounting for the pore pressure at the center of the system, $z=0$, Eq. 36 becomes:

$$P_d(t) \approx \frac{\eta V_{\mathrm{sh}}\zeta}{2k_0}, \tag{38}$$

where P_d is the approximated pore pressure for drained conditions (with $\mathrm{De} \ll 1$). Dividing Eq. 38 by σ_n gives a non-dimensional pressure to overburden ratio:

$$\frac{P_d}{\sigma_n} = \frac{\eta V_{\mathrm{sh}}\zeta}{2k_0\sigma_n}. \tag{39}$$

When $P_d/\sigma_n \ll 1$, liquefaction is not expected, because the compaction induced pore pressure is significantly smaller than the applied external stress, σ_n. When $P_d/\sigma_n \geq 1$ liquefaction is possible, because the evolving pore pressure may reach and even surpass the value of σ_n. On calculation of the pressure-to-overburden ratio from Eq. 39 for the simulations, it is found that in simulations D1–D5 $P_d/\sigma_n < 1$ and, indeed, no liquefaction is observed. In simulations D6 and D7, $P_d/\sigma_n \approx 1$ but the pore pressure maxima are still observed to be smaller than σ_n. For simulations D8–D9, $P_d/\sigma_n > 10$, and pore pressure maxima exceed σ_n. However, these maxima occur in highly localized zones, a situation that is shown to be insufficient to cause complete loss of shear strength and liquefaction. In simulations D11–D12, $P_d/\sigma_n > 100$, and the pore pressure is shown to exceed σ_n in relatively large zones, and to cause liquefaction (Figs. 12e and 14e). Note that simulation D10 is not taken into account here because it has $\mathrm{De} = 1$.

It is concluded that the condition $P_d/\sigma_n > 1$ is not sufficient for liquefaction, however it is still expected that larger ratios will lead to larger chances of liquefaction. Our simulations show that when $P_d/\sigma_n > 100$ liquefaction occurs (simulations D11 and D12). It is proposed that the threshold of 100 is suitable for use as a statistical indicator of the chance of compaction being fast enough in a large enough area during the course of shear strain application. In that sense it is possible to rewrite Eq. 39 as

$$\mathrm{LP}_d = \lambda\frac{\eta V_{\mathrm{sh}}\zeta}{2k_0\sigma_n}, \tag{40}$$

where LP_d is the liquefaction potential for drained conditions, and $\lambda \ll 1$ is an empirically determined factor, chosen to make $\mathrm{LP}_d = 1$ align with the onset of liquefaction. The value of LP_d in accordance with Eq. 40 with $\lambda = 0.01$ exactly distinguishes between simulations that do not generate liquefaction and are characterized by $\mathrm{LP}_d < 1$, and simulations that generate liquefaction and are characterized by $\mathrm{LP}_d > 1$ (Table 1). Yet it is not completely clear whether and how λ scales with system size and system dimensionality.

To estimate the liquefaction potential of field cases consider, for example, a layer of saturated soil buried at depth 10 m (this is also the distance to the boundary, ζ) of permeability $10^{-10}\mathrm{m}^2$. For liquefaction to occur, the excess pore pressure should reach the initial effective stress at depth of 10 m, which is $\sim$0.15 MPa. According to Eq. 40 with $\lambda = 0.01$, for $\mathrm{LP}_d > 1$, the peak ground velocity (PGV) should be $V_{\mathrm{sh}} > 0.3$ m/s. Indeed, Kostadinov and Towhata (2002) estimated that the minimum PGV that may generate soil liquefaction is 0.1 m/s. This observation

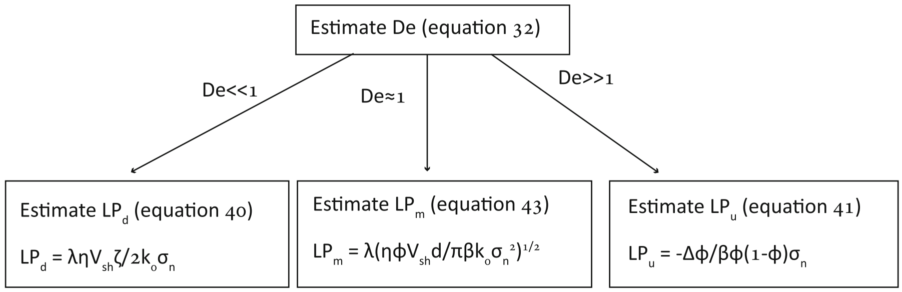

Figure 20
Diagram suggesting paths for estimating liquefaction potential for grains–fluid systems under shear

indeed suggests that in the field, also, λ may be approximated as 10^{-2}.

When De $\gg$ 1, evolution of the average pore pressure in the system is elastic-like and follows Eq. 34. Here, liquefaction potential may be estimated by use of the non-dimensional pressure-to-overburden ratio:

$$\mathrm{LP}_u = -\frac{\Delta\Phi}{\beta\Phi(1-\Phi)\sigma_n}. \tag{41}$$

Liquefaction is expected when $\mathrm{LP}_u \geq 1$. For our undrained initially loose simulation U14, Fig. 16a shows that a porosity reduction of $\Delta\Phi = -2 \times 10^{-4}$ has led to liquefaction. Such a porosity reduction gives $\mathrm{LP}_u \gtrsim 1$ in Eq. 41. Note that a statistical factor is not required here, because Eq. 34 is for the average pore pressure, and because, in simulation U14, the pore pressure homogenizes rapidly within the system, $\mathrm{LP}_u \geq 1$, which means that the pore pressure is of the order of the applied normal stress throughout the whole system.

To estimate the liquefaction potential of a field case with De $\gg$ 1, consider, for example, a thin gouge layer within a fault zone that is buried at depth of 1 km, and is bounded by undrained blocks. It is still assumed that the initial pore pressure within the gouge is hydrostatic. For liquefaction of the gouge, the pore pressure should reach a value of $\sigma_n = 15$ MPa. Assuming the initial porosity of the gouge is 0.1, then, according to Eq. 41, to achieve $\mathrm{LP}_u = 1$, the reduction of porosity should be $\Delta\Phi = -6 \times 10^{-4}$.

When De $\approx$ 1, the evolution of pore pressure is expected to be determined both by viscous-like and elastic-like behavior. In accordance with the approximate model presented by Goren *et al.* (2010, their Appendix B), it is suggested that under such conditions the pore pressure in these mixed-mode systems evolves as:

$$P(z,t) \approx \sqrt{\frac{\eta\Phi V_{\mathrm{sh}} d}{\pi\beta k_0}}. \tag{42}$$

For our simulation D10 with De = 1, Eq. 42 predicts $P = 233$ MPa. This prediction gives an order of magnitude approximation under the assumption that deformation is localized at the system's center (Goren *et al.*, 2010, their Appendix B). In simulation D10 the deformation zone is more widespread and the maximum pore pressure that was generated is 80 MPa. To estimate liquefaction potential, Eq. 42 is divided by σ_n and the statistical nature of the pore-pressure evolution is taken into account by use of the factor λ, similarly to Eq. 40:

$$\mathrm{LP}_m = \lambda\sqrt{\frac{\eta\Phi V_{\mathrm{sh}} d}{\pi\beta k_0 \sigma_n^2}}. \tag{43}$$

For simulation D10, and again using $\lambda = 0.01$, Eq. 43 gives $\mathrm{LP}_m \approx 0.1$. Indeed, high pore pressure that surpasses σ_n is generated, but only in localized zones, and complete loss of shear strength is not observed in this simulation.

7. Conclusions

In this work, a fully coupled model for the mechanics of fluid-filled granular media is developed from two components: A continuum formulation that describes the evolution of pore pressure in response to granular matrix deformation, and a granular dynamics algorithm that solves the grain dynamics. The resulting fully coupled model is extremely general, because it is capable of simulating a variety of loading scenarios leading to both reversible and irreversible granular matrix deformation, with a variety of drainage conditions for the pore fluid. Furthermore, in the coupled model we do not explicitly implement the law of effective stress on the micro (granular) level, but apply to the grains forces that arise from the pressure gradient in the pore fluid. Yet, we have validated that the effective stress law arises macroscopically. To the best of our knowledge this is the first time that the micro origin of the macro effective stress law has been demonstrated.

Analysis of the pore-fluid formulation together with simulation results reveals that evolution of pore pressure may be described as having two types of end-member behavior, "viscous-like" and "elastic-like". These two types of behavior control pore fluid pressurization and depressurization and the dominant terms in the pore-pressure equation. The choice of which mechanism dominates depends on the Deborah number, De, which determines whether the system is effectively drained or undrained. When drainage is good ($\mathrm{De} \ll 1$), pore-pressure evolution is viscous-like, because it is a function of the volumetric strain rate (pore volume strain rate), and it depends on the fluid viscosity and the inverse of the permeability. When drainage is poor ($\mathrm{De} \gg 1$), pore-pressure evolution is elastic-like, with pore pressure variations being a function of the overall volumetric strain (pore volume strain). Here, the pore pressure is also a function of fluid compressibility. Depending on the system variables and the boundary conditions, pore-pressure evolution may follow one of these end-members, or be a mixture of the two.

Simulations of fluid-filled granular layers under constant normal stress and constant shear velocity reveal that pressurization and liquefaction may occur in initially densely-packed layers also, as long as the boundaries are drained. Such conditions were previously often believed to be resistant to liquefaction (Seed *et al*., 1976). Here we show that liquefaction events can occur under such conditions, because viscous-like pore-pressure evolution (that arises when some drainage exists) is a function of the instantaneous rate of change of porosity and has "no memory" of the initial void ratio of the layer. Simulations with initially densely-packed undrained boundaries show "dilatancy hardening" with pore pressure reduction and an increase of the resistance of the layer to shear. Shear of loose initial-packing under undrained conditions leads to a steady-state liquefaction upon very small volumetric strain (which may not be measurable in the laboratory).

Finally, we conclude the manuscript by addressing the two questions that were posed in the "Introduction":

1. what is the physics behind the pore-pressure control of the shear strength? and
2. what processes alter the pore pressure?

To answer the first question we have seen that when pore pressure rises to the value of the applied normal stress, then the force exerted by pressure gradients across the grains may be large enough to counterbalance the solid stresses, and thus acts to detach stress chains and separate previously contacting grains. When a large enough region experiences this loss of grain contact, frictional resistance to sliding of the layer is suppressed and shear is accommodated within the pressurized fluid phase. The answer to the second question is that grain compaction causes the pore pressure to rise and grain divergence causes the pore pressure to decrease. The magnitude of pore pressure change depends on both the volumetric strain rate under well-drained conditions and on the absolute volumetric strain under undrained conditions.

Acknowledgments

RT acknowledges the support of the CNRS INSU program, the regional REALISE program, the ANR SISCA program, and the European SAFELAND program. We thank the anonymous reviewers for their constructive comments.

Appendix 1: Pore Fluid Pressure Evolution for $\mathrm{De} \ll 1$

In this section, the evolution of pore pressure is studied for drained boundaries with $\mathrm{De} \ll 1$. Under such conditions, the time-dependent term in Eqs. 15 and 18 becomes negligible compared with the diffusion term because $\mathrm{De} \ll 1$ in the non-dimensional Eq. 30. Equation 15 then becomes:

$$\nabla \cdot [k(\mathbf{x},t)\nabla P(\mathbf{x},t)] = \eta \nabla \cdot \mathbf{u_s}(\mathbf{x},t). \tag{44}$$

Formulation similar to Eq. 44 was developed by Iverson (1993) for drained conditions. For the 1D case, after integration, Eq. 44 becomes:

$$\frac{\partial P(z,t)}{\partial z} = \frac{\eta}{k_0} u_{sz}(z,t) + C(t), \tag{45}$$

where $C(t)$ is an integration factor, $k(z, t)$ is approximated as the permeability scale factor, k_0, and u_{sz} is the horizontally averaged z component of the solid velocity. In order to express the pressure as a function of the temporal derivative of the porosity, $\partial\Phi/\partial t$ as in Eq. 18, we use the 1D form of Eq. 17:

$$\frac{\partial u_{sz}}{\partial z} = \frac{1}{1-\Phi}\frac{\partial \Phi}{\partial t}. \tag{46}$$

Integrating Eq. 46 between the center of the layer at $z = 0$ and some distance z from the center (Fig. 7) results in:

$$\begin{aligned}
\int_0^z \frac{\partial u_{sz}(z',t)}{\partial z'}\mathrm{d}z' &= \int_0^z \frac{1}{1-\Phi(z',t)}\frac{\partial \Phi(z',t)}{\partial t}\mathrm{d}z' \\
&= \int_0^z -\frac{\partial[\ln(1-\Phi(z',t))]}{\partial t}\mathrm{d}z' \\
&= -\frac{\partial}{\partial t}\int_0^z \ln(1-\Phi(z',t))\mathrm{d}z' \\
&\approx -\frac{\partial}{\partial t}\int_0^z \left(-\Phi(z',t) - \frac{\Phi(z',t)^2}{2}\right)\mathrm{d}z' \\
&\approx -\frac{\partial}{\partial t}\int_0^z -\Phi(z',t)\mathrm{d}z' \\
&= \frac{\partial \langle \Phi(z,t)\rangle}{\partial t} z,
\end{aligned} \tag{47}$$

where $\langle \Phi(z,t)\rangle$ is the average porosity between the system's center and distance z from the center. Equation 47 then leads to the relationship:

$$u_{sz}(z,t) = u_{sz}(0,t) + \frac{\partial\langle\Phi(z,t)\rangle}{\partial t} z. \tag{48}$$

Substituting Eq. 48 in Eq. 45 results in:

$$\frac{\partial P(z,t)}{\partial z} = \frac{\eta}{k_0}\frac{\partial\langle\Phi(z,t)\rangle}{\partial t} z + C_1(t). \tag{49}$$

Integrating Eq. 49 between the layer's center and distance z leads to:

$$P(z,t) = P(0,t) + \frac{\eta}{k_0}\frac{\mathrm{d}\langle\Phi(\mathrm{z},\mathrm{t})\rangle}{\mathrm{d}t}\frac{z^2}{2} + C_1(t)z, \tag{50}$$

where the rate of change of the average porosity, $\mathrm{d}\langle\Phi(z,t)\rangle/\mathrm{d}t$, is approximated as uniform in space. Requiring complete drainage across the boundaries, i.e. $P(\zeta,t) = P(-\zeta,t) = 0$, Eq. 50 leads to:

$$P(z,t) = -\frac{\eta}{2k_0}\frac{\mathrm{d}\langle\Phi(\zeta,t)\rangle}{\mathrm{d}t}\left(\zeta^2 - z^2\right). \tag{51}$$

References

E. Aharonov and D. Sparks. *Rigidity phase transition in granular packings*. Phys. Rev. E, *60*(6):6890–6896, 1999. doi:10.1103/PhysRevE.60.6890.

E. Aharonov and D. Sparks. *Shear profiles and localization in simulations of granular materials*. Phys. Rev. E, *65*(5), 2002. doi:10.1103/PhysRevE.65.051302.

M. H. Anders, E. Aharonov, and J. J. Walsh. *Stratified granular media beneath large slide blocks: Implications for mode of emplacement*. Geology, *28*(11):971–974, 2000.

R. Bachrach, A. Nur, and A. Agnon. *Liquefaction and dynamic poroelasticity in soft sediments*. J. Geophys. Res., *106*(B7): 13515–13526, 2001.

M. A. Biot. *General theory for three-dimensional consolidation*. J. Appl. Phys., *12*(155), 1941.

M. L. Blanpied, D. A. Lockner, and J. D. Byerlee. *An earthquake mechanism based on rapid sealing of faults*. Nature, *358*(6387): 574–576, 1992.

A.-M. Boullier, E.-C. Yeh, S. Boutareaud, S.-R. Song, and C.-H. Tsai. *Microscale anatomy of the 1999 Chi-Chi earthquake fault zone*. Geochem. Geophys. Geosy., *10*, 2009. doi:10.1029/2008GC002252.

G. Castro. *Liquefaction and cyclic mobility of saturated sand*. J. Geotech. Eng. Div., ASCE, *101*(6):551–569, 1975.

K. O. Cetin, N. Isik, and B. Unutmaz. *Seismically induced landslide at Degirmendere Nose, Izmit bay during Kocaeli (Izmit)-Turkey earthquake*. Soil Dyn. Earthquake Eng., *24*(3):189–197, 2004. doi:10.1016/j.soildyn.2003.11.007.

P. A. Cundall and O. D. L. Strack. *A discrete numerical model for granular assemblies*. Géotechnique, *29*(1):47–65, 1979.

M. B. Das. *Principles of Soil Mechanics*. PWS-Kent, Boston, Mass., 1993.

U. El Shamy and M. Zeghal. *A micro-mechanical investigation of the dynamic response and liquefaction of saturated granular soils*. Soil Dyn. Earthquake Eng., *27*(8):712–729, 2007. doi:10.1016/j.soildyn.2006.12.010.

W. D. L. Finn, D. J. Pickering, and P. L. Bransby. *Sand liquefaction in triaxial and simple shear tests*. J. Soil Mech. Found. Div. Proc., *97*(4):639–659, 1971.

E. G. Flekkøy, A. Malthe-Sørenssen, and B. Jamtveit. *Modeling hydrofracture*. J. Geophys. Res., *107*(B8), 2002. doi:10.1029/2000JB000132.

E. J. Gabet and S. M. Mudd. *The mobilization of debris flows from shallow landslides*. Geomorphology, *74*:207–218, 2006. doi:10.1016/j.geomorph.2005.08.013.

V. K. Garga and H. Zhang. *Volume changes in undrained triaxial tests on sands*. Can. Geotech. J., *34*:762–772, 1997.

L. Goren, E. Aharonov, D. Sparks, and R. Toussaint. *Pore pressure evolution in deforming granular material: A general formulation and the infinitely stiff approximation*. J. Geophys. Res., *115*(B09216), 2010. doi:10.1029/2009JB007191.

R. M. Iverson. *Differential-equations governing slip-induced pore-pressure fluctuations in a water-saturated granular medium*. Math. Geol., *25*(8):1027–1048, 1993.

R. M. Iverson and R. G. LaHusen. *Dynamic pore-pressure fluctuations in rapidly shearing granular-material*. Science, *246*(4931):796–799, 1989.

R. M. Iverson, M. E. Reid, N. R. Iverson, R. G. LaHusen, M. Logan, J. E. Mann, and D. L. Brien. *Acute sensitivity of landslide rates to initial soil porosity*. Science, *290*(5491):513–516, 2000. doi:10.1126/science.290.5491.513.

Ø. Johnsen, R. Toussaint, K. L. Måløy, and E. G. Flekkøy. *Pattern formation during air injection into granular materials confined in a circular Hele-Shaw cell*. Phys. Rev. E, *74*(1), 2006. doi:10.1103/PhysRevE.74.011301.

Ø. Johnsen, R. Toussaint, K. J. Måløy, E. G. Flekkøy, and J. Schmittbuhl. *Coupled air/granular flow in a linear Hele-Shaw cell*. Phys. Rev. E, *77*(1), 2007. doi:10.1103/PhysRevE.77.011301.

Ø. Johnsen, C. Chevalier, A. Lindner, R. Toussaint, E. C. K. J. Måløy, E. G. Flekkøy, and J. Schmittbuhl. *Decompaction and fluidization of a saturated and confined granular medium by injection of a viscous liquid or a gas*. Phys. Rev. E, *78*(5), 2008. doi:10.1103/PhysRevE.78.051302.

P. Jop, Y. Forterre, and O. Pouliquen. *A constitutive law for dense granular flows*. Nature, *441*(7094):727–730, 2006. doi:10.1038/nature04801.

F. Kawakami and A. Asada. *Damage to the ground and earth structures by the Niigata earthquake of June 16,1964*. Soil and Foundation, *6*(1):14–30, 1966.

M. V. Kostadinov and I. Towhata. *Assessment of liquefaction-inducing peak ground velocity and frequency of horizontal ground shaking at onset of phenomenon*. Soil Dyn. Earthquake Eng., *22*(4):309–322, 2002. doi:10.1016/S0267-7261(02)00018-0)

V. G. Kozlov, A. A. Ivanova, and P. Evesque. *Sand behavior in a cavity with incompressible liquid under vertical vibrations*. Europhys. Lett., *42*(3):413–418, 1998.

S. L. Kramer. *Geotechnical earthquake engineering*. Prentice Hall, Inc., Upper Saddle River, New Jersey, 1996.

D. A. Lockner and J. D. Byerlee. *Dilatancy in hydraulically isolated faults and the suppression of instability*. Geophys. Res. Lett., *21*(22), 1994.

C. Marone, C. B. Raleigh, and C. H. Scholz. *Frictional behavior and constitutive modeling of simulated fault gouge*. J. Geophys. Res., *95*:7007–7025, 1990.

S. McNamara, E. G. Flekkøy, and K. J. Måløy. *Grains and gas flow: Molecular dynamics with hydrodynamic interactions*. Phys. Rev. E, *61*(4):4054–4059, 2000.

S. A. Miller and A. Nur. *Permeability as a toggle switch in fluid-controlled crustal processes*. Earth Planet. Sci. Lett., *183*:133–146, 2000.

P. L. Moore and N. R. Iverson. *Slow episodic shear of granular materials regulated by dilatant strengthening*. Geology, *30*(9): 843–846, 2002.

M. J. Niebling, E. G. Flekkøy, K. J. Måløy, and R. Toussaint. *Sedimentation instabilities: Impact of the fluid compressibility and viscosity*. Phys. Rev. E, *82*(5), 2010. doi:10.1103/PhysRevE.82.051302.

A. Nur and J. D. Byerlee. *An exact effective stress law for elastic deformation of rock with fluids*. J. Geophys. Res., *76*(26):6414–6419, 1971.

Y. Okada and H. Ochiai. *Coupling pore-water pressure with distinct element method and steady state strengths in numerical triaxial tests under undrained conditions*. Landslides, *4*:357–369, 2007. doi:10.1007/s10346-007-0092-1.

T. Osswald. *Polymer Processing Fundamental*. Hanser/Gardner, Cincinnati, Ohio, 1998.

W. H. Peacock and H. B. Seed. *Sand liquefaction under cyclic loading simple shear conditions*. J. Soil Mech. Found. Div. Proc., *94*(SM3):689–708, 1968.

O. Pouliquen, C. Cassar, P. Jop, Y. Forterre, and M. Nicolas. *Flow of dense granular material: towards simple constitutive laws*. J. Stat. Mech: Theory Exp., JUL 2006. doi:10.1088/1742-5468/2006/07/P07020.

S. R. Pride. Relationships between seismic and hydrological properties. In Y. Rubin and S. S. Hybbard, editors, *Hydrogeophysics*, pages 253–291. Springer, Netherlands, 2005.

J. F. Richardson. Incipient fluidization and particulate system. In J. F. Davidson and D. Harrison, editors, *Fluidization*, pages 25–64. Academic Press, London, 1971.

P.-Y. F. Robin. *Note on effective pressure*. J. Geophys. Res., *78*(14):2434–2437, 1973.

L. Rondon, O. Pouliquen, and P. Aussillous. *Granular collapse in a fluid: role of the initial volume fraction*. Physics of Fluids. 2011, accepted

J. W. Rudnicki and C. H. Chen. *Stabilization of rapid frictional slip on a weakening fault by dilatant hardening*. J. Geophys. Res., *93*(B5):4745–4757, 1988.

M. O. Saar and M. Manga. *Depth dependence of permeability in the Oregon Cascades inferred from hydrologic, thermal, seismic and magnetic modeling constraints*. J. Geophys. Res., *109*(B04204), 2004. 10.1029/2003JB002855.

A. Sagy and E. E. Brodsky. *Geometric and rheological asperities in an exposed fault zone*. J. Geophys. Res., *114*, 2009. doi:10.1029/2008JB005701.

J. Samuelson, D. Elsworth, and C. Marone. *Shear induced dilatancy of fluid saturated faults: experiment and theory*. J. Geophys. Res., 2009. Submitted.

A. Sawicki and J. Mierczynski. *Developments in modeling liquefaction of granular soils, caused by cyclic loads*. Appl. Mech. Rev., *59*:91–106, 2006. doi:10.1115/1.2130362.

J. Schäfer, S. Dippel, and D. E. Wolf. *Force Schemes In Simulations If Granular Materials*. J. Phys. I France, *6*:5–20, 1996.

C. H. Scholz. *Velocity anomalies in dilatant rock*. Science, *201*(4354):441–442, 1978.

C. H. Scholz. *The Mechanics of Earthquakes and Faulting*. Cambridge University Press, Cambridge, UK, 2002.

C. H. Scholz, L. R. Sykes, and Y. P. Aggarwal. *Earthquake prediction—physical basis*. Science, *181*(4102):803–810, 1973.

H. B. Seed. *Soil liquefaction and cyclic mobility evaluation for level ground during earthquakes*. J. Geotech. Geoenviron. Eng. Div., ASCE, *105*:201–255, 1979.

H. B. Seed and K. L. Lee. *Liquefaction of saturated sand during cyclic loading*. J. Soil Mech. Found. Div. Proc., ASCE, *92*(SM6): 105–134, 1966.

H. B. Seed, J. Lysmer, and P. P. Martin. *Pore-water pressure changes during soil liquefaction*. J. Geotech. Eng. Div., ASCE, *102*(4):323–346, 1976.

P. Segall and J. R. Rice. *Dilatancy, compaction, and slip instability of fluid-infiltrated fault*. J. Geophys. Res., *100*(B11):22155–22171, 1995.

A. Snieder and A. van der Beukel. *The liquefaction cycle and the role of drainage in liquefaction*. Granular Matter, *6*, 2004. doi: 10.1007/s100035-0030151-9.

K. Soga. *Soil liquefaction effects observed in the Kobe earthquake of 1995*. Proceedings Of The Institution Of Civil Engineers-Geotechnical Engineering, *131*(1):34–51, 1998.

K. Terzaghi. *Theoretical Soil Mechanics*. John Wiley, New York, 1943.

J. L. Vinningland, Ø. Johnsen, E. G. Flekkøy, R. Toussaint, and K. J. Måløy. *Granular Rayleigh–Taylor instability: Experiments and simulations*. Phys. Rev. Lett., *99*(4), 2007a. doi:10.1103/PhysRevLett.99.048001.

J. L. Vinningland, Ø. Johnsen, E. G. Flekkøy, R. Toussaint, and K. J. Måløy. *Experiments and simulations of a gravitational granular flow instability*. Phys. Rev. E, *76*(5), 2007b. doi: 10.1103/PhysRevE.76.051306.

J. L. Vinningland, O. Johnsen, E. G. Flekkøy, R. Toussaint, and K. J. Måløy. *Size invariance of the granular Rayleigh–Taylor instability*. Phys. Rev. E, *81*(4), 2010. doi:10.1103/PhysRevE.81.041308.

M. Vucetic. *Cyclic threshold shear strains in soils*. J. Geotech. Eng., ASCE, *120*(12):2208–2228, 1994.

J. Walder and A. Nur. *Porosity reduction and crustal pore pressure development*. J. Geophys. Res., *89*(B13):11539–11548, 1984.

H. F. Wang. *Theory of Linear Poroelasticity with Applications to Geomechanics and Hydrogeology*. Princeton University Press, Princeton, NJ, 2000.

T. L. Youd. *Compaction of sands by repeated shear straining*. J. Soil Mech. and Found. Eng. Div., ASCE, *98*:709–725, 1972.

O. C. Zienkiewicz, A. H. C. Chan, M. Pastor, B. A. Schrefler, and T. Shiomi. *Computational Geomechanics with Special Reference to Earthquake Engineering*. J. Wiley, Chichester, 1999.

(Received June 30, 2010, revised February 28, 2011, accepted March 30, 2011, Published online June 9, 2011)

JOURNAL OF GEOPHYSICAL RESEARCH, VOL. 115, B09216, doi:10.1029/2009JB007191, 2010

Pore pressure evolution in deforming granular material: A general formulation and the infinitely stiff approximation

L. Goren,[1] E. Aharonov,[2] D. Sparks,[3] and R. Toussaint[4]

Received 7 December 2009; revised 20 April 2010; accepted 29 April 2010; published 30 September 2010.

[1] The physics of deformation of fluid-filled granular media controls many geophysical systems, ranging from shear on geological faults to landslides and soil liquefaction. Its great complexity is rooted in the mechanical coupling between two deforming phases: the solid granular network and the fluid-filled pore network. Often deformation of the granular network leads to pore fluid pressure (PP) changes. If the PP rises enough, the fluid-filled granular media may transition from a stress-supporting grain network to a flowing grain-fluid slurry, with an accompanying catastrophic loss of shear strength. Despite its great importance, the mechanisms and parameters controlling PP evolution by granular shear are not well understood. A formulation describing the general physics of pore fluid response to granular media deformation is developed and used to study simple scenarios that lead to PP changes. We focus on the infinitely stiff end-member scenario, where granular deformation is prescribed, and the PP responds to this deformation. This end-member scenario illustrates the two possible modes of pore fluid pressurization: (1) via rapid fluid flow when fluid drainage is good and (2) via pore volume compaction when drainage is poor. In the former case the rate of deformation controls PP evolution, while in the latter case, fluid compressibility is found to be an important parameter and the amount of pressurization is controlled by the overall compaction. The newly suggested fluid-induced mechanism (mechanism 1) may help explain observations of liquefaction of initially compact soils and shear zones.

Citation: Goren, L., E. Aharonov, D. Sparks, and R. Toussaint (2010), Pore pressure evolution in deforming granular material: A general formulation and the infinitely stiff approximation, *J. Geophys. Res.*, *115*, B09216, doi:10.1029/2009JB007191.

1. Introduction

[2] Soils, unconsolidated rocks, and fault gouge may be described as porous skeletons composed of contacting grains. Often the pores are filled with fluid. The grains and the fluid form two intertwined networks: the grains connect via frictional contacts forming a heterogeneous deformable solid network, while the fluid flows in the complementary network of pores. The coupled solid-fluid system may deform in response to applied stresses, and deformation naturally arises on all timescales: from slow compaction in response to sediment load, to catastrophic failure during earthquakes and landslides. The granular network may deform elastically or through irreversible rearrangements (e.g., pore collapse). Such deformation changes the pore volume and by that affects the pore fluid pressure (PP). On the other hand, gradients in PP exert forces that may cause grains to move and the solid network to deform. The coupling between the solid matrix deformation and the value of PP is possibly the most important aspect of solid-fluid coupling: elevated PP modifies the way in which saturated granular soils and rocks respond to stresses, and often controls devastating natural phenomena such as earthquakes [e.g., *Sleep and Blanpied*, 1992], landslides [e.g., *Voight and Faust*, 1982; *Iverson et al.*, 1997] and soil liquefaction [*Das*, 1993; *Kramer*, 1996]. A continuum view of how PP modifies the system response to stress is formulated in the law of effective stress [*Terzaghi*, 1943]. The most important aspect of this law is the fact that the shear resistance, τ, of saturated granular material decreases linearly with increasing PP, P, since $\tau \propto \sigma - P$, where σ is the confining stress [*Terzaghi*, 1943; *Scholz*, 1990]. Therefore, the ability of saturated soils to resist shear is crucially dependent on the state of their PP: under normal conditions, when $P < \sigma$, grain-networks behave like solids that can sustain shear stresses. However, if for some reason the PP is elevated to a level where $P = \sigma$ the shear resistance vanishes, and 'liquefaction' occurs, a situation in which the grain-fluid system flows like a fluid in response to even small shear stresses. When PP within a landslide shear zone approaches the confining stress, the slide may accelerate catastrophically. When fault gouge material experiences high

[1]Department of Environmental Sciences and Energy Research, Weizmann Institute of Science, Rehovot, Israel.
[2]Institute of Earth Sciences, Hebrew University, Jerusalem, Israel.
[3]Department of Geology and Geophysics, Texas A&M University, College Station, Texas, USA.
[4]IPGS, CNRS and University of Strasbourg, EOST, Strasbourg, France.

0148-0227/10/2009JB007191

values of PP, the dramatic reduction of shear resistance may lead to dynamic acceleration and an earthquake in response to background tectonic stresses that were previously sustained by the fault resistance to sliding. In soils, an increase in PP leading to liquefaction may cause collapse of previously supported infrastructure.

[3] Traditionally, the mechanics of fluid-filled soils, landslides' shear zone and gouge material are studied separately. Indeed, a major difference between these three systems is their characteristic depth. While soil liquefaction is a phenomenon of the very shallow crust and is usually restricted to few tens of meters below the surface, the depth of landslides' shear zones ranges between several meters to few kilometers [e.g., *Sidle and Ochiai*, 2006], and the depth of fault gouge is restricted to the seismogenic zone, normally 2–30 km. The different depths result in differences in the effective confining stresses. This range of depth is also accompanied by a range of drainage conditions [*Saar and Manga*, 2004].

[4] Despite depth and drainage differences, the basic coupled mechanics of grains and fluid may be applied similarly to soils, shear zones, and gouge layers. Indeed, it will be shown here that the formulation of pore fluid response to granular matrix deformation is depth independent. For that reason, conclusions from various studies (some of them reviewed in Appendix A) that deal with pore fluid pressurization for one system may be applied also to the other systems. Therefore the term 'liquefaction' is used here to address the general case of PP equals the confining stress, regardless of the geological setting (soil, landslides' shear zone, and gouge layers). Caution should be practiced when interpreting the results, as the PP required to liquefy soils is smaller by orders of magnitude than that required to completely liquefy gouge layers. In the rest of the introduction, the importance of PP to soil liquefaction and pressurization along gouge layers is reviewed separately, but the mechanics controlling PP evolution is presented and discussed uniformly.

[5] Soil liquefaction [*Das*, 1993; *Kramer*, 1996] is triggered by and contributes to the devastation of earthquakes, and may cause collapse of infrastructure foundations, and initiate landslides. In the process of soil liquefaction, seismic waves induce cyclic loading, which causes the PP to rise. As a consequence, the granular system, which under normal conditions behaves like a solid that resists shear, loses its shear resistance and may flow as a fluid. As a result, liquefied soil can no longer support the infrastructure that is rooted in it and a catastrophic collapse of buildings, roads, bridges and other structures with foundations may take place (e.g., damage during earthquakes at Niigata, 1964 [*Kawakami and Asada*, 1966], or Izmit, 1999 [*Cetin et al.*, 2004]). In some earthquakes, the damage caused by liquefaction exceeds the damage by direct ground acceleration. For example, the 1995 earthquake in Kobe, Japan, caused liquefaction that resulted in more than 5500 deaths, and an estimated economic loss of over $US 130 billion [*Scawthorn and Yanev*, 1995].

[6] Since liquefaction models are a practical necessity in geotechnical engineering, phenomenological models of coupled solid-fluid deformation have been developed (for a review, see *Sawicki and Mierczynski* [2006]). These models are usually based on continuum mixture theory formulations, and use experimental data for model calibration. A major effort to determine the mechanisms involved in earthquake-induced soil liquefaction by comparing centrifuge experiment with phenomenological numerical models took place as part of the VELACS project [*Popescu and Prevost*, 1995]. None of the models accurately predict the set of experimental outcomes and by themselves show a wide and inconsistent range of predictions [*Manzari et al.*, 1994]. Recently, more sophisticated phenomenological models have improved the predictability of PP buildup and dissipation [*Zienkiewicz et al.*, 1999].

[7] Catastrophic pore fluid pressurization may occur not only in response to cyclic loading induced by earthquakes, but also as a result of continuous shearing of fluid-filled granular layers. This is the most studied scenario for liquefaction within shear zones of landslides and gouge-filled faults. In these cases, drainage conditions and porosity evolution were shown to control PP evolution and thus layer strength. Dynamic dilation and compaction of gouge and shear zone material are shown to be a function of shearing velocity [*Marone et al.*, 1990] and stress conditions [*Iverson et al.*, 2000; *Aharonov and Sparks*, 2002]. When the fault is sealed dilation often leads to stable sliding as it causes PP reduction and fault hardening [*Scholz*, 1990; *Segall and Rice*, 1995; *Moore and Iverson*, 2002], while shear-enhanced compaction of under-compacted gouge may lead to extreme weakening and unstable sliding [*Blanpied et al.*, 1992]. Pore fluid pressurization and migration also control communication between fault zones and earthquakes sequencing [*Yamashita*, 1999; *Miller and Nur*, 2000].

[8] In terms of the physics of the granular-fluid system, a matrix of granular media may deform elastically through small reversible deformation at grain contacts, and/or plastically through irreversible rearrangements (e.g., pore collapse). The term poroplasticity [*Kherbouche et al.*, 1995] is used here to describe such irreversible deformation of granular media in a way that modifies the shape and size of pores and the contact network between grains, and is unrelated to microscopic dislocation glide; that is, rearrangements take place by grains sliding and rolling relative to each other, and thus change the matrix configuration. The traditional approach suggests that poroplasticity may lead to fluid pressurization and may cause liquefaction [*Sawicki and Mierczynski*, 2006]. More recently a different view on the mechanics of liquefaction was suggested: poroelasticity was offered to be the possible cause of liquefaction induced by earthquakes [*Bachrach et al.*, 2001]. Sections 1.1 and 1.2 briefly review poroplastic and poroelastic approaches and demonstrate that the physical understanding of the mechanisms by which matrix deformation generates large enough PP for soils and gouge layers to liquefy is not complete. The rheological regime that controls PP evolution, poroplasticity or poroelasticity, is still debated and so are the relevant boundary conditions (drained and undrained), and the importance of physical parameters such as fluid compressibility.

1.1. Poroplastic Path to Liquefaction: Current State of Understanding

[9] The poroplastic view of liquefaction relates the generation of high PP to irreversible collapse of pore volume

under undrained conditions [*Sawicki and Mierczynski*, 2006]. This mechanism is supported by laboratory experiments showing that when loose sediments compact under cyclic shear [*Casagrande*, 1936; *Youd*, 1972], PP rises under undrained conditions [*Castro*, 1969]. Many models of poroplastic deformation assume specific deformation laws of the porous configuration: in the context of soil liquefaction with matrix compaction induced by mechanical vibrations [*Snieder and van der Beukel*, 2004], in relation to crustal processes with material precipitation within pores [*Walder and Nur*, 1984], and in the context of gouge material with porosity that depends on slip [*Yamashita*, 1999] and slip velocity [*Segall and Rice*, 1995; *Samuelson et al.*, 2009].

[10] Recently, fully coupled grain-scale models of grains and pore fluid were developed to study the relation between general deformation of a granular matrix and soil liquefaction [e.g., *El Shamy and Zeghal*, 2007; *Okada and Ochiai*,2007; *Li et al.*, 2007]. Such models use the discrete element method and are capable of simulating both poroelastic and poroplastic grain rearrangements. Here we review two of these studies that demonstrate the inconsistency in the assumed physics of soil liquefaction: (1) *El Shamy and Zeghal* [2007] study a drained system (where the fluid is allowed to flow freely out of the top boundary) with forcing induced by cyclic shear acceleration at the base of the system and assume that pore fluid is completely incompressible, an assumption that follows many engineering interpretation of experiments [e.g., *Garga and Zhang*, 1997; *Kozlov et al.*, 1998]. (2) *Okada and Ochiai* [2007] study an undrained system (with impermeable boundaries) placed under contractive strain, and assume a compressible pore fluid. Both studies report the generation of high enough PP for liquefaction to occur, while the latter study emphasizes that high PP was generated only in initially loosely packed systems. Thus, these two works study the same problem but assume different physics (incompressible versus compressible fluid) and different boundary conditions (drained versus undrained). The results of *Okada and Ochiai* [2007] can be interpreted within the classical framework of soil liquefaction, as they observe high PP when compacting a loosely packed undrained granular system. However, the results of *El Shamy and Zeghal* [2007] are somewhat unexpected because they observe liquefaction under drained conditions with incompressible fluid. Indeed, a similar model that is described by *Itasca Consulting Group Inc.* [2005], stresses that liquefaction cannot be simulated with an incompressible fluid because then the model "does not include a mechanism for generation of pore pressure under strain." In section 6 we supply a physical explanation for this apparent violation of the classical view of liquefaction and show that the two models of *El Shamy and Zeghal* [2007] and *Okada and Ochiai* [2007] represent different end-members of the same physical system.

1.2. Poroelastic Path to Liquefaction: Current State of Understanding

[11] Poroelastic theory for coupled solid-fluid deformation [*Terzaghi*, 1943; *Biot*, 1941, 1956a, 1956b, 1962; *Skempton*, 1960; *Wang*, 2000] assumes infinitely small reversible deformations, (an assumption better suited for rocks and cohesive matter than for granular media) and calculates solid deformation and PP. The poroelastic view attributes PP variations to the coupling between the elastic deformation of pores and the porous flow induced by the passage of P-waves [*Bachrach et al.*, 2001]. A Biot based model is developed by *Bachrach et al.* [2001], which shows that compressible fluid and low shear modulus of the granular matrix may lead to PP that exceeds the loading. A similar formulation, but without inertial terms, is developed by *Wang* [2000] for the general study of PP response to cyclic loading from a poroelastic point of view. Section 3 shows that PP rise using this mechanism may lead to soil liquefaction only in the very top of the sediment column, and to gouge liquefaction only if the fluid was initially highly pressurized.

1.3. Overview

[12] The diversity of models and approaches and the ongoing debates regarding the basic physics of liquefaction indicate that a coherent physical theory that explains how PP evolves in response to general deformation of the granular matrix is still missing. Such a unifying theory should be able to explain as particular cases the various field, experimental and numerical observations and the links between existing models. It should also address some basic questions that were left unanswered: What is the role of fluid compressibility [*Garga and Zhang*, 1997]? Can liquefaction take place under drained conditions [*Das*, 1993]? And how does liquefaction occur in initially over-compacted soils [*Soga*, 1998]?

[13] The work presented here aims to do exactly that. In order to achieve this goal, we first develop a general theory and then apply it within the scope of the infinite stiffness approximation, where the granular deformation is prescribed and the pore fluid responds to this deformation, without affecting solid matrix deformation. The study of this simple end-member case allows derivation of analytical solutions for the mechanics of pore fluid pressurization, and comparison to numerical solutions. The behavior of this end-member situation is simple but yet rich enough to highlight the mechanisms that control liquefaction.

[14] In this paper we develop a mass and momentum conservation based formulation for the general PP response to granular matrix deformation in section 2. This formulation is not restricted to a particular type of deformation and may be used to study both elastic reversible processes and irreversible plastic deformation. The question of poroelastic versus poroplastic rheology is discussed in section 3. Then, to study pore fluid behavior under the infinite stiffness approximation, section 4 describes the application of the formulation to a simple system of uniform grains immersed in fluid and subjected to shear loading. Section 5 analyzes the equation that lies at the heart of the pore fluid formulation, and reveals different physical processes that control the evolution of PP. One of these processes may explain liquefaction events in initially over-consolidated granular material under drained conditions. Analysis and implications are discussed in section 6, and we present our conclusions in section 7. In Appendix A we show that our formulation for the pore fluid pressure is a generalization of previous models and thus we can uncover the missing links between them. In

Appendix B we develop a general analytic solution for the basic equation that describes pore fluid pressurization.

2. Theoretical Model

[15] In this section, mass and momentum conservation laws are used for the development of an equation describing the spatial and temporal evolution of excess pore fluid pressure in response to granular or porous matrix deformation. Let Φ be the porosity, t the time, ρ_s and ρ_f the mass densities of the bulk material of the grains and of the fluid, respectively, and $\mathbf{u_s}$ and $\mathbf{u_f}$ the grains and fluid velocities, respectively. The velocities are considered at a representative scale for Darcy's law; that is, they are defined for mesoscopic volumes containing at least a few grains. First, mass conservation equations are written for the grains and for the fluid:

$$\frac{\partial[(1-\Phi)\rho_s]}{\partial t} + \nabla \cdot [(1-\Phi)\rho_s \mathbf{u_s}] = 0, \tag{1}$$

$$\frac{\partial[\Phi\rho_f]}{\partial t} + \nabla \cdot [\Phi\rho_f \mathbf{u_f}] = 0, \tag{2}$$

where $\nabla\cdot$ is a divergence operator related to grains/fluid advective processes. The quantity $\Phi(\mathbf{u_f} - \mathbf{u_s})$ corresponds to the Darcy velocity [*Anghel et al.*, 2006], i.e.,

$$\Phi(\mathbf{u_f} - \mathbf{u_s}) = -\frac{k}{\mu}\nabla P, \tag{3}$$

where k is the permeability, μ is the fluid viscosity and P is the excess (over hydrostatic) fluid pressure. Equation (3), Darcy's law, is derived from Stoke's equation, and is a reduced form of the momentum equation under the assumption of negligible fluid inertia. The fluid density is given by the fluid state equation:

$$\rho_f = \rho_0(1 + \beta P), \tag{4}$$

where ρ_0 is the fluid density at a reference hydrostatic pressure level, and β is the adiabatic fluid compressibility, $\beta = (1/\rho_f)(\partial\rho_f/\partial P)$. Using the adiabatic compressibility means assuming no significant heat exchange between the overpressured and underpressured zones during fast motion. We assume that grain compressibility is negligible relative to the fluid compressibility, as expected for natural sand filled with fluid such as water, so that ρ_s can be approximated as constant, and equations (1) to (4) lead to

$$\beta\Phi\frac{\partial P}{\partial t} = \nabla \cdot \left[(1+\beta P)\frac{k}{\mu}\nabla P\right] - (1+\beta P)\nabla \cdot \mathbf{u_s} - \beta\Phi\mathbf{u_s} \cdot \nabla P. \tag{5}$$

This derivation is based on the same basic principles as the approach used successfully to model instabilities in the flow of granular media and fluids [*Vinningland et al.*, 2007a, 2007b; *Johnsen et al.*, 2006, 2007, 2008], and hydrofracture [*Flekkøy et al.*, 2002]. The value of the excess PP, P, has, for the cases considered, an upper bound set approximately by the difference between the lithostatic and hydrostatic stresses, $\sigma_d = (\rho_s - \rho_f)gh$, where h is the depth at which matrix deformation occurs. Indeed, when $P = \sigma_d$ the effective stress vanishes, and liquefaction may occur. For that reason the analysis presented here considers the case of

$$\beta P \le \beta\sigma_d \ll 1. \tag{6}$$

Taking fluid compressibility of $\beta = 4.5 \times 10^{-10}$ Pa^{-1} [*Garga and Zhang*, 1997, and references therein], equation (6) bounds $\sigma_d \ll 2.22$ GPa and $h \ll 150$ km. This restriction on h does not limit the analysis since soil liquefaction is a phenomenon of the shallow crust, and fault gouge material is restricted by the base of the seismogenic zone. It should be noted that here we consider a single fluid with low compressibility, such as water, in the pore space. If the pore space is filled with water/air mixture, the mixture compressibility is expected to increase significantly with respect to pure water and equation (6) might not hold. This situation is not considered in the present paper. Following (6), equation (5) is rewritten as

$$\beta\Phi\frac{\partial P}{\partial t} = \nabla \cdot \left[\frac{k}{\mu}\nabla P\right] - \nabla \cdot \mathbf{u_s} - \beta\Phi\mathbf{u_s} \cdot \nabla P. \tag{7}$$

The first and fourth term of equation (7) compose together the Lagrangian derivative of the PP, the second term describes PP diffusion and the third term may be viewed as the forcing, due to spatial differences in grain velocities.

[16] To investigate the relative magnitude of the different terms in equation (7), a non-dimensional analysis is performed. Let us define the characteristic magnitude of the variables in the model: $P = \hat{P}/\beta$, $\mathbf{u_s} = \hat{\mathbf{u}}_\mathbf{s} u_0$, $k = \hat{k}k_0$, and $t = \hat{t}t_0$, where the $\hat{}$ notation denotes non-dimensional variables, and u_0, k_0, and t_0 are the velocity, permeability, and timescale factors, respectively. The divergence arising from equations (1) and (2) represents grain-scale rearrangements. Therefore, the derivatives in these operators are scaled by d^{-1}, a characteristic grain diameter, and $\nabla\ \cdot = \hat{\nabla}_1 \cdot /d$. However, the gradient operator in equation (3) represents a larger length scale, over which Darcy law applies. Therefore the derivatives in this operator are scaled by l_k^{-1}, the PP diffusion length scale, and $\nabla = \hat{\nabla}_2/l_k$. l_k is bounded from the top by h, and is presumably much larger than d. A natural choice for l_k is $\sqrt{Dt_0}$, where $D = k_0/\beta\mu\Phi$ is the PP diffusion coefficient, and $t_0 = d/u_0$ is the timescale of deformation. Assigning the non-dimensional variables in equation (7) results in

$$\frac{\partial\hat{P}}{\partial\hat{t}} = \frac{D}{l_k u_0}\hat{\nabla}_1 \cdot (\hat{k}\hat{\nabla}_2\hat{P}) - \frac{1}{\Phi}\hat{\nabla}_1 \cdot \hat{\mathbf{u}}_\mathbf{s} - \frac{d}{l_k}\hat{\mathbf{u}}_\mathbf{s} \cdot \hat{\nabla}_2\hat{P}. \tag{8}$$

[17] In equation (8), the coefficients of both the second and the fourth terms may be expressed as functions of either a Peclet number, or a Deborah number, which are identical to each other: $D/l_k u_0 = \sqrt{\mathrm{Pe}^{-1}} = \sqrt{\mathrm{De}_d^{-1}}$, and $d/l_k = \sqrt{\mathrm{Pe}} = \sqrt{\mathrm{De}_d}$. The Peclet number, $\mathrm{Pe} = du_0/D$, expresses the ratio between the rate of advection, u_0, and the rate of PP diffusion across a single grain, D/d [*McNamara et al.*, 2000]. The Deborah number, $\mathrm{De}_d = t_d/t_0$, is defined as the ratio of relaxation timescale and a characteristic process timescale [*Osswald*, 1998, p. 54]. Here, the relaxation timescale, $t_d = d^2/D$, is the timescale for PP diffusion across a single grain,

and the characteristic process timescale, t_0, is the timescale of deformation.

[18] In the following, we use the Deborah number notation, De_d, where subscript d is added because later in this paper an additional relaxation timescale will be considered. De_d is termed the grain Deborah number. There are two limits to equation (8), one when $\mathrm{De}_d \gg 1$, and then the second diffusion term in equation (8) is negligible, and one when $\mathrm{De}_d \ll 1$, and then the last term in equation (8) is negligible. The case of $\mathrm{De}_d > 1$ is an unnatural end-member. Assuming pore fluid water, Carman-Kozeny permeability ($k \propto d^2$), and deformation rate <10 m/s, this end-member occurs only if grain size in unrealistically small (the order of 100 nm). In fact, for most natural cases, and in particular for the cases considered in this paper, $\mathrm{De}_d \ll 1$. As a result, the fourth term (the gradient part of the Lagrangian derivative) in equation (8) may be neglected. Equation (8) may then be rewritten as

$$\frac{\partial \hat{P}}{\partial \hat{t}} = \sqrt{\mathrm{De}_d^{-1}}\hat{\nabla}_1 \cdot (\hat{k}\hat{\nabla}_2\hat{P}) - \frac{1}{\Phi}\hat{\nabla}_1 \cdot \hat{\mathbf{u}}_\mathbf{s}, \tag{9}$$

where only three terms are left. In a dimensional form, equation (9) reads

$$\frac{\partial P}{\partial t} = \frac{1}{\beta\Phi\mu}\nabla \cdot [k\nabla P] - \frac{1}{\beta\Phi}\nabla \cdot \mathbf{u}_\mathbf{s}. \tag{10}$$

[19] Such a non-dimensional analysis is not commonly performed in engineering applications of soil liquefaction. Instead, the first time dependent term in equation (10) is normally neglected due to the small value of fluid compressibility, β [e.g., *Garga and Zhang*, 1997; *Kozlov et al.*, 1998]. However, a simple thought experiment can demonstrate its importance: Consider a sealed system, with initially uniform pressure, that is loaded uniformly. The diffusive term in equation (10) is thus zero. If the time dependent term would have been neglected, then equation (10) would reduce to $\nabla \cdot \mathbf{u}_\mathbf{s} = 0$; that is, no deformation could take place due to fluid resistivity to both flow and compression.

[20] The form of the forcing term in equation (10) is intuitive in the framework of poroplasticity: when a fluid-filled granular system compacts and pore volume collapses, $\nabla \cdot \mathbf{u}_\mathbf{s} < 0$, and the PP is expected to rise. When the system dilates, $\nabla \cdot \mathbf{u}_\mathbf{s} > 0$, and the PP will drop. Furthermore, the form of the forcing as dependent on the local grain velocities suits a straightforward plugging of equation (10) in a model of coupled grains and fluid implemented with discrete elements method of the form of *Okada and Ochiai* [2007].

[21] It is sometimes convenient to express the forcing term as a function of the porosity evolution rather than the divergence of the solid grains velocity. From grain mass conservation, equation (1):

$$(1 - \Phi)\nabla \cdot \mathbf{u}_\mathbf{s} = \frac{\partial \Phi}{\partial t} + \mathbf{u}_\mathbf{s} \cdot \nabla\Phi. \tag{11}$$

When the initial porosity and the rate of porosity evolution are assumed uniform [e.g., *Walder and Nur*, 1984; *Snieder and van der Beukel*, 2004] $\mathbf{u}_\mathbf{s} \cdot \nabla\Phi = 0$ and $(1 - \Phi)\nabla \cdot \mathbf{u}_\mathbf{s} = \partial\Phi/\partial t$. Under these restrictions equation (10) may be rewritten as

$$\frac{\partial P}{\partial t} = \frac{1}{\beta\Phi\mu}\nabla \cdot [k\nabla P] - \frac{1}{\beta\Phi(1-\Phi)}\frac{\partial \Phi}{\partial t}. \tag{12}$$

[22] Formulations similar to our equations (10) or (12) arise in other works dealing with the response of PP to specific situations of granular and porous matrix deformation [*Walder and Nur*, 1984; *Wang*, 2000; *Samuelson et al.*, 2009], some of them specifically in the context of soil liquefaction [*Bachrach et al.*, 2001; *Snieder and van der Beukel*, 2004]. Appendix A demonstrates how these models may be directly compared to our formulation.

3. Poroelastic Pore Fluid Pressurization and Liquefaction

[23] As the formulation presented here is not restricted to a specific rheology (poroelastic or poroplastic), the possibility of generating high PP with a poroelastic mechanism is next examined. For that, we revisit a formulation developed by *Wang* [2000] describing one-dimensional spatiotemporal evolution of PP in response to temporal stressing of a fluid-filled porous material [*Wang*, 2000, equations 3.65 and 6.14]:

$$\frac{\partial P}{\partial t} = \frac{k}{\mu S}\frac{\partial^2 P}{\partial z^2} - \gamma\frac{\partial \sigma_{zz}}{\partial t}, \tag{13}$$

where S is the uniaxial specific storage in Pa^{-1}, γ is the dimensionless loading efficiency, and σ_{zz} is the external elastic loading stress in Pa. $k/\mu S$ is a space and time constant diffusion coefficient, and $\gamma\partial\sigma_{zz}/\partial t$ is the forcing term. Appendix A shows that equation (13) is equivalent to our equation (10) when we assume that $\nabla \cdot \mathbf{u}_\mathbf{s}$ occurs by elastic deformation only, and also demonstrates the equivalency between equation (13) and the formulation of *Bachrach et al.* [2001] under the assumption of negligible inertia. Thus, any conclusion drawn from the analysis in this section applies also to the formulation discussed in section 2. Equation (13) is most suitable for investigating the poroelastic liquefaction hypothesis because its forcing term is given in the form of time dependent elastic stress loading, such as a seismic pressure wave. Indeed, *Wang* [2000] studied the response of equation (13) to loading by stress wave.

[24] *Wang* [2000] solved analytically equation (13) in a half-space, with a forcing, σ_{zz}, of the form

$$\sigma_{zz}(0, t) = -\sigma_0 \exp(i\omega t) \tag{14}$$

where σ_0 is the amplitude of the pressure wave and ω is the loading frequency. The top of the domain is taken as drained and hence $P(z = 0, t) = 0$. Figure 1 shows the resultant PP magnitude, $|P|$, scaled by $\gamma\sigma_0$, as a function of the scaled depth, z/l_k. Note that the maximum value of the loading efficiency, γ, is 1. This maximum value corresponds to the case of low shear modulus for which *Bachrach et al.* [2001] find the maximum value of PP. Figure 1 and *Wang*'s [2000] analysis indicate that when the loading efficiency is maximal, the maximum value of PP obtained in a fluid-filled poroelastic medium when a seismic P-wave passes is

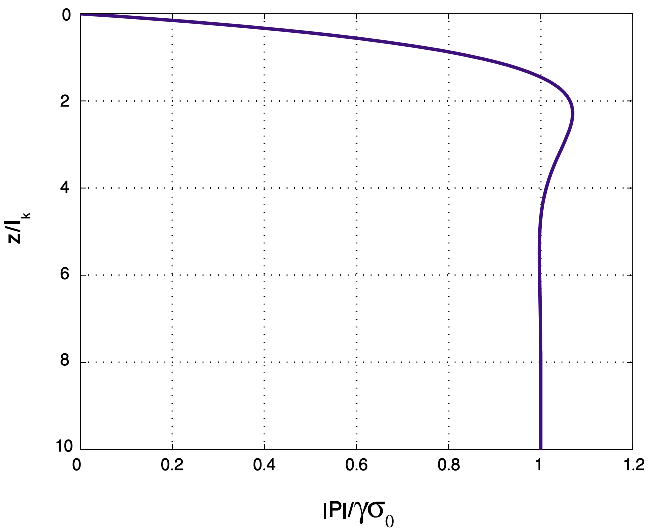

Figure 1. Half-space solution of system of equations (13) and (14), describing the spatial evolution of PP in a poroelastic material under periodic stress loading and drained top. Maximum magnitude of PP, $|P|$, is plotted as a function of normalized depth. $|P|$ is bounded by $1.07\gamma\sigma_0$, where $\gamma \leq 1$ is the loading efficiency and σ_0 is the amplitude of the pressure wave forcing. The relation between $|P|$ and σ_0 indicates that a poroelastic mechanism for liquefaction (see text) is limited to the very top of the soil column. Adopted from *Wang* [2000, Figure 6.11], with permission from Princeton University Press.

bounded by $1.07\sigma_0$. That is, the PP cannot exceed the stress wave amplitude by more than 7%.

[25] For liquefaction to occur, PP must reach lithostatic values [*Sawicki and Mierczynski*, 2006]. If we consider a saturated soil column with a thickness of 1 m, the lithostatic pressure at its base is about 25 kPa, while the hydrostatic pressure is 10 kPa. Therefore there is a need to generate excess of $P = 15$ kPa for liquefaction to occur at a depth of 1m. For the poroelastic liquefaction to occur, the forcing magnitude then must be 14 kPa, two orders of magnitude larger than typical amplitudes of seismic pressure waves [*Bachrach et al.*, 2001]. If we consider a fault gouge at depth of 15 km, the excess PP needed for complete liquefaction is about 0.2 GPa. The excess PP generated by the poroelastic mechanism with a forcing wave of 100 Pa is a negligible fraction of the needed value. These simple examples indicate that the poroelastic path to liquefaction is applicable only for the top few centimeters of the grains-fluid column, or when PP is initially very close to lithostatic values. Therefore, in section 4 we turn back to study the classical poroplastic volume collapse mechanism using a simple prescribed plastic matrix deformation model.

4. Infinite Stiffness Approximation

[26] The formulation presented so far is applicable to a general fully coupled system. But in order to actually solve the fully coupled grain-fluid deformation, another equation for the evolution of solid grain momentum should be prescribed. In this equation, PP gradients exert forces on the granular matrix [e.g., *McNamara et al.*, 2000], sometimes referred to as seepage forces [*Mourgues and Cobbold*, 2003; *Rozhko et al.*, 2007]. However, here we first solve a simpler scenario, the infinitely stiff system, which means that the matrix deformation is externally prescribed and the PP only responds to this deformation. The reason we do not immediately solve also the other direction (that of the deformation of the solid matrix in response to PP gradients), is twofold: First, because currently there is no first principles based theory that predicts the general (elastic and plastic) granular matrix deformation induced by a PP field that varies spatially and temporally. Moreover, currently there is not even a first principles based theory that predicts the deformational response of a dry granular matrix to general loading [*Forterre and Pouliquen*, 2008]. To overcome this limitation, previous works that solve for the fully coupled system with a continuum approach use phenomenological relations to describe the porosity evolution in response to external loading and PP variations [e.g., *Snieder and van der Beukel*, 2004; *Samuelson et al.*, 2009] and in rocks [*Hamiel et al.*, 2005]. Consequently, they are restricted to a specific type of deformation, material properties, and boundary conditions. A second possible method to obtain a general solution for the effect of PP variation on the matrix deformation, and thus a fully coupled solution for the general deformation of grains-fluid system, is via a granular dynamics algorithm [e.g., *McNamara et al.*, 2000; *El Shamy and Zeghal*, 2007; *Okada and Ochiai*, 2007]. The second reason to use the infinitely stiff approximation is that it may be solved analytically, and although it is a simple end-member, its solution already provides a wealth of behaviors that should be considered as the basis for understanding the fully coupled system.

[27] The infinite stiffness approximation assumes that local pore volume collapse and expansion arc externally prescribed and are characterized by $\nabla \cdot \mathbf{u_s} < 0$ in equation (10) or $\dot{\Phi} < 0$ in equation (12). These will lead to pore fluid pressurization and depressurization and to the generation of PP gradients. In a fully coupled formulation the pressure gradients will oppose the pore collapse deformation by exerting a force that will act to push the pore walls aside in the case of compaction and push the pore walls inward in the case of expansion. Thus, the PP gradients somewhat relax the source of pressurization. For that reason the maximum PP within a fully coupled system is limited by the order of magnitude of the confining stress that drives pore volume change. In that sense the magnitude of the PP achieved under the infinite stiffness approximation serves as an upper bound with respect to a fully coupled system.

4.1. Application to Shearing of Fluid-Filled Uniform Granular System

[28] Here we explore the physical behavior of equation (10) under poroplastic conditions. This exploration is a first step in mapping the conditions that will cause liquefaction by irreversible pore volume collapse during shear of a granular system. For that, a simple system of hexagonally packed uniform grains immersed in fluid is studied (Figure 2). Packed uniform grains were previously considered theoretically [e.g., *Rowe*, 1962; *Iverson*, 1993], experimentally [e.g., *Iverson and Lahusen*, 1989; *Frye and Marone*, 2002], and

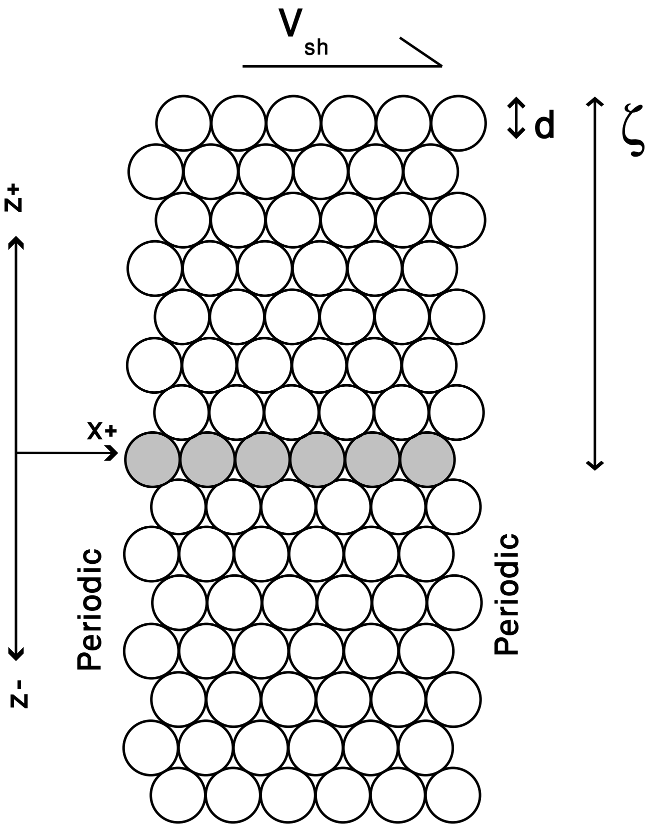

Figure 2. Model geometry for section 4.1. A hexagonal packing of fluid-filled granular material is being subjected to a constant shear velocity, V_{sh}. Shear displacement is accommodated along a single row marked by the grey grains. The boundaries along the x direction are periodic, and therefore, $\partial \mathbf{u_{sx}}/\partial x = 0$; d is a grain diameter, ζ is the distance to the boundaries, and 2ζ is system thickness.

numerically [*Makedonska et al.*, 2010]. In the system we consider here, the top boundary is sheared at a constant shear velocity, V_{sh}, in the $+x$ direction. The system is assumed to respond by localized shear deformation along one row of grains (Figure 3a, sliding row in grey). Along the x direction the system is assumed periodic and hence the divergence of the velocity in equation (10) is reduced to $\nabla \cdot \mathbf{u_s} = \partial \mathbf{u_{sz}}/\partial z$, where $\mathbf{u_{sz}}$ is the z component of the solid grains velocity, and the problem becomes one dimensional. The porosity, Φ, and the granular velocity perpendicular to the shear direction, $\mathbf{u_{sz}}$, of the sliding row of grains are functions of time, t (and thus of displacement, x):

$$\begin{aligned} \mathbf{u_{sz}} &= V_{sh}\frac{[\cos(\pi/3) - V_{sh}t'/d]}{A} \\ \Phi &= 1 - \frac{\pi}{4A} \\ A &= \sqrt{1 - [\cos(\pi/3) - V_{sh}t'/d]^2}. \end{aligned} \quad (15)$$

where $t' = (t + x'/V_{sh}) \bmod (d/V_{sh})$, and $0 \le x' \le d$ depends on the initial conditions as explained below. The simulated domain of thickness 2ζ is assumed to be buried at depth h (where $2\zeta \le h$), so that excess PP of $P = \sigma_d$ is interpreted as resulting in zero effective stress and the onset of liquefaction. The shearing row is located at distance ζ from the boundaries of the system.

[29] In the simulations, we aim to study the influence of the drainage boundary conditions on the evolution of PP. For that, there is a need to define an additional Deborah number, $\mathrm{De}_\zeta = t_\zeta/t_0$, termed the system Deborah number. De_ζ expresses the ratio between $t_\zeta = \zeta^2/D$, the timescale of PP diffusion over the system half thickness, and t_0, the timescale of deformation. When $\mathrm{De}_\zeta \ll 1$, PP can easily diffuse from the shearing row to the boundaries in the timescale of deformation, and as a result the PP along the shearing row feels the drainage conditions on the boundaries. When $\mathrm{De}_\zeta \gg 1$, the PP diffusion front originating along the shearing row does not reach the boundaries in the timescale of deformation. Therefore, the PP along the shearing row is indifferent to the drainage conditions along the boundaries.

[30] Three scenarios are tested. In the first two cases ζ is relatively small and therefore $\mathrm{De}_\zeta \ll 1$: In a *drained* system, a constant PP of $P = 0$ is assumed at the top of the system, as if an open fracture drains the buried domain at its top. In an *undrained* system, zero fluid flux across the top boundary is assumed, simulating an impermeable layer that lies on top of the domain. In these two cases the bottom boundary is assumed undrained. In the third case, ζ is relatively large resulting in $\mathrm{De}_\zeta \gg 1$. In this case the prescribed boundary conditions have no effect of the evolution of PP within the shearing row. The third case is termed *boundary-independent*. Table 1 summarizes the parameters used in the simulations.

[31] Two types of initial conditions are studied: In the first, denoted here as *dense packing*, the sliding row is initially in a hexagonal configuration (Figure 3a, sliding row in grey), and $x' = 0$. In this case, sliding is accompanied by initial dilation until a cubic configuration is reached along the sliding row. Then, the system compacts until hexagonal packing is reached again. A full period is the duration between two consecutive hexagonal configurations. In the second initial condition, termed here *loose packing*, the sliding row is initially placed in a cubic configuration with respect to the row below it (Figure 4a), and $x' = 0.5d$. In this case, the system first compacts to a full hexagonal configuration and then dilation along the sliding row brings it back to a cubic configuration. Here a full period is the duration between two consecutive cubic configurations.

[32] The set of equations (10) and (15) together with Carman-Kozeny equation (Table 1) for the relation between porosity and permeability are solved numerically using a 1D Crank-Nicholson scheme.

4.1.1. Dense Initial Packing

[33] First, the case of dense initial grain packing is studied; that is, all rows are initially hexagonally packed.

4.1.1.1. Drained

[34] Simulation results show that when the system is drained, the excess PP, initially taken as zero, becomes negative when the system starts to dilate as it shears (Figure 3b, red curve). As deformation continues, fluid influx from the top boundary, driven by the pressure gradient that forms between the top of the domain and the location of deformation, decreases the magnitude of this negative value. When a cubic configuration is reached; that is, the system has slid to its maximal porosity, PP is zero again. During compac-

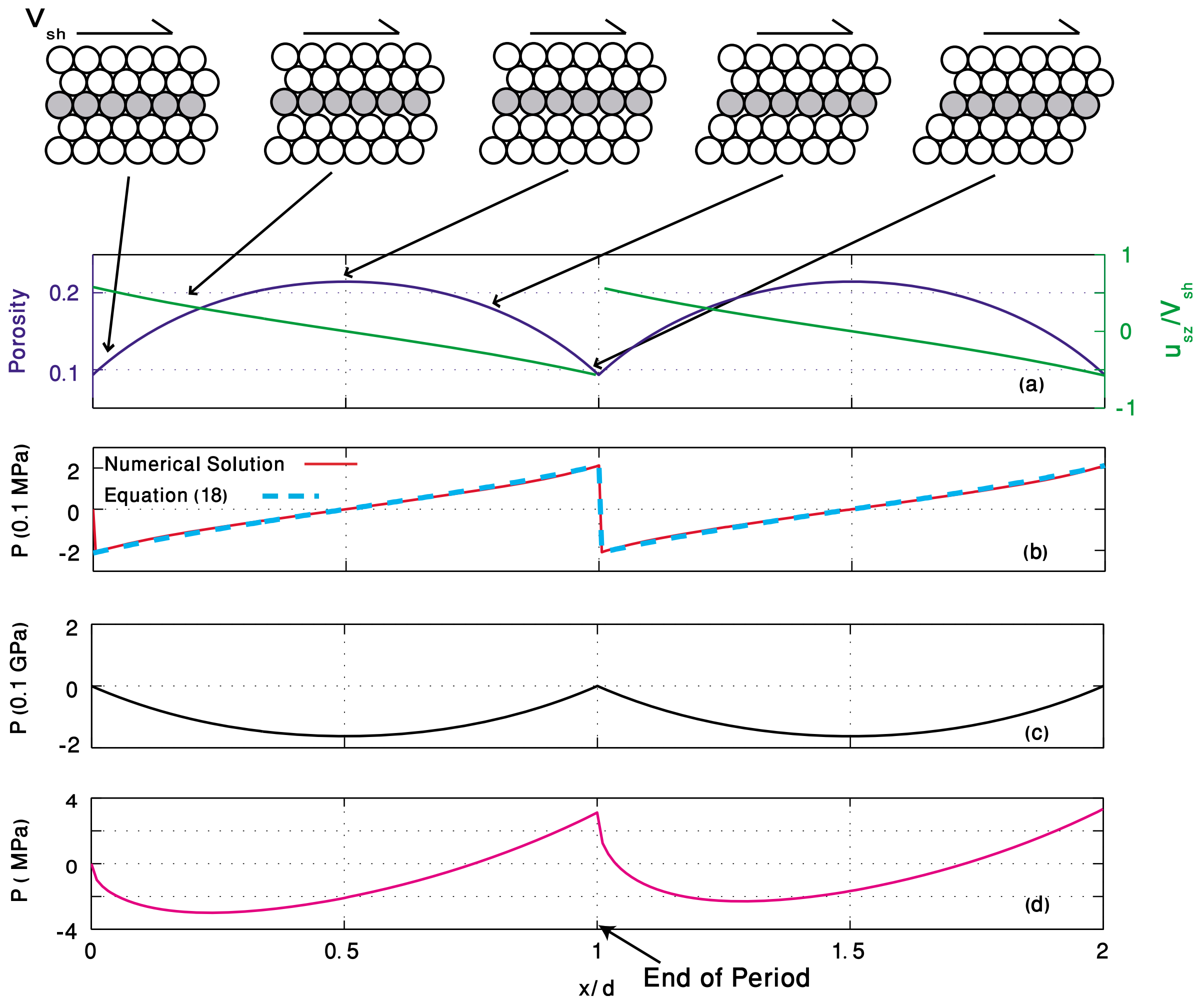

Figure 3. Simulation results of shearing of initially densely packed fluid-filled granular material at a constant shear velocity, V_{sh}, with parameters from Table 1. Shear is accommodated in a localized manner along a single sliding row, depicted by grey filled discs. The system first dilates to a cubic packing and then compacts back to a hexagonal packing. Dilation and compaction induce time and space dependent porosity, permeability and granular velocity. (a) Evolution of porosity (blue) and $\mathbf{u_{sz}}/V_{sh}$ (green) along the sliding row as a function of the horizontal displacement, x, scaled by grain diameter, d. (b) PP evolution along the sliding row, when the top boundary is drained. Maximum PP of 0.21 MPa is attained at the end of the period and corresponds to zero effective stress at depth of around 14 m. Red curve is the simulation results and turquoise dashed curve is an analytical prediction following equation (18). (c) PP evolution along the sliding row when the top boundary is undrained, showing that PP becomes increasingly negative when the system dilates and then returns to zero upon compaction. (d) PP evolution along the sliding row when $\mathrm{De}_\zeta \gg 1$ (boundary-independent). A combination of the two previous regimes is observed with maximum positive PP of 3.3 MPa at the end of the second period.

tion, PP rises until it gets to its maximal value when the system is back in hexagonal packing.

4.1.1.2. Undrained

[35] For an undrained system, the excess PP becomes increasingly negative during dilation and returns to zero when the system compacts again (Figure 3c). This occurs because during dilation the pore volume expands and $\nabla \cdot \mathbf{u_s} > 0$. With no fluid supply from the boundaries, the average PP must decrease. During compaction $\nabla \cdot \mathbf{u_s} < 0$, and PP increases back to the initial zero value. Since PP is negative throughout this simulation, overpressure is not generated. In fact the opposite is true as fluid becomes underpressured.

4.1.1.3. Boundary Independent

[36] The third scenario, of a large system with $\mathrm{De}_\zeta \gg 1$, shows PP evolution that is a combination of the drained and the undrained regimes (Figure 3d). Initially, the PP evolves similarly to an undrained system. However, the effect of fluid flow oriented toward the shearing row compensates for the negative value, so that minimum PP is attained before cubic packing, and PP increases to positive value at the end of the period similar to a drained system.

4.1.2. Loose Initial Packing

[37] Next, initially loose (cubic) packing systems are sheared. During the first half of the period, for all boundary

Table 1. Model Parameters for Section 4.1

Symbol		Value
β	Water compressibility	4.5×10^{-10} Pa^{-1}
μ	Water viscosity	10^{-3} Pa s
d	Grain diameter	5×10^{-4} m
2ζ	Layer thickness for drained and undrained	0.01 m
	Layer thickness for boundary-independent	4 m
V_{sh}	Shearing velocity	0.1 m/s
Φ_{min}	Porosity of hexagonal packing	0.093
k	Permeability (Carman-Kozeny)	$d^2\Phi^3/180(1-\Phi)^2$ m^2
D	Diffusion coefficient	$D_c = k_{min}/\beta\mu\Phi_{min} = 32.45$ m^2/s
l_k	PP diffusion length scale	$\sqrt{D_c t_0} = 0.4$ m[a]
De_d	Grain Deborah number	$t_d/t_0 = 1.54 \times 10^{-6}$[a]
De_ζ	System Deborah number for drained and undrained	$t_\zeta/t_0 = 1.54 \times 10^{-4}$[a]
	System Deborah number for boundary-independent	$t_\zeta/t_0 = 24.7$[a]

[a]Calculated with D_c.

conditions, the system compacts and PP increases. Maximum values are attained in the middle of the period when the systems are in hexagonal configuration (Figure 4). We next review the systems behavior during the second half of the period, when they dilate back to cubic packing.

4.1.2.1. Drained

[38] When a drained system starts dilating in the second half of the period, PP first drops to a negative value and then rises back to zero due to fluid influx from the boundary (Figure 4b).

4.1.2.2. Undrained

[39] For the undrained system, in the second half of the period, when dilation starts, PP returns to zero from its maximal value (Figure 4c, black curve). Here, excess PP is positive throughout the simulation.

4.1.2.3. Boundary Independent

[40] Simulations of a large system with $\mathrm{De}_\zeta \gg 1$ shows that in the second half of the period, upon dilation, PP decreases to a negative value, but the period ends with an increasing trend (Figure 4d). The overall evolution of PP is a combination of the drained and the undrained regimes, with minimum PP occurring not immediately upon initiation of dilation, like in a drained system and not at the end of the period like in an undrained system, but somewhere in between.

4.1.3. Results

[41] We have performed six simulations with two different initial conditions (loose and compacted), two system sizes, and two boundary conditions (drained and undrained). Several insights arise. When an undrained layer with $\mathrm{De}_\zeta \ll 1$ is sheared, then only negative PP is generated when the packing of grains is initially dense. But when the packing is initially loose pore fluid is pressurized and reaches 0.16 GPa, a value corresponding to σ_d at depth of 10 km, or alternatively, a value that reduces the effective stress along gouge material buried at depth of 15 km by more than 70%. It should be remembered that under the infinite stiffness approximation used here, the value of PP is not limited, and it is simply a function of the matrix deformation. In this framework, soil liquefaction at shallower depth is expected to take place early in the period. For example, reaching $P = \sigma_d$ at a depth of 10 m requires the generation of excess PP of 0.15 MPa, which occurs after 1% of a period ($t = 0.01d/V_{sh}$). When the infinite stiffness assumption is relaxed, the value of maximum PP is expected to be bounded by the order of magnitude of the confining stress, because PP gradients between the system interior and exterior will act to oppose further pore volume compaction and limit pressurization to the exact value that dynamically balances the forces acting to compact pore volume.

[42] In contrast, when some drainage exists pore fluid pressurization (to positive values) occurs even when the granular matrix is initially dense (or over-consolidated, as is called in soil mechanics), since shear involves first dilation and then compaction. For the completely drained system, with $\mathrm{De}_\zeta \ll 1$, excess PP becomes positive simultaneously with the initiation of compaction, and reaches a maximum of 0.21 MPa (for Table 1 parameters) corresponding to the effective normal stress at depth of 14 m. When $\mathrm{De}_\zeta \gg 1$, the PP becomes positive after some delay from the onset of compaction, and reaches a maximum of 3.3 MPa (for dense packing), corresponding to the effective stress at depth of 220 m. In these cases pore fluid pressurization occurs even for initially dense systems as long as there is a compaction phase that follows the dilation.

5. Physics of the PP Equation

[43] In light of our simulation results, we turn to analyze the behavior of the PP equation (10) under different drainage regimes.

5.1. Drained Boundary Conditions

[44] When the boundaries are well drained, fluid may flow freely into or out of the system, and PP gradients should evolve between the layer interior and the boundaries. (Here the boundary is maintained at a constant PP). Moreover, since $\mathrm{De}_d \ll 1$, the non-dimensional equation (9) reveals that the diffusion term is large, and the first time dependent term may be neglected relative to it. The PP equation (10) may then be approximated as

$$\nabla \cdot [k(\mathbf{x},t)\nabla P(\mathbf{x},t)] = \mu \nabla \cdot \mathbf{u_s}(\mathbf{x},t). \tag{16}$$

This form of PP response under drained conditions agrees with a Biot-based formulation by *Iverson* [1993]. In the 1D case, equation (16) may be expressed as

$$\frac{\partial P(z,t)}{\partial z} = \frac{\mu}{k(z,t)} \mathbf{u_{sz}}(z,t) + C(t), \tag{17}$$

where $C(t)$ is an integration factor. Note that equations (16) and (17) are independent of the fluid compressibility, β.

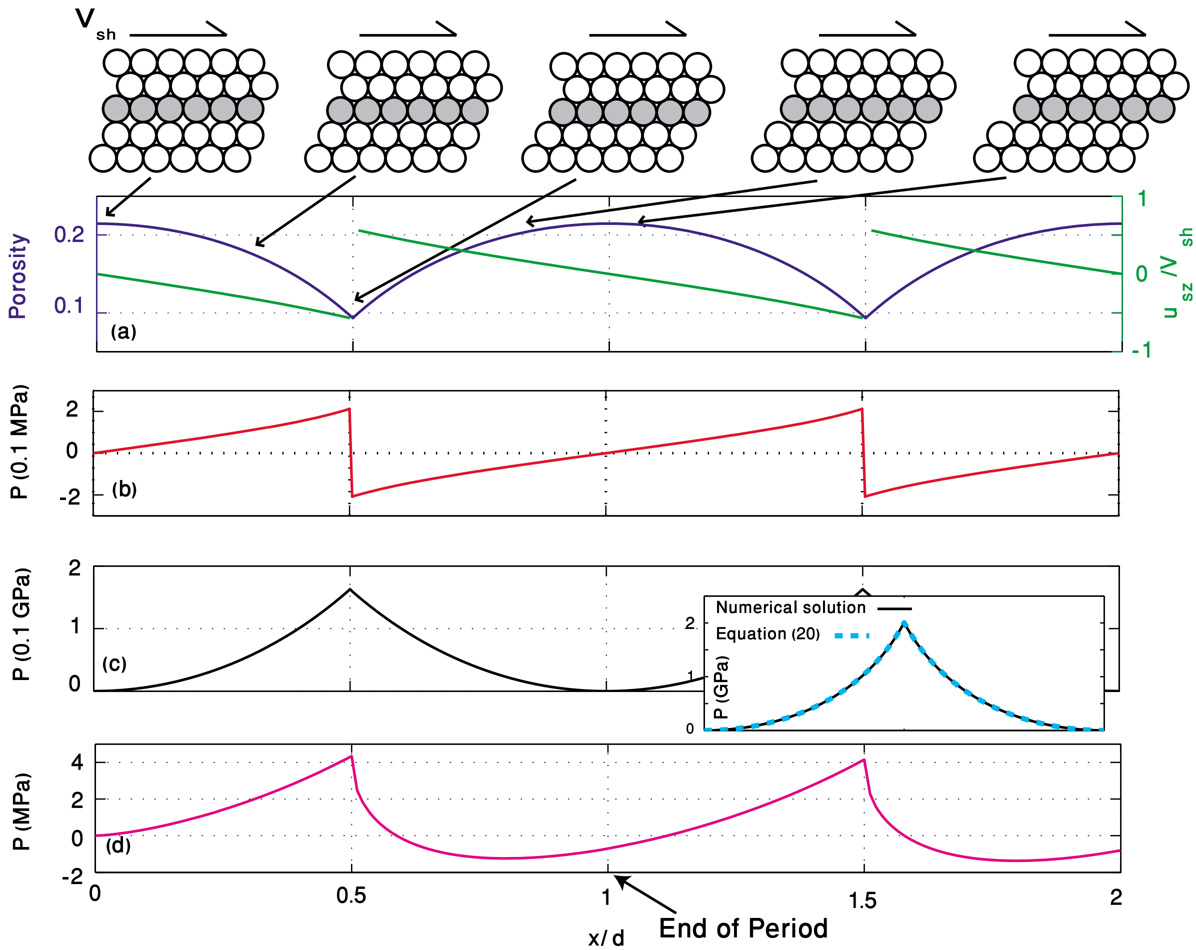

Figure 4. Simulation results of shearing of loosely packed fluid-filled granular material at a constant shear velocity, V_{sh}, with Table 1 parameters. Shear is accommodated in a localized manner along a single sliding row, depicted by grey filled discs. The system first compacts from a cubic configuration to a hexagonal configuration and then dilates back to cubic order. (a) Evolution of porosity (blue) and $\mathbf{u}_{sz}$ (green) along the sliding row as a function of the horizontal displacement, x, scaled by grain diameter, d. (b) PP along the sliding row that accommodates compaction and dilation with drained top evolves similarly to shearing of dense packing (Figure 3b), but with a shift of half period. (c) PP evolution along the sliding row with undrained top showing pore fluid pressurization with maximum of 0.16 GPa, corresponding to zero effective stress at a depth greater than 10 km, in the middle of the period. The inset shows simulation results (black curve) for PP evolution along the sliding row when the permeability is zero throughout the system to oppress PP diffusion, and analytical prediction (turquoise dashed curve) following equation (20) that assumes no diffusion. (d) PP evolution along the sliding row when $\mathrm{De}_\zeta \gg 1$, showing a combination of the two previous regimes.

This corresponds to a regime where the fluid may be considered as incompressible.

[45] The evolution of PP in our drained simulations (with $\mathrm{De}_\zeta \ll 1$) should follow equation (17). The pressure gradient may be estimated as $\partial P/\partial z = -P/\zeta$, and the PP along the sliding row is then approximated as

$$P = -\frac{\mu\zeta}{k}\mathbf{u}_{sz}. \qquad (18)$$

The PP evolution according to equation (18) is compared to the numerical solution (Figure 3b, dashed turquoise curve). The parameters are taken from Table 1, and the permeability $k = k_{\min}$ is taken as the permeability resulting from the porosity of the hexagonal packing that is constantly preserved in the simulations, on top of the sliding row. Excluding the very onset of the motion that is governed by the time dependent term of equation (10), the analytical approximation, equation (18), and the numerical solution match.

[46] Equation (18) reveals that in the drained case the value of the PP along the shearing row depends linearly on the fluid viscosity, μ, the distance to drainage, ζ, and on the inverse of the permeability k^{-1}. For Carman-Kozeny law (Table 1), $k \propto d^2$, and thus $P \propto d^{-2}$. All these dependencies, together with fluid compressibility independency, were verified in a parametric sensitivity study.

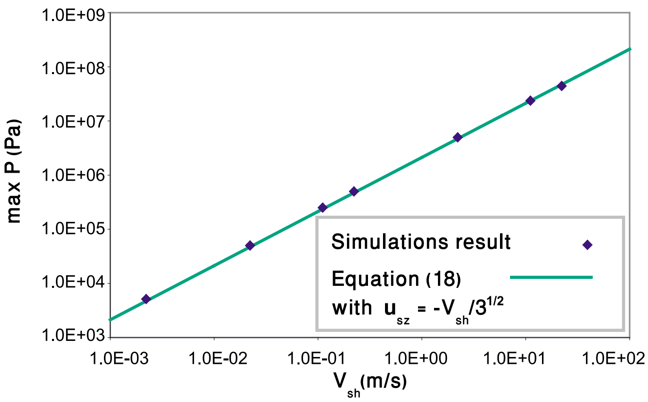

Figure 5. Simulation results with drained conditions (diamonds) for the relation between shear velocity V_{sh} and the maximum value of PP attained at the end of a shearing period. Analytical curve is based on equation (18) assuming $\mathbf{u_{sz}} = -V_{sh}/\sqrt{3}$ (see text), Table 1 parameters and permeability, $k_{\min}$, induced by hexagonal packing porosity (solid line). The slope of the linear relation between P and V_{sh} is a function of fluid viscosity, distance to drainage and inverse of permeability.

[47] Using equation (15), another dependency may be established: The maximum value for the PP, $P_{\max}$, is attained at the end of the period, when $t' = d/V_{sh}$. Assigning this value of t' in equation (15), it is found that $\mathbf{u_{sz}}$ $(t' = d/V_{sh}) = -V_{sh}/\sqrt{3}$. Using this $\mathbf{u_{sz}}$ in equation (18) predicts a linear relation between $P_{\max}$ and shear velocity, V_{sh}, as depicted in Figure 5.

5.2. Undrained Boundary Conditions

[48] When the boundaries are undrained, fluid cannot flow into or out of the granular layer, and fluid mass is conserved. Under such conditions, no pressure gradients arise across the boundaries. If the quantity of interest is the average value of PP within the layer, then the second diffusion term in equation (10) becomes zero (due to both averaging and zero pressure gradients on the boundaries). The average PP is then approximated as

$$P(t) = -\frac{1}{\beta}\int_0^t \frac{\nabla\cdot\mathbf{u_s}(t')}{\Phi(t')}\,dt', \tag{19}$$

where P depends on the fluid compressibility, β.

[49] The PP evolution in our undrained simulations is expected to follow equation (19). Evaluating $\nabla \cdot \mathbf{u}$ as $\mathbf{u_{sz}}/d$ and assigning the expressions for $\mathbf{u_{sz}}$ and Φ from equation (15):

$$\begin{aligned} P &= -\frac{1}{\beta}\left\{\frac{\pi}{4}\ln\left[\frac{\pi-4A}{\pi-4}\right]+A-1\right\} \\ A &= \sqrt{1-\left[\cos(\pi/3)-V_{sh}t'/d\right]^2}. \end{aligned} \tag{20}$$

Comparison between equation (20) and the numerical solution assuming the PP does not diffuse away from the shearing row shows good fit (Figure 4c, inset). Equation (20) indicates that in the absence of PP diffusion, P is independent of the shearing velocity, V_{sh}, but is a function of the inverse fluid compressibility, β^{-1}. Small β will increase the PP.

5.3. Boundary Independent

[50] When the system Deborah number is large, $\mathrm{De}_\zeta \gg 1$, then the PP within the layer is indifferent to the type of imposed drainage boundary conditions. Since the boundaries are remote from the system interior, relatively mild pressure gradients are expected to arise, and none of the terms in equation (10) may be neglected. Here, the evolution of PP results from the competition between pressurization and depressurization induced by the time dependent term of equation (10) and fluid flow originating from the diffusion term of equation (10).

[51] Our large-system simulations should follow this case. It is possible to derive an analytic solution for the full equation (10), under the restrictions of equation (15), and assuming that the diffusion coefficient is constant with time, i.e., $D = D_c = k_{\min}/\beta\mu\Phi_{\min}$. Appendix B shows this derivation, and Figure 6 presents the comparison between the analytic solution and a boundary-independent simulation conducted with an imposed constant diffusion coefficient D_c along its shearing row. The analytic prediction reveals that the characteristic pressure scale for the evolving PP may be expressed as $d/\beta\sqrt{\pi D_c t_0}$. For the parameters of Table 1 this scale is ~1.5 MPa, which is the order of magnitude of PP that is found in Figure 6.

6. Discussion

[52] This section discusses the physics of PP evolution in response to granular matrix deformation as concluded from our theoretical analysis and our simulations. We also discuss the implications of this physics to numerical, experimental and natural systems. First, we consider the mechanisms that control PP evolution based on the formulation presented in section 2 and the analysis presented in section 5. The basic equations for the PP evolution, equations (10) and (12), predict two different physical mechanisms that compete in controlling the evolution of PP, but their relative contribution is determined by the parameters and boundary conditions of the system. The two mechanisms are PI, porosity-change-induced pressurization and depressurization, and FI, flow-induced pressurization and depressurization.

6.1. Pressurization Mechanisms

6.1.1. Mechanism PI

[53] Mechanism PI operates under undrained conditions. Here, pore fluid that cannot escape and is trapped within a shrinking pore volume is pressurized (Figure 7a), while pore fluid that is trapped in an expanding pore volume is depressurized. The evolution of the average PP will follow equation (19), and the magnitude of pressurization and depressurization is controlled by the fluid compressibility, and by the overall pore volume change, $\Delta\Phi$, that is expressed by $\int_0^t \nabla \cdot \mathbf{u_s}(\mathbf{x}, t')dt'$ in equation (19). In that sense this mechanism holds memory of previous states of porosity.

6.1.2. Mechanism FI

[54] Mechanism FI operates under well-drained conditions, and is less intuitive. Because of mass conservation,

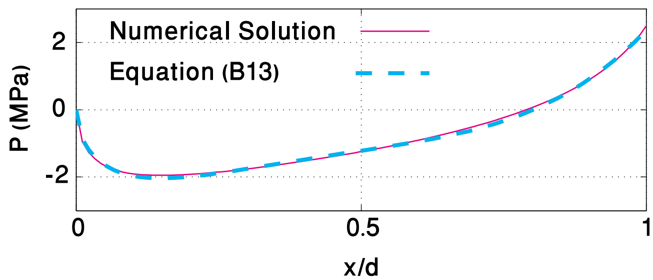

Figure 6. PP along the shearing row for large system with $De_\zeta \gg 1$, when the diffusion coefficient is assumed constant $D_c = k_{min}/\beta\mu\Phi_{min}$. Purple curve is simulation results, and the dashed turquoise curve is the analytic prediction following equation (B13).

convergence (or divergence) of grains causes the pore fluid that resides between the grains, to flow out of (or into) this region (Figure 7b). Because of fluid momentum conservation (here Darcy law), pressure gradients must arise between the location of converging (or diverging) grains and the surrounding, to generate these flows. Here, PP evolves from the arising pressure gradients, and is governed by equations (16) and (17). The magnitude of the generated pressure gradient depends on the rate of grains convergence or divergence, as expressed by ∇ - $\mathbf{u_s}$ in equation (16). This mechanism holds no memory of previous states of porosity but pressurization depends on the instantaneous rate of pore deformation. Although it is not commonly considered as a mechanism for liquefaction, flow-induced PP evolution may lead to significant pressurization with PP that becomes high enough to fully support the normal stress [*Iverson and Lahusen*, 1989]. Moreover, because of its 'lack of memory', this mechanism may lead to generation of high PP even when an initially dense granular matrix is sheared. Indeed, upon shearing an over-compacted layer, it will first dilate (Figure 7b, left to center), and then oscillate around its critical porosity [*Aharonov and Sparks*, 2002; *Gabet and Mudd*, 2006]. In the oscillatory stage, any compaction phase, with $\nabla \cdot \mathbf{u_s} < 0$, will lead to pressurization despite the fact that the instantaneous

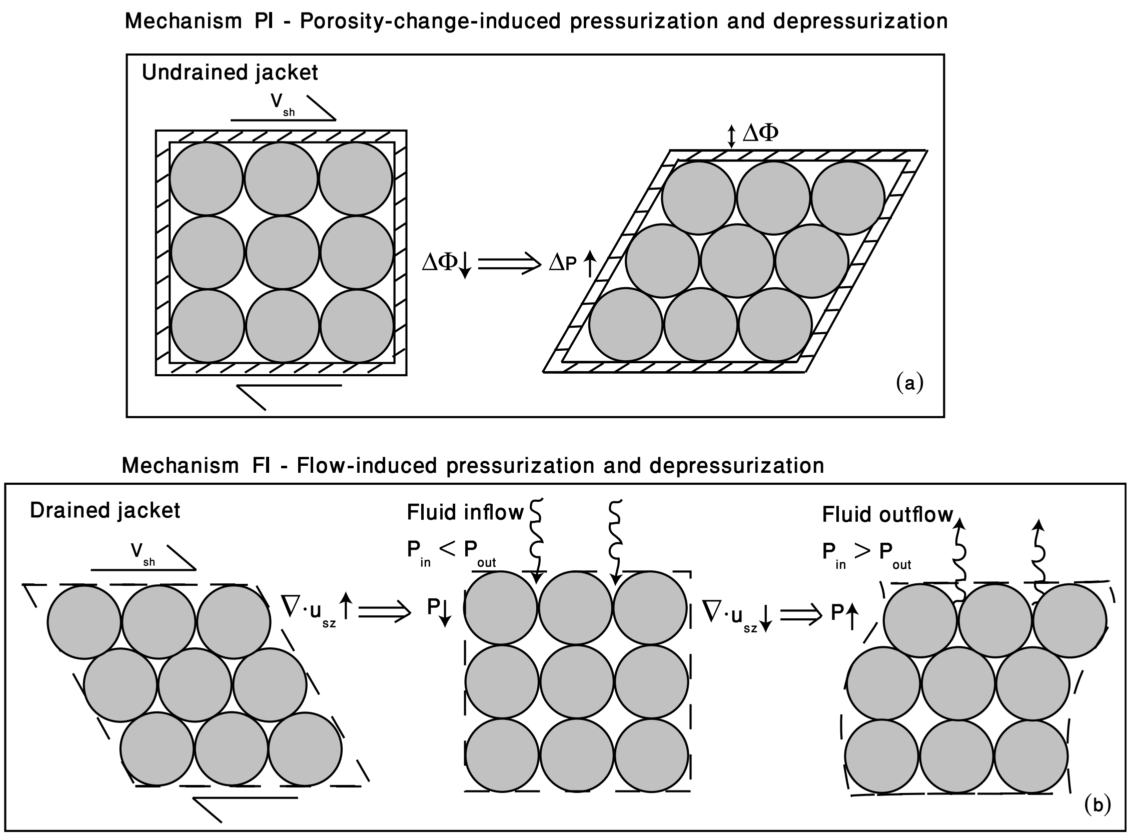

Figure 7. Two mechanisms control the evolution of PP in equation (10). (a) When fluid is trapped within a deforming pore volume (here, due to the undrained boundaries marked by double solid lines), any change of pore volume will cause the PP to evolve following mechanism PI. Compaction will lead to pressurization, and dilation will lead to depressurization. The magnitude of PP change depends on the overall change of porosity and on the inverse of fluid compressibility. (b) When fluid may flow freely in response to matrix deformation, (here, due to the well drained boundaries marked by dashed lines), PP evolution results from fluid flow following mechanism FI. Pressurization is a function of the instantaneous rate of matrix deformation. Upon dilation (left to center), fluid will flow into the system. In order to facilitate this flow, pressure gradient must arise with low pressure within the system interior. Upon compaction (center to right), fluid escapes from the system, and opposite PP gradient arises with higher PP in the system interior.

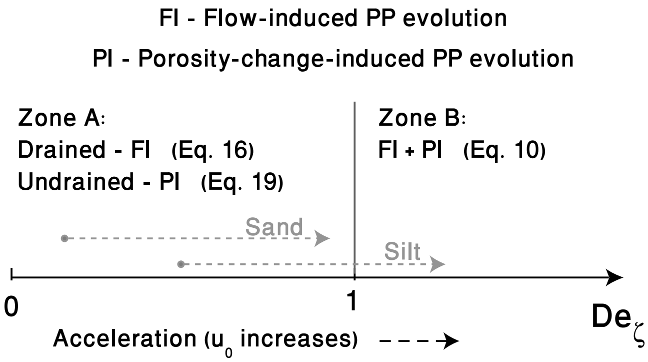

Figure 8. PP evolution mechanisms as a function of the system Deborah number, $\mathrm{De}_\zeta = t_\zeta/t_0$, where t_ζ is the timescale of PP diffusion across the whole layer and t_0 is the timescale of deformation. When $\mathrm{De}_\zeta \gg 1$ (zone B), both pressurization mechanisms operate simultaneously, like the case of boundary-independent simulations from section 4.1. When $\mathrm{De}_\zeta \ll 1$ (zone A), the boundary conditions determine the PP evolution mechanism: Under undrained conditions, mechanism PI (porosity-change-induced) will dominate, and when the boundaries are drained, mechanism FI (flow-induced) will control the evolution of PP. The dashed grey lines show how the PP evolution mechanism changes during the acceleration of deformation in the nucleation stage of earthquakes. Upon acceleration De_ζ increases. Note that the starting points of the dashed lines are not to scale. See text for the evolution of sand and silt.

porosity may be significantly larger than the initial porosity (Figure 7b, center to right).

6.1.3. Relative Importance of Pressurization Mechanisms

[55] The relative importance of the two pressurization mechanisms for a specific system depends on both its properties and on its boundary conditions. These may have different characteristics, such as a strong contrast between internal and boundary permeabilities. The internal properties determine De_ζ, the system Deborah number, that expresses the ability of PP to diffuse across the whole layer in the timescale of deformation. When $\mathrm{De}_\zeta \gg 1$ the drainage boundary conditions are not felt by the fluid within the system, and when $\mathrm{De}_\zeta \ll 1$, drainage boundary conditions are well-felt by the pore fluid. For the boundary conditions, we consider here only the two end-members of completely drained boundaries that are connected to a constant pressure reservoir, and completely undrained boundaries that prevent fluid inflow and outflow. The exact combination of De_ζ, and boundary conditions determines which of the two PP evolution mechanisms will dominate.

[56] We present here a simple two-stage scheme that determines which mechanism for PP evolution will dominant, based on De_ζ, and the boundary conditions: (1) Evaluate De_ζ. If $\mathrm{De}_\zeta \gg 1$, then both mechanisms of PP evolution, PI and FI, operate together (like the boundary-independent simulations that are tested in section 4.1), and there is no need to deal with the boundary conditions. If $\mathrm{De}_\zeta \ll 1$, there is a need to move to the next stage. (2) Evaluate the drainage boundary conditions. If they are drained then the dominant mechanism is FI, flow-induced PP evolution. If they are undrained then mechanism PI will dominate. Figure 8 summarizes this scheme by presenting the dominant mechanism of PP evolution along a De_ζ axis.

[57] To illustrate the physics of these combinations, look at the last situation of $\mathrm{De}_\zeta \ll 1$ (zone A in Figure 8), and undrained boundary conditions. In such a case, when the system undergoes compaction or dilation, pore fluid cannot flow away or into the system. However, PP can equilibrate within the system because PP can reach as far as the boundaries in the timescale of deformation. As a result, the evolution of the average PP will follow mechanism PI. Next in the discussion we apply this scheme to numerical, experimental, and natural systems.

6.2. Applications to Grains and Pore Fluid Modeling and Experiments

[58] When modeling a finite system of grains and fluid, the system parameters and boundary conditions are determined in advance. If the layer is thin, and PP diffusion can reach the boundaries in the timescale of deformation ($\mathrm{De}_\zeta \ll 1$), but it is undrained, so that pore fluid cannot flow into or out of the layer, then mechanism PI, of pressurization by change of pore volume, will dominate. Therefore, fluid compressibility must be accounted for, but diffusive effects may be neglected, and the relevant equation to solve is (19). Pore fluid pressurization is expected only if the system is compacting with respect to its initial porosity, and the magnitude of PP is proportional to the inverse of fluid compressibility and to the amount of compaction.

[59] When modeling a thin drained layer, pore fluid can flow between the system interior and exterior. In order to facilitate this flow, pressure gradients arise between the system interior and the boundaries (assumed to be maintained at some constant pressure). The dominant PP evolution mechanism will be FI, flow-induced pressurization. Accounting for fluid compressibility will only introduce a short-lived transient effect, and if this effect is not of interest it is sufficient to solve Poisson equation (16). Pore fluid pressurization is expected when the system compacts with respect to any former state and not necessarily with respect to the initial state. Generated PP is linearly proportional to the compaction rate, fluid viscosity, distance to drainage, and the inverse of permeability.

[60] When the simulated layer is thick, and PP diffusion cannot reach the boundaries in the timescale of deformation, $\mathrm{De}_\zeta \gg 1$ (boundary-independent), the drainage conditions along the boundaries do not affect the system dynamics and both pressurization mechanisms, PI and FI, operate simultaneously. In this case, both the diffusive term and the time dependent term with fluid compressibility should be accounted for, and the full fluid equation (10) should be solved (Figure 8).

[61] In light of these insights, we may now turn to analyze the two numerical models of *El Shamy and Zeghal* [2007] and *Okada and Ochiai* [2007] that are presented in section 1.1. *El Shamy and Zeghal* [2007] report the occurrence of liquefaction under drained conditions and with incompressible fluid. Such conditions are predicted to cause pressurization by mechanism FI due to pore fluid flow across the boundaries. *Okada and Ochiai* [2007] report the occur-

rence of liquefaction when compacting loose, undrained system, with compressible fluid. Such conditions lead to mechanism PI of PP evolution due to pore volume compaction. Thus, these two models simulate the two end-member mechanisms that are included in equation (10).

[62] Interpretation of experimental results should follow a similar scheme. *Samuelson et al.* [2009] performed a series of experiments, shearing fluid-filled granular material using a triaxial pressure vessel in a double direct shear configuration. We briefly revisit here their system, in order to demonstrate the applicability of our analysis to experiments. The parameters in the experimental system are $\zeta = 2 \times 10^{-3}$ m, $d = 1.27 \times 10^{-4}$ m, $u_0 = 10^{-6} - 10^{-4}$ m/s, $\Phi = 0.2$, and $k = 4.2 \times 10^{-14}$ m^2. PP was kept constant on the boundaries. This combination of parameters leads to a drained system, with $\mathrm{De}_\zeta \ll 1$ (zone A in Figure 8). As a result, mechanism FI is expected to control PP evolution. Since *Samuelson et al.*'s [2009] experiments start with a well-compacted grain layer that dilates with shear, a transient negative PP leading to hardening is expected, similar to the effect observed in the beginning of our drained simulation (Figure 3b, red curve). However, with the parameters used in their experiments, this transient effect should last $< t_\zeta = 8.6 \times 10^{-6}$ s, while the sampling rate was 10^{-4} s. Therefore, it is expected that no dilatancy hardening will be observed. Indeed, *Samuelson et al.* [2009] report that "little if any dilatant hardening" occurs in their experiments.

6.3. Application to Natural Systems

[63] The formulation for the PP response to general granular matrix deformation, developed in section 2, is depth independent, and does not assume in advance the exact system properties and its boundary conditions. Therefore, it is next applied to analyze the mechanisms that control PP evolution in different field settings with granular layers that reside at various depths and are characterized by different boundary conditions: landslides' shear zones, fault gouge layers, and soils.

6.3.1. Liquefaction of Shear Zones

[64] As a first natural system we consider shear zones that accommodate large shear strain, similar to the uniform grain system that is studied in section 4.1. Critical state theory predicts, and experiments have shown, that during shear, loose soils contract while dense soils dilate [*Casagrande*, 1936]. In the past, it was suggested that liquefaction only occurs when loose granular material compacts, which lead to the conclusion that while loosely packed shear zones may liquefy due to grain collapse leading to PP rise, dense shear zones inhibit liquefaction as they do not allow pore fluid to be pressurized [*Iverson et al.*, 2000]. Indeed, here we find that if the shear zone of a landslide (with parameters similar to those studied in section 4.1) is confined by impermeable barriers, then the PP evolution within it will follow mechanism PI. In that case, only initially loose shear zones may become pressurized enough to facilitate mobilization of a landslide into a debris flow, as discussed by *Iverson et al.* [2000].

[65] However, in many cases, natural shear zones are initially highly compacted. It was observed that during shear motion at the base of landslides and also during earthquakes, the strain is large enough for the shear zone to dilate, and reach its critical porosity [*Iverson*, 2005]. That is, an over-compacted shear zone will first dilate, and then after the first several centimeters to several meters of displacement [*Iverson*, 2005; *Garagash and Rudnicki*, 2003] its porosity will oscillate around some steady state value. Such oscillations include also compacting phases, not with respect to the initial over-compacted configuration, but with respect to the critical porosity. If the shear zone is well drained, then mechanism FI, of flow-induced pressurization, may operate, causing significant PP increase during compaction phrases, and potentially leading to liquefaction and acceleration of shear.

[66] *Gabet and Mudd* [2006] report on debris flows mobilization from initially dense soils, and claim that this observation is not well understood since "it is generally accepted that liquefaction only occurs in soils that have porosity greater than the critical-state porosity" [*Gabet and Mudd*, 2006, p. 213], i.e., by mechanism PI. Following their observation, *Gabet and Mudd* [2006] reviewed the possibility that initially dense landslides first slide a limited distance, being arrested by PP reduction due to dilation, but then PP is rebuilt and triggers a second sliding phase, this time from an initially loose configuration. The second phase leads to liquefaction and to debris flow mobilization. *Gabet and Mudd* [2006] further find a correlation between debris flow mobilization and fines/sand ratio. They suggest that soils with a small ratio are mobilized due to their high hydraulic conductivities allowing for rapid fluid inflow and PP rise that leads to the second sliding phase. Following the analysis presented here, it is suggested that initially dense well-drained soils suck in pore fluid during dilation, thus allowing PP rise by mechanism FI during any short compactive stage that follows the initial dilative phase. Mechanism FI may then be responsible for mobilization of debris flow in initially dense shear zones, formulating a continuous version of the mechanics proposed by *Gabet and Mudd* [2006].

6.3.2. Soil Liquefaction

[67] Next we address the mechanism of PP evolution during soil liquefaction. The classical view of soil liquefaction attributes the rise of PP to cyclic strain of the soil skeleton [*Sawicki and Mierczynski*, 2006]. The formulation developed in section 2 is general and does not assume specific forcing, but the analysis of shearing uniform grain system presented in section 4.1 is built upon continuous shearing. We claim here that if the cyclic strain is large enough to allow both dilation and compaction of a single grain layer (shear deformation $\geq$ grain radius), then the behavior observed for continuous shearing is analogous to cyclic shearing. Still, positive PP may evolve only if the soil experiences some compaction during its deformation, but the feasibility and magnitude of compaction depend strongly on the initial porosity and on the duration of the applied force, that are beyond the scope of this paper. Here we discuss the mechanisms by which PP may evolve given an optimal deformation of the soil skeleton.

[68] We start by analyzing the conditions and mechanisms for soil liquefaction induced by the passage of seismic shear waves. We account for pore water and use water compressibility and viscosity from Table 1. The porosity is taken to be $\Phi = 0.46$, which corresponds to medium void ratio for 3D packing of spheres [*Okada and Ochiai*, 2007]. We analyze the situations of medium sand and of silt with grain diameter of $d = 5 \times 10^{-4}$ and 5×10^{-5} m, respectively, and

corresponding permeabilities of $k = 10^{-10}$ and 10^{-14} m^2. These permeabilities are smaller than predicted by Carman-Kozeny (in particular for the silt) as it is assumed that grain size is not completely uniform. The velocity of deformation is taken to be the peak ground velocity (PGV) induced by the seismic waves. We use $u_0 = 0.1$ m/s, which is estimated to be the minimal PGV to induce liquefaction [*Kostadinov and Towhata*, 2002]. We further assume that the source of liquefaction lies at a depth of 5 m, and this is also the distance to the drained boundary, $\zeta = 5$. For these parameters, the system Deborah number is $\mathrm{De}_\zeta = 10.34$ for the sand, and $\mathrm{De}_\zeta = 1.034 \times 10^4$ for the silt, so that for both soil types $\mathrm{De}_\zeta > 1$, and PP cannot reach the boundaries in the timescale of deformation. Following the scheme presented above, both mechanisms of PP evolution, PI and FI, should be considered (zone B in Figure 8).

[69] Larger permeability and smaller PGV will lead to smaller De_ζ, and may potentially lead to PP evolution by mechanism FI. However, such conditions are also expected to decrease the magnitude of the evolving PP, because in accordance with equation (18), the PP depends linearly on the PGV, and inversely on the permeability. For example, if the permeability of the medium sand is as large as $k = 10^{-9}$ m^2, and the PGV is $u_0 = 0.01$ m/s, then $\mathrm{De}_\zeta = 0.1034$. In such a case only mechanism FI of flow-induced pressurization will be of importance. However, the maximum PP, according to equation (18) is 0.05 MPa, while the excess PP needed for liquefaction at depth of 5 m is 0.075 MPa.

[70] This simple analysis shows that the process of soil liquefaction should be evaluated via an outline similar to the boundary-independent system and that both mechanisms of PP evolution, FI and PI, are predicted to operate together. Because mechanism FI contributes to the evolution of PP, we predict that positive PP may evolve even if the soil is not strictly compactive, as long as some transient compaction occurs, similar to the case studied in Figure 4d. A possible documented example of such a scenario comes from the liquefaction event in Kobe, Japan, that followed the 1995 Great Hanshin Earthquake (M = 6.9). *Soga* [1998] reviewed the damage in the port facilities that were built on reclaimed island. It was found that soils that were vibro-compacted, and therefore are not expected to be compactive, were still liquefied.

6.3.3. Sliding Nucleation along Faults

[71] Finally in the discussion we address the evolution of PP during the stage of sliding nucleation along fault zones. Many fault zone systems are characterized by strong permeability and configuration contrasts between the gouge material and the surrounding blocks, so that the gouge layer may be considered as the granular system while the surrounding blocks impose the drainage boundary conditions. We consider here a well-compacted gouge layer of thickness $2\zeta = 0.1$. During the nucleation stage the deformation velocity accelerates, and as a result the timescale of deformation, t_0, decreases. Since the pressurization mechanism depends on t_0, it may change during the nucleation stage. The dashed grey lines in Figure 8 present this change.

[72] At the initial stage of nucleation, assuming $u_0 = 10^{-5}$ m/s, $\mathrm{De}_\zeta \ll 1$ for both the sand and the silt that were considered previously. Therefore, they are located in zone A of Figure 8, where the boundary conditions dictate the pressurization mechanism that will operate. If the confining blocks are impermeable, PP will evolve following mechanism PI according to changes of pore volume, and if the layer is initially over-compacted, negative excess PP will develop in response to any dilation, resulting in hardening. If the confining blocks are highly fractured and allow for communication with a fluid reservoir, then the PP will evolve following mechanism FI; that is, fluid inflow will compensate for the newly generated pore volume, and hardening will not occur [*Samuelson et al.*, 2009]. Upon acceleration, De_ζ increases, and when $u_0 = 0.1$ m/s, the sand remains in zone A, but the silt moves to zone B. Thus, the PP evolution within the silt gouge will become dependent on both mechanisms, FI and PI, regardless of the boundary conditions. Therefore, for small grain size, if the boundaries were previously drained and they remain so, and if dilation of the gouge continues during acceleration, some hardening is expected due to the fact that the systems moves from zone A to zone B in Figure 8, and mechanism PI starts to affect the system. This will introduce a force that acts to slow down the earthquake. If the boundaries were previously undrained and they become drained (e.g., by fracturing during sliding) then the initial negative PP will relax, but only after some delay.

7. Conclusions

[73] This paper presents a formulation describing pore fluid pressurization and flow in response to general granular matrix deformation, and is thus applicable to both elastic reversible deformation and to finite irreversible deformation. The formulation is used to examine the conditions and processes by which pore fluid pressure evolves to large enough values that may lead to liquefaction of soils and shear zones.

[74] It is found that the relative degree of drainage expressed by a Deborah number and by the boundary conditions is of great importance for the evolution of pore pressure (PP). There are two end-member mechanisms for PP evolution: FI, flow-induced pressurization and depressurization, and PI porosity-change-induced pressurization and depressurization. The first mechanism is newly offered, while the second mechanism was previously suggested to control PP evolution, though it was not completely understood. The system Deborah number, $\mathrm{De}_\zeta = t_\zeta/t_0$, expresses the ratio between the timescale of relaxation by PP diffusion across the layer and the timescale of deformation. When $\mathrm{De}_\zeta \ll 1$ then the type of boundary conditions determine which of the pressurization mechanisms operate. If the boundaries are undrained, PI dominates and pore fluid pressurization occurs only for initially loose granular matrices and is highly dependent on fluid compressibility, with faster pressurization for smaller compressibility. Under such conditions pressurization is not correlated to the rate of deformation but to the overall volumetric compaction. If the boundaries are drained, FI dominates and pore fluid pressurization occurs due to arising pressure gradients in response to pore fluid flow. In this pressurization mechanism PP may rise also in initially dense granular matrices during any later compaction stage that follows dilation. Here, PP depends on the compaction velocity, fluid viscosity, system permeability and distance to drainage, but is independent of fluid compressibility. This regime may explain liquefaction phenomena in initially dense and well drained soils and shear zones, conditions that were previously thought to be liquefaction resistant

despite field evidences showing otherwise [e.g., *Soga*, 1998; *Gabet and Mudd*, 2006]. When the system is large, or when deformation is rapid, $De_\zeta \gg 1$, and both fluid compressibility and the rate of deformation control the evolution of pore fluid pressure.

Appendix A: Comparison With Other Models

[75] Here, our equations (10) and (12) are compared to other models studying the response of PP to granular or porous matrix deformation. To facilitate comparison, the notation of this paper is adopted where possible.

A1. Elastic Formulations

[76] *Wang* [2000] presents two equivalent poroelastic formulations for the temporal and spatial evolution of PP in response to elastic forcing in a fluid-filled porous material. The first formulation describes the forcing as a temporal evolution of stress and is presented in equation (13). The second formulation describes the forcing in terms of temporal evolution of strain:

$$\frac{\partial P}{\partial t} = \frac{kM}{\mu}\frac{\partial^2 P}{\partial z^2} - \alpha M \frac{\partial \epsilon_{zz}}{\partial t}. \tag{A1}$$

Equation (A1) follows *Wang* [2000, equation (6.18)] with notation simplification following *Wang* [2000, equations (3.37) and (3.64)]. Where M is Biot's modulus and α is Biot-Willis coefficient. When grains are assumed incompressible, $M = 1/\beta\Phi$ and $\alpha = 1$ [*Wang*, 2000, Table 3.2]. Therefore equation (A1) may be rewritten as

$$\frac{\partial P}{\partial t} = \frac{k}{\mu\beta\Phi}\frac{\partial^2 P}{\partial z^2} - \frac{1}{\beta\Phi}\frac{\partial \epsilon_{zz}}{\partial t}. \tag{A2}$$

This form is equivalent to our equation (10), since the forcing term $\partial\epsilon_{zz}/\partial t$, representing the one dimensional strain rate, may be rewritten as $\partial \mathbf{u_{sz}}/\partial z$. For example, for a periodic strain of the form $\epsilon_{zz} = \epsilon_0 \exp(i\omega t)$, the corresponding grains velocity will be $\mathbf{u_{sz}} = \int_z (\partial\epsilon_{zz}/\partial t)dz = i\epsilon_0 \omega z \exp(i\omega t)$. It is a surprising result that equation (A2) that was developed from a purely elastic point of view, is in fact equivalent to our equation (10), which did not assume elasticity. The only difference is *Wang*'s [2000] assumption of uniform permeability in the diffusion term (first term on the righthand side) of equation (A2), which does not necessarily hold for the general formulation of equation (10).

[77] *Bachrach et al.* [2001] present a study of the propagation of pressure waves in a poroelastic material induced by stress forcing using Biot's equations. Next, the equivalency between *Bachrach et al.*'s [2001] formulation and equation (13) (which follows *Wang*'s [2000] equation (6.14)) is demonstrated under the assumption of negligible inertia, an assumption that is discussed in the following. Combining *Bachrach et al.*'s [2001] equations (7) and (11) and neglecting inertial terms, it is found that

$$\frac{\partial P}{\partial t} = \frac{k}{\mu}2D\left(1 - \alpha\frac{2\alpha D}{H}\right)\frac{\partial^2 P}{\partial z^2} - \frac{2\alpha D}{H}\frac{\partial \sigma}{\partial t}. \tag{A3}$$

As before, $\alpha = 1$, is the Biot-Willis coefficient for incompressible grains. $D = (2\beta\Phi)^{-1}$ and $H = K_\nu^{(u)} = K_\nu + (\beta\Phi)^{-1}$, where $K_\nu^{(u)}$ and K_ν are the undrained and drained uniaxial bulk moduli, respectively. H and D are resolved following their definition by *Bachrach et al.* [2001] and under the assumption of incompressible solid grains. Assigning the expressions for α, H and D into equation (A3) results in

$$\frac{\partial P}{\partial t} = \frac{k}{\mu}\frac{1}{\beta\Phi + K_\nu^{-1}}\frac{\partial^2 P}{\partial z^2} - \frac{1}{K_\nu^{(u)}\beta\Phi}\frac{\partial \sigma}{\partial t}. \tag{A4}$$

Following *Wang* [2000, equation (3.52)], $\beta\Phi + K_\nu^{-1} = S$, and following *Wang* [2000, equation (3.85) and Table 3.2], $(K_\nu^{(u)}\beta\Phi)^{-1} = \gamma$. Thus, it is shown that equation (A4) (which is an inertia free version of Biot's equations, as expressed in *Bachrach et al.*'s [2001] equations (7) and (11)) is identical to *Wang*'s [2000] equation (6.14) and to our equation (13).

[78] Next, we wish to determine the limits for the validity of our assumption of negligible inertia. For that, *Bachrach et al.*'s [2001] equations (7) and (11) are reviewed:

$$\begin{aligned} \rho_b\frac{\partial^2 v}{\partial t^2} + \rho_f\frac{\partial^2 w}{\partial t^2} &= \frac{\partial \sigma}{\partial z} \\ \rho_f\frac{\partial^2 v}{\partial t^2} + m\frac{\partial^2 w}{\partial t^2} &= \frac{\partial P}{\partial z} + \frac{\mu}{k}\frac{\partial w}{\partial t}, \end{aligned} \tag{A5}$$

where ρ_b is the density of the fluid-filled porous material, m is a coupling coefficient, and v and w are the displacement field of the solid matrix and fluid, respectively. Introducing scale factors for each of the variables: $v = w_0\hat{v}$, $w = w_0\hat{w}$, $\sigma = P_0\hat{\sigma}$, $P = P_0\hat{P}$, $z = L\hat{z}$, and $t = t_0\hat{t}$, where $t_0 = (2\pi f)^{-1}$, and f is the forcing frequency in s^{-1}. Assigning the scale factors in equation (A5), dropping the ˆ notation, and considering the magnitude of the densities ρ_f, ρ_b and the coupling coefficient, m, to be of the same order:

$$\begin{aligned} \frac{w_0\rho_f L(2\pi f)^2}{P_0}\left(\frac{\partial^2 v}{\partial t^2} + \frac{\partial^2 w}{\partial t^2}\right) &= \frac{\partial \sigma}{\partial z} \\ \frac{w_0\rho_f L(2\pi f)^2}{P_0}\left(\frac{\partial^2 v}{\partial t^2} + \frac{\partial^2 w}{\partial t^2}\right) &= \frac{\partial P}{\partial z} + \frac{\mu w_0 L(2\pi f)}{kP_0}\frac{\partial w}{\partial t}. \end{aligned} \tag{A6}$$

Taking $\rho_f = 10^3$ kg m^{-3}, $L = 1$ m, $P_0 = 100$ Pa, and $w_0 = 10^{-7}$ m following the values used by *Bachrach et al.* [2001], it is found that the acceleration terms, left-hand side of equation (A6), are important only for frequencies of an order ≥100 Hz, and may be neglected for smaller frequencies (a conclusion that also agrees with an analysis by *Iverson* [1993]). Thus, for smaller frequencies, *Bachrach et al.*'s [2001] formulation is equivalent to *Wang*'s [2000] equation (6.14) formulation, which by itself was shown to be similar to our equation (10).

A2. Non-Elastic Formulations

[79] *Walder and Nur* [1984] study processes of PP generation due to porosity reduction, accounting also for non-elastic deformation [*Walder and Nur*, 1984, equation (5)]:

$$\frac{\partial P}{\partial t} = \frac{k}{\mu\Phi(\beta + \beta_\Phi)}\nabla^2 P - \frac{1}{\Phi(\beta + \beta_\Phi)}\frac{\partial \Phi}{\partial t}_{irrev}. \tag{A7}$$

In this formulation, $\beta_\Phi = (1/\Phi)\ (\partial\Phi/\partial P)$ is the elastic pore compressibility, and $(\partial\Phi/\partial t)_{irrev}$ is the irreversible porosity evolution. With some algebraic transformation equation (A7) may be rewritten as

$$\frac{\partial P}{\partial t} = \frac{k}{\mu\Phi\beta}\nabla^2 P - \frac{1}{\Phi\beta}\left(\frac{\partial\Phi}{\partial t}_{rev} + \frac{\partial\Phi}{\partial t}_{irrev}\right), \quad \text{(A8)}$$

where the pore compressibility was expanded as $\beta_\Phi = (1/\Phi)\ (\partial\Phi/\partial t)_{rev}\ (\partial t/\partial P)$, and $(\partial\Phi/\partial t)_{rev}$ is the reversible component of the porosity change. Equation (A8) resembles our equation (12) under the assumption of space independent permeability. The forcing term of equation (A8) that is divided between reversible and irreversible porosity reduction is expressed as a single term in our equation (12). Therefore the forcing terms are identical up to a factor of $(1 - \Phi)$. This factor results from the different definitions of Darcy's velocity: *Walder and Nur* [1984] use $\mathbf{u_f} = -\frac{k}{\mu\Phi}\nabla P$ as if the matrix is stationary, while our formulation assumes that Darcy's velocity is given by equation (3).

[80] This appendix demonstrates that former formulation of PP generation by porous or granular matrix deformation may be reduced to our equations (10) or (12). That is, the formulations of *Wang* [2000], *Bachrach et al.* [2001], *Walder and Nur* [1984], and the formulations of *Snieder and van der Beukel* [2004] and *Samuelson et al.* [2009] that are not discussed here, all describe the temporal evolution of PP as a combination of a diffusion term and a forcing term.

Appendix B: Analytical Prediction for a Boundary-Independent System

[81] In this appendix we derive an analytical prediction for the temporal and spatial evolution of PP, for the model of fluid-filled uniform granular material, packed in hexagonal packing, under constant shear velocity, that is presented in section 4.1. This solution applies to the case of a large system with $\mathrm{De}_\zeta \gg 1$ (boundary-independent). The prediction is derived by solving equation (10) under the assumption of constant diffusion coefficient, $D_c = k_{\min}/\beta\mu\Phi_{\min}$, and using the evolution of granular velocity and porosity from equation (15). The equation to be solved is

$$\frac{\partial P}{\partial t} = D_c\frac{\partial^2 P}{\partial z^2} - \frac{1}{\beta}F(z,t), \quad \text{(B1)}$$

where $F(z, t)$ expresses the forcing $\nabla \cdot u_{sz}/\Phi$ that is concentrated along $z = 0$ (the shearing row), and is defined as

$$F(z,t) = \delta(z)V_{sh}\cdot u_F(t), \quad 0 < t < t_0 = d/V_{sh}, \quad \text{(B2)}$$

and

$$u_F(t) = \frac{u_{sz}}{\Phi} = \frac{(0.5 - t/t_0)}{\sqrt{1-(0.5-t/t_0)^2 - \pi/4}}. \quad \text{(B3)}$$

$\delta(z)$ is Dirac delta function with units of m^{-1}, that stands for the $\nabla\ \cdot$ operator in equation (10). The solution of equation (B1) for $P(z, t)$ may be expressed using a Green's function by the integral [*McKenzie and Brune*, 1972]

$$P(z,t) = -\frac{1}{2\beta\sqrt{D_c\pi}}\int_0^t\int_{-\infty}^{\infty}\exp\left[-\frac{(z-z_i)^2}{4D(t-t_i)}\right]\frac{F(z_i,t_i)}{\sqrt{t-t_i}}dz_i dt_i. \quad \text{(B4)}$$

Assigning $F(z_i, t_i)$ from equation (B2), equation (B4) is evaluated as [*McKenzie and Brune*, 1972]

$$P(z,t) = -\frac{V_{sh}}{2\beta\sqrt{D\pi}}\int_0^t\exp\left[-\frac{z^2}{4D(t-t_i)}\right]\frac{u_F(t_i)}{\sqrt{t-t_i}}dt_i. \quad \text{(B5)}$$

To solve equation (B5), we first expand $u_F(t_i)$ as a third order power series of t_i using its third order interpolation polynomial, i.e., $u_F\ (t_i) = \sum_{j=0}^{j=3} a_j(t_i)^j$. In the next stage, $u_F(t_i)$ is rewritten as a third order power series of $(t - t_i)$, $u_F(t_i) = \sum_{j=0}^{j=3} b_j(t - t_i)^j$, where $b_j = b_j(t)$ is found by solving the system of linear equations:

$$\begin{aligned} b_0(t) &= a_0 + a_1 t + a_2 t^2 + a_3 t^3 \\ b_1(t) &= -a_1 - 2a_2 t - 3a_3 t^2 \\ b_2(t) &= a_2 + 3a_3 t \\ b_3(t) &= -a3, \end{aligned} \quad \text{(B6)}$$

and equation (B5) is rewritten as

$$P(z,t) = -\frac{V_{sh}}{2\beta\sqrt{D\pi}}\int_0^t\exp\left[-\frac{z^2}{4D(t-t_i)}\right]\frac{\sum_{j=0}^{j=3} b_j(t-t_i)^j}{\sqrt{t-t_i}}dt_i. \quad \text{(B7)}$$

Next, the following dimensionless variables are defined [*McKenzie and Brune*, 1972]:

$$\begin{aligned} \hat{P} &= \frac{\beta\sqrt{\pi Dd/V_{sh}}}{d}P \\ \hat{t}_i &= t_i/t_0 \\ \hat{t} &= t/t_0 \\ \hat{z} &= \frac{1}{\sqrt{2D_c t_0}}z \end{aligned} \quad \text{(B8)}$$

and equation (B7) may be written in a non-dimensional form:

$$\begin{aligned} \hat{P}(\hat{z},\hat{t}) &= -\frac{1}{2}\int_0^{\hat{t}}\exp\left[-\frac{\hat{z}^2}{2(\hat{t}-\hat{t}_i)}\right]\frac{\sum_{j=0}^{j=3} b_j(\hat{t})(\hat{t}-\hat{t}_i)^j}{\sqrt{\hat{t}-\hat{t}_i}}d\hat{t}_i \\ &= -\left(b_0(\hat{t})\frac{1}{2}\int_0^{\hat{t}}\exp\left[-\frac{\hat{z}^2}{2(\hat{t}-\hat{t}_i)}\right]\frac{1}{\sqrt{\hat{t}-\hat{t}_i}}d\hat{t}_i\right) \\ &\quad -\left(b_1(\hat{t})\frac{1}{2}\int_0^{\hat{t}}\exp\left[-\frac{\hat{z}^2}{2(\hat{t}-\hat{t}_i)}\right]\frac{(\hat{t}-\hat{t}_i)}{\sqrt{\hat{t}-\hat{t}_i}}d\hat{t}_i\right) \\ &\quad -\left(b_2(\hat{t})\frac{1}{2}\int_0^{\hat{t}}\exp\left[-\frac{\hat{z}^2}{2(\hat{t}-\hat{t}_i)}\right]\frac{(\hat{t}-\hat{t}_i)^2}{\sqrt{\hat{t}-\hat{t}_i}}d\hat{t}_i\right) \\ &\quad -\left(b_3(\hat{t})\frac{1}{2}\int_0^{\hat{t}}\exp\left[-\frac{\hat{z}^2}{2(\hat{t}-\hat{t}_i)}\right]\frac{(\hat{t}-\hat{t}_i)^3}{\sqrt{\hat{t}-\hat{t}_i}}d\hat{t}_i\right) \\ &= -[b_0(\hat{t})I_0 + b_1(\hat{t})I_1 + b_2(\hat{t})I_2 + b_3(\hat{t})I_3], \end{aligned} \quad \text{(B9)}$$

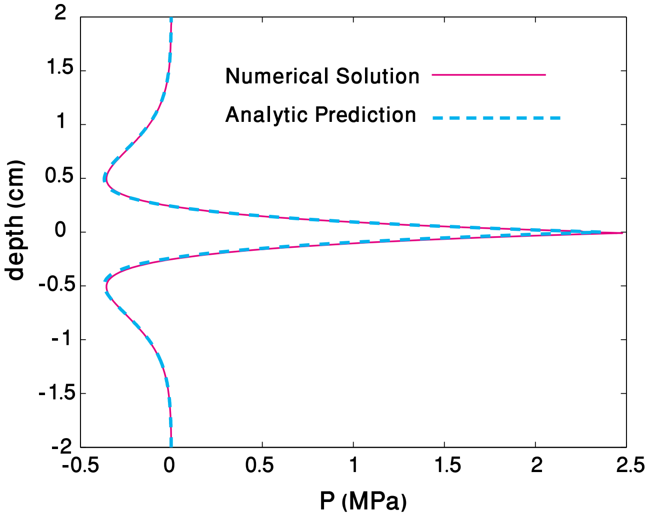

Figure B1. Spatial distribution of PP for a large system (with $\mathrm{De}_\zeta \gg 1$) at the end of the period, $\hat{t} = 1$. The shearing row is in the middle of the domain. Purple curve is simulation results, and dashed turquoise curve is the analytical prediction for $P(z, d/V_{sh})$ following equations (B6)–(B12).

where I_i are the integrals. The solution for I_0 from *McKenzie and Brune* [1972] is

$$I_0 = \sqrt{\hat{t}}\exp\frac{-\hat{z}^2}{2\hat{t}} - \hat{z}\sqrt{\frac{\pi}{2}}\operatorname{erfc}\left(\frac{\hat{z}}{\sqrt{2\hat{t}}}\right). \tag{B10}$$

Integrals $I_1 - I_3$ can be integrated by parts and reduced to I_0 as follows:

$$\begin{aligned} I_1 &= \frac{1}{2}\int_0^{\hat{t}} \exp\left[-\frac{\hat{z}^2}{2(\hat{t}-\hat{t}_i)}\right]\frac{(\hat{t}-\hat{t}_i)}{\sqrt{\hat{t}-\hat{t}_i}}d\hat{t}_i \\ &= -\frac{1}{2}\int_{\hat{t}}^0 \exp\left[-\frac{\hat{z}^2}{2\tau}\right]\tau^{1/2}d\tau \\ &= -\frac{1}{2}\left[\left(\frac{2}{3}\tau^{3/2}\exp\left[-\frac{\hat{z}^2}{2\tau}\right]\right)\Big|_{\hat{t}}^0 - \frac{2}{3}\frac{\hat{z}^2}{2}\int_{\hat{t}}^0 \exp\left[-\frac{\hat{z}^2}{2\tau}\right]\tau^{-1/2}d\tau\right] \\ &= \frac{1}{3}\left[\hat{t}^{3/2}\exp\left[-\frac{\hat{z}^2}{2\hat{t}}\right] - \hat{z}^2 I_0\right]. \end{aligned} \tag{B11}$$

Similarly, it can be shown that

$$\begin{aligned} I_2 &= \frac{1}{5}\left[\hat{t}^{5/2}\exp\left[-\frac{\hat{z}^2}{2\hat{t}}\right] - \hat{z}^2 I_1\right] \\ I_3 &= \frac{1}{7}\left[\hat{t}^{7/2}\exp\left[-\frac{\hat{z}^2}{2\hat{t}}\right] - \hat{z}^2 I_2\right]. \end{aligned} \tag{B12}$$

Equations (B6) and (B7)–(B12) give a full solution for $\hat{P}(\hat{z}, \hat{t})$. Evaluating $\hat{P}(\hat{z}, \hat{t})$ along the shearing row gives

$$\begin{aligned} P(0,\hat{t})\frac{\beta\sqrt{\pi D d/V_{sh}}}{d} = -\frac{1}{105}\sqrt{(\hat{t})}(582.929 - 1885.66\hat{t} \\ + 2667.73\hat{t}^2 - 1524.38\hat{t}^3) \end{aligned} \tag{B13}$$

where the coefficient of the interpolation polynomial for $u_F(\hat{t})$ are $a_0 = 5.5517$, $a_1 = -26.938$, $a_2 = 47.638$ and $a_3 = -31.758$. Figure 6 compares equation (B13) with boundary-independent simulation results conducted with a constant diffusion coefficient, D_c. Figure B1 compares the spatial pattern of PP at the end of the period ($\hat{t} = 1$) between boundary-independent simulations and the analytical prediction presented here.

[82] **Acknowledgments.** We thank Amotz Agnon and Michael Tsesarsky for fruitful discussions. We also wish to thank André Niemeijer, the Associate Editor, and an anonymous reviewer for constructive reviews that helped greatly in improving the manuscript.

References

Aharonov, E., and D. Sparks (2002), Shear profiles and localization in simulations of granular materials, *Phys. Rev. E*, *65*(5), 051302, doi:10.1103/PhysRevE.65.051302.

Anghel, D. V., M. Strauss, S. McNamara, E. G. Flekkøy, and K. J. Måløy (2006), Erratum: Grains and gas flow: Molecular dynamics with hydrodynamic interactions [Phys. Rev. E 61, 4054 (2000)], *Phys. Rev. E*, *74*(2), 029906, doi:10.1103/PhysRevE.74.029906.

Bachrach, R., A. Nur, and A. Agnon (2001), Liquefaction and dynamic poroelasticity in soft sediments, *J. Geophys. Res.*, *106*(B7), 13,515–13,526, doi:10.1029/2000JB900474.

Biot, M. A. (1941), General theory for three-dimensional consolidation, *J. Appl. Phys.*, *12*, 155, doi:10.1063/1.1712886.

Biot, M. A. (1956a), Theory of propagation of elastic waves in a fluid-saturated porous solid. I. Low-frequency range, *J. Acoust. Soc. Am.*, *28*, 168–178, doi:10.1121/1.1908239.

Biot, M. A. (1956b), Theory of propagation of elastic waves in a fluid-saturated porous solid. II. Higher frequency range, *J. Acoust. Soc. Am.*, *28*, 179–191, doi:10.1121/1.1908241.

Biot, M. A. (1962), Mechanics of deformation and acoustic propagation in porous dissipative media, *J. Appl. Phys.*, *33*(4), 1482–1498, doi:10.1063/1.1728759.

Blanpied, M. L., D. A. Lockner, and J. D. Byerlee (1992), An earthquake mechanism based on rapid sealing of faults, *Nature*, *358*(6387), 574–576, doi:10.1038/358574a0.

Casagrande, A. (1936), Characteristics of cohesionless soils affecting the stability of slopes and earth fills, *J. Boston Soc. Civ. Eng.*, *23*, 13–32.

Castro, G. (1969), *Liquefaction of Sands*, *Harvard Soil Mech. Ser.*, vol. 87, Harvard Univ., Cambridge, Mass.

Cetin, K. O., N. Isik, and B. Unutmaz (2004), Seismically induced landslide at Degirmendere Nose, Izmit bay during Kocaeli (Izmit)-Turkey earthquake, *Soil. Dyn. Earthquake Eng.*, *24*(3), 189–197, doi:10.1016/j.soildyn.2003.11.007.

Das, M. B. (1993), *Principles of Soil Mechanics*, PWS-Kent, Boston, Mass.

El Shamy, U., and M. Zeghal (2007), A micro-mechanical investigation of the dynamic response and liquefaction of saturated granular soils, *Soil. Dyn. Earthquake Eng.*, *27*(8), 712–729, doi:10.1016/j.soildyn.2006.12.010.

Flekkøy, E. G., A. Malthe-Sørenssen, and B. Jamtveit (2002), Modeling hydrofracture, *J. Geophys. Res.*, *107*(B8), 2151, doi:10.1029/2000JB000132.

Forterre, Y., and O. Pouliquen (2008), Flows of dense granular media, *Annu. Rev. Fluid Mech.*, *40*, 1–24, doi:10.1146/annurev.fluid.40.111406.102142.

Frye, K. M., and C. Marone (2002), The effect of particle dimensionality on granular friction in laboratory shear zones, *Geophys. Res. Lett.*, *29*(19), 1916, doi:10.1029/2002GL015709.

Gabet, E. J., and S. M. Mudd (2006), The mobilization of debris flows from shallow landslides, *Geomorphology*, *74*, 207–218, doi:10.1016/j.geomorph.2005.08.013.

Garagash, D. I., and J. W. Rudnicki (2003), Shear heating of a fluid-saturated slip-weakening dilatant fault zone: 1. Limiting regimes, *J. Geophys. Res.*, *108*(B2), 2121, doi:10.1029/2001JB001653.

Garga, V. K., and H. Zhang (1997), Volume changes in undrained triaxial tests on sands, *Can. Geotech. J.*, *34*, 762–772, doi:10.1139/cgj-34-5-762.

Hamiel, Y., V. Lyakhovsky, and A. Agnon (2005), Rock dilation, nonlinear deformation, and pore pressure change under shear, *Earth Planet. Sci. Lett.*, *237*(3–4), 577–589, doi:10.1016/j.epsl.2005.06.028.

Itasca Consulting Group, Inc. (2005), PFC3D (Particle Flow Code in 3 Dimensions), version 3.1., Minneapolis, Minn.

Iverson, R. M. (1993), Differential-equations governing slip-induced pore-pressure fluctuations in a water-saturated granular medium, *Math. Geol.*, *25*(8), 1027–1048, doi:10.1007/BF00911548.

Iverson, R. M. (2005), Regulation of landslide motion by dilatancy and pore pressure feedback, *J. Geophys. Res.*, *110*, F02015, doi:10.1029/2004JF000268.

Iverson, R. M., and R. G. LaHusen (1989), Dynamic pore-pressure fluctuations in rapidly shearing granular-materials, *Science*, *246*(4931), 796–799, doi:10.1126/science.246.4931.796.

Iverson, R. M., M. E. Reid, and R. G. LaHusen (1997), Debris-flow mobilization from landslides, *Annu. Rev. Earth Planet. Sci.*, *25*, 85–138, doi:10.1146/annurev.earth.25.1.85.

Iverson, R. M., M. E. Reid, N. R. Iverson, R. G. LaHusen, M. Logan, J. E. Mann, and D. L. Brien (2000), Acute sensitivity of landslide rates to initial soil porosity, *Science*, *290*(5491), 513–516, doi:10.1126/science.290.5491.513.

Johnsen, Ø., R. Toussaint, K. L. Måløy, and E. G. Flekkøy (2006), Pattern formation during air injection into granular materials confined in a circular Hele-Shaw cell, *Phys. Rev. E*, *74*(1), 011301, doi:10.1103/PhysRevE.74.011301.

Johnsen, Ø., R. Toussaint, K. J. Måløy, E. G. Flekkøy, and J. Schmittbuhl (2007), Coupled air/granular flow in a linear Hele-Shaw cell, *Phys. Rev. E*, *77*(1), 011301, doi:10.1103/PhysRevE.77.011301.

Johnsen, Ø., C. Chevalier, A. Lindner, R. Toussaint, E. C. K. J. Måløy, E. G. Flekkøy, and J. Schmittbuhl (2008), Decompaction and fluidization of a saturated and confined granular medium by injection of a viscous liquid or a gas, *Phys. Rev. E*, *78*(5), 051302, doi:10.1103/PhysRevE.78.051302.

Kawakami, F., and A. Asada (1966), Damage to the ground and earth structures by the Niigata earthquake of June 16,1964, *Soil Found.*, *6*(1), 14–30.

Kherbouche, R., J. F. Shao, F. Skoczylas, and J. P. Henry (1995), On the poroplastic behavior of porous rocks, *Eur. J. Mech. A, Solids*, *14*(4), 577–587.

Kostadinov, M. V., and I. Towhata (2002), Assessment of liquefaction-inducing peak ground velocity and frequency of horizontal ground shaking at onset of phenomenon, *Soil. Dyn. Earthquake Eng.*, *22*(4), 309–322, doi:10.1016/S0267-7261(02)00018-0.

Kozlov, V. G., A. A. Ivanova, and P. Evesque (1998), Sand behavior in a cavity with incompressible liquid under vertical vibrations, *Europhys. Lett.*, *42*(4), 413–418, doi:10.1209/epl/i1998-00264-2.

Kramer, S. L. (1996), *Geotechnical Earthquake Engineering*, Prentice Hall, Upper Saddle River, N. J.

Li, X., X. Chu, and D. Sheng (2007), A saturated discrete particle model and characteristic-based SPH method in granular materials, *Int. J. Numer. Methods Eng.*, *72*, 858–882, doi:10.1002/nme.2037.

Makedonska, N., L. Goren, D. Sparks, and E. Aharonov (2010), What controls the effective friction of shearing granular media?, in *Meso-Scale Shear Physics in Earthquake and Landslide Mechanics*, edited by Y. H. Hatzor, J. Sulem, and I. Vardoulakis, pp. 191–203, CRC Press, Boca Raton, Fla.

Manzari, M. T., K. Arulanandan, and R. F. Scott (1994), VELACS project: A summary of achievements, in *Proceedings From the Fifth U.S.-Japan Workshop on Earthquake Resistant Design of Lifeline Facilities and Countermeasures Against Liquefaction*, edited by T. D. O'Rourke and M. Hamada, *Tech. Rep. NCEER-940-0026*, pp. 389–404, Natl. Cent. for Earthquake Eng. Res., State Univ. of N. Y. Buffalo, Buffalo.

Marone, C., C. B. Raleigh, and C. H. Scholz (1990), Frictional behavior and constitutive modeling of simulated fault gouge, *J. Geophys. Res.*, *95*, 7007–7025, doi:10.1029/JB095iB05p07007.

McKenzie, D., and J. N. Brune (1972), Melting on fault planes during large earthquakes, *Geophys. J. R. Astron. Soc.*, *29*, 65–78.

McNamara, S., E. G. Flekkøy, and K. J. Måløy (2000), Grains and gas flow: Molecular dynamics with hydrodynamic interactions, *Phys. Rev. E*, *61*(4), 4054–4059, doi:10.1103/PhysRevE.61.4054.

Miller, S. A., and A. Nur (2000), Permeability as a toggle switch in fluid-controlled crustal processes, *Earth Planet. Sci. Lett.*, *183*, 133–146, doi:10.1016/S0012-821X(00)00263-6.

Moore, P. L., and N. R. Iverson (2002), Slow episodic shear of granular materials regulated by dilatant strengthening, *Geology*, *30*(9), 843–846, doi:10.1130/0091-7613(2002)030<0843:SESOGM>2.0.CO;2.

Mourgues, R., and P. Cobbold (2003), Some tectonic consequences of fluid overpressures and seepage forces as demonstrated by sandbox modelling, *Tectonophysics*, *376*(1–2), 75–97, doi:10.1016/S0040-1951(03)00348-2.

Okada, Y., and H. Ochiai (2007), Coupling pore-water pressure with distinct element method and steady state strengths in numerical triaxial tests under undrained conditions, *Landslides*, *4*, 357–369, doi:10.1007/s10346-007-0092-1.

Osswald, T. (1998), *Polymer Processing Fundamental*, Hanser Gardner, Cincinnati, Ohio.

Popescu, R., and J. H. Prevost (1995), Comparison between VELACS numerical class—A predictions and centrifuge experimental soil test-results, *Soil. Dyn. Earthquake Eng.*, *14*(2), 79–92, doi:10.1016/0267-7261(94)00038-I.

Rowe, P. W. (1962), The stress-dilatancy relation for static equilibrium of an assembly of particles in contact, *Proc. R. Soc. London, Ser. A*, *269*, 500–527, doi:10.1098/rspa.1962.0193.

Rozhko, A. Y., Y. Y. Podladchikov, and F. Renard (2007), Failure patterns caused by localized rise in pore-fluid overpressure and effective strength of rocks, *Geophys. Res. Lett.*, *34*, L22304, doi:10.1029/2007GL031696.

Saar, M. O., and M. Manga (2004), Depth dependence of permeability in the Oregon Cascades inferred from hydrologic, thermal, seismic and magnetic modeling constraints, *J. Geophys. Res.*, *109*, B04204, doi:10.1029/2003JB002855.

Samuelson, J., D. Elsworth, and C. Marone (2009), Shear-induced dilatancy of fluid-saturated faults: Experiment and theory, *J. Geophys. Res.*, *114*, B12404, doi:10.1029/2008JB006273.

Sawicki, A., and J. Mierczynski (2006), Developments in modeling liquefaction of granular soils, caused by cyclic loads, *Appl. Mech. Rev.*, *59*, 91–106, doi:10.1115/1.2130362.

Scawthorn, C., and P. I. Yanev (1995), Preliminary report 17 January 1995, Hyogo-ken Nambu, Japanese earthquake, *Eng. Struct.*, *17*(3), 146–157, doi:10.1016/0141-0296(95)00041-5.

Scholz, C. H. (1990), *The Mechanics of Earthquakes and Faulting*, Cambridge Univ, Press, Cambridge, U. K.

Segall, P., and J. R. Rice (1995), Dilatancy, compaction, and slip instability of fluid-infiltrated fault, *J. Geophys. Res.*, *100*(B11), 22,155–22,171, doi:10.1029/95JB02403.

Sidle, R. C., and H. Ochiai (2006), *Landslides Processes, Prediction, and Land Use*, *Water Resour. Monogr. Ser.*, vol. 18, AGU, Washington, D. C.

Skempton, A. W. (1960), Terzaghi's discovery of effective stress, in *From Theory to Practice in Soil Mechanics*, edited by L. Bjerrum et al., pp. 42–53, John Wiley, New York.

Sleep, N. H., and M. L. Blanpied (1992), Creep, compaction and the weak rheology of major faults, *Nature*, *359*(6397), 687–692, doi:10.1038/359687a0.

Snieder, A., and A. van der Beukel (2004), The liquefaction cycle and the role of drainage in liquefaction, *Granul. Matter*, *6*, 1–9, doi:10.1007/s10035-003-0151-9.

Soga, K. (1998), Soil liquefaction effects observed in the Kobe earthquake of 1995, *Proc. Inst. Civ. Eng. Geotech. Eng.*, *131*(1), 34–51, doi:10.1680/igeng.1998.30004.

Terzaghi, K. (1943), *Theoretical Soil Mechanics*, doi:10.1002/9780470172766, John Wiley, New York.

Vinningland, J. L., Ø. Johnsen, E. G. Flekkøy, R. Toussaint, and K. J. Måløy (2007a), Granular Rayleigh-Taylor instability: Experiments and simulations, *Phys. Rev. Lett.*, *99*(4), doi:10.1103/PhysRevLett.99.048001.

Vinningland, J. L., Ø. Johnsen, E. G. Flekkøy, R. Toussaint, and K. J. Måløy (2007b), Experiments and simulations of a gravitational granular flow instability, *Phys. Rev. E*, *76*(5), 051306, doi:10.1103/PhysRevE.76.051306.

Voight, B., and C. Faust (1982), Frictional heat and strength loss in some rapid landslides, *Geotechnique*, *32*(1), 43–54, doi:10.1680/geot.1982.32.1.43.

Walder, J., and A. Nur (1984), Porosity reduction and crustal pore pressure development, *J. Geophys. Res.*, *89*(B13), 11,539–11,548, doi:10.1029/JB089iB13p11539.

Wang, H. F. (2000), *Theory of Linear Poroelasticity With Applications to Geomechanics and Hydrogeology*, Princeton Univ. Press, Princeton, N. J.

Yamashita, T. (1999), Pore creation due to fault slip in a fluid-permeated fault zone and its effect on seismicity: Generation mechanism of earthquake swarm, *Pure Appl. Geophys.*, *155*, 625–647, doi:10.1007/s000240050280.

Youd, T. L. (1972), Compaction of sands by repeated shear straining, *J. Soil Mech. Found. Design*, *98*, 709–725.

Zienkiewicz, O. C., A. H. C. Chan, M. Pastor, B. A. Schrefler, and T. Shiomi (1999), *Computational Geomechanics With Special Reference to Earthquake Engineering*, John Wiley, Chichester, U. K.

E. Aharonov, Institute of Earth Sciences, Hebrew University, Givat Ram, Jerusalem 91904, Israel. (einatah@cc.huji.ac.il)

L. Goren, Department of Environmental Sciences and Energy Research, Weizmann Institute of Science, Rehovot 76100, Israel. (liran.goren@weizmann.ac.il)

D. W. Sparks, Department of Geology and Geophysics, Texas A&M University, College Station, TX 77843-3115, USA. (sparks@geo.tamu.edu)

R. Toussaint, IPGS, CNRS and University of Strasbourg, EOST, 5 rue René Descartes, F-67000 Strasbourg CEDEX, France. (renaud.toussaint@eost.u-strasbg.fr)

ISPRS Journal of Photogrammetry and Remote Sensing 70 (2012) 39–55

Contents lists available at SciVerse ScienceDirect

ISPRS Journal of Photogrammetry and Remote Sensing

journal homepage: www.elsevier.com/locate/isprsjprs

Correlation of multi-temporal ground-based optical images for landslide monitoring: Application, potential and limitations

J. Travelletti [a,b], C. Delacourt [c], P. Allemand [d], J.-P. Malet [a,*], J. Schmittbuhl [a], R. Toussaint [a], M. Bastard [a]

[a] Institut de Physique du Globe de Strasbourg, CNRS UMR 7516, Université de Strasbourg/EOST, 5 rue René Descartes, 67084 Strasbourg Cedex, France
[b] GEOPHEN – LETG, CNRS UMR 6554, Université de Caen Basse-Normandie, Caen, France
[c] Institut Universitaire Européen de la Mer, CNRS UMR 6538, Université de Bretagne Occidentale, Brest, France
[d] Laboratoire des Sciences de la Terre, CNRS UMR 5570, Université de Lyon and Ecole Normale Supérieure, Lyon, France

ARTICLE INFO

Article history:
Received 7 February 2011
Received in revised form 14 March 2012
Accepted 19 March 2012
Available online 27 April 2012

Keywords:
Image cross-correlation
Image matching
Landslide
Time-lapse photography
Displacement monitoring

ABSTRACT

The objective of this work is to present a low-cost methodology to monitor the displacement of continuously active landslides from ground-based optical images analyzed with a normalized image correlation technique. The performance of the method is evaluated on a series of images acquired on the Super-Sauze landslide (South French Alps) over the period 2008–2009. The image monitoring system consists of a high resolution optical camera installed on a concrete pillar located on a stable crest in front of the landslide and controlled by a datalogger. The data are processed with a cross-correlation algorithm applied to the full resolution images in the acquisition geometry. Then, the calculated 2D displacement field is orthorectified with a back projection technique using a high resolution DEM interpolated from Airborne Laser Scanning (ALS) data. The heterogeneous displacement field of the landslide is thus characterized in time and space. The performance of the technique is assessed using differential GPS surveys as reference. The sources of error affecting the results are then discussed. The strongest limitations for the application of the technique are related to the meteorological, illumination and ground surface conditions inducing partial or complete loss of coherence among the images. Small movements of the camera and the use of a mono-temporal DEM are the most important factors affecting the accuracy of the ortho-rectification of the displacement field. As the proposed methodology can be routinely and automatically applied, it offers promising perspectives for operational applications like, for instance, in early warning systems.

1. Introduction

Displacement monitoring of unstable slopes is a crucial tool for the prevention of hazards. It is often the only solution for the survey and the early-warning of large landslides that cannot be stabilized or that may accelerate suddenly. The choice of an adequate monitoring system depends on the landslide type and size, the range of observed velocity, the required frequency of acquisition, the desired accuracy and the financial constraints. Displacement monitoring techniques applied to landslides can be broadly subdivided in two main groups: geodetic and remote-sensing techniques.

Geodetic surveying consist in detecting geometrical changes in the landslide topography by measuring geometric parameters such as angles, distances or differences in elevation (e.g. levelling, tacheometry; Naterop and Yeatman, 1995). These techniques necessitate the installation of targets in and outside the landslide and in measuring their position at different times. They have the advantage to be very accurate (0.2–2.0 cm) with a high potential of automation (Malet et al., 2002; Jaboyedoff et al., 2004; Foppe et al., 2006). Furthermore, many authors demonstrated the efficiency of permanent (Malet et al., 2002) and non-permanent (Squarzoni et al., 2005; Brunner et al., 2007) differential Global Positioning System (dGPS) for landslide monitoring with a centimetric accuracy during any daytime and weather conditions. However, because landslides can show highly variable displacement rates in time and space according to the local slope conditions (bedrock geometry, distribution of pore water pressures), the major drawbacks of the geodetic techniques are (1) to provide only discrete point measurements of the displacement and (2) the costs of installation and maintenance of the survey network. They are usually only justified in the case of a real risk for the population.

Remote-sensing techniques are interesting tools to obtain spatially-distributed information on kinematics (Delacourt et al., 2007) and can be operational from spaceborne, airborne and ground-based platforms. Remote-sensing techniques give the

* Corresponding author.
E-mail addresses: julien.travelletti@unistra.fr (J. Travelletti), jeanphilippe.malet@eost.u-strasbg.fr (J.-P. Malet).

0924-2716/$ - see front matter © 2012 International Society for Photogrammetry and Remote Sensing, Inc. (ISPRS) Published by Elsevier B.V. All rights reserved.
http://dx.doi.org/10.1016/j.isprsjprs.2012.03.007

possibility to discriminate stable and unstable areas and to map sectors within the landslide with different kinematics from a regional to a local scale. They are also useful tools for a process-based analysis of the deformation field affecting the slope (Casson et al., 2005; Teza et al., 2008; Oppikofer et al., 2008). In the last decades, the development of ground-based platforms for landslide monitoring at the local scale provided many advantages over spaceborne and airborne platforms despite a shorter spatial coverage (Corsini et al., 2006). The geometry and frequency of acquisitions are more flexible and adaptable to any type of local environment. In addition permanent installations of ground-based platforms allow continuous monitoring (Casagli et al., 2004; Delacourt et al., 2007). Three main categories of ground-based remote sensing techniques are used in landslide monitoring: Ground-Based Synthetic Aperture Radar Interferometry (GB-InSAR), Terrestrial Laser Scanning (TLS) and Terrestrial Optical Photogrammetry (TOP). A non-exhaustive review of the main advantages and disadvantages of these techniques is presented in Table 1. Detailed reviews of the application of GB-InSAR and TLS to landslides can be found in Corsini et al. (2006), Tarchi et al. (2003), Jaboyedoff et al. (2010), Teza et al. (2007, 2008) and Monserrat and Crosetto (2008). A state-of-the art of the application of TOP to landslide and related geomorphological processes is given below.

TOP is a technique with implementation, operating and equipment costs much lower than GB-InSAR and TLS. The technique consists in acquiring digital RGB images represented using a matrix of intensity values (brightness) recorded at each pixel of the Charge Coupled Device (CCD) of the camera from a spot very close to the ground (Jiang et al., 2008). In the last decades, camera self-calibration and analytical processing techniques allow the use of non-metric cameras and of simplified camera calibration algorithms to compute digital elevation models using the principle of stereoscopic views (Mikhail et al., 2001; Jiang et al., 2008). In the current state, the application of terrestrial images for landslide monitoring is mostly related to the production of DEMs for image ortho-rectification and sediment budget analysis (Bitelli et al., 2004; Pesci et al., 2004; Cardenal et al., 2008), and more recently to the characterization of the slope morpho-structure (Lim et al., 2005; Sturzenegger and Stead, 2009).

Using matching techniques, two-dimensional displacement fields can be derived by tracking objects in two images acquired at different time. So far, image correlation techniques have been applied only on aerial and satellite images (e.g. SPOT, QuickBird, OrbView, EROS) for the creation of landslide displacement maps (Casson et al., 2003; Delacourt et al., 2004; LePrince et al., 2008; Debella-Gilo and Kääb, 2011). The use of image correlation on terrestrial images has not been as popular for permanent landslide monitoring as in other application fields such as in solid and fluid mechanics for the characterization of the deformation pattern of soil/rock samples (White et al., 2003; Chambon et al., 2003; Küntz et al., 2007) or for the monitoring of other natural processes such as ice glaciers (Corripio, 2004; Fallourd et al., 2010; Maas et al., 2008) or volcanoes (Honda and Nagai, 2002). Only Delacourt et al. (2007) demonstrated an efficient application of TOP for landslide monitoring which consisted in the determination of the landslide boundaries and in the qualitative estimation of the spatial variability of displacement at the La Clapière landslide (French Alps) with an image acquisition system installed at 1-km distance.

Generally, the 2D displacements (in pixels) evaluated by the correlation algorithm have an accuracy of about 0.2 pixels (Casson et al., 2005; Delacourt et al., 2007) in the image plane, corresponding to an accuracy of millimeters to several centimeters for distances of about 100 m in the local coordinate system (Kraus and Waldhäusl, 1994).

The objective of this work is therefore to evaluate the potential and the limitations of TOP for the permanent monitoring of landslides using image correlation techniques. The dataset of images available for the Super-Sauze landslide (South French Alps) for the period 2008–2009 is used. First, the steps in the data acquisition and data processing (image correlation, ortho-rectification) are presented and the results are evaluated using the displacement of benchmarks measured by dGPS. Second, the main advantages and disadvantages of the method and the influence of external factors on the precision and the accuracy of the results are discussed.

Throughout this work, the accuracy is defined as the systematic difference between a measured quantity and the true value, and precision is defined as the random difference between multiple measurements of the same quantity.

Table 1
Relative advantages and disadvantages of GB-InSAR, TLS and TOP for landslide monitoring.

Techniques	Relative advantages	Relative disadvantages
GB-InSAR	High data accuracy possible (millimetric accuracy)	Requires large initial investment
	Monitoring during night and any type of weather conditions	Skilled crew required for operation
	Atmospheric effects can be corrected (permanent scatterers)	Displacement along line of sight
	Potential for high level of automation in acquisition and post-processing	Fails in detecting large and rapid displacements (signal decorrelation)
		Sensitive to changes in acquisition geometry and surface state variations
TLS	High data accuracy possible 1–4 cm (at 100 m range); 30 cm (at 1000 m range)	Requires large initial investment if buying
	Provides an easily understandable image	Skilled crew required for operation
	Potential for high level of automation in acquisition	Computation of the true 3D displacements require specific algorithms optimized for calculations on large 3D point clouds
		Large amount of computational resources for spatial data visualization
		Automated data post-processing difficult
TOP	High data accuracy possible from millimeters to a few centimeters at 100 m range	Adverse weather and illumination changes affect image quality
	Provides an easily understandable image	Not operating during the night
	Low initial and operating costs	Very sensitive to changes in acquisition geometry and surface state variations
	Low energy supply (passive sensors)	Ortho-rectification using accurate DEM is necessary for quantitative analysis
	Potential for high level of automation in acquisition and post-processing	Ground control points necessary for camera calibration
	Simple camera calibration	
	Simple matching algorithms available to produce DEMs and to compute 2D displacement fields	

2. Experimental site: the Super-Sauze landslide

To evaluate the potential of correlation of ground-based images for landslide monitoring, the dataset available at the Super-Sauze landslide, triggered in the Callovo-Oxfordian black marls of the South French Alps (Alpes-de-Haute-Provence, France; Fig. 1) is used. The landslide is located in the upper part of the Sauze torrential catchment. In the 1960s, the area was affected by rock falls in the scarp area. The fallen material composed of rocky panels progressively transformed into a silty-sandy matrix integrating marly fragments of heterogeneous sizes through successive weathering cycles (Malet, 2003). From the 1970s until today, the landslide material is gradually filling a torrential stream with a typical range of displacement rate comprised between 1 and 3 cm day^{-1} on average and possible acceleration of up to 40 cm day^{-1} (Malet et al., 2002). In 2007, the mudslide extents over a distance of 920 m between an elevation of 1980 m at the scarp and 1760 m at the toe with an average width of 135 m and a average slope of 25°. The total volume is estimated at 560,000 m^3 (Travelletti and Malet, 2012).

The kinematics of the landslide is currently monitored by differential Global Positioning System (dGPS), Terrestrial Laser Scanning (TLS) and by a remote camera monitoring system. This instrumentation consists in a low-cost D70 Nikon reflex digital camera installed on a concrete pillar located on a stable crest in front of the landslide at a distance of 300 m from the lower part and 900 m from the main scarp (Fig. 1A, B, and C). The acquisition system is controlled by a data logger (Campbell CR10) and the power is provided by a 40 W solar panel. The characteristics of the acquisition are presented in Table 2. Every four days, a series of images is acquired at 11:00, 12:00, 13:00 and 14:00 GMT in order to increase the probability of acquiring at least one image with good meteorological and illumination conditions. Each photograph (6 Mb) is stored in the Nikon native file format (NEF – Nikon Electronic Format) to avoid any loss of information.

3. Methodology

The steps in the data processing workflow consist in (1) correlating the images by pairs in their original acquisition geometry and (2) orthorectifying the calculated displacement fields using a high-resolution digital elevation model interpolated from airborne LiDAR data. The images presenting the best ground texture contrast and the most homogeneous lightening are manually selected. The detailed methodology is summarized in Fig. 2 and described below.

3.1. Principle of the image correlation technique

The 2D displacement field is obtained by correlating two optical images acquired at different time. The image correlation technique is based on the automatic identification of identical texture patterns within an image by maximizing a correlation function (Lewis, 1995; Baratoux et al., 2001; Debella-Gilo and Kääb, 2011). Its principle adapted for landslide kinematics analysis is described in (Delacourt et al., 2007). Visible ground features have to be superimposed on two successive images on stable parts located outside the landslide. On the areas affected by landslide movements, the visible and recognizable features are shifted by the displacements. In order to quantify the ground displacements, a correlation window is defined on a reference (often the oldest) image. The corresponding window is searched in a pre-defined explored area belonging to the second image. The starting point of this explored area is the expected position of the window with the assumption that no displacement occurred between two acquisitions. The process is repeated for each pixel of the reference image. The Euclidean distance between the reference point and the matching point represents the displacement amplitudes in the image plane. By modifying the zone of interest, it is then possible to determine the displacements at various positions within the images. It is important to note that the normalized cross-correlation technique cannot track objects that start to rotate significantly or are affected by important perspective distortions (Lewis, 1995).

The size of the correlation window is a compromise between the desired accuracy on the displacement estimates and the spatial resolution of the velocity field (Delacourt et al., 2007). An increase of the size of the correlation window ensures a good signal to noise ratio and thus a good precision, but the accuracy on the displacement estimates decreases because of their averaging on a larger correlation window. This compromise is difficult to define when some parts of the landslide are well represented in terms of ground texture while other parts are not. Hierarchical correlation techniques allow one to overcome this problem by automatically changing the physical size of the correlation window and of the explored area during the correlation computations. The physical size is defined as the effective landslide surface covered by the correlation window (Rohály, 2002; El Alaoui and Ibn-Elhaj, 2009).

In this work, a sub-pixel hierarchical correlation technique is used (Hild, 2003; Chambon, 2003). The RGB images are first converted in gray-scale images to which a 3×3 pixel Sobel convolution matrix is applied to highlight the ground surface texture. The gradient values are then correlated (Chambon, 2003). Four successive degradations of the image resolution are applied following a pyramidal approach for changing the physical size of the correlation window and of the explored area by down-sampling the gradient values of the full resolution image (D'Antone, 1995; Kumar and Banerjee, 1998) (Fig. 3). The optimum sizes of the correlation window (16×16 pixels) and of the explored area (32×32 pixels) were identified with a trial and error procedure. These parameters are constant during the correlation computation. The correlation starts with the lowest resolution image in order to determine the largest displacements. Then the location of the pixel with the maximum cross-correlation value is used as the centre of the zone of interest for the next correlation step at a higher resolution. The spatial location of the maximum correlation value in the highest resolution image is thus progressively better estimated (Fig. 3). Ignoring high resolution information at the first computational step decreases the probability to reach a local minimum of the correlation function and, consequently, to obtain a wrong matching in the correspondence solution (El Alaoui and Ibn-Elhaj, 2009). In addition, this approach ensures very often a higher probability of detecting a reliable correlation peak (Anandan et al., 1993). The sub-pixel displacement is computed after the correlation at the highest resolution image. An iterative procedure is used to find the maxima of the correlation function interpolated with a bi-parabolic formula and with a maximization procedure based on the simplex method (Press et al., 1997; Chambon, 2003).

The correlation results consist in matrices of displacement Δu and Δv along the u- and v-axes in the image plane with their associated correlation index (Fig. 3). Because the pixel size is not constant in the image due to the oblique acquisition, the displacement field correlated in the image plane cannot be directly interpreted in terms of metric displacements. Therefore an orthorectification procedure is necessary for a quantitative analysis of the displacement fields.

3.2. Ortho-rectification of the displacement field using high-resolution digital elevation models (DEMs)

The orthorectification procedure consists in transforming the central projection of the image into an orthogonal view of the

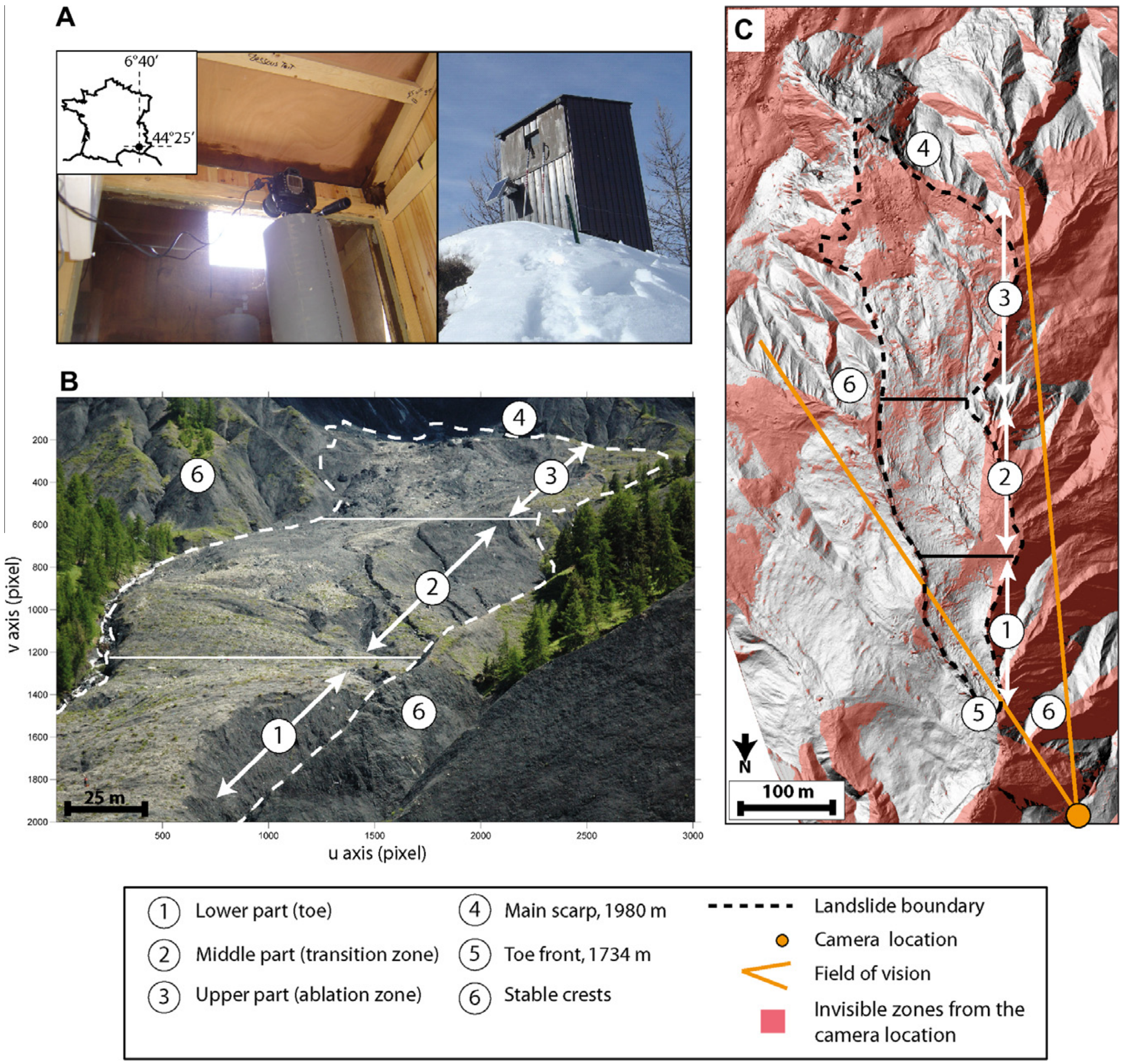

Fig. 1. Overview of the Super-Sauze landslide (South French Alps). (A) Monitoring system by terrestrial optical photography. (B) Image acquired by the monitoring system presenting the different parts of the landslide from the camera location. (C) View of the landslide morphology in the local coordinate system on a shaded relief computed with a 0.25 m resolution DEM interpolated from an airborne LiDAR survey (ALS) acquired in July 2009. The invisible areas from the camera location are indicated.

Table 2
Characteristics of the camera acquisition systems.

Type of camera	Single-lens reflex Nikon digital camera
Effective pixels	6.1 million
Image sensor	RGB CCD, 23.7 × 15.6 mm
Image size	3008 × 2000 pixels
Sensitivity	400 iso
Focal length	52 mm
Shutter speed	1/800
Storage media	CompactFlash™ (CF) Card
Storage system	NEF (Nikon RAW)

ground by correcting the effects of various distortion sources such as camera orientation, topographic effects and lens characteristics (Kraus and Waldhäusel, 1994). In terrestrial photogrammetry, distortions induced by topography effects are the most important due to the oblique acquisition of the images. The orthorectification converts the initial (u, v) and the final $(u + \Delta u, v + \Delta v)$ positions of the displacement vectors in a local coordinate system. The conversion is possible if a digital elevation model (DEM) of the object is available in order to relate two-dimensional pixel positions in the image plane to three-dimensional points in a local coordinate system using parametric approaches (Hemmleb and Wiedemann, 1997).

In our approach, the rotation angles defining the external orientation of the camera are first determined using the relationship between the image coordinates (u, v) and the local coordinate systems (X, Y, Z) given by the collinearity equations (Bonneval, 1972; Kraus and Waldhäusl, 1994). These equations are based on the principle that each point in the local coordinate system is projected with a straight line through the projection center (origin of the camera) into the image plane. Knowing the exact location of the camera and assuming that the principal point is at the center

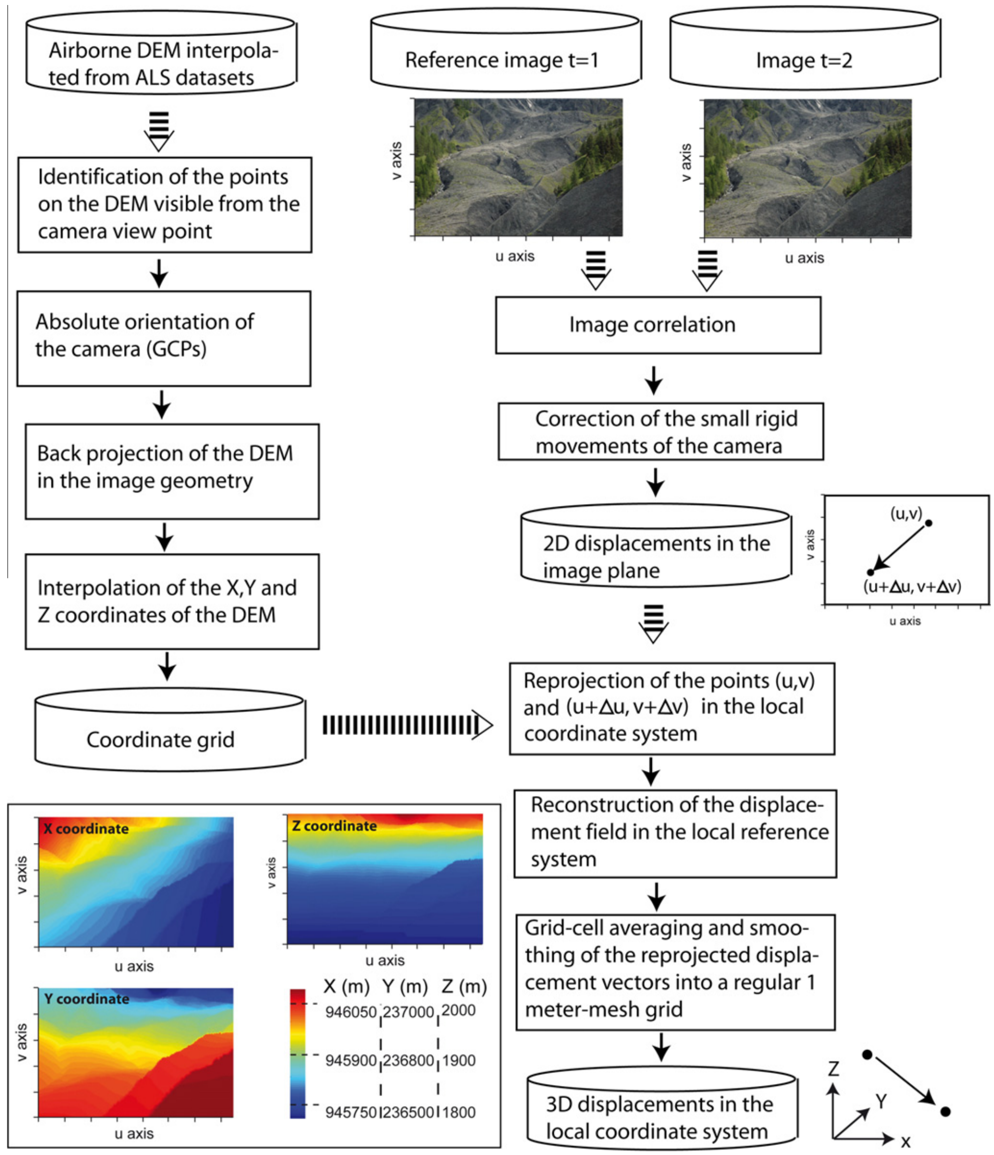

Fig. 2. Flowchart of the methodology.

of the image, the external angle and the effective focal length defining the absolute orientation and the internal parameter of the camera, respectively, can be determined with help of Ground Control Points (GCPs; Heikkila and Silven, 1997; Corripio, 2004).

In our case, a series of 95 pairs of GCPs distributed on the image plane and in the local reference system were measured with dGPS (Fig. 4). The centers of the GCPs are positioned in the local coordinate system with an average 3D accuracy of 0.02 m and a standard deviation of 0.01 m. The coordinates (u, v) of the GCPs in the image plane are determined by manual picking with an estimated accuracy of about 2 pixels. Among the 95 GCPs, 45 are used to compute the external parameters and 40 are kept to calculate the accuracy of the transformation (Section 5.2.1). A least mean square minimization technique based on a Direct Linear Transformation (DLT) and Singular Value Decomposition (SVD) between observed and calculated GCPs in the image plane is used to determine the external and internal parameters that satisfy the collinearity equations (Abdel-Aziz and Karara, 1971; Heikkila and Silven, 1997).

Then, two DEMs (0.25 m mesh-size, 3D error of 0.07 m) interpolated from Airborne Laser Scanning (ALS) dense point clouds acquired in October 2007 and July 2009 are used to orthorectify the displacements. A back projection of the DEMs is applied in the image plane using the external and internal parameters of the camera previously determined with the GCPs (Mikhail et al., 2001; Corripio, 2004). Only the points of the DEM visible from the camera viewpoint are back projected to avoid duplicate points in the same position in the image plane. The sightline method is used to identify the visible points (Fig. 1C; Fisher, 1991; Franklin and Rav, 1994). About 57% of the landslide area is visible from the camera view point. No displacements can be determined in the invisible areas. The 3D coordinates of the projected DEMs are then linearly interpolated in the image plane to allocate a triplet of X, Y, Z coordinates to each initial point (u, v) and each final point $(u + \Delta u, v + \Delta v)$ of the correlated displacements. A re-projection of the displacement vector components in the local reference system is then applied. The displacement components in the local coordinate system are finally averaged and smoothed in a regular grid with a mesh size of 1 m.

The use of a mono-temporal DEM for the orthorectification of the initial point (u, v) and the final point $(u + \Delta u, v + \Delta v)$ of the displacement vectors is a strong hypothesis that the global landslide morphology remains constant over the period. It affects the accuracy

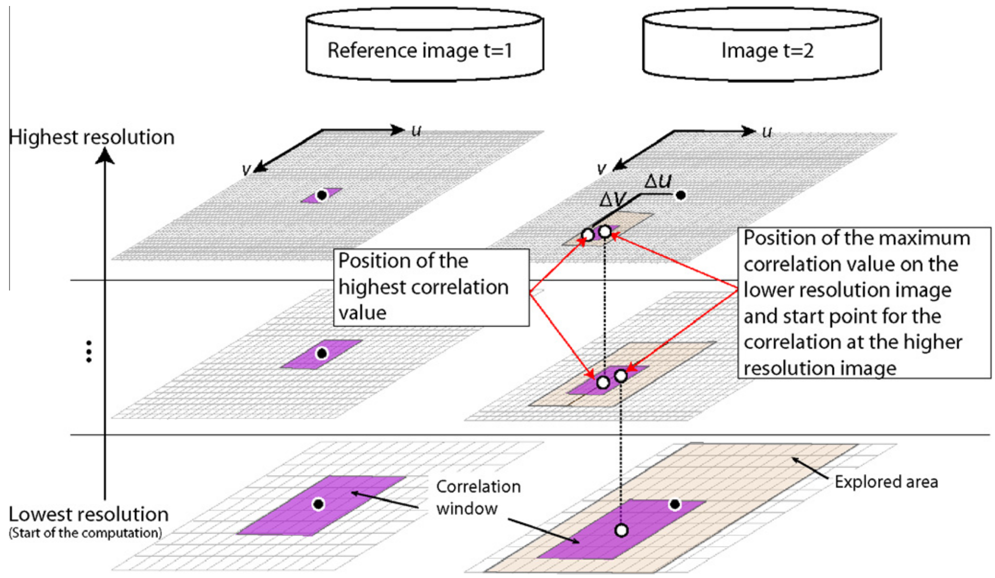

Fig. 3. Principle of normalized hierarchical image correlation.

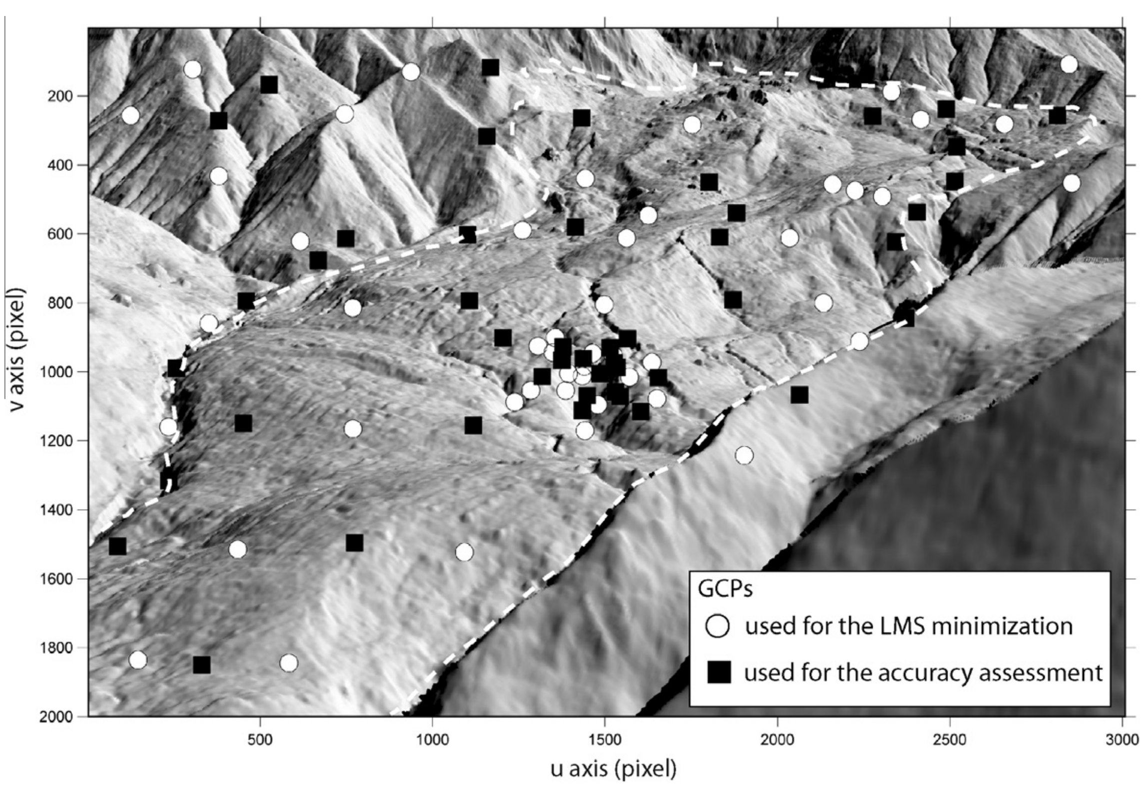

Fig. 4. Location of the Ground Control Points (GCPs), used for the Least Mean Square minimization (LMS) and for the accuracy analysis, plotted on a shaded relief image. The shaded relief image is produced by interpolating the shaded relief values of the ALS DEM of 2009 projected into the image plane.

of the transformation of the displacement vector in the local coordinate system. However, it will be further demonstrated that this method is still a relevant estimation for our purpose with reference to the amplitude of the observed displacements (Section 4.2).

3.3. Image resolution at the terrain surface

The effective (e.g. ground) pixel size is one of the limiting parameters for the accuracy of the correlation (Fig. 5A). It determines the minimum theoretical displacement that can be detected for a pixel-level correlation. Below this displacement threshold, the accuracy solely depends on the accuracy of the sub-pixel correlation. The effective pixel size depends on (1) the distance between the object and the camera and (2) the angle of incidence which is defined as the complementary angle between the line of sight of the camera and the normal to the terrain surface (Fig. 5B). A low incidence angle means that the line of sight is nearly tangential to the topography.

Globally, the incidence angle on the landslide ranges from 0° to 40° and the pixel size varies from 1×10^{-2} m^2 in the lower part (at

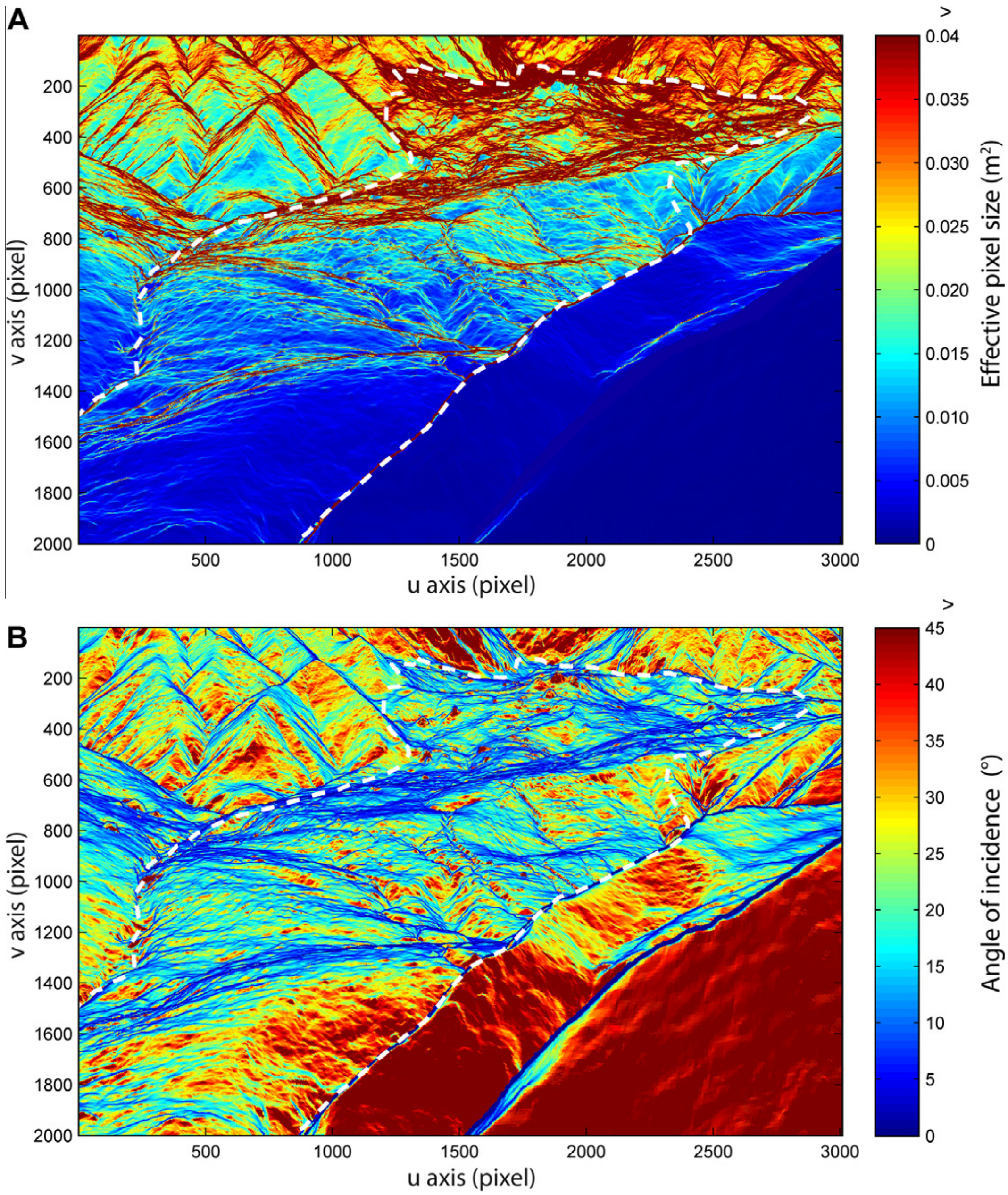

Fig. 5. Characteristics of the images: (A) Effective pixel size calculated with the ALS DEM of 2009 projected to image geometry (in m^2); (B) Angle of incidence (in degrees).

an average distance of 300 m) to 3×10^{-2} m^2 in the upper part of the landslide (at an average distance of 900 m; Fig. 5A and B). The upper part is characterized with a pixel size often larger than 0.04 m^2, especially in areas where the angle of incidence is less than 5°. Therefore the lowest accuracy is expected in this region because the detection of small Δv and Δu displacements can correspond to important ΔX, ΔY, ΔZ metric displacement. Approximately half of the number of pixels in the image plane inside the landslide area show a metric sensitivity of less than 0.17 m for 1 pixel displacement along the v-axis and of less than 0.07 m along the u-axis. The minimum displacements for a pixel-level correlation in the u and v-direction are 0.04 and 0.06 m, respectively, in the lower part of the landslide and 0.09 and 0.11 m in the upper part. In areas where the incidence angle is less than 5°, the minimum displacement that can be detected drastically increases. Therefore no strong confidence is given to areas whose incidence angle is lower than 5°.

3.4. Post-processing: displacement filtering

Filtering criteria are necessary to remove the badly correlated points and improve the signal to noise ratio (Casson et al., 2003; Berthier et al., 2005; Wangensteen et al., 2006; Debella-Gilo and Kääb, 2011). Three criteria are used in this work to filter aberrant displacements in the image plane coordinate system and in the local coordinate system. They are based on:

1. The value of the correlation peak coefficient: loss of coherence can occur during the computations because changes in surface states between a reference image and the correlated image are high, resulting thus in low correlation coefficients. Defining a threshold value has the consequence to increase the percentage of realistic displacements. A high threshold coefficient of $r = 0.6$ was selected to remove the badly correlated points. However, the correlation peak coefficient alone is not a sufficient

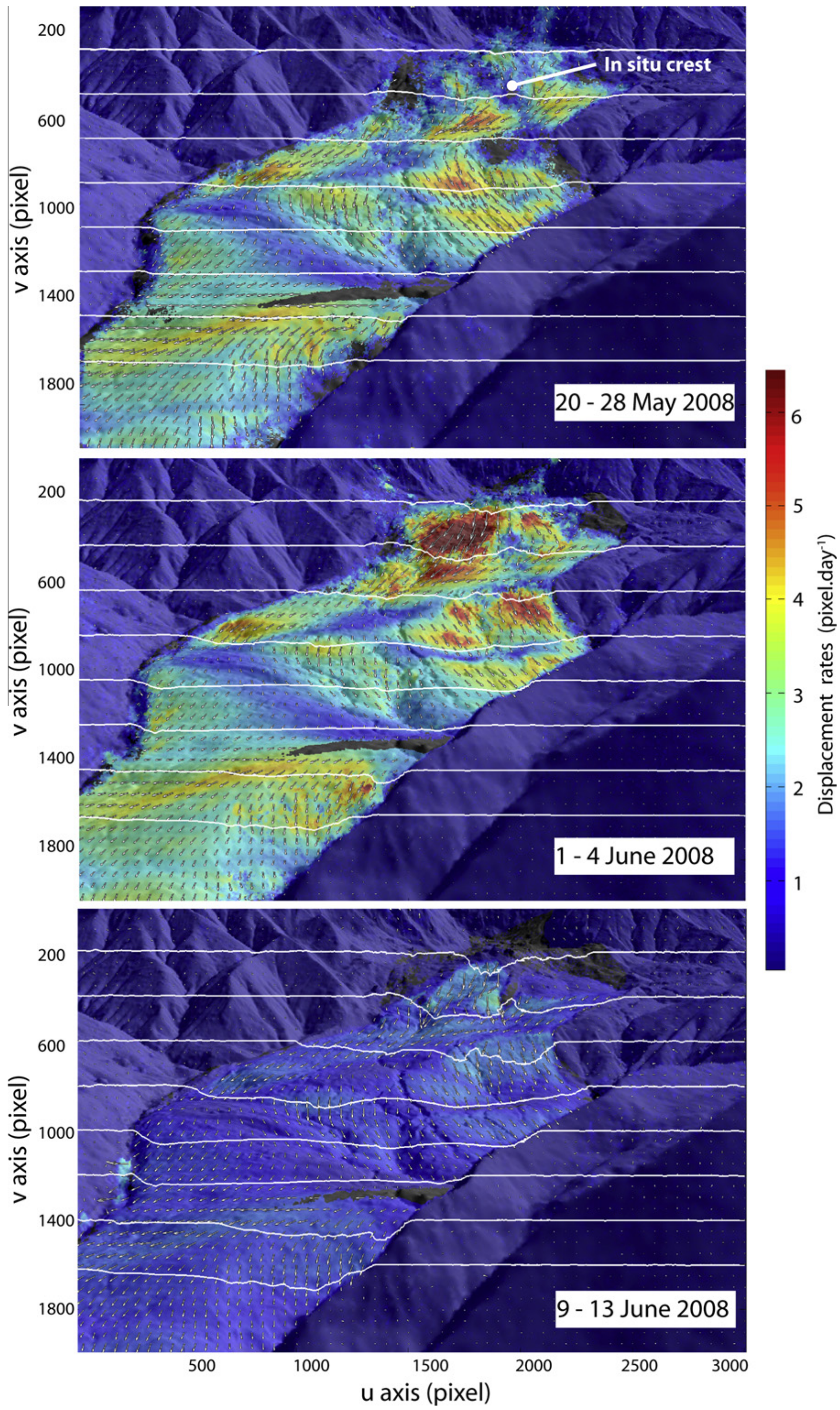

Fig. 6. Displacement rate amplitude (color) and direction (arrow) in the image plane and cumulated displacements along eight profiles crossing the landslide over the period 20 May–25 June 2008. In order to highlight the displacement direction, the arrow length is normalized for each image.

discriminating criterion because some points can display a high correlation coefficient even if they do not represent the same object (e.g. two trees or large stones having the same geometry; Casson et al., 2005).

2. The value of displacement amplitude and direction: points characterized by upslope displacement and important displacement amplitude with reference to a priori knowledge on the landslide kinematics are filtered.
3. The displacements assigned to invisible points from the camera viewpoint because of small orthorectification errors in the conversion to the local coordinate system.

The amount of filtered correlated points varies greatly according to the season; a test carried out with images pairs of 23–27 July 2008 (summer season) and 19–23 October 2008 (autumn season) indicates a number of remaining point post-filtering of

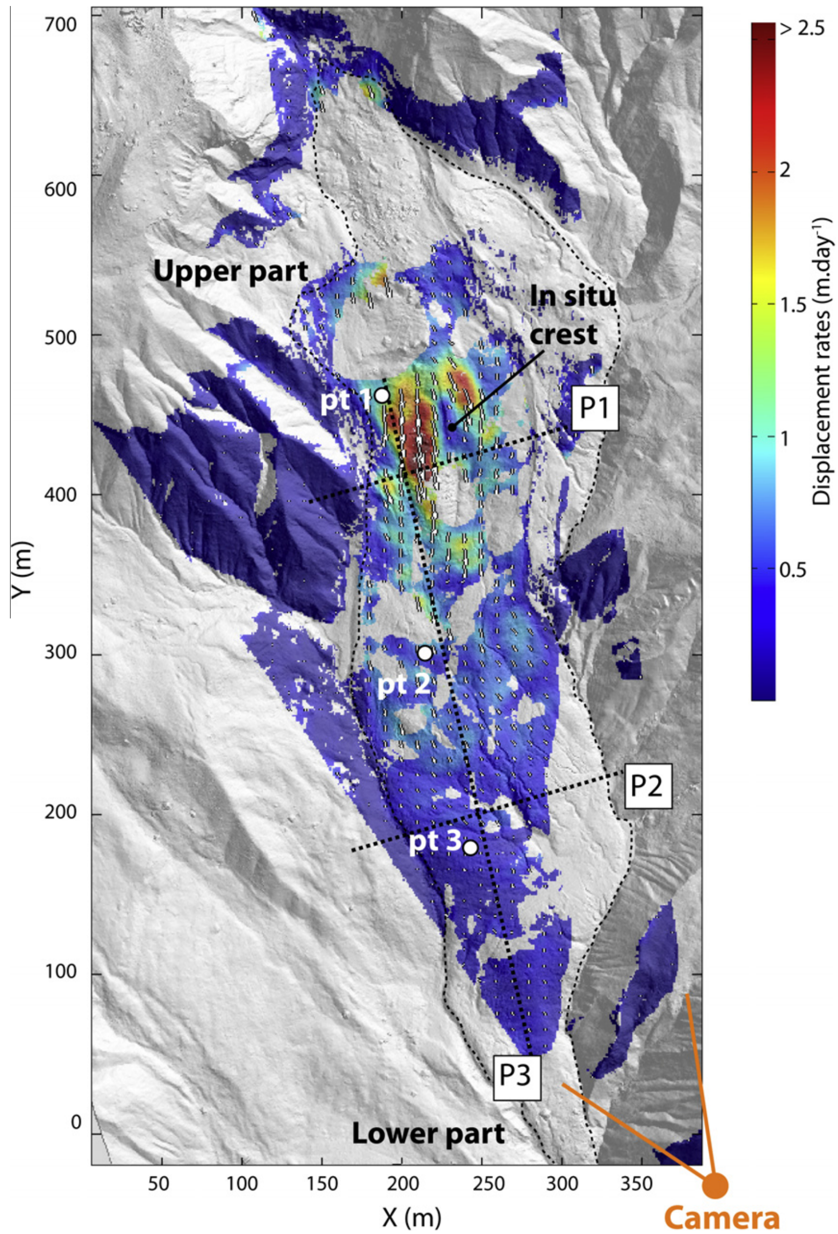

Fig. 7. Displacement rates for the period 1–4 June 2008. The profiles P1, P2 and P3 refer to Fig. 8 and the locations pt 1, pt 2 and pt 3 refer to Fig. 12.

80–90% for the summer period and of only 50% for the autumn period. This is mainly explained by the different illumination conditions (especially low sun elevations in autumn) which affect the quality of the correlation. This aspect will be discussed further in Section 6.1.3.

The upper part of the landslide is most affected by the filtering. This area generally shows a percentage of remaining values lower than in the middle and lower parts of the landslide. This is explained by the fact that the upper part has a more chaotic morphology. Consequently the effects of illumination changes are more important than in the middle and the lower parts, especially in autumn. In addition, the angle of incidence in this area can be low (5–10°) and thus sensitive to slight movements of the camera.

4. Results

4.1. Displacement maps of the landslide

A set of images over the period May–July 2008 is used to illustrate the potential of the technique for the characterization of the kinematics during an acceleration period triggered by high rainfall amounts and a fast melting of the snow cover.

Fig. 6 shows an example of displacement rate (in pixels day^{-1}) of the ground surface in the image plane derived from image pairs of 20–28 May 2008, 1–4 June 2008 and 9–13 June 2008. The reference is the image of 20 May 2008. The contrast in displacement rates between the landslide area and the stable area gives confidence on the calculated velocity field. One can notice that the

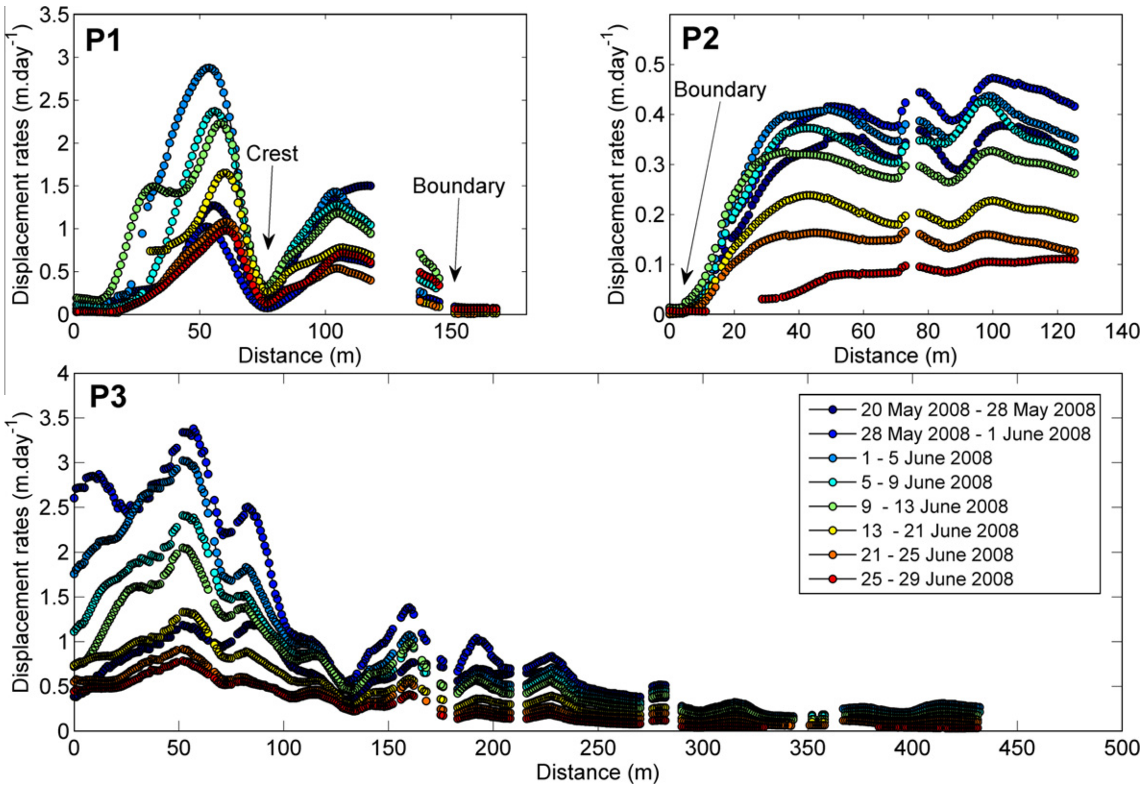

Fig. 8. Profiles of displacement rates in the upper (P1), middle (P2) and lower (P3) parts of the landslide. The location of the profiles is indicated in Fig. 7.

pattern of displacement rate is heterogeneous spatially and temporally. The upper part of the landslide displays the highest velocity ranging from 1 to 7 pixels day^{-1} while the lower part displays velocity of less than 4 pixels day^{-1}. No quantitative comparisons can be carried out at this stage because the pixel sizes vary strongly in the image (Fig. 5A). From the 20 May 2008 to the 13 June 2008, cumulated displacements of up to 110 pixels are observed in the upper part. The maximum displacement rate is observed around the 1st June. Then the landslide decelerates to a displacement rate of about 1 pixel day^{-1}.

Some local specific displacement patterns are also clearly highlighted. For instance, the presence of a stable *in situ* crest located in the landslide body is perfectly identified in the correlated images.

Fig. 7 presents the amplitude of the 3D orthorectified displacement rates for the period 1–4 June 2008 in the local coordinate system. The difference of kinematics between the upper (up to 3 m day^{-1}) and the lower (up to 1 m day^{-1}) parts becomes more evident than in the image plane. The geometrical effect induced by the presence of the stable *in situ* crest on the landslide kinematics is also clearly pointed out. The temporal evolution of the displacement rates is illustrated with two transversal profiles and one longitudinal profile on Figs. 7 and 8. In particular, the difference of displacement rates between the upper and the lower part of the landslide is pointed out.

The precision of the computed displacements is assessed by testing a null hypothesis on the stable areas (Berthier et al., 2005; Casson et al., 2003). Only the points with a correlation coefficient $r > 0.8$ are taken into account. In the image plane coordinate system, the average error μ ranges from 0.5 to 0.9 pixels with standard deviation σ of 0.3 to 1.2 pixels for the image pairs between 20 May 2008 and 25 June 2008. In the local coordinate system, the average error μ ranges from 0.03 to 0.11 m with standard deviation σ of 0.10–0.31 m for the image pairs between 20 May 2008 and 25 June 2008.

4.2. Comparison with dGPS displacements

Sixty benchmarks distributed in the stable parts and on the landslide body were monitored by dGPS (horizontal and a vertical average accuracy of ±0.02 and ±0.05 m) to estimate the accuracy and validate the displacements obtained from image correlation. In total, 219 dGPS measurements are available for the period 2008–2009. In order to validate the displacements computed in the image plane, the dGPS benchmarks are projected to the image plane using the collinearity equations. The pixel displacements derived by image correlation are then averaged in a perimeter of 16 pixels around each benchmark. The results are presented in Fig. 9A. A correlation coefficient of $r = 0.98$ is found between dGPS measurements and image correlation, and an average relative accuracy of 11% is determined (Fig. 9C). In order to validate the metric displacements in the local coordinate system, the orthorectified displacements are averaged in an area of 4 m^2 around each benchmark and compared with the dGPS displacements. A correlation coefficient of $r = 0.95$ is found (Fig. 9B), and an average relative accuracy of 20% is determined (Fig. 9D). The reason why the correlation coefficient in the orthorectified case is lower than in the pixel case is believed to be related to the accuracy of the DEM used for orthorectification. This will be discussed in Section 5.2.2.

5. Discussion: sources of errors

The major sources of errors affecting the displacement calculations and thus limiting the efficiency of TOP for an operational landslide monitoring can be classified in two groups: (i) the parameters affecting the image correlation computation and (ii) the external parameters influencing the orthorectification procedure.

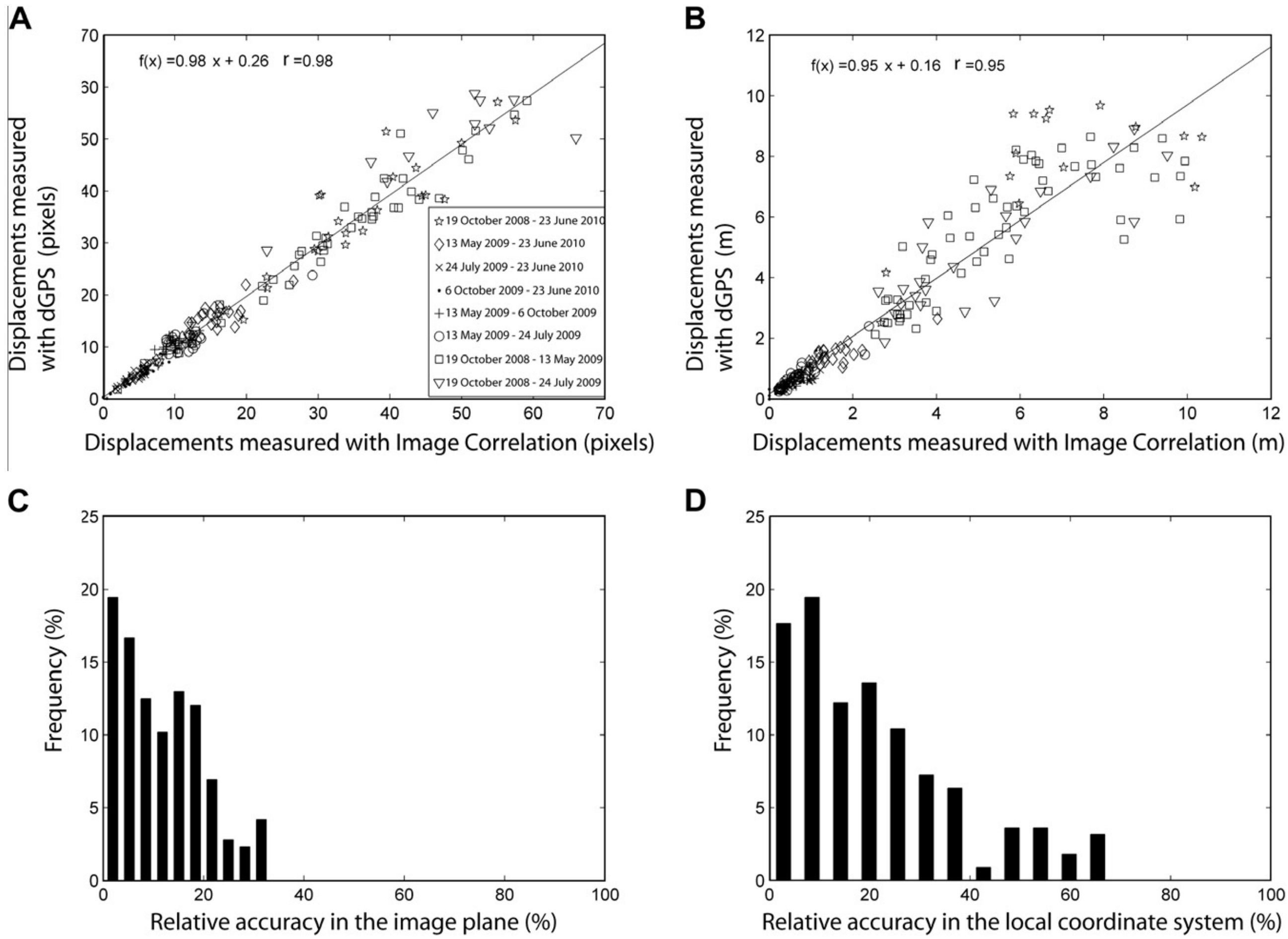

Fig. 9. Assessment of the accuracy of the image correlation technique. Relationships between the displacements observed by image correlation and the displacements measured by dGPS on sixty benchmarks in the image plane (A) and in the local coordinate system (B). Relative accuracy of the image correlation technique in the image plane (C) and in the local coordinate system (D).

5.1. Sources of errors affecting the image correlation computation

5.1.1. Accuracy and precision of the image correlation algorithm

One limitation of the image correlation technique is directly linked to the correlation algorithm and the sub-pixel interpolation method (Debella-Gilo and Kääb, 2011). A series of experimental tests were carried out to assess the precision of the image correlation technique. The series of tests allow one to investigate the influence of the size of the correlation window and of the level of noise observed in the images. Homogeneous imposed displacements (systematically equal to a multiple of pixels to avoid image resampling; Chambon et al., 2003) are applied to pairs of images to create synthetic images. Furthermore, three levels of Gaussian noise were added to the original images with a mean noise level of zero and variances σ^2 of 10^{-4}, 10^{-3} and 10^{-2} (Fig. 10A). Then the image correlation technique is applied to the original image taken as reference and to the synthetic image with different sizes of correlation windows (5, 10, 16, 20, 30 and 50 pixels). For each correlation window, fifteen imposed displacements were calculated with amplitudes ranging from 1 to 23 pixels along the u and v-directions. The analysis was conducted by comparing the noisy synthetic images with the reference image. In the optimal case, the measured displacement would be identical to the imposed displacement.

Each image correlation analysis revealed displacement differences distributed close to zero (mean accuracy of 5×10^{-4} pixels). As observed by Hild (2003), the precision of the correlation algorithm mainly depends on the pixel fraction of the displacement. Larger correlation windows produce less scattered displacements and therefore improve the precision. By plotting the standard deviation of the calculated displacements against the size of the correlation window, the influence of the correlation window size can be pointed out (Fig. 10B). For very low level of noise, the precision is less than 0.1 pixels for a size of correlation window greater than 5×5 pixels. For higher level of noise, the precision is more dependent on the size of the correlation window. As homogenous displacement fields were imposed to the image, the accuracy (average misfit) is similar for small and large correlation windows. In reality, the displacement field becomes more heterogeneous at higher resolution. Therefore, an increase of the size of the correlation window implies a decrease of the spatial resolution but, as shown in these tests, an increase of the precision.

5.1.2. Influence of ground surface state

The time lag between two image acquisitions is one of the critical factors that affect the correlation computation. This time has to be long enough to increase the signal (e.g. landslide displacement) but short enough to preserve the tracked features (Berthier et al., 2005). Loading of the snowpack on the ground during winter, surface erosion due to fast snow melting and the development of water-saturated ponds in spring, weathering of the objects, growing of grass and large deformations are environmental processes that significantly modify the surface state during a year. Such correlation error sources are characterized by very low correlation

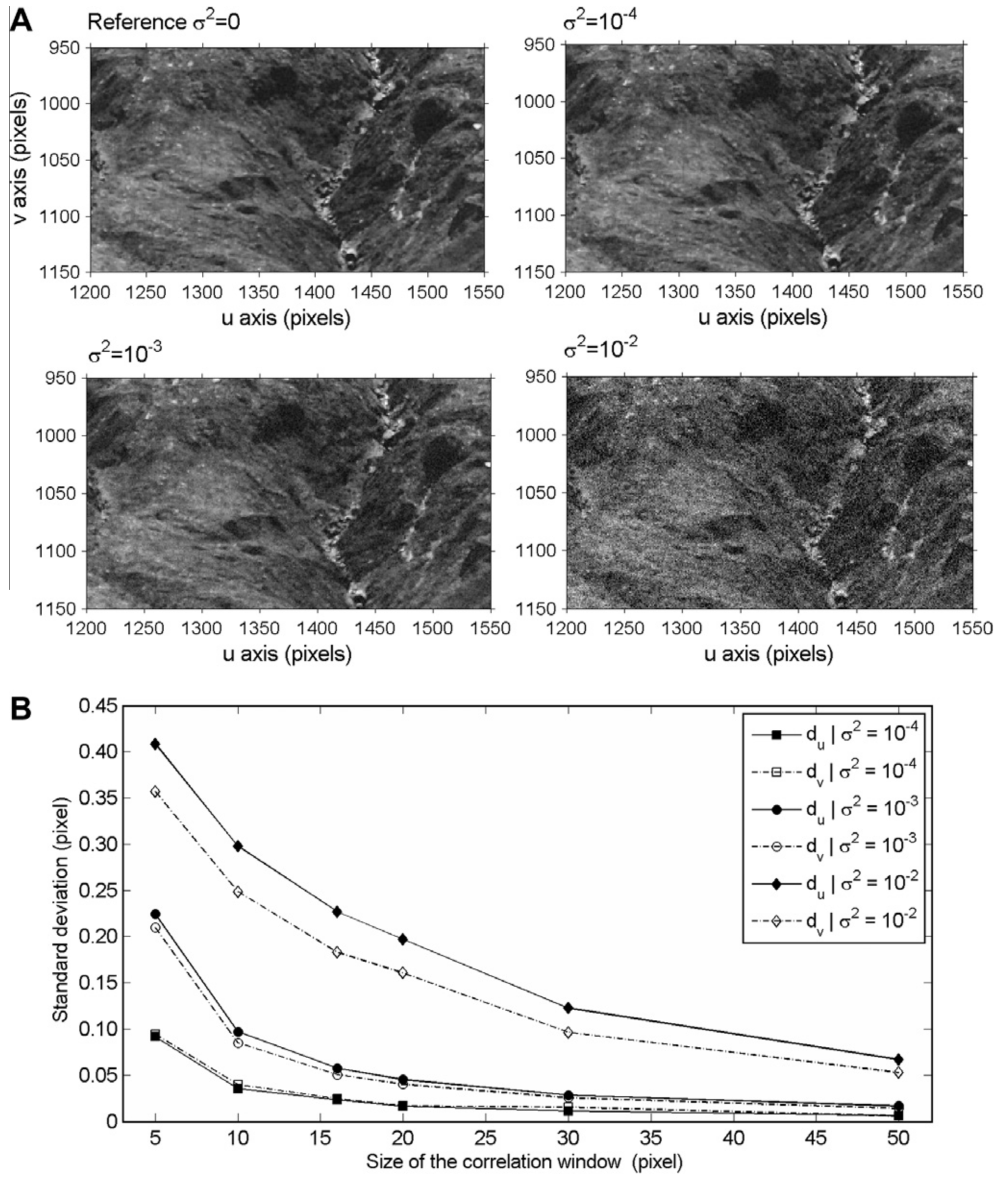

Fig. 10. Precision of the correlation algorithm. (A) Examples of different level of Gaussian noise introduced in the images; (B) Precision of the hierarchical correlator in the u and v direction as a function of different levels of Gaussian noise (σ_n^2) and different sizes of the correlation window.

coefficients, very large displacement amplitudes or randomly-distributed displacement directions in comparison to the neighbor pixels (Fig. 11). On average, about 20–25% of the points are usable from one year to the next year (using a correlation window of 16×16 pixels with a correlation coefficient threshold of 0.8). Consequently, the construction of long time series of displacements with the image correlation technique is a difficult task. The range of cumulated displacement rates observed over a period of 16 months (May 2008–September 2009) is illustrated by tracking the displacement at three locations in the upper (pt 1), middle (pt 2) and lower (pt 3) parts of the landslide in the direct vicinity of benchmark measured by dGPS (Fig. 7). In our case, the cumulated displacements of the year 2009 are adjusted on those of 2008 using GCPs measured with dGPS at the vicinity of the points pt 1, pt 2 and pt 3. The monitoring of some benchmarks with geodetic techniques is necessary to combine displacement patterns observed in image pairs acquired over the period May 2008–September 2009 (74 pairs of images). After the acceleration period of spring 2008, the displacement rates are decreasing to relative constant values of about 0.02 m day^{-1} in the lower and middle parts and 0.05 m day^{-1} in the upper part computed over the period July to October 2008 (Fig. 12).

5.1.3. Influence of illumination conditions

The difference observed in RGB intensities in various images acquired with various solar illumination angles is an important limiting factor essentially in terms of changes of the shadow areas (Berthier et al., 2005). In order to assess the influence of illumination conditions on the image correlation results, two experiments are carried out.

The first experiment consists in correlating images acquired at different times within a day. Four photographs acquired at 11:00, 12:00, 13:00 and 14:00 GMT in a period of low displacements (<0.02 m day^{-1}, August 2009) under clear sky conditions are correlated. The results indicate that illumination changes can lead to an average μ and a standard deviation σ of pixel-level error of μ_{1h} = 1.31 and σ_{1h} = 0.03, μ_{2h} = 1.35 and σ_2 = 0.12, μ_{3h} = 1.89 and σ_{3h} = 0.18 pixel for time-interval acquisition of 1, 2 and 3 h,

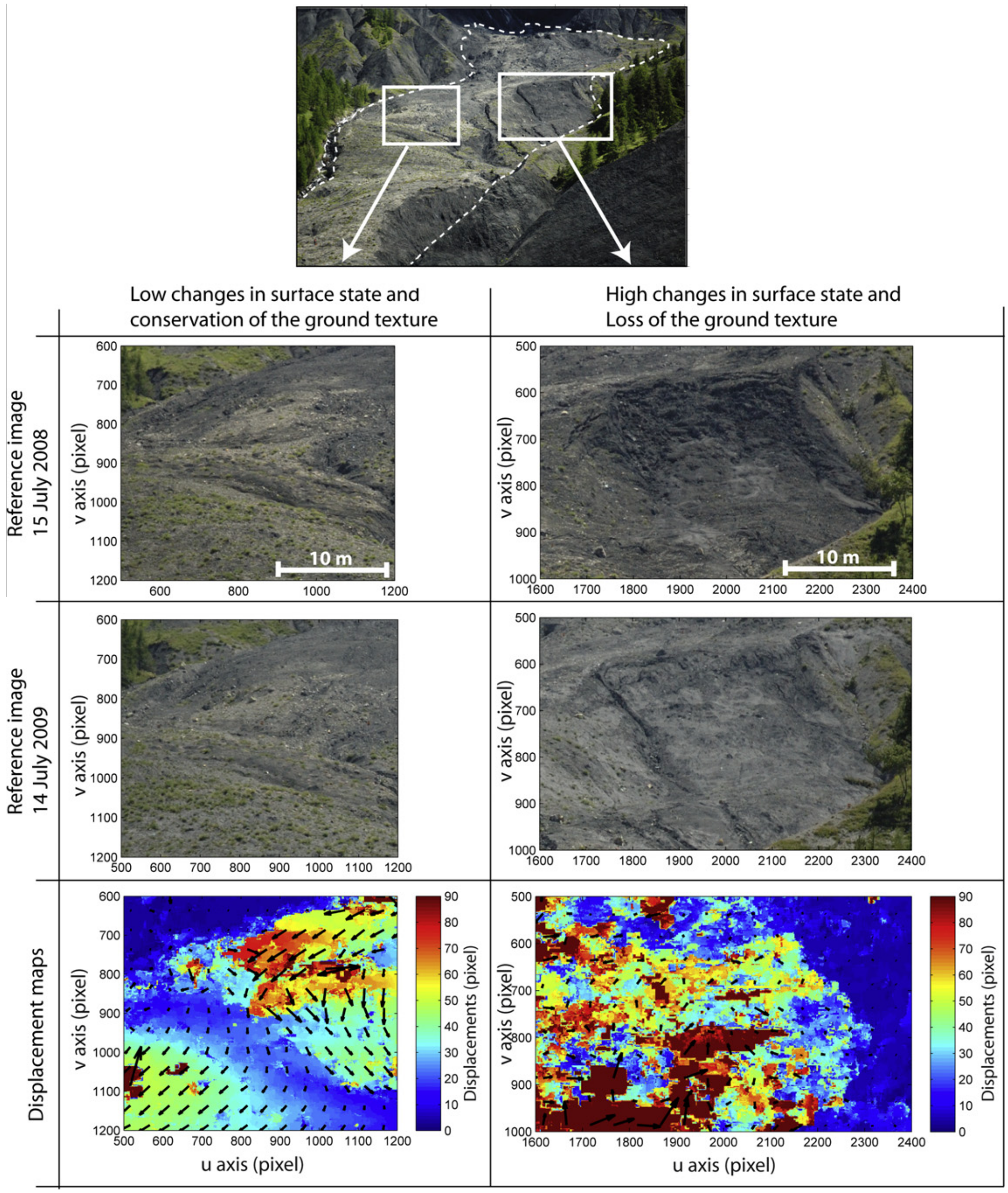

Fig. 11. Example of results for the correlation of two images acquired with one year interval (15 July 2008–14 July 2009), at the same solar time and with clear sky conditions. The incoherency of the displacements is clearly identifiable due to strong surface texture changes (inhomogeneous amplitude and direction of the displacement vectors).

respectively. The results demonstrate that the correlation of images acquired in nearly similar illumination conditions can display a pixel-level precision.

The second experiment consists in creating synthetic images with different shadow intensities as a function of the sun azimuth and elevation (Burrough and McDonnell, 1998). Only the shadows created by direct solar illumination are analyzed assuming clear-sky conditions. The effects of reflected and diffuse illuminations are neglected. Ninety-seven shaded relief images were created with different artificial illuminations (e.g. Fig. 4). Because a preference is given to correlate images taken when the sun elevation is maximal (Delacourt et al., 2007), a shaded relief image with a sun elevation of 65° and a sun azimuth of 250° (illumination coming from the South-West in July at 12:00 GMT) is chosen as the reference image for the correlation. The reference image is correlated with the shaded relief images. The mean correlation coefficient is used to characterize the influence of illumination changes on the image.

As expected, the correlation of the synthetic images indicates that the correlation coefficient strongly depends on the sun elevation and the sun azimuth (Fig. 13). Illumination coming from the opposite direction of the one of the reference (sun azimuth of 120°) with low elevation angles (<30°; end of the daytime in autumn) provides the less reliable correlation results. This finding is in agreement with Table 2 which indicates that the amount of interpretable displacements is lower in the autumn season than in the summer season (lower correlation coefficients). Therefore, correlation of images with a too large time-lapse has to be avoided

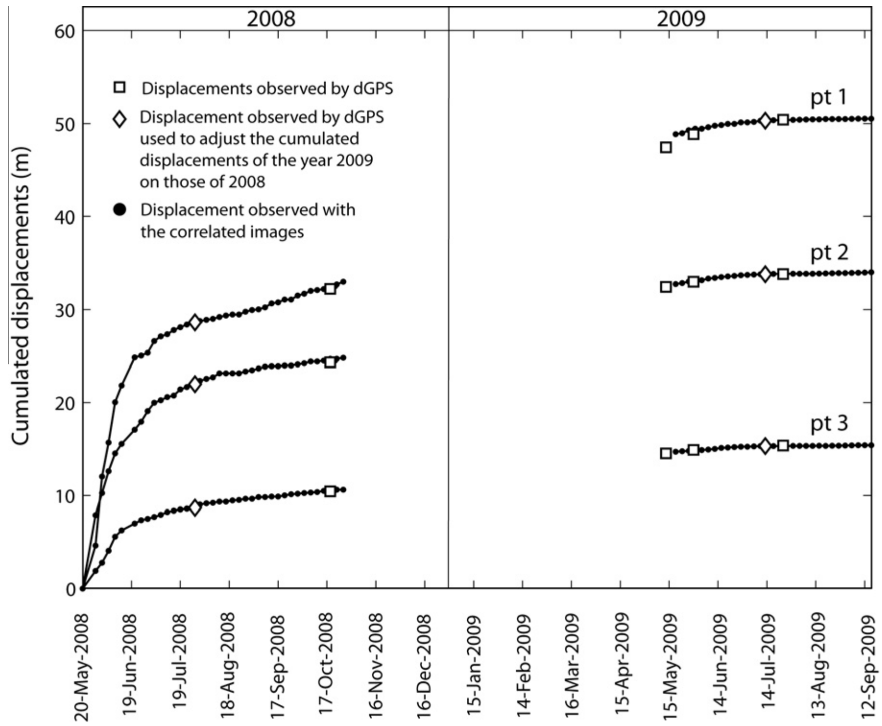

Fig. 12. Cumulated displacements at three locations in the upper (pt 1), middle (pt 2) and lower (pt 3) parts of the landslide. The location of the points is indicated in Fig. 7.

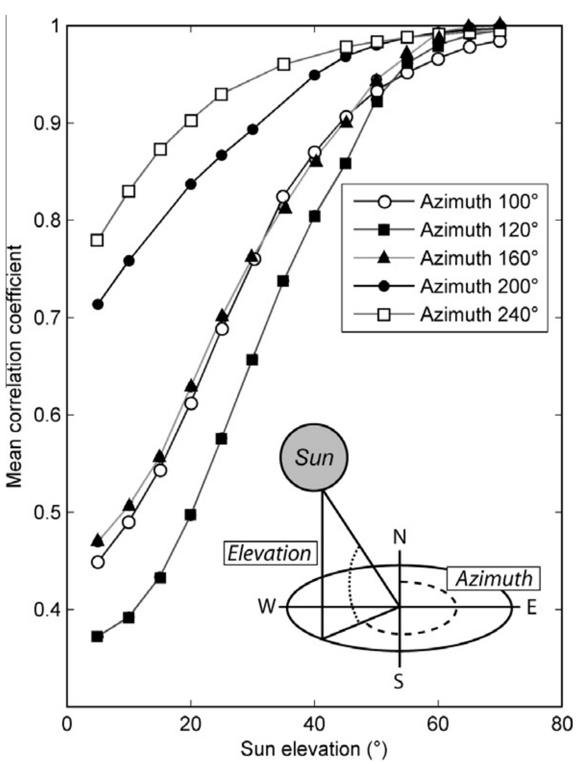

Fig. 13. Influence of illumination conditions as a function of the sun elevation and azimuth on the mean correlation coefficient.

to minimize illumination effects. A possible alternative is to correlate images under diffuse illumination (cloudy day) thus providing a more homogenous lightning. At the opposite, correlation of images acquired at the same solar time during the day and when the sun elevation is maximal is optimal.

In order to compensate for the loss of reliable results in certain areas of the landslide due to strong illumination and ground surface changes, displacements can be interpolated from more reliable neighbor results according to a weight depending on the correlation coefficient (Niebling et al., 2010).

5.2. Sources of errors affecting the ortho-rectification procedure

5.2.1. Influence of camera orientation

The accuracy of the camera orientation is a parameter affecting both the image geometry and the accuracy of the orthorectification (Mikhail et al., 2001). If changes in external orientation of the camera are small, the image geometry is not significantly affected. Consequently a homogeneous component in the correlated displacement field is visible in the image plane (Fig. 14A). This misfit can be significant in the areas where the expected displacements are low or null such as in the stable parts. This systematic error can be corrected assuming a rigid translation of the image by removing the average Δu and Δv misfits (observed on the stable parts of the images such as stable crests or on reference targets located outside the landslide; Fig. 1B and A; Fallourd et al., 2010). Nevertheless this correction is not fully optimal, because the geometric deformations caused by the slight movements of the camera depend on the object distance. Therefore, after correction of the homogeneous component in the image plane, an average residual misfit of about 0–2 pixels is observed.

In order to evaluate the accuracy of the external orientation that influences the orthorectification quality, forty GCPs (not introduced in the minimization processes of Section 3.2.3) are used. The shift between the projected and the observed GCP positions in the image plane is thus determined (Fig. 14B). A mean shift error of −0.20 and −0.08 pixel with a standard deviation of 1.59 and 1.51 pixels, respectively, in the u and v-directions is obtained (Table 3). The accuracy of the external parameters in the orthorectification procedure in the local coordinate system is calculated by comparing the back-projected GCPs identified in the image plane

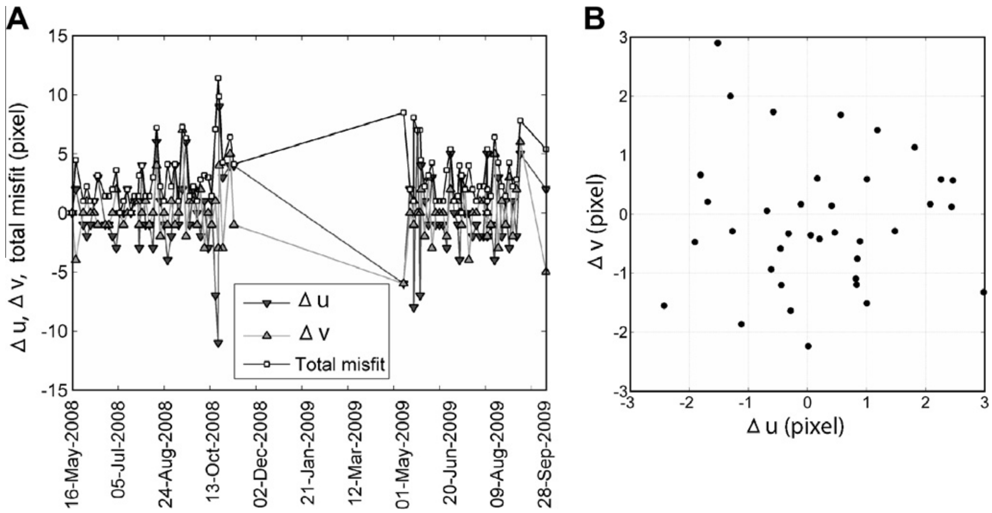

Fig. 14. Assessment of the accuracy of the camera orientation. (A) Average homogenous components due to slight movement of the camera. (B) Residual Δu and Δv misfits between projected and observed GCPs after the least square minimization.

Table 3
Mean value (μ) and standard deviation (σ) of the absolute accuracy for the projection in the image plane and the back-projection in the local coordinate system. n is the number of GCPs used for the calculation of the accuracy.

Image plane (n = 40)	μ (pixel)	σ (pixel)
u	0.20	1.59
v	−0.08	1.51
Local coordinate system (i = 11)	μ (m)	σ (m)
X	0.07	0.41
Y	−0.13	0.53
Z	0.01	0.29

with the GCP positions measured with DGPS and located in the stable parts. The absolute accuracy in X, Y and Z coordinates are presented in Table 3. Because most of GCPs in the stable parts are located in the background of the image where the ground pixel size is about 0.20 m, the mean 3D error (0.14 m) and the standard deviation (0.56 m) of the positioning are not representative of the areas of the landslide located closer to the camera (300 m). Nevertheless, because the standard deviation of the GCPs located in the image plane is close to the accuracy of the GCP picking, the determination of the camera orientation is considered acceptable. Furthermore, the good coherence between the shaded relief images (Fig. 4) and the true images (Fig. 1B) shows that the quality of the determination of the camera orientation is satisfying.

5.2.2. Influence of the DEM

In order to evaluate the influence of the DEM on the orthorectified displacements, the displacements of the period 1–4 June 2008 originally orthorectified with the DEM of October 2007 (Fig. 7) are compared with those orthorectified with the DEM of July 2009 (Fig. 15A and B). The observed differences in displacement are presented relative to the displacement orthorectified with the DEM of 2007. The differences vary spatially in the landslide area. Despite some areas displaying differences in displacement larger than 75%, the average difference is 21% which is very similar to the differences observed with the dGPS measurements (Fig. 9D). As a consequence, the influence of the DEM on the accuracy of the displacement is more important than the influence of the camera orientation, the image resolution and changes in illumination conditions. For large displacements, morphologic changes become significant and the errors on the displacements increase. The computation of multi-temporal DEMs for each image is therefore a pre-requisite to improve the accuracy of the orthorectified displacements. Nevertheless, in case of a translational landslide characterized by low changes in elevation, the use of the same DEM constitutes still an acceptable 1st-order estimate.

6. Conclusion

The potential of multi-temporal correlation of ground-based images for landslide monitoring has been assessed using the dataset available on the Super-Sauze landslide (South French Alps). A methodology to compute displacement rates both in the image plane coordinate system and in the local coordinate system is proposed.

The results demonstrated clearly the potential and the limitations of this technique by identifying the heterogeneous displacement field of the landslide in space and in time. The camera monitoring allowed to characterize displacements of up to 3 m day^{-1} during an acceleration period, and displacement of about 0.02 m day^{-1} over the decelerating period of July to September. The results are in good agreement with previous knowledge on the landslide kinematics and are in very good agreement with benchmark displacements measured by dGPS.

For objects located in a range of 300–900 m from the camera location, this study showed that the pixel size can vary from 0.005 to 0.04 m^2 according to the resolution of the image (2000 × 3008 pixels) and the angle of incidence of the line of sight. The orientation of the line of sight to the ground surface has to be considered before installing a permanent monitoring system. Areas of low incidence angles (<5°) are very sensitive to small movements of the camera. Therefore, the angle should be as perpendicular as possible to the mean displacement vector of the landslide. 3D displacements of less than 0.04 and 0.06 m in the lower part of the landslide and 0.09 and 0.11 m in the u and v-directions over a period of four days are impossible to detect without the use of sub-pixel correlation algorithms. However, the sources of errors due to small movement of the camera and the use of a mono-temporal DEM are the main limiting factors. A regular acquisition of multi-temporal DEMs through airborne or Terrestrial Laser Scanning or stereoscopic photogrammetric views is believed to be a priority to significantly improve the accuracy of the technique. The errors induced by the sub-pixel correlation algorithm are thus insignificant compared to the influences of the other parameters cited previously.

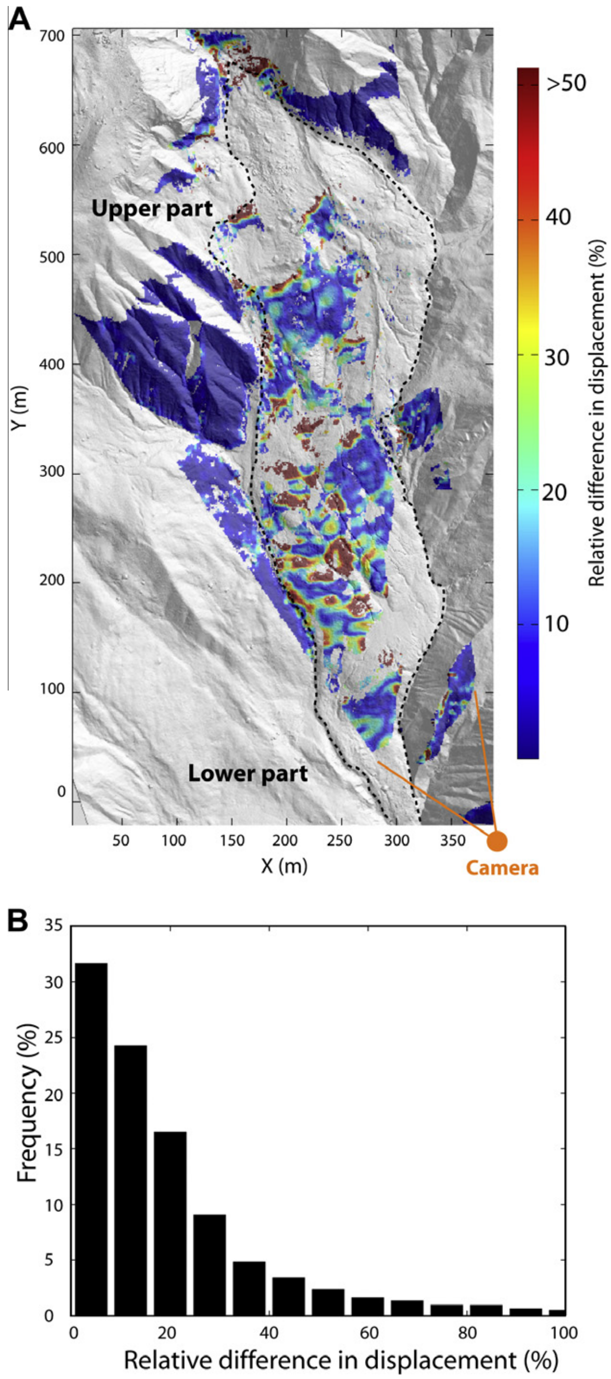

Fig. 15. Influence of the DEM on the orthorectification of the displacement field. (A) Relative difference between the displacement field of the 1st–4th of June orthorectified with a DEM of 2007 and a DEM of 2009. (B) Histogram of the relative differences.

The strongest limitations are independent of the acquisition system. They are related to the meteorological and illumination conditions and the ground surface changes inducing partial or complete loss of coherence between image pairs. During the winter season (from the months November to May), the presence of snow impedes reliable correlation results while excessive ground displacements between two consecutive years impede valid displacement measurements even if the images are acquired during the same solar time.

The results demonstrate that image correlation techniques implemented in permanent monitoring system are particularly interesting for monitoring landslides characterized by annual pluri-decimetric displacements. In addition, this low-cost technique is a very suitable alternative for inaccessible landslides or areas without access to power supply. Furthermore, because the proposed methodology does not require GCPs except for the calibration of the camera and for combining displacement patterns observed in image pairs acquired over two years, the methodology can be routinely and automatically applied to new image pairs. Therefore this work offers very promising perspectives for operational applications which can be potentially integrated in early warning systems by considering additional efforts in direct data transmission. Finally, inversion of the displacement field could be developed to characterize the macroscopic rheological properties of the landslide material.

Acknowledgments

This work was supported by the European Commission within the Marie Curie Research and Training Network '*Mountain risks: from prediction to management and governance*' (2007–2010, Contract MCRTN-035798) and by the FP7 Large-scale Integrating Project '*Safeland: Living with landslide risk in Europe*'' (2009–2012, Contract 226479). The ortho-images and the airborne LiDAR data of the Super-Sauze landslide have been acquired by the Sintegra company in 2007 and by the Helimap System service in 2009. The authors would like to acknowledge André Stumpf (University of Strasbourg, France and University of Twente, Netherlands) and Sabrina Rothmund (University of Stuttgart, Germany) for their help in the field. Special thanks are also due to Bas van Dam (Utrecht University, Netherlands) who designed the automatic monitoring system. The authors are also grateful to Prof. C. Gökçeoğlu and an anonymous reviewer for their constructive comments.

References

Abdel-Aziz, Y.I., Karara, H.M., 1971. Direct linear transformation into object space coordinates in close-range photogrammetry. In: Proc. Symposium on Close-Range Photogrammetric Systems, ASP, Falls Church, VA, 5–10 April, pp. 1–18.

Anandan, P., Bergen, R.J., Hanna, K.J., Hanna, K.J., 1993. Hierarchical model-based motion estimation. In: Sezan, L. (Ed.), Image Sequence Analysis. Kluwer, Dordrecht, pp. 237–252.

Baratoux, D., Delacourt, C., Allemand, P., 2001. High-resolution digital elevation models derived from Viking Orbiter images: method and comparison with Mars Orbiter Laser Altimeter Data. Journal of Geophysical Research 106 (E12), 32927–32941.

Berthier, E., Vadon, H., Baratoux, D., Arnaud, Y., Vincent, C., Feigl, K.L., Rémy, F., Legrésy, B., 2005. Surface motion of mountain glaciers derived from satellite optical imagery. Remote Sensing of Environment 95 (1), 14–28.

Bitelli, G., Dubbini, M., Zanutta, A., 2004. Terrestrial laser scanning and digital photogrammetry techniques to monitor landslides bodies. International Archives of Photogrammetry, Remote Sensing and Spatial Information Sciences 35 (Part B5), 246–251.

Bonneval, H., 1972. Levés topographiques par photogrammétrie aérienne. Photogrammétrie Générale: Tome 3, Collection Scientifique de l'Institut Géographique National, Eyrolles, Paris.

Brunner, F., Macheiner, K., Woschitz, H., 2007. Monitoring of deep-seated mass movements. In: Proceedings of the Third International Conference on Structural Health Monitoring of Intelligent Infra-structure (SHMII-3), Vancouver, Canada, 13–16 November, 7p. (on CDROM).

Burrough, P.A., McDonnell, R.A., 1998. Principles of Geographical Information Systems. Oxford University Press, New York.

Cardenal, J., Mata, E., Perez-Garcia, J.L., Delgado, J., Andez, M.A., Gonzalez, A., Diaz-de-Teran, J.R., 2008. Close-range digital photogrammetry techniques applied to landslide monitoring. International Archives of Photogrammetry, Remote Sensing and Spatial Information Sciences 37 (Part B8) (on CDROM).

Casagli, N., Farina, P., Leva, D., Tarchi, D., 2004. Application of ground-based radar interferometry to monitor an active rock slide and implications on the emergency management. In: Evans, S.G., Scarascia-Mugnozza, G., Strom, A., Hermanns, R.L. (Eds.), Landslides from Massive Rock Slope Failure, Proceedings of the NATO Advanced Research Workshop on Massive Rock Slope Failure – New Models for Hazard Assessment, Celano, Italy, 16–21 June, Springer, Berlin, pp. 351–360.

Casson, B., Baratoux, D., Delacourt, D., Allemand, P., 2003. Seventeen years of the "La Clapière" landslide evolution analysed from ortho-rectified aerial photographs. Engineering Geology 68 (1–2), 123–139.
Casson, B., Delacourt, C., Allemand, P., 2005. Contribution of multi-temporal sensing images to characterize landslide slip surface – application to the La Clapière Landslide (France). Natural Hazards and Earth System Sciences 5, 425–437.
Chambon, G., 2003. Caractérisation expérimentale du frottement effectif des zones de faille. Ph.D. Thesis, Earth Sciences, Université Paris XI-Orsay, Paris.
Chambon, G., Schmittbuhl, J., Corfdfir, A., Vilotte, J.-P., Rous, S., 2003. Shear with comminution of a granular material: microscopic deformations outside the shear band. Physical Review E 68 (1), 1–8.
Corripio, J.G., 2004. Snow surface albedo estimations using terrestrial photography. International Journal of Remote Sensing 25 (24), 5705–5729.
Corsini, A., Farina, P., Antonello, G., Barbieri, M., Casagli, N., Coren, F., Guerri, L., Ronchetti, F., Sterzai, P., Tarchi, D., 2006. Space-borne and ground-based SAR interferometry as tools for landslide hazard management in civil protection. International Journal of Remote Sensing 27 (12), 2351–2369.
D'Antone, I., 1995. Hierarchical correlation for track finding. Nuclear Instrument and Methods in Physics Research 356 (2–3), 476–484.
Debella-Gilo, M., Kääb, A., 2011. Sub-pixel precision image matching for measuring surface displacements on mass movements using normalized cross-correlation. Remote Sensing of Environment 115 (1), 130–142.
Delacourt, C., Allemand, P., Berthier, E., Raucoules, D., Casson, B., Grandjean, P., Pambrun, C., Varel, E., 2007. Remote-sensing techniques for analysing landslide kinematics: a review. Bulletin de Société Géologique 178 (2), 89–100.
Delacourt, C., Allemand, P., Casson, B., Vadon, H., 2004. Velocity field of the "La Clapière" landslide measured by the correlation of aerial and Quick-Bird satellite images. Geophysical Research Letters 31 (L15619), 1–5.
El Alaoui, M.I., Ibn-Elhaj, E., 2009. A robust hierarchical motion estimation algorithm in noisy image sequences in the bispectrum domain. Signal Image and Video Processing 3 (3), 291–302.
Fallourd, R., Vernier, F., Friedt, J.-M., Martin, G., Trouvé, E., Moreau, L., Nicolas, J.-M., 2010. Monitoring temperate glacier with high resolution automated digital cameras – application to the Argentière Glacier. International Archives of Photogrammetry Remote Sensing and Spatial Information Sciences 38 (Part 3B), 1–23.
Fisher, P.F., 1991. First experiments in viewshed uncertainty: the accuracy of the viewshed area. Photogrammetric Engineering & Remote Sensing 57 (10), 1321–1327.
Foppe, K., Barth, W., Preis, S., 2006. Autonomous permanent automatic monitoring system with robot-tacheometers. In: Proc. XXIII International FIG Congress 'Shaping the Change' (FIG-2006), Münich, Germany, 8–13 October, 12p. (on CDROM).
Franklin, W.R., Rav, C.K., 1994. Higher isn't necessarily better: visibility algorithms and experiments. In: Waugh, T.C., Healey, R.G. (Eds.), Proceedings of the Sixth International Symposium on Spatial Data Handling 'Advances in GIS Research' (SDH'94), Edinburgh, Scotland, vol. 2. Taylor & Francis, London, pp. 751–770.
Heikkila, J., Silven, O., 1997. A four-step camera calibration procedure with implicit image correction. In: Proceedings of the IEEE Computer Society Conference on Computer Vision and Pattern Recognition (CVPR'97), San Juan, Puerto Rico, 17–19 June, pp. 1106–1112.
Hemmleb, M., Wiedemann, A., 1997. Digital rectification and generation of orthoimages in architectural photogrammetry. International Archives of Photogrammetry and Remote Sensing 32 (Part 5C1B), 261–267.
Hild, F., 2003. Mesure de champs de déplacement par corrélation d'images et applications en mécanique des solides. Notes de Cours IPSI. Laboratoire de Mécanique et de Technologie, Université Paris 6, France.
Honda, K., Nagai, M., 2002. Real-time volcano activity mapping using ground-based digital imagery. ISPRS Journal of Photogrammetry and Remote Sensing 57 (1–2), 159–168.
Jaboyedoff, M., Oppikofer, T., Abellan, A., Derron, M.-H., Loye, A., Metzger, R., Pedrazzini, A., 2010. Use of LiDAR in landslide investigations: a review. Natural Hazards 2010, 1–24. http://dx.doi.org/10.1007/s11069-010-9634-2.
Jaboyedoff, M., Ornstein, P., Rouiller, J.-D., 2004. Design of a geodetic database and associated tools for monitoring rock-slope movements: the example of the top of Randa rockfall scar. Natural Hazards and Earth System Science 4, 187–196.
Jiang, R., Jauregui, D.V., White, K., 2008. Close-range photogrammetry applications in bridge measurement: literature review. Measurement 41 (8), 823–834.
Kraus, K., Waldhäusl, P., 1994. Photogrammetry: Fundamentals and Standard Processes. Hermès, Paris.
Kumar, S., Banerjee, S., 1998. Development and application of a hierarchical system for digital particle image velocimetry to free-surface turbulence. Physics of Fluids 10 (1), 160–177.
Küntz, M., Jolin, M., Bastien, J., Perez, F., Hild, F., 2007. Digital image correlation analysis of cracks behavior in a reinforced concrete beam during a load test. Canadian Journal of Civil Engineering 33 (11), 1418–1425.
LePrince, S., Berthier, E., Ayoub, F., Delacourt, C., Avouac, J.-P., 2008. Monitoring earth surface dynamics with optical imagery. EOS Transactions 89 (1), 1–5.
Lewis, J.P., 1995. Fast normalized cross-correlation. Vision Interface 10 (1), 120–123.
Lim, M., Petley, D.N., Rosser, N.J., Allison, R.J., Long, A.J., Pybus, D., 2005. Combined digital photogrammetry and time-of-flight laser scanning for monitoring cliff evolution. The Photogrammetric Record 20 (110), 109–129.
Maas, H.-G., Schwalbe, E., Dietrich, R., Bässler, M., Ewert, H., 2008. Determination of spatio-temporal velocity fields on glaciers in West-Greenland by terrestrial image sequence analysis. International Archives of Photogrammetry, Remote Sensing and Spatial Information Science 37 (Part B8), 1419–1424.
Malet, J.-P., 2003. Les glissements de type écoulement dans les marnes noires des Alpes du Sud. Morphologie, fonctionnement et modélisation hydromécanique. Ph.D. Thesis, Earth Sciences, Université Louis Pasteur, Strasbourg.
Malet, J.-P., Maquaire, O., Calais, E., 2002. The use of global positioning system techniques for the continuous monitoring of landslides. Geomorphology 43 (1–2), 33–54.
Mikhail, E., Bethel, J.S., McGlone, J.C., 2001. Introduction to Modern Photogrammetry. John Wiley & Sons Inc., New York.
Monserrat, O., Crosetto, M., 2008. Deformation measurement using terrestrial laser scanning data and least squares 3D surface matching. ISPRS Journal of Photogrammetry and Remote Sensing 63 (1), 142–154.
Naterop, D., Yeatman, R., 1995. Automatic measuring system for permanent monitoring: solexperts geomonitor. Proceedings of 4th International Symposium on Field Measurements in Geomechanics (FMGM-1995), Bergamo, 18–23 April, pp. 417–424.
Niebling, M.J., Flekkøy, E.G., Måløy, K.J., Toussaint, R., 2010. Mixing of a granular layer falling through a fluid. Physical Review E 82 (1), 1–16.
Oppikofer, T., Jaboyedoff, M., Kreusen, H.-R., 2008. Collapse at the eastern Eiger flank in the Swiss Alps. Nature Geoscience 1 (8), 531–535.
Pesci, A., Baldi, B., Bedin, A., Casula, G., Cenni, N., Fabris, M., Loddo, F., Mora, P., Bacchetti, M., 2004. Digital elevation models for landslide evolution monitoring: application on two areas located in the Reno River Valley (Italy). Annals of Geophysics 47 (4), 1339–1353.
Press, W.H., Flannery, B.P., Teukolsky, S.A., Vetterling, W.T., 1997. Numerical Recipes. Cambridge University Press, New York.
Rohály, J., Frigerio, F., Hart, D.P., 2002. Reverse hierarchical PIV processing. Measurement Science and Technology 13 (7), 984–996.
Squarzoni, C., Delacourt, C., Allemand, P., 2005. Differential single-frequency GPS monitoring of the La Valette landslide (French Alps). Engineering Geology 79 (3–4), 215–229.
Sturzenegger, M., Stead, D., 2009. Close-range terrestrial digital photogrammetry and terrestrial laser scanning for discontinuity characterization on rock cuts. Engineering Geology 106 (3–4), 163–182.
Tarchi, D., Casagli, N., Fanti, R., Leva, D.D., Luzi, G., Pasuto, A., Pieraccini, M., Silvano, S., 2003. Landslide monitoring by using ground-based SAR interferometry: an example of application to the Tessina landslide in Italy. Engineering Geology 68 (1–2), 15–30.
Teza, G., Galgaro, A., Zaltron, N., Genevois, R., 2007. Terrestrial laser scanner to detect landslide displacement fields: a new approach. International Journal of Remote Sensing 28 (16), 3425–3446.
Teza, G., Pesci, A., Genevois, R., Galgaro, A., 2008. Characterization of landslide ground surface kinematics from terrestrial laser scanning and strain field computation. Geomorphology 97 (3–4), 424–437.
Travelletti, J., Malet, J.-P., 2012. Characterization of the 3D geometry of flow-like landslides: a methodology based on the integration of multi-source data. Engineering Geology 128, 30–48.
Wangensteen, B., Guomundsson, A., Eiken, T., Kääb, A., Farbrot, H., Etzelmüller, B., 2006. Surface displacements and surface estimates for creeping slope landforms in Northern and Eastern Iceland using digital photogrammetry. Geomorphology 80 (1–2), 59–79.
White, D.J., Take, W.A., Bolton, M.D., 2003. Soil deformation measurement using particle image velocimetry (PIV) and photogrammetry. Géotechnique 53 (7), 619–631.

Multi-temporal terrestrial photogrammetry for landslide monitoring

J. Travelletti, J.-P. Malet, J. Schmittbuhl, R. Toussaint, M. Bastard
Institut de Physique du Globe de Strasbourg, CNRS UMR 7516, University of Strasbourg (EOST), 5 rue René Descartes, 67084 Strasbourg Cedex, France. E-mail : julien.travelletti@unistra.fr

C. Delacourt
Université Européenne de Bretagne, Institut Universitaire Européen de la Mer, CNRS UMR 6538, University of Brest, Brest, France.

P. Allemand
Laboratoire des Sciences de la Terre, Université Lyon et Ecole Normale Supérieure, Lyon, France

D.B. van Dam
Faculty of Geosciences, Department of Physical Geography, Utrecht University, Utrecht, Netherlands.

ABSTRACT: The objective of this work is to present an inexpensive method to monitor the displacement pattern of slow-moving landslides from terrestrial oblique optical images analyzed with a Digital Image Correlation (DIC) technique. The performance of the method is evaluated on the Super-Sauze landslide (South French Alps). The image monitoring system consists in a low-cost optical camera installed on a concrete pillar located on a stable crest in front of the landslide and controlled by a datalogger.
To estimate the planimetric ground displacement that occurred between several images acquired over the same area at several different times, a cross-correlation algorithm using a multi-resolution approach is used. The correlation is first calculated in the image plane of the camera in terms of pixel displacements and direction. Then, a method based on the collinearity equations to orthorectify and georeference the displacements field in the local coordinate system with a high resolution DEM is used.
In the image plane of the camera, the displacement pattern is clearly identified. The maximum of displacement amplitudes is identified in spring 2008 after important rainfalls and snow melting. The amplitude and direction of pixel displacements indicate displacement fields with different kinematics between the upper and the lower part of the landslide. The total amplitude of displacements decreases from the upper part (10.5 m in 4 days) to the lower part of the mudslide (1.1 m in 4 days). The normal landslide activity is recovered with an average daily velocity of about 0.01 $m.day^{-1}$ between end of July and October 2008. Horizontal cumulated displacements for 2008 reach 38 m for the upper part and 7 m for the lower part.
If the landslide is mainly translational without excessive changes in elevation, the same DEM can be used to estimate the displacements in the local coordinate system. The changes in meteorological conditions (snow, clouds, rain storm), in surface conditions (important ground deformations) and in illumination conditions are the main limitations that have to be taken into account to integrate this technique in an early warning system.

1 INTRODUCTION

The kinematics characterization of landslides is a prior to understand landslide mechanism for hazards and risk assessments. Because such natural processes are very sensitive to climatic conditions, their behavior is permanently changing in time and in space, thus making the characterization of landslide kinematics difficult with conventional and punctual geodetic measurements like tacheometry, extensometry and GPS surveys. The application of optical correlation methods is thus particularly efficient for monitoring the spatial heterogeneity of landslide displacements (Kääb, 2002; Casson et al., 2003; Delacourt et al., 2007; LePrince et al., 2008). The performance of the correlation technique on aerial (eg. IGN) and high-resolution satellite images (eg. SPOT, QuickBird, OrbView, EROS) is widely demonstrated for landslide monitoring (Casson et al., 2003; Delacourt et al., 2004; LePrince et al., 2008). However, the acquisition frequency and the spatial resolution of aerial and satellite images are some typical parameters that cannot be controlled by the user. These drawbacks can be very problematic in function of the size and the dynamics of the landslide. Correlation of optical terrestrial images is a good complementary method to aerial and satellite imaging and classical landslide monitoring techniques. Optical terrestrial images can be acquired from a fixed location, generally in front of the landslide with a high resolution and a frequency adapted to the landslide velocity. The images are systematically acquired in exactly the same geometry.

Terrestrial digital images are commonly used to generate accurate Digital Elevation Models (DEMs) for 3D morphological analysis and ortho-rectification of images (Cardenal et al., 2008). The camera system is generally installed for a short period and removed after each acquisition. Therefore only a few examples demonstrated its potential for continuous monitoring of landslides kinematics (eg. Delacourt et al., 2007). This work precisely attempts to present a low-cost permanent monitoring system to characterize the displacement pattern of slow moving landslides from terrestrial multi-temporal optical images acquired in the Super-Sauze mudslide. The Digital Image Correlation (DIC) techniques, the georeferencing procedure and the associated accuracy are explained. Finally the results of the landslide displacements in the image plane and in the local reference system for the monitoring period of 2008 are presented and discussed.

2 EXPERIMENTAL SITE: THE SUPER-SAUZE MUDSLIDE

The Super Sauze mudslide is located in the Callovo-Oxfordian black marls of the Southern French Alps (Alpes-de-Haute-Provence, France). Its extents over a distance of 920 m between an elevation of 2105 m at the crown and 1736 m at the toe with an average width of 150 m and a average slope of 25° (Figure 1). Last estimations of the total volume is evaluated at 560,000 m^3 (Travelletti & Malet, submitted).
The mudslide is gradually covering a torrential stream located downstream with typical range of velocity between 1 to 3 $cm.d^{-1}$ and acceleration peak until 40 $cm.d^{-1}$ in the spring season (Malet et al., 2002). The kinematics of the landslides is currently monitored by DGPS survey, terrestrial laser scanning and the permanent camera monitoring system.

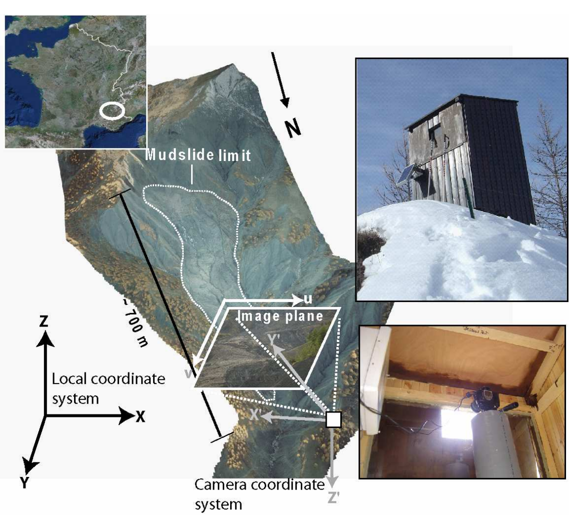

Figure 1.View of the Super-Sauze mudslide, the camera monitoring system and the different coordinates system involved in the georeferencing procedure.

3 METHODOLOGY

3.1 Instrumentation

The monitoring system consists of a low-cost D70 Nikon non metric reflex digital camera (about 1500 €) installed on a concrete pillar located on a stable crest in front of the mudslide at a distance of 300 m from the lower part and 900 m from the upper part of the mudslide (Figure 1). The acquisition system is controlled by a datalogger (CR10) and the power is provided by a 40 W solar panel. The characteristics of the acquisitions are presented in Table 1. The focused of the camera lens is set to manual. The frequency of acquisition is four days. An acquisition consists in four photographs registered at 11:00 a.m., 12:00 p.m., 13:00 p.m. and 14:00 p.m in order to get at least one image taken during good meteorological conditions. Each photograph (6 Mb) is stored in a native file format without any loss of information.

Table 1. Camera acquisitions characteristics

Type of Camera	Single-lens reflex digital camera
Effective Pixels	6.1 million
Image Sensor	RGB CCD, 23.7 x 15.6 mm
Image Size	3008 x 2000
Principal point	(1504 ,1000)
Sensitivity	400 iso
Focal length	52 mm
Shutter speed	1/8000
Storage Media	CompactFlash™ (CF) Card
Storage System	NEF (RAW)

3.2 Processing

3.2.1 Digital Image Correlation (DIC)

Different terminologies exist in the literature to designate methods searching for the greatest correspondence between two signals like Particle Image Velocimetry (PIV), Correlation Image velocimetry (CIV) and Digital Image Correlation (DIC). DIC is the most used terminology for applications in geosciences.

The correlation principle is to recognize identical intensity distribution patterns on a reference image and a second image after displacements. Most of DIC techniques are based on a maximization of a normalized cross-correlation function due to the reliability and the simplicity of the method (Lewis, 1995; Debella-Gilo and Kääb, in press). The function is solved either in the spatial domain or in the frequency domain by using FFT algorithm (Hild et al. 1999). The normalized cross-correlation function for two discretely sampled images is defined as:

$$\Phi(u,v)=\frac{\sum_{x,y}[f(x,y)-\bar{f}_{u,v}][t(x-u,y-v)-\bar{t}]}{\left\{\sum_{x,y}[f(x,y)-\bar{f}_{u,v}]^2\sum_{x,y}(t(x-u,y-v)-\bar{t})^2\right\}^{0.5}} \quad (1)$$

f contains the image intensity distribution of the reference image. $\bar{f}_{u,v}$ is the mean of $f(x,y)$ in the region under the feature. $\bar{t}$ is the mean value of the correlation window. $\Phi(u, v)$ is the cross-correlation function. If $\Phi(u, v)$ is equal to 0, there is no relationship between the matching entities. If $\Phi_{fg}(u, v)$ is equal to 1, the matching is maximal. The Euclidean distance between the coordinates of the reference point and the matching points represents the displacements magnitude in the image plane. By changing the zone of interest, it is then possible to determine displacements at various positions inside the images. In this study, the use of a multi-resolution correlation algorithm with subpixel accuracy is motivated by the necessity:

- to minimize incoherent results due to changes in landslide surface aspect (soil moisture changes, soil surface weathering) and changes in illumination
- to identify and characterize heterogeneous distributed displacement fields.

The correlation algorithm is based on:

- successive degradations of image resolution for changing the physical size of the interest zone. The correlator starts at the lowest resolution image for determining global displacements, then the location of the maximum cross-correlation is used as a start point for the next correlation with a higher resolution to determine local displacements.
- correlation of gradient values by using an edge detection algorithm (Sobel or Prewitt operators), applied on the images to identify object texture (Chambon et al., 2003).

The sub-pixel displacement is computed using an iterative procedure in order to find the maximum of the correlation function interpolated with a bi-parabolic formula between the pixel centers. The maximisation procedure is based on the simplex method (Press et al., 1997). For a thorough description of the multi-resolution correlator and the sub-pixel computation, see Bastard (2009) and Chambon (2003).

The correlation algorithm and the pre and post-processing steps are written in C++ and Matlab programming languages.

3.2.2 Georeferencing

Because the pixel resolution depends on the distance between the landslide and the camera and on the terrain orientation relative to the line of sight of the camera, the displacements field determined in the image plane cannot be directly interpreted in metric displacements. However, a quantitative analysis is possible if a DEM is available to relate two-dimensional pixel positions in the image plane to three-dimensional points in the local coordinate system. The DEMs are usually produced with stereoscopic pair of images taken at the same time (Mikhail et al., 2001; Casson et al., 2003). This method required the installation of at least two terrestrial cameras at different viewpoints. In order to overcome this problem, a DEM interpolated from airborne LiDAR data set (0.25 m mesh size with a planimetry accuracy of 0.15 m and an elevation accuracy of 0.10 m) is used assuming that the landslide morphology remains constant with time. This strong hypothesis will obviously affect the accuracy of the displacements converted in the local coordinate system. However, it will be further demonstrated that this method is still a good estimation.

The external parameters of the camera are first determined. Then a projective transformation in the image plane is applied on the DEM to allocate a 3D position at each 2D pixel coordinates.

3.2.2.1 External parameters of the camera

The relationship between the image coordinates (u,v) and the local coordinates system (X,Y,Z) is given by the classical form of the collinearity equations (Mikhail et al., 2001):

$$u = u_0 - f\,\frac{m_{11}(X - X_C) + m_{12}(Y - Y_C) + m_{13}(Z - Z_C)}{m_{31}(X - X_C) + m_{32}(Y - Y_C) + m_{33}(Z - Z_C)} \quad (2)$$
$$v = v_0 - f\,\frac{m_{21}(X - X_C) + m_{22}(Y - Y_C) + m_{23}(Z - Z_C)}{m_{31}(X - X_C) + m_{32}(Y - Y_C) + m_{33}(Z - Z_C)}$$

The origin of the image plane system is located at the upper left corner of the image (Figure 1). (u_0,v_0) are the coordinates of the principal point. (X_C,Y_C,Z_C) are the coordinates referring to the camera station in the local coordinate system. f is the focal length of the camera. The X-axis is defined along the W-E direction and the Y-axis along the S-N direction in the local coordinate system. The Z-axis is the elevation perpendicular to the plane (X,Y). m_{ij} are the components of the rotation matrix **M** that defines the external parameters of the camera. **M** is constructing by using three sequential rotation angles: ω around the X-axis, φ around the once-rotated Y-axis and κ around the twice-rotated Z-axis:

$$\mathbf{M} = \begin{pmatrix} \cos\varphi\cos\kappa & \cos\omega\sin\kappa + \sin\omega\sin\varphi\cos\kappa & \sin\omega\sin\kappa - \cos\omega\sin\varphi\cos\kappa \\ -\cos\varphi\sin\kappa & \cos\omega\cos\kappa - \sin\omega\sin\varphi\sin\kappa & \sin\omega\sin\kappa + \cos\omega\sin\varphi\sin\kappa \\ \sin\varphi & \sin\omega\cos\varphi & \cos\omega\cos\varphi \end{pmatrix} \quad (3)$$

The estimation of the three independent angles involved in the rotation matrix is the most sensitive part in camera calibration (Mikhail et al., 2001). In order to compute the external parameters of the camera, Ground Control Points (GCPs) identified both in the image plane and in the local coordinate system are used as input data for a self calibration. 95 pairs of GCPs distributed on the image plane and in the local reference system were measured using a Differential Global Positioning System (DGPS) (Fig 2). The GCPs are measured in the local coordinate system with an average 3D accuracy of 0.02 m and a standard deviation of 0.01 m. The GCPs coordinates (u_i,v_i) in the image plane are determined by manual picking with an estimated accuracy of about 2 pixels. Among the 95 GCPs, 45 are used to compute the rotation matrix **M** and 40 are kept for the accuracy analysis. Equ. 2 is then used to obtain the calculated image coordinates of the GCPs using the ground positions of the GCPs. A least mean squares minimization between observed and calculated GCPs in the image plane using Singular Value Decomposition allows to determine the rotational matrix **M** that satisfies the system of Equ. 2 (Heikkilä and Silven, 1997). The camera location measured by DGPS, the focal length (constant for each acquisition) and the central points coordinates (u_0,v_0) provided by the manufacturer are included in the least mean squares minimization to better constrain the rotation matrix computation.

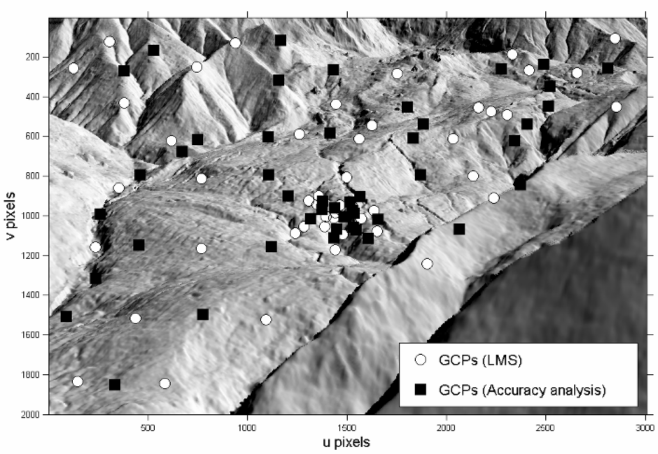

Figure 2. Location of the GCPs in a synthetic image for the Least Mean squared Minimization (LMS) and for the accuracy analysis. The synthetic image is produced by interpolation of the hillshade values of the DEM projected in the image plane.

3.2.2.2 Projection of the DEM in the image plane

Once the rotation matrix **M** is determined, Equ. 2 is applied on the whole DEM. In order to avoid the projection of duplicate points in the same position in the image plane, the points of the DEM invisible from the camera view point C (X_C,Y_C, Z_C) are identified. This step is computed using the sightline method (Fisher, 1994; Franklin and Ray, 1994). The sightline ***S*** is defined as the straight line from the camera location (X_C,Y_C,Z_C) to the position P (X,Y,Z) located in the gridded DEM. ***S*** is defined as follows:

$$\begin{bmatrix} s_x \\ s_y \\ s_z \end{bmatrix} = \begin{bmatrix} x \\ y \\ z \end{bmatrix} + k \begin{bmatrix} x - x_c \\ y - y_c \\ z - z_c \end{bmatrix} \quad , k \in IR \quad (4)$$

If a point of the sightline between the camera location C and the position P goes below the DEM surface ($Z < Z_{DEM}$), P is invisible from the camera location.

Once the visible points of the DEM are projected in the image plane, a linear interpolation is used to associate the X,Y,Z coordinates for each pixel location (u,v) of the image plane. The georeferencing in the local coordinate system of the displacement field determined with the DIC technique can be then applied.

4 ACCURACY ANALYSIS

4.1 Accuracy of the multi-resolution correlator

The accuracy of the multi-resolution correlator was assessed by applying homogeneous synthetic displacement fields on a real image as suggested by Chambon et al. (2003). Three different levels of gaussian noise are added on the synthetic displaced image. The mean Gaussian noise is fixed to null and the variance σ_n^2 is fixed to 10^{-4}, 10^{-3} and 10^{-2} respectively. The DIC is then applied on the real image and the synthetic displaced image. The difference between the calculated displacements and the imposed displacements allow to determine the accuracy of the correlator algorithm (Figure 3). As observed by Hild et al. (1999), the accuracy of the algorithm mainly depends on the pixel fraction of the displacement. For fifteen tests realized with a magnitude of imposed displacements between 1 to 23 pixels, the accuracy of the correlator varies between ± 0.5 pixels for the highest degree of noise and ± 0.1 pixels for the lowest degree of noise.

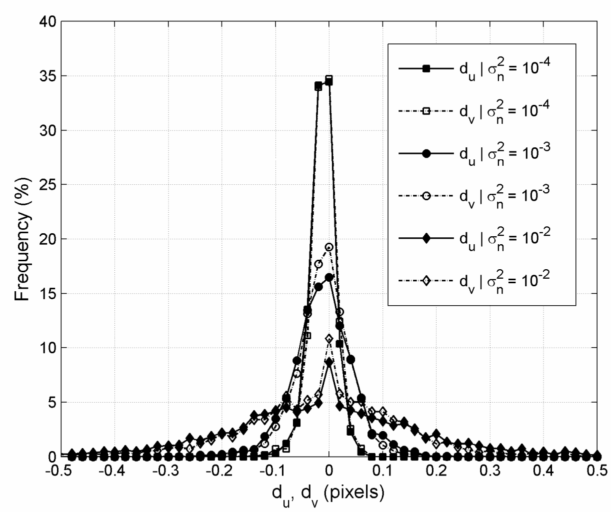

Figure 3. Accuracy of the hierarchical correlator in u and v directions in function of different levels of Gaussian noise (σ_n^2).

4.2 *Influence of the image resolution*

The effective pixel size is a limiting parameter for the correlation accuracy (Figure 4). The pixel size depends on (i) the distance between the terrain surface and the camera and (ii) the angle of incidence which is defined as the complementary angle between the line of sight of the camera and the normal terrain surface. The pixel size determines the minimum theoretical displacement that can be detected by the DIC technique for pixel-level correlation.

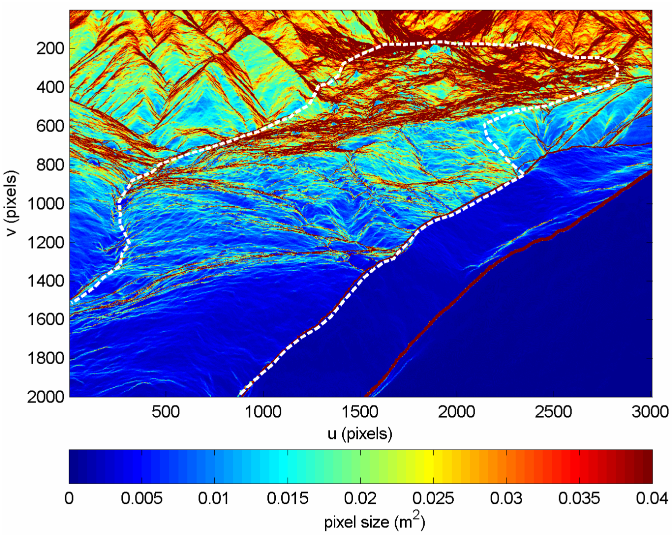

Figure 4. Effective pixel size

The pixel size varies from 1.10^{-2} m^2 in the lower part to 3.10^{-2} m^2 in the upper part of the landslide. Minimum displacements for pixel-level correlation in *u* and *v*-direction of 0.15 m and 0.08 m in the lower part of the landslide and 0.30 and 0.10 m in the upper part are found (Figure 5A, B). Below these displacement thresholds, the accuracy mainly depends on the sub-pixel correlation accuracy.

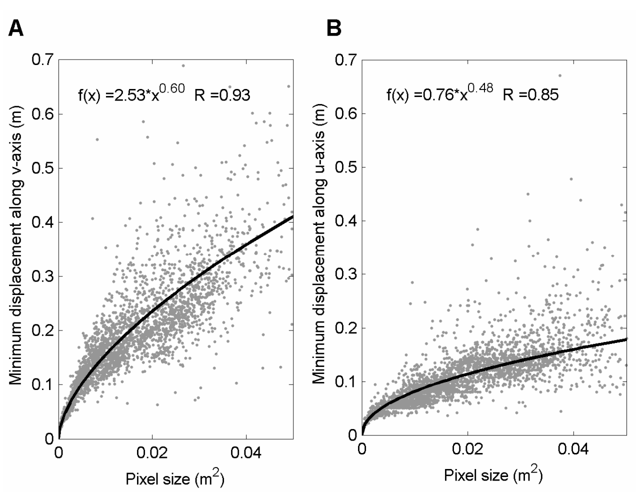

Figure 5. Minimum displacements for pixel-level correlation A) along v and B) along u-axis in function of the pixel size

4.3 *Accuracy of the external parameters*

The 40 GCPs not introduced in the minimization processes are used to evaluate the absolute accuracy of the rotational matrix **M** (Equ. 3). The shift between the projected and the observed GCPs positions in the image plane is determined (Figure 6). A mean shift error of -0.20 pixel and -0.08 pixel with a standard deviation of 1.59 pixel and 1.51 pixels in *u* and *v* direction respectively is found (Table 2). Because the standard deviation is close to the accuracy of the GCPs picking, the solution is judged acceptable.

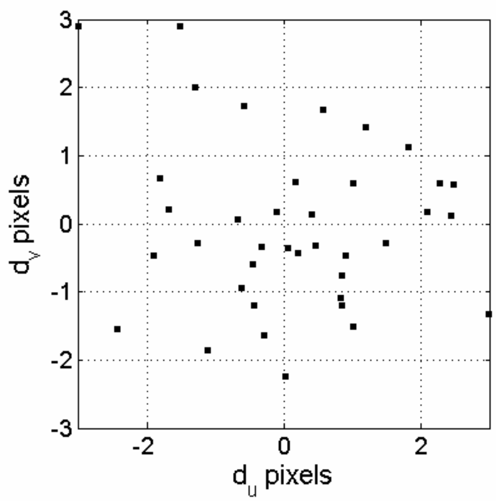

Figure 6. Residual *du* and *dv* misfits between projected and observed GCPs after the minimization.

To control the overall quality of the transformation, a synthetic image of the landslide is reproduced by interpolating the shaded relief value computed in the DEM. Regarding the accuracy of the transformation matrix and the realism of the synthetic image, the results are satisfying (Figure 2; Figure 6).

Slight external parameters changes (movements of the camera) can lead to the occurrence of a homogeneous component in the calculated displacements field in the image plane. These artefacts can be corrected with an automatic routine by removal of the misfit determined in the stable part of the mudslide on the whole computed displacements. Then the accuracy of the displacement in the image plane is assessed by a null test over stable areas by looking at the residual (Casson et al., 2005).

4.4 *Accuracy of the georeferencing*

The accuracy of the georeferencing in the local coordinate system is calculated by comparing the back-projected GCPs with their DGPS position located in the stable part of the landslide where no geomorphic change occurred. The absolute accuracy in *X, Y* and *Z* coordinate are presented in Table 2.

Table 2. Mean μ and standard deviation σ of the absolute accuracy for the projection in the image plane and the back-projection in the local coordinate system

Image plane (n=40)	μ (pixels)	σ (pixels)
u	0.20	1.59
v	-0.08	1.51
Local coordinate system (n=11)	μ (m)	σ (m)
X	0.07	0.41
Y	-0.13	0.53
Z	0.01	0.29

5 RESULTS

5.1 Displacement field in the image plane

41 pairs of images are correlated for the year 2008. The residual misfit after correction of slight movements of the camera is evaluated at about 1 pixel on average and corresponds to an estimation of the displacement accuracy in the image plane.

Loss of coherence is observed in areas where changes of surface texture are too important. Consequently, some points present unreliable displacements characterized with an amplitude and a direction very different from the neighboring points (eg. displacements going upslope). Such points can be thus easily detected and removed (Casson et al. 2005). Aberrant results are also removed according to their correlation coefficient. A correlation threshold coefficient has been fixed to 0.75. Below it, displacements are not considered reliable.

In spring 2008, persistent rainfalls and a fast melting of the snow cover were the main causes of an important acceleration. This acceleration could be measured by the DIC technique from the 20th of May when the snow cover on the landslide completely melt. Figure 7 shows the displacement field in the image plane the 20th of May and the cumulated displacements for 9 profiles crossing the landslide between the 20th of May and the 25th June. The profiles at positions *v* of 200 and 400 clearly point out the stable crest in the center of the upper part (u = 2000 and v = 400) where cumulated displacements are null. On both sides of the crest, the largest pixels velocities are observed. They reach 6 pixels.day^{-1} at the peak of the acceleration at the beginning of June 2008. In one month, cumulated displacements reach 110 pixels in the upper part. Figure 8B shows the cumulated displacement of fours points (Points 1, 2, 3 and 4) respectively located in the upper, medium, lower and stable part of the mudslide. The major mudslide displacements occur in the spring season when the ground water level reached its maximum level. Then, the normal landslide activity is recovered with an average daily velocity of 0 to 1 pixel.day^{-1}.

Figure 7. Displacement field computed at the 20th May and cumulated displacements over the acceleration period of the mudslide. The location of the points 1, 2, 3 and 4 are referring to Figure 8.

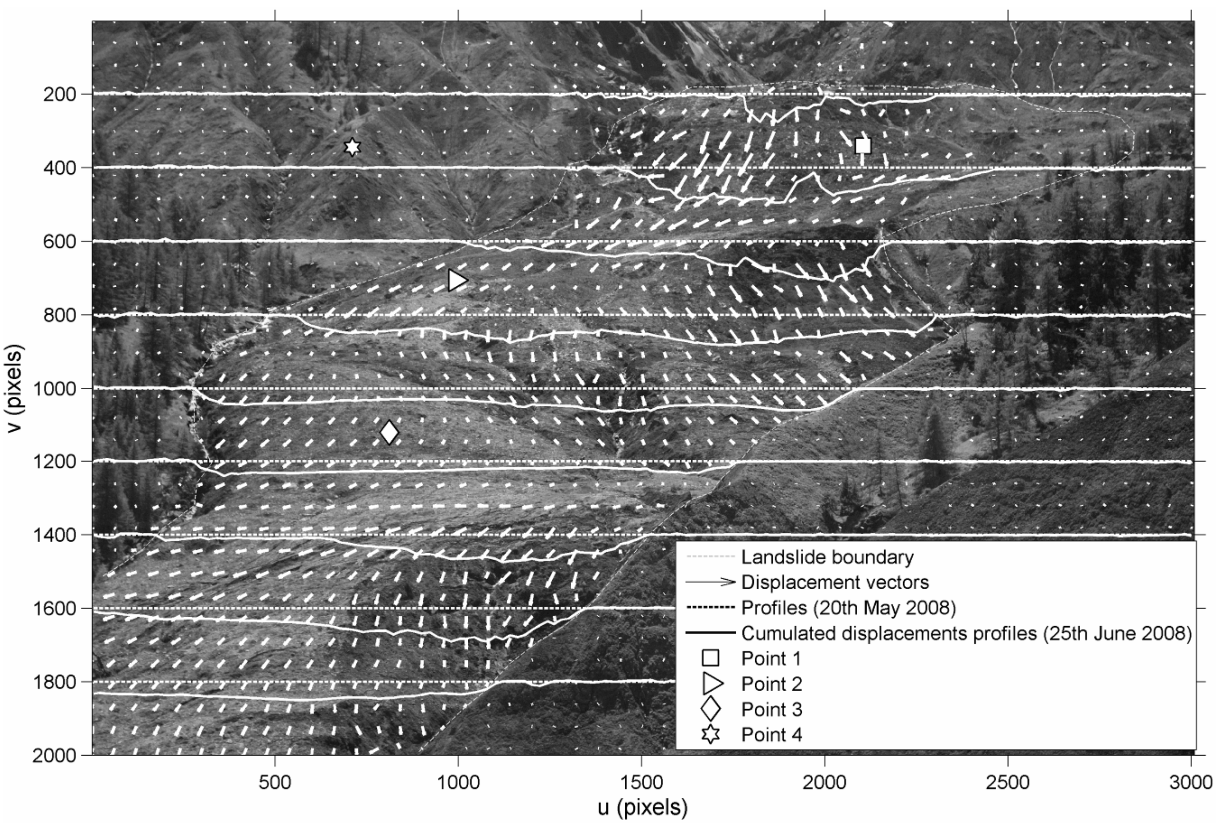

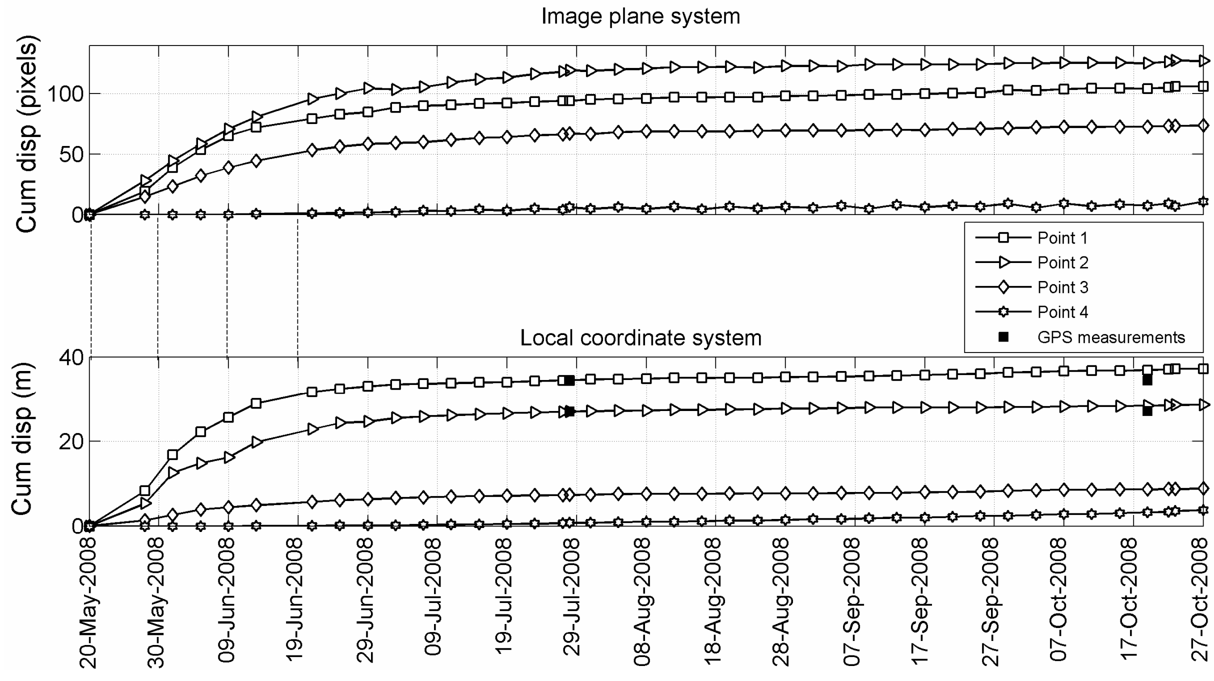

Figure 8. Cumulated displacements of points (1, 2, 3 and 4) located in the upper, medium, lower and stable part of the mudslide in the image plane system and in the local coordinate system in 2008. Their location is shown in Figure 7.

5.2 Displacement field in the local coordinate system

The horizontal displacements of the 20th of May corroborate the previous analysis in term of metric displacements. The displacements field varies temporally and spatially. The total amplitude of displacements decreases from the upper part (10.5 m in 4 days) to the lower part of the mudslide (1.1 m in 4 days) as shown by the points 1,2,3 and 4 in Figure 10 in the local coordinate system.

The normal landslide activity is recovered with an average daily velocity of about 0.01 m.day^{-1} between the end of July and October 2008. Horizontal cumulated displacements reach 38 m in the upper part (Points 1, Figure 8) and 7 m in the lower part (Points 3). No significant velocity change is observed during that period.

The accuracy of the converted displacement is assessed by a null test over stable areas. 95 % of the points located in motionless area present a residual displacement less than 0.30 m which is in agreement with the analyses of section §4.2. The global accuracy of the technique is better defined by comparing the displacements obtained with the DIC technique and displacement measured with the DGPS monitoring (Figure 9). The accuracy varies between 10 to 20%. The constant DEM used for the georeferencing and slight movements of the camera are the main causes of the error. When displacements are large, morphologic changes are significant. Consequently, the accuracy of the method decreases.

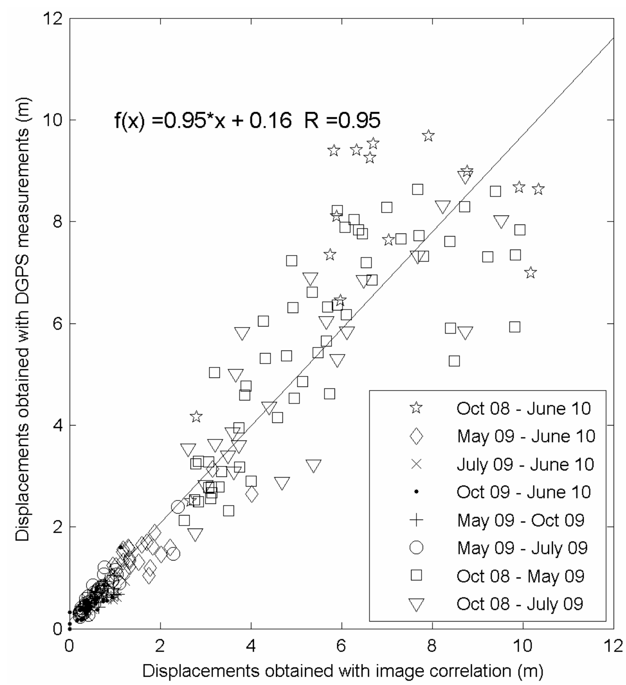

Figure 9. Accuracy and validation of the DIC technique by comparing the displacements obtained with the DIC technique with the displacements obtained with the DGPS monitoring.

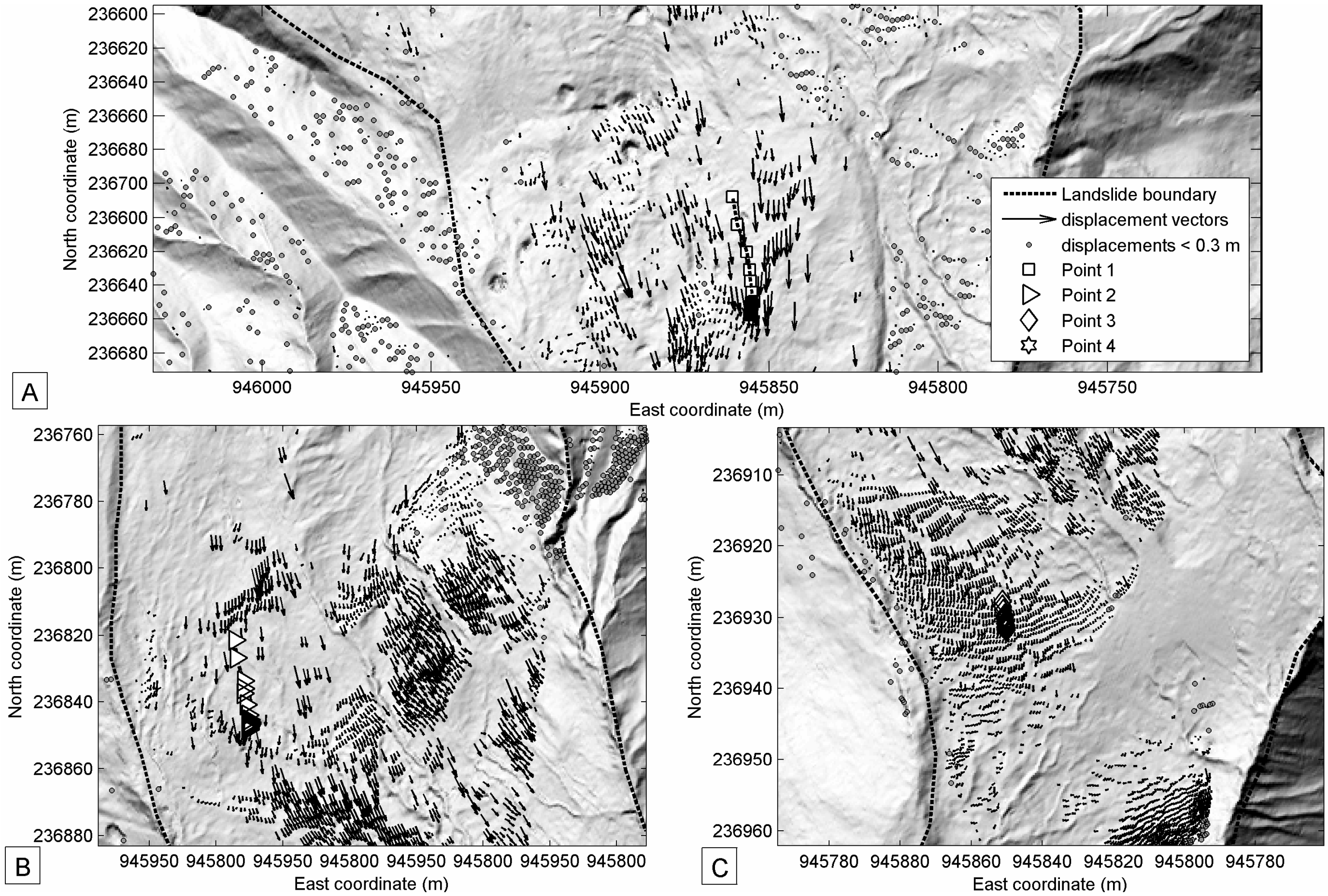

Figure 10. Displacement field for the 20th May 2008 in the local coordinate system in the upper part (A), in the middle part (B) and in the lower part (C) of the mudslide. The trajectories of the points 1, 2, 3 and 4 are also shown. Their cumulated displacements are presented in Figure 8.

6 DISCUSSION AND CONCLUSION

The examples presented in this paper demonstrated the efficiency of the low cost monitoring system based on DIC technique.

If the landslide is mainly translational without excessive changes in elevation, the same DEM can be used to estimate the displacements in the local coordinate system. The accuracy of the converted displacements will obviously depends on the accuracy and the resolution of the DEM. Refining the internal parameters of the camera (eg. radial distortion) might not significantly increase the accuracy because the constant DEM and the slight external parameters changes are the major sources of uncertainties in this method. Acquisitions of several accurate DEMs during the year and a systematic adjustment of the external parameters on fixed control points for each image acquisition would improve the displacement accuracy in the local coordinate system.

Despite its simplicity, the technique is limited by important changes in meteorological conditions (snow, clouds, rain storm), in surface conditions (important ground deformations due to rapid landslides) and in illumination conditions (changes in shadow length and orientation, only operational during the daytime) which drastically affect the correlation accuracy. These aspects have to be taken into account for integrating this technique in an early warning system. Development is also needed for direct data transfer.

ACKNOWLEDGEMENTS

This work was supported by the European Commission within the Marie Curie Research and Training Network '*Mountain Risks: from prediction to management and governance*' (2007-2010, Contract MCRTN-035798). The authors would like to acknowledge Andre Stumpf (Faculty of Geo-Information Science and Earth Observation, Netherlands) and Sabrina Rothmund for their help on the field. The authors thank Dr. Supper (Geological society of Austria) for his help in improving the manuscript.

REFERENCES

Bastard M., 2009. Caractérisation de la cinématique de glissement de terrain par technique de correlation d'image optique. Master thesis. University of Strasbourg (EOST). Institut de Physique du Globe, Strasbourg, France.

Cardenal J., Mata E., Perez-Garcia J.L., Delgado J., Andez M.A., Gonzalez a., Diaz-de-Teran J.R. 2008. Close Range Digital Photogrammetry Techniques applied to Landslide Monitoring. International Archives of the Photogrammetry, *Remote sensing and Spatial Information Sciences*. Vol XXXVII. Part B8.

Casson B., Baratoux D., Delacourt C., Allemand P. 2003. La Clapière" landslide motion observed from aerial differential high resolution DEM. *Engineering Geology*. **68**: 123-139.

Casson B., Delacourt C., Allemand, P. 2005 ; Contribution of multi-temporal sensing images to characterize landslide slip surface – Application to the La Clapière Landslide (France). *Natural Hazards and Earth System Sciences* **5**: 425-437.

Chambon G. 2003. Caractérisation expérimentale du frottement effectif des zones de faille. PHD Thesis. Université Paris XI Orsay, ENPC, pp. 204.

Chambon, G., Schmittbuhl, J., Corfdir, A., Vilotte, J.-P., Roux, S. 2003. Shear with comminution of a granular material: microscopic deformations outside the shear band, *Phys. Rev*. E 68, 011304.

Debella-Gilo M., Kääb A. in press. Sub-pixel precision image matching for measuring surface displacements on mass movements using normalized cross-correlation. *Remote Sensing of Environment*.

Delacourt, C., Allemand P., Casson B., Vadon H. 2004. Velocity field of the "La Clapiere" landslide measured by the correlation of aerial and Quick-Bird satellite images, *Geophys. Res. Lett*. **31**: 1-5.

Delacourt, C., Allemand, P., Berthier, E., Raucoules, D., Casson, B., Grandjean, P., Pambrun, C., Varel, E. 2007. Remote-sensing techniques for analysing landslide kinematics: a review. *Bulletin de Société Géologique* **178**: 89-100.

Fisher, P.F., 1991. First experiments in viewshed uncertainty: The accuracy of the viewshed area. *Photogrammetric Engineering Remote Sensing*, **57**: 1321-1327.

Franklin, W.R., and C.K. Rav, 1994. Higher isn't necessarily better: Visibility algorithms and experiments, Proceedings of-the 6th International Symposium on Spatial Data Handling, Edinburgh, Scotland **2**: 751-770.

Heikkila J. and Silven O. 1997. A four-step camera calibration procedure with implicit image correction. *IEEE Comput. Soc*: 1106-1112.

Hilds F., 2003. Mesure de champs de déplacement par corrélation d'images et applications en mécanique des solides, Notes de cours IPSI. Laboratoire de Mécanique et Technologie, CNRS-UMR 8535, Université Paris 6, France.

Kääb, A. 2002. Monitoring high-mountain terrain deformation from repeated air- and spaceborne optical data: Examples using digital aerial imagery and ASTER data, *J. Photogramm. Remote Sens*., **57**(1-2): 39–52.

LePrince S., Berthier E., Ayoub F., Delacourt C., Avouac J.-P. 2008. Monitoring Earth Surface Dynamics With Optical Imagery. *Eos* **89** (1): 1-5.

Lewis, J.P., 1995. Fast normalized cross-correlation, *Vision Interface*: 120-123.

Malet, J.-P., Maquaire, O., Calais, E. 2002. The use of Global Positioning System for the continuous monitoring of landslides. Application to the Super- Sauze earthflow (Alpes-de-Haute-Provence, France). *Geomorphology*, **43**: 33-54.

Mikhail, E., Bethel, J. S., and McGlone, J. C. 2001: Introduction to Modern Photogrammetry, Hardcover edition, New-York, 479.

Press, W. H., B. P. Flannery, S. A. Teukolsky, et W. T. Vetterling. 1997. Numerical Recipes in C, The Art of Scientific Computing, Second Edition, Cambridge Univ. Press, New York.

Travelletti J. & Malet J-P. Characterization of the 3D geometry of flow-like landslides: a methodology based on the integration of multi-source data. *Submitted in Engineering Geology*.

Julien Travelletti[(1)], Christophe Delacourt[(2)], Jean-Philippe Malet[(1)], Pascal Allemand[(3)], Jean Schmittbuhl[(1)], Renaud Toussaint[(1)]

Performance of image correlation techniques for landslide displacement monitoring

(1) Institut de Physique du Globe de Strasbourg, CNRS UMR 7516, Université de Strasbourg, Ecole et Observatoire des Sciences de la Terre, 5 rue Descartes, F-67084 Strasbourg, France. Email: jeanphilippe.malet@unistra.fr

(2) Laboratoire Domaines Océaniques, CNRS UMR 6538, Université de Bretagne Occidentale, Institut Universitaire Européen de la Mer, Rue Dumont d'Urville, F-29280 Plouzané, France.

(3) Laboratoire de Géologie de Lyon – Terre, Planète, Environnement, CNRS UMR 5276, Université de Lyon 1 et Ecole Normale Supérieure de Lyon, 2 rue Raphaël Dubois, F-69622 Villeurbanne Cedex, France.

Abstract The objective of this work is to present the applicability of image correlation techniques (applied to very-high resolution terrestrial optical photographs and to very dense Terrestrial Laser Scanning (TLS) point clouds) to monitor the displacement of continuously active landslides. The method has been developed to characterize the kinematics of very active landslides with cumulated displacement of several decimeters per year. The monitoring system consists in a high resolution optical camera installed on a concrete pillar located on a stable crest in front of the Super-Sauze landslide (South East French Alps) and on repeated TLS acquisitions over the period 2008-2009. The data are processed with a cross-correlation algorithm applied on the full resolution images (photographs and DEMs produced from the TLS data) in the acquisition geometry. Then, the calculated 2D displacement field is ortho-rectified with a back projection technique. The method allows to characterize the heterogeneous displacement field of the landslide in time and space, and to produce displacement maps. The performance of the technique is assessed using as reference differential GPS surveys of a series of benchmarks.

The sources of error affecting the results are discussed. Because the proposed methodology can be routinely and automatically applied, it offers promising perspectives for operational applications like, for instance, in early warning systems.

Keywords image cross-correlation; image matching; time-lapse acquisition; displacement monitoring; LiDAR, landslide

Introduction

Displacement monitoring of unstable slopes is a crucial tool for the prevention of hazards. It is often the only solution for the survey and the early-warning of large landslides that cannot be stabilized or that may accelerate suddenly. The choice of an adequate monitoring system depends on the landslide type and size, the range of observed velocity, the required frequency of acquisition, the desired accuracy and the financial constraints. Displacement monitoring techniques applied on landslides can be broadly subdivided in two main groups: geodetic and remote-sensing techniques.

Geodetic surveying consist in detecting geometrical changes in the landslide topography by measuring geometric parameters such as angles, distances or differences in elevation (e.g. levelling, tacheometry). These techniques necessitate the installation of targets in and outside the landslide and in measuring their position at different times. They have the advantage to be very accurate (0.2 to 2.0 cm) with a high potential of automation (Malet et al., 2002; Jaboyedoff et al., 2004; Foppe et al., 2006). However, because landslides can show highly variable displacement rates in time and space according to the local slope conditions (bedrock geometry, distribution of pore water pressures), the major drawbacks of the geodetic techniques are (1) to provide only discrete point measurements of the displacement and (2) the costs of installation and maintenance of the survey network.

Remote-sensing techniques are interesting tools to obtain spatially-distributed information on the kinematics (Delacourt et al., 2007) and can be operational from spaceborne, airborne and ground-based platforms. Remote-sensing techniques give the possibility to discriminate stable and unstable areas and to map sectors within the landslide with different kinematics from a regional to a local scale (Casson et al., 2005; Teza et al., 2008; Oppikofer et al., 2008). Three main categories of remote sensing techniques, either operated from terrestrial or airborne platforms, are used in landslide monitoring: Synthetic Aperture Radar Interferometry (InSAR), Laser Scanning (LiDAR) and Optical Photogrammetry (OP).

The objective of this work is to highlight the possible applications and limitations of cross-correlation techniques applied both on airborne and terrestrial LiDAR point clouds and on very-high resolution optical images. Several datasets of multi-source images acquired on the La Valette and Super-Sauze landslides (South French Alps) over the period 2007-2010 from different platforms are analysed. The influence of external factors on the precision and the accuracy of the results are discussed. Throughout this work, the accuracy is defined as the systematic difference between a measured quantity and the true value, and precision is defined as the random difference between multiple measurements of the same quantity.

Principle of the Image Correlation technique

Using matching techniques, two-dimensional displacement fields can be derived by tracking objects in two images acquired at different time. The technique is based on the automatic identification of identical texture patterns within an image by maximizing a correlation function (Lewis, 1995). Its principle adapted for landslide kinematics analysis is described in Delacourt et al. (2007).

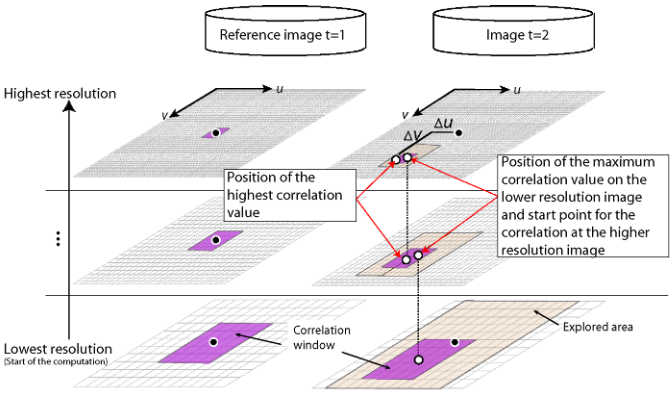

Figure 1 Principle of the normalized hierarchical image correlation technique.

Visible ground features have to be superimposed on two successive images on stable parts located outside the landslide. On the areas affected by landslide movements, the visible and recognizable features are shifted by the displacements. In order to quantify the ground displacements, a correlation window is defined on a reference (often the oldest) image. The corresponding window is searched in a pre-defined explored area belonging to the second image (Fig. 1). The starting point of this explored area is the expected position of the window with the assumption that no displacement occurred between two acquisitions. The process is repeated for each pixel of the reference image. The Euclidean distance between the reference point and the matching point represents the displacement amplitudes in the image plane. By modifying the zone of interest, it is then possible to determine the displacements at various positions within the images. It is important to note that the normalized cross-correlation technique cannot track objects that start to rotate significantly or are affected by important perspective distortions (Lewis, 1995).

The size of the correlation window is a compromise between the desired accuracy on the displacement estimates and the spatial resolution of the velocity field (Delacourt et al., 2007). An increase of the size of the correlation window ensures a good signal to noise ratio and thus a good precision, but the accuracy on the displacement estimates decreases because of their averaging on a larger correlation window. This compromise is difficult to define when some parts of the landslide are well represented in terms of ground texture while others parts are not. Hierarchical correlation techniques allow one to overcome this problem by automatically changing the physical size of the correlation window and of the explored area during the correlation computations. The physical size is defined as the effective landslide surface covered by the correlation window (Rohaly, 2002; Aloui & Ibn-Elhaj, 2009).

So far, Image Correlation techniques have been applied only on aerial and satellite images (e.g. SPOT, QuickBird, OrbView, EROS) for the creation of landslide displacement maps (Casson et al., 2003; Delacourt et al., 2004; LePrince et al., 2008; Debella-Gilo & Kääb, 2010).

Characteristics of the hierarchical cross-correlation technique used in this work

In this work, a sub-pixel hierarchical correlation technique is used (Hild, 2003). The original images are first converted in gray-scale images on which a 3x3 pixel Sobel convolution matrix is applied to highlight the ground surface texture. The gradient values are then correlated (Chambon, 2003). Four successive degradations of the image resolution are applied following a pyramidal approach for changing the physical size of the correlation window and of the explored area by down-sampling the gradient values of the full resolution image (Kumar & Banerjee, 1998) (Fig. 1). The optimum sizes of the correlation window and of the explored area are identified with a trial and error procedure. The correlation starts with the lowest resolution image in order to determine the largest displacements. Then the location of the pixel with the maximum cross-correlation value is used as the centre of the zone of interest for the next correlation step at a higher resolution. The spatial location of the maximum correlation value in the highest resolution image is thus progressively better estimated (Fig. 1). Ignoring high resolution information at the first computational step decreases the probability to reach a local minimum of the correlation function and, consequently, to obtain a wrong matching in the correspondence solution (Aloui & Ibn-Elhaj, 2009). In addition, this approach ensures very often a higher probability of detecting a reliable correlation peak. The sub-pixel displacement is computed after the correlation at the highest resolution image. An iterative procedure is used to find the maxima of the correlation function interpolated with a bi-parabolic formula and with a maximization procedure based on the simplex method (Press et al., 1997).

The correlation results consist in matrices of displacement Δu and Δv along the u- and v-axes in the image plane with their associated correlation index (Fig. 1). In case of orthorectified airborne images, the pixel size is constant, only the effective pixel size at the ground has to be calculated to estimate metric displacements. In case of terrestrial images, the pixel size is not constant in the image due to the oblique acquisition; the displacements field correlated in the image plane cannot be directly interpreted in terms of metric displacements and an orthorectification procedure is compulsory for a quantitative analysis.

Application 1: Image Correlation of terrestrial photographs

A set of images acquired at the Super-Sauze landslide over the period May–July 2008 is used to illustrate the potential of the technique for the characterization of the kinematics during an acceleration period (Travelletti et al., in press).

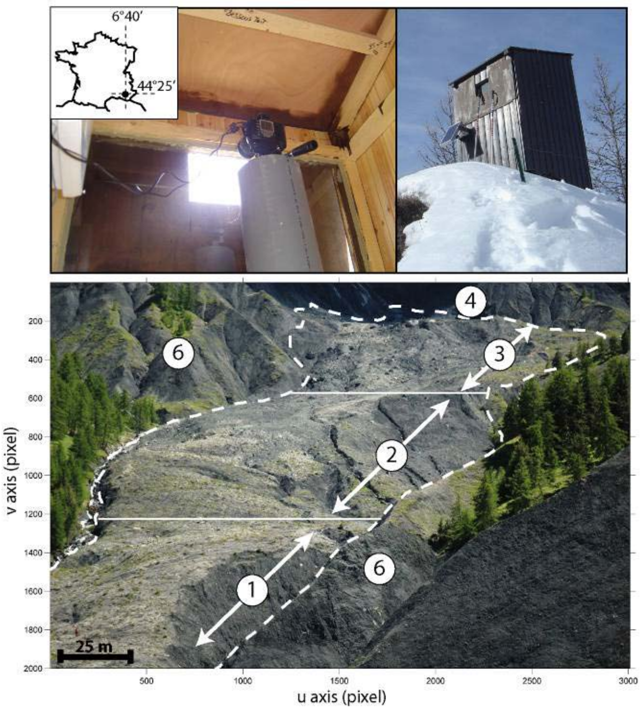

Figure 2 Monitoring system with a very-high resolution camera installed in front of the Super-Sauze landslide on a stable crest. Top: Monitoring system. Bottom: Image acquired by the monitoring system presenting the different parts of the landslide from the camera location. The numbers refers to: (1): Lower part (toe) of the landslide, (2) Middle part (transition zone), (3) Upper part (abalation zone), (4) Main scarp (1980 m), (5) Front (1734 m), (6) Stable crests.

Figure 2 presents the monitoring system installed in front of the landslide. The instrumentation consists in a low-cost D70 Nikon reflex digital camera installed on a concrete pillar located at a distance of 300 m from the lower part and 900 m from the main scarp (Fig. 2A, B). The acquisition system is controlled by a datalogger and the power is provided by a 40 W solar panel. Every four days, a serie of images is acquired at 11:00, 12:00, 13:00 and 14:00 GMT.

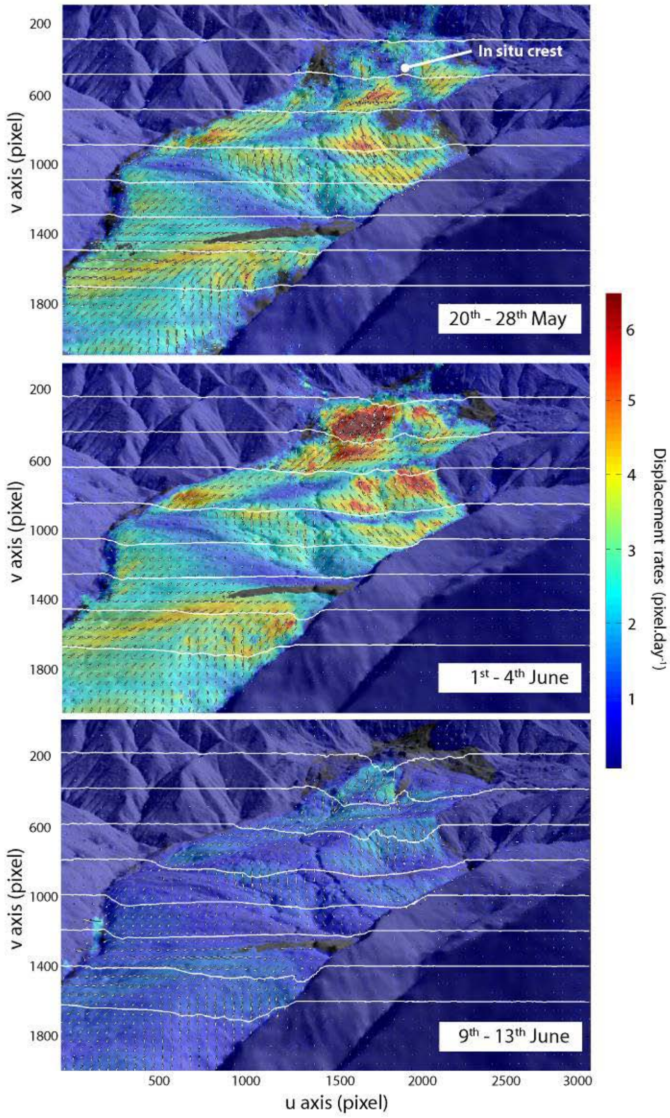

Figure 3 Displacement rates amplitude (color) and direction (arrows) in the image plane and cumulated displacements along eight profiles crossing the landslide over the period 20 May-25 June 2008. In order to highlight the displacement direction, the arrow length is normalized for each image.

Figure 3 shows an example of displacement rates (in pixel.day^{-1}) of the ground surface in the image plane derived from image pairs of 20–28 May 2008, 1–4 June 2008 and 9 June–13 June 2008. The reference is the image of 20 May 2008. The contrast in displacement rates between the landslide area and the stable area gives confidence on the calculated velocity field. One can notice that the pattern of displacement rate is heterogeneous spatially and temporally.

The upper part of the landslide displays the highest velocity ranging from 1 to 7 pixels.day^{-1} while the lower part displays velocity of less than 4 pixels.day^{-1}. From the 20 May to the 13 June, cumulated displacements up to 110 pixels are observed in the upper part. The maximum of displacement rate is observed around the 1st June. Then the landslide decelerates to displacement rate of about 1 pixel.day^{-1}. No quantitative comparisons can be carried out at this stage because the pixel sizes vary strongly in the image (Fig. 4).

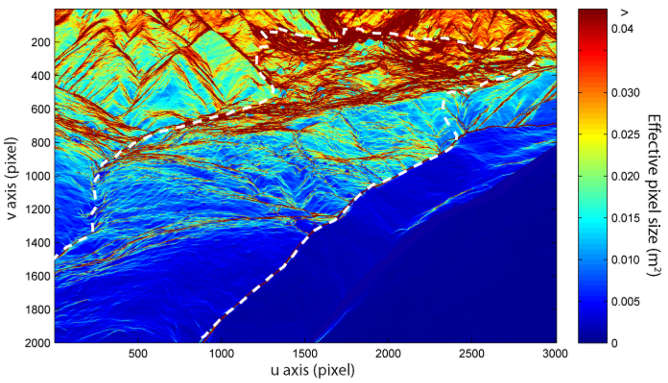

Figure 4 Effective pixel size calculated for the optical images by using an airborne laser scanning DEM acquired in 2009 and projected in the image geometry (in m²).

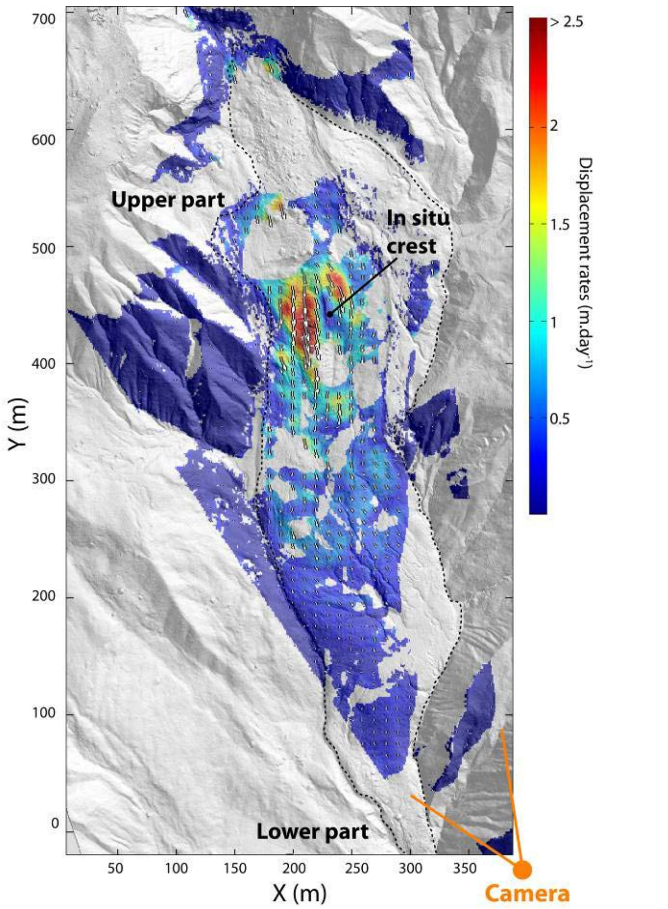

Figure 5 Displacement rates map for the period 1-4 June 2008 in the local geographic coordinate system.

The displacement fields computed in the image plane are then orthorectified in a local geographic coordinate system by transforming the central projection of the image into an orthogonal view of the ground using the collinearity equations (Kraus & Waldhaüsel, 1994). The details of the methodology are explained in Travelletti et al. (in press). Figure 5 presents the amplitude of the 3D orthorectified displacement rates for the period 1–4 June. The difference of kinematics between the upper (until 3 m.day^{-1}) and the lower (until 1 m.day^{-1}) parts is important The geometrical effect induced by the presence of the stable *in-situ* crest on the landslide kinematics is also clearly pointed out.

The precision of the computed displacements is assessed by performing a null hypothesis on the stable areas. Only the points with a correlation coefficient $r > 0.8$ are taken into account. In the image plane coordinate system, the average error μ ranges from 0.5 to 0.9 pixels with standard deviation σ of 0.3 to 1.2 pixels for the image pairs between the 20 May and the 25 June 2008. In the local coordinate system, the average error μ ranges from 0.03 m to 0.11 m with standard deviation σ of 0.10 to 0.31 m for the image pairs between the 20 May and the 25 June 2008. The performance of the method has been evaluated by comparing the displacements derived from the image correlation, and the displacement monitored by dGPS on several benchmarks distributed in the stable parts and on the landslide. A correlation coefficient of $r=0.95$ is found on 219 measurements and an average relative accuracy of 20% is determined (Travelletti et al., in press)

Application 2: Image Correlation of terrestrial LiDAR point clouds (TLS)

The potential of terrestrial LiDAR (TLS) for the monitoring of geomorphologic processes has been demonstrated in the last years, mainly for defining the structure of rocky slopes susceptible to rockfalls and rockslides (Abelan et al., 2009; Oppikofer et al., 2009) or characterizing the dynamics of ice glaciers (Avian et al., 2009) and landslides (Teza et al., 2008). Automatic matching algorithms applicable to TLS data have started to be developed because of their capability to fully exploit all the geometric information available in the point clouds. The approach is to find correspondences among typical features located in multi-temporal point clouds assuming that the tracked object has a constant geometry in time and/or a perfectly rigid behaviour.

Correlation techniques can be applied on repeated TLS acquisitions in order to characterize the 3D displacement field. The hypothesis is that for objects scanned from a unique view point, simple 2D correlation functions can be applied on multi-temporal point clouds and yield the same range of accuracy than complex and time-consuming 3D surface matching algorithms (Teza et al., 2008). The performance of the cross-correlation algorithm is tested on datasets acquired at the toe of the Super-Sauze landslide. A long-range terrestrial laser scanner Optech ILRIS-3D has been used for the monitoring (Travelletti et al., submitted).

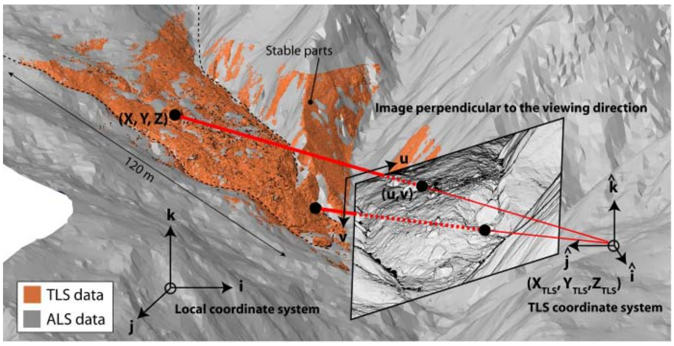

Figure 6 View of the scanned area at the Super-Sauze landslide from the TLS base station, and schematic presentation of the projective projection applied on the TLS point clouds with the different coordinate systems involved in the procedure. The alignment of the stable parts of TLS point clouds on the ALS (airborne laser scanner) point cloud is indicated.

Ten acquisitions were acquired between October 2007 and May 2010 for the same base station at an average distance of 100 m from the landslide toe (Fig. 6). At this distance, the laser diameter on the ground surface is estimated between 3 to 5 cm. Only the last return pulse is registered to maximize the number of points reflected on the ground surface. The average point density at the ground surface varies from 153.0 pts.m^{-2} to 234.9 pts.m^{-2} with a standard deviation up to 351.7 pts.m^{-2} and a maximal density of 1148.3 pts.m^{-2}.

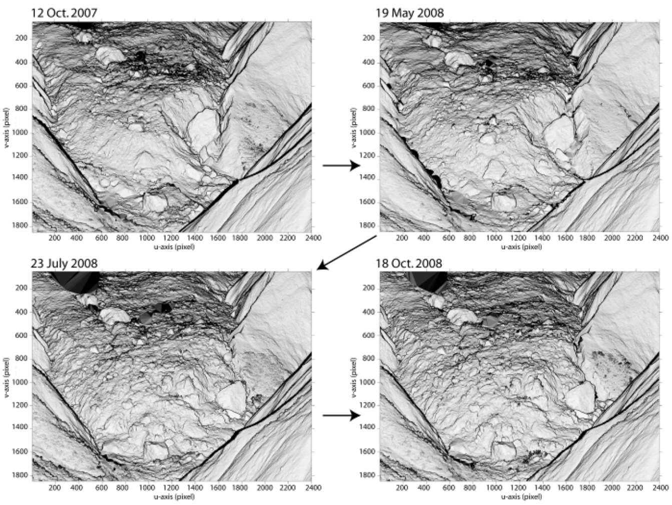

Figure 7 Images derived from the gradient calculation on the TLS point clouds for the period October 2007 – October 2008 at Super-Sauze. The morphology of the landslide toe is very well represented and the progression of the landslide toe is highlighted.

Filtering of vegetation and co-registration of the point clouds have been carried out with the software Polyworks 11 (Innovmetric, 2009). A projective transformation is used to represent the entire geometrical information in a plan perpendicular to the viewing direction of the laser scan using the collinearity equations (Kraus and Waldhaüsel, 1994). The point density varies from 0.78 to 0.94 pt.pixels^{-1} with a relatively low standard deviation of 0.18 pt.pixel^{-1}. The distance between the point clouds to the position of the laser scanner is then determined and linearly interpolated in a regular grid. Because the correlation function gives better results where the input data contains regions of rapidly varying pixel information (Duffy and Hughes-Clarke, 2005), the norm of the 2D gradient in *u* and *v* directions of the distance between the point clouds and the TLS station is calculated for emphasizing the morphology of the landslide. The generated images are then converted in grey-scale values (16 bits) and are used as inputs for the image correlation algorithm (Fig. 7).

The computed displacements are generally well reproduced for all periods of acquisition. Two acquisition periods (July-October 2008, July-October 2009) are presented to illustrate the performance of the approach and the behaviour of the landslide (Fig. 8). For the period July - October 2008, displacements between 0.5 and 1.5 m are observed, corresponding to an average displacement rate of 0.6 to 1.7 cm.day^{-1}. The displacement field displays significant spatial heterogeneities. The largest displacements are detected in the front of the toe where the slope gradient increases. The detachment of a toe compartment is also highlighted in the front.

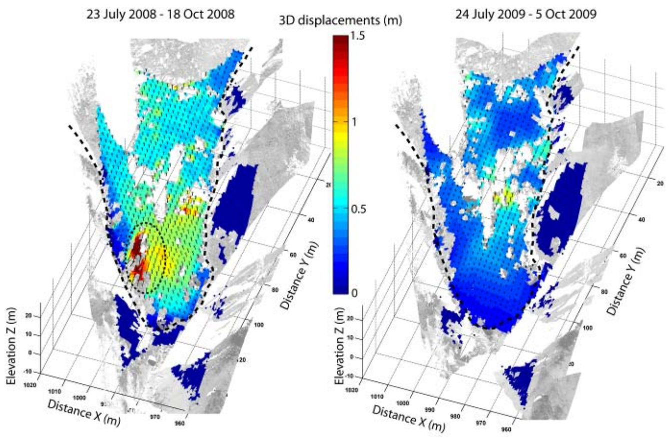

Figure 8 3D displacements field obtained by TLS measurements related to the acquisition periods of July-October of the years 2008 and 2009. The dashed circle indicates the detachment of compartment at the front of the toe.

During the period July-October 2009, the landslide displays a very different kinematics both in terms of magnitude and spatial distribution. Displacements are shorter and range from 0.1 m at the front to 0.6 m in the upper part, corresponding to an average displacement rate of 0.1 to 0.8 cm.day-1.

The computed displacements are validated by comparing the displacement values to dGPS observations of a series of blocks easily recognizable in the TLS point clouds. This comparison allows evaluating the accuracy of the approach by taking into account the noise in the data with the co-registering errors between two acquisitions.

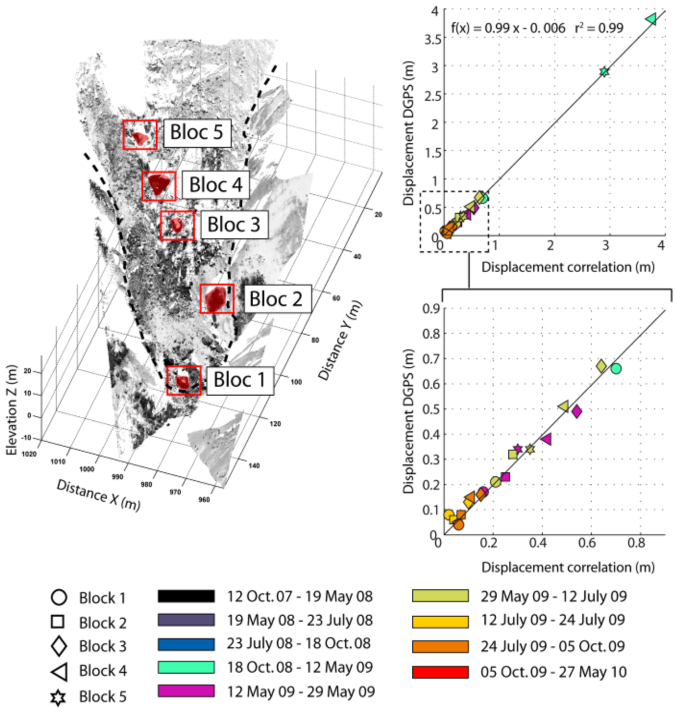

Figure 9 Comparison and validation of the displacements obtained by correlation with dDGPS observations on a series of blocks.

The displacements perfectly correlate (r^2=0.99), and a mean error and a standard deviation of 0.04 m and 0.03 m are determined (Fig. 9). This results show that the error due to the co-registering is about 3 cm.

Application 3: Image Correlation of airborne LiDAR point clouds (ALS)

A similar approach can be used for the creation of displacements maps from repeated airborne LiDAR point clouds (ALS). In this case, the landslide of La Valette is taken as example to illustrate the potential of the technique. Two DEMs with one-metre mesh size are interpolated from airborne LiDAR data acquired in Octobre 2007 and July 2009. The average point density at the ground surface varies from 0.7 pts.m^{-2} to 7.2 pts.m^{-2} with a standard deviation up to 12.1 pts.m^{-2}. Two complementary pieces of information are directly derived from the DEMs (Fig. 10):

+ the elevation differences (Z component) indicating an accumulation of mass in the transit zone;
+ the horizontal displacement field (E-N components) obtained by correlating the 2D gradient of the topography with a size of the correlation window of 20 m; the results indicate a decrease of the displacement magnitudes from the transit zone to the accumulation zone where nearly null displacements are observed.

The landslide behavior is controlled by a drainage system installed to stabilize the accumulation zone. Consequently, an increase of strain and an accumulation of mass occur near the Serre road demonstrating that the drainage system might not be the best solution to control the long term behavior of the slope.

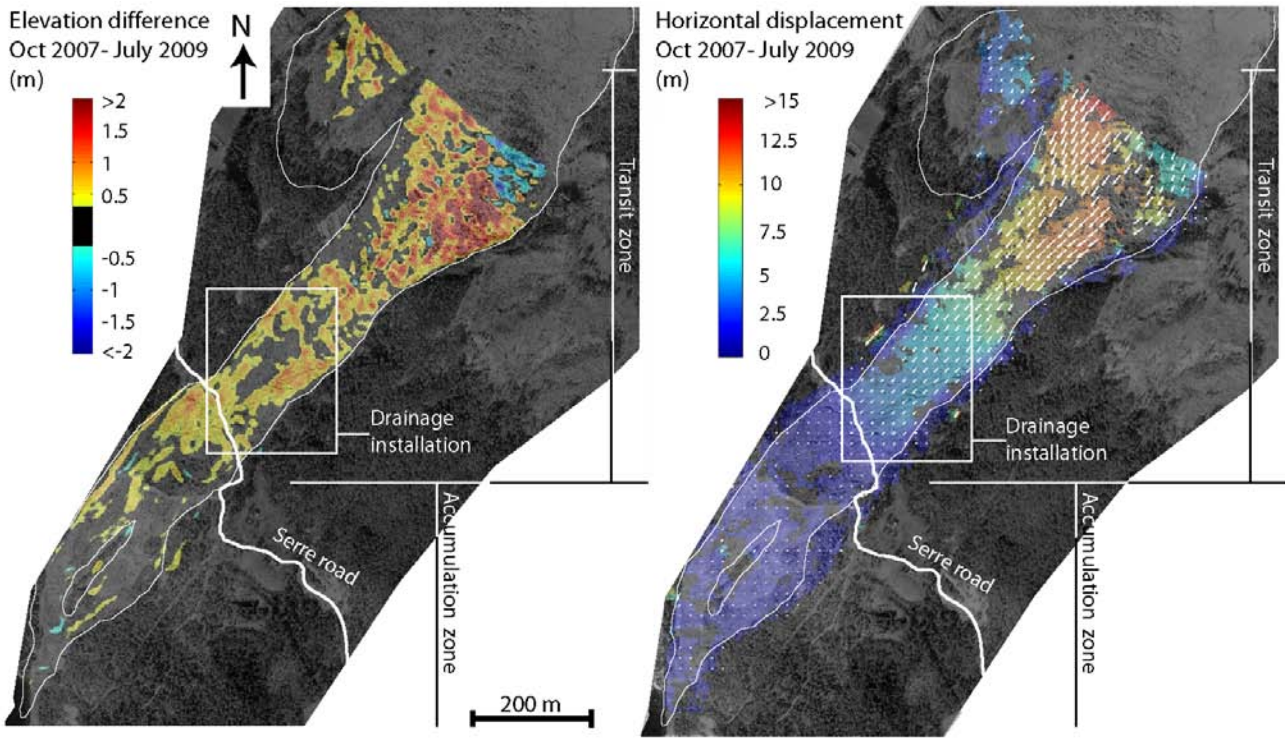

Figure 10 Displacement field calculated at the La Valette landslide from two airborne LiDAR acquisitions in October 2007 and July 2009.Left: Displacement field in the Z direction indicating changes in elevation, and possible zones of material accumulation or erosion. Right: Displacement field in planimetry indicating changes in distribution of mass.

Conclusion

The potential of Image Correlation technique applied to multi-temporal terrestrial photographs or airborne or terrestrial LiDAR point clouds has been evaluated using datasets available on the Super-Sauze and La Valette landslides (South French Alps). Operational methodologies are available to compute displacement rates both in the image plane coordinate system and in local geographic coordinate systems. The technique allows to clearly characterize heterogeneous displacement field of landslides in space and in time, with a high detection thresholds (cm.day^{-1}). The displacements maps computed from the images are in good agreement with local information on the displacement rates observed with classical geodetic techniques such a dGPS.

Using terrestrial images, the effect of pixel size at the ground (according to the distance to the target), the incidence of the line of sight to the ground and the resolution of the image are limiting factors to detect low displacement rates. Moreover, areas of low incidence angles (<5°) are very sensitive to small movements of the acquisition platform, that can partly be corrected. Other limiting factors for optical images are related to the meteorological and illumination conditions and the ground surface changes inducing partial or complete loss of coherence between image pairs.

The results demonstrate that Image Correlation techniques implemented in permanent monitoring system are particularly interesting for monitoring landslides characterized by annual pluri-decimetric displacements. This work offers very promising perspectives for operational applications which can be potentially integrated in early warning systems by considering additional efforts in direct data transmission. Finally, inversion of the displacement field could be developed to characterize the macroscopic rheological properties of the landslide material.

Acknowledgments

This work was partly supported by the European Commission under the Marie Curie Contract '*Mountain Risks: from prediction to management and governance*' (FP6, MCRTN-035798; 2007-2010), and the European Project FP7 '*SafeLand: Living with landslide risk in Europe*' (2009-2012). The authors are grateful to Mr. Grzegorz Skupinski (University of Strasbourg) for his support in the acquisition of the Terrestrial Laser Scanning data.

References

Abellán, A., Jaboyedoff, M., Oppikoffer, T., Vilaplana, J. M., (2009). Detection of millimetric deformation using a terrestrial laser scanner: experiment and application to a rockfall event. Natural Hazards Earth System Sciences, 9, 365-372.

Avian, M., Kellerer-Pirklbauer, A., Bauer, A. (2009). LiDAR for monitoring mass movements in permafrost environments at the cirque Hinteres Langtal, Austria, between 2000 and 2008. Natural Hazards Earth System Sciences, 9, 1087-1094.

Casson B., Delacourt C., Allemand, P. (2005). Contribution of multi-temporal sensing images to characterize landslide slip surface – Application to the La Clapière Landslide (France). Natural Hazards and Earth System Sciences, 5, 425-437.

Casson, B., Baratoux, D., Delacourt, D., Allemand, P. (2003). "La Clapière" landslide motion observed from aerial differential high resolution DEM. Engineering. Geology, 68, 123-139.

Chambon, G. (2003). Caractérisation expérimentale du frottement effectif des zones de faille. PhD Thesis. Université Paris XI Orsay, ENPC.

Debella-Gilo M., Kääb, A. (2010). Sub-pixel precision image matching for measuring surface displacements on mass movements using normalized cross-correlation. Remote Sensing of Environment (2010).

Delacourt, C., Allemand P., Casson B., Vadon H. (2004). Velocity field of the "La Clapiere" landslide measured by the correlation of aerial and Quick-Bird satellite images. Geophysical. Research Letters, 31, 1-5.

Delacourt, C., Allemand, P., Berthier, E., Raucoules, D., Casson, B., Grandjean, P., Pambrun, C., Varel, E. (2007). Remote-sensing techniques for analysing landslide kinematics: a review. Bulletin de Société Géologique, 178, 89-100.

Duffy, G.P., Hughes-Clarke, J.E. (2005). Application of spatial cross correlation to detection of migration of submarine sand dunes. Journal of Geophysical Research, 110, 1-11.

El Alaoui. M.I., Ibn-Elhaj, E. (2009). A robust hierarchical motion estimation algorithm in noisy image sequences in the bispectrum domain. Signal Image and Video Processing, 3, 291-302.

Foppe, K., Barth, W., & Preis, S. (2006). Autonomous Permanent Automatic Monitoring System with Robot-Tacheometers. Proceedings of of the XXIII International FIG Congress, Munich, Germany.

Hild, F. (2003). Mesure de champs de déplacement par corrélation d'images et applications en mécanique des solides. Notes de cours IPSI. Laboratoire de Mécanique et Technologie, CNRS-UMR 8535, Université Paris 6, France.

InnovMetric, (2009). PolyWorks User's Manual - 3-D scanner and 3-D digitizer software from InnovMetric Software Inc., http://www.innovmetric.com/

Jaboyedoff, M., Ornstein, P., Rouiller, J.-D. (2004). Design of a geodetic database and associated tools for monitoring rock-slope movements: the example of the top of Randa rockfall scar. Natural Hazards and Earth System Science, 4, 187-196.

Kraus, K., Waldhäusl, P. (1994). Photogrammetry, Fundamentals and Standard processes. vVol . 1. Hermès (editor), Paris.

Kumar, S., Banerjee, S., (1998). Development and application of a hierarchical system for digital particle image velocimetry to free-surface turbulence. Physics of Fluids, 10, 160-177.

LePrince, S., Berthier, E., Ayoub, F., Delacourt, C., & Avouac, J.- P. (2008). Monitoring earth surface dynamics with optical imagery. Eos, 89, 1-5.

Lewis, J.P., (1995). Fast normalized cross-correlation. Vision Interface, 120-123.

Malet, J.-P., Maquaire, O., Calais, E. (2002). The use of global positioning system techniques for the continuous monitoring of landslides. Geomorphology, 43, 33-54.

Oppikofer, T., Jaboyedoff, M., Kreusen H.-R. (2008). Collapse at the eastern Eiger flank in the Swiss Alps. Nature Geoscience, 8, 531-535.

Oppikofer, T., Jaboyedoff, M., Blikra, L. H, Derron, M. H., Metzger, R. (2009). Characterization and monitoring of the Aknes rockslide

using terrestrial laser scanning. Natural Hazards and Earth System Sciences, 9, 1003-1019.
Press, W.H., Flannery, B.P., Teukolsky, S.A., Vetterling, W.T. (1997). Numerical Recipes. Cambridge University Press, New York.
Rohaly, J., Frigerio F., Hart D. P. (2002). Reverse hierarchical PIV processing. Measurement Science and Technology, 13, 984-996.
Teza, G., Pesci, A., Genevois, R., Galgaro, A. (2008). Characterization of landslide ground surface kinematics from terrestrial laser scanning and strain field computation. Geomorphology, 97, 424-– 437.
Travelletti, J., Delacourt, C., Toussaint, R., Allemand, P., Malet J.-P., Schmittbuhl, J., Bastard, M. 2011 (in press) Correlation of multi-temporal ground-based images for landslide monitoring: application, potential and limitations. International Journal of Photogrametry and Remote-Sensing, 25p. (in press).
Travelletti, J., Malet J.-P., Delacourt, C., (submitted, in review). Multi-date correlation of Terrestrial Laser Scanning data for the characterization of landslide kinematics. Geomorphology, 15p. (in review).

Journal of Structural Geology 45 (2012) 1–2

Contents lists available at SciVerse ScienceDirect

Journal of Structural Geology

journal homepage: www.elsevier.com/locate/jsg

Editorial

Foreword to Special Issue: “Fault Zone Structure, Mechanics and Evolution in Nature and Experiment”

1. Foreword

Tectonic faults in the Earth’s upper crust are geometrically complex zones of localized deformation and rock damage that evolve over wide length- and time-scales. Fault zones influence a range of crustal processes including fluid flow, mechanical strength, basin evolution, and earthquake nucleation, propagation and arrest. Because of this, fault zones motivate considerable academic and commercial research, and have been the focus of a large body of work involving field observations, theory, numerical simulations, experiments and seismology.

Despite recent progress, significant aspects of fault zone structure and evolution remain poorly understood. Uncertainties remain as to the main deformation mechanisms that are active during the seismic cycle. It is also largely unclear how deformation is partitioned between principal faults and adjacent regions of off-fault damage, and to what extent associated fluid flow is influenced by varying fracture modes in different lithologies. A further problem concerns the evolution of fault roughness and fault rock granularity during slip and how this impacts on fault mechanical behavior. Some of these issues are discussed in this Special Issue of the *Journal of Structural Geology* which arises from a session held at the European Geosciences Union (EGU) General Assembly in Vienna, April 2011. The contributions in this volume highlight some of the complexity of natural fault systems. Common themes that link many of the contributions are the relationships between fault zone structure and fault dynamics, and the importance of fault zone structure for sub-surface fluid flow, particularly in fractured carbonates. The 11 papers here are divided in to two parts, although the subdivision is somewhat arbitrary given the multidisciplinary nature of many of the contributions. Papers in Part I, *Fault zone structure and evolution*, deal mainly with field characterization of fault zones at outcrop to regional scales, and associated observations of fault rock microstructures. Papers in Part II, *Fault roughness and brittle rock damage*, present field and experimental constraints on the geometry and mechanical properties of fault slip surfaces, pulverized and sheared fault rocks, and cataclastic deformation bands.

Part I. Fault zone structure and evolution

Agosta et al. describe the structure and deformation mechanisms of shallowly exhumed normal fault zones in clay-bearing conglomerates and carbonate grainstones from the Granada Basin in Spain. Clay smearing and cataclasis were particularly important deformation mechanisms in the conglomerates, whereas jointing, pressure solution and local brecciation surrounding slip surfaces dominated in the carbonate grainstones. Overall, they suggest that the fault zones acted as combined conduit-barrier systems to fluid flow. *Petracchini et al.* present observations of small faults and fractures that cut well-bedded marly and pelagic carbonates of the Cingoli anticline in Italy, a potential analog for carbonate reservoirs in the nearby Po Plain and Adriatic Sea. They identify several distinct sets of largely strata-bound pressure solution seams that formed during compaction and bedding-parallel flexural slip, leading them to propose a model in which faults developed relatively late during the folding process by linkage of bedding surfaces and pressure solution seams. The authors also discuss the role that such structures, below the typical seismic resolution, may have on subsurface fluid flow in folded upper-crustal carbonate sequences of this kind. *Reyer et al.* describe faults with centimeter- to meter-scale offsets cutting both carbonate and clastic sediments in the Northwest German Basin. Their field and laboratory measurements indicate that only fault zones in carbonates have well-defined damage zones with higher fracture densities compared to background fractures in the wall rocks. This leads the authors to suggest that fault zones in carbonates will promote sub-surface fluid flow to a greater extent than fault zones in clastic sedimentary rocks. *Fondriest et al.* present field and microstructural observations of a fault zone exhumed from <2 km depth crosscutting dolostones in the Southern Alps of Italy. They focus on cataclasites in the millimeter- to centimeter-thick slipping zones of the principal, as well as subsidiary faults, and find widespread evidence for fault rock fluidization, injection and clast size sorting. They conclude, in part by comparison to a seismically-active fault in dolostones, that the microstructures formed during seismic slip. The final paper by *Rutter et al.* synthesizes previous observations from the large-displacement Carboneras fault zone in south-eastern Spain, and presents new age determinations and a new geological map to better constrain its geological character and movement history. The structure of the ~ 1 km wide Carboneras fault zone consists of two main fault strands, each containing multiple fault gouge zones enclosing elongate tracts of wall rock lithologies. The authors suggest that the fault zone formed as part of a transform system associated with slab retreat during closure of the Alboran Sea in the western Mediterranean region.

Part II. Fault roughness and brittle rock damage

Candela et al. use terrestrial laser-scanning to measure the roughness of the Dixie Valley normal fault in Nevada, USA. They find that

0191-8141/$ – see front matter © 2012 Published by Elsevier Ltd.
http://dx.doi.org/10.1016/j.jsg.2012.11.001

the roughness of the main slip surface is self-affine in character, meaning that it appears smoother at larger scales of observation. Their field measurements of the dimensions of elongate fault rock lenses leads the authors to develop a model in which the self-affine property of the fault roughness is controlled by linkage of a myriad of overlapping slip surfaces during fault zone growth. *Renard et al.* monitor surface roughness evolution and infra-red emissions during analogue friction experiments involving blocks of halite sliding over a sandpaper base. They show that gouge production during the experiments is highly heterogeneous, involving fracturing and formation of elongate striations in the slip direction, as well as migration of gouge particles in various directions with respect to the slip vector. Accumulation of gouge during the experiments resulted in a gradual decrease in the friction coefficient. Finally, the authors compare the geometry and distribution of wear materials in the experiments with the striations commonly observed on natural fault surfaces. *Doan et al.* perform dynamic loading experiments using a split Hopkinson pressure bar containing granite samples with varying amounts of pre-existing fracture damage. They find that pulverization of the granite is easier to achieve in the case of extensive pre-existing damage. Comparison of the experimental data with fracture propagation theory suggests that the strain rate required to pulverize the granite samples is a power law of initial fracture density. Their results imply that pulverized rocks in the field may result from a positive feedback process during successive earthquake loading events. *Dyer et al.* analyze the particle size distributions of gouge materials, and surface roughness of fractures, produced in a granite sample during a triaxial loading experiment. They find that the power law exponent of the particle size distribution increases systematically towards zones of intense comminution associated with fractures and small faults. In contrast, they find no relationship between the surface roughness of fractures and degree of comminution, although opening-mode fractures are slightly rougher than those with small shear offsets. They conclude for the analyzed granite sample that there is no correlation between the particle size distribution of gouge materials and the roughness of fractures that bound such zones of gouge. *Cilona et al.* present field and laboratory observations of deformation bands formed in porous carbonate grainstones of the Majella anticline in Italy, with the aim of understanding the deformation mechanisms active during their development under natural and experimental conditions. By evaluating the various roles of pressure solution, grain crushing and fracturing, they conclude that there are important differences in the deformation mechanisms active during formation of natural and experimental deformation bands in carbonates. Deformation bands are also the subject of the final paper by *Imber et al,* who present observations of conjugate deformation bands cutting unconsolidated sands and gravels in McKinleyville, California. The deformation bands formed at <50 m depth ahead of the propagating tip of the McKinleyville thrust fault. The authors use a trishear model of fault propagation folding combined with published mechanical data for high-porosity sandstones to test whether the deformation bands may have formed parallel to lines of no finite elongation or parallel to zero extension directions. They conclude that neither of these possibilities adequately explains the orientation of deformation bands in McKinleyville, and instead suggest that the deformation bands most likely formed in an orientation consistent with the Mohr-Coulomb failure criterion, or in an orientation bound by the Mohr-Coulomb failure criterion and zero extension directions.

We would like to thank the authors and reviewers of the papers for their contributions and the staff at Elsevier and the Journal of Structural Geology for their help during compilation of the Special Issue.

S.A.F. Smith, Managing Guest Editor*
Istituto Nazionale di Geofisica e Vulcanologia (INGV), Seismology and Tectonophysics Section, 605 Via di Vigna Murata, 00143, Rome, Italy

F. Agosta, Guest Editor
Department of Sciences, University of Basilicata, Basilicata, Italy

R. Toussaint, Guest Editor
Institut de Physique du Globe de Strasbourg, CNRS, University of Strasbourg, Strasbourg, France

R.E. Holdsworth, Guest Editor
Department of Earth Sciences, Durham University, Durham, England

* Corresponding author. Tel.: +39 0651 860 730.
E-mail address: steven.smith@ingv.it (S.A.F. Smith)

Title:

Dynamic Development of Hydrofracture

Authors:

Irfan Ghani

Tektonophysik, Institut für Geoswissenschaften, Johannes Gutenberg Universität Mainz, Germany.

Daniel Koehn

School of Geographical and Earth Sciences, University of Glasgow, UK.

Renaud Toussaint

Institute of Globe Physics in Strasbourg, CNRS / University of Strasbourg, 5 rue Descartes, 67084 Strasbourg Cedex, France

& Centre for Advanced Study at the Norwegian Academy of Science and Letters, Drammensveien 78, 0271 Oslo, Norway.

Cees Willem Passchier

Tektonophysik, Institut für Geoswissenschaften, Johannes Gutenberg Universität Mainz, Germany.

Key Point:

Hybrid discrete-continuum formulation is developed to model natural hydro-driven fracturing.

Pore pressure diffusion is crucial in pattern formation.

Abstract:

Many natural examples of complex joint and vein networks in layered sedimentary rocks are hydro-fractures that form by a combination of pore fluid overpressure and tectonic stresses. In this paper, a two-dimensional hybrid hydro-mechanical formulation is proposed to model the dynamic development of natural hydrofractures. The numerical scheme combines a Discrete Element Model (DEM) framework that represents a porous solid medium with a supplementary Darcy based pore-pressure diffusion as continuum description for the fluid. This combination yields a porosity controlled coupling between an evolving fracture network and the associated hydraulic field. The model is tested on some basic cases of hydro-driven fracturing commonly found in nature i.e., fracturing due to local fluid overpressure in rocks subjected to hydrostatic and nonhydrostatic tectonic loadings. In our models we find that seepage forces created by hydraulic pressure gradients together with poroelastic feedback upon discrete fracturing play a significant role in subsurface rock deformation. These forces manipulate the growth and geometry of hydrofractures in addition to tectonic stresses and the mechanical properties of the porous rocks. Our results show characteristic failure patterns that reflect different tectonic and lithological conditions and are qualitatively consistent with existing analogue and numerical studies as well as field observations. The applied scheme is numerically efficient, can be applied at various scales and is computational cost effective with the least involvement of sophisticated mathematical computation of hydrodynamic flow between the solid grains.

Index Terms:

0500 COMPUTATION GEOPHYSICS

0545 Modeling

0550 Model verification and validation

0560 Numerical solutions

5100 PHYSICAL PROPERTIES OF ROCKS

5104 Fracture and flow

5112 Microstructure

5114 Permeability and porosity

Keywords:

DEM, Hydrofracture, fluid-solid dynamics, pore pressure diffusion, pattern formation.

1) Introduction:

Brittle deformation of rocks in association with over pressured fluid plays an important role in the geophysical, geochemical and structural mechanics of the Earth's crust in a wide variety of geological settings [*Fyfe et al.*, 1978]. A number of fluid expansion mechanisms e.g., burial compaction, clay dehydration, organic matter decomposition and aquathermal expansion as well as impermeable rock units which behave as seal to subterraneous fluid flow render the pore fluid overpressure, which if in excess of the least principal stress ($P_f > \sigma_3$) may lead to load parallel or load oblique tension fracturing (figure 1) in depths of the Earth's crust.

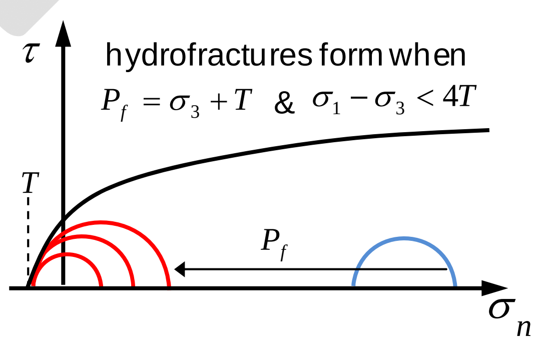

Fig. 1: Mohr diagram of tensile failure due to fluid overpressure. The blue Mohr circle represents the initial state of stress with zero fluid pressure. The Mohr circle moves towards the left hand side (red circles) as a result of fluid overpressure, which results in tensile/shear failure.

The mechanism of hydrofracturing has great implications in the interpretation of field observations and for the prediction of natural or industrial problems in a broad range of research disciplines. After pioneering work of [*Hubbert and Willis*, 1957; *Hubbert and Rubey*, 1959] which explored pore fluid pressure as an important factor for small scale hydrofracturing in tectonic processes, significant efforts have been made in the development of theoretical fundamentals [*Biot et al.*, 1986; *J M Cleary and Illinois State Geological Survey.*, 1958; *Daneshy*, 1973; *Secor*, 1965; *Valkó and Economides*, 1995]. Apart from theoretical aspects, a significant amount of analytical and numerical solutions have also been put forward by many investigators to address this coupled process in a qualitative and quantitative manner [*M P Cleary and Wong*, 1985; *Flekkøy et al.*, 2002; *Gordeyev and Zazovsky*, 1992; *Meyer*, 1986; *Tzschichholz et al.*, 1994; *Yu.N*, 1993].

Most of the previous numerical tools are built on continuum approaches and consider fluid flow in fractures of simple geometry (penny-shaped elliptical or vertical cracks) using the theory of linear elasticity. Much of these approaches however, lack the constitutive relationship of explicit coupling between the solid and fluid being considered separately and makes strong approximations upon complex flow and deformation interaction arising from brittle failure, material disorder and inhomogeneity present at various scales in geo-pressurized problems. Some porosity controlled models [*Boone and Ingraffea*, 1990; *Flekkøy et al.*, 2002; *Mourgues* *and Cobbold*, 2003; *Olson et al.*, 2009; *Wangen*, 2002] revealed that the potential response of inherent poroelastic mechanics is an important parameter in hydro-driven rock failure, where the seepage forces caused by pore pressure gradients [*Engelder and Lacazette*, 1990; *Rozhko*, 2010; *Rozhko et al.*, 2007] in porous rocks affect the driving stress for fracture initiation and growth. Regardless of the underlying driving agent hydrofracturing is a complex process which incorporates the dynamic coupling of at least three sub-processes [*Adachi et al.*, 2007]; 1) Restructuring of rock skeleton upon elastic/in-elastic strain. 2) Corresponding alteration of both the permeability and the interstitial fluid pressure. 3) Further mechanical deformation leading to fracture propagation with concurrent variation in the pore or fracture filled fluid pressure.

Inspired by [*Flekkøy et al.*, 2002] we extended the work of [*Koehn et al.*, 2005] to a hybrid discrete-continuum constitutive modeling approach. The scheme emphasizes the evolution of rock failure in the light of underlying synergistic evolution of rock permeability upon fracture growth and the consequent change in interstitial pore pressure. The hypothesis is that porosity effective pore pressure diffusion along the pressure gradient is critical for the formation of discrete opening mode fractures and thus may influence the propagation of hydrofractures at large scale in porous rocks under controlled strain conditions.

The present paper evaluates the theoretical aspects of the numerical scheme for some basic configurations to which analogue and analytical studies are present i.e., hydrofracturing in homogeneous porous media under hydrostatic and non-hydrostatic conditions. In the following section we give details of the fluid-solid two-way coupling scenario of the scheme. In section 3 the validation of the solution is given and in section 4 implementations of the method is illustrated by means of simulation examples related to simple geometrical problems. Finally, results from this study are pointed out in section 5. The Alternative Direction Implicit procedure for the solution of the continuum diffusion is given in the Appendix-A.

2) Formulation

The simulations implemented in this study constitute of a special solution of the Darcy based Navier Stoke's equation and its coupling with a discrete poroelastic medium. The basic assumption is that the poroelastic feedback is behaving according to Biot's poroelastic theory within a linear elastic regime. This connects pore-scale force balanced hydro-physics with the evolution of the effective pressure gradient in a porous rock. Once a fracture initiates, the overall behavior of the model becomes plastic and Biot's compressibility is no longer applicable [*Flekkøy et al.*, 2002]. The numerical scheme can encounter the displacement of discrete particles or deformation of a solid matrix directly. In this way the hydrodynamics evolve intrinsically with irreversible micro deformation in a solid matrix through the use of the Kozeny-Carman porosity-permeability relation.

The solution procedure adopted for this coupled problem is based on the same basic principles that were successfully used in simulations to model instabilities in fluid filled granular media [*Johnsen et al.*, 2006, 2007, 2008; *McNamara et al.*, 2000]. The same type of hybrid models was also used to model gravitational instabilities in Rayleigh-Taylor like situations with grains falling in a gas [*J. L. Vinningland et al.*, 2007a, 2007b, 2009a, 2009b, 2010], or a fluid [*Niebling et al.*, 2010a, 2010b; *Vinningland et al.*, 2012], and in situations of aerofracturing, i.e. injection of gas in granular media [*Niebling et al.*, 2012a, 2012b]. It was shown to reproduce lubrication in sheared fault gouges due to the presence of an interstitial fluid [*Goren et al.*, 2010, 2011] and a variant of two fluid models is used to model fluidizes beds [*Jackson*, 2000] and saturated landslides [*Denlinger and Iverson*, 2001; *Spickermann et al.*, 2012]. In the following subsections we outline the idealizations employed to set up the hybrid model and describe the model components along with the formulation of constitutive equations. Then we turn to the solution of the fluid-solid interaction, deformation mechanism and finally the assumptions made in this study.

2.1) Methodology:

The numerical scheme is built on a 2D hybrid Particle-Lattice model of unit dimension that utilizes a small-scale triangular discrete spring network code inherited from the software 'Latte' (part of the modeling environment 'Elle', [*Bons et al.*, 2007; *Koehn et al.*, 2005]) as a deformation isotropic porous material. The discrete lattice is then coupled with a continuum fluid phase presented by a stationary square grid of equivalent or larger dimension (figure 2).

The computation is governed by a set of two differential equations, one deals with the translation (elastic deformation) of solid particles and the second solves the time dependent diffusion of fluid pressure according to local strain rates through a poro-elasto-plastic relationship. For a given configuration of the pressure field and the solid particles, the respective constitutive equations are approximated separately by two different numerical procedures. The elastic media is relaxed by a standard over-relaxation algorithm containing kinematic boundary conditions ($n \cdot u = 0$) for boundary particles, while the Pressure ADI routine is used for the solution of the pressure diffusion in a continuum grid (Appendix-A).

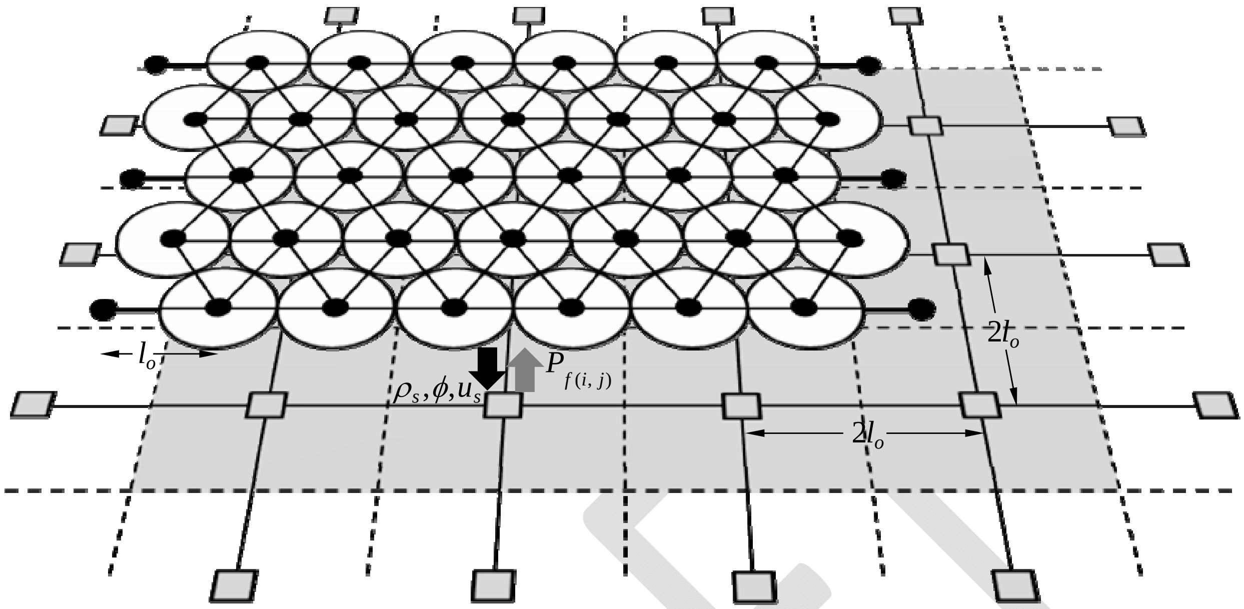

Fig 2. Schematic diagram of the hybrid hydro-elastic model, illustrates overlapping regions in physical space comprising the DEM lattice and the continuum grid.

With a local mass to momentum conservation, the scheme embodies coupling between the solid and the Darcy continuum description. The porosity dependent evolution of the pressure gradient imparts fluid drag forces at the particles of the discrete model. Permeability is treated as an implicit fluid flow property and is an output of the discrete model as a function of change in local porosity where the change in porosity is determined by the translational movement of mass centers of the particles.

2.2) Discrete elastic model

The 2D DEM model is assembled by coupling a triangular network of volume-less linear elastic springs with a particle model where disk shaped particles of constant radius superpose the nodes of the triangular structure. The particle model has its genesis from molecular dynamic models and represents the discrete quantities of the solid material, whereas following Hook's law of interaction the spring lattice model inherits the micro-mechanical physics between the nodes. This setup thus mimics isotropic elastic behavior of solid materials and can be used to model deformation problems in systems described by linear elastic theory. The intrinsic stiffness constant k of linear springs is related to macro-scale elastic material-parameters (E, v) through the consistency measures of strain energy between the 2-D elastic lattice of the triangular network and solid continua [*Flekkøy et al.*, 2002].

$$k = \frac{\sqrt{3}}{2} El \tag{1}$$

where l corresponds to the thickness of the 2D particle-lattice model.

The model produces plain strain deformation and a large-scale average stress tensor can be determined from the local deformations of elastic springs for each time step Δt. Springs can break when a prescribed tensile stress threshold is overcome to exhibit discrete mode-1 fractures in the material. Broken springs are removed from the elastic network, whereas the respective particles still retain repulsive forces to accommodate the successive tension. The breaking strength of springs is related to the mode-I stress intensity factor K_I, a key parameter that gives stress singularities at crack tips and does depend on the size of micro cracks in the material [*Flekkøy et al.*, 2002].

$$K_I = \sigma_I \sqrt{\pi a} \ , \tag{2}$$

where σ_I is the critical mode-I driving stress for the relative displacement of fracture walls and a is the length of micro cracks in an isotropic medium. The porous model is assumed to be homogeneous corresponding to its elastic properties on large scale, however inherent disorder ubiquitous in natural media can be quenched through characteristic distributions of material properties on particles or annealed disorder (Griffith's micro cracks and other defects at grain scale) can be introduced by modifying the elastic properties of mechanical springs. It has been indicated that fracture patterns observed both in field and laboratory studies can be replicated by implying the realistic normal distribution of strength threshold in DEM models [*Malthe-Sørenssen et al.*, 1998a, 1998b; *Walmann et al.*, 1996].

To avoid rigid body translation the elastic system is confined (closed system) by elastic walls at the boundaries. The walls behave as linear elastic springs and exercise a force on the confronted particles proportional to their distance. For instance, the force by a lateral wall on particle i contacted at $x = x_w$ is

$$f_i = \begin{cases} -k_w(x_i + r_i - x_w)n_i & \text{if } x_i + r_i - x_w > 0 \\ 0 & \text{else} \end{cases} \qquad (3)$$

where r_i is the particle radius, n_i is a unit vector normal to the wall and k_w is a spring constant for particle wall interaction.

2.3) 2D Pressure diffusion field

With negligible fluid inertia, a time dependent macroscopic diffusion equation is derived that contains mass and momentum conservation in the bulk simulation of particle and continuum dynamics. The output is an interstitial fluid flow expressed in terms of a porosity dependent pressure gradient, which makes the computation simple and efficient. We start with the continuity equations (both for solid and fluid) at a characteristic scale of a grain diameter.

$$\partial_t\left[(1-\phi)\rho_s\right] + \nabla\cdot\left[(1-\phi)\rho_s u_s\right] = 0 \qquad (4)$$

$$\partial_t(\phi\rho_f) + \nabla\cdot(\phi\rho_f u_f) = 0 \tag{5}$$

where ρ_s, ρ_f are the densities and u_s, u_f the velocities of the solid particles and fluid respectively and ϕ is the local porosity. The Darcy equation for the segregation of fluid and solid gives a local fluid seepage u_f for a pressure drop described by the local permeability on a unit area that is larger than the grain diameter.

$$\phi(u_f - u_s) = -\frac{K}{\mu}\nabla P \tag{6}$$

where μ and P stand for the fluid viscosity and pressure, whereas the local permeability K is expressed as a function of the local solid fraction ρ according to the empirical Kozeny-Carman relation for a Darcy like regime.

$$K(\rho) = \frac{d^2(1-\rho)^3}{180\rho^2} \tag{7}$$

where d is the particle diameter and 1/180 is an empirical constant valid for packing of spheres. Similar to the quenched noise in elastic material constants, a distribution of hydraulic particle size can be treated as an epoxy to intrinsic hydraulic heterogeneity (solid fraction, permeability) in the continuum routine. In general, a larger particle area will result in low permeability and high pressure gradient and eventually an overall larger fluid drag force at the local fixed scale of reference and vise versa. To get a fully consistent picture, the fluid adiabatic compressibility β is included into the continuity equation according to the fluid state equation i.e., proportional approximation of the fluid density to pressure:

$$\rho_f = \rho_o(1+\beta P)\ , \tag{8}$$

where ρ_o denotes the fluid density at some reference pressure. Substituting ρ_f and u_f into equation (5) and eliminate $\partial_t\phi$ from the subsequent equation we end up with the following diffusion equation for the non-hydrostatic pressure P, with an approximation of finite solid compressibility relative to fluid.

$$\phi\beta(\partial_t P + u_s \nabla \cdot P) = \nabla \cdot \left[\left(1+\beta P\right) \frac{K}{\mu} \nabla P \right] - \left(1+\beta P\right) \nabla \cdot u_s \ . \tag{9}$$

The left hand side of equation (9) is the Lagrangian derivative of pore pressure, the first term on the right hand side describes the Darcy diffusion of the fluid pressure relative to particles and the third term in the equation is distinguished as source term. The source term facilitates a pressure change as a function of a change in the particle solid fraction if particles move apart in the local reference scale of Darcy flow. For a detailed dimensional and non-dimensional derivation of the continuum equation presented above see the reference [*Gidaspow*, 1994; *Goren et al.*, 2010, 2011].

The assumption of omitted fluid inertia is evident in equation (9), where the fluid flow is described by the pressure field $P(x, y)$ only. This diffusive-advective description of the fluid flow is valid when the Reynold's number $\mathrm{Re} = u_f d \, {}^{\rho_f}\!/_{\mu}$ is small, where μ is dynamic viscosity of the fluid, d the particle size (diameter). The Reynold's number will be small if particles are small as is in the considered casees of dense model. Assuming the validity of the current approach a priori, one can also evaluate the condition of $\mathrm{Re} < 1$ using Darcy's law i.e., $\mathrm{Re} = -(Kd \, {}^{\rho_f}\!/_{\mu^2}) \nabla P$ in the simulations (which is true for all the cases subjected d here). As far as the particle movement (fracture aperture) is comparable to the diameter of particles, the above assumption of negligible fluid inertia is valid. However, if the fracture aperture becomes broader (sub-particle scale) the fluid inertia becomes important. This not only affects the particle-fluid coupling but also the fluid dynamics and in this case an equation describing the flow of fluid momentum, like the Navier-Stokes equation is required [*McNamara et al.*, 2000]. Nevertheless, this approach is also valid for flow fields at large Reynold's numbers [*Beetstra et al.*, 2007].

2.4) Two way solid-continuum interaction

The DEM lattice is blanketed over the continuum grid in a way that the boundaries of the two parallelized lattices coincide with each other. With the lattice constant of the continuum grid set to be twice as large as that of the discrete lattice, this setup incorporates the "cloud in a cell" method (figure 3) to facilitate the two-way interaction between the porous matrix and the hydrodynamic phase. The particle density ρ and velocity u are estimated locally on the continuum grid in each iteration as a function of the local mean particle density specified by a linear tent weight function upon four nearest grid nodes.

$$\rho(r_o) = \sum_i^n s(r_i - r_o) \tag{10}$$

$$u(r_o) = \sum_i^n u_i s(r_i - r_o) \tag{11}$$

where subscript i stands for particle number and the smoothing function $s(r - r_o)$ satisfies the weighted distribution of particle mass relative to its position.

$$s(r - r_o) = \begin{cases} \left(1 - \dfrac{w_1}{\Delta x}\right)\left(1 - \dfrac{w_2}{\Delta y}\right) & \text{if } w_1 < \Delta x,\ w_2 < \Delta y \\ 0 & \text{otherwise} \end{cases} \tag{12}$$

where $r(x, y)$ and $r_o(x_o, y_o)$ are the positions of the particle and the continuum node respectively, $w_1 = |x - x_o|$ and $w_2 = |y - y_o|$ are the relative distances.

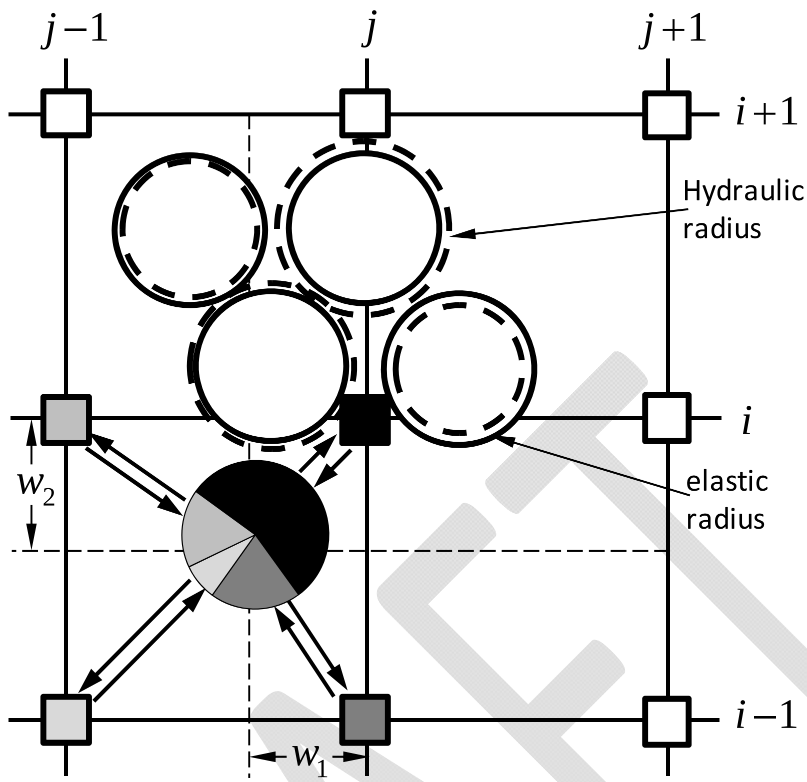

Fig. 3. General overview of the twofold function of the numerical setup. Polar arrows illustrate the linear interpolation of particle area weight (grayish color code) to surrounding grid nodes and in turn the time dependent drag force from grid nodes to encountered particles.

With this configuration, the fluid drag force f_p on each particle encountered by a fluid continuum cell can also be deduced by averaging the pressure gradient at the respective continuum node.

$$f_p = -\sum_k s\left(r_i - r_k\right)\left(\frac{\nabla P}{\rho_n}\right)_k \tag{13}$$

where k runs over four nearest grid nodes. This definition guarantees the mutual and balanced attribution of the pressure force f_p to solid particles from the continuum grid and the density/momentum contribution of the grains to the respective continuum unit cell as determined by equation (20) below.

In the coupled scheme, fluid pressure gradients that are approximated between fixed continuum nodes produce effective stresses at the particles of the DEM lattice. This steers the particles to displace and leads to stretching of the connected elastic springs, which ultimately break and be demonstrated as explicit fracturing when the imposed effective stress exceeds a given tensile stress threshold. Upon the formation of discrete cracks, rearrangement of the particles in the elastic medium (i.e., fracture opening) devise local changes in the background void space of the system, which in turn affects the permeability to be used in the successive step to determine the fluid pore pressure field. This evolution of fluid pore pressure again provides feedback to the stress field in the system and leads to fracture propagation or opening as a function of the particle dynamics. The procedure is repeated until both the continuity equation and the discrete grains are relaxed. The flowchart for one complete cycle of the algorithmic scheme is given in figure 4.

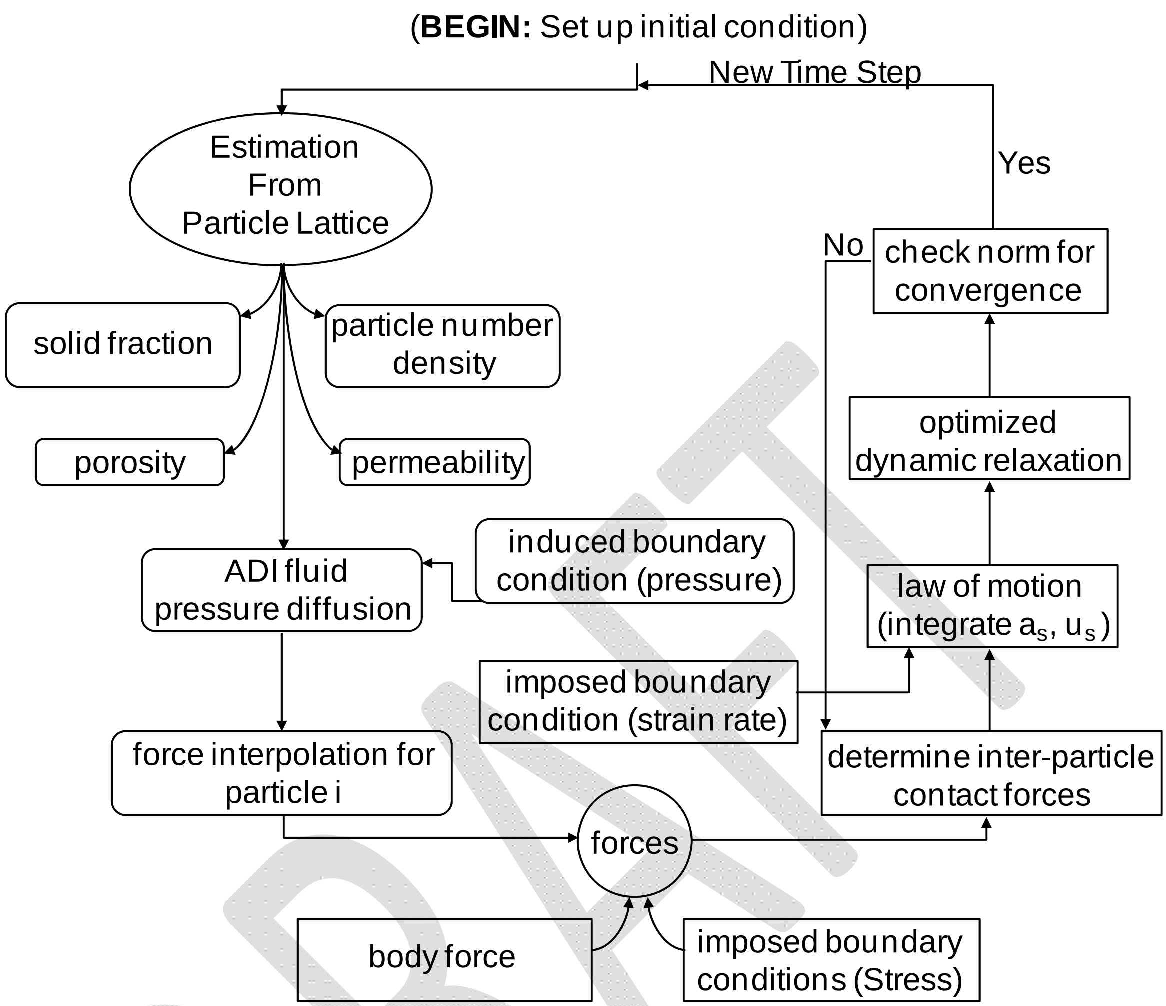

Fig. 4. Flowchart for the complete cycle of the algorithmic scheme.

2.5) Deformation mechanics

The translation motion of the initially relaxed solid particles (solid-solid interaction) is managed by the momentum exchange between solid and fluid phases in a unit volume cell dV (with unit third dimension) of the coupled system on account of-the inter-particle contact force f_e (either connected with a spring or repulsive force), fluid force f_p and gravity loading f_g.

$$m\frac{dV}{dt} = f_e + f_p + f_g \tag{14}$$

where the forces f_e being aligned along the connected elastic springs are characterized by spring constant k_{ij} times the actual distance between the centroid of the particles minus the equilibrium distance a_{ij}.

$$f_e = \sum_j k_{ij} \left(| a_{ij} | - (x_i - x_j) \right) \cdot \hat{n}_{ij} \tag{15}$$

where x_i and x_j are the positions of the connected particles, $\hat{n}_{ij}$ is unit vector pointing from the centroid of particle i to particle j and the sum runs over all the connected neighbors j. The fluid force f_p that acts on the surface normal dA of the unit cell is a result of the fluid flow due to the pressure gradient and is given as:

$$f_p = -\int P dA \tag{16}$$

where P is the local fluid pressure, which is the sum of the hydrostatic pressure $\rho_f gz$ and extraneous pressure P_o. The term gravitational force f_g incorporates the gravity effects of both the fluid and solid masses where the former together with the hydrostatic part of pressure determines the effective stress $\sigma_{eff} = (\rho_s - \rho_f) gz$ on the solid particles.

$$f_g = \rho_s \cdot \rho dV \cdot g + \rho_f \cdot \phi dV \cdot g \tag{17}$$

In the geological realm a transient hydrofracturing is likely to take place by a pore pressure P in excess to σ_{eff}. However, for the considered linear elastic model that exhibits deformation in a quasi-static fashion we only need to assume pore pressure deviations from the lithostatic pressure. This has been achieved by introducing the effect of gravity in form of lithostatic stress and results in the calculated stresses minus the lithostatic pressure. The inferred gravity force on a single cylindrical particle i of volume $V_s = \pi r^2 h$ with base area $A_s = \pi r^2$, where $h = 1$ is the thickness in the third dimension is:

$$f_i^g = \rho_s \pi R_i^2 g s \tag{18}$$

with

$$s = \frac{2}{3}\frac{E_m}{E_R}\frac{A_m}{A_R} \tag{19}$$

where ρ_s is the material mass density, $R_i = r_i \times S$ with S the dimension of the real system. E_m, E_R and A_m, A_R stand for the Young's Moduli and areas of particles in the model and the real system respectively. The factor 2/3 in equation (19) is derived using the expedient strain-stress relation ($\sigma_{\mathrm{v}} = \frac{E\upsilon}{(1+\upsilon)(1-2\upsilon)}\varepsilon_h + \frac{E(1-\upsilon)}{(1+\upsilon)(1-2\upsilon)}\varepsilon_{\mathrm{v}}$) from the generalization of Hooke's law for a 2D plane strain problem assuming $\upsilon = 1/3$ and zero lateral deformation. This is essential in order to acquire a compatible one dimensional lithostatic stress $\sigma_{\mathrm{v}} = \rho g h$ for the isotropic 2D linear elastic solid.

By considering the local fluid velocity a rival of the local particle velocity i.e., high viscous fluid and substituting the respective constitutive force terms in equation (14) one can derive the following force-balance equation, which exhibits an explicit coupling between granular motion and fluid flow in the unit cell ($dV = 1/\rho_n$).

$$m_s\left[1 + \frac{\rho_f \phi}{\rho_s(1-\phi)}\right]\frac{du_s}{dt} = F_i - \frac{\nabla P}{\rho_n} + \rho_{eff} V_s g \ , \tag{20}$$

where ρ_n is the particle number density, $\rho_{eff} = \rho_s - \rho_f$ is the effective mass density and g the gravity. This is the translational equation of each individual particle dragged with velocity u_s in the absence of any frictional and tangential effects. The mass m_s in the left term accounts for the summation of fluid mass to each individual solid particle as a function of the local porosity to particle number density ratio.

2.6) Assumptions

The assumptions made in order to keep the proposed scheme amenable are:

- The fluid-solid friction force at the surface of the solid particles is not considered, therefore the pressure gradient ΔP is the only agent that produces a drag force (in the direction of fluid flow) on particles.
- The fluid is considered to be purely viscous and therefore any effect like thermal evolution of the fluid (a pivotal factor in the development of subsurface overpressure e.g., dehydration of sediments in intrusive zones in particular) is not taken into account.
- The locally interpolated solid fraction on the 2D continuum grid is multiplied by 2/3. With this factor we obtain a good mapping of the 2D porosity on the corresponding 3D equivalent (prerequisite for the 3D Kozeny-Carman permeability) with a match between closed packed configurations and the empty configurations [*McNamara et al.*, 2000]. Without this correction the qualitative behavior is comparable but quantities like fracture speed, propagation or the flux for certain pressure gradients can change by a prefactor, roughly up to a factor 2.
- Analytically the Kozeny-Carman relation works as long as the solid fraction is greater than zero, but a solid fraction of 0.15 or less presents a solid-fluid composite mainly as a fluid and is thus inconsistent with the Kozeny-Carman relation (originally established for dense granular media). We thus chose to apply a threshold to a permeability of a medium

with a solid fraction of 0.15 (e.g., in a broader fracture aperture). The main purpose of limiting the solid fraction and hence permeability to this upper value is to allow larger time steps and improve the speed of the model. Effectively, the zones of the model where the permeability is equal to large values correspond to almost homogeneous pressure zones. The exact value of this cutoff does not affect the pattern formation significantly, as different values of the cutoff have been tested (between 0.25 and 0.05) without any significant changes [*Johnsen et al.*, 2006; *Jan Ludvig Vinningland et al.*, 2007a].

3) Model verification

We first test the linearity of the porosity controlled Darcy flow field and the associated pressure forces on each particle. If we consider compressible water as fluid in the pore space, the evolution of seepage forces in the simulations (figure 5) validates the theoretical aspects of the scheme. A reference model of unit dimension is taken as a porous rock where the solid skeleton is composed of 11500 disc-shaped adhesive particles. The system is confined mechanically at all boundaries whereas hydraulically it is restrained only at the side boundaries. Neglecting any gravitational loading a hydraulic gradient i is established in the system by setting the bottom boundary at a constant pressure input (normalized $P = 1.0$) and fixing the top boundary at 0.0 pressure respectively. The pressure input value is kept suitably low in order not to produce fractures.

Two series of simulations are conducted to test the model by considering a homogeneous (figure 5a) and a heterogeneous (figure 5b) porous rock respectively. In the heterogeneous case a seal is inserted in the model. The seal is represented by a horizontal layer of low permeability with a thickness of 0.1 with lower boundary at 0.2 and upper boundary at 0.3. In the test simulations, initially a high pressure gradient is concentrated in the vicinity of the source boundary, therefore only the intimate particles are subject to resultant seepage forces and consolidate along the direction of the pressure drop. However, after 5000 time steps the pressure gradient becomes linear and the fluid approaches a steady state flow condition in the homogeneous model. In the heterogeneous medium a strong pressure drop develops across the layer of relative low permeability. Two linear regimes develop, one below the seal with a relatively steep gradient and one above the seal with a relatively gentle gradient. Consequently vertical seepage forces of high contrast in magnitude are measured at the seal boundaries (figure 6).

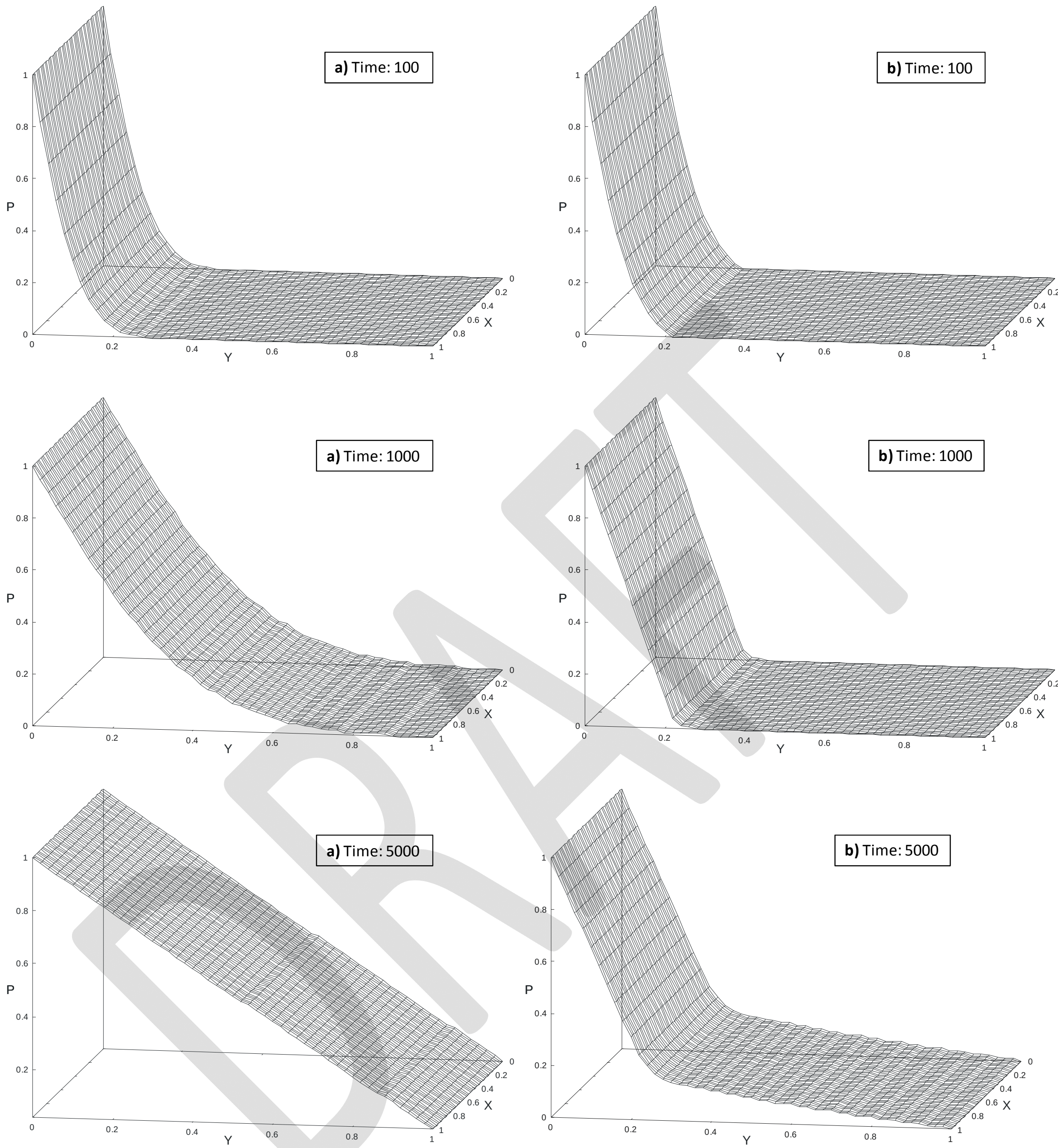

Fig. 5. Normalized pore pressure profiles at different time steps, (a) in a homogeneous porous medium, (b) in a heterogeneous porous medium accompanying a horizontal seal of low porosity at position $0.2-0.3$ on the y-axis (vertical axis).

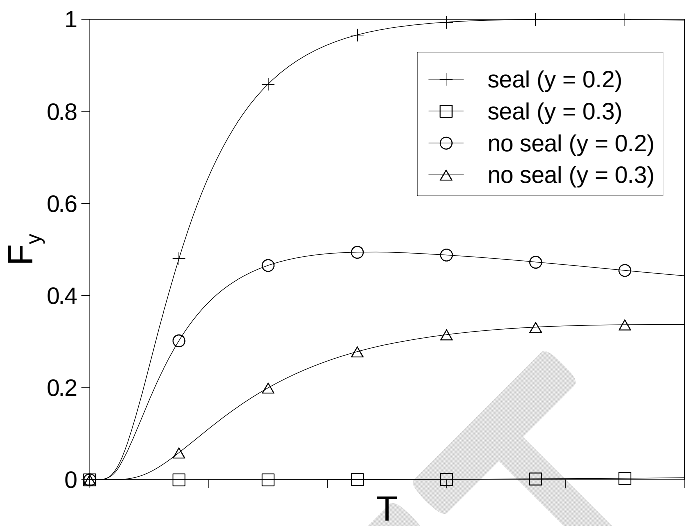

Fig. 6. Overall evolution of the vertical seepage forces as a function of time ($T:1000$) for a homogeneous system and at the lower and upper boundary contacts of the seal in a heterogeneous system. The forces display a sharp contrast in magnitude in the heterogeneous case, whereas in the homogeneous medium the forces show a gradual increase in pressure force. Both the heterogeneous and homogeneous cases reach a steady state condition.

4) Model implementation

In the following sections we show two different test cases to illustrate the development of hydro-fractures in the model.

- Foremost, we discuss fracturing in a homogeneous medium where fractures develop around a point source (fluid is injected locally) in the absence of external deformation. We investigate the fracture pattern that develops as a function of fluid pressure gradients under isotropic diffusion of the fluid pressure. In addition we analyze the influence of changes in background porosity and study the state of stress during fracturing in detail. Later, the likely influence of background non-hydrostatic stress states (i.e., uniaxial vertical loading and pure shear deformation) on the growth of hydrofracture is also examined.

- In the second set of two simulations, we advance to simulate fracture patterns due to local pressure sources in the presence of gravity and tectonic strains. In these cases we use examples where seepage forces develop due to a local increase in pore pressure caused by local perturbations in the stress state. In this case the tectonic strain conditions will control the different fracture patterns.

In each test the model starts from a fully relaxed state and is loaded in small steps afterwards. According to the boundary conditions loading includes increase of fluid pressure in the fluid lattice, vertical loading due to gravity or horizontal loading due to tectonic strains by moving the boundary walls. The mechanical and hydraulic boundary conditions vary accordingly with respect to the underlying problem to imitate laboratory and field conditions.

4.1) Point source in a homogeneous porous medium

In these simulations the fluid pressure is increased at a point source with a constant rate ($P/_{\Delta t}$) at the centre of a homogeneous and isotropic poro-elastic domain. The model is mechanically confined and bears no-flow boundary conditions. In these simulations the hydrofracturing process shows two stages, fracture initiation and episodic fracture growth until the system reaches a steady state (Fig. 7).

The accumulation of fluid pressure at the point source generates an isotropic pressure gradient in the surrounding which contributes to the evolution of the effective stresses and deforms the porous rock elastically as a function of Biot’s poro-elastic coefficient. The rock experiences micro fracturing from the concentration of stress on relatively weak rock elements. The discrete fractures nucleate at the source location and tend to propagate into the undisturbed region (Fig. 7a). At this stage, tension cracking accommodates the strain in the system and results in stress relief and a potential local change in porosity when particles are pushed away by the pressure force and fractures open. This cycle is repeated following the two-way temporal and spatial feedback between hydraulic pressure field and elastic field on account of induced fracturing in the porous matrix until a steady state condition is acquired and fracturing ceases. The symmetry of the developing fracture pattern at the point of injection is a function of a circular extension around the fluid source. The symmetric pattern validates the homogeneous existence of pore pressure in the rock matrix. The seepage forces that develop due to the pressure diffusion modify the force balance in the porous rock sample, which deterministically drives the discrete tensile crack growth along the pressure gradient and results in a regular fracture geometry.

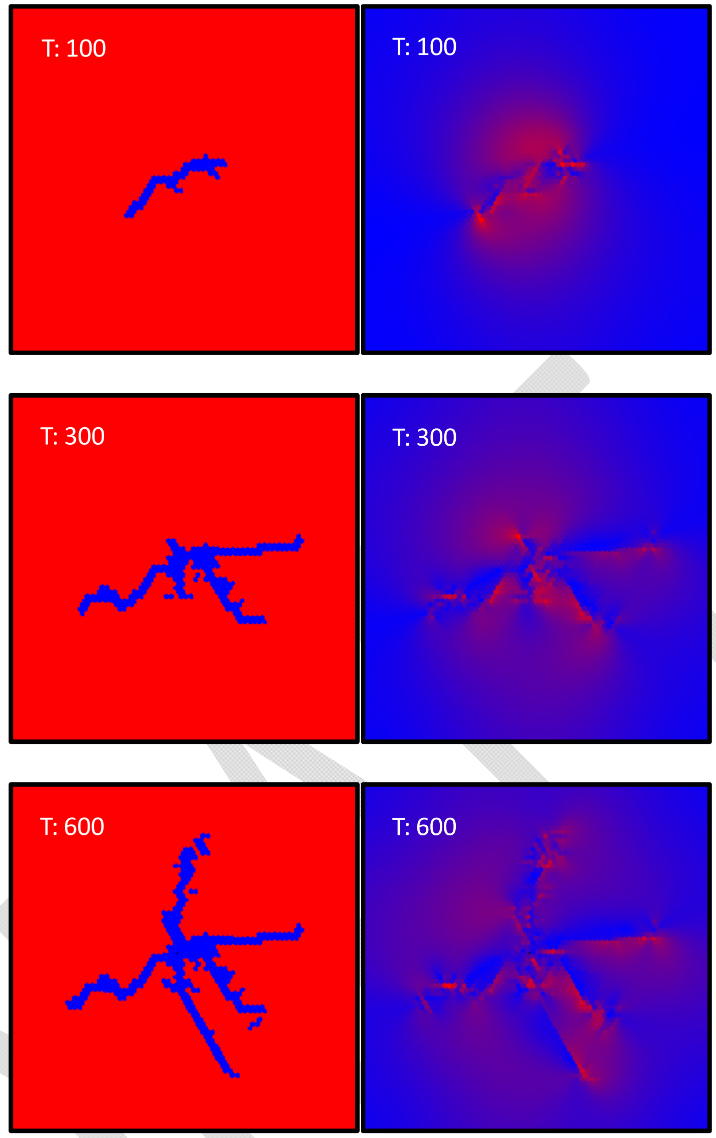

Fig. 7a. The figures on the left hand side show the development of circular hydro-fractures (T= model time, blue particles have broken bonds) by a point source overpressure. The figures on the right hand side show the same simulations and illustrate the associated differential stress states of the model at the respective failure stages (red=high; blue=low differential stress).

Figure 7b shows the evolution of the effective mean stress in the model (positive mean stress is extensional) as a function of time and the growth of broken bonds with time for the simulation shown in figure 7a. In the first steps of the model the effective mean stress increases in a non-linear fashion due to the diffusive nature of the pore fluid pressure. Once the tensile strength of the material is reached the rock fractures suddenly and the stress drops significantly. Subsequently the stress increases slowly, which is followed by subsequent failure events. Finally fracture growth ceases and the mean stress reaches a steady state. Because the shown stress is an average of a larger area in the model the fracturing continues locally even though the mean stress has already reached equilibrium.

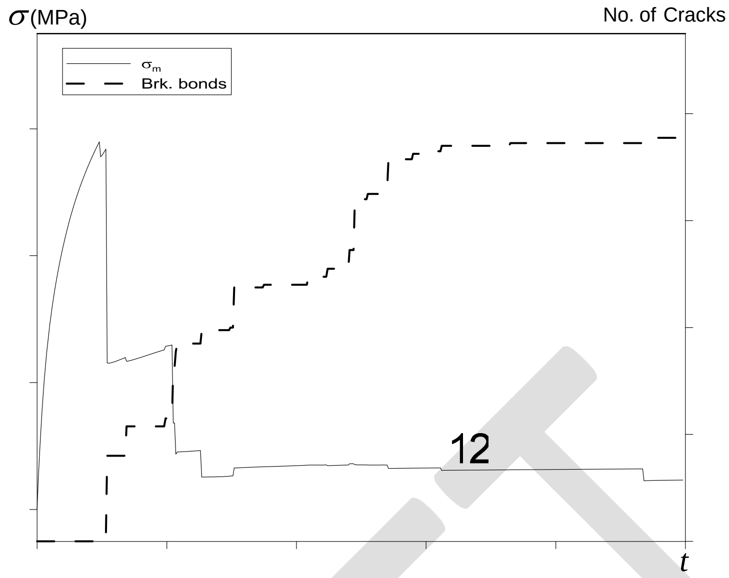

Fig. 7b. Graph shows oscillations in effective mean stress and associated number of broken bonds in the model. The stress shows the episodic evolution of the fluid pressure. Positive effective mean stress in the model is defined as extensional stress.

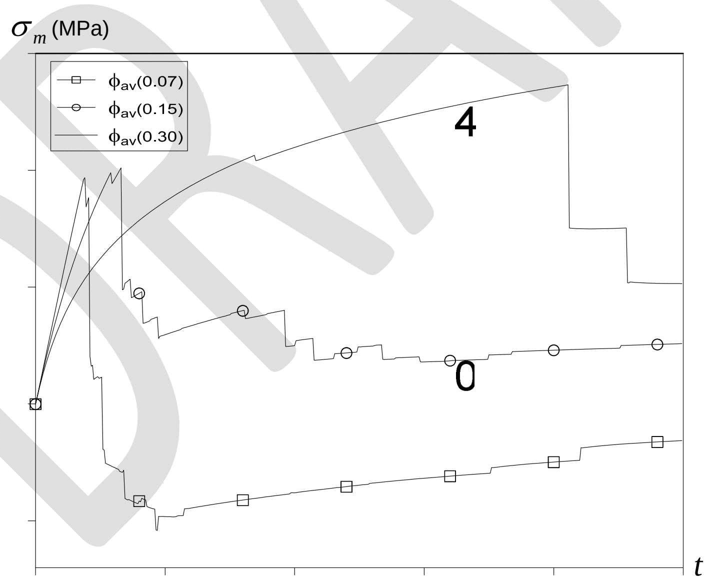

Fig. 8. Mean stress as a function of background rock porosity, where an increase in porosity results in a lower driving force because the pressure can diffuse faster. Note: –ve sign in the model is annotated for compressive stress and +ve sign for extensional stress.

Under the same fluid injection rate a quantitative comparison of the mean stresses in rock samples with different background porosities is given in figure 8. The graphs in figure 8 show the evolution of the effective mean stress field and the fracturing behavior of the rock as a function of porosity. Rocks that inherit low porosity entail the production of high seepage forces to drive tensile failure at comparable low average tensile stress. A low average stress illustrates that the stress in a low porosity rock will be very localized around the point source. The stress drop associated with failure of the material will be relatively large. In addition the state of stress may be altered in these low porosity rocks due to friction along developing fractures (solid-solid coupling), where the overall stress regime may become compressive (figure 8). Subsequently small isolated shear or hybrid extension-shear fractures can develop near the end of the primary dilational fractures when fracturing happens relatively early in low porosity rocks. When the porosity becomes larger the initial loading of the system due to the fluid input becomes successively more non-linear (Fig. 8) up to a point where the pressure just diffuses out of the system without the creation of fractures.

We also simulated a number of examples (Appendix-B, Appendix-C) with the similar hydraulic setup but different external boundary conditions. The developing fracture patterns closely resemble the results observed experimentally by [*Bruno and Nakagawa*, 1991; *Doe and Boyce*, 1989] in rock type material. The simulations manifest the effective influence of pore pressure on the likelihood of tensile failure and the corresponding fracture propagation under non-hydrostatic stress conditions in homogenous sedimentary rocks.

4.2) Hydrofracturing in a homogeneous medium under gravity loading

In the second set of simulations, we reproduce the patterns of hydrofracturing caused by a local pore fluid overpressure under non-hydrostatic tectonic loadings of gravity and lateral stresses and found the results consistent with [*Rozhko et al.*, 2007]. The problem is analogous to various geological systems (magmatic intrusions, hydrothermal venting, volcanoes etc.), which yield a local perturbation in the effective stress field with the induction of localized pore overpressure.

Figures 9 and 10 show simulations with a local point source at the bottom of the model, where the former sustains a stress regime of horizontal extension and the later horizontal compression. The model material is homogeneous and the gravitational loading is followed by equation (18). In order to incorporate the effect of gravitational loading, the model is subjected to a two-stage deformation in both cases. First, the model is let to settle under uniaxial gravitational loading assuming the model is 1 km in depth with fixed side walls, a rock density of 2.5 kg/m^3, Young modulus of 80GPa and Poisson ratio of 1/3. This setup yields a global stress anisotropy where vertical and horizontal stresses differ due to Poisson effects. Secondly, we apply a lateral extension or compression with a relative small horizontal strain rate in order to have a fluid dominated effective state of stress in the rock. A hydraulic anisotropy is produced in the simulations by inducing a pressure drop with a zero assigned pressure at the upper boundary and no flow boundary conditions at the side-walls.

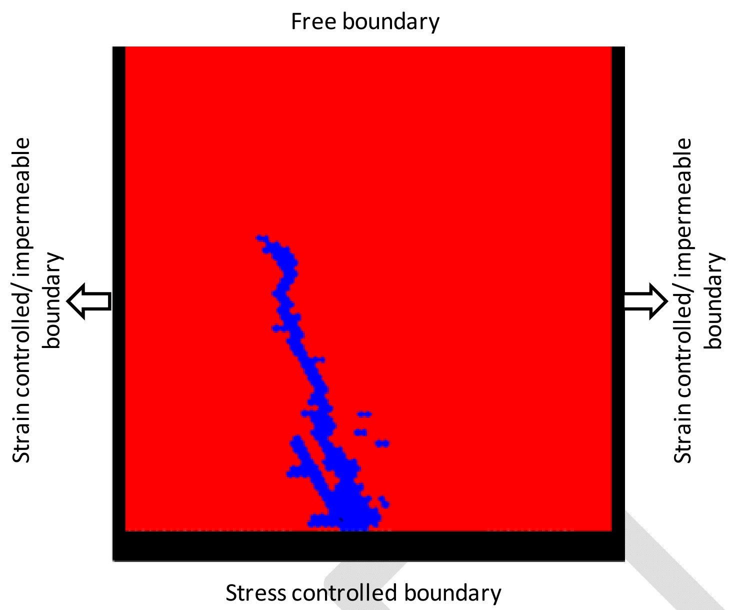

Fig. 9. Vertical hydrofracture in a rock model subjected to lateral extensional strain. A vertical gravitational load is applied to the system and fluid is injected at a point source in the middle of the system at the lower boundary.

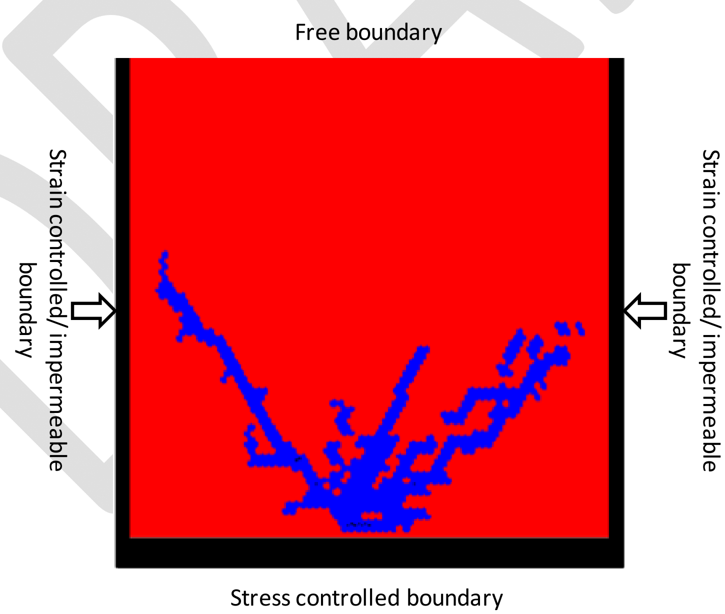

Fig. 10. Conjugate shear fractures under compressive state of stress. A vertical gravitational load is applied to the system and fluid is injected at a point source in the middle of the system at the lower boundary.

The system that is loaded with a gravitational body force experiences buoyancy forces i.e., $P = (\rho_s - \rho_f)gz$ in equation (9) with the reduction in effective stresses due to an increase in local pore pressure. This gradient may lead to a quasi-static fracture propagation through parts of the model.

The failure patterns illustrated in figures 9 and 10 are consistent with the different forces that are applied. Fracturing nucleates in the areas where fluid pressures are high (point source at the bottom of the models). The fractures propagate upwards reflecting the gravitational loading of the system. The horizontal tectonic forces produce almost vertical extensional mode I crack like failure when the system is extending (figure 9) and conjugate shear failure when the system is under compression (figure 10). Even though the source of the fracturing is a high fluid pressure in both cases the pattern that develops is strongly influenced by the heterogeneous stress field due to gravity and tectonic loading. This is clearly illustrated when figure 7a is compared, since figure 7a has the same fluid boundary condition with a point source as figures 9 and 10 but the fracture pattern is very different in the later cases due to the external stress field.

Discussion and conclusion

Discrete fractures or instant opening of existing cracks as a function of fluid overpressure drive perturbations in permeability, change the state of stress and the corresponding release of strain energy on the scale of pores. In this contribution we present a hybrid numerical solution based on first principles rather than on empirical constitutive relationship with ad hoc fitting parameters to model natural examples of hydrofractures. First principles constitute the equation of state separately for the fluid and the solid and the pore scaled forces balance to describe interactions. The scheme thus combines the pertinent features of both continuum and DEM descriptions, and examines the dynamic coupling between porous flow and diagenetic process through fracture mechanics as a response to an applied pressure gradient across the system.

It appears likely that the interplay between the temporal and spatial evolution of the pore pressure and tectonic/gravitational stresses manipulate hydro-fracturing and the corresponding permeability changes. Our model shows an evolution of the deformation dependent permeability illustrating that in hydro-mechanical systems permeability is a nonlinear and time dependent parameter where fracturing localization is very important. The system reacts to forcing and produces the permeability that it needs to allow the fluid pressure to diffuse. It has manifested that small-scale diagenetic events can have adequate impact on the pressure field and in turn the fracture geometry. In our model this effect is achieved by the idealized hydro-mechanical constitutive relation of Kozeny-Carman permeability through a weighted interpolated function. In this relation even small displacements of particles can lead to significant changes in the local solid density and thus the Darcy fluid flow.

It has been perceived that several key features (flow rate upon compaction, yield surface, strain softening and hardening etc.) of critical soil mechanics (CSSM) are inconsistent with the observed porosity and pressure dependent deformation behavior of porous rocks [*Cuss et al.*, 2003; *Gerogiannopoulos and Brown*, 1978; *Ling et al.*, 2002; *Wong et al.*, 1992; *Wong et al.*, 1997]. Therefore, the use of Kozeny-Carman relation (originally developed for soils) for the evolution of the permeability field in the presented model is justified. However, concerns may rise where porosity-permeability relations deviate from the trend of the basic equation [*Zhu and Wong*, 1997] e.g., fracturing in subsurface impermeable rocks causes enhancement in the permeability in contrast to permeable rocks which bear a reduction in permeability. In this case one can pursue either of the following two ways:

1. Use different modified forms of the permeability dependence on the porosity both for ductile and brittle dominated deformation zones using the assumption of linearity between porosity and log permeability with defined parametric values from experimental data [*Sheldon et al.*, 2006].

2. When approximating the local dimension of induced fracture (aperture), a modified form of the porosity-permeability relationship can be derived from the cubic law of fluid flow in fractures [*Steefel and Lasaga*, 1994].

The simulated results validate the generality of the scheme implying that linear Darcy flow has an effective factor in the process of hydrofracturing, and the results are in good agreement with previously reported laboratory and field studies. The numerical scheme can qualitatively replicate some typical quasi-static field examples of hydrofractures when different modeling approaches are applied. Representative example problems constitute fracturing in homogeneous and heterogeneous porous rocks analogous to hydraulic fracturing in pressurize boreholes and natural fracture patterns due to local fluid overpressure. Simulation results illustrate that the diffusion of fluid pressure is a crucial mechanism that interacts with the effective stress field under different geological conditions and produces fracture geometries like branching fractures at point sources, vertical and shear hydrofractures under tensional/compressional tectonic settings.

The presented routine defines a fast approach both for qualitative and quantitative estimation of hydro-driven deformation problems at micro scale. The method can also be used to analysis large scale problems with the suitable selection of none dimensional parameters. In general, gravity loading and the associated non-hydrostatic stress fields along with mechanical heterogeneity in the lithology can have a vital influence over the evolution of buoyant effective forces and thus the hydrofracture patterns. Therefore future work will attempt to integrate these physical parameters in order to determine the appropriate geological conditions when analyzing natural vein and joint networks in real reservoirs.

The presented scheme is also capable to model 3D hydrofracturing, which may have more significant advantages in understanding the complex growth of fractures under the influence of 3D heterogeneity and non-hydrostatic conditions. The only change required is the interpolation of local mass density and velocity over a cubical unit volume of a 3D continuum grid using the same assigned tent function. In the future we intend to couple the derived continuum code with a newly developed 3D next-nearest particle lattice code “Melange” [*Sachau and Koehn*, in press].

Appendix-A: ADI - 2D Pressure Diffusion

The ADI method is time implicit. With symmetric discretization in time i.e., between a forward and backward step, this methods is unconditionally stable and the precision is better than with a purely forward in time implicit method [*Press*, 1992].

The two-dimensional pressure diffusion equation (9) can be rewritten as

$$\frac{\partial P(\vec{r},t)}{\partial t} = \left(1+\beta P\right)\frac{K(\vec{r},t)}{\beta\mu\phi(\vec{r},t)}\left[\frac{\partial^2 P(\vec{r},t)}{\partial x^2}+\frac{\partial^2 P(\vec{r},t)}{\partial y^2}\right]-\frac{1}{\beta\phi(\vec{r},t)}g(\vec{r},t) \qquad \text{(A1)}$$

where $g(\vec{r},t)$ is the source term and $\vec{r}$ stands for position in space. This is a second-order parabolic partial differential equation.

Corresponding to the time and space discretization of the 2D pressure continuum using forward difference with time on the left-hand side and central difference with space on the right hand side of equation (A1).

$$\frac{P_{i,j}^{n+\frac{1}{2}}-P_{i,j}^{n}}{\Delta t} = (1+\beta P)\frac{k_{i,j}}{\beta\mu\phi_{i,j}}\left[\frac{P_{i+1,j}-2P_{i,j}+P_{i-1,j}}{(\Delta x)^2}+\frac{P_{i,j+1}-2P_{i,j}+P_{i,j-1}}{(\Delta y)^2}\right]-\frac{1}{\phi\beta}g_{i,j} \qquad \text{(A2)}$$

where i, j and n are the indices in the x, y, and t directions respectively.

The main idea of the ADI method is to reduce the 2-D problem into a succession of two one-dimensional problems by proceeding one time step from n to $n+1$ in two sub-time steps (figure i). The first half-step (n to $n+\frac{1}{2}$) is taken implicitly in the x-direction and explicitly in the y-direction followed by the second half-step ($n+\frac{1}{2}$ to $n+1$) that is taken implicitly in the y-direction and explicitly in the x-direction.

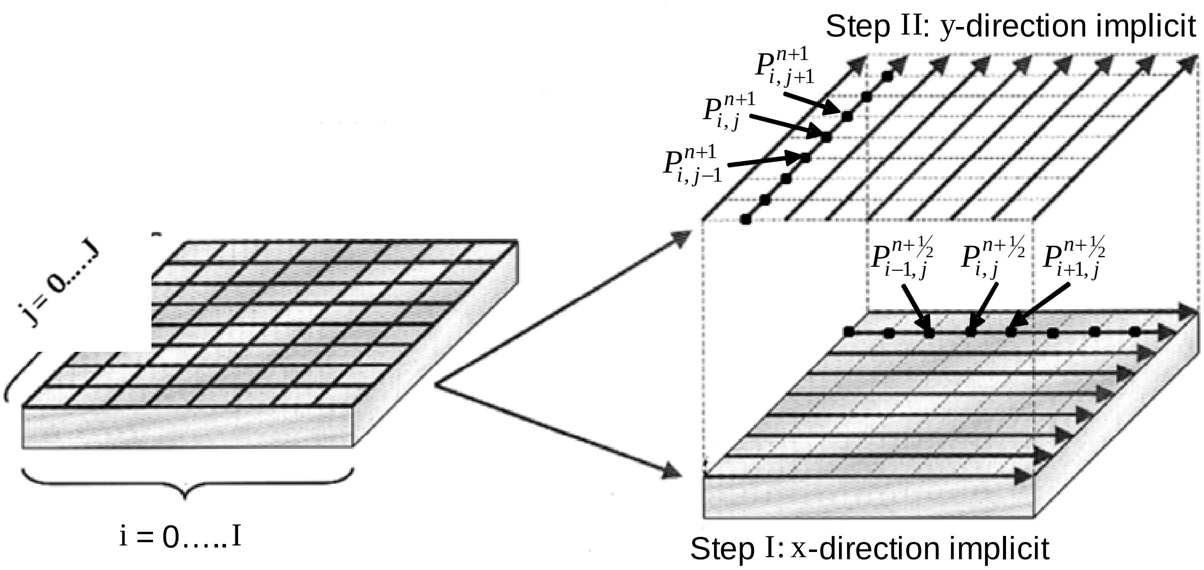

Fig. (I). Schematic diagram of ADI solution of Finite-difference pressure continuum, after [*Wang and Chen*, 2001].

Detailed differential equations in stage-1 for each j at marched time $n+½$ and the corresponding tridiagonal system of equations for the respective one-dimensional problem can be derived in form of matrix equation of dimension I:

$$-\alpha_{i,j}P_{i+1,j}^{n+½}+(1+2\alpha_{i,j})P_{i,j}^{n+½}-\alpha_{i,j}P_{i-1,j}^{n+½}=\gamma_{i,j}P_{i,j+1}^{n}+(1-2\gamma_{i,j})P_{i,j}^{n}+\gamma_{i,j}P_{i,j-1}^{n}-\frac{\Delta t}{2\phi\beta}g_{i,j} \qquad \text{(A3)}$$

$$\begin{bmatrix} 1 & 0 & 0 & \dots & \dots & 0 \\ -\alpha_{i,j} & 1+2\alpha_{i,j} & -\alpha_{i,j} & 0 & \dots & \dots \\ 0 & \dots & \dots & \dots & \dots & 0 \\ \dots & \dots & 0 & -\alpha_{i,j} & 1+2\alpha_{i,j} & -\alpha_{i,j} \\ 0 & \dots & \dots & 0 & 0 & 1 \end{bmatrix} \begin{bmatrix} P_{0,j}^{n+1/2} \\ P_{1,j}^{n+1/2} \\ \dots \\ \dots \\ P_{I,j}^{n+1/2} \end{bmatrix} = \begin{bmatrix} 1 & 0 & 0 & \dots & \dots & 0 \\ \gamma_{i,j} & 1-2\gamma_{i,j} & \gamma_{i,j} & 0 & \dots & \dots \\ 0 & \dots & \dots & \dots & \dots & 0 \\ \dots & \dots & 0 & \gamma_{i,j} & 1-2\gamma_{1,j} & \gamma_{i,j} \\ 0 & \dots & \dots & 0 & 0 & 1 \end{bmatrix} \begin{bmatrix} P_{i,0}^{n} \\ P_{i,1}^{n} \\ \dots \\ \dots \\ P_{i,J}^{n} \end{bmatrix} - \frac{\Delta t}{2\phi\beta} g_{i,j} \qquad \text{(A4)}$$

$i = 0,1,\dots\dots, I;\ j = 0,1,\dots\dots, J$

where

$$\alpha_{i,j} = (1+\beta P)\frac{K_{i,j}\Delta t}{2\mu\beta\phi_{i,j}(\Delta x)^2} \quad \text{and} \quad \gamma_{i,j} = (1+\beta P)\frac{K_{i,j}\Delta t}{2\mu\beta\phi_{i,j}(\Delta y)^2}$$

By analogy, stage-II of the ADI method for each i at time $n+1$, is expressed in tridiagonal system of dimension J:

$$-\gamma_{i,j}P_{i,j+1}^{n+1/2} + (1+2\gamma_{i,j})P_{i,j}^{n+1/2} - \gamma_{i,j}P_{i,j-1}^{n+1/2} = \alpha_{i,j}P_{i+1,j}^{n} + (1-2\alpha_{i,j})P_{i,j}^{n} + \alpha_{i,j}P_{i-1,j}^{n} - \frac{\Delta t}{2\phi\beta} g_{i,j} \qquad \text{(A5)}$$

$$\begin{bmatrix} 1 & 0 & 0 & \dots & \dots & 0 \\ -\gamma_{i,j} & 1+2\gamma_{i,j} & -\gamma_{i,j} & 0 & \dots & \dots \\ 0 & \dots & \dots & \dots & \dots & 0 \\ \dots & \dots & 0 & -\gamma_{i,j} & 1+2\gamma_{i,j} & -\gamma_{i,j} \\ 0 & \dots & \dots & 0 & 0 & 1 \end{bmatrix} \begin{bmatrix} P_{i,0}^{n+1} \\ P_{i,1}^{n+1} \\ \dots \\ \dots \\ P_{i,J}^{n+1} \end{bmatrix} = \begin{bmatrix} 1 & 0 & 0 & \dots & \dots & 0 \\ \alpha_{i,j} & 1-2\alpha_{i,j} & \alpha_{i,j} & 0 & \dots & \dots \\ 0 & \dots & \dots & \dots & \dots & 0 \\ \dots & \dots & 0 & \alpha_{i,j} & 1-2\alpha_{i,j} & \alpha_{i,j} \\ 0 & \dots & \dots & 0 & 0 & 1 \end{bmatrix} \begin{bmatrix} P_{0,j}^{n+1/2} \\ P_{1,j}^{n+1/2} \\ \dots \\ \dots \\ P_{I,j}^{n+1/2} \end{bmatrix} - \frac{\Delta t}{2\phi\beta} g_{i,j} \qquad \text{(A6)}$$

$i = 0,1,\dots\dots, I;\ j = 0,1,\dots\dots, J$

Implementing the Gauss-algorithm with a Dirichlet boundary condition, the derived tridiagonal system of equation (A4) is solved J times and equation (A6) by I times.

Appendix-B:

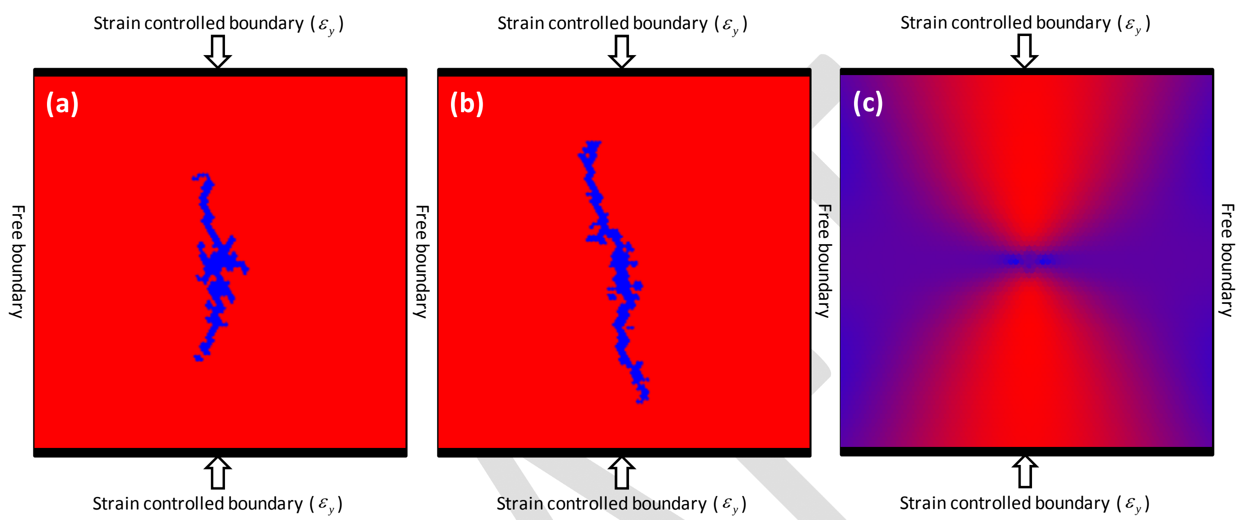

Fig. (II). Different patterns of hydro-fractures in a situation where a constant point source is injected in a homogeneous media under different remote stresses: (a) with relative smaller σ_y, the results show the initial development of circular fracturing at the source location (centre) with elongated fractures oriented parallel to the axis of the applied stress. In contrast to the pattern shown in (a), in (b) a larger σ_y dominates the overall pattern and results only in sub-vertical oriented fractures parallel to the main stress axis and through the source location (central). (c) The figure shows the state of stress field at the onset of fracturing, where the red color code represents high differential stress and blue low differential stress.

Appendix-C:

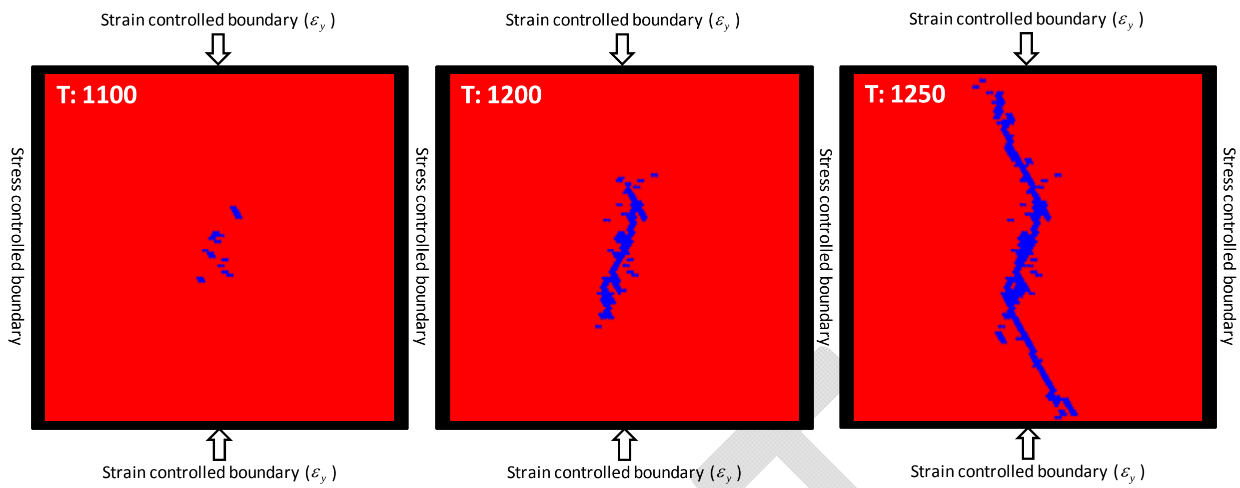

Fig. (III). This figure shows a time series illustrating the influence of the local pore overpressure on brittle failure in a pure shear stress regime. In this case the extension fractures develop at the source location (centre) and link up with shear fractures onwards the edges of the simulation box (time steps T increase from left to right).

Acknowledgement:

We are deeply grateful to Till Sachau for his valuable discussions. This study was carried out within the framework of DGMK (German Society for Petroleum and Coal Science and Technology) research project 718 "Mineral Vein Dynamics Modelling", which is funded by the companies ExxonMobil Production Deutschland GmbH, GDF SUEZ E&P Deutschland GmbH, RWE Dea AG and Wintershall Holding GmbH, within the basic research program of the WEG Wirtschaftsverband Erdöl- und Erdgasgewinnung e.V. We thank the companies for their financial support and their permission to publish these results.

References

Adachi, J., E. Siebrits, A. Peirce, and J. Desroches (2007), Computer simulation of hydraulic fractures, *International Journal of Rock Mechanics and Mining Sciences*, *44*(5), 739-757.

Beetstra, R., M. A. van der Hoef, and J. A. M. Kuipers (2007), Drag force of intermediate Reynolds number flow past mono- and bidisperse arrays of spheres, *AIChE Journal*, *53*(2), 489-501.

Biot, M. A., L. Masse, and W. L. Medlin (1986), A Two-Dimensional Theory of Fracture Propagation, *SPE Production Engineering*, *1*(1), 17-30.

Bons, P. D., D. Koehn, and M. W. Jessell (2007), *Microdynamics Simulation*, Springer.

Boone, T. J., and A. R. Ingraffea (1990), A numerical procedure for simulation of hydraulically-driven fracture propagation in poroelastic media, *International Journal for Numerical and Analytical Methods in Geomechanics*, *14*(1), 27-47.

Bruno, M. S., and F. M. Nakagawa (1991), Pore pressure influence on tensile fracture propagation in sedimentary rock, *International Journal of Rock Mechanics and Mining Sciences & Geomechanics Abstracts*, *28*(4), 261-273.

Cleary, J. M., and Illinois State Geological Survey. (1958), *Hydraulic fracture theory*, [s.n.], Urbana.

Cleary, M. P., and S. K. Wong (1985), Numerical simulation of unsteady fluid flow and propagation of a circular hydraulic fracture, *International Journal for Numerical and Analytical Methods in Geomechanics*, *9*(1), 1-14.

Cuss, R. J., E. H. Rutter, and R. F. Holloway (2003), The application of critical state soil mechanics to the mechanical behaviour of porous sandstones, *International Journal of Rock Mechanics and Mining Sciences*, *40*(6), 847-862.

Daneshy, A. A. (1973), On the Design of Vertical Hydraulic Fractures, *SPE Journal of Petroleum Technology*, *25*(1), 83-97.

Denlinger, R. P., and R. M. Iverson (2001), Flow of variably fluidized granular masses across three-dimensional terrain 2. Numerical predictions and experimental tests, *J. Geophys. Res.*, *106*(B1), 553-566.

Doe, T. W., and G. Boyce (1989), Orientation of hydraulic fractures in salt under hydrostatic and non-hydrostatic stresses, *International Journal of Rock Mechanics and Mining Sciences & Geomechanics Abstracts*, *26*(6), 605-611.

Engelder, T., and A. Lacazette (1990), Natural hydraulic fracturing, paper presented at Rock Joints: Proceedings of the international symposium on rock joints, A.A. Balkema, Rotterdam, Loen, Norway.

Flekkøy, E. G., A. Malthe-Sorenssen, and B. Jamtveit (2002), Modeling hydrofracture, *J Geophys Res-Sol Ea*, *107*(B8).

Fyfe, W. S., N. J. Price, and A. B. Thompson (1978), *Fluids in the earth's crust: their significance in metamorphic, tectonic, and chemical transport processes*, Elsevier Scientific Pub. Co.

Gerogiannopoulos, N. G., and E. T. Brown (1978), The critical state concept applied to rock, *International Journal of Rock Mechanics and Mining Sciences & Geomechanics Abstracts*, *15*(1), 1-10.

Gidaspow, D. (1994), *Multiphase Flow and Fluidization: Continuum and Kinetic Theory Descriptions*, Academic Press.

Gordeyev, Y. N., and A. F. Zazovsky (1992), Self-similar solution for deep-penetrating hydraulic fracture propagation, *Transport in Porous Media*, *7*(3), 283-304.

Goren, L., E. Aharonov, D. Sparks, and R. Toussaint (2010), Pore pressure evolution in deforming granular material: A general formulation and the infinitely stiff approximation, *J. Geophys. Res.*, *115*(B9), B09216.

Goren, L., E. Aharonov, D. Sparks, and R. Toussaint (2011), The Mechanical Coupling of Fluid-Filled Granular Material Under Shear, *Pure and Applied Geophysics*, *168*(12), 2289-2323.

Hubbert, M. K., and D. G. Willis (1957), Mechanics Of Hydraulic Fracturing *Petroleum Transactions, AIME*, *210*, 153-168.

Hubbert, M. K., and W. W. Rubey (1959), Role Of Fluid Pressure In Mechanics Of Overthrust Faulting: I. Mechanics of Fluid-Filled Porous Solids And Its Application To Overthrust Faulting, *Geological Society of America Bulletin*, *70*(2), 115-166.

Jackson, R. (2000), *The Dynamics of Fluidized Particles*, Cambridge University Press.

Johnsen, R. Toussaint, K. J. Måløy, and E. G. Flekkøy (2006), Pattern formation during air injection into granular materials confined in a circular Hele-Shaw cell, *Physical Review E*, *74*(1), 011301.

Johnsen, R. Toussaint, K. J. Måløy, E. G. Flekkøy, and J. Schmittbuhl (2007), Coupled air/granular flow in a linear Hele-Shaw cell, *Physical Review E*, *77*(1), 011301.

Johnsen, C. Chevalier, A. Lindner, R. Toussaint, E. Clement, K. J. Maloy, E. G. Flekkoy, and J. Schmittbuhl (2008), Decompaction and fluidization of a saturated and confined granular medium by injection of a viscous liquid or gas, *Phys Rev E Stat Nonlin Soft Matter Phys*, *78*(5 Pt 1), 6.

Koehn, D., J. Arnold, and C. W. Passchier (2005), Fracture and vein patterns as indicators of deformation history: a numerical study, *Geological Society, London, Special Publications*, *243*(1), 11-24.

Ling, H., D. Yue, V. Kaliakin, and N. Themelis (2002), Anisotropic Elastoplastic Bounding Surface Model for Cohesive Soils, *Journal of Engineering Mechanics*, *128*(7), 748-758.

Malthe-Sørenssen, A., T. Walmann, B. Jamtveit, J. Feder, and T. Jøssang (1998a), Modeling and characterization of fracture patterns in the Vatnajökull glacier, *Geology*, *26*(10), 931-934.

Malthe-Sørenssen, A., T. Walmann, J. Feder, T. Jøssang, P. Meakin, and H. H. Hardy (1998b), Simulation of extensional clay fractures, *Physical Review E*, *58*(5), 5548-5564.

McNamara, S., E. G. Flekkøy, and K. J. Måløy (2000), Grains and gas flow: Molecular dynamics with hydrodynamic interactions, *Physical Review E*, *61*(4), 4054-4059.

Meyer, B. R. (1986), Design Formulae for 2-D and 3-D Vertical Hydraulic Fractures: Model Comparison and Parametric Studies, in *SPE Unconventional Gas Technology Symposium*, edited, 1986 Copyright 1986 Society of Petroleum Engineers, Inc., Louisville, Kentucky.

Mourgues, R., and P. R. Cobbold (2003), Some tectonic consequences of fluid overpressures and seepage forces as demonstrated by sandbox modelling, *Tectonophysics*, *376*(1–2), 75-97.

Niebling, M. J., E. G. Flekkoy, K. J. Maloy, and R. Toussaint (2010a), Mixing of a granular layer falling through a fluid, *Phys Rev E Stat Nonlin Soft Matter Phys*, *82*(1 Pt 1), 7.

Niebling, M. J., E. G. Flekkøy, K. J. Måløy, and R. Toussaint (2010b), Sedimentation instabilities: Impact of the fluid compressibility and viscosity, *Physical Review E*, *82*(5), 051302.

Niebling, M. J., R. Toussaint, E. G. Flekkøy, and K. J. Måløy (2012a), Dynamic aerofracture of dense granular packings, *Physical Review E* **86**, 061315.

Niebling, M. J., R. Toussaint, E. G. Flekkøy, and K. J. Måløy (2012b), Numerical studies of aerofractures in porous media, *Revista Cubana de Fysica* **29**, 1E, 1E66.

Olson, J. E., S. E. Laubach, and R. H. Lander (2009), Natural fracture characterization in tight gas sandstones: Integrating mechanics and diagenesis, *AAPG Bulletin*, *93*(11), 1535-1549.

Press, W. H. (1992), *Numerical recipes in C: the art of scientific computing*, Cambridge University Press.

Rozhko, A. Y. (2010), Role of seepage forces on seismicity triggering, *J Geophys Res-Sol Ea*, *115*.

Rozhko, A. Y., Y. Y. Podladchikov, and F. Renard (2007), Failure patterns caused by localized rise in pore-fluid overpressure and effective strength of rocks, *Geophys. Res. Lett.*, *34*(22), L22304.

Sachau, T., and D. Koehn (in press), 'Melange': A viscoelastic lattice-particle model applicable to the lithosphere, *Geochemistry Geophysics Geosystems*.

Secor, D. T. (1965), Role of fluid pressure in jointing, *Am J Sci*, *263*(8), 633-646.

Sheldon, H. A., A. C. Barnicoat, and A. Ord (2006), Numerical modelling of faulting and fluid flow in porous rocks: An approach based on critical state soil mechanics, *J Struct Geol*, *28*(8), 1468-1482.

Spickermann, A., R. Toussaint, J. Travelletti, J. P. Malet, and T. W. J. Van Asch (2012), A grain-fluid mixture model to characterize the dynamics of active lanslides in fine-grained soils, *J Geophys Res-Sol Ea*.

Steefel, C. I., and A. C. Lasaga (1994), A coupled model for transport of multiple chemical species and kinetic precipitation/dissolution reactions with application to reactive flow in single phase hydrothermal systems, *Am J Sci*, *294*(5), 529-592.

Tzschichholz, F., H. J. Herrmann, H. E. Roman, and M. Pfuff (1994), Beam model for hydraulic fracturing, *Physical Review B*, *49*(10), 7056-7059.

Valkó, P., and M. J. Economides (1995), *Hydraulic fracture mechanics*, Wiley.

Vinningland, J. L., Ø. Johnsen, E. G. Flekkoy, R. Toussaint, and K. J. Maloy (2007a), Experiments and simulations of a gravitational granular flow instability, *Phys Rev E Stat Nonlin Soft Matter Phys*, *76*(5 Pt 1), 27.

Vinningland, J. L., Ø. Johnsen, E. G. Flekkøy, R. Toussaint, and K. J. Måløy (2007a), Experiments and simulations of a gravitational granular flow instability, *Physical Review E*, *76*(5), 051306.

Vinningland, J. L., Ø. Johnsen, E. G. Flekkøy, R. Toussaint, and K. J. Måløy (2007b), Granular Rayleigh-Taylor Instability: Experiments and Simulations, *Physical Review Letters*, *99*(4), 048001.

Vinningland, J. L., Ø. Johnsen, E. G. Flekkoy, R. Toussaint, and K. J. Maloy (2009a), Granular Rayleigh-Taylor instability, paper presented at 6th international conference on micromechanics of granular media, powder and grains, AIP.

Vinningland, J. L., Ø. Johnsen, E. G. Flekkoy, R. Toussaint, and K. J. Maloy (2009b), Granular Rayleigh Taylor instability, paper presented at Traffic and Granular Flow conference 2007, Orsay, 2009.

Vinningland, J. L., Ø. Johnsen, E. G. Flekkøy, R. Toussaint, and K. J. Måløy (2010), Size invariance of the granular Rayleigh-Taylor instability, *Physical Review E*, *81*(4), 041308.

Vinningland, J. L., R. Toussaint, M. Niebling, E. Flekkøy, and K. Måløy (2012), Family-Vicsek scaling of detachment fronts in granular Rayleigh-Taylor instabilities during sedimentating granular/fluid flows, *The European Physical Journal - Special Topics*, *204*(1), 27-40.

Walmann, T., A. Malthe-Sørenssen, J. Feder, T. Jøssang, P. Meakin, and H. H. Hardy (1996), Scaling Relations for the Lengths and Widths of Fractures, *Physical Review Letters*, *77*(27), 5393-5396.

Wang, T.-Y., and C. C.-P. Chen (2001), Thermal-ADI: a linear-time chip-level dynamic thermal simulation algorithm based on alternating-direction-implicit (ADI) method, in *Proceedings of the 2001 international symposium on Physical design*, edited, pp. 238-243, ACM, Sonoma, California, United States.

Wangen, M. (2002), Effective permeability of hydrofractured sedimentary rocks, in *Norwegian Petroleum Society Special Publications*, edited by G. K. Andreas and H. Robert, pp. 61-74, Elsevier.

Wong, T.-f., H. Szeto, and J. Zhang (1992), Effect of Loading Path and Porosity on the Failure Mode of Porous Rocks, *Applied Mechanics Reviews*, *45*(8), 281-293.

Wong, T.-f., C. David, and W. Zhu (1997), The transition from brittle faulting to cataclastic flow in porous sandstones: Mechanical deformation, *J. Geophys. Res.*, *102*(B2), 3009-3025.

Yu.N, G. (1993), Growth of a crack produced by hydraulic fracture in a poroelastic medium, *International Journal of Rock Mechanics and Mining Sciences & Geomechanics Abstracts*, *30*(3), 233-238.

Zhu, W., and T.-f. Wong (1997), The transition from brittle faulting to cataclastic flow: Permeability evolution, *J. Geophys. Res.*, *102*(B2), 3027-3041.

Special Section: MUSIS

R. Toussaint*
K. J. Måløy
Y. Méheust
G. Løvoll
M. Jankov
G. Schäfer
J. Schmittbuhl

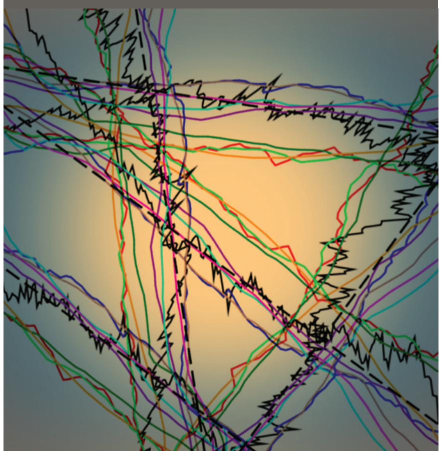

In disordered porous media, two-phase flow can be fractal across some scales, due to capillarity, gravity, and viscosity. This, with the boundary conditions, determines the flow stability. We present a short review and an example of upscaling, expressing a dynamic control over the macroscopic pressure–saturation relationship and residual saturation.

R. Toussaint and J. Schmittbuhl, IPGS, CNRS, Univ. of Strasbourg, Strasbourg, France; K.J. Måløy, G. Løvoll, and M. Jankov, Physics Dep., Univ. of Oslo, Oslo, Norway; Y. Méheust, Géosciences Rennes, Univ. of Rennes 1, Rennes, France; G. Løvoll, Det Norske Veritas AS, Research and Innovation, Høvik, Norway; G. Schäfer, LHYGES, CNRS, Univ. of Strasbourg, Strasbourg, France; R. Toussaint and Y.Y. Méheust, Centre for Advanced Study, Norwegian Academy of Science and Letters, Oslo, Norway. *Corresponding author (renaud.toussaint@unistra.fr).

Vadose Zone J.
doi:10.2136/vzj2011.0123
Received 3 Oct. 2011.

Two-Phase Flow: Structure, Upscaling, and Consequences for Macroscopic Transport Properties

In disordered porous media, two-phase flow of immiscible fluids (biphasic flow) is organized in patterns that sometimes exhibit fractal geometries across a range of length scales, depending on the capillary, gravitational, and viscous forces at play. These forces, as well as the boundary conditions, also determine whether the flow leads to the appearance of fingering pathways, i.e., unstable flow, or not. We present a short review of these aspects, focusing on drainage and summarizing when these flows are expected to be stable or not, what fractal dimensions can be expected, and in which range of scales. We based our review on experimental studies performed in two-dimensional Hele–Shaw cells or addressing three-dimensional porous media by use of several imaging techniques. We first present configurations in which solely capillary forces and gravity play a role. Next, we review configurations in which capillarity and viscosity are the main forces at play. Eventually, we examine how the microscopic geometry of the fluid clusters affects the macroscopic transport properties. An example of such an upscaling is illustrated in detail: for air invasion in a monolayer glass-bead cell, the fractal dimension of the flow structures and the associated scale ranges depend on the displacement velocity. This controls the relationship between saturation and the pressure difference between the two phases at the macroscopic scale. We provide in this case expressions for dynamic capillary pressure and residual fluid-phase saturations.

The physics of two-phase flows in porous media is a complex and rich topic, with obvious applications to the hydraulics of the vadose zone, be it water infiltration, evaporation, or the transport of dense nonaqueous-phase liquids down to the aquifers (Dridi et al., 2009). Hydrogeologists and soil scientists aim at relating volumetric flow, pressure head, and water content at the Darcy scale, which is a mesoscale above which the medium and the flow are described by continuous mathematical fields. They also need to predict the front displacement of the injected fluids, its localizing or nonlocalizing character, and the fluid mass distribution behind it. The basic laws of multiphase flows treated at the mesoscopic scale as a continuum require a closure of simultaneous flow according to Darcy's law. A key point of this closure is a functional relation between the capillary pressure and (water) saturation in the form of retention curves; another key point is the dependence of the relative permeabilities on saturation.

The physics community has been mostly concerned with characterizing and understanding flow structures and patterns from the pore scale and up. These structures and processes have a major impact on the retention curves (see, e.g., the review by Blunt, 2001). Notably, viscous fingering may have a strong influence on retention curves, resulting in dynamic saturation–pressure curves in porous media, as we show below.

These flow structures can vary from compact to ramified and fractal (Lenormand et al., 1988; Lenormand, 1989; Måløy et al., 1985; Méheust et al., 2002; Sandnes et al., 2011; Holtzman and Juanes, 2010). One major issue is to simplify this complexity by keeping just enough information to describe the relevant physics at the relevant scale for the flow considered without discarding essential information. For example, the simple invasion percolation model is sufficient to model the flow structure obtained under slow drainage conditions.

The fact that such simple models can describe simple features of complex systems arises from the property of universality in critical states: many physical dynamic systems, governed by a competition of simple forces with a disorder in thresholds, are in the vicinity of so-called critical points in statistical physics, as discussed, e.g., by Domb (1996) or Feder (1988). These are characterized by scale invariance across some ranges and fractal dimensions, and by critical exponents determining how characteristic lengths that limit the fractal ranges depend on the system size or driving speed. An interesting aspect of such critical points is that the corresponding exponents and fractal dimensions do not depend on the small-scale details of the system but are controlled by how the system is invariant under some form of upscaling. Consequently, many systems differing at small scale are characterized by the same critical exponents: they are said to belong to the same universality class. This allows complex systems to be described sometimes using simple computer models.

The porous body of a piece of soil or rock consists of pores and fracture networks of different length scales and shapes, whose permeability presents large spatial variations. These structures can be correlated at large scale (see, e.g., Brown, 1995; Zimmerman and Bodvarsson, 1996; Méheust and Schmittbuhl, 2003; Neuville et al., 2010a) or present a finite correlation length (Neuville et al., 2010b). The variations in permeability result in flow channeling (see, e.g., Brown, 1987, 1995; Drazer and Koplik, 2002; Méheust and Schmittbuhl, 2000, 2001, 2003; Neuville et al., 2010a, 2011, 2012a, 2012b) and a potential permeability anisotropy (Méheust and Schmittbuhl, 2000, 2001). In general, the soil or rock is a dynamic medium where the porosity can be modified by the fluids involved due to chemical reactions and desorption–adsorption mechanisms (Szymczak and Ladd, 2011), in addition to the fluid pressure and the mechanical stress acting on the porous medium (Johnsen et al., 2006; Goren et al., 2010, 2011). The chemical composition and nano- or microscale structure of the rock further determines the wetting properties of the fluids, which is crucial for the capillary front advancement in two-phase flow. For example, when a fluid with high viscosity is displaced in a porous medium by a fluid with a lower viscosity, the displacing fluid tends to channel through the paths of lower flow resistance, thereby forming pronounced fingers. The physical properties of the fluids play an important practical role in natural flows: e.g., in soil and groundwater, the identification of pollution sources is difficult due to the fact that organic pollutants can rapidly migrate down to the bottom of the aquifer or along paths different from the water (Benremita and Schäfer, 2003).

In addition, when the porous medium is deformable, branching structures can be observed with transitions to fracturing of the porous medium (Lemaire et al., 1993; Cheng et al., 2008; Sandnes et al., 2011; Holtzman and Juanes, 2010; Chevalier et al., 2009; Johnsen et al., 2006; Varas et al., 2011) or the formation of fingers, channels, or bubbles in it (Johnsen et al., 2006, 2008a, 2008b; Kong et al., 2011; Vinningland et al., 2007a, 2007b, 2010, 2012; Niebling et al., 2010a, 2010b).

In this review, we have addressed the detailed structure and dynamics of two-phase flow in fixed and disordered porous media based on pore-scale experiments. We have limited the discussion mostly to drainage, i.e., to situations where a nonwetting fluid displaces a wetting one—even though imbibition, where a wetting fluid invades a nonwetting one, is of equal practical importance. The discussion is limited to media that are isotropic and homogeneous at large scales and to cases where chemical reactions and adsorption or desorption between the fluids and the porous medium can be neglected. The structures of clusters of the moving fluid and the dynamics of drainage in porous media depend on several parameters such as the density difference, the surface tension, the wetting properties, the viscosities, and the flow rates of the fluids involved. The various forces at play dominate at different length scales, and their interplay gives rise to separate scaling regimes. Upscaling, which consists of relating the pore-scale description to properties defined at the Darcy scale or even at the macroscopic scale, is a central topic within hydrology and petroleum engineering.

Only by understanding the scaling of the structures and dynamics within each regime, and the crossover lengths involved, is it possible to perform upscaling. The structures involved are typically fractal within some scaling range; their fractal dimension depends on length scales and often result from fluctuations occurring at smaller scales. At the end of this short review is an example of upscaling of recent experimental data; the experiments in question were aimed at studying the crossover between capillary and viscous fingering in a quasi-two-dimensional (monolayer) porous medium.

This review summarizes the results of a series of works, published mostly in physics journals, that are of interest to model flow in the vadose zone or in general in hydrology. We also illustrate, using simple examples, what type of microstructure and what properties of fingering of the flow control upscaling and the dynamic dependence of macroscopic capillary pressure on microscopic flow.

Capillary and Gravitational Effects

When drainage occurs within the limit of infinitely slow displacement velocities, the pressure drop across the porous medium is controlled by the capillary pressure drop across the interface between the two fluids. The criterion for advancement of the interface into a given pore is that the capillary pressure drop is larger than the capillary pressure threshold needed to invade the pore neck that separates that pore from the already-invaded adjacent pore. The value of the capillary pressure threshold fluctuates from pore neck to pore neck, with a distribution function determined by the geometry of the porous medium. In the case of zero gravity or for a horizontal, two-dimensional porous medium, the next pore throat or neck to be invaded will be, among the pores that touch the interface, the one whose pore throat has the smallest capillary pressure threshold. This idea is the basis of the invasion percolation algorithm (de Gennes and Guyon, 1978; Chandler et al., 1982; Wilkinson and Willemsen, 1983) where random numbers representing the capillary pressure threshold values are distributed on a lattice and where the front is moved at each time step at the location along the interface corresponding to the smallest threshold value. The fact that the fluid front always moves at the most easily invaded pore neck and nowhere else is actually not always true in real flows, even if it is a good approximation. What drives the advancement of the front is the capillary pressure buildup in the fluid. The capillary pressure will not relax immediately after invasion of a new pore but is controlled by a back-contraction of the fluid interface. This is the reason for the so-called Haines jumps, which may lead to invasion of several pores in one jump (Haines, 1930; Måløy et al., 1992; Furuberg et al., 1996).

When the displaced fluid is incompressible (or lowly compressible), trapping takes place. Trapping is very important in two dimensions (Wilkinson and Willemsen, 1983) but much less significant in three dimensions. Experiments addressing capillary fingering in two-dimensional model systems were first performed by Lenormand et al. (1988) and Lenormand (1989), who found a mass fractal dimension of the invaded structures equal to $D_c = 1.83$, which is consistent with the results of numerical simulations based on invasion percolation (in the version of the model allowing trapping of the invaded fluid) (Wilkinson and Willemsen, 1983). In three dimensions, several experiments have been performed (Chuoke et al., 1959; Paterson et al., 1984a, 1984b; Chen et al., 1992; Frette et al., 1994; Hou et al., 2009; Mandava et al., 1990; Nsir et al., 2012; Yan et al., 2012). The fractal dimension found at small scale (2.0–2.6) is compatible with the dimension $D = 2.5$ found in three-dimensional invasion percolation models (Wilkinson and Willemsen, 1983).

Even though the capillary fingering structure is fractal, in practice it is well described by a fractal dimension only within a window of length scales ranging from the pore size up to a crossover length on a larger scale. In the case where the density difference between the two fluids is different from zero but where viscous forces are small compared with the others, this crossover length corresponds to a scale at which the capillary threshold fluctuations become of the same order of magnitude as the difference in hydrostatic pressure drop between the two fluids. This means that the crossover will always occur when the fluid structures become large enough. When a lighter fluid is displacing a heavier one from above at a slow flow rate resulting in low viscous forces, a stable displacement is observed. In this case, the displacing fluid does not finger its way through the displaced fluid; the crossover length sets the width of the rough interface between the two fluids (Birovljev et al., 1991; Méheust et al., 2002; Løvoll et al., 2005) parallel to the average flow direction.

Gravitational effects can easily be accounted for in the invasion percolation model by mapping the system onto a problem where the capillary threshold values are modified linearly by the hydrostatic pressure difference between the two fluids (Wilkinson, 1984; Birovljev et al., 1991; Auradou et al., 1999). By using this theory of percolation in a gradient, Wilkinson (1984, 1986) predicted theoretically the scaling of the front width ξ observed in a gravitational field as

$$\frac{\xi}{a} \propto \mathrm{Bo}^{-\nu/(\nu+1)} \qquad [1]$$

where the Bond number $\mathrm{Bo} = \Delta\rho g a^2/\gamma$ is the ratio of the difference of the hydrostatic pressure drops in the two fluids on the length scale of a single pore to the capillary pressure drop, ν is the critical exponent associated with correlation length divergence in percolation theory ($\nu = 4/3$ in two dimensions; Wilkinson, 1984), $\Delta\rho$ is the density difference between the fluids, g is gravitational acceleration, a is the characteristic pore size, and γ is the surface tension between the two fluids. Gravitationally stabilized fluid fronts occurring during very slow two-dimensional drainage have been studied both experimentally and by computer simulations (Birovljev et al., 1991). The results were found to be consistent with the theoretical prediction of Wilkinson (1984). When a lighter fluid is injected into a heavier fluid from below (Frette et al., 1992; Birovljev et al., 1995; Wagner et al., 1997), gravitational fingering of the displacing fluid through the displaced fluid occurs. A scaling behavior consistent with Eq. [1] has also been found in this unstable case: the characteristic length scale ξ then corresponds to the width of the unstable gravitational fingers, perpendicularly to the average flow direction. The same simple mapping to invasion percolation as described above can also be performed in the case of slow displacement in a rough fracture joint filled with particles (Auradou et al., 1999).

When comparing systems with different capillary pressure threshold distributions, Eq. [1] needs to be modified. From the phenomenology of the invasion process that we have explained above, it is quite intuitive that a gravity-stabilized front in a porous medium presenting a narrow capillary noise (i.e., a narrow distribution of the capillary thresholds) will give a flatter front than a porous medium with a wide capillary noise. Instead of Eq. [1], it has therefore been suggested to take into account a dimensionless fluctuation number $F = \Delta\rho g a/W_t$, in which capillary fluctuations are accounted for in terms of the width W_t of the capillary pressure distribution (Auradou et al., 1999; Méheust et al., 2002). Experiments to check the dependence of the displacement process on the capillary noise (W_t) are difficult because controlling the distribution of threshold capillary pressures in the medium in a systematic way is not straightforward. These experiments therefore remain to be done.

Capillary and Viscous Effects

The crossover between capillary fingering and regimes for which viscous effects are dominant was first studied in the pioneering work of Lenormand et al. (1988). He classified the different flow structures in a phase diagram depending on the viscosity contrast $M = \mu_i/\mu_d$ between the fluids and the capillary number $\mathrm{Ca} = \Delta P_{visc}/\Delta P_{cap}$, which is the ratio of the characteristic viscous pressure drop at the pore scale to the capillary pressure drop; μ_i and μ_d

are the viscosities of the injected and displaced fluid, respectively. From the Darcy equation, the capillary number can be evaluated as

$$\mathrm{Ca}=\frac{\Delta P_{\mathrm{visc}}}{\Delta P_{\mathrm{cap}}}=\frac{a\nabla P_{\mathrm{visc}}}{\gamma/a}=\frac{\mu a^2 v}{\kappa\gamma} \qquad [2]$$

where ΔP_{visc} is the viscous pressure drop at pore scale a, evaluated from the viscous pressure gradient ∇P_{visc}, κ is the intrinsic permeability of the medium, v is the seepage velocity associated with the imposed flow rate of the displaced fluid, μ is the viscosity of the most viscous fluid, and γ/a is the typical capillary pressure drop across the interface. Lenormand identified three flow regimes: (i) stable displacement, for which the interface roughness is not larger than one linear pore size, (ii) capillary fingering, which was discussed above, and (iii) viscous fingering, which occurs when large-scale fingers of the displacing fluid develop inside a more viscous defending fluid, resulting in a much faster breakthrough of the displacing fluid. It is important to keep in mind that the observed structures will depend on the length scale considered. For large systems, it is therefore not meaningful to talk about a sharp transition in a phase diagram between capillary and viscous fingering because both structures will always be present, i.e., capillary fingering at small length scales and either viscous fingering or stable displacement at large length scales. When the two fluids involved have different viscosities, the viscous pressure drop between two points along the fluid interface will typically be different in the two fluids. This viscosity contrast will produce a change in the capillary pressure along the fluid interface, therefore playing a role similar to that of density contrasts in the presence of a gravitational field (see above). At sufficiently large length scales, the difference in the viscous pressure drop between the two sides of the interface will become larger than the typical fluctuations in the capillary pressure threshold. This means that at sufficiently large length scales, and thus for a sufficiently large system, viscous pressure drops, rather than capillary forces associated with random capillary thresholds, determine the most likely invaded pores; consequently, viscous fingering will always dominate at sufficiently large scales when a viscous fluid is injected into another more viscous fluid. At these large scales, and in the absence of stabilizing gravitational effects, two-dimensional flows exhibit tree-like branched displacement structures with a mass fractal dimension $D_{\mathrm{v}} = 1.6$ (Måløy et al., 1985). The fractal dimension of the front, or growing hull, was found experimentally to be around 1, close to the growing interface dimension in diffusion-limited aggregation models (Feder, 1988).

Méheust et al. (2002) have introduced a generalized fluctuation number

$$F=\frac{\Delta\rho g a-a\mu v/\kappa}{W_{\mathrm{t}}} \qquad [3]$$

which is the ratio of the typical total pressure drop in the fluids over one pore, including both viscous and gravitational pressure drops, to the width of the capillary pressure threshold distribution W_{t}. The experiments by Méheust et al. (2002), identical to those by Birovljev et al. (1991) but performed at larger flow rates and therefore under significant viscous effects, showed that the characteristic width of the rough interface parallel to the macroscopic flow could be characterized by the fluctuation number according to an equation analogous to Eq. [1]:

$$\frac{\xi}{a}\propto F^{-\nu/(\nu+1)} \qquad [4]$$

where the exponent $\nu/(1 + \nu) = 4/7$ is consistent with percolation theory ($\nu = 4/3$) in two dimensions. Because the viscous pressure field is not homogeneous like the gravitational field, this result is not obvious. Note that in this case, ξ can be interpreted as the length scale at which the sum of the viscous and gravitational pressure drops becomes of the same order of magnitude as the spatial fluctuations of the capillary pressure threshold. In terms of the fluid–fluid interface, ξ corresponds to the crossover scale between capillary fingering structures at small scale and the stabilized structure, which is linear (dimension 1) at large scales. When the displacement is large enough for viscous forces to play a role, the fractal dimension typical of viscous fingering structures is also seen at intermediate scales (Méheust et al., 2002). Even in the case where the two fluids involved have the same viscosity, the width of the front was found to be consistent with Eq. [4] (Frette et al., 1997). As observed in the experiments of Frette et al. (1997), the effect of trapping turns out, at least in two dimensions, to be of central importance. The trapped islands result in a decrease in the relative permeability of the invaded fluid, which is equivalent to having a fluid with a higher viscosity (as was shown by Frette et al. [1997] by the comparison to simulations allowing trapping or not, with growth along the whole external perimeter of the invader or restricted to the hull). This is the effect responsible for the well-known decreasing dependence of a soil's matric potential on its water content. This result is consistent with the scaling relation Eq. [4], which is expected from theoretical arguments for percolation in a stabilizing gradient (Xu et al., 1998; Wilkinson, 1984; Lenormand, 1989). Note that other scaling relations have been derived theoretically and observed experimentally by other researchers, as reported by Xu et al. (1998). As mentioned above, when a viscous fluid is injected into a two-dimensional medium filled with a more viscous fluid, viscous fingers occur. The scaling of the finger width was studied experimentally by Løvoll et al. (2004) and Toussaint et al. (2005). The measurements were found to be consistent with a scaling law in the form

$$\frac{\xi}{a}\propto \mathrm{Ca}^{-1} \qquad [5]$$

This result is different from the scaling laws that can be explained from the theory of percolation in a gradient, as observed from stabilizing viscous or gravitational forces. In the experiments of Løvoll et al. (2004) and Toussaint et al. (2005), contrary to what happens in a pressure field arising from gravitational effects (as in Méheust et al.. 2002), the viscous pressure field was highly inhomogeneous, constant in front of the fingers, and screened by the fingers behind the invasion front (i.e., the pressure gradient concentrated around the finger tips and decayed behind the finger tips in the stagnant zones). This may explain why the behavior expected from percolation in a gradient is not observed, but a rather simpler one is observed instead. Note, however, that scaling laws based on the theory of percolation in a gradient are still expected for some types of unstable flows (Xu et al., 1998).

The scaling law, Eq. [5], can be explained from a simple mean field argument: consider an approximation for the pressure field for which the pressure gradient ∇P is homogeneous around the mobile sites at the boundary between the two fluids. Let us consider two of these sites, separated by a distance l along the direction of ∇P; the difference between the drops in viscous pressure across the interface at the two sites is $l\nabla P \sim l\mathrm{Ca}\gamma/a^2$. This relation holds not only when the viscosity of one fluid can be neglected with respect to that of the other one (for example, for air and water), in which case a nonzero viscous pressure difference between the two sites occurs in the defending liquid only and the definition of the capillary number is given by Eq. [2]. It also holds in the general case of two viscous fluids, in which case the capillary number can be defined from Eq. [2] by replacing the viscous pressure difference by the difference in the viscous pressure drop across the interface at the two sites, or equivalently by the differential viscous pressure drop $|\Delta P_\mathrm{v}^{(\mathrm{i})} - \Delta P_\mathrm{v}^{(\mathrm{d})}|$, where the $|\Delta P_\mathrm{v}|$ are the viscous pressure differences between the two sites in each of the phases and the superscripts (i) and (d) denote the invading and defending phases, respectively. If the differential viscous pressure difference between these two sites exceeds the characteristic random fluctuations of the capillary pressure threshold from one pore throat to another along the interface, then the viscous pressure field is dominant in determining at which of the two points considered new pores are going to be invaded. On the contrary, if the random fluctuations of capillary threshold exceed the differential viscous pressure drop between the two points, then this random pressure difference component dominates. Assuming that its magnitude W_t is of the same order as the average capillary pressure value, γ/a, we conclude that capillary effects are expected to dominate for scales l such that $l\mathrm{Ca}\gamma/a^2 < \gamma/a$, whereas viscous effects will dominate for larger scales, such that $l\mathrm{Ca}\gamma/a^2 > \gamma/a$; this explains the observed crossover scale $\xi = a/\mathrm{Ca}$ between the structures characteristic of capillary fingering and those characteristic of viscous fingering. Using a pore-scale simulation where they could tune capillary noise, Holtzman and Juanes (2010) determined a phase diagram of the displacement regime (capillary or viscous fingering) as a function of capillary noise and capillary number, and observed the same crossover, which they explained in a similar manner, only expressing the prefactor for the scaling law of the crossover scale in terms of typical capillary pressure threshold fluctuations rather than in terms of the mean capillary pressure threshold (that is, they did not assume that $W_\mathrm{t} \sim \gamma/a$).

An Example of Upscaling from Capillary to Viscous Fingering

In many situations of nonmiscible biphasic flow in porous media, the flow gets organized in fingering structures (preferential paths); in these unstable configurations, the fluids arrange in fractal geometries with nontrivial fractal dimensions depending on the observation scale, and the scale range across which each dimension is observed depends on the imposed boundary conditions (such as the macroscopic fluxes). This microscopic structuring has far-reaching consequences for the upscaled relationships between, for example, saturation and the pressure difference between the two phases.

An example of such a situation was mentioned briefly above: if gravity is negligible, only capillarity and viscosity play a role in the flow; when a fluid of lower viscosity displaces a more viscous one, the fluid–fluid interface is unstable due to viscous pressure gradients increasing at the most advanced parts of the invader so that fingers naturally arise. The development of such an interface instability occurring during drainage was studied optically in Hele–Shaw cells at several controlled injection rates (Løvoll et al., 2004; Toussaint et al., 2005). Air was injected into an artificial porous medium composed of a monolayer of immobile glass beads sandwiched between two glass plates and initially filled with a wetting dyed glycerol–water solution. The Hele–Shaw cell dimensions were denoted as length L by width W by height H, with $H = 1$ mm being the cell thickness as well as the typical glass bead diameter; flow was imposed along the length L, with impermeable lateral boundaries defining a channel of width W (see Fig. 1). An occupancy (also termed occupation probability) was defined in the reference frame moving at the average finger speed between the system boundaries; in that reference, the invasion structure is seen as a finger fluctuating during the experiment behind its stationary tip: for each point in this reference frame, the proportion of time when this point is occupied by the invading fluid is a measure of the occupancy. It was shown in these experiments that the pathway of the air, defined as the locations where the occupancy probability exceeded half its maximum value, was a finger of width λW positioned in the center of the channel, with $\lambda = 0.4$. This was attributed to a similarity between the process of selection of the pore throats to be invaded and a dielectric breakdown model of exponent 2 (Niemeyer et al., 1984), that is, a growth process in which the growth velocity is proportional to the gradient of the driving effect to the power of 2. The presence of a disorder in the capillary threshold turns out to be important to enforce a boundary condition analogous to a growth probability along the invader proportional to $[(P - P_\mathrm{air})/a]^2$, with a field P satisfying the Laplace equation due to mass conservation. This result was justified theoretically by computing the average invasion speed, taking into account the width of the

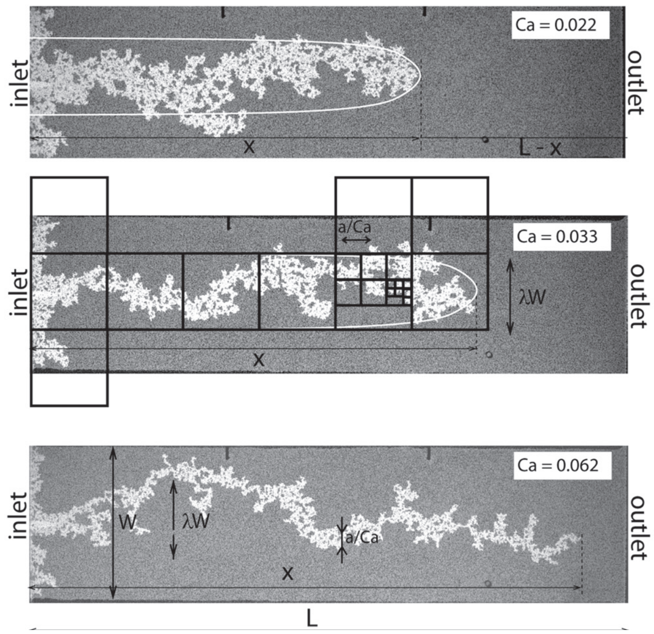

Fig. 1. Invasion structure of a fluid with a low viscosity (white) into a much more viscous one (dark grey) during drainage in an artificial, two-dimensional, porous medium of width W and extent L at three different extraction speeds. The position of the invasion tip is denoted x. Characteristic crossover scales between fractal regimes, λW and a/Ca, separate a straight finger structure, a viscous fingering geometry, and a capillary fingering geometry down to the pore scale a. The black squares of various dimensions in the central figure illustrate the types of boxes used in the box counting measure of the fractal dimension: for boxes of a certain side size l, the number of boxes $N(l)$ needed to cover the structure are counted. This is done for various sizes, from system size down to pixel size. The scaling of this number as a function of the size, $N(l) \sim l^{-D}$ defines the mass fractal dimension D. The sizes W and a/Ca turn out to be the limits of scale ranges with well-defined fractal dimensions: D = 1.00 above W, D_v = 1.60 between W and a/Ca, and D_c = 1.83 below (modified from Løvoll et al., 2011).

capillary threshold distribution (Toussaint et al., 2005). This type of invasion structure is illustrated in Fig. 1.

From approximations of the shape of the pressure around this finger, mostly controlled by the viscous pressure drop, an upscaled pressure–saturation relation can be derived (Løvoll et al., 2010).

Indeed, the pressure presents to first order a linear viscous pressure drop from the tip of the invasion cluster, at position x, to the outlet of the system, at position L. Across the rest of the system, the pressure gradient is screened by the finger, rendering the pressure in the wetting fluid essentially constant at a value close to the sum of the air pressure and the entrance pressure γ/a. Hence, the pressure difference between the two phases, with a pressure in the wetting fluid P_w measured at the outlet, the one in the nonwetting phase equal to the atmospheric pressure P_{nw}, and a correction to this entrance pressure, can be written as

$$\Delta P^* = P_{nw} - P_w - \frac{\gamma}{a} = (L-x)\nabla P \quad [6]$$

$$= (L-x)\frac{\Delta P_{visc}}{a} \quad [7]$$

$$= (L-x)\frac{\Delta P_{cap}\mathrm{Ca}}{a} \quad [8]$$

$$= (L-x)\frac{\gamma \mathrm{Ca}}{a^2} \quad [9]$$

where ΔP_{visc} and ΔP_{cap} are considered at the pore scale. Thus, there is a linear relationship between the viscous pressure drop across the cell and the distance between the tip of the finger and the outlet.

In addition, the relationship between saturation and the capillary number can be inferred from the fractal structure of the nonwetting invading fluid. At scales above the width λW, the finger is a linear structure of dimension 1. Between the scale λW and a/Ca, the structure has a viscous fingering geometry of fractal dimension D_v = 1.60 (Måløy et al.,1985; Løvoll et al., 2004). Between the crossover scale a/Ca and the pore scale a, the structure has a capillary fingering geometry of fractal dimension D_c = 1.83. Hence, the total number of pores invaded by the nonviscous fluid N_{nw} can be evaluated as a function of these fractal dimensions, the ratio of the finger length to its width, $x/\lambda W$, and the ratios of the latter length to the two other lengths, the crossover length and the pore size. This leads to

$$N_{nw} = \frac{x}{\lambda W}\left(\frac{\lambda W}{a\mathrm{Ca}^{-1}}\right)^{D_v}\left(\frac{a\mathrm{Ca}^{-1}}{a}\right)^{D_c} \quad [10]$$

Together with the relationship between the total number of pores N_{tot} and the characteristic model dimensions,

$$N_{tot} = \frac{LW}{a^2} \quad [11]$$

and the relationship between the wetting-phase saturation S_w and nonwetting-phase saturation S_{nw},

$$S_{nw} = 1 - S_w = \frac{N_{nw}}{N_{tot}} \quad [12]$$

Eq. [10] leads to

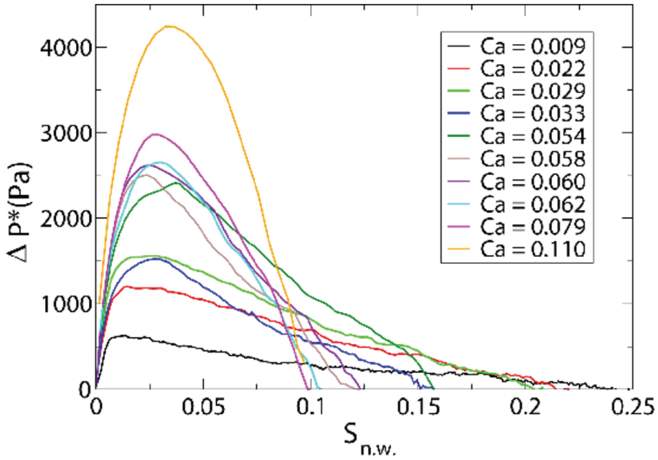

Fig. 2. Dependence of the pressure difference between the two phases and the saturation of the invading fluid after removal of the average capillary pressure drop, $\Delta P^* = P_{nw} - P_w - \gamma/a$ where P_{nw} is the non-wetting-phase pressure, P_w is the wetting-phase pressure, and γ/a is the average capillary pressure, at different injection speeds (adapted from Løvoll et al., 2011).

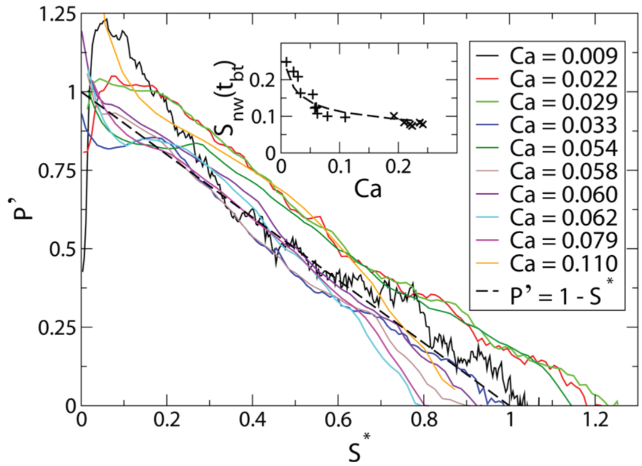

Fig. 3. The collapse of the relationship between the reduced pressure difference (between the two phases), $P' = a^2\Delta P^*/(\gamma L\mathrm{Ca})$, and the reduced saturation of the invading fluid, $S^* = \lambda^{1-D_v}(a/W)^{-2+D_v}\mathrm{Ca}^{D_c-D_v} S_{nw}$, at different injection speeds, shows the influence of the structure on the upscaling. Note that plots corresponding to lower capillary number (Ca) values have been rescaled more and therefore appear more noisy; the dashed curve is the prediction, and the inset shows the residual saturation at breakthrough (adapted from Løvoll et al., 2011).

$$\begin{aligned}1 - S_w &= S_{nw}\\ &= \lambda^{D_v-1}\left(\frac{a}{W}\right)^{2-D_v}\mathrm{Ca}^{D_v-D_c}\left(1-\frac{a^2\Delta P^*}{\gamma L\mathrm{Ca}}\right)\end{aligned} \quad [13]$$

This relationship allows all the pressure difference curves measured as a function of saturation in the set of experiments performed by Løvoll et al. (2010) to collapse onto a unique master curve for capillary numbers ranging from around 0.008 to 0.12. Note that the rescaled pressure $P^* = a^2\Delta P^*/\gamma L\mathrm{Ca} = (\Delta P^*/M)/(\Delta P_{visc}/a)$ is simply the ratio of the gradient in viscous pressure defined at the scale of the model to the gradient in viscous pressure defined at the pore scale. Apart from the normalization by $\Delta P_{visc}/a$, it is nothing other than what is usually defined at the scale L of the experimental model as the capillary pressure. In other words, Eq. [13] defines the dependence on the Darcy or seepage velocity of what is commonly denoted as dynamic capillary pressure, measured at scale L. This example shows how both viscous and capillary effects play a role in constraining the geometry of the invasion structures, resulting in a dynamic capillary pressure, as it is traditionally called (Hassanizadeh et al., 2002), that is simply due to the upscaling of the invasion structure, with only capillary and viscous effects seen at the representative elementary volume scale and without any dynamic capillary or wetting effects occurring at the pore scale.

Figures 2 and 3 illustrate, respectively, the raw measurements at several injection speeds and how Eq. [13] allows these curves of saturation vs. pressure to collapse: with a reduced saturation $S^* = \lambda^{1-D_v}(a/W)^{-2+D_v}\mathrm{Ca}^{D_c-D_v} S_{nw}$ and the rescaled pressure $P' = a^2\Delta P^*/\gamma L\mathrm{Ca} = (\Delta P^*/M)/(\Delta P_{visc}/a)$, Eq. [13] predicts that $P' = 1 - S^*$, which is the theoretical straight line in Fig. 3. This is well followed by the experimental data collapse.

The viscous pressure drop across the cell drops linearly as the finger progresses into the cell, from a maximum value of $\gamma L\mathrm{Ca}/a^2$ at the beginning of the invasion, down to 0 at breakthrough of the invasion finger. In Eq. [13], the wetting saturation is indeed initially 1, as it should be at initial total saturation, but we also obtain the final and maximum value of the residual wetting saturation as

$$1 - S_{wr} = S_{nwr} = \lambda^{D_v-1}\left(\frac{a}{W}\right)^{2-D_v}\mathrm{Ca}^{D_v-D_c} \quad [14]$$

This relation between the residual saturation and the capillary number is indeed consistent with the observed residual saturations, as shown in the inset of Fig. 3.

Besides the relation between saturation and the macroscopic pressure difference between the phases, other macroscopic relations can be obtained via upscaling, as, e.g., in some situations, the relative permeability. For example, in other experiments where both fluids were injected at the same time, with both drainage and imbibition occurring in the flow simultaneously, the trapped structures of wetting fluids were observed to be fractal up to a certain cutoff depending on the imposed flux (Tallakstad et al., 2009a, 2009b). A scaling law was observed for the relative permeability of the wetting viscous fluid in these experiments, with an observed dependence on the imposed flux that can be expressed as $\kappa_{rel} \propto \mathrm{Ca}^{-1/2}$.

The upscaling explaining the cutoff and the structures were allowed to explain this measured scaling law.

For the pure imbibition case, the macroscopic capillary pressure also presents a dynamic dependence: it was found by Stokes et al. (1986) and Weitz et al. (1987) that the fingering also occurs when the lower viscous fluid displaces the more viscous one, and that the finger width scales as $Ca^{-1/2}$, a result that is still largely unexplained.

Conclusions

We have discussed the local flow structures that are observed experimentally during drainage in a disordered porous medium. When the viscosity contrast between the two fluids is high (as for air displacing water), the flow structures are fractal, with a fractal dimension that depends on the observation scale. At small scales, capillary fingering exhibits a fractal dimension of 1.8 for two-dimensional media and between 2 and 2.6 for three-dimensional media. At larger scales, a branched structure characteristic of viscous fingering is seen, with a fractal dimension of 1.6 for two-dimensional systems. The crossover between the two behaviors occurs at a length scale for which the differential viscous pressure drop equals the typical capillary pressure threshold in the medium. This means that for horizontal flow, unstable viscous fingering is always seen at large enough scales, even if the medium exhibits no permeability heterogeneities at the Darcy scale. From the definition of the crossover length, it follows that it scales as the inverse of the capillary number, which explains why experiments performed at a given experimental scale and at very slow flow rates have evidenced capillary fingering, while those performed at very large flow rates have evidenced viscous fingering. As for the effect of gravity, it can be to either destabilize or stabilize the interface, depending on which fluid is the densest. In the latter case, it acts against capillary effects and, when the displacing fluid is the most viscous, against the destabilizing viscous forces, resulting in an amplitude of the interface roughness that scales as a power law of the generalized fluctuation number (or generalized Bond number $Bo - Ca$, as introduced by Méheust et al., 2002). In horizontal two-dimensional flows, viscous fingering is observed to occur up to another characteristic length that is a fixed fraction of the width of the medium. Upscaling of the local flow structures is possible once the fractal dimensions typical of the flow regimes and the relevant length scale range for each of them are known. We have given an example of how the measured capillary pressure can be related theoretically to water saturation, a relation that is confirmed by measurements. In that example, the capillary pressure measured at the scale of the experimental setup exhibits dynamic features, i.e., a dependence on the flow rate, that is fully explained by the geometry of the upscaling, without any dynamic effects in the physical capillary pressure as defined at the pore–interface scale.

Acknowledgments

This work was supported by the CNRS through a French–Norwegian PICS grant, the Alsace region through the REALIZE program, and the Norwegian NFR.

References

Auradou, H., K.J. Måløy, J. Schmittbuhl, A. Hansen, and D. Bideau. 1999. Competition between correlated buoyancy and uncorrelated capillary effects during drainage. Phys. Rev. E 60:7224–7234. doi:10.1103/PhysRevE.60.7224

Benremita, H., and G. Schäfer. 2003. Transfert du trichloréthylène en milieu poreux à partir d'un panache de vapeurs. C. R. Mec. 331:835–842. doi:10.1016/j.crme.2003.08.006

Birovljev, A., L. Furuberg, J. Feder, T. Jøssang, K.J. Måløy, and A. Aharony. 1991. Gravity invasion percolation in two dimensions: Experiment and simulation. Phys. Rev. Lett. 67:584–587. doi:10.1103/PhysRevLett.67.584

Birovljev, A., G. Wagner, P. Meakin, J. Feder, and T. Jøssang. 1995. Migration and fragmentation of invasion percolation clusters in two-dimensional porous media. Phys. Rev. E 51:5911–5915. doi:10.1103/PhysRevE.51.5911

Blunt, M.J. 2001. Flow in porous media: Pore-network model and multiphase flow. Curr. Opin. Colloid Interface Sci. 6:197–207. doi:10.1016/S1359-0294(01)00084-X

Brown, S.R. 1987. Fluid flow through rock joints: The effect of surface roughness. J. Geophys. Res. 92(B2):1337–1347. doi:10.1029/JB092iB02p01337

Brown, S.R. 1995. Simple mathematical model of a rough fracture. J. Geophys. Res. 100(B4):5941–5952. doi:10.1029/94JB03262

Chandler, R., J. Koplik, K. Lerman, and J.F. Willemsen. 1982. Capillary displacement and percolation in porous media. J. Fluid Mech. 119:249–267. doi:10.1017/S0022112082001335

Chen, S., K.H. Kim, F. Qin, and A.T. Watson. 1992. Quantitative NMR imaging of multiphase flow in porous media. Magn. Reson. Imaging 10:815–826. doi:10.1016/0730-725X(92)90417-X

Cheng, X., L. Xu, A. Patterson, H.M. Jaeger, and S.R. Nagel. 2008. Towards the zero-surface-tension limit in granular fingering instability. Nat. Phys. 4:234–237. doi:10.1038/nphys834

Chevalier, C., A. Lindner, M. Leroux, and E. Clément. 2009. Morphodynamics during air injection into a confined granular suspension. J. Non-Newtonian Fluid Mech. 158:63–72. doi:10.1016/j.jnnfm.2008.07.007

Chuoke, R.L., P. van Meurs, and C. van der Poel. 1959. The instability of slow, immiscible, viscous liquid–liquid displacement in permeable media. Trans. Am. Inst. Min. Metall. Pet. Eng. 216:188–194.

de Gennes, P.G., and E. Guyon. 1978. Lois generales pour l'injection d'un fluide dans un milieu poreux aléatoire. J. Mec. 17:403–432.

Domb, C. 1996. The critical point: A historical introduction to the modern theory of critical phenomena. Taylor and Francis, London.

Drazer, G., and J. Koplik. 2002. Transport in rough self-affine fractures. Phys. Rev. E 66:026303. doi:10.1103/PhysRevE.66.026303

Dridi, L., I. Pollet, O. Razakarisoa, and G. Schäfer. 2009. Characterisation of a DNAPL source zone in a porous aquifer using the Partitioning Interwell Tracer Test and an inverse modelling approach. J. Contam. Hydrol. 107:22–44.

Feder, J. 1988. Fractals. Plenum Press, New York.

Frette, O.I., K.J. Måløy, J. Schmittbuhl, and A. Hansen. 1997. Immiscible displacement of viscosity-matched fluids in two-dimensional porous media. Phys. Rev. E 55:2969–2975. doi:10.1103/PhysRevE.55.2969

Frette, V., J. Feder, T. Jøssang, and P. Meakin. 1992. Buoyancy-driven fluid migration in porous media. Phys. Rev. Lett. 68:3164–3167. doi:10.1103/PhysRevLett.68.3164

Frette, V., J. Feder, T. Jøssang, P. Meakin, and K.J. Måløy. 1994. Fast, immiscible fluid–fluid displacement in three-dimensional porous media at finite viscosity contrast. Phys. Rev. E 50:2881–2890. doi:10.1103/PhysRevE.50.2881

Furuberg, L., K.J. Måløy, and J. Feder. 1996. Intermittent behavior in slow drainage. Phys. Rev. E 53:966–977. doi:10.1103/PhysRevE.53.966

Goren, L., E. Aharonov, D. Sparks, and R. Toussaint. 2010. Pore pressure evolution in deforming granular material: A general formulation and the infinitely stiff approximation. J. Geophys. Res. 115(B09216). doi:10.1029/2009JB007191

Goren, L., E. Aharonov, D. Sparks, and R. Toussaint. 2011. The mechanical coupling of fluid-filled granular material under shear. Pure Appl. Geophys. 168:2289–2323. doi:10.1007/s00024-011-0320-4

Haines, W.B. 1930. Studies in the physical properties of soil: V. The hysteresis effect in capillary properties, and the modes of moisture distribution associated therewith. J. Agric. Sci. 20:97–116. doi:10.1017/S002185960008864X

Hassanizadeh, S.M., M.A. Celia, and H.K. Dahle. 2002. Dynamic effect in the capillary pressure–saturation relationship and its impacts on unsaturated flow. Vadose Zone J. 1:38–57.

Holtzman, R., and R. Juanes. 2010. Crossover from fingering to fracturing in deformable disordered media. Phys. Rev. E 82:046305. doi:10.1103/PhysRevE.82.046305

Hou, J., Z.Q. Li, S.K. Zhang, X.L. Cao, Q.J. Du, and X.W. Song. 2009. Computerized tomography study of the microscopic flow mechanism of polymer flooding. Transp. Porous Media 79:407–418. doi:10.1007/s11242-008-9330-9

Johnsen, Ø., C. Chevalier, A. Lindner, R. Toussaint, E. Clément, K.J. Måløy, et al. 2008a. Decompaction and fluidization of a saturated and confined granular medium by injection of a viscous liquid or a gas. Phys. Rev. E 78:051302. doi:10.1103/PhysRevE.78.051302

Johnsen, Ø., R. Toussaint, K.J. Måløy, and E.G. Flekkøy. 2006. Pattern formation during central air injection into granular materials confined in a circular Hele–Shaw cell. Phys. Rev. E 74:011301. doi:10.1103/PhysRevE.74.011301

Johnsen, Ø., R. Toussaint, K.J. Måløy, E.G. Flekkøy, and J. Schmittbuhl. 2008b. Coupled air/granular flow in a linear Hele–Shaw cell. Phys. Rev. E 77:011301. doi:10.1103/PhysRevE.77.011301

Kong, X.-Z., M. Holzner, F. Stauffer, and W. Kinzelbach. 2011. Time-resolved 3D visualization of air injection in a liquid-saturated refractive-index-matched porous medium. Exp. Fluids 50:1659–1670. doi:10.1007/s00348-010-1018-6

Lemaire, E., Y.O.M. Abdelhaye, J. Larue, R. Benoit, P. Levitz, and H. van Damme. 1993. Pattern formation in noncohesive and cohesive granular media. Fractals 1:968–976. doi:10.1142/S0218348X93001040

Lenormand, R. 1989. Flow through porous media: Limits of fractal patterns. Proc. R. Soc. London Ser. A 423:159–168. doi:10.1098/rspa.1989.0048

Lenormand, R., E. Touboul, and C. Zarcone. 1988. Numerical models and experiments on immiscible displacements in porous media. J. Fluid Mech. 189:165–187. doi:10.1017/S0022112088000953

Løvoll, G., M. Jankov, K.J. Måløy, R. Toussaint, J. Schmittbuhl, G. Schäfer, and Y. Méheust. 2010. Influence of viscous fingering on dynamic saturation–pressure curves in porous media. Transp. Porous Media 86:305–324. doi:10.1007/s11242-010-9622-8

Løvoll, G., Y. Méheust, K.J. Måløy, E. Aker, and J. Schmittbuhl. 2005. Competition of gravity, capillary and viscous forces during drainage in a two-dimensional porous medium, a pore scale study. Energy 30:861–872. doi:10.1016/j.energy.2004.03.100

Løvoll, G., Y. Méheust, R. Toussaint, J. Schmittbuhl, and K.J. Måløy. 2004. Growth activity during fingering in a porous Hele–Shaw cell. Phys. Rev. E 70:026301. doi:10.1103/PhysRevE.70.026301

Måløy, K.J., J. Feder, and T. Jøssang. 1985. Vicous fingering fractals in porous media. Phys. Rev. Lett. 55:2688–2691. doi:10.1103/PhysRevLett.55.2688

Måløy, K.J., L. Furuberg, J. Feder, and T. Jøssang. 1992. Dynamics of slow drainage in porous media. Phys. Rev. Lett. 68:2161–2164. doi:10.1103/PhysRevLett.68.2161

Mandava, S.S., A.T. Watson, and M.E. Carl. 1990. NMR imaging of saturation during immiscible displacements. AIChE J. 36:1680–1686. doi:10.1002/aic.690361108

Méheust, Y., G. Løvoll, K.J. Måløy, and J. Schmittbuhl. 2002. Interface scaling in a two-dimensional porous medium under combined viscous, gravity, and capillary effects. Phys. Rev. E 66:051603. doi:10.1103/PhysRevE.66.051603

Méheust, Y., and J. Schmittbuhl. 2000. Flow enhancement of a rough fracture. Geophys. Res. Lett. 27:2989–2992. doi:10.1029/1999GL008464

Méheust, Y., and J. Schmittbuhl. 2001. Geometrical heterogeneities and permeability anisotropy of rough fractures. J. Geophys. Res. 106(B2):2089–2102. doi:10.1029/2000JB900306

Méheust, Y., and J. Schmittbuhl. 2003. Scale effects related to flow in rough fractures. Pure Appl. Geophys. 160:1023–1050. doi:10.1007/PL00012559

Neuville, A., R. Toussaint, and J. Schmittbuhl. 2010a. Fracture roughness and thermal exchange: A case study at Soultz-sous-forêts. C. R. Geosci. 342:616–625. doi:10.1016/j.crte.2009.03.006

Neuville, A., R. Toussaint, and J. Schmittbuhl. 2010b. Hydro-thermal coupling in a self-affine rough fracture. Phys. Rev. E 82:036317. doi:10.1103/PhysRevE.82.036317

Neuville, A., R. Toussaint, and J. Schmittbuhl. 2011. Hydraulic transmissivity and heat exchange efficiency of open fractures: A model based on lowpass filtered apertures. Geophys. J. Int. 186:1064–1072. doi:10.1111/j.1365-246X.2011.05126.x

Neuville, A., R. Toussaint, and J. Schmittbuhl. 2012a. Fracture aperture reconstruction and determination of hydrological properties: A case study at Draix (French Alps). Hydrol. Processes 26:2095–2105. doi:10.1002/hyp.7985

Neuville, A., R. Toussaint, J. Schmittbuhl, D. Koehn, and J. Schwarz. 2012b. Characterization of major discontinuities from borehole cores of the black consolidated marl formation of Draix (French Alps). Hydrol. Processes 26: 2085–2094. doi:10.1002/hyp.7984

Niebling, M.J., E.G. Flekkøy, K.J. Måløy, and R. Toussaint. 2010a. Mixing of a granular layer falling through a fluid. Phys. Rev. E 82:011301. doi:10.1103/PhysRevE.82.011301

Niebling, M.J., E.G. Flekkøy, K.J. Måløy, and R. Toussaint. 2010b. Sedimentation instabilities: Impact of the fluid compressibility and viscosity. Phys. Rev. E 82:051302. doi:10.1103/PhysRevE.82.051302

Niemeyer, L., L. Pietronero, and H.J. Wiesmann. 1984. Fractal dimension of dielectric breakdown. Phys. Rev. Lett. 52:1033. doi:10.1103/PhysRevLett.52.1033

Nsir, K., G. Schäfer, R. di Chiara Roupert, O. Razakarisoa, and R. Toussaint. 2012. Laboratory experiments on DNAPL gravity fingering in water-saturated porous media. Int. J. Multiphase Flow 40:83–92. doi:10.1016/j.ijmultiphaseflow.2011.12.003

Paterson, L., V. Hornof, and G. Neale. 1984a. Visualization of a surfactant flood of an oil-saturated porous medium. SPE J. 24:325–327. doi:10.2118/11598-PA

Paterson, L., V. Hornof, and G. Neale. 1984b. Water fingering into an oil-wet porous medium saturated with oil at connate water saturation. Rev. Inst. Fr. Pet. 39:517–522.

Sandnes, B., E.G. Flekkøy, H.A. Knudsen, K.J. Måløy, and H. See. 2011. Patterns and flow in frictional fluid dynamics. Nat. Commun. 2:288. doi:10.1038/ncomms1289

Stokes, J.P., D.A. Weitz, J.P. Gollub, A. Dougherty, M.O. Robbins, P.M. Chaikin, and H.M. Lindsay. 1986. Interfacial stability of immiscible displacement in a porous medium. Phys. Rev. Lett. 57:1718. doi:10.1103/PhysRevLett.57.1718

Szymczak, P., and A.J.C. Ladd. 2011. Instabilities in the dissolution of a porous matrix. Geophys. Res. Lett. 38:L07403. doi:10.1029/2011GL046720

Tallakstad, K.T., H.A. Knudsen, T. Ramstad, G. Løvoll, K.J. Måløy, R. Toussaint, and E.G. Flekkøy. 2009a. Steady-state two-phase flow in porous media: Statistics and transport properties. Phys. Rev. Lett. 102:074502. doi:10.1103/PhysRevLett.102.074502

Tallakstad, K.T., G. Løvoll, H.A. Knudsen, T. Ramstad, E.G. Flekkøy, and K.J. Måløy. 2009b. Steady-state, simultaneous two-phase flow in porous media: An experimental study. Phys. Rev. E 80:036308. doi:10.1103/PhysRevE.80.036308

Toussaint, R., G. Løvoll, Y. Méheust, K.J. Måløy, and J. Schmittbuhl. 2005. Influence of pore-scale disorder on viscous fingering during drainage. Europhys. Lett. 71:583. doi:10.1209/epl/i2005-10136-9

Varas, G., V. Vidal, and J.C. Geminard. 2011. Morphology of air invasion in an immersed granular layer. Phys. Rev. E 83(6):061302. doi:10.1103/PhysRevE.83.061302

Vinningland, J.L., Ø. Johnsen, E.G. Flekkøy, R. Toussaint, and K.J. Måløy. 2007a. A granular Rayleigh–Taylor instability: Experiments and simulations. Phys. Rev. Lett. 99:048001. doi:10.1103/PhysRevLett.99.048001

Vinningland, J.L., Ø. Johnsen, E.G. Flekkøy, R. Toussaint, and K.J. Måløy. 2007b. Experiments and simulations of a gravitational granular flow instability. Phys. Rev. E 76:051306. doi:10.1103/PhysRevE.76.051306

Vinningland, J.L., Ø. Johnsen, E.G. Flekkøy, R. Toussaint, and K.J. Måløy. 2010. Size invariance of the granular Rayleigh–Taylor instability. Phys. Rev. E 81:041308. doi:10.1103/PhysRevE.81.041308

Vinningland, J.L., R. Toussaint, M. Niebling, E.G. Flekkøy, and K.J. Måløy. 2012. Family–Viscek scaling of detachment fronts in granular Rayleigh–Taylor instabilities during sedimentating granular/fluid flows. Eur. Phys. J. Spec. Topics 204:27–40.

Wagner, G., A. Birovljev, J. Feder, and T. Jøssang. 1997. Fragmentation and migration of invasion percolation clusters: Experiments and simulations. Phys. Rev. E 55:7015–7029. doi:10.1103/PhysRevE.55.7015

Weitz, D.A., J.P. Stokes, R.C. Ball, and A.P. Kushnick. 1987. Dynamic capillary pressure in porous media: Origin of the viscous-fingering length scale. Phys. Rev. Lett. 59:2967. doi:10.1103/PhysRevLett.59.2967

Wilkinson, D. 1984. Percolation model of immiscible displacement in the presence of buoyancy forces. Phys. Rev. A 30:520–531. doi:10.1103/PhysRevA.30.520

Wilkinson, D. 1986. Percolation effects in immiscible displacement. Phys. Rev. A 34:1380–1391. doi:10.1103/PhysRevA.34.1380

Wilkinson, D., and J.F. Willemsen. 1983. Invasion percolation: A new form of percolation theory. J. Phys. A 16:3365–3376. doi:10.1088/0305-4470/16/14/028

Xu, B., Y.C. Yortsos, and D. Salin. 1998. Invasion percolation with viscous forces. Phys. Rev. E 57:739–751. doi:10.1103/PhysRevE.57.739

Yan, J., X. Luo, W. Wang, F. Chen, R. Toussaint, J. Schmittbuhl, et al. 2012. An experimental study of oil secondary migration in a three dimensional porous space. AAPG Bull. (in press).

Zimmerman, R., and G. Bodvarsson. 1996. Hydraulic conductivity of rock fractures. Transp. Porous Media 23:1–30. doi:10.1007/BF00145263

PHYSICAL REVIEW E **70**, 026301 (2004)

Growth activity during fingering in a porous Hele-Shaw cell

Grunde Løvoll,[1,2] Yves Méheust,[3,2,1] Renaud Toussaint,[1,3] Jean Schmittbuhl,[2] and Knut Jørgen Måløy[1]
[1]*Department of Physics, University of Oslo, Norway*
[2]*Laboratoire de Géologie, École Normale Supérieure, Paris, France*
[3]*Department of Physics, NTNU Trondheim, Norway*
(Received 9 October 2003; revised manuscript received 10 February 2004; published 9 August 2004)

We present in this paper an experimental study of the invasion activity during unstable drainage in a two-dimensional random porous medium, when the (wetting) displaced fluid has a high viscosity with respect to that of the (nonwetting) displacing fluid, and for a range of almost two decades in capillary numbers corresponding to the transition between capillary and viscous fingering. We show that the invasion process takes place in an active zone within a characteristic screening length λ from the tip of the most advanced finger. The invasion probability density is found to only depend on the distance z to the latter tip and to be independent of the value for the capillary number Ca. The mass density along the flow direction is related analytically to the invasion probability density, and the scaling with respect to the capillary number is consistent with a power law. Other quantities characteristic of the displacement process, such as the speed of the most advanced finger tip or the characteristic finger width, are also consistent with power laws of the capillary number. The link between the growth probability and the pressure field is studied analytically and an expression for the pressure in the defending fluid along the cluster is derived. The measured pressure is then compared with the corresponding simulated pressure field using this expression for the boundary condition on the cluster.

DOI: 10.1103/PhysRevE.70.026301 PACS number(s): 47.20.Gv, 47.55.Mh, 47.54.+r, 47.55.−t

I. INTRODUCTION

Different types of unstable fluid displacements in porous media play an important role in many natural and commercial processes [1,2]. Development of a better understanding of these processes therefore has a broad scientific interest as well as potentially huge economical benefits. The complex patterns observed in such processes have been extensively studied and modeled over the last decades; see [1–7] and references therein.

The geometry of the displacement structures observed in immiscible two-phase flow is in general controlled by the competition between viscous forces, gravitational forces, and capillary forces; those various forces act on scales ranging from the pore scale to the system size. The relative wettabilities, viscosities, and densities of the fluids, as well as the heterogeneity of the underlying porous media, play an important role in the competition process. The relative magnitudes of viscous and capillary forces (on pore scale) are quantified through the dimensionless *capillary number* Ca $=(\mu_w\, v_f\, a^2)/(\gamma\, \kappa)$ where μ_w is the viscosity in the wetting (displaced) fluid, v_f is the filtration speed, a is the characteristic pore size, γ is the interface tension, and κ is the permeability of the porous medium.

In this paper we address a drainage experiment in which nonwetting air displaces a high-viscous wetting glycerin/water solution in a horizontal two-dimensional porous medium; hence, gravity has no influence on the displacement. The porous medium consists of a Hele-Shaw cell filled with a random monolayer of monodisperse glass beads. We investigate the crossover regime between the regime of slow displacement for which capillary forces control the dynamics of the invasion process and the geometry of the resulting invasion structure (capillary fingering), and that of fast displacements where viscous forces are dominant (viscous fingering). We emphasize on the dependence of the invasion probability density ϕ, or activity, on the distance to the most advanced finger tip along the interface. The invasion probability density ϕ is the growth probability of the invasion structure; it is fundamental because both the structure and dynamics are controlled by this function. Growth probability has been discussed extensively in the past for diffusion limited aggregation (DLA) simulations [8–13] where it was found to be the multifractal distribution of the harmonic measure [11–14]. A strong analogy exists between the structures obtained by DLA and viscous fingering, as was first pointed by Paterson [15]. Both processes obey the Laplacian growth equation

$$\nabla^2 P = 0, \tag{1}$$

$$v \propto -\nabla P, \tag{2}$$

where P denotes the diffusing field—i.e., the probability density of random walkers in DLA or the pressure in viscous fingering—and v denotes the speed of the interface. However, both processes differ in that accreting particles of fixed size are added one by one in DLA, at a random location set by the growth probability proportional to $-\nabla P$, whereas in an empty Hele-Shaw cell, which is a regular porous medium of constant permeability, the growth process is deterministic and full layers are invaded along the whole interface, with a local velovity set by $-\nabla P$. In the absence of surface tension, Mullins-Sekerka instabilities develop in the deterministic Laplacian growth problem, leading to cusp singularities of the interface in a finite time [16]. This instability is regularized by the smallest scales accessible to the system, and another difference between DLA and viscous fingering in regular porous media is the nature of this so-called ultraviolet regularization, set by surface tension in viscous fingering or by the particle size in DLA. The boundary value at the interface is given by surface tension γ for viscous fingering, $P \propto -\gamma/r$, where r is the local curvature of the boundary between both fluids, in contrast to DLA where it is set to constant P. These differences lead to very different structures in channel geometry—namely, stationary solutions corresponding to a Saffman-Taylor regular interface propagating at constant velocity in the case of viscous fingering in Hele-Shaw cells [7,17,18], as opposed to branched structures in the case of DLA [19,20]. In radial geometries however, solutions of both problems display branching and tip splitting, and some authors have argued that none of the above-mentioned differences affect the large scale structure and that viscous fingering patterns are identical to coarse grained DLA clusters [21]. Using the recently developed Hastings-Levitov formalism of iterated conformal maps [22], the relationship between DLA and deterministic Laplacian growth has been intensely investigated [22–28]. Although the issue for Laplacian growth is still controversial [24–26], it seems that DLA, Laplacian growth and viscous fingering in Hele-Shaw cells display indeed the same large-scale structure in radial geometry, with fractal dimensions respectively determined as $D=1.713\pm0.0003$ [29], $D=1.7$ [27], and $D=1.70\pm0.03$ [17].

The process of viscous fingering during drainage in a *random* porous medium, under study in the present paper, is *a priori* distinct from the above cases: although the pressure field satisfies the Laplace equation (1) at large scales, the presence of glass beads in the Hele-Shaw cell affects the viscous fingering process, modifying significantly the pressure boundary condition along the interface between the two fluids, with respect to the empty Hele-Shaw cell case. Fundamentally, the local interface curvature controlling the capillary pressure drop depends on the local pore geometry and is independent of the large-scale curvature, and distributed sizes of pore throats lead to a random distribution of capillary pressure thresholds inside the porous medium. These capillary pressure threshold values introduce a lower cutoff for the invasion probabilities, even for fast flows. In the slow displacement limit for which $v_f \simeq 0$, the invasion process is entirely controlled by the fluctuations of the capillary threshold distribution inside the porous medium [6,30]. For finite displacement velocities, as this study will show, the growth process is in this case intermediate between the one-by-one feature of DLA and the layer-by-layer characteristic of Laplacian growth: in the system studied here, several pores along the interface are invaded simultaneously, although not all of them—see Fig. 3—and it takes a finite time to invade a full pore. This pore-scale randomness in viscous fingering results in branched structure as well in channel geometry, as shown on Fig. 2, in contrast with the Saffman-Taylor fingers obtained in empty Hele-Shaw cells [7]. This might also be the reason why the measured fractal dimensions of viscous fingering patterns in radial geometry are reported slightly lower in random porous media similar to the one used here, $D=1.62$ [31], than in empty Hele-Shaw cells, $D=1.70$ [18].

Imbibition experiments (wetting fluid displacing a nonwetting fluid) were previously performed in a quasi-two-dimensional system [32,33], where the width of the viscous fingers was measured to scale with the capillary number as [32,33] $w_f \propto \mathrm{Ca}^{-0.5}$. This scaling relation was explained by a strong dynamic component of the capillary pressure [33]. We do not observe a strong dynamic component of the capillary pressure in our experiments (see below). The geometry of the invader for drainage is also significantly different from the invader structure of imbibition [32–35].

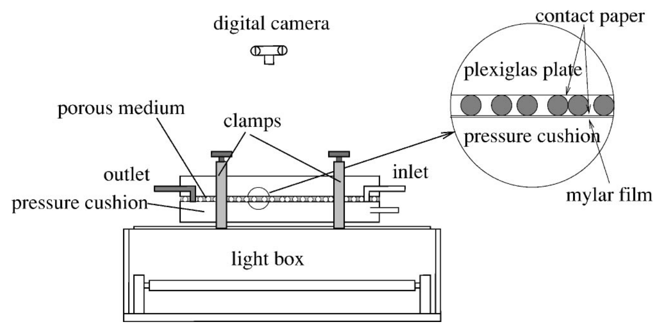

FIG. 1. Sketch of the experimental setup with the light box for illumination, the porous model, and the digital camera. The porous medium is sandwiched between two contact papers and kept together with a "pressure cushion."

In this study we study experimentally the growth probability density $\phi(z)$ as a function of the distance z (in the flow direction) from the most advanced finger tip and its dependence on the extraction speed (or capillary number). We also investigate experimentally the mass density $n(z)$ along the flow direction of the invader and confront the behavior of the measured $\phi(z)$ and $n(z)$ to what we expect from analytical arguments. A calculation of the z dependence of the pressure on the surface of the invader is presented, which yields the z dependence of the capillary pressure and shows a direct link with the measured growth probability density. Pressure measurements are performed in the model and compared with pressures simulated by solving the Laplace equation with this pressure boundary condition. Other features characteristic of the displacement, such as outermost tip velocity and the width of the invasion fingers, are also investigated.

The present article is organized as follows. We first present the experimental method (Sec. II). We then discuss the experimental results (Sec. III), and prospects (Sec. IV) before concluding (Sec. V).

II. EXPERIMENTAL METHOD

The experimental setup is shown in Fig. 1. The porous model consists of a monolayer of glass beads of diameter $a=1$ mm which is randomly spread between two contact papers [31,36]. The model is a transparent rectangular box of dimensions $L\times W$ and thickness a.

Two models of widths $W=430$ mm and $W=215$ mm have been used in the experiments; their other characteristics were identical. They are respectively referred to in the rest of the article as the "wide" and "narrow" models.

To prevent bending of the model a 2-cm-thick glass plate and a 2-cm-thick Plexiglas plate are placed on top of the model. To squeeze the beads and the contact paper together with the upper plate, a Mylar membrane mounted on a 2.5-cm-thick Plexiglas plate, below the model, is kept under a

3.5-m water pressure as a "pressure cushion." The upper and lower plates are kept together by clamps, and the side boundaries are sealed by a rectangular silicon rubber packing. Milled inlet and outlet channels are made in the upper Plexiglas plate. The distance between the inlet and outlet channels defines the length of the model, $L=840$ mm. One should also note that a few beads are removed from a small region near the center of the inlet channel, to initiate the invader in the center of the inlet. This is done to avoid edge effects appearing when the invader grows to the lateral boundaries of the model. The porosity of the models is measured to be 0.63 and the permeability is $\kappa=(0.0166\pm0.0017)\times10^{-3}$ cm^2 $=(1685\pm175)$ darcy.

The defending wetting fluid used in all our experiments is a 90%–10% by weight *glycerol-water* solution dyed with 0.1% Negrosine to increase the contrast between the colored fluid and the invader. *Air* is used as the invading nonwetting fluid. The *wetting* glycerol-water solution has a viscosity of $\mu_w\approx0.165$ Pa s and a density of $\rho_w=1235$ kg m^{-3} at room temperature. The corresponding parameters for the *nonwetting* air are $\mu_{nw}=1.9\times10^{-5}$ Pa s and $\rho_{nw}=116$ kg m^{-3}. The viscous ratio is thus $M=\mu_{nw}/\mu_w\sim10^{-4}$. The surface tension between these two liquids is $\gamma=6.4\times10^{-2}$ N m^{-1}. The temperature in the defending fluid is controlled and measured at the outlet of the model during each experiment, so as to accurately estimate the viscosity of the wetting fluid.

The absolute pressure in the wetting liquid is measured in the outlet channel and at a point at a distance of 280 mm (in the flow direction) from the inlet channel and 38 mm from the left boundary (looking in the flow direction) using Honeywell 26PCA Flow-Through pressure sensors.

The invader is visualized by illuminating the model from below with a light box and pictures are taken at regular intervals with a Kodak DCS 420 CCD camera, which is controlled by a computer over a SCSI connection. This computer records both the pictures and the pressure measurements. Each image contains 1536×1024 pixels, which corresponds to a spatial resolution of 0.55 mm per pixel or ~3.22 pixels per pore (1 mm^2); the color scale contains 256 gray levels. The gray level distribution of the image presents two peaks corresponding, respectively, to the white air-filled and dark gray glycerol-filled parts of the image. The image is filtered so as to obtain a clear boundary between the two phases, through a scheme that mainly consists in removing the background and thresholding at a gray level value between the two latter peaks. All further image treatments are performed on the resulting black and white image.

To check possible dynamic components of the capillary pressure we performed gravity stabilized experiments by keeping the experimental model vertical [36] and extracting the glycerol/water mixture from the bottom of the model. The capillary pressure was measured by recording the pressure in the model as the stabilized fluid front approaches the sensor. No systematic dynamic effect on the capillary pressure was found. For the low injection rates the width of the fronts was further used to estimate the minimum and width W_c of the capillary pressure threshold distribution.

Throughout the paper the following coordinate system is used: (x,z') is the orthonormal frame describing the porous medium plane, with z' the spatial coordinate in the direction of the flow (positive in flow direction). The position of the most advanced finger tip is denoted z'_{tip}; its speed along the z' axis is denoted $v_{tip}=\dot{z}'_{tip}$. The position along the z' axis computed with respect to that of the most advanced finger tip is $z=z'_{tip}-z'$. Those coordinates are indicated in Figs. 2 and 3.

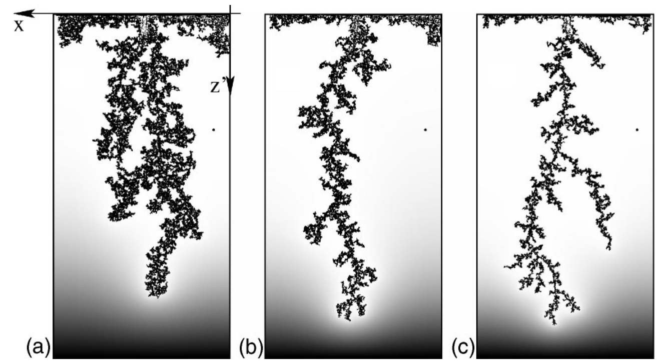

FIG. 2. Displacement structures obtained for different withdrawal rates: (a) Ca=0.027, (b) Ca=0.059, and (c) Ca=0.22. The images have been treated to separate the two phases. The black frame denotes the outer boundaries of the model, while the black spot close to the right edge of the model denotes the position of the pressure sensor. The simulated pressure field is shown superimposed on the image. Dark shadings correspond to low pressures while light shadings correspond to high pressure.

III. RESULTS

We present 12 experiments using the wide model for values of the capillary number Ca ranging from 1.4×10^{-2} to 3.6×10^{-1} and 5 experiments using the narrow model for capillary numbers ranging from 3.3×10^{-2} to 1.9×10^{-1}. The latter series was conducted to check system size dependences. For every experiment, we have carefully investigated the invasion process.

Figure 2 displays air clusters observed for the same porous medium, at three different flow rates. The complex structure of the air clusters is drawn in black. The particles of the porous medium are not shown. The defender—i.e., the glycerin/water solution—is drawn using a scale of grays ranging from white around the air cluster to black near the setup outlet; these shadings represent the intensity of the numerically estimated pressure field in the defending fluid (see Sec. III A). Figure 2(a) addresses an experiment carried out at a small rate (Ca=0.027). It displays a fat cluster where capillary forces dominate the dynamics of the invasion process, leading to a so-called *capillary fingering*. At larger displacement rates [Ca=0.22, Fig. 2(c)], the "fingers" appear thinner and less internal trapping of the defender is observed. This regime is dominated by viscous forces and is generally labeled as *viscous fingering*. For intermediate capillary numbers [Ca=0.059, Fig. 2(b)], the aspect of the cluster includes both geometries: capillary fingering at small scale and viscous fingering at large scale.

The pressure field around the clusters exhibits a fingerlike structure that has analogies to Saffman-Taylor fingers, as will

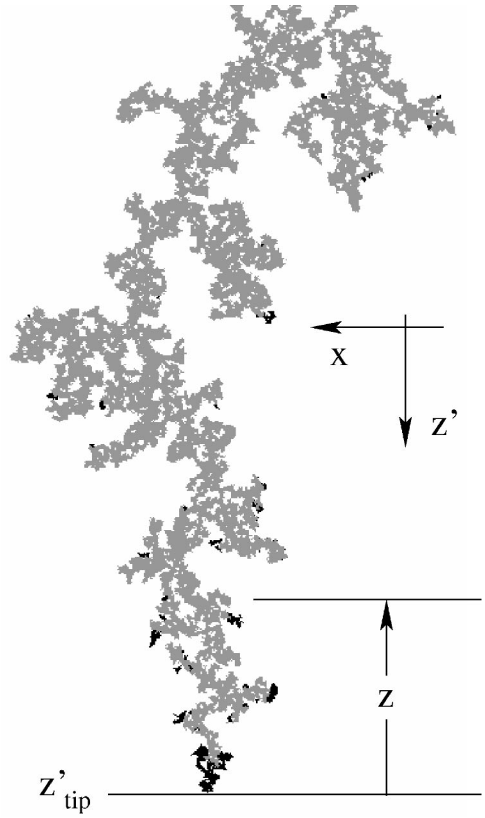

FIG. 3. Two consecutive images taken at a time interval $\Delta t \simeq 15$ during the experiment at Ca=0.059, drawn on top of each other. The invaded regions in the first image are painted light gray, the growth areas obtained by subtracting the first picture from the other one are painted black. The coordinate system used throughout the paper is also shown.

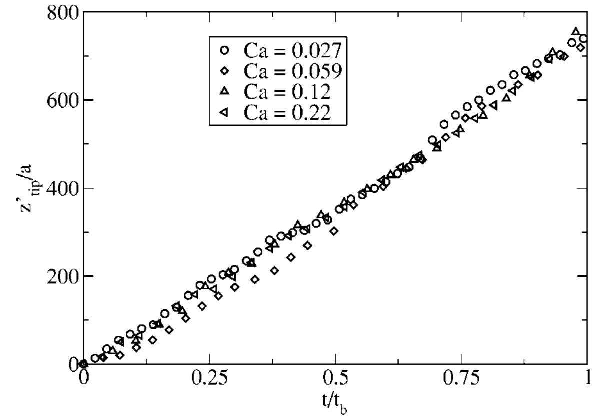

FIG. 4. Plot of the position of the most advanced finger tip, z'_{tip}, as a function of time. Data from the wide model. The time is rescaled by dividing with the break through time t_b, which is the time the most advanced finger reaches the outlet channel. The values of t_b are 5347 s, 1204 s, 476 s, and 256 s for capillary numbers Ca equal to 0.027, 0.059, 0.12, and 0.22, respectively.

be discussed in Sec. IV. Accordingly, the displacement exhibits obvious capillary-number-dependent features, which are discussed in detail in Sec. III B below. In Sec. III A, we focus on the relation between the growth activity, the frozen structure left behind, and the pressure field in front of the fingers.

A. Relation between growth activity, frozen structure, and fluid pressures

The growth activity has been investigated by measuring the growth probability density $\phi(z)$ from series of images and performing pressure measurements.

1. Definition of growth probability density $\phi(z)$ and mass density $n(z)$

To investigate the growth process, images have been taken with constant time delay Δt between each image. The tip position of the longest finger is identified to find the coordinate system (x,z) and to be able to calculate the speed of the longest finger. The differential growth between two images is found by a direct image subtraction between two subsequent images. After the subtraction we typically have a collection of invaded pores representing the growth (see Fig. 3). The growth density $\phi^*(z)$ is defined as the average number of filled pores within $[z,z+\Delta z]$ divided with Δz. After an initial regime corresponding to the time needed for the longest finger to propagate a distance of the order of the width of the porous medium W, $\phi^*(z)$ is found to be fairly independent of time up to a few percents variations. In a given experiment with constant Ca, $\phi^*(z)$ is then averaged over all images excluding this initial regime, to obtain a good average of the stationary growth function. The growth probability density $\phi(z)=K\phi^*(z)$, where K is a normalization constant, is then found by normalizing $\phi^*(z)$ with respect to z so that

$$\int_0^L \phi(z)dz = 1. \tag{3}$$

Note that, in the remainder of the paper, z is in units of pore size ($a=1$ mm).

The mass density of the frozen structure $n(z)$ is defined as the average number of filled pores within $[z,z+\Delta z]$ divided with Δz. The average is taken over all images in a given experiment with constant Ca. Both $n(z)$ and $\phi(z)$ appeared to be fairly robust with respect to the width Δz of the analysis strips used to compute them.

2. Growth activity and the frozen structure left behind

For all experiments, the speed of the most advanced finger tip was observed to be fairly constant. Figure 4 shows the position of the most advanced finger tip, $z'_{\rm tip}$, for different capillary numbers. After a short initial stage, the speed of the fingers saturates to a constant average value. Linear fits to the behavior $z'_{\rm tip}$ as a function of time outside the initiation stage provide an average finger tip speed v_{tip} for all experiments.

The measured invasion probability density function $\phi(z)$ is plotted in Fig. 5 as a function of the distance to the finger tip for the two system sizes on a linear-logarithmic plot. An exponential-like decay is seen for $z<W/2$ with a deviation

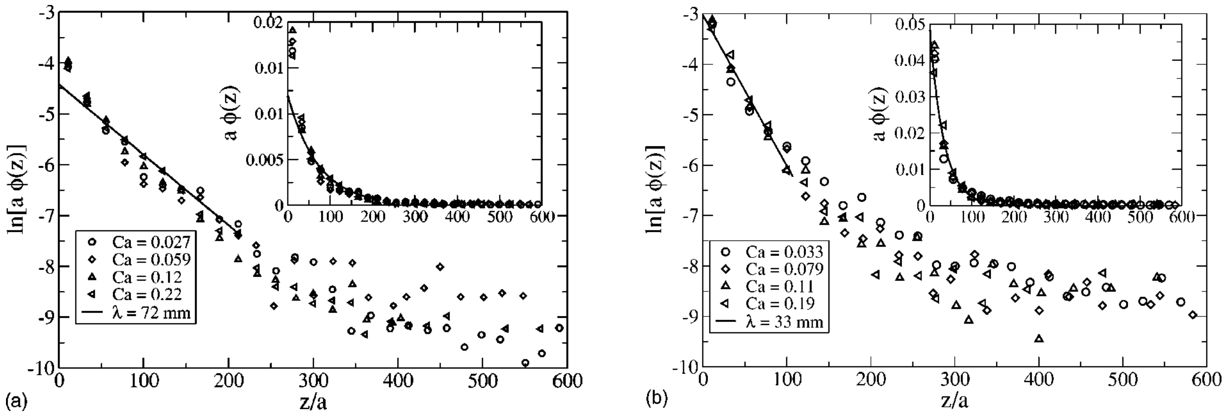

FIG. 5. Linear-logarithmic plot of the invasion probability density $\phi(z)$ as a function of the distance z to the finger tip (insets are double linear plots of the same invasion probability density). (a) Data from the wide experimental model and (b) from the narrow model. The solid lines in the curves correspond to the model function $\ln(Be^{-z/\lambda})$ obtained from linear regression over $\ln[a\cdot\phi(z)]$ for $z<W/2$, where $\phi(z)$ is the average measured invasion probability density. Note that $\phi(z)$ are averages of all the datasets and not only the sets shown in the graphs above. The average screening length λ is estimated from this fit.

from exponential behavior for larger lengths. A characteristic decay length or "screening length" λ is estimated from linear fits to the linear-logarithmic data for $z<W/2$ (see Fig. 5). As we can see from these plots a nice data collapse is obtained, indicating that the invasion probability density $\phi(z)$ and, thus, the screening length λ are independent of the capillary number for a given system. On the other hand, when comparing the two systems, the screening length λ depends on the system size: $\lambda=(72\pm10)$ mm for the wide model and $\lambda=(33\pm5)$ mm for the narrow model. The actual shape of function ϕ also seems to be weakly dependent on the system size.

Relating the mass of the frozen structure, $n(z)$, to the invasion probability density $\phi(z)$ and confronting the obtained relation to experimental results provides new insights into the displacement process. The total number of invaded pores in a time interval $[t,t+\Delta t]$ is $R\Delta t$, where R is the number of invaded pores per time unit. For a given flow rate Q, R is related to Q and to the characteristic pore volume V_{pore} by the relation $Q=RV_{\text{pore}}$, so that

$$R=\frac{W}{a^2}v_f, \tag{4}$$

where W is the width of the system, a is the characteristic pore size, and v_f is the Darcy or filtering velocity of the wetting fluid; for a given porous medium and fluid pair $v_f\propto\text{Ca}$. The number of invaded pores in the analysis strip defined by $z\in[z,z+\Delta z]$ during time interval $[t,t+\Delta t]$ is then $R\Delta t\phi(z)\Delta z$. The tip position z'_{tip} is further given by $z'_{\text{tip}}(t)=z'_0+v_{\text{tip}}t$ where v_{tip} is the speed of the finger tip (assumed to be constant) and $z'_0=z'_{\text{tip}}(t=0)$. This is a fairly good approximation after a short initial regime as seen in Fig. 4.

The total number of invaded pores in an analysis strip of width Δz at a distance z from the finger tip is thus given by

$$n(z)\Delta z=R\int_{t_0}^{t}\phi[z(t')]\Delta z\,dt', \tag{5}$$

where t_0 is the time at which $z'_{\text{tip}}=z'$. Taking advantage of the linear relation between the coordinate z and tip speed v_{tip}, $z(t)=z'_{\text{tip}}(t)-z'_{\text{tip}}(t_0)=(t-t_0)v_{\text{tip}}$, Eq. (5) becomes

$$n(z)=\frac{R}{v_{\text{tip}}}\int_0^z\phi(\tilde z)d\tilde z\equiv\frac{R}{v_{\text{tip}}}\Phi(z). \tag{6}$$

Using Eq. (4) we finally obtain the relation between the linear density of invaded pores (or "cluster-mass" density), $n(z)$, to the cumulative invasion probability density distribution $\Phi(z)$:

$$n(z)=n_{\text{Ca}}\Phi(z), \tag{7}$$

where

$$n_{\text{Ca}}=\frac{W\gamma\kappa}{\mu_w a^4}\frac{\text{Ca}}{v_{\text{tip}}}. \tag{8}$$

The characteristic average mass density can also be related to the filtration velocity: $n_{\text{Ca}}=(W/a^2)(v_f/v_{\text{tip}})$. Equation (7) is confirmed by Fig. 6, where $n(z)/n_{\text{Ca}}$ is plotted as a function of z/a. All experimental plots collapse, confirming that there is one single cumulative probability distribution $\Phi(z)$ for the system for all experiments at different extraction speeds. The function $\Phi(z)$, computed as an average function from all cumulative probability functions for the various experiments, is plotted in Fig. 6 as a plain line. Note that n_{Ca} and consequently $n(z)$ are capillary number dependent, which is directly visible on Fig. 2. The explicit dependence of the saturation mass density on Ca will be plotted in Fig. 9(a). The inset of Fig. 6 shows $1-n(z)/n_{\text{Ca}}$ on a linear-logarithmic scale. The solid lines represents $1-\Phi(z)$ and the dashed lines $1-e^{-z/\lambda}$ which would be the model function for a pure exponential ϕ (λ is the screening length evaluated before).

From the results presented above we conclude that the active invasion zone is defined by a screening length λ which is constant for a given porous media and liquid pair and at a range of capillary numbers of two decades. However, we expect this result to be valid only for sufficiently high filtration speed v_f. Indeed, on the one hand, the capillary fingering regime ($\text{Ca}\simeq0$) corresponds to an invasion that is controlled by fluctuations in the capillary threshold pressures, so that

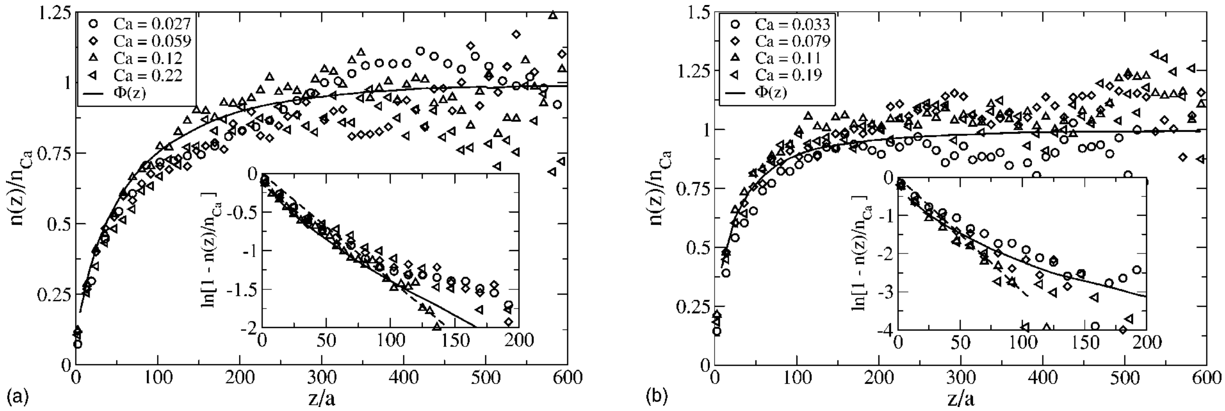

FIG. 6. Plot of the rescaled average mass density of nonwetting fluid $n(z)/n_{\mathrm{Ca}}$, where $n_{\mathrm{Ca}} \propto \mathrm{Ca}/v_{\mathrm{tip}}$, inside the model as a function of the distance to the tip of the most advanced finger z: (a) the wide model and (b) the narrow model. The average cumulative invasion probability function $\Phi(z)$ is plotted on top of the curves for comparison in the two cases. The insets of (a) and (b) show the plots $\ln[1-n(z)/n_{\mathrm{Ca}}]$ as a function of z. The solid lines in the insets correspond to $\ln[1-\Phi(z)]$, and the dashed lines have the slope $1/\lambda$ where λ is the screening length of $\phi(z)$ found from Fig. 5—i.e., respectively, $\lambda=(72\pm10)$ mm and (33 ± 5) mm for the wide model and narrow model.

invasion occurs along the whole front [6,30]. There is no well-defined finger tip or growth direction in that limit. The width of the capillary threshold pressure distribution W_c is larger than the viscous pressure drop over the whole system and defining a screening length or active zone is not meaningful.

When the length of the system is larger than its width, it is found from both pressure measurements and simulations that the decay in pressure into the structure from the longest finger occurs on a length scale of the order of the width of the system (see Fig. 2). We therefore expect W and not L to be the relevant length scale for the decay of the pressure field close to the tip. Viscous forces can therefore be considered to dominate capillary pressures if the following criteria are met:

$$W_c < \frac{W\mu v_f}{\kappa}, \tag{9}$$

or if we assume $W_c \sim \langle P_c \rangle \approx \gamma/a$, where $\langle P_c \rangle$ is the average capillary pressure (which is the case here):

$$\mathrm{Ca} > a/W. \tag{10}$$

For our system $a/W \sim 10^{-3}$, which is an order of magnitude smaller than our lowest capillary number.

On the other hand, for situations where the "pure viscous fingering" in a random porous media has been reached, there is no trapping of wetting liquid inside the fingers, which reached the lower one-pore width limit (at $\mathrm{Ca}\approx 0.2$ in our system). Whether the screening length or active zone has the same width or behaves identically as for lower capillary numbers is not clear. We believe that the screening by the most advanced finger is a viscous effect, which remains important as the displacement speed increases. In this one-pore limit, however, the tip speed dependence on the capillary number is modified, as will be further detailed in Sec. III B.

3. Relation between the growth probability density $\phi(z)$ and the fluid pressure

Figure 7 shows the dependence of the pressure difference $\Delta P(z)=P(z)-P(\infty)$ in the wetting liquid as a function of the distance z to the outermost tip for different capillary num-

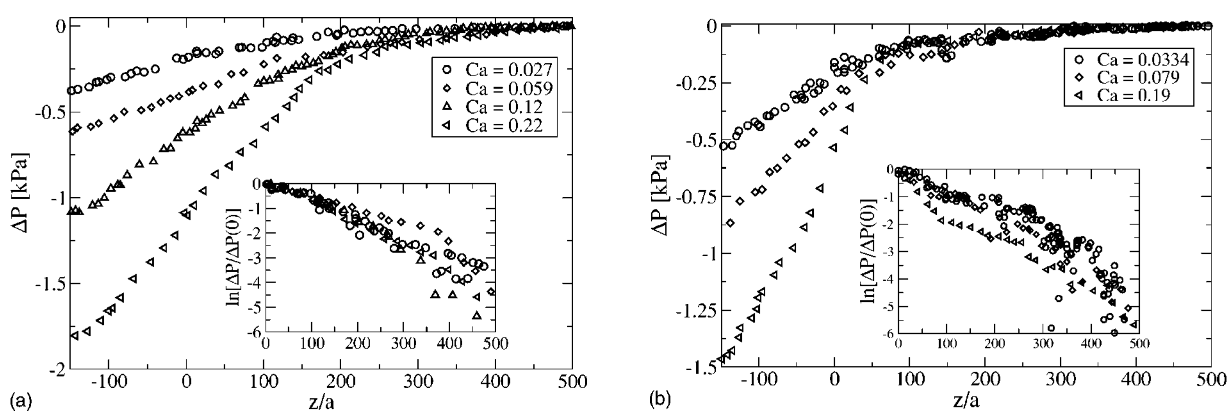

FIG. 7. Plot of the pressure difference $\Delta P(z)=P(z)-P(\infty)$ measured by the pressure sensor located in the position $(x_s, z_s')=(38\ \mathrm{mm},\ 280\ \mathrm{mm})$. The inset is the same data plotted in a semilogarithmic plot where $P(z)$ is scaled with $\Delta P(0)=P(z=0)-P(\infty)$ to illustrate the decay of the pressure field. (a) is for the wide model and (b) is for the narrow model.

bers. Here $P(\infty) \equiv P_0 - P_c(\infty)$ is the liquid pressure along the interface far behind the finger tip, with P_0 the pressure in the nonwetting liquid and $P_c(\infty)$ the capillary pressure in this stagnant zone. It is important to note that the pressure $P(z)$ is measured on the side of the model (indicated in Fig. 2) while the fingers are propagating in the central part of the model (Fig. 2).

The pressure seems to be linearly dependent on the distance from the tip during a first stage before the tip reaches the sensor. In a second stage, after the finger tip has passed the sensor, pressure relaxes and reaches the value $P(\infty)$. A closer inspection of the pressure curves (see Fig. 7) shows that there is no clear systematic dependence of the pressure relaxation on the capillary number. The pressure difference $P(z) - P(\infty)$ decays with approximately the same length for the different capillary numbers (see inset of Fig. 7). This indicates that the details of the internal structure of the "fingers" do not have a strong influence on the pressure field on large scales.

The pressure measurements are related to the invasion activity by the following considerations. Let us consider the local speed of an interface located in an arbitrary pore throat between two pores, one filled with air and the other with the wetting liquid. Let $P(x,z)$ be the pore pressure in the wetting liquid and $P_t(x,z)$ be the capillary pressure threshold value to invade that pore. Note that this is different from the pressure $P(z)$ defined as the pressure measured on the side of the model at the sensor position. The pore throat at position (x,z) is passed under the condition that the pressure difference $P_c(x,z) = P_0 - P(x,z)$ is larger than the capillary threshold pressure $P_t(x,z)$ at this position. If invasion occurs, a characteristic value of the speed of the interface will be

$$v(x,z) = \frac{2\kappa}{\mu}\frac{P_0 - P(x,z) - P_t(x,z)}{a}. \tag{11}$$

In this equation we have used the permeability of the porous media κ as an approximation for the average single pore permeability to get the right order of magnitude. Let $N(P_t(x,z))$ be the capillary pressure distribution. For the sake of simplicity, we assume a flat capillary pressure distribution with lower limit $P_t^{\min}$, upper limit $P_t^{\max}$, and width W_c. Under the condition that the viscous pressure drop over a pore a does not exceed W_c (which we have checked by means of numerical simulations), the expectational value of the interface velocity (average value over the capillary threshold distribution), while the pore is getting invaded, will be

$$\begin{aligned}\langle v(x,z)\rangle &= \frac{1}{P_0 - P(x,z) - P_t^{\min}}\int_{P_t^{\min}}^{P_0 - P(x,z)} \frac{2\kappa}{a\mu}[P_0 - P(x,z) \\ &\quad - P_t(x,z)]dP_t \\ &= \frac{\kappa}{a\mu}[P_0 - P(x,z) - P_t^{\min}]. \end{aligned}\tag{12}$$

Here, $P_t^{\min}$ is the minimum of the distribution for capillary threshold; when $P_0 - P(x,z)$ goes to that minimum, the expectational value for the speed of the interface goes to zero. The growth probability density $\phi(x,z)$ for the invasion structure within a time $[t, t+\Delta t]$ at a position (x,z) is proportional to $\langle v(x,z)\rangle$ times the probability $p(x,z)$ that the throat gets invaded; hence,

$$\phi(x,z) = C\langle v(x,z)\rangle p(x,z), \tag{13}$$

where C is a normalization constant, which we can find by integrating the above equation along the invasion front:

$$\int_S \phi(x,z)dl = C\int_S \langle v(x,z)\rangle p(x,z)dl \tag{14}$$

$$1 = \frac{C}{a}\int_S a\langle v(x,z)\rangle p(x,z)dl = \frac{C}{a}Q, \tag{15}$$

where Q is the flow rate, and thus

$$C = \frac{a}{Q}. \tag{16}$$

Since we have assumed a flat capillary threshold distribution of width W_c, the probability that the pore at position (x,z) gets invaded is

$$p(x,y) = \frac{1}{W_c}[P_0 - P(x,z) - P_t^{\min}]. \tag{17}$$

From Eqs. (12)–(17) we obtain, for the growth probability density $\phi(x,z)$ in position (x,z),

$$\phi(x,z) = \frac{\kappa}{Q\mu W_c}[P_0 - P_t^{\min} - P(x,z)]^2. \tag{18}$$

Averaging this expression over x and introducing the number of interface sites at a distance z from the tip, $f(z)$, we obtain the invasion probability density $\phi(z)$ as

$$\phi(z) = f(z)\langle \phi(x,z)\rangle_x, \tag{19}$$

$$\phi(z) = f(z)\frac{\kappa}{Q\mu W_c}[P_0 - P_t^{\min} - \langle P(x,z)\rangle_x]^2, \tag{20}$$

for which we have assumed that $P(x,z)$ is a function of z only (lowest-order approximation). Equation (20) yields

$$\langle P(x,z)\rangle_x = P_0 - P_t^{\min} - \left(\frac{\phi(z)}{f(z)}\frac{QW_c\mu}{\kappa}\right)^{1/2}, \tag{21}$$

which can be rewritten by introducing the relation between the flow rate and the capillary number. Accordingly the average pressure in the wetting fluid in the immediate vicinity of the interface and at position z is related to the activity $\phi(z)$ according to

$$\langle P(x,z)\rangle_x = P_0 - P_t^{\min} - \left(\mathrm{Ca}\gamma\, W_c\frac{W}{a}\frac{\phi(z)}{f(z)}\right)^{1/2}. \tag{22}$$

Let us now look closer at the "snapshots" of the experiments shown in Fig. 2. For $z=0$, the last correction term in Eq. (22) is 170 Pa for the fastest experiment ($\mathrm{Ca}=0.22$) and 65 Pa for the slowest experiments ($\mathrm{Ca}=0.027$). At the same moment, the imposed external pressures in the outlet channel are 3055 Pa for the fastest and 625 Pa for the slowest experi-

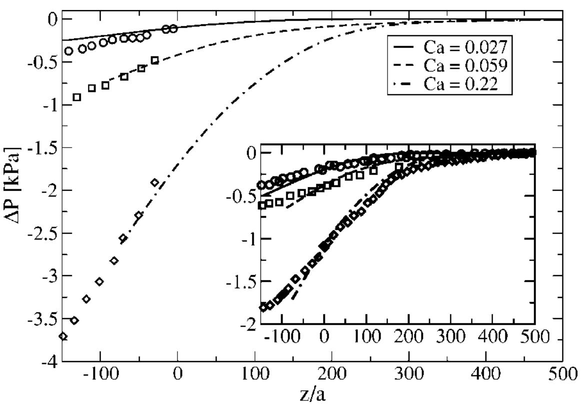

FIG. 8. The simulated pressure along the line with $x_s = 38$ mm (corresponding to the x coordinate of the pressure sensor) for the invasion structures in Fig. 2. The data points in the main graph show the corresponding pressures measured at the outlet sensor. In the inset we plot scaled simulation data with corresponding pressure data measured inside the model at $(x_s, z_s') = (38\text{ mm}, 280\text{ mm})$.

ments. The minimum capillary pressure is estimated to 373 Pa and the width of the capillary distribution to 200 Pa. This indicates that the correction term in Eq. (22) should not be neglected. In Fig. 2 is shown the gray-scale map of the pressure field at a particular time, simulated from the displacement structures obtained experimentally. A very strong screening is seen for all injection rates. The large-scale structure of the pressure field in the vicinity of tip of the longest finger looks visually very similar even if the invader structure is quite different. In the simulations of the pressure field we have used Eq. (22) to set the proper boundary conditions. The pressure field has been calculated by solving the Laplace equation for the pressure using a conjugate gradient method [37]. We used the boundary condition given by Eq. (22) on the cluster and the inlet line. As boundary condition on the outlet we used the pressure $P(\infty) - \Delta P_{\text{tot}}$, where $-\Delta P_{\text{tot}}$ is the total viscous pressure drop imposed in the corresponding experiment at that moment. To obtain $P(\infty) = P_0 - P_c(\infty)$, the capillary pressure $P_c(\infty)$ was measured in the experiments for large values of z. Figure 8 shows the simulated pressure $\Delta P(x_s, z) = P(x_s, z) - P(\infty)$ as a function of the z coordinate relative to the tip position defined as previously, at a fixed lateral position x_s corresponding to the x coordinate of the pressure sensor. It is important to note that this is somewhat different from the experiments since the pressure is measured at different z' positions, but at the same time—i.e., with a fixed geometry of the invasion cluster—while in the experiments the pressure is measured at a fixed z' position, at different times corresponding to various stages of the invasion cluster. The length scale of the decay of the pressure for $z > 0$ is very similar in the experiments and the simulations (see comment below). However, the pressure difference $\Delta P(z)$ in the simulations is lower than the $\Delta P(z)$ measured by the sensor [at position $(x_s, z_s') = (38\text{ mm}, 280\text{ mm})$] in the model (see Fig. 7). This is due to the strong boundary effects of the pressure close to the outlet channel: the tips in the simulations situations are very close to this boundary along which the pressure is fixed (see Fig. 2), while in the situations corresponding to the measurements at $z < 0$ plotted in Fig. 7, the outlet boundary was far ahead of the finger tip, and the pressure boundary condition was equivalent to an imposed gradient at infinite distance. To check the importance of this boundary effect on the magnitude of the pressure difference, the simulated pressure has been compared with the pressure difference $\Delta P(z)$ evaluated from measurements at the outlet channel, as the finger tip progressed further than the stage corresponding to the simulations. The agreement in Fig. 8 between the simulated pressure and the data points corresponding to the outlet channel measurements is then satisfactory.

To compare the length scale of the decay of the pressure for $z > 0$ between the simulations and the experiment, we then compare the pressure data measured inside the model at the sensor position to the simulation data scaled by a factor such as $\Delta P(x_s, z=0)$, which would be equal in experiments and simulations. Such a rescaling of the simulation pressure profile simply corresponds to the result of an identical simulation still carried on the invasion clusters of Fig. 2, with identical boundary conditions derived from the growth density function for the pressure along the clusters, but where the imposed pressure along the bottom boundary is such that the pressure at point (x_s, z'_{tip}) would coincide with the pressure measured in the experiments when the tip passed at the same height as the sensor—-i.e., when $z'_{\text{tip}} = z'_s$. This ensures that the pressure gradient and pressure value in the region around the tip of the invading cluster are of the same order in these rescaled simulations and in the experimental stages corresponding to $z \sim 0$ in Fig. 7, which is a first-order technique to correct for the strong boundary effect and compare with these experimental situations where the bottom boundary is much farther away. The pressure measured in the experiments at sensor position and this scaled simulation data are plotted in the inset of Fig. 8. This comparison shows that the decay in the pressure happens at comparable length scales in the simulations and experiments.

Eventually, the local structure of the finger and the lateral x distance from the invader to the pressure sensor will also have an important influence on the pressure field. The difference in the pressure field between the left and the right side of the finger (looking in the flow direction) in Fig. 2 illustrates this point. The deviation between the experimental data points and the simulations for the lowest capillary number of the main part of Fig. 8 may be explained by this effect. As the lateral position x_{tip} of the invading structure moves during the experiment and is importantly varying from an experiment to the next, this effect also explains the important dispersion of the scaled pressure drops $\Delta P(z)/\Delta P(0)$ observed in the inset of Fig. 7(b).

B. Capillary-number-dependent features

As stated in the introduction to Sec. III, Fig. 2 clearly shows that some features of the invading cluster depend on the capillary number. The mass $n(z)$ of the invasion cluster obviously decreases with increasing capillary number; in relation to this, the speed of the most advanced finger tip, v_{tip}, increases with the capillary number, and there is a systematic trend for fingers to become thinner as capillary number in-

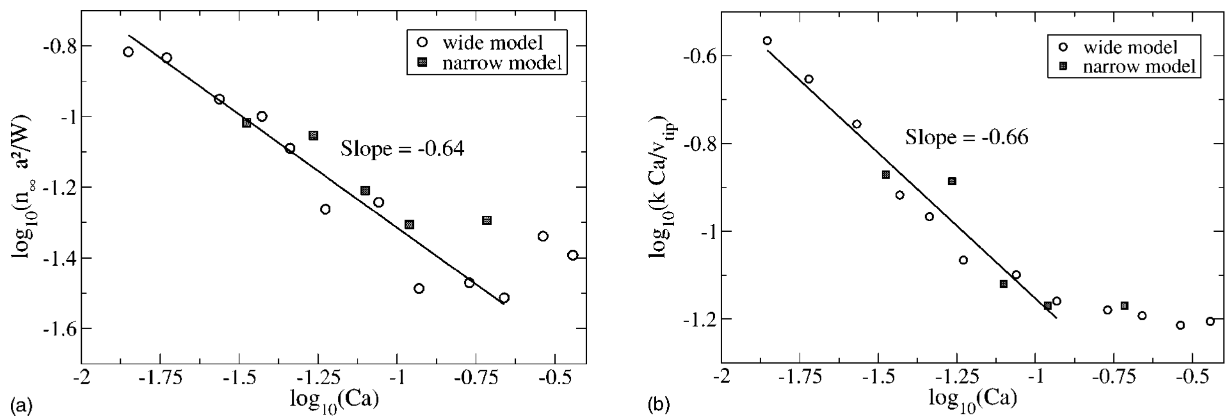

FIG. 9. Double logarithmic plots of (a) the saturated mass density n_∞ and (b) of the speed of the most advanced finger, $v_{\rm tip}$, as a function of the capillary number, for the two sets of experiments. Both plots are consistent with a scaling in the form $n_\infty \propto \mathrm{Ca}/v_{\rm tip} \propto \mathrm{Ca}^{-\alpha}$, with $\alpha \approx 0.65$.

creases. In the following we first present results relative to the "mass density" in the stagnant zone, n_∞, and to the velocity of the most advanced finger tip, $v_{\rm tip}$. In the end we discuss the results relative to measurements of the characteristic width of the fingerlike structures, the definition of which is not as straightforward and clear as those of n_∞ and $v_{\rm tip}$.

The evolution of the average mass density in the stagnant zone n_∞ as a function of the capillary number is presented in Fig. 9(a) on a double-logarithmic scale. The data are consistent with a scaling law in the form $n_\infty \propto \mathrm{Ca}^{-\alpha}$, with a scaling exponent $\alpha \approx 0.65$ for both the wide and narrow models. Here n_∞ has been measured by fitting the function $n_\infty[1-\exp(-z/\lambda)]$ with both parameters free to our measured $n(z)$ data. As a result of the dependence of the mass of the invasion cluster on the capillary number [Fig. 9(a)], the speed of the most advanced finger tip, $v_{\rm tip}$, is expected to depend on the filtration speed or capillary number in a nonlinear way. The saturated mass density and the speed of the most advanced finger are related to each other through Eq. (7), according to

$$v_{\rm tip} \propto \frac{\mathrm{Ca}}{n_\infty}. \tag{23}$$

Based on that argument, $\mathrm{Ca}/v_{\rm tip}$ should therefore scale in the same way as n_∞ with respect to the capillary number. In Fig. 9(b), the quantity $k \cdot \mathrm{Ca}/v_{\rm tip}$ is plotted as a function of Ca on a double-logarithmic scale, where $k=1$ m/s. The plot is consistent with the expected scaling (23) and the result for the mass density presented above.

The study of the dependence of the finger width on the capillary number is somewhat less straightforward, because our invading clusters structures exhibit extensive branching and display "fingers" both at small scales as "capillary fingers" and at large scales as "viscous fingers." Thus, a precise definition of a finger, and furthermore a finger width, is not an easy task for those structures. A possible method to determine the viscous finger width would consist in finding the characteristic crossover length between geometric features characteristic of viscous fingering and those characteristic of capillary fingering from the density-density correlation function of the structures. However, as a result of the small difference in fractal dimension between the two regimes, 1.83 ± 0.01 [6,30] for capillary fingering and 1.62 ± 0.04 [31,38] for viscous fingering, larger systems would be necessary for this method to be accurate enough. An experimental determination of the characteristic width w_f for viscous fingers was previously obtained for *imbibition* experiments [32], for which the characteristic finger width can be defined and found in a more straightforward manner. The obtained scaling was $w_f \propto \mathrm{Ca}^{-0.5}$. In those imbibition experiments, the finger width w_f was measured as the average length of cut segments perpendicular to the flow direction. This method can also be applied in our experiments, but due to the small scale fractal nature of the invasion front, trapping of wetting fluid inside the fingers and capillary fingering on small length scales, it is not obvious which length scales are being probed with this method. The results that we obtain are plotted as a function of the capillary number in Fig. 10. Clusters of wetting liquid trapped behind the displacement front have been removed from the picture prior to analysis. We then define the front width w_f as the average over z and time of

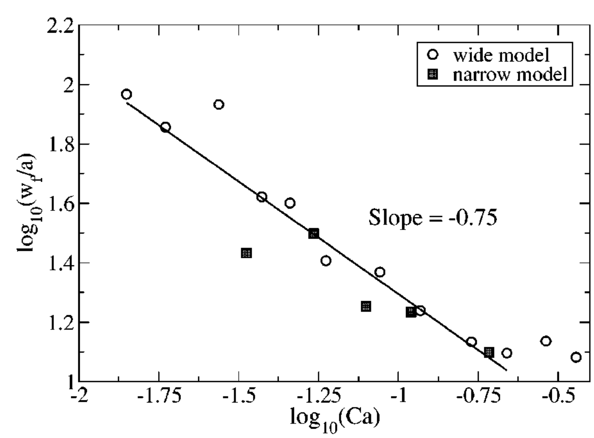

FIG. 10. Double-logarithmic plot of the measured characteristic width of the fingerlike structures as a function of the capillary number, for both the wide and narrow models. The data are consistent with a scaling of the finger width in the form $w_f \propto \mathrm{Ca}^{-\beta}$, with $\beta \approx 0.75$.

the length of the intersects between the invasion cluster emptied from these trapped regions and cuts perpendicular to the flow direction.

The measurements are consistent with a scaling law in the form $w_f \propto \mathrm{Ca}^{-\beta}$, with $\beta \approx 0.75$. This is significantly different from what was measured for imbibition. It also differs significantly from the scaling law expected from theoretical arguments for percolation in a destabilizing gradient [39,40] for two-dimensional systems: $w_f \propto \mathrm{Ca}^{-\beta}$ with $\beta = 0.57$. In our experiments, the destabilizing field (pressure) is highly inhomogeneous, which may explain why the behavior expected from the percolation in a gradient theory is not really observed.

From Figs. 9 and 10, the observed scalings appear to be valid for a limited range of capillary numbers. For high capillary numbers the observed scaling breaks down for Ca ≈ 0.2, which corresponds to situations where the characteristic finger width has reached the one pore limit. At the other limit, for small capillary numbers it is not clear if we reach the lower limit in capillary number. But we expect that the observed scaling breaks down for capillary numbers smaller than the criteria given in Eq. (10), $\mathrm{Ca} \sim 10^{-3}$. As a result of this, it should be noted that the measured exponents α and β only are meaningful for intermediate capillary numbers between the crossovers to the high- and low-capillary-number regimes and that the length scale for the low-capillary-number crossover is system size dependent. Our measured values should therefore be considered as lower bounds for the exponents rather than correct values since inclusion of data points in the crossover regimes will lead to underestimated values for the exponents. For more precise measurements of these exponents experiments on larger systems are needed.

IV. DISCUSSION AND PROSPECTS

Following a procedure similar to that used by Arneodo *et al.* [19] to study the statistical average properties of off-lattice DLA simulations in a linear channel, we introduce an average occupancy map $\pi(x,z)$. Let $g(x,z)$ be the invader occupation function equal to 1 when the local pore is air filled or 0 when it is liquid filled. For any position (x,z) (where z is relative to the tip position), $\pi(x,z)$ corresponds to the average over all times, of the invader occupation function. Points closer than W from the inlet are excluded from this average, since the geometry of the invading structure is expected to be strongly influenced by the central point injection technique in that zone. Similarly to the average DLA situation [19], this average occupancy map saturates to a maximum value $\pi_{\max}$ around the central line $x = W/2$, at distances z larger than W behind the tip position. For $z > W$, $\pi(x,z)$ fluctuates around an average saturated occupancy $\pi(x)$, which is independent of z. This average saturated occupancy is approximated for each experiment by averaging the invader occupation function over all times and all $z > W$. The quantity $\pi(x)$ depends on the capillary number, as expected since by definition $\int_0^W \pi(x)dx \simeq a^2 n_{\mathrm{Ca}}$.

However, the shape of this function, apart from a different $\pi_{\max}$, seems reasonably independent of the capillary number

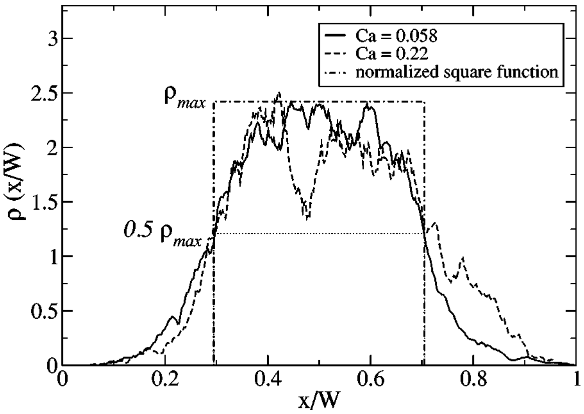

FIG. 11. Normalized average saturated occupation density for five experiments in the thin model at two different capillary numbers. Both functions present an effective width around $0.4W$.

when $\mathrm{Ca} > 0.03$. This is demonstrated in Fig. 11, where the normalized saturated occupancy function for the thin model, $\rho(x/W) = W\pi(x)/\int_0^W \pi(x)dx$, is displayed for five experiments at Ca=0.058 and five experiments at Ca=0.22. The characteristic width of this function is obtained by using two definitions introduced by Arneodo *et al.* [19], $\int_0^W \pi(x)dx/\pi_{\max}$ or $(x^+ - x^-)$ where $\pi(x^+) = \pi(x^-) = 0.5\pi_{\max}$. Both definitions for both capillary numbers lead to a characteristic width around $0.4W$ (Fig. 11). The mean occupancy profile or average envelope, defined as the contour level $\pi(x,z) = 0.5\pi_{\max}$, presents some similarities to the shape of a Saffman-Taylor finger corresponding to the same saturation width [7]. Similar contour levels observed in off-lattice DLA simulations correspond to a characteristic selected width $0.62W$ [19,20] and present some similarities with the corresponding Saffman-Taylor finger, although the detailed shape differs [20]. The pressure field recorded at some distance exceeding $0.2W$ of the invader structure [41] is also consistently comparable to the pressure field around such a Saffman-Taylor finger, which arises from the fact that the Laplace equation controlling the pressure field is sensitive to the coarse external shape of the invader's boundary, rather than to the details of the branched structure inside this average envelope.

Inside the average envelopes, at intermediate scales the structures correspond to "DLA-like" viscous fingers. On these length scales the viscous pressure differences in the fluid are significant compared to the width of the capillary pressure thresholds distribution W_c. The structure is fractal [41], with a fractal dimension identical to that previously measured in viscous fingering experiments in random porous media similar to ours 1.62 ± 0.04 [31]. On length scales smaller than characteristic finger width w_f, the viscous pressure drops are small compared to W_c. Inside the fingers the structures correspond to capillary fingering with a fractal dimension 1.83 ± 0.01 [30]. The cutoff length w_f between these two regimes is about the same size as the trapped wetting clusters. The saturation level of the envelope width seems insensitive to Ca when $\mathrm{Ca} > 0.03$ [41]. This implies that the saturated mass dependence Ca displayed in Fig. 9 results from the decrease of the characteristic finger width w_f with the capillary number (Fig. 10). The structures therefore look more branched and thin at higher capillary numbers (Fig. 2), even if they still occupy the same characteristic zone in the linear cells.

The similarity between viscous fingering and DLA [8] was first proposed by Paterson [15] and is based on the equivalence between the probability field for DLA and the pressure field in the viscous fingering case. They both seem to obey Laplace's equation with similar boundary condition, Eqs. (1) and (2). However, the characteristic of the intermediate scales in our viscous fingering experiments displays fundamental differences from DLA growth models: the obtained saturation width $0.4W$ is significantly below the result $0.60W$ obtained from off-lattice DLA simulations [19,20] and also lower than the width $0.5W$ obtained for on-lattice DLA simulations [19] or for a Saffman-Taylor finger in a empty Hele-Shaw cell at high capillary numbers [7]. Average widths higher than $0.5W$ are reported in empty thin cells [18], depending on the capillary number and on the ratio of the cell thickness over width, which affects the role of a wetting oil film left behind the invasion front. The displacement regimes that we have studied correspond to what the authors of Ref. [18] would refer to with their notations as $1/B \sim 1000-10\,000$ and $w/b=200$, for which their experiments would display selected widths larger than $0.5W$ according to Fig. 3in their article [18]. The observed fractal dimension of the viscous fingering structures in a random porous medium similar to ours, 1.62 ± 0.04 [31], is also somewhat smaller than 1.7, the fractal dimension in radial viscous fingering in empty Hele-Shaw cells [17], in radial Laplacian growth [27], or in DLA [20,29]. This shows experimentally that there are some fundamental differences between these processes and viscous fingering in random porous media. Many works have recently focused on generalizations of Laplacian growth processes and DLA and put evidence on the fact that the fractal dimension or even the fractality of the grown structure depends on the precise boundary condition, growth rate, fraction of the perimeter growing simultaneously, and shot noise at the interface boundary [22–28]. The difference between these models shows the importance of the precise growth conditions along the interface. In the present experiments, the disordered porous material creates a nontrivial growth condition along the interface, dependent on the local pressure level, pressure gradient, and of a quenched disorder in the capillary pressure thresholds.

The fact that in these experiments the width of the mean occupancy profile and fractal dimension are below the DLA case make it more similar to another type of generalized DLA models—namely, dielectric breakdown models (DBM's). In the DBM the growth probability of the structures is proportional to a power higher than unity of the pressure gradient [20,42]. To better support the comparison to these various models, the precise determination of the average occupancy maps and fractal dimension(s) of the structure, as a function of capillary number and system size, is the subject of ongoing work [41].

V. CONCLUSION

We have studied the dynamics of the invasion process observed during drainage in a two-dimensional porous medium, for extraction speeds that result in an unstable fingering of the displacing nonwetting fluid into the displaced wetting fluid.

Our main finding is that for a given porous medium, the displacement is controlled by an invasion probability density that only depends on the distance of the point where it is measured to the tip of the most advanced finger tip and is independent of the capillary number. The decay of this invasion probability density, $\phi(z)$, defines an active zone for the invasion process, outside of which the viscous pressure field can be considered to be screened by the invasion structure. In particular, parts of the invasion structure lying outside this active zone are frozen and do not evolve in time any more. The size of the active zone, of characteristic screening length, λ, was found to be independent of the capillary number for a wide range of injection rates. In addition, experiments carried out on models with two different widths suggested that the invasion probability density appears to be capillary number independent, its actual shape being possibly fixed by the system size. While the invasion process is described by an invasion probability density that is independent of the capillary number, the invasion speed and displaced volume in the stagnant zone were found to scale on the capillary according to power laws, $n_\infty \propto \mathrm{Ca}/v_{\mathrm{tip}} \propto \mathrm{Ca}^{-0.65}$.

Current work [41] was also reported on the mean occupancy density behind the most advanced tip, which also seems to be a function of shape independent of the capillary number as soon as $\mathrm{Ca} > 0.03$, although its average value is capillary number dependent. The ratio of characteristic width of such density map over the system width was found around 0.4, which is significantly below the result corresponding to DLA simulations (0.6).

The link between the growth probability and the pressure field has been studied. An expression for the pressure boundary condition relating the pressure on the interface of the invader to the growth probability density function on the cluster, $\phi(z)$, has been calculated. The measured pressure has been compared to the corresponding simulated pressure by solving the Laplace equation for the pressure field using this expression for the boundary condition on the cluster. Good agreement is found between the simulations and the experiments.

System size dependences should be subject to further investigations, both experimentally and by means of computer simulations.

ACKNOWLEDGMENTS

This work was supported by NFR, the Norwegian Research Council, VISTA, the Norwegian academy of science and Letters' research program with Statoil, and the French/Norwegian collaboration PICS.

[1] J. Bear, *Dynamics of Fluids in Porous Media* (American Elsevier, New York, 1972).
[2] F. A. L. Dullien, *Porous Media Fluid Transport and Pore Structure*, 2nd ed. (Academic, San Diego, 1992).
[3] M. Sahimi, Rev. Mod. Phys. **65**, 1393 (1993).
[4] M. Sahimi, *Flow and Transport in Porous Media and Fractured Rock* (VCH Verlagsgesellschaft GmbH, Weinheim, Germany, 1995).
[5] R. Lenormand, E. Touboul, and C. Zarcone, J. Fluid Mech. **189**, 165 (1988).
[6] R. Lenormand and C. Zarcone, Transp. Porous Media **4**, 599 (1989).
[7] P. G. Saffman and G. Taylor, Proc. R. Soc. London, Ser. A **245**, 312 (1958).
[8] T. A. Witten and L. M. Sander, Phys. Rev. Lett. **47**, 1400 (1981).
[9] M. Plischke and Z. Racz, Phys. Rev. Lett. **53**, 415 (1984).
[10] M. Plischke and Z. Racz, Phys. Rev. Lett. **54**, 2054 (1985).
[11] P. Meakin, A. Coniglio, H. E. Stanley, and T. A. Witten, Phys. Rev. A **34**, 3325 (1986).
[12] T. C. Halsey, P. Meakin, and I. Procaccia, Phys. Rev. Lett. **56**, 854 (1986).
[13] C. Amitrano, A. Coniglio, and F. di Liberto, Phys. Rev. Lett. **57**, 1016 (1986).
[14] B. B. Mandelbrot, J. Fluid Mech. **62**, 331 (1974).
[15] L. Paterson, Phys. Rev. Lett. **52**, 1621 (1984).
[16] B. Shraiman and D. Bensimon, Phys. Rev. A **30**, 2840 (1984).
[17] E. Sharon, M. G. Moore, W. D. McCormick, and H. L. Swinney, Phys. Rev. Lett. **91**, 205504 (2003).
[18] M. G. Moore, A. Juel, J. M. Burgess, W. D. McCormick, and H. L. Swinney, Phys. Rev. E **65**, 030601 (2002).
[19] A. Arneodo, J. Elezgaray, M. Tabard, and F. Tallet, Phys. Rev. E **53**, 6200 (1996).
[20] E. Somfai, R. C. Ball, J. P. DeVita, and L. M. Sander, Phys. Rev. E **68**, 020401 (2003).
[21] L. M. Sander, P. Ramanlal, and E. Ben-Jacob, Phys. Rev. A **32**, 3160 (1985).
[22] M. B. Hastings and L. S. Levitov, Physica D **116**, 244 (1998).
[23] B. Davidovitch, H. G. E. Hentschel, Z. Olami, I. Procaccia, L. M. Sander, and E. Somfai, Phys. Rev. E **59**, 1368 (1999).
[24] F. Barra, B. Davidovitch, A. Levermann, and I. Procaccia, Phys. Rev. Lett. **87**, 134501 (2001).
[25] F. Barra, B. Davidovitch, and I. Procaccia, Phys. Rev. Lett. **65**, 046144 (2002).
[26] H. G. E. Hentschel, A. Levermann, and I. Procaccia, Phys. Rev. E **66**, 016308 (2002).
[27] A. Levermann and I. Procaccia, Phys. Rev. E **69**, 031401 (2004).
[28] M. G. Stepanov and L. S. Levitov, Phys. Rev. E **63**, 061102 (2001).
[29] B. Davidovitch, A. Levermann, and I. Procaccia, Phys. Rev. E **62**, R5919 (2000).
[30] R. Lenormand and C. Zarcone, Phys. Rev. Lett. **54**, 2226 (1985).
[31] K. J. Måløy, J. Feder, and T. Jøssang, Phys. Rev. Lett. **55**, 2688 (1985).
[32] J. P. Stokes, D. A. Weitz, J. P. Gollub, A. Dougherty, M. O. Robbins, P. M. Chaikin, and H. M. Lindsay, Phys. Rev. Lett. **57**, 1718 (1986).
[33] D. A. Weitz, J. P. Stokes, R. C. Ball, and A. P. Kushnick, Phys. Rev. Lett. **59**, 2967 (1987).
[34] R. Lenormand, C. Zarcone, and A. Sarr, J. Fluid Mech. **135**, 337 (1983).
[35] R. Lenormand, J. Phys.: Condens. Matter **2**, SA79 (1990).
[36] Y. Méheust, G. Løvoll, K. J. Måløy, and J. Schmittbuhl, Phys. Rev. E **66**, 051603 (2002).
[37] G. G. Batrouni and A. Hansen, J. Stat. Phys. **52**, 747 (1988).
[38] J.-D. Chen and D. Wilkinson, Phys. Rev. Lett. **55**, 1892 (1985).
[39] R. Lenormand, Proc. R. Soc. London, Ser. A **423**, 159 (1989).
[40] Y. C. Yortsos, B. Xu, and D. Salin, Comput. Geosci. **5**, 257 (2001).
[41] R. Toussaint, G. Løvoll, Y. Méheust, K. J. Måløy, and J. Schmittbuhl (unpublished).
[42] J. Mathiesen and M. H. Jensen, Phys. Rev. Lett. **88**, 235505 (2002).

EUROPHYSICS LETTERS 15 August 2005

Europhys. Lett., **71** (4), pp. 583–589 (2005)
DOI: 10.1209/epl/i2005-10136-9

Influence of pore-scale disorder on viscous fingering during drainage

R. Toussaint[1,3], G. Løvoll[1], Y. Méheust[2], K. J. Måløy[1] and J. Schmittbuhl[3]

[1] *Department of Physics, University of Oslo - PO Box 1048 Blindern N-0316 Oslo, Norway*
[2] *Department of Physics, NTNU Trondheim - N-7491 Trondheim, Norway*
[3] *Institut de Physique du Globe, UMR 7516 5 rue René Descartes, 67084 Strasbourg, France*

received 18 April 2005; accepted 24 June 2005
published online 22 July 2005

PACS. 47.20.Gv – Viscous instability.
PACS. 47.54.+r – Pattern selection; pattern formation.
PACS. 47.55.Mh – Flows through porous media.

Abstract. – We study viscous fingering during drainage experiments in linear Hele-Shaw cells filled with a random porous medium. The central zone of the cell is found to be statistically more occupied than the average, and to have a lateral width of 40% of the system width, irrespectively of the capillary number Ca. A crossover length $w_f \propto Ca^{-1}$ separates lower scales where the invader's fractal dimension $D \simeq 1.83$ is identical to capillary fingering, and larger scales where the dimension is found to be $D \simeq 1.53$. The lateral width and the large-scale dimension are lower than the results for Diffusion Limited Aggregation, but can be explained in terms of Dielectric Breakdown Model. Indeed, we show that when averaging over the quenched disorder in capillary thresholds, an effective law $v \propto (\nabla P)^2$ relates the average interface growth rate and the local pressure gradient.

Viscous-fingering instabilities in immiscible two-fluid flows in porous materials have been intensely studied over the past 50 years [1], both because of their important role in oil recovery processes, and as a paradigm of simple pattern forming system. Their dynamics is controlled by the interplay between viscous, capillary and gravity forces. The ratio of viscous forces to the capillary ones at pore scale is quantified by the capillary number $Ca = \mu v_f a^2/(\gamma\kappa)$, where a is the characteristic pore size, v_f is the filtration velocity, γ the interfacial tension, κ the permeability of the cell, and μ the viscosity of the displaced fluid, supposed here much larger than the viscosity of the invading one.

There is a strong analogy between viscous fingering in porous media and Diffusion Limited Aggregation (DLA), as was first pointed out by Paterson [2]. Indeed, both processes of DLA and viscous fingering in empty Hele-Shaw cells belong to the family of Laplacian Growth Models, *i.e.* obey the Laplacian growth equation $\nabla^2 P = 0$, with an interfacial growth rate $v \propto -\nabla P$, where P is the diffusing field, *i.e.* the probability density of random walkers in DLA, or the pressure in viscous fingering. Despite differences as, respectively, a stochastic and deterministic growth, and boundary conditions as, respectively, $P = 0$ or $P = -\gamma/r$

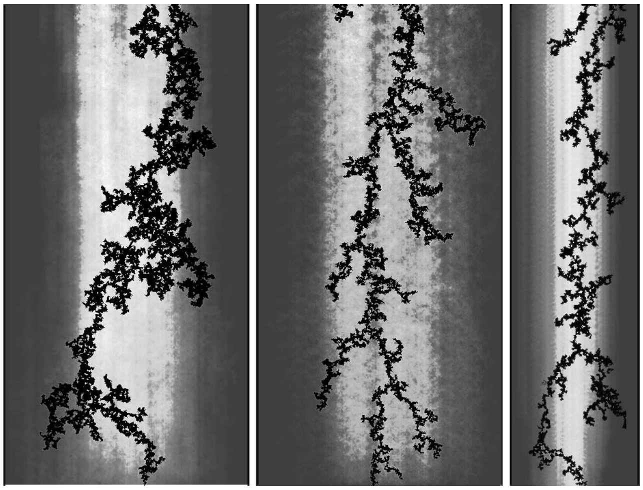

Fig. 1 – Invasion clusters on thresholded images at capillary numbers $Ca = 0.06$ (a) and 0.22 (b, c), for $W/a = 210$ (a, b) and 110 (c), with displayed system lateral boundaries. The superimposed gray map shows the occupancy probability $\pi(x, z)$ of the invader, in a moving reference frame attached to the most advanced invasion tip and to the lateral boundaries.

with r the interfacial curvature, it is admitted that these processes belong to the same universality class [2–4]. In radial geometry these processes lead to fractal structures of dimensions $D = 1.70 \pm 0.03$ [5], 1.713 ± 0.0003 [6], and 1.7 [4], respectively, in viscous fingering in empty Hele-Shaw cells, DLA, and numerical solutions of deterministic Laplacian growth. The two numerical models have been re-explored recently using stochastic conformal mapping theory [3, 4, 6]. However, in Hele-Shaw cells filled with disordered porous materials similar to the one used here, a lower fractal dimension $D = 1.58 \pm 0.09$ has been measured [7].

In straight channels, DLA gives rise to fractal structures of dimension 1.71, occupying on average a lateral fraction $\lambda = 0.62$ of the system width W [8]. Viscous fingering in empty Hele-Shaw cell converge towards the Saffman Taylor (ST) solution [9], with a uniformly propagating fingerlike interface covering a fraction $\lambda = 0.5$ of the system width at large capillary numbers [9, 10], selected by the interfacial tension [11].

For straight channels with a disordered porous medium, viscous fingering with a non-wetting invader leads to a branched structure that depends on Ca, on the observation scale and on the system size (fig. 1). Løvoll *et al.* [12] recently investigated the growth activity of the invading fluid in such systems, and showed that up to statistical fluctuations, the characteristic number of pores invaded at a given longitudinal distance behind the most advanced tip is a stationary quantity (denoted $n(z)$ in [12]). In this letter, we extend the experimental characterization of the probability occupancy function of the invader, and obtain a universal invasion probability function $\pi(x, z)$, which in reduced coordinates is independent of capillary numbers and system sizes. This function represents the fraction of invaded pores in the reference frame of the stationary process. To our knowledge, this is the first experimental attempt to reach such a quantity, and represents a technical challenge due to the required high number of experiments, and the need for the development of good automation techniques for image data processing. We also characterize in detail the fractal geometry of the invasion structure, and its different regimes at different scales. In this letter, we also provide a theoretical argument which takes into account the influence of the disorder in the capillary thresholds along the invasion front, and we establish that if indeed at high capillary number, the process is well described by DLA as often suggested [2], there is also at intermediate Ca a regime where the flow in *random* porous media is better described by another Laplacian model, namely a Dielectric Breakdown Model (DBM) with $\eta = 2$ —the interfacial growth rate is $v \propto (\nabla P)^\eta$ in DBM, $\eta = 1$ corresponding to DLA. This theoretical argument leads to estimates of the fractal dimensions of the invader, and of the lateral fraction λ characteristizing the geometry of the invasion probability function, which are compatible with the experimental results.

In the experiments, linear Hele-Shaw cells of thickness $a = 1\,\mathrm{mm}$ were filled at 38% with a monolayer of randomly located immobile glass beads of diameter a, between which air displaces a solution of 90% glycerol - 10% water of much larger viscosity $\mu = 0.165\,\mathrm{Pa\cdot s}$, wetting the beads and walls of the cell, *i.e.* in drainage conditions (experimental technique similar to [12]). The interfacial tension and the permeability of the cell are, respectively, $\gamma = 0.064\,\mathrm{N\cdot m^{-1}}$ and $\kappa = 0.00166 \pm 0.00017\,\mathrm{mm}^2$. We investigate regimes ranging from capillary to viscous fingering ($0.01 < Ca < 0.5$), in cells with impermeable lateral walls and dimensions $W \times L \times a$, with widths perpendicularly to the flow direction $W/a = 110$, 215 and 430, and a length $L/a = 840$. The cell is set horizontally, so that gravity is irrelevant. A constant filtration rate of water-glycerol is ensured by a controlled gravity-driven pump.

Pictures of the flow pattern are taken from the top, and treated to extract the invading air cluster (with pixels of size $0.55a$), as the black clusters in fig. 1. In ref. [12], we have shown that the invasion process is stationary, up to fluctuations arising from the disorder in pore geometries. To extract the underlying average stationary behavior, all quantities are then analyzed in the reference frame (x, z) attached to the lateral boundaries at $x = 0$ and $x = W$, and to the foremost propagating tip at $z = 0$, z pointing against the flow direction (this tip indeed propagates at a roughly constant speed v_{tip} [12]). Average quantities at any position (x, z) of the tip-related frame, are defined using all stages and points of the invasion process, excluding regions closer than $W/2$ from the inlet or outlet, to avoid finite-size effects.

The average occupancy map $\pi(x, z)$ is defined as follows: for each time (or each picture), we assign the value 1 to the coordinate (x, z) if air is present there, 0 otherwise. $\pi(x, z)$ obtained as the time average of such occupancy function, is displayed as gray map in fig. 1. This definition would coincide, in the limit of large systems, with the mean occupancy introduced for DLA by Arneodo *et al.* [8,13]. Next we compute the average number of occupied pores per unit length at a distance z behind the tip, $n(z)$, which is related to π as $n(z) = (1/a^2) \int_0^W \pi(x, z)\,\mathrm{d}x$. We show in fig. 2(a), a data collapse for all experiments, at different capillary numbers Ca and three system widths W, of $n(z)/n_{Ca} = \Phi(2z/W)$, where $n_{Ca} = (W/a^2)v_f/v_{tip}$ [12]. The underlying scaling function Φ is a function increasing from 0 at $z = 0$ towards 1 at $z = +\infty$, as granted by conservation of the displaced fluid for a statistically stationary process [12]. Φ is evaluated in fig. 2(a) as an average over all experiments and sizes.

We also characterize the lateral structure of the invader in the frozen zone, $z > W$, where less than 10% of the invasion activity takes place since $\Phi(2) > 0.9$. We define over this zone a distribution in reduced coordinates $\rho(x) = [W/(a^2\, n_{Ca})]\, \pi(x, \infty) = (v_{tip}/v_f)\, \pi(x, \infty)$, so that $\int_0^W \rho(x)\mathrm{d}x/W \simeq 1$. This quantity, presented in fig. 2(b) for an average over five experiments at capillary numbers $Ca = 0.06$ and 0.22 for $W/a = 215$, and for four experiments with $0.06 < Ca < 0.22$ for $W/a = 110$, seems also reasonably independent of system size and capillary number, as is $n(z)/n_{Ca}$ —fig. 2(a). We notice a certain dispersion around the average, but no systematic trend over size or capillary number. An interesting geometrical characteristic of this underlying lateral occupation density is the fraction λ of the system, occupied by the invader at saturation, which is evaluated as in [8]: $\lambda = 1/\rho_{max}$, or alternatively $\lambda = (x^+ - x^-)/W$, where $\rho(x^+) = \rho(x^-) = \rho_{max}/2$. Both definitions, for a regular function

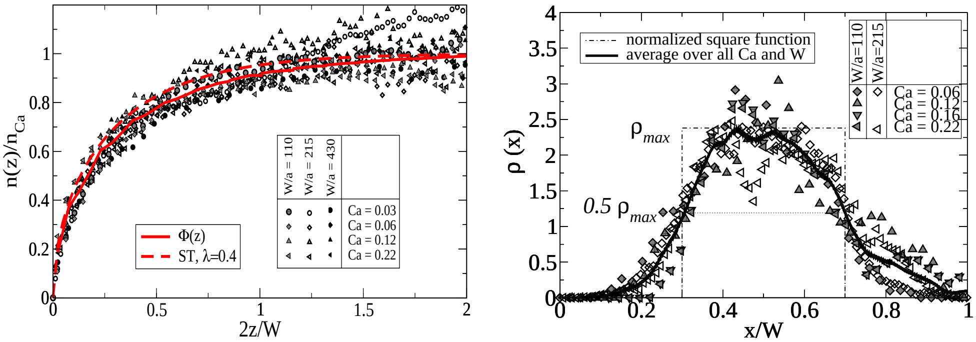

Fig. 2 – Scaled invader's density, after projections along directions parallel or perpendicular to the average flux, as a function of reduced coordinates scaled by the system width W. (a) Scaled density $n(z)/n_{Ca}$ as a function of $2z/W$, scaled longitudinal distance to the most advanced tip, for three system sizes and four capillary numbers. The lines are the experimental averages, and the theoretical Saffman Taylor solution for a single finger occupying a lateral fraction $\lambda = 0.4$ of the system. (b) Normalized density as a function of the scaled lateral coordinate, $\rho(x)$, with half-maximum reached over a width $0.4W$.

$\rho(x)$ determined by averaging over capillary numbers and sizes, lead to $\lambda \simeq 0.4 \pm 0.02$ as shown in fig. 2(b): this is significantly smaller than the off-lattice DLA result $\lambda = 0.62$ [8,14].

The 2D occupancy map $\pi(x,z)$ itself, displayed as gray map in fig. 1, has a maximum $\pi_{max} = \rho_{max} v_f / v_{tip}$, along a line at $(x = W/2, z > W)$. Similarly to Arneodo's procedure [8], we determine the support of $\pi > \pi_{max}/2$, displayed in fig. 3(a) and (b), which corresponds to the most often occupied region. Within the noise error, the shape of this region resembles the theoretical ST curve corresponding to $\lambda = 0.4 \pm 0.05$ [9] (gray lines in fig. 3). For such a theoretical ST finger, this curve would also coincide with another observable determined in this study, namely the scaled longitudinal density of invader. As seen in fig. 2(a), there are also similarities between the two processes for this other observable, *i.e.* between the scaled longitudinal density $\Phi(z)$ determined for the fingering process in disordered media studied here (continuous line), and this theoretical ST curve corresponding to $\lambda = 0.4$ (dashed line). Systematic deviations from the mathematical ST solution at $\lambda = 0.4$ might nonetheless exist

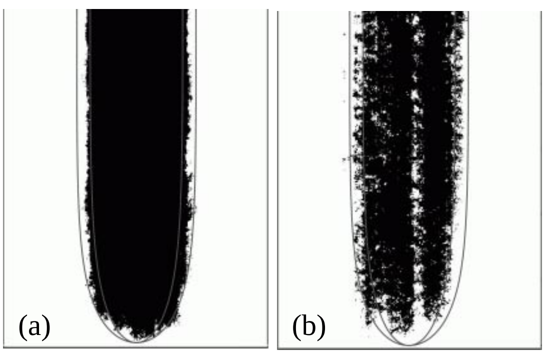

Fig. 3 – (a) Average occupation density map of the invader thresholded at half-maximum, for a system size $W/a = 215$, in the reference frame attached to the tip position, at $Ca = 0.06$ (a) and 0.22 (b), compared to ST curves for $\lambda = 0.35$ and 0.45.

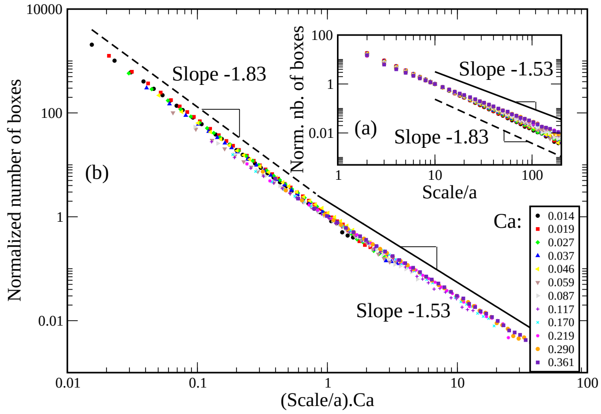

Fig. 4 – Small- and large-scale fractal dimension of the invasion cluster at various capillary numbers, determined by box-counting. (a) Insert: number of boxes as function of the scale. (b) Data collapse for all capillary numbers after rescaling the box size by Ca: evidence of crossover scale $w_f \sim Ca^{-1}$ separating a small-scale capillary fractal dimension 1.83, and a large viscous scale one 1.53.

for these two observables, accordingly to what has been seen between the DLA envelopes and the corresponding ST solution at $\lambda = 0.62$ [14].

The mass fractal dimension of the invasion clusters is analyzed by box-counting. $N(s)$ is the number of boxes of size s to cover the invader. Figure 4 displays a normalized distribution $N(s)/N(a/Ca)$ as a function of $(s/a) \cdot Ca$ for various capillary numbers. By linear regression of this collapsed log-log data, we find that $N(s) \sim s^{-1.83\pm0.01}$ for small scales $s < a/Ca$, and $N(s) \sim s^{-1.53\pm0.02}$ for larger scales. The result can be explained by the following approximations. The distribution of pore throats sizes results in a distribution of capillary pressure thresholds P_t, $g(P_t)$, of characteristic width W_t. Consider a box of size w_f along the cluster boundary in the active zone, such that $w_f \cdot \nabla P_b = W_t$, where ∇P_b is a characteristic pressure gradient. At scales $s < w_f$, viscous pressure variations are lower than capillary threshold fluctuations, and the most likely invaded pores correspond to the lowest random thresholds, which corresponds to capillary fingering, thus leading to $D = 1.83$ (similarly to capillary fingering experiments [15], or to invasion percolation model [16]). Conversely, at larger sizes ($s > w_f$), the invasion activity is determined essentially by the spatial variations of ∇P_b. Assuming that ∇P_b scales as the imposed $\nabla P(-\infty) \propto Ca$, *i.e.* neglecting the geometry variations between different speeds, w_f scales as $W_t/\nabla P_b \propto a/Ca$, as confirmed by the data collapse in fig. 4(a). Such a scaling law, $w_f/a \propto Ca^{-1}$ before saturating at large Ca, is also consistent with another experimental determination of w_f, illustrated in fig. 9 of ref. [12].

Eventually, we sketch a possible explanation for the width selection $\lambda = 0.4$ and the large-scale fractal dimension $D = 1.53 \pm 0.02$, which are smaller than their counterparts in DLA, respectively, 0.62 and 1.71. Neglecting the small-scale permeability variations leads to a Laplacian pressure field in the defending fluid. The boundary condition for the pressure field is then $\nabla P(z = -\infty) = -\mu v_f/\kappa$, and $\nabla P(x = 0, W) \cdot \hat{x} = 0$, where $\hat{x}$ is the unit vector along x. The dynamics of the process is then entirely controlled by the boundary condition along the invading fluid, *i.e.* by the capillary pressure drop across the meniscus in the pore neck and the pressure gradient in the invaded fluid. For a given pressure difference at pore scale between the invading air at P_0, and the pressure P_1 in the glycerol-filled pore, we decompose $P_0 - P_1 = \Delta P_v + P_c$, where ΔP_v is a viscous pressure drop in the pore neck, and the capillary pressure drop is $P_c = \gamma/r + 2\gamma/a$, where the in- and out-of-plane curvature of the interface are, respectively, r and $a/2$. As a meniscus progresses between neighboring beads, its curvature goes through a minimum r_m in the pore neck. The meniscus will be able to pass the neck if the pressure drop $P_0 - P_1$ exceeds the threshold $P_t = P_c(r_m)$. For the sake of simplicity, the probability distribution of the thresholds $g(P_t)$ is considered flat, between P_{min} and P_{max}, with $W_t = P_{max} - P_{min}$ and $g(P_t) = \theta(P_t - P_{min})\theta(P_{max} - P_t)/W_t$, where θ is the Heaviside function. In the pure capillary fingering limit $Ca \to 0$, the pressure field P is homogeneous in the defending fluid, and a pore is invaded when $P_0 - P$ reaches the minimum threshold along the boundary, close to P_{min}. At higher capillary number, we want to relate the invasion rate to the local capillary threshold, and to the pressure P_1 in the liquid-filled pore nearest to the interface. If $P_0 - P_1 < P_t$, the meniscus adjusts reversibly in the pore neck, and the next pore is not invaded. Conversely, if $P_0 - P_1 > P_t$, the pore will be invaded, and most of the invasion time is spent in the thinnest region of the pore neck. A characteristic interface velocity can be evaluated by the Washburn equation [17] at this point: $v \sim -(2\kappa/\mu a)(P_0 - P_1 - P_t)\theta(P_0 - P_1 - P_t)$, where the Heaviside function results from a zero invasion velocity if the pore is not invaded. Hypothesizing that only the average growth rate controls the process, independently of the particular realization of random thresholds, the growth rate averaged over all possible pore neck configurations, is

$$\begin{aligned}\langle v \rangle &= \int \frac{-2\kappa}{\mu a}(P_0 - P_1 - P_t)\theta(P_0 - P_1 - P_t)g(P_t)dP_t \\ &= -(\kappa/\mu a)\theta(P_0 - P_1 - P_{min}) \times \\ &\quad \times\{[(P_0 - P_1 - P_{min})^2/W_t]\theta[P_{max} - (P_0 - P_1)] + \\ &\qquad +2[P_0 - P_1 - (P_{min} + P_{max})/2]\theta[P_0 - P_1 - P_{max}]\}. \qquad (1)\end{aligned}$$

At moderate capillary numbers, such as $P_0 - P_1 < P_{max}$, if we assume that the capillary pressure drop is around $P_c = P_{min}$ when the invasion meniscus is at the entrance of the pore neck, we note that $(P_0 - P_{min} - P_1)/a = \Delta P_v/a \sim \nabla P/2$, and eq. (1) implies that the growth rate goes as $\langle v \rangle = -a\kappa/(4\mu W_t)(\nabla P)^2$. This effective quadratic relationship between the average growth rate and the local pressure gradient arises from the distribution of capillary thresholds, and means that such invasion process should be in the universality class of DBM with $\eta = 2$, rather than DLA (DBM, $\eta = 1$). Indeed, in DBM simulations in linear channels, λ is a decreasing function of η (as in related deterministic problems, as viscous fingering in shear-thinning fluids [18], or η-model [19]), and Somfai *et al.* [14] report $\lambda \simeq 0.62$ and 0.5 for, respectively, $\eta = 1$ and 1.5, so that the observed $\lambda = 0.4$ is consistent with $\eta = 2$. The fractal dimension of DBM is also a decreasing function of η, and $\eta = 2$ corresponds $D = 1.4 \pm 0.1$ [20], which is close to the observed $D = 1.53 \pm 0.02$ in our experiments.

Note that at high capillary numbers such that locally $P_0 - P_1 \gg P_{max}$, the threshold fluctuations are not felt by the interface, and eq. (1) leads to $\langle v_{inv} \rangle = -(\kappa/\mu)\nabla P$, which would correspond to a classic DLA process. We have checked by numerically solving the Laplace equation with the experimental clusters as boundaries that all experiments performed here were at moderate enough capillary number to have $P_0 - P_1 < P_{max}$ all along the boundary [12], *i.e.* the quadratic law $\langle v \rangle = -a\kappa/(4\mu W_t)(\nabla P)^2$ is expected to hold.

Even at moderate Ca, deviations from the DBM model with $\eta = 2$ could be observed for significantly non-flat distribution of the capillary thresholds in the random porous medium, for which eq. (1) would lead to a more complicated dependence of the growth rate v on ∇P, reflecting the details of this distribution, and not simply a power law effective relationship. It would be interesting in future work to explore numerically and experimentally the detailed effect of non-flat capillary threshold distributions on the selected fractal dimension, average width occupied in the system, and total displaced mass $n_{Ca}(Ca)$ (reported in [12] for the present work), to extract the influence of the disorder on the best capillary number to select in order to maximize the efficiency of the extraction process.

* * *

We acknowledge with pleasure fruitful discussions with E. G. FLEKKØY, A. LINDNER, A. HANSEN and E. SOMFAI, and support from the PICS program granted by NFR and CNRS, and from the REALISE program.

REFERENCES

[1] BENSIMON D., KADANOFF L. P., LIANG S., SHRAIMAN B. I. and TANG C., *Rev. Mod. Phys.*, **58** (1986) 977.
[2] PATERSON L., *Phys. Rev. Lett.*, **52** (1984) 1621.
[3] STEPANOV M. G. and LEVITOV L. S., *Phys. Rev. E*, **63** (2001) 061102.
[4] LEVERMANN A. and PROCACCIA I., *Phys. Rev. E*, **69** (2004) 031401.
[5] SHARON E., MOORE M. G., MCCORMICK W. D. and SWINNEY H. L., *Phys. Rev. Lett.*, **91** (2003) 205504.
[6] DAVIDOVITCH B. D., LEVERMANN A. and PROCACCIA I., *Phys. Rev. E*, **62** (2000) R5919.
[7] HINRICHSEN E. L., MÅLØY K. J., FEDER J. and JØSSANG T., *J. Phys. A*, **22** (1989) L271.
[8] ARNEODO A., ELEZGARAY J., TABARD M. and TALLET F., *Phys. Rev. E*, **53** (1996) 6200.
[9] SAFFMAN P. G. and TAYLOR G., *Proc. Soc. London, Ser. A*, **245** (1958) 312.
[10] TABELING P., ZOCCHI G. and LIBCHABER A., *J. Fluid Mech.*, **177** (1987) 67.
[11] MCLEAN J. W. and SAFFMAN P. G., *J. Fluid Mech.*, **102** (1981) 445.
[12] LØVOLL G., MÉHEUST Y., TOUSSAINT R., SCHMITTBUHL J. and MÅLØY K. J., *Phys. Rev. E*, **70** (2004) 026301.
[13] ARNEODO A., COUDER Y., GRASSEAU G., HAKIM V. and RABAUD M., *Phys. Rev. Lett.*, **63** (1989) 984.
[14] SOMFAI E. and BALL R. C., *Phys. Rev. E*, **68** (2003) 020401.
[15] LENORMAND R. and ZARCONE C., *Phys. Rev. Lett.*, **54** (1985) 2226.
[16] CHANDLER R., KOPLIK J., LERMAN K. and WILLEMSEN J. F., *J. Fluid Mech.*, **119** (1982) 249.
[17] WASHBURN E. W., *Phys. Rev.*, **17** (1921) 273.
[18] LINDNER A., BONN D., CORVERA POIRÉ E., BEN AMAR M. and MEUNIER J., *J. Fluid Mech.*, **469** (2002) 237.
[19] BEN AMAR M., *Phys. Rev. E*, **51** (1995) R3819.
[20] MATHIESEN J. and JENSEN M. H., *Phys. Rev. Lett.*, **88** (2002) 235505.

Transp Porous Med (2011) 86:305–324
DOI 10.1007/s11242-010-9622-8

Influence of Viscous Fingering on Dynamic Saturation–Pressure Curves in Porous Media

G. Løvoll · M. Jankov · K. J. Måløy · R. Toussaint · J. Schmittbuhl · G. Schäfer · Y. Méheust

Received: 15 February 2010 / Accepted: 12 July 2010 / Published online: 7 August 2010

Abstract We report on results from primary drainage experiments on quasi-two-dimensional porous models. The models are transparent, allowing the displacement process and structure to be monitored in space and time during primary drainage experiments carried out at various speeds. By combining detailed information on the displacement structure with global measurements of pressure, saturation and the capillary number Ca, we obtain a scaling relation relating pressure, saturation, system size and capillary number. This scaling relation allows pressure–saturation curves for a wide range of capillary numbers to be collapsed on the same master curve. We also show that in the case of primary drainage, the dynamic effect in the capillary pressure–saturation relationship observed on partially water saturated soil samples might be explained by the combined effect of capillary pressure along the invasion front of the gaseous phase, and pressure changes caused by viscous effects in the wetting fluid phase.

Keywords Drainage · Dynamic capillary pressure · Saturation · Water retention · Viscous effects · Rescaling

G. Løvoll (✉) · M. Jankov · K. J. Måløy
Department of Physics, University of Oslo, P.O. Box 1048, Blindern, 0316 Oslo, Norway
e-mail: grunde.lovoll@fys.uio.no

R. Toussaint · J. Schmittbuhl
Institut de Physique du Globe (IPGS), CNRS and University of Strasbourg (EOST), Strasbourg, France

G. Schäfer
Laboratoire d'Hydrologie et de Géochimie de Strasbourg, UMR 7517 CNRS-Université de Strasbourg, 1 rue Blessig, 67083 Strasbourg Cedex, France

Y. Méheust
Geosciences Rennes (UMR CNRS 6118), Université Rennes 1, Rennes, France

G. Løvoll
Det Norske Veritas, Research and Innovation, Veritasveien 1, 1322 Høvik, Norway

1 Introduction

Different types of fluid displacements in porous media play important roles in many natural and commercial processes (Bear 1972; Dullien 1992; Sahimi 1995). Various multiphase problems have been studied and modelled over the last decades (see Bear 1972; Lenormand 1989; Dullien 1992; Sahimi 1995 and references therein).

The morphology of the displacement structures observed in immiscible two phase flow are in general controlled by the competition between viscous forces, gravitational forces and capillary forces; those various forces act on scales ranging from the pore scale to the system size. The relative wettabilities, viscosities and densities of the fluids, as well as the heterogeneity of the underlying porous media, could all play important roles in the competition process (Lenormand 1989; Måløy et al. 1985; Homsy 1987; Hulin et al. 1987; Birovljev et al. 1991; Måløy et al. 1992; Frette et al. 1997).

In order to characterize two phase flow in porous media, it is common practice to define a set of dimensionless numbers that quantify fluid pair characteristics. One such number is the viscosity ratio $M = \mu_{\mathrm{nw}}/\mu_{\mathrm{w}}$, where μ_{nw} is the dynamic viscosity of the non-wetting fluid and μ_{w} is the dynamic viscosity of the wetting fluid. The relative magnitudes of viscous and capillary forces (on the pore scale) are quantified by the *capillary number* Ca:

$$\mathrm{Ca} = \frac{\mu_{\mathrm{w}}\, v_{\mathrm{f}}\, a^2}{\gamma\, \kappa} \tag{1}$$

where v_{f} is the Darcy velocity or specific discharge, a is the characteristic pore size, γ is the interface tension and κ is the intrinsic permeability of the homogeneous and isotropic porous medium. The specific discharge, or filtration velocity, v_{f}, is $v_{\mathrm{f}} = Q/A$ where Q is the volumetric flow rate and A is the cross-section area perpendicular to the flow. In drainage, i.e. flow regimes where the non-wetting fluid replaces the wetting one, three limit flow regimes can be reached by tuning M and Ca (Lenormand et al. 1983, 1988; Lenormand 1989). If the flow rate is sufficiently low ($\mathrm{Ca} \ll 1$), one reaches the capillary fingering regime (Lenormand et al. 1983; Lenormand and Zarcone 1985), for which the displacement structure is controlled solely by the fluctuations in the capillary threshold pressures. This regime is shown to have strong analogies to invasion percolation (Lenormand and Zarcone 1985; Chandler et al. 1982; Wilkinson and Willemsen 1983), and the invasion structure is fractal Mandelbrot (1982); Feder (1988) with a fractal dimension $D_{\mathrm{c}} = 1.83 \pm 0.01$ (Lenormand and Zarcone 1985, 1989). If the invasion rate is high, the displacement is either stable or unstable depending on the viscosity contrast M. If a fluid with high viscosity is invading a fluid with low viscosity ($M \geq 1$), the resulting pressure field due to the viscous dominated displacement will act against the growth of the invasion front, leading to stabilization of the displacement front at a finite width (Saffman and Taylor 1958; Lenormand et al. 1988; Lenormand 1989; Frette et al. 1997; Xu et al. 1998). On the other hand, if the invading fluid is the less viscous one, the displacement is unstable and falls in the viscous fingering regime (Saffman and Taylor 1958; Måløy et al. 1985; Homsy 1987). The invasion structure is fractal with a fractal dimension $D_{\mathrm{v}} \simeq 1.53$ (Måløy et al. 1985; Toussaint et al. 2005).

At intermediate capillary numbers, the viscous and capillary forces dominate on different length scales. At small scales capillary forces dominate the problem so that the invasion structure locally is that of capillary fingering, whereas viscous forces dominate the problem at larger scales, resulting in a morphology typical of viscous fingering at larger scales. The crossover length-scale between these two regimes l_{c} scales with the capillary number as:

$$l_{\mathrm{c}} = \beta \frac{a}{\mathrm{Ca}}. \tag{2}$$

Where the proportionality factor $\beta \simeq 1$ (Løvoll et al. 2004; Toussaint et al. 2005), in the following we will use: $l_c = a/\mathrm{Ca}$. Note that this experimental result is different from the theoretical result for invasion percolation in a destabilizing gradient (Yortsos et al. 1997; Xu et al. 1998). Above this crossover length scale, the flow is destabilized by viscous forces and the displacement takes place in narrow-branched channels (for $M < 1$). Viscous fingering in disordered porous media is different from standard Saffman–Taylor fingering (Saffman and Taylor 1958), obtained in empty straight channels (Hele-Shaw cells), where the fingers are compact and occupy $1/2$ of the system width W. In contrast, in disordered porous media these structures are branched, the invasion structure is fractal (Måløy et al. 1985) and it has been demonstrated that the invasion structure occupies a smaller fraction of the system ($0.4\ W$) (Løvoll et al. 2004; Toussaint et al. 2005).

Many authors in the 'physics community' have been mostly concerned with characterizing and understanding displacement patterns and local flow properties. Hydrogeologists and soil scientists, on the other hand, have studied such systems with the goal of finding empirical laws relating saturation and capillary pressure at the Darcy scale, that is, a meso-scale at which the medium and the flow are described by continuous mathematical fields. The basic laws of multiphase flows treated at mesoscopic scale as a continuum require a closure of partial-flow Darcy relations. The key point of this closure is a functional relation between the capillary pressure (in a water–air system) and (water) saturation in the form of retention curves. The basic assumption underlying this continuous theory of multiphase flow is that for a given porous medium and a wetting-/nonwetting-liquid pair there is a well-defined relation between capillary pressure and saturation as found from quasi-static measurements on representative volumes. The best known mathematical models to describe the relationship are those of Leverett (1941), Brooks and Corey (1964) and Van Genuchten (1980). In these models, the model parameters are fit parameter and they are functions of the characteristics of the pore space, such as the pore size distribution and the degree of connectivity of the network. As found in the early 1960s, the retention curves may also depend on the direction and on the 'displacement history' of the water–air front, further on referred as hysteresis effects (Poulavissilis 1962; Mualem 1976, 1984; Kool and Parker 1987; Parker and Lenhard 1987; Luckner and Van Genuchten 1989; Lenhard et al. 1993; Stauffer and Kinzelbach 2001). Based on the parameterization procedure proposed by Parker et al. (1987), the known retention curves of a porous sample are often used to obtain capillary pressure–saturation curves for the different fluid pairs present in a multiphase system (e.g. Helmig 1997; Bohy et al. 2006). Later studies have demonstrated that hysteresis effects are not the only additional influence on this relationship and they show that there are considerable dynamic effects on the measured capillary pressure curves (Hassanizadeh and Gray 1988; Bourgeat and Panfilov 1998; Hassanizadeh et al. 2002; Dahle et al. 2005). Based on the results of former experimental studies Smiles et al. (1971), Stauffer (1977) and Hassanizadeh et al. (2002) suggested to account for dynamic effects on the retention curves by complementing the capillary pressure obtained under hydrostatic equilibrium conditions, depending on the water saturation of the soil sample, with a dynamic pressure term expressed by a lumped parameter times the variation of water saturation over time.

The present article addresses the gap between (i) capillary pressure as understood in the framework of a pore scale description and modeling of drainage, and (ii) capillary pressure as measured at the global scale of a sample or as described in Darcy-scale models. We present results from drainage experiments on synthetic quasi two-dimensional porous media, in which non-wetting air displaces a highly viscous wetting glycerol/water solution; hence, gravity has no influence on the displacement. We investigate the crossover regime between the regime of slow displacement (capillary fingering), and fast displacement (viscous fingering). By using transparent quasi two-dimensional porous media as our porous media, optical methods are used to observe and analyse the local and global displacement geometry and how it changes with capillary number. The combination of local and global information allow us to perform *upscaling* of our data from the pore scale to the scale of our experimental porous media. In this manner, we are able to relate pressure, saturation, capillary number and system size.

2 Experimental Setup

The presented experiments are performed on quasi two-dimensional porous media. The thickness of the cells containing this porous medium is $a = 1$ mm, and corresponds to the diameter of the fixed glass beads composing the solid matrix of this porous medium. The porous medium is initially completely filled with a wetting liquid, which is displaced by a non-wetting fluid (primary drainage).

The porous medium is made of a random mono layer of glass beads: glass beads are poured on the sticky side of a contact paper (see Fig. 1). When the surface is completely filled with beads, excess beads are removed, leaving a random mono-layer of beads. The sticky paper is attached to a Plexiglas plate that has milled inlet and outlet channels 5 mm wide and 8 mm deep. The model is sealed off at the edges with silicon glue, thus forming a rectangular porous medium of width W and length L.

When glue is applied, another sticky paper is placed (glue down) on top of the glass bead layer. The resulting quasi two-dimensional porous medium can be filled with a liquid through the channels in the Plexiglas plate (see Fig. 1). The model is then placed (horizontally) with the beads down and clamped to a frame with an integrated pressure cushion. This pressure cushion ensures that the position of each bead is fixed and that the porous medium is always only one bead diameter thick (Fig. 1). The pressure cushion is filled with water and kept under hydrostatic pressure. The transparent model is placed and secured on top of a light-box. The porosity ϕ and intrinsic permeability κ are measured for all the models. Average values are: $\phi = 0.62 \pm 0.02$ and $\kappa = (0.017 \pm 0.002) \cdot 10^{-3}\text{cm}^2$ ($\approx 1800 \pm 200$ Darcy).

The wetting liquid is either a 80–20% or a 90–10% by weight *glycerol–water* solution, dyed with 0.1% *Negrosine*, and the invading fluid is *air*. At room temperature, the wetting

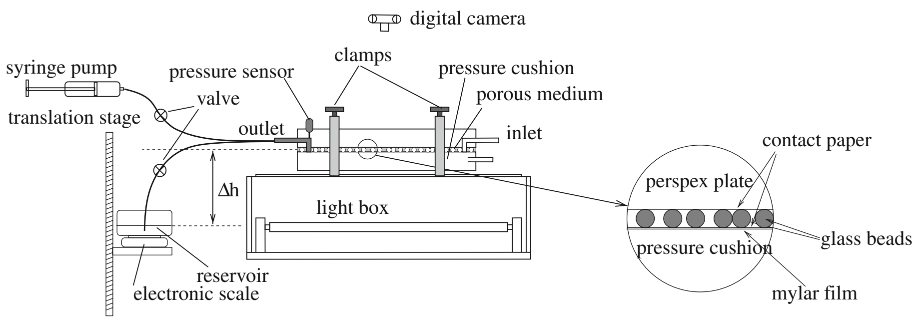

Fig. 1 Sketch of the experimental rig used for the flow experiments. The two-dimensional porous model is clamped to a light-box and kept in place by a pressure cushion

glycerol–water solutions have measured viscosities of $\mu_\mathrm{w} \approx 0.050$ Pa.s and 0.165 Pa.s and densities of ρ_w = 1,209 and $1,235\,\mathrm{kg\,m^{-3}}$, respectively. The corresponding parameters for the non-wetting air are $\mu_\mathrm{nw} = 1.9 \cdot 10^{-5}$ Pa s and $\rho_\mathrm{nw} = 1.20\,\mathrm{kg\,m^{-3}}$. The viscous ratio is thus $M = \mu_\mathrm{nw}/\mu_\mathrm{w} \sim 10^{-4}$, which is low enough to render the pressure gradient negligible in the non-wetting liquid. The surface tension (γ) between the two liquids is $\gamma_{BC} = 6.4 \cdot 10^{-2}\,\mathrm{N\,m^{-1}}$ (Vedvik et al. 1998). Two different liquid mixtures are used in order to tune the viscosity contrast of the fluids while maintaining the wetting properties. The 80–20% *glycerol–water* solution is used in the experiments presented in Sect. 3 while the 90–10% solution is used in the experiments presented in Sect. 4. In all experiments presented in Sect. 4, the temperature in the displaced wetting liquid is measured to enable control of the viscosity of the wetting liquid (and thus, of the capillary number).

The collected data consist of pressure measurements, pictures of the displacement structure and the extracted liquid volume. The absolute pressure in the wetting liquid is measured at the outlet channel (Fig. 1) using a *Honeywell 26PCA* or a *Sensor Technics 26PC0100 Flow Through* pressure sensor. Images are taken with a *Kodak DCS 420* or a *Nikon D200* digital camera. The extracted volume of wetting fluid is also recorded. All the data were collected and synchronized by a computer.

In this article, results from two model sizes are presented. All the experiments presented in Sect. 3, are performed on a model with W = 200 mm and L = 350 mm (called the *small model*). Besides this, in Sect. 4 we present results from a set of experiments for which L = 840 mm and W = 215 mm (called the *large model*).

Results from two fundamentally different types of experiments are presented: (i) quasi-static and (ii) constant flow rate experiments. In the first case, the flow is driven by slowly changing the pressure difference over the model. In the second case, a preset constant flow rate is imposed by means of a syringe pump or a tailored gravity pump (Méheust et al. 2002; Løvoll et al. 2004) (see Fig. 1). Since the observed structure is highly dependent on the imposed flow rate, the latter method has the advantage that invasion happens at a constant well-defined capillary number. This ensures that the length scales characteristic of the present flow regimes stay constant during the experiments (Løvoll et al. 2004; Toussaint et al. 2005).

3 Saturation–Pressure Relation: From Capillary Fingering to Viscous Fingering

As mentioned in the previous section, two different types of primary drainage experiments were performed. In the first set of experiments, the pressure difference across the model was controlled, and we performed slow (quasi-static) capillary fingering experiments. In the second set of experiments, a faster constant flow rate was imposed to investigate the transition to viscous fingering. This was done on the same model as the quasi-static experiments, using a syringe pump. This allowed to perform constant flow rate (Ca) experiments with the capillary number as tuning parameter. These two sets of experiments were carried out with the same porous model (of dimensions 1 mm × 200 mm × 350 mm), and will be presented in this section.

A third set of experiments, also at imposed capillary number, was performed, in which we analysed optically the invasion structure, simultaneously to the retention–saturation dependence. This was done in a larger model, of dimensions 1 mm × 840 mm × 215 mm. The results of these experiments and their treatment to obtain a model of the velocity dependence of the curves will be presented in Sect. 4.

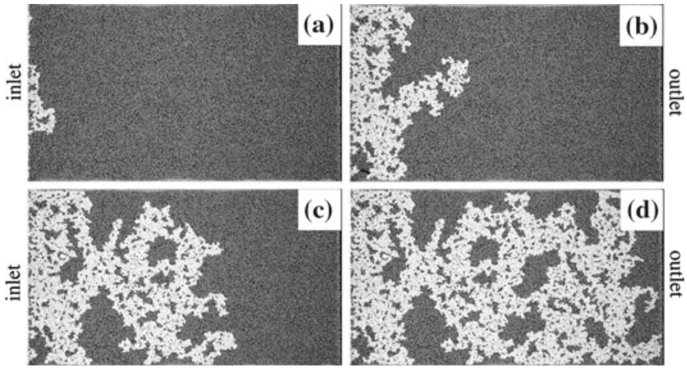

Fig. 2 Snapshots showing the evolution of a quasi static drainage experiment. The wetting glycerol–water solution is dark and the air appear as white. The experiment is driven by slowly increasing the pressure difference over the system. The snapshots **a**, **b**, **c** and **d** are taken at ∼23.0, 15.3, 7.7 and 0 h before breakthrough, respectively. The total time from start to breakthrough was ∼48 h. The snapshots are indicated in the saturation–pressure curve on Fig. 3

3.1 Quasi-Static Experiments Under Imposed Pressure Head

Figure 2 shows a selected set of images from a single quasi-static drainage experiment. The sequence a–d shows the invader from the start of invasion up to just before 'breakthrough', i.e. when the invader reaches the outlet channel. The invading cluster is typical of capillary fingering (Lenormand and Zarcone 1985), it spans the whole system width and leaves behind trapped droplets of wetting fluid, of various sizes (only limited by the system size). The snapshots in Fig. 2 are also referred to in the corresponding saturation–pressure curve in Fig. 3. In this experiment, the pressure drop over the system was changed slowly by keeping the atmospheric pressure at the inlet, while slowly lowering an open reservoir connected to the model outlet by tubes fully filled with the low compressible wetting fluid: this imposes a pressure drop corresponding to the hydrostatic pressure drop in the outlet tube (the vertically movable reservoir is indicated in Fig. 1). In order to minimize any additional pressure drop in the system due to fluid friction in the viscous fluid (dynamic effects), the reservoir is displaced vertically by small increments, and kept at rest between two successive increments until the fluids are not flowing anymore. At this point, the pressure at the setup outlet is constant and related to the atmospheric pressure P_{atm} and to the altitude of the reservoir (referenced with respect to the outlet's altitude) through the law of hydrostatic pressure. As the setup inlet is open to the air, the pressure there is P_{atm}, so the deviation of the pressure at the outlet from the atmospheric pressure also happens to be the pressure head between the setup inlet and outlet. Since the viscosity of the air is negligible with respect to that of the liquid, that pressure head is also the sum of the capillary pressure and of the pressure head through the viscous liquid. This way of driving the system is what we call 'quasi-static'. As described in the previous section, we measure the amount of liquid extracted from the model and the pressure at the setup outlet (gauge pressure sensor). From these mass measurements, the saturation of the non-wetting liquid (S_{nw}) is calculated as a function of time. By combining the calculated saturation with pressure measurements, a standard saturation–pressure curve is obtained. Pressure–saturation data from the experiment addressed in Fig. 2 are plotted in Fig. 3. As can be seen in Fig. 3, the pressure measurements exhibit notable fluctuations during the drainage process. The sudden

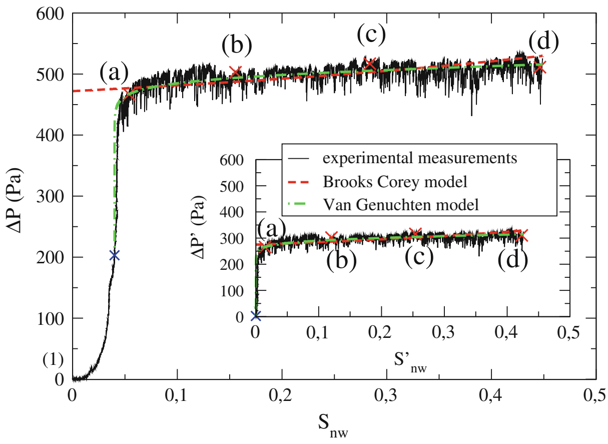

Fig. 3 Pressure–saturation curve from a quasi-static primary drainage experiment. The plotted pressure is the pressure difference over the model (from invasion front to outlet channel). The pressure was measured with a single gauge sensor in the outlet channel where the pressure recorded before the invasion process starts is used as reference. The plotted data were taken from the experiment shown in Fig. 2, the corresponding images are indicated by red crosses on the graph **a**–**d** from left to right. The subplot indicates the modified pressure and saturation, with a reference taken at the moment indicated by the blue cross, after the invader has filled a grain free buffer region in the Hele-Shaw cell, when the interface between the two fluids reaches the boundary of the granular medium. The two curves plotted are Brooks-Corey (*dashed*) and Van Genuchten (*dot-dashed*) models fitted on the data in the subplot—and reported on the main figure. This saturation-pressure curve seems consistent with a behaviour typical of soil samples

(random) jumps seen around the plateau corresponding to the hydrostatic pressures imposed by the reservoir happen during the dynamic stages, that is just after each displacement increment of the reservoir and before the flow has ceased, as the fluid interface (invasion front) penetrates new pores. During these dynamic stages, the measured pressure is different from that imposed at the setup outlet by the reservoir under static conditions. In order to invade a pore, the capillary pressure has to exceed the *capillary threshold pressure* for that pore throat. As this happens the capillary pressure decreases rapidly, the pore is filled with the invading fluid and the fluid interface in the surrounding pores retracts in order to adjust to the new capillary pressure. The size of these pressure jumps is random since the capillary thresholds are randomly distributed (Måløy et al. 1992; Furuberg et al. 1996). All pore necks in the system have an associated capillary threshold pressure. These threshold pressures are determined by the local pore geometry, the surface tension between the fluids, and the local wettability. Therefore, for a given porous medium and fluid pair the thresholds will have a given distribution. During drainage, a subset of this distribution is probed before the invader percolates the system (Auradou et al. 1999; Schmittbuhl et al. 2000; Auradou et al. 2003). If the experiment is driven by slowly increasing the pressure difference between the air and the liquid phase over the model, the invasion process starts once the pressure has reached the lowest pressure in the capillary threshold pressure distribution. For the data plotted in Fig. 3, this corresponds to the steep increase in pressure as air start invading the system. As the pressure is slowly increased further a larger portion of the threshold distribution becomes available for invasion, and while the pressure slowly changes, the non-wetting fluid invades the system and the saturation of non-wetting fluid increases, until the air percolates the system at breakthrough. Therefore, for 'quasi-static' experiments, relatively large changes in saturation occur for small pressure increases once the pressure is established at values well inside the capillary threshold distribution. One can directly compare the pressure saturation curve of these quasi-static tests in grain-filled Hele-shaw cells to standard models from the hydrology literature: denoting the effective water saturation as

$$S_{\mathrm{e}} = \frac{S_{\mathrm{w}} - S_{\mathrm{wr}}}{1 - S_{\mathrm{wr}}} = \frac{1 - S_{\mathrm{nw}} - S_{\mathrm{wr}}}{1 - S_{\mathrm{wr}}},$$

where S_{wr} is the residual water saturation, the Brooks–Corey model (Brooks and Corey 1964) is normally written as

$$p_{\mathrm{c}} = p_{\mathrm{d}}\, S_{\mathrm{e}}^{1/\lambda},$$

where p_{c} is the capillary pressure of the soil sample at the Darcy scale and p_{d} is the air entry pressure. A least-square fit of the reduced data to this model is shown in Fig. 3. The corresponding fit parameters are: $p_{\mathrm{d}} = 275$ Pa, $\lambda_{BC} = 3.1$, and $S_{\mathrm{wr}} = 0$. Typically, for soils, λ stands between 0.2 and 3, the highest values corresponding to highly non-uniform grain-size distribution. The fact that we obtain a value close to the higher naturally occurring values, is consistent with the fact that the nearest neighbour distance, in such layers of beads put at random on a sticky plate, is certainly highly non-uniform compared to a three-dimensional packing of grains stacked under gravity. Given the value of the interfacial tension γ, the entrance pressure corresponds to a minimal curvature in the largest pore necks of $r_{\|} = \gamma / p_{\mathrm{d}} = 0.25$ mm, which is of the order of a quarter of bead size: this is consistent with the expected order of magnitude for such a packing. The fact that S_{wr} is obtained at its smallest possible value, 0, can be explained by the fact that apart from the large fluctuations, no trend of any upward curvature of the pressure–saturation curve can be seen in Fig. 3.

Another common model for such curves is the Van Genuchten water retention function (Van Genuchten 1980),

$$p_{\mathrm{c}} = \frac{1}{\alpha_{\mathrm{vg}}} \left(S_{\mathrm{e}}^{\frac{n}{1-n}} - 1 \right)^{\frac{1}{n}}$$

A fit to this model is shown as the dash-dotted curve in Fig. 3, and leads to Van Genuchten parameters $\alpha_{\mathrm{vg}} = 0.0029\,\mathrm{Pa}^{-1}$ and $n = 9.9$. The value obtained for α_{vg} is consistent with that of a soil, the value of n is a few times larger than the one usually obtained for three-dimensional natural soils. This can be presumably attributed to differences in the packing, and notably the fact that the transition from the steeply growing part of the curve, up to point (a), into a plateau with fluctuations, is quicker than for many natural three-dimensional soils, most likely due to the fact that only one diameter of beads is represented in the packing. From a general point of view, it is interesting to note that this two dimensional medium presents a quasi-static pressure–saturation curve (and model parameters) somewhat similar to what could be expected for its three dimensional counterpart, and presumably represents well the processes at play in tests on opaque three-dimensional media.

3.2 Experiments Under Finite Imposed Flow Rate

As mentioned previously, we have also driven the system at constant capillary number by means of a syringe pump. In this case, a constant flow rate is imposed, and the pressure over the model will at any time be the pressure needed to maintain the flow rate. Figure 4 shows the saturation–pressure data curve for syringe pump driven experiments at different imposed flow rates. The black curve in Fig. 4 shows a slowly driven experiment, at Ca $= 0.01$. It exhibits the same initial pressure buildup in the beginning of the experiment as for the 'quasi-static' experiment (Fig. 3). When the average capillary threshold pressure is reached

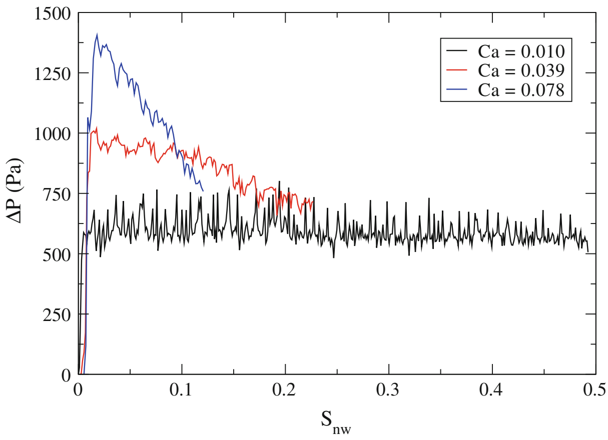

Fig. 4 Saturation–pressure curves from three primary drainage experiments on the *small* model, driven at constant flow rate (constant Ca) by a syringe pump. S_{nw} is the saturation of the system in the non-wetting fluid (air), related to the saturation in wetting fluid (water–glycerol) S_{w} by $S_{\mathrm{nw}} = 1 - S_{\mathrm{w}}$. The total duration of the drainage experiments are ∼2.4 h, ∼10 min. and ∼3 min for Ca = 0.010, 0.039 and 0.078, respectively

the pressure fluctuates more strongly around this constant value during the whole drainage process. The two other curves shown in Fig. 4 present similar results for faster syringe pump driven experiments. These curves still show the random pressure fluctuations caused by the variation of capillary pressure thresholds. Additionally, compared to quasi-static drainage curves, the slope of the drainage curve is 'reversed' by the boundary conditions imposed on fluid velocities (constant flow rate): after the initial pressure buildup, the pressure is steadily decreasing while the air saturation increases. This feature was also observed with different boundary conditions in some numerical studies of dynamic fingering (Dahle et al. 2005). As already known and shown in other studies (Hassanizadeh et al. 2002; Dahle et al. 2005), we observe here that for a given porous medium there is no one-to-one relation between the saturation and the pressure over the system. Boundary conditions and dynamic effects have a significant impact on the pressure versus saturation relation. In the next section, we shall look at dynamic effects more closely.

4 Relating Capillary Number, Saturation, Pressure and System Size

We now turn to the results from experiments carried at different imposed flow rate on the large model (1 mm × 215 mm × 840 mm). Dynamic capillary pressure as measured in water retention experiments (Hassanizadeh et al. 2002) is often defined as the total pressure difference over the porous medium (ΔP), or some spatial average of the pressure over one of the present phases (Dahle et al. 2005) (see discussion in Sect. 5). The total pressure difference is a combination of capillary pressure along the invasion front (P_{c}) and the pressure head caused by viscous effects (ΔP_{v}) (Washburn 1921)

$$\Delta P = P_{\mathrm{c}} + \Delta P_{\mathrm{v}} \tag{3}$$

In drainage, the capillary pressure is essentially unaffected by the speed of the flow and system size (Méheust et al. 2002), except in details, since the pores invaded are not exactly the same (this is, however, not the case in fast imbibition, see (Weitz et al. 1987)). The order of magnitude of this capillary pressure does not change in time and as demonstrated in Sect. 3 it can be treated as randomly fluctuating around a well-defined average value. However, the viscous part (ΔP_{v}) is dependent on finite size effects and invasion speed. In the following, the reported measured pressure (P) is, therefore, equal to the viscous pressure drop:

$$P = \Delta P_{\mathrm{v}} \tag{4}$$

It is obtained from our measurements by using the pressure just before breakthrough (t_{bt}) as reference null pressure $P(t_{\mathrm{bt}}) \equiv 0$.

In Fig. 5, snapshots of the invasion structure are shown for four different drainage experiments. The experiments are all performed at constant flow rate and the snapshots are such that the viscous pressure drop (P) across the cell is the same in all snapshots. These pictures do also illustrate how the saturation of the non-wetting liquid changes with capillary number.

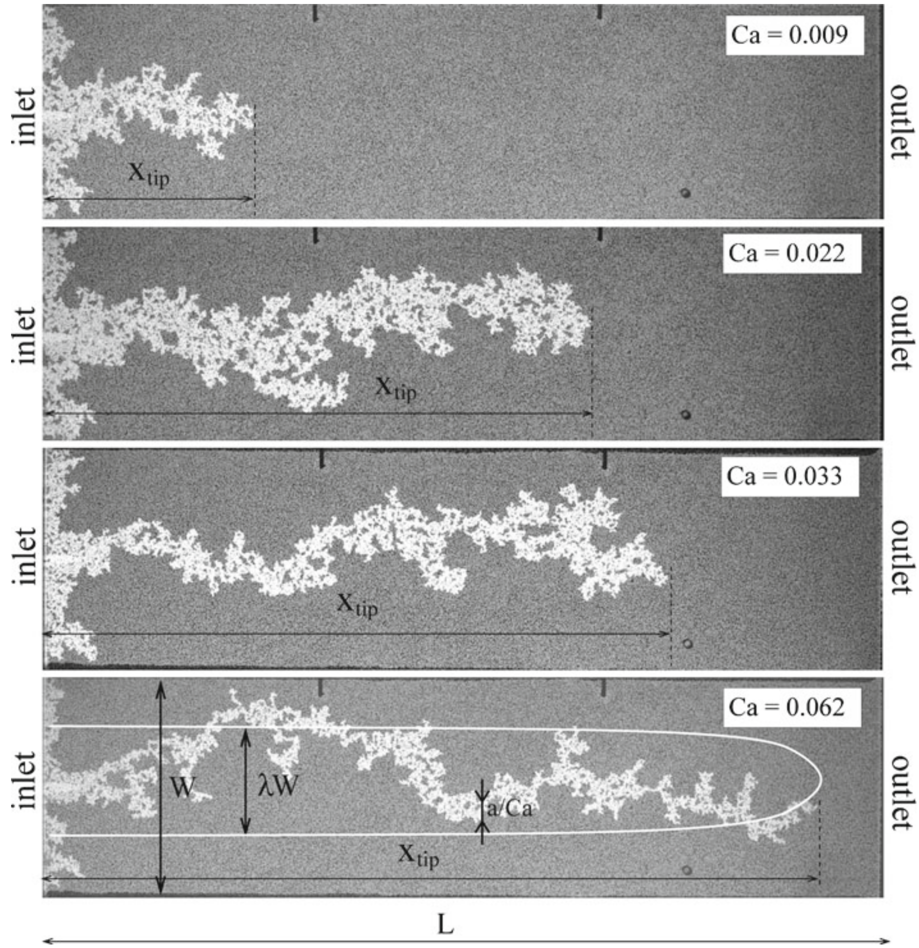

Fig. 5 Images of experiments taken at different withdrawal rates (expressed by the capillary numbers). The viscous pressure difference over the model is $P \sim 490$ Pa in all the pictures. The invasion structure is initiated in the center of the flow cell by creating a small 'notch' in the porous medium at the centre of the inlet. On the lower image relevant length scales are indicated

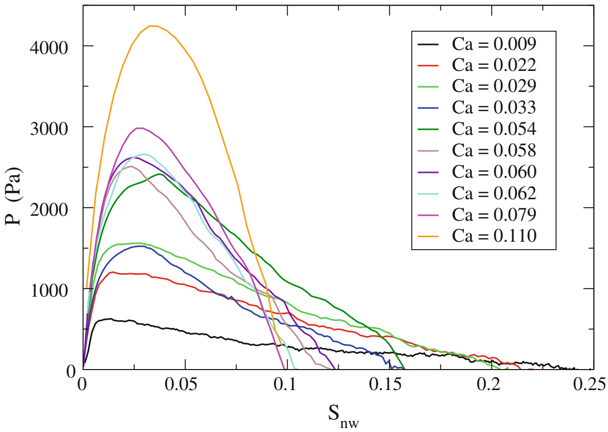

Fig. 6 Pressure (see Eq. 4) as a function of the non-wetting fluid saturation (S_{nw}) for some experiments on the *large* model. The initial pressure buildup is due to inertia in the liquid. The effect is explained in Appendix A

As the invasion rate increases, the invasion structure gets thinner, which again leads to lower saturation of the invading non-wetting liquid. The pressure versus air-saturation (S_{nw}) plots for these drainage experiments are shown in Fig. 6. After the initial pressure buildup, these experiments show the same behaviour as the two 'fast' syringe driven experiments in the previous section (Fig. 4).

If the system is big enough, viscous effects will always dominate the problem at larger length scales. The crossover length scale is given by Eq. (2), $l_c = a/\mathrm{Ca}$. Above this length scale, the viscous pressure drop dominates over capillary threshold fluctuations and the displacement dynamics is in the viscous fingering regime. Where displacement will take place in narrow channels and branched loop-less structures, as shown in Fig. 5 (Løvoll et al. 2004; Toussaint et al. 2005). At scales below this, capillary fluctuations dominate the dynamics, and the resulting structure is characteristic of the capillary fingering regime, with droplets of wetting fluid remaining trapped in loops of the invading non wetting fluid. Looking at pictures from four experiments at different speeds and at the same P (Fig. 5), it is obvious that the viscous pressure drop is related to the position of the most advanced finger and the capillary number. Earlier studies have also shown that the invasion structure is screened by the advancing invasion front and that the propagation speed of the invasion front is fairly constant (Løvoll et al. 2004; Toussaint et al. 2005). The process is thus stationary in a referential attached to the advancing finger tip. All the invasion happens in a zone close to this tip. As was obtained in a detailed analysis of the pressure field, measuring at several points around the invader in each experiment (Løvoll et al. 2004), the pressure is roughly constant behind the finger tip, and the viscous pressure gradient in front of the invasion structure is essentially constant. The viscous pressure is thus (to the first order) a linear function of the distance from the outlet to the most advanced finger:

$$P = \overline{\nabla P}(L - x_{\mathrm{tip}}) \tag{5}$$

where $\overline{\nabla P}$ is the average viscous pressure gradient and x_{tip} is the tip position of the most advanced fingertip (indicated on Fig. 5). $\overline{\nabla P}$ can be approximated by Darcy's law:

$$\overline{\nabla P} = \frac{\mu_{\mathrm{w}} v_{\mathrm{f}}}{\kappa} \tag{6}$$

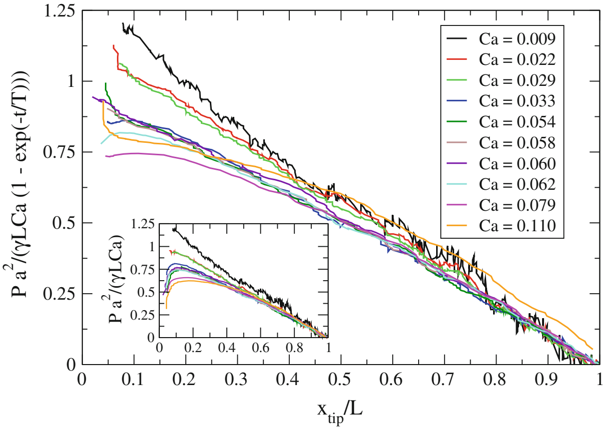

Fig. 7 Data collapse of pressure data as function of x_{tip}/L, where the initial pressure buildup is corrected with the method outlined in Appendix A using $T = 114$ s. The *inset* shows scaled pressure data without initial pressure correction

Consequently, we can write the pressure change caused by viscosity effects as:

$$P = \frac{\mu v_{\text{f}}}{\kappa}(L - x_{\text{tip}}) = \frac{\gamma \text{Ca}}{a^2}(L - x_{\text{tip}}), \tag{7}$$

where we have used the expression of the capillary number, Eq. 1. This allows to express the ratio of x_{tip} to the system length L as a function of pressure and capillary number:

$$1 - \frac{x_{\text{tip}}}{L} = \frac{a^2}{\gamma L \text{Ca}} P \tag{8}$$

where we recall that P is the measured viscous pressure drop over the system (see Eq. 4).

In the inset of Fig. 7, the rescaled pressure $a^2 P/(\gamma\, L\, \text{Ca})$ is plotted as a function of the reduced finger tip position x_{tip}/L for a range of capillary numbers. The pressure drop across the model can also be corrected for the inertia of the fluid during the initial acceleration. In Appendix A, we show how these initial inertial effects lead to a multiplicative factor $(1 - e^{-t/T})$ for the time-dependent pressure, where T is the time characteristic of the initial pressure buildup. A way to correct for these inertial effects is then, after the determination of T by a least square fit, to represent the corrected pressure $P/(1 - e^{-t/T})$ rather than the measured pressure. This is shown in Fig. 7. Based on the argument above, we introduce the dimensionless reduced pressure:

$$P^* \equiv P \frac{a^2}{\gamma L \text{Ca}} \left(1 - e^{-t/T}\right)^{-1} = 1 - \frac{x_{\text{tip}}}{L} \tag{9}$$

Using our knowledge of the morphology of the invading cluster in the transition from viscous- to capillary-fingering (Løvoll et al. 2004; Toussaint et al. 2005), a relation for the non-wetting liquid saturation (S_{nw}) as a function of finger tip position x_{tip}, capillary number (Ca) and the width of the system W can also be derived. This is done by counting the number of invaded pores N_{inv} as a function of x_{tip}/L. Earlier studies (Løvoll et al. 2004; Toussaint et al. 2005) have shown that the invasion typically takes place in a limited region in the center of the channel. The width of this region is λW, where W is the width of the system and $\lambda \simeq 0.4$. Above this scale, we have a linear channel where the displacement structure could be considered homogeneous. Inside this channel (of width λW), two flow regimes are present depending on the length scale considered. At large scales (between λW and l_c) the flow structure is that of viscous fingering, which is a treelike structure with branches and no loops. The viscous fingering structure is a fractal with a fractal dimension $D_v \simeq 1.53$ (Toussaint et al. 2005). At smaller scales, capillary forces dominate the flow process and the displacement structure is that of capillary fingering. Capillary fingering is also fractal, with fractal dimension $D_c \simeq 1.83$ (Wilkinson and Willemsen 1983; Lenormand and Zarcone 1985). The relevant length scales in the problem are sketched in Fig. 5. The argument below is thus valid when:

$$a \ll \frac{a}{\mathrm{Ca}} = l_c \ll \lambda W \tag{10}$$

When the most advanced finger tip is at x_{tip}, the invasion has taken place in a channel of area $\lambda W x_{\mathrm{tip}}$. This channel is composed of $x_{\mathrm{tip}}/(\lambda W)$ square zones of linear size λW. In each of these zones the invading viscous fingering structure goes through $(\lambda W \mathrm{Ca}/a)^{D_v}$ square boxes of linear size a/Ca. And in each such box, the invader occupies on average $[(a/\mathrm{Ca})/(\alpha a)]^{D_c} = (\alpha \mathrm{Ca})^{-D_c}$ pores of linear size αa, with α a geometrical pre factor, of order of magnitude 1 (indicating that the average pore volume is *not* exactly a^3 but rather $(\alpha a)^3$). The total number of invaded pores is thus:

$$\begin{aligned} N_{\mathrm{inv}}(x_{\mathrm{tip}}) &= \frac{x_{\mathrm{tip}}}{\lambda W}\left(\frac{\lambda W \mathrm{Ca}}{a}\right)^{D_v}(\alpha \mathrm{Ca})^{-D_c} \\ &= \frac{x_{\mathrm{tip}}(\lambda W)^{D_v-1}}{a^{D_v}}\alpha^{-D_c}\mathrm{Ca}^{D_v-D_c} \end{aligned} \tag{11}$$

The total volume accessible to the fluid is $W La\phi$ and the average pore volume is $(\alpha a)^3$. The saturation of the non-wetting fluid, S_{nw}, can thus be written as:

$$\begin{aligned} S_{\mathrm{nw}} &= \frac{N_{\mathrm{inv}}(\alpha a)^3}{W La\phi} \\ &= \frac{x_{\mathrm{tip}}}{L}\frac{a^{2-D_v}}{\phi}\frac{(\lambda W)^{D_v-1}}{W}\alpha^{(3-D_c)}\mathrm{Ca}^{D_v-D_c} \end{aligned} \tag{12}$$

This relation can be inverted to obtain a dimensionless reduced saturation S^* which is a reduced variable of the tip position, x_{tip}/L. It relates to the dimensional saturation of the wetting fluid, S_{nw} , according to:

$$S^* \equiv \frac{x_{\mathrm{tip}}}{L} = S_{\mathrm{nw}}\,\alpha^{(D_c-3)}\frac{\phi}{\lambda^{D_v-1}}\left(\frac{W}{a}\right)^{2-D_v}\mathrm{Ca}^{D_c-D_v} \tag{13}$$

Based on Eqs. 9 and 13, we predict that P^* and S^* are related through the relation:

$$P^* = 1 - S^* \tag{14}$$

This is indeed the case to a large extent, as shown in Fig. 8. The satisfactory character of this data collapse for the reduced pressure drop versus reduced saturation at various speeds can be seen when comparing Fig. 8 to the raw data presented in Fig. 6. In addition, the above arguments can be applied to the particular state $P^* = 0$, i.e. at breakthrough, when the invading non wetting fluid reaches the outlet, at $x_{\mathrm{tip}} = L$. The saturation reached at this time gives the final saturation which can be retrieved before the invader reaches the outlet, and thus gives an estimate of the efficiency of the invasion process before breakthrough.

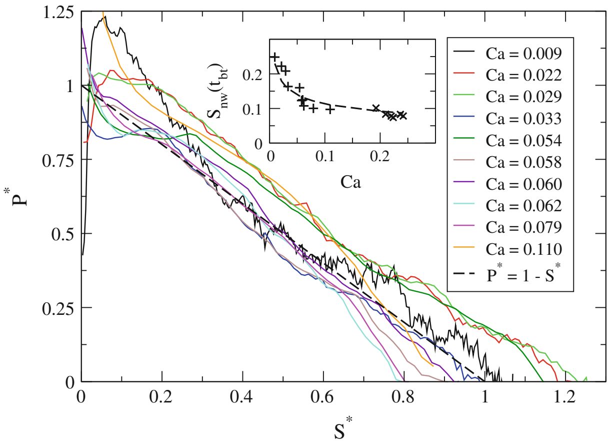

Fig. 8 Data collapse of saturation versus pressure curves from experiments performed at capillary numbers between $9 \cdot 10^{-3}$ and $1.1 \cdot 10^{-1}$. The collapse is obtained by plotting P^* as a function of S^*. The collapse is consistent with the prediction in Eq. 14; it is indicated by the *dashed line*. Compare this to the original data shown in Fig. 6. The only 'free parameter' in the data collapse is the geometrical pre-factor α, $\alpha = 0.75$ is used in the collapse. The *inset* shows the saturation of the non-wetting fluid (S_{nw}) at breakthrough time (t_{bt}) as a function of the capillary number. The *dashed line* in the inset is the breakthrough saturation predicted by Eq. 15

This point corresponds to the prediction $S^* = 1$, i.e. according to Eq. 13, to a final non-wetting saturation S_{nw} at breakthrough

$$S_{\mathrm{nw}}(t_{\mathrm{bt}}) = \alpha^{(3-D_{\mathrm{c}})} \frac{\lambda^{D_{\mathrm{v}}-1}}{\phi} \left(\frac{a}{W}\right)^{2-D_{\mathrm{v}}} \mathrm{Ca}^{D_{\mathrm{v}}-D_{\mathrm{c}}}. \tag{15}$$

and a water residual saturation $S_{\mathrm{w}} = 1 - S_{\mathrm{nw}}$ that reads accordingly. This prediction for the final air saturation as a function of the speed of the invasion process Ca is shown in the inset of Fig. 8 as a dashed curve. The measurements of the final invader saturation at breakthrough for experiments carried out at various capillary numbers, represented as the crosses, are in good agreement with this prediction.

5 Discussion

The theory leading to the scaling relation between pressure and saturation in Eq. (14) is valid for a limited range of capillary numbers, for high viscous contrast and for systems without gravity. The limits in capillary numbers are given in Eq. 10. We believe that the upper limit in capillary number is $\mathrm{Ca} \approx 1/10$ which implies that our largest reported capillary number $\mathrm{Ca} = 0.11$ is close to this limit. For higher capillary numbers, the width of the viscous fingers is close to the pore scale and there is no capillary fingering structure at smaller scales. This would imply that the saturation is independent of the capillary number at higher flow rates and is constant for all Ca higher than the ones satisfying Eq. (10). This observation is consistent with the measured breakthrough saturation shown in the inset of Fig. 8 where the saturation level seems to be fairly constant for capillary numbers above ~ 0.1. At the other end of the scale range, it is the size of the system that sets the limit. When the capillary number is low enough for the crossover length scale to reach the system width ($l_{\mathrm{c}} \approx \lambda W$) (see Fig. 2), there is no crossover from capillary to viscous fingering: a constant breakthrough saturation is obtained. In our case, this corresponds to $\mathrm{Ca} \approx 1/100$ which is of the order of the smallest presented capillary number.

It should also be noted that the invading cluster is fractal for all capillary numbers and the saturation, therefore, depends on the width W. At finite flow rates, the system size determines the importance of viscous effects (dynamic effects). A given capillary number Ca will result in a crossover length scale $l_c = a/\mathrm{Ca}$. Above this length scale viscous effects will dominate the problem. This observation raises a question on the general validity of the *representative elementary volume* (*REV*) assumption commonly used in Darcy scale modeling.

The data collapse of experimental measurements presented in Fig. 8 displays a certain dispersion. The quality of this collapse becomes evident when it is compared to the raw saturation–pressure data shown in Fig. 6. Figure 7 shows that the collapse of the pressure data is good, so the main scatter in the collapse of Fig. 8 results from the saturation data. Even if there is scatter in the saturation data, we will claim that no systematic trend is visible. The experiments are carried out on disordered media, and the morphology of the invasion structures are statistically fractals. On such a small systems, noise is expected. For these model systems there are also boundary effects at the inlet and outlet. The arguments leading to Eq. 12 assume that the process is stationary, and they do not take boundary effects into account. If one looks at Fig. 5, it is evident that there are boundary effects near the inlet channel and that the saturation there is different from the saturation further into the model. In addition to this, the saturation in the frontal region is different from the stationary part left behind the advancing front, so when the invasion front reaches the outlet channel, the saturation will be lower in the vicinity of that channel than the saturation away from it. Earlier studies (Løvoll et al. 2004; Toussaint et al. 2005) have shown that the size of the active frontal region is of the order of the system width. At breakthrough there is, therefore, a region at a distance $\propto W$ where the saturation is lower than in the 'completely invaded' parts of the system. It is, therefore, crucial that the system be large enough to average out these fluctuations and minimize end effect. Therefore, when designing such experiment, we would suggest that one ensures that $L \geq 4W$ and in addition that the system be wide enough so that the Eq. 10 allows for a sufficiently large range of available capillary numbers.

As said earlier, the pressure (or dynamic capillary pressure) is often measured between two points, one in one phase, the other in the other one. Commonly, this is done practically at the inlet and outlet. However, some authors (Hassanizadeh et al. 2002; Dahle et al. 2005) define the dynamic capillary pressure as being the difference between the (spatial) average pressure in one phase, and the average pressure in the other one. Although this definition is easy to use in a numerical system, it is difficult to use in practice in an experimental system, where the pressure in the two phases is normally known only at a limited set of measurement points. We have measured (Løvoll et al. 2004; Toussaint et al. 2005) that the pressure in the wetting liquid is roughly spatially linearly decreasing in front of the invading tip, and roughly constant (equal to P_c) on the sides behind the tip, this is an approximation, see (Løvoll et al. 2004) for details of the pressure modeled and measured around the air fingers. The pressure in the continuous air phase is roughly constant. Consequently, the spatial average of the air pressure is P_{atm}, and the average pressure in the wetting phase is dominated by the pressure ahead of the tip, i.e. the term

$$\int_{x_{\mathrm{tip}}}^{L} dx \left(P_{\mathrm{atm}} + P_c + P \cdot \frac{x - x_{\mathrm{tip}}}{L - x_{\mathrm{tip}}} \right) \Big/ \left(\int_{x_{\mathrm{tip}}}^{L} \mathrm{d}x \right) = P_{\mathrm{atm}} + P_c + P/2.$$

Here, this difference between the average pressures in both phases average should be around

$$P/2 + P_c,$$

when the measured total variation across the cell is

$$\Delta P = P + P_c.$$

Both should be qualitatively the same in terms of dependence on the flow speed, system size, etc. As with the measurements presented here, the 'dynamic capillary pressure' is expected to be system size dependent. In our case, the invading structure is screened from the viscous pressure field by the active zone near the most advanced finger (Løvoll et al. 2004). This implies that in the frontal region there is a spatial trend in the capillary pressure along the fingers: the capillary pressure in the fingertips (where invasion is happening) is larger than further back. This has been reported in earlier studies (Løvoll et al. 2004), and the effect is also present in the classic Saffman–Taylor solution (Saffman and Taylor 1958).

It is also interesting to note that the models proposed by the authors of references Hassanizadeh et al. (2002) and Dahle et al. (2005) include a linear dependency of the time derivative of the saturation ($\partial S/\partial t$) in the definition of the 'dynamic capillary pressure'. It is important to mention that for a system of volume V and porosity ϕ, $\partial S/\partial t = Q\phi/V$, so that $\partial S/\partial t \propto$ Ca. This effect, reported by Hassanizadeh et al. (2002) and Dahle et al. (2005), is indeed a viscous effect (Niessner and Hassanizadeh 2008), and for high viscous contrasts the proportionality factor has been derived in Sect. 4.

In the scaling theory developed in Sect. 4, the invader morphology at small scales is used to predict 'Darcy scale' behaviour. We, therefore, believe that this type of argument could be very useful for Darcy scale modeling. Our results also demonstrate that for flow conditions where the morphology of the invader is fractal, the saturation–pressure relation is system size dependent. Therefore, in a sense there is no such thing as a hydrodynamic 'continuum scale' in fractal systems. Our approach is thus rather a way to understand the problem at the relevant scales than a model for large scale continuum modelling. In real reservoir modelling, one also has to consider effects and problems not included in our theory. At larger length scales, inhomogeneities in the porous media are expected and will play an important role. This implies that the relevant length scales will be different in the different parts of the system. The invasion speed and thus the capillary number can vary in space and time. In addition, in three dimensional systems, gravity and fluid density differences can be very important. When dealing with systems where gravity is important, viscous effects will still be important (Hill 1952; Saffman and Taylor 1958; Méheust et al. 2002) and in this class of problems also the ratio of the relevant forces can be used to predict the relevant length scales of the displacement process (Wilkinson 1984; Chaouche et al. 1994a,b; Birovljev et al. 1991; Méheust et al. 2002). Another limitation in our study is the high viscous contrast between the phases. In this respect, we would like to point out that there will generally be a high viscous contrast in systems where one of the phases is a gas, and that similar arguments have been successfully applied to systems where the viscous contrast were smaller (Frette et al. 1997; Aker et al. 2000).

In contrast to models used to describe standard water retention tests in soil samples, there are no semipermeable membranes at the inlet- and outlet-channel in the models used in this study. This makes it impossible to statically increase the pressure over the sample in order to reach the low water saturations commonly seen in published retention curves (Leverett 1941; Brooks and Corey 1964; Van Genuchten 1980; Lenhard et al. 1993; Hassanizadeh et al. 2002). This choice for our models was motivated by the idea that the lack of semi permeable membranes has the advantage of being more 'realistic', in the sense that in real reservoir systems small volumes are *not* restricted by semi permeable membranes. On the contrary, when using semi permeable membranes the system can be forced into a state which is 'out of reach' in real systems where the application of a large pressure somewhere near a given sample volume would lead to the non-wetting liquid being forced into the surrounding porous medium, without further decrease of the water saturation in the sample volume in question.

6 Concluding Remarks

Results from drainage experiments on transparent quasi-two-dimensional porous models have been reported. The reduced data were used to obtain standard pressure–saturation curves.

By using different ways of driving the invasion process, we can control the dynamic component of the pressure head and explain the experimentally observed dynamic effects by relating them to theoretical arguments. Indeed, by combining detailed information on the displacement structure with global measurements of pressure and saturation, we have derived a scaling relation relating pressure, saturation, system size and the capillary number Ca. By applying this pressure–saturation scaling relation, curves for a range of capillary numbers have been collapsed onto a system size- and Ca-independent master capillary curve. We believe that this study can have a significant impact on the understanding of the impact of dynamic effects on retention curves, and it is our hope that that the size dependence could be applied in reservoir scale modelling.

Acknowledgments We would like to thank Henning A. Knudsen and Eirik G. Flekkøy for useful discussions and suggestions. We would also like to thank the Norwegian Research council for financial support of the project. Financial support for this research from the program REseau Alsace de Laboratoires en Ingénierie et Sciences pour l'Environnement (REALISE) is also gratefully acknowledged. R. T. and Y. M. acknowledge support from CNRS for traveling between France and Norway, under a french–norwegian PICS program.

Appendix

A Pressure Adjustments

The 'gravity pump' used in the experiments consists of an open reservoir connected to the model and located a height H below the model (Méheust et al. 2002). The equation of motion for the liquid is:

$$\rho L A \phi \frac{dv}{dt} = \rho g H A - vR \tag{16}$$

where R is the total hydraulic resistance to flow. The total resistance is dominated by the resistance of the tube and valve connecting the model and the reservoir. We will therefore neglect the resistance of the porous medium. Solving the velocity $v(t)$ with the boundary conditions $v(t = 0) = 0$ and $v(t \gg T) = v_{\mathrm{f}}$, one gets:

$$v(t) = \frac{gH\rho A}{R}(1 - e^{-\frac{tR}{\rho LA\phi}}) = v_{\mathrm{f}}(1 - e^{-\frac{t}{T}}) \quad (17)$$

where $T = LA\phi\rho/R$ is a system specific relaxation time. By using Darcy's law and an effective pressure gradient set by the pressure drop exerted over the distance between the most advanced finger tip position $x = x_{\mathrm{tip}}$ and the outlet at $x = L$ we get:

$$v = -\frac{\kappa}{\mu_{\mathrm{w}}}\nabla P \simeq \frac{\kappa}{\mu_{\mathrm{w}}}\frac{P}{L - x_{\mathrm{tip}}} \quad (18)$$

Combining Eqs. 17 and 18, and the definition of the capillary number (1) yields:

$$P(t) = \frac{\mu_{\mathrm{w}}}{\kappa}v_{\mathrm{f}}(1 - e^{-\frac{t}{T}})(L - x_{\mathrm{tip}}) \approx \frac{\mathrm{Ca}\gamma}{a^2}(1 - e^{-\frac{t}{T}})(L - v_{\mathrm{tip}}t) \quad (19)$$

where the speed of the advancing finger tip v_{tip} is assumed constant. The latter Eq. 19 can be used to correct for the initial pressure buildup. This is done by fitting Eq. 19 to the measured $P(t)$ with T and v_{tip} as fitting parameters. We estimate a single characteristic T by averaging the calculated T-values. This value is then used to correct for the initial pressure buildup, see Figs. 7 and 8.

References

Aker, E., Måløy, K.J., Hansen, A.: Viscous stabilization of 2D drainage displacements with trapping. Phys. Rev. Lett. **84**(20), 4589–4592 (2000)

Auradou, H., Måløy, K.J., Schmittbuhl, J., Hansen, A.: Drainage in a rough gouge-filled fracture. Transp. Porous Media **50**, 267–305 (2003)

Auradou, H., Måløy, K.J., Schmittbuhl, J., Hansen, A., Bideau, D.: Competition between correlated buoyancy and uncorrelated capillary effects during drainage. Phys. Rev. E **60**(6), 7224–7234 (1999)

Bear, J.: Dynamics of Fluids in Porous Media. American Elsevier Publishing Company, New York (1972)

Birovljev, A., Furuberg, L., Feder, J., Jøssang, T., Måløy, K.J., Aharony, A.: Gravity invasion percolation in 2 dimensions—experiment and simulation. Phys. Rev. Lett. **67**(5), 584–587 (1991)

Bohy, M., Dridi, L., Schäfer, G., Razakarisoa, O.: Transport of a mixture of chlorinated solvent vapors in the vadose zone of a sandy aquifer. Vadose Zone J. **5**, 539–553 (2006)

Bourgeat, A., Panfilov, M.: Effective two-phase flow through highly heterogeneous porous media: capillary nonequilibrium effects. Computat. Geosci. **2**(3), 191–215 (1998)

Brooks, R.H., Corey, A.T.: Hydraulic Properties of Porous Media Hydrology Paper 3. Colorado State University, Fort Collins, Colorado (1964)

Chandler, R., Koplik, J., Lerman, K., Willemsen, J.F.: Capillary displacement and percolation in porous media. J. Fluid Mech. **119**, 249–267 (1982)

Chaouche, M., Rakotomalala, N., Salin, D., Xu, B., Yortsos, Y.C.: Invasion percolation in a hydrostatic or permeability gradient: experiments and simulations. J. Fluid Mech. **119**, 249–267 (1994a)

Chaouche, M., Rakotomalala, N., Salin, D., Xu, B., Yortsos, Y.C.: Invasion percolation in a hydrostatic or permeability gradient: experiments and simulations. Phys. Rev. E **49**(5), 4133–4139 (1994b)

Dahle, H.K., Celia, M.A., Hassanizadeh, S.M.: Bundle-of-tubes model for calculating dynamic effects in the capillary-pressure-saturation relationship. Transp. Porous Media **58**(1–2), 5–22 (2005)

Dullien, F.A.L.: Porous Media Fluid Transport and Pore Structure, 2nd edn. Academic Press Inc, San Diego (1992)

Feder, J.: Fractals. Plenum Press, New York (1988)

Frette, O.I., Maløy, K.J., Schmittbuhl, J., Hansen, A.: Immiscible displacement of viscosity-matched fluids in two-dimensional porous media. Phys. Rev. E **55**(3), 2969–2975 (1997)

Furuberg, L., Måløy, K.J., Feder, J.: Intermittent behavior in slow drainage. Phys. Rev. E **53**(1), 966–977 (1996)

Hassanizadeh, S.M., Gray, W.: High-velocity flow in porous-media by Hassanizadeh and Gray—Reply. Transp. Porous Media **3**(3), 319–321 (1988)

Hassanizadeh, S.M., Celia, M.A., Dahle, H.K.: Dynamic effect in the capillary pressure—saturation relationship and its impacts on unsaturated flow. Vadose Zone J. **1**, 38–57 (2002)

Helmig, R.: Multiphase Flow and Transport Processes in the Subsurface, A Contribution to the Modeling of Hydrosystems. Springer (Environmental Engineering), Berlin (1997)

Hill, S.: Channelling in packed columns. Chem. Eng. Sci. **1**, 247–253 (1952)
Homsy, G.M.: Viscous fingering in porous media. Annu. Rev. Fluid Mech. **19**, 271–311 (1987)
Hulin, J.P., Clément, E., Baudet, C., Gouyet, J.F., Rosso, M.: Quantative analysis of an invading-fluid front under gravity. Phys. Rev. Lett. **61**(3), 333–336 (1987)
Kool, J.B., Parker, J.C.: Development and evaluation of closed form expressions for hysteretic soil hydraulic properties. Water Resour. Res. **23**, 105–114 (1987)
Lenhard, R.J., Johnson, T.G., Parker, J.C.: Experimental observations of nonaqueous-phase liquid subsurface movement. J. Contam. Hydrol. **24**, 79–101 (1993)
Lenormand, R.: Flow through porous media: limits of fractal patterns. Proc. R. Soc. Lond. A **423**, 159–168 (1989)
Lenormand, R., Zarcone, C.: Invasion percolation in an etched network: measurement of a fractal dimension. Phys. Rev. Lett. **54**(20), 2226–2229 (1985)
Lenormand, R., Zarcone, C.: Capillary fingering: percolation and fractal dimension. Transp. Porous Media **4**, 599–612 (1989)
Lenormand, R., Zarcone, C., Sarr, A.: Mechanisms of the displacement of one fluid by another in a network of capillary ducts. J. Fluid Mech. **135**, 337–353 (1983)
Lenormand, R., Touboul, E., Zarcone, C.: Numerical models and experiments on immiscible displacement in porous media. J. Fluid Mech. **189**, 165–187 (1988)
Leverett, M.C.: Capillary behaviour in porous solids. Trans. AIME **142**, 152–169 (1941)
Løvoll, G., Méheust, Y., Toussaint, R., Schmittbuhl, J., Måløy, K.J.: Growth activity during fingering in a porous Hele-Shaw cell. Phys. Rev. E **70**(2), 026301 (2004)
Luckner, L., Van Genuchten, M.T.H.: A consistent set of parametric models for the two-phase flow of immiscible fluids in the subsurface. Water Resour. Res. **25**, 2187–2193 (1989)
Måløy, K.J., Feder, J., Jøssang, T.: Viscous fingering fractals in porous media. Phys. Rev. Lett. **55**, 2688–2691 (1985)
Måløy, K.J., Furuberg, L., Feder, J., Jøssang, T.: Dynamics of slow drainage in porous-media. Phys. Rev. Lett. **68**(14), 2161–2164 (1992)
Mandelbrot, B.B.: The Fractal Geometry of Nature. W.H. Freeman, New York (1982)
Méheust, Y., Løvoll, G., Måløy, K.J., Schmittbuhl, J.: Interface scaling in a 2D porous medium under combined viscous, gravity and capillary effects. Phys. Rev. E **66**, 51603–51615 (2002)
Mualem, Y.: A new model for predicting the hydraulic conductivity of unsaturated porous media. Water Resour. Res. **12**, 512–513 (1976)
Mualem, Y.: A modified depend-domain theory of hysteresis. Soil Sci. **137**, 283–291 (1984)
Niessner, J., Hassanizadeh, S.M.: A model for two-phase flow in porous media including fluid-fluid interfacial area. Water Resour. Res. **44**(8), w08439 (2008). doi:10.1029/2007WR006721
Parker, J.C., Lenhard, R.J.: Model for hysteretic constitutive relations governing multiphase flow 1 Saturation-pressure relations. Water Resour. Res. **23**, 2187–2196 (1987a)
Parker, J.C., Lenhard, R.J., Kuppusami, T.: A parametric model for constitutive properties governing multiphase flow in porous media. Water Resour. Res. **23**, 618–624 (1987b)
Poulavissilis, A.: Hysteresis of pore water, an application of concept of independent domains. Soil Sci. **93**, 405–412 (1962)
Saffman, P.G., Taylor, G.: The penetration of a fluid into a porous medium or Hele-Shaw cell containing a more viscous liquid. Proc. Soc. Lond. Ser. **A 245**, 312–329 (1958)
Sahimi, M.: Flow and Transport in Porous Media and Fractured Rock. VCH Verlagsgesellschaft mbH, Weinheim, Germany (1995)
Schmittbuhl, J., Hansen, A., Auradou, H., Måløy, K.J.: Geometry and dynamics of invasion percolation with correlated buoyancy. Phys. Rev. E **61**(4), 3985–3995 (2000)
Smiles, D., Vachaud, G., Vauclin, M.: A test of the uniqueness of the soil moisture characteristics during transient non-hysteretic flow of water in a rigid soil. Soil Sci. Soc. Am. J. **35**, 534–539 (1971)
Stauffer, F.: Einfluss der kapillaren Zone auf instationre Drainagevorgnge, Bericht R 13–77 (Diss ETH Nr. 5931). IHW ETH Zrich (1977)
Stauffer, F., Kinzelbach, W.: Cyclic hysteretic flow in porous medium column: model, experiment, and simulations. J. Hydrol. **240**, 264–275 (2001)
Toussaint, R., Løvoll, G., Meheust, Y., Måløy, K.J., Schmittbuhl, J.: Influence of pore-scale disorder on viscous fingering during drainage. Europhys. Lett. **71**(4), 583–589 (2005)
Van Genuchten, M.T.: A closed-form equation for predicting the hydraulic conductivity of unsaturated soils. Soil Sci. Soc. Am. J. **44**, 892–898 (1980)
Vedvik, A., Wagner, G., Oxaal, U., Feder, J., Meakin, P., Jøssang, T.: Fragmentation Transition for Invasion Percolation in Hydraulic Gradients. Phys. Rev. Lett. **80**(14), 3065–3068 (1998)
Washburn, E.W.: The dynamics of capillary flow. Phys. Rev. **17**, 273–283 (1921)

Weitz, D.A., Stokes, J.P., Ball, R.C., Kushnick, A.P.: Dynamic capillary-pressure in porous media—origin of the viscous fingering length scale. Phys. Rev. Lett. **59**(26), 2967–2970 (1987)
Wilkinson, D.: Percolation model of immiscible displacement in the presence of buoyancy forces. Phys. Rev. A **34**(1), 520–531 (1984)
Wilkinson, D., Willemsen, J.F.: Invasion percolation: a new form of percolation theory. J. Phys. A **16**, 3365–3376 (1983)
Xu, B., Yortsos, Y.C., Salin, D.: Invasion percolation with viscous forces. Phys. Rev. E **57**(1), 739–751 (1998)
Yortsos, Y.C., Xu, B., Salin, D.: Phase diagram of fully developed drainage in porous media. Phys. Rev. Lett. **79**(23), 4581–4584 (1997)

Transp Porous Med (2010) 84:569–585
DOI 10.1007/s11242-009-9521-z

Effects of Pressure Oscillations on Drainage in an Elastic Porous Medium

M. Jankov · G. Løvoll · H. A. Knudsen · K. J. Måløy · R. Planet · R. Toussaint · E. G. Flekkøy

Received: 17 March 2009 / Accepted: 16 December 2009 / Published online: 22 January 2010

Abstract The effects of seismic stimulation on the flow of two immiscible fluids in an elastic synthetic porous medium is experimentally investigated. A wetting fluid is slowly evacuated from the medium, while a pressure oscillation is applied on the injected non-wetting fluid. The amplitude and frequency of the pressure oscillations as well as the evacuation speed are kept constant throughout an experiment. The resulting morphology of the invading structure is found to be strongly dependent on the interplay between the amplitude and the frequency of the applied pressure oscillations and the elasticity of the porous medium. Different combinations of these properties yield morphologically similar structures, allowing a classification of structures that is found to depend on a proposed dimensionless number.

Keywords Drainage displacement · Elasticity · Porous material · Stimulated flow · Two-phase flow · Capillary forces · Viscous forces

1 Introduction

The observed increase of oil recovery in the production wells affected by seismic activity triggered the research of alternative ways in stimulating removal of the residual oil in reservoirs (Beresnev and Johnson 1994; Beresnev et al. 2005). The attempts that have been made, so far, in the investigation on a possible increase in the extraction of organic hydro-carbons

M. Jankov (✉) · G. Løvoll · H. A. Knudsen · K. J. Måløy · E. G. Flekkøy
Department of Physics, University of Oslo, P.O. Box 1048, Blindern, 0316 Oslo, Norway
e-mail: mihailo.jankov@fys.uio.no

R. Planet
Departament d'Estructura i Constituents de la Matèria, Universitat de Barcelona, Marti i Franquès 1, 08028 Barcelona, Spain

R. Toussaint
Institut de Physique du Globe de Strasbourg, CNRS, Université Louis Pasteur, 5 rue Descartes, 67084 Strasbourg Cedex, France

range from the use of surfactants to reduce the surface tension between the phases (Fountain et al. 1991; Pennell et al. 1994) to the use of elastic waves (Beresnev and Johnson 1994; Reddi and Challa 1994; Roberts et al. 2003) and ultra-sonic waves (Roberts et al. 2001). The research has been developing in both experimental (Roberts et al. 2001; Li et al. 2005) and theoretical directions (Hilpert et al. 2000; Iassonov and Beresnev 2003; Hilpert 2007; Pride et al. 2008).

The objective of this study is an experimental investigation of the impacts of seismic stimulation on horizontal flow of two immiscible fluids in a small scale elastic porous medium. The properties of this stimulated drainage process are compared with established knowledge and placed in the context of non-stimulated drainage. Recall that, generally, a non-stimulated displacement in the horizontal plane is controlled by capillary and viscous forces (Lenormand et al. 1983). As one of the phases is being removed from the medium, the other one advances creating the invasion pattern. Depending on which force dominates the flow and the properties of the fluids (e.g., viscosity and density contrast, wettability) different geometries of the invading structure can be achieved (Lenormand et al. 1988; Toussaint et al. 2005; Løvoll et al. 2005).

A horizontal displacement of a wetting by a nonwetting fluid in the capillary regime results in capillary fingering structures that are well reproduced by the invasion percolation (IP) algorithm (Chandler et al. 1982; Wilkinson and Willemsen 1983; Lenormand and Zarcone 1985, 1989; Lenormand et al. 1988). Fast displacement of the same two fluids is governed by the viscous forces. An invasion of a fluid that is more viscous than the defending fluid, results in a stable displacement (Dullien 1992; Lenormand et al. 1988; Aker et al. 2000). Injecting a less viscous non-wetting fluid gives viscous fingering (Saffman and Taylor 1958; Måløy et al. 1985; Lenormand et al. 1988; Løvoll et al. 2004). However, at intermediate outflow velocities, the invading patterns exhibit similarity with the IP patterns on a small scale, whereas on larger scales the displacement structures resemble geometries characteristic for the viscous fingering regime (Toussaint et al. 2005). In a non-horizontal system, gravity and density contrast between the fluids result in a variety of displacement structures (Wilkinson 1984; Birovljev et al. 1991; Wagner et al. 1997; Méheust et al. 2002).

In this study, the focus is shifted from a non-stimulated flow to stimulated drainage in a horizontally placed elastic porous medium. The stimulation consists of a pressure oscillation applied to the non-wetting fluid, while the wetting fluid is being slowly removed from the porous matrix. Systematically changing the amplitude and the frequency of the pressure oscillations, different morphologies of the invading cluster can be achieved. The shape changes from invasion percolation-like, through different finger-like structures ending with a fragmented, and cloud-like structure as the amplitude of the oscillations is increased. The observed change in the flow patterns is strongly coupled to the elasticity of the system as it responds to the pressure perturbations.

In order to put the oscillatory pressure stimulation in a field context, we look into seismic waves. A seismic wave consists of two components, the so-called S- and P-wave. The S-wave corresponds to a shear (transverse) wave of the rock matrix. In a system with fluids and matrix of different densities, the S-wave generates body forces (Pride et al. 2008). We focus on the compressional component of the seismic wave, the P-wave, and its effects on the soft inclusions in the system. A passing P-wave corresponds to a homogeneous compression or dilatation, over scales smaller than the wave length.

When a large scale homogeneous compression is imposed from the boundary over a system with soft inclusions, the stress variation will be larger around the inclusions (Eshelby 1957). If a soft fluid, like air, is trapped in a rock, these pockets will amplify the amplitude of the pressure oscillation corresponding to the P-wave. This pressure oscillation will thus

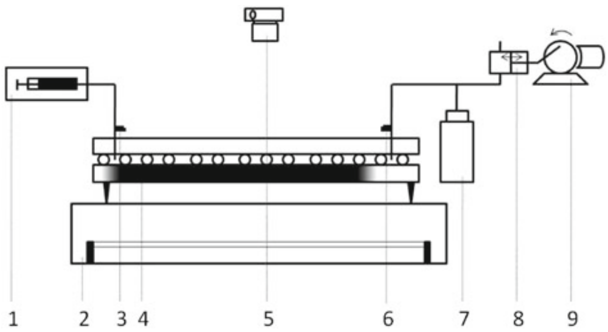

Fig. 1 Schematic view of the vertical cross-section of the experimental setup. 1—syringe pump, 2—light box, 3—outlet pressure sensor, 4—porous matrix and the water cushion on the bottom, 5—camera, 6—inlet pressure sensor, 7—container for pressure amplitude regulation, 8—air pump, and 9—DC motor that operates the air pump

be larger than in the surrounding, resonating due to the compressibility heterogeneity, and will emit secondary pressure waves penetrating in the surrounding medium like a diffusion wave, according to Biot's theory (Biot 1962; Pride 2005). This is the situation analogous to our experiments.

This article is organized as follows. Section 2 presents the experimental setup and provides the experimentally measured elasticity properties of the porous medium. The boundary conditions are presented in detail as they are novel to this setup as compared to work on non-stimulated systems. Section 3 is a theoretical treatment of the physics of the process. The elastic properties of the model are discussed, and a dimensionless number that serves as relevant parameter in the system is given. Section 4 gives in-depth experimental results and, based on visual appearance, proposes a classification of the obtained structures.

2 Experimental Setup and Methodology

The core of the experimental model is the porous matrix and the tubing system, through which the flow is controlled. A schematic view of the model is shown in Fig. 1.

2.1 Porous Matrix: Elastic Properties

The experiments are performed with a quasi-two-dimensional laboratory made porous medium. It consists of a randomly distributed monolayer of 1 mm diameter glass beads between two sheets of transparent contact paper. The size of the contact paper sheets is 50 cm × 50 cm. The beads are poured on the lower contact paper sheet to cover the entire area of it. The active area of the porous matrix, a 35 cm × 20 cm rectangle, is sealed off by silicon glue before adhering the top contact paper sheet onto the beads. The top panel of the porous matrix is then slit to provide the access and the escape openings for fluids. A dissected view of the porous matrix is given in Fig. 2. The porosity and the permeability of the porous medium are measured to be $\phi_0 = 0.63$ and $\kappa = 1.9 \times 10^{-5}$ cm^2, respectively, and the volume of a single pore is approximately 1 mm^3. The upper contact paper is glued to a transparent $50 \times 50 \times 2$ cm^3 Plexiglas plate. There are two channels, 0.5 cm wide and 0.8 cm deep on the bottom of the Plexiglas plate that are aligned with the openings on the matrix, allowing access to the model volume. The Plexiglas plate with the porous layer is

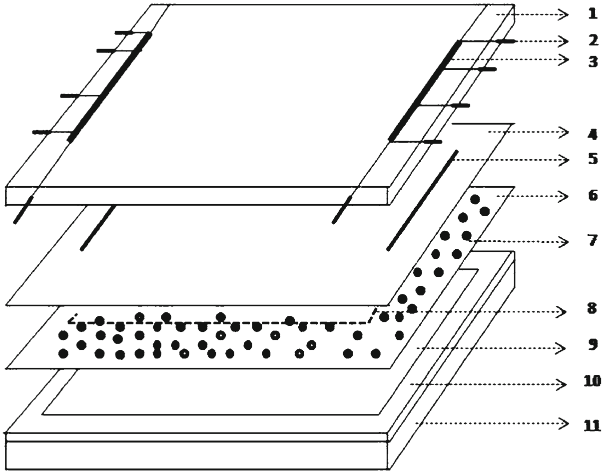

Fig. 2 Schematic view of the porous model: 1—upper Plexiglas plate, 2—inlet/outlet tubing connector, 3—inlet/outlet channel, 4—upper adhesive paper sheet, 5—slit, 6—lower adhesive sheet, 7—monolayer of glass beads, 8—silicone filling (defines the geometry of the active matrix), 9—mylar film, 10—aluminum rim, and 11—lower Plexiglas plate. Elements 9, 10, and 11 define the pressure cushion

clamped to a "water cushion", the pressure from which impedes horizontal movement of the glass beads and helps in keeping the temperature of the system homogeneous, thus keeping the viscosities of the fluids constant throughout experiments (Frette et al. 1997).

The model construction allows for a certain elasticity. The change in the porous matrix volume and the pressure of the fluid is measured while the matrix is being over-saturated from an external reservoir. The fluid volume in the matrix is

$$V(p) = V_0 + \delta V(p), \tag{1}$$

where $V_0 = V(p_{\text{atm}})$ is volume at the reference pressure (atmospheric pressure), and $\delta V(p)$ is the change in the volume due to the applied over-pressure ($\delta p = p - p_{\text{atm}}$). The volume change is found to be linear in the pressure change,

$$\frac{\delta V(p)}{V_0} = \xi \frac{\delta p}{p_{\text{atm}}}, \tag{2}$$

where ξ is the elasticity coefficient of the porous medium. In the pressure range relevant to our experiments, its value is measured to $\xi = 0.38$. Using Eq. 2 and by expressing the volume as $V(p) = Ah(p)\phi(p)$, where A is the area, $h(p)$ the height, and $\phi(p)$ the porosity of the medium, Eq. 1 is rewritten as

$$\phi(p)h(p) = \phi_0 h_0 \left(1 + \xi \frac{\delta p}{p_{\text{atm}}}\right), \tag{3}$$

where $\phi(p_{\text{atm}}) = \phi_0$ and $h(p_{\text{atm}}) = h_0$. This means that the change in the fluid volume due to the imposed pressure results in the alteration of the porosity and the height of the system.

2.2 Boundary Conditions

The prime objective with the setup is to study an on-average slow drainage process under oscillatory driving pressure. A custom built pump system is made for this purpose, see Fig. 1.

Initially, the model is filled with the wetting fluid that is essentially incompressible. During an experiment, this fluid is withdrawn from the model at a constant flow rate. The boundary condition on the model outlet is thus defined by the constant outflow rate, corresponding to a constant pressure gradient at the outlet. Without oscillations the inlet side may be left open to air, and during drainage the pressure of the wetting fluid inside the model is lowered with respect to the surrounding atmospheric pressure. In order to oscillate the pressure on the inlet side, the opening is attached to an air cavity of variable size. This cavity is, in turn, open to surrounding air through a pin-hole, which serves as an air supply and makes the air pressure, on average, equal to the surrounding atmospheric pressure. A larger opening is directly connected to an air pump; a piston that moves back and forth within a cylinder. The motion of the piston compresses and expands the air in the cavity, resulting in an oscillating air pressure at the inlet of the porous matrix. This pressure is monitored, and by tuning the size of the cavity and the piston motion, the desired amplitude of the air pressure oscillations is realized. The oscillatory frequency is given by the piston's frequency.

2.3 Experimental Procedure

The porous medium is placed in the horizontal plane over a light box. At the beginning of each experiment, the porous matrix is fully saturated with the wetting phase. As the wetting fluid, a 80–20% by mass glycerol-water solution dyed with 0.1% nigrosine is used. The viscosity of the wetting fluid is $\eta_{\mathrm{w}} = 0.11\,\mathrm{Pa\,s}$ and the density is $\rho_{\mathrm{w}} = 1,209\,\mathrm{kg/m^3}$. The nonwetting phase is air with viscosity $\eta_{\mathrm{nw}} = 1.9 \times 10^{-5}\,\mathrm{Pa\,s}$. The measured value of surface tension between the phases is $\gamma = 6.4 \times 10^{-2}$ N/m. The wetting fluid is withdrawn at a constant rate $Q = 0.022\,\mathrm{ml/min}$. The pressure in the nonwetting fluid is oscillated with pressure amplitudes up to 4,300 Pa and frequencies (f): 0.2, 0.9, and 4.0 Hz.

The starting point of an experiment is defined as the time when air enters the porous matrix. The invading structure evolves with time as the non-wetting fluid advances in the pores occupied by the wetting fluid. The experiment ends when the invading structure reaches the outlet channel. The geometry of the invading cluster at the breakthrough (i.e., when the invading fluid reaches the outlet channel) represents a fingerprint of the drainage process performed under the oscillating pressure conditions at given frequency and amplitude. An example of three different invading structures achieved for three different amplitudes is shown in Fig. 3.

The time evolution of the invasion is recorded by a digital camera (*Nikon D70 S*) placed above the model. The pictures are taken at 3 min time intervals and the resolution of the images is 3008 × 2000 pixels (70 pixels/cm).

The pressure is recorded at both the inlet and the outlet. In air, a *Honeywell 176PCHD214* and in the liquid, a *Honeywell flow through 26PCA* sensor are used. The pressure sensors are connected with a desktop computer through either a *Keithley (2000)* voltmeter or a *National Instruments Data Acquisition (DAQ)* card.

3 Physics of the Process

In drainage processes, the created pattern, the displacement efficiency, and other characteristics of the process depend on the interplay between the forces involved. The relative strength of capillary and viscous forces determines whether a process is capillary fingering or viscous fingering. In non-horizontal systems, the role of gravity would have to be taken into account, but it can be neglected for the current study of horizontal flows. In our experiments, the oscillatory

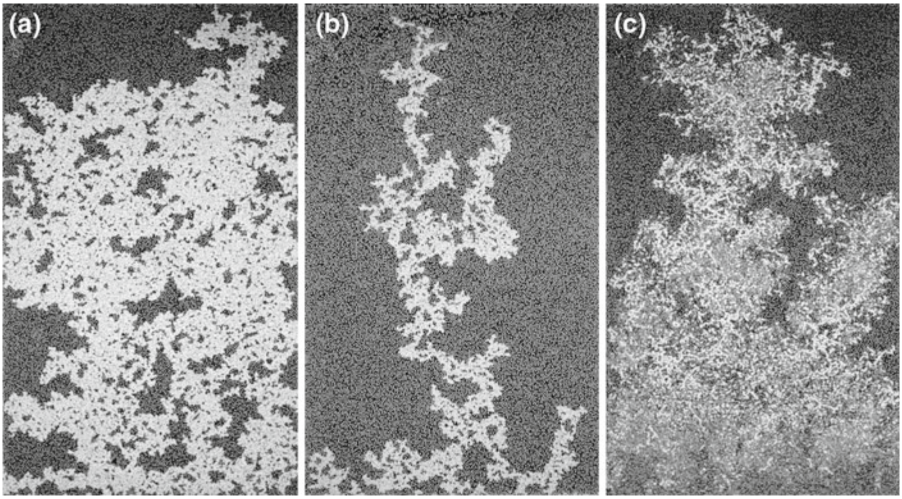

Fig. 3 Examples of breakthrough images of the invading cluster created in a drainage process stimulated with the oscillating pressure. The applied frequency is 0.2 Hz and the amplitudes of the oscillating component vary. The structures shown on the images A, B, and C are created at 20, 560, and 3,700 Pa, respectively. The outflow rate of the wetting fluid is $Q = 0.022$ ml/ min. The dark area on the images represents the wetting fluid, while the white area is the invading air cluster

pressure needs to be compared with the other forces to understand its effect. Before turning to this point in Sect. 3.2, we briefly recapitulate some key points about capillary fingering.

On the pore scale, advancement of the displacement front means the invasion of pore after pore, thus overcoming the capillary pressure threshold in each of the invaded pores. The capillary pressure obeys the Young–Laplace law,

$$p_c = p_{nw} - p_w = \gamma \left(\frac{1}{R_1} + \frac{1}{R_2} \right). \tag{4}$$

The p_{nw} and p_w terms represent the pressures of the nonwetting and the wetting phases, respectively, γ is the interfacial tension, and R_1 and R_2 are principal radii of curvature. In the experiments, the typical pore space is of size a, and the capillary pressure is approximated by $p_c \approx \gamma/a$.

In a very slow drainage process, the front invades the largest pores first, since they exert the least resistance. The growth of the displacing cluster is discontinuous (Haines 1930; Morrow 1970; Måløy et al. 1992; Furuberg et al. 1996), and is characterized by so-called *bursts* or Haines jumps. Before a burst, the pressure builds up until the easiest pore is invaded, and subsequently a certain number of pores is occupied at once. The burst lasts as long as the pressure difference in the advancing part of the interface is large enough to overcome the capillary thresholds in the neighboring pores. After the burst the pressure in the invading fluid builds up again until it is large enough to overcome the capillary pressure barrier in another pore throat along the front.

The movement of the fluid through the medium is characterized by the flow velocity, which is related to the viscous pressure gradient by the Darcy law. For the wetting fluid,

$$\mathbf{v} = -\frac{\kappa}{\eta_w} \nabla p, \tag{5}$$

where, $\mathbf{v}$ is so-called seepage or Darcy's velocity and κ is the permeability of the system. The ratio between viscous and capillary forces is represented through the capillary number. The capillary number is defined as a ratio of the viscous and capillary pressure drop over the pore length,

$$\mathrm{Ca} = \frac{\Delta p}{p_\mathrm{c}} = \frac{\eta v a^2}{\gamma \kappa}. \tag{6}$$

Our experiments are performed with a low background speed, so that the capillary number is small enough to keep the flow in the capillary fingering regime (Wilkinson and Willemsen 1983; Lenormand and Zarcone 1985). However, the capillary number does not include the effects of pressure oscillations. Since the porous medium is elastic, the pressure oscillations cause back and forth motion of the fluids locally, and this alters the local ratio between viscous and capillary forces. An additional dimensionless number is needed to account for this; a number which includes the elastic properties.

3.1 Pressure Skin-Depth in an Elastic, Quasi-Two-Dimensional Porous Medium

The elasticity of the system allows for some volume changes within each oscillatory cycle. In a much stiffer system, the pressure variations would propagate through the entire system, but here the volume changes causes the pressure to attenuate over a certain distance ahead of the front. The distance from the front to which the defending fluid is affected by pressure oscillations is estimated in the following.

For an arbitrary volume of fluid within the porous matrix constrained with δx, δy, and $h(p)$ in x, y, and z directions, respectively, the mass flow through the vertical surface defined by δy and $h(p)$ (assumed perpendicular to the flow) is

$$\Phi = \rho_\mathrm{f}\, \phi(p)\, h(p)\, \delta y\, u. \tag{7}$$

The ρ_f term is the density of the wetting fluid, and u is the fluid velocity through the vertical surface. If the designated volume contains fluid of mass M, then

$$M = \rho_\mathrm{f}\, \phi(p)\, h(p)\, \delta x\, \delta y, \tag{8}$$

which means that the surface density $\rho_\mathrm{s} = M/(\delta x \delta y)$ becomes

$$\rho_\mathrm{s} = \rho_\mathrm{f} \phi(p) h(p). \tag{9}$$

The mass conservation law for the surface density is

$$\partial_\mathrm{t}(\rho_\mathrm{s}) + \nabla \cdot (\rho_s \mathbf{u}) = 0. \tag{10}$$

Note that the actual fluid velocity $\mathbf{u}$, which is related to the Darcy velocity $\mathbf{v}$ as $\mathbf{v}/\phi(p)$ (Anghel et al. 2006; Flekkøy et al. 2001), enters here and yields

$$\partial_\mathrm{t}(\rho_\mathrm{f}\phi(p)h(p)) + \nabla \cdot \left(\rho_\mathrm{f}\phi(p)h(p)\frac{\mathbf{v}}{\phi(p)}\right) = 0. \tag{11}$$

By inserting the expressions for $\phi(p)h(p)$ and $\mathbf{v}$, Eqs. 3 and 5, respectively, we obtain

$$\partial_\mathrm{t}\left(\rho_\mathrm{f}\phi_0 h_0\left[1 + \frac{\xi\delta p}{p_\mathrm{atm}}\right]\right) - \nabla \cdot \left(\rho_\mathrm{f} h(p)\frac{\kappa}{\eta_\mathrm{w}}\nabla p\right) = 0. \tag{12}$$

Due to the incompressibility of the fluid ρ_f is considered constant. In the time derivative term, the pressure p in $\delta p = p - p_\mathrm{atm}$ is the only time-dependent quantity. In the spatial derivative

κ, $h(p)$, and ∇p are all ,in principle, position-dependent. However, we approximate this by assuming the permeability κ to be constant and claiming that the spatial variation in height ($\xi h_0 \delta p / p_{\text{atm}} = h(p) - h_0$) in Eq. 12 is negligibly small compared to the model thickness h_0; therefore, $h(p) \approx h_0$. This gives

$$\frac{\rho_{\text{f}} \phi_0 h_0 \xi}{p_{\text{atm}}} \partial_{\text{tp}} - \frac{\rho_{\text{f}} \kappa h_0}{\eta_{\text{w}}} \nabla \cdot \nabla p = 0. \tag{13}$$

Rearranging the terms, Eq. 13 can be written in the form of a diffusion equation

$$\partial_{\text{tp}} = D \nabla^2 p \tag{14}$$

with the diffusion constant

$$D = \frac{\kappa p_{\text{atm}}}{\eta_{\text{w}} \phi_0 \xi}. \tag{15}$$

In order to estimate the pressure skin-depth in the direction of flow, we solve Eq. 14 assuming invariance in the transverse direction; i.e., $p = p(x, t)$. The boundary conditions are (i) for the inlet: $p(0) = P \cos(\omega t) + p_{\text{atm}}$, where P and $\omega = 2\pi f$ are the amplitude and angular frequency of the applied oscillation and (ii) for the outlet: taking the limit at infinity: $\nabla p_\infty = -v_0 \eta_{\text{w}} / \kappa$.

The solution for $p(x, t)$ (which may be verified by direct inspection) is the real part of

$$p = P e^{i(kx - \omega t)} + p_{\text{atm}}, \tag{16}$$

where the wave number is

$$k = \frac{\sqrt{2}}{2}(1 + i) \sqrt{\frac{\omega \eta_{\text{w}} \phi_0 \xi}{p_{\text{atm}} \kappa}}. \tag{17}$$

The imaginary part of k gives the damping. The length over which the pressure is reduced to $1/e$ is thus

$$x_{\text{s}} = \frac{1}{\text{Im } k} = \sqrt{\frac{2 p_{\text{atm}} \kappa}{\omega \eta_{\text{w}} \phi_0 \xi}}. \tag{18}$$

This pressure skin-depth depends on the frequency of the oscillations. The behavior of the fluid pressure ahead of the invasion front is illustrated in Fig. 4.

3.2 Fragmentation Number

Due to the pressure oscillations and elasticity, there is back and forth movement of the front (Fig. 5). The forward–backward displacement of the front within each pressure oscillatory cycle will result in fragmentation of the invading cluster if the displacement is large enough.

The fragmentation generally occurs when the menisci move backwards within an oscillatory cycle. The likeliness of the fragmentation is higher when the frontal displacement is large relative to the typical pore size, hence the fragmentation number is defined as a ratio of the backward traveling distance (Δx^-) and the pore size (a)

$$F = \frac{\Delta x^-}{a}. \tag{19}$$

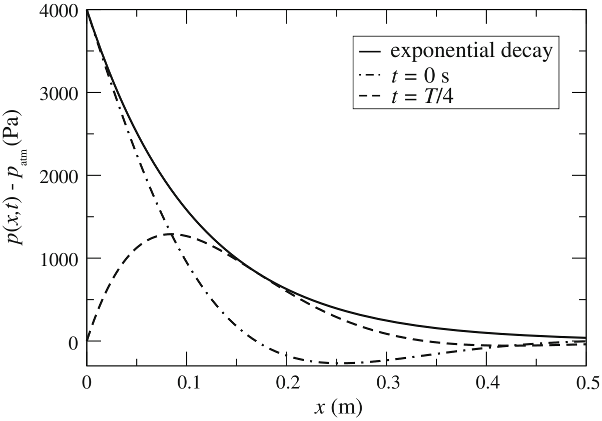

Fig. 4 Pressure wave propagation in the defending fluid as a function of the distance ahead of the invasion front. The *dash-dot line* represents the decay of the pressure amplitude with distance at time $t = 0$, the *dashed line* represents the pressure decay with distance at $t = T/4$ ($T = 1/f$) and the *solid line* represents the exponential decay of the pressure oscillation amplitude (*envelope*). The initial amplitude of the oscillation is 4,000 Pa, and the frequency is 0.2 Hz

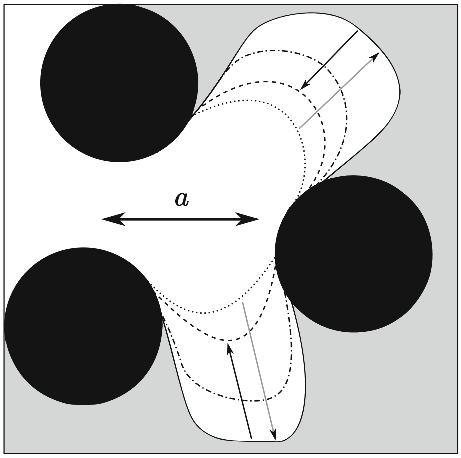

Fig. 5 Schematic view of frontal displacement due to the imposed pressure oscillations on the pore scale. The gray arrow represents the direction of the forward displacement(Δx^+). The *black arrow* represents the direction of the backward displacement of the front (Δx^-). The *dashed lines* schematically show successive positions of the front as it is being displaced due to the pressure oscillations in the nonwetting phase

The backward traveling distance can be expressed as

$$\Delta x^- \approx \frac{1}{\omega}\frac{\kappa P}{\eta_w x_s}, \tag{20}$$

where the first term represents the time scale of the motion, and the second term is an approximation of the velocity of the meniscus. The fragmentation number

$$F = \frac{1}{\omega}\frac{\kappa P}{\eta_w x_s a} = \sqrt{\frac{P^2 \kappa \phi_0 \xi}{4\pi f \eta_w p_{atm} a^2}} = c\frac{P}{\sqrt{f}}. \tag{21}$$

is then proportional to the pressure oscillation amplitude and inversely proportional to the square root of the frequency. In our experiments, the model and fluid parameters (i.e., elasticity coefficient, permeability, pore size, porosity, and viscosity) are held constant, giving $c = 5.7 \times 10^{-5}$ ($\mathrm{Pa}^{-1}\mathrm{s}^{-1/2}$) in Eq. 21.

In order to relate our fragmentation number to a real world situation, we resort to Biot's (Biot 1962) theory of pressure wave propagation in a fluid-saturated porous material. As shown in Pride (2005), similarly to our case, pressure propagation in a porous material is described by a diffusion equation with the diffusion coefficient D_r. For the situations, where a considerable contribution to the compressibility comes from the soft fraction in the porous medium (e.g., fluid with possibly trapped air bubbles), the diffusion coefficient can be written as

$$D_{\mathrm{r}} = \frac{\kappa_{\mathrm{r}}}{\beta\eta}, \tag{22}$$

where κ_{r} is the permeability of the porous medium, β is the compressibility, and η is the viscosity of the soft medium. Analogously to our quasi-two-dimensional case, the fragmentation number for a real, three-dimensional porous material can be calculated as:

$$F = \frac{\kappa_{\mathrm{r}} P}{a\eta\sqrt{2D_{\mathrm{r}}\omega}}. \tag{23}$$

Consider a seismic wave with a pressure amplitude $P = 10^3$ Pa and frequency of 1 Hz, corresponding to a moderate seismic event or to an oscillation created artificially in a nearby well (Shearer 1999). For a porous material filled with water, where the compressibility of water is $\beta = 10^{-10}\,\mathrm{Pa}^{-1}$, and the permeability of the solid matrix is $\kappa_{\mathrm{r}} = 10^{-11}\,\mathrm{m}^2$, with pores of size $a = 10^{-5}$ m, using Eq. 23, the calculated value of F is 0.07. This value is in the same range as the values calculated for the synthetic porous medium used in the experiments.

4 Results and Discussions

The design of the experimental set-up allows independent tuning of amplitudes and frequencies of the pressure oscillations. The oscillatory frequency and the amplitude are chosen at the beginning and kept fixed throughout each experiment. In this study, three different frequencies and a relatively large range of amplitudes are used. The frequencies are 0.2, 0.9, and 4.0 Hz. For each frequency the amplitudes range from around 20 to approximately 4,000 Pa. The typical capillary pressure for the set-up used in the study is around 60 Pa. For each used frequency, there is also a characteristic pressure skin-depth. The skin-depths are 10.7, 5.0, and 2.4 cm for 0.2, 0.9, and 4.0 Hz, respectively (see Eq. 18).

The outflow rate is kept low thus minimizing the effects of the viscous forces and maintaining the background flow of the fluid in the capillary regime. Lower values of Q would not affect the morphology of the invading cluster. In contrast, a considerable increase in Q would lead to a crossover of the background flow from the capillary to the viscous regime therefore affecting the morphology before the stimulation is even applied (Løvoll et al. 2004).

The objective of the study is the analysis of the effects of the pressure oscillations on the invading cluster geometry at break-through, when the invading cluster reaches its maximal size. The breakthrough images are shown in Fig. 6.

In general, it is observed that the applied oscillations change the overall geometry of the invading cluster. The extent of the change relative to the geometry of the invading cluster in a non-stimulated drainage strongly depends on the chosen combination of the amplitude and the frequency of the oscillation (see Fig. 3). There are four different flow regimes identified. Each of the regimes is characterized by a typical morphology of the invading cluster. In order to classify the geometrical characteristics of each regime, the global saturation (S_{nw}) with the non-wetting fluid at breakthrough is measured. In order to characterize the stimulation, the fragmentation number F is also evaluated in each case.

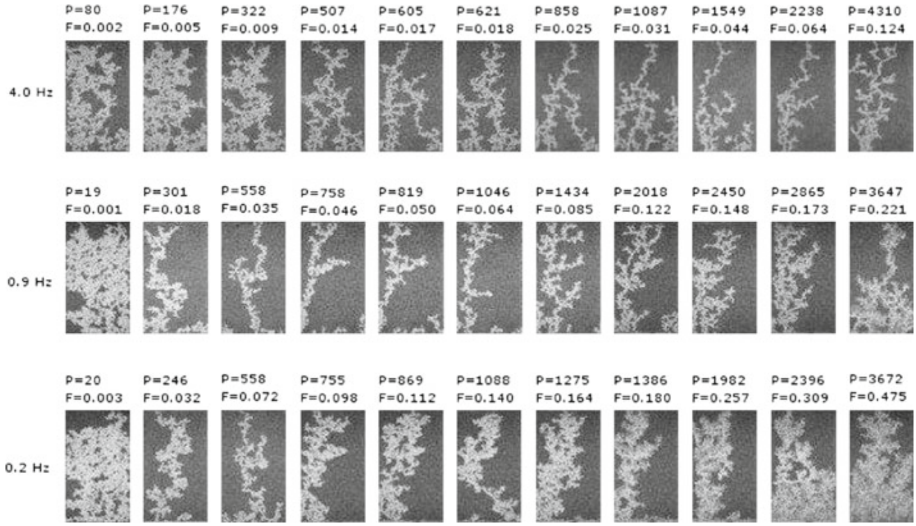

Fig. 6 Breakthrough images of all experiments. The numbers above individual images indicate the amplitude of the pressure oscillations given in Pa (*top row*) and the fragmentation number (F) in the *bottom row*. The numbers 0.2, 0.9, and 4.0 refer to the frequency of the oscillations (Hz) at which the experiments are carried out. The flow direction is from the bottom of each individual image and up

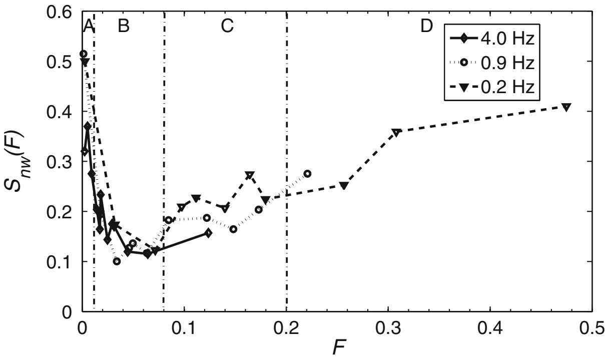

Fig. 7 Saturation (ratio of the matrix volume occupied with the non-wetting fluid to the total volume of the voids) as a function of the fragmentation number ($S_{\mathrm{nw}}(F)$). The *solid line* connects data points from the experiments where the oscillatory frequency is 4.0 Hz, the dotted line marks the 0.9 Hz experiments and the *dashed line* connects the data points from the 0.2 Hz experiments. The *vertical* (*dash-dot*) *lines* divide the graph into sections that correspond to different flow regimes (*A*—capillary fingering, *B*—fingering, *C*—fragmentation, and *D*—foam formation)

4.1 Saturation

The differences in the geometry of the invading cluster for different flow regimes largely reflect in the non-wetting saturation (S_{nw}) at breakthrough. The outflow rate (Q) and the fragmentation number (F) can be tuned independently. In all experiments, the outflow rate is kept constant. For this constant outflow rate, the breakthrough time (t_{b}) and the saturation ($S_{\mathrm{nw}} = Qt_{\mathrm{b}}/(V_0\phi)$) depend on the fragmentation number. The saturation as a function of the fragmentation number ($S_{\mathrm{nw}}(F)$) is given in Fig. 7.

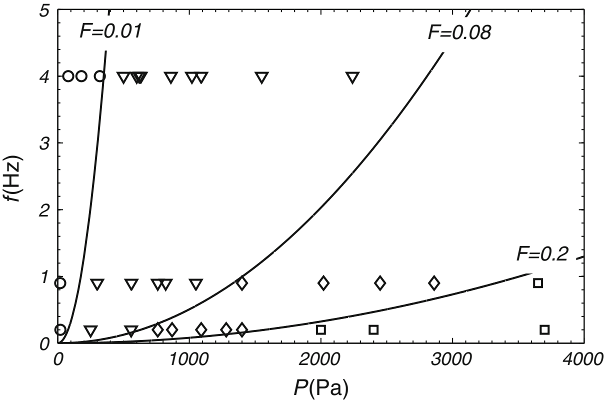

Fig. 8 Phase diagram. The *solid lines* represent the borders between the phases based on the calculated values of the fragmentation number $\left(f = (\frac{cP}{F})^2\right)$. Different *symbols* represent four geometries of the invading cluster (0—capillary fingering, ∇–finger-like structure, ⋄—fragmented structure, and □—structure where foam is present)

The data collapse suggests that the fragmentation number is the controlling parameter. Different levels of saturation in the porous medium can be achieved by choosing the amplitude and frequency of the oscillations to match the fragmentation number that corresponds to the desired saturation.

4.2 Phase Diagram and Invading Cluster Morphology

The classification of the flow regimes is based on the fragmentation number, and is summarized on a phase diagram given in Fig. 8.

4.2.1 Capillary Fingering

In the experiments performed in a relatively low amplitude regime, the breakthrough clusters resemble the structures typically observed in the so-called capillary fingering regime (Fig. 9), in which the pore throats with the lowest capillary pressure thresholds are invaded first. This behavior is somewhat expected because the backwards traveling distance of the menisci is much smaller than the average pore size. In these cases, the impact of the pseudo-seismic stimulation is low or non-existing. This sort of geometry typically occurs in the experiments where F is up to 0.01, independently of the applied frequency.

4.2.2 Finger-Like Geometry

The finger-like structures were typically achieved for $F's$ ranging from 0.01 to 0.08. Generally, the structure is either a result of a simultaneous growth of multiple fingers on different parts of the invading front or just a single finger that spans the matrix. The single-finger-like geometries resemble viscous fingering (Fig. 10).

Regardless of their number, there is also a noticeable difference in the thickness of the individual fingers when the amplitude is changed. The thickest fingers are obtained for relatively

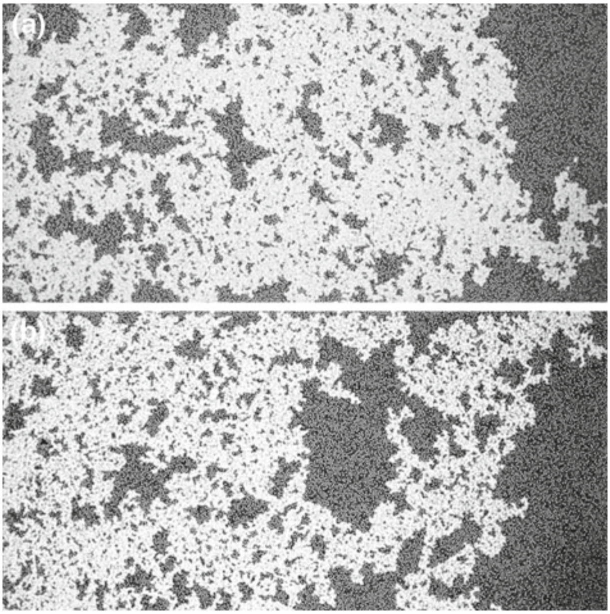

Fig. 9 Comparison of an invading cluster geometry achieved in a low amplitude and frequency experiment (**a**) with typical capillary fingering structure (**b**). The stimulation tends to generate more compact invading structures (smaller sizes of the trapped clusters) than those characteristic for the capillary fingering regime. The direction of the flow is from the left- to the right-hand side

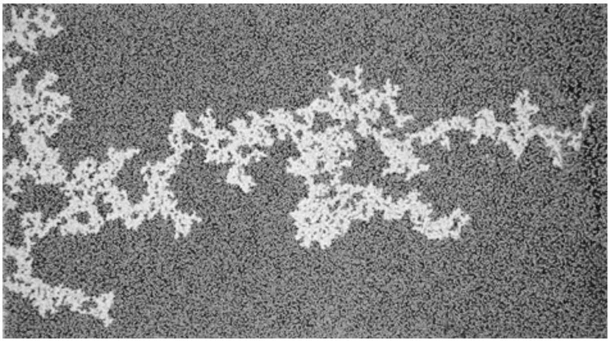

Fig. 10 Example of a single-finger-like invading cluster. The displacing structure is elongated and typically have relatively low number of branches that grow sideways with respect to the main finger. The thickness of the fingers varies, and is generally larger than the thickness of the fingers observed in the viscous regime. The direction of the flow is from the left- to the right-hand side

low amplitude experiments. As an example, images from two experiments performed at different fragmentation numbers are shown in Fig. 11.

A similar increase in thickness is observed when the speed of a drainage process in the viscous regime without oscillations is decreased (Toussaint et al. 2005).

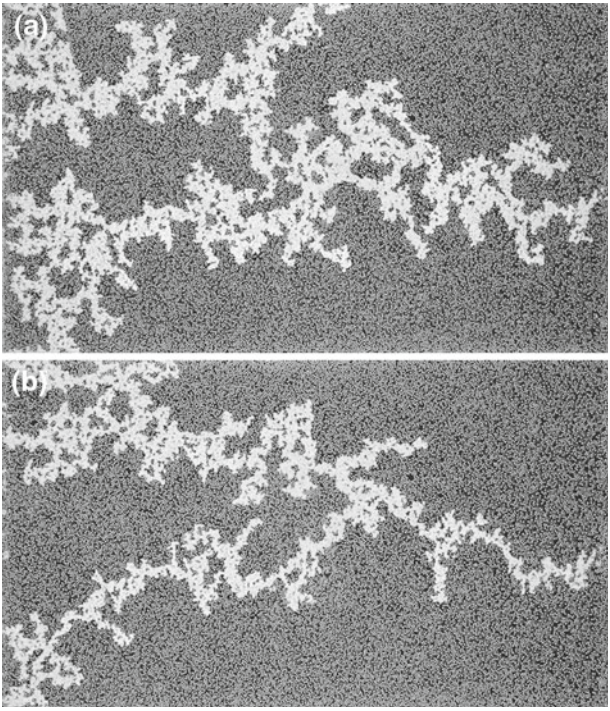

Fig. 11 Comparison of two finger-like structures achieved at $F = 0.018$ (**a**) and $F = 0.025$ (**b**) in the 4 Hz series. The thickness of the fingers is distinguishable, while the general shape is preserved to a great extent. The direction of the flow is from the left- to the right-hand side

4.2.3 Fragmented Geometry

Another prominent feature is the fragmentation or discontinuation of the invading cluster. The fragmentation is present in the cases when F is larger than 0.08. Typically, the fragmentation takes place along the front line, and is particularly pronounced ahead of the most advanced part of the front. Initially, the fragmented structures largely resemble the single-finger-like structures with branches that laterally grow off the main structure. The level of fragmentation depends on F. For the F values on the higher end of the spectrum (values closer to 0.2), the effects of fragmentation are very well visible. A comparison of two fragmented invading structures with the different F values is shown in Fig. 12.

4.2.4 Geometries with Foam

Finally, when F exceeds 0.2 fragmentation dominates the invasion and small air bubbles are introduced in the wetting phase. The trapping of the air bubbles in the defending fluid is defined as foam formation. In the current set-up and the range of achievable fragmentation numbers, the foam formation is present in a very few cases and related to $F's$ larger than 0.2, which corresponds to the largest amplitude experiments in the 0.2 and 0.9 Hz series. Typically, foam forms along the front line and is being left behind as the invading cluster grows and fragments. In the cases, where a considerable amount of foam is formed, there

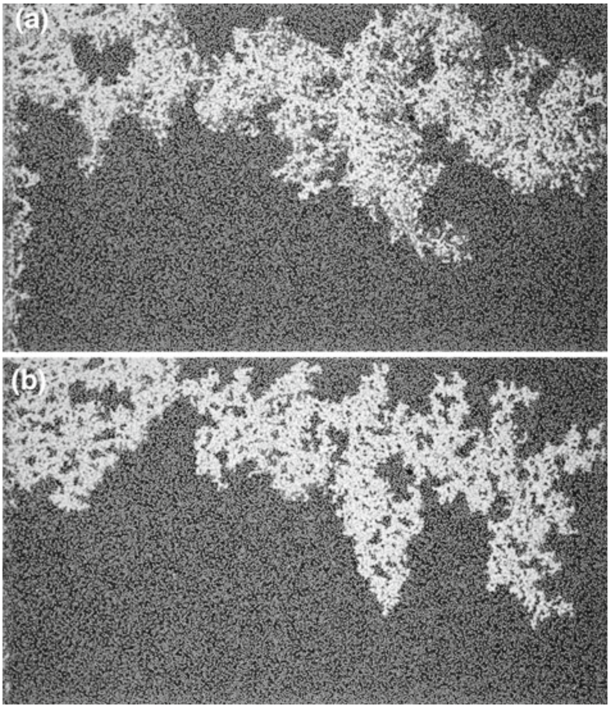

Fig. 12 Difference in the level of fragmentation depending on the F values. The example (**a**) represents a displacement cluster achieved for $F = 0.18$. The entire structure is heavily disconnected, and the fragmentation is not localized, but rather present in the entire displacing structure. In the example (**b**), the value of F is on its lower end ($F = 0.098$). The level of fragmentation is very low and the fragments are located mostly around the top part of the invading cluster. The direction of the flow is from the left- to the right-hand side

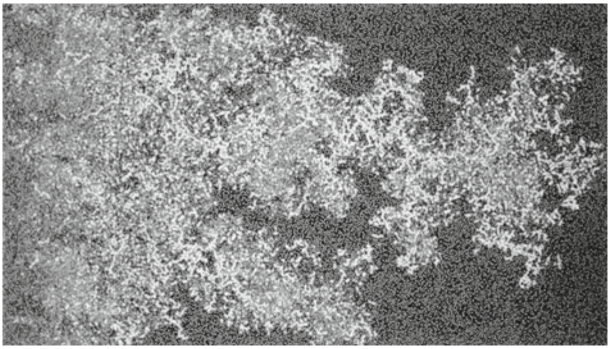

Fig. 13 Example of a displacement cluster with foam. This experiment is carried out at the maximal F achievable for the described experimental set-up. The amount of formed foam varies from experiment to experiment and depends on the fragmentation number. In the cases, where the F values were relatively smaller the foam forms in a smaller quantity. The direction of the flow is from the left- to the right-hand side

is a lack of a well-connected invading cluster and a clearly distinguishable front line due to excessive fragmentation. The displacing structure appears as a cloud-like formation. A typical example of a cluster with a considerable amount of foam is shown in Fig. 13.

5 Conclusions

The effects of pseudo-seismic stimulation on a slow quasi-two-dimensional drainage process in an elastic porous medium are addressed. It is found that the pressure stimulation of the drainage process alters the flow regime in which the wetting fluid is evacuated from the porous medium. The change in the flow regime due to applied pressure oscillation results in a change of the morphological characteristics of the invading structure. The degree of the impact greatly depends on the intensity of the stimulation and the elasticity of the porous medium. The stimulation consisting of the oscillatory amplitudes and frequencies that result in small incursions of the oscillating menisci into the wetting phase has a very little or no impact on the geometry of the displacing structure. In contrast, the stimulation that produces larger incursions of the menisci within an oscillatory cycle leads to a dramatic change in the flow regime. The differences in the flow regimes then result in notably different geometries of the invading structure.

There are four distinguishable flow regimes followed with four regime specific geometries for the used range of amplitudes and frequencies. The classification of the observed morphologies is based on the proposed fragmentation number and the characteristic level of residual saturation (at breakthrough). The phase diagram shows that the proposed fragmentation number can be used to differentiate and characterize the flow regimes. The morphological differences of the invading structures for different regimes result in various levels of saturation with non-wetting fluid. The data collapse obtained when the residual saturation is plotted as function of the fragmentation number suggests that the fragmentation number is the relevant controlling parameter.

Acknowledgments M. Jankov, G. Løvoll, and H. A. Knudsen acknowledge support from NFR (Norwegian Research Council) through a PETROMAKS grant. R. Planet acknowledges Ministerio de Ciencia y Tecnología (Spain) for a grant associated to the project BQU2003-05042-C02-02. R. Touissant acknowledges the support of REALISE.

References

Aker, E., Måløy, K.J., Hansen, A.: Viscous stabilization of 2D drainage displacements with trapping. Phys. Rev. Lett. **84**, 4589–4592 (2000)

Anghel, D.-V., Strauss, M., Flekkøy, E.G., McNamara, S., Måløy, K.J.: Structure formation and instability in a tube of sand (vol. 87, p. 134302, 2001). Phys. Rev. Lett. **97**, 059902 (2006)

Beresnev, I.A., Johnson, P.A.: Elastic-wave stimulation of oil production: a review of methods and results. Geophysics **59**, 1000–1017 (1994)

Beresnev, I.A., Vigil, R.D., Li, W.Q., Pennington, W.D., Turpening, R.M., Iassonov, P.P., Ewing, R.P.: Elastic waves push organic fluids from reservoir rock. Geophys. Res. Lett. **32**, L13303 (2005)

Biot, M.A.: Mechanics of deformation and acoustic propagation in porous media. J. Appl. Phys. **33**, 1482–1498 (1962)

Birovljev, A., Furuberg, L., Feder, J., Jøssang, T., Måløy, K.J., Aharony, A.: Gravity invasion percolation in 2 dimensions: experiment and simulation. Phys. Rev. Lett. **67**, 584–587 (1991)

Chandler, R., Koplik, J., Lerman, K., Willemsen, J.F.: Capillary displacement and percolation in porous media. J. Fluid Mech. **119**, 249–267 (1982)

Dullien, F.A.L.: Porous Media Fluid Transport and Pore Structure. Academic Press, San Diego (1992)

Eshelby, J.D.: The determination of the elastic field of an ellipsoidal inclusion, and related problems. Proc. R. Soc. Lond. Ser. A **241**(1226), 376–396 (1957)

Flekkøy, E.G., McNamara, S., Måløy, K.J., Gendron, D.: Structure formation and instability in a tube of sand. Phys. Rev. Lett. **87**, 134302 (2001)

Fountain, J.C., Klimek, A., Beikirch, M.G., Middleton, T.M.: The use of surfactants for in situ extraction of organic pollutants from a contaminated aquifer. J. Hazard. Mater. **28**, 295–311 (1991)

Frette, O.I., Måløy, K.J., Schmittbuhl, J.: Immiscible displacement of viscosity-matched fluids in two-dimensional porous media. Phys. Rev. E **55**, 2969–2975 (1997)

Furuberg, L., Måløy, K.J., Feder, J.: Intermittent behavior in slow drainage. Phys. Rev. E **53**, 966–977 (1996)

Haines, W.B.: Studies in the physical properties of soil. V. The hysteresis effect in capillary properties, and the modes of moisture distribution associated therewith. J. Agric. Sci. **20**, 97–116 (1930)

Hilpert, M.: Capillarity-induced resonance of blobs in porous media: Analytical solutions, Lattice-Boltzmann modeling, and blob mobilization. J. Colloid Interface Sci. **309**, 493–504 (2007)

Hilpert, M., Jirka, G.H., Plate, E.J.: Capillarity-induced resonance of oil blobs in capillary tubes and porous media. Geophysics **65**, 874–883 (2000)

Iassonov, P.P., Beresnev, I.A.: A model for enhanced fluid percolation in porous media by application of low-frequency elastic waves. J. Geophys. Res. **108**, 2138 (2003)

Lenormand, R., Zarcone, C.: Invasion percolation in an etched network: measurement of a fractal dimension. Phys. Rev. Lett. **54**, 2226–2229 (1985)

Lenormand, R., Zarcone, C.: Capillary fingering: percolation and fractal dimension. Transp. Porous Media **4**, 599–612 (1989)

Lenormand, R., Zarcone, C., Sarr, A.: Mechanisms of the displacement of one fluid by another in a network of capillary ducts. J. Fluid Mech. **135**, 337–353 (1983)

Lenormand, R., Touboul, E., Zarcone, C.: Numerical models and experiments on immiscible displacement in porous media. J. Fluid Mech. **189**, 165–187 (1988)

Li, W.Q., Vigil, R.D., Beresnev, I.A., Iassonov, P., Ewing, R.: Vibration-induced mobilization of trapped oil ganglia in porous media: experimental validation of a capillary-physics mechanism. J. Colloid Interface Sci. **289**, 193–199 (2005)

Løvoll, G., Méheust, Y., Toussaint, R., Schmittbuhl, J., Måløy, K.J.: Growth activity during fingering in a porous Hele–Shaw cell. Phys. Rev. E **70**, 026301 (2004)

Løvoll, G., Méheust, Y., Måløy, K.J., Aker, E., Schmittbuhl, J.: Competition of gravity, capillary and viscous forces during drainage in a two-dimensional porous medium: a pore scale study. Energy **30**, 861–872 (2005)

Måløy, K.J., Feder, J., Jøssang, T.: Viscous fingering fractals in porous media. Phys. Rev. Lett. **55**, 2688–2691 (1985)

Måløy, K.J., Furuberg, L., Feder, J., Jøssang, T.: Dynamics of slow drainage in porous-media. Phys. Rev. Lett. **68**, 2161–2164 (1992)

Méheust, Y., Løvoll, G., Måløy, K.J., Schmittbuhl, J.: Interface scaling in a two-dimensional porous medium under combined viscous, gravity and capillary effects. Phys. Rev. E **66**, 051603 (2002)

Morrow, N.R.: Physics and thermodynamics of capillary action in porous media. Ind. Eng. Chem. **62**, 32–56 (1970)

Pennell, K.D., Jin, M.Q., Abriola, L.M., Pope, G.A.: Surfactant enhanced remediation of soil columns contaminated by residual tetrachloroethylene. J. Contam. Hydrol. **16**, 35–53 (1994)

Pride, S.R.: Relationship between seismic and hydrological properties. In: Rubin, Y., Hubard, S.S. Hydrogeophysics, Springer, Netherlands (2005)

Pride, S.R., Flekkøy, E.G., Aursjø, O.: Seismic stimulation for enhanced oil recovery. Geophysics **73**, 023–035 (2008)

Reddi, L.N., Challa, S.: Vibratory mobilization of immiscible liquid ganglia in sands. J. Environ. Eng. **120**, 1170–1190 (1994)

Roberts, P.M., Sharma, A., Uddameri, V., Monagle, M., Dale, D.E., Steck, L.K.: Enhanced DNAPL transport in a sand core during dynamic stress stimulation. Environ. Eng. Sci. **18**, 67–79 (2001)

Roberts, P.M., Esipov, I.B., Majer, E.L.: Elastic-wave stimulation of oil reservoirs: promising EOR technology?. Lead. Edge **22**, 448–453 (2003)

Saffman, P.G., Taylor, G.: The penetration of a fluid into a porous medium or Helle-Shaw cell containing a more viscous fluid. Proc. R. Soc. A **245**, 312–329 (1958)

Shearer, P.M.: Introduction to Seismology. Cambridge University Press, Cambridge (1999)

Toussaint, R., Løvoll, G., Méheust, Y., Måløy, K.J., Schmittbuhl, J.: Influence of pore-scale disorder on viscous fingering during drainage. Europhys. Lett. **71**, 583–589 (2005)

Wagner, G., Birovljev, A., Meakin, P., Feder, J., Jøssang, T.: Fragmentation and migration of invasion percolation clusters: experiments and simulations. Phys. Rev. E **55**, 7015–7029 (1997)

Wilkinson, D.: Percolation model of immiscible displacement in the presence of buoyancy forces. Phys. Rev. A **30**, 520–531 (1984)

Wilkinson, D., Willemsen, J.F.: Invasion percolation: a new form of percolation theory. J. Phys. A **16**, 3365–3376 (1983)

Steady-State Two-Phase Flow in Porous Media: Statistics and Transport Properties

Ken Tore Tallakstad,[1] Henning Arendt Knudsen,[1] Thomas Ramstad,[2,3] Grunde Løvoll,[1] Knut Jørgen Måløy,[1] Renaud Toussaint,[4] and Eirik Grude Flekkøy[1]

[1]Department of Physics, University of Oslo, P.B. 1048 Blindern, NO-0316 Oslo, Norway
[2]Department of Physics, Norwegian University of Science and Technology, NO-7491 Trondheim, Norway
[3]Numerical Rocks AS, Stiklestadveien 1, NO-7041 Trondheim, Norway
[4]Institut de Physique du Globe de Strasbourg, UMR 7516 CNRS, Université de Strasbourg, 5 rue René Descartes, F-67084 Strasbourg Cedex, France

(Received 16 October 2008; published 18 February 2009)

We study experimentally the case of steady-state simultaneous two-phase flow in a quasi-two-dimensional porous media. The dynamics is dominated by the interplay between a viscous pressure field from the wetting fluid and bubble transport of a less viscous, nonwetting phase. In contrast with more studied displacement front systems, steady-state flow is in equilibrium, statistically speaking. The corresponding theoretical simplicity allows us to explain a data collapse in the cluster size distribution as well as the relation $|\nabla P| \propto \sqrt{\mathrm{Ca}}$ between the pressure gradient in the system and the capillary number.

DOI: 10.1103/PhysRevLett.102.074502 PACS numbers: 47.56.+r, 47.55.Ca, 47.55.dd, 89.75.Fb

Different types of immiscible multiphase fluid flow in porous media play an important role in many natural and commercial processes [1–3]. The complex fluid patterns observed in such processes have been extensively studied and modeled over the past decades; see [1–5], and references therein.

The vast majority of work up to now has focused on invasion processes: either pure drainage or pure imbibition. These inherently transient processes give different displacement patterns and are classified into capillary fingering [6], viscous fingering [5,7–12], and stable front displacement [13,14]. These are nonstationary processes, and to understand them in a broader context there is a need to understand the stationary case which has received far less attention: steady-state flow, which is in equilibrium in the sense that average flow properties and distribution functions are invariant in time. This stationary system is in statistical equilibrium although it is a dissipative process; an external energy input balances the internal energy loss to maintain the equilibrium.

With some notable exceptions, there is to our knowledge very little pore scale experimental data available for such problems [15]. The Payatakes group did pore scale steady-state experiments using network models etched in glass [16] and later theoretical modeling predicting the nonlinearity of such flows [17]. In addition, some numerical work has focused on a steady-state regime: a pore scale lattice Boltzmann study by Gunstensen and Rothman [18] and network simulations at larger scales by Knudsen *et al.* and Ramstad *et al.* [19–22].

In this Letter, we experimentally demonstrate that an equilibrium flow situation results after simultaneous injection of two fluids into a porous medium. This allows for the combination of mean-field approximations of local quantities and energy dissipation considerations. As a result, we analytically obtain the highly nontrivial steady-state pressure-flow-rate relationship. Furthermore, in contrast to transient flows, steady-state mass conservation gives a normalization condition based on flow rate rather than saturation. From this we derive a scaling law of the cluster size distributions of nonwetting fluid.

Our system is shown in Fig. 1. The horizontal porous model consists of a monolayer of glass beads of diameter $a = 1$ mm, which are randomly spread between two transparent contact papers [7,13]. The model dimensions are $L \times W = 85 \times 42\ \mathrm{cm}^2$, with thickness a and volume $V = aLW$. The porosity and absolute permeability are measured to be $\phi_0 = 0.63$ and $\kappa_0 = (1.95 \pm 0.1) \times 10^{-5}\ \mathrm{cm}^2$, respectively. The wetting fluid used is a 85%–15% by

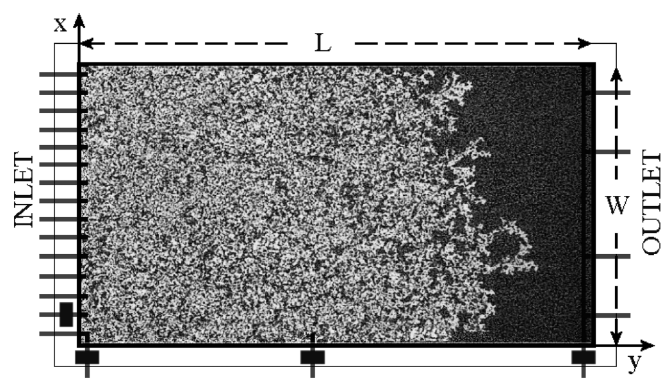

FIG. 1. Depicted inside the model frame ($L \times W = 85 \times 42\ \mathrm{cm}^2$) is the initial transient stage of an experiment. There are 15 independent inlet holes with tubes and syringes attached. Every second syringe injects the wetting phase; the others inject the nonwetting one. An outlet channel with four exit holes allows the fluid mix to leave the system. Three *SensorTechnics 26PC0100G6G* flow-through pressure sensors (indicated by the solid rectangles) are attached alongside the model at the positions $y = 0, L/2, L$. Additionally, one pressure sensor is attached to the first "air" tube from the bottom.

weight *glycerol-water* solution dyed with 0.1% Negrosine and has a viscosity $\mu_w = 0.11$ Pa s at room temperature. *Air* is used as the nonwetting fluid with viscosity $\mu_{nw} = 1.9 \times 10^{-5}$ Pa s, giving a viscosity ratio $M = \mu_{nw}/\mu_w \sim 10^{-4}$. The surface tension is measured to be $\gamma = 6.4 \times 10^{-2}$ N m^{-1}.

The tuning parameter in the experiments is the total flow rate, i.e., the sum of the flow rate of the wetting and nonwetting fluid, and can during steady state be written as $Q_{\rm tot} = Q_w + Q_{nw} = (8 + 7)Q_0$, where Q_0 is the flow rate from every single syringe.

Gray scale images of the flow structure are taken at regular intervals with a *Pixelink Industrial Vision PL-A781* digital camera. An image contains 3000×2208 pixels, corresponding to a spatial resolution of ~0.19 mm per pixel (27 pixels in a pore of size 1 mm^2). All analysis is done on the basis of black and white thresholded images [14] and the measured pressure signals.

The porous model is initially saturated with the wetting phase. An experiment is started by injecting the fluid pair from every other inlet hole. The initial structure consists of bubbles or clusters of air distributed over various sizes, but always much smaller than the system size. The clusters are embedded in a background field of percolating wetting fluid. Usually, the smallest air clusters are immobile and trapped, whereas larger clusters are mobile and propagate in the porous medium. However, trapped clusters can be mobilized when they coalesce with larger migrating clusters, and migrating clusters can be fragmented and thereby trapped.

We divide an experiment into two regimes. A *transient* regime where the mix of nonwetting clusters and wetting fluid gradually fills up the model, as seen in Fig. 1. During this time, the measured average pressure difference between $y = 0$ and $y = L$, ΔP_L, increases. This is due to the presence of more and more air clusters trapped in the system, effectively lowering the relative permeability for the viscous wetting fluid. At some characteristic time, shortly after both phases are produced at the outlet, ΔP_L starts to fluctuate around a constant value. This marks the start of the *steady-state* (or statistically stationary) regime. The whole model now contains a homogeneous mix of the two phases, transported through the model without "long time" flow parameter changes.

Through six experiments we have studied how the measured steady-state pressure difference ΔP_L varies with the capillary number Ca, defined as

$$\mathrm{Ca} = \frac{\mu_w Q_w a^2}{\gamma \kappa_0 A}, \tag{1}$$

where $A = Wa$ is the cross-sectional area. This is shown in Fig. 2, for a span in the Ca number of roughly two decades. The steady-state pressure fluctuations are Gaussian, indicating that ΔP_L results from a sum of independent, local pressure differences over scales smaller than the system size. It is evident that the pressure is consistent with a power law in the Ca number $\Delta P_L \propto \mathrm{Ca}^\beta$, where the exponent is found to be $\beta = 0.54 \pm 0.08$. This is a nontrivial result, and we will return to the discussion shortly.

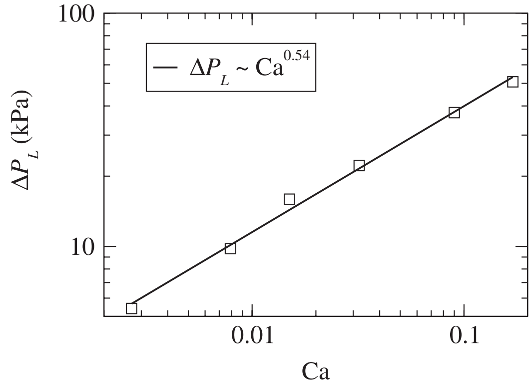

FIG. 2. Mean pressure difference ΔP_L during steady state as a function of Ca. The fluctuations in ΔP_L are of the order of 1 kPa, i.e., very small compared to the mean values. A power law dependence is found, with exponent $\beta = 0.54 \pm 0.08$.

A general trend in the experiments, in passing from high to low Ca numbers, is that the size or area of the largest air clusters increases. This means that the geometry of the clusters depends on the steady-state pressure gradient. To quantify this, we have found the normalized probability distributions of cluster extension in the x and y directions, $P(l_x)$ and $P(l_y)$, respectively (see Fig. 3). We define the extension lengths l_x and l_y as the sides of the smallest rectangle (bounding box) that can contain a cluster. For clarity, l_y lays parallel whereas l_x lays transverse to the average flow direction.

Analysis shows that, for a cluster of a given area s, the extension lengths have well defined means $\langle l_x \rangle$ and $\langle l_y \rangle$ increasing monotonically with s [23]. The corresponding

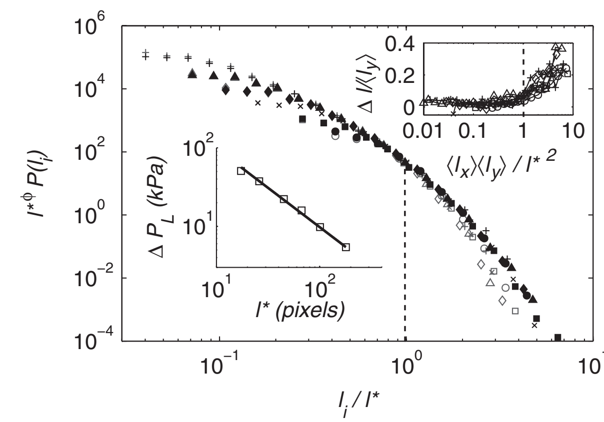

FIG. 3. Air cluster extension length distributions $P(l_y)$ (filled markers) and $P(l_x)$ (empty markers), collapsed by the rescaling $l^{*\phi} P(l_i)$ vs l_i/l^*, where $i \in \{x, y\}$ and $\phi = 2.8$. The dashed vertical line at $l_i = l^*$ indicates the start of the different cutoff behavior in the two directions. The lower left inset shows (solid line) $\Delta P_L \propto 1/l^*$ with the corresponding experimental values (squares). The upper right inset shows $\Delta l/\langle l_y \rangle$ vs $\langle l_x \rangle \langle l_y \rangle / l^{*2}$, where $\Delta l = \langle l_y \rangle - \langle l_x \rangle$.

standard deviations are small and proportional to these means (relatively 20%) for all $\langle l_x \rangle$ and $\langle l_y \rangle$ values [23]. Furthermore, we find that $\langle l_x \rangle = \langle l_y \rangle$ up to a characteristic length scale in the system l^*. Above l^*, $\langle l_y \rangle > \langle l_x \rangle$, as shown in the upper right inset in Fig. 3. The exact same behavior is seen in the distributions $P(l_x)$ and $P(l_y)$. Figure 3 shows, for the same Ca numbers used previously, a collapse of the $P(l_x)$ and $P(l_y)$ distributions by the rescaling $l^{*\phi}P(l_i)$ vs l_i/l^*. The scaling exponent $\phi = 2.8 \pm 0.3$ is taken as the value that gives the best collapse. Apart from the expected crossover when the extension lengths reaches the pore length scale a, the collapse is very good. The above results reveal important information of our system, particularly that there is only one length scale l^*, dependent on the pressure difference ΔP_L, that controls the steady-state displacement structure.

In the following, we shall give a simple and minimal scaling theory for the purpose of predicting the exponents β and ϕ from Figs. 2 and 3 respectively.

Consider a nonwetting cluster in the porous medium surrounded by flowing viscous wetting fluid. The cluster perimeter is made up of several menisci standing in different pores. A single meniscus at a particular position has a surface pressure given by the pressure difference of the nonwetting and wetting fluid on each side. The nonwetting fluid pressure is assumed constant inside the cluster due to its low viscosity, whereas the wetting fluid pressure is position-dependent, decreasing in the y direction. The neighboring pores inside and outside the meniscus can be either imbibed or drained, respectively, if the surface pressure exceeds one of the capillary pressure thresholds for imbibition or drainage. The imbibition and drainage threshold pressures depend on pore geometry and are thus distributions due to the randomness of the porous medium [24].

If all menisci along the perimeter are in mechanical equilibrium, the cluster is *immobile*. This is typically the case for clusters with only a small l_y extension. However, for large enough l_y, the viscous pressure drop on the wetting side of the perimeter is sufficient for a migration step to take place. Migration is the process of drainage in one pore and imbibition in another along the perimeter. The result of several migration steps is that the cluster moves and perhaps also changes shape. The onset of migration will depend on the difference between the mean threshold pressure for drainage and imbibition [24], a pressure we denote $\bar{P}_t$. Furthermore, $\bar{P}_t$ predicts a characteristic length of extension l^* for cluster *mobility*

$$|\nabla P| l^* = \Delta P_L \frac{l^*}{L} = \bar{P}_t, \tag{2}$$

where we make the mean-field assumption that the pressure gradient $|\nabla P|$ is constant. The scaling of the last equality in Eq. (2) is verified experimentally, as shows the lower left inset in Fig. 3. Note that l^* also determines when clusters become unstable against breakup, since the mechanism of cluster mobilization is the same as that of cluster fragmentation. This is important because it links the single crossover length that collapses both $P(l_i)$ distributions in Fig. 3 to the extension of mobilized clusters. Particularly, it means that the characteristic l_x extension of mobilized clusters is l^*.

Equilibrium conditions require the total dissipation in the system to be balanced by the work rate done through the external pressure drop: $Q_{\text{tot}}\Delta P_L = D_f$. In obtaining D_f, we assume that the main contribution to dissipation is in the volume of the wetting fluid and that the dissipation in the nonwetting fluid is negligible. Visual observation indicates that most of the wetting fluid is restricted to flow through narrow channels at some typical spacing. The motion and configuration of the nonwetting clusters seem to show that the channel width is of the order of a pore size $\sim a$ and that the permeability in between channels is made relatively low by the presence of lowly mobile nonwetting clusters. Motivated by these observations, we define a dissipative wetting fluid volume:

$$V_{\text{dis}} = LA_{\text{dis}} = La^2 \frac{W}{l^*} = \frac{aV}{l^*}, \tag{3}$$

where l^* is taken as the spacing between channels, making W/l^* the number of channels through the system. This simplification of channel flow of the wetting fluid is a strong assumption, but supporting numerical simulations also show that the dissipative volume is constrained to a small fraction of the total volume, changing with the flow rate.

Since the overall interface area between the wetting and nonwetting phase is fluctuating around a constant value in steady state, changes in the potential energy stored in the interfaces do not contribute to the average dissipation, and we are justified in writing

$$Q_{\text{tot}}\Delta P_L = D_f = -\int_{V_{\text{dis}}} dVu|\nabla P| = \frac{\mu_w}{\kappa_0}\int_{V_{\text{dis}}} dVu^2, \tag{4}$$

where we have applied Darcy's law locally, in the dissipative part of the wetting fluid. Taking the local Darcy velocity $u = (Q_w/A)(V/V_{\text{dis}})$ as a constant, and using Eqs. (3), (1), and (2), respectively, we obtain

$$\Delta P_L = \frac{8\gamma V l^*}{15a^3 A}\text{Ca} \Rightarrow |\nabla P|^2 = \frac{8\gamma \bar{P}_t}{15a^3}\text{Ca}, \tag{5}$$

i.e., $|\nabla P| \propto \sqrt{\text{Ca}}$, consistent with the exponent β in Fig. 2. An alternative interpretation of this result is that the wetting fluid experiences an effective permeability, assuming a Darcy law $\kappa_{\text{eff}}(\text{Ca}) = \mu_w Q_w / A|\nabla P|$, due to the flow of air:

$$\kappa_{\text{eff}}^2 = \frac{15\gamma}{8a\bar{P}_t}\kappa_0^2\text{Ca}. \tag{6}$$

We turn now to the distributions of cluster extension lengths and the found exponent ϕ. From the collapses in Fig. 3, it is seen that the distributions can be written

$$P_i(l) = l^{-\phi} h_i(l/l^*), \tag{7}$$

where the cutoff functions $h_i(x)$ are dominating. Note that this scaling form should be expected to hold only for l above the lower cutoff scale $\sim a$. To obtain ϕ, we use the fact that the nonwetting flow rate is an imposed quantity and must in steady state be equal to the accumulated flow of all mobile clusters on the average. The contribution of a single cluster of extent l to the total nonwetting flow rate is $alU(l)$, where $U(l)$ is the average center of mass velocity. Further, the average number of clusters of extension $(l, l + dl)$ that intersects any given cross section A is given as $dlP_i(l)Nl/L$. Hence we can write

$$Q_{nw} = \frac{aN}{L} \int_a^\infty dl l^2 U(l) P_i(l), \tag{8}$$

where N is the total number of clusters. This number is measured and found to depend only weakly, at most logarithmically, on Q_{nw}. For simplicity, N will be treated as a constant in the following.

To obtain $U(l)$, we make the general assumption that it is linear in Q_{nw} and has some functional dependence on l/l^*:

$$U(l) = \frac{Q_{nw}}{A} f(l/l^*). \tag{9}$$

As a first-order approximation, $f(x)$ would be a step function, since clusters of size $l < l^*$ usually are immobile. By Eqs. (7) and (9) and the substitution $x = l/l^*$, Eq. (8) can be written

$$1 = l^{*(3-\phi)} \frac{aN}{V} \int_{a/l^*}^\infty dx x^{2-\phi} f(x) h_i(x). \tag{10}$$

Since the right-hand side of Eq. (10) must be independent of l^*, we obtain $\phi = 3$ consistent with the experimental value in Fig. 3.

In conclusion, experiments have been done on two-phase flow in a porous medium under steady-state conditions. In contrast to invasion processes and other inherently transient phenomena of two-phase flow, steady state is in a statistical sense an equilibrium situation. Whereas the description of transient behavior is a whole range of separate loosely attached cases, depending on flow parameters, the description and formalism for steady state should be more integrated and universal. Our work explores a part of its parameter space, and we find a robust power law behavior: Pressure increases as $\Delta P_L \propto \mathrm{Ca}^{0.5}$, alternatively for permeability $\kappa_{\mathrm{eff}} \propto \mathrm{Ca}^{0.5}$.

The power law is valid over roughly two decades, but there should be cutoffs for large and small flow rates. For high flow rate, the cutoff cluster size will approach the pore size, and from that point the permeability must reach a plateau. The same is the case for flow rates low enough that the largest clusters are limited by the system size. These limits were not realized experimentally, but in numerical work these cutoffs have been seen [20,22].

The scaling behavior of the system was explained by theoretical arguments, relying on a high viscosity ratio. Numerical work with a lower viscosity ratio (steady state but somewhat different boundary conditions) indicates a lower exponent: $\Delta P_L \propto \mathrm{Ca}^{\beta'}$, where $\beta' < 0.5$ [20]. We conjecture that the presented theory is a limiting case and thus is suitable as a starting point for further theoretical developments, aiming at incorporating the more complex case where the two fluids have more similar viscosities.

The work was supported by NFR through PETROMAKS, a CNRS PICS, an ANR ECOUPREF project, and a regional REALISE program. A special thanks to Alex Hansen for useful comments.

[1] J. Bear, *Dynamics of Fluids in Porous Media* (Elsevier, New York, 1972).
[2] F. A. L. Dullien, *Porous Media Fluid Transport and Pore Structure* (Academic, San Diego, 1992), 2nd ed.
[3] M. Sahimi, *Flow and Transport in Porous Media and Fractured Rock* (VCH Verlagsgesellschaft mbH, Weinheim, 1995).
[4] R. Lenormand, E. Touboul, and C. Zarcone, J. Fluid Mech. **189**, 165 (1988).
[5] P. G. Saffman and G. Taylor, Proc. R. Soc. A **245**, 312 (1958).
[6] R. Lenormand and C. Zarcone, Phys. Rev. Lett. **54**, 2226 (1985).
[7] G. Løvoll, Y. Meheust, R. Toussaint, J. Schmittbuhl, and K. J. Måløy, Phys. Rev. E **70**, 026301 (2004).
[8] L. Paterson, Phys. Rev. Lett. **52**, 1621 (1984).
[9] K. J. Måløy, J. Feder, and T. Jøssang, Phys. Rev. Lett. **55**, 2688 (1985).
[10] J. P. Stokes, D. A. Weitz, J. P. Gollub, A. Dougherty, M. O. Robbins, P. M. Chaikin, and H. M. Lindsay, Phys. Rev. Lett. **57**, 1718 (1986).
[11] J.-D. Chen and D. Wilkinson, Phys. Rev. Lett. **55**, 1892 (1985).
[12] R. Toussaint, G. Løvoll, Y. Meheust, K. J. Måløy, and J. Schmittbuhl, Europhys. Lett. **71**, 583 (2005).
[13] O. I. Frette, K. J. Måløy, J. Schmittbuhl, and A. Hansen, Phys. Rev. E **55**, 2969 (1997).
[14] Y. Meheust, G. Løvoll, K. J. Måløy, and J. Schmittbuhl, Phys. Rev. E **66**, 051603 (2002).
[15] M. J. Oak, L. E. Baker, and D. C. Thomas, J. Pet. Technol. **42**, 1054 (1990).
[16] D. G. Avraam and A. C. Payatakes, J. Fluid Mech. **293**, 207 (1995).
[17] M. S. Valavanides and A. C. Payatakes, Adv. Water Resour. **24**, 385 (2001).
[18] A. K. Gunstensen and D. H. Rothman, J. Geophys. Res. **98**, 6431 (1993).
[19] H. A. Knudsen, E. Aker, and A. Hansen, Transp. Porous Media **47**, 99 (2002).
[20] H. A. Knudsen and A. Hansen, Phys. Rev. E **65**, 056310 (2002).
[21] H. A. Knudsen and A. Hansen, Europhys. Lett. **65**, 200 (2004).
[22] T. Ramstad and A. Hansen, Phys. Rev. E **73**, 026306 (2006).
[23] K. T. Tallakstad, G. Løvoll, H. A. Knudsen, T. Ramstad, and K. J. Måløy (to be published).
[24] H. Auradou, K. J. Måløy, J. Schmittbuhl, and A. Hansen, Transp. Porous Media **50**, 267 (2003).

An experimental study of secondary oil migration in a three-dimensional tilted porous medium

Jianzhao Yan, Xiaorong Luo, Weimin Wang, Renaud Toussaint, Jean Schmittbuhl, Guy Vasseur, Fang Chen, Alan Yu, and Likuan Zhang

ABSTRACT

A three-dimensional physical experiment was conducted to study secondary oil migration under an impermeable inclined cap. Light-colored oil was released continuously at a slow rate of about 0.1 mL/min from a point at the base of an initially water-saturated porous model. With buoyancy as a primary driving force, a vertical cylindrical shape of an oil migration pathway was observed first, and then a layer-shaped lateral migration pathway was observed beneath the top inclined sealing plate once the oil cluster had reached the top cap. Magnetic resonance imaging was used to observe the migration processes—for example, morphology of the migration pathway, intermittency of oil bubbles, and variation of oil saturation within the migration paths. Results show that the snap-off phenomenon (related to fast local imbibition processes) occurred more commonly during vertical migration than it did during lateral migration. The lateral migration pathway that parallels to the top inclined cap has a typical vertical thickness of 2 to 4 cm (0.8–1.6 in.) (i.e., roughly 40–80 pores). This thickness is consistent with the prediction derived from scaling laws related to pore size and Bond number. Along the lateral migration direction, the sectional area and the horizontal width of the migration pathway fluctuate significantly, although the average oil saturation along the pathway remains almost the same. After stopping the initial oil injection, the sectional area of the migration pathway shrinks significantly. Therefore, we believe that this significant shrinking of the migration

Manuscript received August 31, 2010; provisional acceptance June 16, 2011; revised manuscript received August 22, 2011; final acceptance September 9, 2011.
DOI:10.1306/09091110140

AUTHORS

Jianzhao Yan ~ *Key Laboratory of Petroleum Resources Research, Institute of Geology and Geophysics, Chinese Academy of Science, Beijing, China 100029; yjzh27@163.com*

Jianzhao Yan is a postdoctoral graduate at the Institute of Geology and Geophysics, Chinese Academy of Science, Beijing. He received B.S. and M.S. degrees in petroleum engineering and development from the China University of Petroleum and his Ph.D. in petroleum geology from the Institute of Geology and Geophysics, Chinese Academy of Science. His interests now include theoretical and experimental analyses of secondary hydrocarbon migration, enhancement of oil recovery, and the use of nuclear magnetic resonance in the petroleum industry.

Xiaorong Luo ~ *Key Laboratory of Petroleum Resources Research, Institute of Geology and Geophysics, Chinese Academy of Science, Beijing, China 100029; luoxr@mail.iggras.ac.cn*

Xiaorong Luo is a research scientist at the Chinese Academy of Sciences and has B.S. and M.S. degrees in geology from Northwestern University, China, and a Ph.D in geophysics from the University of Montpellier, France. His research interests focus on experimental and numerical modeling, geopressuring, and hydrocarbon migration and accumulation.

Weimin Wang ~ *School of Electronics Engineering and Computer Science, Peking University, Beijing, China 100871; wmw@263.net.cn*

Weimin Wang has a Ph.D. in radiophysics and is a professor at the School of Computer Science and Electronics Engineering at Peking University. He has been working on the research of magnetic resonance imaging in porous media since 1997. His research covers the imaging method, hardware design, and image processing of magnetic resonance imaging.

Renaud Toussaint ~ *IPGS (Institut de Physique du Globe de Strasbourg), CNRS (Centre National de la Recherche Scientifique), University of Strasbourg, 5 rue Descartes, Strasbourg, France 67000; renaud.toussaint@unistra.fr*

Renaud Toussaint is a CNRS (Centre National de la Recherche Scientifique) researcher in geophysics at IPG Strasbourg (Institut de Physique du Globe de Strasbourg), working on fluid mechanics in porous media and flow and fracture of mixtures of fluids and granular solids. He studied mathematics, theoretical physics (master's degree from the Ecole Normale Supérieure de Lyon [ENS de Lyon], aggregation of mathematics), and geophysics (master's from IPG Paris, Ph.D. from the University of Rennes I). He developed his postdoctoral models of complex flows in the physics departments of the Universities of Oslo and Trondheim.

Jean Schmittbuhl ~ *IPGS (Institut de Physique du Globe de Strasbourg), CNRS (Centre National de la Recherche Scientifique), University of Strasbourg, 5 rue Descartes, Strasbourg, France 67084; Jean.Schmittbuhl@unistra.fr*

Jean Schmittbuhl has been a CNRS (Centre National de la Recherche Scientifique) senior scientist at IPG Strasbourg (Institut de Physique du Globe de Strasbourg) since 2004. He has a master's degree in geosciences from ENS Paris and in physics from the University of Paris 6, an aggregation in geology, a Ph.D. in physics from the University of Paris 6 (1994), and a habilitation in geophysics (University of Paris 7, 2001). His main research interest is in physics of geologic processes (e.g., fluid flow, fracture, friction), combining experimental and numerical approaches.

Guy Vasseur ~ *Sisyphe, UMR7619, University Pierre et Marie Curie, Paris Cedex 05, France 75252; guy.vasseur@upmc.fr*

Guy Vasseur received an engineering degree from Ecole Polytechnique (Paris) in 1963 and a doctorat d'etat (Ph.D.) from the University of Paris in 1971. He then became a senior scientist of Centre National de la Recherche Scientifique and worked at the universities of Montpellier 2 and Paris 6 in various domains of geophysics. His main domain of competence is the modeling of heat and mass transfer in the earth's crust.

Fang Chen ~ *State Key Laboratory of Magnetic Resonance and Atomic and Molecular Physics, Wuhan Institute of Physics and Mathematics, Chinese Academy of Sciences, Hubei, Wuhan, China 430071; chenfang040@sina.com*

Fang Chen received his Ph.D. in nuclear magnetic resonance from the Wuhan Institute of Physics and Mathematics, the Chinese Academy of Sciences, in 2004 and he has held a senior engineer position in this institute since 2010. From 2004 to 2010, he served as a magnetic resonance imaging research and development engineer for the Beijing Wandong Medical Equipment

pathway is the main reason why only a relatively small volume of oil and gas has been lost during secondary migration.

INTRODUCTION

Secondary migration is the movement of hydrocarbons as a separate fluid through water-saturated rocks, faults, or fractures. Lateral secondary migration in a specific carrier bed is considered to be the major process accounting for large-scale oil and gas accumulations in most reservoirs (Schowalter, 1979; Thomas and Clouse, 1995). However, secondary migration typically occurs during a long geologic period and is impossible to be observed directly in situ. In the field, it is also very difficult to locate or identify any active migration pathway as well as the remaining structure left after the migration. Therefore, a laboratory experiment gives a unique means of observing real oil and gas migration processes in porous media and studying the transport mechanism (Schowalter, 1979; Dembicki and Anderson, 1989; Catalan et al., 1992).

As commonly expected, hydrocarbon lateral migration actually occurs three-dimensionally (3-D) within strata, bounded by sealing rocks (Schowalter, 1979; England et al., 1987; Hindle, 1997; Carruthers and Ringrose, 1998). Because of the limitations of experimental model building and observation technique capability, it is difficult to design a proper 3-D model to simulate secondary migration processes. Most published experiments dealing with lateral migration were based on one-dimensional or two-dimensional (2-D) models (Emmons, 1921; Lenormand et al., 1988; Catalan et al., 1992; Thomas and Clouse, 1995; Wagner et al., 1995, 1997; Meakin et al., 2000; Tokunaga et al., 2000; Zhang et al., 2003; Hou et al., 2004, 2005; Luo et al., 2004; Løvoll et al., 2004, 2010; Toussaint et al., 2005), which may not reflect the complexity of hydrocarbon lateral migration within the carrier-seal system. Therefore, the main objective in this study is to conduct a 3-D physical experiment using a relatively large box model that should be closer to reality than the previous experiments to investigate the characteristics of oil migration in a 3-D space.

A few physical experiments of 3-D immiscible flow have been done and published by others under very different experimental conditions (system size) and with limited observational device capability. Frette et al. (1992) conducted an experiment in a glass box to study the migration process of a nonwetting phase driven by buoyancy. The glass box was filled with cylindrical grains of Röhm Plexiglas Formmasse 7N Glasklar (poly[methylmethacrylate] [PMMA]) and saturated with dibutyl-phthalate as the nonwetting phase. The model was transparent because PMMA and dibutyl-phthalate have the same refraction index, allowing the internal structure of the migration pathway to be observed directly. Stöhr et al. (2003) used the planar laser-induced fluorescence (PLIF) technique to simultaneously visualize the 3-D pore-scale flow of two immiscible liquid phases in porous media. Although the PLIF technique is capable of reconstructing the 3-D fluid-flow pathway and can observe the internal structure and morphology directly by selecting the solid and liquid phases with the same refractive index, some strict requirements for the nature of the porous medium and the fluid were not satisfactorily met by this technique. The x-ray absorption technique (Selle et al., 1993) and ultrasonic technique (Thomas and Clouse, 1995) were also tentatively used to observe the migration pathway structure in a porous model and to measure oil saturation, but only for the quasi-2-D media. Sharma et al. (1997) and Hou et al. (2009) used an x-ray computed tomography (CT) technique to observe fluid flow and measure fluid saturation in the 3-D porous medium. Although this CT technique has a high resolution, it is unsuitable to be applied to a large migration model because the field of view is limited (Seright et al., 2002; Turner et al., 2004).

Comparing all the techniques mentioned above, magnetic resonance imaging (MRI), which is a nondestructive probing technique, has innate advantages for observing the migration pathway geometry (Luo et al., 2004, 2008) and measuring oil saturation within the 3-D migration path (Miao et al., 2004). It can directly detect fluids and their flow pattern through the pores (Koptyug et al., 2002) and is not affected by the shape, transparency, and refraction index of the media (Wang et al., 1996). Mandava et al. (1990) used MRI to observe two-phase flow and estimate the fluid saturation in porous media, and Wang et al. (1996) proved that MRI is a suitable method to evaluate residual oil saturation in cores. Fukushima (1999) introduced MRI to observe the fluid velocity field, diffusion processes, and modification of the porous medium. Koptyug et al. (2002) applied MRI to study gas flow and diffusion in a glass bead packing model.

For this article, we focused on the 3-D effects of secondary oil migration and studied the lateral migration pathway characteristics through the physical experiments by designing a large 3-D packing porous medium box-shaped model. Dyed oil was used as a nonwetting phase to conduct the physical secondary migration experiments with the 3-D box model. The MRI technique was applied to observe the migration pathway morphology and to measure oil saturation within the migration pathways.

Company, Limited. His research interests include nuclear magnetic resonance, magnetic resonance imaging, and porous material studies.

Alan Yu ~ *BHP Billiton Petroleum, Geoscience Specialist Group, 1360 Post Oak Boulevard, Houston, Texas 77560; Alan.A.Yu@bhpbilliton.com*

Alan Yu specializes in integrated petroleum system analysis and is currently the principal geologist at BHP Billiton Petroleum. He earned his B.S. degree (1982) in petroleum geology from Northeastern Petroleum University, China, and his Ph.D. (1992) in basin modeling from the University of South Carolina (USC). After a 2-year postdoctoral research at USC, Alan joined the industry in 1994 and has since been working on petroleum exploration and production supports in basins worldwide, including the Gulf of Mexico, South America, Africa, Canada, Southeast Asia, and Australia, for predrill predictions of hydrocarbon charge, fluid quality, pore pressure, top seal integrity and capacity, subsalt sediment seismic velocity, and reservoir quality. Alan has published more than 30 articles in related areas and has been a member of AAPG since 1990.

Likuan Zhang ~ *Key Laboratory of Petroleum Resources Research, Institute of Geology and Geophysics, Chinese Academy of Science, Beijing, China 100029; zhanglikuan1979@163.com*

Likuan Zhang is a postdocral researcher at the Institute of Geology and Geophysics, Chinese Academy of Sciences. He received his B.S. degree in petroleum geology from Jilin University, China, and his Ph.D from the Institute of Geology and Geophysics, Chinese Academy of Sciences. His research interests concern fluid flow in fault zones, numerical basin modeling, and hydrocarbon migration in petroleum systems.

ACKNOWLEDGEMENTS

This study was supported mainly by the Chinese National Science Foundation (40772090, 40902041) and partly by BHP Billiton (L1295XV00) and the University of Strasbourg, France.
The AAPG Editor thanks the three anonymous reviewers for their work on this paper.

EDITOR'S NOTE

Color versions of Figures 1, 3, 8, and 12 can be seen in the online version of this paper.

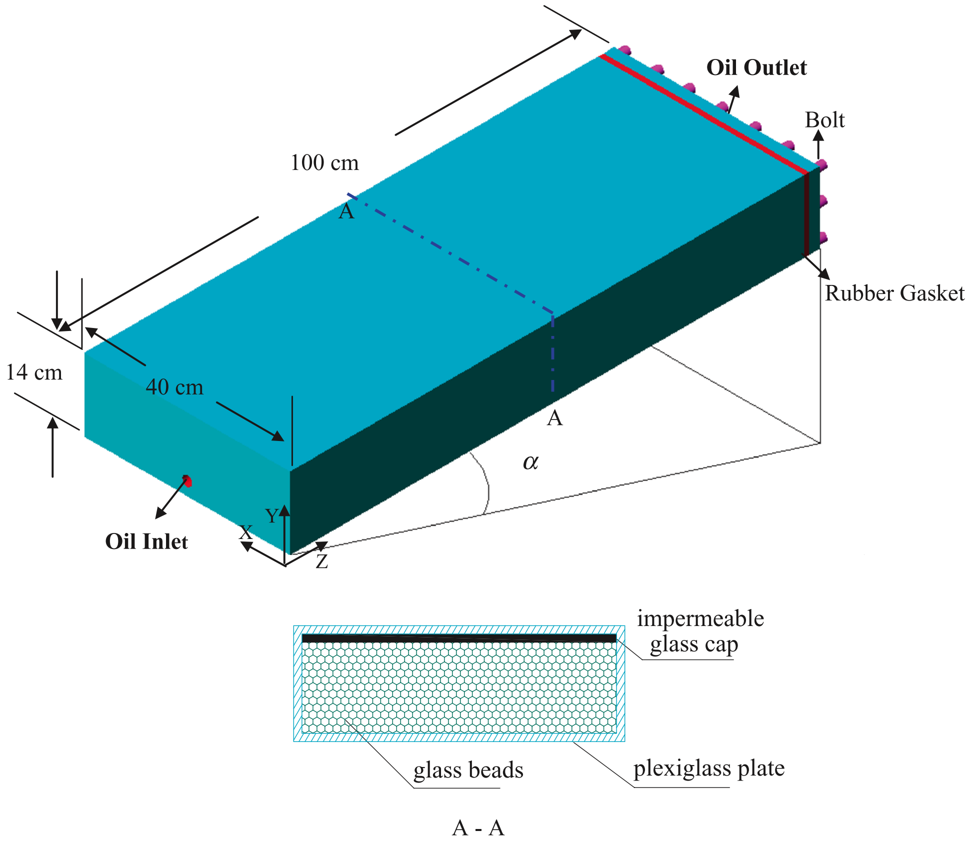

Figure 1. Sketch of the box model.

Some insightful outcomes, including the lateral migration pathway thickness, which agrees with the theoretical value, and vertical and horizontal hydrocarbon migration morphology, were obtained through this experiment measurement under the given condition of an impermeable top inclined cap and the limitation of the experimental settings.

PHYSICAL EXPERIMENT PREPARATION AND OBSERVATION METHODS

Sample Preparation

A plane-parallel 3-D box model of 100 × 40 × 14 cm^3 (6.1 × 2.4 × 0.9 $in.^3$) has been constructed (Figure 1). The length of 100 cm (39 in.) was selected to ensure that oil can migrate laterally far enough without being impacted by boundary limit; the horizontal width of 40 cm (16 in.) was based on the inner diameter of the MRI testing chamber that is about 50 cm (20 in.) wide; the height of 14 cm (6 in.) was chosen to make sure that the thickness of the lateral migration pathway is not affected by the size of the model and also to keep a reasonable weight and size of the model because we had to move around the entire model for measurements. The box is a 1-cm (0.4-in.)-thick plexiglass plate, selected because it is a nonmagnetic material for MRI and possesses sufficient mechanical strength to hold the model. The base inlet plate and four sides of the box were glued together, whereas the outlet plate (dimensions 40 × 14 × 1 cm^3 [2.4 × 0.9 × 0.06 $in.^3$]) was left removable so that the model could be filled with glass beads conveniently. The outlet plate and the sides were connected with nylon bolts and sealed with a back-shaped rubber gasket under pressure during the experiment. The tubes for fluid flow were installed in the inlet and outlet plates. The glass plate was used so that the oil migration pathway would not be affected by a different wettability of the boundary compared with the porous medium (Thomas and Clouse, 1995).

Glass beads with diameters of 0.4 to 0.6 mm were used in the experiment as porous medium. To make sure that they were water wet, all glass beads used were carefully washed with acid and alkaline solutions and then heated to a temperature of 500°C for at least 30 min (Luo et al., 2004).

When filling the box with the glass beads, the 3-D box model was first positioned vertically and filled with water. The outlet plate was removed, and a special sieve was fastened on top of the model. The mixture of glass beads and water was then poured into the sieve, and the glass beads were deposited uniformly and continuously so that the porous medium was as homogeneous as possible. At the same time, the sides of the model were knocked with a rubber hammer around the model in a continuous and uniform way to make sure that the glass beads were closely packed. After filling the glass beads, the back-shaped rubber gasket and the outlet plate were placed onto the top of the model and bolted to seal the model carefully.

The permeability of the medium is 189.7 μm^2, and the radii of pores are in the range of 0.185 to 0.225 mm, as measured by Hou et al. (2004). Once the model was entirely saturated with water (of density ρ = 1000 kg/m^3), it was placed obliquely with a horizontal angle (α) of 36° during the experiment (see Figure 1). Dyed kerosene oil with a density (ρ) of 778 kg/m^3 was injected into the model through the base inlet tube at the bottom by a micropump at a constant rate of 0.1 mL/min. Given this open-design system, a normal pore pressure is expected within the box, and the excess water consequently was driven out of the box through the outlet tube. The interfacial tension between the oil and water was measured to be γ = 0.0289 N/m. Because the oil was dyed red, the movement of oil could be traced visually as well in the vicinity of the box limits.

The Magnetic Resonance Imaging Methods of Observation

The Wandong medical 1.5T superconducting MRI system was used to observe the migration process in the experiment. The presence of ^{1}H in both oil and water induces MRI signals while scanning through the migration pathway. Because of the molecular structural difference between water and oil, the relaxation rates of ^{1}H in oil and water are different, and the relaxation rate of ^{1}H associated with water molecules is quicker than that in oil. That is, when water-soluble Mn^{2+} is added to water, the relaxation rate of ^{1}H in water molecules increases, but the relaxation rate of ^{1}H in oil remains unchanged (Chang et al., 1993; Wang et al., 1996). Therefore, the Mn^{2+} (0.7 g/L) solution could be added to water to distinguish the oil MRI signal from that of water. We confirmed that adding Mn^{2+} to water did not change the interfacial tension between water and oil.

Because the box model occupies a significant part in the MRI testing chamber, the scanning parameter options were set as follows: the largest available magnetic coil and a field of view of 384 × 384 mm^2, which corresponded to a slice resolution of 1.5 mm. These scanning conditions imposed by the size of the model have an impact on the resolution of the scanner because the image quality and the signal-to-noise ratio decrease with the increase of both the coil size and the field of view (Mei et al., 2008). Therefore, an image noise reduction process (or a filter) is required to reprocess the scanned images. After analyzing the signal distribution of the migration pathway, a noise reduction filter based on adjacent pixels was adopted as described here. First, the noise threshold (T_h) was set as the maximum value of signal in the clear-of-oil areas near the migration pathway, and then a threshold concerning the eight neighboring pixels in 2-D space was applied while ensuring the presence of oil. This threshold (n_k) was set to 3. If the pixel gray value of images was smaller than T_h, the pixel was considered as a noise point and its gray value was set to 0. In addition, the number (n) of the adjacent pixels whose gray value was larger than T_h was counted. If n was larger than n_k, the pixel was considered as a point covered by oil and its gray value was confirmed; otherwise, it was considered as a noise point and its gray value was also set to 0. Figure 2 shows the results of the migration pathway image before and after this noise reduction procedure. It demonstrated that the noise was filtered out

Figure 2. The contrast of image before and after noise reduction.

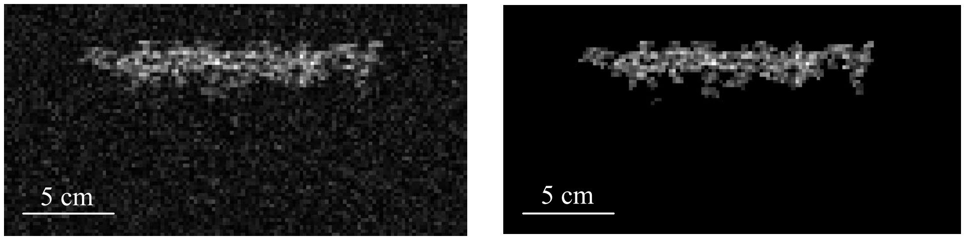

almost completely from the background image, whereas the characteristics of the dominant migration pathway are preserved.

Another processing step needed is to eliminate the different image results because of the scans taken at different times. A linear transformation was applied to normalize all slice signals before reconstructing the 3-D migration pathway.

Also, to measure and calibrate the oil saturation value within the migration pathway from the MRI images, a small glass tube filled with 100% oil was placed along with the model and scanned at the same time as the migration path and used for the oil saturation calibration.

In a preliminary experiment, the longitudinal relaxation time (T1) and the transverse relaxation time (T2) of an oil-saturated glass bead packing similar to the model were measured using the inversion recovery method and echo-spin method, respectively (Tyryshkin et al., 2003). The T1 was found to be 1011 ms and T2 to be 810 ms. The fast-spin echo-proton density weight image sequence was selected here in this work to scan the migration pathway. According to the measured relaxation times from above, echo time (TE) and repetition time (TR) were set, respectively, to 108 ms and 9000 ms. Accordingly, conditions for the spin density image—for example, TR >> T1 and TE << T2 (Xiao et al., 1995)—were satisfied. The acquisition time for each slice is proportional to TR, and it was about 13.73 s in our experiment.

Under these given conditions, the MRI signal varies linearly as a function of the volumetric oil concentration. The oil saturation within the migration pathway can thus be quantitatively estimated from MR images (Miao et al., 2004). The gray level of the image is just proportional to the proton density (in oil), and oil saturation in the migration pathway can be calculated as (Chen et al., 1992; Luo et al., 2004) shown below:

$$s = y/(B \times \phi) \times 100\% \tag{1}$$

where s is the oil saturation; y is the gray level of the migration pathway; B is the gray level of the calibration; and ϕ is the porosity of the model, which is about 0.36, calculated by measuring the total volume and the water volume filling the pore space in the glass tube.

During the scanning process, the thickness of the slice and the interval between the slices were set to be 3.0 and 0.3 mm, respectively. The resolution along the slice was 1.5 mm × 1.5 mm (size of a pixel).

This 3-D physical experiment lasted about 6 days (150 hr), and Table 1 gives the progressive steps of the experiment. Although the model was placed obliquely at 36° during oil migration, it was set horizontally when the migration pathway was being scanned by MRI, a constraint caused by the scanning device.

EXPERIMENTAL RESULTS

The experiment on secondary migration in our 3-D physical model was conducted successfully. The migration process and pathway morphology were observed visually and recorded through MRI images, and the oil saturation within the migration path was computed based on the MR images.

Qualitative Observation by Visual Inspection and by Magnetic Resonance Imaging

Results Observed Visually

Because injected oil was dyed, the process of oil migration and the morphology of the oil pathway

Table 1. The Process of the Experiment

Time (hr)	Description
0–3	Oil migrated vertically and reached the glass cap; the vertical migration pathway was scanned.
4–37	Oil migrated laterally and broke through the outlet plate; the lateral migration pathway (trapped under the top cover) was scanned.
38–44	Migration pathway evolved while oil was being injected, and the migration pathway was scanned.
45–121	Oil migrated driven by buoyancy without oil being injected, and the residual migration pathway formed.
121–123	Residual migration pathway was scanned.
124–150	Oil was injected into the model again, and the migration pathway was scanned.

were initially observed by visual inspection. Because the model is not completely transparent through the glass bead column, the migration pathway along the vertical path could not be detected optically before the oil front had reached the impermeable top inclined cap. As soon as the oil front had reached the top inclined cap, oil started to move laterally under the top inclined glass plate. Note that the development of the migration pathway is not a continuous process but commonly occurs through sudden jumps that are similar to the so-called Haines jumps (Morrow, 1970). The migration feature of such jumps was caused by the motion of the oil migration front paused from time to time, although the oil was continuously injected. Although the front was stagnant, the pathway became thicker and therefore tended to develop transversely, and consequently, new fingers emerged from this enlarged head. Several fingers are commonly present in the front of the lateral migration path, and these fingers could merge or split from time to time. In some instances, water was trapped in the migration pathway when two fingers, especially two nonadjacent fingers, coalesced. Figure 3 is a picture of the migration pathway taken by a digital camera. It shows that the migration pathway was meandering and very irregular in shape. The horizontal width of the migration cluster fluctuated significantly along the main direction of the lateral migration. The front of the fingers did not touch the edges on the sides of the model horizontally, which proved that oil could migrate transversely freely without any constraints because of the boundaries of the box model.

Results Observed by Magnetic Resonance Imaging

The Whole Migration Pathway

The entire 3-D migration pathway was reconstructed using the MRI slices (Figure 4). Figure 4A presents the top view image to show the entire migration pathway morphology along the direction parallel to the top glass cap. It shows that many small fingers developed along the main pathway and some water-saturated areas (e.g., migration shadows) were formed. Generally, the width of the horizontal migration path decreased along the direction of lateral migration, and its mean value (ξ) was measured to be about 8.36 cm (3.3 in.). Figure 4B is the lateral view image (vertical cross section of the model) to illustrate the change of thickness of the migration pathway along the lateral migration direction. It shows that the oil had

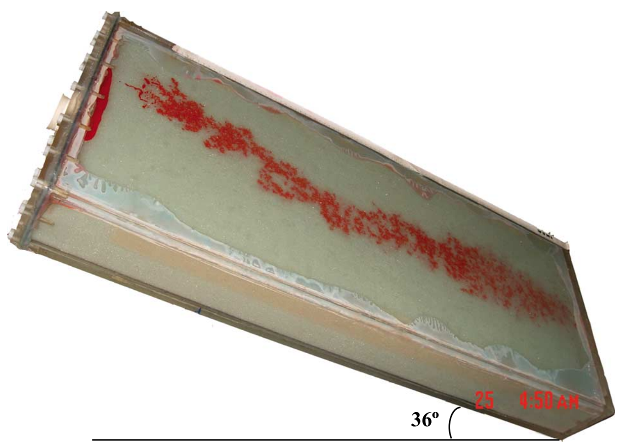

Figure 3. Picture of the lateral migration pathway.

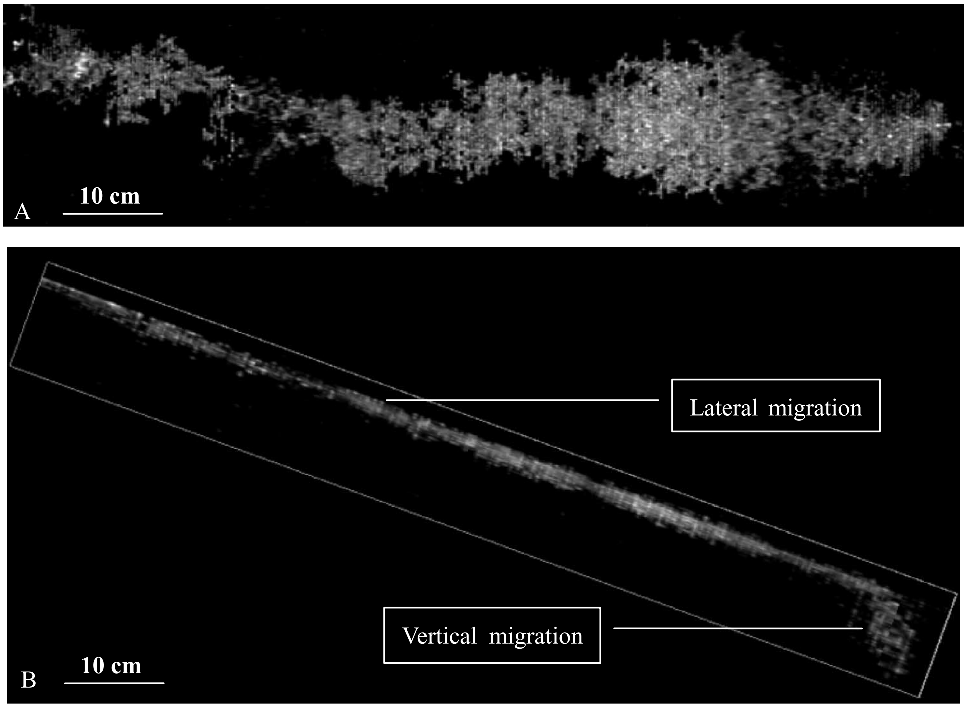

Figure 4. The whole three-dimensional migration pathway. (A) Top view image to show the entire lateral migration pathway morphology. (B) Lateral view image to show the change of the thickness of the lateral migration pathway.

migrated upward first from the point of injection into the model, and then changed its direction once the oil front reached the impermeable top inclined cap. The lateral migration pathway is a thin layer-shaped zone, parallel to the top inclined cap, with a generally stable vertical thickness (H) of 2 to 4 cm (0.8–1.6 in.) in the lateral migration direction under the given conditions of the 3-D box geometry and experiment settings. A closer examination of the inside texture of the lateral migration pathway with nearly constant thickness showed that it consisted of many small clusters of complex morphology embedded within the bounding volume parallel to the top inclined impermeable cap, as could be observed when rotating the 3-D image.

Vertical Migration Pathway and Snap Off

The first movement of oil after injection into the model was upward, driven by buoyancy. The vertical pathway was scanned several times using MRI after the front had reached the top cap. The shape of the vertical migration pathway was roughly cylindrical, and many little fingers were present around the main pathway (Figure 5A). The vertical migration pathway shrank and snapped off obviously when the oil front reached the location point 53 cm (21 in.) away from the inlet plate, and most of the pathway split into oil drops or small oil bands (Figure 5B). With continuing injection, it then was refilled while the migration front moved farther forward (Figure 5C). Compared with Figure 5B, the size of the vertical pathway in Figure 5C was increased, but it was still smaller than the size of the vertical pathway when the oil front was initially reached (Figure 5A). The initial lateral pathway shrank and snapped off at the beginning point of the lateral migration pathway (or the end of vertical migration), whereas the vertical pathway was refilled (see Figure 5C).

Lateral Migration Front

During lateral oil migration, the migration pathway was scanned at the different locations along the lateral migration direction so that the 3-D migration pathway could be reconstructed according to these scanned 2-D slices (Figure 6), and the oil migration phenomenon and behavior could be recorded clearly during the migration process. Panels A and B of Figure 6 show the 3-D migration front when it was at location points 41 and 70 cm (16 and 28 in.), respectively, laterally away from the inlet plate. As shown in Figure 6A, new fingers

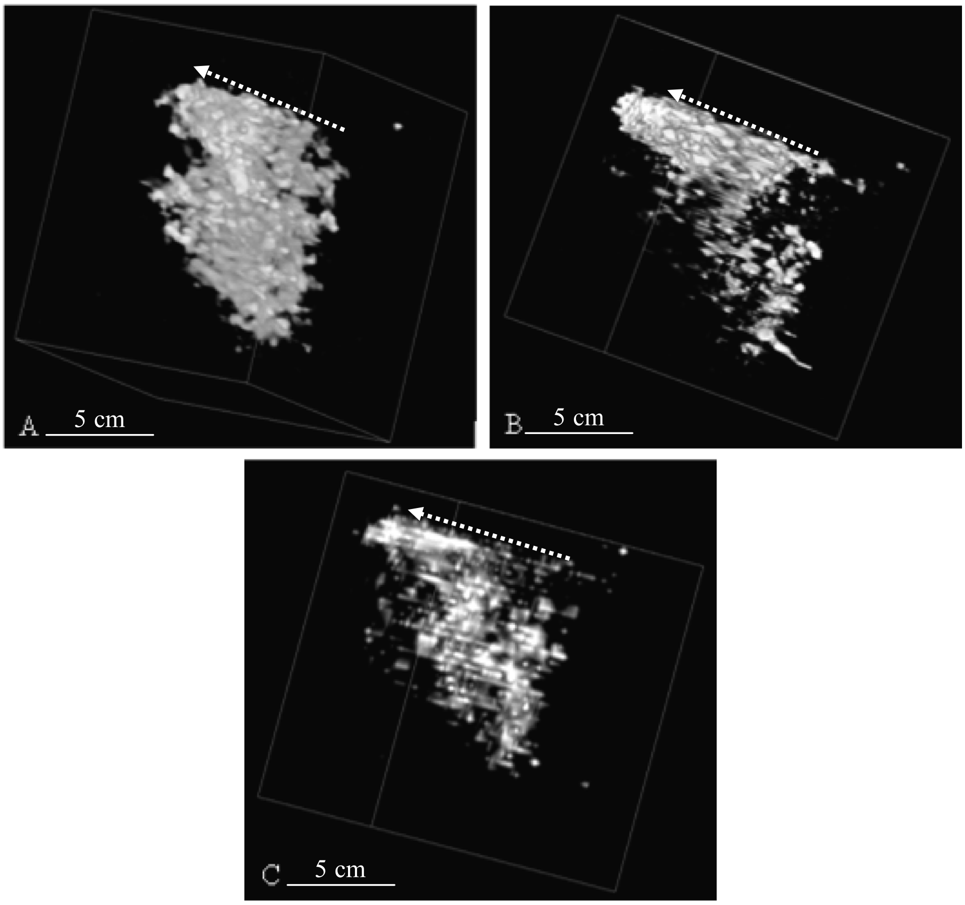

Figure 5. The three-dimensional vertical migration pathways at different periods. The dotted line indicates the location of the impermeable cap, and the arrow indicates the lateral migration direction. (A) When the front just reached the cap, the vertical migration pathway was roughly cylindrical. (B) When the front migrated laterally, the vertical migration pathway snapped off obviously. (C) The migration pathway was refilled.

were formed suddenly along the oil front once the migration front became thicker and started to move transversely. Figure 6B shows the coalescence of oil fingers and its consequent effect of a trapped area, where no oil had migrated into and left behind the migration front, as well as the splitting of fingers after coalescence.

The Lateral Migration Path Evolution with Time

The migration pathway was also scanned repeatedly at the same location to observe the migration path development with time. Figure 7 shows the slices taken at the location point 30 cm (12 in.) away from the inlet plate at moments when the lateral oil front arrived at location points 53 (Figure 7A), 70

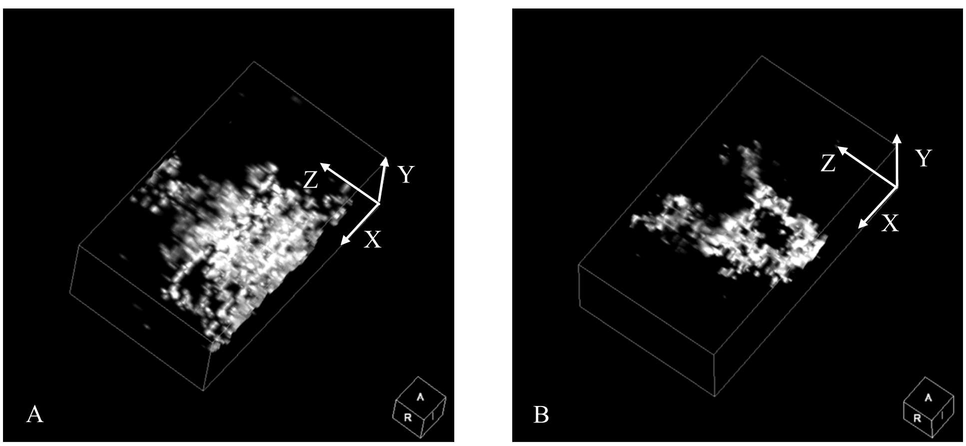

Figure 6. The three-dimensional migration front of lateral pathway at different locations. Oil migrated along the Z axis direction. (A) New fingers formed suddenly along the front. (B) The image emphasizes the splitting of fingers after coalescence.

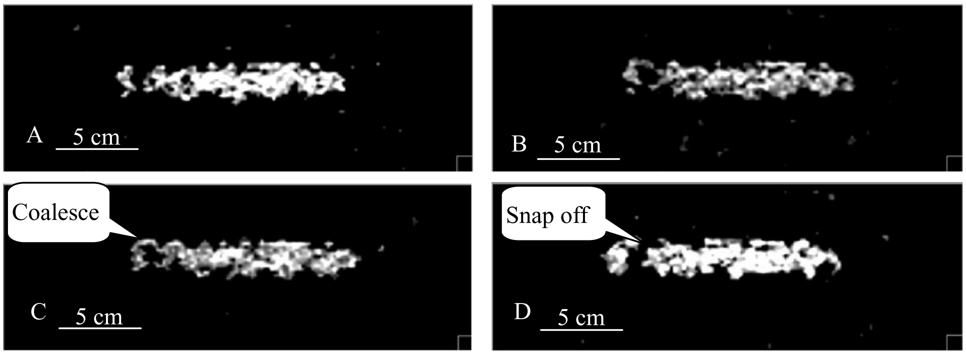

Figure 7. The evolution of the lateral migration pathway along a slice 30 cm (12 in.) away from the inlet.

(Figure 7B), and 84 cm (Figure 7C) (21, 28, and 33 in., respectively) and the outlet point (Figure 7D). These slices show that the overall morphology of the pathway remained almost the same during the lateral migration, but the coalescences (Figure 7B, C) and snap-offs occurred locally (Figure 7A, D) within the 3-D migration pathway.

Quantitative Observation by Magnetic Resonance Imaging

Size of the Lateral Migration Pathway and Oil Saturation within the Pathway

After the migration front had reached the top end of the model in the experiment, the entire migration pathway was scanned and oil saturation within the migration pathway was calculated according to the 2-D MRI slices. To observe the 3-D pathway size and shape and oil saturation distribution, a 2-D slice was taken for every 10 cm (4 in.) along the lateral migration direction, starting from the location of 25 cm (10 in.) (167 pixels) away from the inlet plate of the model (Figure 8). Figure 8 shows that the thickness of the lateral migration pathway was stable at a constant value of approximately 2 to 4 cm (0.8–1.6 in.) vertically in the Y direction. On the contrary, the horizontal width (in the X direction) of the lateral migration pathway fluctuated greatly along the lateral migration direction Z. The entire lateral migration pathway did not consist of a single connected pore layer beneath the top inclined glass cap, but instead had many small fingers developed surrounding the main survived path, and the ends of the upward fingers reached the glass cap. Figure 8 also shows that the oil saturation distribution was heterogeneous in the lateral migration pathway. The oil saturation within most areas was between 40 and 60%, and it could reach 80% only at a few points. Comparing the oil saturation within this 3-D lateral migration pathway with the vertical migration pathway (Luo et al., 2004, 2008), the oil saturation distribution was not artificially affected by the glass cap in the lateral migration pathway. Figures 9 and 10 are plots of the sectional area of the lateral migration pathway and average oil saturation within the pathway, respectively, with the distance along the lateral migration (in the Z direction). The sectional area of the lateral migration pathway fluctuated significantly, having a maximum value of 14 cm^2 (2.2 $in.^2$) and a

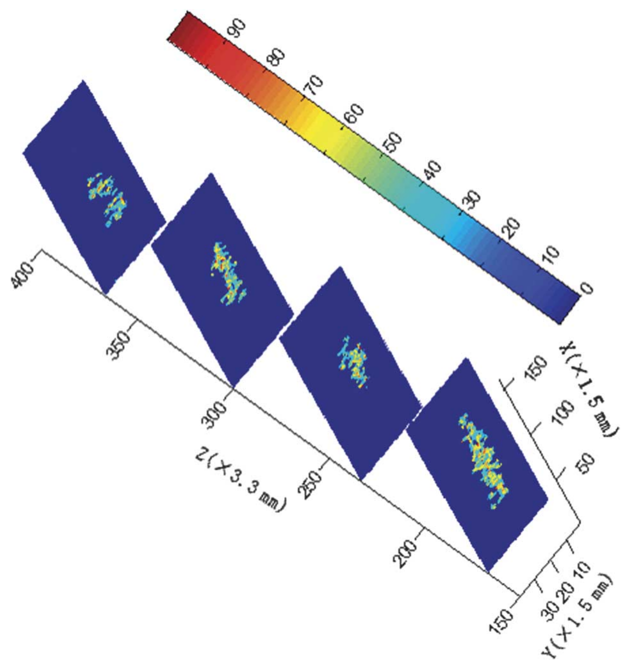

Figure 8. Oil saturation distribution in the lateral migration pathway.

minimum of only 1 cm^2 (0.2 $in.^2$), but the average oil saturation remains relative stable at about 47%.

Size of the Migration Pathway and Oil Saturation at Different Stages

Previous researchers Zhang et al. (2003) and Luo et al. (2004) noticed in their experiments that oil saturation within the pathway varies according to various migration stages, for example, from 70 to 80% during the growing stage to 25 to 35% during the shrinking stage. Therefore, both the migration pathway morphology and oil saturation within the pathway at the different stages were considered during this 3-D physical experiment.

We scanned the migration pathway at location point 45 cm (17.8 in.) away from the inlet plate of the model at various stages of oil injection, as follows: (1) during initial injection when the first pathway formed, (2) during the residual oil stage after injection stopped, and (3) during reinjection stage after the pause of injection. Figure 11 shows the results of the sectional area of the pathways and the average oil saturation in the pathways. The sectional area of residual pathway was significantly smaller than it was when the migration pathway initially formed. The sectional area was increased again when the oil was reinjected, but it was still smaller than the initial stage. Although oil saturation with the initial injection is the largest and the reinjection stage is still larger than it was in the residual stage, the differences of oil saturation among different stages are not large.

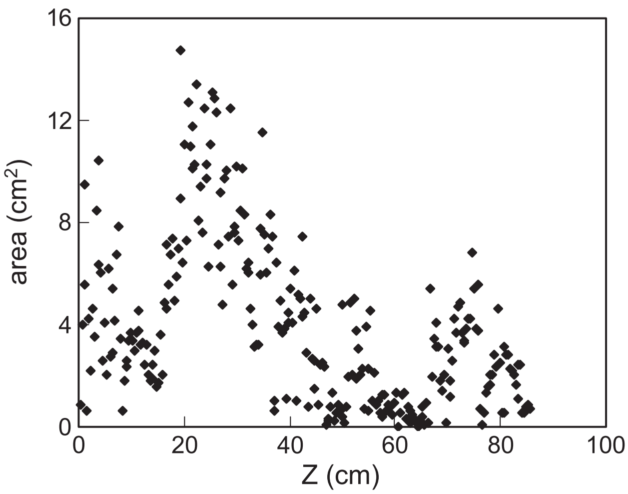

Figure 9. Section area curve along the lateral Z migration direction.

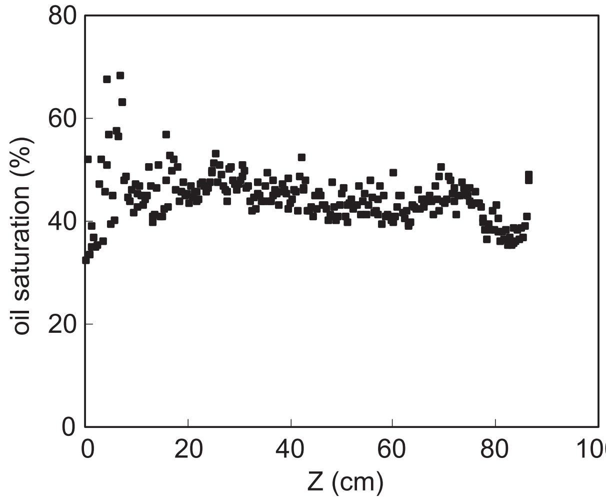

Figure 10. The average oil saturation within the migration pathway varies in the lateral Z migration direction.

DISCUSSION

The aforementioned MRI images show that the lateral migration pathways beneath an impermeable top cap appear as a sheet with a certain thickness that seems like those formed in 2-D Hele-Shaw equipment (Hou et al., 2005) and different from those expected in a 3-D space (Thomas and Clouse, 1995). Therefore, it is necessary to discuss the agreement between theory and measurements for the morphology of the migration pathways.

Previous studies (Tokunaga et al., 2000; Luo et al., 2004; Luo, 2011) indicate that the dimensionless Bo (Wilkinson, 1984, 1986), describing the relationship between buoyancy and interfacial forces at pore scale, provides a suitable characterization of the migration pathway. In our experiment, Bo can be estimated as

$$Bo = \frac{\Delta p_{\mathrm{grav}}}{\Delta p_{\mathrm{int}}} = \frac{\Delta \rho g a^2 \sin \alpha}{\gamma} \tag{2}$$

where Δp_{grav} and Δp_{int} are hydrostatic pressure difference and interfacial pressure difference, respectively; $\Delta\rho$ = 222 kg/m^3 is the density difference of

Figure 11. Characters of the migration pathways at different stages.

Item	Migration	Residual	Reinjection
Slice			
Area (cm^2)	2.16	0.65	0.98
Saturation (%)	40.6	36.9	37.8

the oil and water; $g = 9.8$ m/s^2 is the gravity acceleration; $a = 4.1 \times 10^{-4}$ m is the mean pore diameter; and $\gamma = 0.0289$ N/m is the interface tension between oil and water. So $Bo = 7.44 \times 10^{-3}$. In contrast with the vertical migration pathway, the lateral migration pathway can be assimilated to a 2-D one because the thickness of the lateral migration pathway remained stable at 2 to 4 cm (0.8–1.6 in.). The vertical extent (V) of the lateral migration pathway can be scaled as

$$V \approx a/Bo \tag{3}$$

because of the balance between the buoyancy force and capillary force. The thickness perpendicular to the inclined cap is thus

$$H = V\cos\alpha \approx a\cos\alpha/Bo \tag{4}$$

so H is expected to be approximately 5 cm (~2 in.). The measured lateral migration pathway thickness, between 2 and 4 cm (0.8–1.6 in.), roughly agrees with the theoretical value. These results suggest that the 3-D experimental lateral migration study can be divided into two subsets of 2-D experiments. One is to study the thickness of the migration pathway when the 2-D model is placed obliquely and vertically, as used in the experiment of Thomas and Clouse (1995); the other is to study the morphology of the migration pathway under the impermeable cap when the 2-D model is placed obliquely and horizontally, as used in the study by Birovljev et al. (1995).

The snap-off effect was found both in the vertical migration pathway and in the lateral one. The refilling of the vertical migration pathway after the snap-off and the alternating of coalescence and splitting meant that there may be cyclical changes in the migration pathway. However, this phenomenon appeared to occur more frequently in the vertical migration pathway than in the lateral one. This may be caused by the interplay between local pinning forces and buoyancy leading to the snap-off of the migration pathway (Wagner et al., 1995, 1997), and the effect of the buoyancy in the vertical migration pathway was stronger than that in the lateral migration pathway.

The fractal dimension was measured using the box-counting method. Before fractal dimension computation, the slices were filtered using the method mentioned in section 2 and transformed into binary images. The lateral migration pathway is covered with boxes with a size of λ. The box is empty if it covers none of the migration pathway. The number (N) of non-empty boxes is counted. A series of N is obtained as a function of gradually changing choices of K, and points (λ_i, N_i) are drawn in a double logarithm coordinate system (Figure 12). The fractal dimension is equal to the negative slope of the linear section of the fitting line between the box size and the box number. As shown in Figure 12, the fitting line can be divided into three sections. At a small scale (section 1, from 1 to 11 pixels), the migration pathway was dominated only by the porous disorder and the fractal dimension is 2.2 ± 0.3, which roughly agrees with the value 2.50 that is expected for capillary fingering and consistent with 3-D invasion percolation models (Wilkinson, 1986). At a medium scale (section 2 in Figure 12), at scales between H and ξ, the migration pathway is essentially a thick plate parallel to the cap, that is, it is dominated by the porous disorder and the buoyancy at the same time and the fractal dimension is approximately 1.9. Up

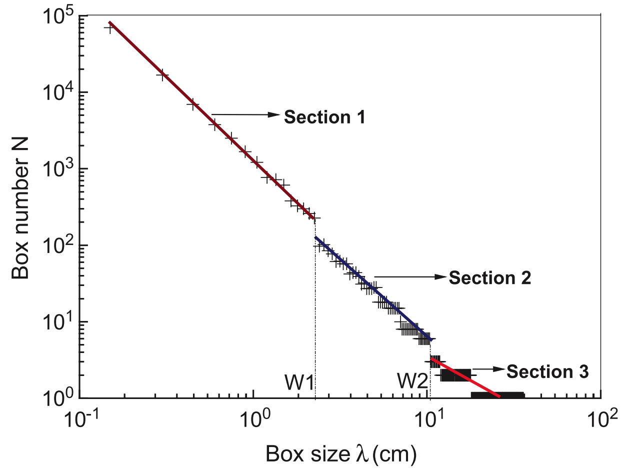

Figure 12. The number of boxes required to cover the oil structure as a function of the linear box size. This number is determined numerically for any possible size λ of the size of a cubic box, in entire pixels, by paving the three-dimensional space with such boxes and counting how many boxes cover the oil structure. This box number procedure allows determination of the mass fractal dimension of the structure: a fractal set of dimension D leads to a law $N(\lambda) \sim \lambda^{-D}$. In bilogarithmic representation, three linear sections (power laws) are identified on the obtained box counts for every size λ (crosses). These linear sections correspond to small, middle, and large scales, respectively. They have slopes determined by linear fitting, corresponding to respective fractal dimensions approximately 2.2, 1.9, and 1. The scales separating these three fractal dimensions are determined from the observed separation in linear regimes of the crosses as W1 = 2.25 cm (0.9 in.) separating small and medium scales and W2 = 9.9 cm (3.9 in.) separating medium and large scales. These observed values are consistent with the predicted values of H and ξ, which are expected to separate scales where different types of forces are in competition, and different fractal dimensions.

to the large error bar inherent to the narrow scale range in this analysis, this is compatible with a large scale (larger than H, section 3 in Figure 12); the migration pathway was dominated only by the buoyancy and looks like an upward linear structure, which is reflected by its fractal dimension that is almost 1. The separation scale W1 = 2.25 cm (0.9 in.) between sections 1 and 2 (left dash-dotted line in Figure 12) is close to the vertical thickness of the lateral migration pathway H approximately 2 to 4 cm (~0.8–1.6 in.). The second separation scale W2 between sections 2 and 3 is 9.9 cm (3.9 in.) (right dash-dotted line in Figure 12), which is close to the mean width, ξ, of the lateral migration pathway.

With the average oil saturation in the migration pathway of each slice and the sectional area of the migration pathway, the oil volume within such a slice can be calculated as

$$v_s = \bar{S}_s \times A_s \times T \times \phi \tag{5}$$

in which $\bar{S}_s$ is the average oil saturation of such a splice in the migration pathway, A_s is the sectional area of the migration pathway, and T is the splice thickness of the slice. Although the part between two splices cannot be MRI scanned because the interval between splices is much smaller than the splice thickness, the oil volume in the gaps between splices can be interpolated from the two neighboring slices:

$$v_G = \frac{(A_s + A_{s+1})}{2} \times \frac{\left(\bar{S}_s + \bar{S}_{s+1}\right)}{2} \times G \times \phi \tag{6}$$

where G is the gap between the two neighboring slices. The oil volume in the whole model is obtained as

$$v_o = \sum_{s=1}^{n} V_s + \sum_{G=1}^{n-1} V_G \tag{7}$$

where n is the total number of splices.

The oil volume is computed according to slice oil saturation and the area is 82.17 mL. However, the actual injected oil volume is computed by multiplying the injection rate by the injection time, which is 96.4 mL. The computed oil volume is slightly less than the actual injected oil volume and can be explained two ways. One is that pure oil is used as the calibration, which shows that the magnetic resonance signal relaxes slower than the oil in the pores, and makes the calculated saturation less than the actual one. The other is that the smallest connected features of the migration pathway may be suppressed during slice filtering.

Accurate estimates of the losses occurring during secondary oil migration are a vital part of valid exploration assessments (Lewan et al., 2002; Luo et al., 2004, 2007, 2008). Secondary oil migration is a very complex process (McNeal, 1961; Harms, 1966; Berg, 1975; Schowalter, 1979). The ratio between the migration pathway and the carrier is small, but it can change from 1 and 10% (Schowalter, 1979; England et al., 1987; Dembicki and Anderson, 1989; Catalan et al., 1992), which makes the estimates of residual oil saturation from different researchers inconsistent (Schowalter, 1979; England et al., 1987; Dembicki and Anderson, 1989; Hirsch and Thompson, 1995) and makes accurate estimates of the losses occurring during secondary migration difficult. Carruthers and Ringrose (1998) pointed out that determining the oil-rock contact volumes is the basic work for accurate estimates of the losses occurring during secondary oil migration. Combined with our study, oil-rock contact volumes can be evaluated based on the thickness and width of the pathway during the lateral migration process. Knowing the oil saturation distribution, the oil losses can be estimated easily. Although oil saturation in the residual pathway was slightly lower than that obtained when the pathway was forming, the residual migration pathway size shrinks greatly and the section area of the residual migration pathway is about 30% of the initial pathway. Shrinking of the pathway after stopping injection appears to be the main reason for the occurrence of small losses during secondary oil migration.

CONCLUSIONS

Compared with the cylindrical shape of the vertical migration pathway, the lateral migration pathway was a layer-shaped zone under and parallel to the impermeable inclined cap. Under the given experimental conditions, the thickness of the lateral migration pathway, perpendicularly to the impermeable cap, was approximately a constant value between 2 and 4 cm (0.8 and 1.6 in.), whereas its horizontal width measured perpendicular to the slope of the cap fluctuated significantly.

The MRI was successfully used to observe the morphology of the secondary migration pathway in this 3-D experiment and to measure the size of the pathway and the oil saturation within the path. Oil saturation was heterogeneous in the lateral migration pathway but was almost not affected by the cap. The oil saturation of most regions was between 40 and 60%, and could reach 80% only at a few points. The average oil saturation was stable at 47% following the lateral migration direction.

Dominated by porous disorder, buoyancy, or the interplay between them, the mass fractal dimension of the lateral migration pathway was measured to be between 2 and 2.5 at scales smaller than the thickness H, consistent with 3-D capillary fingering; approximately 1.9 at scales between the pathway thickness H, consistent with 2-D capillary fingering or fully 2-D structures; its width ξ, consistent with the 2-D capillary fingering or fully 2-D structures; and approximately 1 above ξ, corresponding to a linear uprising geometry of the pathway.

REFERENCES CITED

Berg, R. R., 1975, Capillary pressure in stratigraphic traps: AAPG Bulletin, v. 59, no. 6, p. 939–959.

Birovljev, A., G. Wagner, P. Meakin, J. Feder, and T. Jøssang, 1995, Migration and fragmentation of invasion percolation clusters in two-dimensional porous media: Physical Review E, v. 51, no. 6, p. 5911–5915, doi:10.1103/PhysRevE.51.5911.

Carruthers, D., and P. Ringrose, 1998, Secondary oil migration: Oil-rock contact volume, flow behavior and rates, *in* J. Parnell, ed., Dating and duration of fluid flow and fluid-rock interaction: Geological Society (London) Special Publication 144, p. 205–220, doi:10.1144/GSL.SP.1998.144.01.16.

Catalan, L., W. F. Fu, I. Chatzis, A. Francis, and L. Dullien, 1992, An experimental study of secondary oil migration: AAPG Bulletin, v. 76, no. 5, p. 638–650.

Chang, C. T., S. Mandava, A. T. Watson, S. Sarkar, and C. M. Edwards, 1993, The use of agarose gels for quantitative determination of fluid saturations in porous media: Magnetic Resonance Imaging, v. 11, no. 5, p. 717–725.

Chen, S., K. H. Kim, F. Qin, and A. T. Watson, 1992, Quantitative NMR imaging of multiphase flow in porous media: Magnetic Resonance Imaging, v. 10, no. 5, p. 815–826.

Dembicki, H. J., and M. J. Anderson, 1989, Secondary migration of oil: Experiments supporting efficient movement of separate, buoyant oil phase along limited conduits: AAPG Bulletin, v. 73, no. 8, p. 1018–1021.

Emmons, W. H., 1921, Experiments on accumulation of oil in sands: AAPG Bulletin, v. 5, p. 103–104.

England, W. A., A. S. Mackenzie, D. M. Mann, and T. M. Quigley, 1987, The movement and entrapment of petroleum fluids in the subsurface: Journal of the Geological Society (London), v. 144, no. 2, p. 327–347, doi:10.1144/gsjgs.144.2.0327.

Frette V., J. Feder, T. Jøssang, and P. Meakin, 1992, Buoyancy-driven fluid migration in porous media: Physical Review

Letters, v. 64, no. 21, p. 3164–3167, doi:10.1103/PhysRevLett.68.3164.

Fukushima, E., 1999, Nuclear magnetic resonance as a tool to study flow: Annual Review of Fluid Mechanics, v. 31, p. 95–123.

Harms, J. C., 1966, Stratigraphic traps in a valley fill, western Nebraska: AAPG Bulletin, v. 50, p. 2119–2149, doi:10.1306/5D25B711-16C1-11D7-8645000102C14865D.

Hindle, A. D., 1997, Petroleum migration pathways and charge concentration: A three-dimensional model: AAPG Bulletin, v. 81, no. 9, p. 1451–1481.

Hirsch, L. M., and A. H. Thompson, 1995, Minimum saturations and buoyancy in secondary migration: AAPG Bulletin, v. 79, no. 5, p. 696–710.

Ho, 1999, Nuclear magnetic resonance as a tool to study flow: Annual Review of Fluid Mechanics, v. 31, p. 95–123.

Hou, P., B. Zhou, and X. R. Luo, 2004, Experimental studies on pattern of secondary oil migration pathway: Science in China (Series D Earth Sciences), v. 34, no. S1, p. 162–168, doi:CNKI:SUN:JDXK.0.2004-S1-018.

Hou, P., X. L. Luo, B. Zhou, and N. X. Zhang, 2005, An experimental study of episodic oil migration: Xinjiang Petroleum Geology, v. 26, no. 1, p. 33–35, doi:CNKI:SUN:XJSD.0.2005-01-009.

Hou, J., Z. Q. Li, S. K. Zhang, X. L. Cao, Q. J. Du, and X. W. Song, 2009, Computerized tomography study of the microscopic flow mechanism of polymer flooding: Transport in Porous Media, v. 79, no. 3, p. 407–418, doi:10.1007/s11242-008-9330-9.

Koptyug, I. V., A. V. Matveev, and S. A. Vltobelli, 2002, NMR studies of hydrocarbon gas flow and dispersion: Applied Magnetic Resonance, v. 22, no. 2, p. 187–200.

Lenormand, R., E. Zarcone, and E. Touboul, 1988, Numerical models and experiments on immiscible displacements in porous media: Journal of Fluid Mechanics, v. 189, p. 165–187, doi:10.1017/S0022112088000953.

Lewan, M. D., M. E. Henry, D. K. Higley, and J. K. Pitman, 2002, Material-balance assessment of the New Albany–Chesterian petroleum system of the Illinois Basin: AAPG Bulletin, v. 86, no. 5, p. 745–778, doi:10.1306/61EEDB8E-173E-11D7-8645000102C1865D.

Løvoll, G., Y. Méheust, R. Toussaint, J. Schmittbuhl, and K. J. Måløy, 2004, Growth activity during fingering in a porous Hele Shaw cell: Physical Review E., v. 70, p. 026301, doi:10.1103/PhysRevE.70.026301.

Løvoll, G., M. Jankov, K. J. Måløy, R. Toussaint, J. Schmittbuhl, G. Schäfer, and Y. Méheust, 2010, Influence of viscous fingering on dynamic saturation-pressure curves in porous media: Transport in Porous Media, v. 86, no. 1, p. 305–324, doi:10.1007/s11242-010-9622-8.

Luo, X. R., 2011, Simulation and characterization of pathway heterogeneity of secondary hydrocarbon migration: AAPG Bulletin, v. 95, no. 6, p. 881–898.

Luo, X. R., F. Q. Zhang, S. Miao, W. Wang, Y. Huang, B. Zhou, D. Loggia, and G. Vasseur, 2004, Experimental verification of oil saturation and loss during secondary migration: Journal of Petroleum Geology, v. 27, no. 3, p. 241–251.

Luo, X. R., B. Zhou, S. X. Zhao, F. Q. Zhang, and G. Vasseur, 2007, Quantitative estimates of oil losses during migration: Part I. The saturation of pathways in carrier beds: Journal of Petroleum Geology, v. 30, no. 4, p. 375–387.

Luo, X. R., J. Z. Yan, B. Zhou, P. Hou, W. Wang, and G. Vasseur, 2008, Quantitative estimates of oil losses during migration: Part II. Measurement of residual oil saturation in migration pathways: Journal of Petroleum Geology, v. 31, no. 2, p. 179–190, doi:10.1306/11191010027.

Mandava, S. S., A. Ted Watson, and M. E. Carl, 1990, NMR imaging of saturation during immiscible displacements: American Institute of Chemical Engineers Journal, v. 36, no. 11, p. 1680–1686, doi:10.1002/aic.690361108.

McNeal, R. P., 1961, Hydrodynamic entrapment of oil and gas in Bisti field, San Juan County, New Mexico: AAPG Bulletin, v. 45, no. 3, p. 315–329.

Meakin, P., G. Wagner, A. Vedvik, H. Amundsen, J. Feder, and T. Jossang, 2000, Invasion percolation and secondary migration: Experiments and simulations: Marine and Petroleum Geology, v. 17, no. 7, p. 777–795, doi:10.1016/S0264-8172(99)00069-0.

Mei, L. X., H. Wang, and G. L. Li, 2008, A two-channel surface coil for vertebral imaging on low-field MRI systems: Chinese Journal of Magnetic Resonance, v. 25, no. 1, p. 33–38, doi:CNKI:SUN:PPXZ.0.2008-01-004.

Miao, S., F. Q. Zhang, T. J. Li, X. L. Luo, and P. Hou, 2004, Application of NMR imaging technique to quantitative observation and analysis on hydrocarbon migration pathway: Acta Petrolei Sinica, v. 25, no. 3, p. 44–47.

Morrow, N. R., 1970, Physics and thermodynamics of capillary action in porous media: Industrial and Engineering Chemistry, v. 62, no. 6, p. 32–56, doi:10.1021/ie50726a006.

Schowalter, T. T., 1979, Mechanics of secondary hydrocarbon migration and entrapment: AAPG Bulletin, v. 63, no. 5, p. 723–760.

Selle, O. M., J. I. Jensen, S. Øyvind, T. Andersen, B. Nyland, and T. M. Broks, 1993, Experimental verification of low-dip, low-rate, two-phase (secondary) migration by means of x-ray absorption, *in* J. Parnell, A. H. Ruffell, and N. R. Moles, eds., Geofluids ’93: Contributions to an international conference on fluid evolution, migration and interaction in rocks: Torquay, England, British Gas, p. 72–75.

Seright, R. S., J. Liang, W. B. Lindquist, and J. H. Dunsmuir, 2002, Characterizing disproportionate permeability reduction using synchrotron x-ray computed microtomography: Society of Petroleum Engineers Annual Technical Conference and Exhibition, SPE Paper 71508, 13 p., doi:10.2523/71508-MS.

Sharma, B. C., W. E. Brigham, and L. M. Castanier, 1997, CT imaging techniques for two-phase and three-phase in-situ saturation measurements: Tulsa, Oklahoma, U.S. Department of Energy, National Petroleum Technology Report SUPRI TR 107, 114 p.

Stöhr, M., K. Roth, and B. Jähne, 2003, Measurement of 3-D pore-scale flow in index-matched porous media: Experiments in Fluids, v. 35, no. 2, p. 159–166, doi:10.1007/s00348-003-0641-x.

Thomas, M. M., and J. A. Clouse, 1995, Scaled physical model of secondary oil migration: AAPG Bulletin, v. 79, no. 1, p. 19–29, doi:10.1306/64ED87BE-1724-11D7-8645000102C1865D.

Tokunaga, T., K. Mogi, O. Matsubara, H. Tosaka, and K. Kojima, 2000, Buoyancy and interfacial force effects on two-phase displacement patterns: An experimental study: AAPG Bulletin, v. 84, no. 1, p. 65–74, doi:10.1306/C9EBCD65-1735-11D7-8645000102C1865D.

Toussaint, R., G. Løvoll, Y. Méheust, K. J. Måløy, and J. Schmittbuhl, 2005, Influence of pore-scale disorder on viscous fingering during drainage: Europhysics Letters, v. 71, p. 583, doi:10.1209/epl/i2005-10136-9.

Turner, M. L., L. Knüfing, C. H. Arns, A. Sakellariou, T. J. Senden, A. P. Sheppard, R. M. Sok, A. Limaye, W. V. Pinczewski, and M. A. Knackstedt, 2004, Three-dimensional imaging of multiphase flow in porous media: Physica A, v. 339, p. 166–172, doi:10.1016/j.physa.2004.03.059.

Tyryshkin, A. M., S. A. Lyon, A. V. Astashkin, and A. M. Raitsimring, 2003, Electron spin relaxation times of phosphorus donors in silicon: Physical Review B, v. 68, no. 19, p. 193207.1–193207.4.

Wagner, G., A. Birovljev, P. Meakin, J. Feder, and T. Jøssang, 1995, Migration and fragmentation of invasion percolation clusters in two-dimensional porous media: Europhysics Letters, v. 31, no. 3, p. 139–144, doi:10.1209/0295-5075/31/3/003.

Wagner, G., A. Birovljev, J. Feder, and T. Jøssang, 1997, Fragmentation and migration of invasion percolation clusters: Experiments and simulations: Physical Review E, v. 55, no. 6, p. 7015–7029, doi:10.1103/PhysRevE.55.7015.

Wang, W. W., D. J. Lang, and W. Lie, 1996, The application of NMR imaging to the studies of enhanced oil recovery in China: Magnetic Resonance Imaging, v. 14, no. 5, p. 951–953, doi:10.1016/S0730-725X(96)00192-0.

Wilkinson, D., 1984, Percolation model of immiscible displacement in the presence of buoyancy forces: Physical Review A, v. 30, no. 1, p. 520–531, doi:10.1103/PhysRevA.30.520.

Wilkinson, D., 1986, Percolation effects in immiscible displacement: Physical Review A, v. 34, p. 1380–1391, doi:10.1103/PhysRevA.34.1380.

Xiao, L. Z., Y. R. Du, and C. H. Ye, 1995, NMR spin density micro-imaging for rock samples: Acta Physico-Chimica Sinaca, v. 11, no. 3, p. 196–198.

Zhang, F. Q., X. L. Luo, S. Miao, W. M. Wang, B. Zhou, and Y. Z. Huang, 2003, The patterns and its effects factors of secondary hydrocarbon migration: Petroleum Geology and Experiment, v. 25, no. 1, p. 69–75, doi:cnki:ISSN:1001-6112.0.2003-01-011.

Journal of Petroleum Science and Engineering 86–87 (2012) 237–245

Contents lists available at SciVerse ScienceDirect

Journal of Petroleum Science and Engineering

journal homepage: www.elsevier.com/locate/petrol

Testing oil saturation distribution in migration paths using MRI

Jianzhao Yan [a,*], Xiaorong Luo [a], Weimin Wang [b], Fang Chen [c], Renaud Toussaint [d], Jean Schmittbuhl [d], Guy Vasseur [e], Likuan Zhang [a]

[a] Key Laboratory of Petroleum Resources Research, Institute of Geology and Geophysics, Chinese Academy of Science, Beijing, 100029 China
[b] School of Electronics Engineering and Computer Science, Peking University, Beijing, 100871 China
[c] State Key Laboratory of Magnetic Resonance and Atomic and Molecular Physics, Wuhan Institute of Physics and Mathematics, Chinese Academy of Sciences, Wuhan, 430071 China
[d] IPGS(Institute de Physique du Globe de Strasbourg), CNRS(Centre National de la Recherche Scientifique), University of Strasbourg, 5 rue Descartes, Strasbourg, 67000 France
[e] Sisyphe, UMR7619, University Pierre et Marie Curie, Paris Cedex 05, 75252 France

A R T I C L E I N F O

Article history:
Received 11 January 2011
Accepted 25 March 2012
Available online 5 April 2012

Keywords:
MRI
Oil saturation
Calibration
DICOM
Migration path

A B S T R A C T

Magnetic Resonance Imaging (MRI) method allows to observe the distribution of different fluids in situ in porous media, and to measure oil and water saturation. Although this technique has great advantages compared to others, there remains large space for assessing the method and improving the accuracy of measurement. Using MRI, the oil secondary migration paths are scanned to measure the saturation distribution during the laboratory experiments. The resulting map can be calibrated using a device with the same pore structure as the probed sample and fully saturated with oil. This device is scanned with the probed sample at the same time in order to calibrate the saturation. The Spin-echo multi-slices sequence (SEMS) is adopted for MRI to ensure that the oil saturation in migration paths is accurately measured. The relevant spatial resolution of the mapping is defined according to the concept of REV (representative elementary volume). The oil saturation resulting from data obtained using different image formats are compared and the resulting saturation evaluation is compared to direct bulk saturation measurements. This comparison demonstrates that the calculated MRI oil saturation using DICOM image format is quite accurate, with a relative error less than 2%.

1. Introduction

Physical experiment is an important means of observing the hydrocarbon migration phenomenon and studying the migration mechanism (Dembicki and Anderson, 1989; Catalan et al., 1992; Tukunaga et al., 2000; Zeng and Wang, 2003; Zhang et al., 2003a; Zhang et al., 2004). For interpreting these experiments, it is important to evaluate the oil saturation occurring in the migration channel. Moreover the oil saturation gives an important basis for the quantitative evaluation of the migration losses and for the estimation of potential reservoir (Hirsch and Thompson, 1995; Luo et al., 2004, 2007, 2008).

Many conventional methods of measuring oil saturation, including distillation, chromatography (Tang and Cui, 2007) and water washing method (Dembicki and Anderson, 1989), have been proposed as listed in Table 1. These methods are essentially destructive, i.e. samples are destroyed to measure the oil saturation in the porous medium so that the oil saturation cannot be dynamically monitored. Besides, all results measured with conventional methods are average oil saturation (Chen et al., 1992; Nicula et al., 1998), which makes difficult to assess the spatial distribution of oil in the porous medium (Baldwin and Yamanashi, 1989). So in the recent decades, scientists have developed some new non-destructive technologies, such as optical techniques and ray attenuation method in order to test the spatial distribution of fluid saturation in biphasic flows in porous media. Optical techniques, including light reflection method (LRM) (Van Geel and Sykes, 1994; Fishman et al., 1998; O'Carroll et al., 2004) and light transmission method (LTM) (Hoa, 1981; Darnault et al., 1998; Darnault et al., 2001; Conrad et al., 2002; Bob et al., 2008; Tallakstad et al., 2009) are low cost, easy to fulfill, but only apply to quasi2D transparent media. Compared with conventional light sources, both Gamma rays and X-rays have a relatively strong penetrability and apply to opaque media such as soil and rock (Høst-Madsen and Jensen, 1992; Liu et al., 1992; Ursin, 1992; Illangasekare, et al., 1995; Imhoff et al., 1996; Dicarlo et al., 2000; Hill et al., 2002; Oostrom et al., 2003; Bsavaraj et al., 2005; Oostrom et al., 2005). But as for optical methods, they are half-space measuring methods, and only apply to 2D plate models with low thickness. Computer tomography (CT) methods using Gamma or X-ray attenuation can realize actual 3D local measurement of non-transparent medium without limitation of medium shapes (Sharma et al., 1997; Mogensen et al., 2005; Rangel-German et al., 2006). However, since the absorption and attenuation of X-ray mainly depend on the local density of the porous media (i.e. matrix + fluid) but not on fluids themselves, it is hard to distinguish between fluids. Therefore the CT Gamma or X-ray method is not well adapted to observe the oil and water in porous medium (Edelstein et al., 1988; Li et al., 2007). Methods of 3D imaging based on the detection of a fluid in specific points using optical fibers have also been developed (Gupta and Verma, 2009; Nsir et al., 2012). This is not

* Corresponding author.
E-mail address: yjzh27@163.com (J. Yan).

0920-4105/$ – see front matter © 2012 Elsevier B.V. All rights reserved.
doi:10.1016/j.petrol.2012.03.027

Table 1
Comparison between saturation measurement methods.

r (mm)	0.08	0.2–0.4	0.4–0.6	0.6–0.8	0.8–1.0	1.0–1.2	1.5–2.0	2.0–2.5	0
T_2 (ms)	294	668	810	868	920	956	987	1028	1151

*Grain size of zero represents a pure oil sample.

field measurement, but point ones, since each measuring point requires a specific design to be mounted.

Compared with the above methods, MRI method has huge advantages in testing oil saturation. First, as a non-destructive and non-invasive method, MRI has a high testing precision[12] and can be used to monitor the saturation change during the experimental process; second, MRI provides a much better contrast to distinguish the fluids between them than CT because it detects the fluids in the porous medium directly; third, MRI does not require a particular shape, realizing 3D spatial quantitative measurement in a real sense; and last, MRI allows to see through opaque rocks, unlike optical methods only suitable for Hele Shaw cells.

Many researchers have measured oil saturation by detecting H^+ density using MRI since 1990s (Baldwin and Yamanashi, 1989; Mandava et al., 1990; Chardaireriviere and Roussel, 1991; Chen et al., 1992; Enwere and Archer, 1992; Chang et al., 1993; Mogensen et al., 2005). Washburn and Madelin (2010) adopted Na element to conduct MRI to distinguish between the water phase and the oil phase, and tested the distribution of water-phase saturation with MRI. Most of the tests, however, were carried out in one-dimensional space. Graue et al. (2001) have given the oil distribution in 2D MRI slices, but the test principle and image processing were not described.

Secondary migration of oil and gas in basins is an extremely heterogeneous process (McNeal, 1961; Harms, 1966; Smith, 1966; Berg, 1975; Schowalter, 1979), and heterogeneous path is found even in homogeneous porous media as long as the gravitational or viscous contrast between the two fluids destabilizes the invasion process (Frette et al., 1997; Méheust et al., 2002; Luo et al., 2004; Løvoll et al., 2004; Toussaint et al., 2005; Løvoll et al., 2010; Nsir et al., 2012). Therefore, real-time measurement of shape features of the migration path and the change of its interior oil saturation is an essential basic work for research of hydrocarbon migration mechanism. Miao et al. (2004) and Zhou et al. (2005) have adapted the MRI method to define oil saturation during the oil migration process. They calibrated the measurements using pure oil filled in a small glass tube as calibration, but they didn't consider the possible matrix effect: this effect results in a significant difference between in-pore oil and pure oil estimate from transverse relaxation rate and the overall accuracy should take into account this effect.

This paper focuses on the technique of using MRI to measure oil saturation in heterogeneous oil clusters inside a porous medium. Experiments are conducted in a glass tube initially saturated with water where oil migrates, while another glass tube filled with glass beads and fully saturated with oil is used as the calibration. This allows measuring the oil saturation and its distribution inside the path of different type of patterns. Such patterns have been measured and classified by Yan et al. (in press). The paper also makes a comparative analysis of differences in oil saturation calculated according to data sources of different image formats, and validates the techniques by comparison with independently measured global saturation results.

2. Measurement principle

In the experiments, the SEMS was used to scan the samples and the relaxation process of MRI signal can be described as (Mandava et al., 1990):

$$M(\omega, T_E) = M_0(\omega)\exp\left(-\frac{T_E}{T_2}\right)\left(1-\exp\left(-\frac{T_R}{T_1}\right)\right) \tag{1}$$

in which, ω is the resonance frequency, M is the observed magnetic intensity, $M_0$is the inherent magnetic intensity, T_E is the echo time, T_R is the repeat time, T_1 is the longitudinal relaxation time, and $T_2$is the transverse relaxation time. T_1 and T_2 are dependent on the properties of matter and the surrounding environment; T_E and T_R can be set in the MRI sequence. If $T_R \gg T_1$ and $T_E \ll T_2$, the observed magnetic intensity is close to the inherent one:

$$M(\omega, T_E) \approx M_0(\omega) \tag{2}$$

The gray value of the obtained images is in direct proportion to the proton density:

$$M_0(\omega) = kN\left(H^+\right) \tag{3}$$

which is the basis for oil saturation testing with MRI (Edelstein et al., 1988; Chen et al., 1992).

During the scan of the probed sample with MRI, if a calibration is carried out aside with a known oil saturation (S'), then for the calibration sample, as well:

$$M'\left(\omega', T_E'\right) \approx M_0'\left(\omega'\right) \tag{4}$$

in which, M' and M_0' are the observed magnetic intensity and inherent magnetic intensity of the calibration respectively. The oil saturation of the probed sample and of the calibration sample are called respectively $S$and S', Considering $\omega = \omega'$ and $T_E = T_E'$, the oil saturation in the samples can be evaluated by the oil saturation in the calibration:

$$S = \frac{M(\omega, T_E)}{M'(\omega, T_E)} S' \tag{5}$$

Mn^{2+} allows to distinguish MRI signal of oil from that of water by shortening water transverse relaxation time. In the oil and water two-phase displacement experiments, H^+ in both oil and water can incur MRI signal, but affected by the molecular structure, the relaxation rates of two MRI signals are different, namely, the relaxation of H^+ spin in water molecules is quicker than that in oil. Under addition of water-soluble Mn^{2+} in water, the relaxation time of H^+ in water

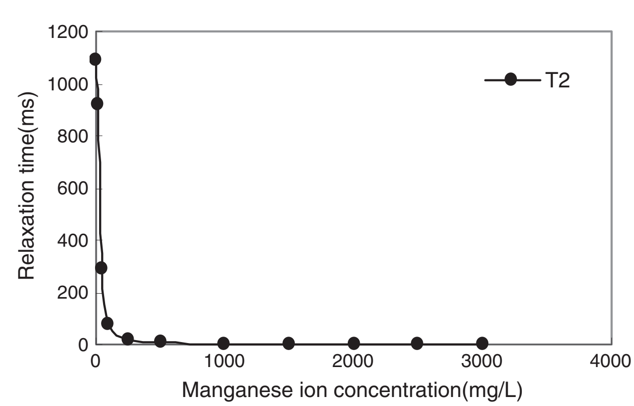

Fig. 1. Water transverse relaxation time as a function of Mn^{2+} concentration in tested porous medium.

molecule will become even shorter, while that in oil remains unchanged (Chang et al., 1993). Fig. 1 describes the dependence of the transverse relaxation time of manganese water solution on the Mn^{2+}concentration, in experimental conditions (i.e. in pores between piled glass beads of 0.6 mm–0.8 mm grain size). As can be seen in Fig. 1, the relaxation times fall dramatically with Mn^{2+} for small concentrations. When Mn^{2+}concentration above 700 mg/L, water relaxation times become much shorter than those of oil (T_1 and T_2 for oil are respectively 1024 ms and 868 ms, whereas for manganese water T_1 ~ 7 ms and T_2~3.5 ms). Under such conditions, it is possible to isolate the MRI signal of oil and neglect the one of the manganese water solution. Setting the T_E to values interval between manganese water and oil transverse relaxation time, i.e. $T_{2w} \ll T_E \ll T_{2o}$, and keeping $T_R$above the longitudinal relaxation time of oil, $T_{1o} \ll T_R$, allows to neglect the contribution of H^+ in water molecule to MRI signal, and to record the inherent magnetic intensity from the oil molecules.

Oil saturation is measured by comparing MRI signal intensity of the probed sample with that of the calibration.

3. Effect of the porous matter structure of the calibration sample on the determination of the oil relaxation time

The accurate measurement of oil saturation requires oil relaxation time in calibration to be the same as in the probed sample.

As pointed out by Kenyon (1992), the transverse relaxation of fluid in pore medium is governed by free relaxation, surface relaxation and diffusion relaxation:

$$\frac{1}{T_2} = \frac{1}{T_{2bulk}} + \rho_2 \frac{s}{v} + \frac{D(\gamma G T_E)^2}{12} \tag{6}$$

in which, T_{2bulk} is the transverse relaxation time of free fluid, ρ_2 is the transverse relaxation intensity, s/v is the specific surface, D is the magnetic diffusion coefficient , γ is the gyromagnetic ratio, and G is the field intensity gradient. The first item on the right side of Eq. (6) represents the transverse relaxation rate of the free fluid, far from liquid/solid boundaries; the second term represents the surface relaxation rate, while the third term represents the magnetic diffusion relaxation rate. As can be seen in the equation, compared with a pure fluid and its free relaxation time, the fluid in porous medium is partly bounded to the solid, affected by surface relaxation mechanisms, and the transverse relaxation time will be shortened. In general, the diffusion relaxation mechanism does not cause significant differences between the calibration and testing sample in transverse relaxation time, and if short enough T_E is adopted to conduct the MRI, the influence of diffusion relaxation can be neglected.

In the present experiment, we use oil as displacement phase fluid and a porous medium fully saturated with oil as a calibration sample, $T_2 = T_2'$ and $S' = 100\%$, so the Eq. (5) can be deducted as:

$$S = \frac{M(\omega, T_E)}{M'(\omega, T_E)} \tag{7}$$

The specific surface of the porous medium is a decreasing function of the pore radius (Pape et al., 2009), namely, the pore radius will affect the transverse relaxation of fluid in the porous media. To quantitatively evaluate the effect of surface relaxation on the relaxation time, we tested the transverse relaxation time of pure free oil and of the oil in pores of glass bead piling body of different grain sizes (Table 2), by adopting the multi-echo spin echo sequence (CPMG) (Wang et al., 2008). It can be seen from Table 2 that, with the decrease of the glass bead size, the transverse relaxation time shortens clearly. In order to eliminate this influence, the sample and the calibration should be filled with the glass beads with same size.

4. Sample making and testing method and flow

We conducted secondary migration experiments in a glass tube of length 55 cm and inner diameter 2.6 cm. To build the migration model, we adopted the wet filling method (Hou et al., 2004): first, one end of the glass tube was plugged with a rubber plug and filled with water, next a mixture of glass beads and water was poured into the tube, which was beaten and shaken from time to time. Eventually when the top surface of the filled glass beads was 1 cm away from the top end, the tube was plugged with another rubber plug, which led to get the model fully saturated with water. The diameter of the glass beads used was 0.6–0.8 mm. Oil was dyed red so that its movement could be traced directly optically. The calibration tube used in the experiment, with the same specification as the tube model, was also filled with the same size glass beads using the wet filling method, but it was saturated with dyed oil.

Dyed oil was injected into the glass tube from the top end while the water was expelled through the bottom plug. Injection was stopped when the height of the oil column reached 24 cm and the glass tube was inverted upside down. Oil migrated upwards driven by the buoyancy and the migration pattern could be observed visually as narrow rising strings (Luo et al., 2004). After 10 minutes, the migration front almost reached the top end of the glass tube and the tube was moved

Table 2
Relaxation time of oil in glass bead pores of different grain sizes r.

Category	Sub-category		Disadvantage	Advantage
Conventional method	Distillation method and Chromatography method Water washing method		1. Samples are destroyed after the measurement and saturation cannot be monitored during the experiment 2. Just the bulk average saturation was given and the saturation spatial distribution cannot be reflected 3. Water washing method is only suitable to unconsolidated porous media	Direct, reliable, and usually used as the verification of other saturation measurement methods
Non-destructive method	Optical method	Light reflection method Light transmission method	1. Half quantitative and empirical parameters are usually used 2. only suitable to transparent 2-dimensional porous media	Non-destructive and can be used to monitor saturation changes; low cost and easy to fulfill
	Ray attenuation method	Normal 2D method	Only suitable to 2-dimensional porous media	Apply to actual rock slices
		Computed tomography (CT) method	The testing signal depends on rather solid porous media than the fluids themselves.	Real 3D positioning measurement; apply to actual rock

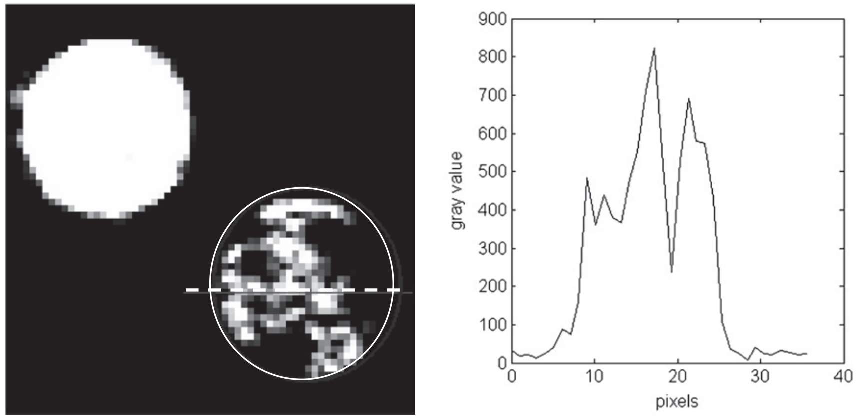

Fig. 2. MRI slice (cross section at the middle of the tube) and gray level distribution (In Fig. 2A, the pixel size is 1 mm*1 mm).

horizontally in the middle of the MRI testing chamber. The calibration sample was put closely and parallel to the tested sample.

The MRI scanner used in the experiment is Wandong 1.5 T superconducting MRI scanner at a proton frequency of 63.89 MHz. According to the measured T_1 and T_2 values of oil in the piling glass bead pores, we set T_R to 6000 ms and set T_E as the minimum value allowed by the meter: 15 ms. We also set the slice thickness (T) as 2 mm and interval between slices (G) as 0.2 mm. It took 52 minutes to complete once scan.

5. MRI image processing

Since NMR imaging results from measurements of weak signals, the effect of noise should be taken into consideration when calculating oil saturation with MRI. Fig. 2A is the MRI slice along the horizontal direction, perpendicular to the vertical migration direction, and Fig. 2B is the gray level distribution along the dotted line marked in the slice. In Fig. 2A, the white disk in the upper left corresponds to the calibration sample; the white part in the lower right corresponds to the migration path; and the white circle marks the position of to-be-measured glass tube in the image. As seen from Fig. 2B, the gray level in the path in not homogeneous, and even outside of the main migration path, the gray value is not zero, which is commonly called noise. Comparing Fig. 2A with Fig. 2B, it can be seen that the noise in non-oil area inside the glass tube is consistent with the noise outside the tube, indicating that the NMR signal of manganese water has been completely shielded.

The background noise level can be estimated by measuring the gray value of image in an oil-empty area (Chen et al., 1992), defined as a rectangular area besides the testing sample: From the gray values of each pixel point in such area, the background level is computed as the average valueB_n:

$$B_n = \frac{1}{j}\sum_{i=1}^{j} g_i \tag{8}$$

in which j is number of pixels in the rectangular area, and $g_i$is the gray level of the pixel of index i. $B_n$is about 28 and far smaller than the signal of oil. In order to lower the effect of the noise, Eq. (7) can be modified as:

$$S = \frac{M(\omega, T_E) - B_n}{M'(\omega, T_E) - B_n} \tag{9}$$

Attention must be paid to the image format when computing the saturation according to MRI. The default image format of MRI is DICOM (Digital Imaging and Communications in Medicine) 3.0 format. The DICOM image output by Wandong superconducting MRI meter has a 12 digits dynamics, i.e. 4096 gray levels. Commonly used image processing software, such as ACDSee and Photoshop, cannot support DICOM image format. To facilitate the image display and

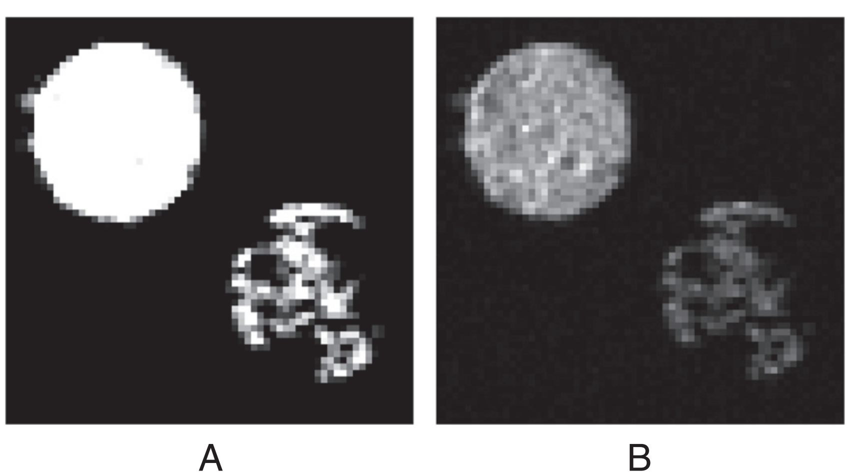

Fig. 3. Effect of window widths and levels on the image format conversion from DICOM to BMP. A: window and level were adjusted to make the migration path clearest; B: the window width covering the whole signal ranges.

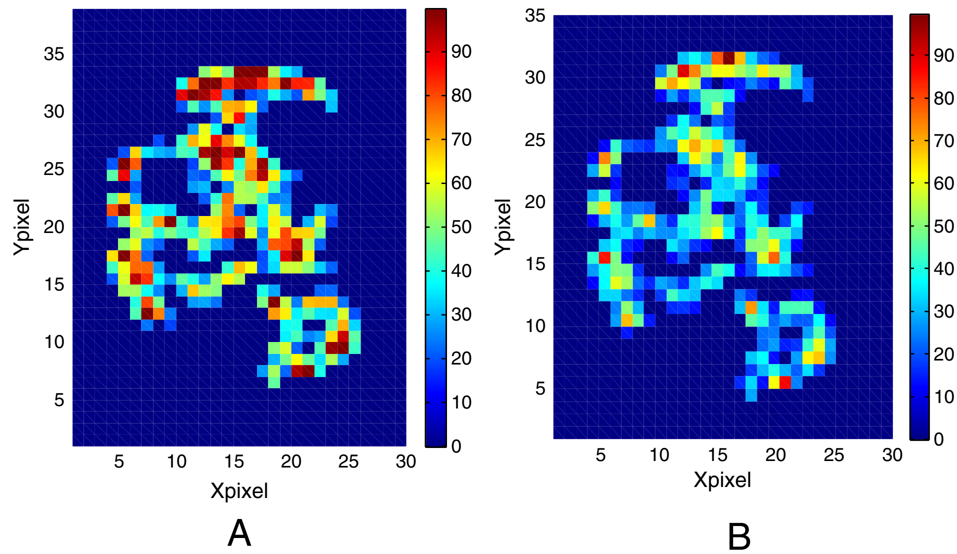

Fig. 4. Effect of window widths and levels on oil distribution. Oil saturation in Fig. 4A and B were calculated according to Fig. 3A and B respectively.

processing, windowing display technology is often used to convert DICOM format into BMP format (or TIF format) (Nakashima and Kamiya, 2007; Groesel et al., 2009). This procedure normally implies to choose a zone in the DICOM image, used for a gray level conversion into the BMP or TIF format. As will be illustrated hereafter, caution has to be paid on the choice of this window in practice, since this affects the type of transform and the quality of the quantitative saturation assessment obtained by the whole treatment chain. The conversion from DICOM format into BMP format is usually partially linear (appendix). The setting of window width and level can directly influence the relative distribution of gray values at each pixel point of the converted BMP format image.

Two sets of window and level were compared when converting DICOM image into BMP image. In a first test, the window and level were adjusted to make the migration path clearest and to generate the BMP format image (Fig. 3A). In a second test, image format was converted from DICOM to BMP while the window width covering the whole signal ranges (Fig. 3B). The oil saturation distribution was calculated according to Fig. 3A and B respectively (Fig. 4A and B). In Fig. 4A and B, the average oil saturations in migration path are 48.15% and 35.13% respectively; it is clear that, the selection of windows directly influences the calculation results of oil saturation. By comparing the oil saturation distribution diagram calculated in BMP format (Fig. 4) with that calculated directly in DICOM format (Fig. 5), it can be found that, only when the window covers the whole pixel interval, both diagrams can match well. This choice should thus always be preferred for a quantitative saturation estimate – even though it may reduce the brightness and contrast of the converted image, which is not the most favorable for the direct observation of the structure of the migration path (Fig. 3).

6. Assessment of the MRI saturation measurement precision in a porous medium model

To check the reliability and determine the accuracy of the oil saturation measurement with MRI, a comparison is done of the total oil mass calculated from the determined saturation distribution with the total oil mass injected into the model.

The glass tube was first fully filled with water, with two ends closed by rubber plugs. Then water was poured out and its volume v_t was measured. The glass tube was refilled with manganese water with a Mn^{2+} concentration of 700 mg/L, and the mixture of glass beads of 0.6–0.8 mm grain diameter and manganese water was poured into the glass tube. The top end of the glass was blocked with a rubber plug, and total mass of the model $m_1$was weighed. A certain amount of oil was injected into the glass tube model, and then the glass tube and the calibrating tube underwent a complete MRI scanning at the same time. Calculating the average oil saturation in migration path of each slice and the sectional area of migration path with the DICOM format image, the oil volume of such slice can be calculated as:

$$v_s = \bar{S_s} * A_s * T * \phi \tag{10}$$

in which, S_s^- is the average oil saturation of such slice in migration path, A_s is the sectional area of migration path, T the slice thickness and ϕ is the porosity of the model. Though the part between two slices cannot be MRI scanned, since the interval between slices is much smaller

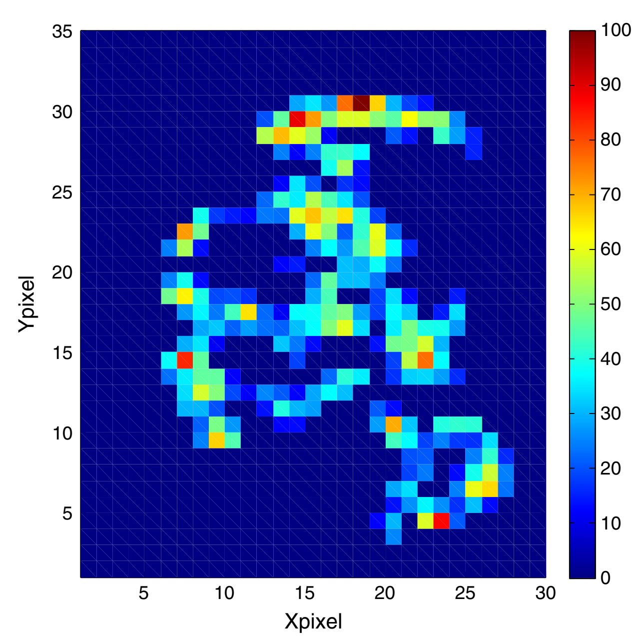

Fig. 5. Oil Saturation distribution calculated in DICOM image format directly.

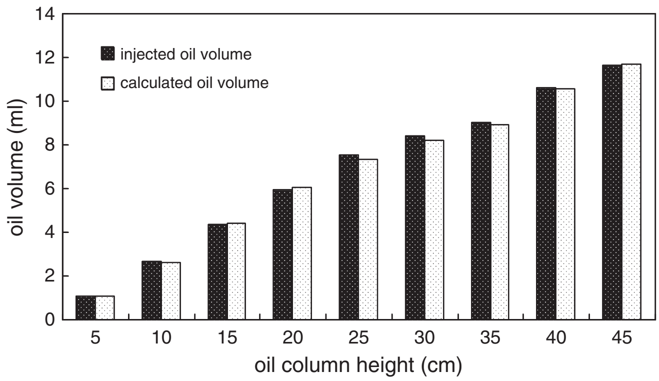

Fig. 6. Comparison of the actually injected oil volume and the calculated total oil volume. The whole migration path was scanned again once the path front migrated upwards 5 cm.

than the slice thickness, the oil volume in the gaps between slices can be interpolated from the two neighboring slices:

$$v_G = \frac{(A_s + A_{s+1})}{2} * \frac{(\bar{S}_s + \bar{S}_{s+1})}{2} * G * \phi \tag{11}$$

with n is the total number of the slices, the oil volume in the whole model is obtained as:

$$v_o = \sum_{s=1}^{n} V_s + \sum_{G=1}^{n-1} V_G \tag{12}$$

In the next step, an increment of oil volume is further injected, and the whole measurement chain described above is determined. A total of nine complete scans of the experiments are conducted. After the completion MRI tests, the glass beads were taken out from the glass tube model, washed tidily and dried, after that the total mass m_2 of the glass beads, glass tube and rubber plugs is measured. Then the volume of manganese water in the glass tube model is determined as:

$$v_p = \frac{m_1 - m_2}{\rho_{Mn}} \tag{13}$$

in which, ρ_{Mn} is the mass density of a 700 mg/Lconcentrated manganese water. The porosity of the glass tube model is calculated from these volumes as $\phi = 0.36$.

A direct comparison of the calculated total oil volume with the actually injected oil volume, in Fig. 6, demonstrates a very good match.

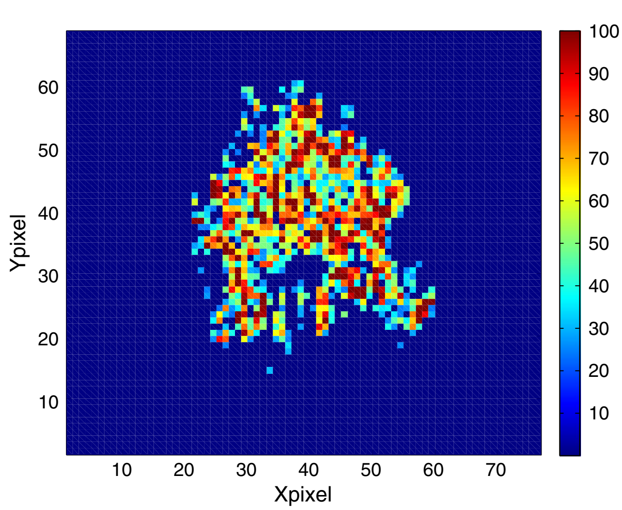

Fig. 7. Oil saturation distribution in finger migration path at the middle of the tube.

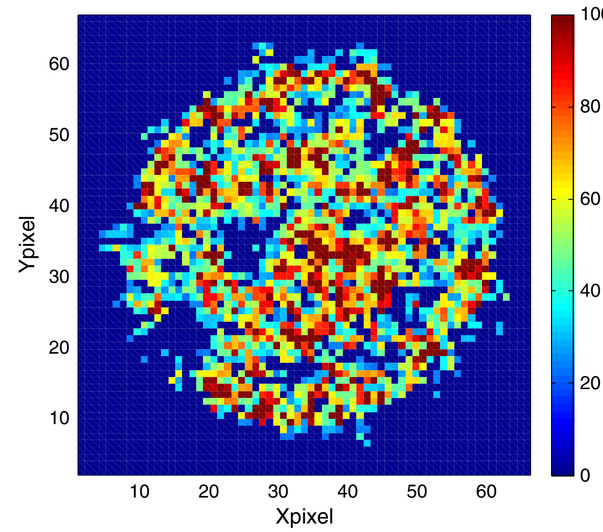

Fig. 8. Oil saturation distribution in piston migration path at the middle of the tube.

The average relative error between the direct measurements and MRI derived measurements, among the nine groups of data, is only 1.57%.

Since the type of oil pattern may vary from stable (piston-like) to unstable (finger) as a function of injection velocity (Tukunaga et al., 2000; Luo et al., 2004), it is important to discuss the accuracy of saturation measurements as a function of migration pattern. Finger pattern and respectively piston migration pattern were observed when oil was injected from the bottom of the glass tube at injection flux of respectively 1.0 ml/min and 4.0 ml/min. Figs. 7 and 8 show the oil saturation in one slice of the finger and piston migration path respectively. For finger migration path, the calculated total oil volume is 32.4 ml whereas the actually injected oil volume is 33 ml, so that the average relative error between them is 1.82%. For piston migration path, the calculated total oil volume is 78.7 ml whereas the actually injected oil volume is 78 ml separately, so that the average relative error between them is 0.9%.

These indicate a very good reliability of the method described here for calculating oil saturation using MRI.

7. Discussion

Like the porosity and permeability, the saturation is an average physical parameter depending on the measurement scale. Chardaireriviere and Rousse (1991) adopted high-field MRI to improve the spatial resolution when testing fluid saturation, with the minimum pixel of 100 μm × 100 μm × 50 μm, but it does not mean that the highest spatial resolution is the best choice to adopt. If the spatial resolution was high enough, the local oil saturation should in principle anywhere be either 0 or 100% according to the presence of either water or oil in a pore, which should reflect the smallest details of the structure of the oil distribution at small scales in the pores, but this choice leads to very noisy measurements. The proper measurement scale can be decided according to the concept of REV (Bear, 1972). On the one hand, the REV shall be small enough to fully reflect the change of spatial distribution of oil saturation on the path, and on the other hand, the REV also shall be large enough to eliminate the effect of the smallest scales, i.e. the effect of the structure of each pore on the determined oil saturation. Fig. 9 is the distribution of signal intensity of the calibrating tube fully saturated with oil by testing with different spatial resolutions at the same place. The saturation is homogeneous in the calibration tube, and the choice of the measurement scale should allow recovering an almost homogeneous signal at the REV scale, erasing the small scale variations of the porosity. It can be seen in Fig. 9 that, when the resolution is too high, e.g. the pixel reaches 0.25 mm*0.25 mm, the signal intensity fluctuates

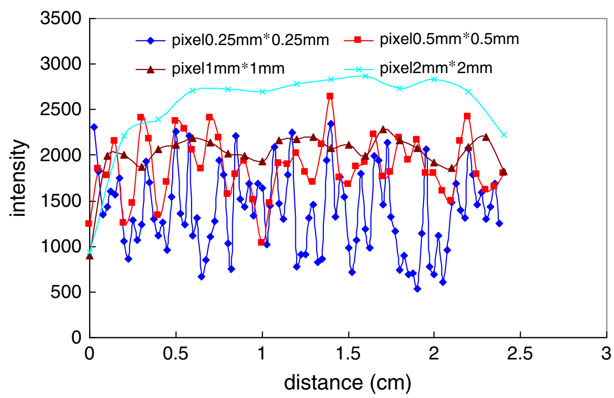

Fig. 9. Effect of MRI resolutions on the distribution curves of MRI signal intensity as a function of position.

dramatically with the change of spatial position; when the pixel reaches 1 mm*1 mm, the signal intensity basically reaches stability and the influence of porous media structure is eliminated. Consequently, in the tests mentioned in this paper, all MRI resolutions are set as 1 mm*1 mm. It should be pointed out that the proper measurement scale should be determined again by a similar procedure if the size of the glass beads is changed. The intensity of the signal increases while the pixel size increasing because larger pixel covers more oil.

Another question is whether the vertical migration path does occur in the columns during the scan time when the tubes lie on their long side in the MRI chamber. Catalan et al. (1992) computed the minimum height ($h_{\min}$) of oil column for migration as:

$$h_{\min} = \frac{(P_{dr} - P_{imb})}{g(\rho_w - \rho_o)} \tag{14}$$

$$P_{dr(w/o)} = P_{dr(w/a)} \frac{\sigma_{(w/o)} \cos\theta}{\sigma_{(w/a)}} \tag{15}$$

$$P_{imb(w/o)} = P_{imb(w/a)} \frac{\sigma_{(w/o)} \cos\theta}{\sigma_{(w/a)}} \tag{16}$$

in which $P_{dr}$and $P_{imb}$are drainage and imbibition capillary pressures respectively, w/ameans water–air system, w/omeans the water–oil system, the interface tension of water–oil system $\sigma_{(w/o)}$and water–air system $\sigma_{(w/a)}$are 0.0289 N/m and 0.072 N/m, the contact angle for water–oil system θ is 30º, $\rho_w = 1014$ kg/m^3 is the density of manganese water, $\rho_o = 792$ kg/m^3 is the density of oil, and $g = 9.80 m/s^2$ is the gravity acceleration. The drainage and imbibition capillary pressures were 1079 Pa and 638 Pa respectively for the water–air system when the glass bead diameter was 0.72 mm (Catalan et al., 1992). The average diameter used in our experiment is very close 0.72 mm. So the drainage and imbibition capillary pressures (1079 Pa and 638 Pa respectively) can be used to predict the minimum height of the oil column for migrating for our experiment.

$$P_{dr(w/o)} = 1079 \times 0.0289 \times \cos(30^{\circ})/0.072 = 375.1\text{Pa}$$

$$P_{imb(w/o)} = 638 \times 0.0289 \times \cos(30^{\circ})/0.072 = 221.8\text{Pa}$$

and from Eq. (14):

$$h_{\min} = (375.1 - 221.8)/[9.8 \times (1014 - 792)] = 0.07\text{m}$$

While the glass tube was placed horizontally, the maximum height of oil column is equal to the inner diameter of the tube ($2.6 cm$), which is obviously smaller than$h_{\min}$. Consequently, oil should not migrate significantly during the MRI scan when the glass tube is horizontal, and the MRI pictures should hardly be affected by such fluid flow.

For more precision of the saturation measurements, the MRI signals of manganese water and oil can be compared quantitatively. In the porous medium, while T_1 and $T_2$of oil is 1024 ms and 868 ms, T_1 and T_2 of manganese water are just 6.88 ms and 3.45 ms. When T_R and $T_E$are equal to 6000 ms and 15 ms respectively, according to Eq. (1), for manganese water, we can get:

$$M^w = 0.0129 * M_0^w \tag{17}$$

in which, M^w and $M_0{}^w$are the observed magnetic and inherent magnetic intensity and of manganese water respectively. For oil, we also can get:

$$M^o = 0.9801 * M_0^o \tag{18}$$

in which, M^o and $M_0{}^o$are the observed magnetic and inherent magnetic intensity and of oil respectively. The inherent magnetic intensity of $H^+$is decided by the abundance of hydrogen atoms. In water (H_2O), the abundance of hydrogen atoms is 11.11%, in oil ($CH_3(CH_2)_nCH_3$, n = 8–16), the abundance of hydrogen atoms is from 14.17% to 15.28%, which is slightly larger than the abundance of hydrogen atoms in water. So the difference of inherent magnetic intensity between water and oil is small. Thus, comparing Eq. (17) with Eq. (18), the MRI signal of water is much smaller than the one of oil, and can be neglected. The result of quantitative analysis is consistent with the observation (Fig. 2). If the signals of water want to be shielded, the following condition is needed:

$$T_2^w << T_E << T_2^o \tag{19}$$

in which, T_2^w and T_2^o are the transverse relaxation time of water and oil respectively.

8. Conclusions

Compared with the testing methods of fluid saturation commonly used before, MRI can make accurate measurements of oil saturation and its 3D spatial distribution in porous media. Considering various kinds of possible influencing factors, a procedure of measure was developed, and it was established that the oil saturation calculated by MRI has a relatively high precision with the average relative error less than 2.0%.

When adopting the gray values of MRI to calculate oil saturation, it is better to directly use the original image in DICOM format; or when the windowing technology is used to convert DICOM format into BMP format to calculate oil saturation, the window must cover the gray value distribution interval of the whole image. Besides the image format, the measurement resolution also should be selected carefully according to the concept of REV.

MRI technology can be used not only to observe the structural form of migration path, but also to quantitatively analyze the distribution of oil saturation, and it has broad application potentials in experiments of secondary migration and even fluid flow in porous medium. For actual rocks, the probed sample itself can be used as the calibration. After the rock saturated fully with oil being scanned by MRI as the calibration signal, it was scanned again when saturated oil is being displaced by water, while keeping the testing conditions and rock's position unchanged. The saturation distribution can be computed by comparing the MRI signal of the two scans. The detailed determination of the saturation distribution in actual rocks is the subject of ongoing work.

Acknowledgements

This study was supported mainly by Chinese National Major Fundamental Research Developing Project (2011CB201105), Chinese National Natural Science Foundation (41102079), Chinese National Key Scientific and Technological Project (2011ZX08005-004), and partly by the University of Strasbourg, France.

Appendix A

DICOM is a set of communication format of imaging in medicine formulated by ACR (American College of Radiology) and NEMA (National Electrical Manufacturers Association), aiming to unify the interface calibration for equipment of different manufacturers. DICOM image is a kind of gray-level image, and the image file contains two parts — file header and data element. It may be 8 digits, 12 digits or 16 digits. Windowing display technology is often used to convert a DICOM format into BMP format (or TIF format). The so-called windowing display is to specify a gray-level window, and according to the following equation, convert linearly the image in such window area into the largest display scope of the display device, and the image data higher or lower than the limits of window are set as the maximum or the minimum, respectively (Zhang et al., 2003b).

$$G(V) = \begin{cases} 0 & V < c - \frac{w}{2} \\ \frac{g_m}{w}\left(V + \frac{w}{2} - c\right) & c - \frac{w}{2} \le V \le c + \frac{w}{2} \\ g_m & V > c + \frac{w}{2} \end{cases}$$

In the above equation, $G$is the gray value of BMP image, $V$is the gray value of DICOM image, $w$is window width (scope of displaying image), $c$is the window level (central value of the display area), and $g_m$is the maximum value of image gray value.

References

Baldwin, B.A., Yamanashi, W.S., 1989. Detecting fluid movement in reservoir core with medical NMR imaging techniques. SPE Reservior Eng. 4 (2), 207–212.

Bear, J., 1972. Dynamics of fluids in porous media. Elsevier, Dover, New York, pp. 19–20.

Berg, R.R., 1975. Capillary pressure in stratigraphic traps. AAPG Bull. 59 (6), 939–959.

Bob, M.M., Brooks, M.C., Mravik, S.C., Wood, A.L., 2008. A modified light transmission visualization method for DNAPL saturation measurements in 2-D models. Adv. Water Resour. 31 (5), 727–742.

Bsavaraj, M.G., Gupta, G.S., Naveen, K., Rudolph, V., Bali, R., 2005. Local liquid holdups and hysteresis in a 2-D packed bed using X-ray radiography. AIChE 51 (8), 2178–2189.

Catalan, L., Xiao, W.F., Chatzis, I., Dullien, F.A.L., 1992. An experimental study of secondary oil migration. AAPG Bull. 76 (5), 638–650.

Chang, C.T., Mandava, S., Watson, A.T., Sarker, S., Edwards, C.M., 1993. The use of agarose gels for quantitative determination of fluid saturations in porous media. Magn. Reson. Imaging 11 (5), 717–725.

Chardaireriviere, C., Roussel, J.C., 1991. Use of a high magnetic field to visualize and study fluids in porous media. Magn. Reson. Imaging 9 (5), 827–832.

Chen, S.H., Qin, F.F., Kim, K.-H., Watson, A.T., 1992. NMR Imaging of multiphase flow in porous media. Paper SPE 24670-MS presented at 1992 Annual Technical Conference and Exhibition, Washington, D.C., 4-7 October.

Conrad, S.H., Glass, R.J., Peplinski, W.J., 2002. Bench-scale visualization of DNAPL remediation processes in analog heterogeneous aquifers: Surfactant floods and in situ oxidation using permanganate. J. Contam. Hydrol. 58, 13–49.

Darnault, C.J.G., Throop, J.A., DiCarlo, D.A., Rimmer, A., Steenhui, T.S., Pralange, J.-Y., 1998. Visualization by light transmission of oil and water contents in transient two-phase flow fields. J. Contam. Hydrol. 31 (3–4), 337–348.

Darnault, C.J.G., DiCarlo, D.A., Bauters, T.W.J., Jacobson, A.R., Throop, J.A., Montemagno, C.D., Parlange, J.-Y., Steenhuis, T.S., 2001. Measurement of fluid contents by light transmission in transient three-phase oil–water–air systems in sand. Water Resour. Res. 37 (7), 1859–1868.

Dembicki, H.J.R., Anderson, M.J., 1989. Secondary migration of oil: Experiments supporting efficient movement of separate, buoyant oil phase along limited conduits. AAPG Bull. 73 (8), 1018–1021.

Dicarlo, D.A., Bauters, T.W.J., Steenhuis, T.S., Parlange, J.-Y., Bierck, B.R., 2000. High-speed measurements of three-phase flow using synchrotron X rays. Water Resour. Res. 33 (4), 569–576.

Edelstein, W.A., Vinegar, H.J., Tutunjian, P.N., Roemer, P.B., Mueller, O.M., 1988. NMR Imaging for Core Analysis, paper SPE 18272-MS presented at 1988 Annual Technical Conference and Exhibition, Houston, Texas, 2-5 October.

Enwere, M.P., Archer, J.S., 1992. NMR Imaging for Water/Oil Displacement in Cores Under Viscous-Capillary Force Control. Paper 24166-MS presented at 1992 SPE/DOE Enhanced Oil Recovery Symposium, Tulsa, Oklahoma, 22-24 April.

Fishman, M., Guarnaccia, J., Enfield, C., Wood, L., 1998. DNAPL infiltration and distribution in subsurface: 2D experiment and modeling approach. First International Conference on Remediation of Chlorinated and Recalcitrant Compounds: Nonaqueous-Phase Liquids, vol. 2, pp. 37–42.

Frette, O.I., Måløy, K.J., Schmittbuhl, J., Hansen, A., 1997. Immiscible displacement of viscosity matched fluids in two-dimensional porous media. Phys. Rev. E 55 (3), 2969–2975.

Graue, A., Aspene, S.E., Moe, R.W., Baldwin, B.A., Moradi, A., Stevens, J., Tobola, D.P., 2001. MRI Tomography of saturation development in fractures during waterfloods at various wettability conditions, paper SPE 71506-MS presented at 2001 SPE Annual Technical Conference and Exhibition, New Orleans, Louisiana, 30 September-3 October.

Groesel, M., Gfoehler, M., Peham, C., 2009. Alternative solution of virtual biomodeling based on CT-scans. J. Biomech. 42 (12), 2006–2009.

Gupta, B.D., Verma, R.K., 2009. Surface plasmon resonance-based fiber optic sensors: principle, probe designs, and some applications. J. Sensors 15.

Harms, J.C., 1966. Stratigraphic traps in a valley fill, western Nebraska. AAPG Bull. 50, 2119–2149.

Hill III, E.H., Kupper, L.L., Miller, C.T., 2002. Evaluation of path-length estimators for characterizing multiphase systems using polyenergetic X-ray absorptiometry. Soil Sci. 167 (11), 703–719.

Hirsch, L.M., Thompson, A.H., 1995. Minimum saturation and buoyancy in secondary migration. AAPG Bull. 79, 696–710.

Hoa, M.T., 1981. A new method allowing the measurement of rapid variations of the water content in sandy porous media. Water Resour. Res. 17 (1), 41–48.

Høst-Madsen, J., Jensen, K.H., 1992. Laboratory and numerical investigations of immiscible flow in soil. J. Hydrol. 135 (1–4), 13–52.

Hou, P., Zhou, B., Luo, X.R., 2004. Analysis on Patterns of Secondary Hydrocarbon Migration Pathways. Sci. Chin. (Volume D - Geosci.) 34 (Supplement 1), 162–168.

Illangasekare, T.H., Ramsey, J.L., Jenson, K.H., Butts, M., 1995. Experimental study of movement and distribution of dense organic contaminants in heterogeneous aquifers. J. Contam. Hydrol. 20 (1–2), 1–25.

Imhoff, P.T., Thyrum, G.P., Miller, C.T., 1996. Dissolution fingering during the solubilization of nonaqueous phase liquids in saturated porous media: 2. Experimental observations. Water Resour. Res. 32 (7), 1929–1942.

Kenyon, W.E., 1992. Nuclear megnatic resonance as a petrophysical measurement. Nucl. Geophys. 6 (2), 153–157.

Li, L.Q., Marica, F., Chen, Q., MacMillan, B., Balcom, B.J., 2007. Quantitative discrimination of water and hydrocarbons in porous media by magnetization prepared centric-scan SPRITE. J. Magn. Reson. 186 (2), 282–292.

Liu, Y.P., Steenhuis, T.S., Parlange, J.-Y., Bierck, B.R., Selker, J.S., 1992. High intensity X-ray and tensiometer measurements in rapidly changing preferential flow fields. Soil Sci. Soc. Am. J. 57 (5), 1188–1192.

Løvoll, G., Méheust, Y., Toussaint, R., Schmittbuhl, J., Måløy, K.J., 2004. Growth activity during fingering in a porous Hele Shaw cell. Phys. Rev. E. 70 (2), 026301.

Løvoll, G., Jankov, M., Måløy, K.J., Toussaint, R., Schmittbuhl, J., Schäfer, G., Méheust, Y., 2010. Influence of viscous fingering on dynamic saturation-pressure curves in porous media. Transp. Porous Media 86 (1), 305–324.

Luo, X., Zhang, F., Miao, S., Wang, W., Huang, Y., Zhou, B., Loggia, D., Vasseur, G., 2004. Experimental verification of oil saturation and loss during secondary migration. J. Petrol. Geol. 27 (3), 241–251.

Luo, X.R., Zhou, B., Zhao, S.X., Zhang, F.Q., Vasseur, G., 2007. Quantitative estimates of oil losses during migration. Part I: the saturation of pathways in carrier beds. J. Petrol. Geol. 30 (4), 375–387.

Luo, X.R., Yan, J.Z., Zhou, B., Wang, W., Vasseur, G., 2008. Quantitative estimates of oil losses during migration. Part II: measurement of residual oil saturation in migration pathways. J. Petrol. Geol. 31 (2), 179–190.

Mandava, S.S., Watson, T.A., Edwards, C.M., 1990. NMR imaging of saturation during immiscible displacements. AIChE 36 (11), 1680–1686.

McNeal, R.P., 1961. Hydrodynamic entrapment of oil and gas in Bisti field, San Juan County, New Mexico. AAPG Bull. 45, 315–329.

Méheust, Y., Løvoll, G., Måløy, K.J., Schmittbuhl, J., 2002. Interface scaling in a two-dimensional porous medium under combined viscous, gravity and capillary effects. Phys. Rev. E 66 (5), 051603.

Miao, S., Zhang, F.Q., Li, T.J., Luo, X.R., Hou, P., 2004. Application of NMR Imaging Technique to Quantitative Observation and Analysis on Hydrocarbon Migration Pathway. Acta Petrol. Sin. 25 (3), 44–47.

Mogensen, K., Stendy, E., Zhou, D., 2005. Studies of waterflooding in low-permeable chalk by use of X-ray CT Scanning. J. Petrol. Sci. Eng. 32 (1), 1–10.

Nakashima, Y., Kamiya, S., 2007. Programs for the analysis of three-dimensional pore connectivity and anisotropic tortuosity of porous rocks using X-ray computed tomography image data. J. Nucl. Sci. Technol. 44 (7), 1233–1247.

Nicula, S., Brancolini, A., Cominelli, A., Mantica, S., 1998. Blending magnetic resonance imaging and numerical simulation. Paper SCA 9819.

Nsir, K., Schäfer, G., Di Chiara Roupert, R., Razakarisoa, O., Toussaint, R., 2012. Laboratory experiments on DNAPL gravity fingering in water-saturated porous media. Int. J. Multiphase Flow 40, 83–92.

O'Carroll, D.M., Bradford, S.A., Abrioba, L.M., 2004. Infiltration of PCE in a system containing spatial wettability variations. J. Contam. Hydrol. 73 (1–4), 39–63.

Oostrom, M., Dane, J.H., Wietsma, T.W., 2005. Removal of carbon tetrachloride from a layered porous medium by means of soil vapor extraction enhanced by desiccation and water table reduction. Vadose Zone J. 4, 1170–1182.

Oostrom, M., Hofstee, C., Lenhard, R.J., Wietsma, T.W., 2003. Flow behavior and residual saturation formation of injected carbon tetrachloride in unsaturated heterogeneous porous media. J. Contam. Hydrol. 64 (1–2), 93–112.

Pape, H., Arnold, J., Pechnig, R., Clauser, C., Talnishnikh, E., Anferova, S., Blümich, E., 2009. Permeability prediction for low porosity rocks by mobile NMR. Pure Appl. Geophys. 166, 1125–1163.
Rangel-German, E., Akin, S., Castanier, L., 2006. Multiphase-flow properties of fractured porous media. J. Petrol. Sci. Eng. 51 (3–4), 192–213.
Schowalter, T.T., 1979. Mechanics of secondary hydrocarbon migration and entrapment. AAPG Bull. 3 (5), 723–760.
Sharma, B.C., Brigham, W.E., Castainier, L.M., 1997. CT imaging techniques for two-phase and three-phase in-situ saturation measurements. report SUPRI TR 107. Stanford University.
Smith, D.A., 1966. Theoretical considerations of sealing and non-sealing faults. AAPG Bull. 50, 363–374.
Tang, H.J., Cui, K.H., 2007. Reservoir Physics. Petroleum industry, Beijing, pp. 89–94.
Tallakstad, K.T., Knudsen, H.A., Ramstad, T., Løvoll, G., Måløy, K.J., Toussaint, R., Flekkøy, E.G., 2009. Steady-state two-phase flow in porous media: statistics and transport properties. Phys. Rev. Lett. 102, 074502.
Toussaint, R., Løvoll, G., Méheust, Y., Måløy, K.J., Schmittbuhl, J., 2005. Influence of pore-scale disorder on viscous fingering during drainage. Europhys. Lett. 71 (4), 583.
Tukunaga, T., Mogi, K., Matsubara, O., Tosaka, H., Kojima, K., 2000. Buoyancy and interfacial force effects on two phase displacement patterns: an experimental study. AAPG Bull. 84 (1), 65–74.
Ursin, J.R., 1992. Detection of fluid saturation levels in porous media using gamma-ray tomography. J. Petrol. Sci. Eng. 7 (3-4), 197–308.
Van Geel, P.J., Sykes, J.F., 1994. Laboratory and model simulations of a LNAPL spill in a variably-saturated sand: 1. Laboratory experiment and image analysis techniques. Contam. Hydrol. 17, 1–25.
Wang, H.Z., Zhang, X.l., Wu, J., 2008. Magnetic resonance imaging test tutorial. China science, Beijing, pp. 90–95.
Washburn, K.E., Madelin, G., 2010. Imaging of multiphase fluid saturation within a porous material via sodium NMR. J. Magn. Reson. 202 (1), 122–126.
Yan, J., Luo, X., Wang, W., Toussaint, R., Schmittbuhl, J., Vasseur, G., Chen, F., Yu, A., and Zhang, L., An experimental study of oil secondary migration in a three-dimensional tilted porous medium. AAPG Bull., in press.
Zeng, J.H., Wang, J., 2003. Mechanisms and Physical Simulation of Hydrocarbon Migration. Petroleum industry, Beijing, pp. 1–187.
Zhang, F.Q., Luo, X.R., Miao, S., Wang, W.M., Zhou, B., Huang, Y.Z., 2003a. Patterns and Influencing Factors of Secondary Hydrocarbon Migration. Petrol. Exp. Geol. 25 (1), 69–75.
Zhang, F.Q., Luo, X.R., Miao, S., Wang, W.M., Zhou, B., 2004. Experiments on Forming Process of Dominant Path for Secondary Hydrocarbon Migration & Mechanisms Analysis. Chin. J. Geol. 39 (2), 159–167.
Zhang, Y.S., Zhao, Z.F., Chen, F.M., 2003b. DIB Display Technique for DICOM-based Medical Images. Appl. Res. Comput. 2, 75–76.
Zhou, B., Hou, P., Wang, W.M., Luo, X.R., 2005. Oil Saturation Analysis in Migration Passways with NMR Imaging Technique. Pet. Explor. Dev. 32 (6), 78–81.

International Journal of Multiphase Flow 40 (2012) 83–92

Contents lists available at SciVerse ScienceDirect

International Journal of Multiphase Flow

journal homepage: www.elsevier.com/locate/ijmulflow

Laboratory experiments on DNAPL gravity fingering in water-saturated porous media

Khalifa Nsir [a], Gerhard Schäfer [a,*], Raphaël di Chiara Roupert [a], Olivier Razakarisoa [a], Renaud Toussaint [b]

[a] Laboratoire d'Hydrologie et de Géochimie de Strasbourg (LHyGeS), UMR 7517, Université de Strasbourg/EOST, Centre National de la Recherche Scientifique (CNRS), 1 rue Blessig, 67084 Strasbourg, France

[b] Institut de Physique du Globe (IPGS), UMR 7516, Université de Strasbourg/EOST, CNRS, 5 rue René Descartes, 67084 Strasbourg, France

ARTICLE INFO

Article history:
Received 15 March 2011
Received in revised form 6 December 2011
Accepted 8 December 2011
Available online 16 December 2011

Keywords:
Gravity-driven instabilities
Immiscible displacement
Porous medium
DNAPL
Optical fibers
Residual saturation

ABSTRACT

Laboratory experiments were carried out at the Darcy scale to investigate the gravity-driven fingering phenomenon of immiscible two-phase flow of water and a dense nonaqueous-phase liquid (DNAPL) such as trichloroethylene (TCE). Rate-controlled displacement experiments were performed on a homogenous sand-filled column under various displacement conditions. Several system parameters (e.g. flow rate, flow mode (upward flow, downward flow) and mean grain-size diameter of the porous medium) were varied in the experimental programme. Optical fiber sensors were developed to quantify the spatial distribution of the advancing displacement front in a given control section of the experimental device. Following each experiment, multi-point measurements of the remaining TCE saturation were obtained by *in situ* soil sampling. The resulting DNAPL distribution was heterogeneous even though the medium was homogeneous sand. Higher DNAPL injection rates and lower medium permeability both reduced gravity fingering. This is because viscous forces stabilize the advancing front with pressure gradients increasing as function of the injection rate and decreasing as function of the permeability. Average residual TCE saturations obtained by mass-balance in the experiment after a complete drainage–imbibition cycle were influenced by the mean grain-size diameter of the porous medium but were not affected by the flow mode of the primary drainage process.

1. Introduction

Characterization and quantification of the migration of immiscible liquids in ground-water are topics that have received considerable attention in recent years. Recent studies of two-phase immiscible flows have been motivated by the need to treat spills and leaks of so-called dense nonaqueous-phase liquids (DNAPLs), such as trichloroethylene (TCE), which can severely impact the quality of subsurface water supplies (Kueper and Frind, 1989; Birovljev et al., 1991; Fayers and Zhou, 1996; Bettahar et al., 1999; Benremita and Schäfer, 2003; Bohy et al., 2004). Unstable immiscible displacement can form viscous, capillary, and/or gravity fingers. These fingers propagate rapidly, causing early breakthrough relative to stable displacement (Brailovsky et al., 2006).

The current physical understanding of fingering processes has been developed primarily through linear stability analysis (Yao and Hendrickx, 2001). While this theory provides information about the displacement process under unstable conditions and the practical growth rate of fingers for small amplitude perturbations, it neither predicts nor explains many significant features observed in laboratory experiments. The assumptions inherent to the linear analysis are somewhat limiting with respect to actual field conditions. Fingering processes were initially studied in 2D experiments, such as empty Hele–Shaw cells, as in the fundamental work of Saffman and Taylor (1958). These cells are composed of two closely spaced parallel plates, and the motion of fluids in the system is mathematically analogous to that of two-dimensional flow in a porous medium. Later on, porous media was added between the plates of Hele–Shaw cells for better reproduction of the random character of porous geometry. Observations from laboratory experiments on instabilities have allowed researchers to both test the predictions of the linear stability theory for fingers and to discover a number of unexpected features of fingering flow fields, in which instabilities arise from the presence of gravity (Frette et al., 1997), viscosity (Løvoll et al., 2004; Toussaint et al., 2005; Løvoll et al., 2011), both gravity and viscosity (Méheust et al., 2002; Nicholl and Glass, 2005) or capillarity when the displacement is very slow (Lenormand and Zarcone, 1989; Ferer et al., 2007; Christophe et al., 2010).

Laboratory studies have also been conducted on soil columns to characterize the behavior of DNAPL displacement in saturated porous media and to better understand the complexities of DNAPL migration in environmental media (Khataniar and Peters, 1992; Riaz and Tchelepi, 2006; Tullis and Wright, 2007; Schwille, 1988)

* Corresponding author.
E-mail address: schafer@unistra.fr (G. Schäfer).

0301-9322/$ - see front matter © 2011 Elsevier Ltd. All rights reserved.
doi:10.1016/j.ijmultiphaseflow.2011.12.003

conducted large column experiments (1 m high, 0.4 m diameter) with perchloroethylene (PCE) in a low-permeability saturated sand ($K = 2 \times 10^{-4}$ m s^{-1}). He found that the PCE front was not uniform or even bulb-shaped. Instead, the PCE penetrated as tendrils or fingers in the interior of the sand body. Schwille (1988) also investigated PCE penetration into water-saturated glass beads with diameters ranging from 0.49 to 0.7 mm. The DNAPL was observed to penetrate into the saturated zone in a finger-like stream. Anderson et al. (1992) described the common occurrence of DNAPLs in the saturated zone of aquifers in the form of fingered plumes and pools that cause erratic contaminant distributions. Glass and Nicholl (1996) reported that a complicated pattern of interacting fingers resulted from their stratified soil experiments; and this limited the number of isolated fingers for which velocity and diameter data could be collected. To explore the wetting phase saturation levels in fingers, Geiger and Durnford (2000) and Dicarlo (2004) conducted one-dimensional fingering experiments using small cylindrical columns in which they examined the variation in DNAPL saturation along the finger length. Their results suggested that the propagating fingertip is near full saturation, and the saturation level decreases in the direction of the finger tail. Glass et al. (2000) used a high-resolution light transmission method to investigate gravity-destabilized non-wetting phase invasion (CO_2 and trichloroethylene) in a macro-heterogeneous porous medium. They observed a series of fingers and pools, behind the growing front, as a sequence of gravity-stabilized and gravity-destabilized displacements within the heterogeneous medium.

To describe the two-phase liquid–liquid displacement in a porous medium, various dimensionless parameters such as the capillary number N_c (ratio of viscous to capillary forces), the viscosity ratio M (ratio between the displaced fluid viscosity and the displacing fluid viscosity), and the Bond number N_b (ratio of gravity to capillary forces) are commonly used in the literature (Gioia and Urciuolo, 2006). These numbers are defined as follows:

$$N_c = \frac{v\mu_w}{\sigma_{ow}\cos\theta} \tag{1}$$

where v is the Darcy velocity (L T^{-1}), μ_w (M L^{-1} T^{-1}) is the dynamic viscosity of the wetting fluid, σ_{ow} (M T^{-2}) is the interfacial tension between the non-wetting (oil) and wetting fluid (water) and θ (–) is the contact angle at the solid–water–DNAPL interface;

$$M = \frac{\mu_1}{\mu_2} \tag{2}$$

where μ_1 (M L^{-1} T^{-1}) is the dynamic viscosity of the displacing fluid and μ_2 (M L^{-1} T^{-1}) is the dynamic viscosity of the displaced fluid, and

$$N_b = \frac{\Delta\rho g a^2 \cos(\alpha + \pi)}{\sigma_{ow}\cos\theta} \tag{3}$$

where $\Delta\rho$ (M L^{-3}) is the difference between the density of displacing fluid and the density of displaced fluid, g (L T^{-2}) is gravitational acceleration, a (L) is the mean grain diameter of the porous medium, and α (–) is the angle formed by the flow vector and gravity vector. When gravity forces are involved, the Bond number can be either positive or negative, depending on the value of α. The common convention is that N_b is considered positive when flow is gravity-stabilized, whereas N_b is considered negative when the gravity acting to destabilize the displacement. In the context of vertical gravity-driven DNAPL migration in porous media, N_b is usually negative.

When two liquids are in contact in a porous medium, the denser fluid tends to sink to the bottom, and the upward force that this heavier fluid exerts on the lighter fluid to balance its weight is known as the buoyancy force. In the absence of buoyancy forces, the fluid patterns formed by immiscible displacement of a wetting fluid by a non-wetting fluid can be divided into three regimes (stable, viscous fingering, and capillary fingering regimes) separated by an intermediate transition zone. Lenormand et al. (1983) developed a phase diagram used to identify the location of the different regimes, and thus of the transitional region between them, in an M, N_c space. Ewing and Berkowitz (1998) noted that the phase diagram relating viscous, capillary, and stable flow regimes should contain a third dimension to account for gravity and buoyancy forces, given by the Bond number N_b.

The quantitative parameters previously described have also been applied to estimate the mobility of DNAPLs in porous media in terms of temporal variation of DNAPL saturation profiles during immiscible displacements (Pennell et al., 1996; Helen and Paul, 1997; Hunt et al., 1998; Theodoropoulou et al., 2005; Glen et al., 2006). Several methods have been used to study fluid saturations during the immiscible fluid displacement process. In the past, resistivity measurements (Leverett, 1939) and microwave absorption (Parsons and Marathon, 1975) provided area-average fluid saturations. More recently, techniques such as radioisotope tracing/Gamma cameras (Zhang and Smith, 2001), X-ray tomography methods (Glass et al., 2000) were able to deliver two-dimensional projections of the fluid saturation distribution and provide real-time visualization of the advancing front. In these cases, the ability to reproduce physical measurements was excellent. However, if excellent images were obtained and the exact macroscopic structure of fingers has to be provided, the application of this method was limited to either 2D flow cells, or fairly small 3D flow. One general conclusion from water-flooding investigations is that DNAPL saturation in porous media strongly depends on the interfacial tension between the immiscible liquids, the wettability of the solids with respect to the immiscible liquids, and the pore water velocity attained during water flooding (Nguyen et al., 2006).

The aforementioned methods have not provided enough accurate data for a conclusive study of displacement instability processes. In addition, few experimental studies on immiscible displacement have considered buoyancy forces, and relevant data from experiments depicting the development of DNAPL gravity fingering are thus needed. Additionally, there is still no clear experimental evidence on the effect of flow rates, mode flow (gravity-stabilized, gravity-destabilized), and texture of the porous medium on the occurrence of this phenomenon. A consistent issue is that natural porous media are opaque, and we need to look at the pore scale to understand to understand how the fingers evolve.

The overall aim of the present work is to quantify displacement instabilities in a saturated homogeneous porous medium. The experimental approach is original as it is based on the use of optical fibers to quantify locally the arrival times of the DNAPL/water front at different points within a control section of the porous medium. The column experiments comprise a series of drainage experiments with TCE as the non-wetting fluid and water as the wetting fluid. A second set of experiments focus on a complete drainage–imbibition cycle to remobilize the TCE entrapped during the primary drainage in the porous medium. Various displacement configurations were considered for study of the influence of specific model parameters on the displacement process, such as the direction of flow, the velocity of the displacing fluid, and the texture of the porous medium. The experiments were analyzed with respect to both distribution of water/DNAPL front velocities, and the DNAPL saturation in the column. In addition, conclusions about displacement instability were then drawn.

2. Materials and methods

2.1. Experimental setup

Laboratory experiments were conducted on a transparent glass column with a total length of 68 cm and an inner diameter of

10 cm. Two porous media were used: medium sand and fine sand. The characteristic properties of both porous media, such as intrinsic permeability (k), mean grain size diameter (d_{50}), uniformity coefficient (U), and porosity (η) were determined experimentally (Table 1).

Trichloroethylene (TCE) was chosen as the DNAPL for the experiments because it is among the most frequently detected contaminants in subsurface environments. At 20 °C, TCE has a density of 1.463 g/cm^3, a viscosity of 0.0056 g/s/cm, and a solubility in water of 1300 mg/L (Jellali et al., 2003). In the column experiments, a dye (Organol Red BS) was added to TCE to allow visual detection of the DNAPL during the experiments; the dye concentration was approximately 5 mg/L. Organol Red BS is highly soluble in TCE, and does not modify its chemical and physical properties in the range of concentrations applied (Jellali et al., 2001). A high-accuracy peristaltic pump with Teflon tubing and interchangeable heads for flow rates up to 200 mL/min was used to inject the displacing fluid in the sand-filled column. A 2-cm layer of coarse sand was placed at the top and bottom of the sand column to ensure uniform flow conditions in the inlet and outlet sections of the studied sand column. Pressures at the inlet and outlet were measured using a pressure transducer (Cerabar T-PMC131). Eight optical fiber sensors were developed (see Section 2.2) to measure the arrival time of the DNAPL front at different points within a section located halfway up the column. The measurement recordings were acquired using an Agilent 34970A Data Acquisition device connected to a personal computer. The experimental setup used for running the displacement experiments is illustrated in Fig. 1.

The experimental setup was designed to produce a controlled and well-defined injection of TCE in an initially water-saturated homogeneous porous medium. Filling of the column was carried out with dry sand added regularly and successively in layers of several centimeters to a 10-cm deep water layer at the bottom of the sand column, which was then mixed from bottom to top with a thin rigid rod. Next, the sides of the glass column were gently tapped to encourage the sand to settle tightly. This method was previously demonstrated by Nsir (2009) to yield packed columns with highly reproducible and uniform physical properties. To ensure that the sand filling had the same perfect water-wet characteristics in each run, the glass column was refilled with fresh sand for each experiment. Before the start of each displacement experiment, the column was flushed with de-aired water to ensure complete water saturation of the sand, and to measure the hydraulic conductivity of the sand column. Once steady water flow was achieved, TCE was injected through the injection port of the packed column at a constant flow rate. The outlet section of the column was kept at a constant water pressure. The optical fiber sensors might disturb locally the flow field but the effect of their emplacement has no major impact on the conclusions drawn about displacement instability as their emplacements in the porous medium were not changed during the different studied displacement scenarios.

Two displacement modes were studied in the experiments, referred to as vertical-upward and vertical-downward displacement later on in the study. In the first set of studies, drainage experiments were run in which TCE was the non-wetting fluid and water the wetting fluid. Here, the displacement is generally unstable according to the contrast of density and the unfavorable viscosity ratio M ($M = 0.58 < 1$) that existed between the immiscible fluids. The second set of experiments is primary drainage followed by water flooding to mobilize the TCE entrapped in the porous medium. The system constitutes a complete drainage–imbibition cycle. To reach residual TCE saturations, a large range of water flow rates was used. In practice, the critical value of the capillary number at which oil recovery becomes significant has been found to be in the range of between 10^{-5} and 10^{-4}. As the capillary number in our experiments is typically in the order of 10^{-6} for ordinary water flooding, flow rate varied in the laboratory experiment from 40 up to 170 mL/min, corresponding to a capillary number N_c of 4.1×10^{-6} to 16.8×10^{-6}. Residual TCE saturation after imbibition (water-flooding) was examined under a range of experimental conditions, including direction of flow (upward or downward), displacing fluid velocity, and the mean pore size (medium or fine sand). Tables 2 and 3 summarize the different parameters varied in drainage experiments and experiments conducted to study drainage–imbibition cycle, respectively.

A major issue in the experimental studies was how to quantify the preferential pathways of DNAPL during its migration in a saturated porous medium. The fingering process was recorded using specially designed optical fiber sensors to measure the arrival time of the water/DNAPL front at eight points in a control section located halfway up the column. To obtain visual information on the fingering events that appeared in the sand column, digital images were taken of the red-colored DNAPL blobs observed at the glass wall of the column. For each displacement experiment, the DNAPL breakthrough at the column outlet was determined by measuring the quantity of TCE leaving the column. The extent of local DNAPL saturation was determined by collecting and analyzing sand cores after each experiment (see Section 2.3).

2.2. Optical fiber sensors

The experiment used optical fibers to quantify the DNAPL migration pathways through the saturated sand. This technique, widely used in industrial applications, can act as an active sensing mechanism and is generally referred to as an intrinsic optical fiber sensor. Similar sensors have found application in chemical, biochemical, biomedical, and environmental sensing (Sharma and Guptal, 2006; Gupta and Verma, 2009). The general structure of the developed optical fiber sensor is shown in Fig. 2. It consists of an LED as the optical source, an optical fiber that transfers the optical signal, an optical detector (a photodiode), and processing electronics.

The sensing principle is based on the change of optical intensity modulation along the optical fiber. The tool converts the presence of a DNAPL into modified optical characteristics of the emitted signal. The original prototype version of the optical fiber sensor was conceived by VEGAS (Versuchseinrichtung für Grundwasser- und Altlastensanierung) of the University of Stuttgart (Barczewski and Marschall, 1992). As part of the PhD thesis of Nsir (2009), further improvements were undertaken to obtain a robust and sensitive tool for detecting the presence of DNAPL in porous media.

An optical fiber consists of a central core (through which light is guided) embedded in an outer cladding with a slightly lower refractive index. They are covered by a plastic jacket to mechanically protect the fiber and exclude stray light. Light transmission through an optical fiber occurs due to internal reflection at the core/cladding interface. Any change in reflection can be detected by a change in transmission. Because reflection depends on the refractive index of the medium surrounding the fiber, removing a portion of the cladding creates a zone that can detect DNAPL, due to the different refractive indices of water ($n_w = 1.33$) and

Table 1
Properties of the porous media used in the experiments.

	Intrinsic permeability K (m^2)	Mean grain diameter d_{50} (mm)	Uniformity coefficient U (–)	Porosity (η)
Medium sand	9×10^{-11}	0.43	2.1	0.43
Fine sand	5×10^{-12}	0.17	2.3	0.40

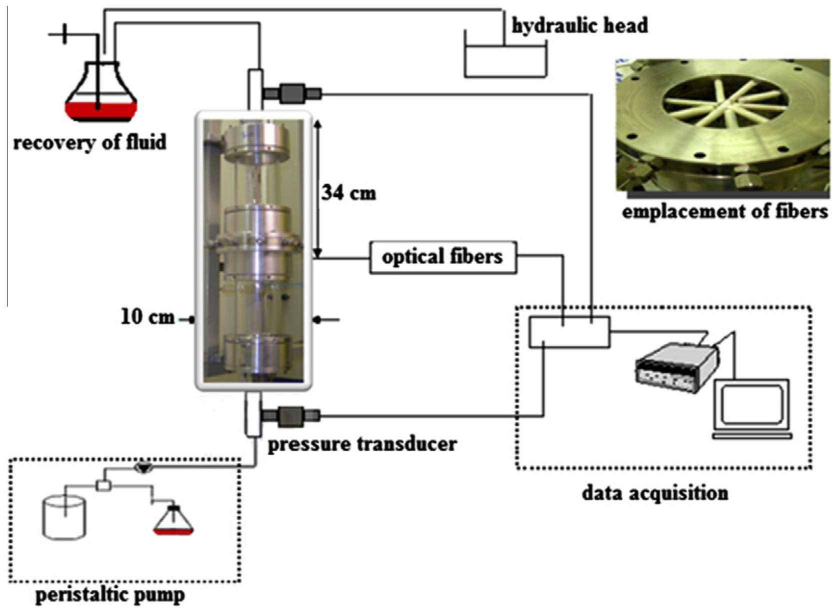

Fig. 1. Schematic representation of the experimental setup.

Table 2
Characteristics of drainage experiments.

	Porous medium	Flow mode	N_c	M	N_b
Experiment 1	Medium sand	Upward	4.1×10^{-6}	0.58	2.7×10^{-5}
Experiment 2	Medium sand	Downward	4.1×10^{-6}	0.58	-2.7×10^{-5}
Experiment 3	Medium sand	Downward	7.5×10^{-6}	0.58	-2.7×10^{-5}
Experiment 4	Fine sand	Downward	4.1×10^{-6}	0.58	-4.2×10^{-6}

Table 3
Characteristics of drainage–imbibition cycle experiments.

	Porous medium	Drainage flow mode	Displacement condition	Imbibition flow mode	Displacement condition
Experiment 1	Medium sand	Upward	Stabilizing gravity effect	Downward	Stabilizing gravity effect
Experiment 2	Medium sand	Upward	Stabilizing gravity effect	Upward	Destabilizing gravity effect
Experiment 3	Medium sand	Downward	Destabilizing gravity effect	Downward	Stabilizing gravity effect
Experiment 4	Medium sand	Downward	Destabilizing gravity effect	Upward	Destabilizing gravity effect
Experiment 5	Fine sand	Downward	Destabilizing gravity effect	Downward	Stabilizing gravity effect

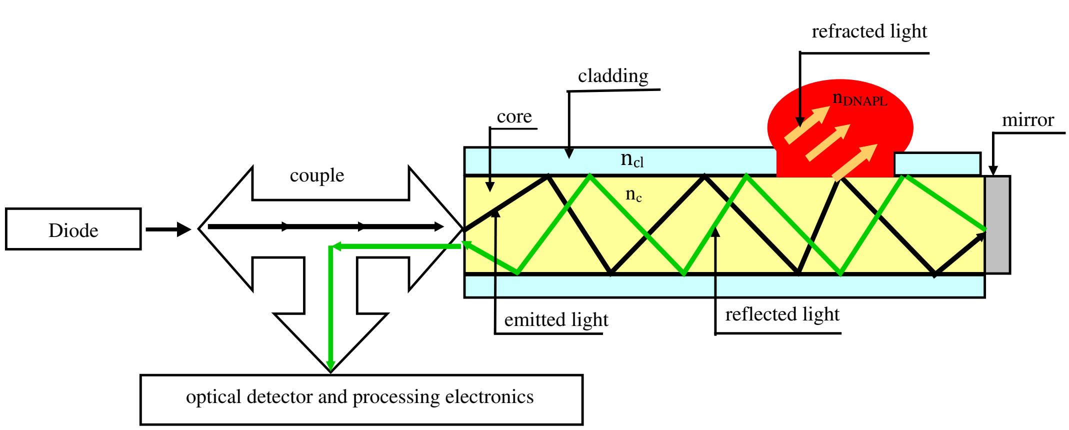

Fig. 2. Principle of the developed optical fiber sensor. n_{cl} and n_c are the refractive indices of the cladding and core of the optical fiber, respectively.

DNAPL (n_{DNAPL} = 1.46). Therefore, light intensity modulation can be brought about by refraction of rays in the DNAPL surrounding the modified cladding region.

The experimental work uses an all-silica multimode fiber with core/cladding/jacket external diameters of 600/675/690 μm. The optical fibers were approximately 50 cm long. The sensing element was prepared by decladding a small portion of the optical fiber (about 1 cm in length), which was then cleaved at its end face. Next, the polished surface of the end face was coated with a thin aluminum layer to create a mirror, using monomer vapor phase deposition (Nsir, 2009). The *in situ* deposition of the chemically active metal (aluminum) on the polished surface of fiber is achieved by suspending it in the monomer vapor phase deposition. The output face of the fiber is placed in front of a crucible filled with boil-off and heated to above 1000 °C. Evaporation of aluminum was carried out under a pressure of about 10^{-7} atm. The coating and adhesion of the metal to the fiber surface were of high quality.

The developed sensors do not indicate of what percent of the proportion of DNAPL was in contact with the sensitive part of the fiber. They react for primary droplets of DNAPL being in contact with the sensitive part of the fiber. Therefore, detection of DNAPL in any sensor emplacement does not mean that surface surrounding of the sensing element is completely impregnated by DNAPL. An estimate of DNAPL saturation is thus not possible with the actual fiber tool.

2.3. Quantification of DNAPL saturation

For each drainage experiment, a total volume of TCE corresponding to approximately 70% of the pore volume of the packed sand was injected into the column at a constant flow rate of 40 mL/min. The amount of TCE entrapped in the porous medium was determined by mass balance of DNAPL inflow and outflow.

Residual saturations of TCE were established in the water-saturated sand column after a complete drainage–imbibition cycle. First, TCE was injected into the saturated porous medium, as in the drainage experiment. The flow direction was then reversed, and water was pumped through the column to displace the mobile TCE phase. To minimize the removal of entrapped TCE by dissolution the water injected into the sand-filled column did not exceed three times the total pore volume. If no TCE mobilization was observed after flushing with the chosen flow rate, an increased flow rate was applied to the sand column. For each flow rate, the DNAPL recovered in the effluent was collected in glass vials, and the volume of TCE displaced as free product measured. The average TCE saturation in the column was calculated per difference.

At the end of each displacement experiment (drainage experiment/complete drainage–imbibition cycle) the sand was sampled to obtain vertical profiles of local (entrapped/residual) TCE saturations in the saturated porous medium. Because of the emplacement of fibers, the sampling was achieved only above the sensor control section of the column. Local TCE saturations at various lateral positions and at different depths of the sand column were quantified using a soil sampler that probed a volume of roughly 2 cm^3 (Nsir, 2009). The sampling grid used for this process was very fine (5 cm spacing) in the vertical direction. At each sampling depth, one sample was taken on the axis of the column and two others on opposite points of the edges of the column section. TCE was extracted from these samples with methanol, and was measured by GC/FID.

3. Results and discussion

3.1. Arrival time of the water/DNAPL front for a low injection rate

To determine whether displacement instabilities occur, the arrival times of the DNAPL front were recorded at different points of the control section ($z = -34$ cm) during a drainage experiment conducted at a low injection rate of 40 mL/min, for both vertical-upward and vertical-downward flow modes. A normal distribution was fit to the arrival times, and normalized by the mean arrival time (Fig. 3). All sensors placed in the control section of the column detected DNAPL for both gravity-destabilized and gravity-stabilized flow. This may be explained by the fact that only a small portion of the sensitive part of fiber may have been in contact with DNAPL droplets. In the case of the downward flow mode, the arrival times of the DNAPL/water front varied widely, and their distribution is non-uniform. A standard deviation of nearly 70 s was obtained, whereas in the case of upward flow mode a standard deviation of only 9 s was calculated. This large difference is principally caused by density-driven fingering that develops in the case of the vertical-downward displacement. The low injection rate makes viscous forces negligible, so the capillary and buoyancy forces together dictate the movement of the advancing fluid. Given the contrast of both density and viscosity between the two fluids, the injected non-wetting fluid (TCE) prefers to move along preferential paths with low capillary resistances, thereby forming pronounced fingers. Capillary fingers, if formed, would be converted into gravity fingers as they elongated. A vertically oriented macroscopic finger may result that is composed of a sequence of larger cluster of entrapped TCE. In the case of vertical-upward displacement, gravity plays a stabilizing role in the migration of DNAPL and compensates for the destabilizing viscosity ratio M that exists between the two fluids. Under this condition, the water/TCE interface moves as a piston-like flow, and as a result, the recorded arrival times are very close together. This is consistent with the digital images taken of the red-colored TCE blobs observed at the glass wall of the column (Fig. 4). In the case of downward flow, TCE front was observed as small droplets or globules forming fingers and numerous protuberances, as described by Zhang and Smith (2001). In the case of upward flow, the TCE front followed a compact path as a succession of homogeneous layers alternating with thin discontinuities. This layering is an artifact of the packing method employed in the experiments. Here, N_b becomes positive in the system and its value of 2.7×10^{-5} seems to be sufficient to generate a stable displacement regime independently of the values of both capillary number ($N_c = 4.1 \times 10^{-6}$) and unfavorable viscosity ratio ($M = 0.58$).

In case of downward displacement, buoyancy forces speed up the downward movement of the TCE on account of its higher density as compared to water (Fig. 4b). Thus, the displacing fluid moves much faster than in the vertical-upward case, and a premature breakthrough time is established. This behavior was experimentally confirmed, with TCE breaking through at the outlet section of the column at nearly 30 min and 22 min for upward displacement and downward displacement, respectively.

3.2. Average DNAPL saturation

The average TCE saturations calculated by mass balance over the entire column are quite different for upward and downward

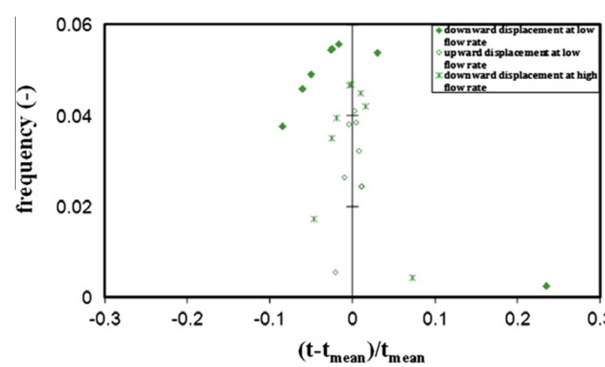

Fig. 3. Measured dimensionless arrival times of DNAPL front in both vertical-upward flow mode and downward flow mode at low DNAPL injection rate and in downward flow mode at high DNAPL injection rate (t_{mean} is the average arrival time of DNAPL front): case of drainage of water-saturated medium sand.

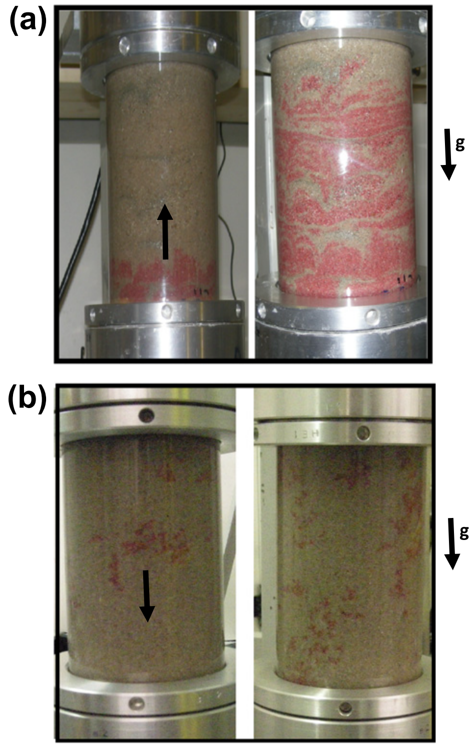

Fig. 4. TCE front observed on the column wall at the beginning (5 min) and the end of experiment: (a) case of upward drainage of water-saturated medium sand at low DNAPL injection flow rate; (b) case of downward drainage of water-saturated medium sand at low DNAPL injection flow rate.

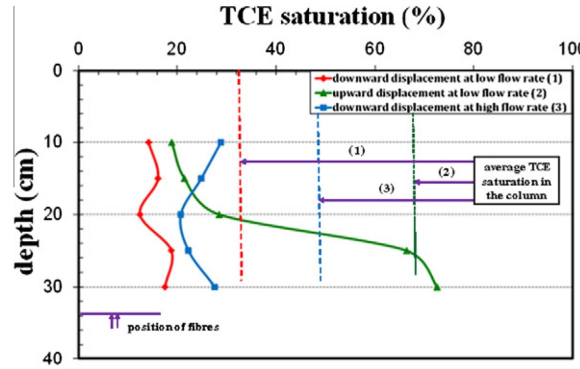

Fig. 5. Measured TCE saturation as function of depth and average TCE saturation in the column at the end of experiment for both vertical-upward and vertical-downward drainage of water-saturated medium at low DNAPL injection flow rate and vertical-downward drainage of water-saturated medium sand at high DNAPL injection flow rate.

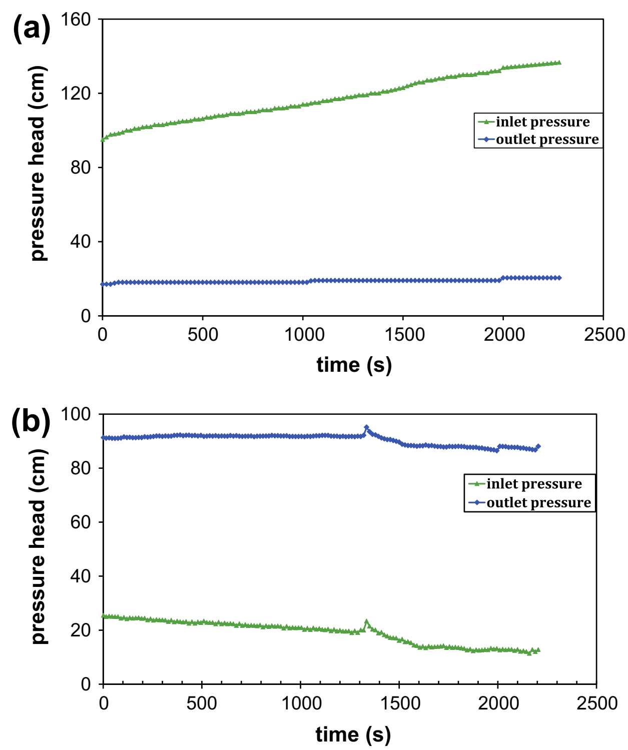

Fig. 6. Measured inlet and outlet pressure head as functions of time: (a) case of vertical-upward drainage of water-saturated medium sand at low DNAPL injection flow rate; and (b) case of vertical-downward drainage of water-saturated medium sand at low DNAPL injection flow rate.

displacements (Fig. 5), and these observations confirm that density contrast plays a significant role in the migration of a DNAPL in a porous medium, particularly at low DNAPL injection rates. In the experiments, we determined an average TCE saturation of about 66% in the case of upward displacement, but only 33% for downward displacement. Furthermore, soil samples taken at the end of each drainage experiment clearly indicate that the TCE saturation front behavior is abrupt in the case of upward water displacement varying from 20% to 70% at a depth between 10 and 30 cm. In the case of downward displacement, the TCE saturations are more or less uniformly distributed over the sampling depths and are characterized by a low saturation of about 16% (see Fig. 5). This difference is mainly due to the stable growth during upward displacement, whereas downward displacement is characterized by flow instabilities. The interactions between the capillary, buoyancy, and viscous forces result in a complex flow pattern characterized by ramified features as observed in Fig. 4b.

3.3. DNAPL pressure at the inlet section

Although the DNAPL saturation describes the distribution of displacement fluids in the porous medium, it is the pressure build-up that significantly determines the displacement of one fluid by another. Thus, to better understand the interplay between global pressure behavior and displacement condition (stable or unstable), the inlet TCE pressure was measured in the laboratory experiment for upward and downward displacement. Fig. 6a and b summarizes the TCE pressure measured as a function of time at the inlet section of the soil column for the cases of upward displacement and downward displacement, respectively. The boundary pressure applied to the outlet section of the experimental system corresponded to a water height of 18 cm and 86 cm, respectively. As shown in Fig. 6a, the pressure at the inlet section increased with time in the case of vertical upward displacement. Thus, the water/DNAPL interface is stabilized by the gravity effect in this case. This confirms the findings of Løvoll et al. (2005). The potentially destabilizing influence of the viscosity ratio was not significant. The pressure increase is therefore caused by the high density of the invading fluid, which overrides the decrease in viscous pressure drop during the displacement of the less viscous DNAPL.

Downward displacement of water by TCE is an unstable displacement, with a much more irregular front and several gravity fingers. The interplay between hydrostatic pressure and viscous pressure varies under this condition of displacement and results in an overall decrease of the inlet TCE pressure. As shown in

Fig. 6b, the measured pressure decreases as the less viscous and denser fluid invades the system due to the constant TCE injection rate. Here, buoyancy forces are destabilizing and dominate the movement, resulting in typical DNAPL fingers in the displaced fluid. The macroscopic water/DNAPL interface is therefore no longer horizontal and many throats become blocked by the capillary effects. The number of active invasion paths is therefore low, and the flow section of DNAPL is reduced. The contribution of viscous pressure is also limited and is dominated by the contribution of the higher density of the invading fluid. Combination of all of these effects results in the decreased inlet pressure.

3.4. Influence of the DNAPL injection rate on gravity fingering

The DNAPL injection rate is one of the key factors in displacement of water by DNAPL and controls the balance between the buoyancy, viscous, and capillary forces. Low injection rates yield more opportunities for capillary effects and buoyancy effects to acting in displacement, and the viscous forces are basically limited. It has been previously shown that under a low injection rate, the vertical-downward displacement of water by TCE gives rise to several fingers. Development of fingers is mainly caused by the destabilizing effect of the gravitational forces that dominate the displacement process in this situation. The invasion of a saturated porous medium by TCE is only partial, and the resulting distribution of the pollutant is thus inhomogeneous. To study the effect of increasing the injection rate on the occurrence of instability phenomena during downward flow mode, a displacement experiment was performed with a doubled DNAPL injection rate.

The statistical description of the measured arrival times shows that their distribution is quite similar to the one obtained for upward displacement at a low flow rate (see Fig. 3). The standard deviation is about 17 s, which is significantly less than that obtained for the case of downward displacement of water by TCE at a low rate (standard deviation equal to 70 s) and similar to that observed in the case of upward movement (stable case, standard deviation equal to 9 s). Thus, the increase in the injection rate significantly stabilizes the displacement. The displacement pattern has more resemblance to the compounding pattern for the vertical-upward displacement recorded at low flow rate. This can be explained by the fact that the high DNAPL injection rate is related to a high-pressure gradient, and when the pressure gradient is high enough, and then both the capillary and buoyancy forces might be effectively neglected. Here N_b is negative (-2.7×10^{-5}) and the viscosity ratio M is always unfavorable, but an increase of the capillary number (N_c increases from 4.1×10^{-6} to 7.5×10^{-6}) seems to lead to a transition to a stable displacement regime which can be referenced in the 3D diagram proposed by Ewing and Berkowitz (Ewing and Berkowitz, 1998). This result is rather surprising, because DNAPL has a lower viscosity, and one would expect a faster injection rate to destabilize the fronts even more. The motion may be unstable, but the shape of the finger head is such that it hits most of the sensors in a moderate amount of time, whereas the untouched parts of the flow are located in the zones without sensors. Alternatively, the separation between a TCE finger and water may cover a longer distance at high speed, which then becomes comparable to or larger than the cell size.

TCE saturations obtained at high injection rate are shown as function of depth in Fig. 5. The TCE saturations are globally higher than those obtained in the case of low injection rate. The average TCE saturation is now increased to 47%. The corresponding profiles also display fewer irregularities than those obtained in the case of downward drainage conducted at a low injection rate. As the flow rate increases, the advancing DNAPL/water front behavior becomes more abrupt.

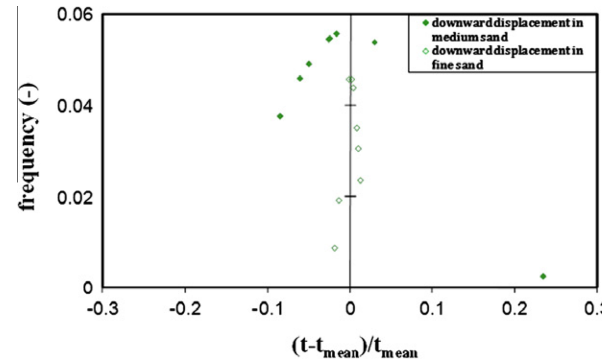

Fig. 7. Measured dimensionless arrival times of the water/DNAPL front in both medium sand and fine sand: case of vertical-downward water displacement at low DNAPL injection flow rate (40 mL/min).

3.5. Effect of permeability on gravity fingering

To study the effect of the intrinsic permeability of the porous medium on the gravity fingering process, a second displacement experiment was performed using fine sand and applying the same low DNAPL injection rate as in the first experiment. The intrinsic permeability of the fine sand is approximately eighteen times lower than that of the medium sand. Fig. 7 shows the comparison of measured dimensionless arrival times of the TCE front (during the downward displacement of water by TCE) carried out in fine sand to those obtained in the medium sand. In the case of the fine sand, statistical analysis of the determined distribution of front arrival times yields a nearly uniform distribution. The standard deviation in this case is only 12 s, in comparison to the 70 s recorded in the case of displacement of water by TCE in the medium sand. Because the permeability is primarily controlled by the pore-throat size, changing the size of the mean grain diameter of the sand has a larger effect on drainage displacement behavior due to the increase in capillarity effects (Yao and Hendrickx, 2001). One might expect that the growth of gravity-driven fingers would be nearly suppressed under this condition of displacement. Although buoyancy forces dominate the displacement especially at low DNAPL injection rates and the Bond number is negative, the capillary number ($N_c = 4.1 \times 10^{-6}$) is closer to the absolute value of Bond number ($|N_b| = 4.2 \times 10^{-6}$) in the case of displacement in fine sand than in the case of displacement in medium sand (($|N_b| = 2.7 \times 10^{-5}$). Indeed, a lower mean grain size of the porous medium is directly translated to a lower absolute value of the Bond number (see Eq. (3)). This might explain the reduction in the potential contribution of buoyancy forces to the development of fingering processes in low-permeability porous media. Furthermore, when an evolving finger propagates in fine sand, the finger velocity may be slowed down until the non-wetting phase pressure increases enough to overcome the local increase in capillarity effects, which is apparently sufficient to stabilize the displacement front. Indeed, the destabilizing effect of the unfavorable viscosity ratio on the displacement was not completely overcome and formation of local fingers that we did not observe might have occurred.

Based on these observations, we may assert that when the Bond number is negative but have the same magnitude as the capillary number, may corresponding to a stable displacement region that we can refine in the 3D diagram proposed by Ewing and Berkowitz (1998).

3.6. Residual DNAPL saturations

Residual TCE saturations were measured in the sand-filled column after a complete drainage–imbibition cycle. Four configuration cycles related to the applied flow mode (vertical-upward flow, vertical-downward flow) in both primary drainage and water-flooding processes were carried out in the medium sand. The primary drainage was initially carried out under a stable displacement condition using a constant vertical-upward DNAPL flow rate. This resulted in a high initial TCE saturation, whereas the vertical-downward primary drainage gave rise to a small initial TCE saturation in the saturated porous medium (see Section 3.2). After each drainage experiment, water was then either injected from bottom to top, which reproduced an unstable gravity condition, or from top to bottom in a second experiment, allowing buoyancy forces to play a maximum stabilizing role in the water flooding process. In addition, one complete drainage–imbibition cycle was conducted in the fine sand (see Table 3). In this case, both primary drainage and water-flooding displacements were performed in the direction of the gravity forces. Section 3.5 clearly showed that stable conditions were achieved during the drainage process even for a destabilized-gravity condition and unfavorable viscosity ratios between the two fluids.

A large range of water flow rates was applied to mobilize the DNAPL entrapped in the porous medium after primary drainage. Corresponding entrapped TCE saturation in the porous medium was measured by mass balance as described in Section 2.3. The water flow rate was varied (up to approximately four times the initial flow rate) by increasing the water injection rates from 40 to 170 mL/min, corresponding to a capillary number N_c ranging from 4.1×10^{-6} to 16.8×10^{-6}.

Fig. 8 summarizes the observed average TCE saturations as a function of the capillary number (N_c) for the four drainage–imbibition cycles conducted in the medium sand and for the one cycle performed in both the fine and medium sand under the same flow mode. It should be noted that, independent of the primary drainage condition (stable or unstable), the average residual TCE saturations quantified in the medium sand were lowest for downward water-flooding and highest for upward water-flooding at the lowest capillary number of 4.1×10^{-6}. For a high initial TCE saturation in the porous medium (66%), the remaining TCE saturation is only 18% for downward water-flooding against 45% when a upward water-flooding was applied. This result is in good agreement with the findings of Helen and Paul (1997). In the case of upward water-flooding, the viscous forces are counteracted by buoyancy forces at the lowest water-flooding rates, and a large fraction of the TCE remains in the pores. However, buoyancy forces push the DNAPL droplets downward when the water is injected from the top. Whereas the buoyancy forces are cooperative forces in the downward water-flooding and are combined with the capillary and viscous forces to displace the DNAPL droplets, the buoyancy forces are subtractive forces in the case of upward displacement and compete the capillary and viscous forces that mobilize the entrapped DNAPL. Furthermore, the remaining TCE saturations in the medium sand for both flow modes applied during water-flooding tend to decrease as N_c increases. This indicates that both the capillary and buoyancy forces are overcome by the viscous forces at high injection flow rates, and therefore, the mobilization of TCE becomes independent of the chosen flow mode. On the other hand, it can be noted that residual TCE saturations obtained at high capillary numbers were slightly different for both water-flooding directions, whereas their values were fairly equal for the two primary drainage directions and followed the same water-flooding mode. Regardless of the initial saturation in the porous medium, the average residual TCE saturation was stabilized around 20% and 12% for upward water-flooding and downward water-flooding, respectively. Therefore, it can be concluded that residual TCE saturations are directly related to the imbibition flow mode and are independent of the initial distribution of DNAPL in the porous medium.

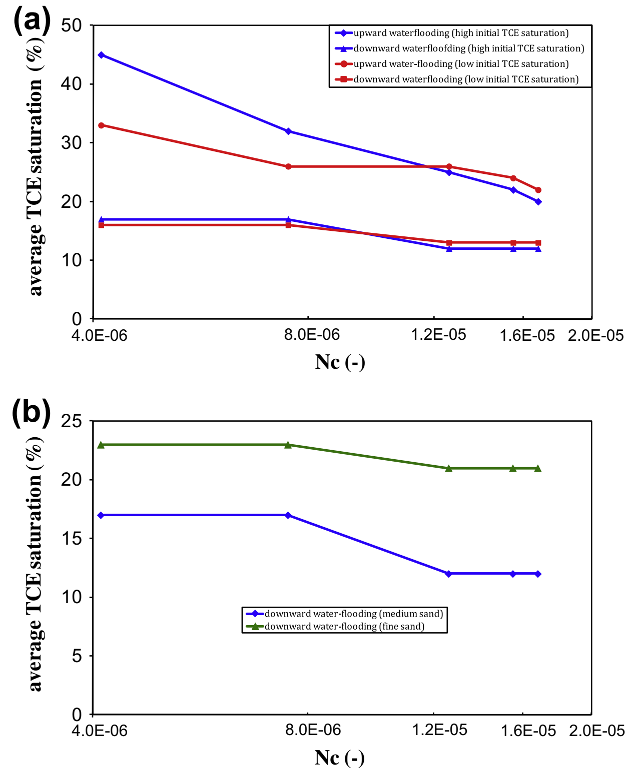

Fig. 8. Average TCE saturations as a function of the capillary number N_c: (a) four drainage–imbibition cycles performed in medium sand and (b) one drainage–imbibition cycle performed in medium and fine sand under the same flow modes.

As shown in Fig. 8b, the residual TCE saturation determined at the lowest capillary number ($N_c = 4.1 \times 10^{-6}$) for the fine sand was slightly higher than that observed in the medium sand. The initial difference of about 5% increases with increasing capillary number. At higher capillary numbers, residual TCE saturation is reduced to 20% in the fine sand, and 13% in the medium sand. This may be explained by the fact that, with decreasing mean grain size of the porous medium, capillary forces become dominant and lead to a significant quantity of TCE being captured in the porous medium, even when viscous forces increase during water-flooding at high flow rates.

Fig. 9a and b shows the measured local TCE saturations at a centre point and two point edges of a column transect as a function of depth for downward water-flooding displacement and upward water-flooding displacement in the medium sand, respectively. In the case of downward water-flooding, the residual TCE saturation seems to be more homogeneous along the whole section of the soil column because the measured TCE saturation values on the axis and edges (two opposite points) of the soil column are closer to each other at most sampling depths than those obtained in the case of upward-water flooding. Despite favorable viscosity ratios existing between the immiscible fluids, fingering driven by destabilizing density may be formed (Lenormand and Zarcone, 1985; Lenormand, 1989). The shape of these fingers might be different to those observed during gravity destabilizing primary drainage. During downward water-flooding, as the displacing fluid (water) is lighter than the displaced fluid (TCE), the TCE/water interface is kept stable, and water most likely crosses the entire section of the sand-filled column. Consequently, the major part of the entrapped TCE in the porous medium is mobilized downwards at the same rate. However, due to the unstable gravity condition in the case of upward water-flooding, water flows upwards along preferential paths and leaves behind a heterogeneous spatial

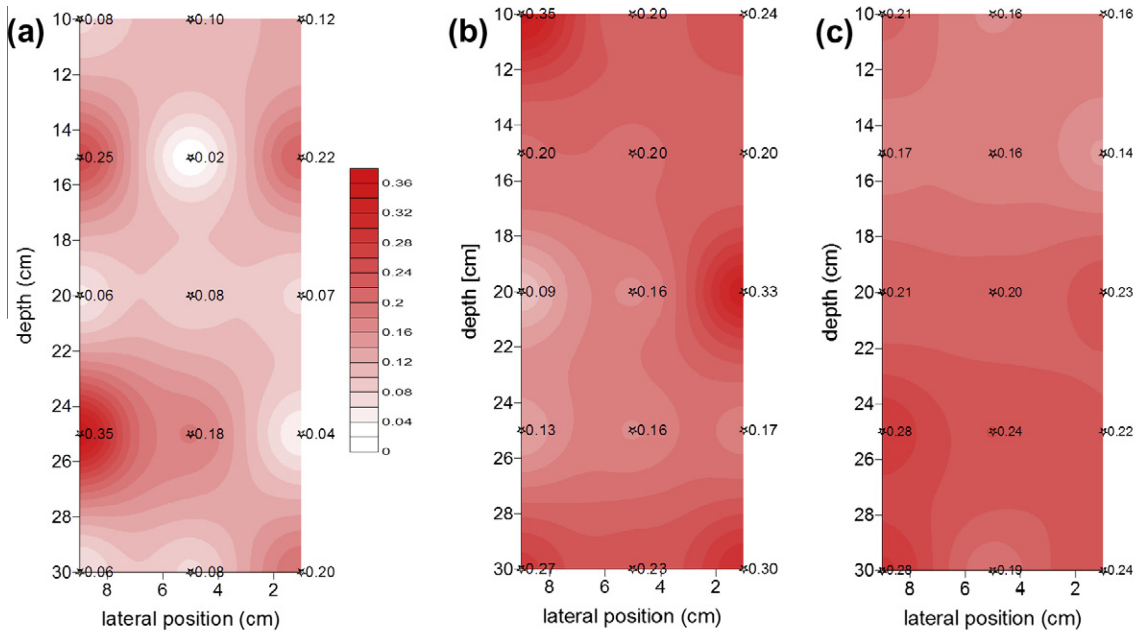

Fig. 9. Residual TCE saturation at different positions of the column section as function of depth: (a) downward water-flooding displacement and (b) upward water-flooding displacement in the medium sand, and (c) downward water-flooding displacement in the fine sand.

distribution of an amount of TCE in the sand. This is shown as an example for a depth of $z = -15$ cm (with $z = 0$ corresponding to the top of the column). A low residual TCE saturation of only 2% was measured, indicating the preferential pathways of water, whereas at another sampling point located at the same depth, a high residual TCE saturation of nearly 25% was quantified, illustrating a region not in contact with the water flush.

The residual TCE saturation measured in the fine sand as a function of depth at different points of the column section (centre point and two point edges) are shown in Fig. 9c. The residual TCE saturation appears to be more uniformly distributed than in the medium sand. For a given depth, the difference between TCE saturation values in the axis and along the wall of the column is lower than 5%. Furthermore, the average residual TCE saturation varies between 16% and 24% along the total sampling height. This indicates that, due to the dominating capillary forces in the fine sand (as previously stated), the immiscible front of displacement is almost abrupt.

4. Conclusion

In this study, optical fiber sensors were developed to quantify DNAPL gravity-driven fingering in a water saturated homogeneous porous medium. The influence of several hydrodynamic parameters (such as direction of flow, velocity of displacing fluid, and texture of the porous medium) on the instability displacement process was evaluated during various displacement configurations (drainage experiment and complete drainage–imbibition cycle).

DNAPL front arrival times recorded halfway up in a column filled with medium sand were more spread out in downward drainage than those obtained in the case of upward drainage, showing evidence of preferential path growth for the non-wetting fluid in the saturated porous medium. Here, the spatial distribution of the measured DNAPL saturation was rather inhomogeneous. As expected, buoyancy forces help to stabilize the displacement during the vertical-upward drainage, however, they enhance the unstable displacement and may lead to gravity-driven fingers in the case of a downward displacement. It is worthwhile to note that the velocity of front displacement and the permeability of the porous medium may fundamentally affect the occurrence of gravity fingers and may even entirely suppress the fingering process during immiscible downward displacement. The experimental results highlight that, even for a gravity-destabilized condition, the displacement of the immiscible front was more stable in the case of a high DNAPL injection rate, and entrapped DNAPLs were nearly uniformly distributed in the saturated medium sand. This happens because viscous forces become dominant over buoyancy forces. This stabilizing effect is evident in laboratory experiments, but it is very hard to achieve in a real applied situation. Additionally, it was also concluded from the experimental results that downward migration of the DNAPL in a sand with fine texture leads to an enhanced stabilization of the immiscible front in the saturated porous medium. Here, the small pores of the fine sand accentuate the local capillary pressure in the pores, which slows down the front displacement and makes it more uniform.

The experimentally obtained residual DNAPL saturations clearly indicate that upward water-flooding displacement leads to higher quantities of entrapped DNAPL than during downward displacement of water by DNAPL. It was also found that residual DNAPL saturation is a decreasing function of the capillary number N_c, which confirms the findings of earlier studies. Subsequently, the difference in permeability between the fine sand and the medium sand significantly impacts the values of residual DNAPL saturation. Furthermore, the residual DNAPL saturations measured in the case of the fine sand were much more uniformly distributed over the depth than in the medium sand. In an upcoming paper, the experimental data will be used to validate a recently developed numerical grain size distribution based pore-throat model (Nsir and Schäfer, 2010) to compute the water/DNAPL displacement at the pore scale.

Acknowledgements

Financial support for this research was received from the programme REALISE (REseau Alsace de Laboratoires en Ingénierie et Sciences pour l'Environnement). The Région Alsace, the GDR «Hydrodynamique et Transferts dans les Hydrosystèmes

Souterrains » (INSU-CNRS), and the Conseil Scientifique de l'Université Louis Pasteur Strasbourg are gratefully acknowledged. Furthermore, the authors would like to thank the anonymous reviewers for their valuable comments and suggestions, which helped to improve the article significantly.

References

Anderson, M.R., Johnson, R.L., Pankow, J.L., 1992. Dissolution of dense chlorinated solvents into groundwater. 3. Modeling contaminant plumes from fingers and pools of solvent. Environ. Sci. Technol 5, 901–908.

Barczewski, B., Marschall, P., 1992. Development and application of a light fiber fluorimeter for tracer tests. In: Hôtzl, H., Werner, A. (Eds.), Tracer Hydrology. Balkema, Rotterdam, pp. 3–39.

Benremita, H., Schäfer, G., 2003. Quantification du transfert de trichloroéthylène en milieu poreux à partir d'un panache de vapeurs vers la nappe d'eau souterraine. C.R. Méc. 331 (12), 835–842.

Bettahar, B., Ducreux, J., Schäfer, G., Van Dorpe, V., 1999. Surfactant enhanced in situ remediation of LNAPL contaminated aquifers: large scale studies on a controlled experimental site. Transp. Porous Med. 37, 276–286.

Birovljev, A., Furuberg, L., Feder, J., Jøssang, T., Måløy, K.J., Aharony, A., 1991. Gravity invasion percolation in 2 dimensions-experiment and simulation. Phys. Rev. Lett. 5, 584–587.

Bohy, M., Schäfer, G., Razakarisoa, O., 2004. Caractérisation de zones sources de DNAPL à l'aide de traceurs bisolubles: mise en évidence d'une cinétique de partage. C.R. Géosci. 336, 799–806.

Brailovsky, I., Babchin, A., Frankel, M., Sivashinsky, G., 2006. Fingering instability in water–oil displacement. Transp. Porous Med. 63, 363–380.

Christophe, C., Hugues, B., Annie, C., 2010. Drainage in two-dimensional porous media: from capillary fingering to viscous flow. Phys. Rev. E, 82, 046315.

Dicarlo, D.A., 2004. Experimental measurements of saturated overshoot on infiltration. Water Resour. Res, 40, W04215.

Ewing, R.P., Berkowitz, B., 1998. A generalized growth model for simulating initial migration of dense non-aqueous phase liquids. Water Resour. Res. 34, 611–622.

Fayers, F.J., Zhou, D., 1996. On the importance of gravity and three-phase flow in gas displacement processes. J. Petrol. Sci. Eng. 15, 321–341.

Ferer, M., Bromhal, G.S., Smith, D.H., 2007. Crossover from capillary fingering to compact invasion for two-phase drainage with stable viscosity ratios. Adv. Water Resour. 30, 284–299.

Frette, O.I., Måløy, K.J., Schmittbuhl, J., Hansen, A., 1997. Immiscible displacement of viscosity-matched fluids in two-dimensional porous media. Phys. Rev. E 3, 2969–2975.

Geiger, S.L., Durnford, D.S., 2000. Infiltration in homogeneous sands and a mechanistic model of unstable flow. Soil Sci. Soc. Am. J. 64, 460–469.

Gioia, F., Urciuolo, M., 2006. Combined effect of Bond and capillary numbers on hydrocarbon mobility in water saturated porous media. J. Hazard. Mater. 133, 218–225.

Glass, R.J., Nicholl, M.J., 1996. Physics of gravity fingering of immiscible fluids within porous media: an overview of current understanding and selected complicating factors. Geoderma 70, 133–163.

Glass, R.J., Conrad, S.H., Peplinski, W., 2000. Gravity destabilized non-wetting phase invasion in macroheterogneous porous media: experimental observations of invasion dynamics and scale analysis. Water Resour. Res. 36, 3121–3137.

Glen, R., Boyd, D., Ana, M., Gómez, O., Minghua, L., Husserl, J., 2006. Effects of initial saturation on properties modification and displacement of tetrachloroethene with aqueous isobutanol. J. Contam. Hydrol. 88, 69–91.

Gupta, B.D., Verma, R.K., 2009. Surface plasmon resonance-based fiber optic sensors: principle, probe designs, and some applications. J. Sensors 15.

Helen, E.D., Paul, V.R., 1997. Influence of viscous, gravitational, and capillary forces on DNAPL saturation. Ground Water 35, 261–269.

Hunt, J.R., Sitar, N., Udell, K.S., 1998. Nonaqueous phase liquid transport and cleanup. I. Analysis of mechanisms. Water Resour. Res. 8, 1247–1258.

Jellali, S., Muntzer, P., Razakarisoa, O., Schäfer, G., 2001. Large scale experiment on transport of trichloroethylene in a controlled aquifer. Transp. Porous Media 44, 145–163.

Jellali, S., Benremita, H., Muntzer, P., Razakarisoa, O., Schäfer, G., 2003. A large-scale experiment on mass transfer of trichloroethylene from the unsaturated zone of a sandy aquifer to its interfaces. J. Contam. Hydrol. 60, 31–53.

Khataniar, S., Peters, E.J., 1992. The effect of reservoir heterogeneity on the performance of unstable displacements. SPE Reservoir Eng. 7, 263–281.

Kueper, B.H., Frind, E.O., 1989. An overview of immiscible fingering in porous media. J. Contam. Hydrol. 2, 95–110.

Lenormand, R., 1989. Flow through porous media: limits of fractal patterns. Proc. Roy. Soc. Lond. Ser. A, Math. Phys. Sci. 423, 159–168.

Lenormand, R., Zarcone, C., 1985. Invasion percolation in an etched network: measurement of a fractal dimension. Phys. Rev. Lett. 54, 2226.

Lenormand, R., Zarcone, C., 1989. Capillary fingering: percolation and fractal dimension. J. Porous Media 4, 599–612.

Lenormand, R., Zarcone, C., Sarr, A., 1983. Mechanisms of displacement of one fluid by another fluid in a network of capillary ducts. J. Fluids Mech. 135, 337–353.

Leverett, M.C., 1939. Flow of oil–water mixtures through unconsolidated sands. Trans. Am. Inst. Min. Metall. Pet. Eng 132, 149–171.

Løvoll, G., Méheust, Y., Toussaint, R., Schmittbuhl, J., Måløy, K.J., 2004. Growth activity during fingering in a porous Hele Shaw cell. Phys. Rev. E 70, 026301.

Løvoll, G., Méheust, Y., Måløy, K.J., Aker, E., Schmittbuhl, J., 2005. Competition of gravity, capillary and viscous forces during drainage in a two-dimensional porous medium, a pore scale study. Energy 30, 861–872.

Løvoll, G., Jankov, M., Måløy, K.J., Toussaint, R., Schmittbuhl, J., Schäfer, G., Méheust, M., 2011. Influence of viscous fingering on dynamic saturation-pressure curves in porous media. Transp. Porous Med. 86 (1), 305–324, doi:10.1007/s11242-010-9622-8.

Méheust, M., Løvoll, G., Måløy, K.J., Schmittbuhl, J., 2002. Interface scaling in a two-dimensional porous medium under combined viscous, gravity and capillary effects. Phys. Rev. E, 66, 051603.

Nguyen, V.H., Sheppard, A.P., Knackstedt, A.A., Pinczewski, W.V., 2006. The effect of displacement rate on imbibition relative permeability and residual saturation. J. Petrol. Sci. Eng. 52, 54–70.

Nicholl, M.J., Glass, R.J., 2005. Experimental observations of gravity-driven fingering during immiscible displacements within a rough-walled fracture. Vadose Zone J. 4, 1123–1151.

Nsir, K., 2009. Etude expérimentale et numérique de la migration des polluants non miscibles à l'échelle de Darcy. PhD thesis, Université de Strasbourg, France, 207.

Nsir, K., Schäfer, G., 2010. A pore-throat-model based on grain size distribution to quantify gravity-dominated DNAPL instabilities in water saturated homogeneous porous medium. C.R. Geosci. 342, 881–891.

Parsons, R.W., Marathon, O.C., 1975. Microwave attenuation – a new tool for monitoring saturations in laboratory flooding experiments. SPE J. 15, 302–310.

Pennell, K., Pope, G., Abriola, L., 1996. Influence of viscous and buoyancy forces on the mobilization of residual tetrachloroethylene during surfactant flushing. Environ. Sci. Technol 30, 1328–1335.

Riaz, A., Tchelepi, H.A., 2006. Influence of relative permeability on the stability characteristics of immiscible flow in porous media. Transp. Porous Med. 64, 315–338.

Saffman, P.G., Taylor, G., 1958. The penetration of a fluid into a porous medium or Hele–Shaw cell containing a more viscous liquid. Proc. Roy. Soc. Lond., Ser. A 245, 312–329.

Schwille, F., 1988. Dense Chlorinated Solvent in Porous and Fractured Media: Model Experiments. Translated from the German by Pankow. J.F. Lewis Publishers, Boca Raton, Florida, pp. 1–146.

Sharma, A.K., Gupta1, B.D., 2006. Fibre-optic sensor based on surface plasmon resonance with Ag–Au alloy nanoparticle films. Nanotechnology 17, 124–131.

Theodoropoulou, M.A., Sygouni, V., Karoutsos, V., Tsakiroglou, C.D., 2005. Relative permeability and capillary pressure functions of porous media as related to the displacement growth pattern. Int. J. Multiphase Flow 31, 1155–1180.

Toussaint, R., Løvoll, G., Méheust, Y., Måløy, K.J., Schmittbuhl, J., 2005. Influence of pore-scale disorder on viscous fingering during drainage. Europhys. Lett. 71, 583–589.

Tullis, B.P., Wright, .S.J., 2007. Wetting front instabilities: a three-dimensional experimental investigation. Transport Porous Medium 70, 335–353.

Yao, T., Hendrickx, J.M., 2001. Stability analysis of the unsaturated water flow equation. 2. Experimental verification. Water Resour. Res. 7, 1875–1881.

Zhang, Z.F., Smith, J.E., 2001. The velocity of DNAPL fingering in water-saturated porous media: laboratory experiments and a mobile–immobile–zone model. J. Contam. Hydrol. 49, 335–353.

Approche expérimentale et numérique des instabilités de déplacement d'un DNAPL en milieu poreux saturé à l'échelle de Darcy

K. NSIR[a,b], G. SCHÄFER[a,b], O. RAZAKARISOA[a,b], R. TOUSSAINT[c], J. SCHMITTBUHL[c]

a. Institut de Mécanique des Fluides et des Solides (IMFS), 2 rue Boussingault, 67000 STRASBOURG
b. Laboratoire d'Hydrologie et de Géochimie de Strasbourg (LHyGeS), UMR 7517, CNRS – Université de Strasbourg, 1 rue Blessig, 67084 STRASBOURG Cedex.
c. Institut de Physique du Globe de Strasbourg (IPGS), UMR 7516, CNRS – Université de Strasbourg, 5 Rue René Descartes, 67084 STRASBOURG Cedex.

Résumé :

L'étude porte sur une quantification des instabilités de déplacement d'un DNAPL (Dense Non Aqueous Phase Liquid) en milieu poreux homogène et saturé en eau. L'approche expérimentale repose sur la mesure des vitesses d'arrivée du DNAPL dans une colonne de laboratoire à différents points d'une section de contrôle au moyen des fibres optiques et sur la cartographie in situ des saturations locales en DNAPL. La simulation numérique du processus de drainage (eau/DNAPL) est abordée par une approche de type réseau des pores et capillaires.

Abstract :

This study is focussing on the quantification of the instability of DNAPL (Dense Non Aqueous phase Liquid) displacement in homogenous and water saturated porous media. The experimental approach is based on both the measurement of the velocity of DNAPL arrival in a laboratory column at different points of a control section by means of optic fibres and on the in situ mapping of local DNAPL saturations. The drainage process is numerically simulated by a network model of bodies and throats.

Mots clefs: déplacement, instabilité, DNAPL, milieu poreux, réseau discret, fibres optiques

1 Matériels et méthodes

Les expériences ont été conduites sur une colonne de laboratoire. Des capteurs à fibres optiques ont été mis au point pour quantifier les cheminements préférentiels d'un DNAPL (Dense Non Aqueous phase Liquid) dans un milieu poreux saturé à partir de la mesure de la vitesse d'arrivée de la phase à différents points d'une section de contrôle de la colonne. L'approche mathématique retenue est basée sur une représentation du milieu poreux comme un ensemble des pores et des capillaires de formes géométriques simples. La résolution des équations d'écoulement permet de déterminer les saturations en DNAPL ainsi que les pressions lors du déplacement.

1.1 Capteurs à fibre optique

Une fibre optique est constituée de 2 couches, le cœur et la gaine, avec des indices de réfraction différents. De ce fait, il y a des réflexions totales qui retiennent la lumière dans la fibre. Lorsqu'on enlève la gaine, la propriété de conduire la lumière, dépendra de l'indice de réfraction du milieu qui entoure le cœur. Ce type d'intervention sur la fibre crée une zone sensible qui permet la détection d'un DNAPL dans un milieu poreux saturé en eau due à la différence des indices de réfraction entre l'eau (n_{eau} = 1.33) et le DNAPL (n_{DNAPL} = 1.46). A l'extrémité de la zone sensible, un miroir est mis en place pour réfléchir la lumière conduite dans la fibre. La quantification de l'atténuation de la lumière réfléchie renseigne sur la présence ou non du DNAPL. Chacun de huit capteurs à fibre optique utilisés comporte une fibre optique modifiée, une photodiode, un séparateur des faisceaux lumineux et un module de mesure de la lumière réfléchie.

1.2 Dispositif expérimental et protocole

Le dispositif expérimental est composé de deux colonnes en verre (ϕ = 10 cm ; L = 34 cm) raccordées par une pièce jointive en acier inoxydable pour la mise en place de 8 fibres optiques dans le milieu poreux (figure 1). L'entrée et la sortie de la colonne sont équipées de deux capteurs de pression de type PMC131 permettant la mesure de la pression relative dans une gamme de pression entre 0 et 200 mbar. Les modules de mesure branchés aux fibres ainsi que les capteurs de pression sont connectés à une centrale d'acquisition des données (Agilent 34970A). Le milieu poreux choisi est le sable H2F, fournie par la société Friedrich en Allemagne. Ce milieu a une porosité d'environ 40%, une conductivité hydraulique de l'ordre de 0.08 cm/s et une masse volumique apparente de 1.59 g/cm^3. Le DNAPL utilisé est le trichloréthylène (TCE). Il s'agit d' un composé organo-chloré moins visqueux que l'eau dont la masse volumique est de 1.462 g/cm^3.

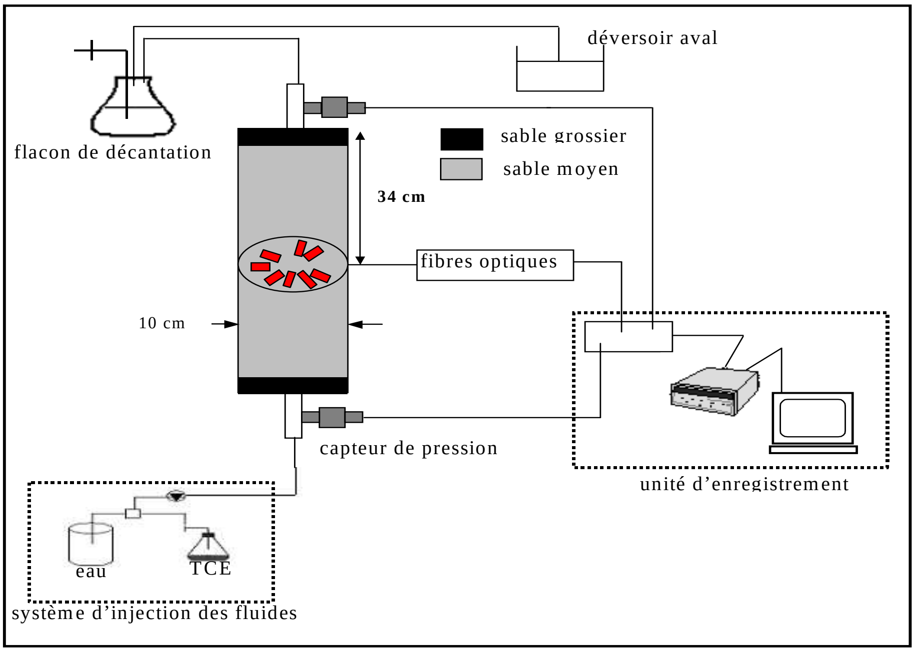

FIG. 1– Dispositif expérimental

L'injection des fluides à travers l'orifice d'entrée de la colonne est assurée par une pompe péristaltique fournissant un débit maximal de 100 ml/min. La pompe est reliée aux réservoirs des fluides par l'intermédiaire d'une vanne à trois voies permettant de sélectionner successivement l'arrivée de chacun des fluides. Deux modes de déplacement ont été étudiés: le déplacement vertical ascendant (cas stable) et le déplacement vertical descendant (cas instable). Le volume du TCE injecté dans la colonne est de 1.5 litres ; le débit pratiqué dans les essais est de l'ordre de 40 ml/min. A la fin de chaque expérience, 3 échantillons de sable ont été prélevés tous les 5 cm à différentes positions de la colonne (un au centre et deux proches de la paroi) moyennant un micro-prélèveur peu perturbateur. L'échantillonnage est effectué uniquement sur le module supérieur du dispositif expérimental (module placé au-dessus de la section du contrôle). Sur la section proche de la section de contrôle, 10 prélèvements supplémentaires aux points qui coïncident éventuellement avec les emplacements des zones sensibles des fibres optiques ont été effectués. Les échantillons de sable ont été ensuite analysés par la méthode de chromatographie en phase gazeuse pour quantifier les saturations locales en TCE**.**

1.3 Modèle discret de type réseau des pores et des capillaires

1.3.1 Géométrie du réseau

Le milieu poreux est représenté par un réseau tridimensionnel des pores et des capillaires. Les pores sont sphériques et constituent la porosité du milieu poreux. Les capillaires sont de formes cylindriques et présentent des rayons plus faibles que les pores. La taille des rayons des pores et des capillaires est générée d'une manière aléatoire selon une loi de distribution statistique [9]

$$g(x)=\begin{cases} x/x_2^2 \exp(-x/x_2^2)\,, & \text{si } x \le x_3 \\ 0 & \text{, si } x \succ x_3 \end{cases} \tag{1}$$

avec $x = r - r_{min}$, $x_2 = r_{moy} - r_{min}$ et $x_3 = r_{max} - r_{min}$, r réfère au rayon du pore ou du capillaire généré à partir de la loi de distribution, r_{min}, r_{moy}, r_{max}, représentent respectivement le rayon minimum, moyen et maximum des pores ou des capillaires. La longueur L_{ij} d'un capillaire reliant deux pores adjacents de rayon r_i et r_j est $L_{ij} = L - (r_i + r_j)$ où L est la distance séparant les centres de deux pores qui est supposée constante dans le réseau.

1.3.2 Algorithmes du processus de drainage eau/DNAPL

La modélisation du processus de drainage a nécessité d'implémenter des règles d'invasion [5]. Les effets de la capillarité dans les pores sont négligés et une interface unique sur la limite entre un pore et un capillaire est prise en compte [8]. De ce fait, la tension interfaciale joue un rôle uniquement lorsque les pores adjacents sont complètement remplis par deux fluides différents [7]. Considérons deux pores adjacents, l'un rempli par la phase non mouillante (DNAPL) et l'autre par la phase mouillante (eau). Lorsque la pression motrice de déplacement augmente, l'interface eau/DNAPL devient instable et il y aura lieu une avancée rapide de l'interface une fois la pression capillaire est affranchie [1]. Ce mécanisme est simulé par le modèle en définissant une pression seuil nécessaire pour que l'interface se déplace dans le capillaire. Cette pression capillaire seuil P_c définie comme la différence de pression entre les deux phases à travers l'interface est donnée par la loi de Young-Laplace [2]

$$P_c = \frac{2\sigma\cos\theta}{r} \tag{2}$$

où θ est l'angle de contact, σ (N/m) correspond à la tension interfaciale entre les fluides et r (m) est le rayon du capillaire.

1.3.3 Equations d'écoulement

Les fluides étant considérés incompressibles, l'application de la conservation de la masse pour chaque pore i du réseau conduit à l'équation suivante :

$$\sum_j Q_{ij} = 0 \tag{3}$$

où Q_{ij} (cm^3 /s) est le flux sortant du pore i vers les pores voisins j, qui est donné par la loi de Poiseuille

$$Q_{ij}^{\alpha} = G_{ij}^{\alpha}(P_i - P_j),\ \text{si } z_i = z_j \tag{4a}$$

$$Q_{ij}^{\alpha} = G_{ij}^{\alpha}(P_i - P_j - \rho^{\alpha} L_{ij} g),\ \text{si } z_i \prec z_j \tag{4b}$$

$$Q_{ij}^{\alpha} = G_{ij}^{\alpha}(P_i - P_j + \rho^{\alpha} L_{ij} g),\ \text{si } z_i \succ z_j \tag{4c}$$

où z est la cote du pore considéré et G_{ij} est la conductance du capillaire contenant une phase fluide α

$$G_{ij}^{\alpha} = \frac{\pi r_{ij}^4}{8\mu^{\alpha} L_{ij}}\ . \tag{5}$$

P_i et P_j sont les pressions dans les pores i et j, r_{ij} est le rayon du capillaire, μ^{α} et ρ^{α} sont respectivement la viscosité et la masse volumique de la phase α. La substitution de l'équation (4) dans (3) conduit à un système d'équations linéaires qui peut être reformulé sous forme matricielle

$$A_{ij} X_i = B_i \tag{6}$$

où A_{ij} est une matrice ayant comme termes les conductances des capillaires et X_i correspondent aux éléments inconnus du vecteur pression. Le vecteur B_i contient les termes connus issus des conditions aux limites. La résolution du système d'équations est effectuée par la méthode de gradient conjugué préconditionné. Les pressions calculées sont ensuite utilisées pour déterminer les saturations en DNAPL dans les pores. Le pas du temps T_{min} choisi correspond au temps minimal nécessaire pour un remplissage complet d'un pore en phase non mouillante. En tenant compte du champ des saturations en DNAPL S^n au pas de temps précédant, le nouveau champ des saturations S^{n+1} est déterminé comme suit :

$$S_i^{n+1} = S_i^n + \frac{Q_i \times T_{min}}{V_i} \tag{7}$$

où Q_i est le flux entrant dans le pore i et V_i correspond au volume du pore.

2 Résultats

2.1 Distribution des vitesses d'arrivée du front de déplacement

Les phénomènes observés dans les deux cas de déplacement sont différentes et illustrent le rôle majeur de la gravité sur la stabilité de déplacement. La figure 2 montre les résultats d'une analyse statistique de la distribution des vitesses d'arrivées du DNAPL dans la section de contrôle pour les deux cas de déplacement. Les vitesses enregistrées pour le cas de déplacement descendant sont étalées ; leur distribution est plutôt non uniforme. Cette forte variation des vitesses est essentiellement due aux instabilités gravitaires de déplacement qui conduisent à une répartition non uniforme du DNAPL dans le milieu poreux saturé.

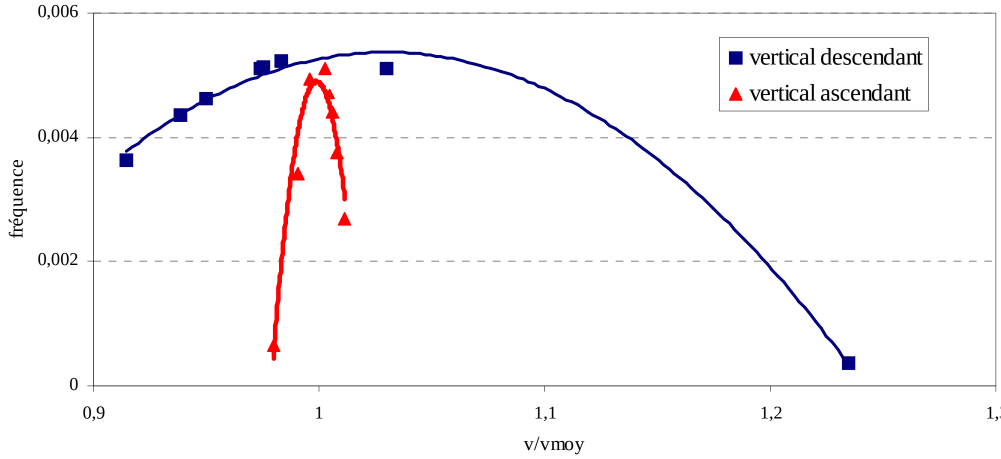

FIG. 2 – Distribution des vitesses d'arrivée du TCE normalisés par rapport à la vitesse moyenne (v_{moy}) dans la section de contrôle pour les deux cas de déplacement

Compte tenu du contraste de densité et de viscosité entre les deux fluides, le TCE tend à emprunter des chemins où la résistance au déplacement est moins élevée [3, 4, 6]. De ce fait, le DNAPL forme des digitations bien marquées. Dans le cas de déplacement ascendant, la gravité joue un rôle stabilisateur dans la migration du DNAPL et compense le rapport défavorable de la viscosité entre les deux fluides. Le déplacement eau/TCE est de type piston et par conséquent les vitesses d'arrivée enregistrées sont rapprochées. Les saturations en TCE quantifiées sur la section proche des emplacements des fibres (figure 3) confirment indirectement ces observations. En effet, une saturation de l'ordre de 2 % pourrait être une zone où le front de TCE est passé tout récemment. Cependant, les saturations élevées, par exemple 12 à 17 %, marquent les zones de passage préférentiel du TCE caractérisant des temps d'arrivée précoces du DNAPL dans la section de contrôle.

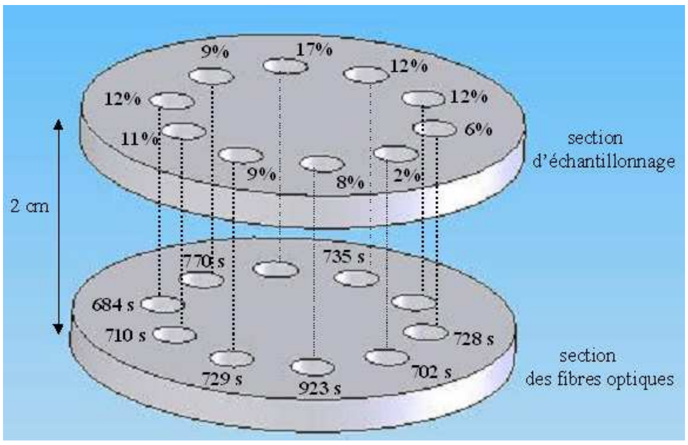

FIG. 3. – Temps d'arrivée du DNAPL dans la section de contrôle et saturations en DNAPL correspondantes aux emplacements des fibres optiques (cas du déplacement descendant)

2.2 Répartition des saturations en TCE dans le milieu poreux saturé

Le profil des saturations en TCE obtenu à proximité de la paroi de la colonne présente un front abrupt dans le cas du déplacement ascendant cependant il est irrégulier dans le cas de déplacement descendant (figure 4). D'autre part, les valeurs des saturations enregistrées sont plus faibles dans le cas du déplacement descendant. En effet, la saturation maximale en TCE ne dépasse pas 30% pour ce cas de déplacement. Les forces de gravité présentent donc une influence importante sur les phénomènes de digitations lors de la migration verticale du DNAPL dans le milieu poreux saturé. Ces forces stabilisent le front avec une distribution homogène du DNAPL lors du déplacement ascendant. Dans le cas inverse, le champ de saturation devient fortement hétérogène

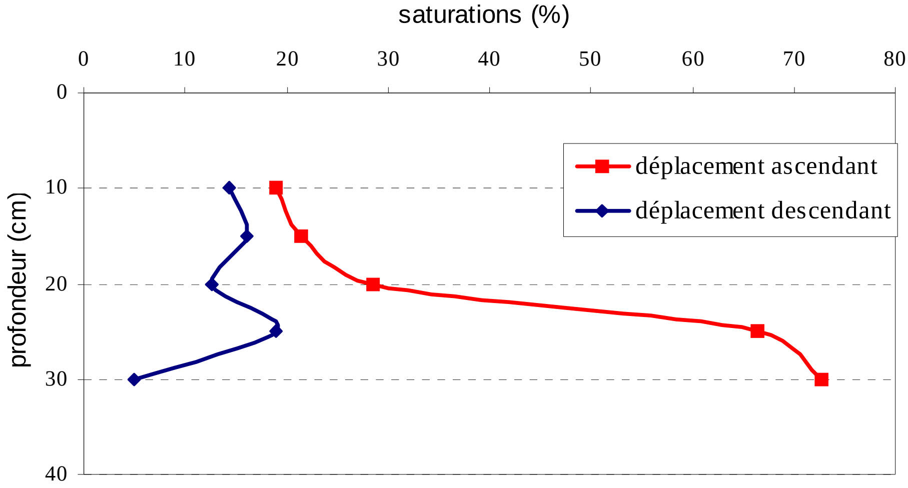

FIG. 4 – Profils des saturations en TCE en fonction de la profondeur pour les deux cas de déplacement

2.3 Simulation numérique des instabilités de déplacement eau/DNAPL

Le modèle développé est utilisé pour simuler les deux cas de déplacement eau/TCE. Afin de s'approcher des conditions de l'expérience, une condition de Neumann (flux imposé) a été choisie sur la limite amont. Le débit injecté (Q = 0.015 ml/min) est défini au niveau de chaque pore appartenant à cette section d'entrée. La limite aval du réseau correspond à une condition de Dirichlet où la pression est maintenue constante (P = 0) sur toutes les pores de cette limite. Le réseau simulé comporte 10 ×10 ×20 pores. Les paramètres caractérisant la distribution de la taille des pores et des capillaires du réseau (R_{min},R_{moy},R_{max}) sont respectivement (0.6,1.2,1.8) et (0.2,0.4,0.6) mm. La distance L séparant les centres de deux pores adjacents est de 6 mm. L'occupation du réseau en TCE pour les deux cas de déplacements est illustrée dans la figure 5. Compte tenu des résultats obtenus, nous constatons que le modèle reproduit qualitativement les cheminements préférentiels observés sur colonne de laboratoire. En effet, la répartition du DNAPL obtenue pour le cas de déplacement ascendant est relativement uniforme. Le DNAPL injecté remplit la majorité des pores à différentes tailles et dans toutes les directions. Cependant, la répartition du DNAPL est ramifiée dans le cas du déplacement descendant. La phase envahissante suit les chemins menant aux pores ayant une grande taille et aux canaux ayant une pression capillaire seuil minimale.

3 Conclusions et perspectives

Le dispositif expérimental tel qu'il a été conçu a permis de fournir des informations quantitatives et précises sur les instabilités de déplacement de drainage eau/DNAPL. Les phénomènes observées ont été reproduits qualitativement au moyen du modèle discret développé. La prochaine étape consistera à paramétrer le modèle réseau pour le milieu poreux utilisé dans l'expérimentation afin de pouvoir simuler les expériences et comparer les résultats numériques et expérimentaux. Nous envisageons aussi de réaliser une étude similaire du processus de l'imbibition couplée au drainage et quantifier les saturations résiduelles en DNAPL dans les différents cas de déplacement (stable et instable).

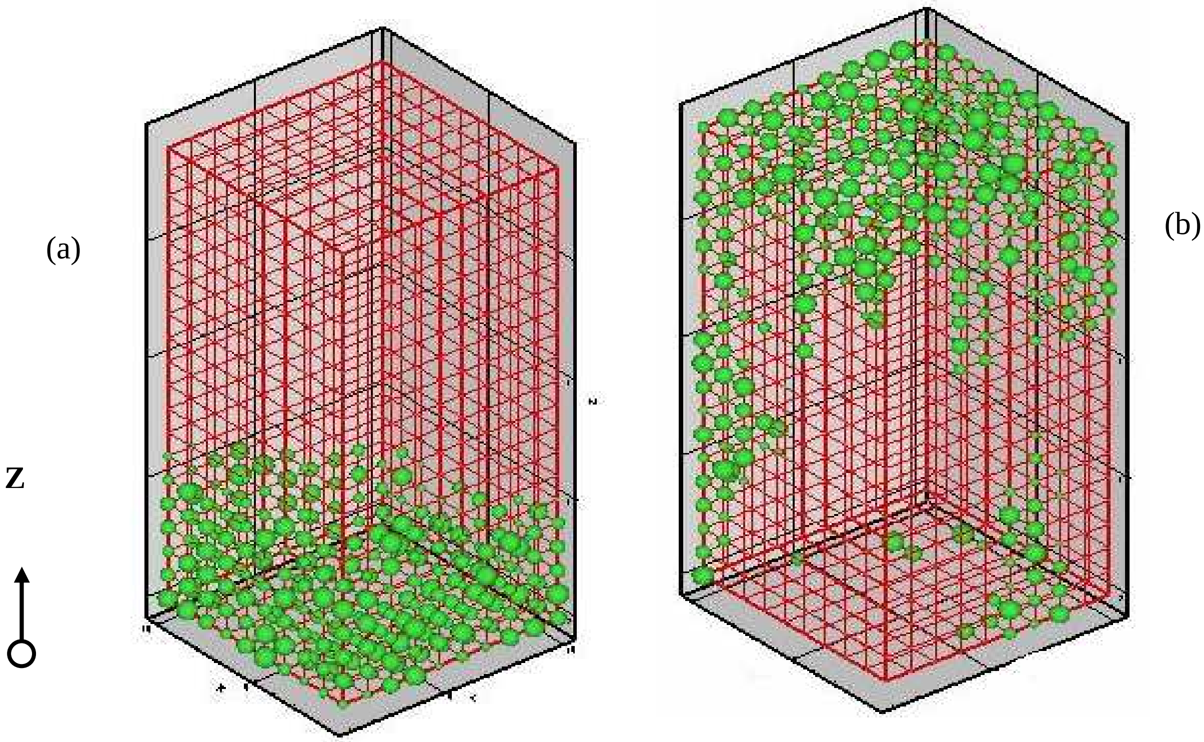

FIG. 5 – Occupation du réseau en TCE (sphères en vert) pour la même séquence de déplacement (envahissement de 700 pores du réseau) pour les cas de déplacement ascendant (a) et descendant (b)

Remerciements

Ces travaux ont reçu le soutien financier du REseau Alsace de Laboratoires en Ingénierie et Sciences pour l'Environnement (REALISE), du GDR «Hydrodynamique et Transferts dans les Hydrosystèmes Souterrains » et du Conseil Scientifique de l'Université Louis Pasteur de Strasbourg. Nous tenons à adresser nos sincères remerciements à M. Olivier Gregut, Ingénieur de Recherche CNRS à l'IPCMS et M. Joseph Rapp, Assistant Ingénieur CNRS à l'IMFS pour leur participation active à la mise au point des capteurs à fibre optique.

Références

[1] Ahmadi A., Aigueperse A. and Quintard M., Upscaling of nowetting phase residual transport in porous edia: A network approch, Transport in Porous Media, 43, 309-353, 2001.
[2] Dullien F.A.L., Porous media, fluid transport and pore structure, Academic, San Diego, California, 1992
[3] Grunde L., Yves M., Knut J.M., Eyvind A. and Schmittbuhl J., Competition of gravity, capillary and viscous forces during drainage in a two-dimensional porous medium, a porous scale study, Energy, 30, 861-872, 2005.
[4] Helen E.D., and Paul V.R., Influence of viscous, gravitational, and capillary Forces on DNAPL saturation, Ground Water, 35, 261-269, 1997.
[5] Koplik J. and Lasseter T.J., Two phase flow in random network models of porous media, SPE, 89-100, 1985.
[6] Kueper B.H. and Frind E.O., An overview of immiscible fingering in porous media, Journal of contaminant Hydrology, 2, 95-110, 1989.
[7] Lenormand R., Zarcone C. and Sarr A., Mechanisms of displacement of one fluid by another fluid in a network of capillary ducts, Journal Fluids Mechanisms, 135, 337-353, 1983.
[8] Nordhaug H.F., Celia M.and Dahle H.K., A pore network model for calculation of interfacial velocities, Advances in Water Resources, 26, 1061-1074, 2003.
[9] Singh M. and Mohenty K., Dynamic network for drainage through three dimensional porous materials, Chemical Engineering Science 58, 1-18, 2003.

HYDROLOGICAL PROCESSES
Hydrol. Process. **26**, 2085–2094 (2012)
Published online 23 February 2011 in Wiley Online Library
(wileyonlinelibrary.com) DOI: 10.1002/hyp.7984

Characterization of major discontinuities from borehole cores of the black consolidated marl formation of Draix (French Alps)

A. Neuville,[1]* R. Toussaint,[1] J. Schmittbuhl,[1] D. Koehn[2] and J.-O. Schwarz[2,3]

[1] *IPGS; Université de Strasbourg/EOST, CNRS; 5 rue Descartes, 67000 Strasbourg, France*
[2] *Johannes Gutenberg Universität Mainz, Institut für Geowissenschaften, Becherweg 21, 55099 Mainz, Germany*
[3] *Earth System Research Center, Mainz, Germany*

Abstract:

A quantitative description of rock discontinuities present in subsurface cores that were drilled (down to 20 m) in the marls of the Laval and Moulin catchments near Draix (France) is presented. Three kinds of discontinuities are studied: those fully open, those open but filled with clay rich material and those sealed with calcite. With a laser profiler, the topography of facing sides of typical discontinuities was measured with a normal resolution of 1 µm. The probability distribution of the elevation of each surface are obtained and shown to be normal. Possible self-affine scaling invariance of the topography were explored. The mineralogical content of an interface between the marl bulk and the embedded calcite vein is also investigated using X-ray computed tomography. Implication of this study for water transport in such discontinuities is addressed in a companion paper in the same issue. Copyright © 2011 John Wiley & Sons, Ltd.

KEY WORDS fracture; Draix; self-affinity; optical profiler; X-ray computed tomography

Received 19 July 2009; Accepted 13 December 2010

INTRODUCTION

In catchments like the Laval and Moulin ones, located near Draix, in the South French Alps mass movements frequently occur in the black consolidated marl formation ("Terres Noires") (Fressard *et al*., 2009). The landslides are often due to water driven processes. Indeed, water causes a chemo-mechanical weathering of the rock, which modifies the geometry of the subsoil and the mechanical stability of the rocks and slopes. For a given solid stress along an interface prone to sliding, the decrease of effective pressure leads to an increase of the ratio of tangential stress over effective pressure, bringing this ratio closer to a Coulomb sliding threshold, which increases the slope failure potential (Terzaghi, 1936; Iverson and Reid, 1992). High pore pressure may also trigger hydraulic fracturing which can increase the size of the fractures and enhance downslope movements of blocks along the fractures. If water does not seep into the bedrock, it may trigger debris flows (Yamakoshi *et al*., 2009) and important surface runoffs which carry a significant amount of material (Antoine *et al*., 1995; Mathys, 2006).

In order to understand the Draix landslides, five boreholes were drilled at the top of a stable interfluve, between the Laval and Moulin catchments (Figure 1). Among them is the borehole SC1 which was completely cored showing numerous major discontinuities. Hydraulic studies in the surrounding area (Cosandey *et al*., 2007) and studies where tracer tests between these boreholes are performed (Garel *et al*., 2009; Lofi *et al*., 2011) show that the fractured marl has a significant role in the hydraulic balance. At field scale, mass losses of water complicates the permeability estimation of the fractured bedrock. At core scale, hydraulic tests are also difficult to perform as the permeability is due to large discontinuities intercepting the core while the rock matrix (marl) has a negligible permeability.

The permeability of each main discontinuity of the Draix fractured bedrock is probably highly influenced by their precise geometry as the hydraulic behaviour of rough open fractures is significantly affected by the fracture roughness (Brown, 1987; Barton *et al*., 1997; Glover *et al*., 1997; Méheust and Schmittbuhl, 2000; Plouraboué *et al*., 2000; Drazer and Koplik, 2002; Méheust and Schmittbuhl, 2003; Auradou *et al*., 2005). This was also shown by studies about fracture morphology that were carried out in parallel with experiments aiming at measuring their hydraulic behaviour (Hakami and Larsson, 1996; Vicente *et al*., 2002).

This article focuses on how to measure and characterize the topography of the surfaces of typical discontinuities sampled during coring. The knowledge of the fracture side topography is a first step towards a description of the hydraulic behaviour of the Draix formation, which is done in a companion paper in the same issue (Neuville *et al*., 2011), hereafter referred as Paper 2.

* Correspondence to: A. Neuville, EOST, Université de Strasbourg, France. E-mail: amelie.neuville@unistra.fr

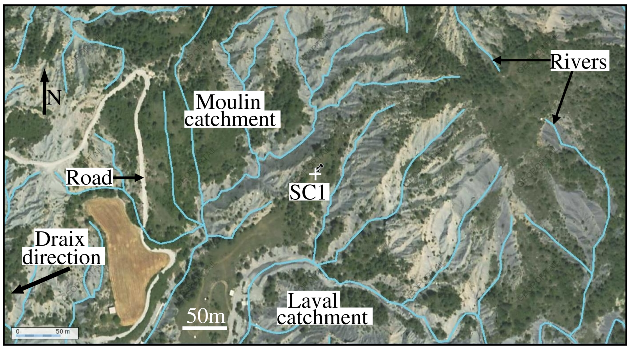

Figure 1. Aerial photography and river locations, modified after www.geoportail.fr (Geoportail, 2007–2009), showing the surroundings of the well SC1 (indicated by the label SC1, located at longitude 06°21′43″E and latitude 44°08′30″N in the WGS84 standard). The surrounding catchments are the Laval and Moulin ones. The nearest town is Draix, located at 1·6 km south-east from the well SC1

This article is organized as follows: in Section "Core Log Description and Localization of the Studied Discontinuities", a description of the drilling procedure is given, as well as the definition of morphological units of the core. The location of the four studied discontinuities is also presented. These discontinuities are described in a qualitative way in Section "Qualitative Description of the Discontinuities". Section "Measurement of the Morphology of the Discontinuity Sides" shows the topography measurements that have been performed on the facing surfaces of each discontinuities using a laser profiler. An X-ray computer tomography (CT) has also been used to image the mineralogical content of an interface between marl and an embedded calcite vein. In Section "Statistical Characterization of the Roughness of the Discontinuity Surfaces", a statistical study of the topography fluctuations is presented.

CORE LOG DESCRIPTION AND LOCALIZATION OF THE STUDIED DISCONTINUITIES

The studied discontinuities come from a coring of 10 cm in diameter, extracted from the SC1 borehole (20 m deep) and located between the Laval and Moulin catchments near Draix, French Alps (Figure 1). One should keep in mind that the sample collected from the well might not be fully representative of the whole bedrock as it is only a local sampling. Due to the heterogeneity of the subsoil and stress field, local open discontinuities exist, the stress being then transmitted through the contact zones of the discontinuities. Studying the discontinuities requires the cores to be recovered as intact as possible, which was possible owing to special care during SC1 drilling. More specifically, a triple tube core barrel was used, which consists in two embedded external metallic tubes and an internal transparent plastic tube. In this system, only the external metallic tube rotates while both inner tubes are fixed, so that there is little rotation or vibration of the core (Wyllie, 1999). The core was directly stored in the inner plastic tube, so that most of the infill and fractured parts was recovered (excepted maybe at the end and beginning of each core). Plastic tubes were then quickly sealed so that the moisture content was kept, preventing the dessication of the marl during the storage time. Moreover, the second metallic tube also prevents the core from being damaged by the drilling fluid (here: water). As the cores were studied at ambient air and because of core handling, crumbled marl or clayey infill might have been damaged. The study of the surface was therefore performed only on parts of the core fairly resistant to dessication and manipulations. Despite all these precautions, coring might, however, slightly modify the open discontinuities. In any case, the coring does not modify sealed discontinuities that will also be of interest to characterize for the morpholog y characterization.

From cores and well logs (Lofi *et al.*, 2011), the local stratigraphy is divided into three major units (Figure 2a) (Bondabou, 2007; Mery, 2008). Below 6·3 m, the core consists of a consolidated matrix intercepted by large discontinuities and altered zones. The matrix is a compact black marl which was described as resistant, structured and cohesive by Maquaire *et al.*, 2002. The consolidated part of the core is divided into two units: the lowest is unit 1 (Figure 2a) which shows numerous sealed veins, filled with recrystallized calcite, probably issued from water flow from surrounding zones richer in carbonates (Cras, 2005; Bondabou, 2007). Lying above unit 1 is unit 2 which is intercepted by open fractures and discontinuities filled with clayey materials. Above 6·3 m the cores are less consolidated. Just above the consolidated marls lays a transition zone, unit 3b, with highly altered marl. The top part of the core is unit 3 which consists of unconsolidated layers with soft clay and limon.

In unit 2, two discontinuities (F9 and F6) respectively located at depths 9·3 and 6·6 m are studied (Figure 2). The Discontinuity F9 is open while F6 is filled with debris and clay. In unit 3, a sample (C14) consisting mainly of calcite, located in an altered zone, at 14·6 m depth is also studied, as well as a sample (C12) consisting of two very thin calcite veins embedded into the marl of less than 1 mm thick, located around 12 m depth. Samples C10 and C17 are other examples of calcite veins.

QUALITATIVE DESCRIPTION OF THE DISCONTINUITIES

Description of the open discontinuity

F9 is an open discontinuity which is studied. It is located inside a compact dark gray marl which follows approximately the schistosity with an apparent dip of 42° with respect to the plane perpendicular to the core direction, i.e. roughly the horizontal plane (angle measured on the sample with an inclinometer, with a precision of ±0·5°). The discontinuity F9 looks scarcely altered (Figure 2) with many complementary reliefs appearing on both surfaces once one of the surfaces is translated. Facing oxided zones on both sides (Figure 3a) are signs of water circulation. The presence of these oxides shows

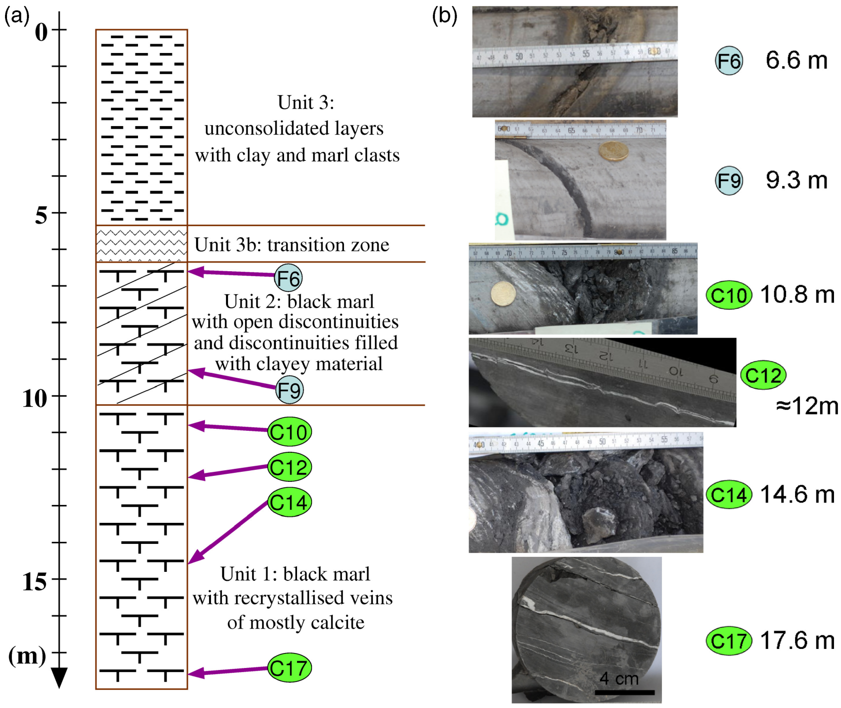

Figure 2. (a) Stratigraphic log after the indications of J. Ortega and J.-P. Malet. (b) Picture of typical discontinuities with depth. Scale on the pictures is given by the ruler in centimeter

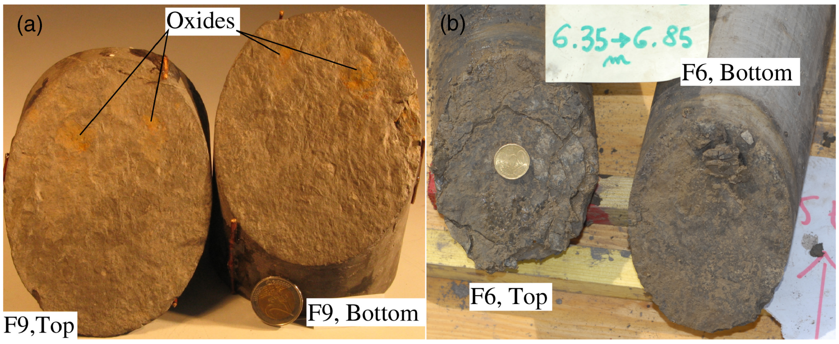

Figure 3. (a) Facing surfaces of the discontinuity F9. Oxidized zones can be observed on both faces. (b) Facing surfaces of the discontinuity F6, covered with a layer of clay. This layer was removed before studying the topography of the surfaces

that this discontinuity existed before the borehole was drilled.

Description of the discontinuity filled with debris and clay

The second discontinuity studied in unit 2 is the discontinuity F6, which is also located in a compact dark gray marl, following approximately the schistosity. Contrary to F9, F6 shows clear signs of degradation (Figure 3b). F6 is surrounded with a layer of marl which is oxidized (darker region on Figure 2b). This discontinuity was filled with clay and marl fragments which are presumably coming from a local water circulation (Cras, 2005; Bondabou, 2007). When observing the discontinuity F6 just after it was taken out of the plastic tube, it was seen that both sides were covered with a 2 mm-thick clay layer (Figure 3b). The morphology and composition of such a layer is definitively very sensitive to any *in situ* water content or flow change. As our study stands at ambient air, this layer would have been modified by dessication. Consequently, we chose to study the topography of the competent rock surface, which appeared once the clay layer had been washed out.

Description of sealed discontinuities

Several veins filled with calcite intersect the cores, in particular in unit 1 (Figure 2). The thickness of the calcite joints ranges from less than 0·1 mm to about 15 mm. A simple case would be that the discontinuity consists in a single fracture filled with calcite. In that case, assuming the morphology to remain constant during the calcite crystallization, the calcite vein would be a direct cast of the fracture aperture. However, observing the content of these sealed zones excludes this hypothesis: indeed they seem to be formed during a series of crystallization episodes. Complex zones that consist of several anastomosed parallel calcite veins are frequent in unit 1 (e.g. zones C10, C12 and C14 in Figure 2b); individual calcite veins are therefore hardly visible. Parallel fractures, either open or sealed, located in C17 sample (Figure 2b), suggest that the calcite vein concentrates stresses in the vicinity of the vein in the embedding rock, provoking new fractures along the interface, which will be filled at a later time. Therefore, these sealed zones, which seem to have formed during several opening/crystallization episodes, are too complex to be seen as casts of single pre-existing fractures. However, independently from the formation scenario, each complex zone could become a single open transport zone, if the calcite is later dissolved.

In particular, two zones, C14 and C12 (Figures 2 and 4), which are located in unit 1, are studied. The calcite discontinuity, C14, is studied by laser profilometry on both sides. As C14 is a core fragment detached from the consolidated part of the core, the orientation of the joint in the core is not known. Therefore the sides are arbitrarily assigned as bottom and top. In addition, to understand the connection between the calcite content and the *in situ* interface between the sealed discontinuity and the surrounding marl, an X-ray CT was performed on a similar calcite vein, C12.

Figure 4. Profile picture of the calcite vein, C14, located at 14 m depth near the complex zone shown in Figure 2b. The picture shows the typical thickness of the calcite vein and the complexity of the sample because of multi-layer structure

MEASUREMENT OF THE MORPHOLOGY OF THE DISCONTINUITY SIDES

Laser profiler measurement of the surfaces

The topography of surface pairs of the discontinuities F6, F9 and C14 was obtained (Figures 5, 6, 7) using a laser profiler (Méheust, 2002; Schmittbuhl *et al*., 2008). The instrument sends a vertical laser beam (diameter 30 µm) towards the surface. If the surface is diffusive enough, the two charge-coupled devices (CCD) located on each side of the laser head are able to register the position of the diffusion spot on the surface. A calibration procedure, which is carried out before each measurement, provides a measure of the distance between the laser head and the reflecting surface with a precision of 1 µm. The measurement is carried on-the-flight, while the laser head moves along a regular planar array above the scanned surface. The grid mesh size of the measured topography of F9 and F6 sides is 40 ± 2 µm $\times$ $40 \pm 0{\cdot}1$ µm in the horizontal plane and the vertical precision of the measured topography is about 1 µm. However, in this study, the horizontal plane resolution is reduced for F6 by a cubic interpolation to a mesh of 200 µm $\times$ 200 µm. The morphology of the surfaces of the calcite vein C14 was also measured with the profiler with an in-plane resolution of 150 µm $\times$ 150 µm.

When doing the topography measurement of the F9 and F6 surfaces, each surface was fixed approximately horizontally. After the surface measurement was finished, a mean plane was fitted by a least mean square method on a relevant subset (i.e. without taking into account notches or outliers) of the measured surface. A rotation of the axes is then performed to get the so called $x - y$ plane aligned with the mean plane of the surface. A translation along the z-axis is also applied relevant so that the average of the height values is equal to $\langle h \rangle = 0$. In Figures 5, 6

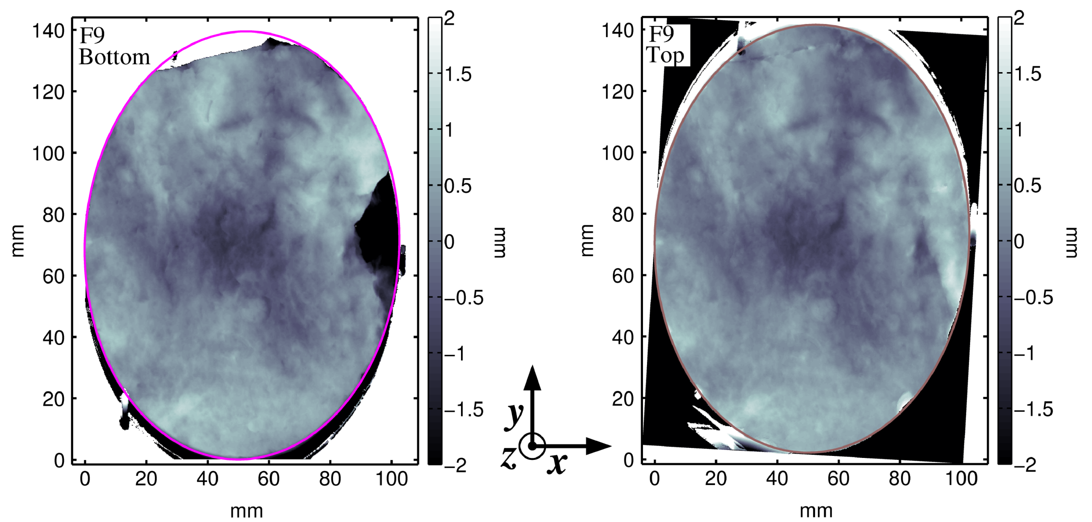

Figure 5. Topography of both facing internal F9 surfaces, measured by the laboratory profiler and shown once the axes are rotated and shifted so that the mean plane (obtained by a least mean square method) of the surface corresponds to the $x - y$ plane. The top surface (on the right) is presented after rotation of 180° around the y-axis, in order to stress the similarity between top and bottom surfaces. A rotation of 3·3° around the z-axis was also performed in order to maximize the correspondence between similar patterns of the top and bottom surfaces. On both figures the complementary asperities are therefore located at the same coordinates, and because of the rotation around the y-axis, they are shown with the same level of grey. Elliptic fits of the core boundary are also plotted for both surfaces (same ellipse size for both cores)

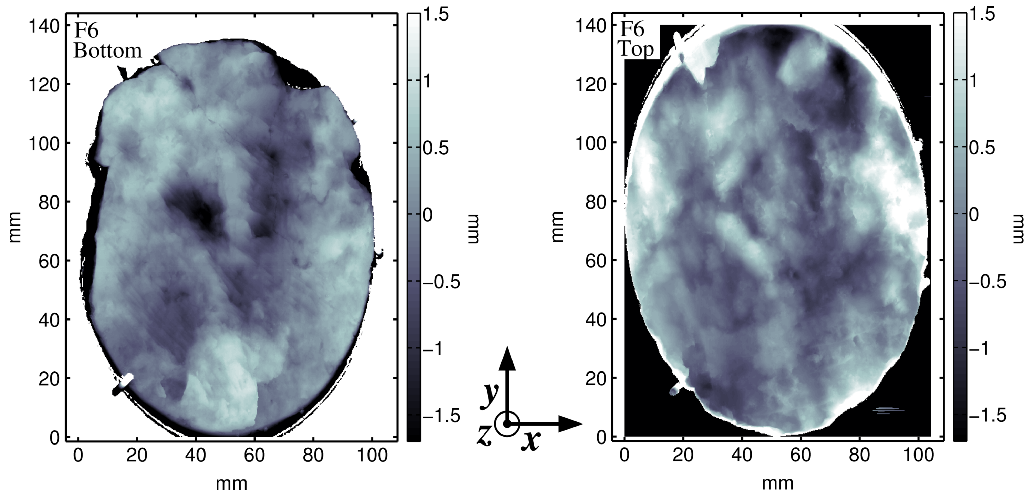

Figure 6. Topography (measured by the laser profiler) of both facing F6 surfaces, presented after treatments similar to those applied to F9 in Figure 5. Here no clear correlation between the two sides is visible, therefore no rotation around the z-axis has been performed

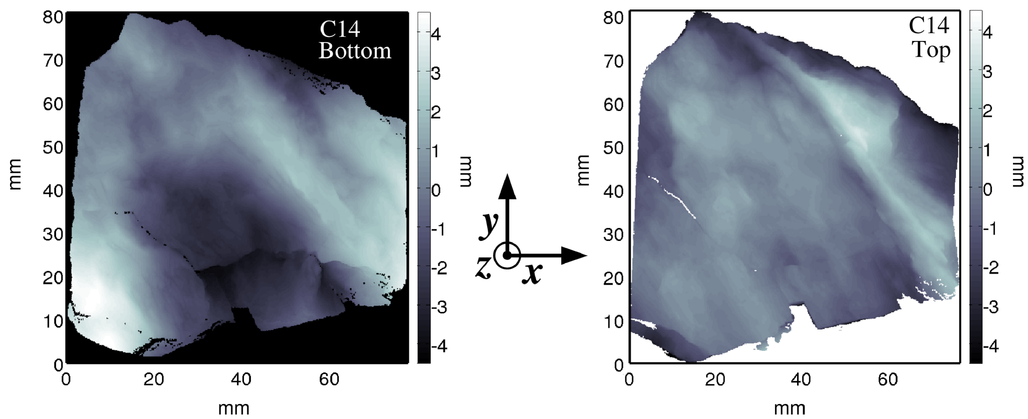

Figure 7. Topography of the external sides of the calcite vein C14, measured by the laser profiler, shown after each trend of the surfaces was removed. The top surface is presented after rotation of 180° around the y-axis, in order to see the similarities between top and bottom surfaces

and 7, the x and y axes define the mean plane of the surface, the z-axis being perpendicular.

For the open discontinuities, like F6 or F9, the top and bottom surfaces which are studied are located on two different parts of core, whose relative position is *a priori* lost. On the contrary, for the sealed discontinuity C14, the topography of each side of a single rock piece has to be measured. Therefore, if, when doing the topography measurements, there exists a rigid reference frame common for both sides, one can infer their relative position (Paper 2). To this aim, sample C14 was docked within a rigid box.

Detailed study of the interface between calcite sealed discontinuities and the marl bulk using X-ray CT

Observing sample C14, (Figure 4), it was noticed that the interface between calcite and marl was not a clear boundary but rather a zone of alternating calcite and black marl layers, each being thinner than 0·5 mm. To check the volumetric structure of the transition from the vein to the surrounding embedding marl, the sample C12, which contains two very thin calcite layer ($\leq$1 mm), was investigated by X-ray CT.

Figure 8a shows an example of a bidimensional (2D) slide extracted from the tridimensional (3D) measurement (axes $x - y - z$ provided by the CT device). The X-rays transmitted by the material are sensitive to the local density (e.g. see references related to tomography principle in Zhang *et al.*, 2004): the dark parts of Figure 8a correspond to low density areas. The calcite, whose density is $2{\cdot}7 \times 10^3$ kg/m^3, looks brighter than the dry marl, which has a density of about $2{\cdot}3 \times 10^3$ kg/m^3 (Carmichael, 1990). For this measurement, the calcite layers were approximately oriented along the y-z plane. The resolution is given by isotropic grid meshes of 90·2 μm × 90·2 μm × 90·2 μm.

A density evolution was observed in the direction approximatively perpendicular to the calcite vein, i.e. along x-profiles (Figure 8b). As the calcite infill is not a perfect plane, the beginning of each x-profiles was adjusted so that $x = 0$ when the density is below 3% of the calcite density. Figure 8b shows the variability of such density profiles. Density profiles were then averaged, over a set of 18 × 70 profiles, respectively for the z and y axes, separated by steps of 4·5 mm along z and 90·2 μm along y (Figure 9). The calcite density in dimensionless units is about 1 while the marl density is

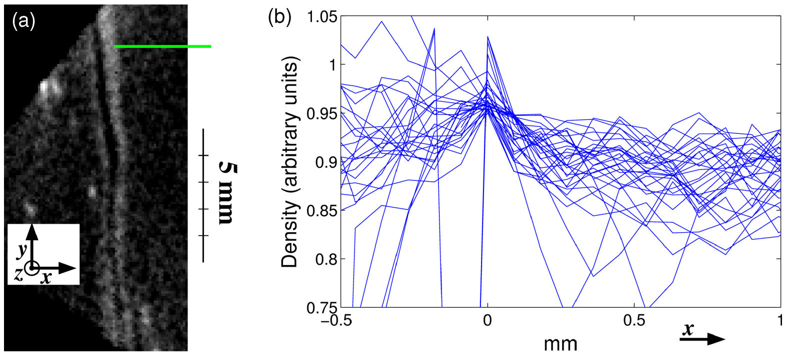

Figure 8. (a) Slide obtained from 3D X-ray computed tomography of the calcite veins contained in C12 (Figure 2b). The calcite veins are approximately parallel to the y-z plane. The thickness of these veins is less than 1 mm. The line shows an example of an x-profile along which the density was studied. (b) 70 density profiles oriented along the x-axis, perpendicularly to the approximate mean plane of the calcite vein embedded in C12, showing the variability of the density. For all these profiles, the x-axis is shifted so that $x = 0$ corresponds to a density below 3% of the density of the calcite. The density is normalized by the calcite density

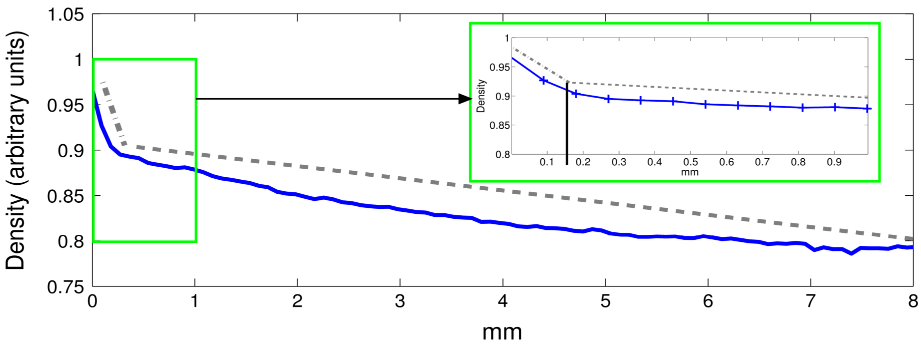

Figure 9. The density profile shown is the average of 1260 profiles similar to the ones shown in Figure 8b, taken across the whole surface of the calcite vein, distributed over a surface about 6 mm × 70 mm. Two density gradients, underlined by the dotted lines, are observed at the transit from the calcite density to the marl density: a sharp transition, extending over 0·15 mm (see blow up) and a smoother one, extending over several millimeters

about 0·8. Figure 9 shows that the transition from a zone rich in calcite to a zone poor in calcite occurs in two steps: a very sharp evolution over roughly 0·15 mm (less than two grid meshes), and a smoother evolution over several mm. The zone rich in calcite probably results from precipitation of water rich in carbonates into an open discontinuity. The other zone would corresponds to a zone with mostly marl and little calcite, which could come from precipitation of water rich in carbonates after the water has diffused into the porosity of the marl bulk.

With a higher resolution, it would be interesting to use these profiles, select a given threshold and determine the topography of the interface at this threshold (see for instance Noiriel, 2005). As we observed that this vein could not be easily separated from the surrounding marl — certainly due to the calcite content in the marl and the absence of a sharp transition in calcite content — it was then not possible to perform a compared study of such surface determined by density thresholding, and the same one measured by laser profilometry.

STATISTICAL CHARACTERIZATION OF THE ROUGHNESS OF THE DISCONTINUITY SURFACES

A statistical study along the topography variations of the discontinuity sides is presented here. The goal is to obtain a geometrical model of the asperities in terms of magnitude, density and spatial correlations that could possibly be extended at larger scales.

Statistical characterization of F9 discontinuity sides

As seen on the probability distribution function shown in Figure 10a, computed for F9, the elevation of both discontinuity sides follows a normal distribution having a standard deviation of $0{\cdot}4 \pm 0{\cdot}05$ mm. The maximum difference of elevation for the bottom and top sides is about 2·7 mm.

In order to compare potential anisotropy directions in the scaling laws of the top and bottom F9 surfaces, the surfaces are oriented relatively to one another (see details in paper 2). The autocorrelation function of the morphology elevation is computed for each side of F9 (see Marache *et al.*, 2002 or Méheust and Schmittbuhl, 2000, 2003 for comparable study on natural fractures). Estimates are done without taking into account major flaws along the external boundary of the core that are due to damage during coring. The autocorrelation C_2 is computed in the real domain and defined by the square root of the second moment of the elevation difference:

$$C_2(\vec{\Delta}) = \sqrt{\langle [z(\overrightarrow{OM} + \vec{\Delta}) - z(\overrightarrow{OM})]^2 \rangle} \qquad (1)$$

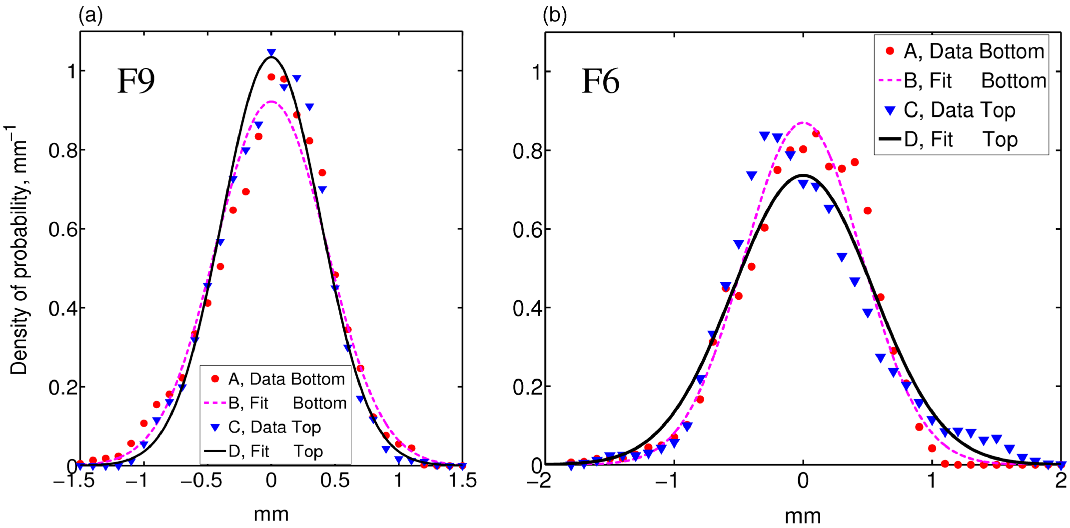

Figure 10. Probability density of the elevation of the bottom (A) and top (C) sides and their normal probability fits (B, D), for (a) F9 and (b) F6. For plots A, B, C, D, mean value is 0 mm and RMS is (a) $0{\cdot}4 \pm 0{\cdot}05$ mm and (b) $0{\cdot}5 \pm 0{\cdot}05$ mm

where z is the local elevation with respect to the mean plane, $\vec{\Delta}(\Delta_x, \Delta_y)$ the lag vector (i.e. characteristic distance at which the correlation is computed), and $\langle\rangle$ indicates that the average is computed over all the possible spatial points M so that $z(\overrightarrow{OM})$ and $z(\overrightarrow{OM} + \vec{\Delta})$ are defined. Self-affine properties of surfaces were tested by checking if (Barabàsi and Stanley, 1995):

$$C_2(\Delta) = C_2(\Delta_0)\left(\frac{\Delta}{\Delta_0}\right)^{\zeta} \tag{2}$$

is fulfilled, where ζ is the Hurst exponent, Δ_0 is 1 mm and Δ is the norm of $\vec{\Delta}$.

Figure 11 shows the 1D plot of $\log_{10}[C_2(\Delta)/\Delta_0]$ as a function of $\log_{10}[\Delta/\Delta_0]$ for two directions (hereafter demonstrated as being the directions showing the largest anisotropy): $\theta = 10°$, $\theta = -80°$, where θ is the angle between the x-axis and $\vec{\Delta}$. A linear trend has been fitted for lags ranging from 0·04 mm to 7 mm, for these directions. As Equation (2) translates into:

$$\log_{10}\left[\frac{C_2(\Delta)}{\Delta_0}\right] = \zeta \log_{10}\left[\frac{\Delta}{\Delta_0}\right] + \log_{10}\left[\frac{C_2(\Delta_0)}{\Delta_0}\right] \tag{3}$$

the linearity of such a plot indicates that the surface is self-affine in the θ direction, and ζ and $C_2(\Delta_0)$ can be deduced. In order to show the variability of ζ and $C_2(\Delta_0)$ as a function of θ, a polar plot of both parameters is also shown (Figure 12), where $C_2(\Delta_0)$ is obtained from interpolation of C_2 at 1 mm. The Hurst exponent computed so, slightly varies (amplitude of $\pm 0{\cdot}02$) around 0·69 (bottom side) or 0·74 (top side) according to the direction. The value $C_2(\Delta_0)$ also regularly varies (amplitude of $\pm 0{\cdot}02$ mm) around 0·09 mm (top side) and 0·11 mm (bottom side), with extrema for θ equals to 10° and −80°.

The linearity of $\log_{10}[C_2(\Delta)/\Delta_0]$ potentially does not fit over all the ranges of Δ. In order to be able to observe possible multiple trends over various ranges of Δ, a representation of $\log_{10}[C_2(\Delta)/\Delta_0]$ as a function of the polar coordinates $(\log_{10}(\Delta/l_p), \theta)$ (Ebner *et al.*, 2010) is also shown (Figure 13), where l_p is 0·04 mm, i.e. the smallest pixel size used for topography measurement. If the surface is isotropic and self-affine over all the observed ranges, then the isovalue lines are a family of circles regularly distributed. An anisotropic self-affine surface would translate in a family of equally distributed and noncircular isovalue lines. Figure 13a, computed for the topography of the bottom side of F9, shows that the variations of the Hurst exponent and $C_2(\Delta_0)$ are of secondary order. A very similar figure was also obtained for the top side of F9. For both surfaces, the fit of the scaling laws can finally approximatively be done by $\log_{10}[C_2(\Delta)/\Delta_0] = 0{\cdot}75\log_{10}[\Delta/\Delta_0] - 1{\cdot}07$, i.e. $\zeta = 0{\cdot}75$ and $C_2(\Delta_0) = 0{\cdot}09$ mm, from $\Delta = 0{\cdot}04$ mm to 7 mm.

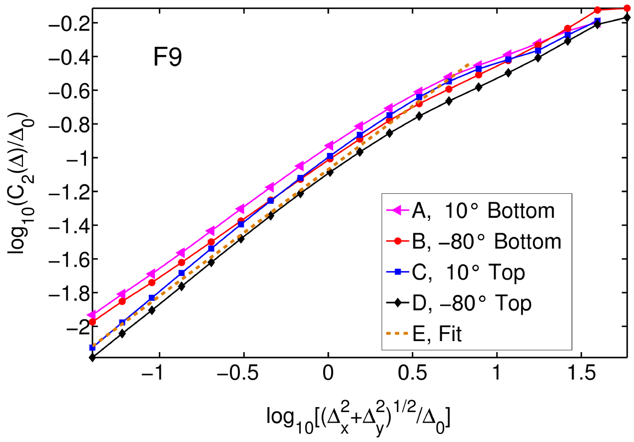

Figure 11. Plot of $\log_{10}[C_2(\Delta)/\Delta_0]$ as a function of $\log_{10}[\Delta/\Delta_0]$, computed for discontinuity F9, in directions θ equal to 10° and 80°, for the bottom side (A, B) and top side (C, D), respectively. Plot E is a linear fit $\log_{10}[C_2(\Delta)/\Delta_0] = 0{\cdot}75\log_{10}[\Delta/\Delta_0] - 1{\cdot}07$, i.e. $\zeta = 0{\cdot}75$ and $C_2(\Delta_0) = 0{\cdot}09$ mm, plotted from $\Delta = 40$ μm to $\Delta = 7$ mm. Δ and C_2 are in millimeters, and $\Delta_0 = 1$ mm

Estimating the Hurst exponent with the C_2 method requires a linear fit of Equation (3). As the data contains inherent noise, the Hurst exponent determined therefore

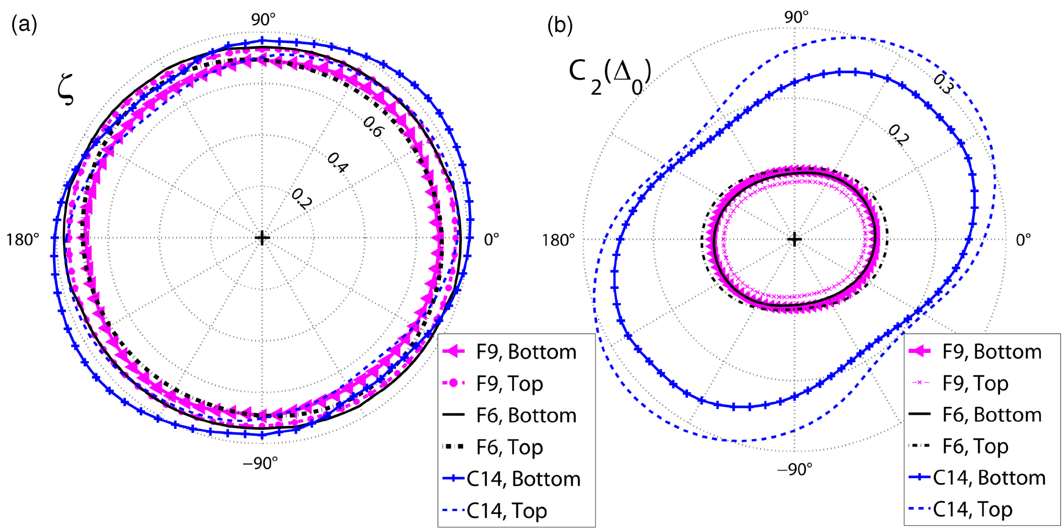

Figure 12. Polar plot of the Hurst exponent ζ (a) and $C_2(\Delta_0)$ in millimeter (b), as functions of θ for the topography of the top and bottom sides, according to the angle, for the F9, F6 and C14 discontinuities as indicated by the labels. Note that the F6, F9 and C14 discontinuities are not oriented relatively to one another, on the contrary to each side relatively of a given pair

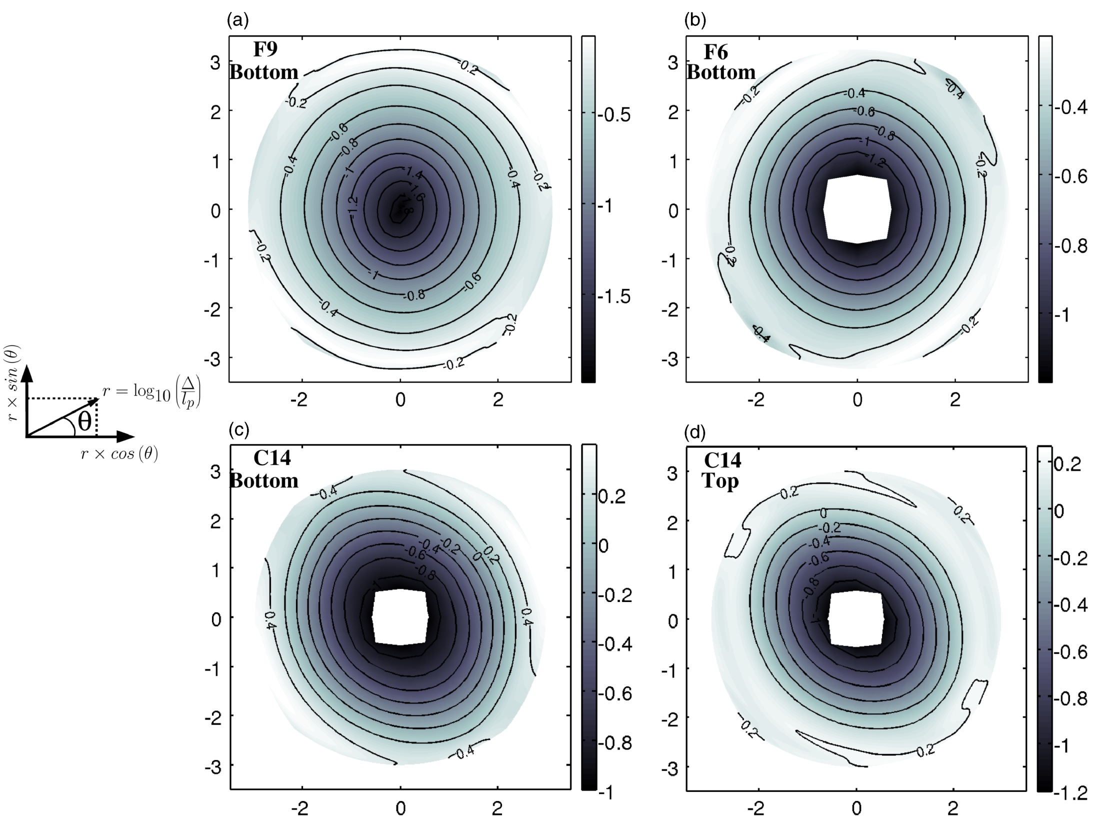

Figure 13. Representation of $\log_{10}[C_2(\Delta)/\Delta_0]$ as a function of the polar coordinates $(\log_{10}(\Delta/l_p), \theta)$, where l_p is the pixel size used for topography measurement (0·04 mm), computed for the topography of the bottom side of F9 (a), F6 (b), C14 (c) and top side of C14 (d). Δ, C_2 are in millimeters, and $\Delta_0 = 1$ mm. At first order, the isovalue lines are families of circles approximatively regularly distributed, showing that the surfaces are nearly isotropic and self-affine over all the observed ranges. At second order, C14 is slightly more anisotropic (especially the top one). Note that the range of isovalues is different between the surfaces, with higher C_2 values for the C14 sides

depends on the fitting method and, above all, on the chosen range of Δ used to perform the fit. The C_2 method might underestimate the Hurst exponent (Schmittbuhl *et al.*, 1995b; Renard *et al.*, 2006), but has the advantage of being easily applied in 2D on the whole natural surfaces. The study is in any case limited by the sample size and the sampling resolution.

Statistical characterization of F6 discontinuity sides

The probability distribution function of the elevation was computed for both sides of F6 (Figure 10b). Both probability distribution functions can be fitted with a normal probability density function having a standard deviation of $0{\cdot}5 \pm 0{\cdot}05$ mm. This result shows that the elevation is slightly more variable than that of F9 sides which are less altered. The function $\log_{10}[C_2(\Delta)/\Delta_0]$ as a function of $\log_{10}[\Delta/\Delta_0]$ (Figure 14) was also plotted for two directions corresponding to the directions θ showing the largest anisotropy for each side. In fact, as for F9, the anisotropy of the bottom side of F6 is barely pronounced (Figure 13b). A similar plot for the top side both has been made, showing that correlation of the top side is very similar to the bottom one. Both surfaces are also self-affine, from roughly 0·3 to 10 mm. The Hurst exponent computed for these ranges, regularly varies (amplitude of $\pm$0·02) around 0·70 (bottom side) or 0·76 (top side), according to the angle (Figure 12a). The $C_2(\Delta_0)$ value also regularly varies (by $\pm$0·02 mm) around 0·12 mm (top side) and 0·10 mm (bottom side) (Figure 12b). Note that this scaling law is very close to that of the F9 sides, and as most observed fracture surfaces (Bouchaud, 1997).

Statistical characterization of C14 discontinuity sides

C_2 was computed for the sides of discontinuity C14, and $\log_{10}[C_2(\Delta)/\Delta_0]$ was plotted as a function of $\log_{10}[\Delta/\Delta_0]$ for two directions θ (Figure 14). A linear trend can be observed from 0·3 to 10 mm, which means that a self-affine law can be fitted. As shown by Figure 12, for both C14 surfaces, C_2 is slightly anisotropic, with $C_2(\Delta_0)$ values progressively varying according to the direction around 0·23 (by an amplitude of $\pm$0·04 mm) for the bottom side and around 0·26 (by an amplitude of $\pm$0·06 mm) for the top side, with extremal values around θ equal to $\pm 45°$. The Hurst exponent also shows an anisotropy, as it varies according to the direction (amplitude of $\pm$0·06) around 0·70 (top) and 0·76 (bottom). Note that the side measurements are relatively oriented to one another (Paper 2), so that the directions of anisotropy can be compared between both surfaces. The difference to an isotropic self-affine surface can be fully observed in Figures 13c and d which show $\log_{10}[C_2(\Delta)/\Delta_0]$ as a function of the polar coordinates $(\log_{10}(\Delta/l_p), \theta)$ for both surfaces. It also shows that the anisotropy direction slightly evolves with the range of scales and that the range of C_2 values is larger for the top surface than for the bottom one. By observing the rock sample, it was noticed that this anisotropy might correspond to a crystallization occurring along a preferential direction. It the anisotropy is considered as a second order effect, a rough common self-affine fit can be proposed with $\zeta = 0{\cdot}75$ (similarly to F9 and F6), and $C_2(\Delta_0) = 0{\cdot}25$ mm (more than twice higher than the value for F6 and F9).

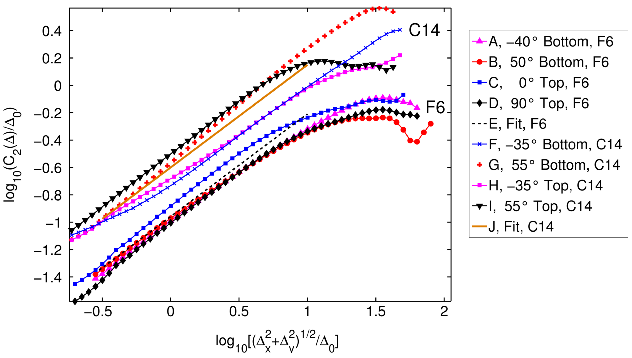

Figure 14. Plot of $\log_{10}[C_2(\Delta)/\Delta_0]$ as a function of $\log_{10}[\Delta/\Delta_0]$, for the top and bottom sides of F6 (A, B, C, D) and C14 (F, G, H, I), for various directions θ, as indicated by the labels. Plot E is the linear fit for F6 sides, $\log_{10}[C_2(\Delta)/\Delta_0] = 0{\cdot}75\log_{10}[\Delta/\Delta_0] - 0{\cdot}96$, i.e. $\zeta = 0{\cdot}75$ and $C_2(\Delta_0) = 0{\cdot}11$ mm. Plot J is the linear fit for C14 sides, $\log_{10}[C_2(\Delta)/\Delta_0] = 0{\cdot}75\log_{10}[\Delta/\Delta_0] - 0{\cdot}6$, i.e. $\zeta = 0{\cdot}75$ and $C_2(\Delta_0) = 0{\cdot}25$ mm. Δ and C_2 are in millimeters, and $\Delta_0 = 1$ mm

CONCLUSION

A careful coring allowed us to study the surface morphology of the typical discontinuities present in the bedrock underlying the potential landslide zones near Draix (French Alps). Three sets of discontinuities have been distinguished: the fully open discontinuities, those filled by altered material and clay, and those sealed with calcite. Measurements with a laser profiler have provided statistical properties of the surface. It was observed that the probability density of the boundary elevation of the open (F9) and clay filled (F6) discontinuities is normal, with similar RMS for top and bottom sides. It was also shown that the surfaces of F6 and F9 are self-affine under a limited range, with little variation of the Hurst exponent and prefactor according to the direction for each pair of surfaces. The surfaces of the sealed discontinuity C14 were also shown to be self-affine, for a range of scale 0·3 mm to 1 cm, with visible variation of the Hurst exponent according to the direction. For each surface, the Hurst exponent range around $0{\cdot}75 \pm 0{\cdot}05$, which is of the same order than the one previously observed for various rocks (Power *et al.*, 1987; Cox and Wang, 1993; Schmittbuhl *et al.*, 1993, 1995a). Such a multi-scaling property allows further modeling of transport properties (Paper 2). The measurement by X-ray CT provided quantitative volumetric information, in particular about the thickness of the calcite–marl interface. The transition from calcite to marl density occurs in two steps: a sharp transition occurring on about 0·15 mm, followed by a smooth transition of several millimeters.

ACKNOWLEDGEMENTS

The authors would like to thank José Ortega for his help for the geological description of the core, as well as Grégory Bièvre for helpful information about the SC1 drilling. We also would like to thank Alain Cochard, Jean-Philippe Malet, Julien Travelletti, Alexandre Remaître and Émilie Garel for fruitful discussions, and Alain Steyer for technical support. We thank the ANR Triggerland, as well as the SISCA and REALISE programs for their financial support.

REFERENCES

Antoine P, Giraud A, Meunier M, van Asch T. 1995. Geological and geotechnical properties of the "Terres Noires" in Southeastern France:

weathering, erosion, solid transport and instability. *Engineering Geology* **40**: 223–234.

Auradou H, Drazer G, Hulin J, Koplik J. 2005. Permeability anisotropy induced by the shear displacement of rough fracture walls. *Water Resources Research* **41**(9): 1–10.

Barabàsi AL, Stanley H. 1995. *Fractal Concepts in Surface Growth*, 2nd edn. Cambridge University Press: Cambridge, UK; 366.

Barton C, Hickman S, Morin R, Zoback M, Finkbeiner T, Sass J, Benoit D. 1997. Fracture permeability and its relationship to in-situ stress in the Dixie Valley, Nevada, geothermal reservoir. In *Twenty-Second Workshop on Geothermal Reservoir Engineering*, vol. SGP-TR-155. Stanford University: Stanford, California.

Bondabou K. 2007. Étude géologique et structurale d'un massif marneux fracturé sur le site expérimental de Draix (Alpes du Sud). Rapport de master, Département de l'Enseignement des Sciences de la Terre et de l'Environnement de Montpellier.

Bouchaud E. 1997. Scaling properties of cracks. *Journal of Physics: Condensed Matter* **9**: 4319–4344.

Brown S. 1987. Fluid flow through rock joints: the effect of surface roughness. *Journal of Geophysical Research* **92**(B2): 1337–1347.

Carmichael R. 1990. *Practical Handbook of Physical Properties of Rocks and Minerals*, 2nd edn. CRC Press Inc.: Boca Raton, FL USA.

Cosandey C, Mathys N, Maquaire O, Esteves M. 2007. Les marnes, roches imperméables? Processus générateurs des crues dans les marnes noires de la région de Digne-les-Bains. In *Actes des JSIRAUF*, Hanoï.

Cox B, Wang J. 1993. Fractal surfaces: measurement and application in earth sciences. *Fractal* **1**(1): 87–115.

Cras A. 2005. Étude de la dynamique de fonctionnement hydrologique des bassins versants torrentiels marneux. Apport du traçage naturel. Thèse de doctorat, Université d'Avignon et des Pays de Vaucluse.

Drazer G, Koplik J. 2002. Transport in rough self-affine fractures. *Physical Review E* **66**: 026303.

Ebner M, Toussaint R, Schmittbuhl J, Koehn D, Bons P. 2010. Anisotropic scaling of tectonic stylolites: a fossilized signature of the stress field? *Journal of Geophysical Research*. DOI:10.1029/2009JB006649. **110**: B06403.

Fressard M, Maquaire O, Malet JP, Klotz S, Grandjean G. 2009. Morpho-structure and triggering conditions of the Laval landslide developed in clay-shales, Draix catchment (South French Alps). In *Landslide Processes. From Geomorphologic Mapping to Dynamic Modelling*, Remaître A, Malet J-P, Bogaard T (eds). CERG, Strasbourg: France; 111–114.

Garel E, Marc V, Emblanch C, Debieche TH, Malet JP, Klotz S. 2009. Flow characterization in fractured black marls by single well pulse injection tests (Alpes-de-Haute-Provence, France). In *Landslide Processes. From Geomorphologic Mapping to Dynamic Modelling.*, Remaître A, Malet J-P, Bogaard T (eds). CERG, Strasbourg: France; 111–114.

Geoportail. 2007–2009. http://www.geoportail.fr. ® 2007–2009, IGN-BRGM. [Accessed: 2009].

Glover P, Matsuki K, Hikima R, Hayashi K. 1997. Fluid flow in fractally rough synthetic fractures. *Geophysical Research Letters* **24**(14): 1803–1806.

Hakami E, Larsson E. 1996. Aperture measurements and flow experiments on a single natural fracture. *International Journal of Rock Mechanics & Mining Sciences* **33**(4): 395–404.

Iverson R, Reid M. 1992. Gravity-driven groundwater flow and slope failure potential 1. Elastic effective-stress model. *Water Resources Research* **28**(3): 925–938.

Lofi J, Pezard P, Loggia D, Garel E, Gautier S, Merry C, Bondabou K. 2009. Geological discontinuities, main flow path and chemical alteration in a marly hill prone to slope instability: assessment from petrophysical measurements and borehole image analysis. *Hydrological Processes* in press, DOI: 10.1002/hyp.7997.

Maquaire O, Ritzenthaler A, Fabre D, Ambroise B, Thiery Y, Truchet E, Malet JP, Monnet J. 2002. Caractérisation des profils de formations superficielles par pénétrométrie dynamique à énergie variable: application aux marnes noires de Draix (Alpes-de-Haute-Provence, France). Characterisation of alteration profiles using dynamic penetrometry with variable energy. Application to weathered black marls, Draix (Alpes-de-Haute-Provence, France). *Comptes Rendus Geosciences* **334**(11): 835–841. DOI:10.1016/S1631-0713(02)01788-1.

Marache A, Riss J, Gentier S, Chilès JP. 2002. Characterization and reconstruction of a rock fracture surface by geostatistics. *International Journal for Numerical and Analytical Methods in Geomechanics* **26**(9): 873–896.

Mathys N. 2006. Analyse et modélisation à différentes échelles des mécanismes d'érosion et de transport de matériaux solides. Cas des petits bassins versants de montagne sur marne (Draix, Alpes-de-Hautes-Provence). Thèse de doctorat, INP Grenoble.

Méheust Y. 2002. Écoulement dans les fractures ouvertes. Thèse de doctorat, Université Paris Sud.

Méheust Y, Schmittbuhl J. 2000. Flow enhancement of a rough fracture. *Geophysical Research Letters* **27**: 2989–2992.

Méheust Y, Schmittbuhl J. 2003. Scale effects related to flow in rough fractures. *Pure and Applied Geophysics* **160**(5–6): 1023–1050.

Mery C. 2008. Étude pétrographique et d'imagerie en forage d'un massif marneux fracturé sur le site expérimental de Draix. Rapport de master, Département de l'Enseignement des Sciences de la Terre et de l'Environnement de Montpellier.

Neuville A, Toussaint R, Schmittbuhl J. 2009. Fracture aperture reconstruction and determination of hydrological properties: a case study at Draix (French Alps). *Hydrological Processes* in press, DOI: 10.1002/hyp.7985.

Noiriel C. 2005. Contribution à la détermination expérimentale et à la modélisation des différents processus contrôlant l'évolution géochimique, structurale et hydrodynamique des roches fissurées carbonatées. Thèse de doctorat, École des Mines de Paris.

Plouraboué F, Kurowski P, Boffa JM, Hulin JP, Roux S. 2000. Experimental study of the transport properties of rough self-affine fractures. *Journal of Contaminant Hydrology* **46**: 295–318.

Power W, Tullis T, Brown S, Boitnott G, Scholz C. 1987. Roughness of natural fault surfaces. *Geophysical Research Letters* **14**(1): 29–32.

Renard F, Voisin C, Marsan D, Schmittbuhl J. 2006. High resolution 3 D laser scanner measurements of a strike-slip quantify its morphological anisotropy at all scales. *Geophysical Research Letters* **33**(4): L04305.

Schmittbuhl J, Gentier S, Roux S. 1993. Field measurements of the roughness of fault surfaces. *Geophysical Research Letters* **20**(8): 639–641.

Schmittbuhl J, Schmitt F, Scholz C. 1995a. Scaling invariance of crack surfaces. *Journal of Geophysical Research* **100**(B4): 5953–5973.

Schmittbuhl J, Steyer A, Jouniaux L, Toussaint R. 2008. Fracture morphology and viscous transport. *International Journal of Rock Mechanics & Mining Sciences* **45**: 422–430.

Schmittbuhl J, Vilotte J, Roux S. 1995b. Reliability of self-affine measurements. *Physical Review E* **51**: 131–147.

Terzaghi K. 1936. The shearing resistance of saturated soils and the angle between the planes of shear. In *Proceedings, 1st International Conference on Soil Mechanics and Foundation Engineering*, 1. Cambridge, USA; 54–56.

Vicente SM, Ribeiro e Sousa L, Hack R. 2002. Laboratory study of geomechanical and hydro-mechanical characterisation of discontinuities. *News Journal International Society for Rock Mechanics (ISRM)* **7**(2): 9–15.

Wyllie D. 1999. *Foundations on Rock*, 2nd edn. Spon Press: London, UK.

Yamakoshi T, Mathys N, Kiotz S. 2009. Time-lapse video observation of erosion processes on the black marls badlands in the Southern Alps, France. *Earth Surface Processes and Landforms* **34**(2): 314–318.

Zhang S, Lai Y, Zhang X, Pu Y, Yu W. 2004. Study on the damage propagation of surrounding rock from a cold-region tunnel under freeze-thaw cycle condition. *Tunnelling and Underground Space Technology* **19**: 295–302.

HYDROLOGICAL PROCESSES
Hydrol. Process. **26**, 2095–2105 (2012)
Published online 23 February 2011 in Wiley Online Library
(wileyonlinelibrary.com) DOI: 10.1002/hyp.7985

Fracture aperture reconstruction and determination of hydrological properties: a case study at Draix (French Alps)

A. Neuville,* R. Toussaint and J. Schmittbuhl
IPGS; Université de Strasbourg/EOST, CNRS; 5 rue Descartes, 67000 Strasbourg, France

Abstract:

We propose two techniques for fracture aperture reconstruction. The first one is a correlation technique that estimates the normal aperture or the tangential shift across a discontinuity whose sides present geometrical similarities. The only required material is a pair of appropriately controlled images of each side. Here, the images are maps of the corresponding side topography, obtained from laser profilometry. Assuming a purely normal opening, it is possible, from two corresponding sides of a given discontinuity in a core log, to infer the precise geometry of the in situ aperture. The second technique allows to retrieve the three-dimensional geometry of a sealed discontinuity from non-independent topography measurements of both sides. Both techniques are applied to discontinuities extracted from a core drilled down to 20 m in a fractured marl formation at Draix (French Alps). The probability density functions of the aperture of the sealed and open discontinuities are shown to be Gaussian. At the sample scale, the sealed fracture aperture is self-affine, while the open one shows a cross-over from a self-affine regime at very small scales to an uncorrelated regime at largest scales. After extrapolating those scaling laws at the scale of the whole formation, we discuss when the aperture roughness affects the hydraulic properties of the Draix fractured bedrock. The overall estimated permeability is significant ($10^{-9} - 10^{-8}$ m^2), consistently with some previous indirect inferences. Copyright © 2011 John Wiley & Sons, Ltd.

KEY WORDS fracture; aperture reconstruction; Draix; self-affinity; hydraulic; optical profiler

Received 11 March 2010; Accepted 13 December 2010

INTRODUCTION

Many physical processes occurring in fractured rocks depend on the individual fracture apertures: for instance, the hydraulic flow (e.g. Auradou *et al.*, 2005, 2006; Brown, 1987; Drazer and Koplik, 2002; Méheust and Schmittbuhl, 2001; Pyrak-Nolte *et al.*, 1988; Schmittbuhl *et al.*, 2008; Tsang and Tsang, 1987; Zimmerman and Bodvarsson, 1996), the tracer dispersion (e.g. Drazer and Koplik, 2002; Plouraboué *et al.*, 1998; Roux *et al.*, 1998) or the heat transfer (e.g. Muralidhar, 1990; Neuville *et al.*, 2010a; Walkup and Horne, 1985). Therefore, it is important to be able to reconstitute the volumetric geometry of apertures, knowing both the average opening and the fracture roughness. The hydraulic properties are notably highly influenced by the ratio between roughness amplitude and mean aperture (e.g. Al-Yaarubi *et al.*, 2005; Brown, 1987; Méheust and Schmittbuhl, 2001).

This paper shows how to reconstruct, at laboratory scale, the aperture of open fractures and the thickness of veins, in order to estimate the hydraulic behaviour of a fractured bedrock. The studied discontinuities are extracted from a core drilled in the fractured marl of Draix (French Alps), an experimental site exploited to understand landslide processes (Fressard *et al.*, 2009). At laboratory scale, aperture reconstruction of fracture has previously been explored in various ways depending if the fracture fully intercepts the sample (providing two sample pieces) or not. Some of the methods allow to obtain the aperture fluctuations directly: for instance, X-ray computer tomography measurements (e.g. Noiriel, 2005) or resin injection into the fracture (e.g. Gentier and Hopkins, 1997; Hakami and Larsson, 1996). In the study by Hakami and Larsson, 1996, the sample was then sliced perpendicularly to the fracture, and the aperture was measured on each slide using images obtained from an optical microscope. If both sides of the fracture are separated, the aperture fluctuations can also be obtained indirectly, by measuring the topography of facing fracture surfaces whose relative position is ensured by a common reference frame (e.g. the boundaries of the sample). For instance, it was done using transparent casts of each surfaces, whose morphology can be obtained through light attenuation properties (e.g. Isakov *et al.*, 2001), and also by measuring the morphology of surfaces using mechanical or laser profilers (e.g. Lee and Cho, 2002; Sakaguchi *et al.*, 2008; Sharifzadeh *et al.*, 2008; Vicente *et al.*, 2002). In some of the previously cited studies, the average aperture is either *a priori* known, especially when the sample fully embodies the fracture, or arbitrarily fixed: for instance, when both fracture sides are assumed to be in contact. When the sample is entirely intercepted by the discontinuity, providing two separated

* Correspondence to: A. Neuville, EOST, Université de Strasbourg, Strasbourg, France. E-mail: amelie.neuville@unistra.fr

sides whose relative position is unknown, the average aperture is tricky to estimate. Such open discontinuities, showing no contact at sample scale between both sides can typically be found in samples extracted from a core drilled in fractured bedrocks (e.g. Genter and Traineau, 1996; Lofi *et al.*, 2011). For a sealed discontinuity, the situation is different. Boundary geometry can be directly measured if the embedding material can be removed. However, even in this case, the volumetric geometry is lost when both surface elevations are not measured in a common reference frame. In Section "Aperture Reconstruction" of this paper, we detail two methods, respectively, dedicated to open and sealed discontinuities, allowing the reconstruction of both the average aperture and the roughness variation of a discontinuity. The first method requires the analyse of the correlations between the surfaces, provided that these correlations exist. For a sealed discontinuity, the relative positioning is ensured by attaching the sample to a specific frame when measuring each surface topography. Both methods are illustrated on experimental discontinuities whose surface elevations were previously measured with a laser profiler (Neuville *et al.*, 2011), hereafter referred as Paper 1), providing an accurate knowledge of each surface topography. In Section "Statistical Characterization of the Apertures", a statistical study of the fluctuations of the resulting apertures is presented, and the scaling laws governing the aperture roughness are determined. In Section "Hydraulic Properties of the Draix Formation", the hydraulic behaviour of various discontinuities is determined, and the observed scaling laws are used to obtain the large-scale hydraulic properties of the formation.

APERTURE RECONSTRUCTION

Reconstruction of the aperture of an open discontinuity with correlated sides

Topography of the sides at zero relative displacement. Let us consider a brittle elastic fracturing that creates two sides with complementary morphologies (or asperities). If the displacement induced by the fracturing is zero, then each surface asperity is in contact with the corresponding asperity on the other surface, as shown in Figure 1a. Note that this state might be fictitious if the relative displacement occurs at the same time as the fracturing. In practice, during the bedrock history, the discontinuity morphology might be modified due to chemo-mechanical processes; hence, the correlation between both surfaces may disappear. Let us consider that despite a probable alteration of the fracture, enough complementary asperities may still be observed.

Present displacement indicated by the borehole boundaries. When the drilling is performed, the intercept between the drill and both sides of the fracture is very likely to provide information about the relative position

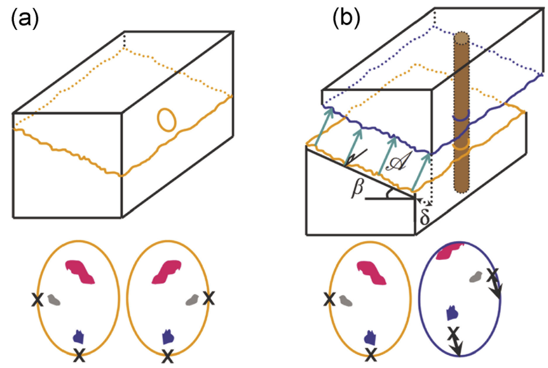

Figure 1. Comparison of the elliptic intercept of a drill before (a) and after (b) a normal shift of a discontinuity. In (b), the location of the elliptic boundary of the core with respect to the similar facing patterns (see step v in Figure 2) are compared, hence $\vec{\delta}$ is obtained; β is the angle between the normal to the mean plane of the discontinuity and the core axis

of the fracture sides at the drilling time. Both complementary sides might have been shifted relatively to each other. Handling the sample, and moving both sides relatively to each other, one can — in principle — restore contact between the complementary asperities (i.e. as defined above, the state of the fracture at zero displacement). In general, once the asperities are in contact, the boundaries of the facing sides no longer fit. When the fracture is not perpendicular to the cylindrical core axis, the intersection between the discontinuity mean plane and the boundary of the drill provides surfaces with elliptic boundaries. This only assumes that $\beta \neq 0$, where β is defined as the angle between the normal to the mean discontinuity plane and the core axis (Figure 1b). Let $\vec{\delta}$ be the projection of the true vector displacement field between surfaces, in the fracture mean plane (defined here as the plane fitted by a least mean square method of the surface topography). It can be measured from the shift of the elliptical boundaries once the complementary asperities are in contact. The vector field $\vec{\delta}$, that will further be called the in-plane shift, allows to reconstitute the true field of relative displacements of the fracture sides, under some simple geometrical assumptions.

Displacement history. If the fracture opened in shear mode, i.e. with relative displacement parallel to the average plane, then $\vec{\delta}$ is uniform and its norm directly provides the shear value. Let us now consider the other end member, i.e. a fracture that opened in mode I, whose sides moved along a direction normal to the mean plane. When the axis of the drill is not perpendicular to the mean discontinuity plane ($\beta \neq 0$), the more the fracture is open, the more the facing patterns will appear shifted once the core is extracted from the drill (Figure 1b). In this case, the field $\vec{\delta}$ is also uniform. Knowing the angle β and the norm δ (Figure 2), the average aperture $\mathscr{A}$, measured in the direction perpendicular to the mean discontinuity plane, can be deduced: $\mathscr{A} = \delta / \tan\beta$. The angle β can be measured directly on the considered discontinuity using an inclinometer, once the core is extracted from the soil. Moreover, this measurement allows to check if both sides of the open discontinuity are indeed parallel on average, as it should indeed be for pure mode I opening. In the next part, we show how $\vec{\delta}$ may be evaluated.

Quantitative evaluation of the in-plane shift $\vec{\delta}$ by image correlation. Let us consider two sides of an open discontinuity, assumed to be parallel *in situ*. It is also assumed that correlations between both sides are visible: typically, some similar patterns in the topography can be observed on both surfaces. Some patterns may also be identified because of similar colours (like oxidized parts). Estimate of the in-plane shift $\vec{\delta}$ can be done using either maps of the topography, or any top view images resulting from any technique (like photos) where the similar patterns to be correlated are visible. In Figure 2, the procedure used to deduce δ from the topography measurement is presented. Once the measurement of the topography is known (step i) (e.g. using a profiler, or other techniques that can produce scaled three-dimensional data), a change of coordinates is done, performing a rotation of the initial axes, in order to get the so called $x - y$ plane aligned with the mean plane of the surface (Figure 2, step ii). Then a rotation of 180° around the y-axis of one of the surfaces is performed (Figure 2, step iii). Then it is assumed that only a 1D rotation around the z axis and a two-dimensional (2D) translation of the top surface axes (Figure 2, step iv) are required to position the facing asperities at the same coordinates. This 2D transformation can theoretically be obtained in several ways: either minimization of volume difference between similar zones, or inter-correlation (e.g. Brown, 1992; Wilson and Theriot, 2006) of images or surface elevations. However, if both surfaces are not similar enough, with possible outliers in the measurement, we have found that the volume minimization method was not reliable (i.e. clear mismatch of the facing patterns). A simple method to implement is to inspect visually both maps of elevation as images and to select N pairs of points of

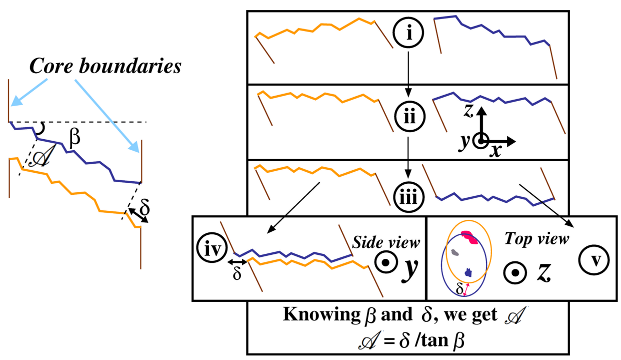

Figure 2. The displacement is assumed here to be normal to the mean plane of the discontinuity. The diagram shows the major five steps of the process. (i) Measurement of the surface topographies. (ii) Detrending by rotation of the surfaces; after this rotation, the mean surface plane, computed by a least mean square method, defines the x-y plane. (iii) Rotation of 180° of the top surface around the y-axis. (iv) Asperity correlation and linear transformation (in-plane rotation and translation) to adjust the two sides one against the other; this step requires similarities between both sides. (v) Fit of the elliptic boundaries of the sample cores. In this processing, the mean planes of each discontinuity sides are assumed to be initially parallel, like for the F9 discontinuity

coordinates (x_i^B, y_i^B) and (x_i^T, y_i^T) (one from each image), that are confidently identified as corresponding points of two homologous asperities. The isometry Ω to be applied is determined by a least square minimization, i.e. minimization of $\sum_{i=1}^{N}[\sqrt{(x_i^B - x_i^{T'})^2 + (y_i^B - y_i^{T'})^2}]$ where $(x_i^{T'}, y_i^{T'}) = \Omega(x_i^T, y_i^T)$. Then, the in-plane projection of the intercept between the core an the discontinuity are actually fitted with an identical ellipse for both sides (Figure 2, step v). Once the image registration is made, each top and bottom corresponding point of the elliptical boundaries is shifted of $\vec{\delta}$. By comparing the positions of both fitted ellipses, an estimate of the variability of the field $\vec{\delta}$ can be estimated and, if it is uniform (corresponding therefore to a relative translation of the sides without rotation), the in-plane shift δ is obtained.

Application of the method to a real discontinuity from Draix borehole. The natural discontinuity which is studied here is the one called F9, extracted from a drill in marl at Draix (French Alps) (Paper 1). F9 is an open discontinuity in the sense that no infill material was observed and no contact zone between the top and bottom parts of the discontinuity is known at the core scale.

The topography of both sides of F9 is known from the measurement with an optical profiler (Paper 1). Actually, F9 shows very similar top and bottom surfaces. Once step ii and iii are performed, one searches the best transformation to be applied so that similar patterns are facing. The transformation obtained by selecting pairs of points provided a good match of the similar patterns, as shown in Figure 3. The elliptical boundaries of the surfaces can indeed be fitted with an ellipse of identical size for the top and bottom sides, but with different centre and orientation. Comparing the position of those ellipses once the corresponding patterns match, it was found that the transformation to be applied to transform one of the ellipse to the other was mostly a translation and a negligible rotation: $\vec{\delta}$ is approximately uniform. The translation was determined as equal to $\delta = 2{\cdot}085 \pm 0{\cdot}05$ mm.

As no striation was seen on the surfaces, it was deduced that fractures opened in mode I, with a displacement normal to the fracture plane. This mode is coherent with a fracturing due to a pore pressure increase (hydraulic fracturing). Many other mechanisms can also lead to such tensile fractures, as local contraction of the material due to, e.g. temperature change, drying, chemical change. The oxidation shows that independently of the origin of the fracture, water circulated in it after its creation. The angle β was measured as $\beta = 42°$, which implies $\mathscr{A}_{F_9} = \delta/\tan\beta \simeq 2{\cdot}3 \pm 0{\cdot}1$ mm.

The final step is to reconstruct the volumetric aperture, knowing the average aperture, as well as the fluctuation of both surface elevations around their mean plane. Hence, both surface elevations are interpolated on the same $(x - y)$ grid (using transformed coordinates, after steps i to iii shown in Figure 2 are performed). Finally, the detailed aperture field of

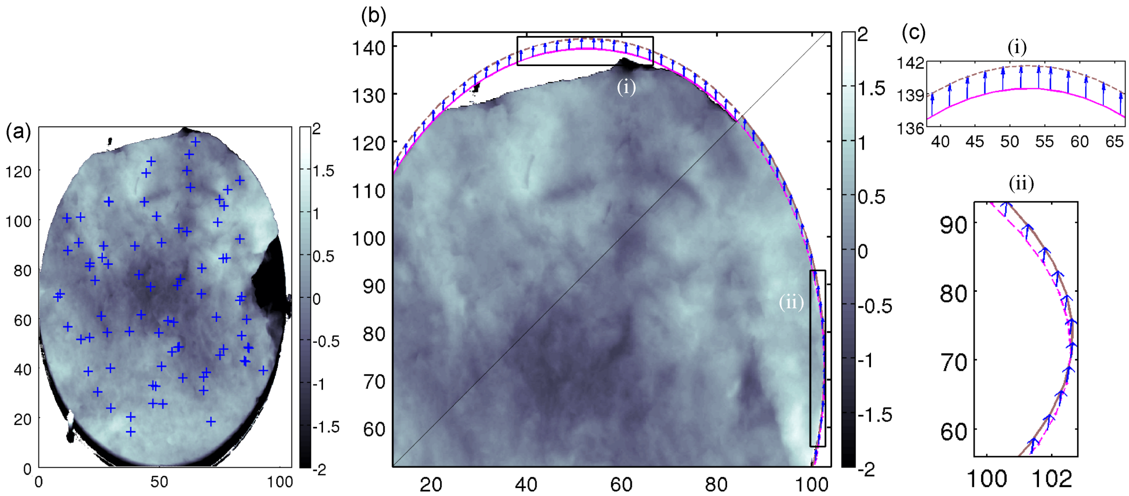

Figure 3. (a) Points selected on the bottom surface of F9. Points corresponding to the similar asperities were also selected on the F9 top surface. Using these points, cross-correlation was done in order to position both surfaces relatively to one another. (b) Topography of both sides of the discontinuity F9. Composite picture formed of two parts: topography of the bottom side shown on the top left, topography of top side on the bottom right, positioned by maximization of the cross-correlations. It shows that similar patterns are at the same coordinates, while the ellipses fitting both elliptical boundaries are shifted by $\vec{\delta}$. (c) Blow-ups (i) and (ii) show that $\vec{\delta}$ is approximately homogeneous

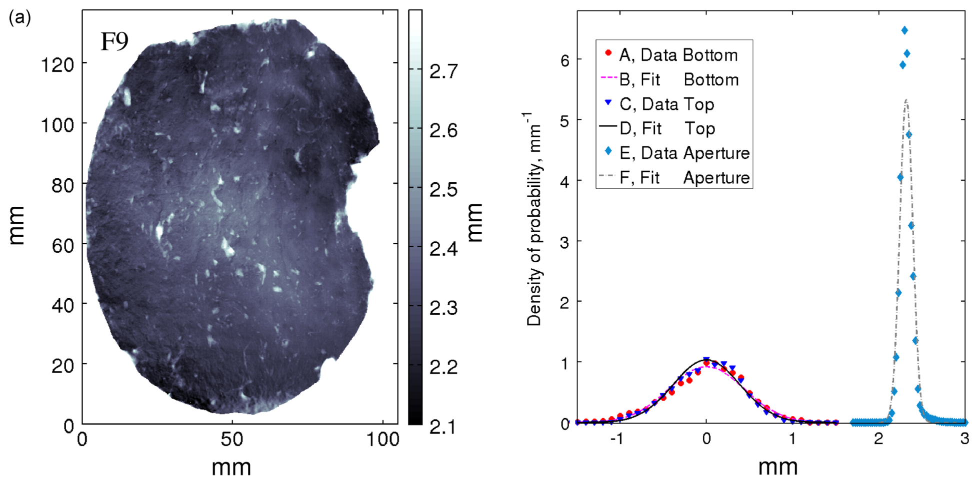

Figure 4. (a) Aperture of discontinuity F9 issued from the laser profiler topography measurement and reconstruction from image correlation. (b) Probability density functions of the elevation of the bottom (A) and top surfaces (C), and aperture (E) of F9, and their normal probability fits (B, D, F). For A, B, C, D, mean value is 0 mm and RMS (root mean square) is about 0·4 mm. For E, F, mean value is 2·3 mm and RMS is about 0·08 mm. The measurements for the plots A, B, C, D are described in Paper 1

F9 shown in Figure 4 is obtained. In this figure, it can be seen that the aperture in the central zone is about 0·2 mm larger than on the border of the core, and that some small zones of about 3 mm^3 show a locally larger aperture than the one in the surroundings. This may correspond to local rupture of asperities.

Reconstruction of the thickness of a sealed discontinuity

For a sealed discontinuity, which has been isolated from the matrix, the aperture can be visually appreciated, but remains to be fully quantified. This can be achieved by measuring the elevation on each side of the sample, so as to deduce its thickness by appropriate transformations (Figure 5). A critical condition for such a procedure to provide meaningful results is that both topography measurements share a common reference frame, which may be adequately done by wedging the vein into a rigid box of known geometry (Figure 5). First, the topography of one surface (called top) is determined together with the boundaries of the box ($A_1\ B_1\ C_1\ D_1$). Second, the box is flipped upside down and the topography of the other surface (bottom) is similarly measured. It is then possible to transform coordinates from the global frame — given by the profiler — to the local frames $\mathcal{R}_1$ and $\mathcal{R}_2$, which are associated with, the top and bottom boundaries of the box, as shown in Figure 5. To do so, a precise knowledge of the box geometry is also mandatory. The use of a rectangular parallelepiped box greatly eases this procedure (see practical protocol in the Appendix). Once the topography is known in frames $\mathcal{R}_1$ and $\mathcal{R}_2$, as well as the relative position of both these frames, the aperture can finally be obtained.

This procedure was applied to a natural discontinuity, called C14 in Paper 1, extracted from a drill at Draix (French Alps). C14 refers to a discontinuity sealed with

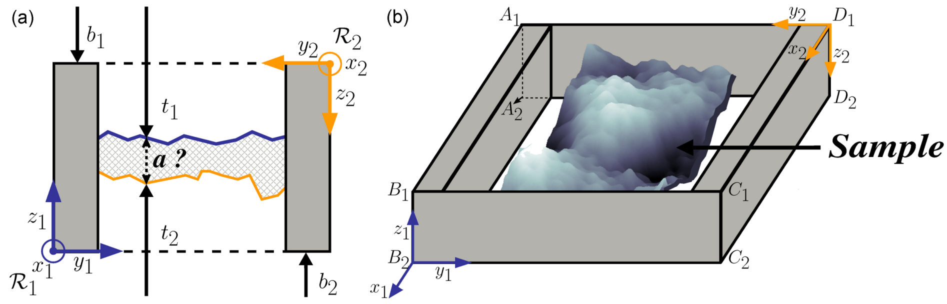

Figure 5. Drawings of a sealed discontinuity wedged in a rigid frame (box): (a) side view, (b) perspective view. By measuring the topography of both surfaces, t_1 and t_2, as well as the box boundaries, b_1 and b_2, the three-dimensional geometry of the discontinuity can be deduced

calcite, *in situ* embedded into marl, which was studied after removing the surrounding bulk marl. This discontinuity was then wedged in a box, and the topography of each side was measured with an optical profiler, allowing to reconstruct its thickness geometry, shown in Figure 6.

The error of the in-plane relative positioning between frames $\mathcal{R}_1$ and $\mathcal{R}_2$ translates into an error on the discontinuity aperture, which has been estimated by two independent reconstructions. This error is on average 0·2 mm, and increases with the slope of the aperture. Most of the uncertainty on the aperture comes from the boundaries of the box not being exactly rigid and orthogonal, which can be improved by using a box designed better than for this exploratory test.

STATISTICAL CHARACTERIZATION OF THE APERTURES

Characterization of the aperture morphology of an open discontinuity

The aperture field of F9 ranges between 2 and 3 mm (Figure 4). Its probability density function (Figure 4b, E) is approximately normal (Figure 4b, F) with a standard deviation of 0·08 mm around the mean aperture $\mathscr{A} =$ 2·3 mm. The standard deviation of the aperture is about five times lower than the standard deviation of the elevation of each side, which is 0·4 mm (Paper 1, recalled in Figure 4b, A, B, C, D). This result already shows that the facing surface topographies are highly correlated. Further comparison between the top and bottom surface topographies is done by analysing their scaling properties.

The scaling law of the aperture has been determined exactly with the same auto-correlation expression as for the topographies (Paper 1, Section "Statistical Characterization of the Roughness of the Discontinuity Surfaces"),

$$C_2(\vec{\Delta}) = \sqrt{\langle [f(\overrightarrow{OM} + \vec{\Delta}) - f(\overrightarrow{OM})]^2 \rangle} \qquad (1)$$

where f is the function to be analysed (here, the aperture), $\vec{\Delta}(\Delta_x, \Delta_y)$ the lag vector (i.e. characteristic distance at which the correlation is computed), $\langle\rangle$ indicates that the average is computed over all the possible spatial points M so that $f(\overrightarrow{OM})$ and $f(\overrightarrow{OM} + \vec{\Delta})$ are defined, and Δ_0 is here chosen to be 1 mm. The self-affinity was checked in the same way as in Paper 1, i.e. by plotting $C_2(\Delta)$ as a function of Δ in a log–log representation: if such a plot is linear, the slope provides a direct determination of the Hurst exponent. This has been plotted in 1D (Figure 7), for given directions θ, defined as the angle between the x-axis and $\vec{\Delta}$, and in 2D (Figure 8), in order to check the isotropy of the scaling law. Figure 7

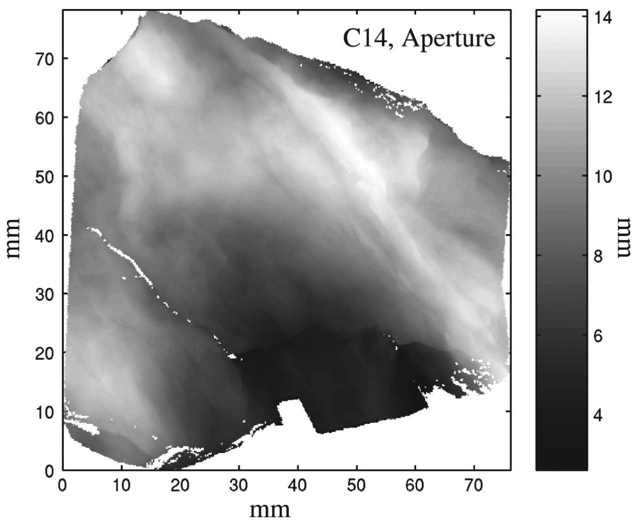

Figure 6. Reconstructed aperture field of C14. Units are in millimeters

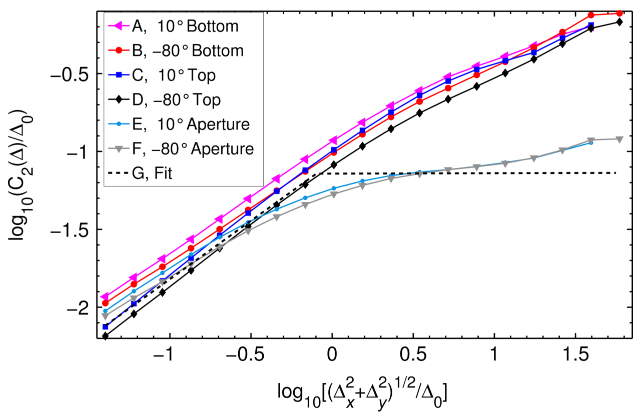

Figure 7. Plot of $\log_{10}[C_2(\Delta)/\Delta_0]$ as a function of $\log_{10}[\Delta/\Delta_0]$, for discontinuity F9, in directions θ equal to 10° and −80°, for the bottom side (A, B), top side (C, D), and aperture (E, F), respectively. The measurements for the plots A, B, C, D are described in Paper 1. The fit curve shows the suggested model for the F9 aperture: it is self-affine from $\Delta = 0{\cdot}04$ mm to $\Delta = 0{\cdot}8$ mm with a slope of 0·75 and $C_2(0{\cdot}1 \text{ mm}) = 17$ µm; then for Δ values higher than 0·8 mm it reaches a plateau characterized with $C_2(\Delta > 0{\cdot}8 \text{ mm}) = 0{\cdot}07$ mm. Δ, C_2 are in millimeters, and $\Delta_0 = 1$ mm

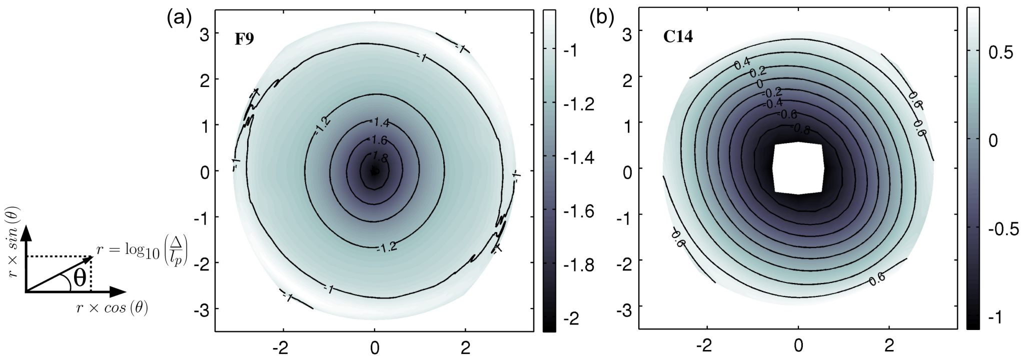

Figure 8. Representation of $\log_{10}[C_2(\Delta)/\Delta_0]$ as a function of the polar coordinates $(\log_{10}(\Delta/l_p), \theta)$, where l_p is 0·04 mm, computed for the apertures F9 (a) and C14 (b). For C9 and C14, the isovalue lines are a family of slightly elongated circles, showing that both apertures are isotropic at first order. Note that, at second order, C14 is slightly more anisotropic; and also that C_2 values are higher for C14 than for F9. These lines are regularly distributed for C14, showing that the aperture is self-affine over all the observed ranges, while F9 aperture shows only a self-affine law at very small scales. Δ and C_2 are in millimeters

shows that the scaling law property of the discontinuity aperture, plotted for two directions, is rather different from that of each side, whose scaling curves (A, B, C, D) are recalled for comparison. While those were observed to be self-affine at least from 0·04 to 7 mm (Paper 1), the aperture (E, F) exhibits a self-affine property only on a very short range of scales (from 0·04 to 0·8 mm). At larger scales, the auto-correlation C_2 for the F9 aperture tends to saturate, with a smooth cross-over at the transition between both regimes. Similar analytic and numerical scaling curves were discussed, e.g. by Auradou *et al*., 2006; Brown, 1995; Glover *et al*., 1998; Méheust and Schmittbuhl, 2003; Ogilvie *et al*., 2006; Plouraboué *et al*., 1995, who studied the aperture obtained from two self-affine surfaces matching at large scales and independent at small scales. In our case, the mismatch at small scales is isotropic and would correspond to small scale surface damaging, while the large-scale match probably reflects the initial match of the fracture boundaries. Here, the Hurst exponent characterizing the self-affinity at small scales is difficult to estimate robustly, due to the very short range where the self-affinity can be observed. The fit proposed in Figure 7 has a slope (Hurst exponent) of 0·75. This is in accordance with the results presented in Paper 1, where it was shown that both sides of F9 have a self-affine geometry characterized by a Hurst exponent of 0·75. Figure 8a, is a 2D plot of $\log_{10}[C_2(\Delta)/\Delta_0]$ as a function of the polar coordinates $(\log_{10}(\Delta/l_p), \theta)$ ($l_p = 0{\cdot}04$ mm). It shows that the scaling properties of the aperture are roughly the same in any direction, which was also the case for the facing surfaces.

Scaling law of the thickness of the sealed discontinuity

The calcite joint studied, C14, has a thickness ranging from about 3 to 14 mm. This thickness (shown in Figure 6), mostly around 1 cm, is relatively variable due to the anastomose of multiple calcite layers (Figure 4 in Paper 1).

C_2 was computed for aperture C14, and Figure 9 shows the 1D plot of $\log_{10}[C_2(\Delta)/\Delta_0]$ as a function of $\log_{10}[\Delta/\Delta_0]$ for two directions (hereafter demonstrated as being close to the directions showing the largest

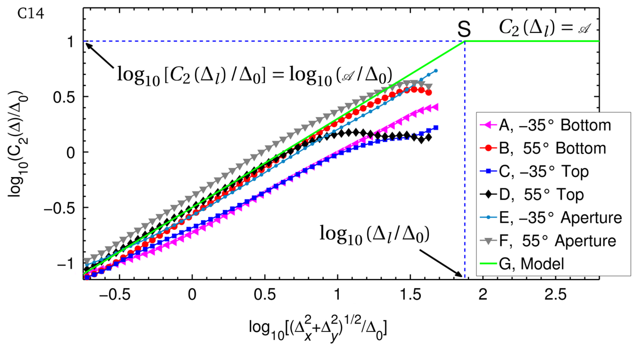

Figure 9. Plot of $\log_{10}[C_2(\Delta)/\Delta_0]$ as a function of $\log_{10}[\Delta/\Delta_0]$, for the C14 discontinuity, in directions θ equal to $-35°$ and $55°$, for the bottom side (A, B), top side (C, D), and thickness (E, F), respectively. The measurements for the plots A, B, C, D are described in Paper 1. Plot G shows the suggested geometrical model applied at small and large scales. Point S is the intersection between the scaling law $\log_{10}[C_2(\Delta)/\Delta_0] = -0{\cdot}5 + 0{\cdot}8\log_{10}[\Delta/\Delta_0]$ and $C_2(\Delta) = \mathscr{A} = 1$ cm. Assuming that the fluctuation of the aperture cannot be larger than the average $\mathscr{A}$, the self-affine law is considered to show a cut-off at scales larger than the correlation length $\Delta_l = 75$ mm, which is the abscissa of S; Δ and C_2 are in millimeters, and $\Delta_0 = 1$ mm

anisotropy): $\theta = -35°$ and $\theta = 55°$. A linear trend can be observed from 0·3 to 25 mm, which means that a self-affine law can be fitted. As shown in Figure 10, C_2 for C14 is slightly anisotropic, as was the case for its surfaces, with $C_2(\Delta_0)$ values progressively varying (amplitude of $\pm 0{\cdot}08$) according to the direction, around 0·34 mm, with extremal values around θ equal to $-50°$ and 40°. The Hurst exponent also shows an anisotropy (however less pronounced), as it varies around 0·78 according to the direction, by $\pm 0{\cdot}04$. Note that the sides and the aperture measurements are oriented relatively to one another (see Section "Reconstruction of the Thickness of a Sealed Discontinuity"), so that the directions of anisotropy can be compared between both surfaces and the aperture. The difference to an isotropic self-affine surface can be fully observed in Figure 8b, from the fact that the isovalues are elongated circles. It can also be noticed that the anisotropy direction slightly evolves according to the range of scales. Ignoring these second order effects leads to a global Hurst exponent of about 0·8 for the aperture and 0·75 for the individual sides, whose scaling

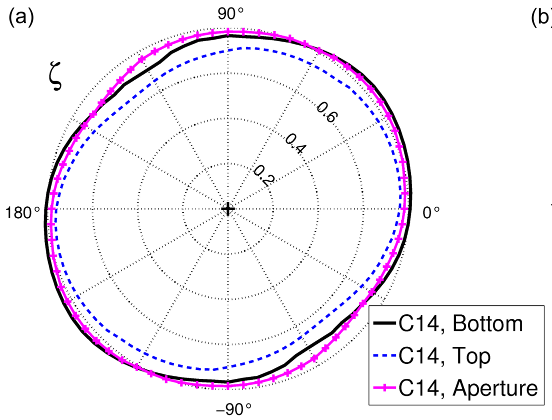

Figure 10. Polar plot of ζ (a) and $C_2(\Delta_0)$ in millimeter (b) as functions of θ, for the topography of the sides, and aperture, as indicated by the labels, for C14 discontinuity. The ellipsoidal shape of the curves shows how anisotropic the scaling are

curves (Figure 9, A, B, C, D) are recalled for comparison (Paper 1). $C_2(\Delta_0)$ of aperture C14 is however shown to be larger than the one of its sides (Figure 10b), which simply shows that the spatial variability at 1 mm of the aperture is larger than the variability of the topography of both sides. This is a behaviour opposite to what is observed for discontinuity F9, whose aperture shows less fluctuations than its sides. C14 is an example of discontinuity with two independent sides which are both self-affine with approximately the same Hurst exponent, which provides a thickness which is self-affine over the same range of scales as that of the sides.

HYDRAULIC PROPERTIES OF THE DRAIX FORMATION

Description of the parameters influencing the permeability of a fractured bedrock

The aim is to estimate the present permeability k of the Draix fractured bedrock at large scale. Open fractures, like F9, will play a significant role in the permeability. The bedrock being essentially intact marl, the permeability in the perpendicular direction of the mean plane fracture is supposed to be negligible in comparison to the in-plane permeability. An increase of permeability might also come from the dissolution of sealed discontinuities of the type previously considered (C14), or even from simple washing of less consolidated clay filled discontinuities (like F6 discontinuity, studied in Paper 1), which also exist along the drill. The estimate of the permeability requires the evaluation of the density of open and sealed discontinuities along the core, as well as their orientation. The morphology of the discontinuities also greatly influences the permeability, as was shown, for instance, with numerical simulations of the hydraulic flow, performed on synthetic apertures (e.g. Al-Yaarubi *et al.*, 2005; Auradou *et al.*, 2005; Brown, 1987; Drazer and Koplik, 2002; Méheust and Schmittbuhl, 2001; Méheust and Schmittbuhl, 2003; Zimmerman and Bodvarsson, 1996). Among the numerically explored aperture models, isotropic rough apertures showing self-affinity at any scale, or at limited scale (e.g. Brown, 1987; Méheust and Schmittbuhl, 2001; Méheust and Schmittbuhl, 2003; Neuville *et al.*, 2010a,b; Zimmerman and Bodvarsson, 1996), have been compared, in term of permeability, to apertures with flat sides. Those simulations, using the Reynolds equation in the permanent and laminar regimes, under the lubrication approximation (e.g. Zimmerman and Bodvarsson, 1996), have shown that, if $\sigma/\mathscr{A}$ is small enough (where σ is the root mean square of the aperture field), the cubic law (e.g. Zimmerman and Main, 2004)

$$k = \frac{N\mathscr{A}^3}{12} \tag{2}$$

is valid, where N is the density of isotropic fractures (number of fractures per length unit), of same orientation and mean aperture $\mathscr{A}$. The study of the aperture morphology of the open and sealed discontinuities can therefore be used to determine if that cubic law can be applied to Draix. It is first needed to extrapolate to the scale of the formation the statistical properties observed at the sample scale. Since the determined aperture correlations are almost isotropic, the associated permeability is isotropic along the discontinuity mean plane. However, since most observed fractures display quite similar directions, the permeability in the direction normal to these fractures would rather be the one of the bulk marl.

Hydraulic contribution of the open discontinuities

F9 is assumed to have an aperture representative of all the open fractures in the formation. It was shown that the average aperture is about $\mathscr{A}_{F_9} = 2{\cdot}3$ mm, with very little variations around this mean (Figure 4): $\sigma_{F_9}/\mathscr{A}_{F_9} < 0{\cdot}04$. The aperture was also shown to follow a self-affine law at very small scales (less than 1 cm), and to be statistically invariant at larger scales. Méheust and Schmittbuhl, 2003, for instance, showed that the hydraulic behaviour, under lubrication approximation, for fracture apertures with such scaling characteristics are controlled by the self-affinity. Therefore, the behaviour of F9 can be deduced from numerical simulations performed over numerous self-affine apertures (Neuville *et al.*, 2010b), showing $\sigma/\mathscr{A} < 0{\cdot}04$. It was shown that the hydraulic behaviour computed for a fracture with such a small $\sigma/\mathscr{A}$ ratio can be approximated by that of a parallel plate model with aperture $\mathscr{A}$, with a precision better than 99% on the hydraulic aperture.

Counting the number of open discontinuities visible along the core for fractured unit 2, which is the unit where open discontinuities are numerous, we get approximately four discontinuities over 4 m, i.e. $N_o \simeq 1$ open discontinuity per metre. From equation (2), the permeability is thus of order $k = 10^{-9}$ m^2 in the direction of the fractured bedrock. That means that unit 2 is highly permeable. Apertures of some of the open fracture might however be different from 2·3 mm, with a slightly different orientation, which might result into a different permeability.

Potential hydraulic contribution of sealed discontinuities and of discontinuities containing debris and clay

Using calcite vein C14, the hydraulic permeability increase, if such calcite veins were dissolved, can be estimated. The main question to determine the large-scale permeability associated to this fracture, is to upscale the geometrical parameters of the aperture. The observed small scale is self-affine, as already stated in Section “Scaling Law of the Thickness of the Sealed Discontinuity”, with an average $\mathscr{A} = 1$ cm, a Hurst exponent of 0·8 and a pre-factor $C_2(\Delta_0) \simeq 0{\cdot}3$ mm. Assuming simply that this self-affine character of the aperture is obeyed up to the largest scales L (several meters or more), would lead to a similar average $\mathscr{A} = 1$ cm, and fluctuations between apertures within this zone, of the order of $C_2(L) \simeq 0{\cdot}3(L/\Delta_0)^{0{\cdot}8}\Delta_0 \simeq 79$ mm, for $L = 1$ m, i.e. much larger than the average aperture. This would correspond an aperture field with numerous negative values, i.e. mainly patches of overlap between the faces. This picture is not physically sound, which shows that an aperture field with such average cannot be self-affine up to such large scales. We thus discard it. The next hypothesis to perform the upscaling, in order of simplicity, is that the observed self-affinity holds, up to the scale where some contact points between the faces arise. Above this, the fluctuation magnitude has to saturate at a maximum value, of the order of the average aperture. Mathematically, this criterion allows to determine at which scale, Δ_l, this saturation holds: when $C_2(\Delta_l) = \mathscr{A} = 1$ cm. Thus, the relationship $\log_{10}[C_2(\Delta_l)/\Delta_0] = -0{\cdot}5 + 0{\cdot}8\log_{10}[\Delta_l/\Delta_0]$ provides $\Delta_l = 75$ mm (see abscissa of point S in Figure 9). Note that this behaviour is consistent with the morphology of natural fractures, for which the aperture tends to be statistically invariant at large scales (e.g. Isakov *et al.*, 2001; Plouraboué *et al.*, 1995).

The hydraulic behaviour is determined for a self-affine variable fracture (i.e. for scales smaller than 75 mm), using the Reynolds equation in the permanent and laminar regime, with the lubrication approximation (e.g. Zimmerman and Bodvarsson, 1996), solved with finite differences (e.g. Méheust and Schmittbuhl, 2000, 2003; Schmittbuhl *et al.*, 2008; Neuville *et al.*, 2010a,b). As no correlations in the fracture aperture are expected above a scale of 75 mm, the hydraulic behaviour of the fracture at the formation scale is likely to be identical to that of a self-affine fracture of size 75 mm × 75 mm (length over width). Figure 11 shows an example of (a) a synthetic isotropic aperture field of size 75 mm × 75 mm with $\zeta = 0{\cdot}8$ and mean aperture $\mathscr{A} = 1$ cm and (b) an extract of the aperture C14, of size 52 mm × 58 mm with $\zeta = 0{\cdot}8$ and $\sigma/\mathscr{A} = 0{\cdot}3$. For the synthetic case, the root-mean square aperture variation, σ, is fixed by the maximum possible value permitting to avoid contact between the fracture sides (which results in this case in $\sigma \simeq 0{\cdot}46\mathscr{A}$).

Figure 12 shows the corresponding hydraulic flow, q which is defined as the norm of the local hydraulic flux. It is shown in dimensionless units, being normalized by $12\eta l_x/\Delta P$, where $l_x = 75$ mm is the fracture length, η is the dynamic viscosity, and ΔP is the pressure difference imposed between the inlet and the outlet of the fracture. Owing to the spatial variability of the aperture, the hydraulic flow is also variable in space. For those

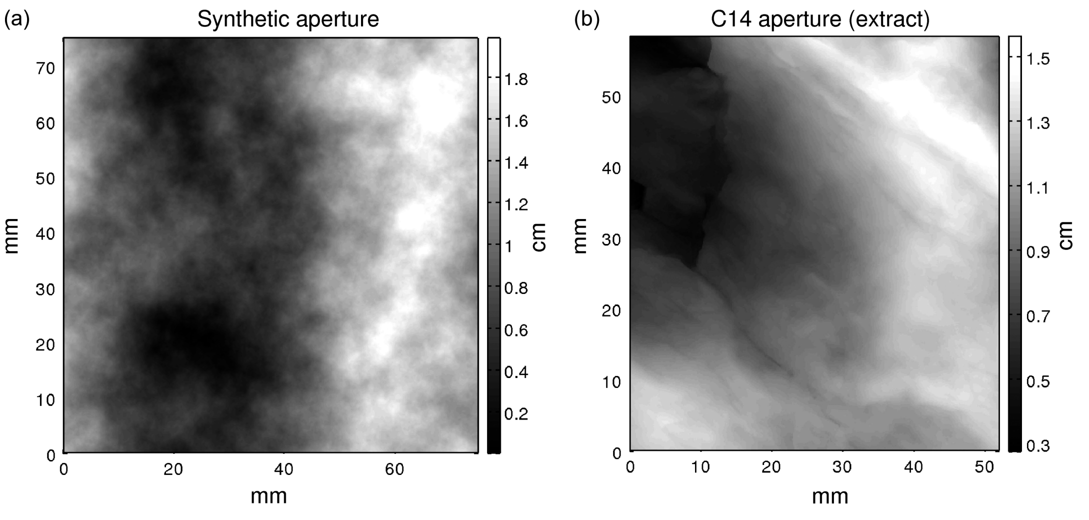

Figure 11. Square map of (a) an isotropic synthetic aperture field with $\zeta = 0{\cdot}8$, $\sigma = 0{\cdot}46$ cm, and $\mathscr{A} = 1$ cm and (b) an extract of the aperture field C14, that shows $\zeta = 0{\cdot}8$, $\sigma/\mathscr{A} = 0{\cdot}3$. Dark areas correspond to thinner apertures while light areas correspond to larger apertures

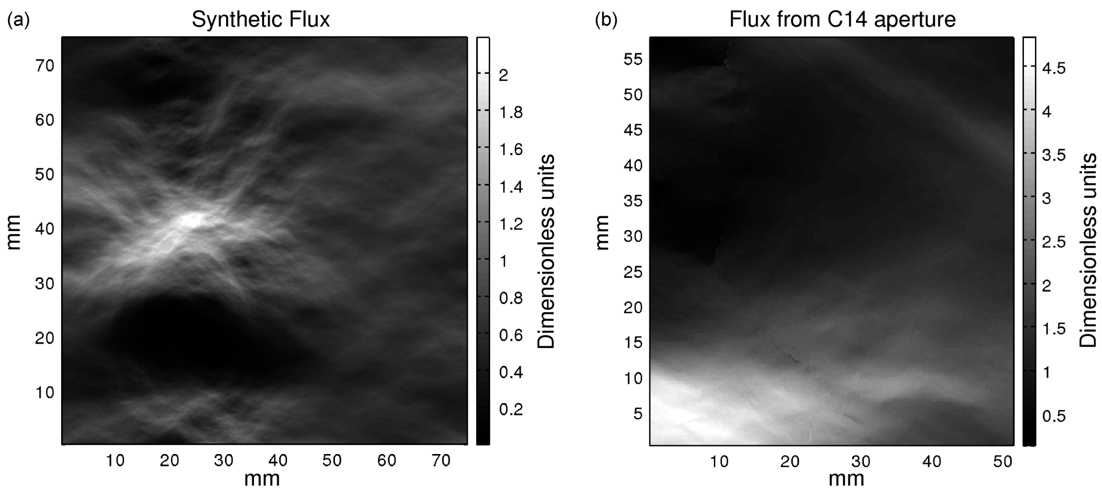

Figure 12. Map of the normalized hydraulic flow computed, from (a) the synthetic aperture field shown in Figure 11a, and (b) the real field shown in Figure 11b. The plane coordinates are in millimeters and the hydraulic flow field in arbitrary units (depending on the pressure gradient). The average hydraulic aperture of these fields are (a) $H = 0{\cdot}68$ cm and (b) $H = 0{\cdot}9$ cm. Dark areas correspond to quasi-static fluid while light areas correspond to larger hydraulic flow

examples, the average hydraulic aperture, defined by $H = \langle -q12\eta \frac{l_x}{\Delta P}\rangle^{\frac{1}{3}}$, is for case (i) $H = 0{\cdot}7$ cm, and for case (ii) $H = 0{\cdot}9$ cm, which means that those fractures are less permeable than parallel plates separated by a constant aperture $\mathscr{A} = 1$ cm. From studies previously made on numerous rough fractures (e.g. Al-Yaarubi *et al.*, 2005; Brown, 1987; Méheust and Schmittbuhl, 2001; Neuville *et al.*, 2010b; Patir and Cheng, 1978; Zimmerman and Bodvarsson, 1996), it is known that the hydraulic aperture for an isotropic fracture with $\sigma/\mathscr{A} > 0{\cdot}45$ and $\mathscr{A} = 1$ cm is likely to be $H \simeq 0{\cdot}9$ cm under lubrication hypothesis. Counting the number of sealed discontinuities visible on the core for fractured unit 1, which is the unit where sealed discontinuities are numerous, we get approximately five discontinuities over five meters, i.e. a density $N_s^{\max} \simeq 1$ sealed discontinuity per metre. However, it is not sure that all the fractures will re-open at the same time. If only one such fracture re-opens along the core in unit 1, then $N_s^1 = 0{\cdot}2$ sealed discontinuity per meter, which implies $k = 10^{-8}$ m^2 in the direction of the fractured marl. This value is significantly larger than the permeability of the open fracture ($k = 10^{-9}$). As sealed discontinuities show a multiple layer structure (Section "Qualitative Description of the Discontinuities" in Paper 1), one could also conceive that only part of the layers would be dissolves, providing thinner apertures.

CONCLUSION

Two techniques for the aperture reconstruction of discontinuities have been developed. The first one, suited to fully open discontinuities at the scale of the core log, is based on correlating the detailed morphology of their sides. Using this method, the aperture of one of the open discontinuities located in the marl bedrock of Draix has been determined. The three-dimensional thickness of such a discontinuity was also computed using measurements of the surface elevations with a laser profiler. The relative spatial positioning of the top and bottom elevation measurements was necessary for reconstructing the thickness of the vein, and was ensured by docking the rock sample into a rigid frame with a known geometry. The ratio between the amplitude of the roughness and the mean aperture was found to be very small for the open discontinuity, contrary to what was obtained fore the sealed discontinuity. The scaling laws of the aperture and thickness of respectively the open and sealed discontinuities were also obtained. The thickness of the vein is self-affine, with similar Hurst and pre-factor values as the ones of its sides. On the contrary, the open discontinuity presents two non-independent self-affine surfaces, leading to an aperture which is only self-affine at very small scales and uncorrelated at larger scales. From these geometrical properties, macroscopic hydraulic transport properties of open and sealed discontinuities could be assessed using, in the first case, a simple planar fracture model, and, in the second case, finite difference simulations for self-affine apertures. This allowed us to come to an estimate of macroscopic permeability values for these sets of discontinuities: $k = 10^{-9}$ m^2 for the open ones, and potentially $k = 10^{-8}$ m^2 for the ones currently sealed, in case the material inside would dissolved or washed away. It means that the fractured marl is potentially highly permeable.

ACKNOWLEDGEMENTS

The authors would like to thank José Ortega for his help for the geological description of the core, as well as Grégory Bièvre for helpful information about the SC1 drilling. We also would like to thank Alain Cochard, Jean-Philippe Malet, Julien Travelletti, Alexandre Remaître and Émilie Garel for fruitful discussions, and Alain

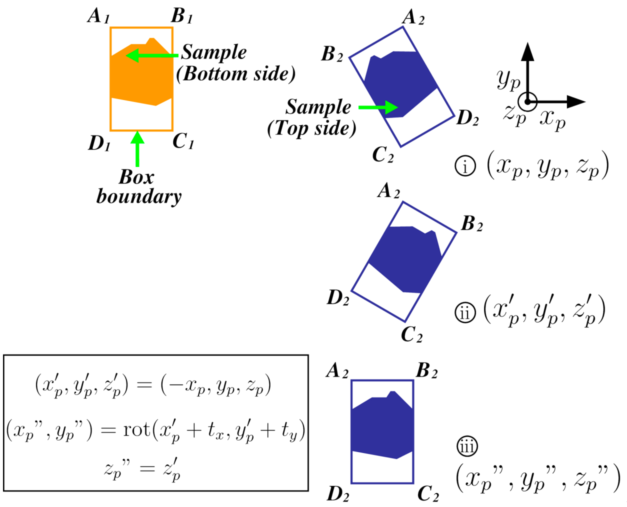

Figure 13. Schematic view of the transformations to be performed, step by step, to bring both measured topographies in a common frame. The sample and the box are viewed from the top (same as the profiler view)

Steyer for technical support. We thank the ANR Triggerland, as well as the SISCA and REALISE programs for their financial support.

APPENDIX: EXPERIMENTAL PROTOCOL TO CHANGE FRAMES WHEN MEASURING THE APERTURE USING THE TOPOGRAPHY OF A SEALED DISCONTINUITY

This is an appendix to Section "Reconstruction of the Thickness of a Sealed Discontinuity", where it is explained how to reconstruct the aperture of a sealed discontinuity from topography measurement of its surfaces. This is achieved if both topography measurements share a common reference frame, which may be adequately done by wedging the vein into a rigid box of known geometry. A truly rectangular parallelepiped box greatly eases the procedure. First, the topography of one surface (called top) is determined together with the boundaries of the box (A_1 B_1 C_1 D_1, Figure 13, top left). Second, the box is flipped upside down and the topography of the other surface (bottom) is similarly measured (Figure 13, step i). It is then possible to transform coordinates from the global frame — given by the profiler — to the local frames $\mathcal{R}_1$ and $\mathcal{R}_2$, where $\mathcal{R}_1$ and $\mathcal{R}_2$ are the frames associated with, respectively, the top and bottom boundaries of the box, as shown in Figure 5. With a parallelepiped box, it simply remains to bring A_1 B_1 C_1 D_1 in correspondence with A_2 B_2 C_2 D_2 (corresponding points of the top surface), thus obtaining new set (x''_p, y''_p, z''_p) of coordinates for the top surface. This is done with a rotation of 180° around the y-axis of the top surface (Figure 13, step ii), followed by an in-plane translation and rotation (Figure 13, step iii). Finally, knowing the box thickness, the aperture can be deduced by an appropriate subtraction of the top and bottom measurements.

REFERENCES

Al-Yaarubi A, Pain C, Grattoni C, Zimmerman R. 2005. Navier-Stokes simulations of fluid flow through a rock fracture. In *Dynamics of Fluids and Transport in Fractured Rocks*, vol. 162, Faybishenko B, Witherspoon P, Gale J (eds). American Geophysical Union: Washington, DC; 55–64. AGU Monograph.

Auradou H, Drazer G, Boschan A, Hulin JP, Koplik J. 2006. Flow channeling in a single fracture induced by shear displacement. *Geothermics* **35**(5–6): 576–588.

Auradou H, Drazer G, Hulin J, Koplik J. 2005. Permeability anisotropy induced by the shear displacement of rough fracture walls. *Water Resources Research* **41**(9): 1–10.

Brown LG. 1992. Survey of image registration techniques. *ACM Computing Surveys* **24**(4): 325–376.

Brown S. 1987. Fluid flow through rock joints: the effect of surface roughness. *Journal of Geophysical Research* **92**(B2): 1337–1347.

Brown S. 1995. Simple mathematical model of a rough fracture. *Journal of Geophysical Research* **100**(B4): 5941–5952.

Drazer G, Koplik J. 2002. Transport in rough self-affine fractures. *Physical Review E* **66**: 026303.

Fressard M, Maquaire O, Malet JP, Klotz S, Grandjean G. 2009. Morpho-structure and triggering conditions of the Laval landslide developed in clay-shales, Draix catchment (South French Alps). In *Landslide Processes. From Geomorphologic Mapping to Dynamic Modelling*, Remaître A, Malet J-P, Bogaard T (eds). CERG, Strasbourg: France; 111–114.

Genter A, Traineau H. 1996. Analysis of macroscopic fractures in granite in the HDR geothermal well EPS-1, Soultz-sous-Forêts, France. *Journal of Volcanology and Geothermal Research* **72**(1–2): 121–124.

Gentier S, Hopkins D. 1997. Mapping fracture aperture as function of normal stress using a combination of casting, image analysis and modeling techniques. *International Journal of Rock Mechanics and Mining Sciences & Geomechanics Abstracts* **34**(3–4): 359.

Glover P, Matsuki K, Hikima R, Hayashi K. 1998. Synthetic rough fractures in rocks. *Journal of Geophysical Research B: Solid Earth* **103**(5): 9609–9620.

Hakami E, Larsson E. 1996. Aperture measurements and flow experiments on a single natural fracture. *International Journal of Rock Mechanics & Mining Sciences* **33**(4): 395–404.

Isakov E, Ogilvie SR, Taylor CW, Glover PWJ. 2001. Fluid flow through rough fractures in rocks I: high resolution aperture determinations. *Earth and Planetary Science Letters* **191**(3–4): 267–282.

Lee H, Cho T. 2002. Hydraulic characteristics of rough fractures in linear flow under normal and shear load. *Rock Mechanics and Rock Engineering* **35**(4): 299–318.

Lofi J, Pezard P, Loggia D, Garel E, Gautier S, Merry C, Bondabou K. 2011. Geological discontinuities, main flow path and chemical alteration in a marly hill prone to slope instability: assessment from petrophysical measurements and borehole image analysis. *Hydrological Processes* in press, DOI: 10.1002/hyp.7997.

Méheust Y, Schmittbuhl J. 2000. Flow enhancement of a rough fracture. *Geophysical Research Letters* **27**: 2989–2992.

Méheust Y, Schmittbuhl J. 2001. Geometrical heterogeneities and permeability anisotropy of rough fractures. *Journal of Geophysical Research* **106**(B2): 2089–2012.

Méheust Y, Schmittbuhl J. 2003. Scale effects related to flow in rough fractures. *Pure and Applied Geophysics* **160**(5–6): 1023–1050.

Muralidhar K. 1990. Flow and transport in single rock fractures. *Journal of Fluid Mechanics* **215**: 481–502. DOI:10.1017/S0022112090002725.

Neuville A, Toussaint R, Schmittbuhl J. 2010a. Fracture roughness and thermal exchange: A case study at Soultz-sous-forêts. *Comptes Rendus Geoscience* **342**(7–8): 616–625. DOI:10.1016/j.crte.2009.03.006.

Neuville A, Toussaint R, Schmittbuhl J. 2010b. Hydro-thermal flows in a self-affine rough fracture. **82**: 036317. DOI: 10.1103/PhysRevE.82.036317.

Neuville A, Toussaint R, Schmittbuhl J, Koehn D, Schwarz J. 2011. Characterization of major discontinuities from borehole cores of the black consolidated marl formation of Draix (French Alps). *Hydrological Processes* in press, DOI: 10.1002/hyp.7984.

Noiriel C. 2005. *Contribution à la détermination expérimentale et à la modélisation des différents processus contrôlant l'évolution géochimique, structurale et hydrodynamique des roches fissurées carbonatées*. Thèse de doctorat, École des Mines de Paris.

Ogilvie S, Isakov E, Glover P. 2006. Fluid flow through rough fractures in rocks II: A new matching model for rough rock fractures. *Earth and Planetary Science Letters* **241**(3–4): 454–465.

Patir N, Cheng H. 1978. An average flow model for determining effects of three-dimensional roughness on partial hydrodynamic lubrication. *Journal of Lubrication Technology* **100**: 12–17.

Plouraboué F, Hulin JP, Roux S, Koplik J. 1998. Numerical study of geometrical dispersion in self-affine rough fracture. *Physical Review E* **58**(3): 3334–3346.

Plouraboué F, Kurowski P, Hulin JP, Roux S, Schmittbuhl J. 1995. Aperture of rough cracks. *Physical Review E* **51**(3): 1675–1685.

Pyrak-Nolte L, Cook N, Note D. 1988. Fluid percolation through single fractures. *Geophysical Research Letters* **15**(11): 1247–1250.

Roux S, Plouraboué F, Hulin JP. 1998. Tracer dispersion in rough open cracks. *Transport in Porous Media* **32**(1): 97–116.

Sakaguchi K, Tomono J, Okumura K, Ogawa Y, Matsuki K. 2008. Asperity height and aperture of an artificial tensile fracture of metric size. *Rock Mechanics and Rock Engineering* **41**(2): 325–341. DOI:10.1007/s00603-005-0102-3.

Schmittbuhl J, Steyer A, Jouniaux L, Toussaint R. 2008. Fracture morphology and viscous transport. *International Journal of Rock Mechanics & Mining Sciences* **45**: 422–430.

Sharifzadeh M, Mitani Y, Esaki T. 2008. Rock joint surfaces measurement and analysis of aperture distribution under different normal and shear loading using GIS. *Rock Mechanics and Rock Engineering* **41**(2): 299–323.

Tsang Y, Tsang C. 1987. Channel model of flow through fractured media. *Water Resources Research* **23**(3): 467–479.

Vicente SM, Ribeiro e Sousa L, Hack R. 2002. Laboratory study of geomechanical and hydro-mechanical characterisation of discontinuities. *News Journal International Society for Rock Mechanics (ISRM)* **7**(2): 9–15.

Walkup GJ, Horne R. 1985. Forecasting thermal breakthrough of reinjected water using a dispersion-retention model for tracer test interpretation. In *International Symposium - Geothermal Energy, Part II*, vol. 9, Geothermal Resources Council Transactions. Conference Paper; 369–374.

Wilson C, Theriot J. 2006. A correlation-based approach to calculate rotation and translation of moving cells. *IEEE Transactions on Image Processing* **15**(7): 1939–1951.

Zimmerman R, Bodvarsson G. 1996. Hydraulic conductivity of rock fractures. *Transport in Porous Media* **23**(1): 1–30.

Zimmerman R, Main I. 2004. Hydromechanical behaviour of fractured rocks, *Mechanics of Fluid-saturated Rocks*, vol. 89 of International Geophysics Series, Elsevier, Academic press: London, UK; 363–421.

Hydrothermal coupling in a self-affine rough fracture

A. Neuville,* R. Toussaint, and J. Schmittbuhl

Institut de Physique du Globe de Strasbourg (IPGS), CNRS, and Université de Strasbourg (EOST), 5 rue Descartes, 67000 Strasbourg, France

(Received 31 March 2010; published 21 September 2010)

The influence of the multiscale fracture roughness on the heat exchange when a cold fluid enters a fractured hot solid is studied numerically on the basis of the Stokes equation and in the limit of both hydrolubrication and thermolubrication. The geometrical complexity of the fracture aperture is modeled by small self-affine perturbations added to a uniform aperture field. Thermal and hydraulic properties are characterized via the definition of hydraulic and thermal apertures both at microscopic and macroscopic scales and obtained by comparing the fluxes to the ones of flat fractures. Statistics over a large number of fracture configurations provide an estimate of the average behavior and its variability. We show that the long-range correlations of the fracture roughness induces strong channeling effects that significantly influence the hydraulic and thermal properties. An important parameter is the aspect ratio (length over width) of the fracture: we show, for example, that a downstream elongated rough fracture is more likely to inhibit the hydraulic flow and subsequently to enhance the thermal exchange. Fracture roughness might, in the opposite configuration, favor strong channeling which inhibits heating of the fluid. The thermal behavior is in general shown to be mainly dependent on the hydraulic one, which is expressed through a simple law.

DOI: 10.1103/PhysRevE.82.036317 PACS number(s): 47.56.+r, 44.05.+e, 47.11.Bc, 44.30.+v

I. INTRODUCTION

Among situations where heat exchange between a passing fluid and a fractured medium is of central importance, geothermics is an intensively developing field. Deep enhanced geothermal systems (EGSs) are based on the energy extraction obtained when a cold fluid is injected from the surface inside a hot fractured massif at depth and extracted after circulation in the open fractures possibly artificially created from an hydraulic or chemical stimulation (e.g., the EGS pilot plant in Soultz-sous-Forêts, France [1–4]).

The efficiency of the heat exchange depends on the balance between conductive and convective heat fluxes. The former is mainly dependent on the geometry of each individual interface, i.e., facing fracture surfaces, but the latter is definitively related to the hydraulic properties of the fracture network, which results from the network connectivity and the fracture permeability.

Hydraulic conductivity of fractured rocks has been intensively studied for different motivations. For instance, the hydraulic properties of the crystalline aquifer of Ploemeur, France have been studied by Le Borgne *et al.* [5] to address water supply issues. Another example is the mitigation of radionuclide migration which has been forecasted in the case of the repository site for nuclear wastes storage in Äspö, Sweden on the basis of a discrete fracture network [6]. The modeling of the transport properties of fracture networks is actually a very active research area. A classical approach is to model the flow paths via parallel interacting flat fractures [7]. More advanced studies address the effects of the connectivity and correlations of the fractures (e.g., in Refs. [8,9]).

In many models of hydraulic or hydrothermal flow developed so far, the geometry of each fracture of the network is nevertheless considered as simple, e.g., as parallel plates with a simple geometry of the edge as an ellipse or a polyhedron. This is the case in most fracture network models used for geothermal [10] or for fluid transport applications [8,9]. The nontrivial character of the fracture aperture geometry is however very likely to influence the fracture flow given their complex real geometry. Most natural fracture surfaces are indeed self-affine objects. Surprisingly, the complexity of the multiscale properties of the fractures has some remarkable simplicity, in the sense that their Hurst exponent is very robustly around 0.8 [11]. Exceptions however exist like for fractures in sandstones where the Hurst exponent is 0.5 [12,13] or in glassy ceramics which show an exponent close to 0.4 [14].

The aperture between fracture surfaces is subsequently far from flat in particular if facing fracture surfaces are uncorrelated, at least at small scales [15,16]. A rough self-affine aperture is indeed defined between two uncorrelated self-affine fracture surfaces or between two identical self-affine fractures translated tangentially to their average plane by a translation larger than the scale under study. Self-affine apertures have been shown to be responsible for tortuous flow path. The related channeling of the fluid flow was experimentally observed in rough fractures [17,18] and modeled using lubrication approximation with Reynolds equation (e.g., [13,19–22]). The applicability of such an approximation has been studied, e.g., in Refs. [23–25]. Extension of this situation was considered, for example, by Plouraboué *et al.* [26] where the Reynolds equation is coupled to the chemical convection-diffusion study. More advanced hydraulic simulations including the solving of the Navier-Stokes equation have been proposed either considering simplified geometry [23,27] or more recently within a realistic fracture geometry [28–32]. However, these recent simulations require heavy computations (although different methods are available) and are therefore not fully compatible with statistical

*amelie.neuville@unistra.fr

approaches where a large number of realizations are necessary.

Beyond the problem of mass flow in rough fractures, different kinds of numerical simulations have already been proposed to account for hydrothermal coupling. As a first approach, analytical solutions have been obtained to compute the heat flux along parallel circular cracks embedded in a three-dimensional (3D) infinite medium using simplified heat equations [33]. At large scale and for long-term predictions, models like that of Bataillé *et al.* [10] have been proposed to predict the response of geothermal reservoirs. This type of finite-element model includes conduction and free and forced convection, but reduces the geometry of the hydraulic network to a double permeability distribution to account for both matrix and fracture transport. A variety of more complex models have also been proposed like the modeling of a 3D network of fractures organized according to geological observations and completed with stochastic fractures for underdetermined parts of the model [34], or that for Soultz-sous-Forêts, France by Rachez *et al.* [35] or that of Kolditz and Clauser [36] for Rosemanowes, UK.

In the present study, we focus on the hydrothermal coupling at the fracture scale where the channeling effect is expected to affect not only the fluid transport properties, but also the heat flux properties, as suggested by Kolditz and Clauser [36] who proposed that the discrepancy between classical heat model predictions and real observations could be due to flow channeling resulting from fracture roughness. We aim at obtaining from the microscopic analysis of the flow at scales of the fracture asperities the macroscopic parameters (i.e., the hydraulic transmissivity and the characteristic thermalization length) that govern the efficiency of the fluid mass and heat transport through the overall fracture. This will allow us to coarse grain the description of the effect of microscopic asperities, i.e., the fracture roughness, on the hydraulic and thermal behavior in large-scale network models as the ones mentioned above. The upscaling from the microscopic asperity scale to the fracture scale is done via a systematic statistical analysis of the macroscopic flow parameters, for a large set of stochastic synthetic fracture surfaces, described with a few key parameters for such apertures: average aperture and standard deviation. The macroscopic parameters obtained after the upscaling reduce to two: the hydraulic transmissivity, characterizing the fluid mass transport, and the other one characterizing the efficiency of the heat exchange between the rock and the fluid. This exchange is expressed via the characteristic length R in a macroscopic law of type

$$(\boldsymbol{q}/\|\boldsymbol{q}\|) \cdot \nabla_2 \bar{T} - (\bar{T} - T_r)/R = 0, \tag{1}$$

with $\bar{T}$ as a fluid temperature, T_r as the temperature in the surrounding rock, $\boldsymbol{q}$ as the fluid flux integrated over the fracture thickness, and ∇_2 as the two-dimensional (2D) gradient operator along the fracture plane. The hydrothermal modeling is performed as in [3]. The present study is in the framework of the lubrication approximation [37] which implies that the Reynolds number is small and that the fracture walls are locally flat enough to provide a mainly in-plane velocity field, with a negligible component normal to the mean fracture plane. We propose to extend the lubrication approximation to the thermal fluxes. By balancing heat conduction and forced convection we obtain a three-dimensional temperature law which will then be reduced to a 2D temperature equation by averaging it along the thickness of the fracture as proposed, e.g., by Turcotte and Schubert [38].

Section II describes our geometrical model of the fracture aperture based on a self-affine scaling invariance. In Sec. III, using lubrication approximations, we obtain the bidimensional pressure and thermal equations when a cold fluid is injected through a fracture in a stationary regime. As a first step, the temperature within the surrounding rock is supposed to be hot and constant (in time and space), and the density of the fluid is considered as constant. We show that at a coarse-grained scale, the 2D equation for heat flux is identical to the one for parallel plates [Eq. (1)], but with a characteristic thermalization length associated with an aperture (named thermal aperture), different from the geometrical aperture (also often labeled as the mechanical aperture). Other relevant quantities are defined to describe the hydraulic and thermal behaviors at local and macroscopic scales. The numerical approach is described in detail in Sec. IV. Equations are discretized using a finite difference scheme and solved with a biconjugate gradient method. The numerical hydraulic and thermal results are, respectively, set out in Secs. IV and V. In each of these sections, we first describe the results for a given fracture morphology (locally and macroscopically), then averaged trends of macroscopic parameters that are observed statistically from large sets of synthetic fractures.

II. DESCRIPTION OF THE ROUGHNESS OF THE FRACTURE APERTURE

The roughness of a self-affine surface is statistically invariant upon an isotropic scaling within its mean plane (x,y), while on the perpendicular direction z the scaling is anisotropic. Indeed, it is statistically invariant under the scaling transformation $x \to \lambda x,\ \ y \to \lambda y,\ \ \Delta z \to \lambda^{\zeta} z$ [39–41], where ζ is called roughness exponent or Hurst exponent. A self-affine geometrical model has been experimentally shown to be a realistic description of natural rock surfaces [11,16,42,43], with Hurst exponent equal at large scale to $\zeta \simeq 0.8$ for many kinds of natural fractures and material surfaces [42–45] and $\zeta \simeq 0.5$ for sandstones [46,47]. It is important to note that a self-affine surface having a roughness exponent smaller than 1 is asymptotically flat at large scales [48]. Accordingly, a self-affine topography can be seen as a perturbation of a flat interface. On the other end of the scales, the local slope of a self-affine surface diverges at small scales, and the maximum slope of such surface is determined by the lower cutoff of the self-affine behavior—corresponding, e.g., to granular diameter when present. In principle, modeling a flow boundary condition along such surface requires us to check that the macroscopically obtained result does not depend on such lower cutoff.

The aperture is the space between the facing fracture surfaces. Our study is limited to the case where two noncorrelated fracture surfaces with the same roughness exponents are facing each other. Subsequently the aperture $a(x,y)$ is also a self-affine function with the same Hurst exponent which fulfills the following property [39,40]:

$$\lambda^{\zeta}\,\text{Prob}(\lambda^{\zeta}\Delta a,[\lambda\Delta x,\lambda\Delta y]) = \text{Prob}(\Delta a,[\Delta x,\Delta y]), \qquad (2)$$

where $\text{Prob}(\Delta a,[\Delta x,\Delta y])$ is the probability to get an aperture difference Δa between two points separated by the distance $[\Delta x,\Delta y]$, λ is an arbitrary scaling factor, and ζ is the roughness exponent.

The self-affine aperture field is numerically obtained by first generating a white noise $\epsilon(x,y)$ [49] on a grid of size $2n_x \times 2n_y$ with a square mesh size d. Then the statistical spatial correlations are introduced by multiplying the 2D Fourier transform of the white noise $\tilde{\epsilon}(k_x,k_y)$ by $\|\boldsymbol{k}\|^{(-1-\zeta)}$ [50], where $\boldsymbol{k}$ is the wave vector. When desired, a lower cutoff length scale l_c can be introduced by filtering as follows: if $\|\boldsymbol{k}\| \geq \pi/l_c$, $\tilde{a}(k_x,k_y)=0$. Finally, we perform the inverse Fourier transform of $\tilde{a}(k_x,k_y)$ and normalize it to get a synthetic aperture $a(x,y)$ with an average A and a root mean square (RMS) σ. Using different seeds of the random generator of the white noise, it is possible to generate independent self-affine aperture morphologies showing different patterns, even if they share the same roughness exponent chosen equal to $\zeta=0.8$, the same mean aperture A, and the same RMS σ. The upper limit of σ is provided by the condition of positive aperture, i.e., we prevent contact between the fracture faces to keep a constant simple boundary geometry of the domain where the equations are solved. In practice a is imposed to range between 10^{-4} and 10, which leads to $0.7 > \sigma/A > 10^{-3}$. The typical grid sizes that were used are 1024×1024, 1024×2048, and 1024×512. The mesh size d has been adjusted to get a sufficient numerical precision of the temperature solution in the case of a parallel plate configuration where an analytical solution is known. The numerical stability of the solutions has also been tested against slight shifts of the mesh position on an oversampled self-affine aperture field, $2n_x \times 2n_y = 2^{12} \times 2^{12}$, and against the introduction of a lower cutoff l_c of the self-affine perturbations varying between the mesh size and ten times the mesh size: the determined flow and temperature fields were found to be independent of such small-scale modifications.

III. HYDRAULIC AND THERMAL FLOW EQUATIONS

A. Hydraulic flow

We consider the steady flow of a Newtonian fluid at low Reynolds number, so that the viscous term of the Navier-Stokes equation dominates the inertial one. The Navier-Stokes equation is therefore reduced to the Stokes equation [51,52]

$$\boldsymbol{\nabla} P = \eta \Delta \boldsymbol{v}, \qquad (3)$$

where η is the dynamic viscosity, $\boldsymbol{v}$ is the velocity of the fluid, and P is the pressure deviation from the hydrostatic profile (i.e., the hydraulic head which is equal to the pressure corrected by the gravity effect). To be in the framework of the lubrication approximation [37], besides small Reynolds number, we also consider fractures with flat enough sides as

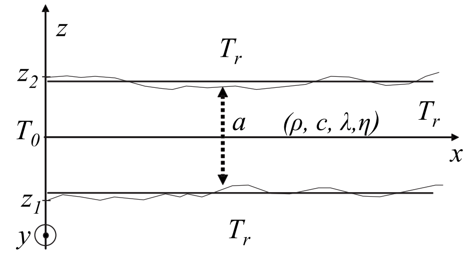

FIG. 1. 2D sketch of the fracture model with parameter definitions. x axis is along the mean hydraulic flow, y axis is along the mean fracture plane but perpendicular to the main hydraulic flow, and z axis denotes the out-of-mean fracture plane direction. $z=z_1$ and $z=z_2$ are the average positions of the facing fracture surfaces. $a(x,y)$ is the fracture aperture. T_r is the temperature of the solid, supposed to be homogeneous and constant, T_0 is the fluid temperature at the inlet. Fluid properties are ρ, c, χ, and η, which are, respectively, density, heat capacity, thermal diffusivity, and dynamic viscosity.

mentioned above (i.e., with small local slopes). Therefore, fluid velocity vectors get negligible z components (normal to the mean fracture plane), and accordingly the velocity field is dominated by in-plane components. The unitary vector $\hat{\boldsymbol{x}}$ is aligned with the macroscopic imposed pressure gradient (see Fig. 1); $z_1(x,y)$ and $z_2(x,y)$ are the bottom and top fracture coordinates, with $z_2 - z_1 = a$. Under these approximations, the pressure dependence is $P(x,y)$ and the velocity $\boldsymbol{v}$ is oriented along the unitary vector $\hat{\boldsymbol{v}}(x,y)$. By integrating the Stokes equation with the boundary conditions, $\boldsymbol{v}(z_{1,2})=\boldsymbol{0}$, we get a local parabolic law in z (Fig. 2) [25]:

$$\boldsymbol{v}(x,y,z) = \frac{\boldsymbol{\nabla_2} P(x,y)}{12\eta}(z-z_1)(z-z_2), \qquad (4)$$

where $\boldsymbol{\nabla_2} = \hat{\boldsymbol{x}}\frac{\partial}{\partial x} + \hat{\boldsymbol{y}}\frac{\partial}{\partial y}$ is the in-plane gradient operator.

Integrating Eq. (4) along z leads to expressing the hydraulic flow through the fracture thickness $\boldsymbol{q}$ as

$$\boldsymbol{q} = -\frac{a^3}{12\eta}\boldsymbol{\nabla_2} P. \qquad (5)$$

Furthermore, we assume the fluid to be incompressible, i.e., $\boldsymbol{\nabla_2}\cdot\boldsymbol{q}=0$, which leads to the Reynolds equation [19]

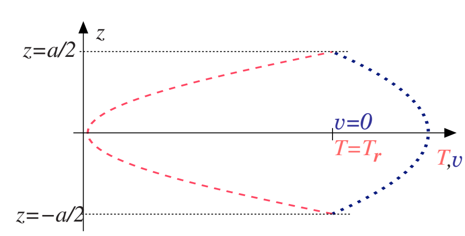

FIG. 2. (Color online) Local velocity quadratic profile (short dashed line) and temperature quartic profile (long dashed line) inside a fracture [with coefficients from Eqs. (9) and (4)]; arbitrary abscissa units. Along the contact with the fracture, $\boldsymbol{v}=\boldsymbol{0}$ and $T=T_r$.

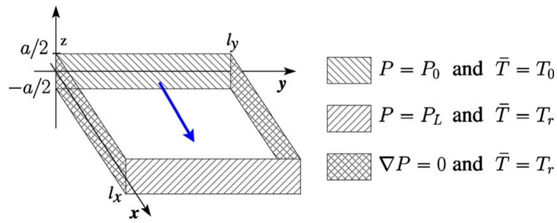

FIG. 3. (Color online) Fracture model with pressure and temperature boundary conditions.

$$\nabla_2 \cdot (a^3 \nabla_2 P) = 0. \tag{6}$$

As boundary conditions of this equation (Fig. 3), we impose the pressure at the inlet and outlet of the fracture (if $x=0$, $P=P_0$, and if $x=l_x$, $P=P_L$, with $P_0 > P_L$) and consider impermeable sides (no mass exchange with the rock matrix) at $y=0$ and $y=l_y$.

B. Thermal flow

In this work, we neglect the natural convection that happens in fractured rocks when the fluid density is thermally sensitive, as studied, for instance, by Bataillé *et al.* [10]. Natural convection might happen within the thickness of the fracture (owing to the temperature difference between the fracture boundary and the core of the flow along the gravity direction) and at large scale when the fracture is nonhorizontal. For the sake of simplicity, we consider that the forced fluid flow studied here is only weakly affected by density changes. A quantitative criterion of this assumption is given by the comparison of the pressure differences ΔP forcing the flow and that generated by the temperature changes: $\Delta P \gg g\alpha_T \rho \Delta T$, with g as the gravity, α_T as the fluid coefficient of thermal expansion, ρ as the fluid density, and ΔT as the temperature differences in the system. We also assume that the Prandtl number of the fluid is sufficiently high for the flow to be dominated by hydrodynamic effects rather than thermal effects.

Since our focus is to understand how the macroscopic mass and heat flows are affected by the fracture roughness in the stationary limit, we do not consider time and space variations of the temperature in the rock: the fracture sides are assumed to be permanently hot at the fixed temperature T_r. This simplification is valid if we consider either long time scales, i.e., when the rock temperature profiles stabilizes, or time scales shorter than that of the hosting rock evolution. Taking the slow temperature evolution of the hosting rock into account would require us to combine the present study with a nonstationary conductive heat solver for the rock, which is beyond the scope of this paper. In principle, to model these intermediate time scales, the macroscopic parameters controlling the heat exchange determined in this paper could be utilized in a hybrid model, coupling the heat diffusion-advection in the fluid with the heat diffusion in the solid.

Local energy conservation implies that the fluid temperature is controlled by the balance between thermal convection and conduction inside the fluid, which reads as (with heat source due to friction between fluid layers being neglected) [53]

$$\boldsymbol{v} \cdot \nabla T = \chi \Delta T, \tag{7}$$

where χ is the thermal diffusivity of the fluid and T is the fluid temperature. We extend the lubrication approximation (cf. Sec. I) by considering that the slopes of the fracture morphology are small enough to provide conduction at the rock interface locally oriented along $\hat{z}$. This implies that the out-of-plane conduction term is dominant in front of the in-plane ones. Otherwise, $v_z \partial T/\partial z$ can be neglected in $\boldsymbol{v}\cdot\nabla T$ since out-of-plane velocity v_z is negligible. Accordingly the leading terms in Eq. (7) are the conduction along the $\hat{z}$ axis and the in-plane convection terms, and this reduces to

$$\frac{\partial^2 T}{\partial z^2} = \frac{v_x}{\chi}\frac{\partial T}{\partial x} + \frac{v_y}{\chi}\frac{\partial T}{\partial y}. \tag{8}$$

For the boundary conditions, we assume that the fluid temperature is equal to the rock temperature along the fracture sides,

$$T(x,y,z_{1,2}) = T_r,$$

and far from the fracture inlet,

$$T(x,y,z) \underset{x\to\infty}{\longrightarrow} T_r.$$

The temperature of injection at the inlet is T_0, so that $T(0,y,z)=T_0$ (for any y and z). By assuming that $\beta = q_x \partial T/\partial x + q_y \partial T/\partial y$ is only a function of x and y, the following quartic expression of T is a solution of Eq. (8):

$$T(x,y,z) = T_r - \frac{\beta(x,y)}{2a^3\chi}(z-z_1)(z-z_2)(z-\sqrt{5}z_1)(z-\sqrt{5}z_2). \tag{9}$$

For the particular case of symmetric apertures around an average plane, i.e., where $z_1=-z_2=a/2$, this reduces to $T = -3\beta(z^4/6 - a^2z^2/4 + 5a^4/96)/(a^3\chi) + T_r$. By uniqueness of the solution for given boundary conditions (the problem is well posed), this quartic law is the only solution of Eq. (7). The temperature profile along z is illustrated together with the velocity profile in Fig. 2.

The energy conservation equation [Eq. (7)] is integrated along the z direction through the thickness of the fracture (as done for the hydraulic description), which provides an in-plane description of the thermal balance. First, we estimate the advected energy flux. For this, we note by c the fluid specific heat capacity and U_0 its internal energy density at $T=T_0$, and write the internal energy density U as $U=U_0 + \rho c(T-T_0)$. Integrating along the fracture thickness (i.e., along the z axis) leads to the internal energy flux per unit volume $\boldsymbol{f}(x,y) = \int U \boldsymbol{v} dz$, which can be expressed as

$$\boldsymbol{f}(x,y) = [U_0 + \rho c(\bar{T} - T_0)]\boldsymbol{q}(x,y), \tag{10}$$

where $\bar{T}$ is a weighted average temperature defined as

$$\bar{T}(x,y) = \frac{\int_a v(x,y,z)T(x,y,z)dz}{\int_a v(x,y,z)dz}, \tag{11}$$

with $\bar{T}(0,y)=\bar{T}_0=T_0$ at the inlet. The heat source coming from the advected energy is then given by $-\nabla_2 \cdot \boldsymbol{f}$. Using the mass conservation equation, $\nabla_2 \cdot \boldsymbol{q}=0$, leads to

$$\nabla_2 \cdot \boldsymbol{f} = \rho c \boldsymbol{q} \cdot \nabla_2 \bar{T}. \tag{12}$$

The advected energy flux balances the conductive flux through the upper and lower fracture walls. To evaluate the thermal conductive flow oriented along the outgoing normal to the fracture walls $\hat{\boldsymbol{n}}$, the lubrication approximation (cf. Sec. I), leads to $\hat{\boldsymbol{n}} \simeq \pm \hat{\boldsymbol{z}}$. Let φ_w be the projection of the conductive flow along $\hat{\boldsymbol{n}}$, evaluated along the walls, at $z_{1,2}$. The Fourier law provides $\varphi_w = -\chi \rho c \frac{\partial T}{\partial z}\big|_{z=z_{1,2}} \hat{\boldsymbol{z}} \cdot \hat{\boldsymbol{n}}$. Inserting Eqs. (9) and (4) to Eq. (11) leads to $\frac{\partial T}{\partial z}\big|_{z=z_{1,2}} = (\bar{T}-T_r)\frac{70}{17a}\hat{\boldsymbol{z}} \cdot \hat{\boldsymbol{n}}$. The Nusselt number $\mathrm{Nu}=-\varphi_w/\varphi_{ref}=70/17$ is used to characterize the efficiency of the present heat exchange compared to the reference heat flow $\varphi_{ref}=\chi \rho c (T_r-\bar{T})/a$, which occurs in situations with only conduction. The energy net flux,

$$\nabla_2 \cdot f + 2\varphi_w = 0, \tag{13}$$

can finally be expressed as

$$\boldsymbol{q} \cdot \nabla_2 \bar{T} + 2\frac{\chi}{a}\mathrm{Nu}(\bar{T} - T_r) = 0. \tag{14}$$

For the boundary conditions of the two-dimensional field $\bar{T}$, we assume that the fluid is injected at a constant temperature $\bar{T}(0,y)=T_0$ colder than the rock, and we consider the length of the fracture to be long enough to get the fluid at the same temperature as the rock at the end of it: $\bar{T}(l_x,y)=T_r$. On the contrary, temperature settings along the boundaries $y=0$ and $y=l_y$ have no influence since the hydraulic flow is null there [see Eq. (6)].

Let the reference case be a fracture modeled with two parallel plates separated by a constant aperture $a_\parallel$ (i.e., no self-affine perturbation). In this case, the gradient of pressure is constant all along the fracture, as well as the hydraulic flow, which is equal to $\boldsymbol{q}_\parallel = -\Delta P a_\parallel^3/(12 l_x \eta)\hat{\boldsymbol{x}}$, where the subscript $\parallel$ denotes results valid for parallel plates and $\Delta P = P_L - P_0$. Under these conditions Eq. (14) is invariant along y and can be written as

$$\frac{\partial \bar{T}_\parallel}{\partial x} + \frac{(\bar{T}_\parallel - T_r)}{R_\parallel} = 0, \tag{15}$$

where the thermal length $R_\parallel$ characterizes the distance at which the fluid reaches the temperature of the surrounding rock:

$$R_\parallel = \frac{a_\parallel \|\boldsymbol{q}_\parallel\|}{2\,\mathrm{Nu}_\parallel \chi} = -\frac{\Delta P}{l_x}\frac{a_\parallel^4}{24\eta\,\mathrm{Nu}_\parallel \chi}, \tag{16}$$

with $\mathrm{Nu}_\parallel = 70/17 \simeq 4.12$. Then the analytical solution of Eq. (15) for parallel plates is

$$\bar{T}_\parallel - T_r = (T_0 - T_r)\exp\left(-\frac{x}{R_\parallel}\right). \tag{17}$$

For rough fractures, we aim at using Eq. (17) as a proxy of the average temperature profile $\bar{\bar{T}}$ along the flow and defining an effective macroscopic thermal length R as

$$\bar{\bar{T}} - T_r = (T_0 - T_r)\exp\left(-\frac{x}{R}\right). \tag{18}$$

C. Definition of microscopic and macroscopic apertures

Different types of fracture apertures can be defined. The most obvious one is the geometrical aperture, but effective apertures such as hydraulic or thermal aperture can also be introduced. The latter are defined on the basis of an inversion on a specific model like the parallel plate model. For instance, the hydraulic aperture is deduced from the knowledge of the fluid flow through the fracture, and it represents the aperture of a parallel plate model that reproduces the observed fluid flow. Equivalently a thermal aperture can be introduced as the aperture of a parallel plate model that reproduces a similar thermal profile. A spatial scale has to attach to define the hydraulic or thermal equivalent behavior, in particular for a multiscale geometry. Since we aim at understanding the upscaling of the fracture properties, we will introduce two specific scales: the smallest one, i.e., the grid size of the discretization, and the largest one, i.e., the system size. The smallest will be referred to as the microscopic or local scale and small letters will be used for their labeling, and the largest will be referred to as the macroscopic scale and described with capital letters.

We already use the microscopic geometrical or mechanical aperture a and its spatial average, i.e., the macroscopic geometrical aperture: $A=\langle a(x,y)\rangle_{x,y}$. The microscopic hydraulic aperture is defined as from Eq. (5) [19,54]

$$h = \left(\|\boldsymbol{q}\|\frac{12\eta}{\left|\frac{\Delta P}{l_x}\right|}\right)^{1/3}. \tag{19}$$

It depends on the local hydraulic flow $\boldsymbol{q}$ and can be related to the local pressure gradient $\|\nabla P\|$ and local aperture a as

$$h = a\left(\frac{\|\nabla P\|}{\frac{\Delta P}{l_x}}\right)^{1/3}. \tag{20}$$

If the local pressure gradient $\|\nabla P\|$ is smaller than the macroscopic gradient $\Delta P/l_x$, then $h(x,y) < a(x,y)$, which means that locally the hydraulic conductivity is lower than expected from its local mechanical aperture. The macroscopic hydraulic aperture H can also be defined at the system scale from the average hydraulic flow $Q_x=\langle \boldsymbol{q} \cdot \boldsymbol{n_x}\rangle_{x,y}$:

$$H = \left(Q_x \frac{12\eta}{\left| \frac{\Delta P}{l_x} \right|} \right)^{1/3}. \qquad (21)$$

Macroscopic and microscopic hydraulic apertures are related since H is actually proportional to the cubic root of the third-order moment of h: $H = \langle h(x,y)^3 \rangle_{x,y}^{1/3}$, which is proportional to the first-order moment of the hydraulic flux to power of 1/3. If $H/A > 1$, then the fracture is more permeable than parallel plates separated by $a(x,y) = A$.

The macroscopic thermal aperture is defined from a one-dimensional temperature profile $\bar{\bar{T}}(x)$ along the forced pressure gradient direction [see Eq. (18)] where the average temperature is defined as

$$\bar{\bar{T}}(x) = \frac{\int_{l_y} u_x(x,y)\bar{T}(x,y)dy}{\int_{l_y} u_x(x,y)dy}. \qquad (22)$$

It is an average of $\bar{T}$ along the width of the fracture l_y, weighted by the local fluid velocity $u_x(x,y) = q_x(x,y)/a(x,y)$ which is the ratio of the x component of the local flux over the local fracture aperture. Then, by fitting the parallel plate temperature solution [Eq. (18)] to the average temperature profile $\bar{\bar{T}}(x)$, we get the macroscopic thermal length R. In practice the fit is computed from a least-squares minimization, for abscissa from $x=0$ to the minimum x value, so that $|(\bar{\bar{T}} - T_r)/(T_0 - T_r)| < 2 \times 10^{-6}$. The macroscopic thermal aperture Γ is then defined by analogy to the parallel plate solution [Eq. (16)] as

$$\Gamma = \left(- R \times 24\eta \,\mathrm{Nu}\, \chi \frac{l_x}{\Delta P} \right)^{1/4} = A(R^*)^{1/4}, \qquad (23)$$

where $R^* = R/R_\parallel$ is the normalized thermal length. At a coarse-grained scale, the rough fracture is thermally equivalent to parallel plates separated by the constant aperture $a(x,y) = \Gamma$. Indeed, both will exhibit the same thermal length R under the same macroscopic pressure gradient $\Delta P/l_x$.

The microscopic thermal aperture γ can also be introduced after defining a local thermal length r. Similarly to the definition of a microscopic hydraulic aperture from the local pressure gradient, or local flux, rather than the macroscopic pressure difference, or macroscopic flux, we estimate the local thermal length from a local temperature gradient rather than a large-scale pressure difference. Equation (14) can be rewritten as

$$\boldsymbol{q} \cdot \boldsymbol{\nabla}_2(\ln[\bar{T}^*]) + \frac{\|\boldsymbol{q}\|}{r} = 0, \qquad (24)$$

with

$$r = \frac{a\|\boldsymbol{q}\|}{2\,\mathrm{Nu}\,\chi}, \qquad (25)$$

which is an estimate of the gradient along $\hat{\boldsymbol{s}}$, the local hydraulic flow direction. Finally, the local thermal aperture γ can be defined by [consistently with Eq. (16)]

$$\gamma = \left(- r \times 24\eta \,\mathrm{Nu}\, \chi \frac{l_x}{\Delta P} \right)^{1/4}. \qquad (26)$$

A link between macroscopic and microscopic thermal apertures can also be shown as follows: at first order, considering that the average of $\|\boldsymbol{q}\|$ is very close to the average of q_x then the local length of reference would be equal to $\tilde{r} = -[\partial \ln(\bar{\bar{T}}^*)/\partial x]^{-1}$. On the other hand, integrating Eq. (18) between zero and significant length L results in $R = -(\{\ln[\bar{\bar{T}}^*(L)] - \ln[\bar{\bar{T}}^*(0)]\}/L)^{-1}$, which shows the link between macroscopic and microscopic thermal apertures: $R = L[\int_0^L (-1/\tilde{r})dx]^{-1}$, i.e., $R = \langle r^{-1} \rangle^{-1} \propto \langle (a\|\boldsymbol{q}\|)^{-1} \rangle^{-1}$, according to Eq. (25).

For parallel plates, all microscopic apertures are equal and also equal to the macroscopic ones: $h = a = \gamma = H = \Gamma = A$. For rough fractures, this is definitively not the case since the local apertures vary spatially inside the fracture. We will see in the next section how all these apertures are influenced by the roughness amplitude of the fracture aperture, for which we will emphasize on two main parameters: the normalized root-mean-square deviation σ/A of the geometrical aperture and the aspect ratio of the fracture $J = l_x/l_y$, i.e., the ratio of the downstream length of the fracture l_x over its width l_y.

D. Dimensionless quantities

Dimensionless positions, apertures, pressure, temperature, and hydraulic flow are defined as follows:

$$x^* = \frac{x}{d}, \quad y^* = \frac{y}{d},$$

$$a^* = \frac{a}{A}, \quad H^* = \frac{H}{A}, \quad \Gamma^* = \frac{\Gamma}{A},$$

$$P^* = -\frac{(P - P_0)}{2d}\frac{l_x}{\Delta P},$$

$$\bar{T}^* = \frac{\bar{T} - T_r}{T_0 - T_r},$$

$$\boldsymbol{q}^* = -\frac{12\eta l_x}{\Delta P A^3}\boldsymbol{q}, \qquad (27)$$

where d is the mesh size of the aperture grid. Otherwise, we note that in the dimensionless temperature, the difference between the injection temperature T_0 and the rock temperature T_r intervenes only as a factor of proportionality.

IV. HYDRAULIC FLOW SIMULATIONS

A. Description of the pressure solver

The Reynolds and temperature equations [Eqs. (6) and (14)] are numerically solved by using a finite difference scheme. The pressure P, the hydraulic flow $\boldsymbol{q}$, and temperature $\bar{T}$ are discretized on a grid of $n_x \times n_y$ points with a mesh size of $2d$ i.e., half of the aperture grid points. In the following, when indices (i,j) are positive integers, they refer to node positions where an aperture, a pressure, and a temperature are defined on the contrary to the noninteger node position ($i \pm 0.5$ or $j \pm 0.5$) where only an aperture is defined.

The Reynolds equation [Eq. (6)] is discretized and solved in the same way as by Méheust and Schmittbuhl [20]: we use finite differences centered on a square mesh of lattice step size $2d$, and the linear equation system is inverted using an iterative biconjugate gradient method [49]. The chosen pressure drop along the fracture length is $\Delta P^* = P^*_{n_x,j} - P^*_{1,j} = 1 - n_x$ for $1 \leq j \leq n_y$. The hydraulic flow $\boldsymbol{q}^*_{i,j} = (q^*_{i,jx}, q^*_{i,jy}, 0)$ is computed from the pressure field as

$$q^*_{i,jx} = -\frac{a^{*3}_{i,j}}{2}(P^*_{i+1,j} - P^*_{i-1,j}),$$

$$q^*_{i,jy} = -\frac{a^{*3}_{i,j}}{2}(P^*_{i,j+1} - P^*_{i,j-1}).$$

For a parallel plate configuration (i.e., modeling without self-affine perturbation), $q^*_{i,j_x} = 1$ and $q^*_{i,j_y} = 0$ everywhere in the fracture.

B. Example of a microscopic hydraulic aperture field

An example of a fracture aperture is shown in Fig. 4(a). It is generated as explained in Sec. II on a 1024×512 grid and has a RMS equal to $\sigma/A = 0.25$. The hydraulic flow computed inside this morphology is shown in Fig. 4(b), as well as the microscopic hydraulic apertures [Fig. 4(c)]. In this case, the hydraulic flow exhibits a strong channeling as previously described by Méheust and Schmittbuhl [20]. The microscopic hydraulic apertures can be observed not to be simply correlated with the aperture field.

The link between microscopic mechanical apertures a and the microscopic hydraulic apertures h is given in Fig. 5, where the scale shows the corresponding occurrence probability of each local configuration. We see that the normalized mechanical and hydraulic aperture values are distributed around a characteristic point: $(h/A, \langle a \rangle/A) = (1,1)$. Nevertheless, the correlation between both apertures is not simple. Some of the highest density values are located below and above the straight line which represents $h = a$. Accordingly, the permeability can locally be lower or higher than what is given by an average Poiseuille law. The scattering around the straight line shows that, at one point, the local flow is not determined by the local mechanical aperture, but is influenced by all the surrounding microscopic mechanical apertures. From computations with other σ's, we notice that the lower the roughness amplitude is, the closer to (1,1) the cloud is.

C. Variability of the macroscopic hydraulic aperture

The dimensionless macroscopic hydraulic aperture is measured for our fracture example as $H/A = 0.94$ (ordinate of the cross in Fig. 5). $H/A < 1$ means that the fracture permeability is reduced compared to the one of parallel plates having the same mechanical aperture A, without any self-affine perturbation. For the same morphology pattern (Fig. 4), we examine how the roughness amplitude influences the macroscopic hydraulic aperture by changing σ/A (cf. Sec. II). In Fig. 6 we see that the macroscopic hydraulic aperture is close to 1 when $\sigma/A = 0.05$, which corresponds to a quasiflat aperture. When the roughness amplitude increases, H decreases,

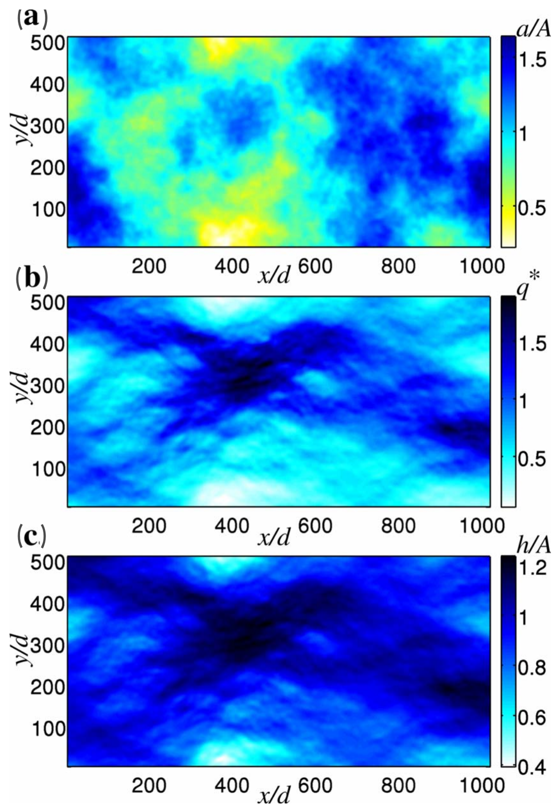

FIG. 4. (Color online) (a) Self-affine aperture with $\sigma/A = 0.25$. (b) Dimensionless hydraulic flow norm computed with the aperture of (a), having for dimensionless hydraulic aperture $H^* = 0.94$. (c) Microscopic hydraulic apertures, computed from the third root of the hydraulic flow shown in (b).

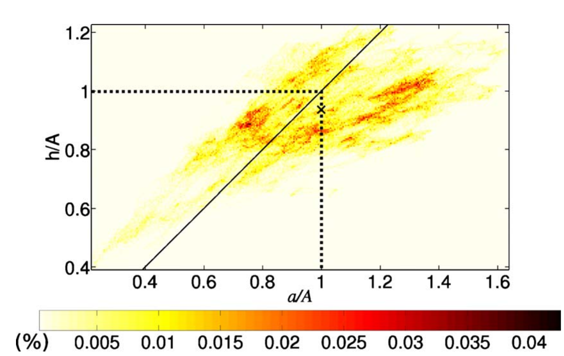

FIG. 5. (Color online) 2D histogram of the link between the microscopic hydraulic aperture and the microscopic mechanical aperture for the fracture shown in Fig. 4 (the scale indicates the probability in percent); the cross has for coordinates $(H/A, \langle a \rangle/A) = (0.94, 1)$. The straight line is $h = a$, which is the equality given by a local Poiseuille law.

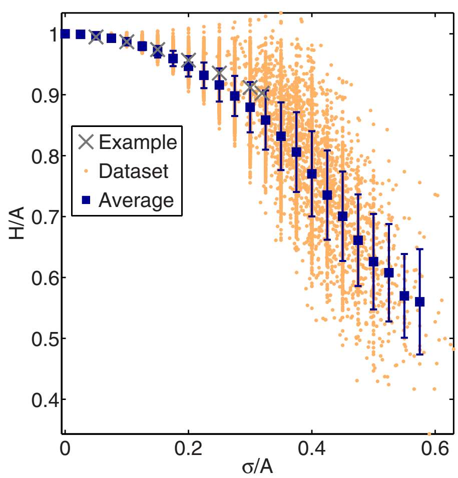

FIG. 6. (Color online) Macroscopic hydraulic aperture H/A versus σ/A for fractures with aspect ratio $l_x/l_y=2$; crosses, variation of the hydraulic aperture by increasing the roughness amplitude σ/A for the aperture shown in Fig. 4; dots, cloud of computed data (about 20 000 aperture realizations); squares, average hydraulic behavior with variability bars. On average, $H/A<1$: the permeability is smaller than expected from the Poiseuille law in parallel plate apertures.

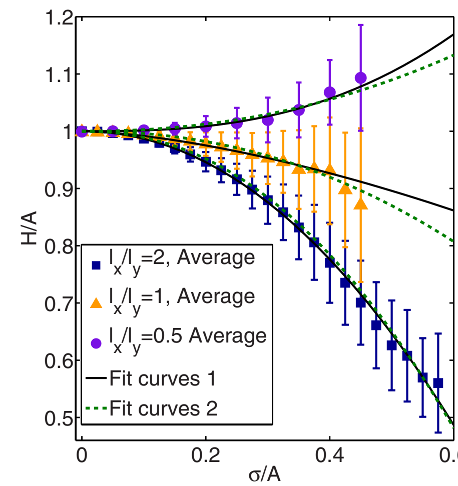

FIG. 7. (Color online) Macroscopic hydraulic aperture versus σ/A, for three aspect ratios $J=l_x/l_y$. Averages computed from data are shown with symbols, with error bars, corresponding to plus or minus the standard deviation (see how the average is computed in Sec. IV C). $J=l_x/l_y=2$ shows an enhanced flow (same data as presented in Fig. 6); $J=1$ shows on average a slightly inhibited flow, i.e., $H\leq A$ (computed from a cloud of about 1300 points); for $J=0.5$, on average, higher permeability is observed (computed from a cloud of about 900 points). Continuous curves are fitting models (1) $H/A=1+\alpha(\frac{\sigma}{A})^{\kappa}$, with parameters (κ,α) equal to $(2.05,-1.46)$, $(1.57,-0.31)$, $(2.69,0.67)$, respectively, for J equal to 2, 1, and 0.5. Dotted curves are obtained with fitting models (2) $H/A=1-\mu[\log_2(J)+\delta](\frac{\sigma}{A})^{\kappa}$, with $(\mu,\delta,\kappa)=(0.98,0.59,2.16)$, for the three curves.

which means that this morphology pattern tends to inhibit the hydraulic flow and makes the fracture permeability decrease.

For various realizations with the same σ/A value, various hydraulic behaviors may happen owing to the channel variability in the hydraulic flow. In Fig. 6, we plot the dimensionless macroscopic hydraulic apertures H/A versus σ/A (for about 20 000 computations with 1700 different fracture aperture patterns). Here, each fracture has the same size as the fracture shown in Fig. 4 where $l_x/l_y=2$. We compute the mean hydraulic apertures inside windows of size $0.025\sigma/A$, and each plotted bar represents twice the standard deviation of H/A inside the corresponding windows. We see that, for most cases, the permeability is reduced. For $\sigma/A<0.25$, the hydraulic aperture is still quite close to A, and the dispersivity is relatively small even if some configurations show a flow enhancement owing to the fracture roughness: $H>A$ [20]. Then, for higher RMS, the average of H/A decreases significantly on average (up to 50%) with σ/A, but with a higher variability of the results.

D. Influence of the fracture aspect ratio on the hydraulic flow

To get a complete description, we now modify one additional parameter: the aspect ratio of the fracture, by changing the ratio of the fracture length over its width, $J=l_x/l_y$. Figure 7 shows the same kind of average plots of H/A as a function of σ/A but for three different aspect ratios: $J=2$ (square symbols), which is the one presented in Fig. 6, $J=1$ (triangle), and $J=0.5$ (disks). Since less simulations were done for $J=1$ and $J=2$ (see the legend in Fig. 7), few apertures show $\sigma/A>0.45$, and therefore no average points are represented in these cases. For square systems ($J=1$) and downstream elongated fracture ($J\geq 1$), H/A is on average smaller than 1 (i.e., inhibiting hydraulic flow compared to the one through parallel plates separated by the same opening A), whereas for systems wider perpendicularly to the pressure gradient direction, H/A is on average higher than 1. A qualitative explanation might be that it is statically more likely to get a large-scale connecting channel for a wide and short fracture ($J<1$) rather than for a thin and long fracture ($J>1$). In other words, qualitatively, channels are rather in parallel in wide fractures and in series in long ones. For square systems which should be isotropic and providing as many perpendicular and parallel channels, we see that when the roughness amplitude increases, the hydraulic aperture gets on average slightly smaller than A. We can suspect that there would exist an aspect ratio J_{inv}, so that the hydraulic aperture is on average independent of the fracture roughness magnitude: $H/A=1$ for any σ/A. Following the model proposed below in Sec. IV E, we get $J_{inv}\simeq 0.65\pm 0.05$. For any J value, we see that the higher the ratio σ/A is, the higher the variability of the behaviors is, especially for square systems which exhibit both high ($H>A$) and low ($H<A$) permeabilities for the same roughness magnitude.

E. Model of the average macroscopic hydraulic aperture

One of the main questions we want to address here is the relationship between the macroscopic hydraulic aperture H and the microscopic mechanical aperture field $a(x,y)$. The knowledge of the mechanical aperture field $a(x,y)$ provides us the following bounds for H: $\langle a^{-3}\rangle^{-1}<H^3<\langle a^3\rangle$—the lower case corresponds to a system of aperture fluctuations purely aligned in series, and the upper one corresponds to fluctuations purely aligned in parallel [55]. However, $a(x,y)$ is rarely known and subsequently $\langle a^{-3}\rangle^{-1}$ and $\langle a^{3}\rangle$ are difficult to estimate.

From Fig. 7, σ/A and J appear to be important parameters controlling the macroscopic hydraulic aperture of the fracture H. Reference [20] proposed a first model of the H behavior as $H/A=1+\alpha(\frac{\sigma}{A})^{\kappa}$. Here, we similarly model the average hydraulic aperture curves corresponding to each aspect ratio (continuous curves in Fig. 7) and find (κ,α) successively equal to $(2.05,-1.46)$, $(1.57,-0.31)$, and $(2.69,0.67)$, respectively, for J equal to 2, 1, and 0.5. Depending on the sign of α, we get a permeability either lower or higher than that expected with flat plates. Then we fit these three behaviors by a more general model which includes the aspect ratio variation, with three parameters (μ,δ,κ) to be optimized: $H/A=1-\mu[\log_2(J)+\delta](\frac{\sigma}{A})^{\kappa}$. With $(\mu,\delta,\kappa)=(0.98,0.59,2.16)$, we get the three dotted lines in Fig. 7 which are acceptable fits of the average trend. However, it has to be highlighted that the real hydraulic aperture of a specific surface is possibly very different from this average value (see the size of variability bars in Fig. 7), especially at high σ/A.

Other models for numerical or experimental hydraulic apertures have been proposed in the literature [19] as $(H/A)^3=1-C_1\exp(-C_2A/\sigma)$ or $(H/A)^3=1/[1+C_3(2A/\sigma)^{1.5}]$, where C_{1-3} are constants, but the shape of these functions does not fit well our averaged points, and these fits are not presented here.

V. THERMAL FLOW SIMULATIONS

A. Description of the temperature solver

The temperature equation [Eq. (14)] is discretized as

$$q^*_{i,j_x}(\bar{T}^*_{i+1,j}-\bar{T}^*_{i-1,j})+q^*_{i,jy}(\bar{T}^*_{i,j+1}-\bar{T}^*_{i,j-1})+\frac{4d}{R_\parallel}\frac{\bar{T}^*_{i,j}}{a^*_{i,j}}=0, \tag{28}$$

where $(i,j)\in[|2,n_x-1|]\times[|2,n_y-1|]$ and $R_\parallel$ is the thermal length expected by neglecting the roughness amplitude [see Eq. (16)]. The boundary conditions are

$$1\le j\le n_y,\quad \bar{T}^*_{1,j}=1,\quad \bar{T}^*_{n_x,j}=0,$$

$$2\le i\le n_x-1,\quad \bar{T}^*_{n_x,j}=0,\quad \bar{T}^*_{n_x,j}=0.$$

The system is solved in the same way as the pressure system (Sec. IV A). Two limiting numerical factors intervene for the efficiency of the discretization scheme: the mesh step d has to be sufficiently small to capture with a sufficient accuracy the relative variations of $\bar{T}-T_r$ over a lattice step. In practice, the mesh step used in this paper is chosen as $d=R_\parallel/50$. We checked that dividing this mesh size by 2 did not change significantly the computed temperature field. The second numerical limit is that the system size l_x has to be larger than $20R_\parallel$ to avoid a possible numerical instability (mostly with the aperture grid size 1024×2048, which is

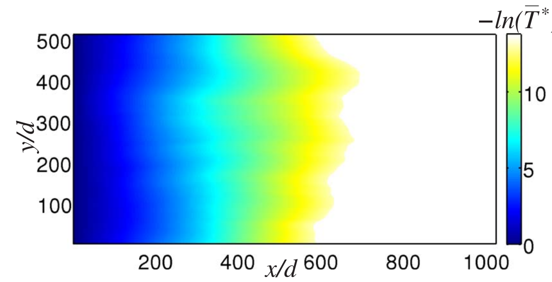

FIG. 8. (Color online) $-\ln(\bar{T}^*)$, opposite of the logarithm of the temperature field $\bar{T}^*$ computed from the aperture morphology pattern shown in Fig. 4 with a very low roughness amplitude: $\sigma/A=0.05$. The hydraulic aperture of this fracture is $H/A=0.99$. The temperature field exhibits a normalized thermal length equal to $R^*=0.97$ and a thermal aperture of $\Gamma/A=0.99$.

more likely to exhibit a longer thermal length, as explained in Sec. V E). If not, the fluid passing the fracture is so slowly warmed up that the condition $\bar{T}^*_{n_x,j}=0$ at the outlet badly represents the condition imposed in principle at infinity in the channel, and this boundary condition imposed at a physically too short distance from the inlet cannot be fulfilled without numerical artifact. To face this problem in such rare situations, we duplicate the aperture grid to get a longer system length and impose the same macroscopic pressure gradient, and the rock temperature at the new end: $\bar{T}^*_{2\cdot n_x,j}=0$.

B. Example of a local microscopic temperature field

For a nearly constant aperture ($\sigma/A=0.05$), we numerically obtain a temperature law close to an exponential downstream profile (Fig. 8), as we expect from Eq. (17). The 2D temperature field shown in Fig. 9(a) ($\sigma/A=0.25$) is computed from the aperture and its previously computed hydrau-

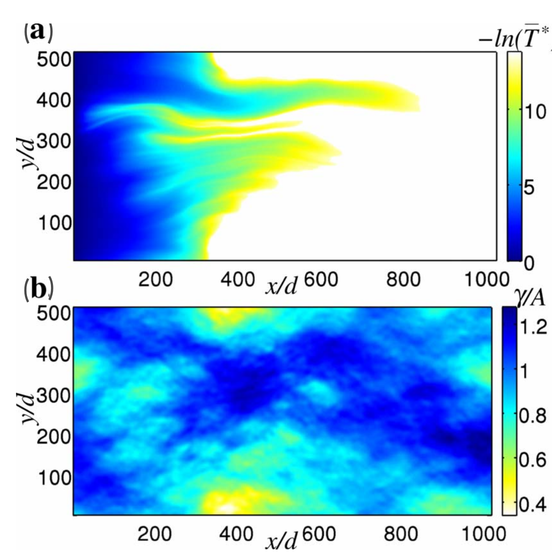

FIG. 9. (Color online) (a) $-\ln(\bar{T}^*)$, opposite of the logarithm of the 2D temperature field, computed from the apertures in Fig. 4(a) ($\sigma/A=0.25$). (b) Normalized local thermal aperture γ/A associated with the temperature field shown in (a).

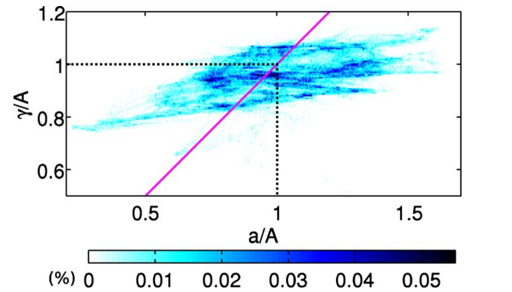

FIG. 10. (Color online) 2D histogram in percent of the fracture shown in Fig. 4 as a function of the local thermal aperture γ and local aperture a (the shading indicates the probability density). The straight line is $\gamma = a$. The dispersivity of the cloud around the line shows that there is no simple link between the local aperture and the thermal one.

lic flow field, shown in Fig. 4(b). We see that it can be observed that the fluid is getting inhomogeneously warm, with channelized features. The thermal channel begins in a zone where the hydraulic flow coming from the inlet converges [Fig. 4(b)]. The local normalized thermal aperture γ/A [map shown in Fig. 9(b)] exhibits less pronounced channel effect than in Fig. 9(a). Figure 10 is the plot of the local microscopic thermal apertures γ/A versus the local apertures a/A, using a shading showing the occurrence density in the $(\gamma/A, a/A)$ space. The dispersivity of the cloud around the line $\gamma = a$ shows that there is no simple link between the local aperture and the thermal one. A similar plot (Fig. 11) allows us to observe the correlation between the local microscopic thermal apertures and the local microscopic hydraulic apertures. It shows a good correlation of the local thermal aperture and the local hydraulic aperture (i.e., the cloud is close to the straight line $\gamma = h$). Note that it is more probable (59%) to have $\gamma > h$, which corresponds to a heat exchange locally less efficient than what is expected from a parallel plate model which is equivalent in permeability.

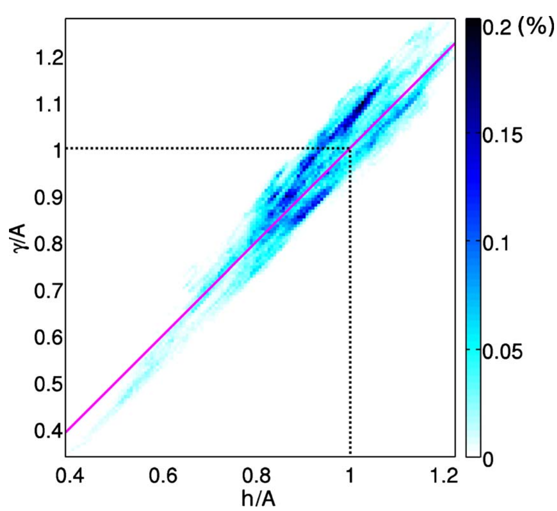

FIG. 11. (Color online) 2D Histogram in percent of the fracture shown in Fig. 4 as a function of the local thermal aperture γ and local hydraulic aperture h (the scale indicates the probability in percent). The straight line is $\gamma = h$; the localization of the cloud around the line shows a good correlation between γ and h.

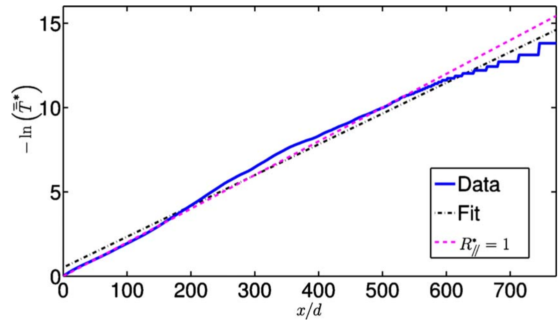

FIG. 12. (Color online) Continuous curve, $-\ln(\bar{\bar{T}}^*)$, opposite of the logarithm of the temperature field computed from the temperature field $\bar{T}$ shown in Fig. 9. Dashed-dotted curve, linear fit of curve A (from $x/d = 0$ to $x/d = 772$), which provides the thermal length: $-\ln(\bar{\bar{T}}^*) = x/1.09 + 0.6$, i.e., $R^* = 1.09$. Dashed curve, $-\ln(\bar{\bar{T}}_\parallel^*)$, opposite of the logarithm of the temperature law for the same fracture modeled without self-affinity perturbation (i.e., parallel plates), which has for thermal length $R_\parallel^* = 1$.

C. Variability of the macroscopic thermal aperture

The average temperature $\bar{\bar{T}}$ [see definition in Eq. (22)] is a semilocal property which shows how the thermal behavior evolves on average along the pressure gradient direction. The shape of $\bar{\bar{T}}(x)$ (Fig. 12) is close to an exponential law, but with a thermal length R slightly different from the fracture without self-affine perturbation (i.e., parallel plates). This thermal length is computed from the slope of the linear regression of $\ln[\bar{\bar{T}}(x)]$ (see Sec. III C). In the example displayed in Fig. 12, the thermal length is $R_\parallel^* = 1.09$, which results in an equivalent thermal aperture of $\Gamma^* = 1.02$.

In Fig. 13, the crosses illustrate the roughness amplitude influence on the thermal aperture for the morphology pattern

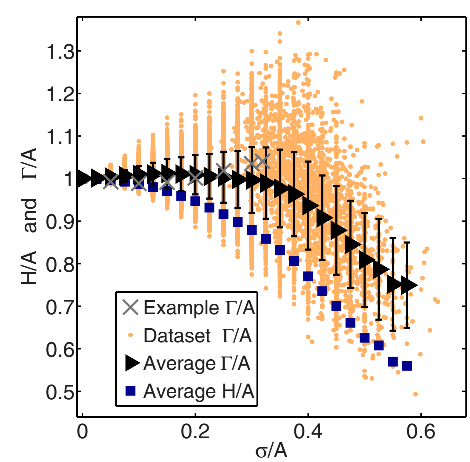

FIG. 13. (Color online) Crosses, variation of the thermal aperture Γ/A by increasing the roughness amplitude σ/A for the aperture pattern shown in Fig. 4; dots, cloud of computed data (about 20 000 points) for fractures with aspect ratio $l_x/l_y = 2$; triangles, average thermal behavior with variability bars of the cloud; squares, average hydraulic aperture H/A versus σ/A, recalled here for comparison.

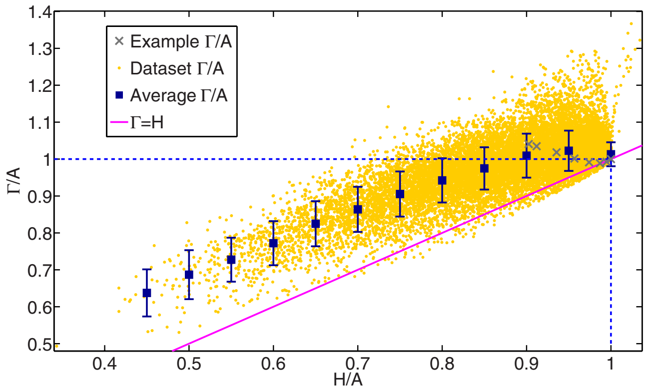

FIG. 14. (Color online) Normalized thermal aperture Γ/A versus H/A for fractures with aspect ratio $l_x/l_y=2$. Crosses, variation of the thermal aperture by increasing the roughness amplitude for the aperture pattern shown in Fig. 4(a) versus H/A; dots, cloud of computed data (about 20 000 points); squares, average thermal behavior with variability bars. Continuous curve, $\Gamma/A=H/A$, which holds for parallel plates separated by $a(x,y)=H$.

shown in Fig. 4(a), whose relief is amplified by changing the σ value (see Sec. II). For this example, Γ vs σ is not monotonic. The dimensionless thermal length is close to 1 when $\sigma/A=0.05$, which corresponds to a quasiflat aperture. When the roughness amplitude is big enough ($\sigma>0.1$), Γ increases with σ and is higher than 1, which means that this morphology pattern tends to inhibit the thermal exchange. In Fig. 14, the crosses show the thermal aperture versus H/A using the same data as for the plots shown by crosses in Figs. 6 and 13.

D. Variability of the thermal behavior

Statistical thermal results are computed for numerous cases (more than 20 000) whose macroscopic hydraulic apertures are presented in Sec. IV C for various σ/A values. Similarly, a normalized average macroscopic thermal aperture, Γ/A, and its standard deviation is obtained as functions of σ/A. The resulting Γ/A for the aspect ratio $J=2$ is displayed in Fig. 13, with bars representing the double of the standard deviation. For the same normalized roughness amplitude σ/A, various thermal behaviors may happen, especially for $\sigma/A>0.25$, with channels appearing or not and dimensionless thermal lengths higher or lower than 1. At first order, both the macroscopic thermal (Fig. 13, triangles) and hydraulic average apertures (Fig. 13, squares) are decreasing as functions of σ. This trend is significantly more pronounced for H than for Γ. The thermal results are compared with systems equivalent in permeability (same normalized hydraulic aperture) in Fig. 14 which presents the normalized thermal aperture versus the hydraulic aperture with the average points computed inside windows of size $0.05H/A$. The most striking result is that roughness inhibits thermalization: nearly all the cloud is above the continuous curve $\Gamma=H$, which means that the thermalization of the fluid (thermalization is obtained when the fluid temperature reaches the rock one) is inhibited compared to what we expect from the hydraulic behavior. At the same time, we note that, on average, $\Gamma/A<1$, i.e., most of the apertures exhibit an enhanced thermalization compared to what would be expected with a model of flat fractures separated by A, i.e., having the same geometric (or mechanical) aperture.

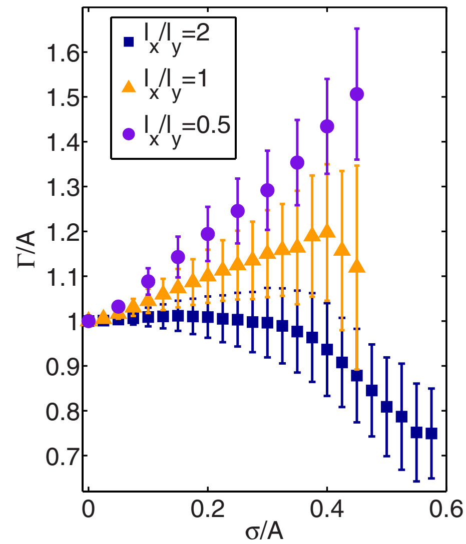

FIG. 15. (Color online) Averages of the normalized thermal aperture Γ/A and their deviation bars versus σ/A for various aspect ratios $J=l_x/l_y$, as indicated by the labels. See how the average is computed in Sec. IV C.

E. Influence of the fracture aspect ratio on the thermal behavior

We complete our study by computing the averaged thermal apertures for two other aspect ratios, J, by using the hydraulic flows computed in Sec. IV D. The averaged values of the thermal apertures, with the variability bars (defined similarly to what is done in Sec. V D) for $J\in\{0.5,1,2\}$ are plotted in Figs. 15 and 16. When Γ/A is plotted as a function of σ/A (Fig. 15), various thermal behaviors are observed, according to the aspect ratio, with high variability, particularly when $\sigma/A>0.25$. On the contrary to fractures with aspect ratio equal to $J=2$ (described in Sec. V D) the ones with J in $\{0.5,1\}$ are more likely to inhibit the thermalization compared to flat fractures with the same mechanical aperture ($\Gamma/A>1$).

Figure 16 shows the average of Γ/A versus H/A. Contrarily to what can be observed for Γ/A vs σ/A (Fig. 15), the average curves Γ/A vs H/A are roughly independent on the aspect ratio. This shows that the hydraulic aperture is a better parameter than the roughness σ/A to assess the thermal properties. The thermal aperture is systematically larger than the hydraulic aperture ($\Gamma>H$). It means that once the permeability is known, e.g., by pumping tests, using a parallel plate model separated by H for estimating the thermal behavior overestimates the efficiency of the heat exchange: the fluid needs indeed a longer distance to be thermalized than expected from flat fractures with the same permeability. On average Γ/A vs H/A is monotonic (Fig. 16), i.e., this average dependence displays a simpler behavior than for a particular case of morphology of varying amplitude (e.g., Fig. 14, crosses).

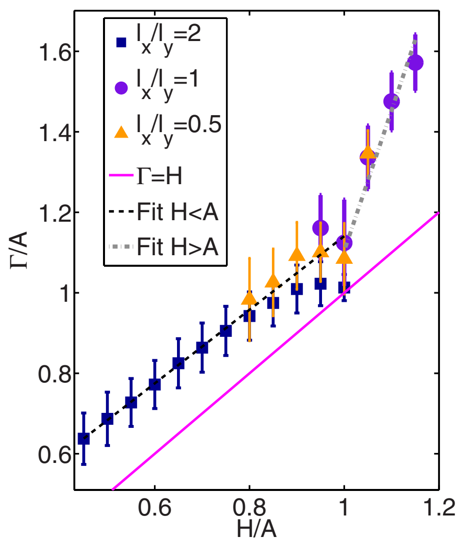

FIG. 16. (Color online) Averages of the normalized thermal aperture Γ/A and their deviation bars versus H/A for various aspect ratios $J=l_x/l_y$, as indicated by the labels (see how the average is computed in Sec. IV C). Models lines are $\Gamma=0.9H+0.2A$ for $H<A$ and $\Gamma=3.5H-2.4A$ for $H\geq A$; no continuity condition between both lines is imposed.

Going more into details, Fig. 16 also shows that for $H/A>1$, the slope of Γ vs H is steeper than for $H/A<1$; both parts of the curve can be modeled with straight line fits (dotted and dotted-dashed curves). This could be interpreted as follows: fractures with high hydraulic apertures provide high velocities, so that fluid particles need to go further to reach the rock temperature. Fractures with small hydraulic apertures $H/A<1$ might be dominated by small mechanical apertures (fences) providing small velocities, which leads to thermal apertures closer to the line $\Gamma=H$.

VI. DISCUSSION AND CONCLUSION

A. Model limits and possible extension

Despite the hydraulic lubrication hypothesis, which implies notably a low Reynolds number, the fluid velocity should not be too small. Indeed, the velocity drives the in-plane thermal convection, which is supposed to be large compared to the in-plane thermal conduction. This can be quantified by the Péclet number (ratio between the characteristic times of diffusion and advection): our model is valid at low in-plane Péclet number. Therefore, owing to in-plane conduction, the thermal channeling effect might be reduced especially in the case of high temperature contrast along the channel and very low hydraulic flow. This homogenization might be reinforced if the fluid temperature is still inhomogeneous but very close to the rock temperature: in this case the in-plane conduction inside the fluid might be as high as the conduction between rock and fluid. Free convection (temperature dependence of ρ), which is not taken into account here, may also intervene, especially for thick fractures [56].

In practice, some 3D effects might happen as the lubrication approximation is not necessarily respected owing to the rock morphology (e.g., [23,24]). In natural cases, the roughness amplitude σ/A covers a large range across the natural cases, from small to large values according to the type of rock and fractures. For instance, we recently measured the roughness amplitude of natural fractures in black marl at borehole scale, and we obtained values of $\sigma/A<0.04$ for one and $\sigma/A=0.3$ for another one [22]. Some other values, typically $\sigma/A>0.4$, have also been reported, for instance, in granitic rocks [57,58]. If the cases with large roughness amplitudes also correspond to large local slopes (angle between the fracture side and the average plane), it is likely that the Reynolds equation and 2D temperature equation do not apply so well to these cases, and that the results reported here are only approximate for those.

When the fracture morphology is highly developed, due to more surface exchange, the rock might locally provide better heat exchange. The assumption of averaging thermal phenomena in two dimensions has been studied, e.g., by Volik *et al.* [59] and Sangaré *et al.* [60], who considered only conduction. The 3D solving of the full Navier-Stokes and heat advection-diffusion equations is also possible, for example, with a coupled lattice-Boltzmann method [61]. However, considering the complexity of fracture morphology from very small scales to large ones requires heavy computations, which makes statistical results difficult to obtain. When convection also acts, 3D effects lead to zones decoupled from the main mass and heat flux, as the fluid might be blocked into eddies (off lubrication regime) provoked by sharp morphologies [23,29–32] (like Moffatt eddies [62]). It has indeed to be noticed that even when low-pressure gradient is imposed, turbulent flow might be observed due to high roughness amplitude. This effect is complementary to observations made at high Reynolds number [63–66], when even a very low roughness amplitude of the wall induces turbulent flow.

All the results about the thermal aperture may also be influenced by the thermal boundary conditions. In particular we have assumed that T_r is constant. Spatial variations of T_r can easily be taken into account by changing the boundary conditions of the thermal equation while temporal variations require to model the rock getting colder in the surrounding (consequences of the rock diffusivity). In time, the hypothesis of constant temperature T_r holds either for very short durations when the regime is transitory or for longer durations, at quasistationary regime, when the rock temperature evolves very slowly and the fluid temperature adapts fast. This is the case if the solid is much more thermally diffusive than the fluid, which is quite true in our case: for instance, the ratio of the granite thermal diffusivity over the water one is 5.9. We could check the time evolution by using another numerical approach based on lattice-Boltzmann methods [61], which allows us to solve both the rock and fluid temperatures and takes into account the contrast of thermal diffusivity. For a fracture with an aperture of a few millimeters, T_r can be considered as constant at transitory regime for durations much less than 1 min. Conversely it also holds for longer durations after a quasistationary regime is reached, which can happen after minutes or years, according to the properties of the system (e.g., distance to the heat source and injection point). Time variation of T_r can also be taken into account by coupling our model to a thermal diffusion model in the rock, using alternately both models in time. Similarly, it is possible to couple our code to another one modeling the change in the geometry of the fracture (e.g., because of stress or chemical reactions).

B. Conclusion

We have proposed a model of thermal exchange between a Newtonian fluid and a hot rock inside a rough fracture under a given pressure gradient. The flow considered was assumed to be at low Reynolds number, in laminar regime, so that Stokes equation and lubrication approximations hold for the mass flow equations and for the temperature advection in the heat transport equation. We have then set from basic principles the mass and heat transport equations, expressed them in a 2D form, discretized them by finite differences, and solved the resulting systems by biconjugate gradient methods. The whole numerical scheme can be used with any variable aperture field without contact (for instance, obtained from real rock surfaces). Here, apertures have been chosen to be numerically generated, in order to get statistically significant results over more than 20 000 realizations. The aperture fields are modeled as many natural ones, namely, as self-affine with a Hurst exponent of 0.8, with various ratios of the aperture fluctuations over the average aperture and three different aspect ratios of the fracture. The hydraulic and thermal behaviors are quantified with both local and macroscopic apertures: h, γ, and H,Γ.

The plot of H as function of σ/A exhibits some trends according to the aspect ratio, and we have been able to find model curves. However, around these model curves, the hydraulic behavior is very variable and, therefore, knowing the roughness amplitude, σ/A, these model curves may not be reliably combined with a model of another phenomenon dominated by the hydraulic aperture, such as the thermal exchange. The macroscopic thermal aperture Γ vs the roughness amplitude is also highly variable, despite trends that are visible on average according to the aspect ratio. The fracture, taking into account its roughness, is either less or more permeable than model of flat parallel plates with the same mechanical aperture.

At local and macroscopic scales, hydraulic apertures are badly correlated with mechanical apertures. On the contrary, hydraulic apertures are highly correlated with thermal apertures, showing that the thermal behavior is mostly determined by the hydraulic one for rough fractures. Compared to flat fractures with equivalent permeability, for a rough aperture, the fluid almost systematically needs a longer distance to reach the temperature of rock ($\Gamma > H$): the heat exchange is less efficient. A practical implication of this general result is that when fracture aperture is assessed on the field based on hydraulic transmissivity measurement, obtained, e.g., by pumping tests, the efficiency of the thermal exchange assessed from flat fracture models is systematically overestimated. Using the laws $\Gamma=0.9H+0.2A$ if $H<A$ and $\Gamma=3.5H-2.4A$ for $H\geq A$ (Fig. 16) should allow us to correct this overestimation.

Another important result is that the derived temperature in rough channels, when averaged, behaves according to the solution of the macroscopic equation that would be used for flat apertures [Eq. (14)]. The local roughness of the fracture can therefore be coarse grained. Doing so, the structure of Eq. (14) is kept; it is simply necessary to adjust both the hydraulic transmissivity and the thermal length (or the Nusselt number). For instance, this coarse-grained approach based on parallel plate laws with adjusted Nusselt numbers can be used for hydraulic and thermal models of fracture networks.

ACKNOWLEDGMENTS

We thank E. G. Flekkøy, S. Roux, K. J. Måløy, J. Andrade, Jr., H. Auradou, A. Genter, and J. Sauze for fruitful discussions. We thank the European EHDRA program, as well as the ANR ECOU-PREF and the REALIZE programs for their financial support.

[1] A. Gérard, A. Genter, T. Kohl, P. Lutz, P. Rose, and F. Rummel, Geothermics **35**, 473 (2006).
[2] A. Neuville, R. Toussaint, and J. Schmittbuhl, Proceedings of the EHDRA Scientific Conference, 2006 (unpublished).
[3] A. Neuville, R. Toussaint, and J. Schmittbuhl, C. R. Geosci. **342**, 616 (2010).
[4] J. Sausse, C. Dezayes, A. Genter, and A. Bisset, Proceedings of the 33rd workshop on Geothermal Reservoir Engineering, Stanford University, CA, 2008 (unpublished).
[5] T. Le Borgne, O. Bour, J. Dreuzy, P. Davy, and F. Touchard, Water Resour. Res. **40**, W03512 (2004).
[6] V. Cvetkovic, S. Painter, N. Outters, and J. Selroos, Water Resour. Res. **40**, W02404 (2004).
[7] A. Jupe *et al.*, Geothermics **24**, 403 (1995).
[8] J.-R. De Dreuzy, C. Darcel, P. Davy, and O. Bour, Water Resour. Res. **40**, W01502 (2004).
[9] P. Adler and J.-F. Thovert, *Fractures and Fracture Networks* (Kluwer Academic, Dordrecht, 1999).
[10] A. Bataillé, P. Genthon, M. Rabinowicz, and B. Fritz, Geothermics **35**, 654 (2006).
[11] E. Bouchaud, J. Phys.: Condens. Matter **9**, 4319 (1997).
[12] L. Ponson, H. Auradou, M. Pessel, V. Lazarus, and J.-P. Hulin, Phys. Rev. E **76**, 036108 (2007).
[13] Y. Méheust and J. Schmittbuhl, Pure Appl. Geophys. **160**, 1023 (2003).
[14] D. Bonamy, L. Ponson, S. Prades, E. Bouchaud, and C. Guillot, Phys. Rev. Lett. **97**, 135504 (2006).
[15] F. Plouraboué, P. Kurowski, J.-P. Hulin, S. Roux, and J. Schmittbuhl, Phys. Rev. E **51**, 1675 (1995).
[16] A. Neuville, R. Toussaint, J. Schmittbuhl, D. Koehn, and J. Schwarz, special issue of Hydrolog. Process. (to be published).
[17] Y. Méheust and J. Schmittbuhl, Geophys. Res. Lett. **27**, 2989 (2000).
[18] F. Plouraboué, P. Kurowski, J.-M. Boffa, J.-P. Hulin, and S.

Roux, J. Contam. Hydrol. **46**, 295 (2000).
[19] S. Brown, J. Geophys. Res. **92**, 1337 (1987).
[20] Y. Méheust and J. Schmittbuhl, J. Geophys. Res. **106**, 2089 (2001).
[21] J. Schmittbuhl, A. Steyer, L. Jouniaux, and R. Toussaint, Int. J. Rock Mech. Min. Sci. **45**, 422 (2008).
[22] A. Neuville, R. Toussaint, and J. Schmittbuhl, special issue of Hydrolog. Process. (to be published).
[23] S. Brown, H. Stockman, and S. Reeves, Geophys. Res. Lett. **22**, 2537 (1995).
[24] V. Mourzenko, J.-F. Thovert, and P. Adler, J. Phys. II **5**, 465 (1995).
[25] R. Zimmerman and I.-W. Yeo, *Geophysical Monograph* (American Geophysical Union, Washington, D.C., 2000), Vol. 122, p. 213.
[26] F. Plouraboué, J.-P. Hulin, S. Roux, and J. Koplik, Phys. Rev. E **58**, 3334 (1998).
[27] R. Zimmerman and G. Bodvarsson, Transp. Porous Media **23**, 1 (1996).
[28] G. Drazer and J. Koplik, Phys. Rev. E **66**, 026303 (2002).
[29] D. Brush and N. Thomson, Water Resour. Res. **39**, 1085 (2003).
[30] A. Al-Yaarubi, C. Pain, C. Grattoni, and R. Zimmerman, in *Dynamics of Fluids and Transport in Fractured Rocks*, edited by B. Faybishenko, P. Witherspoon, and J. Gale, AGU Monograph Vol. 162 (American Geophysical Union, Washington, D.C., 2005), pp. 55–64.
[31] D. Boutt, G. Grasselli, J. Fredrich, B. Cook, and J. Williams, Geophys. Res. Lett. **33**, L21402 (2006).
[32] M. Cardenas, D. Slottke, R. Ketcham, and J. Sharp, Jr., Geophys. Res. Lett. **34**, L14404 (2007).
[33] N. Heuer, T. Kupper, and D. Windelberg, Geophys. J. Int. **105**, 659 (1991).
[34] S. Gentier, X. Rachez, C. Dezayes, A. Hosni, A. Blaisonneau, A. Genter, and D. Bruel, Proceedings of the EHDRA Scientific Conference, 2005 (unpublished).
[35] X. Rachez, S. Gentier, and A. Blaisonneau, Proceedings of the EHDRA Scientific Conference, 2007 (unpublished).
[36] O. Kolditz and C. Clauser, Geothermics **27**, 1 (1998).
[37] O. Pinkus and B. Sternlicht, *Theory of Hydrodynamic Lubrication* (McGraw-Hill, New York, 1961).
[38] D. Turcotte and G. Schubert, *Geodynamics*, 2nd ed. (Cambridge University Press, Cambridge, England, 2002), Chap. 6, pp. 262–264.
[39] K. Falconer, *Fractal Geometry: Mathematical Foundation and Application* (Wiley, New York, 1990).
[40] J. Feder, *Fractals* (Plenum, New York, 1988).
[41] F. Plouraboué, S. Roux, J. Schmittbuhl, and J.-P. Vilotte, Fractals **51**, 1675 (1995).
[42] J. Schmittbuhl, S. Gentier, and S. Roux, Geophys. Res. Lett. **20**, 639 (1993).
[43] J. Schmittbuhl, F. Schmitt, and C. Scholz, J. Geophys. Res. **100**, 5953 (1995).
[44] W. Power, T. Tullis, S. Brown, G. Boitnott, and C. Scholz, Geophys. Res. Lett. **14**, 29 (1987).
[45] B. Cox and J. Wang, Fractals **1**, 87 (1993).
[46] J. Boffa, C. Allain, and J.-P. Hulin, Eur. Phys. J.: Appl. Phys. **2**, 281 (1998).
[47] Y. Méheust, Ph.D. thesis, Université Paris Sud, 2002.
[48] S. Roux, J. Schmittbuhl, J.-P. Vilotte, and A. Hansen, EPL **23**, 277 (1993).
[49] W. Press, S. Teukolsky, W. Vetterling, and B. Flannery, *Numerical Recipes* (Cambridge University Press, New York, 1992).
[50] M. Sahimi, Phys. Rep. **306**, 213 (1998).
[51] G. Stokes, Trans. Cambridge Philos. Soc. **8**, 287 (1846).
[52] G. Batchelor, *An Introduction to Fluid Dynamics* (Cambridge University Press, New York, 1967).
[53] L. Landau and E. Lifchitz, *Physique Théorique, Mécanique des Fluides*, 3rd ed. (Ellipses, Moscow, 1994), Chap. 5, p. 280.
[54] R. W. Zimmerman, S. Kumar, and G. S. Bodvarsson, Int. J. Rock Mech. Min. Sci. Geomech. Abstr. **28**, 325 (1991).
[55] M. J. Beran, *Statistical Continuum Theories* (Interscience, New York, 1968).
[56] H. Murphy, J. Geophys. Res. **84**, 6121 (1979).
[57] E. Hakami and E. Larsson, Int. J. Rock Mech. Min. Sci. **33**, 395 (1996).
[58] M. Vicente Silvestre, L. Ribeiro e Sousa, and R. Hack, News J., Int. Soc. Rock Mech. **7**, 9 (2002).
[59] S. Volik, V. Mourzenko, J.-F. Thovert, and P. Adler, Transp. Porous Media **27**, 305 (1997).
[60] D. Sangaré, J.-F. Thovert, and P. M. Adler, J. Appl. Phys. **104**, 074915 (2008).
[61] A. Neuville, R. Toussaint, and J. Schmittbuhl (unpublished).
[62] H. Moffatt, J. Fluid Mech. **18**, 1 (1964).
[63] J. Nikuradse, VDI-Forschungsh. **356**, 1-35 (1932).
[64] G. Barenblatt, A. Chorin, and V. Prostokishin, Proc. Natl. Acad. Sci. U.S.A. **94**, 773 (1997).
[65] E. Skjetne, A. Hansen, and J. Gudmundsson, J. Fluid Mech. **383**, 1 (1999).
[66] P. Goldenfeld, Phys. Rev. Lett. **96**, 044503 (2006).

Geophysical Journal International

Geophys. J. Int. (2011) **186,** 1064–1072 doi: 10.1111/j.1365-246X.2011.05126.x

Hydraulic transmissivity and heat exchange efficiency of open fractures: a model based on lowpass filtered apertures

Amélie Neuville,* Renaud Toussaint and Jean Schmittbuhl

Institut de Physique du Globe de Strasbourg (IPGS), CNRS, and University of Strasbourg (EOST), 5 rue Descartes, 67000 Strasbourg, France. E-mail: renaud.toussaint@unistra.fr

Accepted 2011 June 25. Received 2011 June 18; in original form 2010 November 10

GJI Marine geosciences and applied geophysics

SUMMARY

Natural open joints in rocks commonly present multiscale self-affine apertures. This geometrical complexity affects fluid transport and heat exchange between the flowing fluid and the surrounding rock. In particular, long range correlations of self-affine apertures induce strong channelling of the flow which influences both mass and heat advection. A key question is to find a geometrical model of the complex aperture that describes at best the macroscopic properties (hydraulic conductivity, heat exchange) with the smallest number of parameters. Solving numerically the Stokes and heat equations with a lubrication approximation, we show that a low pass filtering of the aperture geometry provides efficient estimates of the effective hydraulic and thermal properties (apertures). A detailed study of the influence of the bandwidth of the lowpass filtering on these transport properties is also performed. For instance, keeping the information of amplitude only of the largest Fourier length scales allows us to reach already an accuracy of 9 per cent on the hydraulic and the thermal apertures.

Key words: Fourier analysis; Numerical approximations and analysis; Fractals and multifractals; Heat flow; Hydrothermal systems; Fracture and flow.

1 INTRODUCTION

Mass and heat transport in natural fractures and joints are important in many contexts, notably in crystalline or carbonate rocks. Indeed, in addition to Darcian transport characteristic of many porous media (Bear 1972), the structure of some porous media involves a large range of scales and shapes (Dullien 1992), and networks of fractures sometimes carry a very significant part of the fluid in the rocks, affecting significantly the transport dynamics (Sahimi 1995a,b; Adler & Thovert 1999). Models of fluid transport in fractures of various shapes have been obtained analytically and numerically (Zimmerman & Bodvarsson 1996; Zimmerman & Main 2004; Méheust & Schmittbuhl 2001). The understanding of the transport in these units is of key importance to model oil transport in carbonate reservoirs, water or pollutant transport in calcareous or granitic rocks, as for example, in water resource reservoirs (Ploemeur, France— Le Borgne *et al.* 2004) or around nuclear waste storage facilities in granitic rocks (Aspö, Sweden—Andersson *et al.* 2004)—see for example, a recent review in Faybishenko *et al.* (2005).

For deep enhanced geothermal plants, which are a developing carbon-free energy producing technology, the geometry of the heat exchanger is also often dominated by a few large fracture zones. This is the case, for instance, in the granitic formation between the injection and extraction wells of the pilot power plant of Soultz-sous-Forêts, France (Dezayes *et al.* 2010), developed by the European project EHDRA (European Hot Dry Rock Association) over the last 30 years. Even in such a case, the heat exchanger does not consist of only few large fractures, but of interconnected large and small fractures regrouped in fracture zones (Genter & Traineau 1996; Sausse 2002). Such complexity can be described using an interconnected fracture network, as for example, in the works of Bruel & Cacas (1992); Bruel (1995); Kohl & Hopkirk (1995); Kohl *et al.* (1995); Jupe *et al.* (1995); Hayashi *et al.* (1999); Kolditz & Clauser (1998); Watanabe & Tahahashi (1995). In such networks, most modellings propose simple models for single fracture units. We propose in this study to focus on such a single element, and to see how its own geometrical complexity affects its heat and mass transport properties. We will describe a simple way to capture the effect of this complexity. Ideally, this study could be used to parameterize the hydraulic and thermal properties of each element of a fracture network—combining deterministic and stochastic aspects to include at best the partial pieces of information on the network geometry and the geometric features of these units.

More specifically, the basic models of flow or heat exchange often consider that the joints have a simple geometry, like a volume between two parallel fracture surfaces. Self-affine geometry was however observed for most natural surfaces in fractures (Brown & Scholz 1985; Bouchaud 1997; Power & Durham 1997; Neuville *et al.* 2011b), faults (Power *et al.* 1987; Renard *et al.* 2006; Candela

*Now at: Department of Physics, University of Oslo, P.O. Box 1048, Blindern, NO-0316 Oslo, Norway.

et al. 2009) or stylolites (Schmittbuhl *et al.* 2004; Koehn *et al.* 2007; Ebner *et al.* 2009a,b). Thus, more realistic models of fractures have been proposed, which often consist in one of the two following models: the void between two identical self-affine fracture surfaces, opened and shifted with respect to each other, or the void between two statistically independent self-affine surfaces. Both geometries have been observed, for example, in natural cases, like the joints present at depth in a marl formation analysed in Draix (Neuville *et al*. 2011a,b).

Models already exist on how the self-affine characteristics of fracture surfaces affect on average the hydraulic and transport properties. For example, studies have been carried out on series of fractures with a certain aperture and roughness amplitude (Méheust & Schmittbuhl 2001; Neuville *et al.* 2010b).

For an open fracture, a key question to model its hydraulic transmissivity and the efficiency of the heat exchange is how to capture its geometric complexity with a small number of geometric parameters. In practice, some knowledge about the geometry of a fracture can be acquired by the study of core logs (e.g. Neuville *et al.* 2011a,b) at scales between micrometers and centimetres—some scaling hypothesis being required to extrapolate the large scale aperture. Unfortunately, such logs are rare. Generally, subsurface imaging methods, as surface seismic or electromagnetic methods, or localization of acoustic emissions during fluid injection, give some large scale information on the geometry of a particular fracture (e.g. Sausse *et al.* 2010). With such information at various scales, a central question is how to determine the transmissivity of a particular joint or fracture.

In this manuscript, we will show that both the thermal and hydraulic properties of transport in a self-affine fracture are largely determined by the large scale Fourier modes of its aperture.

2 EXISTING MODELS OF FLOW IN VARIABLE APERTURE FIELDS

For the simplest geometries of parallel plates, the stationary flow of Newtonian fluids is characterized by its hydraulic transmissivity described by the cubic law (Zimmerman & Bodvarsson 1996; Zimmerman & Main 2004), that is, j, the fluid flux integrated across the aperture follows

$$j = -[H^3/(12\eta)]\nabla P, \tag{1}$$

where H is the distance between the plates, η the fluid dynamic viscosity, ∇P the gradient of the deviation from hydrostatic pressure.

For apertures of any shape, at low speeds (in the Stokes regime), j is proportional to ∇P (Zimmerman & Bodvarsson 1996). The transmissivity of the fracture is characterized by its hydraulic aperture H, defined as follows: for a given pressure drop, H would be the distance between parallel plates leading to the observed flux, following eq. (1). For rough fractures, the hydraulic aperture H differs from the geometric aperture, $A = \langle a \rangle$, which is the spatial average of the aperture field $a(x, y)$, with (x, y) Cartesian coordinates in the fracture mid-plane. It was shown (Beran 1968) that in general, the hydraulic aperture H is bounded by $1/\langle a^{-3} \rangle \leq H^3 \leq \langle a^3 \rangle$, where $\langle . \rangle$ refers to space averaging. The lower bound corresponds to apertures varying in series along the flow, and the upper one to variations in parallel.

To avoid the explicit computations of the hydraulic flow in complex aperture fields, approximated computations of H have been proposed, based on several moments of the aperture field distribution (Brown 1987; Méheust & Schmittbuhl 2001). Classical parameters are the average of the aperture field, A, and the standard deviation, $\sigma = \left(\langle a^2 \rangle - \langle a \rangle^2\right)^{1/2}$ (Patir & Cheng 1978; Brown 1987; Zimmerman & Bodvarsson 1996; Méheust & Schmittbuhl 2001; Al-Yaarubi *et al.* 2005). Several expressions have been obtained analytically and numerically, for various models of apertures presenting small fluctuations as for example, sinusoidal or sawtooth profiles (Zimmerman & Bodvarsson 1996; Zimmerman & Main 2004), or in self-affine fractures (Méheust & Schmittbuhl 2001, 2003). Notably, for small aperture variations, $\sigma/A \ll 1$, it was shown that to second order in σ/A (Méheust & Schmittbuhl 2003; Zimmerman & Main 2004), $H^3 = A^3[1 - (3/2)(\sigma/A)^2]$. The result at larger order depends on the type of correlations of the aperture field considered (Méheust & Schmittbuhl 2001; Zimmerman & Main 2004). Statistical characterizations of H/A (its mean and dispersion) have been realized for a large number of self-affine apertures as functions of σ/A (Neuville *et al.* 2010b).

Fluid transport in rough fractures is marked by channeling flow, as has been observed experimentally (Tsang 1984; Méheust & Schmittbuhl 2000; Plouraboué *et al.* 2000). It was shown that among all the Fourier modes of the aperture, only a few large scale modes play an important role for the hydraulic properties of self-affine fractures (Schmittbuhl *et al.* 2008). In this manuscript, we will study such filter-based approximation for the hydraulic transmissivity of fractures, and precisely quantify its precision depending on the number of modes kept.

Concerning the thermal exchange behaviour in rough fractures, several models have been developed, notably in the context of geothermal reservoir modelling (Hayashi *et al.* 1999). Many models consider thermal and mass flux in networks of simple fractures (Jupe *et al.* 1995; Kohl & Hopkirk 1995; Kohl *et al.* 1995; Bruel 1995; Kolditz & Clauser 1998). Each fracture in these models is a simple object, for example, with parallel plane walls. In such geometries, analytical solutions exist (Gringarten & Sauty 1975; Rodemann 1979; Heuer *et al.* 1991). As was however underlined by Hayashi *et al.* (1999), Kolditz & Clauser (1998), the complexity of mechanical effects as poroelastic or thermoelastic ones, modifying the geometry of the fractures is likely to influence the flow geometry and the heat coupling. The hydrothermal properties of complex fault zones have been studied with variations of porosity, permeability and thermal conductivity (Rosener *et al.* 2007). With realistic self-affine apertures, it was shown that the thermal coupling between the fluid and rock is affected by the induced channelling, for example, in large fractures connecting the wells of Soultz-sous-Forêts (Neuville *et al.* 2010a).

To our knowledge, there has been no study so far of the specific influence of the different Fourier modes of the aperture on the thermal exchange efficiency.

3 APERTURE AND FLOW MODEL

In natural rocks, the surfaces of fractures and joints are often found to be self-affine, most of them with a Hurst exponent around 0.8 (Schmittbuhl *et al.* 1993, 1995; Bouchaud 1997). If two such independent surfaces are facing each other, the aperture in-between will also be self-affine, with an identical Hurst exponent. Similarly, if a self-affine fracture surface is created, and the sides of the fracture are opened and sheared, the aperture will be self-affine at scales below the amount of shear (Plouraboué *et al.* 1995). The determination of the detailed morphology of the open volume in a fracture or a joint is difficult to perform *in situ*, and seldom done beyond the characterization of an average aperture. Recently, we have performed such a study on a natural example of rock (black marl) analysed from a log core, and indeed found some example of self-affine aperture fields at the scale of observation (10 cm) (Neuville *et al.* 2011a,b).

The average aperture A of such self-affine channels is not sufficient to characterize entirely their properties in terms of hydraulic transport and heat exchange efficiency between the rock and fluid (Schmittbuhl *et al.* 2008; Neuville *et al.* 2010b). Even if the additional knowledge of the aperture roughness amplitude σ provides a better estimate of these properties, the dispersion between the different realizations of fractures with a given (σ, A) is still large (Neuville *et al.* 2010b). We will see here how, for a specific self-affine fracture, the gradual degradation of the resolution with a lowpass spatial filter provides a good determination of the fluid mass transport and fluid-rock heat exchange properties.

Specifically, we will consider synthetic self-affine aperture fields $a(x, y)$ with a Hurst exponent of $\zeta = 0.8$, determined as follows (Méheust & Schmittbuhl 2001): on a grid of lattice step d, with $L_x \times L_y = 512d \times 1024d$ points regularly spaced in (x, y), a white noise $\epsilon(x, y)$ is randomly generated. The 2-D (2-D) Fourier transform of this noise $\tilde{\epsilon}(k_x, k_y)$ is evaluated, and multiplied by a scale dependent factor to obtain a varying field $\tilde{\psi}(k_x, k_y) = (k_x^2 + k_y^2)^{(-1-\zeta)/2}\tilde{\epsilon}(k_x, k_y)$ (Adler & Thovert 1999). The inverse Fourier transform provides a self-affine function $\psi(x, y)$ with the desired Hurst exponent. Normalizing it and adding it to a homogeneous value results in a self-affine aperture field of the chosen average aperture A and standard deviation σ. Such an example of aperture, with $\sigma/A = 0.35$, is shown on Fig. 1. The flow considered is at low Reynolds number, that is, in the Stokes regime, and the aperture variations are assumed small compared to the average aperture, so that a lubrication approximation allows to locally integrate the flux through the aperture thickness. The integrated flow $q = \int v(x, y, z)dz$ relates to the 2-D pressure gradient (e.g. Zimmerman & Bodvarsson 1996) as

$$q(x, y) = -\frac{a^3}{12\eta}\nabla P, \tag{2}$$

and it satisfies the 2-D incompressibility equation: $\nabla \cdot q = 0$. The boundary conditions correspond to constant pressures imposed at $x = 0$ and at $x = L_x$, and impermeable sides parallel to the x direction. After discretization on the grid, these equations are solved using a biconjugate gradient method (Press *et al.* 1992). The 3-D velocity $v(x, y, z)$ is related to $q(x, y)$ as

$$v(x, y, z) = q(x, y)[z_1(x, y) - z][z - z_2(x, y)]/a(x, y)^3, \tag{3}$$

where z_1 and z_2 are the out of plane coordinates of the fracture sides, related to the aperture by $z_2 - z_1 = a$. Since the flow only depends on the aperture, for simplicity, one considers here apertures symmetric around their mid-planes, that is, such as $z_2 = -z_1 = a/2$.

The obtained integrated flow q, for the aperture of Fig. 1, is shown on Fig. 2. The grey scale is proportional to $q^* = q/q_{\text{ref}}$,

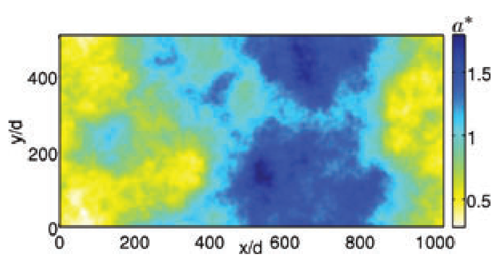

Figure 1. Self-affine synthetic aperture field with a normalized roughness amplitude $\sigma/A = 0.35$. The aperture field is normalized by its average, that is, the map corresponds to $a(x, y)/A$. d is a lattice step of arbitrary dimensions.

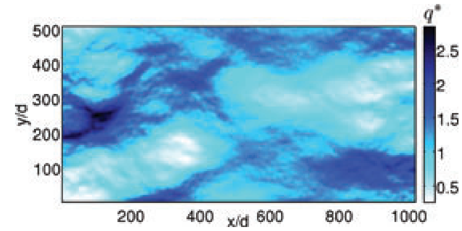

Figure 2. Integrated flow field q/q_{ref} in the aperture displayed: the colour code is proportional to the norm of the flow.

where q_{ref} is the integrated flux between parallel plates spaced by the same average A, with the same imposed macroscopic gradient and viscosity. Note that the aperture dependence of the flow is complex: for instance, at coordinates (600, 300), q very low, while a is quite large.

Profiles of the velocity along planes perpendicular to the fracture mid-plane, perpendicular or parallel to the average flow direction, are shown on Figs 3(a) and (b). These velocities have been scaled by v_{refmax}, the maximum velocity between parallel plates with the same geometric aperture. The heat transport is modelled by considering that in-plane advection entirely balances out-of-plane thermal conduction (Neuville *et al.* 2010b). Defining a thickness-averaged temperature weighted by the velocity,

$$\bar{T} = \int v(x, y, z)T(x, y, z)dz \Big/ \int v(x, y, z)dz, \tag{4}$$

these approximations lead to the following diffusion-advection equation for the thickness-averaged temperature (Neuville *et al.* 2010b)

$$q \cdot \nabla\bar{T} + 2(\chi/a)\,\text{Nu}(\bar{T} - T_{\text{r}}) = 0, \tag{5}$$

where T_{r} is the rock temperature, χ is the thermal diffusivity of the fluid and $\text{Nu} = 70/17$ the Nusselt number in a Poiseuille flow for a fracture. This partial differential equation is also discretized by finite-differences and solved by a biconjugate gradient method (Neuville *et al.* 2010b). The temperature field obtained in this way for our example is shown on Fig. 4. The colour scale corresponds to $-\ln(\bar{T}^*)$, with a dimensionless temperature

$$\bar{T}^* = (\bar{T} - T_{\text{r}})/(\bar{T}_{\text{inlet}} - T_{\text{r}}), \tag{6}$$

where $\bar{T}_{\text{inlet}}$ is the average temperature $\bar{T}(x = 0)$ imposed at the inlet of the fracture, which corresponds to the injection of cold fluid. The 3-D temperature field, according to the thermal lubrication approximation, is

$$\begin{aligned} T(x, y, z) &- T_{\text{r}} \\ &= (q \cdot \nabla\bar{T})/(2\chi a^3)(z - z_1)(z - z_2)(z - \sqrt{5}z_1)(z - \sqrt{5}z_2) \end{aligned} \tag{7}$$

Cross-sections of this temperature along the same planes as those used for the flow velocity are shown on Figs 5(a) and (b)—with a dimensionless representation $T^* = (T - T_{\text{r}})/(\bar{T}_{\text{inlet}} - T_{\text{r}})$.

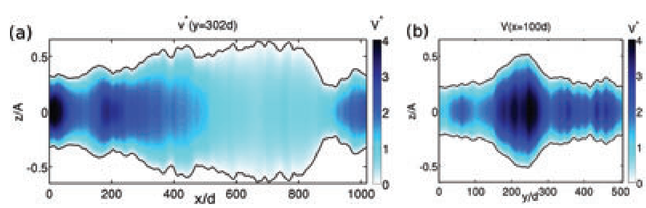

Figure 3. Cross-section of the flow field $v(x, y, z)/v_{\text{refmax}}$ across the aperture displayed, (a) parallel (at $y = 302d$) and (b) perpendicular (at $x = 100d$) to the flow direction.

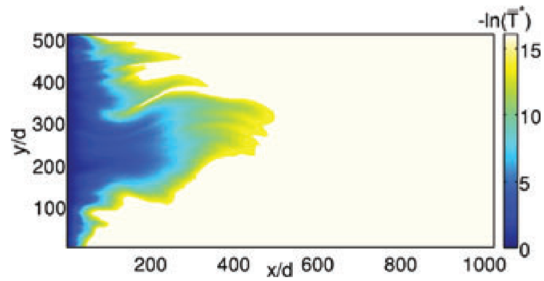

Figure 4. Integrated temperature field $-\ln(\bar{T}^*)$.

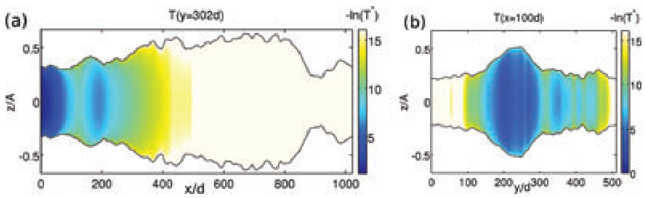

Figure 5. Cross-section of the temperature field $-\ln(T^*)$, (a) parallel (at $y = 302d$) and (b) perpendicular to the flow direction (at $x = 100d$).

4 FILTER BASED FLOW APPROXIMATION ON AN EXAMPLE

For any aperture field $a(x, y)$, with an integer n called a filtering radius, the lowpass filtered field $a_n(x, y)$ is defined as follows from the 2-D Fourier transform $\tilde{a}(k_x, k_y)$ of the aperture field

$$\begin{cases} \left(\frac{k_x L_x}{2\pi}\right)^2 + \left(\frac{k_y L_y}{2\pi}\right)^2 \geq n^2 \rightarrow \left\|\tilde{a}_n\left(k_x, k_y\right)^2\right\| = 0 \\ \left(\frac{k_x L_x}{2\pi}\right)^2 + \left(\frac{k_y L_y}{2\pi}\right)^2 < n^2 \rightarrow \left\|\tilde{a}_n\left(k_x, k_y\right)^2\right\| = \left\|\tilde{a}\left(k_x, k_y\right)^2\right\|. \end{cases} \quad (8)$$

The real space aperture field $a_n(x, y)$ is obtained by inverse Fourier transform of $\tilde{a}_n$ so defined. For a discretized aperture of size $L_x \times L_y$, (k_x, k_y) are wavevectors, and $(n_x, n_y) = (k_x L_x/(2\pi), k_y L_y/(2\pi))$ are integer wavenumbers. The filtering radius sets the number of large wavelength modes kept—see Fig. 6: for instance, for $n = 1$, only the homogeneous aperture mode $(n_x, n_y) = (0, 0)$ is kept in $a_1 = A$. For $n = 2$, the modes $(n_x, n_y) \in \{(0, 0); (0, 1); (1, 0); (1, 1); (-1, 1)\}$ are kept [together with the complex conjugate modes, that is, the opposite wavenumbers, (0,−1), (−1,0), (−1,−1), (1,−1)]. We consider here the example of the self-affine fracture shown on Fig. 1. Applying the proposed lowpass filter of order n generates apertures which are self-affine down to the scale L_y/n [or for any shape L_x and L_y, down to the scale $\min(L_x, L_y)/n$]. The $n = 2$ and $n = 4$ filtered aperture fields are shown on Fig. 7.

4.1 Hydraulic behaviour

The same finite-difference numerical scheme as described previously is used to compute the flow field in these filtered apertures, according to eqs (2, 3). The resulting flow velocity, integrated through the aperture is shown on Fig. 8. Two cross-sections of the velocity field across the thickness are also computed and shown on Fig. 9. The comparison of these flow field structures to the results with the full resolution of the aperture roughness (Figs 2 and 3) shows that the main features of the flow field are obtained from the computation of the flow in the filtered aperture. Thus, solving for the flow field in a lowpass filtered aperture seems to reproduce the main features of the flow. To evaluate more quantitatively the quality of

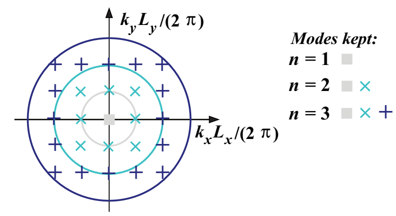

Figure 6. Representation of the lowpass spatial filter applied for filtering radii $n = 1$, $n = 2$ and $n = 3$: wavenumbers (n_x, n_y) of the Fourier modes kept.

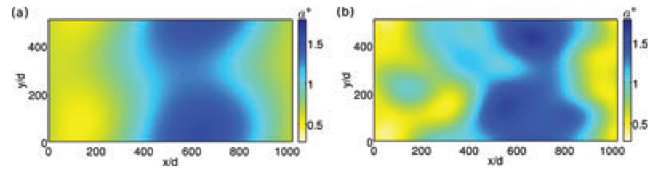

Figure 7. (a) Filtered aperture field a/A with the 3 main Fourier modes and conjugates, that is, a filtering radius $n = 2$, and (b) with a filtering radius $n = 4$.

this approximation, the hydraulic aperture H_n is evaluated for the filtered apertures, as a function of the filtering radius n. The relative difference between H_n and the hydraulic aperture with full resolution of the geometric aperture, H_{ref}, is shown on Fig. 10(a). Clearly, this curve converge quickly. The reference aperture for this joint is such as $H_{\mathrm{ref}}/A = 0.816$, and this limit as n grows is quickly approached by H_n/A. The trivial case of parallel plates corresponds to the $n = 1$ filtered case, for which $H/A = 1$ by definition, and for which $(H_1 - H_{\mathrm{ref}})/H_{\mathrm{ref}} = 22$ per cent. Already, including the four main modes in addition to the average aperture ($n = 2$) brings this relative accuracy to 0.8 per cent: a very clear improvement, despite the small number of modes considered. In this example, all hydraulic apertures computed with radii $n > 6$ are closer than 0.2 per cent from the full resolution H_{ref}. The tendency observed in this

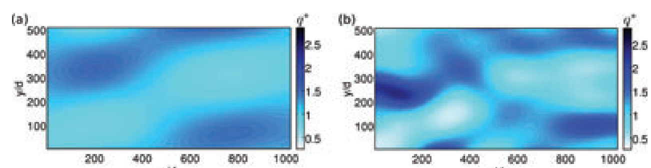

Figure 8. Dimensionless hydraulic flux q/q_{ref} in the filtered apertures, with filtering radii of respectively (a) $n = 2$ and (b) $n = 4$.

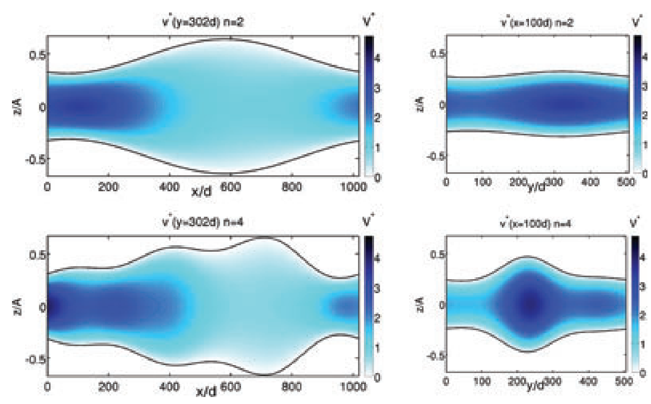

Figure 9. Cross-section of the flow v/v_{refmax} in the $n = 2$ (top panel) and $n = 4$ (bottom panel) filtered aperture, (left-hand side) along the flow, at $y = 302d$ and (right-hand side) perpendicularly to the flow, at $x = 100d$.

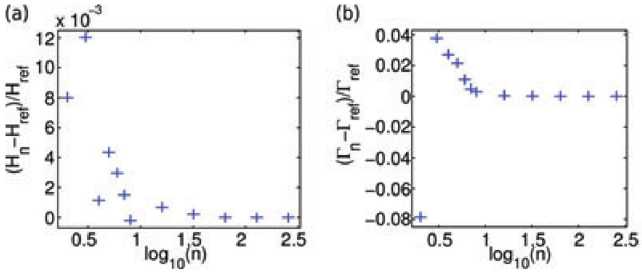

Figure 10. (a) Hydraulic and (b) thermal apertures as a function of the filter degree n (for $n \in \{2-8, 16, 32, 64, 128, 256\}$) relative to the fully rough case.

example, that H_n is overestimated at small n with respect to H_{ref}, is not systematic for all apertures: for some other cases, $H_{\mathrm{ref}} > A$, and H_n is rather underestimated.

4.2 Thermal behaviour

Similarly to the approach taken for the velocity, we compute the temperature field in large scale filtered apertures. The resulting thickness-averaged temperature field $\bar{T}$ is represented on Fig. 11. The corresponding cross-sections are represented on Fig. 12. The scaling factors and the shading scales are identical to those used on Figs 4 and 5. The similarities with these figures show how the large scales control the channelling of the energy transport to a great extent. To quantify the quality of the filtering approximation, a macroscopic quantity, named as the thermal aperture Γ_n , is evaluated in the apertures filtered at order n. At a coarse-grained scale, the temperature gap between the fluid and the rock evolves exponentially as a function of the travel distance in the channel. The inverse

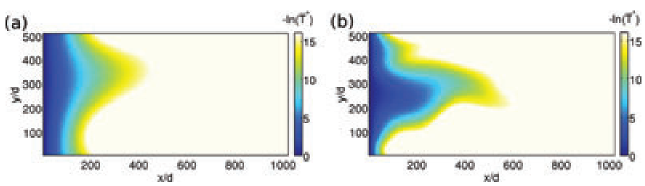

Figure 11. Temperature (integrated across the thickness) in a filtered aperture field, with filtering radii of respectively (a) $n = 2$ and (b) $n = 4$. The colour scale represents $-\ln(\bar{T}^*)$, the logarithm of the scaled temperature $\bar{T}^*$.

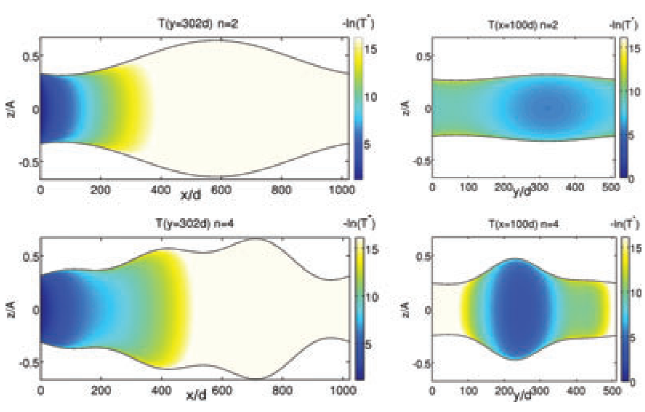

Figure 12. Cross-section of the scaled temperature in the $n = 2$ (top panel) and $n = 4$ (bottom panel) filtered aperture, (left-hand side) along the flow, at $y = 302d$ and (right-hand side) perpendicular to the flow, at $x = 100d$.

of the slope of the linear fit in a semilogarithmic representation of the temperature gap provides us a characteristic thermalization distance (Neuville *et al.* 2010b). This length characterizes the exponential evolution of the fluid temperature toward the rock one. The thermal aperture is then defined as the aperture between two parallel plates leading to the same characteristic thermalization distance (Neuville *et al.* 2010b). This characterizes the efficiency of the thermal exchange between the fluid and the surrounding rock. As an approximation to the thermal aperture of the rough aperture at full resolution, Γ_{ref}, we consider the thermal aperture of the filtered aperture fields Γ_n. The relative difference between Γ_n and the hydraulic aperture with full resolution of the geometric aperture, Γ_{ref}, is shown on Fig. 10(b). Here, $\Gamma_{\mathrm{ref}}/A = 0.886$, that is, the thermal aperture of the rough joint is $(\Gamma_1 - \Gamma_{\mathrm{ref}})/\Gamma_{\mathrm{ref}} = 11.4$ per cent below the parallel plate case ($n = 1$). Considering the first largest Fourier modes ($n = 2$), the relative error of the approximation drops to 8 per cent, and with the next largest wavelength ($n = 3$), below 4 per cent. The speed of convergence of the filter-based approximation is slightly slower than for the hydraulic aperture. For $n \geq 6$, the precision of the approximation is better than 0.11 per cent.

5 PRECISION OF THE FILTER-BASED APPROXIMATION, STATISTICS OVER THE APERTURES

The previous analysis of the accuracy of the filter approximation was for a particular aperture. We will study statistically the convergence of the hydraulic and thermal apertures as a function of the filter radius n over many realizations. For this purpose, 300 realizations of statistically independent synthetic self-affine apertures (with the same Hurst exponent 0.8) are created. Each realization is characterized by a roughness amplitude σ and an average aperture A. These 300 realizations are grouped in five values of σ/A, $\{0.1, 0.2, 0.3, 0.4, 0.5\}$, with at least 50 realizations in each group. The filtered hydraulic and thermal apertures are computed with filtering radii from $n = 1$ (flat) to $n = 11$ (around 100 largest scale Fourier modes)—see Fig. 13.

For each of the filtered morphologies, the flux and temperature are solved, the hydraulic aperture H_n and thermal aperture Γ_n are extracted, and compared to their counterparts for the unfiltered fields, H_{ref} and Γ_{ref}. The roughness amplitude of the filtered aperture, σ_n, is also compared to that of the unfiltered aperture, σ. The resulting

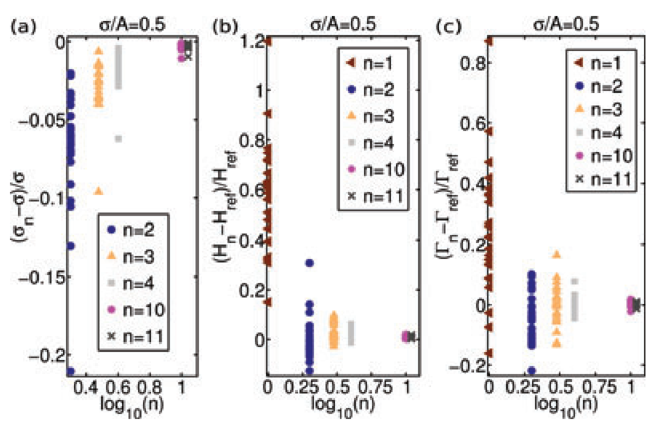

Figure 13. Relative error on: (a) the aperture fluctuation σ_n, (b) the hydraulic aperture, and (c) the thermal aperture, as a function of the degree of the filter, for large aperture fluctuations ($\sigma/A = 0.5$). Cloud of values obtained over 50 independent realizations.

values as functions of the filter radius n are shown on Fig. 13, for the group with the largest roughness, $\sigma/A = 0.5$. For these examples, the maximum relative error on the hydraulic aperture is 120 per cent for $n = 1$ (flat plates), and 20 per cent for $n = 2$ (4 largest modes). On the thermal one, the maximum relative error is 60 per cent for $n = 1$, and 20 per cent for $n = 2$. Obviously, adding even only the largest modes of the roughness increases sensibly the resolution of the hydraulic and thermal properties of the fracture model. The error on the amplitude of the roughness due to the filtering is at maximum 13 per cent for $n \geq 2$. The value for $n = 1$ is not displayed, being by construction always equal to $(\sigma_1 - \sigma_{\mathrm{ref}})/\sigma_{\mathrm{ref}} = -1$.

These values are maximal values, and the characteristic amplitude of the relative error can be computed by evaluating $\sigma[\mathrm{e}_n]$, the root mean square of these relative errors over each group of values of σ/A: the dispersion of the relative errors on hydraulic apertures, $\sigma\,[\mathrm{e}(H_n)] = \sqrt{\langle[(H_n - H_{\mathrm{ref}})/H_{\mathrm{ref}}]^2\rangle}$ and on thermal ones, $\sigma\,[\mathrm{e}(\Gamma_n)] = \sqrt{\langle[(\Gamma_n - \Gamma_{\mathrm{ref}})/\,\Gamma_{\mathrm{ref}}]^2\rangle}$, are displayed as functions of n for each of the five groups on Fig. 14. The error dispersion logically increases as a function of the roughness amplitude σ/A, and fast decreases as a function of the filtering radius. The largest value of $\sigma[\mathrm{e}_n]$, obtained for the group $\sigma/A = 0.5$, drops below 4 per cent on the hydraulic aperture for $n \geq 3$, and on the thermal aperture for $n \geq 4$.

One can directly compute analytically the error made on local values of the aperture $a(x, y)$ by the lowpass filtering procedure, and show that it presents a power law of n as an upper bound, $E(n) \sim n^{-\zeta}$, where ζ is the Hurst exponent of the aperture field. Technically, the rate of convergence of the Fourier series of the aperture field $a(x, y)$ is determined as follows, from its Fourier transform

$$a(x, y) = \sum_{k} \tilde{a}(k_x, k_y) e^{-2i\pi(k_x x + k_y y)}. \tag{9}$$

In this series, the error done on the aperture by omitting the terms of the lowpass filter of order n, defined by eq. (8), is

$$E(n) = \sum_{k \geqslant n.2\pi/L} \tilde{a}(k, \theta) e^{-2i\pi(kr\cos(\theta-\theta\prime))}, \tag{10}$$

where (k, θ) and $(r, \theta\prime)$ are the radial representations of the vectors (k_x, k_y) and (x, y). The self-affinity of a implies that for $k \neq 0$, its 2-D Fourier transform scales as $\tilde{a}(k, \theta) \sim Ck^{-1-\zeta}$. Hence, for large enough n, the sum of the modes comprising the error can be upper bounded as follows, and evaluated using a continuous integral:

$$E(n)^2 \leq \sum_{k \geqslant n.2\pi/L} \|\tilde{a}(k, \theta)\|^2 \tag{11}$$

$$\simeq \sum_{k \geqslant n.2\pi/L} C^2 k^{-2-2\zeta} \tag{12}$$

$$\simeq [C^2 L^2/(4\pi^2)] \int_{n.2\pi/L}^{+\infty} k^{-2-2\zeta} 2\pi k dk \tag{13}$$

$$\simeq [C^2 L^2/(2\pi(-1-2\zeta))](2\pi/L)^{-2\zeta} n^{-2\zeta}, \tag{14}$$

which shows that the convergence of the n-lowpass filtered aperture behaves as $E(n) \sim n^{-\zeta}$.

Given this power-law dependence of the error on n for the local geometric aperture, it is plausible that the errors done on the hydraulic and thermal apertures present similar power-law behaviour on n, the filtering radius. This hypothesis is consistent with the data, as shown on Figs 14(a) and (b): the bilogarithmic representation of the dispersion of these errors as a function of the filtering radius is reasonably linear, with a central value around 2 for the slope of the linear regressions (exponent) corresponding to $\sigma\,[e_n] \sim n^{-2}$ for both errors on hydraulic and thermal apertures – $\sigma[\mathrm{e}(H_n)]$ and $\sigma[\mathrm{e}(\Gamma_n)]$, defined above. The determined power laws with exponent 2 and prefactors obtained by linear regression in these two figures are also displayed on Figs 14(a) and (b). These simulations have been performed on elongated fractures of in-plane aspect ratio $J = L_x/L_y = 2$, where x is along the average flow direction and y transverse to it (z being the thickness). It has been shown that the hydraulic and thermal properties of a fracture potentially depend on this aspect ratio (Neuville *et al.* 2010b). The same analysis as above has also been performed on fractures of aspect ratio $J = L_x/L_y = 1$ (square fractures) and 0.5 (large ones). The results are qualitatively similar to those obtained for the elongated fractures. Up to roughness amplitudes $\sigma/A = 0.4$, the error dispersion of the filter-based approximation drops below 3 per cent for $n \geq 2$ for the hydraulic aperture, and below 4 per cent for the thermal aperture for $n \geq 3$—see Fig. 14(c), for the case of $\sigma/A = 0.4$ (other values behave similarly, with smaller errors). The error dispersions also behave reasonably as power laws of the filtering radius, $\sigma[\mathrm{e}_n] \sim n^{-2}$, as shows the comparison with the fits displayed as continuous lines.

Eventually, the quality of the approximation done by reducing the aperture to the largest Fourier modes can be tested on the following example: similarly to the work done in Neuville *et al.* (2010b), one can look at the deviation in hydraulic and thermal apertures from a parallel plate model, as a function of the normalized roughness amplitude (for elongated fractures with $J = 2$). The average and standard deviation of H/A and Γ/A as functions of σ/A are evaluated from 300 independent simulations, each being approximated

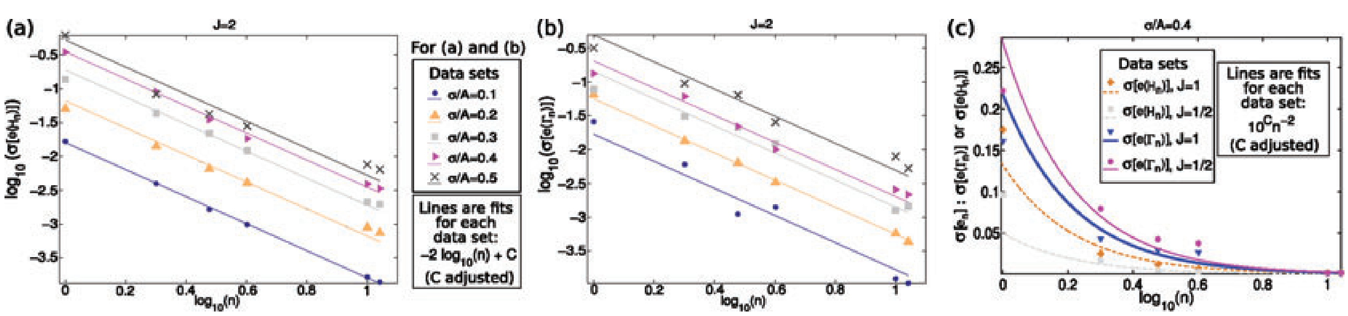

Figure 14. Dispersion of the relative errors, $\sigma[\mathrm{e}_n]$ (for $n \in \{1-4, 10, 11\}$) on (a) the hydraulic aperture, (b) the thermal aperture, as a function of the degree of the filter, for different aperture fluctuations from $\sigma/A = 0.1$ to 0.5, in bilogarithmic representation, with aspect ratio $J = 2$. Straight lines correspond to a power-law behaviour $\sigma[\mathrm{e}_n] \sim n^{-2}$, corresponding to the central value of linear regressions over each data set in bilogarithmic space. On (c), the same is shown in lin–log representation for $J = L_x/L_y$=1 or 1/2, and aperture fluctuations $\sigma/A = 0.4$.

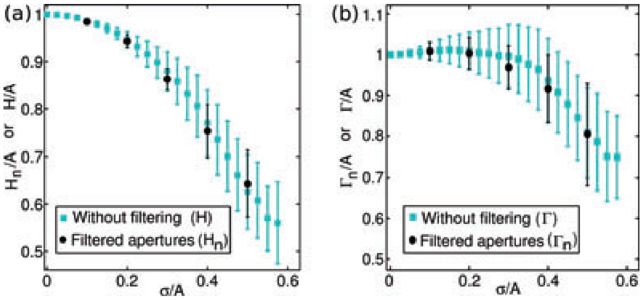

Figure 15. Statistical results over numerous synthetic apertures in simulations (with $J = 2$): (a) hydraulic aperture (average and error bars given by plus or minus the root mean square) and (b) thermal aperture, as functions of the roughness amplitude: comparison between the $n = 4$ filter (with 300 aperture field realizations) and the full scale description of the aperture (with 20×10^3 aperture field realizations).

by its filtered aperture with $n = 4$ radius. This is compared to the results with the full scale description of the aperture for 20×10^3 independent simulations (Fig. 15). This figure shows that the full-resolution dependence is not distinguishable for this feature from the results obtained in the filtered aperture (black circles).

6 DISCUSSION

Many length scales and time scales intervene when considering the hydraulic and heat transport into a self-affine fracture. Here, the self-affine property of the aperture is supposed to hold for a range of scales, up to the size of the fracture, which is higher than the cut-off length scale introduced in our frequency lowpass Fourier truncation. In practice, the self-affinity property stops at large scales either for geometrical reasons (Neuville *et al.* 2011a), or for instance if the facing topographies are decorrelated at small scales and correlated at large scales (Méheust & Schmittbuhl 2003; Plouraboué *et al.* 1995, and references therein). In relation to the Stokes flow approximation, the surface is considered smooth below a certain cut-off. If the aperture is also self-affine below this cut-off, this small scale roughness is neglected. The exact role of these small details is studied for example, by Skjetne *et al.* (1999). The detailed study of this in terms of heat exchange is a current track for future work under development (e.g. using lattice Boltzmann methods – Neuville 2010). In the systems we consider, the cut-off of the Fourier filter is much higher than the mean fracture aperture, and also higher than the characteristic thermalization distance (which is proportional to the velocity). For such systems, the Péclet number, defined by vL_x/χ is high enough so that in-plane advective heat flux is dominant compared to the in-plane diffusive process. It also means that the typical length scale in the fracture plane below which diffusive transport dominates over the advective one, χ/v, is much smaller than the Fourier filter cut-off.

The rock temperature is also supposed to be constant and uniform. This is true for very short time scales when the regime is transitory, or for longer scales at quasi-stationary regimes. Indeed, as the thermal diffusivity of the rock is higher than the fluid one, the fluid temperature evolves faster than that of the rock.

Eventually, the current simulations have all been performed with self-affine aperture fields characterized by a Hurst exponent $\zeta = 0.8$, commonly observed on rock discontinuities. On some joints or rock types, this Hurst exponent changes: for example, $\zeta = 0.5$ was measured for natural sandstone surfaces (Méheust & Schmittbuhl 2003; Ponson *et al.* 2007). To generalize this study to other self-affine joints, a natural question is the impact of this Hurst exponent on the quality of the proposed filtering approach. Performing the whole statistical study carried out here for many different Hurst exponents would be out of the scope of this manuscript, but a hint on this question can be obtained from the convergence of the lowpass filter of the Fourier series describing the aperture field a. As was shown earlier, for a given roughness amplitude σ, the error on the local aperture made by a lowpass filter of order n decays faster than $n^{-\zeta}$. Thus, the convergence of the filtered aperture towards the real aperture field is faster for larger Hurst exponents. The computation of mass and heat flux in better approximated aperture fields is expected to capture better the transport features: the larger the Hurst exponent, the better the quality of the proposed filter-based approximation should be.

7 CONCLUSION

Rough aperture fields with a Hurst exponent of $\zeta = 0.8$ correspond to often encountered empty fracture geometries in natural rocks. For such joints, channelling effects affect the flow, and lead to non-trivial hydraulic properties (ratio of the flow over the macroscopic pressure gradient) and efficiency of the thermal exchange between a flowing fluid and the surrounding: these are different from the properties that would correspond to straight channels with flat sides with identical average geometric aperture. A key question, for a given fracture, is what parameters should be kept to model these properties with a sufficient accuracy, while retaining the smallest number of free parameters. We have shown here that the largest scales of the aperture control these properties.

Retaining only the variability at the largest scales (4 modes on top of the average) for example, allows us to reach already an accuracy of 9 per cent over the hydraulic and thermal aperture. Operationally, applying a Fourier filtering of the aperture keeping only the largest Fourier length scales, and solving for the hydraulic and thermal transport in such smoothed aperture fields, provides an excellent approximation to compute the hydraulic and thermal aperture of a given aperture field. If a measurement method determines these few large scale modes, a good deterministic model of these thermal and mass transport properties can be obtained.

ACKNOWLEDGMENTS

We wish to thank H. Auradou, Y. Méheust, F. Cornet, D. Amitrano, A. Genter, E. Flekkøy, A. Cochard and P. Baud for fruitfull discussions. We also acknowledge the financial support of the ANR ECCO, ANR TRIGGERLAND, INSU, and of the Alsace region through the REALISE program.

REFERENCES

Adler, P. & Thovert, J.-F., 1999. *Fractures and Fracture Networks,* Kluwer Academic Publishers, Dordrecht, The Netherlands.

Al-Yaarubi, A., Pain, C., Grattoni, C. & Zimmerman, R., 2005. Navier-Stokes simulations of fluid flow through a rock fracture, in *Dynamics of Fluids and Transport in Fractured Rocks,* AGU Monograph, Vol. 162, pp. 55–64, eds Faybishenko, B., Witherspoon, P. & Gale, J., American Geophysical Union, Washington, DC.

Andersson, P., Byegard, J., Tullborg, E., Doe, T., Hermanson, J. & Winberg, A., 2004. In situ tracer tests to determine retention properties of a block scale fracture network in granitic rock at the Äspö Hard Rock Laboratory, sweden, *J. Contam. Hydrol.,* **70**(3–4), 271–297.

Bear, J., 1972. *Dynamics of Fluids in Porous Media,* Elsevier, New York, NY.

Beran, M.J., 1968. *Statistical Continuum Theories,* Interscience, New York.

Bouchaud, E., 1997. Scaling properties of cracks, *J. Phys.: Condens. Matter,* **9,** 4319–4344.

Brown, S., 1987. Fluid flow through rock joints: the effect of surface roughness, *J. geophys. Res.,* **92**(B2), 1337–1347.

Brown, S. & Scholz, C.H., 1985. Broad bandwidth study of the topography of natural rock surfaces, *J. geophys. Res.,* **90**(B2), 12 575–12 582.

Bruel, D., 1995. Heat extraction from forced fluid flow through stimulated fractured rock masses: application to the Rosemanowes Hot Dry Rock reservoir, *Geothermics,* **24**(3), 361–374, doi:10.1016/0375-6505(95)00014-H.

Bruel, D. & Cacas, M.C., 1992. Numerical modelling technique: contribution to the Soultz HDR project, *Geotherm. Sci. Tech.,* **3,** 267–279.

Candela, T, Renard, F., Bouchon, M., Brouste, A., Marsan, D. & Schmittbuhl, J., 2009. Characterization of fault roughness at various scales: implications of three-dimensional high resolution topography measurements, *Pure appl. Geophys.,* **166**(10–11), 1817–1851.

Dezayes, C., Genter, A. & Valley, B., 2010. Structure of the low permeable naturally fractured geothermal reservoir at Soultz, *C. R. Geosci.,* **342**(7–8), 517–530.

Dullien, F., 1992. *Porous Media Fluid Transport and Pore Structure,* 2nd edn, Academic, San Diego, CA.

Ebner, M., Koehn, D., Toussaint, R., Renard, F. & Schmittbuhl, J., 2009a. Stress sensitivity of stylolite morphology, *Earth planet. Sci. Lett.,* **277**(3–4), 394–398.

Ebner, M., Koehn, D., Toussaint, R. & Renard, F., 2009b. The influence of rock heterogeneity on the scaling properties of simulated and natural stylolites, *J. Struct. Geol.,* **31,** 72–82.

Faybishenko, B., Witherspoon, P. & Bodvarsson, G., 2005. Emerging issues in fractured-rock flow and transport investigations: introduction and overview, in *Dynamics of Fluids and Transport in Fractured Rocks,* AGU Monograph, Vol. 162, pp. 1–11, eds Faybishenko, B., Witherspoon, P. & Gale, J., American Geophysical Union, Washington, DC.

Genter, A. & Traineau, H., 1996. Analysis of macroscopic fractures in granite in the HDR geothermal well EPS-1, Soultz-sous-Forêts, France, *J. Volc. Geotherm. Res.,* **72**(1–2), 121–124.

Gringarten, A.C. & Sauty, J., 1975. A theoretical study of heat extraction from aquifers with uniform regional flow, *J. geophys. Res.,* **80**(35), 4956–4962.

Hayashi, K., Willis-Richards, J., Hopkirk, R. & Niibori, Y., 1999. Numerical models of HDR geothermal reservoirs – a review of current thinking and progress, *Geothermics,* **28**(4-5), 507–518.

Heuer, N., Kupper, T. & Windelberg, D., 1991. Mathematical model of a Hot Dry Rock system, *Geophys. J. Int.,* **105**(3), 659–664.

Jupe, A. *et al.*, 1995. Modelling of a European prototype HDR reservoir, *Geothermics,* **24**(3), 403–419.

Koehn, D., Renard, F., Toussaint, R. & Passchier, C., 2007. Growth of stylolite teeth patterns depends on normal stress and finite compaction, *Earth planet. Sci. Lett.,* **257,** 582–595.

Kohl, T. & Hopkirk, R., 1995. "FRACURE" – A simulation code for forced fluid flow and transport in fractured, porous rock, *Geothermics,* **24**(3), 333–343.

Kohl, T., Evans, K., Hopkirk, R.J. & Rybach, L., 1995. Coupled hydraulic, thermal and mechanical considerations for the simulation of Hot Dry Rock reservoirs, *Geothermics,* **24**(3), 345–359.

Kolditz, O. & Clauser, C., 1998. Numerical simulation of flow and heat transfer in fractured crystalline rocks: application to the Hot Dry Rock site in Rosemanowes (U.K.), *Geothermics,* **27**(1), 1–23.

Le Borgne, T., Bour, O., de Dreuzy, J., Davy, P. & Touchard, F., 2004. Equivalent mean flow models for fractured aquifers: insights from a pumping test scaling interpretation, *Water Resour. Res.,* **40**(3), doi:10.129/2003WR002436.

Méheust, Y. & Schmittbuhl, J., 2000. Flow enhancement of a rough fracture, *Geophys. Res. Lett.,* **27,** 2989–2992.

Méheust, Y. & Schmittbuhl, J., 2001. Geometrical heterogeneities and permeability anisotropy of rough fractures, *J. geophys. Res.,* **106**(B2), 2089–2012.

Méheust, Y. & Schmittbuhl, J., 2003. Scale effects related to flow in rough fractures, *Pure appl. Geophys.,* **160**(5–6), 1023–1050.

Neuville, A., 2010. Comportement hydro-thermique d'un écoulement de fluide dans une fracture rugueuse: Modélisation et application à des massifs fracturés, *PhD thesis*, Université de Strasbourg.

Neuville, A., Toussaint, R. & Schmittbuhl, J., 2010a. Fracture roughness and thermal exchange: a case study at Soultz-sous-Forêts, *C. R. Geosci.,* **342**(7–8), 616–625.

Neuville, A., Toussaint, R. & Schmittbuhl, J., 2010b. Hydro-thermal flows in a self-affine rough fracture, *Phys. Rev. E,* **82,** 036317, doi:10.1103/PhysRevE.82.036317.

Neuville, A., Toussaint, R. & Schmittbuhl, J., 2011a. Fracture aperture reconstruction and determination of hydrological properties: a case study at Draix (French Alps), *Hydrol. Processes,* in press, doi: 10.1002/hyp.7985.

Neuville, A., Toussaint, R., Schmittbuhl, J., Koehn, D. & Schwarz, J., 2011b. Characterization of major discontinuities from borehole cores of the black consolidated marl formation of Draix (French Alps), *Hydrol. Processes,* in press, doi: 10.1002/hyp.7984.

Patir, N. & Cheng, H., 1978. An average flow model for determining effects of three-dimensional roughness on partial hydrodynamic lubrication, *J. Lubr. Technol.,* **100,** 12–17.

Plouraboué, F., Kurowski, P., Hulin, J.-P., Roux, S. & Schmittbuhl, J., 1995. Aperture of rough cracks, *Phys. Rev. E,* **51**(3), 1675–1685.

Plouraboué, F., Kurowski, P., Boffa, J.-M., Hulin, J.-P. & Roux, S., 2000. Experimental study of the transport properties of rough self-affine fractures, *J. Contam. Hydrol.,* **46,** 295–318.

Ponson, L., Auradou, H., Pessel, M., Lazarus, V. & Hulin, J.-P., 2007. Failure mechanisms and surface roughness statistics of fractured Fontainebleau sandstone, *Phys. Rev. E,* **76**(3), 036108, doi:10.1103/PhysRevE.76.036108.

Power, W.L. & Durham, W.B., 1997. Topography of natural and artificial fractures in granitic rocks: implications for studies of rock friction and fluid migration, *Int. J. Rock Mech. Min. Sci.,* **37,** 979–989.

Power, W.L., Tullis, T.E., Brown, S.R., Boitnott, G.N. & Scholz, C.H., 1987. Roughness of natural fault surfaces, *Geophys. Res. Lett.,* **14,** 29–32.

Press, W., Teukolsky, S., Vetterling, W. & Flannery, B., 1992. *Numerical Recipes,* Cambridge University Press, New York, NY.

Renard, F, Voisin, C., Marsan, D. & Schmittbuhl, J., 2006. High resolution 3D laser scanner measurements of a strike-slip quantify its morphological anisotropy at all scales, *Geophys. Res. Lett.,* **33,** L04305, doi:10.1029/2005GL025038.

Rodemann, 1979. *Modellrechnungen zum Wärmeaustausch in einem Frac.,* p. 90, Report No. 81990, Niedersächsisches Landesamt für Bodenforschung (NLfB), Hannover.

Rosener, M., Géraud, Y., Vaunat, J. & Fritz, B., 2007. Damage zone integration into fault models: implication on heat and mass transfer during geothermal exploitation, in *Proceedings of the EHDRA Scientific Conference*. GEIE Exploitation Minière de la Chaleur, Kutzenhausen, France.

Sahimi, M., 1995a. Flow phenomena in rocks – from continuum models to fractals, percolation, cellular-automata, and simulated annealing, *Rev. Mod. Phys.,* **65,** 1393–1534.

Sahimi, M., 1995b. *Flow and Transport in Porous Media and Fractured Rock,* VCH, Mannheim.

Sausse, J., 2002. Hydromechanical properties and alteration of natural fracture surfaces in the Soultz granite (Bas-Rhin, France), *Tectonophysics,* **348**(1-3), 169–185.

Sausse, J., Dezayes, C., Dorbath, L., Genter, A. & Place, J., 2010. 3D model of fracture zones at Soultz-sous-Forêts based on geological data, image logs, induced microseismicity and vertical seismic profiles, *C. R. Geosci.,* **342**(7–8), 531–545.

Schmittbuhl, J., Gentier, S. & Roux, S., 1993. Field measurements of the roughness of fault surfaces, *Geophys. Res. Lett.,* **20**(8), 639–641.

Schmittbuhl, J., Schmitt, F. & Scholz, C., 1995. Scaling invariance of crack surfaces, *J. geophys. Res.,* **100**(B4), 5953–5973.

Schmittbuhl, J., Renard, F., Gratier, J.P. & Toussaint, R., 2004. Roughness of stylolites: implications of 3D high resolution topography measurements, *Phys. Rev. Lett.,* **93,** 238501, doi:10.1103/PhysRevLett.93.238501.

Schmittbuhl, J., Steyer, A., Jouniaux, L. & Toussaint, R., 2008. Fracture morphology and viscous transport, *Int. J. Rock Mech. Min. Sci.,* **45,** 422–430.

Skjetne, E., Hansen, A. & Gudmundsson, J.S., 1999. High-velocity flow in a rough fracture, *J. Fluid Mech.,* **383,** 1–28.

Tsang, Y., 1984. The effect of tortuosity on fluid flow through a single fracture, *Water Resour. Res.,* **20**(9), 1209–1215.

Watanabe, K. & Takahashi, H., 1995. Parametric study of the energy extraction from hot dry rock based on fractal fracture network model., *Geothermics,* **24**(3), 223–236, doi:10.1016/0375-6505(94)00049-I.

Zimmerman, R. & Bodvarsson, G., 1996. Hydraulic conductivity of rock fractures, *Transp. Porous Media,* **23**(1), 1–30.

Zimmerman, R. & Main, I., 2004. Hydromechanical behaviour of fractured rocks, in *Mechanics of Fluid-Saturated Rocks,* Vol. 89 of International geophysics series, pp. 363–421, Academic Press, London.

C. R. Geoscience 342 (2010) 616–625

Contents lists available at ScienceDirect

Comptes Rendus Geoscience

www.sciencedirect.com

Surface geosciences (Hydrology–hydrogeology)

Fracture roughness and thermal exchange: A case study at Soultz-sous-Forêts

Rugosité de fracture et échange thermique : étude de cas à Soultz-sous-Forêts

Amélie Neuville [a,*,b], Renaud Toussaint [a,b], Jean Schmittbuhl [a,b]

[a] *UMR CNRS 7516, institut de physique du globe de Strasbourg, 5, rue Descartes, 67084 Strasbourg cedex, France*
[b] *EOST, université de Strasbourg, Strasbourg, France*

ARTICLE INFO

Article history:
Received 11 November 2008
Accepted after revision 17 March 2009
Available online 10 June 2009

Written on invitation of the Editorial Board

Keywords:
Fracture
Roughness
Lubrication
Heat exchange
Soultz-sous-Forêts
France

Mots clés :
Fracture
Rugosité
Lubrification
Échange de chaleur
Soultz-sous-Forêts
France

ABSTRACT

Heat exchange during laminar flow in an open fracture is studied numerically on the basis of the Stokes equation in the limit of hydrothermal lubrication. We examine the influence of fracture roughness on hydraulic permeability and heat flux through the fracture sides when a cold fluid is injected into a homogeneous hot host rock. Spatial temperature fluctuations inside the fluid are studied assuming the temperature of the rock to be constant and the fracture aperture to be self-affine. An application to the case study at the deep geothermal reservoir of Soultz-sous-Forêts, France, is presented. Finally, a thermal model based on sparse spatial information of the geometrical aperture is successfully proposed to reproduce the response of the fracture.

RÉSUMÉ

L'échange de chaleur en régime laminaire est étudié numériquement dans une fracture ouverte sur la base de l'équation de Stokes, dans la limite de l'hypothèse de lubrification hydrothermique. Nous observons l'influence de la rugosité sur la perméabilité hydraulique, ainsi que sur le flux de chaleur à travers les parois de la fracture, quand un fluide froid est injecté dans une roche mère ayant une température chaude homogène. Les fluctuations de la température du fluide sont étudiées en supposant que la température de la roche est constante et la fracture auto-affine. Une application au cas d'étude du réservoir de géothermie profonde à Soultz-sous-Forêts, France, est présentée. Finalement, nous proposons un modèle thermique basé sur la connaissance spatiale réduite de l'ouverture géométrique, qui reproduit bien la réponse de la fracture.

1. Introduction

Modeling of the fluid transport in low permeable crustal rocks is of central importance for many applications (Neuman, 2005). Among them is the monitoring of the geothermal circulation in the project of Soultz-sous-Forêts, France, (Bachler et al., 2003) where the heat exchange especially occurs through open fractures in granite (Gérard et al., 2006).

Numerous hydrothermal models have already been proposed. For simple geometries, some analytical solutions are known: e.g., the cases of parallel plates (Turcotte and

* Corresponding author.
E-mail address: amelie.neuville@eost.u-strasbg.fr (A. Neuville).

1631-0713/$ – see front matter © 2009 Académie des sciences. Published by Elsevier Masson SAS. All rights reserved.
doi:10.1016/j.crte.2009.03.006

Schubert, 2002) or flat cylinders (Heuer et al., 1991). More complex models exist as well like the models of three-dimensional (3D) networks of fractures reproducing geological observations and possibly completed with stochastical distributions of fractures (e.g. in Soultz-sous-Forêts, France, (Gentier, 2005; Rachez et al., 2007) or in Rosemanowes, UK (Kolditz and Clauser, 1998)). Nevertheless, the geometry of each fracture is generally simple. Kolditz and Clauser (1998) have however suspected that differences between heat models and field observations could be due to channeling induced by the fracture roughness or the fracture network. Channeling of the fluid flow owing to fracture roughness has indeed already been experimentally observed and studied (Méheust and Schmittbuhl, 2000; Plouraboué et al., 2000; Schmittbuhl et al., 2008; Tsang and Tsang, 1998).

Here, we limit our study to the fracture scale and we will show only one example of thermal behavior, among other simulations we completed (Neuville et al., submitted). The specificity of our hydrothermal model is to take into account the different scale fluctuations of the fracture morphology. We aim at bringing out the main parameters, which control the hydraulic and thermal behavior of a complex rough fracture. The perspective is to propose a small set of effective parameters that could be introduced within simplified elements for an upscaled network model.

We first describe our geometrical model of the fracture aperture thanks to self-affine apertures. Then, using lubrication approximations, we obtain the bidimensional (2D) pressure and thermal equations when a cold fluid is injected through the fracture in a stationary regime. The temperature within the surrounding rock is supposed to be hot and constant in time and space. The fluid density is also supposed to be constant.

We apply our numerical model to the case study at Soultz-sous-Forêts and we show for this case an example of the computed hydraulic and thermal behavior. Finally, we aim at bringing out what is the minimal geometrical information needed to get the dominant behavior of the hydraulic and thermal fields. This last approach is based on spatial low pass Fourier filtering of the geometrical aperture field.

2. Modeling

2.1. Roughness of the fracture aperture

We consider that the mean fracture plane is described by the $(\hat{x},\hat{z})$ coordinates and the perpendicular direction is $\hat{y}$ (Fig. 1) – where the hat notation refers to unit vectors along the (x,y,z) axis. It has been shown that a possible geometrical model of natural rough fractures consists in self-affine surfaces. A surface described by a function $y = f(x,z)$ is self-affine if it is statistically invariant under the scaling transformation $x \to \lambda x$, $z \to \lambda z$ and $y \to \lambda^{\zeta} y$, where ζ is called the roughness exponent or Hurst exponent. Such surfaces are therefore statistically invariant upon an isotropic scaling within their mean plane while along the perpendicular direction, the scaling is anisotropic (e.g. Brown and Scholz, 1985; Cox and Wang, 1993; Power et al.,

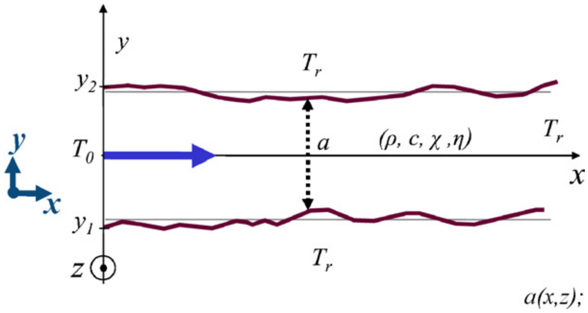

Fig. 1. Schematic fracture with variable aperture *a(x,z)*; ρ, c, χ, η are respectively the following fluid properties: density, heat capacity, thermal diffusivity and dynamic viscosity.

Fig. 1. Schéma de fracture ayant une ouverture variable *a(x,z)*; ρ, c, χ, η sont les propriétés respectives suivantes du fluide : densité, capacité thermique, diffusivité thermique et viscosité dynamique.

1987; Schmittbuhl et al., 1993, 1995). Most fracture surfaces in heterogeneous material exhibit a Hurst exponent equal to $\zeta = 0.8$ (Bouchaud, 1997; Santucci et al., 2007; Schmittbuhl et al., 1993, 1995). Sandstone fractures, however, show $\zeta = 0.5$ (Boffa et al., 1998; Méheust, 2002).

It is important to note that a self-affine surface having a roughness exponent smaller than one is asymptotically flat at large scales (Roux et al., 1993). Accordingly, the self-affine topography can be seen as a perturbation of a flat interface. When the lubrication approximation (Pinkus and Sternlicht, 1961) holds, in particular with smooth enough self-affine perturbations or highly viscous fluid, only the local aperture controls the flow and not the local slope of the fracture. The accuracy of the lubrication approximation, compared to the full Navier-Stokes resolution, was studied in Al-Yaarubi et al. (2005). Under this assumption, the only required geometrical input is the aperture field (also called the geometrical aperture); there is no need to know the geometry of each facing fracture surfaces. The aperture between two uncorrelated self-affine fracture surfaces having the same roughness exponent is as well self-affine (Méheust and Schmittbuhl, 2003). Thus, we generate the numerical apertures by using self-affine functions.

Several independent self-affine aperture morphologies can be generated with the same roughness exponent chosen equal to $\zeta = 0.8$. They exhibit various morphology patterns according to the chosen seed of the random generator (Méheust, 2002). The mean geometrical aperture A and the root-mean square deviation σ (RMS) of an aperture $a(x,z)$ are defined as

$$A = \frac{\iint a \ dxdz}{l_x \cdot l_z} \text{ and} \tag{1}$$

$$\sigma^2 = \frac{\iint a^2 dxdz}{l_x \cdot l_z} - A^2 \tag{2}$$

with l_x the length and l_z the width of the fracture. To keep the boundary geometry of the domain as simple as possible, we do not allow any contact area (i.e. no local aperture equal to zero). This is obtained by considering a large enough aperture average to get strictly positive aperture fields.

It has to be noted that our hydrothermal model can be applied to other geometrical models (i.e. different from a self-affine model), which might be more relevant depending on the geological context.

2.2. Physics of hydraulic flow

The hydraulic flow is obtained under the same hypotheses and solved in the same way as in Méheust and Schmittbuhl (2001). We use finite differences, and the system of linear equations is inverted using an iterative biconjugate gradient method (Press et al., 1992).

We impose a pressure drop across the system and study the steady state flow of a Newtonian fluid at low Reynolds number, so that the viscous term dominates the inertial one in the Navier-Stokes equation (Batchelor, 2002; Stokes, 1846):

$$\vec{\nabla} P = \eta \Delta \vec{u}^{3D} \tag{3}$$

where η is the dynamic viscosity, u^{3D} the velocity of the fluid and P is the pressure deviation from the hydrostatic profile (or the hydraulic head equal to the pressure corrected by the gravity effect). To be in the framework of the lubrication approximation (Pinkus and Sternlicht, 1961), we consider fractures with constant enough apertures together with a small Reynolds number. In doing so, the velocity vector of the fluid flow has negligible components normal to the mean fracture plane. We consider that the macroscopic pressure gradient is imposed along $\hat{x}$; $\hat{z}$ is therefore perpendicular to the mean flow direction. Accordingly, the fluid velocity follows a parabolic law (e.g. Iwai, 1976) (Fig. 2):

$$\vec{u}^{3D}(x,y,z) = \frac{\vec{\nabla}_2 P}{2\eta}(y-y_1)(y-y_2) \tag{4}$$

where y_1 and y_2 are the local fracture sides coordinates and $\vec{\nabla}_2$ is the gradient operator in the fracture plane. The hydraulic flow through the fracture aperture follows a cubic law:

$$\vec{q}(x,z) = \int_a \vec{u}^{3D}(x,y,z)dy = -\frac{a^3}{12\eta}\vec{\nabla}_2 P \tag{5}$$

and the bidimensional (2D) velocity $\vec{u}$ is defined from the average of the velocity $\vec{u}^{3D}$ over the aperture with

$$\vec{u}(x,z) = \frac{1}{a(x,z)}\int_a \vec{u}^{3D}(x,y,z)dy = -\frac{a^2}{12\eta}\vec{\nabla}_2 P \tag{6}$$

Furthermore, considering the fluid to be incompressible, the Reynolds equation is obtained: $\vec{\nabla}_2(a^3\vec{\nabla}_2 P) = 0$. As boundary conditions of this equation, we impose the pressure at the inlet and outlet of the fracture (if $x = 0$, $P = P_0$ and if $x = l_x$, $P = P_{lx}$, with $P_0 > P_{lx}$) and consider impermeable sides at $z = 0$ and $z = l_z$.

2.3. Physics of thermal exchange

On the basis of a classical description (e.g. Ge, 1998; Turcotte and Schubert, 2002), we aim at modeling the fluid temperature when cold water is permanently injected at the inlet of a hot fracture at temperature T_0. As the conduction inside the rock is not taken into account (hypothesis of infinite thermal conduction inside the rock), the fracture sides are supposed to be permanently hot at the fixed temperature T_r. This hypothesis should hold for moderate time scales (e.g. minutes), after the fluid injection has stabilized, and before the rock temperature has significantly changed, or alternatively once the whole temperature bedrock is stabilized (which depends on the boundary condition of the entire region). For time scales implying evolution of the rock temperature, our model should be coupled to a model of the rock temperature evolution.

The fluid temperature is controlled by the balance between thermal convection and conduction inside the fluid, which reads (Landau and Lifchitz, 1994): $\vec{u}^{3D} \cdot \vec{\nabla} T = \chi \Delta T$ where χ is the thermal diffusivity of the fluid and T the fluid temperature. We extend the local lubrication approximation by considering that the slopes of the fracture morphology are small enough to limit the conduction only along the y-axis. We suppose that the leading terms are the conduction along the y-axis and the in-plane convection (since there is no fluid velocity component along $\hat{y}$). Indeed, the off-plane free convection has been shown to be negligible (its magnitude is of the order of km/year (Bataillé et al., 2006)). So, the previous equation reduces to:

$$\frac{\partial^2 T}{\partial y^2} = \frac{\vec{u}_x^{3D}}{\chi}\frac{\partial T}{\partial x} + \frac{\vec{u}_z^{3D}}{\chi}\frac{\partial T}{\partial z} \tag{7}$$

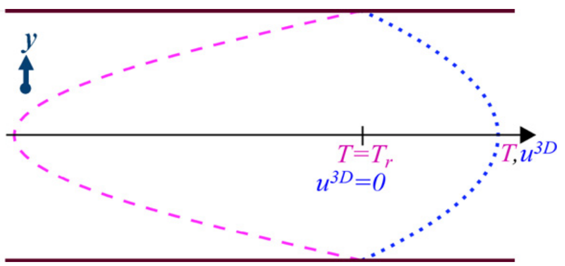

Fig. 2. Local velocity quadratic profile (dotted line) and temperature quartic profile (dashed line) inside a fracture across the aperture at the mesh scale. Along the fracture sides, $u^{3D} = 0$ and $T = T_r$, and the roots of the polynoms given by Eqs. (4) and (8) are respected.

Fig. 2. Profil local parabolique de vitesse (ligne pointillée) et profil local quartique de température (ligne tiretée) dans la fracture, à travers l'ouverture. Le long des bords, $u^{3D} = 0$ et $T = T_r$ et les racines des polynômes donnés par les Éqs. (4) et (8) sont respectées.

where $\vec{u}_x^{3D}$, $\vec{u}_z^{3D}$ are the in-plane components of the fluid velocity. The fluid is supposed to be at rock temperature along the fracture sides, and sufficiently far from the inlet. When we integrate Eq. (7) along the fracture aperture, we assume that $\beta = q_x(\partial T/\partial x) + q_z(\partial T/\partial x)$ is independent of y, where q_x and q_z are the in-plane component of $\vec{q}$ defined in Eq. (5). Accordingly, we find that the temperature solution has a quartic profile (Fig. 2) along the fracture aperture:[1]

$$T = -\frac{\beta}{2a^3\chi}(y-y_1)(y-y_2)(y-\sqrt{5}y_1)(y-\sqrt{5}y_2) + T_r \quad (8)$$

where y_1 and y_2 are the local fracture sides coordinates.

Similarly to what is done for the hydraulic flow, we solve the thermal equation by integrating it along the fracture aperture (following the lubrication approximation extended to the thermal field). In particular, when doing the balance of the energy fluxes, we express the advected free energy flux as $\rho c \int_a u^{3D}(x,y,z)[T(x,y,z) - T_0]dy$. Accordingly, we introduce:

$$\overline{T}(x,z) = \frac{\int_a u^{3D}(x,y,z)T(x,y,z)dy}{\int_a u^{3D}(x,y,z)dy} \quad (9)$$

which is an average of the temperature profile weighted by the local norm of velocity. We also use the Nusselt number $Nu = \varphi_r/\varphi_{ref}$ which compares the efficiency of the heat flow along the fracture boundaries:

$$\varphi_r = \mp \chi\rho c \frac{\partial T}{\partial y}\bigg|_{y=y_1,y_2} \quad (10)$$

to the mesoscopic heat flow at the fracture aperture scale without convection: $\varphi_{ref} = \chi\rho c(T_r - \overline{T})/a$. Using the polynomial expression of T (in Eq. (8) and the definition of $\bar{T}$, we get $\beta = 140\chi(T_r - \overline{T})/(17a)$ and Nu = 70/17. Eq. (7) leads then to:

$$\vec{q}\cdot\vec{\nabla}_2\overline{T} + 2\frac{\chi}{a}Nu(\bar{T} - T_r) = 0, \quad (11)$$

Boundary conditions are: $\overline{T}(0,z) = T_0$ at the inlet and $\overline{T}(l_x,z) = T_r$ at the outlet (with l_x large enough). Any boundary condition for the temperature along $z = 0$ or $z = l_z$ can be used as the hydraulic flow $\vec{q}$ is null there.

We discretize this equation by using a first order finite difference scheme and finally get $\bar{T}$ by inverting the system using a biconjugated gradient method (Press et al., 1992).

It is finally possible to get the three-dimensional temperature field T anywhere within the fluid by using the previous β expression and the quartic profile (Eq. (8). Fig. 3 illustrates an example of temperature field at a given $z = z_0$, $T(x,y,z = z_0)$, obtained in that way from a given bidimensional field $\bar{T}$. Along any given cut at $x = x_0$, the temperature (represented by the color scale) follows a quartic law (Fig. 2). The boundaries between the colors are isotherms.

[1] We compared our method to another algorithm based on a Lattice Boltzmann (LB) method, which does not reduce Navier-Stokes to a Stokes equation and does not hypothesize any lubrication approximation, in order to solve the velocity and temperature fields. The finite diffusivity of the rock is also taken into account. From those results, it appears that the analytical parabolic and quartic approximations (with the proper coefficients) of the respective fields are indeed consistent within a 5% error bar with the LB results.

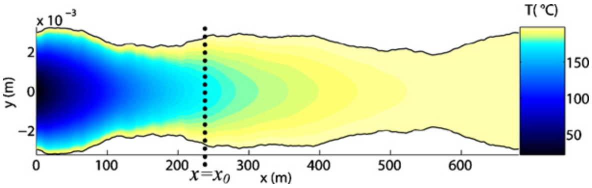

Fig. 3. Example of temperature $T(x,y,z = z_0)$ inside a variable aperture between $\pm a(x,y,z = z_0)/2$, computed from $\bar{T}$ shown in Fig. 7, at $z = 700$ m. The color scale is linear.

Fig. 3. Exemple de température $T(x,y,z = z_0)$ à travers l'ouverture variable, entre $\pm a(x,y,z = z_0)/2$, calculé d'après $\bar{T}$ illustré Fig. 7, en $z = 700$ m. L'échelle de couleur est linéaire.

2.4. Definition of characteristic quantities describing the computed hydraulic and thermal fields

2.4.1. Comparison to modeling without roughness

If we consider a fracture modeled by two parallel plates separated by a constant aperture A, then the gradient of pressure is constant all along the fracture as well as the hydraulic flow which is equal to:

$$\vec{q}_{//} = -\frac{\Delta P}{l_x}\frac{A^3}{12\eta}\hat{x} \quad (12)$$

where the subscript // is for parallel plate conditions and $\Delta P = P_{lx} - P_0$. Under these conditions, the analytical solution of Eq. (11) is:

$$\overline{T}_{//} = (T_0 - T_r)\exp\left(-\frac{x}{R_{//}}\right) + T_r \quad (13)$$

where $R_{//}$ is a thermal length describing the distance at which the fluid typically reaches the temperature of the surrounding rock. We have:

$$R_{//} = \frac{A\|\vec{q}_{//}\|}{2Nu\chi} = -\frac{\Delta P}{l_x}\frac{A^4}{24\eta Nu\chi} = \frac{APe}{Nu} \quad (14)$$

where Pe is the Péclet number defined by $Pe = \|\vec{q}_{//}\|/2\chi$. Pe expresses the magnitude of the convection with respect to the conduction.

For rough fractures, we want to study whether the temperature profiles along x at a coarse grained scale can still be described by Eq. (13) and, if so, what is the impact of the fracture roughness on the thermal length R.

2.4.2. Hydraulic aperture

The hydraulic flow can be macroscopically described using the hydraulic aperture H (Brown, 1987; Zimmerman et al., 1991), defined as the equivalent parallel plate aperture to get the macroscopic flow $\langle q_x\rangle$ under the pressure gradient $\Delta P/l_x$:

$$H = \left\langle -q_x\frac{12\eta l_x}{\Delta P}\right\rangle^{1/3}, \quad (15)$$

where the quantity under bracket is the spatial average over x and y. Note that the hydraulic aperture H is an effective measure that can be estimated from hydraulic tests whereas the geometrical aperture A is deduced from a direct measurement of the fracture geometry. If H/A is higher than 1, then the fracture is more permeable than parallel plates separated by A. Hydraulic apertures can also be defined locally as:

$$h(x,z) = \left(-q_x(x,z)\frac{12\eta l_x}{\Delta P}\right)^{1/3} \quad (16)$$

Local geometrical and hydraulic apertures are denoted here with small letters while the corresponding macroscopic variables (mean geometrical and hydraulic aperture) are in capital letters.

2.4.3. Thermal aperture

For the thermal aspect, once $\bar{T}$ is known, we aim at defining a thermal length R like in Eq. (13). To do that, we define $\bar{\bar{T}}$, a z-average temperature which varies only along the forced gradient direction x, and weighted by the 2D fluid velocity u_x to fulfill energy conservation:

$$\bar{\bar{T}}(x) = \frac{\int_{l_z} u_x(x,z)\bar{T}(x,z)dz}{\int_{l_z} u_x(x,z)dz} \quad (17)$$

Then, based on the flat plate temperature solution (Eq. (13), we do a linear fit of $ln[(\bar{\bar{T}} - T_r)/(T_0 - T_r)]$ plotted as a function of x, and we use the slope of this fit to get the characteristic thermal length R. This fit is computed over the zone where the numerical precision of the fitted quantities is sufficient (larger than $ln[2 \times 10^{-6}]$). Similarly to the parallel plate case (Eq. (14)), the thermal length R can be used to define a thermal aperture Γ:

$$R = -\frac{\Delta P}{l_x}\frac{\Gamma^4}{24\eta Nu\chi} \quad (18)$$

which means that a fracture modeled by parallel plates separated by a distance Γ provides the same averaged thermal behavior as the rough fracture of mean geometrical aperture A.

3. Case study at Soultz-sous-Forêts (France)

3.1. Computation of apertures, hydraulic and thermal fields

Let us consider the GPK3 and GPK2 wells of the deep geothermal drilling near Soultz-sous-Forêts (France), which are separated by a distance of about 600 m at roughly 5000 m of depth. From hydraulic tests (Sanjuan et al., 2006), it has been shown that the hydraulic connection between both wells is relatively direct and straight. Sausse et al. (Sausse et al., 2008) showed that actually a fault is linking GPK3 (at 4775 m) to GPK2. This fault zone consists of a large number of clusters of small fractures (most apertures ranges around 0.1 mm) (Sausse et al., 2008) which probably lead to complex hydraulic streamlines and heat exchanges. We study here a simplified model of this connecting fault zone between the wells using one single rectangular rough fracture. The size of the studied fracture is $l_x \times l_y = 680 \times 1370$ m^2. Individual fracture apertures are typically of the order of 0.2 mm (Genter and Jung, private communication) while the fracture zone is rather thicker (10 cm) (Sausse et al., 2008). To account for this variability of the fault zone aperture, we use a probabilistic model with the following

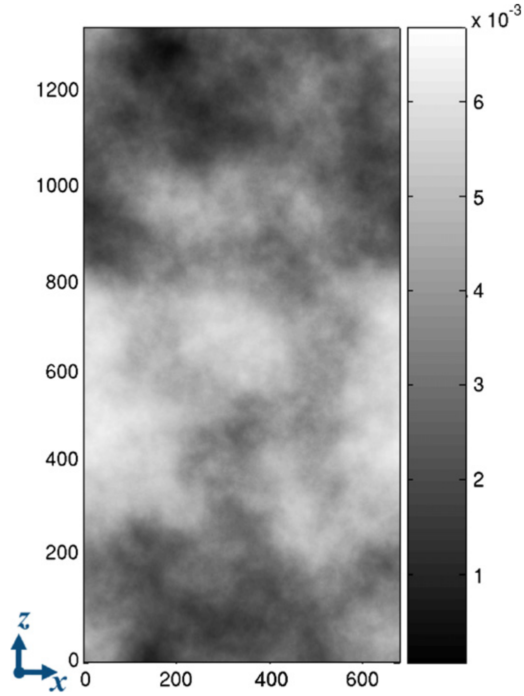

Fig. 4. Aperture field with mean aperture A = 3.60 mm and variability of the aperture σ = 1.23 mm (σ/A = 0.34). The color bar represents the aperture in meters, the side units are plane spatial coordinates (x,z), also in meters.

Fig. 4. Champ d'ouverture de moyenne A = 3.60 mm et de RMS σ = 1.23 mm (σ/A = 0.34). La barre de couleur indique les valeurs d'ouverture en mètres et les valeurs sur les bords sont les coordonnées spatiales (x,z), aussi en mètres.

macroscopic properties: a mean aperture A equal to 3.60 mm and its standard deviation to σ = 1.23 mm. Fig. 4 shows an example of a self-affine aperture randomly generated with the required parameters.

With little knowledge about the pressure conditions along the boundaries of this model, we assume that the two facing sides along x of this rectangular fracture correspond to the inlet and outlet of the model where the pressure is homogeneous, respectively P_0 and P_{lx}. In other words, we assume the streamlines to be as straight as possible between both wells.

The pressure gradient $\Delta P/l_x$ is chosen as -10^{-2} bar/m, which corresponds to about six bars between the bottom of both wells. The dynamic viscosity is chosen to be 3×10^{-4} Pa/s (reference value for pure water at 10 Pa and 100 °C in Spurk and Aksel (2008)). The Reynolds number rescaled with the characteristic dimensions of the fracture (Méheust and Schmittbuhl, 2001) is equal to $Re' = (\rho u_x a^2)/(\eta.l_x) = 0.026$ and the Péclet number is $Pe = 3.8 \times 10^4$.

Then, we solve the hydraulic flow in the fracture domain and obtain the 2D velocity field, $\vec{u}$ defined in Eq. (6). Fig. 5 shows the spatial fluctuations of $||\vec{u}||$. For information, a parallel plate model separated by the chosen aperture A would predict a homogeneous fluid velocity of 3.6 m/s and a thermal length $R_{//}$ = 33.3 m. As we see in Fig. 5, the 2D velocity field exhibits interesting features: the fluid is rather immobile along the upper and lower borders of the fracture (close to $z = 0$ and $z = l_x$) while

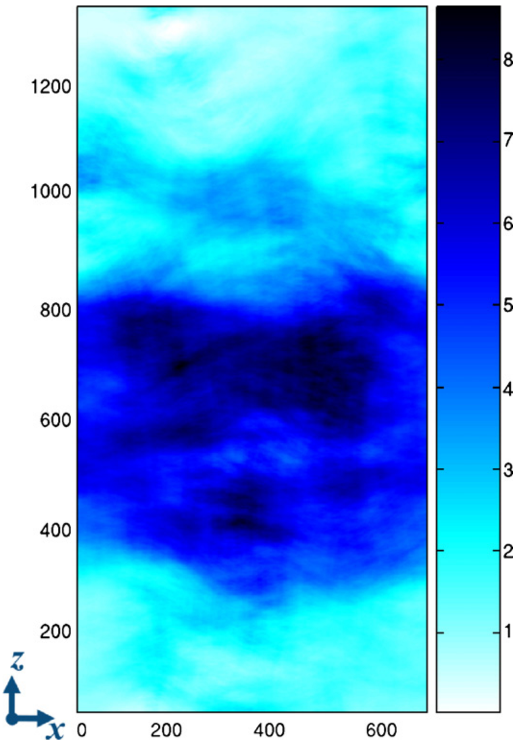

Fig. 5. Color map of u, the 2D velocity field norm in m/s. Dark areas correspond to very high velocity while light areas show static fluid. A linear pressure gradient is imposed between the left and right of the fracture. The spatial coordinates are in meters.

Fig. 5. Carte de u, la norme du champ de vitesse 2D en m/s. Les zones sombres correspondent à une forte vitesse tandis que les zones claires indiquent un fluide immobile. Un gradient de pression linéaire est imposé entre les bords gauche et droit de la fracture. Les coordonnées spatiales sont en mètres.

most of the fluid flows very quickly through a channel in the middle of the fracture.

The macroscopic hydraulic aperture is deduced from the local hydraulic flow estimate (Eq. (15)): H = 3.73 mm, which is slightly higher than the mean mechanical aperture A = 3.60 mm. Therefore, this fracture is more permeable than parallel plates separated by A. In other words, the fracture is geometrically thinner than what one would expect from the knowledge of H possibly inverted from an hydraulic test. However, the local hydraulic apertures h (Eq. (16)) range from nearly 0 to 5.43 mm (Fig. 6).

From the average estimate of the fluid velocity, we can go back to our approximation of a linear inlet, even if the fracture is not vertical and does not intersect the well on a very long distance. We might estimate this distance from the following argument. The flow rate observed at Soultz is about $Q = 20$ L/s. Thus, using a velocity of about u = 3.6 m/s and a fracture aperture equal to 3.6 mm implies that the well crosses such fractures over a cumulated length of about (neglecting the well radius):

$$L = \frac{Q}{uA} = \frac{20 \times 10^{-3}}{3.6 \times 3.6 \times 10^{-3}} \approx 1.5\mathrm{m}$$

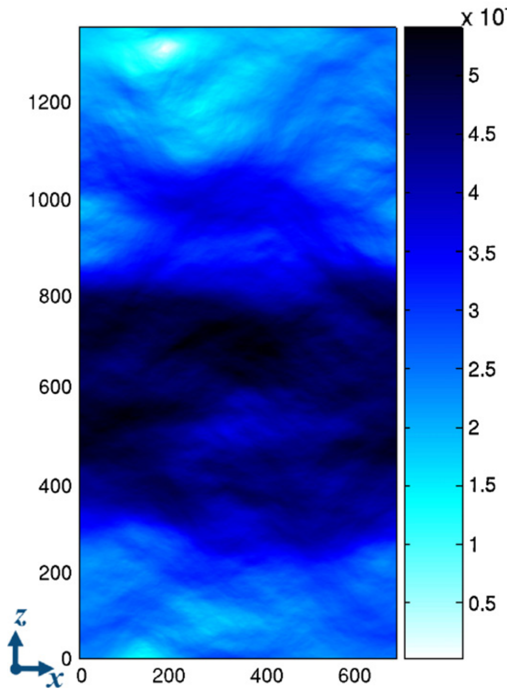

Fig. 6. Color map of the local hydraulic aperture in metres computed from the variable aperture and velocity field shown in Figs. 4 and 5. The spatial coordinates are in meters.

Fig. 6. Carte de l'ouverture hydraulique locale en mètres, calculée d'après le champ d'ouverture variable de la Fig. 4 et le champ de vitesse de la Fig. 5. Les coordonnées spatiales sont en mètres.

which is effectively much smaller than the boundary size. However, we expect the presence of connecting fractures between the well and the fault zone to be sufficiently permeable to define an effective linear inlet of constant effective pressure. All the results presented here are valid under any dimensioning which keeps the ratio $l_x/R_{//}$ constant (here equal to 20.5): for instance, the results apply for l_x = 690 m, A = 10 mm and $\Delta P/l_x = -1.7 \times 10^{-4}$ bar/m (using the same fluid parameters), which leads to a Poiseuille velocity of about 0.46 m/s.

As we see, $\bar{T}$ is very inhomogeneous and also exhibits channeling. The chosen inlet temperature is T_0 = 60 °C, the rock temperature is T_r = 200 °C (Fig. 7) and the fluid diffusivity is χ = 0.17 mm^2/s (corresponding to water at T = 100 °C, from Taine et Petit (2003). Note that the rock temperature will evolve over time in contrast to the one of our approximations. Indeed, the rock thermal diffusivity is about 1 mm^2/s which is larger than the fluid diffusivity (χ = 0.17 mm^2/s) but not sufficiently to be fully neglected.

However, $\bar{T}$ is rather different from a parallel plate solution. Indeed, the solution is not invariant in $\hat{z}$. Different temperature profiles function of x are shown in Fig. 8. Two end-member types of behavior are plotted: temperature profiles at z = 960 m (curve iv) and z = 700 m (curve v). The temperature difference can be larger than 100 °C in the inlet region. Even rather far from the inlet, for example at x = 200 m, the temperature difference can still be of the order of 17 °C (200.0 °C for z = 960 m, and 183.4 °C for z = 700 m). The temperature field $T(x,y,z = 700\ \mathrm{m})$ for this

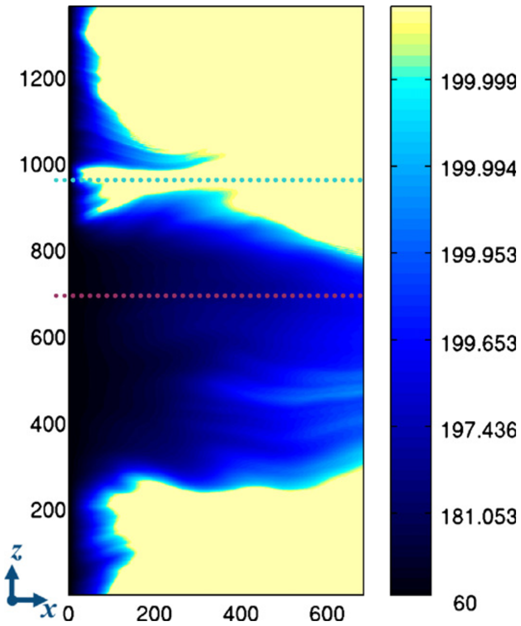

Fig. 7. Map of the averaged temperature field $\bar{T}$ in Celsius degrees (°C). The color bar changes exponentially; thus small variations slightly below the temperature rock (200 °C) are highly visible. The dotted lines indicate the location of the profiles of temperature $\bar{T}(x, z = z_0)$ shown in Fig. 8, for z = 960 m and z = 700 m. The spatial coordinates are in meters.

Fig. 7. Carte du champ de température moyennée $\bar{T}$ en degrés Celcius (°C). L'échelle de couleur varie exponentiellement ; les petites variations en dessous de la température de la roche (200 °C) sont donc très visibles. Les lignes en pointillées indiquent la position des profils de température $\bar{T}(x, z = z_0)$ montrés sur la Fig. 8, en z = 960 m et z = 700 m. Les coordonnées spatiales sont en mètres.

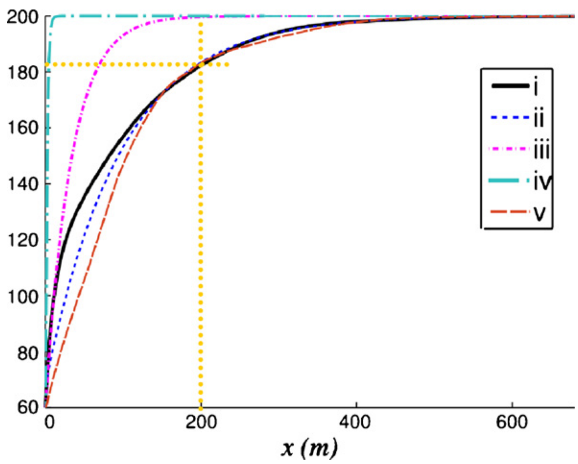

Fig. 8. Fluid 1D temperature in °C as function of x. The continuous curve (i) shows the computed temperature $\bar{\bar{T}}$. The dashed curve (ii) is the fit of curve (i) with an exponential function. The dot dashed curve (iii) is the fluid 1D temperature by neglecting the self-affinity perturbation (inside flat parallel plates). The curves (iv) and (v) are the profiles of temperature $\bar{T}(x, z = z)$ for respectively z = 960 m and z = 700 m (Fig. 7).

Fig. 8. Température 1D en degrés en fonction de x. La courbe continue (i) est le profil calculé $\bar{\bar{T}}$. La courbe tiretée (ii) est la régression de la courbe (i) avec une fonction exponentielle. La courbe (iii) est la température 1D obtenue en négligeant la perturbation auto-affine (modèle de plaques parallèles). Les courbes (iv) et (v) sont les profils de température $\bar{T}(x, z = z)$ respectivement en z = 960 m et z = 700 m (Fig. 7).

set of parameters is shown in Fig. 3, where we see how the temperature evolves along the x-axis, away from the mean plane. Temperature profiles can be compared to the one obtained for a parallel plate model where plates are separated by the aperture A (curve iii) which reads from Eqs. (13) and (17): $\bar{\bar{T}}_{//} = \bar{T}_{//}$.

Following this model (curve iii), the fluid should be at 199.7 °C at x = 200 m. If we compare $\bar{\bar{T}}_{//}$ to the averaged observed temperature $\bar{\bar{T}}$ (defined in Eq. (13)) (Fig. 8, curve i), we see that $\bar{\bar{T}}_{//}$ is not representative of the end-member types of behavior. We model $\bar{\bar{T}}$ by using an adapted parallel law $\bar{\bar{T}}_{\text{mod}}$ (curve ii), which is an exponential law with a suitable thermal length R:

$$\bar{\bar{T}}_{\text{mod}} = (T_0 - T_r)\exp\left(-\frac{x - x_0}{R}\right) + T_r \qquad (19)$$

where R = 97 m (i.e. 2.9 × $R_{//}$) and x_0 = −10 m. As we do a least square fit on a semi-log space to obtain the parameters R and x_0, the beginning of the fit in the linear-linear space is not accurate. We see that the distance between wells (600 m in our case study) is about six times larger than R. However, owing to channeling the fluid temperature will not necessarily be in full equilibrium with the rock temperature at the out well. The thermal aperture is equal to Γ = 4.7 mm, which is rather different from the geometrical aperture A = 3.6 mm. A larger thermal aperture (compared to the geometrical one) means an inhibited thermalization on average.

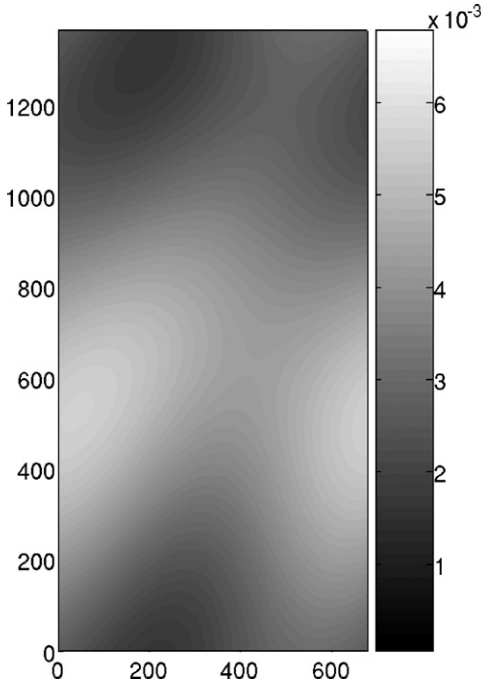

Fig. 9. Map of the coarse-grained fracture aperture in metres, obtained by a very low pass filtering of the aperture (Fig. 4) keeping only the zero and first Fourier modes along x and z. The spatial coordinates are in meters.

Fig. 9. Carte de l'ouverture géométrique à faible résolution spatiale, en mètres, obtenue en filtrant l'ouverture (Fig. 4), en ne gardant que la moyenne et les premiers modes de Fourier sur x et z. Les coordonnées spatiales sont en mètres.

3.2. Temperature estimation with few parameters

The knowledge of the spatial correlations rather than all the details of the geometrical aperture seems to be a key parameter to evaluate the hydraulic flow and the temperature of the fluid in a rough fracture. Indeed, the macroscopic geometrical aperture A brings too little information to characterize the heat exchange at the fracture scale. By contrast, it is impossible in particular for field measurements to know in detail the spatial variability of the local geometrical aperture A. Therefore, we propose to characterize the macroscopic geometrical properties with more than a single value, using several parameters describing the largest spatial variations. Numerically, it is possible to obtain them by filtering the fracture aperture field in the Fourier domain.

Fig. 9 shows the aperture field displayed in Fig. 4 once it has been filtered with the following criterion: only the Fourier coefficients fulfilling

$$\left(\frac{k_x}{2\pi}l_x\right)^2 + \left(\frac{k_z}{2\pi}l_z\right)^2 < 2^2 \tag{20}$$

are kept, where k_x and k_z are the wave vector coordinates along respectively the x and z-axes. Since the Fourier transform is discrete, it means that we only keep the Fourier components corresponding to the wave number $(n_x, n_z) = (2\pi/(k_x.l_x), 2\pi/(k_z.l_z))$ in {(0,0);(0,1);(1,0);(1,1)} (i.e. the average A and the first Fourier modes along x and z are left).

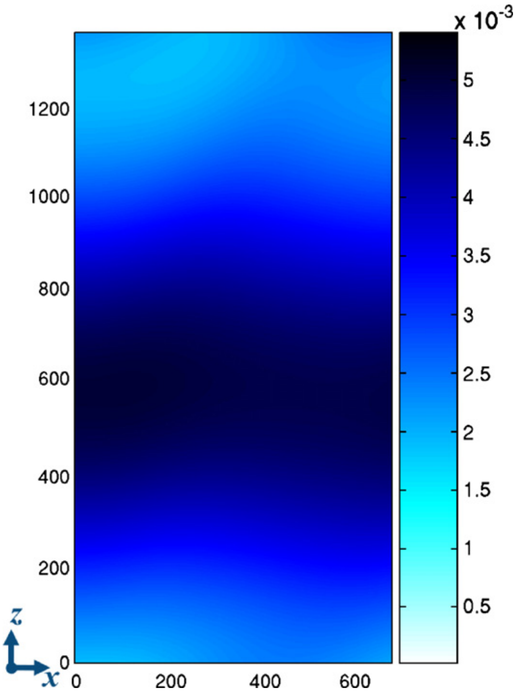

Fig. 10. Map of the local hydraulic aperture in meters, obtained from the filtered geometrical aperture shown in Fig. 9. This figure has to be compared to Fig. 6 (same color bar). The spatial coordinates are in meters.

Fig. 10. Carte de l'ouverture hydraulique en mètres obtenue d'après les ouvertures géométriques filtrées de la Fig. 9. Ce champ est comparable à celui de la Fig. 6 (même échelle de couleur). Les coordonnées spatiales sont en mètres.

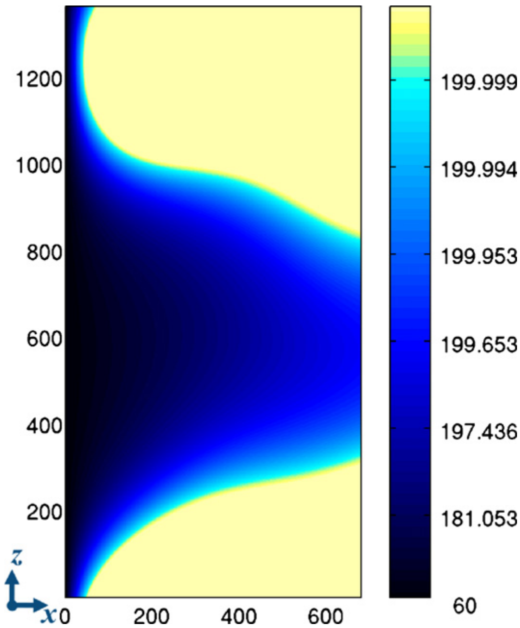

Fig. 11. Map of the temperature field obtained using the previous coarse-grained aperture and its corresponding hydraulic results (Figs. 9 and 10). The color scale is in °C and it changes exponentially. The spatial coordinates are in meters.

Fig. 11. Carte de température obtenue en utilisant les ouvertures filtrées et les résultats hydrauliques correspondant (Fig. 9 et 10). L'échelle de couleur, en °C, varie exponentiellement. Les coordonnées spatiales sont en mètres.

Let us assume that we only have these data available to evaluate the hydraulic flow and heat exchange. Using the same method and the same parameters as previously, we compute the pressure field corresponding to the filtered aperture field. In Fig. 10, we show the hydraulic aperture field we obtain. As we see, the high hydraulic aperture channel in the middle of the figure remains, while high frequency variations are removed. These large scale fluctuations of the hydraulic flow, computed from the knowledge of a very limited set of Fourier modes of the geometrical aperture, might be obtained from field measurements. Then, the corresponding temperature field shown in Fig. 11 is computed. The main features of the thermal field (Fig. 7) are still visible: the main channel is at the same position and the values are of the same order of magnitude. Despite small local differences, this substitution model gives a relevant description of what thermally happens.

4. Conclusions

We propose a numerical model to estimate the impact of the fracture roughness on the heat exchange at the fracture scale between a cold fluid and the hot surrounding rock. We assume the flow regime to be permanent and laminar. The numerical model is based on a lubrication approximation for the fluid flow (Reynolds equation). We also introduce a "thermal lubrication" approximation, which leads to a quartic profile of the temperature across the aperture. It is obtained by assuming that the in-plane convection is dominant with respect to the in-plane conduction (i.e. high in-plane Péclet number). The lubrication approximation implies also that the off-plane convection is neglected; subsequently, the heat conduction initiated by the temperature difference between the rock and the fluid is supposed to be the major off-plane phenomenon.

Our model shows that the roughness of the fracture can be responsible for fluid channeling inside the fracture. In this zone of high convection, the heat exchange is inhibited, i.e., the fluid needs a longer transport distance to reach the rock temperature. Spatial variability of the temperature is characterized on average by a thermal length and a thermal aperture.

In this article, we illustrate our modeling by a case study at the geothermal reservoir of Soultz-sous-Forêts, France, with a rough aperture which leads to inhibited thermal exchanges owing to a strong channeling effect, in the sense that the characteristic thermal length in this stationary situation is longer in rough fractures than in flat ones with the same transmissivity. Qualitatively, this can be attributed to the localization of the flow inside a rough fracture: most of the fluid flows through large aperture zones at faster velocity than the average, which leads to longer thermalization distances.

We performed simulations for about 1000 other aperture fields (not illustrated here) compatible with the macroscopic observations, of the same type as shown here. A general property holds for all these aperture fields: the thermal exchanges are always inhibited in rough fractures, compared to a fracture modeled by parallel plates with the same macroscopic hydraulic transmissivity (Neuville et al., submitted) (same H).

From the numerical solutions, we see that the mean geometrical aperture provides too little information to characterize the variability of the fluid flow and fluid temperature. In contrast, the knowledge of the dominant spatial variation of the geometrical aperture field (here obtained by keeping only the largest scale fluctuations using low pass Fourier filtering) provides interesting information about the spatial pattern of the hydraulic and thermal fields. The macroscopic spatial correlation of the aperture is shown to be an important parameter ruling the hydrothermal behavior. Note that we considered a self-affine model for the aperture roughness, but other types of geometrical descriptions of this roughness (given either by constraints from field measurements, or other kind of geometrical models), could be also considered using the type of simulations described here.

Acknowledgements

We thank Albert Genter, Reinhard Jung Marion, Patrick Nami, Marion Schindler, Eirik G. Flekkøy, Stéphane Roux, Jose S. Andrade Jr. and Yves Méheust for fruitful discussions. This work has been supported by the EHDRA project, the REALISE program and the French Norwegian PICS project.

References

Al-Yaarubi, A.H., Pain, C.C., Grattoni, C.A., Zimmerman, R.W., 2005. Navier-Stokes simulations of fluid flow through a rock fracture, Dynamics of fluids and transport in fractured rock, AGU Monograph 162 ed. by B. Faybishenko, P.A. Witherspoon, and J. Gale, Amer. Geophys. Union, Washington, DC, pp. 55–64.

Bachler, D., Kohl, T., Rybach, L., 2003. Impact of graben parallel faults on hydrothermal convection – Rhine graben case study. Phys. Chem. Earth 28, 431–441.

Bataillé, A., Genthon, P., Rabinowicz, M., Fritz, B., 2006. Modeling the coupling between free and forced convection in a vertical permeable slot: Implications for the heat production of an Enhanced Geothermal System. Geothermics 35, 654–682.

Batchelor, G.K., 2002. An introduction to fluid dynamics. Cambridge University Press, Cambridge, UK, 615 p.

Boffa, J.M., Allain, C., Hulin, J.P., 1998. Experimental analysis of fracture rugosity in granular and compact rocks. Eur. Phys. J. Appl. Phys. 2, 281–289.

Bouchaud, E., 1997. Scaling properties of cracks. J. Phys. Cond. Matter 9, 4319–4344.

Brown, S.R., 1987. Fluid flow through rock joints: the effect of surface roughness. J. Geophys. Res. 92, 1337–1347.

Brown, S.R., Scholz, C.H., 1985. Broad bandwidth study of the topography of natural rock surfaces. J. Geophys. Res. 90, 12575–12582.

Cox, B.L., Wang, J.S.Y., 1993. Fractal surfaces: measurement and application in earth sciences. Fractal 1, 87–115.

Ge, S., 1998. Estimation of groundwater velocity in localized fracture zones from well temperature profiles. J. Volcanol. Geothermal Res. 84, 93–101.

Gentier, S., Rachez, X., Dezayes, C., Hosni, A., Blaisonneau, A., Genter, A. Bruel, D., 2005. Thermohydro-mechanical modelling of the deep geothermal wells at Soultz-sous-Forêts, Proceedings of EHDRA scientific conference.

Gérard, A., Genter, A., Kohl, T., Lutz, P., Rose, P., Rummel, F., 2006. The deep EGS (Enhanced geothermal System) project at Soultz-sous-Forêts (Alsace, France). Geothermics 35, 473–483.

Heuer, N., Küpper, T., Windelberg, D., 1991. Mathematical model of a Hot Dry Rock system. Geophys. J. Int. 105, 659–664.

Iwai, K., 1976. Fundamental Studies of Fluid Flow through a single fracture, Ph.D. Thesis, University of California, Berkeley.

Kolditz, O., Clauser, C., 1998. Numerical simulation of flow and heat transfer in fractured cristalline rocks: application to the hot dry rock site in Rosemanowes (U.K.). Geothermics 27, 1–23.

Landau, L., Lifchitz, E., 1994. Physique théorique mécanique des fluides, 3rd Ed. Ed. MIR-Ellipses, Paris, France, 280 p.

Méheust, Y., 2002. Écoulements dans les fractures ouvertes, Ph.D. thesis Université Paris Sud.

Méheust, Y., Schmittbuhl, J., 2000. Flow enhancement of a rough fracture. Geophys. Res. Lett. 27, 2989–2992.

Méheust, Y., Schmittbuhl, J., 2001. Geometrical heterogeneities and permeability anisotropy of rough fractures. J. Geophys. Res. 106, 2089–2102.

Méheust, Y., Schmittbuhl, J., 2003. Scale effects related to flow in rough fractures, PAGEOPH 160, 1023–1050.

Neuman, S., 2005. Trends, prospects and challenges in quantifying flow and transport through fractured rocks. Hydrogeol. J. 13, 124–147.

Neuville, A., Toussaint, R., Schmittbuhl, J., Hydrothermal coupling in a self-affine rough fracture, submitted to PRE (2010).

Pinkus, O., Sternlicht, B., 1961. Theory of hydrodynamic Lubrication. Mc Graw-Hill, New York, 465 p.

Plouraboué, F., Kurowski, P., Boffa, J.M., Hulin, J.P., Roux, S., 2000. Experimental study of the transport properties of rough self-affine fractures. J. Contaminant Hydrology 46, 295–318.

Power, W.L., Tullis, T.E., Brown, S.R., Boitnott, G.N., Scholz, C.H., 1987. Rhougness of natural fault surfaces. Geophys. Res. Lett. 14, 29–32.

Press, W.H., Teukolsky, S.A., Vetterling, W.T., Flannery, B.P., 1992. Numerical Recipes. Cambridge University Press, New York, USA, 994 p.

Rachez, X., Gentier, S., Blaisonneau, A., 2007. Current status of BRGM modeling activities at the Soultz EGS reservoir: hydro-mechanical modeling of the hydraulic stimulation tests and flow and transport modelling of the in-situ tracer test, proceedings of EHDRA scientific conference.

Roux, S., Schmittbuhl, J., Vilotte, J.P., Hansen, A., 1993. Some physical properties of self-affine rough surfaces. Europhys. Lett. 23, 277–282.

Sanjuan, B., Pinault, J.L., Rose, P., Gerard, A., Brach, M., Braibant, G., et al., 2006. Tracer testing of the geothermal heat exchanger at Soultz-sous-Forets (France) between 2000 and 2005. Geothermics 35, 622–653.

Santucci, S., Måløy, K.J., Delaplace, A., Mathiesen, J., Hansen, A. Haavig Bakke, J.Ø., Schmittbuhl, J., Vanel, L., Ray, P., 2007. Statistics of fracture surfaces, Physical Review E 75, 016104 6p.

Sausse, J., Dezayes, C., Genter, A., Bisset, A., 2008. Characterization of fracture connectivity and fluid flow pathways derived from geological

interpretation and 3D modelling of the deep seated EGS reservoir of Soultz (France), Proceedings, thirty-third workshop on Geothermal Reservoir Engineering, Stanford, California.
Schmittbuhl, J., Gentier, S., Roux, S., 1993. Field measurements of the roughness of fault surfaces. Geophys. Res. Lett. 20, 639–641.
Schmittbuhl, J., Schmitt, F., Scholz, C., 1995. Scaling invariance of crack surfaces. J. Geophys. Res. 100, 5953–5973.
Schmittbuhl, J., Steyer, A., Jouniaux, L., Toussaint, R., 2008. Fracture morphology and viscous transport. Int. J. Rock Mech. Min. Sci. 45, 422–430.
Spurk, J.H., Aksel, N., 2008. Fluid Mechanics, 2nd Ed. Springer, Berlin, Germany, 516 p.
Stokes, G.G., 1846. On the theories of the internal friction of fluids in motion, and of the equilibrium and motion of elastic solids. Trans. Cambr. Phil. Soc 8, 287–319.
Taine, J., Petit, J.P., 2003. Transferts thermiques, 3rd Ed. Dunod, Paris, France, 449 p.
Tsang, Y.W., Tsang, C.F., 1998. Flow channeling in a single fracture as a two-dimensional strongly heterogeneous permeable medium. Water Resour. Res. 25, 2076–2080.
Turcotte, D.L., Schubert, G., 2002. Geodynamics, 2nd Ed. Cambridge University Press, Cambridge, UK, pp. 262–264.
Zimmerman, R.W., Kumar, S., Bodvarsson, G.S., 1991. Lubrication Theory Analysis of Rough-Walled Fractures. Int. J. Rock. Mech. 28, 325–331.

interpretation and 3D modelling of the deep seated EGS reservoir of Soultz (France), Proceedings, thirty-third workshop on Geothermal Reservoir Engineering, Stanford, California.
Schmittbuhl, J., Gentier, S., Roux, S., 1993. Field measurements of the roughness of fault surfaces. Geophys. Res. Lett. 20, 639–641.
Schmittbuhl, J., Schmitt, F., Scholz, C., 1995. Scaling invariance of crack surfaces. J. Geophys. Res. 100, 5953–5973.
Schmittbuhl, J., Steyer, A., Jouniaux, L., Toussaint, R., 2008. Fracture morphology and viscous transport. Int. J. Rock Mech. Min. Sci. 45, 422–430.
Spurk, J.H., Aksel, N., 2008. Fluid Mechanics, 2nd Ed. Springer, Berlin, Germany, 516 p.
Stokes, G.G., 1846. On the theories of the internal friction of fluids in motion, and of the equilibrium and motion of elastic solids. Trans. Cambr. Phil. Soc 8, 287–319.
Taine, J., Petit, J.P., 2003. Transferts thermiques, 3rd Ed. Dunod, Paris, France, 449 p.
Tsang, Y.W., Tsang, C.F., 1998. Flow channeling in a single fracture as a two-dimensional strongly heterogeneous permeable medium. Water Resour. Res. 25, 2076–2080.
Turcotte, D.L., Schubert, G., 2002. Geodynamics, 2nd Ed. Cambridge University Press, Cambridge, UK, pp. 262–264.
Zimmerman, R.W., Kumar, S., Bodvarsson, G.S., 1991. Lubrication Theory Analysis of Rough-Walled Fractures. Int. J. Rock. Mech. 28, 325–331.

EC Contract SES6-CT-2003-502706

PARTICIPANT ORGANIZATION NAME: UMR CNRS ULP 7516

Related with Work Package…………

Related with Working Group…………

EFFECTS OF THE ROUGHNESS OF A FRACTURE ON THERMAL EXCHANGE

Amélie Neuville, Renaud Toussaint, Jean Schmittbuhl
Institut de Physique du Globe de Strasbourg, UMR CNRS ULP 7516
EOST, Université Louis Pasteur, 5 Rue René Descartes, 67084 Strasbourg, France
e-mail: amelie.neuville@eost.u-strasbg.fr
(Draft Version)

ABSTRACT

Heat exchange during laminar flow in an open fracture is studied numerically on the basis of the Stokes equation in the limit of hydro-thermal lubrication. We study the influence of fracture roughness on hydraulic permeability and heat flux through the fracture sides when a cold fluid is injected into a homogeneous hot host rock. As a first step, the temperature rock is supposed to be constant so that we only deal with the spatial temperature evolution inside the fluid. We use realistic aperture geometry and parameters to illustrate our modeling. Then we show a simplified thermal simulation by using only little spatial information about the hydraulic flow.

INTRODUCTION

The modeling of the fluid transport in low permeable crustal rocks is of central importance for many applications (Neuman, 2005). Among them is the monitoring of the geothermal circulation in the project of Soulz-sous-Forêts, France (Bachler et al, 2003), where the heat exchange especially occurs through open fractures in granite (Gérard et al., 2006).

Numerous hydro-thermal simulations have already been proposed: some analytical solutions are known for simple geometry like parallel plates (e.g. Turcotte & Schubert, 2002), flat circular cylinders (Heuer et al., 1991). It exists as well more complex models, for instance: modeling occurring through a tridimensional network of fractures organized according to geological observations eventually added with stochastical fractures (like in Soultz-sous-Forêts, France, e.g. Gentier et al., 2006; Rachez et al., 2007 or in Rosemanowes, U.K., Kolditz & Clauser, 1998). Nevertheless, the geometry of each fracture itself is simple and in Kolditz and Clauser, 1998 it is suspected that some differences between the heat model and what is observed could be due to fracture channeling from roughness and network channeling. Channeling of the fluid flow has indeed already been experimentally observed (e.g Méheust & Schmittbuhl, 2000; Plouraboué et al., 2000) within rough fracture.

Here, we focus on the fracture scale, and the specificity of our hydro thermal model is to take into account the different scale variations of the fracture morphology. We aim at bringing out the main parameters which change the hydraulic and thermal behavior and quantifying the results. The further idea would be to take into account the roughness in network model by simply correcting macroscopic parameters.

We first describe our model of fracture thanks to self-affine apertures. Then, using lubrication approximations, we obtain bidimensional (2D) pressure and thermal equations when a cold fluid is injected through a fracture in a stationary regime. The temperature within the surrounding rock is supposed to be hot and constant (in time and space), with the fluid density being constant. We assume that at a coarse grained scale, the one dimensional (1D) basic equation for heat flux is identical to the one for parallel plates, but with a suitable characteristic thermal length which is different from the one computed with the mechanical aperture.

The numerical hydraulic and thermal results are illustrated for a given fracture morphology by trying to use realistic parameters (roughly inspired by the one of Soultz-sous-Forêts). Then we aim at bringing out what hydraulic information we need to have an idea of the thermal field. Thus we roughly estimate the temperature field by using only restricted spatial information about the hydraulic field (here obtained thanks to spatial Fourier filtering).

MODELING

Roughness of the fracture aperture

It has been shown that a possible geometrical model of rough fractures consists in using self affine surfaces, statistically invariant upon an isotropic scaling within their mean plane while on the perpendicular direction, the scaling is anisotropic (e.g. Brown & Scholz, 1985, Power et al., 1987; Cox & Wang, 1993; Schmittbuhl et al, 1993; Schmittbuhl et al 1995). To simplify the notation, we consider that the mean fracture plane (Figure 1) is described by the $(\hat{x},\hat{z})$ coordinates and perpendicular direction is $\hat{y}$. Such a self affine surface is invariant under the scaling transformation $x\rightarrow \lambda x$, $z\rightarrow \lambda z$ and $y\rightarrow\lambda^{\zeta} y$, where ζ is called the roughness exponent or Hurst exponent. Many rock surfaces exhibit a Hurst exponent equal to $\zeta=0.8$ (granite, etc) (Bouchaud, 1997, Schmittbuhl et al, 1993, Schmittbuhl et al, 1995; Santucci et al., 2007) or to $\zeta=0.5$ (sandstone) (Boffa et al., 1998; Méheust, 2002).

It is important to note that a self-affine surface having a roughness exponent inferior to 1 is asymptotically flat at large scales (Roux et al., 1993). Accordingly, the self-affine topography can be seen as a perturbation of a flat interface. Due to the lubrication approximation (Pinkus & Sternlich, 1961), which holds with smooth enough self affine perturbations, we will see that only the local aperture controls the problem. Therefore, the only input is the aperture field (also called geometrical aperture). The difference between two uncorrelated self-affine fracture sides having the same roughness exponent is as well a self-affine function (Méheust & Schmittbuhl, 2003). Thus we generate numerical apertures by using self-affine functions.

Several independent self-affine aperture morphologies are generated with the same roughness exponent chosen equal to $\zeta = 0.8$. They exhibit various pattern morphologies, various root-mean square deviations (RMS, denoted as σ), mean geometrical apertures A and size (length l_x and height l_z). The local aperture can be expressed as $a(x,z) = A + \sigma.a'(x,z)$, where A is the spatial average of a,

$\sigma = \left(\iint a^2 dxdz\right) / (l_x \cdot l_z) - A^2$ and a' is a self-affine perturbation having ζ as exponent, with a spatial average being null and a RMS equal to one. To keep simple boundary geometry of the domain where the equations are solved (i.e. where the aperture is not null), we do not allow any contact area by probing a range of strictly positive normalized aperture fields.
It has to be noticed that our hydro-thermal model can be applied to other variable aperture which might be more relevant depending on the geological context.

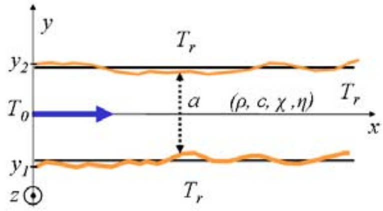

Figure 1: Schematic fracture with variable aperture a(x,z); ρ, c, χ, η *are respectively the following fluid properties: density, heat capacity, thermal diffusivity and dynamic viscosity.*

Hydraulic flow

The hydraulic flow is obtained under the same hypotheses and solved in the same way as in Méheust & Schmittbuhl, 2001: we use finite differences, and the system of linear equations is inverted using an iterative biconjugate gradient method (Press et al., 1992).
We impose the pressure drop across the system, and study the steady state flow of a Newtonian fluid at low Reynolds number, so that the viscous term of the Navier-Stokes dominates the inertial one (Stokes, 1856; Batchelor, 1967): $\vec{\nabla} P = \eta \Delta \vec{v}$, where η is the dynamic viscosity, $\vec{v}$ the velocity of the fluid and P is the pressure deviation from the hydrostatic profile (or the hydraulic head, equal to the pressure corrected by the gravity effect). To be in the framework of the lubrication approximation (Pinkus & Sternlich, 1961), besides small Reynolds number, we consider fractures with flat enough sides. Therefore, the velocity vectors get negligible components normal to the mean fracture. We consider that a macroscopic forced pressure gradient imposed along the $\hat{x}$ axis; $\hat{y}$ is denoted as the axis perpendicular to the mean fracture plane, and $\hat{z}$ is the in plane unit vector perpendicular to the mean flow direction. This leads us to express the velocity as a parabolic law (e.g. Iwai, 1976) (Figure 2):

$$\vec{v}(x,y) = \frac{\vec{\nabla}_2 P}{2\eta}(y-y_1)(y-y_2) \text{ [Eq. 1]},$$

where y_1 and y_2 are the fracture sides coordinates and $\vec{\nabla}_2$ is the gradient operator in the fracture plane. The hydraulic flow through the fracture aperture is (cubic law):

$$\vec{q}(x,z) = \int_a v(x,y,z)dy = -\frac{a^3}{12\eta}\vec{\nabla}_2 P \text{ [Eq. 2]},$$

and the bidimensional (2D) velocity is defined from the average of the velocity over the aperture with

$$\vec{u}(x,z) = -\frac{a^2}{12\eta}\vec{\nabla}_2 P \text{ [Eq 3]}.$$

Furthermore, considering the fluid to be incompressible, the Reynolds equation is obtained: $\vec{\nabla}_2(a^3\vec{\nabla}_2 P) = 0$. As boundary conditions of this equation, we impose the pressure at the inlet and outlet of the fracture (if $x = 0$, $P = P_0$ and if $x = l_x$, $P = P_L$, with $P_0 > P_L$) and consider impermeable sides at $z = 0$ and $z = l_z$.

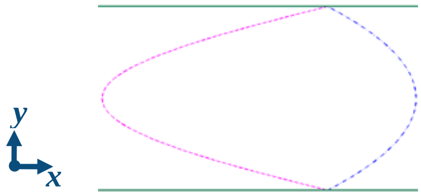

Figure 2: Velocity quadratic profile (dashed line) and temperature quartic profile (dot-dashed line) inside a fracture along the aperture; arbitrary abscissa units. Along the fracture sides, v=0 *and* T=T$_r$, *and the roots of the polynoms given by equations 1 and 4 are respected.*

Thermal exchange

On the basis of a classical description (e.g. Turcotte & Schubert, 2002), we aim at modeling the fluid temperature when cold water is permanently injected at the inlet of the hot fracture at temperature T_0. As the conduction inside the rock is not taken into account (hypothesis of infinity thermal conduction inside the bedrock), the fracture sides are supposed to be permanently hot at the fixed temperature T_r. This hypothesis should hold for moderate time scales (e.g., months), after the fluid injection has stabilized, and before the rock temperature has significantly changed. The fluid temperature is controlled by the balance between thermal convection and conduction inside the fluid, which reads (Landau & Lifchitz, 1994): $\vec{v} \cdot \vec{\nabla} T = \chi \Delta T$ where χ is the thermal diffusivity of the fluid and T the fluid temperature. We extend the lubrication approximation by considering that the slopes of the fracture morphology are small enough to provide conduction oriented along y axis. We suppose that the leading terms are conduction along y axis and in plane convection (no velocity component along $\hat{y}$); the vertical free convection (order of magnitude is km/year from Bataillé et al, 2006) as well as the fluid conduction along $\hat{x}$ and $\hat{z}$ axes are neglected, so that the previous equation is reduced to :

$$\frac{\partial^2 T}{\partial y^2} = \frac{v_x}{\chi}\frac{\partial T}{\partial x} + \frac{v_z}{\chi}\frac{\partial T}{\partial z} \text{ [Eq. 4]}.$$

The fluid temperature is supposed to be the one of the rock along the fracture sides, and the fluid is supposed to reach the temperature rock at a long enough distance. When we integrate this quantity along the fracture aperture we assume that $\beta = q_x \frac{\partial T}{\partial x} + q_z \frac{\partial T}{\partial z}$ is mainly dependent on *(x,z)* (few dependence on z if we are away from the fracture sides), where q_x and q_z are the x and z component of $\vec{q}$ defined in Eq. 2. In this way, we find that the temperature solution has a quartic profile (Figure 2) along the fracture aperture [1]:

$$T = -\frac{\beta}{2a^3\chi}(y-y_1)(y-y_2)(y-\sqrt{5}y_1)(y-\sqrt{5}y_2) + T_r \text{ [Eq.5]},$$

where y_1 and y_2 are the fracture sides coordinates.

---

1 We develop as well another kind of algorithm based on Lattice Boltzmann method, which requires very few hypotheses, in order to solve the velocity and temperature fields. From those results it appears that the respective parabolic and quartic solutions (with the proper coefficients) are indeed right more or less 5%.

Similarly to what we do for the hydraulic flow, we solve the thermal equation by integrating it along the fracture aperture (consequence of the lubrication approximation extended for the thermal aspect). In particular, when doing the balance of the energy flux, we express the advected free energy flux as $\vec{\nabla}_2\left(\rho c\int_a v(x,y,z)\left[T(x,y,z)-T_0\right]dy\right)$. Consistently with this energy budget, we introduce the relevant quantity $\overline{T}$ which is an average temperature weighted by the velocity:

$$\overline{T}(x,z)=\frac{\int_a v(x,y,z)T(x,y,z)dy}{\int_a v(x,y,z)dy} \quad \text{[Eq. 6]}.$$

We also use the Nusselt number $Nu=-\varphi_r/\varphi_{ref}$ which compares the efficiency of the present heat flow at the fracture side $\varphi_r=-\chi\rho c\left.\frac{\partial T}{\partial y}\right|_{y=z_1,z_2}$ and the mesoscopic flow at the fracture aperture scale without convection: $\varphi_{ref}=\chi\rho c\left(T_r-\overline{T}\right)/a$. Using the polynomial expression of T (Eq. 5) and $\overline{T}$ definition, we get $Nu=\frac{70}{17}$. Rearranging the simplified equation of thermal convection and conduction balance (Eq. 4), we get the final equation to be solved:

$$\vec{q}\cdot\vec{\nabla}_2\overline{T}+2\frac{\chi}{a}Nu\left(\overline{T}-T_r\right)=0 \quad \text{[Eq. 7]},$$

with boundary conditions $\overline{T}(0,z)=T_0$ at the inlet and $\overline{T}(z)\xrightarrow{x\to\infty}T_r$ at the outlet. Moreover any boundary condition can be used along $z=0$ or $z=l_z$, as the hydraulic flow is null there.
We discretize this equation by using a first order finite differences scheme and finally get $\overline{T}$ by inversing the system using a conjugated gradient method (Press et al., 1992).

Characterization of the computed hydraulic and thermal fields

Comparison to modeling without roughness

If we consider a fracture modeled with two parallel plates separated by a constant aperture A, then the gradient of pressure is constant all along the fracture as well as the hydraulic flow which is equal to:

$\vec{q}_{//}=-\frac{\Delta P}{l_x}\frac{A^3}{12\eta}\hat{x}$, where the subscript // denotes results valid for parallel plates and $\Delta P = P_L - P_0$. Under these conditions the analytical solution of Eq. 7 for parallel plates is:

$$\overline{T}_{//}=(T_0-T_r)\exp\left(-\frac{x}{R_{//}}\right)+T_r \quad \text{[Eq. 8]},$$

where $R_{//}$ is a thermal length describing the distance at which the fluid reaches the temperature of the surrounding rock. It is defined by:

$$R_{//}=\frac{A\left\|\vec{q}_{//}\right\|}{2Nu\,\chi}=-\frac{\Delta P}{l_x}\frac{A^4}{24\eta Nu\,\chi}=\frac{APe}{Nu} \quad \text{[Eq. 9]},$$

where Pe is the Peclet number defined by $Pe=\left\|\vec{q}_{//}\right\|/2\chi$. Pe expresses the convection importance compared to the conduction. For rough fractures, we want to study whether the temperature profiles can still be described by Eqs. 7 and 8 at a coarse grained case. If this is the case within some approximation, the goal of our study becomes to understand how the roughness affects the thermalization, and more precisely to quantify the suitable thermalization length R: when the modeled temperature profile is fitted by an exponential profile similar to Eq. 8, we obtain a suitable thermal length R that depends on the fracture morphology.

Hydraulic aperture

The hydraulic flow can be macroscopically quantified with the hydraulic aperture H (Brown, 1987; Zimmerman, 1991), defined as the equivalent parallel plate aperture to get the macroscopic flow $\langle q_x\rangle$ under the pressure gradient $\Delta P/l_x$:

$$H=\left\langle -q_x\frac{12\eta l_x}{\Delta P}\right\rangle^{1/3} \quad \text{[Eq. 10]},$$

where the quantity under bracket like $\langle q_x\rangle$ is the spatial average of what is inside the brackets. On the field this H value is probably a quantity which can be determined by hydraulic tests while A is the value we get an idea of using optical or geometrical measurements. If H/A is higher than 1, then the fracture is more permeable than parallel plates separated by $a(x, y) = A$. As the hydraulic aperture can be inhomogeneous, we define as well a local hydraulic aperture with:

$$h(x,z)=\left(-q_x(x,z)\frac{12\eta l_x}{\Delta P}\right)^{1/3} \quad \text{[Eq. 11]}.$$

Local quantities (geometrical and hydraulic apertures) are denoted with small letters and macroscopic variables (mean geometrical and hydraulic aperture) are in capital letters.

Thermal length

For the thermal aspect, once $\overline{T}$ is known, we aim at defining a thermal length R. To do that, we first define $\overline{\overline{T}}$, a 1D temperature which varies in the forced gradient direction, fulfilling the energy conservation:

$$\overline{\overline{T}}(x)=\frac{\int_a u_x(x,z)\overline{T}(x,z)dz}{\int_a u_x(x,z)dz} \quad \text{[Eq. 12]}.$$

It is the average of $\overline{T}$ along the width of the fracture l_z, weighted by u_x which is the x component of the 2D velocity (defined in Eq. 3).

Then, based on the flat plate temperature solution (Eq. 8), we do a linear regression of $\ln\left[\left(\overline{\overline{T}}-T_r\right)/\left(T_0-T_r\right)\right]$ plotted as a function of x, and we use the slope of this model line to get the characteristic thermal length R. The regression is computed with least square minimization for abscissa from $x=0$ to the minimum x value so that $\left|\frac{\overline{\overline{T}}-T_r}{T_0-T_r}\right|<2\cdot10^{-6}$.

This thermal length can be linked to a “thermal aperture” Γ by using a similar definition to the one given in Eq. 9 :

$$R=-\frac{\Delta P}{l_x}\frac{\Gamma^4}{24\eta Nu\,\chi}$$

It means that parallel plates separated by the proper aperture Γ will provide the same averaged thermal behavior as the rough plates.

APPLICATION

Example of computed hydro-thermal fields

Let us consider the wells GPK3 and GPK2 near Soultz-sous-Forêts, which are separated by a distance of about 600m at about 5000 m of depth. From hydraulic tests (Sanjuan et al., 2006), it has been shown that the hydraulic connection is relatively direct between both wells: (Sausse et al., 2008) a fault zone consisting on clusters of small fractures would link GPK3 (interception at 4775m) and GPK2. That probably leads to complex hydraulic streamlines and heat exchanges. We study a simplified case with one single fracture and roughly straight streamlines between both wells (linear flow). Then we use parameters (geometrical aperture and pressure gradient) which are probably slightly different from the ones observed or used in practice at Soultz-sous-Forêts.

Figure 3 shows an example of self-affine aperture, randomly generated and dimensioned so that the mean aperture A is equal to $3.60\ mm$ and its standard deviation is $\sigma = 1.23\ mm$.

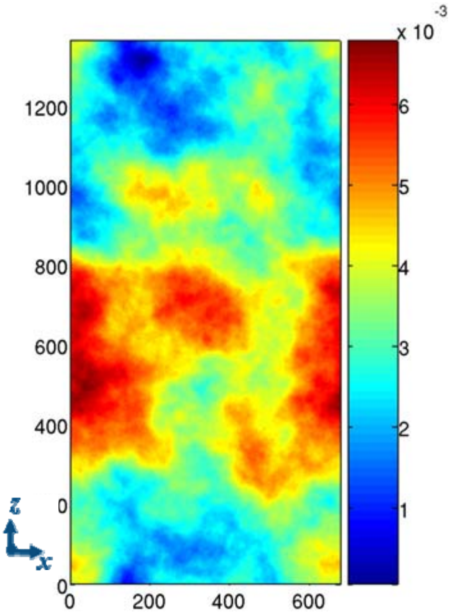

Figure 3 Aperture field with mean aperture A=3.60 mm and variability of the aperture σ=1.23 mm (σ/A=0.34). The color bar represents the aperture in m, the side units are plane spatial coordinates (x,z), also in m.

Then we solve the hydraulic flow in this variable morphology and obtain the 2D velocity field u (Figure 4 shows norm of u, defined in Eq.3) by dimensioning it with $\Delta P/l_x=-10^{-2} bar/m$, which corresponds to about 6 *bars* between the bottom of both wells. The dynamic viscosity is chosen equal to $4\text{x}10^{-4}\ Pa/s$ (reference value for pure water at $10\ Pa$ and $100°C$ from table in Spurk & Aksel, 2008). The size of the studied fracture is l_x x $l_y=683.3\text{x}1366.5$ and using the parallel plate model separated by A, the 2D-velocity expected from the quadratic law is 3.6 m/s and the thermal length is $R_{//}=33.3m$.

As we see, the 2D velocity field exhibits quite high contrasts: the fluid is rather immobile at the upper and lower borders of the fracture (close to $z=0$ and $z=l_x$) while most of the fluid flows very quickly through a channel in the middle of the fracture.

The macroscopic hydraulic aperture is $3.73\ mm$, which is slightly higher than the mean mechanical aperture A. Therefore, this whole fracture is more permeable than parallel plates separated by A. That means as well that this fracture is mechanically thinner than what we would expect from the knowledge of H. However, if the measurement of the hydraulic aperture is local (see in Figure 5), then h ranges from nearly 0 to $5.43\ mm$.

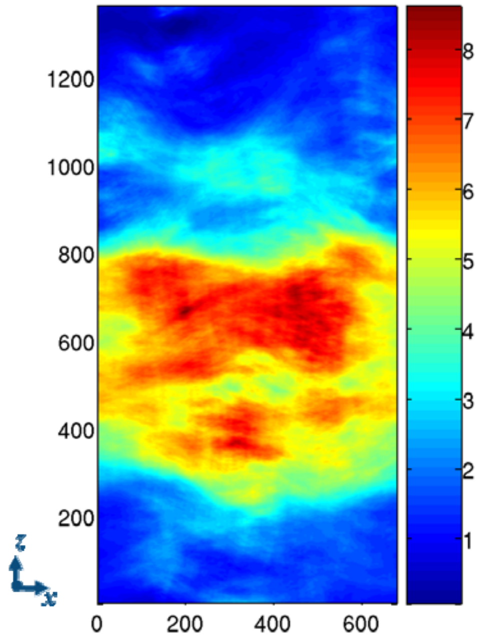

Figure 4: Color map of the velocity field in m/s. Red areas correspond to very high velocity while dark blue areas show static fluid. A linear pressure gradient is imposed between the left and right of the fracture. Spatial coordinates are in m.

It has to be noticed that many individual fracture apertures observed in Soultz are rather thinner ($0.2\ mm$) (Genter & Jung, private communication) while the fracture zone is rather thicker (10cm) (Sausse et al., 2008) and that the pressure gradient is probably higher than what is applied here – however the friction along the well itself may diminishes the pressure difference applied at the well head–. In our simulation, we have to work with small enough velocities (moderate Reynolds number) and we need to fix the pre-supposed macroscopic ratio between convection and conduction (thermal Peclet number). We quantify it indirectly thanks to the ratio $l_x/R_{//}$. $R_{//}$, defined in Eq. 9, is the characteristic thermal length depending on the average aperture, pressure gradient and fluid parameters which can be computed without knowing the exact morphology. All the results we present are still valid under any dimensioning which keeps $l_x / R_{//}$ constant (here equal to 20.5): for instance another dimensioning for other purpose could be $l_x=691m$, $A=10mm$ and $\Delta P/l_x=-1.7\text{x}10^{-4} bar/m$ (using the same fluid parameters).

The wells does not inject/pump water all along the fracture height (straight streamlines are only an approximation) and the fracture zone between GPK2 and GPK3 is not vertical. The flowrate observed at Soultz is about $Q=20L/s$, which is probably carried by several fractures. Thus, using a velocity of about $u=5m/s$ and a fracture aperture equal to $5mm$ means that the well crosses such fractures over a cumulated length of about (by neglecting the well radius):

$$L = \frac{Q}{VA} = \frac{20\times10^{-3}}{5\times5\times10^{-3}} \approx 80cm\ .$$

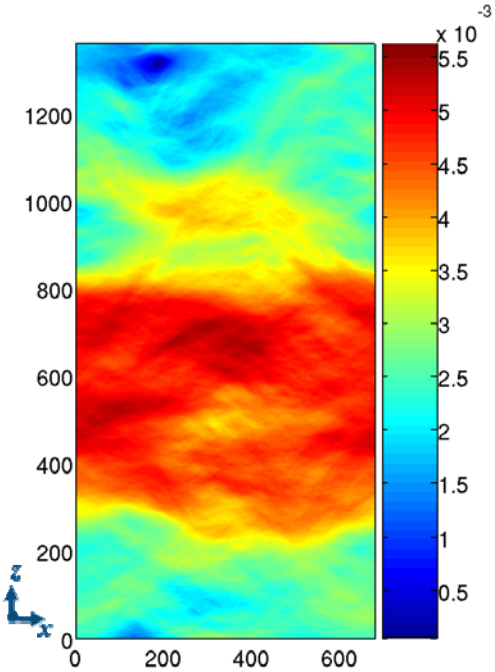

Figure 5: Color map of the local hydraulic aperture in m computed from the variable hydraulic flow and aperture. Spatial coordinates are in m.

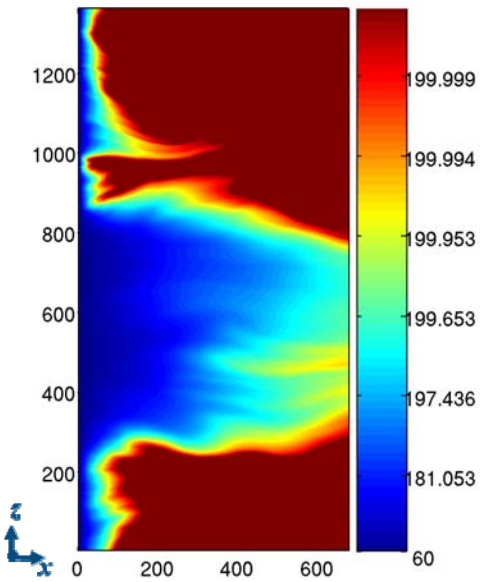

Figure 6: Map of the averaged temperature field $\overline{T}$ in Celsius degrees (°C). The color bar changes exponentially; thus small variations slightly below the temperature rock (200°C) are highly visible. Spatial coordinates are in m.

Figure 6 shows the temperature field $\overline{T}$ computed inside the variable aperture using the variable hydraulic flow. As we see, $\overline{T}$ is very inhomogeneous and exhibits channeling.
The chosen inlet temperature is $T_0=60°C$, the rock temperature is $T_r=200°C$ and the fluid diffusivity is $\chi=0.17mm^2/s$ (water reference value at $T=100°$, from table in Taine & al., 2003). In practice, the rock temperature will evolve because the rock thermal diffusivity is about $1mm^2/s$, while we considerer it as far larger compared to the fluid one (so that T_r is kept constant). Using these parameters we see that the pumping well located at $600m$ within the illustrated fracture geometry is far enough to get hot water.

However, $\overline{T}$ is rather different from what we expect from parallel plates, especially because this field is not at all invariant along $\hat{z}$. That is quantitatively well illustrated in Figure 7 where we plot some profiles of temperature along x for $z=970m$ (plot iv) and $z=703m$ (plot v). For example, at $x=200m$, the fluid is $200°C$ hot in $z=970m$, while in $z=703m$ the temperature is only $183°C$. Let us compare these 1D temperature profiles along x to the one obtained inside parallel plates separated by the aperture A which reads:

$$\overline{\overline{T}}_{//} = (T_0 - T_r)\,exp\left(-\frac{x}{R_{//}}\right) + T_r \quad \text{[Eq. 13].}$$

Following this model (plot iii) the fluid should be as well at $200°C$ in $x=200m$. If we compare $\overline{\overline{T}}_{//}$ to the averaged observed temperature $\overline{\overline{T}}$ (defined in Eq. 12) (Figure 7, plot i), we see that $\overline{\overline{T}}_{//}$ is not well representative. Therefore, we model $\overline{\overline{T}}$ by using an adapted parallel law $\overline{\overline{T}}_{mod}$ (plot ii) which is an exponential law with a suitable thermal length R:

$$\overline{\overline{T}}_{mod} = (T_0 - T_r)\,exp\left(-\frac{x - x_0}{R}\right) + T_r \quad \text{[Eq. 14],}$$

where $R=96.6m$ (i.e. 2.9x$R_{//}$) and $x_0=9.8m$. Due to the choice of the minimization to obtain parameters R and x_0 (least square applied on the semi-log plot), the beginning of the fit curve is not accurate. The thermal aperture is therefore equal to $\Gamma=4.7\ mm$, which is rather different from the geometrical aperture $A=3.6\ mm$. A larger thermal aperture (compared to the geometrical one) means an inhibited thermalization on average.

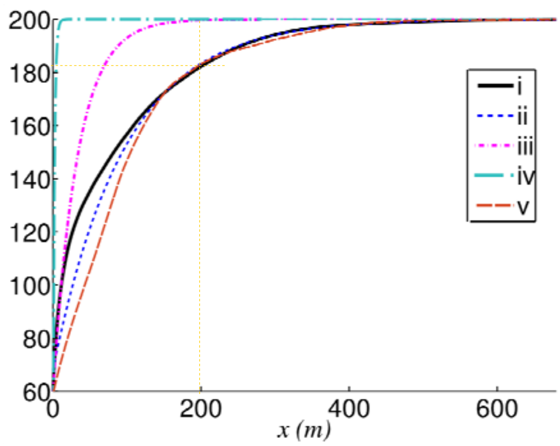

Figure 7 Fluid 1D temperature in °C in function of x. The continuous black curve (i) shows the computed temperature $\overline{\overline{T}}$. The blue dashed curve (ii) is the model of curve (i) with an exponential function. The dot dashed magenta curve (iii) is the fluid 1D temperature by neglecting the self-affinity perturbation (inside flat parallel plates). The curves (iv) and (v) are profiles of temperature $\overline{T}(x,z)$ for respectively z=970m and z=703m.

Temperature estimation with few parameters

The spatial correlation of the hydraulic aperture seems to be a key parameter to evaluate the temperature field. The macroscopic hydraulic aperture H brings too few information to characterize the heat exchange, while it is quite useless to know in detail the spatially variable hydraulic aperture h (which is by the way impossible on the field). Therefore we propose to characterize the hydraulic aperture with only the largest spatial variations. Numerically, it is possible to obtain them by filtering the hydraulic field in Fourier domain with the following criterion: only the Fourier coefficients so that $\left(\frac{k_x}{2\pi}l_x\right)^2+\left(\frac{k_z}{2\pi}l_z\right)^2<2^2$ are kept, where k_x and k_y are the coordinates of the wave number. Considering that the Fourier transform is discrete, it means that only the average and the first Fourier modes along x and z are left. The hydraulic aperture field displayed in Figure 5 is therefore reduced to the field $h_f(x,z)$ shown in Figure 8 (with the same color scale). As wee see, the middle channel remains, while high frequency variations are removed.

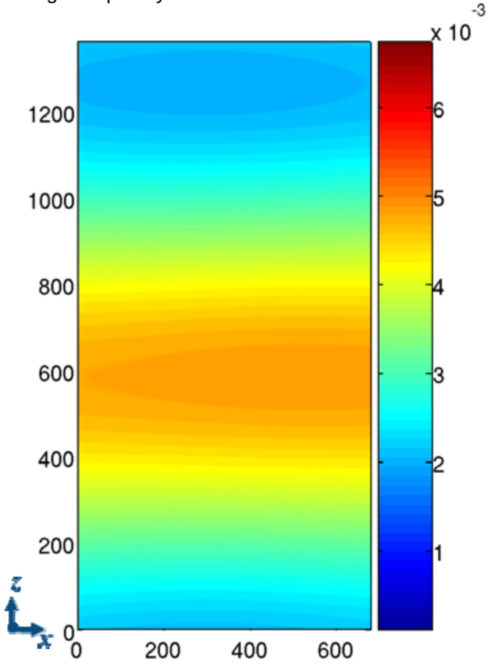

Figure 8: Map of the simplified hydraulic aperture h_f in m. Here, it is obtained by Filtering the previous hydraulic aperture: average and 1st Fourier modes along x and y are left. The spatial coordinates are in m.

Such low frequency variations might be obtained with field measurement. Let us assume that we only have this data to evaluate the heat exchange.

A quick and simple approximation of the thermal field is to use the exponential law with a local variable length of reference $R_f(x,y)$ which change accordingly to the local hydraulic aperture $h_f(x,z)$. $R_f(x,y$ is defined similarly to $R_{//}$ in Eq. 4 by putting $h_f(x,z)$ in place of A:

$$\overline{T}_f(x,y)=(T_0-T_r)\exp\left(-\frac{x}{R_f(x,y)}\right)+T_r \text{ [Eq. 15]}$$

where $R_f(x,y)=-\frac{\Delta P}{l_x}\frac{[h_f(x,y)]^4}{24\,\eta Nu\,\chi}$ [eq. 16].

From this last expression, we obtain the thermal field shown in Figure 9. The main spatial channel of the complete thermal field (Figure 6) is still visible, and even if the fluid temperature evolves slightly differently (quicker), it may roughly give an idea of what thermically happens.

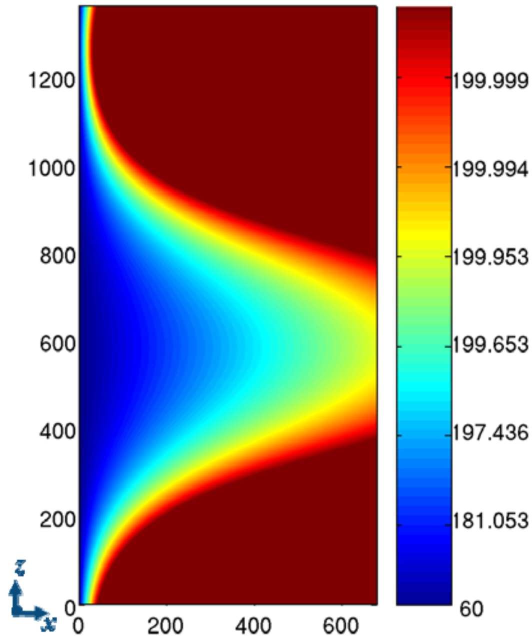

Figure 9: Map of the simplified temperature field $\overline{T}_f$ obtained using the previous filtered aperture (fig. 8) in the exponential law. Color scale is in °C and it changes exponentially.

CONCLUSION AND COMPLEMENT

We propose a numerical model to estimate the heat exchange at the fracture scale between cold fluid and hot surrounding rock. We supposed to be in permanent laminar regime and the numerical model is based on a lubrication approximation for the fluid flow (Reynolds equation). We introduce a “thermal lubrication” approximation which leads us to a quartic profile of the temperature across the aperture. It is obtained by assuming that in plane convection is dominant compared to in plane conduction (low in plane Peclet number). Moreover, due to the lubrication approximation, the out plane convection is neglected and the heat conduction initiated by the difference of temperature between rock and fluid is supposed to be the major out plane phenomenon.

Our model shows that the roughness of the fracture can be responsible for fluid channeling inside one single fracture. In this zone of high convection the heat exchange is inhibited: the fluid needs a longer distance to reach the rock temperature. Besides, the temperature evolution is inhomogeneous along the fracture height. We characterize it on average thanks to a thermal length and a thermal aperture which change according to the morphology.

In this proceeding, we only illustrate a case of rough aperture which leads to inhibited thermalization with a long channeling. With other apertures (not illustrated here) we observe that roughness may also locally highly reduce the convection (because of barriers of rock perpendicular to the main flow) which locally enhances the heat exchange (high conduction compared to convection).

In any case, we notice that the temperature distribution is strongly affected by the hydraulic flow.

By characterizing the hydraulic and thermal exchange with reduced parameters, we see that average value of the geometrical aperture provide too little information to characterize the fluid temperature. In contrast, the

knowledge of the main spatial variation of the hydraulic aperture (here observed by keeping only the very low spatial frequencies using Fourier filtering) brings interesting information about the spatial thermal field.
Moreover knowing the real distance covered by fluid particles may improve the temperature estimation. Indeed, it seems that the thermal field evolves exponentially along the trajectory lines. That brings back to the notion of tortuosity of the flow inside the fracture.
If the main variations of the geometrical field are known, it is also possible to compute the hydro-thermal fields in the same way as we have explained in the “Modeling” part. The main spatial hydro-thermal features can be obtained using apertures fields presenting various features (self affine or not). The macroscopic spatial correlation of the aperture is probably an important parameter ruling the hydro-thermal behavior.

We thank Albert Genter, Reinhard Jung Marion, Patrick Nami and Marion Schindler for discussion about this modeling.

REFERENCES

Bachler, D., Kohl, T., Rybach, L., (2003), Impact of grabenparallel faults on hydrothermal convection – rhine graben case study. *Phys. Chem. Earth,* **28**, 431-441.

Bataillé, A., Genthon, P., Rabinowicz, M. & Fritz, B. (2006), Modeling the coupling between free and forced convection in a vertical permeable slot: Implications for the heat production of an Enhanced Geothermal System, *Geothermics*, **35**, 654–682

Batchelor, G.K. (1967), An introduction to fluid dynamics, (*Cambridge University Press*, Cambridge)

Boffa, J.M., Allain C. & Hulin, J.P. (1998), Experimental analysis of fracture rugosity in granular and compact rocks. *Eur. Phys. J. Appl. Phys.,* **2**, 281-289.

Bouchaud, E. (1997), Scaling properties of cracks. *J. Phys. Cond. Matter,* **9**, 4319-4344

Brown, S. R. (1987), Fluid flow through rock joints : the effect of surface roughness. *J. Geophys. Res.,* **92**, 1337-1347

Brown, S.R. & Scholz, C.H. (1985), Broad bandwidth study of the topography of natural rock surfaces. *J. Geophys. Res.,* **90**, 12575-12582.

Cox, B. L. & Wang, J.S.Y. (1993), Fractal surfaces : measurement and application in earth sciences, *Fractal*, **1**, 87-115

Gentier, S., Rachez, X. Dezayes, C. Hosni, A., Blaisonneau, A, Genter, A. & Bruel, D. (2005), Thermohydro-mechanical modelling of the deep geothermal wells at Soultz-sous-Forêts. *Proceedings of EHDRA scientific conference.*

Gérard, A., Genter, A., Kohl, T., Lutz, P., Rose, P. & Rummel, F. (2006), The deep EGS (Enhanced geothermal System) project at Soultz-sous-Forêts (Alsace, France), *Geothermics*, **35**, 473-483

Heuer, N. Küpper, T. & Windelberg, D. (1991), Mathematical model of a Hot Dry Rock system, *Geophys. J. Int.,* **105**, 659-664

Iwai, K., (1976), Fundamental Studies of Fluid Flow Through a Single Fracture, Ph.D. Thesis, University of California, Berkeley.

Kolditz, O. & Clauser, C. (1998), Numerical simulation of flow and heat transfer in fractured cristalline rocks : application to the hot dry rock site in Rosemanowes (U.K.), *Geothermics,* **27** (1), 1-23

Landau, L. & Lifchitz, E. (1994), Physique théorique mécanique des fluides, 3è éd., p. 280

Méheust, Y. & Schmittbuhl, J. (2000) Flow enhancement of a rough fracture. *Geophys. Res. Lett.,* **27**, 2989-2992

Méheust Y. & Schmittbuhl, J. (2001), Geometrical heterogeneities and permeability anisotropy of rough fractures. *J. Geophys. Res.* **106**, 2089-2102

Méheust, Y. & Schmittbuhl, J. (2003), Scale effects related to flow in rough fractures. *PAGEOPH* **160 (5-6)**, 1023-1050

Méheust, Y. Ph.D. thesis, (2002), Ecoulements dans les fractures ouvertes, Université Paris Sud.

Neuman, S., (2005), Trends, prospects and challenges in quantifying flow and transport through fractured rocks. *Hydrogeol. J.*, **13**, 124-147.

Pinkus, O. & Sternlich, B. (1961), Theory of hydrodynamic Lubrication, Mc Graw-Hill, New York

Plouraboué, F., Roux, S. Schmittbuhl, J., Vilotte, J.P. (1995), Geometry of contact between self-affine surfaces, *Fractals*, **3** (1), 113-122

Plouraboué, F., Kurowski, P., Boffa, J.M., Hulin, J.P. & Roux, S. (2000), Experimental study of the transport properties of rough self-affine fractures, *J. of Contaminant Hydrology*, **46**, 295-318

Power, W. L., Tullis, T.E. Brown, S.R, Boitnott, G.N. & Scholz, C.H. (1987), Rhougness of natural fault surfaces, *Geophys. Res. Lett*., **14**, 29-32

Press, W. H., Teukolsky, S. A., Vetterling, W. T. & Flannery, B.P. (1992), Numerical Recipes (*Cambridge University Press*, New York)

Rachez, X., Gentier, S. & Blaisonneau, A. (2007), Current status of BRGM modeling activities at the Soultz EGS reservoir: hydro-mechanical modeling of the hydraulic stimulation tests and flow and transport modelling of the in-situ tracer test. *Proceedings of EHDRA scientific conference*

Roux, S., Schmittbuhl, J., Vilotte, J.P. & Hansen, A. (1993), Some physical properties of self-affine rough surfaces. *Europhys. Lett.,* **23**, 277-282.

Sanjuan, B., Pinault, J.L., Rose, P. Gerard, A., Brach, M., Braibant, G., Crouzet, C., Foucher, J.C., Gautier, A & Touzelet, S. (2006), Tracer testing of the geothermal heat exchanger at Soultz-sous-Forets (France) between 2000 and 2005, *Geothermics,* **35**, (5-6), 622-653

Santucci, S., Måløy, K.J., Delaplace, A., Mathiesen, J., Hansen, A., Haavig Bakke, J.Ø., Schmittbuhl, J., Vanel, L., & Ray, P. (2007), Statistics of fracture surfaces Physical Review E, **75** (1), 016104

Sausse, J., Dezayes, C., Genter, A. & Bisset, A. (2008), Characterization of fracture connectivity and fluid flow pathways derived from geological interpretation and 3D modelling of the deep seated EGS reservoir of Soultz (France). *Proceedings, thirty-Third workshop on Geothermal Reservoir Engineering, Stanford, California*.

Schmittbuhl, J., Gentier S. & Roux, S. (1993), Field measurements of the roughness of fault surfaces. *Geophys. Res. Lett.*, **20**, 639-641

Schmittbuhl, J. Schmitt, F & Scholz, C (1995), Scaling invariance of crack surfaces. *J. Geophys. Res.,* **100**, 5953-5973

Spurk, J. H. & Aksel, N. (2008), Fluid Mechanics, 2nd ed., (*Springer)*, p.516

Stokes, G.G. (1846), On the theories of the internal friction of fluids in motion, and of the equilibrium and motion of elastic solids. *Trans. Cambr. Phil. Soc,* **8**, 287-319

Taine J. & Petit, J.P. (2003), Transferts thermiques, 3rd ed., (*Dunod*), p.449

Turcotte, D. L. & Schubert, G. (2002) Geodynamics, 2nd ed. (*Cambridge University Press*), Chap. 6, p.262-264

Zimmerman, R. W., Kumar, S. & Bodvarsson, G. S. (1991) Lubrication Theory Analysis of Rough-Walled Fractures, *Int. J. Rock. Mech.,* **28**, 325-331.

Available online at www.sciencedirect.com
ScienceDirect
International Journal of Rock Mechanics & Mining Sciences 45 (2008) 422–430
International Journal of Rock Mechanics and Mining Sciences
www.elsevier.com/locate/ijrmms

Fracture morphology and viscous transport

J. Schmittbuhl*, A. Steyer, L. Jouniaux, R. Toussaint

Institut de Physique du Globe de Strasbourg, UMR 7516, 5 rue René Descartes, 67084 Strasbourg Cedex, France

Received 15 February 2007; received in revised form 28 June 2007; accepted 2 July 2007
Available online 24 September 2007

Abstract

The morphology of a fracture in a granite block is sampled using a high resolution profiler providing a 3999×4000 pixel image of the roughness. We checked that a self-affine model is an accurate geometrical model of the fracture morphology on the basis of a spectral analysis. We also estimated the topothesy of the experimental surface to be $l_r \approx 2 \times 10^{-7}$ mm and the roughness exponent to be $\zeta \approx 0.78$. A finite difference scheme of the Stokes equation with a lubrication approximation was used to model the viscous flow through a fracture aperture defined as the gap between the experimental fracture surface and a flat plane. We finally compare our numerical results to experimental measurements of the flux through the fracture of a glycerol/water mixture (to be at sufficiently low Reynolds number where Stokes equations holds) changing the average aperture of the fracture. The comparison is successful despite a limited resolution of the experimental measurements. Interestingly we show that only long wavelengths of the fracture morphology control the fracture hydraulic conductivity.

Keywords: Fracture roughness; Fluid flow; Hydraulic conductivity

1. Introduction

The modelling of the fluid transport in low permeable crustal rocks is of central importance for many applications [1]. Among them is the monitoring of the geothermal circulations in the project of Soultz-sous-Forêt, France [2]. The transit time of the brines into the natural and induced fractures between injection and production wells has to be carefully estimated in order to provide precise estimates of the production running time. Water flux controls both the heat transfer to the fluid and the cooling of the massif [3–5].

As shown from previous studies [5–7] only a few important fractures, closely associated in clusters [8] are controlling the fluid exchange between wells. Accordingly the study of the flow within a single fracture appears of central interest. It is also important for large scale numerical simulations of the convective circulation in the massif [9,10]. Up to now, only very simple models for fractures, i.e. parallel plates models, have been considered, ignoring the impact of the fracture morphology on the fracture transmissivity [5].

For a parallel plate model, the steady state solution of the Navier–Stokes equations for incompressible laminar flow yields the cubic law, where the volumetric flow rate Q depends linearly on the macroscopic pressure gradient in the flow direction, and is proportional to the cube of the plate separation a:

$$Q = -L_y \frac{a^3}{12\eta} \nabla P, \tag{1}$$

where L_y is the width of the fracture perpendicular to flow and η is the fluid viscosity [11,12].

In this study, we are interested in the influence of a realistic geometry of the fracture on its hydraulic permeability [13–21]. The morphology of fresh fractures is sampled and compared to a geometrical model that can be used in numerical codes for the fluid flow. We will also use the measured aperture profile as boundary conditions for numerical simulations. A contrario, the existence of a simple geometrical model of fracture morphology will allow to generate many realizations of synthetic fracture aperture, and thus study systematic effects when good

*Corresponding author. Tel.: +33 3 90 24 03 41; fax: +33 3 90 24 01 25.
E-mail address: Jean.Schmittbuhl@eost.u-strasbg.fr (J. Schmittbuhl).

1365-1609/$ - see front matter
doi:10.1016/j.ijrmms.2007.07.007

statistics are needed. Our goal is to show that realistic fracture morphology can be introduced as a perturbation of the parallel plate model. However we show that strong influences on the transport properties might emerge owing to the long spatial correlations of the asperities morphology even in the limit of laminar flows. We have to mention that we assume that altered fractures partly coated with secondary minerals are still correctly described by a similar geometrical model [22–24]. In any case, as long as the coating process redistribute masses within a finite range, the geometrical model considered will properly describe the large scale morphology of the fracture aperture—i.e., at first, only small scale modifications of the aperture profile will happen. This large scale morphology will be shown to strongly control the fracture transmissivity, and the morphological model for fresh fracture is thus hopefully also relevant for the transmissivity of altered fractures.

We limit ourself to viscous flow characterized by low Reynolds number ($Re \ll 1$) although turbulence might develop at high flow rate [25,26]. The Reynolds number Re that can be defined from the Navier–Stokes equation is the ratio of the inertial terms to the terms describing the viscous forces. It is typically defined as: $Re \approx (\rho/\eta)\ u_{\parallel} l_h$ where ρ is the fluid density, $u_{\parallel}$ is a characteristic velocity along the mean fracture plane direction and l_h the characteristic aperture of the fracture [27]. A more precise estimate of the Reynolds number that compares only terms of the Navier–Stokes equation along the mean fracture plane direction is: $Re^* = Re\ l_h/l_{\parallel}$ where $l_{\parallel}$ is a characteristic length scale for flow variations along the mean fracture plane [23]. Since the aspect ratio of fracture is typically very small (see Section 2.3), we obtain: $Re^* \ll Re$.

We also assume that the lubrication approximation holds, i.e. that the velocity components in the direction transverse to the average fracture plane can be neglected. By integrating the Stokes equation over transverse direction, a further simplification of the Stokes equation emerges leading to a local cubic law. According to detailed analysis of the range of validity of the Stokes equation and this lubrication approximation [27], for the experiments performed here at Reynolds numbers (Re) ranging from 0.001 to 0.25, this Stokes lubrication approximations should be valid. Accordingly flow properties are only a function of the local apertures and not of the aperture gradients. This property implies that open fractures with different pairs of surface fractures, one on the top $z^+(x,y)$ and one on the bottom $z^-(x,y)$, but with the same aperture field $a(x,y) = z^+(x,y) - z^-(x,y)$, will have the same hydraulic behavior. Among this set of equivalent fractures, a semi-fracture, made of a rough surface facing a flat plate can be defined as $z^+(x,y) = a(x,y)$ and $z^-(x,y) = 0$. This equivalent semi-fracture will show the same aperture field. We will base our experimental approach on this property and reduce our problem to such a semi-rough fracture. The flat plate is chosen to be transparent (PMMA) which allow to follow optically tracers if necessary (e.g. in ongoing experiments on reactive fluids).

At larger Reynolds numbers where the Stokes equation would not hold any more, an alternative numerical approach would be to use directly the Navier–Stokes equation in the three dimensional fracture geometry. This has been shown to produce results in agreement with experimental flow in natural fractures [20,21]. The scope of the present work is on smaller Reynolds numbers where the treatment of the full Navier–Stokes equation is not required. Relatively to these studies [20,21], the present work focuses on a finer statistical description of the fracture morphology, and on the influence of the various modes of wavelength of the fracture morphology on the transport properties. We will show indeed that the largest wavelengths of the fracture opening control its hydraulic conductivity.

2. Fracture morphology

2.1. Roughness measurement

We studied the viscous flow imposed inside a fresh fracture that extends over an area of 10 cm × 10 cm. Grains are typically millimetric (0.5 mm). The fracture was obtained from a mode I failure under a three point bending load of a 10 cm × 10 cm × 20 cm granite block from Lanhélin, France. The fracture was initiated from a linear initial notch that was machined in the middle of the block before triggering the breaking procedure, and crossed the sample dynamically. The granite is a two-mica granite containing both muscovite and biotite, and K-felspars [23].

To get a fast and precise topography measurement of the fracture surfaces, we used an optical profiler (see Fig. 1) [23,28]. The instrument provides a height measurement without any contact of the surface which allows a fast on-flight acquisition of the topography (up to 70 points per second). However this technique requires not to measure

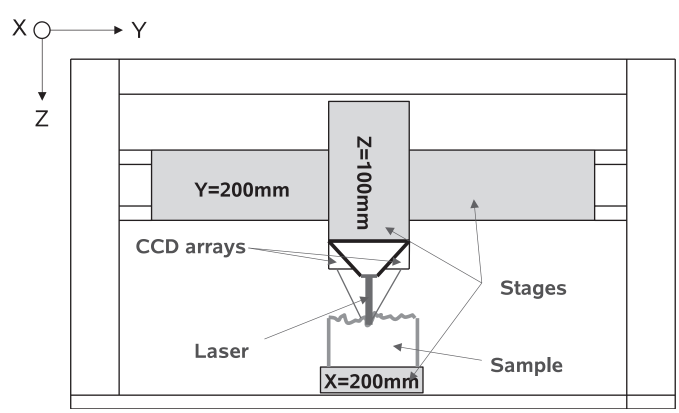

Fig. 1. Sketch of the optical profiler. The laser sensor sends a laser beam of 30 μm in diameter normally to the surface and records diffuse reflection from two ccd arrays. Height is deduced from a triangulation estimate. The sensor is attached to the Z-axis which is vertical and moved horizontally by the Y-axis, over the sample. The X-axis is the second horizontal translation stage that moves the sample. Maximum range of each translation stage is explicited. Their mechanical resolution is 1 μm.

the original fracture but a cast of the fracture made of an optically homogeneous material. To do this, we apply a blue silicon resin (RTV 1570) on the granite surface and turn it out after drying to get a perfect counter molding of the granite surface. The use of a silicon cast aims at suppressing optical artifacts that might come from significant variations of the reflectivity when passing different minerals along the granite surface. Indeed, the silicon is uniformly blue and rather equally diffusive providing a high quality measurement of the fracture morphology. Therefore very high resolution map of the fracture can be obtained.

In the present study, a 3999×4000 image of the complete fracture surface is obtained with a vertical resolution of $2\,\mu$m (see Fig. 2). The map consists of almost 16 millions pixels providing one of the highest image resolution ever obtained for a fracture surface. The mesh of the horizontal grid (i.e. along the (X, Y) plane) is $24\,\mu\text{m} \times 24\,\mu\text{m}$ and the total area is $95.952 \times 95.976\,\text{mm}^2$. A mean plane estimated from a least square fit has been removed.

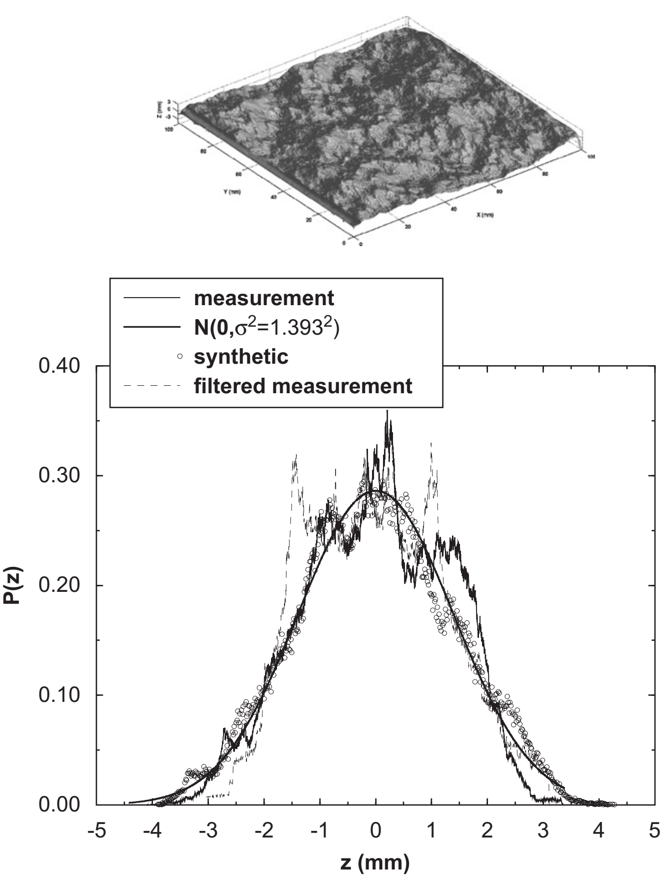

Fig. 2. Top: 3D map of the silicon cast of a fresh granite fracture sampled with the optical profiler. The resolution of the map is 3999×4000 with a mesh of $24\,\mu\text{m} \times 24\,\mu\text{m}$. On the left side of the image (low X), the initial machined notch is visible. Bottom: height distribution of the fracture topography. The best Gaussian fit for the whole distribution is plotted as: $N(0,\sigma^2) = (1/\sigma\sqrt{2\pi})\exp(-z^2/2\sigma^2)$ with $\sigma = 1.393$ mm. Height distribution of the synthetic fracture topography presented in Fig. 5 is added for comparison as the height distribution of the filtered measured surface shown in Fig. 8.

The fracture surface shows a very rich distribution of asperities of any size (see the fractal dimension measured in [29] and the return probability measured in [30]), the aspect ratio of the asperities (i.e. height over lateral extension) being very small. To be more precise, an asperity can be defined as a connected surface entirely above the mean plane, the height of the asperity is the maximum z-coordinate of this surface, and its lateral extension refers to the x- or y-extent of the orthogonal projection of this surface on the mean plane.

2.2. Height statistics

The height distribution is computed and shown in Fig. 2. Even with a very large amount of data (i.e. 15 996 000 data points), the Gaussian fit obtained from a least square fit, is a raw approximation. The rms of the Gaussian model provides an estimate of the height fluctuations: $\sigma = 1.393$ mm (see Fig. 2). An extended description of the height statistics, in particular the departure from a Gaussian statistics, is proposed in [31].

To characterize the possible spatial correlations of the height fluctuations, we computed the Fourier power spectrum of the topography $P(k) = |\tilde{z}(k)|^2$ where k is the wave number. This is also the Fourier transform of the height–height correlation: $P(k) = \tilde{C}(k)$ where $C(\delta) = \langle h(x)h(x+\delta)\rangle_x - \langle h^2\rangle_x$ (see Fig. 3). A power law behavior is a good fit over more than three decades. The average phase spectrum $\langle\phi(k)\rangle$ is also plotted in Fig. 3. It shows the average over the y-axis of phase spectrum $\phi(k_x)$ of profiles extracted along x-axis. Phases almost average to zero for most wave numbers k showing their randomness. At low wave-numbers (i.e. low k), phases still show large fluctuations indicating that phases might be spatially correlated and not fully random.

2.3. Geometrical model

A self-affine surface is a possible geometrical model for roughness topographies of fractures as shown in several previous studies [22,30,32,33]. Self-affinity is a scaling invariance property that reads as:

$$\begin{cases} x \to \lambda x, \\ y \to \lambda y, \\ z \to \lambda^{\zeta} z, \end{cases} \tag{2}$$

where λ is a scaling factor and ζ is the roughness exponent. As can be seen from Eq. (2), the scaling transformation is supposed to be isotropic within the mean plane (x, y) since the scaling factors are the same along x and y axes. Accordingly the fracture propagation direction is assumed not to influence the fracture roughness [18,23]. On the contrary, the scaling is anisotropic along the out of plane direction z. Indeed, the scaling factor is not the same along the mean plane (x, y) compared to the out of plane direction z. For the latter direction, the roughness

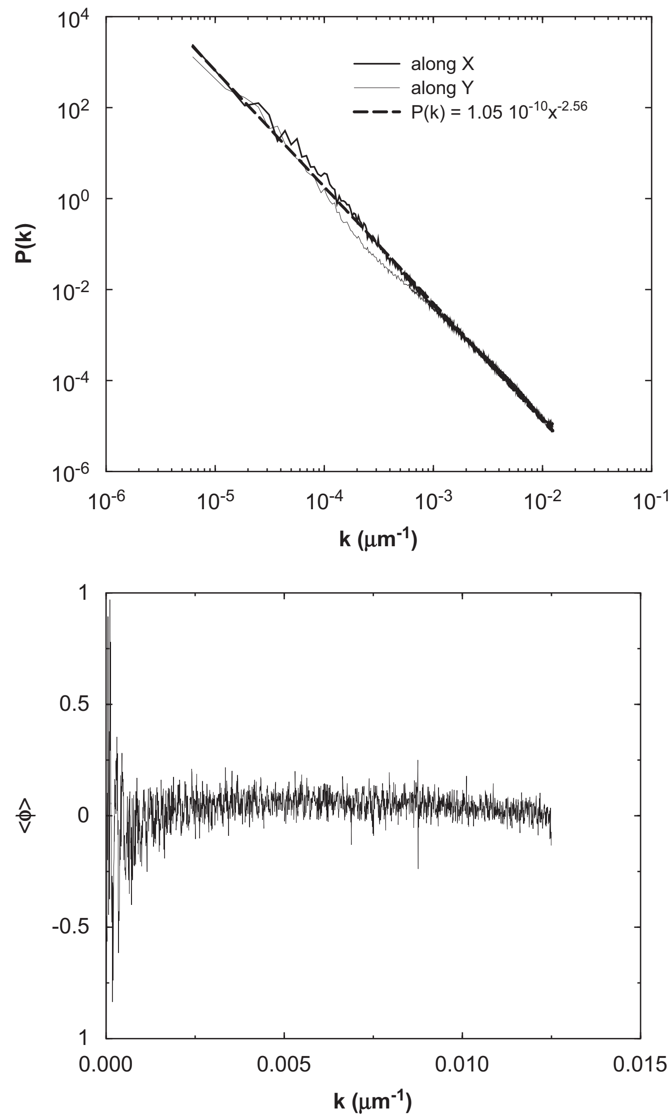

Fig. 3. Top: Fourier spectra of the fracture morphology. Spectra are computed from 2D profiles extracted along either x or y direction (respectively, parallel or perpendicular to the crack propagation) and then averaged over all the extracted profiles along the same direction [30]. The best power law fit is given: $P(k) = 1.05 \times 10^{-10} x^{-2.56}$ with $P(k)$ in µm^3 (error bars are 5×10^{-11} for the prefactor and 0.05 for the exponent). Bottom: Phase spectra have been computed along the X-direction and averaged over the Y-direction. Phases are qualitatively distributed randomly.

exponent ζ describes how anisotropic is the property. When being equal to one, the property is isotropic and corresponds to a fractal. When the roughness exponent is different from one (i.e. classically between 0 and one), the scaling is anisotropic and the surface is self-affine.

If a surface $z(x, y)$ shows such a self-affine behavior, it can be shown that its 1D Fourier power spectrum fulfils the relation [30]: $P(k) \propto k^{-1-2\zeta}$ and the phase spectrum is supposed to be flat and uncorrelated. Fig. 3 shows how good is the self-affine model for a high-resolution measurement of a fracture surface. The estimate of the roughness exponent from a Fourier method, is $\zeta \approx 0.78$.

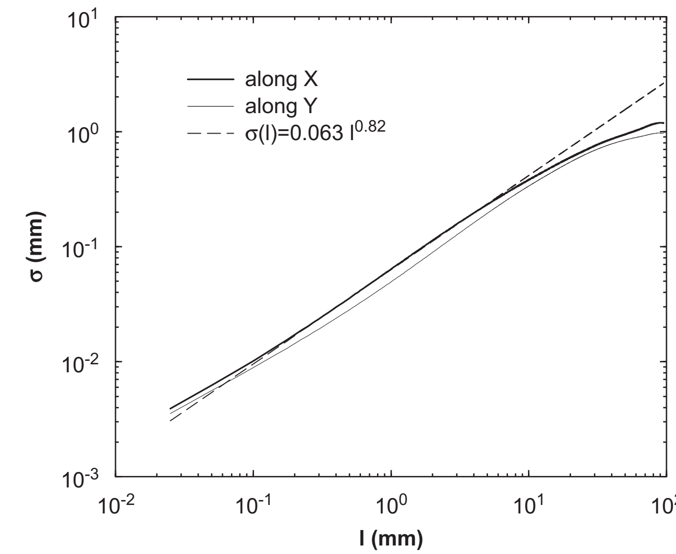

Fig. 4. Scaling of the rms $\sigma(l)$ of the fracture topography along x- and y-axis. The best fit of the form $\sigma(l) = l_r^{1-\zeta} l^{\zeta}$ defines the roughness exponent $\zeta \approx 0.82$ and the topothesy $l_r \approx 2 \times 10^{-7}$ mm.

The self-affine property is also visible in the real space when computing the rms of the height fluctuations over a variable length scale l:

$$\sigma^2(l) = \langle z^2(x, y) \rangle_l - \langle z(x, y) \rangle_l^2. \tag{3}$$

Fig. 4 shows the scaling of the rms of the experimental surface. A self-affine surface shows a scaling of the second moment as: $\sigma(l) = l_r^{1-\zeta} l^{\zeta}$ where the prefactor l_r defines the topothesy of the surface. We estimate $l_r \approx 2 \times 10^{-7}$ mm which is very small. The topothesy corresponds physically to the length scale for which the slope of the surface is one: $\sigma(l_r) = l_r$ [34]. Accordingly the local slope of the surface is always significantly smaller than one for the range of scales that we explored, i.e. from 0.03 to 100 mm, as shown on Fig. 4. It is of interest to note that having an extremely small topothesy is very consistent with a lubrication approximation. Indeed, the topothesy is the length scale for which $l_\parallel \approx t_h$. For scales larger that l_r, one expects $l_h/l_\parallel \ll 1$. Since l_r is very small, at all considered length scales ($l \gg l_r$), the lubrication approximation is valid: $u_h \ll u_\parallel$.

2.4. Synthetic fracture surfaces

The knowledge of the roughness exponent and the topothesy allows the numerical construction of synthetic surfaces [16,18]. Indeed, from the Fourier transform $\tilde{R}(k)$ of a random field or white noise of magnitude $l_r^{1-\zeta}$, it is possible to apply a fractional integration in the Fourier domain by multiplying the Fourier transform by the wavenumber to the power $-1-\zeta$: $\tilde{h}(k) = k^{-1-\zeta} \tilde{R}(k)$ and get a synthetic fracture surface after applying an inverse Fourier transform.

Fig. 5 shows an example of a synthetic surface of size 512×512 with comparable statistical parameters to the

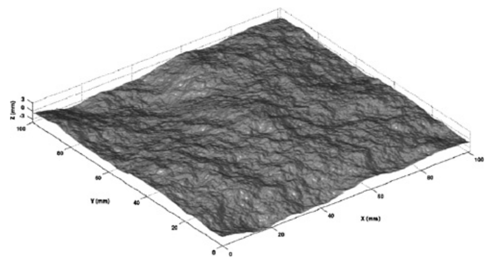

Fig. 5. Synthetic fracture surface (512×512) with a roughness exponent $\zeta = 0.82$ and a topothesy $l_r = 2 \times 10^{-7}$ mm.

measured surface. The height distribution of it is shown in Fig. 2. Mean and root mean square are equal to those of the measured surface.

3. Numerical modeling of a viscous flow

3.1. Stokes flow

As mentioned in the introduction, we limit our study to viscous flow. Extension of the present work to higher Reynolds number will be addressed by a future work.

To study the viscous flow in a rough fracture, we developed a numerical simulation based on the Stokes equation [18,19]. As mentioned earlier, the rough aperture is considered as the void between a rough fracture surface a facing flat plane. In such a case, the height fluctuations of the fracture surface are identical to that of the aperture:

$$a(x,y) = Z(x,y) = z(x,y) + a_{\mathrm{m}}, \tag{4}$$

where $Z(x,y)$ is the height measurement of the topography in the reference frame of the upper flat plane and $z(x,y)$ is the height fluctuations of zero mean ($\langle z(x,y)\rangle_{\text{fracture}} = 0$) and a_{m} is the so-called mechanical aperture which corresponds to the average aperture of the fracture: $\langle a(x,y)\rangle_{\text{fracture}} = a_{\mathrm{m}}$.

As shown in several studies [16,18], if the local aperture $a(x,y)$ is slowly varying (i.e. $\partial_x a \ll 1$), the lubrication approximation is valid. As a consequence, a local cubic law holds for the local flow rate:

$$\mathbf{q}(x,y) = -\frac{a(x,y)^3}{12\eta}\boldsymbol{\nabla} P, \tag{5}$$

where $\mathbf{q}(x,y) = \int_{a(x,y)} \mathbf{v}(x,y,z)\,\mathrm{d}z$ and $\mathbf{v}(x,y,z)$ is the local fluid velocity. In doing so, the problem becomes two dimensional. It can be shown that the local flow rate is conservative: $\boldsymbol{\nabla}\cdot\mathbf{q} = 0$ which leads to the Reynolds lubrication equation that is numerically solved:

$$\boldsymbol{\nabla}\cdot\left(\frac{a(x,y)^3}{12\eta}\boldsymbol{\nabla} P\right) = 0. \tag{6}$$

The pressure field is solved using a finite difference scheme [18] and a bi-conjugated gradient method for the matrix inversion [35]. The pressure field $P(x,y)$ is described on grid twice coarser than the aperture field $a(x,y)$. We reduce the resolution of the measured aperture field to a 1000×1000 resolution by under-sampling because of numerical limitations which slightly reduces the scaling range of the aperture but has no influence on the self-affine property of it. Boundary conditions are defined as follow: a pressure drop ΔP is imposed along the x-axis between the inlet and outlet while no flux exists through the lateral boundaries.

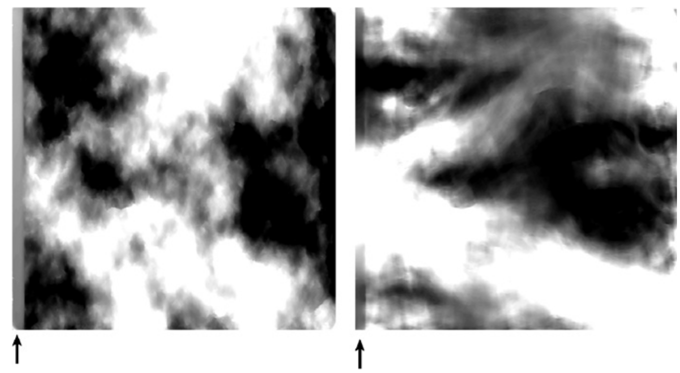

Fig. 6. Left: gray level image of the fracture aperture (white corresponds to large aperture). Right: gray level map of the modulus of the local flux $|\mathbf{q}(x,y)|$ (white is for large flux). The global imposed flux is from left to right. The notch is visible on the left side of the images and marked by an arrow.

The result of the simulation in terms of modulus of the local flux $|\mathbf{q}(x,y)|$ for $a_{\mathrm{m}} = a_{\mathrm{m}}^{\mathrm{c}}$ is shown in Fig. 6. The critical mechanical aperture $a_{\mathrm{m}}^{\mathrm{c}}$ is defined as the smallest mechanical aperture to get only the highest asperity of the rough fracture surface in rigid contact to the facing plane. For the measured rough fracture, $a_{\mathrm{m}}^{\mathrm{c}} = 3.37$ mm.

Fig. 6 compares the aperture fluctuations to the local flux fluctuations. Both sub-images differ in their general aspect: aperture fluctuations show a rich, long range correlated, but isotropic pattern [18]. On the contrary, flux patches are anisotropic and a channeling effect is clearly visible. It is of interest to note that the region of maximum aperture on the upper side of the picture does not correspond to a maximum of the local flux. This shows the importance of large scale properties of the aperture to get extended channel where most of the flux takes place.

We also computed the hydraulic conductivity of the fracture as: $K = \eta Q/\Delta P$ since the system is square ($L_x = L_y$). If a cubic law were holding at large scale for any aperture of the fracture, we would expect the hydraulic conductivity to behave as: $K = a_{\mathrm{m}}^3/12$ where a_{m} is the mechanical aperture. To check the validity of such a large scale cubic law, we plotted in Fig. 7 the ratio $12K/a_{\mathrm{m}}^3$ which should be equal to one for a perfect cubic law. A significant departure from the cubic law is observed at small closure of the fracture ($a_{\mathrm{m}} \approx a_{\mathrm{m}}^{\mathrm{c}}$). Influence of the pressure drop orientation has been explored in [18,19].

3.2. Dominant role of large scale asperities

In comparison to an experimental approach, the numerical modelling allows to study explore with a new path, the role of the fracture roughness on the fluid flow.

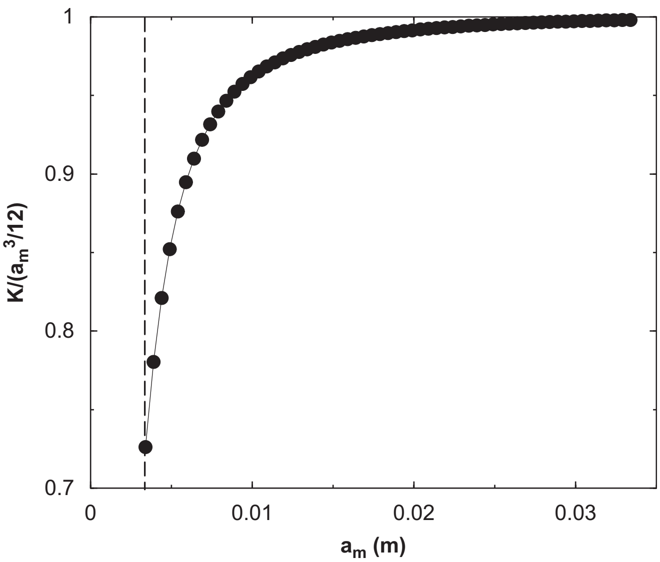

Fig. 7. Ratio of the hydraulic conductivity K and expected hydraulic conductivity from a cubic law $a_{\mathrm{m}}^{3}/12$ as a function of the mechanical aperture a_{m}. The vertical dashed line indicates the aperture at rigid contact $a_{\mathrm{m}}^{\mathrm{c}}$.

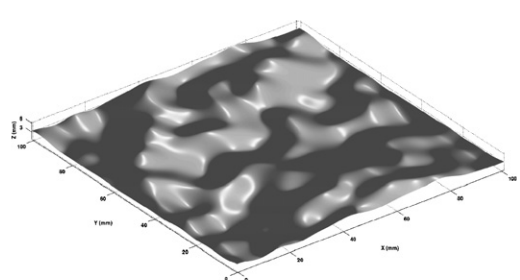

Fig. 8. Example of a low-pass filter applied to the experimental surface. The cutoff frequency is $k_{\mathrm{c}}/k_{\mathrm{min}} = 8$ which corresponds to eight Fourier modes. The height distribution of the surface is shown in Fig. 2.

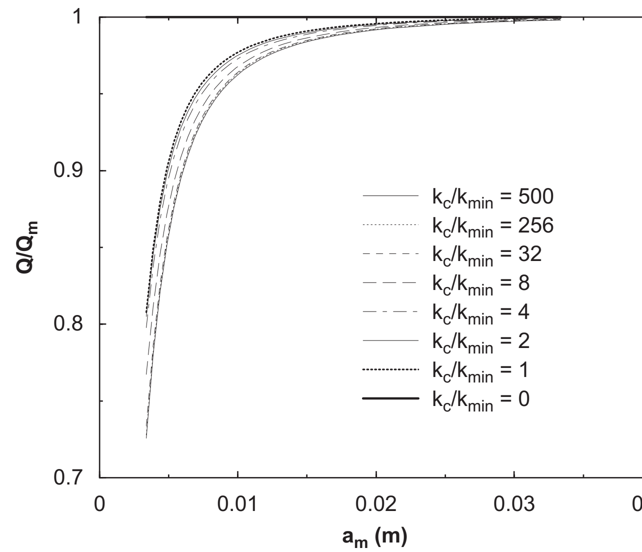

Fig. 9. Evolution of the aperture filtering on the departure to the cubic law. The ratio of the flow rate and the flow rate deduced from the cubic law ($Q_{\mathrm{m}} = a_{\mathrm{m}}^{3}/12\eta\Delta P$) as a function of the mechanical aperture. The aperture is filtered from a low-pass filter in the Fourier domain at $k = k_{\mathrm{c}}$. Only the two first Fourier modes of the aperture field are responsible for most of the departure from the cubic law.

Indeed, it is possible to show that long wavelength modes of the aperture fluctuations are controlling the fluid flux. For this purpose we artificially filtered the aperture field and studied the impact of the filtering on the hydraulic conductivity of the fracture. The filter is applied in the Fourier domain as a low-pass filter. Each modulus of the Fourier transform of the experimental aperture field that has a wavenumber k smaller than a cut-off wavenumber k_{c} is set to zero. An inverse Fourier transform provides a smoothened aperture field as illustrated in Fig. 8 for $k_{\mathrm{c}} = 8k_{\mathrm{min}}$ where k_{min} is the smallest wavenumber of the surface. Therefore only eight Fourier modes in both directions k_x and k_y (i.e. 64 modes in total) are not equal to zero. Note that a direct measurement with a poor spatial resolution could provide similar results but if it were done on a much larger sample to get a large statistics of the large wavenumber topography fluctuations.

We then solve the Stokes equation and search for the evolution of the dimensionless flux Q/Q_{m} where Q_{m} is the expected flux from the cubic law. Fig. 9 shows the effect of the filtering on the flux. It is of interest to see that already for $k_{\mathrm{c}} = 2k_{\mathrm{min}}$ (i.e. two Fourier modes in each direction) which is a very smoothened version of the aperture field, most of the difference with the cubic law is obtained. Then increasing k_{c} provides more and more details of the full response $k_{\mathrm{c}} = 500k_{\mathrm{min}}$. Accordingly, the knowledge of the aperture does not need to be described with a high resolution but it has to be measured on large wavelength. However, the exact value of the contact condition $a_{\mathrm{m}} = a_{\mathrm{m}}^{\mathrm{c}}$ requires a very precise description of the highest asperity.

4. Experimental modelling

To check the validity of the Stokes equation to describe the flow in a rough fracture we conducted laboratory experiments that enable a direct check of the numerical results.

The experimental setup is described in Fig. 10. It consists of a fracture permeameter where the fluid flux is imposed using a peristaltic pump in the range: $0-3\,\mathrm{l\,min}^{-1}$ (similar to the numerical simulations). Pressure difference between the inlet and outlet of the fracture is measured using two piezo-electric Honeywell 24PC sensors at the bottom of the input and output containers. The accuracy of the pressure measurement is 0.2 Pa (i.e. 0.02 mm of water). To get a stabilized measurement (no influence of the pump vibration), the pressure difference is sampled at a 1 Hz frequency during 6 min. The pump is also run 15 min before any measurements to get a thermal equilibrium of the fluid.

In our setup, the mechanical aperture a_{m} is an adjustable parameter. It is set with a precision of 0.2 mm. Indeed, a waterproof connection between the upper Plexiglas plate facing the rough fracture surface and the rest of the setup

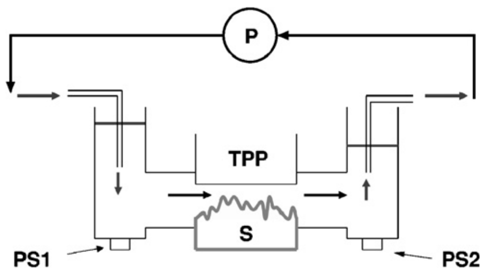

Fig. 10. Sketch of the experimental setup: fracture sample (S), transparent Plexiglas plate (TPP), peristaltic pump (P), pressure sensors (PS1, PS2).

allows a vertical motion of the plate. Two bubble levels ensure parallel positions of the upper plate and the mean fracture plane. Indeed the mean fracture plane has been extracted from the roughness measurement and its crosses with the granite block boundaries, drawn on the block (with an angular resolution of 0.3°). A first bubble level is then attached to this mean fracture plane. A second bubble level is set on the upper Plexiglas plate. The comparison of the two bubble levels ensures the parallel position of the facing interfaces.

We chose a viscous fluid to be at low Reynolds number (i.e. laminar Stokes flow). Accordingly we used a glycerol/water mixture (90%/10%). Its density has been measured: $\rho = 1200\,\mathrm{kg\,m^{-3}}$. The kinematic viscosity has also been measured and its sensitivity to temperature: $\eta(T) \approx 0.22 - 5.5\times10^{-3}\,\mathrm{T}$ in $\mathrm{kg\,m^{-1}\,s^{-1}}$ with T in Celsius degree. These parameters are similar to those used in the simulation.

The corresponding Reynolds number can be evaluated as $Re = \rho a_{\mathrm{m}} Q/(La_{\mathrm{m}})/\mu = \rho Q/L\mu$, with $L = 0.1\,\mathrm{m}$ the lateral extent of the fracture, and lies in the range between 0.006 and 0.25 for the fluxes used experimentally, ranging from 6×10^{-7} to $2.5\times10^{-5}\,\mathrm{m^3\,s^{-1}}$. At such Reynolds number below 1, both the Stokes equation and lubrication approximation are expected to be valid [27].

As a first check of the Stokes flow, we checked the reversibility of the flow changing the flux direction for a given mechanical aperture a_{m} (see Fig. 11 that shows the flux Q as a function of the pressure drop ΔP). Twenty different values of the imposed flux are performed providing an accurate estimate of the relationship between flux and pressure drop. The reversibility is very good. It comes to excellent if the influence of the temperature on the viscosity is considered.

As a second check, we plotted similar quantities, Q versus ΔP, but for 10 different experiments for five apertures (two experiments per aperture but changing the flow direction). We see that the linearity between the flux Q and the pressure drop ΔP is fulfilled over the range of explored fluxes. We also confirm the reversibility of the flow from the symmetry of the figures when changing the flow direction (Fig. 12).

Finally we report the obtained ratio of the flux Q and the pressure drop ΔP as a function of the mechanical aperture (see Fig. 13). Twenty four experiments are reported. They were done with a relative error of the translation measurement of 0.25 mm. Since they are performed at slightly different temperatures, a temperature correction has been introduced using the measured temperature sensitivity of the viscosity to estimate the flux at the average temperature of 23.1 °C.

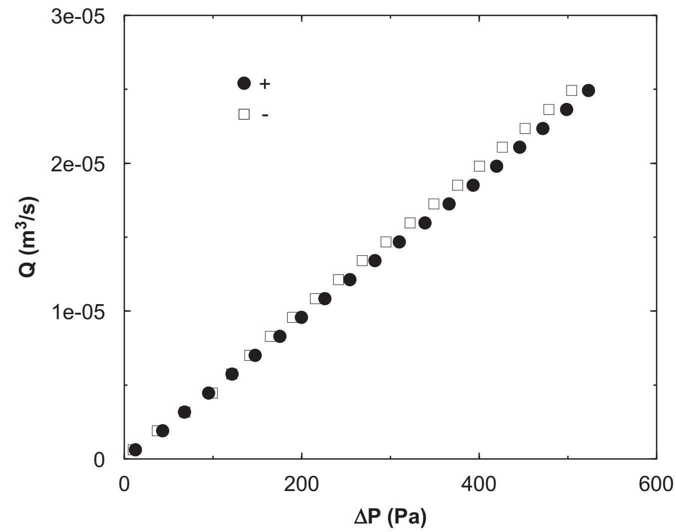

Fig. 11. Reversibility test: The flux Q is plotted versus the pressure drop ΔP between the inlet and the outlet for the minimum possible aperture. Two set of experiments are reported: one for a direction of the flux labelled + and one for the opposite direction of the flux labelled −. No correction for the temperature variation has been introduced though experiments were done with a 0.5 °C temperature difference which correspond to a 3% difference in viscosity. Only the sign of the pressure drop has been changed for experiments in direction −.

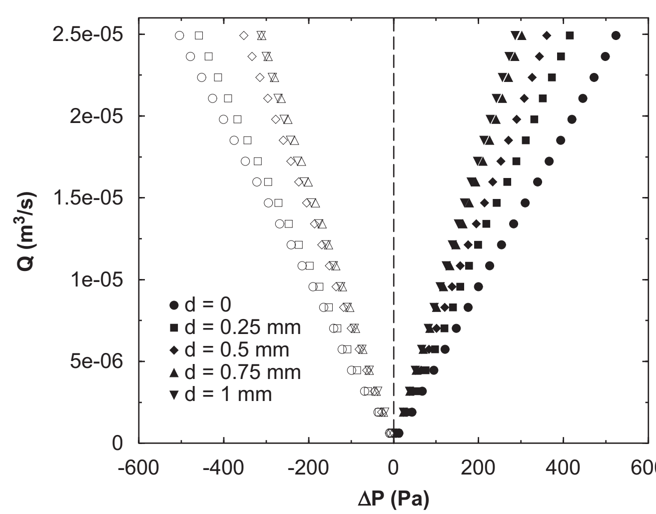

Fig. 12. Influence of the imposed shift d on the flow rate Q versus pressure drop ΔP behavior. For each mechanical aperture $a_{\mathrm{m}} = a_{\mathrm{m}}^{\mathrm{c}} + d$, 20 steps of the imposed flux have been performed (from 6.27×10^{-7} to $2.49\times10^{-5}\,\mathrm{m^3\,s^{-1}}$) in each direction + and −. Only experiments for d between 0 and 1 mm are reported here.

Experimental results show an increase of the ratio hydraulic conductivity $Q/\Delta P$ (which is proportional to the hydraulic conductivity) for an increase of the mechanical

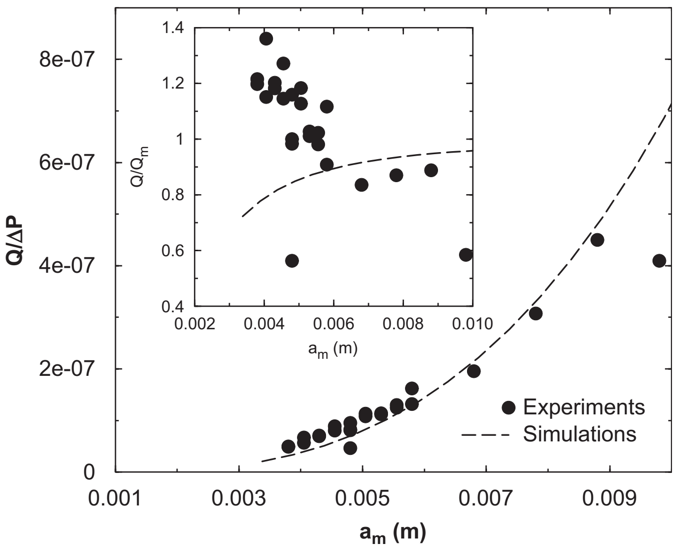

Fig. 13. Comparison between experiments and simulations: evolution of the ratio of the flux $|Q|$ and the pressure difference ΔP for 24 experiments. Experiments have a relative error for a_m^c of 0.25 mm. The critical mechanical aperture obtained from a contact test, has been found to be $a_m^c = 3.8$ mm which is slightly higher than the value obtained from the topography measurement $a_m^c = 3.37$ (i.e. from the measurement of the highest asperity). Simulations were performed for a viscosity $\eta = 0.112\,\mathrm{kg\,m^{-1}\,s^{-1}}$ to get a satisfactory match with absolute experimental data (i.e. slightly higher than the experimentally measured values). Inset shows the ratio Q/Q_m for the same experimental and numerical data.

aperture. At low mechanical aperture, experimental data (i.e. black circles in Fig. 13) exhibit a clear trend and experiments at the same aperture but in opposite flow directions, show very consistent results. For comparison, the results from numerical simulations are added in Fig. 13. They are in good agreement with the experimental results despite the scattering of the experimental data. However the departure from the cubic law being of a small effect with the experimentally explored parameters and owing to the limited quality of the experimental data (i.e. too large error bar on the contact condition, a_m^c), we could not observe clearly the departure as described in the previous numerical section (see inset in Fig. 13).

5. Conclusions

We measured the topography of a fresh fracture surface at very high resolution (almost 16 millions pixels). We confirmed that a self-affine model provides a nice description of the fracture geometry that can be used for many modellings where the fracture geometry might play a significant role: fluid flow, thermal advection and diffusion, chemical interaction like erosion or precipitation, exchange surface measurement, etc.

Fracture roughness is shown to have a significant influence on the flow through its aperture. More precisely we show that only very large wavelengths of the aperture fluctuations control most of the hydraulic conductivity in the limit of a viscous flow and a sufficiently open fracture. This observation suggests that only very coarse-grain measurement of the fracture aperture is required to describe the hydraulic fracture aperture. Indeed we show that only four modes of the Fourier transform of the aperture fluctuations account for most of the departure to the cubic law at small aperture. On the contrary, the knowledge of the mechanical aperture is very much controlled by the measurement of the largest asperities of the fracture topography. Unfortunately the later will be described by the tail of the topography distribution which requires a precise and intense geometrical characterization.

Acknowledgments

We thank Yves Méheust, Grégor Duval, Amélie Neuville and Samuel Maucourant for fruitful discussions. The project has been supported by the European EHDRA program and the french ECCO-PNRH and ECCO-ECOUPREF programs.

References

[1] Neuman S. Trends, prospects and challenges in quantifying flow and transport through fractured rocks. Hydrogeol J 2005;13:124–47.

[2] Bachler D, Kohl T, Rybach L. Impact of graben-parallel faults on hydrothermal convection—rhine graben case study. Phys Chem Earth 2003;28:431–41.

[3] Murphy H. Convective instabilities in vertical fractures and faults. J Geophys Res 1979;84(B11):6121–30.

[4] Glover PWJ, Matsuki K, Hikima R, Hayashi K. Fluid flow in synthetic rough fractures and application to the hachimantai geothermal hot rock test site. J Geophys Res 1998;103(B5):9621–35.

[5] Tournier C, Genthon P, Rabinowicz M. The onset of natural convection in vertical fault planes: consequences for the thermal regime in crystalline basements and for heat recovery experiments. Geophys J Int 2000;140:500–8.

[6] Benderitter Y, Elsass P. Structural control of deep fluid circulation at the soultz hdr site, france: a review. Geotherm Sci Technol 1995;4(4): 227–37.

[7] Evans K, Genter A, Sausse J. Permeability creation and damage due to massive fluid injection into granite at 3.5 km at soultz: I. Borehole observations. J Geophys Res 2005;110(B04203):0–19.

[8] Genter A, Traineau H, Ledésert B, Bourgine B, Gentier S. Over 10 years of geological investigations within the hdr soultz project, france. In: Proceedings of the World geothermal congress 2000. Kyushu-Tohoku; 2000. p. 3707–12.

[9] Fontaine F, Rabinowicz M, Boulègue J. Permeability changes due to mineral diagenesis in fractured crust: implications for hydrothermal circulation at mid-ocean ridges. Earth Planet Sci Lett 2001;184: 407–25.

[10] Zhao C, Hobbs B, Mühlhaus H, Ord A, Lin G. Convective instability of 3-d fluid saturated geological fault zones heated from below. Geophys J Int 2003;155:213–20.

[11] Bodin J, Delay F, de Marsily G. Solute transport in a single fracture with negligible matrix permeability: 2. Mathematical formalism. Hydrogeol J 2003;11:434–54.

[12] Brush D, Thomson N. Fluid flow in synthetic rough-walled fractures: Navier–Stokes, Stokes, and local cubic law simulations. Water Resour Res 2003;39(4):1085.

[13] Brown SR. Fluid flow through rock joints: the effect of surface roughness. J Geophys Res 1987;92:1337–47.

[14] Plourabou F, Kurowski P, Hulin J, Roux S, Schmittbuhl J. Aperture of rough crack. Phys Rev E 1995;51:1675.

[15] Hakami E, Larsson E. Aperture measurements and flow experiments on a single fracture. Int J Rock Mech Min Sci Geomech Abstr 1996;33(4):395–404.
[16] Adler P, Thovert J. Fractures and fracture networks. The Netherlands: Kluwer; 1999.
[17] Méheust Y, Schmittbuhl J. Flow enhancement of a rough fracture. Geophys Res Lett 2000;27:2989–92.
[18] Méheust Y, Schmittbuhl J. Geometrical heterogeneities and permeability anisotropy of rough fractures. J Geophys Res 2001;106(B2):2089–102.
[19] Méheust Y, Schmittbuhl J. Scale effects related to flow in rough fractures. PAGEOPH 2003;160(5&6):1023–50.
[20] Zimmerman R, Al-Yaarubi A, Pain C, Grattoni C. Non-linear regimes of fluid flow in rock fractures. Int J Rock Mech Min Sci 2004;41(3):384.
[21] Al-Yaarubi A, Pain C, Grattoni C, Zimmerman R, Navier–Stokes simulations of fluid flow through a rock fracture. In: Dynamics of fluids and transport in fractured rocks, vol. 162 of AGU Monograph; 2005. p. 55–64.
[22] Schmittbuhl J, Gentier S, Roux S. Field measurements of the roughness of fault surfaces. Geophys Res Lett 1993;20:639–41.
[23] Y. Méheust, Écoulements dans les fractures ouvertes, PhD thesis, Université Paris Sud; 2002.
[24] Schmittbuhl J, Chambon G, Hansen A, Bouchon M. Are stress distributions along faults the signature of asperity squeeze? Geophys Rev Lett 2006;33:L13307.
[25] Gutfraind R, Hansen A. Study of fracture permeability using lattice gas automata. Transp Porous Media 1995;18:131–49.
[26] Qian J, Zhan H, Zhao W, Sun F. Experimental study of turbulent unconfined groundwater flow in a single fracture. J Hydrol 2005;311: 134–42.
[27] Zimmerman RW, Bodvarsson GS. Hydraulic conductivity of rock fractures. Transp Porous Media 1996;23:1–30.
[28] Renard F, Schmittbuhl J, Gratier JP, Meakin P, Merino E. The three-dimensional roughness of stylolites in limestones. J Geophys Res 109 (2004) 10.1029/2003JB002555.
[29] Bouchaud E, Lapasset G, Planés J. Fractal dimension of fractured surfaces: a universal value? Europhys Lett 1990;13:73–9.
[30] Schmittbuhl J, Schmitt F, Scholz C. Scaling invariance of crack surfaces. J Geophys Res 1995;100:5953–73.
[31] Santucci S, Mathiesen J, Måløy KJ, Hansen A, Schmittbuhl J, Vanel L, Delaplace A, Bakke JØH, Ray P. Statistics of fracture surfaces. Phys Rev E 2007;75:016104.
[32] Brown SR, Scholz CH. Broad bandwidth study of the topography of natural rock surfaces. J Geophys Res 1985;90:12575–82.
[33] Bouchaud E. Scaling properties of cracks. J Phys Cond Matter 1997;9:4319–44.
[34] Simonsen I, Vandembroucq D, Roux S. Wave scattering from self-affine surfaces. Phys Rev E 2000;61:5914–7.
[35] Press WH, Teukolsky SA, Vetterling WT, Flannery BP. Numerical recipies. New York: Cambridge University Press; 1992.

EC Contract SES6-CT-2003-502706

PARTICIPANT ORGANIZATION NAME: CNRS

Synthetic 2nd year report

Related with Work Package…………

HYDRO-THERMAL FLOW IN A ROUGH FRACTURE

A. Neuville, R. Toussaint, J. Schmittbuhl

**Institut de Physique du Globe de Strasbourg, CNRS-UMR7516, 5 rue René Descartes, 67084 Strasbourg Cedex*

e-mail: Jean.Schmittbuhl@eost.u-strasbg.fr

ABSTRACT

Heat exchange during laminar flow is studied at the fracture scale on the basis of the Stokes equation. We used a synthetic aperture model (a self-affine model) that has been shown to be a realistic geometrical description of the fracture morphology. We developed a numerical modelling using a finite difference scheme of the hydrodynamic flow and its coupling with an advection/conduction description of the fluid heat. As a first step, temperature within the surrounding rock is supposed to be constant. Influence of the fracture roughness on the heat flux through the wall, is estimated and a thermalization length is shown to emerge. Implications for the Soultz-sous-Forêts geothermal project are discussed.

INTRODUCTION

The modelling of the fluid transport in low permeable crustal rocks is of central importance for many applications (Neuman, 2005). Among them is the monitoring of the geothermal circulation in the project of Soulz-sous-Forêts, France (Bachler et al, 2003). The transit time of the water into the main fractures between injection and extraction wells has to be carefully estimated in order to provide precise estimates of the experiment duration. Water flux controls both the heat transfer to the fluid and the cooling of the massif (Murphy, 1979; Glover et al, 1998; Tournier et al, 2000). As shown from previous studies (Benderitter and Elsass, 1995; Tournier et al, 2000) only a few important fractures are controlling the fluid exchange between wells. Accordingly the study of the flow within a single fracture appears of central interest. It is also important for large scale numerical simulations of the convective circulation in the massif (Fontaine et al, 2001; Zhao et al, 2003). Up to now, only very simple models for fractures, like the parallel plates model, have been considered, ignoring the impact of the fracture morphology on the fracture transmitivity (Tournier et al, 2000).

In this study, we are interested in the influence of a realistic geometry of the fracture on its hydro-thermal response. Several studies have addressed the permeability of rough fractures (Brown, 1987; Plouraboué et al, 1995; Hakami and Larsson, 1996; Adler and Thovert, 1999; Méheust and Schmittbuhl, 2000, 2001, 2003). Our goal is to show that realistic fracture morphology can be introduced as a perturbation of the parallel plate model and have a strong influence on the heat transport properties even in the limit of laminar flow.

MODEL DESCRIPTION

Aperture model

A self-affine surface is a possible geometrical model for roughness topographies of fractures as shown in several previous studies (Brown and Scholz, 1985; Schmittbuhl et al, 1993; Schmittbuhl et al, 1995, Bouchaud, 1997). Self-affinity is a scaling invariance property that reads as: $x \to \lambda x$, $y \to \lambda y$, $z \to \lambda^{\zeta} z$ where λ is a scaling factor and ζ is the roughness exponent. As can be seen the scaling transformation is supposed to be isotropic within the mean plane *(x,y)* since the scaling factors are the same along *x* and *y* axes. The scaling factor, (λ) is not the same along the mean plane *(x,y)* and the out of plane direction *z,* (λ^{ζ}). For the latter direction, the roughness exponent ζ describes how anisotropic is the property. Figure 1 shows an example of a synthetic self-affine aperture field *a(x,y)*. In this case, the aperture defined as the volume between two facing fracture surfaces, is also self-affine (Méheust and Schmittbuhl, 2003).

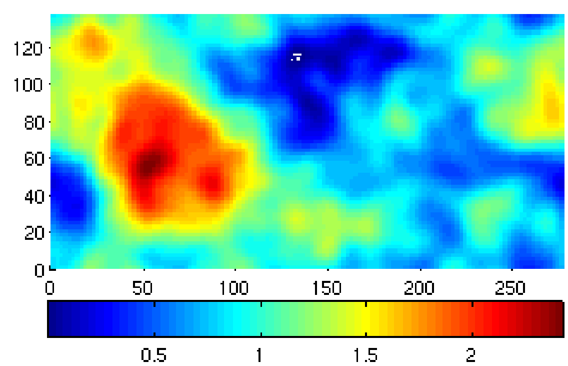

Figure 1: Sample of a synthetic self-affine aperture field a(x,y) (in mm): red corresponds to largest apertures and blue to quasi-closed areas. The rms of the aperture field is 0.46mm.

Fluid flow model

To study the viscous flow in a rough fracture, we developed a numerical simulation based on the Stokes equation for low Reynolds number (Méheust and Schmittbuhl, 2001; 2003):

$$\vec{\nabla} P = \eta \Delta \vec{v}$$

where *P* is the fluid pressure, η the fluid viscosity and *v* the Eulerian fluid velocity.

In the limit of small aperture variations ($\|\vec{\nabla} a\| \ll 1$) , the lubrication approximation might hold and the local flux per unit length is then related to the local pressure gradient:

$$\vec{u} = -\frac{a^3}{12\,\eta}\vec{\nabla} P$$

This leads to the Reynolds equation which is a two dimensional approximation of the local flux within the fracture aperture:

$$\vec{\nabla}.(a^3 \vec{\nabla} P) = 0$$

We used a finite difference scheme to solve the Reynolds equation with a conjugated gradient method. Precision was set to 10^{-15}. Figure 2 shows the result of the computation for the aperture field shown in Fig. 1 when the fluid is injected from the left side. Upper and lower boundary are closed. The fracture is supposed to be horizontal.

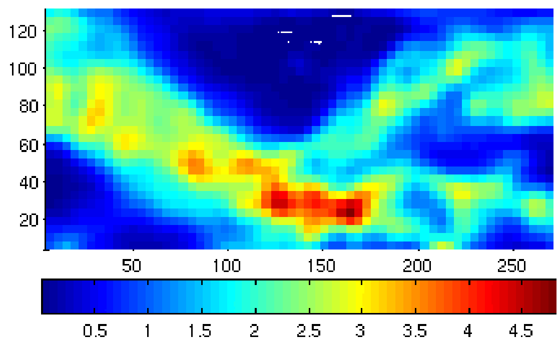

Figure 2: Map of the normalized local flux for the aperture field shown in Fig. 1. Red areas correspond to maximum fluxes and blue regions to immobile zones.

It is of important to note the strong channelling of the flow which is induced by the fracture roughness. Despite isotropic aperture fluctuations along the mean fracture plane, as shown in Fig. 1, most of the flow occurs in a significant sub-part of the fracture. This localization of the flow stems from the long range correlations included in the aperture fluctuations. A direct consequence is the clear separation between hydraulically active and inactive zones with a non-direct mapping between aperture magnitude and local flux. In other terms, at a mesoscopic scale, mechanical and hydraulical apertures might strongly differ even if the average aperture is well defined and constant over the whole fracture.

Heat flow model

We include heat flow in our modelling to describe the temperature field within the fracture when the fluid is injected at a different temperature from the surrounding rock. T_0 is the temperature of the fluid at the inlet of the fracture and T_w is that of the rock. As a first step in our modelling, we assume the temperature of the rock to be homogeneous. We also consider a stationary condition.

Conduction describes the heat flow between two regions of different temperature and fulfills the Fourier law: $\vec{q} = -\lambda \vec{\nabla} T$ that relates linearly the heat flux *q* and the temperature gradient by the mean of the thermal conductivity λ. Convection is due to fluid motion and it is described by the estimate of the advected heat. From the energy conservation law (Landau and Lifchitz, 1994), conduction effects balance convective effects and the local temperature within the fluid fulfills:

$$\chi \Delta T = \vec{v}.\vec{\nabla} T$$

where *v* is the fluid velocity and χ the thermal diffusivity.

For the fluid flow modelling we based our approach on the lubrication approximation which relies on an averaging procedure over the thickness of the aperture. Similarly, we propose a "thermal lubrication" approximation which is based on the average of the temperature over the fracture thickness, weighted by the local fluid velocity:

$$\bar{T}(x,y) = \frac{\int_a v(x,y,z)\,T(x,y,z)\,dz}{\int_h v(x,y,z)\,dz}$$

We also introduce the Nusselt number $Nu = -j_w / q_{ref}$ which compares, when no convection holds, two estimates of the conductive flux: the local flux at the boundary of the fracture $j_w = -\lambda \left(\frac{\partial T}{\partial z}\right)_{z=a/2}$ and the mesoscopic flux at the fracture thickness scale $q_{ref} = \lambda \frac{T_w - \bar{T}}{a}$.

Finally, assuming that the horizontal conduction is negligible when compared to the vertical conduction and that the vertical convection is limited, the local average temperature $\bar{T}(x,y)$ is obtained from the following equation:

$$a\bar{\vec{v}}.\vec{\nabla}\bar{T} + 2\frac{\chi}{a}Nu(\bar{T} - T_w) = 0$$

We discretized this equation using a first order finite difference scheme and solved it using also a conjugated gradient method. Fig. 3 shows the fluid temperature field for the fracture aperture described in Fig. 1 and in horizontal position. The cold fluid is injected from the left side within the fracture which is assumed to be embedded in hot rock at a homogeneous temperature.

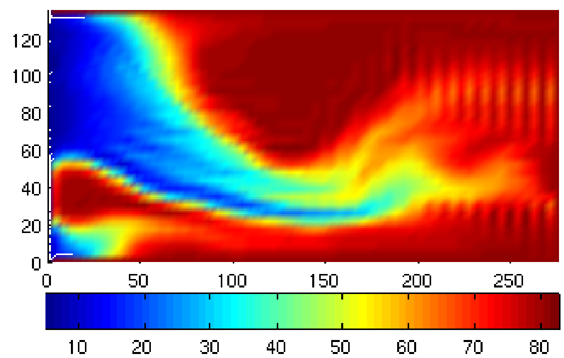

Figure 3: Map of the normalized temperature within the fracture shown in Fig. 1. The surrounding rock is hotter than the injected fluid. Low temperature zones are in blue and hot zones in red.

The channelling effect of the temperature field is very significant and directly related to the channelling of the fluid flow (for a convection dominated regime). Accordingly the temperature is far from homogeneous in the fracture though its aperture is constant on average. It therefore emphasizes the importance of aperture fluctuations on the heat exchange between the cold fluid and the hot rock.

Influence of the fracture roughness can be monitored from the comparison with the parallel plate case with the same average aperture, *i.e.* same mechanical aperture. The temperature profile along the fluid flow direction (x direction) can be analytically computed in the case of parallel plate boundary conditions. It reads as:

$\bar{T} - T_w = (T_0 - T_w)\exp(-x/l_{ref})$ where $l_{ref} = \frac{Pe}{Nu}$.

The Peclet number is defined as: $Pe = \frac{\bar{v}\, a}{2\chi}$. Therefore a characteristic length exists in the problem: l_{ref}. It describes the typical length scale for the fluid to be in thermal equilibrium with the surrounding rock. Accordingly this is a thermalization length. Figure 4 shows the temperature profile for the parallel plate model and its comparison with profiles for rough fractures. It is of interest to note that rough fractures still show a similar trend but the thermalization length is significantly larger (smaller increase of the temperature within the fracture). In other words, cold fluid migrates further into the fracture in the rough case compared to the parallel plate case owing to the channeling effect.

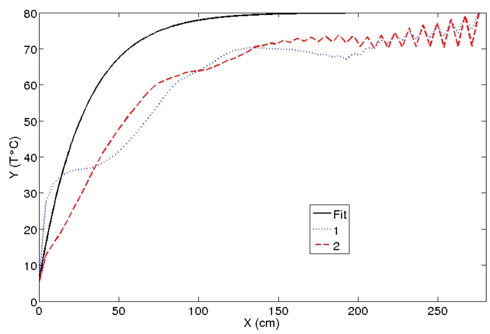

Figure 4: Temperature profiles (T(x)) for the parallel plate case (exponential curve in black) and two different synthetic fractures (blue and red curves).

At large scales, numerical oscillations emerge which stems from a too loose spatial discretization of the thermalization length scale.

CONCLUSIONS

We propose a numerical model to estimate the heat exchange at the fracture scale between a cold fluid and hot surrounding rock. The numerical model is based on a lubrication approximation for the fluid flow and a "thermalization lubrication" approximation for the temperature evolution. Gravity is neglected since we are dealing with horizontal fractures but could be included from a redefinition of the pressure to include hydrostatic contributions.

Our model shows that fracture roughness is responsible for channelling effects. Fluid flow is dominant in a significant subpart of the fracture where head advection is important. Accordingly, temperature distribution is strongly affected by small fluctuations of the fracture aperture.

On-going work addresses implications for the Soultz-sous-Forêts HDR project where large sub-horizontal fractures are controlling the fluid transfer from the injection well (GPK3) and the extraction wells (GPK2 and GPK4). For this purpose we link our fracture model to a large scale dipolar model of the fluid flow.

REFERENCES

Adler, P., Thovert, J., (1999). Fractures and Fracture Networks. Kluwer academic publishers, The Netherlands.

Bachler, D., Kohl, T., Rybach, L., (2003). Impact of graben-parallel faults on hydrothermal convection - rhine graben case study. *Phys. Chem. Earth* **28**, 431-441.

Benderitter, Y., Elsass, P., (1995). Structural control of deep fluid circulation at the soultz hdr site, france: a review. *Geotherm. Sci. Technol.* **4** (4), 227-237.

Bouchaud, E., (1997). Scaling properties of cracks. *J. Phys.: Cond. Matter* **9**, 4319-4344.

Brown, S.R., (1987). Fluid flow through rock joints: the effect of surface roughness. *J. Geophys. Res.* **92**, 1337-1347.

Brown, S.R., Scholz, C.H., (1985). Broad bandwidth study of the topography of natural rock surfaces. *J. Geophys. Res.* **90**, 12575-12582.

Fontaine, F., Rabinowicz, M., Boulègue, J., (2001). Permeability changes due to mineral diagenesis in fractured crust: implications for hydrothermal circulation at mid-ocean ridges. *Earth Planet. Sci. Lett.* **184**, 407-425.

Glover, P.W.J., Matsuki, K., Hikima, R., Hayashi, K., (1998). Fluid flow in synthetic rough fractures and application to the hachimantai geomthermal hot rock test site. *J. Geophys. Res.* **103** (B5), 9621-9635.

Hakami, E., Larsson, E., (1996). Aperture mearurements and flow experiemnts on a single fracture. *Int. J. Rock Mech. Min. Sci. & Geomech.* Abstr. **33** (4), 395-404.

L. Landau E. Lifchitz, (1994). Physique théorique mécanique des fluides, 3rd ed.

Méheust, Y., Schmittbuhl, J., (2000). Flow enhancement of a rough fracture. *Geophys. Res. Lett.* **27**, 2989-2992.

Méheust, Y., Schmittbuhl, J., (2001). Geometrical heterogeneities and permeability anisotropy of rough fractures. *J. Geophys. Res.* **106** (B2), 2089-2102.

Méheust, Y., Schmittbuhl, J., (2003). Scale effects related to flow in rough fractures. *PAGEOPH* **160** (5-6), 1023-1050.

Murphy, H., (1979). Convective instabilites in vertical fractures and faults. *J. Geophys. Res.* **84** (B11), 6121-6130.

Neuman, S., 2005. Trends, prospects and challenges in quantifying flow and transport through fractured rocks. *Hydrogeol. J.* **13**, 124-147.

Plouraboué, F., Kurowski, P., Hulin, J., Roux, S., Schmittbuhl, J., (1995). Aperture of rough crack. *Phys. Rev. E* **51**, 1675.

Schmittbuhl, J., Gentier, S., Roux, S., (1993). Field measurements of the roughness of fault surfaces. *Geophys. Res. Lett.* **20**, 639-641.

Tournier, C., Genthon, P., Rabinowicz, M., (2000). The onset of natural convection in vertical fault planes: consequences for the thermal regime in cristalline basements and for heat recovery experiments. *Geophys. J. Int.* **140**, 500-508.

Zhao, C., Hobbs, B., Mühlhaus, H., Ord, A., Lin, G., (2003). Convective instability of 3-d fluid saturated geological fault zones heated from below, Geophys. J. Int. 155, 213-220.

Fracture of disordered solids in compression as a critical phenomenon. I. Statistical mechanics formalism

Renaud Toussaint* and Steven R. Pride†
Géosciences Rennes, Université de Rennes 1, 35042 Rennes Cedex, France

(Received 14 November 2001; revised manuscript received 13 June 2002; published 27 September 2002)

This is the first of a series of three articles that treats fracture localization as a critical phenomenon. This first article establishes a statistical mechanics based on ensemble averages when fluctuations through time play no role in defining the ensemble. Ensembles are obtained by dividing a huge rock sample into many mesoscopic volumes. Because rocks are a disordered collection of grains in cohesive contact, we expect that once shear strain is applied and cracks begin to arrive in the system, the mesoscopic volumes will have a wide distribution of different crack states. These mesoscopic volumes are the members of our ensembles. We determine the probability of observing a mesoscopic volume to be in a given crack state by maximizing Shannon's measure of the emergent-crack disorder subject to constraints coming from the energy balance of brittle fracture. The laws of thermodynamics, the partition function, and the quantification of temperature are obtained for such cracking systems.

DOI: 10.1103/PhysRevE.66.036135 PACS number(s): 62.20.Mk, 46.50.+a, 46.65.+g, 64.60.Fr

I. INTRODUCTION

When rocks and other disordered-solid materials are in compression and then have an additional deviatoric strain applied to them, small stable cracks irreversibly appear at random throughout the material. Each time the deviatoric strain is increased, more cracks appear. In the softening regime following peak stress, a sample will unstably fail along a plane localized at an angle relative to the principal-stress direction. We have accumulated evidence suggesting that such localization is a continuous phase transition.

This is the first of three articles that develops a statistical mechanics that allows the possible phase transitions in a cracking solid to be investigated. Many studies have assumed that, fracture is a thermally-activated process and have used a statistical mechanics based on thermal fluctuations [1–5]. However, our interest here is with "brittle fracture" in which cracks appear irreversibly and in which thermal fluctuations play no role. For this problem, the statistics of the fracture process is entirely due to the initial quenched disorder in the system.

A considerable literature has developed for so-called "breakdown" phenomena in systems having quenched disorder and zero temperature [6–23]. In particular, the burned-fuse [6–8], spring-network [9–11] and fiber-bundle [12–17] analog models for fracture have all been shown to yield various types of scaling laws prior to the point of breakdown [18–23]. Our work is different in that we directly treat the fracture problem (not an analog model of it) assuming that all of the statistics is due to quenched disorder. We obtain the probability of emergent damage states by maximizing Shannon's entropy subject to appropriate constraints. This approach has recently been proven exact in the special case of fiber bundles [24].

The principal conclusion of our present theory is that at a critical-strain point, there is a continuous phase transition from states where cracks are uniformly distributed to states where coherently oriented cracks are grouped into conjugate bands. Several facts justify classifying such band formation as a critical phenomenon.

First, the localization of the cracks into bands spontaneously breaks both the rotational and translational symmetries of the material even though our model Hamiltonian preserves these same symmetries. The entropy of the material remains continuous and the ensemble of the most probable states becomes degenerate at the localization transition; i.e., prior to localization, the most probable state is the intact state, while right at the transition, certain banded states acquire the same probability as the intact state. Further, an autocorrelation length associated with the aspect ratio of the emergent-crack bands diverges in the approach to the critical point. Unfortunately, quantitative laboratory measurements of how the bands of cracks coalesce and evolve in size and shape prior to the final localization point do not presently exist. We speculate in the third article of this series on how such measurements might be performed.

Our explanation of localization based on the physics of interacting cracks is distinct from the bifurcation analysis of Rudnicki and Rice [25] in which localization is a consequence of a proposed phenomenological elasto-plasticity law. Our work provides a method for obtaining such a plasticity law from the underlying physics.

II. THE PROBABILISTIC NATURE OF THE FRACTURE PROBLEM

Rocks are a disordered collection of grains in cohesive contact. The grains have varying shapes and sizes with typical grain sizes in the range of 10–100 μm but sometimes considerably larger. The contacts between the grains are generally weaker than the grains themselves and have strengths and geometries that vary from one contact to the next. When deviatoric (i.e., shear) strain is applied to a rock, grain con-

*Present address: Department of Physics, University of Oslo, P.O. Box 1048 Blindern, 0316 Oslo 3, Norway. Email address: Renaud.Toussaint@fys.uio.no
†Email address: Steve.Pride@univ-rennes1.fr

tacts begin to break. In what follows, a broken grain contact will be called a "crack." Such a break is a stress-activated irreversible process. Once a grain contact is broken, there is no significant healing that occurs. Cracks are not arriving and disappearing due to thermal fluctuations. This fact makes our definition of statistical ensembles quite different from that in the usual application of statistical mechanics to molecular systems, as we now go on to discuss.

A. Creating a statistical ensemble

We imagine dividing a huge (formally infinite) system into mesoscopic volumes that will be called "mesovolumes." Because the materials of interest here have a wide range of grain-scale disorder, many different crack states will emerge in the various mesovolumes once energy has been put into the system and cracking begins. These various mesovolumes and the crack states they contain comprise the ensembles in our theory.

In order to be specific with our ideas, we now introduce a simple model of the initial disorder and emergent-crack states. The purpose of this special model in the present paper is to motivate how ensembles are formed; however, the model Hamiltonian developed in Paper II will be based upon it.

In the model, each mesovolume is divided into N identical cells, where a cell has dimensions on the order of a grain size and where N is a large number such as 10^{2D} or more with D the system's dimension. In each cell, only a single grain contact is allowed to break. The local order parameter (explicitly defined in Paper II) characterizes both the orientation and the length of such a broken grain contact. In the present paper, an order-parameter description is not yet necessary. Prior to breaking, all cells are assumed to have the same elastic moduli.

The quenched disorder is in how the grain-contact breaking energy $\mathcal{E}(\boldsymbol{x})$ is distributed in the cells $\boldsymbol{x}$ of a mesovolume. We assume that only a fraction of the nominal grain-contact area is actually cemented together, and that the degree of cementation from one contact to the next is random. Thus, the breaking energies $\mathcal{E}(\boldsymbol{x})$ are random variables independently sampled from a distribution $\pi(\mathcal{E})$ having support on $[0,\Gamma d^{D-1}]$ where Γ is the surface-energy density of the mineral, d is the nominal linear dimension of a grain contact, and d^{D-1} is the grain-contact area in D dimensions. The quenched-disorder distribution $\pi(\mathcal{E})$ can have any assumed form.

We now define an infinite collection of distinct mesovolumes by allowing for every conceivable way that $\mathcal{E}(\boldsymbol{x})$ may be distributed in a mesovolume. Putting this collection together forms the infinite rock mass whose properties we are interested in determining. Each mesovolume so defined is a deterministic system and upon slowly applying the same strain tensor $\boldsymbol{\varepsilon}$ to all the mesovolumes, each will undergo a deterministic cracking scenario and end up in a well-defined crack state. We denote each of the possible final crack states with an index j. A principal goal of the present paper is to obtain the occupation probabilities p_j of these various crack states that are simply the fraction of the mesovolumes in the system that are in the state j.

We can understand how the various crack states emerge by appealing to a form of Griffith's [26] criterion. A cell will break only if the change in the elastic energy due to the break is greater than or equal to the bond-breaking energy $\mathcal{E}(\boldsymbol{x})$. If $\mathbf{C}_a$ is the effective elastic-stiffness tensor of the entire mesovolume that holds after the break occurs and if $\mathbf{C}_b$ is the stiffness tensor that held before the break, Griffith's criterion can be stated,

$$\ell^D \boldsymbol{\varepsilon}:(\mathbf{C}_b-\mathbf{C}_a):\boldsymbol{\varepsilon}/2>\mathcal{E}, \tag{1}$$

where $\boldsymbol{\varepsilon}$ is the strain tensor characterizing the entire mesovolume at the moment of the break and ℓ^D is the volume of a mesovolume. This particular statement is an approximation based on an assumed linear elasticity and absence of residual strain after unloading, but a general statement will be derived in Sec. III B. Since the mesovolume with an extra crack is more compliant than without it, the weakest cells will begin to break even after the slightest of applied strain.

Yet an emergent-crack state is not just a trivial consequence of the $\mathcal{E}(\boldsymbol{x})$ distribution in a mesovolume. Cracks aligned along bands concentrate stress allowing even large barriers $\mathcal{E}(\boldsymbol{x})$ to be overtaken along the band. In the present model, this means that placing cracks along bands produces a larger change in the elastic moduli of the mesovolume than placing cracks in more random positions. Thus, at least above some applied strain level, we expect the banded states to emerge as the ones that are significantly present in a rock system. Nonbanded states at large strain are much more special. They can come only from mesovolumes in which the weak cells making up the state are all surrounded by strong cells.

A key idea here is that each mesovolume embedded in the system experiences the same global strain tensor and, as such, has a crack state statistically independent from the other mesovolumes. This is only valid so long as the emergent bands of organized cracks have a dimension ξ that is small relative to the size ℓ of the mesovolume. Screening effects due to destructive strain interactions between incoherently oriented cracks cause the far-field strain from a local crack structure to fall off with distance r even more rapidly than the $(\xi/r)^D$ fall off in an uncracked material. But even in the thermodynamic limit of infinite system sizes, the required statistical independence of the mesovolumes breaks down right at the critical strain where divergent bands of cracks become important. The conclusion is that although our ensemble-based statistics is valid in the approach to localization, it is incapable of describing the post-localization physics.

B. Macroscopic observables

In the laboratory experiments to which we apply our theory, a sample is immersed in a reservoir from which either uniform stress or strain conditions can be applied to the sample's exterior surface $\partial\Omega$. The macroscopic strain tensor $\boldsymbol{\varepsilon}$ is defined in terms of the displacement $\mathbf{u}$ at points on $\partial\Omega$ as

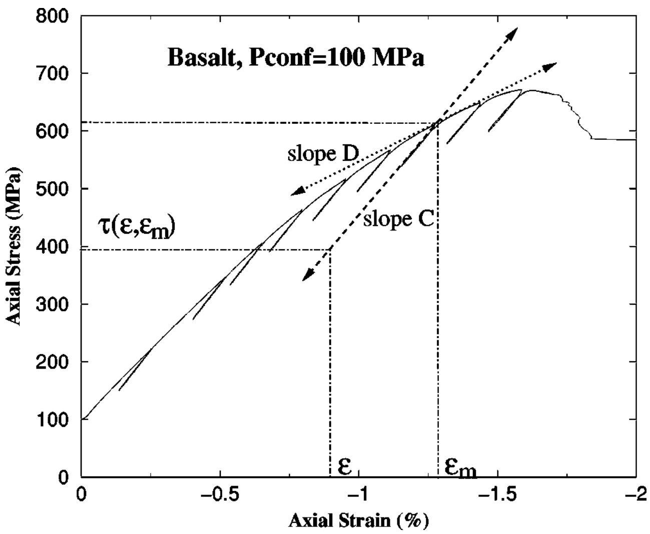

FIG. 1. Stress-strain data courtesy of David Lockner of the USGS Menlo Park. The slope measured upon loading a sample is defined by **D** while that measured upon unloading and/or reloading the sample is defined by **C**.

$$\boldsymbol{\varepsilon}=\frac{1}{L^D}\int_{\partial\Omega}\mathbf{n}\mathbf{u}\,dS \tag{2}$$

where **n** is the outward normal to the sample's surface and L^D is the volume of the sample in D dimensions. This definition of deformation thus corresponds to the volume average of the local deformation tensor $\nabla\mathbf{u}(\boldsymbol{x})$ defined at interior points $\boldsymbol{x}$ of the sample. It will soon be shown to be conjugate to the macroscopic stress tensor $\boldsymbol{\tau}$ in the expression for the work carried out on the sample. If strain (rather than stress) is the control variable, the displacements at points $\boldsymbol{x}$ of the external surface $\partial\Omega$ are given by $\mathbf{u}=\boldsymbol{x}\cdot\boldsymbol{\varepsilon}$.

As shown in Fig. 1, a typical compression experiment starts with the sample in a pure hydrostatic pressure state and then systematically increases the deformation in the axial direction, keeping the radial "confining" pressure p_c constant. Other ways of controlling the radial stress during the experiment are to keep a constant ratio between axial and radial stress, or to impose a constant radial deformation. So long as the confining pressure does not become so large as to induce a brittle-to-ductile transition [28], these various experiments all result in the same type of localized structure at large axial strains. When axial strain is monotonically increased, cracks arrive at each strain increment and the deformation and stress changes are related as

$$d\boldsymbol{\tau}=\frac{d\boldsymbol{\tau}}{d\boldsymbol{\varepsilon}}:d\boldsymbol{\varepsilon}=\mathbf{D}:d\boldsymbol{\varepsilon}, \tag{3}$$

where the fourth-order tensor **D** is called the tangent-stiffness tensor. This tensor defines the slopes between the various stress and strain components as the sample is being loaded and is an experimental observable.

If at some point in the stress history the axial pressure is reduced, we follow a different deformation path as seen in the figure due to the fact that no new cracks are created. Such an unloading experiment defines the elastic (or secant) stiffness tensor **C**,

$$d\boldsymbol{\tau}=\mathbf{C}:d\boldsymbol{\varepsilon}. \tag{4}$$

We model the unloading/reloading paths as being entirely reversible and in so doing neglect the small hysteresis due to friction along the opened cracks.

In order to distinguish loading paths (with crack creation) from unloading paths (without crack creation), all properties are explicitly taken to depend on two strain variables; namely, the maximum strain $\boldsymbol{\varepsilon}_m$ having been applied to a sample, and the current strain $\boldsymbol{\varepsilon}$ that is different than the maximum only if the sample has been subsequently unloaded. Note that even if $\boldsymbol{\varepsilon}$ and $\boldsymbol{\varepsilon}_m$ are written as tensors, they each correspond to only one scalar degree of freedom along the loading/unloading paths, since the radial components can always be expressed in terms of the axial components via the type of radial control employed (e.g., $p_c=\text{const}$ in a standard triaxial test).

The stress tensor $\boldsymbol{\tau}$ corresponds to the volume average of the local stress tensor $\mathbf{T}(\boldsymbol{x})$ that satisfies $\nabla\cdot\mathbf{T}(\boldsymbol{x})=\mathbf{0}$ at interior points $\boldsymbol{x}$; i.e., $\boldsymbol{\tau}=L^{-D}\int_\Omega\mathbf{T}(\boldsymbol{x})dV$ and is a function of the current and maximum strains $\boldsymbol{\tau}=\boldsymbol{\tau}(\boldsymbol{\varepsilon},\boldsymbol{\varepsilon}_m)$ as shown in Fig. 1. By averaging the elastostatic identity $\nabla\cdot(\mathbf{T}\boldsymbol{x})=\mathbf{T}$ over the mesovolume we further have that $\boldsymbol{\tau}=L^{-D}\int_{\partial\Omega}\mathbf{n}\cdot\mathbf{T}\boldsymbol{x}dS$.

The work density dU performed on the sample when there is an increment in strain $d\boldsymbol{\varepsilon}$ is in both cases of loading and unloading

$$dU=\frac{1}{L^D}\int_{\partial\Omega}\mathbf{n}\cdot\mathbf{T}\cdot d\mathbf{u}\,dS \tag{5}$$

$$=\boldsymbol{\tau}:d\boldsymbol{\varepsilon}. \tag{6}$$

To obtain Eq. (6) from (5), we have written the controlled displacements on a sample's surface as $d\mathbf{u}=\boldsymbol{x}\cdot d\boldsymbol{\varepsilon}$ where the strain increment $d\boldsymbol{\varepsilon}$ is uniform over $\partial\Omega$. Thus, dU corresponds to the volume average of the local work density $\mathbf{T}(\boldsymbol{x}):d\nabla\mathbf{u}(\boldsymbol{x})$.

The total energy U per unit sample volume that goes into the sample during the loading up to a maximum strain tensor $\boldsymbol{\varepsilon}_m$ is then

$$U(\boldsymbol{\varepsilon}_m)=\int_{\boldsymbol{\varepsilon}_0}^{\boldsymbol{\varepsilon}_m}\boldsymbol{\tau}(\boldsymbol{\varepsilon}',\boldsymbol{\varepsilon}'):d\boldsymbol{\varepsilon}', \tag{7}$$

where $\boldsymbol{\varepsilon}_0$ is the strain associated with the initial isotropic stress. If after loading to $\boldsymbol{\varepsilon}_m$, the sample is unloaded back to a current strain of $\boldsymbol{\varepsilon}$, we have the general expression

$$U(\boldsymbol{\varepsilon},\boldsymbol{\varepsilon}_m)=U(\boldsymbol{\varepsilon}_m)+\int_{\boldsymbol{\varepsilon}_m}^{\boldsymbol{\varepsilon}}\boldsymbol{\tau}(\boldsymbol{\varepsilon}',\boldsymbol{\varepsilon}_m):d\boldsymbol{\varepsilon}'. \tag{8}$$

If the sample is unloaded back to the initial stress, corresponding to a possibly nonzero residual strain $\boldsymbol{\varepsilon}^{\text{res}}$, a last experimental observable is the energy $Q(\boldsymbol{\varepsilon}_m)=U(\boldsymbol{\varepsilon}^{\text{res}},\boldsymbol{\varepsilon}_m)$

(per unit sample volume) that went into crack creation and that is lost during the loading process .

C. Ergodic hypothesis

We have shown above that the experimentally measurable variables of energy density U, deformation $\boldsymbol{\varepsilon}$, and applied stress $\boldsymbol{\tau}$ correspond to volume averages of each field throughout a system. Our ergodic hypothesis amounts to assuming that the systems we work with are sufficiently large that such volume averages can be replaced by ensemble averages

$$U=\sum_j p_j E_j, \quad \boldsymbol{\varepsilon}=\sum_j p_j \boldsymbol{\varepsilon}_j, \quad \boldsymbol{\tau}=\sum_j p_j \boldsymbol{\tau}_j. \tag{9}$$

Here, E_j is the average work per unit mesovolume required to take an initially uncracked mesovolume from zero strain to the strain tensor $\boldsymbol{\varepsilon}_j$. A similar definition holds for $\boldsymbol{\tau}_j$. In both the definition of E_j and $\boldsymbol{\tau}_j = dE_j/d\boldsymbol{\varepsilon}_j$, the average is over the initial quenched-disorder distribution.

So long as each mesovolume contains crack states that have no significant influence on the neighboring mesovolumes (formally valid only in the thermodynamic limit), the sum over the collection of mesovolumes (ensemble averaging) is equivalent to a volume integral over the entire system. In practice, we will only ever consider ensembles that have by definition $\boldsymbol{\varepsilon}_j=\boldsymbol{\varepsilon}$; however, we could equivantly immerse each mesovolume in a uniform stress-tensor reservoir and allow $\boldsymbol{\varepsilon}_j$ to vary from state to state.

III. THERMODYNAMICS OF CRACK POPULATIONS

A. Fundamental postulate

The fracture-mechanics problem of counting how many of the initial mesovolumes can be led to the same crack state appears to be hopelessly intractable. Fortunately, it also appears to be unnecessary for systems containing initial quenched disorder. Upon putting deviatoric strain energy into such a system, the emergent-crack states j will, on the one hand, attempt to mirror this quenched disorder with weakest cells breaking first; however, due to the energetics of the crack interactions, many different types of initial mesovolumes may be led to the same crack state which results in nonuniform crack-state probabilities p_j even if the quenched-disorder distribution is uniform.

We state our fundamental postulate as follows: *The probability p_j of observing a mesovolume to be in crack state j can be determined by maximizing Shannon's [27] measure of disorder*

$$S=-\sum_j p_j \ln p_j, \tag{10}$$

subject to constraints involving the macroscopic observables that derive from the energetics of the fracture mechanics. That entropy is to be maximized can be expected since the quenched disorder allows all states to be present in a sufficiently large system. In recent work [24], we have demonstrated that this postulate yields exact results for the special case of fiber bundles with global-load sharing.

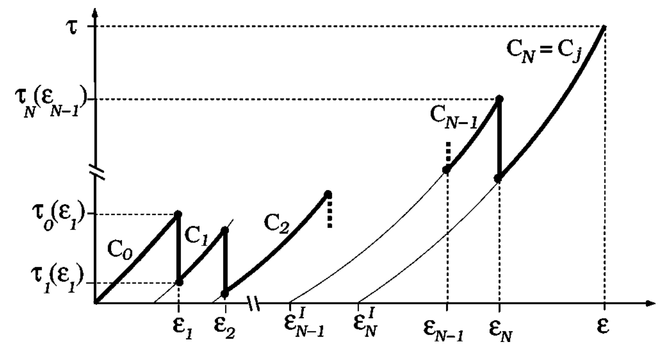

FIG. 2. The heavy line is the actual path followed during the steady application of axial strain. Each vertical drop in stress corresponds to the arrival of a crack.

The constraints are what give the dimensionless function S defined by Eq. (10) all the thermodynamic information about our cracking system and must explicitly involve the independent variables of S. Such independent variables are determined by establishing the first law of thermodynamics for a system cracking in compressive shear.

B. The work of creating a crack state

To obtain the first law, it is first necessary to define the detailed energy balance for each crack state and to understand how the work E_j required to create state j depends on both the actual strain $\boldsymbol{\varepsilon}$ and on the maximum-achieved strain $\boldsymbol{\varepsilon}_m$.

1. Griffith's criterion and crack-state energy

Consider a given mesovolume with a deterministic distribution of breaking energies $\mathcal{E}(\boldsymbol{x})$ assigned to each cell $\boldsymbol{x}$ of the mesovolume. Starting from a state of isotropic strain $\boldsymbol{\varepsilon}_0$, we slowly apply an additional axial deformation and monitor how one crack after another enters the mesovolume until the final strain tensor $\boldsymbol{\varepsilon}$ and final crack state j are arrived at. Lets say that this state j has a total of $\mathcal{N}$ cracks associated with it.

Figure 2 details the history of how the stress (and, therefore, work) might evolve in the mesovolume as strain is applied and cracks arrive. Initially, the mesovolume will elastically deform according to the stiffness tensor $\mathbf{C}_0$ (no cracks yet present) until the first crack arrives at the strain tensor $\boldsymbol{\varepsilon}_1$ with an associated drop in the mesovolume's stress. Lets say the bond-breaking energy of this first crack was $\mathcal{E}_1$. The mesovolume will now have a different overall stiffness tensor $\mathbf{C}_1$ and will elastically deform with these new moduli until the second crack arrives and so on until all $\mathcal{N}$ cracks have entered and the mesovolume has attained its final stiffness tensor of $\mathbf{C}_j=\mathbf{C}_{\mathcal{N}}$. The final tensor $\mathbf{C}_j$ depends on both the location and orientation of these $\mathcal{N}$ cracks in addition to their number.

At some intermediate stage having n cracks, the stress tensor $\boldsymbol{\tau}_n(\boldsymbol{\varepsilon})$ is defined by integrating $d\boldsymbol{\tau}=\mathbf{C}_n(\boldsymbol{\varepsilon}'):d\boldsymbol{\varepsilon}'$ from $\boldsymbol{\varepsilon}_n^{\mathrm{res}}$ to $\boldsymbol{\varepsilon}$, where $\boldsymbol{\varepsilon}_n^{\mathrm{res}}$ is the "residual" deformation observed upon unloading the sample back to zero stress as shown in the figure. We have

$$\boldsymbol{\tau}_n(\boldsymbol{\varepsilon}) = \int_{\boldsymbol{\varepsilon}_n^{\mathrm{res}}}^{\boldsymbol{\varepsilon}} \mathbf{C}_n : d\boldsymbol{\varepsilon}'. \tag{11}$$

The elastic energy density corresponding to this state at deformation $\boldsymbol{\varepsilon}$ is similarly

$$E_n^{\mathrm{el}}(\boldsymbol{\varepsilon}) = E_n^{\mathrm{res}} + \int_{\boldsymbol{\varepsilon}_n^{\mathrm{res}}}^{\boldsymbol{\varepsilon}} \boldsymbol{\tau}_n(\boldsymbol{\varepsilon}') : d\boldsymbol{\varepsilon}', \tag{12}$$

where E_n^{res} represents the residual elastic energy that remains in the system when the state with n cracks is unloaded to zero applied stress. These residual (zero stress) quantities are present whenever plastic deformation occurs within a grain contact. After a sample elastically returns to zero applied stress, such plastic deformation remains and, accordingly, there is an elastic stress field surrounding any crack that experienced plastic deformation. The strain energy associated with such local residual stress is what constitutes the residual energy E_n^{res}.

When the nth crack arrives in a strain-controlled experiment, there is no change in the strain $\boldsymbol{\varepsilon}_n$ and thus no external work performed. However, there is a change in stiffness (and possibly residual strain) resulting in an associated stress drop $\Delta \boldsymbol{\tau}_n = \boldsymbol{\tau}_{n-1}(\boldsymbol{\varepsilon}_n) - \boldsymbol{\tau}_n(\boldsymbol{\varepsilon}_n)$, and a drop in the stored elastic energy density $\Delta E_n^{\mathrm{el}} = E_{n-1}^{\mathrm{el}}(\boldsymbol{\varepsilon}_n) - E_n^{\mathrm{el}}(\boldsymbol{\varepsilon}_n)$. Energy conservation requires the elastic energy reduction to exactly balance the work performed in opening the crack so that

$$-\Delta E_n^{\mathrm{el}} + \frac{\mathcal{E}_n + K_n}{\ell^D} = 0, \tag{13}$$

where $\mathcal{E}_n$ is the bond-breaking work performed at the grain contact of the nth crack, K_n is the energy that went into acoustic emissions when the crack arrived and/or expended in any mode II frictional sliding or plastic deformation at the grain contact (K_n is a positive "loss" term), and, as earlier, ℓ^D is the volume of a mesovolume. Because K_n is positive, we can rewrite Eq. (13) as an inequality

$$\frac{K_n}{\ell^D} = \Delta E_n^{\mathrm{el}} - \frac{\mathcal{E}_n}{\ell^D} \geqslant 0, \tag{14}$$

which is a general statement of Griffith's criterion. Upon appealing to linear elasticity (elastic stiffnesses independent of strain level) and putting the residual deformation to zero (no plasticity inside the cracks), we arrive at the convenient statement $\ell^D \boldsymbol{\varepsilon}_n : (\mathbf{C}_{n-1} - \mathbf{C}_n) : \boldsymbol{\varepsilon}_n / 2 \geqslant \mathcal{E}_n$ given earlier.

The work performed between the arrival of the nth and the $(n+1)$th crack is defined,

$$W_n = \int_{\boldsymbol{\varepsilon}_n}^{\boldsymbol{\varepsilon}_{n+1}} \boldsymbol{\tau}_n(\boldsymbol{\varepsilon}') : \boldsymbol{\varepsilon}' = E_n^{\mathrm{el}}(\boldsymbol{\varepsilon}_{n+1}) - E_n^{\mathrm{el}}(\boldsymbol{\varepsilon}_n). \tag{15}$$

Thus, the total work required to reach the final strain $\boldsymbol{\varepsilon}$ is the sum (cf. Fig. 2)

$$E_j^p = \sum_{m=0}^{\mathcal{N}} W_n, \tag{16}$$

where by convention $W_{\mathcal{N}}$ is the work performed after the arrival of the last crack to get to the final deformation $\boldsymbol{\varepsilon}$. The superscript p on E_j^p is simply indicating that this is the work for one particular realization of the quenched disorder. Rewriting the sum by introducing Eqs. (15) and (13), then gives

$$\begin{aligned} E_j^p &= E_{\mathcal{N}}^{\mathrm{el}}(\boldsymbol{\varepsilon}) - E_0^{\mathrm{el}}(\boldsymbol{\varepsilon}_0) + \sum_{n=1}^{\mathcal{N}} \Delta E_n^{\mathrm{el}} \\ &= E_j^{\mathrm{el}}(\boldsymbol{\varepsilon}) + \sum_{n=1}^{\mathcal{N}} \frac{\mathcal{E}_n + K_n}{\ell^D} - E_0^{\mathrm{el}}(\boldsymbol{\varepsilon}_0), \end{aligned} \tag{17}$$

where $E_0^{\mathrm{el}}(\boldsymbol{\varepsilon}_0)$ is the small and physically unimportant amount of energy that is stored in the initial isotropic strain field. Equation (17) is the natural statement that the work performed in creating state j at strain $\boldsymbol{\varepsilon}$ is the sum of the elastic energy density stored in the material in the final state plus the energy irreversibly expended during the opening of each crack.

Both the loss term K_n and the residual energies E_j^{res} (contained in E_j^{el}) are potentially a function of the point in strain history at which a grain contact actually breaks; e.g., most models one might propose for plastic deformation at a grain contact are dependent on the applied stress level. However, modeling such plastic processes seems uncertain at best. We thus assume that at least for those crack states significantly contributing to any phase transition (states with lots of cracks), the stress-history dependence of K_n is, on average, negligible. Further, since the residual strain in brittle-fracture experiments is never more than a few percent of the peak-stress deformation and since the essence of the localization process does not seem to lie in E_j^{res}, we assume that $E_j^{\mathrm{res}} \ll \Sigma_n \mathcal{E}_n$. With these approximations, the work density E_j^p depends only on the final state j, the final strain $\boldsymbol{\varepsilon}$ (through E_j^{el}), and the breaking energies $\mathcal{E}_n$.

The energy density E_j needed later in our probability law is obtained by further averaging over the quenched disorder in the breaking energies $\mathcal{E}_n$ to give

$$E_j = E_j^{\mathrm{el}}(\boldsymbol{\varepsilon}) + \gamma_j(\boldsymbol{\varepsilon}_m) \frac{\mathcal{N}_j}{\ell^D} - E_0^{\mathrm{el}}(\boldsymbol{\varepsilon}_0). \tag{18}$$

Here, $\mathcal{N}_j = \mathcal{N}$ is the total number of cracks in state j and γ_j is the average energy required to break a single grain contact where the average is over all cells throughout all mesovolumes led to state j. This γ_j can be different for different final crack states. It will also be greater at greater values of the maximum strain $\boldsymbol{\varepsilon}_m$ because, according to Griffith, the cells comprising j can break at higher energy levels when the strain is greater. The first term in Eq. (18) corresponds to the purely reversible elastic energy and therefore depends only on the actual strain state $\boldsymbol{\varepsilon}$.

2. Specific expression for E_j

To facilitate the development in Paper II and to be more specific, we now use Griffith's criterion to develop an expression for E_j that is based on linear elasticity. When the nth crack arrives, the linear-elastic variant of the Griffith criterion gives that

$$\mathcal{E}_n < \ell^D \boldsymbol{\varepsilon}_n : (\mathbf{C}_{n-1} - \mathbf{C}_n) : \boldsymbol{\varepsilon}_n / 2 \tag{19}$$

$$< \ell^D \boldsymbol{\varepsilon}_m : (\mathbf{C}_{n-1} - \mathbf{C}_n) : \boldsymbol{\varepsilon}_m / 2, \tag{20}$$

where as earlier $\boldsymbol{\varepsilon}_n$ is the strain point on the load curve where the nth crack arrives while $\boldsymbol{\varepsilon}_m$ is the final maximum strain level of the experiment. The second inequality follows from the first since an extra crack always reduces the stiffness of a mesovolume. For any particular mesovolume in state j, the average energy required to break a contact γ_j^p thus satisfies

$$\gamma_j^p \equiv \frac{1}{\mathcal{N}_j} \sum_{n=1}^{\mathcal{N}_j} \mathcal{E}_n < \frac{\ell^D}{2\mathcal{N}_j} \boldsymbol{\varepsilon}_m : (\mathbf{C}_0 - \mathbf{C}_j) : \boldsymbol{\varepsilon}_m , \tag{21}$$

where the right-hand side comes from summing Eq. (20). Since this inequality is independent of the history, every mesovolume that is led to state j must satisfy it. We may thus write γ_j in the form

$$\gamma_j = f_j \frac{\ell^D}{2\mathcal{N}_j} \boldsymbol{\varepsilon}_m : (\mathbf{C}_0 - \mathbf{C}_j) : \boldsymbol{\varepsilon}_m , \tag{22}$$

where the fraction f_j is bounded as $0 < f_j < 1$. We next demonstrate that the variation of f_j from one state to the next is so small as to be neglected altogether.

A tighter lower bound for f_j is obtained by considering crack states j having $\mathcal{N}_j$ noninteracting cracks. Since the cracks do not interact to concentrate stress, all of the $\mathcal{N}_j$ cells that broke had their breaking energies somewhere in the range $0 \leqslant \mathcal{E} \leqslant \delta E = \ell^D \boldsymbol{\varepsilon}_m : \delta \mathbf{C} : \boldsymbol{\varepsilon}_m / 2$, where $\delta\mathbf{C}$ is the change in the stiffness tensor due to the arrival of a single noninteracting crack and δE is the associated change in the elastic energy. Since the breaking energies are independent random variables taken from the distribution $\pi(\mathcal{E})$, we obtain

$$\gamma_j = \frac{\int_0^{\delta E} e\, \pi(e)\, de}{\int_0^{\delta E} \pi(e)\, de} \tag{23}$$

for noninteracting crack states j.

We now appeal to a specific form for the probability distribution $\pi(\mathcal{E})$. Initially, our rocks are intact and it is expected that more grain contacts are entirely bonded ($\mathcal{E} = \Gamma d^{D-1}$) than entirely unbonded ($\mathcal{E} = 0$). We thus assume a monotonic distribution $\mathcal{E}^k$ with $k > 0$ satisfying the normalization $\int_0^{\Gamma d^{D-1}} \pi(e)\, de = 1$ so that

$$\pi(\mathcal{E}) = \frac{(k+1)}{\Gamma d^{D-1}} \left(\frac{\mathcal{E}}{\Gamma d^{D-1}} \right)^k = c\, \mathcal{E}^k. \tag{24}$$

Using this π, the average energy required to break a contact in a noninteracting crack state is

$$\gamma_j = \frac{k+1}{k+2} \delta E = \frac{q}{2} \ell^D \boldsymbol{\varepsilon}_m : \delta \mathbf{C} : \boldsymbol{\varepsilon}_m , \tag{25}$$

where we have defined $q = (k+1)/(k+2)$. All dependence on the underlying quenched-disorder distribution in our theory is confined to the constant q which for any $k > 0$ is in the range $[0.5,1]$.

Since for noninteracting states $\mathbf{C}_0 - \mathbf{C}_j = \mathcal{N}_j \delta\mathbf{C}$, a comparison of Eqs. (25) and (22) shows that $f_j = q$ for all the noninteracting states. For the interacting states, the prefactor f_j must be slightly greater because now stress concentration can allow stronger cells to break. It is thus concluded that for all states, the f_j of Eq. (22) are bounded as $q \leqslant f_j < 1$ which when compared to how $\mathcal{N}_j$ varies from state to state can be considered negligible. From here on, we simply take $f_j = q$ for all states.

The essential physics for the average amount of work that goes into building up any given crack state j is thus captured by

$$E_j(\boldsymbol{\varepsilon}, \boldsymbol{\varepsilon}_m) = E_j^R(\boldsymbol{\varepsilon}) + E_j^I(\boldsymbol{\varepsilon}_m), \tag{26}$$

$$E_j^R(\boldsymbol{\varepsilon}) = \frac{1}{2} \boldsymbol{\varepsilon} : \mathbf{C}_j : \boldsymbol{\varepsilon}, \tag{27}$$

$$E_j^I(\boldsymbol{\varepsilon}_m) = \frac{q}{2} \boldsymbol{\varepsilon}_m : (\mathbf{C}_0 - \mathbf{C}_j) : \boldsymbol{\varepsilon}_m , \tag{28}$$

where the superscripts R and I denote respectively the reversible and irreversible part of the energy. The intact hydrostatic energy $E_0^{\mathrm{el}}(\boldsymbol{\varepsilon}_0)$ has been neglected since it does not involve cracks and, therefore, cannot influence the probability of the various crack states.

C. The laws of our crack-based thermodynamics

Using the ergodic hypothesis discussed earlier, the average energy density in a disorded solid can be written $U = \Sigma_j p_j E_j$. We are interested in how U changes when increments in $\boldsymbol{\varepsilon}$ and $\boldsymbol{\varepsilon}_m$ are applied to the system.

In general, a small increment in U can be written as

$$dU = \sum_j E_j dp_j + \sum_j p_j dE_j . \tag{29}$$

The first term involving the probability change is entirely due to crack creation. Some mesovolumes that were in less cracked states prior to the increment, are transformed to state j during the increment, while mesovolumes that were in state j, are transformed to other more cracked states. If in the increment, the number of mesovolumes arriving in state j is different than the number leaving, there is a change dp_j in the occupational probability of that state. Such changes are the only way to change the disorder in the system, so that

$$\sum_j E_j dp_j = T dS \tag{30}$$

is the work involved in changing the system's disorder via crack production. The proportionality constant T is formally a temperature and will be treated in detail.

Using the decomposition $E_j(\boldsymbol{\varepsilon},\boldsymbol{\varepsilon}_m)=E_j^R(\boldsymbol{\varepsilon})+E_j^I(\boldsymbol{\varepsilon}_m)$, we can write the second term of Eq. (29) as

$$\sum_j p_j dE_j=\sum_j p_j dE_j^R+\sum_j p_j dE_j^I. \tag{31}$$

The first part is due to purely elastic (reversible) changes in each mesovolume and may be further written

$$\sum_j p_j dE_j^R=\boldsymbol{\tau}:d\boldsymbol{\varepsilon}, \tag{32}$$

where $\boldsymbol{\tau}$ is the average stress tensor acting on the mesovolumes. This result can be verified by appealing either to Eq. (27) or to the more general statement of Eq. (12).

The second part $\Sigma_j p_j dE_j^I$ represents the average work performed in creating cracks in just the final strain increment $d\boldsymbol{\varepsilon}_m$. Some of the initial mesovolumes led to state j at maximum strain $\boldsymbol{\varepsilon}_m+d\boldsymbol{\varepsilon}_m$ had all their cracks in place before the final strain increment, while others had cracks arrive in the final increment. We write

$$\sum_j p_j dE_j^I=\boldsymbol{g}:d\boldsymbol{\varepsilon}_m, \tag{33}$$

where the tensor $\boldsymbol{g}$ has units of stress but is quite distinct from the stress tensor $\boldsymbol{\tau}$.

The "first law" for the rock mass is then

$$dU=\boldsymbol{\tau}:d\boldsymbol{\varepsilon}+\boldsymbol{g}:d\boldsymbol{\varepsilon}_m+TdS, \tag{34}$$

with the formal definitions

$$\boldsymbol{\tau}=\left.\frac{\partial U}{\partial\boldsymbol{\varepsilon}}\right|_{\boldsymbol{\varepsilon}_m,S},\quad \boldsymbol{g}=\left.\frac{\partial U}{\partial\boldsymbol{\varepsilon}_m}\right|_{\boldsymbol{\varepsilon},S},\quad\text{and}\quad T=\left.\frac{\partial U}{\partial S}\right|_{\boldsymbol{\varepsilon},\boldsymbol{\varepsilon}_m}. \tag{35}$$

The natural variables of the fundamental function U are $(S,\boldsymbol{\varepsilon},\boldsymbol{\varepsilon}_m)$. Equivalently if S is treated as the fundamental function, then $S=S(U,\boldsymbol{\varepsilon},\boldsymbol{\varepsilon}_m)$ which means that the constraints placed on the maximization of S must involve U, $\boldsymbol{\varepsilon}$, and $\boldsymbol{\varepsilon}_m$.

The "second law" of this crack-based thermodynamics is that $dS\geqslant 0$ (equal to zero only if $d\boldsymbol{\varepsilon}_m=0$ so that no cracks are created) while a "third law" may be proposed by simply defining $T=0$ when $S=0$. The system will have zero emergent disorder before cracks begin to arrive and so our third law states that the temperature T starts at zero and then increases in magnitude as the number of cracks in the system increases from zero. The justification for this postulate comes *a posteriori* when it is found that in order to have zero probability for a mesovolume being in anything but the uncracked state $(S=0)$, we must have that $T=0$.

D. The probability distribution

To obtain the probability of observing a mesovolume to be in crack state j, we maximize $S=-\Sigma_j p_j \ln p_j$ subject to the constraint that $\Sigma_j p_j=1$, and to the additional constraints that $\boldsymbol{\varepsilon}_j=\boldsymbol{\varepsilon}$, $\boldsymbol{\varepsilon}_{mj}=\boldsymbol{\varepsilon}_m$, and $\Sigma_j p_j E_j=U$. These constraints define our canonical ensemble. Other ensembles can be defined by considering other constraints involving $\boldsymbol{\varepsilon}$, $\boldsymbol{\varepsilon}_m$, and U; however, since all ensembles yield identical average properties in the thermodynamic limit, we elect to work only with the canonical ensemble due to its analytical convenience.

This maximization problem is solved using Lagrange multipliers to obtain the Boltzmannian

$$p_j=\frac{e^{-E_j/T}}{Z},\quad\text{where}\quad Z=\sum_j e^{-E_j/T}, \tag{36}$$

and where the parameter T is exactly the partial derivative $\partial U/\partial S|_{\boldsymbol{\varepsilon},\boldsymbol{\varepsilon}_m}$ called "temperature."

E. The free energy and its derivatives

Any equilibrium physical property that depends on the distribution of cracks throughout the system can be obtained from the partition function Z given by Eq. (36).

To do so, a thermodynamic potential F called the free-energy density is introduced that is related to Z by

$$F(\boldsymbol{\varepsilon},\boldsymbol{\varepsilon}_m,T)=-T\ln Z(\boldsymbol{\varepsilon},\boldsymbol{\varepsilon}_m,T). \tag{37}$$

This potential F is the Legendre transform with respect to S of the total-energy density $U=U(\boldsymbol{\varepsilon},\boldsymbol{\varepsilon}_m,S)$ as can be seen from

$$U-TS=\sum_j p_jE_j+T\sum_j p_j\ln p_j=-T\ln Z\sum_j p_j=F, \tag{38}$$

where we used that $\ln p_j=-E_j/T-\ln Z$.

When $(\boldsymbol{\varepsilon},\boldsymbol{\varepsilon}_m,T)$ are the independent variables, the first law can be obtained by taking the total derivative of Eq. (37)

$$\begin{aligned}dF&=-T\frac{dZ}{Z}-\ln Z\,dT\\&=-T\sum_j\left[-\frac{dE_j(\boldsymbol{\varepsilon},\boldsymbol{\varepsilon}_m)}{T}+E_j\frac{dT}{T^2}\right]p_j-\ln Z\,dT\\&=(F-U)\frac{dT}{T}+\sum_j p_j[dE_j^R(\boldsymbol{\varepsilon})+dE_j^I(\boldsymbol{\varepsilon}_m)]\\&=-SdT+\boldsymbol{\tau}:d\boldsymbol{\varepsilon}+\boldsymbol{g}:d\boldsymbol{\varepsilon}_m,\end{aligned} \tag{39}$$

where we have used the definitions that $\boldsymbol{\tau}_j=dE_j^R(\boldsymbol{\varepsilon})/d\boldsymbol{\varepsilon}$ and $\boldsymbol{g}_j=dE_j^I(\boldsymbol{\varepsilon}_m)/d\boldsymbol{\varepsilon}_m$.

With $\beta=1/T$, the various thermodynamic functions are related to the partial derivatives of $\ln Z(\boldsymbol{\varepsilon},\boldsymbol{\varepsilon}_m,\beta)$ as

$$-\frac{\partial\ln Z}{\partial\beta}=\sum_j E_jp_j=U, \tag{40}$$

$$-\frac{1}{\beta}\frac{\partial \ln Z}{\partial \boldsymbol{\varepsilon}} = \sum_j \boldsymbol{\tau}_j p_j = \boldsymbol{\tau}, \tag{41}$$

$$-\frac{1}{\beta}\frac{\partial \ln Z}{\partial \boldsymbol{\varepsilon}_m} = \sum_j \boldsymbol{g}_j p_j = \boldsymbol{g}. \tag{42}$$

These results, along with $S=\ln Z+\beta U$, are used in Paper III.

IV. TEMPERATURE

The temperature is a well-defined essential part of our quenched-disorder statistics. Through the probability law $p_j = e^{-E_j/T}/Z$, the temperature quantifies the energy scale that separates probable from improbable states and how this energy scale evolves with strain. No other meaning should be read into T. We now demonstrate how to exactly obtain T.

A. Evolution of temperature with strain

The only way energy enters the system is by performing work on the external surface. Thus, the general relation $dU = \boldsymbol{\tau}:d\boldsymbol{\varepsilon}$ holds for either loading or unloading situations. This previously unused fact provides a differential equation for $T=1/\beta$ that permits everything about our system to be exactly known once an order-parameter based model for $E_j(\boldsymbol{\varepsilon},\boldsymbol{\varepsilon}_m)$ is determined and the functional sums defining $Z(\boldsymbol{\varepsilon},\boldsymbol{\varepsilon}_m,\beta)=\sum_j e^{-\beta E_j(\boldsymbol{\varepsilon},\boldsymbol{\varepsilon}_m)}$ are performed.

The temperature and entropy only evolve along load paths defined by $\boldsymbol{\varepsilon}=\boldsymbol{\varepsilon}_m$ and only such paths need be considered in what follows. Using $dU=\boldsymbol{\tau}:d\boldsymbol{\varepsilon}$, the first law [Eq. (34)] can then be rewritten as

$$TdS+\boldsymbol{g}:d\boldsymbol{\varepsilon}=0. \tag{43}$$

Since it always requires energy to break contacts, we have that $\boldsymbol{g}:d\boldsymbol{\varepsilon}>0$ and consequently $TdS<0$. Furthermore, since the entropy (disorder) necessarily grows during the crack-creation process (at least initially), the temperature of our system is negative (at least initially).

The load path of a standard triaxial experiment is when axial strain ε_z monotonically increases while the radial confining stress $\tau_x=\tau_y=-p_c$ remains constant. Along this path, all properties evolve only as a function of ε_z. With $Z(\boldsymbol{\varepsilon},\boldsymbol{\varepsilon}_m,\beta)$ considered as known, the radial deformation components can be expressed in terms of the axial deformation by using the two equations

$$\beta p_c = \left.\frac{\partial \ln Z}{\partial \varepsilon_x}\right|_{\boldsymbol{\varepsilon}_m=\boldsymbol{\varepsilon}} = \left.\frac{\partial \ln Z}{\partial \varepsilon_y}\right|_{\boldsymbol{\varepsilon}_m=\boldsymbol{\varepsilon}}$$

to obtain the two functions

$$\varepsilon_x = f_x(\beta,\varepsilon_z) \quad \text{and} \quad \varepsilon_y = f_y(\beta,\varepsilon_z) \tag{44}$$

that are valid only along the load path.

We now write dU in two different ways. First, $dU = \boldsymbol{\tau}:d\boldsymbol{\varepsilon}$ is evaluated along the load path to obtain

$$dU=\tau_z d\varepsilon_z - p_c(df_x+df_y). \tag{45}$$

Second, we use the fact that $U=U(\beta,\boldsymbol{\varepsilon},\boldsymbol{\varepsilon}_m)$ to obtain

$$dU=\frac{\partial U}{\partial \beta}d\beta+\left(\frac{\partial U}{\partial \varepsilon_z}+\frac{\partial U}{\partial \varepsilon_{mz}}\right)d\varepsilon_z+\left(\frac{\partial U}{\partial \varepsilon_x}+\frac{\partial U}{\partial \varepsilon_{mx}}\right)df_x + \left(\frac{\partial U}{\partial \varepsilon_y}+\frac{\partial U}{\partial \varepsilon_{my}}\right)df_y. \tag{46}$$

Upon equating Eqs. (45) and (46) we obtain a first-order nonlinear differential equation for β

$$a(\beta,\varepsilon_z)\frac{d\beta}{d\varepsilon_z}+b(\beta,\varepsilon_z)=0, \tag{47}$$

where a and b are given by

$$a=\frac{\partial U}{\partial \beta}+\left(p_c+\frac{\partial U}{\partial \varepsilon_x}+\frac{\partial U}{\partial \varepsilon_{mx}}\right)\frac{\partial f_x}{\partial \beta}+\left(p_c+\frac{\partial U}{\partial \varepsilon_y}+\frac{\partial U}{\partial \varepsilon_{my}}\right)\frac{\partial f_y}{\partial \beta}, \tag{48}$$

$$b=-\tau_z+\frac{\partial U}{\partial \varepsilon_z}+\frac{\partial U}{\partial \varepsilon_{mz}}+\left(p_c+\frac{\partial U}{\partial \varepsilon_x}+\frac{\partial U}{\partial \varepsilon_{mx}}\right)\frac{\partial f_x}{\partial \varepsilon_z} + \left(p_c+\frac{\partial U}{\partial \varepsilon_y}+\frac{\partial U}{\partial \varepsilon_{my}}\right)\frac{\partial f_y}{\partial \varepsilon_z}. \tag{49}$$

We are to use $\tau_z=-\beta^{-1}\partial \ln Z/\partial \varepsilon_z$ and $U=-\partial \ln Z/\partial \beta$ in these expressions for a and b once the function $Z(\boldsymbol{\varepsilon},\boldsymbol{\varepsilon}_m,\beta)$ has been determined. Furthermore, all partial derivatives are to be evaluated along the load curve; i.e., at $\varepsilon_{mx}=f_x(\beta,\varepsilon_z)$, $\varepsilon_{my}=f_y(\beta,\varepsilon_z)$, and $\varepsilon_{mz}=\varepsilon_z$.

B. Initial conditions

In order to integrate Eq. (47), initial conditions must be provided. The initial conditions of our so-called "third law" (i.e., the intact conditions that $\beta=-\infty$ when $\varepsilon_z=0$) are not well-defined for β. Thus, Eq. (47) must be integrated not from the intact state, but from a state that contains at least a few cracks so that $\beta\neq-\infty$.

Accordingly, we define "one-crack" initial conditions by considering the point in strain history where on average throughout the ensemble of mesovolumes, there is one crack in each mesovolume. If there are N cells in a mesovolume, the probability of any given cell to be broken somewhere in the ensemble is then $P_1=1/N$. This same probability can also be obtained from Griffith's criterion by integrating the quenched-disorder distribution of Eq. (24) to obtain $P_1 = [\delta E_1/(\Gamma d^{D-1})]^{k+1}$, where $\delta E_1=\ell^D \boldsymbol{\varepsilon}_1:\delta\mathbf{C}:\boldsymbol{\varepsilon}_1/2$ is the elastic energy change due to a single isolated crack and where $\boldsymbol{\varepsilon}_1$ is the strain tensor at which on average there is a single crack in each mesovolume. Thus, we have $\boldsymbol{\varepsilon}_1:\delta\mathbf{C}:\boldsymbol{\varepsilon}_1 = 2\Gamma d^{D-1}/(N^{1/(k+1)}\ell^D)$ that can be used to obtain an expression for the initial axial strain ε_{z1} at which on average there is one crack per mesovolume.

To obtain the inverse temperature β_1 corresponding to this initial strain, the exact probability of observing a particular type of crack state is determined and compared to our temperature-dependent Boltzmannian. The particular states we choose to analyze are, for simplicity, those having precisely one broken cell.

The probability p_j of a state consisting of one broken cell and $N-1$ unbroken cells can be written as

$$p_j = P_1(1-P_1)^{N-1}\Pi_{\boldsymbol{x}}[1-\delta P(\boldsymbol{x})], \tag{50}$$

where P_1 is again the probability of having a single broken cell and $(1-P_1)^{N-1}$ is the probability of having $N-1$ broken cells in the absence of other cracks. Thus, the product $\Pi_{\boldsymbol{x}}[1-\delta P(\boldsymbol{x})]$ is the probability that no cells broke due to the strain perturbations caused by the presence of a first broken cell, where $\boldsymbol{x}$ represents distance from this first broken cell. We define $\delta E_2(\boldsymbol{x})$ as the elastic energy change in a mesovolume when a second cell breaks solely in the perturbed strain field emanating from a first broken cell. This energy varies with the separation distance $|\boldsymbol{x}|$ between the two cracks as $|\boldsymbol{x}|^{-D}$. We have

$$\delta P(\boldsymbol{x}) = \int_0^{\delta E_2(\boldsymbol{x})} \pi(e)\,de = \left(\frac{\delta E_2(\boldsymbol{x})}{\Gamma d^{D-1}}\right)^{k+1} = \frac{c_2}{|\boldsymbol{x}|^{D(k+1)}}, \tag{51}$$

where Eq. (24) was used for π and where c_2 depends on both the overall applied strain and the angle from the first-crack's orientation to the second crack. Since δP is small compared to one (restricting to models where cracks are smaller than the cell size Λ, since the separation distance $|\boldsymbol{x}|$ always exceeds it), we have

$$\Pi_{\boldsymbol{x}}[1-\delta P(\boldsymbol{x})] = 1 - \frac{1}{\ell^D}\int_{|\boldsymbol{x}|>\Lambda} \frac{c_2}{|\boldsymbol{x}|^{D(k+1)}}\, d^D\boldsymbol{x} \tag{52}$$

and since $k>0$, this spatial integral over the mesovolume can be neglected in the thermodynamic limit.

The conclusion is that

$$p_j = P_1(1-P_1)^{N-1} = p_0 \frac{P_1}{1-P_1} = p_0 e^{-\ln(N-1)}, \tag{53}$$

where $p_0 = (1-P_1)^N$ is the probability of the entirely intact state. This can be compared to our probability law where, from Eqs. (26)–(28), we have

$$p_j = p_0 \exp\left[\beta_1 \frac{(1-q)}{2} \boldsymbol{\varepsilon}_1 : \delta\mathbf{C} : \boldsymbol{\varepsilon}_1\right]. \tag{54}$$

Thus, the inverse temperature that holds when $\boldsymbol{\varepsilon} = \boldsymbol{\varepsilon}_1$ is

$$\beta_1 = -\frac{\ell^D N^{1/(k+1)} \ln(N-1)}{(1-q)\Gamma d^{D-1}}. \tag{55}$$

C. Approximate approach to the temperature

The approach just taken in defining the initial conditions suggests a convenient way of obtaining an approximate expression for the temperature.

Consider "dilute" states j where cracks do not significantly interact. In this case, the probability P_m that any one cell has broken when the maximum strain tensor is at $\boldsymbol{\varepsilon}_m$ is again just the cumulative distribution $P_m = [\ell^D \boldsymbol{\varepsilon}_m : \delta\mathbf{C} : \boldsymbol{\varepsilon}_m / (2\Gamma d^{D-1})]^{k+1}$. In this case, the probability of observing a noninteracting state j consisting of $\mathcal{N}_j$ cracks is $p_j = P_m^{\mathcal{N}_j}(1-P_m)^{(N-\mathcal{N}_j)}$ where we have forgone the analysis of the preceeding section demonstrating that the unbroken-cell probabilities are negligibly influenced by the strain perturbations from the $\mathcal{N}_j$ broken cells (at least for $k>0$). We may write

$$p_j = p_0 \exp\left[-\ln\left(\frac{1}{P_m} - 1\right)\mathcal{N}_j\right], \tag{56}$$

where $p_0 = (1-P_m)^N$ is the probability of the unbroken state.

For such dilute states, the Hamiltonian of Eq. (26) is written (with $\boldsymbol{\varepsilon}_m = \boldsymbol{\varepsilon}$) as

$$E_j = \frac{1}{2}\boldsymbol{\varepsilon}_m : \mathbf{C}_0 : \boldsymbol{\varepsilon}_m - \frac{(1-q)}{2}\boldsymbol{\varepsilon}_m : \delta\mathbf{C} : \boldsymbol{\varepsilon}_m \mathcal{N}_j \tag{57}$$

so that our probability law predicts

$$p_j = p_0 \exp\left[\frac{\beta(1-q)}{2}\boldsymbol{\varepsilon}_m : \delta\mathbf{C} : \boldsymbol{\varepsilon}_m \mathcal{N}_j\right]. \tag{58}$$

Upon using $1/P_m = [2\Gamma d^{D-1}/(\ell^D \boldsymbol{\varepsilon}_m : \delta\mathbf{C} : \boldsymbol{\varepsilon}_m)]^{k+1}$ and equating Eqs. (58) and (56), the temperature is identified

$$\beta(\boldsymbol{\varepsilon}_m) = \frac{-2\ln\{[2\Gamma d^{D-1}/(\ell^D \boldsymbol{\varepsilon}_m : \delta\mathbf{C} : \boldsymbol{\varepsilon}_m)]^{k+1} - 1\}}{(1-q)\boldsymbol{\varepsilon}_m : \delta\mathbf{C} : \boldsymbol{\varepsilon}_m}. \tag{59}$$

This expression for β has the expected behavior that $\beta = -\infty$ when $\boldsymbol{\varepsilon}_m = 0$, and that β is a negative and increasing function of $\boldsymbol{\varepsilon}_m$ up to the strain point $P_m = 1/2$ where it smoothly goes to zero. For $P_m > 1/2$, β is a positive and increasing function of $\boldsymbol{\varepsilon}_m$. Our probability law with β negative predicts the intact state to have the greatest probability, while when $P_m > 1/2$ and β is positive, the most probable state jumps to every cell being broken. Although such a phase transition occurs in fiber bundles [24], we demonstrate in Paper III using the exact differential equation for temperature, that the localization transition always occurs prior to this divergent-temperature transition.

We emphasize that Eq. (59) is an approximation to the extent that due to the long-range nature of elastic interactions, one can never truly define a noninteracting state. We use it to obtain an order-of-magnitude idea of the temperature at a given strain. But it should always be considered preferable to obtain the temperature by integrating the exact Eq. (47) from the first-crack (or other exact) initial conditions.

V. CONCLUSIONS

The present theory of fracture in disordered solids works from the postulate that the probability p_j of observing a mesovolume in a given emergent-crack state j and at a given applied strain can be determined by maximizing Shannon's measure of the emergent-crack disorder subject to constraints that come from the energy balance of brittle fracture. These constraints are what allow nonuniform probability distributions to occur. The validity of this postulate can be demonstrated in simpler cases [24] by integrating the probability distribution through history, but its general validity in the case of rocks with interacting cracks remains an open problem. Our approach to answering this question is to use the statistical mechanics that follows from our maximal-disorder postulate to make predictions about the physical properties of real systems and to compare such predictions to laboratory data.

ACKNOWLEDGMENTS

The authors thank S. Roux and M. Holschneider for useful discussions in the early stages of this work, and D. Lockner for sharing both his data and knowledge of the fracture process. R.T. received financial support from the TMR network "Fractal Structures and Selforganization" through EEC Grant No. FMRXCT980183.

[1] R. L. Blumberg Selinger, Z. G. Wang, W. M. Gelbart, and A. Ben-Shaul, Phys. Rev. A **43**, 4396 (1991).
[2] J. B. Rundle and W. Klein, Phys. Rev. Lett. **63**, 171 (1989).
[3] Z. G. Wang, U. Landman, R. L. Blumberg Selinger, and W. M. Gelbart, Phys. Rev. B **44**, 378 (1991).
[4] L. Golubović and A. Peredera, Phys. Rev. E **51**, 2799 (1995).
[5] P. Meakin, in *Statistical Models for the Fracture of Disordered Media*, edited by H. Hermann and S. Roux (Elsevier, Amsterdam, 1990).
[6] G. G. Batrouni and A. Hansen, Phys. Rev. Lett. **80**, 325 (1998).
[7] L. de Arcangelis and H. J. Herrmann, Phys. Rev. B **39**, 2678 (1989).
[8] P. M. Duxbury, P. L. Leath, and P. D. Beale, Phys. Rev. B **36**, 367 (1987).
[9] S. Arbabi and M. Sahimi, Phys. Rev. B **47**, 695 (1993); M. Sahimi and S. Arbabi, *ibid.* **47**, 703 (1993); **47**, 713 (1993).
[10] M. Sahimi and S. Arbabi, Phys. Rev. Lett. **77**, 3689 (1996).
[11] H. J. Herrmann, A. Hansen, and S. Roux, Phys. Rev. B **39**, 637 (1989).
[12] M. Kloster, A. Hansen, and P. C. Hemmer, Phys. Rev. E **56**, 2615 (1997).
[13] A. Hansen and P. C. Hemmer, Phys. Lett. A **184**, 394 (1994).
[14] P. C. Hemmer and A. Hansen, J. Appl. Mech. **59**, 909 (1992).
[15] S. D. Zhang and E. J. Ding, Phys. Rev. B **53**, 646 (1996).
[16] D. Sornette, J. Phys. A **22**, L243 (1989).
[17] Y. Moreno, J. B. Gómez, and A. F. Pacheco, Phys. Rev. Lett. **85**, 2865 (2000); Physica A **296**, 9 (2001).
[18] L. de Arcangelis, A. Hansen, H. J. Herrmann, and S. Roux, Phys. Rev. B **40**, 877 (1989).
[19] A. Hansen, E. L. Hinrichsen, and S. Roux, Phys. Rev. B **43**, 665 (1991).
[20] *Statistical Models for the Fracture of Disordered Media*, edited by H. J. Herrmann and S. Roux (North-Holland, Amsterdam, 1990).
[21] S. Zapperi, P. Ray, H. E. Stanley, and A. Vespignani, Phys. Rev. Lett. **78**, 1408 (1997).
[22] S. Zapperi, P. Ray, H. E. Stanley, and A. Vespignani, Phys. Rev. E **59**, 5049 (1999).
[23] J. V. Andersen, D. Sornette, and K. T. Leung, Phys. Rev. Lett. **78**, 2140 (1997).
[24] S. R. Pride and R. Toussaint, Physica A **312**, 159 (2002).
[25] J. W. Rudnicki and J. R. Rice, J. Mech. Phys. Solids **23**, 371 (1975).
[26] A. A. Griffith, Philos. Trans. R. Soc. London, Ser. A **221**, 163 (1920).
[27] C. Shannon, Bell Syst. Tech. J. **27**, 373 (1948).
[28] M. S. Paterson, *Experimental Rock Deformation—the Brittle Field* (Springer-Verlag, Berlin, 1978).

Fracture of disordered solids in compression as a critical phenomenon. II. Model Hamiltonian for a population of interacting cracks

Renaud Toussaint* and Steven R. Pride†
Géosciences Rennes, Université de Rennes 1, 35042 Rennes Cedex, France
(Received 14 November 2001; revised manuscript received 13 June 2002; published 27 September 2002)

To obtain the probability distribution of two-dimensional crack patterns in mesoscopic regions of a disordered solid, the formalism of Paper I requires that a functional form associating the crack patterns (or states) to their formation energy be developed. The crack states are here defined by an order parameter field representing both the presence and orientation of cracks at each site on a discrete square network. The associated Hamiltonian represents the total work required to lead an uncracked mesovolume into that state as averaged over the initial quenched disorder. The effect of cracks is to create mesovolumes having internal heterogeneity in their elastic moduli. To model the Hamiltonian, the effective elastic moduli corresponding to a given crack distribution are determined that includes crack-to-crack interactions. The interaction terms are entirely responsible for the localization transition analyzed in Paper III. The crack-opening energies are related to these effective moduli via Griffith's criterion as established in Paper I.

DOI: 10.1103/PhysRevE.66.036136 PACS number(s): 62.20.Mk, 46.50.+a, 46.65.+g, 64.60.Fr

I. INTRODUCTION

In triaxial-stress experiments on rocks in the brittle regime, the onset of a macroscopic localization of deformation is usually observed around peak stress [c.f. Bésuelle [1] for a review]. Such departure from a macroscopically uniform deformation regime is intrinsically beyond the capacities of a mean-field theory, and so a specific model is developed here that takes the orientational nature of crack-to-crack interactions into account.

This is the second paper in a series of three dedicated to exploring how the physical properties of disordered solids evolve as they are led to failure in a state of compression. The goal of this paper is to obtain a reasonable form for the Hamiltonian $E_j(\boldsymbol{\varepsilon},\boldsymbol{\varepsilon}_m)$ which is defined as the average work required to lead an intact region at zero deformation to the crack state denoted by j when the maximum applied strain is $\boldsymbol{\varepsilon}_m$ and where the final strain $\boldsymbol{\varepsilon}$ is possibly different than $\boldsymbol{\varepsilon}_m$ due to a final unloading. This Hamiltonian must be expressed in terms of the spatial distribution of the local order parameter that is the variable used to characterize the population of cracks in each mesovolume of a huge disordered-solid system.

Most existing lattice models explore the dynamics of scalar order parameters either representing the breakdown of elastic spring or beam networks under tensile stress [2], or of fuse networks [3]. The analogies between such scalar models and fracture of disordered media has been widely discussed [4]. One advantage of our approach is the ability to explore interactions based on a fully tensorial description of the stress perturbations produced by each crack. Another is its ability to yield analytical rather than only numerical results. Using E_j in the partition function established in Paper I, it is possible to explore the crack patterns that emerge in compressive settings for which isolated cracks appear in an intrinsically stable manner no matter their size [5], and for which macroscopic localization is a collective phenomenon due to the energetic organization of small cracks as opposed to an instability associated with the largest defects. In the present paper, we retain the leading-order effects of oriented-crack populations interacting in two-dimension (2D). The overriding importance of the long-range elastic interactions leaves hope that 3D generalizations would not yield qualitatively different critical behavior.

*Present address: Department of Physics, University of Oslo, P.O. Box 1048 Blindern, 0316 Oslo 3, Norway. Email address: Renaud.Toussaint@fys.uio.no

†Email address: Steve.Pride@univ-rennes1.fr

II. PRINCIPLES OF THE MODEL

A. Order-parameter definition

We now elaborate on the crack model introduced in Paper I. Each mesovolume of a huge rock system is discretized into a square network of diamond-shaped cells of size Λ (grain sizes) and only a single crack is potentially present in each cell. A crack is located at the center of the cell and has a length d somewhere within the support $[0,d_m]$, where d_m is the maximum crack length (a fixed parameter of the system) required to satisfy $d_m<\Lambda$. In the perturbative treatment of the crack interactions developed herein, $\epsilon=(d_m/\Lambda)^D$ is taken to be a small number, where D is the number of space dimensions (in the present model, $D=2$). The local order parameter $\varphi(\boldsymbol{x})$ associated with each cell $\boldsymbol{x}$ is taken to have an amplitude $\psi=|\varphi|=(d/d_m)^D$ and has a sign that indicates whether the crack is oriented at $+45°$ or $-45°$ relative to the principal stress direction (the so-called "axial direction"). The model is summarized in Fig. 1

The restriction that cracks are either at $\pm 45°$ and have lengths less than the grain dimensions is of course a great simplification compared to what is found inside of real rocks. However, we only need to characterize the essential features of a crack population that contribute to localization phenomena and, to this extent, it appears overly complicated to

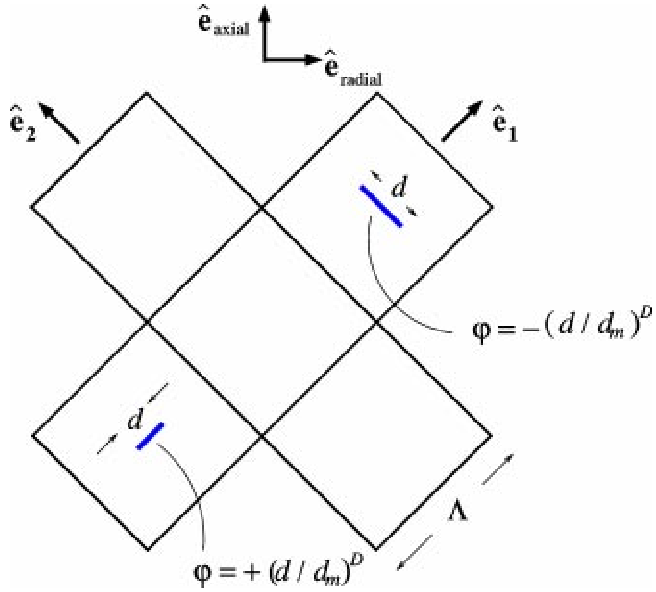

FIG. 1. Part of the diamond network of cells that comprise a mesovolume. Each cell has the linear dimension Λ and is only allowed to contain one crack. The maximum length of any crack is d_m and this length is assumed to be sufficiently small that $(d_m/\Lambda)^D \ll 1$. The amplitude of the order parameter is by definition $\psi = |\varphi| = (d/d_m)^D$, where d is the length of the crack found in the cell, while the sign of φ indicates the orientation of the crack as shown.

model the amazing variety of crack geometries encountered in real rocks [6,7]. The localization transition involves spontaneous breaking of symmetries both under translation and parity (inversion of the minor stress axis) as is seen from the structure of the shear bands emerging in the post-peak-stress regime [8]. The essential feature of any proposed order parameter is that it must reflect and quantify the amount of local symmetry breaking and our simple model with cracks at either $\pm 45°$ does just this.

Furthermore, there is evidence both from acoustic-emissions monitoring [9] and from direct observation after unloading [10], that cracks developing prior to peak stress do not exceed an extent of a few grains diameters. This is principally because the grain contacts that break are much weaker than the grains and have a finite length so that cracks arriving in compression do so stably [5]. Crack coalescence is not explicitly allowed for. However, since several neighboring cells in a line may all contain cracks of the same sign, the long-range elastic effect of long (coalesced) cracks is effectively allowed for. Our picture of the final shear bands experimentally observed in the post-peak-stress regime is that they were created by unstable sliding along a band weakened in the pre-peak-stress regime by a concentration of coherently oriented cracks [8]. Our model allows small cracks to stably concentrate *en échelon* along conjugate bands relative to the principal-stress direction; however, it does not model the final unstable rupture along a given band.

B. Formation energy of a crack pattern

It has been established in Paper I that to a reasonable approximation, the work required to form a crack state, as averaged over the initial disorder, separates into one part representing the work required to break the grain contacts, and a second part representing the elastic energy stored in the cracked solid. This was expressed in Eqs. (26)–(28) of Paper I as

$$E_j = \frac{q}{2}\boldsymbol{\varepsilon}_m : (\mathbf{C}_0 - \mathbf{C}_j) : \boldsymbol{\varepsilon}_m + \frac{1}{2}\boldsymbol{\varepsilon} : \mathbf{C}_j : \boldsymbol{\varepsilon}. \tag{1}$$

The first term of Eq. (1) is the energy spent in the irreversible formation of the crack state j averaged over quenched disorder and was obtained through an application of Griffith's principle. The parameter q derives from the quenched-disorder distribution and lies in the range $[1/2,1]$ (see Sec. III B 2 of Paper I). The second term is the reversibly-stored elastic energy with $\mathbf{C}_j$ being the elastic-stiffness tensor of state j.

Our principal task is therefore to model the way that cracks and collective crack-states affect the overall elastic moduli of a mesovolume. This requires detailed knowledge of the stress (or strain) field throughout the mesovolume in the presence of arbitrary crack populations, and we treat this need using the following approximations. First, since the cracks in the model are isolated one to each cell, their main effect regarding the far-field stress is to change the elastic moduli of their embedding cell. Such a change is modeled assuming the cracks to be penny-shaped ellipsoidal cavities. We ignore how such ellipses change shape when the applied stress is unloaded/reloaded since linear elasticity alone captures the principle effect of how the rock becomes weaker due to strategic placement of cracks in cells. Since a crack occupies a limited extent of a cell, the modification of the moduli is small compared to the moduli of the intact cell so that the resulting far-field stress field can be developed as a Born series. It is in the third term of this development that crack-to-crack interactions are first allowed for. Higher-order interactions (three cracks simultaneously interacting and so on) are negligible to the extent that $\epsilon = (d_m/\Lambda)^D$ can be considered small.

III. ELASTIC ENERGY

The goal of this section is to determine the elastic energy E_j^{el} stored in a mesovolume occuping the region Ω and containing the crack state j (which denotes the spatial distribution of $\varphi(\boldsymbol{x})$ at all points $\boldsymbol{x}$ of Ω) when a displacement corresponding to a uniform strain tensor $\boldsymbol{\varepsilon}^{(0)}$ is applied on the external surface $\partial\Omega$ of the mesovolume.

A. Elastic energy of a weakly heterogeneous solid

The effect of the crack field $\varphi(\boldsymbol{x})$ is to perturb the stiffness tensor of each cell as $\mathbf{C}(\boldsymbol{x}) = \mathbf{C}^0 + \delta\mathbf{c}[\varphi(\boldsymbol{x})]$, where $\mathbf{C}^0$ denotes the moduli of an uncracked cell (assumed uniform for all cells), and where $\delta\mathbf{c}(\boldsymbol{x})$ is a small perturbation due to the possible presence of a crack as characterized by $\varphi(\boldsymbol{x})$. It is established in the Appendix that the nonzero components of $\delta\mathbf{c}$ are typically smaller than those of $\mathbf{C}^0$ by a factor $\epsilon = (d_m/\Lambda)^D \ll 1$. Our problem is to resolve an elasticity boundary-value problem in a region Ω containing a weakly heterogeneous stiffness tensor $\mathbf{C}(\boldsymbol{x})$.

The displacement boundary conditions are given as

$$\forall \boldsymbol{x} \in \partial\Omega, \quad \mathbf{u}(\boldsymbol{x}) = \boldsymbol{\varepsilon}^{(0)} \cdot \boldsymbol{x}, \tag{2}$$

where $\boldsymbol{x}$ denotes distance from the center of the mesovolume. Elastostatic equilibrium requires that

$$\partial_j \tau_{ij} = C^0_{ijkl} \partial_j \partial_k u_l + \partial_j [\delta c_{ijkl} \partial_k u_l] = 0 \tag{3}$$

throughout Ω, where summation over repeated indices is assumed both here and throughout. Due to the linearity of the problem, we use the elastostatic Green tensor $\mathbf{G} = G_{ij} \hat{\boldsymbol{x}}_i \hat{\boldsymbol{x}}_j$ for a uniform material which is a solution of

$$C^0_{ijkl} \partial_j \partial_k G_{lm}(\boldsymbol{x}, \boldsymbol{x}') + \delta_{im} \delta^D(\boldsymbol{x} - \boldsymbol{x}') = 0, \tag{4}$$

$$\forall \boldsymbol{x} \in \partial\Omega, \quad G_{ij}(\boldsymbol{x}, \boldsymbol{x}') = 0. \tag{5}$$

The components $G_{ij}(\boldsymbol{x}, \boldsymbol{x}')$ define the ith component of the displacement at $\boldsymbol{x}$ induced by a unit point force acting along the j axis at $\boldsymbol{x}'$. Here, δ_{ij} is the Kronecker symbol, and δ^D is the D-dimensional Dirac distribution.

The solution for the displacements when no cracks are present is simply $\mathbf{u}^{(0)}(\boldsymbol{x}) = \boldsymbol{\varepsilon}^{(0)} \cdot \boldsymbol{x}$ throughout all of Ω. Thus, it is a straightforward excercise to demonstrate that the total displacement $\mathbf{u}$ in the presence of the cracks satisfies the following integral equation:

$$u_i(\boldsymbol{x}) = u_i^{(0)}(\boldsymbol{x}) + \int_\Omega G_{ij}(\boldsymbol{x}, \boldsymbol{x}') \partial_{k'} [\delta c_{jklm} \partial_{l'} u_m](\boldsymbol{x}') d^D \boldsymbol{x}', \tag{6}$$

where $\partial_{i'}$ denotes the partial derivative relative to the coordinate x_i'. Using ϵ as the argument of a series expansion, we write the displacements as $\mathbf{u} = \mathbf{u}^{(0)} + \mathbf{u}^{(1)} + \cdots \mathbf{u}^{(n)} + O(\epsilon^{(n+1)})$, where each $\mathbf{u}^{(m)}$ is $O(\epsilon^m)$. Collecting terms at each order of ϵ in Eq. (6) gives the following recursion relation:

$$u_i^{(n+1)}(\boldsymbol{x}) = \int_\Omega G_{ij}(\boldsymbol{x}, \boldsymbol{x}') \partial_{k'} [\delta c_{jklm} \partial_{l'} u_m^{(n)}](\boldsymbol{x}') d^D \boldsymbol{x}'. \tag{7}$$

The boundary conditions used to define $\mathbf{G}$ guarantee that for all $n > 0$, the displacements $\mathbf{u}^{(n)}$ are zero on the boundary $\partial\Omega$.

The quantity we are specifically seeking to establish is the elastic energy density $E^{\mathrm{el}} = \ell^{-D} \int_\Omega \frac{1}{2} \boldsymbol{\tau}(\boldsymbol{x}) : \boldsymbol{\varepsilon}(\boldsymbol{x}) d^D \boldsymbol{x}$, where we recall that ℓ is the linear dimension of a mesovolume. The definitions of the strain $\varepsilon_{ij} = \frac{1}{2}(\partial_i u_j + \partial_j u_i)$ and stress $\tau_{ij} = (C^0_{ijkl} + \delta c_{ijkl}) \varepsilon_{kl}$ give immediately the following relations:

$$\varepsilon_{ij}^{(n)} = \frac{1}{2}(\partial_i u_j^{(n)} + \partial_j u_i^{(n)}), \tag{8}$$

$$\tau_{ij}^{(n)} = C^0_{ijkl} \varepsilon_{kl}^{(n)} + \delta c_{ijkl} \varepsilon_{kl}^{(n-1)}, \tag{9}$$

$$E^{(n)} = \frac{1}{2\ell^D} \sum_{a=0}^{n} \int_\Omega \boldsymbol{\tau}^{(n-a)} : \boldsymbol{\varepsilon}^{(a)} d^D \boldsymbol{x}, \tag{10}$$

with the convention $\boldsymbol{\varepsilon}^{(-1)} = 0$. In the last expression, the fact that $\mathbf{u}^{(a)} = 0$ on the boundary for all $a > 0$ guarantees that after integrating by parts,

$$\int_\Omega \boldsymbol{\tau}^{(n-a)} : \boldsymbol{\varepsilon}^{(a)} d^D \boldsymbol{x} = \int_\Omega \boldsymbol{\tau}^{(n-a)} : \boldsymbol{\nabla} \mathbf{u}^{(a)} d^D \boldsymbol{x}$$

$$= \int_{\partial\Omega} \mathbf{n} \cdot \boldsymbol{\tau}^{(n-a)} \cdot \mathbf{u}^{(a)} d^{D-1} \boldsymbol{x} = 0,$$

where we used the facts that the stress tensor is symmetric and solenoidal. The nth term of the total elastic energy is then

$$E^{(n)} = \frac{1}{2} \overline{\boldsymbol{\tau}^{(n)}} : \boldsymbol{\varepsilon}^{(0)}, \tag{11}$$

where the upper bar denotes a volume average over Ω.

The first term of the elastic energy is independent of the φ field, and corresponds to the physically unimportant amount of energy

$$E^{(0)} = \frac{1}{2} \boldsymbol{\varepsilon}^{(0)} : \mathbf{C}^{(0)} : \boldsymbol{\varepsilon}^{(0)} \tag{12}$$

stored in the intact state.

For the higher orders $n \geqslant 1$, $\boldsymbol{\tau}^{(n)}$ is expressed by Eq. (9), and the same argument as above using the fact that $\mathbf{u}^{(n)} = 0$ on $\partial\Omega$ eliminates a term:

$$E^{(n)} = \overline{\boldsymbol{\varepsilon}^{(n)}} : \mathbf{C}^{(0)} : \boldsymbol{\varepsilon}^{(0)} + \frac{1}{2} \overline{\boldsymbol{\varepsilon}^{(n-1)} : \delta \mathbf{c}} : \boldsymbol{\varepsilon}^{(0)} = \frac{1}{2} \overline{\boldsymbol{\varepsilon}^{(n-1)} : \delta \mathbf{c}} : \boldsymbol{\varepsilon}^{(0)}. \tag{13}$$

The second term of the developement,

$$E^{(1)} = \frac{1}{2} \boldsymbol{\varepsilon}^{(0)} \overline{: \delta \mathbf{c} :} \boldsymbol{\varepsilon}^{(0)}, \tag{14}$$

represents only a local dependance on $\delta \mathbf{c}$ (and therefore on the crack field) since it does not involve nested integrals over two different positions. It will be shown to represent only the contribution of the average crack porosity to the stiffness of the rock.

The third term of the development is where the desired crack-to-crack interactions arrive. Using the symmetry of $\delta \mathbf{c}$ under the inversion of its two first or last indices, and Eq. (7) to have an integral form of $\mathbf{u}^{(1)}$, Eq. (13) transforms to

$$2\ell^D E^{(2)} = \int \partial_b u_a^{(1)}(\boldsymbol{x}) \delta c_{abcd}(\boldsymbol{x}) \varepsilon_{cd}^{(0)} d^D \boldsymbol{x}$$

$$= \int \int \varepsilon_{cd}^{(0)} \delta c_{abcd}(\boldsymbol{x}) \partial_b G_{aj}(\boldsymbol{x}, \boldsymbol{x}')$$

$$\times \partial_{k'} \delta c_{jklm}(\boldsymbol{x}') \varepsilon_{lm}^{(0)} d^D \boldsymbol{x} d^D \boldsymbol{x}'. \tag{15}$$

This term accounts for the way that a crack present at $\boldsymbol{x}'$ energetically interacts with a different crack at $\boldsymbol{x}$. This is the nonlocal interaction term that is ultimately responsible for the localization transition. The higher terms of the Born development can be neglected for our purposes.

B. Elastic energy as explicit function of the crack field

To establish the terms of the Born-approximated elastic energy as explicit functions of both the crack state φ and the imposed strain $\boldsymbol{\varepsilon}^{(0)}$, a few definitions are first introduced.

The principal axes of $\boldsymbol{\varepsilon}^{(0)}$ are along $(\hat{\mathbf{e}}_{\mathrm{radial}},\hat{\mathbf{e}}_{\mathrm{axial}})$ as denoted in Fig. 1. Our square network of cells is rotated $+45°$ from this orthonormal basis. We work here in the coordinates $(\hat{\mathbf{e}}_1,\hat{\mathbf{e}}_2)$ of the square network so that the applied-strain takes the form

$$\boldsymbol{\varepsilon}^{(0)}=\frac{1}{2}\begin{pmatrix}\Delta & \gamma\\ \gamma & \Delta\end{pmatrix}, \tag{16}$$

where $\Delta=\varepsilon_{\mathrm{radial}}+\varepsilon_{\mathrm{axial}}$ and $\gamma=-(\varepsilon_{\mathrm{radial}}-\varepsilon_{\mathrm{axial}})$ are the imposed dilatation and shear strain.

For convenience, we assume the intact material to be isotropic. Taking $\lambda+2\mu$ as the stress unit, where (λ,μ) are the Lamé parameters of the material, and using the usual tensor-to-matrix mapping of the indices $(11)\to 1$; $(22)\to 2$; $(12)\to 3$, the fourth-order stiffness tensor of the intact material takes the form

$$\mathbf{C}^0=\begin{pmatrix}1 & 2\alpha-1 & 0\\ 2\alpha-1 & 1 & 0\\ 0 & 0 & 1-\alpha\end{pmatrix}, \tag{17}$$

where

$$\alpha=\frac{\lambda+\mu}{\lambda+2\mu} \tag{18}$$

is a material-dependent constant in the range $[0.5,1]$.

The deviation $\delta\mathbf{c}$ of this tensor due to the possible presence of a crack in a cell separates into an isotropic contribution independent of the crack's orientation, and into an anisotropic orientation-dependent contribution. In the Appendix, we demonstrate that

$$\delta\mathbf{c}(\boldsymbol{x})=\epsilon[\mathbf{A}\varphi(\boldsymbol{x})+\mathbf{B}|\varphi(\boldsymbol{x})|], \tag{19}$$

$$\mathbf{A}=\begin{pmatrix}\eta_2-\eta_1 & 0 & 0\\ 0 & \eta_1-\eta_2 & 0\\ 0 & 0 & 0\end{pmatrix}, \tag{20}$$

$$\mathbf{B}=\begin{pmatrix}-\eta_1 & -(2\alpha-1)\eta_2 & 0\\ -(2\alpha-1)\eta_2 & -\eta_1 & 0\\ 0 & 0 & -(1-\alpha)\eta_3\end{pmatrix}, \tag{21}$$

where (η_1,η_2,η_3) are positive constants expressed in the Appendix in terms of the Lamé parameters.

Making the necessary contractions over the indices, we easily obtain the trivial (crack independent) energy $E^{(0)}$ using Eqs. (12), (16), and (17). For later convenience, this result is best written in matrix form as

$$E^{(0)}=\frac{1}{2}(\Delta,\gamma)\cdot\mathbf{M}_0\cdot(\Delta,\gamma)^T, \tag{22}$$

$$\mathbf{M}_0=\begin{pmatrix}\alpha & 0\\ 0 & 1-\alpha\end{pmatrix}. \tag{23}$$

Using the auxiliary field

$$\psi(x)=|\varphi(x)| \tag{24}$$

denoting the amplitude of each crack, one similarly obtains [using Eqs. (14) and (19)–(21)]

$$\begin{aligned}E^{(1)}&=\frac{\epsilon}{2}[\boldsymbol{\varepsilon}^{(0)}:\mathbf{A}:\boldsymbol{\varepsilon}^{(0)}\overline{\varphi}+\boldsymbol{\varepsilon}^{(0)}:\mathbf{B}:\boldsymbol{\varepsilon}^{(0)}\overline{\psi}]\\ &=\frac{1}{2}(\Delta,\gamma)\cdot\mathbf{M}_1\cdot(\Delta,\gamma)^T,\end{aligned} \tag{25}$$

with

$$\mathbf{M}_1=-\epsilon\overline{\psi}\begin{pmatrix}\kappa_2 & 0\\ 0 & \kappa_3\end{pmatrix}, \tag{26}$$

$$\kappa_2=\frac{\eta_1}{2}+\frac{2\alpha-1}{2}\eta_2, \tag{27}$$

$$\kappa_3=(1-\alpha)\eta_3. \tag{28}$$

The term proportional to $\overline{\varphi}$ has algebraically canceled due to the symmetry of the problem under parity; inversion of the minor axis $\hat{\mathbf{e}}_{\mathrm{radial}}$ flips the orientation of cracks, and therefore changes the sign of $\overline{\varphi}$, while the energy remains necessarily unchanged. The surviving term is negative and proportional to $\overline{\psi}$, and accounts for the softening of the mesovolume due to the presence of cracks. This dependence on the total number of cracks is the only order-parameter dependent effect to first order.

Last, the crack-interaction term of principal interest can be readily expressed from Eqs. (15) and (19) as

$$\begin{aligned}-2\ell^D E^{(2)}=&\,\epsilon^2\varepsilon_{cd}^{(0)}\varepsilon_{kl}^{(0)}A_{abcd}A_{ijkl}f_{aibj}\\ &+2\epsilon^2\varepsilon_{cd}^{(0)}\varepsilon_{kl}^{(0)}A_{abcd}B_{ijkl}g_{aibj}\\ &+\epsilon^2\varepsilon_{cd}^{(0)}\varepsilon_{kl}^{(0)}A_{abcd}B_{ijkl}h_{aibj},\end{aligned} \tag{29}$$

where the fourth-order tensors $\mathbf{f},\mathbf{g},\mathbf{h}$ are functionals of φ and defined as

$$f_{aibj}=\int d^D\mathbf{x}\int d^D\mathbf{x}'\,G_{ai}(\boldsymbol{x},\boldsymbol{x}')\,\partial_b\varphi\partial_{j'}\varphi, \tag{30}$$

$$g_{aibj}=\int d^D\mathbf{x}\int d^D\mathbf{x}'\,G_{\{ai\}}(\boldsymbol{x},\boldsymbol{x}')\,\partial_b\varphi\partial_{j'}\psi, \tag{31}$$

$$h_{aibj}=\int d^D\boldsymbol{x}\int d^D\boldsymbol{x}'\,G_{ai}(\boldsymbol{x},\boldsymbol{x}')\partial_b\psi\partial_{j'}\psi. \qquad (32)$$

In the second term, the reciprocity of the Green function $G_{ai}(\boldsymbol{x},\boldsymbol{x}')=G_{ai}(\boldsymbol{x}',\boldsymbol{x})$ is used as well as the notation $G_{\{ai\}}=(G_{ai}+G_{ia})/2$.

The Green tensor needed here satisfies the Dirichlet conditions of Eq. (5) and can be obtained, in principle, from the infinite-space Green tensor via the image method. However, this transforms $E^{(2)}$ into an infinite series (one term for each image), and makes the functional integrations of Paper III analytically hopeless. To remedy this problem, the Green function with a periodic instead of zero boundary condition is used as ersatz. Since $\mathbf{u}^{(1)}$ is only affected close to the boundaries by this replacement, this approximation will be considered valid for the evaluation of the volume integral $E^{(2)}$.

The double integrals of Eqs. (30)–(32) are most easily expressed using the 2D finite-Fourier transform

$$\tilde{F}(\boldsymbol{k})=\int_\Omega d^D\boldsymbol{x}F(\boldsymbol{x})e^{-i\boldsymbol{k}\cdot\boldsymbol{x}}, \qquad (33)$$

$$F(\boldsymbol{x})=\frac{1}{\ell^D}\sum_{\boldsymbol{k}}\tilde{F}(\boldsymbol{k})e^{i\boldsymbol{k}\cdot\boldsymbol{x}}, \qquad (34)$$

where the sum over the wave vectors $\boldsymbol{k}$ is over $\{\boldsymbol{k}=2\pi n_i/\ell\hat{\mathbf{e}}_i;\ \forall i,n_i\in\mathbb{Z}\}$ with an upper cutoff given by $\max n_i>\ell/\Lambda$ that reflects the fact that the order parameter cannot vary on scales smaller than cell sizes Λ. Since the Green function used is defined with periodic boundary conditions, it satisfies $G_{ai}(\boldsymbol{x},\boldsymbol{x}')=G_{ai}(\boldsymbol{x}-\boldsymbol{x}')$. Its Fourier transform is easily established, and upon recalling that $(\lambda+2\mu)$ is adopted as the stress unit, reads

$$\tilde{\mathbf{G}}(\boldsymbol{k})=\frac{1}{(1-\alpha)\boldsymbol{k}^2}(\mathbf{I}-\alpha\hat{\boldsymbol{k}}\hat{\boldsymbol{k}}), \qquad (35)$$

$$\hat{\boldsymbol{k}}=\frac{\boldsymbol{k}}{\|\boldsymbol{k}\|}, \qquad (36)$$

where $\mathbf{I}$ is the identity tensor. This is real and symmetric, as is $\mathbf{G}(\boldsymbol{x})$ itself. Since φ and ψ are real fields, one has $\tilde{\varphi}(-\boldsymbol{k})=\tilde{\varphi}^*(\boldsymbol{k})$ and $\tilde{\psi}(-\boldsymbol{k})=\tilde{\psi}^*(\boldsymbol{k})$. Using these relations, together with the identity $\int_\Omega d^D\boldsymbol{x}e^{i\boldsymbol{k}\cdot\boldsymbol{x}}=\ell^D\delta_{\boldsymbol{k}}$, the integrals of Eqs. (30)–(32) become the following sums

$$f_{aibj}=\frac{1}{\ell^D}\sum_{\boldsymbol{k}\neq 0}|\tilde{\varphi}(\boldsymbol{k})|^2\hat{k}_j\hat{k}_b(\delta_{ia}-\alpha\hat{k}_i\hat{k}_a) \qquad (37)$$

$$g_{aibj}=\frac{1}{\ell^D}\sum_{\boldsymbol{k}\neq 0}\mathrm{Re}[\tilde{\varphi}(\boldsymbol{k})\tilde{\psi}^*(\boldsymbol{k})]\hat{k}_j\hat{k}_b(\delta_{ia}-\alpha\hat{k}_i\hat{k}_a), \qquad (38)$$

$$h_{aibj}=\frac{1}{\ell^D}\sum_{\boldsymbol{k}\neq 0}|\tilde{\psi}(\boldsymbol{k})|^2\hat{k}_j\hat{k}_b(\delta_{ia}-\alpha\hat{k}_i\hat{k}_a), \qquad (39)$$

where Re denotes the real part of a complex quantity and where $\hat{k}_i$ denotes the ith component of $\hat{\mathbf{k}}=\boldsymbol{k}/\|\boldsymbol{k}\|$. With the following definitions associated with the orientation of $\boldsymbol{k}$:

$$\theta_{\boldsymbol{k}}=(\hat{\boldsymbol{e}}_1,\boldsymbol{k}), \qquad (40)$$

$$u_{\boldsymbol{k}}=\cos(2\theta_{\boldsymbol{k}})=\cos^2\theta_{\boldsymbol{k}}-\sin^2\theta_{\boldsymbol{k}}=\hat{k}_1^2-\hat{k}_2^2, \qquad (41)$$

$$v_{\boldsymbol{k}}=\sin(2\theta_{\boldsymbol{k}})=2\cos\theta_{\boldsymbol{k}}\sin\theta_{\boldsymbol{k}}=2\hat{k}_1\hat{k}_2, \qquad (42)$$

the remaining contraction in Eq. (29) over the eight indices $(abcdijkl)$ is performed. The calculation is a bit long but without surprise and finally produces

$$E^{(2)}=\frac{1}{2}(\Delta,\gamma)\cdot\mathbf{M}_2\cdot(\Delta,\gamma)^T, \qquad (43)$$

$$\mathbf{M}_2=\frac{-\epsilon^2}{(1-\alpha)\ell^{2D}}\begin{pmatrix} a & b\\ b & c\end{pmatrix}, \qquad (44)$$

where the components a, b, and c are defined,

$$a=\sum_{\boldsymbol{k}\neq 0}a_{\boldsymbol{k}};\quad b=\sum_{\boldsymbol{k}\neq 0}b_{\boldsymbol{k}};\quad c=\sum_{\boldsymbol{k}\neq 0}c_{\boldsymbol{k}}, \qquad (45)$$

$$a_{\boldsymbol{k}}=(1-\alpha u_{\boldsymbol{k}}^2)\kappa_1^2|\tilde{\varphi}_{\boldsymbol{k}}|^2+2(1-\alpha)u_{\boldsymbol{k}}\kappa_1\kappa_2\,\mathrm{Re}(\tilde{\varphi}_{\boldsymbol{k}}\tilde{\psi}_{\boldsymbol{k}}^*)+(1-\alpha)\kappa_2^2|\tilde{\psi}_{\boldsymbol{k}}|^2,$$

$$b_{\boldsymbol{k}}=-\alpha u_{\boldsymbol{k}}v_{\boldsymbol{k}}\kappa_1\kappa_3\,\mathrm{Re}(\tilde{\varphi}_{\boldsymbol{k}}\tilde{\psi}_{\boldsymbol{k}}^*)+(1-\alpha)v_{\boldsymbol{k}}\kappa_2\kappa_3|\tilde{\psi}_{\boldsymbol{k}}|^2,$$

$$c_{\boldsymbol{k}}=(1-\alpha v_{\boldsymbol{k}}^2)\kappa_3^2|\tilde{\psi}_{\boldsymbol{k}}|^2,$$

with κ_2,κ_3 defined in Eqs. (27), (28) and κ_1 a new material-dependent constant,

$$\kappa_1\hat{=}\frac{\eta_1-\eta_2}{2}. \qquad (46)$$

IV. SURFACE FORMATION ENERGY

Next, we must account for the energy E_j^I that irreversibly went into creating the cracks of a given crack state j at a maximum deformation $\boldsymbol{\epsilon}_m$. In Paper I, this contribution was obtained using Griffith's criterion as

$$E_j^I=\frac{q}{2}\ell^D\boldsymbol{\epsilon}_m:(\mathbf{C}_0-\mathbf{C}_j):\boldsymbol{\epsilon}_m, \qquad (47)$$

where q derives from the quenched disorder and is bounded as $0.5\leqslant q<1$. The derivation of this statement implicitly assumed that all cracks were the same length. In the present treatment, cracks are allowed to have any length in the range $0\leqslant d\leqslant d_m$. It is a straightforward exercise to demonstrate that if the breaking energies for each possible length d are all sampled from the same quenched-disorder distribution, then Eq. (47) again holds. We forego such a demonstration. In the notation of the present paper we may thus state that

$$E[\varphi]^I = q(E^{(0)} - E^{\mathrm{el}}[\varphi]) = -q(E^{(1)} + E^{(2)})[\varphi], \quad (48)$$

where $E^{(1)}$ and $E^{(2)}$ are the terms of the Born-development given by Eqs. (25) and (43) upon replacing the current strain parameters Δ and γ by the maximum-achieved strain Δ_m and γ_m.

V. TEMPERATURE

Although not required as part of the Hamiltonian model, we now give an explicit in Δ_m, γ_m approximate expression for the temperature by using Eq. (59) of Paper I. This temperature was derived in Paper I assuming only a single crack size. Unfortunately, the result does not easily generalize to multiple crack sizes and so we simply take $d = d_m$ to obtain the estimate

$$\ell^D T(\Delta_m, \gamma_m) = -\frac{(1-q) d_m^D e_1(\Delta_m, \gamma_m)}{\ln\{[\zeta/e_1(\Delta_m, \gamma_m)]^{q/(1-q)} - 1\}}, \quad (49)$$

where $e_1 d_m^D$ is how much the first-Born elastic energy in a mesovolume is reduced when a crack of length d_m is introduced [c.f. Eqs. (25) and (26)]. The energy density $e_1(\Delta_m, \gamma_m)$ is defined as

$$e_1(\Delta_m, \gamma_m) = \frac{1}{2}(\kappa_2 \Delta_m^2 + \kappa_3 \gamma_m^2), \quad (50)$$

while ζ is a dimensionless ‘‘fracture toughness’’ parameter defined as

$$\zeta \equiv \frac{\Gamma}{(\lambda + 2\mu) d_m}. \quad (51)$$

There is a phase transition when $(\zeta/e_1)^{q/(1-q)} = 2$ and T diverges so that all crack states become equally probable.

We now consider whether such a phase transition is expected in laboratory experiments on rocks. The order of magnitude values $\Gamma \sim 10^2$ J/m^2, $d_m \sim 10^{-5}$ m, $\kappa_2 \sim 1$, and $(\lambda + 2\mu) \sim 10^{10}$ Pa are appropriate for typical grains in rocks so that $\zeta \sim 10^{-3}$. When a rock fails in shear, the accumulated strain is on the order of a percent or two, so that the maximum value of e_1 of interest is also on the order of 10^{-4}. We thus find that at shear failure, $\zeta/e_1 \sim 10$ and so we *a priori* expect the localization transition to occur prior to the temperature-divergence transition. This is more quantitatively demonstrated in Paper III.

VI. SUMMARY

Collecting together both the elastic energy and the surface formation energy, we obtain at last the Hamiltonian to be used in performing ensemble averages over crack states in the next paper. We write this Hamiltonian in the final form

$$E_j(\boldsymbol{\varepsilon}, \boldsymbol{\varepsilon}_m) = E^R(\boldsymbol{\varepsilon})[\varphi] + E^I(\boldsymbol{\varepsilon}_m)[\varphi],$$

$$E^R(\boldsymbol{\varepsilon})[\varphi] = E^0(\Delta, \gamma) + E^{\mathrm{av}}(\Delta, \gamma)[\varphi] + E^{\mathrm{int}}(\Delta, \gamma)[\varphi],$$

$$E^I(\boldsymbol{\varepsilon}_m)[\varphi] = -q\{E^{\mathrm{av}}(\Delta_m, \gamma_m)[\varphi] + E^{\mathrm{int}}(\Delta_m, \gamma_m)[\varphi]\},$$

where (Δ, γ) are the isotropic and shear strain components of the current strain tensor $\boldsymbol{\varepsilon}$, and (Δ_m, γ_m) are similar quantities referring to the maximum achieved strain $\boldsymbol{\varepsilon}_m$. The energy E^0 is the trivial elastic energy of the uncracked state

$$E^0(\Delta, \gamma) = \frac{1}{2}\{\alpha \Delta^2 + (1-\alpha)\gamma^2\},$$

where α is a dimensionless elastic constant in the range [0.5,1] defined by Eq. (18).

The next term in the Born development is $E^{\mathrm{av}} = E^{(1)}$, which depends only on the volume average $\overline{\psi}$, which is the fraction of cracked cells in the crack state φ and is thus entirely independent of the spatial fluctuations of φ. Its dependence on the strain (Δ, γ) is

$$E^{\mathrm{av}}(\Delta, \gamma)[\varphi] = -\frac{1}{2}[\kappa_2 \Delta^2 + \kappa_3 \gamma^2]\epsilon \overline{\psi}.$$

We defined $\epsilon = (d_m/\Lambda)^D$ to be a small parameter, where $D = 2$ is the number of space dimensions in the model, and d_m, Λ, and ℓ as respectively the linear sizes of the largest crack, a unit cell, and a mesovolume. The three coefficients κ_i are positive dimensionless material-dependent constants defined by Eqs. (27), (28), and (46).

The interaction energy $E^{\mathrm{int}} = E^{(2)}$ involve a quadratic matrix operator $P_{\boldsymbol{k}}$ that, for each nonzero wave vector $\boldsymbol{k}$, mixes together the Fourier modes of both φ and ψ:

$$E^{\mathrm{int}}(\Delta, \gamma)[\varphi] = \frac{-\epsilon^2}{2(1-\alpha)\ell^{2D}} \sum_{\boldsymbol{k} \neq 0} (R_{\boldsymbol{k}}^T \cdot P_{\boldsymbol{k}} \cdot R_{\boldsymbol{k}} + I_{\boldsymbol{k}}^T \cdot P_{\boldsymbol{k}} \cdot I_{\boldsymbol{k}}),$$

$$R_{\boldsymbol{k}} = [\mathrm{Re}(\tilde{\varphi}_{\boldsymbol{k}}); \mathrm{Re}(\tilde{\psi}_{\boldsymbol{k}})]^T,$$

$$I_{\boldsymbol{k}} = [\mathrm{Im}(\tilde{\varphi}_{\boldsymbol{k}}); \mathrm{Im}(\tilde{\psi}_{\boldsymbol{k}})]^T,$$

$$P_{\boldsymbol{k}} = \begin{bmatrix} L_{\boldsymbol{k}} & M_{\boldsymbol{k}} \\ M_{\boldsymbol{k}} & N_{\boldsymbol{k}} \end{bmatrix},$$

where Re and Im represent the real and imaginary part of a complex number. The components $L_{\boldsymbol{k}}$, $M_{\boldsymbol{k}}$, $N_{\boldsymbol{k}}$ depend both on the applied-strain parameters (maximum or actual ones), and the wave vector $\boldsymbol{k}$. In anticipation of Paper III, it is convenient to introduce

$$\omega = \frac{\kappa_3}{\kappa_1} \frac{\gamma}{\Delta}$$

as the shear-strain variable and to define the parameter

$$c = \kappa_2/\kappa_1 = 1 + \frac{2\mu(\lambda+\mu)(\lambda_+ 2\mu)}{\lambda^3},$$

where $c>1$. The components of the matrix $P_{\boldsymbol{k}}$ are then

$$L_{\boldsymbol{k}}(\Delta,\omega)=\Delta^2\kappa_1^2(1-\alpha u_{\boldsymbol{k}}^2),$$

$$M_{\boldsymbol{k}}(\Delta,\omega)=\Delta^2\kappa_1^2 u_{\boldsymbol{k}}[(1-\alpha)c-\alpha v_{\boldsymbol{k}}\omega],$$

$$N_{\boldsymbol{k}}(\Delta,\omega)=\Delta^2\kappa_1^2[(1-\alpha)c^2+2(1-\alpha)cv_{\boldsymbol{k}}\omega + (1-\alpha v_{\boldsymbol{k}}^2)\omega^2],$$

where $u_{\boldsymbol{k}}=\cos(2\theta_{\boldsymbol{k}})$ and $v_{\boldsymbol{k}}=\sin(2\theta_{\boldsymbol{k}})$ are functions that characterize the orientation of $\boldsymbol{k}$ through its polar angle $\theta_{\boldsymbol{k}}$.

Note that all terms contributing to the Hamiltonian have been written in a dimensionless form in which energy density E_j, like stress, is measured in units of $(\lambda+2\mu)$.

APPENDIX: EFFECTIVE MODULI OF A CRACKED CELL

A crack is modeled here as an elongated ellipse having a major axis of length d and a minor axes of length w in the limit that $w/d \ll 1$ which corresponds to a so-called "penny-shaped" crack. Its long axis is by convention oriented along $\hat{\mathbf{e}}_1$ if locally $\varphi>0$, and along $\hat{\mathbf{e}}_2$ if $\varphi<0$. The unit cell is a square whose sides are colinear with $(\hat{\mathbf{e}}_1;\hat{\mathbf{e}}_2)$, and has a size $\Lambda \gg d$ since the crack is taken to be small. The interior of the crack is supposed to be much more compliant than the embedding matrix and all plastic deformation will be ignored; i.e., there is no residual stress or strain allowed for in the cracked system when it is unloaded to zero applied stress.

Denoting as usual the volume average of a quantity with an overbar, we seek to determine the elastic-stiffness tensor $\mathbf{C}$ of a cell as defined through the relation

$$\overline{\tau_{ij}}=C_{ijkl}\overline{\varepsilon_{kl}}. \tag{A1}$$

The region inside the crack is occupied by a uniform material of stiffness $\mathbf{C}^1$ while the intact matrix surrounding the crack is occupied by a material of stiffness $\mathbf{C}^1$. Upon denoting v the volume fraction of the crack in the cell, we obtain directly

$$\overline{\tau_{ij}}=(1-v)C^0_{ijkl}\overline{\varepsilon^0_{kl}}+vC^1_{ijkl}\overline{\varepsilon^1_{kl}}. \tag{A2}$$

Eshelby [11] demonstrates that the strain $\boldsymbol{\varepsilon}^1$ inside an elliptic inclusion is uniform while Wu [12] relates this strain to the strain at infinity by a tensor $\mathbf{T}$,

$$\overline{\varepsilon^1_{ij}}=T_{ijkl}\varepsilon^\infty_{kl}. \tag{A3}$$

With cracks considered as small inclusions in their embedding cell ($v\ll 1$), the approximation $\boldsymbol{\varepsilon}^\infty \simeq \overline{\boldsymbol{\varepsilon}}$ is valid to leading order in the above, so that

$$\overline{\varepsilon^0_{ij}}=W_{ijkl}\overline{\varepsilon_{kl}}, \tag{A4}$$

$$(1-v)W_{ijkl}=(\delta_{ik}\delta_{jl}-vT_{ijkl}). \tag{A5}$$

Using Eqs. (A3) and (A4) for the average deformation in and out of the inclusion, Eq. (A2) has the desired linear form of Eq. (A1) with an effective stiffness tensor given by

$$C_{ijkl}=C^0_{ijkl}-v(C^0_{ijmn}-C^1_{ijmn})T_{mnkl}\simeq C^0_{ijkl}-vC^0_{ijmn}T_{mnkl}. \tag{A6}$$

This approximation is justified under the hypothesis that the material inside the inclusion (air) is far more compliant than the host material (solid silicate). These relations are valid in any space dimension D . The two-dimensional case of interest to us here can be obtained from the three-dimensional Wu-Eshelby results by working with a three-dimensional ellipsoidal inclusion having semiaxes of linear dimension $a=d/2$; $b=w/2$; and $c=h/2$ embedded within a cell of dimension $\Lambda\times\Lambda\times h$ in the limit that $h\gg\Lambda$. In this limit, the three-dimensional problem becomes one in two dimensions.

Wu expresses his tensor $\mathbf{T}$ in terms of a tensor $\mathbf{S}$ defined by Eshelby,

$$T_{ijij}=\frac{1}{2(1-2S_{ijij})} \quad \text{when} \quad i\neq j, \tag{A7}$$

$$\begin{pmatrix} T_{1111} & T_{1122} & T_{1133}\\ T_{2211} & T_{2222} & T_{2233}\\ T_{3311} & T_{3322} & T_{3333}\end{pmatrix} = \begin{pmatrix} 1-S_{1111} & -S_{1122} & -S_{1133}\\ -S_{2211} & 1-S_{2222} & -S_{2233}\\ -S_{3311} & -S_{3322} & 1-S_{3333}\end{pmatrix}^{-1}. \tag{A8}$$

The Eshelby [11] tensor components are defined

$$S_{1111}=Qa^2I_{aa}+RI_a, \tag{A9}$$

$$S_{1122}=Qb^2I_{ab}-RI_a, \tag{A10}$$

$$S_{1212}=\frac{Q}{2}(a^2+b^2)I_{ab}+\frac{R}{2}(I_a+I_b), \tag{A11}$$

with similar expressions for the remaining components obtained through the permutation of a,b,c and 1,2,3. In the notation of the present paper, the various parameters of Eqs. (A9)–(A11) are defined

$$Q=\frac{3}{8\pi(1-\sigma_p)} \quad \text{and} \quad R=\frac{1-2\sigma_p}{8\pi(1-\sigma_p)}, \tag{A12}$$

where $\sigma_p=\lambda/2(\lambda+\mu)$ is the Poisson's ratio of the solid material (assumed isotropic), and

$$I_a=2\pi ab\int_0^\infty \frac{du}{(a^2+u)D}, \tag{A13}$$

$$I_{aa}=2\pi ab\int_0^\infty \frac{du}{(a^2+u)^2D}, \tag{A14}$$

$$I_{ab}=\frac{2}{3}\pi ab\int_0^\infty \frac{du}{(a^2+u)(b^2+u)D}, \tag{A15}$$

with $D=\sqrt{(a^2+u)(b^2+u)}$ and $I_c=I_{ac}=I_{bc}=I_{cc}=0$. Similar expressions are obtained for I_b and I_{bb} by replacing a and b in the above. These elliptic integrals are evaluated to the leading order in the small aspect ratio $\delta=b/a$ which gives

$$I_a=4\pi\delta,\quad I_b=4\pi(1-\delta), \tag{A16}$$

$$I_{aa}=\frac{4\pi}{3a^2}2\delta,\quad I_{bb}=\frac{4\pi}{3b^2},\quad I_{ab}=\frac{4\pi}{3a^2}(1-2\delta). \tag{A17}$$

Defining parameters q and r by

$$q=4\pi Q=\frac{3}{2(1-\sigma_p)}\quad \text{and}\quad r=4\pi R=\frac{1-2\sigma_p}{2(1-\sigma_p)}, \tag{A18}$$

we obtain that to the leading order in $1/\delta$,

$$T_{1212}=\frac{3}{4q}\frac{1}{\delta}, \tag{A19}$$

$$T_{2211}=\frac{\frac{q}{3}-r}{r\left(1+\frac{q}{3}-r\right)}\frac{1}{\delta}, \tag{A20}$$

$$T_{2222}=\frac{1}{r\left(1+\frac{q}{3}-r\right)}\frac{1}{\delta}. \tag{A21}$$

All remaining components of $\mathbf{T}$ are either $O(1)$ and therefore negligible, or are unimportant for the components of $\mathbf{C}$ related to directions 1 and 2.

To get finally the deviation $\delta\mathbf{c}$ of the effective elastic moduli of the cracked cell through Eq. (A6), we note first that

$$v=\frac{4\pi}{3}\frac{abc}{\Lambda^2 h}=\frac{2\pi}{3}\frac{a^2}{\Lambda^2}\frac{b}{a}=\frac{\pi}{6}\frac{d^2}{\Lambda^2}\delta=\frac{\pi}{6}\epsilon\psi\delta, \tag{A22}$$

where we recall that $d=2a$ is the crack's length, $w=2b$ its width, and δ its aspect ratio. It is through this expression that the small parameter $\epsilon=(d_m/\Lambda)^2\ll 1$ enters the Born series. Note that $\psi=|\varphi|=(d/d_m)^2$ characterizes the extent of the crack. The third dimension of $h=2c$ goes to infinity in order to obtain the two-dimensional limit of this three-dimensional system.

Replacing q and r by their expressions in terms of the Lamé parameters λ,μ, and using by convention $(\lambda+2\mu)$ as the stress unit, the crack-induced perturbations of the cell moduli are

$$\delta c_{2222}=-v C^0_{2222}T_{2222}=-\frac{\pi}{6}\epsilon\psi\frac{\lambda+2\mu}{\mu}, \tag{A23}$$

$$\delta c_{1111}=-v C^0_{1122}T_{2211}=-\frac{\pi}{6}\epsilon\psi\frac{\lambda^2}{\mu(\lambda+2\mu)}, \tag{A24}$$

$$\delta c_{1122}=-v C^0_{1122}T_{2222}=-\frac{\pi}{6}\epsilon\psi\frac{\lambda}{\mu}, \tag{A25}$$

$$\delta c_{2211}=-v C^0_{2222}T_{2211}=-\frac{\pi}{6}\epsilon\psi\frac{\lambda}{\mu}, \tag{A26}$$

$$\delta c_{1212}=-v(C^0_{1212}T_{1212}+C^0_{1221}T_{2112})=-\frac{\pi}{6}\epsilon\psi\frac{1}{2}\frac{\mu}{\lambda+\mu}, \tag{A27}$$

with all other terms being zero except those obtained by the necessary symmetries under exchange of the two first or two last indexes.

Using the dimensionless constants α defined in Eq. (18) and introducing the positive dimensionless coefficients η_i,

$$\eta_1=\frac{\pi}{6}\frac{\lambda^3+\mu(\lambda+2\mu)^2}{\lambda\mu(\lambda+2\mu)},$$

$$\eta_2=\frac{\pi}{6}\frac{\lambda+2\mu}{\lambda},$$

$$\eta_3=\frac{\pi}{12}\frac{\lambda+2\mu}{\lambda+\mu}, \tag{A28}$$

we obtain at last the deviation of the elastic moduli of a cell containing a crack with long axis oriented along $\hat{\mathbf{e}}_1$ (corresponding to a positive φ),

$$\delta\mathbf{c}=\begin{pmatrix} \eta_2-2\eta_1 & -(2\alpha-1)\eta_2 & 0\\ -(2\alpha-1)\eta_2 & -\eta_2 & 0\\ 0 & 0 & -(1-\alpha)\eta_3\end{pmatrix}\epsilon\psi. \tag{A29}$$

The expression for both possible orientations of the cracks is straightforward. Orienting the crack along $\hat{\mathbf{e}}_2$ instead $\hat{\mathbf{e}}_1$ is equivalent to exchanging the one and two indices in the components of $\delta\mathbf{c}$, which results in an exchange of the components δc_{1111} and δc_{2222}, all remaining components of $\delta\mathbf{c}$ being unaffected by this change. Separating both expressions of $\delta\mathbf{c}$ into symmetric and antisymmetric parts, and noting that $\delta\mathbf{c}=0$ trivially when $\varphi=0$ (no crack), we obtain the general expression used in Eqs. (19)–(21).

[1] P. Bésuelle, Ph.D. thesis, Université Joseph Fourier–Grenoble I, 1999, and references therein for a review.
[2] S. Arbabi and M. Sahimi, Phys. Rev. B **47**, 695 (1993); M. Sahimi and S. Arbabi, *ibid.* **47**, 703 (1993); **47**, 713 (1993).
[3] G. G. Batrouni and A. Hansen, Phys. Rev. Lett. **80**, 325 (1998).
[4] *Statistical Models for the Fracture of Disordered Media*, edited by H. J. Herrmann and S. Roux (North-Holland, Amsterdam, 1990).
[5] D. A. Lockner, in *Rock Physics and Phase Relations, A Handbook of Physical Constants*, edited by T. J. Ahrens (American Geophysical Union, Washington, DC, 1995), and references therein.
[6] R. L. Kranz, Tectonophysics **100**, 449 (1983).
[7] M. L. Batzle, G. Simmons, and R. W. Siegfried, J. Geophys. Res. B **85**, 7072 (1980).
[8] M. S. Paterson, *Experimental Rock Deformation—the Brittle Field* (Springer-Verlag, Berlin, 1978).
[9] D. A. Lockner, J. D. Byerlee, V. Kuksenko, A. Ponomarev, and A. Sidorin, in *Fault Mechanics and Transport Properties of Rocks*, edited by B. Evans and T. F. Wong (Academic Press, San Diego, 1992).
[10] K. Mair, I. Main, and S. Elphick, J. Struct. Geol. **22**, 25 (2000).
[11] J. D. Eshelby, Proc. R. Soc. London, Ser. A **241**, 376 (1957).
[12] T. T. Wu, Int. J. Solids Struct. **2**, 1 (1966).

Fracture of disordered solids in compression as a critical phenomenon. III. Analysis of the localization transition

Renaud Toussaint* and Steven R. Pride†
Géosciences Rennes, Université de Rennes 1, 35042 Rennes Cedex, France

(Received 14 November 2001; revised manuscript received 13 June 2002; published 27 September 2002)

The properties of the Hamiltonian developed in Paper II are studied showing that at a particular strain level a ''localization'' phase transition occurs characterized by the emergence of conjugate bands of coherently oriented cracks. The functional integration that yields the partition function is then performed analytically using an approximation that employs only a subset of states in the functional neighborhood surrounding the most probable states. Such integration establishes the free energy of the system, and upon taking the derivatives of the free energy, the localization transition is shown to be continuous and to be distinct from peak stress. When the bulk modulus of the grain material is large, localization always occurs in the softening regime following peak stress, while for sufficiently small bulk moduli and at sufficiently low confining pressure, the localization occurs in the hardening regime prior to peak stress. In the approach to localization, the stress-strain relation for the whole rock remains analytic, as is observed both in experimental data and in simpler models. The correlation function of the crack fields is also obtained. It has a correlation length characterizing the aspect ratio of the crack clusters that diverges as $\xi \sim (\boldsymbol{\varepsilon}_c - \boldsymbol{\varepsilon})^{-2}$ at localization.

DOI: 10.1103/PhysRevE.66.036137 PACS number(s): 62.20.Mk, 46.50.+a, 46.65.+g, 64.60.Fr

I. INTRODUCTION

In Paper II of this series, we obtained the Hamiltonian $E_j(\boldsymbol{\varepsilon},\boldsymbol{\varepsilon}_m)$ of a population of interacting cracks which is the energy necessary to lead a mesovolume of a disordered-solid system from uncracked and unstrained initial conditions, to a final crack state j at a maximum imposed strain $\boldsymbol{\varepsilon}_m$ that is possibly different than the actual strain $\boldsymbol{\varepsilon}$ if the system has been subsequently unloaded. Using this Hamiltonian, we prove here that at a well-defined strain $\boldsymbol{\varepsilon}_c$, the system undergoes a phase transition to bands of coherently oriented cracks.

To study the nature of this localization transition, we must evaluate the partition function Z from which all physical properties depending on the crack distribution are obtained through differentiation. In Paper I, it was established that Z takes a standard form

$$Z(\boldsymbol{\varepsilon},\boldsymbol{\varepsilon}_m,T)=\sum_j e^{-E_j(\boldsymbol{\varepsilon},\boldsymbol{\varepsilon}_m)/T}, \tag{1}$$

despite the fact that it derives from the initial quenched disorder in the grain-contact strengths and has nothing to do with fluctuations through time. The possible crack states j for a mesovolume are defined by a local order parameter $\varphi(\boldsymbol{x})$ distributed at each cell $\boldsymbol{x}$ of a regular square network of identical cells. The amplitude of $\varphi(\boldsymbol{x})$ corresponds to the length of a local crack (always less than cell dimensions), and its sign indicates its orientation ($\pm 45°$ relative to the principal-stress axis).

Our approach for performing the sum over states begins by determining which fields φ maximize the Hamiltonian. Because the temperature in strain-controlled experiments is negative, such maximizing states are the dominant terms in Eq. (1). Any change in the nature of the maximizing crack fields or in the nature of the Hamiltonian in their neighborhood (e.g., the vanishing of a second derivative) corresponds to a phase transition.

In Sec. II, the localization transition is identified and the geometrical nature of the crack fields in the ''functional neighborhood'' surrounding the maximizing states defined. In Sec. III, we sum only over this subset of all states to obtain an analytical approximation of Z. In Sec. IV, the free energy $F=-T\ln Z$ is differentiated with respect to $\boldsymbol{\varepsilon}$ and T to determine both the sustained stress $\boldsymbol{\tau}$, the energy U, and the entropy S. In the approach to localization, no singularities are present in either F or any of its derivatives with respect to strain or temperature which demonstrates, among other things, that the stress/strain relation is analytic up to (and including) localization. In Sec. V, an external field J is introduced that couples to φ permitting an autocorrelation function to be obtained. All singularities at localization are in the second (and higher) derivatives of F with respect to J with the consequence that the correlation length diverges as $\xi \sim (\boldsymbol{\varepsilon}_c-\boldsymbol{\varepsilon})^{-2}$.

II. PRINCIPLE OF THE TRANSITION

A. Extrema of the Hamiltonian

We now determine the most probable states by maximizing the Hamiltonian $E_j(\boldsymbol{\varepsilon},\boldsymbol{\varepsilon}_m)$ along the load path $\boldsymbol{\varepsilon}=\boldsymbol{\varepsilon}_m$. From the summary of Paper II, we have

$$E_j=E^0(\boldsymbol{\varepsilon}_m)+(1-q)\{E^{\rm av}(\boldsymbol{\varepsilon}_m)[\varphi]+E^{\rm int}(\boldsymbol{\varepsilon}_m)[\varphi]\},$$

where E^0 is the energy of the intact material, $E^{\rm av}$ is the energy due to the crack field when crack interactions are

*Present address: Department of Physics, University of Oslo, P.O. Box 1048 Blindern, 0316 Oslo 3, Norway. Email address: Renaud.Toussaint@fys.uio.no
†Email address: Steve.Pride@univ-rennes1.fr

neglected, and $E^{\rm int}$ is the energy due to crack interactions. The parameter q derives from the quenched-disorder distribution and is bounded as $1/2 \leqslant q < 1$.

That the Hamiltonian must be maximized and not minimized comes from the temperature parameter being negative as was quantitatively established in Sec. IV of Paper I. Because we assume the system is intact before strain is applied, it is a fact of our model that the intact state is always the most probable. For this to hold true, the temperature must be negative in strain-controlled experiments because the arrival of cracks at constant strain always reduces the energy in a mesovolume.

1. Mean-field terms

A mean-field simplification of the model built in Paper II would reduce the Hamiltonian to the sole term

$$E^0 + (1-q)E^{\rm av} = \frac{1}{2}[\alpha\Delta^2 + (1-\alpha)\gamma^2] - (1-q)\epsilon\overline{\psi}[\kappa_2\Delta^2 + \kappa_3\gamma^2],$$

where Δ is the strain dilatation, γ the shear strain, and α and κ_i are combinations of the elastic moduli all as defined in Paper II. The second term is strictly negative and represents the weakening of the rock due to the crack porosity which is proportional to $\overline{\psi}$, the volume average of the positive field $\psi = |\varphi|$. Therefore, this mean-field Hamiltonian is maximum when $\overline{\psi} = 0$, which uniquely corresponds to the uniform intact state $\psi = \varphi = 0$.

2. Interaction term

The interesting term is the interaction energy $E^{\rm int}$. As defined in the summary of Paper II (the reader should consult this summary for the definitions of all the terms in what follows), $E^{\rm int}$ is a sum over wave numbers $\boldsymbol{k}$ of orthogonal quadratic forms involving $R_{\boldsymbol{k}}$ and $I_{\boldsymbol{k}}$, which are vectors containing the $\boldsymbol{k}$-space Fourier modes of the order-parameter fields φ and ψ. The sign of these forms is determined by the sign of the two eigenvalues of the symmetric matrices $P_{\boldsymbol{k}}$. For any $\boldsymbol{k}$, at least one of the eigenvalues is positive, since $[1,0]\cdot P_{\boldsymbol{k}}\cdot[1,0]^T = L_{\boldsymbol{k}} = \Delta^2\kappa_1^2(1-\alpha u_{\boldsymbol{k}}^2) > 0$, where $1/2 < \alpha < 1$ and $u_{\boldsymbol{k}}$ is a cosine. To determine the sign of the second eigenvalue, it is sufficient to take the determinant of $P_{\boldsymbol{k}}$. Using $u_{\boldsymbol{k}}^2 + v_{\boldsymbol{k}}^2 = 1$, it is straightforward to show that

$$\det|P_{\boldsymbol{k}}| = \Delta^4\kappa_1^4(1-\alpha)[c v_{\boldsymbol{k}} + \omega]^2. \tag{2}$$

This is strictly positive for every $\boldsymbol{k}$, except when

$$v_{\boldsymbol{k}} = \sin(2\theta_{\boldsymbol{k}}) = -\omega/c, \tag{3}$$

in which case the determinant and second eigenvalue are zero. The vanishing of the determinant is thus independent of the norm of $\boldsymbol{k}$, and takes place at either of two conjugate angles $\theta_{\boldsymbol{k}}^+ = \arcsin(-\omega/c)/2$ or $\theta_{\boldsymbol{k}}^- = \pi/2 - \arcsin(-\omega/c)/2$, where $\theta_{\boldsymbol{k}}$ represents the angle between $\boldsymbol{k}$ and the crack-orientation vector $\hat{\boldsymbol{e}}_1$. The directions in $\boldsymbol{k}$ space at which the determinant vanishes will be denoted by the unit vectors $\hat{\boldsymbol{k}}^\pm$. Thus, the matrices $P_{\boldsymbol{k}}$ are positive definite; i.e., they have two strictly positive eigenvalues, except for those particular wave vectors lying along one of the two directions for which they become positive degenerate. The eigenvector of $P_{\boldsymbol{k}}$ associated with the zero eigenvalues is easily computed to be $[1, -M_{\boldsymbol{k}}/L_{\boldsymbol{k}}]^T$.

The positive-definite quadratic forms of $E^{\rm int}$ are multiplied by a negative constant which implies that the maximum of $E^{\rm int}$ occurs when $\tilde{\varphi}_{\boldsymbol{k}} = \tilde{\psi}_{\boldsymbol{k}} = 0$ for every nonzero $\boldsymbol{k}$ with the exception of those $\boldsymbol{k}$ satisfying Eq. (3). At these degenerate angles, the Fourier modes of φ and ψ are related as

$$\tilde{\varphi}_{\boldsymbol{k}} = -\frac{L_{\boldsymbol{k}}}{M_{\boldsymbol{k}}}\tilde{\psi}_{\boldsymbol{k}}. \tag{4}$$

Now, the definition of the auxiliary field $\psi_x = |\varphi_x|$ imposes a series of constraints between $\tilde{\varphi}_{\boldsymbol{k}}$ and $\tilde{\psi}_{\boldsymbol{k}}$. The simplest is obtained by noting that the space integrals of φ^2 and ψ^2 must be the same which is equivalent to

$$\sum_{\boldsymbol{k}} (\tilde{\psi}_{\boldsymbol{k}}\tilde{\psi}_{-\boldsymbol{k}} - \tilde{\varphi}_{\boldsymbol{k}}\tilde{\varphi}_{-\boldsymbol{k}}) = 0. \tag{5}$$

For a crack-state maximizing $E^{\rm int}$, this condition further requires that

$$(\tilde{\varphi}_0^2 - \tilde{\psi}_0^2) + \sum_{\substack{\boldsymbol{k}=k\hat{\boldsymbol{k}}^\pm \\ k\neq 0}} \left(1 - \frac{M_{\boldsymbol{k}}^2}{L_{\boldsymbol{k}}^2}\right)\tilde{\varphi}_{\boldsymbol{k}}\tilde{\varphi}_{-\boldsymbol{k}} = 0. \tag{6}$$

It will be seen momentarily that along the directions $\hat{\boldsymbol{k}}^\pm$, the factors $1 - M_{k\hat{\boldsymbol{k}}^\pm}^2/L_{k\hat{\boldsymbol{k}}^\pm}^2$ are equal, and that this quantity is an increasing function of the shear-strain parameter $\omega = (\kappa_3\gamma)/(\Delta\kappa_1)$, starting at a strictly negative value when $\omega = 0$ (no shear deformation yet applied), and reaching 0 at a particular value ω_c. For every wave vector, $\tilde{\varphi}_{\boldsymbol{k}}\tilde{\varphi}_{-\boldsymbol{k}} = \|\tilde{\varphi}_{\boldsymbol{k}}\|^2$ is trivially positive, and the definition of ψ also requires that $\tilde{\varphi}_0^2 - \tilde{\psi}_0^2 \leqslant 0$ for any crack state. From Eq. (6), we can conclude that for $\omega < \omega_c$, the only crack-states maximizing the interaction term $E^{\rm int}$ must satisfy both $\tilde{\varphi}_0^2 = \tilde{\psi}_0^2$ and, for every nonzero $\boldsymbol{k}$, $\tilde{\varphi}_{\boldsymbol{k}} = \tilde{\psi}_{\boldsymbol{k}} = 0$. Such a maximum thus corresponds to a spatially uniform crack field.

At the degenerate point $\omega = \omega_c$, the set of maximizing crack states goes through a drastic change. Any nonzero Fourier mode of φ and ψ along the directions $\hat{\boldsymbol{k}}^\pm$ no longer modifies $E^{\rm int}$ so long as $\tilde{\varphi}_0^2 = \tilde{\psi}_0^2$; i.e., so long as the crack field has the same sign over the entire mesovolume. This degeneracy of $E^{\rm int}$ at $\omega = \omega_c$ is at the origin of the localization phase transition.

The critical value ω_c, and the corresponding wave vectors $\boldsymbol{k}$ for which nonzero Fourier modes of φ and ψ do not contribute to $E^{\rm int}$, are determined from the two conditions

$$\det(P_{\boldsymbol{k}}) = 0, \tag{7}$$

$$L_{\boldsymbol{k}}^2 - M_{\boldsymbol{k}}^2 = 0. \tag{8}$$

Using the solution of Eq. (7) given by Eq. (3) in the definitions of $L_{\boldsymbol{k}}$ and $M_{\boldsymbol{k}}$ given in the summary of Paper II, Eq. (8) then becomes an equation for ω_c,

$$[\omega_c^2-(c^2-1)]\left[\omega_c^2+\frac{(1-\alpha)}{\alpha}c^2\right]=0. \tag{9}$$

From the definitions of Paper II, we have $c>1$ while $1/2<\alpha<1$. Thus, Eqs. (7)–(8) can only be satisfied by

$$\omega=\omega_c^{\pm}=\pm\sqrt{c^2-1}, \tag{10}$$

$$\sin(2\theta_{\boldsymbol{k}})=-(\sqrt{c^2-1})/c. \tag{11}$$

With a radial confining pressure maintained constant, and a positive shear stress $\tau_{\text{axial}}>\tau_{\text{radial}}$, the strain components of the rock satisfy $\varepsilon_{\text{axial}}<\varepsilon_{\text{radial}}$ and $\varepsilon_{\text{axial}}<0$ so that $\omega=(\kappa_3/\kappa_1)(\varepsilon_{\text{axial}}-\varepsilon_{\text{radial}})/(\varepsilon_{\text{axial}}+\varepsilon_{\text{radial}})$ is a positive and monotonically increasing function of the axial stress, until the rock possibly exhibits some positive volumetric strain (we will later show that this does not occur prior to localization), where this quantity diverges to $+\infty$ and increases further starting from $-\infty$. All of this establishes that Eqs. (7) and (8) have no solution until the first solution $\omega=\omega_c^+$ is reached. At this particular strain value, nonzero Fourier modes of φ and ψ having any wave vector lying in one of the two directions defined by Eq. (11) can be added to a mesovolume with no change in the interaction energy.

For quartz as the rock mineral,

$$\frac{\kappa_1}{\kappa_3}\omega_c^+=\left(\frac{\varepsilon_{\text{axial}}-\varepsilon_{\text{radial}}}{\varepsilon_{\text{axial}}+\varepsilon_{\text{radial}}}\right)_c\simeq 12,$$

so that we find $(\varepsilon_{\text{axial}}/\varepsilon_{\text{radial}})_c\simeq-1.2$ at the transition. Our model thus predicts the localization transition to occur after a sign reversal of $\varepsilon_{\text{radial}}$ but prior to the point where $\Delta=\varepsilon_{\text{axial}}+\varepsilon_{\text{radial}}$ changes sign. These results are consistent with what is observed in usual triaxial mechanical experiments (e.g., [1–3]).

It can now be algebraically verified using the definitions of $L_{\boldsymbol{k}}$ and $M_{\boldsymbol{k}}$ given in Paper II, that $1-M^2_{k\hat{\boldsymbol{k}}^{\pm}}/L^2_{k\hat{\boldsymbol{k}}^{\pm}}$ does not depend on the norm $\boldsymbol{k}$ nor on which of the two directions $\hat{\boldsymbol{k}}^{\pm}$ is selected. Further, it increases monotonically from a negative value to reach zero when $\omega=\omega_c^+$ (facts used in obtaining the above results).

B. Structure at the localization transition

The goal here is to define the geometric nature of the states maximizing E^{int} at the strain point ω_c. Necessary conditions on the structure of the degenerate states were just given and these are easily made into sufficient conditions. First, the degenerate states must correspond to crack fields of constant sign. They thus satisfy everywhere $\psi=\varphi$ or $\psi=-\varphi$ or, equivalently, $\tilde{\psi}_{\boldsymbol{k}}=\tilde{\varphi}_{\boldsymbol{k}}$ or $\tilde{\psi}_{\boldsymbol{k}}=-\tilde{\varphi}_{\boldsymbol{k}}$. Considering this together with the necessary conditions of Eqs. (4) and (7), requires that the degenerate states be one of two types: (1) $\varphi>0$ everywhere and the only possible nonzero Fourier modes of φ have wave vector directions that satisfy $N_{\boldsymbol{k}}/M_{\boldsymbol{k}}=M_{\boldsymbol{k}}/L_{\boldsymbol{k}}=-1$; or (2) $\varphi<0$ everywhere and the wave vector directions satisfy $N_{\boldsymbol{k}}/M_{\boldsymbol{k}}=M_{\boldsymbol{k}}/L_{\boldsymbol{k}}=+1$. Using again the definitions of $L_{\boldsymbol{k}},M_{\boldsymbol{k}},N_{\boldsymbol{k}}$ given in the summary of Paper II, the first type of degenerate mode corresponds to wave vectors satisfying $\sin(2\theta_{\boldsymbol{k}})=-\sqrt{c^2-1}/c$ and $\cos(2\theta_{\boldsymbol{k}})=-1/c$, while the second type of mode has the same sine requirement, but an opposite value for the cosine. Using $\hat{\boldsymbol{k}}^+$ to represent the wave vector direction corresponding to the first condition, and $\hat{\boldsymbol{k}}^-$ the wave vector direction for the second condition, we conclude that the emergent degenerate crack states consist either of right-inclined cracks with spatial fluctuations forming bands perpendicular to $\hat{\boldsymbol{k}}^+$, or of left-inclined cracks forming bands perpendicular to $\hat{\boldsymbol{k}}^-$. Such geometry is sketched in Fig. 1.

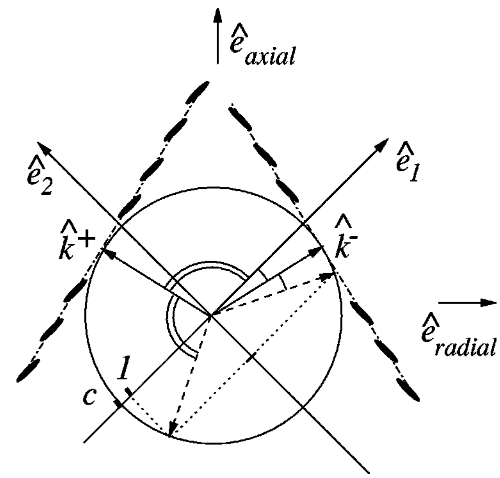

FIG. 1. A part of the conjugate bands emerging at the critical strain. The bands perpendicular to $\hat{\boldsymbol{k}}^+$ are exclusively composed of right-inclined cracks, while those perpendicular to $\hat{\boldsymbol{k}}^-$ contain only left-inclined cracks.

These two sets of crack modes are conjugate to each other; i.e., symmetric to each other under inversion of the radial axis. Since they become statistically important as $\omega\to\omega_c$, whereas the intact state or uniform states are the important states prior to ω_c, the system spontaneously breaks its symmetry at the transition, which is characteristic of a continuous phase transition.

Further, the angle formed by these bands is at $45°-|\theta_{\hat{k}^-}|$ from the axial direction. Using Eq. (11) and the definitions of κ_1 and κ_2 in terms of the Lamé parameters, it is found that this angle is typically between 15° and 35° depending on the rock mineral [4] considered which is consistent with laboratory experiments.

Finally, we note that these special crack bands that leave E^{int} unchanged, make a negative contribution to the Hamiltonian through the mean-field energy E^{av} that is proportional to $\overline{\psi}$. Due to the r^{-D} range of elastic interactions, E^{int} is independent of the norm of $\boldsymbol{k}$ (it depends only on its orientation). Thus, the spatial variation of the bands perpendicular to their lateral extent has no influence on E^{int}; it only affects E^{av} through the number of cracks present. For large systems and a narrow band of only a few cell widths, $\overline{\psi}=\Lambda\ell/\ell^2$

$=\Lambda/\ell$, where Λ and ℓ are the linear size of a cell (grain) and of a mesovolume. Thus, such a thin band makes a negligible contribution to $\overline{\psi}$ for large systems, and is energetically equivalent to the intact state. However, states with numerous and/or wide bands can make a non-negligible contribution to $\overline{\psi}$ and are, therefore, less probable. So this transition indeed corresponds to "localized" structures. Only those states with a small number of small width bands along the special directions are the statistically emergent ones as is observed in actual experiments on rocks.

III. OBTAINING THE PARTITION FUNCTION

The sum over crack states in Eq. (1) is equivalent to the functional integration

$$Z=\int\left(\prod_{\boldsymbol{x}\in\Omega} d\varphi_{\boldsymbol{x}}\right)e^{-E[\varphi,\boldsymbol{\varepsilon},\boldsymbol{\varepsilon}_m]/T}. \tag{12}$$

Since our Hamiltonian is expressed in terms of the Fourier modes $\tilde{\varphi}_{\boldsymbol{k}}$, it is shown in standard textbooks [5,6] that Z further transforms to

$$Z=\int d\tilde{\varphi}_0\prod_{\boldsymbol{k}\in\Upsilon}(d\tilde{\varphi}^R_{\boldsymbol{k}}d\tilde{\varphi}^I_{\boldsymbol{k}})e^{-E[\tilde{\varphi}_{\boldsymbol{k}},\boldsymbol{\varepsilon},\boldsymbol{\varepsilon}_m]/T}, \tag{13}$$

where $\tilde{\varphi}^R_{\boldsymbol{k}}$ and $\tilde{\varphi}^I_{\boldsymbol{k}}$ are the real and imaginary part of $\tilde{\varphi}_{\boldsymbol{k}}$, and Υ is a half space of the set of the wave vectors corresponding to the nonzero modes; i.e., corresponding in two dimensions to the discrete set $(k_1,k_2)=(2\pi\ell/n_1,2\pi\ell/n_2)$ with $(n_1,n_2)\in\mathbb{Z}^2$. There is a small-wavelength cutoff given by $\max(|n_1|;|n_2|)<\ell/\Lambda$ that ensures that φ does not vary on scales smaller than that of a cell, and there is the arbitrary criterion $k_1>0$ made to divide this space into two symmetrical parts. Equation (13) is valid up to a multiplicative constant that has no physical importance since the properties of a system correspond to the derivatives of the free energy $F=-T\ln Z$.

An analytic approximation for Z is obtained by performing the functional integration over a properly chosen subset of all the possible crack states. The definition of this subset is based on what was learned in the preceeding section; namely, that among the states having a given nonzero crack occupation $\overline{\psi}$, the most probable are the uniform states, and precisely at the phase transition, certain banded states may arrive at almost no energy cost, and these emergent states also have the same sign over space. Thus, the geometrical characteristic of all such states in the "functional neighborhood" of the minimizing state is that in each one, all cracks are oriented in the same direction (either left or right). This property justifies making a so-called "constant-sign" (or "mean-phase") approximation for the partition function in which only those states in which the sign does not change in space will be considered. This still includes a huge range of states in which φ spatially varies. The excluded states in this approximation are guaranteed to have lower probabilities than the included ones and, as such, should have a negligible influence on the physical properties of the system. In this aproximation, the Fourier modes of the auxiliary ψ field are trivially related to those of φ as either $\tilde{\psi}_{\boldsymbol{k}}=\tilde{\varphi}_{\boldsymbol{k}}$ for the positive states, or $\tilde{\psi}_{\boldsymbol{k}}=-\tilde{\varphi}_{\boldsymbol{k}}$ for the negative states.

We now rescale the temperature as $T=\Lambda^D T'/\ell^D$. From the definition $T=\partial U/\partial S$ and the fact that U is an energy density independent of ℓ while S is extensive and thus increases as ℓ^D, we have that T scales as ℓ^{-D}. In taking the thermodynamic limit in what follows, it is convenient to work with the purely intensive parameter T' (that is independent of ℓ). Our partition function within the constant-sign approximation then takes the form

$$\begin{aligned}Z\simeq&\int_+\mathcal{D}\varphi\exp\left\{\frac{-\ell^D}{\Lambda^D T'}\left[d+e\left(\frac{\tilde{\varphi}_0}{\ell^D}\right)+\sum_{\boldsymbol{k}\in\Upsilon}w^+(\boldsymbol{k})\left|\frac{\tilde{\varphi}_{\mathbf{k}}}{\ell^D}\right|^2\right]\right\}\\&+\int_-\mathcal{D}\varphi\exp\left\{\frac{-\ell^D}{\Lambda^D T'}\left[d+e\left(\frac{\tilde{\varphi}_0}{\ell^D}\right)\right.\right.\\&\left.\left.+\sum_{\boldsymbol{k}\in\Upsilon}w^-(\boldsymbol{k})\left|\frac{\tilde{\varphi}_{\mathbf{k}}}{\ell^D}\right|^2\right]\right\},\end{aligned} \tag{14}$$

where $\mathcal{D}\varphi$ is a compact notation for the functional measure $d\tilde{\varphi}_0\Pi_{\mathbf{k}\in\Upsilon}(d\tilde{\varphi}^R_{\mathbf{k}}d\tilde{\varphi}^I_{\mathbf{k}})$, and where $\int_+$ and $\int_-$ represent integration over the subsets of φ fields that are everywhere either positive or negative. The quantities $d,e,$ and $w^\pm$ are defined in the summary of Paper II as

$$d=\frac{1}{2}[\alpha\Delta^2+(1-\alpha)\gamma^2], \tag{15}$$

$$e=-\frac{\epsilon}{2}[\kappa_2(\Delta^2-q\Delta_m^2)+\kappa_3(\gamma^2-q\gamma_m^2)], \tag{16}$$

$$\begin{aligned}w^\pm(\boldsymbol{k})=-\frac{\boldsymbol{\epsilon}^2}{(1-\alpha)}[&(L_{\boldsymbol{k}}\pm 2M_{\boldsymbol{k}}+N_{\boldsymbol{k}})(\boldsymbol{\varepsilon})\\&-q(L_{\boldsymbol{k}}\pm 2M_{\boldsymbol{k}}+N_{\boldsymbol{k}})(\boldsymbol{\varepsilon}_m)].\end{aligned} \tag{17}$$

Recall that the values of the actual strain $\boldsymbol{\varepsilon}$ intervening in the probability distribution and in the partition function are those along the load curve for which $\boldsymbol{\varepsilon}=\boldsymbol{\varepsilon}_m$. Their formal distinction only plays a role when partial derivatives of the free energy are taken to define stress. We note then that the value of $w^\pm$ at $\boldsymbol{\varepsilon}=\boldsymbol{\varepsilon}_m$ is $w^\pm=-(1-q)\boldsymbol{\epsilon}^2[1,\pm 1]\cdot P(\boldsymbol{k})\cdot[1,\pm 1]^T/(1-\alpha)$ and since we have shown that P is a positive-definite matrix, and that the temperature T' is negative, we have that $w^\pm/T'$ in Eq. (14) is strictly positive.

The symmetry of the problem under the parity transformation (inversion of the radial axis) guarantees that both integrals in Eq. (14) are equal. Accordingly, only the first integral over positive crack states will be treated. This integral separates into products of Gaussian integrals with the only remaining coupling between the Fourier modes coming from the complicated constraints on the integration domain boundaries that are what guarantee φ to have the same sign everywhere in real space, and ψ to lie within $[0,1]$. But in order to study any singular behavior of the free energy F in the vicinity of localization, Z is determined in the thermodynamic limit in which both the system size and mesovolume size ℓ are taken to be infinite. In this limit, the complicated integration bounds in $\boldsymbol{k}$-space are not relevant. The integration can be carried out entirely on $\mathbb{R}^+$ for $\tilde{\varphi}_0/\ell^D$, and $\mathbb{R}$ for each of the variables $\tilde{\varphi}^R_{\boldsymbol{k}}/\ell^D$, $\tilde{\varphi}^I_{\boldsymbol{k}}/\ell^D$ without changing the result because the contribution to these integrals in the thermodynamic limit comes from the immediate neighborhood of $\tilde{\varphi}_0/\ell^D=0$ and $\tilde{\varphi}_{\boldsymbol{k}}/\ell^D=0$.

A technical proof of this can be obtained as follows: using $\mathbb{R}^+$ and $\mathbb{R}$ as the integration domains produces an upper bound for Z since this includes every positive crack field. A lower bound can be obtained by reducing the integration domain to a subset of the set of all positive crack fields in which $0<\tilde{\varphi}_0<\ell^D$ and $\Sigma_{\boldsymbol{k}\in\Upsilon}(|\tilde{\varphi}^R_{\boldsymbol{k}}|+|\tilde{\varphi}^I_{\boldsymbol{k}}|)\leqslant\min[\tilde{\varphi}_0/\sqrt{2},(\ell^D-\tilde{\varphi}_0)/\sqrt{2}]$. Integrating mode by mode over this polyhedra, the result can be shown to be asymptotically equivalent to the result of the upper bound in the limit where ℓ^D becomes infinite. This exercise is left to the attention of the reader.

Thus, no coupling between the $\boldsymbol{k}$ modes exists in the thermodynamic limit, and our approximation of the partition function takes the convenient form

$$Z\simeq 2z_0z_1\prod_{\boldsymbol{k}\in\Upsilon}[z(\boldsymbol{k})^2], \tag{18}$$

where $z_0=e^{-\ell^D d/\Lambda^D T'}$ and

$$z_1=\int_{x\in\mathbb{R}^+}dx e^{-\ell^D ex/\Lambda^D T'}, \tag{19}$$

$$z(\boldsymbol{k})=\int_{x\in\mathbb{R}}dx\, e^{-\ell^D w^+(\boldsymbol{k})x^2/\Lambda^D T'}. \tag{20}$$

In the limit $\ell\to+\infty$, these two integrals become

$$z_1\sim\Lambda^D T'/(\ell^D e), \tag{21}$$

$$z(\boldsymbol{k})\sim\sqrt{\pi\Lambda^D T'/[\ell^D w^+(\boldsymbol{k})]}. \tag{22}$$

Using Eq. (18), one then obtains the free-energy density in the thermodynamic limit

$$F=-T'(\ln Z)\Lambda^D/\ell^D\sim d+\frac{\Lambda^D T'}{\ell^D}\sum_{\boldsymbol{k}\in\Upsilon}\ln\left(\frac{\ell^D w^+(\boldsymbol{k})}{\Lambda^D T'}\right). \tag{23}$$

The contribution z_1 has vanished in this limit due to the fact that $x\ln x\to 0$ as $x\to 0$. This is a technical consequence of the fact that for states composed of a few single bands, $\bar{\psi}$ vanishes in the thermodynamic limit, as commented upon in the previous section.

IV. SYSTEM PROPERTIES AT LOCALIZATION

The remaining task is to link this free energy to the observables of the system by taking the partial derivatives of F in the limit as localization is approached.

The two partial derivatives of primary interest are those that give the dimensionless entropy density $s=\Lambda^D S/\ell^D$ and the stress $\boldsymbol{\tau}$. From Paper I, we have

$$-s=\left.\frac{\partial F}{\partial T'}\right|_{\boldsymbol{\varepsilon},\boldsymbol{\varepsilon}_m} \quad\text{and}\quad \boldsymbol{\tau}=\left.\frac{\partial F}{\partial\boldsymbol{\varepsilon}}\right|_{T',\boldsymbol{\varepsilon}_m}.$$

The free energy of Eq. (23) is rewritten by replacing the sum over the wave vectors $\Sigma_{\boldsymbol{k}\in\Upsilon}$ with a continuous integral $\ell^D/(2\pi)^D\int_0^{2\pi/\Lambda}k\,dk\int_0^{\pi}d\theta$. After performing the trivial integration over dk we have

$$F=d+\frac{T'}{2}\left[I-\pi\ln\left(-\frac{\Lambda^D T'}{\ell^D}\right)\right], \tag{24}$$

where I is the integral

$$I=\int_{-\pi/2}^{\pi/2}\ln(-w^+)d\theta. \tag{25}$$

The integrand w^+ is a temperature-independent strain function so that $-\partial F/\partial T'$ gives

$$s=-\frac{I}{2}+\frac{\pi}{2}\left[1+\ln\left(-\frac{\Lambda^D T'}{\ell^D}\right)\right], \tag{26}$$

while from $F=U-T's$

$$U=d+\frac{\pi}{2}T'. \tag{27}$$

Since d represents the linear elastic response of an intact rock, and T' decreases from zero to negative values as damage accumulates, this expression shows that the average energy decreases due to the presence of cracks and is thus consistent with the negative curvature of the strain/stress load curve observed experimentally.

Before addressing how s and F (and their derivatives) behave at localization, we first establish the stress and temperature behavior at localization.

A. Mechanical behavior at localization

Consider the stress components $\sigma=-2\partial F/\partial\gamma$ and $p=-2\partial F/\partial\Delta$, where σ (shear stress) and p (pressure) are both positive and related to the axial and radial stress components as

$$-\sigma=\tau_a-\tau_r,\quad\text{and}\quad -p=\tau_a+\tau_r. \tag{28}$$

In standard laboratory experiments, the axial stress τ_a varies while the radial stress $\tau_r=-p_r$ is kept constant. The strain components γ (shear strain) and Δ (dilatation) are similarly related to the axial and radial strain as

$$\gamma=\varepsilon_a-\varepsilon_r,\quad\text{and}\quad \Delta=\varepsilon_a+\varepsilon_r. \tag{29}$$

Using the definition of w^+ [Eq. (17)] along with the definitions of $L_{\boldsymbol{k}}$, $M_{\boldsymbol{k}}$, and $N_{\boldsymbol{k}}$ given in the summary of Paper II, we differentiate the integral I with respect to the actual strain variables, evaluate along the load path ($\Delta_m=\Delta$ and $\gamma_m=\gamma$), use the definition $\omega=\omega_3\gamma/\Delta$ with the new constant $\omega_3=\kappa_3/\kappa_1$ and make the change of integration variables $z=\tan^{-1}\theta$ to obtain exactly

$$\partial_\gamma I=\frac{\omega_3}{(1-q)\Delta}\partial_\omega I, \tag{30}$$

$$\partial_\Delta I=\frac{1}{(1-q)\Delta}(2\pi-\omega\partial_\omega I), \tag{31}$$

where $q=1-1/(k+2)$ is the constant associated with the exponent $k\geqslant 0$ of the quenched disorder distribution, and the integral $\partial_\omega I$ is defined

$$\partial_\omega I=\int_{-\infty}^{+\infty}\frac{\partial_\omega g}{g}\frac{dz}{1+z^2}, \tag{32}$$

with $g(\omega,z)$ given by

$$\begin{aligned} g(\omega,z)=&[1-\alpha-2(1-\alpha)c+(1-\alpha)c^2+\omega^2]z^4\\ &+[4\alpha\omega+4(1-\alpha)c\omega]z^3+[2+2\alpha+2(1-\alpha)c^2\\ &-2(2\alpha-1)\omega^2]z^2+[-4\alpha\omega+4(1-\alpha)c\omega]z+1\\ &-\alpha+2(1-\alpha)c+(1-\alpha)c^2+\omega^2. \end{aligned} \tag{33}$$

Thus, the shear stress and pressure can be written as

$$\sigma=-2(1-\alpha)\gamma-\frac{T'}{\Delta}\frac{\omega_3}{(1-q)}\partial_\omega I(\omega), \tag{34}$$

$$-p=2\alpha\Delta+\frac{T'}{(1-q)\Delta}[2\pi-\omega\partial_\omega I(\omega)]. \tag{35}$$

The integral $\partial_\omega I$ is solved using the residue theorem once the roots z of the quartic $g(\omega,z)$ have been found.

This quartic decomposes into the exact form

$$g(\omega,z)=[z-\zeta(\omega)][z-\zeta^*(\omega)]u(\omega,z), \tag{36}$$

$$u(\omega,z)=\rho(\omega)[z-\xi(\omega)][z-\xi^*(\omega)], \tag{37}$$

where the star indicates taking the complex conjugate. The roots $\zeta(\omega)$ and $\zeta^*(\omega)$ both merge to the real axis in the approach to localization $\omega\to\omega_c$, while the other two roots $\xi(\omega)$ and $\xi^*(\omega)$ remain complex at localization.

There are thus three simple poles $\zeta(\omega)$, $\xi(\omega)$, and i contributing to $\partial_\omega I$ if the loop is closed in the upper-half z plane so that the residue theorem yields

$$\begin{aligned}\frac{\partial_\omega I}{\pi}=&\frac{\partial_\omega g(\zeta)}{\mathrm{Im}\{\zeta\}u(\zeta)[1+\zeta^2]}+\frac{\partial_\omega g(\xi)}{\rho\,\mathrm{Im}\{\xi\}[\xi-\zeta][\xi-\zeta^*][1+\xi^2]}\\ &+\frac{\partial_\omega g(i)}{[i-\zeta][i-\zeta^*]u(i)},\end{aligned} \tag{38}$$

where Im designates taking the imaginary part. We are interested in evaluating this integral (and therefore, the roots ζ and ξ and the function ρ) only in the approach to localization; i.e., when $\delta\omega=\omega-\omega_c$ can be considered small. In this limit, the second and third terms of Eq. (38) (the residues from ξ and i) have numerators and denominators that are both order 0 in $\delta\omega$ so that it suffices to know the behavior

$$\xi(\omega)=\xi_0+\xi_1\delta\omega, \tag{39}$$

$$\rho(\omega)=\rho_0+\rho_1\delta\omega. \tag{40}$$

However, the residue related to ζ is proportional to $\delta\omega$ in both the numerator and the denominator which requires knowledge of this root to second order

$$\zeta(\omega)=\zeta_0+\zeta_1\delta\omega+\zeta_2\delta\omega^2. \tag{41}$$

The various strain-independent constants ξ_i, ρ_i, and ζ_i are all known groupings of the elastic constants derived from Eqs. (33), (36), and (37). The final result for the integral after an enormous algebraic reduction is

$$\partial_\omega I=I_c+I_1\delta\omega, \tag{42}$$

where the constants I_c and I_1 are exactly

$$I_c=2\pi\frac{\sqrt{c^2-1}}{c^2}\quad\text{and}\quad I_1=2\pi\frac{2-c^2}{c^4}. \tag{43}$$

1. Stress and strain at localization

The shear stress and pressure may be written as

$$\sigma=\sigma_0+\sigma^{\mathrm{int}}\quad\text{and}\quad p=p_0+p^{\mathrm{int}},$$

where $\sigma_0=-2(1-\alpha)\gamma$ and $p_0=-2\alpha\Delta$ are the trivial linear variations of the uncracked material. We have just shown that at localization ($\delta\omega=0$), the nontrivial shear stress due to cracks and crack interaction is

$$\sigma_c^{\mathrm{int}}=-\frac{2\pi\omega_3T_c'}{(1-q)\Delta_c}\frac{\sqrt{c^2-1}}{c^2}<0, \tag{44}$$

while the nontrivial pressure is

$$p_c^{\mathrm{int}}=-\frac{2\pi T_c'}{(1-q)\Delta_c c^2}<0. \tag{45}$$

That these critical values are both negative follows because T_c' (scaled temperature at localization) is negative and Δ_c (total dilatation at localization) will soon be shown to be negative. Equations (44) and (45) say that the presence of cracks has lowered both shear stress and pressure relative to an intact material at the same strain. This is indeed what is observed in experiments.

To quantify the nature of Δ_c, we use that the confining pressure p_r is a known positive constant in standard experiments on rocks so that

$$p_r = -\alpha\Delta_c + (1-\alpha)\gamma_c - \frac{T_c'[2\pi - (\omega_c+\omega_3)I_c]}{2(1-q)\Delta_c}. \quad (46)$$

Together with $\omega_c = \omega_3\gamma_c/\Delta_c$, this represents an equation for Δ_c,

$$\left[\alpha - (1-\alpha)\frac{\omega_c}{\omega_3}\right]\Delta_c^2 + p_r\Delta_c + \frac{T_c'[2\pi-(\omega_c+\omega_3)I_c]}{(1-q)} = 0. \quad (47)$$

Because T' varies with strain, we have that T_c' is also a function of Δ_c so that Eq. (47) is more than a simple quadratic in Δ_c. To obtain an order-of-magnitude estimate of T_c', we use the approximate temperature expression based on noninteracting cracks,

$$\frac{1}{T_c'} = -\frac{2\Lambda^2}{d_m^2(1-q)[\kappa_2+\kappa_3(\omega_c/\omega_3)^2]\Delta_c^2} \times \ln\left\{\left[\frac{2\Gamma}{(\lambda+2\mu)d_m\Delta_c^2[\kappa_2+\kappa_3(\omega_c/\omega_3)^2]}\right]^{q/(1-q)} - 1\right\}. \quad (48)$$

After putting Eq. (48) into Eq. (47), Δ_c is numerically determined using Newton's method. The predicted Δ_c is negative for the range of confining pressure p_r of interest and remains negative for all ranges of elastic moduli found in rocks. The signs of the various terms in Eq. (47) imply that the transition happens when the temperature has sufficiently departed from zero, but is still negative. Typical results from the numerical evaluation are $T_c' \sim -10^{-2}(\lambda+2\mu)$, which confirms the rough estimate given in Sec. V of Paper II. The typical value for Δ_c is a few percent; i.e., the order of magnitude experimentally observed at peak stress [7].

The conclusion is that at localization, both dilatation Δ_c and shear strain $\gamma_c = \omega_c\Delta_c/\omega_3$ are negative while $|\gamma_c| \gg |\Delta_c|$. This demonstrates that the radial strain $\varepsilon_r = \Delta_c - \gamma_c$ is positive at localization, which is also consistent with experimental observations.

2. Stress, strain, and temperature derivatives at localization

We now address how the stress and strain components, as well as the temperature are changing with the negative of axial strain $\varepsilon = -\varepsilon_a = -(\Delta+\gamma)/2$ at localization.

In the approach to localization we write $\Delta = \Delta_c + \delta\Delta$, $\gamma = \gamma_c + \delta\gamma$, and $T' = T_c' + \delta T'$ using the exact differential equation for temperature to define $\delta T'$ in what follows (not the approximation). The condition that p_r is constant requires that

$$\delta\Delta\left\{-\alpha + \frac{T_c'[2\pi-(2\omega_c+\omega_3)I_c-(\omega_c+\omega_3)\omega_c I_1]}{2(1-q)\Delta_c^2}\right\} + \delta\gamma\left\{1-\alpha+\frac{T_c'\omega_3[I_c+(\omega_c+\omega_3)I_1]}{2(1-q)\Delta_c^2}\right\} - \frac{\delta T'}{2(1-q)\Delta_c}\{2\pi-(\omega_c+\omega_3)I_c\} = 0,$$

which along with $-2\delta\varepsilon = \delta\Delta + \delta\gamma$ gives

$$\frac{1}{2}\frac{d\Delta}{d\varepsilon} = \frac{2(1-q)(1-\alpha)\Delta_c^2/T_c' + \omega_3[I_c+(\omega_c+\omega_3)I_1] + \Delta_c/(2T_c')[2\pi-(\omega_c+\omega_3)I_c]dT'/d\varepsilon}{-2(1-q)\Delta_c^2/T_c' + 2\pi - 2(\omega_c+\omega_3)I_c - (\omega_c+\omega_3)^2 I_1}, \quad (49)$$

$$\frac{1}{2}\frac{d\gamma}{d\varepsilon} = \frac{2(1-q)\alpha\Delta_c^2/T_c' - 2\pi + (2\omega_c+\omega_3)I_c + (\omega_c+\omega_3)\omega_c I_1 - \Delta_c/(2T_c')[2\pi-(\omega_c+\omega_3)I_c]dT'/d\varepsilon}{-2(1-q)\Delta_c^2/T_c' + 2\pi - 2(\omega_c+\omega_3)I_c - (\omega_c+\omega_3)^2 I_1}. \quad (50)$$

To obtain an exact expression for $dT'/d\varepsilon$ (within the context of having employed the mean-phase approximation), we use the formalism of Sec. IV A of Paper I to write

$$\left[\partial_{T'}U + \left(\partial_\Delta U + \partial_{\Delta_m}U + \frac{p}{2}\right)\partial_{T'}\Delta + \left(\partial_\gamma U + \partial_{\gamma_m}U + \frac{\sigma}{2}\right)\partial_{T'}\gamma\right]\frac{dT'}{d\varepsilon} + \left(\partial_\Delta U + \partial_{\Delta_m}U + \frac{p}{2}\right)\partial_\varepsilon\Delta + \left(\partial_\gamma U + \partial_{\gamma_m}U + \frac{\sigma}{2}\right)\partial_\varepsilon\gamma = 0. \quad (51)$$

Using Eq. (27) for U, we have $\partial_{T'}U = \pi/2$, $\partial_\Delta U = \alpha\Delta = -p_0/2$, $\partial_\gamma U = (1-\alpha)\gamma = -\sigma_0/2$, $\partial_{\Delta_m}U = 0$, and $\partial_{\gamma_m}U = 0$ so that the temperature derivative at localization is given by

$$\frac{1}{2}\frac{dT'}{d\varepsilon} = \frac{[(2\pi-\omega_c I_c)(1-\alpha)+\omega_3 I_c\alpha]2(1-q)\Delta_c + \omega_3(\omega_c+\omega_3)(2\pi I_1+\omega_3 I_c^2)T_c'/\Delta_c}{-[2\pi-(\omega_c+\omega_3)I_c]^2 + (1-q)\pi[-2(1-q)\Delta_c^2/T_c' + 2\pi - 2(\omega_c+\omega_3)I_c - (\omega_c+\omega_3)^2 I_1]}. \quad (52)$$

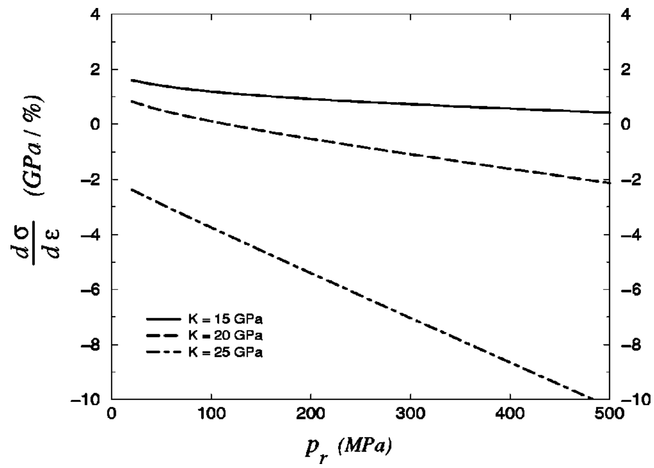

FIG. 2. The localization value of the axial tangent modulus $d\sigma/d\varepsilon$ as a function of the radial confining pressure p_r. The three curves represent different assumed bulk moduli for the mineral. The other rock properties are $\Gamma=10$ J/m^2, $d_m=10$ μm, $\mu=15$ GPa, and $q=3/4$.

This derivative is numerically calculated to be finite and negative for the ranges of elastic moduli and radial confining pressures of interest, thus indicating that the localization transition always preceeds the phase transition where the temperature diverges to $-\infty$. Since rocks fail immediately after localization, the temperature-divergence transition is not observed in rock experiments.

Last, we determine the variation of the stress components with axial strain ε at localization. Since p_r is constant, we have that $dp/d\varepsilon=d\sigma/d\varepsilon=-d\tau_a/d\varepsilon$. These derivatives define the so-called "tangent modulus" given by

$$\frac{1}{2}\frac{d\sigma}{d\varepsilon}=-\frac{\omega_3}{2(1-q)}\frac{I_c}{\Delta_c}\frac{dT'}{d\varepsilon}+\frac{T_c'\omega_3(I_c+\omega_c I_1)}{2(1-q)\Delta_c^2}\frac{d\Delta}{d\varepsilon}-\left[(1-\alpha)+\frac{T_c'}{2(1-q)\Delta_c^2}\omega_3^2 I_1\right]\frac{d\gamma}{d\varepsilon},\qquad(53)$$

where the derivatives $d\Delta/d\varepsilon$, $d\gamma/d\varepsilon$, and $dT'/d\varepsilon$ have been given above.

In Fig. 2, we plot how $d\sigma/d\varepsilon$ varies with radial confining pressure for various values of the elastic constants. The plot shows that for a sufficiently large ratio of bulk to shear modulus, the axial pressure is always decreasing at localization, which means that it has already passed through the stress maximum. However, for sufficiently small bulk moduli and at low confining pressures, localization can also occur prior to peak stress. Thus, peak stress and localization are distinct in our theory. Localization can occur in either the hardening or softening regime depending on the bulk modulus and confining pressure. When localization occurs in the softening regime (large bulk modulus), the strain/stress curve around peak stress is necessarily an analytic (quadratic) function, whereas when it occurs in the hardening regime (small bulk modulus with small confining pressure), the peak stress presumably corresponds to a sharper variation as microcracks start to coalesce along a weakened band and unstable failure sets in. These predictions are consistent with the experimental observations.

B. Entropy and its derivatives at localization

The exact result $\partial_\omega I=I_c+I_1\delta\omega$ with I_c and I_1 as given by Eq. (43) means that the integral I of Eq. (25) is itself both finite and continuous in the limit as $\delta\omega\to 0$. Because it has further been shown that T' remains finite and continuous at localization, Eqs. (24) and (26) then show that both the free energy and the entropy (and all of their derivatives with respect to strain) remain finite and continuous as $\delta\omega\to 0$. This demonstrates exactly that the localization transition is a continuous phase transition and allows us to classify it as a critical point.

V. CORRELATION FUNCTION

A. Derivation of a diverging correlation length

The qualitative study of Sec. II B leads to the conclusion that the localization transition is associated with the creation of conjugate bands of coherently oriented cracks. In this final section, the statistical correlation between cracks will be quantitatively addressed.

The autocorrelation function is defined as

$$G(\boldsymbol{x},\boldsymbol{y})=\langle\varphi(\boldsymbol{x})\varphi(\boldsymbol{y})\rangle-\langle\varphi(\boldsymbol{x})\rangle\langle\varphi(\boldsymbol{y})\rangle\qquad(54)$$

and will be determined using a standard method of statistical mechanics [5,6,8]. First, the Hamiltonian $E[\varphi]$ is generalized to include an additional coupling of the local field $\varphi(\boldsymbol{x})$ with an aribitrary field $J(\boldsymbol{x})$ coming from some external source

$$E'[\varphi,J]=E[\varphi]-\int_{\boldsymbol{x}\in\Omega}d^D\boldsymbol{x}J(\boldsymbol{x})\varphi(\boldsymbol{x}).\qquad(55)$$

The partition function becomes then a functional of the external field

$$Z[J]=\int\prod_{\boldsymbol{x}\in\Omega}(d\varphi_x)e^{-E'[\varphi,J]/T}\qquad(56)$$

and the averages involved in Eq. (54) are obtained by taking functional derivatives of $Z[J]$ with respect to J and then letting the external field go to zero; i.e.,

$$\langle\varphi(\boldsymbol{x})\rangle=\lim_{J\to 0}\frac{T}{Z}\frac{\delta Z}{\delta J(\boldsymbol{x})},\qquad(57)$$

$$\langle\varphi(\boldsymbol{x})\varphi(\boldsymbol{y})\rangle=\lim_{J\to 0}\frac{T^2}{Z}\frac{\delta^2 Z}{\delta J(\boldsymbol{x})\delta J(\boldsymbol{y})}.\qquad(58)$$

Since the original Hamiltonian is most easily handled in Fourier form, the external coupling will be expressed as

$$-\int_{x\in\Omega} d^D\boldsymbol{x}\, J(\boldsymbol{x})\varphi(\boldsymbol{x})$$
$$=-\frac{1}{\ell^D}\left(\tilde{J}_0\tilde{\varphi}_0+2\sum_{\boldsymbol{k}\in\Upsilon}\tilde{J}^R_{\boldsymbol{k}}\tilde{\varphi}^R_{\boldsymbol{k}}+2\sum_{\boldsymbol{k}\in\Upsilon}\tilde{J}^I_{\boldsymbol{k}}\tilde{\varphi}^I_{\boldsymbol{k}}\right), \tag{59}$$

where the superscripts R and I refer once again to the real and imaginary parts of a complex quantity. The functional derivatives relative to $J(\boldsymbol{x})$ must then be expressed by their counterparts in Fourier space,

$$\frac{\delta}{\delta J(\boldsymbol{x})}=\sum_{\boldsymbol{k}\in\Upsilon\cup\{0\}}\left(\frac{\delta\tilde{J}^R_{\boldsymbol{k}}}{\delta J(\boldsymbol{x})}\frac{\partial}{\partial\tilde{J}^R_{\boldsymbol{k}}}+\frac{\delta\tilde{J}^I_{\boldsymbol{k}}}{\delta J(\boldsymbol{x})}\frac{\partial}{\partial\tilde{J}^I_{\boldsymbol{k}}}\right)$$
$$=\sum_{\boldsymbol{k}\in\Upsilon\cup\{0\}}\left(\cos(\boldsymbol{k}\cdot\boldsymbol{x})\frac{\partial}{\partial\tilde{J}^R_{\boldsymbol{k}}}-\sin(\boldsymbol{k}\cdot\boldsymbol{x})\frac{\partial}{\partial\tilde{J}^I_{\boldsymbol{k}}}\right). \tag{60}$$

The modified partition function will again be determined using the constant-sign approximation, but now the presence of the external field breaks the symmetry between the sum over positive and negative crack fields, so that both terms need to be kept in the generalization of Eq. (14). This leads to a slightly more complicated version of Eq. (18) for the expression of Z in the thermodynamic limit

$$Z\simeq z_0\left\{z_1^+\prod_{\boldsymbol{k}\in\Upsilon}\left[z_R^+(\boldsymbol{k})z_I^+(\boldsymbol{k})\right]+z_1^-\prod_{\boldsymbol{k}\in\Upsilon}\left[z_R^-(\boldsymbol{k})z_I^-(\boldsymbol{k})\right]\right\}, \tag{61}$$

where z_0 is again the trivial intact term, and where

$$z_1^\pm=\int_{x\in\mathbb{R}^+}dx\, e^{-(e\ell^D\pm\tilde{J}_0)x]/\Lambda^D T'}, \tag{62}$$

$$z_R^\pm(\boldsymbol{k})=\int_{x\in\mathbb{R}}dx\, e^{-[-2\tilde{J}^R_{\boldsymbol{k}}x+\ell^D w^\pm(\boldsymbol{k})x^2]/\Lambda^D T'}, \tag{63}$$

with $z_I^\pm(\boldsymbol{k})$ having the same form as $z_R^\pm(\boldsymbol{k})$ after replacing $\tilde{J}^R_{\boldsymbol{k}}$ with $\tilde{J}^I_{\boldsymbol{k}}$. In the following, the forms implying derivatives with respect to $\tilde{J}^I_{\boldsymbol{k}}$ are to be implicitly understood as having the same forms as their counterparts with respect to $\tilde{J}^R_{\boldsymbol{k}}$ (these imaginary components will not be explicitly written out).

The integrals are easily performed giving

$$z_1^\pm=\Lambda^D T'/[e\ell^D\pm\tilde{J}_0], \tag{64}$$

$$z_R^\pm(\boldsymbol{k})=\exp\left[\frac{(\tilde{J}^R_{\boldsymbol{k}})^2}{\Lambda^D\ell^D w^\pm(\boldsymbol{k})T'}\right]\sqrt{\frac{\pi\Lambda^D T'}{\ell^D w^\pm(\boldsymbol{k})}}. \tag{65}$$

The first derivatives of Z with respect to the external field are then

$$\frac{\partial Z}{\partial\tilde{J}_0}=z_0\left\{-\frac{\Lambda^D T'}{(e\ell^D+\tilde{J}_0)^2}z_1^+\prod_{\boldsymbol{k}\in\Upsilon}\left[z_R^+(\boldsymbol{k})z_I^+(\boldsymbol{k})\right]+\frac{\Lambda^D T'}{(e\ell^D-\tilde{J}_0)^2}z_1^-\prod_{\boldsymbol{k}\in\Upsilon}\left[z_R^-(\boldsymbol{k})z_I^-(\boldsymbol{k})\right]\right\}, \tag{66}$$

$$\frac{\partial Z}{\partial\tilde{J}^R_{\boldsymbol{k}}}=z_0\left\{z_1^+\prod_{\boldsymbol{k}\in\Upsilon}\frac{2\tilde{J}^R_{\boldsymbol{k}}}{\Lambda^D\ell^D w^+(\boldsymbol{k})T'}\left[z_R^+(\boldsymbol{k})z_I^+(\boldsymbol{k})\right]+z_1^+\prod_{\boldsymbol{k}\in\Upsilon}\frac{2\tilde{J}^R_{\boldsymbol{k}}}{\Lambda^D\ell^D w^-(\boldsymbol{k})T'}\left[z_R^-(\boldsymbol{k})z_I^-(\boldsymbol{k})\right]\right\}. \tag{67}$$

Letting the external field go to zero, both of these terms disappear, so that using the chain rule of Eq. (60), the average of the crack variable φ at any point $\boldsymbol{x}$ in a mesovolume is given by Eq. (57) to be

$$\langle\varphi(\boldsymbol{x})\rangle=0.$$

As expected, there is no spontaneous symmetry breaking prior to the transition.

Consequently, the autocorrelation function reduces to only the second derivatives of Z in Eq. (58). Differentiating Eqs. (66)–(67) with respect to $\tilde{J}_0$, $\tilde{J}^R_{\boldsymbol{k}'}$ and $\tilde{J}^I_{\boldsymbol{k}'}$, and taking the limit where J goes uniformly to zero leads to

$$\frac{\partial^2 Z}{\partial\tilde{J}^R_{\boldsymbol{k}}\partial\tilde{J}^R_{\boldsymbol{k}'}}=\frac{\partial^2 Z}{\partial\tilde{J}^I_{\boldsymbol{k}}\partial\tilde{J}^I_{\boldsymbol{k}'}}=\left[\frac{1}{w^+(\boldsymbol{k})}+\frac{1}{w^-(\boldsymbol{k})}\right]\frac{2Z_0\delta_{\boldsymbol{k}\boldsymbol{k}'}}{\Lambda^D\ell^D T'},$$

$$\frac{\partial^2 Z}{\partial\tilde{J}_0^2}=\frac{2\Lambda^D T'}{\ell^{3D}e^3}Z_0,$$

where $Z_0=Z[0]$ is the original partition function without external source. All the remaining cross derivatives go to zero,

$$\frac{\partial^2 Z}{\partial\tilde{J}^R_{\boldsymbol{k}}\partial\tilde{J}^I_{\boldsymbol{k}'}}=\frac{\partial^2 Z}{\partial\tilde{J}^R_{\boldsymbol{k}}\partial\tilde{J}_0}=\frac{\partial^2 Z}{\partial\tilde{J}^I_{\boldsymbol{k}}\partial\tilde{J}_0}=0.$$

Through the chain rules of Eq. (60), these equalities show that the autocorrelation function has the form $G(\boldsymbol{x};\boldsymbol{y})=G(\boldsymbol{x}-\boldsymbol{y})$ due to the symmetry of the problem under translation for an infinite system. The Fourier transform $G(\boldsymbol{x};\boldsymbol{y})=\sum_{\boldsymbol{k}}\tilde{G}_{\boldsymbol{k}}e^{i\boldsymbol{k}\cdot(\boldsymbol{x}-\boldsymbol{y})}/\ell^D$ is thus given by

$$\tilde{G}_{\boldsymbol{k}}=2\Lambda^D T'\left[\frac{1}{w^+(\boldsymbol{k})}+\frac{1}{w^-(\boldsymbol{k})}\right] \tag{68}$$

when $\boldsymbol{k}\neq 0$. The special value $\tilde{G}_0=2\Lambda^{3D}T'^3/e^3\ell^{3D}$ does not play any role in the thermodynamic limit.

In real space, the autocorrelation function is obtained by an inverse Fourier transform:

$$G(\boldsymbol{x})=\frac{1}{4\pi^2}\int_0^{2\pi/\Lambda}k\,dk\int_0^{2\pi}d\theta\,\tilde{G}(\boldsymbol{k})e^{i\boldsymbol{k}\cdot\boldsymbol{x}}. \tag{69}$$

Using $\tilde{G}(-\boldsymbol{k})=\tilde{G}(\boldsymbol{k})$ which is a consequence of $w^{\pm}$ being π-periodic functions, and working in polar coordinates $\boldsymbol{x}=(x,\theta_x)$ and $\boldsymbol{k}=(k,\theta)$, the angular integral is divided into two symmetric domains which gives

$$G(x,\theta_x)=\int_0^{2\pi/\Lambda}\frac{k\,dk}{2\pi^2}\int_{\theta_x}^{\theta_x+\pi}d\theta\tilde{G}(k,\theta)\cos[kx\cos(\theta-\theta_x)].$$

Since $w^{\pm}$ and therefore $\tilde{G}$ only depend on the angular part of $\boldsymbol{k}$, the integral over $k=|\boldsymbol{k}|$ yields

$$G(x,\theta_x)=\int_{\theta=\theta_x}^{\theta_x+\pi}d\theta\frac{\tilde{G}(\theta)}{2\pi^2}\times\left\{\frac{2\pi}{\Lambda x\cos(\theta-\theta_x)}\sin\left(\frac{2\pi x\cos(\theta-\theta_x)}{\Lambda}\right)+\frac{1}{x^2\cos^2(\theta-\theta_x)}\left[\cos\left(\frac{2\pi x\cos(\theta-\theta_x)}{\Lambda}\right)-1\right]\right\}.$$

For $x\gg\Lambda$, this integral is dominated by a neighborhood of $\theta=\theta_x+\pi/2$, of angular size $c_1\Lambda/x$ with c_1 a constant of order unity. The function $\tilde{G}(\theta)$ is almost constant over this small neighborhood, and this integral can be well approximated as

$$G(x,\theta_x)=\frac{\tilde{G}(\theta_x+\pi/2)}{\Lambda^2}I_G\left(\frac{x}{\Lambda}\right),$$

with the dimensionless integral I_G defined as

$$I_G(u)=2\pi^2\int_{\theta=0}^{\pi}d\theta\left\{\frac{2\pi\sin[2\pi u\cos(\theta)]}{u\cos(\theta)}+\frac{\{\cos[2\pi u\cos(\theta)]-1\}}{u^2\cos^2(\theta)}\right\}.$$

An asymptotic study of this oscillating integral for $u\gg1$ shows that $I_G(u)\sim c_2/u$, with c_2, a positive constant of order unity. Reformulating Eq. (68) with

$$h(\theta)=2c_2T'\left[\frac{1}{w^+(\theta+\pi/2)}+\frac{1}{w^-(\theta+\pi/2)}\right] \quad (70)$$

gives the real space autocorrelation function in the form

$$G(x,\theta_x)\sim h(\theta_x)\frac{\Lambda}{x}. \quad (71)$$

This establishes that along any direction, the autocorrelations decay as Λ/x (for two points separated by a significant number of grains, $x\gg\Lambda$).

Concerning the angular dependence of G, the symmetry of the system under parity leads to $w^-(\theta)=w^+(\pi/2-\theta)$ [which can also be verified directly from the definitions of $w^{\pm}$ and the dependencies of $L_{\boldsymbol{k}},M_{\boldsymbol{k}},N_{\boldsymbol{k}}$ on $u_{\boldsymbol{k}}=\cos(2\theta)$ and $v_{\boldsymbol{k}}=\sin(2\theta)$ given in paper II, together with the fact that the parity symmetry keeps v constant but changes the sign of u].

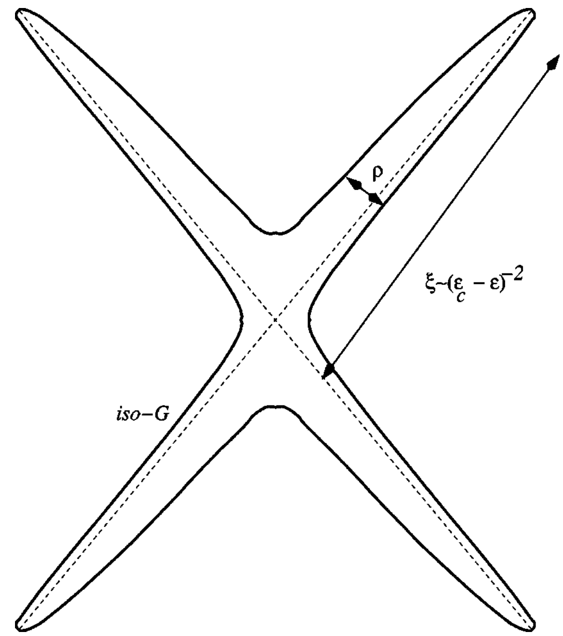

FIG. 3. Form of an isoautocorrelation curve in the approach to the localization transition.

This, along with the π periodicity of $w^{\pm}$, shows that G is symmetric under parity; i.e., $G(x,\pi/2-\theta_x)=G(x,\theta_x)$.

The angular dependence is best shown by considering curves of isocorrelations $G(x,\theta_x)=c_3$, where c_3 is constant along a curve. Such curves obey $x=\Lambda h(\theta_x)/c_3$. The direct study of the function w^+ shows that it admits quadratic maxima along the directions $\theta^+[\pi]$, scaling as $\max(w^+)=w^+(\theta^+[\pi])=-a(\delta\omega)^2$ when the transition is approached, where a is a positive constant. This comes from the fact that E^{int} is degenerate exclusively for the critical angles $\theta^{\pm}$, at reduced strain ω_c. Outside a small neighborhood of $\theta^+[\pi]$, w^+ remains bounded. The definition of h and the exchange under parity of $w^{\pm}$ shows then that such an isocorrelation curve has four branches (spikes) along the directions $\pm\theta^+\pm\pi/2$, whose extent ξ diverge to $+\infty$ as

$$\xi\sim2\Lambda(-T')\frac{c_2}{ac_3}(\omega_c-\omega)^{-2}\sim c_4\Lambda(\varepsilon_c-\varepsilon)^{-2}. \quad (72)$$

The fact that w^+ remains bounded outside any small neighborhood of $\theta^+[\pi]$ also means that the width ρ of the branches remains finite; i.e., that the aspect ratio of the branches ξ/ρ also diverges as $(\varepsilon_c-\varepsilon)^{-2}$. This is qualitatively illustrated in Fig. 3. This prediction can be interpreted as corresponding to the formation of clusters of microcracks having aspect ratios ξ/ρ that diverge as the cracks organize into long thin structures along which the sample will ultimately fail to form the experimentally observed shear bands.

B. Experimental measurement of ξ

It would certainly be desirable to have direct experimental verification of whether the crack bands have aspect ratio that diverge as $1/(\varepsilon_c-\varepsilon)^2$. Unfortunately, there are many practical problems that have prevented the direct measurement of the autocorrelation function of cracks in materials like rocks. We comment here on three types of measurements that either have or could be used to quantify the autocorrelation.

First, following ideas used by Davy and Bonnet [9] in interpreting their sandbox shear experiments, one can measure the local deformation of a large sample by covering the surface with pixels and monitoring the shear strain of each pixel. The total shear strain of the system is then approximated by taking the average over the surface pixels. If the system deformation is plotted as a function of the pixel size, it is expected that when the pixels are smaller than the emergent band structures, the system deformation will decrease as a power law of increasing pixel size as was observed by Bonnet and Davy. However, at a particular pixel size there is a crossover to a constant system deformation as pixel size increases. The pixel size at the crossover point is at least an indirect measurement of the correlation length ξ above which a volume-averaged description of the system holds with properties independent of the pixel size.

Second, a direct measurement of the autocorrelation between cracks can in principle be obtained via acoustic-emissions monitoring [10]. However, the present resolution of this method (millimeters in centimeter-scale specimens) and the difficulty in determing the mode of the individual crack events prevents having a satisfactory sampling for statistical analysis. It seems that improvements on these present limitations are possible.

Last, by analogy with the probing of spin populations by electromagnetic waves to study the ferro/paramagnetic transitions, it should be possible to send plane sound waves through a system and measure the scattering cross section as the waves scatter from the structure of the evolving microcrack population. We have not yet obtained the rigorous connection between such a measured cross section and the Fourier transform of our autocorrelation function; however, such a relation almost certainly exists. No experimental attempts to measure the correlation function of cracking systems in this manner has been attempted to our knowledge.

VI. CONCLUSION

We now summarize the principal results that have emerged in our study. First, we have demonstrated that at a well-defined strain point $\omega=\omega_c$, thin bands of coherently oriented cracks can be added to the system at no energetic cost. Such localized structures break the symmetry that held when $\omega<\omega_c$ and correspond to a phase transition that we named the ''localization transition.'' It was demonstrated that the free energy F and entropy of the system remain continuous and finite at the localization transition which justifies calling it a critical-point phenomena. Such continuity also demonstrates that the stress/strain behavior of the rock is entirely analytic up to and including localization. The only divergence at localization is in the second derivatives of F with respect to the external field J. The consequence is that the correlation length (aspect ratio) of the emergent-crack clusters diverges as $(\omega_c-\omega)^{-2}$. Presumably, if the ''mean-phase'' approximation had not been invoked and if order-parameter contributions proportional to φ^3 and higher had been retained in the Hamiltonian through a renormalization scheme, then a nontrivial exponent on this scaling law might emerge.

The mechanical behavior of the system at localization exhibits many qualities observed in actual experiments on rocks. First, the stress components at localization are reduced relative to their values if the rock had remained intact. The total dilatation Δ_c remains negative at localization, even though the radial strain is positive. With radial confining stress kept constant, the tangent moduli $d\sigma/d\varepsilon$ are, most normally, negative at localization indicating that the load curve has already gone through a smooth quadratic peak stress prior to localization. Nonetheless, for rocks with a sufficiently low bulk modulus and at sufficiently low confining pressures, the localization can occur in the hardening regime, presumably followed by a sharp peak stress corresponding to the unstable coalescence of cracks as the sample fails along a shear band. These results are consistent with what experimentalists observe.

Using the exact differential equation that controls the temperature in the theory, it has been demonstrated that the temperature is becoming even more negative at localization that means that the temperature is always finite at localization. Unfortunately, the exact value T_c of the temperature at localization is difficult to obtain because it is a result of integrating the differential equation from the initial conditions. Although this could be done numerically, we have instead used an approximate value of T_c based on a noninteracting crack model.

By far the most important signature of the localization transition is the divergence of the aspect ratio of the crack clusters. As reported, no definitive experimental work has yet been performed to test this prediction and we hope that experimentalists take this as a challenge.

[1] W.F. Brace, B.W. Paulding, Jr., and C. Scholz, J. Geophys. Res. **71**, 3939 (1966).

[2] R.N. Schock, H.C. Heard, and D.R. Stephens, J. Geophys. Res. **78**, 5922 (1973).

[3] C.H. Scholz, J. Geophys. Res. **73**, 1417 (1968).

[4] J. Bass, in *Mineral Physics and Crystallography. A Handbook of Physical Constants*, edited by T. J. Ahrens (American Geophysical Union, Washington, DC, 1995).

[5] M. Le Bellac, in *Des Phénomènes Critiques aux Champs de Jauge*, 2nd ed. (CNRS, Paris, 1990).

[6] N. Goldenfeld, *Lectures on Phase Transitions and the Renormalization Group*, Frontiers in Physics (Addison-Wesley Reading, MA, 1992).

[7] M.S. Paterson, *Experimental Rock Deformation—the Brittle Field* (Springer-Verlag, Berlin, 1978).

[8] J.J. Binney, N. Dowrick, A. Fisher, and M. Newman, *The Theory of Critical Phenomena* (Clarendon Press, Oxford, 1992).

[9] P. Davy and E. Bonnet, J. Geophys. Res. (to be published).

[10] D. Lockner, in *Rock Physics and Phase Relations. A Handbook of Physical Constants*, edited by T.J. Ahrens (American Geophysical Union, Washington, DC, 1995), pp. 127–147.

ELSEVIER

Physica A 312 (2002) 159 – 171

PHYSICA A

www.elsevier.com/locate/physa

Thermodynamics of fiber bundles

Steven R. Pride[a,*], Renaud Toussaint[b]

[a] Géosciences Rennes, Université de Rennes 1, 35042 Rennes Cedex, France
[b] Department of Physics, University of Oslo, P.O.Box 1048 Blindern, 0316 Oslo, Norway

Received 28 February 2002

Abstract

A recent theory that determines the properties of disordered solids as the solid accumulates damage is applied to the special case of fiber bundles with global load sharing and is shown to be exact in this case. The theory postulates that the probability of observing a given emergent damage state is obtained by maximizing the emergent entropy as defined by Shannon subject to energetic constraints. This theory yields the known exact results for the fiber-bundle model with global load sharing and holds for any quenched-disorder distribution. It further defines how the entropy evolves as a function of stress, and shows definitively how the concepts of temperature and entropy emerge in a problem where all statistics derive from the initial quenched disorder. A previously unnoticed phase transition is shown to exist as the entropy goes through a maximum. In general, this entropy-maximum transition occurs at a different point in strain history than the stress-maximum transition with the precise location depending entirely on the quenched-disorder distribution. © 2002 Elsevier Science B.V. All rights reserved.

Keywords: Fiber bundles; Entropy maximization; Phase transitions

PACS: 46.50.+a; 46.65.+g; 62.20.Mk; 64.60.Fr

1. Introduction

The fiber-bundle model with global load sharing is a simple model for failure in tension introduced almost 80 years ago [1–3] and having received considerable attention and extensions over the past 15 years [4–19]. Although this model may have little pertinence to real fibrous systems such as a rope breaking in tension, it is of interest because it possesses exact analytical properties.

* Corresponding author. Fax: +33-2-23-23-60-90.
E-mail addresses: steve.pride@univ-rennes1.fr (S.R. Pride), renaud.toussaint@fys.uio.no (R. Toussaint).

PII: S0378-4371(02)00816-6

In recent work [20–22], we have developed a general statistical theory for determining the properties of a disordered solid that is accumulating irreversible damage due to cracking under stress. The ensembles in this theory are created by considering different realizations of the quenched disorder in the local breaking strength of the material. Such realizations are made either for the system as a whole, or of more pertinence to real systems, by dividing a given system into smaller "mesovolumes" and letting each mesovolume correspond to a different realization of the quenched disorder. The ensembles so obtained have nothing to do with thermal fluctuations (molecular dynamics). Given a system with such quenched disorder, our theory determines the probability of emergent crack states by maximizing Shannon's measure of disorder subject to constraints coming from the energetics of the fracture process.

In the present paper, we apply this theory to the specific problem of fiber bundles with global load sharing and demonstrate that for any quenched-disorder distribution, it yields the known exact results. Furthermore, a previously unnoticed phase transition is demonstrated to exist where entropy goes through a maximum. This phase transition is distinct from the well-known stress maximum transition and was noticed in the present theory because of the prominent role played by entropy.

However, the importance of our theory is not that it yields a new result in this old model, but that it applies and yields analytical results about phase transitions for any quasi-static damage model; albeit, for models involving crack interactions, approximate treatment of the functional integrations may be required to obtain analytical results (such as renormalization or mean-field approximations). Using our theory, we recently treated the problem of how the mechanical properties of rocks change due to cracks arriving and interacting in compressive shear [20–22]. We analytically demonstrated that the localization transition observed in experiments is a second-order phase transition.

2. Thermodynamics

Our theory was originally developed for a disordered solid under the influence of a stress tensor. For fiber bundles, a much simpler scalar theory applies and so in this section, the formalism is rederived in this simplified context.

A fiber bundle is depicted in Fig. 1. A collection of N fibers are stretched between two rigid supports. One support is held fixed, while the other is free to displace. A load F_N is applied to the bundle through the free support so that the fibers are in a state of tension. In this paper, the load F_N will always be normalized by N to define the overall tension $\tau = F_N/N$. Each non-broken fiber in a bundle has the same length L. If, when $\tau = 0$, this length is L_0, then the measure of strain is $\varepsilon = L/L_0 - 1$. Experiments may be performed on the bundle either by controlling τ or ε.

Each of the fibers has the same Young's modulus which is taken to be unity so that the axial strain ε of each fiber is identical to the tension in the fiber. The N fibers have strengths $\varepsilon_1, \varepsilon_2, \ldots, \varepsilon_N$ which are independent random variables sampled from a distribution $p(\varepsilon)$, whose cumulative distribution is defined $P(\varepsilon) = \int_0^\varepsilon p(x)\,dx$. As the strain ε of the bundle is increased, the individual fibers will break once their tension (strain) gets to their fixed strength threshold. The assumption of "global load sharing"

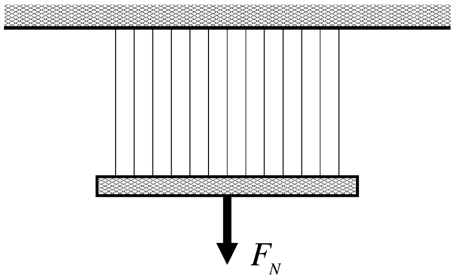

Fig. 1. A bundle of N fibers stretched between two rigid supports with a load F_N applied through the free support.

is that when one of the fibers breaks at fixed load, all the other fibers will extend by the same amount thus increasing the tension in each of the surviving fibers so that the load as a whole is always supported entirely by the surviving fibers. All of this defines the fiber bundle model with global load sharing. Of interest are the mechanical properties of such bundles as averaged over all possible realizations of the fiber strengths.

We first need to know the probability p_j of observing one of the realizations to be in a particular state j of damage when the ensemble as a whole is at an applied strain ε. In the fiber bundle model, a damage state j is defined by which of the N fibers are broken. One could define j using a local order parameter that is 1 if a fiber is intact and 0 if the fiber is broken.

Our theory postulates that the fraction p_j of all realizations observed to be in state j is obtained by maximizing Shannon's measure of disorder

$$S = -\sum_j p_j \ln p_j \tag{1}$$

subject to constraints. Such constraints must involve the independent variables of S. To identify the independent variables, we consider how both S and the average energy in the ensemble of bundles change as the strain is increased.

When ε increases to $\varepsilon + \mathrm{d}\varepsilon$, there is both a work carried out in reversibly stretching the fibers and an additional work carried out due to irreversible fiber breaks. Due to breaking, some of the members of the ensemble (individual realizations of the disorder) will be led out of their current damage state and into state j, while others that were in state j will transfer to still different states. If there is a difference in the number of members entering and leaving state j, there will be a change $\mathrm{d}p_j$ in the occupation probability of state j and such changes are what cause Shannon's disorder measure S to change.

The average energy density (average energy normalized by N) in the ensemble is given by $U = \sum_j p_j E_j$. Here, E_j is the energy density required to create state j at imposed strain ε and as averaged over all members that have been led to state j. Depending on the breaking strengths of a given realization, the work performed in arriving at state j can be different. It is through E_j that all dependence on the quenched-disorder distribution enters the problem. The change that occurs when ε increases to

$\varepsilon + \mathrm{d}\varepsilon$ is

$$\mathrm{d}U = \sum_j E_j \,\mathrm{d}p_j + \sum_j p_j \,\mathrm{d}E_j \,. \tag{2}$$

The first term is the energy expended in changing the disorder over the collection of realizations. It is thus proportional to the disorder change and can be written as

$$T \,\mathrm{d}S = \sum_j E_j \,\mathrm{d}p_j \,. \tag{3}$$

The second term is written

$$f \,\mathrm{d}\varepsilon = \sum_j p_j \,\mathrm{d}E_j \tag{4}$$

and represents both the reversible stretching energy in those members that did not experience breaks during the deformation increment, as well as the irreversible energy changes due to all the breaks that did not result in a net change in the occupation numbers of each state.

This decomposition of the energy increment can be thought of as follows. When breaks occur throughout the ensemble of realizations as ε increases to $\varepsilon + \mathrm{d}\varepsilon$, there is a flow of members between the states. This flow involves energy changes due to fibers breaking in the interval $\mathrm{d}\varepsilon$. It may be resolved into a uniform "incompressible" part whose associated energy is included within $f\,\mathrm{d}\varepsilon$ as well as a non-uniform "compressible" part associated with more members arriving in a given state than are leaving that state. The energy associated with the non-uniform flow between states is entirely contained in $T\,\mathrm{d}S$.

From these expressions it may be concluded that if U is to be treated as a fundamental function, then $U = U(S, \varepsilon)$, or equivalently if S is to be treated as the fundamental function then $S = S(U, \varepsilon)$. In other words, the independent variables that must be involved in the constraints on the maximization of S are U and ε. The proportionality constants T and f are defined

$$T = \left(\frac{\partial U}{\partial S}\right)_\varepsilon \quad \text{and} \quad f = \left(\frac{\partial U}{\partial \varepsilon}\right)_S \,. \tag{5}$$

The state function f is something different than the overall tension τ since we also have that $\tau\,\mathrm{d}\varepsilon = \mathrm{d}U$. Thus, in general, $(\tau - f)\,\mathrm{d}\varepsilon = T\,\mathrm{d}S$ so that $f \neq \tau$ due to fibers breaking in a positive increment $\mathrm{d}\varepsilon$. If strain were to be decreased, fibers do not break and so $\mathrm{d}S = 0$ and the state function f would be defined using only the purely elastic part of the energy changes $\mathrm{d}E_j$. Changes in f in this case are equivalent to changes in τ. Last, since we have taken S to be extensive (proportional to N) while U is a density independent of N, T comes out being proportional to $1/N$. This choice is made so that factors of N do not clutter the equations that follow.

The constraint involving ε is that each non-broken fiber throughout the entire ensemble has the same length which implies $\varepsilon_j = \varepsilon$. The constraint involving U is that $U = \sum_j p_j E_j$. Carrying out the maximization of S subject to these constraints using Lagrangian multipliers gives the probability distribution as

$$p_j(\beta,\varepsilon) = \frac{e^{-\beta E_j(\varepsilon)}}{Z(\beta,\varepsilon)} , \tag{6}$$

where $\beta = 1/T$ and where the partition function Z is defined

$$Z(\beta,\varepsilon) = \sum_j e^{-\beta E_j(\varepsilon)} . \tag{7}$$

The free energy $F = F(\beta,\varepsilon)$ in this ensemble (for this set of constraints) is the Legendre transform of U with respect to S; i.e., $F = U - TS$. Differentiation then gives

$$dF = \beta^{-2} S \, d\beta + f \, d\varepsilon . \tag{8}$$

Upon introducing $U = \sum_j p_j E_j$ and $S = -\sum_j p_j \ln p_j$ into the Legendre transform $F = U - S/\beta$ and using that $\ln p_j = -\beta E_j - \ln Z$ we obtain the standard result

$$\beta F = -\ln Z . \tag{9}$$

Thus, the standard canonical ensemble emerges in this problem where quenched disorder alone (not molecular fluctuations) is responsible for the existence of ensembles.

An important question in such an approach is whether anything precise can be said about the temperature $T = 1/\beta$. Indeed, β can formally be found as the solution of a differential equation. This differential equation is obtained from the previously stated but unused fact that $dU = \tau \, d\varepsilon$ which can be written

$$\tau = \frac{dU}{d\varepsilon} = \sum_j \frac{dp_j}{d\varepsilon} E_j + \sum_j p_j \frac{dE_j}{d\varepsilon} . \tag{10}$$

Now from Eq. (6), we obtain that

$$\frac{dp_j}{d\varepsilon} = \left[-\frac{dE_j}{d\varepsilon} \beta - E_j \frac{d\beta}{d\varepsilon} - \frac{d\ln Z}{d\varepsilon} \right] p_j , \tag{11}$$

while from Eqs. (8) and (9)

$$\frac{d\ln Z}{d\varepsilon} = -F \frac{d\beta}{d\varepsilon} - \beta \frac{dF}{d\varepsilon} = -U \frac{d\beta}{d\varepsilon} - \beta f . \tag{12}$$

Since each member is at the same ε, each member has its own τ_j, and so $\tau = \sum_j p_j \tau_j$. We then obtain the differential equation for β in the form

$$a \frac{d\beta}{d\varepsilon} + b\beta + c = 0 \tag{13}$$

with coefficients given by

$$a = \sum_j p_j E_j (U - E_j), \quad b = \sum_j p_j E_j \left(f - \frac{dE_j}{d\varepsilon} \right),$$

$$c = \sum_j p_j \left(\frac{dE_j}{d\varepsilon} - \tau_j \right) . \tag{14}$$

Since $p_j = p_j\ (\beta, \varepsilon)$, this equation is non-linear and thus difficult to solve. In the present work, we demonstrate that a proposed function $\beta = \beta(\varepsilon)$ exactly satisfies this equation and thus is the true "fiber-bundle" β. To make progress, we next obtain E_j and τ_j for the specific problem of fiber bundles with global load sharing.

3. Fiber bundle model

Fig. 2 details the history of how the overall tension τ might evolve when controlled variations in ε are applied to a bundle having fiber strengths $\varepsilon_1, \varepsilon_2, \ldots, \varepsilon_N$. In this particular example, $n = 3$ fibers have broken when the strain is at ε.

The load on the bundle is equally shared by the $N - n$ surviving fibers so that

$$\tau_n = \varepsilon\left(1 - \frac{n}{N}\right) \tag{15}$$

which is a relation independent of the history; i.e., it depends only on the actual state of the bundle through the number of broken fibers n, and not on the breaking thresholds $\varepsilon_1, \varepsilon_2, \ldots, \varepsilon_n$.

The total work density E_j^p for states j consisting of n broken fibers is the area under the charging curve in a particular realization (the area under the solid line in Fig. 2)

$$E_j^p = \int_0^{\varepsilon} \tau(x)\,\mathrm{d}x = \sum_{m=0}^{n} \int_{\varepsilon_m}^{\varepsilon_{m+1}} \tau_m(x)\,\mathrm{d}x = \sum_{m=0}^{n}\left(1 - \frac{m}{N}\right)\left(\frac{\varepsilon_{m+1}^2}{2} - \frac{\varepsilon_m^2}{2}\right),$$

where from Eq. (15) we have used $\tau_m(x) = x(1 - m/N)$ and where by convention $\varepsilon_{n+1} = \varepsilon$ is the final applied strain. A direct recursion gives exactly

$$E_j^p = \left(1 - \frac{n}{N}\right)\frac{\varepsilon^2}{2} + \sum_{m=1}^{n} \frac{\varepsilon_m^2}{2N}\,. \tag{17}$$

The first term here is the elastic energy that can be reversibly recovered upon decreasing the strain while the second term represents the energy irreversibly consumed in the breaking process. Both contributions can be directly visualized in Fig. 2.

Eq. (17) is next averaged over the quenched disorder to obtain the average energy E_j needed to create state j. Each breaking threshold ε_m is an independant variable, randomly distributed according to $p(\varepsilon_m)$ under the condition that $0 \leqslant \varepsilon_m \leqslant \varepsilon$. They are therefore distributed according to the probability density $p(\varepsilon_m)/P(\varepsilon)$ where the normalization factor accounts for the fact that the upper limit ε is independent of the threshold values ε_m. Thus, averaging over the quenched-disorder gives

$$h(\varepsilon) = \left\langle \frac{\varepsilon_m^2}{2} \right\rangle_{\text{q.d.}} = \frac{1}{P(\varepsilon)} \int_0^{\varepsilon} \frac{x^2}{2}\, p(x)\,\mathrm{d}x\,, \tag{18}$$

where $h(\varepsilon)$ designates the average energy that is lost when each fiber breaks.

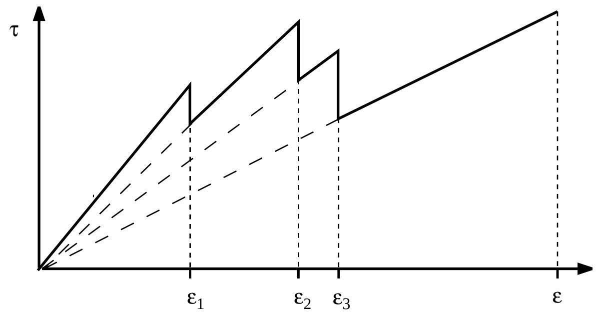

Fig. 2. A strain-controlled experiment. The solid line is the load path followed during the experiment. The dashed lines represent the path that would be followed if strain were to be decreased at some point during the experiment. When a fiber breaks at constant ε, the load τ must be reduced as represented by the vertical drops.

The average work density (Hamiltonian) required to create the state j, averaged over all realizations of the quenched disorder is then in general

$$E_j = \left(1 - \frac{n_j}{N}\right)\frac{\varepsilon^2}{2} + \frac{n_j}{N}h(\varepsilon) = \frac{\varepsilon^2}{2} - \frac{n_j}{N}\left[\frac{\varepsilon^2}{2} - h(\varepsilon)\right] . \tag{19}$$

For example, under the special assumption that the breaking strengths are randomly sampled from a uniform distribution on $0 \leqslant \varepsilon_m \leqslant 1$, we have that $p(\varepsilon) = 1$, $P(\varepsilon) = \varepsilon$, $h(\varepsilon) = \varepsilon^2/6$, and $E_j = \varepsilon^2/2 - (n_j/N)\varepsilon^2/3$.

4. Average properties

We now apply the above theory and determine the thermodynamic functions as a function of applied strain ε. The following analysis is valid for any properly normalized quenched-disorder distribution $p(\varepsilon)$.

The cumulative distribution $P(\varepsilon) = \int_0^\varepsilon p(x)\,\mathrm{d}x$ is the probability that any one fiber has broken when the strain is at ε. Thus, the fraction of all possible realizations having n_j broken fibers and $N - n_j$ unbroken fibers is exactly

$$p_j^{\text{exact}} = (1 - P)^{N - n_j} P^{n_j}. \tag{20}$$

This distribution may be written as

$$p_j^{\text{exact}} = p_0 \exp\left[-n_j \ln\left(\frac{1 - P}{P}\right)\right] , \tag{21}$$

where $p_0 = (1 - P)^N$ is the probability of the unbroken state $j = 0$. Upon using the Hamiltonian of Eq. (19), the postulate of entropy maximization predicts this same distribution to be given by

$$p_j = p_0 \exp\left[n_j \frac{\beta}{N}\left(\frac{\varepsilon^2}{2} - h\right)\right] , \tag{22}$$

where $p_0 = \exp(-\beta\varepsilon^2/2)/Z$ is the probability of the unbroken state.

These two distributions are both Boltzmannians in the number n_j of broken fibers and are identical if the temperature $T = 1/\beta$ is given by

$$\beta(\varepsilon) = \frac{-N}{\varepsilon^2/2 - h(\varepsilon)} \ln\left(\frac{1 - P(\varepsilon)}{P(\varepsilon)}\right) . \tag{23}$$

If it can be shown that this β satisfies the differential equation of Eq. (13), then our theory is exact when applied to fiber bundles with global load sharing.

From the definition $P(\varepsilon)h(\varepsilon) = \int_0^\varepsilon p(x)x^2/2\,\mathrm{d}x$, one has $h(\varepsilon) < \varepsilon^2/2$ for any distribution $p(\varepsilon)$. Thus, $\beta(\varepsilon)$ is a negative increasing function up to the strain point $\varepsilon = \varepsilon_\beta$ where it smoothly goes to zero. The inflection point ε_β is obtained from the condition that $P(\varepsilon_\beta) = \frac{1}{2}$ and defines a previously unnoticed phase transition that will be shown to be distinct from the transition at peak stress. When $\varepsilon > \varepsilon_\beta$, β becomes a positive increasing function of ε.

There are two key average properties upon which all the thermodynamic functions depend; namely, the average fraction of broken fibers in each bundle $\langle n_j/N\rangle$ and the average of this fraction squared $\langle (n_j/N)^2\rangle$. Using the exact probabilities of Eq. (21) [which is equivalent to using the β of Eq. (23) in our probability law], one obtains

$$\left\langle \frac{n_j}{N} \right\rangle = \sum_j p_j \frac{n_j}{N} = \sum_{n=0}^{N} c_n^N \frac{n}{N} P^n (1-P)^{N-n} , \tag{24}$$

where $c_n^N = N!/[n!(N-n)!]$ defines the number of ways of selecting n objects from a group of N distinguishable items. The binomial theorem states that

$$(x+y)^N = \sum_{n=0}^{N} c_n^N x^n y^{N-n} . \tag{25}$$

Upon differentiating this equation with respect to x and then multiplying by x/N, gives that when $x = P$ and $y = 1 - P$

$$\left\langle \frac{n_j}{N} \right\rangle = P \tag{26}$$

which is a known result consistent with the meaning of P. Differentiating a second time yields

$$\left\langle \left(\frac{n_j}{N}\right)^2 \right\rangle = P^2 + \frac{P(1-P)}{N} . \tag{27}$$

Using these two results, the other averages defining the thermodynamic variables are easily read off.

The average stress $\tau(\varepsilon)$ is thus obtained to be

$$\tau = \sum_j p_j \tau_j = (1-P)\varepsilon \tag{28}$$

which is initially an increasing function of ε having the slope

$$\frac{d\tau}{d\varepsilon} = 1 - P - \varepsilon p \,. \tag{29}$$

This slope goes to zero and the stress has a maximum at any strain point ε_τ that is a solution of $1 - P(\varepsilon_\tau) - \varepsilon_\tau p(\varepsilon_\tau) = 0$; i.e., at the point(s) where

$$\varepsilon_\tau p(\varepsilon_\tau) = 1 - \int_0^{\varepsilon_\tau} p(x)\, dx \tag{30}$$

admits a solution. This is a known exact result [4,10]. In general, we can expect that $\varepsilon_\tau \neq \varepsilon_\beta$. The condition required for equality of these strain points is that simultaneously $\varepsilon p(\varepsilon) = \frac{1}{2}$ and $\int_0^\varepsilon p(x)\, dx = \frac{1}{2}$ which for monotonic distribution functions $p(\varepsilon)$ can only occur with the uniform distribution $p(\varepsilon) = 1$ in which case $\varepsilon_\tau = \varepsilon_\beta = \frac{1}{2}$ and the two transitions coincide. If $p(\varepsilon)$ is a monotonic increasing function of ε, then $\varepsilon_\tau < \varepsilon_\beta$ while if it is a decreasing function of ε, then $\varepsilon_\tau > \varepsilon_\beta$. For non-monotonic distributions, there can be an arbitrary number of stress maximas and Eq. (30) can have either no solutions or multiple solutions [10]. The nature of the phase transitions at the distinct strain points ε_β and ε_τ is discussed in the following section.

The average energy in the ensemble is

$$U = \sum_j p_j E_j = (1-P)\frac{\varepsilon^2}{2} + hP \,. \tag{31}$$

Again recalling the definition of h from Eq. (18) gives

$$\frac{dU}{d\varepsilon} = (1-P)\varepsilon - p\,\frac{\varepsilon^2}{2} + \frac{d(hP)}{d\varepsilon} = \tau \tag{32}$$

which is also the equation that gives the differential equation for temperature. This is sufficient for demonstrating that the $\beta(\varepsilon)$ of Eq. (23) satisfies its differential equation. Nonetheless, as a consistency test, the coefficients a, b, and c defined in Eq. (14) will be derived and the differential equation will explicitly be shown to be satisfied.

To obtain the state function f, we need first

$$\frac{dE_j}{d\varepsilon} = \varepsilon - \frac{n_j}{N}\left[\varepsilon - \frac{p}{P}\left(\frac{\varepsilon^2}{2} - h\right)\right] \,. \tag{33}$$

From Eq. (4) and the Lemma of Eq. (26), we then have

$$f = \sum_j p_j \frac{dE_j}{d\varepsilon} = (1-P)\varepsilon + p\left(\frac{\varepsilon^2}{2} - h\right) \,. \tag{34}$$

The variation of the entropy is obtained from the energy balance as

$$\frac{dS}{d\varepsilon} = \beta\left(\frac{dU}{d\varepsilon} - f\right) = Np \ln\left(\frac{1-P}{P}\right) \,. \tag{35}$$

Together with the initial condition $S(0)=0$, this is readily integrated to give

$$S=-N[P\ln P+(1-P)\ln(1-P)]\,. \tag{36}$$

This expression is the classical Shannon result for a set of N random variables in two possible states having probabilities P and $1-P$, which is precisely the case of the fiber bundle with global sharing. This is another consistency check. This entropy S increases from zero [total certainty that every member is intact] and goes smoothly through a maximum [total uncertainty as to what state a member may be in] at the same strain point $P(\varepsilon_\beta)=1/2$ where β goes to zero. After the smooth maximum, S decreases to reach zero if $P(\varepsilon)$ reaches 1 in which case there is total certainty that each member is entirely broken. We note that Eq. (36) can also be directly obtained from the Shannon formula upon applying the binomial theorem.

Finally, the free energy F is again obtained from its Legendre transform definition $F=U-S/\beta$ to be

$$F=\frac{\varepsilon^2}{2}-\left(\frac{\varepsilon^2}{2}-h\right)\frac{\ln(1-P)}{\ln(1-P)-\ln P}\,. \tag{37}$$

At the point ε_β defined by $P(\varepsilon_\beta)=\frac{1}{2}$, the free energy diverges due to the fact that $\beta(\varepsilon_\beta)=0$ while $S(\varepsilon_\beta)$ remains finite. So long as $\varepsilon_\beta\neq\varepsilon_\tau$, the free energy does not diverge when (if) $\varepsilon=\varepsilon_\tau$. In passing, we also note that

$$Z=[(1-P)^h P^{-\varepsilon^2/2}]^{N/(\varepsilon^2/2-h)} \tag{38}$$

is the exact expression of the partition function.

With the above results established, we now obtain the coefficients a,b,c of the differential equation for the temperature as

$$a=-\frac{1-P}{N}\left(Ph^2-\frac{\varepsilon^2}{2}\right)^2,\quad b=\frac{1-P}{N}\left(Ph^2-\frac{\varepsilon^2}{2}\right)\left(P\varepsilon-p\,\frac{\varepsilon^2}{2}+ph\right),$$

$$c=-p\left(h-\frac{\varepsilon^2}{2}\right)\,. \tag{39}$$

Using these together with Eq. (23) for β and its derivative

$$\frac{\mathrm{d}\beta}{\mathrm{d}\varepsilon}=-\frac{Np}{P(1-P)(h-\varepsilon^2/2)}+N\ln\left(\frac{1-P}{P}\right)\left[\frac{\varepsilon+(h-\varepsilon^2/2)p/P}{(h-\varepsilon^2/2)^2}\right] \tag{40}$$

shows that the differential equation $a\,\mathrm{d}\beta/\mathrm{d}\varepsilon+b\beta+c=0$ is exactly satisfied and that our theory gives exact results for this model.

5. Phase transitions

5.1. The entropy maximum transition

The strain point ε_β defined by $P(\varepsilon_\beta)=\frac{1}{2}$ is where simultaneously $\beta=0$, the entropy is a maximum, and the free energy diverges. It is distinct from the stress-maximum transition(s) at ε_τ. The interpretation of $\varepsilon = \varepsilon_\beta$ as a phase transition is natural, since the most probable configuration of a bundle suddenly jumps from being entirely intact to entirely broken. What are the measurable manifestations of this transition at ε_β?

Since the entropy is a maximum at this point, the fluctuations between realizations should also be a maximum as we now demonstrate. Define the fraction of broken fibers in state j to be $\rho_j = n_j/N$, and define the average of this fraction to be $\rho = \langle \rho_j \rangle = P$ where $P = P(\varepsilon)$ is again the probability of a fiber being broken. The quantity of interest here is the root-mean-square fluctuation $\Delta\rho$ in the fraction of broken fibers given by

$$\Delta\rho = \sqrt{\langle \Delta\rho_j^2 \rangle} = \sqrt{\langle \rho_j^2 \rangle - \rho^2} = \frac{\sqrt{P(1-P)}}{\sqrt{N}} \tag{41}$$

which indeed goes through a maximum at $P(\varepsilon_\beta) = \frac{1}{2}$ as expected. This maximum is something that can be directly measured in numerical experiments on fiber bundles but has never before been commented on. The reason it has been discovered in the present theory is because entropy and temperature are explicitly present. We encourage someone to numerically measure $\Delta\rho$ and to verify that it is a maximum at the transition point ε_β. Recall that for monotonic quenched-disorder distributions, if $p(\varepsilon)$ is a decreasing function (more weak fibers than strong fibers), then $\varepsilon_\beta < \varepsilon_\tau$. So the numerical observation in this case should be that $\Delta\rho$ goes through a maximum prior to peak stress. Equivalent comments hold when $p(\varepsilon)$ is an increasing function and $\varepsilon_\beta > \varepsilon_\tau$.

The other fluctuations that are potentially of interest include the root-mean-square stress fluctuation

$$\Delta\tau = \sqrt{\langle \Delta\tau_j^2 \rangle} = \sqrt{\langle \tau_j^2 \rangle - \tau^2} = \varepsilon\Delta\rho \tag{42}$$

and the root-mean-square energy fluctuation

$$\Delta U = \sqrt{\langle \Delta E_j^2 \rangle} = \sqrt{\langle E_j^2 \rangle - U^2} = \left(\frac{\varepsilon^2}{2} - h \right) \Delta\rho \, , \tag{43}$$

but since these are simply proportional to $\Delta\rho$ it seems that the interesting signature of this phase transition is the maximum in $\Delta\rho$.

The "order" of this transition is not classically defined in the Ehrenfest scheme; however, it seems inappropriate to call it a continuous transition because the free energy is singular at ε_β as shown above. Nonetheless, in the limit as $\varepsilon \to \varepsilon_\beta$ the singular part of F diverges according to the scaling law

$$F_s = -\frac{\ln 2}{8} \frac{[\varepsilon_\beta^2 - h(\varepsilon_\beta)/2]}{p(\varepsilon_\beta)} (\varepsilon - \varepsilon_\beta)^{-1} \tag{44}$$

which has a (trivial) universal exponent. Since F and its derivatives are difficult to numerically measure, the principle manifestation of this phase transition remains $\Delta\rho$ going through a maximum at a point $\varepsilon_\beta \neq \varepsilon_\tau$.

5.2. The stress maximum transition

The phase transition at peak stress $\varepsilon = \varepsilon_\tau$ is the one that researchers up to now have focused on. Since S and its derivatives remain continuous and finite there, an attempt to classify this transition as being first-order or second-order is meaningless. The label of "continuous" transition seems the most appropriate.

There is universality at this transition due to the fact that for any monotonic analytic quenched-disorder distribution, $\tau(\varepsilon)$ is a smooth analytic function so that upon developing this function in the neighborhood of its maximum one is guaranteed $|\tau - \tau(\varepsilon_\tau)| \sim |\varepsilon - \varepsilon_\tau|^2$ with the exponent of course being independent of the distribution $p(\varepsilon)$ or other model parameters. Such development of an analytic function about a critical point is the way any mean-field theory acquires a universal scaling law. However, Kloster, Hansen and Hemmer [10] do demonstrate that a non-analytic quenched-disorder distribution can lead to highly non-analytic stress-strain behavior that thus falls outside the quadratic universality class. Also, in other damage models in which elastic interaction between cracks (damage points) is important, the simple observation of a model exhibiting an averaged stress maximum does not by itself guarantee an exactly quadratic stress-strain relation in the neighborhood of the maximum. Such a relation may be non-analytic due to a diverging correlation length in the correlation between cracks.

The quadratic stress maximum means that $\mathrm{d}\varepsilon/\mathrm{d}\tau$ diverges as $|\tau - \tau(\varepsilon_\tau)|^{-1/2}$ [11,19]. Accordingly, the average rate at which the fraction of broken fibers increases with stress $\mathrm{d}\rho/\mathrm{d}\tau = p\,\mathrm{d}\varepsilon/\mathrm{d}\tau$ also diverges as $|\tau - \tau(\varepsilon_\tau)|^{-1/2}$ [4,15]. Using additional considerations not developed in this paper, one can further show that the average size of avalanches also diverges as $|\tau - \tau(\varepsilon_\tau)|^{-1/2}$ [10,15,17], and that the distribution $D(\Delta)$ of the size Δ of the avalanches scales as $D(\Delta) \sim \Delta^{-5/2}$ [6,7,10,17] at the stress maximum. These are the principal observable characteristics of the stress-maximum transition.

6. Summary and conclusions

Two principal results have been obtained in this paper. First, it was demonstrated that for any quenched-disorder distribution used in the fiber-bundle model with global load sharing, the probability of the emergent damage states may be exactly calculated by maximizing Shannon's entropy subject to constraints. It is through the constraints that the nature of the quenched-disorder distribution enters the macroscopic thermodynamics.

Second, a previously unnoticed phase transition occurs in the fiber-bundle model with global load sharing when the entropy goes through a maximum. This phase transition is distinct from the stress-maximum transition; although, for the uniform quenched-disorder distribution, the two transitions coincide. The principle manifestation of this transition is that the root-mean-square fluctuation in the number of broken fibers will go through a maximum, which is a quantity that can be directly measured in numerical experiments.

To conclude, we postulate that the probability of emergent states can always be calculated through entropy maximization for any damage model of interest including models in which there is elastic interaction between the local damage (order) parameters. Damage models with order-parameter interactions are not normally considered amenable to analytical treatment; however, using our approach a rather standard canonical-ensemble partition function emerges and the various functional integration procedures available for studying the partition function in the neighborhood of critical points may be employed.

Such generality is the principal utility of our approach. A concern is the ability to produce an expression for the model temperature. The temperature can be found in principle as the solution of a well-posed initial-value problem. Unfortunately, the differential problem is highly non-linear and thus difficult to solve. Because stress maxima and entropy maxima do not normally coincide, a stress-maximum transition may be studied by simply assuming the temperature to be well behaved in the neighborhood of the stress maxima. But if an explicit expression for the temperature is desired, the following approach can be employed.

In models involving crack interactions, there are always a subset of dilute states in which the interactions are negligible. The exact probabilities of such states can usually be determined from the quenched-disorder distribution alone. A comparison between the probabilities calculated from entropy maximization and such exact probabilities then determines the model temperature to be used in the Boltzmannian. With the temperature so defined, and with a proper model Hamiltonian in hand, the partition function can be analyzed.

References

[1] F.T. Peirce, J. Text. Ind. 17 (1926) 355.
[2] H.E. Daniels, Proc. R. Soc. A 183 (1945) 404.
[3] B.D. Coleman, J. Appl. Phys. 29 (1958) 968.
[4] J.V. Andersen, D. Sornette, K.W. Leung, Phys. Rev. Lett. 78 (1997) 2140.
[5] H.E. Daniels, Adv. Appl. Probab. 21 (1989) 315.
[6] A. Hansen, P.C. Hemmer, Phys. Lett. A 184 (1994) 394.
[7] P.C. Hemmer, A. Hansen, J. Appl. Mech. 59 (1992) 909.
[8] R.C. Hidalgo, F. Kun, H.J. Herrmann, Phys. Rev. E 65 (2002) 032502.
[9] R.C. Hidalgo, F. Kun, H.J. Herrmann, Phys. Rev. E 64 (2001) 066122.
[10] M. Kloster, A. Hansen, P.C. Hemmer, Phys. Rev. E 56 (1997) 2615.
[11] F. Kun, S. Zapperi, H.J. Herrmann, Eur. Phys. J. B 17 (2000) 269.
[12] D. Krajcinovic, M.A.G. Silva, Int. J. Solids Struct. 18 (1982) 551.
[13] I.L. Menezes-Sobrinho, A.T. Bernardes, J.G. Moreira, Phys. Rev. E 63 (2001) 025104(R).
[14] L. Moral, Y. Moreno, A.F. Pacheco, Phys. Rev. E 63 (2001) 066106.
[15] Y. Moreno, J.B. Gomez, A.F. Pacheco, Phys. Rev. Lett. 85 (2000) 2865.
[16] Y. Moreno, J.B. Gomez, A.F. Pacheco, Physica A 274 (1999) 400.
[17] S. Roux, A. Delaplace, G. Pijaudier-Cabot, Physica A 270 (1999) 35.
[18] S. Roux, Phys. Rev. E 62 (2000) 6164.
[19] D. Sornette, J. Phys. A 22 (1989) L243.
[20] R. Toussaint, S.R. Pride, Phys. Rev. E 2002, to be submitted.
[21] R. Toussaint, S.R. Pride, Phys. Rev. E 2002, to be submitted.
[22] R. Toussaint, S.R. Pride, Phys. Rev. E 2002, to be submitted.

PHYSICAL REVIEW E **71**, 046127 (2005)

Interacting damage models mapped onto Ising and percolation models

Renaud Toussaint*
Department of Physics, University of Oslo, P. O. Box 1043 Blindern, 0316 Oslo, Norway

Steven R. Pride†
Earth Science Division, Lawrence Berkeley National Laboratory, 1 Cyclotron Road, MS 90-1116, Berkeley, California 94720, USA
(Received 16 March 2004; revised manuscript received 1 February 2005; published 21 April 2005)

We introduce a class of damage models on regular lattices with isotropic interactions between the broken cells of the lattice. Quasistatic fiber bundles are an example. The interactions are assumed to be weak, in the sense that the stress perturbation from a broken cell is much smaller than the mean stress in the system. The system starts intact with a surface-energy threshold required to break any cell sampled from an uncorrelated quenched-disorder distribution. The evolution of this heterogeneous system is ruled by Griffith's principle which states that a cell breaks when the release in potential (elastic) energy in the system exceeds the surface-energy barrier necessary to break the cell. By direct integration over all possible realizations of the quenched disorder, we obtain the probability distribution of each damage configuration at any level of the imposed external deformation. We demonstrate an isomorphism between the distributions so obtained and standard generalized Ising models, in which the coupling constants and effective temperature in the Ising model are functions of the nature of the quenched-disorder distribution and the extent of accumulated damage. In particular, we show that damage models with global load sharing are isomorphic to standard percolation theory and that damage models with a local load sharing rule are isomorphic to the standard Ising model, and draw consequences thereof for the universality class and behavior of the autocorrelation length of the breakdown transitions corresponding to these models. We also treat damage models having more general power-law interactions, and classify the breakdown process as a function of the power-law interaction exponent. Last, we also show that the probability distribution over configurations is a maximum of Shannon's entropy under some specific constraints related to the energetic balance of the fracture process, which firmly relates this type of quenched-disorder based damage model to standard statistical mechanics.

DOI: 10.1103/PhysRevE.71.046127 PACS number(s): 46.50.+a, 46.65.+g, 62.20.Mk, 64.60.Fr

I. INTRODUCTION

The physics of breakdown processes that lead, for example, to stress-induced catastrophic failure of both man-made and geological structures, remains an ongoing subject of research. Stress-induced fracture of a homogeneous material containing a geometrically simple single flaw has been studied since the work of Griffith [1] and is now well understood. However, the breakdown of heterogeneous structures, in which the local mechanical properties are randomly distributed in space and/or time, continues to present challenges despite the many advances over the last 15 years [2]. The difficulty is in characterizing and quantifying the effects of interaction between the multitude of constituents.

Most of the knowledge about these types of systems has been obtained from lattice network simulations. One of the most well-studied lattice network models is the 80 year old fiber bundle model (FBM) [3–6] that describes the rupture of bundles of parallel fibers. This model originally considered elastic fibers of identical elastic constant, breaking when their elongation exceeds individual thresholds distributed according to a given uncorrelated random distribution. A global load sharing rule (GLS) is assumed by which the load carried by a fiber is uniformly distributed to the surviving fibers when it breaks. Analytical results for this model have been obtained [7–11] that concern the average load-deformation properties [7–9], the distribution of avalanches [10], or the relationship between such quenched-disorder based models and standard statistical mechanics [11].

The original FBM model with global load sharing has been generalized to allow for nonuniform load sharing rules, considered either as purely local load sharing (nearest-neighbor interactions), in which case distribution of avalanches and mechanical properties have been analytically studied [12–14], or as power laws of distance from the failed fiber, which have been studied numerically [15,16].

Closely related to these models of fiber bundles in elastic interaction, many studies have addressed fuse networks [17–25], or networks of isotropic damage with interactions having the range of the elastostatic Green function [26–28].

The classification of lattice breakdown processes as critical-point phenomena is still subject to debate [9,29–37]. Local load sharing models are usually understood as breaking through a process similar to a first-order transition [29], while models with long-range elastic interactions or GLS are analyzed either as a critical-point transition [9,29,30,35], or as a spinodal nucleation process [31,38]. The issue depends on whether the accumulated damage has a correlation length that diverges as a power law of the average deformation in the approach to macroscopic failure. Numerical evidence in

*Electronic address: Renaud.Toussaint@fys.uio.no; URL: http://folk.uio.no/renaud/
†Electronic address: srpride@lbl.gov

the literature suggests that the nature of the correlation length in the approach to failure depends on the specific model being analyzed, the damage interaction range, and the type of quenched-disorder distribution considered. A major difficulty of such attempts to classify the breakdown process is that no analytical form for the distribution of the damage configurations at a given external load is available (at least that has a firm basis). Numerical simulations of the scaling behavior of avalanches are limited in size due to computational restrictions which makes critical-point analysis difficult.

It is proven here that quasistatic interacting damage models such as the FBM, that possess randomly quenched local breaking thresholds, can be mapped onto percolation, Ising, or generalized Ising models depending on the range of the damage interaction. Our demonstration holds in the limit of small damage; i.e., under the restriction that the stress perturbation emanating from each broken cell is much smaller than the average stress in the system. More specifically, the change in elastic energy in the system at fixed imposed boundary deformation due to damage that arrives is the sum of a mean-field softening term proportional to the number of damaged cells, and an additive function over pairs of damaged cells that is small compared to the mean-field softening terms. This corresponds to the general validity conditions of a Born approximation. In real solids accumulating damage, the cracks represent only small local changes in the elastic moduli, and so this weak perturbation limit has direct practical importance.

The stress-induced emergent-damage distribution is proven to be a Boltzmannian with a temperature (probabilistic energy scale) that is an explicit analytical function of both the applied deformation and the quenched-disorder threshold probability distribution funtion (PDF). The damage-model Hamiltonian is shown to have an Ising form with coupling constants that have explicit functional dependence on the applied deformation, the quenched-disorder PDF, and the nature of the damage interaction (nearest neighbor or long range). The critical point of the Ising model is of course well known. So for a given numerical simulation or laboratory experiment, one can use the expressions for the coupling constants developed here to determine how the system is evolving in coupling-parameter space as deformation increases and thus be able to predict the nature of any phase transition that might arrive (first order, continuous, or no transition). Knowing whether catastrophic failure (i.e., damage correlation-length divergence) is an imminent possibility has practical application.

We have recently proposed a statistical theory for the localization of oriented fractures that emerge and elastically interact when the system has a shear stress applied to it [39–41]. The distribution of the emergent crack states was obtained using the postulate that the fracture arrival would maximize Shannon's entropy under constraints representing the energetic balance of the process. In the present work, we do not make this postulate but instead prove its validity by direct integration over the damage evolution. The present work also presents more general ranges of interaction. However, unlike our previous work, the present analysis is for a purely isotropic (scalar) description of damage interaction. The interaction of real fractures in an anisotropic load, where microfractures present high aspect ratios, necessarily requires a tensorial elastic description as in our earlier work [39–41].

The organization of the paper is as follows. In Sec. II, we introduce (and justify in the Appendix) the general type of scalar damage models that are considered. In Sec. III, the probability of each damage configuration is obtained by integrating over all paths that lead to it. In Sec. IV, we establish the relationship between these configurational distributions and standard statistical mechanics, which allows the standard toolbox of statistical mechanics to be applied to damage models entirely based on quenched disorder. These analytical developments will then be utilized in Sec. V to establish that fracture processes in such damage models are isomorphic to percolation for GLS (Sec. V A), or to the Ising model for nearest-neighbor interactions (Sec. V B). This allows us to isolate some transition points in these models, and to predict the nature of the correlation length in the approach to the transition. We will also discuss in Sec. V C the case of damage models with arbitrary power-law decay of the interactions, and show how they are related to generalized Ising models, which can themselves be mapped onto standard ones via renormalization of the coupling constants. The results are summarized and discussed in a concluding section.

II. DEFINITION OF THE DAMAGE MODELS CONSIDERED

Our models reside on a regular lattice of dimension D (e.g., a square lattice in $D=2$). Each cell of the lattice has a location x within the set Ω of cells making up the lattice, and has a state described by a local order parameter φ_x, where $\varphi_x=0$ if the cell is intact and $\varphi_x=1$ if it is broken. There is a local stress and strain associated with each cell. The cells elastically interact with each other; however, such interaction must be isotropic for the present analysis to apply. A configuration of damage is described as a damage field φ corresponding to the set of N local variables $\varphi \equiv \{\varphi_x\}_{x\in\Omega}$ where $N=N(\Omega)$ is the total number of cells in the system.

Our systems are initially uniform by hypothesis; i.e., they have a homogeneous damage field $\varphi=0$ at zero strain and stress and each cell starts with the same elastic moduli. Strain is progressively applied through the application of a uniform normal displacement l at the edges of the system. A cell breaks at constant applied l when the energy required to break it (which is a random quenched threshold sampled from a probability distribution function) just equals the reduction in stored elastic energy in the lattice due to the break.

A key requirement of the models treated here is that the stress perturbation emanating from a broken cell must be weak enough that a first Born approximation holds; i.e., stress interaction between any two broken cells is allowed for while simultaneous interaction between three or more broken cells is not. This approximation is valid whenever the stress perturbation due to a broken site is much smaller than the mean stress in the system.

One specific realization of such a "weak damage" model is an appropriately defined fiber bundle model. In the model, a set of N elastic fibers are stretched between a free rigid plate and an elastic half space. The rigid plate is displaced by a controlled amount l that puts the fibers in tension. Once fibers begin to break, elastic interactions occur through the elastic solid. As demonstrated in the Appendix, such interactions will be weak if either (1) the elastic solid is much stiffer than the fiber material, or (2) the fibers are much longer than wide and are sufficiently widely placed. In the limit that the elastic half space becomes rigid, this model reduces to the classic global load sharing fiber bundle.

Another realization is a uniform isotropic solid divided into N cells. Uniform displacements l are applied to the limiting faces of the lattice in such a way that the material is in a state of uniform dilation. The damage that arrives is assumed to change the isotropic moduli without creating anisotropy in the process. For example, the damage might be modeled as a spherical cavity that opens at the center of the cell thus reducing the elastic moduli of that cell. The weak interaction is guaranteed if the change in the cell modulus is small. We emphasize that the assumption of weak damage holds for any configuration of damage over the underlying lattice, including damage states with large fractions of broken cells.

As demonstrated in the Appendix, the energy E_p reversibly stored in such systems when the system is in a damage state φ at the applied loading level l is

$$E_p[\varphi,l] = (C_0 + C_1 + C_2)l^2, \tag{1}$$

$$C_0 = N, \tag{2}$$

$$C_1 = -c\sum_{x\in\Omega} \varphi_x, \tag{3}$$

$$C_2 = -\varepsilon\sum_{x,y} J_{xy}\varphi_x\varphi_y, \tag{4}$$

where c is a positive constant in the range $0<c\leqslant 1$ that is independent of the damage or deformation state, ε is a small positive parameter in the range $0<\varepsilon/c\ll 1$ that controls the strength of the stress perturbations, and J_{xy} are $O(1)$ coupling constants that allow for the load redistribution between cells at positions x and y when a cell is broken. Various spatial ranges for J_{xy} are considered including (1) global load sharing in which case $J_{xy}=0$; (2) local load sharing in which case $J_{xy}=\alpha>0$ is a constant of order unity for pairs xy of nearest neighbors, 0 otherwise; (3) elastic load sharing in which case $J_{xy}\sim(\ell/|x-y|)^D$ where ℓ is the lattice step size; and (4) fiber-bundle elastic sharing with fibers interacting through an elastic plate in which case $D=2$ and $J_{xy}\sim\ell/|x-y|$ (see the Appendix).

The local load sharing case (2) can in principle happen in a fiber bundle stretched between plates enduring both elastic and plastic deformations capable of screening the stress perturbations caused by broken fibers to only nearest neighbors, which always can carry some load if damaging them only decreases their elastic constant (i.e., $c<1$). We treat case (2) for the sake of generality and do not specify the detailed constitutive relations required for it to be realized in practice.

The cost in surface energy to break any of the cells (which represents either the energy required to create new surface area within a cell or to break a fiber) is a random variable fixed *ab initio*, with no spatial correlations between the different cells. The breaking energy is thus a quenched uncorrelated disorder, described by a probability distribution function $p(e)$ for which $p(e)de$ is the probability that a cell's surface energy is in $[e,e+de]$, and having a cumulative distribution $P(e)=\int_0^e p(z)dz$. For a given realization of each cell's surface energy e_x, there is thus a certain total surface energy

$$E_s[\varphi] = \sum_{x\in\Omega} e_x(1-\varphi_x) \tag{5}$$

associated with each damage field $\varphi=\{\varphi_x\}_{x\in\Omega}$.

Given that $B\subset\Omega$ is a certain subset of locations, the notation φ^B refers to the state where this subset is broken and its complementary intact; i.e., $\varphi_x^B=1$ for every $x\in B$, and $\varphi_x^I=0$ for every $x\in I=B^C$.

As the external deformation l is increased, damage evolution is ruled by Griffith's principle: Given the system in a certain configuration φ^B and deformation l, it can undergo a transition towards a more broken state $\varphi^{B\cup\{x\}}$ that differs from the previous state by one additional broken cell at x, if the release in potential energy is equal to the surface energy cost of the new break; i.e., if

$$\Delta E_p[\varphi^B,x,l] = e_x, \tag{6}$$

where

$$\Delta E_p[\varphi^B,x,l] = E_p[\varphi^B,l] - E_p[\varphi^{B\cup\{x\}},l] = \left(c+\varepsilon\sum_y J_{xy}\varphi_y\right)l^2. \tag{7}$$

If $e_x>\Delta E_p[\varphi^B,x,l]$ for any surviving cell $x\in I$, there is no break and the deformation can be further increased while the system remains in the same state φ^B. If a break happens in cell x, which leads to the new state φ^E where $E=B\cup\{x\}$ while the external deformation l is kept constant, there is a possibility of avalanche at fixed l if there is some $y\in E^C$ such that

$$\Delta E_p[\varphi^E,y,l] \geqslant e_y. \tag{8}$$

If there is more than one possible location satisfying Eq. (8), the one that breaks is determined by maximizing the energy release; i.e., its location corresponds to

$$\Delta E_p[\varphi^E,y,l] - e_y = \max_{z\in E^C}(\Delta E_p[\varphi^E,z,l] - e_z). \tag{9}$$

The avalanche test [Eq. (8)] is then computed again until the system stabilizes in a given configuration.

Eventually, although we have chosen to base the evolution of our damage model on minimization of energy, we note that the formal integration of path probabilities presented in the following sections could similarly be obtained as well for the case of a rule based on force thresholds, with at any given external deformation a force carried per intact fiber equal to an average one, plus perturbations due to the already broken fibers. However, this approach will not be pursued here.

III. PROBABILITY DISTRIBUTION OF DAMAGE STATES

The probability of occurrence of any damage configuration φ is now determined when the system is at a given external deformation l that was reached monotonically (l as defined here does not include any elastic unloading).

More specifically, in the previous section, we have defined a deterministic rule for the evolution of our studied systems. Given a particular realization of the quenched disorder (QD) over each lattice cell, and an initially intact state, the system experiences a progressive damage that builds up as the external deformation is increased. Given a specific emergent damage configuration over the lattice, and a final elongation l, we determine here what fraction of all possible realizations of the QD lead to the given damage state at the given deformation. By definition, this probability of occurrence integrates over all possible ways (and orders) through which this configuration arises at final l. Consequently, the probability distribution over configurations that we obtain contains no information about the order at which the cells broke.

The PDF we obtain thus corresponds to the classical quantity estimated in numerical simulations of deterministic systems with QD in the damage thresholds; namely, given N_r realizations of the QD, a specific damage configuration is realized n_r times, and the probability of occurrence of this configuration is estimated as the fraction n_r/N_r at large N_r.

We will first summarize the results for the simplest case, global load sharing, which was performed in [11], and which will serve as a basis for a perturbative treatment to include the effect of interactions.

A. Global load sharing

In this case, the interaction term of Eq. (4) is $C_2=0$ for any configuration, and from Eq. (7), $\Delta E_p[\varphi,x,l]=cl^2$ regardless of the state φ and new break location x considered.

Each of the cells then shares the same level of deformation l, and the probability for any one of them to be broken is simply (from the cumulative surface energy distribution)

$$P_0 = P(e < cl^2) = \int_0^{cl^2} p(z)dz, \qquad (10)$$

independently of the state of the other cells since there are no interactions between them, and each fiber simply sustains the mean-field deformation l, which was reached monotonically from zero.

The probability of being in a given configuration φ with n cells broken out of N is then

$$P[\varphi,l] = P_0(l)^n[1 - P_0(l)]^{N-n}. \qquad (11)$$

This corresponds to the behavior of a so-called "two-state system" in which each of the N independent sites has a probability $P_0(l)$ of being broken and $1-P_0(l)$ of being intact.

To avoid confusion, note that the above probability is the probability of reaching a *specific configuration* φ at l, which specifies the state of every cell, and depends only on the number of broken cells n in the state φ in this GLS case. Accordingly, the probability $P[n,l]$ of reaching *any* state with n broken cells can be obtained by adding this probability $P[\varphi,l]$ for every state φ containing n broken cells out of N, so that $P[n,l]=N!/[(N-n)!n!]P_0(l)^n[1-P_0(l)]^{N-n}$.

The consequences of this distribution function for the mechanical behavior and correlation length at the transition point of macroscopic rupture will be developed in Sec. V A As a consistency check, we will then show that the derived ensemble-averaged mechanical response of the system has exactly the known form [7] for a fiber bundle in global load sharing, in the limit of large sizes N.

Note that working at an imposed deformation level l, rather than an imposed total force τ over the bundle, results in the local deformation level of each cell being that imposed on the entire system. Considering instead an imposed total force τ carried by the bundle would require global information on the total number of broken cells n in order to know the elongation of each cell (and hence the force carried by each surviving cell). In the present notation, the force carried by an intact cell is $dE/dl=2l$, the one carried by a damaged cell is similarly $2(1-c)l$, so that the total force carried by the bundle is $\tau=(N-nc)2l$. If we impose the total force τ on the bundle as an external control parameter, the probability for any cell to break would depend both on τ and on the past history of the bundle, through the dependence of the individual elongations (or forces) on the number n of already broken cells, since $l=\tau/[2(N-nc)]$. Considering the imposed total force τ as a control parameter allows us to compute the statistics of avalanches [10,12,13], but involves more complicated expressions to obtain the probability of states at a fixed global force level [7]. This led us to choose here to work instead at imposed global deformation l, which immediately makes the states of the cells at given elongation independent random variables from each other in the GLS case. The advantage of this choice in the case of interactions of variable ranges, where these events are no longer statistically independent, is that we will be able to analytically explore the effect of these interactions by a perturbative treatement from the simple Eq. (11) above.

B. Local load sharing

1. Damage-state probability distribution

We now consider the case where each broken cell increases the local deformation by an amount $\alpha\varepsilon l$ on each of its nearest neighbors; i.e., $J_{xy}=\alpha$ for each nearest-neighbor pair, or $J_{xy}=0$ for more distant cells.

Note that for a given cell x, the potential energy release defined in Eq. (7), $\Delta E_p[\varphi,x,l]$, is a growing function of both the deformation l and the subset of cracked cells φ considered; i.e., if we consider two subsets $B\subset D$ and $x\in D^C$, then $\Delta E_p[\varphi^D,x,l]\geqslant\Delta E_p[\varphi^B,x,l]$. Physically, this inequality means that the local load over each cell increases with the external load imposed, and that any cell breaking anywhere else induces an additional increase in local load. This inequality will play a key role in obtaining the damage-state probability distribution.

To aid the pedagogic development, we first derive the probability of occurrence of a configuration φ^B with n isolated broken cells forming a subset B, which do not share any common nearest neighbors. There are zn nearest neighbors to these n cells (in a subset F corresponding to the boundary of broken cells) where z is the coordination number of the lattice considered. There are then $N-(z+1)n$ cells completely isolated from the broken ones in the subset $(B\cup F)^C$. For a cell x having broken from an intermediate stage φ^A with $A\subset B$, at an intermediate external load $h \in [0,l]$, the change in the stored energy satisfies $\Delta E_p[\varphi^A,x,h]=ch^2\leqslant cl^2$. For every cell having survived, we have either $\Delta E_p[\varphi^B,x,l]=(c+\alpha\varepsilon)l^2$ if $x\in F$ (x is on the boundary of the broken cell set), or $\Delta E_p[\varphi^B,x,l]=cl^2$ if $x \in (B\cup F)^C$ (x is completely disconnected from the broken cell set). Applying Griffith's principle [Eq. (6)] to every cell and intermediate deformation $h\in[0,l]$, and using the monotony of $\Delta E_p[\varphi,x,l]$ in both l and φ, we obtain that a necessary and sufficient condition for all cells in B to be broken is that their surface-energy thresholds were below cl^2, while those of their neighbors in F were above $(c+\alpha\varepsilon)l^2$, and the remaining ones in $(B\cup F)^C$ above cl^2. Defining

$$P_1(l) = P(e < (c+\alpha\varepsilon)l^2) = \int_0^{(c+\alpha\varepsilon)l^2} p(z)dz, \tag{12}$$

this then implies that

$$P[\varphi,x] = P_0^n(1-P_1)^{zn}(1-P_0)^{N-(z+1)n} \tag{13}$$

is the probability of occurrence of such a configuration.

We now pass to the more general case. In the argument, we obtain upper and lower bounds for the probability of some arbitrary damage state, and then demonstrate that in the limit $\varepsilon/c\ll 1$, the two bounds converge to the unique probability distribution of interest.

For any configuration φ, u_k is defined as the number of intact cells with k broken nearest neighbors and n_k as the number of broken cells with k broken neighbors. If n out of the N cells are broken, we have $\Sigma_k n_k=n$ and $\Sigma_k u_k=N-n$. The way the above quantities are associated with any particular configuration is illustrated in Fig. 1.

For a cell x that broke from an intermediate state $\psi\subset\varphi$ with k already broken neighbors in ψ, at an external load h, we have

$$\Delta E_p[\psi,x,h] = (c+k\alpha\varepsilon)h^2. \tag{14}$$

Using again the monotony of ΔE_p, a necessary and sufficient condition for any intact cell $y\in B^C$ to have survived is that its threshold exceeded $\Delta E_p[\varphi,y,l]$. The probability for each of these independent statistical events to occur is expressed as $1-P_k(l)$, where

$$P_k(l) = P(e < (c+k\alpha\varepsilon)l^2). \tag{15}$$

For any cell that broke $x\in B$, we note that they have broken with certainty at the ultimate deformation l if the external load was sufficient to trigger their break without the help of overload due to breaks of the other ones; i.e., they have broken with certainty if their energy threshold was below $\Delta E_p(\varphi^{\emptyset},x,l)=cl^2$ where $\emptyset$ denotes the empty set (no broken cells). Furthermore, if every threshold in B was below cl^2,

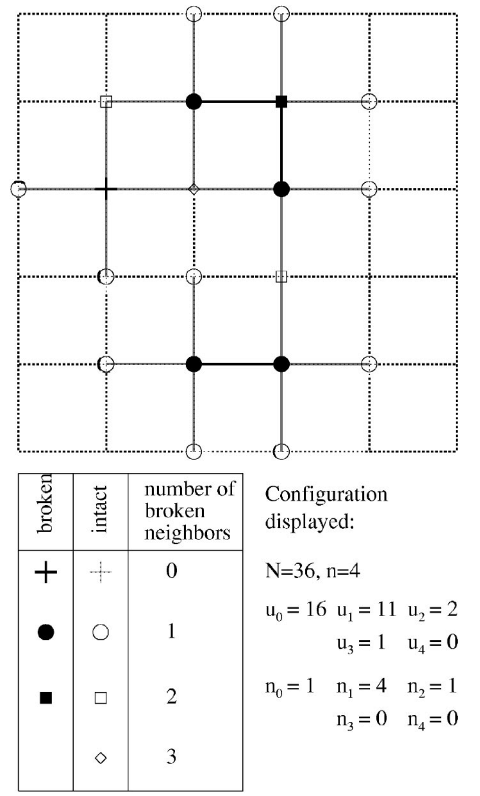

FIG. 1. Typical configuration and associated connectivity measures.

except a particular one $x\in B$ which has k_x broken neighbors in the considered configuration φ^B and has a breaking energy between cl^2 and $(c+k_x\alpha\varepsilon)l^2$, the k_x neighbors of this considered cell x will have broken with certainty at the ultimate load l, so that x will also break with certainty under the effect of the overload due to its broken neighbors. The probability that this individual threshold broke under the sole effect of the overload due to its neighbors can be expressed

$$\Delta P_{k_x} = P_{k_x}(l) - P_0(l). \tag{16}$$

Thus, a lower bound for the probability of occurrence of the configuration φ^B can be expressed as

$$P[\varphi^B,l] > \left[P_0^n + \left(\sum_{x\in B} P_0^{n-1}\Delta P_{k_x}\right)\right]\prod_{k\in N}(1-P_k)^{u_k}, \tag{17}$$

where the index k runs formally to N; however, $u_k=0$ when $k>z$ (the coordination number of the lattice).

For any cell $x\in B$ that broke, its associated energy threshold was necessarily lower than $\Delta E_p[\varphi^{B\setminus\{x\}},x,l]$ where $B\setminus\{x\}$ denotes the set B with cell $\{x\}$ excluded from it. Thus, an upper bound for the probability of occurrence of the configuration under study is

$$\begin{aligned} P[\varphi^B,l] &< \left[\prod_{x\in B} P_{k_x}\right]\prod_k (1-P_k)^{u_k} \\ &= \left[\prod_{x\in B}(P_0+\Delta P_{k_x})\right]\prod_k(1-P_k)^{u_k}. \end{aligned} \tag{18}$$

For a continuous PDF over thresholds (which guarantees no jumps in the cumulative distribution P and is the only restriction placed on the PDF), ΔP_k is a quantity of order ε, and P_0 is of order 1. In the limit of a Born model (weak stress perturbations for which $\varepsilon / c \ll 1$), the upper and lower bounds for the probability of occurrence are identical to order ε. We have thus established in this framework that

$$P[\varphi,l] = \prod_{m=0}^{\infty} P_m{}^{n_m} \prod_{k=0}^{\infty} (1-P_k)^{u_k}. \tag{19}$$

2. Identification of a surface tension and cohesion energy

The above can be reexpressed for small interactions $\varepsilon \ll 1$ by a Taylor expansion of the cumulative QD distribution as

$$\Delta P_k(l) = \gamma(l)k, \quad \text{where } \gamma = p(cl^2)\alpha\varepsilon l^2. \tag{20}$$

Then, Eq. (19) becomes

$$\ln P[\varphi,l] = \ln\left[\prod_{m=0}^{\infty}(P_0+\gamma m)^{n_m}\prod_{k=0}^{\infty}(1-P_0-\gamma k)^{u_k}\right] \tag{21}$$

$$\begin{aligned}&\simeq n\ln P_0 + (N-n)\ln(1-P_0) \\ &\quad + \frac{\gamma}{P_0}\sum_{m=1}^{\infty} m n_m - \frac{\gamma}{1-P_0}\sum_{k=1}^{\infty} k u_k \\ &= n\ln P_0 + (N-n)\ln(1-P_0) \\ &\quad + 2\frac{\gamma}{P_0}n_I - \frac{\gamma}{1-P_0}n_S,\end{aligned} \tag{22}$$

where in the state φ considered, n is the number of broken sites, and n_I and n_S refer, respectively, to the number of internal bonds between pairs of broken cells and the number of boundary bonds between broken and intact cells.

These probabilities are thus of the form

$$P[\varphi,l] = P[\varphi^{\emptyset}]e^{n\ln[P_0/(1-P_0)]+2n_I\gamma/P_0-n_S\gamma/(1-P_0)} \tag{23}$$

with the probability of the intact state

$$P[\varphi^{\emptyset}] = (1-P_0)^N. \tag{24}$$

The probabilities are thus classic Boltzmann distributions $P[\varphi^{\emptyset}]e^{-H}$ where

$$-H[\varphi,l] = \ln\left[\frac{P_0}{(1-P_0)}\right]n + 2\frac{\gamma}{P_0}n_I - \frac{\gamma}{1-P_0}n_S. \tag{25}$$

For no interactions, $\gamma=0$ and the above reduces to the global load model of Eq. (11). Since n and n_I can be formally interpreted as volume integrals over the interior of clusters of broken cells, and n_S as a surface integral along the boundary of these clusters, we can make the following analogies to the quantities of classical statistical physics:

$$\ln[P_0/(1-P_0)] \to -\mu/T \quad \text{(chemical potential)}, \tag{26}$$

$$2\frac{\gamma}{P_0} \to \frac{-e}{T} \quad \text{(bulk energy)}, \tag{27}$$

$$\frac{\gamma\ell}{1-P_0} \to \frac{\gamma_S}{T} \quad \text{(surface tension)}, \tag{28}$$

where ℓ is the lattice step size. The first term in Eq. (25) accounts for the average energy required to break a cell, the second term for an increase in the probability of finding some clusters of connected cracks due to positive interactions between them, and the third term for a decrease in the probability of finding clusters with a long interface between cracked and noncracked regions due to the fact that intact cells along the boundary are more likely to have broken from overloading from cracked neighbors, thus leading to even more fractured states.

In the beginning of the process, the two first terms dominate, and to leading order

$$-H[\varphi,l] = (\ln P_0)n + 2\frac{\gamma}{P_0}n_I. \tag{29}$$

C. Arbitrary-range interactions

As long as screening effects are absent or neglected (as they are in the present model of weak interactions), the above arguments based on Griffith's principle and the monotony of ΔE_p in φ and l extend directly to the case of arbitrary ranges of interactions.

At external deformation l, a cell x (1) has broken with certainty if the external load alone could break it, i.e., if its associated surface energy is lower than cl^2; and (2) is intact with certainty if the external load plus the load perturbation due to the broken cells in the final configuration could not break it at final deformation, i.e., if its surface energy is higher than $(c+\varepsilon\Sigma_y J_{xy}\varphi_y^B)l^2$. Denoting

$$P_0 = P(e < cl^2), \tag{30}$$

$$\begin{aligned}\Delta P_x &= P\left(e < \left(c+\varepsilon\sum_y J_{xy}\varphi_y^B\right)l^2\right) - P(e<cl^2) \\ &= p(cl^2)\varepsilon l^2 \sum_y J_{xy}\varphi_y^B,\end{aligned} \tag{31}$$

a necessary condition to end up at a certain configuration φ^B at deformation l is that all surviving cells $x \in B^C$ in that configuration have their threshold above $(c+\varepsilon\Sigma_y J_{xy}\varphi_y^B)l^2$, and all cells that broke $x\in B$ have their threshold below $(c+\varepsilon\Sigma_y J_{xy}\varphi_y^B)l^2$. Thus,

$$P[\varphi^B,l] < \prod_{x\in B}(P_0+\Delta P_x)\prod_{z\in B^C}(1-P_0-\Delta P_z) \tag{32}$$

provides an upper bound for the probabilities in the case of arbitrary ranges of interaction.

Conversely, a sufficient condition to end up in this configuration is that all surviving cells have their threshold above $(c+\varepsilon\Sigma_y J_{xy}\varphi_y^B)l^2$, and that the broken cells either (1) have all their thresholds below cl^2; or (2) all but one located at x have such thresholds, the last one breaking only due to the overload from the others; i.e., the last one has its threshold bounded by $cl^2 < e < (c+\varepsilon\Sigma_y J_{xy}\varphi_y^B)l^2$. This gives a lower bound for the probability of the configuration φ^B,

$$P[\varphi^B,l] > \sum_{x\in B}(P_0+\Delta P_x)\prod_{y\in B\setminus\{x\}}P_0\prod_{z\in B^C}(1-P_0-\Delta P_z). \tag{33}$$

As earlier, both lower and upper bounds coincide to order ε, so that upon Taylor expanding $\ln P[\varphi,l]$ to this order, we again obtain the Boltzmannian $P[\varphi,l]=P[\varphi^{\emptyset}]e^{-H[\varphi,l]}$ with an intact probability given again by $P[\varphi^{\emptyset}]=(1-P_0)^N$ and

$$-H[\varphi,l] = \ln[P_0/(1-P_0)]n + \frac{p(cl^2)\varepsilon l^2}{P_0}\sum_{xy}J_{xy}\varphi_x\varphi_y - \frac{p(cl^2)\varepsilon l^2}{1-P_0}\sum J_{xy}\varphi_x(1-\varphi_y). \tag{34}$$

In the beginning of the process, the two first terms once again dominate and

$$-H[\varphi,l] = \ln[P_0]n + \frac{p(cl^2)\varepsilon l^2\sum_{xy}J_{xy}\varphi_x\varphi_y}{P_0}. \tag{35}$$

This expresses the equivalence between this most general weakly interacting damage model and an Ising model with generalized interaction rules.

IV. EQUIVALENCE WITH A MAXIMUM ENTROPY POSTULATE

We now obtain these same probability distributions using the standard entropy maximization argument. The reason for doing this is to make explicit connection to usual thermostatistics and to define a partition function from which all thermodynamic properties of interest may be obtained through differentiation.

It is convenient to introduce the index j to denote each possible damage configuration φ. We postulate that the probability distribution function over configurations j maximizes Shannon's disorder [42]

$$S = -\sum_j p_j \ln p_j \tag{36}$$

subject to the constraints

$$\sum_j p_jE_j = U, \quad \sum p_jn_j = n, \quad \sum_j p_j = 1, \quad \forall\ j, \quad l_j = l, \tag{37}$$

where U is the total average energy that has been put into the system and n is again the average number of broken cells. The validity of this maximization postulate will be directly demonstrated in what follows. However, independent of the formal demonstration, one can anticipate that Shannon entropy should be maximized since the initial quenched disorder in the breaking energies allows each possible damage configuration to be accessible. The constraints allow for the content of the Griffith principle and are what make certain emergent damage states more probable than others.

Throughout the remainder of the paper, p_j denotes the probability of finding a configuration j over all possible realizations of the qd, when the system has been brought to average deformation l starting from an initially intact state. The term n_j now refers to the total number of cracks in the configuration j, while n is the statistical average of n_j. A few classical results can directly be derived from these assumptions:

$$p_j = \frac{e^{-\beta(E_j-\mu n_j)}}{Z}, \tag{38}$$

$$Z \equiv \sum_j e^{-\beta(E_j-\mu n_j)},$$

where $\beta=\partial S/\partial U|_{l,n}$ and $\beta\mu=-\partial S/\partial n|_{l,U}$. From these one further has

$$G \equiv -\ln(Z)/\beta,$$

$$G = U - S/\beta - \mu n,$$

$$dG = \tau\, dl - Sd(1/\beta) - n\, d\mu,$$

$$dU = \tau\, dl + dS/\beta + \mu\, dn, \tag{39}$$

where

$$\tau = \sum_j p_j\tau_j \quad \text{and} \quad \tau_j \equiv \frac{dE_j}{dl}. \tag{40}$$

The thermodynamic parameters β and μ are obtained here by comparing Eq. (38) to the earlier probabilities obtained by direct integration over the microstate space.

The PDF over configurations is a maximum of Shannon's entropy under the above constraints, if and only if there are two constants (β,μ) such that

$$H_j - \beta(E_j-\mu n_j) = \text{const} \quad \forall\ j \tag{41}$$

with H_j given by Eq. (34). From Eqs. (1)–(4) and Eq. (34), we have

$$-H_j = \ln\left(\frac{P_0}{1-P_0}\right)n_j + \frac{p(cl^2)\varepsilon l^2}{P_0}\sum_{xy}J_{xy}\varphi_x\varphi_y - \frac{p(cl^2)\varepsilon l^2}{1-P_0}\sum_{xy}J_{xy}\varphi_x(1-\varphi_y),$$

$$E_j = \left(N - cn_j - \varepsilon\sum_{xy}J_{xy}\varphi_x\varphi_y\right)l^2,$$

$$\sum_{xy}J_{xy}\varphi_x(1-\varphi_y) = -\sum_{xy}J_{xy}\varphi_x\varphi_y + n_j\sum_r J_r, \tag{42}$$

where translational invariance of $J_{xy}=J_{r=|\mathbf{y}-\mathbf{x}|}$ has been assumed. Equation (41) then requires

$$\beta = \frac{p(cl^2)}{P_0(1-P_0)}, \tag{43}$$

$$\mu = \frac{1}{\beta}\ln\left[\frac{P_0}{(1-P_0)}\right] - l^2\left(c + \varepsilon P_0 \sum_r J_r\right). \qquad (44)$$

Thus, the PDF over configurations indeed maximizes entropy [Eq. (36)] under the constraints of Eq. (37), with no unknowns. The inverse temperature and chemical potential depend on the deformation level through Eqs. (43) and (44). They are well defined analytical functions of l and the model parameters considered, the qd distribution via P_0, and the interaction coupling J_r. So the usual machinery of equilibrium statistical mechanics [Eqs. (38) and (39)] is valid and can be used for any of our damage models.

The autocorrelation function $\langle \varphi_x \varphi_y \rangle$ can therefore be obtained in the standard way by (1) defining a new Hamiltonian $E'_j = E_j + \Sigma_x Q_x \varphi_x$ that incorporates a coupling with a formal external field Q_x; (2) evaluating the associated generalized partition function Z'; and (3) performing second-order derivatives with respect to the external field,

$$\langle \varphi_x \varphi_y \rangle = \frac{1}{\beta^2 Z'} \left. \frac{\partial^2 Z'}{\partial Q_x \partial Q_y} \right|_{Q\equiv 0}. \qquad (45)$$

Second-order derivatives of the free energy G with respect to β and μ can also be directly related to variances of the number of broken cracks n_j and the potential energy E_j, but these standard derivations are left to the reader.

Note that the coupling constants J_r above are nonrandom functions of r. All randomness has been integrated over, giving rise to the Boltzmann distribution and the two statistical parameters β and μ. An alternative approach used by other authors on similar systems, namely, random fuse networks, would be to not integrate over the underlying quenched disorder, but to instead map the quasistatic evolving system onto a random field Ising model [43] with zero temperature. In this case, the underlying quenched disorder would manifest as randomness in the coupling parameters of some Hamiltonian function that must be minimized to obtain the realized configurations. This is an alternative approach quite distinct from the one used here. Our approach is the usual one of equilibrium statistical mechanics, in which the coupling constants are nonrandom functions, but there are many configurations in the neighborhood of the minimum of the Hamiltonian H that are of statistical importance in determining the average properties of the system.

The energy yardstick $1/\beta$ (temperature) that decides whether a given configuration is statistically significant behaves regularly throughout the damage process (at least for continuous QD distributions). In the case of a uniform QD on [0,1], it will take the particularly simple form $1/\beta = P_0(1-P_0)$, starting from zero and going back to it, with a maximum when $P_0 = 1/2$. The chemical potential μ behaves regularly as well.

V. APPLICATIONS

A. Global load model

A consistency check of the results in Sec. IV is now performed for the case of the simple global load sharing model. From Eqs. (43) and (44) with $J_r = 0$, we have

$$E_j = (N - cn_j)l^2, \qquad (46)$$

$$\beta(E_j - \mu n_j) = -\ln\left[\frac{P_0}{1-P_0}\right]n_j + \frac{p(cl^2)}{P_0(1-P_0)}[(N-cn_j)l^2 + cn_j l^2]$$
$$= \ln\left[\frac{P_0}{1-P_0}\right]n_j + f(l). \qquad (47)$$

Independently, we also have the direct result from Eq. (11)

$$p_j = P_0^{n_j}(1-P_0)^{N-n_j} = P_0 e^{-n_j \ln[P_0/(1-P_0)]}. \qquad (48)$$

Thus, the Boltzmann distribution Eq. (38) with temperature and chemical potential given by Eqs. (43) and (44) is indeed identical to the known solution Eq. (48), which confirms the validity of the expressions for β and μ.

It is also instructive to look at all terms in the first law Eq. (39) to see exactly what they represent. The values of the average quantities in this simplest model can be obtained using the lemma

$$\sum_j P_0^{n_j}(1-P_0)^{N-n_j} n_j = NP_0,$$

which is demonstrated by applying the operator $x\partial/\partial x$ to the binomial theorem,

$$(x+y)^N = \sum_{n=0}^{N} \frac{N!}{(N-n)!n!} x^n y^{N-n} = \sum_j n_j x^{n_j} y^{N-n_j},$$

and then taking $x = P_0$ and $y = 1 - P_0$. Using Eqs. (36), (37), (40), (46), and (48), one obtains

$$n = P_0 N, \qquad (49)$$

$$U = \sum_j P_0^{n_j}(1-P_0)^{N-n_j}(N - cn_j)l^2 = N(1-cP_0)l^2, \qquad (50)$$

$$S = -N[P_0 \ln P_0 + (1-P_0)\ln(1-P_0)], \qquad (51)$$

$$\tau_j = \frac{dE_j}{dl} = (N - cn_j)2l, \qquad (52)$$

$$\tau = N(1-cP_0)2l. \qquad (53)$$

Taking the derivatives of these quantities yields

$$dn = N\, dP_0, \qquad (54)$$

$$dS = \ln\left[\frac{P_0}{1-P_0}\right] dP_0,$$

$$\mu\, dn = \left(\frac{P_0(1-P_0)}{p(cl^2)} \ln\left[\frac{P_0}{1-P_0}\right] - cl^2\right) N\, dP_0,$$

$$\frac{dS}{\beta} = -\frac{P_0(1-P_0)}{p(cl^2)} \ln\left[\frac{P_0}{1-P_0}\right] N\, dP_0,$$

$$\mu\, dn + \frac{dS}{\beta} = -cl^2 N\, dP_0,$$

$$\tau\, dl = N(1 - cP_0)2l\, dl,$$

$$\mu\, dn + \frac{dS}{\beta} + \tau\, dl = N(1 - cP_0)2l\, dl - cl^2N\, dP_0,$$
$$= d[N(1 - cP_0)l^2] = dU,$$

which is a consistency check for the validity of the first law [Eq. (39)]. The average mechanical behavior of this model, as well as the evolution of entropy and formal temperature, are illustrated in Fig. 2 for flat QD distributions between 0 and $l_{\max}$ and for various values of c (the parameter that controls the relative change in stiffness due to a cell breaking).

Most importantly for our present purposes, since the probabity P_0 of having a site broken in this model is independent of the configuration and site location, the global load sharing damage model is exactly equivalent to the percolation model with occupation probability $P_0(l)$. There is a critical-point phase transition in this model, when $P_0(l_c)=1/2$, for which S goes through a maximum $S=N\ln 2$. The correlation length diverges then as

$$\xi \sim |P_0(l) - 1/2|^{-\nu} \tag{55}$$

with $\nu=4/3$ in dimension $D=2$ [44]. We have in general

$$P_0(l) - P_0(l_c) \sim p(cl_c^2)(l - l_c) \tag{56}$$

and thus

$$\xi \sim |l - l_c|^{-4/3}. \tag{57}$$

In pathological cases, special QD distributions satisfy $p(cl_c^2)=0$ so that $P_0(l)-P_0(l_c)\sim(l-l_c)^{\alpha}$ with $\alpha\neq 1$. This results in

$$\xi \sim |l - l_c|^{-4\alpha/3}. \tag{58}$$

Note that in Ref. [11], we have treated this model with $c=1$, which did not change anything in the nature of the transition, but only changed the minimum stiffness associated with the most damaged configuration where $\tau_{\min}=2N(1-c)l$, and, consequently, the position or existence of a peak stress in the average mechanical response $\tau(l)$. This is seen in Fig. 2(b): the existence, and the position of a possible peak-stress position relative to the percolation transition (black dot $l/l_{\max}=1/\sqrt{2}$), depends on the particular model considered. However, the divergence of the correlation length and the associated critical-point nature of the percolation transition are insensitive to c.

The present approach does not allow a direct exploration of the avalanche distributions as the critical point is approached. This is because the probability distribution over configurations was obtained at each elongation l by averaging over all realizations of the quenched disorder. To obtain directly a result on avalanches, on the contrary, correlations between successive elongations should be considered for each realization of the QD, and the average over the QD should only be considered afterward. Our damage model nonetheless behaves as a fiber bundle with GLS for which results about the avalanche distribution have been determined [10,12,13].

B. Local load model

In this case, $J_{xy}=\alpha$ when x,y are nearest neighbors, and zero otherwise. To make explicit connection to the Ising model in its usual form, we map the order parameter onto $\{-1,1\}$ by defining $\sigma=2\varphi-1$. The probability distribution over configurations is then

$$P[\sigma,l] = \exp\left[\beta\left(E\sum_x \sigma_x + J\sum_{\langle xy\rangle}\sigma_x\sigma_y\right)\right] \Big/ Z, \tag{59}$$

where $\langle xy\rangle$ denotes a sum on nearest neighbors only. This is exactly the classical Ising model, with coupling constant and external field given by

$$\beta J = \frac{\alpha p(cl^2)\varepsilon l^2}{4P_0(1 - P_0)}, \tag{60}$$

$$\beta E = \frac{1}{2}\ln\left[\frac{P_0}{1 - P_0}\right] + \frac{2\alpha p(cl^2)\varepsilon l^2}{P_0}. \tag{61}$$

The critical point of this model is at [45]

$$(\beta J_c, \beta E) = (A_c, 0)$$

with $A_c=\ln(1+\sqrt{2})/2$. The external field βE starts at infinitely negative values, and ends up at infinitely positive ones. It evolves continuously and thus necessarily crosses $E=0$ at the l_c satisfying, from Eq. (61),

$$P_0(l_c)\{\ln[1 - P_0(l_c)] - \ln[P_0(l_c)]\} = 4\alpha p(cl_c^2)\varepsilon l_c^2. \tag{62}$$

The mean-field percolation result of $P_0(l_c)=1/2$ is thus recovered when the coupling vanishes ($\alpha=0$), which is a consistency check.

More generally, for nonzero nearest coupling constants α, the system will undergo a first-order transition if at l_c satisfying Eq. (62) the formal inverse temperature satisfies

$$\beta(l_c)J = \frac{\alpha p(cl_c^2)\varepsilon l_c^2}{4P_0(l_c)[1 - P_0(l_c)]}$$
$$= \frac{\ln[1 - P_0(l_c)] - \ln[P_0(l_c)]}{16[1 - P_0(l_c)]} > A_c. \tag{63}$$

Depending on the value of $\beta(l_c)J$, the system can display four types of behavior, which are schematically depicted in Fig. 3.

(i) For many QD distributions, the first value of l_c satisfying Eq. (62) occurs for very small values of $P_0(l_c)$, which correspond to small values of $2\alpha p(cl_c^2)\varepsilon l_c^2$, since $x\ln[(1-x)/x]\to 0^+$ when $x\to 0$. In this case, $\ln\{[1-P_0(l_c)]/P_0(l_c)\}/[1-P_0(l_c)]\simeq -\ln[P_0(l_c)]\geqslant 1$, and the condition of Eq. (63) is satisfied. The system thus goes through a first-order phase transition at this l_c and there is a discontinuous jump in the average number of broken cells and the average stress (which are related to first derivatives of the free energy with respect to l or μ, and are similar to the average number of spins up in an Ising model) [46]. The correlation length increases up to the transition but remains finite. All of this behavior for such local load models has been documented in the literature [12,13,15].

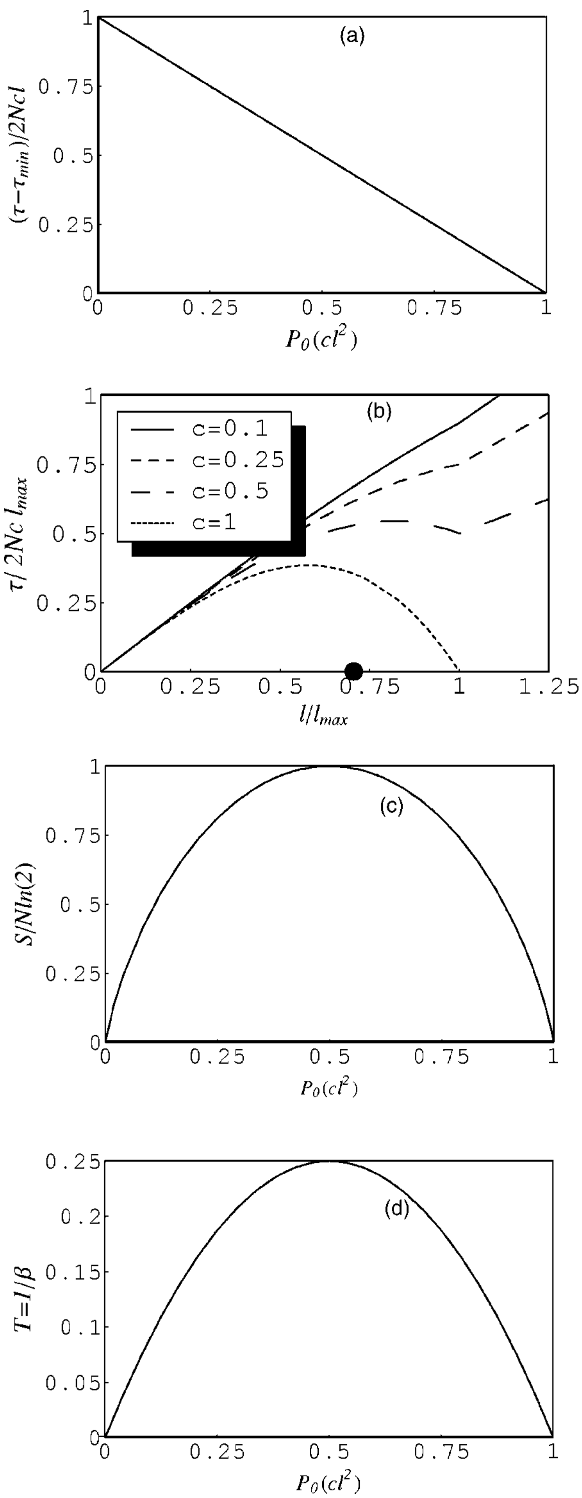

FIG. 2. Thermodynamic and mechanical response as a function of imposed deformation for the global load sharing model: (a) the difference between the average Young's modulus τ/l and the minimum Young's modulus $\tau_{\min}/l$ (which holds in the entirely damaged configuration); (b) average stress for a few particular models (the black dot is the percolation critical-point transition); (c) Shannon entropy; and (d) temperature.

However, three other behaviors are also possible if $\beta(l_c)J < A_c$ at the point l_c at which the external field vanishes [Eq. (62)]. Whether this occurs is controlled by the type of QD distribution and the value of the coupling constant α. When $\beta(l_c)J < A_c$, no first-order transition is encountered and one can further classify the transition into three subcategories.

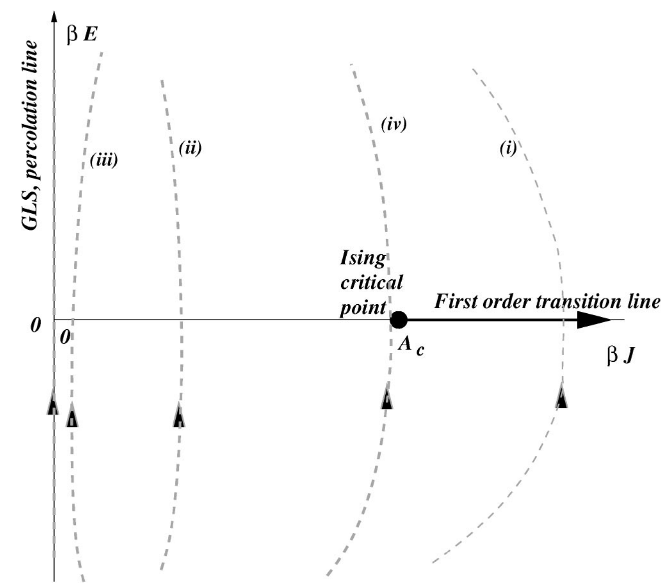

FIG. 3. Possible paths in the space of coupling constants of Ising models, under increasing imposed elongation associated with different local load sharing damage models.

(ii) If $\beta(l_c)$ has a finite value of order unity, significantly below A_c, the system simply goes continuously through l_c, without discontinuity in sustained load or average number of cracks. The correlation length remains finite.

(iii) If $\beta(l_c)J \ll 1$ (which should happen for vanishing α), the distribution over configurations is dominated by the external field, and the system essentially behaves as a percolation model going through the percolation transition. Although there should be corrections due to the nonzero character of $\beta(l_c)J$, these might be smaller than the finite size corrections in numerical realizations, and the correlation length would then be found to diverge up to the system size as $\xi \sim |l-l_c|^{-4/3}$.

(iv) Finally, if $\beta(l_c)J \sim A_c^-$, the system comes close to the critical point of the Ising model at l_c, and the correlation length should diverge correspondingly as in an Ising system whose temperature comes close to $1/A_c = T_c$ from above, while the external field changes sign. The slope of the average mechanical curve $\tau(l)$ should also locally diverge around l_c. The exponents associated with the divergence of ξ as a function of $(l-l_c)$ depend on the way the critical point is approached as a function of l. For values of l such that $\beta E(l) \ll 1$, we write $1/\beta(l)J \sim T_c + f(l)$, and $\xi \sim |T(l)-T_c|^{-\nu} = |f(l)|^{-\nu}$ where $\nu=1$ for the two dimensional (2D) Ising model. The correlation length therefore diverges as $|l-l_c|^{-\nu}$, unless the temperature has a quadratic minimum in l close to l_c in which case it diverges as $|l-l_c|^{-2\nu}$.

C. Power-law decay

We last consider the general case of stress perturbations decaying as power laws of the distance to broken cells,

$J(x) \sim \alpha(x/d)^{-\gamma}/\Phi(\gamma)$, where α is of order unity, d is the lattice constant, and $\Phi(\gamma)=\Sigma_{y\neq x}(|y-x|/d)^{-\gamma}$ is a normalizing factor (which depends on the lattice size if $\gamma > D$, where D is the system dimension). To be consistent, the models considered here are biperiodic of linear size L, and the interactions are put to 0 for distances above L. This type of model, considered for example by Hidalgo *et al.* [15,16], allows us to span ranges between purely global sharing (when $\gamma=0$) to the local sharing limit ($\gamma\to\infty$). Equations (42)–(44) show that this model leads to probability distributions over configurations of the form

$$P[\sigma,l] = \exp\left[\beta\left(E\sum_x \sigma_x + \sum_{x\neq y} J(|x-y|)\sigma_x\sigma_y\right)\right] \Big/ Z, \tag{64}$$

which is a generalized long-range Ising model with coupling constants and external field given by

$$\beta J(r) = \frac{\alpha p(cl^2)\varepsilon l^2}{4P_0(1-P_0)}\frac{(r/d)^{-\gamma}}{\Phi(\gamma)}, \tag{65}$$

$$\beta E = \frac{1}{2}\ln\left(\frac{P_0}{1-P_0}\right) + \frac{\alpha p(cl^2)\varepsilon l^2}{2P_0}. \tag{66}$$

Note that although the case $\gamma\to\infty$ is isomorphic to the local load sharing model introduced in the previous section, the global load sharing model of Sec. V A corresponds to $\alpha=0$, but not to the exponent $\gamma=0$. The presence of the quadratic coupling makes this latter case isomorphic to a Curie-Weiss model, which is the mean-field theory of Ising models.

Such long-range Ising models are still an open area of research, with the precise value of the critical point for any power-law interaction not precisely known. Nonetheless, it has been proposed [46–48] that one can classify the criticality into two categories depending on whether $\gamma > D$ or $\gamma < D$. In the shorter-range case, $\gamma > D$, this model admits a traditional thermodynamic limit when $L\to\infty$. Although $\Phi(\gamma)$ diverges when $L\to\infty$, the thermodynamic limit is well defined once $\Phi(\gamma)$ is introduced into the coupling constants $J(r)=(r/d)^{-\gamma}/\Phi(\gamma)$. Thus, the free or internal energy per lattice site, entropy, and magnetization all admit a finite limit when $L\to\infty$, and are functions of β and the external field E. As $\gamma\to\infty$ in the thermodynamic limit, Eq. (65) reduces to the result of the standard Ising model [Eq. (60)] and so

$$\lim_{\gamma\to\infty} \beta_c = \ln(1+\sqrt{2})/2.$$

It has also been shown [48] that as $\gamma\to D^+$, $\beta_c \sim 1$. Thus, for γ/D in the range $[1^+,\infty]$, β_c is bound between 1 and $\ln(1+\sqrt{2})/2$. However, more precise details of how β_c varies with γ in this range are not presently available.

In the other category of longer-range interactions where γ/D lies in $[0,1^-]$, the only thing certain is that when $\gamma/D=0$, the Curie-Weiss model is obtained for which β_c is also of order unity. It has thus been conjectured that all power-law interactions for which $\gamma/D<1$ should be in the Curie-Weiss universality class [49]. The Curie-Weiss model corresponds to the mean-field coupling $J_{xy}=1/N$, independently of x and y, where N is the total number of cells in the system. For the Curie-Weiss model, the PDF over state configurations is $P[\sigma]\propto\exp[\beta(E\Sigma_x\sigma_x+\Sigma_{xy}\sigma_x\sigma_y/N)] \propto \exp\{\beta[E\Sigma_x\sigma_x+(\Sigma_x\sigma_x)^2/2N]\}$.

All this suggests the following classifications of our damage models.

(1) If the coupling constant is small ($\alpha \ll 1$), the damage model is close to the percolation model so that in the approach to the transition at elongation l_c, the correlation length behaves as $\xi\sim|l-l_c|^{-\nu}$, with $\nu=4/3$.

(2) For non-negligible coupling constants α, in the shorter-range case $\gamma > D$, we recover the same three possible behaviors as described above for the local load sharing rule.

(3) In the longer-range case where $\gamma < D$, we again recover the same four types of scenarios depending on the ratio $\beta(l_c)/A_c$ (as discussed in the local load sharing case). The model behaves as percolation when $\alpha \ll 1$. Otherwise, the behavior is determined by the ratio $\beta(l_c)/A_c$. Note that A_c is of order unity, but depends on the particular exponent γ and on the system size. If $\beta(l_c)/A_c<1$, the system behaves continuously and no transition is observed. If $\beta(l_c)/A_c>1$, there is a discrete jump in both the average number of broken cells and the sustained load. The correlation length remains finite in both of these two cases. Only the limiting case of $\beta(l_c)/A_c\sim1$ corresponds to a second-order phase transition. In any of these cases, for large enough systems, the Curie-Weiss description holds according to Refs. [46–48]. Accordingly, if there is any divergence of correlation length due to the system coming close to $\beta(l_c)/A_c\sim1$ at $E=0$, the associated exponents should be those of the Curie-Weiss mean-field critical point ($\nu=1/2$), and not the Ising one.

These results can be compared to numerical-simulation results in the literature for related models. In fiber-bundle models with power-law interactions [15], a transition has been found as a function of the interaction exponent γ that is consistent with the above analysis, predicting mean-field behavior for the long-range case $\gamma < D$, and Ising-like behavior in the short-range case $\gamma > D$. Typical configurations prior to breakdown for this type of system are displayed in Fig. 5 of Ref. [15], and look very similar to percolation configurations close to the transition in the case $\gamma=0$, displaying smaller and smaller cluster sizes (characteristic of the autocorrelation length) and compact configurations as γ increases above D. This is coherent with a mean-field behavior close to percolation transition in the first case, as opposed to a first-order transition (analogous to Ising model crossing $E=0$ below T_c) when $\gamma < D$. This analogy is even more apparent in Fig. 7, bottom, of Ref. [16], where an extension of this model was considered, with time-delayed fiber breaking process in addition to power-law decaying interactions [16].

Burned fuse models, in which the interactions between burned fuses decay as $1/r^D$, exhibit diverging autocorrelation lengths at breakdown, with $\xi\sim|l-l_c|^{-\nu}$, where l is the imposed voltage, and ν is equal to the percolation exponent [44], $\nu=4/3$ in 2D [22,50] or 0.88 in 3D [51]. Roux *et al.* [50] showed that in the limit of "infinitely large" disorder, such models are isomorphic to percolation models. When the disorder is less pronounced, stress concentration leads to regimes of localizing damage. At low disorders, stress concentration entirely dominates, and fuses burn in clusters of size scaling as the lattice step, leading to a so-called "total localization regime." At intermediate disorders, fuses burn essentially in regions that scale as the lateral size of the system (size in the direction perpendicular to the main current flow), *a priori* much larger than the lattice step, which constitutes the "soft localization regime" [22,52]. It has been shown [22,51] that such a process is still in the percolation universality class, in the sense that there is still a growing autocorrelation length with an exponent identical to the percolation one. Based on the fact that these soft localizing regimes are in the percolation universality class, coupled with the large-scale profile of damage in the system, Hansen *et al.* [22] related the roughness of the final fracture spanning through the system to the autocorrelation length exponent, based on arguments of percolation in a gradient, and this properly predicts the Hurst exponent of the final damage fronts, in both 2D and 3D. The morphology of the connected "fracture" at breakdown is oriented, and different from percolating clusters in the percolation model. This is related to the anisotropic character of interactions in the burned fuse model; i.e., the current perturbation from a burned fuse varies as a dipolar field decaying as $1/r^D$, but also having an orientational aspect not included in the models under study in this paper. This anisotropic aspect is absent from the models discussed here, but the fact that the autocorrelation length exponent is similar to the ones of percolation is coherent with the fact that long-range systems are in the percolation universality class. Burned fuse systems are at the overlap between short- and long-range interactions, in the sense that they correspond to $\gamma=D$.

Last, fiber bundles connected to elastic plates, where $\gamma=1$ and $D=2$, have been numerically studied in Ref. [28] and an autocorrelation length exponent of $\nu\simeq 1.54$ numerically determined. The discrepancy between this result and the percolation or Curie-Weiss critical-point result might presumably result from finite-size effects making this model ($\gamma=1$) still significantly different from the Curie-Weiss one ($\gamma=0$), or from the fact that the stress perturbation in this numerical model might have been too large for the interactions to be considered weak (a requirement for the validity of the present analysis).

VI. CONCLUSIONS

We have treated a class of damage models having weak isotropic interactions between cells that become damaged in the lattice. A quenched disorder is present in the rupture energies for each lattice cell, and the evolution of damage is ruled by the Griffith principle. Averaging over all possible realizations of the underlying quenched disorder, the probability distribution of each possible damage configuration was obtained as a function of the deformation externally applied to the system.

The exact calculation is analytically tractable in the case of a global load sharing model, and it has been shown to be isomorphic to a percolation model. This corresponds to the behavior of a system totally dominated by the underlying disorder, where the next cell to break is always the weakest one. Spatial interactions added to the system modify this picture, since the overload created by broken cells induces some degree of spatial ordering that competes with the weakest cell mechanism. By limiting ourselves to small overloads compared to the average load of the system, it was possible to obtain the probability of damage configurations as integrated over all realizations of the quenched disorder.

In this weak interaction limit, the resulting probability distributions were shown to be Boltzmannians in the number of broken cells and in the stored elastic energy. This type of distribution maximizes Shannon's entropy under constraints related to the energetic balance of the fracture process, and we have demonstrated the formal relationship between our quenched-disorder damage models and the standard distributions arising in equilibrium statistical mechanics. This then allows the standard toolbox of statistical mechanics to be applied to our damage models.

Our systems map onto three types of possible behaviors: (1) percolation models in the case of interactions so weak they may be neglected; (2) Ising models for non-negligible short-range interactions; and (3) Curie-Weiss mean-field theory for non-negligible long-range interactions. The temperature and external field in the partition function of our models are analytical functions that depend on the particular sharing rule, on the type of quenched disorder considered, and on the average elongation (or deformation) externally loaded onto the system. The path followed in the Ising control parameter space when the load is increased from 0 depends on the qd distribution and the load sharing rule. When the formal external field changes sign, a phase transition is possible. This can correspond to a first-order phase transition, a percolationlike transition, or an Ising critical-point transition, depending on the value of the formal temperature during the transition.

The systems studied here are limited to isotropic load perturbations. We have earlier studied oriented crack models in [39–41], which correspond to anisotropic load perturbations that depend on the orientation of the crack opened in the lattice. Those earlier studies were based on an entropy-maximum assumption. The hypotheses of the present work extend directly to oriented systems, and so the present paper justifies the entropy-maximum assumption postulated in our earlier work. The precise value of the temperature, and the physical interpretation of the functional forms given in [39–41], should be modified according to the results of this paper. Such modifications will, however, result in identical functional forms relating the configuration space and the PDF over configurations, and thus the present work confirms the existence of a phase transition in such an oriented crack model, with an associated divergence exponent of the autocorrelation length $\nu=2$.

Experimentally, the emergence of correlated damage at large scale has an important influence on the macroscopic rupture of a heterogeneous object. For example, the roughness of natural fracture surfaces, whose universality has long been observed experimentally [53], has recently been related to the behavior of the divergence of the damage correlation length at the approach to breakdown [22]. Damage correlated at large scale should also leave a signature on elastic wave scattering through the damaged material. The knowledge of the behavior of a damage autocorrelation function, as fracturing progresses, is thus experimentally relevant in monitoring the approach to macroscopic failure or shear banding through the use of elastic-scattering experiments.

APPENDIX: RECOVERABLE ENERGY AS A FUNCTION OF THE DAMAGE STATE

The argument here will be specific to a fiber bundle model. However, as noted in the text, other weak damage models will also be controlled by the same type of stored-energy function obtained here.

Define a fiber bundle as (initially) N fibers stretched between a free rigid plate and an elastic half space. The rigid plate has a controlled displacement l applied to it that stretches the fibers and the elastic half space. As a fiber breaks at fixed l, the force it held will be transmitted to the other fibers through the elastic half space.

A fiber at point $\mathbf{x}$ is stretched a distance $\ell_{\mathbf{x}}$. Where that fiber is attached to the elastic half space, the surface of the half space is displaced by an amount $u_{\mathbf{x}}$. Thus, at those places $\mathbf{x}$ where fibers exist, we have

$$l = \ell_{\mathbf{x}} + u_{\mathbf{x}}. \tag{A1}$$

The fiber at point $\mathbf{x}$ exerts a force on the elastic half space that is

$$\frac{f_{\mathbf{x}}}{A_F} = Y_F(1-\varphi_{\mathbf{x}})\frac{\ell_{\mathbf{x}}}{L_F}, \tag{A2}$$

where A_f is the cross-sectional area of the fiber (assumed to be independent of the extension), L_F is the inital length of each fiber, and Y_F is the Young's modulus of each fiber. The local order parameter $\varphi_{\mathbf{x}}$ is 0 if the fiber is intact and 1 if broken.

The Green function for point forces acting on the surface of an elastic half space [54] yields

$$u_{\mathbf{x}} = u_3(\mathbf{x}) = \frac{1-\sigma_s^2}{\pi Y_s}\sum_{\mathbf{y}\neq\mathbf{x}}\frac{f_{\mathbf{y}}}{|\mathbf{y}-\mathbf{x}|} \tag{A3}$$

$$= \frac{1-\sigma_s^2}{\pi}\frac{Y_F}{Y_s}\frac{A_F}{L_F}\sum_{\mathbf{y}\neq\mathbf{x}}\frac{(1-\varphi_{\mathbf{y}})}{|\mathbf{y}-\mathbf{x}|}\ell_{\mathbf{y}}, \tag{A4}$$

where Y_s is the Young's modulus and σ_s the Poisson's ratio of the elastic solid. In general, the displacement at a point $\mathbf{x}=(x_1,x_2,x_3)$ within the elastic solid (where $x_3=0$ defines the surface) due to a point force acting at a point $\mathbf{y}=(y_1,y_2,0)$ on the surface [i.e., $\mathbf{f}(\mathbf{x})=f_{\mathbf{y}}\delta(\mathbf{x}-\mathbf{y})\hat{\mathbf{3}}$] is given by

$$u_1 = \frac{1+\sigma_s}{2\pi Y_s}\left[\frac{(x_1-y_1)x_3}{r^3} - \frac{(1-2\sigma_s)(x_1-y_1)}{r(r+x_3)}\right]f_{\mathbf{y}}, \tag{A5}$$

$$u_2 = \frac{1+\sigma_s}{2\pi Y_s}\left[\frac{(x_2-y_2)x_3}{r^3} - \frac{(1-2\sigma_s)(x_2-y_2)}{r(r+x_3)}\right]f_{\mathbf{y}}, \tag{A6}$$

$$u_3 = \frac{1+\sigma_s}{2\pi Y_s}\left[\frac{x_3^2}{r^3} + \frac{2(1-\sigma_s)}{r}\right]f_{\mathbf{y}}, \tag{A7}$$

where

$$r = [(x_1-y_1)^2 + (x_2-y_2)^2 + x_3^2]^{1/2}. \tag{A8}$$

Putting $x_3=0$ in the expression for $u_3(\mathbf{x};\mathbf{y})$ and then summing over all $\mathbf{y}$ yields the expression for the displacement $u_{\mathbf{x}}$ of the surface.

We now define the dimensionless number

$$\varepsilon = \frac{(1-\sigma_s^2)}{\pi}\frac{Y_F}{Y_s}\frac{A_F}{L_F L_P}, \tag{A9}$$

where a length L_P has been defined as

$$\frac{1}{L_P} = \sum_{\mathbf{y}\neq\mathbf{x}}\frac{1}{|\mathbf{y}-\mathbf{x}|}; \tag{A10}$$

i.e., this sum is independent of which point $\mathbf{x}$ is considered. Assuming either that the elastic half space is stiffer than the fibers, or that each fiber has a length much greater than its width, or that fibers are spaced far enough apart that L_p is large, allows ε to be considered a small number. Since the fiber bundle is assumed to be made of a finite number N of fibers, there is no divergence to L_P.

Using these definitions along with $u_{\mathbf{x}}=l-\ell_{\mathbf{x}}$ and iterating Eq. (A4) once to get the leading order in ε contribution gives

$$\frac{\ell_{\mathbf{x}}}{l} = 1 + \varepsilon\left(-1 + \sum_{\mathbf{y}\neq\mathbf{x}}\frac{L_P}{|\mathbf{y}-\mathbf{x}|}\varphi_{\mathbf{y}}\right) + O(\varepsilon^2). \tag{A11}$$

The elastic strain energy reversibly stored in each surviving fiber is then

$$E_{\mathbf{x}} = \frac{1}{2}f_{\mathbf{x}}\ell_{\mathbf{x}} = \frac{1}{2}\frac{A_F Y_F}{L_F}l^2(1-\varphi_{\mathbf{x}})\left(\frac{\ell_{\mathbf{x}}}{l}\right)^2 \tag{A12}$$

$$= \frac{1}{2}\frac{A_F Y_F}{L_F}l^2\left\{1-\varphi_{\mathbf{x}} + 2\varepsilon\left[-1+\varphi_{\mathbf{x}} + \sum_{\mathbf{y}\neq\mathbf{x}}\frac{L_P}{|\mathbf{y}-\mathbf{x}|}\varphi_{\mathbf{y}}(1-\varphi_{\mathbf{x}})\right]\right\}, \tag{A13}$$

where terms of $O(\varepsilon^2)$ have been dropped. Thus, upon summing over all the fibers we obtain the total energy E_F stored in the fibers as a function of the damage state

$$E_F = \sum_{\mathbf{x}} E_{\mathbf{x}} = \frac{1}{2}\frac{A_F Y_F}{L_F}l^2\left[(1-2\varepsilon)N - (1-4\varepsilon)\sum_{\mathbf{x}}\varphi_{\mathbf{x}} - \varepsilon\sum_{\mathbf{x},\mathbf{y}\neq\mathbf{x}} J_{\mathbf{xy}}\varphi_{\mathbf{x}}\varphi_{\mathbf{y}}\right], \tag{A14}$$

where the coupling constant is defined as

$$J_{\mathbf{xy}} = \frac{2L_P}{|\mathbf{y}-\mathbf{x}|}. \tag{A15}$$

This form of the fiber energy is consistent with what was defined in the text.

We now demonstrate that the energy recoverably stored in the elastic solid makes no important modification to E_F. The strain energy in the solid is given by

$$E_s = \frac{Y_s}{2(1+\sigma_s)} \int_{x_3>0} d^3\mathbf{x} \sum_{\mathbf{y}\neq\mathbf{x}} \left(e_{ik}e_{ik} + \frac{\sigma_s}{1-2\sigma_s} e_{ll}^2 \right), \tag{A16}$$

where summation over the indices is assumed and where the strain tensor is defined as

$$e_{ik}(\mathbf{x};\mathbf{y}) = \frac{1}{2}\left(\frac{\partial u_i(\mathbf{x};\mathbf{y})}{\partial x_k} + \frac{\partial u_k(\mathbf{x};\mathbf{y})}{\partial x_i} \right). \tag{A17}$$

The displacements are given by Eqs. (A5)–(A7).

From these equations, the strain at points $\mathbf{x}$ inside the elastic solid takes the leading order in ε form

$$e_{ik} = \varepsilon l L_P \left[c_{ik} + \varepsilon \sum_{\mathbf{y}\neq\mathbf{x}} \frac{f_{ik}(\mathbf{x}-\mathbf{y})}{|\mathbf{x}-\mathbf{y}|^2} \varphi_{\mathbf{y}} \right], \tag{A18}$$

where the constant tensor c_{ik} has units of inverse-length squared and the average strain tensor throughout the elastic solid is $\varepsilon l L_P c_{ik}$. The perturbation term due to the broken fiber volume integrates to zero. The tensor f_{ik} has no dependence on the norm $|\mathbf{x}-\mathbf{y}|$; however, this fact is immaterial since f_{ik} plays no important role.

Upon forming the required products for the integrand in Eq. (A16), and using the fact that terms linear in the broken-fiber perturbations integrate to zero, one obtains that the energy stored in the elastic solid is

$$E_s = \frac{1}{2} \frac{A_F Y_F}{L_F} l^2 \varepsilon V L_p \left(c_{ik}c_{ik} + \frac{\sigma_s}{1-2\sigma_s} c_{ll}^2 \right) [1 + O(\varepsilon^2)], \tag{A19}$$

where V is the volume integrated over (assumed finite). In other words, any energy stored in the elastic solid that is due to the interaction between fibers is ε^2 smaller than the leading order contribution which itself can be considered small. The leading order contribution depends only on the average number of broken fibers and thus does not alter the analytical form of Eq. (A14). Thus, the energy stored in the elastic solid plays no essential role in the damage model.

[1] A. A. Griffith, Philos. Trans. R. Soc. London, Ser. A **221**, 163 (1920).
[2] *Statistical Models for the Fracture of Disordered Media*, edited by H. J. Herrmann and S. Roux (North-Holland, Amsterdam, 1990).
[3] H. E. Daniels, Proc. R. Soc. London, Ser. A **183**, 404 (1945).
[4] H. E. Daniels, Adv. Appl. Probab. **21**, 315 (1989).
[5] B. D. Coleman, J. Appl. Phys. **29**, 968 (1958).
[6] F. T. Peirce, J. Text. Inst. **17**, 355 (1926).
[7] D. Sornette, J. Phys. A **22**, L243 (1989).
[8] D. Sornette, J. Phys. I **2**, 2089 (1992).
[9] J. V. Andersen, D. Sornette, and K. T. Leung, Phys. Rev. Lett. **78**, 2140 (1997).
[10] P. C. Hemmer and A. Hansen, J. Appl. Mech. **59**, 909 (1992).
[11] S. R. Pride and R. Toussaint, Physica A **312**, 159 (2002).
[12] A. Hansen and P. C. Hemmer, Phys. Lett. A **184**, 394 (1994).
[13] M. Kloster, A. Hansen, and P. C. Hemmer, Phys. Rev. E **56**, 2615 (1997).
[14] S. D. Zhang and E-jiang Ding, Phys. Rev. B **53**, 646 (1996).
[15] R. C. Hidalgo, Y. Moreno, F. Kun, and H. J. Herrmann, Phys. Rev. E **65**, 046148 (2002).
[16] O. E. Yewande, Y. Moreno, F. Kun, R. C. Hidalgo, and H. J. Herrmann, Phys. Rev. E **68**, 026116 (2003).
[17] J. O. H. Bakke, J. Bjelland, T. Ramstad, T. Stranden, A. Hansen, and J. Schmittbuhl, Phys. Scr., T **106**, 65 (2003).
[18] G. G. Batrouni and A. Hansen, Phys. Rev. Lett. **80**, 325 (1998).
[19] L. de Arcangelis and H. J. Herrmann, Phys. Rev. B **39**, 2678 (1989).
[20] L. de Arcangelis, A. Hansen, H. J. Herrmann, and S. Roux, Phys. Rev. B **40**, 877 (1989).
[21] P. M. Duxbury, P. L. Leath, and P. D. Beale, Phys. Rev. B **36**, 367 (1987).
[22] A. Hansen and J. Schmittbuhl, Phys. Rev. Lett. **90**, 045504 (2003).
[23] A. Hansen, E. L. Hinrichsen, and S. Roux, Phys. Rev. B **43**, 665 (1991).
[24] S. Zapperi, H. J. Herrmann, and S. Roux, Eur. Phys. J. B **17**, 131 (2000).
[25] S. Zapperi, H. J. Herrmann, and S. Roux, Fractals **11**, 327 (2003).
[26] G. G. Batrouni, A. Hansen, and J. Schmittbuhl, Phys. Rev. E **65**, 036126 (2002).
[27] H. J. Herrmann, A. Hansen, and S. Roux, Phys. Rev. B **39**, 637 (1989).
[28] J. Schmittbuhl, A. Hansen, and G. G. Batrouni, Phys. Rev. Lett. **90**, 045505 (2003).
[29] Y. Moreno, J. B. Gomez, and A. F. Pacheco, Physica A **296**, 9 (2001).
[30] Y. Moreno, J. B. Gómez, and A. F. Pacheco, Phys. Rev. Lett. **85**, 2865 (2000).
[31] S. Zapperi, P. Ray, H. E. Stanley, and A. Vespignani, Phys. Rev. Lett. **78**, 1408 (1997).
[32] S. Zapperi, P. Ray, H. E. Stanley, and A. Vespignani, Phys. Rev. E **59**, 5049 (1999).
[33] S. Zapperi, A. Vespignani, and H. E. Stanley, Nature (London) **388**, 658 (1997).
[34] F. Kun, S. Zapperi, and H. J. Herrmann, Eur. Phys. J. B **17**, 269 (2000).
[35] D. Sornette and J. V. Andersen, Eur. Phys. J. B **1**, 353 (1998).
[36] G. Caldarelli, F. D. Di Tolla, and A. Petri, Phys. Rev. Lett. **77**, 2503 (1996).
[37] V. I. Räisänen, M. J. Alava, and R. M. Nieminen, Phys. Rev. B **58**, 14288 (1998).
[38] J. B. Rundle and W. Klein, Phys. Rev. Lett. **63**, 171 (1989).
[39] R. Toussaint and S. R. Pride, Phys. Rev. E **66**, 036135 (2002).
[40] R. Toussaint and S. R. Pride, Phys. Rev. E **66**, 036136 (2002).
[41] R. Toussaint and S. R. Pride, Phys. Rev. E **66**, 036137 (2002).
[42] C. E. Shannon, Bell Syst. Tech. J. **27**, 373 (1948).
[43] M. Barthelemy, R. da Silveira, and H. Orland, Europhys. Lett.

57, 831 (2002).
[44] D. Stauffer and A. Aharony, *Introduction to Percolation Theory*, 2nd ed. (Taylor and Francis, London, 1994).
[45] K. Huang, *Statistical Mechanics*, 2nd ed. (Wiley, New York, 1987).
[46] S. A. Cannas, P. M. Gleiser, and F. A. Tamarit, available at http://tero.fis.uncor.edu/~cannas/papers/bookchapter3.pdf
[47] S. A. Cannas, A. C. N. de Magalhaes, and F. A. Tamarit, Phys. Rev. B **61**, 11521 (2000).
[48] S. A. Cannas and F. A. Tamarit, Phys. Rev. B **54**, R12661 (1996).
[49] Even if not all nonlocal models belong to the Curie-Weiss universality class: for example, the 1D Kac model, with interactions as $-L^{-1}\exp(-x/L)$, where the limit $L \to \infty$ is taken after the thermodynamic limit, obeys the van der Waals equation of state: C. J. Thompson, *Classical Equilibrium Statistical Mechanics* (Clarendon Press, Oxford, 1988), p. 95.
[50] S. Roux, A. Hansen, H. Herrmann, and E. Guyon, J. Stat. Phys. **52**, 237 (1988).
[51] T. Ramstad, J. Ø. H. Bakke, J. Bjelland, T. Stranden, and A. Hansen, e-print cond-mat/0311606.
[52] R. Toussaint and A. Hansen, e-print cond-mat/0403217.
[53] E. Bouchaud, J. Phys.: Condens. Matter **9**, 4319 (1997).
[54] L. D. Landau and E. M. Lifshitz, *Theory of Elasticity*, 3rd ed. (Pergamon Press, New York, 1986).

STATISTICAL MECHANICS OF INTERACTING FIBER BUNDLES

Renaud Toussaint
Department of Physics, University of Oslo, P.O.Box 1048 Blindern, N-0316 Oslo, Norway.

ABSTRACT

We consider quasistatic fiber bundle models with weak interactions, i.e. where the perturbation emanating from every broken fiber is small compared to the mean-field imposed average deformation of the bundle. Classical load sharing rules are considered, namely purely local, purely global or decaying as a power-law of distance. All fibers have identical spring constants, reducing to zero after their irreversible break, which happens at a random threshold picked ab initio independently for every fiber from a quenched disorder (q.d.) distribution. Initially, all fibers are intact and as the buffer plates are progressively separated, with a controlled displacement between them, fibers break one after the other. We are interested in the probability distribution of configurations of broken fibers, averaged over all possible realizations of the underlying q.d. (i.e. over all possible values of the set of threshold distributions). This configurational distribution is accessed via integration over the independent variables of the system, i.e. through mapping the threshold set space onto the configurational space, via paths corresponding to the deterministic evolution of bundles characterized by each set of realized q.d., up to a certain imposed elongation. Using a perturbational approach allows to obtain this configurational distribution exactly to leading order in the interactions. This maps this fiber bundle systems onto classical statistical mechanics models, namely percolation, standard Ising models or generalized Ising models depending on the range of the interactions chosen in the load sharing rule. This relates unambiguously such q.d. based systems to standard classical mechanics, which allows the use of the associated toolbox to derive various observables of the system, as e.g. correlation lengths. The thermodynamic parameters formally equivalent to temperature and chemical potential, are analytically expressed functions of the externally imposed deformation, with functional dependences depending on the load sharing rule and the particular choice of the q.d. distribution.

1 INTRODUCTION

The physical process of brittle failure under external load has long been studied, and is well understood in the case of a homogeneous solid (Griffith [1]), but the behavior of mechanically heterogeneous systems is still an open subject of research. The difficulty arises from the necessity of quantifying the effect of randomness in the mechanical properties of many interacting constituents. Despite many advances over the last 20 years [2], no analytical unified description of such breakdown processes of heterogeneous materials is available at the moment. Most results in this field are obtained from lattice models, e.g., spring or beam networks, or fuse networks, scalar analog of the elastic problem [2]. These simulations led to an understanding of the experimentally well-established Hurst exponent of fracture surfaces [3]: 0.8 in the case of three dimensional fracture, with a cross-over to 0.5 at small scales (see Bouchaud for a review [4]), or 0.6 for the roughness of a fracture front in interfacial brittle failure in mode I (Schmittbuhl and Måløy [5]). Fiber bundle models, first introduced by Daniels [6] and Coleman [7], are among the most studied paradigms of simplified lattice models of breakdown processes in heterogeneous materials. They consist of a bundle of parallel fibers set under tension between two buffer plates, with random elongation thresholds for breaking, and a model-dependent load sharing rule. This rule states how the load carried by a fiber is redistributed when it breaks among the surviving fibers, and reflects the physical properties of the buffer plates: purely rigid, elastic, or more complicated. The most commonly considered rules are the Global Sharing Rule (GLS), where the load is uniformly distributed among all fibers, and the Local Sharing Rule (LLS), where broken fibers only overload the nearest surviving fibers. Analytical solutions are available in these two extreme cases for the average load curve (Sornette [8] for GLS) or the statistics of avalanches (Hemmer, Hansen and Kloster [9,10,11]). For more general load sharing rules, like these corresponding to plates responding elastically or transferring the load as a power-law of distance to broken fibers, only numerical solutions are available [12].

In the present paper, we will present a formal analytical mapping of such quasistatic q.d. based models onto standard statistical mechanics models, namely percolation, Ising and generalized Ising models, depending on the particular disorder distribution and load sharing rule adopted. Specifically, we will consider any possible particular (initial) realization of the q.d. describing the set of breaking thresholds of the fibers, and compute to which configuration of broken and intact fibers each realization leads when the initially intact system is monotonically extended from zero to a given fixed extension. Considering then the ensemble of possible realizations of the q.d., we will obtain the probability distribution of the possible damage configurations at the considered extension, as the frequency of occurrence of each configuration among all possibles, averaged over all realizations of the q.d.. Insodoing, we will show that in the limit of small interactions, the emerging configurational distribution can be expressed as Boltzmannians of a simple functional of the damage field, and relate these distribution to standard statistical mechanics. The equivalent of temperature, which will be here a probabilistic energy scale, and external field setting the average fraction of broken fibers, will be obtained analytically from the underlying q.d., load sharing rule and extension achieved.

Relating analytically the well known Fiber Bundle Models to such classical models of statistical mechanics is important in the sense that it allows to use the traditional toolbox of standard statistical mechanics, and possibly to classify the possible transitions corresponding to localization of disorder and/or macroscopic rupture. Indeed the classification of rupture processes as second or first order transitions, or spinodal nucleation processes, is still a subject of debate. The difficulty of such classification in this problem lies in the absence of analytical form for the probability distribution of configurations of broken elements, apart from the simplest cases (GLS,LLS). Although such probability distributions in similar systems have been proposed [13], they were in general postulated, whereas we will here derive this distribution directly from first principles of evolution rules, incorporating the choice of a load sharing rule and threshold distribution.

We also underline that we will only consider quasistatic models, in which the disorder is quenched ab initio, and in which there is no evolution of microstate when the external parameter, imposed average elongation, is kept fixed. This should be relevant to describe systems where the inverse imposed strain rate is significantly lower than any characteristic time for thermal transition from a fracture state to another at fixed external elongation, solely due to molecular motion (otherwise thermal rupture models with quenched disorder should be considered, which is described in the GLS case e.g. by Politi [14]). It is interesting to note that, when averages over all possible realizations of the q.d. are considered, classical Boltzmannian distributions still arise despite the absence of any evolution of the system at fixed boundary conditions: mapping the initial q.d. distribution over configurational distributions of damage states, via deterministic rules, still gives rise to classical statistical mechanics solutions.

We have already shown the relationship between classical statistical mechanics and quasistatic fiber bundle models in the restricted framework of global sharing rule (Pride and Toussaint [15]), or in interacting fiber bundle models, with an energy based evolution rule (Toussaint and Pride [16]). Here we show that the particular choice of energy or force based evolution rule does not alter the main results, and use a rule directly comparable to most numerical models.

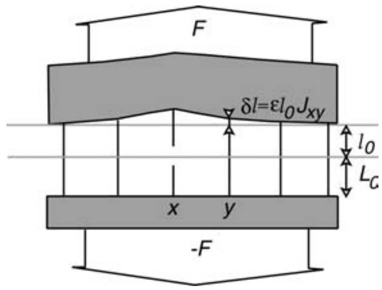

Figure 1: Sketch of a fiber bundle between a rigid and a deformable plate, with the imposed raw elongation l_0 plus the elongation perturbation profile due to a broken fiber at location x.

2 MODEL DESCRIPTION AND EVOLUTION RULES

We consider the following generic models: an ensemble of parallel fibers are attached between parallel plates, at locations placed on the sites $\{x\}$ of a square lattice of dimensions $N = a \times a$, with the lattice step considered as length unit. The fibers are supposed to have identical length L_0 at rest, and to present the same spring constant, set to one which fixes the force unit. A fiber thus carries a force $f = l$, up to a threshold t above which the fibers breaks irreversibly, so that afterwards $f = 0$ independently of l. This threshold is picked ab initio independently for each fiber, from a distribution $p(t) = dP(t)/dt$ where the cumulative distribution $P(t)$ denotes the probability for a threshold to be below t. From the initial rest state, the plates are separated while kept parallel, and the minimum distance between them, $L_0 + l_0$, is increased in infinitesimal steps. The lower plate is modelled as perfectly rigid, while the upper one is allowed to have more complicated mechanical properties, which is reflected in the load sharing rule between the fibers. When a fiber is broken at a location x, this creates a force pertubation $-l_0$ on the corresponding site along the plates boundaries, compared to the raw homogeneous force per site l_0 that would be exerted by a bundle of intact fibers (counted positively in the direction from the plates towards the bundle). This force perturbation possibly creates a deformation of the plate boundary, illustrated in Fig. 1, if the plate is deformable,

$$\delta l(y) = \varepsilon J(||y - x||) l_0, \tag{1}$$

where we have assumed isotropy and invariance of the system under translation. This is conceptually realized by considering biperiodic boundary conditions along the lattice boundaries, with thresholding of the interactions for separations exceeding the linear lattice dimension a. We assume that $\varepsilon \ll 1$, and $0 \leq J(r) \leq 1$ for any separation r. The fact that $\delta l \ll l_0$ is granted if the plates are significantly stiffer than the fiber bundle, e.g. if they are rigid or elastic with a Young modulus much higher than the fibers' spring constant divided by the elementary lattice site area. The load sharing rule is then univoquely defined by the function $J(r)$. Classically considered cases are: perfectly rigid plates (GLS), with $J(r) \equiv 0$ [8,9], or the opposite case (LLS), where $J(r) = 0$ for any separation r, except $J(r = 1) = 1$, i.e. interactions are only carried between nearest neighbors [10,11]. Power-law decay have also been considered [12] where $J(r) \sim r^{-\alpha}$, the special case of $\alpha = 1$ corresponding to a purely elastic plate [17]. Note also that an elastic sheet put under extension, where circular flaws smaller than a lattice step nucleate when a threshold in local strain is achieved, will present such power-law strain perturbations emanating from every flaw with $\alpha = 2$, which is thus a special case of the models discussed here.

The evolution rule of the system is as follows: for a certain quenched realization of the q.d. in the set of rupture thresholds$\{t_x\}$, the bundle is monotonically brought from zero to a macroscopic elongation l_0. Each time that the local elongation $l_0 + \delta l(x)$ of some fiber at x reaches its breaking threshold t_x, this fiber breaks irreversibly at l_0 kept fixed. The local elongations are then updated on all fibers according to Eq. (1). If this leads to breakage of other fibers, the one corresponding to the minimum of $t_x/[l_0 + \delta l(x)]$ is removed, and this avalanche procedure is iterated up to the point where all thresholds of surviving fibers are above their elongation. This completely defines a deterministic path for the state of the bundle as function of l_0 for each possible realization of the q.d.. The state of the bundle is referred to by an order parameter field $\varphi = \{\varphi_x\}$, with locally $\varphi_x = 0$ for an intact fiber, and $\varphi_x = 1$ for a broken one. For different realizations of the q.d., a priori different bundle states φ will be obtained for identical final elongations l_0. For each possible state φ and elongation, we define $P[\varphi, l_0]$ as the frequency of occurence of φ at final elongation l_0, over all possible realizations of the initial q.d. – i.e. when the deterministic experiment is performed ab initio as many times as there are possible q.d. realizations. We are interested in computing the configurational probability distribution $P[\cdot, l_0]$ for every elongation, and the associated average mechanical properties.

3 RESULTS

We first consider the simple Global Load Sharing rule. Considering a fiber state φ, each fiber is brought at the same elongation l_0 independently of the remaining ones. Thus, the probability for this fiber to be broken is $P_0 = P(l_0)$, and the probability that it has survived is $1 - P_0$, independently of the other fibers. The state of each fiber at l_0 are then independent random variables, and the probability of a given state φ, which specifies the state of each fiber in every location, is simply $P[\varphi, l_0] = P_0^n(1-P_0)^{N-n}$ where $n = \sum_x \varphi_x$ is the number of broken fibers in the state considered, and $N - n$ the number of surviving ones. The configurational probability distribution is thus simply given by a site percolation model with probability of occupancy P_0.

The average fraction of broken fibers at l_0 is thus P_0, and the mechanical properties are also directly obtained: Since the total force carried by the bundle is $F[\varphi, l_0] = l_0 \sum_x (1 - \varphi_x)$, its average value over all realizations of the q.d. is $F = N l_0 (1 - P_0)$, which is also the mechanical behavior of a fiber bundle in GLS with imposed total force (rather than elongation), in the limit of large sizes $N \to \infty$ [8,9]. If $F(l_0)$ presents a single maximum, this corresponds to a peak stress, which a priori does not coincide with the percolation transition happening at $P_0 = 1/2$. We notice that this configurational probability can also be cast under the form $P[\varphi, l_0] = \exp[-\ln[(1 - P_0)/P_0] \sum_x \varphi_x]/Z$ where Z is a normalization factor.

For more general Load Sharing Rules, i.e. for non-zero sharing functions J, the configurational probability distribution can also be obtained by perturbation, through the following reasoning: we consider a given state φ and final elongation l_0. The elongation of each fiber in the final state, $l(x) = l_0[1+\varepsilon \sum_y J(||y-x||)]$, is by construction the maximum elongation that this fiber has reached from the initial state. We also have $l(x) \geq l_0$. We utilize these two facts to first obtain an upper bound of the probability $P[\varphi, x]$ via these arguments: if any fiber x such as $\varphi_x = 1$ in the considered φ state had a threshold such as $t_x > l(x)$, this particular fiber should survive and the state φ is not reached. Conversely, if there is any x such as $\varphi_x = 0$ in the considered state, having a threshold below $t_x < l(x)$, this fiber should break and the final state will also not be reached. Consequently, a necessary condition to reach the state φ at l_0 is that each fiber such as $\varphi_x = 1$ has a threshold realized below $l(x)$, and each one such as $\varphi_x = 0$ had a threshold above $l(x)$. The probability of these two events to happen for each fiber threshold is $P(t < l(x)) = l_0 + l_0 \varepsilon \sum_y J(||y - x||) = P_0 + \delta P_x$, and $P(t > l(x)) = 1 - P_0 - \delta P_x$, where by Taylor expansion of the cumulative distribution P around l_0 we define $\delta P_x = \varepsilon l_0 \sum_y J(||y - x||)p_0$, with $p_0 = p(l_0) = dP/dx(l_0)$. An upper bound to the probability of observing the considered state φ is thus

$$P[\varphi, l_0] \leq \prod_{\{x/\varphi_x=1\}} (P_0 + \delta P_x) \prod_{\{z/\varphi_z=0\}} (1 - P_0 - \delta P_z). \tag{2}$$

A lower bound can be obtained by expressing a set of sufficient conditions on the individual thresholds for the considered state φ to be reached at l_0: if all fibers such as $\varphi_x = 1$ had a threshold below l_0, while all the others had their thresholds above $l(x)$, the state φ will be reached with certainty. In addition, other nonoverlapping subsets of the ensemble of realized thresholds lead with certainty to the considered state: if all fibers such as $\varphi_x = 0$ have thresholds realized above $l(x)$, all fibers such as $\varphi_x = 1$ but one have thresholds below l_0, and the last one has a threshold between l_0 and $l_0 + \delta l(x)$, the first ones are intact with certainty, the second ones are broken with certainty under the effect of the basic mean field elongation, and thus the last considered fibers also breaks with certainty due to the elongation perturbations coming from the other broken ones. Adding the measures of these nonoverlapping subsets in the q.d. space (corresponding to the set of thresholds), we obtain a lower bound seeken for:

$$P[\varphi, l_0] \geq \left\{ [\prod_{\{x/\varphi_x=1\}} (P_0)] + [\sum_{\{x/\varphi_x=1\}} \delta P_x \prod_{\{y \neq x/\varphi_y=1\}} (P_0)] \right\} \prod_{\{x/\varphi_x=0\}} (1 - P_0 - \delta P_x). \tag{3}$$

To leading order $O(\varepsilon)$, these lower and upper bounds are identical, so that the above determines exactly the probability of occurence of configurations φ that we look for, with interactions included through a perturbation analysis. This can be expressed more easily by considering the logarithm of the above: to leading order in the interactions ε, $P[\varphi, l_0] = e^{-H[\varphi,l_0]}/Z$ with Z a normalization factor, and

$$H[\varphi, l_0] = \ln\left(\frac{1-P_0}{P_0}\right) \sum_x \varphi_x - \frac{\varepsilon p_0 l_0}{P_0} \sum_{xy} J_{xy} \varphi_x \varphi_y + \frac{\varepsilon p_0 l_0}{1-P_0} \sum_{xy} J_{xy} \varphi_x (1 - \varphi_y) \tag{4}$$

In this function, the first leading term corresponds to the mean field GLS result, and is analog to a chemical potential, influencing the average number of broken fibers at a given level. The second term reflects the tendency of damage to cluster due to stress perturbations, and is thus analog to a bulk energy. The third term arises from the fact that it is less likely for a fiber to be intact if it interacts with many broken ones. In the LLS model, this positive term would arise only at the boundary between broken and non broken clusters, and is thus analog to an interfacial tension.

It is possible to extract a formal temperature arising from all possible realizations of the initial q.d., directly related to the variance of elastic energy over all realized systems, by noting that the elastic energy in the ensemble of fibers is $E = (1/2)\sum_x (1-\varphi_x)(l_0 + \delta l(x))^2 \simeq l_0^2/2 \sum_x (1-\varphi_x) + l_0^2 \varepsilon \sum_{xy} J(||y-x||)(1-\varphi_x)\varphi_y$, so that we can express $H[\varphi] = (E[\varphi] - \mu \sum_x \varphi_x)/T$ up to a constant, with a unique possible choice for the formal temperature and chemical potential, $T = 2P_0(1-P_0)l_0/p_0$ and $\mu = 2(P_0(1-P_0)l_0/p_0)\ln[P_0/(1-P_0)] - (l_0^2/2)[1+(4P_0-1)\varepsilon \sum_x J(||x||)]$. If desired, it is then possible to use standard statistical mechanics techniques to derive from a potential defined as $-T\ln(Z)$, the statistical characteristics of the system as mechanical characteristics (sustained force by the bundle, averaged over all realizations of the q.d.), average number of broken fibers, Shannon entropy or autocorrelation function of the system [16].

Last, we note that Eq. (4) maps these models onto well-known ones: defining a spin $\sigma_x = 2\varphi_x - 1$, we can express $H = -\beta I \sum_x \sigma_x - \beta j J_{xy} \sum_{xy} \sigma_x \sigma_y$ with an external field $\beta I = \ln[(1 -$

$P_0)/P_0]/2 - (\varepsilon p_0 l_0/2P_0)\sum_x J(||x||)$ and coupling factor $\beta j = \varepsilon p_0 l_0/[4P_0(1-P_0)]$: this corresponds to generalized Ising models of coupling constant jJ_{xy}, and reduces to standard Ising model for LLS, and percolation for GLS. Such models have a critical point at zero external field, and a certain value of coupling factor βj_c. When the external field βI reverses sign, the coupling factor has a certain unique value βj_r, and such model should go through a percolation-like transition, if $\beta j_r \ll \beta j_c$, a first order transition if $\beta j_r > \beta j_c$, a second-order transition if $\beta j_r \sim \beta j_c$, or no transition if $0 < \beta j_r < \beta j_c$.

4 CONCLUSION

For quasistatic interacting fiber bundle models with quenched disorder in the breaking thresholds, we have shown analytically how to obtain the probability distribution over damage configurations, when all possible realizations of the initial quenched disorder are considered. We have mapped these q.d. based models onto paradigms of classical statistical physics, namely percolation, standard or generalized Ising models for respectively, global, local or arbitrary decaying load sharing rules. The functional dependence of the coupling parameters over the elongation reached has been explicited analytically as forms which depend on the q.d. distribution and the load sharing rule considered. This allows to obtain the possible phase transitions in such systems depending on these: second order ones associated to percolation, Ising or generalized Ising critical points, first order ones associated to (possibly generalized) Ising models, or none. This exact analytical mapping should be confronted to direct numerical testing in future work.

5 REFERENCES

[1] A.A. Griffith, *Philos. Trans. Roy. Soc. London A*, vol. 221, pp. 163 (1920).
[2] H.J. Herrmann and S. Roux, eds, *Statistical models for the fracture of disordered materials* (North-Holland, Amsterdam) (1990).
[3] A. Hansen and J. Schmittbuhl, Phys. Rev. Lett., vol. 90, 045504 (2003).
[4] E. Bouchaud, J. Phys. Condens. Matt. vol. 9, p.4319 (1997).
[5] J. Schmittbuhl and K.J. Måløy, Phys. Rev. Lett., vol. 78, p.3888 (1997).
[6] H.E. Daniels, Proc. Roy. Soc. A vol. 183, p.404 (1945).
[7] B.D. Coleman, J. Appl. Phys. vol. 29, p.968 (1958).
[8] D. Sornette, J. Phys. A vol. 22, p.L243 (1989).
[9] P.C. Hemmer and A. Hansen, Journal of Applied Mechanics, vol. 59, p.909 (1992).
[10] A. Hansen and P.C. Hemmer, Phys. Lettt. A, vol. 184, p.394 (1994).
[11] M. Kloster and A. Hansen and P.C. Hemmer, Phys. Rev. E, vol. 56, p.2615 (1997).
[12] R.C. Hidalgo, Y. Moreno, F. Kun and H.J. Herrmann, Phys. Rev. E, vol. 65, 046148 (2002).
[13] R.L. Blumberg-Selinger, Z.G. Wang, W.M. Gelbart and A. Ben-Shaul, Phys. Rev. A, vol. 43, p.4396 (1991).
[14] A. Politi, S. Ciliberto and R. Scorretti, Phys. Rev. E, vol. 66, 026167 (2002).
[15] S.R. Pride and R. Toussaint, Physica A, vol. 312, p.159 (2002).
[16] R. Toussaint and S.R. Pride, Cond-mat/0403412, preprint (2004).
[17] J. Schmittbuhl, A. Hansen, and G. G. Batrouni, Phys. Rev. Lett. vol. 90, 045505 (2003).

Mean-field theory of localization in a fuse model

Renaud Toussaint*
Institut de Physique du Globe de Strasbourg, CNRS, UMR 7516, 5 rue Descartes, F-67084 Strasbourg Cedex, France

Alex Hansen†
Department of Physics, Norwegian University of Science and Technology, N-7491 Trondheim, Norway
(Received 28 November 2005; published 3 April 2006)

We propose a mean-field theory for the localization of damage in a quasistatic fuse model on a cylinder. Depending on the quenched disorder distribution of the fuse thresholds, we show analytically that the system can either stay in a percolation regime up to breakdown, or start at some imposed current, to localize starting from the smallest scale (lattice spacing), or instead go to a diffuse localization regime where damage starts to concentrate in bands of width scaling as the width of the system, but remains diffuse at smaller scales. Depending on the nature of the quenched disorder on the fuse thresholds, we derive analytically the phase diagram of the system separating these regimes and the current levels for the onset of these possible localizations. We compare these predictions to numerical results.

DOI: 10.1103/PhysRevE.73.046103 PACS number(s): 62.20.Mk, 46.50.+a, 46.65.+g, 64.60.Cn

I. INTRODUCTION

To understand breakdown processes in brittle systems with elastic interactions between the elements, and disorder in the material properties, fuse networks are often studied [1,2]. Such simplified models correspond to a scalar approximation of elasticity, i.e., retain the presence of long-range interactions, and such lattice models can be conveniently studied numerically, with the possibility to control *a priori* the probability distribution function (p.d.f.) characterizing the disorder in the rupture thresholds [1]. Fuse models allow us to study the impact on breakdown processes, of parameters as the disorder in material properties, and of size effects (the ratio of system size over lattice spacing, or over grain size for a natural system). We will present here a detailed study of the fuse model implemented on a network forming a long cylinder, and show how three different breakdown regimes are accessible to it depending on the nature of the quenched disorder (q.d.) in the rupture thresholds, and on the system size.

Related studies have already been performed on fuse models implemented on square lattices [3]. The present work extends these studies to the case of rectangular systems, with an extent L_y importantly exceeding the dimension L in the direction perpendicular to the main current flow. This extension will allow us to show how three types of breakdown processes can emerge in it, which will be termed as an entirely localized regime, a diffuse localization regime, and a percolationlike one. We will develop an analytical mean-field theory, allowing us to classify which regime dominates the final breakdown, as a function of the system size, and of the characteristics of the quenched disorder. The three possible regimes are illustrated in Fig. 1. The total localization regime corresponds to the breakdown propagating between close or nearest neighbors. The percolationlike regime corresponds to systems where a significant fraction of the entire set of fuses have blown before the system becomes nonconducting. The diffuse localization regime corresponds to a system where the burned-out fuses concentrate in a band of size comparable with the system width, but where the damage is distributed diffusely inside this band, without necessarily propagating to the close neighbors of the already burned fuses.

An important motivation of this study is to characterize the scaling law between the system size, and the characteristic size where damage localizes in the so-called "diffuse localization" regime. This scaling law has an important theoretical impact on the understanding of the origin of the geometrical characteristics of natural fracture surfaces. Indeed, in general the main contribution (so far) to the science of fracture by the physics community over the last 20 years is the discovery that brittle fracture surfaces are self-affine [4]. Self-affinity implies statistical invariance of fracture surfaces under the rescaling of length scales parallel to the average fracture plane by a factor λ and rescaling of the out-of-plane length scale by a factor λ^{ζ}, where ζ is the Hurst or roughness exponent. In 1990, based on experimental investigations of brittle aluminum fracture surfaces, Bouchaud *et al.* [5] proposed that the roughness exponent has a *universal* value close to 0.8. This value has been reported in many later investigations, see, e.g., [6–9]. In Refs. [8,9], a small-scale regime governed by a different roughness exponent was reported in addition to the "usual" regime characterized by a roughness exponent of 0.8, see [10] for a review. There have been several attempts at finding a theoretical explanation for the universal roughness exponents, see [11–14].

Using the fuse model as paradigm for brittle fracture [1,2], Hansen and Schmittbuhl [14] have recently proposed that the roughness exponent ζ is related to the exponent ν controlling the divergence of the autocorrelation length of the emerging damage, ξ, as function of the control parameter: more explicitly, in the case of a burned fuse model, noting V the imposed global voltage difference, and V_c the voltage at complete electrical failure, $\xi \sim |V-V_c|^{-\nu}$. Hansen

*Email address: Renaud.Toussaint@eost.u-strasbg.fr
†Email address: Alex.Hansen@ntnu.no

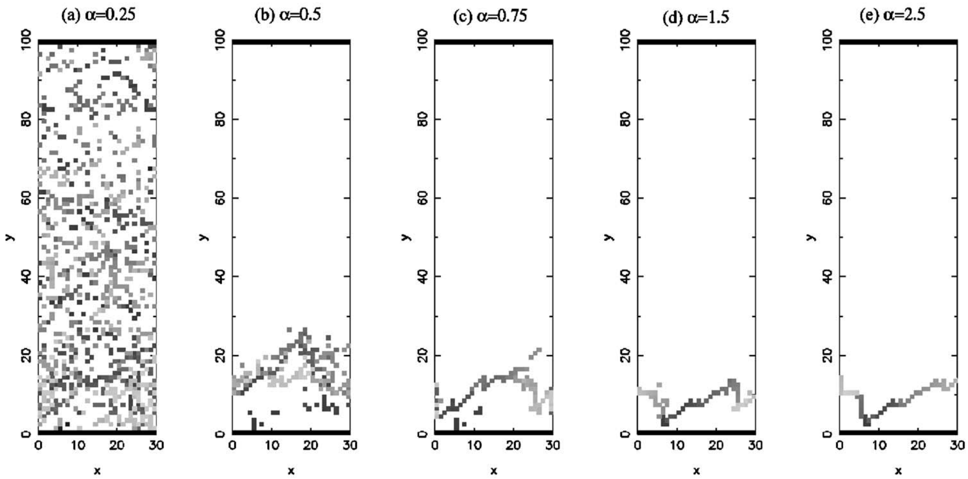

FIG. 1. Configuration of burned fuses in an elongated network at system breakdown, for five realizations with a decreasing quenched disorder from (a)–(e): the distribution of the fuse thresholds t is of the type $p(t) \sim t^{\alpha-1}$ for $0 < t < 1$, with α indicate. In the white region is a nondisplayed diamond lattice of intact fuses, inclined at 45° with respect to the bus bars at the top and bottom, with a lattice step $\ell = 1$. Burned fuses are marked by gray squares, with a gray index turning from dark to light in chronological order. In cases (d) and (e), order dominates and the rupture proceeds almost always via nearest neighbors: this is an ordered rupture, with a *total localization* of damage. In case (a), disorder is large and the breakdown process is dominated by the distributed location of weakest flaws: this is a *percolationlike* filling, with a finite fraction of bonds to break to reach the system breakdown. In cases (b) and (c), rupture does not proceed via nearest neighbors, and looks diffuse at scales below $L = 30\ell$, the lateral x size of the system. Broken bonds are nonetheless localized in a band of vertical size w comparable to the horizontal width L of the system: this is the *diffuse localization* regime.

and Schmittbuhl [14] proposed the existence of a scaling relationship between these two exponents, $\zeta = 2\nu/(1+2\nu)$ in such breakdown problems. This relationship was numerically checked for a fuse model in two dimensions, where the exponent ν was numerically measured, and found to be close to that of percolation, $\nu = \frac{4}{3}$ [15], leading to the roughness exponent $\zeta \approx 8/11$. However, large-scale simulations by Nukala *et al.* [16] gave $\nu = 1.56$ and high-precision measurements of the roughness exponent gives $\zeta = 0.74 \pm 0.03$ [17]. Using the value 1.56 in the relation $\zeta = 2\nu/(1+2\nu)$ gives 0.76. In three dimensions, one finds $\nu = 0.83 \pm 0.04$ [18], and $\zeta = 0.62 \pm 0.05$ [19]. The same reasoning for brittle fracture, based on the same scaling relationship, and an auto correlation divergence exponent $\nu = 2$ [20], leads to the roughness exponent $\zeta = \frac{4}{5}$ for brittle fracture, in excellent agreement with the experimental measurements [5]. Central to this theory is the scaling law $w \sim L/\ell$ between the width of a concentrated damage zone w and the size of the system L, where ℓ is the lattice constant. One of the aims of this paper is to explain the origin of this scaling law.

The fuse model consists of a lattice of Ohmic resistors with identical conductances placed between two bus bars, where each bond carries an electrical current up to a threshold t above which the bond burns irreversibly. Each of these local random thresholds t are fixed initially and taken independently of each other from the p.d.f. $p(t)$, which entirely characterizes the uncorrelated quenched disorder present in this system.

For square systems, the phase diagram of this system was established numerically and through order statistics arguments [3] depending of two parameters α and β characterizing the quenched disorder distribution tails in the limit of zero or infinite thresholds, as $p(t) \sim t^{\alpha-1}$ where $t \to 0$ and $p(t) \sim t^{-\beta-1}$ when $t \to \infty$. We will consider here such systems in a cylindrical geometry, i.e. a periodic band of finite width $L \gg \ell$, where ℓ is the lattice constant placed between two bus bar at distances $L_y \gg L$, and derive analytically the equivalent of this phase diagram as function of α and L/ℓ, at $L_y/\ell \gg 1$–we will only consider here power-law distributions with an upper cutoff, corresponding to $\beta \to \infty$ in the previous terminology. With respect to this previous work, we extend the study in two ways: we consider elongated systems, and in detail the anisotropic aspect of the current perturbation generated by burned fuses.

The derivation of the phase diagram of such a paradigmatic model is important in several respects. It allows first to clarify the role of disorder and system geometry on this particular simple breaking model. Moreover, there have been recent studies focusing on isomorphisms between classical statistical mechanics models, and breakdown models such as burned fuse models [21] or quasistatic fracture models [22,23]. The determination of the phase diagram of such simple breakdown models, as function of the quenched disorder and system geometry, should help in the future to theoretically scrutinize these isomorphisms, by comparison of the phase diagrams of the known systems.

In the next section, we present the basic assumptions for and philosophy of our statistical analysis of the fuse model. In Section III we calculate the shape of the current distribution around a region of burned-out fuses. We then present in Section IV the spatial probability distribution of subsequent fuse burn-outs. The main result of the calculation is presented in Fig. 4. Depending on the disorder exponent α, and on the system size, there are three possible breakdown regimes: (1) A percolationlike phase where no localization occurs and where a finite fraction of the total number of fuses needs to burn out in order for the conductance of the lattice to drop to zero in the infinite-lattice limit; (2) a diffuse localization phase where a damage zone develops, with a width w proportional to the width of the lattice L; and (3) a complete localization phase where a single crack evolves without damage around it. These regimes are illustrated in Fig. 1. We do not in this paper discuss the phase diagram with respect to the second disorder exponent β. In Sec. V, we compare our analysis to numerical results on the fuse model. We summarize our findings in Sec. VI.

II. MODEL UNDER STUDY AND BASIC ASSUMPTIONS

At any stage of the rupture process, we will assume that the local currents in the fuse model are determined through a continuous approximation, as the solution of the conservation of charge $\nabla \cdot \boldsymbol{j}=0$ under boundary conditions $\boldsymbol{j} \to j_e \hat{y}$ when $y \to \pm L_y/2$ [the band is L-periodic in the x direction, $(\hat{x},\hat{y})$ are the unit vectors]. The current density is of the form $\boldsymbol{j}(\boldsymbol{r})=-c(\boldsymbol{r})\nabla\phi(\boldsymbol{r})$, with a conductance $c(\boldsymbol{r})$ equal to unity in the intact cells, and zero in the broken ones.

After the first fuse has burnt at a certain current level j_e at a position defined as the origin, we are interested in the average change of external current necessary to break the next element: since the problem is linear, for a given geometry of burnt elements, the current flow for any other value of the external current j' is simply $(j'/j_e)\boldsymbol{j}(\boldsymbol{r})$. For a given realization of the quenched disorder $t(\boldsymbol{r})$ [such as $t(\boldsymbol{r}) > j_e$ at every location], the next fuse will burn when a first threshold is reached by the local current, i.e., when the external current reaches

$$j_n = j_e \min_{\boldsymbol{r}}\left(\frac{t(\boldsymbol{r})}{j(\boldsymbol{r})}\right), \tag{1}$$

at a position $\boldsymbol{r}_n$ corresponding to the realization of this minimum. If $j_n > j_e$, the applied external current has to be increased by a finite value for the next fuse to burn. On the contrary, if $j_n \leqslant j_e$, there is an avalanche and the next fuse burns immediately if the external current is not reduced immediately during the first burn-out to this lower value j_n.

We are also interested in the geometric characteristics of the relative position of the next burnt fuse with respect to the first one: over all realizations of the quenched disorder, we define the probability distribution over this relative position of the next burnt fuse as $\mu(\boldsymbol{r}_n)$. Three scenarii will be shown to happen, depending on the random mean square distance of the next burnt fuse to the previous one, $d^2=\int \boldsymbol{r}_n^2 \mu(\boldsymbol{r}_n) d\boldsymbol{r}_n$: (1) $d \sim +\infty$ and the process remains diffuse, resembling a percolation process. (2) $d \sim \ell$, i.e., it is a function of the lattice spacing, independent of the system width L. This is the onset of a complete localization, i.e., the current perturbation created by the broken cell is such that the rupture will propagate mainly from nearest neighbor to nearest neighbor up to complete breakdown of the system. (3) $d \sim L$, which is the onset of a regime which we define as "diffuse localization:" damage starts to concentrate in a band of a width in the y direction comparable to the system size in the x direction, L, but the closest neighbors of the previously burnt cell are not significantly favorized. This is the regime where the scaling arguments of [14] should apply.

If the system remains in the diffuse regime, the spatial correlations of the damage are not significant, and we are entitled to consider a mean-field approximation to study the subsequent history of the process: if the last fuse has burnt at a location $\boldsymbol{r}_0$ at a current level j_e, the probability distribution over the location of the next fuse burning is approximated as the probability obtained from a situation where a single fuse has burnt at $\boldsymbol{r}_0$, under the condition that all of the remaining thresholds were above j_e.

To estimate the average level of current necessary to trigger the next fuse burning and the statistical properties of its location, we extend the arguments of Roux and Hansen [24]: By convention, any level of local current j in the system will be expressed through a reduced dimensionless variable $s=(j-j_e)/j_e$, the ratio of the current perturbation generated by the last fuse burnt, over the average imposed current level. We next define $n(s)\Delta s$ as the number of cells experiencing a local current between $j_e(1+s)$ and $j_e(1+s+\Delta s)$, where $\Delta s \ll 1$ is a small parameter. Defining as $\Omega(s,\Delta s)$ the region experiencing that local current level, we have

$$n(s) = \lim_{\Delta s \to 0} \frac{1}{\ell^2 \cdot \Delta s} \int_{(x,y) \in \Omega(s,\Delta s)} dx\, dy. \tag{2}$$

The average value m of the external current leading to the next burn-out is, from Eq. (1), the average value of the minimum over all cells of the random variable $y=t/(1+s)$—Eq. (1),

$$m = \left\langle \min_{\{s=n\Delta s, \boldsymbol{r} \in \Omega(s,\Delta s)/n \in \mathbb{Z}\}} \frac{t(\boldsymbol{r})}{1+s} \right\rangle. \tag{3}$$

At a given level of current perturbation s, we define $P(y,s)$ as the cumulative probability of the random variable $y=t/(1+s)$, given that $t > j_e$. This last condition reflects the fact that the intact fuses experiencing a current $j_e(1+s)$ have survived, up to the burning point of the fuse creating the dipolar perturbation we look at. This is straightforwardly

$$P(y,s) = \frac{P[y(1+s)] - P(j_e)}{1-P(j_e)} \mathrm{He}[y(1+s) - j_e], \tag{4}$$

where He is the Heaviside function, and P is the cumulative distribution of thresholds.

As shown in Appendix, A, where we extended some statistical results of Gumbel [25], m satisfies the implicit equation

$$\int_s n(s) P(m,s) ds = 1. \tag{5}$$

We also show in this Appendix that $\mu(\boldsymbol{r}_n) \alpha P(m, s(\boldsymbol{r}_n))$, where m is the solution of the above equation, i.e., that $n(s)P(m,s)\Delta s$ is the probability that the next bond would break in $\Omega(s,\Delta s)$. Thus, if we find $(s_{max},\Delta s)$ such as the integral in the above has a significant support only in $[s_{max}, s_{max}+\Delta s]$—i.e., $\int_{s_{max}}^{s_{max}+\Delta s} n(s)P(m,s)ds=1$, the next break will almost certainly happen in the spatial region $\Omega(s_{max},\Delta s)$, and the geometric properties of this spatial ensemble are representative of the ones of the spatial distribution over all possible locations of the next broken bond, i.e., the random mean square distance to the next broken bond will be evaluated as

$$d^2 = \int_{(x,y)\in\Omega(s_{max},\Delta s)} (x^2+y^2)dx\,dy. \tag{6}$$

III. NUMBER DENSITY OF CELLS OVER THE LEVEL OF CURRENT PERTURBATION

We will now compute the mass $n(s)\Delta s$ and shape $\Omega(s,\Delta s)$ of each region carrying a certain value of the local current magnitude in $[j_e(1+s),j_e(1+s+\Delta s)]$. The local current, after a unit has fused somewhere, is written as $\boldsymbol{j}(\boldsymbol{r}) = j_e\hat{y}+\delta\boldsymbol{j}(\boldsymbol{r})$, with a perturbation $\delta\boldsymbol{j}(\boldsymbol{r})=-\nabla\phi$ and a potential field satisfying Laplace equation $\nabla^2\phi=0$ under Neumann boundary conditions, $\nabla\phi=0$ when $y\to\pm L_y$ and $\hat{n}\nabla\phi=j_e\hat{n}\hat{y}$ along the surface of the broken element (elementary lattice cell), where $\hat{n}$ is the elementary vector normal to it. Since $L\ll L_y$, this current perturbation will be approximated as the one in an infinitely long cylinder, i.e., the long-range condition used will be $\nabla\phi=0$ when $y\to\pm\infty$, and x periodicity with a period L. We will then also use the coordinate system where the last burnt fuse is at the origin. Furthermore, from a distance of a few lattice size and above, the shape of the lattice cell is no more relevant, and this elementary current perturbation is itself approximated as the solution of this problem with a spherical fused element of diameter ℓ: ϕ satisfies in circular coordinates, $\hat{n}\nabla\phi(r=\ell/2,\theta)=j_e\sin(\theta)$. For sufficiently large systems $L/\ell\gg 1$, this particular potential can itself be constructed as

$$\phi = -j_e\pi\ell^2\hat{y}\nabla G/2, \tag{7}$$

where G is the solution of the Poisson equation in L-periodic boundary conditions in the x direction, satisfying $\Delta G = \delta(x,y)$ and $G(x+L,y)=G(x,y)$: indeed, along the surface of the elementary circle of diameter ℓ, we have $\nabla G \simeq \hat{r}/2\pi r$, and with $\hat{r}$ the elementary radial vector, and θ the angle between $\hat{x}$ and $\hat{r}$,

$$\hat{\boldsymbol{r}}\cdot\nabla(\hat{y}\nabla G) = \hat{\boldsymbol{r}}\nabla[\sin(\theta)/2\pi r] = -2\sin(\theta)/\pi\ell^2.$$

The complete expression of G in such periodic boundary conditions is after Morse and Feshbach [26],

$$G(x,y) = \frac{1}{4\pi}\ln\left[4\sin^2\left(\frac{\pi x}{L}\right)+4\sinh^2\left(\frac{\pi y}{L}\right)\right]. \tag{8}$$

Eventually, at a sufficient distance from a broken cell $r\gg\ell$, we have $\delta j\ll j_e$ and $j(\boldsymbol{r})\simeq\sqrt{[j_e\hat{y}+\delta\boldsymbol{j}(\boldsymbol{r})]}\simeq j_e+\delta j(\boldsymbol{r})$, where $\delta j(\boldsymbol{r})=\hat{y}\delta\boldsymbol{j}(\boldsymbol{r})$—which is a classical expression for the dipolar perturbation emanating from a burned fuse in such models, see, e.g., [27]. The magnitude of the current perturbation is thus determined from the above Eqs. (7) and (8) as

$$\delta j(x,y)/j_e = \frac{\pi^2\ell^2}{2L^2}f(2\pi x/L, 2\pi y/L), \tag{9}$$

with

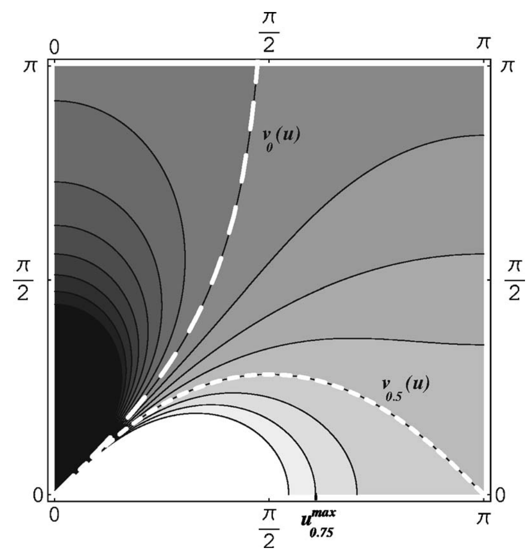

FIG. 2. Contour map of the elementary current perturbation due to a burnt fuse at the origin. The long-dashed curve corresponds to a 0 perturbation, the short-dashed one meets a saddle point at $(\pi,0)$, and corresponds to $f(u,v)=0.5$.

$$f(u,v) = \frac{1-\cos(u)\cosh(v)}{[\cosh(v)-\cos(u)]^2}. \tag{10}$$

A contour map of the dimensionless current perturbation $f(u,v)$ is displayed in Fig. 2.

Since this perturbation $f(u,v)$ is a pair in both its arguments, only a zone $[0,\pi]^2$ was represented. The system is 2π periodic in the x direction. Two special contours were highlightened: $f(u,v)=0$ is the long-dashed curve. On the displayed region, points to the right of this line experience an increased current due to the burnt fuse at the origin, and conversely the current is screened for those to the left of it. This zero perturbation contour correspond to $v_0(u) = \text{a}\cosh[1/\cos(u)]$, which has a support on u mod $[2\pi] \in[-\pi/2,\pi/2]$ and an asymptot $v_0(u)\to+\infty$ when $u\to\pm\pi/2$. The other contour goes through a saddle point of f in $(u,v)=(0,\pi)$, and corresponds to $f(u,v)=0.5$, or $v_{0.5}(u) = \text{a}\cosh(\sqrt{2-\cos^2 u})$.

The regions $\Omega(s,\Delta s)$ that we want to characterize geometrically, which support a perturbation of current such as $s<\delta j/j_e<s+\Delta s$, correspond to the regions between two neighboring lines of the contour map in Fig. 2. The number of the cells in such regions, defined in Eq. (2), is shown in Appendix B to be of the form

$$n(s) = \frac{2L^4}{\pi^2\ell^4}g(2L^2 s/\pi^2\ell^2), \tag{11}$$

where the dimensionless quantity g, function of its dimensionless argument, is numerically evaluated and plotted as a continuous line in Fig. 3. The numerical evaluation is based on analytical expressions detailed in Appendix B, where the asymptotic behaviors of this function g are also derived, which are plotted in Fig. 3.

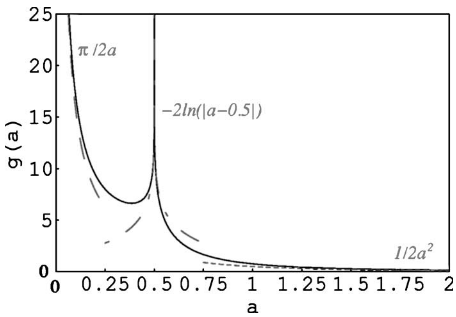

FIG. 3. Dimensionless number density of cells as function of the level of current perturbation, and asymptotic forms in dashed, at infinite distance ($a=0$), around the saddle point $\left(a=\frac{1}{2}\right)$ and in the region close to the burnt fuse ($a\to\infty$).

IV. REGION OF MOST PROBABLE NEXT EVENT

We have now derived the number of cells associated with each current level, $n(s)$, characterizing the interactions in this system, and need to consider some specific quenched disorder to determine the typical separation between two subsequent burning fuses. With a quenched disorder distribution of power-law type $P(t)=t^{\alpha}$ on $0\leqslant t\leqslant 1$, with $\alpha\geqslant 0$, we obtain the cumulative distribution for thresholds to be below m, for the fuses that were still intact at current j_e, through Eq. (4), as

$$P(m,s)=\frac{m^{\alpha}(1+s)^{\alpha}-j_e^{\alpha}}{1-j_e^{\alpha}}\mathrm{He}[m(1+s)-j_e]. \qquad (12)$$

We divide the space with respect to the last burned fuse in three zones, noted Ω_c, Ω_d, and Ω_f, and have to solve the implicit Eq. (5) to find both the most probable region out of these three where the next break will happen, and the most probable value of the external current m at which the next fuse will burn. This equation becomes

$$\left(\int_{\Omega_c}+\int_{\Omega_d}+\int_{\Omega_f}\right)n(s)P(m,s)ds=1. \qquad (13)$$

By definition, Ω_c is a region of fuses close to the last burned one, with the largest positive current perturbation, such as $f(u,v)>L/(2\pi^2\ell)$. All such fuses lie within a distance $r<\sqrt{(L\ell)}$ of the last burned one, where we recall that ℓ is the lattice step and L is the x dimension of the system.

Ω_d is a region defined with moderate and finite current perturbations, where $L/(2\pi^2\ell)>f(u,v)>\frac{1}{4}$. The typical distance r from the origin of the current perturbation, over the zone Ω_d, is such as $\sqrt{(L\ell)}<r<\pi L$.

Last, Ω_f is a region of weak to negative current perturbation, defined by the implicit equation $f(u,v)<\frac{1}{4}$. It will be shown that when this region dominates the left-hand side of Eq. (13), the leading contribution to it comes from points sitting at a characteristic distance r to the last burned fuse, scaling with the system size as $r\sim L_y$.

In Appendix C, we analyze in detail the three terms of Eq. (13), and reformulate it as

$$H_c(\lambda)+H_d(\lambda)+H_f(\lambda)=\frac{2\varepsilon(1-j_e^{\alpha})}{j_e^{\alpha}}, \qquad (14)$$

where $\lambda=m/j_e$, with j_e, m the values of te external current at the last break and at the most probable next one, $\varepsilon=\pi^2\ell^2/(2L^2)$ and H_c, H_d, H_f are proportional to the integrals in Eq. (13) over the regions Ω_c, Ω_d, and Ω_f.

We will classify the regime of the system according to the dominant term in the left-hand side of Eq. (14): If H_f dominates, the system remains in a diffuse regime where there are no noticeable spatial correlations in the pattern of burnt fuse. If H_c dominates, this signifies the onset of a complete localization regime where the damage will develop in a concentrated zone scaling as the lattice size ℓ, and propagate through the system, tearing it with jumps between successive events close to this smallest scale. Last, the dominance of H_d would denote the onset of a diffuse localization regime, where the characteristic distance d between the burnt fuse scales as L, the system's width.

Thus, following as the imposed current increases, which of the three terms dominates in Eq. (14), allows us to understand when damage starts to localize, and at which spatial scale. This allows us to classify, as function of the system dimensions L_x/ℓ, L_y/ℓ and of the quenched disorder, characterized by α, in which localization regime the system ends up in.

It is shown in Appendix C that in the early stages of the process, at small j_e, H_f dominates the solution of Eq. (14), owing to the singularity of $n(s)$ around $s\sim 0$ (zero current perturbation line), and this equation reduces to

$$\lambda^{\alpha}-1=\frac{1-j_e^{\alpha}}{N_{cells}j_e^{\alpha}}. \qquad (15)$$

Since the first break is typically for $j_1^{\alpha}=1/N_{cells}$, this equation predicts a second break typically at

$$\lambda_1^{\alpha}-1=1, \qquad (16)$$

i.e., the second break should happen on average at $j_2=\lambda_1 j_1=(1+1)^{1/\alpha}j_1=(2/N_{cells})^{1/\alpha}$. Since $j_2>j_1$, the process is stable and there is a finite gap in the external current to trigger the next fuse burning. Since H_f is dominated by the asymptote of zero current perturbation (noted h_4 and h_6 in Appendix C), corresponding to the long dashed curve in Fig. 2, which spans the whole y range of the system, the next fuse is likely to burn at a distance scaling as $d\sim L_y$ from the first one, i.e., the system remains in a diffuse regime, with no noticeable correlations between the locations of the burnt fuses: the size of the system wins compared to the attractive feature of the current concentration around the last burnt fuse, in a Flory-type argument. We can then proceed with this mean-field theory to treat the later stages of the process.

As long as H_f dominates Eq. (14), Eq. (15) remains valid, and by recurrence, we show in Appendix C that the nth fuse burns on average when the external current is such as

$$j_n^{\alpha}=(n/N_{cells}):. \qquad (17)$$

As long as this is the case, the nth weakest bonds are the most likely to be the n first burnt ones.

For threshold distributions characterized by a very large disorder, i.e., in the limit $\alpha \to 0$, it is shown in Appendix C that $H_f(\lambda)$ always dominates in the solution of Eq. (14), up to the moment where $j_e^\alpha = \frac{1}{2}$. In this limit, the nth fuse burning corresponds to the nth weakest threshold, and this lasts until the entire system is broken due to burned fuses percolating through the system. In this case, the process remains diffuse, in a percolationlike regime, up to the moment where $P(j_e) = \frac{1}{2}$, which corresponds to the critical percolation threshold. This means that in this limit of nonrenormalizability of the q.d. distribution, and very large disorder, the process is equivalent to a bond-percolation process, which was shown by Roux *et al.* [28].

On the contrary, for very small disorder, in the limit $\alpha \to +\infty$, we show in Appendix C that $H_c(\lambda)$ dominates, and even that the contribution of the nearest neighboring cells on the sides of the last burnt fuse dominate the integral: thus, the next fuses to burn are the ones carrying the highest current perturbation, and from the asymptotic expression of $H_c(\lambda)$ derived in Appendix C, and Eq. (14), the level of next break is set by

$$\lambda = \frac{2^{1/\alpha}}{j_e s(\alpha)^{1/\alpha}}, \tag{18}$$

where

$$s(\alpha) = \int_{\ell/4\pi L}^{1/4\pi} \frac{(1+\gamma)^\alpha}{2\gamma^2} d\gamma. \tag{19}$$

This happens in a controlled way, i.e., for $\lambda > 1$ if α is still sufficiently small so that $s(\alpha) < 2N = 2/j_e^\alpha$, or through immediate avalanches $\lambda < 1$ in the opposite case. This is the limit of no disorder, where all bonds share the same threshold, and the concentration of current around the first broken one is the significant parameter controlling the process in this case: the rupture proceeds from the smallest scales, expanding through nearest neighbors from the initial seed to tear the system apart. This corresponds to a classical rupture process, analog to the rupture of a perfectly elastic and homogeneous material (no disorder), where the stress concentration at the tips of an initial default leads to the rupture of the system when the load is increased—in a stable way or not, depending on the load level—the situation known from one century in linear elastic fracture mechanics, treated by Griffith and Inglis [29].

Between these two extreme cases, in the range of finite α, the system can be driven to a third regime if H_d dominates in the solution of Eq. (14): correlations in the damage start to be significant, but the characteristic distance to the preceding burnt fuses is in a range between $\sqrt{L\ell}$ and L, and does not scale as the lattice constant ℓ: this is the regime which we refer to as "diffuse localization."

We determine a lower value α_m of the exponent of the q.d. distribution separating systems entirely equivalent to percolation up to breakdown, and these leading to diffuse localization, as follows: as long as the percolation regime holds, the value of the external current, and the size of the jumps λ in it, are determined by Eq. (17). This regime goes on as long as $H_d(\lambda)$ can indeed be neglected in front of $H_f(\lambda)$. If both terms become equal, the system transits towards the diffuse localization regime, which is shown in Appendix C to correspond to leading order in $1/N_{cells}$, to the condition

$$\frac{\alpha}{2} \ln\left(\frac{L}{\ell}\right) = 2\frac{1-j_e^\alpha}{j_e^\alpha}. \tag{20}$$

If this condition is not met at the percolation threshold $j_e^\alpha = \frac{1}{2}$, i.e. if

$$\alpha < \alpha_m = \frac{4}{\ln(L/\ell)}, \tag{21}$$

the system always remains in the percolation universality class. If on contrary $\alpha > \alpha_m$, the system undergoes a transition towards diffuse localization at a typical external current

$$j_t = 1/[1 + \alpha \ln(L/\ell)/4]^{1/\alpha}. \tag{22}$$

Similarly, we determine an upper cutoff α_M of the exponent of the q.d. distribution, above which complete localization will prevail about the diffuse one. By equating $H_f(\lambda)$ and $H_c(\lambda)$, with λ evaluated from the percolation regime expression in Eq. (15), we show in Appendix C that this upper cutoff satisfies the implicit equation

$$\frac{s(\alpha_M) - 2\pi L/\ell}{\alpha_M} = \frac{\ln(L/\ell)}{2}. \tag{23}$$

From the expression of s, the equation above has a single solution at $\alpha_M = 1$. If $\alpha > 1$, the system will transit towards complete localization at a characteristic current level

$$j_t = 1/\{1 + [s(\alpha) - 2\pi L/\ell]/2\}^{1/\alpha}. \tag{24}$$

Eventually, if $L/\ell < e^4 \simeq 54$, the above would lead to $\alpha_M < \alpha_m$, and no diffuse localization is obtained for any value of α. There is instead a transition directly from the percolation regime below $\alpha < \alpha_d$ to a regime leading to complete localization for $\alpha > \alpha_d$, with

$$s(\alpha_d) - \frac{2\pi L}{\ell} = \frac{\pi}{\varepsilon} \ln\left(\frac{1}{a_m}\right)(\lambda_{perco}^\alpha - 1) = 2. \tag{25}$$

where λ_{perco} is estimated by Eq. (15). For $\alpha > \alpha_d$, the system starts a complete localization at a current level given by Eq. (24).

To summarize the above results, a phase diagram of the system, showing the regime through which it will go to final breakdown, is shown in Fig. 4. The value of α_d was determined numerically from Eq. (25). A visual representation of sequences of burning fuses, for small systems, in five points of this phase diagram, illustrating the three regimes, is given in Fig. 1.

The above can be compared, in the limit of infinitely large systems, to the numerical analysis carried by Hansen *et al.* [3]: using the notations of this paper, $\alpha = \phi_0$, and $1/\phi_\infty = 0$, and the system goes from a disorderless regime A when $\alpha > \alpha_M = 1$ to a scaling regime B with diffuse damage and localization when $\alpha < \alpha_M$. The difference between the critical exponent separating the two regimes, which is $\alpha_M = 1$ in the present case, and $\phi_0 = 2$ in the models of [3], is believed to come from the elongated character of the systems considered here ($L_y \gg L$).

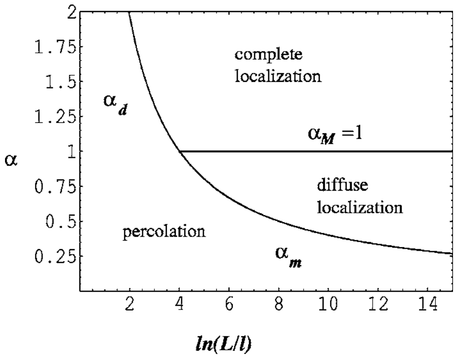

FIG. 4. Phase diagram of the system displaying the regime through which it will go to macroscopic breakdown, as a function of the system's width and exponent characterizing the fuse threshold distribution.

Some remarks can be done on the succession of approximations carried to establish this phase diagram: Most of these approximations correspond to keeping the leading order in the inverse of the number of lattice cells in the lateral dimension, ℓ/L, for systems of infinite anisotropic ratio (such as $L/L_y \to 0$). These approximations already take into account finite size effects, since they keep finite ℓ/L. They should thus be valid as long as these numbers are $\ell \ll L$, and $L \ll L_y$. Evaluating the following terms corresponding to higher orders of the parameters ℓ/L and L/L_y, in order to estimate the quality of the asymptotic expansions reduced to leading order, is beyond the scope of the present work. In this analytical development, there is however an approximation that does not fall in this category of asymptotic expansion: in order to evaluate whether the system departs from the percolationlike regime, as more and more fuses are burned and the system has stayed so far in this regime, we have considered separately the current perturbation triggered by each burned fuse. This is perfectly justified in the early stages of the process, where since the process is in a percolationlike regime, successively burned fuses are at distances of order L_y from each other, and almost do not interact. However, as the density of burned fuses increases, it can become finite (for sizes and q.d. where the process always remains in a percolation like regime, the density reaches eventually a large fraction, in principle, the percolation threshold). In this situation of a high fraction of burned fuses, the approximation corresponding to evaluate the local current as a homogeneous background j_e, superimposed to the perturbation emanating from a single burned fuse (the last burned one), becomes of lower quality, due to the existence of multiple close burned fuses anywhere in the system. Overcoming this limitation at high fractions of burned fuses, would require to take into account a large number of perturbation sources. This task seems more suitable for a purely numerical approach: a main scope of this paper is to carry out the analytical development in terms of extreme statistics for a mean-field theory going beyond the purely homogeneous description of damage (i.e., incorporating a homogeneous term plus a local perturbation). Carrying out analytically the details of the calculation while keeping the track of every local perturbation is beyond the scope of this work. The result of this approximation is mainly to underestimate the number of close perturbation sources anywhere in the system as the process goes on: thus, this overestimates the weight of the probability to break far from the existing sources, H_f, and underestimates the probability to enter a diffuse localization or a total localization regime. Thus, the mean-field theory presented here should predict properly the transition between "total" and "diffuse" localization regime, but should overestimate the domain of the "percolationlike" regime: in Fig. 4, the left line should be located at smaller sizes. This approximation seems to overestimate the transition size L/ℓ by a finite factor not exceeding an order of magnitude, as will be shown in the next section.

Eventually, we note that in the diffuse localization regime, the process looks uncorrelated at the lattice constant scale, i.e., looks like a percolation system, but the arguments developed in this paper show that damage starts to concentrate in a band of width scaling as the width of the system L. An argument based on percolation in a gradient corresponding to the structure of the damage concentration at the scale of the system can then be applied to describe the breakdown process, which sustains the arguments developed in [14] to explain the origin of the roughness of the ultimate breakdown connected fronts in this regime.

Qualitatively, the phase diagram shown above supports the idea that the failure of natural macroscopic heterogeneous systems is dominated by either the "total localization," or the "diffuse localization" regime. Indeed, macroscopic materials are often systems much larger than the typical scale of the disorder, i.e., systems with a high ratio of system size over cell size, L/ell. In such regime, the present work predicts that the percolation regime vanishes. More precisely, in this limit, the percolation regime would only subsist in the limit of nonnormalizable threshold distribution, corresponding to $\alpha \to 0$. So the present work predicts that the breakdown of such system is "totally localizing" at low disorder, or "diffusely localizating" at a larger one. This picture is consistent with the fracture properties of natural objects: when the fracturing solid is more homogeneous, or has only moderately disordered toughness properties, corresponding to large values of α, the rupture is initiated on the weakest flaws, and the fracture propagates from nearest neighbor to nearest neighbor: this is the classical picture of linear elastic fracture mechanics of a homogeneous solid, described here as "total localization." The fracture of such a regular object, as, e.g., a crystal, leaves a flat, or close to flat, fracture surface, as seen in Fig. 1(e). Conversely, when the toughness properties of the breaking solid are more scattered, i.e., at smaller α, when the heterogeneous solid is more disordered, the rupture proceeds according to the "diffuse localization" regime [illustrated in Fig. 1(b)]: this corresponds to the rough post mortem fracture surfaces observed in most natural materials, found to be self-affine with a universal roughness of 0.8.

V. COMPARISON TO NUMERICAL SIMULATIONS

We now turn to confront this theory to numerical simulations of the fuse model. We consider rectangular models of

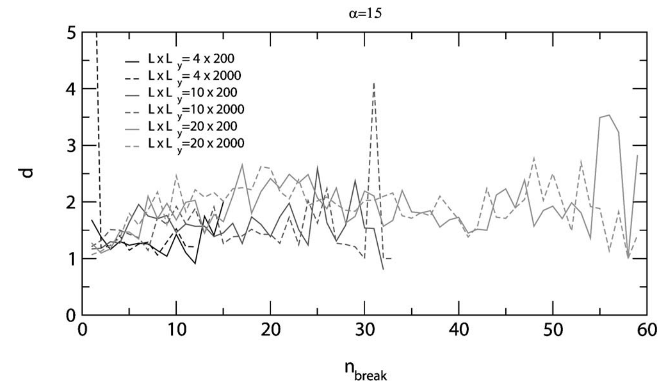

FIG. 5. Total localization: distance between successive burning events, as a function of their index, averaged over 50 realizations. For a quenched disorder exponent $\alpha=1.5$, this distance remains of order unity, irrespectively of the dimensions L and L_y of the lattice.

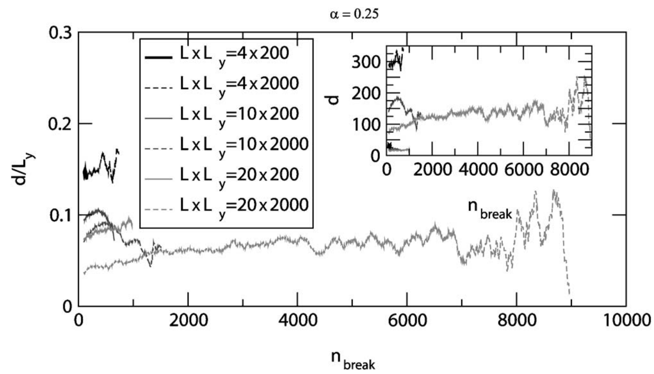

FIG. 6. Fuse threshold distribution corresponding to exponent $\alpha=0.25$: percolation universality class. Distance between successive burning fuses, divided by the lattice elongation L_y, averaged over 50 realizations and 200 successive events. Irrespectively of the lattice dimensions, this distance is comparable to L_y (of order $L_y/10$ here). Note that this corresponds depending on the lattice dimensions, to an average distance d equal to 20–200 lattice units, as the inset shows, and equal to 1–10 times L.

$L\times L_y$ cells, with high aspect ratios L_y/L in order to be close to the infinitely long cylinder considered so far. The lattice constant ℓ is now considered as unit length, the models considered are periodic along the transverse x direction, and the rows of nodes at both lattice boundaries are set to two constant potential values, with a voltage drop ΔU between both regularly increased from 0. The rows of fuses are inclined at 45° with respect to the x and y directions. Current conservation (Kirchhoff equation) is required at each node, and the current through each fuse at location r connecting neighboring nodes with a local potential drop ΔV between them, is ΔV if the fuse is intact, or 0 if the fuse is burned. This allows for each configuration of burned and intact fuses, to obtain by solving a linear system the voltage at each node, and the corresponding current map as $j(r)=C(r)\Delta U$, where $C(r)$ depends on the configuration of burned and intact fuses. The linear inversion is performed via a conjugate gradient algorithm [Hestenes-Stiefel, Eqs. (32)–(38) in Ref. [30]]. Initially, the system is entirely intact and random thresholds of maximum sustainable current $j_t(r)$ are picked from the quenched disorder distribution, independently for each fuse. At any stage of the process, the location r of the next fuse to burn and the corresponding value of the external current ΔU is obtained as $\Delta U=\min_s[j_t(s)/C(s)]=j_t(r)/C(r)$.

An example of configurations and the history of burning fuses is displayed in Fig. 1, for systems of size $L\times L_y=30\times 100$, and values of α between 0.25 and 2.5. The characteristic features of the three regimes are examplified in these cases.

For various values of L, L_y and of the exponent α characterizing the quenched disorder, we look at the distance d between two successive events, as function of its occurrence number in the succession of events up to total failure of the system (when a connected line separated the upper and lower boundaries of the system). This distance is averaged over 50 realizations.

The characteristic situation corresponding to $\alpha>1$ is illustrated for the case of $\alpha=1.5$ in Fig. 5: the distance between successive events is from a very early stage of order of a few unities, irrespectively, of the sizes L (4, 10, 20) and L_y (200 and 2000) considered. This regime was referred above as total localization.

On the contrary, for low exponents α corresponding to larger disorder, the typical situation is illustrated in Fig. 6 by the case of $\alpha=0.25$: Simulations have been performed using lattice elongations $L_y=200$ and $L_y=2000$, and widths $L=4$, 10 and 20. The distance between successive events has been averaged over 50 simulations. Even so, this quantity is still highly fluctuating, and an additional running average over 200 successive events is performed in order to extract the proper slow varying average of this distance. These high fluctuations are easily explainable: this regime is expected to be in the universality class of percolation, where the distribution of this distance at any stage is non-negligible for all possible distances in the lattice. Assuming consequently that the root of the variance of this distribution is of the same order as its average, the central limit theorem ensures that the root of the variance of the averaged distance over 50 realizations is still of the order $\frac{1}{7}$ of its average, which still corresponds to a high noise to signal ratio. The resulting average distance is plotted in Fig. 6, scaled by the lattice elongation L_y in the main figure, or directly in lattice constant units in the insert. This distance is found out to vary slightly during the process, and shows 50% variations between the different probed widths L, but the main result is that the average d is of order $0.1L_y$, i.e. scales with L_y: this is consistent with the prediction of the previous sections, that systems of infinite elongation L_y are isomorphic to percolation, i.e., that the distribution of burnt-out fuses is homogeneous, irrespectively of the configuration of the already burned fuses—which would predict for a very elongated system $L_y\to\infty$, an average distance between successive events $d\sim\int_0^{L_y}\int_0^{L_y}dy_1dy_2|y_1-y_2|/L_y^2=L_y/3$. The fact that we observe $d\sim L_y/10$ rather than $L_y/3$ can be understood as a finite size effect: less cells far away from the last fuse burning are likely to present the minimum ratio t/j, which increases the likelihood of having a next burned fuse in the zone of significant current perturbation, closer to the last burned fuse.

We have also analyzed the behavior of the system for $\alpha=0.5$, where according to Eq. (21), in the limit of $L_y\to\infty$ one

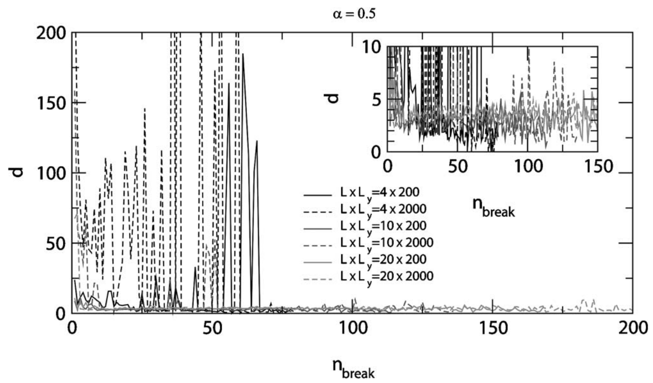

FIG. 7. $\alpha=0.5$: features of localization, or of percolation, depending on L and L_y: Localization (short distance between successive events) is seen for larger L and smaller L_y, whereas episodes with distances significantly larger than L are observed for short L and large L_y. Data averaged over 50 simulations.

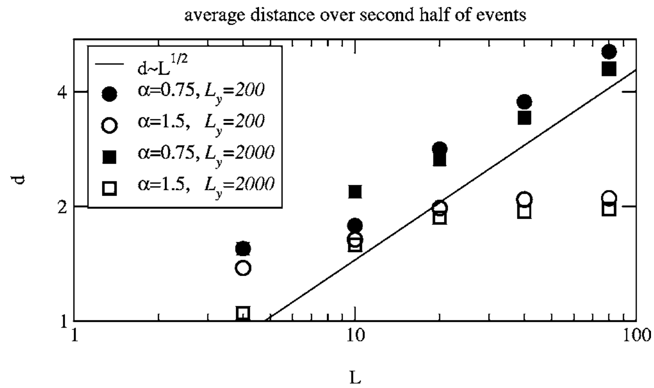

FIG. 8. Distinction between total and diffuse localization: at elongations $L_y=200$ or 2000, average distance d between successive events, for the second half of events, as function of the lateral size L of the system, on a bilogarithmic scale. Over the numerically accessible range as L grows, d is seen to saturate for $\alpha=1.5$, corresponding to total localization. For $\alpha=0.75$, $d/L^{1/2}$ does not vanish, corresponding to diffuse localization.

expects a percolationlike behavior for $L<e^{4/0.5}\sim 2980$, or a diffuse localization behavior for larger system width. The average distance for $L=4$, 10, 20 and $L_y=200$ and 2000 is displayed in Fig. 7—the inset represents the same data on a smaller scale. A qualitative interpretation of these results can be presented as follows: focusing first on the least elongated systems ($L_y=200$), the average distance is for $L=10$ and 20 of a few units, but the thinest systems, $L=4$, display a more complicated behavior: after an initial decrease, the distance displays episodes where its magnitude is around a few unities, alternated with episodes of order L_y. This can be interpreted as a case on the verge between localizing or nonlocalizing, i.e., as a case sitting around the line separating percolation from the localizing regime in Fig. 4. The value $L=4$ is considerably smaller than the predicted $L\simeq 2980$ for infinitely elongated system. This presumably results from the underestimate in the analytical calculations, of the localizing and/or nonlocalizing separation due to the high fraction of burned fuse close to the breakdown process, and from strong finite-size effects at finite L_y, as explained in the previous Section.

The presence of important finite size effects is confirmed by the fact that for more elongated systems, $L_y=2000$, such episodes where the average distance significantly exceeds the width of the system occur even more for the case $L=4$, and appear also for the case $L=10$, while they are absent from the case $L=20$: presumably, the boundary between localizing and percolating systems is around $L=10$ in that case. This means at finite elongations L_y, this boundary for any α corresponds to significantly smaller L than value predicted for infinitely elongated systems. This finite size effect is observed to diminish for increasing elongations, as expected: the larger is the elongation L_y, the larger is the transition width L. Due to numerical costs, it seems, however, difficult to evaluate numerically, in the limit $L_y\to\infty$ where this finite size effects would vanish, the exact transition value for the x-size separating non localizing systems and systems with diffuse localization, for example for such q.d. at $\alpha=0.5$. From the above, at finite L_y, this transition size at $\alpha=0.5$ is bounded between $L=10$ (numerical observation for $L_y=2000$) and $L\simeq 2980$ [theoretical upper bound from the mean field approach, Eq. (21)]. For practical numerical purposes at moderate system sizes, we note that such systems get into localizing regimes for x-system sizes L/ℓ at one to two orders of magnitude than the previously derived upper bound, Eq. (21).

Eventually, in the localizing regimes, we need to distinguish between what was referred to as diffuse or total localization in Sec. IV: total localization was defined as a case where the most probable break after departing from percolation, would happen in the zone referred to as (1), i.e. corresponding to a distance r/ℓ from the last burned fuse smaller than $\sqrt{L/\ell}$. Diffuse localization corresponds to cases where the next event would happen preferentially in zone (2), at moderate current perturbations, which corresponds to distances r/ℓ from the last burned fuse ranging from $\sqrt{L/\ell}$ up to a few L/ℓ. A criterion to distinguish numerically between these two regimes is thus to look, for a fixed large elongation L_y, whether the dependence of the average distance between successive events over the system width is such as $d/\sqrt{L\ell}$ vanishes at large L, or on the contrary remains finite or diverges. In Fig. 8, the average distance between successive events was evaluated over 50 simulations and over the second half of the events before complete breakdown, which is in the localization regime for all cases probed. This average distance seems lowly sensitive to $L_y=200$ or 2000 (20% difference or less between both sizes), but the scaling as function of L shows that this distance saturates rapidly for $\alpha=0.75$, while it grows approximately as $\sqrt{L}$ for $\alpha=1.5$. The extent over which this power law corresponds to slightly more than a decade for L, which is the maximum achievable numerically since the elongation L_y has to exceed significantly L to be in the considered framework. This result is thus consistent with a transition from diffuse to total localization between $\alpha=0.75$ and $\alpha=1.5$—the theory for $L_y\to\infty$ predicts this transition at $\alpha=1$. To pinpoint more accurately the precise value of the transition exponent [between 0.75 and 1.5 is not easy numerically]: this would require *a priori* to look at the scaling of $d(L)$ over more orders of magnitudes, for numerous α inbetween, which would represent a significant numerical cost and was not the main objective of this work, performed mainly as a numerical check of the analytical derivations carried out in the previous sections.

VI. CONCLUSION

The main results of the analytical calculation presented in this paper are to be found in Fig. 4: There are three distinct phases of the fracture process depending on the disorder exponent α and on the ratio between the width of the lattice L and the lattice constant ℓ when the lattice is a cylinder of infinite length. The first regime is a percolationlike regime where the distance between successive failing fuses is completely random. In the second regime, named diffuse localization, the controlling parameter is L/ℓ, while in the third regime, complete localization, the controlling length is ℓ.

To summarize the numerical results of Sec. V, regimes corresponding to percolation, diffuse and total localization have been clearly identified. The transition from diffuse to total localization is consistent with the predicted $\alpha=1$. The transition from percolation universality class to localizing regimes is seen to happen under increase of either the exponent α of the quenched disorder power-law distribution, or the width of the system, as predicted by the theory. Nonetheless, the transition width for a given exponent was found significantly smaller for the systems of finite elongation studied than for the infinite elongation system considered analytically. This discrepancy was observed to be lower when the elongation L_y increased, and presumably corresponds to important finite size effects. The transition from diffuse to total localization is consistent with the predicted $\alpha=1$, irrespectively of the system's elongation.

Hence, in the diffuse localization phase, we expect a smooth variation of the damage profile scales L, while there is still no strong localization driving the burned fuse to merge at the lattice constant scale: the region where arguments based on the percolation in gradient should apply. In this case, the shape of the dipolar current perturbation (Fig. 2), leads to most probable relative positions (x,y) of the next burned fuse relative to the last one, for which x and y are of the same order of magnitude, which is at the origin of the smooth quadratic maximum of the damage profile as function of y, as observed in [14]: This confirms the scaling arguments used to relate to roughness exponents and correlation length divergence exponents in such systems.

APPENDIX A: STATISTICAL LEMMAS

Consider p different types of random variables y, characterized by their cumulative distributions $P_i(y)$ and probability density functions $p_i(y)=dP_i(y)/dy=P_i'(y)$, for $i=1,\ldots,p$. Next, consider an ensemble of n_1 random variables distributed according to p_1, n_2 according to $p_2,\ldots,n_p$ according to n_p. In the limit where $N=\Sigma_{i=1}^{p} n_i \gg 1$, we wish to characterize

$$m=\langle \min_{\{i=1,\ldots,p,j=1,\ldots,n_i\}} y_{i,j}\rangle. \tag{A1}$$

The probability that some particular variable number j of type i, $y_{i,j}$, would be equal to x, while all others are larger, is

$$p_i(x)[1-P_i(x)]^{n_i-1}\prod_{j\neq i}[1-P_j(x)]^{n_j}. \tag{A2}$$

The probability that any of the variables of type i would be the smallest and equal to x, is the above times a factor n_i. Thus, the wanted quantity may be written as

$$\begin{aligned} m &= \int x\, dx \sum_{i=1}^{p}\left[n_i p_i(x)[1-P_i(x)]^{n_i-1}\prod_{j\neq i}[1-P_j(x)]^{n_j}\right] \\ &= \int x\, dx \frac{d}{dx}\left[\prod_{j=1}^{p}[1-P_j(x)]^{n_j}\right] \\ &= \int dx\left[\prod_{j=1}^{p}[1-P_j(x)]^{n_j}\right]. \end{aligned} \tag{A3}$$

Setting $p=1$ in Eq. (A3), we have that

$$m=\int dx[1-P_1(x)]^N. \tag{A4}$$

Since the function $1-P_1(x)$ decreases continuously from 1 to 0, for large n the product $[1-P_1(x)]^N$ is equal to 1 for $x<x_c$, up to a certain cutoff x_c, above which it becomes vanishingly small. The integral Eq. (A4) is then simply equal to x_c. We determine x_c by invoking the standard saddle point approximation, which leads to the equation

$$\frac{p_1'(x_c)}{p_1(x_c)}=(N-1)\frac{p_1(x_c)}{1-P_1(x_c)} \tag{A5}$$

for x_c. By using l'Hôpital's rule, $p_1'/p_1 \approx p_1/P_1$, this equation reduces to the condition $NP(x_c)=1$. Using $m=x_c$, we have [25]

$$NP_1(m)=1. \tag{A6}$$

Generalizing this result to $p>1$, we find by invoking the saddle point approximation for Eq. (A3), the equation

$$\sum_{i=1}^{p}\left(\frac{n_i p_i(m)}{1-P_i(m)}\right)'=\left(\sum_{j=1}^{p}\frac{n_j p_j(m)}{1-P_j(m)}\right)^2. \tag{A7}$$

If we now set $1-P_j(m)\approx 1$ as $P_j(m)\ll 1$, and use l'Hôpital's rule,

$$\frac{\sum_{i=1}^{p} n_i p_i'(m)}{\sum_{j=1}^{p} n_j p_j(m)} \approx \frac{\sum_{i=1}^{p} n_i p_i(m)}{\sum_{j=1}^{p} n_j P_j(m)}, \tag{A8}$$

Eq. (A7) reduces to

$$\sum_{j=1}^{p} n_j P_j(m)=1, \tag{A9}$$

which generalizes Eq. (A6).

In the case of an infinite number of random variables indexed by a continuous parameter s, the equivalent of Eq. (A9) is

$$\int_s n(s)P(m,s)ds = 1. \tag{A10}$$

The probability Q_i that the minimum variable would be of type i (for a discrete set of random variables), is from the above

$$Q_i = \int dx\left[n_i p_i(x)[1-P_i(x)]^{n_i-1}\prod_{j\neq i}[1-P_j(x)]^{n_j}\right]. \tag{A11}$$

The same argument shows that $[1-P_i(x)]^{n_i-1}\Pi_{j\neq i}[1-P_j(x)]^{n_j}$ is equivalent to 1 when $x<m$, or 0 when $x>m$. Thus,

$$Q_i = \int_{x=-\infty}^{m} dx\, n_i p_i(x) = n_i P_i(m). \tag{A12}$$

For a continuous set of random variables, the probability that the minimum variable would correspond to an index $s \in [s_1, s_2]$ is then

$$Q_{[s_1,s_2]} = \int_{s_1}^{s_2} n(s)P(m,s)ds. \tag{A13}$$

APPENDIX B: DENSITY OF CELLS PER LEVEL OF SUSTAINED CURRENT

To compute $n(s)$, we will use an explicit expression $v_a(u)$ of the contours of isoperturbation, shown in Fig. 2 defined implicitly as

$$f(u,v_a(u)) = a. \tag{B1}$$

Inverting this expression from Eqs. (10) and (B1), comes the following: if $a<0$, there are two points of abcissa u satisfying this. Their ordinates are

$$v_a^{\pm}(u) = \text{a}\cosh\left[\frac{2a-1}{2a}\cos(u) \pm \sqrt{\frac{\cos^2(u)}{4a^2}+\frac{\sin^2(u)}{a}}\right]. \tag{B2}$$

These functions are defined for

$$u \bmod[2\pi] \in [-u_a^{max}, u_a^{max}],$$

with $u_a^{max}=\text{a}\cos[4a/(4a-1)]$. If $0<a<0.5$, there is a single defined function $v_a(u)$ satisfying Eq. (B1) for any u, which is the positive alternative of the above Eq. (B2). Last, if $a>0.5$, the expression of $v_a(u)$ is identical, but once again this function has a finite support $u \bmod[2\pi] \in [-u_a^{max}, u_a^{max}]$, with $u_a^{max}=\text{a}\cos(1-1/a)$. Some examples of these auxiliary quantities were set in Fig. 2.

To compute $n(s)$, we reformulate the condition $j\in[j_e(1+s), j_e(1+s+\Delta s)]$ as $f(u,v)\in[a,a+\Delta a]$ where $a=2L^2 s/(\pi^2\ell^2)$ and $\Delta a=2L^2\Delta s/(\pi^2\ell^2)$ from Eq. (9), which through a Taylor expansion of $f(u,v)$ in v around $v_a(u)$ defines

$$\Omega(s,\Delta s) = \{(u,v)/v \in [v_a(u)-w_a(u)\Delta a, v_a(u)]\}, \tag{B3}$$

$$w_a(u) = -1/\frac{\partial f}{\partial v}[u,v_a(u)], \tag{B4}$$

and thus $n(s)=\frac{1}{\Delta s\ell^2}\int_{(x,y)\in\Omega(s,\Delta s)}dx\,dy$ can be expressed as

$$n(s) = \frac{2L^4}{\pi^2\ell^4}g(2L^2 s/\pi^2\ell^2), \tag{B5}$$

where

$$g(a) = \int_{u=0}^{\min(u_a^{max},\pi)} w_a(u)du. \tag{B6}$$

This number density $g(a)$ was numerically evaluated from the above and displayed in Fig. 3. We will also derive below the asymptotic behavior of this function around the special values $a\sim 0$, infinitely away from the burnt fuse, $a\to+\infty$, around for the near neighbors of the broken fuse, and $a\sim 0.5$, around the saddle point ($u=\pi$, $v=0$). As will be shown straightforwardly, these asymptots, displayed in Fig. 3, are

$$g(a)\sim_{a\to 0}\pi/2|a|, \tag{B7}$$

$$g(\delta a+1/2)\sim_{\delta a\to 0} -2\ln(|\delta a|), \tag{B8}$$

$$g(a)\sim_{a\to\pm\infty}1/2a^2. \tag{B9}$$

Indeed, from Eq. (10),

$$w_a(u) = -1/\frac{\partial f}{\partial v}[u,v_a(u)] = \frac{[\cosh(v_a(u))-\cos(u)]^3}{\sinh(v_a(u))[\cos^2(u)+\cos(u)\cosh(v_a(u))-2]}, \tag{B10}$$

where $v_a(u)$ is given by Eq. (B2).

Developing the above around $a\sim 0^+$ to main order in a is a direct exercise which leads to $w_a(u)\sim -1/a$ when $u\in[\pi/2,\pi]$, and $|w_a(u)|\ll 1/a$ for $u\in[0,\pi/2]$. The integration of $w_a(u)$ in Eq. (B6) leads then to the asymptotic value in Eq. (B7).

Conversely, around $a\sim+\infty$, $f(u,v)\sim 2(u^2-v^2)/(u^2+v^2)^2 = 2\cos(2\theta)/r^2$, where $u/r=\cos\theta$ and $v/r=\sin\theta$. Then, defining,

$$I(a) = \int_{u>0,v>0,f(u,v)<a} du\,dv,$$

we have

$$g(a) = -dI(a)/da, \tag{B11}$$

and in polar coordinates

$$I(a) = \int_{\theta=0}^{\pi/4}\int_{r=0}^{\sqrt{2\cos(2\theta)/a}} r\,dr\,d\theta = 1/2a, \tag{B12}$$

leading to the asymptotic form $g(a)\sim 1/2a^2$, Eq. (B9).

Eventually, around $\delta a=a-\frac{1}{2}\sim 0$, we reformulate the condition $f(u,v)\in[1/2-\delta a, 1/2]$ by a Taylor expansion of f to second order in v: $\delta f = f(u,v) - 1/2 = f(u,v) - f[u, v_{0.5}(u)] \sim \partial_v f[u, v_{0.5}(u)]\delta v + \partial_{vv} f[u, v_{0.5}(u)]\delta v^2/2$. The first term dominates if $\delta a < |2(\partial_v f)^2/\partial_{vv} f|$ and then $0 < \delta f < \delta a$ is equivalent to $0 < \delta v < -\delta a/\partial_v f$. When $\delta a > 2(\delta_v f)^2/\partial_{vv} f$, we will have $|\delta f| < \delta a$ if $0 < \delta v < \sqrt{\delta a/\partial_{vv} f}$. From Eqs. (B2) and (B10), $v_{0.5}(u) = \sqrt{2 - \cos^2(u)}$, and $\partial_v f[u, v_{0.5}(u)]$ has a single zero in $u = \pi$ (saddle point), $\partial_v f \sim (\pi - u)/4$, whereas $\partial_{vv} f[u, v_{0.5}(u)]$ remains finite, tending towards a finite value α when $u \to \pi$. Thus, we have

$$\int_{u,v/f(u,v)\in[0.5-\delta a,0.5]} du\,dv, \tag{B13}$$

$$\simeq \delta a \int_0^{\pi - \sqrt{\delta a/8\alpha}} \frac{-4du}{\pi - u} + O(\delta a),$$

$$\simeq -2\delta a \ln(\delta a) + O(\delta a). \tag{B14}$$

Differentiating this expression with respect to δa shows that $g(0.5 - \delta a) \sim -2\ln(\delta a)$, for $\delta a \to 0^+$. Similar arguments lead to the same asymptotic form for a negative δa, i.e., to the asymptotic form in Eq. (B8).

APPENDIX C: SPATIAL DIVISION OF THE INTEGRAL CHARACTERIZING EXTREME STATISTICS

Here, we present the details of the subterms intervening in the implicit Eq. (5), which determine both the region of the most probable next break with respect to the previous one, and the most probable jump in external current to reach this next break.

We have to solve the implicit Eq. (5), with a derived distribution

$$P(m,s) = \frac{m^\alpha (1+s)^\alpha - j_e^\alpha}{1 - j_e^\alpha} \mathrm{He}(m(1+s) - j_e). \tag{C1}$$

coming from the assumed quenched disorder distribution, $P(t) = t^\alpha$ on $0 \leq t \leq 1$, with $\alpha \geq 0$, transformed into a conditional probability of breaking for fuses having so far survived, using Eq. (4).

In the integrand of Eq. (5), $n(s)$ is expressed as function of $g(a)$ through Eq. (11), and we approximate this last function by its asymptotic forms Eqs. (B7)–(B9) around the singularities and in the tail of highest perturbations. We divide the support of the integral in seven zones.

(1) In the neighboring cells carrying maximum current, such as $r/\ell < c$ where c is a finite large number. The nearest neighbors on the sides of the last broken cell carry the maximum current, $\delta j/j_e = f(2\pi\ell/L, 0)\pi^2\ell^2/2L^2 = \frac{1}{4}$, corresponding to an upper cutoff $a_M = L^2/2\pi^2\ell^2$. Close to the origin, the current perturbation falls as $1/r^2$, and this close zone is then defined by the condition $a_M/c^2 < f(u,v) < a_M$.

(2) The cells carrying a current such as $\frac{3}{4} < f(u,v) < c^2/2\pi^2$. On the x axis, from Eq. (10), these conditions correspond to $2L/c < x < \mathrm{a}\cos(-\frac{1}{3})L/2\pi \simeq L/3$. We require that these two defined first zones have a common boundary, which by equating the cutoffs of f sets $c^2 = L/\ell$.

(3) A zone around the saddle point, defined as $\frac{1}{4} < f(u,v) < \frac{3}{4}$.

(4) A zone such as $a_m < f(u,v) < 1/4$. This zone includes the far-range from the last broken fuse, on which the current is slightly increased by its presence. The lower cutoff a_m is determined by the y extent of the system (length of the band), which was so far omitted. When the finite aspect of L_y is taken into account, the current perturbation derived from boundary conditions at infinity, Eqs. (9) and (10) is still valid in boundary conditions corresponding to setting the global current through the top and bottom plate, i.e.,

$$\int_{x=-L/2}^{L/2} \hat{y}\boldsymbol{j}(x, \pm L_y/2)dx/L = j_o.$$

Indeed, we find for $L_y \gg L$, that

$$f(u, \pi L_y/L) \simeq -\cos(u)/\cosh(\pi L_y/L)$$
$$\simeq -\cos(u)\exp(-\pi L_y/L),$$

whose integral is zero for $u \in [-\pi, \pi]$. However, when counting the number of cells sustaining a given current, the condition $|y| < L_y/2$ should be added to derive $n(s)$. From the above, $n(s)$ is unmodified when $a > a_m = \exp(-\pi L_y/L)$, or when $a < -a_m$, but in the neighborhood of zero for $-a_m < a < a_m$, $n(s)$ has to be modified according to

$$g(a) = \frac{1}{a}[\mathrm{a}\cos(-a/a_m) - \pi/2]. \tag{C2}$$

This function is pair, and increasing for $a \geq 0$ from $g(0) = 1/a_m$ to $g(a_m) = \pi/2a_m$.

(5) A tiny zone of vanishing current perturbation, $-a_m < f(u,v) < a_m$, for which $n(s)$ has just been determined.

(6) A far-range zone where the current is screened by the last burnt fuse, $-1 < f(u,v) < -a_m$.

(7) A zone of a highly screened current, $-a_M < f(u,v) < -1$.

The zones corresponding to regions defined as Ω_c, Ω_d, and Ω_f in Sec. IV, are, respectively, regions (1)–(7). They correspond to regions, which are with respect to the last break, either close to it, at distances comparable with the lattice step, or diffusively close, at distances comparable to the width of the system L_y, or "far," at distances comparable with the system size $L_y \gg L_x$. Dividing here in seven subregions, will allow us to use asymptotic forms of the seven corresponding subintegrals.

We will classify the regime of the system according to the zone where most of the integral in Eq. (5) is realized: We expect this zone to be either (4)–(6), in which case the system remains in a diffuse regime where there are no noticeable spatial correlations in the pattern of burnt fuse, or (1), which signifys the onset of a complete localization regime where the damage will develop in a concentrated zone scaling as the lattice size ℓ, and tear through the system starting from this smallest scale, or (2) and (3), which would denote the onset of a diffuse localization regime, where the characteristic distance d between the burnt fuse scales as L, the system's width.

Noting $\varepsilon=\pi^2\ell^2/2L^2$ and $\lambda=m/j_e$, where j_e, m are the values of the external current at last break and for the next one, Eq. (5) is then equivalent to

$$\sum_{i=1}^{7} h_i(\lambda) = \frac{2\varepsilon(1-j_e^\alpha)}{j_e^\alpha}, \tag{C3}$$

where with

$$p(a,\lambda) = \mathrm{He}[\lambda(1+\varepsilon a)-1], \tag{C4}$$

the h functions are defined from the above zones, asymptotic behaviors of $n(s)$ and the q.d. distribution as

$$h_1(\lambda) = \int_{a_M/c^2}^{a_M} \frac{(1+\varepsilon a)^\alpha\lambda^\alpha - 1}{2a^2} p(a,\lambda)da, \tag{C5}$$

$$h_3(\lambda) = \int_{-1/4}^{1/4} 2\ln\left(\frac{1}{|\delta a|}\right)\{[1+\varepsilon(0.5+\delta a)]^\alpha\lambda^\alpha - 1\} \times p(0.5+\delta a,\lambda)d\delta a, \tag{C6}$$

$$h_4(\lambda) = \int_{a_m}^{1/4} \frac{\pi[(1+\varepsilon a)^\alpha\lambda^\alpha - 1]}{2|a|} p(a,\lambda)da, \tag{C7}$$

$$h_5(\lambda) = \int_{-a_m}^{a_m} \frac{1}{a}[\mathrm{a}\cos(-a/a_m) - \pi/2]p(a,\lambda)da, \tag{C8}$$

and h_2 has the same integrand as h_1, but a support, respectively, on $[3/4, c^2/2\pi^2]$, h_6 has the same integrand as h_4 and bounds $[-1,-a_m]$, h_7 has the same integrand as h_1 and has a support $[-a_M,-1]$.

We first note that the term on the right-hand side of Eq. (C3) is in the first stages of the process of a large number, since the first fuse burns at an average value of the external current j_1 such as $j_1^\alpha=1/N_{cells}=\ell^2/LL_y$, so that $2\varepsilon(1-j_1^\alpha)/j_1^\alpha \simeq \pi^2 L_y/L \gg 1$. It becomes a number of order ε when $j_0^\alpha \simeq \frac{1}{2}$.

We first look for solutions corresponding to an increase in the external current, i.e., we look at the behavior of the h functions for $\lambda \geq 1$. The Heaviside terms can, therefore, be neglected for $h_1,\ldots,h_5$. Expanding the integrands to first order in ε, and keeping the leading orders in $c=\sqrt{L/\ell}$, we obtain

$$h_1(\lambda) = \varepsilon[s(\alpha)\lambda^\alpha - 2\pi(c^2-1)], \tag{C9}$$

where

$$s(\alpha) = \int_{1/4\pi c^2}^{1/4\pi} \frac{(1+\gamma)^\alpha}{2\gamma^2} d\gamma, \tag{C10}$$

$$h_2(\lambda) = \frac{2}{3}(\lambda^\alpha - 1) + \frac{\alpha\varepsilon}{2}\ln\left(\frac{c^2}{2\pi}\right)\lambda^\alpha, \tag{C11}$$

$$h_3(\lambda) \simeq [\ln(4)+1](\lambda^\alpha - 1) + \frac{\alpha\varepsilon}{2}\lambda^\alpha, \tag{C12}$$

$$h_4(\lambda) \simeq \frac{\pi}{2}\ln(1/a_m)(\lambda^\alpha - 1) + \frac{\alpha\varepsilon\pi}{8}\lambda^\alpha, \tag{C13}$$

$$h_6(\lambda) \simeq \left[\frac{\pi}{2}\ln(1/a_m)(\lambda^\alpha - 1) + \frac{\alpha\pi}{2}\left(1-\frac{1}{\lambda}\right)\lambda^\alpha\right] \times \mathrm{He}[\lambda(1+\varepsilon a_m)-1]. \tag{C14}$$

The other h functions can be shown to be negligible in front of these, and are not displayed here. In the early stages of the process, the first terms of h_4 and h_6 will dominate, i.e., the singularity of n around $s\sim 0$ corresponding to the furthest zone of the last break will be preponderant, and the threshold to the next break will be set by

$$\pi\ln\left(\frac{1}{a_{min}}\right)(\lambda^\alpha - 1) = 2\varepsilon\frac{1-j_e^\alpha}{j_e^\alpha}, \tag{C15}$$

$$\text{i.e.,}\quad \lambda^\alpha - 1 = \frac{1-j_e^\alpha}{N_{cells}j_e^\alpha}, \tag{C16}$$

which corresponds to Eq. (15).

This leads to a second break happening on average when $j_2=\lambda_1 j_1=(1+1)^{1/\alpha}j_1=(2/N_{cells})^{1/\alpha}$. As long as the process remains in a diffuse regime where burned fuse are far away from each other, at distances comparable with the y extent of the system L_y, we can go on with this mean-field theory, and use the same arguments to evaluate the probability of finding the next $(n+1-th)$ burned fuses with respect to the previously burned ones. In this situation, the fuses of interest are far from the already burned ones (h_4 and h_6 dominate the integral), and thus have thresholds above j_e, the external current reached so far. We can then use the same arguments, replacing the average current at first break j_1 by the average external current level at the nth break j_n, to obtain by reccurrence that $j_n=(n/N_{cells})^{1/\alpha}$, which corresponds to Eq. (17). Indeed, by definition, $j_{n+1}=\lambda_n j_n$, and from Eq. (C16),

$$\lambda_n^\alpha - 1 = 1/(N_{cells}j_n^\alpha) = 1/n. \tag{C17}$$

Thus, $\lambda_n=[(n+1)/n]^{1/\alpha}$ and $j_{n+1}=[(n+1)/N_{cells}]^{1/\alpha}$, establishing the result by recurrence. Note that this result is a simple consistency check of the present theory: In this percolation regime, the concentration of the current around the broken fuses is negligible, and the level j_{n+1} of $(n+1)$-th break should be given by the average minimum of the thresholds of the entire system, under the condition that all of them have survived up to the current j_n. This formulates as $P(j_{n+1}|j_{n+1}>j_n)=(j_{n+1}^\alpha-j_n^\alpha)/(1-j_n^\alpha)=1/N_{cells}$, which is exactly Eq. (C16).

A careful analysis of the above functions shows that in the limit y, these first terms of h_4 and h_6 always dominates: they are larger by a factor $\ln(1/a_m)=L_y/L$ than the other terms proportional to $(\lambda^\alpha-1)$, and all of the corrections proportional to ε vanish. Thus, in this limit, H_f dominates Eq. (14), and no localization happens. This lasts during the whole process (as long as the interactions between already burned fuses are weak enough for this mean-field theory to apply), and in this limit of large disorder $\alpha\to 0$, the process remains diffuse, in a percolationlike regime, up to the moment where $j_e^\alpha=\frac{1}{2}$, i.e., when $P(j_e)=\frac{1}{2}$, which corresponds to the critical percolation threshold.

On the contrary, for $\alpha \to +\infty$, $s(\alpha)$ is diverging faster than all prefactors of λ^{α} in the above, and $h_1(\lambda)$ defined in Eq. (C9), i.e., dominates the left-hand side in Eq. (C3), i.e., $H_c(\lambda)$ dominates in Eq. (14), thus leading to a level of the next break set by $h_1(\lambda)=2\varepsilon(1-j_e^{\alpha})/j_e^{\alpha}$, i.e., Eq. (18). In this case, the next fuses to burn will be the ones carrying the highest current perturbation, i.e., the near neighbors on the sides of the first one [moreover, $s(\alpha)$ is dominated by the contribution between $1/4\pi$ and $1/4\pi/2^2$, i.e., in this limit $\alpha \to \infty$, the nearest neighbors will burn with certainty].

In the range of finite α, the system can be driven to a third regime if h_2 or h_3 dominate in Eq. (C3): correlations in the damage start to be significant, but the characteristic distance to the preceding burnt fuses is in a range between $\sqrt{L\ell}$ and L, and does not scale as the lattice constant ℓ: this is the regime which we refer to as diffuse localization.

We have shown above that in the early stages of the process, for a finite disorder, i.e., at finite α, the system starts in a percolationlike regime, i.e., that H_c (h_2 and h_3) dominate in Eq. (C3). This can be the case up to the percolation transition, when $P(j_e)=\frac{1}{2}$, for large enough disorder, i.e., small α. But as the weakest bonds are broken, the process can transit to one of the two other regimes: either the "total localization regime," where rupture proceeds via jumps between successive burned fuses, whose size d is close to the lattice spacing, $d \ll \sqrt{(L\ell)}$. Either the diffuse localization regime, characterized by a distance d between successive bonds scaling typically such as $\sqrt{(L\ell)} \ll d \ll L_y$ when $L \to \infty$ and $L_y \to \infty$. This transition towards the diffuse localization regime should happen when H_d stops being small compared to H_c, while H_f remains negligible compared to these. Technically, this transition can be determined by equating $H_c(\lambda)=H_d(\lambda)$, which corresponds to leading order to $h_2(\lambda)=h_4(\lambda)+h_6(\lambda)$ [it can be shown that the contribution of the saddle point $h_3(\lambda)$ is always negligible in front of $h_2(\lambda)$ as long as $c^2=L/\ell \gg 1$]. From Eqs. (C11), (C13), and (C14) corresponds to leading order in $1/N_{cells}$ to the condition

$$\frac{\alpha}{2}\ln\left(\frac{L}{\ell}\right)=2\frac{1-j_e^{\alpha}}{j_e^{\alpha}}, \tag{C18}$$

which corresponds to Eq. (20). As detailed in Sec. IV, if this condition is not met at the percolation transition when $j_e^{\alpha}=\frac{1}{2}$, the system stays in the percolationlike regime, whereas if this condition is met before and H_c is still negligible, the system transits towards the diffuse localization regime before breakdown: from Eq. (C18), this transition never happens if $\alpha < \alpha_m = \frac{4}{\ln(L/\ell)}$, which corresponds to Eq. (12).

To characterize the boundary between transition to total localization, and diffuse localization, i.e., to obtain Eq. (23), we have considered whether indeed $H_c(\lambda)$ is still small compared to $H_d(\lambda)$, with λ approximated by its value at the percolation threshold, i.e., fixed by Eq. (15) with $j_e^{\alpha}=\frac{1}{2}$. Expressing in this way the condition $h_1(\lambda)=h_2(\lambda)$, with the detailed expressions in Eqs. (C9)–(C11), together with the definitions $a_m=\exp(-\pi L_y/L)$, $\varepsilon=\pi^2\ell^2/2L^2$ and $c^2=L/\ell$, leads to Eq. (23).

The estimate of the current value, Eq. (24), where the system transits towards total localization when $\alpha>1$, is obtained by equating $h_1(\lambda)=h_4(\lambda)+h_6(\lambda)$, and by noting that the last term of $h_4(\lambda)$ dominates the right-hand side.

Eventually, Eq. (25), which determines the boundary between the percolationlike regime and the total localization regime in the $\alpha - L/\ell$ space, is obtained by equating $h_1(\lambda)=h_4(\lambda)+h_6(\lambda)$, with λ evaluated from its value at percolation threshold, i.e., fixed by Eq. (15), with $j_e^{\alpha}=\frac{1}{2}$.

[1] *Statistical Models for the Fracture of Disordered Media*, edited by H. Herrmann and S. Roux (Elsevier, Amsterdam, 1990).
[2] L. de Arcangelis, S. Redner, and H. J. Herrmann, J. Phys. (Paris), Lett. **46**, L585 (1985).
[3] A. Hansen, E. L. Hinrichsen, and S. Roux, Phys. Rev. B **43**, 665 (1991).
[4] B. B. Mandelbrot, D. E. Passoja, and A. J. Paullay, Nature (London) **308**, 721 (1984).
[5] E. Bouchaud, G. Lapasset, and J. Planès, Europhys. Lett. **13**, 73 (1990).
[6] K. J. Måløy, A. Hansen, E. L. Hinrichsen, and S. Roux, Phys. Rev. Lett. **68**, 213 (1992).
[7] J. Schmittbuhl, F. Schmitt, and C. H. Scholz, Geophys. Res. Lett. **100**, 5953 (1995).
[8] P. Daguier, S. Henaux, E. Bouchaud, and F. Creuzet, Phys. Rev. E **53**, 5637 (1996).
[9] P. Daguier, B. Nghiem, E. Bouchaud, and F. Creuzet, Phys. Rev. Lett. **78**, 1062 (1997).
[10] E. Bouchaud, J. Phys.: Condens. Matter **9**, 4319 (1997).
[11] A. Hansen, E. L. Hinrichsen, and S. Roux, Phys. Rev. Lett. **66**, 2476 (1991).
[12] J. E. Bouchaud and S. P. Bouchaud, Phys. Rev. B **50**, 17752 (1994).
[13] J. P. Bouchaud, E. Bouchaud, D. S. Fisher, S. Ramanathan, and J. R. Rice, J. Mech. Phys. Solids **50**, 1703 (2002).
[14] A. Hansen and J. Schmittbuhl, Phys. Rev. Lett. **90**, 045504 (2003).
[15] D. Stauffer and A. Aharony, *Introduction to Percolation Theory* (Taylor, London, 1992).
[16] P. K. V. V. Nukala, S. Šimunović, and S. Zapperi, J. Stat. Mech: Theory Exp., P08001 (2004).
[17] J. Ø. H. Bakke, J. Bjelland, T. Ramstad, T. Stranden, A. Hansen, and J. Schmittbuhl, Phys. Scr., T **106**, 65 (2003).
[18] T. Ramstad, J. Ø. H. Bakke, J. Bjelland, T. Stranden, and A. Hansen, Phys. Rev. E **70**, 036123 (2004).
[19] G. G. Batrouni and A. Hansen, Phys. Rev. Lett. **80**, 325 (1998).
[20] R. Toussaint and S. R. Pride, Phys. Rev. E **66**, 036135 (2002); **66**, 036136 (2002); **66**, 036137 (2002).
[21] M. Barthelemy, R. da Silveira, and H. Orland, Europhys. Lett. **57**, 831 (2002).

[22] R. Toussaint and S. R. Pride, Phys. Rev. E **71**, 046127 (2005).
[23] S. R. Pride and R. Toussaint, Physica A **312**, 159 (2002).
[24] S. Roux and A. Hansen, Europhys. Lett. **11**, 37 (1990).
[25] E. Gumbel, *Statistics of Extremes* (Columbia University Press, New York, 1958).
[26] P. Morse and H. Feshbach, *Methods of Theoretical Physics* (McGraw-Hill, New York, 1953), Vol. 2, p. 1236.
[27] M. Barthelemy, R. Da Silveira, and H. Orland, Europhys. Lett. **57**, 831 (2002).
[28] S. Roux, A. Hansen, H. Herrmann, and E. Guyon, J. Stat. Phys. **52**, 237 (1988).
[29] B. Lawn, T. R. Wilshaw, B. R. Lawn, and T. R. Wilshaw, *Fracture of Brittle Solids* (Cambridge University Press, Cambridge, 1993).
[30] G. Batrouni and A. Hansen, J. Stat. Phys. **52**, 747 (1988).

Local Waiting Time Fluctuations along a Randomly Pinned Crack Front

Knut Jørgen Måløy,[1] Stéphane Santucci,[1] Jean Schmittbuhl,[2] and Renaud Toussaint[2]
[1]*Fysisk Institutt, Universitetet i Oslo, P.O. Boks 1048 Blindern, N-0316 Oslo 3, Norway*
[2]*Institut de Physique du Globe de Strasbourg, UMR 7516, 5 rue René Descartes, F-67084 Strasbourg Cedex, France*
(Received 26 August 2005; published 30 January 2006)

The propagation of an interfacial crack along a heterogeneous weak plane of a transparent Plexiglas block is followed using a high resolution fast camera. We show that the fracture front dynamics is governed by local and irregular avalanches with very large size and velocity fluctuations. We characterize the intermittent dynamics observed, i.e., the local pinnings and depinnings of the crack front by measuring the local waiting time fluctuations along the crack front during its propagation. The deduced local front line velocity distribution exhibits a power law behavior, $P(v) \propto v^{-\eta}$ with $\eta = 2.55 \pm 0.15$, for velocities v larger than the average front speed $\langle v \rangle$. The burst size distribution is also a power law, $P(S) \propto S^{-\gamma}$ with $\gamma = 1.7 \pm 0.1$. Above a characteristic length scale of disorder $L_d \sim 15$ μm, the avalanche clusters become anisotropic providing an estimate of the roughness exponent of the crack front line, $H = 0.66$.

DOI: 10.1103/PhysRevLett.96.045501 PACS numbers: 62.20.Mk, 05.45.Df, 61.43.−j, 81.40.Np

The physics community has recently paid a lot of attention to the study of damaging processes [1–3]. This interest is motivated not only by the practical benefits to many engineering domains, but also from a more fundamental point of view, by the diverse challenging questions brought forward, in particular, in statistical physics [4]. The role of heterogeneities during crack propagation is of central importance since they induce local pinnings of the crack front and subsequently trigger a very complex history of the fracture in the material. One of the consequences of this phenomenology is the roughness of fracture surfaces left by the crack. Indeed, cracks in heterogeneous media exhibit a self-affine morphology, with long range correlations. The associated roughness exponent was found to be very robust for different materials, over a broad range of length scales [5–11], and was further conjectured to be universal [7,8]. A recent work [2,12] suggests that the origin of these self-affine long range correlations comes from the elastic interactions within the damage zone and proposes a link between the roughness exponent and the critical exponent ν for the correlation length of the damage clusters. More generally, front propagation in random media has become a challenging problem related to the dynamics of interfaces in many different physical systems theoretically connected, such as crack fronts [11], magnetic domain walls [13], or wetting contact lines [14–16], where elasticity and disorder compete to shape the interface.

In order to shed some light on the interactions between the crack front and material heterogeneities, a simplification to a two dimensional configuration—an interfacial crack—has been proposed both experimentally [17,18] and theoretically [12,19]. The interfacial configuration provides a higher resolution since all locations of the crack front belong to the same plane. Moreover, using a transparent material and a high resolution fast camera, the detailed complex crack dynamics can be captured, following the crack front with a high precision both in time and space [20]. So far experiments have been focused on the fracture front line morphology leading to the estimated roughness exponent $\zeta = 0.55 \pm 0.03$ [17], followed up by a longer study showing $\zeta = 0.63 \pm 0.03$ [18]. First attempts have been recently performed to analyze the interfacial crack front dynamics [20,21]. These studies have shown that the fracture front propagation is intermittent and can be described in terms of a Family-Vicsek scaling [22] with a roughness $\zeta = 0.6$ and a dynamic exponent $\kappa = 1.2 \pm 0.2$.

In this Letter, we study a system first studied experimentally by Schmittbuhl and Måløy [17,20]. Whereas previous studies focused on the morphology of the interfacial crack [17], we focus on the local crack dynamics, and on the distribution in both time and space of the waiting time during pinning events. To address this problem, we introduce a new analysis procedure in order to study the local waiting time fluctuations. The improved experimental techniques and resolution allow us to show that the dynamics of the fracture front is driven by local irregular avalanches with very large size and velocity fluctuations, and anisotropic shapes whose scaling is directly linked to the self-affine scaling of the crack front itself. This new set of experiments also confirms earlier results on such systems [17,20].

We describe here experiments where two Plexiglas plates are annealed together to create a single block with a weak interface [17]. The plates are of dimensions: 32 cm × 14 cm × 1 cm and 34 cm × 12 cm × 0.4 cm, and annealed together at 205 °C under several bars of normal pressure. Before annealing, both plates are sandblasted on one side with 50 μm steel particles or 100 μm glass beads. Sandblasting introduces a random topography which induces local toughness fluctuations during the annealing procedure. We have measured the profile of a sandblasted Plexiglas surface, using a white light interferometry technique (performed at SINTEF-Oslo laboratory) and found that the local irregularities have a characteristic size about 15 μm [23]. While the upper Plexiglas plate is clamped to a stiff aluminum frame, a press applies a normal displacement to the lower one (1 cm thick) at a constant low speed which results in a stable crack propagation in mode I [17]. The fracture front is observed with a high resolution fast camera mounted on a microscope. Two different cameras have been used, a Kodak Motion Korder Analyzer CCD camera which records up to 500 frames per second (fps) with a 512×240 pixel resolution, and lately a much more powerful one, a Photron Ultima CMOS camera. Using this camera at a spatial resolution of 1024×512 pixels, and an acquisition rate of 1000 fps we can follow the stable crack front during more than 12 s (recording up to 12 288 images). Different experiments have been performed varying the acquisition hardware, the microscope magnification corresponding to a pixel size between 1.7 to 10 μm, and the average front line speed ranging from 0.35 to 40 μm/s. It is important to note that in all cases, the pixel size is smaller than the size of the local irregularities of about 20 μm due to the sandblasting process.

In order to analyze the local waiting time fluctuations and the burst dynamics, we propose the following procedure: the fracture front lines extracted from image analysis of the digital pictures [see Fig. 1(a)] are added to obtain a waiting time matrix $\mathbf{W}(\mathbf{x}, \mathbf{y})$. This matrix has the dimension of the original image and an initial value equal to zero. We add the value 1 to the matrix element w corresponding to each pixel of the detected front line position (x, y). This procedure is performed for all frames of a given experiment in order to obtain the final waiting time matrix $\mathbf{W}(\mathbf{x}, \mathbf{y})$. A gray scale map of this matrix is shown in

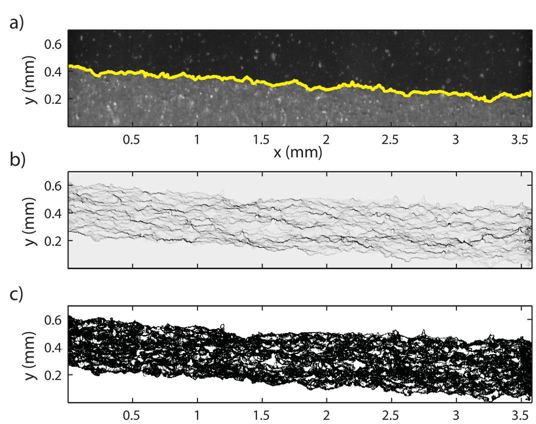

FIG. 1 (color). (a) Typical example of a picture recorded by the high speed camera (Photron Ultima) during an experiment with an average crack front speed $\langle v \rangle = 28.1\ \mu\mathrm{m\,s^{-1}}$, and a pixel size $a = 3.5\ \mu$m. The solid line represents the interface separating the uncracked (in black) and cracked parts extracted after image analysis. (b) Gray scale map of the waiting time matrix deduced from 10 000 front positions recorded at a rate of 1000 fps. The darker parts show the longer waiting times. (c) Spatial distribution of clusters (in white) corresponding to velocities 10 times larger than the average crack front speed.

Fig. 1(b). The spatially random toughness along the weak interface generates a rough crack line in pinning the crack front [Fig. 1(a)], and triggers a rich burst activity on a wide range of length scales. The numerous and various regions of gray levels suggest this intermittent dynamics [Fig. 1(b)]. It is important to mention that the image recording is so fast that there are basically no holes in the waiting time matrix $\mathbf{W}(\mathbf{x}, \mathbf{y})$, i.e., no regions of zero values (apart from below the first front, above the last one, and a few artifacts due to impurities in the sample). Then, we can deduce from $\mathbf{W}(\mathbf{x}, \mathbf{y})$, a matrix $\mathbf{V}(\mathbf{x}, \mathbf{y})$ of the local normal speed of the interface at the time when the front went through a particular position, by computing the inverse value of the corresponding matrix element w of $\mathbf{W}(\mathbf{x}, \mathbf{y})$ multiplied by the ratio of the pixel size a and the typical time between two images δt. Therefore, we can associate to each pixel corresponding to the crack line in each image, a local front velocity $v = \frac{1}{w}\frac{a}{\delta t}$. Finally, we can obtain the probability distribution functions of the local waiting time w and the local front velocity v by estimating the occurrence number of each measured waiting time or velocity on all the pixels in all the fracture front line images. The velocity distribution $P(v/\langle v \rangle)$ is shown in Fig. 2 in a log-log scale. A data collapse is obtained for all different experimental conditions by scaling the local velocity v with the average crack front speed $\langle v \rangle$ which varies from one experiment to another. A clear power law behavior of the velocity distribution $P(v/\langle v \rangle) \sim (v/\langle v \rangle)^{-\eta}$ is observed for velocities larger than $\langle v \rangle$ with a crossover to a slowly increasing function for velocities smaller than $\langle v \rangle$. A linear fit to the experimental data for $v/\langle v \rangle > 1$ gives a slope $-\eta = -2.55 \pm 0.15$. The inset of the figure shows a double logarithmic plot of the corresponding waiting time distribution $P(w/\langle w \rangle)$, where w is the waiting time, and $\langle w \rangle$ the average waiting time for each experiment. A linear

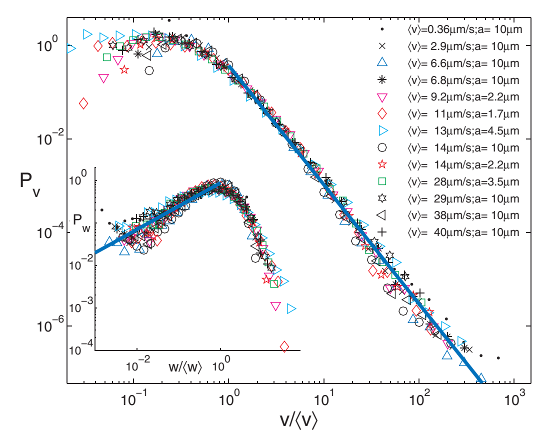

FIG. 2 (color). The velocity distribution $P(v/\langle v \rangle)$ as a function of the scaled velocity $v/\langle v \rangle$ for different experimental conditions (various average crack front speeds $\langle v \rangle$ and pixel sizes a). A fit (solid line) to all data for $v > \langle v \rangle$ has a slope -2.55. Inset shows the corresponding waiting time distribution $P(w/\langle w \rangle)$ as a function of the scaled waiting time $w/\langle w \rangle$. The solid line represents a fit to all the data for $w < \langle w \rangle$ with a slope 0.55.

fit to the experimental data for $w < \langle w \rangle$ has a slope 0.55 ± 0.15, consistent with the exponent $\eta - 2$ deduced from the velocity distribution. The power law distribution of the local velocities confirms once again previous observations, revealing a nontrivial underlying dynamics as observed on a fast video recording. It is important to note that even though the first moment of the velocity fluctuations $\langle v \rangle$ exists, the second and higher moments are ill defined and dominated by the largest velocity fluctuations. In an earlier work, the velocity distribution was investigated with a different method, based on the distance between subsequent fronts at a given time interval [20]. However, such a method proved out to produce results depending on the time interval chosen. Indeed, a short time between the front only gave contribution from the high velocity part of the distribution while a long time between the fronts gave a peak around the average velocity only. By using the concept of waiting time introduced in the present Letter, we are able to measure both high and low velocities. In the present case there exists a well defined length scale a at which the velocity can be measured. Using different magnification of the microscope, we have checked the robustness of our procedure and shown the reproducibility of our results for different pixel sizes.

In order to analyze the local burst activity, we consider a thresholded matrix generated from the velocity matrix $\mathbf{V}(\mathbf{x}, \mathbf{y})$, by setting the matrix elements v equal to one for $v > C\langle v \rangle$ and zero elsewhere, where C is a constant of the order of a few unities. Figure 1(c) shows the spatial distribution of clusters of different sizes obtained from a thresholded matrix with a threshold level $C = 10$. The white clusters correspond to velocities 10 times larger than the average crack front speed $\langle v \rangle$. Then, we can extract from this thresholded velocity matrix the size distribution of the high velocity bursts. The clusters connected to the first and last front, and thus belonging to the upper and lower white parts are excluded from the analysis.

On Fig. 3, the cluster size distribution $P(S/\langle S \rangle)$ is shown for different experiments at a given threshold value $C = 3$. First, we show a data collapse for all the different experiments performed by rescaling the clusters size S with the average burst size $\langle S \rangle$. Moreover, we clearly observe that the burst size distribution $P(S/\langle S \rangle)$ follows a power law with an exponent $\gamma = 1.7$ proving that the burst dynamics occurs on all length scales. We have checked that this critical behavior, and, in particular, the exponent $\gamma = 1.7 \pm 0.1$, is really robust: normalizing by the average burst size $\langle S \rangle$, we can rescale all the different distributions corresponding to diverse experimental conditions and a wide range of threshold level values $2 < C < 20$ (see inset of Fig. 3).

We expect a connection between the spatial scaling of the bursts, and the self-affine scaling of the front line itself on large scales. To investigate this, we have for each cluster S chosen the smallest rectangular bounding box enclosing it. The size of the bounding box gives the length scale L_y of the clusters along the growth direction and the length scale L_x of the clusters along the average front line orientation. Figure 4 shows the dependence of the average size $\langle L_y \rangle$ on the length scale $\langle L_x \rangle$ in a double logarithmic plot, for a wide range of threshold values $2 < C < 20$, averaged over all the different experimental conditions (different pixels sizes and average crack front speeds). We clearly see that the avalanche clusters become anisotropic above a characteristic length scale $L_d \sim 15$ μm. This typical size corre-

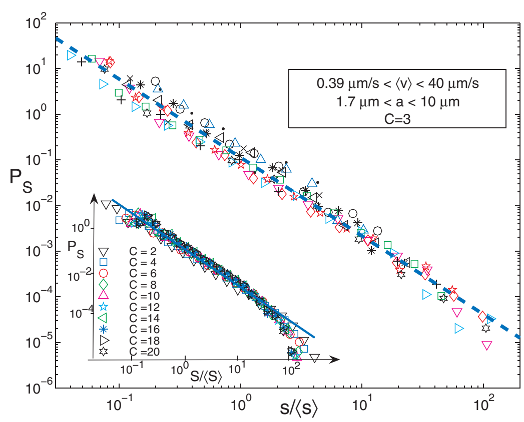

FIG. 3 (color). Burst size S distribution $P(S/\langle S \rangle)$, normalized by the average burst size $\langle S \rangle$, for different experimental conditions (the various symbols correspond to those on Fig. 2). The bursts detected for each experiment correspond to clusters of velocities 3 times larger than the average crack front speed. A fit on all the data (dashed line) gives a slope equal to 1.71. Inset: Normalized bursts size distribution $P(S/\langle S \rangle)$ averaged over all the different experimental conditions, for a wide range of different threshold levels C. A fit to all the data, cutting the largest clusters at which a cutoff appears due to the lack of statistics (solid line), gives a slope equal to 1.67.

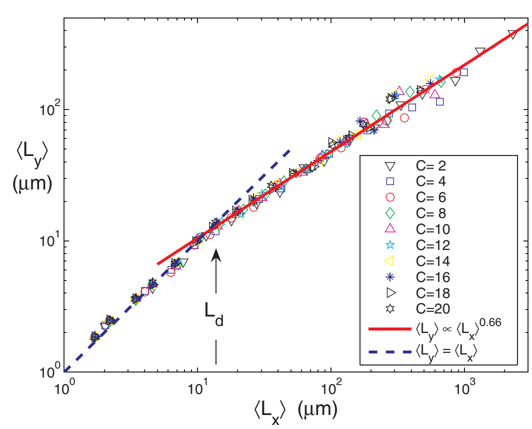

FIG. 4 (color). Average length scale $\langle L_y \rangle$ as function of the length scale $\langle L_x \rangle$, for different threshold levels C, averaged over all the different experiments performed. The solid line is a fit to the data points for $L_x > 15$ μm and has a slope $H = 0.66$, consistent with the roughness exponent of the fracture front line. The dotted line represents the curve $\langle L_y \rangle = \langle L_x \rangle$ and serves as a guide for the eye.

sponds to the correlation length for the disorder introduced by the sandblasting technique [23]. Below L_d, the local toughness is marked by the same individual asperity and as a result the thresholded velocity bursts appear isotropic. A fit to the data points for $L_x > 15$ μm gives a slope $H = 0.66$ consistent with previous independent estimates of the roughness exponent $\zeta = 0.63 \pm 0.03$ for the fracture front line. This result shows that the system exhibits self-affine scaling with the same roughness exponent ζ for the local burst as the fracture front line and brings a new confirmation of the roughness exponent found in our experiment, which is different and higher than most present theoretical or numerical predictions [19,24–26].

As mentioned in the introduction, the scaling behavior of elastic interfaces in random media is involved in various physical systems. Actually, the discrepancy between the theoretical and measured roughness exponent has also been reported recently, for contact lines of helium-4 [14] and water meniscus [15,16] propagating on rough substrates. It confirmed that the Joanny–de Gennes model [27], usually proposed to describe the contact lines dynamics which leads to the same kind of equation of motion for crack fronts [28], is not sufficient [16]. Interestingly the roughness exponents found, respectively, equal to 0.56 ± 0.03 and 0.52 ± 0.04, are close to the fracture front line roughness. Besides, for the helium-4 meniscus, power law avalanche size distributions have been measured with exponents γ from 0.99 to 1.3, depending on the contact angle, which is different from the exponent $\gamma = 1.7$ found in our experiments. However, avalanches are defined by Prevost *et al.* [14] based on subtraction between fronts, which is different from the present technique, and this γ exponent could be sensitive to such a definition.

Recent simulations based on a quasistatic model and interpreted as a stress weighted percolation problem [12], give for the first time consistent results with the experimental roughness and dynamic exponent [20,21]. The insensitivity of the velocity distribution in our experiments on the average velocity of the front gives support to the quasistatic assumptions used in these simulations. However, the simulated process zone was not observed in our experiments above the micrometer scale. It should be mentioned that dynamical effects have also been introduced in a model [26] with a full elastodynamic description where elastic waves may trigger instabilities and modify the roughness of the crack front, leading to the value $\zeta = 0.5$ [29].

No theory or simulations so far have investigated the local velocity or the burst fluctuations. It will be of great interest to perform these analyses on the numerical models for a direct comparison with our experimental work. This will hopefully clarify the importance of dynamical effects in modeling the fracture front propagation.

We thank A. Hansen, E. G. Flekkøy, and J. P. Vilotte for fruitful discussions, and E. L. Hinrichsen at SINTEF-Oslo for his hospitality. This work was supported by the CNRS/NFR PICS program, the NFR Petromax and SUP program, and the french programs ACI "RNCC" and ACI "ALEAS."

[1] F. Célarié, S. Prades, D. Bonamy, L. Ferrero, E. Bouchaud, C. Guillot, and C. Marlière, Phys. Rev. Lett. **90**, 075504 (2003).
[2] A. Hansen and J. Schmittbuhl, Phys. Rev. Lett. **90**, 045504 (2003).
[3] I. Afek, E. Bouchbinder, E. Katzav, J. Mathiesen, and I. Procaccia Phys. Rev. E **71**, 066127 (2005).
[4] H. J. Herrmann and S. Roux, *Statistical Models for Fracture of Disordered Media* (Elsevier, Amsterdam, 1990).
[5] B. B. Mandelbrot, D. E. Passoja, and A. J. Paullay, Nature (London) **308**, 721 (1984);
[6] S. R. Brown and C. H. Scholz, J. Geophys. Res. **90**, 12 575 (1985).
[7] E. Bouchaud, G. Lapasset, and J. Planés, Europhys. Lett. **13**, 73 (1990).
[8] K. J. Måløy, A. Hansen, E. L. Hinrichsen, and S. Roux, Phys. Rev. Lett. **68**, 213 (1992).
[9] J. Schmittbuhl, S. Gentier, and S. Roux, Geophys. Res. Lett. **20**, 639 (1993).
[10] J. Schmittbuhl, F. Schmitt, and C. H. Scholz, J. Geophys. Res. **100**, 5953 (1995).
[11] E. Bouchaud, J. Phys. Condens. Matter **9**, 4319 (1997).
[12] J. Schmittbuhl, A. Hansen, and G. Batrouni, Phys. Rev. Lett. **90**, 045505 (2003).
[13] S. Lemerle *et al.*, Phys. Rev. Lett. **80**, 849 (1998).
[14] A. Prevost, E. Rolley, and C. Guthmann, Phys. Rev. B **65**, 064517 (2002).
[15] S. Moulinet, C. Guthmann, and E. Rolley, Eur. Phys. J. E **8**, 437 (2002).
[16] S. Moulinet, A. Rosso, W. Krauth, and E. Rolley, Phys. Rev. E **69**, 035103(R) (2004).
[17] J. Schmittbuhl and K. J. Måløy, Phys. Rev. Lett. **78**, 3888 (1997).
[18] A. Delaplace, J. Schmittbuhl, and K. J. Måløy, Phys. Rev. E **60**, 1337 (1999).
[19] J. Schmittbuhl, S. Roux, J. P. Vilotte, and K. J. Måløy, Phys. Rev. Lett. **74**, 1787 (1995).
[20] K. J. Måløy and J. Schmittbuhl, Phys. Rev. Lett. **87**, 105502 (2001).
[21] S. Santucci, K. J. Måløy, R. Toussaint, and J. Schmittbuhl, NATO ASI Geilo Proceedings (to be published).
[22] F. Family and T. Vicsek, J. Phys. A **18**, L75 (1985).
[23] S. Santucci, K. J. Måløy, R. Toussaint, and J. Schmittbuhl (to be published).
[24] J. P. Bouchaud, E. Bouchaud, G. Lapaset, and J. Planes, Phys. Rev. Lett. **71**, 2240 (1993).
[25] S. Roux and A. Hansen, J. Phys. I **4**, 515 (1994).
[26] S. Ramanathan and D. Fisher, Phys. Rev. B **58**, 6026 (1998).
[27] J. F. Joanny and P. G. de Gennes, J. Chem. Phys.**81**, 552 (1984).
[28] H. Gao and J. R. Rice, J. Appl. Mech. **56**, 828 (1989).
[29] E. Bouchaud, J. P. Bouchaud, D. S. Fisher, S. Ramanathan, and J. R. Rice, J. Mech. Phys. Solids **50**, 1703 (2002).

SELF-AFFINE SCALING

DURING INTERFACIAL CRACK FRONT PROPAGATION

Stéphane Santucci, Knut Jørgen Måløy,
Fysisk Institutt, Universitetet i Oslo,
P. O. Boks 1048 Blindern, N-0316 Oslo 3, Norway.

Renaud Toussaint and Jean Schmittbuhl.
Institut de Physique du Globe de Strasbourg - UMR 7516,
5, rue René Descartes, 67084 Strasbourg Cedex, France.

Abstract.

We have performed an experimental study of slow crack front propagation through a weak plane of a transparent Plexiglas block. Spatial random toughness fluctuations along the weak interface generate a rough crack line in pinning locally the crack front, and leads to an intermittent dynamics of the crack front line. Using a high speed and high resolution camera we are able to capture the features of this complex dynamics.

A new analysis procedure is proposed in order to measure the waiting time fluctuations, and study the local burst dynamics and structure along the crack front during its propagation. First, we confirm previous results [1]: the fracture front dynamics is governed by local and irregular avalanches with very large size and velocity fluctuations, and can be described in terms of a Family-Vicsek scaling with a roughness exponent $\zeta \simeq 0.6$ and a dynamic exponent $\kappa \simeq 1.2$. Then, focusing in particular on the avalanches structure, we show that the system exhibits self-affine scaling with the same roughness exponent ζ for the local burst and the fracture front line itself.

Key words: Interfacial fracture, depinning transition, self-affinity, dynamic scaling.

1. Introduction

Since the pioneering work of Mandelbrot, Passoja and Paullay [2], it is now well established that crack surfaces are self-affine objects. The scaling properties of the morphology of cracks manifest themselves through self-affine long range correlations [2, 3, 4, 5, 6, 7, 8, 9] with a roughness exponent which is found to be very robust for different materials and a broad range of length scales. However, the physical role played by the heterogeneities which lead to these self-affine long range correlations is not well understood.

In recent years front propagation in disordered media has become a challenging problem trying to describe the dynamics of interfaces in many different physical systems such as crack fronts [9], magnetic domain walls [10], or wetting [11].

Actually there exists few experimental data describing crack front propagation through heterogeneous material, essentially due to the difficulty of making direct observation and following the crack front line. Indeed, the crack front line growing in a 3d heterogeneous medium has itself a 3-d shape with different in-plane and out-of-plane roughnesses, respectively $\zeta_{||}$ and $\zeta_{\perp}$. Therefore, the interfacial crack front problem simplifies the 3-d original one, both experimentally [12, 13] and theoretically [14]. Since the crack front is constrained geometrically to lie in the plane where the motion is driven by the stress transmitted through the two elastic plates, it is possible to perform direct visualization and to follow the fracture front line. So far most experiments on fracture front lines have been focused on the fracture front line morphology leading to the estimated roughness exponent $\zeta = 0.55 \pm 0.03$ [12], followed up by a longer study leading to $\zeta = 0.63 \pm 0.03$ [13]. Recently the interfacial crack front propagation has started to be investigated [1]. This study has shown that the fracture front line dynamics is intermittent - the depinning on asperities triggers local instabilities- and can be described in terms of a Family-Vicsek scaling [15] with a roughness exponent $\zeta = 0.6$ and a dynamic exponent $\kappa = 1.2$. In contrast to earlier numerical and theoretical studies [8, 16, 17, 18], recent numerical simulations interpreted as a stress-weighted percolation problem [19] give consistent results on the experimental roughness and dynamic exponents.

In this work, we went further on in the investigation of the local dynamics and this study appears as the continuation of the experimental work initiated by Måløy and Schmittbuhl [1]. In the first part, we will recall the experimental set-up and the sample preparation that permits us the direct observation of an in-plane crack front which propagates into the annealing plane of two transparent polymethylmethacrylate (PMMA) plates [12]. It is important to underline that now, using a really powerful high speed and high resolution camera (Photron Ultima), we are able actually to capture the details of the complex crack front dynamics. Then, in order to analyze the local burst dynamics and in particular to extract the local waiting time fluctuations, we propose in the second section a new analysis procedure. Both this analysis and the fast video recording confirm the previous observations and results, showing that the dynamics of the fracture front is driven by local and irregular avalanches with very large size and velocity fluctuations. In this paper we would like to focus on the scaling of the crack front line. We will first confirm that the development of the crack roughness follows a Family-Vicsek scaling and then examining in details the structure of the local avalanches we will show that the system exhibits self-affine scaling with the same roughness exponent ζ for the whole set of local bursts, and for the fracture front line itself. More details concerning the dynamics and in particular the velocity and waiting time fluctuations will be given elsewhere [20].

2. Experimental procedure

2.1. SAMPLE PREPARATION

Two Plexiglas plates ($32 \times 14 \times 1cm$ & $34 \times 12 \times 0.4cm$) are annealed together at $205°C$ during 30 *mn* under several bars of normal pressure, in order to create a single block with a weak interface. Before the annealing procedure both plates are sand-blasted on one side with $50\mu m$ steel particles or $100\mu m$ glass beads. Sand-blasting introduces a random topography which induces local toughness fluctuations during the annealing process. In order to estimate the characteristic size of the local heterogeneities arising from the sand-blasting process, we have measured the profile of a sand-blasted Plexiglas surface, using a white light interferometry technique (performed at SINTEF laboratory). We found that these local irregularities have an upper cut-off size estimated as $18 \pm 2\mu m$.

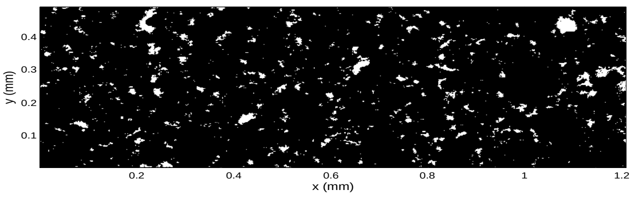

Figure 1. Two dimensional map of a sand blasted PMMA surface: white patches correspond to asperities higher than $0.85\mu m$, which corresponds to the standard deviation of the height of this profile.

The two key points of the procedure are *the transparency* of the material allowing *the direct observation* of the fracture front, and *the random toughness* introduced along the interface which generates a rough crack line in pinning the crack front.

2.2. MECHANICAL AND OPTICAL SET-UP

While the upper Plexiglas plate is clamped to a stiff aluminium frame, a press applies a normal displacement to the lower one (1 cm thick) corresponding to a crack opening in mode I configuration (pure tensile mode) at a low and constant rate $\sim 10\mu m.s^{-1}$.

A high speed and high resolution camera (Photron Ultima) mounted on a microscope allows us to follow the slow crack front propagation. Using this camera at a spatial resolution of 1024×512 pixels, and an acquisition rate of 1000 f.p.s. we can follow the crack front during $\simeq 12s$ (obtaining $\simeq$ 12000 images). In this work, we will focus in particular on a given experiment with an average crack front speed $\langle v \rangle = 28.1\mu m/s$ an a pixel size $a = 3.5\mu m$. It is important

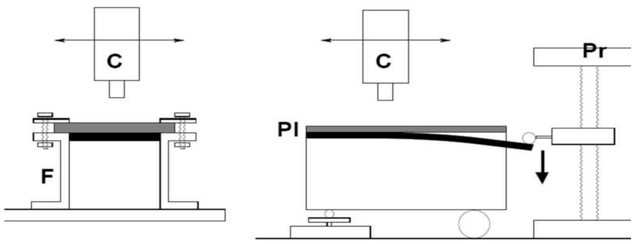

Figure 2. Sketch of the experimental setup: a thick PMMA plate (PL) is clamped into a rigid frame (F). A normal displacement is imposed by a press (Pr) on the thin plate with a cylindrical rod. A high speed and high resolution camera (C) mounted on a microscope follows the crack front propagation.

to notice that the pixel size is smaller than the characteristic scale of these local heterogeneities, estimated as $18 \pm 2\mu m$ arising from the sand-blasting process. In a forthcoming paper [20], we will present using an extended set of data that all of these preliminary results are stable while changing the experimental conditions (varying both the average front line speed and the pixel size).

3. Analysis procedure and results

3.1. SCALING ANALYSIS OF THE CRACK FRONT

Image analysis is performed to extract the crack front by computing the gradient of the gray levels. A typical result is shown on figure 3. The front position being

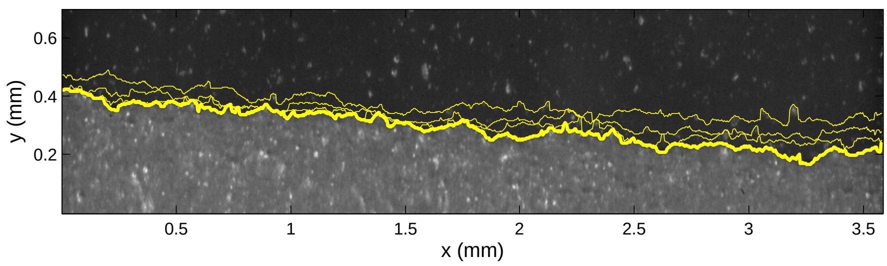

Figure 3. Typical example of a picture recorded by the high speed camera (Photron Ultima) during an experiment with an average crack front speed $\langle v \rangle = 28.1 \mu m.s^{-1}$. The pixel size is $a = 3.5\mu m$. During this experiment, the camera recorded in total 9000 frames with a time delay of $1ms$ for each picture. The crack front propagates from bottom to top. The thick solid line represents the interface separating the uncracked (in black) and cracked parts extracted after image analysis. We superimpose 3 fracture front positions for later times (0.5, 1 and $2s$), suggesting the crack pinning and the burst activity.

defined as the contrast interface between the uncracked (in black) and cracked parts is given by $y = h(x, t)$.

The power spectrum $P(k)$ of the deviations from the mean front position $h(x) - \langle h(x) \rangle$, averaged over all the crack front position detected during an experiment (in this case 9000 fronts), as function of the wave number k, is shown on figure 4. The slope of the best fit $P(k) \propto k^{-(1+2\zeta)}$ gives an estimation of the roughness exponent $\zeta = 0.54 \pm 0.06$. This value for the roughness exponent is consistent with previous careful estimations $\zeta = 0.55 \pm 0.05$ [12] and $\zeta = 0.63 \pm 0.03$ [13], where it has been extensively checked for fronts at rest over a much larger range of scales (around 3.5 decades), and using several techniques.

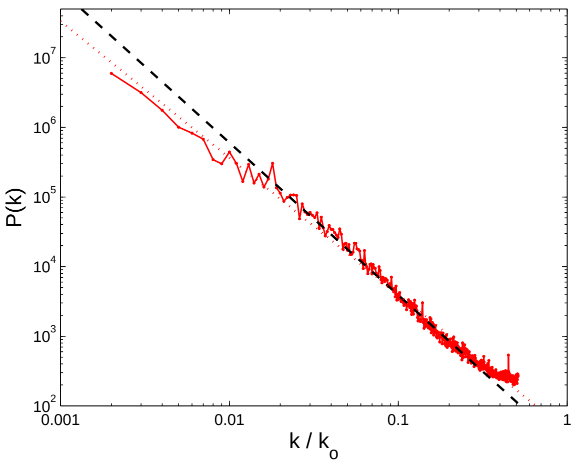

Figure 4. Power spectrum of the deviations from the mean front position $h(x) - \langle h(x) \rangle$ as function of the reduced wave number k/k_o with $k_0 = 2\pi/(3.5\mu m)$ averaged over 9000 crack front positions detected. The lines correspond respectively to the best fits $P(k) \propto k^{-(1+2\zeta)}$ of all the spectrum (dotted line), and excluding small and high wave number, $0.25 \geq k/k_o \geq 10^{-2}$ (dashed line). An average over the slopes of the fits gives an estimation of the roughness exponent: $\zeta = 0.54 \pm 0.06$. The reduced quantity is $k_0 = 2\pi/(3.5\mu m)$. The vertical axis is arbitrary.

Moreover, we confirm that the development of the crack roughness follows rather well the Family-Vicsek scaling ansatz with a roughness exponent $\zeta = 0.6$ and a dynamic exponent $\kappa = 1.2 \pm 0.2$. Considering the power spectrum of the relative position $\Delta h(x, t) = h(x, t) - h_i$, where $h_i = h(x, t_i)$ is the initial front, the Family-Vicsek scaling ansatz can be written in the following way.

$$P(k, \Delta t) = \Delta t^{(1+2\zeta)/\kappa} G(k \Delta t^{1/\kappa}) \qquad \text{with} \qquad G(x) \propto \begin{cases} b & x \ll c \\ x^{-(1+2\zeta)} & x \gg c \end{cases}$$

where $\Delta t = t - t_i$ is the time delay between the analyzed images, b and c are characteristic constants.

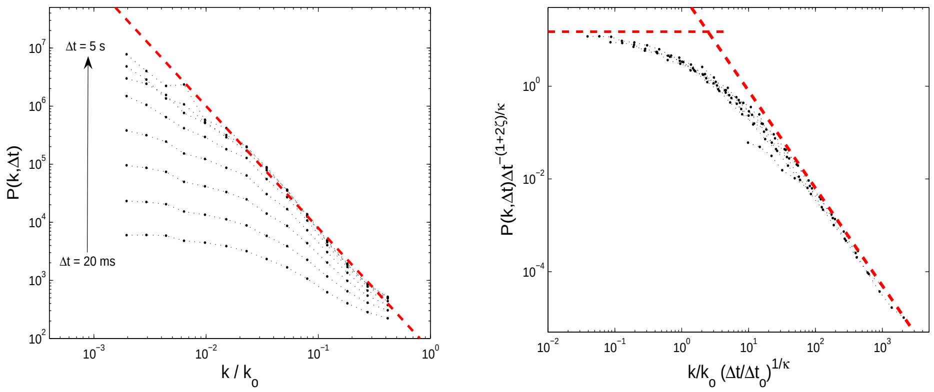

Figure 5. Left: Power spectrum of the relative position $\Delta h(x, t)$ as function of the reduced wave number k/k_o with $k_0 = 2\pi/(3.5\mu m)$ for logarithmically increasing time delays $\Delta t = t - t_i$, from $\Delta t = 20ms$ to $\Delta t = 5s$. Right: Data collapse for the scaling function $G(k\Delta t^{1/\kappa}) = P(k, \Delta t)\Delta t^{-(1+2\zeta)/\kappa}$, showing a dynamic Family-Vicsek scaling with a roughness exponent $\zeta = 0.54$ and a dynamic exponent $\kappa = 1$. The power spectra of the relative position $\Delta h(x, \Delta t) = h(x, t) - h(x, t_i)$ have been averaged over 4000 different initial front $h_i = h(x, t_i)$. The dashed lines are guides for the eyes and have a slope of -2.1. The horizontal axis correspond to reduced dimensionless quantities k/k_0, t/t_0, with $k_0 = 2\pi/(3.5\mu m)$, and $\Delta t_0 = 1ms$. The vertical axis are arbitrary.

On Fig. 5 to the left, we show the power spectrum of the relative position $\Delta h(x, t)$ for logarithmically increasing time delays Δt, from $\Delta t = 20ms$ to $\Delta t = 5s$, averaged over 4000 different initial front $h(x, t_i)$. When increasing the time delays Δt, we observe a crossover behaviour from a flat spectrum - indicating that no spatial correlations are present at small time delays Δt -, towards a power law behaviour at larger times Δt, consistent with the self-affine long range correlations previously observed $P(k) \propto k^{-(1+2\zeta)}$ with a roughness exponent $\zeta = 0.54$. Then, we plot on figure 5 to the right, the scaling function $G(k\Delta t^{1/\kappa}) = P(k, \Delta t)\Delta t^{-(1+2\zeta)/\kappa}$ as a function of $k\Delta t^{1/\kappa}$ with a roughness exponent $\zeta = 0.54$ previously measured. A satisfying data collapse is obtained for a dynamic exponent $\kappa = 1$. Performing the same procedure for different experiments leads to the following estimation for the dynamic exponent $\kappa = 1.2 \pm 0.2$ with a roughness exponent of $\zeta = 0.6$, consistent with previous experimental results [1].

3.2. WAITING TIME MATRIX **W** AND LOCAL FRONT VELOCITY MATRIX **V**

In order to study the local burst dynamics during the slow crack propagation we have computed a waiting time matrix $\mathbf{W}(\mathbf{x}, \mathbf{t})$. The fracture front lines extracted from image analysis of the digital pictures (see Fig. 3) were added to obtain a waiting time matrix **W**. This matrix has the dimension of the original image and an initial value equal to zero. We add the value 1 to the matrix element w

corresponding to each pixel of the front line position detected. This procedure has been performed for all frames of a given experiment in order to obtain the final waiting time matrix **W** for each experiment. Then, a local normal speed of the interface $\mathbf{V}(\mathbf{x}, \mathbf{t})$ can be deduced by computing the matrix of the inverse waiting time w times the ratio of the pixel size a on the typical time between two images δt. Therefore, we can associate to each pixel corresponding to the crack line in each image, a local front velocity $v = \frac{a}{w\delta t}$.

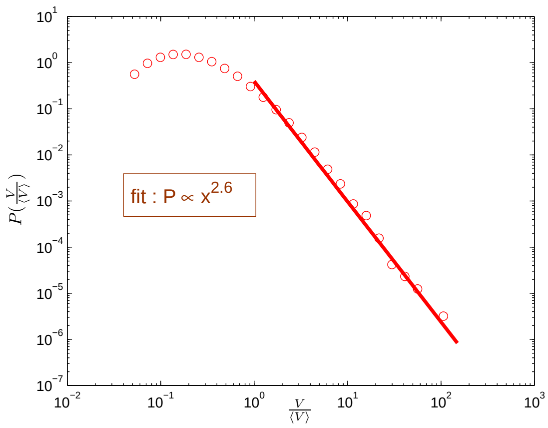

Figure 6. Distribution of the local front velocity normalized by the average crack speed $\frac{v}{\langle v\rangle}$ for an experiment with an average crack front speed $\langle v\rangle = 28.1\mu m/s$. The solid line represents a fit for velocities 2 times larger than the average crack front speed $\langle v\rangle$ and has a slope of -2.6.

Finally, we can obtain the probability distribution functions of the local waiting time w and the local front velocity v, in estimating the occurrence number of each measured waiting time or velocity on all pixels in all fracture front line images. A typical example of a distribution $P(\frac{v}{\langle v\rangle})$ of the local front velocity v, obtained for an experiment with an average crack front speed $\langle v\rangle = 28.1\mu m/s$ is shown on Fig. 6, in log-log scale. For velocities larger than the average crack front speed $\langle v\rangle$, we clearly observe that the local front velocities are power law distributed $P(v/\langle v\rangle) \propto (v/\langle v\rangle)^{-\eta}$ with an exponent $\eta \simeq 2.6$. This power law behaviour for the velocity distribution reveals a rich and non trivial underlying dynamic as one can observe on a fast video recording that the crack front is growing through irregular avalanches on all length scales. Since in this study we would like to focus on the local burst dynamic, more details concerning the velocity and waiting time fluctuations will be given elsewhere [20], and now we are going to examine in particular the structure of the local avalanches.

3.3. LOCAL BURST STRUCTURE

In order to analyze the local burst activity, let us consider the velocity matrix **V**. We can generate a clipped velocity matrix from **V** by setting the matrix elements v equal to one for $v > C \cdot \langle v \rangle$ and zero elsewhere. We present on Fig. 7 the spatial distribution of clusters of different sizes S obtained from the clipped matrix for a clip level $C = 8$. The white clusters correspond to velocities eight times larger than the average front speed $\frac{v}{\langle v \rangle} > C = 8$, which was for this experiment $\langle v \rangle = 28.1 \mu m.s^{-1}$. The clusters connected to the first and the last front, and thus belonging to the upper and lower white parts are excluded from the analysis.

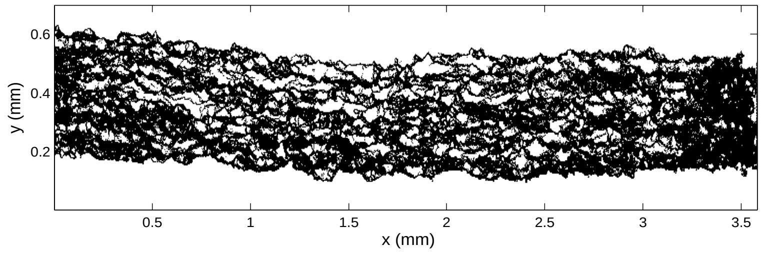

Figure 7. Spatial distribution of clusters size S. White clusters correspond to velocities $v > C \cdot \langle v \rangle$ with a clip level $C = 8$, during an experiment with an average crack front speed $\langle v \rangle = 28.1 \mu m.s^{-1}$. The pixel size is $a = 3.5 \mu m$. The crack front propagates from bottom to top.

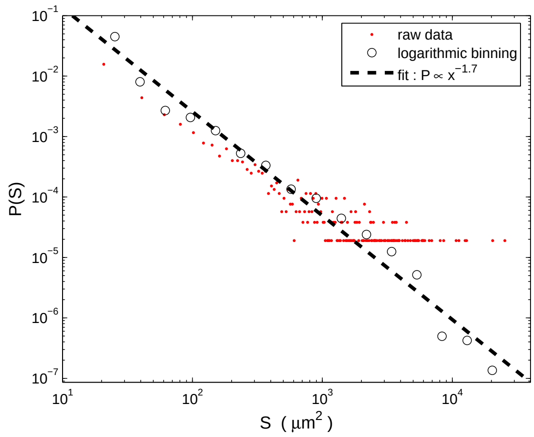

Figure 8. Distribution of the burst sizes S for an experiment with an average crack front speed $\langle v \rangle = 28.1 \mu m.s^{-1}$ and a pixel size $a = 3.5 \mu m$. The clip level used here $\frac{v}{\langle v \rangle} > C = 8$. Notice that the logarithmic binning allows to extract the scaling law underlying the large statistics, over a large range of event sizes. The dashed line represents the best fit $P(S) \propto S^{-\gamma}$ and gives an exponent $\gamma = 1.7$

In Fig.8, the cluster sizes S distribution $P(S)$ is given in a double logarithmic scale. We clearly observe a power law behaviour $P(S) \propto S^{-\gamma}$ with an exponent $\gamma = 1.7$ proving that the burst dynamics occurs on all length scales. We have checked that this critical behaviour, and in particular the exponent γ, is really stable: normalizing by the average burst size $\langle S \rangle$, we can rescale all the different distributions corresponding to diverse experimental conditions and a wide range of clip level values (see [20] for more details).

We expect a correlation between the burst structure on small scales and the self-affine scaling of the crack front line on larger scales. In order to investigate the spatial scaling on small scales in detail, we have for each cluster S chosen the smallest bounding box enclosing it. The size of the bounding box gives the length scale L_y of the clusters along the growth direction and the length scale L_x of the clusters in the direction of the average fracture frontline.

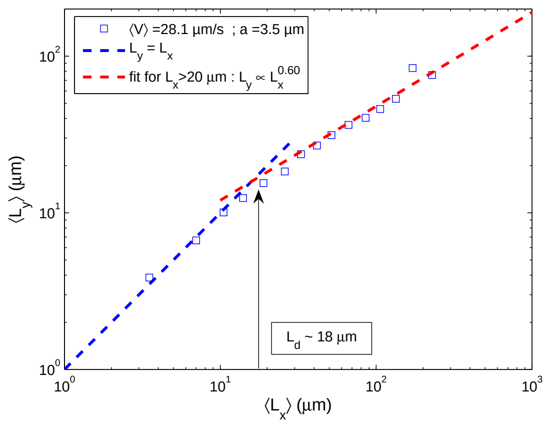

Figure 9. Average length scale $\langle L_y \rangle$ in function of the average length scale $\langle L_x \rangle$. The dashed line is a fit to the data points for $L_x > 20$ μm and has a slope 0.60 consistent with the roughness exponent of the fracture front line. The dotted line represents the curve $y = x$ and serves as a guide for the eye.

Figure 9 shows the dependence of the average length scale $\langle L_y \rangle$ as function of $\langle L_x \rangle$ in a double logarithmic plot for the same previous experiment ($\langle v \rangle = 28.1 \mu m.s^{-1}$, and $a = 3.5 \mu m$), for a given clip value $C = 8$. We clearly see that the avalanche clusters become anisotropic above a characteristic length scale $L_d \sim 18 \mu m$. This typical size can be interpreted as a correlation length for the disorder introduced by the sand-blasting technique as we have observed previously on Fig. 1. Below L_d the local toughness is marked by the same individual asperity and as a result the clipped velocity bursts appear isotropic. A linear fit of the data points for $L_x > 20 \mu m$ gives a slope 0.60 consistent with the roughness exponent $\zeta = 0.63 \pm 0.03$ of the fracture front line itself. This result shows that the system exhibits self-affine scaling with the same roughness exponent ζ for the local dynamic bursts as for the fracture front line itself, and brings a new confirmation of the roughness exponent determined in such interfacial crack experiments. It is important to note that most present theoretical and numerical works predict a lower value for this roughness exponent [8, 16, 17, 18].

4. Conclusion

We have performed an experimental study of slow interfacial crack front propagation. This work confirms previous experimentals results [1]: the fracture frontline dynamics can be described in terms of a Family-Vicsek scaling with a roughness exponent $\zeta \simeq 0.6$ and a dynamic exponent $\kappa \simeq 1.2$. Moreover, we have observed that this dynamics is driven by local and irregular avalanches whose size and velocity are power law distributed. We show that the dynamics and the structure of the local bursts are playing a crucial role for the scaling and the dynamics of the crack front itself. In particular, above a typical size $L_d \sim 20\mu m$, the burst size scales differently in the direction parallel and normal to the fracture front with an exponent consistent with the roughness exponent of the fracture front $\zeta \simeq 0.6$. However, if it appears consistent to interpret this result as finite size effect related to the disorder, more experimental work is needed to control and change the typical disorder size, in order to be conclusive and affirm that this cut-off length scale really corresponds to the quenched disorder correlation length introduced by the sand-blasting procedure.

Recent simulations interpreted as a stress-weighted percolation problem [19] give consistent results with the experimental roughness and dynamic exponent measured, in contrast to earlier numerical and theoretical studies [8, 16, 17, 18]. However so far, no theory or simulations have examined the dynamics and in particular the local burst activity of the crack line, and therefore it appears of central importance to develop these numerical studies.

Acknowledgements

We acknowledge E.L. Hinrichsen, M. Fleissner, and SINTEF laboratories in Oslo for their hospitality, permitting us to perform the white light interferometry measurements. We also thank L. Vanel, O. Ramos, A. Hansen, E.G. Flekkøy, and J.P. Vilotte for fruitful discussions. This work was supported by the CNRS/NFR PICS program, and the NFR Petromax and SUP program.

References

1 K. J. Måløy and Jean Schmittbuhl. *Phys. Rev. Lett.*, **87**, 105502 (2001)

2 B. B. Mandelbrot, D. E. Passoja, and A. J. Paullay. *Nature*, **308**, 721 (1984);

3 S. R. Brown and C. H. Scholz. *J. Geophys. Res.*, **90**,12575 (1985);

4 E. Bouchaud, G. Lapasset, and J. Planés. *Europhys. Lett.*, **13**, 73 (1990);

5 J. Schmittbuhl, S. Gentier, and S. Roux. *Geophys. Res. Lett.*, **20**, 639 (1993);

6 B. L. Cox and J. S. Y. Wang. *Fractals*, **1**, 87 (1993);

7 K. J. Måløy, A. Hansen, E. L. Hinrichsen, and S. Roux. *Phys. Rev. Lett.*, **68**, 213 (1992);

8 J. Schmittbuhl, F. Schmitt, and C. H. Scholz. *J. Geophys. Res.*, **100**, 5953 (1995).

9 E. Bouchaud. *J. Phys*, **9**, 4319 (1997).

10 S. Lemerle, J. Ferr, C. Chappert, V. Mathet, T. Giamarchi and P. Le Doussal *Phys. Rev. Lett.*, **80**, 2849, (1998).

11 E. Rolley, C. Guthmann, R. Gombrovisch and V. Repain, *Phys. Rev. Lett.*, **80**, 2865, (1998).

12 J. Schmittbuhl and K. J. Måløy. *Phys. Rev. Lett*, **78**, 3888 (1997);

13 A. Delaplace, J. Schmittbuhl, and K. J. Måløy. *Phys. Rev. E*, **60**, 1337 (1999); J. Schmittbuhl, A. Delaplace, and K. J. Måløy. *In Physical Aspects of Fracture.* (eds E. Bouchaud), (Kluwer Academic Publishers, 2001)

14 J. Schmittbuhl, S. Roux, J. P. Vilotte and K. J. Måløy.*Phys. Rev. Lett.*, **74**, 1787 (1995).

15 F. Family and T. Vicsek. *J. Phys. A*, **18**,L75 (1985).

16 J. P. Bouchaud, E. Bouchaud, G. Lapaset, and J. Planes. *Phys. Rev. Lett.*, **71**, 2240 (1993).

17 S. Roux and A. Hansen. *J. Phys. I*, **4**, 515, (1994).

18 S. Ramanathan and D. Fisher. *Phys. Rev. B*, **58**, 6026 (1998);

19 J. Schmittbuhl, A. Hansen and G. Batrouni. *Phys. Rev. Lett.*, **90**, 045505, (2003)

20 K. J. Måløy, S.Santucci, R.Toussaint and J. Schmittbuhl. submitted to *Phys. Rev. Lett.*

Deformation of the crack front during propagation in some disordered medium: theoretical and experimental studies

N. Pindra[1], V. Lazarus[2], J.B. Leblond[1], J. Schmittbuhl[3], R. Toussaint[3]

[1]*UPMC Univ Paris 6, CNRS, UMR 7190, Institut Jean Le Rond d'Alembert, Boite courrier 161-2, 4 Place Jussieu, F-75005, Paris, France;*
[2]*UPMC Univ Paris 6, Univ Paris-Sud, CNRS, UMR 7608, Lab FAST, Bat 502, Campus Univ, F-91405, Orsay, France;*
[3]*Institut de Physique du Globe de Strasbourg, UMR 7516 CNRS 7516, 5, rue René Descartes, F-67084 Strasbourg, France*

Abstract: In heterogeneous disordered materials, a straight crack front experiences toughness fluctuations during its propagation that generate geometric fluctuations. Their long time statistical behavior has been studied by Lazarus et al. (JMPS, 2008) using Bueckner-Rice weight function theory. In particular, the evolution of the auto-correlation function, power spectrum and variance of the front fluctuations have been derived. The aim here is to compare these results to some experiments performed on transparent plexiglas blocks with the same apparatus as in Schmittbuhl and Maloy (PRL, 1997) by measuring the amplitude evolution of the crack front fluctuations in addition to the self-affinity roughness parameters.

In a perfectly ideal homogeneous material, an initial straight crack front remains straight during propagation. But in an heterogeneous disordered materials, it becomes rough. The aim of the present paper is to derive an analytical description of the evolution of this roughness and to compare it to experimental results. The assumption of quasi-static brittle crack propagation will be done.
Among the experimental works, one may cite on the one hand, the pioneer work of Daguier *et al.* [2] in which the crack front is obtained postmortem, the crack surface being marked by ink and on the other hand, the works of Delaplace, Maloy and Schmittbuhl [8, 3] in transparent plexiglas in which the crack front can be observed in situ during its evolution. They deal mainly with the universal self-affine character of the crack front. The roughness exponent ξ was measured between 0.5 and 0.6. Here, we have again used the experimental framework of [8, 3] to measure the time evolution of the fluctuations in addition to its roughness.
All the theoretical studies of the statistical properties of the crack front performed in quasi-static, use Bueckner[1]-Rice[7] weight function theory, also called line elastic models, to evaluate the stress intensity factors along the perturbed crack front. Among them, one may distinguish two groups depending on the type of the advance law used. The first ones [9, 10, 6] deal with crack advance governed

by *brittle* fracture Irwin's criterion with a slightly heterogeneous toughness. This criterion is a *threshold* type one: the crack propagates only if the stress intensity factor becomes equal to the local toughness. In particular, by a first order analysis the roughness exponent was derived and found to be $\xi = 0.37$ or $\xi = 0.5$ depending on the papers. This apparent discrepancy will be considered further. The second group deals with crack advance governed by Paris' law (*fatigue* or *subcritical* fracture). It is a *time dependent* type criterion: the rate of crack advance is proportional to a power law of the stress intensity factor. Lazarus, Leblond and coauthors have performed the study of a tensile tunnel-crack [4] and of a tensile semi-infinite interfacial crack [6]. Contrary to the case of threshold advance law, their first order study in crack advance was not sufficient to obtain the crack front roughness. However Adda-Bedia and Katzav [5] performed the second order study for a semi-infinite crack and obtained $\xi = 0.5$.
Here, the work of Pindra, Lazarus and Leblond [6] is applied to experiments made with the same framework as Delaplace, Maloy and Schmittbuhl [8, 3]. For Irwin's advance law, using Bueckner-Rice formulation for a semi-infinite crack subjected to line loading on its faces, the evolution of the variance and power spectrum, so as the roughness exponent are derived and compared to previous theoretical results of Schmittbuhl, Vilotte and coauthors [9, 10]. Then, comparison with experiments are performed, not solely on the roughness exponent as in previous papers but also on the evolution of the crack front amplitude.

1 Experiments

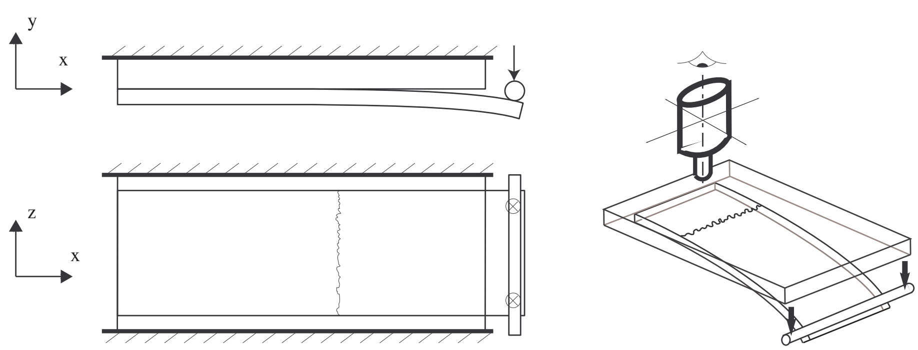

Figure 1: Two PMMA plates sintered together: a thick clamped one (21 cm long, 11 cm wide, and 1 cm thick) and a thin one (23 cm $\times$ 9 cm $\times$ 0.6 cm) subjected to a normal displacement.

The experimental framework is the one still used by Delaplace, Maloy and Schmittbuhl [8, 3]. Two PMMA transparent plates are sandblasted and annealed together by increasing temperature to obtain one block with a weak plane where the crack will propagate. The larger plate is clamped. A normal displacement is applied to the smaller one that creates a stable propagating crack in the weak plane of the specimens (fig. 1). The crack front is observed with a microscope at several stages of the propagation.

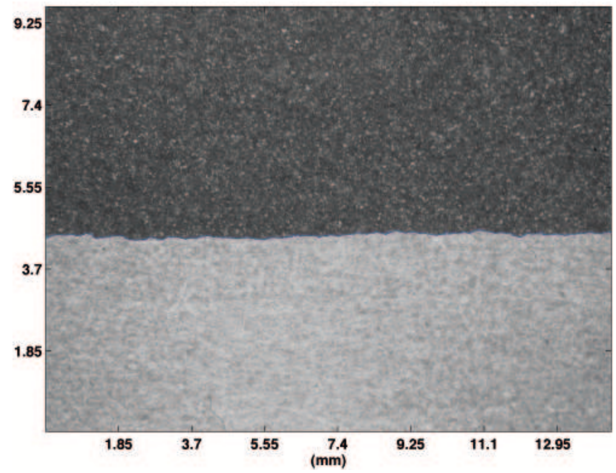

Figure 2: Experimental picture of the crack front for one equilibrium position. In blue the extracted crack front

By image treatment, one extracts the position of the crack fronts at different time steps (fig. 2). The front becomes rough because of the toughness fluctuations introduces by the sandblasting.

2 Theoretical determination of the roughness

2.1 Evolution of the perturbation of the crack fronts

Since [6] is a general paper (an interfacial crack, several type of loadings, fatigue and fragile fracture are considered), and hence is quiet complicated, we give here the reasoning in the particular case of an homogeneous medium ($\varepsilon = 0$), the particular line loading of the experiments, brittle fracture, although most of the results can be directly (but not painlessly) derived from the paper.
Let us consider a semi-infinite plane crack in an infinite homogeneous linear elastic medium. Line tractions $\pm P\vec{e}_y$ are applied on the crack faces at a distance a of the crack front (fig. 3). We suppose that for each equilibrium position of the crack front, Irwin's criterion is satisfied, that is:

$$K(M) = K_c(M) \tag{1}$$

at each point M of the crack front. Here $K(M)$ is the stress intensity factor (SIF) and $K_c(M)$ the toughness, both at point M.

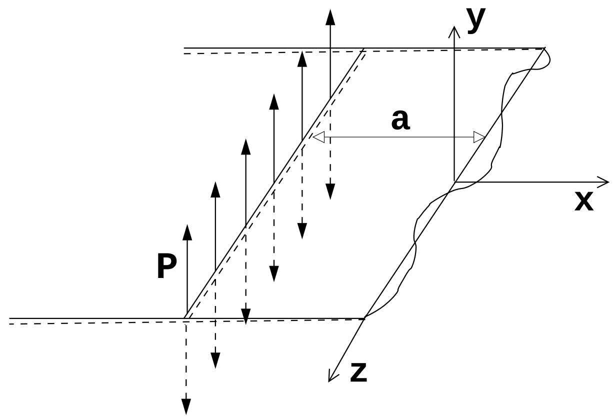

Figure 3: Semi-infinite plane crack with a slightly perturbed crack front and line tractions at a distance a of the crack front

If the toughness is uniform, the crack front remains straight during propagation. The SIF along the crack front are then :

$$K = P\sqrt{\frac{2}{\pi a}} \tag{2}$$

so that the loading corresponding to position a of the front verifies :

$$P = K_c\sqrt{\frac{\pi a}{2}} \tag{3}$$

Notice that the propagation is stable, in the sense that the loading has to be increased for the crack to advance (a increases).
Now introduce some small fluctuations of the toughness :

$$K_c(z,x) = \overline{K}_c(1+\kappa(z,x)), \quad |\kappa| \ll 1 \tag{4}$$

It produces small fluctuations $\delta a(z,a)$ and $\delta K(z,a)$ of the crack front position $a(z,a)$ and of the SIF $K(z,a)$ (see fig. 3) so that :

$$\left\{ \begin{array}{lllll} a(z,a) & \equiv & a+\delta a(z,a), & |\delta a(z,a)| & \ll & a \\ K(z,a) & \equiv & K(a)+\delta K(z), & |\delta K(z,a)| & \ll & K(a) \end{array} \right. \tag{5}$$

where a and $K(a)$ denote their mean values.
Expanding Irwin's criterion (1) to first order and identifying terms of order 0 and 1, one gets :

$$\left\{ \begin{array}{l} K(a) = K_c \\ \\ \dfrac{\delta K(z,a)}{K(a)} = \kappa(z,a) \end{array} \right. \tag{6}$$

Now we use Bueckner [1]-Rice [7] formalism, expanded to line tractions as in [6], to express the perturbed SIF to first order in δa :

$$\frac{\delta K(z,a)}{K(a)} = -\frac{1}{2a}\delta a(z,a) + \frac{1}{2\pi}\mathrm{PV}\int_{-\infty}^{\infty}\frac{\delta a(z',a)-\delta a(z,a)}{(z'-z)^2}\mathrm{d}z' \tag{7}$$

Inserting equation (7) into (6.2) and taking the Fourier transform of the equation, one gets:

$$\delta\hat{a}(k,a) = -\frac{2a\hat{\kappa}(k,a)}{1+|ka|} \tag{8}$$

2.2 Statistical study of the deformation of the front

We consider a large number of random possible realizations of the heterogeneous medium and the crack geometry. Statistical invariance of the functions $\kappa(z,x)$ in the direction z and x, and $\delta a(z,a)$ in the direction z being assumed, the two point auto-correlation functions of these functions depend only on the relative position of the points considered:

$$E\left[\kappa(z_1,a)\kappa(z_2,a)\right] = \mathcal{K}(z_2-z_1) \tag{9}$$

$$E\left[\delta a(z_1,a)\delta a(z_2,a)\right] = \mathcal{A}(z_2-z_1,a) \tag{10}$$

where $E[X]$ denotes the mathematical expectation of any quantity X. The functions $\mathcal{K}(z)$ and $\mathcal{A}(z,a)$ can be identified with the average values of $\kappa(z',a)\kappa(z'+z,a)$ and $\delta a(z',a)\delta(z'+z,a)$ over the crack front, provided an ergodic hypothesis is made. The function $\mathcal{A}(z,a)$ and its z -Fourier transform $\widehat{\mathcal{A}}(k,a)$ (the spectral density of the perturbation) provide statistical information about the geometry of the crack front.

Using the property that

$$\widehat{\mathcal{A}}(k,a) = \frac{1}{2\pi}\int_{-\infty}^{\infty} E\left[\delta\hat{a}(k_1,a)\delta\hat{a}(-k,a)\right]\mathrm{d}k_1 \tag{11}$$

and equation (8), one obtains the power spectrum of the perturbation of the crack front :

$$\widehat{\mathcal{A}}(k,a) = \frac{4a^2}{(1+|ka|)^2}\widehat{\mathcal{K}}(k) \tag{12}$$

For $a \gg a_0$ this yields :

$$\begin{cases} \widehat{\mathcal{A}}(k,a) = \dfrac{4}{k^2}\widehat{\mathcal{K}}(k), \quad \text{for } k \neq 0 \\ \\ \widehat{\mathcal{A}}(0,a) = 4\widehat{\mathcal{K}}(0)a^2 \end{cases} \tag{13}$$

Taking the inverse Fourier transform of equation (12), one gets for $a \gg a_0$:

$$\mathcal{A}(z,a) \sim \frac{4}{\pi}a\widehat{\mathcal{K}}(0) \tag{14}$$

The squared fluctuation $\sigma(z,a) \equiv E\left[(\delta a(z,a) - \delta a(0,a))^2\right]^{1/2}$ can also be derived. For $a \gg a_0$ and $z \gg b$, b being the correlation length of κ ($b = 0$ for white noise):

$$\sigma(z,a)^2 \sim 4\widehat{\mathcal{K}}(0)z \tag{15}$$

2.3 Roughness exponent

Suppose that the toughness fluctuation are given by a white noise: $\widehat{\mathcal{K}}(k) = \widehat{\mathcal{K}}_0 = Cst.$. Equations (13) or (15) gives the value of the so-called wandering or roughness exponent :

$$\xi = 0.5 \tag{16}$$

However, numerical simulations performed in [10] using also Bueckner-Rice formula (7) yield two different values: $\xi = 0.37$ as in [9] and $\xi = 0.5$, the first value being obtained if in their simulations $\delta a_{max} > b$ and the second if $\delta a_{max} < b$. The difference hence is due to the numerical parameters used. May be that for $\delta a_{max} > b$, the results are in fact illicit since Bueckner-Rice formula, that supposes the perturbation and all is derivatives small, is then no more valid for $\frac{\partial \delta a}{\partial z} \sim \frac{\delta a_{max}}{b} > 1$. Moreover, physically it may be more pertinent to suppose that $\delta a_{max} < b$ when the crack front is trapped, as in the experiments by fluctuations of thoughness (roughness smaller than the typical size of the zones of higher thoughness). Whatever, further investigations are under study to clarify this point.

3 Comparison experiments and theoretical results

3.1 Power spectrum evolution

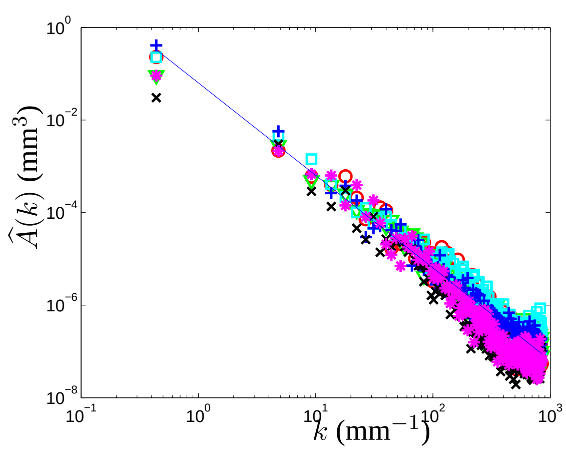

Figure 4: Power spectrum. Marker lines: for several crack fronts with a between 35 mm and 100 mm. Continuous line: $\widehat{\mathcal{A}}(k) \propto k^{-1-2\xi}$, $\xi = 0.5$.

In figure 4, the experimental power spectrum $k \rightarrow \widehat{\mathcal{A}}(k,a)$ evolution is given for several crack positions a. Several remarks can be done:

1. For all the fronts considered, $\widehat{\mathcal{A}}(k,a)$ is independent of a. This is in agreement with the behavior for large a obtained in eq. (13).

2. The roughness exponent as in previous measures is near $\xi = 0.5$ in agreement with our theoretical prediction.

3.2 Variance evolution

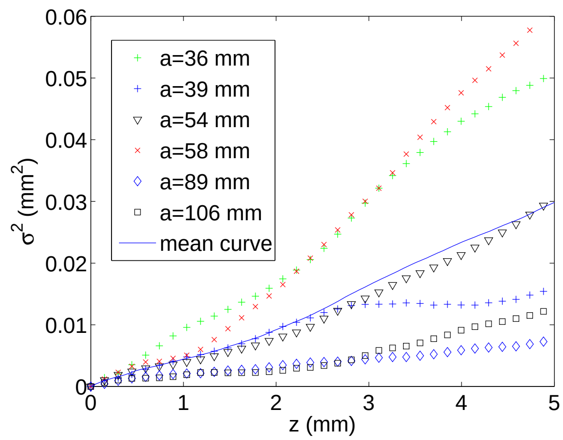

Figure 5: Variance. Marker lines: for several crack front with a between 36 mm and 58 mm. Continuous line: the mean of all these values

In figure 5, the experimental evolution of the variance is given. One notices that:

1. The values for several front oscillates around the mean value during propagation. This corresponds to fluctuations of each position of the front around a steady state situation, due to the heterogeneities.

2. The steady state situation observed is also in agreement with the long time behavior of the variance found in equation (15).

3. The mean value varies linearly with z as predicted by equation (15). Hence one retrieves a roughness exponent of $\xi = 0.5$.

4 Conclusion

We considered a semi-infinite crack embedded in an infinite elastic medium subjected to traction line loading on its faces. Using Bueckner-Rice weight function theory for this geometry (elastic line model), the power spectrum and the variance

of the crack fluctuations arising from small toughness fluctuations has been derived analytically. In particular, a roughness exponent of $\xi = 0.5$ has been found in contradiction with some previous numerical works but in agreement with the results found by [10] in the case of small roughness amplitude toward the correlation length of the thoughness fluctuations.
In spite of the approximations made in the theoretical modelization (finite geometry replaced by infinite one, uniform displacement loading along the line replaced by uniform force loading), one recovers at least qualitatively the experimental behavior in particular for the steady state situation and for the value of the roughness exponent.

References

[1] H. F. Bueckner. Weight functions and fundamental fields for the penny-shaped and the half-plane crack in three-space. *International Journal of Solids and Structures*, 23(1):57–93, 1987.

[2] P. Daguier, E. Bouchaud, and G. Lapasset. Roughness of a crack front pinned by microstructural obstacles. *EPL (Europhysics Letters)*, 31(7):367–372, 1995.

[3] A. Delaplace, J. Schmittbuhl, and K. J. Måløy. High resolution description of a crack front in a heterogeneous plexiglas block. *Physical Review E (Statistical Physics, Plasmas, Fluids, and Related Interdisciplinary Topics)*, 60(2):1337–43, 1999.

[4] E. Favier, V. Lazarus, and J.-B. Leblond. Statistics of the deformation of the front of a tunnel-crack propagating in some inhomogeneous medium. *Journal of the Mechanics and Physics of Solids*, 54(7):1449–1478, 2006.

[5] E. Katzav and M. Adda-Bedia. Roughness of tensile crack fronts in heterogenous materials. *Europhysics Letters*, 76(3):450–456, 2006.

[6] N. Pindra, V. Lazarus, and J.-B. Leblond. Slight in-plane perturbation of a system of two coplanar parallel tensile slit-cracks. In 9 au 12 septembre à Gdansk, editor, *SolMech2008*, 2008.

[7] J. R. Rice. First-order variation in elastic fields due to variation in location of a planar crack front. *ASME Journal of Applied Mechanics*, 52(3):571–579, 1985.

[8] J. Schmittbuhl and K. J. Måløy. Direct observation of a self-affine crack propagation. *Physical Review Letters*, 78(20):3888–91, 1997.

[9] J. Schmittbuhl, S. Roux, J. P. Vilotte, and K.-J. Maloy. Interfacial crack pinning: effect of nonlocal interactions. *Physical Review Letters*, 74(10):1787–1790, 1995.

[10] J. Schmittbuhl and J.-P. Vilotte. Interfacial crack front wandering: influence of quenched noise correlations. *Physica A*, 270(1-2):42–56, 1999.

Crackling dynamics during the failure of heterogeneous material: Optical and acoustic tracking of slow interfacial crack growth

S. Santucci[1,2,3], M. Grob[4], R.Toussaint[4,5], J. Schmittbuhl[4,5], A. Hansen[6], K. J. Måløy[1]

[1]Physics Dpt, Oslo University, Norway; [2]Physics of Geological Processes, Oslo University, Norway; [3] Laboratoire de Physique, Ecole Normale Superieure de Lyon, Lyon, France; [4]Institut de Physique du Globe de Strasbourg, Strasbourg, France;[5]EOST, University of Strasbourg, Strasbourg, France; [6] Physics Dpt, NTNU, Trondheim, Norway;

1. Introduction

The failure of heterogeneous materials has been extensively studied in the recent past (see the recent reviews [1, 2] and references therein). Those various studies have been motivated by the numerous practical benefits to many engineering fields, but also by the fundamental questions brought forward in particular in statistical physics [1, 2]. Indeed, they belong clearly to a more general framework concerning the dynamics of elastic disordered systems, concerning many different physical situations, such as crack fronts [3, 4], magnetic domain walls in disordered ferromagnets [5], or wetting contact lines on rough substrates [6], where elasticity and disorder are competing to shape the interface.
A fracture front propagating in a 3d heterogeneous medium has itself a 3-d shape with different in-plane and out-of-plane roughnesses, denoted respectively $\zeta_{||}$ and $\zeta_{\perp}$. In order to simplify this problem and shed some light on the interactions between the crack front and material heterogeneities, a simplification to a two dimensional configuration — an interfacial crack, where the crack front is constrained to propagate within a weak heterogeneous plane of a 3d block — has been proposed both experimentally [7, 8] and theoretically [4].

In this work, we will focus on this simpler configuration, studying both the structure and the dynamics of those planar cracks. Indeed, using a transparent material and both a high resolution fast camera and two microphones, the detailed complex crack dynamics can be fully captured. Indeed we can follow the propagation of the crack front along a weak heterogeneous plane of a transparent block with a high precision both in time and space.
First, we will show that the fracture front displays a complex, jerky dynamics also called "Crackling Noise": the fracture dynamics is governed by irregular avalanches with very large size and velocity fluctuations. We characterized the intermittent dynamics observed - the local pinnings and depinnings of the crack front- by measuring both the acoustic emission and the local waiting time fluctuations along the crack front during its propagation.
Then, we will focus on the morphology of the interfacial crack fronts - at rest, in order to obtain a high resolution in the description of those interfaces - by studying in details the scaling properties of the front.

2. A complex dynamics: "Crackling Noise"

2.1 Experimental set-up and method

We describe here experiments where two Plexiglas plates are annealed together to create a single block with a weak interface, as shown on Fig. 1. (for more details see [7-10]). The Plexiglas plates have the following dimensions: the main plate is 16 cm long, 14 cm large and 1 cm thick; the other ones are a set of 17 cm long, 0.4 cm thin and 1 cm wide bands. Before annealing, both plates are sandblasted on one side with 200 μm large glass beads. Sandblasting introduces a random topography which induces local toughness fluctuations during the annealing procedure. Another consequence of the blasting process is that the transparency of the Plexiglas plates is lost: light scatters because of the microstructures created. However, after annealing, the newly formed block recovers its transparency, since the contrast of the refraction index along the interface disappears, allowing a direct observation of the crack interface when opening the block in mode 1.

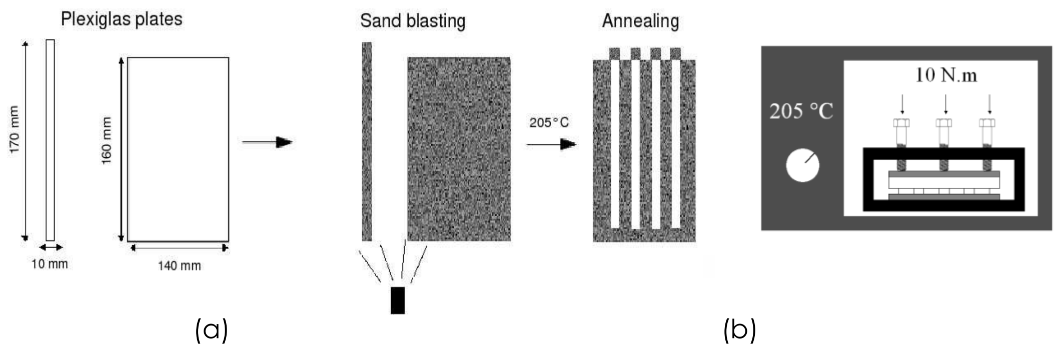

Figure 1: Sample preparation procedure. The Plexiglas plates are sand-blasted and sintered together to form new single blocks. (a) The blasting procedure creates roughness fluctuations on the plate surface that control the local toughness during the annealing process. It also induces a loss of transparency by unpolishing the surfaces. Transparency is however recovered thanks to the sintering process. (b) Sintering process: in white, the PMMA sample; in gray, the two aluminum plates; in black, the solid frame with the screws to apply a torque of = 10 N.m. The whole block is put in an oven at 205°C during 30 minutes.

Then, we impose a normal displacement at a constant speed (between 1 μm/s up to 100 μm/s) to the lower plate, resulting in stable crack propagation in mode I. A sketch of the experimental set-up is shown in Fig. 2. Using a high speed camera (Photron Ultima) mounted on top of a microscope, up to 12288 consecutive images of the crack advance can be recorded with a spatial resolution of 1024 x 512 pixels (1 pixel ≈ 10 x 10 μm2) at an acquisition rate of 1000 frames per second (fps). It is important to notice that the width of the image acquired by the fast camera is adjusted to the width of the PMMA band, and therefore we can capture the full dynamics of the front. Moreover using two contact microphones (Wide Band acoustic sensors in the ultrasonic range 100kHz - 1MHz), placed on top of the thick Plexiglas plate, on the sides of the band, we record simultaneously at an acquisition rate of 1MHz the acoustic emissions during the propagation of the crack.

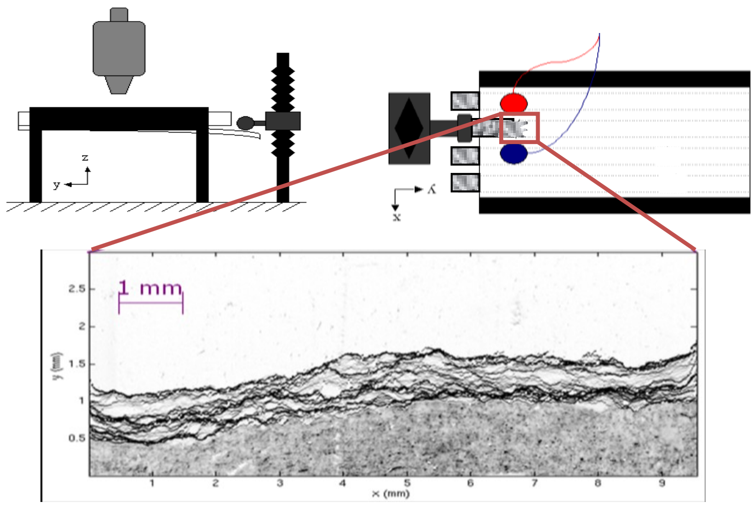

Figure 2: Sketch of the experimental setup (top left: side view; top right: view from above). The thick plate of the sample (in white) is clamped into a rigid aluminum frame (in black). A cylindrical rod imposes a displacement of the thin Plexiglas band at a constant speed. The crack propagates in the y direction and is observed from above using a high speed camera mounted on a microscope. Moreover, using two microphones, placed on top of the thick Plexiglas plate on the sides of the band, we can record simultaneously the acoustic emissions during the propagation of the crack. The figure shows a typical image recorded by the high resolution fast camera during an experiment with an average crack front speed ‹V› ≈ 200 µm/s. We superimpose 6000 fronts recorded at an acquisition rate of 1000 fps.

2.2 A complex intermittent dynamics: "Crackling Noise"

On Fig.2, we show a typical image recorded by the high resolution fast camera during an experiment with an average crack speed ‹V› ≈ 200 µm/s. Moreover, we superimpose on the same figure 6000 fronts recorded by the fast camera at a frame rate of 1000 fps. The spatially random toughness along the weak interface generates a rough crack line in pinning the crack front, and triggers a rich burst activity on a wide range of length scales. The various regions of gray levels (the darker parts show the longer waiting time) reveal this complex dynamics.

We characterized the intermittent dynamics observed, i.e. the local pinnings and depinnings of the crack front by measuring the local waiting time fluctuations along the interface during its propagation [10]. This analysis allowed us to define local velocity at each point of the front during its propagation, and finally avalanches or quakes, as clusters of large local velocities.

On Fig.3, we show the spatio-temporal map of the local velocity of the front, suggesting once again an intermittent dynamics on a wide range of temporal and length scales. These (optically detected) quakes can be ranked in catalogs with analogous characteristics to seismicity catalogs (epicenter location, time of occurrence and rupture area of each quake). Interestingly, in a recent work [11], we have shown that the spatial and temporal distributions of the events for our experimental quake catalogs share similar statistical features to those observed for large scale, real seismicity data, suggesting a tight link between this laboratory experimental model and natural events.

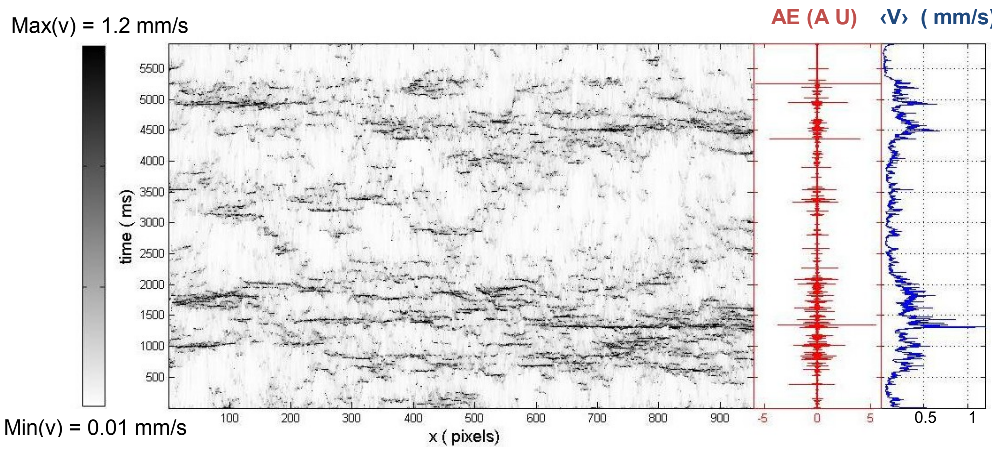

Figure 3: (a) Spatio-temporal of the local velocity of the crack front during its propagation within the weak heterogeneous plane of the Plexiglas block at an average speed of ‹V› ≈ 200 µm/s. (b) Acoustic emissions continuously recorded by one contact microphone, output signal in volts (Arbitrary Units) (Wide Band acoustic sensor 100kHz - 1MHz) at 1MHz during the crack propagation. (c) The average crack front speed shows an intermittent dynamics.

We also show on Fig 3. an acoustic signal that was acquired continuously (during the same experiment) at a rate of 1 MHz using a wide-band acoustic sensor in the ultrasonic range 100kHz-1MHz. We clearly observe a qualitative correlation between the acoustic activity and the propagation of the front. Work is in progress in order to build catalogs of acoustic events, pursuing the statistical analysis of both acoustic and optical bursts in order to investigate in detail the correlation between the acoustic emissions and the propagation of the front. In particular, we are currently measuring the acoustic energy released for each optical events and comparing their statistical features.

2.3 An ideal experimental system

We have shown here that our experimental set-up allows to fully capture the complex crackling dynamics of a fracture front propagating along a weak heterogeneous interface. We used a double experimental technique developing a simultaneous acoustic and optical tracking of the failure of the block. This experimental study appears relevant both in Earth sciences and statistical physics. Indeed, it is an ideal system for testing the various theoretical description proposed in the literature [12-14] in order to clarify the role of the disorder and in particular the elastic interactions between the heterogeneities within the material which give rise to such a complex intermittent behavior.

After studying the crackling dynamics of interfacial crack fronts, let us examine now the morphology of those interfaces.

3. A complex morphology
- Different self-affine behavior at small and large scales-

3.1 Motivation

Since the pioneering work of Mandelbrot et al [15] revealing the self-affine character of fracture surfaces of metals, numerous studies have been devoted to the morphological properties of crack surfaces (see the reviews [1, 2]). In particular, the roughness exponent characterizing this self-affinity was shown to be very robust and further on conjectured to be Universal [1, 16, 17]. This apparent Universality led to interpret the fracture of heterogeneous materials within the framework of critical phenomena [1, 18]- following the work of Ertas and Kardar for a very different system i.e. the motion of vortex lines in superconductors [19]. In this approach, the failure of heterogeneous material appears as a depinning transition of an elastic line through a disordered landscape, and the crack surface corresponds to the trace left by the front during its propagation.

Although qualitatively appealing, this description failed to reproduce quantitatively the scaling exponents experimentally observed and therefore triggered an upsurge of studies [1]. Despite the plethoric literature concerning the morphology of rough crack surfaces, a clear understanding of the role of material heterogeneities leading to those self-affine long range correlations is still lacking, with up to now an apparent disagreement between the scaling exponents obtained both theoretically and numerically and those measured experimentally [1, 2, 4, 7, 8, 20, 21, 22]. In particular, the morphological properties of in-plane cracks - which were proposed to simplify the original 3d problem remain a very controversial issue. Indeed, the in-plane roughness exponent measured experimentally till now ζ^{exp}~0.6 [7, 8, 23] is significantly larger than the one predicted either theoretically via renormalization group calculations or numerical simulations ζ^{th}~0.39 [4, 20, 21, 22]. A percolation-like approach recently proposed [12, 13] to account for the local damage ahead of the crack front was able for the first time to reproduce the scaling behavior of those interfacial fronts. However, this description has been tremendously debated [24, 25].

Therefore, it appears of crucial importance to clarify this controversy by obtaining a clear and detailed experimental description of the scaling behavior of those planar cracks.

3.2 Experimental set-up and method

We will focus here on the morphology of the interfacial crack fronts at rest in order to obtain a high resolution description of the height fluctuations of the interface. The experimental set-up is identical to the one described in the previous section. We just changed the dimensions of the Plexiglas plates (32 cm x 14 cm x 1 cm and 34 cm x 12 cm x 0.4 cm), and the loading procedure: we impose a normal displacement to the lower plate, resulting in a stable crack propagation in mode I; when the front has advanced of a few millimeters (typically 5 mm), the plate is unloaded in order to arrest the front. Then, we take high resolution pictures of the crack interface using a Nikon camera (3871 x 2592 pixels) mounted on a microscope, placed itself on a translation stage that can move in the direction parallel and perpendicular to the propagation plane (x,y). During each loading stop, the table is translated along the front x-axis, and neighboring pictures are taken.

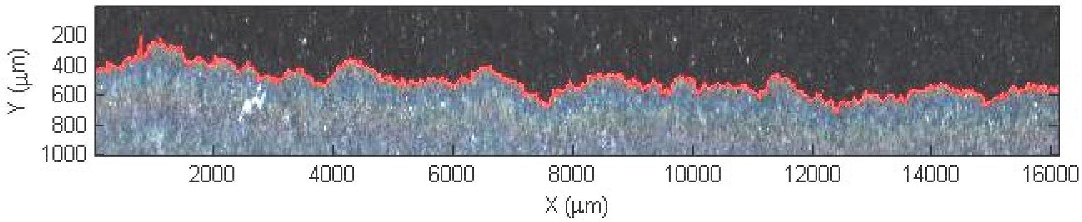

Figure 1 : Assembling up to 15 high resolution pictures of an interfacial crack front at rest provides a large front description with around 16 000 data points and a pixel size of 1 μm.

The assemblage of up to 15 high resolution pictures of an interfacial crack front at rest provides a large front description with around 16 000 data points and a pixel size of a = 1 μm. This procedure was repeated 20 times in order to obtain 20 different and independent fracture fronts. The total length of each analyzed crack was around 16 mm, with a typical example shown on Fig.1. Finally, in order to modify the heterogeneities within the weak plane of the block, we prepared different samples using glass beads of different diameters during the sand-blasting procedure, respectively $Ø_1 \sim 50$ μm and $Ø_2 \sim 200$ μm.

3.3 A complex self-affine behavior

We aim at characterizing the scaling properties of the height fluctuations of the interfacial crack fronts $\Delta h(\delta) = h(x+\delta) - h(\delta)$. On Fig. 4, we plot the standard deviation σ of the height fluctuations $\Delta h(\delta)$ of the crack interfaces as a function of the scale δ for samples roughened with glass beads of diameter $Ø_2 \sim 200$ μm during the blasting procedure.

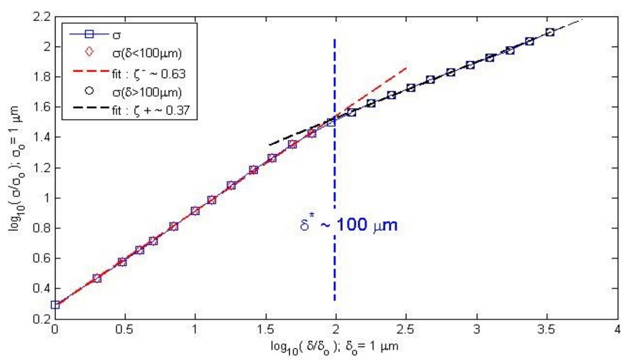

Figure 2 : Scaling behavior of interfacial crack fronts at rest. We plot the standard deviation σ of the height fluctuations Δh(δ) of the crack interfaces as a function of the scale δ. The glass beads used for preparing the samples – blasting and roughening of the Plexiglas plates – had a diameter of $Ø_2 \sim 200$ μm.

At small scales, below $\delta^* \sim 100$ µm, we observe a self-affine scaling behavior $\sigma(\delta<\delta^*) \sim \delta^{\zeta-}$ with a roughness exponent around $\zeta^- \sim 0.63$ which is in agreement with previous observations [7, 8] and the percolation-like approach recently proposed [12, 13] to account for the local damage ahead of the crack front.
However, interestingly, at scales larger than $\delta^* \sim 100$ µm, we observe a cross-over to another scaling regime $\sigma(\delta > \delta^*) \sim \delta^{\zeta+}$ with a smaller roughness exponent $\zeta^+ \sim 0.37$. It is important to emphasize that this is the first time that such a scaling regime is reported for in-plane crack fronts. Moreover, this value appears in agreement with the prediction of a depinning model [4, 20, 21, 22].
In order to analyze in more details this scaling behavior at large scales, we define height fluctuations at a given scale as $\Delta h(\delta,x)=h(x+\delta)-h(x)$, and propose to examine the statistical distribution of the height fluctuations $P[\Delta h(\delta)]$ on that range of scales $\delta > \delta^* \sim 100$µm .

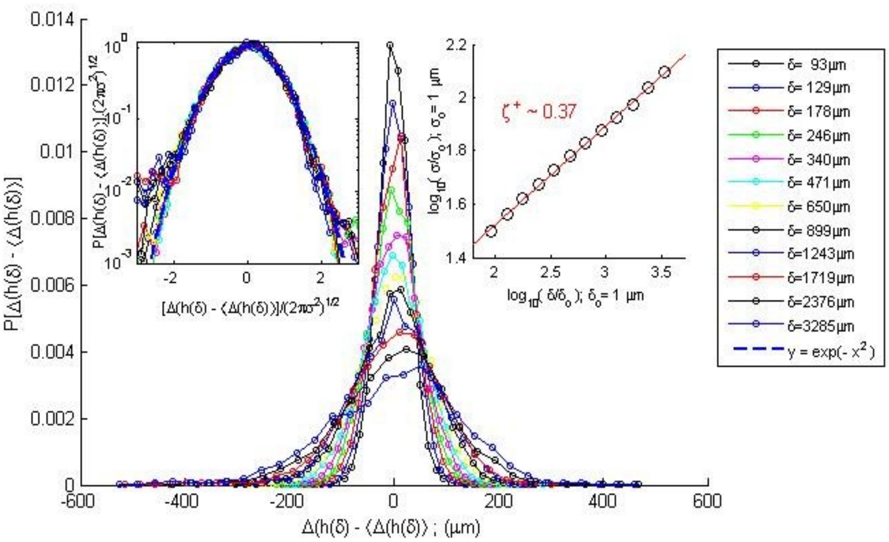

Figure 3 : Statistical distributions of the height fluctuations $\Delta h(\delta)$-$\langle\Delta h(\delta)\rangle$, for logarithmically increasing length scales δ. We observe on that range of scales (δ ≥ 100 µm) that the statistical distributions $P[\Delta h(\delta)-\langle\Delta h(\delta)\rangle]$ follow a Gaussian shape, with a width increasing with the range of scales studied δ. The self-affine behavior of those distributions enters through the scaling behavior of the standard deviation σ of the height fluctuations $\Delta h(\delta)-\langle\Delta h(\delta)\rangle$, $\sigma \sim \delta^{\zeta+}$, with a roughness exponent $\zeta^+ \sim 0.37$, as we can observe on the inset top-right. The Gaussian statistics is confirmed in the figure top-left where we observe a collapse of all the various distributions when plotting on a semilog scale $P[\Delta h(\delta)-\langle\Delta h(\delta)\rangle].(2\pi\sigma^2)^{1/2}$ as a function of $[\Delta h(\delta)-\langle\Delta h(\delta)\rangle]/(2\pi\sigma^2)^{1/2}$. The blue dotted line represents the curve $y=\exp(-x^2)$ and fits perfectly the experimental rescaled distributions.

It is important to remark that our experimental data set is large enough to perform such a direct reliable measurement. In Fig.2, we show the distributions of the height fluctuations for logarithmically increasing length scales δ. On that range of scales, above δ^*, $\delta>\delta^*\sim100\mu m$, we clearly observe that the distributions $P[\Delta h(\delta)]$ follow a Gaussian statistics. The self-affine character of the height fluctuations of the fronts appears through the scaling behavior of the standard deviation σ of those distributions $P[\Delta h(\delta)]$, $\sigma \sim \delta^{\zeta+}$ with a unique roughness exponent $\zeta^+ \sim 0.37$.

3.4 Effect of the disorder and the material microstructure

Let us now examine and discuss the crossover length scale δ^* separating the large and small scale behavior of the height fluctuations. In order to check the effect of disorder and material microstructure on the scaling behavior of the interfacial crack fronts, we modified the heterogeneities within the weak plane of the block, preparing different samples using glass beads of different diameters $Ø_1 \sim 50$ µm and $Ø_2 \sim 200$ µm for the blasting procedure.

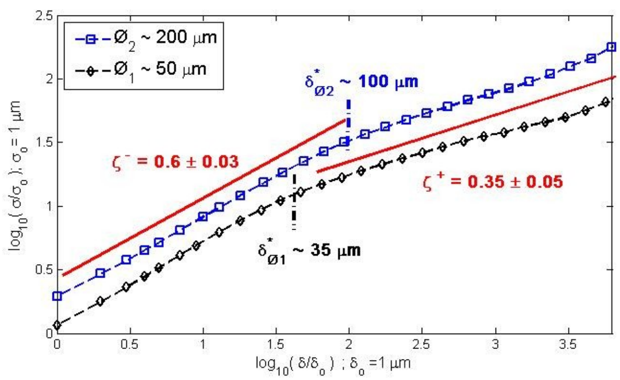

Figure 4 : Effect of disorder on the self-affine scaling of interfacial crack fronts. We plot the standard deviation σ of the height fluctuations Δh(δ) of the crack interfaces as a function of the scale δ. We analyzed two different sets of data, prepared with glass beads of different diameters respectively $Ø_1$~50µm and $Ø_1$~200µm.

We show on Fig.4. the scaling behavior of the interfacial crack fronts for those different samples. We observe mainly the same features as on previous figure with the two different scaling behaviors separated by a characteristic size respectively $\delta^*_{Ø1} \sim 35$ µm, and $\delta^*_{Ø2} \sim 100$ µm. It is important to note that the scaling regime at small scales up to the characteristic sizes $\delta^*_{Ø1}$ and $\delta^*_{Ø2}$ can be associated to the material heterogeneities. Indeed, when using larger glass beads for roughening the Plexiglas plates, the amplitude of the height fluctuations of the fronts increases (vertical shift of the blue curves) as well as the scaling range at small scales, providing a roughness exponent $\zeta^- \sim 0.6$ up to the scale $\delta^*_{Ø2} \sim 100$ µm. It is important to notice that those results appear by analogy, in agreement with recent experimental observations on 3-d fracture surfaces of phase separated glasses [26]. However, more work is needed, in order to obtain a characterization of the disorder produced by the indentation impacts during the blasting process and finally to be able to compare this typical size δ^* (separating the two different scaling regimes) with the typical scale of the heterogeneities. In particular, it appears important to study the influence of the crack growth velocity, the mechanical properties of the plates on this typical size $\delta^*$and its eventual link to the damage process zone [27].

4. Conclusion

Finally, we can conclude by insisting on the fact that our high resolution experimental set-up allows to obtain a detailed description of the failure of heterogeneous materials. Indeed, we can fully capture the crack dynamics by observing directly the interface with a high resolution fast camera, and recording simultaneously the acoustic emissions during the front propagation along a weak heterogeneous plane of a transparent Plexiglas block.

The role of heterogeneities during crack propagation is of central importance since they induce local pinnings of the crack front and subsequently trigger a very complex burst activity, characterized by avalanches, spanning over a broad range of temporal and length scales. This intermittent dynamics also called "crackling noise" is also suggested from the acoustic emission accompanying the failure process. Another consequence of this phenomenology is the roughness of fracture surfaces left by the crack. Indeed, cracks in heterogeneous media exhibit a self-affine morphology, with long range correlations. In particular, we have shown here that the interfacial crack fronts follow different scaling regime at small and large scales. For scales larger than a typical size δ^*, that could be interpreted as a characteristic size of disorder, we observed a self-affine regime with a roughness exponent $\zeta^+ = 0.35 \pm 0.05$ much smaller than the value measured up to now and observed here at small scales $\zeta^- = 0.6 \pm 0.03$. Those different scaling regimes can be understood within the framework of recent statistical models [28].

5. References

[1] E. Bouchaud, J. Phys. Condens. Matter, volume 9, 4319, (1997).

[2] M. Alava, P.K.V.V Nukala, and S. Zapperi, Adv. Phys., 55, 349, (2006).

[3] H. Gao and J. R. Rice, J. Appl. Mech. 56, 828 (1989).

[4] J. Schmittbuhl, S. Roux, J.P. Vilotte, and K.J. Maloy, Phys. Rev. Lett. 74, 1787 (1995);

[5] G. Bertotti, G. Durin, and A. Magni, J. Appl. Phys. 75,5490 (1994); G. Durin and S. Zapperi, Phys. Rev. Lett. 84, 4705 (2000).

[6] D. Ertas and M. Kardar, Phys. Rev. E 49, R2532 (1994); E. Rolley, C. Guthmann, R. Gombrowicz, and V. Repain, Phys. Rev. Lett. 80, 2865 (1998);

[7] J. Schmittbuhl and K. J. Måløy, Phys. Rev. Lett. 78, 3888, (1997).

[8] A. Delaplace, J. Schmittbuhl, and K. J. Måløy, Phys. Rev. E 60, 1337 (1999).

[9] K. J. Måløy and J. Schmittbuhl, Phys. Rev. Lett. 87,105502 (2001).

[10] K. J. Måløy, S. Santucci, J. Schmittbuhl, and R. Toussaint, Phys. Rev. Lett. 96, 045501, (2006);

[11] M. Grob, J. Schmittbuhl, R. Toussaint, L.Rivera, S. Santucci, K. J. Måløy to be published in Pure Appl. Geophys. (2008) .

[12] A. Hansen and J. Schmittbuhl, Phys. Rev. Lett. 90, 045504 (2003).

[13] J. Schmittbuhl, A. Hansen, and G. G. Batrouni, Phys. Rev. Lett. 90, 045505 (2003).

[14] D. Bonamy, S. Santucci, L. Ponson, PRL 101, 045501 (2008).

[15] B. B. Mandelbrot, D. E. Passoja, and A. J. Paullay, Nature (London) 308, 721 (1984);

[16] E. Bouchaud, G. Lapasset, and J. Planes, Europhys. Lett. 13, 73 (1990).

[17] K. J. Måløy, A. Hansen, E. L. Hinrichsen, and S. Roux, Phys. Rev. Lett. 68, 213 (1992).

[18] O. Narayan and D. S. Fisher, Phys. Rev. B 48, 7030 (1993).

[19] D. Ertas and M. Kardar, Phys. Rev Lett. 69, 929 (1992);

[20] S. Ramanathan, D. Ertas, D. Fisher, Phys. Rev. Lett. 79, 873 (1997).

[21] A. Tanguy, M. Gounelle and S. Roux, Phys. Rev. 58, 1577 (1998);

[22] A. Rosso and W. Krauth, Phys. Rev. E {\bf 65}, 025101(R) (2002);

[23] P. Daguier, E. Bouchaud and G. Lapasset, Europhys. Lett., 31 (7), pp. 367-372 (1995)

[24] M. Alava and S. Zapperi, Phys. Rev. Lett. 92, 049601 (2004).

[25] J. Schmittbuhl, A. Hansen, and G. G. Batrouni, Phys. Rev. Lett. 92, 049602 (2004).

[26] D. Dalmas, A. Lelarge and D. Vandembroucq, arxiv:0712.4197.

[27] S. Morel D. Bonamy, L. Ponson, and E. Bouchaud, Phys. Rev. E 78, 016112 (2008).

[28] S. Santucci, M. Grob, R. Toussaint, J. Schmittbuhl, A. Hansen, K. J. Måløy, to be submitted

Pure appl. geophys. 166 (2009) 777–799
0033–4553/09/050777–23
DOI 10.1007/s00024-004-0496-z

Pure and Applied Geophysics

Quake Catalogs from an Optical Monitoring of an Interfacial Crack Propagation

M. Grob,[1] J. Schmittbuhl,[1] R. Toussaint,[1] L. Rivera,[1] S. Santucci,[2,3] and K. J. Måløy[3]

Abstract—Using an experimental setup which allows to follow optically the propagation of an interfacial crack front in a heterogeneous medium, we show that the fracture front dynamics is governed by local and irregular avalanches with large velocity fluctuations. Events defined as high velocity bursts are ranked in catalogs with analogous characteristics to seismicity catalogs: time of occurence, epicenter location and energy parameter (moment). Despite differences in the fracturing mode (opening for the experiments and shear rupture for earthquakes), in the acquisition mode and in the range of time scales, the distributions of moment and epicenter jumps in the experimental catalogs obey the same scaling laws with exponents similar to the corresponding distributions for earthquakes. The record-breaking event analysis also shows very strong similarities between experimental and real seismicity catalogs. The results suggest that the dynamics of crack propagation is controlled by the elastic interactions between microstructures within the material.

Key words: Crack front dynamics, asperity, microseismicity catalogs, analog model.

1. *Introduction*

In observational seismology, attempts to characterize earthquake ruptures have motivated numerous studies from the very early stages (Reid, 1910). The description of small earthquakes is often reduced to a source-point description given by a set of simple parameters: time of occurrence, source location, seismic moment or magnitude, possibly focal mechanism (Clinton *et al*., 2006). Despite this crude information, organized in well-known seismic catalogs, these simple parameters have provided extremely useful earthquake features like the Gutenberg-Richter magnitude-frequency relationship (Gutenberg and Richter, 1944). A complementary approach is to analyze the properties

[1] Institut de Physique du Globe de Strasbourg, UMR 7516 CNRS, EOST/Université de Strasbourg, 5 rue René Descartes, F-67084 Strasbourg Cedex, France.
[2] Physics of Geological Processes, University of Oslo, PO Box 1048, Blindern, N-0316 Oslo, Norway.
[3] Physics Institut, University of Oslo, PO Box 1048, Blindern N-0316 Oslo, Norway.

of interactions between earthquakes (Bak *et al.*, 2002; Kagan, 2002; Ziv *et al.*, 2003; Corral, 2004; Davidsen and Paczuski, 2005; Bizzarri and Belardinelli, 2008). It has been shown for instance that the spatiotemporal evolution of earthquakes in a specific region exhibits a fractal pattern resulting from a dynamical process and expressing a hierarchical organization of events in space and time (Marsan *et al.*, 2000; Davidsen *et al.*, 2006).

Seismic inversions of slip history during large earthquakes have been an important step in the description of the rupture process (Wald *et al.*, 1991; Bouchon *et al.*, 2000). The complete fault region associated to the earthquake is then considered. Slip history inversions provide important features of the rupture propagation: fault geometry, rupture length, rupture speed, time rise, rupture width, etc. However, they rely on strong assumptions like simple fault models for kinematic inversions (Kikuchi and Kanamori, 1991) or simple friction processes for dynamic inversion (Ide and Takeo, 1997; Fukuyama *et al.*, 2003) and subsequently provide low resolution or speculative images of the rupture complexity. Statistics from these inversions however allow more precise statistical relationships such as the ones linking the seismic moment M_0 to the three geometric quantities characterizing the rupture: Its length L, its width W and the average slip on the fault u (Kanamori and Anderson, 1975; Wells and Coppersmith, 1994; Mai and Beroza, 2000). In general, all these relationships can be approximated by a power law and exponents are found to be mostly universal (Scholz, 2002; Kagan, 1999). New tools to account for the full complexity of the earthquake rupture are required and under development (Mai and Beroza, 2002; Aochi and Fukuyama, 2002; Tinti *et al.*, 2005; Rubin and Ampuero, 2007).

Fracture complexity has also been addressed in the mechanical community, particularly since the pioneer work of Mandelbrot *et al.* (1984). In particular, scaling properties of fractures in heterogeneous materials were discovered (Bouchaud, 1997). For instance, the roughness of fracture surfaces in heterogeneous media exhibits a self-affine morphology. The associated roughness exponent is found to be very robust for different materials such as steel or aluminium alloy (Måløy *et al.*, 1992; Bouchaud *et al.*, 1993) or fault rocks (Schmittbuhl *et al.*, 1993, 1995). Experiments were also carried out to investigate the interactions between the crack front and the material heterogeneities (Daguier *et al.*, 1995). In a simplified two-dimensional configuration, studies of the crack front that is constrained geometrically in a plane, both theoretically (Schmittbuhl *et al.*, 2003a, 2003b) and experimentally (Schmittbuhl and Måløy, 1997; Delaplace *et al.*, 1999) were performed. The front line morphology is shown to exhibit scaling invariances (Schmittbuhl and Måløy, 1997; Delaplace *et al.*, 1999; Santucci *et al.*, 2007). More recent studies were performed to describe the crack front dynamics (Schmittbuhl *et al.*, 2001; Santucci *et al.*, 2006; Måløy *et al.*, 2006). These works show that the crack propagation is controlled by the pinning and depinning of the front owing to local asperities. The fracture front dynamics is then governed by local and irregular avalanches of varying sizes and velocities.

In this article, we propose a link between the fracture dynamics analyzed at the laboratory scale and the earthquake dynamics extracted from a subset of the Southern California catalog (SHLK catalog). The core of the study is the construction of laboratory-scale catalogs of events or quakes from an optical monitoring of an interfacial crack front propagation in a heterogeneous medium. Using a transparent material (Plexiglas), the experimental setup allows to follow visually at high spatial resolution and continuously in time, the rupture process. The first part of the paper describes the sample preparation and how the experimental setup works. The next section explains the image processing of the raw crack front pictures in order to obtain the parameters needed to build the quake catalogs made of several thousands of events. Since we aim at comparing our experimental results to natural seismicity data, we show in a following section the results of statistical tools typically applied to natural seismicity data when applied to the experimental data. Finally a discussion of the reliability of analogies or differences between experimental and natural data is proposed.

2. *An Interfacial Rupture Experiment*

2.1. *Sample Preparation*

The samples are built from two types of transparent polymethylmethacrylate (PMMA) plates: The main plate is 16-cm long, 14-cm large and 1-cm thick; the others are a set of 17-cm long, 0.4-cm thin and 1-cm wide bands. One surface of each plate is first sand-blasted with glass beads of diameter ø = 200 μm or 500 μm. The thick plate is then assembled to a set of four thin plates (see Fig. 1(a)), sand-blasted surfaces facing each other, and placed under a normal homogeneous load, so that the remaining air is expelled from the contact area when the PMMA sandwich is loaded. The loading frame for the sample preparation is made of two parallel aluminium plates between which the Plexiglas plates sandwich is placed. Twelve screws are used to exert a normal load on the sample (see Fig. 1(b)). The torque applied when tightening the screws is equal to 10 N.m.

To anneal the plate assembly, the whole block (sample + press) is put in an oven at 205°C during 30 minutes, which allows the Plexiglas plates to adhere. The thermal annealing process produces a cohesive interface along the former boundary between the two plates which is weaker than the bulk PMMA (the critical stress intensity factor K_c, also called fracture toughness, for the growth of our interfacial crack is around 40 kPa.m$^{1/2}$, more than 55 times smaller than in the bulk). Thus this sample preparation constrains the block to break along an interfacial fracture during mode I crack. Figure 1 summarizes the sample preparation procedure.

An important feature of the interface preparation is the sand-blasting procedure that induces a random topography on the PMMA surface to be annealed and accordingly controls the local toughness during annealing. Another consequence of the sand-blasting technique is that the transparency of the Plexiglas plates is lost: light scatters because of

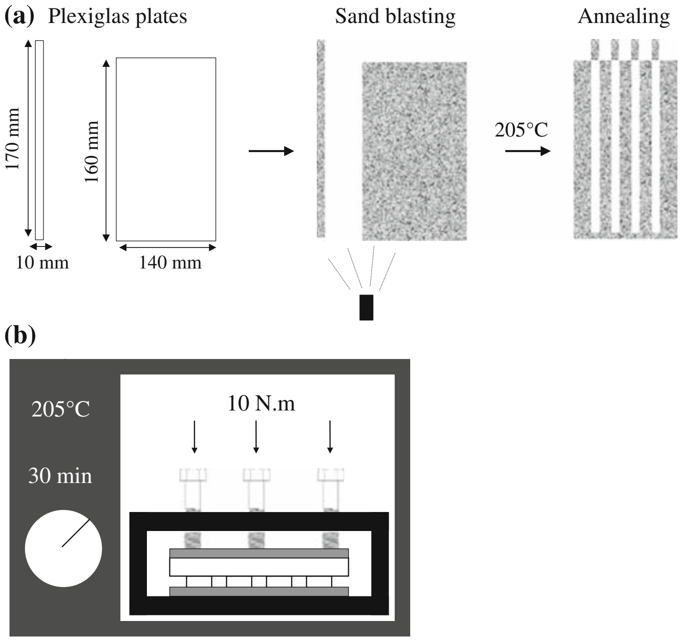

Figure 1
(a) Sample preparation procedure. Plexiglas plates are sand-blasted and sintered together to form a new single block. Sandblasting creates roughness fluctuations on the plate surface that control the local toughness during the annealing process. It also induces a loss of transparency by unpolishing the surfaces. Transparency is however recovered thanks to the sintering process. (b) Scheme of the loading system: In white, the PMMA sample; in gray, the two aluminium plates; in black, the solid frame with the screws to apply a torque $N =$ 10 N.m. The whole block is put in an oven at 205°C during 30 minutes.

the microstructures introduced by the sand-blasting. Nonetheless after annealing, the newly formed block recovers its transparency since contrast of the refraction index along the interface disappears.

2.2. *Setup*

The thick PMMA plate is clamped to a stiff aluminium frame. The thin plates are pulled apart thanks to a rod that presses on the excess length of the thin Plexiglas bands. A diagram of the setup is displayed in Figure 2. The loading translation stage is controlled by a stepping motor that applies a continuous descent of the rod at a speed in the range: 100–200 μm.s^{-1} (in our configuration, the mean crack velocity is proportional to the speed of the rod motion). The normal displacement imposed to the lower Plexiglas plate induces a stable mode I crack propagation along the artificially introduced weak plane of the sample. The crack propagation is stable since the total energy of the system decreases with the crack advance, owing to the plate geometry (it would not be the case

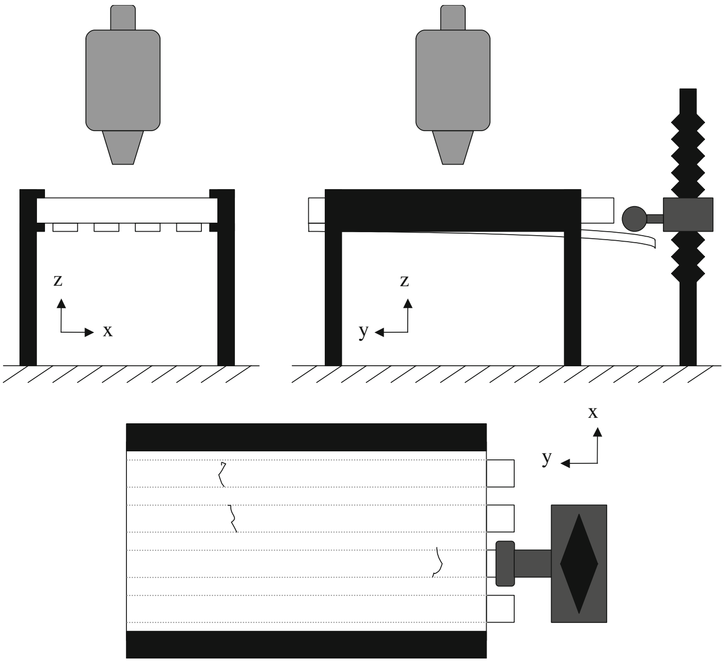

Figure 2
Sketch of the experimental setup (*top left:* Front view; *top right:* Side view; *bottom:* View from above). The thick plate of the sample (in white) is clamped into a rigid aluminium frame (in black). A cylindrical rod imposes a displacement of the thin Plexiglas band. The crack propagates in the y direction and is observed from above using a high speed camera mounted on a microscope (in light gray).

for a crack in an infinite elastic medium). Indeed the energy per unit of front length can be found from simple beam theory (LAWN, 1993):

$$U_E = \frac{Ed^3h^2}{8{c_r}^3}, \tag{1}$$

where E is the Young modulus, d the thickness of the lower plate, h the displacement of the rod and c_r the distance between the position of the crack and the point of application of the loading force. The energy release rate G, also called driving force, is a measure of the mechanical energy for an increment of crack extension, therefore the following expression for the energy release rate can be deduced:

$$G = -\frac{dU_E}{dc_r} = \frac{3Ed^3h^2}{8{c_r}^4}. \tag{2}$$

Equation (2) shows that the energy of the system decreases when the crack extension c_r increases. The fracture is accordingly controlled by the displacement of the loading rod. The loading value to reach for the front to start moving is of the order of a few tens of Newton.

The propagation of the crack front is followed optically with an optical microscope. Using a high-speed camera mounted on top of a microscope, up to 12288 consecutive images of the crack advance can be recorded with a spatial resolution of 1024×512 pixels (1 pixel $\approx 10 \times 10\ \mu m^2$) at an acquisition rate of 1000 frames per second (fps) which corresponds to an acquisition duration of 12 seconds. To provide sufficient light intensity at this small closure time (1 ms), the sample is lighted from below using optical fibers linked to an intense light source. These optical fibers contain lens elements at their end that allow the light source to focus on the crack front. The width of the image acquired by the fast camera is adjusted to the width of the PMMA band. After the opening of the sample, light rescatters in the fractured part of the sample because of the microstructures previously introduced on the PMMA plates. The open part of the sample looks opaque whereas the sintered region is still transparent. The transition between these two areas corresponds to the crack front (see Fig. 3(a)).

3. *Image Processing*

3.1. *Front Extraction*

Images of the interfacial fracture are divided in two parts: A bright zone which is the cracked and open area (microstructures along the interface scatter the light of the newly open surface) and a dark region which is still soldered and transparent. The image processing aims at extracting the shape of the transition zone between the bright and dark areas of the picture which corresponds to the crack front. Some white spots ahead of the fracture front appear on the image (see the dark part of the photo in Figure 3(a)). This is due to flaws created by the sand-blasting but located slightly inside the Plexiglas plates which scatter the light. In an attempt to remove these flaws in the fracture front images, a subtraction of a background picture taken before any opening is performed systematically. An example of the resulting image is displayed in Figure 3(b). Some flaws are still visible, however the contrast has been markedly enhanced. The gray level histogram of the image is clearly bimodal (Fig. 3(c)): The peaks represent the two different regions of the image. The picture is then clipped at the threshold level that separates these two lobes (Fig. 3(d)). The norm of the gradient of the segmented image is computed to search for the boundaries (Fig. 3(e)). Isolated clusters of pixels that might appear are removed by keeping only the largest cluster that percolates from the left to the right edge of the picture (Fig. 3(f)) to obtain the front path. More details about the last four steps of the image processing can be found in Delaplace *et al.* (1999). Figure 3(g) shows the extracted front superimposed on the raw image. A zoom on the preceding picture is done to show the resolution of the extracted front (cf. Fig. 3(h)). The absolute position of the front deduced from the images of the high-speed camera is accurate within 3 to 4 pixels (that is to say within 30 to 40 μm). Indeed the position of the front can move from 1 to 4 pixels if, for instance, the

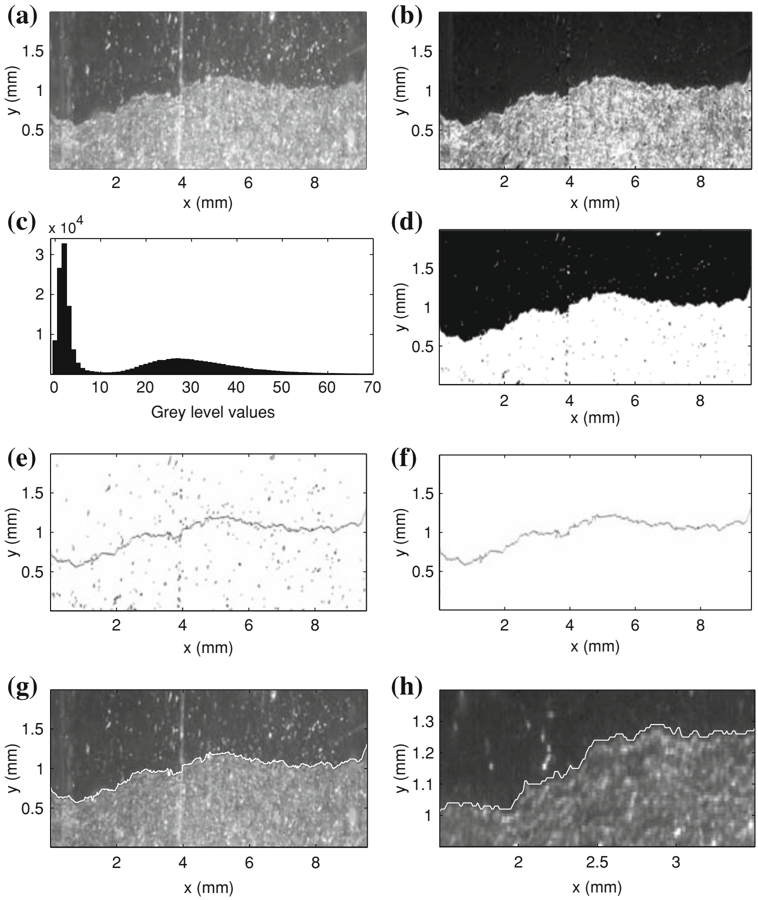

Figure 3
(a) Example of raw image taken with the high speed camera. (b) Example of the resulting picture of a subtraction between two raw images. (c) Gray level histogram of the preceding picture. (d) Image after thresholding. (e) Gradient of the clipped image. (f) Extraction of the percolating cluster from the gradient picture. (g) Extracted front (white line) superimposed on its corresponding raw image. (h) Zoom on the extracted front.

threshold level on the histogram is changed by ± 1, or if the front is defined by the maximum or minimum y position of pixels at a given x along the percolating front (the cluster that goes from one side to the other of the thresholded picture) (DELAPLACE *et al.*, 1999). The relative position along the front is however obtained at a much smaller precision (computed as the difference between the standard deviations of two extracted fronts with a shift in the threshold level) which is around 0.2 μm. Its irregular shape is explained by the fact that the front is pinned by local zones of high toughness during the propagation and becomes rough.

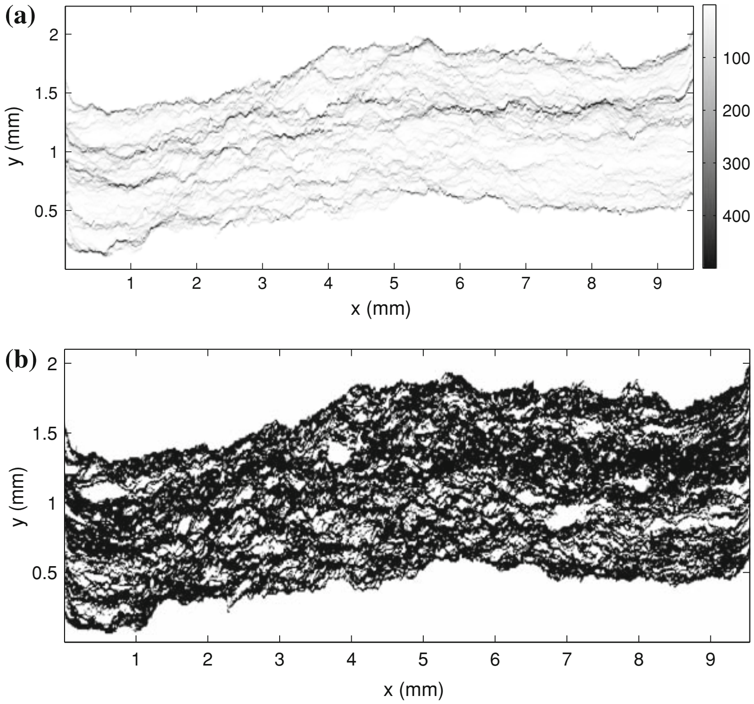

Figure 4
(a) Gray scale map of the waiting time matrix for one experiment deduced from 5908 fronts recorded at a rate of 1000 fps. The darker spots show the longer waiting times. (b) Spatial distribution of clusters (in white) for velocities 10 times larger than the average front speed (here $\langle V \rangle = 214$ μms^{-1}).

3.2. *Quake Definition*

In order to analyze the burst dynamics of the interfacial crack propagation and define rupture quakes, the fracture front lines extracted from image processing are added to form the waiting time matrix W (MÅLØY *et al.*, 2006, 2005). This matrix has the same size as the raw images and initial values equal to zero for all its elements. The value 1 is added to the matrix elements W_{ij} corresponding to pixels where a front line position (x, y) is detected. If several successive fronts are observed at the same particular position, the matrix elements W_{ij} at this position increases by one for each encountered front. This procedure was done for all frames of a given experiment to obtain the final waiting time matrix W (Fig. 4(a)). The waiting times estimate the amount of time during which the front was stuck at a precise position. The local speed of the crack front at the time when it passes a particular position (x, y) can be deduced from W by the inverse value of the corresponding matrix element W_{ij} multiplied by the ratio of the pixel linear size a (typically 10 μm) over the typical time δt between two pictures (0.001 s). The velocity matrix V is therefore defined as $V_{ij} = \frac{1}{W_{ij}} \frac{a}{\delta t}$, thus associating a local crack front speed to

Table 1

Table of parameters for the five experiments described in the article. ø is the diameter of the beads used for the sand-blasting of the sample. Nb stands for number

Experiment	ø(μm)	Duration (*s*)	$\langle V\rangle$ (μms^{-1})	*c* levels	Nb of clusters	Catalog
A	200	5.908	214	5	1990	A1
				10	2454	A2
				20	2583	A3
B	500	8.001	295	3	4756	B1
				7	6423	B2
				10	6321	B3
C	500	6.158	276	4	3736	C1
				10	4709	C2
				13	4623	C3
D	200	9.150	163	8	2290	D1
				11	2248	D2
				15	2168	D3
E	200	7.720	199	6	2995	E1
				14	3755	E2
				18	3827	E3

each pixel of the crack front in each image. It is important to mention that the image recording is performed so fast that there is basically no hole in the waiting time matrix, i.e., no element equal to zero (except below the first front, above the last one, and a few artefacts due to initial flaws in the sample).

In order to define events (or quakes), the velocity matrix V is clipped by setting its elements V_{ij} equal to 1 if $V_{ij} > c\langle V\rangle$ and 0 elsewhere, where c is a constant of the order of a few unities (MÅLØY *et al.*, 2006, 2005). Each region or cluster where the crack penetrates at a front speed larger than a few times the average front velocity is considered as an event or quake. Figure 4(b) is an example of the thresholded matrix with $c = 10$. The white clusters correspond to regions where the crack front speed is 10 times larger than the average front velocity $\langle V\rangle$. These zones are defined as quakes. The clusters connected to the first and last fronts, belonging to the upper and lower white zones in the figure, are excluded from the analysis.

3.3. *Quake Catalogs*

This data processing is applied to five experiments (named A, B, C, D and E) with different parameters. Table 1 summarizes the parameters for all experiments. Three different c values are used to threshold the velocity matrix corresponding to each experiment. We thus have fifteen data sets of events. The aim now is to build catalogs from these data sets that could be compared to real seismicity data catalogs. The most utilized quantities are: The time of occurrence, the location of hypocenter and an energy parameter of the event (seismic moment or magnitude).

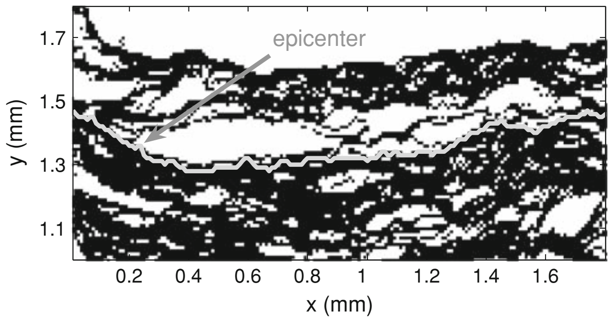

Figure 5
Determination of an epicenter for one event (white cluster) of the experimental catalog. The light gray line is the first front that enters the cluster. The arrow points to the pixel where the front touches the cluster, which defines the epicenter of the event.

For each event of each data set, the time of occurrence is found by searching for the first pixel in time that is attached to the considered cluster (Fig. 5). The time of occurrence t in ms is calculated considering the beginning of the experiment as the original time.

The epicenter of an event is given by the position (x, y) of this first pixel (Fig. 5). As the crack front propagation is constrained in a plane, the z coordinate is considered constant and equal to 0 in a first approximation. As the y axis is the direction of propagation of the crack front, a strong link exists between the time and the y coordinate of the epicenter. Hence the spatial position of the event is mainly given by the x coordinate.

The moment M of an event is given by the area of the event (which is the total number of pixels belonging to the cluster) multiplied by a characteristic opening which is assumed to be constant. The parameter M is then directly proportional to the area of the event. The three parameters t, the couple (x, y) and M, build up a quake catalog for our experiments. In total, fifteen quake catalogs named A1, A2, A3, B1, B2, B3, C1, C2, C3, D1, D2, D3, E1, E2 and E3, were created from the velocity matrix of five different experiments, each thresholded with three various level values (Table 1).

Figure 6 shows the locations of the epicenters of events superimposed on the thresholded velocity matrix for experiment A2. The diameter of the circles representing the quakes is proportional to the logarithm of the area of the clusters. Only events with $\log_{10}(M) > 1.5$ are displayed for a better visibility. The good agreement between the circles and the corresponding cluster contributes to validate the method used to build the catalogs. For a better readability, the logarithm of the moment M is denoted m in the following.

3.4. *Quake Maps*

As first qualitative analyses, some maps are drawn from the catalogs. Figure 7 shows the locations of epicenters for the three experimental catalogs from experiment A and for

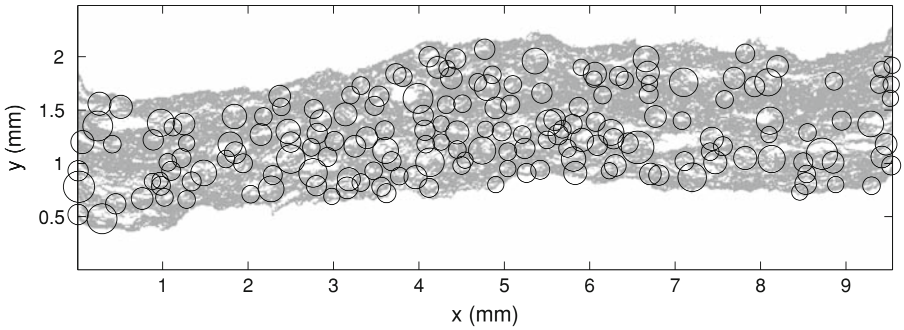

Figure 6
Epicenter localization superimposed on the thresholded velocity matrix for experiment A2. The diameters of the circles are proportional to the logarithm of the area of the clusters. Only events with $\log_{10}(M) > 1.5$ are shown for a better visibility.

one catalog from experiment B, as examples. The diameter of the circles is proportional to m. Differences can be seen between the three experimental catalogs generated from the same experiment concerning the size of the events and their localization. They are due to the removal of pixels when increasing the c level, thus dividing some large clusters into smaller ones. An effect of clustering can be observed on the maps: gaps appear in the distribution of the events.

The density of events can vary from one experiment to another. For instance, the density of events is higher for experiment B than for experiment A. This may be related to the velocity of propagation of the crack front which is larger for experiment B. The particle size used for sand-blasting the sample for experiment B is also larger than that for sample A. It can also affect the density of events by varying the toughness on the interface.

Another way of demonstrating a possible effect of clustering is to display events on a time versus x coordinate map. Figure 8 represents this spatio-temporal distribution of events for two catalogs (diameters of circles are proportional to m). The clustering effect is clearly visible on both maps: several events follow each other in time in a small zone along the x axis. This means that the advance of the crack front is very irregular and controlled by the ability of the front to go through a local region of high toughness. Indeed the front is stopped in some places because of local high toughness bounds on the interface. When it manages to penetrate the front can advance over some distance with a high velocity, which helps breaking other bounds before being stuck again.

4. *Comparison between Experimental Results and Real Seismicity Data*

4.1. *The SHLK Catalog*

To compare our experimental catalogs and real seismicity data, a subset of the Southern California catalog, the SHLK catalog (data available at http://www.data.scec.

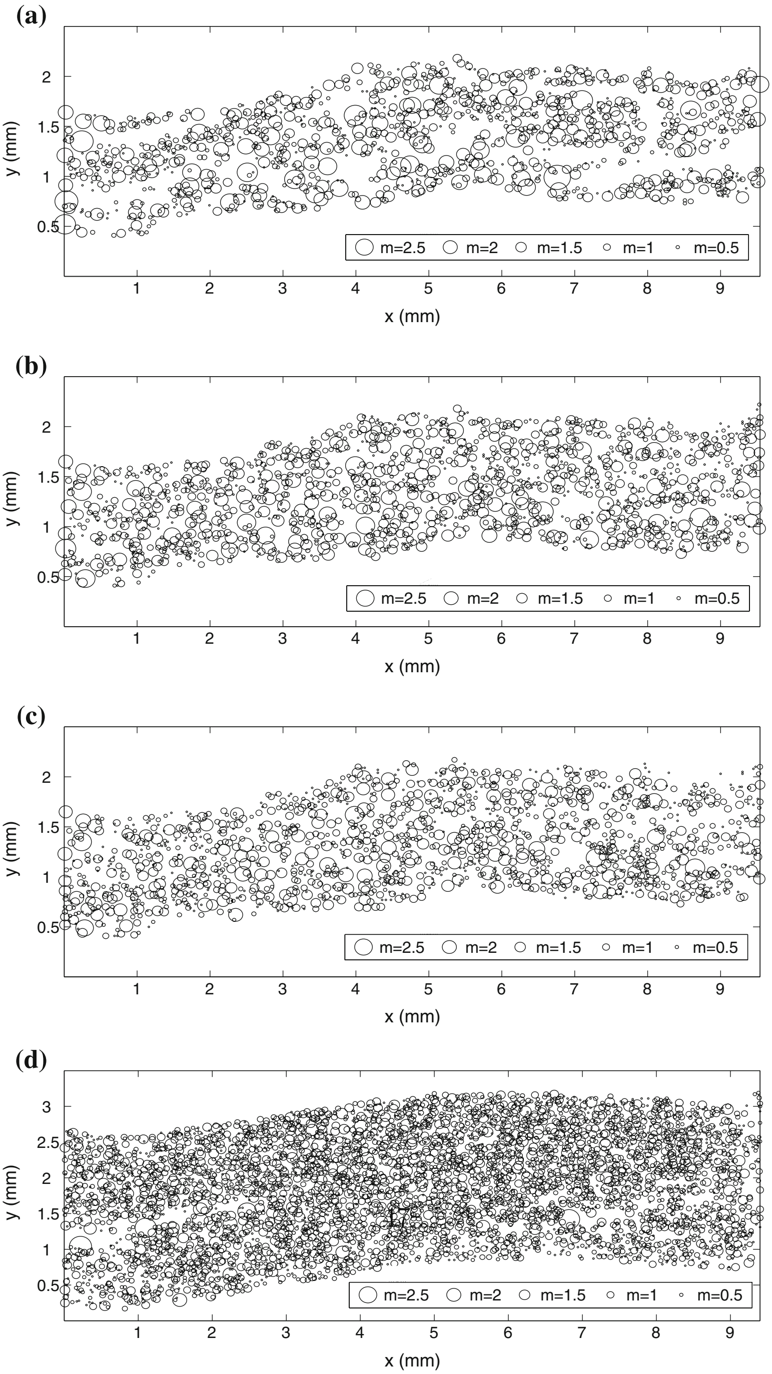
(a)
(b)
(c)
(d)
y (mm)
x (mm)
m=2.5
m=2
m=1.5
m=1
m=0.5

◀

Figure 7

Epicenters location of events for the three experimental catalogs from experiment A and the catalog B3 from experiment B. The diameters of the circles are proportional to the logarithm m of the area of the clusters. (a) Catalog A1. (b) Catalog A2. (c) Catalog A3. (d) Catalog B3.

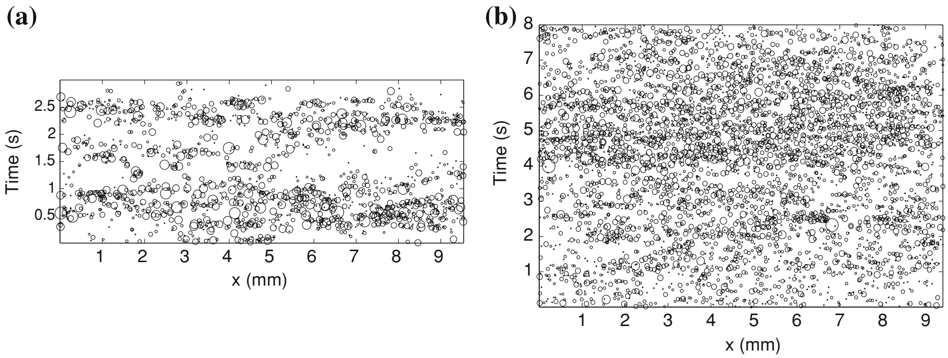

Figure 8

Spatio-temporal distribution of events for two experimental catalogs: (a) A2 and (b) B3. The diameter of the circles representing the events is proportional to the parameter m.

org/ftp/catalogs/SHLK/), is used. This catalog is built with earthquakes from a region of high seismicity. It is considered as complete for earthquakes with a magnitude larger than 2.5 (the distribution of magnitudes larger than 2.5 follow the Gutenberg-Richter relationship). The SHLK catalog is also homogeneous from January 1984 to December 2002: The seismometers in Southern California are spatially well distributed and worked continuously during this period. Davidsen and Paczuski (2005) and Davidsen *et al.* (2006) used it for their analyses and, as we wanted to compare their results to ours, we limited our own analysis to the same area (120.5°W,115.0°W) × (32.5°N,36.0°N), giving 22217 events to be considered. A detailed description of the catalog can be found in Shearer *et al.* (2005).

The exact date and time of occurrence of an earthquake are given with a precision reaching a thousandth of a second. The time of occurrence of events in the experimental catalogs is also precise up to 1 ms, although the real seismicity data catalog covers almost twenty years whereas the experiments only last a few seconds. The location of hypocenters is specified by three coordinates: latitude, longitude and depth. The configuration is clearly three-dimensional, on the contrary to the experiment in which the coordinates (x, y, z) simplify to the couple (x, y) because z is constant. Regarding the energy parameter, only the magnitude was available in the chosen catalog. The seismic moment (units in N.m) was calculated with the following relationship between seismic moment and magnitude:

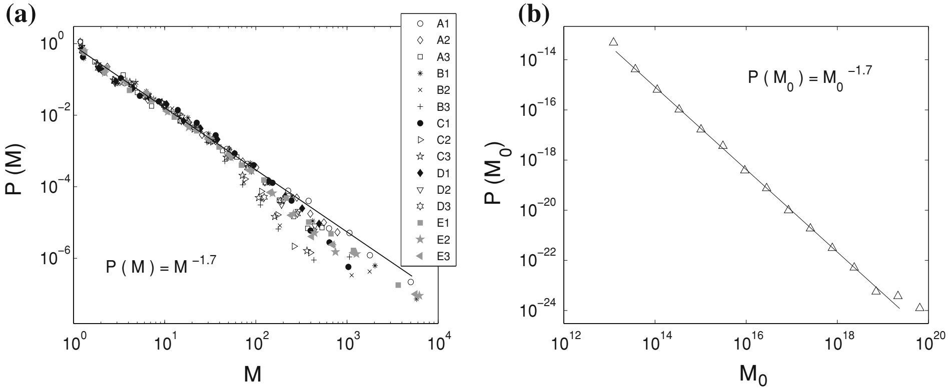

Figure 9

(a) Burst size M distributions $P(M)$ for the fifteen experimental catalogs. A fit on all the data for $0 \leq m \leq 2$ (black line) gives a slope of 1.7. A cut-off appears around $m = 2$ for large c values because of the lack of statistics for the largest clusters. (b) Seismic moment distribution $P(M_0)$ for a subset of the California seismicity catalog. The black curve shows a fit of the data with a slope equal to 1.7.

$$\log_{10}(M_0) = \frac{3}{2}M_w + 9.1, \tag{3}$$

where M_w is the so-called moment magnitude (Kanamori, 1977) given in the catalog. The seismic moment is a quantity that combines the cracked area S with the amount of fault offset D and the shear modulus μ: $M_0 = \mu S\, D$. The analogy between the moment defined for the events in the experiments and the seismic moment is discussed in the last section of this paper.

4.2. Moment Distribution

Figure 9(a) shows the noncumulative quake-size distributions $P(M)$ for the fifteen experimental catalogs. A log binning was used to build the distributions which were also normalized by the total number of events for a better comparison of all the data. A robust result is found for all experiments and for the different values of c as all the data collapse. The power-law behavior of the distribution $P(M) \propto M^{-\gamma}$ proves that the burst dynamics occurs at all length scales. A fit of the data to a power-law function gives a slope equal to 1.7. A large scale cut-off appears for all the curves although at different m values, due to the lack of statistics. The exponent $\gamma = 1.7$ is comparable to exponents already found in earlier works for experiments based on the same mechanical setup over a wider range of experimental conditions (Måløy *et al.*, 2006). The authors in Måløy *et al.* (2006) used samples sand-blasted with smaller-sized beads than the ones used for the experiments described in this paper and the average front line speeds they found were also much smaller ($0.3\mu\text{m.s}^{-1} \leq \langle v \rangle \leq 40\,\mu\text{m.s}^{-1}$). However, the fact that the value of the exponent determined for our new data is similar to the results of former experiments from Måløy *et al.* (2006) contributes to validate the technique.

As a first comparison between our experimental catalogs and real seismicity data, Figure 9(b) displays the noncumulative seismic moment distribution $P(M_0)$ of earthquakes taken from the SHLK catalog. The power-law behavior of $P(M_0)$ can be related to one well-known scaling law in seismology, the Gutenberg-Richter relationship (GUTENBERG and RICHTER, 1944) between seismic moment M_0 and frequency of earthquakes:

$$P(M_0) \propto M_0^{-1-\beta}, \tag{4}$$

where $P(M_0)$ is the frequency-moment distribution. The value β was found to equal 2/3 and proven to be very robust over different regions (GUTENBERG and RICHTER, 1944; SCHOLZ, 2002). Hence the exponent $\gamma = 1.7$ found for the experimental catalogs is similar to the exponent of the Gutenberg-Richter relationship (equation (4)) for earthquakes of the SHLK catalog.

4.3. *Epicenter Jump Distribution*

After having analyzed the size distribution of events, we focus on the spatial distances or "jumps" $\Delta r_i = \sqrt{(x_{i+1} - x_i)^2 + (y_{i+1} - y_i)^2}$ between successive events with epicenter coordinates (x_i, y_i) and (x_{i+1}, y_{i+1}). Following the work of DAVIDSEN and PACZUSKI (2005), the probability density function of the jumps $P_L(\Delta r)$ is measured for the fifteen experimental catalogs. The result can be seen in Figure 10. The straight line with a slope equal to 0.6 is displayed as a guide to the eye. A cut-off is reached around $r \approx L/2$ because of the finite spatial size of the considered areas. DAVIDSEN and PACZUSKI (2005) applied this method to characterize spatial clustering of earthquakes to the SHLK catalog. The distribution of jumps for the California catalog is superimposed to the experimental ones in the graph 10 (black triangle curve). It decays like the other curves with a trend also following a power law with an exponent $\lambda = 0.6$. Despite differences in the coordinates of hypocenters (the y coordinate in the experimental catalogs is closely related to the time and hypocenters of earthquakes are given for a 3-D configuration), a good correlation between the distributions of jumps for experimental events and real earthquakes can be observed.

4.4. *Record-breaking Event Analysis*

Another comparison between experimental and real data is conducted with a method developed by DAVIDSEN *et al.* (2006). They introduce the notion of record-breaking event. An event B is considered as a record with respect to an earthquake A if no event takes place in the spatial disc with radius AB centered on A during the time interval $[t_A, t_B]$ with $t_A < t_B$. Each record B is characterized by the distance $l = AB$ and the time interval (or waiting time) $T = t_B - t_A$ between the two earthquakes. Each event in the catalog has its own sequence of records (or recurrences). DAVIDSEN *et al.* (2006) tested this method on

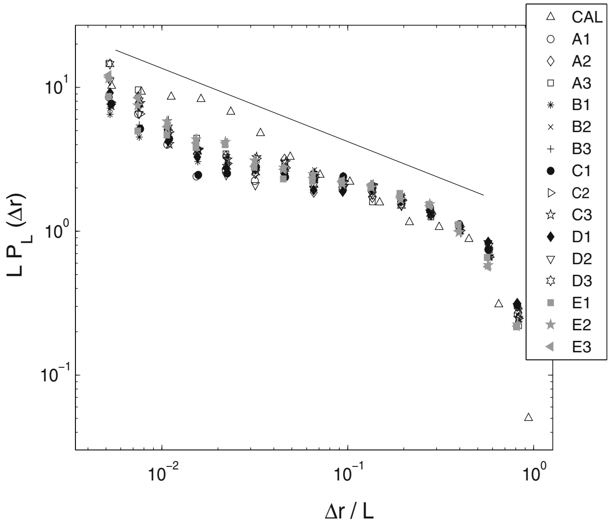

Figure 10

Distribution of jumps $P_L(\Delta r)$ for the fifteen experimental catalogs and a subset of the Southern California seismicity catalog rescaled by the longest size of the considered area L. Distances $\Delta r < 2$ km for the California catalog and $\Delta r < 40$ μm for the experimental catalogs have been discarded because of uncertainties in the locations of hypocenters. The solid black line has a slope $\lambda = 0.6$ and is shown as a guide to the eye.

the SHLK catalog. They found that the probability density functions of distances l and of recurrence times T both follow power laws spanning a few decades.

An analogy can be made here between our experiment and real seismology. Our mode I setup must to be compared to a mode II fault in friction: The y axis in the experiments is related to the time for the slipping fault (the y-coordinate value would represent a slip), while the x axis must be linked with space. The catalogs built from the experiments were processed in order to obtain a sequence of records for each cluster event but considering only the x coordinate as a position of the epicenters. Figure 11(a) shows the probability density function $P_x(l_x)$ of distances l_x of recurrent events for the different experiments. All distributions collapse and follow a power-law decay over several decades with an exponent $\delta \approx 1.1$. This value of the slope is close to the value found by Davidsen *et al.* (2006) for the Southern California seismicity catalog ($\approx$1.05). The probability density functions are independent of the experiments and the threshold level c proving the robustness of the process. The cut-off appearing between 4 and 5 mm is induced by the finite size of the system. The limit of linearity for the left side of the curves is due to location errors of the epicenters (distances below 40 μm, which corresponds to 4 pixels, are unreliable). The record-breaking event analysis was also applied to five experimental catalogs (A2, B1, C2, D1 and E3) considering only events with a moment parameter larger or equal to a certain value of m. Figure 11(b) shows the distributions $P_{x,\ m}(l_{x,\ m})$ resulting from this analysis. The

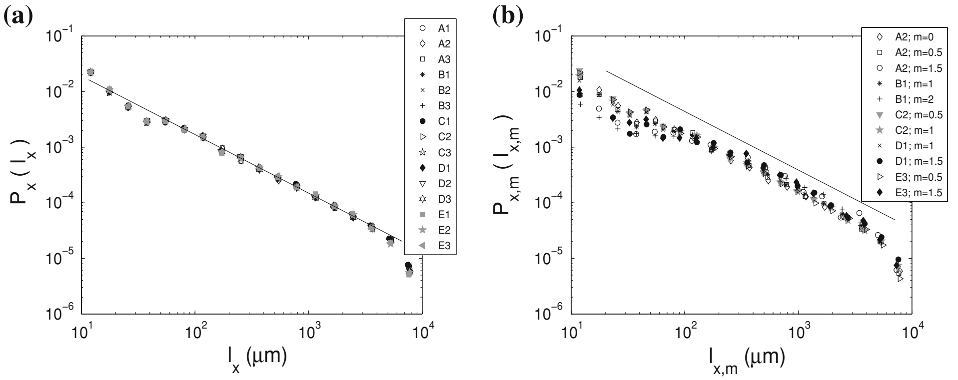

Figure 11

(a) Distribution $P_x(l_x)$ of distances l_x of recurrent events considering only the positions of epicenters on the x axis for the fifteen experimental catalogs. The straight line has a slope of 1.1. (b) Distribution $P_{x,\, m}(l_{x,\, m})$ of distances $l_{x,\, m}$ for five catalogs (A2, B1, C2, D1 and E3) varying the threshold moment m. Only events with moments greater or equal to m are considered. Data for $m = 0$ cover the whole catalog. The black line corresponds to a power law with an exponent equal to 1.1.

black straight line is a reminder of the power law with an exponent $\delta = 1.1$. The linear part of the curves for intermediate distances follows this power-law behavior. The cut-off at 4–5 mm is still observable but the peaks of the curves on the left side now vary slightly with the moment (the larger the moment threshold, the larger the minimum distance limit).

The distributions $P_x(T_x)$ for the time intervals T_x were also calculated for the record-breaking events obtained considering only the x position of the epicenters. They are shown in Figure 12(a). They obey a power law with an exponent $\alpha = 0.95$ when fitting the data for the intermediate values of recurrent times. Davidsen *et al.* (2006) found an exponent $\alpha \approx 0.9$, which is very close to our result. The variations from the general trend appearing for small T_x (between 3 and 4 ms) are due to inaccuracy concerning the time of occurrence of the events. The cut-off for large T_x indicates an upper limit of the waiting times. Figure 12(b) displays the distributions $P_{x,\, m}(T_{x,\, m})$ of recurrent times $T_{x,\, m}$ for five experimental catalogs (A2, B1, C2, D1 and E3) varying the moment threshold m. A collapse of the data is observed for intermediate $T_{x,\, m}$ values. The straight line has a slope of 0.95. Contrary to Davidsen *et al.* (2006) $P_{m,\, x}(T_{x,\, m})$ is not independent of m: The cut-off indicating a lower limit of the recurrent times varies with this threshold value. A fanning of the curves can be observed for large $T_{x,\, m}$ with the varying moment thresholds. For increasing m value, the range of the power-law regime decreases. The shift of the distributions from the power law of slope 0.95 for the experimental catalogs is probably due to the incompleteness of these catalogs. The lack of enormous events is closely related to the front propagation velocity or to the local variations of the toughness on the interface.

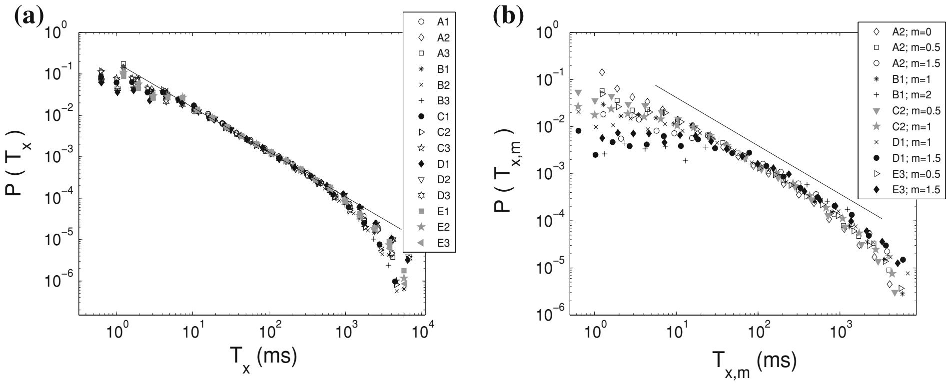

Figure 12
(a) Distribution $P_x(T_x)$ of recurrent time intervals T_x for the fifteen experimental catalogs when analyzed considering only the x-coordinate position of the events. The straight line has a slope $\approx$ 0.95. (b) Distribution $P_{x,m}(T_{x,m})$ of waiting times $T_{x,m}$ for five catalogs (A2, B1, C2, D1 and E3) varying the threshold moment m. Only events with moments larger or equal to m are taken into account. For $m = 0$ the whole catalog is involved. The black line corresponds to the power law with a slope of 0.95.

5. *Discussion*

In the previous section we compared the spatial and temporal analyses made on the experimental quake catalogs and those applied to seismicity catalogs. The distributions of size of quakes and epicenter jumps obey power laws such as the distributions of magnitude and spatial distances between epicenters of earthquakes. The record-breaking analysis of the experimental catalogs and that of the SHLK catalog also show strong analogies: The distributions of distances and waiting times between a quake and its recurrent events both follow a power-law decay. Furthermore the values of the scaling law exponents for the experimental catalogs and real seismicity data are quite close. A good data collapse can be observed between the five experiments performed on five samples with different original sand-blasting (200 μm and 500 μm bead size). No sign of a possible influence of the preparation difference can be found in the graphs. However, more experiments on samples sand-blasted with various-sized beads are needed to draw a significant conclusion on the influence of the size of disorder introduced over the crack propagation.

All these scaling properties illustrate that the dynamics of crack propagation at large scales is controlled by microstructures within the material. The good agreement between experimental and real seismicity catalogs tends to suggest that the global dynamics of rupture propagation depends on the interactions between events. These interactions are controlled by the long-range elastic coupling between heterogeneous microstructures (Ramanathan and Fisher, 1998; Schmittbuhl *et al.*, 2003a, 2003b). Indeed the modeling of Schmittbuhl *et al.* (2003b) for a quasistatic propagation of a crack front along a heterogeneous interface was compared successfully to experimental data of the same experiment presented in this paper. This fracture model describes the crack tip as a region of interactions between microcracks. Results from another modeling, based on an elastic contact line description (BONAMY *et al.*, 2008), were also compared with some experimental results presented here. Both modelings capture the role of the pinning and depinning of the crack front with long-range elastic coupling (RAMANATHAN and FISHER, 1998; SCHMITTBUHL *et al.*, 2003a, 2003b). These models have also been used to describe large-scale mode II ruptures (PERFETTINI *et al.*, 2001).

One main point of discussion for the comparison between the experimental catalogs and real seismicity data is the fracturing mode. Indeed an earthquake is modelled by a mode II or III shear rupture whereas the fracture experiment described in this paper is in mode I (opening). Attempts were already made to find analogies between mode I and mode II/III fracturation. GAO and RICE (1989) showed that mathematically the 2-D problem of an antiplane rupture along a frictional fault is governed by the same equations as the mode I perturbed crack-front problem. The numerical model of crack-front propagation of SCHMITTBUHL *et al.* (2003a), based on that of GAO and RICE (1989), was compared to former experiments based on the same mechanical setup described in this paper. Here the experimental data are directly compared to real seismicity data assuming an analogy between the moment for mode I and for mode II/III. The moment is directly proportional to the area since the opening is assumed to be constant (the elastic deformation gradient at the crack tip is presumed to be on a very small region, considering the size of an event). This is not the case for the seismic moment where the fault offset D varies.

As a perspective, the experiment presented here can be useful for the particular study of tensile cracks. Several authors (COX and SCHOLZ, 1988; PETIT and BARQUINS, 1988; YAMASHITA, 2000; DALGUER *et al.*, 2003) have shown through field observations, laboratory experiments or numerical simulations, that the three modes of rupture can coexist during an earhquake. They show that an array of microscopic tensile cracks initiate the rupture in the material or appear around a pre-existing macroscopically ruptured zone to form an initial damage zone. Under continued deformation increasingly more of these tensile cracks form until linkage occurs and the large-scale rupture then propagates in modes compatible with the global load possibly different from the microscopic mode I. Our experiment can be used to study the initiation and propagation of these mode I cracks at small scales that take place as a first stage during material breaking before fault growth (LEI *et al.*, 2000, 2004).

Another perspective for our experiment could be the study of properties of slow earthquakes (OBARA, 2002; ROGERS and DRAGERT, 2003; SCHWARTZ and ROKOSKY, 2007). Since our experiments involve not only dynamical events (*i.e.*, local unstable events which produce acoustic emission) but also very slow events compared to Rayleigh speed owing to the viscous rheology of the PMMA both in the bulk and along the contact plane, our experiment could be used as a paradigm for slow earthquakes. In this context it is of interest to note that we produce slow quakes without fluid presence contrasting to the first explanations for the slow earthquakes (SZELIGA *et al.*, 2004; MCCAUSLAND *et al.*, 2005;

SHELLY *et al.*, 2006; DOUBRE and PELTZER, 2007; ITO *et al.*, 2007). BRODSKY and MORI (2007) analyzed the static stress drop of slow and ordinary earthquakes, their ratio of slip to fault length. They conclude that the differences between dynamic and quasi-static rupture can explain the occurrence of ordinary earthquakes or slow ones. These authors write that the distinction between both types of earthquakes results from their ability to jump over rough patches on the fault plane, which corresponds exactly to the pinning and depinning of our experimental crack front. MELBOURNE *et al.* (2005) with inversion of GPS data for the 2003 Cascadia slow earthquake also found spatially localized non-uniform slip and evoked stress drop as a constraint for rupture mechanism.

In conclusion, the quake catalogs derived from the optical monitoring of a crack propagation experiment have strong similar scaling properties with real seismicity catalogs. This result yields a possible explanation of the rupture propagation mechanism: The rupture front is trapped by local asperities and its depinning involves local instabilities. Heterogeneities in the medium thus play a crucial part in the fracture propagation. The advantage of the experiment presented in this paper is the possibility to follow optically and continuously over an extended range of time scales, the propagation of the rupture thanks to the use of a transparent material, which can not be done for earthquake faults. Consequently analyzes of the experimental data offer good implications with which to address the question of earthquake mechanisms in complex media.

Acknowledgements

The authors would like to thank P. Srutarshi, G. Daniel and M. Bouchon for fruitful discussions regarding this project. The authors are also grateful to A. Bizzarri, S. Stanchits and S. Vinciguerra for their useful review of the manuscript. This work was supported by the programs ANR CATT MODALSIS and PICS "France/Norway".

REFERENCES

AOCHI, H. and FUKUYAMA, E. (2002), *Three-dimensional nonplanar simulation of the 1992 Landers earthquake*, J. Geophys. Res. *107*(B2), 2035.

BAK, P., CHRISTENSEN, K., DANON, L., and SCANLON, T. (2002), *Unified scaling law for earthquakes*, Phys. Rev. Lett. *88*(17), 178501.

BIZZARRI, A. and BELARDINELLI, M. (2008), *Modelling instantaneous dynamic triggering in a 3-D fault system: Application to the 2000 June South Iceland seismic sequence*, Geophys. J. Internat. *173*, 906–921.

BONAMY, D., SANTUCCI, S., and PONSON, L. (2008), *Crackling dynamics in material failure as the signature of a self-organized dynamic phase transition*, Phys. Rev. Lett. *101*, 045501.

BOUCHAUD, E. (1997), *Scaling properties of cracks*, J. Physics: Condensed Matter, *9*(21).

BOUCHAUD, E., LAPASSET, G., PLANÈS, J., and NAVEOS, S. (1993), *Statistics of branched fracture surfaces*, Phys. Rev. B *48*(5), 2917–2928.

BOUCHON, M., TOKSÖZ, N., KARABULUT, H., BOUIN, M.-P., DIETRICH, M., AKTAR, M., and EDIE, M. (2000), *Seismic imaging of the 1999 Izmit (Turkey) rupture inferred from the near-fault recordings*, Geophys. Res. Lett. *27*(18), 3013–1016.

BRODSKY, E. and MORI, J. (2007), *Creep events slip less than ordinary earthquakes*, Geophys. Res. Lett. *34*, L16309.

CLINTON, J., HAUKSSON, E., and SOLANKI, K. (2006), *An evaluation of the SCSN moment tensor solutions: robustness of the M_W magnitude scale, style of faulting and automation of the method*, Bull. Seismol. Soc. Am. *96*(5), 1689–1705.

CORRAL, A. (2004), *Long-term clustering, scaling and universality in the temporal occurrence of earthquakes*, Phys. Rev. Lett. *92*(10), 108501.

COX, S. and SCHOLZ, C. (1988), *Rupture initiation in shear fracture of rocks: An experimental study*, J. Geophys. Res. *93*(B4), 3307–3320.

DAGUIER, P., BOUCHAUD, E., and LAPASSET, G. (1995), *Roughness of a crack front pinned by microstructural obstacles*, Europhys. Lett. *30*(7), 367–372.

DALGUER, L., IRIKURA, K., and RIERA, J. (2003), *Simulation of tensile crack generation by three-dimensional dynamic shear rupture propagation during an earthquake*, J. Geophys. Res. *108*(B3), 2144–2167.

DAVIDSEN, J., GRASSBERGER, P., and PACZUSKI, M. (2006), *Earthquake recurrence as a record-breaking process*, Geophys. Res. Lett. *33*, L11304.

DAVIDSEN, J. and PACZUSKI, M. (2005), *Analysis of the spatial distribution between successive earthquakes*, Phys. Rev. Lett. *94*, 048501.

DELAPLACE, A., SCHMITTBUHL, J., and MÅLØY, K. (1999), *High resolution description of a crack front in a heterogeneous Plexiglas block*, Phys. Rev. Lett. *60*(2), 1337–1343.

DOUBRE, C. and PELTZER, G. (2007), *Fluid-controlled faulting process in the Asal Rift, Djibouti, from 8 yr of radar interferometry observations*, Geology *35*(1), 69–72.

FUKUYAMA, E., MIKUMO, T., and OLSEN, K. (2003), *Estimation of the critical slip-weakening distance: theoritical background*, Bull. Seismol. Soc. Am. *93*(4), 1835–1840.

GAO, H. and RICE, J. (1989), *A first-order perturbation analysis of crack trapping by arrays of obstacles*, ASME J. Appl. Mech. *56*, 828–836.

GUTENBERG, B. and RICHTER, C. (1944), *Frequency of earthquakes in California*, Bull. Seismol. Soc. Am. *34*, 185–188.

IDE, S. and TAKEO, M. (1997), *Determination of constitutive relations of fault slip based on seismic wave analysis*, J. Geophys. Res. *102*(B12), 27379–27391.

ITO, Y., OBARA, K., SHIOMI, K., SEKINE, S., and HIROSE, H. (2007), *Slow earthquakes coincident with episodic tremors and slow slip events*, Science *315*, 503–506.

KAGAN, Y. (1999), *Universality of the seismic moment-frequency relation*, Pure Appl. Geophys. *155*(2), 641–655.

KAGAN, Y. (2002), *Aftershock zone scaling*, Bull. Seismol. Soc. Am. *92*, 537–573.

KANAMORI, H. (1977), *The energy release in great earthquakes*, J. Geophys. Res. *82*(B20), 2981–2988.

KANAMORI, H. and ANDERSON, D. (1975), *Theoritical basis of some empirical relations in seismology*, Bull. Seismol. Soc. Am. *65*(5), 1073–1095.

KIKUCHI, M. and KANAMORI, H. (1991), *Inversion of complex body waves*, Bull. Seismol. Soc. Am. *81*(6), 2335–2350.

LAWN, B., *Fracture of Brittle Solids* (Cambridge Univ. Press 1993) second edition.

LEI, X., KUSUNOSE, K., RAO, M., NISHIZAWA, O., and SATOH, T. (2000), *Quasi-static fault growth and cracking in homogeneous brittle rock under triaxial compression using acoustic emission monitoring*, J. Geophys. Res. *105*(B3), 6127–6139.

LEI, X., MASUDA, K., NISHIZAWA, O., JOUNIAUX, L., LIU, L., MA, W., SATOH, T., and KUSUNOSE, K. (2004), *Detailed analysis of acoustic emission activity during catastrophic fracture of faults in rock*, J. Struct. Geol. *26*, 247–258.

MAI, P. and BEROZA, G. (2000), *Source scaling properties from finite-fault-rupture models*, Bullet. Seismol. Soc. Am. *90*(3), 604–615.

MAI, P. and BEROZA, G. (2002), *A spatial random field model to characterize complexity in earthquake slip*, J. Geophys. Res. *107*(B11), 2308.

MÅLØY, K., HANSEN, A., HINRICHSEN, E., and ROUX, S. (1992), *Experimental measurements of the roughness of brittle cracks*, Phys. Rev. Lett. *68*(2), 213–215.

MÅLØY, K., SANTUCCI, S., SCHMITTBUHL, J., and TOUSSAINT, R. (2006), *Local waiting time fluctuations along a randomly pinned crack front*, Phys. Rev. Lett. *96*(4).

MÅLØY, K., TOUSSAINT, R., and SCHMITTBUHL, J. (2005), *Dynamics and structure of interfacial crack fronts, Proc. 11th Internat. Congress on Fracture*, page 6.

MANDELBROT, B., PASSOJA, D., and PAULLAY, A. (1984), *Fractal character of fracture surfaces of metal*, Nature *308*, 721–722.

MARSAN, D., BEAN, C., STEACY, S., and MCCLOSKEY, J. (2000), *Observation of diffusion processes in earthquake populations and implications for the predictability of seismicity systems*, J. Geophys. Res. *105*(B12), 28081–28094.

MCCAUSLAND, W., MALONE, S., and JOHNSON, D. (2005), *Temporal and spatial occurrence of deep non-volcanic tremor: from Washington to northern California*, Geophys. Res. Lett. *32*, L24311.

MELBOURNE, T., SZELIGA, W., MILLER, M., and SANTILLAN, V. (2005), *Extent and duration of the 2003 Cascadia slow earthquake*, Geophys. Res. Lett. *32*, L04301.

OBARA, K. (2002), *Nonvolcanic deep tremor associated with subduction in southwest Japan*, Science *296*, 1679–1681.

PERFETTINI, H., SCHMITTBUHL, J., and VILOTTE, J.-P. (2001), *Slip correlations on a creeping fault*, Geophys. Res. Lett. *28*(10), 2137–2140.

PETIT, J.-P. and BARQUINS, M. (1988), *Can natural faults propagate under mode ii conditions?* Tectonics *7*(6), 1243–1256.

RAMANATHAN, S. and FISHER, D. (1998), *Onset of propagation of planar cracks in heterogeneous media*, Phys. Rev. B *58*(10), 6026–6046.

REID, H., *The California earthquake of April 18, 1906*. In *Report of the State Earthquake Investigation Committee*, vol. II (Carnegie Institution of Washington 1910).

ROGERS, G. and DRAGERT, H. (2003), *Episodic tremor and slip on The Cascadia subduction zone: The chatter of silent slip*, Science *300*, 1942–1943.

RUBIN, A. and AMPUERO, J.-P. (2007), *Aftershock asymmetry on a bimaterial interface*, J. Geophys. Res. *112*, B05307.

SANTUCCI, S., MÅLØY, K., TOUSSAINT, R., and SCHMITTBUHL, J., *Self-affine scaling during interfacial crack front propagation*. In *Proc. Dynamics of Complex Interconnected Systems: Networks and Bioprocesses*, NATO ASI Geilo (Springer 2006).

SANTUCCI, S., MATHIESEN, J., MÅLØY, K., HANSEN, A., SCHMITTBUHL, J., VANEL, L., DELAPLACE, A., HAAVIG BAKKE, J., and RAY, P. (2007), *Statistics of fracture surfaces*, Phys. Rev. E *75*(1), 016104.

SCHMITTBUHL, J., DELAPLACE, A., and MÅLØY, K., *Propagation of an interfacial crack front in an heterogeneous medium: Experimental observations*. In *Proc. NATO Advanced Study Institute on Physical Aspects of Fracture*, pages 353–369 (Kluwer Academic Publishers 2001).

SCHMITTBUHL, J., DELAPLACE, A., MÅLØY, K., PERFETTINI, H., and VILOTTE, J. (2003a), *Slow crack propagation and slip correlations*, Pure Appl. Geophys. *160*(5–6), 961–976.

SCHMITTBUHL, J., GENTIER, S., and ROUX, S. (1993), *Field measurements of the roughness of fault surfaces*, Geophys. Res. Lett. *20*(8), 639–641.

SCHMITTBUHL, J., HANSEN, A., and BATROUNI, G. (2003b), *Roughness of interfacial crack fronts: stress-weighted percolation in the damage zone*, Phys. Rev. Lett. *90*(4).

SCHMITTBUHL, J. and MÅLØY, K. (1997), *Direct observation of a self-affine crack propagation*, Phys. Rev. Lett. *78*(20), 3888–3891.

SCHMITTBUHL, J., SCHMITT, F., and SCHOLZ, C. (1995), *Scaling invariance of crack surfaces*, J. Geophys. Res. *100*(B4), 5953–5973.

SCHOLZ, C., *The Mechanics of Earthquakes and Faulting* (Cambridge Univ. Press 2002) second edition.

SCHWARTZ, S. and ROKOSKY, J. (2007), *Slow slip events and seismic tremor at circum-Pacific subduction zones*, Rev. Geophys. *45*, RG3004.

SHEARER, P., HAUKSSON, E., and LIN, G. (2005), *Southern California hypocenter relocation with waveform cross-correlation, Part 2: Results using source-specific station terms and cluster analysis*, Bull. Seismol. Soc. Am. *95*(3), 904–915.

SHELLY, D., BEROZA, G., IDE, S., and NAKAMULA, S. (2006), *Low-frequency earthquakes in Shikoku, Japan, and their relationship to episodic tremor and slip*, Nature, *442*, 188–191.

SZELIGA, W., MELBOURNE, T., MILLER, M., and SANTILLAN, V. (2004), *Southern Cascadia episodic slow earthquakes*, Geophys. Res. Lett. *31*, L16602.

Tinti, E., Spudich, P., and Cocco, M. (2005), *Earthquake fracture energy inferred from kinematic rupture models on extended faults*, J. Geophys. Res. *110*, B12303.

Wald, D., Helmberger, D., and Heaton, T. (1991), *Rupture model of the 1989 Loma Prieta earthquake from the inversion of strong-motion and broadband teleseismic data*, Bull. Seismol. Soc. Am. *81*(5), 1540–1572.

Wells, D. and Coppersmith, K. (1994), *New empirical relationships among magnitude, rupture length, rupture width, rupture area and surface displacement*, Bull. Seismol. Soc. Am. *84*(4), 974–1002.

Yamashita, T. (2000), *Generation of microcracks by dynamic shear rupture and its effects on rupture growth and elastic wave radiation*, Geophys. J. Internat. *143*, 395–406.

Ziv, A., Rubin, A., and Kilb, D. (2003), *Spatiotemporal analyzes of earthquake productivity and size distribution: observations and simulations*, Bull. Seismol. Soc. Am. *93*(5), 2069–2081.

(Received April 1, 2008, revised September 16, 2008, accepted January 8, 2009)
Published Online First: May 20, 2009

A LETTERS JOURNAL EXPLORING THE FRONTIERS OF PHYSICS

November 2010

EPL, **92** (2010) 44001
doi: 10.1209/0295-5075/92/44001

www.epljournal.org

Fracture roughness scaling: A case study on planar cracks

S. SANTUCCI[1,2,3(a)], M. GROB[4], R. TOUSSAINT[4], J. SCHMITTBUHL[4], A. HANSEN[5] and K. J. MALØY[3]

[1] *Laboratoire de Physique, UMR CNRS 5672, Ecole Normale Supérieure de Lyon 46 allée d'Italie, F-69007 Lyon, France, EU*
[2] *Physics of Geological Processes, Oslo University - 1048 Blindern, N-0316 Oslo, Norway*
[3] *Fysisk Institutt, Universitetet i Oslo - 1048 Blindern, N-0316 Oslo, Norway*
[4] *Institut de Physique du Globe de Strasbourg, UMR CNRS 7516, EOST/Université de Strasbourg 5 rue René Descartes, F-67084 Strasbourg Cedex, France, EU*
[5] *Institutt for fysikk, Norges teknisk-naturvitenskapelige Universitet - N-7491 Trondheim, Norway*

received 13 October 2010; accepted 2 November 2010
published online 18 November 2010

PACS 46.50.+a – Fracture mechanics, fatigue and cracks
PACS 68.35.Ct – Interface structure and roughness

Abstract – Using a multi-resolution technique, we analyze large in-plane fracture fronts moving slowly between two sintered Plexiglas plates. We find that the roughness of the front exhibits two distinct regimes separated by a crossover length scale δ^*. Below δ^*, we observe a multi-affine regime and the measured roughness exponent $\zeta_{\parallel}^{-} = 0.60 \pm 0.05$ is in agreement with the coalescence model. Above δ^*, the fronts are mono-affine, characterized by a roughness exponent $\zeta_{\parallel}^{+} = 0.35 \pm 0.05$, consistent with the fluctuating line model. We relate the crossover length scale to fluctuations in fracture toughness and the stress intensity factor.

Since the pioneering work of Mandelbrot *et al.* [1] demonstrating the self-affine character of fracture surfaces of metals, numerous studies have been devoted to the morphology of fracture surfaces [2,3]. In particular, the roughness exponent $\zeta_{\perp}$ characterizing this self-affinity was shown to be very robust and further on conjectured to be universal [4] with $\zeta_{\perp} \sim 0.8$ over a large set of materials and conditions [2–5] and up to very large scales [6]. In the weak disorder limit when toughness fluctuations are small compared to stress loading fluctuations, there are data suggesting that $\zeta_{\perp}$ takes on a smaller value, 0.4 [7,8]. A first attempt at investigating the origin of a universal fracture roughness exponent in the quasistatic propagation limit was made by Hansen *et al.* [9] who suggested that in two dimensions it might be related to the directed polymer problem. This idea was further developed by Räisänen *et al.* [10]: the fracture surface follows the surface that minimizes the integrated strength of the intact material. Numerical studies based on this idea gave a roughness exponent $\zeta_{\perp} = 0.41 \pm 0.02$. A different idea was proposed by Bouchaud *et al.* [11]. In their picture, the fracture surface is the "footprint" of a passing fluctuating elastic line —the fracture front— moving through a disordered three-dimensional landscape. This powerful idea opened up for the existence of *two* roughness exponents: one describing the roughness orthogonal to the average crack plane $\zeta_{\perp}$ and another describing the roughness of the front in the average roughness plane $\zeta_{\parallel}$ [12].

In order to simplify the 3d configuration, Schmittbuhl *et al.* [13] proposed a numerical model where the crack front is constrained to propagate along a weak plane (suppressing the out-of-plane roughness). The in-plane roughness exponent was found equal to $\zeta_{\parallel} = 0.35$, and later on, refined to $\zeta_{\parallel} = 0.39$ by Rosso and Krauth [14]. Even though such a fluctuating line approach [15] can match several scaling exponents related to the crack front dynamics [16], it fails at reproducing the in-plane roughness exponent $\zeta_{\parallel}$ measured up to now around 0.6 [17–19]. We will adress precisely this problem in the present letter, insisting on the fact that the fluctuating line model is typically a perturbative approach assuming the local slope of the front to be small, and ignoring crack coalescence [20]. A theory based on a mapping of the fracture process to a correlated percolation one [21,22] considered precisely the latter aspect. Numerical simulations based on this model gave $\zeta_{\parallel} = 0.6$, substantially larger than the value found based on the fluctuating line model but consistent

(a) E-mail: stephane.santucci@ens-lyon.fr

with the experimental results obtained up to now. The coalescence model also clarified the controversy over the concept of self-affinity [23–25].

The goal of the present letter is to address the possible coexistence of two roughness scaling regimes in the case of in-plane fracture. We analyze stable mode-I fracture fronts propagating along the sandblasted and sintered contact plane between two PMMA plates [16–19,26]. An important contribution to our analysis comes from the compilation of numerous observations at different resolutions. We observe that the planar cracks follow two distinct scaling regimes, multi-affine at small scales and mono-affine at larger ones, characterized by different roughness exponent $\zeta_{\parallel}^{-}=0.60$ and $\zeta_{\parallel}^{+}=0.35$, respectively. We show that those two regimes are separated by a well-defined crossover length δ^{*} controlled by a balance between the stress intensity factor variability along the fracture front and fluctuations in the fracture toughness. Below δ^{*}, the value of the roughness exponent is in agreement with the prediction of the coalescence model $\zeta_{\parallel}=0.60$, while the large-scale exponent is consistent with the value predicted by the fluctuating line model, $\zeta_{\parallel}=0.39$. We argue in the second part of the paper why *both* theories may be correct in describing the experiment, but operating at different length scales.

Experiments. – The experimental setup allows for a stable mode-I crack propagation along a weak plane in a PMMA block from a displacement imposed normally [17]. Toughness fluctuations along the weak plane are artificially introduced during the sample preparation, which consists of annealing two sandblasted PMMA plates. In order to modify the toughness fluctuations, we changed the type and the size of the blasting particles using glass beads of diameters around $\varnothing_1 \sim 50\mu$m, $\varnothing_2 \sim 200\mu$m, and $\varnothing_3 \sim 300\mu$m and a glass-aluminum powder with a typical particle size around $S \sim 50\,\mu$m. We also changed the loading speed and procedure, with interfaces recorded during their propagation at various velocities. In order to obtain a multi-high-resolution description of the fronts, we considered fracture fronts at rest. During those experiments, after a slow crack propagation, the sample was unloaded in order to arrest the crack. Then, we took high-resolution pictures (3871×2592 pixels) of the front at rest (fig. 1) using a digital camera mounted on an optical microscope. Using a translation stage that can move the microscope in the x-direction parallel to the front (and perpendicular to the fracture propagation direction y) neighboring pictures were taken. Up to 15 high-resolution pictures were then assembled resulting in fracture fronts with around 25000 data points and a pixel size $a=0.48\,\mu$m. To remove acquisition artifacts, different resolutions of the front description were obtained by changing the magnification of the optical zooms (see fig. 1). This results in images of the same fracture at resolutions, 4, 2, 1 and $0.48\,\mu$m per pixel with, respectively, around 4000, 8000, 16000 and 25000 data points per image. This procedure was repeated 20 times in order to obtain 20 independent fracture fronts. The actual total length of each analyzed crack was around 15 mm.

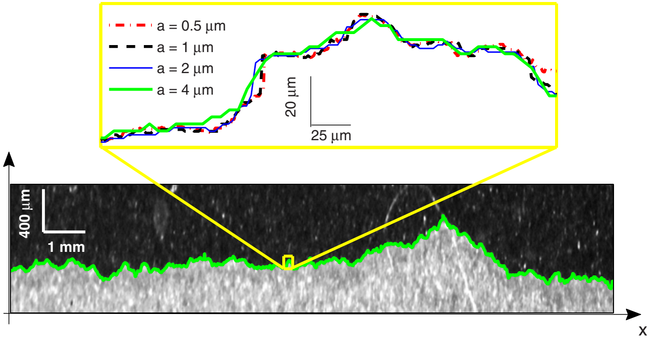

Fig. 1: (Colour on-line) A typical fracture (using glass beads of a diameter $\varnothing_1 \sim 50\mu$m for roughening the samples) and a zoom of the crack front $y(x)$ to emphasize the effect of the optical resolution given by the pixel size a.

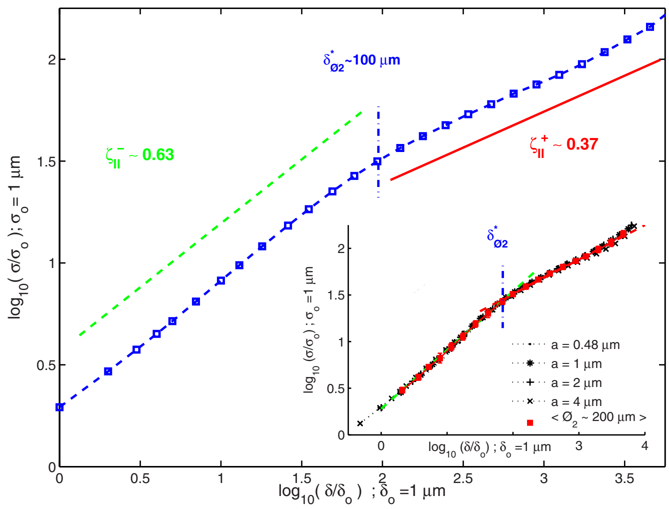

Fig. 2: (Colour on-line) Scaling behavior of the rms σ of the height fluctuations $\Delta y(\delta)$ with two different roughness exponents $\zeta_{\parallel}^{-}\sim 0.63$ and $\zeta_{\parallel}^{+}\sim 0.37$, below and above the typical scale $\delta^{*}\sim 100\,\mu$m, respectively. The inset shows that this scaling is independent of the image resolution a.

Two scaling regimes. – We analyze the height fluctuations of the crack fronts $\Delta y(\delta)=y(x+\delta)-y(x)$ where $y(x)$ is the advance of the front along the y-direction at position x. We will first consider fracture fronts at rest for samples prepared with $200\,\mu$m glass beads. Then, we will prove the universality of our results showing the same analysis for various experimental conditions. In fig. 2, we examine the scaling behavior of the root mean square (rms) of the height fluctuations $\sigma(\delta)=\langle \Delta y^2(\delta)\rangle^{1/2}$. At small scales below $\delta^{*}\sim 100\,\mu$m, we observe a self-affine scaling behavior: $\sigma(\delta)\propto \delta^{\zeta_{\parallel}^{-}}$ with a roughness exponent $\zeta_{\parallel}^{-}=0.60\pm 0.05$. This is consistent with previous experimental measurements [16–19] and the value predicted by the coalescence model [22]. However, at scales larger

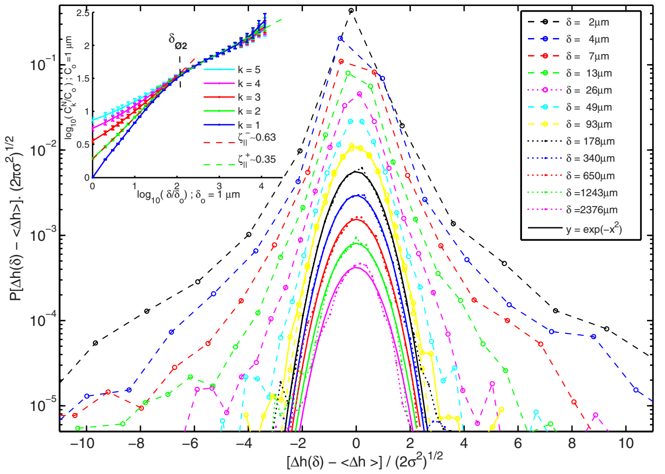

Fig. 3: (Colour on-line) We observe two different scaling regime of the normalized structure functions $C_k^N(\delta)=C_k(\delta)/R_k^G(\delta)$ separated by the crossover $\delta^* \sim 100\,\mu$m. The corresponding p.d.f. of the height fluctuations $\Delta y(\delta)$ are shown in the inset where we plot in semi-log $P[\Delta' y(\delta)].\sqrt{2\pi\sigma^2}$ *vs.* $[\Delta' y(\delta)]/\sqrt{2\sigma^2}$ for increasing length scales δ, shifted vertically for visual clarity. Above δ^*, the lines $f(x)=e^{-x^2}$ fit the parabolic shape of the Gaussians.

than δ^*, we observe a crossover to another scaling regime with a smaller roughness exponent $\zeta_{\|}^{+}=0.35\pm0.05$. This value corresponds to the fluctuating line model prediction $\zeta_{\|}=0.39$ [14]. Due to the limited scaling range for $\delta>\delta^*$, our data do not rule out a possible slow crossover to a flat front (no disorder regime), at large scales [27]. In the inset of fig. 2, we demonstrate the robustness of our results by showing that the two different scaling regimes and the crossover length scale observed are independent of the sampling resolution of the interface.

In order to study in more details those different scaling behaviors, we develop a multi-scaling analysis [26] by performing a direct measurement of the p.d.f. $P[\Delta' y]$ of the height fluctuations $\Delta' y(\delta)=\Delta y(\delta)-\langle\Delta y\rangle$ and computing their structure functions $C_k(\delta)=\langle|\Delta y(\delta)|^k\rangle_x^{1/k}$. In fig. 3 we show the distributions of the height fluctuations $P[\Delta' y(\delta)]$ for logarithmically increasing length scales δ. Above the characteristic length scale $\delta^*\sim 100\,\mu$m, the shape of the distributions is Gaussian, while for smaller length scales, we observe long tails consistent with a non-Gaussian and multi-affine scaling. Indeed, we show that the structures functions $C_k(\delta)$ —when normalized by the set of values $R_k^G=\sqrt{2}\left(\Gamma\left(\frac{k+1}{2}\right)/\sqrt{\pi}\right)^{1/k}$ corresponding to the ratios $R_k^G=C_k^G(\delta)/C_2^G(\delta)$ obtained for a Gaussian and mono-affine signal (see [26] for details)— collapse and follow a self-affine scaling with a unique roughness exponent $\zeta_{\|}^{+}=0.35\pm0.05$ corresponding to the elastic line prediction. Below δ^*, the fanning of the structure functions confirms the deviation to the Gaussian statistics and reveals an effective multi-affine behavior consequence of the heterogeneities along the interface leading to steep crack front slopes. A fit to $C_2(\delta)$ on that range gives $\zeta_{\|}^{-}=0.60\pm0.05$, in agreement with the coalescence model [22].

Crossover length scale. – We now investigate what controls the crossover length δ^*. We base our discussion on the Griffith criterion that assumes a balance between the stress intensity factor K and the fracture toughness, K_c. We introduce a mean-field argument to describe the stress intensity factor variation in the direction of the propagation around the average position of the front $\bar{y}$: $K(y)=K_0(\bar{y})+K'(y-\bar{y})$, where $K'=\partial K/\partial y$ is the average local gradient of the stress intensity factor. Then, the toughness of the asperities along the weak plane is supposed to be random around an average K_c^* and uncorrelated beyond the asperity size δ_c. We assume that $K_0(\bar{y})=K_c^*$ and that the fluctuation of the toughness over the front width $\sigma(\delta_c)$ reads as $K_c(\bar{y}\pm\sigma(\delta_c))=K_c^*\pm\Delta K_c(\delta_c)$, where ΔK_c is the magnitude of the toughness fluctuations on scale equal or larger than δ_c. Finally, we estimate the width of the crack front $\sigma(\delta_c)$ to be the typical scale in the y-direction at which the failure criterion is met: $K(\bar{y}+\sigma(\delta_c))\approx K_c(\bar{y}+\sigma(\delta_c))$. Hence at a first order, we get an estimate of the front width at the asperity scale as a function of the magnitude of the toughness fluctuations ΔK_c and the local stress gradient K': $\sigma(\delta_c)=\Delta K_c/K'$. Due to the self-affinity of the front with a roughness exponent $\zeta_{\|}$, our argument leads to an estimate of the prefactor of this scaling as

$$\sigma(\delta)=\sigma(\delta_c)\left(\frac{\delta}{\delta_c}\right)^{\zeta_{\|}}=\left(\frac{\Delta K_c}{K'}\right)\left(\frac{\delta}{\delta_c}\right)^{\zeta_{\|}}. \qquad (1)$$

An important consequence is that the scaling of the fracture front will be hidden in the no disorder limit: when either the toughness disorder disappears ($\Delta K_c\to 0$) or when the loading gradient becomes very large ($K'\to\infty$).

We now address the estimate of the local slope of the crack front at the asperity scale, *i.e.*, $\sigma(\delta_c)/\delta_c$. Two cases emerge. First, if the local slope is small, $\sigma(\delta_c)\ll\delta_c$, the front may be described using a perturbative approach. We expect in this case that the fluctuating line model to be valid, leading to a roughness exponent $\zeta_{\|}^{+}\approx 0.39$. We note here that $\sigma(\delta)\ll\delta$ is valid for all $\delta>\delta_c$ if it is fulfilled for δ_c due to the self-affinity of the front. The second situation occurs when $\sigma(\delta_c)\geqslant\delta_c$. In this case, we assume the coalescence model to be valid with a roughness exponent $\zeta_{\|}^{-}=0.6$. Hence, the slope at a scale δ scales as $\sigma(\delta)/\delta\propto\delta^{\zeta_{\|}^{-}-1}$, which means that it decreases with increasing δ. This implies that there is a scale δ^* at which the slope $\sigma(\delta^*)/\delta^*=\alpha$ with $\alpha<1$, and where the fluctuating line model is assumed to take over. Subsequently, we estimate

$$\delta^*=\left(\frac{\Delta K_c}{\alpha K'}\right)^{1/(1-\zeta_{\|}^{-})}\delta_c^{-\zeta_{\|}^{-}/(1-\zeta_{\|}^{-})}. \qquad (2)$$

This length scale δ^* is different to the Larkin length [28] separating various pinning regimes [29] of an elastic line in

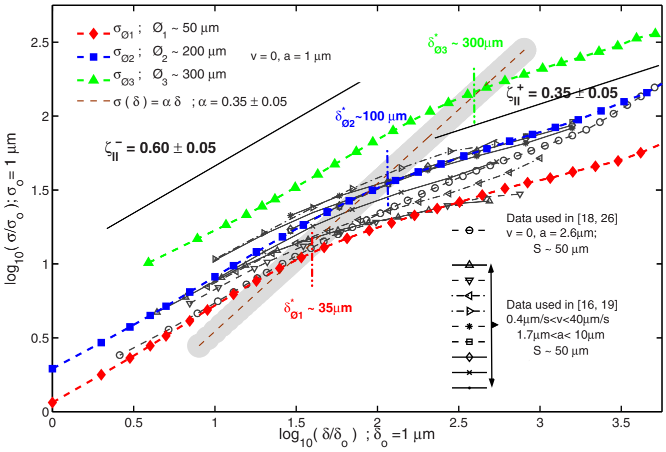

Fig. 4: (Colour on-line) Effect of disorder on the scaling of interfacial crack fronts. We plot the rms σ of the height fluctuations Δy as a function of the scale δ for crack fronts at rest and samples blasted with glass beads of various diameters $\varnothing_1 \sim 50\mu$m, $\varnothing_2 \sim 200\mu$m and $\varnothing_3 \sim 300\mu$m. The line $\sigma(\delta) = 0.35\,\delta$ separates the two scaling regimes. To insist on the robustness of our results, we add various data obtained during previous experiments with many different experimental conditions: glass-aluminium powder with a typical size around $S \sim 50\,\mu$m and crack front propagating at various velocities v [16,18,19,26].

a random medium. It rather corresponds to the onset of steep front slopes or overhangs (fig. 1) leading to deviations to the Gaussian and mono-affine scaling of the fronts (fig. 3), and therefore limiting the range of validity of the elastic line models. In fig. 4 we plot $\sigma(\delta^*)/\delta^* = \alpha$ for $\alpha = 0.35$ and check that it accounts for the crossover between the two scaling regimes for the various experiments performed in different conditions. We conclude that the crossover length scale δ^* is a function of the asperity size δ_c, the toughness fluctuations ΔK_c and the stress intensity factor gradient K'. Following the above arguments, the measure of the crossover δ^* provides an estimate of the link between the magnitude of the toughness fluctuations ΔK_c and the asperity size δ_c knowing the loading conditions K'. The crossover δ^* depends on ΔK_c and K' through a power law with a positive exponent $1/(1-\zeta_{\parallel}^{-}) \approx 5/2$, very different from its variation with δ_c, $-\zeta_{\parallel}^{-}/(1-\zeta_{\parallel}^{-}) \approx -3/2$. Also the crossover δ^* is not expected to scale linearly with the asperity size δ_c as suggested in [30] except if the toughness fluctuations are proportional to the asperity size: $\Delta K_c \propto \delta_c$.

Disorder effect. – In order to check the effect of disorder and material microstructure (*i.e.* ΔK_c and δ_c), we modified the heterogeneities of the sintered interface between the two Plexiglas plates by preparing different samples using glass beads of different diameters $\varnothing_1 \sim 50\mu$m, $\varnothing_2 \sim 200\mu$m and $\varnothing_3 \sim 300\mu$m.

We show in fig. 4 the scaling behaviour of the interfacial crack fronts with those various types of disorder that influence the toughness fluctuations (unfortunately the measurement of the link between sandblasting particle size and toughness fluctuations was not possible). We observe mainly the same features as in previous figures with the two different scaling behaviours separated by a characteristic size, respectively, $\delta^*_{\varnothing_1}$, $\delta^*_{\varnothing_2}$ and $\delta^*_{\varnothing_3}$. For instance, when using smaller glass beads ($\varnothing_1 \sim 50\,\mu$m), the amplitude of the height fluctuations of the fronts decreases (vertical shift) as well as the scaling range at small scales providing a roughness exponent $\zeta_{\parallel}^{-} \sim 0.6$ up to the scale $\delta^*_{\varnothing_1} \sim 35\mu$m. We checked that all observations are independent of the sampling resolution, and the analysis techniques (see fig. 2 and fig. 3). Moreover, we also verified on fig. 4 that those results are consistent with the morphology of planar cracks obtained during previous experiments [16,18,19,26] with various conditions concerning both the sample preparation (glass beads mixed with an aluminum powder with a wider size distribution) and the fracturing process with both crack front at rest ($v = 0$) or propagating at various velocities ($0.4\,\mu$m/s $< v < 40\,\mu$m/s).

Conclusion. – We have analyzed the scaling properties of long planar crack fronts moving along a rough interface between two sintered Plexiglas plates. We identified two scaling regimes separated by a length scale δ^* that depends on the ratio of the local stress drop and the local toughness disorder. Above δ^*, the fronts are mono-affine, characterized by a roughness $\zeta_{\parallel}^{+} = 0.35 \pm 0.05$, consistent with the fluctuating line model. Below δ^*, we see a different scaling regime, multi-affine, with a roughness exponent $\zeta_{\parallel}^{-} = 0.60 \pm 0.05$. The later roughness exponent is in agreement with the coalescence model. A similar picture may explain observations for the scaling of crack surfaces [7,30–32] suggesting that crack coalescence is the mechanism operating at small scales corresponding to the process zone while the fluctuations of the elastic front line is the dominating one at larger scales.

* * *

We thank D. Bonamy, E. Bouchaud, J. Mathiesen, S. Roux, L. Vanel, M. Adda-Bedia, C. Marlière, S. Zapperi, M. Alava and L. Laurson for helpful discussions.

REFERENCES

[1] Mandelbrot B. B., Passoja D. E. and Paullay A. J., *Nature*, **308** (1984) 721.
[2] Bouchaud E., *J. Phys.: Condens. Matter*, **9** (1997) 4319.
[3] Alava M. K., Nukala P. K. V. V. and Zapperi S., *Adv. Phys.*, **55** (2006) 349.
[4] Bouchaud E. *et al.*, *Europhys. Lett.*, **13** (1990) 73.
[5] Måløy K. J. *et al.*, *Phys. Rev. Lett.*, **68** (1992) 213.

[6] Renard F. *et al.*, *Geophys. Res. Lett.*, **33** (2006) L04 305.
[7] Bonamy D. *et al.*, *Phys. Rev. Lett.*, **97** (2006) 135504.
[8] Ponson L. *et al.*, *Phys. Rev. Lett.*, **97** (2006) 125501.
[9] Hansen A. *et al.*, *Phys. Rev. Lett.*, **66** (1991) 2476.
[10] Räisänen V. I. *et al.*, *Phys. Rev. Lett.*, **80** (1998) 328.
[11] Bouchaud J. P. *et al.*, *Phys. Rev. Lett.*, **71** (1993) 2240.
[12] Daguier P. *et al.*, *Europhys. Lett.*, **31** (1995) 367.
[13] Schmittbuhl J. *et al.*, *Phys. Rev. Lett.*, **74** (1995) 1787.
[14] Rosso A. and Krauth W., *Phys. Rev. E*, **65** (2002) R025101.
[15] Bonamy D. *et al.*, *Phys. Rev. Lett.*, **101** (2008) 045501.
[16] Måløy K. J. *et al.*, *Phys. Rev. Lett.*, **96** (2006) 045501.
[17] Schmittbuhl J. and Måløy K. J., *Phys. Rev. Lett.*, **78** (1997) 3888.
[18] Delaplace A. *et al.*, *Phys. Rev. E*, **60** (1999) 1337.
[19] Måløy K. J. and Schmittbuhl J., *Phys. Rev. Lett.*, **87** (2001) 105502.
[20] Bouchaud E. *et al.*, *J. Mech. Phys. Solids*, **50** (2002) 1703.
[21] Hansen A. and Schmittbuhl J., *Phys. Rev. Lett.*, **90** (2003) 045504.
[22] Schmittbuhl J. *et al.*, *Phys. Rev. Lett.*, **90** (2003) 045505.
[23] Alava M. K. and Zapperi S., *Phys. Rev. Lett.*, **92** (2004) 049601.
[24] Schmittbuhl J. *et al.*, *Phys. Rev. Lett.*, **92** (2004) 049602.
[25] Hansen A. *et al.*, *Phys. Rev. E*, **75** (2007) 03102.
[26] Santucci S. *et al.*, *Phys. Rev. E*, **75** (2007) 016104.
[27] Katzav E., Adda-Bedia M. and Derrida B., *EPL*, **78** (2007) 46006.
[28] Blatter *et al.*, *Rev. Mod. Phys.*, **66** (1994) 1125.
[29] Tanguy A. and Vettorel T., *Eur. Phys. J. B*, **38** (2004) 71.
[30] Dalmas D. *et al.*, *Phys. Rev. Lett.*, **101** (2008) 255501.
[31] Morel S. *et al.*, *Phys. Rev. E*, **78** (2008) 016112.
[32] Daguier P. *et al.*, *Phys. Rev. Lett.*, **78** (1997) 1062.

Local dynamics of a randomly pinned crack front during creep and forced propagation: An experimental study

Ken Tore Tallakstad,[1] Renaud Toussaint,[2] Stephane Santucci,[3] Jean Schmittbuhl,[2] and Knut Jørgen Måløy[1]
[1]*Department of Physics, University of Oslo, PB 1048 Blindern, NO-0316 Oslo, Norway*
[2]*Institut de Physique du Globe de Strasbourg, UMR 7516 CNRS, Université de Strasbourg, 5 rue René Descartes, F-67084 Strasbourg Cedex, France*
[3]*Laboratoire de Physique, Ecole Normale Suprieure de Lyon, CNRS UMR 5672, 46 Alle d'Italie, F-69364 Lyon Cedex 07, France*
(Received 7 September 2010; revised manuscript received 24 January 2011; published 14 April 2011)

We have studied the propagation of a crack front along the heterogeneous weak plane of a transparent poly(methyl methacrylate) (PMMA) block using two different loading conditions: imposed constant velocity and creep relaxation. We have focused on the intermittent local dynamics of the fracture front for a wide range of average crack front propagation velocities spanning over four decades. We computed the local velocity fluctuations along the fracture front. Two regimes are emphasized: a depinning regime of high velocity clusters defined as avalanches and a pinning regime of very low-velocity creeping lines. The scaling properties of the avalanches and pinning lines (size and spatial extent) are found to be independent of the loading conditions and of the average crack front velocity. The distribution of local fluctuations of the crack front velocity are related to the observed avalanche size distribution. Space-time correlations of the local velocities show a simple diffusion growth behavior.

DOI: 10.1103/PhysRevE.83.046108 PACS number(s): 62.20.mt, 46.50.+a, 68.35.Ct

I. INTRODUCTION

The failure of heterogeneous materials has a vast importance in geophysical systems, industrial applications, and, of course, fundamental physics. This subject is far from understood and has been studied extensively over the years [1–3]. Of key importance for brittle materials is the competition between pinning forces due to local material heterogeneities and elastic forces due to outer applied stress, resulting in a complex roughening of fracture surfaces. In general, this competition triggers a rich history dependence of the fracture process. Up until quite recently, a broad range of experimental and simulation studies have been concerned with the morphology of either fracture surfaces in the case of three-dimensional solids [4], or interfacial crack fronts for planar fracture [5–7]. In both geometries it has been well established that the fracture roughness exhibits self-affine scaling properties [8–11]. To this end, theoretical approaches have been suggested: the fluctuating line model [12,13], where the interface is seen as an elastic string propagating in a rough morphology, being pinned with different strengths at different positions and also the stress weighted percolation approach [14] with a damage zone ahead of the crack.

In this study, we will pay attention to the dynamics of fracture propagation. Owing to the material heterogeneities, the motion is complex and characterized by abrupt jumps separated by periods of rest. Both the jumping and the resting behavior span a large range of time scales. This dynamics is often referred to as *crackling noise* [15]. Apart from the direct observation of fracture [16–19], such intermittent dynamics embody also large-scale activity in earthquakes [20–22], acoustic emission during material failure (fiberglass [23], rocks [24], paper [25], etc.), magnetic domain wall motion (Barkhaussen noise) [26], wetting contact line motion on a disordered substrate [27,28], and imbibition fronts in porous media [29].

Studies on fracture propagation often characterize the complex dynamics through related effective average quantity due to the difficulties of direct observation and/or insufficient resolution of the spatiotemporal behavior at local scale. In contrast we use here a transparent poly(methyl methacrylate) (PMMA) model for an in-plane mode-I fracture well suitable for capturing optically detailed intermittent behavior with high precision in both time and space [5].

The present work is a completion and substantial extension of the experimental study presented by Måløy *et al.* in Ref. [17], where the concept of the waiting time matrix was introduced; a consistent way of obtaining the local velocity field of the propagation of a pinned interface. Statistical analysis, based on the waiting time matrix, of avalanche behavior in fracture front propagation has since been followed up by simulations. Bonamy *et al.* [30] quantitatively reproduced the intermittent crackling dynamics observed in experiments, using a crack line model based on linear-elastic fracture mechanics extended to disordered materials. Using a similar string model, but with pure quasistatic driving and zero average propagation velocity, Laurson *et al.* [31] have recently proposed a scaling relation connecting the global activity with the observed local avalanches, connecting the dynamics at large and small scales. Further they found that the aspect ratio of local avalanches is consistent with recent experimental advances of multiscale roughness analysis [7]. Experimentally, Grob *et al.* [32] have, through the terminology of seismic catalogs, been able to compare the dynamics of interfacial crack propagation to what is found in shear rupture for earthquakes.

Most of the previous studies mentioned in the above paragraph address only rapid event statistics for a fracture propagation that is forced by the imposed boundary conditions (critical fracture propagation). What we present here is more elaborate and general in the sense that we consider intermittency in *both* high and low velocity regimes of crack propagation using two different methods of external loading: (1) constant opening velocity of the crack and (2) creep relaxation of a crack maintained at a constant opening distance. While it is easy to imagine that these different boundary conditions will give a very different global behavior, we are surprised to find that the local dynamics is similar in every respect. This is shown by statistical analysis of high and low velocity events, referred to as depinning and pinning clusters, respectively, and by considering the autocorrelation of the velocity field. The vanishingly small time correlations have been related to the time evolution of the width of the fracture front [16]. We see that it follows simple diffusion growth. Another important finding is that the pinning and depinning size distributions are described by the same power-law exponent. Moreover, we propose a relationship between the different power-law exponents describing the fracture process, thus linking velocity fluctuations with spatial avalanches.

This paper is organized as follows. In Sec. II we describe in detail the experimental setup, including sample preparation, loading conditions, and optical setup. We then present the results in Sec. III starting with the distribution of local velocities along the fracture front (Sec. III A). In Sec. III B we obtain the autocorrelation functions in time and space for these velocities. Finally, in Sec. III C we give the main statistical analysis of spatial clusters that we eventually show to be linked to the local velocity distribution in Sec. III A. Section IV summarizes the paper with concluding remarks.

II. EXPERIMENTAL SETUP

A. Sample preparation

The experimental setup [5,6,32] is shown in Fig. 1. The fracture sample is made out of two transparent Plexiglas (PMMA) plates: a thicker plate with dimensions $(l_1,w_1,h_1) = (30,14,1)$ cm and a thinner plate with dimensions $(l_1,w_2,h_2) = (30,10,0.4)$ cm for the length, width, and thickness, respectively. The plates are then sandblasted on one side using glass beads ranging between 50 and 300 μm in diameter. Sandblasting introduces random roughness on the originally "flat" surface. This causes light to be scattered in all directions from these microstructures, hence transparency of the plate is lost and it becomes opaque. The plates are then clamped together in a pressure frame, with the sandblasted sides facing each other. The pressure frame is made of two parallel aluminum plates, exerting a normal homogeneous pressure on both sides of the PMMA. Finally, the pressure frame is put in a ceramic temperature controlled oven at 205 °C for 30–50 min. This annealing or sintering procedure creates new polymer chains between the two plates and the resulting PMMA block is now fully transparent. The new layer created between the two plates are weaker than the bulk PMMA, so that we obtain a weak plane with quenched disorder in which the fracture can propagate. This system is ideal for direct visual observation since the fractured part of the sample immediately becomes opaque whereas the unfractured part remains transparent. The sharp and high contrast boundary between transparent and opaque parts thus defines the fracture front.

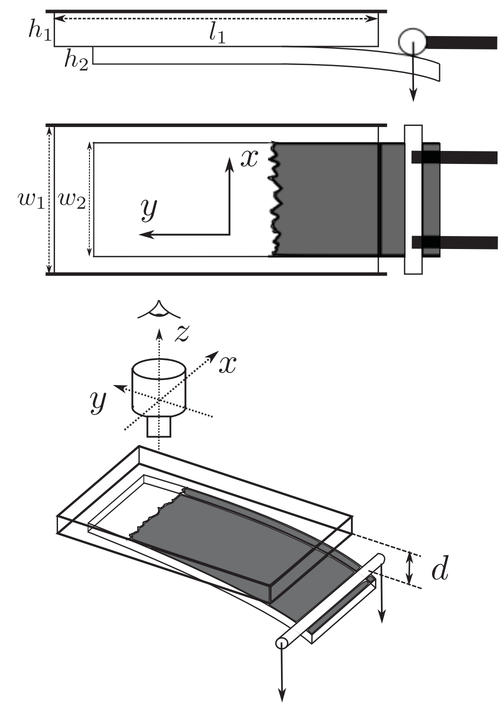

FIG. 1. Sketch of the experimental setup. Two PMMA plates with dimensions $(l_1,w_1,h_1) = (30,14,1)$ cm and $(l_1,w_2,h_2) = (30,10,0.4)$ cm are sintered together, creating a weak in-plane layer for the fracture to propagate. Fracture is initiated by lowering a cylindrical press bar, controlled by a step motor, onto the lower plate. The uncracked part of the sample is transparent, whereas the cracked part has lost transparency hence creating a good contrast at the fracture front. The fracture front is imaged from above by a digital camera. The deflection d (z direction) between the plates is indicated in the lower panel. The fracture plane is (x,y), where the x direction is transverse to the average direction of fracture propagation whereas the y direction is parallel to the average direction of fracture propagation.

The rough surface generated by the sandblasting technique depends on the volume flux of the beads, the kinetic energy of the beads, the bead size, and the total time of the sand blasting. It is important to note that there is no obvious direct link between the bead size and the characteristic size of the disorder. The rough surface will, after annealing, give local toughness fluctuations. The strength of these fluctuations will depend on the sintering time. The relationship between the disordered morphology of the plates and the toughness fluctuations is very difficult to access experimentally. However, we know that the toughness fluctuations will change when the disorder of the plates changes [7]. In Ref. [33] a white-light interferometry technique was used to measure the rough surface, sandblasted with 50–100 μm particles, and it was found that the local heterogeneities had a characteristic size of ~15 μm. Other samples have been studied through a microscope [6] where the random position of the defaults and the maximum size of the defaults was seen to roughly correspond to the bead size ~50 μm. However, we emphasize that the image pixel resolution is smaller (~1–5 μm) and the largest length scales considered (~10^3 μm) are much larger than the sample disorder.

Two different PMMA samples, characterized by the glass bead diameter, have been used in our experiments. Sample 1 has been sandblasted with 100–200 μm beads whereas sample 2 has been sandblasted with 200–300 μm beads. Both samples where sintered in the oven for 50 min.

B. Mechanical setup and loading conditions

The thick plate of the PMMA block is mounted on a rigid aluminum frame, also containing a camera setup for imaging. The mode-I fracture is induced by a normal displacement of the thin plate pushed by a cylindrical press bar, as shown in Fig. 1. Indicated is also the definition of our coordinate system, where (x,y) is the fracture plane: the x direction is transverse to the average direction of fracture propagation whereas the y direction is parallel to the average direction of fracture propagation. The deflection d is defined as the plate separation at the position of the press bar. A bit of glycerol is put on the contact between the plate and the press bar to reduce any friction and prevent shear loading. The press bar is mounted to a force gage on a vertical translation stage controlled by a step motor so that it can be moved up and down in the z direction. Through the force gage we are able to monitor the force exerted on the lower plate during an experiment. To ensure a homogeneous loading, all components of the experimental setup are mounted on a rigid plane aluminum plate and leveled. Particularly, a level is used on the thin plate to ensure that it is perfectly horizontal. If not, adjustments are made to make it so. This is also done with the press bar, thus any gradient in the loading should not exist.

We use two sets of loading conditions.

(1) The imposed deflection d (see Fig. 1) as a function of time t is given by

$$d(t) = v_p t, \tag{1}$$

where v_p is the velocity of the press bar. Throughout the experiment we can measure the force F on the lower plate at the position of the press bar. As an example, the force development during an experiment is shown in the upper panel of Fig. 2(a). Initially there is a period of linear increase, corresponding to pure elastic bending of the lower plate. At some point, indicated by the dashed line, linear behavior is deviated and fracturing occurs. After some transient period, the force decays only slowly in time as the fracture propagates in the sample. The corresponding linear increase of the deflection is shown in the bottom panel. We will refer to these loading conditions as *constant velocity boundary conditions* (CVBC).

(2) The deflection is given by

$$d(t) = \begin{cases} v_p t & \text{for} \quad t < t_{\text{stop}} \\ \text{const.} & \text{for} \quad t > t_{\text{stop}} \end{cases}, \tag{2}$$

where t_{stop} marks the time at which the step motor controlling the pressbar is switched off (i.e., $v_p = 0$). We will refer to these loading conditions as *creep boundary conditions* (CBC) since it is seen that the fracture front continues to propagate at "creepingly slow" velocities over several days after t_{stop}. An example is shown in Fig. 2(b) where we see a logarithmic decay of the force while the deflection is maintained as constant. Motivated by the different global behavior of the fracture in CVBC and CBC, we have performed experiments using both loading conditions to study the local dynamics.

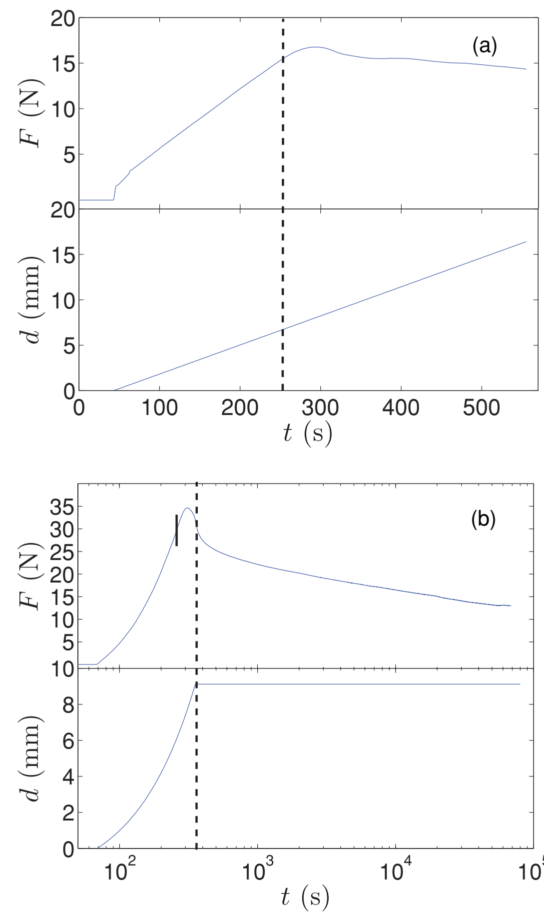

FIG. 2. (Color online) (a) Constant velocity boundary conditions (CVBC). Upper panel shows the force development $F(t)$ on the lower plate as it is bent by the pressbar. The dashed line indicates the onset of fracturing. Lower panel shows the linear increase of the deflection $d(t)$. (b) Creep boundary conditions (CBC). Same as in (a) but $F(t)$ and $d(t)$ are in a semilog scale. The short, solid line in the upper panel indicates the onset of fracturing, whereas the dashed line indicates the time at which the pressbar is stopped and maintained in a constant position according to Eq. (2).

C. Optical setup

A small central region, at the millimeter scale, of the front propagation is followed in time using a high-speed digital camera mounted on a microscope. The large width of the bent PMMA plate (10 cm) ensures that the central region of interest is not influenced by finite size effects (see Fig. 3). In one experiment between 12 000 and 30 000 frames are captured using either the *Photron Fastcam-Ultima APX* (512 × 1024 pixels) or the *Pixelink Industrial Vision PL-A781* (2200 × 3000 pixels). High-resolution images (∼ 1–5 μm/pixel) are captured at a high frame rate relative to the average propagation velocity of the crack front (see Table I). This is important as the local fluctuations in velocity can range over several decades. As large amounts of data are accumulated, we only have the possibility to follow the fracture

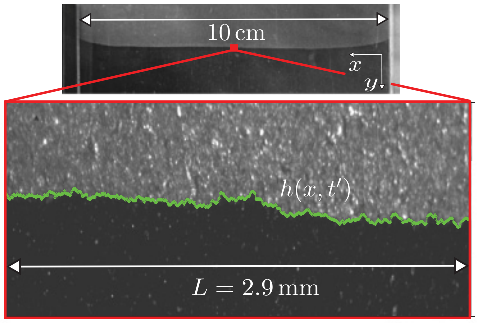

FIG. 3. (Color online) Fracture frontline $h(x,t')$ at some time t', superimposed on the corresponding raw image. Direction of propagation is from top to bottom. System size L in the x direction is indicated. The framed raw image corresponds to a tiny central part of the full sample as seen in the upper panel.

front over short time windows compared to the long-time global development in the examples shown in Fig. 2. Both in the case of CBC and CVBC these time windows are small enough so that the average propagation velocity of the crack front is considered constant. Also for CBC we did several experiments with very different average velocity [Fig. 2(b)] during the same loading periods. The span of the time windows will of course vary depending on the average velocity, but the y distance (parallel to direction of propagation) covered by the crack front is roughly $\sim 500\,\mu$m in all our experiments. Note that the average initial y position of the crack front is varied on the order of several centimeters between different experiments. Finally, image capture is initiated only after onset of the fracture process.

The obtained grayscale images of the fracture front contain two parts: a dark and a bright region, corresponding, respectively, to the uncracked and the cracked part of the sample. The gray level distribution of the image thus presents two distinct peaks. Image analysis is performed to obtain the coordinates of the fracture front line, $h(x,t)$, separating the two regions. This is done by thresholding the grayscale image at the local minimum of the gray level histogram, between the bright and dark peak. We then obtain a black and white image from which the front can easily be extracted. We always obtain a very good contrast between the cracked and uncracked part of the sample; the extracted fronts are very robust with respect to perturbations in the chosen threshold. For a more detailed description of the front extraction and image treatment see Refs. [6,32].

Figure 3 shows an extracted front line $h(x,t)$ superimposed on the corresponding raw image. Its roughness is due to local pinning asperities of high toughness, created as a result of the sandblasting and annealing procedure as explained earlier. Occasionally, on small scales close to the pixel resolution, the front shows local overhangs and is not always a single valued function of x. However, the number of overhangs per front and the scale at which they occur are small; hence we construct the single valued front $h(x,t)$ by keeping only the most advanced y coordinate at the front line for a given x coordinate. Arbitrarily we could also have chosen the least advanced y coordinate. Single valued fronts are constructed to simplify the statistical analysis, which has shown not to influence the results.

TABLE I. Parameters of the different experiments, sorted after the average propagation velocity of the front $\langle v \rangle$: System size L (x direction), image timestep δt gives the time delay between the capture of two subsequent images, resolution a gives the pixel resolution of an image, displacement type denotes the set of boundary conditions used, and the last column indicates the sample number. Sample 1 has been sandblasted with 100–200 μm beads whereas sample 2 has been sandblasted with 200–300 μm beads.

	$\langle v \rangle$ (μm/s)	L (μm)	δt (s)	a (μm/pixel)	Displacement type	Sample no.
Expt. 1	0.028	6700	1	2.24	CBC	2
Expt. 2	0.15	6700	5×10^{-1}	2.24	CBC	2
Expt. 3	0.42	5600	2×10^{-2}	5.52	CVBC	2
Expt. 4	1.36	5600	2×10^{-2}	5.52	CBC	2
Expt. 5	2.4	2865	8×10^{-3}	2.83	CVBC	1
Expt. 6	10.1	2865	2×10^{-3}	2.83	CBC	1
Expt. 7	23	2865	2×10^{-3}	2.83	CVBC	1
Expt. 8	141	2842	5×10^{-4}	2.83	CVBC	1

III. RESULTS

The rough fracture front exhibits self-affine scaling properties [8–11,13,14] together with a complex avalanche-like motion with very large velocity fluctuations. Due to the large temporal and spatial variations in front velocity it is not straightforward to analyze the local dynamics by a simple front subtraction procedure. Therefore we characterize this complex behavior by measuring the local waiting time fluctuations of the crack front during its propagation, following the procedure introduced first in Ref. [17]. We compute a so-called *waiting time matrix* (WTM) [29,30,32], which is a pinning time map with elements w, giving the amount of time the front is pinned down or fixed at a particular position (x,y) in time step units. As explained in Appendix A, the local velocity v at a given position is given as $v = a/(w\,\delta t)$. Using $h(x,t)$ and the WTM, it is then straightforward to obtain the local velocities along a fracture front $v(x,t)$. Furthermore, by computing $v(x,t)$ for all time steps, we build the spatiotemporal velocity map $V_t(x,t)$. The average velocity $\langle v \rangle$ is defined as the average over all elements of $V_t(x,t)$ (i.e., the total average over all fronts).

Presented below are the results of eight experiments (both CBC and CVBC), spanning a broad average propagation velocity range, where we have characterized the local dynamics. The total duration of an experiment is within the range of 4 seconds to 7 hours, whereas the average distance of front propagation, is $\sim 500\,\mu$m in all cases. The details of each experiment can be found in Table I. Additionally we will also compare the present data to previous experiments from Ref. [17].

A. Distribution of local velocities

A grayscale map of the waiting time matrix is shown for a CBC experiment in Fig. 4. The dark regions correspond to a high waiting time and thus a low velocity, and vice versa for bright regions. The dark low velocity regions are seen to occur as irregularly shaped "lines," separated by brighter compact

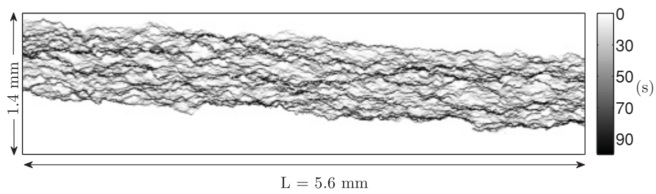

FIG. 4. Waiting time matrix of a CBC experiment, $\langle v\rangle = 1.36$ μm/s. The map results from the extraction of 24 576 front lines at a rate of 50 fps. Dark regions correspond to a high waiting time and thus a low velocity, and vice versa for bright regions, as shown in the colorbar indicating the amount of time (in seconds) the front has been fixed at a given position. Black pinning lines are visible, with bright depinning regions in between. The system size L is indicated.

regions referred to as high velocity avalanches. The wide span of waiting times shown by the colorbar, together with their irregular distribution in space, is direct visual confirmation of the complex dynamics found in this system. Furthermore, the visual impression of the WTM for a CBC experiment compared to a CVBC experiment is identical. The similarity of the local dynamics in CBC and CVBC experiments is also confirmed in our analysis, as we will return to.

From the local velocities along all front lines $V_t(x,t)$ we can compute the normalized probability density function (PDF) $P(v)$. By rescaling every local velocity with the average propagation velocity $v/\langle v\rangle$, we obtain a data collapse for all experiments as shown in Fig. 5. In this figure the results from all experiments in Table I are put on top of previous experiments from Ref. [17]. It was found that

$$P(v/\langle v\rangle) \propto (v/\langle v\rangle)^{-\eta}, \quad \text{for} \quad v/\langle v\rangle > 1, \tag{3}$$

with the exponent $\eta = 2.55 \pm 0.15$. It is important to note that the PDF $P(v)$, computed here directly from $V_t(x,t)$, is exactly the same quantity as the PDF of the local front velocity v found by estimating the occurrence number of each measured velocity on all the pixels in all the fracture front line images, as defined in Ref. [17]. The result in Eq. (3), primarily obtained for CVBC, is now extended to the case of creep experiments. It is indeed very stable over the different experiments, considering the wide range of average velocities. We emphasize that Fig. 5 provides quantitative confirmation on the similarity between the local dynamics for CBC and CVBC experiments.

At this point we divide the velocity distribution in two and define a *pinning* regime for $v/\langle v\rangle < 1$ and a *depinning* regime for $v/\langle v\rangle > 1$, as indicated in Fig. 5. The Fig. 5 inset shows the corresponding PDF of waiting times $P(w/\langle w\rangle)$. Through Eq. (A2) the two distributions are related by $P(v)dv = P(w)dw$ [cf. Eq. (35)], giving $P(w/\langle w\rangle) \propto (w/\langle w\rangle)^{\eta-2}$ for $w/\langle w\rangle < 1$. Note that the waiting time distribution decays very fast in the pinning regime compared to the depinning regime.

B. Space and time correlations

The power-law distribution of the local velocities confirms the visual impression of a nontrivial local dynamics of the fracture process. As mentioned earlier, the front propagates through high velocity bursts of different sizes. An important question is thus how the local velocities along and between different front lines are correlated in space and time.

We define the normalized autocorrelation function $G(\Delta x)$ and $G(\Delta t)$ for the local velocities on all front lines $v(t,x)$ in space and time as

$$G(\Delta x) = \left\langle \frac{\langle [v(x+\Delta x,t) - \langle v\rangle_x][v(x,t) - \langle v\rangle_x]\rangle_x}{\sigma_x^2} \right\rangle_t, \tag{4}$$

$$G(\Delta t) = \left\langle \frac{\langle [v(x,t+\Delta t) - \langle v\rangle_t][v(x,t) - \langle v\rangle_t]\rangle_t}{\sigma_t^2} \right\rangle_x, \tag{5}$$

where $\langle v\rangle_x$ and σ_x is the spatial average and standard deviation, respectively, at a given time in $V_t(x,t)$, whereas $\langle v\rangle_t$ and σ_t are the temporal average and standard deviation, respectively, for a given position in $V_t(x,t)$. The outer brackets in Eqs. (4) and (5) denotes an average over all different realizations in time and space, respectively (i.e., over all columns and rows in the V_t matrix).

In Fig. 6 the spatial correlation function $G(\Delta x)$ is shown for all experiments listed in Table I. It is more or less evident that correlation functions obtained from the same sample are grouped together, independently of the average propagation velocity and loading condition. By fitting the data with power-law functions with an exponential cutoff we get

$$G(\Delta x) \propto \Delta x^{-\tau_x} \exp(-\Delta x/x^*), \tag{6}$$

where $\tau_x = 0.53 \pm 0.12$ is the average exponent and $x^* = \{92,131\}$ μm is the average cutoff or correlation length of the local velocities in the x direction, for samples 1 and 2, respectively. The quality of the fits is not perfect, as can be seen in Fig. 6, but they represent each group of correlation functions fairly well. It is to be noted that extracting well-defined correlation lengths is not trivial in our data. Other estimators of Eq. (4) are possible to use (e.g., the power spectrum method).

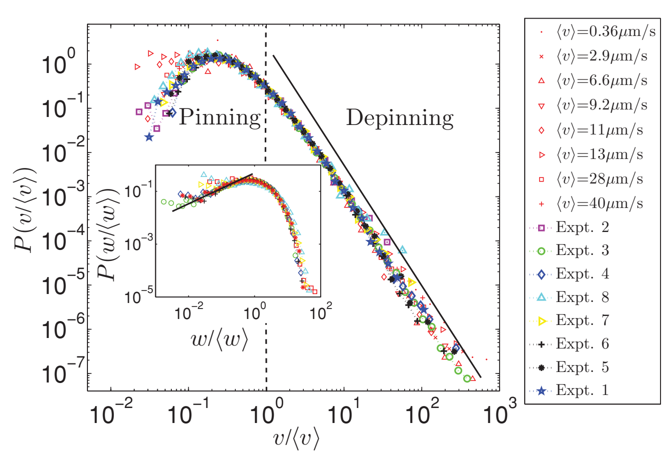

FIG. 5. (Color online) Distribution of local velocities $P(v/\langle v\rangle)$ rescaled by the average propagation velocity for various experimental conditions: A range of roughly four decades in average crack front velocity including both CBC and CVBC experiments. In the legend, symbols labeled with different average velocities are results from Ref. [17]. A fit to all the data for $v > \langle v\rangle$ shows power-law behavior with an exponent -2.55. Inset shows the corresponding waiting time distribution $P(w/\langle w\rangle)$. The exponent transforms in this case to 0.55.

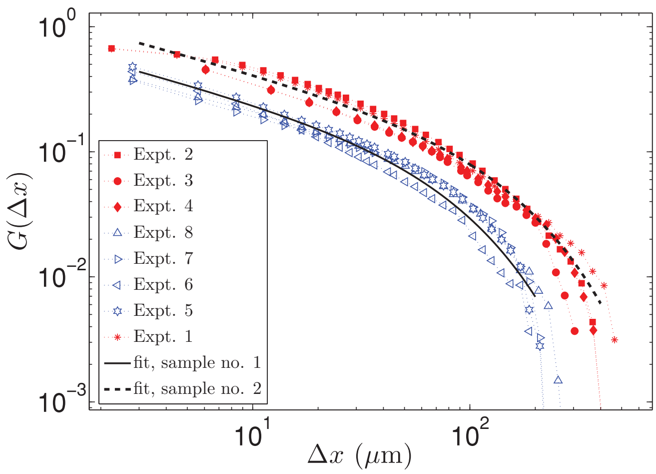

FIG. 6. (Color online) Space correlation functions $G(\Delta x)$. Functions from the same sample are grouped together (sample 2: filled markers, sample 1: open markers). A power law with exponential cutoff has been fitted to each group of correlation functions, as indicated by the solid and dashed lines for samples 1 and 2, respectively (see text).

In Fig. 7(a) the time correlation function $G(\Delta t)$ is shown for all experiments listed in Table I. For each experiment, functional fits analog to Eq. (6) have been made. Using the average value of the power-law exponent $\tau_t \approx 0.43$ and different cutoff correlation times t^*, a good collapse is obtained. We note also that t^* is small; typically more than two orders of magnitude smaller than the duration of an experiment. The inset shows the scaling of the correlation time with the average propagation velocity

$$t^* = y^*/\langle v\rangle, \tag{7}$$

where $y^* \approx 7\,\mu$m. The proportionality constant y^* has the dimension of a length since the scaling exponent equals minus unity. This length scale is on the order of the pixel resolution a and also within the disorder limit. Hence y^* is very small and might be influenced both by resolution and disorder effects. For comparison we calculate $G(\Delta y)$ directly, that is, the velocity autocorrelation in space along the direction of propagation, defined similarly to Eq. (4) and shown in Fig. 7(b). We find no power-law decay in this case, but the drop to zero correlation occurs between 10–20 μm consistently with y^*. Correlation functions from the same sample are shown using filled and empty markers for samples 2 and 1, respectively. Within the interval $\{a,20\}$ μm, where a is the image resolution, the sample grouping is not so clear as in the case for $G(\Delta x)$ as shown in the inset, but the same initial trend is observed. This can be attributed to resolution effects and the very small correlation lengths. Thus at the time and length scales we are looking at, the local velocities are considered uncorrelated in the y direction.

Since the local fluctuations control the global advancement of the crack, it is of interest to consider the evolution of the width of the fracture front in time. This growth process is known to depend on the system correlations. It has been shown previously [34] that uncorrelated growth processes such as simple diffusion, Brownian motion, and so on, can be described by a growth exponent $\alpha = 1/2$. For the present case we define the *root-mean-square* (RMS) value of the front width $\Delta h(t)$ as

$$\langle \Delta h(t)^2\rangle^{\frac{1}{2}} = \langle([h(x,t+t_0)-\bar{h}]-[h(x,t_0)-\bar{h}_0])^2\rangle^{\frac{1}{2}}_{x,t_0}, \tag{8}$$

where $h(x,t_0)$ is an initial front line and $\bar{h}$ indicates a positional average height at a given time. This differs somewhat from the usual situation of a front growth from an initially flat front. In our case the front width is defined as the fluctuations from an initially rough line which corresponds to the geometry of the

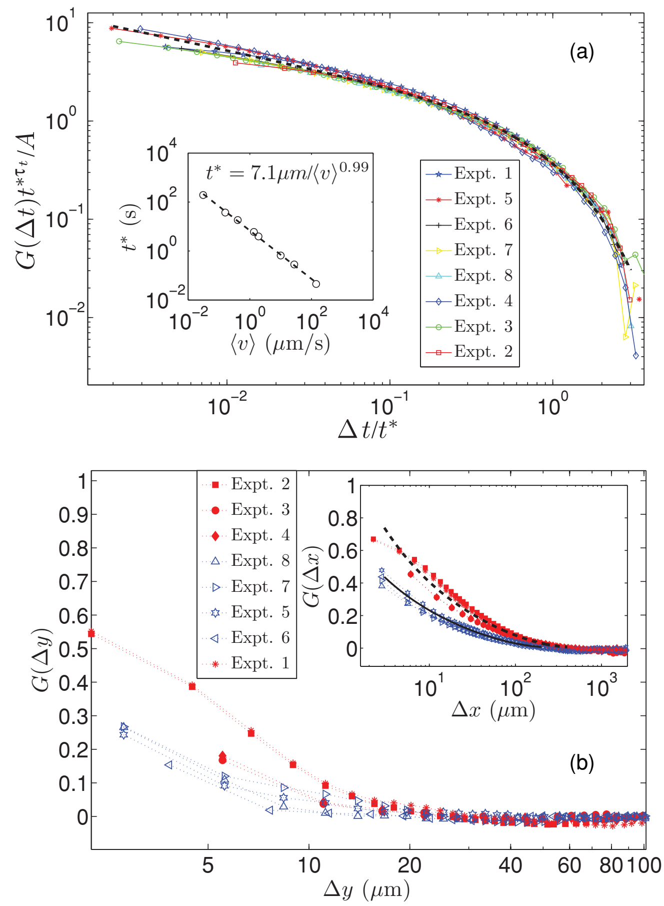

FIG. 7. (Color online) (a) Time correlation functions collapsed onto each other according to a power law with an exponential cutoff $G(\Delta t) = A\Delta t^{-\tau_t}\exp(-\Delta t/t^*)$. The exponent is $\tau_t \approx 0.43$. Inset shows the scaling between the crossover correlation time and average propagation velocity $t^* \approx 7\,\mu\text{m}/\langle v\rangle$. (b) Space correlation function $G(\Delta y)$ with logarithmic Δy axis. Consistently with (a) and Eq. (7), the local velocities become uncorrelated after only a short distance (~10–20 μm) in the y direction. Correlation functions from experiments performed on samples 2 and 1 have filled and open markers, respectively. To some extent we see also here a grouping of experiments from the same sample. The difference is, however, not as clear as for the spatial correlations along the transverse x axis (subparallel to the fronts), on the inset showing $G(\Delta x)$ with logarithmic x axis. The reason might be that the drop to zero correlation occurs close to the resolution scale for $G(\Delta y)$.

front at the onset of the experiment. The front width is related to the autocorrelation of local velocities in time. By rewriting Eq. (8) and using that $h(t+t_0) - h(t_0) = \int_{t_0}^{t+t_0} v(t')dt'$ we obtain

$$\begin{aligned}\langle \Delta h(t)^2 \rangle &= \langle [h(x,t+t_0) - h(x,t_0)]^2 \rangle - (t\langle v \rangle)^2 \\ &= \int_{t_0}^{t+t_0} \int_{t_0}^{t+t_0} \langle v(n)\, v(m) \rangle dm\, dn - (t\langle v \rangle)^2. \quad (9)\end{aligned}$$

By substituting $n + \Delta t = m$ and using Eq. (5) we get

$$\begin{aligned}&\langle \Delta h(t)^2 \rangle \\ &= \int_{t_0}^{t+t_0} \int_{t_0-n}^{t+t_0-n} \langle v(n)\, v(n+\Delta t) \rangle d\Delta t\, dn - (t\langle v \rangle)^2 \\ &= \sigma_t^2 \int_{t_0}^{t+t_0} dn \int_{t_0-n}^{t+t_0-n} d\Delta t\, G(\Delta t). \quad (10)\end{aligned}$$

As argued above, we consider the local velocities uncorrelated in time. The regime where $G(\Delta t)$ behaves as a power law is very short, and should only affect $\Delta h(t)$ on very small time scales.

Thus we approximate the autocorrelation function with the Dirac delta function $G(\Delta t) \approx \delta(\Delta t)$ which gives

$$\langle \Delta h(t)^2 \rangle \propto t \Rightarrow \langle \Delta h(t)^2 \rangle^{\frac{1}{2}} \sim t^{\alpha}, \quad (11)$$

with the growth exponent $\alpha = 1/2$. Figure 8 shows the scaling of the front width as a function of time for all experiments. We find, indeed, a growth exponent $\alpha = 0.55 \pm 0.08$ consistent with Eq. (11), as indicated by the fitted dashed line. The large-scale crossover is an effect of a limited system size in the direction of crack propagation. Our direct measurement of the growth exponent also agrees with the indirect measures in Refs. [16,33], where the front width power spectrum was analyzed at different times and interpreted in terms of a Family-Vicsek scaling, with a dynamic exponent $\kappa = 1.2$ and a roughness exponent $\delta = 0.6$ giving $\alpha = \delta/\kappa = 0.5$.

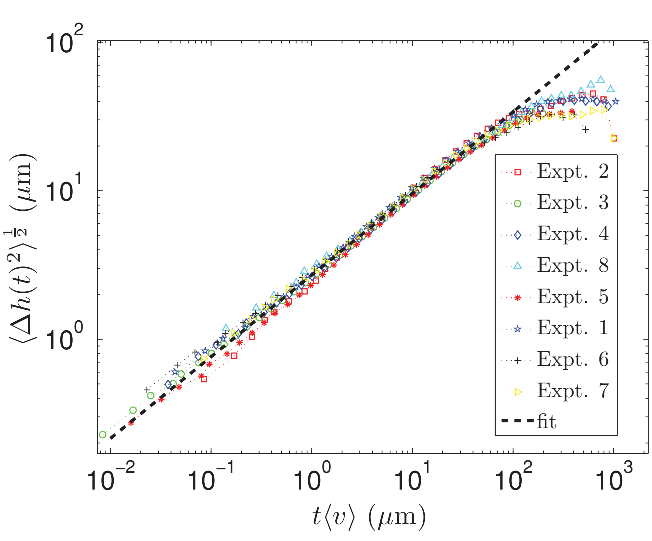

FIG. 8. (Color online) Scaling of the front width as a function of time, rescaled with the average velocity. The dashed line corresponds to $\langle \Delta h(t)^2 \rangle^{\frac{1}{2}} \propto t^{0.55}$.

Due to the one-to-one correspondence between velocity and waiting time [Eq. (A2)], the above analysis of correlations could just as well have been performed using the latter quantity. Calculating $G(\Delta x)$, $G(\Delta t)$, and $G(\Delta y)$ using w, we obtain approximately the same trends and correlation lengths as for v. We turn now to the statistics of the dynamical avalanches in the pinning and depinning regimes.

C. Cluster analysis

1. Spatial map of clusters

As discussed earlier, the local dynamics of the fracture front is a mix of pinning lines where the front is fixed or only moves slowly, and sudden propagation in high velocity jumps or bursts. The statistics in both the pinning and depinning regimes will be shown to be scale invariant and characterized by equal scaling exponents. To study both these regimes we apply a thresholding procedure to the velocity matrix $V(x,y)$ and obtain a thresholded binary matrix V_C

$$V_C = \begin{cases} 1 & \text{for} \quad v \geqslant C \langle v \rangle \\ 0 & \text{for} \quad v < C \langle v \rangle \end{cases}, \quad (12)$$

for the depinning regime and

$$V_C = \begin{cases} 1 & \text{for} \quad v \leqslant \frac{1}{C} \langle v \rangle \\ 0 & \text{for} \quad v > \frac{1}{C} \langle v \rangle \end{cases}, \quad (13)$$

for the pinning regime. Here C is a threshold constant of the orders of a few unities. An example of a thresholded matrix V_C in both regimes is shown, in Fig. 9. The geometrical characteristics of the two regimes can be seen quite clearly. Depinning clusters (high velocity regions) are compact and extend somewhat longer in the x direction than in the y direction. Pinning clusters (low velocity regions) have also a long x direction extension, but are very narrow in the y direction on the other hand. Thus they can be described almost like irregularly curved lines in the fracture plane. From Eq. (12) it is clear that the cluster size decreases with increasing values of the threshold parameter C in both regimes. Obviously one must choose reasonable values of C in the two regimes as the number of clusters goes to one and zero when C is very small or very large, respectively.

In order for the thresholding of the velocity matrix to be consistent, it is important to note that the average velocity must be constant in time to avoid clusters from being affected by a size gradient. Thus we ensure that the duration of image capture is short enough for the global development of the average velocity to be approximated as constant for CBC and CVBC experiments.

2. Size distribution of clusters

We will denote the size or area of a cluster, for both pinning and depinning, S. Figure 10 shows for $C = 3$ the normalized probability density function (PDF) of the sizes $P(S)$, respectively for all experiments. There are several aspects to emphasize about these figures. First of all, the distributions show a power-law decay, with a cutoff for large sizes S. Furthermore, the distributions fall on top of each other, meaning that they span the same range of cluster sizes, independently of the average propagation velocity. Neither is

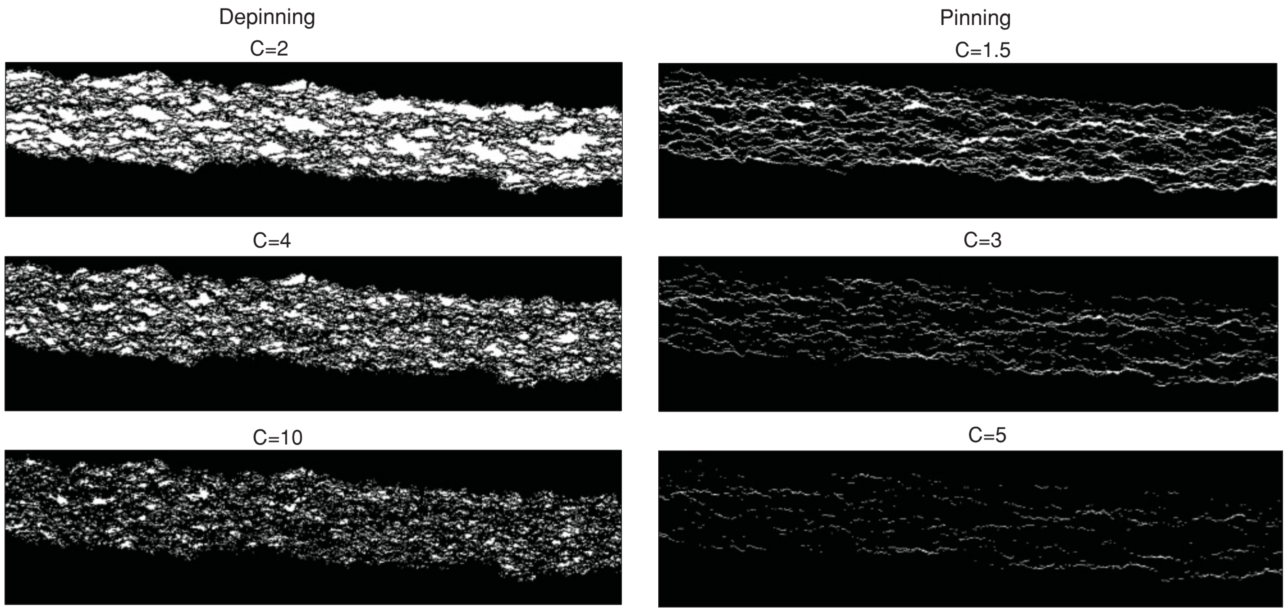

FIG. 9. Thresholded matrix V_C $(5600 \times 1400)\mu$m in the depinning (left) and pinning (right) regime for a CBC experiment with $\langle v \rangle = 1.36$ μm/s. White clusters correspond to velocities C times larger than $\langle v \rangle$ for the depinning case, whereas white clusters or lines correspond to velocities C times less than $\langle v \rangle$ for the pinning case.

there a clear indication that the PDF cutoffs depend on the correlation length x^*. It is thus reasonable to average cluster data from all the experiments to improve, in particular, the tail of the distribution. Finally, the distributions from both CBC and CVBC experiments cannot be distinguished. Thus the distributions seem to indicate that the local dynamics are very similar in the two cases, despite very different boundary conditions. We will, in the following, quantify the properties of these distributions.

Figure 11 shows the averaged $P(S)$ distributions for a threshold range $C = 2$–12 in the pinning regime. It is clear that the distributions follow a power law with an exponential-like cutoff. Furthermore it is evident and to be expected that the size of the largest clusters (i.e., the cutoff cluster size) decreases with increasing values of the threshold level. A similar behavior is found for the PDFs of cluster sizes in the depinning regime, but the cutoff size is generally larger due to the cluster geometry. In contrast to what was done in Ref. [17], where the distributions were rescaled by the average cluster

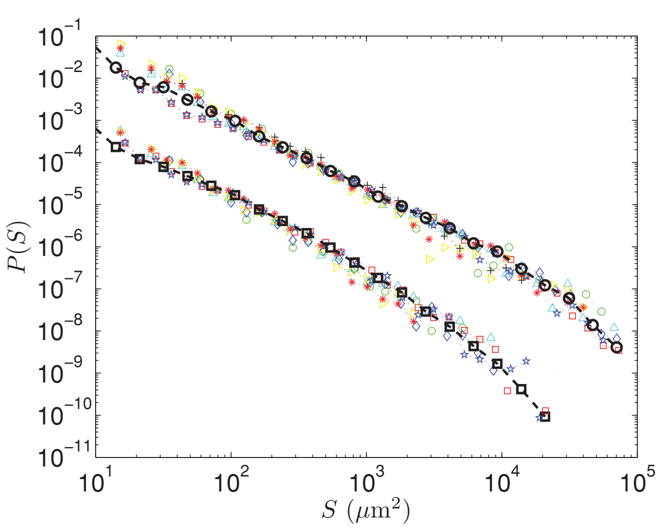

FIG. 10. (Color online) Probability distribution function $P(S)$ for all experiments using a threshold $C = 3$. A distribution averaged over all experimental conditions is also included for the depinning (dashed line and circular markers) and pinning regime (dashed line and square markers). The pinning size distributions have been shifted along the y axis to enhance visual clarity.

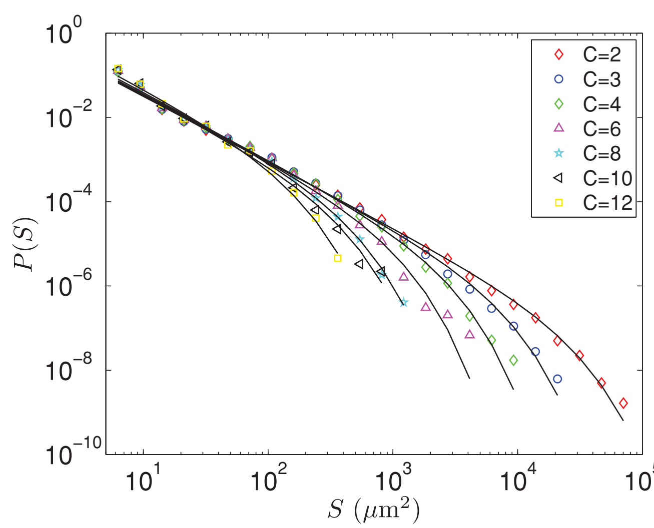

FIG. 11. (Color online) Distributions of pinning clusters $P(S)$ averaged over all different experimental conditions, for a threshold range $C = 2$–12. Solid lines show the fits corresponding to a power law with an exponential cutoff.

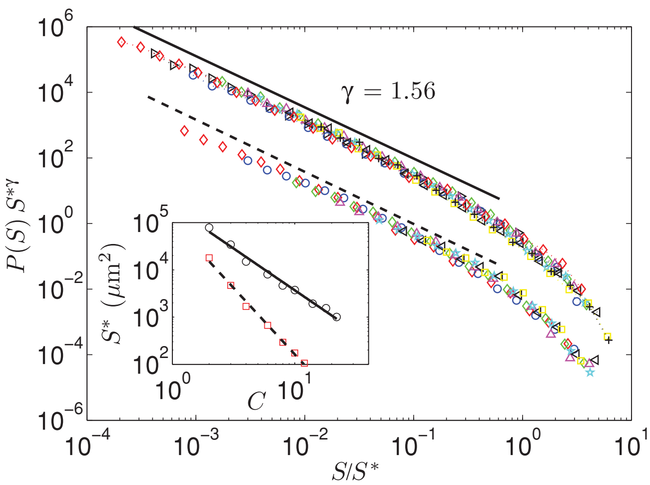

FIG. 12. (Color online) Collapsed $P(S)$ distributions averaged over all different experimental conditions for both depinning (upper set of data) and pinning (lower set of data). The pinning distributions have been shifted relative to the depinning distributions by a factor 0.01 for visual clarity. Depinning and pinning thresholds are in the range $C = 2$–22 and $C = 2$–12, respectively. The dashed and the solid lines both have the slope $\gamma = 1.56$. Inset shows the scaling between the cutoff S^* and the threshold C for the depinning (solid line $\sigma_d = 1.77$) and pinning regime (dashed line $\sigma_p = 2.81$).

size ($P(S/\langle S\rangle)$), we choose to fit the distributions according to the function

$$P(S) \propto S^{-\gamma}\exp(-S/S^*), \tag{14}$$

where S^* is the cutoff cluster size and γ the power-law exponent. This is shown for the pinning regime in Fig. 11, where the fitted solid lines are plotted on top of the averaged experimental data (similar fits have been obtained for the depinning regime). We find that in *both* regimes, the cluster size PDF scales with an average exponent $\gamma = 1.56 \pm 0.04$. Using this exponent and the fitted values for the cutoff cluster size we obtain a data collapse in both velocity regimes for the full range of available threshold values, as shown in Fig. 12. Furthermore we find a scaling relation between the cutoff cluster size S^* and the threshold level C, as shown in the inset of Fig. 12. For the depinning regime it is given by

$$S^* \propto C^{-\sigma_d}, \tag{15}$$

where $\sigma_d = 1.77 \pm 0.16$. Similarly, we obtain for the pinning regime.

$$S^* \propto C^{-\sigma_p}, \tag{16}$$

where $\sigma_p = 2.81 \pm 0.23$.

The exponent $\gamma = 1.56$ is somewhat lower, but consistent with the previously reported value in Ref. [17] ($\gamma = 1.7 \pm 0.1$), in which the distributions were rescaled by the average cluster size in the absence of a pronounced cutoff size. A later check using the rescaling as explained in the above paragraph does show to lower the exponent also for the old data. We would like to mention that our experimentally obtained exponents γ and σ_d are in excellent agreement with the recent numerical study of high velocity clusters in planar crack front propagation by Laurson *et al.* [31]. They used an empirical value of $\sigma_d = 1.8$ to describe the relationship between the cutoff size and the threshold. Their value of the size exponent $\gamma = 1.5$ is explained theoretically from the decomposition of a global avalanche (collective movement of the front as a whole) into local clusters. The experimental equivalent to the suggested numerical approach is to study how the fluctuations of the spatially averaged instantaneous velocity $\langle \frac{\partial h}{\partial x}(x,t)\rangle_x$ relates to the distribution of local clusters that we observe here. We do not consider global avalanches in this study, but it is certainly available in our data and is a work in progress. In this respect, we would also like to explore the suggested link between macroscopic loading conditions and the cutoff length scale of the global front dynamics [35,36].

It should also be noted that our results for the local cluster size distributions further provide quantitative confirmation of the similarity between the local dynamics for the CBC and the CVBC experiments. A recent local elastic thermal model by Kolton *et al.* [37] also showed a similar dynamic between the subcritical and the critical regimes. This model, however, only contains elastic interactions with the nearest neighbors. In our experiments we expect the nonlocal elastic interaction to be of central importance for the dynamics.

3. *Scaling relations*

The collapse in Fig. 12 shows that the scaling in Eqs. (15) and (16) are well satisfied. If we first consider the depinning regime, it is possible to relate the exponents σ_d and γ of the cluster size distribution [Eq. (14)] to the exponent η characterizing the spatiotemporal distribution of local velocities [Eq. (3)]. The latter distribution is obtained from $V_t(x,t)$, that is, the velocity map in space and time of all front lines [Eq. (A3) and Fig. 18(b)], thus the space-time fraction covered by local velocities between v and $v + dv$ is $P(v)dv$. One may also define the spatial distribution of local velocities, obtained from the spatial map of local velocities $V(x,y)$ [Eqs. (A1) and (A2)], denoted $R(v)$. The fraction of (x,y) space covered by local velocities between v and $v + dv$ is then $R(v)dv$. As shown in Appendix B, there is a relationship between these two probability density functions. Using Eq. (B5) gives

$$R(v) = \frac{P(v)}{\langle v\rangle}\, v \sim v^{-\eta+1}, \quad \text{for} \quad v > \langle v\rangle. \tag{17}$$

The cumulative distribution of $R(v)$, from a given threshold C and up to the highest velocity, equals the area fraction that these velocities occupy out of the total area swept by the fracture front. In terms of threshold level we then get

$$R_c(v \geqslant C) = \int_C^\infty R(v)\,dv \sim C^{-\eta+2}. \tag{18}$$

The same area fraction can also be expressed through the cluster size distribution, hence we obtain

$$R_c(v \geqslant C) = \frac{N\langle S\rangle}{A_{x,y}} \tag{19}$$

$$\propto N\int_{S_{\rm low}}^\infty S P(S)\,dS, \tag{20}$$

where $A_{x,y}$ is the total area in the (x,y) plane where the fracture has propagated, N is the total number of clusters, $\langle S\rangle$ is the average cluster size, and $S_{\rm low}$ is the pixel size or some other lower cutoff. Substituting $P(S) = B\, S^{-\gamma} \exp(-S/S^*)$, where B is the normalization factor, in the above integral, we obtain for $\langle S \rangle$

$$\frac{1}{B} = \int_{S_{\mathrm{low}}}^{\infty} S^{-\gamma} \exp(-S/S^*)\, dS, \tag{21}$$

$$\langle S \rangle = B \int_{S_{\mathrm{low}}}^{\infty} S^{1-\gamma} \exp(-S/S^*)\, dS, \tag{22}$$

where S^* is the cutoff cluster size. Considering the normalization factor, we get by substituting $x = S/S^*$

$$\frac{1}{B} = S^{*1-\gamma} \int_{S_{\mathrm{low}}/S^*}^{\infty} x^{-\gamma} \exp(-x)\, dx. \tag{23}$$

Since the lower limit is very small and $\gamma = 1.56 > 1$, the power-law part of the integrand will dominate and the contribution from the upper cutoff is negligible. Thus we approximate

$$\frac{1}{B} \approx S^{*1-\gamma} \int_{S_{\mathrm{low}}/S^*}^{\infty} x^{-\gamma} dx \sim S^{*1-\gamma} \frac{S_{\mathrm{low}}^{1-\gamma}}{S^{*1-\gamma}} = S_{\mathrm{low}}^{1-\gamma}, \tag{24}$$

which is independent of S^*. For the average cluster size we then obtain

$$\langle S \rangle \propto S^{*2-\gamma} \int_{S_{\mathrm{low}}/S^*}^{\infty} x^{1-\gamma} \exp(-x)\, dx. \tag{25}$$

Since $\gamma - 1 = 0.56 < 1$, this integral will converge at the lower end, to a value independent of S_{low} as long as $S_{\mathrm{low}}/S^* \ll 1$. Thus from Eq. (15), we obtain

$$\langle S \rangle \propto S^{*2-\gamma} \propto C^{-\sigma_d(2-\gamma)}, \tag{26}$$

where $\sigma_d(2-\gamma) = 0.79$. Equation (26) is experimentally verified for $C > 3$, as shown in Fig. 13.

The number of clusters N depends on the threshold level in a nontrivial manner. This is shown in the inset of Fig. 13.

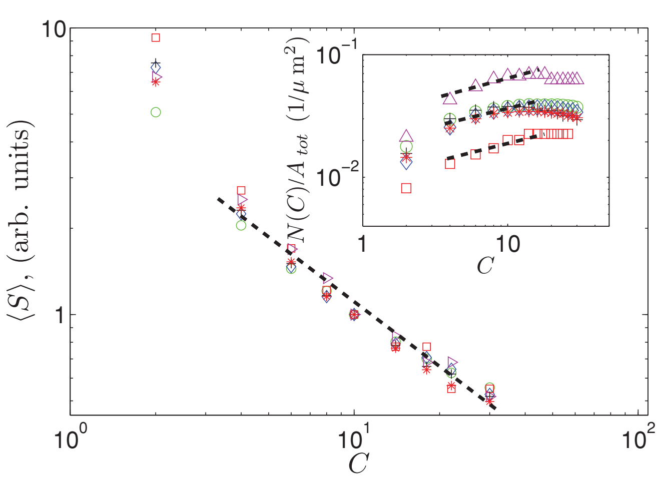

FIG. 13. (Color online) Average cluster size $\langle S \rangle$ obtained from the image analysis vs. threshold level C. The dashed line shows a power-law fit for $3 < C < 30$, with the exponent $-\sigma_d(2-\gamma) = -0.75$. Inset shows the number of clusters as a function of threshold level for the various experiments. The dashed lines all have the average slope $\chi = 0.28$.

We see, however, that in the interval $3 < C < 16$ the number of clusters can be approximated by

$$N(C) \sim C^{\chi}, \tag{27}$$

where $\chi = 0.28$. Inserting Eqs. (18), (26), and (27) into Eq. (19) we obtain the following scaling relation

$$C^{-\eta+2} \sim C^{-\sigma_d(2-\gamma)+\chi}, \tag{28}$$

leading to a quantitative link between the exponent of local velocity distribution and the exponent of the event size distribution

$$\eta = \sigma_d(2-\gamma) - \chi + 2. \tag{29}$$

Inserting numbers in the above equation ($\eta = 2.55$, $\gamma = 1.56$, $\chi = 0.28$) we get that $\sigma_d = 1.88$, in good agreement with the empirically found value of $\sigma_d = 1.8$. Strictly speaking this result is only valid for $3 \leqslant C \leqslant 16$. If we now turn to the pinning regime, we note that from Eqs. (15) and (16), $\sigma_p \approx \sigma_d + 1$, although we cannot derive it from a theoretical argument. The pinning threshold values spans a velocity interval ($v/\langle v \rangle < 0.5$), in which the $P(v/\langle v \rangle)$ distribution does not follow a power law (Fig. 5). Thus a similar scaling argument to the depinning regime, based on simple power-law behaviors of all dependent variables, is not very likely to hold.

4. Cluster morphology

A depinning cluster of size S can be further decomposed into two extension lengths l_x, transverse to the average direction of front propagation and l_y, parallel to the average direction of front propagation, by fitting a bounding box. A bounding box is the smallest rectangle that can enclose the cluster, with sides l_x and l_y as shown in the left panel of Fig. 14(a). As mentioned earlier, the pinning cluster geometry can be characterized as an irregularly curved line with a much larger extension in the x direction compared to the y direction. Due to this feature, l_y is not a good measure, and badly overestimates the y-direction extension. This is shown in Fig 14(b) where bounding boxes for both pinning and depinning clusters are shown. Thus for pinning clusters we use l_x in the x direction and the average cross-sectional width l_{yw} as a measure of the y-direction extension, as shown in the right panel of Fig. 14(a). Analysis shows that for a cluster of size S, either depinning or pinning, the extension lengths have well-defined means $\bar{l}_x$, $\bar{l}_y$, and $\bar{l}_{yw}$ increasing monotonically with S. Note here that the bar denote the mean only over a narrow range of S and is not the overall mean. The corresponding standard deviations are small and proportional to these means. Due to the different definitions of l_y and l_{yw}, their absolute value cannot be compared directly. From analysis we find that, after an initial transient, $\bar{l}_y$ and $\bar{l}_{yw}$ do scale similarly but with different prefactors for depinning clusters. This is a consistency check between using either a bounding box or the cross-sectional width to describe the y-direction extension. Thus l_{yw} is a reasonable measure for the y-direction extension of pinning clusters.

Figure 15 shows the scaling of the different extension lengths with the cluster size in the two regimes. In all cases there are differences between small (pixel resolution up to $S \sim 100\,\mu\mathrm{m}^2$) and large-scale behavior. In the case of

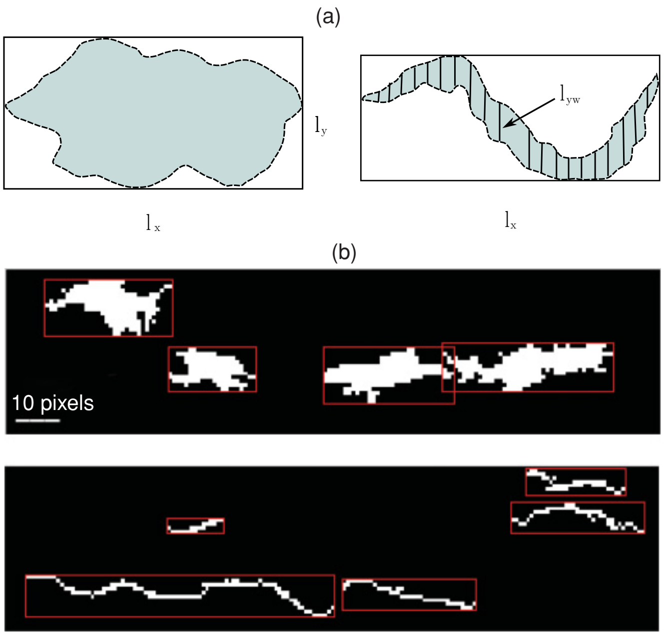

FIG. 14. (Color online) (a) Left panel shows a bounding box with sides l_x and l_y embedding a depinning cluster. In this case the bounding box is a good measure of the linear extension of the cluster. Right panel shows a bounding box embedding a pinning cluster. In this case l_x gives a reasonable linear extent measure, however, l_y does not due to the irregular curvature (somewhat exaggerated in the figure) and to the narrow width in the y direction. To characterize this width we use instead the average cross sectional width l_{yw}. (b) Upper and lower panels show bounding boxes for depinning and pinning clusters, respectively, from one experiment.

depinning, for small S values, $\bar{l}_x$ and $\bar{l}_y$ scale more or less similarly indicating that clusters are isotropic at these scales. In the case of pinning, $\bar{l}_{yw}$ is very small and stays constant while $\bar{l}_x$ scales almost like the depinning cluster size. This is consistent with the characteristic linear geometry observed in the pinning regime. However, the small-scale behavior ranges only over one decade, and might be affected both by resolution and disorder effects, so we do not have much information at these scales. The large-scale behavior spans close to three decades in S and displays robust scaling in all cases. From Fig. 15 we obtain the following relationship between extension lengths and cluster size

$$\bar{l}_x \propto S^{\alpha_x}, \qquad \bar{l}_y \propto S^{\alpha_y}, \qquad \bar{l}_{yw} \propto S^{\alpha_{yw}}, \tag{30}$$

for $S > 100\,\mu\text{m}^2$ where $\alpha_x = 0.62 \pm 0.04$ is considered equal in both velocity regimes, $\alpha_y = 0.41 \pm 0.06$ in the depinning regime and $\alpha_{yw} = 0.34 \pm 0.05$ in the depinning regime. The exponents in both regimes confirm the visually observed anisotropy of cluster extension. Note also the very small y-direction maximum extension ($\bar{l}_{yw} \sim 25\,\mu$m) of pinning clusters, resulting from a small proportionality factor in the scaling relation. Furthermore we obtain approximately from the exponents in Eq. (30) that $S \sim \bar{l}_x\bar{l}_y \sim \bar{l}_x\bar{l}_{yw}$, meaning that the ratio of the approximated area from the extension lengths to the real cluster area is scale independent. From Eq. (30) we get the following x and y direction aspect ratio:

$$\bar{l}_y \propto \bar{l}_x^{\alpha_y/\alpha_x}, \qquad \bar{l}_{yw} \propto \bar{l}_x^{\alpha_{yw}/\alpha_x}, \tag{31}$$

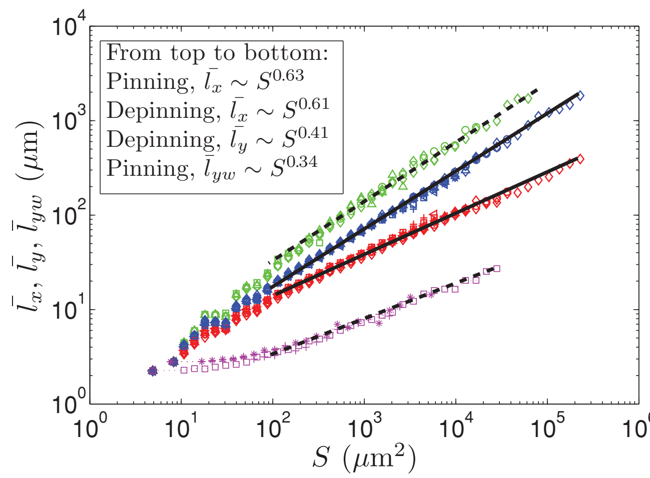

FIG. 15. (Color online) Linear extent of pinning and depinning clusters as a function of cluster size for the full span of threshold levels and averaged over all experimental conditions. The slopes of the different fitted lines (dashed: pinning clusters, solid: depinning clusters) are indicated in the caption. Note that there in all cases are initial transients up to $S \approx 100\,\mu\text{m}^2$.

where $\alpha_y/\alpha_x = 0.66$ and $\alpha_{yw}/\alpha_x = 0.55$ for the depinning and pinning regime, respectively. It was suggested in Refs. [17] and in [38] that α_y/α_x could be another measure of the roughness of the self-affine fracture front, in agreement with previous experimental measurements of the roughness exponent. However, in a very recent experimental work [7] on planar crack growth, there has been two roughness exponents observed acting at different scales; a small-scale roughness with exponent ∼0.6 and a large-scale roughness with exponent ∼0.4, with a crossover depending on the fracture toughness fluctuations and the stress intensity factor. This trend has also been seen for the aspect ratio of depinning clusters in the simulation study by Laurson *et al.* [31]. In the experimental case, on the other hand, considering that the length scale of this roughness crossover is comparable with the $\bar{l}_x$ range in our case, we find no traces of such behavior in the aspect ratio of depinning clusters. This point thus warrants further consideration.

Finally, we discuss the marginal distributions of the extension lengths (i.e., for all cluster sizes) in the two regimes denoted $P(l_x)$, $P(l_y)$, and $P(l_{yw})$. For clarity we mention again that l_x scales similarly with S in the two regimes only separated by a small difference in the proportionality factor, whereas l_y (describing the depinning regime) and l_{yw} (describing the pinning regime) are treated separately. The insets in Figs. 16(a) and 16(b) show the extension length distributions $P(l_x)$ and $P(l_y)$, respectively, in the pinning regime. The corresponding pinning cluster distributions display similar behavior, except that the $P(l_{yw})$ distribution is entirely dominated by a cutoff function. This is due to the very narrow y-direction span of pinning clusters. We define the following distributions for the extension lengths

$$P(l_x) \propto l_x^{-\beta_x} D(l_x/l_x^*), \tag{32}$$

$$P(l_y) \propto l_y^{-\beta_y} D(l_y/l_y^*), \tag{33}$$

$$P(l_{yw}) \propto l_{yw}^{-\beta_{yw}} D(l_y/l_y^*), \tag{34}$$

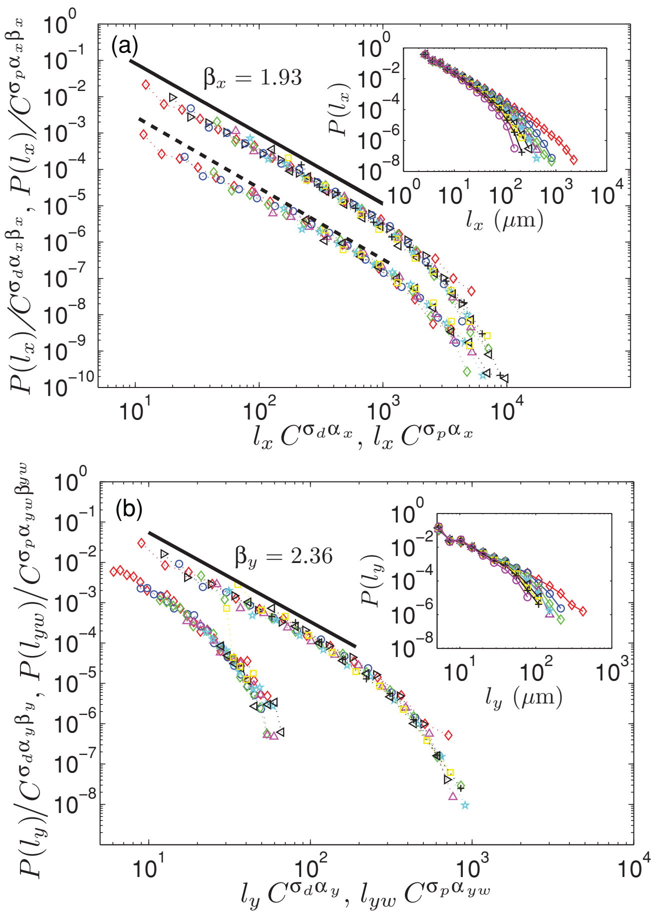

FIG. 16. (Color online) (a) Collapsed $P(l_x)$ distributions averaged over all different experimental conditions for both depinning (upper set of data) and pinning (lower set of data). The pinning distributions have been shifted relative to the depinning distributions by a factor of 0.05 for visual clarity. Depinning and pinning thresholds are in the range $C = 2$–30 and $C = 2$–12, respectively. The solid and dashed lines both have the slope $\beta_x = 1.93$. Inset shows for the case of depinning the threshold dependence for the unscaled distributions. (b) Collapsed $P(l_y)$ and $P(l_{yw})$ distributions averaged over all different experimental conditions for the depinning (upper set of data) and pinning (lower set of data) regime, respectively. The pinning distributions have been shifted relative to the depinning distributions by a factor of 0.1 for visual clarity. Thresholds are in the range $C = 2$–30 and $C = 2$–12 for depinning and pinning, respectively. The solid line has the slope $\beta_y = 2.36$. Inset shows for the case of depinning the threshold dependence for the unscaled distributions.

where $D(x)$ is some cutoff function decaying faster to zero than any power of l_x, l_y, or l_{yw} when $x > 1$ and constant otherwise. The β exponents above can be predicted from our previous results for the cluster size distribution. From statistics we know that the relation between the PDFs of two random variables b and c, one-to-one related, can be expressed as

$$P(b) = P(c)\frac{dc}{db}. \tag{35}$$

In our case S, l_x, l_y, and l_{yw} is not one-to-one related, but since the means $\bar{l}_x$, $\bar{l}_y$, and $\bar{l}_{yw}$ have only small standard deviations, the PDFs $P(l_x)$, $P(l_y)$, and $P(l_{yw})$ should at least be approximated by Eq. (35). For $P(l_x)$ we get by inserting Eqs. (14) and (30) into Eq. (35)

$$\beta_x = \frac{\gamma + \alpha_x - 1}{\alpha_x}, \tag{36}$$

where $\beta_x = 1.93$. Similarly we obtain $\beta_y = 2.36$ and $\beta_{yw} = 2.65$. For the depinning regime we obtain for the cutoffs in Eqs. (32) and (33) by using Eqs. (15) and (30)

$$l_x^* \propto C^{-\sigma_d\alpha_x}, \qquad l_y^* \propto C^{-\sigma_d\alpha_y}. \tag{37}$$

For the pinning regime we obtain for the cutoffs in Eqs. (32) and (34) by using Eqs. (16) and (30)

$$l_x^* \propto C^{-\sigma_p\alpha_x}, \qquad l_{yw}^* \propto C^{-\sigma_p\alpha_{yw}}. \tag{38}$$

The extension length distributions in both velocity regimes are collapsed according to Eqs. (32) through (34) as shown in Figs. 16(a) and 16(b). In the x direction, transverse to the direction of crack propagation, the distribution in both regimes scale with the same exponent, similarly to what was found for the cluster size distribution. The only difference between the two distributions is the proportionality factor in the cutoff length, as explained earlier. We see that along the direction of crack propagation the depinning [$P(l_y)$] and pinning [$P(l_{yw})$] distributions are quite different, in the sense that all power-law behavior is suppressed by the cutoff function in the latter distribution. This is understandable since the span of l_{yw} values is no more than one decade.

In Sec. III B we discussed various correlation functions of the spatiotemporal velocity field. In particular, it was seen that the local velocities had correlation lengths of the order ~100 and 10 μm in the x and y directions, respectively. One would expect the correlation lengths in some sense to control the extent of pinning and depinning clusters. This dependence is nontrivial since a cluster in this context is artificially constructed by thresholding the velocity field. No clear relation is found between the cutoff size of the pinning and depinning clusters, and the correlation length extracted from the autocorrelation function of the velocity field. However, since the clusters are obtained from thresholded velocities, it is also possible to look at the autocorrelation function of thresholded velocities rather than the one of the continuous velocity signal. In ongoing work we consider such correlation functions $G_C(\Delta x)$ [Eq. (4)], obtained from discretized signals $v_C(x,t)$ where the local velocities along each front line are now thresholded with a threshold C according to Eq. (12). A preliminary analysis indicates the existence of a correlation length roughly proportional to l_x^* [Eq. (37)], meaning that both quantities evolve similarly with the threshold C.

Furthermore, in the x direction we could see clear sample differences in the correlation lengths, even though they were within the same order of magnitude (Fig. 6). Analyzing carefully both size and extension length distributions of individual experiments, and not average distributions as presented above, we could not recognize such trends. In this respect it is also important to mention that for individual experiments, the cutoff behavior in the distributions are not well pronounced due to the lack of large-scale statistics. Even when considering the above limitations, we can say that the geometry of pinning lines are qualitatively consistent with the observed correlation lengths. Thus it seems that the vanishingly small correlation length in the y direction, describes the low-value part of the local velocity distribution.

IV. CONCLUSION

The local dynamics of an in-plane mode-I fracture have been studied experimentally using high-resolution monitoring of the front line advances. Indeed the transparency of the PMMA enable us to follow the fracture process using a high-speed camera. Fracture is induced by fixing the upper plate, while applying a force on the lower plate from a pressbar controlled by a step motor. Experiments are performed using two sets of boundary conditions: (1) constant driving velocity on the pressbar, giving a linear deflection in time between the plates (CVBC) and (2) fixed deflection between the plates (CBC), resulting in a slow creep motion of the fracture front.

Disorder is introduced in the fracture plane by a sand-blasting and sintering procedure, resulting in heterogeneous fluctuations of the local toughness. The competition between the toughness fluctuations and the long-range damping elastic forces results in a rough fracture front with self-affine scaling properties. In this study we have considered the local dynamics of the fracture front over a wide range of average propagation velocities ($0.028 < \langle v \rangle < 141$) μm/s. The local velocity field is obtained through the waiting time matrix and gives a spatiotemporal distribution with a large power-law tail for high velocities described by an exponent $-\eta = -2.55$. The fracture front advance, displays pinning, and avalanches with a broad range of velocity scales. Our results show that the local dynamics is similar in every respect for the two different boundary conditions. This is an important and nontrivial result considering the very different behavior in the global large-scale propagation. Additionally, no dependence on the average propagation velocity for different experiments is found.

The average autocorrelation of local velocities have been studied in both spatial directions, and also in time along the direction of crack propagation. We find that the velocities are correlated up to $\sim$100 μm transverse to the direction of crack propagation, and $\sim$10 μm (i.e., close to the spatial resolution) and thus uncorrelated in the direction of crack propagation. Within these general trends we have seen that there are differences in the autocorrelation function from sample to sample, but no dependence on the loading condition or average propagation velocity. Relating the autocorrelation of velocities in time to the evolution of the front width gives a growth exponent of $\alpha = 1/2$ similar to simple diffusion, a process such as Brownian motion.

The local dynamics have been studied through a statistical analysis of local avalanche events. We have observed that the cluster properties are independent of both loading conditions and average velocity of the crack front. The depinning cluster size distribution show scale invariance, described by an exponent $-\gamma = -1.56$, in agreement with previous experimental [17] and numerical results [30,31]. Surprisingly the same result is found also for the pinning regime. Furthermore, we have in this study seen that the cluster size distribution scaling is truncated by an upper cutoff, depending on the threshold value. We have shown that the cutoff essentially is controlled by the total distribution of local velocities. Particularly for the depinning regime we have obtained a scaling law relating the cluster size exponent γ to the exponent η describing the local velocity distribution.

Clusters have, in both velocity regimes, been further decomposed into extension lengths in the x and y directions. We have demonstrated that the distributions of these extension lengths are consistent with their size distribution. The aspect ratio of depinning clusters follows a power law with the exponent $\alpha_y/\alpha_x = 0.66$ indicating that the clusters are anisotropic and extending longer transverse to the direction of propagation than in the direction of crack propagation. We have yet to obtain experimentally a relationship between the extension of depinning clusters and the roughness of the fracture front. This is a topic that warrants further work.

The pinning clusters were found to display a very strong anisotropy, extending far in the x direction as opposed to the very short y-direction extension. This is qualitatively in agreement with the found velocity correlation lengths in the two directions, thus indicating that these lengths describe the spatial correlations of low velocities.

ACKNOWLEDGMENTS

This work was supported by the Norwegian Research Council, a French Norwegian PICS program of the CNRS, the INSU, and the French ANR SUPNAF grant. The authors thank A. Hansen and O. Lengline for stimulating discussions.

APPENDIX A: THE WAITING TIME MATRIX

The waiting time matrix (WTM) is a robust procedure that enables a comparison of both different experiments at different time and space resolution, and also with numerical simulations of similar systems. It can be applied to any propagating interface [29,30,32], and is particularly suited for estimating the local velocity of pinned interfaces which are dominated by low speeds. Below, we will explain the procedure in detail.

The coordinates of the extracted front lines $h(x,t)$, introduced in Fig. 3, can be represented in matrix form as $H[x,h(x,t)] = 1$ and 0 elsewhere, with a matrix size equal to the captured image size. We define the WTM W as the sum of all front matrices H

$$W(x,y) = \sum_t H[x,h(x,t)], \tag{A1}$$

where the sum runs over all discrete times t. Note that W is an integer matrix, so to get the true waiting time, the time step δt must be multiplied to each matrix element w. An example of front line addition is shown in Fig. 17.

From above it is clear that the WTM procedure gives a *spatial* map that accounts for the amount of time spent by the front at a given pixel, thus reflecting the local dynamics of the interface. However, avoiding holes in the WTM implies a high enough sampling rate so that the movement of the front position is at maximum one pixel between two subsequent images. Second, it also requires a small noise from the imaging device. Finally, care must be taken in preparing the sample. Indeed, impurities and surface scratches are not transparent,

$$t_1 \quad \begin{bmatrix} 0&0&0&0&0&0&0&0&0&0&0&0&0 \\ 1&0&0&0&0&0&0&1&0&0&0&0&1 \\ 0&1&0&0&1&0&1&0&1&0&0&1&0 \\ 0&0&1&1&0&1&0&0&0&1&1&0&0 \\ 0&0&0&0&0&0&0&0&0&0&0&0&0 \\ 0&0&0&0&0&0&0&0&0&0&0&0&0 \end{bmatrix}$$

$$t_2 \quad \begin{bmatrix} 0&0&0&0&0&0&0&0&0&0&0&0&0 \\ 2&0&0&0&0&0&0&1&0&0&0&0&1 \\ 0&2&0&0&1&0&1&1&2&0&0&2&1 \\ 0&0&2&2&1&1&1&0&0&2&2&0&0 \\ 0&0&0&0&0&1&0&0&0&0&0&0&0 \\ 0&0&0&0&0&0&0&0&0&0&0&0&0 \end{bmatrix}$$

$$t_3 \quad \begin{bmatrix} 0&0&0&0&0&0&0&0&0&0&0&0&0 \\ 2&0&0&0&0&0&0&1&0&0&0&0&1 \\ 1&2&0&0&1&0&1&1&2&0&0&3&2 \\ 0&1&3&3&1&1&2&1&1&2&3&0&0 \\ 0&0&0&0&1&2&0&0&0&1&0&0&0 \\ 0&0&0&0&0&0&0&0&0&0&0&0&0 \end{bmatrix}$$

FIG. 17. (Color online) Example of the computation of the waiting time matrix $W(x,y)$ [Eq. (A1)]. All fronts are added to an originally empty matrix in time step unit. Indicated above is the addition of front lines in three timesteps t_1 (red), t_2 (blue), and t_3 (green).

but rather reflect light and may thus artificially alter the extracted front shape. In our case, experiments are devised so that the front is propagating in a steady manner both before and after the short interval of image capture. To avoid transient effects at the beginning and at the end of the image recording, we typically clip between 200–500 front lines in the start and end of the generated WTM.

From the WTM we can construct the local velocity matrix in *space* $V(x,y)$. Matrix elements represent the normal speed of the fracture front at the time it went through a particular position

$$v = \frac{1}{w}\frac{a}{\delta t}. \tag{A2}$$

From the local velocity matrix $V(x,y)$, we can also obtain the local velocity along each front $h(x,t)$

$$v(x,t) = V[x,h(x,t)]. \tag{A3}$$

By computing $v(x,t)$ for every time step, we build the *spatiotemporal* velocity map $V_t(x,t)$. We then define the average propagation velocity of the front $\langle v\rangle$ as the average taken over all elements in the matrix $V_t(x,t)$. The development of the front in time for a given x position is shown in Fig. 18(a), also indicating how the velocity is approximated from the WTM. One realization of the local velocity fluctuations along a front line is shown in Fig. 18(b).

APPENDIX B: VELOCITY PDF TRANSFORMATION

In transforming from the spatiotemporal map $V_t(x,t)$ [Eq. (A3) and Fig. 18(b)] to the spatial map $V(x,y)$ [Eqs. (A1) and (A2)] with the PDFs $P(v)$ and $R(v)$, respectively, we can express the space traveled through at speed v over a time dt as $dy = v\,dt$. The area in (x,y) space where the front travels at speed u between v and $v+dv$ corresponds to the total area of fracture propagation, $A_{x,y}$, multiplied by the fraction of the area corresponding to this speed

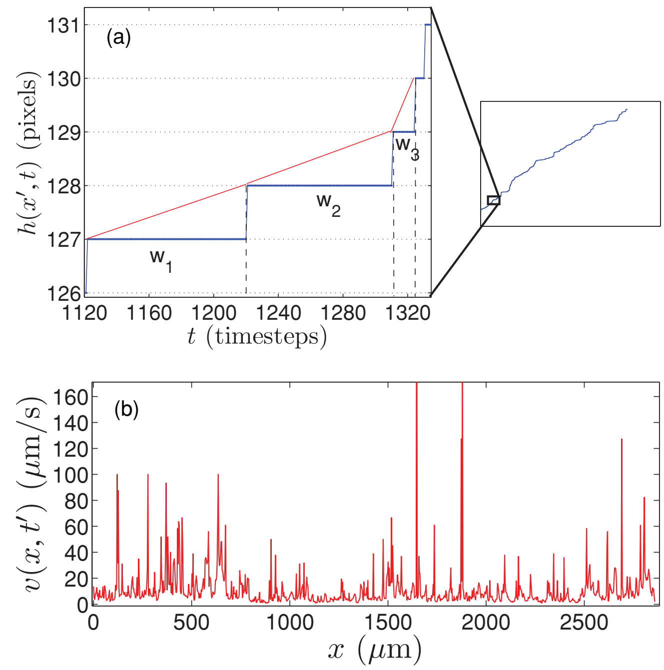

FIG. 18. (Color online) (a) Pixel level zoom in of a front line $h(x',t)$ at a given position x' as function of time. Indicated are three waiting times w_1, w_2, and w_3 separated by a one-pixel jump. As an example, note that all captured fronts from $h(x',t_0)$ to $h(x',t_0+w_1)$ are given the same constant velocity $v_1 \propto 1/w_1$ in making the jump from pixels 127 to 128 along the y axis. This approximation means that the front position increases linearly during this time interval, as indicated. (b) Local velocity fluctuations $v(x,t')$ along the front line $h(x,t')$.

$$\int_{v<u(x,y)<v+dv} dx\,dy = A_{x,y} R(v)\,dv. \tag{B1}$$

This area is related to the area covered by the fronts traveling at that speed in the spatiotemporal map, expressed using the variable change between y and t

$$\int_{v<u(x,y)<v+dv} dx\,dy = \int_{v<u(x,t)<v+dv} dx\,v\,dt. \tag{B2}$$

Eventually, this last area is directly related to the distribution $P(v)$, with the same argument as for the spatial map: Denoting $A_{x,t}$ the total area of the spatiotemporal map, we can write

$$\int_{v<u(x,t)<v+dv} dx\,dt = A_{x,t} P(v)\,dv. \tag{B3}$$

Inserting Eqs. (B1) and (B3) into Eq. (B2) leads to

$$A_{x,y} R(v) dv = A_{x,t} P(v) v dv. \tag{B4}$$

Furthermore it can be shown that $A_{x,y}/A_{x,t} = \langle v\rangle$, thus eventually

$$v\,P(v)\,dv = \langle v\rangle R(v)\,dv. \tag{B5}$$

[1] B. Lawn, *Fracture of Brittle Solids* (Cambridge University Press, Cambridge, England, 1993).

[2] M. J. Alava, P. K. V. V. Nukala, and S. Zapperi, Adv. Phys. **55**, 349 (2006).

[3] D. Bonamy, J. Phys. D: Appl. Phys. **42**, 214014 (2009).

[4] E. Bouchaud, J. Phys. Condens. Matter **9**, 4319 (1997).

[5] J. Schmittbuhl and K. J. Måløy, Phys. Rev. Lett. **78**, 3888 (1997).

[6] A. Delaplace, J. Schmittbuhl, and K. J. Måløy, Phys. Rev. E **60**, 1337 (1999).

[7] S. Santucci, M. Grob, A. Hansen, R. Toussaint, J. Schmittbuhl, and K. J. Måløy, Euro. Phys. Lett. **92**, 44001 (2010).

[8] L. Ponson, D. Bonamy, and E. Bouchaud, Phys. Rev. Lett. **96**, 035506 (2006).

[9] D. Bonamy, L. Ponson, S. Prades, E. Bouchaud, and C. Guillot, Phys. Rev. Lett. **97**, 135504 (2006).

[10] S. Santucci, K. J. Måløy, A. Delaplace, J. Mathiesen, A. Hansen, J. O. Haavig Bakke, J. Schmittbuhl, L. Vanel, and P. Ray, Phys. Rev. E **75**, 016104 (2007).

[11] J. Schmittbuhl, A. Hansen, and G. G. Batrouni, Phys. Rev. Lett. **90**, 045505 (2003).

[12] J. P. Bouchaud, E. Bouchaud, G. Lapasset, and J. Planes, Phys. Rev. Lett. **71**, 2240 (1993).

[13] J. Schmittbuhl, S. Roux, J. P. Vilotte, and K. J. Måløy, Phys. Rev. Lett. **74**, 1787 (1995).

[14] A. Hansen and J. Schmittbuhl, Phys. Rev. Lett. **90**, 045504 (2003).

[15] J. Sethna, K. Dahmen, and C. Myers, Nature (London) **410**, 242 (2001).

[16] K. J. Måløy and J. Schmittbuhl, Phys. Rev. Lett. **87**, 105502 (2001).

[17] K. J. Måløy, S. Santucci, J. Schmittbuhl, and R. Toussaint, Phys. Rev. Lett. **96**, 045501 (2006).

[18] S. Santucci, L. Vanel, and S. Ciliberto, Phys. Rev. Lett. **93**, 095505 (2004).

[19] A. Marchenko, D. Fichou, D. Bonamy, and E. Bouchaud, Appl. Phys. Lett. **89**, 093124 (2006).

[20] B. Gutenberg and C. F. Richter, *Seismicity of Earth and Associated Phenomena* (Princeton University Press, Princeton, NJ, 1954).

[21] A. Corral, Phys. Rev. Lett. **92**, 108501 (2004).

[22] A. P. Mehta, K. A. Dahmen, and Y. Ben-Zion, Phys. Rev. E **73**, 056104 (2006).

[23] A. Garcimartín, A. Guarino, L. Bellon, and S. Ciliberto, Phys. Rev. Lett. **79**, 3202 (1997).

[24] J. Davidsen, S. Stanchits, and G. Dresen, Phys. Rev. Lett. **98**, 125502 (2007).

[25] J. Koivisto, J. Rosti, and M. J. Alava, Phys. Rev. Lett. **99**, 145504 (2007).

[26] D. Spasojevi, S. Bukvić, S. Milošević, and H. E. Stanley, Phys. Rev. E **54**, 2531 (1996).

[27] A. Prevost, E. Rolley, and C. Guthmann, Phys. Rev. B **65**, 064517 (2002).

[28] S. Moulinet, A. Rosso, W. Krauth, and E. Rolley, Phys. Rev. E **69**, 035103 (2004).

[29] R. Planet, S. Santucci, and J. Ortín, Phys. Rev. Lett. **102**, 094502 (2009).

[30] D. Bonamy, S. Santucci, and L. Ponson, Phys. Rev. Lett. **101**, 045501 (2008).

[31] L. Laurson, S. Santucci, and S. Zapperi, Phys. Rev. E **81**, 046116 (2010).

[32] M. Grob, J. Schmittbuhl, R. Toussaint, L. Rivera, S. Santucci, and K. J. Måløy, Pure Appl. Geophys. **166**, 777 (2009).

[33] S. Santucci, K. J. Måløy, R. Toussaint, and J. Schmittbuhl, *Interconnected Biosensor Systems: Networks and Bioprocesses* (Kluwer, Amsterdam, 2006).

[34] A. L. Barabasi and H. E. Stanley, *Fractal Concepts in Surface Growth* (Cambridge University Press, New York, 1995).

[35] L. Ponson and D. Bonamy, Int. J. Fract. **162**, 21 (2010).

[36] A. Rosso, P. Le Doussal, and K. J. Wiese, Phys. Rev. B **75**, 220201 (2007).

[37] A. B. Kolton, A. Rosso, T. Giamarchi, and W. Krauth, Phys. Rev. Lett. **97**, 057001 (2006).

[38] K. J. Måløy, R. Toussaint, and J. Schmittbuhl, in 2005 *Proceedings of the ICF11, 11th International Conference on Fracture, Torino* (Springer, Dordrecht, The Netherlands, 2006).

Non Gaussian fluctuationsof crack front velocity

Ken Tore Tallakstad[1], **Renaud Toussaint** [2,4], **Stephane Santucci** [3,4], **and Knut JørgenMåløy**[1,4]

[1] - Department of Physics, University of Oslo, PB 1048 Blindern, NO-0316 Oslo, Norway

[2] - Institut de Physique du Globe de Strasbourg, UMR 7516 CNRS, Université de Strasbourg, 5 rue Rene Descartes, F-67084 Strasbourg Cedex, France

[3] - Laboratoire de Physique, ÉcoleNormaleSupérieure de Lyon, CNRS UMR5 672, 46 Alléed'Italie, 69364 Lyon cedex 07, France

[4] - Centre for Advanced Study at The Norwegian Academy of Science and Letters, Drammensveien 78, 0271 N-Oslo, Norway

Dated: July 16, 2012

Abstract

We study the velocity fluctuations of an in-plane rough crack front propagating along the weak heterogeneous plane of two sintered Plexiglas plates. The transparency allows for direct imaging of the crack propagation, and thus, the spatio-temporal velocity field has been obtained at a very high spatial and temporal resolution. The local velocity of the interfacial crack front follows a fat tail distribution, with a power law exponent $1 + \alpha = 2.6 \pm 0.15$ (1, 2). Here, we study the implications of such a fat tail distribution on the global average velocity fluctuations. We observe that the crack front velocity when averaged over larger and larger uncorrelated spatial domains does not follow the Central Limit Theorem (CLT), but rather displays a non-Gaussian statistics. The distribution of the global crack front velocity is characterized by an asymmetric shape with a fat tail, and can be well fitted by a so-called *stable Levy* distribution.

Introduction

The failure and fracturing of materials has obvious implications in everyday life and in the industry. Such mechanical process takes place on a very broad range of length scales from atomic to geological scales (3). In heterogeneous materials, the competition between pinning forces at local asperities of high toughness and long-range elastic forces due to external loading results in rough self-affine fractures morphology, extensively studied both numerically and experimentally over the years (4, 5), and leads as well to an intermittent crack front propagation (6). Thanks to a high-speed camera, it was shown that for such interfacial crack in Plexiglas, the probability density function (PDF) of the local crack front velocities has a fat tail spanning several orders of magnitude above the average (2). Moreover, Tallakstad et al. (1) demonstrated that the intermittent avalanche behavior is intimately linked to this fat tail in the PDF.

The present study extends the analysis of our high-resolution data from (1), as we here consider the temporal fluctuations of the spatially averaged global velocity. We have access to local information due to the transparency of our fracture sample. The main motivation for a coarsening, studying both small and large scale is the comparison to other systems where only averaged large-scale data is available. Our experiments thus allow us to address two very general questions, important also in other areas of physics: 1) to what extent is the PDF of a global random variable affected by the detailed information of its underlying local random variables? 2) How do the statistics of global random variables depend on the measurement scale? These questions are usually difficult to answer, mainly for two reasons. Firstly, fluctuations are usually only available at a large scale, averaged in space and time. This applies not only for fracture problemsbutfor most Crackling Noise (7) systems. Consequently, it is neither not easy to assess the importance of possible local correlations.Secondly, PDF's of global random variables tend to follow the central limit theorem (CLT) at the large scale. Thus individual random variables can be drawn from completely different distributions themselves, and yet, by the CLT, their sum or average will converge to the bell shaped Gaussian. A particularly illustrating example is the study by Planet et al (8) of the average velocity of imbibition fronts in a rough Hele-Shaw cell. Below a certain correlation length, the velocity fluctuations are non-Gaussian and the comparison with Gumbel statistics (9) is made, whereas above this length, a clear convergence to the Gaussian law is observed.

We show that for the case of our fracture experiments, independently of loading conditions and average propagation velocity, the global velocity PDF does not converge to a Gaussian. This breakdown of the Central Limit Theorem (CLT) can only be explained by the diverging variance and fat tail of the underlying *local* velocity PDF.

Experimental setup

The experimental setup is shown in Fig. 1, and described in large detail in (1). The fracture sample is made of two transparent Plexiglas (PMMA) plates, sandblasted on one side using glass beads ranging between 50 μm and 300 μm in diameter. This introduces random roughness (50μm in size) on the originally "flat" surface, and causes light to be scattered in all directions from these micro-asperities. Thus, the transparency of the plates is lost and they become opaque. The plates are then clamped together in a pressure frame, with the sandblasted sides facing each other. Finally, the pressure frame is put in a ceramic temperature controlled oven at 205 degrees Celsius, for 30−50 min. This annealing procedure creates new polymer chains between the two plates and the resulting PMMA block is now fully transparent. However, the new interface created between the two plates is weaker than the bulk PMMA, resulting in a weak plane with quenched heterogeneities where the fracture will propagate. This system is ideal for direct visual observation since the fractured part of the sample immediately becomes opaque whereas the unfractured part remains transparent. The sharp and high contrast boundary between transparent and opaque parts thus defines the fracture front, *h(x,t)*.

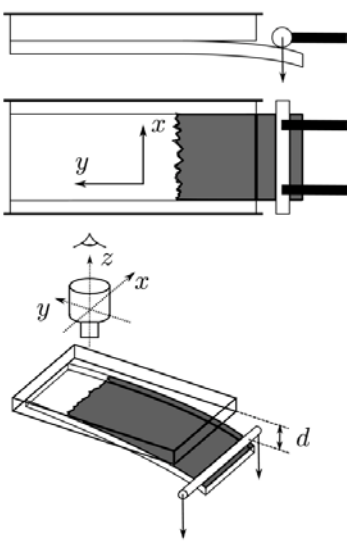

***Figure** 1: From (1). Sketch of the experimental setup. Two PMMA plates with dimensions (30,14,1) cm and (30,10,0.4) cm are sintered together, creating a weak in-plane layer for the fracture to propagate. Fracture is initiated by lowering a cylindrical press bar, controlled by a step motor, onto the lower plate. The uncracked part of the sample is transparent, whereas the cracked part has lost transparency hence creating a good contrast at the fracture front. The fracture front is imaged from above by a digital camera. The deflection d (z-direction) between the plates is indicated in the lower panel. The fracture plane is (x,y), where the x-direction is transverse to the average direction of fracture propagation whereas the y-direction is parallel to the average direction of fracture propagation.*

We use two sets of loading conditions to propagate the fracture in a Plexiglas sample: 1)the press-bar is displaced with a constant velocity, and thus the imposed deflection *d* (see Fig. 1) increases linearly as function of time t. We refer to these loading conditions as constant velocity boundary conditions (CVBC); 2) An initial deflection is obtained by displacing the press-bar with a constant velocity. As soon as the fracture starts to propagate, the motor is switched off, and the press-bar is kept at this fixed position, giving a constant deflection throughout the experiment. We refer to these loading conditions as creep boundary conditions (CBC), since the fracture front continues to propagate at "creepingly slow" velocities over several days after the press-bar is stopped.

A small central region, at the millimeter scale, of the front propagation is followed in time using a high- speed and high-resolution digital camera mounted on a microscope. The large width of the Plexiglas plate (10 cm) ensures that the central region of interest is not influenced by finite size effects (see Fig. 2). In one experiment between 12 000 and 30 000 frames are captured using either the PhotronFastcam-Ultima APX (512 × 1024 pixels) or the Pixelink Industrial Vision PL-A781 (2200 × 3000 pixels). High-resolution images (2.5 μm/pixel) are captured at high frame rate relative to the total average propagation velocity of the crack front<*v*>. This is important as the local fluctuations in velocity can range over several decades. As large amounts of data are accumulated, we only have the possibility to follow the fracture front over short time windows. Both in the case of CBC and CVBC, these time windows are small enough so that the average propagation velocity of the crack front is considered constant. The span of the time windows will of course vary, depending on <*v*>, but the *y*-distance (parallel to direction of propagation) covered by the crack front is roughly 500 μm in all our experiments.

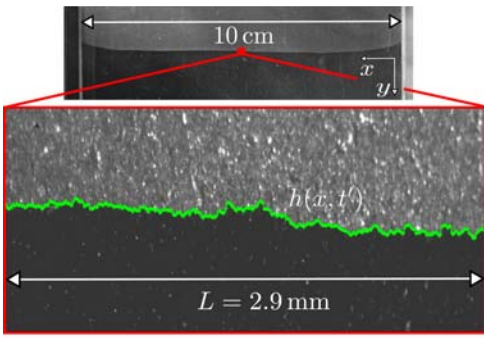

Figure 2:*From (1). Fracture front h(x,t') at some time t', superimposed on the corresponding raw image. Direction of propagation is from top to bottom. System L in the x-direction is indicated. The framed raw image corresponds to a tiny central part of the full sample as seen in the upper panel.*

Local fluctuations

In (1) and (2), the local fluctuations of this fracture system was studied. We summarize here, the most important results. The starting point of the analysis is to obtain the local velocity field v(x,t) obtained by calculating the so-called Waiting Time Matrix (1). In short, for each imaged crack front, one generates a binary matrix with unit entries at the crack front interface, and zeros elsewhere. These matrices are then added for all the crack fronts, and one obtains a waiting time map of the crack front, where a single matrix entry, w, corresponds to the number of timesteps the front has spent at a given pixel. The local velocity at this point is then approximated as, v=a/(w.dt), where a and dtis the pixel and temporal resolution respectively.

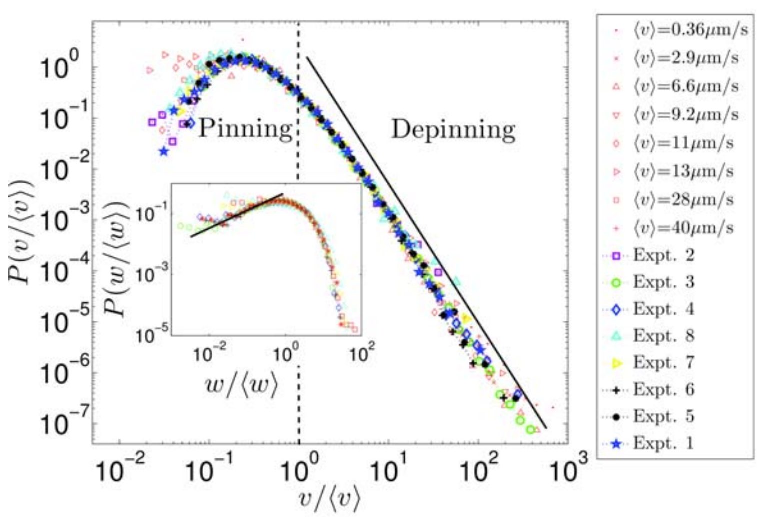

Figure 3: *From (1). Distribution of local velocities P(v/<v>) rescaled by the average propagation velocity for two different experimental loading conditions. In the legend, symbols labeled with different average velocities are results from (2). A fit to all the data for v ><v> shows power law behavior with an exponent -2.6. Inset shows the corresponding waiting time distribution P(w/<w>). The exponent transforms in this case to 0.6.*

Figure 3 shows the marginal PDF $P(v/<v>)$ of $v(x,t)$ for experiments performed for both CVBC and CBC, and a range of almost four decades in average crack front velocity $<v>$. It is clearly seen that all distributions collapse, and that they display a fat tail with a power law exponent. The tail exponent $1+\alpha$ is measured $1+\alpha = 2.6$. Since the exponent $\alpha<2$, the second central moment of this PDF will diverge, and thus also the variance. This is a crucial resultthat will affect the global fluctuations of the crack velocity,as we will show later on.

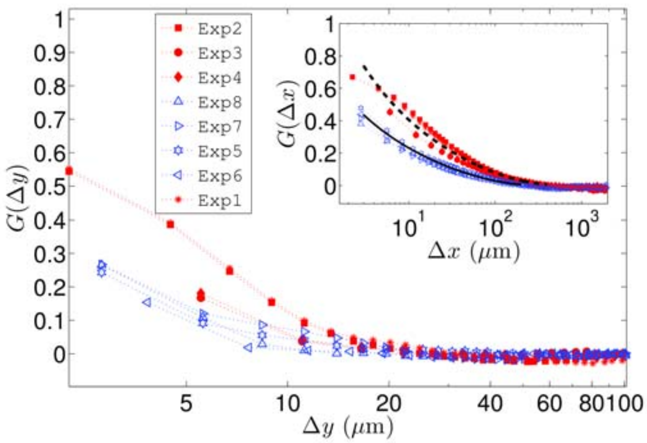

Figure 4: From (1). Spatial correlation function $G(\Delta y)$ with logarithmic Δy axis. Correlation functions from experiments performed on two different samples have filled and open markers respectively. To some extent, we see grouping of experiments from the same sample. The difference is however not as clear as for the spatial correlations along the crack front, as shown in the inset for $G(\Delta x)$ with logarithmic Δx-axis.

It is also of importance to consider possible correlations in the *x*- and *y*- direction respectively. The autocorrelation function [see (1)] of the local velocity in *x*- and *y*-direction (transverse to, and along the direction crack propagation respectively), $G(\Delta x)$ and $G(\Delta y)$ is shown in Fig. 4. Experiments are performed on two different Plexiglas samples, as indicated by solid and open markers. It is clear that in both directions, experiments from the same sample group together. The slight difference in disorder from sample to sample, due to the sandblasting procedure, may be one reason explaining this. In any case, the differences between the autocorrelation functions from the two samples are relatively small. In general we conclude the following [see (1) for more details]: 1) for Δy, i.e along the direction of propagation, the local velocity is close to uncorrelated with a decorrelation length of roughly $y^* \sim 10$µm, close to the resolution scale at ~ 2.5 µm. 2) for Δx, i.e transverse to the direction of propagation, the local velocity is correlated up to a length of roughly $x^* \sim 150$ µm. This is well above the resolution- and disorder scale (~ 15-50µm), however much below the system size($x^* \sim L / 50$). It is to be noted that the range of correlations $(x^*, y^*)=(150, 10)$µm is much smaller than the propagated area of the crack front during an experiment $(L, L_y) = (6000, 500)$µm.

Global fluctuations

With full knowledge of the local statistics, we turn now to the study of the global velocity. The spatially averaged velocity $V_l(t)$, at length scale l (pixel units, *x*-direction) is $\mathbf{V}_l(t) = \frac{1}{l}\sum_{i=1}^{l} v(x_i, t)$

In the case of $l=L$, this corresponds to full spatial average in the local spatio-temporal velocity field $v(x,t)$. To reduce the averaging scale to $l=L/3$ for instance,we divide the matrix $v(x,t)$ into three boxes, taking the spatial average within each box and finally putting all three temporal signals together into one. This is shown in the left panel of Fig. 5. In this procedure of splitting the statistics into smaller boxes, we assume that each box is an independent realization, i.e uncorrelated, $l > x^*$ (note that $L = 50\, x^*$, corresponding to a maximum of 50 independent boxes). When the assumption of independence holds, this procedure is a way to significantly increase the statistics.

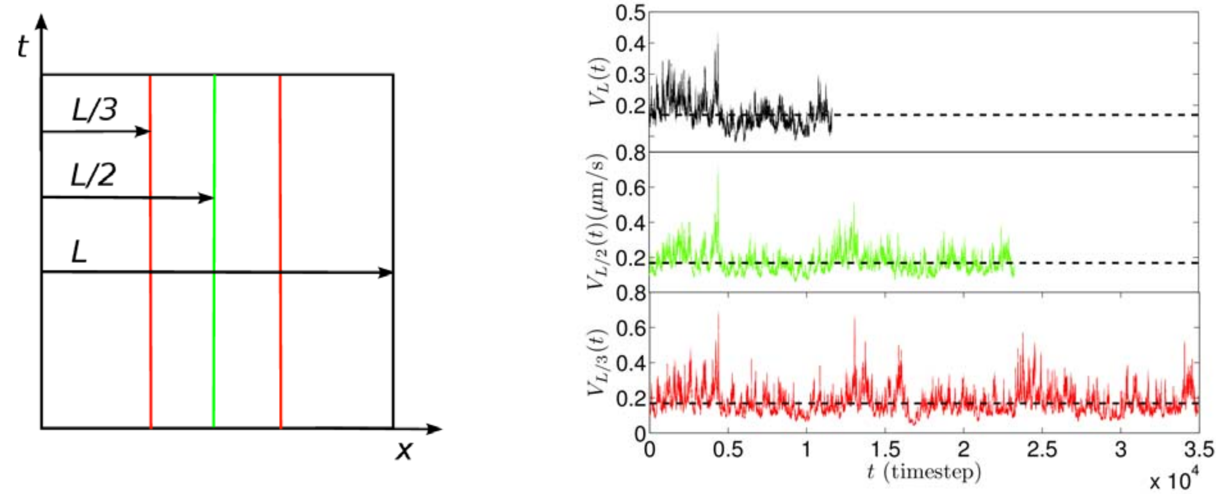

Figure 5: *(Left panel) Schematic illustration of how the local velocity field v(x,t) is divided into boxes to obtain the spatially averaged velocity* $V_l(t)$*. For l=L, there is one box at the width of the system size. The corresponding experimental signal is shown in the upper right panel. For l=L/2, v(x,t) is divided in two boxes and stacked in time, generating double the statistics, as shown in the middle right panel. For l=L/3, v(x,t) is divided in three boxes and stacked in time, generating triple the statistics, as shown in the lower right panel. The dashed line shows the total space-time average* $<v>$*. It is clear that for all the scales shown, the statistics is asymmetric with extreme events above the average.*

For one experiment, we show in the right panel of Fig. 5, the average velocity $V_l(t)$, at three different scales, all well above the correlation length. Already by visual inspection of this signal, the main conclusions can be drawn: The distribution of $V_l(t)$ is asymmetric around the average value (dashed line), and there are extreme events even at this large scale. Normally, following the central limit theorem, one would expect a convergence to the Gaussian law. This is however not the case as seen in Fig. 6, where we show the centered and normalized PDF of $V_l(t)$, $R([V-<V>]/\sigma)$, for several experiments and several scales above the correlation length. Here, σ is the standard deviation of $V_l(t)$.

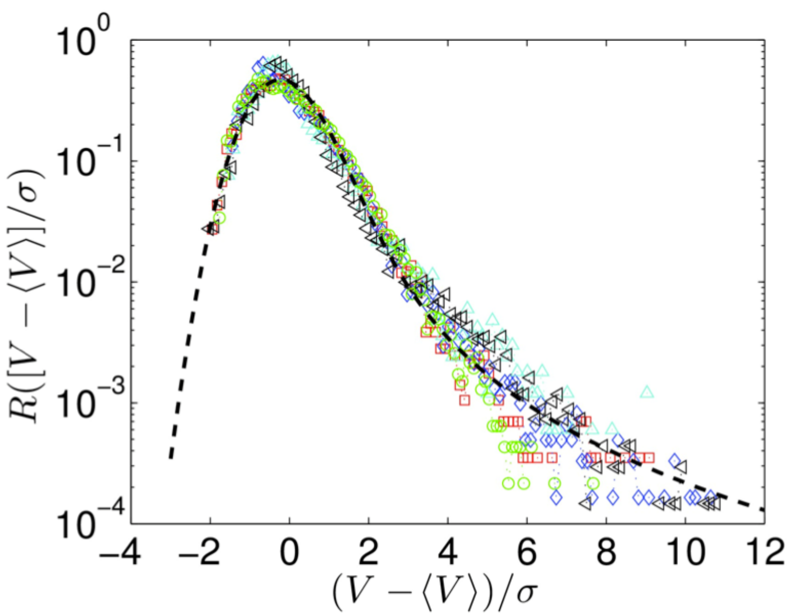

Figure 6: *PDF* $R([V-<V>]/\sigma)$ *of the global velocity* $V_l(t)$*, for different experiments at scales l/x* = [40, 20, 13], in semi-log scale. Note that even at these large scales, well above the correlation length (l>13x*), the statistics is clearly non-Gaussian. The dashed line shows the PDF of a fitted stable Levy distribution, and compares very well with the data.*

We thus clearly observe the convergence to a Non-Gaussian distribution. To understand this, one must consider a generalized version of the central limit theorem. It states, very roughly, that if the PDF of the individual summands (the local velocities) has a diverging variance, the PDF of the summed or averaged variable (the global velocity) should converge to a so-called *stable Levy* law (10, 11). The Levy PDF can be similar to a Gaussian in the central part, but has a much slower decay in the tails.

Unfortunately, the stable Levy PDF is rarely analytically expressible (10). Our fracture data fulfill the assumptions behind this generalized CLT.Moreover, the main property of this Levy law is that the fat tail is preserved from small to large scale, meaning that one should be able to measure α also at a global scale -provided enough statistics. This has been extensively studied in a recent work, where we predict the full shape of our global velocity fracture distribution from the generalized CLT (11). Here we simply show that by using the same exponentα found for the local velocity PDF (1, 2), and fitting a scale parameter to the Levy distribution, we obtain the fit shown as a dashed line in Fig. 6. The comparison to our experimental data is highly satisfactory.

Conclusion

We have demonstrated the non-Gaussian nature of the velocity fluctuations of a crack front propagating along the weak heterogeneousplane of a Plexiglas block. The local velocity fluctuations span a range of roughly four decades, and display a fat tail with a power law exponent. The PDF of the spatially averaged global velocity measured at larger and larger scalesconverges to a non-Gaussian distribution with an asymmetric shape and a fat tail, even well above any spatial correlations in the local velocity. This breakdown of the Central Limit Theorem is due to the fat tail of the local velocity PDF. The PDF observed at large scale compares indeed very well with a stable Levy distribution (11).

References

(1) K. T. Tallakstad, R. Toussaint, S. Santucci, J. Schmittbuhl, and K. J.Måløy. *Local dynamics of a randomly pinned crack front during creep and forced propagation: An experimental study.* Phys. Rev. E, 83(4):046108, Apr 2011.

(2) K. J. Måløy, S. Santucci, J. Schmittbuhl, and R. Toussaint. *Local waiting time fluctuations along a randomly pinned crack front.* Phys. Rev. Lett., 96(4):045501, Jan 2006.

(3) B. R. Lawn. *Fracture of Brittle Solids - Second Edition.* Cambridge University Press, 1993.

(4) D. Bonamy. *Intermittency and roughening in the failure of brittle heterogeneous materials.* J. Phys. D: Appl. Phys., 42:214014, 2009.

(5) E. Bouchaud, G. Lapasset, and J. Planès. *Fractal dimension of fractured surfaces: A universal value?*Europhys. Lett., 13(1):73, 1990.

(6) J. Schmittbuhl and K. J. Måløy. *Direct observation of a self- affine crack propagation.* Phys. Rev. Lett., 78(20):3888–3891, May 1997 .

(7) J. P. Sethna, K. A. Dahmen, and C. R. Myers. *Crackling noise.* Nature (London), 410(2001):242–250.

(8) R. Planet, S. Santucci, and J. Ortin. *Avalanches and Non-Gaussian Fluctuations of the Global Velocity of Imbibition Fronts.* Phys. Rev. Lett. 102, 094502 2009.

(9) E. Bertin. *Global Fluctuations and Gumbel Statistics.*Phys. Rev. Lett. 95, 170601 Oct 2005.

(10) V. V. Uchaikin and V. M. Zolotarev. *Chance and Stability - Stable Distributions and their Applications* (VSP BV, The Netherlands, 1999).

(11) K. T. Tallakstad, R. Toussaint, S. Santucci, and K. J. Måløy. *The non-Gaussian nature of fracture, and the survival of fat-tail exponents.* Submitted to Phys. Rev. Lett. July 2012.

Non-Gaussian Nature of Fracture and the Survival of Fat-Tail Exponents

Ken Tore Tallakstad,[1] Renaud Toussaint,[2,3] Stephane Santucci,[4,3] and Knut Jørgen Måløy[1,3]

[1]Department of Physics, University of Oslo, PB 1048 Blindern, NO-0316 Oslo, Norway

[2]Institut de Physique du Globe de Strasbourg, UMR 7516 CNRS, Université de Strasbourg, 5 Rue René Descartes, F-67084 Strasbourg Cedex, France

[3]Centre for Advanced Study, The Norwegian Academy of Science and Letters, Drammensveien 78, NO-0271 Oslo, Norway

[4]Laboratoire de Physique, Ecole Normale Supérieure de Lyon, CNRS UMR 5672, 46 Allée d'Italie, 69364 Lyon Cedex 07, France

(Received 11 July 2012; revised manuscript received 24 January 2013; published 2 April 2013)

We study the fluctuations of the global velocity $V_l(t)$, computed at various length scales l, during the intermittent mode-I propagation of a crack front. The statistics converge to a non-Gaussian distribution, with an asymmetric shape and a fat tail. This breakdown of the central limit theorem (CLT) is due to the diverging variance of the underlying local crack front velocity distribution, displaying a power law tail. Indeed, by the application of a generalized CLT, the full shape of our experimental velocity distribution at large scale is shown to follow the stable Levy distribution, which preserves the power law tail exponent under upscaling. This study aims to demonstrate in general for crackling noise systems how one can infer the complete scale dependence of the activity—and extreme event distributions—by measuring only at a global scale.

DOI: 10.1103/PhysRevLett.110.145501 PACS numbers: 62.20.mt, 46.50.+a, 68.35.Ct

The failure of heterogeneous materials is a complex process taking place on a very broad range of scales, from the separation of atomic bonds to the nucleation and growth of micro- and macrovoids, even up to earthquakes and fault dynamics [1,2]. The competition between pinning forces, at local asperities of high toughness, and long range elastic forces due to loading, results both in a rough fracture morphology, with self-affine scaling properties [3–5], and a complex intermittent dynamics. The velocity fluctuations are very large, containing sudden avalanches that span a wide range of sizes and durations [6–8]. Such a complex spatiotemporal dynamics, generically called crackling noise [9], arises also in a wide variety of other physical systems, for instance, magnetic domain wall motion in disordered ferromagnets [10], vortex lines in type-II superconductors [11], and dislocation lines in defective crystalline solids [12]. However, in most systems, experimentally, one usually cannot access the local information, as for instance a front position as a function of space and time, $h(x, y, t)$. Thus, the crackling dynamics can only be characterized at a global scale via the measurement of a global, i.e., spatially averaged, quantity. This is particularly the case for the fracture of disordered materials, where the damaging processes are usually monitored indirectly via the recording of acoustic emissions [13–15], since the materials considered are usually opaque and the crack fronts have a complex three-dimensional structure, therefore preventing a direct observation.

We overcome such difficulty by using a transparent model where the crack is constrained to propagate along a weak heterogeneous interface [7]. Thus, using a high resolution fast camera, we extract, in all details, the local spatiotemporal crack front dynamics. Specifically, we have shown previously that the dynamics is governed by avalanches with very large size and velocity fluctuations, following a fat-tail distribution with a power law exponent $1 + \alpha = 2.6 \pm 0.15$, and thus has a diverging variance [6,7]. This theoretically implies the breakdown of the usual central limit theorem (CLT) [16]. In the present Letter, we exploit our detailed local information and go further on the investigation of such complex dynamics at larger scales.

We focus now on the global crack growth, which displays an intermittent behavior, as a consequence of the local burst motion of the front. We study in particular the fluctuations of the global velocity $V_l(t)$, spatially averaged at different length scales, and show that they do not converge to the usual Gaussian statistics. Interestingly, recent theoretical and experimental results [17–19] have underlined the importance of long range spatial correlations in the statistics of a global variable, showing that such fluctuations can follow a general Gumbel distribution—asymmetric with an exponential tail—when the measuring window is comparable to the correlation length, while above such a characteristic length scale, a clear convergence to the Gaussian statistics is observed.

In contrast, as observed in our experiments, the deviation from the Gaussian law does not arise from finite size effects, but is due to the diverging second moment of underlying local crack front velocity probability distribution function (PDF). As a consequence, the PDF of the sum, or average, of such local random variables does not converge to a Gaussian, but rather to a stable Levy distribution [16,20]. Indeed, by using a generalization of the CLT, we can predict the full nature of the global velocity fluctuations, characterized by the fat-tail scaling exponent

α and an asymmetry parameter β. The main implication of this generalized CLT is the preservation of local information also at large scale; i.e., α survives averaging and can be measured, given good enough statistics. Furthermore this can be exploited to predict the scaling of extremes and of the individual summands in the global variable. This is, to the best of our knowledge, the first time such Levy distributions and their formalism are reported and used in the case of fracture.

We observe directly, with a high resolution fast camera, a crack front propagating slowly (0.1–100 μm/s) along a weak heterogeneous interface of a Plexiglas block. It is made of two weakly sintered sandblasted plates having dimensions of (27, 14, 1) cm and (30, 12, 0.4) cm. The roughening procedure generates heterogeneities in the range of ~15–50 μm [21]. The crack front propagation is imaged at a very high spatial (up to 3000 pixels, with a pixel size of $a \approx 2.5$ μm) and temporal resolution (up to 40 000 images recorded at a rate varying from 1 up to 1000 fps), relative to its velocity fluctuations. The imaged area, covered by the crack front, corresponds to roughly (6×0.5) mm transverse to, and along, the direction of propagation, respectively. The quasi–mode-I crack growth is obtained by imposing a normal displacement on the bottom plate while the upper plate is fixed to an aluminum frame [7]. Independently of the loading conditions [7], the time of observation is small enough, so that the average velocity of crack propagation in space and time is constant during an experiment.

The local velocity along the crack front $h(x,t)$ is computed from the waiting time at a given position $w(x,y)$ [6,7], i.e., the discrete number of time units the front has spent at a given pixel. The local velocity of the front is then obtained for each front at each time step as $v(x,t) = a/w[x, h(x,t)]\delta t$, where a is the pixel size and δt is the time resolution. This constitutes a local velocity space-time map, where the global velocity $V_l(t)$, spatially averaged over line segments of length l (pixels) in the x direction, can be measured at any scale l: $V_l(t) = \langle v(x,t)\rangle_l \equiv \frac{1}{l}\sum_{i=1}^{l} v(x_i,t)$ with temporal mean $\langle V_l\rangle_T = \frac{1}{T}\sum_{j=1}^{T} V_l(t_j)$, and an estimated standard deviation $\sigma^2 \equiv \langle (V_l - \langle V_l\rangle_T)^2\rangle_T$, where T is the total number of time steps of the signal. To check that our results are independent of the specific way the global velocity is obtained, we compare them when suitable (see Figs. 2 and 3) to those obtained when the global velocity is instead computed directly, through the time derivative of the spatially averaged crack front position at scale l, $U_l(t) = d\langle h(x,t)\rangle_l/dt$. This is typically what is done in low resolution crackling noise experiments.

The local velocity fluctuations, in space and time, along the crack front, for $v > \bar{v}$, follow a power-law distribution, $P(v/\bar{v}) \propto (v/\bar{v})^{-(\alpha+1)}$ with $\alpha = 1.6 \pm 0.15$, independently of the loading conditions and average crack front velocity [7]. Since the mean $\bar{v} \equiv \int_0^\infty vP(v)dv$ is well defined for $\alpha > 1$ we have $\bar{v} = \langle V_l\rangle_T = \bar{V}_l \equiv \int_0^\infty V_l\Psi(V_l)dV_l$ for sufficiently large T, where $\Psi(V_l)$ is the PDF of V_l. Local fluctuations occur over a very broad interval, as observed on a typical space-time map of the velocity field $v(x,t)$, shown in Fig. 1, and thus lead to a complex intermittent dynamics of the global crack growth $V_l(t)$.

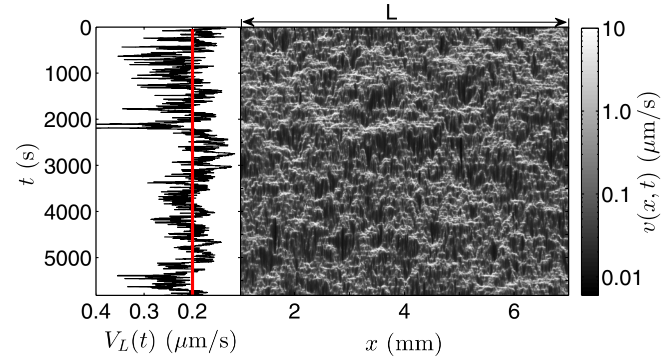

FIG. 1 (color online). The spatiotemporal velocity field $v(x,t)$ during a fracture experiment (right panel). The corresponding spatially averaged signal $V_L(t) = \langle v(x,t)\rangle_L$, over the full system size L (left panel). The solid red line indicates the full space-time average velocity $\langle V_L\rangle_T = \bar{v}$.

The variance of a sum of independent and identically distributed random variables equals the sum of their individual variances [16,20], i.e,, $\langle(\sum_{i=1}^{l} v_i - \langle\sum_{i=1}^{l} v_i\rangle_T)^2\rangle_T \sim l\langle\langle(v-\bar{v})^2\rangle_l\rangle_T$, in the large T limit. Under such assumptions and by multiplying with $1/l^2$, we obtain the relationship between the global velocity V_l at scale l and the local velocity v,

$$\sigma^2 = \langle(V_l - \bar{V}_l)^2\rangle_T \sim \frac{1}{l}\langle\langle(v-\bar{v})^2\rangle_l\rangle_T. \tag{1}$$

For large T, the variance estimators of v can be replaced with an integral over the underlying PDF (see the Supplemental Material [22]),

$$\left(\frac{\sigma}{\bar{v}}\right)^2 \sim \frac{1}{l}\int_0^{z^*}(z-1)^2 G(z) z^{-(1+\alpha)}dz, \tag{2}$$

where $z = v/\bar{v}$ and $G(z) = P(z)z^{1+\alpha}$ is the lower cutoff function of $P(z)$, ensuring the convergence in the lower limit [because $G(z)$ is finite for $z \ll 1$]. In the upper limit [$G(z) \sim 1$ for $z \gg 1$], this integral will diverge if $z^* \to \infty$ for $\alpha < 2$. However, since σ is only estimated over a scale l and sampled over a finite number of realizations T, z^* must be finite, and given by the largest velocities that are sampled from $P(z)$ to generate the global velocity V_l. Thus, as argued in Ref. [22], $z^*\bar{v}$ can be represented by the average maximum velocity at scale l, i.e., $\langle v_{\max}^l(t)\rangle_T \equiv \langle\max\{v(x_i,t); i = 1,\ldots,l\}\rangle_T$. From extreme value theory, the PDF of $v_{\max}^l$ will converge to the so-called Fréchet distribution, with mean [16,20,22]

$$\langle v_{\max}^l\rangle_T \sim l^\gamma, \quad \text{where } \gamma = 1/\alpha. \tag{3}$$

We use $z^* = \langle v^l_{\max}\rangle_T/\bar{v}$ as an upper limit in Eq. (2) giving

$$(\sigma/\bar{v}) \sim l^{-\xi} \quad \text{with} \quad \xi = 1 - \frac{1}{\alpha}. \tag{4}$$

Note that for $\alpha < 2$, Eq. (4) predicts non-Gaussian statistics. For uncorrelated data, such a scaling provides an indirect way of measuring the power law exponent in the fat tail of the local variables distribution. Usually in experiments, high resolution data are unavailable. This measure should thus prove particularly useful in general.

Figure 2 shows the scaling behavior of both $\langle v^l_{\max}\rangle_T$ and σ, normalized by $\bar{v}$ for different experiments [7], as functions of l, rescaled by the correlation length x^*. Indeed, due to the interplay between sample disorder and elastic interactions, the local velocities are correlated along the crack front, up to a characteristic scale $x^* \sim 150\ \mu$m [7]. Our data appear in excellent agreement with the expected scaling behavior, providing the exponent and $\xi = 0.42 \pm 0.02$ leading to $\gamma = 0.58 \pm 0.03$ and $\alpha = 1.7 \pm 0.1$, consistent with the value previously reported [6,7]. Interestingly, we observe a different regime with a deviation to the expected scaling behavior for $\sigma < l/x^*$, whereas $\langle v_{\max}\rangle_t$ maintains the scaling prediction even at scales below l/x^*. Hence, measuring the spatial dependence of σ or $\langle v^l_{\max}\rangle_T$, at a few large scales, allows us to determine the tail shape of the underlying local distribution. This is also confirmed when $\sigma(l)$ is obtained from $U_l(t)$, as shown in black circular markers in the lower panel of Fig. 2.

To predict the full shape of the global velocity PDF, measured at various scales l, consider now the normalized global velocity $V' = (V_l(t) - \langle V_l(t)\rangle_T)/b_l$, where b_l [cf. Eq. (7)] is a normalization constant. We show in the upper panel of Fig. 3, the PDF $\Psi(V')$ for three experiments, at different space-time average velocities [7]: $\langle V_l\rangle_t = \bar{v} = 0.15\ \mu$m/s, $\bar{v} = 1.36\ \mu$m/s, and $\bar{v} = 141\ \mu$m/s. The global velocity V_l has been obtained over four different length scales l, at least 1 order of magnitude above the correlation length x^*, so that $l/x^* \approx \{40, 20, 13, 10\}$. We observe a clear data collapse of our experimental PDFs, showing a non-Gaussian behavior of the temporal fluctuations of the global velocity $V_l(t)$, with an asymmetric shape and an asymptotic fat tail for large positive values. It is important to underline that this behavior is independent of the loading conditions or average propagation velocity of the crack front. Some dispersion in the tail between the experiments is observed, however, within the limits of uncertainty in α, and can be traced back to small variations in the tail for the experimental $P(v/\bar{v})$ PDFs. The lower panel in Fig. 3 shows $\Psi(V')$, where V' is now obtained through $U_l(t)$, also including more points in the tail due to slightly higher statistical significance in those data. It is evident that the two ways of obtaining the global velocity produce highly consistent results.

The fat-tail decay, observed for the local velocity distribution with $\alpha + 1 = 2.7 < 3$, produces the divergence of the integral in Eq. (2), and thus leads to the breakdown of the usual CLT. However, we can explain these results by invoking a generalization of the CLT, in particular that the fat tail, seen in Fig. 3, of the experimental data should decay with a power law exponent $1 + \alpha$. It states that an average variable V of a number of independent random variables v with an asymptotic power law tail distribution $1/|v|^{\alpha+1}$, where $\alpha < 2$, (and therefore having infinite

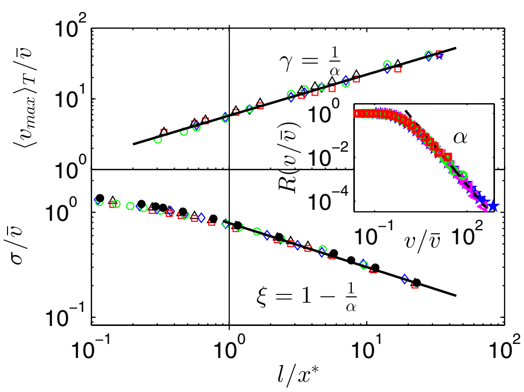

FIG. 2 (color online). Average maximum velocity (upper panel) $\langle v^l_{\max}\rangle_T/\bar{v}$ and standard deviation (lower panel) $\sigma/\bar{v}$ of $V_l(t)$ as functions of the measuring window rescaled by the correlation length l/x^*. The upper solid line corresponds to the slope $\gamma = 1/1.7 \approx 0.58$. The lower solid line is a fit of Eq. (4) for $l/x^* > 3$, giving $\xi = 0.42 \pm 0.03$ and thus $\alpha = 1.7 \pm 0.1$. Circular black markers show, for one experiment, $\sigma(l)$, obtained from $U_l(t)$ (smoothed over 15 time steps) as defined in the text. The inset shows the cumulative PDF of the local velocity $R(v/\bar{v})$. The dashed line is a fit to the asymptotic tail, using $\alpha = 1.7$, to obtain λ^+ as defined in the text.

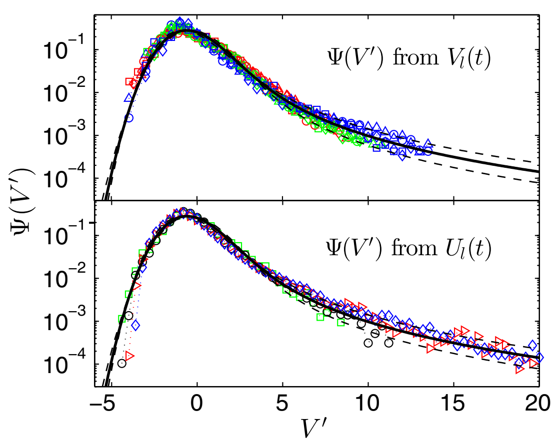

FIG. 3 (color online). PDF $\Psi(V')$ of the global velocity $V_l(t)$ (upper panel) for three different experiments, shown as dark gray, light gray, and black (red, green, and blue), at four different averaging scales $l/x^* \in \{40, 20, 13, 10\}$, in semilog representation. For one of these experiments (blue), we obtain $\Psi(V')$ from $U_l(t)$, smoothed over 15 time steps, at the same averaging scales (lower panel). The solid lines show the PDF $\Psi(V'; 1.7, 1)$, obtained from Eq. (5), whereas the dashed lines correspond to $\Psi(V'; 1.7 \pm 0.1, 1)$, displaying the effect of the variations in α.

variance) will tend to a so-called alpha stable Levy distribution [23] $\Psi(V; \alpha, \beta, c, \delta)$ as the number of individual variables v, used to obtain the average V, grows [16,20]. Generally not analytically expressible, Ψ contains four parameters and is defined through the inverse Fourier transform of its characteristic function Φ,

$$\Psi(V; \alpha, \beta, c, \delta) = \frac{1}{2\pi}\int_{-\infty}^{\infty} \Phi(k)\exp(-iVk)dk, \quad (5)$$

$$\Phi(k) = \exp\left\{ik\delta - |ck|^{\alpha}\left[1 + i\beta\frac{k}{|k|}\tan\left(\frac{\pi}{2}\alpha\right)\right]\right\}, \quad (6)$$

for $\alpha \neq 1$. Here, V is the random variable (in our case the global velocity), α is the index of the distribution giving the exponent of the asymptotic power law tail $(\alpha + 1)$, and $\beta \in [-1, 1]$ is the so-called skewness parameter and a measure of asymmetry. Note in this context that the usual skewness, given by the third moment of the distribution [20], is not well defined for $\alpha < 2$ due to the divergence of the second and higher order moments. The shift parameter δ gives the peak position for a symmetric distribution, whereas c is a scale factor characterizing its width. For $\alpha > 1$, it is possible to reduce the number of varying parameters in Ψ by the following normalization of V [20]:

$$V' = \frac{V_l - \langle V_l\rangle_T}{b_l} \quad \text{with} \quad b_l = \left(\frac{\pi(\lambda^+ + \lambda^-)}{2\Gamma(\alpha)\sin(\alpha\pi/2)}\right)^{1/\alpha} l^{1/\alpha - 1}. \quad (7)$$

Here, b_l is proportional to the standard deviation, and with this normalization V' will be centered around zero, leading to $\delta = 0$, and $c = 1$. In Eq. (7), Γ is the gamma function, whereas the constants λ^+ and λ^- characterize the asymptotic behavior on the positive and negative axes, respectively, of the cumulative distribution function of v: $R(v \to \infty) = \lambda^+ v^{-\alpha}$, and $1 - R(v \to -\infty) = \lambda^-|v|^{-\alpha}$. The skewness parameter is given as $\beta = \frac{\lambda^+ - \lambda^-}{\lambda^+ + \lambda^-}$, which has its extreme value of 1 in the case of non-negative summands v [20], as is the case here, leading to $\lambda^- = 0$ and thus, $\beta = 1$. Finally, from the cumulative PDF $R(v/\bar{v})$, shown by the dashed line in the inset in Fig. 2, we obtain $\lambda^+ \approx 1.4$. Thus, our experimental data should converge to the distribution $\Psi(V'; 1.7, 1, 1, 0) \equiv \Psi(V'; 1.7, 1)$, shown as a solid line in Fig. 3. The comparison is highly satisfactory.

Finally, we examine the rate of convergence to such a stable law, when the measuring length scale increases from the micron to the millimeter scale, below and above the correlation length, respectively. This evolution is shown in Fig. 4, represented in log-log form, for the scales $l/x^* \approx \{3, 1, 0.5, 0.2, 0.05\}$, and shifted systematically for visual clarity. The solid lines show the corresponding Levy distribution $\Psi(V'; 1.7, 1)$. The convergence to the Levy law is clear, as soon as the measuring window is larger than the correlation length x^*. However more strikingly, the fat tail of the velocity distribution survives clearly the upscaling.

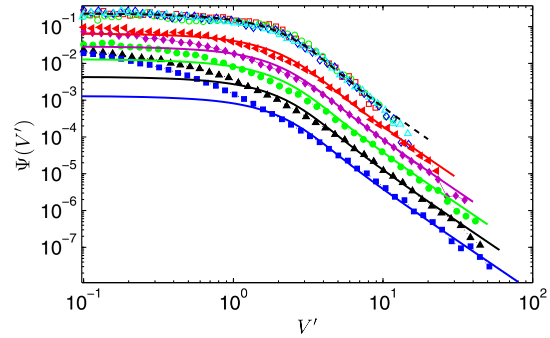

FIG. 4 (color online). PDF $\Psi(V')$ for one experiment in log-log representation, at the scales $l/x^* \approx \{40, 20, 13, 10\}$ (upper collapsed curves, empty markers), and in filled markers from top to bottom, at $l/x^* \approx \{3, 1, 0.5, 0.2, 0.05\}$, respectively. The latter distributions with the theoretical curves, $\Psi(V'; 1.7, 1)$ shown as solid lines, have been shifted for visual clarity.

This shows very explicitly, the validity of the generalized CLT for the fracture velocity statistics.

We have analyzed the intermittent propagation of a crack front along a heterogeneous plane in a Plexiglas block, focusing on the temporal fluctuations of the global velocity, i.e., spatially averaged at various length scales. We have shown how the fat tail of the local crack front velocity leads to the breakdown of the central limit theorem, with anomalous scaling behaviors of the average maximum velocity $\langle v_{\max}^l\rangle_T$ and variance σ of $V_l(t)$, and thus non-Gaussian fluctuations also at the large scale. Moreover, we have demonstrated how the generalized version of the CLT must be applied, in order to predict the full global distribution of crack front velocities.

The authors thank J. Bergli, L. Angheluta, and A. Hansen for fruitful discussions, and also Mark Veillette for his MATLAB routine to integrate stable distributions [24]. The work was supported by the Norwegian Research Council, the University of Strasbourg, and ENS-Lyon.

[1] M. J. Alava, P. K. V. V. Nukala, and S. Zapperi, Adv. Phys. **55**, 349 (2006).
[2] D. Bonamy and E. Bouchaud, Phys. Rep. **498**, 1 (2011).
[3] L. Ponson, D. Bonamy, and E. Bouchaud, Phys. Rev. Lett. **96**, 035506 (2006).
[4] S. Santucci, K. J. Måløy, A. Delaplace, J. Mathiesen, A. Hansen, Jan Oistein Haavig Bakke, J. Schmittbuhl, L. Vanel, and P. Ray, Phys. Rev. E **75**, 016104 (2007).
[5] J. Schmittbuhl and K. J. Måløy, Phys. Rev. Lett. **78**, 3888 (1997).
[6] K. J. Måløy, S. Santucci, J. Schmittbuhl, and R. Toussaint, Phys. Rev. Lett. **96**, 045501 (2006).
[7] K. T. Tallakstad, R. Toussaint, S. Santucci, J. Schmittbuhl, and K. J. Måløy, Phys. Rev. E **83**, 046108 (2011).
[8] K. J. Måløy and J. Schmittbuhl, Phys. Rev. Lett. **87**, 105502 (2001).
[9] J. Sethna, K. Dahmen, and C. Myers, Nature (London) **410**, 242 (2001).

[10] D. Spasojevi, S. Bukvić, S. Milošević, and H. E. Stanley, Phys. Rev. E **54**, 2531 (1996).
[11] G. Blatter, M. V. Feigel'man, V. B. Geshkenbein, A. I. Larkin, and V. M. Vinokur, Rev. Mod. Phys. **66**, 1125 (1994).
[12] F. F. Csikor, C. Motz, D. Weygand, M. Zaiser, and S. Zapperi, Science **318**, 251 (2007).
[13] A. Garcimartín, A. Guarino, L. Bellon, and S. Ciliberto, Phys. Rev. Lett. **79**, 3202 (1997).
[14] J. Davidsen, S. Stanchits, and G. Dresen, Phys. Rev. Lett. **98**, 125502 (2007).
[15] J. Koivisto, J. Rosti, and M. J. Alava, Phys. Rev. Lett. **99**, 145504 (2007).
[16] D. Sornette, *Critical Phenomena in Natural Sciences* (Springer-Verlag, Berlin, 2000).
[17] E. Bertin, Phys. Rev. Lett. **95**, 170601 (2005).
[18] S. Joubaud, A. Petrosyan, S. Ciliberto, and N. B. Garnier, Phys. Rev. Lett. **100**, 180601 (2008).
[19] R. Planet, S. Santucci, and J. Ortín, Phys. Rev. Lett. **102**, 094502 (2009).
[20] V. V. Uchaikin and V. M. Zolotarev, *Chance and Stability-Stable Distributions and Their Applications* (VSP BV, The Netherlands, 1999).
[21] S. Santucci, M. Grob, A. Hansen, R. Toussaint, J. Schmittbuhl, and K. J. Måløy, Europhys. Lett. **92**, 44001 (2010).
[22] See Supplemental Material at http://link.aps.org/supplemental/10.1103/PhysRevLett.110.145501 for details on Eqs. (1)–(4).
[23] This family of distributions is in some communities referred to simply as stable distributions. In such a case, the term stable Levy is reserved for the special case of $\alpha = 1/2$ [20].
[24] M. Veillette, http://math.bu.edu/people/mveillet/html/alphastablepub.html.

Importance of extreme events in a sum of random variables

Ken Tore Tallakstad,[1] Renaud Toussaint,[2,3] Stephane Santucci,[4] and Knut Jørgen Måløy[4]

[1] *Department of Physics, University of Oslo, PB 1048 Blindern, NO-0316 Oslo, Norway*
[2] *Institut de Physique du Globe de Strasbourg, UMR 7516 CNRS, Université de Strasbourg, 5 rue René Descartes, F-67084 Strasbourg Cedex, France*
[3] *Centre for Advanced Study at The Norwegian Academy of Science and Letters, Drammensveien 78, 0271 N-Oslo, Norway*
[4] *Laboratoire de Physique, Ecole Normale Supérieure de Lyon, CNRS UMR5 672, 46 Allée d'Italie, 69364 Lyon cedex 07, France*

(ΩDated: December 14, 2012)

DEFINITIONS

Consider a set of independent and identically distributed random variables x given by the probability density function (PDF)

$$P(x) = \alpha x_m^\alpha \, x^{-(1+\alpha)} \ , \qquad \text{where} \ \ x \geq x_m , \tag{1}$$

and cumulative distribution function (CDF)

$$R(x' \geq x) = x_m^\alpha \, x^{-\alpha} \ , \tag{2}$$

where x_m is the lower limit of x. For $1 < \alpha < 2$ the mean $\bar{x} = \int_0^\infty xP(x)dx$ and variance $\sigma^2 = \int_0^\infty (x-\bar{x})^2 P(x)dx$ is given by

$$\bar{x} = \frac{\alpha}{\alpha - 1} x_m , \qquad \sigma^2 = \infty \ . \tag{3}$$

Note that for $\alpha < 2$, the variance or second moment of $P(x)$ diverges. In this particular example we chose x to be distributed according to a power law, or the so called *Pareto* distribution, due to its simplicity. However, we underline that the results in the following sections will be valid also in a more general case ($P(x) = f(x)x^{-(1+\alpha)}$, where $f(x)$ is slowly varying), as long as the asymptotic tail of the PDF of x is a power law.

We then consider the sum and the maximum value of l elements drawn from the $P(x)$,

$$X_l = \sum_{i=1}^{l} x_i \ , \tag{4}$$

$$M_l = \max(x_i, i = 1, ..., l) \ . \tag{5}$$

EXTREME VALUE STATISTICS (EVS)

From the Fisher – Tippett – Gnedenko theorem in EVS [1], it follows that for large l, the cumulative distribution function of M_l will converge to the so called *Frechet* distribution, for *any* PDF of x with a power law tail:

$$F(M_l' \leq M_l) = \exp\left[- \left(\frac{M_l - m}{s} \right)^{-\alpha} \right] \ , \tag{6}$$

with PDF,

$$G(M_l) = \frac{\alpha}{s} \left(\frac{M_l - m}{s} \right)^{-(1+\alpha)} \exp\left[- \left(\frac{M_l - m}{s} \right)^{-\alpha} \right] \ , \tag{7}$$

where m is a location parameter and s is a scale parameter depending on l as we will return to. Note that the fat tail exponent α emerges both in the EVS and the local statistics of x, i.e, both $P(x)$ and $G(M_l)$ has the same fat tail as their argument goes to infinity. It can also be shown that for $\alpha > 1$, the mean of M_l is given by

$$\bar{M_l} = \int_0^\infty M_l G(M_l) dM_l = m + s\Gamma(1 - 1/\alpha) \ , \tag{8}$$

where Γ is the Gamma function. The scale parameter s dependence on l, can be deduced by realizing that $R(x)$ and $F(M_l)$ are related. For some value M_l^*, M_l' is smaller than M_l^*, only if all x_i are smaller than M_l^*. From the condition of independence, this probability is simply

$$F(M_l' \leq M_l^*) = [R(x' \leq M_l^*)]^l \ , \tag{9}$$

$$= [1 - R(x' \geq M_l^*)]^l \ . \tag{10}$$

For $l \gg 1$, this can be approximated as

$$F(M_l' \leq M_l^*) = \exp[-lR(x' \geq M_l^*)] \ , \tag{11}$$

$$\exp\left[- \left(\frac{M_l^* - m}{s} \right)^{-\alpha} \right] = \exp[-l x_m^\alpha M_l^{*-\alpha}] \ . \tag{12}$$

and we obtain

$$m = 0, \qquad s = x_m l^{1/\alpha} \ . \tag{13}$$

Thus, from Eq. (8), the mean maximum value of x in a set of l elements, $\bar{M_l}$, is given by

$$\bar{M_l} = \Gamma(1 - 1/\alpha) x_m l^{1/\alpha} \ . \tag{14}$$

IMPORTANCE OF THE MAXIMUM IN A SUM

In [2] it is shown how much weight M_l carries in the sum X_l. For $\alpha > 1$ and large l, the expectation value

($E[...]$) of the ratio X_l/M_l reads

$$E\left[\frac{X_l}{M_l}\right] = \frac{1}{1-\alpha}\left(1-\Gamma(1/\alpha)l^{1-1/\alpha}\right), \quad (15)$$

$$\approx \frac{1}{\alpha-1}\Gamma(1/\alpha)l^{1-1/\alpha} \; . \quad (16)$$

The $E[X_l/M_l] \sim l^{1-1/\alpha}$ scaling illustrates well how dominant the maximum value is, in a sum of power law distributed elements, compared to the standard $E[X_l/M_l] \sim l$ behaviour, observed for Gaussian variables, where each element carries the same weight.

Finally we address the question of what is the typical upper limit among l elements of x_i, when we obtain T different realizations of X_l. Knowing that M_l is distributed according to Eq. (7) in the large l limit, its estimated mean will converge to the true mean for a large number of realizations T and $\alpha > 1$. Now, what is the probability for x_i not to exceed $\bar{M}_l$, among T realizations of X_l? Evaluating Eq. (6) with $M_l = \bar{M}_l$ [Eq. (8)] gives

$$F(M' \leq \bar{M}_l) = \exp(-\Gamma(1-1/\alpha)^{-\alpha}) \; . \quad (17)$$

Thus for $\alpha = 1.7$, $F(M' \leq \bar{M}_l) \approx 0.8$. That is, roughly 80% of the x_i drawn from $P(x)$ to generate X_l, will not exceed $\bar{M}_l$ at this α. At an even larger limit, say twice the mean value we obtain $F(M' \leq 2\bar{M}_l) \approx 0.9$, and a similar scaling with l: $2\bar{M}_l \sim l^{1/\alpha}$.

From the above considerations, we thus conclude that in generating T realizations of X_l, $P(x)$ is sampled up to an upper limit, corresponding to the average maximum velocity, $\bar{M}_l \sim l^{1/\alpha}$, with $\sim 80\%$ confidence. Note also that if one chooses a higher confidence interval in the upper limit of $P(x)$, the scaling with l is preserved. An upper sampling limit of $P(x)$ is useful, because one can quantify diverging moments in terms of numerical estimators. As an example, we take the variance of $P(x)$ for $\alpha < 2$. The mean is well defined, whereas the true variance σ^2 diverges [Eq. (3)]. However, it is possible to estimate the variance in a series of l elements drawn from $P(x)$, sampled over a total of T different realizations,

$$\langle\langle(x-\bar{x})^2\rangle_l\rangle_T \equiv \frac{1}{T}\sum_{j=1}^{T}\frac{1}{l}\sum_{i=1}^{l}(x_{i,j}-\bar{x})^2 \; . \quad (18)$$

It is now possible to use the definition of the true variance and integrate over the PDF, as long as the upper limit of the integral is truncated at the upper sampling limit of $P(x)$, here chosen to be $\bar{M}_l$. Thus, the sampled variance should be approximately given by

$$\langle\langle(x-\bar{x})^2\rangle_l\rangle_T \sim \int_0^{\bar{M}_l}(x-\bar{x})^2 P(x)dx \; , \quad (19)$$

$$\sim l^{2/\alpha-1} \; . \quad (20)$$

[1] S. Kotz and N. L. Johnson, *Breakthroughs in Statistics: Foundations and Basic Theory* (Springer-Verlag, 1992).

[2] D. Sornette, *Critical Phenomena in Natural Sciences* (Springer-Verlag, Berlin Heidelberg, Germany, 2000).

Earth and Planetary Science Letters 331–332 (2012) 215–223

Contents lists available at SciVerse ScienceDirect

Earth and Planetary Science Letters

journal homepage: www.elsevier.com/locate/epsl

Interplay of seismic and aseismic deformations during earthquake swarms: An experimental approach

O. Lengliné [a,e,*], J.E. Elkhoury [b], G. Daniel [c], J. Schmittbuhl [a], R. Toussaint [a,e], J.-P. Ampuero [b], M. Bouchon [d]

[a] Institut de Physique du Globe de Strasbourg, CNRS et Université de Strasbourg (EOST), France
[b] Seismological Laboratory, Caltech, Pasadena, USA
[c] Magnitude, Research and Development, Centre Regain, Sainte-Tulle, France
[d] ISTERRE, CNRS et Université Joseph Fourier, Grenoble, France
[e] Centre for Advanced Study at the Norwegian Academy of Science and Letters, Oslo, Norway

ARTICLE INFO

Article history:
Received 13 November 2011
Received in revised form 5 March 2012
Accepted 13 March 2012
Available online 13 April 2012

Editor: P. Shearer

Keywords:
Earthquake swarms
Aseismic slip

ABSTRACT

Observations of earthquake swarms and slow propagating ruptures on related faults suggest a close relation between the two phenomena. Earthquakes are the signature of fast unstable ruptures initiated on localized asperities while slow aseismic deformations are experienced on large stable segments of the fault plane. The spatial proximity and the temporal coincidence of both fault mechanical responses highlight the variability of fault rheology. However, the mechanism relating earthquakes and aseismic processes is still elusive due to the difficulty of imaging these phenomena of large spatiotemporal variability at depth. Here we present laboratory experiments that explore, in great detail, the deformation processes of heterogeneous interfaces in the brittle-creep regime. We track the evolution of an interfacial crack over 7 orders of magnitude in time and 5 orders of magnitude in space using optical and acoustic sensors. We explore the response of the system to slow transient loads and show that slow deformation episodes are systematically accompanied by acoustic emissions due to local fracture energy disorder. Features of acoustic emission activities and deformation rate distributions of our experimental system are similar to those in natural faults. On the basis of an activation energy model, we link our results to the Rate and State friction model and suggest an active role of local creep deformation in driving the seismic activity of earthquake swarms.

1. Introduction

Numerous observations of a correlation between seismic activity enhancements and slow slip transients in the Earth crust have been reported in various tectonic locations (Crescentini et al., 1999; Linde et al., 1996; Liu et al., 2007; Lohman and McGuire, 2007; Segall et al., 2006) and in geothermal areas (Bourouis and Bernard, 2007; Takada and Furuya, 2010). Also, observations of postseismic slip and aftershocks following large earthquakes are manifestations of transient deformation coupled with abundant earthquake activity (Perfettini and Avouac, 2004). A central question is whether or not these two different mechanical responses of faults, i.e. seismic and aseismic slips, occur on closely located zones. If they are, one expects a strong interaction between the two processes.

In some cases, the seismic signal concurrent with slow slip events is characterized as tectonic tremors or low frequency earthquakes, as observed in subduction zones (Ito et al., 2007; Obara et al., 2004; Rogers and Dragert, 2003) or in transform tectonic settings like the San Andreas Fault (SAF) (Nadeau and Dolenc, 2005; Shelly, 2010; Vidale and Shearer, 2006). The aseismic nucleation phase of mainshocks has also been related to foreshocks, as in the case of the 1999 Izmit earthquake (Bouchon et al., 2011) or the 2011 Tohoku-Oki earthquake (Ando and Imanishi, 2011; Kato et al., 2012; Miyazaki et al., 2011). Seismic events associated with aseismic slip are generally located on fault planes suggesting that they represent a dynamic shear instability on the sliding interface (La Rocca et al., 2009; Shelly et al., 2009). Geodetic inversions suggest that the aseismic motion occurs on the same fault plane as the seismic events (Lohman and McGuire, 2007). However the deformation signal recorded at the surface by GPS and/or InSAR instruments only provides a macroscopic view of the deformation process at depth. Details of the aseismic slip distribution are often lacking due to the limited resolution, unless the aseismic slip occurs at the Earth surface (Doubre and Peltzer, 2007).

The close spatial and temporal occurrence of both seismic and aseismic slip suggests a causal relation between the two phenomena. Nonetheless, the causal mechanism is not straightforward as earthquakes can both trigger and be triggered by slow slip events (Du et al., 2003; Perfettini and Avouac, 2004). It might also be that both aseismic and seismic slips are manifestations of a common deformation process. In

* Corresponding author. Institut de Physique du Globe de Strasbourg, CNRS et Université de Strasbourg (EOST), France.
URL: lengline@unistra.fr (O. Lengliné).

0012-821X/$ – see front matter © 2012 Elsevier B.V. All rights reserved.
doi:10.1016/j.epsl.2012.03.022

this case, the seismic signal can be seen as the signature of patches on the fault plane deforming dynamically whereas the geodetic observation represents an integrated signal over all the deforming sites. Therefore, the deformation on a fault plane takes place over a wide range of speeds. This is supported by observations of heterogeneous postseismic slip on the SAF inferred from the analysis of repeating earthquake sequences (Lengliné and Marsan, 2009). The dynamic events represent the high velocity tail of the slip speed distribution while its average produces the observed geodetic signal.

The contribution of earthquakes to the total amount of slip released during transient episodes is generally small (Lohman and McGuire, 2007). Despite being located on a common interface, accurate spatial location of the seismic activity relative to the aseismic slip is difficult to obtain. The heterogeneity of mechanical and physical properties of the interface might control the partition between seismic and aseismic slips, the interface being envisioned as a collection of brittle patches (asperities) embedded in an otherwise creeping region which accommodates slow slip (Linde et al., 1996; Lohman and McGuire, 2007; Perfettini et al., 2010; Wech et al., 2009). The concentration of asperities, or brittle patches, governs the relative importance of dynamic failures in the deformation process. It is also readily possible that temperature produces a broad scale effect on the slip partition over the interface and thus constrains the transition between brittle and ductile rheology.

The physics of both seismic and aseismic processes is not straightforward as it involves a complex problem on a spatially heterogeneous medium with a large number of degrees of freedom and short and long range interactions. Several numerical models have tried to reproduce the evolution of such systems but computations are extremely demanding and time consuming and limited to only large scale heterogeneities (Kaneko et al., 2010), or to the quasi-dynamic approximation (Ariyoshi et al., in press; Hillers et al., 2007). Analog laboratory experiments overcome these difficulties as space–time integrations are performed by the deforming system without any model requirement. Here, we investigate the slow (creep) and fast (acoustic) deformations produced by the propagation of an interfacial brittle-creep crack. Our experimental setup is a much simpler configuration than that of a complex fault zone system but the fundamental processes of interest, the interplay of slow deformation and brittle fracture on the same heterogeneous interface, remain similar. Our setup allows the simultaneous monitoring of both acoustic activity and the detailed geometrical evolution of the fracture. We show that seismic and aseismic events co-exist in the system and their activity rates are highly correlated. This suggests that seismic activity during swarm episodes is driven by the elastic loading of asperities by local aseismic deformations.

2. Experimental setup

2.1. Sample preparation

To prepare each sample, we use two transparent PMMA (poly methyl methacrylate) plates of dimensions $20\times10\times1.0$ cm and $23\times2.8\times0.5$ cm (Fig. 1). First, we sand-blast one surface of the narrow plate with glass beads of diameter $\phi\in[180-300]$μm. We clean the blasted plate to remove any electrically attached glass beads. Then we assemble the two plates in a stiff metallic loading cell with the blasted surface facing one of the surfaces of the thick plate. Finally, we impose a homogeneous normal load on the assembled plates and heat the loaded sample to 190°C for 45 min to anneal the plates. The thermal annealing produces a cohesive interface, weaker than the bulk, along which the sample will break under load. The sand-blasting introduces random roughness to the plate surface that controls the heterogeneity of local strength along the interface. It also induces microstructures on the plate surface that make the surface opaque. The newly formed block, after annealing, recovers its transparency since the contrast of the refraction index along the interface disappears (see (Grob et al., 2009; Lengliné et al., 2011a) for details). Interestingly PMMA exhibits a brittle behavior at short time scales and is semi-brittle or even plastic at longer times. Macroscopically this long time scale regime is described by a ductile rheology. PMMA shows a time–temperature equivalence desirable for addressing either high temperature processes or very long term evolution (Ward and Hadley, 1993). This richness of the PMMA rheology enables the observation of a brittle-creep rupture regime. It provides an attractive analogy for the study of numerous time-dependent mechanisms in the Earth crust as those originating at the brittle–ductile transition.

2.2. Mechanical loading

Once the sample is ready, we clamp the widest PMMA plate to a stiff aluminum frame. A stepping motor applies the loading over the top side of the narrow plate in a direction normal to the plate interface (Fig. 1). We measure the vertical displacement of the loading point with a linear variable differential transformer (LVDT) with a resolution of 1.3 μm. The vertical displacement imposed on the narrower plate induces stable mode I propagation of a planar fracture along the prescribed weak interface. We impose a variation of the loading speed, $\dot{u}(t)$, to simulate a variation of the external driving force. We performed 14 experiments where we applied various forms of temporal transients, namely a step increase, a bump increase and a sinusoidal of the loading speed imposed by the stepping motor. All these transient loads produced broad scale variation of the front speed (e.g. Fig. 2, see also Supplementary material) and they could be interpreted as an analog for far field stress perturbations caused, for example, by pore fluid pressure, magmatic intrusion or mantle flow.

2.3. Optical events

We monitor the fracture front propagation using a fast camera (CamRecord 600) with up to 1000 fps or a slow speed camera (Nikon D700) with up to 5 fps to follow the progression of the front position over longer time scales (Fig. 1). Optical images of the interfacial rupture show dark and bright regions corresponding to open crack and unbroken parts of the sample respectively. Image processing determines the transition between dark and bright areas that defines the fracture front. We first compute the difference between each image and the first image of the experiment. The image difference highlights the fracture front while removing permanent artifacts. Then, grayscale images are transformed into black and white images according to a gray level threshold separating bright and dark regions. Then, we calculate the gradient in the direction of front propagation to highlight the transition zone. We finally extract connected pixels from the gradient images that correspond to the front position, $a(x,t)$. The front propagates along the y axis with the origin defined at the loading point and is positive in the direction of crack propagation. The x axis is perpendicular to y and defines the coordinate of a point along the front and $\bar{a}(t)$ is the mean position of the

Fig. 1. a: side view of the experimental setup. The bottom plate is separated from the upper one using a loading force applied by a rod connected to a stepping motor. The upper PMMA plate is attached to a stiff aluminum frame (short dashed lines). The load causes a deflection u of the bottom plate and the propagation of an interfacial crack. The crack front is located at distance $\bar{a}$ from the loading point. The front advance is monitored by a high or slow speed camera set in vertical position, perpendicular to the crack plane. b: detailed bottom view of the sample and the loading axis. The dark gray zone corresponds to the cracked zone. The multiple black areas show the acoustic sensors of the linear array.

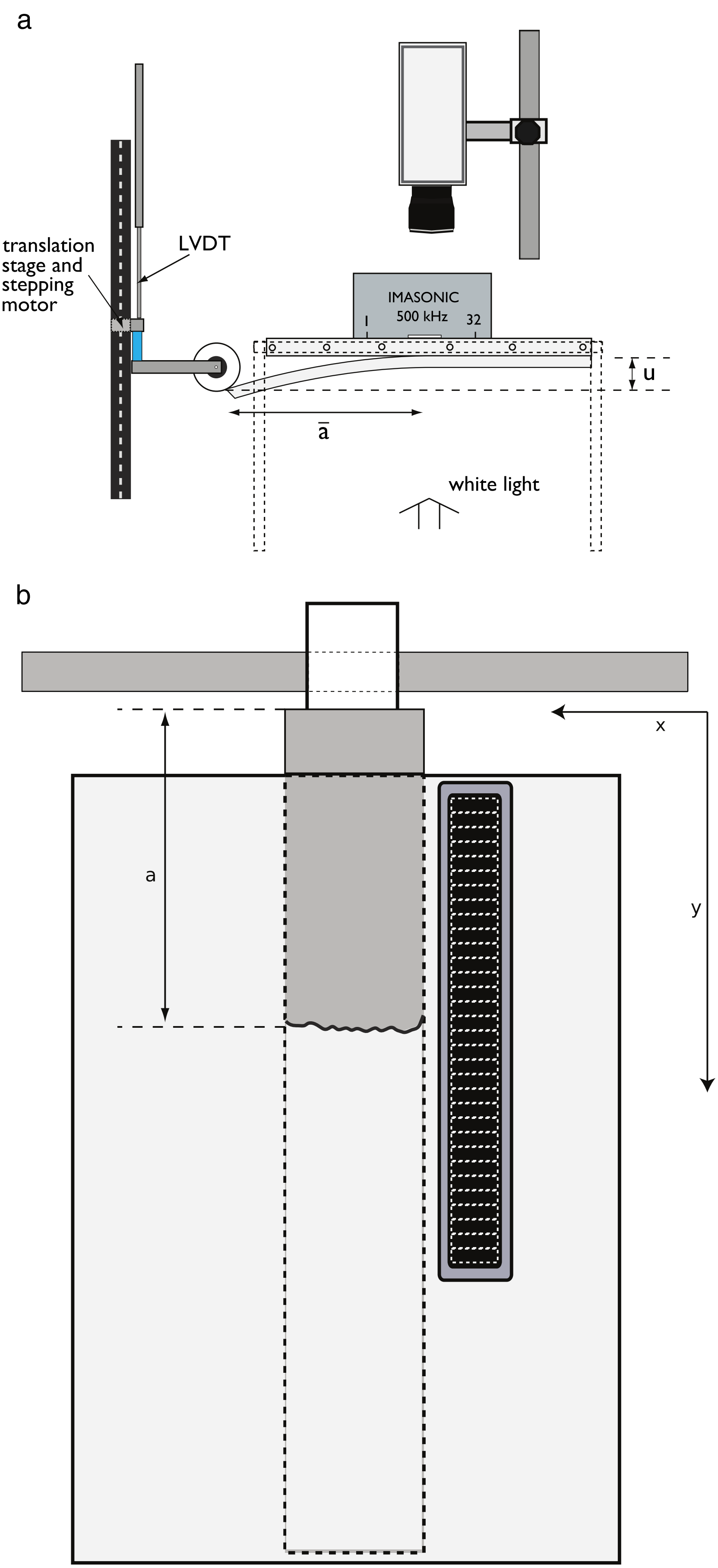
a
translation stage and stepping motor
LVDT
IMASONIC
500 kHz
1
32
u
ā
white light
b
x
y
a

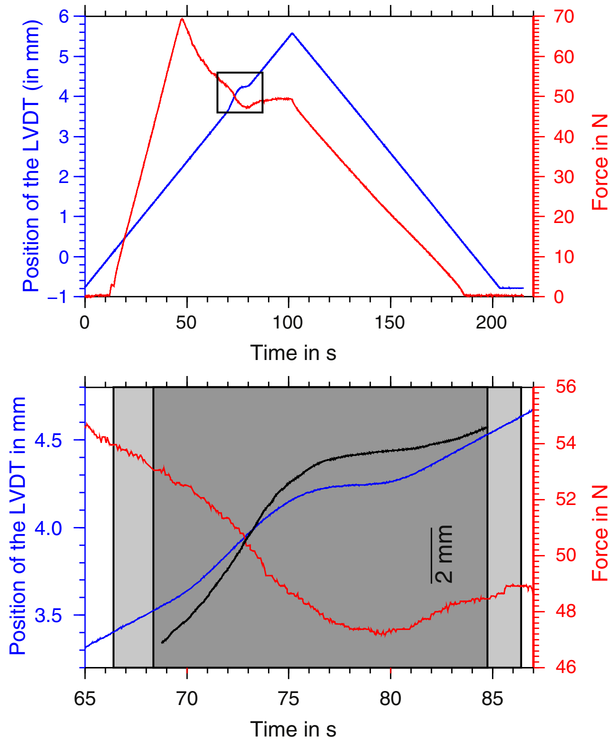

Fig. 2. Evolution of the loading force (red), and the loading displacement (blue) during an experiment. The crack is supposed to start moving at $t=45$ s as evidenced by the force peak. The black box on the top figure represents a zoom displayed on the bottom figure. A transient variation of speed is superimposed to a constant loading displacement rate between t = 65 s to 85 s (the black line corresponds to the average front position). Camera and acoustic time windows are displayed respectively as dark gray and light gray shaded areas.

front at time t (see Måløy et al., 2006 and Grob et al., 2009 for details). We compute the local speed of the crack as the pixel size divided by the time spent by the front in each pixel (Fig. 3). We extract the pixels with the highest speeds from the local movements of the front. The broad scale variation of the front velocity could be compared to slow events recorded by geodetic instruments in a tectonic context. The patches of higher than average deformation speed could be considered as analogous to local creeping episodes or slow slip events. They represent slow deformation episodes that locally exceed the macroscopic deformation rate. We follow the procedure detailed by Grob et al. (2009) to define such events. We define an "optical event" (OE) as a cluster of connected pixels which velocity exceeds a prescribed speed threshold, v_{th}. Here we adopt $v_{th}=10\times<v>$, where $<v>$ is the mean velocity of the crack during an experiment. Although these optical events have higher velocities than most of the deforming sites, they remain slow deformation episodes compared to dynamic events (the average speed $<v>\simeq 500$ μms^{-1}, far from the Rayleigh wave speed, $V_r\simeq 1.7\ 10^9$ μms^{-1}). These optical events are characterized by a Gutenberg–Richter power law with a slope similar to that of tectonic earthquakes (Grob et al., 2009). This Gutenberg–Richter relation might also be related to the magnitude–frequency scaling inferred for slow-slip events (Wech et al., 2010).

2.4. Acoustic events

The crack propagation produces acoustic activity that we monitor with a 32 elements linear array of piezo-electric sensors. Sensors are located on a line parallel to the plate axis and sensors separation is 3 mm (see Fig. 1). The typical distance between the closest acoustic sensor and the border of the plate is 1 cm. The sensors peak frequency response is ~500 kHz and all channels are continuously recorded at 5 MHz. For each experiment, we extract the acoustic signal recorded in the two closest acoustic sensors to the fracture front line. We

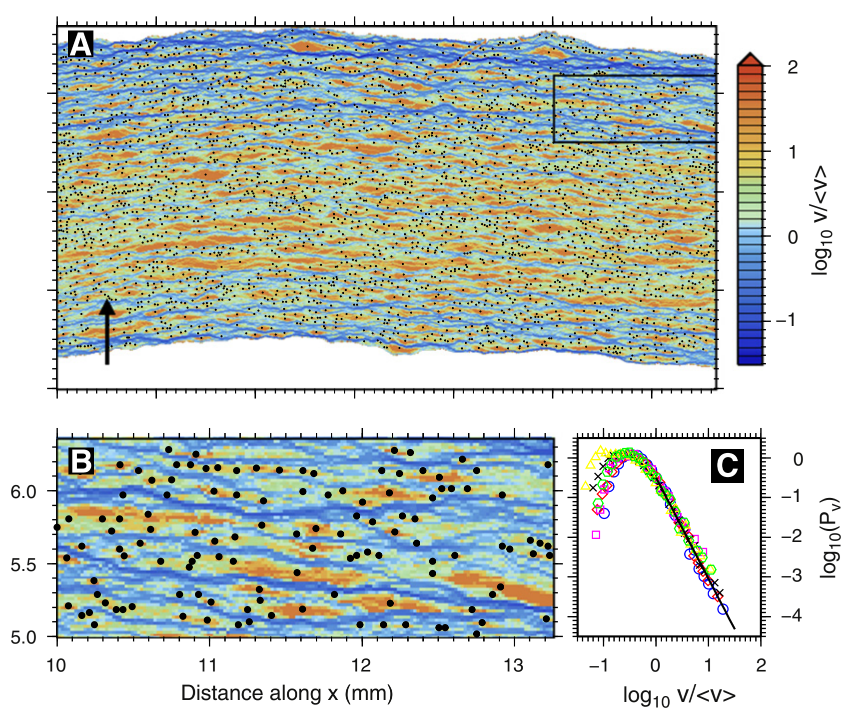

Fig. 3. A: Map of the local speeds of the front. Image scale is given by the length of the vector showing the front propagation direction which is 1.3 mm long. The front propagates from bottom to top. We observe small scale fluctuations of the crack front speed. Black dots represent hypocenters of optical events obtained after thresholding the velocity map and are displayed at the centroid of the corresponding high velocity cluster. B: Zoom on a subzone of the interface located in the black rectangle in A. C: Probability density functions (pdfs) of the local velocities computed for 6 experiments. We observe a power law decay of the pdfs for $v>\langle v\rangle$ with an exponent $\nu=-2.55$ compatible with Måløy et al. (2006).

manually trigger the acquisition of the acoustic data, which is synchronized with the camera time sequence. The recordings of the acoustic signals last, in our experiments, for a maximum of 50 s.

We use a short-term-average to long-term-average ratio (STA/LTA) to detect acoustic events (AE) in the recorded acoustic signal (Earle and Shearer, 1994). This procedure is similar to that applied to earthquake data. In our case, we use shorter time windows tailored to our short signal durations and high frequency acquisition rate. The STA window length is 20μs, the LTA window length is 100μs and the threshold for setting an STA/LTA detection is 2.0. An event must be detected simultaneously on the two closest channels to be considered in our analysis. We show an example of the acoustic signal recorded during one experiment in Fig. 4. The typical duration of the recorded events is on the order of 100 μs. The performance of the detection algorithm is illustrated in Fig. 5. As expected, the detection of events is associated with high amplitudes of the recorded signal on the two closest channels. AEs result from the fracturing of geometrical asperities over the interface. We estimate the typical spatial scale of these failures to be less than several microns (the largest AE is generated during an optical event that has maximum dimensions of ~600 μm by 30 μm). We observe non-uniformly distributed clustering of acoustic and optical activity (Fig. 5). The temporal coincidence of AEs and OEs is important but not systematic (Fig. 5). It is attributed to AEs that are too small to be optically detected, OEs that are genuinely aseismic, and clusters of AEs that are lumped into a single large OE.

3. Results

3.1. Distribution of inter-event time

Our results suggest the presence of clustering of the acoustic activity (Fig. 5). We quantify this clustering by calculating the distribution of inter-event times of successive AEs for all 14 experiments. We only considered AE when the loading rate was nearly constant in order to avoid mixing populations recorded during different loading rates. Inter-event times are normalized by the average AE rate of each experiment (the average AE rate for the different experiments, is on the order of 10^2 events/s). The probability density functions (pdf) for all the experiments are well approximated by a gamma function (Fig. 6). The displayed gamma distribution is obtained from averaging the parameters of each individual fit. Fig. 6 also includes the inter-event time distribution for the ISC worldwide catalog for earthquakes with magnitude M > 5.5 in the period 1975–2004. Temporal clustering has been well documented for earthquakes and is suggested to be a result of interactions among earthquakes (Corral, 2004; Hainzl et al., 2006; Molchan, 2005; Saichev and Sornette, 2007). The normalization of the interevent time is obtained similarly by the average seismic event rate (on the order of 1 event/day). The good agreement between the gamma distribution and the pdf obtained from our experimental data is similar to that for earthquake data (Corral, 2004) or AE recorded during

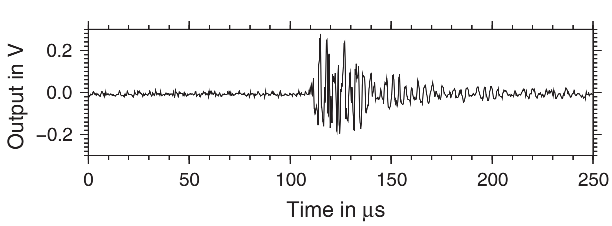

Fig. 4. Example of recorded signal of an acoustic event (AE). We observed a modification of the frequency content associated with the arrival of the AE wave train. The duration of the AE on the displayed channel is around 100μs. Sampling rate is 5 MHz.

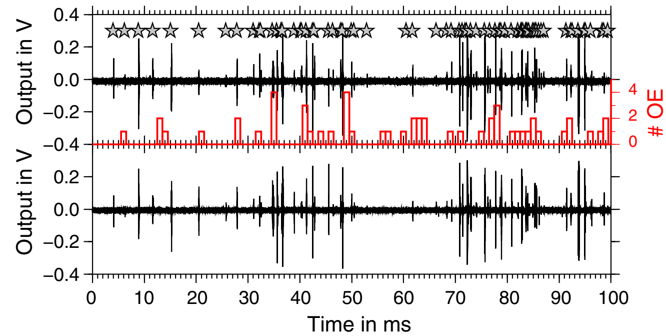

Fig. 5. Acoustic records of two channels during 100 ms. We observe on these two channels an abundant activity as attested by the numerous peaks in the acoustic signals. Stars mark the identification of events after automatic processing of the two signals by a STA/LTA procedure and matching common detection. Rate of optical events recorded during the same time period is plotted in red.

rock fracture experiments (Davidsen et al., 2007). It suggests that the mechanism responsible for the seismic activity in fault systems or rock fractures shares strong similarities with our experiment, which can be seen as an analogous system for seismicity interactions. We interpret the decay at short time scale as the emergence of an Omori–Utsu law describing interactions among events while the distribution evolves to an exponential distribution representative of a Poisson process at longer time scales (Saichev and Sornette, 2007).

3.2. Power-law distribution of local velocity

We calculate the pdf of the local velocities following (Måløy et al., 2006) for six of the experiments where we used the fast video camera at high sampling rate. We only analyze, for these experiments, time windows with an almost constant large scale velocity. The local velocity is normalized by the average velocity of the crack, $<v>$. Front velocities exhibit significant fluctuations at small scales (Fig. 3). For $v > <v>$ the pdf shows a power law decay with exponent 2.55 consistent with previous works (Lengliné et al., 2011a; Måløy et al., 2006). This power law behavior of the deformation rate at small scale, in our experiment, has to be compared to the observed behavior in natural fault systems. For instance, in southern California,

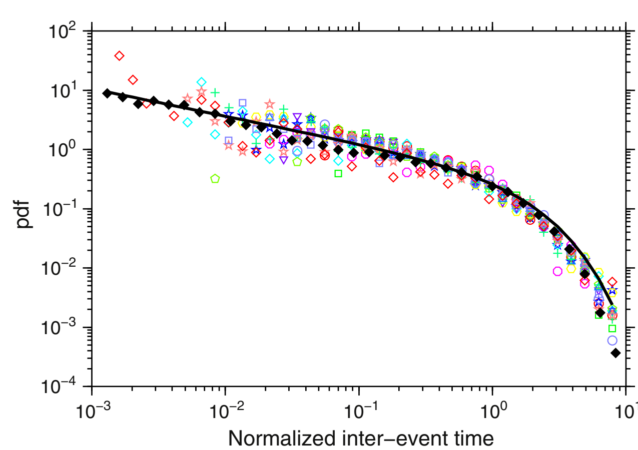

Fig. 6. Distribution of normalized inter-event time for all experiments. Each experiment is represented by a different color. The best gamma distribution fitting all the experiments, is represented by a black curve: $p(\tau) = C\tau^{\gamma-1}e^{-\tau/\beta}$, where $C = 0.44$, $\beta = 1.8$ and $\gamma = 0.54$. Black filled diamonds show the inter-event time distribution computed from the ISC worldwide catalog for earthquakes with magnitude M > 5.5.

fault slip rates are found to obey such a power law scaling where the fault system is characterized by slow slip rates (Meade, 2007). This comparison suggests that a second relation between our experiments and natural fault behavior can be proposed and that the scaling behavior is a general feature of slowly deforming media in the presence of heterogeneities.

3.3. Lateral migration of the deformation velocity

Migration of the fracture velocity along the crack front direction is analogous to the dip-parallel slip propagation revealed by tremors in subduction zone (Ghosh et al., 2010; Shelly et al., 2007). In most experiments, high loading rates or low recording acquisition rates do not allow us to distinguish migration patterns confidently as interactions among sites are numerous and occur over short time intervals. We find indications of along-front migration with tractable velocities for long enough times during experiments where loading rates are the lowest (Fig. 8). High velocity clusters appear in streaks that suggest the progression of the rupture in the direction perpendicular to the crack front propagation. The migration velocity of these high velocity streaks is on the order of 2 cm/s (Fig. 8). During this time interval, the crack front propagated at a typical velocity of 400 μm/s. We note that this migration speed is higher than the crack front speed. Taking 10–100 km/h as a typical range of dip-parallel tremor migration (Ghosh et al., 2010; Shelly et al., 2007), and 10 km/day as an estimate of along-strike speed of the slow slip event (e.g. Bartlow et al., 2011), the ratio of these two velocities is in the range 25–250. The velocity ratio obtained in our experiment is on the order of 50, well within the range obtained in subduction zones.

3.4. An interplay of seismic and aseismic local deformations

The evolution of the acoustic emission (AE) rate, the spatial average velocity of the crack front and the optical event (OE) rate are similar (Fig. 7). AE, OE rates and the average front velocities are computed for intervals of 0.2 s. A clear temporal relation between these three quantities at this large scale can be inferred: the AE and OE rates closely follow the macroscopic variation of crack front speed. The brittle fracture propagation generating acoustic emission and creep deformation co-exist in the same zone and are active at the same time.

We calculate the affine relation connecting the average front speed and the AE rate for all experiments. The residuals of the linear relation are small and symmetrically distributed suggesting a linear

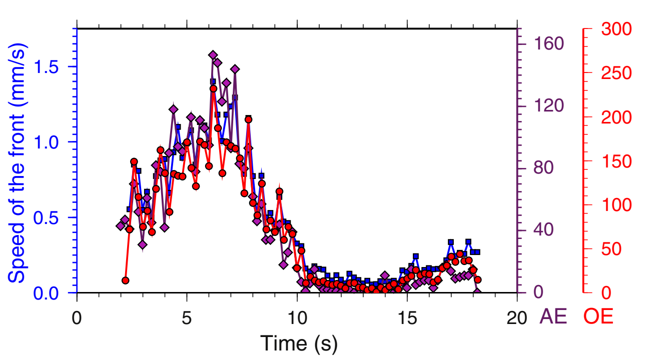

Fig. 7. Evolution of the rate of AE (purple diamonds), of the average crack front speed (blue squares) and of the optical event (OE) rate (red circles) as a function of time. Rate is computed for interval of 0.2 s for a time period encompassing the loading transient shown in Fig. 2. We observe that the rates of AE and OE are well correlated with the variation of the crack front speed at this broad time scale.

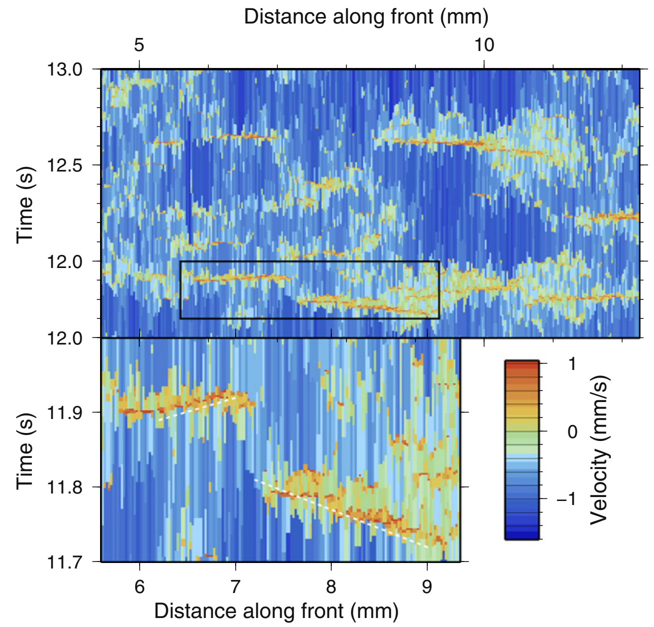

Fig. 8. Top: crack front speed as a function of time and position along front during one experiment. High velocities appear as streaks that extend along the crack front direction. Bottom left: zoom that corresponds to the space time domain delimited by the black rectangle in the upper figure. White dashed lines show the migration during two high velocity episodes. Slope of these lines gives an estimated migration speed of the order of 2 cm/s.

relation between AE rate and crack velocity. This is attested by the correlation coefficient, ρ, computed for each experiment between these two variables. The correlation coefficient is defined as $\rho=\sigma_{xy}/\sigma_x\sigma_y$, with σ_{xy} the covariance of the AE rate with the front speed and σ_x and σ_y the standard deviations of the AE rate and the front speed. The correlation coefficient, ρ for a 0.2 s window and for our 14 experiments ranges from $\rho=0.75$ to 0.97 and with a mean value of 0.87.

We now focus on smaller time scales relevant to acoustic activity and slow movement of the crack front. The crack front velocity shows important fluctuations at small scales, although being smooth and rather continuous when observed at large scale. These fluctuations result from the heterogeneous nature of the interface and the elastic interactions along the crack front line. We investigate the temporal relation between OE and AE recorded during the 6 experiments which show the highest acoustic activity and the best resolved crack advance. The cross-correlation function, $C(\Delta t)$, between the rate of AE, $r_{\mathrm{AE}}(t)$, and the rate of optical events, $r_{\mathrm{OE}}(t)$ is

$$C(\Delta t)=\frac{1}{\sqrt{C_{\mathrm{AE}}C_{\mathrm{OE}}}}\sum_{t_0}^{t_f} r_{\mathrm{OE}}(t+\Delta t)\times r_{\mathrm{AE}}(t), \tag{1}$$

where C_{AE} and C_{OE} are the auto-correlations values at zero lag time of the AE and the OE rates, respectively. For both AE and OE, rates are computed as the number of events detected in time intervals of 5 ms from time t_0 to time t_f (the mean is removed from the time-series). The maximum correlation between the two types of signals is at zero lag time (Fig. 9). It shows that the acoustic activity occurs mostly in a short time span around the aseismic deformation. The quasi-symmetric shape of the correlation function also suggests that optical events both precede and follow acoustic activity during the course of an experiment highlighting the close interplay between these two modes of deformation. The slight asymmetrical shape of $C(\Delta t)$ (Fig. 9) also suggests that a higher rate of OE occurs following

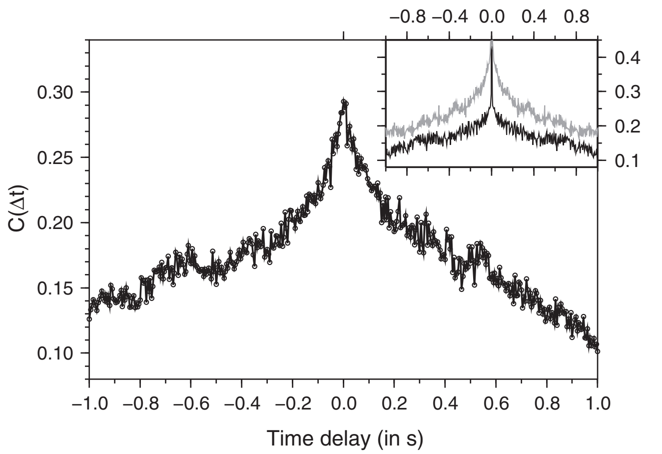

Fig. 9. Cross-correlation function $C(\Delta t)$ between the rate of acoustic events (AE) and the rate of optical events (OE). AE rate and OE rate are computed as the number of events during intervals of 5 ms and mean is remove from the time-series. The cross-correlation function corresponds to an averaged function computed over 6 experiments. We observe that the maximum of the correlation function is found at zero time lag. We also notice the increase of the correlation function around the peak, suggesting that OE is clustered in time for some duration before and after an AE. The inset figure shows the normalized autocorrelation functions for the AE (black curve) and the OE (gray curve). Both functions show some increase around zero time lag supporting the interplay between these two modes of deformation.

AE than preceding it, similar to postseismic slip observed after large earthquakes (e.g. Hsu et al., 2006).

4. Discussion

In our experiments, the average fracture speed obeys the Arrhenius law at the macroscopic or global scale (Lengliné et al., 2011b). Such an evolution has been inferred in numerous experimental systems reproducing slow deformations of rocks and other materials (Atkinson, 1984). In our experiment, this expression relates the crack front speed propagation, V, to an activation energy mechanism and can be expressed as

$$V = V_0 exp\left(\frac{-Q}{k_B T}\right). \tag{2}$$

V_0 is the product of a frequency of attempt to break molecular bonds and the jump distance, k_B is the Boltzmann constant and T is the temperature. The activation energy of the process is Q

$$Q = Q_0 - G\alpha^2, \tag{3}$$

where Q_0 is the activation energy in the absence of applied stress, G is the energy release rate and α is the typical length scale of the atomistic fracturing process. The stress dependence in Eq. (3) is similarly often written in terms of the stress intensity factor, K, at the crack tip. It follows that by controlling the imposed loading rate on the system we modify the value of the energy release rate (equivalently stress intensity factor) at the crack tip. In this sense, simulated transient deformation processes mimic the increase of the deformation speed recorded during swarm episodes (Lohman and McGuire, 2007) or slow slip events in subduction zones (Rogers and Dragert, 2003). The formulation of the crack speed in Eq. (2) has been proposed to be the physical basis of the rate and state friction model widely considered in fault mechanics (e.g. Nakatani, 2001; Rice et al., 2001). If we consider a volumetric process, the corresponding expression to Eq. (3) is

$$Q = Q_0 - \tau_c\alpha^3 \tag{4}$$

where the stress dependence is written in terms of the average shear stress, τ_c along asperity contacts. α^3 is the activation volume of the process. Following (Rice et al., 2001), we call σ_c the average normal stress on contact zones, defined as: $\tau_c/\sigma_c = \tau/\sigma$, with τ and σ being the large scale stresses. It follows from Eq. (2)

$$V = V_0 exp\left(\frac{-Q_0 + \tau_c\alpha^3}{k_B T}\right) \tag{5}$$

leading to:

$$\tau = \sigma\left[\frac{Q_0}{\alpha^3\sigma_c} + \frac{k_B T}{\sigma_c\alpha^3} ln\left(\frac{V}{V_0}\right)\right] \tag{6}$$

where V is interpreted in terms of slip rate on the fault plane. Eq. (6) has a similar form to the empirical relation of the rate and state friction model with $a = k_B T/\sigma_c\alpha^3$ and the state dependent variable represented by $Q_0/\alpha^3\sigma_c$ (Rice et al., 2001). It follows that the progressive evolution of the front position in our system can be viewed as a similar mechanical problem to the evolution of slip on a fault plane with the same constitutive equation. The quasi-static evolution of an anti-plane shear rupture is governed by similar formulations to mode I fractures (Gao and Rice, 1986; Schmittbuhl et al., 2003). Thus, we consider our mode I fracture problem analogous to shear ruptures. Therefore our experimental setup is relevant for addressing the mechanics of simplified fault models as studied numerically by (Gao et al., 1991; Perfettini et al., 2003). Provided this analogy, the crack front advance $a(x,t)$ is analogous to the slip along fault $\delta(x,t)$. However each point of the interface that breaks is completely unloaded due to the geometry of our experimental setting. Therefore, we have no repeating failure of the same patch contrary to natural faults and AE stress drops are total. However, earthquake stress drops are usually a small fraction of the total stress (e.g. Kanamori, 1994). Nevertheless, in both systems, AE and earthquake still represent a dynamic failure mode, which makes them comparable. Following the approach presented by (Dieterich, 1994), we propose to relate the AE rate to the stress history of our system. We assume an interface composed of a population of sources that generate AE. We hypothesize that the duration of nucleation of these sources is longer than the duration of stress variations imposed to the system. Hence, the seismicity rate, R, varies exponentially with the shear stress change $\Delta\tau$ imposed on the system (Beeler and Lockner, 2003; Cochran et al., 2004; Dieterich, 1994; Helmstetter and Shaw, 2009),

$$R = r\,exp\left(\frac{\Delta\tau}{a\sigma}\right) \tag{7}$$

where r is a reference seismicity rate. The analogy mentioned above between shear stress τ and the energy release rate G, suggests that in our experiment:

$$R = r\,exp\left(\frac{\alpha^2\Delta G}{k_B T}\right), \tag{8}$$

Notice that Eq. (8) is the same expression of that for the speed of the crack as a function of G obtained by combining Eqs. (2) and (3): $V = V_0^* exp(\alpha^2 G/k_B T)$ with $V_0^* = V_0 exp(-Q_0/k_B T)$. Therefore we have a direct linear relation between AE rate R and speed of the crack V: $R \propto V$, (Fig. 7). This relation can also be recovered from a trivial argument. Supposing a density of asperities ρ_{asp} over the interface, a front advance, Vdt, will cover $dN = Vdt\rho_{asp}L_x$ asperities leading as well to $R = dN/dt \propto V$. At the system size, this relation provides a link between acoustic activity and periods of high deformation. At smaller scales, the same mechanism is applicable as the acoustic activity is influenced by local important deformations episodes (OE) (Fig. 9).

Such local creeping episodes are similar to the small localized creep events observed on the San-Andreas fault by Scholz et al. (1969).

We emphasize that the deformation recorded at the surface of the Earth during transient episodes should be viewed as the macroscopic integration of sequences of creep events. On large spatial scales, the creep events formed the observed large scale behavior and correspond to the macroscopic observation of the transient slip speed variation. Such a view is similar to the concept developed by Scholz et al. (1969) where the deformation is modeled as the integration of discrete sites subject to time-dependent strength. The acoustic deformation being recorded only represents the part of the deformation corresponding to zones that fail dynamically. This model is fully compatible with our observations. We also remark that sites do not fail independently as attested by the local close temporal activity between creep events and acoustic events. As proposed by Scholz et al. (1969), it is readily possible that creep events recorded at our experimental scale are also formed of small acoustic events such that down-scaling might exist up to the microscopical level associated with the discrete breakage of single molecular bonds.

5. Conclusion

We analyze the coupled evolution of acoustic activity and slow deformation during the propagation of brittle-creep fractures in a heterogeneous medium. Our unique experimental setup addresses the relation between seismic and aseismic slips along natural faults. It provides an original characterization of slow deformation processes which are difficult to capture on faults at depth. Numerous statistical features of the deformation observed in natural systems are reproduced by our experiments like the gamma distribution of interevent times and the power law distribution of slip rates. We show that the acoustic activity (dynamic events) is part of the deformation process and it occurs over a widely distributed range of speeds including slow slip. Also, small scale observations of the deformation reveal coexistence between creep and acoustic events in the same mechanical system. The small scale complex dynamics lead to a macroscopic integrated signal of the deformation that shows a smooth and continuous deformation speed that correlates with the rate of acoustic events.

Acknowledgments

We thank K. J. Måløy, K. T. Tallakstad, S. Santucci, M. Grob, F. H. Cornet, J.P. Avouac, D. R. Shelly, M. Aktar and H. Karabulut for fruitful discussions. We also thank the editor and two anonymous reviewers for their suggestions and A. Steyer for technical support. We acknowledge the support of ANR grant SUPNAF and of NSF grant EAR-1015698.

Appendix A. Supplementary data

Supplementary data to this article can be found online at doi:10.1016/j.epsl.2012.03.022.

References

Ando, R., Imanishi, K., 2011. Possibility of Mw 9.0 mainshock triggered by diffusional propagation of after-slip from mw 7.3 foreshock. Earth Planets Space 63, 767–771.

Ariyoshi, K., Matsuzawa, T., Ampuero, J.-P., Nakata, R., Hori, T., Kaneda, Y., Hino, R., Hasegawa, A., in press. *Migration process of very low-frequency events based on a chain-reaction model and its application to the detection of preseismic slip for megathrust earthquakes*. Earth, Planets and Space.

Atkinson, B.K., 1984. Subcritical crack growth in geological materials. J. Geophys. Res. 89, 4077–4114 (Jun.).

Bartlow, N.M., Miyazaki, S., Bradley, A.M., Segall, P., 2011. Space–time correlation of slip and tremor during the 2009 Cascadia slow slip event. Geophys. Res. Lett. 38, 18309.

Beeler, N.M., Lockner, D.A., 2003. Why earthquakes correlate weakly with the solid earth tides: effects of periodic stress on the rate and probability of earthquake occurrence. J. Geophys. Res. 108, 2391.

Bouchon, M., Karabulut, H., Aktar, M., Özalaybey, S., Schmittbuhl, J., Bouin, M.-P., 2011. Extended Nucleation of the 1999 M_w 7.6 Izmit Earthquake. Science 331, 877.

Bourouis, S., Bernard, P., 2007. Evidence for coupled seismic and aseismic fault slip during water injection in the geothermal site of Soultz (France), and implications for seismogenic transients. Geophys. J. Int. 169, 723–732.

Cochran, E.S., Vidale, J.E., Tanaka, S., 2004. Earth tides can trigger shallow thrust fault earthquakes. Science 306, 1164–1166.

Corral, A., 2004. Long-term clustering, scaling, and universality in the temporal occurrence of earthquakes. Phys. Rev. Lett. 92, 108501.

Crescentini, L., Amoruso, A., Scarpa, R., 1999. Constraints on slow earthquake dynamics from a swarm in central Italy. Science 286 (5447), 2132–2134.

Davidsen, J., Stanchits, S., Dresen, G., 2007. Scaling and universality in rock fracture. Phys. Rev. Lett. 98, 125502.

Dieterich, J., 1994. A constitutive law for rate of earthquake production and its application to earthquake clustering. J. Geophys. Res. 99, 2601–2618.

Doubre, C., Peltzer, G., 2007. Fluid-controlled faulting process in the Asal rift, Djibouti, from 8 yr of radar interferometry observations. Geology 35 (1), 69–72.

Du, W.-, Sykes, L.R., Shaw, B.E., Scholz, C.H., 2003. Triggered aseismic fault slip from nearby earthquakes, static or dynamic effect? J. Geophys. Res. 108, 2131.

Earle, P.S., Shearer, P.M., 1994. Characterization of global seismograms using an automatic-picking algorithm. Bull. Seismol. Soc. Am. 84 (2), 366–376.

Gao, H., Rice, J.R., 1986. Shear stress intensity factors for a planar crack with slightly curved front. J. Appl. Mech. 53, 774.

Gao, H., Rice, J.R., Lee, J., 1991. Penetration of a quasi-statistically slipping crack into a seismogenic zone of heterogeneous fracture resistance. J. Geophys. Res. 96, 21535–21548.

Ghosh, A., Vidale, J.E., Sweet, J.R., Creager, K.C., Wech, A.G., Houston, H., Brodsky, E.E., 2010. Rapid, continuous streaking of tremor in Cascadia. Geochem. Geophys. Geosyst. 11, 12010.

Grob, M., Schmittbuhl, J., Toussaint, R., Rivera, L., Santucci, S., Måløy, K.J., 2009. Quake catalogs from an optical monitoring of an interfacial crack propagation. Pure Appl. Geophys. 166, 777–799.

Hainzl, S., Scherbaum, F., Beauval, C., 2006. Estimating background activity based on interevent-time distribution. Bull. Seismol. Soc. Am. 96, 313–320.

Helmstetter, A., Shaw, B.E., 2009. Afterslip and aftershocks in the rate-and-state friction law. J. Geophys. Res. 114, B01308.

Hillers, G., Mai, P.M., Ben-Zion, Y., Ampuero, J.-P., 2007. Statistical properties of seismicity of fault zones at different evolutionary stages. Geophys. J. Int. 169, 515–533.

Hsu, Y.-J., Simons, M., Avouac, J.-P., Galetzka, J., Sieh, K., Chlieh, M., Natawidjaja, D., Prawirodirdjo, L., Bock, Y., 2006. Frictional afterslip following the 2005 Nias–Simeulue earthquake, Sumatra. Science 312, 1921–1926.

Ito, Y., Obara, K., Shiomi, K., Sekine, S., Hirose, H., 2007. Slow earthquakes coincident with episodic tremors and slow slip events. Science 315, 503.

Kanamori, H., 1994. Mechanics of earthquakes. Annu. Rev. Earth Planet. Sci. 22, 207–237.

Kaneko, Y., Avouac, J.-P., Lapusta, N., 2010. Towards inferring earthquake patterns from geodetic observations of interseismic coupling. Nat. Geosci. 3, 363–369.

Kato, A., Obara, K., Igarashi, T., Tsuruoka, H., Nakagawa, S., Hirata, N., 2012. Propagation of slow slip leading up to the 2011 mw 9.0 Tohoku-Oki earthquake. Science 335 (6069), 705–708.

La Rocca, M., Creager, K.C., Galluzzo, D., Malone, S., Vidale, J.E., Sweet, J.R., Wech, A.G., 2009. Cascadia tremor located near plate interface constrained by S minus P wave times. Science 323, 620.

Lengliné, O., Marsan, D., 2009. Inferring the coseismic and postseismic stress changes caused by the 2004 $M_w = 6$ Parkfield earthquake from variations of recurrence times of microearthquakes. J. Geophys. Res. 114, B10303.

Lengliné, O., Schmittbuhl, J., Elkhoury, J., Ampuero, J.P., Toussaint, R., Måløy, K.J., 2011a. Down-scaling of fracture energy during brittle creep experiments. J. Geophys. Res. 116.

Lengliné, O., Toussaint, R., Schmittbuhl, J., Elkhoury, J.E., Ampuero, J.-P., Tallakstad, K.T., Santucci, S., Måløy, K.J., 2011b. Average crack front velocity during subcritical fracture propagation in a heterogeneous medium. Phys. Rev. E 84.

Linde, A.T., Gladwin, M.T., Johnston, M.J.S., Gwyther, R.L., Bilham, R.G., 1996. A slow earthquake sequence on the San Andreas fault. Nature 383, 65–68 (Sep.).

Liu, Y., Rice, J.R., Larson, K.M., 2007. Seismicity variations associated with aseismic transients in Guerrero, Mexico, 1995 2006. Earth Planet. Sci. Lett. 262, 493–504.

Lohman, R.B., McGuire, J.J., 2007. Earthquake swarms driven by aseismic creep in the Salton Trough, California. J. Geophys. Res. 112, B04405.

Måløy, K.J., Santucci, S., Schmittbuhl, J., Toussaint, R., 2006. Local waiting time fluctuations along a randomly pinned crack front. Phys. Rev. Lett. 96, 045501.

Meade, B.J., 2007. Power-law distribution of fault slip-rates in southern California. Geophys. Res. Lett. 342, L23307.

Miyazaki, S., McGuire, J.J., Segall, P., 2011. Seismic and aseismic fault slip before and during the 2011 off the Pacific coast of Tohoku earthquake. Earth Planets Space 63, 637–642.

Molchan, G., 2005. Interevent time distribution in seismicity: a theoretical approach. Pure Appl. Geophys. 162, 1135–1150.

Nadeau, R.M., Dolenc, D., 2005. Nonvolcanic tremors deep beneath the San Andreas fault. Science 307 (5708), 389.

Nakatani, M., 2001. Conceptual and physical clarification of rate and state friction: frictional sliding as a thermally activated rheology. J. Geophys. Res. 106, 13347–13380.

Obara, K., Hirose, H., Yamamizu, F., Kasahara, K., 2004. Episodic slow slip events accompanied by non-volcanic tremors in southwest Japan subduction zone. Geophys. Res. Lett. 31, L23602.

Perfettini, H., Avouac, J.-P., 2004. Postseismic relaxation driven by brittle creep: a possible mechanism to reconcile geodetic measurements and the decay rate of aftershocks, application to the Chi-Chi earthquake, Taiwan. J. Geophys. Res. 109, B02304.

Perfettini, H., Schmittbuhl, J., Cochard, A., 2003. Shear and normal load perturbations on a two-dimensional continuous fault: 1. Static triggering. J. Geophys. Res. 108, 2408.

Perfettini, H., Avouac, J.-P., Tavera, H., Kositsky, A., Nocquet, J.-M., Bondoux, F., Chlieh, M., Sladen, A., Audin, L., Farber, D.L., Soler, P., 2010. Seismic and aseismic slip on the central Peru megathrust. Nature 465, 78–81.

Rice, J., Lapusta, N., Ranjith, K., 2001. Rate and state dependent friction and the stability of sliding between elastically deformable solids. J. Mech. Phys. Solids 49, 1865–1898.

Rogers, G., Dragert, H., 2003. Episodic tremor and slip on the Cascadia subduction zone: the chatter of silent slip. Science 300, 1942–1943.

Saichev, A., Sornette, D., 2007. Theory of earthquake recurrence times. J. Geophys. Res. 112, B04313.

Schmittbuhl, J., Delaplace, A., Måløy, K.J., Perfettini, H., Vilotte, J.P., 2003. Slow crack propagation and slip correlations. Pure Appl. Geophys. 160, 961–976.

Scholz, C.H., Wyss, M., Smith, S.W., 1969. Seismic and aseismic slip on the San Andreas fault. J. Geophys. Res. 74, 2049.

Segall, P., Desmarais, E.K., Shelly, D., Miklius, A., Cervelli, P., 2006. Earthquakes triggered by silent slip events on Kīlauea volcano, Hawaii. Nature 442, 71–74.

Shelly, D.R., 2010. Migrating tremors illuminate complex deformation beneath the seismogenic San Andreas fault. Nature 463, 648–652.

Shelly, D.R., Beroza, G.C., Ide, S., 2007. Complex evolution of transient slip derived from precise tremor locations in western Shikoku, Japan. Geochem. Geophys. Geosyst. 8, 10014.

Shelly, D.R., Ellsworth, W.L., Ryberg, T., Haberland, C., Fuis, G.S., Murphy, J., Nadeau, R.M., Bürgmann, R., 2009. Precise location of San Andreas Fault tremors near Cholame, California using seismometer clusters: slip on the deep extension of the fault? Geophys. Res. Lett. 36, L01303.

Takada, Y., Furuya, M., 2010. Aseismic slip during the 1996 earthquake swarm in and around the Onikobe geothermal area, NE Japan. Earth Planet. Sci. Lett. 290, 302–310.

Vidale, J.E., Shearer, P.M., 2006. A survey of 71 earthquake bursts across southern California: exploring the role of pore fluid pressure fluctuations and aseismic slip as drivers. J. Geophys. Res. 111, B05312 (May).

Ward, I.M., Hadley, D.W., 1993. An Introduction to the Mechanical Properties of Solid Polymers. Wiley.

Wech, A.G., Creager, K.C., Melbourne, T.I., 2009. Seismic and geodetic constraints on Cascadia slow slip. J. Geophys. Res. 114, B10316.

Wech, A.G., Creager, K.C., Houston, H., Vidale, J.E., 2010. An earthquake-like magnitude-frequency distribution of slow slip in northern Cascadia. Geophys. Res. Lett. 372, L22310 (Nov.).

Downscaling of fracture energy during brittle creep experiments

O. Lengliné,[1] J. Schmittbuhl,[1] J. E. Elkhoury,[2] J.-P. Ampuero,[2] R. Toussaint,[1] and K. J. Måløy[3]

Received 25 October 2010; revised 22 May 2011; accepted 6 June 2011; published 27 August 2011.

[1] We present mode 1 brittle creep fracture experiments along fracture surfaces that contain strength heterogeneities. Our observations provide a link between smooth macroscopic time-dependent failure and intermittent microscopic stress-dependent processes. We find the large-scale response of slow-propagating subcritical cracks to be well described by an Arrhenius law that relates the fracture speed to the energy release rate. At the microscopic scale, high-resolution optical imaging of the transparent material used (PMMA) allows detailed description of the fracture front. This reveals a local competition between subcritical and critical propagation (pseudo stick-slip front advances) independently of loading rates. Moreover, we show that the local geometry of the crack front is self-affine and the local crack front velocity is power law distributed. We estimate the local fracture energy distribution by combining high-resolution measurements of the crack front geometry and an elastic line fracture model. We show that the average local fracture energy is significantly larger than the value derived from a macroscopic energy balance. This suggests that homogenization of the fracture energy is not straightforward and should be taken cautiously. Finally, we discuss the implications of our results in the context of fault mechanics.

Citation: Lengliné, O., J. Schmittbuhl, J. E. Elkhoury, J.-P. Ampuero, R. Toussaint, and K. J. Måløy (2011), Downscaling of fracture energy during brittle creep experiments, *J. Geophys. Res.*, *116*, B08215, doi:10.1029/2010JB008059.

1. Introduction

[2] Heterogeneities in geological media have a strong impact on deformation processes in Earth's crust that are difficult to assess. Indeed, deformation is often multiscaled due to numerous local rheological variations (e.g., variability of rocks, mineralogy) and geometrical discontinuities (e.g., faults). These discontinuities are themselves often characterized by complex morphologies that lead to local stress concentrations [*Okubo and Aki*, 1987; *Schmittbuhl et al.*, 2006]. Microstructures like grains, cracks and mineral assemblage also contribute to the inhomogeneity of rock structures [*Scholz*, 2002; *Paterson and Wong*, 2005].

[3] Measurements of large-scale crustal deformation, usually done at the Earth surface, e.g., by GPS and Insar [*Blewitt*, 2007; *Simons and Rosen*, 2007], allow limited constraints on the deformation at small scales, in particular at depth. Measurements in laboratory rock mechanics experiments suffer from the same limitations as sensors are located at the surface of rock specimens. Macroscopic information averaged over the sample size might be different from direct observations at the smaller scales at which the physical mechanism responsible for the deformation is at play.

[4] Creep of faults and rocks produces smooth and continuous deformation when recorded at the system size, at large scales along faults [e.g., *Titus et al.*, 2006] and at small scales during creep laboratory tests [*Heap et al.*, 2009]. However, the presence of microearthquakes and transient deformation in creeping faults [*Lengliné and Marsan*, 2009] and acoustic emission (AE) in laboratory experiments [*Lei et al.*, 2000; *Heap et al.*, 2009] suggest that the deformation process is more intermittent and distributed over a wide range of velocities. The deformation induced by microearthquakes is generally not significant, although damage-related inelastic deformation contributes to the global deformation [*Wang et al.*, 2010].

[5] The differences in behavior between macroscopic and microscopic deformations highlight the importance of analyzing the physical processes at local scales at which observations can unambiguously be linked to a given mechanism. Moreover these differences question homogenization procedures, i.e., the upscaling of physical parameters from microscopic to macroscopic scales. The focus of our study is the relation between macroscopic smooth creep deformation and microscopic complex intermittent dynamics during crack propagation experiments. We address the link between macroscopic and microscopic scales where local strength heterogeneities are important.

[6] Creep deformation results from subcritical crack growth mechanisms and plays a significant role in time-

[1]Institut de Physique du Globe de Strasbourg, IPGS, UMR 7516, CNRS, Université de Strasbourg, Strasbourg, France.
[2]Division of Geological and Planetary Sciences, California Institute of Technology, Pasadena, California, USA.
[3]Department of Physics, University of Oslo, Oslo, Norway.

0148-0227/11/2010JB008059

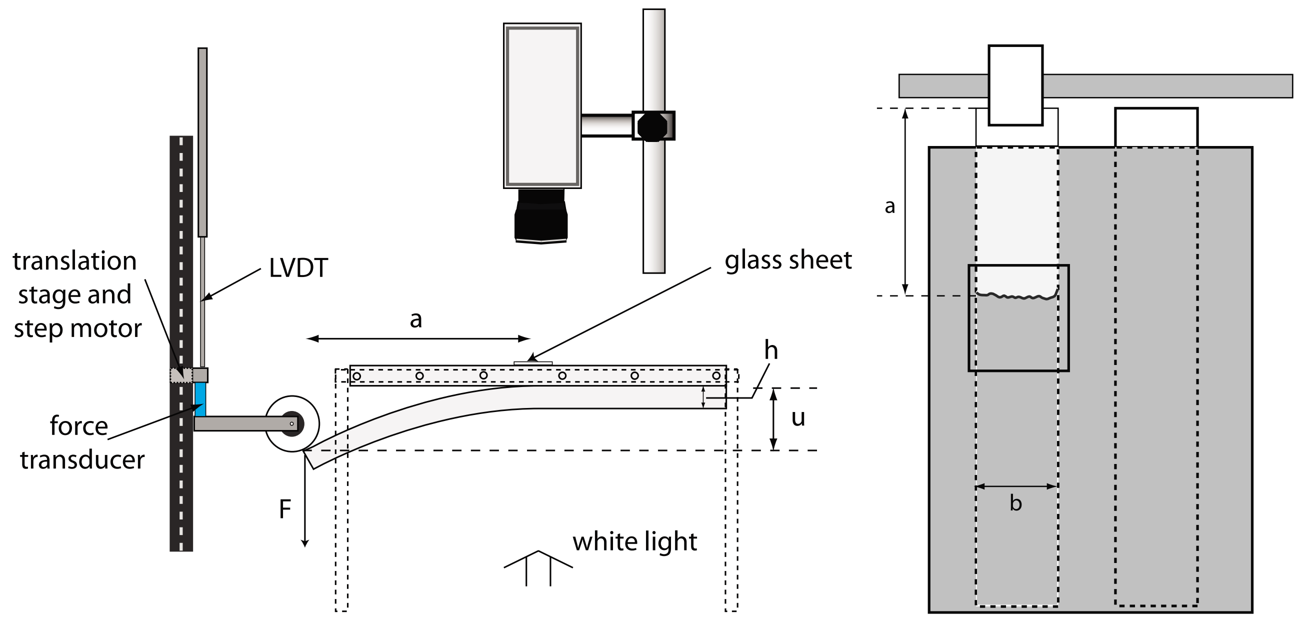

Figure 1. (left) Side view and (right) top view of the experimental setup. A stiff aluminum frame is attached to the upper PMMA plate. The bottom plate is separated from the upper one using a loading force F applied by a rod connected to a stepping motor. The load causes a deflection u of the bottom plate and the propagation of a mode 1 crack. The crack front is located at distance $\overline{a}$ from the free end. The front advance is monitored by a high-speed camera set in vertical position, perpendicular to the crack plane. Lower plate height and width are noted h and b respectively.

dependent failure of rocks [*Atkinson*, 1984]. Among the numerous models of creep, the brittle creep model results from time-dependent microfracturing at the crack tip [*Scholz*, 1968a]. The smooth large-scale response in this model is a statistical response of a complex population of interacting microcracks [*Scholz*, 2002; *Lockner*, 1993; *Baud and Meredith*, 1997]. The time dependence might result from chemical processes like corrosive mechanisms. In particular, rocks feature a strong action of water on Si-O bonds. For polymers or metals, lateral motion of atomic kinks along the crack front, microplasticity or diffusion induce strength variation in time [*Lawn*, 1975; *Atkinson and Meredith*, 1987a]. This time dependence of slow kinetic crack propagation is usually well represented by a thermally activated mechanism where the strain rate obeys an Arrhenius law dependent on the energy release rate G (i.e., the energy available to drive the crack per unit area) [*Lawn*, 1993]. In this approach, the crack growth is directly influenced by environmental factors (applied stress, temperature, chemical concentrations) that affect the free energy, and thus the energy barrier, via numerous competing mechanisms like stress corrosion, diffusion, dissolution, plasticity and thermal effects [*Atkinson and Meredith*, 1987a; *Lawn*, 1993]. Experimentally, several empirical relations have been often reported to divide the slow crack propagation in three main characteristic regimes [*Freiman*, 1984]: (1) at very slow velocity, external variables are dominant and result in an increasing speed of crack growth with increasing G; (2) a weak stress sensitive regime follows where transport is limiting, and (3) at higher stress crack growth kinetics is little influenced by environment.

[7] The energy release rate G is thus of primary importance when studying the creep mechanism and its scaling effect. G is often associated with a critical energy release rate G_c defined from the Griffith energy balance concept: the energy release rate equals the energy available to drive the crack per unit area $G = G_c$. Such fracture energy criterion is relevant to many geological processes like fault rupture or dike propagation [e.g., *Rice and Simons*, 1976; *Rubin*, 1993]. Estimation of G_c is difficult and relies on laboratory rock experiments [*Wong*, 1982] or earthquake rupture modeling using recorded waveforms or geological observations. Most measurements of the fracture energy are associated with a macroscopic quantity defined as a system size representative value, hence ignoring all fluctuations of G_c present at smaller scales. Here, we examine the relation between the macroscopic quantity and the smaller-scale variations in G_c. We do not investigate dynamic rupture (e.g., earthquakes) but slow, creeping fractures. This slow regime is relevant to many geophysical phenomena such as earthquake nucleation [*Bouchon et al.*, 2011], slow slip events and postseismic slip [e.g., *Das and Scholz*, 1981].

[8] We present a series of quasi-static mode 1 fracture experiments performed on an experimental setting introduced by *Schmittbuhl and Måløy* [1997], *Delaplace et al.* [1999], and *Grob et al.* [2009]. The system allows to track a propagating crack in a brittle heterogeneous medium. We use samples of polymethylmethacrylate (PMMA), which, contrary to polycrystalline rocks, are transparent and allow for direct observation of crack deformation at the scale of the heterogeneities. The high temporal and spatial resolution of the experiment provides detailed information on

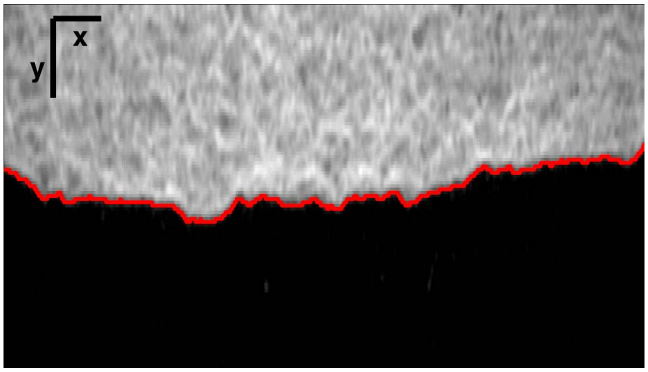

Figure 2. Zoom on the crack front displaying the difference between an image at the onset of the experiment and the current image of the front. During the experiment the crack front propagates from the top to bottom. The bright area marks the zone which is already cracked while in the dark area the two plates are still in contact (i.e., uncracked). The front line $a(x, t)$ is superimposed on the image as a red line. Scales are provided by two black segments which are 1 mm and 0.5 mm long respectively in the x and y directions.

the deformation process induced by the crack at the microscopic scale.

[9] We first present the macroscopic behavior of the fracture and an estimation of the relationship between fracture energy and average fracture velocity at the sample scale [*Scholz*, 1968a]. The brittle creep propagation of the crack is characterized by an intermittent dynamics at the microscopic scale and is well modeled by an activation energy mechanism. Then, we present the microscopic behavior of the fracture front roughness, the local fracture velocity and the local fluctuations of the energy release rate along the crack front line. The microscopic distribution of fracture energies spreads over a wide range and is directly linked to the disordered morphology of the interface. The fracture energy determined at the local scale is on average higher than the fracture energy computed at the global scale. This highlights the importance of local defects in controlling the rupture process in heterogeneous media. It also suggests that homogenization of the fracture energy is not straightforward and should be taken cautiously.

2. Experimental Setup

2.1. Sample Preparation

[10] We use two transparent PMMA plates of dimensions 20 × 10 × 1.0 cm and 23 × 2.8 × 0.5 cm (Figure 1). First, we sand blast one surface of the narrow plate with glass beads of diameter $\phi \in [180–300]$ μm. We clean the blasted plate to remove any electrically attached glass beads. Then we assemble the two plates in a stiff metalic loading cell with the blasted surface facing a surface of the larger plate. Finally, we impose an homogeneous normal load on the assembled plates and heat the loaded sample at 190°C for 45 minutes to anneal the plates. The thermal annealing produces a weak cohesive interface along which the sample breaks in mode 1. The sand blasting introduces the random roughness of the plate surface that controls the local strength along the weak interface. It also induces microstructures at the plate surface which make the sample opaque, but the newly formed block, after annealing, recovers its transparency since the contrast of the refraction index along the interface disappears.

[11] We choose PMMA in our experiment because (1) it is easy to handle and has a high transparency adequate for optical imaging, (2) its low Young modulus (3.2 GPa) allows fine tuning of small stress changes under imposed deformation, and (3) its surface energy, substantially larger than that of glass [*Brace and Walsh*, 1962; *Katsamanis and Delides*, 1988], limits the propagation of cracks at low applied stress. These combined properties enable a better control of the experimental system. Another advantage of PMMA compared to glass is its lower melting point which allows the welding of the PMMA plates at a much lower temperature and accordingly in an oven with a better temperature monitoring. In addition to these technical motivations, PMMA exhibits viscoelastic behavior. It is brittle at short time scales and semibrittle or even plastic at longer times. Macroscopically this long time scale regime is described by a ductile rheology. PMMA shows a time-temperature equivalence which is a very nice property for addressing either high temperature processes or very long term evolution. This richness of the PMMA rheology enables the observation of a mixed rupture regime macroscopically. It provides an attractive analogy for the study of numerous time-dependent mechanisms in the Earth's crust as those originating at the brittle-ductile transition. However, natural materials are generally very disordered at all scales due to the presence of microcracks, grains, pores and different minerals [*Bean*, 1996] that may increase the energy absorbed in the damage zone. Our PMMA material does not exhibit such strong disorder, and consequently the expected energy consumed around the crack tip by local plastic deformations is reduced.

2.2. Acquisition and Image Processing

[12] Once the sample is ready, we clamp the widest PMMA plate to a stiff aluminum frame. A stepping motor applies the loading over the top side of the narrow plate in a direction normal to the plate interface (Figure 1). We measure the vertical displacement of the loading point with a linear variable differential transformer (LVDT) and the loading force by an STC 1205 traction/compression transducer. Displacement and force are measured with a resolution of 1.3 μm and 2.4×10^{-3} N respectively. The vertical displacement imposed on the narrower plate induces stable propagation of a mode 1 planar fracture along the prescribed weak interface. We monitor the fracture front propagation using a fast optical camera (CamRecord 600) with up to 1000 fps. Images have a maximum dimension of 1024 × 1280 pixels and sample resolution is ~20 μm/pixel. For some experiments, we use a slow speed camera (Nikon D700) with up to 5 fps to follow the progression of the average front position over long time scales (Figure 1).

[13] Optical images of the interfacial mode 1 rupture show dark and bright regions respectively corresponding to open crack and unbroken parts of the sample (Figure 2). Image processing determines the transition between dark and bright areas that defines the fracture front. We first compute the difference between each image and the first image of the experiment. The image difference highlights the fracture front while removing permanent artifacts. Then, gray scale images are transformed into black and white images according

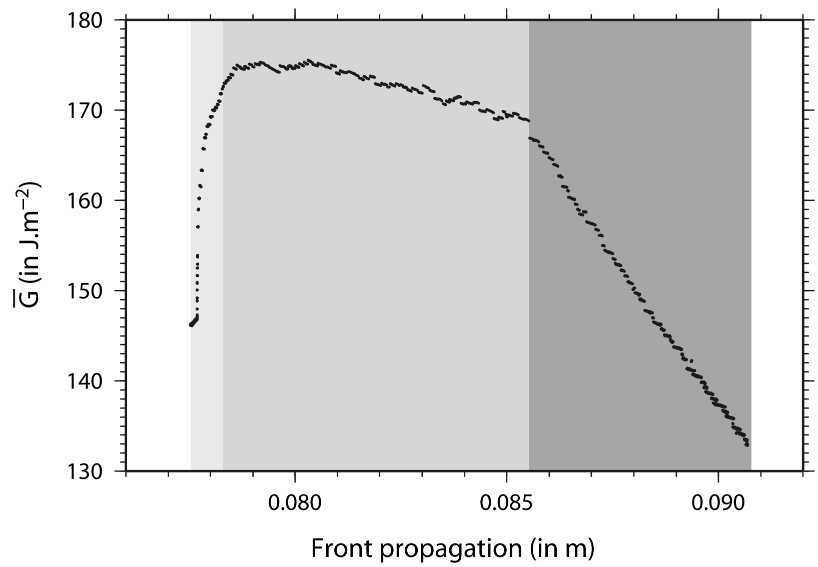

Figure 3. Evolution of $\overline{G}$ during a mode 1 fracture experiment as a function of the crack front position. During this experiment, the sample is loaded at a constant speed. The front starts to move slowly and $\overline{G}$ increases (light gray area) up to a nearly constant value when the crack front velocity reaches a steady state value (gray area). The loading point position is finally set to a constant value and $\overline{G}$ decreases (dark gray area) before the loading point moves back to its initial position at the end of the experiment (in a part of the curve not displayed here).

to a gray level threshold separating bright and dark regions. Then, we compute the gradient in the direction of front propagation to highlight the transition zone. We finally extract connected pixels from the gradient images that correspond to the front position $a(x, t)$ (Figure 2). The front propagates along the y axis with the origin defined at the load point and is positive in the sense of crack propagation. The x axis is perpendicular to y and defines the coordinate of a point along the front (see *Måløy et al.* [2006] and *Grob et al.* [2009] for details).

2.3. Loading Procedure

[14] The loading rate is constant during an experiment but different among the experiments, ranging from 6 μm/s to 300 μm/s. The crack advance for each experiment is on the order of 1 cm. We imposed a small transient load in one of the experiments. In several experiments we set the loading velocity to zero during the last stage to explore the fracture propagation under a fixed load point displacement (i.e., relaxation test). Here the average crack front velocity ranges from zero, at rupture initiation, to hundreds of μm/s. The rupture velocity in all experiments is much lower than the Rayleigh wave speed of the PMMA ($V_r \sim 1.7 \times 10^9$ μm/s).

3. Macroscopic Behavior

3.1. Energy Release Rate Evolution

[15] The macroscopic mechanical energy release rate during mode 1 crack propagation $\overline{G}$ is related to the total strain energy U stored in the system by [*Lawn*, 1993]

$$\overline{G}(t) = -\frac{1}{b}\frac{dU(t)}{d\overline{a}(t)}, \tag{1}$$

where b is the plate width (Figure 1) and $\overline{a}(t)$ is the average position of the front, i.e., the spatial average of each profile $a(x, t)$. Owing to the geometry of our setup, $\overline{G}$ can be estimated by beam theory. In the approximation of small, purely elastic deformation and neglecting the weight of the plate, small compared to the loading force, the force F and load point displacement u (the deflection at the free end of the beam), are related by [*Lawn*, 1993]

$$F = \frac{E\,b\,h^3}{4\,\overline{a}^3}u, \tag{2}$$

where E is the Young's modulus and h the height of the lower PMMA plate. We observe a linear relation between the observed average front position as a function of the predicted position (i.e., $[u/F]^{1/3}$) that proves the validity of the elastic beam theory applied to our experiments (equation (2)). The energy stored in the plate is

$$U = \frac{uF}{2}. \tag{3}$$

Combining equations (1) to (3) we obtain

$$\overline{G} = \frac{3\,E\,h^3}{8}\frac{u^2}{\overline{a}^4}. \tag{4}$$

This is the usual expression of the energy release rate for a simple cantilever beam under imposed displacement and neglecting mode 2 loading [*Lawn*, 1993]. Equation (4) can be written in terms of the observables F, u and $\overline{a}$ as

$$\overline{G} = \frac{3\,F\,u}{2\,b\,\overline{a}} \tag{5}$$

using equation (2). We prefer expression (5) instead of (4) because it involves measured variables raised to lower powers, which reduces the uncertainties. We track the evo-

Table 1. Macroscopic Energy Release Rate Determined for All Seven Experiments Performed With the Fast Speed Camera[a]

Experiment	$\overline{G}_c$	$\langle \overline{G} \rangle$	$\overline{G}_{area}$
1	174	148	144
2	122	118	126
3	153	140	123
4	147	142	113
5	182	173	167
6	130	122	115
7	190	182	159

[a]The values of the fracture energies $\overline{G}_c$ are obtained by taking the maximum of $\overline{G}$ computed from equation (5) for each experiment. We also report the mean energy release rates during the crack propagation obtained by the beam theory $\langle \overline{G} \rangle$ and by integration under the deflection-force space $\overline{G}_{area}$. All values are in $J.m^{-2}$.

lution of $\overline{G}$ (equation (5)) during crack propagation as F, u and a are continuously monitored (Figure 3).

[16] The crack propagates at steady speed when the macroscopic energy release rate $\overline{G}$ reaches a plateau that defines the macroscopic fracture energy $\overline{G}_c$ (Figure 3), consistently with a macroscopic Griffith equilibrium. $\overline{G}_c$ is in the range 122 $J \cdot m^{-2}$–190 $J \cdot m^{-2}$ for the set of experiments presented here. The fracture front also propagates during the relaxation regime (final stage of the experiment in Figure 3) with decreasing velocity. This propagation happens while $\overline{G} < \overline{G}_c$, which is not predicted by the Griffith theory with time-independent $\overline{G}_c$.

[17] We also estimate the global energy release rate directly from equation (1). The strain energy loss due to the crack propagation is the area ΔA defined in the deflection-force (u - F) space, between the loading and unloading curves. We numerically integrate ΔA and divide it by the crack length increase $\Delta \overline{a}$ and the plate width b. This approach provides an independent estimate $\overline{G}_{area}$ and validates the beam approach employed above under the assumption of a constant energy release rate during the entire crack propagation regime. We report the energy release rates and fracture energies for a subset of experiments in Table 1. Although some discrepancies exist between the two methods, we observe that a simple elastic beam model is appropriate to first order. Typical uncertainties in G are on the order of 7.5% given the uncertainties in F, u, b and a (typical values are $F = 30 \pm 0.2\,N$, $u = 10^{-2} \pm 10^{-6}$ m, $b = 2.8 \pm 0.2$ cm and $\overline{a} = 10 \pm 0.2$ cm). This relative uncertainty in $\overline{G}$ partially accounts for the small differences observed between the two methods used for its calculation. However, discrepancies might also be due to viscoelastic effects and yielding at the crack tip which contribute to energy loss during crack propagation but are neglected in our calculation. These effects are unfortunately difficult to estimate and we did not attempt to quantify their importance. It is worth noting that fracture energies in PMMA are of the same order of magnitude as those for rocks in mode 1 experiments at room conditions [*Atkinson and Meredith*, 1987b] and significantly higher than those for minerals [*Scholz*, 2002].

3.2. Brittle Creep Crack Propagation Model

[18] The crack propagation we observe at $\overline{G} < \overline{G}_c$ is not accounted for by the Griffith criterion (Figure 3). This is particularly pronounced towards the end of experiments where the loading displacement is fixed, which induces crack propagation at decreasing speed while $\overline{G}$ also decreases. Many mechanisms produce time-dependent subcritical crack advance where the velocity v follows an Arrhenius law [*Wiederhorn and Bolz*, 1970]

$$v(G) = v_o \exp\left[\frac{\beta G - E'}{RT}\right], \tag{6}$$

where G is the energy release rate, E' is an energy barrier, R is the universal gas constant and T is the temperature. β and v_o are material-dependent empirical constants and the energy release rate G is directly linked to the stress intensity factor K by $K = \sqrt{G\,E}$ in plane stress.

[19] We consider our fracture interface as a set of discrete sites of varying energy release rate along which the crack front line is pinned [*Scholz*, 1968b]. We describe the energy release rate by a probability density function $f(G, \overline{G})$. It is the probability of a point along the front line to have an energy release rate G given an average energy release rate $\overline{G}$ along the front. The probability distribution arises from the interplay between local toughness fluctuations on the interface and elastic interactions among sites of the front line. Equation (6) is understood as the local propagation criterion. It can be viewed as proportional to the inverse time to failure for a site locally loaded by a constant energy release rate G. The average crack front velocity $d\overline{a}/dt$ is defined by

$$\frac{d\overline{a}}{dt} = \int_{G=-\infty}^{+\infty} f\left(G, \overline{G}\right) v(G) dG. \tag{7}$$

[20] We assume a normal distribution for $f(G, \overline{G})$ with mean $\overline{G}$ and standard deviation σ_G [*Scholz*, 1968a]:

$$\frac{d\overline{a}}{dt} = \int_{-\infty}^{+\infty} \frac{v_0}{\sqrt{2\pi}\sigma_G} \exp\left[-\frac{1}{2}\left(\frac{G-\overline{G}}{\sigma_G}\right)^2 + \frac{\beta G - E'}{RT}\right] dG, \tag{8}$$

which integrates to

$$\frac{d\overline{a}}{dt} = v_o \exp\left[\frac{\beta \overline{G} - E'}{RT} + \frac{\beta^2 \sigma_G^2}{2R^2\,T^2}\right] = \overline{v}_o \exp\left[\frac{\beta}{R\,T}\overline{G}\right], \tag{9}$$

where $\overline{v}_o = v_o \exp\left[\frac{\beta^2\sigma_G^2}{2R^2T^2} - \frac{E'}{RT}\right]$. Equation (9) plainly shows that the evolution of the crack front velocity at the macroscopic scale is described by the same functional form as in the microscopic scale (equation (6)). Equation (9) implies $\overline{v} \propto \exp(\overline{G})$ independently of the loading conditions, extending its validity to the entire duration of the experiment. Equation (9) also reproduces the average evolution of the crack speed as a function of the macroscopic energy release rate $\overline{G}$ (Figure 4). It is also applicable when $du/dt = 0$. Since $\overline{a}(t)$ is small in the creeping regime, we use a first-order expansion around the initial position $\overline{a}_0$:

$$\overline{G}(\overline{a}) = \overline{G}_0 + \frac{d\overline{G}(\overline{a}_0)}{d\overline{a}}(\overline{a} - \overline{a}_0), \tag{10}$$

where $\overline{a}_0$ is the average position of the front at the onset of the creeping regime and $\overline{G}_0 = \overline{G}(\overline{a}_0)$. Substituting into (9), we get

$$\frac{d\overline{a}}{dt} = \overline{v}'_o \exp[-C_0\overline{a}], \tag{11}$$

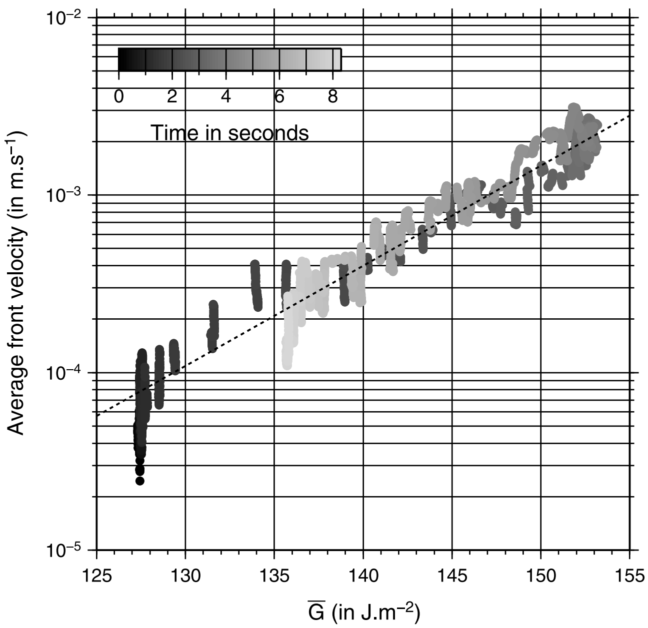

Figure 4. Variation of the average crack velocity $d\overline{a}/dt$ as a function of the average energy release rate $\overline{G}$ for an experiment conducted with the high-speed camera. The gray scale refers to the time since the start of the recording. During the entire crack propagation, from the initiation phase up to the relaxation phase, the best fit using equation (6), displayed as a dashed line, provides a good description of the data. It suggests that the crack propagation is a process driven by time-dependent brittle creep.

where $\overline{v}'_o = \overline{v}_o \cdot \exp(5\beta\, \overline{G}_0/RT)$ and $C_0 = 4\beta\, \overline{G}_0/RT\overline{a}_0$. After integration we get

$$\overline{a}(t) - \overline{a}_0 = \frac{1}{C_0} \ln[C_0 \overline{v}'_0 (t - t_0) + \exp(C_0)], \tag{12}$$

where t_0 is the time at the onset of the creeping regime.

[21] We also investigate the prediction of the model in the case $du/dt \neq 0$. When the front reaches a steady state regime, the crack propagates with $\overline{G} = constant$. This condition is similar to the Griffith energy criterion. A propagation with a constant energy release rate is described from equation (4) by

$$\overline{G} = \frac{u^2}{\overline{a}^4} \frac{3Eh^3}{8} \qquad \text{and} \qquad a(u) = \sqrt{u} \left(\frac{3Eh^3}{8\overline{G}} \right)^{1/4}. \tag{13}$$

Equation (12) provides a good description of the macroscopic evolution of the crack front in the relaxation regime (Figure 5, bottom) and equation (13) provides a good description in the forced regime (Figure 5, top). The macroscopic evolution of the front advance is well reproduced by a subcritical crack growth mechanism (Figures 4 and 5) that explains the propagation of the crack even for an energy release rate (or similarly the stress intensity factor) lower than the interface fracture energy (or similarly the toughness). It is also valid even when the front is propagating at a constant speed. In order to supplement our estimation of the fracture energy, next we present a procedure to estimate G at the local scale.

4. Microscopic Behavior

4.1. Scaling of the Fracture Front

[22] So far, we only considered straight crack fronts. These are expected if the toughness is uniform along the interface. However, departures from the straight front geometry suggest lateral variation of material resistance due to the sand blasting procedure applied during the sample preparation (Figure 6). The morphology of propagating interfacial cracks has been intensely studied [*Schmittbuhl and Måløy*, 1997; *Delaplace et al.*, 1999] and reproduced numerically [*Schmittbuhl et al.*, 2003a]. The in-plane morphology of crack fronts is self-affine and can be characterized by a roughness exponent. We show that a similar scaling of the fracture front morphology exists in our experiments. The Fourier transform of each front line, for a given experiment, is computed after detrending and tapering the original profile $a(x, t)$. We then obtain the average power spectrum representative of all fronts in this experiment (Figure 6). We observe a power law decay of the power spectrum in agreement with a self-affine morphology and the roughness exponent is in agreement with previously reported values (H = 0.6) [*Santucci et al.*, 2010]. Variable geometry of the crack front line suggests that heterogeneities over the interface should be taken into account when evaluating the fracture energy.

4.2. Distribution of Local Velocities

[23] The waiting time spent by the crack front at each local site is power law distributed [*Måløy et al.*, 2006]. The intermittent dynamics at the microscopic scale is also indirectly evidenced in rocks during creep tests [e.g., *Heap et al.*, 2009]. The recording of acoustic emissions during a slow macroscopic deformation suggests that at the local scale the deformation is distributed over a wide range of velocities. Figure 7 shows, for two experiments, the probability density function (pdf) of v obtained by the procedure described by *Måløy et al.* [2006]. The broad distribution of local speeds, spanning more than 2 orders of magnitude, highlights the irregular nature of the fracturing process at the small scale.

4.3. Local Energy Release Rate

4.3.1. Nonstraight Front Geometry

[24] We follow a first-order analysis based on a perturbation method for nearly straight crack fronts, valid for small relative variations of the fracture energy [*Gao and Rice*, 1989]. This approach is valid in our experiments since front lines are straight at first order. Furthermore, the model adequately reproduces the morphology of experimentally propagating cracks, although a discrepancy in the value of the roughness exponent remains [*Schmittbuhl et al.*, 2003a]. However, this approach ignores crack coalescence, which can play a role in redistributing stresses ahead of the crack front [*Hansen and Schmittbuhl*, 2003; *Schmittbuhl et al.*, 2003b]. Here we assume that the elastic front line model represents the dominant process. The first-order

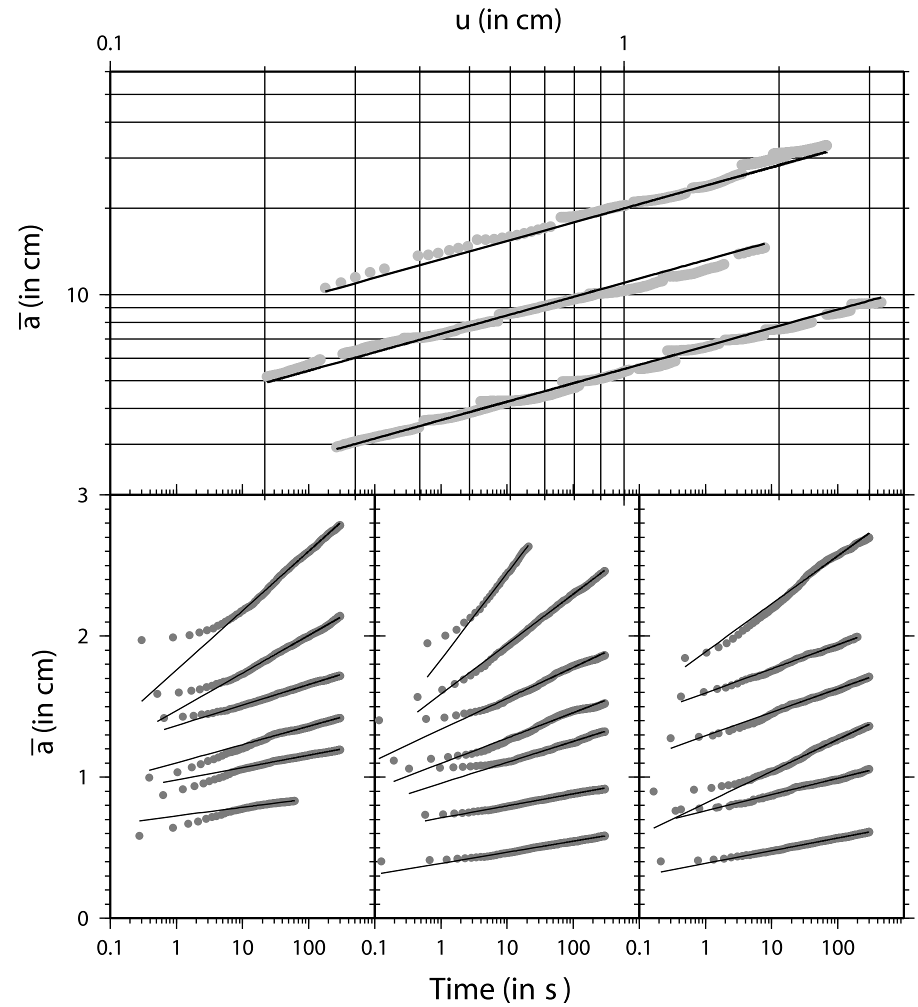

Figure 5. (top) Variation of the average crack front position $\overline{a}$ as a function of the loading point displacement u. The gray points refer to data recorded from different samples. For each sample we carried out several experiments. The best fit using equation (13) is displayed as a black line for each sample. Crack front positions are shifted vertically for each sample in order to enhance the visibility. (bottom) Evolution of the average front position $\overline{a}$ during the relaxation regime (gray dots). The x axis is the time after we stopped the loading. For each experiment, the best fit using equation (12) is displayed as a black line. A good match of the fitted line to the data is observed after several seconds which marks a transition period from the previous regime. Each of the three bottom images represents a different sample. For each experiment, the vertical axis is shifted in order to enhance visibility.

approximation of the energy release rate of an almost straight crack is [*Gao and Rice*, 1989]

$$G(x_i, t_k) = \overline{G}(t_k)(1 + \gamma(x_i, t_k)) \tag{14}$$

for a given front at time t_k. $\overline{G}(t_k)$ is the energy release rate computed from the average front position at time t_k and $\gamma(x_i, t_k)$ is the contribution from elastic interactions due to local fluctuations of the front position given by

$$\gamma(x, t) = \frac{1}{\pi}\mathcal{PV}\int_{-\infty}^{+\infty} \frac{a(x', t) - a(x, t)}{(x - x')^2} dx', \tag{15}$$

where $\mathcal{PV}$ denotes the principal value. This expression is the Hilbert transform of the local slope of the front [*Ampuero and Rubin*, 2008], which explains why small-scale variations in the $\gamma(x)$ profile are larger than in the $a(x)$ profile. The discretized version of equation (15) is

$$\gamma(x_i, t_k) = \frac{1}{\pi}\sum_{j=-l/2, j\neq i}^{l/2} \frac{a(x_j, t_k) - a(x_i, t_k)}{(x_j - x_i)^2} \,.\, dl, \tag{16}$$

where dl is the width of a pixel and l is the width of the picture. A small error may arise in the determination of γ for points close to the edge of the images of the fracture front. Since the decay of the elastic kernel with distance is fast ($\propto 1/x^2$), the loss of information at the edge only affects a small region near the edge of the picture. The computation of γ, as presented in equation (16), assumes a half plane crack in an infinite body. If the finite height of the plate is taken into account, the elastic kernel transitions from the $1/x^2$

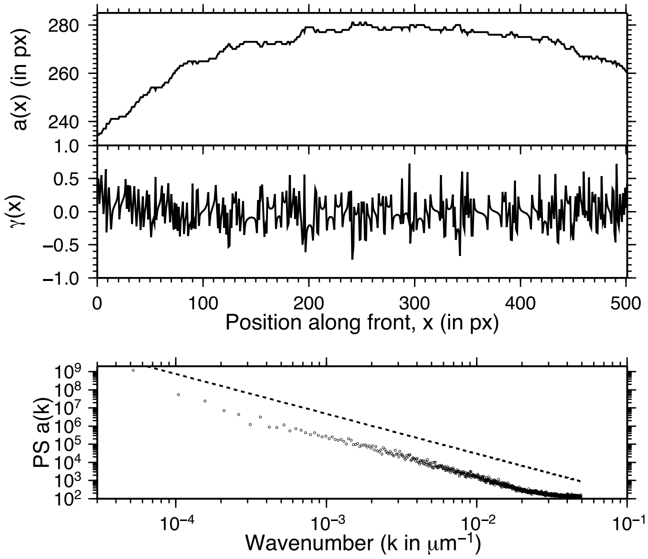

Figure 6. (top) Example of front position $a(x)$ extracted from a picture captured with the high-speed camera. Distances are in pixels and the size of a pixel is ~21 μm. The difference between the less advanced and the farthest advanced point on the front is slightly less than 1 mm whereas the front length is ~1.1 cm. (middle) The γ values corresponding to the front line displayed above and computed using equation (16). We observe sharp fluctuations of γ which are correlated with local variations of the slope of the front $a(x)$. (bottom) Averaged power spectrum (PS) of the front morphology over all fronts extracted during an experiment. We observe a clear power law decay of the PS which shows the presence of fluctuations of $a(x, t)$ at all spatial scales and is representative of the self-affine nature of the crack front morphology. The dashed line indicates a power law decay function with an exponent of −2.2, consistent with a roughness exponent H = 0.6.

behavior of equation (15) to a faster (exponential) decay at distances x larger than the plate height. We calculate the local value of γ at the middle of a front line in order to quantify the impact of the truncation and the finite height. We progressively extend the bounds of the summation up to $l/2$. Two different front lines originating from two different experiments are processed in this way to represent the typical convergence of γ as a function of the integration range. We observe that ~90% of the final estimate of γ is recovered in the first 100 pixels which corresponds to a dimension of 2 mm (Figure 8). This shows that γ is controlled by the closest neighboring sites. The infinite medium approach is valid since the length scale influencing the estimate of γ is smaller than all other dimensions of the plate. An example of a γ profile for a given front is shown in Figure 6.

4.3.2. 1-D Time Evolution

[25] The matrix $\gamma(x, t)$ represents normalized fluctuations of the energy release rate at any time and position along the front. The mean of the γ distribution, along a given front line, for a given image, is zero by definition. We track the evolution of $\gamma(x_0, t)$ for a particular position, x_0, along the front (Figure 9). The local movement of the front $a(x_0, t)$

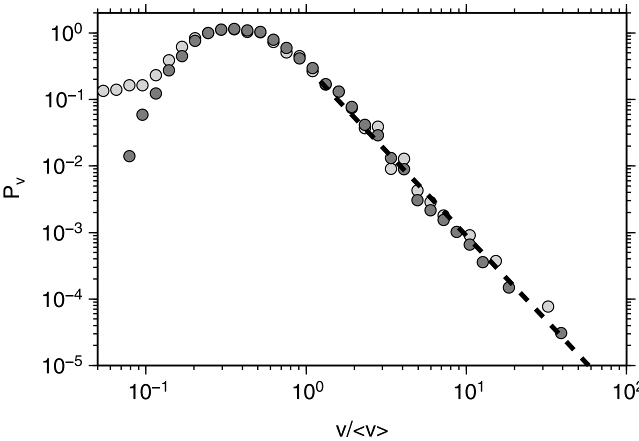

Figure 7. Probability density function of the local speed computed for two different experiments (light and dark gray circles). All velocities are normalized by the average crack propagation velocity in order to compare experiments. We clearly observe a power law decay of the pdf above $v/\langle v \rangle = 1$. The dashed line indicate a power law decay with exponent −2.55 as found by *Måløy et al.* [2006].

reveals potential correlations between the evolution of γ and local variations of a (Figure 9).

[26] The local motion of the front is not continuous but rather exhibits a stick-slip pattern with long resting periods followed by jumps of the front position (Figures 7 and 9). In contrast, the large-scale evolution of the average crack position is continuous.

4.3.3. 2-D Maps

[27] The energy release rate increases at pinned positions along the front line. This increase has two contributions: (1) a large-scale contribution from the external loading applied to the system (increase of the load point deflection) and (2) local contributions resulting from local elastic interaction due to the differential movement of neighboring points. As G increases, it rises the probability of the local site

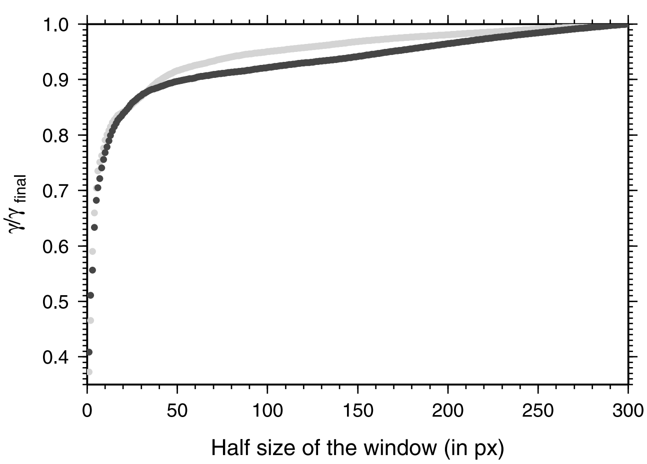

Figure 8. Convergence of γ to its final estimate as a function of the half size of the window used to compute it. This convergence is tested on two different front lines taken from two different experiments. Convergence is fast: ~90% of the final estimate of γ is recovered in the first 100 pixels (2 mm).

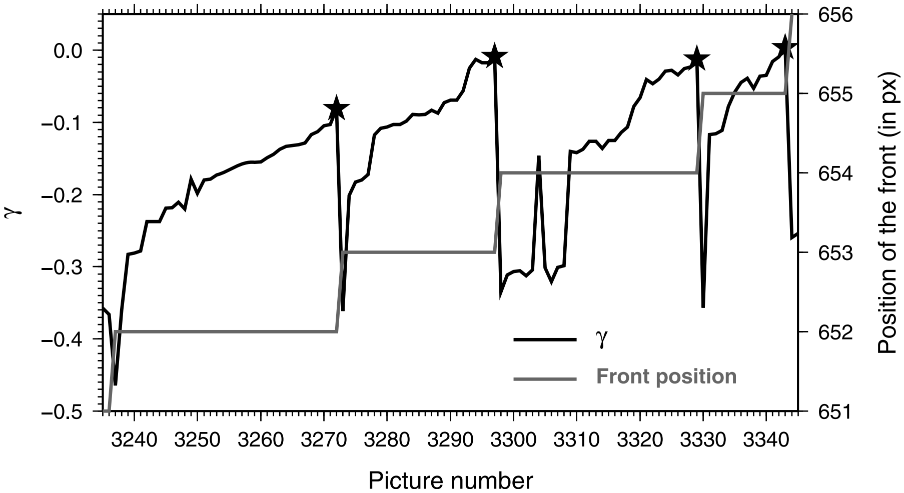

Figure 9. Evolution of γ (black line) and front position (gray line) for a given position along front and during ~8 s. Stars represent the last values of γ at a given front position and are defined as γ_c.

to fail in the next time interval as defined by equation (6). This probability increases until G reaches G_c, at which point the local site breaks. Accordingly, we define γ_c as the last value of γ just before a local variation of the front position and we estimate the fracture energy at this site as

$$G_c(x_i, a(x_i, t_k^*)) = \overline{G}(t_k^*)(1 + \gamma(x_i, a(x_i, t_k^*))), \qquad (17)$$

where t_k^* is the time at which γ_c was reached. It is important to note that $\overline{G}(t_k^*)$ is obtained from the measurement of the average position of the front $\overline{a}(t_k^*)$. Any variation of γ taking place during the time interval between estimating γ_c and the local front advance is neglected. These microscopic estimates of the fracture energy are lower bounds, since there is a finite probability that the local site actually breaks with $G < G_c$ according to the Arrhenius model described earlier. In order to get an insight on collective processes that take place at the local scale during the crack propagation, we show two examples of a spatiotemporal map $\gamma(x, t)$ in Figure 10. These maps are subregions of the effectively recorded areas (both in time and space) taken from two different experiments representative of the two propagation regimes, at fixed loading point (relaxation regime) and constant loading rate respectively.

[28] Notable features emerging from Figure 10 are summarized below:

[29] 1. At a given time (horizontal line), only a few points are at $G = G_c$, and most points have $G < G_c$ for both forced ($\overline{G} = \overline{G}_c$) and relaxation regimes. Observation of the intermittent failure of local sites during slow crack propagation is a direct measurement of a brittle/creep behavior. As most of the sites along the front line are below G_c, the macroscopic estimate of fracture energy $\overline{G}_c$ is an average among local values of G that are mainly below the critical state ($\overline{G} \neq \overline{G}_c$). Therefore, the macroscopic fracture energy is a lower estimate compared to the microscopic values.

[30] 2. Large collective failure events (numerous black points on the same horizontal line) corresponding to a burst of activity in a relatively short time interval occur at discrete periods. These fast local movements arise from a connected set of unstable positions along the front. A burst of unstable positions appears when the local G is equal or higher than the fracture energy of all sites of the cluster. This scenario typically occurs after breaking a strong local asperity (high G_c value). The front then travels in a region with lower G_c up to a new arrest position that corresponds to the next accessible equilibrium position.

[31] 3. Despite very different average velocities and loading regimes, strong similarities exist between the patterns of the two maps. The main difference between the two loading regimes arises from the waiting time between each successive move of the front at a particular local site. Time intervals between two successive moves are much larger in the relaxation regime (frame rates in Figure 10 are 125 fps and 1000 fps for the relaxation and the forced regime respectively). The shorter time intervals observed in the forced regime are related to a higher loading rate at each local site.

4.4. Influence of Fluctuations in Toughness

4.4.1. Large-Scale Fluctuations

[32] The front geometry has a long wavelength curvature due to a large-scale variation of the fracture energy at the interface. The annealing condition in the sample during its preparation is not perfectly homogeneous. Transient heat diffusion from the sides of the plates to the center of the sample is possibly responsible for such curvature. As a consequence, edges of the plate have higher strength than the center. We used this large-scale curvature of the front line to infer the large-scale variation of the fracture energy along the x direction. The largest Fourier mode of the front is a single cosine function of the form $a(x) = A_0 + 2A_1 \cos(\pi x/b)$ where x is the coordinate along the front direction and b is the width of the plate [*Gao and Rice*, 1989]. Griffith criterion holds everywhere along the crack front (G very close to G_c), with G_c being the local fracture energy at each site. It follows from [*Gao and Rice*, 1989]

$$\sqrt{\tilde{G}} = \sqrt{\tilde{G}_0}\left[\frac{1}{A_0} - \frac{\pi}{L}\right] A_1, \qquad (18)$$

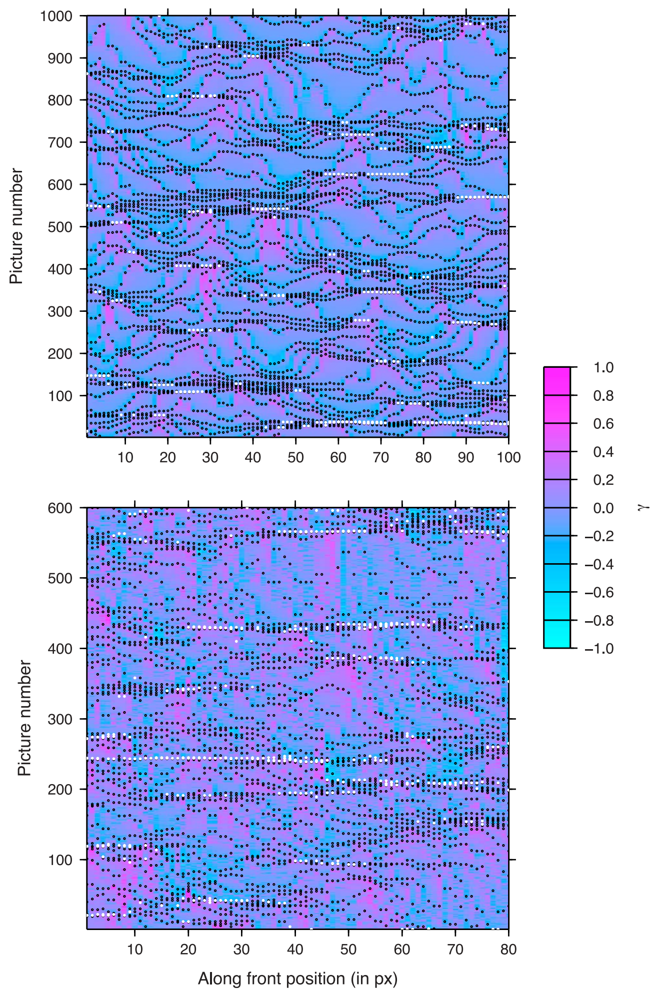

Figure 10. Zooms on a subspace of γ matrix obtained using equation (16) for two experiments recorded with the fast video camera at (top) 125 fps and (bottom) 1000 fps. Time axis is vertical and is oriented from bottom to top. Note that the time interval between two pictures is not the same for the two maps (8 s and 0.6 s). The top image is obtained while the front is relaxing (i.e., u = *constant*) while the bottom image was obtained while the front was propagating at constant velocity. Black dots correspond to last positions of the front before a local move and thus define G_c as expressed in equation (17). White dots correspond to estimation of G_c obtained from only one measure, thus reflecting the non-equilibrium position of the front at these locations.

where $\tilde{G}$ and $\tilde{G}_0$ are the Fourier modes of order 1 and 0 respectively. The variation of fracture energy at long wavelength between the center of the plate and its border is

$$\frac{G_c^{center}}{G_c^{border}} \approx \left(\frac{b - \pi A_1}{b + \pi A1}\right)^2 \tag{19}$$

for $A_0 \gg b/\pi$ which is the case for our experiments. As A_1 is on the order of several hundred of micrometers and b is ~2 cm, the long wavelength shape of the front is explained by a variation of fracture energy along the plate on the order of 10%.

4.4.2. 2-D Toughness Fluctuations

[33] We estimate spatial maps of local fracture energies $G_c(x,\ a(x))$, i.e., everywhere along the interface, from equation (17) (Figure 11). The local fracture energy is broadly distributed over the range 18 to 395 $J.m^{-2}$, clearly expressing the heterogeneity of local fracture energies (Figure 11). Interface roughness δz is obtained from a broken sample, previously peeled off (Figure 11). The analyzed interface does not correspond to the same area where the G_c map was computed but the statistical properties of the interface morphology are assumed to be representative of the whole sample interface. The morphology of the interface was measured by a laser profilometer with spatial and vertical resolution of 10 μm and ~1 μm respectively (Figure 11). Height fluctuations δz have a standard deviation of several of μm.

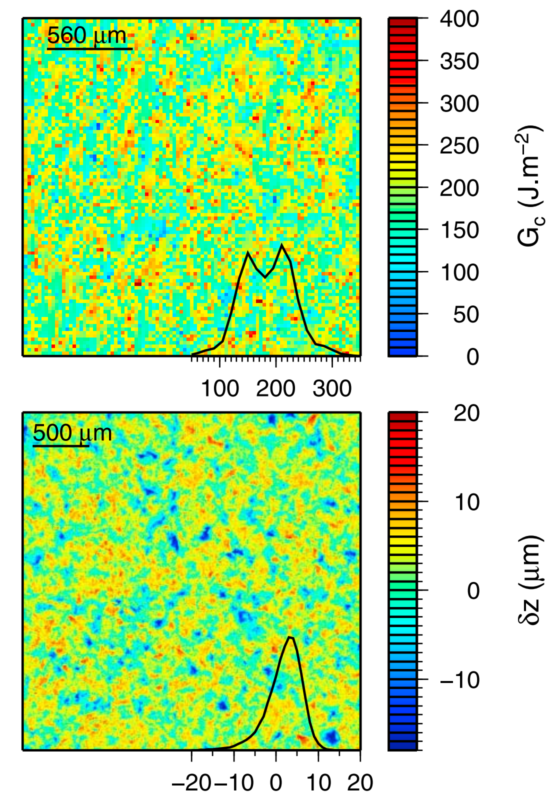

Figure 11. (top) Zoom on a map of local fracture energy G_c computed using equation (17). During this experiment the crack propagates from bottom to top. We clearly observe an heterogeneous distribution of G_c which appears as a random field although a correlation among sites can be identified. The few holes (3% of total number of pixels) that exist at some places in the map, because of a too low frame rate, have been filled by linear interpolation. The inset graph represents the distribution of fracture energy for all sites of the main picture. (bottom) Map of a sample interface morphology $\delta\ z$ of a similar size to the one represented for the fracture energy. An heterogeneous distribution of $\delta\ z$ is clearly visible with an amplitude of variation of several tens of micrometers. The inset graph represents the distribution of the interface height $\delta\ z$.

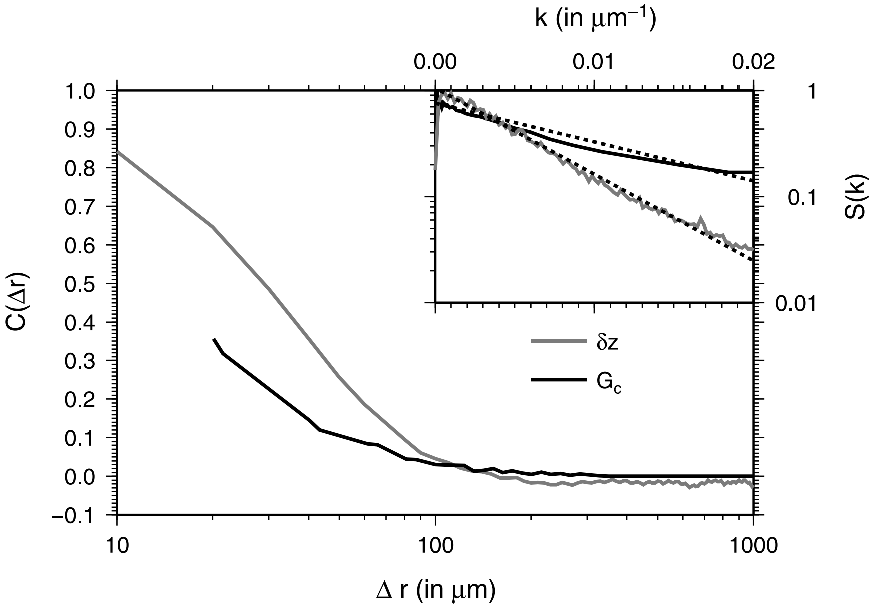

Figure 12. Averaged correlation functions $C(\Delta r)$ as a function of the distance Δr between two points along the interface. Correlations are averaged from stripes computed along the front direction and perpendicular to it. The gray line denotes the correlation function computed for the interface morphology whereas the black line represents the correlation functions of the fracture energy. The inset shows the two power spectra $S(k)$ from which correlation functions are computed. The best exponential fit for each function $S(k)$ is plotted as a dashed line. The correlation lengths inferred from these fits are r_c = 188 μm and 84 μm for the height and fracture energy respectively. The values are in agreement with the lengths where the correlations functions $C(\Delta r)$ get uncorrelated.

[34] Local toughness variations arise from the squeezing of local asperities along the interface. We extract all profiles of G_c and δz along the front propagation direction and perpendicular to it. The power spectra $S(k)$ is averaged over the two in-plane directions for both the distributions of G_c and δ_z. The autocorrelation function $C(\Delta r)$ is then obtained as the inverse Fourier transform of the power spectrum:

$$C(\Delta r) = \int_{-\infty}^{\infty} S(k) e^{j2\pi k\tau}\, dk, \tag{20}$$

where k is the wavenumber. Figure 12 shows correlation functions of the fracture energy and the surface morphology along with their power spectra $S(k)$. The autocorrelation functions of G_c and δz decrease with distance (Figure 12). The decrease is faster for G_c than for δz. The power spectra shows an exponential form although we cannot exclude a model with power law decay associated with a cutoff length. An exponential of the form $S(k) \propto \exp(-k/k_c)$ is an adequate fit. The length scale $1/k_c$ is the correlation length, the distance beyond which the distribution becomes uncorrelated. For the front morphology we find $1/k_c \sim 188$ μm. The distribution of G_c is characterized by a smaller correlation length ~84 μm ~4 pixels. These cutoff length scales can also be appraised from the correlation functions as we observe that $C(\Delta r)$ gets around 0 above these distances. Although the cutoff length is not the same, the exponential decay is observed for both G_c and δ_z. The existence of a finite correlation length for G_c and δz does not necessarily imply that an approach using a representative element volume (REV) could be valid at scales greater than this length scale. Long range interactions, owing to elastic forces applied over long distances results in an interplay between the toughness fluctuations and these elastic forces. This is well demonstrated by the self-affine nature of the crack front line observed previously (section 4.1).

5. Scaling of the Fracture Energy

[35] The observation that most points along the crack front have energy release rate $G < G_c$ indicates that the macroscopic estimate of the fracture energy $\overline{G}_c$ is different from the fracture energy at the local scale. We test this proposition by comparing G_c at the local and the global scales. In particular, we address whether the macroscopic toughness is a simple arithmetic average of the distribution of local toughness. In such a case, an homogenization procedure is quite straightforward and $G_c = \langle G_c \rangle$, i.e., the local variations of material resistance are simply scattered around the global value and the average of the distribution is equal to the global value. We calculate normalized distributions of G_c as well as global estimations of $\overline{G}_c$, obtained with equation (5) for each experiment (Figure 13). We only consider for the estimates of G_c those locations where the front was present during more than one time interval. The estimate involves only values at equilibrium positions and thus related to the interface property [*Roux et al.*, 2003]. We also calculate the normalized distribution of G computed from equation (14) (Figure 13). The distribution of local energy release rate is wide and is centered on the macroscopic estimate of the fracture energy. This is expected from

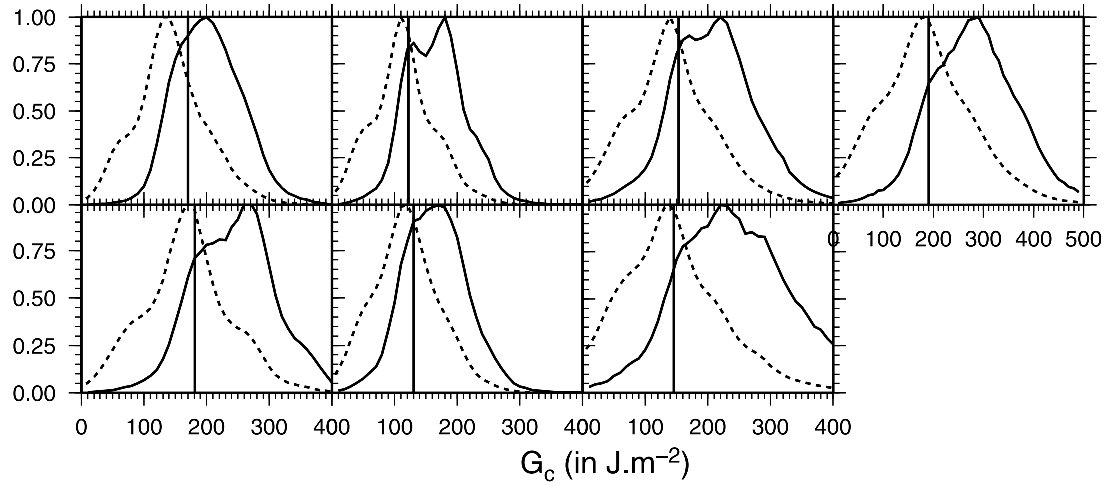

Figure 13. Distributions of G_c (black line), G (dash line) for all seven experiments carried with the fast video camera. The vertical black lines is the value of the macroscopic fracture energy $\overline{G}_c$. We systematically observe that the microscopic distribution of G_c is centered on higher value than their respective macroscopic estimates.

equation (14) and equation (16), because γ has zero mean. Accordingly, the distribution of G should be approximately centered on the global value $\overline{G}$, as observed. A more interesting feature emerges when analyzing the distribution of local fracture energy G_c (Figure 13). We clearly observe that the average of local fracture energy $\langle G_c \rangle$ is higher than the macroscopic estimate of the fracture energy $\overline{G}_c$. We recall that the macroscopic estimate of the fracture energy $\overline{G}_c$ is defined as the maximum value of the $\overline{G}$ reached during the crack propagation. Such higher values of G_c compared to $\overline{G}_c$ are observed for all experiments and the distribution of G_c is systematically shifted to higher values compared to the global $\overline{G}_c$. This indicates that G_c samples the subset with the highest values of G. For a pinned position of the front, γ increases with time leading to higher values at the end of the time interval, just before the local advance of the front. Therefore, γ_c are on average higher than γ and the distribution of G_c is shifted towards higher values compared to G. It is worth noting that the shift to higher values, going from macroscale to microscale, does not depend of any particular choice of calculating $\overline{G}$. For example, equations (4) and (5) produce a similar shift of $\langle G_c \rangle$ compared to $\overline{G}_c$ because G_c values are computed using $\overline{G}$ from equation (14). The observed toughening effect at the microscopic scale is thus independent on a particular calculation of $\overline{G}$. The same argument is also valid when considering the variation of $\overline{G}$ owing to the uncertainties of the parameters defining $\overline{G}$. Despite these uncertainties, local values of G_c will still be, on average, higher than $\overline{G}_c$. We note however that the amplitude of this toughening depends on the macroscopic value of the energy release rate.

[36] There are some known geophysical scaling problems where a simple arithmetic mean (average) is not relevant for an upscaling of the problem. For example, bulk permeability of a heterogeneous material is bounded from above by the arithmetic mean and below by the harmonic average [*Zimmermann and Main*, 2004]. Contrary to the case of the permeability, for which the Darcy's law allows to make the transition link between scales, an equivalent expression does not exist in our problem. This prevents us to define the particular averaging procedure relevant in our system. Nevertheless, we test several forms of mean of our values of G_c. We compute the harmonic, the geometric and the arithmetic means of the microscopic distribution of fracture energy for each experiment. We observe for all experiments that all types of average are systematically overestimating the macroscopic value. This suggests that scaling effects are non trivial and related to the observation scale and the mechanism of brittle creep as proposed.

6. Implications for Fault Mechanics

6.1. Link Between Crack Modes

[37] Several analogies can be drawn between our mode 1 fracture experiment and deformation processes in the crust. Tensile failure of natural materials occurs during dyke propagation and during secondary microcracking surrounding shear fractures. The mechanical process in our experiments is not limited to tensile fracture. The role of heterogeneities along a fault plane has similar consequences on the local values of the stress intensity factor (or energy release rate). An expression similar to equation (14) exists for mode 2 and mode 3 cracks when ignoring second-order coupling among shear modes [*Gao et al.*, 1991]. The only difference with the mode 1 expression is a constant coefficient dependent on the Poisson ratio. One could refer to *Schmittbuhl et al.* [2003a] for an extended discussion on the relation between rupture modes.

6.2. Importance of the Process Zone

[38] Fracture in rock samples or faults exhibit a process zone that encompasses a region with complex microcracking because of the high stress field around the crack tip. Significant energy is dissipated in the formation of the process zone and in the frictional work on these microcracks. This energy loss is much higher than the surface energy associated with the separation of the two blocks in contact. As the size of the process zone is observed to

increase with fault length, a scaling argument suggests that the energy release rate dissipated in the process zone also increases with the fault/system size [*Scholz*, 2002]. This results in an apparent scaling of the fracture energy with the system size, where the fracture energy includes all sources of energy dissipations [e.g., *Abercrombie and Rice*, 2005]. Our system does not involve a pronounced process zone because of the small bulk disorder. As a consequence, estimates of the fracture energy in our experiments are close to the surface energy, in contrast to earthquake data where the growth of the process zone and friction greatly influence the dissipation process. Our observations do not directly address the issue of the scaling of G_c with system size. The size of our system is fixed by the sample size (plate dimensions) and does not vary. The difference of fracture energy that we observe results from the change of the observation scale and not the sample scale.

6.3. Slow Slip Events

[39] Our observations provide a guide for understanding the simultaneous presence of acoustic emissions and smooth deformation during creep experiments in rock samples [e.g., *Heap et al.*, 2009]. Such brittle creep behavior is possible due to the heterogeneous nature of the interface which produces, at the local scale, a complex pattern of ruptures (see Figure 10) because of elastic interactions. It is a competition between sites with subcritical or critical propagation (pseudo stick-slip crack advances) resulting in an average (macroscopic) steady deformation. This mode of rupture implies a variation of the fracture energy with observation scale. The fracture energy computed at the sample scale actually integrates all points along the front line and thus is an average among sites that are at $G = G_c$ (only a few points) and a majority of points that are pinned along the interface under unloading conditions with $G < G_c$. A higher proportion of sites along the front line are at $G = G_c$ when the loading speed is increased, and subsequently the crack speed. The difference between $\overline{G_c}$ and $\langle G_c \rangle$ vanishes when the speed of the crack approaches the Rayleigh wave speed. The deformation rate is an important factor that affects the large-scale estimate $\overline{G_c}$ while faintly modifying estimates at local scales. In the case of a dynamic crack, in our model, at a given time step, all points along the front line are moving. Our definition of the local fracture energy implies that at all time steps and for every position along front, the energy release rate is equal to the fracture energy. Averaging over all local estimates produces the exact same value as the macroscopic one $\overline{G_c} = \langle G_c \rangle$. Our results are more closely related to slow deformation processes occurring in the Earth crust rather than dynamic events, like creeping of fault segments, nucleation phase of earthquakes, postseismic slip or slow slip processes. The fracture energy for slow ruptures in the earth are lower (by few orders of magnitude) compared to values reported for dynamic fractures of the same size. This is the case for a creep event along the San Andreas fault reported by *Rice and Simons* [1976]. This is also suggested from the low slip to size ratio of slow events [e.g., *Ide et al.*, 2007], which combined with *Rice and Simons* [1976, equation (67)] yields low values of fracture energy compared to regular earthquake. These studies however do not resolve the spatial distribution of fracture energy on the fault plane during the slow events which would make possible the comparison with macroscopic estimates as in our study.

7. Conclusion

[40] We provide a direct description of brittle creep crack propagation at different observational scales. At the local scale, the fracturing process is intermittent and is characterized by a complex fracture front morphology and a wide range of local crack velocities. At a given time, a mixture of slow and fast ruptures can be observed simultaneously. This complex pattern results from the presence of heterogeneities along the crack interface together with significant elastic interactions. When observed at the macroscopic scale, the variability of the local scales disappears and the crack propagation is smooth. This suggests that macroscopic observation of slow deformation processes (for example for rocks samples or faults) should be analyzed in the light of the heterogeneous nature of the material. Therefore, the fracture energy depends on the observation scale and its macroscopic estimate is lower than the average over local values.

[41] **Acknowledgments.** We gratefully acknowledge fruitful discussions with K.T. Tallakstad, V. Lazarus, N. Pindra, S. Santucci, S. Roux, J.P. Leblond, M. Bouchon, H. Karabulut, P. Meredith, P. Baud, and M. Heap and experimental support by Alain Steyer. This research is funded by ANR grant SUPNAF. J.E.E. was supported by a Caltech Seismological Laboratory fellowship. J.E.E. and J.P.A. were partially supported by the National Science Foundation (grant EAR-1015698). We thank Ian Main, the Associate Editor, and an anonymous reviewer for useful suggestions. Some figures were drawn with GMT software [*Wessel and Smith*, 1995].

References

Abercrombie, R. E., and J. R. Rice (2005), Can observations of earthquake scaling constrain slip weakening?, *Geophys. J. Int.*, *162*, 406–424, doi:10.1111/j.1365-246X.2005.02579.x.

Ampuero, J.-P., and A. M. Rubin (2008), Earthquake nucleation on rate and state faults: Aging and slip laws, *J. Geophys. Res.*, *113*, B01302, doi:10.1029/2007JB005082.

Atkinson, B. K. (1984), Subcritical crack growth in geological materials, *J. Geophys. Res.*, *89*, 4077–4114, doi:10.1029/JB089iB06p04077.

Atkinson, B. K., and P. G. Meredith (1987a), The theory of subcritical crack growth with applications to minerals and rocks, in *Fracture Mechanics of Rocks*, pp. 111–166, Academic, San Diego, Calif.

Atkinson, B. K., and P. G. Meredith (1987b), Experimental fracture mechanics data for rocks and minerals, in *Fracture Mechanics of Rocks*, pp. 477–525, Academic, San Diego, Calif.

Baud, P., and P. G. Meredith (1997), Damage accumulation during triaxial creep of Darley Dale sandstone from pore volumometry and acoustic emission, *Int. J. Rock Mech. Min. Sci.*, *34*(3–4), 24.e1–24.e10, doi:10.1016/S1365-1609(97)00060-9.

Bean, C. J. (1996), On the cause of 1/f-power spectral scaling in borehole sonic logs, *Geophys. Res. Lett.*, *23*, 3119–3122, doi:10.1029/96GL02922.

Blewitt, G. (2007), GPS and space-based geodetic methods, in *Treatise on Geophysics*, vol. 3, *Geodesy*, pp. 351–390, Elsevier, New York.

Bouchon, M., H. Karabulut, M. Aktar, S. Ozalaybey, J. Schmittbuhl, and M.-P. Bouin (2011), Extended nucleation of the 1999 mw 7.6 Izmit earthquake, *Science*, *331*(6019), 877–880, doi:10.1126/science.1197341.

Brace, W. F., and J. B. Walsh (1962), Some direct measurements of the surface energy of quartz and orthoclase, *Am. Mineral.*, *47*, 1111–1122.

Das, S., and C. H. Scholz (1981), Theory of time-dependent rupture in the earth, *J. Geophys. Res.*, *86*, 6039–6051, doi:10.1029/JB086iB07p06039.

Delaplace, A., J. Schmittbuhl, and K. J. Måløy (1999), High resolution description of a crack front in a heterogeneous plexiglas block, *Phys. Rev. E*, *60*, 1337–1343.

Freiman, S. W. (1984), Effects of chemical environments on slow crack growth in glasses and ceramics, *J. Geophys. Res.*, *86*, 4072–4076.

Gao, H., and J. R. Rice (1989), A first-order perturbation analysis of crack trapping by arrays of obstacles, *J. Appl. Mech.*, *56*, 828–836.

Gao, H., J. R. Rice, and J. Lee (1991), Penetration of a quasi-statistically slipping crack into a seismogenic zone of heterogeneous fracture resistance, *J. Geophys. Res.*, *96*, 21,535–21,548.
Grob, M., J. Schmittbuhl, R. Toussaint, L. Rivera, S. Santucci, and K. J. Måløy (2009), Quake catalogs from an optical monitoring of an interfacial crack propagation, *Pure Appl. Geophys.*, *166*, 777–799.
Hansen, A., and J. Schmittbuhl (2003), Origin of the universal roughness exponent of brittle fracture surfaces: Stress-weighted percolation in the damage zone, *Phys. Rev. Lett.*, *90*, 045504, doi:10.1103/PhysRevLett.90.045504.
Heap, M. J., P. Baud, P. G. Meredith, A. F. Bell, and I. G. Main (2009), Time-dependent brittle creep in Darley Dale sandstone, *J. Geophys. Res.*, *114*, B07203, doi:10.1029/2008JB006212.
Ide, S., G. C. Beroza, D. R. Shelly, and T. Uchide (2007), A scaling law for slow earthquakes, *Nature*, *447*, 76–79, doi:10.1038/nature05780.
Katsamanis, F. G., and C. G. Delides (1988), Fracture surface energy measurements of PMMA: A new experimental approach, *J. Phys. D Appl. Phys.*, *21*, 79–86, doi:10.1088/0022-3727/21/1/012.
Lawn, B. R. (1975), An atomistic model of kinetic crack growth in brittle solids, *J. Mater. Sci.*, *10*, 469–480, doi:10.1007/BF00543692.
Lawn, B. R. (1993), *Fracture of Brittle Solids*, Cambridge Univ. Press, New York.
Lei, X., K. Kusunose, M. V. M. S. Rao, O. Nishizawa, and T. Satoh (2000), Quasi-static fault growth and cracking in homogeneous brittle rock under triaxial compression using acoustic emission monitoring, *J. Geophys. Res.*, *105*, 6127–6139, doi:10.1029/1999JB900385.
Lengliné, O., and D. Marsan (2009), Inferring the coseismic and postseismic stress changes caused by the 2004 $m_w = 6$ Parkfield earthquake from variations of recurrence times of microearthquakes, *J. Geophys. Res.*, *114*, B10303, doi:10.1029/2008JB006118.
Lockner, D. (1993), Room temperature creep in saturated granite, *J. Geophys. Res.*, *98*, 475–487, doi:10.1029/92JB01828.
Måløy, K. J., S. Santucci, J. Schmittbuhl, and R. Toussaint (2006), Local waiting time fluctuations along a randomly pinned crack front, *Phys. Rev. Lett.*, *96*, 045501, doi:10.1103/PhysRevLett.96.045501.
Okubo, P. G., and K. Aki (1987), Fractal geometry in the San Andreas fault system, *J. Geophys. Res.*, *92*, 345–356, doi:10.1029/JB092iB01p00345.
Paterson, M. S., and T. Wong (2005), *Experimental Rock Deformation - The Brittle Field*, 2nd ed., Springer, New York.
Rice, J. R., and D. A. Simons (1976), The stabilization of spreading shear faults by coupled deformation-diffusion effects in fluid-infiltrated porous materials, *J. Geophys. Res.*, *81*, 5322–5334, doi:10.1029/JB081i029p05322.
Roux, S., D. Vandembroucq, and F. Hild (2003), Effective toughness of heterogeneous brittle materials, *Eur. J. Mech. Solids*, *22*, 743–749.
Rubin, A. M. (1993), Tensile fracture of rock at high confining pressure: Implications for dike propagation, *J. Geophys. Res.*, *98*, 15,919–15,935.
Santucci, S., M. Grob, R. Toussaint, J. Schmittbuhl, A. Hansen, and K. J. Maløy (2010), Fracture roughness scaling: A case study on planar cracks, *Europhys. Lett.*, *92*, 44001, doi:10.1209/0295-5075/92/44001.
Schmittbuhl, J., and K. J. Måløy (1997), Direct observation of a self-affine crack propagation, *Phys. Rev. Lett.*, *78*, 3888–3891.
Schmittbuhl, J., A. Delaplace, K. J. Måløy, H. Perfettini, and J.-P. Vilotte (2003a), Slow crack propagation and slip correlations, *Pure Appl. Geophys.*, *160*, 961–976.
Schmittbuhl, J., A. Hansen, and G. G. Batrouni (2003b), Roughness of interfacial crack fronts: Stress-weighted percolation in the damage zone, *Phys. Rev. Lett.*, *90*, 045505, doi:10.1103/PhysRevLett.90.045505.
Schmittbuhl, J., G. Chambon, A. Hansen, and M. Bouchon (2006), Are stress distributions along faults the signature of asperity squeeze?, *Geophys. Res. Lett.*, *33*, L13307, doi:10.1029/2006GL025952.
Scholz, C. H. (1968a), Microfracturing and the inelastic deformation of rock in compression, *J. Geophys. Res.*, *73*, 1417–1432, doi:10.1029/JB073i004p01417.
Scholz, C. H. (1968b), Mechanism of creep in brittle rock, *J. Geophys. Res.*, *73*, 3295–3302, doi:10.1029/JB073i010p03295.
Scholz, C. H. (2002), *The Mechanics of Earthquakes and Faulting*, Cambridge Univ. Press, New York.
Simons, M., and P. A. Rosen (2007), Interferometric synthetic aperture radar geodesy, in *Treatise on Geophysics*, vol. 3, *Geodesy*, pp. 391–446, Elsevier, New York.
Titus, S. J., C. DeMets, and B. Tikoff (2006), Thirty-five-year creep rates for the creeping segment of the San Andreas Fault and the effects of the 2004 Parkfield earthquake: Constraints from alignment arrays, continuous global positioning system, and creepmeters, *Bull. Seismol. Soc. Am.*, *96*(4), S250–S268, doi:10.1785/0120050811.
Wang, L., S. Hainzl, S. Ozeren, and Y. Ben-Zion (2010), Postseismic deformation induced by brittle rock damage of aftershocks, *J. Geophys. Res.*, *115*, B10422, doi:10.1029/2010JB007532.
Wessel, P., and W. H. F. Smith (1995), New version of the generic mapping tools released, *Eos Trans. AGU*, *76*, 329–329, doi:10.1029/95EO00198.
Wiederhorn, S. M., and L. H. Bolz (1970), Stress corrosion and static fatigue of glass, *J. Am. Ceram. Soc.*, *53*, 543–548, doi:10.1111/j.1151-2916.1970.tb15962.x.
Wong, T. (1982), Shear fracture energy of westerly granite from postfailure behavior, *J. Geophys. Res.*, *87*, 990–1000.
Zimmermann, R., and I. Main (2004), Hydromechanical behaviour of fractured rocks, in *Mechanics of Fluid-Saturated Rocks*, pp. 363–422, Elsevier, London.

J.-P. Ampuero and J. E. Elkhoury, Division of Geological and Planetary Sciences, California Institute of Technology, 1200 E. California Blvd., MC 252-21, Pasadena, CA 91125, USA. (ampuero@gps.caltech.edu; elkhoury@gps.caltech.edu)

O. Lengliné, J. Schmittbuhl, and R. Toussaint, Institut de Physique du Globe de Strasbourg, IPGS, UMR 7516, CNRS, Université de Strasbourg, 5 rue René Descartes, F-67084 Strasbourg, France. (olivier.lengline@eost-u.strasbg.fr; jean.schmittbuhl@eost-u.strasbg.fr; renaud.toussaint@eost-u.strasbg.fr)

K. J. Måløy, Department of Physics, University of Oslo, PB 1048, Blindern, N-0316 Oslo, Norway. (maloy@fys.uio.no)

Average crack-front velocity during subcritical fracture propagation in a heterogeneous medium

Olivier Lengliné, Renaud Toussaint, and Jean Schmittbuhl
IPGS, EOST, CNRS, Université de Strasbourg, 5 rue René Descartes, F-67084, Strasbourg, France

Jean E. Elkhoury and J. P. Ampuero
Seismological Laboratory, California Institute of Technology, Pasadena, CA 91125, USA

Ken Tore Tallakstad, Stéphane Santucci,* and Knut Jørgen Måløy
Department of Physics, University of Oslo, PB 1048 Blindern, NO-0316 Oslo, Norway
(Received 16 February 2011; revised manuscript received 15 June 2011; published 9 September 2011)

We study the average velocity of crack fronts during stable interfacial fracture experiments in a heterogeneous quasibrittle material under constant loading rates and during long relaxation tests. The transparency of the material (polymethylmethacrylate) allows continuous tracking of the front position and relation of its evolution to the energy release rate. Despite significant velocity fluctuations at local scales, we show that a model of independent thermally activated sites successfully reproduces the large-scale behavior of the crack front for several loading conditions.

DOI: 10.1103/PhysRevE.84.036104 PACS number(s): 46.50.+a, 62.20.M−

I. INTRODUCTION

The mechanisms responsible for the onset and evolution of fracture propagation are of central importance for the assessment of failures in man-made structures and natural materials such as rocks, sea ice, and wood [1–4]. In the general context of fracture mechanics, several regimes of behavior are often reported. According to the Griffith energy balance concept, in a quasistatic regime, the energy release rate G is roughly constant and equal to a material-dependent critical energy release rate, $G \sim G_{gr}$ [5]. G_{gr} is the free energy per unit surface area associated with the creation of new crack surfaces. The kinetic energy becomes important in unstable configurations or during fast loading leading to a dynamic regime [6,7]. In the slow, unstable regime (i.e., rupture velocity smaller than the Rayleigh wave speed), the crack propagation speed is roughly proportional to the difference between G and G_{gr} (e.g., [8]) and strongly controlled by loading conditions (imposed stress or imposed displacement, loading rate) and material rheology. Modeling approaches in these cases are typically based on the linear elastic fracture mechanics (LEFM) approximation [9].

A generalization of the Griffith concept of fracturing, in the framework of irreversible processes, allows for the propagation of fractures at speeds below that of the Rayleigh wave for energy release rate lower than G_{gr} [10]. In consequence the slow kinetic crack propagation is usually referred to as subcritical crack growth or the subcritical regime. Statistical physics models suggest that this subcritical regime is governed by a thermally activated mechanism where the strain rate often obeys an Arrhenius law, i.e., corresponds to a Boltzmannian of the gap to a critical energy level $G_c - G$ [5,11,12]. The crack growth is directly influenced by environmental factors (applied stress, temperature, chemical concentrations) affecting the free energy, and thus the energy barrier, via numerous competing mechanisms like stress corrosion, diffusion, dissolution, and plasticity [1,5]. Several experimental empirical relations have been reported that divide slow crack propagation into three main characteristic regimes depending on the crack speed [13]. These regimes reflect the competition between crack growth velocity and diffusion of species at the crack tip. At very slow velocity, external variables are dominant and an increase in G results in an increase in the speed of crack growth. A weak stress-sensitive regime follows where transport is limited. At higher stress, the crack growth kinetics becomes similar to that in the case with no environmental effects.

Other relations besides the Arrhenius law have also been reported to describe slow crack growth. These relations are generally inferred from fitting an empirical relation to experimental data on a G-$\bar{v}$ diagram, where $\bar{v}$ is the crack velocity. Such relations involve power laws with small exponents [14], or large exponents when the crack propagation is more sensitive to chemical reaction rates [15,16]. To simplify the relationship between strain rate (i.e., crack-front advance) and stress, some models consider the crack propagation speed as roughly proportional to the difference between G and an energy release rate threshold, or to a power law of this difference, i.e., a Paris law (e.g., [17–19]).

The Arrhenius form of the kinetic fracture evolution is appealing as it has a certain universality associated with statistical mechanics. It is related to any thermally activated mechanism at the molecular scale and can be derived from first principles as the theory of process rates [5]. Such a relation is also supported by experimental data [1,20], and if the dependence of the free energy G on the strain can be adequately linearized, a logarithmic time dependence of the strain, and force, can be derived. This is observed for many systems under creep like granular systems displaying a temporal logarithmic deformation (or force) during slow relaxation [21–23].

For heterogeneous materials, crack propagation is, however, influenced by local variations of the material properties, microstructures, thermal fluctuations, and the development of

*Present address: Laboratoire de Physique, CNRS UMR 5672, Ecole Normale Supérieure de Lyon, 46 allée d'Italie, 69364 Lyon Cedex 07, France.

a process zone [24]. The interplay of the different contributions to the crack growth makes its analysis a complex problem. It is indeed difficult to discriminate the part of each contribution by observing the evolution of a crack advance at a microscopic level. The failure of brittle materials with weak flaws is typically described by Weibull statistics of the flaw strengths which relies on the weakest-link approach and extreme-value statistics [25]. Quasibrittle materials exhibit a departure from the Weibull statistics for which ductile behavior around the crack tip imposes an representative elementary volume (REV) of non-negligible size compared to the sample size. These materials show significant scaling or size effects, in particular at very low loading rates [26].

The interfacial crack propagation configuration has long been a favorable experimental setting for fine monitoring of crack propagation. It consists of a single cantilever beam configuration with fracture propagation along a weak interface. It was the first setup to enable measurements of fracture energy in brittle materials like mica [27]. In the case of quasibrittle materials [e.g., polymethylmethacrylate) (PMMA)], it provided the first detailed observation of the morphology of the crack front [28,29]. The distribution of local velocities of the crack front displays an intermittent behavior at small scales [30,31]. The scaling properties of the crack front remain unchanged in both the high and slow speed limits at the local dynamic [31]. This suggests that a common mechanism might be operating in these two regimes. This was the case for both the front's geometrical properties (scaling of the front roughness) and the time and space scaling properties of the velocity fluctuations. The interfacial configuration is also favorable for numerical simulations since it reduces the roughening of the crack front to an in-plane problem. Two modeling approaches have been proposed: (1) a microscopic description of the crack front as a continuous line [8,32–34] and (2) fiber bundle models in which a discrete population of active sites are competing under various interaction rules [35–39].

Here, we focus on the experimental description of the spatially averaged velocity of the crack front in the interfacial fracture configuration, under various loading conditions. Our heterogeneous medium consists of an interface between two PMMA plates with small toughness fluctuations [40]. Each local asperity is a site of a depinning transition that leads to a progressive local advance of the crack front. We optically monitor the global evolution of the crack by taking advantage of the transparency of our sample. We explore the regimes of small loading rates (up to 1 mm/s) and relaxation at fixed load point displacement. First, we compare the average crack velocity to the loading velocity or the energy release rate for both loading regimes. Then we show that the large-scale evolution of the crack-front velocity can be explained by a simple model of a population of statistically independent but temperature-sensitive microscopic active sites, slowly evolving, following an Arrhenius law. Numerical solutions of the model correctly describe the experimental behaviors for time scales spanning over six orders of magnitude for both loading types. The parameters of the subcritical crack-growth law provide a characteristic size of the individual breaking bond. For our case, we obtain a length scale of 10^{-11} m for PMMA comparable to the separation of individual molecular elements and much smaller than the scaling of the fracture front (10^{-5} to 10^{-2} m) similar to the scales determined for granite [41], paper [42], and numerous other materials [12].

In addition to the numerical solutions, we derive simple analytical expressions for the two loading regimes under several approximations. Notably, we find a slow time-logarithmic relaxation. We also show that $G \sim G_{gr}$, for imposed loading rates, results from an Arrhenius law with stress-activated microscopic sites and linear elasticity that describe the dependence of the stress on the large-scale geometry.

II. EXPERIMENTAL ANALYSIS

A. Sample preparation

We use two PMMA plates of dimensions $20 \times 10 \times 1.0$ cm^{3}and $23 \times 2.7\times$ cm^3. First, we sandblast one surface of the narrower plate with glass beads of diameter ϕ ($\phi \in$ [180–300] μm). The blasted plate is cleaned to remove any electrically attached glass beads. Then, we assemble the two plates in a stiff aluminum frame with the blasted surface facing a surface of the larger plate. Finally, we subject the assembled plates to a homogeneous normal load of 3 MPa and heat the assembly in an oven at 190 °C for 45 min to anneal the plates. The thermal annealing produces a cohesive interface that is weaker than the bulk and constrains the sample to break along the prescribed interface. The glass bead blasting introduces random heterogeneities in the surface topography that provides surface roughness and controls the local strength at the interface. The induced microstructure at the interface makes the sample opaque. However, the newly formed block, after annealing, recovers its transparency since contrast of the refractive index along the interface disappears.

B. Acquisition and image processing

We clamp the large plate of the fully healed sample to a stiff aluminum frame. A stepping motor applies the loading to the tip of the narrow plate normal to the plate surface (Fig. 1). The contact on the plate is imposed by a freely rotating rod (using ball bearings), made of low-friction-coefficient material (polyamide PA 6.6). We measure the vertical displacement at the loading point using a linear variable differential transformer (LVDT) and the force load by an STC 1205 traction-compression transducer. Displacement and force are measured to a resolution of 1.3 μm and 2.4×10^{-3} N, respectively. The vertical displacement imposed on the narrower sample induces the stable propagation of a planar fracture along the prescribed interface. The loading velocity varies for each experiment within the range [6–600] μm/s and is zero during creep tests. This leads to null front velocities at the start of experiments and maximum front velocities on the order of 3.0×10^3 μm/s. The total advance of the crack front achieved during an experiment is typically on the order of 1.0 cm.

We monitor the fracture front optically using a Nikon D700 camera with up to ∼5 frames per second to follow the crack front propagation (Fig. 1). The optical images are 4256×2832 pixels and of a resolution in the range [5–10] μm/pixel. The optical images of the interfacial rupture are divided into bright and dark regions representing the cracked open and unbroken sections of the sample respectively. To obtain the

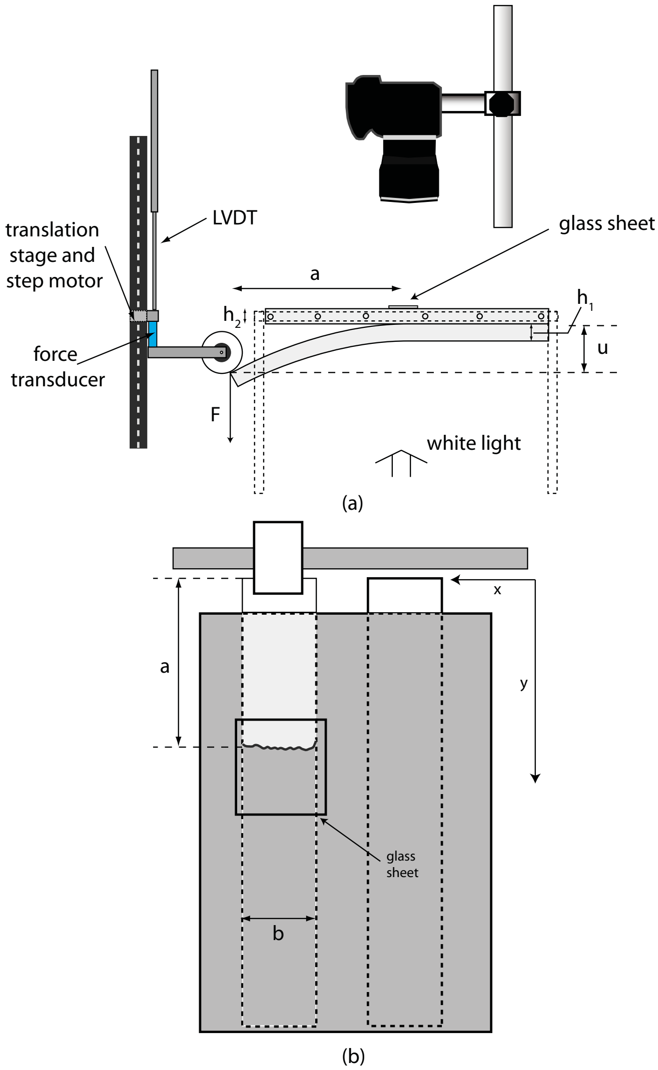

FIG. 1. Side view (top) and top view (bottom) of the experimental setup. A stiff aluminum frame is attached to the upper PMMA plate. The lower plate is separated from the upper one by a load F applied by a rod connected to a stepping motor. The rod can freely rotate around its axis. The load causes a deflection u of the bottom plate and the propagation of an interfacial crack. The crack front is located at the average distance $\bar{a}$ from the free end ($\bar{a}$ is obtained as the spatial average of the distance a along the front). Front advance is monitored by a camera set in vertical position, perpendicular to the crack plane. We add glycerol between the upper plate and a thin glass sheet located above the crack front to enhance the optical contrast of the pictures. The narrow plate thickness and width are denoted h_1 and b, respectively, while the large plate thickness is denoted h_2.

transition between the bright and dark regions that represents the fracture front, we first compute the difference of the grayscale maps between each image and the first image of the experiment. This first step highlights the difference between two consecutive time stamps of the fracture process while removing permanent artifacts associated with index variations in the material. Then, we transform the grayscale images to black and white according to a threshold that represents the gray level separation between the bright and dark regions. The fracture front $a(x,t)$ is the largest cluster of connected pixels with nonzero gradient. The front propagates on average along the y axis where the origin is defined at the free end of the plate and is positive in the direction of propagation. The x axis is perpendicular to the y axis and defines the coordinate of a point along the front, t is time, and $a(x,t)$ is the y position of the front at lateral position x and time t. We compute the average front position $\bar{a}(t)$ from each profile $a(x,t)$ [30,40].

C. Typical run of an experiment

All experiments start with no initial deflection, i.e., the loading point is not in contact with the narrow PMMA plate. Then the stepping motor moves the loading point at controlled speed V_l. Once contact is achieved between the loading point and the plate, both the force F at the free end of the plate and the deflection u increase. The force increase leads to the initiation of crack movement while the loading point continues to move at constant velocity. The duration of this constant-loading-velocity regime is inversely proportional to V_l. The fracture front speed decreases once we stop the stepping motor ($V_l = 0$, at $t = t_{\text{stop}}$). We typically monitor the evolution of the fracture fronts for about 5 min. Monitoring lasted for more than 18 h for one of our experiments. We unload the sample by moving the loading point backward to its initial position, leading to the arrest of the front. The next experiment starts where the previous one ends until the front reaches the end of the plate. We performed all experiments at room temperature ($T \in [22.2\text{–}24.4]\,^\circ$C) and used two completely independent experimental setups run by different groups, with no noticeable discrepancies in the results.

An example of typical experimental measurements is shown in Fig. 2. Here, the sample was continuously loaded at 62 μm/s during 230 s. Rupture initiates at $t \sim 190$ s, as evidenced by the onset of the front movement and the deviation of the force from the linear trend. We observe an increase in the crack velocity as long as the sample is continuously loaded. We then maintain the loading point at a fixed position at time $t_{\text{stop}} = 230$ s as indicated by the vertical gray line (Fig. 2). The front velocity exhibits a deceleration while the force is decreasing when the loading point velocity is set to zero. We performed all the experiments following the same scheme presented in Fig. 2.

III. EXPERIMENTAL OBSERVATIONS

In the following subsections we report on the behavior of the average front positions with time in the two loading regimes, at constant loading velocity, or at constant loading position, and show that they follow simple laws. In subsequent sections, we derive these laws on a theoretical basis and interpret their parameters in a physical context.

A. Constant loading velocity

In the constant-loading-velocity regime, we observe an initiation phase which precedes the propagation of the crack at an almost constant velocity (Fig. 2). The evolution of the front position $\bar{a}$ as a function of the loading point displacement u is shown in Fig. 3. We only show data for $t < t_{\text{stop}}$ where the dynamics of the crack is driven by the applied load at constant velocity. We observe that the evolution of $\bar{a}$ is well approximated by a fit of the form $\bar{a}(u) \propto \sqrt{u}$ (dashed lines in Fig. 3) for each of our samples.

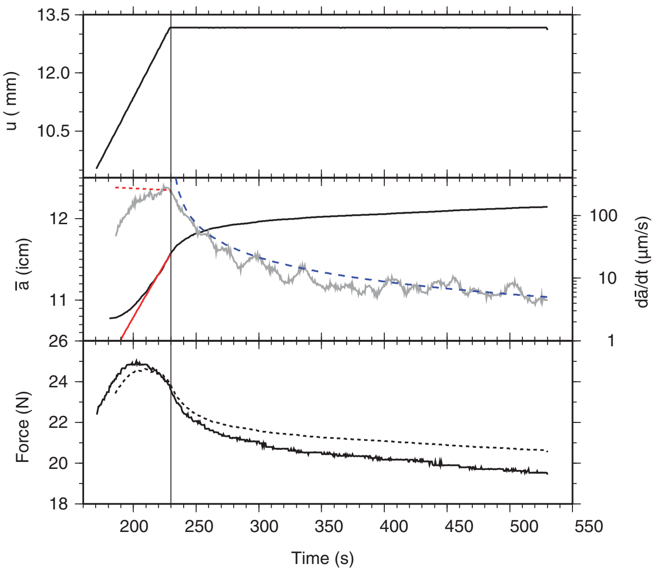

FIG. 2. (Color online) Top: Variation of loading point position u as a function of time during an experiment. At time $t = 230$ s, the loading point is maintained in a fixed position. Middle: Variation of the average front position $\bar{a}$ as a function of time (black solid line) and evolution of the crack front velocity $d\bar{a}/dt$ (gray solid line). The red solid and short-dashed lines represent a fit to the average front position and velocity, respectively, according to Eq. (19). The blue long-dashed line is a fit to the crack velocity in the relaxation regime following Eq. (26). Bottom: Variation of force as a function of time (black solid line) and force predicted by the beam theory (gray dashed line) using (5) with $E = 3.2$ GPa and $b = 2.84$ cm, which are the measured properties of the plate. For all figures, the vertical gray line denotes the time at which the loading was stopped and separates the imposed velocity regime from the relaxation regime.

B. Constant-deflection condition

Now we turn to the relaxation regime characterized by a constant deflection u ($t > t_{\mathrm{stop}}$). We observe a progressive deceleration of the front (Fig. 2). In order to precisely describe the evolution of the front position in this particular regime, we set $\bar{a}_0 = \bar{a}(t_{\mathrm{stop}})$ and we represent the evolution of the front position $\bar{a}(t) - \bar{a}_0$ for time since t_{stop}. We observe a logarithmic evolution of the front advance for large times (Fig. 4). We propose to fit the advance of the front by a logarithmic relation of the form

$$\bar{a}(t - t_{\mathrm{stop}}) - \bar{a}_0 = A \ln\left(\frac{t - t_{\mathrm{stop}}}{t^*} + 1\right), \qquad (1)$$

where t^* is a characteristic time and A an empirical constant. Equation (1) provides a good fit (Fig. 4). We obtain typical values of t^* on the order of 1–10 s, while typical values of A are on the order of 10^{-4}–10^{-3} m. We also report the evolution of the front position during this relaxation regime for an experiment lasting more than 18 h (Fig. 4). The propagation of the front remained small (∼2 cm) even for this long-term experiment. The logarithmic evolution of the crack front contrasts with the previous regime of constant loading velocity. The large-scale progression of the front must be dominated by a process capable of capturing such distinct behaviors.

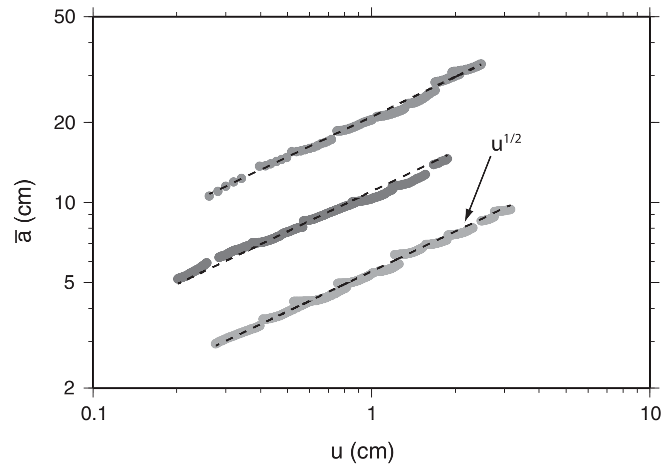

FIG. 3. Variation of the crack front position $\bar{a}$ as a function of the loading point displacement u. The gray points refer to recorded data from different samples. For each sample we carried out several experiments. The best fit using $\bar{a}(u) \propto u^{1/2}$ is displayed as a dashed line for each sample. Crack-front positions are shifted vertically for each sample in order to enhance the visibility (by a prefactor corresponding respectively to a factor 0.5 for the lowest and 2 for the highest curves). We see that for each sample and for each experiment the observed behavior is in good agreement with the fitted trend. Notice, however, that the crack initiation does not seem well approximated by this trend.

IV. SUBCRITICAL CRACK PROPAGATION MODEL

A. Thermally activated microscopic process

We assume that the crack propagation is governed, at the local scale, by a subcritical mechanism based on an Arrhenius law [14]. Owing to thermal fluctuations large enough to overcome the fracture energy barrier of individual bonds, the fracture propagates at slow speed. This contrasts with the Griffith approach where no propagation is allowed below the Griffith energy release rate G_{gr} (or below the Griffith stress intensity factor K_{gr} following an Irwin criterion [5]). The fracture energy barrier fluctuates in space but it is constant at a characteristic microscopic scale α, which is a length scale associated with individual degrees of freedom of the microscopic fracturing process. At zero loading, we consider that the magnitude of the barrier is related to the local critical energy release rate $\alpha^2 G_c$. This aspect of a quenched fluctuating zero-loading barrier relates material properties to G_c. The energy gap is also dependent on the elastic mechanical energy around the crack tip which is described by the local energy release rate $\alpha^2 G$. Such models of coupled thermal noise and spatial disorder have been previously investigated in some theoretical approaches of fiber bundle models and irreversible crack growth [43,44]. The probability for an individual asperity to go beyond the barrier $\Delta G = G_c - G$ per period characteristic of the microscopic thermal motion τ_B is the Boltzmannian of the relative elastic energy $\alpha^2 \Delta G$. The Arrhenius relation governing the local fracture velocity $v = d\,a/dt$ can thus be written as

$$v(G, G_c) = \psi \exp(-\alpha^2 \Delta G / k_B T), \qquad (2)$$

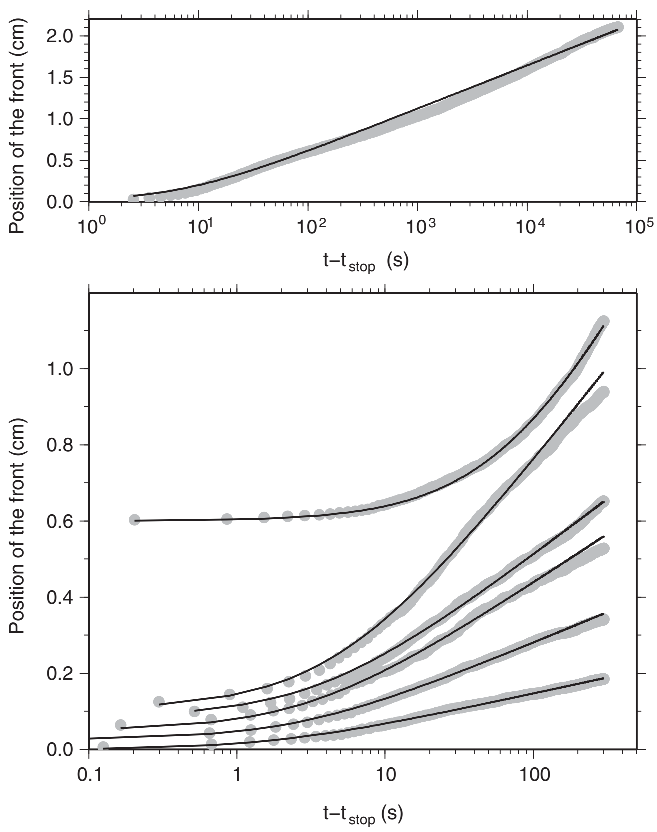

FIG. 4. Evolution of the average front position $\bar{a}(t) - \bar{a}_0$ during several relaxation experiments as a function of time $t - t_{\rm stop}$. The observed front position is represented by gray dots while the best fits using (1) are displayed as continuous dark lines. Traces have been shifted vertically in order to enhance visibility. The experiment displayed on the top figure lasted more than 18 h (the time representation scale is different from the one in the bottom figure).

where ψ is a constant of proportionality equal to α/τ_B, T is the absolute temperature (in kelvin), and k_B is the Boltzmann constant.

B. Population of independent microscopic sites

We propose a model for the average crack velocity based on a statistical approach. The behavior of the weak interface is assumed to be dominated at large scales by a discrete set of independent microscopic sites. We obtain the large-scale evolution law of the crack-front speed by integrating Eq. (2) over all local microscopic sites at a given time. Such an integration is not straightforward as there might exist correlations among local values of G and G_c. Fluctuations in G results from the crack front roughening around its average position $\bar{a}$ [32] and a perpendicular, large-scale, stress gradient due to bending of the loading plate. For the fracture energy G_c, the quenched fluctuations result from the sample preparation. Such fluctuations introduce correlation over a finite length of local velocities [31]. We hypothesize that at the macroscopic scale, above these correlation lengths, the average (or large-scale) evolution of the front is governed by a law similar to Eq. (2) but involving only large-scale average quantities. $\bar{G}$ describes the average loading along the front and $\bar{G}_c$ describes the upscaled energy barrier at the front scale. The critical size of the degree of freedom, α, is preserved. For example, in a simple model where all parameters were statistically independent and G and G_c could be described by two independent normal distributions with respective means $\bar{G}$ and $\bar{G}_c$ and root mean squares σ_G and σ_{G_c}, we would get

$$\bar{v} = \chi \exp[-\alpha^2(\bar{G}_c - \bar{G})/k_B T], \tag{3}$$

where

$$\chi = \psi \exp\left[\frac{\alpha^4(\sigma_G^2 + \sigma_{G_c}^2)}{2k_B^2 T^2}\right]$$

We acknowledge that, at small scales, G and G_c are not statistically independent and that intermittent behavior, large fluctuations of velocity, and spatial correlations in G and in G_c have been observed and described in detail (e.g., [30,31]). Nonetheless, we assume that the upscaling leads to a simple form as in Eq. (3). The upscaling could result from a discretization scale above which asperities could be considered independent. This discretization scale could be analogous to the REV introduced by Bažant and Pang [45] for quasibrittle materials. Within each REV, the effective failure of the asperity is considered as a purely thermally activated and stress-dependent process. This model is not continuous in contrast to the contact line approach [8,32–34]. It can rather be compared to fiber bundle models [35–39] or interacting damage models [46–49] but with a nondirect stress redistribution.

For simplicity, we ignore mechanical interactions among microscopic sites in describing the dynamics of the upscaled spatially averaged velocity. Only the mechanical energy release rate, controlling the upscaled velocity, depends on the large-scale average front position. The upscaling of Eq. (2) leads to a similar form with only upscaled energy release rates and energy barrier [Eq. (3)]. This assumption will be checked by comparing this simple model to our experimental observations. Below we show that the model holds for the relaxation regime and also for the forced regime.

C. A cantilever configuration

We estimate the average energy release rate $\bar{G}$ using classical elastic plate theory, neglecting fluctuations of the front position around an average front position $\bar{a}$. The average energy release rate from the elastic strain energy, U_E, stored in the loading plate is

$$\bar{G} = -\frac{1}{b}\frac{dU_E}{d\bar{a}}, \tag{4}$$

where b is the width of the plate [5]. The linear relation between the applied force F and the deflection of the beam u from one-dimensional (1D) beam theory is

$$F = \frac{uEbh^3}{4\bar{a}^3}, \tag{5}$$

where E is the Young modulus of the narrow plate and $1/h^3 = 1/h_1^3 + 1/h_2^3$ is an equivalent thickness resulting from our asymmetric configuration (see [5] and details in the Appendix, where we also estimate both mode I and mode II loading). This leads to the following expression of the elastic energy:

$$U_E = F\frac{u}{2}. \tag{6}$$

Combination of Eqs. (4), (5), and (6) gives an estimation of the average energy release rate in our system,

$$\bar{G} = \frac{3u^2 E h^3}{8\bar{a}^4}. \tag{7}$$

D. Macroscopic evolution law

We derive the expression for the evolution of the crack-front velocity by combining Eqs. (3) and (7),

$$\bar{v} = \frac{d\bar{a}}{dt} = \chi \exp\left(\frac{\alpha^2}{k_B T}\left[\frac{3u^2 E h^3}{8\bar{a}^4} - \bar{G}_c\right]\right). \tag{8}$$

Equation (8) is the differential equation that governs the motion of the front in our experimental configuration. This equation takes different forms depending on the loading scheme, which manifest in the expression of the time-dependent imposed deflection $u(t)$. We explored two particular loading conditions imposed on the experimental system, namely, a constant-loading-velocity condition and a fixed-deflection condition.

As a first check, we computed the average crack-front velocity $\bar{v}(t)$. We smoothed $\bar{a}(t)$ values with a window running along time and then dividing each incremental position by the time interval between successive images. We estimated $\bar{G}$ at each time interval from Eq. (7). The average crack-front velocity is shown in Fig. 5 as a function of the average energy release rate $\bar{G}$ using Eq. (7). We clearly observe that

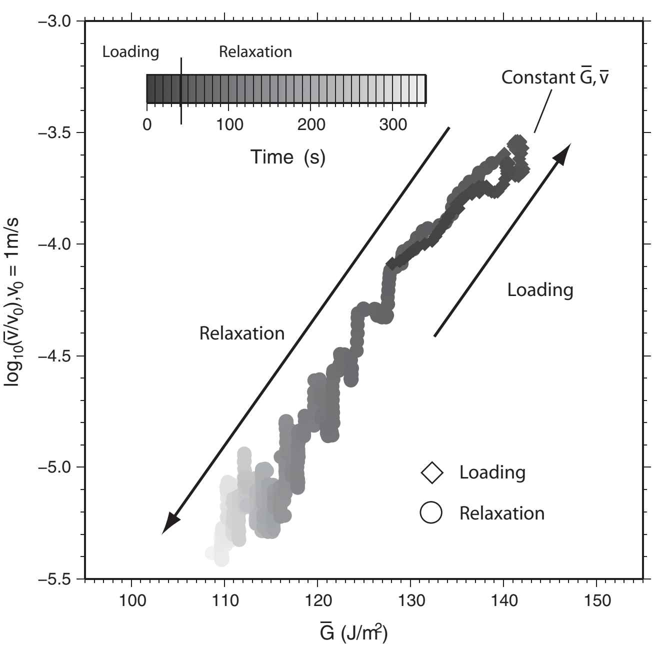

FIG. 5. Variation of the logarithm of the average crack-front velocity as a function of the average energy release rate during an experiment. The grayscale refers to time since the picture acquisition starts. Both loading regimes (constant loading velocity, diamonds, and relaxation regimes, circles) are included. We see the increase of $\bar{G}$ and $\bar{v}$ during the constant-loading-velocity regime, the stabilization of $\bar{G}$ while the front is propagating at almost constant speed, and the decrease of $\bar{G}$ and $\bar{v}$ during the relaxation process. The linear relationship between $\bar{G}$ and $\log_{10}(v)$ is observed during all these phases.

a linear relationship [$\ln(\bar{v})$ vs $\bar{G}$] is a reasonable proxy of the complete behavior of the experiment where the sample undergoes multiple loading cycles: first a constant-loading-velocity condition followed by a constant-deflection condition. We also notice that $\bar{G}$ is almost constant while the front velocity $\bar{v}$ reaches a nearly steady value. The linear relationship [$\ln(\bar{v})$ vs $\bar{G}$] is valid for all 13 experiments shown in Fig. 6. The horizontal shift in $\bar{G}$ between experiments results from variations of the fracture energy $\bar{G}_c$ from plate to plate. Large-scale variations of the fracture energy on a given plate are also expected. It results from the annealing process during sample preparation, since temperature, plate thickness, and normal load applied on the sample are not perfectly uniform and may vary among plates [50]. As $\bar{G}_c$ cannot be solely estimated from our experimental results (due to its coupling with χ), we set an arbitrary characteristic reference velocity in our experiments $v_{\rm ref}$ and searched for an estimate of a reference energy release rate $\bar{G}^{\rm ref} = \bar{G}(v_{\rm ref})$ for each experiment that provides the best superposition of all experimental curves [see Fig. 6(b)]. Following Eq. (3), we get

$$\ln(\bar{v}/v_{\rm ref}) = \frac{\alpha^2(\bar{G} - \bar{G}^{\rm ref})}{k_B T} \tag{9}$$

for each experiment. We set the reference velocity to 10^{-4} m/s, which is a typical order of magnitude of the crack-front velocity in our experiments. Although values of $\bar{G}^{\rm ref}$ depend on the particular choice of $v_{\rm ref}$, the variation of $\bar{G}^{\rm ref}$ among experiments remained constant regardless of the choice of $v_{\rm ref}$. We report values of $\bar{G}^{\rm ref}$ in Fig. 7. We used $k_B = 1.38 \times 10^{-23}$ J/K and $T = 300$ K and obtained the value of α by least squares fitting over all experiments: $\alpha = 2.5 \times 10^{-11}$ m. α is the characteristic length scale at which the elementary fracturing process is expected to occur. This implies that the rupture process is governed by mechanisms operating at the scale of the bond distance between atoms. This is consistent with the underlying physics of the Arrhenius law, where each individual degree of freedom in the system can break with a certain probability set by thermodynamics to be a Boltzmann distribution. These individual degrees of freedom probably correspond to individual molecules crossing through the weak interface.

The estimated reference energy release rate $\bar{G}^{\rm ref}$ has a median and mean of 133 and 137 J/m^2 respectively with 20% fluctuations (Fig. 7). Such a range of variation is compatible with sample preparation variability (plate thickness fluctuation, non-fully-homogeneous annealing procedure, sandblasting variability, etc.) and is also consistent with results obtained in [50]. Furthermore, variations of $\bar{G}^{\rm ref}$ are found to be small for experiments that are performed on the same PMMA plate and close to each other (i.e., consecutive experiments that were initiated just one after the other on a small region of the plate) but with significant differences when changing plates or exploring very different zones of the same plate [Fig. 6(a)]. It therefore suggests that the horizontal shift observed on Fig. 6(a) between experiments results from variations in $\bar{G}_c$.

Other relations linking the crack speed to the energy release rate have been proposed. These are (1) $\bar{v} \sim e^{-E' k_B T} G^{n/2}$ [15] and (2) transforming ΔG in (3) into $\Delta G^{-\mu}$, where the exponent μ arises from possible 3D paths taken by the crack

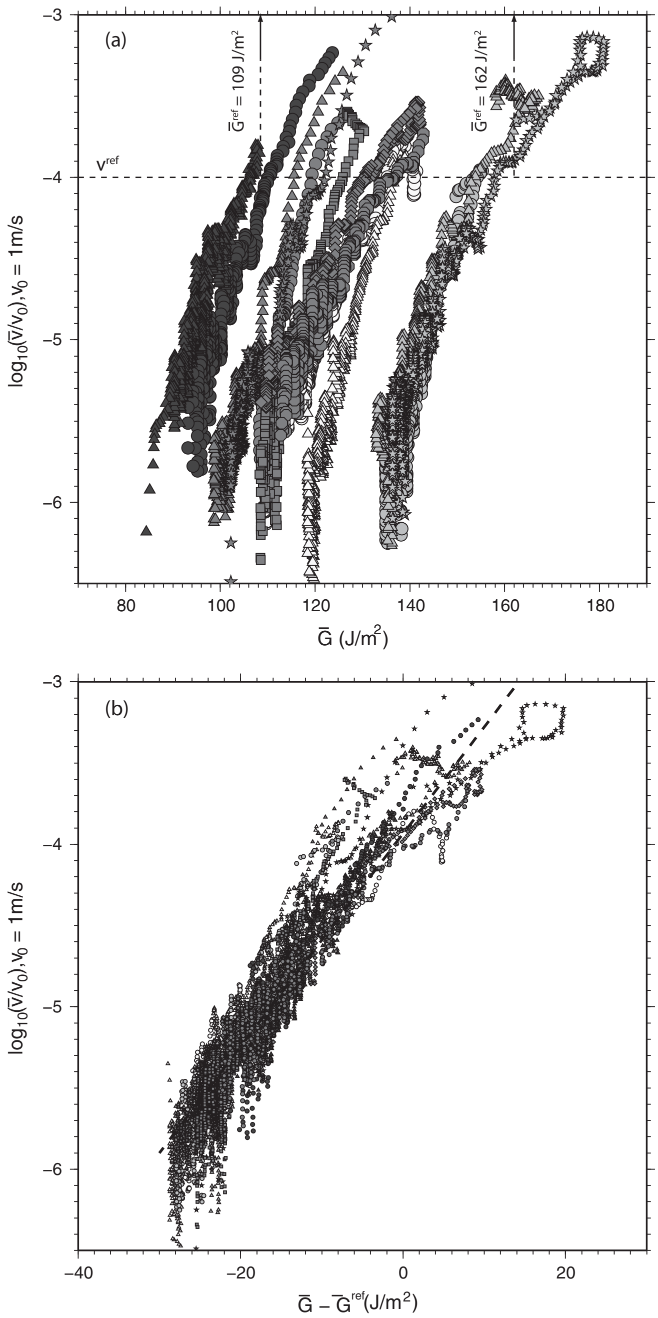

FIG. 6. (a) Variation of the logarithm of the average crack-front velocity as a function of the average energy release rate. All experiments are reported in this figure and are distinguished by gray levels and symbols. Similar gray levels indicate experiments performed in the same region of one specific plate (short separation distance between fracture onsets). The reference velocity v_{ref} used to estimate $\bar{G}^{\mathrm{ref}}$ is shown as a horizontal black line. Upper and lower bounds of $\bar{G}^{\mathrm{ref}}$ are indicated with arrows. (b) Superimposition of all experiments when plotted as a function of $\bar{G} - \bar{G}^{\mathrm{ref}}$. The dashed line represents the best-fitted model. The slope of this line is related to the value of α and is $\alpha^2/k_B T$.

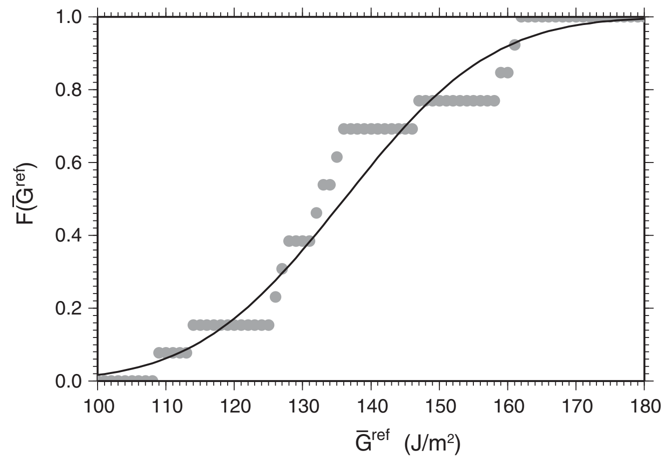

FIG. 7. Cumulative distribution function of the estimated values of $\bar{G}^{\mathrm{ref}}$ for all experiments (gray dots). Values are distributed between 109 and 162 J/m^2 with a mean of 137 J/m^2. The dark curve represents the expected cumulative distribution function for a normal distribution with similar mean and standard deviation as inferred from our experimental data.

[41,51]. Our experimental data do not allow us to discriminate among these different formulations. We consider the simple Arrhenius law introduced in Eq. (3), where the energy barrier is linearly related to the difference between G and G_c, a relevant model of the fracture process for our experiments. Indeed, it fits our experimental data over several orders of magnitude of average crack speed (Fig. 6).

V. NUMERICAL SOLUTIONS

We solve the Arrhenius law [Eq. (3)] with the prescribed loading and dependence of $\bar{G}$ on $\bar{a}$ and u [Eq. (8)] to obtain predictions of the evolution, for each experiment, of the front position, the loading force, and the energy release rate. This allows a second check on the validity of the activated energy mechanism to describe the crack-front propagation. Unfortunately, setting $u = V_l t$ or $u = \text{const}$ in Eq. (8) does not lead to analytical solutions. Therefore, we proceed to solve Eq. (8) numerically.

We first introduce a characteristic speed v_1 defined as

$$v_1 = \chi \exp\left(-\frac{\alpha^2 \bar{G}_c}{k_B T}\right) \tag{10}$$

$$= v_{\mathrm{ref}} \exp\left(-\frac{\alpha^2 \bar{G}^{\mathrm{ref}}}{k_B T}\right). \tag{11}$$

Then, we introduce dimensionless variables $\bar{a}' = \bar{a}/\lambda$ and $t' = t/\tau$ that transform Eq. (8) into a simpler form. In the *forced regime* we introduce

$$\lambda = \alpha \frac{V_l}{v_1}\left(\frac{3Eh^3}{8k_B T}\right)^{1/2}, \tag{12}$$

$$\tau = \frac{\lambda}{v_1}, \tag{13}$$

which lead to

$$\frac{d\bar{a}'}{dt'} = \exp\left(\frac{t'^2}{\bar{a}'^4}\right), \tag{14}$$

where $u = V_l t$.

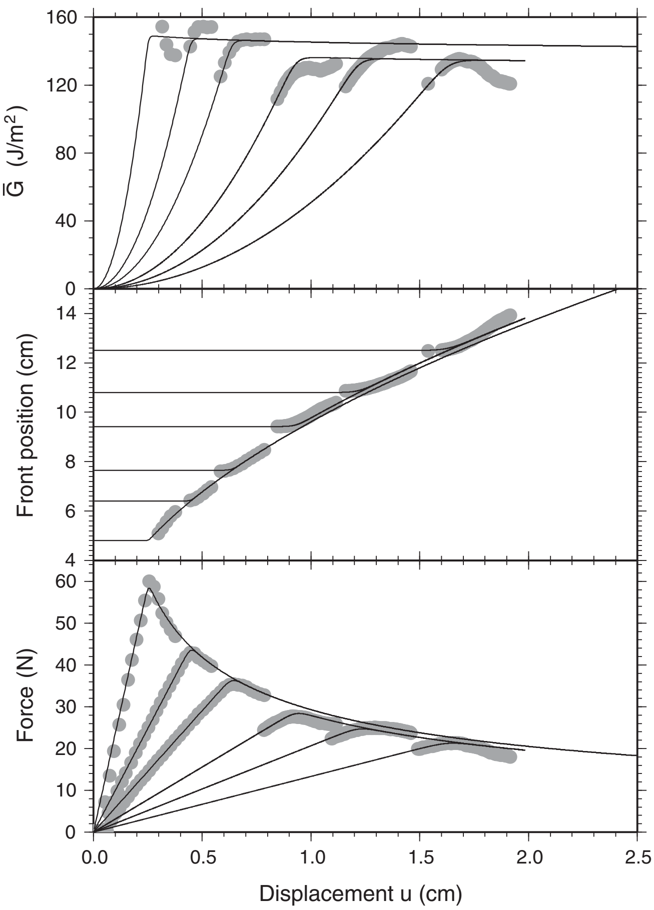

FIG. 8. Variation of force F, front position $\bar{a}$, and energy release rate $\bar{G}$ obtained during six experiments (gray points) carried out in the forced regime. The results of the numerical integration of Eq. (14) are drawn as black lines. The model captures most of the features observed in our experiments, such as the peak value of the force and its occurrence time. It also captures the appearance of a Griffith regime, i.e., the fact that $\bar{G}$ is close to constant at large enough crack speed.

We use Eq. (5) to compute the force from the front position. We numerically solve Eq. (14) using a simple Euler model with a constant time step. We found that the evolution of $\bar{a}$ and F can both be well reproduced as solutions of Eq. (14) when we set $\alpha = 2.5 \times 10^{-11}$ m and $\bar{G}^{\mathrm{ref}} = 152$ J/m^2. These values fall in the range of estimated parameters (Fig. 7) and represent acceptable results. We should note that α and $\bar{G}^{\mathrm{ref}}$ are not well constrained as they are highly correlated. A change in α can be balanced by a change in $\bar{G}^{\mathrm{ref}}$. The evolution of force, front position, and $\bar{G}$ along with numerical solutions of Eq. (14) are shown in Fig. 8 for six experiments. The loading velocity is $V_l = 310$ μm/s for the first three experiments and $V_l = 62$ μm/s for the remaining three experiments. The width of the plate is 2.84 cm and the Young modulus of the PMMA plate is $E = 3.2$ GPa. All solutions with a common loading velocity tend to align on the same curve after a sufficiently long time. This results from the common time dependence of Eq. (14) in all experiments with the same loading velocity. Differences arise from the variation of the initial front position at the start of the experiment. Our numerical model, resulting from the coupling of the cantilever beam configuration of our system and the activated energy mechanism necessary to describe the fracture process, is in good agreement with the evolution of the force, front position, and energy release rate (Fig. 8).

The integration of this thermal activation model with the large-scale elastic mechanics, over these characteristic time scales, with a constant velocity loading, leads to roughly constant values of $\bar{G}$ during the propagation: this means that the fact that $\bar{G} = constant$, i.e., a Griffith regime, results from the direct integration of this subcritical model with a proper forcing in the evaluation of $\bar{G}$.

The numerical model depends on the choice of several parameters (E,b,h) that are affected by uncertainties. It is possible to improve the fits to our data by varying these parameters within their uncertainty range. However, the discrepancy between the model and the data is small and could also be the result of second-order effects affecting the crack propagation (e.g., viscoelastic effects).

We now turn to the *relaxation regime* where the beam deflection is constant. We observe an evolution of the front position (Fig. 4) that is *a priori* not compatible with LEFM theory and the viscous rheology model as used in simulations, e.g., by Bonamy *et al.* [52], which assumed that the transition to zero propagation velocity of the front is sharp when the energy release rate is below the critical energy for fracture propagation (Griffith criterion, zero-temperature limit). We obtain the evolution of the crack front in this relaxation regime by setting $u_{\mathrm{stop}} = V_l t_{\mathrm{stop}}$ in Eq. (8) and solving the dimensionless differential equation:

$$\lambda = \left(\frac{3Eh^3\alpha^2 u_{\mathrm{stop}}^2}{8k_B T}\right)^{1/4}, \tag{15}$$

$$\tau = \frac{\lambda}{v_1}, \tag{16}$$

leading to

$$\frac{d\bar{a}'}{dt'} = \exp\left(\frac{1}{\bar{a}'^4}\right). \tag{17}$$

We keep the same estimate of α and $\bar{G}^{\mathrm{ref}}$, that we obtained in the constant-loading-velocity regime, when solving Eq. (17). We compare the results of the integration of Eq. (17) to the experimental observations shown in Fig. 2. The evolution of the force and front position obtained from the experimental data and from the numerical model are shown Fig. 9. The fit to the front position provided by the integration of Eq. (17) is in close agreement with the observations. We also fitted our numerical model to the long-lasting experiment (18 h of relaxation). As this experiment was performed on a different sample, we calculated $\bar{G}^{\mathrm{ref}}$ and α for this experiment. We obtained our best fit by setting $\alpha = 1.8 \times 10^{-11}$ m and $\bar{G}^{\mathrm{ref}} = 142 J/m^2$ (Fig. 9). Both force and front position are well reproduced by the numerical model [dark continuous line in Figs. 9(a) and 9(b)]. However, the front position departs from the computed position at long times [Fig. 9(b)]. This may imply that additional processes are taking place and affecting the front propagation or that some parameters, considered as constant, did actually vary over the course of this experiment, for instance temperature or the broad scale of the fracture toughness.

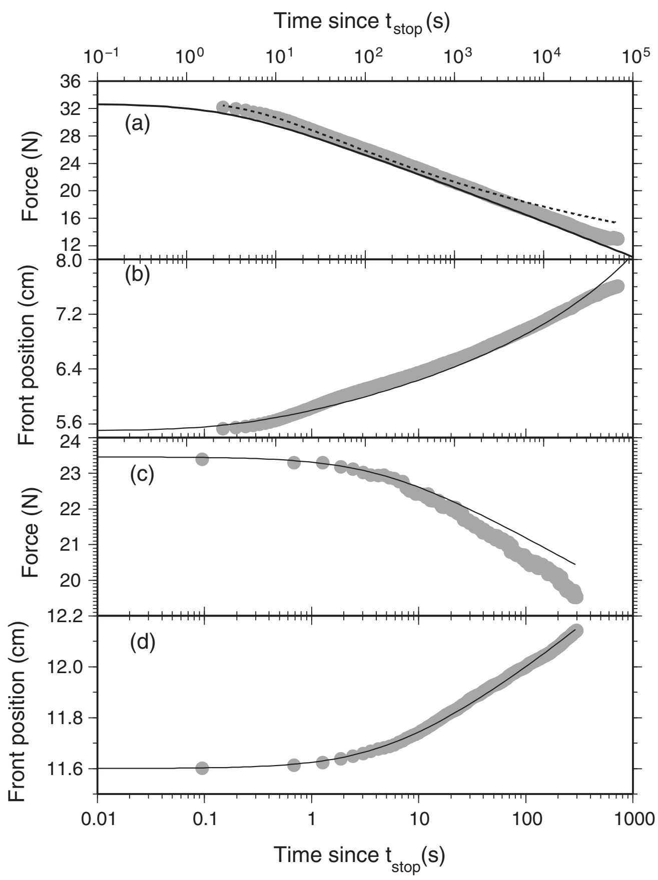

FIG. 9. Variation of force F and front position $\bar{a}$ obtained during the relaxation regime for the experiment displayed on Fig. 2 and for 5 min [gray dots, (c) and (d)]. Results of the numerical integration are represented as black line. Same representation is made for the experiments monitored for more than 18 h in the relaxation regime and is displayed in the two upper graphs [(a) and (b)]. The dashed line shows the evolution of force deduced from the fit of the front position from Eq. (1).

VI. DISCUSSION

Equation (8) governs the large-scale motion of the crack. Unfortunately, it has no analytical solutions for the two loading regimes of interest to our experiments. Nonetheless, we show that two simple approximations lead to analytical expressions of the front advance in close agreement with our experimental observations.

A. Constant-G approximation

Here we focus on the case where the energy release rate can be considered as constant: $\bar{G} = \text{const}$. This condition corresponds to a constant crack velocity $\bar{v} = \text{const}$ [Eq. (3)]. We clearly observe the propagation of the front reaching a quasiconstant velocity during the forced regime ($V_1 = \text{const} \neq 0$) after an initiation phase [Fig. 2(b)]. An initiation phase is expected as the front velocity cannot jump instantaneously from zero to its steady state value. To first order, the energy release rate $\bar{G}$ remains the same in the forced regime, $\bar{G} = G_0$, during the crack propagation.

For a constant energy release rate G, we derive from Eq. (7)

$$\bar{G} = \frac{3E\delta^3}{8}\frac{u^2}{\bar{a}^4} = G_0 = \text{const.} \tag{18}$$

Introducing $A = (\frac{3E\delta^3}{8G_0})^{1/4}$, we get

$$\bar{a}(u) = Au^{1/2}. \tag{19}$$

Therefore a constant energy release rate implies a scaling between the average front position $\bar{a}$ and the deflection u. In fact, Eq. (19) is of the form of the fit used in Fig. 3. It thus provides a physical basis to the empirical relation proposed to fit the data.

On the other hand, the result of Eq. (19) implies that $\bar{v}(t) \propto V_l/\bar{a}$ as $u \propto V_l t$ in the forced regime. The front velocity decreases at constant G as the crack front advances. However, as $\bar{a}$ is small around the initial front position for each incremental experiment along the same sample, $\bar{v}$ is small as well. Finally, it is noticeable in Fig. 8 that the experimental evolution of the energy release rate $\bar{G}$ is almost constant for the entire duration of the investigated range after an initiation period well reproduced by the complete numerical integration of the Arrhenius law [Eq. (8)]. This is also in agreement with the hypothesis of $\bar{G} = \text{const}$ in this forced regime.

B. First-order approximation of G

Now we focus on characterizing the relaxation process ($t > t_{\text{stop}}$). We recall that the loading velocity is zero ($V_l = 0$ for $t > t_{\text{stop}}$) during this time interval. The force decreases with time while the average position of the front continues to increase in a logarithmic fashion (Figs. 2 and 4). We analyze a first-order approximation of the solution assuming that $\bar{a}(t)$ is small in this relaxation regime. We derive a first-order expansion of $\bar{G}$ around some position $\bar{a}_0 = \bar{a}(t_{\text{stop}})$:

$$\bar{G} = G_0 + \frac{d\bar{G}(\bar{a}_0)}{d\bar{a}}(\bar{a} - \bar{a}_0), \tag{20}$$

where $G_0 = \bar{G}(\bar{a}_0)$ and $\frac{d\bar{G}(\bar{a}_0)}{d\bar{a}}$ can be computed from Eq. (7) as

$$\frac{d\bar{G}(\bar{a}_0)}{d\bar{a}} = -\frac{4G_0}{\bar{a}_0}. \tag{21}$$

Replacing (20) and (21) into Eq. (3), we obtain

$$\bar{v} = \chi' \exp\left(-\frac{4\alpha^2 G_0 \bar{a}}{\bar{a}_0 k_B T}\right) \tag{22}$$

with $\chi' = \chi \exp(\alpha^2 \frac{-\bar{G}_c + 5G_0}{k_B T})$. The above equation integrates to

$$\bar{a}(t) = \frac{k_B T \bar{a}_0}{4\alpha^2 G_0} \ln\left[\frac{4\chi' G_0 \alpha^2}{k_B T \bar{a}_0}(t - t_0) + \exp\left(\frac{4G_0\alpha^2}{k_B T}\right)\right], \tag{23}$$

where t_0 and $\bar{a}_0$ are the lower integration limits, corresponding to the initial time and position, respectively, where we consider the creep conditions to apply. The above expression can be simplified by setting $H_0 = \frac{(5G_0 - \bar{G}_c)\alpha^2}{k_B T}$, $\beta = \frac{5G_0 - \bar{G}_c}{4G_0}$, and introducing the characteristic time $t^* = \frac{\beta \bar{a}_0}{H_0 \chi} \exp[-H_0(1 - 1/\beta)]$. This yields

$$\bar{a}(t) - \bar{a}_0 = \frac{\bar{a}_0 \beta}{H_0} \ln\left[\frac{t - t_0}{t^*} + 1\right]. \tag{24}$$

At large times, when $t - t_0 \gg t^*$, the above equation reduces to

$$\bar{a}(t) - \bar{a}_0 \approx \frac{\bar{a}_0 \beta}{H_0} \ln\left(\frac{t - t_0}{t^*}\right), \tag{25}$$

$$\bar{v}(t) \approx \frac{\bar{a}_0 \beta}{H_0} \frac{1}{t - t_0}. \tag{26}$$

Logarithmic relaxation has also been observed in granular media [21]. In rock mechanics, Scholz [16] developed a simple model of creep in heterogeneous media where the collective behavior resulting from local decreases of strength leads to a similar $\propto t^{-1}$ evolution of the deformation rate during the creep regime. The functional form of Eq. (24) is similar to that of Eq. (1) used to describe the evolution of the front in this relaxation regime (Fig. 4). It implies that Eq. (24) also provides a good description of the data and that our first-order approximation is valid in the range investigated in our experiments.

VII. CONCLUSIONS

We explored the average velocity of an interfacial crack under two different loading conditions. These are (1) a forced regime with imposed constant loading velocity and (2) a relaxation regime. Both conditions induce crack velocities much lower than the Rayleigh wave velocity of the material. As often observed for homogeneous or weakly heterogeneous materials, the constant-speed loading regime is compatible with a constant energy release rate, and the relaxation regime is compatible with a logarithmic deformation. The macroscopic evolution of the crack front is smooth and continuous, characteristic of creep processes. This is opposite to what is observed and modeled at the local scale, namely, an intermittency of the fracture process described by a succession of local discrete brittle failures [8,30]. Such "brittle-creep" behavior has been extensively studied in rocks where acoustic emissions are recorded during the otherwise slow global deformation of the sample (e.g., [16,41,53]) or in other materials like paper [12,42,54].

We developed a thermally activated fracture model that consists of a set of independent microscopic sites that break according to an Arrhenius law. The energy barrier is assumed to be a function of the difference between the local energy release rate G and the local critical energy release rate G_c. We show for independent microscopic sites in time and space that the model reduces to 1D where the crack tip advance is controlled by the difference between the average energy release rate $\bar{G}$ and the average critical energy release rate $\bar{G}_c$. The model describes the fracturing process in the subcritical regime as a mechanism sensitive only to the applied stress on the crack tip and the effective toughness of the material. It allows the crack propagation to be driven below the critical energy release rate by statistical stress fluctuations that trigger rupture at the scale of atomic bonds. The typical length scale of the process is on the order of picometers, in agreement with values reported by Ponson [41] for rock samples and by Santucci *et al.* [42] for paper. This suggests that the creeping mechanism we observe is related to breakage at the typical length scale of atomic bonds and that stress fluctuations can trigger rupture of these atomic bonds. The length scale of this process, a few 10^{-11}–10^{-10} m, is much smaller than the correlation length scale of the toughness heterogeneity of the material, typically on the order of the glass bead size used during sample preparation blasting (1×10^{-4} –5×10^{-4} m) [50,55].

All experimental data of the macroscopic evolution of the crack are well explained by the proposed subcritical mechanism despite the different tested loading conditions. Neglect of this temperature effect does not give a correct description of the crack propagation in a constant-deflection regime during relaxation tests. Moreover, several factors that would possibly influence the progression of the crack have been disregarded. They include possible finite mechanical rotation of the plate, viscoelastic flows inside the bulk of the PMMA plate like microbubbles, or chemical processes. The thermally activated model we propose clearly reproduces the evolution of the front during experiments over a large range of time scales (from 10^{-1} to more than 10^4 s) and different loading paths, at least when the average advance of the front, $\bar{a}$, is small compared to its initial position. Therefore, neglected mechanisms have second-order effects on the crack evolution compared to the stress-induced creeping mechanism.

We reproduce the large-scale evolution of the front propagation despite a simple description of the heterogeneous nature of the material. The macroscopic behavior of the interface with spatially fluctuating toughness induced by the sandblasting procedure is represented by an average quantity. This might be due to the limited heterogeneity of the toughness when seen at a centimeter scale, as evidenced by the almost flat geometry of the crack front line (we never observed crack-front distortions bigger than 10% of the system scale). Although heterogeneities are present and are encountered during the crack propagation, the macroscopic scale evolution is well described by the average energy release rate, an average quantity among all local sites. Such large-scale information appears sufficient to predict the overall large-scale dynamics of the propagating crack under various loading regimes.

ACKNOWLEDGMENTS

We acknowledge Alain Steyer for technical support. The project was supported by a French ANR RiskNat SUPNAF grant, by a CNRS French-Norwegian PICS, and by the INSU CESSUR program. J.E.E. was supported by the Caltech Seismological Laboratory. K.J.M. was partly supported by a visiting grant from Strasbourg University.

APPENDIX

In our configuration, the force applied on the plates is mostly tangential to the plates, which contributes to reduce mode II loading: this is achieved by applying the force at the free end of the bent plate with a freely rotating rod (using ball bearings). Furthermore, the rod is made of polyamide PA 6.6 (nylon) and thus has a low friction coefficient. It ensures that minimum shear forces are actually applied on the bending plate

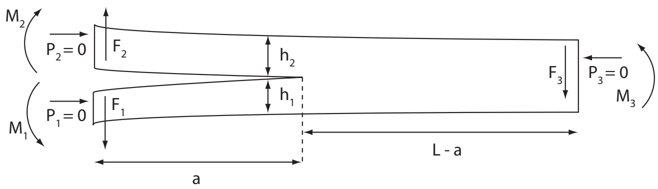

FIG. 10. General configuration of bent plates, adapted from [56] to the configuration used in this work.

and thus limits the existence of mode II fracture component in our experiments.

Even though this tangential force at the free end of the beam is reduced, the loading asymmetry in our configuration, and the unequal thickness of the two plates, may induce some mode II component at the crack tip. This can be precisely evaluated by following the development detailed below. Following the general formulation presented in [56] for a nonsymmetric beam configuration, based on the evaluation of the J integral in a general two-plate configuration, we can calculate precisely the values of the forces per unit length applied on the ends of the plates both normal to the plates, F_1, F_2, and F_3, and tangential, P_1, P_2, and P_3, as well as the torques per unit length with respect to the tip, M_1, M_2, and M_3; see Fig. 10.

The design of the setup guarantees that the tangential components are minimal with respect to the normal ones: we will consider that $P_1 = P_2 = P_3 = 0$. The distance between the tip and the rod being denoted $\bar{a}$, and $F_l = F/b$ the force exerted on the lower plate (F is the total force, and b the plate width; hence the force per unit length is $F_l = F/b$), one writes $F_1 = F_l$, and the torque on the lower plate is $M = M_1 = F_l\bar{a}$. The torques on the upper plate and on the opposite end are $M_2 = F_2\bar{a}$ and $M_3 = F_3(L-\bar{a})$, where L is the plate length. The equilibrium between the forces ensures that $F_1 = F_2 - F_3$, and the one between the torques (nonrotation of the plates) that $M_1 = M_2 + M_3$. Hence, we have

$$F_2 - F_3 = F_l, \tag{A1}$$

$$F_2\bar{a} + F_3(L-\bar{a}) = F_l\bar{a}, \tag{A2}$$

which leads to

$$F_3 = 0, \quad F_2 = F_1 = F_l, \quad M_2 = M_1 = M = F_l\bar{a}.$$

From Eq. (3.7) in Hutchinson and Suo [56] this allows us to obtain separately the values of the stress intensity factors K_I and K_{II} in order to evaluate their relative importance. From the general asymmetric beam configuration and applying the particular boundary condition imposed in our system, we get with the thicknesses of the two plates, $h_1 = 0.5$ cm and $h_2 = 1$ cm, the ratio $\eta = h_1/h_2 = 0.5/1 = 0.5$, and the constants, evaluated from [56],

$$\sin(\gamma) = (6\sqrt{UV})\eta^2(1+\eta), \tag{A3}$$

$$1/V = 12(1+\eta^3), \tag{A4}$$

$$1/U = 1 + 4\eta + 6\eta^2 + 3\eta^3, \tag{A5}$$

$$\omega = 52.1^\circ - 3^\circ\eta, \tag{A6}$$

which leads to

$$V = 0.074, \tag{A7}$$

$$U = 0.21, \tag{A8}$$

$$\gamma = 16^\circ, \tag{A9}$$

$$\omega = 51^\circ. \tag{A10}$$

With these constants, the general formula Eq. (3.7) in [56] reduces to

$$K_I = \frac{\bar{a}F_l}{\sqrt{2h_1^3 V}}\sin(\omega+\gamma), \tag{A11}$$

$$K_{II} = -\frac{\bar{a}F_l}{\sqrt{2h_1^3 V}}\cos(\omega+\gamma). \tag{A12}$$

This yields an estimate of

$$K_{II}/K_I = 0.43.$$

It thus implies that the mode II component is not negligible in our problem. Taking into account the details of this asymmetry leads to the formulation of the energy release rate $\bar{G}$ for a propagation of the crack at the interface between the two plates in our system, in mixed mode. The energy release rate does not separate the rupture modes, which present a similar dependence on $\bar{a}$. The fact that the fracture propagates along the interface is due to a combination of factors: First, K_{II} remains smaller than K_I, which does not favor an out-of-plane branching of the crack. Next, the toughness K_c is smaller along the interface than anywhere else in the bulk of the plates, due to the preparation of the samples, for both modes I and II. It thus favors a propagation of the crack along the interface, as is indeed observed.

Following the general formulation from [56] [or directly from their Eq. (3.6)], the energy release rate per unit length in our system is thus

$$\bar{G} = \bar{G}_I + \bar{G}_{II} \tag{A13}$$

$$= \left(K_I^2 + K_{II}^2\right)/E \tag{A14}$$

$$= \frac{M^2}{2Eh_1^3 V}[\sin^2(\omega+\gamma) + \cos^2(\omega+\gamma)] \tag{A15}$$

$$= \frac{F_l^2\bar{a}^2}{2Eh_1^3}\left[12\left(1 + h_2^2/h_1^2\right)\right] \tag{A16}$$

$$= \frac{6F_l^2\bar{a}^2}{Eh^3}, \tag{A17}$$

where h^3 is defined as

$$\frac{1}{h^3} = \frac{1}{h_1^3} + \frac{1}{h_2^3} \tag{A18}$$

and h_1 and h_2 are respectively the thicknesses of the bottom and the upper plate. This then yields

$$G = \frac{6F^2\bar{a}^2}{Eh^3b^2} = \frac{1}{b}\frac{dU_E}{d\bar{a}}, \tag{A19}$$

which has the opposite sign to Eq. (4) because

$$\left.\frac{dU_E(F)}{d\bar{a}}\right|_F = -\left.\frac{dU_E(u)}{d\bar{a}}\right|_u$$

[4]. Integration of the previous expression shows that

$$U_E = \frac{2F^2\bar{a}^3}{Ebh^3}, \tag{A20}$$

and since due to linear elasticity, the stored elastic energy is

$$U_E = Fu/2,$$

it leads to

$$u = \frac{4F\bar{a}^3}{Eh^3b}, \quad F = \frac{Eh^3bu}{4\bar{a}^3}, \tag{A21}$$

so that

$$\bar{G} = \frac{3u^2Eh^3}{8\bar{a}^4}. \tag{A22}$$

If one used instead an estimate of $\bar{G}$ based on a pure mode I, symmetric loading hypothesis, one would get

$$\bar{G} = \frac{3u^2Eh_1^3}{8\bar{a}^4}. \tag{A23}$$

Taking into account this asymmetry thus leads to a change in the estimate of $\bar{G}$ by a factor

$$\rho = \frac{h_1^3 + h_2^3}{h_2^3}. \tag{A24}$$

As $h_1 = 5$ mm and $h_2 = 1$ cm in our experiments, it then yields $\rho = 1.125$.

[1] B. K. Atkinson, *Fracture Mechanics of Rocks* (Academic Press, San Diego, 1991).
[2] E. Schulson and P. Duval, *Creep and Fracture of Ice* (Cambridge University Press, Cambridge, 2009).
[3] I. Smith, E. Landis, and M. Gong, *Fracture and Fatigue in Wood* (John Wiley & Sons, New York, 2003).
[4] T. L. Anderson, *Fracture Mechanics—Fundamentals and Applications*, 2nd ed. (CRC Press, Boca Raton, FL, 1995).
[5] B. Lawn, *Fracture of Brittle Solids*, 2nd ed. (Cambridge University Press, Cambridge, 1993).
[6] L. Freund, *Dynamic Fracture Mechanics* (Cambridge University Press, Cambridge, 1990).
[7] J. Fineberg and M. Marder, Phys. Rep. **313**, 1 (1999).
[8] D. Bonamy, J. Phys. D **42**, 214014 (2009).
[9] D. Unger, *Analytical Fracture Mechanics* (Dover, New York, 1995).
[10] J. R. Rice, J. Mech. Phys. Solids **26**, 61 (1978).
[11] L. D. Landau and Lifshitz, *Statistical Physics, Part 1*, 3rd ed. (Pergamon, Oxford, 1980).
[12] L. Vanel, S. Ciliberto, P.-P. Cortet, and S. Santucci, J. Phys. D **42**, 214007 (2009).
[13] S. W. Freiman, J. Geophys. Res. **86**, 4072 (1984).
[14] S. M. Wiederhorn and L. H. Bolz, J. Am. Ceram. Soc. **53**, 543 (1970).
[15] R. J. Charles, J. Appl. Phys. **29**, 1549 (1958).
[16] C. H. Scholz, J. Geophys. Res. **73**, 3295 (1968).
[17] E. Favier, V. Lazarus, and J.-B. Leblond, in *Modern Practice in Stress and Vibration Analysis 2003 (MPSVA2003), Glasgow*, edited by M. S. Forum (Trans Tech Publications, Zurich, 2003), Vol. **440-441**, pp. 153–160.
[18] N. Pindra, V. Lazarus, and J.-B. Leblond, J. Mech. Phys. Solids **58**, 281 (2010).
[19] V. Lazarus, J. Mech. Phys. Solids **59**, 121 (2011).
[20] S. N. Zhurkov, Int. J. Fract. Mech. **1**, 311 (1965).
[21] R. R. Hartley and R. P. Behringer, Nature (London) **421**, 928 (2003).
[22] L. Bocquet, E. Charlaix, S. Ciliberto, and J. Crassous, Nature (London) **396**, 735 (1998).
[23] G. Løvoll, K. J. Måløy, and E. G. Flekkøy, Phys. Rev. E **60**, 5872 (1999).
[24] M. Sahimi, *Heterogeneous Materials II: Nonlinear and Breakdown Properties and Atomistic Modeling* (Springer-Verlag, New York, 2003).
[25] W. Weibull, J. Appl. Mech. **18**, 293 (1951).
[26] Z. Bažant, *Scaling of Structural Strength*, 2nd ed. (Butterworth-Heinemann, London, 2005).
[27] J. Obreimoff, Proc. R. Soc. London **127**, 290 (1930).
[28] J. Schmittbuhl and K. J. Måløy, Phys. Rev. Lett. **78**, 3888 (1997).
[29] A. Delaplace, J. Schmittbuhl, and K. J. Måløy, Phys. Rev. E **60**, 1337 (1999).
[30] K. J. Måløy, S. Santucci, J. Schmittbuhl, and R. Toussaint, Phys. Rev. Lett. **96**, 045501 (2006).
[31] K. T. Tallakstad, R. Toussaint, S. Santucci, J. Schmittbuhl, and K. J. Måløy, Phys. Rev. E **83**, 046108 (2011).
[32] H. Gao and J. R. Rice, J. Appl. Mech. **56**, 828 (1989).
[33] J. Schmittbuhl, S. Roux, J.-P. Vilotte, and K. J. Måløy, Phys. Rev. Lett. **74**, 1787 (1995).
[34] S. Ramanathan and D. S. Fisher, Phys. Rev. B **58**, 6026 (1998).
[35] S. R. Pride and R. Toussaint, Physica A **312**, 159 (2002).
[36] R. Toussaint and S. R. Pride, Phys. Rev. E **71**, 046127 (2005).
[37] J. Schmittbuhl, A. Hansen, and G. G. Batrouni, Phys. Rev. Lett. **90**, 045505 (2003).
[38] M. Alava, P. Nukalaz, and S. Zapperi, Adv. Phys. **55**, 349 (2006).
[39] S. Pradhan, A. Hansen, and B. Chakrabarti, Rev. Mod. Phys. **82**, 499 (2010).
[40] M. Grob, J. Schmittbuhl, R. Toussaint, L. Rivera, S. Santucci, and K. J. Måløy, Pure Appl. Geophys. **166**, 777 (2009).
[41] L. Ponson, Phys. Rev. Lett. **103**, 055501 (2009).
[42] S. Santucci, L. Vanel, and S. Ciliberto, Phys. Rev. Lett. **93**, 095505 (2004).
[43] A. Saichev and D. Sornette, Phys. Rev. E **71**, 016608 (2005).
[44] P. Cortet, L. Vanel, and S. Ciliberto, Europhys. Lett. **74**, 602 (2006).
[45] Z. Bažant and S. Pang, J. Mech. Phys. Solids **55**, 91 (2007).
[46] R. Toussaint and S. R. Pride, Phys. Rev. E **66**, 036135 (2002).
[47] R. Toussaint and S. R. Pride, Phys. Rev. E **66**, 036136 (2002).
[48] R. Toussaint and S. R. Pride, Phys. Rev. E **66**, 036137 (2002).
[49] R. Toussaint and A. Hansen, Phys. Rev. E **73**, 046103 (2006).
[50] O. Lengliné, J. Schmittbuhl, J. Elkhoury, J.-P. Ampuero, R. Toussaint, and K. J. Måløy, J. Geophys. Res. **116**, B08215 (2011).
[51] A. B. Kolton, A. Rosso, and T. Giamarchi, Phys. Rev. Lett. **94**, 047002 (2005).
[52] D. Bonamy, S. Santucci, and L. Ponson, Phys. Rev. Lett. **101**, 045501 (2008).

[53] B. K. Atkinson, J. Geophys. Res. **89**, 4077 (1984).

[54] S. Santucci, L. Vanel, and S. Ciliberto, Eur. Phys. J Spec. Top. **146**, 341 (2007).

[55] S. Santucci, K. J. Måløy, R. Toussaint, and J. Schmittbuhl, in *Dynamics of Complex Interconnected Systems: Networks and Bioprocesses*, edited by A. T. Skjeltorp and A. V. Belushkin, NATO Science Series II: Mathematics, Physics and Chemistry Vol. 232 (Springer, Dordrecht, 2006), pp. 49–59.

[56] J. W. Hutchinson and Z. Suo, *Advances in Applied Mechanics* (Academic Press, New York, 1992), Vol. 29, pp. 63–191.

Dynamics and structure of interfacial crack front

Knut Jørgen Måløy[1], Renaud Toussaint[1], and Jean Schmittbuhl[2]
[1]Department of Physics, University of Oslo, P.O.Box 1048 Blindern, N-0316 Oslo, Norway.
[2]Laborato1re de Geologie, UMR 8538 Ecole Normale Superieure,
24 rue Lhomond, 75231 Paris Cedex 05, France

ABSTRACT

The propagation of an interfacial crack front through a weak plane of a transparent Plexiglas block has been studied experimentally. A stable crack in mode I was generated by loading the system by an imposed displacement. The local velocities of the fracture front line have been measured by using an high speed CCD camera. The distribution of the velocities exhibits a power law behavior for velocities larger than the average front velocity <v> with a crossover to a slowly increasing function for velocities lower than <v>. The fluctuations in the velocities reflect an underlying irregular bursts activity with a power law distribution of the bursts. We further found that the size of the local bursts scales differently in the direction parallel to and perpendicular to the fracture front.

1 INTRODUCTION

The propagation of a crack front through a heterogeneous solid is a central question for numerous mechanical problems. The scaling properties of the morphology of brittle cracks manifest themselves through self-affine [1-2] long range correlations [1-11] with a roughness exponent which is found to be very robust for different materials and a broad range of length scales [3-9]. In order to shed light on both the dynamics, the structure and the “universality” [4] of the roughness exponent a simpler problem than the original 3D one has been devised [10-11]. This problem is simpler because the crack front is constrained geometrically to lie in the plane and is driven by the stress field transmitted through two elastic plates. So far most experiments on fracture front lines have been focused on the morphology of the fracture front and less on the detailed dynamic. Recent experimental studies of the in plane fracture problem presented here gave the estimate of the roughness exponent $\zeta=0.55\pm0.05$ [10], and was followed up by a longer study leading to the estimate $\zeta=0.63\pm0.03$ [12]. A recent study of the motion of a helium-4 meniscus along a disordered substrate - a problem related to the motion of the crack line - gave $\zeta=0.56\pm0.03$ [12]. In contrast to the experiments presented here most experiments are performed with instable fractures which exhibit fast propagation with a speed of the order of the speed of sound and a direct observation of the detailed crack front line is usually impossible. The focus of this work is to study the local dynamics of the fracture propagation. The front has in recent work [13] been found to exhibit a Family-Vicksek scaling [14] with a roughness exponent $\zeta=0.63$ and a dynamic exponent $\kappa=1.2$. The results are consistent with recent quasi static simulations [15-16] and with an elastodynamic description [17-18]. In this work we went further on in the study of the local dynamics. We show that the movement of the fracture is controlled by local bursts and that the velocity distribution exhibits a power law behavior with a characteristic speed equal the average front velocity <v>. The dependence of the velocity distribution on the rescaled velocity v/<v> is independent on the average velocity <v> for all experiments (<v> is ranging from 0.36μm/s to 40μm/s). The burst distribution in space was further measured and we found that the size of the bursts scales differently in the normal and the tangential direction to the crack front line.

2 EXPERIMENTAL PROCEDURE

Samples were made of transparent polymethylmethacrylate (PMMA) which makes the fracture front directly observable because of the transparency of the material [10-11]. Each sample was obtained by annealing two plates of dimension 32cm × 14cm × 1cm and 34cm × 12cm × 0.4cm together at 205^{o}C. Both plates were sand blasted on one side with 50μm steel beads before the annealing. The sand-blasting procedure introduces a randomness in the annealed surface with a cutoff in the structure on a length scale of about 50μm. We don't expect correlations in the toughness fluctuations above this length scale. The annealed surface corresponds to a weak surface which the fracture front line will propagate along. The 1cm thick plate was clamped to a stiff aluminum frame and a normal displacement was applied on boundary on the short side of the 0.4 cm thick plate. The fracture front line was observed by a microscope linked to a high speed Kodak Motion Korder Analyzer camera which records up to 500 images per second with a spatial resolution of 512×240 pixels. The experiment was performed with an average front line speed ranging from 0.36μm/s to 40μm/s. In total 8 different experiments were performed with 4367 images which gives all together 34936 fracture front lines to be analyzed.

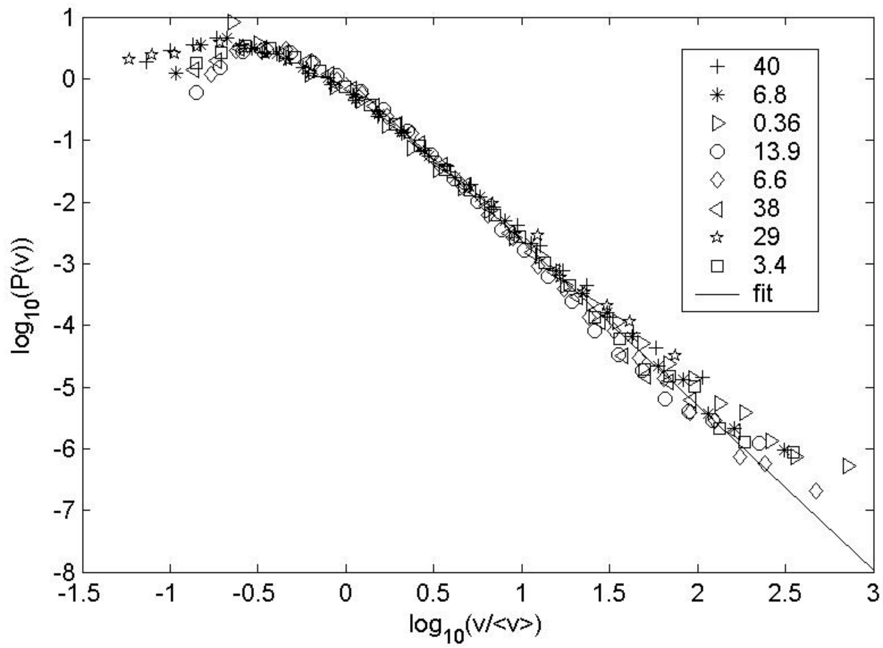

Figure 1: The velocity distribution P(v) as function of v/<v>. The solid line represents a fitting to all data for v > <v> to a linear function and has a slope -2.67. The number inserted in the figure indicates the average speed <v> in μm/s.

The fracture front lines extracted from the digital images were added to obtain a waiting time matrix **M.** The matrix **M** has the same dimension as the images and an initial value equal to zero for all its elements. The addition of the front line to the matrix was performed by adding 1 to the matrix in the positions corresponding to the front line positions. This procedure was done for all 4367 images in the experiment to obtain the final waiting time matrix **M** for each experiment. The local normal speed of the interface at the time when the front went through a particular position is found by the inverse value of the corresponding matrix element of **M** multiplied by K, where K is the ratio between the linear size of the pixel (typical 10μm) and the time between each picture (typical 0.002s). Let **V** the image matrix representing the local speeds. It is important to mention that the image recording was performed so fast that there was basically no holes in the waiting time matrix **M** with value equal to zero (apart from below the first front and above the last front, and some few artifacts due to impurities in the sample). The **V** matrix allows to associate to each pixel representing the front in each image an estimated front velocity v=K/m (where m is an integer). For each possible measured velocity v=K/m, the probability of v is estimated as the occurrence number of this velocity over all pixels in all front images.

3. RESULTS

The velocity distribution P(v) is shown in Fig.1 as function of v/<v> where <v> is the average speed of the fracture front line for the corresponding experiments. A satisfying data collapse is obtained by scaling the local velocity v with the average velocity <v>. A power law behavior of the velocity distribution $P(v) \propto (v/\langle v\rangle)^{-\eta}$ is apparent for velocities larger than <v> with a crossover at low velocities to a slowly increasing function for velocities lower than <v>. The solid line, obtained from a linear fit to the experimental data for v/<v> >1 has a slope $-\eta=-2.67\pm0.10$.

Figure 2: The image shows the distribution of bursts of size s in white for C=10 and an average velocity <v>=29μm/s.

The power law tail in the velocity distribution indicates a non trivial underlying dynamics. This dynamics can also be observed by visual inspection of the fast video recording where irregular jumps occur on all length scales. To analyze the burst activity we will consider the velocity matrix **V**. A clipped matrix was generated from **V** by setting the elements equal to one for v>C<v> and zero elsewhere. Fig. 3 shows the dependence of the distribution N(s) on the connected clusters of size s in the clipped matrix for different values of C. We find a stable result for the distribution for a wide range of C values 4<C<14. A fit of the experimental data to a linear function, gives a slope -1.89±0.10. Assuming a power law behavior $N(s) \propto s^{-\gamma}$ this gives $\gamma=1.89$. As seen in Fig. 2 the typical width of the trapped islands s in the direction normal to the front are limited by the characteristic width of the fracture front line. However the width of the islands l_1 in the direction parallel to the front are typical larger than their width l_2

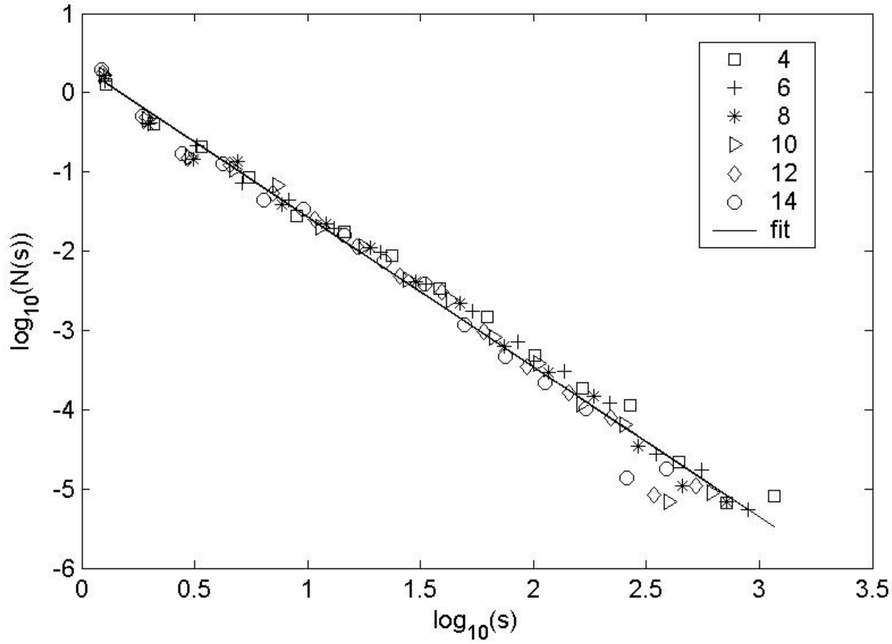

Figure 3: The distribution N(s) for different clip levels averaged over all eight experiments. The numbers inserted in the figure are the clip levels C. The solid line is a linear fitting to the data points and has a slope -1.89.

normal to the front. Since the fracture front is self-affine we want to check if the individual clusters exhibit the same scaling. Fig.4 shows the two distributions $n(l_1)$ and $n(l_2)$ for different clip levels C. The experimental data for both curves are consistent with power laws $n(l_1)\propto l_1^{-\alpha}$ and $n(l_2)\propto l_2^{-\beta}$. Linear fitting of the data gives $\alpha=2.3\pm0.1$ and $\beta=2.5\pm0.1$ respectively. If in addition if the self affinity of the front leads to a scaling relationship $l_2\propto l_1^{\zeta}$, $n(l_1)dl_1=n(l_2)dl_2$ imply the following scaling law:

$$\alpha= \zeta(\beta-1)+1 \qquad (1)$$

By using the fitted results of α and β we find $\zeta=0.86\pm0.20$ which is somewhat higher but consistent with the roughness exponent 0.63 of the fracture front line [11]. The size of an island might as a zero order approximation be written as $s=l_1l_2$. Since s,l_1 and l_2 depend on each other we may assume $n(s)ds=n(l_1)dl_1=n(l_2)dl_2$. From this assumption follows the following scaling law between α,β and γ.

$$\gamma=(1+\beta \zeta)/(1+ \zeta)= (\alpha+ \zeta)/(1+ \zeta)=(\alpha\beta-1)/(\alpha+\beta-2) \qquad (2)$$

By using the measured values of α and β we find $\gamma=1.70\pm0.20$. This value is consistent with the value $\gamma=1.89\pm0.10$ measured directly from the burst size distribution N(s).

4. CONCLUSION

The fast dynamics at small scales are very different from the apparent dynamics at large scales characterized with a smooth creeping motion. We show in this work that the

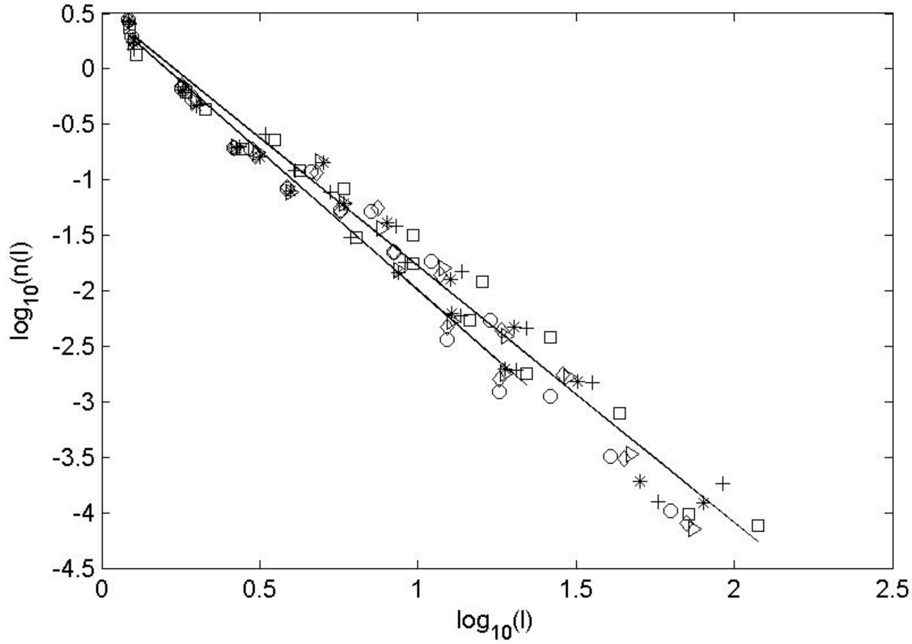

Figure 4:The upper and lower curve shows the distribution $n(l_1)$ and $n(l_2)$ respectively averaged aver all eight experiments. The solid lines are fitting to a linear curves and has slopes -2.5 and -2. 3 respectively. The different symbols reflect the same clip levels as the insert in Fig. 3.

dynamics is controlled by an irregular burst activity with bursts of size s on all length scales but limited by the total width of the fracture front line. The bursts activity has a power law like distribution with an exponent γ=1.89. The lengths l_1 and l_2 of the burst s parallel and normal to the average front line are linked through $l_2 \infty l_1^{\zeta}$ with an exponent ζ consistent with the roughness exponent of the fracture front line. More experiments is however needed to be conclusive on this point due to the uncertainty in the data. The velocity distribution of the fracture front exhibit a nice data-collapse when plotted as function of v/<v> and with power law behavior when v><v> with an exponent η=2.67. A correct modeling of this problem should in addition to give the correct roughness exponent ζ also predict the exponent η and γ found in these experiments.

References

[1] B. B. Mandelbrot, *The fractal geometry of nature,* (W. H. Freeman New York). (1983)
[2] B. B. Mandelbrot, D. E. Passoja, and A. J. Paullay. Nature, **308,** 721, (1984)
[3] S. R. Brown and C. H. Scholz, J. Geophys. Res., **90,** 12575, (1985)
[4] E. Bouchaud, G. Lappaset, and J. Planes. Europhys Lett. **13,** 73, (1990)
[5] K. J. Måløy, A. Hansen, E. L. Henrichsen, and S. Roux. Phs. Rev. Lett., **68,** 68, (1992)
[6] J. Schmittbuhl, S. Gentier, and S. Roux, Geophys. Res. Lett., **20,** 639, (1993)
[7] B. L. Cox, and J. S. Y. Wang. Fractals, **1**, 87, (1993)
[8] W. L. Powel, T. E. Tullis, S. R. Brown, G. N. Boitnott, C. H. Scholz. Geophys. Res. Lett. **14**, 29, (1987)

[9] E. Bouchaud, J. Phys, **9,** 4319, (1997)
[10] J. Schmittbuhl, and K. J. Måløy, Phys. Rev. Lett. **78,** 3888 (1997)
[11] A. Delaplace, J. Schmittbuhl, and K. J. Måløy, Phys. Rev. **E60**, 1337 (1999)
[12] E. Rolley, C. Guthmann, R. Gombrovisch and V. Repain, Phys. Rev. Lett. **80,** 2865, 1998)
[13] K, J, Måløy, and J. Schmittbuhl, Phys. Rev. Lett. **87,** 105502, (2001)
[14] F. Family, and T. Vicsek, J. Phys. A. **18**, L75 (1985)
[15] J. Schmittbuhl, A. Hansen, and G. Batrouni, Phys. Rev. Lett. **90,** 045505 (2003)
[16] A. Hansen, and J. Schmittbuhl, Phys. Rev. Lett, Phys. Rev. Lett, **80,** 045504 (2003)
[17] S. Ramanathan and D. Fisher, Phys. Rev. **B58,** 6026 (1998)
[18] S. Ramanathan and D. Fisher, Phys. Rev. Lett. **79,** 877 (1977).

Earth and Planetary Science Letters 341–344 (2012) 104–113

Contents lists available at SciVerse ScienceDirect

Earth and Planetary Science Letters

journal homepage: www.elsevier.com/locate/epsl

Modelling of stylolite geometries and stress scaling

D. Koehn [a,*], M. Ebner [b], F. Renard [c,d], R. Toussaint [e], C.W. Passchier [f]

[a] School of Geographical and Earth Sciences, University of Glasgow, Gregory building, Lilybank Gardens, Glasgow G12 8QQ, UK
[b] Geological Survey of Austria, Neulinggasse 38, A1030 Vienna, Austria
[c] CNRS-Observatoire, Université Joseph Fourier BP 53, F-38041 Grenoble, France
[d] Physics of Geological Processes, University of Oslo, Norway
[e] Institut de Physique du Globe de Strasbourg (IPGS), CNRS and University of Strasbourg (EOST), 5 rue Descartes, F-67084 Strasbourg Cedex, France
[f] Tectonophysics, Institute of Geosciences, Johannes Gutenberg University, Becherweg 21, 55099 Mainz, Germany

ARTICLE INFO

Article history:
Received 8 June 2011
Received in revised form
30 March 2012
Accepted 23 April 2012
Editor: L. Stixrude
Available online 7 July 2012

Keywords:
stylolite
stress-gauge
compaction
pressure solution
numerical model
self-affinity

ABSTRACT

In this contribution we present numerical simulations of stylolite growth to decipher the effects of initial rock heterogeneity and stress on their morphology. We show that stylolite growth in a rock with a uniform grain size produces different patterns than stylolite growth in a rock with a bimodal grain size distribution. Strong pinning of large heterogeneities produce stylolite structures that are dominated by pronounced teeth, whereas a uniform grain size leads to spikes and a roughness that shows variable wavelengths. We compare the simulated stylolites with natural examples and show that the model can reproduce the real structures. In addition we show that strong pinning in the bimodal case can lead to a linear stylolite roughness growth in contrast to the non-linear growth of stylolites that develop from a uniform noise. In a set of 24 simulations we vary the main principle stress on the stylolite in order to test if our model can reproduce the analytically derived stress-scaling proposed by Schmittbuhl et al. (2004). We compare the calculated stresses with the applied stresses and show that the numerical model and the analytical solution are in good agreement. Our results strengthen the hypothesis that stylolites can be used as strain and stress gauges to estimate not only the orientation of paleo-stresses, but also their absolute values of formation stresses and amounts of compaction.

1. Introduction

Pressure solution is an important deformation mechanism that takes place in the upper parts of the Earth's crust (Rutter, 1983). This mechanism of dissolution, transport and precipitation of material starts as shallow as 90 m during diagenesis in sedimentary basins (Tada and Siever, 1989) and may still be active during high grade metamorphic conditions (Beach, 1979). If the dissolution of material takes place in a localised manner, rough dissolution surfaces develop that are termed stylolites (Fig. 1, Dunnington, 1954; Heald, 1955; Park and Schot, 1968; Guzzetta, 1984; Merino, 1992; Railsback, 1993; Karcz and Scholz, 2003). Stylolites are very common in a variety of mono-mineralic rock types and have several distinct characteristics: they concentrate material that cannot be dissolved as fast as the matrix appearing as dark seams, the surface has a pronounced roughness of peaks or spikes with parallel or inward sloping sides, such that they can be pulled apart without breaking the rock; and this roughness occurs on a range of scales (Fig. 1).

Geologists are interested in stylolites because they are used to estimate the compaction and the stress history in sedimentary basins (Ebner et al., 2009b; Petit and Mattauer, 1995; Rispoli, 1981). The hydrocarbon industry is mainly interested in stylolites because they affect reservoir properties; they can be sealing because of their clay content and reduce porosity and permeability around the stylolite, while they may also act as channelways when fluids travel along the stylolite interface (Fabricius and Borre, 2007; Baron and Parnell, 2007). The use of stylolites to estimate compaction and stress is of great interest to Earth scientists and may be used for basin analysis or tectonic studies in fold and thrust belts. Reliable paleo-stress gauges are rare in geology. For several reasons we are convinced that stylolites can play this role: (1) Stylolites are very common geological structures and (2) the orientation of their teeth track the direction of the main compressive stress, (3) the magnitude of these asperities capture part of the compaction history of the host-rock and (4) it has been demonstrated that the stylolite roughness can be used to estimate absolute stress values, i.e. the mean, differential and the principal stress values (Ebner et al., 2009b, 2010a). A few other

* Corresponding author.
E-mail address: daniel.koehn@glasgow.ac.uk (D. Koehn).

0012-821X/$ - see front matter © 2012 Elsevier B.V. All rights reserved.
http://dx.doi.org/10.1016/j.epsl.2012.04.046

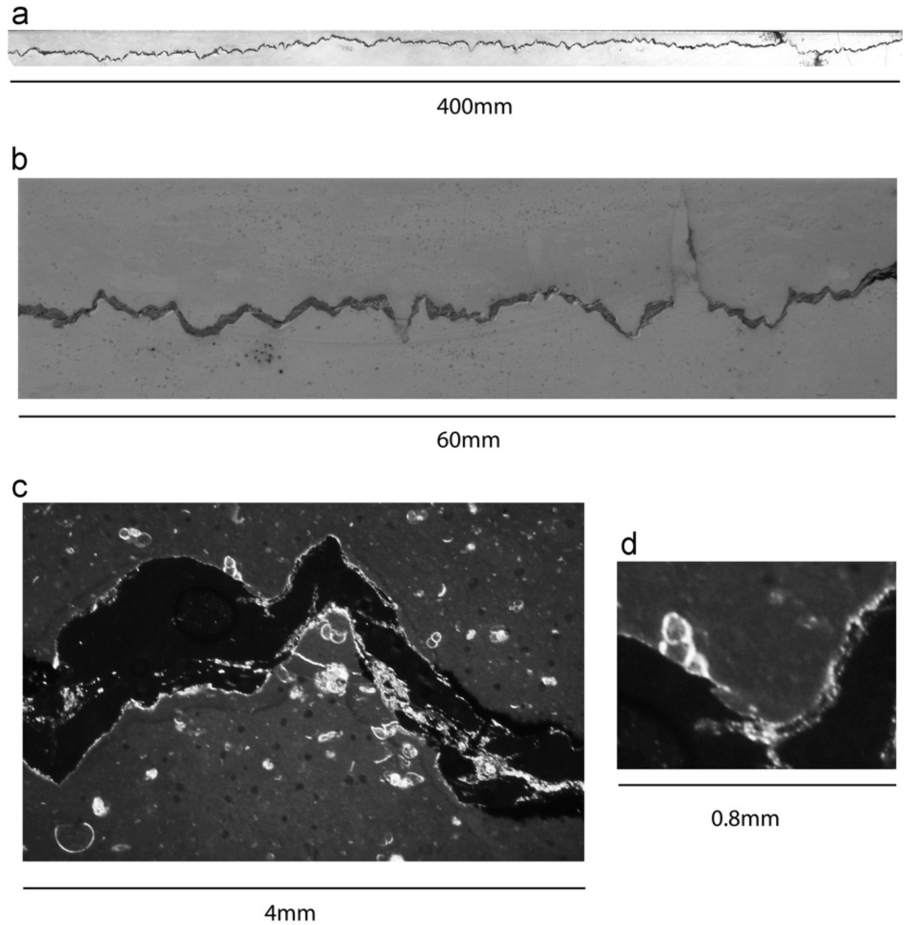

Fig. 1. Example of the same natural stylolite in limestone, at different scales. On the large scale, the stylolite is relatively flat whereas the aspect ratio of the roughness (out-of-plane dimension over in-plane one) increases towards smaller scales from a to c. Between c and d the roughness aspect ratio remains constant.

paleo-stress markers exist, for e.g. the study of calcite twins in rocks (Burkhard. 1993; Lacombe, 2010), but they are generally more sensitive to the stress orientation than to its magnitude. It is useful to develop additional paleo-stress gauges, which can be applied on a variety of rocks, such as stylolites that are present in many sedimentary rocks.

2. The use of stylolites for structural analysis

Stylolite morphology develops according to two main processes. Firstly, an interface can either be initially present in the sediment, such as the interface between two different sedimentary layers or a fracture, or they form by propagation from an initial site of stress concentration that promotes the formation of an anticrack (Fletcher and Pollard, 1981), localise due to chemical effects induced by micas (Aharonov and Katsman, 2009) or localised volume reduction (Katsman et al., 2006). Dissolution may localise on such an interface because an existing interface has better transport properties or because dissolution at the interface is enhanced due to a higher concentration of micas or oxides along the interface. Secondly, such interface may roughen with time, a process that is dependent on local stress conditions and the amount of heterogeneities in the rock. Stylolites can be used in structural analysis to find three parameters: the main compressive stress direction (e.g. Rispoli, 1981; Koehn et al., 2007), the amount of compaction and the product of the differential and mean stress (Ebner et al., 2009b, 2010a). Stylolite teeth (Fig. 2a) are thought to grow parallel to the main compressive stress direction, a hypothesis that was strengthened by recent numerical simulations (Ebner et al., 2009a; Koehn et al., 2007). These simulations show that the lateral position of a tooth along a stylolite interface is random but its shape is strongly deterministic with respect to the orientation of the direction of maximum finite compaction, which is identical with the main compressive stress orientation in homogeneous solids. The amplitude of a stylolite can be used indirectly to calculate the amount of compaction. Although this can be difficult, the non-linear scaling relationship between finite compaction and average stylolite amplitude gives reasonable estimates (Koehn et al., 2007). Without the use of a scaling function one can estimate the amount of dissolved material at the stylolite by using its maximum height, but this requires the observation of this maximum in a few spots, which can be hidden in the rock in some situations. Hence, the maximum height observed corresponds to a lower bound of the dissolution (amount of compaction along the stylolite) that took place, and not necessarily the total one. The scaling function given by Koehn et al. (2007) can be used to estimate compaction; however, the function is non-linear leading to a relatively large uncertainty in the result.

The third and most important value that can be determined from natural stylolites is the product of the differential and mean stress, which can be calculated from the scaling of the stylolite roughness (Renard et al., 2004), based on an analytical solution presented in Schmittbuhl et al. (2004). This analytical solution demonstrates that the stresses acting during stylolite formation can be derived from the stylolite roughness hidden in the crossover-length scale that separates two self-affine scaling

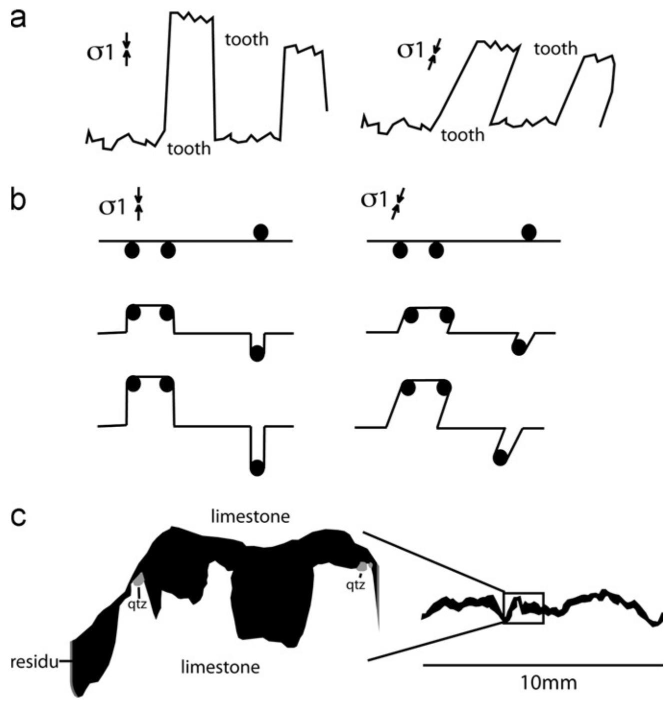

Fig. 2. (a) Sketch showing typical stylolite teeth where the sides of the teeth are oriented parallel to the main compressive stress. In the example on the right hand side the teeth are inclined indicating that the main stylolite plane is oriented at an angle to the smallest principle stress σ_3. (b) Sketch illustrating how stylolite teeth shown in a) can grow if impurities (dark cirlces) pin the interface. (c) Sketch after Ebner et al. (2010b) showing how low solubility quartz grains may pin the sides of teeth in natural stylolites.

regimes well documented for natural stylolites. Ebner et al. (2009b) showed in a study on natural bedding parallel stylolites, which were sampled at different depths in a sedimentary basin, that the measured principal normal stress value increases linearly with the depth of stylolite formation, which supports the analytical solution. These authors also present a method that allows the calculation of the full paleo-stress tensor from the stylolites under favourable conditions. In addition Ebner et al. (2010a) show with a study on tectonic stylolites that these can reveal the difference between all three principal stress components, which is an additional support for the theory of Schmittbuhl et al. (2004).

In order to further test the hypothetical scaling relation of the stylolite roughness as a function to overburden stress, we present two-dimensional numerical simulations of the roughness development of a set of sedimentary stylolites and their sensitivity to stress. First we present different stylolite geometries that develop in a limestone with a constant grain size versus a limestone with a bimodal distribution of grains (or fossils). Then we test the analytical solution of Schmittbuhl et al. (2004) and show with a numerical model (Koehn et al., 2007) how stylolites can be used to attain the full paleo-stress tensor and the paleo-depth of (bedding parallel) stylolite growth in a sedimentary basin. In addition we validate our numerical simulations by showing that they result in stylolite geometries found in nature and we show that the model reproduces the crossover length scale that is predicted by the solution of Schmittbuhl et al. (2004) for a given stress.

3. The stress gauge

Detailed measurements of stylolite roughness (Renard et al., 2004; Ebner et al., 2009b), as well as deterministic models of stylolite formation (Schmittbuhl et al., 2004; Koehn et al., 2007) indicate that the absolute value of the stress can be determined from the roughness of a stylolite. Stylolites are thought to roughen because of the existence of heterogeneities in a rock that dissolve at different rates than the host-rock. In limestone, these heterogeneities may be fossils on a millimetre scale or clay particles, oxide or quartz grains on a micrometre scale. Impurities are localising dissolution and in some cases enable stylolite formation (Aharonov and Katsman, 2009) and collect within the stylolite surface during successive stress driven dissolution of the host-rock. The host-rock dissolves on both sides of the stylolite. If this dissolution is locally heterogeneous, so that one part of the host-rock on one side of the stylolite dissolves slower than the other, the interface starts to become rough (Fig. 2a and b). In an extreme case an impurity like an oxide grain can pin one side of the stylolite host-rock completely, so that this side does not dissolve at all. The pinning particle is then quasi pushed into the host-rock on the other side of the stylolite and a spike develops. For example, Ebner et al. (2010b) have shown with an EBSD analysis that small quartz grains pin corners of some stylolite teeth (Fig. 2c).

The developing stylolite roughness can be accurately described by a self-affine scaling function with a characteristic Hurst or roughness exponent (Brouste et al., 2007; Gratier et al., 2005; Renard et al., 2004; Schmittbuhl et al., 2004). When a rough surface shows a self-affine property, its roughness has a variable amplitude (A) over wavelength (λ) ratio at different scales. A self-affine 1D profile can be described mathematically as invariant under self affine transformations, i.e. anisotropic zooms of any pair of factors (b,b^{α}), where b is real, respectively for the sub-parallel and normal direction to the average surface: A zoom transformation on the surface in the x-direction by $x \rightarrow bx$ and in height by $h \rightarrow b^{\alpha}h$, where x is oriented parallel to the stylolite interface, h is the height of the interface, b is a linear scaling factor and α the Hurst or roughness exponent (Barabasi and Stanley, 1995). If the roughness exponent is smaller than 1.0, the profile is called self-affine: it appears flat on the large scale (cm- to km-scale) and rougher (with larger aspect ratio A/λ of out of plane amplitude over in plane wavelength) on the small scale (mm- to μm-scale). Such a scaling is reproduced by the natural stylolite shown in Fig. 1, where the stylolite seems flat on the larger scale (Fig. 1a, width 40 cm, low ratio A/λ) and appears progressively rougher on the small scale (Fig. 1c and d, width 6 cm and 4 mm, higher ratio A/λ). The main natural scale of the rock shown in Fig. 1 is the grain size, which is 10 μm for most grains (with the exception of large fossils seen in Fig. 1c and d). The grain size is important for compaction estimates as will be explained later on (Koehn et al., 2007; Ebner et al., 2009a). Natural stylolites tend to show not only one but two characteristic roughness exponents. On the large scale the exponent is around 0.5 whereas on the small scale it is close to 1 (Renard et al., 2004; Schmittbuhl et al., 2004). The change from one scaling regime to the other (characterised by different scaling exponents) is relatively sharp. It lies typically on the millimetre length scale and is termed crossover-length (l). An interface with a roughness exponent of about 1.0 is called self-similar, and does not change its roughness aspect ratio A/λ with different scales, which can also be seen in Fig. 1c and d, where the amplitude over wavelength ratio does not change significantly (width 4 mm and 0.8 mm). Schmittbuhl et al. (2004) could show with their analytical solution that these two roughness exponents correspond to two different thermodynamic regimes where surface energy is dominant on the small scale and elastic energy dominant on the large scale, with a well-defined cross-over length at the millimetre scale.

It is important to notice that surface and elastic energies tend to flatten the interface whereas the heterogeneities initially present in the host rock i.e. a quenched noise roughen the interface (Koehn et al., 2007; Schmittbuhl et al., 2004).

The surface energy in the rock stays constant (eq. 2 in Koehn et al., 2007) whereas the elastic energy is a function of the stress field surrounding the stylolite (Eq. (9) in Koehn et al., 2007). When the stress increases because the stylolite grows for example in deeper parts of a sedimentary basin the elastic energy also increases and the cross-over between surface and elastic energy dominated regimes shifts to smaller scales. Hence the influence of surface energies is shifted to smaller scales with increasing stress. Determining the cross-over from natural stylolites thus gives a value for the stress on the stylolite interface. The scaling relation from Schmittbuhl et al. (2004) relates the cross-over length scale (l) with the product of the mean (σ_m) and differential (σ_{dif}) stress according to

$$l = \frac{\gamma E}{\beta} \frac{1}{\sigma_m \sigma_{dif}}, \tag{1}$$

where γ is the surface free energy, E the Young modulus and β a function of the Poisson ratio ($\beta = v(1-2v)/\pi$). In a sedimentary basin with a uniaxial vertical stress component (i.e. zero horizontal displacements) and the horizontal components being a function of the vertical stress component σ_z, Eq. (1) simplifies to (modified after Ebner et al., 2009b)

$$l = \frac{\gamma E}{\kappa} \frac{1}{\sigma_z^2}, \tag{2}$$

where κ is a function of the Poisson ratio ($\kappa = (v)/(3\pi)(((1-2v)^2 (1+v))/((1-v)^2)))$. This scaling relation is only valid for bedding parallel stylolites (sedimentary stylolites), for which the principal horizontal stresses are equal if one assumes no lateral displacement. For tectonic stylolites with 3 different main compressive stresses this solution cannot be applied since in that case the differential stresses vary. An approximation for the complex tectonic case is given in Ebner et al. (2010a). In the present contribution we want to test the scaling relation for sedimentary stylolites with the numerical simulations of Koehn et al. (2007) and illustrate how the stylolite morphology varies with increasing depth in a sedimentary basin. This comparison between natural data (Ebner et al., 2009b), an analytical model (Schmittbuhl et al., 2004) and numerical simulations will allow us to propose that stylolites can be used as stress gauges.

4. Numerical model

We use the numerical model of Koehn et al. (2003, 2006, 2007), Bons et al. (2008) and Ebner et al. (2009a). It is based on a 2D linear elastic lattice spring model where elements can dissolve as a function of surface energy, elastic energy and normal stress at the interface. Dissolution takes place at a predefined surface that is initially smooth (Fig. 3). Particles on the interface are stressed when they are in contact. We calculate the surface energy at the interface and the elastic energy of the particle (Koehn et al., 2007) and use these in addition to the difference between the normal stress at the particle surface and the average normal stress across all particles at the interface to determine how fast the particle dissolves according to (Koehn et al., 2007)

$$D_i = k_i V_s \left(1 - \exp\left(\frac{-\Delta\sigma_n V_s - \Delta\psi}{RT}\right)\right), \tag{3}$$

where D_i is the dissolution rate of particle i, k_i a rate constant, V_s the molecular volume, $\Delta\sigma_n$ the difference in normal stress along the interface, $\Delta\Psi_s$ the difference in Helmholtz free energy of the solid (the sum of elastic and surface energies at a particle) between a curved stressed interface and a flat unstressed interface, R the universal gas constant and T the absolute temperature (in Kelvins). For a derivation of Eq. (3) see Koehn et al. (2003). Note that we are using the difference in normal stress between the average normal stress on all interface particles and the particle's normal stress. We are not using the stress difference between an unstressed surface and a stressed surface. If we use the difference between an unstressed and a stressed surface the normal stress term is too dominant and the crossover does not appear in the simulations. We assume that the interface is constantly dissolving so that diffusion and precipitation of material are not taken into account. However, since we use the normal stress difference between the average stress and the local stress we model a situation where the fluid has a concentration of

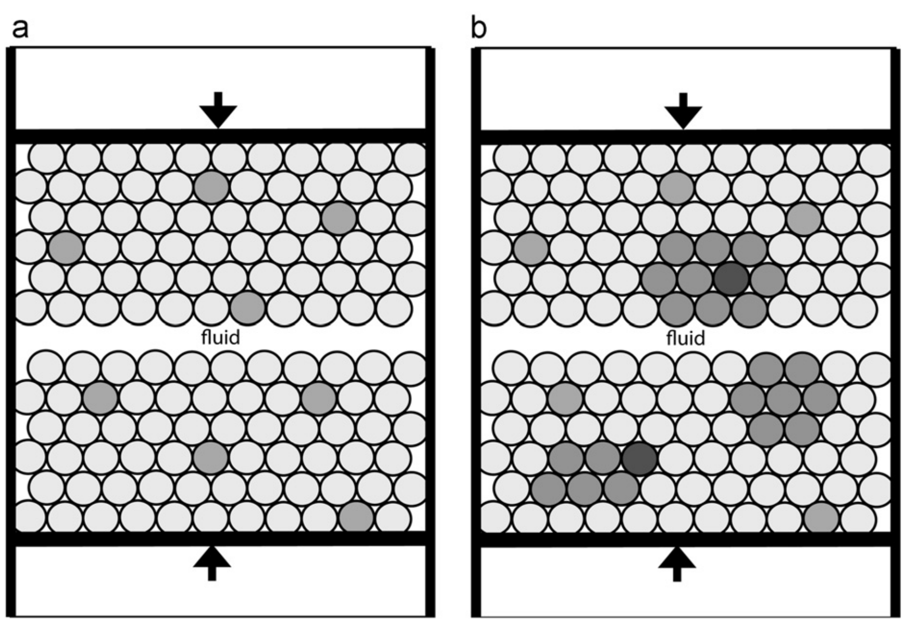

Fig. 3. Model setups for the numerical simulations of stylolite roughening. The sidewalls are confined and the upper and lower walls are pushed inwards. Dissolution takes place along an initially flat line in the centre of the model. Dark particles dissolve slower. (a) Setup for a uniform grain size where the particles in the model may represent grains in the rock. (b) Setup for a bimodal grain size, where the small grains are represented by particles in the model whereas the large grains are defined by clusters of particles.

dissolved material that is proportional to the average normal stress on the stylolite. In this case the system is open assuming that material can be transported away from the stylolite and precipitate to fill pore space; however, the fluid remains saturated on average accounting for the stress state of the rock at a certain depth. Local gradients in fluid saturation along the stylolite are thought to decay fast relative to the stylolite growth. Since diffusion is not taken into account the model does not have a "real" time scale, we cannot predict how fast the stylolite roughens in real time. We only predict how the roughness grows as a function of compaction that is taking place at the stylolite. In addition we are not taking the precise fluid chemistry into account, we are assuming that the fluid chemistry does not vary along the stylolite. Differences in fluid chemistry and different diffusion lengths and time scales will affect how fast the stylolite can grow. However, we argue that the scaling of the roughness does not change even with a change in fluid chemistry.

Roughening of the surface is induced by randomly oriented slower dissolving particles (5%) that pin the interface until they themselves dissolve (Fig. 3a). In the case of a bimodal grain size we include slower dissolving larger grains (or fossils), defined by clusters of particles. These clusters themselves contain a noise on a smaller scale, so that they contain particles that dissolve slower than the cluster itself (Fig. 3b). For the presented simulations the numerical model has two resolutions, the smaller resolution of 184,000 particles, a real physical width of 4 cm and a particle size of 0.1 mm is used for simulations that have a noise and grain size on one scale whereas a larger resolution of 736,000 particles and a real physical width of 8 cm is used for simulations with a bimodal distribution of noise and grain size. Additional parameters are a Poisson ratio of 0.33 (determined by the shape of lattice used), a Young's modulus of 80 GPa and a surface free energy of 0.27 J/m^2 relevant for limestone. The molar volume for calcite is 0.00004 m^3/mol, the temperature is 300 K and the dissolution constant for calcite is 0.0001 mol/(m^{2}s) (Clark, 1966; Renard et al., 2004; Schmittbuhl et al., 2004; Koehn et al., 2007). The deformation is uniaxial with fixed side-walls simulating stylolite formation in a sedimentary basin, the vertical stress is constant for the simulation with a bimodal noise (50 MPa) and is varied between 29 and 92 MPa (29, 41, 50, 57, 64, 71, 80, 92) for simulations with a noise that is only on the particle scale.

5. Results of the simulations

5.1. Comparison of natural and simulated stylolites

We use two different initial setups for the simulations, which are illustrated in Fig. 3. In the first setup we use a random distribution of slower dissolving particles in the model, these are shown as dark particles in Fig. 3a. In all these simulations 5% of particles dissolve 20% slower than the rest. This means that they can pin the surface, but they may dissolve themselves if elastic or surface energies at the tips of spikes become too large or if two slower dissolving particles meet at the interface (Koehn et al., 2007). In the second set of simulations we add larger grains (also 5%) that dissolve 20% slower (Fig. 3b); they are defined as clusters of particles. These larger grains are added on top of the initial distribution of slower dissolving particles. This means that the slower dissolving grains also contain particles that dissolve slower and the noise is bimodal.

The developing geometries are shown in Fig. 4 where we compare the simulated patterns with natural examples. Fig. 4a shows a stylolite that was simulated when using a bimodal noise. The larger grains at the interface are shown in grey. The stylolite geometry clearly reflects the bimodal nature of the noise. The largest grains pin the interface and result in extreme teeth with very straight edges. The stylolite surface between the large grains shows much smaller roughness amplitude that slowly develops into larger wavelengths. This surface is on average still in the middle of the stylolite and resembles the orientation of the initially flat interface where dissolution started. The teeth that are pinned by larger grains have variable height depending on when the pinning grains (clusters of slower dissolving particles in our model setup) meet the interface. The surface on top or at the bottom of the teeth shows a roughness that is similar to the normal stylolite roughness indicating that the pinning grains slowly dissolve themselves. The actual dissolution of the host-rock is indicated by the grey bar on the right hand side of the simulated stylolite. One can observe that the distance between the highest and lowest teeth on each side of the stylolite almost reflects the actual dissolution. Large grains started to pin the interface relatively early and are not yet completely dissolved so that the actual dissolution is still recorded by the stylolite.

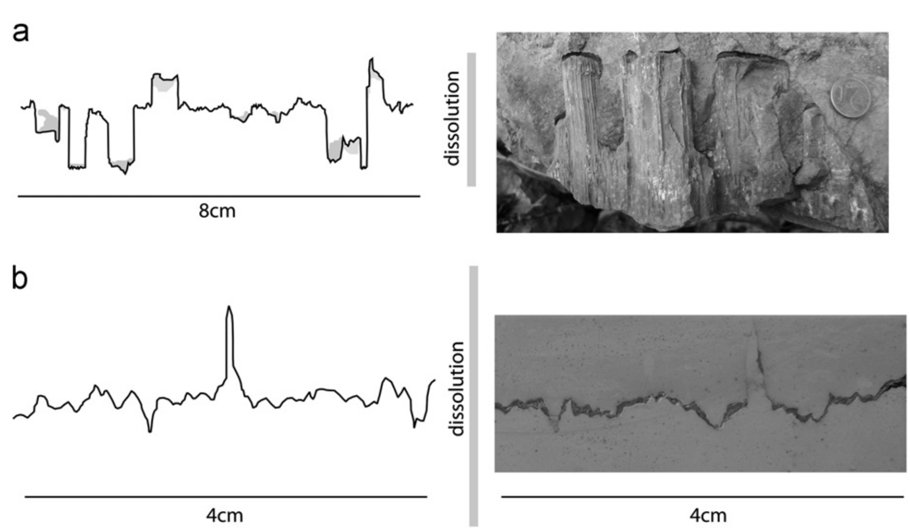

Fig. 4. Results of the numerical simulations of stylolite roughening for (a) a bimodal grain size and (b) a uniform grain size. The actual dissolution of the host rock is indicated with grey vertical bars next to the stylolites. On the right hand side two natural stylolites are shown that may represent similar variations in noise than in the simulations. The grey patches along the stylolite indicate the largest grains that dissolve slower and act as pinning sites for the interface. Note the strong similarity between the numerical simulations and the natural stylolites.

The picture on the right hand side shows a stylolite from the "Muschelkalk" limestone of southern Germany where large fossils pin the interface resulting in large teeth. The noise is clearly bimodal and the simulation captures the geometries of the real stylolite.

Fig. 4b shows a simulation with a noise only on the particles and a similar natural stylolite on the right hand side. The simulated stylolite shows the typical geometry that was discussed in Koehn et al. (2007) and Ebner et al. (2009a, 2009b) with the development of variable wavelengths and amplitudes of roughness. Extreme spikes can develop if single particles pin the interface for a long time, meaning that they probably meet no slowly dissolving particle on the other side of the interface. The spikes are not as straight as the teeth that develop when the noise is bimodal (Fig. 4a). The grey bar on the right hand side of the simulated stylolite shows the actual dissolution and illustrate that dissolution is underestimated when the distance between the highest and lowest tip of the spikes on the stylolite are used to estimate compaction. The picture on the right hand side of Fig. 4b shows a stylolite with a geometry that is very similar to the simulation. This indicates that the noise in the natural example has a relatively constant scale and the grain size is probably relatively uniform which is underpinned by microscopic analysis not shown in this study. In general it can be stated that the numerical model can capture the complex geometries of natural stylolite examples. This implies that the model captures the main characteristics of stylolite growth and is realistic.

5.2. Bimodal noise, stylolite growth and compaction estimates

Fig. 5 shows the progressive growth of a stylolite with pronounced teeth for three different time steps, after 2000, 4000 and 6000 model steps. These steps do not correspond to real time but are a function of the vertical strain and thus the compaction applied to the stylolite. Large grains that pin the surface are shown in grey and the actual amount of host-rock dissolution is shown in grey bars on the right hand side of the three stylolites. Grains that pin the interface are initially relatively close to the starting dissolution surface so that pinning results already in pronounced teeth in the first time step shown ($t=2000$). Parts of these pinning grains survive and pin the surface until the last time step. This means that only initially a small part of the compaction is not recorded by the stylolite but at later stages the teeth record the full amount of dissolved host-rock. This will change once the pinning grains are dissolved themselves and pinning stops. During time steps 2000 and 4000 the stylolite geometry is still controlled by the large pinning grains on the one hand and by the small scale roughness that develops due to pinning on the particle scale. The latter results in the rough stylolite surface in the centre of the stylolite at time step 4000 where a number of wavelengths develop. At time step 6000 the geometry is mainly controlled by the large scale pinning grains since most of these meet with the stylolite interface. Each tip of a tooth contains small rests of these slower dissolving grains. Some of the teeth record almost the full compaction (from

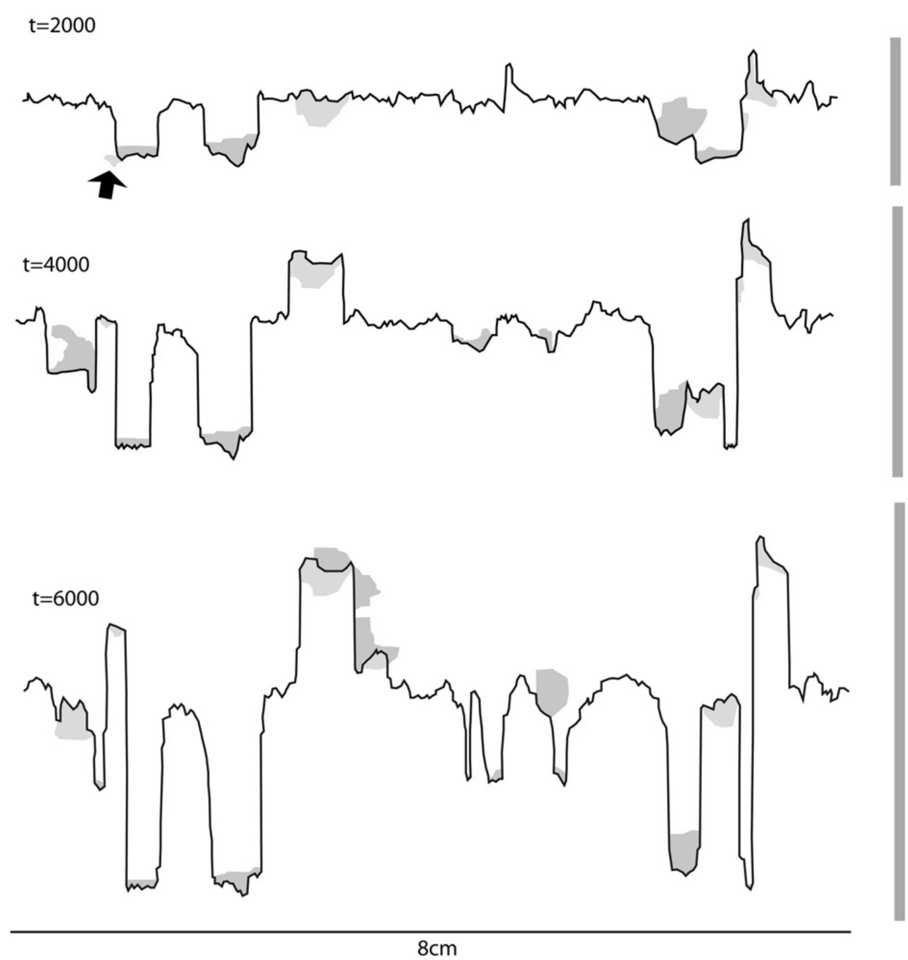

Fig. 5. Time sequence of simulated stylolite growth in a host rock with a bimodal grain size. Note that model steps are proportional to strain increments and amounts of dissolved material and not real time. Bars on the right hand side record the real amount of dissolved material in the simulations. Note how largest grains (grey patches) pin the interface and produce pronounced teeth that record accurately the actual compaction.

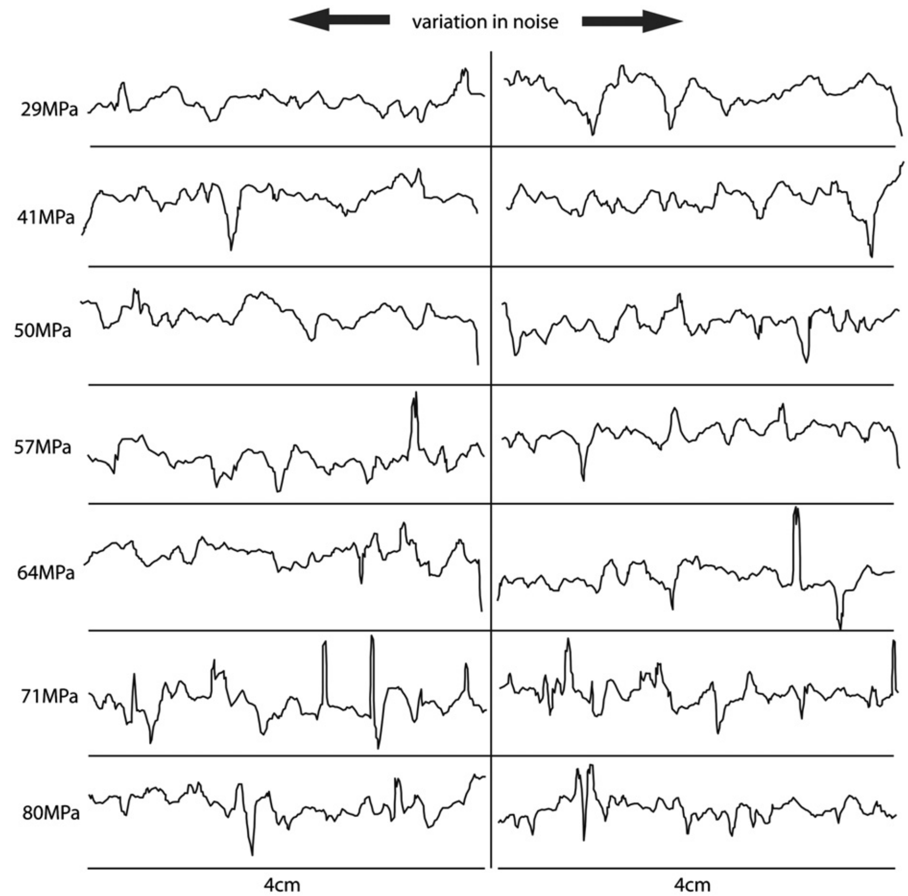

Fig. 6. Two sets of 7 stylolites that developed under increasing normal stress. Right and left hand stylolites only differ in initial random seeds of the quenched noise in the simulations. The relationship between the rough geometries and stresses cannot be visualised, even though there may be an increase in spikes from low to high stresses.

one side) because they met the stylolite relatively early and started to grow from the centre of the stylolite. Others, however, do not really record the full compaction since they either met the interface during a later stage of growth or they met an already developing tooth and are now dissolving the host-rock in the other direction. This can be seen for example at time step 2000, when a small grain on the left hand side of the stylolite meets the left corner of a tooth (see arrow in Fig. 5a). The grain is now "pushing" upwards into the host-rock, the developing tooth meets the original orientation of the interface during time step 4000 and moves upwards at time step 6000. One can use the distance between the highest and lowest tooth in such a stylolite to estimate compaction. Note that unless two slower dissolving grains are positioned next to each other but on opposite sides of the stylolite and pin the interface, each stylolite tooth will only record half of the compaction since they start out from one side of the stylolite (Fig. 5). In contrast to the non-linear growth of stylolites that grow in more uniform rocks (Koehn et al., 2007; Ebner et al., 2009a), a stylolite with a bimodal noise and strongly pinning grains grows linear with a growth exponent of about 1.0—up to the moment where slowly dissolving grains would meet and destroy this large teeth growing in a ballistic (or fast) mode, to get more fluctuating peak growth: a transition to a nonlinear growth similar to the more uniform rock type is then expected.

5.3. Stress scaling

In the last set of simulations, we perform runs with a uniform noise and vary the stress on the stylolite. We model stylolites that grew under a vertical stresses of 29, 41, 50, 57, 64, 71, 80 and 92 MPa. All stylolite simulations run for 8000 model time steps, each stress state is modelled three times. We then analyse the roughness and try to recover the stress from the stylolite morphology using the crossover length, where we average the results of the three different runs per stress state. Examples of the finite stylolite pattern are shown in Fig. 6, where we present two stylolites for each stress state from 29 to 80 MPa. Variations in noise in these cases are only a function of a different random seed of quenched noise, i.e. the heterogeneities in the system for each simulation.

Fig. 6 illustrates the difficulty to see a relationship between the amount of stress that a stylolite experienced and the stylolite roughness directly from the geometry of the roughness. This is also illustrated by the variation in stylolite shape at constant stress depending only on the random distribution of slowly dissolving particles (right versus left hand side in Fig. 6). There may be a general trend from more wavy stylolites at lower stresses to more spiky stylolites at higher stresses, but this relation is not clear. Therefore one has to use statistical tools in order to analyse the stylolite roughness.

In order to determine the scaling of the interface roughness and cross-over length scale from the simulated and natural stylolites we use the Fourier method (e.g. Barabasi and Stanley, 1995; Schmittbuhl et al., 1995). We calculate the Fourier power spectrum $P(k)$ i.e., the square of the modulus of the Fourier transform, as a function of the wave-number k [1/lengthscale (mm^{-1})] for each stylolite pattern. For the simulations we take averages of the power spectra of three runs and plot the resulting average power spectrum as a function of k in log–log space. If the

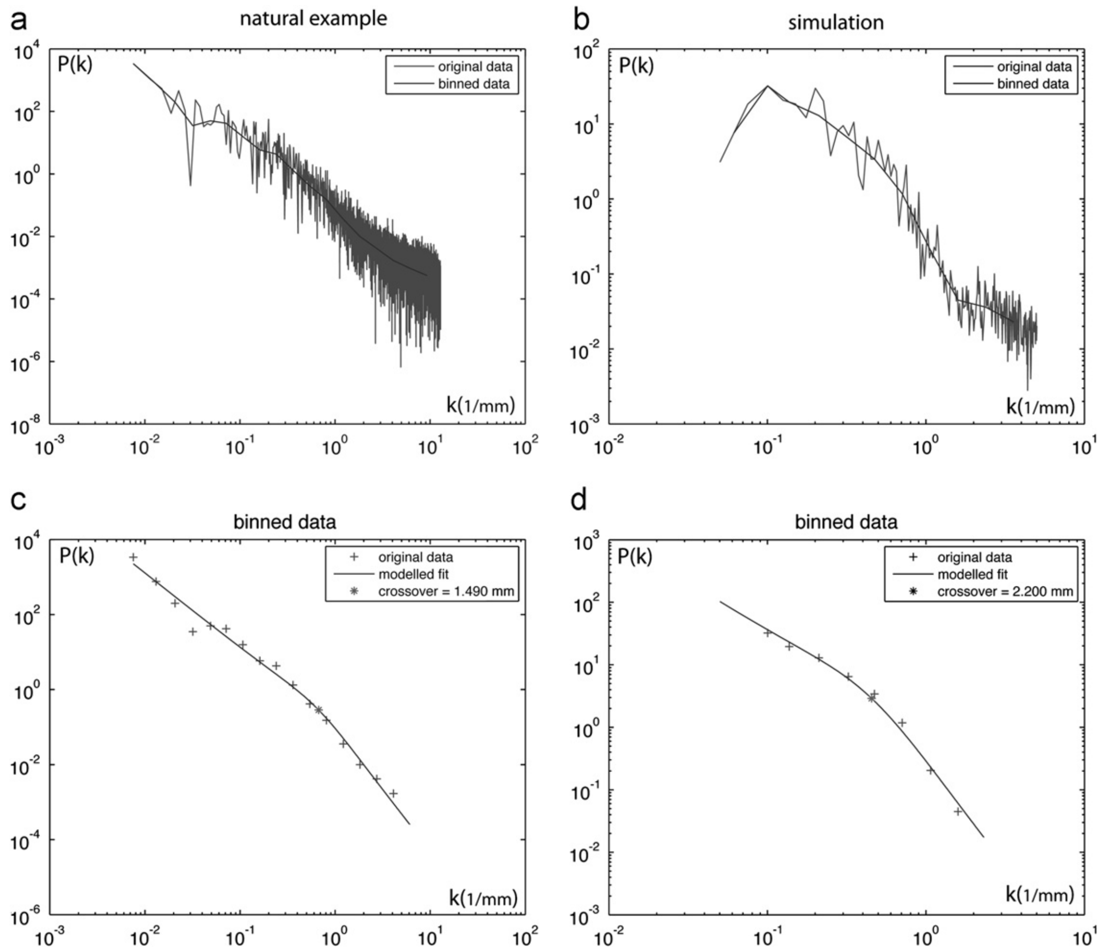

Fig. 7. Fourier analysis of the roughness of stylolites, where the Fourier power spectrum ($P(k)$) is plotted against the wave-number (k), the inverse of the wavelength of the roughness. (a) shows a Fourier analysis of a the natural stylolite shown in Fig. 1, (b) an average of the Fourier analysis of 3 numerical stylolites. (c) and (d) show binned data sets of the Fourier power spectra of (a) and (b) and the presence of a well-defined crossover length scale.

roughness is self-affine the plot shows a linear slope, which is a function of the Hurst exponent (Renard et al., 2004; Schmittbuhl et al., 2004)

$$P(k) \sim k^{-1-2\alpha}. \tag{4}$$

Fig. 7a shows the power spectrum as a function of the wave-number for the natural stylolite of Fig. 1 and Fig. 7b an average of three numerical simulations. Both plots are similar, with the natural data spanning over a wider range of magnitudes than the simulated data but the simulated data having less noise in the signal because it is averaged over three runs. Since the wave-number in the plots is a function of 1/wavelength, the left hand side of the plots represents the larger wavelengths. Here the plots show two slopes, separated by a well-defined crossover wave-length. These two self-affine regimes correspond to the elastic energy dominated regime at the large scale and the surface energy dominated regime at the small scale. On the very right hand side of the two plots the slope becomes flatter at a length scale comparable to the particle size in the model and the drawn bitmap of the natural example. This flat portion of the signal has to be cut off for the analysis of the cross-over length scale. In order to fit a curve to the graphs we bin the data: it becomes clear in Fig. 7c and d that in the binned data set the two slopes become more visible. To avoid bias due to improper fitting of the cross-over-length that separates the two slopes we use a nonlinear least square curve-fitting algorithm in logarithmic space (Ebner et al., 2009b) with predefined roughness exponents of 1.1 and 0.5 for the surface energy and elastic dominated regimes, respectively (Ebner et al., 2009b). The resulting cross-over l is then used for further analysis.

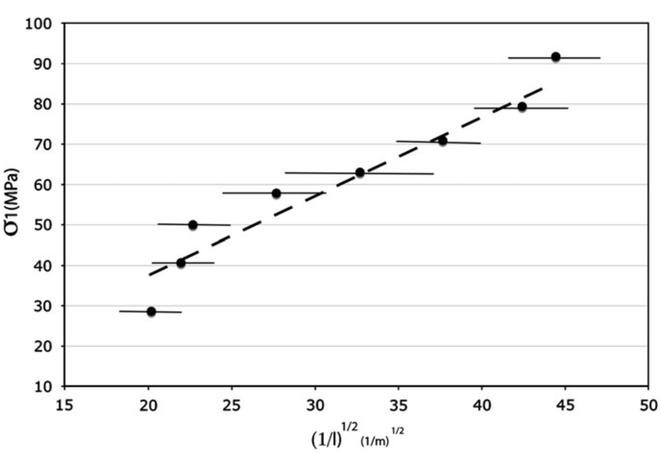

Fig. 8. Plot of the square root of the inverse of the determined crossover length from the numerical simulations against the applied stress following the scaling law of Schmittbuhl et al. (2004). The data plots roughly on a line illustrating that the simulations reproduce the scaling relation. Error bars represent variations in different cross-over length scales found in different simulations.

Fig. 8 shows the result of the 24 simulations where the externally applied vertical stress component of the simulated stylolites is plotted against the inverse of the square root of the cross-over according to the scaling function of Eq. (2). The determined cross-over in the simulations is clearly a function of the stress on the stylolite and shows the right scaling relation:

$$\sigma_z = a\sqrt{1/l}, \tag{5}$$

similar to Eq. (2), since the boundary condition used in these simulations also correspond to a fixed vertical stress and fixed lateral displacement along x, as the one used to derive Eq. (2). The slope (a) of the linear regression line of the data is a function of the input parameters in Eq. (2) of the numerical model. The slope is almost identical with the input parameters of the numerical model (square root of Young's modulus times surface energy divided by κ), which shows that the scaling relation derived analytically and presented by Schmittbuhl et al. (2004) is verified by the numerical stylolite morphologies and is independently produced by the current numerical model presented here. This thus constitutes another completely independent check of this analytical expression, after the comparison of the overload stresses with the one determined from the crossover length for the stylolites investigated by Ebner et al. (2009b) in Southern France.

6. Methodology and application to natural cases

As an example for a paleo-stress calculation, we can use the natural stylolite shown in Fig. 1 and the determined cross-over in Fig. 7c. The calculation gives a vertical stress of about 34 MPa, a horizontal stress of about 13 MPa, a mean stress of 23.5 MPa and a differential stress of 21 MPa. If we assume that the overlying sediments in the basin had a density of about 2.5 kg/cm^3, the paleo-depth of the stylolite was about 1400 m in the basin. The orientation of the teeth or spikes of the stylolite indicates that the direction of the main compressive stress was vertical and that the stylolite formed in the sedimentary basin during burial. A limit with these calculations will always be the uncertainty in the input parameters like the Young's Modulus, Poisson's ratio and the surface free energy at the time of stylolite formation. We used a relatively high Young's Modulus for the numerical simulations (80 GPa). The real limestone may have a lower value of about 50 GPa and this would change the stress and depth estimates (26.5 MPa vertical stress and 1100 m overburden). It is always advisable to use a range of natural stylolites for depth estimates as proposed in the work of Ebner et al. (2009b). In addition to the stress calculation, one can estimate the amount of dissolved material at the stylolite. According to the presented simulations the stylolite shown in Figs. 1 and 4b (right hand side) developed in a host-rock with a relatively uniform grain size. If the stylolite grew in a similar way than the simulations (Fig. 4b) then the dissolved material at the interface is in the order of 3 cm. However, since the grain size in the natural example is about 1/10th of the size of the model particles, the actual amount of dissolved material at the interface is probably larger, because the amount of dissolved material depends on the grain size (Eq. (6)). The scaling relation of Koehn et al. (2007)

$$A = b\left(\frac{w}{L}\right)^{1/0.8} L, \tag{6}$$

where the prefactor b is 10 (factor varies, see Koehn et al. (2007) and Ebner et al. (2009a)), A is the dissolved material (mm), w the mean RMS (root mean square) width of the interface in millimetre (for details of calculation compare Koehn et al. (2007) and Ebner et al. (2009a))and L the grain size (mm), with a grain size of about 0.01 mm for the natural example and a mean width of the interface of 2 mm, results in an estimation of roughly 7.5 cm of material dissolved at the interface or 40 times the mean width of the interface. It is thus not possible to deduce the amount of dissolution directly from the finite interface morphology.

7. Conclusions

We modelled the development of stylolite patterns using a rock matrix that contains either a uniform or a bimodal grain size. Stylolites that developed from a bimodal noise show pronounced teeth with straight edges and grow linearly with a growth exponent of about 1.0. The morphology produced by the simulations is similar to field observations. The distance between the maximum and minimun height of a tooth above and below the original dissolution surface can be used to estimate compaction if pinning starts relatively early during stylolite growth, and pinning grains are not completely destroyed during successive dissolution, thus giving a value that only slightly underestimates the true dissolution along the interface. Stylolites that develop in a rock that has a noise that sits on a uniform grain size may contain spikes but the height of these asperities highly underestimates compaction. For these stylolites the mean width of the interface should be calculated and the scaling law of Koehn et al. (2007) should be used to estimate compaction.

Modelling the growth of stylolites that developed under different normal stresses shows stylolite patterns that can be best distinguished using statistical methods. We use the Fourier method to extract the cross-over length scale from the numerical stylolites, calculate the predicted theoretical vertical stress values and compare them with the actual values used in the numerical simulations. The results are consistent and we can show that the numerical model reproduces the proposed scaling relation, thus our numerical model gives an independent confirmation of the analytical solution of Schmittbuhl et al. (2004). This analytical solution to determine paleo-stress magnitudes from stylolite shapes seems to be robust: the analytical result is verified for sets of stylolites obtained with two independent techniques, namely the ones produced with the current numerical model, and natural examples investigated by Ebner et al. (2009a, 2009b), whose burial stresses were inferred from their relative position in the stratigraphic column. To summarise, comparing numerical simulations with the stylolite shown on Fig. 1b indicates that this stylolite formed during burial in a basin, at depth close to 1400 m, and accommodated about 7.5 cm of dissolution.

Acknowledgements

Koehn and Ebner acknowledge funding by the DFG (KO 2114/5). Toussaint and Renard acknowledge support of a FORPRO CNRS/ANDRA grant.

References

Aharonov, E., Katsman, R., 2009. Interaction between pressure solution and clays in stylolite development: insights from modeling. Am. J. Sci. 309 (7), 607–632.
Barabasi, A.L., Stanley, H.E., 1995. Fractal Concepts in Surface Growth. Cambridge University Press.
Baron, M., Parnell, J., 2007. Relationships between stylolites and cementation in sandstone reservoirs: examples from the North Sea, UK and East Greenland. Sediment. Geol. 194, 17–35.
Beach, A., 1979. Pressure solution as a metamorphic process in deformed terrigenous sedimentary rocks. Lithos 12, 51–58.
Bons, P.D., Koehn, D., Jessell, M.W., 2008. Microdynamics simulation. Lecture Notes in Earth Sciences, 106. Springer, Berlin.
Brouste, A., Renard, F., Gratier, J.P., Schmittbuhl, J., 2007. Variety of stylolites' morphologies and statistical characterization of the amount of heterogeneities in the rock. J. Struct. Geol. 29, 422–434.

Burkhard, M., 1993. Calcite twins, their geometry, appearance and significance as stress–strain markers and indicators of tectonic regime: a review. J. Struct. Geol. 15 (3-5), 351–368.

Clark, S.P.J., 1966. Handbook of Physical Constants. Geological Society of America, New York.

Dunnington, H.V., 1954. Stylolite development post-dates rock induration. J. Sediment. Petrol. 24, 27–49.

Ebner, M., Koehn, D., Toussaint, R., Renard, F., 2009a. The influence of rock heterogeneity on the scaling properties of simulated and natural stylolites. J. Struct. Geol. 31, 72–82.

Ebner, M., Koehn, D., Toussaint, R., Renard, F., Schmittbuhl, J., 2009b. Stress sensitivity of stylolite morphology. Earth Planet. Sci. Lett. 277, 394–398.

Ebner, M., Toussaint, R., Schmittbuhl, J., Koehn, D., Bons, P., 2010a. Anisotropic scaling of tectonic stylolites: a fossilized signature of the stress field? J. Geophys. Res. 115, B06403.

Ebner, M., Piazolo, S., Renard, F., Koehn, D., 2010b. Stylolite interfaces and surrounding matrix material: nature and role of heterogeneities in roughness and microstructural development. J. Struct. Geol. 32, 1070–1084.

Fabricius, I.L., Borre, M.K., 2007. Stylolites, porosity, depositional texture and silicates in chalk facies sediments. Ontong Java Plateau—Gorm and Tyra fields, North Sea. Sedimentology 54, 183–205.

Fletcher, R.C., Pollard, D.D., 1981. Anti-crack model for pressure solution surfaces. Geology 9, 419–424.

Gratier, J.P., Muquet, L., Hassani, R., Renard, F., 2005. Experimental microstylolites in quartz and modeled application to natural stylolitic structures. J. Struct. Geol. 27, 89–100.

Guzzetta, G., 1984. Kinematics of stylolite formation and physics of the pressure-solution process. Tectonophysics 101, 383–394.

Heald, M.T., 1955. Stylolites in sandstones. J. Geol. 63, 101–114.

Katsman, R., Aharonov, E., Scher, H., 2006. A numerical study on localized volume reduction in elastic media: some insights on the mechanics of anticracks. J. Geophys. Res. 111 (B3), B03204.

Karcz, Z., Scholz, C.H., 2003. The fractal geometry of some stylolites from the Calcare Massiccio Formation, Italy. J. Struct. Geol. 25, 1301–1316.

Koehn, D., Arnold, J., Jamtveit, B., Malthe-Sørenssen, A., 2003. Instabilites in stress corrosion and the transition to brittle failure. Am. J. Sci. 303, 956–971.

Koehn, D., Malthe-Sørenssen, A., Passchier, C.W., 2006. The structure of reactive grain boundaries under stress containing confined fluids. J. Chem. Geol. 230, 207–219.

Koehn, D., Renard, F., Toussaint, R., Passchier, C.W., 2007. Growth of stylolite teeth patterns depending on normal stress and finite compaction. Earth Planet. Sci. Lett. 257, 582–595.

Lacombe, O., 2010. Calcite twins, a tool for tectonic studies in thrust belts and stable orogenic forelands, oil & gas science and technology—rev. IFP Energ. Nouv. 65, 809–838.

Merino, E., 1992. Self-organization in stylolites. Am. Sci. 80, 466.

Park, W.C., Schot, E.H., 1968. Stylolites: their nature and origin. J. Sediment. Petrol. 38, 175–191.

Petit, J.P., Mattauer, M., 1995. Paleostress superimposition deduced from mesoscale structures in limestone—the matelles exposure, Languedoc, France. J. Struct. Geol. 17, 245–256.

Railsback, L.B., 1993. Lithologic controls on morphology of pressure-dissolution surfaces (stylolites and dissolution seams) in paleozoic carbonate rocks from the Mideastern United-States. J. Sediment. Petrol. 63, 513–522.

Renard, F., Schmittbuhl, J., Gratier, J.P., Meakin, P., Merino, E., 2004. Three-dimensional roughness of stylolites in limestones. J. Geophys. Res.-Solid Earth 109 (B3).

Rispoli, R., 1981. Stress-fields about strike-slip faults inferred from stylolites and tension gashes. Tectonophysics 75, T29–T36.

Rutter, E.H., 1983. Pressure solution in nature, theory and experiment. J. Geol. Soc. London 140, 725–740.

Schmittbuhl, J., Vilotte, J.P., Roux, S., 1995. Reliability of self-affine measurements. Phys. Rev. E 51, 131–147.

Schmittbuhl, J., Renard, F., Gratier, J.P., Toussaint, R., 2004. Roughness of stylolites: implications of 3D high resolution topography measurements. Phys. Rev. Lett. 93, 238501.

Tada, R., Siever, R., 1989. Pressure solution during diagenesis. Annu. Rev. Earth Planet. Sci. 17, 89–118.

Modeling the growth of stylolites in sedimentary rocks

Alexandra Rolland,[1,2] Renaud Toussaint,[1,3] Patrick Baud,[1] Jean Schmittbuhl,[1] Nathalie Conil,[2] Daniel Koehn,[4] François Renard,[5,6] and Jean-Pierre Gratier[5]

Received 3 December 2011; revised 1 April 2012; accepted 15 April 2012; published 7 June 2012.

[1] Stylolites are ubiquitous pressure solution seams found in sedimentary rocks. Their morphology is shown to follow two self-affine regimes. Analyzing the scaling properties of their height over their average direction shows that (1) at small scale, they are self-affine surfaces with a Hurst exponent around 1, and (2) at large scale, they follow another self-affine scaling with Hurst exponent around 0.5. In the present paper, we show theoretically the influence of the main principal stress and the local geometry of the stylolitic interface on the dissolution reaction rate. We compute how it is affected by the deviation between the principal stress axis and the local interface between the rock and the soft material in the stylolite. The free energy entering in the dissolution reaction kinetics is expressed from the surface energy term and via integration from the stress perturbations due to these local misalignments. The resulting model shows the interface evolution at different stress conditions. In the stylolitic case, i.e., when the main principal stress is normal to the interface, two different stabilizing terms dominate at small and large scales which are linked respectively to the surface energy and to the elastic interactions. Integrating the presence of small-scale heterogeneities related to the rock properties of the grains in the model leads to the formulation of a Langevin equation predicting the dynamic evolution of the surface. This equation leads to saturated surfaces obeying the two observed scaling laws. Analytical and numerical analysis of this surface evolution model shows that the crossover length separating both scaling regimes depends directly on the applied far-field stress magnitude. This method gives the basis for the development of a paleostress magnitude marker. We apply the computation of this marker, i.e., the morphological analysis, on a stylolite found in the Dogger limestone layer located in the neighborhood of the ANDRA Underground Research Laboratory at Bure (eastern France). The results are consistent with the two scaling regimes expected, and the practical determination of the major principal paleostress, from the estimation of a crossover length, is illustrated on this example.

Citation: Rolland, A., R. Toussaint, P. Baud, J. Schmittbuhl, N. Conil, D. Koehn, F. Renard, and J.-P. Gratier (2012), Modeling the growth of stylolites in sedimentary rocks, *J. Geophys. Res.*, *117*, B06403, doi:10.1029/2011JB009065.

1. Introduction

[2] Stylolites are undulated surfaces resulting from localized stress-driven dissolution of some minerals of the rock. Insoluble minerals as clay particles, oxides and organic matters are concentrated in the interface and make stylolites visible. *Bathurst* [1987] describes stylolites as serrated interfaces with an amplitude greater than the diameter of the transected grains giving them a sutured appearance. He makes a difference with dissolution seams or "flaser" which are smooth, undulating, lacking in sutures and fitting around grains instead of cutting through them. Stylolites are most often found in carbonates [*Stockdale*, 1922, 1926, 1936, 1943; *Dunnington*, 1954; *Bushinskiy*, 1961; *Park and Schot*, 1968; *Bathurst*, 1971; *Buxton and Sibley*, 1981; *Railsback*, 1993] but also in sandstones [*Young*, 1945; *Heald*, 1955], shales [*Wright and Platt*, 1982; *Rutter*, 1983], cherts [*Bushinskiy*, 1961; *Iijima*, 1979; *Cox and Whitford-Stark*, 1987] and sometimes in coal [*Stutzer*, 1940]. Stylolites are divided in two groups according (i) to their orientation with respect to the bedding of the surrounding rock or (ii) to the orientation of their "tooth" with respect to the mean plane of the stylolite. The first group shows two types of orientation: stylolites parallel to the bedding plane, designated as sedimentary, and formed under the lithostatic pressure and stylolites oblique or even perpendicular to the bedding,

[1]Institut de Physique du Globe, Université de Strasbourg, CNRS, Strasbourg, France.
[2]ANDRA, Bure, France.
[3]Centre for Advanced Study at the Norwegian Academy of Science and Letters, Oslo, Norway.
[4]School of Geographical and Earth Sciences, University of Glasgow, Glasgow, UK.
[5]ISTerre, CNRS, Joseph Fourier University, Grenoble, France.
[6]Physics of Geological Processes, University of Oslo, Oslo, Norway.

Corresponding author: R. Toussaint, Institut de Physique du Globe, Université de Strasbourg, 5 Rue René Descartes, F-67084 Strasbourg CEDEX, France. (renaud.toussaint@unistra.fr)

designated as tectonic, and depending on the maximum tectonic stress. The tooth orientation is in both cases an indicator of the direction of the incremental displacement which is parallel to the major principal stress in coaxial deformation. The stylolites of the second group are called “slickolites” [*Ebner et al.*, 2010a]. They develop when there is a preferential plane for their growth (bedding or fracture). In this case, the stress is not perpendicular to the mean plane of the stylolite [*Stockdale*, 1922], but the edges of the tooth are subparallel to the maximum principal stress axis. Various studies [*Park and Schot*, 1968; *Renard et al.*, 1997, 2001; *André*, 2003; *Aharonov and Katsman*, 2009] suggest that many parameters play an important role in the stylolite growth such as confining pressure, deviatoric stress, fluid pressure, temperature, shape and assemblage of grains, anisotropy of minerals, rates of dissolution and presence of clay (acting potentially as catalyst for the dissolution).

[3] Only few papers report experiments about stylolites development. Indeed, they are inherently difficult to reproduce as the kinetics of pressure solution processes is very slow [*Rutter*, 1976]. Experiments were conducted either on aggregates [*Cox and Paterson*, 1991; *Den Brok and Morel*, 2001; *Renard et al.*, 2001; *Gratier et al.*, 2005] or with indenter techniques [*Gratier and Guiguet*, 1986; *Gratier*, 1993; *Gratier et al.*, 2004; *Dysthe et al.*, 2002, 2003; *Karcz et al.*, 2008]. *Dysthe et al.* [2002, 2003] used an indenter technique where a sodium chloride crystal was kept in contact with a piston at given pressure and temperature for several months. A fluid at compositional equilibrium with the crystal is trapped between the sample and the indenter. The contact evolved due to pressure solution during the indentation. A power law time dependence with an exponent value of 1/3 as in Andrade creep law was shown to control the indentation rate. The observed microstructures in the contact seem to be different from stylolites. *Karcz et al.* [2008] loaded a halite cone-shaped indenter against a flat silicate surface immersed in an undersaturated brine. Using confocal microscopy techniques, they observed that the evolution of the system is dictated by an interaction between two deformation mechanisms: undercutting dissolution reducing the area of the contact and plastic flow increasing it. Recently, similar experiments were carried out with a brine at chemical equilibrium with the crystal [*Laronne Ben-Itzhak*, 2011]. Emerging evolving islands and channels were observed at the contact. Such islands and channels structures were previously observed at the contacts during experiments on aggregates [*Schutjens and Spiers*, 1999; *Den Brok and Spiers*, 1991]. Other experiments on aggregates were performed by *Gratier et al.* [2005]. They loaded layers of fine quartz sand grains. The experiments lasted several months at 350°C, under 50 MPa of differential stress and in presence of an aqueous silica solution. Microstylolites were created for the first time in the laboratory at the stressed contacts between the quartz grains. An interesting observation is that the stylolites peaks are always located in front of dislocation pits. Consequently, stylolites appear to be localized by the heterogeneities of the mineral. *Den Brok and Morel* [2001] loaded elastically K alum crystals at a controlled temperature and in a saturated K alum solution. A hole was drilled in the middle of the crystals to provide an elastic strain gradient. They observed macroscopic etch grooves on the originally smooth free surfaces of the soluble crystals which disappear when removing the stress. *Koehn et al.* [2004] stressed crystals of $NaClO_3$ in a $NaClO_3$ solution at room temperature. Parallel dissolution grooves developed on their free surface in a 1-D geometry to a 2-D geometry with the coarsening of the pattern. The pressure solution process slowed down or stopped progressively with the increasing concentration of the solution during the experiments. *Gratier et al.* [2004] used a similar technique in which a sample of Bure claystone was kept in contact with a piston, with a saturated brine in the contact, at an imposed pressure and temperature for several months. No evidence of localized pressure solution (dissolution seam) was observed in this case, grain to grain sliding being more efficient in presence of clay. *Renard et al.* [2001] studied chemical compaction of aggregates of halite (salt) mixed with clay. They showed that clay particles enhance pressure solution. Moreover, *Renard et al.* [1997] studied the effect of clay on clay-rich sandstones. They suggested that pressure solution is enhanced by clay because a thick film of water is preserved between clay particles. They also concluded that the depth determines the limiting factor for the process: at great depth, the water film between grains should be thinner and diffusion limits the process. Conversely, at low-depth water films are bigger, transport is easier and the reaction kinetics is the limiting factor.

[4] The clay particles effect on pressure solution was recently simulated in numerical modeling. *Aharonov and Katsman* [2009] used the two-dimensional Spring Network Model to study the stylolites growth in a medium with a uniform clay distribution. They showed that clay plays a role of enhancing pressure solution and that stylolites propagation is possible only when both pressure solution and clay-enhanced dissolution operate together. *Koehn et al.* [2007] developed a new discrete simulation technique that reproduces successfully the roughening of stylolites from a preferential existing surface with no clay. This model is based on molecular dynamics, with a dissolution speed depending on the local free energy that includes stress dependent terms and surface energy terms. Two different spatial regimes arise from this modeling: a small-scale regime where surface energy is dominant with significant fluctuations of the roughness and a large-scale regime where elastic energy dominates. The dependence on the crossover scale between both regime on the imposed stress has been recently investigated numerically [*Koehn et al.*, 2012]. This model shows that the growth of the stylolite tooth follows the main compressive stress direction. The nature and structure of the small-scale disorder for the dissolution properties of grains were systematically analyzed [*Ebner et al.*, 2009a]. Moreover, *Ebner et al.* [2010b] performed detailed microstructural analysis to investigate the interplay between this disorder and the compositional nature of the grains surrounding a stylolite.

[5] Stylolites are localized features for which deformation is purely compactant as for compaction bands [*Mollema and Antonellini*, 1996; *Baud et al.*, 2004; *Katsman et al.*, 2006b; *Tembe et al.*, 2008]. Stylolites and compaction bands development was modeled as anticracks or antimode I fracture [*Fletcher and Pollard*, 1981; *Rispoli*, 1981; *Mollema and Antonellini*, 1996]. *Fletcher and Pollard* [1981] assume that the rate of pressure solution is only a function of the normal stress. They observed an elliptic dissolution

pattern, i.e., more dissolution in the central part of stylolites than at the tips. With these observations they proposed an analogy between propagation of stylolites and propagation of mode I fractures. They observed that the relative displacement between the sides of a stylolite should have the opposite sign than that of a crack, and thus termed their model an anticrack. Note however that cracks can bear zero surface traction, contrary to stylolites. This distinction between crack solutions and stylolites was introduced, and it was shown by *Katsman et al.* [2006a] that, as compaction bands, stylolites are Localized Volume Reduction zones (LVR). The shape of the displacement along stylolites, and how the stress perturbation can be determined from the concept of LVR, is discussed in details by *Katsman* [2010].

[6] In LVR where the dissolution amount is constant across the surface of the LVR, as for a compaction band, the stress enhancement was shown to be that of a dislocation [*Katsman et al.*, 2006a]. In later models [*Katsman*, 2010], it was shown that if more dissolution is allowed in the center of a stylolite, another type of stress enhancement, with a dependence on the distance to the tips analogous to the one for a crack (rather than to a dislocation), can be observed it is given by the Eshelby inclusion problem. Such an increase of the dissolution in the center of a stylolite, where the dissolution does not stop in the already dissolved zone in the middle of the stylolite, can be observed in models with a positive feedback to the dissolution, as for example the one that can be modeled from a clay concentration mechanism [*Aharonov and Katsman*, 2009].

[7] In general, in stylolites, the stress concentrates at the tips and the largest stress is perpendicular to the stylolites. Recent models [*Koehn et al.*, 2007; *Ebner et al.*, 2009b; *Zhou and Aydin*, 2010] suggest that a higher stress concentration at the top of the tooth should be responsible of localized high rates of dissolution. *Benedicto and Schultz* [2010] investigated the topography of stylolites (along-strike trace length, maximum and average amplitudes) from the damaged zone of the Gubbio normal fault zone in central Italy. They showed that the amount of contractional strain accommodated by stylolites as well as their length and their number increase according to the topography parameters. Analyses of cores from boreholes reveal also an increase in stylolite abundance with depth [*Lind*, 1993]. *Fabricius and Borre* [2007] compared formations of chalk from boreholes on the Ontong Java Plateau and in the central North Sea. They showed that the burial stress and the temperature play distinct roles in the burial diagenesis and porosity development of chalk. Pressure solution and physical compaction are controlled by the burial stress while the temperature controls recrystallization and cementation. Moreover, *Lind* [1993] suggests that mineralogical anomaly is an initializing factor in stylolite formation such as burrows, shale clasts or flaser structures. Many studies were conducted on the morphology of sedimentary stylolites [*Renard et al.*, 2004; *Brouste et al.*, 2007; *Ebner et al.*, 2009b]. Morphology analyses can be done on 1-D profiles or 2-D opened surfaces. They consist on studying a stylolitic profile or surface height variations (standard deviation, height differences, power spectrum, average wavelet coefficient spectrum, etc.) over different scales [*Schmittbuhl et al.*, 1995, 2004; *Renard et al.*, 2004]. These analyses reveal two distinct scaling regimes that could be described by power laws. The power laws are a function of a roughness exponent, also called Hurst exponent, inferred to be 1 and 0.5 for small and large scale, respectively [*Renard et al.*, 2004; *Schmittbuhl et al.*, 2004; *Brouste et al.*, 2007; *Ebner et al.*, 2009b]. The two regimes are separated by a crossover length typically around 1 mm [*Renard et al.*, 2004; *Schmittbuhl et al.*, 2004]. For sedimentary stylolites, the two-dimensional (2-D) analysis of their surface does not show any significant in-plane anisotropy reflecting the fact that horizontal stresses are isotropic. *Ebner et al.* [2010a] observed that the profiles of tectonic stylolites show the same geometric attributes as sedimentary ones. Two different regimes are also observed with Hurst exponent around 1 and 0.5 for small and large scale, respectively. However, for tectonic stylolites, the 2-D analysis revealed an anisotropy of the crossover length which varies with the direction in the plane of stylolites. *Ebner et al.* [2010a] argue that this anisotropy develops because the stylolite roughens in an anisotropic in-plane stress field. The vertical and in-plane horizontal stresses are significantly different. In recent papers, stylolites are presented as fossilized signatures of the stress field [*Renard et al.*, 2004; *Schmittbuhl et al.*, 2004; *Ebner et al.*, 2009b, 2010a]. The existence of two scaling regimes for sedimentary stylolites was shown in *Schmittbuhl et al.* [2004] where a brief theoretical derivation was performed. It was shown that the crossover length between both scaling regimes is expected to be dependent on the stress acting on the stylolite during its growth. Their conclusion was that stylolite morphology can be used as a paleostress magnitude indicator. This conclusion was later probed independently on two types of approaches: first, on field data sampled from the same formation at different heights, *Ebner et al.* [2009b] showed that the measured crossover length in the morphology followed the expected scaling with the burial stress, evaluated from the position in the formation. Next, discrete numerical simulations were carried out at different stress magnitudes, allowing for the dissolution of grains along the fluid/rock interface, with free energy depending on interfacial tension and local stress. It was shown that the two expected scaling regimes were observed [*Koehn et al.*, 2007, 2012], and that the crossover length followed the predicted dependence on the far-field stress amplitude [*Koehn et al.*, 2012].

[8] Interfaces between solids and fluids are related to models of stylolitization. In the case where a solid in contact with a fluid is stressed, an instability due to pressure solution was shown theoretically to exist and is called the Asaro-Tiller-Grinfeld (ATG) instability [*Renard et al.*, 2004]. In models of dissolving surfaces with a stress imposed to a solid in contact with a fluid at chemical equilibrium, this instability leads to the growth of initial large-scale modulations of the surface with a wavelength selection obtained through a fastest growing mode. The basic equation depends on the particular boundary conditions, e.g., when two solids with different elastic properties are in contact and submitted to a stress, the interface can undergo a fingering instability led by the contrast between the free energies applied to both solids [*Angheluta et al.*, 2008, 2009, 2010]. The stability analysis can be performed theoretically from expressions for the kinetics using local free energy criteria for the reaction rate [*Renard et al.*, 2004; *Schmittbuhl et al.*, 2004], or global ones [*Bonnetier et al.*, 2009; *Angheluta et al.*, 2008]. Depending on the boundary conditions, this situation is also

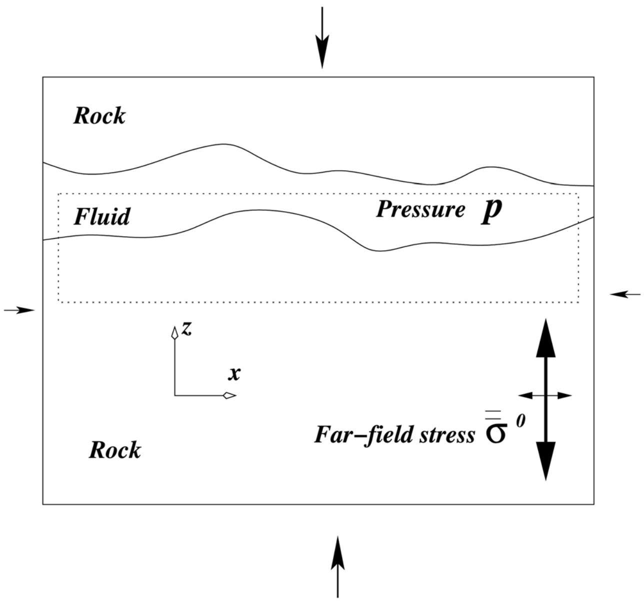

Figure 1. Initial stage of a stylolite: trapped elongated fluid pocket.

found to be unstable for perturbations exceeding a certain wavelength, leading to fingering (e.g., as with large stress tangential to a fluid interface, or a stress normal to fluid interfaces and lateral periodic boundary conditions [*Bonnetier et al.*, 2009]). With other boundary conditions, the surface energy and elastic interactions are found to stabilize the interfaces, which are only destabilized by material noise due to heterogeneities [*Schmittbuhl et al.*, 2004; *Koehn et al.*, 2007]. We will argue in details in the discussion section about the different possibilities applied to the geometry of stylolites, and the fact that stylolites displaying self-affine scaling laws for their height at large scale are compatible with the stabilizing character of elastic forces at large scale. This manuscript provides the technical development and details that lead to the final result that was previously published without derivation, in a condensed form [*Schmittbuhl et al.*, 2004]. It also compares the result of the analytical development to a direct numerical simulation.

[9] In this paper we concentrate on the following questions: (i) is the elastic energy stabilizing or destabilizing, and (ii) what is the significance of the obtained paleostress values? To answer to these questions, we do the following:

[10] 1. We derive the details of the computation leading to the link between the paleostress magnitude and the crossover length between the two scaling regimes. This is performed by a perturbative analysis of the elastic energy around an interface slightly wavy and unaligned with one of the principal stresses. Then we show in details that the mechanics and chemistry allow to relate the small and large-scale behavior of stylolites to known models, with Hurst exponents corresponding to the observed ones.

[11] 2. We finally present and discuss an application in relation with the geological context. This is made on a stylolite from the Bure carbonates and it shows how the predicted scaling regimes can be found, and how to determinate the paleostress from the extracted crossover length.

2. Analytical Approach: Continuous Elastostatic Model for Stylolite Propagation

[12] The rough morphology of stylolites arises from the disorder present in a rock and its impact on the pressure solution process. This disorder is spatially linked to the grains constituting the rock. To understand the impact of this disorder on the chemicomechanical coupling, we will consider the following simplified geometry: the initial stage of the stylolite is modeled as an elongated fluid pocket enclosed between two contactless rough surfaces of infinite extent. The contacts between these two surfaces can in principle modify the geometry of the resulting dissolution surface. However, they are assumed to be sufficiently loose in a stylolite and thus the main morphological results are not affected. This assumption simplifies the problem since the dissolution process, happening on both sides of the stylolite (Figure 1), can be described as the dissolution of a solid half plane in contact with a fluid. With this geometry, the small- and large-scale self-affine behaviors of the dissolution surface and the associated roughness exponents (or Hurst exponents) are well reproduced. The model leads to the characteristic exponents typically observed in previous studies [*Renard et al.*, 2004; *Schmittbuhl et al.*, 2004; *Brouste et al.*, 2007; *Ebner et al.*, 2009b].

[13] The average stylolitic plane is defined along the x and y axis (Figure 2). To have better statistics on the morphology of the studied surfaces, the model is assumed to be invariant by translation along the y axis. It allows to us to describe a larger range of scales at the same numerical cost and to numerically solve the self-affine behavior of the resulting pressure solution surface over a larger number of orders of length scales. The same approach can be considered using invariance by translation along the x axis. In the model we assume a mechanical equilibrium throughout the system and express the dissolution rate as a function of the stress tensor and of the area of interface per unit volume.

2.1. Force Perturbation Related to the Mechanical Equilibrium Along the Fluid-Solid Interface

[14] First, we express the mechanical equilibrium at the solid-fluid interface (Figure 2). The convention adopted is that compressive stresses and compactive strains are negative [*Landau and Lifchitz*, 1986]. The far-field stress applied to the host rock is denoted by $\bar{\bar{\sigma}}^0$. The largest principal stress axis, perpendicular to the average plane of the stylolite, is defined along the z axis. The fluid pocket transmits all the load through itself (the boundary condition of the fluid pocket is approximated as undrained for that respect: if there is any flow, from or into the fluid pocket, it happens slowly, via the lateral ends. If there is any contact between the opposite walls perpendicular to the main fluid direction, the load transmitted through this contact is neglected). The fluid pressure is thus homogeneous and equal to the largest principal stress applied to the host rock, considering the integral of the local stress field $\bar{\bar{\sigma}}$ along an elongated rectangular boundary (dashed line in Figure 1):

$$p = -\sigma^0_{zz} \tag{1}$$

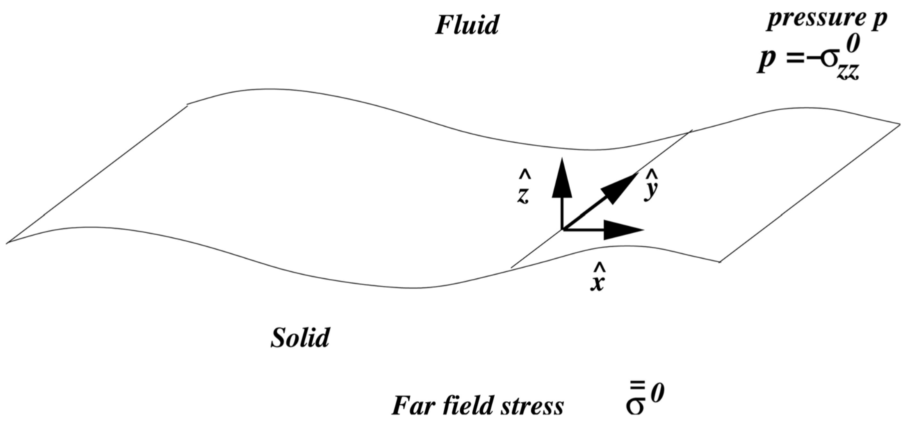

Figure 2. Solid-fluid interface: geometry considered.

Locally, the local stress $\bar{\bar{\sigma}}$ is split between the far-field asymptotic value $\sigma^{0=}$ and a perturbation generated by the irregular nature of the interface $\sigma^{1=}$:

$$\bar{\bar{\sigma}}(x) = \bar{\bar{\sigma}}^{0} + \bar{\bar{\sigma}}^{1}(x) \tag{2}$$

[15] The far-field stress unit vectors $\hat{x}$ and $\hat{z}$ along the x and z axis are assumed to be the principal directions, i.e.,

$$\bar{\bar{\sigma}}^{0} = \sigma_{xx}^{0}\hat{x}\hat{x} + \sigma_{zz}^{0}\hat{z}\hat{z} \tag{3}$$

[16] Here, the notations $\hat{x}\hat{x}$ and $\hat{z}\hat{z}$ correspond to unit matrixes composed from the unit vectors, e.g., as are $\hat{y}\hat{y}$, $\hat{x}\hat{y}$, or $\hat{z}\hat{x}$. This canonical basis for the matrixes is composed from the doublets of unit vectors $\hat{x}, \hat{y}$ and $\hat{z}$. For example, $\hat{x}\hat{z}$ represents the unit matrix with all components equal to zero, apart from a unit in the line corresponding to the x coordinate, and the column corresponding to the z one, so that for a pair of vectors u, v applied to the left and right of this matrix, $u \cdot (\hat{x}\hat{z}) \cdot v = (u \cdot \hat{x})(\hat{z} \cdot v) = u_x v_z$. In other terms, with cartesian components along directions of indexes i and j, and the help of the Kronecker symbol δ, the components of the matrix $\hat{x}\hat{z}$, for example, are: $(\hat{x}\hat{z})_{ij} = \delta_{ix}\delta_{jz}$. This convention to define the canonical basis of matrix space (nine elementary second-order dyadic products like $\hat{x}\hat{z}$) from the three basic unitary vectors of the vectorial space, $\hat{x}, \hat{y}$ and $\hat{z}$ is, for example, defined by *Gonzalez and Stuart* [2008].

[17] For a stylolite, the largest compressive stress axis is normal to its average plane and thus to the average fluid pocket direction:

$$|\sigma_{zz}^{0}| > |\sigma_{xx}^{0}| \tag{4}$$

This relation has strong implications on the stability of the surface pattern emerging from the dissolution process. The far-field deviatoric stress is defined as

$$\sigma_{s}^{0} = (|\sigma_{zz}^{0}| - |\sigma_{xx}^{0}|) = (\sigma_{xx}^{0} - \sigma_{zz}^{0}) \tag{5}$$

To express the force perturbation related to the curved nature of the interface, we define the unit vector $\hat{n}$ normal to the surface pointing toward the fluid. This vector is assumed to be close to the principal stress axis. In the following, we will consider small-angle deviations from a straight surface, and the results will therefore be valid for small surface slopes only. The model presented below aims to describe the onset of the stylolite propagation from a flat surface, and it will also describe the evolution of large wavelength modes, if the aspect ratio of such modes (ratio of the amplitude over the wavelength) stays small, corresponding to small effective slopes at large wavelength.

[18] The interface is described as a single-valued function $z(x)$ and the slopes are assumed to be of the order ϵ, i.e., that $|\partial_{x}(z)| \in O(\epsilon) \ll 1$. Since the normal $\hat{n}$ to the interface of slope $\partial_{x}z$ can be expressed by the conditions of normality to the interface, $\hat{n} \cdot (1, \partial_x z)^T = 0$ (at any order or ϵ), and by its unitary norm $\hat{n}^2 = 1$, it is in general $\hat{n} = (-(\partial_x z)\hat{x} + \hat{z})/\sqrt{1 + (\partial_x z)^2}$. Using the above limit of small slopes, developing in ϵ, we obtain to leading order

$$\hat{n} = \hat{z} - (\partial_x z)\hat{x} + O(\epsilon^2) \tag{6}$$

(The order $O(\epsilon)$ is absent from $\hat{n}$).

[19] The local mechanical equilibrium at the solid-fluid interface is expressed as

$$\sigma \cdot \hat{n} = -p\hat{n} \tag{7}$$

And with equations (1)–(7) the force perturbation (illustrated in Figure 3) becomes

$$\begin{aligned}\delta f(x) = \sigma^1(x) \cdot \hat{n} = \\ &- p\hat{n} - \sigma^0 \cdot \hat{n} \\ &= \sigma_{zz}^{0}[\hat{z} - (\partial_x z)\hat{x}] - \sigma_{zz}^{0}\hat{z} + \sigma_{xx}^{0}(\partial_x z)\hat{x} \\ &= (\sigma_{xx}^{0} - \sigma_{zz}^{0})(\partial_x z)\hat{x} \\ &= \sigma_{s}^{0}(\partial_x z)\hat{x}\end{aligned} \tag{8}$$

2.2. Chemicomechanical Coupling

[20] Next, we express the chemicomechanical coupling. The dissolution speed normal to the solid/fluid interface (in mol.m^{-2}. s^{-1}) is to the first order proportional to the chemical potential $\Delta\mu$ of the chemical product dissolving [*Kassner et al.*, 2001; *Misbah et al.*, 2004; *Schmittbuhl et al.*, 2004; *Koehn et al.*, 2007]:

$$v = m\Delta\mu \tag{9}$$

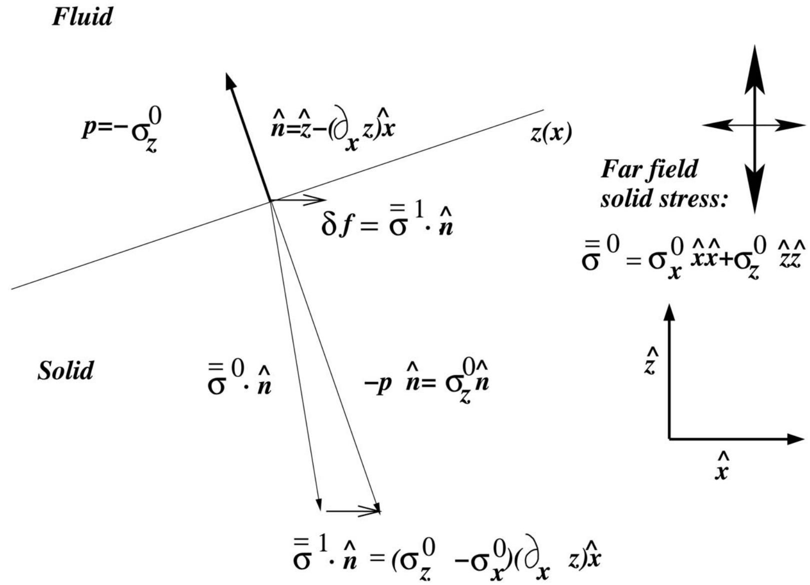

Figure 3. Local mechanical equilibrium along the fluid-solid interface (equation (8)).

where

$$m = k_0\Omega/RT \tag{10}$$

is the mobility of the dissolving species, R = 8.31 J. mol^{-1}. K^{-1} is the universal gas constant, T is the temperature in Kelvin, k_0 is a dissolution rate which can be measured experimentally, and Ω is a molar volume. For calcite, $\Omega \simeq 4 \cdot 10^{-5}$ m^3.mol^{-1} and $k_0 \simeq 10^{-4}$ mol.m^{-2}. s^{-1} for dissolution in water at atmospheric pressure and 298°K [*De Giudici*, 2002; *Schmittbuhl et al.*, 2004]. The difference in chemical potential from the solid state to the fluid state is [*Kassner et al.*, 2001; *Misbah et al.*, 2004; *Koehn et al.*, 2007]

$$\Delta\mu = \Delta\Psi_s + \Omega\Delta P_n + \Omega\gamma\kappa \tag{11}$$

Considering a solid state at given pressure and elastic free energy in chemical equilibrium with the fluid, $\Delta\Psi_s$ and ΔP_n are defined respectively as the change in Helmoltz free energy per mole and the change in stress normal to the interface. The last term corresponds to the surface energy with $\kappa = \partial_{xx}z$, the surface curvature (the inverse of the radius curvature) and γ the surface tension between the solid and the fluid phase. In a particular case, neglecting temperature variation effects and assuming that the fluid composition is in chemical equilibrium with a solid flat surface at normal pressure p and stress σ_{ref}, equation (11) reduces to

$$\Delta\mu = 0 \tag{12}$$

$$\kappa = 0 \tag{13}$$

More generally, by definition [*Kassner et al.*, 2001],

$$\Delta\Psi_s + \Omega\Delta P_n = \Omega\Delta u_e, \tag{14}$$

where

$$\Delta u_e = u_e(\sigma) - u_e^{ref} \tag{15}$$

and

$$u_e = [(1+\nu)\sigma_{ij}\sigma_{ij} - \nu\sigma_{kk}\sigma_{ll}]/4E \tag{16}$$

is the elastic free energy per unit volume with E the Young's modulus and ν the Poisson's ratio of the elastic solid [*Kassner et al.*, 2001; *Landau and Lifchitz*, 1986].

[21] To take into account the dissolution speed variations associated to the morphology of the stylolite, we develop the dissolution speed to the leading order as

$$v = v^0 + v^1 \tag{17}$$

With equations (9)–(16),

$$\begin{aligned} v^0 &= \frac{k_0\Omega^2}{RT}\left(\frac{[(1+\nu)\sigma_{ij}^0\sigma_{ij}^0 - \nu\sigma_{kk}^0\sigma_{ll}^0]}{4E} - u_e^{ref}\right) \\ &= \frac{k_0\Omega^2}{RTE}(\alpha p_0^2 - \alpha_{ref}p_{ref}^2) \end{aligned} \tag{18}$$

The geometrical factor α is computed assuming $\sigma_{xx}^0 = \sigma_{yy}^0 = -p_0 + \sigma_s/3$ and $\sigma_{zz}^0 = -p_0 - 2\sigma_s/3$:

$$\alpha = \frac{9(1-2\nu) + 2(1+\nu)\sigma_s^2/p_0^2}{12} \tag{19}$$

α_{ref} is expressed with a similar expression and characterizes the chemical equilibrium with the fluid at the referential state as a function of the pressure p_{ref} and the shear stress σ_{ref}. Typically, for a limestone with a Young's modulus E = 80 GPa stressed at $p_0 \simeq$ 10 MPa (which corresponds to a few hundred of meters deep in sedimentary rocks) and for a fluid with a chemical composition in equilibrium with the solid, the dissolution speed at the solid-fluid interface in a limestone is of the order of

$$v_n^0 \simeq 10^{-6} \text{ to } 10^{-6} \text{ m.}yr^{-1}.$$

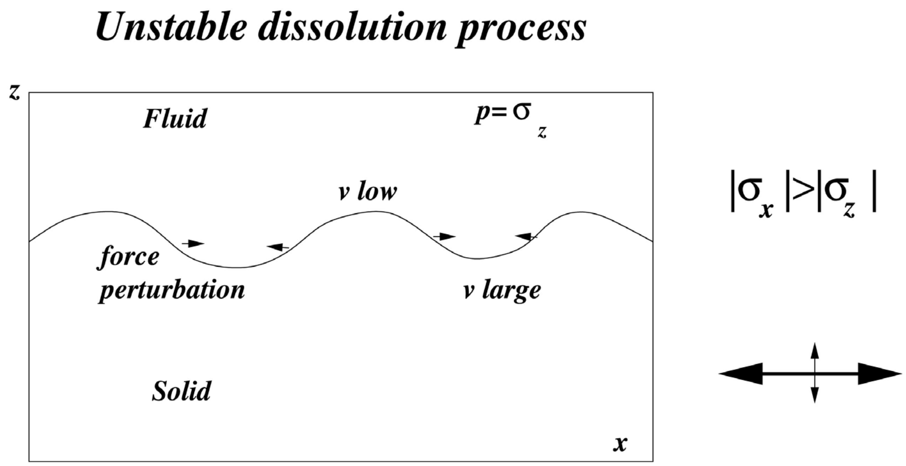

Figure 4. Surface tangential to the largest stress (σ_{xx}) axis: unstable case, Azaro-Tiller-Grinsfeld instability.

2.3. Consequences for the Stability of the Dissolution Process

[22] From the local mechanical equilibrium and the nature of the chemicomechanical coupling, some important considerations can be inferred about the morphological stability of the dissolution surfaces. This behavior depends on the orientation of the surfaces with respect to the far-field stress.

[23] Previously we have shown how to express the force perturbation arising from the mismatch between the solid-fluid interface orientation and the principal axis of the far-field stress tensor $\hat{x}$ (equation (8)).

[24] This relationship holds independently of the relative magnitudes of the principal stresses σ_{xx} and σ_{zz}. If the largest principal stress is tangential to the interface, which is not the case for stylolites, $\sigma_s^0 < 0$ and the sign of $\delta f(x) \cdot \hat{x}$ is opposite to the slope of the interface $\partial_x z$. Such tangential force perturbation is concentrated at the points lying ahead of the average dissolution front (Figure 4). The elastic forces concentrate stress at the valleys of the dissolution front where the free energy is thus higher. This leads to an increased dissolution speed at the points lying ahead of the averaged front. The dissolution propagates downward. The points at the crests, i.e., located behind the averaged dissolution front, show a reduced rate of dissolution thus pushing them further from the average front. The points lying out of the average dissolution plane tend therefore to depart further from the average position. The elastic force is in this situation a destabilizing force. On the contrary, the surface tension tends to stabilize the process by decreasing the surface area by flattening the interface.

[25] The competition between the elastic long-range destabilizing forces and the surface tension short-range stabilizing forces leads to the ATG interface instability. The fastest growing wavelength is determined by the balance between these long-range destabilizing and short-range stabilizing effects. Such instability arising in stressed solids was studied theoretically [*Asaro and Tiller*, 1972; *Grinfeld*, 1986; *Misbah et al.*, 2004] and observed experimentally in stressed soluble crystals immersed in a saturated fluid [*Den Brok and Morel*, 2001; *Koehn et al.*, 2004].

[26] If the largest principal stress lies perpendicular to the interface, as for stylolites, $\sigma_s^0 > 0$ and the sign of $\delta f(x) \cdot \hat{x}$ is the same as the slope of the interface $\partial_x z$. Such tangential force perturbation is concentrated at the points lying behind of the average dissolution front (Figure 5). The elastic forces concentrate stress at the crests of the dissolution front where the free energy is thus higher. This leads to an increased dissolution speed for the points lying behind the averaged front. The dissolution propagates downward. The points at the valleys, i.e., located ahead of the averaged dissolution front, tend to come back to the average position. The elastic force is a stabilizing force in this situation. Here, the surface tension is again a stabilizing process.

[27] Since the long-range elastic force and the short-range surface tension force are stabilizing forces, if the modeled solid properties are purely homogeneous (i.e., homogeneous elastic solid with homogeneous dissolution rate properties), the model predicts the flattening of any initial nonplane surface with time.

[28] Consequently, to model the morphogenesis of stylolites, which are rough surfaces, we will take here into account the disorder linked to the material properties.

2.3.1. Consequence on Initial Evolution of Trapped Fluid Pocket

[29] In summary, the above arguments show that an elementary bump of a flat surface disappears for $\sigma_s > 0$, or grows for $\sigma_s < 0$. Qualitatively, if the argument on the stability of surfaces depending on their orientation on the principal stress axis extends for more local orientations along trapped fluid pockets, one should observe the following. The sides of a fluid pocket lying tangentially to the largest stress should develop instable grooves penetrating into the solid, similarly to the ATG instability case. On the contrary, the sides normal to the largest stress direction should remain relatively flat, apart from the fluctuations due to the disorder. These small variations along the surfaces normal to the principal stress axis, and the penetrations of grooves of characteristic wavelength in the rock along the direction of the weakest stress, should lead to the development of elongated structures, and merge initially separated fluid pockets (or clay-enriched pockets). This qualitative mechanism is illustrated on Figure 6. This expectation of qualitative evolution is indeed compatible with the mechanism of development of anticracks numerically obtained by *Koehn et al.* [2003]. The experimental grooves observed along

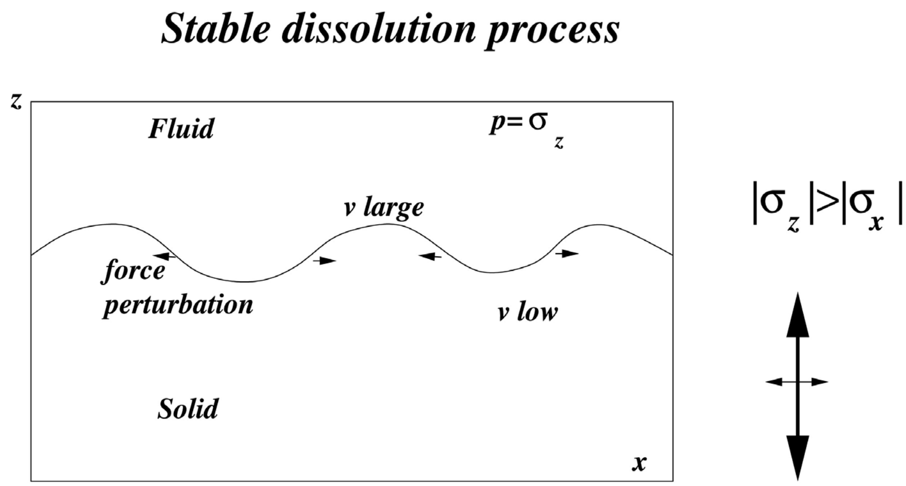

Figure 5. Surface normal to the largest stress (σ_{zz}) axis: stable case.

the free surface on the sides of a fluid-filled cylindrical pocket by *Den Brok and Morel* [2001] also displayed this trend.

2.4. Expression of the Dissolution Speed Perturbation as a Function of the Interface Shape

[30] To model the disorder in the solid we assume that the material properties (related to the solid grains) vary in a random and spatially uncorrelated way. This disorder can originate from the diversity of grain composition, grain size or orientation; i.e., it represents the small-scale heterogeneities present in the rock. For example, the dissolution rate k can be expressed as an averaged term k_0 plus some spatial variations of zero average $\eta(x, z) \cdot k_0$:

$$k = k_0(1 + \eta(x, z(x))) \tag{20}$$

The random variable η is a quenched disorder with no spatial correlations and is characterized by its mean $\langle\eta\rangle = 0$ and its variance $\langle\eta^2\rangle$ assumed to be small enough to keep small local slopes. The dynamics of the dissolving interface $z(x, t)$ can be expressed from equations (9)–(17) as

$$\begin{aligned} v = -\partial_t z &= \frac{k\Omega^2}{RT}(\Delta u_e + \gamma\partial_{xx}z), \\ &= \frac{k_0\Omega^2}{RT}(1+\eta)\Big\{(1+\nu)[(\sigma^0_{ij}+\sigma^1_{ij})(\sigma^0_{ij}+\sigma^1_{ij}) \\ &\quad - \nu(\sigma^0_{kk}+\sigma^1_{kk})^2]/4E - u^e_{ref} + \gamma\partial_{xx}z\Big\} \\ &= \frac{k_0\Omega^2}{RT}\Big\{(1+\nu)[\sigma^0_{ij}\sigma^0_{ij} - \nu(\sigma^0_{kk})^2]/4E - u^e_{ref}\Big\} \\ &\quad + \frac{k_0\Omega^2}{RT}\eta\Big\{(1+\nu)[\sigma^0_{ij}\sigma^0_{ij} - \nu(\sigma^0_{kk})^2]/4E - u^e_{ref}\Big\} \\ &\quad + \frac{k_0\Omega^2}{RT}\Big\{(1+\nu)[2\sigma^0_{ij}\sigma^1_{ij} - 2\nu(\sigma^0_{kk}\sigma^1_{kk})]/4E + \gamma\partial_{xx}z\Big\} \end{aligned} \tag{21}$$

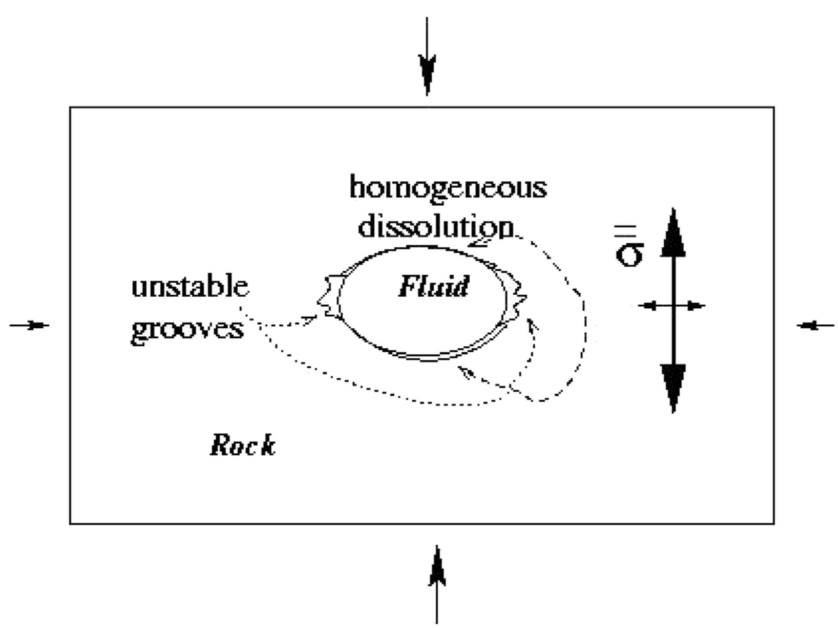

Figure 6. Expected stability or instability of the dissolution front around a trapped fluid pocket.

i.e., using equation (18) for the expression of $\sigma^0_{ij}\sigma^0_{ij} - \nu(\sigma^0_{kk})^2$, a dissolution speed separated between an average homogeneous speed v_0 and a leading order of the perturbations v_1, first order in ϵ as

$$\partial_t z(x,t) = -v_0 - v_1(x,t) \tag{22}$$

with v_0 the dissolution speed given by equation (18) and v_1 a deviation of the dissolution speed with respect to the average dissolution speed v_0 expressed as

$$v^1 = \frac{k_0\Omega^2}{RT}\frac{(\alpha p_0^2 - \alpha_{ref}p_{ref}^2)}{E}\eta(x,z(x)) + \frac{k_0\Omega^2}{RT}\gamma\partial_{xx}z(x) + \frac{k_0\Omega^2}{RT}\left(\frac{[(1+\nu)\sigma^0_{ij}\sigma^1_{ij} - \nu\sigma^0_{kk}\sigma^1_{ll}]}{2E}\right) \tag{23}$$

σ^1 is the stress perturbation mentioned previously in equation (2). It is generated by the surface distribution of the tangential force perturbation $\delta f(x)$ due to the irregular nature of the interface.

[31] The first term is a quenched disorder term leading to the roughening of the interface. The second one is a stabilizing quadratic short-range term arising from the surface tension. The last term can be expressed via a nonlocal kernel from the shape of the interface $z(x)$ by integrating the elastostatic equations in the solid half plane.

2.5. Detailed Form of the Elastic Long-Range Interaction Kernel

[32] The stress perturbation induced by the force perturbation $\delta f(x)$ (equation (8)) exerted on the surface can be determined via the Green function method. Following *Landau and Lifchitz* [1986], the displacement induced by an elementary force $\hat{x}$ applied at the origin (0, 0, 0) on a semi-infinite solid is

$$\begin{aligned}
a_x(x,y,z) &= \frac{1+\nu}{2\pi E}\left\{\frac{2(1-\nu)r+z}{r(r+z)} + \frac{(2r(\nu r+z)+z^2}{r^3(r+z)^2}x^2\right\}\\
a_y(x,y,z) &= \frac{1+\nu}{2\pi E}\left\{\frac{2r(\nu r+z)+z^2}{r^3(r+z)^2}xy\right\}\\
a_z(x,y,z) &= \frac{1+\nu}{2\pi E}\left\{\frac{(1-2\nu)x}{r(r+z)} + \frac{zx}{r^3}\right\}
\end{aligned} \tag{24}$$

where r is the distance relatively to the force application point at (0, 0, 0), i.e., $r^2 = x^2 + y^2 + z^2$. The associated strain applied on the solid is

$$\epsilon^e_{ij} = \frac{1}{2}(\partial_i a_j + \partial_j a_i) \tag{25}$$

and the associated stress is

$$f_{ij}(x,y,z) = \frac{E}{1+\nu}(\epsilon^e_{ij} + \frac{\nu}{1-2\nu}\epsilon^e_{kk}\delta_{ij}) \tag{26}$$

The stress associated to the point force $\hat{x}$ applied on the surface of normal $\hat{z}$ at the origin is equal at the origin itself to $\hat{x}\hat{z} + \hat{z}\hat{x}$.

[33] Since the model treated here is invariant by translation along y, the force perturbation $\delta f(u) = \sigma^0_s(\partial_u z)(u)\hat{x}$ is exerted at any $v \in]-\infty, \infty[$ and the resulting displacement field at (x, y, z), is solely dependent on (x, z) and can be expressed, by linearity of the elastostatics equations (similarly to the elastostatic Green function method detailed in equation (8.14) by *Landau and Lifchitz* [1986]), as a displacement field w of components

$$w_i(x, y=0, z) = \int_{u=-\infty}^{\infty}\int_{v=-\infty}^{\infty} a_i(x-u, -v, z)dudv\,\delta f(u).\hat{x} \tag{27}$$

[34] The associated strain perturbation is

$$\epsilon^p_{ij} = \frac{1}{2}(\partial_i w_j + \partial_j w_i), \tag{28}$$

and the associated stress,

$$\sigma^1_{ij}(x) = \frac{E}{1+\nu}(\epsilon^p_{ij} + \frac{\nu}{1-2\nu}\epsilon^p_{kk}\delta_{ij}) + \delta f(x)(\delta_{ix}\delta_{jz} + \delta_{iz}\delta_{jx})\delta(z), \tag{29}$$

where the first term represents the stress induced by the elastic deformation, and the second one the direct application of the force perturbation on the surface. In the above, the spatial derivative of equation (28) can be exchanged with the integration in equation (27), to obtain

$$\epsilon^p_{ij}(x, y=0, z) = \int_{u=-\infty}^{\infty}\int_{v=-\infty}^{\infty} \epsilon^e_{ij}(x-u, -v, z)dudv\,\delta f(u).\hat{x}. \tag{30}$$

Recalling the expression of the force perturbation, equation (8), from equation (29), the stress perturbation along the surface, at $z = 0$, is thus,

$$\sigma^1_{ij}(x) = \sigma^0_s \cdot p.p.\left[\int_{u=-\infty}^{\infty} du(\partial_u z)(u) * \int_{v=-\infty}^{\infty} f_{ij}(x-u, -v, 0)dv\right] + \sigma^0_s(\partial_x z)(x)(\delta_{ix}\delta_{jz} + \delta_{iz}\delta_{jx}) \tag{31}$$

where p.p. refers to the principal part of the integral. Taking the derivatives of the displacement field (equation (25)), we can calculate the associated stress. Integrating this result along the y axis gives

$$\int_{v=-\infty}^{\infty} f_{ij}(x, -v, 0)dv = -\frac{2\nu}{\pi x}(\delta_{ix}\delta_{jx} + \delta_{iy}\delta_{jy}) \tag{32}$$

and thus,

$$\sigma^1(x) = -\frac{2\nu\sigma^0_s}{\pi}\cdot p.p.[\int_{x'=-\infty}^{\infty} du\frac{(\partial_u z)(u)}{x-u}](\hat{x}\hat{x} + \hat{y}\hat{y}) + \sigma^0_s\cdot(\partial_x z)(x)(\hat{x}\hat{z} + \hat{z}\hat{x}) \tag{33}$$

The elastic energy perturbation associated to the interface deformation can be computed using equation (33) and the relation

$$\sigma^0 = -(p_0 - \sigma^0_s/3)(\hat{x}\hat{x} + \hat{y}\hat{y}) - (p_0 + 2\sigma^0_s/3)\hat{z}\hat{z} \tag{34}$$

It results in

$$u_e^1 = \frac{[(1+\nu)\sigma_{ij}^0\sigma_{ij}^1 - \nu\sigma_{kk}^0\sigma_{ll}^1]}{2E} = \frac{2\nu[(1-2\nu)p_0]}{\pi E} * \sigma_s^0 \cdot p.p.\left[\int_{u=-\infty}^{\infty} du \frac{(\partial_u z)(u)}{x-u}\right] \quad (35)$$

2.6. Dynamic Equation for the Dissolution Interface

[35] The equation (22) rules the dynamics of the interface dissolution. When computed with equation (18), it gives

$$\frac{RT}{k_0\Omega^2}v^1 = \frac{(\alpha p_0^2 - \alpha_{ref}p_{ref}^2)}{E}\eta(x,z(x)) - \gamma\partial_{xx}z(x) + \beta\frac{p_0\sigma_s^0}{E}\cdot p.p.\left[\int_{u=-\infty}^{\infty} du\frac{(\partial_u z)(u)}{x-u}\right] \quad (36)$$

where β is a geometrical factor:

$$\beta = [2\nu(1-2\nu)]/\pi \quad (37)$$

Equation (23) can be expressed in a dimensionless form by using length and time units as

$$L^* = \gamma E/(\beta p_0 \sigma_s) \quad (38)$$

$$\tau = (L^*)^2 RT/(\gamma k_0 \Omega^2) \quad (39)$$

We define the dimensionless variables in the reference frame moving at the average velocity $- v_0$ as

$$z' = [z + (v_0 t)]/L^* \quad (40)$$

$$x' = x/L^* \quad (41)$$

$$t' = t/\tau \quad (42)$$

and the reduced quenched noise as

$$\eta'(x', z'(x,t) - v_0 t/L^*) = [(\alpha p_0^2 - \alpha_{ref}p_{ref}^2)/(\beta p_0\sigma_s)]\eta(x, z(x,t)) \quad (43)$$

The dimensionless stochastic equation for the stylolite growth process is then

$$\partial_{t'}z'(x',t') = \eta'(x', z'(x',t') - v_0\tau t'/L^*) + \partial_{x'x'}z' - p.p.\left[\int_{u=-\infty}^{\infty} du\frac{(\partial_u z')(u)}{x'-u}\right] \quad (44)$$

At large average dissolution speed, the term $v_0\tau t'/L^*$ takes over z quickly and the noise is annealed, becoming mostly time dependent. On the contrary, for sufficiently slow processes such as the extend of the surface roughness over several grains, the noise can be considered as quenched. This is the case here as the changes in η' arising from $z(x, t)$ are significantly larger than the changes due to some variations of the average dissolution front position $v_0\tau t'/L^*$. To the first order, the noise dependence is mainly $\eta'(x', z'(x', t'))$ and the noise will therefore be considered here as quenched.

[36] The dynamic equation then becomes

$$\partial_{t'}z'(x',t') = \eta'(x', z'(x',t')) + \partial_{x'x'}z' - p.p.\left[\int_{u=-\infty}^{\infty} du\frac{(\partial_u z')(u)}{x'-u}\right] \quad (45)$$

Alternatively, in some arbitrary spatial unit ℓ, this can also be written as

$$\partial_t z(x,t) = \eta''(x', z'(x',t')) + \partial_{xx}z - \frac{\ell}{L^*}\int dy\frac{\partial_y z}{x-y} \quad (46)$$

with $L^* = \gamma E/(\beta p_0 \sigma_s)$ and $\tau = \ell^2 RT/(\gamma k_0 \Omega^2)$, the time unit.

2.7. Small-Scale and Large-Scale Behavior of the Model

[37] Elastic interactions can be neglected in equation (46) for small scales such as $\ell \ll L^*$ (the lower limit corresponds to the resolution of the analyzed signal) reducing the model to a Laplacian description:

$$\partial_t z'(x,t) = \partial_{xx}z' + \eta(x, z'(x)) \quad (47)$$

This equation is known as the Edwards Wilkinson model [*Edwards and Wilkinson*, 1982] modified with a quenched random noise. It has been studied in the literature and leads to the growth of self-affine surfaces of roughness $\zeta \sim 1.2$ [*Roux and Hansen*, 1994], in agreement with existing data on stylolites where $\zeta \sim 1.1$ [*Schmittbuhl et al.*, 2004].

[38] Conversely, for large scales $\ell \gg L^*$ (the upper limit corresponds to the system size), surface tension can be neglected reducing equation (46) to a mechanical regime:

$$\partial_t z'(x,t) = -\frac{\ell}{L^*}\int dy\frac{\partial_y z}{x-y} + \eta(x, z'(x)) \quad (48)$$

In this case, the model is similar to known models describing the propagation of an elastic line on a disordered pinning landscape or the propagation of a mode I fracture front in a disordered solid. It leads to the growth of self-affine surfaces of roughness $\zeta \simeq 0.5$ [*Tanguy et al.*, 1998]. In summary, the model derived above predicts the growth of dissolution surfaces with different self-affine characteristics at small scale ($\zeta_1 \sim 1.2$) and large scale ($\zeta_2 \sim 0.5$). The transition between these regimes is expected to occur at a certain crossover length L^*.

3. Numerical Approach: Dynamic Evolution of the Interface

[39] From a purely analytical point of view and via the similarity of asymptotic form of the dynamic equation with known models for large and small scales, we have shown that two different scaling laws are expected for small and large scales, and that the crossover length should depend on the far-field stress magnitude. Independently from this general analytical analysis, we will now show how to solve the problem numerically, i.e., implement the dynamic evolution of the interface with all the large- and small-scale terms and random variables to represent the disorder and analyze the resulting morphogenesis.

3.1. Practical Implementation of the Model

[40] We simulate the dissolution process for a calcite-water interface. This is done in an event-driven discrete lattice code, with algorithms corresponding to a discrete Langevin equation leading to grains getting dissolved one at a time: for each grain along the interface, a time to dissolution is computed from the above Langevin equation, and the grain with the shortest dissolution time is removed. After what, the times are recomputed for all grains along the interface, and the next grain with shortest dissolution time is removed, and so on (see *Renard et al.* [2004] for details of the practical implementation). The selected constants correspond to a calcite-water system, $\gamma = 0.27\ \mathrm{J \cdot m^{-2}}$, $\Omega = 4 \cdot 10^{-5} \mathrm{m^3 \cdot mol^{-1}}$, $\nu = 0.25$, $E = 80$ GPa and $k_0 = 10^{-4} \mathrm{mol \cdot m^{-2} \cdot s^{-1}}$ [*Renard et al.*, 2004]. The chosen physical conditions are $T = 420$ K, $\langle p \rangle = 10$ MPa and $\langle \sigma_s \rangle = 40$ MPa. The amount of quenched noise is associated to the natural variations of grain properties. The typical scale associated to the quenched disorder (or typical grain size) is considered here to be around $\ell = 10\ \mu$m, with no correlation above this scale. This quenched disorder has a standard deviation $\sqrt{\langle \eta^2 \rangle} = [\alpha \ell p_0 / (\beta L^* \sigma_s)] \cdot [(\delta E/E) + (\delta k/k_0) + (\delta\alpha/\alpha)]$ corresponding to some relative variations of the dissolution rate of around 10% (i.e., $\delta k/k_0 \sim 0.1$).

[41] The dimensionless surface dynamic equation without disorder is

$$\partial_t z(x,t) = v_0 + \partial_{xx} z - \frac{\ell}{L^*} \int dy \frac{\partial_y z}{x - y} \tag{49}$$

where $L^* = \gamma E/(\beta p_0 \sigma_s)$, ℓ is the unit length, and $\tau = \ell^2 RT/(\gamma k \Omega^2)$ is the time unit.

[42] We assume a small disorder in the implied quantities (e.g., Young's modulus), that are quenched in the material properties of the rock heterogeneity associated with micrometric grains, typically $\ell = 10\ \mu$m. The interface is supposed to be normal to the largest stress direction (stabilizing elastic interactions).

[43] Considering a perturbation to the first order, in the referential frame of the homogeneously moving average front, $z' = z - v_0 t$, the equation ruling the surface growth becomes

$$\partial_t z'(x,t) = \partial_{xx} z - \ell L^* \int dy \frac{\partial_y z}{x - y} + \eta(x, z(x)) \tag{50}$$

with a quenched random term $\eta(x, z'(x)) = [\alpha \ell p_0 / (\beta L^* \sigma_s)] \cdot [(\delta E/E) + (\delta k/k) - (\delta\alpha/\alpha)]$.

[44] The first and second terms are stabilizing terms. The third term referring to the quenched disorder destabilizes the interface. We perform the simulation of this dynamic equation with both stabilizing terms and quenched noise.

[45] The prefactors in equation (50) depend on the rock type and on the applied stress. In addition to these mappings, the characteristic units are known as function of the rock properties. The crossover scale $L^* = \gamma E/(\beta p_0 \sigma_s)$ is function of the pressure during the growth, through p_0 and σ_s.

[46] Determining the crossover length L^* for natural samples allows to determine such stress value during the growth, and consequently the depth of the rock during the stylolite propagation. Assuming as an order of magnitude $p_0 \sim \sigma_s$ and typical values for the limestone elastic properties and the water calcite reaction rates, $L^* \sim 1$ mm leads to a typical depth of 1 km. *Stylolites* can thus be considered as *fossils of the stress magnitude.*

[47] We solved the dynamic equation (46) with an event-driven algorithm where the fastest dissolving grain is removed at each step. The problem is considered as L-periodic and the long-range elastic kernel $p.p. \int dy \frac{\partial_y z}{x-y} = -p.p. \int dy \frac{z(x)-z(y)}{(x-y)^2}$ is replaced by its finite-size form $-p.p. \int_0^L dy \frac{z(x)-z(y)}{\sin^2(\pi(x-y)/L)} \frac{\pi^2}{L^2}$. This standard form can be obtained by solving the elastostatic equations in the Fourier space and performing an inverse Fourier integration. When a new grain is reached, the realization of its quenched disorder η is evaluated using a Gaussian distribution. For the dissolution surface simulated which is 4096ℓ long, 8,000,000 grains were dissolved.

3.2. Analysis of the Small-Scale and Large-Scale Roughness of the Saturated Interface

[48] The simulation of the calcite-water system leads to the growth of a dissolution interface. Starting from a flat interface and after a certain transient time, the Fourier modes saturate to a characteristic amplitude. A snapshot of the developed stylolitic interface is shown in Figure 7.

[49] This interface fluctuates around the average progressing flat dissolution front. The Fourier power spectrum $\mathrm{P}(k,t) = ||\tilde{z}(k,t)||^2$ of each front $z(x, t)$ is extracted, and the ensemble average of this power spectrum $P(k) = \langle ||\tilde{z}(k)||^2 \rangle$ is obtained for developed interfaces, by averaging over all fronts after 80,000 grains have been dissolved. The expected small- and large-scale self-affine characteristics correspond to the theoretical predictions, as shown in Figure 8. Indeed, the power spectrum is a power law of scale, with two different exponents at large and small scale, and a crossover length around the scale L^*: For $k > 2\pi/L^*$, i.e., at small scale, we have $P(k) \sim k^{-1-2\zeta}$ with $\zeta_S = 1.2$, and for the large scales, the roughness exponent is found to be around $\zeta_L = 0.35$. The straight lines in the bilogarithmic axes (Figure 8) correspond to these power law behaviors, determined by linear regression over the two domains $k > 2\pi/L^*$ and $k < 2\pi/L^*$. The ensemble used for the roughness estimate is the following: it corresponds roughly to 100,000 grain being dissolved after the first 80,000 ones, which are discarded. We thus compute the average power spectral density profiles over all these states, representative of a saturated situation with fluctuations of the Fourier mode amplitude around some characteristic magnitude for each wavelength. The linear regression have been performed in bilogarithmic space on the ranges $0 < \log_{10}(k) < 1.5$ and $2 < \log_{10}(k) < 3$, with k unit of $2\pi/L$, with $L = 4096\ell$ and a grain size $\ell = 10\ \mu$m. The standard error bar provided by the linear regression over this two ranges is around ± 0.2 in slope (i.e., ± 0.1 for the Hurst exponents ζ).

[50] Thus, we find that the scaling of saturated surfaces in this model is compatible with observations made on natural surfaces, and with the previous analytical predictions.

[51] In addition, the dynamic behavior of these models (Edwards Wilkinson in a quenched noise [*Roux and Hansen*, 1994], or elastic string in a disordered landscape [*Tanguy et al.*, 1998]) is known. The prefactor (characteristic time) associated with the dynamics can be evaluated through the previous computations from the rock material properties. The time to saturation at an observation scale of a few

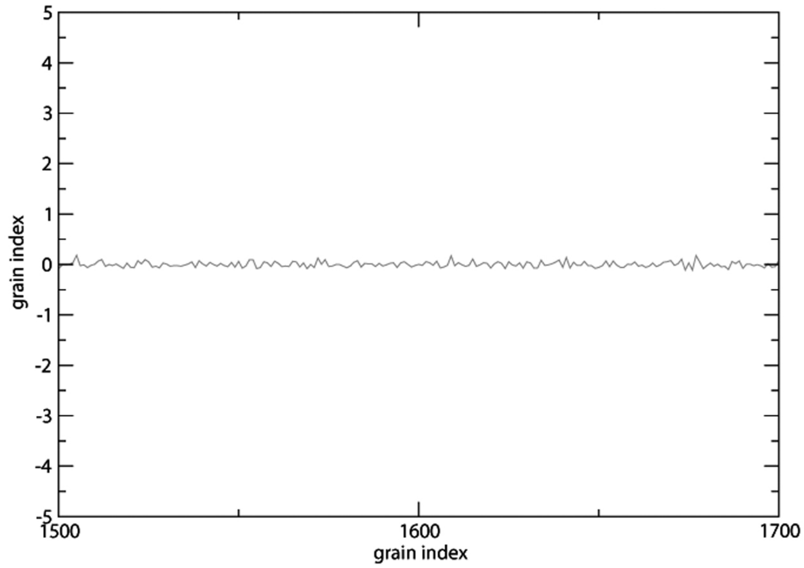

Figure 7. Snapshot of the pressure solution profile.

centimeters is estimated to be around a few thousands of years. The stylolite roughness is hence always in a saturation state for a geologist at small observation scale.

[52] However, for longer systems, e.g., decametric ones, much longer times would be required for saturation. Such long stylolites are sometimes observed but rarely analyzed in terms of scaling of the height. To our knowledge, the only analysis performed on decametric size stylolites [*Laronne Ben-Itzhak*, 2011] showed that these large-scale structures were not saturated. This means that the time during which the stylolitization was active on such very long stylolites was only enough to lead the small scales to saturated amplitude, but not the large ones (above a few tenth of centimeters).

4. Example: Application of the Model to Natural Data

[53] The model is applied to a sedimentary stylolite collected in a core at the ANDRA (National Radioactive Waste Management Agency) Underground Research Laboratory

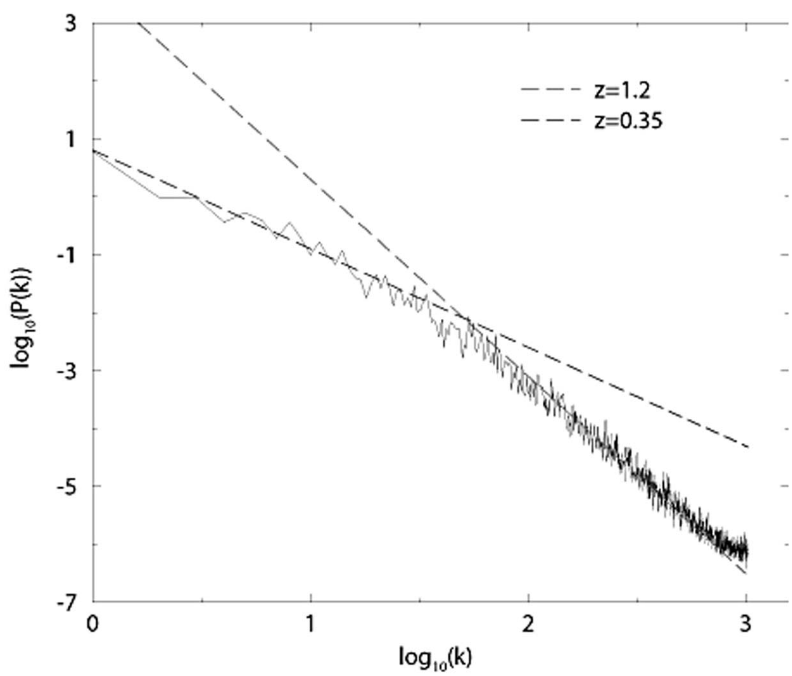

Figure 8. Average power spectrum of simulated stylolitic fronts, in bilogarithmic representation. The k unit is $2\pi/L$, with L = 4096ℓ and a grain size ℓ = 10 μm. The vertical unit is arbitrary. The crossover is obtained at $2\pi/L^*$.

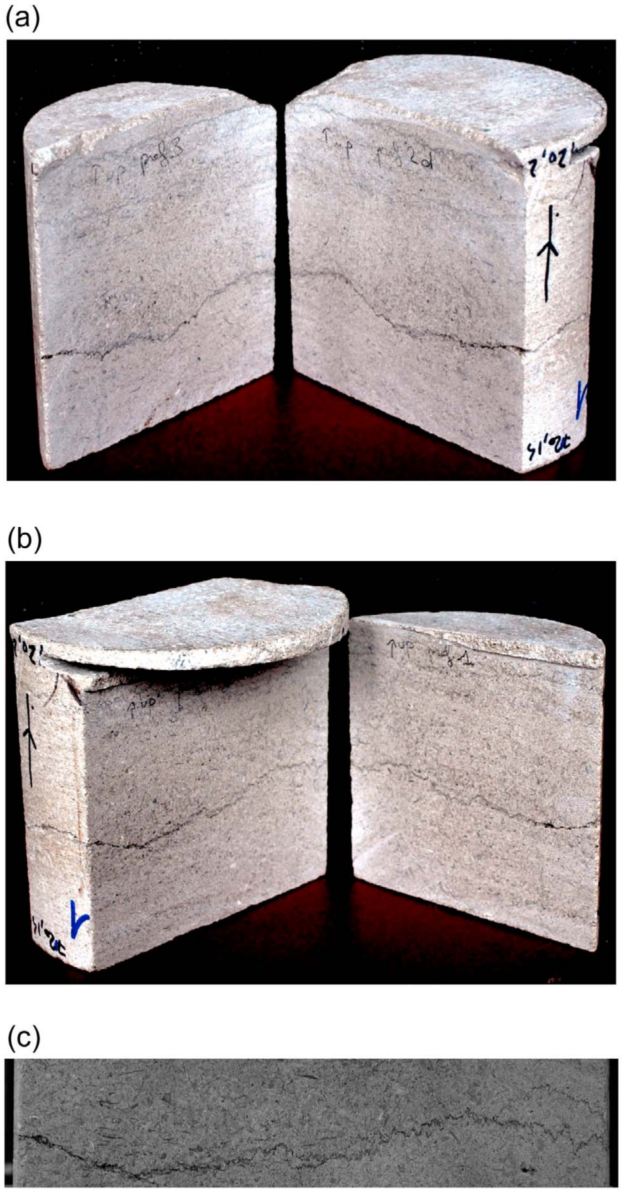

Figure 9. (a, b) A core from the Dogger formation (EST433 well) was cut in three parts to obtain four profiles. Each profile was photographed at high resolution. (c) A close-up of profile 2.

(URL) at Bure in eastern France. The selected sample comes from the borehole EST433 at a depth of 720 m. The host rock is a fine-grained, homogeneous grainstone from the Dogger age. The core was cut in three parts thus giving four profiles for analysis (Figure 9).

[54] Profiles 1 and 2 and profiles 3 and 4 are spaced by 3 mm (thickness of the drilling saw) and profiles 2 and 3 are spaced by 30 mm. Each profile has a length around 90 mm. The stylolites were photographed at a resolution of 30 μm. A systematic method was used to extract profiles from the photographs. It consists on isolating the black pixels constituting the clay particles in the stylolite from photographs converted in grey level pictures. The profiles will be used as functions in the spectral analysis (integral transforms) and thus are required to be single valued. Stylolites show a self-affinity geometry [*Schmittbuhl et al.*, 1995; *Barabási and Stanley*, 1995] meaning that they are statistically invariant under an affine transformation. Thus, for Δx and Δy the horizontal direction amplitude and Δz the vertical direction amplitude: $\Delta x \rightarrow \lambda x\Delta$, $\Delta y \rightarrow \lambda y\Delta$ and $\Delta z \rightarrow \lambda^{\zeta}\Delta z$, where λ can take any value and ζ is the Hurst exponent which describes the scaling invariance [*Schmittbuhl et al.*, 2004; *Renard et al.*, 2004]. As in *Ebner et al.* [2009b] we used both the Fourier power spectrum [*Schmittbuhl et al.*, 1995] and the averaged wavelet coefficient [*Simonsen et al.*, 1998] signal processing methods to analyze the profiles (Figure 10). We used two different methods to check the repeatability of the results. First we calculated the Fourier power spectrum $P(k)$, which is the square of the modulus of the Fourier transform, as a function of the wave number k ($k = 2\pi/L$, where L is the wavelength). The power spectrum expressed as a function of the length for a self-affine profile behaves as $P(L) \simeq L^{2\zeta + 1}$. We calculated also the averaged wavelet coefficient spectrum as a function of the scale a with Daubechies 4 wavelets which behaves as $W(a) \simeq a^{1/2 + \zeta}$.

[55] The results show the two scaling regimes predicted by the theory presented above, described by two different power laws. Figure 11 shows the Fourier power spectrum for the profile 1 as a function of the length L. The raw data are more concentrated at small scale. The lower limit for the length corresponds to the Nyquist length which is the resolution multiplied by 2. As the profiles have a finite size, the upper limit for the analysis (corresponding to small wave number) is given by the size of the profile. To analyze the data, we apply a logarithmic binning so that the weight on each point is equal. To estimate the crossover length, we used a linear-by-part fit with a crossover function changing the scaling law from small to large scale as explained in *Ebner et al.* [2009b]. The averaged wavelet coefficient spectrum (Figure 12) does not require a binning. The same kind of fitting was used to appraise the crossover length L^*.

[56] The intersection between both regimes (whose slopes are imposed by $\zeta_S = 1$ and $\zeta_L = 0.5$ for small and large scale, respectively) gives the crossover length L^*. We summarize the estimated crossover length for all the analyzed profiles with both methods in Table 1. The uncertainties on the crossover length (68% and 44% for Fourier power spectrum and averaged wavelet coefficient respectively) are due to the spatial variability of the intersection between the small and large regimes.

5. Discussion

5.1. Interpretations of the Estimated Paleostress

[57] We discuss three theories about the meaning of the estimated paleostress for the studied sedimentary stylolite:

[58] 1. Present-day stress: If the conditions for pressure solution (lithostatic pressure in competition with the presence of a fluid at an appropriate state of equilibrium) are present, a stylolite should show the present-day state of morphology and is still evolving. This means that we should measure the current applied stress and see the last evolution of the morphology. This can be compared with recent studies where vertical and horizontal stresses were measured in boreholes at Bure [*Wileveau et al.*, 2007; *Gunzburger and Cornet*, 2007] to assess if the estimated stress corresponds to the measured ones.

[59] 2. Evolution stopped: This can occur if the lithostatic stress becomes too small to encourage the process (change in

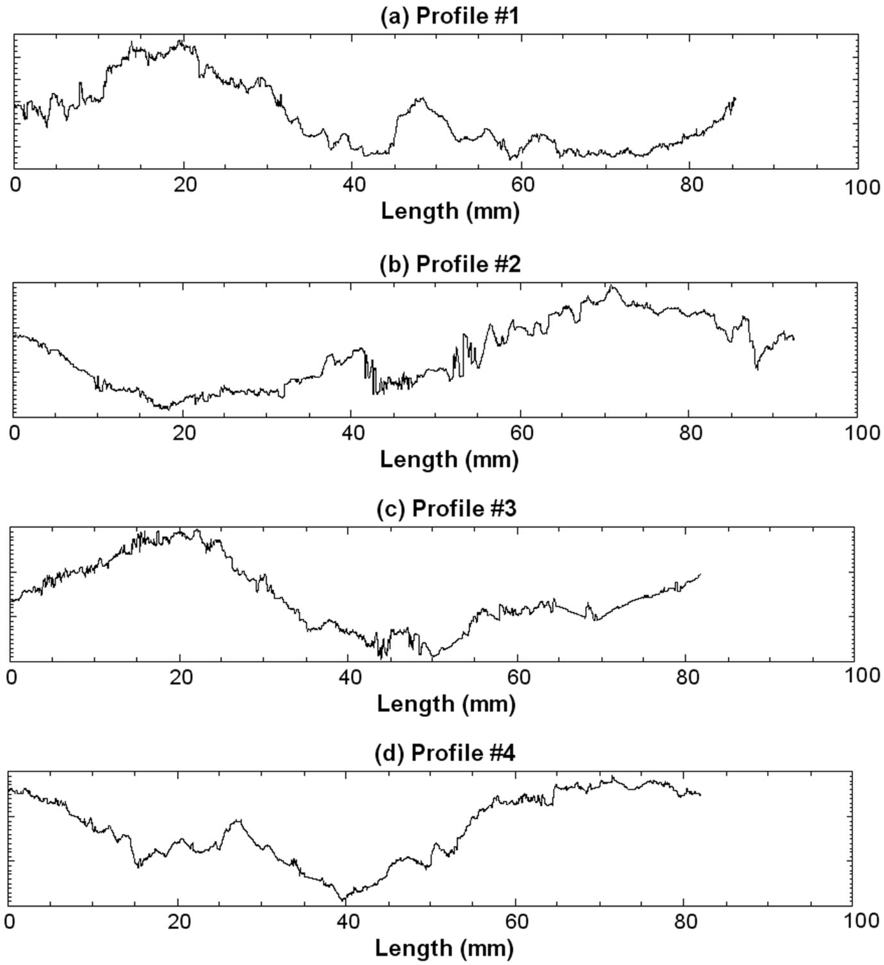

Figure 10. Functions obtained from profiles 1, 2, 3, and 4. A grey-level threshold was imposed on the pictures to isolate the stylolites. The functions were then obtained by selecting the mean limit of the pixels.

the magnitude due to a tectonic phase for example). It can also be associated with the closing of the porosity by recrystallization. Indeed, if the pore size decreases because of recrystallization at the pore surface, the surface tension increases preventing more recrystallization. Thus, the water is getting more charged in dissolved materials and the chemistry of the water changes and can stop the stylolite evolution. Moreover, the decrease of the pore size can limit or stop the fluid flow and close the system.

[60] 3. Reactivation: Both previous theories can act on the history of a stylolite. After its initiation, a stylolite can see its growth stopped by the kind of process we developed just before. If in the geological history an event as emerged soil and/or erosion allows to change the applied stress or to meteoritic fluids to flow in the soil, the system can have its properties changed and pressure solution process can start again until it is stopped or it can still evolve.

[61] These three theories will be discussed with regard to the paleostress results.

5.2. Estimation of the Paleostresses

5.2.1. Hypothesis on the Basin Evolution

[62] To estimate the paleostress from the model developed in this study, we use the average of the crossover lengths

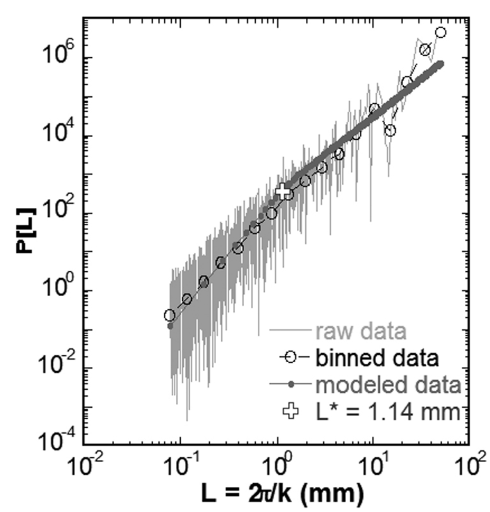

Figure 11. Fourier power spectrum of profile 1. The raw data were binned logarithmically to run a linear-by-part fitting on the data [*Ebner et al.*, 2009b]. Two different scaling regimes are observed at small and large scale with the Hurst exponent around 1 and 0.5, respectively. The fit reveals a crossover length L^* around 1.14 mm.

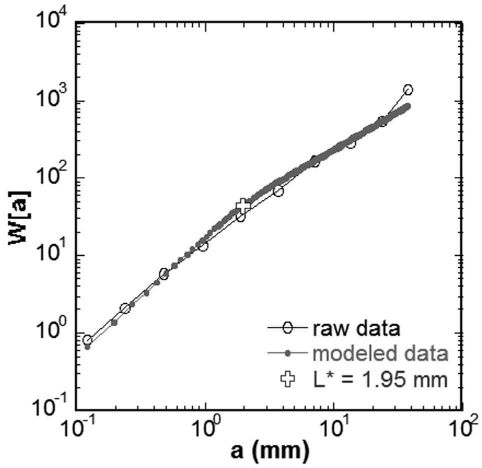

Figure 12. Averaged wavelet coefficient spectrum of profile 1. A linear-by-part fitting was run on the data [*Ebner et al.*, 2009b]. Two different scaling regimes are observed at small and large scale with the Hurst exponent around 1 and 0.5, respectively. The fit reveals a crossover length L^* around 1.95 mm. This is in good agreement with the length inferred using the Fourier power spectrum method.

determined for the four profiles. The crossover length is related to the stresses by equation (38). However, this equation can be simplified by making assumptions on the surrounding rock formation. We use the same assumptions as in *Ebner et al.* [2009b] for the stylolites from Cirque de Navacelle (Cévennes, France) considering that the initiation of stylolites occurs at the early stage of a basin. The major principal stress is vertical (σ_{zz}) as we analyzed a sedimentary stylolite. The principal horizontal stresses are isotropic ($\sigma_{xx} = \sigma_{yy}$). Thus the mean stress p_0 and the shear stress σ_S are

$$p_0 = -(2\sigma_{xx} + \sigma_{zz})/3 \tag{51}$$

$$\sigma_S = \sigma_{xx} - \sigma_{zz} \tag{52}$$

As stylolites are known to develop in the early stage of sedimentation of basins, the strain is assumed to be uniaxial:

$$\sigma_{xx} = \sigma_{yy} = \frac{\nu}{1-\nu}\sigma_{zz} \tag{53}$$

Using equations (51)–(53), equation (38) becomes

$$\sigma_{zz}^2 = \frac{\gamma E}{\alpha\beta L^*} \tag{54}$$

Table 1. Summary of the Crossover Length Found for the Four Profiles Analyzed by Fourier Power Spectrum (FPS) and Average Wavelet Coefficient (AWC)

	Profile				
	1	2	3	4	Average ($\bar{L}^*$)
L^*_{FPS} (mm)	1.14	0.37	0.37	1.13	0.75 ± 0.51
L^*_{AWC} (mm)	1.95	1.52	0.72	1.60	1.45 ± 0.64

Table 2. Summary of the Estimated Paleostress for the Stylolites From the Crossover Length

$\gamma (J \cdot m^{-2})$	$E_{up}(GPa)$	ν	α	β
0.27	36.2 ± 0.4	0.37 ± 0.04	0.32 ± 0.01	0.033 ± 0.007

where

$$\alpha = \frac{1}{3}\frac{(1+\nu)}{(1-\nu)}\frac{(1-2\nu)}{(1-\nu)} \tag{55}$$

is a dimensionless geometrical factor. The geometrical factor β (equation (37)) is $\beta = \nu(1 - 2\nu)/\pi$. Using the average crossover length L^* in equation (54), we can estimate the main principal paleostress σ_{zz}. The Poisson's ratio ν of the host rock was determined by measuring the P and S elastic wave velocities ($\nu = \frac{0.5(V_P/V_S)^2-1}{((V_P/V_S)^2-1)}$). The relative errors for the measurements of V_P and V_S are 1 and 2% respectively [*Benson et al.*, 2005]. The relative error for the Poisson's ratio is thus equal to 12%. Consequently, α and β have error bars equal to 2% and 22%, respectively. The last constant to be determined is the Young's modulus. The next paragraph details our choices for this matter.

5.2.2. Uncertainties on Young's Modulus E

[63] In their paper, *Ebner et al.* [2009b] determined E assuming the vertical stress is equal to the lithostatic stress as in equation (56) where z is the current depth of their samples. They plotted the determined stress as a function of $L^{-1/2}$. The slope of the curve is proportional to $E^{1/2}$ (see equation (54)). They found $E = 15$ GPa which is the lowest acceptable limit for limestones [*Clark*, 1966]. Based on uniaxial loading made in our laboratory, we determined $E = 36.2$ GPa for the rock surrounding the analyzed stylolite. Considering that the limestones from Bure replaced in the geological context of the Paris basin cannot be excessively harder than what we observe today, the value determined in the laboratory is taken as the upper limit for E. Thus we can estimate the paleostress in a small range of E. The values used for the calculation of the paleostress are summarized in Table 2.

[64] To calculate the paleostress σ_{zz}, we take into account the error bars for each parameter. The computed error for the calculation of σ_{zz} is 66% for the Fourier power spectrum method and 54% for the averaged wavelet coefficient method. The results are summarized in Table 3.

Table 3. Results for the Calculation of the Paleostress σ_{zz} Using the Averaged Crossover Length for the Fourier Power Spectrum (FPS) and Average Wavelet Coefficient (AWC) Methods[a]

Paleostress (MPa)	$\bar{L}^*, E_{low}$	$\bar{L}^*, E_{up}$
σ_{FPS}	22.6 ± 14.9	35.1 ± 23.2
σ_{AWC}	16.3 ± 8.8	25.3 ± 13.7

[a]We calculated the paleostress taking into account the variability of the Young's modulus E where E_{low} is the lower limit for the Young's modulus for limestones and E_{up} is the determined Young's modulus for the studied sample.

Table 4. Results for the Calculation of the Depth for the Fourier Power Spectrum (FPS) and Average Wavelet Coefficient (AWC) Methods[a]

Depth (m)	L^*, E_{low}	L^{**}, E_{up}
h_{FPS}	850.1 ± 561.1	1320.3 ± 871.4
h_{AWC}	613.1 ± 331.1	951.7 ± 513.9

[a]We consider an early stage of formation of a sedimentary basin with an overburden made of limestones only.

5.3. Geological Context

[65] By doing some assumptions on the sedimentary overburden, the depth of development of the stylolite can be assessed. The lithostatic pressure σ_{zz} can be expressed as

$$\sigma_{zz} = \rho g h \tag{56}$$

where ρ is the density in g · m^{-3}, g is the Earth's gravity (g = 9.81 m · s^{-2}) and h is the depth in m. We make the assumption that at the initiation of the stylolite, linked to the early stage of formation of the sedimentary basin, the overburden was made of limestones only. Thus, we consider the density of limestones ρ = 2710 g · m^{-3}. The estimated depths of development of the stylolites are summarized in Table 4. The error bars on h are of the same order as for the paleostress.

[66] Now we can wonder what is the interpretation of the estimated paleostress with regard to the three theories exposed previously:

[67] 1. *Wileveau et al.* [2007] and *Gunzburger and Cornet* [2007] measured the vertical stress at Bure which is equivalent to the lithostatic pressure as in equation (56). Our results show that the calculated depth corresponds to the depth where we cored the analyzed stylolite. Thus the studied stylolite is more likely to be still active and to show the present-day stress.

[68] 2. *André et al.* [2010] discussed about a reactivation of the stylolitization during the Tertiary age (end of Cretaceous more precisely) by the change in the stress orientation or by the emergence of the Cretaceous sediments which were eroded and permitted to meteoritic fluid to spread in the sediments. This reactivation process could have acted on the growth of the studied stylolite until today. But still it seems that the theory of the present-day stress is more applicable on that example.

6. Conclusions

[69] Analyzing the local boundary conditions due to the fact that the inside of a stylolite does not sustain shear stress and an elastic surrounding, we derived the dependence of the free energy along a stylolite surface on the shape of the stylolite. Adding up a surface energy term we derived a dynamic surface evolution model for a stylolitic interface. This model, in the situation where a stylolite is perpendicular to the largest principal stress axis—as in most cases—includes terms that lead to the stabilization of the surface dynamics, i.e., to the vanishing of initial perturbations toward a flattening surface. Hence, the presence of disorder linked to the heterogeneities of the material properties is required to explain the rough nature of stylolites. Introducing such noncorrelated quenched disorder, the model predicts the occurrence of two scaling laws. At small scale, a destabilizing disorder competing with a stabilizing surface energy term give a model similar to the Edwards Wilkinson model in a quenched noise leasing to a saturated surface with a Hurst exponent around 1. At large scale, the competition between destabilizing disorder and stabilizing elastic interactions is similar to models of evolution of an elastic interface in quenched disorder leading to a Hurst exponent of 0.5.

[70] The crossover scale between these two scaling regimes was shown to be directly linked to the stress magnitude. Hence, the determination of this crossover and other physical rock properties allows to use stylolites as markers of the paleostress magnitude.

[71] Both scaling laws and the dependence of this crossover scale on the stress magnitude were derived in two ways: by purely analytical derivation and similarity to known models in section 2 and by numerical integration in section 3.

[72] Importantly, it should be noted that the elastic forces, depending on the boundary conditions, can be stabilizing, as here, or destabilizing. The existence of several models and techniques of global or local calculation of the free energy can raise the question of a stabilizing or destabilizing nature of the elastic forces in the context of a stylolite. Independently from the derivation carried out in details in this paper, we note the following argument that can distinguish between stabilizing and destabilizing terms. The only difference between models with stabilizing or destabilizing elastic kernel is the sign of the prefactor in front of the elastic operator in the dynamic equation. However, when this sign is reverted, all large-scale wavelength Fourier modes become unstable (with a selection of fastest growing mode, e.g., as shown in *Misbah et al.* [2004] or *Bonnetier et al.* [2009]). Numerical simulations similar to the ones shown above, with a destabilizing mode, do not lead to any saturation of the amplitude of the large modes at long times, and the Fourier power spectrum at a given time does not display any scaling law at fixed time for the large scales. Thus, the scaling laws observed in field stylolites are compatible with a model where elastic forces are stabilizing: we take this as a good sign of validity of the proposed approximations to take the boundary conditions into account in the proposed model.

[73] The results from both analytical and numerical independent resolutions presented in this study are also consistent with three other independent observations:

[74] 1. The existence of two Hurst exponents at small and large scales, as observed in *Schmittbuhl et al.* [2004], in the stylolites from the log cores of Bure (section 4).

[75] 2. The results of recent molecular dynamic models of dissolution with pressure reliance and surface energy terms in the free energy displaying similar scaling laws and an identical law for the dependence of the crossover length over the applied stress [*Koehn et al.*, 2012].

[76] 3. The model was applied in a previous study to stylolites found at various depths in a limestone formation at Cirques de Navacelles (Cévennes, France). The inferred formation stresses were compatible with the derived weight of overburden at the time of formation [*Ebner et al.*, 2009b].

[77] We show finally on the example of sedimentary stylolites in Bure, how the confinement stress can be derived from morphological studies of stylolites. The ubiquitous nature of these pressure solution features makes them a

versatile marker for paleostress magnitude that can give access to the stress during the growth of stylolites. This easily available paleostress marker opens the way for systematic studies of paleostress in large rock formations for different stylolite families. However, it must be used carefully as the error bars are not minor. An important number of measurement is required to constrain the results. Together with dating indications for the time of occurrence of such stylolites (e.g., times of tectonic events) and current stress assessment methods it opens the way for the determination of stress evolution in large basins, which is a key to understand their evolution.

[78] **Acknowledgments.** We would like to thank M. Ebner, O. Lacombe, F. Cornet, C. Aurière, J. D. Bernard, T. Reuschlé, A. Steyer, E. Aharonov, Y. Bernabé, and J. L. Alves for technical help and discussions. This work was partially funded by the French National Radioactive Waste Management Agency (ANDRA) and supported by a FORPRO grant. The authors would also like to thank the CAPES-COFECUB program for stimulating fruitful discussions.

References

Aharonov, E., and R. Katsman (2009), Interaction between pressure solution and clays in stylolite development: Insights from modeling, *Am. J. Sci.*, *309*, 607–632.
André, G. (2003), Caractérisation des déformations méso-cénozoïques et des circulations de fluides dans l'Est du Bassin de Paris, thesis, Univ. Henri Poincaré, Nancy, France.
André, G., C. Hibsch, S. Fourcade, M. Cathelineau, and S. Buschaert (2010), Chronology of fracture sealing under a meteoritic fluid environment: Microtectonic and isotopic evidence of major Cainozoic events in the eastern Paris Basin (France), *Tectonophysics*, *490*, 214–228.
Angheluta, L., E. Jettestuen, J. Mathiesen, F. Renard, and B. Jamtveit (2008), Stress-driven phase transformation and the roughening of solid-solid interfaces, *Phys. Rev. Lett.*, *100*, 096105, doi:10.1103/PhysRevLett.100.096105.
Angheluta, L., E. Jettestuen, and J. Mathiesen (2009), Thermodynamics and roughening of solid-solid interfaces, *Phys. Rev. E*, *79*, 031601, doi:10.1103/PhysRevE.79.031601.
Angheluta, L., J. Mathiesen, C. Misbah, and F. Renard (2010), Morphological instabilities of stressed and reactive geological interfaces, *J. Geophys. Res.*, *115*, B06406, doi:10.1029/2009JB006880.
Asaro, R., and W. Tiller (1972), Interface morphology development during stress-corrosion cracking: Part I. Via surface diffusion, *Metall. Trans. B*, *3*, 1789–1796.
Barabási, A., and H. Stanley (1995), *Fractal Concepts in Surface Growth*, 388 pp., Cambridge Univ. Press, Cambridge, U. K.
Bathurst, R. G. C. (1971), *Carbonate Sediments and Their Diagenesis*, *Dev. Sedimentol.*, vol. 12, 620 pp., Elsevier, Amsterdam.
Bathurst, R. G. C. (1987), Diagenetically enhanced bedding in argillaceous platform limestones: Stratified cementation and selective compaction, *Sedimentology*, *34*, 749–778.
Baud, P., E. Klein, and T. F. Wong (2004), Compaction localization in porous sandstones: Spatial evolution of damage and acoustic emission activity, *J. Struct. Geol.*, *26*, 603–624.
Benedicto, A., and R. Schultz (2010), Stylolites in limestones: Magnitude of contractional strain accommodated and scaling relationships, *J. Struct. Geol.*, *32*, 1250–1256.
Benson, P. M., P. G. Meredith, E. S. Platzman, and R. E. White (2005), Pore fabric shape anisotropy in porous sandstones and its relation to elastic wave velocity and permeability anisotropy under hydrostatic pressure, *Int. J. Rock Mech. Min. Sci.*, *42*, 890–899.
Bonnetier, E., C. Misbah, F. Renard, R. Toussaint, and J. Gratier (2009), Does roughening of rock-fluid-rock interfaces emerge from a stress-induced instability?, *Eur. Phys. J. B*, *67*, 121–131.
Brouste, A., F. Renard, J. P. Gratier, and J. Schmittbuhl (2007), Variety of stylolites' morphologies and statistical characterization of the amount of heterogeneities in the rock, *J. Struct. Geol.*, *29*, 422–434.
Bushinskiy, G. I. (1961), Stylolites, *Izv. Akad. Nauk. SSSR, Ser. Fiz.*, *8*, 31–46.
Buxton, T. M., and D. Sibley (1981), Pressure solution features in a shallow buried limestone, *J. Sediment. Petrol.*, *51*, 19–26.
Clark, S. P., Jr. (Ed.) (1966), *Handbook of Physical Constants*, Geol. Soc. of New York, New York.
Cox, M. A., and J. L. Whitford-Stark (1987), Stylolites in the Caballos Novaculite, west Texas, *Geology*, *15*, 439–442.
Cox, S. F., and M. S. Paterson (1991), Experimental dissolution-precipitation creep in quartz aggregates at high temperatures, *Geophys. Res. Lett.*, *18*, 1401–1404.
De Giudici, G. (2002), Surface control vs. diffusion control during calcite dissolution: Dependence of step-edge velocity upon solution pH, *Am. Mineral.*, *87*(10), 1279–1285.
Den Brok, S. W. J., and J. Morel (2001), The effect of elastic strain on the microstructure of free surfaces of stressed minerals in contact with an aqueous solution, *Geophys. Res. Lett.*, *28*, 603–606.
Den Brok, S. W. J., and C. Spiers (1991), Experimental evidence for water weakening of quartzite by microcracking plus solution-precipitation creep, *J. Geol. Soc. London*, *148*, 541–548.
Dunnington, H. V. (1954), Stylolite development post-dates rock induration, *J. Sediment. Petrol.*, *24*, 27–49.
Dysthe, D., Y. Podlchikov, F. Renard, J. Feder, and B. Jamtveit (2002), Universal scaling in transient creep, *Phys. Rev. Lett.*, *89*, 246102, doi:10.1103/PhysRevLett.89.246102.
Dysthe, D., F. Renard, J. Feder, B. Jamtveit, P. Meakin, and T. Jøssang (2003), High-resolution measurements of pressure solution creep, *Phys. Rev. E*, *68*, 011603, doi:10.1103/PhysRevE.68.011603.
Ebner, M., D. Koehn, R. Toussaint, and F. Renard (2009a), The influence of rock heterogeneity on the scaling properties of simulated and natural stylolites, *J. Struct. Geol.*, *31*, 72–82.
Ebner, M., D. Koehn, R. Toussaint, F. Renard, and J. Schmittbuhl (2009b), Stress sensitivity of stylolite morphology, *Earth Planet. Sci. Lett.*, *277*, 394–398.
Ebner, M., R. Toussaint, J. Schmittbuhl, D. Koehn, and P. Bons (2010a), Anisotropic scaling of tectonic stylolites: A fossilized signature of the stress field?, *J. Geophys. Res.*, *115*, B06403, doi:10.1029/2009JB006649.
Ebner, M., S. Piazolo, F. Renard, and D. Koehn (2010b), Stylolite interfaces and surrounding matrix material: Nature and role of heterogeneities in roughness and microstructural development, *J. Struct. Geol.*, *32*, 1070–1084.
Edwards, S. E., and D. R. Wilkinson (1982), The surface statistics of a granular aggregate, *Proc. R. Soc. London. Ser. A*, *381*, 17–31.
Fabricius, I. L., and M. K. Borre (2007), Stylolites, porosity, depositional texture, and silicates in chalk facies sediments. Ontong Java Plateau—Gorm and Tyra fields, North Sea, *Sedimentology*, *54*, 183–205.
Fletcher, R. C., and D. D. Pollard (1981), Anticrack model for pressure solution surfaces, *Geology*, *9*, 419–424.
Gonzalez, O., and A. Stuart (2008), *A First Course in Continuum Mechanics*, 394 pp., Cambridge Univ. Press, Cambridge, U. K.
Gratier, J. P. (1993), Experimental pressure solution of halite by an indenter technique, *Geophys. Res. Lett.*, *20*, 1647–1650.
Gratier, J. P., and R. Guiguet (1986), Experimental pressure solution-deposition on quartz grains: The crucial effect of the nature of the fluid, *J. Struct. Geol.*, *8*, 845–856.
Gratier, J. P., L. Jenatton, D. Tisserand, and R. Guiguet (2004), Indenter studies of the swelling, creep and pressure solution of Bure argillite, *Appl. Clay Sci.*, *26*, 459–472.
Gratier, J. P., L. Muquet, R. Hassani, and F. Renard (2005), Experimental microstylolites in quartz and modeled application to natural stylolitic structures, *J. Struct. Geol.*, *27*, 89–100.
Grinfeld, M. A. (1986), Instability of the interface between a nonhydrostatically stressed elastic body and a melt, *Dokl. Akad. Nauk. SSSR*, *290*, 1358–1363.
Gunzburger, Y., and F. H. Cornet (2007), Rheological characterization of a sedimentary formation from a stress profile inversion, *Geophys. J. Int.*, *168*, 402–418.
Heald, M. T. (1955), Stylolites in sandstones, *J. Geol.*, *63*, 101–114.
Iijima, A. (1979), Nature and origin of the Paleogene cherts in the Setogawa Terrain, Shizuoka, central Japan, *J. Fac. Sci. Univ. Tokyo, Sect. 2*, *20*, 1–30.
Karcz, Z., E. Aharonov, D. Ertas, R. Polizzotti, and C. H. Scholz (2008), Deformation by dissolution and plastic flow of a single crystal sodium chloride indenter: An experimental study under the confocal microscope, *J. Geophys. Res.*, *113*, B04205, doi:10.1029/2006JB004630.
Kassner, K., C. Misbah, J. Müller, J. Kappey, and P. Kohlert (2001), Phase-field modeling of stress-induced instabilities, *Phys. Rev. E*, *63*, 036117.
Katsman, R. (2010), Extensional veins induced by self-similar dissolution at stylolites: Analytical modeling, *Earth Planet. Sci. Lett.*, *299*, 33–41.
Katsman, R., E. Aharonov, and H. Scher (2006a), A numerical study on localized volume reduction in elastic media: Some insights on the mechanics of anticracks, *J. Geophys. Res.*, *111*, B03204, doi:10.1029/2004JB003607.
Katsman, R., E. Aharonov, and H. Scher (2006b), Localized compaction in rocks: Eshelby's inclusion and the Spring Network Model, *Geophys. Res. Lett.*, *33*, L10311, doi:10.1029/2005GL025628.

Koehn, D., J. Arnold, B. Jamtveit, and A. Malthe-Sørenssen (2003), Instabilities in stress corrosion and the transition to brittle failure, *Am. J. Sci.*, *303*, 956–971.

Koehn, D., D. K. Dysthe, and B. Jamtveit (2004), Transient dissolution patterns on stressed crystal surfaces, *Geochim. Cosmochim. Acta*, *68*, 3317–3325.

Koehn, D., F. Renard, R. Toussaint, and C. W. Passchier (2007), Growth of stylolite teeth patterns depending on normal stress and finite compaction, *Earth Planet. Sci. Lett.*, *257*, 582–595.

Koehn, D., M. Ebner, F. Renard, R. Toussaint, and C. W. Passchier (2012), Modelling of stylolite geometries and stress scaling, *Earth Planet. Sci. Lett.*, in press.

Landau, L. D., and E. M. Lifchitz (1986), *Theory of Elasticity*, vol. 7, *Course of Theoretical Physics*, 3rd ed., Butterworth-Heinemann, London.

Laronne Ben-Itzhak, L. (2011), Pressure solution and stylolites in carbonate rocks, PhD dissertation, Weizmann Inst. of Sci., Rehovot, Israel.

Lind, I. L. (1993), Stylolites in chalk from leg 130, Ontong Java Plateau, *Proc. Ocean Drill. Program Sci. Results*, *130*, 673–686.

Misbah, C., F. Renard, J. P. Gratier, and K. Kassner (2004), Dynamics of a dissolution front for solids under stress, *Geophys. Res. Lett.*, *31*, L06618, doi:10.1029/2003GL019136.

Mollema, P. N., and M. A. Antonellini (1996), Compaction bands: A structural analog for anti-mode I crack in aeolian sandstone, *Tectonophysics*, *267*, 209–228.

Park, W. C., and E. H. Schot (1968), Stylolites: Their nature and origin, *J. Sediment. Petrol.*, *38*, 175–191.

Railsback, L. B. (1993), Lithologic controls on morphology of pressure-dissolution surfaces (stylolites and dissolution seams) in Paleozoic carbonate rocks from the mideastern United States, *J. Sediment. Petrol.*, *63*, 513–522.

Renard, F., P. Ortoleva, and J. P. Gratier (1997), Pressure solution in sandstones: Influence of clays and dependence on temperature and stress, *Tectonophysics*, *280*, 257–266.

Renard, F., D. Dysthe, J. Feder, K. Bjørlykke, and B. Jamtveit (2001), Enhanced pressure solution creep rates induced by clay particles: Experimental evidence in salt aggregates, *Geophys. Res. Lett.*, *28*, 1295–1298.

Renard, F., J. Schmittbuhl, J.-P. Gratier, P. Meakin, and E. Merino (2004), Three-dimensional roughness of stylolites in limestones, *J. Geophys. Res.*, *109*, B03209, doi:10.1029/2003JB002555.

Rispoli, R. (1981), Stress field about strike-slip faults inferred from stylolites and tension gashes, *Tectonophysics*, *75*, 29–36.

Roux, S., and A. Hansen (1994), Interface roughening and pinning, *J. Phys. I*, *4*, 515–538.

Rutter, E. H. (1976), The kinetics of rock deformation by pressure solution, *Philos. Trans. R. Soc. London A*, *283*, 203–219.

Rutter, E. H. (1983), Pressure solution in nature, theory and experiment, *J. Geol. Soc.*, *140*, 725–740.

Schmittbuhl, J., F. Schmitt, and C. Scholz (1995), Scaling invariance of crack surfaces, *J. Geophys. Res.*, *100*, 5953–5973.

Schmittbuhl, J., F. Renard, J. P. Gratier, and R. Toussaint (2004), Roughness of stylolites: Implications of 3D high resolution topography measurements, *Phys. Rev. Lett.*, *93*, 238501, doi:10.1103/PhysRevLett.93.238501.

Schutjens, P., and C. Spiers (1999), Intergranular pressure solution in NaCl: Grain-to-grain contact experiments under the optical microscope, *Oil Gas Sci. Technol.*, *54*, 729–750.

Simonsen, I., A. Hansen, and O. M. Nes (1998), Determination of the Hurst exponent by use of wavelet transforms, *Phys. Rev. E*, *58*, 2779–2787.

Stockdale, P. B. (1922), *Stylolites: Their Nature and Origin*, *Indiana Univ. Stud.*, *9*, 97 pp.

Stockdale, P. B. (1926), The stratigraphic significance of solution in rocks, *J. Geol.*, *34*, 399–414.

Stockdale, P. B. (1936), Rare stylolites, *Am. J. Sci.*, *32*, 129–133.

Stockdale, P. B. (1943), Stylolites: Primary or secondary?, *J. Sediment. Petrol.*, *13*, 3–12.

Stutzer, O. (1940), *Geology of Coal*, Univ. of Chicago Press, Chicago, Ill.

Tanguy, A., M. Gounelle, and S. Roux (1998), From individual to collective pinning: Effect of long-range elastic interactions, *Phys. Rev. E*, *58*, 1577–1590.

Tembe, S., P. Baud, and T. Wong (2008), Stress conditions for the propagation of discrete compaction bands in porous sandstone, *J. Geophys. Res.*, *113*, B09409, doi:10.1029/2007JB005439.

Wileveau, Y., F. H. Cornet, J. Desroches, and P. Blumling (2007), Complete in situ stress determination in an argillite sedimentary formation, *Phys. Chem. Earth*, *32*, 866–878.

Wright, T. O., and L. B. Platt (1982), Pressure dissolution and cleavage in the Martingsburg Shale, *Am. J. Sci.*, *282*, 122–135.

Young, R. B. (1945), Stylolitic solution in Witwatersrand quartzites, *Trans. Geol. Soc. S. Afr.*, *47*, 137–142.

Zhou, X., and A. Aydin (2010), Mechanics of pressure solution seam growth and evolution, *J. Geophys. Res.*, *115*, B12207, doi:10.1029/2010JB007614.

Available online at www.sciencedirect.com

ScienceDirect

Earth and Planetary Science Letters 257 (2007) 582–595

EPSL

www.elsevier.com/locate/epsl

Growth of stylolite teeth patterns depending on normal stress and finite compaction

Daniel Koehn [a,*], François Renard [b,c], Renaud Toussaint [d], Cees W. Passchier [a]

[a] *Tectonophysics, Institute of Geosciences, University of Mainz, Becherweg 21, 55099 Mainz, Germany*
[b] *LGIT-CNRS-Observatoire, Université Joseph Fourier BP 53, F-38041 Grenoble, France*
[c] *Department of Physics of Geological Processes, University of Oslo, Norway*
[d] *Institut de Physique du Globe de Strasbourg, UMR CNRS 7516, 5 rue Descartes, F-67084 Strasbourg Cedex, France*

Received 21 December 2006; received in revised form 9 March 2007; accepted 11 March 2007
Available online 16 March 2007
Editor: G.D. Price

Abstract

Stylolites are spectacular rough dissolution surfaces that are found in many rock types. They are formed during a slow irreversible deformation in sedimentary rocks and therefore participate to the dissipation of tectonic stresses in the Earth's upper crust. Despite many studies, their genesis is still debated, particularly the time scales of their formation and the relationship between this time and their morphology.

We developed a new discrete simulation technique to explore the dynamic growth of the stylolite roughness, starting from an initially flat dissolution surface. We demonstrate that the typical steep stylolite teeth geometry can accurately be modelled and reproduce natural patterns. The growth of the roughness takes place in two successive time regimes: i) an initial non-linear increase in roughness amplitude that follows a power-law in time up to ii) a critical time where the roughness amplitude saturates and stays constant. We also find two different spatial scaling regimes. At small spatial scales, surface energy is dominant and the growth of the roughness amplitude follows a power-law in time with an exponent of 0.5 and reaches an early saturation. Conversely, at large spatial scales, elastic energy is dominant and the growth follows a power-law in time with an exponent of 0.8. In this elastic regime, the roughness does not saturate within the given simulation time.

Our findings show that a stylolite's roughness amplitude only captures a very small part of the actual compaction that a rock experienced. Moreover the memory of the compaction history may be lost once the roughness growth saturates. We also show that the stylolite teeth geometry tracks the main compressive stress direction. If we rotate the external main compressive stress direction, the teeth are always tracking the new direction. Finally, we present a model that explains why teeth geometries form and grow non-linearly with time, why they are relatively stable and why their geometry is strongly deterministic while their location is random.

Keywords: stylolite; compaction; stress; roughening; scaling

1. Introduction

Dynamic roughening of interfaces is an important research topic in many scientific disciplines. A natural and spectacular example of such processes are stylolites,

* Corresponding author.
E-mail address: koehn@uni-mainz.de (D. Koehn).

0012-821X/$ - see front matter © 2007 Elsevier B.V. All rights reserved.
doi:10.1016/j.epsl.2007.03.015

pairs of dissolution surfaces facing each other, that are found in many rocks, mostly in limestones, and which are often used for ornamental stone. A characteristic feature of stylolite interfaces is their pronounced roughness with "teeth"- or "pen"-like geometries [stylus = pen, [1–5]]. The dark residual material that is collected within the stylolite consists mostly of clay particles [6]. Stylolites have mainly been described qualitatively in Earth Sciences so that dynamic models of their growth and scaling properties are only now emerging [6–8]. However, the development mechanism of their teeth-geometry, with peculiar square peaks (Fig. 1), is up to now not understood.

Stylolites tend to grow perpendicular to the maximum compressive stress direction, and exhibit a pronounced roughness on several scales [3]. Teeth like peaks develop with sides oriented sub-parallel to the maximum stress direction (Fig. 1) [9]. The orientation of stylolites and their teeth is commonly used by geologists as an indicator for the direction of the maximum compressive stress [10–12] and the amplitude of the stylolite roughness is sometimes used as a direct estimate of the compaction that the rock underwent [13]. We use compaction here not only for a reduction in porosity of a rock but also for a vertical shortening of the rock due to the weight of the overlying sediments. Studies on the validity of these "rule of thumb" methods of compaction estimates are clearly missing, and the reason for this is probably the complexity of the development of stylolites. Since stylolites are so complex, there is also an ongoing debate in the literature about ways to classify them.

Fig. 1. Natural stylolites on a limestone quarry surface from the Burgundy area, France. On the large scale the stylolites are planar structures whereas on the small scale they show a pronounced roughness (see inset). Note the steep "teeth" like patterns in the inset.

These features grow as a function of physical and chemical interactions and it is not easy to study them experimentally [14] nor in numerical models [6]. However, experiments or numerical models are needed since field observations alone cannot elucidate the dynamics of the roughening process but only represent snapshots at a given time. Early works in Earth Sciences classify stylolites according to their shape using qualitative methods [3]. However, this classification cannot successfully encompass all stylolite patterns, which can be found in numerous rock types and on a large range of scales [1–3]. Also, these classifications are often not related to any specific material parameters, scaling properties or growth conditions. More promising methods use qualitative descriptions of the stylolite roughness suggesting that they are fractal surfaces [7,15] and self-affine structures [6,8,14]. Here we present new microdynamic simulations of stylolite roughening that allow us to explore the dynamics of the stress induced roughening process in time and space, illustrate stylolite geometries that develop at different scales and propose a process-based explanation for the growth of stylolite teeth. These simulations are based on first principles of physics and chemistry, without any ad hoc phenomenological equation. It should also be underlined that contrarily to previous linearized models [6,8], the model used here allows the exploration of the fully developed structures, i.e. they take into account both, the non-linearities of the system that can be associated to large departures from flat surfaces and the solid–solid contacts occurring through the stylolite.

2. The numerical model

We start with an initially flat interface where dissolution can take place and the solid can only dissolve and not precipitate. The fluid is initially in equilibrium with the solid but becomes undersaturated when the solid is stressed. This flat interface may represent an initial "anticrack", that is assumed to represent the stylolite at an early stage of formation [16,17]. The model is two-dimensional and it assumes that everything that dissolves along the interface is transported instantaneously in the fluid out of the system, i.e. that diffusion in the fluid pocket is not limiting the process, but happens at a much faster time scale than the dissolution itself. Accordingly, the fluid has a constant solute concentration. The applied boundary condition is a constant displacement rate that results in an average stress across the interface. Dissolution is fast enough to relax the stress at the interface so that stresses do not accumulate during a simulation run. Therefore the constant displacement rate boundary condition can be seen as an equivalent to a constant load boundary condition. The model is part of the modelling environment "Elle" [18].

The setup of the model is as follows: two solids are pressed together with a confined fluid layer in between them (Fig. 2). The right and left hand sides of the model are fixed through elastic walls whereas the lower and upper walls of the model are moved inwards at a constant displacement rate. The solid is made up of small particles that are connected via linear elastic springs along a triangular lattice. These elements can represent either a single grain or a pack of smaller grains. At a scale larger than the grains, this network behaves in a classical elastostatic way.

2.1. Thermodynamics and kinetics of stylolite dissolution

Dissolution of the solid takes place in small steps dimensioned in such a way that one single element or particle of the solid is dissolved at every step. Dissolution follows a simple linear rate law

$$D = \mathrm{kV}\left[1 - \exp\left(-\frac{\{\Delta\psi + \Delta\sigma_\mathrm{n}\}V}{\mathrm{RT}}\right)\right], \tag{1}$$

where D is the dissolution velocity of the interface (m s^{-1}), k a dissolution kinetics rate constant (mol m^{-2} s^{-1}), V the molecular volume of the solid (m^3 mol^{-1}), R the universal gas constant (J mol^{-1} °K^{-1}), T the temperature (°K), $\Delta\psi$ (J m^{-3}) the changes in Helmholtz free energy of the solid during dissolution of a solid element, and $\Delta\sigma_n$ (Pa) the normal stress gradients along the interface [further details of the derivation are given in [19,20]]. The Helmholtz free energy takes into account the variations in elastic and in surface energy.

Changes in surface energy are calculated from the curvature of the interface. The surface energy (E^s) per area unit around a single element located at the interface can be expressed as

$$E^\mathrm{s} = \frac{\gamma}{\rho}, \tag{2}$$

where γ is the surface free energy and ρ is the local radius of curvature of the interface. The local curvature is determined using the two neighbours of each element along the interface. The sign of the curvature ρ is such that the interface will become flat. We perform an average across the interface using the local surface energies of elements and those of their neighbours (up to $n=40$ in each direction) with the expression

$$E_i^\mathrm{avs} = \frac{1}{C}\sum_{h=1}^{n}\left(\frac{1}{(2h+1)^2}\sum_{j=0}^{2h+1}E_{i+j-h}^{s}\right), \tag{3}$$

where E_i^avs is now the average surface energy for element i, E_i^s the local surface energy for element i, and E_{i+j-h}^s surface energies of neighbouring elements along the interface, and $C = \frac{\pi^2}{4} - \frac{17}{9} \approx 0.578512$ is a normalization factor that ensures that the average surface energy on all sites is preserved in this averaging procedure. The local surface energies are divided by

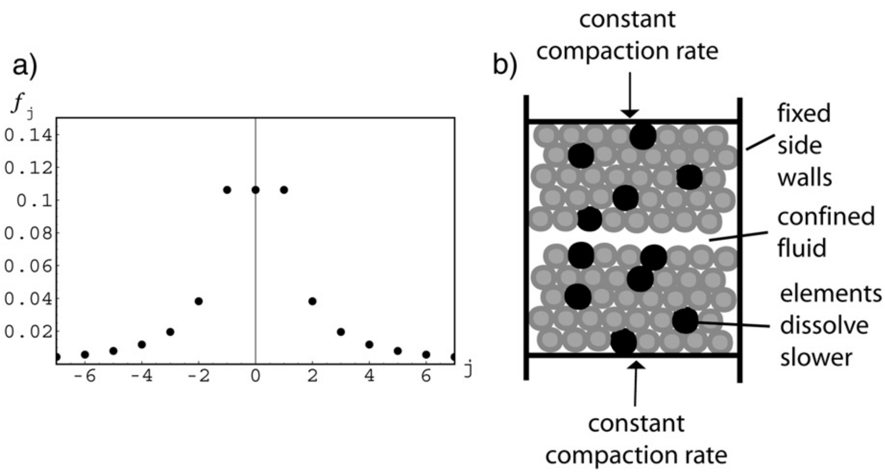

Fig. 2. (a) Weight function used in the coarse graining procedure to evaluate the surface energy. (b) Setup of the numerical model. Side-walls are fixed whereas the upper and lower walls are moved inwards to compact the system. The rock contains two kinds of particles that dissolve at two different rates. This heterogeneity in the dissolution rate represents an initial quenched noise in the rock.

the sum of added elements and their maximum distance (divided by the initial radius of curvature of a particle). This averaging procedure amounts to consider a coarse-grained surface energy, at the scale of a few elements, and allows to avoid artefacts that could arise from the discreteness of the model. In this way, a singular local term E_i^{s} obtained at a corner of the interface is smoothened for E_i^{avs} over a neighbourhood of a few grains. This procedure is commonly used in computational physics to avoid discreteness artefacts [21,22]. The above expression is equivalently represented as a discrete convolution operation

$$E_i^{\mathrm{avs}} = \sum_{-\infty<j<\infty} f_j E_{i+j}^{s}, \tag{4}$$

with a tent function shown in Fig. 2a,

$$f_j = \frac{1}{C}\sum_{k=|j|}^{\infty} \frac{1}{(2k+1)^2} \text{ for } j\neq 0, \text{ and } f_0 = f_1. \tag{5}$$

Keeping the terms up to $n=40$ in this sum, i.e. all terms in the sum of Eq. (4) for $|j|<40$, we are left with an error of only 2% in the tail of the weight function. The value of the normalization constant C is obtained by requiring that the average coarse grained surface energy is equal to the average local surface energy, i.e. it is set up by the condition that

$$\sum_{-\infty<j<\infty} f_j = 1. \tag{6}$$

2.2. Mechanics

The elastic energy and the normal stress at the interface are determined using a lattice spring model for the solid where elements are connected by linear elastic springs. We assume that the solid deforms only elastically without internal plastic deformation, except for the irreversible dissolution events happening at the modelled interface. Stresses in the solid are determined using an over-relaxation algorithm where elements of the model are moved until a new equilibrium configuration is found. The equilibrium configuration is defined by a given relaxation threshold. The net force (F_i) acting on an element i at position x_i is

$$F_i = \sum_{(j)} \kappa\left(|x_i - x_j| - l\right) v_{i,j} + f_{\mathrm{p}}, \tag{7}$$

where the sum is over all neighbours j, κ is a spring constant, l is the equilibrium distance between elements i and j, $v_{i,j}$ is a unit vector pointing from j to i and f_{p} is an external force like the repulsion from a wall.

The elastic energy (E^{el}) is directly evaluated at a node i as

$$E^{\mathrm{el}} = \frac{1}{4V}\sum_{(j)} \kappa\left(|x_i - x_j| - l\right)^2, \tag{8}$$

where $V = \sqrt{3}/2l^2$ is the volume of an elementary cell. It can also be determined from the strain tensor (u_{ik}) that is calculated from the lattice spring model with the expression [23]

$$E^{\mathrm{el}} = \frac{1}{2}\lambda_1\left(\sum_i u_{ii}\right)^2 + \lambda_2\sum_{i,k}(u_{ik})^2, \tag{9}$$

where λ_1 and λ_2 are the Lamé constants. We use the Einstein convention with summation over repeated indices. Differences in elastic energy in Eq. (9) refer to differences between a stressed and a non-stressed element. The Lamé constants are set up by the spring constant, the lattice constant and the triangular lattice configuration, i.e. $\lambda_1 = \sqrt{3}\kappa/(2l)$ and $\lambda_2 = \sqrt{3}\kappa/(4l)$, or equivalently, the Young modulus is $K = \lambda_1 + 2\lambda_2/3 - 2\kappa/(\sqrt{3}l)$, and the Poisson ratio is $v = \lambda_1/(2\lambda_1 + 2\lambda_2) = 1/3$ [24].

Finally the normal stress at the interface is determined from the repulsion of the two solids at the interface where the repulsion only contains normal components, assuming that a fluid film with no shear stress exists at the interface [25]. In order to calculate changes in normal stress along the interface we calculate an average of the normal stress across the whole interface and define differences in stress as the local normal stress minus the average normal stress.

The simulation flow is as follows:

– First the outer walls are moved in a given time step to stress the system.
– Once the upper and lower solids meet at the interface stress builds up. The rate law (Eq. (1)) is then used to calculate if elements can dissolve in the given time step. If not the system is stressed again until the first element can dissolve.
– Once elements dissolve they are removed one at a time and the stress is calculated again. The time that is used up by the dissolution of a single element is averaged to be the time it takes to dissolve that element completely divided by the system size (number of elements in the x-direction). Dissolution

of elements proceeds until the given time is used up and another deformation step is applied. Using a desktop workstation, each simulation lasts between 10 and 30 days; the stress relaxation being the most time consuming part.

2.3. Simulation parameters and disorder

The parameters used in the simulation should mimic those of the natural example (Fig. 1). For our idealized model we use a rock mainly made up of calcite with a molecular volume of 0.00004 m^3/mol, a Young's Modulus of 80 GPa, a Poisson's ration of 0.33 (given by the model configuration), a surface free energy of 0.27 J/m^2, a temperature of 300 K and a dissolution rate constant of 0.0001 mol/(m^2s) [8]. In addition, the displacement rate of the upper and lower boundaries is fixed at a constant value corresponding to strain rates of compaction between 10^{-10} and 10^{-12} s^{-1} (see Fig. 2). Average mean stresses that build up in the model reach values of about 20 MPa and remain constant during a simulation run.

In order to introduce heterogeneities to the system a bimodal variation is set on the dissolution rate constants of the elements. The heterogeneity in the system is set such that 5% of all elements have a dissolution rate constant that is half the rate constant of the other elements, i.e. they dissolve slower and pin the surface. The initial spatial distribution of the rate constants is set using a pseudorandom routine resulting in a probability of 5% of particles dissolving more slowly, picked independently for each site. Using this procedure, a spatial heterogeneity, also called quenched noise, is introduced in the initial rock.

3. Results

3.1. Simulated stylolites and comparison with natural data

At first we compare a simulated stylolite directly with a natural example. Fig. 3 shows a simulation of a roughening stylolite in a model that is 400 elements wide and that has an absolute horizontal size of 40 cm. One element in the model then has a diameter of 1 mm and may represent a single grain in a natural rock. We can compare the simulation with the natural stylolite shown in Fig. 1, especially with the inset. The simulated stylolite has a width that is about 2/3 of the width of the natural stylolite in the inset (see the hammer for the scale).

The simulated stylolite develops in 8000 yr at a compaction rate of 3×10^{-12} s^{-1} and has compacted by 25.6 cm or 64% (original height of the simulated box was 40 cm). Both simulated and natural stylolites are visually very similar. They both produce pronounced teeth with smaller scale roughness in between and on top of the teeth. The height of the teeth (up to about 8 cm) and their width are comparable in the natural and the simulated stylolite implying that both have similar scaling properties. The grain size of the simulated example (1 mm) is larger compared to natural rocks, mainly because we are limited by the calculation time of the model.

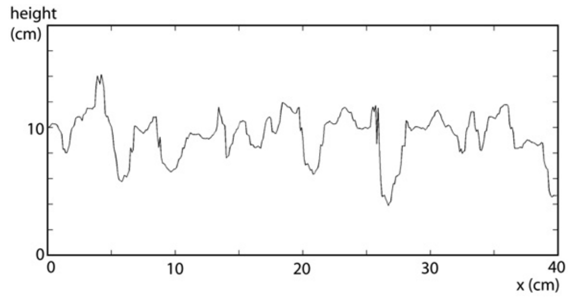

Fig. 3. Simulated stylolite with a width of L=40 cm (1:1). Note similarities between the natural stylolite (in Fig. 1) and the simulated stylolite. Both develop a roughness on different scales and well-developed square teeth structures.

3.2. Initiation of the stylolite roughness by interface pinning along heterogeneities

The stylolite roughness is initiated by elements that dissolve slower. If the model contains no heterogeneity the interface will only become rough on the scale of single elements and remain flat on the larger scale. This is because surface energies and elastic energies are minimized when the surface is flat. Therefore, both of these energies will prevent the surface to roughen and the stylolite to grow [8]. Once the system contains heterogeneity, slower dissolving elements continuously pin the surface and thus make it rougher (Fig. 4). Dissolution takes a longer time to destruct a roughness that is pinned by slower dissolving elements than to flatten an interface with no variation. The roughness is not stable but very dynamic in time since an increasing amount of more slowly dissolving elements are pinning the interface while the solid progressively dissolves. However, the slower dissolving elements themselves may dissolve as well if the roughness produces locally very high surface energies due to a strong curvature of the interface or high elastic energies due to stress concentrations or if two slower dissolving elements meet on opposing interfaces.

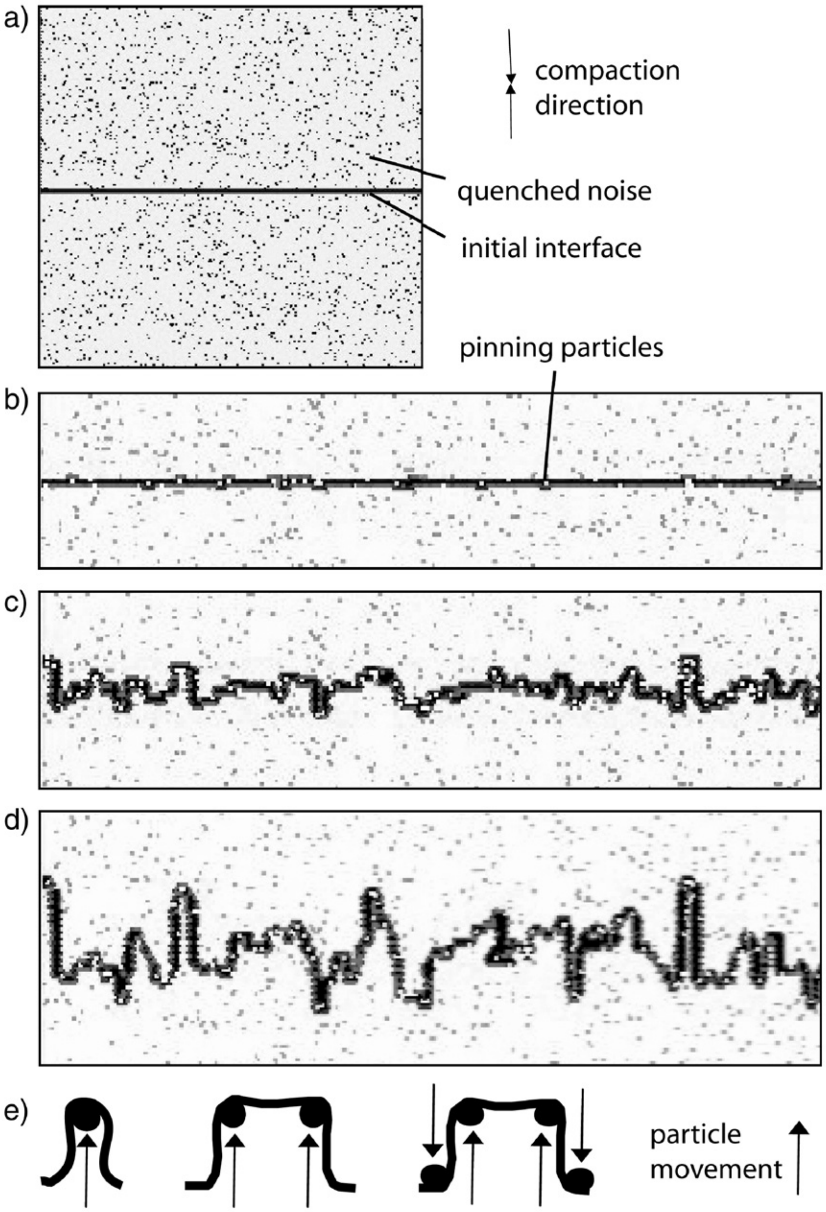

Fig. 4. Particles pinning along the interface. (a) Initial setup of a simulation with the initial interface in the centre and the quenched noise in the background (particles that dissolve twice slower are dark). (b–d) Progressive growth of the roughness and pinning of the interface (particles that pin are white). (e) Structures that develop during pinning: spikes, teeth that are pinned in one direction and teeth that are pinned in two directions.

Dissolution of pinning elements will then reduce the roughness again.

An example of the development of the roughness in a simulation and the effects of interface pinning is illustrated in Fig. 4. Fig. 4a shows the initial random distribution of slower dissolving elements (small dark spots). This heterogeneity is frozen into the system at the beginning and does not change during a simulation (quenched noise). The interface where the stylolite is initiated is shown as a black line. While the solid dissolves, pinning elements are progressively being collected within the interface (small white spots, Fig. 4b to d).

Two end-member patterns develop during the pinning of the interface. On one hand, one or a couple of elements pin very locally and produce local spikes. On the other hand, larger parts of the interface may be pinned between two elements that are further apart.

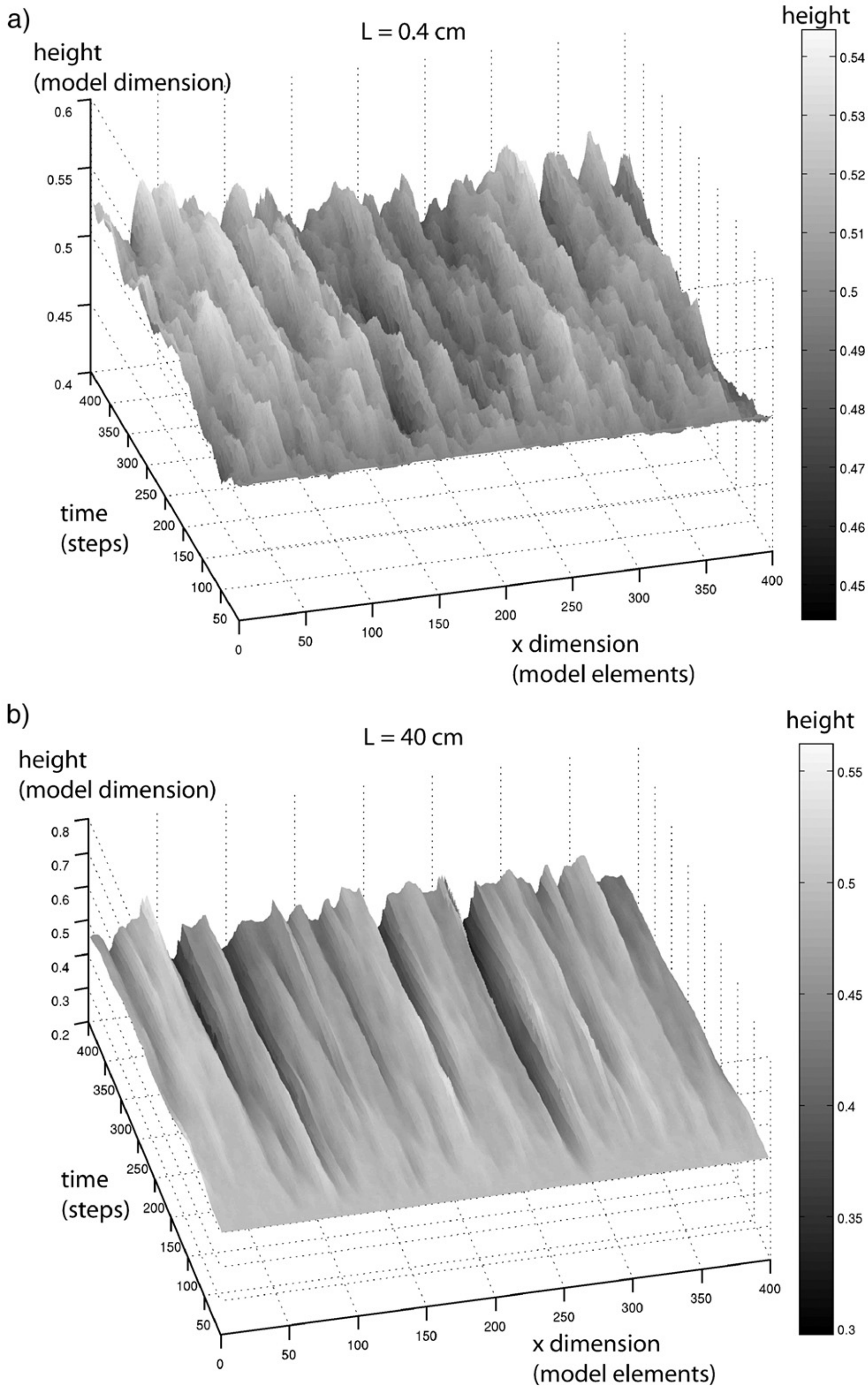

Fig. 5. 3D diagrams showing the growth of two stylolites. (a) Small stylolite that grows in the surface energy dominated regime (x-dimension is $L=0.4$ cm). The growth of the roughness slows down relatively fast and saturates. The growth is very dynamic so that pinning particles are dissolved relatively fast. (b) Large stylolite that grows in the elastic energy dominated regime (x-dimension is $L=40$ cm). The stylolite roughness grows continuously and develops teeth.

These second pattern generates the teeth geometries, typical of stylolites, with teeth having various widths.

Fig. 4e illustrates three different cases of pinning schematically. Single pinning elements produce spikes whereas two pinning elements that pin from the same side produce teeth. The structures grow fastest when elements pin from opposing sides. The interfaces in Fig. 4c and d illustrate the teeth-forming processes presented in Fig. 4e: the interface is made up of single pinning elements, larger teeth where groups of elements pin and steep interfaces where elements pin from opposing sides. The surface structure changes when new pinning elements are collected within the stylolite and when pinning elements are destructed. The amplitude of the stylolite grows during these processes (from Fig. 4b to d) and the wavelength of the interface is also evolving. Small wavelengths can grow very fast (Fig. 4c) whereas the larger wavelengths need longer time to develop (Fig. 4d).

Fig. 5 shows the evolution of the growing roughness of two stylolites through time in 3D diagrams where the *x*-axis shows the amount of elements in the x-direction, the *y*-axis corresponds to the time in model time-steps (here one step corresponds to 20 yr) and the *z*-axis shows the non-dimensional height of the stylolite. The parameters for the two stylolites shown in Figs. 5a and b are the same except for the absolute length (and height respectively). The stylolite shown in Fig. 5a has an *x*-dimension of 0.4 cm whereas the stylolite shown in Fig. 5b has an *x*-dimension of 40 cm.

The differences in absolute initial system size L have an effect on the dominance of elastic versus surface energies during the roughening process. Surface energies become increasingly more important towards smaller scales. This means that the stylolite in Fig. 5a, which is relatively small (L=0.4 cm) with a small grain size of 1 μm, is dominated by surface energies so that elastic energies only play a minor role. The stylolite shown in Fig. 5b however is relatively large (L=40 cm) with a large grain size of 1 mm so that the elastic energy dominates the roughening process and surface energies only play a minor role.

When comparing Fig. 5a and b (note that the *z*-axis scales differently, one unit corresponds to 0.4 cm in a) and to 40 cm in b)), one observes that the roughness forms better developed teeth with steep sides in the case of the larger stylolite (Fig. 5b). The roughness of the smaller stylolite (Fig. 5a) is not growing smoothly but is disrupted quite often and produces neither large amplitude nor well-developed teeth. In addition, the larger stylolite (Fig. 5b) grows progressively while the small stylolite (Fig. 5a) shows an initial increase in roughness that is followed by strong fluctuations in time, where the average roughness amplitude remains more or less constant. These roughness evolutions imply that pinning elements are destroyed when surface energy is high because of very high curvatures of spikes. The interface of the surface energy dominated stylolite therefore contains no larger spikes or teeth and is quite dynamic. Elastic energy on the other hand does not destroy spikes easily. Therefore well-developed teeth structures tend to arise in larger stylolites at the outcrop scale when surface energy is relatively unimportant, whereas we would expect to find less well-developed teeth but rounder structures on the scale of a thin-section, where surface energy is important. In addition we can expect that the crossover between the elastic and the surface energy dominated regimes shifts if the stylolite experiences a different stress or if elastic constants or surface energies of the host-rock are different. High stresses, for example, will result in high elastic energies so that the elastic energy dominated regime shifts towards smaller scales [8]. This effect may be visible in natural stylolites, especially when stylolites grow in rocks with very different elastic properties or surface energies. However, further simulations are needed in order to quantify these relations.

In order to explore the evolution of the roughness amplitude with time, we use signal-processing tools from statistical physics [26], as illustrated in the next section.

3.3. Growth of the roughness with time

The dynamics of a surface roughening process can be described by some basic scaling laws that are the same or at least very similar for different interfaces and surfaces (as e.g., gas–fluid interface motion in non-saturated porous media, propagation of flame fronts, atomic deposition processes, bacterial growth, erosion or dissolution fronts, contact line motion biphasic fronts over disordered pinning substrates, interfacial crack fronts). These laws, discovered by statistical physicists, describe how the amplitude of the roughness grows non-linearly with time, following power laws [26–29].

First we have to define an average value for the amplitude of the roughness of our numerical stylolites for each time step. We use the root mean square method to determine the average width of the stylolite roughness following [26]

$$w(L,t) \equiv \sqrt{\frac{1}{L}\sum_{i=1}^{L}\left[h(i,t)-\bar{h}(t)\right]^2}, \tag{10}$$

where w is the interface width as a function of system size L and time t, h is the height of point i on the interface at time t and $\bar{h}$ the average height of the interface at time t. This function gives an average width of the interface for each time step t and therefore characterizes the growth of the roughness. In our simulations, the system size L is defined as the number of elements in the x-direction. We use model sizes of 200 and 400 elements in the x-direction. The average height of the interface is defined as

$$\bar{h}(t) \equiv \frac{1}{L}\sum_{i=1}^{L} h(i,t). \tag{11}$$

Statistical physics scaling laws [26] have demonstrated that, in many stochastic interfacial systems, roughening interfaces grow following a power law in time with a so-called growth exponent β. This is described by

$$w(L,t) \sim t^{\beta}, \tag{12}$$

where the interface width w is proportional to time t to the power β, for a given system size L. If $\beta=1.0$, the interface grows linearly with time, if β is smaller than 1.0 the interface growth slows down with time. Normal diffusion processes are characterized by $\beta=1/2$, anomalous diffusion processes by $\beta\neq 1/2$, and $0\leq\beta\leq 1$. In addition, for most stochastic interfacial systems the width of roughening interfaces saturates after a critical time t_{crit}. This time increases with the system size L.

When modelling the growth of stylolites, one can expect two scaling regimes in time, first a power law up to time t_{crit} followed by a regime where w remains constant (Fig. 6a). In order to study the dynamics of the roughening process one constructs diagrams of $\log_{10}(w)$ against $\log_{10}(t)$. The increase in width of the interface roughness should follow a straight line where the slope of the line gives the growth exponent β. After a critical time t_{crit} the roughness saturates and the slope vanishes to zero (Fig. 6a).

We studied three simulations (Fig. 6b–d) with this method, where the simulation shown in Fig. 6b has a system size $L=0.4$ cm, the simulation shown in Fig. 6c

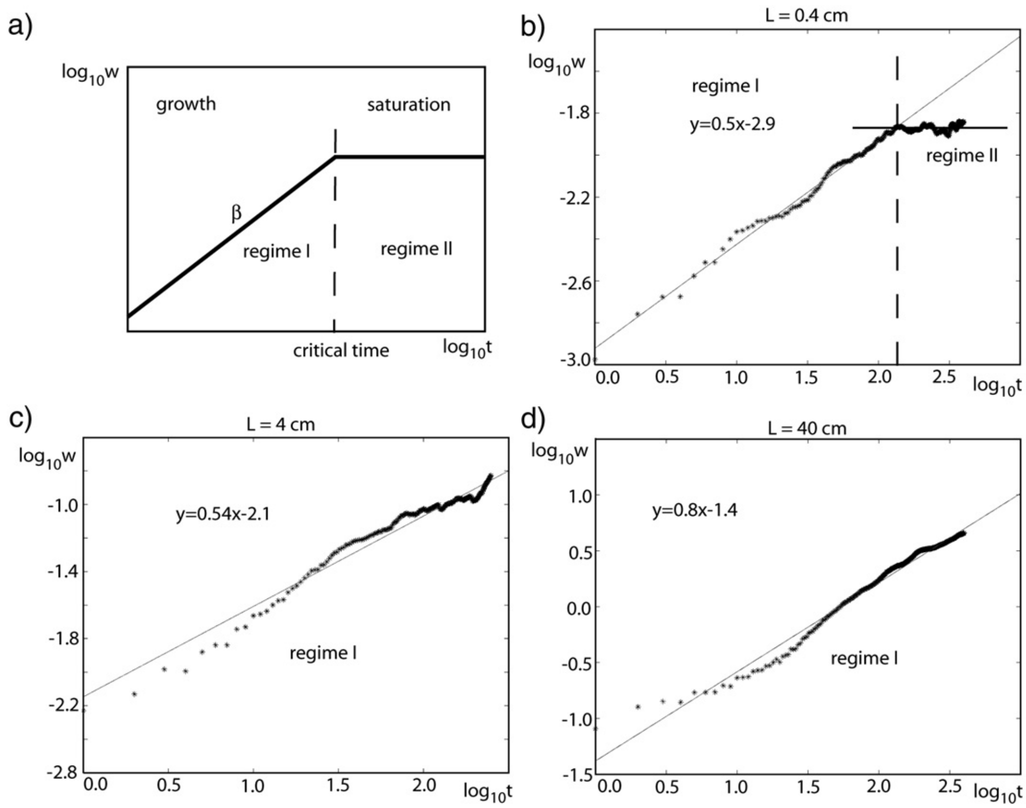

Fig. 6. Log/log diagrams showing the growth of the roughness amplitude w (one unit=0.004 m) against time (t, model steps). (a) Schematic diagram illustrating the two regimes that should develop [26]. Regime I shows a growth that follows a power law in time with a growth exponent β until a critical time. Regime II is characterized by a saturation of the growth so that the roughness amplitude remains constant. (b) Small stylolite ($L=0.4$ cm) that shows both regimes, a power law growth with an exponent of 0.5 in regime I (as slow as a diffusive process) and a crossover regime II where the roughness saturates. (c) Medium sized stylolite ($L=4$ cm) that shows only regime I with a power law growth with an exponent of 0.54. (d) Large stylolite ($L=40$ cm) that shows only regime I with a power law growth with an exponent of 0.8.

has $L=4$ cm and the one shown in Fig. 6d has $L=40$ cm. Figs. 6b and 5a and Figs. 6d and 5b show the same simulations, respectively. The simulated stylolite shown in Fig. 6b shows the expected behaviour with two scaling regimes, the roughness first grows with a roughness exponent of 0.5 and saturates after 2500 yr, where it remains constant close to a value of 50 μm. Going back to Fig. 5a where the growth of the same stylolite is illustrated in 3d, the roughness saturates after 2500 yr, which corresponds to model time step 125. Fig. 6c and d show only the first scaling regime where the increase in roughness amplitude w follows a power law, but w never saturate. That means probably that these two simulations (Figs. 6c, d) did not reach the critical time needed for the roughness to saturate. Taking a look at Fig. 5b where the growing roughness of the stylolite shown in Fig. 6d is illustrated, the roughness width still grows i.e. is not yet saturated.

The three stylolites shown in Figs. 6b–d seem to have different critical times when the roughness saturates but also their growth exponents vary. β increases from the smallest simulation (Fig. 6b) with a value of 0.5 through the medium-sized simulation with a value of 0.54 to the largest simulation with a value of 0.8. These differences may reflect differences of growth regimes that are dominated by either surface energy or by elastic energy, in analogy to the discussion in Fig. 5a and b. The surface energy dominated growth regime (small stylolite, Fig. 6b) has a growth exponent of 0.5 and saturates relatively early. The stylolite shown in Fig. 6c is intermediate, the growth exponent is still small with 0.54 but the roughness does not saturate within the simulated time. The largest stylolite (Fig. 6d) has a significantly larger growth exponent of 0.8, does not saturate, and represents the elastic energy dominated regime.

In terms of natural stylolites the above-mentioned values demonstrate that small stylolites that grow within the surface energy dominated regime grow as slow as a diffusive process (exponent of 0.5) and saturate early so that compaction estimates are almost impossible. However, stylolites that grow within the elastic energy dominated regime grow faster (exponent 0.8) and do not seem to saturate after 8000 yr. They can thus capture part of the compaction of the rock even though their growth is non-linear, and slows down with time. Consequently, rather than using a rule of thumb as a direct proportionality between A, the amplitude of compaction displacement accommodated for around a stylolite, and the stylolite amplitude w, the nonlinear power-law observed for this process where the imposed displacement is linear in time can be utilized to be stated as $(w/l) \sim (t/t_0)^\beta \sim (A/l)^\beta$, with l the relevant physical length, which is here the grain size.

Conversely, for large enough stylolites, as long as the critical saturation time has not been reached at the observed scale, the relationship between the total compaction displacement A and the stylolite amplitude should be of the type

$$A \sim (w/l)^{1/\beta} l. \tag{13}$$

This law should hold until the critical saturation time is reached. Using the proposed scaling law for the large simulation ($L=40$ cm) we obtain the right relation with a slope of 6.6 (Fig. 7) using the root mean square width and a grain size of 1 mm. The stylolite amplitude may finally saturate, but this seems not to happen in 8000 yr for the case of the 40 cm long stylolites that we have studied.

3.4. The teeth structures and their relation with the main compressive stress direction

After characterizing the dynamics of the growth process, we now focus on the orientation of the stylolite teeth. We have demonstrated so far that the teeth mainly develop in the regime where elastic energy is dominant so that well-developed teeth form in the stylolite simulation with a system size $L=40$ cm. The steep sides of the teeth are thought to develop parallel to the main compressive stress and the top of the teeth is

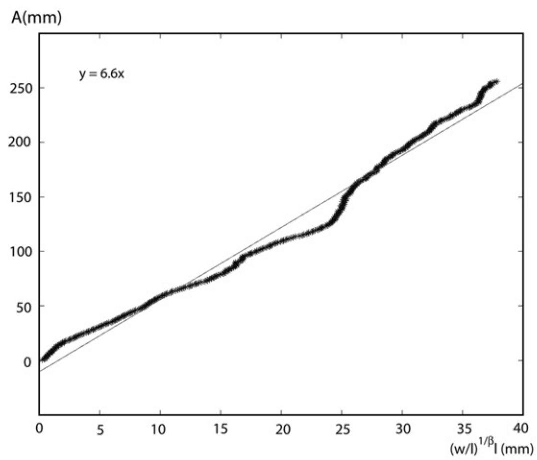

Fig. 7. Proposed scaling relation between the amplitude of compaction around a stylolite (A) and the mean width of the stylolite roughness (w). l corresponds to the grain size and β is the predetermined growth exponent (0.8 in this case). Plot shows the scaling relation for the large stylolite simulation (40 cm long stylolite) using Eq. (13). Theoretically this scaling relation with the determined prefactor of 6.6 can be used to estimate compaction from real stylolites.

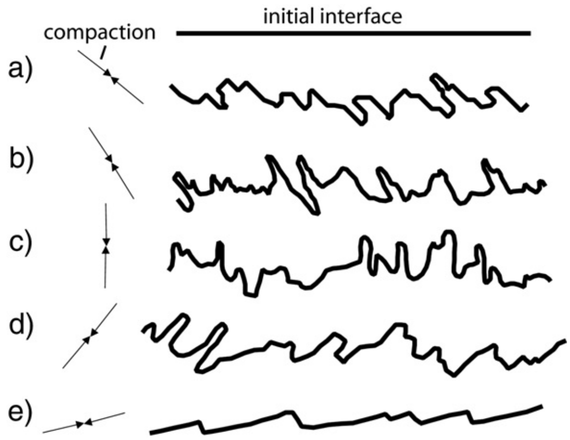

Fig. 8. Stylolite teeth directions track variations of the compression direction. The orientation of the initial interface is given at the top and the direction of the compaction is illustrated at the left hand side. The simulations show that the orientation of the teeth is strongly deterministic and follows the compaction direction.

thought to be oriented perpendicularly to that stress direction.

We test this hypothesis that the teeth track the orientation of the largest principal stress. For the test, we choose again a model with an initially flat dissolution surface that is oriented horizontally with respect to the simulation box but we rotate the compression direction so that the stress field rotates. Theoretically, the teeth should follow the rotated stress field so that one can evaluate the direction of the main compressive stress using the teeth orientation. We use simulations with a system size of 200 elements in the x-direction with an absolute size of $L=10$ cm so that we are in the elastic regime.

The results of the 5 different simulations are shown in Fig. 8a–e where the orientation of the compression direction is shown on the left hand side. Indeed, the teeth do follow the stress directions in all the examples. The sides of the teeth are the best stress direction indicators but even the tops of some teeth tend to orient themselves with respect to the stress. The most extreme example is shown in Fig. 8e where the compression direction has a very low angle with respect to the initial horizontal heterogeneity. The initially horizontal surface has vanished and a stair-step geometry develops with steps that are oriented perpendicular with respect to each other. One set of surfaces corresponds to the sides of the teeth and the other set to the top surface of the teeth.

These simulations demonstrate that stylolite teeth indeed track the direction of the main compressive stress and can therefore be used as stress indicators in natural rocks. One has to note however, that this is only the case

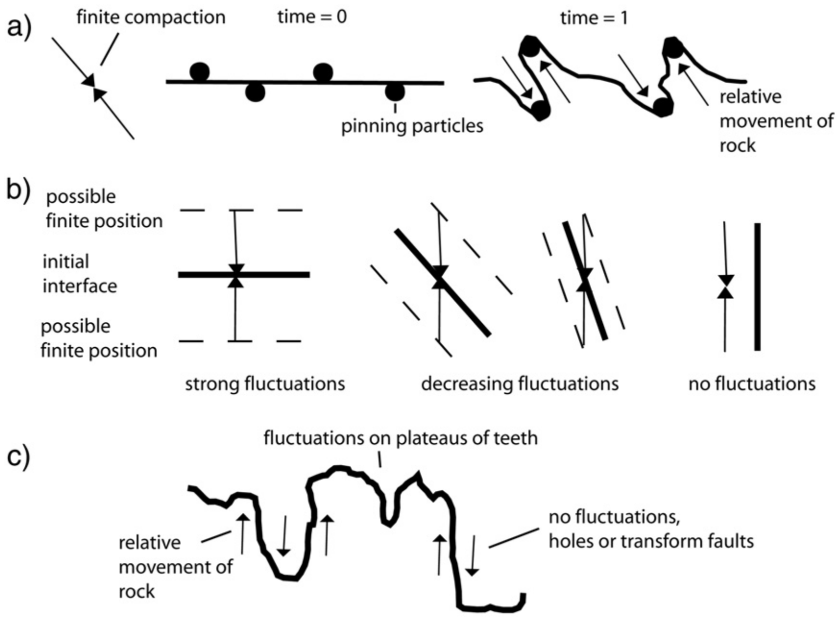

Fig. 9. Model for the development of stylolite teeth. (a) Development of oblique teeth due to pinning particles that record the relative movement of the rock on each side of the interface. (b) Possible fluctuations that may develop on interfaces with different orientations with respect to the main compaction direction. Strongest fluctuations appear on interfaces that are oriented perpendicular with respect to the main compaction direction (arrows). Interfaces that are parallel to the main compaction direction do not show fluctuations. (c) Illustration of these fluctuations on a natural stylolite. The sides of teeth are relatively stable, show no fluctuations and may act as transform faults. Plateaus of teeth are interfaces that show largest fluctuations.

when the stress field does not rotate during stylolite growth and the stress history is not complex.

3.5. Model for the deterministic orientation of stylolite teeth

Our simulations have shown that well-developed stylolite teeth only tend to develop in the elastic regime (Fig. 5). In order to understand the relation between the compaction direction and the orientation of the stylolite teeth, we consider the stress distribution at the interface and the finite compaction. The stress field at the interface for a given time step is directly controlling dissolution. However, just observing the stress field across a stylolite for a single time step is not enough since dissolution and thus a change in the geometry of the interface influences the stress back, dissolution and stress being highly coupled. Therefore we also have to consider the whole stress history and the finite compaction across the interface.

Going back to Fig. 4, one can observe that the location of the teeth is random because it depends on the quenched noise in the background. The second simple observation is that the finite compaction is directly recorded by the pinning of particles (Fig. 4). As long as they pin the interface, they move in the direction of the compaction, which is parallel to the far field compressive stress for a simple homogeneous rock. This scenario does not change when the compaction direction and thus the main compressive stress is not perpendicular to the initial interface (Fig. 9a). Pinning particles still record the rotated compaction direction because they move in that direction. If two pinning elements are close but on opposing sides of the interface they move in opposite directions and a perfect side of a tooth develops recording the compaction direction. If this direction is parallel to the far field main compressive stress, the stylolite also records this stress direction.

Looking at the movement of a whole interface (Fig. 9b), one can see that the total amount that the interface may move perpendicularly to itself depends on its orientation with respect to the compaction direction. An interface that is oriented perpendicularly to the compaction direction can have the largest fluctuations and thus produce a roughness with the largest amplitude. An interface that is oriented at a smaller angle to the compaction direction will not develop importantly in the direction perpendicular to itself. If particles are pinning this interface, it may actually develop steps. The most extreme case is an interface that is oriented parallel to the compaction direction. This interface shows no fluctuations and thus cannot develop a roughness. It cannot even develop steps because particles cannot pin this interface. The interface is very stable and can only act as a transform fault. Therefore the sides of teeth, which reflect such an interface, are very stable and the teeth geometry itself is a natural consequence of the compaction direction (Fig. 9c). Strongly pinning particles are not even necessary for the development of these geometries. Some pinning or a variation in dissolution across the interface is necessary for a roughening of the interface, but once this roughness is initiated and for large scales where the surface energy is not dominant, the typical teeth geometries develop and stay stable without much flickering, i.e. they are strongly deterministic.

Looking at the stress history, we also show that the main compressive stress close to the stylolite is parallel to the main compaction direction. An interface perpendicular to the main compaction direction has a significantly normal stress component and experiences dissolution. For an interface parallel to the main compressive stress, dissolution will only relax the second principle stress that builds up in a laterally confined system. The second principle stress will vanish to zero and in the extreme case a hole can develop. Compaction itself cannot fill the hole because the compaction has the wrong direction. The only possibility to build-up stress again is a flow of material into the hole or a collapse of the teeth. Looking at the stress history, the main compressive stress close to the stylolite and the direction of the finite compaction are parallel. Indeed, the stylolite teeth track this direction.

4. Discussion

In this discussion we first focus on several assumptions used in the simulations. The focus of these simulations is the roughening process of an initially smooth interface, not an investigation of the reason why the dissolution is localized. Therefore we use an initially flat interface were dissolution starts and restrict dissolution to this stylolite surface. Some observations in natural rocks support such a scenario: First, some stylolites do initiate from mica-rich layers. Next, some stylolites with oblique teeth do exist. Stylolites with oblique teeth are most probably initiating from an interface that was oblique with respect to the main compressive stress direction when the stylolite roughness started to grow. However, surely not all stylolites start from given heterogeneities but may localize due to geochemical self-organization [30] or anti-cracking [16]. This is beyond the focus of this current manuscript.

In our simulations, we use a simple description of the noise that initiates the roughening process. As mentioned earlier, the noise is only chemical (a variation in dissolution constants), is set on single particles that have the same size and is distributed with a bimodal distribution. In a real rock, elastic properties and surface energy may also vary, the noise may be on the grain scale or at the scale of smaller heterogeneities and the distribution may be more complicated than bimodal. It is not clear how variations in these parameters may affect the stylolite growth and what kind of noise is present in a real rock. The nature of the noise may influence pinning of the surface and thus may influence the growth and structure of the stylolite [31]. However, since our simulations can reproduce natural stylolites quite realistically, one can argue that the exact nature of the noise is less important than the effects of elastic energy, surface energy and stress.

The collection of slowly dissolving particles within the stylolite interface can have two additional effects: a mechanical change of the interface and a chemical effect that enhances dissolution kinetics. We have not yet taken these possibilities into account. A change in the properties of the interface may theoretically change the growth rate of the stylolite amplitude. However, recent simulations that we performed show no variation in the growth exponents as a function of dissolution constants of pinning particles that are collected within the stylolite. Therefore we expect no change due to a chemical effect. However, a possible mechanical effect was not yet tested.

We assume that the dissolution process is controlled by the reaction kinetics. If the process is diffusion controlled, the time scales in the model may change significantly. The relation between absolute compaction of the rock and the stylolite amplitude should not change, but the compaction rate may be slower.

We apply a constant displacement rate at the model boundaries. This leads to an average mean stress within the model that stays constant during a simulation. The dissolution adjusts to the given displacement rate. This scenario is similar to a constant load boundary condition where the compaction of the rock is a function of the dissolution at the stylolite. We are not yet modelling the development of a stylolite in a dynamic sedimentary basin where the load of the overlying sediments may increase with time.

Another interesting question is how a stylolite grows when the finite strain is rotating. We have demonstrated that stylolite teeth develop by a particle pinning process at the interface and track the direction of the finite compaction. However, this is not necessarily true if the finite strain is rotating because particles at the interface only pin the interface from the moment when they meet the interface to the moment when they dissolve. This means that they are only recording parts of the finite compaction direction. If the stylolite grows in a simple shear dominated rock, the direction of the pinning particles should initially record the direction of the compressive ISA (incremental stretching axes) and then the teeth should rotate. Therefore young teeth do really track the compressive ISA and thus probably also the direction of the compressive stress whereas old teeth rotate. However, if the roughness is dynamic and the stylolite constantly changes its shape, it can always grow new teeth and old teeth will disappear so that the direction of the compressive ISA and the compressive stress are recorded.

5. Conclusions

We have developed a numerical model that can successfully reproduce the roughening of stylolites. The numerical stylolites are very similar, if not identical, to natural stylolites. We propose that the growth of the stylolite roughness is induced by pinning particles that produce a complex interface that evolves dynamically through time. Two different regimes can be separated, a small-scale regime where the roughness fluctuates significantly and a large-scale regime where well-developed teeth patterns grow. The small-scale regime is dominated by surface energy whereas the large-scale regime is dominated by elastic energy. Scaling laws characterizing the dynamic growth of the stylolite roughness as a function of time are proposed. These laws show that the roughness grows in two successive regimes in time, a first regime where the growth follows a power law and a second regime where the roughness growth saturates. These findings are essential for compaction estimates using stylolites, the roughness growth is non-linear in time, slows down with time and may even saturate. A saturated stylolite looses its memory for compaction completely and cannot be used for total compaction or strain rate estimates. We also show with our simulations that the teeth of stylolites do really follow the main compaction direction and may thus indicate the direction of the maximum compressive stress in a homogeneous rock. We show that this strong deterministic geometry of the teeth is a consequence of pinning particles that move in the direction of the finite compaction and of the local stress history at the stylolite interface. Summarizing, the geometry of stylolite teeth can be used by geologists to estimate the direction of the finite compaction or the main compressive stress, but absolute compaction estimates are difficult to perform and may strongly underestimate the real values. In the regime preceding saturation, we utilize the observed nonlinear growth of the roughness amplitude to propose a refined estimate of absolute compaction, Eq. (13), based both on the stylolite roughness amplitude and the size of the dissolving grains (Fig. 7). This can in general be used as a lower bound of total compaction.

Acknowledgements

DK acknowledges funding by the MWFZ Center of Mainz University and the DFG (KO 2114/5-1). This is contribution no. 37 from the Geocycles Cluster funded by the state of Rheinland-Pfalz.

References

[1] P.B. Stockdale, Stylolites: their nature and origin, Indiana University Studies IX, 1922, pp. 1–97.
[2] M.T. Heald, Stylolites in sandstones, J. Geol. 63 (1955) 101–114.
[3] W. Park, E. Schot, Stylolites: their nature and origin, J. Sediment. Petrol. 38 (1968) 175–191.
[4] R. Bathurst, Carbonate sediments and their diagenesis, Elsevier Sci, New York, 1971.
[5] B. Bayly, A mechanism for the development of stylolites, J. Geol. 94 (1986) 431–435.
[6] F. Renard, J. Schmittbuhl, J.-P. Gratier, P. Meakin, E. Merino, Three-dimensional roughness of stylolites in limestones, J. Geophys. Res. 108 (2004) B03209.
[7] Z. Karcz, C.H. Scholz, The fractal geometry of some stylolites from the Calcare Massiccio Formation, Italy, J. Struct. Geol. 25 (2003) 1301–1316.
[8] J. Schmittbuhl, F. Renard, J.-P. Gratier, R. Toussaint, The roughness of stylolites: implications of 3D high resolution topography measurements, Phys. Rev. Lett. 93 (2004) 238501.
[9] J. Suppe, Principles of Structural Geology, Prentice-Hall, New Jersey, 1985, p. 537.
[10] H. Stel, M.J. De Ruig, Opposite vergence of a kink fold and pressure solution cleavage, southeast Spain: a study of the relation between paleostress and fold kinematics, Tectonophysics 165 (1989) 117–124.
[11] J.-P. Petit, M. Mattauer, Plaeostress superimposition deduced from mesoscale structures in limestone: the Matelles exposure, Languedoc, France, J. Struct. Geol. 17 (1995) 245–256.
[12] M. Ebner, B. Grasemann, Divergent and convergent non-isochoric deformation, J. Struct. Geol. 28 (2006) 1725–1733.
[13] D.C.P. Peacock, I.N. Azzam, Development and scaling relationships of a stylolite population, J. Struct. Geol. 28 (2006) 1883–1889.
[14] J. Gratier, L. Muquet, R. Hassani, F. Renard, Experimental microsylolites in quartz and modeled application to natural stylolitic structures, J. Struct. Geol. 27 (2005) 89–100.
[15] C.N. Drummond, D.N. Sexton, Fractal structure of stylolites, J. Sediment. Res. 68 (1998) 8–10.
[16] R.A. Fletcher, D.D. Pollard, Anticrack model for pressure solution surfaces, Geology 9 (1981) 419–424.
[17] R. Katsman, E. Aharonov, H. Scher, Localized compaction in rocks: Eshelby's inclusion and the spring network model, Geophys. Res. Lett. 33 (2006) L10311.
[18] M.W. Jessell, P.D. Bons, L. Evans, T.D. Barr, K. Stüwe, Elle: the numerical simulation of metamorphic and deformation textures, Comput. Geosci. 27 (2001) 17–30.
[19] D. Koehn, J. Arnold, A. Malthe-Sørrenssen, B. Jamtveit, Instabilities in stress corrosion and the transition to brittle failure, Am. J. Sci. 303 (2003) 956–971.
[20] D. Koehn, A. Malthe-Sørenssen, C. Passchier, The structure of reactive grain—boundaries under stress containing confined fluids, Chem. Geol. 230 (2006) 207–219.
[21] S. McNamara, E.G. Flekkoy, K.J. Maløy, Grains and gas flow: molecular dynamics with hydrodynamic interactions, Phys. Rev., E 61 (2000) 4054–4059.
[22] O. Johnsen, R. Toussaint, K.J. Maløy, E.G. Flekkøy, Pattern formation during air injection into granular materials confined in a circular HeLe–Shaw cell, Phys. Rev., E 74 (2006) 011301.
[23] L.D. Landau, E.M. Lifshitz, Theory of Elasticity, Pergamon Press, New York, 1959, p. 134.
[24] E.G. Flekkøy, A. Malthe-Sørrensen, B. Jamtveit, Modeling hydrofracture, J. Geophys. Res. B8 107 (ECV 1) (2002) 1–11.
[25] M.S. Paterson, Nonhydrostatic thermodynamics and its geologic applications, Rev. Geophys. Space Phys. 11 (1973) 355–389.
[26] A.L. Barabási, E.H. Stanley, Fractal concepts in surface growth, Cambridge Univ. Press, New York, 1995.
[27] F. Family, T. Vicsek, Dynamics of fractal surfaces, World Scientific Publishing, Singapore, 1991 New Jersey London Hong Kong.
[28] S. Moulinet, A. Rosso, W. Krauth, E. Rolley, Width distribution of contact lines on a disordered substrate, Phys. Rev., E 69 (2004) 035103(R).
[29] K.J. Maløy, S. Santucci, J. Schmittbuhl, R. Toussaint, Local waiting time fluctuations along a randomly pinned crack front, Phys. Rev. Lett. 96 (2006) 045501.
[30] T. Dewers, P. Ortoleva, A coupled reaction/transport/mechanical model for intergranular pressure solution, stylolites, and differential compaction and cementation in clean sandstones, Geochim. Cosmochim. Acta 54 (1990) 1609–1625.
[31] A. Brouste, F. Renard, J.-P. Gratier, J. Schmittbuhl, Variety of stylolite morphologies and statistical characterization of the amount of heterogeneities in the rock, J. Struct. Geol. 29 (2007) 422–434.

Roughness of Stylolites: Implications of 3D High Resolution Topography Measurements

J. Schmittbuhl

Laboratoire de Géologie, UMR CNRS 8538, Ecole Normale Supérieure, 24, rue Lhomond, F-75231 Paris Cédex 05, France

F. Renard* and J. P. Gratier

LGIT-CNRS-Observatoire, Université J. Fourier, BP 53, F-38041 Grenoble, France

R. Toussaint

Institute of Physics, University of Oslo, PB 1048, Blindern, N-0316 Oslo, Norway

(Received 3 March 2003; revised manuscript received 18 August 2004; published 1 December 2004)

Stylolites are natural pressure-dissolution surfaces in sedimentary rocks. We present 3D high resolution measurements at laboratory scales of their complex roughness. The topography is shown to be described by a self-affine scaling invariance. At large scales, the Hurst exponent is $\zeta_1 \approx 0.5$ and very different from that at small scales where $\zeta_2 \approx 1.2$. A crossover length scale at around $L_c = 1$ mm is well characterized. Measurements are consistent with a Langevin equation that describes the growth of a stylolitic interface as a competition between stabilizing long range elastic interactions at large scales or local surface tension effects at small scales and a destabilizing quenched material disorder.

DOI: 10.1103/PhysRevLett.93.238501 PACS numbers: 91.60.Dc, 62.40.+i, 68.35.Ct, 68.35.Fx

Stylolites are geological patterns that are very common in polished limestones, a material largely used to construct floors and walls of buildings and monuments. They are observed in many sedimentary rocks as thin irregular interfaces that look like printed lines on rock cuts, which is responsible for their name. They are roughly planar structures, typically perpendicular to the geological load (i.e., lithostatic pressure or tectonic maximum compressive stress) and are formed at shallow depths in the Earth's crust during deformation of sedimentary rocks. They result from a combination of stress-induced dissolution and precipitation processes [1] and exist on a very large range of scales, from micrometers to meters. Despite their abundance, stylolites are, as mentioned by Gal *et al.* [2], "among the least well-explained of all pressure-solution phenomena." First, they are complex 3D structures that are often only described from 2D cross sections since they are generally partially sealed [3]. Second, they develop in various geological contexts which lead to very different geometries. Third, they are sometimes transformed because of processes like diagenesis and metamorphism that develop after their initiation.

In this Letter we show the first 3D high resolution topography measurements of natural stylolite interfaces. We characterize the scaling invariance, namely, self-affinity, of the morphology and show the presence of a crossover length scale. We also propose a model based on a Langevin equation that emphasizes the role of the quenched disorder.

The roughness measurements have been performed on three independent stylolite interfaces included in very fine-grained limestone samples from Burgundy area, Vercors, and Jura mountains in France (Fig. 1). The samples have been collected in newly open quarries, thus preserved from late breakage and chemical erosion. The opening procedure was possible for these samples because of the accumulation of undissolved minerals like clays which formed a weak layer along the stylolite interface. The concentration of these minerals provides an estimate of the cumulative strain by dissolution the sample underwent [4]. As shown in Fig. 1, peaks along the interface are randomly distributed in space and of various sizes (up to 1 cm). Large peak magnitudes and local high slopes along the topography make the roughness measurement difficult and challenging.

We used two different profilometers to sample the stylolite roughness. First, with a mechanical profilometer [5] we extracted four profiles of 1030 points each with a horizontal step of $\Delta x = 30\ \mu$m. The mechanical profilometer measures the surface height from the contact of a needle onto the surface (its radius is 25 μm). The vertical resolution is 3 μm over an available range of 5 cm. One of these profiles is shown in Fig. 2. We compare the me-

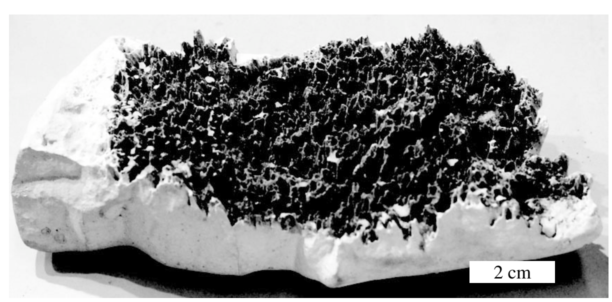

FIG. 1. Picture of a stylolite surface (S12A) in a limestone from Vercors Mountains. Magnitude of the peaks are typically of the order of 6 mm.

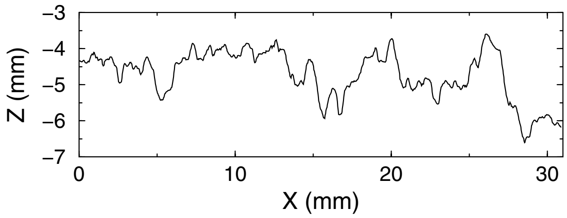

FIG. 2. A 1D profile obtained by a mechanical profilometer (1030 data points $-$ $\Delta x = 30$ μm) along a stylolite surface.

chanical measurements to an optical profiling [6] that is based on a laser triangulation of the surface without any contact. The laser beam is 30 μm wide and horizontal steps between measurement points were $\Delta x = \Delta y = 7$ to 50 μm. The vertical resolution is 2 μm. The latter technique has a high acquisition speed since there is no vertical move, allowing on-flight measurements. However, a successful comparison with mechanical measurements is necessary to ensure that optical fluctuations are true height fluctuations and not material property fluctuations. Three independent samples have been measured at very high resolution: one side of a stylolite from Jura mountains (Sjura) with a resolution 600×600, one side of a stylolite from Burgundy area (S15) with a resolution 8200×4100, and two opposite surfaces of the same stylolite from Vercors mountains shown in Fig. 1 with a resolution 2400×1400 for S12A and 8200×4100 for S12B.

We analyzed the height distribution in terms of self-affinity [7], which states that the surface remains statistically unchanged for the transform: $\Delta x \rightarrow \lambda \Delta x$, $\Delta y \rightarrow \lambda \Delta y$, $\Delta z \rightarrow \lambda^{\zeta} \Delta z$, where λ can take any real value. The exponent ζ is the so-called Hurst exponent. A 1D average wavelet coefficient (AWC) technique [8] has been used to estimate ζ. Indeed, for a self-affine profile, the wavelet spectrum behaves as a power law with a slope $1/2 + \zeta$. AWC spectra clearly exhibit two regimes (Fig. 3). At large length scales, a power-law behavior is observed with a slope of 1, which is consistent with a Hurst exponent of $\zeta_1 = 0.5$. At small length scales, a second power-law behavior is observed with a larger slope (1.7) in agreement with a Hurst exponent $\zeta_2 = 1.2$. The crossover length scale is sharp and defines a characteristic length scale which is slightly different for the three surfaces, $L_c \approx 1$ mm. L_c is several orders of magnitude larger than the grain size and experimental cutoffs. This spectral behavior is observed for both mechanical and optical measurements.

We checked that another analysis technique, namely, the Fourier power spectrum, was providing very consistent results. Figure 4 shows averaged 1D spectra of profiles extracted from the surface Sjura. A self-affine property of the profiles leads to a power-law behavior of the power spectrum as $P(k) \propto k^{-1-2\zeta}$ [7]. Moreover, average spectra of profiles taken along perpendicular directions provide very consistent results (Fig. 4). Isotropy of scaling invariance is confirmed by the circular symmetry of the 2D power spectrum of the surface.

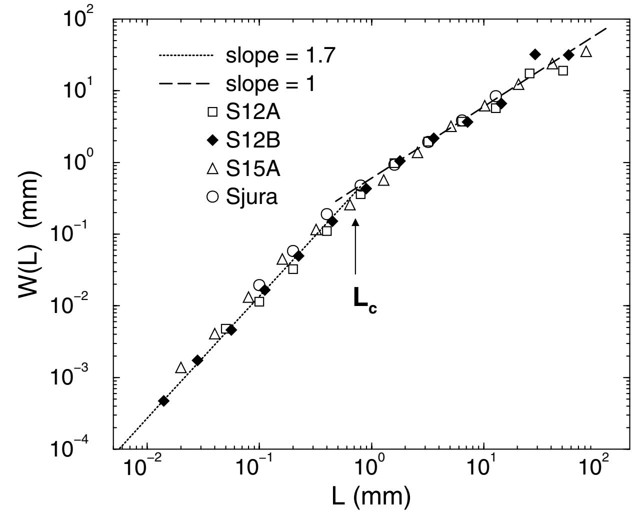

FIG. 3. Averaged wavelet spectra of topographic profiles extracted from four optical maps of stylolite surfaces. Spectra have been normalized to superimpose for large L on the spectrum of S12A.

The second part of the Letter is devoted to a modeling of the stylolite roughening which aims at understanding the origin of the self-affine behaviors and of the characteristic length L_c. The stylolite interface is assumed to be initiated along a boundary between geological beds. More precisely it is approximated as the boundary of a quasiflat and very elongated fluid pore where the trapped fluid is

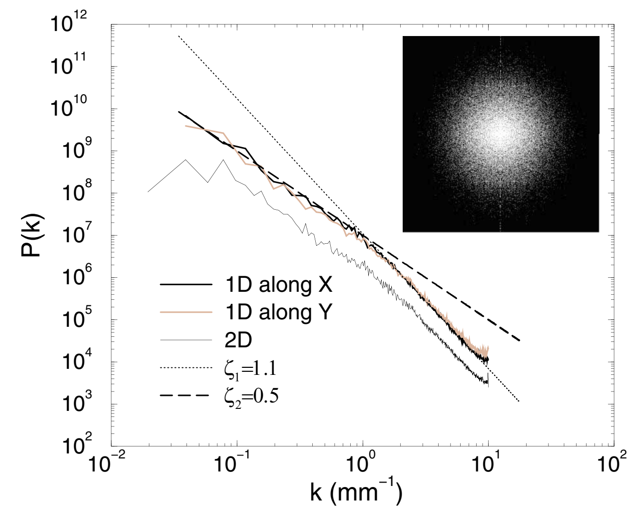

FIG. 4 (color online). Fourier power spectra of 1D topographic profiles oriented along two perpendicular directions (X and Y) and of the full 2D surface. The latter was radially integrated to be compared to the 1D power spectra. Inset: A gray map of the 2D power spectrum. A mirroring technique has been used to reduce nonperiodic edge effects.

assumed to be at lithostatic pressure and the solid, where this pore is embedded, at an average stress $\boldsymbol{\sigma}^0 = \sigma_{zz}^0 \hat{z}\hat{z} + \sigma_{xx}^0(\hat{x}\hat{x} + \hat{y}\hat{y})$, where $\hat{z}$ refers to the direction normal to average stylolite direction and $\hat{x}$ and $\hat{y}$ refer to directions along the average stylolite direction. Since stylolites are on average normal to the largest principal stress direction, $\sigma_s = |\sigma_{zz}^0| - |\sigma_{xx}^0| > 0$.

Possible solid contacts with the mirror surface on the other side of the fluid film are neglected, considering that such contact points concentrate dissolution and disappear. Accordingly, we assume that the stylolite morphology is to first order dominated by a dissolution process between a fluid film and a single elastic solid.

Assuming a free surface profile $z(x, t)$, the normal $\hat{n}$ to the interface pointing toward the solid is, in the limit of small relief, $\hat{n} = \hat{z} - (\partial_x z)\hat{x}$, where plane strain holds. The stress state in the solid is expressed as $\boldsymbol{\sigma} = \boldsymbol{\sigma}^0 + \boldsymbol{\sigma}^1$, where mechanical equilibrium between solid and fluid requires that $\boldsymbol{\sigma}^1 \cdot (-\hat{n}) = -\sigma_s(\partial_x z)\hat{x}$. This stress state results from a surface distribution of tangential force $-\sigma_s(\partial_x z)\hat{x}$ applied on the quasiplanar boundary of the solid by the fluid, so that using Green's elastostatic function [9] and integrating along the y direction, at the surface, $\sigma_{xz}^1 = \sigma_{zx}^1 = \sigma_s(\partial_x z)$ and $\sigma_{xx}^1 = \sigma_{yy}^1 = \sigma_s(2\nu/\pi) \times \int dy(\partial_y z(y))/(x - y)$, all other components being null.

For small reliefs ($||\sigma_1||/||\sigma_0|| \ll 1$) and to the leading order, the elastic free energy $u_e = [(1 + \nu)\sigma_{ij}\sigma_{ij} - \nu\sigma_{kk}\sigma_{ll}]/4E$ can be approximated as $u_e = u_e^0 + u_e^1$ where, from the above, $u_e^0 = \alpha p_0^2/E$, and

$$u_e^1 = -\beta(p_0\sigma_s/E)\int dy(\partial_y z)/(x - y) \tag{1}$$

with an average solid pressure $p_0 = -(2\sigma_{xx}^0 + \sigma_{zz}^0)/3$, and two dimensionless positive constants $\alpha = [9(1 - 2\nu) + 2(1 + \nu)\sigma_s^2/p_0^2]/12$ and $\beta = \nu(1 - 2\nu)/\pi$, where E is an effective Young's modulus, and ν the Poisson coefficient. u_e^0 is the average elastic energy from the global tectonic loading and u_e^1 is its local perturbation that results from the interface topography.

The chemical potential difference at the solid-fluid interface that potentially destabilizes the interface can be written as [10] $\Delta\mu = \Omega(u_e + \gamma\kappa)$ where u_e is the elastic energy per unit volume in the solid, γ is the surface energy, κ is the curvature, and Ω is a molar volume. Gravity effects are supposed to be negligible. We have also assumed that the matrix of the solid, i.e., an assembly of initial sedimentary particles, is sufficiently porous during stylolite initiation to have a bulk diffusion within the material. This assumption is supported by rock thin section observations under an optical microscope [11]. If a bulk diffusion holds in the fluid surrounding the stylolite, the evolution of the interface is directly related to the chemical potential difference: $v_n = m\Delta\mu$ where v_n is the normal dissolution velocity and m is the mobility [10]. We also neglected the chemical potential evolution within the film since we aim only at describing the initiation of the process under drained conditions.

This homogeneous description thus predicts, for small reliefs, $\partial_t z = v_0 + m\Omega(u_e^1 + \gamma\partial_{xx}z)$, with $v_0 = m\Omega u_e^0$. Surface tension is a stabilizing term, but it is important to note that the elastic interaction term, u_e^1, is also stabilizing in the present context. For the present situation, stylolites are perpendicular to the maximum principal stress, and will subsequently be assumed horizontal: $\sigma_s > 0$. Considering an elementary departure from a flat interface, such as a fluid intrusion in the solid, i.e., a bump with a maximum in x, such as $\partial_y z > 0$ for $y < x$, and $\partial_y z < 0$ for $y > x$, u_e^1 is negative in x and reduces the dissolution speed in the bump at x. Accordingly, since the problem is linear, elastic interactions are stabilizing for any corrugations of the interface. For vertical stylolites, the picture is opposite ($\sigma_s < 0$) and elastic interactions are destabilizing leading to the growth of horizontal fingers.

The homogeneous picture predicts the propagation of a planar dissolution interface driven by the average elastic energy u_e^0, with an average speed estimated as $v_0 \approx 8 \times 10^{-6}$ m/yr where we used $m = k\Omega/(RT)$, with a dissolution rate $k \approx 10^{-4}$ mol/m^2/s, $\Omega \approx 4 \times 10^{-5}$ m^3/mol for calcite, R is the universal gas constant, $T \approx 300$ K, $\alpha \approx 0.5$, $E \approx 8 \times 10^{10}$ Pa for limestones, a characteristic stress estimated as $p_0 \approx 25$ MPa, corresponding to a rock at 1 km depth.

To understand the dynamic roughening of stylolites, it is essential to capture the effect of heterogeneities of relevant material properties in the solid, namely ν, E, m, and γ. We assume the relative variation ($\delta E/E$ and others) of these properties to be small, and to correspond to independent random variables associated with each constitutive grain of the rock, which are typically $\ell = 10$ μm sized. At early stages of the process where $\partial_x z \ll 1$, we define the dimensionless surface position with respect to the average plane $z' = (z - v_0 t)/\ell$ and the dimensionless space and time variables $x' = x/\ell$ and $t' = t/\tau$ where $\tau = \ell^2/(\gamma\Omega m)$ to obtain, to the leading order in relative fluctuations and typical slopes, for the roughening interface speed

$$\partial_{t'} z'(x', t') = \partial_{x'x'} z' - \frac{\ell}{L^*}\int dy' \frac{\partial_{y'} z'}{x' - y'} + \eta(x', z'(x')), \tag{2}$$

where $L^* = \gamma E/(\beta p_0 \sigma_s)$ and $\eta = [\alpha\ell p_0/(\beta L^* \sigma_s)] \times [(\delta E/E) + (\delta m/m) - (\delta\alpha/\alpha)]$. In this Langevin equation with quenched noise, the destabilizing random term is balanced by the restoring surface tension term at scales below L^*, and by the restoring elastic interactions at scales above L^*. We propose that this critical scale L^* corresponds to the measured crossover length L_c. For typical limestones, $\gamma = 0.27$ J/m^2 for a water-calcite surface and $\nu \approx 0.25$, so that $\beta \approx 0.04$ and $L^* \approx 0.9$ mm, consistently with the above measured. The other characteristic quantities of interest are $\tau \approx 0.2$ yr, and the characteristic amplitude of the dimensionless noise η is $\rho \approx \alpha\ell p_0/(\beta\lambda^*\sigma_s) \approx 0.2$.

For the Laplacian regime ($L \ll L^*$) and the mechanical regime ($L \gg L^*$), only one of the two restoring terms in Eq. (2) dominates, and these two independent regimes have already been studied. Indeed, the Laplacian regime is nothing other than the Edwards Wilkinson (EW) problem [12] in a quenched noise. In this case the interface is self-affine with an exponent $\zeta_2 \approx 1.2$ [13]. In the mechanical regime, Eq. (2) is analogous to the quasistatic propagation of an elastic line or a mode I fracture front in a disordered material, and the Hurst exponent is $\zeta_1 \approx 0.4$ for a kernel similar to Eq. (1) [14].

The roughening amplitude can be obtained by considering the EW equation with a quenched noise: the characteristic width of the surface measured at scale L, i.e., the saturation width, scales as $w(L)/\ell \approx \rho(L/\ell)^{\zeta_2}$. The saturation time for this width to be achieved from a flat interface defines the characteristic time for the roughness evolution $\tau_s(L)$. Indeed, the dissolution process goes on, with an average speed v_0, as long as $u_e^0 > 0$, and the surface profile fluctuates around the average progressing plane with a correlation time τ_s and a characteristic amplitude $w(L)$. τ_s is such that $\tau_s/\tau \approx (L/\ell)^{\zeta_2/\delta}$, with a dynamic exponent $\delta \approx 0.8$ [13]. With $L \approx 1$ mm, $\ell \approx 10\ \mu$m, and $\zeta_2 \approx 1.2$, this scaling law predicts, up to a constant of order unity, the saturation width at crossover scale $w(L^*) \approx 0.5$ mm and the time to saturation as $\tau_s \approx 200$ yr. This length scale corresponds to the measured one (Fig. 2). The short saturation time implies that observed stylolites have achieved their saturation width over geological time scales. That the width amplitude is also correctly predicted in the mechanical regime could be checked directly, but is granted by the fact that it is correctly predicted in the Laplacian regime, as well as the crossover scale, which determines entirely the prefactor of the scaling law $w(L)$ in the $L > L^*$ regime. In principle, determining L^* and $w(L^*)$ could give two independent constraints on both p_0 and σ_s, which could allow one to determine both the pressure and the differential stress prevailing during the formation of a particular stylolite. However, given the amount of approximations in the involved constants, the only way to test this effect on the crossover wavelength would be to measure stylolites formed in various geological conditions and study the effect of depth and orientation to the main stress.

In conclusion, we presented a quantitative description of stylolite interfaces. The experimental measurements are 3D high resolution descriptions of the topography of natural stylolites. We show that the surfaces are self-affine but with two regimes. At small scales, the Hurst exponent is unexpectedly high, $\zeta_2 = 1.2$, and consistent with a Laplacian regime. At large scales, the stylolites morphology is controlled by long range elastic stress redistributions. In this case the roughening is important with a low Hurst exponent $\zeta_1 = 0.5$. The two regimes are separated by a crossover characteristic length L_c, also predicted by a model based on the description of a stress-induced dissolution, where restoring surface tension effects and elastic interactions compete with a quenched noise. It is important for geological implications to note that L_c is very sensitive to the average stress p_0. Indeed, a measurement of L_c from roughness profiling could provide an estimate of the stress magnitude during the stylolite growth, that is, in the past. Accordingly, stylolites could be considered as stress fossils.

We acknowledge D. Rothman, J. Rice, A. Lobkovsky, B. Evans, Y. Bernabé, B. Goffé, H. Perfettini, P. Meakin, and E. Merino for fruitful discussions.

*Also at Physics of Geological Processes, University of Oslo, Norway.

[1] W. C. Park and E. H. Schot, J. Sediment. Petrol. **38**, 175 (1968).
[2] D. Gal, A. Nur, and E. Aharonov, Geophys. Res. Lett. **25**, 1237 (1998).
[3] Z. Karcz and C. H. Scholz, J. Struct. Geol. **25**, 1301 (2003).
[4] F. Renard *et al.*, J. Geophys. Res. **109**, B03209 (2004).
[5] J. Lopez and J. Schmittbuhl, Phys. Rev. E **57**, 6405 (1998).
[6] Y. Méheust, Ph.D. thesis, University Paris 11, 2002.
[7] A. Barabási and H. Stanley, in *Fractal Concepts in Surface Growth*, edited by A. Barabási and H. Stanley (Cambridge University Press, Cambridge, 1995).
[8] I. Simonsen, A. Hansen, and O. M. Nes, Phys. Rev. E **58**, 2779 (1998).
[9] L. D. Landau and E. M. Lifchitz, *Theory of Elasticity* (Butterworth-Heinemann, London, 1986), 3rd ed.
[10] K. Kassner *et al.*, Phys. Rev. E **63**, 036117 (2001).
[11] E. Carrio-Schaffhauser and S. Raynaud, J. Struct. Geol. **14**, 973 (1992).
[12] S. E. Edwards and D. R. Wilkinson, Proc. R. Soc. London A **381**, 17 (1982).
[13] S. Roux and A. Hansen, J. Phys. I (France) **4**, 515 (1994).
[14] J. Schmittbuhl, S. Roux, J. P. Vilotte, and K. Måløy, Phys. Rev. Lett. **74**, 1787 (1995); S. Ramanathan and D. S. Fisher, Phys. Rev. B **58**, 6026 (1998); A. Tanguy, M. Gounelle, and S. Roux, Phys. Rev. E **58**, 1577 (1998); A. Rosso and W. Krauth, Phys. Rev. E **65**, 025101(R) (2002).

where E is the Young's modulus, γ is the solid-fluid interfacial energy, $\beta = \nu(1-2\nu)/\pi$ is a dimensionless constant with ν the Poisson's ratio, and σ_m and $\sigma_{dv/dh}$ are the mean and differential stresses, respectively. Since the mean stress is the same for both directions, we can reformulate equation (A1) to

$$\sigma_m = \frac{\gamma E}{\beta}\frac{1}{L_v \sigma_{dv}}, \qquad \sigma_m = \frac{\gamma E}{\beta}\frac{1}{L_h \sigma_{dh}}, \tag{A2}$$

and join both equations so that

$$L_v \sigma_{dv} = L_h \sigma_{dh}. \tag{A3}$$

If we now define the differential stresses using the main principal stress components with $\sigma_1 = \sigma_{yy}$, that is, acting normal to the stylolite plane; $\sigma_2 = \sigma_{zz}$, that is, the vertical in-plane stress component; and $\sigma_3 = \sigma_{xx}$, that is, the horizontal in-plane stress component (compare Figure 1B). As $\sigma_{dv} = \sigma_{yy} - \sigma_{zz}$ and $\sigma_{dh} = \sigma_{yy} - \sigma_{xx}$, equation (A3) becomes

$$\frac{L_h}{L_v} = \frac{\sigma_{yy} - \sigma_{zz}}{\sigma_{yy} - \sigma_{xx}}, \tag{A4}$$

and solving for the xx component,

$$\begin{aligned} \sigma_{yy} - \sigma_{xx} &= \frac{L_v}{L_h}\left(\sigma_{yy} - \sigma_{zz}\right), \\ \sigma_{xx} = \sigma_{yy} - \frac{L_v}{L_h}\left(\sigma_{yy} - \sigma_{zz}\right) &= \sigma_{yy} - \frac{L_v}{L_h}\sigma_{yy} + \frac{L_v}{L_h}\sigma_{zz}. \end{aligned} \tag{A5}$$

Part II

[34] For simplification we substitute all material parameters in equation (A1) that are assumed to be constant, according to

$$a = \frac{\gamma E}{\beta}.$$

Then we use equation (A1) for the horizontal crossover,

$$L_h = a\frac{1}{\sigma_m \sigma_{dh}},$$

or

$$\sigma_m \sigma_{dh} = \frac{\sigma_{xx} + \sigma_{yy} + \sigma_{zz}}{3}\left(\sigma_{yy} - \sigma_{xx}\right) = \frac{a}{L_h},$$

and

$$\left(\sigma_{xx} + \sigma_{yy} + \sigma_{zz}\right)\left(\sigma_{yy} - \sigma_{xx}\right) = 3\frac{a}{L_h}. \tag{A6}$$

Now we include equation (A5) in equation (A6) and solve for σ_{yy},

$$\left(2\sigma_{yy} + \sigma_{zz} - \sigma_{yy}\frac{L_v}{L_h} + \sigma_{zz}\frac{L_v}{L_h}\right)\left(\sigma_{yy}\frac{L_v}{L_h} - \sigma_{zz}\frac{L_v}{L_h}\right) = 3\frac{a}{L_h}, \tag{A7}$$

and multiplying the components gives

$$\begin{aligned} 2\sigma_{yy}^2\frac{L_v}{L_h} - \sigma_{yy}^2\left(\frac{L_v}{L_h}\right)^2 + 2\sigma_{yy}\sigma_{zz}\left(\frac{L_v}{L_h}\right)^2 - \sigma_{yy}\sigma_{zz}\frac{L_v}{L_h} \\ - \sigma_{zz}^2\frac{L_v}{L_h} - \sigma_{zz}^2\left(\frac{L_v}{L_h}\right)^2 - 3\frac{a}{L_h} = 0. \end{aligned} \tag{A8}$$

Rearranging equation (A8) to solve a binomial formula gives

$$\sigma_{yy}^2 + \sigma_{yy}\frac{2\sigma_{zz}\left(\frac{L_v}{L_h}\right)^2 - \sigma_{zz}\frac{L_v}{L_h}}{2\frac{L_v}{L_h} - \left(\frac{L_v}{L_h}\right)^2} - \frac{\sigma_{zz}^2\frac{L_v}{L_h} - \sigma_{zz}^2\left(\frac{L_v}{L_h}\right)^2 - 3\frac{a}{L_h}}{2\frac{L_v}{L_h} - \left(\frac{L_v}{L_h}\right)^2} = 0, \tag{A9}$$

and the solution of the binomial formula is then

$$\begin{aligned} \sigma_{yy1,2} = -0.5\frac{2\sigma_{zz}\left(\frac{L_v}{L_h}\right)^2 - \sigma_{zz}\frac{L_v}{L_h}}{2\frac{L_v}{L_h} - \left(\frac{L_v}{L_h}\right)^2} \\ \pm\sqrt{0.25\left(\frac{2\sigma_{zz}\left(\frac{L_v}{L_h}\right)^2 - \sigma_{zz}\frac{L_v}{L_h}}{2\frac{L_v}{L_h} - \left(\frac{L_v}{L_h}\right)^2}\right)^2 - \left(\frac{-\sigma_{zz}^2\frac{L_v}{L_h} - \sigma_{zz}^2\left(\frac{L_v}{L_h}\right)^2 - 3\frac{a}{L_h}}{2\frac{L_v}{L_h} - \left(\frac{L_v}{L_h}\right)^2}\right)}. \end{aligned} \tag{A10}$$

The value of σ_{xx} can be derived from equation (A5).

[35] **Acknowledgments.** J. Nebelsick, M. Maisch, O. W. Vonderschmidt, and T. Sachau are thanked for valuable discussion and support in the field. M. Ebner and D. Koehn acknowledge financial support through DFG project KO2114/5 and the MWFZ of Mainz and the Geocycles Cluster funded by the state of Rhineland-Palatinate. R. Toussaint and J. Schmittbuhl acknowledge the support of a FORPRO grant. We thank both reviewers for thorough reviews and suggestions that helped to improve the manuscript.

References

Angheluta, L., et al. (2008), Stress-driven phase transformation and the roughening of solid-solid interfaces, *Phys. Rev. Lett.*, *100*(9), 096105, doi:10.1103/PhysRevLett.100.096105.

Banda, E., and S. Cloetingh (1992), Europe's lithosphere—Mechanical structure, in *The European Geotraverse*, edited by D. Blundell et al., Cambridge Univ. Press, Cambridge, U.K.

Barabasi, A. L., and H. E. Stanley (1995), *Fractal Concepts in Surface Growth*, 366 pp., Cambridge Univ. Press, Cambridge, U.K.

Bonnetier, E., et al. (2009), Does roughening of rock-fluid-rock interfaces emerge from a stress-induced instability?, *Eur. Phys. J. B*, *67*(1), 121–131.

Bretz, J. H. (1940), Solution cavities in the Joliet limestone of northeastern Illinois, *J. Geol.*, *48*(4), 337–384, doi:10.1086/624897.

Brouste, A., et al. (2007), Variety of stylolites' morphologies and statistical characterization of the amount of heterogeneities in the rock, *J. Struct. Geol.*, *29*(3), 422–434, doi:10.1016/j.jsg.2006.09.014.

Buxton, T. M., and D. F. Sibley (1981), Pressure solution features in a shallow buried limestone, *J. Sediment. Petrol.*, *51*(1), 19–26.

Candela, T., et al. (2009), Characterization of fault roughness at various scales: Implications of three-dimensional high resolution topography measurements, *Pure Appl. Geophys.*, *166*(10/11), 1817–1851.

Capote, R., et al. (2002), The Alpine system north of the Betic Cordillera, in *The Geology of Spain*, edited by W. Gibbons and T. Moreno, 632 pp., Geological Society of London, London.

Casas, A. M., et al. (2000), Syn-tectonic sedimentation and thrust-and-fold kinematics at the intra-mountain Montalban Basin (northern Iberian Chain, Spain), *Geodin. Acta*, *13*(1), 1–17, doi:10.1016/S0985-3111(00)00105-4.

Cooley, J. W., and J. W. Tukey (1965), An algorithm for machine calculation of complex Fourier series, *Math. Comput.*, *19*(90), 297, doi:10.2307/2003354.

Drummond, C. N., and D. N. Sexton (1998), Fractal structure of stylolites, *J. Sediment. Res.*, *68*(1), 8–10.

Dunnington, H. V. (1954), Stylolite development post-dates rock induration, *J. Sediment. Petrol.*, *24*(1), 27–49.

Ebner, M., et al. (2009a), The influence of rock heterogeneity on the scaling properties of simulated and natural stylolites, *J. Struct. Geol.*, *31*(1), 72–82, doi:10.1016/j.jsg.2008.10.004.

Ebner, M., et al. (2009b), Stress sensitivity of stylolite morphology, *Earth Planet. Sci. Lett. 277*, 394–398, doi:10.1016/j.epsl.2008.11.001.

Etzold, A., et al. (1996), Schwäbische Alb—Stratigraphie, Tektonik, Vulkanismus, Karsthydrogeologie, *Z. Geol. Wiss.*, *24*(1/2), 175–215.

Geyer, O. F., and M. P. Gwinner (1991), *Geologie von Baden-Wurttemberg*, 4th ed., 482 pp., Schweizerbart'sche Verlagsbuchhandlung, Stuttgart.

Goshtasby, A. (1986), Piecewise linear mapping functions for image registration, *Pattern Recogn.*, *19*(6), 459–466, doi:10.1016/0031-3203(86)90044-0.

Goshtasby, A. (1988), Image registration by local approximation methods, *Image Vis. Comput.*, *6*(4), 255–261, doi:10.1016/0262-8856(88)90016-9.

Gratier, J. P., et al. (2005), Experimental microstylolites in quartz and modeled application to natural stylolitic structures, *J. Struct. Geol.*, *27*(1), 89–100, doi:10.1016/j.jsg.2004.05.007.

Guzzetta, G. (1984), Kinematics of stylolite formation and physics of the pressure-solution process, *Tectonophysics*, *101*(3–4), 383–394, doi:10.1016/0040-1951(84)90122-7.

Heald, M. T. (1955), Stylolites in sandstones, *J. Geol.*, *63*(2), 101–114, doi:10.1086/626237.

Karcz, Z., and C. H. Scholz (2003), The fractal geometry of some stylolites from the Calcare Massiccio Formation, Italy, *J. Struct. Geol.*, *25*(8), 1301–1316, doi:10.1016/S0191-8141(02)00173-6.

Kley, J., and T. Voigt (2008), Late Cretaceous intraplate thrusting in central Europe: Effect of Africa-Iberia-Europe convergence, not Alpine collision, *Geology*, *36*(11), 839–842, doi:10.1130/G24930A.1.

Koehn, D., et al. (2007), Growth of stylolite teeth patterns depending on normal stress and finite compaction, *Earth Planet. Sci. Lett.*, *257*(3/4), 582–595, doi:10.1016/j.epsl.2007.03.015.

Liesa, C. L., and J. L. Simón (2009), Evolution of intraplate stress fields under multiple remote compressions: The case of the Iberian Chain (NE Spain), *Tectonophysics*, *474*(1/2), 144–159, doi:10.1016/j.tecto.2009.02.002.

Meheust, Y., and J. Schmittbuhl (2001), Flow enhancement of a rough fracture, *Geophys. Res. Lett.*, *27*, 2989–2992.

Park, W. C., and E. H. Schot (1968), Stylolites: Their nature and origin, *J. Sediment. Petrol.*, *38*(1), 175–191.

Pollard, D. D., and R. C. Fletcher (2005), *Fundamentals of structural geology*, 500 pp., Cambridge Univ. Press, Cambridge, U.K.

Press, W. H., et al. (2007), *Numerical Recipes. The Art of Scientific Computing*, 3rd ed., 1256 pp., Cambridge Univ. Press, Cambridge, U.K.

Railsback, L. B. (1993), Lithologic controls on morphology of pressure-dissolution surfaces (stylolites and dissolution seams) in paleozoic carbonate rocks from the mideastern United States, *J. Sediment. Res.*, *63*(3), 513–522.

Railsback, B. L., and L. M. Andrews (1995), Tectonic stylolites in the 'undeformed' Cumberland Plateau of southern Tennessee, *J. Struct. Geol.*, *17*(6), 911–915, doi:10.1016/0191-8141(94)00127-L.

Renard, F., et al. (2004), Three-dimensional roughness of stylolites in limestones, *J. Geophys. Res.*, *109*, B03209, doi:10.1029/2003JB002555.

Renard, F., et al. (2006), High resolution 3D laser scanner measurements of a strike-slip fault quantify its morphological anisotropy at all scales, *Geophys. Res. Lett.*, *33*, L04305, doi:10.1029/2005GL025038.

Rutter, E. H. (1983), Pressure solution in nature, theory and experiment, *J. Geol. Soc.*, *140*(5), 725–740, doi:10.1144/gsjgs.140.5.0725.

Schmittbuhl, J., et al. (1995), Reliability of self-affine measurements, *Phys. Rev. E*, *51*(1), 131–147, doi:10.1103/PhysRevE.51.131.

Schmittbuhl, J., et al. (2004), Roughness of stylolites: Implications of 3D high resolution topography measurements, *Phys. Rev. Lett.*, *93*, 238501, doi:10.1103/PhysRevLett.93.238501.

Schmittbuhl, J., et al. (2008), Fracture morphology and viscous transport, *Int. J. Rock Mech. Min. Sci.*, *45*(3), 422–430, doi:10.1016/j.ijrmms.2007.07.007.

Simon, J. L. (2007), Analysis of solution lineations in pebbles: Kinematical vs. dynamical approaches, *Tectonophysics*, *445*(3/4), 337–352, doi:10.1016/j.tecto.2007.09.003.

Simonsen, I., et al. (2000), Wave scattering from self-affine surfaces, *Phys. Rev. E*, *61*(5), 5914, doi:10.1103/PhysRevE.61.5914.

Stockdale, P. B. (1922), Stylolites: Their nature and origin, *Indiana Univ. Studies*, *9*, 1–97.

Tada, R., and R. Siever (1989), Pressure solution during diagenesis, *Annu. Rev. Earth Planet. Sci.*, *17*, 89–118, doi:10.1146/annurev.ea.17.050189.000513.

Turcotte, D. L. (1997), *Fractals and Chaos in Geology and Geophysics*, 2nd ed., 398 pp., Cambridge Univ. Press, Cambridge, U.K.

P. Bons, Institute for Geosciences, Eberhard Karls University Tübingen, Sigwartstr. 10, D-72076 Tübingen, Tübingen, Germany.

M. Ebner, Geological Survey of Austria, Neulinggasse 38, A-1030 Vienna, Austria. (marcus.ebner@geologie.ac.at)

D. Koehn, Tectonophysics, Institute of Geosciences, Johannes Gutenberg University, Becherweg 21, D-55128 Mainz, Germany.

J. Schmittbuhl and R. Toussaint, EOST, University of Strasbourg, Strasbourg 67081, France.

Earth and Planetary Science Letters 277 (2009) 394–398

Contents lists available at ScienceDirect

Earth and Planetary Science Letters

journal homepage: www.elsevier.com/locate/epsl

Stress sensitivity of stylolite morphology

Marcus Ebner [a,*], Daniel Koehn [a], Renaud Toussaint [b,c], François Renard [d,e], Jean Schmittbuhl [b,c]

[a] Tectonophysics, Institute of Geosciences, Johannes Gutenberg University, Becherweg 21, D-55128 Mainz, Germany
[b] EOST, Université Louis Pasteur, Strasbourg, France
[c] Institut de Physique du Globe de Strasbourg, UMR CNRS 7516, 5 rue Descartes, F-67084 Strasbourg Cedex, France
[d] LGCA-CNRS-Observatoire de Grenoble, Université Joseph Fourier BP 53, F-38041 Grenoble, France
[e] Physics of Geological Processes, University of Oslo, Norway

ARTICLE INFO

Article history:
Received 16 May 2008
Received in revised form 10 September 2008
Accepted 1 November 2008
Available online 28 November 2008

Editor: Dr. C.P. Jaupart

Keywords:
stylolites
roughness
self-affine scaling
morphogenesis
paleo-stress

ABSTRACT

Stylolites are rough surfaces that form by localized stress-induced dissolution. Using a set of limestone rock samples collected at different depths from a vertical section in Cirque de Navacelles (France), we study the influence of the lithostatic stress on the stylolites morphology on the basis of a recent morphogenesis model. We measured the roughness of a series of bedding-parallel stylolites and show that their morphology exhibits a scaling invariance with two self-affine scaling regimes separated by a crossover-length (L) at the millimeter scale consistent with previous studies. The importance of the present contribution is to estimate the stylolite formation stress σ from the sample position in the stratigraphic series and compare it to the crossover-length L using the expected relationship: $L{\sim}\sigma^{-2}$. We obtained a successful prediction of the crossover behavior and reasonable absolute stress magnitude estimates using relevant parameters: depth of stylolite formation between 300 to 600 m with corresponding normal stress in the range of 10–18 MPa. Accordingly, the stylolite morphology contains a signature of the stress field during formation and we thus suggest that stylolites could be used as paleo-stress gauges of deformation processes in the upper crust.

1. Introduction

Stylolites are rough paired surfaces (as illustrated in Fig. 1A), mainly observed in monomineralic sedimentary rocks. The fact that stylolites can be found in a variety of rocks and display a wide range of morphologies, even within a single outcrop, makes comparison and description of natural stylolites a difficult task (Park and Schot, 1968). Early classifications were mainly based on qualitative parameters such as the visual appearance of the interface and the orientation with respect to the bedding (Park and Schot, 1968; Guzzetta, 1984). Moreover, the necessary overburden for the formation of bedding-parallel stylolites is still debated: up to 800–1000 m (e.g. Railsback, 1993) whereas other studies (Tada and Siever, 1989 and references cited therein) report depths as shallow as 90 m for the onset of stylolitization. Stylolites form by localized stress induced dissolution (*e.g.* Stockdale, 1922; Dunnington, 1954; Rutter, 1983). They reflect important diagenetic processes like local mass transfer, compaction, and porosity reduction in sedimentary basins (e.g. Tada and Siever, 1989). They are often used to estimate the amount of dissolved material in the rock (Tada and Siever, 1989), and therefore the total amount of deformation. The long axis of stylolite teeth-like patterns (Fig. 1) is also commonly used to decipher the largest principal compressive stress direction based on field observations (Petit and Mattauer, 1995; Ebner and Grasemann, 2006).

Modeling of stylolite morphogenesis is a challenging task (Gal et al., 1998). When their shape is analyzed at large scales and reduced to a flat penny-shape disk, they have been thought to propagate as anticracks (Fletcher and Pollard, 1981). A significant step in stylolite morphogenesis modeling has been obtained from extended roughness measurements in particular 3D profiling of open stylolites. These data have allowed quantitative approaches based on fractal analysis tools (Drummond and Sexton, 1998) and demonstrated fractal scaling invariance over several orders of magnitude of stylolite roughness (Renard et al., 2004; Schmittbuhl et al., 2004; Gratier et al., 2005; Karcz and Scholz, 2003; Brouste et al., 2007). In addition Schmittbuhl et al. (2004) and Renard et al. (2004) observed the existence of a crossover-length (L) that separates two scaling regimes with different roughness exponents for small and large scales. These scaling regimes are consistent with an interface morphogenesis model (Schmittbuhl et al., 2004; Renard et al, 2004) that describes the growth of a stylolite surface as a competition between two stabilizing forces: long range elastic fluctuations and local surface tension, and a destabilizing force due to the presence of heterogeneities in the material. These heterogeneities are thought to be caused by mineral impurities that induce local fluctuations of the elastic moduli. According to this model, the roughening destabilization is induced by the heterogeneities in the material, whereas surface tension balances the roughening process on small and elastic energies on large scales. The key point in

* Corresponding author. Tel.: +49 6131 3926612; fax: +49 6131 3923863.
E-mail address: ebnerm@uni-mainz.de (M. Ebner).

0012-821X/$ – see front matter © 2008 Elsevier B.V. All rights reserved.
doi:10.1016/j.epsl.2008.11.001

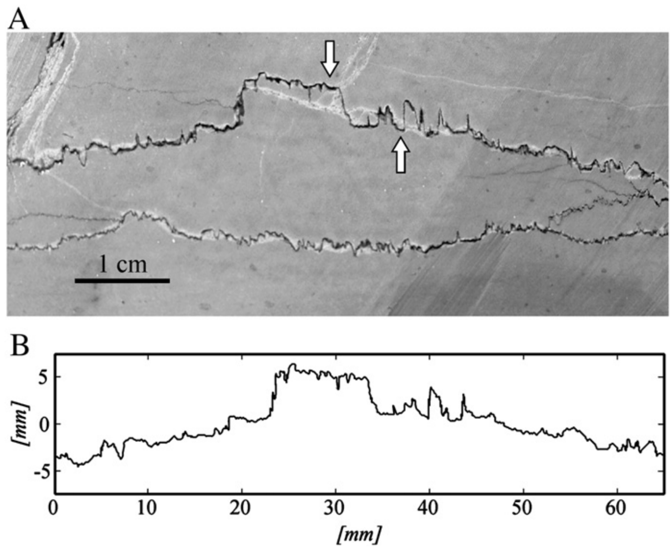

Fig. 1. Bedding-parallel stylolite from Cirque de Navacelles (southern France). A: Plane section of a sample is cut perpendicular to the mean stylolitic plane. Arrow indicates "teeth-like" structures that are oriented parallel to the principal stress direction. B: 1D roughness of the stylolite shown in A after removal of overhangs and linear trend. These data were used to calculate the scaling properties of the roughness.

the modeling is the prediction of the crossover-length L, i.e. a property of the present stylolite geometry, as a function of the stress field during stylolite formation, i.e. the driving paleo-stress. A numerical check of this modeling was proposed by Koehn et al. (2007), which verified the basic assumptions of interrelation between stress orientation and the orientation of stylolite teeth. The motivation of the present work is to examine the link between stylolite morphology and stress magnitude, based on a data set of natural stylolites for which the stress magnitude can be estimated.

2. Stylolite data-set, roughness measurements and analysis

We studied a set of 14 bedding-parallel stylolites from Cirque de Navacelles (southern France), where a 300 m section of flat-lying upper Jurassic limestone crops out (e.g. Bodou, 1976). The investigated succession is an external shelf deposit of the Vocontian Basin that consists mainly of fine-grained (5–40 µm) mudstones and wackestones. The top 100 m is made up of massive Kimmeridgian limestones, whereas the lower 200 m part contains well-bedded Oxfordian mudstones with higher marl content and a slight secondary dolomitisation (Bodou, 1976). The main tectonic overprint in this area is caused by Eocene roughly N–S directed compression from the Pyrenean (e.g. Rispoli, 1981; Petit and Mattauer, 1995). This tectonic phase reactivated subvertical fractures, which trend NE–SW and show a left-lateral displacement. The main tectonic structures are exposed south of the sampling area, but a set of approximately E–W striking vertical stylolites that accompany this tectonic event can be found in the investigated area (Petit and Mattauer, 1995). Such vertical tectonic stylolites were not used or investigated in this study.

The investigated samples were all collected along fresh road-cuts. Only closed interfaces were considered for sampling to avoid overprint due to weathering. In addition, we collected only macroscopically visible stylolites in calcitic limestones for the present study. The samples are very fine-grained mudstones and, for all samples, the porosity is secondary and amounts to less than 10%, in line with high seismic velocities measured (see later). Microstructural investigation of the samples showed that bioclast content is below 5–10% and that clasts do not pin the surface, *i.e.* do not register in the roughness. The bedding parallel stylolites did not initiate along preexisting planes of anisotropy, such as bedding planes, but originated along sites of stress concentration (e.g. clay particles). Microstylolites observed in thin-section frequently revealed tapered terminations as predicted by the anticrack theory (Fletcher and Pollard, 1981). Insoluble materials, including fine-grained clay minerals that have accumulated along the stylolitic interface do not exceed 0.5 mm in thickness (Bodou, 1976). The samples were collected along the vertical profile to systematically investigate the influence of lithostatic stress on stylolite roughness.

Since mechanical opening along the stylolitic interface was not possible for most of the samples, we could not investigate the stylolite surface morphology with a profiler (e.g. Renard et al., 2004). Therefore we examined 2D slabs that displayed the stylolite seam.

All oriented specimens were cut normal to the main stylolitic plane to contain the principal stress direction. Each slab was imaged with an SLR camera (sample size along the cut surface is 10–30 cm with a pixel resolution of 35 µm) without further treatment (see Fig. 1). The signals were extracted from these images using two different methods. In the first method we manually digitized the images using standard drawing software (CorelDraw©). To check the consistency of our method and to avoid bias from human input we used a second method, for which we used simple image analysis tools. For that purpose, we clipped the appropriate value range (i.e. the stylolite) from the histogram of the grayscale image and converted the clipped part to a binary image. This image contains the trace of the stylolite from which the boundary pixels were extracted for further treatment.

The raw 1-D profiles (Fig. 1B) were pre-treated by removing the overhangs to get single valued functions down to the inverse of the Nyquist-frequency (i.e. of twice the pixel size of the digital images). This binning of the raw data was executed using an algorithm that extracts the topmost pixel of the stylolite signal along each vertical column of the image. A reference frame has been defined for each profile, by adjusting its horizontal (x) axis to the global linear trend i.e. a regression over the profile, and the vertical (z) axis is set to have zero mean height. We verified that the signal derived from our stylolite cross-sections shows a scaling behavior similar to extended measurements from 3D topographies by taking side pictures of "opened" stylolites not used in this study, applying the same image extraction technique as described above and comparing the outcome to profiler measurements as suggested by Schmittbuhl et al., (2004).

Results from Schmittbuhl et al. (2004) and Renard et al. (2004) show that stylolite roughness exhibits complex self-affine scaling invariance. A self-affine rough surface is characterized statistically by the fact that points along the surface separated by a distance Δx from each other are typically distant in the direction transverse to the surface by $\Delta h \approx \Delta x^H$, where H is the roughness or Hurst exponent. Indeed two self-affine regimes are observed on stylolites which can be summed up for the average description of the height difference h of points along the surface separated by a distance Δx as:

$$h(\Delta x) \approx A \Delta x^{H_S} g(\Delta x/L) \text{ with } g(u) = \begin{cases} u^0 & \text{if } \quad u \ll 1 \\ u^{H_L - H_S} & \text{if } \quad u \gg 1 \end{cases} \quad (1)$$

where A is a scaling factor g is a scaling function and u is the ratio $\Delta x/L$ with L being a crossover-length. H_S, H_L correspond to the roughness exponents for small and large scales, respectively.

We calculated the Fourier power spectrum P of the stylolite profiles as a function of the wave number k (Renard et al., 2004; Schmittbuhl et al., 2004) (see Fig. 2A). The power spectrum actually exhibits two power law regimes separated by a crossover at a wavenumber $k_L \approx 1$ mm^{-1}. Knowing that the power spectrum of a self-affine profile behaves as: $P(k) \sim k^{-1-2H}$, we can estimate both roughness exponents from the asymptotic behaviors at small and large scales. To verify our results, we used a second independent signal processing technique, the average wavelet coefficient method (AWC), with Daubechies D4 wavelets (Simonsen et al., 1998). The wavelet spectrum of a self-affine function behaves as a power law with an exponent equal to $½ + H$ (see Fig. 2B). Using both methods, our results confirm

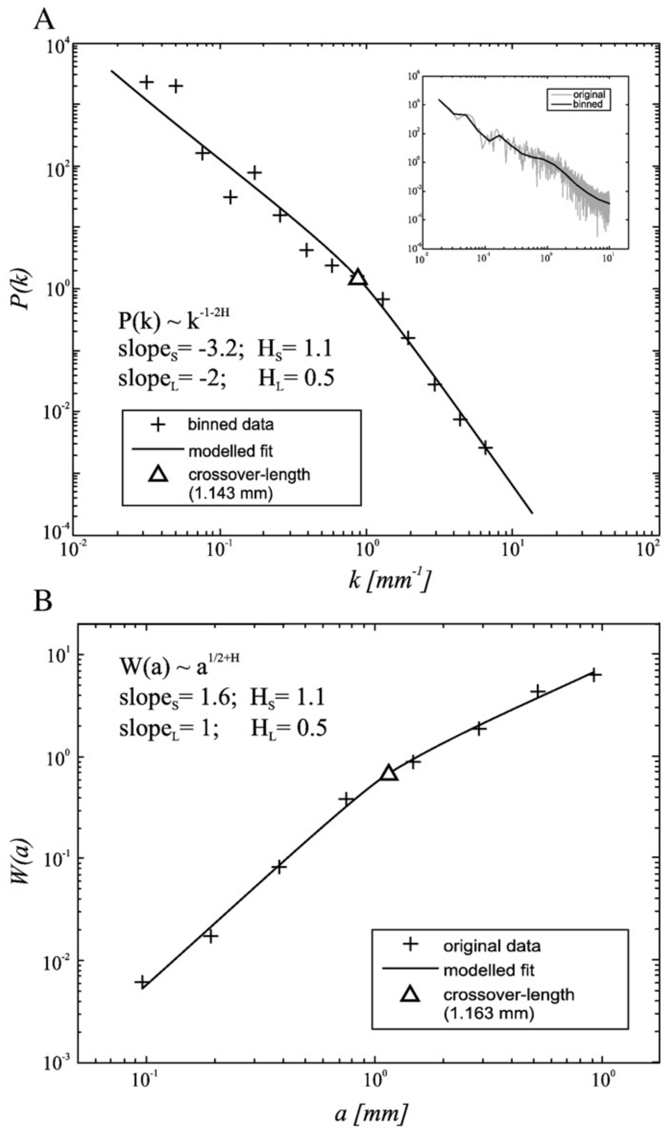

Fig. 2. Scaling of Fourier power and averaged wavelet spectra from 1D stylolite profiles. A: Fourier power spectrum (inset) of the stylolite shown in (A) and logarithmically binned spectrum (crosses) used for nonlinear least square fitting (solid line) with L indicated by a triangle; H_S and H_L denote the roughness exponents of the signal. B: Averaged wavelet spectrum (AWC) of the stylolite (crosses) of (A) with modelled fit (solid line) and L (triangle). Both independent methods reveal similar values for the crossover-length and roughness exponents of individual samples.

the presence of two scaling regimes with H_S~ *1.1* and H_L~*0.5* for small and large length scales respectively.

A sensitive task is to estimate precisely the crossover-lengthscale L. For this, we assumed a linear-by-parts fit of the Fourier or wavelet spectra in the logarithmic space, with a crossover function to change from the small scale branch of the scaling law to the large scale one: More precisely, noting in Fourier space, $x=\ln(k)$ and $f(x)=\ln[P(k)$with $P(k)$ the power spectrum, or alternatively in wavelet space, $x=\ln(a)$ where a is the scale parameter, and $f(x)=\ln[A(a)]$ with $A(a)$ the associated average wavelet coefficient, we fit these spectra to the following model:

$$f(x) = (a_L x + m_L)(1-w(x)) + (a_S x + m_s)w(x) \text{ with } w(x) = \frac{(\tanh(x+L)+1}{2} \quad (2)$$

where $\alpha_{L,S}$ are the exponents of the scaling function for large and small scales (i.e. $\alpha_{L,S}=-1-2H_{L,S}$ in Fourier, and $\alpha_{L,S}=0.5+H_{L,S}$ for the wavelet spectrum), $m_{L,S}$ are the corresponding intercepts with the ordinate and $w(x)$ is the weighting function. We fixed the roughness exponents and searched using a least square algorithm the best estimates of L and $m_{L,S}$. In addition we verified that the obtained parameters did not vary along the interface by performing the scaling analysis over independent parts of the same 1D signal. This procedure allowed a robust investigation of the data. Note that to model the data with an equal importance for the large and small scale, we resample the power spectra with a logarithmic binning, i.e. to get a constant density of data points over the complete spectrum in logarithmic representation.

3. Results

We calculated the crossover-lengths L for all samples from Fourier and wavelet spectra. Fig. 3A shows the correlation between L and the

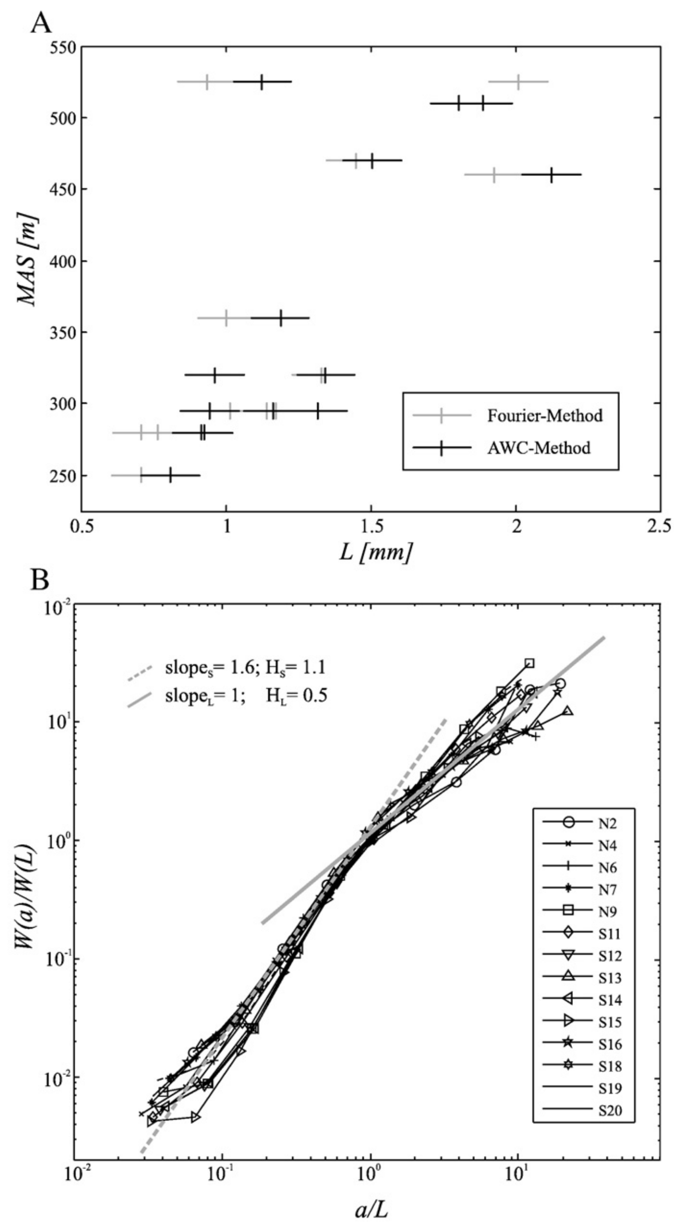

Fig. 3. Crossover-length and scaling data for all samples. A: Relative sample position MAS (=meters above sea-level) versus L for the whole stylolite data set (error-bars indicate the precision of measurements). Notice the increase in L with the sample vertical position in the profile. B: Data collapse for the scaling functions of all samples for the AWC method. L is used to normalize the scaling functions demonstrating that there is one scaling function common to all stylolites investigated.

relative vertical position of the sample in the stratigraphic series. We observe that L decreases from ~2.1 mm near the top (525 m above sea level–MAS) to ~0.7 mm at the bottom of the series (250 m–MAS), which corresponds to a factor 3 for almost 300 m of relative depth. The crossover-length for sample N2 is clearly off the trend (see Fig. 3A) for both methods but the respective roughness exponents are similar compared to the other samples (Fig. 3B). A way to check the consistency of our crossover length-scale estimate is to collapse all data on a single curve (i. e. a uniform scaling function) using L to scale the horizontal distance along the sample and the vertical magnitude of the roughness for all samples (see Fig. 3B for the collapse of the wavelet spectra) as proposed by Renard et al. (2004). The accordance of the collapse is a measurement for the quality of the overall fit of L for all samples. Indeed, a good data collapse should demonstrate that the crossover-lengths used to normalize the data are correct for individual samples. We however notice a systematic offset of ~0.13 mm between estimates of L from the Fourier spectra and that from the wavelet spectra. This systematic offset is of the same order of magnitude as the precision of measurement of L as indicated in Fig. 3A. Error analysis performed by Schmittbuhl et al. (1995) revealed that the Fourier analysis is more sensitive to signal length and self affinity of the signal compared to the AWC analysis (Simonsen et al., 1998) when using synthetic signals with known properties. Hence in the following we correct the Fourier estimates by adding this offset to all the values.

Schmittbuhl et al. (2004) and Renard et al. (2004) established from first principles of mechanics and thermodynamics a model for stylolite growth under the form of a stochastic partial differential equation (a generalized Langevin equation), which successfully described stylolite growth as a competition between material disorder and stabilizing forces such as surface tension and elastic interactions. Hence a possible link between L, surface tension and the state of stress during stylolite formation has been proposed by Schmittbuhl et al. (2004):

$$L = \frac{\gamma E}{\beta \sigma_m \sigma_d} \tag{3}$$

where E is the Young's Modulus, γ is the solid-fluid interfacial energy, $\beta = \nu(1-2\nu)/\pi$ is a dimensionless constant with ν the Poisson's ratio, σ_m and σ_d, are the mean and differential stresses respectively. For the Cirque de Navacelle stylolites, we assumed that the main principal stress is vertical (σ_{zz}), whereas both horizontal stresses are equal and smaller than the vertical stress component. Accordingly, $\sigma_m = 1/3(\sigma_{zz} + 2\sigma_{xx})$ and $\sigma_d = \sigma_{zz} - \sigma_{xx}$. Finally, we consider the strain to be uniaxial (i.e. zero horizontal displacement), which is a reasonable simplification for the early stages of sedimentation in most basins. This allowed us to relate the horizontal and vertical components of stress ($\sigma_{xx} = \sigma_{yy} = \frac{\nu}{1-\nu}\sigma_{zz}$). Expressing the mean and differential stresses as a function of the vertical principal normal stress (σ_{zz}) gives: $\sigma_m \sigma_d = \alpha \sigma_{zz}$ with $a = \frac{1}{3}\left(\frac{1+\nu}{1-\nu}\right)\left(\frac{1-2\nu}{1-\nu}\right)$ Introducing these estimates in Eq. (3) provides a relationship between the crossover L, the surface tension and the principal normal stress component σ_{zz}:

$$L = \frac{\gamma E}{\beta} \cdot \frac{1}{\alpha \sigma_{zz}^2}, \tag{4}$$

if the physical parameters are known. For the surface free energy, we adopted a typical value of a calcite-water interface in limestones, $\gamma = 0.23$ J/m^2 (Wright et al., 2001). We assumed a Poisson's ratio $\nu = 0.25 \pm 0.05$ (Clark, 1966).

The last step is to measure the vertical stress independently of Eq. (4). This is obtained assuming that the vertical stress equals the weight of overburden, i.e. lithostatic stress: $\sigma_{zz} = \rho\, g\, z$ with ρ is the rock-density; g is the acceleration of gravity (9.81 m/s^2), and z the depth. We measured a constant bulk density from our samples of: $\rho = 2.7$ g/cm^3.

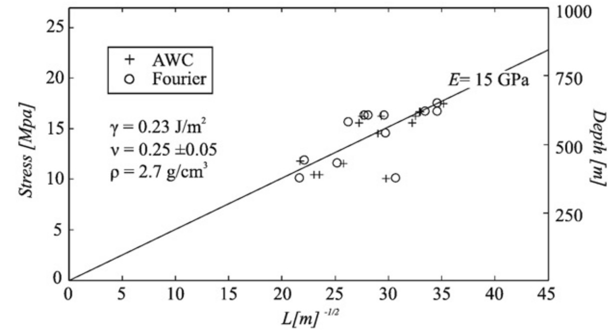

Fig. 4. Plot of a principal normal stress as a function of $L^{-1/2}$. The plot illustrates the linear dependence of the field data and demonstrates that a linear trend for both scaling-methods confirms the analytical solution of Schmittbuhl et al., (2004). The slope of the linear fit of the natural datasets (solid line) correspond to a Young's modulus of 15 GPa for a given set of material properties (ρ, γ, ν) calculated from Eq. (4).

We rearranged Eq. (4) in a way that stress is plotted as a function of $L^{-1/2}$ in order to obtain a linear relationship (Fig. 4). That this plot exhibits such a linear behavior demonstrates the consistency of our model. The plot shown in Fig. 4 suggests that the roughness of bedding-parallel stylolites contains a significant signature of the stress-field during formation of the stylolites. We found that the Young's modulus was $E = 15$ GPa, i.e. the regression line through the data points, which is in line with values measured on limestones (Clark, 1966). Our dataset indicates that the thickness of the overlying rock mass was ~300 m (which can be read from the representation in Fig. 4), which corresponds to ~10 MPa and ~18 MPa of vertical normal stress at the top and bottom of the investigated section, respectively, applying the stated assumptions. The related horizontal normal stresses were then ~4 MPa and ~6.5 MPa.

4. Discussion & Conclusions

To characterize the present material constants, we determined the elastic parameters for two characteristic rock samples using seismic wave velocity measurements under laboratory conditions. From the P and S-wave velocities we calculated the elastic parameters (Jaeger et al., 2007) of two representative samples (ST-17: $E = 86$ GPa, $\nu = 0.09$; N-6: $E = 97$ GPa, $\nu = 0.05$). The elastic parameters are clearly different from the values plotted in Fig. 4. Indeed, during stylolite formation, the rock was softer and the Young's modulus and Poisson's ratio might have been different than for a compacted rock. Given that carbonates are prone to diagenetic alterations that may modify the porosity and thus seismic velocities, especially in the vicinity of a stylolite (Raynaud and Carrio-Schaffhauser, 1992), the elastic parameters derived from our samples may be strongly altered (Anselmetti and Eberli, 1993). Accordingly mechanico-chemical tests to reproduce the observed stylolites using present rock samples would be inappropriate.

Eq. (4) shows that the crossover length is a function of the elastic properties, which are strongly influenced by the rock porosity (e.g. Eberli et al., 2003). It is likely that the elastic parameters evolve with the compaction process, consequently the elastic parameters may change with depth. We do not think that our observed trend in the stylolite crossover is a function of varying elastic parameters. In order to explain such a smooth variation of the crossover over the whole profile by a variation of one of the parameters (Young's modulus, porosity or density) would require that these parameters vary smoothly and linearly with depth, which is not very often the case (compare Eberli et al., 2003). For example a decrease in porosity down-section, i.e. an increase in the Young's modulus, would result in a non-linear *increase* of the crossover-length with depth. This seems to be a second order effect since our data are consistent with a linear relationship (Eq. (4)) and more importantly a *decrease* of L with depth.

Our assumption that elastic parameters are constant throughout the profile implies that the kinetics of the roughening must be fast relative to the progressive burial of rocks so that the stylolite roughness can re-equilibrate with depth. Schmittbuhl et al. (2004) demonstrated that the time to saturate the roughness and thus develop self-affine scaling invariance and a respective crossover-length is in the order of 200 years. Even high accumulation rates in platform carbonates usually do not exceed ~40 m/my i.e. less than 1 cm in 200 years (e.g. McNeill, 2005), which would easily allow the re-equilibration of the roughness. Under the assumption that the timescale for the roughening would be much larger than that for a change in the accumulation of the burial load, styolites would record the terminal stresses before they become inactive. We conclude that our constant Young's modulus assumption seems to fit the data over the investigated range but further investigations are necessary that span greater differences in formation depth. It has to be added that the measured vertical distances between the samples in the section were probably larger during formation of the stylolites due to ongoing compaction of the rock-mass. This effect would result in a telescoping of the data along the ordinate of Fig. 3A and an opposite effect would be noticed in Fig. 4, i.e. the slope through the data would be steeper.

Another assumption used in this study is that all stylolites formed more or less simultaneously, which is indeed questionable. However, if the stylolites formed one after the other when their host rock reached a certain depth in the basin, they would not reveal a difference in crossover-lengths.

It can be further noticed that another petrographical factor, the transition from massif to bedded mudstone layers, does not register in the observed crossovers. We are therefore confident that these large scale heterogeneities played, if any, a negligible role in the scaling of the crossover-length in the investigated section. Additional analysis is necessary to investigate the influence of different lithologies from the same structural level since we only investigated very homogeneous mudstone along the section. In summary we suggest that the systematic variation of the crossover-length in the investigated section is mainly a function of stress. Our results are in line with differential stress/depth relations obtained from in-situ stress measurements and comparable to other paleo-piezometers e.g. calcite twinning (Lacombe, 2007 and references cited therein).

We propose that bedding-parallel stylolites can be considered as quantitative stress gauges because their roughness depicts the stress field during formation. Investigation of a set of samples from different depth allows determining their depth of formation and the absolute stress magnitudes if the assumptions stated above can be adopted.

In this contribution we investigated bedding-parallel stylolites that formed due to lithostatic overburden. This setting allows simplifications that are not valid for stylolites that formed in response to a stress field that has its largest principal stress direction oblique to the Earth's surface. Assessment of the stress field around vertical stylolites needs more prerequisites e.g. a test if the scaling is isotropic as in the case of bedding-parallel stylolites and, further, needs good depth constraints e.g. from independent methods or under favorable circumstances from horizontal stylolites with the method proposed here. Knowledge of these quantities would enable us to investigate stresses around vertical stylolites and thus magnitudes of tectonic loading in the Earth's crust.

Acknowledgements

We thank J.-P. Gratier for his introduction to the field-area and critical discussions. E. Jettestuen is thanked for assistance with image analysis and U. Exner and J. Weller for critical reading of the manuscript. M. Ebner and D. Koehn acknowledge financial support through the DFG project *KO2114/5-1*, the MWFZ of Mainz and the Geocycles Cluster funded by the state of Rhineland-Palatinate.

References

Anselmetti, F.S., Eberli, G.P., 1993. Controls on sonic velocity in carbonates. Pure Appl. Geophys. 141 (2–4), 287–323.

Bodou, P., 1976. Importance of the stylolitic joints in the compaction of limestones. Bull. Centre Rech. Pau-SNPA 10, 627–644.

Brouste, A., Renard, F., Gratier, J.P., Schmittbuhl, J., 2007. Variety of stylolites' morphologies and statistical characterization of the amount of heterogeneities in the rock. J. Struct. Geol. 29 (3), 422–434.

Clark, S.P.J., 1966. Handbook of Physical Constants. Geological Society of New York, New York.

Drummond, C.N., Sexton, D.N., 1998. Fractal structure of stylolites. J. Sediment. Res. 68 (1), 8–10.

Dunnington, H.V., 1954. Stylolite development post-dates rock induration. J. Sediment. Petrol. 24 (1), 27–49.

Eberli, G.P., Baechle, G.T., Anselmetti, F.S., Incze, M.L., 2003. Factors controlling elastic properties in carbonate sediments and rocks. Lead. Edge 22, 654–660.

Ebner, M., Grasemann, B., 2006. Divergent and convergent non-isochoric deformation. J. Struct. Geol. 28 (10), 1725–1733.

Fletcher, R.C., Pollard, D.D., 1981. Anticrack model for pressure solution surfaces. Geology 9 (9), 419–424.

Gal, D., Nur, A., Aharonov, E., 1998. Stability analysis of a pressure solution surface. Geophys. Res. Lett. 25 (8), 1237–1240.

Gratier, J.P., Muquet, L., Hassani, R., Renard, F., 2005. Experimental microstylolites in quartz and modeled application to natural stylolitic structures. J. Struct. Geol. 27 (1), 89–100.

Guzzetta, G., 1984. Kinematics of stylolite formation and physics of the pressure-solution process. Tectonophysics 101, 383–394.

Jaeger, J.C., Cook, N.G.W., Zimmermann, R.W., 2007. Fundamentals of rock mechanics. Blackwell Publishing Ltd, Oxford.

Karcz, Z., Scholz, C.H., 2003. The fractal geometry of some stylolites from the Calcare Massiccio Formation, Italy. J. Struct. Geol. 8, 1301–1316.

Koehn, D., Renard, F., Toussaint, R., Passchier, C.W., 2007. Growth of stylolite teeth patterns depending on normal stress and finite compaction. Earth Planet. Sci. Lett. 257 (3–4), 582–595.

Lacombe, O., 2007. Comparison of paleostress magnitudes from calcite twins with contemporary stress magnitudes and frictional sliding criteria in the continental crust: mechanical implications. J. Struct. Geol. 29 (1), 86–99.

McNeill, D.F., 2005. Accumulation rates from well-dated late Neogene carbonate platforms and margins. Sediment. Geol. 175 (1–4), 73–87.

Park, W.C., Schot, E.H., 1968. Stylolites: their nature and origin. J. Sediment. Petrol. 38 (1), 175–191.

Petit, J.P., Mattauer, M., 1995. Palaeostress superimposition deduced from mesoscale structures in limestone: the Matelles exposure. J. Struct. Geol., 17 (2). Languedoc, France, pp. 245–256.

Railsback, L.B., 1993. Lithologic controls on morphology of pressure-dissolution surfaces (stylolites and dissolution seams) in Paleozoic carbonate rocks from the Mideastern United-States. J. Sediment. Petrol. 63 (3), 513–522.

Raynaud, S., Carrio-Schaffhauser, E., 1992. Rock matrix structures in a zone influenced by a stylolite. J. Struct. Geol. 14 (8–9), 973–980.

Renard, F., Schmittbuhl, J., Gratier, J.P., Meakin, P., Merino, E., 2004. Three-dimensional roughness of stylolites in limestones. J. Geophys. Res.-Sol. Ea. 109, (B03209). doi:10.1029/2003JB002555.

Rispoli, R., 1981. Stress fields about strike-slip faults inferred from stylolites and tension gashes. Tectonophysics 75, 29–36.

Rutter, E.H., 1983. Pressure solution in nature, theory and experiment. J. Geol. Soc. London. 140 (5), 725–740.

Schmittbuhl, J., Vilotte, J.P., Roux, S., 1995. Reliability of self-affine measurements. Phys. Rev. E 58 (1), 131–147.

Schmittbuhl, J., Renard, F., Gratier, J.P., Toussaint, R., 2004. Roughness of stylolites: implications of 3D high resolution topography measurements. Phys. Rev. Lett. 93, (238501). doi:10.1103/PhysRevLett.93.238501.

Simonsen, I., Hansen, A., Nes, O.M., 1998. Determination of the Hurst exponent by use of wavelet transforms. Phys. Rev. E 58 (3), 2779–2787.

Stockdale, P.B., 1922. Stylolites: their nature and origin. Indiana Univ. Stud. 9, 1–97.

Tada, R., Siever, R., 1989. Pressure solution during diagenesis. Ann. Rev. Earth Planet. Sci. 17, 89–118.

Wright, K., Cygan, R.T., Slater, B., 2001. Structure of the (10(1)over-bar4) surfaces of calcite, dolomite and magnesite under wet and dry conditions. Phys. Chem. Chem. Phys. 3 (5), 839–844.

Journal of Structural Geology 31 (2009) 72–82

Contents lists available at ScienceDirect

Journal of Structural Geology

journal homepage: www.elsevier.com/locate/jsg

The influence of rock heterogeneity on the scaling properties of simulated and natural stylolites

Marcus Ebner [a,*], Daniel Koehn [a], Renaud Toussaint [b], François Renard [c]

[a] Tectonophysics, Institute of Geosciences, Johannes Gutenberg University, Becherweg 21, D-55099 Mainz, Germany

[b] Institut de Physique du Globe de Strasbourg, UMR CNRS 7516, EOST, Université de Strasbourg I, 5 rue Descartes, F-67084 Strasbourg, Cedex, France

[c] LGCA-CNRS-Observatoire de Grenoble, Université Joseph Fourier BP 53, F-38041 Grenoble, France & Physics of Geological Processes, University of Oslo, Norway

ARTICLE INFO

Article history:
Received 29 April 2008
Received in revised form
24 September 2008
Accepted 8 October 2008
Available online 1 November 2008

Keywords:
Stylolite
Scaling
Roughness
Compaction
Pressure solution
Quenched noise

ABSTRACT

Stylolites are among the most prominent deformation patterns in sedimentary rocks that document localized pressure solution. Recent studies revealed that stylolite roughness is characterized by two distinct scaling regimes. The main goal of the present study is to decipher whether this complex scaling behavior of stylolites is caused by the composition of the host-rock, i.e. heterogeneities in the material, or is governed by inherent processes on respective scales, namely the transition from a surface energy to an elastic energy dominated regime, as theoretically predicted. For this purpose we have developed a discrete numerical technique, based on a lattice spring model, to simulate the competition between stress, strain, and dissolution during stylolite roughening. We varied systematically the quenched noise, initially present in the material, which controls the roughening. We also changed the size, amount, and dissolution rate of the heterogeneities introduced in our model and evaluated the influence on the scaling exponents. Our findings demonstrate that the roughness and growth exponents are independent of the exact nature of the heterogeneities. We discovered two coinciding crossover phenomena in space and time that separate length and time scales for which the roughening process is either balanced by surface or elastic energies. Our observations are consistent with analytical predictions and with investigations quantifying the scaling laws in the morphology of natural stylolites. The findings presented here can further be used to refine volume loss (compaction) estimates from the finite strain pattern of stylolites.

1. Introduction

Pressure solution in sedimentary rocks results in either intergranular or localized dissolution of material (e.g. Tada and Siever, 1989). The latter is responsible for the formation of stylolites, a frequent deformation pattern in sedimentary rocks (e.g. Stockdale, 1922; Dunnington, 1954; Heald, 1955; Park and Schot, 1968; Buxton and Sibley, 1981; Rutter, 1983; Railsback, 1993). Stylolites are rough interfaces that contain insoluble material (Fig. 1), which is considered to be the residuum of the dissolved rock (Railsback, 1993; and references cited therein). Stylolite initiation is still highly debated (e.g. Tada and Siever, 1989) but several mechanisms have been proposed that are in agreement with field observations: Formation (I) along preexisting anisotropies (Bathurst, 1987) (II) as anticracks (Fletcher and Pollard, 1981) that propagate due to stress concentrations at anticrack tips (even though this idea was challenged recently by Katsman et al., 2006) and (III) by stress induced self-organization (Merino, 1992; Railsback, 1998; Merino et al., 2006).

In the present study we quantify the roughness of simulated stylolites and study their dynamic development independent of the process leading to the localization of dissolution along a plane. Based on recent quantitative methods of stylolite roughness characterization (Renard et al., 2004; Schmittbuhl et al., 2004; Koehn et al., 2007; Ebner et al., in press) we use statistical tools to compare simulated and natural stylolites. In particular we study the influence of initial heterogeneity concentration in the host-rock on a) stylolite roughness, b) dynamic roughness growth and c) the correlation of crossover phenomena in space and time. To integrate the results of our study in the context of quantitative characterization we will first review the basic principles of our approach.

The exact classification of stylolites in the field is a difficult task because there is a wide range of geometries (e.g. Park and Schot, 1968) that are often transitional even within a single outcrop. Many previous studies (Park and Schot, 1968; Buxton and Sibley, 1981; Guzzetta, 1984; Tada and Siever, 1989; Railsback, 1993) used classification schemes that were based on visual descriptions of macroscopic features of stylolites. These classification schemes are

* Corresponding author. Tel.: +49 6131 39 26612; fax: +49 6131 39 23863.
E-mail address: ebnerm@uni-mainz.de (M. Ebner).

0191-8141/$ – see front matter © 2008 Elsevier Ltd. All rights reserved.
doi:10.1016/j.jsg.2008.10.004

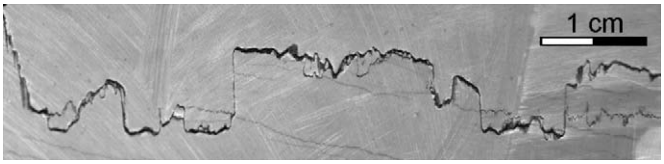

Fig. 1. Plane section of a bedding parallel stylolite in a jurassic limestone from Cirque de Navacelles (southern France). The rough interface is accentuated by a thin clay layer that is considered to be the residuum of the dissolved rock mass.

not quantitative and they are hard to compare since these studies focused on a variety of different aspects of stylolite formation. Recent studies, however (Drummond and Sexton, 1998; Karcz and Scholz, 2003) took a more quantitative approach using fractal concepts to describe the stylolite roughness in a statistical sense. They could describe stylolite roughness with a fractal scaling over several orders of magnitude, which means that their roughness is not dominated by a certain wavelength.

Renard et al. (2004) and Schmittbuhl et al. (2004) demonstrated that bedding parallel stylolite surfaces show a self-affine scaling invariance with characteristic Hurst exponents (also called roughness exponents). A self-affine rough surface is characterized statistically by the fact that points along the surface separated by a distance δx from each other are typically distant in the direction transverse to the surface by $\delta h = \delta x^{\alpha}$, where α is the roughness exponent. It was further noticed that two distinct scaling regimes exist that were characterized by two different Hurst or roughness exponents separated by a crossover-length (L), around the millimeter scale for the analyzed natural stylolites. Above this crossover, all investigated stylolites exhibit a Hurst exponent of about 0.5 meaning that they change relatively fast from being flat features on larger scale to being rough features on the smaller scale. Below the crossover-length the Hurst exponent is about 1.0, which means that the slope, or aspect ratio $\delta z/\delta x$, stays more or less constant. Schmittbuhl et al. (2004) and Renard et al. (2004) established from first principles of mechanics and chemistry a model for stylolite growth under the form of a stochastic partial differential equation (called in this case a generalized Langevin equation). This equation simulates the roughening of a stylolite surface as a competition between stabilizing forces (that keep the surface flat), which are controlled by long range elastic and local surface tension effects, and destabilizing forces (that roughen the interface) that are induced by pinning effects of material heterogeneities. The analytical solution of Schmittbuhl et al. (2004) reproduced the observed scaling behavior of natural stylolites and demonstrated that the two scaling regimes (characterized by the two different Hurst exponents) correspond to two thermodynamic regimes that are dominated by either surface or elastic energies on small and large scales, respectively (Renard et al., 2004; Schmittbuhl et al., 2004; Gratier et al., 2005). Based on the work of Schmittbuhl et al. (2004) it was demonstrated for the first time by Ebner et al. (in press) that the crossover-length of natural stylolites, which should be a function of the stress during stylolite growth, can be used to determine stress magnitudes and burial depth in sedimentary basins. The discrete numerical simulation technique of Koehn et al. (2007) enabled to study the dynamics of the roughening process through time revealing that the stylolite interface width w (defined in detail below) grows as a power law with time ($w \sim t^{\beta}$) with a growth exponent β of 0.5 in the surface energy dominated regime and a growth exponent of 0.8 in the elastic energy dominated regime. In addition the roughness growth may saturate so that the stylolites lose their memory for compaction or finite strain. It is important to notice that the roughness of simulated stylolites in this contribution is produced by heterogeneities in the material that pin the stylolitic interface due to slower dissolution rate constants, which are in competition with the surface and elastic energies which tend to flatten the surface (Koehn et al., 2007). Therefore the obvious question to ask is whether a variation of the quenched noise changes the scaling properties of the stylolitic interface?

Thus, in the present contribution we investigate the influence of different heterogeneities (namely the percentage of pinning particles, their pinning factor (defined below), and their size) on the scaling behavior, dynamic growth, and determined crossover-length of simulated stylolites.

2. Numerical model setup

The numerical technique that we use to simulate stylolite roughening is based on a lattice spring model coupled with a dissolution routine (Koehn et al., 2004, 2006, 2007). The model itself is embedded as a module in the *"Elle"* modeling-platform (Bons et al., 2008).

For computational reasons, to access large systems and analyze scaling laws over a large system size – resolution ratio, we will consider situations spatially invariant along one of the directions tangential to the stylolite – and effectively treat systems with two spatial dimensions. For the same reasons, we assume that the heterogeneity in the rock as well as the statistical properties of the stylolite surface can be represented in a 2D model, as shown in Fig. 2a, which contains a predefined flat interface filled with a confined fluid. Two blocks of particles are separated by a fluid pocket. Such a configuration is expected for example, in the case of a fluid pocket embedded between two low permeability sedimentary layers. This model system represents two solids or rocks that are pressed together by inward moving top and bottom boundaries, whereas the side boundaries remain fixed (uniaxial strain). A quenched noise (denoted by darker particles in Fig. 2a, b) is introduced by assigning a lower dissolution rate constant to a certain fraction of the particles (=pinning particles) and represents material heterogeneities initially present in the host-rock of natural stylolites.

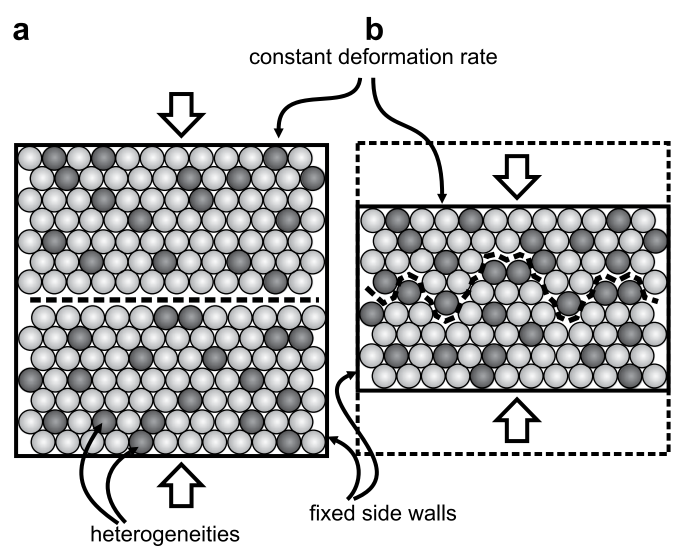

Fig. 2. Simplified sketch of the setup of the numerical model (modified after Koehn et al., 2007). The top and bottom walls of the box are moved inwards simultaneously to stress the system and initiate dissolution along the interface. a) Initial configuration of the setup showing a flat interface (dashed line). b) Configuration after a certain amount of compaction. The interface (dashed line) has developed a distinct roughness, note that the heterogeneities (darker spheres) accumulate along the interface.

2.1. Theory

This section provides only a cursory review on the governing equations of the dissolution process used in the model. For a detailed description and implementation the reader is referred to Koehn et al. (2007) and Bons et al. (2008).

The pressure solution process is discretized in steps of dissolution of entire particles, following a linear rate law (Koehn et al., 2007 and references cited therein) according to

$$D = kV\left[1 - \exp\left(-\frac{\{\Delta\psi + \Delta\sigma_n\}V}{RT}\right)\right] \quad (1)$$

where D is the dissolution velocity of the interface ($\mathrm{m\,s^{-1}}$), k a dissolution kinetics rate constant ($\mathrm{mol\,m^{-2}\,s^{-1}}$), V the molecular volume of the solid ($\mathrm{m^3\,mol^{-1}}$), R the universal gas constant ($8.314\,\mathrm{J\,mol^{-1}\,{}^\circ K^{-1}}$), T the temperature (°K), $\Delta\psi$ (Pa) the changes in Helmholtz free energy density (i.e. the sum of the elastic and surface energy of particles in the discrete network), which accounts for the variations in elastic and surface energies of the solid during dissolution of a solid element, and $\Delta\sigma_n$ (Pa) the differences between the average normal stress along the interface and the local normal stress at a specific location which is due to the repulsion of the solids (Koehn et al., 2007). We assume that the dissolution process is reaction controlled and that the dissolved matter is transported out of the system. This implies that the diffusion may control the absolute time scale of the stylolite growth, but has no local influence on the reaction process and the roughening, which are a function of the amount of compaction and the number of dissolved particles (Koehn et al., 2007). We are not interested in absolute time scales in this contribution.

Surface energies (E^S) of particles are calculated from the local curvature of the interface around each particle, which can be expressed as

$$E^s = \frac{\gamma}{\rho} \quad (2)$$

where γ is the surface free energy and ρ is the local radius of curvature of the interface. We consider a plane strain situation, i.e. an invariance along the third spatial dimension, so one radius along the 2D plane investigated entirely characterizes the curvature of the interface – the radius of curvature along the direction of invariance is infinite, and no surface energy is associated to this direction. The surface energies of individual particles are averaged over their neighbors to avoid artifacts from the discreteness of the model (for details see Koehn et al., 2007).

In the lattice spring model every particle (i) is connected to its neighbors (j) via a triangular linear elastic spring network. The elastic energy (E^{el}) of a single element is given by

$$E^{el} = \frac{1}{4}\sum_{(j)} \kappa\left(|x_i - x_j| - l\right)^2, \quad (3)$$

where the sum is over all neighbors (j), κ is a spring constant and l is the equilibrium distance between elements i and j.

2.2. Basic numerical step

The constitutive equations stated above are implemented as follows:

- Top and bottom walls are moved inwards simultaneously at a given time/deformation step.
- For every deformation step the rate law (Eq. (1)) is used to calculate if individual particles at the interface can dissolve in the given time as soon as the two solids meet.
- When elements dissolve they are removed completely and the system can relax. Relaxation is accomplished by an over-relaxation algorithm that finds the new equilibrium configuration for the lattice. Dissolution of particles can take place as long as the given time for the individual deformation step is not consumed.
- If the deformation time is used up or no particles can dissolve within the given time the system is stressed again by a deformation step.

2.3. Parameters, boundary conditions, limitations

The material parameters we use resemble those of a limestone (e.g. Clark, 1966) and are in line with values used in Renard et al. (2004) and Schmittbuhl et al. (2004): a molar volume of $0.00004\ \mathrm{m^3/mol}$, a Young's Modulus of 80 GPa, a Poisson's ratio of 0.33 (this number is given by the triangular lattice configuration), a surface free energy of $0.27\ \mathrm{J/m^2}$, a temperature of 300 K and a dissolution rate constant of $0.0001\ \mathrm{mol/(m^2\,s)}$. In addition, the displacement rate of the upper and lower boundaries is fixed at a constant value corresponding to a velocity of $10^{-10}\ \mathrm{m\,s^{-1}}$.

The boundary condition can be seen as equivalent to a constant load boundary condition since the dissolution process is fast enough to relax the stresses that build up during a single deformation step. The sidewalls remain fixed during the model runs and there is no wrapping of particles in the x-direction of the model.

We use three basic model setups for which we systematically vary the heterogeneities in the structure. All boxes used have the same number of particles (400 particles) in the x-direction but three different particles' sizes were used 0.01 mm, 0.1 mm and 1 mm, which corresponds to absolute box-sizes of 4, 40 and 400 mm.

To introduce the quenched noise in the simulations a pseudo-random algorithm is used to create a spatial Gaussian distribution of particles that dissolve slower (pinning particles). We varied three parameters of the quenched noise in this study: (i) number of pinning particles in a range from 1 to 20% (ii) dissolution rate constant of pinning particles (from 0.1 to 0.99 normalized to the dissolution rate constant of the matrix, which is 1), which determines the pinning factor and (iii) the absolute size of the heterogeneities which varies with the particle size in the range of 0.01–1 mm.

3. Data analysis and results

The individual model runs are grouped with respect to the particle size of the model and are termed *surface*, *intermediate* and *elastic class* according to the dominance of the energy regime during the roughening process (Koehn et al., 2007). The *surface class* has a particle size of 0.01 mm (box size of 4 mm), the *intermediate class* a particle size of 0.1 mm (box size of 4 cm) and the *elastic class* a particle size of 1 mm (box size of 40 cm). These three classes allow the investigation of a broad range of scales in a sufficient resolution. In nature the particles may resemble actual grains so that the grain size of the rock varies between the different classes. A single simulation with 400 particles in the x-direction may run from 10 to 15 days on 4 cores of a recent workstation, thus limiting the extent of our runs. Fig. 3 shows the roughening of stylolites of these three classes, each with identical quenched noise (5% pinning particles with half the dissolution rate of the matrix) to demonstrate the influence of the absolute box/particle size. The differences in the roughness and the roughness growth can easily be seen when individual steps of different classes are compared and also by following the growth of individual stylolite peaks with time. In the *elastic class* individual peaks grow very continuously whereas in the *surface class* the growth is often disrupted, due to dissolution

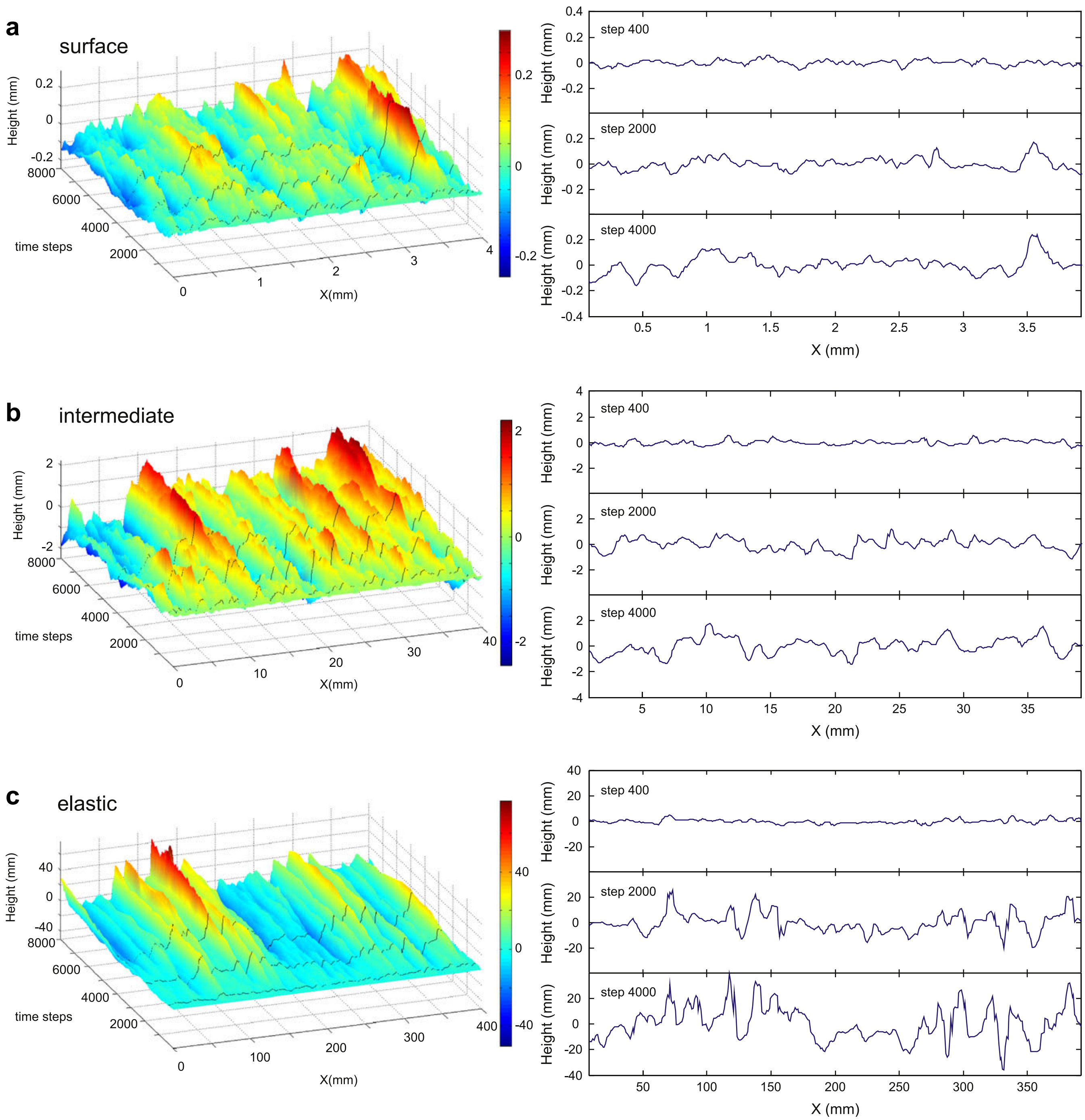

Fig. 3. Growth of three stylolites with similar heterogeneities but different lengths and discretization resolution. Left panels show 3D plots of the stylolite growth from a flat interface until the end of the experiment. Right panels show 3 individual deformation steps (steps 400, 2000 and 4000) corresponding to the solid lines in the 3D plot a) surface class (box size = 0.4 cm) b) intermediate class (box size = 4 cm) c) elastic class (box size = 40 cm); Notice the disrupted growth of the surface class whereas the elastic class exhibits very continuous growth and pronounced peaks and teeth.

of pinning particles as a result of high surface energies along pronounced peaks.

In the following sections we concentrate on the influence of the noise (amount and pinning factor of the noise particles) on 1) the roughness exponents, 2) the growth exponents and 3) the cross-over-length.

3.1. Roughness exponents

To quantitatively characterize the roughness of an individual 1D profile of a stylolite we used concepts from statistical physics (Barabasi and Stanley, 1995), which are briefly introduced in the first part of this section. The methods used here are the same as those of previous studies of natural stylolites (Renard et al., 2004; Schmittbuhl et al., 2004; Gratier et al., 2005; Ebner et al., in press), which facilitates comparison.

The prerequisite for the application of these scaling methods is that the 1D signal of the numerical stylolite obeys a self-affine scaling invariance, which is given by (e.g. Barabasi and Stanley, 1995)

$$f(bx) \sim b^{\alpha} f(x), \tag{4}$$

where $f(x)$ is a single-valued function and the power law exponent α is called *roughness* or *Hurst* exponent and provides a quantitative measurement of the roughness of the signal. A self-affine function must be rescaled differently in x and y directions to obtain a scaling invariance, i.e. horizontal rescaling of the form $x \rightarrow bx$, b being a dilation factor, has to be rescaled in the vertical direction by $y \rightarrow b^{-\alpha}y$ to obtain a scaling invariance. Different statistical methods can be used to evaluate the self-affine character of a signal and to determine the associated roughness exponent. We apply two independent methods in this contribution, the *Fourier method* and the *Average Wavelet Coefficient method*.

The *Fourier method* (e.g. Barabasi and Stanley, 1995; Schmittbuhl et al., 1995) is based on a Fourier transform of the original 1D signal (Fig. 4a). For every 1D signal (every deformation step) the Fourier power spectrum $P(k)$ i.e. the square of the modulus of the Fourier transform, was calculated as a function of the wavenumber k. Plotting $P(k)$ as a function of k in log–log space reveals a linear trend for a self-affine function (Fig. 4b), and the slope is a function of the Hurst exponent through (Renard et al., 2004; Schmittbuhl et al., 2004):

$$P(k) \sim k^{-1-2\alpha}. \tag{5}$$

The *Average wavelet coefficient method* (*AWC*) was used as a second independent method to confirm the scaling results (Simonsen et al., 1998; Hansen et al., 2000). This method is again based on a decomposition of the 1D signal into wavelets, whose amplitude depends on scale and the position. The wavelet transform is defined after Simonsen et al. (1998) by

$$W_{a,b} = \frac{1}{\sqrt{a}}\int_{-\infty}^{\infty} \varphi\left(\frac{x-b}{a}\right) f(x)dx, \tag{6}$$

where φ is the wavelet basis (Daubechies wavelet of order 12), which is parameterized by a scale parameter a and a translation parameter b, and f is the single-valued original function. Finally the wavelet coefficients are averaged over the translation parameter b for every a to obtain the average wavelet coefficient $W(a)$. If the input signal is self-affine, the wavelet transform verifies that the average wavelet coefficient $W(a)$ scales as (Simonsen et al., 1998)

$$W(a) \sim a^{\alpha+1/2}. \tag{7}$$

Plotting the average wavelet coefficients as a function of the scale parameter a in log–log space (Fig. 4c), the slope of the linear regression through the data is again a function of the Hurst exponent.

Using these two statistical methods, we first study the dynamics of the roughness exponents through time during stylolite growth, and then concentrate on their stability with respect to variations of the noise. The roughness exponents increase relatively quickly in the course of a simulation run (Fig. 4d) and become stable after model step 3000 with only minor fluctuations. The *Fourier*- as well as the *AWC-method* shows consistent evolutions and similar values of the roughness exponents. Averages of the plateau values reached (after step 3000) for individual model runs are used as a characteristic value for the roughness exponent for a specific setup. Error bars underline the standard deviation around this average (Fig. 5).

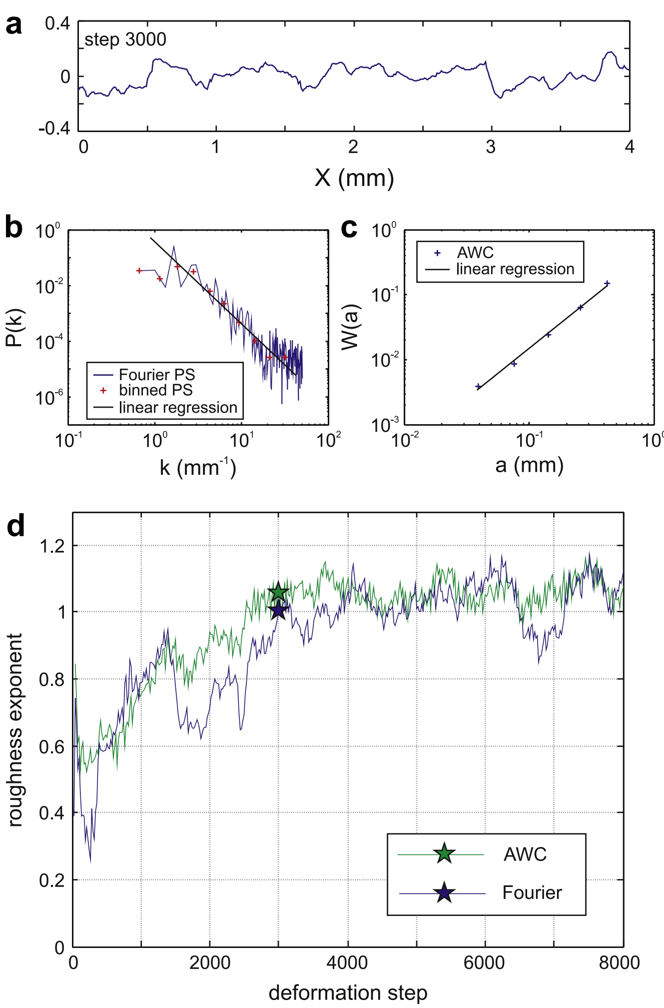

Fig. 4. Roughness characterization of single deformation steps by means of the Hurst exponent. a) 1D profile (deformation step 3000) of the surface class with 5% pinning particles and a dissolution rate constant of $k = 0.4$; b) Fourier power spectrum $P(k)$ of the signal from Fig. 4a plotted as a function of the wavenumber k. Linear regression (solid line) is calculated from the binned spectra (crosses), the slope of the regression is a function of the Hurst exponent, see Section 3.1 for detailed description. c) Wavelet spectra $W(a)$ plotted (crosses) as a function of the scaling parameter a (see average wavelet coefficient method in Section 3.1.). The slope of the linear regression (solid line) is again a function of the Hurst exponent. d) Evolution of the Hurst exponent in the course of an entire experiment for the Fourier and AWC methods. Stars indicate the Hurst exponent of the 1D signal shown in Fig. 4a for the two methods used. Notice the leveling off at a specific Hurst exponent (plateau value) which is characteristic for all simulations.

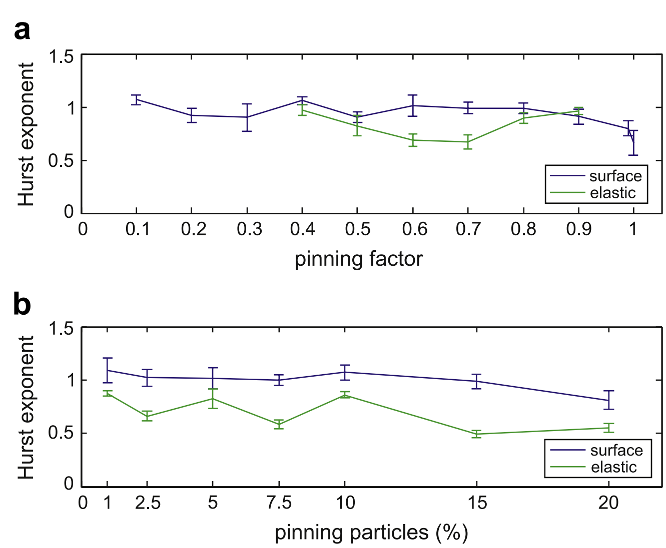

Fig. 5. Composite plots showing the plateau roughness (Hurst exponents) for the surface and elastic classes. a) Hurst exponent plotted versus dissolution rate constants k with a fixed amount of pinning particles of 5% (where $k = 1$ is the dissolution rate of the matrix). b) Hurst exponent plotted versus amount of pinning particles with a dissolution rate constant of $k = 0.5$ for all experiments. The error bars correspond to the standard deviation given by the fluctuation around the plateau values, compare Fig. 4d.

The *surface class* is characterized by consistently high values for the Hurst exponent, i.e. $\alpha \sim 0.9$–1.1, independent of the pinning factor (i.e. the dissolution rate constant k in Eq. (1); cp Fig. 5a) or the amount of pinning particles (Fig. 5b).

The exponents only decrease when the pinning factor of particles is very low (dissolution rate constant >0.9) and the rock becomes homogeneous. The most stable roughness exponents for the surface class are reached in the range 0.1–0.8 for the pinning factor and 1–20% of pinning particles.

The *elastic class* reveals lower Hurst exponents ($\alpha \sim 0.6$–0.9) than the *surface class*. If the pinning factor of particles is very strong, i.e. particles are very resistant to dissolution (below the value 0.4 for the relative dissolution rate constant in Fig. 5a) stress concentrations are locally too high once two pinning particles meet and artifacts develop (usually anticracks that grow laterally emerge from these concentrations, hence modifying the surface topography) in the numerical model within the *elastic class*. Therefore we did not include values below 0.4 from elastic simulations in Fig. 5a. Generally the roughness exponents in the elastic class show stronger fluctuations than those of the surface class. They are relatively stable within a pinning factor range of 0.5–0.8 (Fig. 5a) and 1–20% of pinning particles.

The *surface* and *elastic classes* correspond well to the two scaling regimes found in natural stylolites (Renard et al., 2004; Schmittbuhl et al., 2004) that are separated by a crossover-length at the millimeter scale. The roughness exponents of the surface class ($\alpha \sim 1.1$) are in good agreement with analytical predictions and experimental observations (e.g. Gratier et al., 2005). The *elastic class* displays values for the Hurst exponent ($\alpha \sim 0.6$–0.9) that are higher than exponents from natural examples (Renard et al., 2004; Schmittbuhl et al., 2004; Ebner et al., in press) or analytical predictions, which are generally around 0.5. These analytical predictions are usually based on linear approximations, which are strictly speaking valid as long as the surface morphology is not too developed. The present model does not present any such limitations, and the fully developed situation can thus present a different Hurst exponent from the initial one. The discrepancy with natural data may arise from the large particle (or grain) size that we use in the setup for the elastic class. In nature the grain size is much smaller and corresponds to the values that we use in the surface class.

3.2. Interface growth

In addition to the dynamic development of the roughness exponents the simulations allow us to study how fast the amplitude of the stylolite roughness grows through (model-) time or as a function of the finite strain. First we concentrate on different growth regimes of stylolites, the associated growth exponents and prefactors of scaling functions and then study the variation of these factors as a function of host-rock heterogeneities. In order to quantify the amplitude of the roughness we use the *interface width* (w) that is defined as the root-mean-square fluctuation of the height of the interface for a given time step (Barabasi and Stanley, 1995)

$$w(L,t) \equiv \sqrt{\frac{1}{L}\sum_{i=1}^{L}[h(i,t) - \bar{h}(t)]^2}, \tag{8}$$

where w is the interface width as a function of system size L and time t, h is the height of point i on the interface at time t and $\bar{h}$ the average height of the interface at time t is given by

$$\bar{h}(t) \equiv \frac{1}{L}\sum_{i=1}^{L} h(i,t). \tag{9}$$

In our simulations, the system size L is defined as the number of elements in the x-direction, which is constant for all simulations, i.e. 400 particles. Roughening processes of interfaces in a wide range of fields have been demonstrated to follow a power law in time (e.g. Barabasi and Stanley, 1995) defined by a growth exponent β (given by, $w(L,t) \sim t^{\beta}$). This initial phase of interface growth is usually followed by a second regime during which the interface width reaches a saturation value, w_{sat}, which is directly related to the system size.

Both growth and saturation regimes can be seen in Fig. 6a for an experiment of the surface class with a characteristic growth exponent of $\beta \sim 0.5$. The arrow in Fig. 6a marks the transition from the power law growth regime to the regime where the interface width saturates and stays constant. The *intermediate class* simulations show a similar growth exponent (around 0.5) but do not saturate in the given deformation time. The *elastic class* (Fig. 6b) shows two successive growth regimes, the first being defined by a growth exponent of $\beta \sim 0.5$ up to a crossover interface width followed by a second regime with $\beta \sim 0.8$ without reaching the saturation regime. We suggest the following schematic growth regimes (Fig. 6c) for stylolites: (i) growth in the surface energy dominated regime with an exponential growth defined by $\beta \sim 0.5$ followed by (ii) growth in the elastic energy dominated regime with $\beta \sim 0.8$ and finally reaching (iii) a saturation regime where the interface width stays constant.

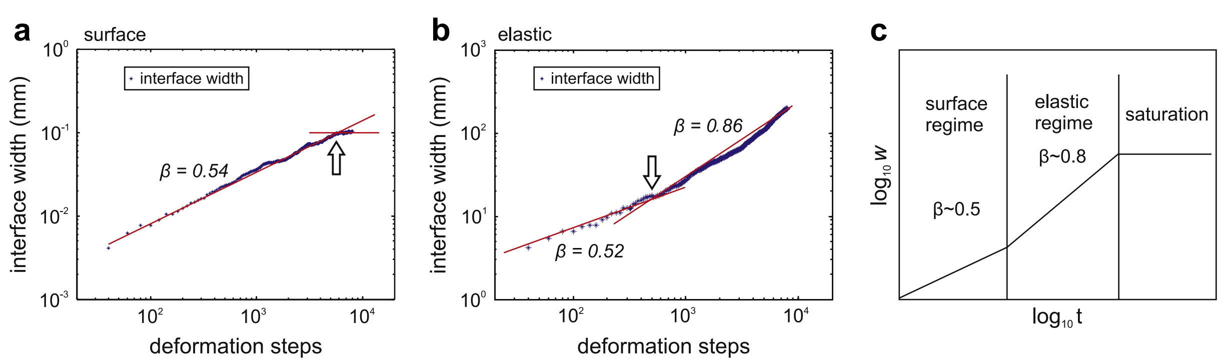

Fig. 6. Interface growth depicted by the interface width (Eq. (8)). a) Log–log plot of the interface width as a function of time in the surface class (5% pinning particles and dissolution rate constant of 0.4). Growth exponent $\beta = 0.5$ is given by the slope of the linear regression (solid line). Notice the saturation point (indicated by arrow) i.e. interface width remains constant during ongoing deformation. b) Log–log plot of the interface width as a function of time in the elastic class (5% pinning particles and dissolution rate constant of 0.4). Notice the two successive growth regimes characterized by an initial growth exponent of $\beta = 0.5$ up to a crossover width (indicated by arrow) followed by an exponent of $\beta = 0.8$; no saturation can be observed within the given simulation time. c) Proposed composite graph of the interface growth of simulated stylolites. Two successive growth regimes separated by a narrow crossover width that are dominated either by surface or elastic energies are followed by a saturation of the interface growth due to correlation introduced by finite size effects.

This strict non-linearity of the interface growth in our simulations suggests that estimated amounts of compaction (here used as synonymous with volume/area loss due to pressure solution) from stylolite amplitude heights (e.g. Tada and Siever, 1989; and references cited therein) only capture a small part of the actual compaction. To cope with this problem, Koehn et al. (2007) demonstrated that the actual displacement can be expressed for the elastic or surface energy dominated growth regimes as a function of the interface width and the growth exponent (as long as the critical saturation time is not reached), given by

$$A \sim (w/l)^{1/\beta} l \tag{10}$$

where, A is the compaction displacement, w the interface width, β the growth exponent (for a certain class) and l the particle size. The slope of this function gives a prefactor for the scaling relation which should remain constant until the saturation time is reached. We call the slope of this relation here and in the subsequent sections *compaction prefactor* because it relates the interface width to the total compaction (Fig. 7). As soon as the saturation time is reached the relation does not hold any more and the function deviates from the linear trend. This effect can be observed in Fig. 7a where the arrow marks the onset of interface width saturation, where compaction continues through but the interface width (x-axis) remains constant. However, if the saturation is not attained (Fig. 7b) the actual compaction can be calculated accurately from the interface width and the growth exponent using Eq. (9).

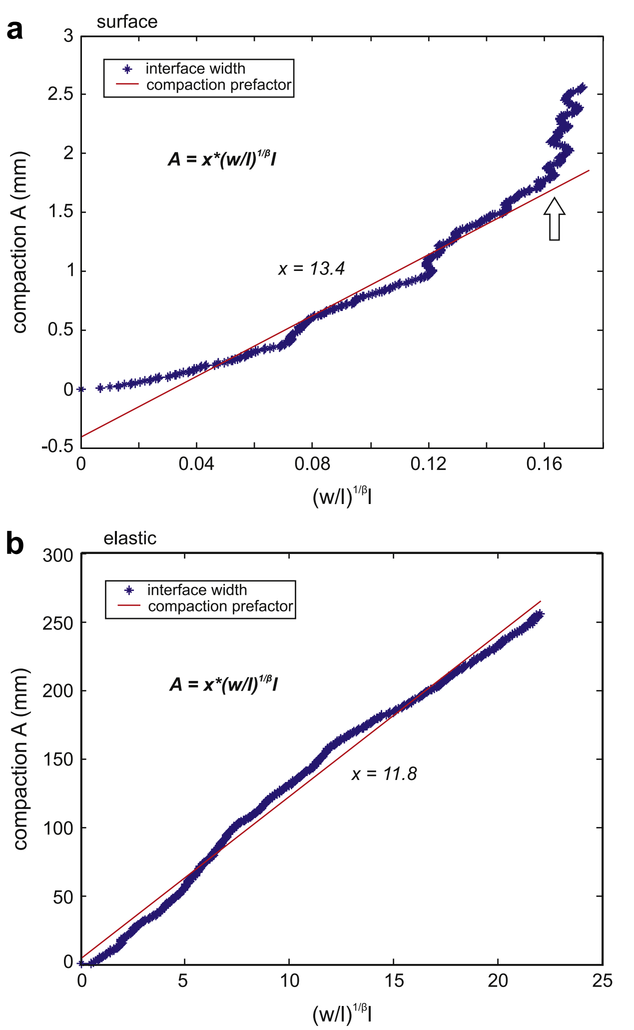

Fig. 7. Total compaction displacement expressed as a linear function (solid line) of the interface width and the compaction prefactor (compare Eq. (10)). a) Surface class experiment (5% pinning particles and dissolution rate constant of $k = 0.4$) demonstrates that the relationship is only valid as long as the interface is not saturated, i.e. strong deviation from linear trend (compare Fig. 6a). b) Elastic class experiment (5% pinning particles and dissolution rate constant of 0.4) reveals an accurate reproduction of the linear relationship (solid line) stated in Eq. (10). No saturation was observed in the given simulation time.

Fig. 8a demonstrates that neither pinning factor nor amount of pinning particles have a strong effect on the growth exponent. The values for the growth exponent cluster around $\beta \sim 0.5$ for the *surface* and *intermediate classes* and around $\beta \sim 0.8$ for the *elastic class*. The compaction prefactors display a higher variability than the growth exponents but no systematic trend can be seen that relates this variation to the pinning factor or amount of pinning particles in the host-rock. Fig. 8c, d shows that there is no significant difference between the three classes of particle sizes used with values for the compaction prefactor in a range between ~12 and ~25. Finally, we compare the maximum interface width normalized by the particle size (w_{max}) that develops during simulations with different heterogeneities (Fig. 8e and f). The largest interface widths are achieved in the *elastic class* with $w_{max} \sim 20$ in contrast to $w_{max} \sim 10$ reached in the *intermediate* and *surface class*. Hence the interface growth displays twice the displacement in the *elastic class* in the given simulation time due to the larger growth exponents than those of the *intermediate* or *surface class*, respectively. For the *surface*, *intermediate* and *elastic classes* the variation of the pinning factor of particles (Fig. 8e) have no considerable influence on the maximum interface width. However the amount of pinning particles has a significant influence on the *surface* and *intermediate class* (Fig. 8f). Both classes show an evident decrease in the maximum interface width with increasing amount of pinning particles. This trend cannot be observed in the *elastic class* (Fig. 8f).

We also tested the influence of the initial shape of the predefined interface separating the two blocks that are pressed together during an experimental run (compare Fig. 2a), which is flat in all the simulation data shown in the preceding sections. To investigate the dynamic roughness evolution of an already rough interface we arbitrarily choose a time/deformation step (t_n) of a simulation run (Fig. 9a) and subtracted the topography (h) of this step from the subsequent time steps similar to $h(t) = h(t_n + m\delta t) - h(t_n)$. This procedure allows investigation of the dynamic evolution of a rough interface by statistically evaluating the difference of the evolving roughness from time t_n onwards (Fig. 9b). Departing from an already rough interface does not change the scaling parameters (growth and roughness exponent) as depicted in Fig. 9. Hence the model setup we choose in this work (i.e. a flat initial interface) can also account for complex initial topographies.

3.3. Crossover-length scales

The crossover-length of stylolite roughness that separates the surface energy dominated regime from the elastic energy dominated regime is a function of the stress during stylolite growth and can be used as paleo-stress gauge (Renard et al., 2004; Schmittbuhl et al., 2004; Ebner et al., in press). It is of fundamental importance to know if this crossover is constant when the heterogeneities in the host-rock vary, because this knowledge would facilitate the use of the crossover-length as a quantitative measure of the stress during formation (compare Ebner et al., in press). In the following section we want to explore how sensitive the crossover-length scale is to variations in the amount and strength of pinning particles. The crossover-length between the two well characterized regimes (i.e. surface energy- and elastic energy-dominated) can be found in the *intermediate class* of our simulations that exhibits two distinct roughness exponents and hence the transition between the two

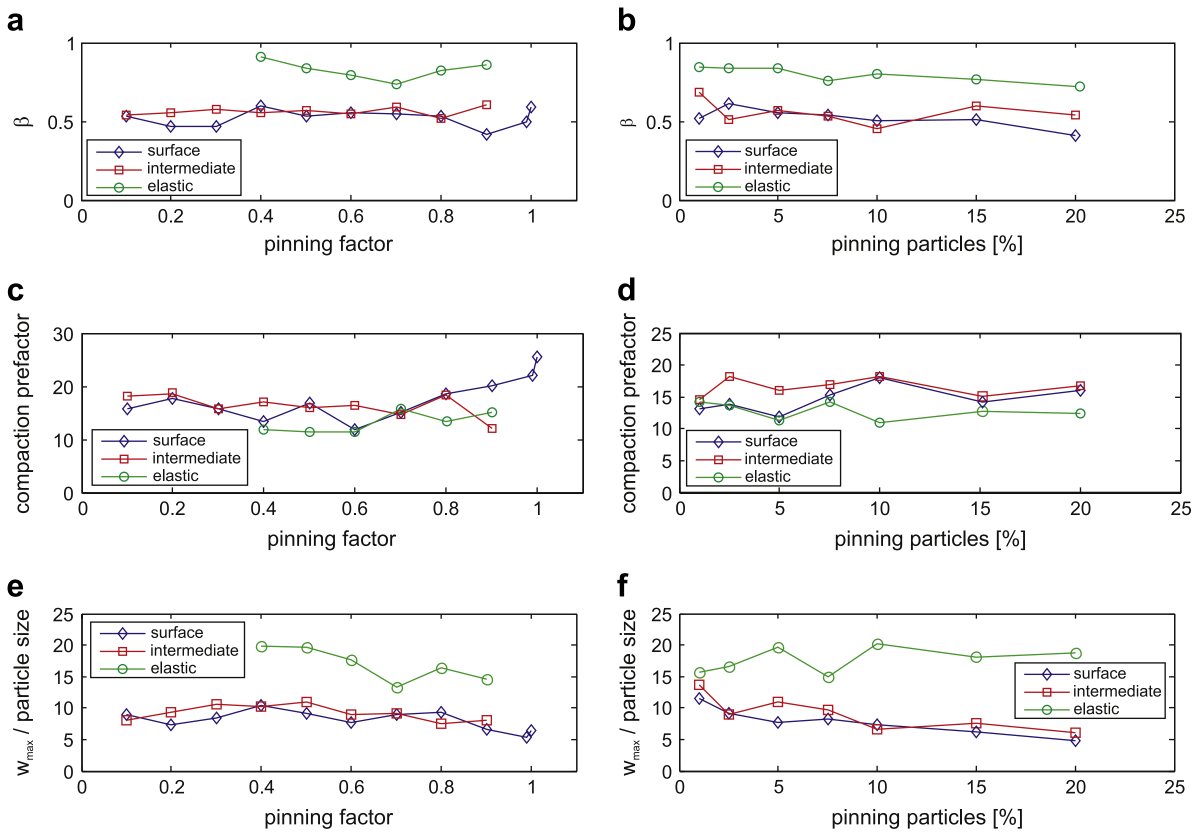

Fig. 8. Cumulative data for the surface, intermediate and elastic classes for: a) Growth exponent versus dissolution rate constant (pinning particles fixed at 5%); b) Growth exponent versus amount of pinning particles (dissolution rate constant fixed at $k = 0.5$); c) Compaction prefactor versus dissolution rate constant (pinning particles fixed at 5%); d) Compaction prefactor versus amount of pinning particles (dissolution rate constant fixed at $k = 0.5$). Maximum interface width normalized by the particle size attained during experimental runs for the *surface*, *intermediate* and *elastic* class e) with changing dissolution rate constant (with 5% pinning particles); f) with changing amount of pinning particles (dissolution rate constant is fixed at 0.5).

scaling regimes (Fig. 10). The Fourier power spectrum of the 1D signal of a stylolite in the intermediate class (Fig. 10b) shows a change from a shallow to a steep slope indicating small and large roughness exponents on large and small scales, respectively. To avoid bias due to improper fitting of the crossover-length we used a nonlinear least square curve fitting algorithm in logarithmic space to model our scaling function (Ebner et al., in press):

$$f(x) = (a_L x + m_L)(1 - w(x)) + (a_S x + m_S)w(x) \tag{11a}$$

and

$$w(x) = \frac{(\tanh(x + L) + 1)}{2}, \tag{11b}$$

where $a_{L,S}$ are the exponents of the scaling function for large and small scales, $m_{L,S}$ the corresponding intercepts with the ordinate and $w(x)$ the weighting function. During this procedure the roughness exponents of our nonlinear model function were fixed according to the roughness exponents ($\alpha_S \sim 1.1$; $\alpha_L \sim 0.5$) reported from natural stylolites (Renard et al., 2004; Schmittbuhl et al., 2004; Ebner et al., in press).

The crossover-lengths obtained for all experiments of the intermediate class are in a range of $L \sim 1.33 \pm 0.09$ mm, the crossover-length usually develops simultaneously with the achievement of the plateau values (compare Fig. 4d). Neither of the quenched noise parameters influenced the crossover-length significantly (Fig. 11).

The time evolution of the roughness presented in the previous section showed that the surface energy dominated regime is characterized by a growth exponent of 0.5 whereas the elastic energy dominated regime is characterized by a growth exponent of 0.8. However, the surface energy dominated growth can be detected at the beginning of the roughness evolution of the elastic energy dominated regime (Fig. 6). Therefore the growth exponents also show a transition (that we term the crossover interface width) between growth in the surface energy dominated regime and growth in the elastic energy dominated regime, similar to the two roughness exponents that are characteristic for these two regimes. The crossover interface width is very consistent for all experiments with $w \sim 1.23 \pm 0.04$ mm, independent of the quenched noise introduced in the system. We did not observe a crossover in the interface growth of the *intermediate* and *surface class* because the interface width in these classes is simply not large enough to reach the elastic growth regime. Due to the very good correlation between the magnitudes of the crossover-length and the crossover interface width (Fig. 11) we argue that both crossovers arise from the same process, namely the transition from a surface energy to an elastic energy dominated regime.

4. Discussion

In the following section we first discuss the influence of the quenched noise on the scaling parameters in our numerical simulations, deal with the relevance of the noise and compare the results to natural stylolites. Secondly, we focus on the crossover phenomena and their significance for the estimate of volume loss along a finite natural stylolite.

The influence of the exact nature of the heterogeneities (i.e. pinning factor, amount and size of pinning particles) on the scaling

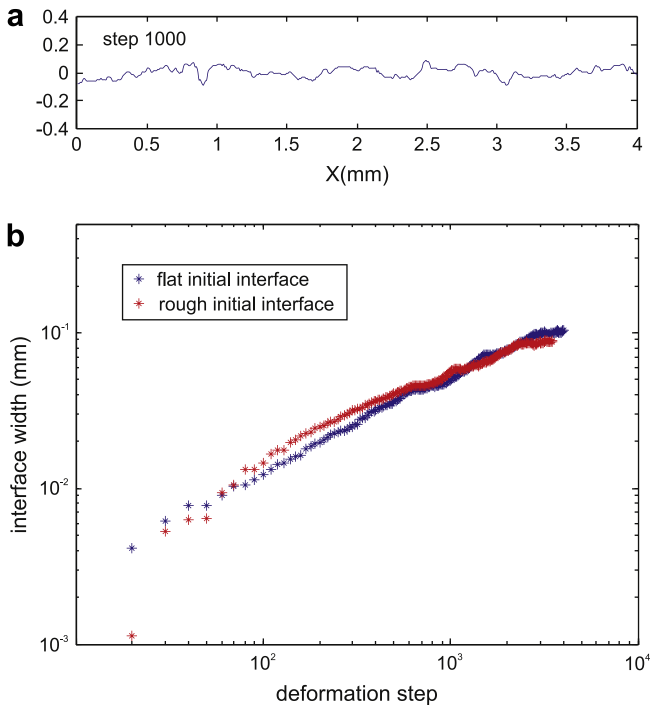

Fig. 9. The influence of the topography of the initial predefined interface on the dynamic roughness evolution. a) Rough initial interface used as starting point to evaluate the interface width evolution on top of this roughness for a *surface class* simulation with 5% pinning particles and a pinning factor of 0.5 (for details see text). b) Comparison of the interface width evolution of an initially flat and rough (see Fig. 9a) interface. Both interfaces show a similar evolution with growth exponents of 0.54 and 0.51 for the flat and rough initial interface respectively. Notice that both growth and the roughness exponents (not shown) are independent of the initial topography of the predefined interface.

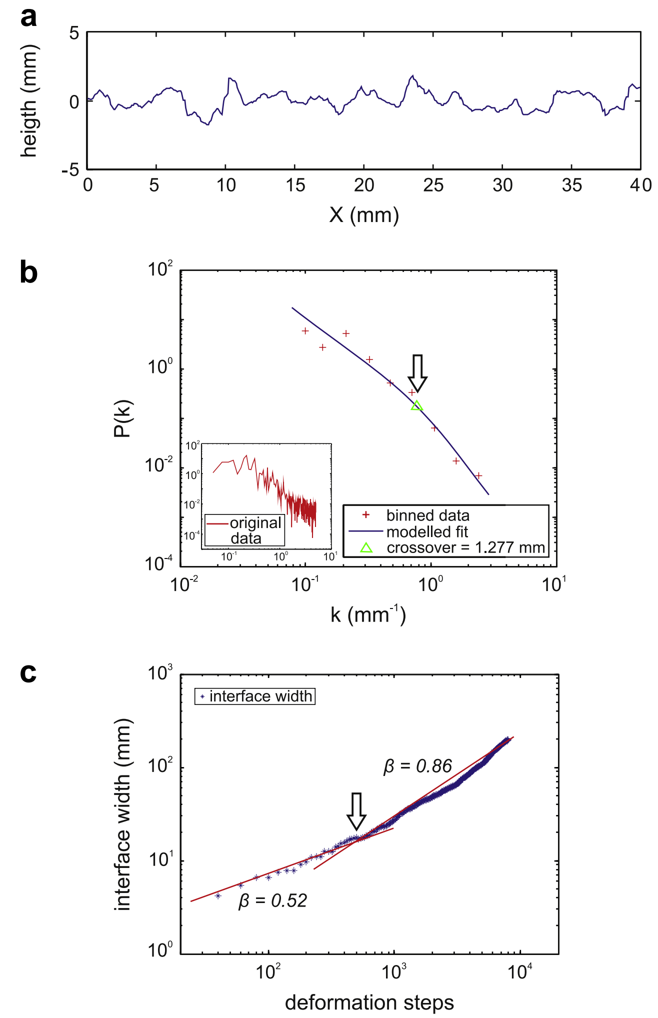

Fig. 10. Crossover phenomena in the roughness scaling and interface growth. a) 1D signal of an experiment from the intermediate class (5% pinning particles; dissolution rate constant $k = 0.4$); b) Fourier power spectrum (inset) of the signal and binned spectra (crosses). A nonlinear model function (for explanation see text) used to minimize the original data (solid line) is used to accurately locate the position of the crossover-length (triangle) $L = 1.27$ mm; c) Log–log plot of the interface width versus time of the elastic class (5% pinning particles and dissolution rate constant $k = 0.4$). Notice the two successive growth regimes characterized by an initial growth exponent of $\beta = 0.5$ up to a crossover width $w = 1.24$ mm followed by an exponent of $\beta = 0.8$. Notice that both crossover scales correspond to the transition from a surface to an elastic energy dominated regime.

exponents can be directly investigated by a close examination of Figs. 5, 8 and 11. The pinning factor has the least influence on the roughness and growth exponents as well as on the crossover scaling (L and w_{cross}), resulting in values that are very consistent over wide ranges of the parameter space. The amount of pinning particles only shows an influence on the maximum interface width w_{max}, which decreases with increasing amount of heterogeneities (Fig. 8f). This fact is in agreement with qualitative observations made on natural stylolites that stylolite amplitudes decrease with the amount of heterogeneities (e.g. Tada and Siever, 1989; and references cited therein). The scaling exponents themselves are independent of the amount of pinning particles. The biggest influence seems to be exerted by the particle sizes. But these differences have been shown to arise (Renard et al., 2004; Schmittbuhl et al., 2004; Koehn et al., 2007) from a transition from surface energy dominated smoothening to elastic energy dominated smoothening. The differences in the scaling exponents between the experimental classes are therefore not caused by the heterogeneities themselves but by the processes that govern the roughening on respective scales. We are thus convinced that the influence of the exact nature of the heterogeneities plays a minor role and that roughening is dominated by an inherent process that depends on the length scale.

The quenched noise we introduced in the different simulations, i.e. changes in the dissolution rate constant that influence the dissolution velocity of a particle (cp. Eq. (1)), represents simple chemical noise as pointed out by Koehn et al. (2007). We are aware that along natural stylolitic interfaces the elastic parameters, surface energies and crystallographic orientations change, in addition to chemical variations. However, the effects of change in these other parameters in our model will ultimately result in a change of the dissolution velocity. We therefore argue that for the developing structure it should make no difference what the exact nature of the noise is, since any particle with a slower dissolution velocity will pin the surface and therefore cause a roughening of the interface.

It was demonstrated that individual natural stylolites from different outcrop localities and lithologies, i.e. different host-rock compositions, reveal the same scaling behavior (e.g. Renard et al., 2004; Schmittbuhl et al., 2004; Ebner et al., in press). Consequently the investigation of these natural stylolites corroborates the evidence that a common underlying mechanism for the roughening of the investigated stylolites can be assumed rather than a roughening that is dominated by the composition of the host-rock.

Nevertheless we do not claim that knowledge of the exact nature or distribution of the material heterogeneities is unimportant. Brouste et al. (2007) have shown that a changing amount of

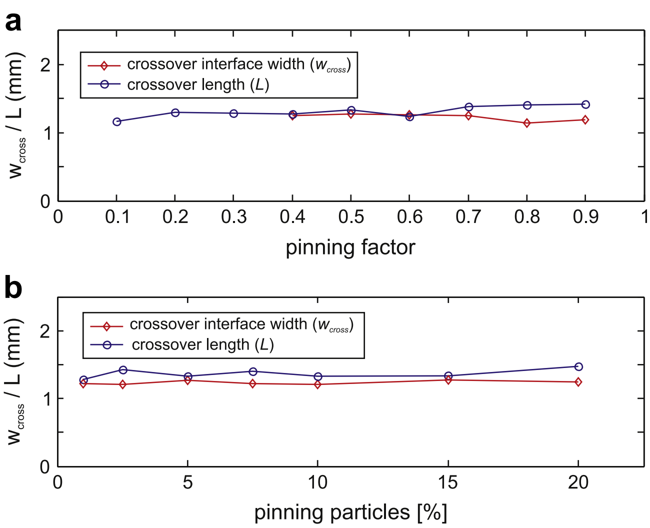

Fig. 11. Crossover-length L and crossover interface width w plotted as a function of the quenched noise. a) Crossover-length (circles) calculated from the Fourier power spectrum (cp. Fig. 10b) and crossover interface width (diamonds) for simulations with different dissolution rate constants. b) Crossover-length (circles) and crossover interface width (diamonds) for simulations with different amounts of pinning particles.

heterogeneities might cause a stylolite to become a non-stationary signal with alternating wavy and flat portions along the interface. This study also demonstrates that correlated quenched noise only influences the stylolite morphology above a crossover-length scale, implying that two scaling regimes, which can be connected to surface and elastic energy dominated roughening (e.g. Renard et al., 2004; Schmittbuhl et al., 2004), can also be found in the case of correlated noise. We have not investigated the effects of irregularly distributed (correlated) noise since the heterogeneities are distributed equally in our model setup.

The roughness data of simulated stylolites presented in this study reveal two self-affine scaling regimes that are separated by a distinct crossover-length of $L \sim 1.3$ mm, which is well in line with investigations of natural stylolites (Renard et al., 2004; Schmittbuhl et al., 2004; Ebner et al., in press). Additionally we have detected a crossover in the growth of the interface during which the initial growth exponent of $\beta \sim 0.5$ up to a crossover interface width of $w \sim 1.23$ mm is replaced by a growth regime with an exponent of $\beta \sim 0.8$. Due to the very good correlation between the magnitudes of the crossover-length and the crossover interface width we argue that both crossovers arise from the same process, namely the transitions from a surface energy to an elastic energy dominated regime. The knowledge of the crossover-length L which can be derived from the finite pattern of a natural stylolite with the above methods is thus equivalent to knowledge of the crossover interface width. This fact has important consequences regarding the assessment of the amount of total compaction of individual stylolites. Substituting the growth exponents and the compaction prefactors found for the two growth regimes in combination with the crossover-length, which separates the two growth regimes (cp. Fig. 10c), into Eq. (10) should allow an approximate reconstruction of the amount of total compaction from finite pattern of a natural stylolites.

5. Conclusions

In the course of this study we evaluated the scaling properties of simulated stylolites, which facilitate a quantitative comparison with natural examples, reproducing their scaling. We observed only minor correlation between the exact nature of the noise introduced in the model or the topography of the predefined interface and the scaling parameters investigated, concluding that inherent processes, i.e. the transition from a surface to an elastic energy dominated regime, control the roughening process.

Nevertheless the amount of heterogeneities has a negative effect on the maximum interface width (w_{max}) achieved during deformation, revealing increasing interface width with decreasing amount of quenched noise. The absolute particle/noise size influences the roughness and growth exponents, which in turn is caused by the transition from a surface to an elastic energy dominated regime. Therefore it is important to know how large the noise or pinning particles are in natural systems. The transition from surface energy as the dominant stabilizing force of the interface to the dominance of elastic energies causes the most significant scaling transitions: (i) the roughness is characterized by two distinct spatial scaling regimes on small and large length scales, respectively; (ii) the interface growth reveals two growth regimes with a growth exponent of $\beta \sim 0.5$ up to a crossover interface width that coincides with the crossover-length L followed by a growth regime with an exponent of $\beta \sim 0.8$ that eventually saturates due to finite size effects; (iii) the crossover interface width w coincides with the crossover-length L and thus allows to accurate reconstruction of the compaction history of finite stylolite patterns.

Our study corroborates the evidence that the simple mechanisms summarized above support analytical predictions and natural observations given in previous studies, and are a convincing cause for the formation of stylolite roughness. However a detailed study on the exact nature and distribution of quenched noise in the host-rocks of natural stylolites would shed light on the origin and initiation of these complex structures.

Acknowledgements

We are indebted to Jean Schmittbuhl for stimulating discussion. T. Blenkinsop is thanked for editorial handling and Z. Karcz and an anonymous reviewer are thanked for critical reading of the manuscript. M. Ebner and D. Koehn acknowledge financial support through the DFG project *KO2114/5-1*, the MWFZ of Mainz and the Geocycles Cluster funded by the state of Rhineland-Palatinate.

References

Barabasi, A.L., Stanley, H.E., 1995. Fractal Concepts in Surface Growth. Cambridge University Press.
Bathurst, R.G.C., 1987. Diagenetically enhanced bedding in argillaceous platform limestones – stratified cementation and selective compaction. Sedimentology 34, 749–778.
Bons, P.D.D., Koehn, D., Jessell, M.W., 2008. Microdynamics simulation. In: Friedmann, G.M., Seilacher, A. (Eds.), Lecture Notes in Earth Sciences, vol. 106. Springer, Berlin, p. 406.
Brouste, A., Renard, F., Gratier, J.P., Schmittbuhl, J., 2007. Variety of stylolites' morphologies and statistical characterization of the amount of heterogeneities in the rock. Journal of Structural Geology 29, 422–434.
Buxton, T.M., Sibley, D.F., 1981. Pressure solution features in a shallow buried limestone. Journal of Sedimentary Petrology 51, 19–26.
Clark, S.P.J., 1966. Handbook of Physical Constants. Geological Society of America, New York.
Dunnington, H.V., 1954. Stylolite development post-dates rock induration. Journal of Sedimentary Petrology 24, 27–49.
Drummond, C.N., Sexton, D.N., 1998. Fractal structure of stylolites. Journal of Sedimentary Research 68, 8–10.
Ebner, M., Koehn, D., Toussaint, R., Renard, F., Schmittbuhl, J. Stress sensitivity of stylolite morphology. Earth and Planetary Science Letters, in press, doi:10.1016/j.epsl.2008.11.001.
Fletcher, R.C., Pollard, D.D., 1981. Anti-crack model for pressure solution surfaces. Geology 9, 419–424.
Gratier, J.P., Muquet, L., Hassani, R., Renard, F., 2005. Experimental microstylolites in quartz and modeled application to natural stylolitic structures. Journal of Structural Geology 27, 89–100.
Guzzetta, G., 1984. Kinematics of stylolite formation and physics of the pressure-solution process. Tectonophysics 101, 383–394.

Hansen, A., Schmittbuhl, J., Batrouni, G.G., de Oliveira, F.A., 2000. Normal stress distribution of rough surfaces in contact. Geophysical Research Letters 27, 3639–3642.

Heald, M.T., 1955. Stylolites in sandstones. Journal of Geology 63, 101–114.

Katsman, R., Aharonov, E., Scher, H., 2006. A numerical study on localized volume reduction in elastic media: some insights on the mechanics of anticracks. Journal of Geophysical Research-Solid Earth 111 B03204.

Karcz, Z., Scholz, C.H., 2003. The fractal geometry of some stylolites from the calcare massiccio formation, Italy. Journal of Structural Geology 25, 1301–1316.

Koehn, D., Dysthe, D.K., Jamtveit, B., 2004. Transient dissolution patterns on stressed crystal surfaces. Geochimica et Cosmochimica Acta 68, 3317–3325.

Koehn, D., Malthe-Sorenssen, A., Passchier, C.W., 2006. The structure of reactive grain-boundaries under stress containing confined fluids. Chemical Geology 230, 207–219.

Koehn, D., Renard, F., Toussaint, R., Passchier, C.W., 2007. Growth of stylolite teeth patterns depending on normal stress and finite compaction. Earth and Planetary Science Letters 257, 582–595.

Merino, E., 1992. Self-organization in stylolites. American Scientist 80, 466.

Merino, E., Calas, A., Fletcher, R.C., 2006. Genesis of self-organized zebra textures in burial dolomites: displacive veins, induced stress, and dolomitization. Geologica Acta 4, 383–393.

Park, W.C., Schot, E.H., 1968. Stylolites: their nature and origin. Journal of Sedimentary Petrology 38, 175–191.

Railsback, L.B., 1993. Lithologic controls on morphology of pressure-dissolution surfaces (stylolites and dissolution seams) in paleozoic carbonate rocks from the Mideastern United-States. Journal of Sedimentary Petrology 63, 513–522.

Railsback, L.B., 1998. Evaluation of spacing of stylolites and its implications for self-organizations of pressure dissolution. Journal of Sedimentary Research 68, 2–7.

Renard, F., Schmittbuhl, J., Gratier, J.P., Meakin, P., Merino, E., 2004. Three-dimensional roughness of stylolites in limestones. Journal of Geophysical Research-Solid Earth 109, B3209.

Rutter, E.H., 1983. Pressure solution in nature, theory and experiment. Journal of the Geological Society of London 140, 725–740.

Schmittbuhl, J., Vilotte, J.P., Roux, S., 1995. Reliability of self-affine measurements. Physical Review E 51, 131–147.

Schmittbuhl, J., Renard, F., Gratier, J.P., Toussaint, R., 2004. Roughness of stylolites: implications of 3D high resolution topography measurements. Physical Review Letters 93, 238501.

Simonsen, I., Hansen, A., Nes, O.M., 1998. Determination of the Hurst exponent by use of wavelet transforms. Physical Review E 58, 2779–2787.

Stockdale, P.B., 1922. Stylolites: their nature and origin. Indiana University Studies 9, 1–97.

Tada, R., Siever, R., 1989. Pressure solution during diagenesis. Annual Review of Earth and Planetary Sciences 17, 89–118.

JOURNAL OF GEOPHYSICAL RESEARCH, VOL. 115, B06403, doi:10.1029/2009JB006649, 2010

Anisotropic scaling of tectonic stylolites: A fossilized signature of the stress field?

Marcus Ebner,[1,2] Renaud Toussaint,[3,4] Jean Schmittbuhl,[3,4] Daniel Koehn,[1] and Paul Bons[5]

Received 26 May 2009; revised 15 October 2009; accepted 13 January 2010; published 19 June 2010.

[1] Vertical stylolites are pressure solution features, which are considered to be caused by horizontal tectonic loading, with the largest principal compressive stress being (sub-) parallel to the Earth's surface. In the present study we analyze the roughness of such tectonic stylolites from two tectonic settings in southern Germany and northeastern Spain, aiming to investigate their scaling properties with respect to the stress during formation. High-resolution laser profilometry was carried out on opened stylolite surfaces of nine samples. These data sets were then analyzed using one- and two-dimensional Fourier power spectral approaches. We found that tectonic stylolites show two self-affine scaling regimes separated by a distinct crossover length (L), as known for bedding parallel stylolites. In addition, tectonic stylolites exhibit a clear in-plane scaling anisotropy that modifies L. Since the largest and smallest crossover lengths are oriented with the sample vertical and horizontal directions (i.e., σ_2 and σ_3) and L is a function of the stress field during formation as analytically predicted, we conclude that the scaling anisotropy of tectonic stylolites is possibly a function of the stress field. Knowledge of this crossover-length anisotropy would enable the reconstruction of the full three-dimensional stress tensor if independent constraints of the depth of formation can be obtained.

Citation: Ebner, M., R. Toussaint, J. Schmittbuhl, D. Koehn, and P. Bons (2010), Anisotropic scaling of tectonic stylolites: A fossilized signature of the stress field?, *J. Geophys. Res.*, *115*, B06403, doi:10.1029/2009JB006649.

1. Introduction

[2] The intriguing variety of pressure solution features and its widespread occurrence in monomineralic rock types have provoked continuous interest in and attention to various geoscience disciplines over the past decades [*Tada and Siever*, 1989]. One of the most prominent and complex pressure solution features is stylolites, which are rough dissolution interfaces that are found in a large variety of sedimentary rocks [*Buxton and Sibley*, 1981; *Dunnington*, 1954; *Heald*, 1955; *Park and Schot*, 1968; *Railsback*, 1993; *Rutter*, 1983; *Stockdale*, 1922; *Tada and Siever*, 1989]. Until recently stylolite morphology has been described qualitatively by the use of a descriptive terminology that groups stylolites into generic classes. One classification uses the orientation of the stylolite plane relative to bedding. Bedding parallel stylolites are supposed to have formed owing to the layer-normal overburden pressure, while tectonic stresses cause the formation of stylolites oblique or perpendicular to bedding [*Park and Schot*, 1968; *Railsback and Andrews*, 1995]. The second classification is based on the orientation of the stylolite teeth relative to the stylolite plane. Here the term "stylolite" is used for teeth at a high angle to the plane, and the term "slickolite" is used for dissolution surfaces where the teeth are distinctly oblique to the dissolution plane [*Bretz*, 1940; *Gratier et al.*, 2005; *Simon*, 2007]. Finally, the shape of the characteristic teeth-like asperities and spikes along the interface has been used to characterize stylolites [*Guzzetta*, 1984; *Park and Schot*, 1968].

[3] More recently, stylolites have been subjected to more rigorous quantitative analyses to characterize the roughness of the stylolite surface [*Brouste et al.*, 2007; *Drummond and Sexton*, 1998; *Ebner et al.*, 2009a–2009b; *Gratier et al.*, 2005; *Karcz and Scholz*, 2003; *Koehn et al.*, 2007; *Renard et al.*, 2004; *Schmittbuhl et al.*, 2004]. It was demonstrated that the one-dimensional (1-D) stylolite roughness obeys a fractal scaling invariance [*Drummond and Sexton*, 1998; *Karcz and Scholz*, 2003]. Investigation of the rough interface of opened stylolite surfaces by means of laser profilometry revealed that the stylolite morphology shows two self-affine scaling regimes with two distinct roughness exponents on their respective scales, which are separated by a characteristic crossover length at the millimeter scale [*Renard et al.*, 2004; *Schmittbuhl et al.*, 2004] for bedding parallel stylolites. Self-affine surfaces define a group of fractals that remain statistically unchanged by the transform, $\Delta x \to b \times \Delta x$, $\Delta y \to b \times \Delta y$, $\Delta z \to b^H \times \Delta z$, where b is a transformation factor that can take any real value and H is

[1]Tectonophysics, Institute of Geosciences, Johannes Gutenberg University, Mainz, Germany.
[2]Now at Geological Survey of Austria, Vienna, Austria.
[3]EOST, University of Strasbourg, Strasbourg, France.
[4]Also at Institut de Physique du Globe de Strasbourg, UMR CNRS 7516, Strasbourg, France.
[5]Institute for Geosciences, Eberhard Karls University Tübingen, Tübingen, Germany.

0148-0227/10/2009JB006649

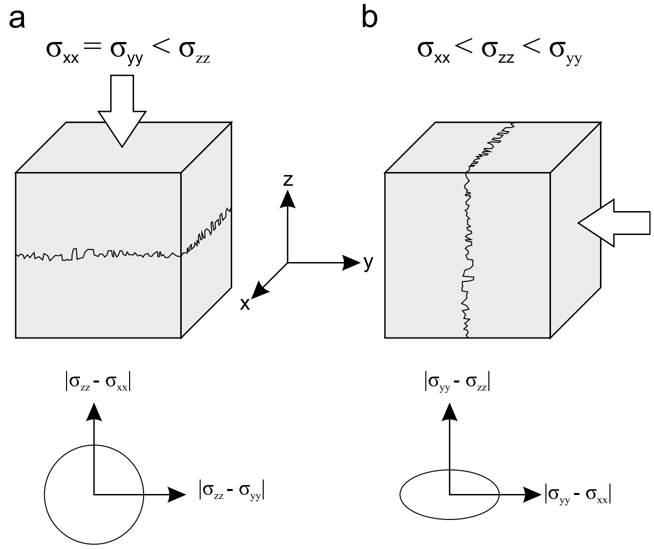

Figure 1. Schematic drawing of the formation stress state for (a) bedding parallel and (b) tectonic stylolites. The largest compressive stress direction (σ_1) is indicated by the white arrow. Below the sketch map an idealized graph of the in-plane differential stress is plotted as a function of the orientation within the stylolite plane. For bedding parallel stylolites (a) the horizontal normal stresses are equal and thus the differential stress is equal in every direction. For tectonic stylolites (b) the in-plane normal stresses are dissimilar and σ_{zz} is generally larger than σ_{xx}. Thus the in-plane differential stress scales inversely with the magnitudes of the σ_{xx} and σ_{zz} directions, having a maximum along the x axis.

the Hurst or roughness exponent [*Barabasi and Stanley*, 1995], which is a quantitative measure of the roughness of the signal.

[4] Analytical and numerical investigations have demonstrated that the growth of the stylolite roughness is induced by heterogeneities in the host rock that pin the interface and is slowed down by two stabilizing forces, the elastic and surface energies. The elastic energy dominates on larger scales and is represented by a small roughness exponent of 0.3 to 0.5, whereas the surface energy is dominant on small scales, with a roughness exponent of about 1 [*Koehn et al.*, 2007; *Renard et al.*, 2004; *Schmittbuhl et al.*, 2004]. The characteristic crossover length (L) that separates these two scaling regimes is a function of the principal normal stress [*Renard et al.*, 2004; *Schmittbuhl et al.*, 2004] on the interface of a bedding parallel stylolite. These analytical predictions were successfully tested by *Ebner et al.* [2009b], who demonstrated, on a set of 13 bedding parallel stylolites from varying stratigraphic depths of a cretaceous succession, that this crossover length decreases with increasing depth (and normal stress) and thus exhibits the analytically predicted behavior. The 1-D scaling of stylolites with two self-affine scaling invariance regimes can be described as the height difference h of points along the surface separated by a distance Δx as [*Ebner et al.*, 2009b]

$$h(\Delta x) \approx A\Delta x^{H_S} g(\Delta x/L) \text{ with } g(u) = \begin{cases} u^0 & \text{if } u \ll 1, \\ u^{H_L - H_S} & \text{if } u \gg 1, \end{cases} \tag{1}$$

where A is a scaling factor, g is a scaling function, and u is the ratio $\Delta x/L$, with L being the crossover length. H_S and H_L correspond to the roughness exponents for small and large scales, respectively. Numerical simulations also demonstrate that the crossover length is very robust with regard to the kind and amount of quenched noise (heterogeneities initially present) in the rock [*Ebner et al.*, 2009a]. Hence, the use of bedding parallel stylolites as a quantitative stress gauge under the assumption of uniaxial strain (zero horizontal displacement) seems to be verified. Investigations of the surface morphology of bedding parallel stylolites showed that their scaling is isotropic within the plane defined by the stylolite [*Renard et al.*, 2004; *Schmittbuhl et al.*, 2004]. This implies that any arbitrary section through the stylolite interface that contains the principal stress direction (i.e., normal to the plane) fully characterizes the complex self-affine roughness of bedding parallel stylolites. A second mechanism claimed to be responsible for the formation of the characteristic roughness is a stress-induced roughening instability along an initially flat solid-solid interface [*Angheluta et al.*, 2008] or a solid-fluid-solid interface [*Bonnetier et al.*, 2009]. In both cases the instability is triggered by elastic stresses acting normal on the interface.

[5] Up to now no study has quantitatively investigated the 3-D topography of tectonic stylolites that formed owing to (sub-)horizontal compression resulting in a vertical stylolite plane. Tectonic stylolites differ in two major characteristics from bedding parallel stylolites. First, the stress field during the formation of tectonic stylolites is nonisotropic, that is, the in-plane normal stresses differ (i.e., $\sigma_{zz} > \sigma_{xx}$), whereas bedding parallel stylolites often have equal in-plane normal stresses $\sigma_{xx} = \sigma_{yy}$ (Figure 1). This implies that the scaling of tectonic stylolites is not invariant within the plane, since the crossover length should scale with the (nonisotropic) stress field as shown analytically [*Schmittbuhl et al.*, 2004]. A second common feature of tectonic stylolites are oblique/tilted teeth with respect to the mean stylolite plane due to overprinting of pre-existing planes of anisotropy such as joints, bedding planes, and other interfaces. Tilting of the teeth with respect to the stylolite plane also influences the morphology because it leads to the dominance of long grooves and ridges [*Simon*, 2007]. These features could lead to an anisotropic scaling of the stylolite interface in addition to variations of the in-plane stresses.

[6] The present study investigates such tectonic stylolites that formed in a vertical orientation. We mainly concentrate on the influence of (i) the orientation of the dissolution surface with respect to the displacement direction and (ii) the formation stress on the scaling properties of natural stylolites in limestones. To accomplish this task we use laser profilometry data on opened interfaces of tectonic stylolites from flat-lying Jurassic limestones of the Swabian Alb in southern Germany and from a Tertiary fold and thrust belt of the Iberian Chain of northeastern Spain.

2. Geological Setting

[7] In this section we give a brief introduction of the investigated field areas in southern Germany and northeastern Spain, which both expose upper Jurassic limestones. The Swabian Alb of southern Germany forms a region of flat-lying, mainly marine Jurassic deposits [*Geyer and*

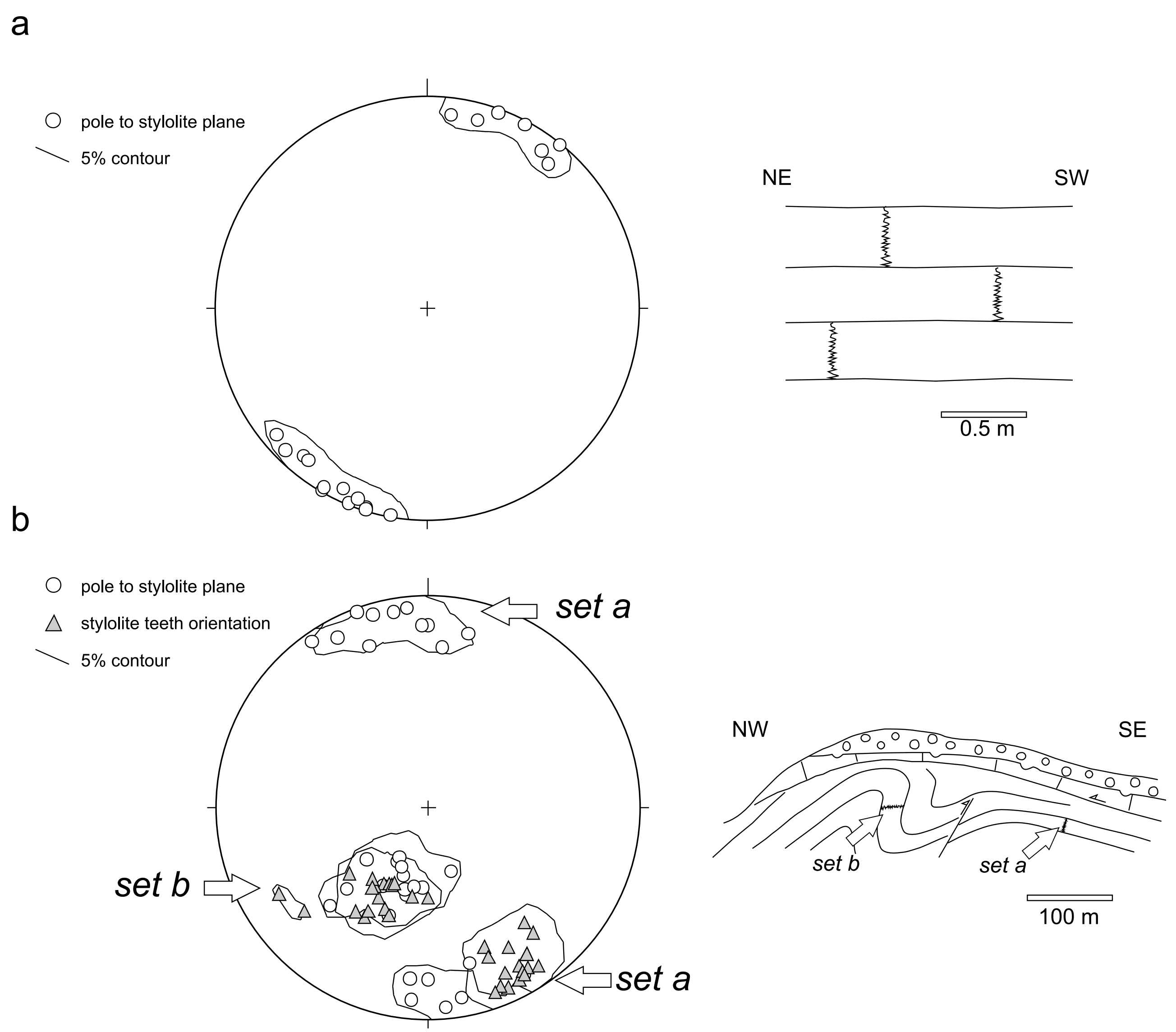

Figure 2. Lower hemispheric equal area projection (Schmidt's net) of the field data and schematic cross sections of the investigated outcrops. (a) The Swabian Alb of southern Germany (n = 22). The sketch at the right shows the flat-lying Jurrassic strata with vertical stylolites limited to individual beds. (b) The Iberian Chain of northeastern Spain (n = 32). The sketch at the right shows a cross section of NE-plunging fold and the positions of sets a and b within the fold. All samples are taken from well-bedded Jurassic strata. In the overlying massif Jurassic limestones (vertical lines) and conglomerates (circles), no stylolites were found. Note that in Figure 2a, only the poles to the stylolite planes are displayed since the shortening direction is normal to that plane. In Figure 2b two populations are shown, which correspond to the two investigated fold limbs. Poles to planes (circles) diverge slightly from the orientation of the long axis of the teeth (triangle). See text for a detailed explanation.

Gwinner, 1991]. The studied sections are located 10 km south of the city of Tübingen and comprise upper Jurassic (Oxfordian to Kimmeridgian) limestones. The basal part of the sections (UTM 32U, E 0515212 m, N 5362240 m) are made up of well-bedded Oxfordian limestones, whereas the upper part of the profile contains massive Kimmeridgian limestones representing a riff facies, with sponges and algae being the main rock-forming species [*Etzold et al.*, 1996; *Geyer and Gwinner*, 1991]. The bedding is (sub-)horizontal, dipping slightly (<5°) to the SE on a regional scale. The principal structural features are ENE-WSW-striking graben structures, which exhibit a mixed-mode displacement, with a major normal and a subordinate dextral component [*Etzold et al.*, 1996; *Geyer and Gwinner*, 1991], and can be attributed to a later compressional phase (see below). The investigated stylolites (samples Sa6/1a, Sa6/1b, and Sa9/2) form vertical planes that trend WNW-ESE with teeth pointing parallel to the surface normal direction, hence recording a NNE-SSW compression (Figure 2a). Additionally, small-scale reverse faults and NNE-SSW-trending joints confirm the same kinematic framework. A younger subordinate set of stylolites not investigated in this study

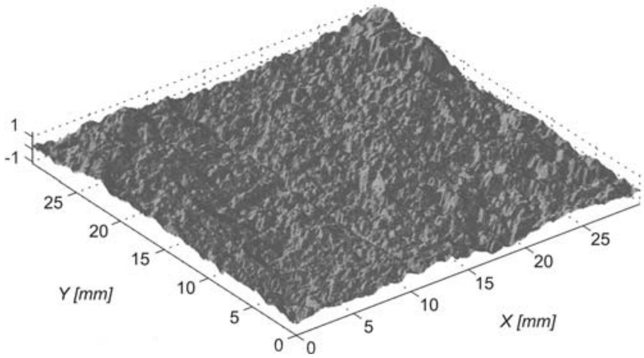

Figure 3. Oblique view of the three-dimensional (3-D) morphology of the surface of an opened stylolite (sample M4/4) reconstructed from optical profilometry. A linear trend is removed from the raw data (compare Figure 4 for details).

form NE-SW-trending vertical stylolite planes that can be related to the prominent dextral graben structures found in the area [*Geyer and Gwinner*, 1991; *Kley and Voigt*, 2008]. Our relative chronological sequence of deformation events is in agreement with data reported by *Kley and Voigt* [2008] demonstrating a change in the stress field from NNE-SSW-directed compression in the late Cretaceous to NW-SE-directed compression in the Neogene. This second compression phase altered neither the shape nor the orientation of the investigated stylolites, since layer parallel shortening did not cause any orientational change and deformation was restricted to stylolite interfaces.

[8] The Iberian Chain of northeastern Spain is located south of the Ebro Basin and trends roughly NW-SE. The succession is composed of up to 6000 m of Mesozoic, mainly Jurassic and Cretaceous, sediments [*Capote et al.*, 2002], although the sequence is significantly reduced, to only 300–400 m, in the investigated area. The investigated area belongs to the Maestrazgo structural domain that forms the transition zone between the NW-SE-striking fold and thrust belt of the Aragon Branch and the NE-SW-striking Catalonian Coastal Ranges. A regional NNW-SSE compression in the sampling area between the small towns of Molinos and Ejulve is indicated by ENE-WSW-striking, 100–1000 m-scale fold trains with the top to the NNW kinematics. The onset of deformation is estimated to be around the Early to Middle Eocene, whereas the deformational peak is assumed to be during the Oligocene [*Capote et al.*, 2002; *Casas et al.*, 2000; *Liesa and Simón*, 2009]. *Liesa and Simón* [2009] report stylolite data that they argue to be attributed to Betic and Guadarrama compressions, both having their deformational peaks during the Oligocene. The investigated section (UTM 30T, E 07111963 m, N 4518336 m) comprises well-bedded limestones in an upper Jurassic upright antiform containing several smaller synforms that plunges 25° to the NW. Stylolites were investigated in a shallow ENE-dipping limb (set A in Figure 2b) and an overturned limb that dips steeply to the SE (set B in Figure 2b). In the eastward-dipping limb of the fold the stylolites (samples M4/1, M4/2, M4/3, and M4/4) track the far-field shortening direction (SSE-NNW) confirmed by field measurements in other outcrops in the area. In the overturned and steeply dipping fold limb the stylolites (samples M4c/1 and M4c/3) are rotated around the fold axis into a shallow dipping orientation (i.e., a counterclockwise or clockwise rotation of 65° around the fold axis would transform the stylolite orientation from one limb into the orientation of the stylolites in the other limb of the fold). Hence, the stylolite formation in this outcrop predates the folding event. In addition, the angle between the stylolite plane and the bedding (not shown) is consistent in both positions of the fold, thus corrugating the evidence that stylolitization predates the folding event. It must be noted that stylolites in sets A and B both form in a vertical orientation. Another important feature is that the stylolite teeth are somewhat oblique (~10°) to the mean stylolite plane, which we interpret as a result of a pressure-solution overprint of a pre-existing joint set that strikes NE-SW, subparallel to the stylolite planes.

3. Methodology

[9] The samples collected in the locations described above were all taken oriented in the outcrop to reconstruct the spatial position of the 3-D stylolite morphology after laser profilometry. For analysis, only "closed" specimens were considered. Stylolite surfaces that were already open in the outcrop and were subjected to an unknown amount of weathering were ignored. The sampled specimens were opened mechanically along the two opposing interfaces of the stylolite. This method causes some negligible damage to the surface due to the interlocking of asperities. The split surfaces were cleaned from any clay material, that is, the residuum of the dissolved rock, with a soft brush and distilled water. Areas that did not exhibit visual mechanical damage were chosen for profilometry.

[10] Optical profilometry is based on a laser triangulation of the surface similarly to previous studies [*Renard et al.*, 2004; *Schmittbuhl et al.*, 2004, 2008]. The triangulation technique uses a laser beam that is focused on the surface of the object, which is monitored by a nearby CCD sensor. The distance between the object and the sensor changes as a function of changes of the angle under which the point of consideration is observed. The distance between the object and the laser head is then calculated from angular relationships [*Schmittbuhl et al.*, 2008]. Before every individual measurement a test run was made to calibrate voltage fluctuations of the laser beam (the volt-height relationship is virtually linear in the chosen range, which gives the estimate of the vertical resolution: small distortions of the profile height, <1%, can be expected.). The laser beam is 30 μm wide and horizontal steps between measurement points were $\Delta x = \Delta y = 25$ μm, with a horizontal precision of 1 μm. The vertical resolution is 2 μm. Maps were constructed by movement of the laser head along parallel profiles over the specimen (Figure 3). Eight samples have been measured at a high resolution ($\Delta x = \Delta y = 25$ μm), with map sizes of 1200 × 1200 (samples M4/1 and M4/4), 1600 × 1600 (samples Sa6/1a, Sa6/1b, M4/2,M4/3, M4c/1, and M4c/3), and 2000 × 2000 measurement points (sample Sa9/2), which correspond to square maps with physical side lengths of 30, 40, and 50 mm. The x and y directions are arbitrary choices parallel to the principal axis of the profilometer. The sample is usually oriented in a way to fit the biggest square

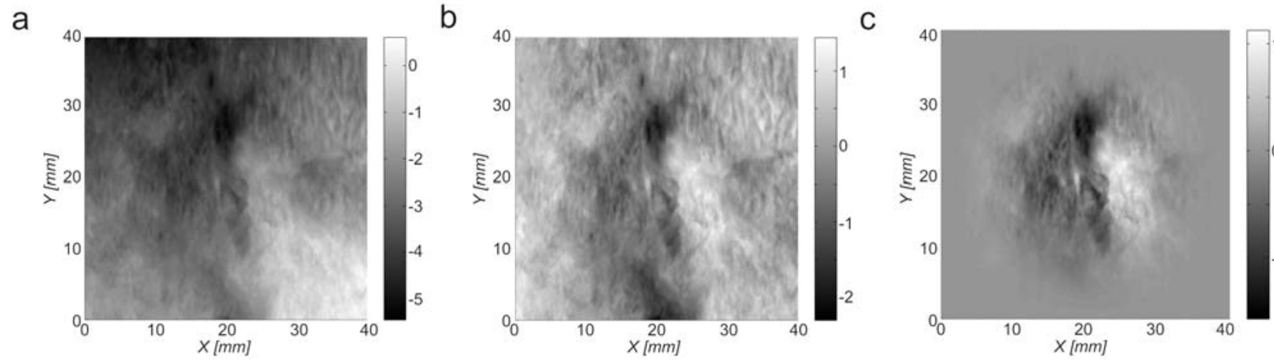

Figure 4. Grayscale maps of sample M4/3: (a) raw data from profilometry (notice a general trend from the top left to the bottom right); (b) detrended data, i.e., the linear trend is removed and the mean height is set to be zero; (c) detrended data modified with a Hanning window technique where the data are forced to taper off to zero at the boundaries (for explanation see text). Light colors correspond to peaks and ridges, and dark colors represent local depressions.

map on the respective stylolite interface. Care was taken that from the orientation of the map x/y direction, the sample orientation could be reconstructed.

[11] Additionally, sample Sa6/1 was measured twice, where the second measurement (Sa6/1b) was rotated 32° clockwise around a vertical axis with respect to the first measurement (Sa6/1a). This was done to test the robustness of the measurements used against possible noise arising from the measurement procedure along discrete profiles. An image registration [*Goshtasby*, 1986, 1988] of the two measurements in the spatial domain revealed the same amount of rotation, 32°, with an uncorrelated noise in the height difference between the two images that arises from the discreteness of the two maps (not shown). This height difference is less than 5% (i.e., the ratio of the standard deviation σ of the height difference to the σ of the height of the surface is 0.063/1.477 mm). Hence, there seems to be no significant error introduced by the measurement procedure.

4. Data Analysis

[12] Before we analyzed the 2-D maps in detail the raw data from the laser profilometry were subjected to a series of pretreatments (Figure 4). First, a mean plane calculated from a least-squares fit was subtracted from the raw data (Figure 4a); that is, the x/y plane was adjusted to a global trend and the vertical (z) axis was set to have zero mean height (Figure 4b). To increase the quality of our Fourier transforms (described below), we used a Hanning window technique [*Karcz and Scholz*, 2003; *Press et al.*, 2007] to force our data to taper to zero at the boundaries (Figure 4c), to reduce spectral leakage (compare Figure 3). This is a standard technique in signal processing, which does not modify the frequency or amplitude of the original signal.

4.1. One-Dimensional Analysis

[13] From the 2-D height field a 1-D profile can be extracted either along the x or y direction or in any arbitrary direction. For an arbitrary 1-D profile $f(x)$ the Fourier transform $F(k)$ can be calculated and the power spectrum $P(k) \sim |F(k)|^2$ of the transform can be plotted as a function of the wave number $k = 2\pi/\lambda$ (m^{-1}), which scales inversely to the wavelength λ [*Renard et al.*, 2004; *Schmittbuhl et al.*, 1995, 2004]. In Figure 5 the averaged spectra of sample M4/3 along the x and y directions of the measured map are shown. The averaged spectra are found by calculating the mean $P(k)$ for every k value over all k profiles in one direction [*Renard et al.*, 2004; *Schmittbuhl et al.*, 2004]. This averaging procedure reduces the noise attached to an individual 1-D profile. A linear slope of the power spectra confirms a self-affine scaling invariance. The power spectrum of a self-affine signal behaves as

$$P(k) \sim k^{-D-2H}, \tag{2}$$

where D is the topological dimension of the signal ($D = 1$ for 1-D profiles) and H is the Hurst exponent. The Hurst exponent can thus be calculated from the slope of the power spectra. When we study the averaged 1-D spectra of a tectonic stylolite along specific directions (Figure 5a), we see that the signal exhibits two slopes, which are separated by a crossover length (L) in agreement with observations on bedding parallel stylolites [*Ebner et al.*, 2009b; *Renard et al.*, 2004; *Schmittbuhl et al.*, 2004]. The two observed scaling regimes have typical Hurst exponents of $H_S \sim 0.5$ and $H_L \sim 1.1$ for the small and large scale (large and small wave number), respectively. These observations indicate that the scaling of bedding parallel stylolites [equation (1)] can be extended to tectonic stylolites (compare Figure 5a). To enable a more detailed comparison of the power spectra of our tectonic stylolites from two different (orthogonal) directions, we normalize the power spectra along the x direction with the power spectrum of the y direction at k = 1 (mm^{-1}), that is, $P_x(k)/P_y[1\ (\text{mm}^{-1})]$ as shown in the inset to Figure 5a. This normalization yields a collapse of the large k values (small scales), but a notable difference for the small k values (large scales), of the scaling functions. This is basically the expression of the shift in cutoff between the two linear subbranches, which is the crossover length L. Figure 5b shows that the calculated cutoff between the scaling regimes and thus the crossover length differ between them. With 1.22 and 0.62 mm for the x and y directions, the crossover length changes by 0.6 mm (Figure 5b). The nonlinear fitting, shown by the solid line in both plots in

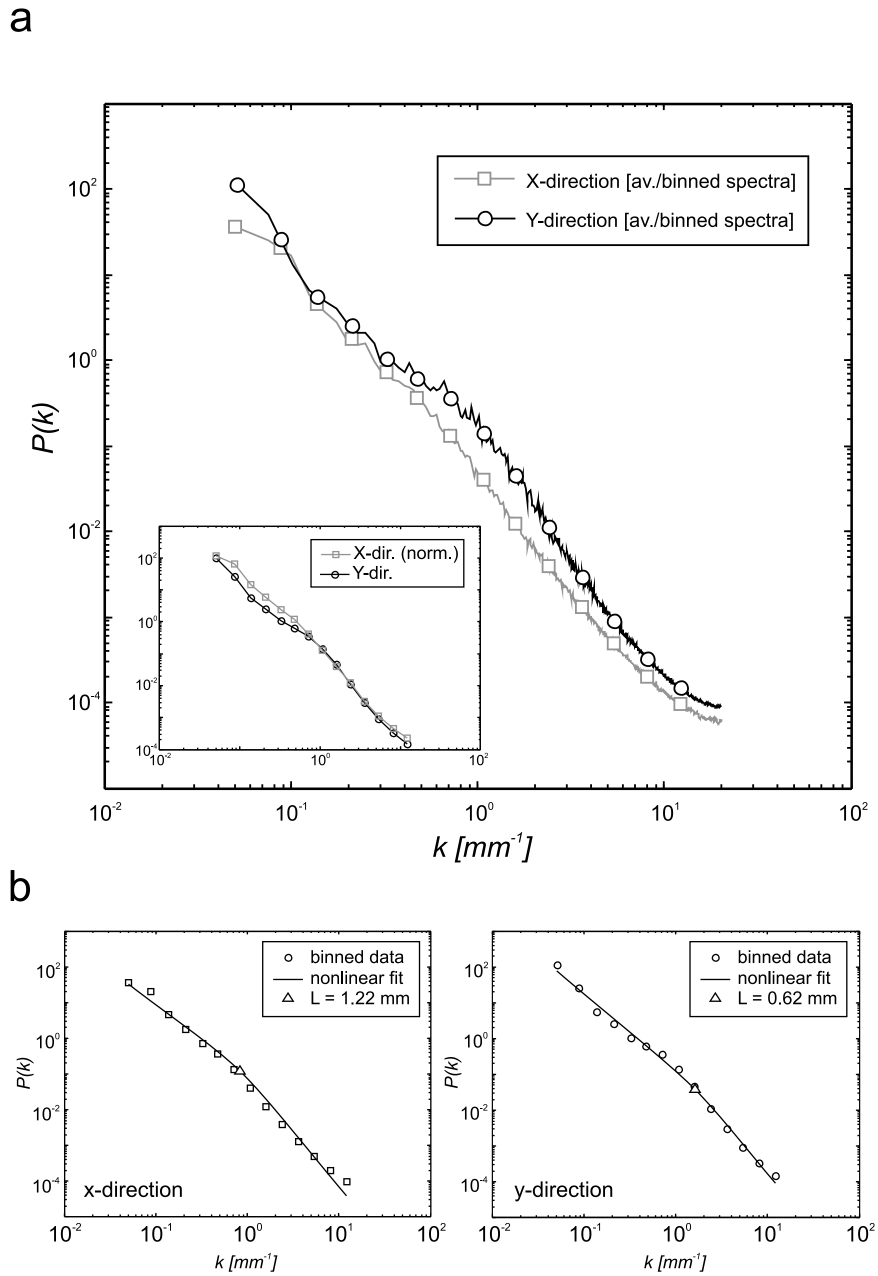

Figure 5. One-dimensional data analysis of sample M4/3. (a) Averaged power spectra $P(k)$ (solid line) and the respective binned spectra (circles) plotted as a function of the wave number along the x and the y direction of the measured map. The inset in (a) again shows the power spectra for both directions but the x direction is now normalized with respect to the y direction, $P_x(k)/P_y(1\ \mathrm{mm}^{-1})$. This yields a collapse of the large k values (small scales). Note that for the small k values (large scales), the scaling functions deviate considerably. (b) Nonlinear fit of the binned spectra for both directions used to estimate the crossover length L (triangle). Along the x direction the crossover length is larger (L = 1.22) than along the y direction (L = 0.62). The slope of the branches of the nonlinear model corresponds to Hurst exponents of 1.1 and 0.5 for small and large scales, respectively.

Figure 5b, is a linear-by-parts least-squares fit in logarithmic space with a weighting function that changes from the small-scale to the large-scale fraction of the scaling law (for details compare *Ebner et al.* [2009b]). This nonlinear model uses a minimization algorithm to find the least-squares fit for the crossover length. The differences found between the two directions also include a discrepancy in the scaling prefactor, that is, a vertical shift of the power spectra, which is clearly higher for all scales in the y direction.

[14] To fully quantify rough surfaces it is necessary to characterize this prefactor of the scaling function and thus obtain a full description of the surface morphology. In the following we use the height-height correlation function to calculate the scaling prefactor. The height-height correlation

function [*Barabasi and Stanley*, 1995] is defined for a function $h(x)$ over the spatial variable x by $C(\Delta x) = [\langle h(x) - h(x + \Delta x)\rangle^2]^{1/2}$, where $\langle\rangle$ denotes the average over the range of x, which estimates the average height difference between two points in the profile separated by a distance Δx. For a self-affine profile the correlation function follows a power law such that $C(\Delta x) \sim t^{1-H}\Delta x^H$, where H is the Hurst exponent and t is the scaling prefactor. The prefactor can be designed as $C(t) = t$ and, thus, denotes a length scale, also known as the topothesy [*Renard et al.*, 2006; *Schmittbuhl et al.*, 2008; *Simonsen et al.*, 2000]. The topothesy corresponds physically to the length scale for which the slope of the rough profile is equal to 1. In other words, t is the theoretical length scale over which the rough profile has a mean slope of 45°. The smaller the t, the flatter the profile appears on a macroscopic scale.

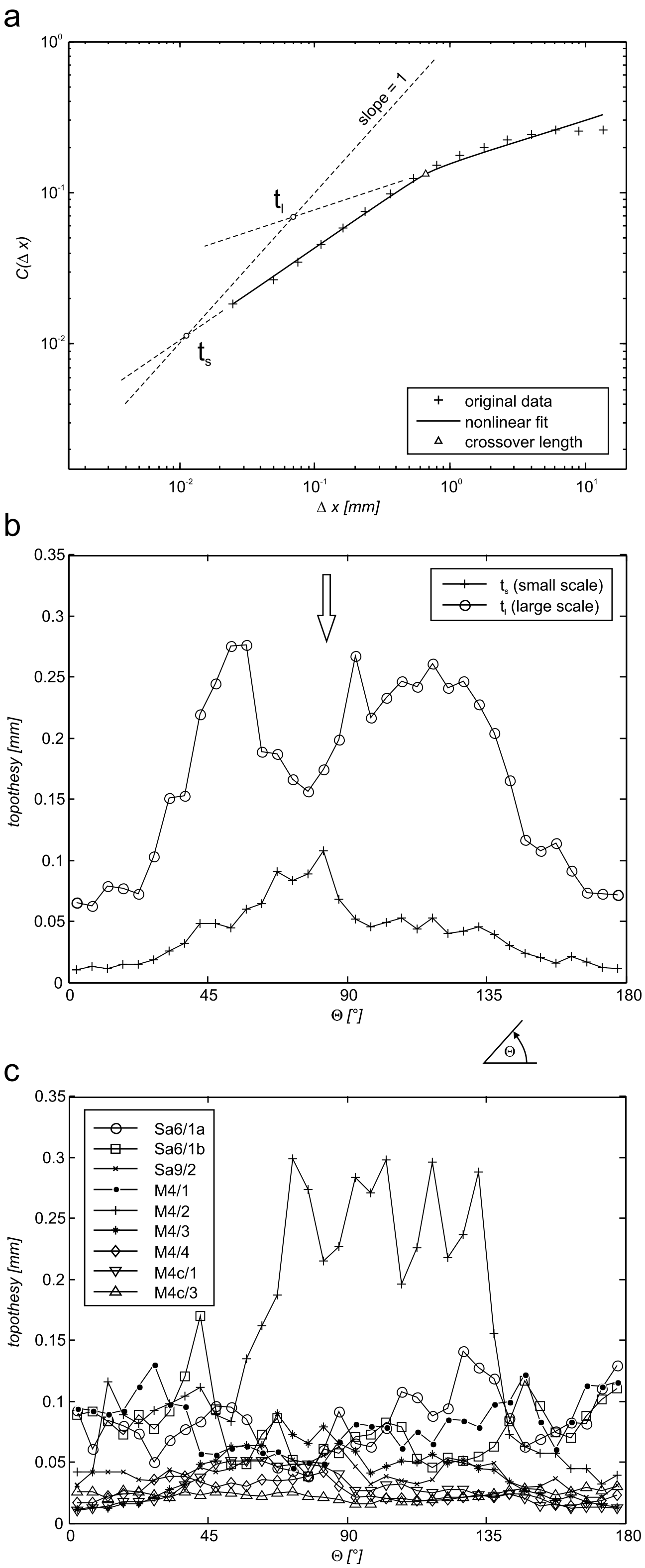

Figure 6. One-dimensional analysis of the scaling prefactor, i.e., the topothesy of tectonic stylolites. (a) A loglog plot of the correlation function $C(\Delta x)$ of a 1-D slice of sample M4/3 oriented parallel to the x direction of the analyzed surface with the nonlinear fit (compare text for details) and the topothesies t_s and t_l for small and large scale subbranches. The topothesy is constructed from the intersection of the linear subbranches with the 1/1 line. (b) The topothesies t_s and t_l of sample M4/3 plotted as a function of Θ, i.e., the counterclockwise angle from the x direction of the map. Note that the correlation functions are averaged over 5° intervals. The arrow indicates the vertical direction projected onto the stylolite plane. Note that only the t_s shows a clear correlation with the sample orientation. (c) The small-scale topothesy t_s for all samples plotted as a function of Θ.

[15] Figure 6a shows a scaling of the correlation function with two linear subbranches separated by a crossover length similar to the scaling of the power spectra shown in Figure 5a, with only the slopes being different. The correlation function shows, similarly to the power spectra, two linear subbranches separated by a distinct crossover length. We use the same nonlinear fitting approach as described previously (with fixed Hurst exponents of 0.6 and 0.3). The different scaling exponents compared to the power spectral approach is in line with the reliability of self-affine measurements performed on synthetic signals [*Candela et al.*, 2009; *Schmittbuhl et al.*, 1995]. Those authors have demonstrated that the correlation function underestimates the input Hurst exponents and thus shows lower values than the power spectra. The scaling prefactor and thus the topothesies t_s and t_l for the small- and large-scale regimes can be found by intersection of the two subbranches of the scaling function with the 1/1 line (Figure 6a). We estimated the topothesy for all orientations on the surfaces (Figures 6b and 6c) and found that there is a weak anisotropy in the scaling prefactor, which shows a correlation, with the highest topothesies being parallel to the horizontal direction in the sample orientation (Figure 6b) for most samples, but this is only visible in the small-scale regime. This observation is similar to what we found from investigation of the power spectra, where the small-scale regime shows very consistent results but the large-scale regime reveals a higher degree of variability; for example, compare the inset in Figure 5a. The small-scale topothesy is shown in Figure 6c. The average topothesies range between 0.05 and 0.15 mm and between 0.15 and 0.3 mm for the small and large scales, respectively.

[16] Both the power spectra (i.e., the cutoff length between the linear subbranches) and the topothesy of a 1-D signal show a considerable degree of anisotropy, which is often obscured owing to the noise associated with an individual

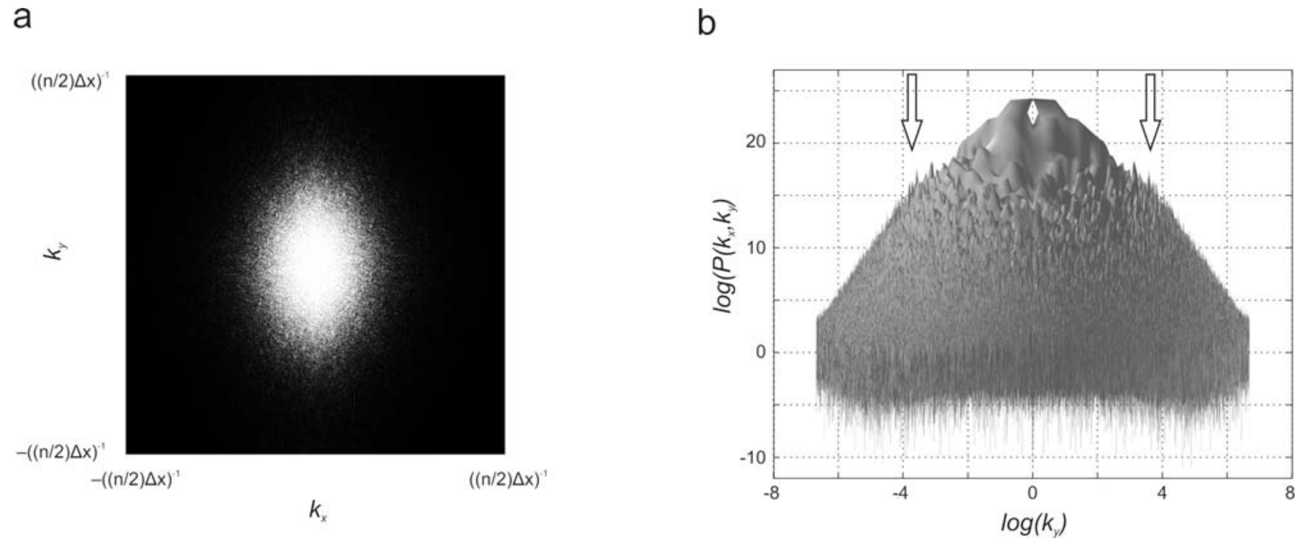

Figure 7. Two-dimensional data analysis of sample M4/3. (a) Two-dimensional Fourier transform plotted on a regular grid as a function of k_x and k_y, which range from $-[(n/2)\Delta x]^{-1}$ to $[(n/2)\Delta x]^{-1}$, where n is the number of measurement points in one direction of the map and Δx is the step size. Note that the zero-frequency component lies in the center of the map. A clear anisotropy of the data can be observed subparallel to the k_y axis (vertical axis). To investigate the power-law scaling exhibited by the 1-D analysis, the 2-D Fourier transform is converted to a double-log space, where $\log(k_x,k_y)$ is plotted as a function of the logarithm of the power spectra. (b) The 2-D power spectra are plotted as a surface whose height corresponds to $\log[P(k_x,k_y)]$. The 3-D surface is viewed along the k_x direction and the arrow indicates the crossover length L, which separates the two scaling regimes, i.e., the two linear subparts of the slope of the cone.

1-D profile. We conclude that to account for this in-plane variation, a 1-D signal fails to capture all scaling characteristics of tectonic stylolites and the choice of the investigated profile is not arbitrary as for bedding parallel stylolites. Hence, tectonic stylolites have a measurable in-plane anisotropy that we want to characterize in detail with a 2-D approach.

4.2. Two-Dimensional Analysis

[17] For the 2-D analysis we used the processed data as described at the beginning of this section (Figure 4c). First, a 2-D Fourier transform, that is, a discrete Fourier transform (DFT) was calculated from the data points of the 2-D height field with the fast Fourier transform algorithm [*Cooley and Tukey*, 1965] implemented in Matlab. Then the discrete Fourier transform is shifted so that the zero-frequency component lies in the center of the spectra and the 2-D power spectum $P(k_x,k_y)$ is again calculated as the square of the absolute magnitude of the Fourier transform. Figure 7a displays a map of the 2-D power spectra $P(k_x,k_y)$ in which the absolute magnitude squared is shown as grayscale values and k_x and k_y range from $-[(n/2) \times \Delta x]^{-1}$ to $[(n/2) \times \Delta x)]^{-1}$, where n is the number of measurement points in one direction of the map and $\Delta x = \Delta y$ is the step size. To investigate the power-law behavior located in the 1-D signals, the 2-D power spectra had to be transformed to a double-logarithmic space originating from the center of the map, that is, the zero-frequency component or the smallest wave number. This is accomplished by translating every value pair (k_x,k_y) by $\log\left(\left|\sqrt{k_x^2+k_y^2}\right|\right)$ along the direction defined by the direction cosine of the position vector (k_x,k_y) with the x axis of the coordinate system and plotting $\log[P(k_x,k_y)]$ on the newly formed logarithmic grid. The central point in this case corresponds to the system size, which imposes the smallest nonzero k. Figure 7b illustrates such a double-log plot of sample M3/4, in which the power spectra are displayed as a 3-D surface. Note that the view direction is along the k_x axis. The slopes of the surface, which roughly describe an elliptical cone, clearly exhibit two linear branches and a distinct crossover region (L) marked by the arrow in Figure 7b. Thus the 3-D representation is consistent with the scaling behavior found from the analysis of the 1-D signal.

[18] For further analysis of the anisotropy we resample the 3-D representation (Figure 7b) with a 2-D logarithmic binning (along k_x and k_y direction), to get a constant density of grid points in double-logarithmic representation (Figure 8a). For this reason a fixed grid that covers the 2-D power spectra with a constant bin size (bs) in logarithmic space [$\log(bs) = 0.4$] in the x and y direction is used to find all k_x,k_y-value pairs that fall into a certain bin, and the mean of all power spectra that belong to these k_x,k_y-value pairs in this bin is then used to define the binned power spectrum. This procedure allows analysis of the data with equal importance for the large and small scales, respectively. In addition, this method smoothes the data by removing the local fluctuations without altering the overall geometry of the 3-D representation that is characterized by the two scaling regimes and the distinct crossover.

[19] We use isopach/contour maps of the binned 2-D power spectra to quantify the degree of anisotropy. Isotropic

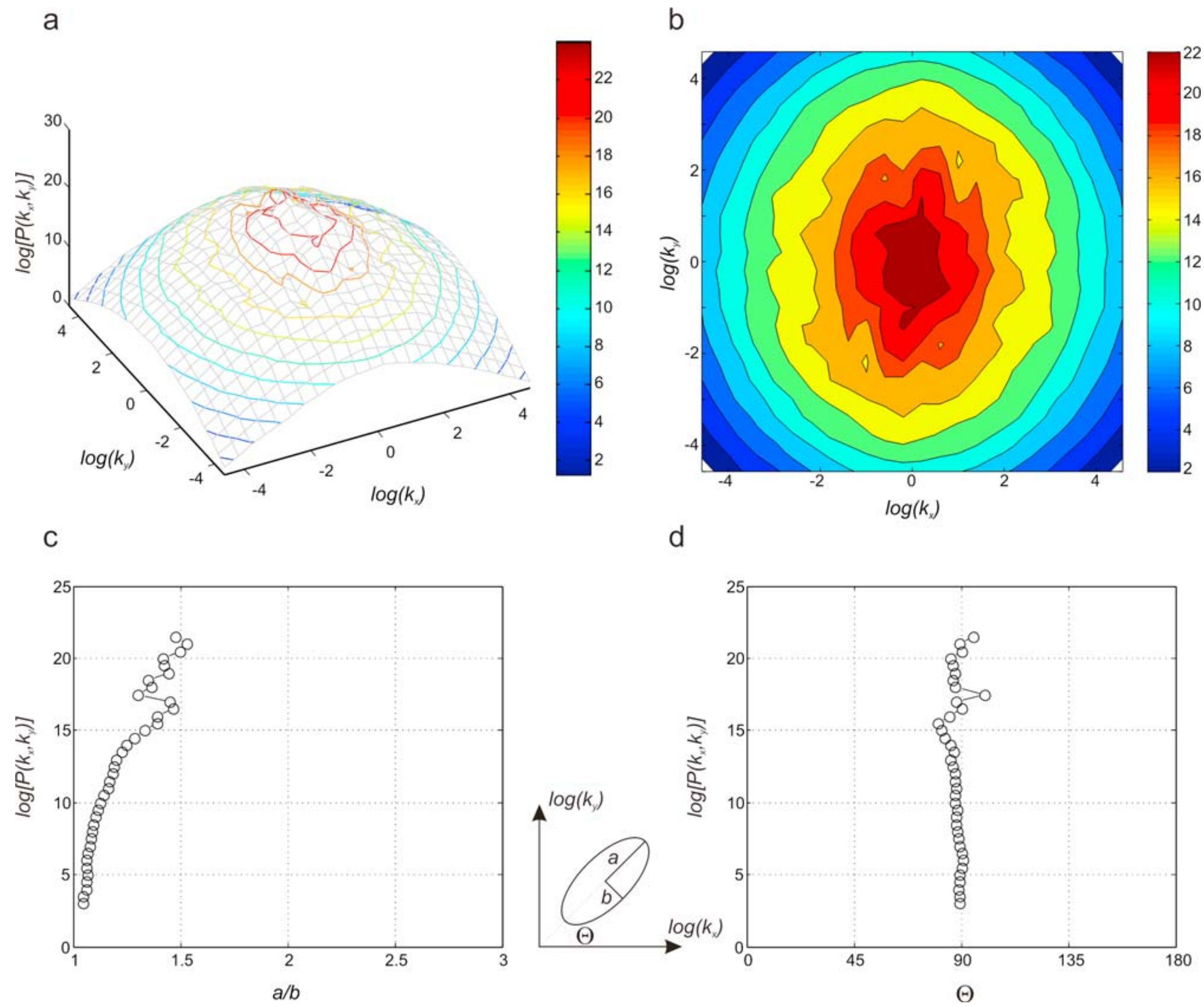

Figure 8. Quantification of the 2-D scaling anisotropy of sample M4/3. (a) Oblique 3-D view of the binned 2-D power spectra (gray mesh) with an overlay of colored contour lines of constant $\log[P(k_x,k_y)]$ values. (b) Map view of the contours calculated from the conic 2-D power spectra. These contours were utilized to calculate best-fitting ellipses using a least-squares approach. (c) Aspect ratio (*a/b*) of the fitted ellipse for every $\log[P(k_x,k_y)]$ contour. An increasing aspect ratio toward the center of the map is characteristic for all samples investigated. (d) Slope (i.e., the counterclockwise angle from the *x* direction of the measured map) of the long axis of the fitted ellipse plotted for the contour intervals.

signals should reveal concentric circular contour lines, which define the same $\log[P(k_x,k_y)]$ value. Concentric circular contour lines would imply that the crossover lengths that separate the self-affine scaling regimes for small and large scales are the same in every direction. Figures 8 show that this is clearly not the case for tectonic stylolites (also compare Figure 7a), where the contour lines reveal an elliptical shape (Figures 8a and 8b). This shape is clearly different from the circular concentric contours found in bedding parallel stylolites [compare, e.g., to Figure 4 of *Schmittbuhl et al.*, 2004]. We use a least-squares criterion to estimate the best-fit ellipse of the individual contour lines. From the best-fit ellipse we calculate the aspect ratio of the principal axis (i.e., *a/b*; where *a* and *b* are the semimajor and semiminor axis of the best fit ellipse) to get a quantitative measure of the anisotropy of the 2-D binned power spectra (Figure 8c). For the direction of the anisotropy we utilize the angle Θ between the long axis (*a*) of the fitted ellipse and the *x* direction of the coordinate system (Figure 8d). For all investigated samples we recognized an increased ellipticity toward the center of the 2-D power spectra but only a moderate or no significant change in orientation of the asymmetry with respect to the position in the power spectra. Note that in this representation (Figure 8a) high contour lines (small wave numbers) correspond to large physical length scales, whereas low contour lines (large wave numbers) correspond to small length scales.

[20] The fact that the large wave numbers display an isotropic power spectrum, that is, an aspect ratio close to 1 (Figure 8c), whereas the small ones show an anisotropic

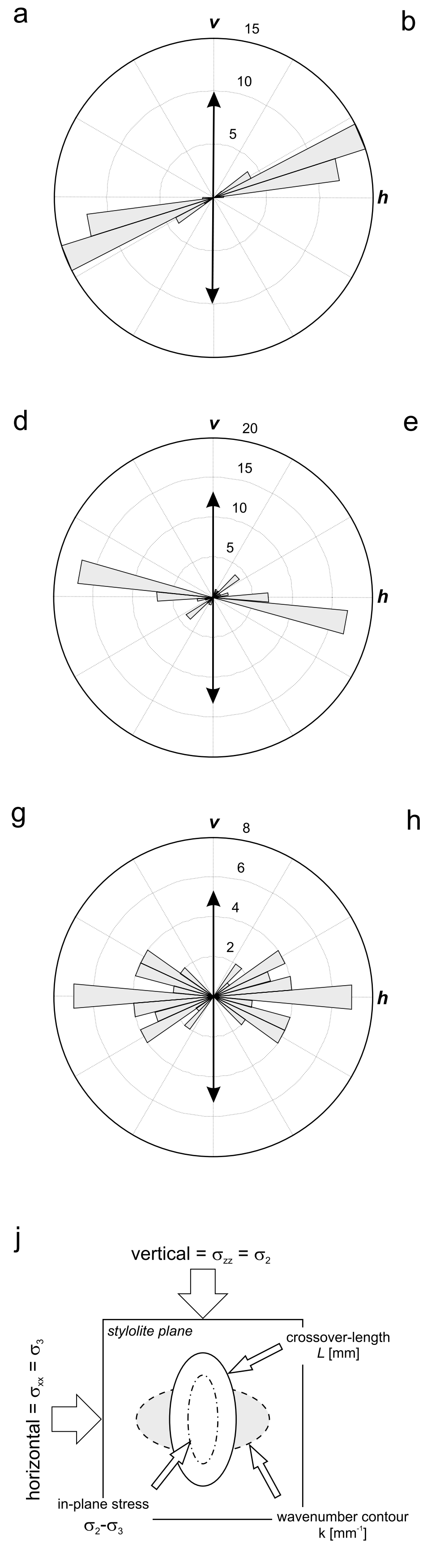
a
b
c
d
e
f
g
h
i
j
v
h
vertical = σ_{zz} = σ_2
horizontal = σ_{xx} = σ_3
stylolite plane
crossover-length
L [mm]
in-plane stress
σ_2-σ_3
wavenumber contour
k [mm^{-1}]

Figure 9

one, is very consistent with the result of the 1-D data analysis (see previous section). This observation is also in agreement with the physical interpretation of the mechanism of stylolite formation and morphogenesis [*Ebner et al.*, 2009b; *Koehn et al.*, 2007; *Renard et al.*, 2004; *Schmittbuhl et al.*, 2004]: At small scales (large wave numbers), the balance between surface tension and disorder controls the shape of stylolites. Both are a priori isotropic along the stylolite. In contrast, the large-scale morphologies (small wave numbers) are normally physically interpreted as resulting from a balance between the elastic field and the material disorder that controls the shape of the stylolites. The fact that an anisotropy is observed at large scales is thus the signature of an in-plane anisotropy of the stress. Since stylolite teeth are normally parallel to the largest stress direction associated with $\sigma 1$, this large-scale anisotropy should be associated with a difference between the two principal values of the in-plane stress components, σ_2 and σ_3.

[21] The orientation of the long axis of the fitted ellipse relative to the vertical orientation of the sample is shown in rose diagrams (Figure 9) for all samples. The long axes of the contours of the power spectrum are associated with a shorter crossover length L (i.e., reciprocal of the wave number) between the large-k isotropic scaling and the small-k anisotropic one (Figure 9j). We see in the next sections that this can be interpreted as a variation of the difference between the largest principal stress (normal to the stylolite plane) and the two in-plane stress components. The principal stress associated with the direction of the long axis should thus be the smallest one, that is, σ_3. Arrows show the orientation of a vertical line projected onto the stylolite plane in its original outcrop orientation. From this representation (Figure 9) it is evident that the vertical direction is roughly normal to the long axis of the anisotropy for all samples except M4c/1 and M4c/3, which formed vertically (see section 2 for details) but were subsequently rotated into a shallow dipping (nonvertical) orientation plane due to folding (Figures 9h and 9i). They thus serve as a cross-check to our findings since the vertical direction in these samples does not coincide with the vertical direction during stylolite formation and the anisotropy is therefore not normal to the present vertical direction in these samples as for samples of the upright limb.

[22] To estimate the crossover length (L) and thus get quantitative information on the stresses during stylolite formation, we again use the elliptical fit as a simplified representation of the 2-D Fourier transform of our data. We assume that the crossover is located at the position of the biggest change in the local slope of the 2-D Fourier transform (compare Figure 7b). We calculate the local slope s as the difference between the long and the short axis (a,b) of the best-fit ellipse for succeeding $\log[P(k_x,k_y)]$ contours $s = (\Delta a + \Delta b)/2$. A plot of the $\log[P(k_x,k_y)]$ contours as a function of the local slope s is shown in Figure 10a. The crossover is defined to lie at the minimum local slope in this representation and the crossover is calculated from the principal axis of the best- fit ellipse at this minimum (Figure 10b). It can be noted that the maximum crossover length coincides quite well with the vertical direction (indicated by the arrow in Figure 10b); this is in agreement with our previous observations that the anisotropy of the power spectra is also oriented (normal) with respect to the sample vertical orientation (compare Figure 9).

[23] Before we discuss the orientation of the anisotropy and the determined crossover length scales in relation to the stress tensor that was present during stylolite growth, we investigate the influence of tilted teeth on the scaling results.

4.3. Synthetic Data Analysis

[24] It is important to prove that the large-scale anisotropy we found in the investigated samples is really related to the stress field during formation and thus exclude the influence of other factors that might also cause a scaling anisotropy. The second important characteristic of tectonic stylolites, as stated in the Introduction, is the occurrence of inclined teeth, that is, slickolites. It is easy to imagine that the ridge and groove morphology of slickolites with highly inclined teeth can causes a difference in the scaling parallel or transverse to these elongated morphological features and, thus, an anisotropy. To systematically investigate the influence of a tilt of the asperities or teeth, we construct synthetic isotropic self-affine surfaces and tilt the teeth around one arbitrary axis. Tilted or inclined asperities are a common feature of slickolites [*Simon*, 2007] and it is commonly assumed that these structures formed when a stylolite overprinted a pre-existing plane of anisotropy in the host rock. In this case the principal stresses are oriented oblique to the pressure solution surface, which was recently proven numerically by *Koehn et al.* [2007]. Synthetic self-affine surfaces can be created following the approaches found in the literature [*Meheust and Schmittbuhl*, 2001; *Turcotte*, 1997]. We follow the method described by *Meheust and Schmittbuhl* [2001], who construct square white-noise maps of size $n = 512$. The self-affine correlation is then introduced by multiplying the modulus of the 2-D Fourier transform of the white noise by the modulus of the wave number raised to the power of $-1 - H$, where H is the roughness exponent.

Figure 9. Rose diagrams of all samples, i.e., a histogram with a constant bin size of 10° plotting the relative orientation of the long axis of the fitted ellipse to the vertical direction of each sample. The arrow in each diagram shows the intersection of the vertical direction of the oriented sample with the mean stylolite plane. (a) Sample Sa6/1a; (b) sample Sa6/1b; (c) sample Sa9/2; (d) sample M4/1; (e) sample M4/2; (f) sample M4/3; (g) sample M4/4; (h) sample M4c/1; (i) sample M4c/3. Note that for all samples the long axis and thus the direction with the smallest crossover length is roughly normal to the vertical direction (except for Figures 8h and 8i; for explanation see text). This direction corresponds typically to the largest differential stress, which is also the smallest in-plane stress. v and h correspond to the vertical and horizontal directions, respectively. (j) Schematic drawing of the relationship among the wave number contour (mm^{-1}) (compare Figure 8), the crossover length L (mm), the principal in-plane stresses, and the sample orientation i.e., horizontal and vertical direction. Refer to text for detailed explanation.

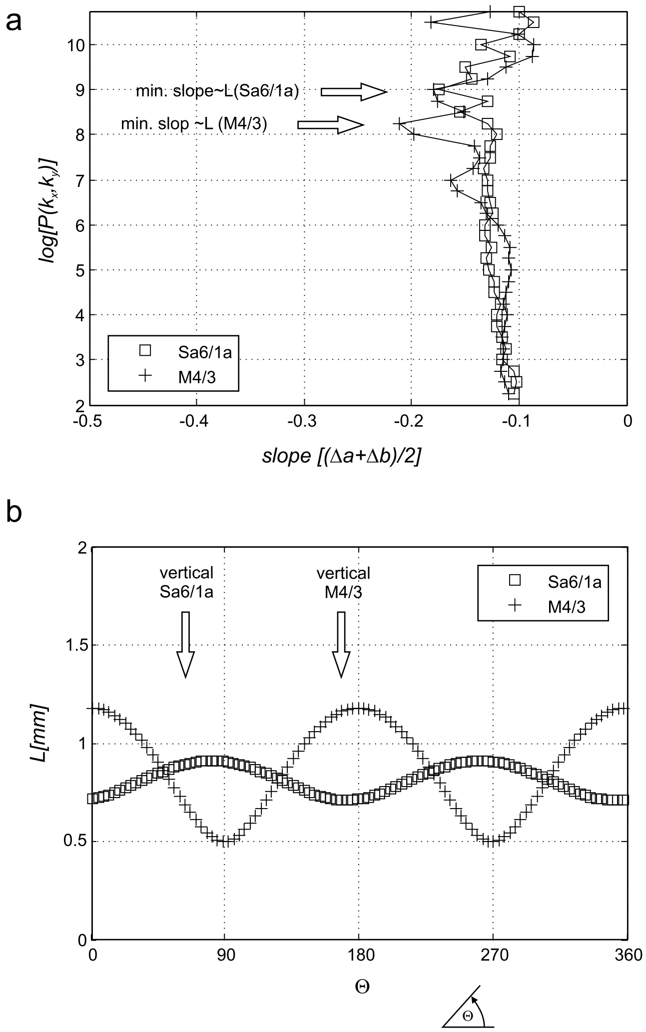

Figure 10. Crossover length from the contour data of the maps for sample M4/3 and Sa6/1a. (a) Slope of the 2-D power spectra calculated as the mean difference between the principal axis of the fitted ellipse (a, b). The biggest change in slope (arrow) is assumed to be the contour at which the crossover is located. (b) The crossover length plotted as a function of the counterclockwise angle from the x direction of the measured map. The vertical direction in the stylolite plane is indicated for both samples and roughly corresponds to the largest crossover length, i.e., the smallest differential stress as shown in Figure 1.

The self-affine surface is obtained from the inverse Fourier transform. The synthetic surface shown in Figure 11a is constructed with a Hurst exponent of $H = 0.5$ and its 2-D Fourier transform has a true isotropic self-affine behavior (compare inset in Figure 11a). A predefined tilt of the roughness is then attained from adding a linear trend along the x axis of the map, which corresponds to a tilt angle α and a subsequent back-rotation around α, that is, multiplying the data with a 3-D rotation matrix of $-\alpha$. Various tilt angles ranging from 1° to 50° were realized from the map shown in Figure 11a. To analyze single-valued functions (with no overhangs), the tilted surfaces are projected on a plane defined by the mean surface. The data were then analyzed as described in section 4.2. The degree (aspect ratio) and orientation (slope) of the anisotropy are displayed in Figures 11b and 11c. It is evident that the original data set is isotropic, with aspect ratios for $\log[P(k_x,k_y)]$ contours close to 1. With small tilt angles, $\alpha < 10°$, an anisotropy for the low $\log[P(k_x,k_y)]$ contours, and thus large wave numbers and small scales exists, which decreases with increasing α. In addition, there is a general increase in the anisotropy in all scales with tilt angles of $\alpha \geq 20°$ (Figure 11b), whereas the orientation is more and more aligned with the rotation/tilt axis (Figure 11c) with increasing tilt angle. The topothesy of the synthetic surfaces does not exhibit a directional anisotropy but reveals a general decrease in the average topothesy with increasing tilt angle, from $t \sim 0.22$ for the original data down to $t \sim 0.09$ for a tilt angle of 50°.

5. Discussion

[25] We have shown that the tectonic stylolites investigated in this study, that is, stylolites that form when the principal compressive stress direction is horizontal, differ fundamentally from bedding parallel stylolites, as they show anisotropic scaling relations. Two self-affine scaling regimes (with Hurst exponents of ~0.5 and ~1.1 for the small and large scales, respectively), which are separated by a crossover length at the millimeter scale, can be found in bedding parallel and tectonic stylolites. The crossover length L scales inversely with the formation stress $L \sim \sigma^{-2}$ for bedding parallel stylolites [*Ebner et al.*, 2009b]. The analytical solution of *Schmittbuhl et al.* [2004] relates the crossover length (L) to the stress field during stylolite formation. Their stress term is a product of mean and differential stress and can be used to calculate the stress magnitudes in addition to determining the principal stress directions. The analytical solution shows that

$$L = \frac{\gamma E}{\beta \, \sigma_m \, \sigma_d}, \tag{3}$$

where E is the Young's modulus, γ is the solid-fluid interfacial energy, $\beta = \nu(1 - 2\nu)/\pi$ is a dimensionless constant with ν the Poisson's ratio, and σ_m and σ_d are the mean and differential stresses, respectively. Since perfect confinement can be assumed (that is, uniaxial strain or zero horizontal displacement) for bedding parallel stylolites, the stresses and thus the crossover length L are independent of the orientation within the stylolite surface (Figure 1a). For a tectonic stylolite with a vertical stylolite plane, the scenario is different (Figure 1b) and it can be assumed that the in-plane stresses are dissimilar. One in-plane principal stress component should be dependent on the amount of overburden and should be oriented vertically, whereas the second stress component should have a horizontal orientation. Since the crossover length L scales inversely with the product of mean and differential stress and the mean stress should be constant, variations of the crossover should reflect variations of the differential stress $|\sigma_1 - \sigma_{\text{in-plane}}|$ [compare to *Schmittbuhl et al.*, 2004]. Therefore the crossover length has to increase from a minimum in the direction of the least principal stress σ_3 (x axis in Figure 1b), and thus the direction of the largest differential stress $|\sigma_1 - \sigma_3|$ to a maximum in an in-plane orientation normal to this direction, which corresponds to the direction of the largest in-plane stress σ_2 (the vertical direction in Figure 1b) and the smallest differential stress $|\sigma_1 - \sigma_2|$. In conclusion, it can be assumed that the orientations of the largest and smallest crossover lengths coincide with the vertical and horizontal direction (i.e., $\sigma_{xx} < \sigma_{zz}$), respectively.

[26] Indeed we found a scaling anisotropy in our data, which shifts the crossover length accordingly (Figure 9). The 1-D analysis (Figure 5) and the 2-D data analysis (Figures 9 and 10) reveal that the long axis of the detected anisotropy is normal to the vertical direction with a crossover length maximum in this direction, implying that σ_2 has a vertical orientation. This observation holds for both investigated areas, although there is a slight deviation of up to ±10° for some samples. Only the samples (M4c/1 and M4c/3 from the overturned fold limb) that formed vertically but experienced a passive rotation subsequently to stylolite formation due to folding (compare Figures 2B, 9H, and 9I) differ significantly. This can be explained by the fact that the stylolite formation occurred prior to folding, as can be concluded from the structural relationships in the field data (Figure 2). Thus the present orientation of the samples in the overturned fold limb does not coincide with the orientation during formation of the stylolites.

[27] We noticed a small difference (<10°) between the orientation of the stylolite teeth and the pole of the mean stylolite plane for the samples from northeastern Spain. This is because the stylolites overprint a pre-existing joint set that is subnormal to the principal shortening direction, which influenced stylolite formation as stated previously. To investigate the effect of the tilt of the stylolite teeth and its contribution to the observed scaling anisotropy, we used synthetic self-affine surfaces that were systematically tilted to get slickolite similar structures as explained previously (Figure 11). The effect of the tilt of the teeth with respect to the mean plane of the stylolite can be characterized by (i) an anisotropy for the large wave numbers, that is, on the scale of individual teeth or asperities for small tilt angles (<10°), and (ii) a general homogeneous increase in the anisotropy for all scales with an increase in the tilt angle for angles >10°. This anisotropy caused by the imposed tilt of the asperities differs significantly from the anisotropy of real stylolites. Therefore we conclude that the 3-D formation stress is the dominant force that influences the scaling anisotropy of the investigated samples. However, one has to

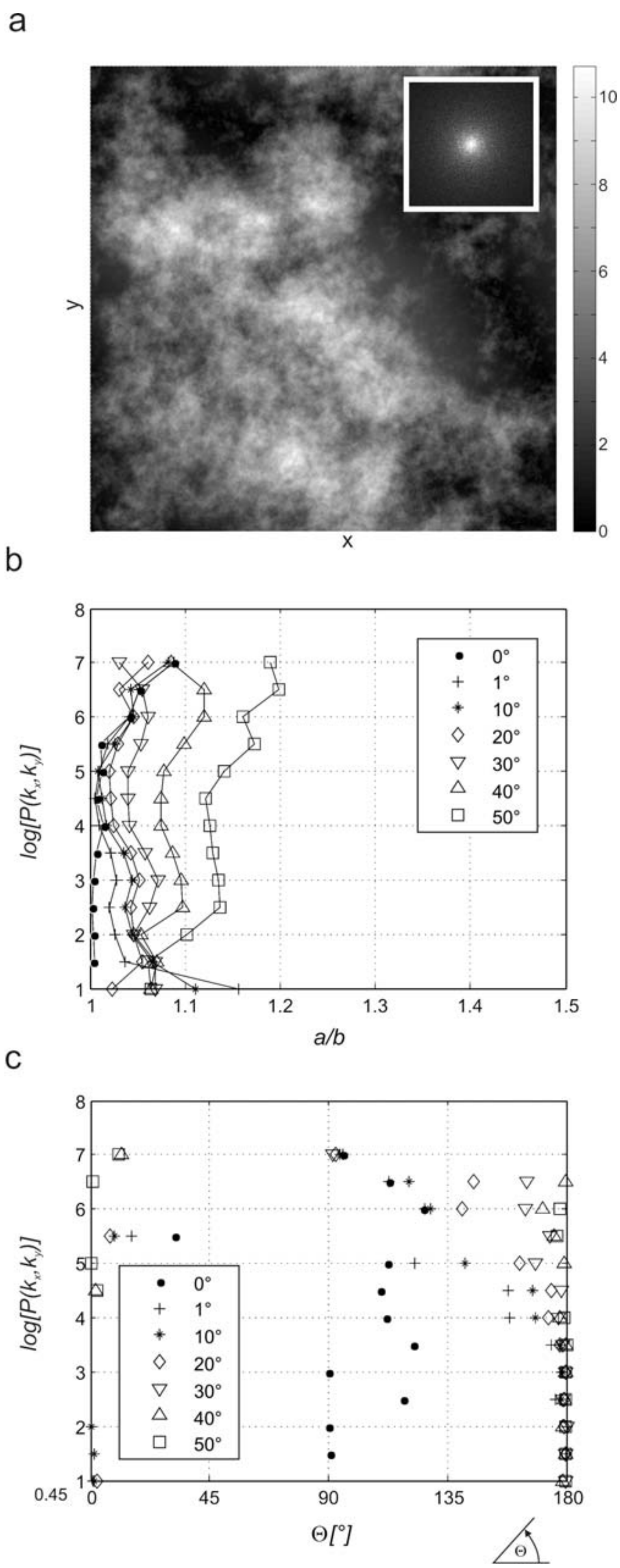

Figure 11. Grayscale map (a) of a synthetic self-affine square surface with a side length of 512 and a Hurst exponent of 0.5. Inset displays a 2-D Fourier transform of that map, which clearly exhibits isotropy with respect to its center, similar to bedding parallel stylolites. This data set is then utilized to construct slickolites, i.e., stylolites with oblique teeth and asperities (see text), with various tilt angles (e.g., 10° corresponds to oblique asperities that are rotated 10° counterclockwise around the x direction with respect to the mean plane of the synthetic surface). (b) Aspect ratio of elliptical fit of synthetic data set. For small tilt angles an anisotropy on small scales (i.e., large wave numbers and low $\log[P(k_x,k_y)]$ contours) can be observed. For large tilt angles a general increase in the aspect ratio over all scales is apparent. (c) Orientation of the long axis of the fitted ellipse (compare Figure 8d). Note the increasing alignment of the long axis of the fitted ellipse toward higher $\log[P(k_x,k_y)]$ contours with increasing tilt angles.

note that tilted teeth imply that the principal stress components are not necessarily oriented within the stylolite plane. Therefore only tectonic stylolites with plane-perpendicular teeth should be used to recalculate principal stress orientations and magnitudes.

[28] The analytical solution [*Schmittbuhl et al.*, 2004] is strictly valid only for 2-D stress cases where the principal stresses parallel to the stylolite plane are invariant along the third direction, which is truly the case for bedding parallel stylolites as discussed by *Ebner et al.* [2009b]. But since a solution for the 3-D case is not available, we argue that equation (3) could serve as an ersatz of a first approximation to calculate the order of magnitude and the difference between the principal stresses for such tectonic stresses. We assume that the crossover length in a specific direction is mainly a function of the stresses in the plane normal to the stylolite surface along the direction of investigation and that the out-of-plane stresses are invariant. This would imply that the differential stresses for the vertical and horizontal directions could be defined as $\sigma_{dv} = \sigma_{yy} - \sigma_{zz}$ and $\sigma_{dh} = \sigma_{yy} - \sigma_{xx}$, and equation (3) can be solved if the depth of stylolite formation and the material properties during stylolite formation are known. For the stylolites from the Swabian Alb, with a vertical crossover of 0.95 mm and a horizontal crossover of 0.7 mm, assuming a Poisson's ratio of 0.25, a surface free energy of calcite of 0.27 J/m^2, a Young's modulus of 14 GPa [*Ebner et al.*, 2009b], and a vertical stress component (σ_2) of 6 MPa (assuming a vertical load of 220 m of sediments with a density of 2.7 g/cm^3, in agreement with sedimentological constraints), the tectonic stress component (σ_1) is about 17.7 MPa and the horizontal in-plane stress (σ_3) component is 1.8 MPa. See the Appendix for details of the calculation. The theoretical stresses of stylolite formation calculated here cannot serve as realistic values since we unjustifiably borrow from the analytical solution for the isotropic case but should give a first-order estimate under the limiting assumptions stated previously. Nevertheless, we would expect stresses during tectonic stylolite formation to be close to the compressive lithospheric strength, that is, $\sigma_1 - \sigma_3 \sim 14$ MPa [*Banda and Cloetingh*, 1992], but much smaller than the uniaxial compressive strength of laboratory measurements for limestones, which are in the range of ~50–200 MPa [*Pollard and Fletcher*, 2005]. Utilizing the solution given in the Appendix, the resulting stress magnitudes are surprisingly close to expected values.

[29] For our samples in Spain we do not calculate the stresses because the principal stresses are quite likely not aligned with the stylolite plane as discussed previously. We argue that even if it were possible to calculate the stresses for tectonic stylolites in a fold and thrust belt like in northeastern Spain, the stresses deduced from stylolites might be completely different form that of the folding event. The main reason is that stylolites probably form rather quickly, of the order of hundreds of years [*Schmittbuhl et al.*, 2004]. This would allow several generations of stylolites to form (revealing different finite orientations) during a single folding event; the analysis of a single set of stylolites would thus result in a snapshot from the geologic history not necessarily revealing the full picture. Even if the stylolites can be attributed to the same kinematic framework as the folding event, both most likely have a rather diverse history in terms of stress.

6. Conclusions

[30] Vertical tectonic stylolites investigated in this study show a 1-D scaling invariance that resembles those of bedding parallel stylolites investigated in previous studies [*Ebner et al.*, 2009b; *Renard et al.*, 2004; *Schmittbuhl et al.*, 2004]. They have a self-affine scaling invariance, which is characterized by a Hurst exponent of 1.1 for long and 0.5 for short scales and a distinct crossover length at the millimeter scale that separates these two scaling regimes.

[31] High-resolution laser profilometry of tectonic stylolites provides quantitative 3-D information on these pressure solution surfaces that enables a 2-D analysis of the surface morphology. We demonstrate that our samples of tectonic stylolites have an anisotropic scaling that is not independent of the orientation of the investigated section within the plane of the stylolite. This anisotropy's main characteristic is a systematic shift of the crossover length that separates the scaling regimes. The presented analysis also confirms that the anisotropy observed in our vertical samples is oriented with respect to the horizontal and vertical direction and thus coincides with the principal stress directions within the stylolite plane for vertical stylolites, for example, σ_2 and σ_3 as depicted in Figure 2B. The long axis of the anisotropy, and thus the smallest crossover length, consistently coincides with the horizontal direction in the stylolite plane, whereas the largest crossover length is found in a vertical section. This observation is consistent with the fact that the horizontal in-plane stress is generally smaller than the vertical in-plane stress, which should be the case for tectonic stylolites (Figure 1B). They are also both smaller than the normal stress oriented perpendicular to the stylolite plane, which should be oriented horizontally. Therefore the crossover length should be smaller in a horizontal section than in a vertical section (equation (3)) using analytical considerations [*Schmittbuhl et al.*, 2004].

[32] In addition, we studied the influence of inclined teeth and asperities on the scaling behavior of stylolites. Using synthetic "slickolites" with various tilt angles, we found that the evolving anisotropy is negligible and clearly different from the anisotropy we observed in the investigated samples. We thus conclude that the scaling anisotropy of the investigated vertical tectonic stylolites can be related to the 3-D formation stress.

Appendix: Stress Calculation

Part I

[33] In this Appendix we show how the tectonic stress (σ_1) and the smaller in-plane stress component (σ_3) can be calculated if the vertical stress component can be approximated using vertical loading conditions. According to equation (A1) the vertical and horizontal crossovers (L_v and L_h) can be calculated by [*Schmittbuhl et al.*, 2004]

$$L_v = \frac{\gamma E}{\beta}\frac{1}{\sigma_m \sigma_{dv}}, \qquad L_h = \frac{\gamma E}{\beta}\frac{1}{\sigma_m \sigma_{dh}}, \tag{A1}$$

Earth and Planetary Science Letters 337–338 (2012) 186–196

Contents lists available at SciVerse ScienceDirect

Earth and Planetary Science Letters

journal homepage: www.elsevier.com/locate/epsl

Upper bound on stylolite roughness as indicator for amount of dissolution

Leehee Laronne Ben-Itzhak [a,b,*], Einat Aharonov [b], Renaud Toussaint [c,d], Amir Sagy [e]

[a] Weizmann Institute of Science, P.O. Box 26, Rehovot 76100, Israel
[b] The Hebrew University of Jerusalem, The Institute of Earth Sciences, Givat Ram, Jerusalem 91904, Israel
[c] Institut de Physique du Globe de Strasbourg, CNRS, University of Strasbourg, 5 rue Descartes, F-67084 Strasbourg Cedex, France
[d] Centre for Advanced Study at the Norwegian Academy of Science and Letters, Drammensveien 78, 0271N-Oslo, Norway
[e] Geological Survey of Israel, 30 Malkhe Israel St., Jerusalem 95501, Israel

A R T I C L E I N F O

Article history:
Received 5 November 2011
Received in revised form
23 April 2012
Accepted 21 May 2012
Communicated by: L. Stixrude
Available online 23 June 2012

Keywords:
stylolites
surface roughening
pressure solution
porosity
LIDAR
Family–Vicsek scaling
surface growth

A B S T R A C T

Stylolites are rough surfaces that form by localized dissolution. Despite their abundance in carbonates and sandstones, and their importance for fluid flow and rock deformation, many fundamental issues concerning their structure and evolution are still unresolved. This manuscript studies the roughening of long parallel stylolites. Here we report measurements of stylolite surface roughness at a scale larger than ever measured before (10^{-2}–10^{1} m). Measurements were performed using ground-based-LIDAR on 6 naturally exposed surfaces of $>$ km long stylolites in Northern Israel, producing a topographic map of the surfaces, from which roughness characteristics were derived. Our results show that for length scales below $\sim$50 cm, the stylolite morphology exhibits self-affine behavior, with a Hurst exponent $H\sim0.65$, consistent with previous studies made on smaller samples. The self-affine behavior changes for measurements made on scales above 50 cm, with H decreasing almost to zero on long length scales. This observed upper-bound of self-affine roughness is measured here for the first time, but has been previously predicted by theory (Ebner et al., 2009b; Koehn et al., 2007). Our measurements support these theoretical models and together with them present a scenario in which the investigated stylolites evolve from preferential dissolution along an existing surface that was initially smooth and progressively roughened with time. Such a mechanism of stylolites growth is different from previously suggested mechanisms for other classes of stylolites, which might propagate sideways from an initial defect. Based on the theoretical roughening model that we adopted, the upper limit to fractality for this class of stylolites may be used as a measure of the amount of dissolution on stylolites. Indeed, the amount of dissolution on the stylolites in our field site, which we calculated from the upper limit to fractality, is comparable to (though slightly larger than) our estimates of dissolution from two additional independent techniques, reflecting compactive strain of $\sim$50%.

1. Introduction

Stylolites are rough dissolution surfaces abundantly found in carbonates and sandstones (Heald, 1955; Kaplan, 1976; Park and Schot, 1968; Stockdale, 1922; Tada and Siever, 1989). They are lined by insoluble material (mainly clay minerals, oxides, and organic matter) which accumulates as the more soluble rock constituents dissolved (Kaplan, 1976; Stockdale, 1922). Stylolites and their surrounding regions are characterized by anomalous porosity and permeability with respect to the host rock, and thus are crucial in determining the deformation and permeability of rocks. In spite of their importance and decades of research, their formation is still not well understood. Specifically, the propagation and development of stylolites, as well as the controls on their lateral extent and teeth-amplitude, is of interest.

Sedimentary stylolites, like their structurally related solution and cleavage seams, are present in several morphological classes (Van der Pluijm and Marshak, 2004): An often-discussed class is isolated stylolites, with well-defined tips and a parabolic dissolution profile (Benedicto and Schultz, 2010; Fletcher and Pollard, 1981; Stockdale, 1922). Another commonly observed class is long, bedding-parallel stylolites, with no apparent tips (Laronne Ben-Itzhak, 2011; Safaricz, 2002; Safaricz and Davison, 2005). The present paper focuses on field measurements, characterization, and modeling of the formation and evolution of this class of long stylolites, with emphasis on multi-scale statistical properties of their teeth amplitude. Modeling together with observations, constrain the physics of evolution of these stylolites, and in this provide much-needed constraints to a scientific issue that lacks experimental measures (since stylolites were never formed in the lab on the large scale).

* Corresponding author at: The Hebrew University of Jerusalem, The Institute of Earth Sciences, Givat Ram, Jerusalem 91904, Israel.
E-mail address: llaronne@gmail.com (L. Laronne Ben-Itzhak).

0012-821X/$ - see front matter © 2012 Elsevier B.V. All rights reserved.
http://dx.doi.org/10.1016/j.epsl.2012.05.026

Since both observations and modeling focus on stylolitic roughness, we review the topic briefly here and in greater detail in Section 2.1: In many field sites, stylolite teeth amplitude displays multiscale roughness characteristics that can be evaluated as statistically self-affine (Ebner et al., 2009b; Karcz and Scholz, 2003; Renard et al., 2004; Schmittbuhl et al., 2004). The statistical properties of a self-affine 1-D profile remain unchanged under a particular scaling transformation (Mandelbrot, 1986). The roughness characteristics of a surface, such as whether it is self-affine or not, or the value of its Hurst exponent, H, which characterizes its self-affinity, or the variation of H with scale, may be used to constrain physical formation mechanisms, by comparing with theory. This has been claimed with regard to stylolites by Ebner et al. (2009a), Renard et al. (2004) and Schmittbuhl et al. (2004). They found two different self-affine regimes, characterized by two different H values, with a crossover between them at the millimeter scale. The two regimes emerge from two mechanisms controlling dissolution: surface energy dominates at smaller scales while elastic strain energy dominates behavior at the larger scales. These two mechanisms tend to smooth the surface while pinned heterogeneities (noise) in the rock are the source for the continued roughening during dissolution. The largest surfaces analyzed in these references were ~10 cm long. Since stylolites are often longer than 10 cm (e.g. Safaricz (2002) and Safaricz and Davison (2005) reported 8.5-m-long stylolites in chalk, Park and Schot (1968) traced stylolites in limestone for over 50 m and in Laronne Ben-Itzhak (2011) the >1 km-long stylolites investigated in this paper are described), studying roughness of stylolites on larger scales may provide additional insights regarding their formation process.

Roughness measurements were performed in this study on surfaces of long stylolites in the "Blanche cliff", Northern Israel. Section 2 of this manuscript presents uniquely long scale measurements (10^{-2}–10^{1} m) that show that stylolite roughness is self-affine up to ~50 cm, where a clear newly recognized crossover to a different behavior appears. In Section 3 we model and explain these observations by using published growth models of stylolites roughening from an initial flat surface (Ebner et al., 2009a; Ebner et al., 2009b; Koehn et al., 2007; Renard et al., 2004; Schmittbuhl et al., 2004). The agreement between the models and the field measurements suggest that long parallel stylolites form on existing, very long (practically infinite) bedding-parallel surfaces undergoing preferential dissolution (e.g., catalyzation of pressure solution on surfaces of higher clay content). This is in contrast to isolated, single stylolites which have been suggested to propagate sideways from an initial defect (e.g., Fletcher and Pollard, 1981; Aharonov and Katsman, 2009). Section 4 explains how these models can be used to calculate the amount of dissolution, A, on stylolites. A is calculated for stylolites in the Blanche site, and is compared to values obtained by two other methods. We end this manuscript by discussing the limitations of our calculations and assumptions, and addressing the question of when roughness measurements can be used as a method for estimation of A on stylolites.

2. Field observations: large scale roughness measurements of stylolites

We focus here on the "Blanche" cliff of the Ein El-Assad Formation (Albian) exposed in Northern Israel (Figs. 1 and 2), due to its unique exposure length (>1 km), and its well developed stylolites (cm-scale teeth amplitude). It is a roughly 50 m thick shallow inner-platform biomicritic limestone formation, with very low porosity (as will be discussed below), that dips gently to the west (Sneh and Weinberger, 2003). This formation

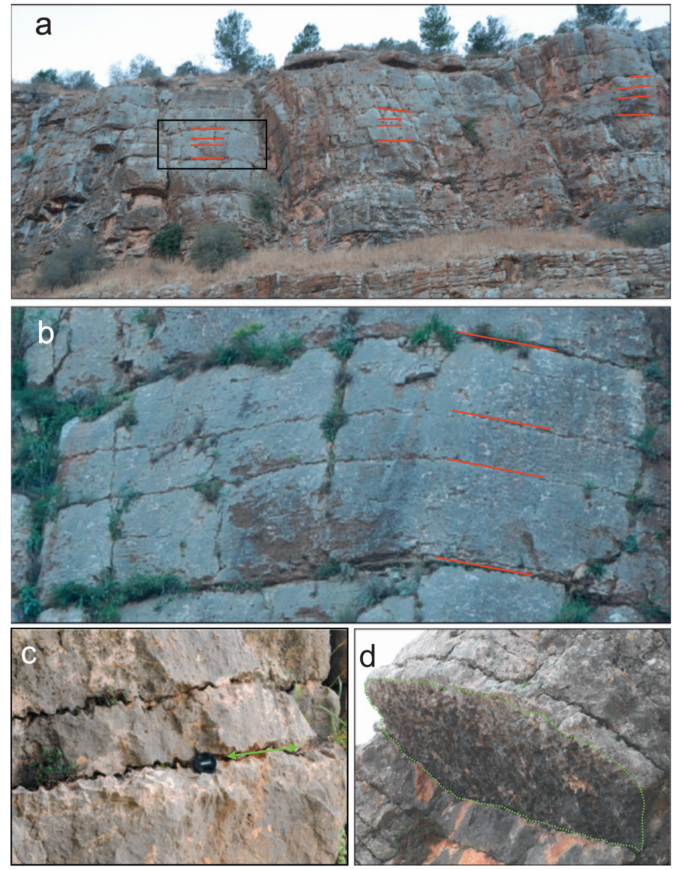

Fig. 1. Photos of the study area: the Blanche cliff, Northern Israel. (a) General view of the cliff with four stylolites (arbitrarily chosen, marked in red) showing they can be traced for a large distance (height of cliff is ~50 m). (b) Zoom on rectangle marked in (a). (c) Zoom-in on two other stylolites, where stylolite cm-scale roughness is evident. (d) An exposed rough surface (of "*in situ* 1", Table 1). (For interpretation of the references to color in this figure legend, the reader is referred to the web version of this article.)

has been covered by ~1000 m of carbonate rocks until middle Eocene (Sneh and Weinberger, 2003), when uplift in the region started. Stylolites probably formed during part or all of this burial period. The cliff is characterized by well developed, very long, bedding parallel stylolites (Fig. 1). The stylolites can be traced through the entire outcrop (>1 km), and most likely continue beyond the exposure. Such remarkable stylolite continuity is observed for the first time and has implications for understanding scales of permeability units and their structural continuity. Several large oil-reservoirs of the same geological age also contain stylolites which are claimed to highly affect porosity (Oswald et al., 1995). At the northern end of the exposure the maximum amplitude and spacing of all observable stylolites (a total of 65) were measured and showed average spacing, $\overline{d}$, of 30 cm (with a standard deviation of 20 cm) (Laronne Ben-Itzhak, 2011). Maximum amplitude and spacing measurements conducted along strike of this outcrop (Fig. 2.7 in Laronne Ben-Itzhak (2011)) showed that the stylolites are similarly developed along their whole length and also maintain constant spacing. These measurements are described in detail in Laronne Ben-Itzhak (2011) as well as in a manuscript in preparation. The observation of constant amplitude suggests that the stylolites were formed on pre-existing layers, with preferential dissolution possibly due to a chemical heterogeneity, such as higher clay content compared to the surrounding rock (Aharonov and Katsman, 2009; Engelder and Marshak, 1985; Fueten et al., 2002; Heald, 1955;

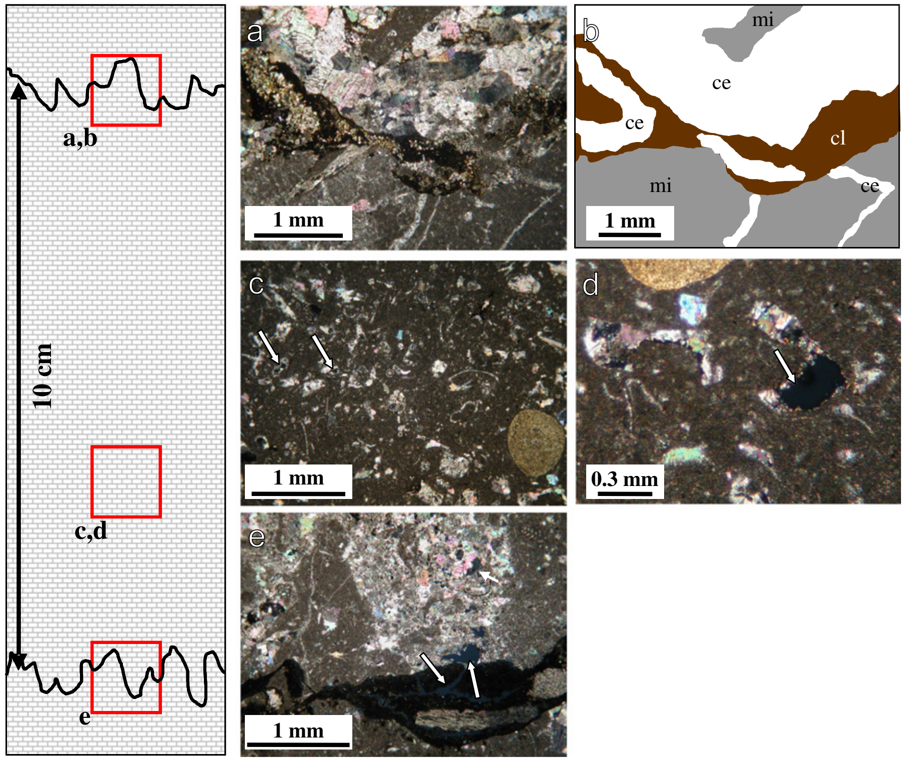

Fig. 2. Thin-section images (CPL, see scale bar on each) of two stylolites (a and e) and the bulk rock in between them (c and d). (b) shows a generalized cartoon, based on (a), with the different regions in the thin-section: mi = micrite; cl = clay; ce = calcite cement. A schematic section showing distances between the samples is plotted on the left. The stylolites in a and e are composed of clay with some calcite cement within the clay areas. Cementation near these stylolites is pervasive and non-selective and could also appear in some veins. In the bulk rock (c, d) calcite cement is selective to the bio-clasts and very few isolated pores are observed (white arrows). Near the stylolite in (e) some porosity is seen within the cemented regions as well as inside the stylolite (white arrows). However, this may be due to unloading, weathering or sample preparation. (For interpretation of the references to color in this figure legend, the reader is referred to the web version of this article.)

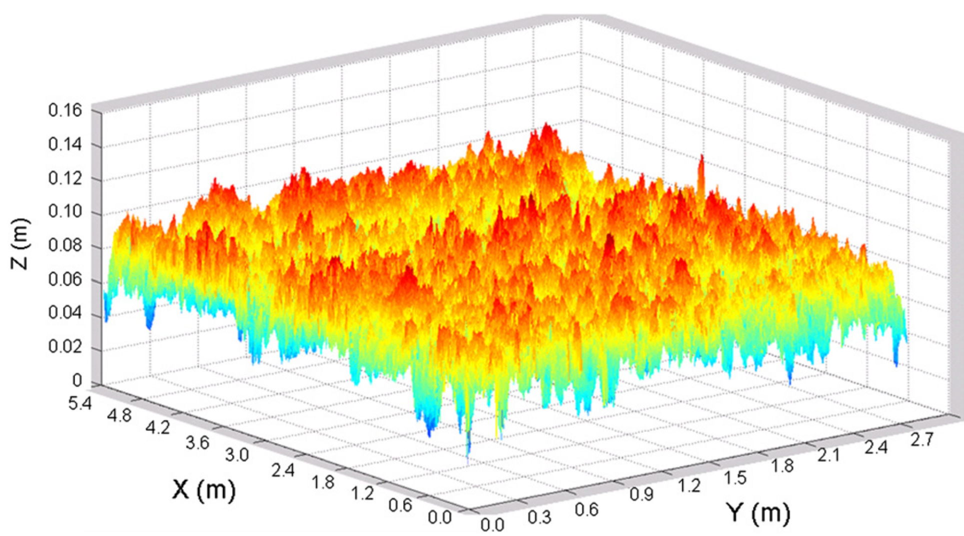

Fig. 3. Topography $h(x,y)-\overline{h}$ ($\overline{h}$ is the average surface height) of one of the scanned surfaces ("rockfall 1", in Table 1) after data interpolation to an *xy* grid.

Laronne Ben-Itzhak, 2011; Thomson, 1959; Van der Pluijm and Marshak, 2004).

On the small scale, Fig. 2 shows thin sections of two stylolites in the Blanche (2a and 2e) and of the bulk rock in between them (2c and 2d). The stylolites are regions composed of clay and calcite cement within them. Near the stylolites pervasive spar-cementation appears and is often asymmetric across the two sides of the stylolite. Cementation away from the stylolites is selective within the bio-clasts with few isolated pores in these clasts. Porosity measurement on thin section images (analysis conducted using ImageJ software) shows it is 1–2% in the bulk rock. Some porosity is seen within the cemented regions near the stylolites as well as inside the stylolite in 2e but is probably an artifact of sample preparation. Presence of calcite cement within the stylolites may indicate that they served as flow paths at some stage (during or after stylolitization).

This paper studies stylolitic roughness as a recorder of stylolitic development. Thus roughness of exposed stylolite surfaces in the Blanche (such as in Fig. 1d) was measured, using Ground-based LIDAR, the Leica HDS3000 Laser scanner. The relative resolution of the scanner was tested using targets with known topography. When a target is scanned from a distance of 20–30 m the scanner provides resolution of $\sim$3 mm in all directions. A single scan provides a cloud with millions of points that are interpolated to generate a topographic map or hundreds of 1D profiles (Fig. 3), allowing a statistical approach when calculating roughness (Sagy and Brodsky, 2009; Sagy et al., 2007). The scan data are rotated so that the mean surface is parallel to the x–y plane. The cloud of points is then interpolated to an x–y grid, in which the topography is represented by $h(x,y)$. Not many large (m-scale) stylolite surfaces are "open" and exposed for scanning, but we found four surfaces that were exposed by blocks falling from below the stylolite (as in Fig. 1b). These surfaces were scanned *in situ* and two other scans were performed on "rockfalls"-m-sized blocks that detached from the cliff. Surfaces with minimum erosion were picked for scanning and the few small eroded regions that remained were not included in the analyzed zones. The measured surfaces range in length from 2.1 to 9.3 m (see Table 1). The obtained measurements of stylolite surface roughness range in scale between 10^{-2} and 10^{1} m, larger than ever measured before. The surfaces have cm-scale teeth amplitude, are symmetric with respect to the surface average plane (in the z-direction) and demonstrate no anisotropy (similar roughness characteristics in the x and y directions), as was found by performing the analyses explained below on length-parallel and width-parallel profiles. Results are presented for length-parallel profiles (Fig. 4 and Table 1) so that larger scales can be studied.

2.1. Characterization of roughness

The surface topography, $h(x,y)$, of the six surfaces described above was analyzed. Characterization of rough surfaces depends on the scale of measurement. One common method is to measure the surface width (in the z-direction) as a function of the lengthscale at which the measurement is made (l). Maximum width ($w_\infty(l)$ according to Schmittbuhl et al. (1995b)) or average width $w(l)$ are commonly used, with the latter calculated by the standard deviation (STD) of height from the average surface height, $\bar{h}$. STD is defined by the root mean square (RMS) method (Barabasi and Stanley, 1995):

$$w(l) \equiv \sqrt{\frac{1}{l}\sum_{i=1}^{l}(h(i)-\bar{h})^2} \quad (1)$$

Here we study 1D profiles measured along the y (defined as the long) direction, so $h(i)$ is the interface height at point i along a profile. The horizontal scale of the measure, which is a moving window of size l, ranges from $2-3$ mm (the distance between two neighboring data points on the 1D profile), to the whole profile length. The average height is a function of this window of measure, defined by its starting position j and its length l: $\overline{h_{j,l}} \equiv \frac{1}{l}\sum_{i=j+1}^{j+l} h(i)$. The procedure is similar to that of Ebner et al. (2009a, 2010b): For each profile we calculate the RMS width, $w_{j,l}$ for any window of size l, starting at position j: $w_{j,l} = \sqrt{\frac{1}{l}\sum_{i=j+1}^{j+l}(h(i)-\overline{h_{j,l}})^2}$.

The RMS width $w(l)$ is then obtained by averaging $w_{j,l}$ over all the possible positions j for windows of size l, in each profile, and over all 1-D profiles on the surface.

When a surface is self-affine, w and l are related by a power law $w(l)\sim l^H$, with an exponent H, the Hurst exponent (Barabasi and Stanley, 1995). This exponent can also be derived using other common methods for surface characterization, such as power spectral density (PSD) as performed on stylolites (e.g. Renard et al., 2004) and on fault surfaces (e.g. Sagy and Brodsky, 2009). We average the 1-D spectra of hundreds of profiles in the x and in the y direction for each surface in order to arrive at a spectral estimate with minimal variance (the noise of our PSD analysis is in the order of 10^{-7}). The PSD, for self affine data, follows a law:

$$\|\tilde{h}_k\|^2 \propto k^{-1-2H} \quad (2)$$

Fig. 4a shows the average width of the measured surfaces, $w(l)$, as a function of l, calculated following Eq. (1). The surfaces' widths follow a self-affine scaling:

$$w(l) \sim l^H \quad (3)$$

with two scaling regimes above and below a crossover length, χ: for measurement windows l smaller than χ, the H has a value of 0.65 ± 0.1 (the error for H is the standard deviation for all data fitted linearly in bilogarithmic space, with logarithmic binning to treat evenly large and small scales, Ebner et al. 2009a). For larger measurement windows, i.e. for $l > \chi$, H decreases to almost zero, i.e. the surface width saturates and does not grow anymore with increasing window of measurement. The crossover length value, of $\chi = 50 \pm 20$ cm, was measured from the intersection between two asymptotes (as shown in the inset of Fig. 4a): a line with a slope $H=0$, that asymptotes the data for $l > \chi$, and a line with a slope $H\sim 0.65$, that fits the data at scales $l < \chi$ (see Table 1). Errors for χ emerge from the uncertainty of the position of the $H=0$ asymptote. The emergence of a clear upper cutoff to the self-affine behavior of

Table 1
Physical and statistical characteristics of six stylolite surfaces from the Blanche cliff, Northern Israel. Hurst exponents of the self-affine scales of each surface were calculated using three independent methods (values in boldface, RMS= root mean square; PSD=power spectral density).

#	Sample name	Dimensions (m)		H, $l<\chi$			χ (m)	$w(\chi)$ (m)	A (m)	
		Length	Width	RMS	PSD	Wavelet			z=0.81	z=1
1	*in situ* 1	2.14	0.20	**0.57**	**0.5**	**0.56**	*0.41* (*0.01*)	*0.013* (*0.001*)	0.33 (0.05)	1.28 (0.24)
2	*in situ* 2	9.32	0.30	**0.72**	**0.67**	–	*0.87* (*0.34*)	*0.022* (*0.007*)	0.17 (0.08)	0.58 (0.34)
3	*in situ* 3	4.80	0.12	**0.63**	**0.68**	–	*0.50* (*0.07*)	*0.013* (*0.002*)	0.19 (0.05)	0.65 (0.22)
4	*in situ* 4	3.30	0.23	**0.75**	**0.82**	**0.8**	*0.39* (*0.06*)	*0.013* (*0.001*)	0.08 (0.01)	0.23 (0.03)
5	rockfall 1	5.37	2.73	**0.64**	**0.67**	–	*0.42* (*0.03*)	*0.011* (*0.001*)	0.14 (0.02)	0.45 (0.09)
6	rockfall 2	2.50	2.14	**0.7**	**0.79**	**0.62**	*0.33* (*0.05*)	*0.012* (*0.001*)	0.10 (0.01)	0.30 (0.05)
	Average (std)			**0.65*** **(0.1)**	**0.7(0.1)**	**0.65 (0.1)**	*0.48** (*0.20*)	*0.014** (*0.004*)	0.15[a,b,] (0.07)	0.50[a] (0.30)

χ and $w(\chi)$ are in italics (see text for explanation on how they were derived, errors are in brackets); A (amount of dissolution) is calculated for two values of the dynamic exponent, z (using l^*=1 mm and α=0.22, see Appendix A) according to Eq. (11) (errors in brackets are due to errors in H, χ, and $w(\chi)$). The last row shows average values of each column and its standard deviation.

[a] These averages are calculated using the average values of H, χ, and $w(\chi)$ (marked by $*$) and are not the average of A calculated for each surface.
[b] This value is 0.13 for l^*=0.5 mm and α=0.28, and 0.18 for l^*=3 mm and α=0.16.

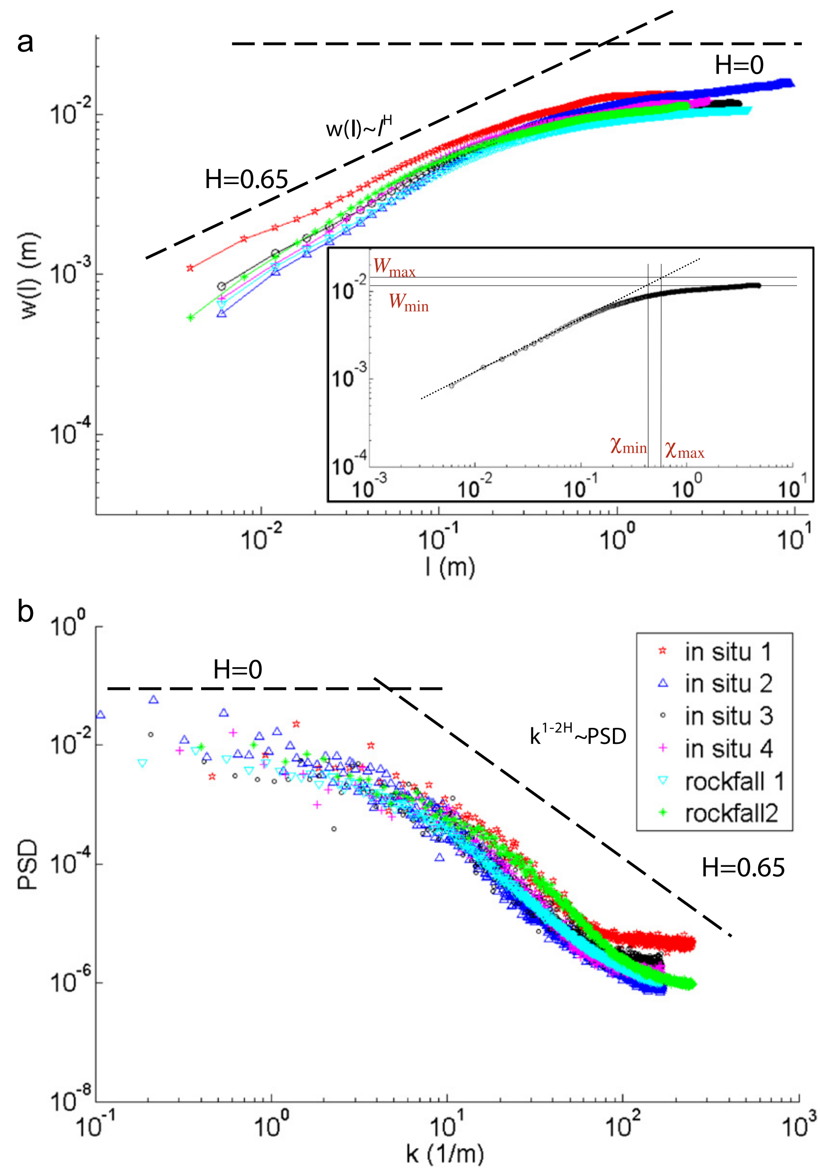

Fig. 4. (a) RMS and (b) PSD analysis of surface roughness of 6 stylolite surfaces in the Blanche cliff (see Table 1 for dimensions and detailed results for each surface; legend refers to both (a) and (b)). The x-axis of the PSD analysis is the wave-number, k (m^{-1}), and equals $(l)^{-1}$. Two scaling regimes are seen: (1) self-affine behavior with $H\sim0.65$ (average of the six surfaces) for scales up to $l\sim50$ cm; and (2) for $l>50$ cm, H decreases to ~0. The value of intersection of these two asymptotes is termed the correlation length, χ. In the inbox we show (an example on surface "*in situ* 3") how the correlation length, χ, is found. An upper and lower estimate of the asymptote for the large scales (where $H=0$) gives the error on χ.

these surfaces means that they appear rough on small scales, but at large enough scales, i.e. viewed from far enough away, where resolution is less than the saturation width (defined as $w(l\geq\chi)$, which is here a few cm) they are smooth. They are significantly smoother at this scale than would simply imply the decrease of the aspect ratio with size, as $w(l)/l\sim l^{H-1}$, if the self affine regime was prolongated (that would imply $w(l)\sim10$ m at $l=$km scale, which is not observed). The PSD analyses presented in Fig. 4b, as well as an additional analysis using the wavelet technique (Simonsen et al., 1998), both provided similar values of H and χ as those calculated by RMS (Table 1).

To avoid possible problems due to the finite size of the profiles before computing their PSD, two refinement methods have been applied: Over each analyzed window, the data was detrended from a linear trend, and the width of the detrended data was analyzed (both in real space to compute $w(l)$, and over each entire profile prior to evaluating its PSD). In addition, to avoid spectral leakage of artifacts due to the finite size limit of the data (and to the non-periodic character of these finite profiles), one can compute the product of the signal with a Hamming window prior to the PSD evaluation (as performed, e.g. by Ebner et al., 2010b). Both of these refinements did not affect significantly the behavior of $w(l)$ or the PSD: the determined small scale exponents were the same up to the error bar.

3. Existing models of stylolite roughening from an initially flat surface

Our roughness measurements can be compared to predictions offered by existing roughening models which assume an initially flat surface and predict how stylolite roughness will develop with time. Rolland et al. (2012) and Schmittbuhl et al. (2004) offer a continuum equation and its analytical solution to describe how stylolite surfaces roughen with time due to a competition

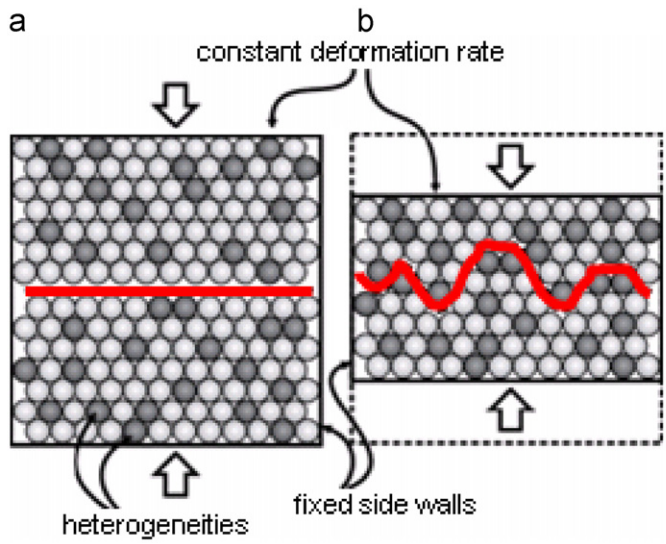

Fig. 5. Modified from Fig. 2 of Ebner et al. (2009a). Simplified sketch of the results from a numerical model that simulates stylolite roughening from an initial flat interface (marked by a red line). (a) Initial setup; and (b) configuration after a certain amount of dissolution and consequent compaction. The darker spheres are "pinning particles" which have a lower solubility. (For interpretation of the references to color in this figure legend, the reader is referred to the web version of this article.)

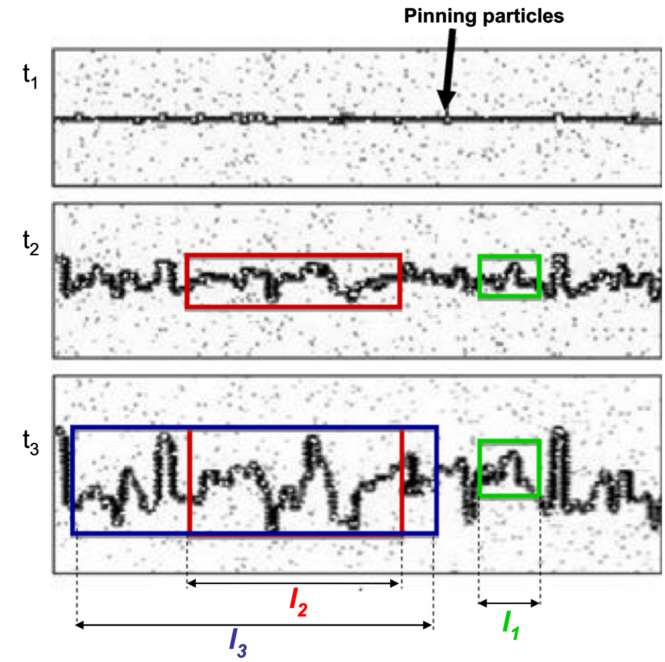

Fig. 6. Simulation results, from a similar model as Fig 5, from Fig. 4 of Koehn et al. (2007) on which we added a schematic illustration of how the maximum amplitude, A_{max} depends on time and on sampling size, l. For example, maximum teeth amplitude in a window size l_2 at t_2 is smaller than at t_3. At a given time A_{max} depends on l up to a critical size, after which it remains constant (e.g. at t_3, for $l>l_2$, A_{max}=const). This dependence on l is characteristic of self-affine surfaces.

between surface energy, elastic energy, and pinned heterogeneities. The evolution of stylolite roughness from an initial flat surface was also simulated by Ebner et al. (2009a, 2009b) and Koehn et al. (2007) using a discrete model. The discrete model presses two rock bodies, made of soluble grains, against each other, with dissolution occurring only on a predefined fluid-filled interface. dissolution is governed by a linear rate law (see Eq. (1) in Ebner et al., 2009a) which depends on the local elastic and surface energies and on the local deviation of normal stress from its average value on the surface. "Quenched noise" in solubility is introduced by assigning a lower dissolution rate constant to a certain fraction of the grains. This is seen in Fig. 5: darker, less soluble grains get pinned and stuck in the interface as dissolution evolves.

Both the analytical and numerical models described above assume *three controlling processes*: The first is that the system has quenched noise (heterogeneities present in the host rock), which causes heterogeneous solubility and is the main drive for roughening. The second is that the process has long-range interactions, provided by elastic surface forces. The third process is diffusion and smoothing of the interface, provided by surface energies. The models presented above quantify stylolite roughness evolution by evolving Fourier or wavelet transforms, or by the evolution of surface average width, w (Eq. (1)) as a function of time, t, and of the sampling size, l.

The evolution of w with t and l according to these models is illustrated schematically in Fig. 6 (where the maximum width, $w_{\infty}(t,l)$, is shown since w is harder to show visually; both quantities evolve in a similar manner (Schmittbuhl et al., 1995b): time in this figure correlates with average dissolution, and with increasing dissolution (from t_1 to t_3) the roughness and width of the surface grows. Yet roughness is also a function of l: at any given time there is a critical sampling size (which grows with time), above which w and w_{∞} are constant. For example, in Fig. 6 this critical size at time t_3 is l_2. This behavior of surface evolution belongs to a universality class of surface growth models of the *Family–Viscek type* (FV), i.e. where the surface dynamics shows a Family–Vicsek scaling (Family and Viscek, 1985, e.g.: Barabasi and Stanley, 1995). Other phenomena such as flame fronts, viscous fingering, sedimentation fronts in granular packings (Vinningland et al., accepted), fluctuations of dipolar chains (Toussaint et al., 2006, 2004), fracture growth, and electrochemical deposition of crystals obey FV scaling.

For many growth processes, the fluctuating quantity is, for a given time, correlated below, and decorrelated above, a certain length scale χ (termed the "correlation length"), so that $w(l)$ follows Eq. (3) for $l<\chi$ but is constant for $l>\chi$. A surface growth process obeys FV scaling if at any time the different laws described above can be collapsed to a single scaling law where $w(l,t)$ and l are solely a function of another power law of $l/\chi(t)$:

$$w(l,t)/l^{\varsigma} \sim f\left(\frac{l}{\chi}\right) \tag{4}$$

In this case, the fact that $w(l)$ is independent of χ for $l<\chi$ implies that $f(u)$ is constant for small u, and $w(l)\sim l^H$ (as in Eq. (3)) implies $\varsigma = H$. In contrast, the fact that the width is decorrelated above χ, i.e. that $w(l,t)$ is constant for $l>\chi$, implies that $f(u)\sim u^{-\zeta}$for $u>>1$.

The upper cutoff for self-affinity, χ, can be described physically as the maximum distance between two points on the surface to still be correlated: heights of points separated by distance $l<\chi$ are positively correlated, while heights of points separated at a distance $l>\chi$ are independent of each other. χ increases as a power-law with dissolution time (or surface evolution time) following:

$$\chi \sim t^{1/z} \tag{5}$$

χ grows according to (5) until it reaches the system size, at which point it saturates. The dynamic exponent, z, in Eq. (5) is related to H via β, another growth exponent (z=H/β) (Barabasi and Stanley, 1995). z and β are not the same for all processes that

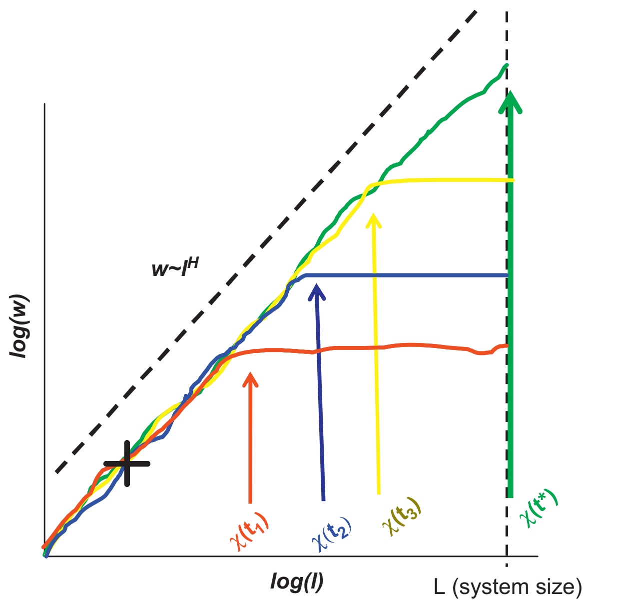

Fig. 7. Schematic log–log plot of $w(l)$ for several times according to roughening models of Ebner et al. (2009a) and Koehn et al. (2007). At any given time $w \sim l^H$ (dotted black line) up to $l=\chi$. At scales larger than χ, w saturates. χ increases with time until it reaches the system size, L (assuming the process has not stopped before). At $\chi=L$ ($t=t^*$) roughness stops evolving though dissolution may still continue.

follow a FV scaling: they depend on the physical and chemical processes (Family and Vicsek, 1985).

The conceptual evolution of Eqs. (3) and (4) is plotted in Fig. 7:

For measurement samples smaller than χ, the width, w, is a power-law of l only, and is *independent of time*, i.e.

$$w(l,t) \sim l^H \quad \text{for} \quad l \leq \chi \tag{6}$$

The width in these small windows will never grow anymore, even though the surface keeps on dissolving and dynamically evolving as a whole, since these small wavelengths have saturated. The black-cross data point in Fig. 7 remains stationary as time progresses, illustrating the above point.

In contrast, Eqs. (4) and (5) dictate that for measurement windows larger than χ:

$$w(l,t) = l^H \left(\frac{l}{\chi}\right)^{-H} \sim (\chi)^H \sim t^{H/Z} \rightarrow \text{for } l \geq \chi \tag{7}$$

The width, w, is *independent of l*. It is constant no matter how large the sampling window is and grows as a power-law of time. The exponent characterizing the early growth is defined as the growth exponent β, i.e. $w(l,t) \sim t^{\beta}$, which establishes the scaling law between β, z and H: $\beta = H/z$.

Eqs. (3) and (4) are scaling equations. In order to relate w concretely to other length scales, we normalize these equations by l^* – the smallest scale for which the self-affinity holds, as explained below.

3.1. Amount of dissolution

We next wish to infer the unknown amount of dissolution, A (in meters), that occurred on the stylolite, from the width measured in models or in the field. This may be done if we assume the dissolution rate (ν) was constant, so that $A=\nu t$, where t represents the time during which dissolution has been active. In order to obtain concrete values from the scaling, we rewrite Eqs. (3) and (4), using l^*, the smallest scale for self-affinity, a geometrical prefactor α, of order 1 (see Appendix A), and $t^* = l^*/\nu$ a time unit, defined by the fact that at time t^*, the correlation length was $\chi(t^*) = l^*$:

$$\frac{w(l)}{l^*} = \alpha\left(\frac{l}{l^*}\right)^H \mathit{for}\ l \leq \chi \tag{8}$$

$$\frac{\chi}{l^*} = \left(\frac{t}{t^*}\right)^{1/z} \tag{9}$$

plugging $t=A/\nu$, and $t^* = l^*/\nu$ into Eq. (9) one obtains a relationship between χ and A:

$$\chi = l^* \left(\frac{A}{l^*}\right)^{1/z} \tag{10}$$

using (10) for $l=\chi$ in (8), one obtains:

$$w(\chi) = \alpha l^* \left(\frac{\chi}{l^*}\right)^H = \alpha l^* \left(\frac{A}{l^*}\right)^{H/Z} \tag{11}$$

Thus in order to calculate A one should solve either Eq. (10) or (11). For this one needs roughness measurements on a scale larger than χ, so as to capture accurately χ or $w(\chi)$. In addition one must derive l^* and α and obtain z from growth models.

The scaling-factor l^* is considered the smallest scale for which the observed self-affinity regime holds. We suggest it reflects the observations that growth of self-affine stylolites follows two regimes: surface energy dominated at small scale (with $H \sim 1.1$), and a crossover at a length-scale $l^* \sim 0.5-3$ mm to an elastic energy dominated regime (with $H \sim 0.5$) (Ebner et al., 2009b; Koehn et al., 2007; Renard et al., 2004). Our measurements have a resolution limit of about 3 mm, thus missing the crossover scale l^*. Using $l^*=0.5$–3 mm in Eq. (8), and using values of w and l from our graphs, one calculates $\alpha=0.36$–0.17 (see Appendix A). Variations in l^* and α change the scaling and A by a relatively small amount (see footnote b to Table 1), and are less influential than changes in z.

The dynamic exponent, z, is predicted by discrete stylolite growth models to be different for the small scale surface energy dominated regime, and for the large scale elastic energy dominated regime (Ebner et al., 2009a; Koehn et al., 2007). In our current study we look at the elastic regime, for which Koehn et al. (2007) and Ebner et al. (2009a) find $H=0.5$, $\beta=0.8$, so that $z=H/\beta=0.625$. It is impossible for us to measure β from the field data, since we have only one snapshot in time, and β requires knowledge of temporal evolution. Thus we take their $\beta=0.8$ and the average value of $H=0.65$ from our measurements, to obtain $z=0.81$. Slightly larger values (between 1 and 2) are theoretically predicted for continuum growth equations of the same universality class (Schmittbuhl et al., 1995a; Tanguy et al., 1998). z is sensitive to the specific growth physics, and not only to the universality class. The value of $z \sim 0.8$ seems most plausible since it emerges from stylolite dynamics models.

4. Implementation of the roughening models to the Blanche stylolites

The measured roughness characteristics (Section 2) are similar to those of the models (Section 3) in that both demonstrate self-affine behavior, characterized by value of H ($H \sim 0.5$, and varies between 0.4 and 0.9 in models (Ebner et al., 2009a; Renard et al., 2004; Schmittbuhl et al., 2004) and $H \sim 0.65 \pm 0.1$ in our measurements), up to a crossover length, χ. For $l \gg \chi$, the theoretical model predicts that H equals zero. Our field measurements for $l \gg \chi$ indeed show a value that is close to zero, as expected for surfaces following a complete FV scaling (Section 5.1 discusses why H is slightly larger than 0 for some of the surfaces). We propose to use the value of χ (or its associated $w(\chi)$) measured on the Blanch stylolites to calculate the average amount of dissolution, A, on them, via the growth models explained above, using Eq. (10) or (11):

$$A = [\frac{w(\chi)}{\alpha l^*}]^{z/H} l^* = [\frac{\chi}{\alpha l^*}]^z l^* \tag{12}$$

Using average values (Table 1): $\chi = 0.48$ (± 0.20) m; $w(\chi) = 0.014$ (± 0.004) m and $H = 0.65$ (± 0.1), and l^* and α equal 1 mm and 0.22, respectively (see Appendix A), we find that for $z = 0.81$, the calculated dissolution is $A = 0.15$ (± 0.07) m. Using a slightly higher value of $z = 1.0$, $A = 0.50$ (± 0.30) m. Detailed results of these calculations (Table 1) demonstrate that the variability of A from one surface to another is much smaller than the sensitivity of A to the selected value of z. For example, for $z = 0.81$, A varies between 0.10 and 0.35 m, whereas A is $2-3$ times higher for $z = 1.0$ compared to $z = 0.81$ for a given surface. With an average spacing, $\overline{d}$, of ~ 30 cm between stylolites in the Blanche cliff (as stated in Section 2) these calculated values of A translate to between 15 cm/(15+30) cm = 33%, and 50 cm/(50+30) cm = 63% average strain (for z values of 0.81 and 1.0, respectively).

A *second* method to calculate A is by *a simplified mass-balance*. This calculation assumes that (1) stylolites are the only source of cement, and (2) the dissolution–precipitation system was closed on the scale of neighboring stylolites, so that all material dissolving on stylolites precipitates in the adjacent porosity. In the Blanche formation, the absence of significant fluid-pathways via fractures (as evident both at the outcrop-scale and in thin-sections, e.g., Fig. 2a, c where the few veins are very local and limited in extent) suggests that assumptions (1) and (2) are plausible. Additional evidence for the suggestion that the system is practically closed, comes from the finding that most calcite precipitation is in close proximity to stylolites, suggesting that the combined process of dissolution–diffusion–precipitation occurred over very short distances (as in Raynaud and Carrioschaffhauser, 1992). On the other hand, the occurrence of calcite cement within the stylolites could indicate that flow (and precipitation) did occur within stylolites at some stage during or after stylolitization.

A crucial variable needed to estimate A from mass balance is the change in porosity from the beginning until the end of the stylolitization period. Current porosity around the stylolites is measured to be close to zero (from thin sections such as Fig. 2). We estimate that the initial porosity, φ, ranged between 0.2 and 0.3. This estimate is based on general carbonate literature and is not possible to make from our thin sections. Assumptions (1) and (2) imply that once the initial porosity was completely shut by cement originating from dissolution on the stylolites, the stylolitization stopped.

The last variable required to calculate A is the distance between adjacent stylolites, d, which determines the size of the sink for cementation: The larger the d, the larger the mass dissolved before stylolitization stops. Using the measured average distance between stylolites from our field site, $\overline{d} = 30$ cm (± 20 cm) we estimate A:

$$A = \frac{\phi \overline{d}}{1-\phi} \approx \frac{0.2{*}30 \text{ cm}}{(1-0.2)} = 7.5 \text{ cm (or} \quad 12 \text{ cm} \quad \text{for} \quad \phi = 0.3)$$

Calculating strain as $A/\overline{d}$, translates to between 20% and 30% strain, and is comparable to our roughness-based estimates with the lower value of z, perhaps slightly underestimating them.

A *third* independent method that can be used to evaluate the amount of dissolution A is by *maximum amplitude of stylolites* (peak-to-peak) measured in 2D in the field, assuming it is a minimum estimate to the amount of dissolution. The maximum amplitude method is used routinely by oil companies to estimate dissolution. We define $A_{\max}(l)$ as the width of a window of length l, as demonstrated in Fig. 6. A similar definition regarding fracture roughness was used by Schmittbuhl et al. (1995b) who defined it as w_∞. $A_{\max}(l = 1$ m) of several selected stylolites in the Blanche cliff was measured in several locations along the exposure (Laronne Ben-Itzhak, 2011), where in each location $A_{\max}$ of 1-m-length sections was measured. For a given stylolite, $A_{\max}(l = 1$ m) was constant along the cliff and its value varied among the stylolites between 2 and 12 cm (Fig. 2.7 in Laronne Ben-Itzhak, 2011). These values are comparable to, or slightly underestimate, the dissolution calculated using $z = 0.81$. Note that $A_{\max}(l)$ is a roughness measure that is expected to depend on l as (Schmittbuhl, 1995b):

$$A_{\max}(l) = w_\infty(l) \sim l^H \tag{13}$$

Similar to w, the increase in $A_{\max}$ with l holds up to $l \sim \chi$, at which point $A_{\max}(l)$ will saturate to a constant value and correlate with the true amount of dissolution. The size of our measurement window ($l = 1$ m) for $A_{\max}$ was larger than our measured $\chi \sim 0.5$ m, and so our estimate obtained from maximum teeth amplitude is expected to reflect the true amount of dissolution.

All three independent methods give similar estimates of A, within an order of magnitude, which we interpret as a good sign of their validity. However it is important to note that both the new correlation-length roughness-based method presented here, and the traditional "maximum teeth amplitude" method, must be made for $l > \chi$, in order to provide a correct estimate! The maximum amplitude method is used routinely by oil companies to estimate dissolution, but they often use $l < \chi$ since cores from drillings are on the scale of centimeters. These are expected to underestimate dissolution, with the amount of underestimation dependent on the scale of the core.

5. Discussion

This paper uses models of stylolite roughening from an initial flat surface to explain measurements performed on long-parallel stylolites in the Blanche cliff, Northern Israel. Roughness analysis on several different stylolitic surfaces from this site showed self-affine stylolites, with $H \approx 0.65$, for length scales below ~ 50 cm. Above this length-scale, H approaches zero, with a robust upper cutoff to fractality termed the "correlation length", χ, that is also predicted by the roughening models.

5.1. The life and death of the Blanche stylolites

The conformity between the roughening models and our measurements agrees with a picture of dissolution occurring preferentially along a surface. This surface was initially smooth and roughened with time. Had stylolitization in the Blanche continued for a long enough time, a self-affine behavior would exist on all scales. The Blanche stylolites are not self-affine on the large scale, which implies that the stylolitization process had stopped at some stage. One reasonable explanation for termination of the stylolitization process could be related to porosity destruction resulting in no place available for precipitation, an option supported by the mass balance calculations presented above. Already in Bathurst, 1975 it was suggested that the growth of a stylolite could stop when the permeability in the adjacent sediment has fallen so low that transport of ions away from the solution film is practically inhibited. The role of stylolites as a local source for cement is well accepted (Ehrenberg, 2006; Finkel and Wilkinson, 1990; Walderhaug and Bjorkum, 2003; Wong and Oldershaw, 1981), but how much of the dissolved material precipitates locally and how much is transported out of the system depends on local conditions and their temporal evolution. The frequency and connectivity of open fractures and the permeability of the bulk control how "open" or "closed" the system is.

Thin-sections of the Blanche (Fig. 2) show that current porosity is very low and not connected both close to the stylolites and at mid-points between adjacent stylolites. Very few small fractures or veins were identified, which also supports the concept of a closed system in which pore fluid has no path out and precipitation occurs near-by. Our observations (few fractures, no remaining porosity, mass balance between dissolution and precipitation) are consistent with the suggestion that the life cycle of stylolites in our case-study was controlled by precipitation: once pore space was completely cemented, the process of stylolitization stopped. Yet one cannot rule out the possibility that dissolution terminated on stylolites due to other condition changes that erased the chemical-potential-gradient drive for the dissolution-precipitation process: i.e. stress, fluid pressure, or fluid compositional changes.

In some of the surfaces H remains slightly larger than 0 for $l>\chi$ (see Fig. 4 and Table 1). It is not clear if H actually approaches zero or if it remains very low due to some inherent large-wavelength roughness of the surface which is unrelated to the stylolitization process. Since our system size is >1 km, which is much larger than the largest measured surface ($\sim$10 m), we cannot rule out that H continues to be small but non-zero for 10 m $< l <$ 1000 m, or that there is another transition to $H=0$ at higher l, above our measurement limit.

5.2. The correlation length, χ

In the present work we measured for the first time the upper bound of self-affinity and the correlation length which were predicted by previous theoretical studies. Previous studies have shown, using smaller surfaces, fractal stylolite roughness over several orders of magnitude, with two different self-affine regimes (Ebner et al., 2009a; Renard et al., 2004; Schmittbuhl et al., 2004). The two regimes have roughness exponents of $H_S\sim1.1$ and $H_L\sim0.5$ for scales smaller than, and larger than, about 1mm, respectively. They were suggested to reflect two competing mechanisms driving dissolution: surface energy and elastic strain energy. The larger scales previously measured, with $H\sim0.5$ (between 0.4 and 0.9), correlate to the smaller scales in our LIDAR measurements, and the part with $H\sim1.1$ $(0.9-1.2)$ is below our resolution. The two regimes discussed in these papers are therefore *not* the two regimes we present, and the correlation length was not measured in these cases either.

These previous stylolite roughness measurements have not measured the upper bound to fractality, either because the largest scale of their measurement was smaller than χ, or because χ had reached the system size. When stylolites are connected by a framework of fractures (such as in the case of Karcz and Scholz, 2003), it may indicate that the system was open, at least to some degree, thus allowing dissolution to continue and roughness to develop to very large correlation lengths. In such a case, it would require very large sampling size to capture χ, or χ may even have reached the system size.

An alternative explanation to why the upper cutoff to fractality has not been reported by others is that not all sedimentary (bedding-parallel) stylolites are formed on existing flat surfaces, as the Blanche stylolites. Other types of stylolite populations have been reported in the literature, such as isolated stylolites, e.g., Fletcher and Pollard (1981). These stylolites probably propagate laterally (Aharonov and Katsman, 2009; Zhou and Aydin, 2010) and their roughness is expected to be more developed in the center and decrease towards the “younger” stylolite edges (Stockdale, 1922).

5.3. Upper bound to fractality: is it a good measure for A?

Estimates of amount of dissolution on stylolites have been performed by various authors (e.g.: Heald, 1955; Kaplan, 1976; Sibley and Blatt, 1976; and Stockdale, 1926). The common methods used are summarized in Table 1. We have presented here an additional method for estimating the amount of dissolution and found that its results are comparable to maximum teeth amplitude and to mass balance calculations. The common method used for evaluating amount of dissolution from cores is by measuring $A_{\max}$. Two issues should be discussed.

5.3.1. When is maximum amplitude a good measure of dissolution amount?

The answer to this question is that $A_{\max}$ (or equivalently w_∞, Schmittbuhl et al., 1995b) is a function of the sampling size l, and is a good measure of dissolution in case the sampling size is larger than χ. If it is smaller it will probably give an underestimate. For example, if we measure $A_{\max}$ for $l=\chi/2$ (assuming $A_{\max}(\chi/2)/A_{\max}(\chi)=w(\chi/2)/w(\chi)$, Schmittbuhl et al., 1995b), the dissolution underestimation would be, according to Eq. (12): $\frac{A_{\max(\chi/2)}}{A_{\max(\chi)}}=\frac{(\chi/2/\alpha l^*)^z l^*}{(\chi/\alpha l^*)^z l^*}=2^{-z}$. For $z=0.81$ the value of measured $A_{\max}$ will be 0.57 of the true value measured when $l>\chi$. In general, the underestimated value would be b^{-z} for measurement size $l=\chi/b$. It is common for oil companies to estimate A using cores a few cm wide. At this scale the teeth heights are expected to be independent of amount of dissolution, since they already saturated (as the cross point in Fig. 7). Unless they are looking at a small amount of dissolution, the estimate from a small core may strongly underestimate the dissolution, with the degree of underestimation worsening with increasing dissolution and with decreasing core size.

Another requirement for $A_{\max}$ to be a good measure of the dissolution amount is that the measured stylolite evolved on a pre-existing surface. If it evolved from a seed and grew laterally, the position from where the sample is taken is expected to have major influence on roughness. It is unknown at this stage how such different stylolite groups can be differentiated when studied in a core, but this is one interesting question to investigate in the future.

A third issue regarding the measure of $A_{\max}$ is that it is expected to give a good estimate for dissolution as long as the most insoluble grains on the interface have not dissolved. Once these most resistant grains are also dissolved, the peak-to-peak measure will start to underestimate dissolution.

5.3.2. Is dissolution amount based on roughness measurements a better estimate than other methods?

The answer to this question is currently no, since the major parameter which is unknown and evaluated only from models is the dynamic exponent, z. This parameter defines the time-dependence of the evolution of roughness. In our calculation we gave a lower and upper estimate of this parameter, which resulted in quite a large range for A (0.15–0.5 m on average). This parameter could be better constrained from field studies of stylolitization evolution with time, or from laboratory experiments but these are obviously not easy to conduct, as stylolites have never been produced in the lab (except on the sub-grain scale by Gratier et al., 2005).

6. Summary and conclusions

In this paper we have presented 3D roughness measurements of stylolite surfaces at a scale larger than ever measured before.

We have compared these measurements to predictions from a model of surface roughening from an initially flat interface. The analyzed surfaces show self-affine characteristics with $H=0.65\pm0.10$ for scales of several mm and up to ~50 cm. Above this scale, H decreases almost to zero, indicating that there is an upper cutoff to the self-affine behavior. The existence of this upper cutoff, termed the "correlation length" (χ), was interpreted as an indicator that the stylolitization process stopped before roughness has saturated. We proposed a scenario in which dissolution and hence roughening stopped when all available porosity around the stylolites was shut down by precipitation originating from the material dissolved on the stylolites, although it is also possible that other causes may have led to dissolution termination. A method for estimating the amount of dissolution on stylolites from their roughness characteristics in cases where χ is much smaller than the stylolites length was presented. Dissolution amount for the Blanche stylolites was calculated and compared to its estimates from two other methods. The agreement between the three independent methods indicates that the upper bound to fractality of stylolites' roughness can indeed indicate the amount of dissolution. An important implication of the agreement between the models and measurements is that it provides support for formation of stylolites, at least in this field site, from roughening of existing surfaces. These surfaces could be perhaps of higher clay content, with clays somehow enhancing pressure solution (Aharonov and Katsman, 2009; Engelder and Marshak, 1985; Fueten et al., 2002; Heald, 1955; Laronne Ben-Itzhak, 2011; Thomson, 1959; Van der Pluijm and Marshak, 2004). This is in contrast to in-plane propagation of stylolites, as suggested for other cases (Aharonov and Katsman, 2009; Fletcher and Pollard, 1981; Mardon, 1988; Nenna and Aydin, 2011; Raynaud and Carrioschaffhauser, 1992).

Acknowledgments

This research was sponsored by ExxonMobil and by an ISF Grant 751/08. We deeply thank Dr. Hagai Ron for help in the field and in coring samples, Dr. Kul Karcz for many discussions and ideas and ExxonMobil for assistance in thin-section preparation.

Appendix A. Calculating prefactors for the roughness relations

Following the two scaling regimes found by Koehn et al. (2007), Ebner et al. (2009b), and Renard et al. (2004), the Hurst exponent for the surface energy-dominated, small-scale regime is termed H_S, and equals ~1, and the Hurst exponent for the strain energy-dominated, large-scale regime is termed H_L (~0.6). Each regime may have different prefactors, α_s and α, and normalization physical length-scales, $l^*_S$and l^*, respectively. The dependence of w on l for these two regimes is therefore:

$$\frac{w(l)}{l^*_S} = \alpha_S\left(\frac{l}{l^*_S}\right)^{H_S} \text{for} \quad l^*_S \le l \le l^* \tag{A1}$$

$$\frac{w(l)}{l^*} = \alpha\left(\frac{l}{l^*}\right)^{H_L} \text{for} \quad l^* \le l \tag{A2}$$

Where l^* is the crossover length-scale between the two regimes.

Using $l=l^*_S$ and assuming $H_S=1$ in Eq. (A1):

$$w(l^*_S) = l^*_S\alpha_S\left(\frac{l^*_S}{l^*_S}\right)^{H_S} = l^*_S\alpha \tag{A3}$$

To find the two prefactors α_s and α we calculate $w(l^*)$ obtained from Eqs. (A1) and (A2), and equate the two values, due to continuity:

$$w(l^*) = l^*_S\alpha_S\left(\frac{l^*}{l^*_S}\right)^1 = l^*\alpha_S \tag{A4}$$

$$w(l^*) = l^*\alpha\left(\frac{l^*}{l^*}\right)^{H_L} = l^*\alpha \tag{A5}$$

Therefore $\alpha=\alpha_S$, and Eqs. (A1) and (A2) can be replaced by Eqs. A6 and A7 for small and large scales, respectively:

$$w(l) = \alpha l \quad \text{for} \quad l^*_S \le l \le l^* \tag{A6}$$

$$w(l) = \alpha l^*\left(\frac{l}{l^*}\right)^{H_L} \quad \text{for} \quad l^* \le l \tag{A7}$$

The small-scale relevant length scale, l^*_S, cannot be calculated and thus cannot be used. It is expected to reflect the heterogeneity in the dissolution process (Ebner et al., 2010a), possibly the size of fossils in the thin sections (Fig. 2), which is ~40 μm on the average. The large-scale characteristic length, l^*, is as stated above, the crossover length scale between the two regimes and its value is approximately 1 mm (Ebner et al., 2009a; Ebner et al., 2009b; Koehn et al., 2007; Renard et al., 2004; Schmittbuhl et al., 2004).

To calculate α from Eq. (A7) we will solve for $l=\chi$ by using the literature values for l^* and the average values we found for $w(\chi)$, χ and H_L (Section 2, Table 1, the latter defined as H throughout the manuscript), which are 0.014 m, 0.48 m and 0.65, respectively:

$$w(\chi) = \alpha l^*\left(\frac{\chi}{l^*}\right)^{H_L} \tag{A8}$$

For $l*=0.001$m, we obtain $\alpha=0.22$; for $l^*=0.0005$m, $\alpha=0.28$; and for $l^*=0.003$m, $\alpha=0.16$. The prefactor α is thus on the order of 1. These values of l^* and α are used for the calculation of A in Section 4.

Appendix B. Parameters used in this manuscript, their symbols and units.

See Table B1.

Table B1

Symbol	Name	Units
H	Hurst exponent	
w	Average "width" of stylolite interface	m
w_∞	Maximum "width" of stylolite interface	m
A_{max}	Maximum teeth amplitude ($=w_\infty$)	m
A	Dissolution amount	m
l	Sampling size	m
L	System size	m
χ	Correlation length	m
t^*	Critical time for which $\chi=L$	s
β	Growth exponent	
z	Dynamic exponent	
l^*	Characteristic scaling parameter	m
α	Geometrical prefactor	
V	Dissolution rate	m/s
$\bar{d}$	Average spacing between stylolites	m
φ	Porosity	

References

Aharonov, E., Katsman, R., 2009. Interaction between pressure solution and clays in stylolite development: insights from modeling. Am. J. Sci. 309 (7), 607–632.
Barabasi, A.L., Stanley, E.H., 1995. Fractal Concepts in Surface Growth. Cambridge Univ. Press, New York.
Bathurst, R.G.C., 1975. Carbonate Sediments and their Diagenesis. Elsevier, Amsterdam 658 pp..

Benedicto, A., Schultz, R.A., 2010. Stylolites in limestone: magnitude of contractional strain accommodated and scaling relationships. J. Struct. Geol. 32, 1250–1256.

Ebner, M., Koehn, D., Toussaint, R., Renard, F., 2009a. The influence of rock heterogeneity on the scaling properties of simulated and natural stylolites. J. Struct. Geol. 31 (1), 72–82.

Ebner, M., Koehn, D., Toussaint, R., Renard, F., Schmittbuhl, J., 2009b. Stress sensitivity of stylolite morphology. Earth Planet. Sci. Lett. 277 (3–4), 394–398.

Ebner, M., Piazolo, S., Renard, F., Koehn, D., 2010a. Stylolite interfaces and surrounding matrix material: nature and role of heterogeneities in roughness and microstructural development. J. Struct. Geol. 32 (8), 1070–1084.

Ebner, M., Toussaint, R., Schmittbuhl, J., Koehn, D., Bons, P., 2010b. Anisotropic scaling of tectonic stylolites: a fossilized signature of the stress field? J. Geophys. Res.-Solid Earth 115 (B06403) 16.

Ehrenberg, S.N., 2006. Porosity destruction in carbonate platforms. J. Petrol. Geol. 29 (1), 41–51.

Engelder, T., Marshak, S., 1985. Disjunctive cleavage formed at shallow depths in sedimentary rocks. J. Struct. Geol. 7 (3/4), 327–343.

Family, F., Viscek, T., 1985. Scaling of the active zone in the Eden process on percolation networks and the ballistic depositional model. J. Phys. A: Math. Gen. 18 (2).

Finkel, E.A., Wilkinson, B.H., 1990. Stylolitization as source of cement in Mississippian Salem Limestone, West-Central Indiana. AAPG Bull. 74 (2), 174–186.

Fletcher, R.C., Pollard, D.D., 1981. Anti-crack model for pressure solution surfaces. Geology 9 (9), 419–424.

Fueten, F., Robin, P.Y.F., Schweinberger, M., 2002. Finite element modelling of the evolution of pressure solution cleavage. J. Struct. Geol. 24 (6-7), 1055–1064.

Gratier, J.P., Muquet, L., Hassani, R., Renard, F., 2005. Experimental microstylolites in quartz and modeled application to natural stylolitic structures. J. Struct. Geol. 27 (1), 89–100.

Heald, M.T., 1955. Stylolite in sandstones. J. Geol. 63 (2), 101–114.

Kaplan, M.Y., 1976. Origin of stylolites. Docl. Acad. Sci USSR, Earth Sci. Sect. 221, 205–207.

Karcz, Z., Scholz, C.H., 2003. The fractal geometry of some stylolites from the Calcare Massiccio Formation, Italy. J. Struct. Geol. 25 (8), 1301–1316.

Koehn, D., Renard, F., Toussaint, R., Passchier, C.W., 2007. Growth of stylolite teeth patterns depending on normal stress and finite compaction. Earth Planet. Sci. Lett. 257 (3-4), 582–595.

Laronne Ben-Itzhak, L., Pressure solution and stylolites in carbonate rocks. Ph.D. Dissertation Thesis, Weizmann Institute of Sciences, Rehovot, 2011.

Mandelbrot, B.B, 1986. Fractals in Physics. Elsevier, Amsterdam.

Mardon, D., Localized pressure solution and the formation of discrete solution seams. Ph. D. Thesis, Texas A&M University, 1988.

Nenna, F.A., Aydin, A., 2011. The formation and growth of pressure solution seams in clastic rocks: A field and analytical study. J. Struct. Geol. 33, 633–643.

Oswald, E.J., Mueller III, H.W., Goff, D.F., Al-Habshi, H., Al-Matroushi Adco, S., 1995. Controls on porosity evolution in Thamama Group Carbonate Reservoirs in Abu Dhabi, U.A.E. Middle East Oil Show, 251–265.

Park, W.C., Schot, E.H., 1968. Stylolites—their nature and origin. J. Sediment. Petrol. 38 (1), 175–191.

Raynaud, S., Carrioschaffhauser, E., 1992. Rock matrix structures in a zone influenced by a stylolite. J. Struct. Geol. 14 (8–9), 973–980.

Renard, F., Schmittbuhl, J., Gratier, J.P., Meakin, P., Merino, E., 2004. Three-dimensional roughness of stylolites in limestones. J. Geophys. Res.-Solid Earth 109 (B3).

Rolland, A., Toussaint, R., Baud, P., Schmittbuhl, J., Conil, N., Koehn, D., Renard, F., Gratier, J.P., 2012. Modeling the growth of stylolites in sedimentary rocks. J. Geophys. Res.-Solid Earth.

Safaricz, M., Pressure solution in chalk. Ph.D. Dissertation Thesis, Royal Holloway University of London, 2002.

Safaricz, M., Davison, I., 2005. Pressure solution in chalk. AAPG Bull. 89 (3), 383–401.

Sagy, A., Brodsky, E.E., 2009. Geometric and rheological asperities in an exposed fault zone. J. Geophys. Res.-Solid Earth 114 (B02301), 15.

Sagy, A., Brodsky, E.E., Axen, G.J., 2007. Evolution of fault-surface roughness with slip. Geology 35, 283–286.

Schmittbuhl, J., Renard, F., Gratier, J.P., Toussaint, R., 2004. Roughness of stylolites: implications of 3D high resolution topography measurements. Phys. Rev. Lett. 93 (23).

Schmittbuhl, J., Roux, S., Vilotte, J.P., Maloy, K.J., 1995a. Interfacial crack pinning: effect of nonlocal interactions. Phys. Rev. Lett. 74 (10), 1787–1790.

Schmittbuhl, J., Schmitt, F., Scholz, C., 1995b. Scaling invariance of crack surfaces. J. Geophys. Res.-Solid Earth 100 (B4), 5953–5973.

Sibley, D.F., Blatt, H., 1976. Intergranular pressure solution and cementation of tuscarora orthoquartzite. J. Sediment. Petrol. 46 (4), 881–896.

Simonsen, I., Hansen, A., Nes, O.M., 1998. Determination of the Hurst exponent by use of wavelet transforms. Phys. Rev. E 58 (3), 2779–2787.

Sneh, A., and R. Weinberger, Geological Map of Israel. Sheet 2-II Metulla, Israel Geological Survey, 2003.

Stockdale, P.B., 1922. Stylolites: their nature and origin. Indiana Univ. Stud. 9, 1–97.

Stockdale, P.B., 1926. The stratigraphic significance of solution in rocks. J. Geol. 34, 399–414.

Tada, R., Siever, R., 1989. Pressure solution during diagenesis. Annu. Rev. Earth Planet. Sci. 17, 89–118.

Tanguy, A., Gounelle, M., Roux, S., 1998. From individual to collective pinning: effect of long-range elastic interactions. Phys. Rev. E 58 (2), 1577–1590.

Thomson, A., Pressure Solution and Porosity. Soc. Econ. Paleontol. Mineral. Special Publication, 1959, pp. 92–110.

Toussaint, R., Flekk y, E.G., Helgesen, G., 2006. Memory of fluctuating Brownian dipolar chains. Phys. Rev. E 74 (5), 051405.

Toussaint, R., Helgesen, G., Flekk y, E.G., 2004. Dynamic roughening and fluctuations of dipolar chains. Phys. Rev. Lett. 93 (10), 108304.

Van der Pluijm, B., Marshak, S., 2004. Earth Structure: An Introduction to Structural Geology and Tectonics. WW Norton &Company 672 pp..

Vinningland, J.L., R. Toussaint, M. Niebling, E.G. Flekkoy, K.J. Maloy, 2012. Family–Vicsek scaling of detachment fronts in Granular Rayleigh Taylor Instabilities during sedimenting granular/fluid flows. Europhys. Lett. Special Topics, 204, 27–40. http://dx.doi.org/10.1140/epjst/e2012-01550-2.

Walderhaug, O., Bjorkum, P.A., 2003. The effect of stylolite spacing on quartz cementation in the Lower Jurassic Sto Formation, southern Barents Sea. J. Sediment. Res. 73 (2), 146–156.

Wong, P.K., Oldershaw, A., 1981. Burial cementation in the Devonian, Kaybob Reef Complex, Alberta, Canada. J. Sediment. Petrol. 51 (2), 507–520.

Zhou, X.X., Aydin, A., 2010. Mechanics of pressure solution seam growth and evolution. J. Geophys. Res.-Solid Earth 115.

Eur. Phys. J. B **67**, 121–131 (2009)
DOI: 10.1140/epjb/e2009-00002-2

THE EUROPEAN PHYSICAL JOURNAL B

Regular Article

Does roughening of rock-fluid-rock interfaces emerge from a stress-induced instability?

E. Bonnetier[1], C. Misbah[2,a], F. Renard[3,4], R. Toussaint[5,6], and J.-P. Gratier[3]

[1] Laboratoire Jean Kuntzmann, Université Joseph Fourier and CNRS, B.P. 53, 38041 Grenoble Cedex 9, France
[2] Laboratoire de Spectrométrie Physique, 140 avenue de la physique, Université Joseph Fourier, and CNRS, 38402, Saint Martin d'Hères, France
[3] Laboratoire de Géodynamique des Chaines Alpines, CNRS-OSUG, Université Joseph Fourier, B.P. 53, 38041 Grenoble, France
[4] Physics of Geological Processes, University of Oslo, Norway
[5] Institut de Physique du Globe de Strasbourg, UMR CNRS 7516, 5 rue Descartes, 67084 Strasbourg Cedex, France
[6] EOST, Université de Strasbourg, France

Received 20 October 2008 / Received in final form 24 November 2008
Published online 9 January 2009

Abstract. Non-planar solid-fluid-solid interfaces under stress are very common in many industrial and natural materials. For example, in the Earth's crust, many rough and wavy interfaces can be observed in rocks in a wide range of spatial scales, from undulate grain boundaries at the micrometer scale, to stylolite dissolution planes at the meter scale. It is proposed here that these initially flat solid-fluid-solid interfaces become rough by a morphological instability triggered by elastic stress. A model for the formation of these unstable patterns at all scales is thus presented. It is shown that such instability is inherently present due to the uniaxial stress that promotes them, owing to the gain in the total elastic energy: the intrinsic elastic energy plus the work of the external forces. This is shown explicitly by solving the elastic problem in a linear stability analysis, and proved more generally without having resort to the computation of the elastic field.

PACS. 91.32.De Crust and lithosphere – 68.35.Fx Diffusion; interface formation – 02.30.Jr Partial differential equations – 91.60.Dc Plasticity, diffusion, and creep

1 Introduction

When a solid is non-uniformly loaded (Fig. 1), its elastic free energy is increased and local gradients of free-energy can induce mass transfer from the most stressed sides of the solid to the least stressed ones, or to other surrounding solids, to minimize the energy increase related to the loading. The interface kinetics of the stressed solid is controlled by the slowest mechanism by which the mass is transported. This configuration is found in many layered industrial materials or natural systems. For example, in the rocks of the Earth's crust, loaded interfaces are widespread: fault surfaces and stylolites (Fig. 2) at a macroscopic scale; grain boundaries and grain free surfaces in a porous medium at the microscopic scale.

Two different geometries can be defined, depending on the orientation of the main compressive stress relative to the loaded interface (Fig. 1).

– When the main compressive stress is parallel to the surface, grooves can develop, this is the Asaro-Tiller-Grinfeld instability [3,11,12,21,23,31], referred to, later in this paper, as "the free-face instability". This instability is well understood theoretically. It has been observed on Helium by Torii and Balibar [33]. It has also been proposed that it could be reproduced experimentally on sodium chlorate single crystals [7]. However, experiments on the same salt do also show that this instability may disappear after some time. This effect might be related to the precipitation of a stress-free skin at the surface of the crystals [5].
– When the main compressive stress is perpendicular to the solid surface, initially flat dissolution surfaces can become rough in the course of time by a dissolution process. Typical natural examples of such squeezed unstable interfaces can be observed in natural rocks. They are called stylolites (Fig. 2). In sedimentary basins, stylolites are observed as rough horizontal interfaces [8,13,24,30,32]. There, the main compressive

[a] e-mail: chaouqi.misbah@ujf-grenoble.fr

stress is vertical and corresponds to the weight of the overburden rocks. In mountain chains, where the main compressive stress corresponds to the horizontal tectonic loading, rough stylolite surfaces are oriented vertically [2,25]. From these basic observations, one may conclude that stress is a key ingredient in stylolite pattern formation [4,17]. In the present study, we call such roughening process "the squeezed interface instability". It differs from the free-face instability by the orientation of the main compressive stress. This second instability is less understood. It has been proposed that the roughening of the interface is controlled by a destabilizing force, the noise initially present in the rock [26,27]. In [9] it was assumed that diffusion occurs along the solid-solid interface and a simple model to describe the instability has been proposed. However, a model that takes into account a more realistic geometry is lacking, together with a systematic derivation of the governing equations. Furthermore, it remains to be shown whether or not a purely elastic instability explains the formation of stylolites. This paper is directed along these lines.

We present a model that shows that squeezed solid-fluid-solid interfaces are unstable due to stress. This situation is less classical than the one usually treated: here two solids are in contact with a thin liquid layer and the weight is transmitted from one solid to the other by the liquid layer. It is thus essential to derive the equations and boundary conditions in this geometry. We must take into account not only the intrinsic elastic energy but also the work due to external forces.

Natural and experimental observations of rough surfaces indicate that stress has a strong control on the evolution of the fluid-solid interfaces: stress gradients are released by dissolution-precipitation or melting solidification processes, which modify the solid texture and induce irreversible deformations (see Fig. 2).

The scheme of this paper is as follows. In Section 2 we briefly review the free interface case. In Section 3 we treat the squeezed interface case by performing a linear stability analysis, and present the main results that reveals an instability driven by stress. In Section 4 we present a more general and formal proof of the instability without having resort to an explicit solution of the elastic field. Section 5 is devoted to a general discussion. Some technical details are presented in an appendix.

2 The free interface case

If the main compressive stress is parallel to the loaded interface (Fig. 1a), grooves can develop on the free surface. This is the well-known Asaro-Tiller-Grinfeld instability [3,11]. It has been found experimentally [7,19,33] that the formation of the grooves occurs on a free surface of various solids in contact with a fluid when a load (or a uniaxial stress [33]) is applied. The grooves can theoretically evolve to fractures that propagate at a subcritical rate [14,16,18,34]. The wavelength of the instability is controlled by a balance between elastic forces, which tend to

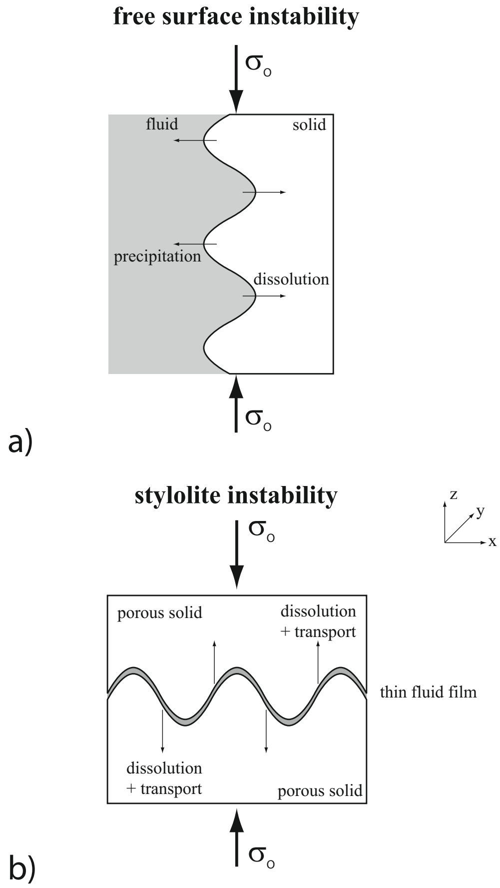

Fig. 1. Morphological instabilities of a solid-fluid interface and effect of the orientation of the main compressive stress. (a) Free-face instability: when a free surface of a solid in contact with a fluid is loaded perpendicular to the surface, grooves can develop through time and even evolve to cracks. This is the Asaro-Tiller-Grinfeld instability. (b) Squeezed interface instability: A typical example is a stylolite, which corresponds to a fluid-filled rock-rock interface loaded perpendicularly to the interface. The mean roughness amplitude of the interface grows with time, which gives their characteristic shapes to the stylolites. In both cases, the fluid phase acts as a reactive medium transporting solutes by diffusion and allowing stress driven dissolution-precipitation processes at the interface with the solid.

roughen the surface, and surface tension, which smoothen it. The characteristic wavelength λ_c of the instability that emerges from a linear stability analysis is

$$\lambda_c = \frac{\pi E \gamma}{\sigma_0^2(1-\nu^2)}, \tag{1}$$

where E is the Young modulus of the solid, γ is the interfacial energy between the solid and the liquid, ν is the Poisson coefficient, and σ_0 is the applied main compressive stress (see Fig. 1). The planar front is unstable if the perturbation wavelength λ is such that $\lambda > \lambda_c$ and it is stable otherwise.

For the case of rocks, in which we are interested here, it has been shown that the transport mechanism may be

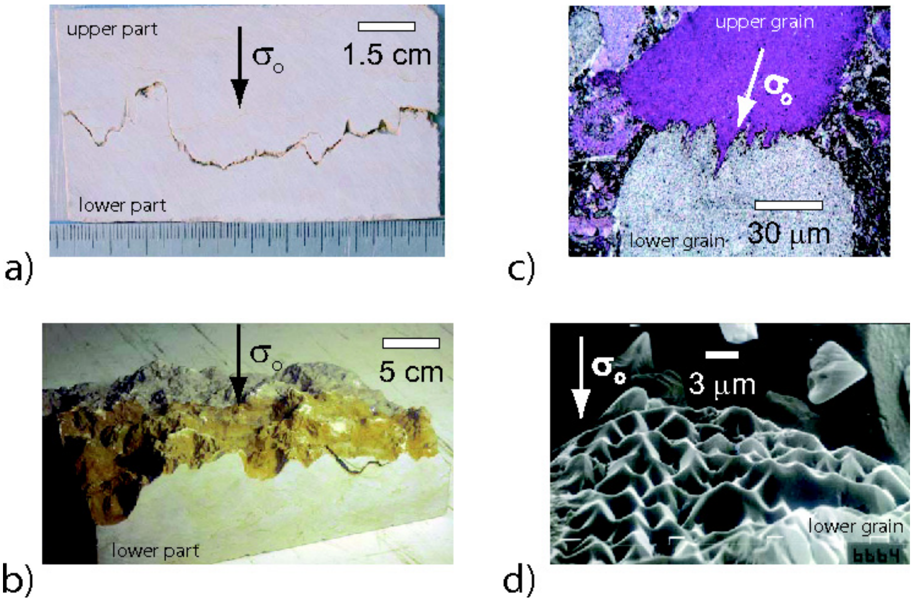

Fig. 2. Various patterns of rough stylolite interfaces at all scales. (a) Stylolite interface in a sedimentary limestone from the Chartreuse Mountains, France. The rough interface pattern formed by stress-enhanced dissolution from an initially flat rock-fluid-rock interface. In this case, the maximum compressive stress σ_0 was perpendicular to the interface. (b) Stylolite surface viewed in 3D after removing the upper part of a limestone, similar to the sample shown in (a). (c) Microscopic observation of a rough grain-grain boundary in a limestone from Mons, Belgium, showing two spherical grains indented into each other. The rough teeth pattern of the interface has formed by a stress-enhanced dissolution process. (d) Scanning Electron Microscope view of a quartz grain surface, after experimentally produced stress-enhanced dissolution against a second quartz grain that has been removed for better visualization. The maximum stress was vertical, and perpendicular to the rough interface. Adapted from [10].

controlled either by dissolution kinetics of the crystal, or diffusion of solutes in the fluid [9,21]. This depends on the nature of rocks, as discussed in [21].

3 The squeezed interface case

3.1 Presentation of the instability

Consider the situation depicted in Figure 3, where the initial surface representing the position of the squeezed interface Γ is set at $z = 0$. The interface contains a thin water film at a pressure p, squeezed between the two solids that have identical linear elastic properties. We consider, for the sake of simplicity, one dimensional deformations along x only, so that the stress and the strain fields are independent of y. Here we shall not describe the mechanisms by which the modulation takes place, but, rather, we are interested to compare the energetic of the initial state (flat) with that of a corrugated one.

Due to the assumption of translational invariance along y, the problem reduces to an effective 2D one where it is convenient to make use of the Airy function $\chi(x, z)$ which is defined in terms of the stress tensor as [20]:

$$\sigma_{xx} = \frac{\partial^2 \chi}{\partial z^2}\, , \sigma_{zz} = \frac{\partial^2 \chi}{\partial x^2}\, , \sigma_{xz} = -\frac{\partial^2 \chi}{\partial x \partial z}. \qquad (2)$$

The Airy function χ obeys a bi-harmonic equation [20]:

$$\nabla^4 \chi = 0. \qquad (3)$$

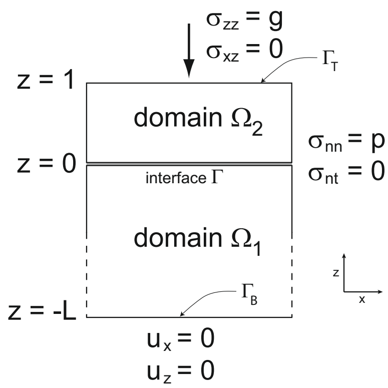

Fig. 3. Geometry of the system: two linear elastic solids with identical moduli are pushed into each other and separated by a thin confined water film at pressure p. The boundaries conditions used in Sections 3 and 4 are given.

Once χ is determined the stress can be computed from the very definition of χ, and the strain is obtained from Hooke's law. It must be emphasized that since we confine ourselves to two dimensional deformations, the strain-stress relation differs from the three dimensional version (as far as the coefficients are concerned). We have in two dimensions the relations

$$\varepsilon_{xx} = \frac{1+\nu}{E}[(1-\nu)\sigma_{xx} - \nu\sigma_{zz}]$$
$$\varepsilon_{zz} = \frac{1+\nu}{E}[(1-\nu)\sigma_{zz} - \nu\sigma_{xx}]$$
$$\varepsilon_{xz} = \frac{1+\nu}{E}\sigma_{xz} \tag{4}$$

where E is the Young's modulus of the solid and ν is the Poisson's ratio. This limit is also known as the plane strain condition.

The interface equation is written as $z = h(x)$. For $h = 0$, $\chi_0 = gx^2/2$ (the subscript '0' refers to the planar interface) is obviously a solution of (3) with $\sigma_{zz} = g$ the only non zero component. This solution satisfies the boundary condition at $z = 1$, and from $\sigma_{nn} = p$, (σ_{nn} is the normal component of the stress, and p is a pressure-like parameter; see Section 4) we obtain $p = g$. This is physically appealing since the equilibrium at the interface, where the force is normal and equal to p, requires a compensation of the applied load g. Apart from a hydrostatic pressure (taken as an origin), both $\sigma_{xx} = 0$ and $\sigma_{xz} = 0$. The pre-strained situation is uniaxial.

Let us now assume that the interface undergoes a virtual displacement $h(x)$ and compute the resulting elastic fields in both solid domains denoted as '1' and '2'. Of course in its great generality this problem is highly nonlinear for an arbitrary h, and can only be dealt with numerically. If one is interested in determining whether or not an interface displacement results in a gain of energy, it may be sufficient to perform a linear stability analysis, a problem which can ba handled analytically.

Because different modes do not interact in the linear regime, it is sufficient to consider only one Fourier component, namely we seek solutions in the form:

$$h = \varsigma e^{iqx} + c.c. \tag{5}$$

where ς is a small parameter, small enough for a linear analysis to make a sense, and q is the perturbation wavenumber. The perturbed Airy function can also be decomposed onto Fourier modes

$$\chi = \varsigma f(z)e^{iqx} + c.c. + \chi_0 \tag{6}$$

where f is a function which is yet unknown. From (3) it follows that f obeys

$$\left[\frac{\partial^2}{\partial z^2} - q^2\right]^2 f = 0. \tag{7}$$

The general solution of which reads

$$f = (Az + B)e^{qz} + (A'z + B')e^{-qz}. \tag{8}$$

The four integrations factors A, A', B, B' are computed from the boundary conditions.

In domain '1' (lower domain) we have

$$f = (A_1 z + B_1)e^{qz} + (A_1' z + B_1')e^{-qz}. \tag{9}$$

In domain '2' we have

$$f = (A_2 z + B_2)e^{qz} + (A_2' z + B_2')e^{-qz}. \tag{10}$$

The eight integration factors are determined by the eight conditions: the normal stress at $z = 1$ is equal to g where the surface there is free from shear. These two conditions read

$$\sigma_{zz}|_{z=1} = g, \quad \sigma_{xz}|_{z=1} = 0. \tag{11}$$

At the interface the normal components on both sides coincide with p, while the tangential components vanish. This amounts to four independent conditions

$$\sigma_{nn}|_{z=0^-} = p, \quad \sigma_{nn}|_{z=0^+} = p,$$
$$\sigma_{nt}|_{z=0^-} = 0, \quad \sigma_{nt}|_{z=0^-} = 0 \tag{12}$$

where $\sigma_{nn} = n_i\sigma_{ij}n_j$ and $\sigma_{nt} = n_i\sigma_{ij}t_j$, with n_i and t_j representing the i^{th} component of the normal and the tangent vectors evaluated at the interface. Note that from zeroth order solution we have seen that $p = g$, so that from now on we shall abandon the p symbol in favor of g.

Finally at the bottom, $z = -L$, we impose a zero displacement condition, namely

$$u_z|_{z=-L} = 0, \;\; u_x|_{z=-L} = 0. \tag{13}$$

Using the Airy function and the definition (2) together with (9) and (10), and expanding the equations to order one in ς we obtain eight equations determining the eight unknowns. The solutions take the form

$$\begin{aligned}
A_1 &= g[e^{-2qL}(2qL + 1) + 3 - 4\nu]/D_1\\
B_1 &= 2ge^{-2qL}[q^2L^2 + 2 + 4\nu^2 - 6\nu]/D_1\\
A_1' &= ge^{-2qL}[1 - 2qL + e^{-2qL}(3 - 4\nu)]/D_1\\
B_1' &= -B_1\\
A_2 &= -g[e^{2q}(2q - 1) + 1]/D_2\\
B_2 &= 2qge^{2q}/D_2\\
A_2' &= -ge^{2q}[e^{2q} - 2q - 1]/D_2\\
B_2' &= -2qge^{2q}/D_2
\end{aligned} \tag{14}$$

where we have set

$$D_1 = (3 - 4\nu)[1 + e^{-4qL}] + 2e^{-2qL}[2q^2L^2 + 8\nu^2 - 12\nu + 5] \tag{15}$$

and

$$D_2 = 2e^{2q}(2q^2 + 1) - 1 - e^{4q}. \tag{16}$$

Having determined these eight constants of integration, the elastic field can be obtained straightforwardly.

3.2 Energy considerations

In this section we will be mainly concerned with the total energy of the system in the deformed and undeformed states. The total energy should contain both the intrinsic part and the work of the external force, g. The energy contribution from the intrinsic part is $1/2 \int_\Omega \sigma d\tau : \varepsilon(u)$

where Ω is the total volume, and the work of the external force is $-\int_{\Gamma_T} gu$, with Γ_T is the upper boundary (see Fig. 3). The total energy is thus

$$E = \frac{1}{2}\int_\Omega \sigma : \varepsilon(u) d\tau - \int_{\Gamma_T} gu. \tag{17}$$

It will be shown in Section 4 that minimization of this energy with respect to u yields the appropriate elastic equations, $\mathrm{div}(\sigma) = 0$ and the boundary conditions (11), (12), and (13). Upon substitution of the equilibrium condition, the relaxed elastic energy will then take the following form

$$E_0 = -\frac{1}{2}\int_\Omega \sigma : \varepsilon(u) d\tau \tag{18}$$

where the subscript '0' is to remind us that the quantity under consideration is the relaxed energy. That this quantity is negative is obvious, since the relaxed energy should be smaller than the non-relaxed one, otherwise there is a trivial solution which would have a zero energy, the one corresponding to a zero displacement.

It remains now to be shown that the variation of this quantity with respect to an interface modulation $\varsigma\cos(qx)$ (produced due to some mass transport) is negative, a signature of the instability. A general proof is presented in Section 4 without resorting to the explicit form of the elastic field. It is also of interest to have an explicit expression of the energy, (and possibly of the chemical potential), if one wishes to study the kinetics of the instability, and provide the appropriate length and time scales of the evolution.

We should remind that σ has a zeroth order contribution due to pre-strain, and in computing the energy E_0 one has to subtract the energy of the pre-strained state, so that the obtained form contains the contribution due to the profile $z = h(x, t)$. In the linear regime of perturbation with respect to h (i.e. the stress is computed up to order h), the energy E_0 assumes a quadratic form. In the general situation where the extent of the upper and lower parts of the sample is finite the energy is lengthy enough so we did not feel it worthwhile to list it here. We give only the limit where $qL \gg 1$ (lower part, below the interface, is large in comparison to lengths of interest):

$$\begin{aligned} E_0 = qg^2\frac{1+\nu}{ED_2}\{&(1-2\nu)\left[1+e^{4q}-2e^{2q}-4q^2e^{2q}\right] \\ &-4qe^{2q}+e^{4q}-1\}\varsigma^2 \end{aligned} \tag{19}$$

where D_2 is a constant defined in equation (16). The above energy is computed per unit period along x and per unit length along y. If the surface energy (39) is taken into account, one has to supplement E_0 with the following contribution

$$E_s = \gamma\int dx\left(\frac{dh}{dx}\right)^2 \tag{20}$$

where we have used the approximation of small perturbation so that the change of arclength from the planar surface configuration is approximated by $(dh/dx)^2$. The cost in surface energy per unit period and unit length in the y direction is thus given by

$$E_s = \gamma q^2\varsigma^2. \tag{21}$$

It can be checked that the right hand side in equation (19) is always negative, signaling an instability. Note that if the work of the external forces in (17) is not included, then the relaxed energy would be the opposite of (18), and therefore E_0 would have been positive in equation (19), signaling a stability instead of instability. This will further be shown in the general treatment in Section 4. In contrast to elasticity, the surface energy is stabilizing. A remark is in order. The comparison of the elastic energy (which is destabilizing) and the surface energy (which is stabilizing) has also a similar spirit as that due Griffith in fracture theory. Indeed, in Griffith theory a crack propagates if its length ℓ exceeds a typical value given by the ratio of the loss of surface energy γ over the gain in elastic energy (crack releases stored elastic energy) $\sim\sigma_0^2/E$. More interesting is that the Griffith condition, according to which a crack propagates when its length exceeds a critical length ℓ_c, is precisely (apart from a numerical factor of order unity) the condition of the ATG instability: the planar front is unstable if the wavelength is larger than λ_c (see Eq. (1)), whereas the Griffith condition states [20] that a crack propagates if its length $\ell > \ell_c = (4/\pi^2)\lambda_c$.

We shall first discuss the two extreme limits of large and short wavenumbers. In these extreme limits the expression takes a very simple form. The first case is, perhaps, the most relevant one for natural systems such as stylolites, where we assume that $q \gg 1$ (short wavelength). This means that we take the limit where the modulation wavelength is small as compared to the interface extent. The energy (per unit period) takes then the form

$$E_0 = -\frac{4(1-\nu^2)}{E}|q|g^2\varsigma^2 \tag{22}$$

which is negative, signaling a morphological instability. Note that we keep $|q|$ in the expression above in order to stress the nonlocal character of the elastic field. Indeed, in real space the quantity $|q|$ leads to a Hilbert transform of $\partial_x h(x)$. More precisely

$$TF^{-1}(|q|h_q) = (1/\pi)\mathcal{P}\int\frac{\partial_{x'}h(x')}{x'-x}, \tag{23}$$

where TF stands for a Fourier transform, and $h_q = TF^{-1}(h)$ (TF^{-1} designates the inverse Fourier transform). The symbol $\mathcal{P}$ refers to the fact that the integral must be taken in the sense of the Cauchy principal value. For a real non singular function $f(x)$ the Cauchy principal value is defined as

$$\mathcal{P}\int_{-\infty}^{\infty}\frac{f(x)}{x}dx \equiv \lim_{\epsilon\to 0}\left[\int_{-\infty}^{-\epsilon}\frac{f(x)}{x}dx + \int_{\epsilon}^{\infty}\frac{f(x)}{x}dx\right]. \tag{24}$$

Let us abbreviate this expression as $pv(f(x)/x)$. Applying TF on both sides of (23), one gets on the left hand side $|q|h_q$, while the right hand side is a convolution providing a product of $TF(\partial_{x'}h(x'))$ and $TF(pv(1/(x'-x)))$. The first term yields iqh_q, while the second one is equal to $-i\pi\,\mathrm{sgn}(q)$ (a classical result of theory of distributions, and can easily be obtained by using the residue theorem), $\mathrm{sgn}(q)$ stands for 'sign of q'. The final result (after accounting for the factor π in (23)) is $q\,\mathrm{sgn}(q)h_q = |q|h_q$, that is identical to the left hand side result.

In the opposite limit ($q \ll 1$) one gets (for $L = 1$)

$$E_0 = -\frac{2(1+\nu)}{15E(1-\nu)} g^2 q^2 (17 - 32\nu)\varsigma^2. \qquad (25)$$

The effect of the confinement leads to a spectrum which begins with q^2 instead of q. This may have, in principle, some significant consequences, as discussed below.

For example, in the non-confined regime the elastic energy (which is $\sim q$) dominates at small q in comparison to the surface energy which behaves as q^2. This means that the instability is always present there. The typical length-scale of the instability is given by balancing the elastic energy $\sim qg^2/E$ with the surface energy $\sim\gamma q^2$ where γ is the surface energy. This leads to a typical length scale $\lambda_c \sim E\gamma/g^2$.

In the confined regime the energy behaves as $-q^2g^2\ell E$ (where for homogeneity reasons we have reintroduced a length scale ℓ representing a typical length of the vertical extent of the solid), precisely like the surface energy regarding the q dependence, $+q^2\gamma$. Since the latter is stabilizing, while the former is destabilizing, an instability may take place only if $\ell > \gamma E/g^2$. g has a dimension of E and can be written as $g = nE$ where n is a dimensionless number smaller than one. We must have then $\ell > \gamma/(nE)$. In most cases γ/E is of the order of an atomic length and n is small enough so we conclude that for all practical purposes the instability takes place.

4 A general framework

In this section, we cast the previous calculation in the framework of a variational analysis. We provide a rigorous mathematical derivation on the stress-induced instability. Unlike the previous derivation, the present result will be obtained without knowing the explicit expression of the elastic field. We restrict ourselves to a 2D situation for simplicity; however, the analysis carries over to the 3D case. We consider a configuration similar to that of Figure 3: a portion of interface Γ separates two pieces of solids Ω_1 and Ω_2 in the rectangle $\Omega = \Omega_1 \cup \Omega_2 \cup \Gamma$.

4.1 Mechanical equilibrium for a fixed interface Γ

We view the rectangle $\Omega = (0,1)\times(0,1)$ as a small slab of solid around an interface and assume periodic boundary conditions on the vertical sides $\Gamma_V = \{0\}\times(0,1)\cup\{1\}\times(0,1)$. We assume that Ω_1 lies below Ω_2 and that both are sufficiently regular open sets (say with Lipschitz boundaries). A vertical load with modulus g is applied to the top boundary Γ_T and the displacement u_1 is fixed on the bottom boundary Γ_B. We use the Einstein summation convention of repeated indices.

The transmission conditions between Ω_1 and Ω_2 models the presence of a very thin layer of fluid in the interface. We assume therefore that the stress tensors σ_1 and σ_2 in Ω_1 and Ω_2 satisfy

$$\sigma_i n_i = p n_i, \quad \text{on } \Gamma,\ i = 1,2,$$

where n_i denotes the outward normal to Ω_i, and where p is the Lagrange multiplier that denotes the (unknown) pressure in the thin layer of fluid. Altogether, the mechanical equilibrium of the system is expressed by the equations

$$\begin{cases} -\mathrm{div}(\sigma_i) = 0 & \text{in } \Omega_i, \\ \sigma_i = A\varepsilon(u_i) & \text{in } \Omega_i, \\ \sigma_2 n_2 = g n_2 & \text{on } \Gamma_T, \\ u_1 = 0 & \text{on } \Gamma_B, \\ u_i \ \text{periodic on } \Gamma_V, \\ \sigma_i n_i = p n_i & \text{on } \Gamma, \end{cases} \qquad (26)$$

where $i = 1,2$, $\varepsilon(u) = 1/2(\nabla u + \nabla u^T)$ is the symmetric strain tensor, and A is the 4×4 tensor of isotropic Lamé coefficients of the solid. Alternatively, the above partial differential equations can be obtained as the Euler Lagrange equations of the following energy functional

$$E_\Gamma(v_1,v_2) = \frac{1}{2}\int_{\Omega_i} A\varepsilon(v_i):\varepsilon(v_i)dx - \int_{\Gamma_T} g n_2 v_2.$$

The set V of admissible displacements V_Γ consists of pairs $(v_1,v_2):\Omega_1\times\Omega_2 \longrightarrow \mathbf{R}^2\times\mathbf{R}^2$ of square integrable functions, with square integrable derivatives, such that

$$\begin{cases} v_1 = 0 \text{ on } \Gamma_T \\ v_1, v_2 \text{ periodic on } \Gamma_V \\ \int_\Gamma v_1 n_1 + v_2 n_2 = 0. \end{cases}$$

Note that the constraint on the normal displacements on Γ is associated with the Lagrange multiplier p introduced above. One easily checks that minimizing E_Γ over V_Γ yields a solution (u_1,u_2) to the corresponding Euler-Lagrange equation (26), which is defined up to a horizontal translation of u_2. To obtain a well-defined solution we further impose the normalization condition

$$\int_{\Gamma_T} u_2 \begin{pmatrix} 1 \\ 0 \end{pmatrix} = 0.$$

4.2 First variation with respect to the interface Γ

In this paragraph, we compute the shape derivative, with respect to variations of the interface Γ, of the elastic energy functional

$$J(\Gamma) = \min_{(v_1,v_2)\in V(\Gamma)} E_\Gamma(v_1,v_2).$$

Denoting (u_1,u_2) the solution of the above variational problem (the actual elastic displacements for the geometry defined by the interface Γ, under the loading g) using (26), and integrating by parts shows that

$$J(\Gamma) = \frac{1}{2}\int_{\Omega_i} A\varepsilon(u_i):\varepsilon(u_i)dx - \int_{\Gamma_T} gn_2u_2$$

$$= -\frac{1}{2}\int_{\Omega_i} A\varepsilon(u_i):\varepsilon(u_i) \tag{27}$$

$$= -\frac{1}{2}\int_{\Gamma_T} gn_2u_2. \tag{28}$$

To differentiate the functional with respect to variations of the shape of Γ, we follow the approach of Murat and Simon [22,28] which we now briefly recall: Consider perturbations of an open set $\omega \subset \mathbf{R}^2$ of the form

$$\omega_t = \omega + t\theta,$$

where $\theta : \mathbf{R}^2 \longrightarrow \mathbf{R}^2$ is a sufficiently smooth function, and t is a small real parameter (the limit $t \to 0$ will be taken eventually).

Let z be a smooth function and consider the functionals, defined respectively as a volume integral and a surface integral

$$J_1(\omega) = \int_\omega z(u)$$

$$J_2(\omega) = \int_{\partial\omega} z(u),$$

where u is the solution of a partial differential equation $Au = 0$ in ω, with boundary conditions $Bu = 0$. The shape derivatives (or functional derivatives) of J_1, J_2 in the direction θ are defined by

$$J_i'(\omega)\theta = \lim_{t\to 0}\frac{J_i(\omega+t\theta)-J_i(\omega)}{t}.$$

When ω and u are sufficiently smooth, one can show that $J_i(\omega+t\theta) = J_i(\omega) + tJ_i'(\omega)\theta + o(t||\theta||)$, and further, that

$$J_1'(\omega)\theta = \int_\omega \partial_u z(u)u' + \int_{\partial\omega} z(u)\theta n, \tag{29}$$

$$J_2'(\omega)\theta = \int_{\partial\omega} \partial_u z(u)u' + \int_{\partial\omega}[Hz(u)+\partial_n z(u)]\theta n, \tag{30}$$

where $\partial_n f(x) = \nabla f(x)n$ is the normal derivative of f. The presence of the mean curvature H on $\partial\omega$ in the derivative of the surface integral J_2 results from taking variations of the surface measure. In these expressions, the local derivative u' of u at $x \in \omega$ is defined by

$$u'(x) = \lim_{t\to 0}\frac{u_t(x)-u(x)}{t},$$

where u_t is the solution to $Au = 0$ in ω_t with the boundary conditions $B_tu_t = 0$.

In our context, we consider perturbations (Ω_1, Ω_2) of the form

$$\Omega_i^t = \Omega_i + t\theta(x,y), \quad i = 1,2,$$

where $\theta : \mathbf{R}^2 \longrightarrow \mathbf{R}^2$ is sufficiently smooth. We assume that θ leaves the outer boundary $\partial\Omega$ fixed, (i.e., θ only modifies the shape of the interface) and that it preserves the volume of each subdomain Ω_i

$$\begin{cases} \theta(x,y) = 0 & \text{on } \partial\Omega \\ |\Omega_i^t| \quad = |\Omega_i| & i=1,2, \end{cases} \tag{31}$$

which imposes that

$$\int_\Gamma \theta n_i = 0. \tag{32}$$

Let (u_1^t, u_2^t) denote the solution to (26) for the configuration Ω_t

$$\begin{cases} \operatorname{div}(Ae(u_i^t)) = 0 & \text{in } \Omega_i^t \\ u_1^t \quad = 0 & \text{on } \partial\Omega_i \cap \Gamma_B \\ A\nabla u_2^t\, n_2 \quad = g\, n_2 & \text{on } \Gamma_T \\ u_i^t \quad \text{periodic on } \Gamma_V & \\ Ae(u_i^t)\, n_i^t \quad = p_t\, n_i^t, & \text{on } \Gamma + t\theta. \end{cases} \quad i=1,2. \tag{33}$$

The local derivatives (u_1', u_2') satisfy

$$\operatorname{div}(Ae(u_i')) = 0 \quad \text{in } \Omega_i \tag{34}$$

and are periodic on the sides Γ_V. The boundary condition (26.d) implies that $u_1' + \theta_n\partial_n u_1 = 0$ on Γ_B, which, given the hypothesis on θ, reduces to

$$u_1' = 0 \quad \text{on } \Gamma_B. \tag{35}$$

In the Appendix, we derive the expression of the shape derivative of $J(\Gamma)$. If $\Gamma \subset (0,1)\times(0,1)$ is a periodic simple curve, sufficiently smooth, one obtains

$$J'(\Gamma)\theta = \frac{1}{2}\int_\Gamma [A\varepsilon(u_1):\varepsilon(u_1) - A\varepsilon(u_2):\varepsilon(u_2)]\theta n_1$$
$$- \int_\Gamma p\,[\operatorname{div}(u_1) - \operatorname{div}(u_2)]\,\theta n_1. \tag{36}$$

In particular, if Γ is the flat interface $\Gamma^0 = (0,1)\times\{y_0\}$, the associated displacements are linear:

$$u_i(x,y) = (0, \frac{g}{\lambda+2\mu}y), \qquad i=1,2.$$

This greatly simplifies the computations (for instance all the terms on Γ_0 involving curvature vanish) and one finds in (36) that $J'(\Gamma_0)\theta = 0$ for any θ, i.e., the flat interface is a local extremum of the elastic energy functional J. We show below that the sign of the second derivative of J with respect to the interface shape variation tells if the extremum is a minimum or a maximum of the energy functional.

4.3 Second variation with respect to Γ

With the notations of the previous section, the second derivative (with respect to the interface shape variation) of a volume integral is given by [29]

$$J_1''(\omega,\theta,\theta) = (J_1')'(\omega,\theta,\theta) - J_1'(\omega)(\nabla\theta)\theta$$
$$= \lim_{t\to 0}\frac{J_1'(\omega+t\theta)\theta - J_1'(\omega)\theta}{t} - J_1'(\omega)(\nabla\theta)\theta.$$

If ω and θ are sufficiently smooth, Simon [29] has shown that

$$J_1(\omega+t\theta)=J_1(\omega)+tJ_1'(\omega)\theta + \frac{t^2}{2}J_1''(\omega,\theta,\theta)+o(t^2||\theta||).$$

For our objective functional in the form $J(\Gamma) = -1/2\int_{\Omega_i} A\varepsilon(u_i):\varepsilon(u_i)$, calculations similar to those presented in the Appendix show that at $\Gamma=\Gamma^0$

$$J''(\Gamma_0,\theta,\theta)=-2\int_{\Omega_i} A\varepsilon(u_i'):\varepsilon(u_i'), \tag{37}$$

which is negative, since the elastic densities $A\varepsilon(u_i'):\varepsilon(u_i')$ are quadratic and positive, and since the fields u_i' do not vanish identically. We can thus conclude that when t is small enough

$$J(\Gamma_0+t\theta)=J(\Gamma_0)+J'(\Gamma_0)\theta+J''(\Gamma_0,\theta,\theta)+O(||\theta||^2) < J(\Gamma_0).$$

In other words, any variation away from the flat interface decreases the value of the total elastic energy, which demonstrates the instability of the flat interface. Had we disregarded the work due to the external force g in equation (27), we would then have obtained an opposite sign (namely $+\frac{1}{2}\int_{\Omega_i} A\varepsilon(u_i):\varepsilon(u_i)$) for the relaxed energy, and thus stability would have been implied.

Finally if the boundary conditions at the bottom surface were different, we may ask the question regarding sensitivity of our conclusion. If, instead of imposing a zero displacement at the bottom surface, we apply a fixed load, as for the upper surface, the conclusion about stability is unchanged. Let us call h the load, then one has to add to (27) the following term $-\int_{\Gamma_B} hn_1v_1$, then following exactly the same manipulations as with the last term in (27) we arrive at the same final conclusion (37). It would be interesting to investigate in the future more general boundary conditions in order to extract the generic conditions that trigger an instability.

5 Discussion

5.1 Effect of external work on the calculation of the total energy

A point which is worth mentioning is that in writing the total energy, we must include both the intrinsic elastic energy and the work due to the external forces. Carelessness (for example not including the work done by surface forces) would be penalized by a fallacious conclusion: the surface would be stable! A simple argument that the external forces must be included is that when we perform a variation of the energy with the respect to the displacement field we must arrive to the appropriate bulk (Lamé equation) and boundary conditions, otherwise, the considered equations would not fulfill mechanical equilibrium. This requirement has guided our considerations.

5.2 Kinetics effects

By comparing the final state to the initial one, we did not include, *de facto*, explicitly the notion of kinetics. It is quite clear that two mechanisms play a major role: dissolution and diffusion in the fluid interstices. This has been treated for the free surface case where it has been shown that both dissolution and diffusion may be limiting factors for rocks [21]. We are planning to include diffusion in the fluid layer, and due to the thin fluid layer, it is likely that diffusion should have a two dimensional character (i.e. like surface diffusion; the diffusion constant should then be renormalized by the fluid layer). We expect the spectrum for the surface fluctuation of diffusion to scale like $D\ell^2q^4$, where ℓ is the fluid thickness, and D is the bulk diffusion constant in the liquid. By comparing to the usual diffusion limited spectrum Dq^2, the effective diffusion should be lowered by a factor of the order of $q\ell \ll 1$ (wavelengths of stylolites are usually much bigger than the fluid thickness).

For example, it has been found in [21] for quartz and other rocks that the dissolution is the slowest mechanisms. Now due to the thin fluid layer, we expect diffusion to compete, if not to limit, the instability. We hope to report along these lines in the near future.

5.3 Chemical potential considerations

We translate now the energy calculations performed in the previous sections in terms of chemical potential, for the sake of future kinetic calculations. The chemical potential of a solid element at the interface is obtained from the energy change with respect to the interface variation. This corresponds to the cost in energy that is needed to create a bump (a volume element) on the interface. More precisely, let E_T denote the sum of the elastic and surfaces energies, then the very definition of the change of the chemical potential is

$$\Delta\mu_T = -\frac{\delta E_T}{\delta V} \tag{38}$$

where δ denotes the functional derivative (derivative with respect to the interface shape variation). Since we limit ourselves to a one dimensional interface, the functional derivative corresponds to variation with respect to the interface profile $h(x)$. It follows that the added (or removed) volume element becomes an area element given by $\delta h dx$, where dx is a fixed interval along the x direction. Thus the chemical potential will be just proportional to $-\frac{\delta E_T}{\delta h}$. The surface energy per unit length along the y direction reads

$$E_s=\gamma\int\left(\left[1+\left(\frac{dh}{dx}\right)^2\right]^{1/2}-1\right)dx \tag{39}$$

and its variation with respect to the profile $h(x)$ is given by

$$\delta E_s = -\gamma \int \frac{d}{dx}\left(\frac{\frac{dh}{dx}}{\left[1+\left(\frac{dh}{dx}\right)^2\right]^{1/2}}\right)dx = -\gamma \int \kappa dx \delta h \tag{40}$$

where we have set

$$\kappa = -\frac{\frac{d^2h}{dx^2}}{\left[1+\left(\frac{dh}{dx}\right)^2\right]^{3/2}} \tag{41}$$

which is nothing but the interface curvature. It follows that the contribution to the chemical potential from surface energy is given by

$$\Delta\mu_s = -\frac{\delta E_T}{\delta V} = \gamma\kappa. \tag{42}$$

The contribution coming from elasticity is more subtle, since the elastic energy is defined in the bulk, while our wish is to define a surface chemical potential. It turns out that one may express the variation of the elastic energy with respect to the interface shape precisely as an integral over the surface, as written above for the surface energy in equation (40). The calculation is given in details in Section 4, and the desired result of the first variation is given by equation (36). In that section please note that δh used above is equivalent to θ multiplied by the normal vector; actually only normal displacements cause a shape change. The change in chemical potential due to stress is thus given by

$$\begin{aligned}\Delta\mu_e = & -\frac{1}{2}\left[A\varepsilon(u_1):\varepsilon(u_1) - A\varepsilon(u_2):\varepsilon(u_2)\right] \\ & + p\left[\mathrm{div}(u_1) - \mathrm{div}(u_2)\right]\end{aligned} \tag{43}$$

where we recall that u_i $(i = 1, 2)$ is the displacement field in medium i (see Fig. 3), ε is the deformation (or strain) tensor given by $\varepsilon(u) = (\nabla u + \nabla u^T)/2$, and A is the fourth order tensor which enters Hooke's law, namely the stress tensor σ is related to the deformation by $\sigma = A\varepsilon$ ($A_{ijkl} = \lambda\delta_{ik}\delta_{jl} + \mu\delta_{il}\delta_{jk}$ where λ and μ are the Lamé coefficients). Finally p is a Lagrange multiplier introduced in Section 4, and plays the role of a pressure like term of the thin fluid layer, but it must be solved for in a consistent manner, as we have seen in Section 4. We have seen that in the linear regime p coincides with the load g.

Note that if there was only one solid bounded by vacuum, or by a liquid, then the chemical potential would simply be given by

$$\Delta\mu_e = \frac{1}{2}A\varepsilon(u):\varepsilon(u) \tag{44}$$

as has been used in other contexts (see for example [14]).

Once the total chemical potential is obtained one can relate it to the kinetics of the interface. The most simple example is that the normal velocity is proportional to minus the chemical potential drop across the interface.

The surface evolution equation (at global equilibrium, as is the case in this problem) – or more precisely the normal velocity of the interface – vanishes if the chemical potential difference vanishes, or equivalently if the energy derivative with respect to the shape vanishes. The second variation of the energy with respect to the interface shape (which is computed in this paper) is proportional to the variation of the chemical potential $\Delta\mu$. It is the second variation of energy with respect to the shape that carries information on stability.

There are three major physical effects that drive the surface evolution: (i) if the interface is in contact with a reservoir of a liquid containing the molecules of the solid, and if one disregards diffusion (say if the attachement/detachment at the surface is the limiting mechanism), then the normal velocity is proportional to the chemical potential difference between two states (say the actual one and the initially flat one), this is the case treated in reference [14], (ii) if the surface dynamics evolves due to surface diffusion (as is probably the case for stylolites), then the surface velocity is proportional to the minus of the Laplacian of the chemical potential drop across the interface $\Delta\mu_T$. This is the case treated in Asaro-Tiller [3], and Yang and Srolovitz [34]. The conclusion about stability is the same in both cases, the difference is encoded in the proportionality pre-factor (which has the same sign in both cases) between the normal velocity and the second derivative of the energy with respect to the shape. (iii) Finally if diffusion in the bulk is included, then the normal velocity will be given by an integral equation, and the Kernel of the integral operator, is proportional to $\Delta\mu_T$ times a propagator (Green's function). The propagator expresses the fact that the dynamics becomes nonlocal (addition of mass at some point at the surface is felt by the molecules in the solution at a distant point-due to depletion-inducing thus a nonlocal self-interaction of the moving boundary). But in all the three cases, the instability is encoded in the sign of the second derivative of the energy (with respect to the interface shape). Of course the precise way the instability evolves later in time, depends on the kinetic mechanisms, but not the existence of the instability itself.

5.4 Instability of solid-solid interfaces: application to stylolites

Solid-solid interface roughening has also been studied, e.g. [1,12], where the two solids have different elastic moduli. There, it was demonstrated that an instability can emerge only if the two solids have different material properties. This markedly differs from our situation where the instability does occur even when the two solids have identical elastic properties. This is traced back to the very difference of the two models: in our case it is the thin fluid layer that transmits the stresses and materializes the interface, while in [12], the interface notion looses its meaning if the two solids have identical material properties (Eqs. (22) and (23) in [12] implies that the elastic energy vanishes exactly for $\chi = 1$, i.e. for identical material properties).

The present model considers a geometry which is close to that of a natural stylolite, where the interface separates two pieces of rock, and is a medium of dissolution in a fluid phase. Quantitative measurements on stylolite surfaces, using a high resolution profilometer, demonstrate that roughening does occur at all scales [27]. The interpretation of this observation is still controversial. It has been proposed that the roughening may be driven by a quenched noise initially present in the rock [6,27]. Here, we propose an alternative mechanism: stylolite might be inherently unstable, and the roughening could be driven by local gradients of strain energy. This interpretation is supported by the observation that stylolite do roughen even in very pure rocks such as chalk, where the amount of heterogeneities (quenched noise) is very low. However, further studies, together with laboratory experiments (mimicking the phenomenon) are needed before drawing more conclusive answers.

6 Conclusion

We have shown that a normal load on a solid-fluid-solid interface leads to an instability when using a boundary condition of transmission of the normal stress. We have shown both explicitly (from linear theory with regard to the perturbation of a flat interface) and from a more general consideration (still within linear perturbation, but without having resort to an explicit solution of the elastic field) that the flat interface is unstable.

When comparing the final state corresponding to a modulated surface with the initial state having a flat surface, we have shown that the modulated surface has lower energy. Given this fact, and the fact related to the Asaro-Tiller-Grinfeld instability, it is appealing to speculate that this should be the case in an for arbitrary geometry and arbitrary boundary conditions, provided that locally the considered moving interface possesses a non zero deviatoric stress component. A mathematical general proof is still lacking.

It must be kept in mind that the present study has introduced two simplifications. (i) The instability wavelength is small as compared with the lateral extent of the interface. This holds for natural interfaces that can be found in rocks, for example stylolites. If it occurs (in some special situation) that this is not the case, then one has to consider the role of lateral boundaries as well. (ii) We have considered a uniaxial stress and not a bi-axial one as occurs in realistic situations. Extensions to more general biaxial pre-stress would be interesting.

Finally, our study has focused on the birth of instability and on the lengthscales that are likely to grow first. Nonlinear effects should become decisive in the course of time as linear theory tells us that the amplitude should grow exponentially with time. How would the final state (if any) look like? How would coarsening (if any) occur, in that how fast is it? These question require a numerical study, and an appropriate way would be to make use of a phase-field model, like in [15].

We acknowledge financial support from the French ministry of research (PPF Dynamique des Systèmes Complexes). The support of Région Rhône Alpes (project Elasticité et Nanostructures) and of the ANR project Géocarbone are also gratefully acknowledged.

Appendix A: Proof of formula (36)

We first recall that the local derivatives u_i' are x-periodic on Γ_V and that $u_1' \equiv 0$ on Γ_B. Taking the shape derivative (29) of the expression (27) of the objective functional, we obtain

$$J(\Gamma)'\theta = -\int_{\Omega_i} A\varepsilon(u_i) : \varepsilon(u_i') \\ -\frac{1}{2}\int_{\partial\Omega_i} A\varepsilon(u_i) : \varepsilon(u_i)\,\theta n_i.$$

Integrating by parts and using the fact that θ vanishes on the boundaries but on Γ shows that

$$J(\Gamma)'\theta = -\int_{\Gamma} A\varepsilon(u_i) n_i u_i' - \int_{\Gamma_T} g\, n_2 u_2' \\ -\frac{1}{2}\int_{\Gamma} A\varepsilon(u_i) : \varepsilon(u_i)\,\theta n_i.$$

On the other hand, taking the shape derivative (30) of (28) yields

$$J(\Gamma)'\theta = \frac{-1}{2}\int_{\Gamma_T} g\, n_2 u_2'.$$

Combining the two previous expressions we obtain

$$\begin{aligned} J(\Gamma)'\theta &= \int_{\Gamma} A\varepsilon(u_i) n_i u_i' + \frac{1}{2}\int_{\Gamma} A\varepsilon(u_i) : \varepsilon(u_i)\,\theta n_i \\ &= \int_{\Gamma} p\, n_i u_i' + \frac{1}{2}\int_{\Gamma} A\varepsilon(u_i) : \varepsilon(u_i)\,\theta n_i. \end{aligned} \quad (45)$$

To eliminate the local derivatives in the above equality, we take the shape derivative of the constraint on the displacements, which is conveniently rewritten

$$\int_{\Gamma} u_i n_i = \int_{\Omega_i} \mathrm{div}(u_i) - \int_{\Gamma_T} u_2 n_2 = 0,$$

and obtain

$$0 = \int_{\Omega_i} \mathrm{div}(u_i') + \int_{\partial\Omega_i} \mathrm{div}(u_i)\,\theta n_i - \int_{\Gamma_T} u_2' n_2.$$

Integrating by parts the first term in the above expression, we arrive at

$$\int_{\Omega_i} u_i' n_i = -\int_{\Gamma} \mathrm{div}(u_i)\,\theta n_i.$$

Finally, injecting this equality in (45) proves (36).

References

1. E. Jettestuen, L. Angheluta, J. Mathiesen, F. Renard, B. Jamtveit, Phys. Rev. Lett. **100**, 096106 (2008)
2. F. Arthaud, M. Mattauer, Bull. Soc. Géol. Fr. **11**, 738 (1969)
3. R.J. Asaro, W.A. Tiller, Met. Trans. **3**, 1789 (1972)
4. R.G.C. Bathurst, *Carbonate sediments and their diagenesis* (Elsevier, Amsterdam, 1971)
5. J. Bisschop, D.K. Dysthe, Phys. Rev. Lett. **96**, 146103 (2006)
6. A. Brouste, F. Renard, J.-P. Gratier, J. Schmittbuhl, J. Struc. Geol. **29**, 422 (2007)
7. S.W.J. Den Brok, J. Morel, Geophys. Res. Lett. **28**, 603 (2001)
8. H.V. Dunnington, J. Sed. Petrol. **24**, 27 (1954)
9. D. Gal, A. Nur, E. Aharonov, Geophys. Res. Lett. **25**, 1237 (1998)
10. J.P. Gratier, L. Muquet, R. Hassani, F. Renard, J. Struc. Geol. **27**, 89 (2005)
11. M. Grinfeld, Sov. Phys. Dokl. **31**, 831 (1986)
12. M.A. Grinfeld, J. Nonlinear Sci. **3**, 35 (1993)
13. M.T. Heald, J. Geol. **63**, 101 (1955)
14. K. Kassner, C. Misbah, Europhys. Lett. **28**, 245 (1994)
15. K. Kassner, C. Misbah, Europhys. Lett. **46**, 217 (1999)
16. K. Kassner, C. Misbah, J. Müller, J. Kappey, P. Kohlert, Phys. Rev. E **63**, 036117 (2001)
17. R. Kerrich, Zentrabl. Geol. Paleontol. **5-6**, 512 (1977)
18. D. Koehn, J. Arnold, A. Malthe-Srenssen, B. Jamtveit, Am. J. Sci. **303**, 656 (2003)
19. D. Koehn, D.K. Dysthe, B. Jamtveit, Geochim. Cosmochim. Acta **68**, 3317 (2004)
20. D.L. Landau, E.M. Lifchitz, *Theory of elasticity*, Butterworth Heinemann (Oxford, UK, 1999)
21. C. Misbah, F. Renard, J.-P. Gratier, K. Kassner, Geophys. Res. Lett. **31**, L06618 (2004)
22. F. Murat, J. Simon, *Sur le contrôle par un domaine géométrique*, Rapport du Laboratoire d'Analyse Numérique, 189, 76015. Université de Paris 6, Paris (1976)
23. P. Nozieres, *The grinfeld instability of stressed crystals*, in *NATO Ad-vanced Research Workshop on Spatio-Temporal Patterns in Nonequilibrium Complex Systems*, edited by P.E. Cladis, P. Palffy-Muhoray, Vol. 21, 1994
24. W.C. Park, E.H. Schot, J. Sedimentary Petrology **38**, 175 (1968)
25. L.B. Railsback, L.M. Andrews, J. Struc. Geol. **17**, 911 (1995)
26. F. Renard, J. Schmittbuhl, J.P. Gratier, P. Meakin, E. Merino, J. Geophys. Res. **108**, B03209 (2004)
27. J. Schmittbuhl, F. Renard, J.P. Gratier, R. Tous-saint, Phys. Rev. Lett. **93**, 238501 (2004)
28. J. Simon, Second variations for domain optimization problems, in *4th Internationial conference on control of distributedparameter systems*, International Series, edited by F. Kappel, K. Kunish, W. Schappacher, Birkhauser, Berlin, 1989
29. J. Simon, *Differenciacion de problemas de con-torno respecto del dominio*, lecture notes available at `http://wwwlma.univ-bpclermont.fr/~simon/pagePubs.html#vardomaine`. Departamento de An'alisis Matem'atico, Universidad de Sevilla, Sevilla (1991)
30. H.C. Sorby, Proc. Royal Soc. London **12**, 538 (1863)
31. D.J. Srolovitz, Acta Metall. **37**, Koehn04621 (1989)
32. P.B. Stockdale, *Stylolites: Their nature and origin*, Ph.D. thesis, Indiana University Studies, 1922
33. R.H. Torii, S. Balibar, J. Low Temp. Phys. **89**, 391 (1992)
34. W.H. Yang, D.J. Srolovitz, Phys. Rev. Lett. **71**, 1593 (1993)

Dynamic Roughening and Fluctuations of Dipolar Chains

Renaud Toussaint,[1] Geir Helgesen,[2] and Eirik G. Flekkøy[1]
[1]Department of Physics, University of Oslo, P.O. Box 1048 Blindern, N-0316 Oslo, Norway
[2]Department of Physics, Institute for Energy Technology, N-2027 Kjeller, Norway
(Received 14 November 2003; published 2 September 2004)

Nonmagnetic particles in a carrier ferrofluid acquire an effective dipolar moment when placed in an external magnetic field. This fact leads them to form chains that will roughen due to Brownian motion when the magnetic field is decreased. We study this process through experiments, theory and simulations, three methods that agree on the scaling behavior over 5 orders of magnitude. The rms width goes initially as $t^{1/2}$, then as $t^{1/4}$ before it saturates. We show how these results complement existing results on polymer chains, and how the chain dynamics may be described by a recent non-Markovian formulation of anomalous diffusion.

DOI: 10.1103/PhysRevLett.93.108304 PACS numbers: 82.70.Dd, 05.40.–a, 83.10.Pp, 83.80.Gv

Existing observations of collective Brownian motion in polymer chains are restricted to averaged behavior in polymer melts or, in the case of single chain observations, subject to ambiguous interpretations. The latter fact is due to the existence of several active mechanisms in these systems, i.e., long-range hydrodynamic as well as dipolar interactions [1]. In this Letter we introduce direct experimental observations of Rouse behavior [2] of single particle chains along with a theoretical analysis to explain why. Recent understanding of the experimental interactions explains why both the hydrodynamic and dipolar interactions are suppressed in our case, as opposed to existing studies. While existing measurements are interpreted in terms of theories based on such interactions our experiment lends itself directly to the simpler Rouse model.

Magnetic holes [3–5] are nonmagnetic micrometer sized spheres suspended in a ferrofluid, much larger than the magnetite nanoparticles in suspension. In an external magnetic field $\mathbf{H}$, these holes acquire an effective dipolar moment equal to the opposite of the dipolar moment of the displaced ferrofluid. When placed between two nonmagnetic glass plates the spheres acquire interactions that may be fine-tuned to produce well defined separation distances and interparticle forces [4]. In a constant field, particles aggregate to form chains.

We study the kinematic roughening of an initially straight chain which is parallel to the glass plates, and much longer than the space between them. This changes the hydrodynamic interaction forces from $1/r$ to $1/r^2$, effectively making them short range, as is the $1/r^4$ behavior of the dipolar forces.

The tunability of the experimental interactions allows us to observe the scaling behavior over a significantly larger range (5 orders of magnitude in the dynamic domain) than has been possible in earlier studies.

In the end we show how the Markovian N-particle description of the entire chain may be contracted to a non-Markovian description of a single particle in the chain. This is done by integrating out all interaction degrees of freedom. What is left is a generalized Langevin equation with long term memory. It has recently been shown how such an equation may be used to predict anomalous diffusion exponents [6], and indeed these exponents coincide with our independent predictions and measurements. This system is the first experimental realization confirming this theory.

The ability of particle chains to change the rheological properties of their carrier fluids has given rise to practical applications and designs such as dampers, hydraulic valves, clutches, and brakes [7]. In constant fields (electric or magnetic, depending on the nature of the dipoles), these chains aggregate laterally [8] due to their thermal fluctuations. Therefore, the precise quantification and understanding of these fluctuations along an *isolated* dipolar chain is an important component to understand the aggregation phenomena in constant fields of magnetorheological [9] or electrorheological [10] fluids, as well as in systems of magnetic holes [11].

We note that also by coating the microspheres with bioactive materials, such as streptavidin [12], they may be used for the direct manipulation of single strands of DNA. For such an application the quantitative control of Brownian fluctuations is essential.

In the experiments monodisperse polystyrene spheres [13] of diameters $a = 3.0$ or 4.0 μm were dispersed in a kerosene based ferrofluid [14] of susceptibility $\chi = 0.8$ and viscosity $\eta = 6 \times 10^{-3}$ Pa s, inside a glass cell of thickness $d = 10$ μm and lateral extent 38×8 mm. A pair of outside coils produced magnetic field strengths up to $H = 20$ Oe. The setup was mounted under an optical microscope with an attached video camera recording four frames per second. Low volume fractions (<1%) of microspheres were used and chains were grown [11] by applying a constant field of about $H = 18$ Oe parallel to the thin ferrofluid layer for about 20 min. Because of the nonmagnetic character of the glass plates, particles are centered midway between them [4].

The cell was searched for long isolated chains of 30–120 spheres. The field was then reduced to a constant value H in the range $2 \leq H \leq 10$ Oe while the motion of one long chain was recorded and analyzed. One pixel of the video image corresponded to 0.5 μm, and the uncertainty in particle position could be reduced to 0.2 μm by utilizing the intensity profile of the pixels showing the particle. The experiments illustrated in Fig. 1 are challenging in part because this accuracy is needed to reveal the scaling behavior of the chains.

In order to obtain an equation of motion for chains we define the lateral displacement of particle i, h_i, from the initial straight line. A particle pair at a separation r and angle θ to the external magnetic field experiences a coupling energy $U = \mu_f \sigma^2(1 - 3\cos^2\theta)/(4\pi r^3)$, where $\sigma = -\pi a^3[\chi/(6 + 4\chi)]\mathbf{H}$ [3,15]. The ratio of the maximum interaction energy over the thermal energy $k_B T$ characteristic of the random forces due to the molecular motion in the solvent is defined as [16] $\lambda = (\mu_f \sigma^2)/(2\pi a^3 kT)$. In Fig. 1 the initial value $\lambda = 866$ is reduced to $\lambda = 24$. Neglecting all magnetic interactions but the nearest neighbor ones and performing a Taylor expansion of the magnetic interaction potential around the minimal energy configuration, a straight line with spacing a, the lateral component of the magnetic force on sphere i is $F_i^M = \alpha(h_{i+1} - 2h_i + h_{i-1})$, with $\alpha = \pi\mu_f \bar{\chi}^2 H^2 a/12 = 6\lambda kT/a^2$. Since the Reynolds number in this system is very small (typically $\mathrm{Re} = 10^{-5}$), the hydrodynamic forces are linear in the particle velocity, and $F_i^H = -\kappa \dot{h}_i$, where $\kappa = 3\pi\eta a$.

Newton's second law for the ith sphere is then

$$m\ddot{h}_i = F_i^M + F_i^H + \zeta_i(t), \qquad (1)$$

where the fluctuating force $\zeta_i(t)$ is due to the molecular nature of the fluid and gives rise to the Brownian motion of the particle. At time scales exceeding the viscous damping time $t_m = m/\kappa = a^2\rho/18\eta \approx 10^{-7}$ s, the inertial term $m\ddot{h}_i$ is negligible. Because of the presence of confining plates, inertial motion in the fluid also decays on this time scale, so that we can neglect any non-Markovian corrections to Eq. (1) as well as such corrections in the fluctuating force [17]. We may therefore write $\langle \zeta_i(t)\zeta_j(0)\rangle = 2\kappa k_B T\delta(t)\delta_{ij}$, where the prefactor reflects the equipartition of particle kinetic energy, i.e., $k_B T = \langle m\dot{h}_i^2\rangle$ [18]. Combining the above equations Eq. (1) can be written

$$\dot{h}_i = \frac{\alpha}{\kappa}(h_{i+1} + h_{i-1} - 2h_i) + \frac{1}{\kappa}\zeta_i(t). \qquad (2)$$

For spatial scales above a, this reduces to the Rouse model, $\kappa\partial h/\partial t = \alpha a^2 \partial^2 h/\partial^2 x^2 + \zeta_i(t)$, famous in polymer dynamics but usually not confirmed by experiments because of hydrodynamic interactions [2]. This also corresponds to the Edwards-Wilkinson equation, model for kinetic interface growth [19].

We consider an isolated chain of N particles and are interested in the dynamic roughening of the chain. To observe this experimentally λ is decreased from a value $\lambda_0 \gg 1$ to a finite value still greater than 1 (so that the chain does not melt).

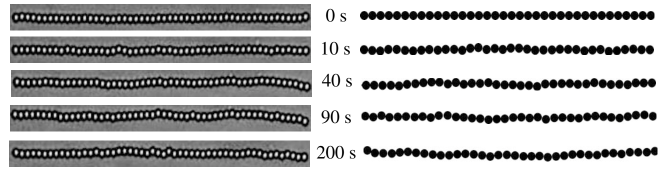

FIG. 1. Typical dynamic roughening of dipolar chains of 52 magnetic holes of diameter 4 μm after a sudden decrease of the external magnetic field: experiments (left) and simulations (right).

It is convenient to describe this by using the discrete space-Fourier transform along the chain $\tilde{h}_n = \frac{1}{N} \times \sum_{j=0}^{N} h_j e^{-2i\pi n j/N}$, for $n = 0 \cdots N-1$. Equation (2) then takes the form

$$\dot{\tilde{h}}_n = -\omega_n \tilde{h}_n + \tilde{\zeta}_n/\kappa, \qquad (3)$$

with the dispersion relation $\omega_n = 2\alpha[1 - \cos(2\pi n/N)]/\kappa$, and random terms obeying $\langle \tilde{\zeta}_m(t)\tilde{\zeta}_n^*(0)\rangle = 2\kappa k_B T\delta(t)\delta_{mn}/N$. Equation (3) is easily solved to give

$$\tilde{h}_n(t) = \tilde{h}_n(0)e^{-\omega_n t} + \int_0^t dt' e^{-\omega_n(t-t')}\tilde{\zeta}_n(t')/\kappa. \qquad (4)$$

Setting $\tilde{h}_n(0) = 0$ and taking the thermodynamic average of the square of the above equation leads to

$$\langle \tilde{h}_n(t)\tilde{h}_m^*(t)\rangle = \frac{k_B T}{\kappa N}\frac{1 - e^{-2\omega_n t}}{\omega_n}\delta_{mn} \qquad (5)$$

for $n \neq 0$, and $\langle |\tilde{h}_0(t)|^2\rangle = (2k_B T/\kappa N)t$. It is seen from Eq. (5) that each Fourier mode is initially in a free diffusion regime, $\langle |\tilde{h}_n(t)|^2\rangle \sim t$, for $t \ll \tau_n = 1/2\omega_n$ and saturates when $t \gg \tau_n = 1/2\omega_n$. The minimum and maximum saturation times are, respectively, $\tau_{N/2} = \tau = \kappa/8\alpha$ and $\tau_1 = N^2\tau/\pi^2$ for the shortest and longest wavelength.

We are interested in the mean square width of the chain $W^2 = \sum_i (h_i - \sum_j h_j/N)^2/N = \sum_{n=1}^{N-1}\langle |\tilde{h}_n|^2\rangle$. When $t \ll \tau$ all Fourier modes are in free diffusion and $W^2 \approx 2k_B T t/\kappa$. This result arises only because of the existence of a shortest wavelength a in the system. In the continuum limit $a \to 0$, $\tau \to 0$ and this regime does not exist. Later on the modes associated with progressively longer wavelengths reach their saturated states, which is reflected in a new scaling behavior of W. By inserting Eq. (5) in the above expression for W^2 it is straightforward to show that it satisfies the Family-Vicsek scaling form $W^2 = NF(t/N^2)$. Moreover, the exact form of F may be obtained. Along with the expressions for τ, κ, and α this gives the result

$$\frac{W^2 H^2 a}{N k_B T} = \begin{cases} \frac{2N}{3\pi\eta}\frac{H^2}{N^2}t & \text{when } t \ll \tau \\ \sqrt{\frac{8}{\pi^3\eta\mu_f\bar{\chi}^2}}\sqrt{\frac{H^2}{N^2}t} & \text{when } \tau \ll t \ll \tau N^2/\pi^2. \\ \frac{2}{\pi\mu_f\bar{\chi}^2} & \text{when } t \gg \tau N^2/\pi^2 \end{cases}$$

The hydrodynamic coupling between the particles and the confining plates was taken into account by renormalizing the drag coefficient as $\eta/\eta_o = 2/[1 - 9a/16d] - 1 = 1.40$ (1.7) for $a = 3$ μm (4 μm) [20]. This scaling law was checked in 15 experiments where chains of $N = 36$ to 59 spheres of diameters 3 or 4 μm were allowed to evolve from states where λ was reduced to values between 2.7 and 267. In Fig. 2 the average of the scaled width $WH\sqrt{a/N}$ is displayed as a function of the scaled time H^2t/N^2. The average is taken both over time intervals of $0.01t$ and over different experiments.

The relevance of the long-range nature of the dipolar interactions and of the linearization of the magnetic interactions was studied via Brownian dynamics simulations, where Eq. (1) without the $m\ddot{h}_0$ term was solved, this time with the full dipolar form of the magnetic interactions computed for every particle pair. A repulsive potential $\sim\exp(-100r/a)$ when $r < a$ was used to prevent any significant overlaps. The average width over 100 simulations was evaluated for $N = 36$, $a = 3$ μm, and $H = 4$ Oe. Figure 2 demonstrates that both the simulations and theoretical results agree with experimental measurements in all three scaling regimes, although the crossover between the $t^{1/2}$ and $t^{1/4}$ regimes extends over a full decade. The $W \sim t^{1/4}$ regime is visible over roughly 2.5 decades. The high variance around the average of W in the saturated regime comes from the small number (three) of experiments that were carried out at this reduced time. Lubrication or cohesion forces between the particles are irrelevant for the collective behavior of these lateral fluctuations, as shown by the agreement between experiments and simulations, where these were absent. This can be attributed to the presence of surfactants in the ferrofluid, preventing flocculation of the particles, and to the fact that lubrication forces act mainly along the direction of separation vectors between neighboring particles, which are close to the field direction, and have thus a negligible contribution to the transverse components studied here [21].

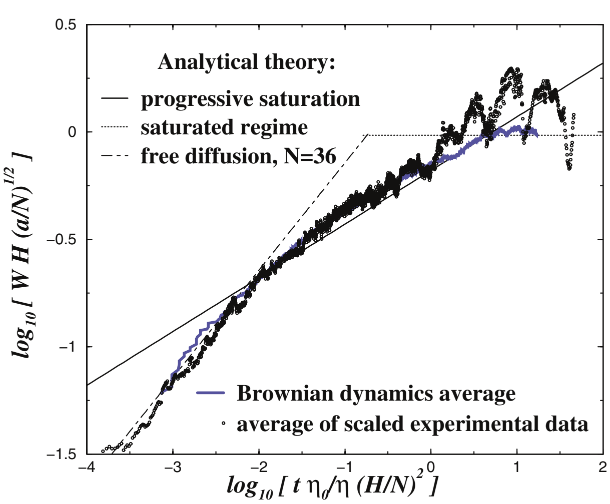

FIG. 2 (color online). Scaling of the random mean square width of the transverse displacements: theory, experiments, and Brownian dynamics result. The units are Oe, μm, μm, and seconds for H, a, W, and t, respectively.

It is also possible to obtain the dynamic scaling from the equilibrium behavior. For this purpose consider the departure Δh_i from an arbitrary initial configuration, i.e., $\Delta h_i(t, t_0) = h_i(t + t_0) - h_i(t_0)$. Using Eq. (4) again we find that the averaged space-Fourier transform of $\Delta h_i(t, t_0)$ obeys

$$\frac{\langle|\Delta\tilde{h}_n(t, t_0)|^2\rangle}{At} = \frac{1 - e^{-\omega_n t}}{\omega_n t}, \qquad (6)$$

where $A = 2k_BT/3\pi\eta aN$. Above we have used the saturation level $\langle|\tilde{h}_n(t_0)|^2\rangle = k_BT/\kappa N\omega_n$ from Eq. (5). Comparing this expression with Eq. (5) shows that the lateral fluctuations at equilibrium behave similarly to the lateral displacements starting from a straight chain during the nonequilibrium roughening stage, but display an amplitude $\sqrt{2}$ times larger and develop 2 times more slowly.

In Fig. 3 we have compared the theory of Eq. (6) to $N = 57$, $a = 3$ μm experiments with $\lambda = 113$ and 18.1, for which $\tau = 0.022$ and 0.14 s. For each t the power spectrum $|\Delta\tilde{h}_n(t, t_0)|^2$, calculated using a Hamming window, was averaged over all possible t_0's in the 30 min the experiment lasted. The agreement between these experiments and this theory, where there are no free parameters, is satisfactory.

Finally, we sketch the structure of the connection between the present problem and the general framework of anomalous diffusion of particles in systems with memory [6]. We consider particle $i = 0$ and use Eq. (1) to integrate out the $i \neq 0$ variables. This does not modify the underlying physics of the system but allows us to map it on a non-Markovian description for this single particle, in a background consisting of both the fluid and the rest of

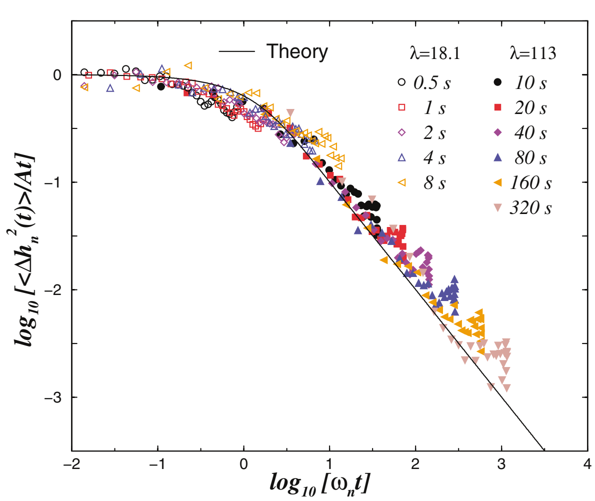

FIG. 3 (color online). Power spectrum of the space-Fourier transform of the fluctuations normalized by time.

the particles, which displays memory effects mathematically incorporated in a response function $\Gamma(t)$. By applying time Fourier transforms and neglecting all but the $i = 0$ mass it is possible to arrive at [21]

$$m\hat{\ddot{h}}_0(\omega) = -m\hat{\Gamma}(\omega)\hat{\dot{h}}_0(\omega) + \hat{F}(\omega), \tag{7}$$

where the time Fourier transform is denoted by hat symbols, $F(t)$ is the fluctuating part of the force, and $\tilde{\Gamma}(\omega) = (4/m)\sqrt{\alpha\kappa/i\omega}$ for $1/\tau_1 \ll \omega \ll 1/\tau$ and $\hat{\Gamma}(\omega) \sim (4/m)\sqrt{\alpha\kappa\tau_1/i}$ for $\omega \ll 1/\tau_1$. The inverse Fourier transform of Eq. (7) is a generalized Langevin equation of the Mori-Lee form [6],

$$m\ddot{h}_0(t) = -m\int_{-\infty}^{t} dt_1\Gamma(t - t_1)\dot{h}_0(t_1) + F(t). \tag{8}$$

From the exact form of $F(t)$ [21] the fluctuation dissipation theorem for such a generalized Langevin equation, $\langle F(t)F(0)\rangle = 2mk_BT\Gamma(|t|)$, can be checked directly. The memory effects and correlations in $F(t)$ come from the interaction between the rest of the chain and the fluid. According to theory [6], the random mean square width of the observed particle's displacement scales at long time as $W^2 \sim t^{1-\alpha}$ if $\hat{\Gamma}(\omega) \sim \omega^{-\alpha}$ in the limit $\omega \sim 0$. Here, the asymptotic behavior of the response function corresponds to $\alpha = 0$ for finite chains and $t > \tau_1$, and to $\alpha = 1/2$ for times below τ_1 ($\tau_1 \to \infty$ when $N \to \infty$). The observed behavior $W^2 \sim t^{1/2}$ for $t \ll \tau_1$ is then in agreement with this theory.

For chains in an unbounded medium, the Zimm model predicts $W \simeq t^{1/3}$ [2], and experiments carried on various magnetorheological fluids report $W \simeq t^{0.35\pm0.05}$ [1]. This behavior is attributed to either hydrodynamic or long-range dipolar interactions. In our system hydrodynamic interactions are suppressed by the walls. This may be understood by noting that the flow in our system is described by a simple Darcy law $v \sim -\nabla P$ at length scales above d, along with $\nabla^2 P = 0$. This implies that a local flow perturbation decays as $1/r^2$ which is faster than the $1/r$ decay, given by the Oseen tensor in an unbounded medium [2]. Since the chain length is typically much larger than d, hydrodynamic interactions are local and do not affect the longer wavelengths of our chain motion. On the other hand, we note that if our experimental and simulation data were truncated as $\log_{10}(H^2t/N^2) \leq -1$ they could support the $W \simeq t^{3/8}$ interpretation made by Furst and Gast [1]. As these authors attribute their exponent 3/8 to long-range dipolar interactions, our results may indicate that such interactions do play a role, but only in a crossover regime to the $W \simeq t^{1/4}$ behavior.

In conclusion, we have established the scaling behavior of confined dipolar chains over 5 orders of magnitude by matching experiments, theory, and Brownian dynamics simulations. We have also related this system to nearby theories of both polymer models, kinetic interface growth, and non-Markovian formulations of anomalous diffusion. This allowed us to show that the quasi-two-dimensional nature of this system reduces it to a Rouse behavior and that this system experimentally validates this recent non-Markovian theory of anomalous diffusion. These results are attractive, in particular, because of the versatility and easy control of the experiments.

[1] E. M. Furst and A. P. Gast, Phys. Rev. E **62**, 6916 (2000); **58**, 3372 (1998); S. Cutillas and J. Liu, Phys. Rev. E **64**, 011506 (2001); A. S. Silva, R. Bond, F. Plouraboué, and D. Wirtz, Phys. Rev. E **54**, 5502 (1996).

[2] A. Y. Grosberg and A. R. Khokhlov, *Statistical Physics of Macromolecules* (AIP Press, New York, 1994).

[3] A. Skjeltorp, Phys. Rev. Lett. **51**, 2306 (1983).

[4] R. Toussaint *et al.*, Phys. Rev. E **69**, 011407 (2004).

[5] A. Skjeltorp and G. Helgesen, Physica (Amsterdam) **176A**, 37 (1991).

[6] R. Morgado, F. A. Oliveira, G. G. Batrouni, and A. Hansen, Phys. Rev. Lett. **89**, 100601 (2002).

[7] *Proceedings of the 5th International Conference on Electro-rheological Fluids, Magneto-rheological Suspensions and Associated Technology*, edited by W. A. Bullough (World Scientific, Singapore, 1996).

[8] T. C. Halsey and W. Toor, J. Stat. Phys. **61**, 1257 (1990); Phys. Rev. Lett. **65**, 2820 (1990); W. R. Toor, J. Colloid Interface Sci. **156**, 335 (1993); J. E. Martin, J. Odinek, and T. C. Halsey, Phys. Rev. Lett. **69**, 1524 (1992).

[9] J. E. Martin, K. M. Hill, and C. P. Tigges, Phys. Rev. E **59**, 5676 (1999); J. Liu *et al.*, Phys. Rev. Lett. **74**, 2828 (1995); M. Fermigier and A. P. Gast, J. Colloid Interface Sci. **154**, 522 (1992); G. Helgesen *et al.*, Phys. Rev. Lett. **61**, 1736 (1988).

[10] S. Fraden, A. J. Hurd, and R. B. Meyer, Phys. Rev. Lett. **63**, 2373 (1989); J. E. Martin, J. Odinek, T. C. Halsey, and R. Kamien, Phys. Rev. E **57**, 756 (1998).

[11] J. Cernak, G. Helgesen, and A. T. Skjeltorp, Phys. Rev. E (to be published).

[12] D. Wirtz, Phys. Rev. Lett. **75**, 2436 (1995).

[13] J. Ugelstad *et al.*, Adv. Colloid Interface Sci. **13**, 101 (1980).

[14] Type EMG 909, produced by FerroTec, 40 Simon Street, Nashua, NH 03060-3075.

[15] B. Bleaney and B. Bleaney, *Electricity and Magnetism* (Oxford University Press, Oxford, 1978).

[16] P. G. De Gennes and P. A. Pincus, Phys. Kondens. Mater. **11**, 189 (1970).

[17] E. G. Flekkøy and D. H. Rothman, Phys. Rev. E **53**, 1622 (1996); Phys. Rev. Lett. **75**, 260 (1995).

[18] F. Reif, *Fundamentals of Statistical and Thermal Physics* (McGraw-Hill, Singapore, 1965).

[19] S. F. Edwards and D. R. Wilkinson, Proc. R. Soc. London A **381**, 17 (1982).

[20] L. P. Faucheux and A. J. Libchaber, Phys. Rev. E **49**, 5158 (1994).

[21] R. Toussaint, E. G. Flekkøy, and G. Helgesen, report.

Memory of fluctuating Brownian dipolar chains

Renaud Toussaint,[1,*] Eirik G. Flekkøy,[2] and Geir Helgesen[3]
[1]Institute of Globe Physics in Strasbourg (IPGS), UMR 7516 CNRS, 5 rue Descartes, F-67084 Strasbourg Cedex, France
[2]Department of Physics, University of Oslo, P.O. Box 1048 Blindern, NO-0316 Oslo, Norway
[3]Institute for Energy Technology, NO-2027 Kjeller, Norway
(Received 19 June 2006; published 20 November 2006)

Nonmagnetic particles in suspension in a ferrofluid act as magnetic holes when an external magnetic field is exerted: They acquire an effective dipolar moment opposing the surrounding one, which induces dipolar magnetic interactions. For a large enough imposed field and particle size, the induced interactions dominate the thermal forces, dipolar chains form. At equilibrium, these chains fluctuate under the effect of brownian noise. When the imposed magnetic field is suddenly decreased, these chains roughen dynamically. We study the time and size scaling of these fluctuations and roughening, and the relationships between the equilibrium and out of equilibrium behavior. We compare the experimental data both to Brownian dynamics simulations, and to a simple theory of semiflexible polymer chains, a generalization of the Rouse model. The scaling behavior of the experiments agree with the predictions of both theory and simulations over 5 orders of magnitudes. The roughening follows three successive regimes: The root mean square width of the chain initially evolves as $W \sim t^{1/2}$, then it enters a subdiffusive regime where $W \sim t^{1/4}$ and eventually it saturates to a level $W \sim N$, where N is the number of particles in the chain. The exact prefactors as a function of the applied field, particle diameter, and temperature are also derived analytically. We also show that this phenomenon can be described equivalently as a non-Markovian diffusion process for a particle in an environment with memory effects. Within this framework, our system is shown to confirm the predictions of theories for anomalous diffusion in systems with memory.

DOI: 10.1103/PhysRevE.74.051405 PACS number(s): 82.70.Dd, 75.50.Mm, 05.40.−a, 83.10.Pp

I. INTRODUCTION

When micrometer sized nonmagnetic spheres are suspended in a magnetized ferrofluid they define magnetic holes that interact very much like magnetic dipoles [1–3]. These dipole interactions may be precisely controlled by the external field. In 1983, Skjeltorp introduced such a system that allowed direct observation by the use of transparent glass plates and perfectly monodisperse Ugelstad spheres [4].

A population of magnetic holes may be brought to organize in a rich variety of structures through their induced dipole interactions [2]. One of the simplest equilibrium structures that can be obtained, is a straight dipolar chain. When the particles are sufficiently small such chains exhibit lateral thermal fluctuations. We have recently described these fluctuations and shown that dipolar chains, or Brownian worms, are described by the Rouse model [5,6] for polymer dynamics. Since hydrodynamic interactions between different chain segments are suppressed by the boundaries the present system in fact realizes the Rouse model more closely than any free polymer, and to our knowledge, any comparable experimental system.

The external control of the interparticle forces allows us to study the roughening of an initially straight chain. We study this dynamic process experimentally by optical microscopy, and we compare it to Brownian dynamics simulations as well as analytical results. As a main result we observe growth exponents that agree well with the predictions [5]: Initially the root-mean-square (rms) width of the chain grows with a diffusive exponent of 1/2 which subsequently crosses over to an exponent of 1/4 before the chain width saturates at an asymptotic value that depends on the chain length. Analytically these exponents are derived from a discrete version of the Edwards-Wilkinson equation [7]—or equivalently, the Rouse model.

Chain fluctuations in equilibrium are closely connected to the dynamic roughening process. We show that the dynamic roughening from an initially straight chain, and the departure from an initially rough state at equilibrium, are two equivalent problems, characterized by the same Family-Vicsek scaling with same roughness and dynamic exponents. Only the prefactor of the mean square chain width is different.

Having derived the discrete Edwards-Wilkinson equation with the coefficients corresponding to our experiment, we turn to an alternative theoretical description by which we identify the dynamic roughening as a process of anomalous diffusion [8]. The long memory effects that are a prerequisite for any process of anomalous diffusion, stem from the propagation of perturbations along the chain, and we compute the observed anomalous diffusion exponent of 1/4.

In general, the lateral fluctuations of dipolar chains have attracted much attention over the past two decades. The systems in which such chains have been studied include in particular magnetorheological [9–12] and electrorheological (ER) suspensions. In these systems, the dipolar moment is fixed inside the particles, in contrast to the present system where the interactions of the nonmagnetic particles only reflect the magnetization of the surrounding fluid. Much of the interest in electrorheological and magnetorheological fluids is based on their ability to form chains under application of an external field, thereby changing the rheology. Technologically these effects may allow the development of dampers,

*Electronic address: renaud.toussaint@eost.u-strasbg.fr

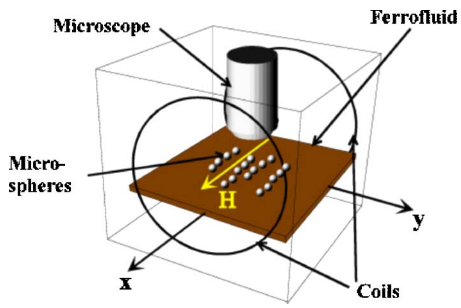

FIG. 1. (Color online) The experimental setup.

hydraulic valves, clutches or brakes [13–17]. Over time chains may aggregate laterally due to their Brownian motion. These effects are analogous to the van der Waals interaction, and have been analyzed by Halsey and Toor as well as Martin *et al.* [18–21]. Therefore, the precise quantification of Brownian motion of *a single* isolated dipolar chain is an important compound to understand the larger scale aggregation phenomena, whether this happens in magnetorheological [22–24] or electrorheological [21,25,26] fluids, or in systems of magnetic holes [27,28].

The paper is organized as follows: in Sec. II, we describe the experimental system under study along with some basic theoretical considerations. In Sec. III, we derive discrete Edwards-Wilkinson equation and the dynamical scaling of a dipolar chain. In Sec. IV, we describe the numerical Brownian dynamic model designed to simulate the chain motion. In Sec. V, we compare the analytical, numerical, and experimental results for the dynamic chain roughening. In the following section, we derive analytically the connections between the out-of-equilibrium roughening problem, and the equilibrium fluctuations. Next, in Sec. VII, we derive the linear response function of the chain, and show how the dynamic scaling may be understood in the theoretical framework of diffusion in systems with memory [8]. The conclusions are eventually summarized in Sec. VIII.

II. THEORETICAL BASIS AND THE EXPERIMENTAL SETUP

The magnetic properties of a ferrofluid stem from suspended magnetite particles which are of nanometer size. Therefore the magnetic properties of the ferrofluid is homogeneous on the scale of the Ugelstad spheres. These spheres are of nonmagnetic polystyrene designed according to Ugelstads technique [4]. They are embedded in a kerosene-based ferrofluid [29] confined between two parallel glass plates with a 10 μm separation (see Fig. 1).

Since the Ugelstad spheres are not magnetized by the external field they represent an effective dipole with a moment approximately equal to and opposite of the dipolar moment of the displaced ferrofluid. We are currently working to quantify this effective moment more precisely. However, to first approximation it may be written $\sigma=-V\bar{\chi}\mathbf{H}$ where χ is the magnetic susceptibility of the ferrofluid, $\mathbf{H}$ the magnetic field, V is the holes volume and $\bar{\chi}=3\chi/(3+2\chi)$ is an effective susceptibility taking into account the demagnetization factor associated with the spherical shape of the particles [30]. In the absence of confining walls the magnetic interaction potential between two holes of diameter a, may be written [30]

$$U=\frac{\mu_f\sigma^2}{4\pi}\frac{1-3\cos^2\theta}{r^3}, \tag{1}$$

where r is the distance between the centers of the spheres, with a separation vector lying at an angle θ to the external magnetic field. The ratio of the magnetic interaction energy to the thermal energy kT is denoted λ, and can be estimated from the above equation as [31]

$$\lambda=\frac{\mu_f\sigma^2}{2\pi a^3kT}=\frac{\mu_f\bar{\chi}^2H^2\pi a^3}{72kT}. \tag{2}$$

When λ exceeds 1, the dipolar interactions lead the particles to organize in long chains parallel to the imposed field. At $\lambda \gg 1$, these chains are essentially straight and rigid, and the particles are in contact. If the external field is suddenly reduced to values that are still greater than 1, Brownian forces from the embedding fluid leads to a dynamic roughening of the chains (see Fig. 2).

In the experiments the polystyrene spheres [4], which were of equal size, had diameters either $a=3.0$ or 4.0 μm. They were dispersed in a kerosene-based ferrofluid [29] of susceptibility $\chi=0.8$ and viscosity $\eta=6\times10^{-3}$ Pa s, inside a glass cell of size 38 mm $\times$ 8 mm $\times$ 10 μm. A pair of outside coils produced a magnetic field parallel to the long axis of the cell with field strength up to $H=20$ Oe. The setup was mounted under an optical microscope using an optical magnification of 20$\times$ and having an attached video camera that recorded to a digital tape recorder at a speed of 25 frames per second. Low volume fractions (1%) of microspheres were used and chains were grown by applying a constant field of about $H=18$ Oe parallel to the thin ferrofluid layer for about 20 minutes [28]. The cell was then searched for long chains containing typically 20–120 spheres which were well separated from neighboring chains in order to avoid interchain interactions. The field was then reduced to a constant value H in the range 2 Oe$\leq H \leq$10 Oe while the motion of one long chain was recorded. The recorded video, which had a frame size of 720$\times$576 pixels, was analyzed with a sampling rate of four frames per second. One pixel of the video image corresponded to 0.5 μm, and the uncertainty in particle position could be reduced to 0.2 μm by utilizing the intensity profile of the pixels showing the particle. The initial roughness of the chains before reducing the field strength was less than the experimental resolution of 0.2 μm, and the time to reduce the magnetic field from the initial to the final value was about 1 s, thus introducing a similar uncertainty in the starting moment of free fluctuations. During an experiment the nonmagnetic particles were centered midway between the upper and lower glass plate of the cell due to magnetic repulsion from the nonmagnetic walls (the magnetic "mirror image" effect) [2]. The experiments illustrated in Fig. 2 are challenging in part because this accuracy is needed to reveal the scaling behavior of the chains.

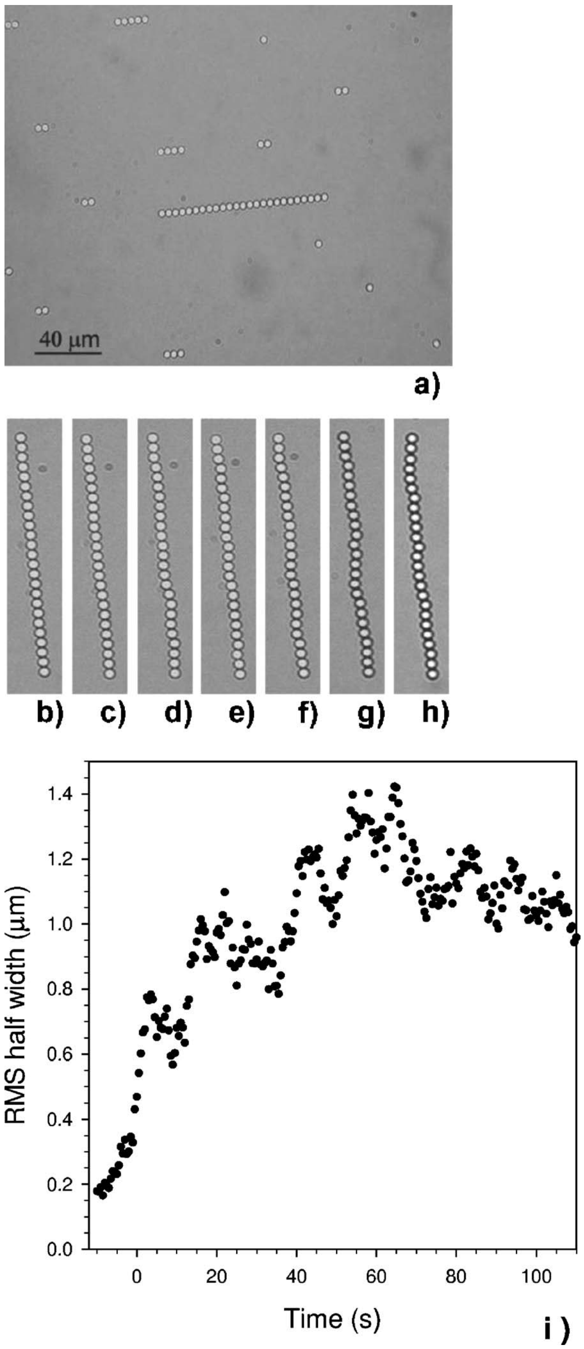

FIG. 2. Dynamic roughening of dipolar chains of magnetic holes of diameter 4 μm after a decrease of the external magnetic field from $\lambda=866$ to $\lambda=24$ at $t=0$. (a) Region with low density of chains, (b) the longest chain 10 s before the field was reduced ($t=-10$ s), (c) $t=0$, (d)–(h) $t=3$ s, 10 s, 30 s, 60 s, and 150 s, respectively. (i) Time evolution of the root-mean-square half-width of the chain.

III. ANALYSIS OF LATERAL FLUCTUATIONS

To obtain the dynamic description of the chain we start from the nearest neighbor interactions and consider departures from the minimum energy configuration of the straight chain.

First we estimate the magnitude of next-nearest-neighbor interactions: From Eq. (1) we see that $U \propto 1/r^3$ and therefore that the ratio of the nearest-neighbor energy to the energy associated with the remaining interactions may be written

$$\frac{U(a)}{\sum_{n=2}^{\infty} U(na)} \approx \frac{aU(a)}{\int_{2a}^{\infty} drU(r)} = 8. \tag{3}$$

This we will take as justification to neglect interactions beyond nearest neighbor ones.

To identify the equation of motion for the position h_i of particle i in the direction normal to the applied field, we perform a Taylor expansion of the magnetic interaction potential in Eq. (1) around the rigid chain reference state. This gives the normal component of the magnetic force acting on sphere i as

$$F_i^M = k_\perp (h_{i+1} - 2h_i + h_{i-1}) \tag{4}$$

$$\text{with } k_\perp = \pi\mu_f \bar{\chi}^2 H^2 a/12, \tag{5}$$

where a is the particle diameter, and H the external applied field. Typically $a \approx 3$ μm, and $H=20$ Oe, so that $k_\perp \approx 1.2 \times 10^{-6}$ kg/s^2.

Since the Reynolds number in this system is very small (using the particle diameter $a=1$ μm and the thermal particle velocity, $\mathrm{Re}=10^{-4}$) the hydrodynamic forces are linear in the particle velocity. Neglecting in a first stage the hydrodynamic interactions between the particles, we write then

$$F_i^H = -f_\perp \dot{h}_i, \tag{6}$$

where $f_\perp = 3\pi\eta a$, with the fluid viscosity $\eta = 6\times 10^{-3}$ Pa s. We will comment further on the influence of the confining cell boundaries on this drag coefficient, and on the influence of the hydrodynamic coupling between the particles in the chain.

Newton's second law for the ith sphere is then

$$m\ddot{h}(x_i) = F_M(x_i) + F_H(x_i) + \tilde{F}_i(t), \tag{7}$$

where we have added also the fluctuating force $\tilde{F}_i(t)$, which is due to the molecular nature of the fluid and gives rise to the Brownian motion of the particle.

The correlation time of $\tilde{F}_i(t)$ cannot exceed the viscous damping time $t_m = m/f_\perp$. This is the time it takes for a particle velocity to decay. An upper bound for t_m in our system is given by $t_m = a^2\rho/18\eta \approx 5\times 10^{-6}$ s, and above this time scale we may assume

$$\langle \tilde{F}_i(t)\tilde{F}_j(0)\rangle = A\,\delta(t)\,\delta_{ij}, \tag{8}$$

where A is a constant. In passing we note that since a force over a particle in general causes inertial motion in the fluid, that will decay only over a finite viscous damping time, the equation of motion for $\{h_i\}$ will also in general have a non-Markovian nature, i.e., the motion of h_i will depend not only the instantaneous forces but the entire history of those forces [32,33]. However, due to the presence of the confining plates the damping time for any inertial motion is simply t_m, and above this time it is correct to neglect the non-Markovian corrections to Eq. (7). This argument can also be given a more rigorous basis by showing that the non-Markovian interface equations, as given in Ref. [32], actually reduces to Eq. (7) in the $t_m \to 0$ limit.

Having established the Markovian nature of our description without this rigor we now determine A. The observation that $\tilde{F}_i$ is independent of F_M allows us to determine A from (7) with the F_M term removed. Following standard textbook [34] procedures we multiply the remainder of Eq. (7) by $\exp[(f_\perp/m)t]$ to obtain the explicit solution $\dot{h}(x_i,t) = \int_{-\infty}^{t} dt' \, 1/m \tilde{F}_i(t') e^{[-(f_\perp/m)(t-t')]}$. If we average the square of this equation, use Eq. (8) and invoke the equipartition principle we obtain $k_B T = \langle m\dot{h}(x_i)^2 \rangle = A/2f_\perp$ which gives

$$A = 2f_\perp k_B T. \tag{9}$$

Combining the above results, and neglecting the inertial terms due to the smallness of t_m, Eq. (7) can be written

$$\dot{h}_i = \frac{k_\perp}{f_\perp}(h_{i+1} + h_{i-1} - 2h_i) + \frac{1}{f_\perp}\tilde{F}_i(t). \tag{10}$$

This is a discrete form of the Edwards-Wilkinson equation, valid when $\lambda \gg 1$ where the quadratic approximation of the potential is valid. For spatial scales above a and times above t_m, the above reduces to the Edwards-Wilkinson equation [7],

$$\frac{\partial h}{\partial t} = \frac{k_\perp a^2}{f_\perp}\frac{\partial^2 h}{\partial x^2} + \frac{1}{f_\perp}\tilde{F}_i(t), \tag{11}$$

also known in polymer dynamics as the Rouse model [6].

A chain of particles may be made arbitrarily straight by applying large external magnetic fields. As an idealization of this situation we shall assume an initially straight chain and ask how it roughens when the external fields are reduced, while $\lambda > 1$, which ensures that the chain does not melt and the Taylor expansion performed above is accurate enough. As a side result we shall also find the equilibrium width of the chain, that results as a balance between the Brownian forces that tends to buckle the chain and the magnetic forces that tend to straighten it out.

For this purpose we will take the discrete Fourier transform of Eq. (10) as a starting point. The Fourier transforms are defined as

$$h_j = h(x_j) = \sum_{n=0}^{N-1} e^{ik_n x_j} h_n,$$

$$h_n = h_{k_n} = \frac{1}{N}\sum_{j=0}^{N} h_j e^{-ik_n x_j}, \tag{12}$$

where

$$x_j = ja, \quad j = 0, 1, \ldots, N-1,$$

$$k_n = \frac{2\pi}{Na} n, \quad n = 0, \ldots, (N-1). \tag{13}$$

The Fourier transform of Eq. (10) may be written

$$\dot{h}_n = -\omega_n h_n + \frac{1}{f_\perp}\tilde{F}_n, \tag{14}$$

where

$$\omega_n = \frac{k_\perp}{f_\perp} 2[1 - \cos(k_n a)]. \tag{15}$$

Equation (14) is easily solved to give

$$h_n(t) = \frac{1}{f_\perp}\int_{-\infty}^{t} dt' \, e^{-\omega_n(t-t')} \tilde{F}_n(t') \tag{16}$$

and correspondingly Eq. (8) takes the form—force:

$$\langle \tilde{F}_n(t) \tilde{F}^*_{n'}(0) \rangle = \frac{2f_\perp k_B T}{N} \delta(t) \delta_{nn'}. \tag{17}$$

The mean square width W^2 is defined as the average of $(h_i - 1/N \Sigma_j h_j)^2$, which by Parseval's identity may be written

$$W^2 = \frac{1}{N}\sum_i \left\langle \left(h_i - \frac{1}{N}\sum_j h_j \right)^2 \right\rangle = \sum_{n>0} \langle |h_n|^2 \rangle. \tag{18}$$

An initially straight particle chain is most conveniently described by setting $\tilde{F}_n(t<0) = 0$. The average of the square of $h_n(t)$ then takes the form

$$\langle |h_n(t)|^2 \rangle = \frac{2k_B T}{N f_\perp}\int_0^t dt' \, e^{-2\omega_n(t-t')} \tag{19}$$

$$= \frac{2k_B T}{f_\perp}\frac{1 - e^{-2\omega_n t}}{2\omega_n} \tag{20}$$

and

$$W^2 = \frac{2k_B T}{N f_\perp}\sum_{n\geq 1}\frac{1 - e^{-2\omega_n t}}{2\omega_n}. \tag{21}$$

When $t \ll 1/\omega_{\max}$ we have $[1 - \exp(-2\omega_n t)]/(\omega_n t) \approx 2$ and

$$W^2 \approx \frac{2k_B T}{f_\perp} t. \tag{22}$$

This result arises only because of the existence of a shortest wavelength a in the system. In the continuum limit $a \to 0$, $\omega_{\max} \to \infty$, and the $t \ll 1/\omega_{\max}$ regime does not exist. Equation (22) describes the superposition of N independent random walks in the h direction, and therefore the $t^{1/2}$ dependence of W is as expected.

When $1/\omega_{\max} \ll t \ll 1/\omega_{\min}$, then $\omega_k t \gg 1$ for large k and $\omega_k t \ll 1$ for small k. Since $[1 - \exp(-2\omega_n t)]/(\omega_n t)$ is of order 1 for the smallest ω_k and $[1 - \exp(-2\omega_n t)]/(\omega_n t) \ll 1$ for large ω_k we see that the sum over wave numbers is dominated by the small ω_k. We can then write $\omega_k \approx (ka)^2/\tau$ where $\tau = f_\perp/k_\perp \approx 0.2(H/20 \text{ Oe})^2$ s. By noting that $\omega_{N-n} = \omega_n$, the mean square width W^2 may be cast in the Family-Vicsek scaling form [35]

$$W^2 = LF\left(\frac{t}{L^2}\right), \tag{23}$$

where

$$F(x) = \frac{k_B T}{2\pi^2 k_\perp a} \sum_{n=1}^{N/2} \frac{1 - e^{-8k_\perp a^2 \pi^2 n^2 x / f_\perp}}{n^2}. \tag{24}$$

This equation has the following physical interpretation. Every mode k_n grows to its equilibrium value on a time scale $1/\omega_n$. At that point there is an equilibrium between the effects of the thermal force $\tilde{F}_i$ and the restoring force F_{M_i}. Since at small times W must be independent of L and at large times, when W has reached its asymptotic value, it must be independent of t, we have that

$$F(x) \sim \begin{cases} x^{1/2} & \text{for small } x, \\ \text{const} & \text{for large } x. \end{cases} \tag{25}$$

From this it follows that

$$W \sim \begin{cases} t^{1/4} & \text{for small } t, \\ L^{1/2} & \text{for large } t. \end{cases} \tag{26}$$

To get the prefactors however, we must evaluate the sums. In the $1/\omega_{\max} \ll t \ll 1/\omega_{\min}$ regime we can replace the sum by an integral to a good approximation. This yields

$$W^2(t) = \frac{2k_B T t}{N f_\perp \Delta k} \int_{2\pi/Na}^{\pi/a} dk \frac{1 - e^{-2\omega_k t}}{\omega_k t}, \tag{27}$$

where $\Delta k = 2\pi/(Na)$. Using the small k expansion for ω_k and a simple substitution we obtain

$$W^2(t) \approx \frac{k_B T \tau}{f_\perp \pi a} \int_0^\infty dk \frac{1 - e^{-k^2 (2a^2 t/\tau)}}{k^2} = \frac{k_B T}{\sqrt{k_\perp f_\perp}} I t^{1/2}, \tag{28}$$

where

$$I = \frac{\sqrt{2}}{\pi} \int_0^\infty dx \frac{1 - e^{-x^2}}{x^2} = \sqrt{\frac{2}{\pi}}. \tag{29}$$

When $t \gg 1/\omega_{\min}$, $e^{-2\omega_n t} \approx 0$ for all n, and

$$W^2 = \frac{2k_B T}{N f_\perp} \sum_{n=1}^{N/2} \frac{1}{\omega_n} \approx \frac{k_B T}{2\pi^2 k_\perp} \frac{L}{a} \sum_{n=1}^{\infty} \frac{1}{n^2}. \tag{30}$$

Using

$$J = \frac{1}{2\pi^2} \sum_{n=1}^{\infty} \frac{1}{n^2} = \frac{1}{12} \tag{31}$$

we may summarize the above as

$$W^2 = k_B T \begin{cases} \dfrac{2}{f_\perp} t & \text{when } t \ll \dfrac{1}{\omega_{\max}}, \\ \sqrt{\dfrac{2}{\pi k_\perp f_\perp}} t^{1/2} & \text{when } \dfrac{1}{\omega_{\max}} \ll t \ll \dfrac{1}{\omega_{\min}}, \\ \dfrac{1}{12 k_\perp} \dfrac{L}{a} & \text{when } t \gg \dfrac{1}{\omega_{\min}}. \end{cases} \tag{32}$$

Noting finally from Eqs. (13) and (15) that $1/\omega_{\max} = \tau/4$ and $1/\omega_{\min} = N^2 \tau / 4\pi^2$, those separation times can be evaluated as $1/\omega_{\max} = 0.06(H/20\text{ Oe})^2$ s and $1/\omega_{\min} = N^2 \cdot 0.06(H/20\text{ Oe})^2$ s.

IV. BROWNIAN DYNAMIC SIMULATIONS

The dynamic roughening of such dipolar chain can also be studied numerically by performing Brownian dynamics simulations. In this model the interaction forces, which act on each particle of the chain, is composed of the dipole-dipole interaction of Eq. (1), a repulsive contact force, and a thermal, fluctuating force from the surrounding fluid. Such a numerical study allows us to study the effects neglected in the analytical derivation above, namely, (1) the finite range of the dipolar interactions beyond nearest neighbor ones. (2) The influence of the nonlinearities in the potential for large departures from a straight chain. (3) The fact that particles are not constantly in contact but have somewhat fluctuating spacings.

Our hydrodynamic regime is strongly damped, which implies that the acceleration term $m_i \ddot{\mathbf{r}}$ is negligible compared to the viscous friction term $\mathbf{F_v} = -\mathbf{f}_\perp \dot{\mathbf{r}}_\mathbf{i}$. The time evolution of each particle in the chain is then given by the force-balance equation

$$f_\perp \dot{\mathbf{r}}_i = -\left(\sum_j \mathbf{F}_m(\mathbf{r}_j - \mathbf{r}_i) \right) + \mathbf{F}_c(\mathbf{r}_j - \mathbf{r}_i) + \tilde{\mathbf{F}}_i(t), \tag{33}$$

where the magnetic interaction force is derived from the pair potential U in Eq. (1), i.e., $\mathbf{F_m}(\mathbf{r}) = -\nabla \mathbf{U}$.

The contact forces are modeled as

$$\mathbf{F}_c(\mathbf{r}) = f_0 \Theta(a - r) \hat{\mathbf{r}} \exp\left(\frac{r - a}{l} - \frac{l}{r - a} \right), \tag{34}$$

where Θ is a Heavyside function, $r-a$ the overlap distance between neighboring particles, l a characteristic distance of overlap, $\hat{\mathbf{r}}$ the radial unit vector, and f_0 the characteristic force magnitude arising from the elastic properties of the particle material. The shape of this interaction is chosen so that this force and its derivative of any order are continuous—although similar results are obtained with the simpler form $\mathbf{F}_c(\mathbf{r}) = f_0 \Theta(a-r) \hat{\mathbf{r}} \exp[(r-a)/(l)]$. In the model, we adopt arbitrarily $l = 0.01a$, and $f_0 = U(r=a, \theta = 0)/a$. By testing several values of these parameters, we have checked that these particular values are irrelevant for the roughening dynamic, as long as $l/a \ll 1$, which ensures that the interactions approximate those of rigid particles.

The hydrodynamic interactions between the plates and the particles cannot be neglected. They are taken into account in the following way.

Since the magnetic interactions between the particles and the nonmagnetic boundaries keep the particles in the middle between the plates, the hydrodynamic coupling between the particles and the plates amount to increasing the friction coefficient by a factor

$$c = 2/(1 - 9a/16d) - 1 = 1.40(1.70) \tag{35}$$

for a=3 μm (4 μm) [36]. Consequently, the viscous friction term is modeled as $\mathbf{F}_v = -f_\perp \dot{\mathbf{r}}_i$, with $f_\perp = 3c\pi\eta a$. Eventually,

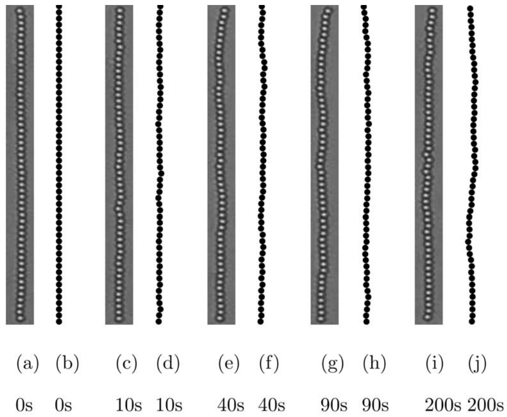

FIG. 3. Typical dynamic roughening of dipolar chains of 52 magnetic holes of diameter 4 μm after a decrease of the external magnetic field from $\lambda = 866$ to $\lambda = 24$ at initial time, experiments (gray) and simulations (black and white).

the hydrodynamic interactions between the particles are neglected, as will be justified further in Sec. V B.

The magnitude of the fluctuating force in the Langevin equation, Eq. (33), is set up by the fluctuation-dissipation theorem, as derived in Eqs. (9), i.e.,

$$\langle \tilde{F}_i(t)\tilde{F}_j(0)\rangle = 2f_\perp k_B T\delta(t)\delta_{ij}. \tag{36}$$

The Langevin equation (33) is directly integrated over time steps Δt as

$$f_\perp[\mathbf{r}_i(t+\Delta t) - \mathbf{r}_i(t)] \tag{37}$$

$$= -\left(\sum_j \mathbf{F}_m[\mathbf{r}_j(t) - \mathbf{r}_i(t)]\right)\Delta t \tag{38}$$

$$+ \mathbf{F}_c[\mathbf{r}_j(t) - \mathbf{r}_i(t)]\Delta t + \Delta\tilde{\mathbf{F}}_i(t), \tag{39}$$

where according to the central limit theorem and Eq. (36), the integrated random variables $\Delta\tilde{\mathbf{F}}_i = \int_t^{t+\Delta t}\tilde{\mathbf{F}}_i(t')dt'$ are uncorrelated Gaussian variable of zero mean and of variance given by

$$\langle \Delta\tilde{F}_i(t)\Delta\tilde{F}_j(t')\rangle = 2f_\perp k_B T\Delta t\delta_{tt'}\delta_{ij}. \tag{40}$$

The time step Δt is chosen so that the average spatial steps do not exceed 0.001 diameters. The simulations are run from an initial state where all particles are in contact and aligned.

As in the experiments, under the effect of thermal noise, the chains roughen until they reach a characteristic fluctuation size. The equilibrium size of these fluctuations depend on the applied field. Five snapshots of a typical simulation are shown in Fig. 3, together with an experiment carried out with similar field parameters. In the experiment, the field was reduced from a strong value corresponding to $\lambda = 866$, to a lower one corresponding to $\lambda = 24$. In the simulation, the initial straight state corresponding to $\lambda \gg 1$ is let to fluctuate according to the Brownian dynamic scheme carried out with restoring magnetic forces at $\lambda = 24$. The visual agreement between simulations and experiments seems satisfying, as shown in Fig. 3.

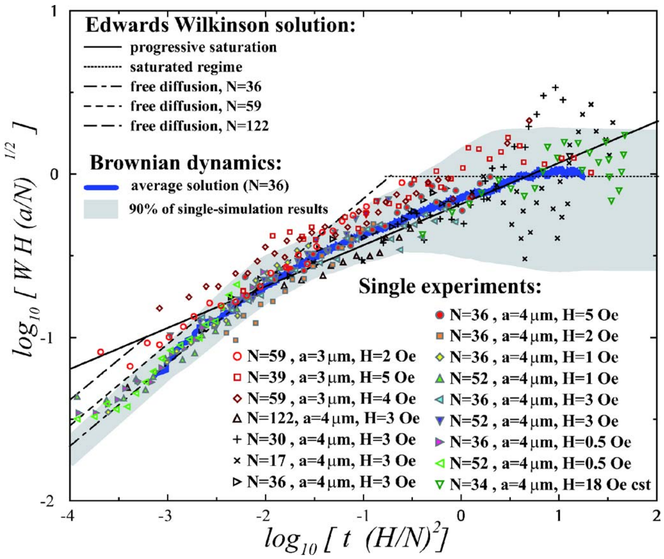

FIG. 4. (Color online) Collapse of the scaled rms of the displacements, as a function of the scaled time: experimental data compared to analytical theory, with average behavior and characteristic variance evaluated from simulations. The units of H, t, and W are, respectively, Oersteds, seconds and μm.

V. COMPARISON BETWEEN THEORETICAL MODEL, SIMULATIONS AND EXPERIMENTS

A. Evolution of the chain width

To characterize the roughening dynamic of the dipolar chains, we extract the root-mean-square width of the lateral coordinates as function of time t after a decrease of the external field from a strong value. Since this system is excited by thermal noise, this width differs between realizations. We record this width as a function of time for each single experiment or numerical realization of Brownian dynamics simulation,

$$W_{sr}(t) = \frac{1}{N}\sum_j h_j^2 \tag{41}$$

The average over realizations of this rms width should correspond to the thermodynamic average $W(t) = \langle W_{sr}\rangle$ derived in Sec. III. In order to check the scaling law derived in Eq. (32), for the width as function of time, we plot the scaled width $WH\sqrt{a/N}$ as function of the scaled time, $tc(H/N)^2$, in Fig. 4. Each symbol represents a different experiment, with a different applied field, particle number or particle diameter, as specified in the figure.

The black continuous lines correspond to the predicted thermodynamic average, evaluated from Eq. (32) with $f_\perp = 3c\pi\eta a$ with c given by Eq. (35). The dashed lines correspond to the initial freely diffusive regime for chains of length 36, 59, and 122. The data collapse of the experimental data in these reduced coordinates is consistent with the analytical model, but the scatter around the thermodynamic average is non-negligible for each of these single experiments, as is expected when no averaging is performed.

To characterize further this scatter around the average, we have performed the following analysis on the Brownian

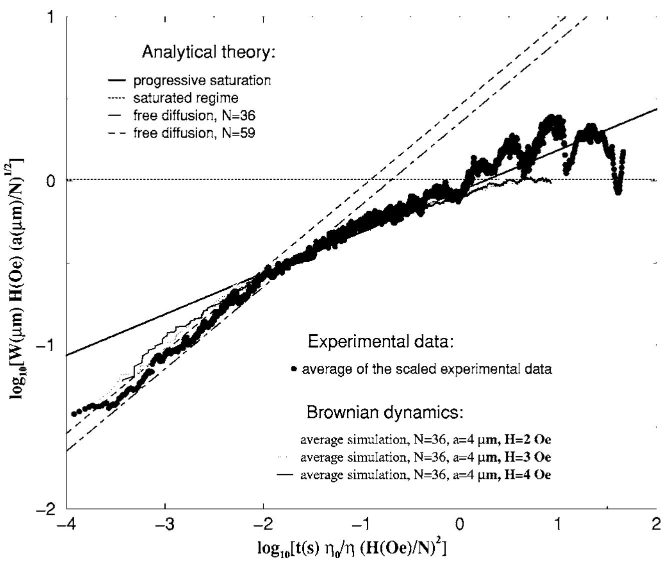

FIG. 5. Scaling of the random mean square width of the transverse displacements: theory, experiments and Brownian dynamics result.

dynamics simulation: From 1000 different runs on 36 particles long chains, we have evaluated the average width over these realizations at a given time, $\langle W_n(t)\rangle$. This is plotted in Figs. 4 and 5 for fields of magnitude $H=2$, 3, and 4 Oe, and particles of 3 μm. These three average sets indeed collapse in reduce coordinates, and correspond reasonably well to the analytical estimates shown as continuous lines.

Each of these simulations nonetheless exhibits a dynamic width $W_n(t)$ departing significantly from the thermodynamic average. At each time, we have evaluated the standard deviation of the width from 1000 simulations, $\sigma(t) = \sqrt{\langle W_n^2(t) - \langle W_n(t)^2\rangle\rangle}$. In reduced coordinates, σ/W at a given scaled time is found to be lowly sensitive to H. The distribution of the width at a given time is essentially Gaussian, and at each time t, $\sqrt{2/\pi}\mathrm{erfc}(2/\sqrt{2})=95\%$ of the widths $W_n(t)$ of single numerical realizations are within $2\sigma(t)$ of the thermodynamic average $\langle W(t)\rangle$.

In Fig. 4, we have represented in gray shading the zone corresponding to this probable interval of 95% of the numerical realizations, $[\langle W(t)\rangle - 2\sigma(t); \langle W(t)\rangle + 2\sigma(t)]$. Indeed, most experimental widths evaluated for single experiments are in this range, i.e., the experimental deviation from the average for a given realization is comparable to the one observed in the Brownian dynamics simulations. So, the data collapse of the experimental reduced width as function of the reduced time seems satisfactory.

To extract the average behavior from the experiments, we performed a running average of the scaled width over all 16 experiments, with a logarithmic binning procedure so as to have 40 points per time decade, i.e., averages over time windows $[t_i, t_{i+1}]$ with $t_{i+1}=\alpha t_i$, with $\alpha=10^{1/40}=1.05$. The resulting average over experiments, represented in black circular symbols in Fig. 5, coincides reasonably well with the Brownian dynamics and analytical results. The larger discrepancies are observed for the largest reduced times, where only a few experiments have been carried out (at large times in the largest fields), and can be interpreted once again as an insufficient number of independent experimental realizations. Moreover, this happens in the region where the variance of the width of a single realization is the largest, due to the fact that the largest wavelengths modes are developed, and that the number of such wavelengths in the system is limited, so that no spatial average smoothens the effect of the fluctuations of these large wavelengths.

The tunability of the characteristic time as function of the applied field in our system allows to effectively sample experimentally more than five decades of reduced times. This allows to distinguish experimentally the three regimes predicted, $W \sim t^{1/2}$, $W \sim t^{1/4}$ and saturation width, each of them being observed over a couple of decades.

B. Irrelevance of hydrodynamic interactions between particles in a confined system

The reason for neglecting the hydrodynamic interactions in this setup is the presence of the plates confining the system dampen such hydrodynamic interactions. Indeed, the corrective force on particle i due to the hydrodynamic interaction with the particle j, moving at velocity v_j with respect to the fluid at infinity, can be estimated as $f_\perp u_{ij}$, where u_{ij} is the characteristic fluid velocity at the center of particle i, that the particle j moving at v_j would create in a fluid medium with no other particles [6]. At scales larger than the plate separation, the pressure field between two parallel plates is Laplacian, i.e., $\nabla^2 P=0$. Indeed, the average fluid velocity between two parallel plates u can be obtained via Darcy's law, $u \propto -\nabla P$ [37], since the ferrofluid is incompressible, $\nabla \cdot u=0$. A moving particle generates a dipolar pressure source perturbation, decaying as $1/r$ and a fluid velocity perturbation decaying as $u \sim -\nabla P \sim 1/r^2$. Thus, the flow perturbation generated by the thermal motion of all particles further than a distance l behaves as $\Sigma_{j>l/a} v_j a^2/(ja)^2$. An upper bound for this corrective velocity contribution can be set as $v_T a/l$ where $v_T \sim \sqrt{k_B T/m}$ is the characteristic thermal velocity magnitude. For large enough l, this correction can be made arbitrarily small, and consequently, the hydrodynamic interactions between particles remain of finite range. Taking into account the hydrodynamic interactions between a few neighboring particles could possibly induce a correction as a prefactor for the rms width of the chain, which, since it only corrects local effects, would not change the exponents.

Indeed, we have observed that the experiments agree well with the theoretically predicted scaling laws $W \sim t^\alpha$. Furthermore, even the prefactor $W(t)/t^\alpha$ is captured by theory and simulations that neglect the hydrodynamic interactions between particles. This shows a posteriori that these interactions are indeed irrelevant for our confined system.

On the other hand, for three-dimensional systems where no confining plates dampen such hydrodynamic pertubations, a particle moving at velocity v induces a flow perturbation decaying as $v \cdot a/r$, as given by the Oseen tensor in an unbounded medium [6]. The sum of these perturbations for particles beyond a certain distance l, $\Sigma_{j>l/a} v_j a/(ja)$, depends on the precise series of velocities v_j, and cannot be trivially bounded. Consequently, hydrodynamic interactions for dipolar chains in unconfined fluids are in general relevant, and their presence leads to a different anomalous diffusion exponent, $W \sim t^{1/3}$ [6]. This can be described by the Zimm model, and experiments carried out on magnetorheological fluids in three-dimensional geometries indeed report $W \sim t^{0.35\pm0.05}$ [9–12].

VI. EQUILIBRIUM FLUCTUATIONS

So far, we have studied how an initially straight chain roughens dynamically when the external field is suddenly lowered to a finite and constant value. This out-of-equilibrium problem corresponds to following the dynamic roughening of our dipolar chain under the effect of a thermal bath turned on initially.

Once the chain reaches equilibrium it is a different problem to characterize the growth away from an arbitrary state of the equilibrium distribution. This problem is hence an equilibrium one, and we will now characterize the spatial and temporal scaling of the autocorrelation function.

The difference between these equilibrium fluctuations and the out-of-equilibrium dynamic roughening problem lies only in the knowledge of the initial state: The roughening process is nonequilibrium because it starts from a nonequilibrium distribution, that is, a distribution of (flat) states that are only a subset of all the equilibrium states. For the equilibrium process we consider the departure from an arbitrary rough state $h(x_j,t_0)$, i.e.,

$$\Delta h(x_j,t,t_0) = h(x_j,t+t_0) - h(x_j,t_0). \tag{42}$$

As in the out-of-equilibrium problem, this quantity starts at 0 at $t=0$. We can characterize the rms width of this departure, as

$$\Delta W^2(t,t_0) = \frac{1}{N}\sum_{j=1}^{N}\left(\Delta h_j - \frac{1}{N}\sum_l \Delta h_l\right)^2 \tag{43}$$

$$= \sum_{n=1}^{N-1} \langle |\Delta\tilde{h}_n(t,t_0)|^2\rangle, \tag{44}$$

where we used Parseval theorem.

To evaluate the contribution of each Fourier mode, we integrate once again the Langevin equation, Eq. (14), to get

$$\Delta h_n(t,t_0) = h_n(t) - h_n(t_0) \tag{45}$$

$$= h_n(t_0)(e^{-\omega_n t} - 1) + \frac{1}{f_\perp}\int_{t_0}^{t_0+t} dt' \, e^{-\omega_n(t_0+t-t')}\tilde{F}_n(t'). \tag{46}$$

Using the expression for the variance of the fluctuating forces, $\langle \tilde{F}_n(t)\tilde{F}^*_{n'}(0)\rangle = 2f_\perp k_B T/N\delta(t)\delta_{nn'}$, we can integrate this to obtain

$$\langle \Delta h_n(t,t_0)^2\rangle = \langle h_n(t_0)^2\rangle(e^{-2\omega_n t} - 2e^{-\omega_n t} + 1) \tag{47}$$

$$+ 2k_B T\int_{t_0}^{t_0+t} e^{-\omega_n(2t_0+2t-2t')}dt' \tag{48}$$

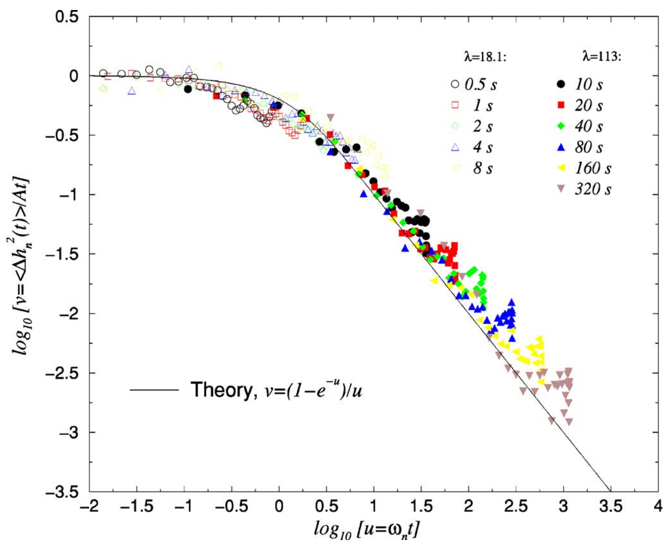

FIG. 6. (Color online) Power spectrum of the fluctuations: scaling of the autocorrelation function in time and space.

$$= \langle h_n(t_0)^2\rangle(e^{-2\omega_n t} - 2e^{-\omega_n t} + 1) \tag{49}$$

$$+ k_B T\frac{(1 - e^{-2\omega_n t})}{\omega_n}. \tag{50}$$

The equilibrium width of mode n is given by Eq. (19) at large times, i.e., $\langle h_n(t_0)^2\rangle = k_B T/\omega_n$. Then the above equation simplifies to

$$\langle \Delta h_n(t,t_0)^2\rangle = 2k_B T(1 - e^{-\omega_n t})/\omega_n. \tag{51}$$

The dynamics of this fluctuating mode is independent of the initial time t_0, reflecting the fact that equilibrium averages are time translational invariant. We note that the time dependence of $\langle \Delta h_n(t,t_0)^2\rangle$ is closely related to the time dependence of the roughening states in Eq. (19): The behavior is in fact identical, only with a doubled prefactor, and a doubled characteristic time. This is linked to the fact that the chain may on the average displace further from an arbitrary state than a straight one.

The above scaling law for the dynamic departure from a given equilibrium configuration was directly checked in two series of experiments, Eq. (51) predicts that

$$\langle [\Delta h_n(t,t_0)]^2\rangle/At = f(u), \tag{52}$$

where $u=\omega_n t$, $f(u)=(1-e^{-u})/u$ and $A=2k_B T$.

The two experiments were performed at fields such that $\lambda=18$ and $\lambda=113$, and we recorded 20 minutes of chain motion, for which we performed the spatial Fourier transform of $\Delta h(x,t,t_0)$. A Hamming window was used to avoid frequency leakage due to the finite chain sizes [38].

We subsequently evaluated the power spectrum $\Delta h_n(t,t_0)^2$ which was averaged over t_0 with a fixed time lapse t. The result is plotted in the scaled form $\langle[\Delta h_n(t,t_0)^2]\rangle_{t_0}/At$ as a function of $u=\omega_n t$ in Fig. 6. Note that each curve actually corresponds to fixed t and variable n. The fact that t varies by more than two orders of magnitude thus gives a five order of magnitude variation in u.

Both experiments at all probed times show a fluctuation spectrum consistent with the theoretical prediction of Eq. (52), which is shown as a continuous line. The initial flat plateau corresponds first to the normal diffusion regime where $f(u) \sim 1$, and then the progressive saturation of the modes is seen as the straight line of slope -1 on the right-hand side, i.e., a power-law decay with $f(u) \sim 1/u$.

Note that the knowledge of the spatial power spectrum $\langle \widetilde{\Delta} h_n^2 \rangle$ and the equilibrium average $\langle h_n^2 \rangle$ given in Eq. (19) allows us also to evaluate the two-point correlation function in space and time. This function is defined as

$$G(x,t) = \langle h(0,0)h(x,t) \rangle, \tag{53}$$

which has the spatial Fourier transform

$$G_n(t) = \langle h_n(0)h_n(t) \rangle. \tag{54}$$

By definition of $\Delta h_n(t)$ with $t_0=0$ we can write

$$\langle \Delta h_n(t)^2 \rangle = \langle h_n(t)^2 \rangle - 2\langle h_n(t)h_n(0) \rangle + \langle h_n(0)^2 \rangle, \tag{55}$$

where the first and last right-hand-side terms are the same equilibrium averages.

Solving for $G_n(t)$ above we immediately get

$$G_n(t) = \langle h_n^2 \rangle - \frac{\langle \Delta h_n(t)^2 \rangle}{2} = k_B T \left(\frac{1}{\omega_n t} - \frac{1 - e^{-2\omega_n t}}{\omega_n} \right)$$
$$= \frac{e^{-2\omega_n t}}{\omega_n} k_B T, \tag{56}$$

where we have used Eq. (51) with $t_0=0$ to substitute for $\langle \Delta h_n(t)^2 \rangle$.

VII. THE MEMORY OF THE BROWNIAN WORM

In this section, we will show that the $W \sim t^{1/4}$ regime can also be understood in terms of anomalous diffusion in a system with memory. We will show how the Markovian description for the entire chain becomes a non-Markovian description when it is formulated for a single particle in the chain.

For such a particle linked to a background constituted of both the solvent and the rest of the chain, the motion is governed by an exterior with long-time memory in the fluctuating force as well as the response function.

The single particle description takes the form of a generalized Langevin equation of the Mori-Lee form [8]:

$$m\ddot{h}_0(t) = -m \int_{-\infty}^{t} dt_1 \Gamma(t-t_1)\dot{h}_0(t_1) + F(t), \tag{57}$$

with $\Gamma(t)$ a linear response function, and $F(t)$ a fluctuating function satisfying the fluctuation dissipation theorem,

$$\langle F(t)F(0) \rangle = m k_B T \Gamma(t). \tag{58}$$

From the theory of anomalous diffusion in such systems with memory, the anomalous diffusion exponent is related to the asymptotic behavior of the linear response function [8]. When the Laplace transform of the response function behaves as $\hat{\Gamma}(\omega) \sim \omega^{-\alpha}$ when $\omega \to 0$, this theory predicts an anomalous diffusion $W^2 \sim t^{1-\alpha}$. We will show that this system indeed follows this theoretical prediction, i.e., that it can be described by an Eq. (57) with the asymptotic behavior $\hat{\Gamma}(\omega) \sim \omega^{-1/2}$. In other words, this alternative description also produces the prediction $W \sim t^{1/4}$, in agreement with the direct treatment above.

A. Generalized Langevin equation for a particle in a Brownian worm

We consider a set of N particles in an immobile solvent. The inertial terms are neglected for every particle. However, for technical purposes we shall take the particle in focus to have a mass initially. This is done to exhibit a known structure of the Langevin equation: eventually, the mass of this particle will also be send to zero.

Thus, we write for every particle j,

$$\delta_{j0} m \ddot{h}_j = -\kappa \dot{h}_j + \alpha(h_{j+1} - 2h_j + h_{j-1}) + \zeta_j, \tag{59}$$

where $\kappa=3\pi\eta a$ and α is the curvature of the magnetic energy with respect to lateral bending, and ζ_j is the uncorrelated Brownian force with a magnitude which is given by dissipation fluctuation theorem

$$\langle \zeta_i(0)\zeta_j(t) \rangle = 2\kappa k_B T \delta_{ij} \delta(t). \tag{60}$$

We Fourier transform this in space

$$f'_n = \sum_{j=1}^{N} f_j e^{-2\pi j n/N}, \quad f_j = \frac{1}{N} \sum_{n=0}^{N-1} f'_n e^{2\pi j n/N}. \tag{61}$$

From here on primes refer to Fourier modes in space, and tildes to Fourier modes in time to simplify notation. We then obtain

$$-m\ddot{h}_0 = \kappa(\dot{h}'_n + \omega_n h'_n) - \zeta'_n = \kappa e^{-\omega_n t} \frac{d}{dt}[h'_n(t) e^{\omega_n t}] - \zeta'_n, \tag{62}$$

where

$$\omega_n = \frac{2\alpha}{\kappa} \left[1 - \cos\left(\frac{2\pi n}{N} \right) \right], \tag{63}$$

i.e., when

$$n \ll N, \quad \omega_n \simeq \omega_1 n^2, \tag{64}$$

where

$$\omega_1 = \frac{\alpha}{\kappa} \frac{(2\pi)^2}{N^2}. \tag{65}$$

Equation (62) is integrated as

$$-h'_n(t) = \int_{-\infty}^{\infty} dt_1 [m\ddot{h}_0(t_1) - \zeta'_n(t_1)] \frac{\Theta(t-t_1) e^{-\omega_n (t-t_1)}}{\kappa}, \tag{66}$$

where Θ is the Heaviside function. Performing an inverse space Fourier transform, we get

$$-h_0(t)=\int_{-\infty}^{\infty}dt_1 m\ddot{h}_0(t_1)\frac{1}{N}\sum_n\frac{\Theta(t-t_1)e^{-\omega_n(t-t_1)}}{\kappa}-\int_{-\infty}^{\infty}dt_1\frac{1}{N}\sum_n\zeta_n'(t_1)\frac{\Theta(t-t_1)e^{-\omega_n(t-t_1)}}{\kappa}.$$

Taking the derivative with respect to time, we obtain

$$\int_{-\infty}^{\infty}dt_1 m\ddot{h}_0(t_1)\sum_n\frac{\delta(t-t_1)-\Theta(t-t_1)\omega_n e^{-\omega_n(t-t_1)}}{\kappa N}=-\dot{h}_0(t)+\int_{-\infty}^{\infty}dt_1\sum_n\zeta_n'(t_1)\frac{\delta(t-t_1)-\Theta(t-t_1)\omega_n e^{-\omega_n(t-t_1)}}{\kappa N}.$$

Using $*$ as a convolution operator we may write the above as

$$m\ddot{h}_0 * G=-\dot{h}_0+\sum_n\zeta_n * G_n, \tag{67}$$

where

$$G_n(t)=\frac{\delta(t)-\Theta(t)\omega_n e^{-\omega_n t}}{\kappa N}, \tag{68}$$

$$G(t)=\sum_n G_n(t). \tag{69}$$

We now perform a time Fourier transform of the above. This transform is defined as

$$\tilde{f}(\omega)=\int_{-\infty}^{\infty}f(t)e^{-i\omega t}dt,\quad f(t)=\frac{1}{2\pi}\int_{-\infty}^{\infty}\tilde{f}(\omega)e^{i\omega t}d\omega. \tag{70}$$

The convolution theorem then yields

$$m\tilde{\ddot{h}}_0(\omega)=-m\tilde{\Gamma}(\omega)\tilde{\dot{h}}_0(\omega)+\tilde{F}(\omega), \tag{71}$$

where

$$m\tilde{\Gamma}(\omega)=1/\tilde{G}(\omega), \tag{72}$$

$$\tilde{F}(\omega)=\sum_n\tilde{\zeta}_n'(\omega)\tilde{G}_n(\omega)/deG(\omega). \tag{73}$$

An inverse Fourier transform, then leads to

$$m\ddot{h}_0(t)=-m\int_{-\infty}^{t}dt_1\Gamma(t-t_1)\dot{h}_0(t_1)+F(t) \tag{74}$$

which is exactly the Mori-Lee generalized Langevin equation [8]. To replace the $+\infty$ upper bound of the integral by t, we have used that the response function is causal, i.e., that $\Gamma(t)=0$ when $t<0$: This is shown explicitly in Appendix A. The fact that the generalized fluctuation dissipation theorem is satisfied, i.e., that

$$\langle F(t)F(0)\rangle=mk_BT\Gamma(t) \tag{75}$$

is verified in Appendix B.

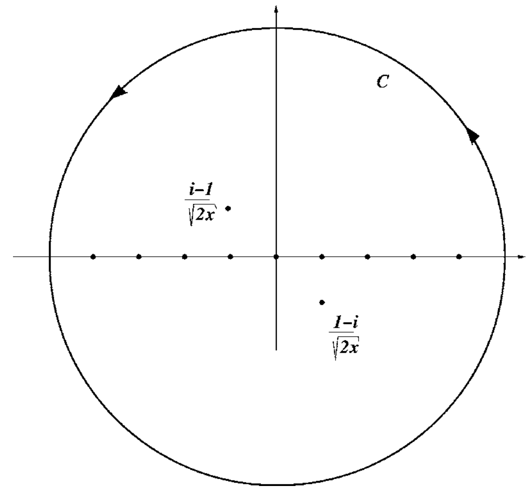

FIG. 7. Contour for integration of the **G** function in the complex plane.

B. Derivation of long time behavior of the linear response function

From Eq. (68) and Bracewell [39] we get immediately

$$\tilde{G}_n(\omega)=\frac{1}{\kappa N}\left(1-\frac{\omega_n}{\omega_n+i\omega}\right)=\frac{i\omega}{\kappa N(\omega_n+i\omega)} \tag{76}$$

and we need to evaluate the discrete sum

$$\tilde{G}(\omega)=\sum_{n=0}^{N-1}\frac{i\omega}{\kappa N(\omega_n+i\omega)}$$

for times $1/\omega$ larger than $\kappa/4\alpha$, so that

$$\tilde{G}(\omega)\approx\sum_{n=0}^{\infty}\frac{i\omega}{\kappa N(\omega_1 n^2+i\omega)}=\frac{i}{\kappa N}I\left(\frac{\omega_1}{\omega}\right), \tag{77}$$

where

$$I(x)=\sum_{n=0}^{\infty}\frac{1}{xn^2+i}=\frac{1}{2i}+J(x) \tag{78}$$

with

$$J(x)=\frac{1}{2}\sum_{-\infty}^{\infty}f(n), \tag{79}$$

$$f(z)=\frac{1}{xz^2+i} \tag{80}$$

$$=\frac{1}{x\left(z-\frac{1-i}{\sqrt{2x}}\right)\left(z+\frac{1-i}{\sqrt{2x}}\right)}. \tag{81}$$

To proceed, note that $\int_C \cot(\pi z)f(z)=0$ for a contour C corresponding to $\mathrm{R}e^{i\theta}$ with R a constant that will be sent to infinity and $\theta\in[0,2\pi[$ (cf. Fig. 7), then by the residue theorem

$$0=\sum_{\text{Res}}\operatorname{cotan}(\pi z)f(z)=\frac{1}{\pi}\sum_{n=-\infty}^{\infty}f(n)+\frac{\operatorname{cotan}(\pi i^{3/2}/\sqrt{x})}{i^{3/2}\sqrt{x}}. \tag{82}$$

So that

$$J(x)=\frac{i\pi}{2}\frac{\operatorname{cotan}(i^{3/2}\pi/\sqrt{x})}{\sqrt{ix}} \tag{83}$$

and from Eq. (77),

$$\widetilde{G}(\omega)=\frac{1}{2\kappa N}g(\pi i^{3/2}\sqrt{\omega/\omega_1}) \tag{84}$$

with

$$g(z)=1+z\operatorname{cotan}(z). \tag{85}$$

The function $g(z)$ is monotonously growing, with limits $g(z)\to 1$ when $z\to 0$, and $g(z)\to \pi z/2$ when $z\to\infty$.

Consequently, for finite chains, the long time limit is given by $\widetilde{G}(\omega\to 0)\sim 1/(2\kappa N)$, if ω_1 is fixed and finite. This corresponds to a normal diffusive behavior.

However, for very long chains, the transient time to reach this saturaton is extremely long, and corresponds to the regime physically probed by the system. This is seen by taking first the $N\to\infty$ limit in the above, so that using $\omega_2=\omega_1 N^1=(2\pi)^2\alpha/\kappa$,

$$\widetilde{G}(\omega)=\frac{\pi^2 i^{3/2}}{4\kappa N}\sqrt{\omega/\omega_1}=\frac{\pi^2 i^{3/2}}{4\kappa}\sqrt{\omega/\omega_2}=\frac{\pi i^{3/2}}{8}\sqrt{\omega/(\alpha\kappa)} \tag{86}$$

for any ω.

Thus, the Fourier transform of the response function is from Eq. (72),

$$\widetilde{\Gamma}(\omega)=\frac{2\kappa}{\pi m}\sqrt{\frac{\omega_2}{i\omega}}=\frac{4}{m}\sqrt{\frac{\alpha\kappa}{i\omega}}, \tag{87}$$

and from Ref. [8], since the Laplace transform $\hat{\Gamma}$ of Γ in the limit of small ω (long times) behaves as

$$\hat{\Gamma}(\omega)\sim\widetilde{\Gamma}(-i\omega)\sim\omega^{-1/2}, \tag{88}$$

we have for the rms displacement of the observed particle,

$$\langle x^2(t)\rangle\propto t^{1-1/2}=t^{1/2} \tag{89}$$

which is nothing but the subdiffusive regime we observe up until saturation. Thus, our system experimentally, analytically, and numerically verifies the theory for anomalous diffusion in systems with memory derived in Ref. [8], and thus provides an experimental realization of this theory.

VIII. CONCLUSION

Chains of dipoles suspended between two plates, roughen dynamically under the effect of thermal disorder when the dipolar interaction is decreased. This dynamic roughening is intimately related to the scaling of the equilibrium fluctuation of these chains. We have studied the dynamic roughening experimentally and theoretically and the equilibrium fluctuations of such chains composed of magnetic holes in a ferrofluid. Their dynamic roughening and fluctuations are shown to behave according to a discrete Rouse model. The rms width of these chains behaves initially as normal diffusion, $W^2\propto t$, then it grows with an anomalous exponent, i.e., $W^2\propto t^{1/2}$ as Fourier modes progressively saturate from the small scales to the large ones. Eventually W reaches an amplitude $W^2\sim N$ at large times. We have derived this behavior analytically, including the prefactors, and verified that the experimental data coincide with the theoretical predictions over five decades in the case of the equilibrium fluctuations. The analytic predictions and experiments also coincide with Brownian dynamic simulations taking into account the nonlinearities of the interaction potential, and the interactions beyond nearest neighbors.

Eventually, we have shown that the Markovian description of the entire Brownian worm can be reduced to a non-Markovian one for a single particle. This description contains a linear response function, with a long time tail decaying as $t^{-\alpha}$ with $\alpha=1/2$. Thus, since these chains experimentally exhibit the anomalous diffusion exponent $1/2=1-\alpha$, predicted by the theory of diffusion in systems with memory, they constitute a first experimental realization of this theory.

APPENDIX A: DERIVATION OF THE REAL-TIME EXPRESSION OF THE RESPONSE FUNCTION

We will now perform the inverse time Fourier transform (TFT) from Eq. (87): for that purpose, we introduce a small parameter ε and write

$$\Gamma(t)=\lim_{\varepsilon\to 0}\frac{1}{2\pi}\frac{2\kappa}{\pi m}\int_{\omega=-\infty}^{\infty}d\omega e^{i\omega t}\frac{i-1}{\sqrt{2}}\frac{\sqrt{\omega_2}}{\sqrt{\omega-i\varepsilon}}. \tag{A1}$$

We define in the complex plane, the square root function $\sqrt{\cdot}$ to have a branch cut along the axis ix, $x>0$, i.e., $\lim_{\delta\to 0^+}\sqrt{i+\delta}=\frac{1+i}{\sqrt{2}}$, and $\lim_{\delta\to 0^+}\sqrt{i-\delta}=\frac{-1-i}{\sqrt{2}}$.

For $t<0$, we close the contour in complex plane by a half-circle in the lower half-plane, and since no singularity is enclosed, $\Gamma(t)=0$ in that case: the response function is causal as desired.

For $t>0$, we get by following the contour in Fig. 8,

$$\begin{aligned}\int_{\omega=-\infty}^{\infty}d\omega\frac{e^{i\omega t}}{\sqrt{\omega-i\varepsilon}}&=\int_{x=+\infty}^{0}idxe^{-xt}\frac{1}{\sqrt{i(x-\varepsilon)+\delta}}\\&\quad+\int_{x=0}^{+\infty}idxe^{-xt}\frac{1}{\sqrt{i(x-\varepsilon)-\delta}}\\&\simeq-2\frac{\sqrt{2}i}{1+i}\int_0^{\infty}\frac{e^{-xt}}{\sqrt{x}}dx=-2\frac{\sqrt{2}i}{1+i}\sqrt{\frac{\pi}{t}}\end{aligned} \tag{A2}$$

and thus from Eq. (23),

$$\Gamma(t)=\Theta(t)\frac{2\kappa\sqrt{\omega_2}}{m\sqrt{\pi^3 t}}=\Theta(t)\frac{4\sqrt{\kappa\alpha}}{m\sqrt{\pi t}}. \tag{A3}$$

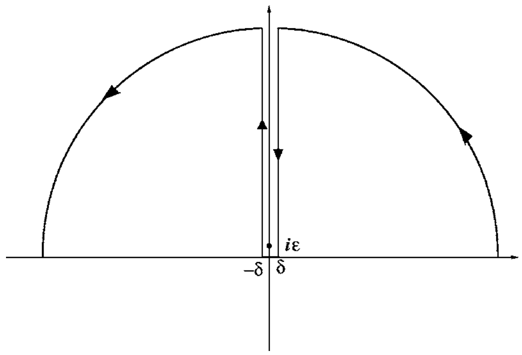

FIG. 8. Contour for the obtention of the linear response function, in the complex plane.

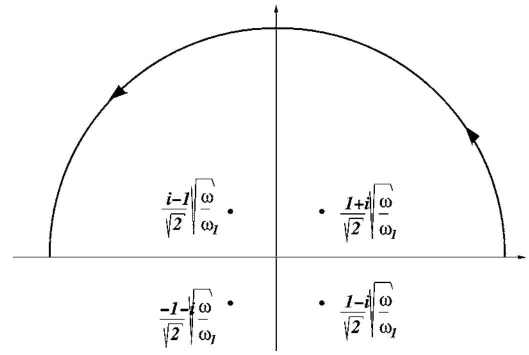

FIG. 9. Contour in the complex plane for the integration of the time autocorrelation of the fluctuating force.

APPENDIX B: AUTOCORRELATION FUNCTION OF THE FLUCTUATING FORCE

We will here check directly the validity generalized fluctuation dissipation theorem for our specific system with memory, i.e., derive Eq. (75).

We will first use the fluctuation dissipation theorem on the basic set of equations, that led to Eq. (60) for the autocorrelation function of the fluctuating force from the fluid on every particle. Performing a space Fourier transform, Eq. (60) translates for the correlations between the Fourier modes of the fluctuating force, to

$$\langle \zeta'_m(t)\zeta'^*_n(0)\rangle = 2Nk_BT\delta_{mn}\delta(t). \tag{B1}$$

We now perform a TFT of $\zeta'_n(t)$ to obtain from the above and Eq. (70),

$$\begin{aligned}\langle \tilde{\zeta}'_m(\omega)\tilde{\zeta}'^*_n(\omega')\rangle &= \int_{-\infty}^{\infty} dt\int_{-\infty}^{\infty} dt' \langle \zeta'_m(t)\zeta'^*_n(t')\rangle e^{-i(\omega t-\omega' t')}\\ &= 2N\kappa k_BT\delta_{mn}\int_{-\infty}^{\infty} dt e^{-i(\omega-\omega')t}\\ &= 4\pi N\kappa k_BT\delta_{mn}\delta(\omega-\omega').\end{aligned} \tag{B2}$$

We will now express the time autocorrelation function of $F(t)$, the total (chain+fluid) fluctuating force on particle 0, defined in Eq. (73): using also Eqs. (76) and (77), we obtain

$$\langle F(t)F^*(0)\rangle = \frac{1}{(2\pi)^2}\int_{-\infty}^{\infty} d\omega\int_{-\infty}^{\infty} d\omega' \frac{4\kappa^2}{\pi^2}\frac{\omega_1}{\omega}\frac{\omega^2}{\kappa^2}\frac{e^{i\omega t}}{N^2} \times\sum_{mn}\frac{\langle \tilde{\zeta}'_m(\omega)\tilde{\zeta}'^*_n(\omega')\rangle}{(\omega_m+i\omega)(\omega_n-i\omega)} \tag{B3}$$

$$= \frac{8\kappa k_BT/\pi^2}{2\pi}\int_{-\infty}^{\infty} d\omega s(\omega)e^{i\omega t} \tag{B4}$$

with

$$\begin{aligned}s(\omega) &= \frac{\omega_1\omega}{N}\sum_n \frac{1}{\omega_n^2+\omega^2}\\ &\simeq \frac{\omega_1\omega}{N}\sum_n \frac{1}{\omega_1^2 n^4+\omega^2}\\ &\simeq \frac{1}{2}\frac{\omega}{\omega_1}\int_{-\infty}^{\infty}\frac{dx}{x^4+\frac{\omega^2}{\omega_1^2}}\\ &= \frac{\pi i\omega}{\sqrt{2}\omega_1}\left(\frac{1}{-i(i-1)}+\frac{1}{i(i+1)}\right)\left(\frac{\omega_1}{\omega}\right)^{3/2}\\ &= \frac{\pi}{\sqrt{2}}\left(\frac{\omega_1}{\omega}\right)^{1/2}\end{aligned} \tag{B5}$$

(see Fig. 9 for the contour adopted in application of the residue theorem). Thus, introducing the notation

$$\langle F(t)F^*(0)\rangle = g(t) \tag{B6}$$

we obtain from Eqs. (87) and (B4)–(B6),

$$\tilde{g}(\omega) = \frac{8\kappa k_BT}{\pi\sqrt{2}}\sqrt{\frac{\omega_1}{\omega}} = 2mk_BT[\tilde{\Gamma}(\omega)+\tilde{\Gamma}^*(\omega)] \tag{B7}$$

which means that

$$\langle F(t)F^*(0)\rangle = 2mk_BT\Gamma(|t|), \tag{B8}$$

where we have used the fact that since the response function is real,

$$\tilde{\Gamma}^*(\omega) = \frac{1}{2\pi}\int_{-\infty}^{\infty}\Gamma(t)e^{i\omega t}dt = \frac{1}{2\pi}\int_{-\infty}^{\infty}\Gamma(-t)e^{-i\omega t}dt \tag{B9}$$

and since it is causal, $\Gamma(t)+\Gamma(-t)=\Gamma(|t|)$. Equation (B8) corresponds to the fluctuation dissipation theorem for a system with memory, as presented in Ref. [8].

[1] A. T. Skjeltorp, Phys. Rev. Lett. **51**, 2306 (1983).
[2] R. Toussaint, J. Akselvoll, G. Helgesen, A. T. Skjeltorp, and E. G. Flekkøy, Phys. Rev. E **69**, 011407 (2004).
[3] A. Skjeltorp and G. Helgesen, Physica A **176**, 37 (1991).
[4] J. Ugelstad and P. Mork, Adv. Colloid Interface Sci. **13**, 101 (1980).
[5] R. Toussaint, G. Helgesen, and E. G. Flekkøy, Phys. Rev. Lett. **93**, 108304 (2004).
[6] A. Y. Grosberg and A. R. Khokhlov, *Statistical Physics of Macromolecules* (AIP Press, New York, 1994).
[7] S. F. Edwards and D. R. Wilkinson, Proc. R. Soc. London, Ser. A **381**, 17 (1982).
[8] R. Morgado, F. A. Oliveira, G. G. Batrouni, and A. Hansen, Phys. Rev. Lett. **89**, 100601 (2002).
[9] E. M. Furst and A. P. Gast, Phys. Rev. E **62**, 6916 (2000).
[10] E. M. Furst and A. P. Gast, Phys. Rev. E **58**, 3372 (1998).
[11] S. Cutillas and J. Liu, Phys. Rev. E **64**, 011506 (2001).
[12] A. S. Silva, R. Bond, F. Plouraboué, and D. Wirtz, Phys. Rev. E **54**, 5502 (1996).
[13] M. R. Jolly, J. W. Bender, and J. D. Carlson, J. Intell. Mater. Syst. Struct. **10**, 5 (1999).
[14] S. F. Dyke, B. F. Spencer, M. K. Sain, and J. D. Carlson, Smart Mater. Struct. **7**, 693 (1998).
[15] *Proceedings of the 5th International Conference on Electrorheological Fluids, Magneto-rheological Suspensions and Associated Technology*, edited by W. A. Bullough (World Scientific, Singapore, 1996).
[16] O. Ashour, C. Rogers, and W. Kordonsky, J. Intell. Mater. Syst. Struct. **7**, 123 (1996).
[17] J. A. Stangroom, Phys. Technol. **14**, 290 (1983).
[18] T. C. Halsey and W. Toor, J. Stat. Phys. **61**, 1257 (1990).
[19] T. C. Halsey and W. Toor, Phys. Rev. Lett. **65**, 2820 (1990).
[20] T. C. Halsey, J. Colloid Interface Sci. **156**, 335 (1993).
[21] J. E. Martin, J. Odinek, and T. C. Halsey, Phys. Rev. Lett. **69**, 1524 (1992).
[22] J. E. Martin, K. M. Hill, and C. P. Tigges, Phys. Rev. E **59**, 5676 (1999).
[23] M. Fermigier and A. P. Gast, J. Colloid Interface Sci. **154**, 522 (1992).
[24] G. Helgesen, A. T. Skjeltorp, P. M. Mors, R. Botet, and R. Jullien, Phys. Rev. Lett. **61**, 1736 (1988).
[25] S. Fraden, A. J. Hurd, and R. B. Meyer, Phys. Rev. Lett. **63**, 2373 (1989).
[26] J. E. Martin, J. Odinek, T. C. Halsey, and R. Kamien, Phys. Rev. E **57**, 756 (1998).
[27] J. Liu, E. M. Lawrence, A. Wu, M. L. Ivey, G. A. Flores, K. Javier, J. Bibette, and J. Richard, Phys. Rev. Lett. **74**, 2828 (1995).
[28] J. Cernak, G. Helgesen, and A. T. Skjeltorp, Phys. Rev. E **70**, 031504 (2004).
[29] Type EMG 909, produced by Ferrofluidics Corporation, 40 Simon St., Nashua, NH 03061.
[30] B. Bleaney and B. Bleaney, *Electricity and Magnetism* (Oxford University Press, Oxford, 1978).
[31] P. G. De Gennes and P. Pincus, Phys. Kondens. Mater. **11**, 1970 (1970).
[32] E. G. Flekkøy and D. H. Rothman, Phys. Rev. E **53**, 1622 (1996).
[33] E. G. Flekkøy and D. H. Rothman, Phys. Rev. Lett. **75**, 260 (1995).
[34] F. Reif, *Fundamentals of Statistical and Thermal Physics* (McGraw-Hill, Singapore, 1965).
[35] F. Family and T. Vicsek, J. Phys. A **18**, L75 (1985).
[36] L. P. Faucheux and A. J. Libchaber, Phys. Rev. E **49**, 5158 (1994).
[37] M. Sahimi, *Flow and Transport in Porous Media and Fractured Rocks* (Wiley-VCH, New York, 1995).
[38] W. H. Press *et al.*, *Numerical Recipes* (Cambridge University Press, New York, 1992).
[39] R. N. Bracewell, *The Fourier Tranform and its Applications*, 3rd ed. (McGraw-Hill, Singapore, 2000).

Interaction model for magnetic holes in a ferrofluid layer

Renaud Toussaint*
Department of Physics, NTNU, N-7491 Trondheim, Norway

Jørgen Akselvoll, Geir Helgesen, and Arne T. Skjeltorp
Institutt for Energiteknikk, N-2007 Kjeller, Norway

Eirik G. Flekkøy
Department of Physics, University of Oslo, N-0316 Oslo, Norway

(Received 30 April 2003; published 30 January 2004)

Nonmagnetic spheres confined in a ferrofluid layer (magnetic holes) present dipolar interactions when an external magnetic field is exerted. The interaction potential of a microsphere pair is derived analytically, with precise care for the boundary conditions along the glass plates confining the system. Considering external fields consisting of a constant normal component and a high frequency rotating in-plane component, this interaction potential is averaged over time to exhibit the average interparticular forces acting when the imposed frequency exceeds the inverse of the viscous relaxation time of the system. The existence of an equilibrium configuration without contact between the particles is demonstrated for a whole range of exciting fields, and the equilibrium separation distance depending on the structure of the external field is established. The stability of the system under out-of-plane buckling is also studied. The dynamics of such a particle pair is simulated and validated by experiments.

DOI: 10.1103/PhysRevE.69.011407 PACS number(s): 82.70.Dd, 75.50.Mm, 75.10.−b, 83.10.Pp

I. INTRODUCTION

The dynamic properties of so-called magnetic holes in ferrofluid layers has been the object of increasing interest over the past 20 years [1–23]. These systems consist of spherical nonmagnetic particles in a carrier ferrofluid, whose size is order of magnitudes (1–100 μm) above the one of the magnetic particles (0.01 μm) in suspension. The ferrofluid appears then as homogeneous at the scale of the large particles—holes— and their effect on the magnetic field can be modeled as a dipolar perturbation, where the magnetic moment is opposite to the one of the displaced ferrofluid [1]. The system is generally confined between glass plates in quasi-two-dimensional layers, whose thickness slightly exceeds the diameter of the holes. The induced dipolar interactions give rise to a rich zoology of physical phenomena, such as crystallization of magnetic holes in constant or oscillating magnetic fields [1–5], order-disorder transitions in those crystals [6–9], or nonlinear phenomena in the dynamics of those systems in low frequency oscillating fields [10–13], commonly described using braid theory [14–18].

The understanding of these systems is important in relation to industrial ferrofluid applications [24,25], or for their potential use in biomedicine [26–28]. The dynamics of these phenomena can also be used indirectly to characterize the ferrofluid's transport properties [29], such as its viscosity. Eventually, the ability to shape the effective pair interaction potentials through the imposed external magnetic field makes these systems good candidates as large analog models to study phase transitions [30], aggregation phenomena [19], or fracture phenomena in coupled granular/fluid systems.

Nonetheless, despite the theoretical studies on similar dual systems such as ferromagnetic particles in a viscous fluid [31,32], and the extensive experimental observations of these magnetic holes, there is a lack of theory describing this detailed effective pair interaction potential. Notably, there has been no satisfying explanation so far for the existence of stable configurations of particle populations with finite separation distances in external fields consisting of a circular rotating in-plane component and a constant normal one (reported in Ref. [2]), or for the existence of out-of-plane buckled structures [8], and no theoretical framework for the influence of the ferrofluid layer thickness (separation of the embedding plates).

We will show here how the magnetic boundary conditions along the confining plates lead to rich effective interaction potentials rendering for those structures, rather than the qualitative magnetohydrodynamic effects proposed in Ref. [2]. In particular, we give an explanation for the existence of a finite equilibrium separation between particles. Theoretical work has already been done along this line [20], but in a reduced case of constant normal field. The present study includes a circular high frequency oscillating field in addition. The potential derived should be an essential brick in all the applications mentioned above of the magnetic holes, and in general this type of contribution of the confining structure should be relevant to any quasi-two-dimensional (2D) colloidal system with a significant dielectric or magnetic permeability contrast between the fluid medium and the confining structure, as in Ref. [33].

In this paper, we first describe the system under study and review briefly the basic modeling assumptions and standard theory. We next derive the instantaneous pair interaction potential with precise care for the magnetic permeability contrast of the boundaries, and average it over the short oscilla-

*Electronic address: Renaud.Toussaint@fys.uio.no

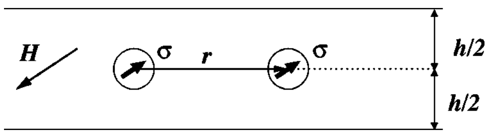

FIG. 1. Pair of nonmagnetic particles in a ferrofluid layer and related effective dipolar moments due to the external magnetic field.

tion periods to get the effective interactions. We turn then to the properties of the equilibrium configurations, sketch a simple dynamical theory, and compare the theoretical and experimental results for the dynamics of a particle pair. Eventually, the three-dimensional aspect of the ferrofluid layers is taken into account to evaluate both gravity-induced corrections and the stability of the system under out-of-plane buckling.

II. SYSTEM UNDER STUDY AND BASIC ASSUMPTIONS

The system considered consists of two nonmagnetic spheres inside a ferrofluid which is homogeneous at their scale, whose susceptibility and magnetic permeability are denoted, respectively, χ_f and $\mu_f = \mu_0(1+\chi_f)$, where $\mu_0 = 4\pi\times 10^{-7}$ H m^{-1}. This ferrofluid is itself embedded between two glass plates considered as perfectly plane, parallel, and nonmagnetic. The magnetic field anywhere between the glass plates is then decomposed between a uniform order zero component resulting from the outer imposed field, plus a perturbation due to the spheres. This perturbation is essentially dipolar: an isolated sphere in a field with a given uniform (constant) boundary value $\boldsymbol{H}$ at infinity provokes a purely dipolar perturbation outside it, generated by an effective dipole as shown in Fig. 1:

$$\boldsymbol{\sigma} = -V\bar{\chi}\boldsymbol{H}, \tag{1}$$

$$\bar{\chi} = \frac{\chi_f}{1+2\chi_f/3}, \tag{2}$$

where $\bar{\chi}$ is an effective susceptibility including a demagnetization factor, i.e., whose precise form results when the boundary conditions for the magnetic field on the surface of the sphere are properly taken into account (see, for example, Refs. [20,34]), SI magnetic units are adopted throughout this paper, $V=\pi a^3/6$ and a refer, respectively, to the volume and diameter of a sphere. This result justifies the name of magnetic holes used for those nonmagnetic spheres, and stays valid to leading order when a system more complicated than an isolated sphere is considered: it holds as soon as the external magnetic field $\boldsymbol{H}$ can be considered as uniform at the scale of a sphere, which will be assumed and commented on further in Sec. VI B.

The average magnetic field inside the ferrofluid $\boldsymbol{H}$ itself is simply related to the external uniform magnetic field imposed outside the glass plates $\boldsymbol{H}^e$ through

$$\boldsymbol{H} = \boldsymbol{H}^e_\parallel + \frac{1}{1+\chi_f}\boldsymbol{H}^e_\perp \tag{3}$$

to fulfill the boundary conditions along the glass-ferrofluid planar interfaces—namely, $\boldsymbol{H}^e_\parallel = \boldsymbol{H}_\parallel$ and $\boldsymbol{B}^e_\perp = \boldsymbol{B}_\perp$ [34,35]—where the parallel and normal components are oriented relative to the glass plates.

The simplest model for a particle pair can be obtained first by neglecting the effect of the nonmagnetic boundaries: considering a couple of two such spheres of identical moments $\boldsymbol{\sigma}$ with a separation vector from center to center $\boldsymbol{r}$, the total interaction energy of the system is, after Bleaney and Bleaney [34],

$$U = \frac{\mu_f}{4\pi}\boldsymbol{\sigma}^2\left(\frac{1-3\cos^2\theta}{r^3}\right), \tag{4}$$

where $r=\|\boldsymbol{r}\|$ and $\theta = \angle(\boldsymbol{r};\boldsymbol{\sigma})$ is the angle between the field and the separation vector.

We consider now external fields composed of a circular in-plane component oscillating at frequency ν, superimposed to a constant normal one. At high enough frequency, the relative displacement of the particles during an oscillation period is negligible compared to its average value, and the time dependence of the separation vector can be decoupled in a slow and a fast varying mode, $\mathbf{r}(t) = \overline{\mathbf{r}}(t) + \delta\mathbf{r}(\overline{\mathbf{r}};t)$, with $\overline{\delta\mathbf{r}} = 0$ and $\delta r \ll \overline{r}$. Throughout the remainder of this paper, bold symbols refer to vectors, lightface ones to their norm, and the upper bar refers to averaged quantities over oscillating time. Moreover, we will now use the additional constraint on $\boldsymbol{r}$ that it should be in-plane under the effect of the glass plates over the microspheres which center them at positions equally separated from the top and bottom boundaries. The presence of the boundaries can indeed be represented by equivalent image dipoles outside the confining plates, as established in Sec. III, which repel the dipole from the boundaries. This constraint will be addressed specifically in Sec. VII to show that this centering magnetic effect is valid in most work cases when no lateral confinement is exerted in the system—Sec. VII B. The possible sink caused by gravity under the density contrast between the microspheres and the fluid is generally negligible—Sec. VII A. Thus, in the reference frame $(\hat{\overline{\mathbf{r}}};\hat{\mathbf{n}}\otimes\hat{\overline{\mathbf{r}}};\hat{\mathbf{n}})$—where hats refer to unit vectors—instantaneous fields read

$$\boldsymbol{H} = H(\cos\phi\sin\alpha;\sin\phi\sin\alpha;\cos\alpha)^T, \tag{5}$$

with definition

$$\cot\alpha = \beta = H_\perp/H_\parallel = H^e_\perp/(1+\chi_f)H^e_\parallel, \tag{6}$$

and $\phi = 2\pi\nu t$. Thus, defining $\gamma = \angle(\overline{\mathbf{r}};\boldsymbol{r})$ comes $\cos^2\theta = \cos^2(\phi-\gamma)\sin^2\alpha = \cos^2(\phi-\gamma)/(1+\beta^2)$, and

$$U(\boldsymbol{r};\phi) = A\frac{a^3}{r^3}[2\beta^2 - 1 - 3\cos(2\phi-2\gamma)], \tag{7}$$

$$\text{with}\quad A = \frac{\mu_f\sigma^2}{8\pi a^3(1+\beta^2)} = \frac{\mu_f\pi a^3\chi^2 H_\parallel^2}{288}. \tag{8}$$

Consider distant enough particles to prevent contact and significant hydrodynamic interactions during an oscillation period of the external field: the neglect of inertial terms allows one to balance magnetic interaction forces and Stokes drag for both particles, which gives, to leading order in $\delta r/\overline{r}$,

$$
\begin{aligned}
3\pi\eta a(\dot{\overline{\mathbf{r}}}+\delta\dot{\mathbf{r}}) &= -\boldsymbol{\nabla} U(\boldsymbol{r}) \\
&= \frac{3Aa^3}{\overline{r}^4}\big[(2\beta^2-1)\hat{\overline{\mathbf{r}}}+3\cos(2\phi)\hat{\overline{\mathbf{r}}} \\
&\quad +2\sin(2\phi)\hat{\mathbf{n}}\otimes\hat{\overline{\mathbf{r}}}\big].
\end{aligned}
\tag{9}
$$

Neglecting inertial terms is easily justified since a large upper bound of Reynold's number can be evaluated as being $\mathrm{Re}=\rho x a^2\nu/\eta \leqslant 10^{-4}$, where $x=\delta r/a$ is the relative amplitude of the oscillations which will be shown straightforwardly to be typically below 10^{-2}, for typical diameters $a=50\ \mu\mathrm{m}$, ferrofluid's viscosity $\eta=9\times10^{-3}$ Pa s and density $\rho=1000\ \mathrm{kg\,m^{-3}}$, and field oscillation frequency $\nu=100$ Hz. Random thermal motion in the ferrofluid is essentially irrelevant at these size scales, as will be shown in Sec. VI B, justifying the use of deterministic dynamics instead of a Brownian one. The above equations (7) and (9) establish that the slow motion $\overline{\mathbf{r}}$ is driven by an effective potential obtained through time averaging over the oscillations of the field, i.e., simply using $\overline{\cos^2\phi}=1/2$ at fixed $\mathbf{r}=\overline{\mathbf{r}}$,

$$
3\pi\eta a\dot{\overline{\mathbf{r}}}=-\boldsymbol{\nabla}\overline{U}(\overline{\mathbf{r}}),
\tag{10}
$$

$$
\text{with}\quad \overline{U}(\overline{\mathbf{r}})=A\frac{a^3}{\overline{r}^3}(2\beta^2-1)
\tag{11}
$$

while small and quick elliptic oscillations are performed:

$$
\delta\mathbf{r}=-\frac{\nu_c}{\nu}\frac{a^5}{\overline{r}^5}\big[3\sin(4\pi\nu t)\overline{\mathbf{r}}+2\cos(4\pi\nu t)\hat{\mathbf{n}}\otimes\overline{\mathbf{r}}\big],
$$

$$
\text{with}\quad \nu_c=\frac{A}{4\pi^2\eta a^3}=\frac{\mu_0(1+\chi_f)\overline{\chi}^2H_\parallel^2}{1152\pi\eta}.
$$

The relative magnitude of the fast oscillations $\delta r/\overline{r}=\nu_c a^5/\nu\overline{r}^5$ are indeed negligible as soon $\nu\gg\nu_c\simeq 0.1$ Hz for typical ferrofluids, $\chi_f=1.9$, $\overline{\chi}=0.84$, $\eta=9\times10^{-3}$ Pa s and fields $H_\parallel=14$ Oe. ν_c, inverse of the viscous relaxation time of the system, is the critical frequency introduced in Ref. [11], above which a particle pair cannot anymore follow the direction of an external rotating field due to the fluid drag. In this paper, we study regimes where $\nu\geqslant 10$ Hz, for which the relative variations of the separation vector are below 1%, and focus on the slow motion of the particles $\overline{\mathbf{r}}(t)$ driven by $\overline{U}(\overline{\mathbf{r}})$.

In this simple picture however, this average potential is a simple central one whose inverse cubic range reflects the dipole-dipole nature of the interactions, and in the absence of any characteristic length scale, this basic model predicts a very simple behavior for the particle pair. Depending on the ratio β of the normal over the in-plane field, either the two particles will repel each other without end if $\beta>\beta_c=1/\sqrt{2}$ or they will attract each other when $\beta<\beta_c$ until the magnetic forces are balanced by contact forces or very short-range hydrodynamic forces sensitive when particles almost touch—when $(r-a)/a$ gets insignificant. This theory is obviously insufficient to render for the finite equilibrium separation distance, sometimes at a few diameters, which is experimentally observed for a whole range of imposed fields [2]. A proper treatment of the boundary conditions of the system along the glass plates, introducing the plate separation as an extra length scale to the problem, will in the following section be shown to remedy this problem.

III. EFFECT OF THE BOUNDARIES ON THE INSTANTANEOUS INTERACTIONS

The boundaries between the ferrofluid and the embedding glass plates are supposed to be perfectly plane. The two microspheres are supposed perfectly centered between the glass plates, and the perturbation of the magnetic field due to the presence of those spheres is modeled as a perturbation due to two identical pointlike dipoles $\boldsymbol{\sigma}=-\overline{\chi}V\boldsymbol{H}$ located at the center of the spheres. To fulfill the magnetic boundary conditions—i.e. the continuity of $H_\parallel$ and $B_\perp$—along the plates, a direct use of the image method (e.g., Weber [36]) shows that this magnetic perturbation between the plates is equal to the field emitted, in an unbounded uniform medium of susceptibility χ_f, by an infinite series of dipoles: the two original ones, at locations defined as $\mathbf{0}$ and $\boldsymbol{x}$, plus an infinite set of images for each of them corresponding to the mirror symmetry across the plane boundaries of the sources and all of the successive images. A magnification factor

$$
\kappa=\frac{\mu_f-\mu_0}{\mu_f+\mu_0}=\frac{\chi_f}{\chi_f+2}
\tag{12}
$$

multiplies the amplitude of the dipolar moments at each symmetry operation, i.e., explicitly defined by the following conditions.

For any dipole source $\boldsymbol{\sigma}$ at position $\boldsymbol{r}_0$, with $\boldsymbol{h}$ the normal separation vector between the plates, an infinite set of dipolar images indexed by $l\in\mathbb{Z}$ is defined by their locations and moments—see Fig. 2:

$$
\boldsymbol{r}_l-\boldsymbol{r}_0=l\boldsymbol{h},
\tag{13}
$$

$$
\boldsymbol{\sigma}_{l_\parallel}=\kappa^{|l|}\boldsymbol{\sigma}_\parallel,
\tag{14}
$$

$$
\boldsymbol{\sigma}_{l_\perp}=\kappa^{|l|}(-1)^{|l|}\boldsymbol{\sigma}_\perp\,.
\tag{15}
$$

The total interaction energy of such a system—where all dipoles do not have anymore the same moment—is (Bleaney and Bleaney [34])

$$
U=\frac{\mu_f}{8\pi}\sum_{b\neq c}\frac{1}{r_{bc}^3}\left[\boldsymbol{\sigma}_b\cdot\boldsymbol{\sigma}_c-\frac{3(\boldsymbol{\sigma}_b\cdot\boldsymbol{r}_{bc})(\boldsymbol{\sigma}_c\cdot\boldsymbol{r}_{bc})}{\boldsymbol{r}_{bc}^2}\right],
\tag{16}
$$

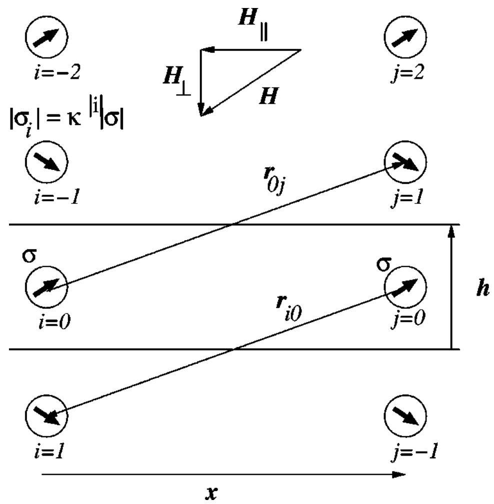

FIG. 2. Image dipoles representing the boundary conditions.

where the sum on the b index runs over the two source dipoles and the one over the c index runs over the whole set of sources and image dipoles, as seen in the preceding section; separation vectors can be considered as constant over the quick variations of $\boldsymbol{\sigma}$, and the upper bars over $\boldsymbol{r}$ are implicit for the remainder.

We will then use the following straightforward geometrical equalities resulting from Eqs. (1), (6), (13)–(15): if the c index represents the lth image of the source b, then

$$\frac{\boldsymbol{\sigma}_b\cdot\boldsymbol{\sigma}_c}{\kappa^{|l|}\sigma^2}=\frac{1+(-1)^l\beta^2}{1+\beta^2}, \tag{17}$$

$$\frac{(\boldsymbol{\sigma}_b\cdot\boldsymbol{r}_{bc})(\boldsymbol{\sigma}_c\cdot\boldsymbol{r}_{bc})}{\kappa^{|l|}\sigma^2\boldsymbol{r}_{bc}^2}=\frac{\beta^2(-1)^l}{1+\beta^2}, \tag{18}$$

$$r_{bc}=|l|h. \tag{19}$$

If on contrary c represents the lth image of one source—as indexed in Fig. 2—and b the other source, then

$$\frac{\boldsymbol{\sigma}_b\cdot\boldsymbol{\sigma}_c}{\kappa^{|l|}\sigma^2}=\frac{1+(-1)^l\beta^2}{1+\beta^2}, \tag{20}$$

$$\frac{(\boldsymbol{\sigma}_b\cdot\boldsymbol{r}_{bc})(\boldsymbol{\sigma}_c\cdot\boldsymbol{r}_{bc})}{\kappa^{|l|}\sigma^2\boldsymbol{r}_{bc}^2}=\frac{[y\cos\phi+\beta(-1)^l l](y\cos\phi+\beta l)}{(1+\beta^2)(y^2+l^2)}, \tag{21}$$

$$r_{bc}=\sqrt{x^2+l^2h^2}, \tag{22}$$

where

$$y=\frac{x}{h} \tag{23}$$

is the ratio of the particle in-plane separation distance to the plate separation. Introducing these equalities in Eq. (16) we get

$$\frac{U}{2Aa^3}=\frac{I_0^{so}}{x^3}+\sum_{l\in\mathbb{Z}^*}\kappa^{|l|}\left[\frac{I_l^{ss}}{|l|^3h^3}+\frac{I_l^{so}}{(x^2+l^2h^2)^{3/2}}\right], \tag{24}$$

$$I_l^{ss}=1-2(-1)^{|l|}\beta^2, \tag{25}$$

$$I_l^{so}=\left[1+(-1)^{|l|}\beta^2 -3\frac{[y\cos\phi+\beta(-1)^{|l|}l](y\cos\phi+\beta l)}{(y^2+l^2)}\right], \tag{26}$$

where A is the constant defined in Eq. (8). The first term, denoted by I_0^{so}, is the direct interaction between the two sources, the next one I_l^{ss} corresponds to the interactions between the sources and their own images, and finally the term I_l^{so} corresponds to the cross interactions between a source and the images of the other one.

IV. TIME-AVERAGED EFFECTIVE INTERACTIONS

A. Derivation of the potential

The $\boldsymbol{H}$ fields consist of a perfectly circular in-plane component $\boldsymbol{H}_\parallel=H_\parallel[(\cos\phi)\hat{\boldsymbol{r}}+(\sin\phi)\hat{\boldsymbol{n}}\otimes\hat{\boldsymbol{r}}]$, and a normal component $\boldsymbol{H}_\perp$ which is maintained constant. During an oscillation of the in-plane field, the only significantly varying quantity in Eq. (16) is the angle ϕ, with once again $\overline{\cos^2\phi}=1/2$.

The term I_l^{ss}, i.e., the interactions between a source and its own images, naturally does not depend on the in-plane separation vector $\boldsymbol{x}$, and produces no net in-plane force. It is worthwhile to note that this would however not be the case for any nonplane interfaces, giving the possibility to quench any geometrical property of the roughness of the interfaces in this potential. In the current hypothesis of purely planar plates, this interaction term is only responsible for a normal centering force, as will be established in Sec. VII B. For the present purpose where the microspheres are constrained on the half-plane between the plates, the in-plane forces are the only relevant ones, and this term is simply discarded in the following.

The remaining terms produce through time average the interaction energy

$$\overline{U}(\boldsymbol{x})=A\frac{d^3}{h^3}u\left(\frac{x}{h}\right), \tag{27}$$

with A the constant defined in Eq. (8), and a dimensionless term

$$u(y)=(2\beta^2-1)y^{-3}+4\sum_{l=1}^{+\infty}\kappa^l\left(\frac{1+(-1)^l\beta^2}{(y^2+l^2)^{3/2}}-\frac{3}{2}\frac{y^2+2(-1)^l l^2\beta^2}{(y^2+l^2)^{5/2}}\right). \tag{28}$$

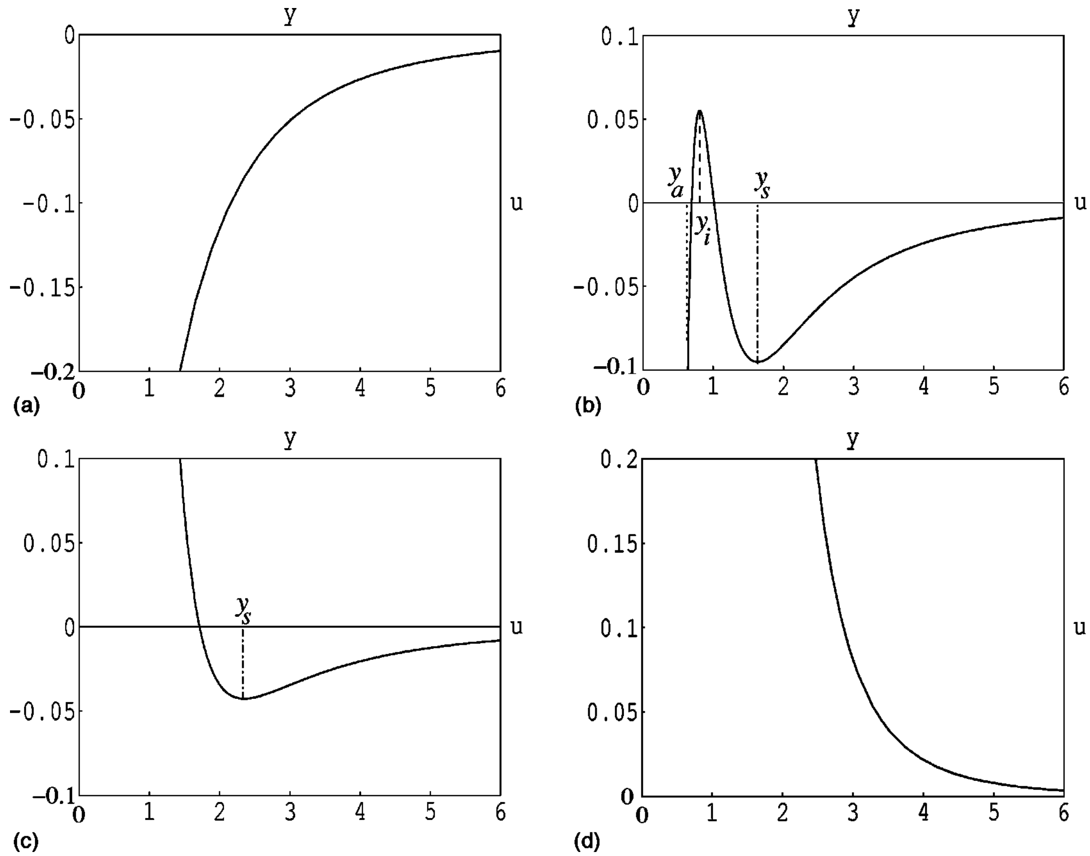

FIG. 3. Possible types of interactions depending on β.

The first term reduces to the expression of the first-order theory of Eq. (11), which is a test of self-consistency, since an infinite medium would be equivalent to the absence of permeability contrast along the plates, $\kappa=0$. The following ones render for the interactions between a source and the images of the other one. Due to the cylindrical symmetry of the problem with a purely circular in-plane field, this interaction is isotropic: the dependence on the separation vector $\boldsymbol{x}$ enters only through its norm $x=hy$.

B. Properties of the isotropic interactions

The introduction of those images is responsible for possible finite separation equilibrium distances for a whole range of β characterizing the imposed magnetic field, as is illustrated in Fig. 3: In this example, a typical susceptibility $\chi_f=1.9$ was considered for the ferrofluid, i.e., $\kappa=0.49$. The four potentials $u(y)$ represented correspond, respectively, to $\beta=0.4$, 0.58, 0.8, 2.1. They were obtained by truncating the sums in Eq. (28) to order $l=10$, which corresponds to a relative error lower than 10^{-3} in u for any y.

The general typology of those potentials can be classified in four cases as will be demonstrated in the following section, separated by three particular values of β, referred to as β_m, β_c, and β_u, which depend only on the susceptibility χ_f.

(a) For $\beta<\beta_m$, u is a monotonically increasing function, and the magnetic forces are purely attractive, thus leading any pair of spheres to contact.

(b) For $\beta_m<\beta<\beta_c$, u presents a short-range attractive core, and presents both a maximum—an unstable equilibrium point—at some distance y_i, typically slightly below 1, and a minimum—a stable equibrium point—at a greater distance y_s, usually above 1.

Two locally stable equilibrium configurations are possible in principle, depending on the ratio $y_a=a/h$ of the particle diameter to the plate separation, and of the initial particle separation y_{init}: if $y_{\text{init}}>y_i$, the particles should end up at the equilibrium separation y_s, which since $y_s>1>y_a$ corresponds to an equilibrium configuration without contact between the particles. If on the contrary $y_{\text{init}}<y_i$, the particles should attract each other and end up in contact at y_a. Since any separation $y<y_a$ is forbidden due to contact forces, this second case is only possible when $y_a<y_i$, i.e., when the ratio of plate separation over particle diameter is sufficiently big. In that case, if the thermal fluctuations are large enough to let the particles go over the energy maximum at y_i with a significant probability over the observation time, only one of the two possible equilibrium configurations will be thermodynamically stable, and the other one will be only metastable. The selection of stability/metastability between the two is determinated by the comparison of $u(y_a)$ and $u(y_s)$.

(c) For $\beta_c<\beta<\beta_u$, u presents only a global minimum, which thus corresponds to a stable equilibrium separation distance y_s. Since generally $y_s>1>y_a$, this equilibrium configuration corresponds to a finite separation distance $hy_s-a>0$.

(d) For $\beta_u < \beta$, u is monotonically decreasing, and the time-averaged magnetic forces are purely repulsive at any separation.

V. EQUILIBRIUM SEPARATION DISTANCE AS FUNCTION OF THE APPLIED FIELD

The separation equilibrium distance y_{eq}—which is stable or not—corresponds to the extrema of the potential, and can be obtained in principle by solving

$$\frac{du}{dy}(y_{eq}) = 0. \tag{29}$$

y_{eq} corresponds to y_s or y_i defined in Sec. IV B, according to the sign of d^2u/dy^2. Derivating Eq. (28) with respect to the scaled separation y leads straightforwardly to

$$\frac{y^4}{3}\frac{du}{dy} = (1-2\beta^2) - 2\sum_{l=1}^{+\infty} \kappa^l \lambda_l(y)[-1+2(-1)^l\beta^2], \tag{30}$$

$$\lambda_l(y) = \frac{(y^2-4l^2)y^5}{(y^2+l^2)^{7/2}}. \tag{31}$$

Equation (30) above is the sum of a term independent of β plus another proportional to β^2. The constant term can be shown to be positive, and the prefactor of β^2 strictly negative, for any possible (y,κ), i.e., any $y>0$, $0\leqslant\kappa<1$. Thus, $du/dy(y,\beta)$ is a monotonic decreasing function of β^2, equal to 0 when

$$\beta_0(y) = \sqrt{\frac{1+2\sum_{l=1}^{+\infty}\kappa^l\lambda_l(y)}{2+4\sum_{l=1}^{+\infty}(-1)^l\kappa^l\lambda_l(y)}}. \tag{32}$$

Thus, for a given field configuration β, and separation y, pair interactions are attractive, i.e., $du/dy>0$, if $\beta<\beta_0(y)$, and conversely if $\beta>\beta_0(y)$. A numerical study of the above function, for any κ, shows that $\beta_0(y)$ is monotonically decreasing from $\beta_c = 1/\sqrt{2}$ to a finite positive minimum $\beta_m(\kappa)$ between $y=0$ to $y_m(\kappa)$, and next monotonically increasing up to a finite limit $\beta_u(\kappa)>\beta_c$ between $y_m(\kappa)$ and $y\to+\infty$.

These considerations allow us to obtain by a direct graphical inversion of $\beta_0(y)$ the possible roots $y_s(\beta)$ and $y_i(\beta)$ for which the interaction forces are zero at a given field geometry β, as shown in Fig. 4 which is obtained for the particular case $\chi_f=1.9$, i.e., $\kappa=0.49$. This nonlinear dependence of the equilibrium separation $y_s(\beta)$ seems more complex than observed in earlier experiments by Helgesen and Skjeltorp [2]. This apparent discrepancy will be resolved in the following section, which is centered on finite-time results.

Defining the three parameters $\beta_m, \beta_c, \beta_u$ identified above as

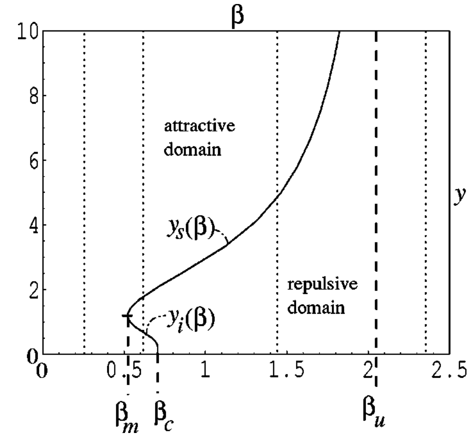

FIG. 4. Equilibrium separation of a pair as a function of the applied field.

$$\beta_c = \beta_0(y=0), \tag{33}$$

$$\beta_m = \min_y \beta_0(y) = \beta_0(y_m), \tag{34}$$

$$\beta_u = \lim_{y\to+\infty}\beta_0(y), \tag{35}$$

these arguments prove that the pair effective potentials belong to one of the four types described in the preceding section.

(a) If $\beta<\beta_m$, the potential is purely attractive at any separation.

(b) If $\beta_m<\beta<\beta_c$, there are two roots to Eq. (29), denoted $y_i(\beta)$ and $y_s(\beta)$: the potential is attractive below y_i or above y_s and repulsive between both.

(c) If $\beta_c<\beta<\beta_u$, the potential presents a single minimum at $y_s(\beta)$.

(d) If $\beta>\beta_u$, the potential is purely repulsive and there is no equilibrium separation.

The definition of β_u above—Eq. (35)—shows also clearly that $\lim_{\beta\to\beta_u^-}(y_s) = +\infty$: in principle, it should be possible to drive a pair of microspheres in an equilibrium configuration with any desirable separation distance. Naturally, since the magnetic interactions decay rapidly with distance, thermal processes or any kind of external perturbation in the fluid flow, or default in the planarity of the plates, will be predominant at large separations, where this theory will become inapplicable.

The dependence of $\beta_c, \beta_u, \beta_m$ on the susceptibility of the ferrofluid (through the parameter κ) is as follows: Replacing $\lambda_l(0)=0$ in Eq. (32) shows that

$$\beta_c = 1/\sqrt{2} \tag{36}$$

independent of κ. Similarly, since $\lim_{y\to+\infty}\lambda_l(y)=1$, β_u is easily summed as

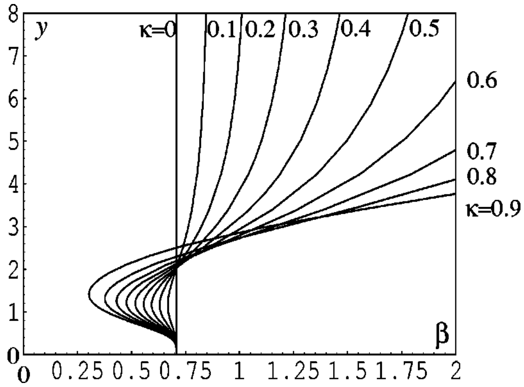

FIG. 5. Equilibrium separation distances as a function of the applied field for various ferrofluids.

$$\beta_u=\frac{1}{\sqrt{2}}\sqrt{\frac{1+2\sum_{l=1}^{+\infty}\kappa^l}{1+2\sum_{l=1}^{+\infty}(-\kappa)^l}}=\frac{1}{\sqrt{2}}\frac{1+\kappa}{1-\kappa}. \quad (37)$$

A numerical study of β_m shows that it decreases monotonically with κ, down to zero when $\kappa\to 1$.

This shows that the range of β over which stable equilibrium distances exist is larger when the susceptibility of the ferrofluid is important (κ increases with χ_f; β_m and β_u are, respectively, decreasing and increasing with κ) up to the limiting case of an infinitely susceptible ferrofluid $\kappa\to 1$ ($\chi_f \gg 1$), for which $\beta_m\to 0$, $\beta_u\to +\infty$, and there is a finite stable equilibrium separation for any ratio β.

The other limiting case $\kappa\to 0$ is obtained directly by discarding the sums in Eq. (32)—their convergence to 0 in that limit for any y is straightforward. This shows that $\lim_{\kappa\to 0}\beta_m=\lim_{\kappa\to 0}\beta_u=\beta_c=1/\sqrt{2}$. Without any permeability contrast along the glass plates, no images are felt and the first-order theory is recovered—the interactions are simply purely attractive when $\beta<\beta_c$, and purely repulsive when $\beta>\beta_c$, with the stable regimes $\beta\in[\beta_m,\beta_u]$ disappearing.

An overall picture of $y_{eq}(\beta)$ for different values of κ distributed regularly between 0 and 0.9 is given in Fig. 5. The sums in Eq. (32) have been truncated to order 10, which results in an accuracy better than 1% for the displayed function $\beta_0(y)$: indeed, functions $\lambda_l(y)$ defined in Eq. (31) can be bounded by $|\lambda_l(y)|<1/(y^2+l^2)^{3/2}$, so that $|\Sigma_{l=N}^{+\infty}\kappa^l\lambda_l(y)|<\Sigma_{l=N}^{+\infty}\kappa^l|\lambda_l(y)|<\kappa^N/(1-\kappa)N^3$, and similarly for $|\Sigma_{l=N}^{+\infty}(-\kappa)^l\lambda_l(y)|$. Thus, neglecting terms from order $N=11$ in the sums, for any $\kappa<0.9$, results in a relative error on $\beta_0(y)$, smaller than $0.9^{11}/(1-0.9)11^3\simeq 0.0023$.

VI. FINITE-TIME THEORY AND EXPERIMENTS

A. Simple time-dependent theory

The preceding section was centered on equilibrium properties of this system, but the relaxation time to reach equilibrium amounts to hours or days in certain configurations, as will be shown here. In order to compare efficiently theoretical and experimental data, we have therefore concentrated on the slow dynamics of this system, starting from hole pairs in contact under the effect of a purely in-plane field $\beta=0$, through the following scheme: neglecting once again the inertial terms, Stokes drag and magnetic interactions are balanced to obtain

$$3\pi\eta a\frac{dx}{dt}=-\frac{d}{dx}\overline{U}(x), \quad (38)$$

where the effective potential includes the images due to the boundaries, Eq. (27). The viscosity η above is renormalized to take into account hydrodynamic interactions with the confining plates, as will be detailed further.

In dimensionless units, this equation leads to

$$\frac{dy}{dt'}=-\frac{d}{dy}u(y), \quad (39)$$

$$\text{with}\quad T=\frac{864\eta}{\mu_0(1+\chi_f)\overline{\chi^2}H_\parallel^2}\frac{h^5}{d^5}, \quad (40)$$

and $y(t')=x/h$, $t'=t/T$, and $u(y)$ is the potential defined in Eq. (28). The characteristic time above lies typically around 30 s–5 min at usual working parameters, as will be shown in the following section, and moreover the potential wells can be pretty flat, thus producing often metastable situations that last from minutes to hours [the driving force close to equilibrium position is proportional to the distance to it times the second derivative of the potential in the well, and $u''(y_s)\to 0$ when $\beta\to\beta_u^-$].

Starting from a pair configuration in contact, and setting at time 0 the field parameters (β ratio and magnitude $H_\parallel$) to a constant value, the time $t'(y)$ to reach a given separation will be directly obtained through numerical integration of the differential equation (39):

$$t'(y)=-\int_{z=a/h}^{y}dz/u'(z). \quad (41)$$

An inverse representation of the above is plotted for a ferrofluid of susceptibility $\chi_f=1.9$. In Fig. 6, the solid thin line represents $y(t')$ at fixed $\beta=0.8$, and in Fig. 7 the dashed lines represent $y(\beta)$ for four characteristic times $t'=0.25$, 1, 4, 16, slowly converging to equilibrium separation $y_s(\beta)$, plotted as a solid line.

To compare this with experiments, the fine tuning of the time dependence requires a refined analysis of the hydrodynamic interactions in the above: since experiments are carried out in cells of width h comparable with the diameter a of the embedded holes—typically h/a lies between 1.1 and 2—a strong hydrodynamic coupling with the confining plates is present. Considering that both particles sit at a fixed fraction z of the plate separation relative to the central position (nonzero z can be obtained in principle between horizontal plates due to the density contrast between the particles and ferrofluid), these interactions are represented according to Ref. [37] by a normalization of the Stokes drag as

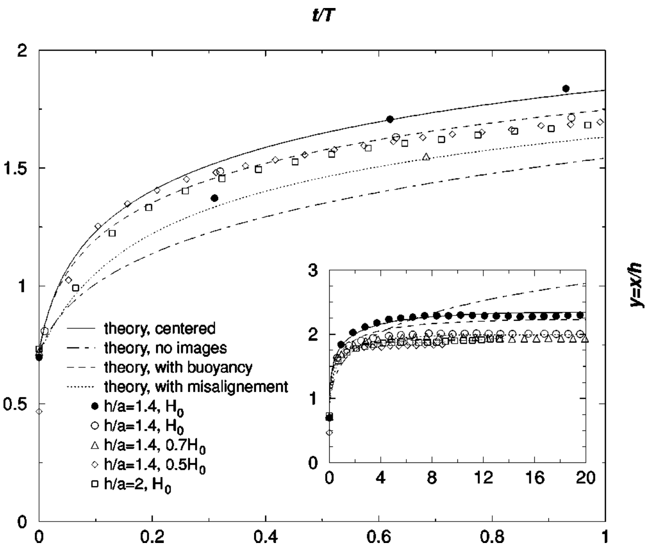

FIG. 6. Scaled separation as a function of time for various field magnitudes and plate separations for $\beta = H_\perp / H_\parallel = 0.8$. The inset represents the same data for longer times.

$$\eta/\eta_0 = f(a/(h+2zh)) + f(a/(h-2zh)) - 1, \quad (42)$$

with η_0 the naked viscosity of the carrier ferrofluid, and

$$f(x) = \left(1 - \frac{9x}{16} + \frac{x^3}{8} - \frac{45x^4}{256} - \frac{x^5}{16}\right)^{-1} + O(x^6). \quad (43)$$

Two experimental cases will be considered here, where $h/a = 1.4$, $z \simeq 0$ and $h/a = 2$, $z \simeq 0.14$, corresponding, respectively, to $\eta/\eta_0 \simeq 2.6$ and 2.4. This is consistent with Faucheux and Libchaber's measures for a confined Brownian motion [37] and with an experimental value $\eta/\eta_0 \simeq 2.4$, which we measured in the $h/a = 1.4$ case by placing 50 μm diameter particles between 70 μm distant plates set up in vertical position, without any magnetic field, and by recording the motion of a single particle under the effect of buoyancy forces. The density of the ferrofluid was $\rho_f = 1.24$ and the one of the polystyrene particles was $\rho_p \simeq 1$. This value is slightly below the theoretical $\eta/\eta_0 \simeq 2.6$, which is consistent with the effect of the Brownian motion of the particle along the normal direction, as analyzed in Ref. [37]. We have chosen to use $\eta/\eta_0 = 2.5$ in the following.

Hydrodynamic interactions between both particles were neglected, which should be a relatively poor approximation for particles close to contact, but become reasonable at separations $x/h > 2$ where most of the time is spent to achieve equilibrium at relatively large separations, and is therefore the most important one in the present context. The typical magnitude of this error can be roughly estimated through the analyses performed by Dufresne *et al.* or Grier and Behrens [21,38] for a close context: they derived for two particles of diameter a, separated by x and at a distance $h/2$ from a single plate, the hydrodynamic corrections to the mobility to first order in x/a and x/h. Considering for simplicity a double contribution for two plates relative to Eq. (13) in Ref. [21], contributions due to the particle-particle interactions become,

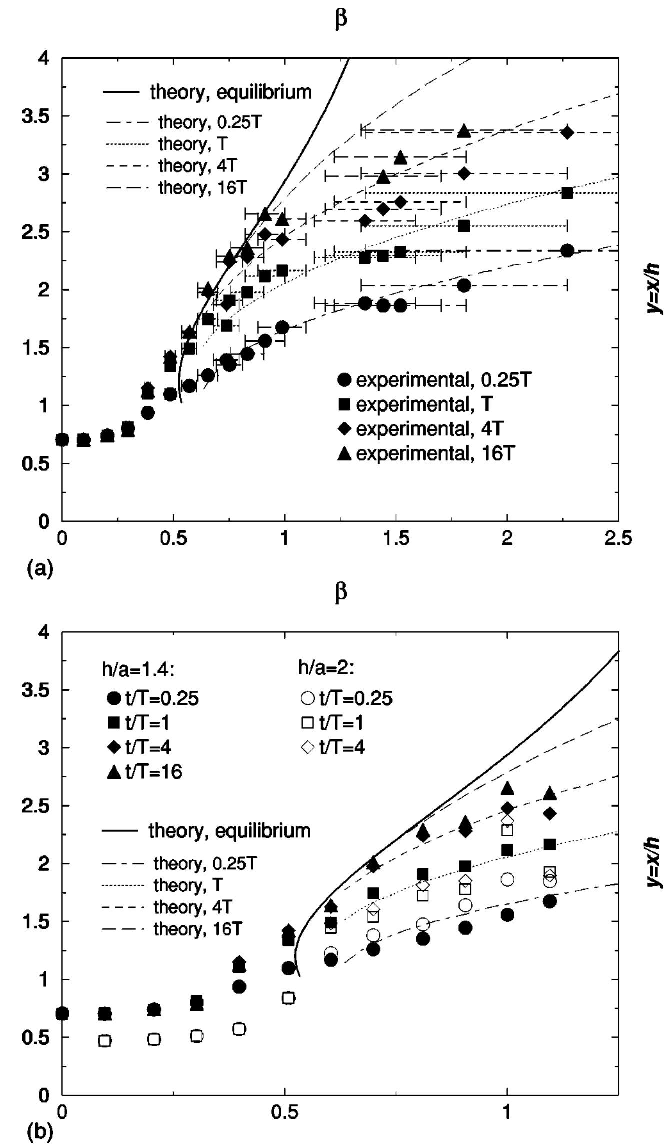

FIG. 7. Separation as a function of time and β for various field configurations, times, and cell sizes: merged data and theory.

for $h/a = 1.4$, $x/h > 2$, less than 30% of the one due to the plates—term $9x/16$ in Eq. (43).

We neglect also the rotational degrees of freedom of the ferrofluid itself, which can lead to the rotation of the nonmagnetic spheres, and induce another type of hydrodynamic interactions between pairs of spheres: in ferrofluids submitted to circular magnetic fields, the rotation of the magnetite particles induces asymmetric stresses in the fluid, which leads to a counterrotation of the magnetic holes [2,23]. The mismatch between this rotational motion of the magnetic holes and the one of the magnetites could in principle induce a vortex in the fluid flow around each of the holes, which would lead to a net hydrodynamic torque over close pairs of holes. Nonetheless, with the ferrofluid and field frequency regime used here ($\nu_f < 100$ Hz), this rotational motion of the holes is so slow that it is hardly detectable. Experimentally, with a similar ferrofluid (kerosene-based, $\chi_f = 0.8$), the hole's frequency was bounded by $\nu_s < 0.01$ Hz. This rotational motion was described theoretically in detail by Miguel and Rubi [23]. Through this theory, for the ferrofluid and field frequencies used here, the frequency of the magnetic holes will straightforwardly be shown to be lower than $\nu_s < 0.05$ Hz. This justifies for the present study the neglect of these rotation-induced hydrodynamic interactions. These interactions would in any case lead to a purely rotational motion of the hole pair, decoupled from the purely central forces induced by the magnetic interactions studied here. Experimentally, some very slow rotational motion of the hole pairs was indeed occasionally observed when the particles were close (nonperiodic, angular velocity always lower than 0.001 Hz), but no systematic trend for its direction or velocity was noted, i.e., this effect was beyond the experimental error.

To obtain the theoretical estimate of the hole's frequency above, the Langevin parameter of the ferrofluid, defined [23] as $\mu = m_0 H / k_B T$, where m_0 is the magnetic moment of the magnetites, is derived from the saturation magnetization of the ferrofluid and its susceptibility [39] as $\mu = 3H/\chi M_{\mathrm{sat}}$. For the ferrofluid used, $\chi = 1.9$, $M_{\mathrm{sat}} = 200$ G, $H = 14$ Oe, and $\mu = 0.26$. This enables us to express the ratio of the hole's frequency over the field's one as [23]

$$\nu_s / \nu_f = -\Phi(\mu - \tanh \mu)/(\mu + \tanh \mu) = -0.00041, \tag{44}$$

where $\Phi = -0.036$ is the magnetite volume fraction of the ferrofluid. For the regime $\nu_f < 100$ Hz where the experiments are carried, the sphere's frequency is thus below $\nu_s = 0.041$ Hz.

B. Experimental results and scaling

We used pairs of $a = 50$ μm diameter neutral polystyrene spheres of density $\rho_p = 1$, designed according to Ugelstad's technique [40], and ferrofluids of susceptibility $\chi_f = 1.9$, density $\rho_f = 1.24$, and viscosity $\eta_0 = 0.009$ Pa s [41], confined in horizontal cells of thickness 70 μm or 100 μm and width of the order of centimeters. The thickness of the cell was obtained by confining plates by quenching a few 70 μm diameter spheres between the two plates clamped together (these spacers were typically half a centimeter distant from each other). The oscillating in-plane and constant normal field were generated by external coils, with a typical magnitude $H_\parallel = H_0 = 14.2$ Oe, with frequencies from 10 to 100 Hz. Magnitudes and phase of the field are accurate up to 1%, which also corresponds to the degree of homogeneity of the in- and out-of-plane fields throughout the entire cell. The direction of the constant field varies slightly along the cell, with a maximum 3° misalignment from the direction normal to the confining planes (these accuracies for the homogeneity and misalignment of the field were obtained directly by considering the geometry of the Helmholtz coils generating the field, whose characteristic extent is 10 cm, together with a 0.5 mm accuracy for the position of the cell inside them). The in-plane motion of the particles was recorded using a microscope and a camera linked to a numerical data analysis setup. The entire experimental setup is described, for example, in Ref. [12]. The samples were prepared with a pure in-plane field to bring the particles in contact, after that the in-plane field was maintained constant and the normal field was set to a constant $H_\perp^e = (1+\chi_f)\beta H_\parallel$. The normal field required typically a few seconds to stabilize. Separation between the particles were then recorded every 10 s, for 30 min. The concentration of the spheres in the entire sample was such that the nearest sphere or spacer would sit at least 20 diameters apart from the observed pair, which was sufficiently dilute not to influence the motion of the observed pair.

1. Time-dependent result at fixed field geometry and discussion

The scaled separation as a function of time is shown in Fig. 6, for five experiments carried out at $\beta = 0.8$, i.e., for the potential represented in Fig. 3(c), which presents a single minimum at $y_s(0.8) = 2.35$. Four experiments were carried out in a $h = 70$ μm thick cell, two of them at identical field amplitudes $H_\parallel = H_0 = 14.2$ Oe and two other at $H_\parallel = 0.7H_0$; $0.5H_0$. The last experiment was carried out in a $h = 100$ μm thick cell, with an in-plane field H_0. These parameters corresponded, respectively, to characteristic times evaluated using Eq. (40) as $T = 32$ s, 63 s, 129 s, and 192 s.

a. Comparison with the theory. The large part of the figure represents the short-time evolution $t < T$ (typically the first minutes) and the encapsulated part shows longer time (typically 30 min). Every data point (separated by 10 s) was used for the early regime, one point out of 2–12 depending on the experiment for the later one. At shorter times, the scaled data collapse reasonably well on the theoretical curve obtained from the theory sketched so far, solid line. The only two main outliers (first filled circle and triangle, $t = 10$ s) presumably corresponded to a weaker normal field in the first few seconds, until it stabilized. For illustration, the first-order theory neglecting the magnetic confinement leads to the dot-dashed curve, obtained using Eq. (41) with a bare potential retaining only the source-source term. This too simple theory clearly differs from data both at short and large times.

b. Corrections due to buoyancy. A third dashed theoretical curve was plotted, corresponding to a slightly refined calculation of the interaction potential, where buoyancy forces due to the density contrast between ferrofluid and particles led to a shift z of the particle pairs from the central midplane of the cell. The relative displacement z/h due to this gravitational correction is evaluated in Sec. VII A as 15% in the weakest fields $0.5H_0$, $h/a = 1.4$ case, and in the thicker layer H_0, $h/a = 2$ case, whereas it should remain around 6% for the thinner cells, higher field H_0 case. The extended potential to take this lateral shift into account is also derived in Sec. VII A, and the dashed curve corresponds to this potential at a fixed shift $z/h = 14\%$, which is the maximum possible in the thin cells, since it would correspond to contact of the particles with one of the plates, coinciding with $z/h = (1 - a/h)/2$ at $h/a = 1.4$. Considering this correction, one would expect the diamond and squares to follow the dashed line, the circles to be close to the solid line, and the triangle to sit in between. This is indeed approximately the case at shorter times for the diamonds and rectangles, and the filled circles fit well with the centered theory, both at short and long times. Nonetheless, it is worth noting that the open circles collapse rather with the lower field experiments than with the filled circles, another experiment carried with identical parameters. This gives an estimate of the reproducibility of these experiments, corresponding roughly to a relative experimental error bar of 10% for the separation at a given time, estimated between open and filled circle cases. The gravity-induced correction discussed above is of order 5% for the separation as a function of the dimensionless time, and the effect of this shift on the magnetic interactions can therefore hardly be distinguished from experimental dispersion in terms of separation. Still, the renormalization of the time due to hydrodynamic interactions with the plates would lead in the thick cell case $h/a=2$ to $\eta/\eta_0 \simeq 1.2$ if the particles were considered as centered, $z/h=0$, instead of the value $\eta/\eta_0=2.5$ that we used and corresponded to the predicted shift in that case, $h/a=2$, $z/h=0.15$. This gravity-induced correction is then clearly sensible for the hydrodynamic corrections, if not so much on the magnetic interactions, since the above incorrect viscosity η would correspond to dividing T by 2, which would double the abscissas of the square data points and drive them way out of the theory and rest of the data. This shows qualitatively that this shift was indeed present in cases $h/a=2$, H_0, and $h/a=1.4$, $0.5H_0$, and that particles sat close to or in contact with a plate in this last case.

c. Corrections due to experimental error on the field directions. The fourth dotted curve represents the theoretical effect of a misalignment of angle $\alpha=2.5°$ between the constant field and the normal direction. A direct generalization of Secs. II to IV to such configurations with a slightly tilted constant field shows that the time-averaged potential is still of the form in Eqs. (25) and (26), with a modified parameter

$$\beta' = \frac{\boldsymbol{H}_\perp^e}{(1+\chi_f)[\boldsymbol{H}_\parallel + \sqrt{2}\sin(\alpha)\cos(\theta)\boldsymbol{H}_\perp^e]} \simeq \beta - \sqrt{2}(1+\chi_f)\beta^2 \sin(\alpha)\cos(\theta), \tag{45}$$

where θ is the angle between the projection of the constant field over the plane and the separation vector. This modified interaction potential leads to a torque tending to align the particle pair with the direction $\theta=0$, and a radial interaction force corresponding to a modified β' in $[\beta-\sqrt{2}(1+\chi_f)\beta^2\sin(\alpha);\beta]$, β' decreasing with time towards the lower limit as the pair aligns with the in-plane constant component of the field. The dotted curve corresponds to this lower limit for a possible misalignment $\alpha=2.5°$, which is evaluated from the above as $\beta'=0.68$.

For the longer-time period shown in the encapsulated part of Fig. 6, an apparent equilibrium position was reached in each experiment after typically $6T$—no more than a 1% relative motion was noticed later when the experiments were conducted for several hours. This equilibrium separation corresponds theoretically to the equilibrium one studied in the preceding section, $y_s(0.8)=2.35$. The high field and thin cell experiments (filled circles) agree well (within 2%) with the theory with a purely normal field (solid line), but discrepancies between solid line and experiments are noticeable at longer times for the four other experiments. A comparison of the data with the dotted line shows that a misalignment of order 2.5° between constant field and normal direction is sufficient to explain these discrepancies: in these experiments, the particle pairs started at a relatively large angle θ from the in-plane component of the constant field, which is why the unmodified theory and experimental data are close for short times. At longer times, the particle pairs aligned with the direction $\theta=0$ and the modified theory $\beta'=0.68$ agree well with the data. An initial rotation of the particle pair and subsequent locking of this direction in a particular one was indeed observed in these experiments.

Brownian motion in the ferrofluid can be proved to be entirely negligible for the relatively large particles and field we worked with, its relative magnitude compared to magnetic interaction energy being $kT/\min\overline{U} \leqslant kT/[A(d^3/h^3)\min u] \simeq 10^{-4}/\min u \leqslant 5\times10^{-3}$ for the fields, particles, and plate separations considered here.

2. Scaled time-dependent results at various field geometries

Experiments were carried out with in-plane field magnitudes H_0 and normal fields jumping at initial time from 0 to $\beta(1+\chi_f)H_0$ with various β from 0 to 3.5. This was done for $a=50$ μm diameter particles and plate separation $h=70$ μm and 100 μm. The results, scaled separation as a function of β, at four values of the scaled time are shown in Fig. 7(a) for the thinner cell. The error bars correspond to a possible misalignment $\alpha=2.5°$ between the constant field and the normal direction: they represent the limits $[\beta-\sqrt{2}(1+\chi_f)\beta^2\sin(\alpha);\beta]$ for the effective β' parameter as explained in the preceding section. For the "c" regime $\beta>\beta_c=1/\sqrt{2}\sim0.7$, theory and experiment agree well for any of the tested field parameters and times.

The solid line represents the theoretical equilibrium value, studied in Sec. V. This is reached within typically $16T$ (8 min for $h/a=1.4$, $H_\parallel=H_0$) for $\beta\leqslant1$, or longer time at higher β. This is the main reason why the upward curvature of the theoretical solid curve at larger values of β is not observed in experimental data, which correspond to finite times, and for which other types of perturbations always enter the picture at very large times and distances.

In Fig. 7(b), we present the results of experiments carried out at two different plate separations, as a function of time and value of β. The error bars have been omitted for readability, and the experimental points represented correspond to a constant field supposed purely normal [i.e., the abscissas are the upper limit of the error bars in Fig. 7(a)]. The experiments carried out in thicker cells, corresponding to weaker magnetic interaction forces, are more sensitive to any perturbations. The relative data collapse for both plate separations at $0.25\,T$ and T when $\beta>\beta_c$ nonetheless show that the separations in this regime scale with plate separation, and not with particle diameter. Apart from the misalignment of the constant field with the normal direction, a possible source for these perturbations is as follows: when the particles come close to equilibrium, in-plane magnetic forces tend to zero, and the particle motion becomes more sensitive to any interactions with the local environment (confining plates)—this being of course even more the case for weaker fields or larger h/a. There seems to be a pinning (friction) of the particles to an absolute plate position at large times. The physical origin of this pinning is possibly due to roughness of the plates (especially when particles are almost in contact), which can quench the particles through the magnetic perturbation due to this roughness (the repulsion effect of a dipole by its images would make a particle sit preferably in positions of larger plate separation), or alternatively when particles are almost in contact with the plates can result in an in-plane component of the hydrodynamic coupling or contact forces responding to buoyancy forces. Instead of plate roughness, the same type of qualitative effects could be due to small impurities in the ferrofluids, starting to stick to the plates or particles at large times, when the chemical surfactant layers around large particles and possible impurities break apart in some points.

For the regime $\beta<\beta_c$, the simple theory presented here would predict that particles stay always in contact at $y=a/d=0.5$ or 0.71 for $\beta<\beta_m\sim 0.55$, and for $\beta_m<\beta<\beta_c$ would either stay in contact if $a/h<y_i(\beta)$ or go to the secondary minimum $y_s(\beta)$ if $y_i(\beta)<a/h$ (the separation between the first and second case happening at $\beta=0.61$ for $a/h=1/1.4$ and $\beta=0.67$ for $a/h=1/2$). Particles seem indeed to be in contact for $\beta\leqslant 0.2$, but start to separate significantly well before β_m. We note also that this separation seems grossly to be proportional to the particle diameter when $\beta\leqslant 0.3$, where some finite separation can already be observed—ordinates of opened and filled symbols are multiples of each other through a factor 100/70—and proportional to plate separation in the regime $\beta_m<\beta<\beta_c$. This shows that an extra physical effect that was not taken into account here generated repulsive forces, whose range is finite but scales with the particle diameter. This effect suppresses then the short-range attraction in the regime $\beta_m<\beta<\beta_c$, so that the particle jumps directly to $y_s(\beta)$, which is always a stable minimum and not a metastable one. For $\beta<\beta_m$, this extra effect starts to separate the particles in proportion to particle diameter. The physical origin of this short-range repulsion should not be the particle-particle hydrodynamic interactions, which should slow down the relative motion rather than result in a net repulsion—see Refs. [38,42]. A probable candidate for this repulsion is rather the magnetic effect of the finite size of the spheres, particularly sensible when particles are close to contact. Even if an isolated nonmagnetic sphere generates a purely dipolar perturbation when it is isolated in a homogeneous susceptible medium, this dipolar perturbation does not fulfill the boundary conditions along the surface of another magnetic sphere, sufficiently close of the first one to feel the heterogeneity of the perturbation at the scale of its diameter, which is naturally the case at a finite separation/diameter ratio. To model this short-range repulsion requires accounting for the magnetic perturbation generated by this nonpointlike character of close enough spherical particles. Though this can be performed by a simple image method for pairs of disks in 2D, one can show that this does not extend to pairs of spheres in 3D, and the proper mathematical description of this perturbation requires the use of a series of spherical harmonics, which was not performed in the present study. To conclude this discussion, we note that this correction seems to be negligible at separations exceeding the sphere diameter $x/a>2$, as shows the agreement between experimental data and the present theory when $\beta>\beta_m$.

Finally, we note that the present results are not contradictory with similar experiments carried out in Ref. [2] with a slightly different ferrofluid, plate separation, and particle size, where it was reported that the equilibrium particle separation is approximately linear in β once the particles start to separate; for example, this is also the case with the present ferrofluid, in the particular case $h/a=1.4$ in the regime $0.3<\beta<1$—see the filled triangles or theoretical curve in Fig. 7(a). This linear property is however shown here to be a mere coincidence, for this does not hold in the same β regime for $h/a=2$, or for any h/a when $\beta>1$, where $y_s(\beta)$ is curved upwards, and any result $y(\beta,t)$ observed at a given finite time t is curved downwards.

VII. GENERALIZATION TO QUASI-2D SYSTEMS

A. Gravity-induced corrections

Although the effect of the dipolar images in the confining plates tends to center particles at a midplane position, the density contrast between the ferrofluid and particles tends to drive the particle out of it for large enough particles. An estimation of this effect can be obtained by considering for each particle the sole effect of its own images plus buoyancy forces—for the simple estimation we look at here, we will neglect the coupling between one source and the images of the other. Extending the analysis performed in Secs. III and IV A to a single dipole lying at a vertical distance z from the center between two horizontal plates, we directly have

$$\overline{U}^{\text{shifted}}(z)=A\frac{a^3}{h^3}u^{\text{shifted}}\left(\frac{z}{h}\right), \tag{46}$$

$$u^{\text{shifted}}(s)=\sum_{l\in\mathbb{Z}^*}\kappa^{|l|}\frac{1-2(-1)^l\beta^2}{|l-[1+(-1)^{l+1}]s|^3}. \tag{47}$$

This potential can be shown to be always centering for any value of β, i.e., to have a single minimum in $s=0$ and to diverge to infinity at $s=\pm0.5$—plate contact for very small particles. Equilibrium between gravity forces and magnetic interactions between the dipole and its images leads to

$$\frac{d\overline{U}^{\text{shifted}}}{dz}=V(\rho_g-\rho_f), \tag{48}$$

i.e.,

$$\frac{du}{ds}=\frac{48(\rho_g-\rho_f)gh}{\mu_f\overline{\chi}^2H_\parallel^2}\frac{h^3}{d^3}. \tag{49}$$

For small separations (i.e, small particles or strong enough fields), a Taylor expansion to first order around the plates' center gives

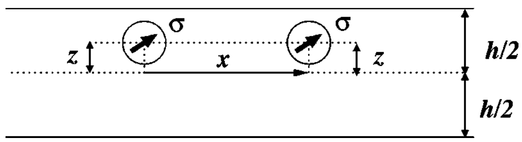

FIG. 8. Shifted hole pairs considered.

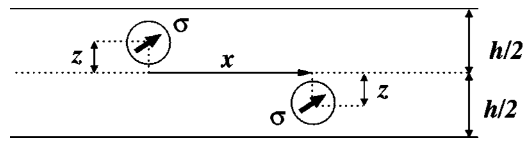

FIG. 9. Tilted hole pairs considered.

$$\frac{du}{ds}=96C(\kappa)(1+2\beta^2)|s|, \tag{50}$$

$$C(\kappa)=\sum_{n\in N}\kappa^{2n+1}/(2n+1)^5, \tag{51}$$

which is valid up to 25% for $s<0.1$. Thus, the displacement looked for can be evaluated as

$$s=z/a=\frac{(\rho_g-\rho_f)gh}{2C(\kappa)(1+2\beta^2)\mu_f\overline{\chi^2}H_\parallel^2}\frac{h^3}{a^3} \tag{52}$$

when this quantity does not exceed 0.1, or directly using Eqs. (49) and (50) otherwise. For the ferrofluid and particles we used, this led, respectively, for $h=70\ \mu$m, $H_\parallel=H_0$, $0.7\,H_0$, or $0.5\,H_0$ and $h=100\ \mu$m, $H_\parallel=H_0$ to $s=0.06$, 0.10, 0.15, and 0.15.

The magnetic interaction potentials were unaffected up to 1% in the $s=0.06$ vertical shift case, and the dashed curve in Fig. 6 was obtained by considering particles at a fixed $s=0.14$ out-of-midplane shift, using a generalized potential obtained for a configuration sketched in Fig. 8 through an extension of the method used in Secs. III and IV A as

$$u_s^{\text{pair}}(y)=(2\beta^2-1)y^{-3}+4\sum_{l=1}^{+\infty}\kappa^l\left(\frac{1+(-1)^l\beta^2}{[y^2+m_s(l)^2]^{3/2}}-\frac{3}{2}\frac{y^2+2(-1)^l m_s(l)^2\beta^2}{[y^2+m_s(l)^2]^{5/2}}\right), \tag{53}$$

$$m_s(l)=l+s[1+(-1)^l]. \tag{54}$$

This $s=0.14$ value was picked to represent the magnetic effect of a shift sufficient to bring particles in contact with the plates in the $h/a=1.4$, $0.5\,H_0$ case. To an accuracy of 1%, the results for $s=0.15$ were very close to this case, the ones for $s=0.06$ very close to pure in-plane situations, and the situation $s=0.10$ fell roughly halfway between both, and were therefore omitted from Fig. 6 for readability.

B. Stability of the plane solutions and buckled configurations

When particles are sufficiently small or fields sufficiently high, the preceding section establishes that the confining plates have an effective repulsive effect on an isolated particle, which is therefore centered on midplane. In the case of a pair of particles, the interactions between one source and the images of the other one might nonetheless modify that picture and make the plane solutions described in this paper unstable, as have been observed in some experiments. Neglecting gravity, we will here generalize the interaction potential to configurations where particle pairs are allowed to tilt on both sides of the midplane, i.e., where both are displaced by the same distance z on both sides of it—cf. Fig. 9. We consider only symmetric situations due to the symmetry of the problem under parity in the absence of gravitational forces. The effective interaction potential is obtained similar to the plane one, and comes as $\overline{U}(x,z)=A(a^3/h^3)u(x/h,z/h)$, where

$$u(y,s)=2\sum_{l=-\infty}^{+\infty}\kappa^{|l|}\left(\frac{1+(-1)^l\beta^2}{[y^2+(l+p_ls)^2]^{3/2}}-\frac{3}{2}\frac{y^2+2(-1)^l(l+p_ls)^2\beta^2}{[y^2+(l+p_ls)^2]^{5/2}}\right)+2\sum_{l\in\mathbb{Z}^*}\kappa^{|l|}[1-2(-1)^l\beta^2]\times\left(\frac{1}{|l+(2-p_l)s|^3}-\frac{1}{|l|^3}\right), \tag{55}$$

$$p_l=1+(-1)^l, \tag{56}$$

which reduces to the previous in-plane solution, Eq. (28), when $s=0$. Contour plots of this pair potential are displayed in Fig. 10 for the ferrofluid used here, $\chi_f=1.9$, and the four types of potentials, $-\beta$ values, are identical to the ones adopted in Sec. IV B. Black and white represent, respectively, $u=-0.2$ and 0.5 in panels (a) and (b), $u=-0.2$ and 1 in (c) and (d), and the gray level linear in u in between. Out-of-plane values represented cover the whole possible range $0\leqslant s\leqslant 0.5$ in (c) and (d), and are restricted to 10% from the midplane in (a) and (b). The in-plane configurations correspond to the bottom axis of those graphs.

In-plane solutions are in principle locally stable if $\partial^2u/\partial s^2(y,0)>0$, otherwise particle pairs will tend to tilt. For both first cases, $\beta<\beta_c$, we note that $\partial^2u/\partial s^2>0$ for any possible (y,s), and any tilt is restored by the magnetic image effect; the plane configurations are indeed stable. As soon as $\beta>\beta_c$, besides the minima $(y,s)=(y_s,0)$ or $(+\infty,0)$ in (c) or (d) case, another local minimum appears at a certain $(y,s)=(0,s_e(\beta))$: particles can be stable at a finite distance on top of each other—the pair tends to align with the large normal field— or if they are close enough to be attracted by this potential minimum but too large $[a>s_e(\beta)$ and $a>h/2]$, contact forces between them and with the confining plates will attract them to a buckled configuration where both particles are in contact with each other, and with one different plate each. Note that $0<s_e(\beta)<0.5$, i.e., very small particles, $a\ll h$, at this second minimum would sit on top of each other, neither in contact between them nor with the

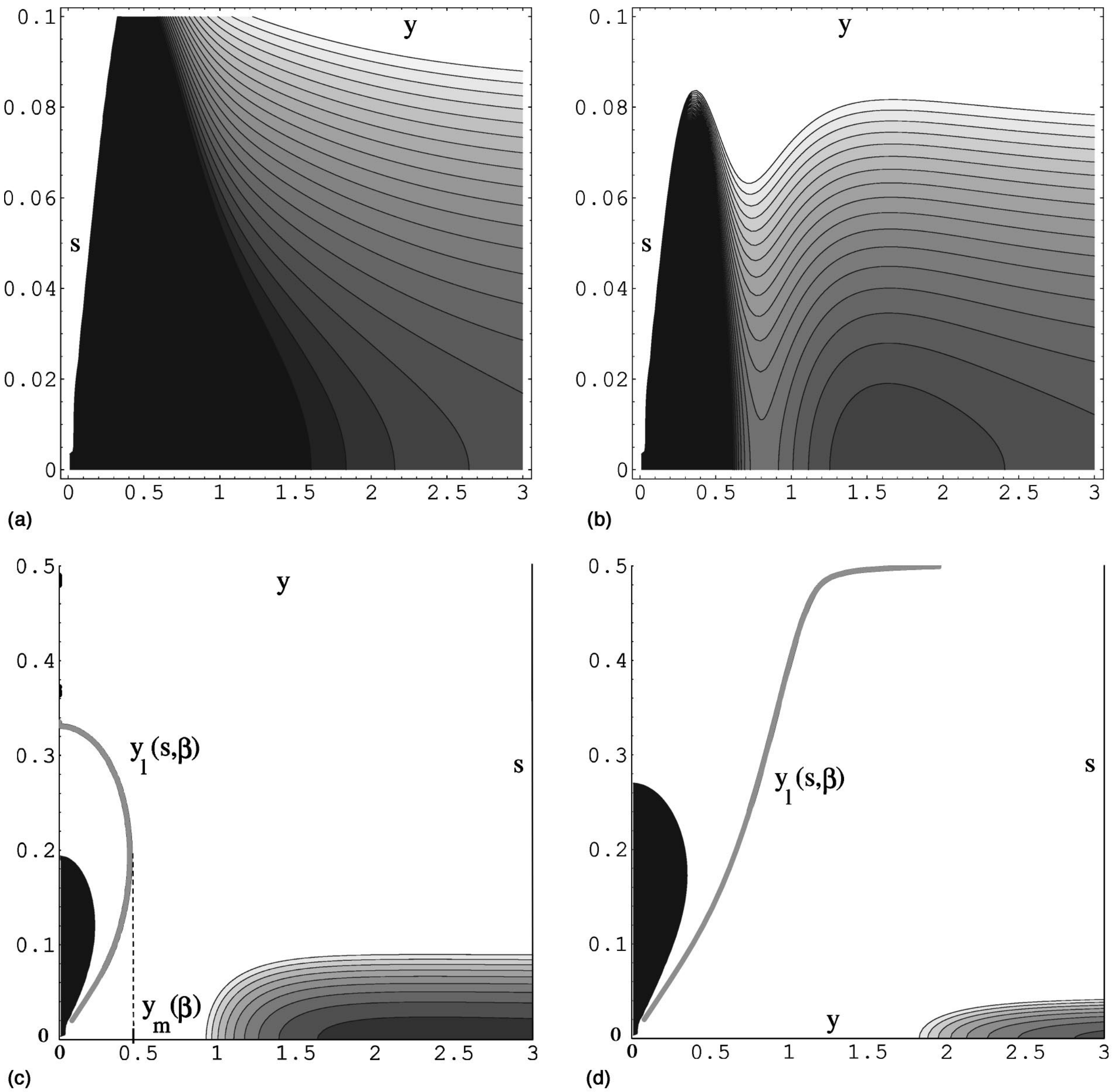

FIG. 10. Contour plots of the interaction potential as a function of in-plane separation y and tilt coordinate s.

plates. The criterion to determine whether particles are attracted by the in-plane solution, or the buckled configurations, is to determine whether the present (y,s) lie in the basin of attraction of one minimum or the other. Both basins of attraction are separated by a ridge of the potential, on which u decreases under the effect of any perturbation of (y,s) apart from the ones directed exactly along its gradient. This boundary between both basins of attraction, noted $y_l(s,\beta)$, was determined numerically and plotted as the gray solid line in Figs. 10(c) and 10(d). We note that the whole axis $(y,0)$ lies in the basin of attraction of the plane minimum, so any particle pair starting with no tilt should end up so. However, at short enough distances y in a c field, or at any in-plane distance in a d field, certain configurations with a finite tilt are attracted by the normal-aligned pair minimum, and will end up in a buckled contact configuration or normal-aligned pair. We have determined for every β the maximum $y_m(\beta) = \max_s y_l(s,\beta)$. For a given β, when $y > y_m(\beta)$, any tilted configuration will be attracted by the in-plane solution, whereas for certain finite tilts at close enough $y < y_m(\beta)$, the pairs will be attracted towards buckled in-contact configurations. The function $y_m(\beta)$ is displayed as the dashed curve in Fig. 11—the solid curve is a reminder of the equilibrium in-plane distances $y_s(\beta), y_i(\beta)$ determined in Sec. V. The function $y_m(\beta)$ diverges when $\beta \to \beta_u^-$, illustrating the fact that in any d-type field, configurations with out-of-plane tilts s close to 0.5, i.e., both particle centers almost along the plates (for small enough particles) will be attracted by the normal-aligned pair mode.

This effect is believed to be responsible for the lattices of buckled chains of particles in contact observed in Ref. [8]. These were observed in pure normal fields ($\beta = +\infty$), and the nontrivial character of the lattices, being hexagonal or square instead of triangular lattices characteristic of attractive inter-

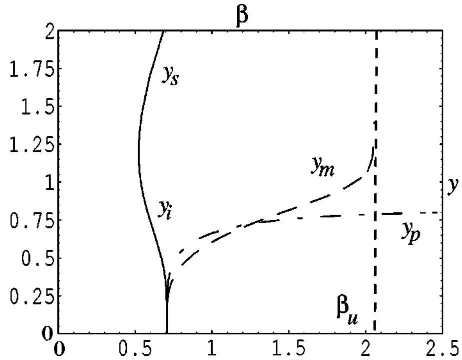

FIG. 11. Stability limits of the in-plane configurations.

actions at any range, can be qualitatively explained by frustration effects: neighboring particles tend to sit in top-down contact configurations, but top-top or down-down configurations are repulsive—cf. shifted potential developed in the preceding section—and therefore lattices with noneven number of particles along the loops, as the triangular one, are disfavored in comparison with those involving even numbers in loops, such as the square or hexagonal ones.

Eventually, the local stability of a plane configuration was investigated in fields of c or d type: the second derivative $\partial^2 u/\partial s^2$ is positive at $s=0$ for large enough distances, and small out-of-plane tilts will be restored by magnetic interactions, but below a certain $y<y_p(\beta)$, $\partial^2 u/\partial s^2(y,s=0)<0$, and the in-plane solution will be locally unstable. However, the preceding section established that this out-of-plane character will be transient, since this case will still be attracted at long times by the in-plane solution. This upper limit $y_p(\beta)$ below which in-plane configurations will go to a transient out-of-plane regime was determined numerically for any β and plotted as the dash-dot curve in Fig. 11.

VIII. CONCLUSIONS

For pairs of magnetic holes in ferrofluid layers of finite thickness, exposed to fast oscillating conic magnetic fields, we have established the effective interaction potential driving their slow motion. The importance of the magnetic permeability contrast between ferrofluid and confining plates on these interactions was demonstrated, and the resulting pair potential analytically derived. This allowed the classification of those interaction potentials into four types, two of which present a secondary minimum at a finite distance. A simple finite-time theory for these non-Brownian microspheres, including the hydrodynamic interactions of the holes with the confining plates, was directly compared and confirmed by experimental results, through data collapse of the scaled separation as a function of scaled time, for various plate separations and field magnitudes. The relaxation time of these systems to reach equilibrium when there is any was typically a few minutes or above. Eventually, we generalized the study to full three dimensions in the layer thickness, and studied the stability of the in-plane configurations. This established that although in-plane configurations are stable at small normal fields, or at large ones and sufficient particle separation, hole pairs can be attracted by another stable configuration of tilted pairs of particles with contact between them and contact with one plate each.

This simple theory renders for so far unexplained observed configurations of magnetic holes, namely, 2D lattices with finite separation or buckled lattices of tilted pairs of particles. In principle, the effect described here in detail should be important in any colloidal system confined in a layer with significant magnetic permeability or dielectric contrast between the fluid and confining structure.

The ability to tune the equilibrium distance at will through the ratio of the normal over in-plane magnitude of the external field makes this magnetic hole system a good candidate for various applications, such as the manipulation of large molecules using the magnetic holes, for example, proteins which would be fixed to one or several holes coated with antigens, the determination of the transport properties of a ferrofluid, or as analog model of systems implying discrete particles of tunable interactions and hydrodynamic coupling to the carrier fluid. The effective pair interactions derived here should be a fundamental brick of any such applications.

[1] A.T. Skjeltorp, Phys. Rev. Lett. **51**, 2306 (1983).
[2] G. Helgesen and A.T. Skjeltorp, J. Magn. Magn. Mater. **97**, 25 (1991).
[3] A.T. Skjeltorp, J. Magn. Magn. Mater. **37**, 253 (1983).
[4] A.T. Skjeltorp, J. Appl. Phys. **55**, 2587 (1984).
[5] A.T. Skjeltorp, Physica B & C **127**, 411 (1984).
[6] A.T. Skjeltorp, Physica A **213**, 30 (1995).
[7] A.T. Skjeltorp, J. Appl. Phys. **57**, 3285 (1985).
[8] A.T. Skjeltorp and G. Helgesen, Physica A **176**, 37 (1991).
[9] G. Helgesen and A.T. Skjeltorp, Physica A **170**, 488 (1991).
[10] G. Helgesen, P. Pieranski, and A.T. Skjeltorp, Phys. Rev. Lett. **64**, 1425 (1990).
[11] G. Helgesen, P. Pieranski, and A.T. Skjeltorp, Phys. Rev. A **42**, 7271 (1990).
[12] G. Helgesen and A.T. Skjeltorp, J. Appl. Phys. **69**, 8277 (1991).
[13] M.C. Miguel and J.M. Rubi, Physica A **231**, 288 (1996).
[14] A.T. Skjeltorp, S. Clausen, and G. Helgesen, J. Magn. Magn. Mater. **226**, 534 (2001).
[15] A.T. Skjeltorp, S. Clausen, and G. Helgesen, Physica A **274**, 267 (1999).
[16] S. Clausen, G. Helgesen, and A.T. Skjeltorp, Int. J. Bifurcation Chaos Appl. Sci. Eng. **8**, 1383 (1998).
[17] S. Clausen, G. Helgesen, and A.T. Skjeltorp, Phys. Rev. E **58**, 4229 (1998).
[18] P. Pieranski, S. Clausen, G. Helgesen, and A.T. Skjeltorp, Phys. Rev. Lett. **77**, 1620 (1996).
[19] G. Helgesen, A.T. Skjeltorp, P.M. Mors, R. Botet, and R. Jullien, Phys. Rev. Lett. **61**, 1736 (1988).
[20] M. Warner and R. Hornreich, J. Phys. A **18**, 2325 (1985).
[21] P. Davies, J. Popplewell, G. Martin, A. Bradbury, and R. Chantrell, J. Phys. D **19**, 469 (1986).

[22] H. Sellers and H. Brenner, PCH, PhysicoChem. Hydrodyn. **11**, 455 (1989).
[23] M.C. Miguel and J.M. Rubi, J. Colloid Interface Sci. **172**, 214 (1995).
[24] R. Chantrell and E. Wohlfart, J. Magn. Magn. Mater. **40**, 1 (1983).
[25] Rosensweig, Annu. Rev. Fluid Mech. **19**, 437 (1987).
[26] J. Ugelstad, P. Stenstad, L. Kilaas, W. Prestvik, R. Herje, A. Berge, and E. Hornes, Blood Purif **11**, 349 (1993).
[27] A. Berge, T. Ellingsen, K. Nustad, S. Funderud, and J. Ugelstad, in *Scientific Methods for the Study of Polymer Colloids and their Applications*, edited by F. Candau and R.H. Ottewill (Kluwer Academic, Dordrecht, 1989), p. 517.
[28] J.B. Hayter, R. Pynn, S. Charles, A.T. Skjeltorp, J. Trewhella, G. Stubbs, and P. Timmins, Phys. Rev. Lett. **62**, 1667 (1989).
[29] J.M. Rubi and M.C. Miguel, Physica A **194**, 209 (1993).
[30] A.T. Skjeltorp, J. Magn. Magn. Mater. **65**, 2 (1987).
[31] A. Laufer, Am. J. Phys. **19**, 275 (1951).
[32] J. Newman and R. Yarbrough, J. Appl. Phys. **39**, 5566 (1968).
[33] G.M. Kepler and S. Fraden, Phys. Rev. Lett. **73**, 356 (1994).
[34] B. Bleaney and B. Bleaney, *Electricity and Magnetism* (Oxford University Press, Oxford, 1978).
[35] H. Knoepfel, *Magnetic Fields: A Comprehensive Theoretical Treatise for Practical Use* (Wiley, New York, 2000).
[36] E. Weber, *Electromagnetic fields: Theory and Applications* (Wiley, New York, 1950), Vol. 1.
[37] L.P. Faucheux and A.J. Libchaber, Phys. Rev. E **49**, 5158 (1994).
[38] D.G. Grier and S. Behrens, in *Electrostatic Effects in Soft Matter and Biophysics*, edited by C. Holm (Kluwer Academic, Dordrecht, The Netherlands, 2001).
[39] R.G. Larson, *The Structure and Rheology of Complex Fluids* (Oxford University Press, New York, 1999), Chap. 8.4.2.
[40] J. Ugelstad and P. Mork, Adv. Colloid Interface Sci. **13**, 101 (1980). Produced under the trade name Dynospheres by Dyno Particles A.S., N-2001 Lillestrøm, Norway.
[41] Type EMG 905, produced by Ferrofluidics Corporation, 40 Simon St., Nashua, NH 03061.
[42] E.R. Dufresne, T.M. Squires, M.P. Brenner, and D.G. Grier, Phys. Rev. Lett. **85**, 3317 (2000).

Progr Colloid Polym Sci (2004) 128: 151–155
DOI 10.1007/b97120

Renaud Toussaint
Jørgen Akselvoll
Geir Helgesen
Eirik G. Flekkøy
Arne T. Skjeltorp

Interactions of magnetic holes in ferrofluid layers

R. Toussaint (✉) · J. Akselvoll
E.G. Flekkøy · A.T. Skjeltorp
Department of Physics,
University of Oslo,
P.O. Box 1048 Blindern,
0316 Oslo, Norway
e-mail: renaud.toussaint@fys.uio.no

J. Akselvoll · G. Helgesen · A.T. Skjeltorp
Physics Department, Institute for Energy Technology, 2027 Kjeller, Norway

Abstract Nonmagnetic microspheres in a ferrofluid layer interact as dipoles in an external magnetic field. With a constant field normal to the layer and an oscillating in-plane field, the spheres stabilize at fixed separations, and can thus be trapped at tunable finite distances. We show analytically how the susceptibility contrast at the system boundary is responsible for this secondary minimum of a pair interaction potential, obtain the effective interaction potential and equilibrium separation as a function of the applied field, and experimentally validate this theory.

Keywords Ferrofluids · Magnetic holes · Rotating magnetic fields · Effective interactions · Confined system

Introduction

Magnetic holes in a carrier ferrofluid are micrometric spherical nonmagnetic particles, whose size is orders of magnitudes above that of magnetites (0.01 μm), so the ferrofluids appears homogeneous on their scale. In the presence of an external magnetic field, they generate dipolar magnetic perturbations, whose moment is the opposite of that of the ferrofluid displaced [1, 2]. This induces dipolar interactions between them, which can be tuned through the type of imposed external field. This system, first invented by Skjeltorp [1], is confined between two nonmagnetic plates, spaced by a fixed distance ranging from one to ten particle diameters. The ability to design and modify the effective interactions in this system enables us to grow crystals of such holes and induce order/disorder transitions in them [1], to study aggregation dynamics of these particles [3], or to study the nonlinear dynamics of such magnetic holes in low-frequency rotating magnetic fields [4]. Understanding these systems is important for ferrofluid industrial applications [5], or their possible use in biomedicine [6]. Nonetheless, there was no satisfactory theoretical description of the effective interactions between holes in magnetic fields composed of a high-frequency rotating in-plane component and a constant normal one, and the existence of stable configurations of particles with a finite distance between them [2] remained unexplained.

Focusing on the boundary conditions of the magnetic fields along the confining plates, we will derive analytically the pair interaction potential in such oscillating fields, and demonstrate for a wide range of them the existence of a secondary minimum whose position depends continuously on the ratio between out-of-plane and in-plane field magnitudes. We will then compare this theory with experiments where the motion of a particle pair is followed.

System presentation and derivation of an effective pair interaction potential

In the presence of a far-range field $\vec{H}$ in a ferrofluid of susceptibility χ, each hole generates a dipolar perturbation of the dipolar moment equal and opposite to that of the displaced ferrofluid,$\vec{\sigma} = -V\chi_e \vec{H}$, where V is the volume of the particle, and $\chi_e = 3\chi/(3+2\chi)$ is the effective susceptibility including a demagnetization factor rendering for the boundary conditions of the magnetic field along the spherical particle boundary [1, 7]. The susceptibility contrast between the ferrofluid and the two planar nonmagnetic confining plates leads to a different dipolar field perturbation from that in the infinite medium expression. According to the image method [8], the boundary conditions for the magnetic field along the plates are fulfilled if in addition to the infinite space expression, the dipolar field emitted in an unbounded medium by an infinite series of dipole images is taken into account. This series consists of mirror images in the plane boundaries of the initial dipoles or of some previous image, by multiplying the magnitude of the dipole at each mirror symmetry operation by an attenuation factor $\kappa = \chi/(\chi+2)$ – see Fig. 1.

The instantaneous interaction potential between a pair of confined particles can then be expressed as [7]

$$U = \frac{\mu}{8\pi}\sum_{i\neq j}\left[\frac{\vec{\sigma}_i\cdot\vec{\sigma}_j}{r_{ij}^3} - 3\frac{(\vec{\sigma}_i\cdot\vec{r}_{ij})(\vec{\sigma}_j\cdot\vec{r}_{ij})}{r_{ij}^5}\right] \tag{1}$$

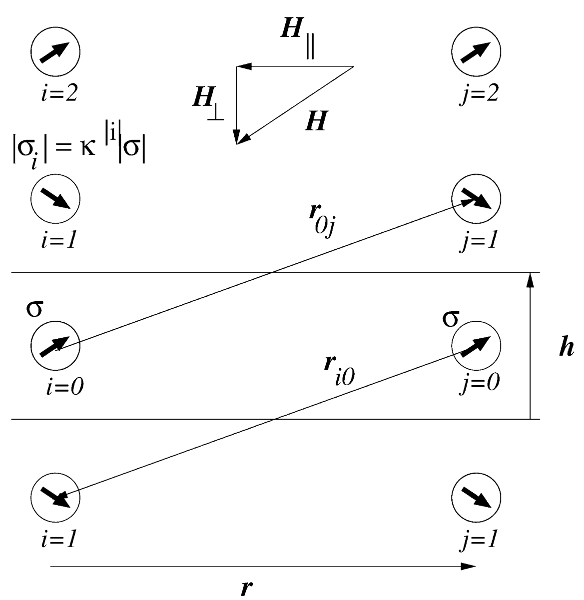

Fig. 1 Pair of nonmagnetic particles in a ferrofluid layer, viewed along the confinement plates, and a series of dipole images accounting for the boundary conditions of the magnetic field along the plates

where μ is the ferrofluid's permeability, the i-index runs over both the source and image dipoles, and the j-index runs only over the two source particles. A detailed analysis shows that the dominant effect for the components of the forces normal to the plates is the interaction between a particle and its own mirror images, which stabilizes the particles midway between the plates. This constraint is therefore adopted throughout this paper and in Fig. 1. Buoyancy forces have also been checked to be negligible for the ferrofluid and particles used in this work.

Decomposing the instantaneous far-range field into its in-plane and normal components $\vec{H}_\perp$ and $\vec{H}_\parallel$, we define the ratio of their magnitudes as $\beta = H_\perp/H_\parallel$, the angle between in-plane component and separation vector as φ, the particle diameter and interplate separation, respectively, as a and h, and the scaled separation as $x = r/h$.

A straightforward analysis of Eq. (1) in the configuration of Fig. 1 leads up to an additive constant to

$$\frac{144h^3U}{\mu\pi a^6\chi_e^2H_\parallel^2} = \sum_{l=-\infty}^{+\infty}\kappa^{|l|}\left[\frac{1+(-1)^{|l|}\beta^2}{(x^2+l^2)^{3/2}} - 3\frac{(y\cos\varphi + l\beta)\left(y\cos\varphi + (-1)^{|l|}l\beta\right)}{(x^2+l^2)^{5/2}}\right]. \tag{2}$$

The term $l=0$ corresponds to the source–source interaction term, already used in previous studies [1, 2], the other terms correspond to interactions between a particle and the images of the other one. For all existing ferrofluids, κ is sufficiently smaller than unity, so the prefactor ensures that the three first images are enough to get a relative precision better than 1% for the potential and its derivatives.

The imposed fields considered consist of a constant component $\vec{H}_\perp$, while $\vec{H}_\parallel$ rotates uniformly at sufficiently high frequency (10–100 Hz in this work). For the micrometric particles considered here ($a = 50\ \mu$m), inertial terms can be neglected, and a characteristic viscous relaxation time can be obtained as the time to separate two particles initially in contact by their size, balancing the Stokes drag with the magnetic interaction forces derived from the potential. Retaining the main term $l=0$ in Eq. (1) leads to an estimate of $T_c = 144\eta/(\mu\chi_e^2 H^2) \approx 5$s, for the ferrofluid [$\eta = 9\times10^{-3}$ Pa s, $\mu = \mu_0(1+\chi)$, $\chi = 1.9$, $\mu_0 = 4\pi\times10^{-7}$ H m^{-1}] and the typical field $H = 10$ Oe considered here. At field rotation frequencies significantly exceeding the inverse relaxation time, the particle's motion can be neglected during a field oscillation, and an effective interaction potential averaged over time can be obtained by replacing simply the φ-dependent terms in Eq. (2) by their average over an oscillation, while the slowly varying separation vector is maintained constant, which leads to the dimensionless effective interaction potential:

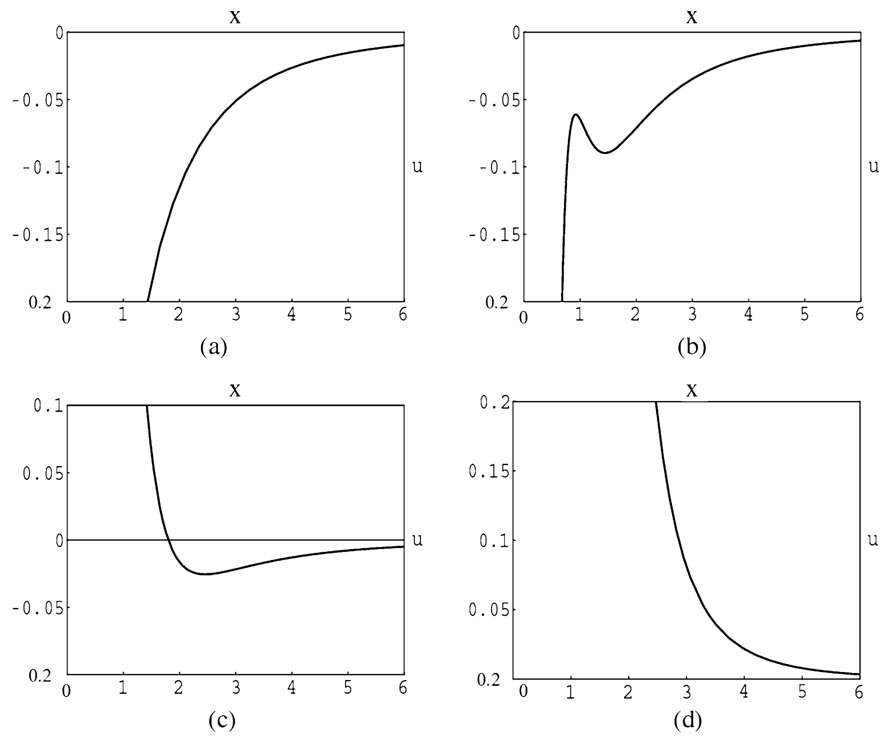

Fig. 2 Four possible types of interaction potentials: **a** $\beta < \beta_m$ purely attractive interactions, **b** $\beta_m < \beta < \beta_c$ interactions with a secondary minimum, **c** $\beta_c < \beta < \beta_u$ interactions with a single equilibrium position at a finite distance, **d** $\beta_u < \beta$ purely repulsive interactions

$$
\begin{aligned}
u(x) &\equiv \frac{144h^3\overline{U}}{\mu\pi a^6\chi_e^2 H_\parallel^2} \\
&= \sum_{l=-\infty}^{+\infty} \kappa^{|l|}\left[\frac{1+(-1)^{|l|}\beta^2}{(x^2+l^2)^{3/2}} - 3\frac{(-1)^{|l|}l^2\beta^2+y^2/2}{(x^2+l^2)^{5/2}}\right].
\end{aligned}
\tag{3}
$$

For a given ferrofluid and field, this central potential can be of four possible types as illustrated in Fig. 2.

At low normal field $\beta < \beta_m$, the interactions are purely attractive up to contact; at higher fields $\beta_m < \beta < \beta_c$, a secondary minimum at finite distance appears, later on in the regime $\beta_c < \beta < \beta_u$ this minimum becomes the only one, and ultimately interactions are purely repulsive for $\beta_u < \beta$. For the ferrofluid used, the equilibrium separation for these effective interactions as a function of β are displayed as a continuous line in Fig. 3.

From Eq. (3), the separating values can be shown to be $\beta_C = 1/\sqrt{2}$, $\beta_u = \beta_c(1+\kappa)/(1-\kappa)$, which is a growing function of the susceptibility diverging to infinity when the susceptibility does, and β_m a function of the susceptibility decreasing regularly from β_c at zero susceptibility to 0 at infinite susceptibility – for the ferrofluid used here, $\beta_m \approx 0.55$ and $\beta_u \approx 2.05$. Neglecting the susceptibility contrast along the plates – terms $l \neq 0$ in Eq. (3) – would correspond to the limiting case $\kappa = 0$, where these three separating values merge, and the interactions are either purely attractive or repulsive. The presence of this susceptibility contrast is thus essential to trap the particles at a given equilibrium distance in this type of field.

In order to confront this theory with experiments, the motion of particle pairs initially in contact in a given field was recorded through time. The dynamical equation ruling the particles in this overdamped regime is obtained by balancing the Stokes drag from the embedding fluid with the magnetic interactions, which leads to $\dot{x} = -u'(x)$, where the dot refers to derivation with respect to $t' = t/T$, the dimensionless time, with $T = 3T_c h^5/a^5$, the unit time. The function $t'(x)$ was then

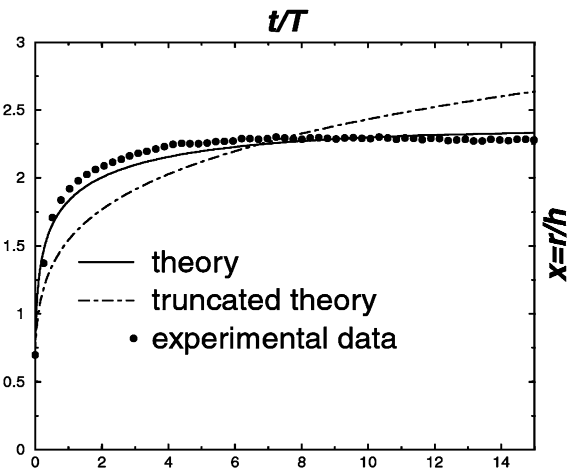

Fig. 3 Scaled separation between a pair of particles as a function of the scaled time, comparison between theory and experiment obtained with an oscillating in-plane field of magnitude $H_\parallel = 14.2$ Oe and a constant normal field $H_\perp = 0.8H_\parallel$

numerically evaluated as the integral of $-1/u'$ from the initial a/h to the actual x value of the scaled separation, to obtain the dashed lines of Fig. 3 and the full line of Fig. 4.

Experiments and results

The experiments were carried using $a = 50$-μm diameter neutral nonmagnetic polystyrene particles designed by Ugelstad's technique [9] and produced under the trademark Dynospheres by Dyno Particles, Lillestrøm, Norway, in a kerozene-based ferrofluid (type EMG905, Ferrofluidics, Nashua, NH, USA). The confining cell consisted of two glass plates 70 μm from each other, and was obtained by slightly pressing the cells together with a few $h = 70$-μm-diameter spacers in-between (of the same composition as the holes). The cell was placed in three pairs of Helmholtz coils, and the particle motion was recorded and digitized from optical microscopy data. The particles were initially brought into contact by applying a fast oscillating purely in-plane field, after which the constant normal field component was added at time zero. The particle pair observed was separated from any other particle or spacer by more than 20 diameters, so as to avoid perturbations.

A typical record of the scaled distance as a function of the scaled time, obtained for a field $H_{||} = 14.2$ Oe, at $\beta = 0.8$, is shown in Fig. 3.

In this case, the unit time is $T = 32$ s, and particles come to the predicted equilibrium distance $r = 2.35h$ after a few minutes. Comparing this data with the present theory (full line) and with the preexisting expression [1, 2] ignoring the effect of the boundary conditions along the nonmagnetic plates (dashed line) we conclusively show the primary importance of this susceptibility contrast in explaining the existence of this secondary minimum.

A range of geometric β parameters of the applied field was explored in a series of experiments with the same setup, and the resulting scaled separation as a function of β, for various characteristic scaled times, is displayed in Fig. 4.

The error bars correspond to an experimental error in β reflecting a possible angle up to 2.5° of the constant field over the normal direction, which is the maximum variation of the field orientation over the cell, calculated from its precise geometry with respect to the external coils. This error effect was calculated to be the major one owing to the slight inhomogeneity of the field along the experimental cell. Once again, in the range $\beta > \beta_m \approx 0.55$ experiments and theory agree fairly well.

The main discrepancy lies in the small but nonzero separation ($x > 50/70$) for $0.3 < \beta < \beta_m \approx 0.55$. This is believed to be due to the effect of the non-point-like character of the magnetic holes for the magnetic field, which should generate higher-order terms in a multipolar expansion at moderate separations r/a – qualitatively, the dipolar perturbation field of a hole does not fulfill proper boundary conditions along the surface of another hole that is close enough, and a repulsive term corresponding qualitatively to taking into account images of one sphere in the other one, similar to the repulsive effect of images in the plane boundaries on its source particle, becomes sensitive at these short distances.

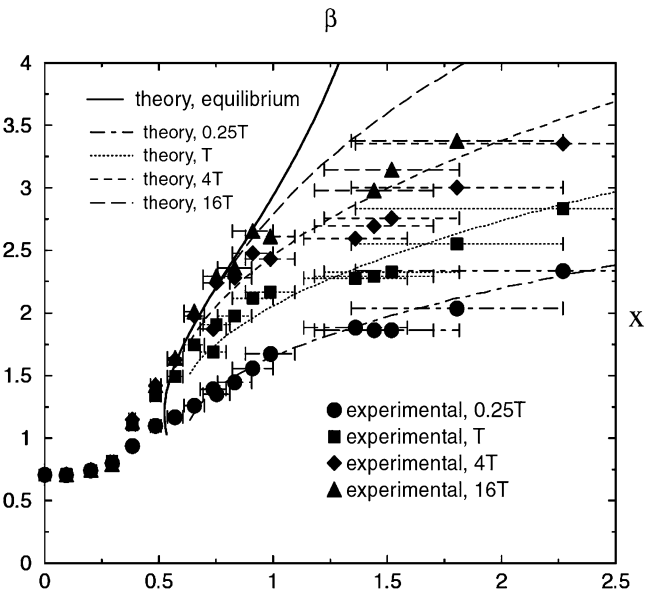

Fig. 4 Scaled distance as a function of the field geometric parameter β, at various values of the scaled time

Conclusions

We have established the effective pair interactions of nonmagnetic particles embedded in a ferrofluid layer confined between two nonmagnetic plates, submitted to magnetic fields including constant normal components and high-frequency oscillating in-plane components. Owing to the susceptibility contrast along the glass plates, a family of potentials displaying a secondary minimum at a finite separation distance has been proven to exist, which should allow us to trap nonmagnetic bodies at tunable distances via the external field.

A system with interactions such as those described here should be relevant for any colloidal suspension of electrically or magnetically polarizable particles constrained in layers. The realization of the detailed effective interaction potentials of this system also makes it a good candidate as an analog model system to study phase transitions [1], aggregation phenomena in complex fluids [4], or fracture phenomena in coupled granular/fluid systems.

References

1. Skjeltorp AT (1983) Phys Rev Lett 51:2306
2. Helgesen G, Skjeltorp AT (1991) J Magn Magn Mater 97:25
3. Helgesen G, Skjeltorp AT, Mors PM, Botet R, Jullien R (1988) Phys Rev Lett 61:1736
4. Helgesen G, Pieranski P, Skjeltorp AT (1990) Phys Rev Lett 64:1425
5. Chantrell R, Wohlfart E (1983) J Magn Magn Mater 40:1
6. Hayter T, Pynn R, Charles S, Skjeltorp AT, Trewhella J, Stubbs G, Timmins P (1989) Phys Rev Lett 62:1667
7. Bleaney B, Bleaney B (1978) Electricity and magnetism. Oxford University Press, Oxford
8. Weber E (1950) Electromagnetic fields: theory and applications, vol 1. Wiley, New York
9. Ugelstad J, Mork P (1980) Adv Colloid Interface Sci 13:101

SELF-ASSEMBLY AND DYNAMICS OF MAGNETIC HOLES

A.T. SKJELTORP[1,2], J. AKSELVOLL[1,2],
K.de LANGE KRISTIANSEN[1,2], G. HELGESEN[1], R. TOUSSAINT[2,3],
E.G. FLEKKØY[2], and J. CERNAK[4]
[1]*Institute for Energy Technology, POB 40, NO-2027 Kjeller, Norway*
[2]*Department of Physics, University of Oslo, NO-0316 Oslo, Norway*
[3]*Department of Physics, NTNU, NO-7491 Trondheim, Norway*
[4]*University P.J. Safarik Kosice, Biophysics Department, Jesenna 5, SK-043 54 Kosice, Slovak Republic*

Abstract

Nonmagnetic particles in magnetized ferrofluids have been denoted magnetic holes and are in many ways ideal model systems to test various forms of particle self assembly and dynamics. Some case studies to be reviewed here include:

- Chaining of magnetic holes
- Braid theory and Zipf relation used in dynamics of magnetic microparticles
- Interactions of magnetic holes in ferrofluid layers

The objectives of these works have been to find simple characterizations of complex behavior of particles with dipolar interactions.

1. Ferrofluids

Figure 1 shows the characteristic features of ideal ferrofluids on different length scales. Ferrofluids consist of coated magnetic nanoparticles dispersed in a carrier liquid. The nanoparticles are so small that they contain only one magnetic domain, i.e. at this length scale it is not energetically favorable to break up into domains as in ordinary bulk magnets. Ferrofluids are in fact an early success story in the commercialization of nanotechnology [1]. In the 1970s, ferrofluids were adopted by the disk drive industry as near-zero friction bearings. Today, ferrofluid bearings are a key component in greatly reducing the incidence of hard-disk failure, and there is also a wide range of other ferrofluid applications. Ferrofluids are often denoted magneto-rheological fluids (MRF) as they may exhibit fast, strong and reversible changes in their rheological properties when a magnetic field is applied. MRF are similar to electro-rheological fluids, but normally much stronger, and more stable and easier to use. Applications of MRF include clutches, damping systems in passenger vehicles, brakes, controllable friction damper that decreases the noise and vibration in washing machines, and seismic mitigation MRF damping systems protecting buildings and bridges from earthquakes and windstorms [2]. Ferrofluids exhibit also many exotic macroscopic phenomena as exemplified in Figure 2.

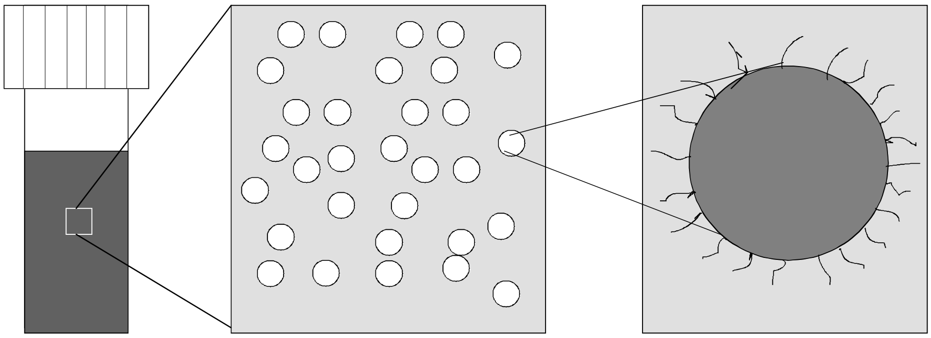

(a) (b) (c)

Figure 1. Schematic picture of ferrofluid on three length scales:
a: On a macroscopic length scale, it resembles an ordinary liquid with a uniform magnetization.
b: On a colloidal length scale, solid nanoparticles dispersed in a liquid.
c: Each particle consists of a single domain magnetic core, e.g. iron oxide, and a surface grafted with polymer chains, particle size ~ 10 nm.

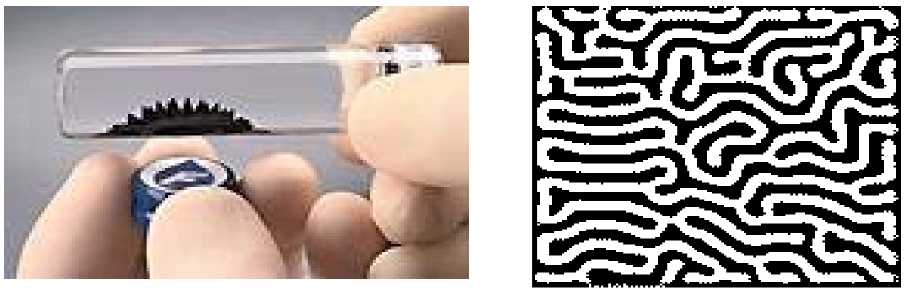

(a) (b)

Figure 2. (a) Surface instability of ferrofluid subject to an external magnetic field (http://www.ferrotec.com/) and (b) a ferrofluid meander in a thin layer.

2. Magnetic Holes

Monodisperse polystyrene spheres dispersed in ferrofluid provide a convenient model system for the study of various order-disorder phenomena [3]. The basis for this is that the spheres displace ferrofluid and behave as magnetic holes [4] with effective moments equal to the total moment of the displaced ferrofluid. The spheres are much larger (1-100 μm) than the magnetic particles (typically 0.01 μm) in the ferrofluid and the spheres therefore move around in an approximately uniform magnetic background. By confining the spheres and ferrofluid between closely spaced microscope slides an essentially two-dimensional many-body system of interacting particles is obtained. This offers the possibilities of observing directly through a microscope a wide range of nonlinear dynamic phenomena and collective processes, as they are easy to produce and to manipulate with external magnetic fields. A simplifying feature of magnetic holes is that their magnetic moments are collinear with an external field at any field strength. This is in contrast with magnetic particles dispersed in non-magnetic fluids where random orientation of the magnetic moments complicates the theoretical treatment of the dynamic and static properties of the particles.

The basic principle for magnetic holes is shown in Figure 3. It is in some sense a magnetic analogue of Archimedes' principle. When a non-magnetic particle is dispersed in a magnetized ferrofluid ($H > 0$), the void produced by the particle possesses an effective magnetic moment M_V equal in size but opposite in direction to the magnetic moment of the displaced fluid

$$M_V = -V\chi_{eff}H\,, \tag{1}$$

where V is the volume of the sphere and $\chi_{eff} = 3\chi/(3+2\chi)$ is the effective volume susceptibility of the ferrofluid. The interaction energy between two spheres with a centre-to-centre separation d is given approximately by the dipolar interaction

$$U = \frac{M_v^2(1-3\cos^2\theta)}{d^3}\ . \tag{2}$$

Here, θ is the angle between the line connecting the centres of the spheres and the direction of the field. Figure 3 illustrates that if the centers of two holes are collinear, they will attract each other, while two holes side by side will repel. Typical examples of structures formed for the two field orientations are shown in Figure 4.

A detailed description of the interaction between the spheres in a lattice is quite complicated. Since the dipolar interaction is of relatively long range, the direct particle interaction goes far beyond the nearest neighbours. In addition, there is an indirect particle-particle interaction mediated via the glass plates confining the system. This "image dipole" effect is caused by the change in the magnetic permeability across the glass plates. Thus the spheres also interact with their image dipoles situated at the opposite side of the ferrofluid-glass interface. This effect causes the lattice to be situated precisely midway between the upper and lower glass plate. As the plate separation is typically 50-100% larger than the diameter of the spheres, the dipole image contribution is relatively small (typically 10% or less) compared with the interaction energy between the real dipoles. Even in the presence of the dipole images, this experimental system may still be considered to be two-dimensional.

It is possible to obtain a thermodynamic system by using small spheres (diameter less than 2 μm) since Brownian motion introduces fluctuations into the system. The controlling parameter for the stability of the structure formation is the ratio of the dipolar energy to the thermal energy:

$$\Gamma = \frac{M_v^2}{d^3k_BT} \tag{3}$$

where d is the (centre-to-centre) separation of the spheres and k_B is Boltzmann's constant.

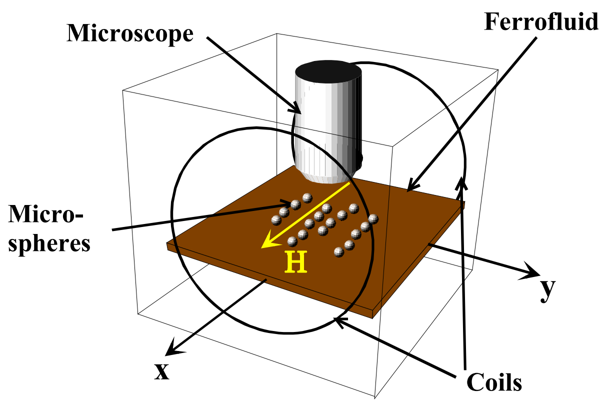

Figure 5. Schematic experimental set-up.

The main advantage of this system is the possibility to tune the strength of the particle-particle interactions. In our case we can create experimental conditions that are close to an ideal point-dipole system, i.e, the particles are spherical, monodisperse, and their resulting induced magnetic moments are oriented in the direction of the external magnetic field. In order to study the importance of dipole-dipole interaction and Brownian motion relative to non-Brownian ballistic drift, we used microspheres with different diameters d = 1.9, 4.0, and 14 μm. In zero external fields the diffusive Brownian motion of the 1.9 μm spheres is clearly visible in the microscope. However, the diffusion of the 14 μm spheres can only be seen by comparing images taken at typically 30 s time lap. The experiments were done with low volume fractions of microspheres, corresponding to coverage of a few percent. Magnetic fields in the range H = 4 – 16 Oe were used. The combination of these fields with the three particle sizes gave rise to values of Γ in the range 8 - 10^4. A typical example of the aggregates that were formed is shown in Figure 6.

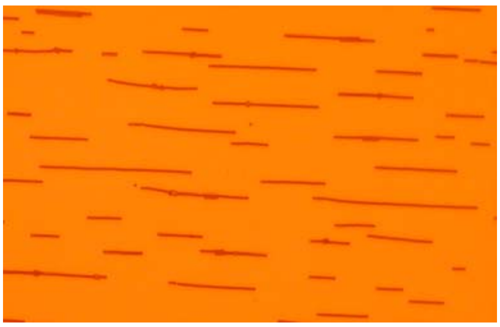

Figure 6. An example of the straight aggregates formed by 4 μm spheres in 10 Oe magnetic field after about 2 hours.

The ability to design and modify the effective interactions in this system enables studies of various phenomena discussed in the next sections.

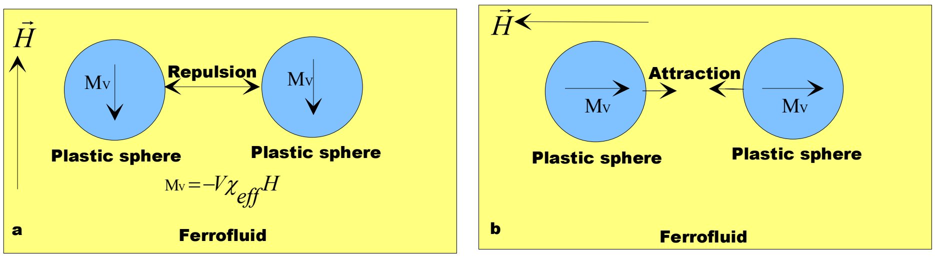

Figure 3. The principle of a magnetic hole in a soft magnet as discussed in the text. (a) Two holes side by side will repel each other. (b) Two holes with the centers collinear with the field lines will attract each other.

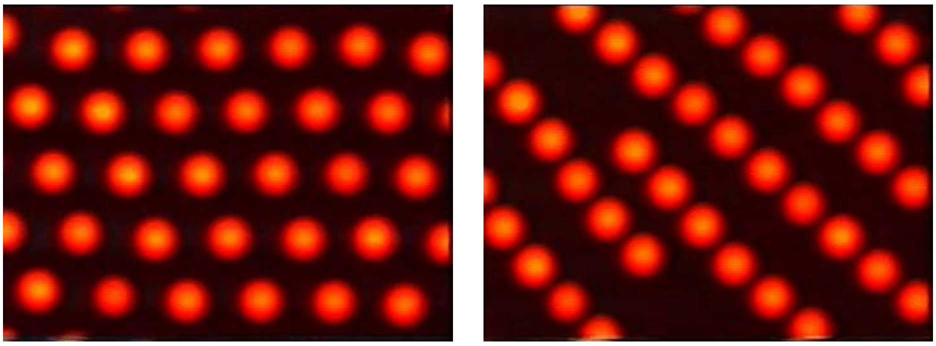

(a) (b)

Figure 4. Structures of 10 μm diameter spheres formed by a magnetic field (a) normal to the layer and (b) parallel to the layer.

3. Aggregation and Chaining of Magnetic Holes

Experimental studies of field induced colloidal aggregation have been carried out earlier, e.g., with paramagnetic microspheres [5,6], magnetic nano-particles [7,8], and electric field-induced association of dielectric particles [9]. The results have essentially confirmed the scaling behavior of the mean cluster size as a function of time [10-12] and it has been possible to scale the temporal size distribution of clusters [5,8,13] into a single universal curve as predicted by dynamic scaling theory [14].

In the present work we have studied the chain formation of non-magnetic microspheres [15] dispersed in thin layer of ferrofluid [16] induced by external magnetic fields, see Figure 5.

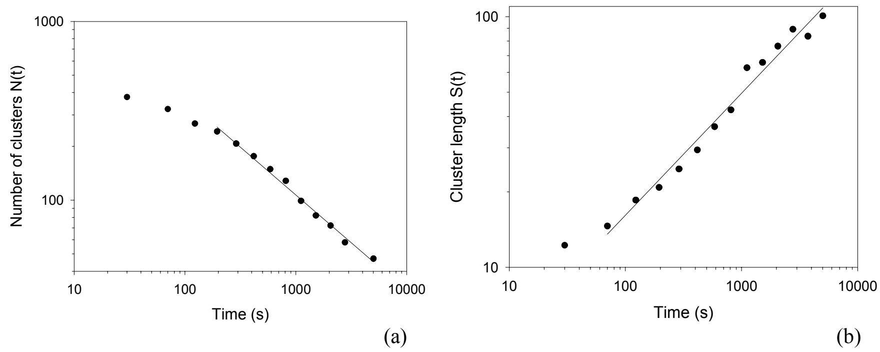

Figure 7. (a) The number of clusters and (b) cluster length versus time for aggregation of 10 μm spheres in a 10 Oe magnetic field. The solid lines are fits to a power law with exponents (a) z' = 0.53 and (b) z = 0.50.

In order to characterize the aggregation process in more detail, the length s of any cluster was determined at different time intervals t relative to the initial time $t = 0$ when the field was turned on. The time dependences of the number of clusters $N(t)$ and mean cluster size (length) $S(t)$ for a typical experiment with d = 4 μm spheres are shown in Figure 7. We see that the data asymptotically follow the power laws $N(t) \sim t^{-z'}$ and $S(t) \sim t^{z}$ with scaling exponents z' = 0.53 and z = 0.50 for $t > 100$ s. Using the dynamical scaling relations for cluster-cluster aggregation [12,14], it was possible to collapse all the cluster size distributions $n_s(t)$ to a scaling function curve [17].

4. Braid Theory and Zipf Relation used in Dynamics of Magnetic Microparticles

Cooperative behavior of interacting microparticles is of great interest both from a fundamental and a practical point of view. The rank-ordering statistics is one way of analyzing such collective diffusive systems [18]. Here we report some results from our studies of a colloidal system of magnetic holes with an experimental set-up like that in Figure 5. Intricate motions of particles in a plane can be illustrated as entangled lines in three-dimensional space-time, Figure 8, and braid theory gives a compact description of these lines [19,20].

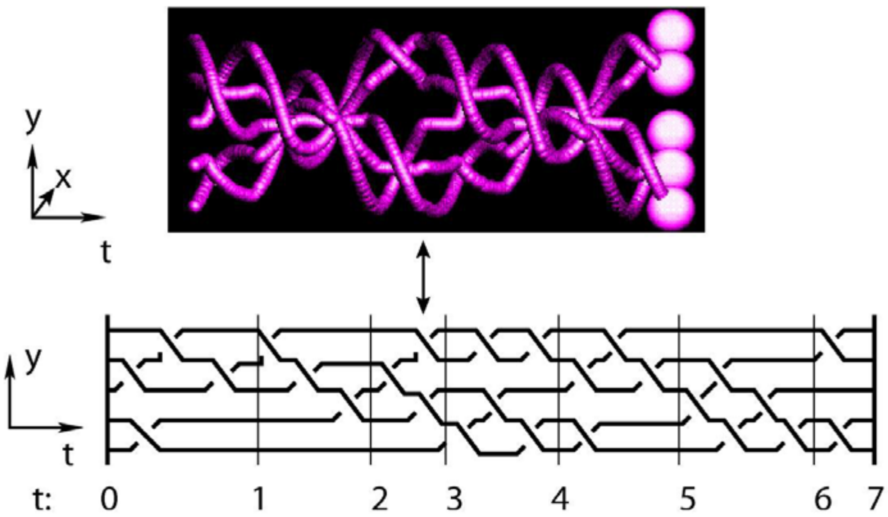

Figure 8. The two-dimensional motion of 5 microspheres is extended to three-dimensional space-time with the trace of each particle in time (upper). Projecting onto (y,t)-axis gives the braid for the motion (lower).

The magnetic holes system consists of 50 μm diameter diamagnetic, polystyrene micro-spheres [15] immersed in a thin layer of ferrofluid [16]. In an external planar, elliptically polarized rotating magnetic field H a microsphere introduces a magnetic hole with apparent magnetic moment given by Eq. (1). The motions of the microspheres can easily be simulated [7] by considering, to first order, the magnetic dipole-dipole interaction between each pair of microspheres and the viscous force on each microsphere.

By varying the angular velocity of the magnetic field and its anisotropy, we observe a rich diversity of patterns. Here we will focus on non-ordered behavior. The structure and complexity of the braids formed by the traces of the moving particles can be captured by calculating a few characteristic numbers. One of these is found by transforming the braid into a positive permutation braid [22] and use that as a measure of the systems dynamical mode. Then we apply rank-ordering statistics on these permutation braids, i.e., count all the different modes and rank them. Figure 9 shows a plot of the frequency of occurrence of the permutation braid $\phi(r)$ vs. rank r. This graph show a power law dependence, according to the Zipf relation [23] $\phi(r) \sim r^{\gamma}$ with $\gamma = 1.2$ for about two decades in r. Attempts to understand the origin of this relation were connected to the structure of hierarchical systems [24].

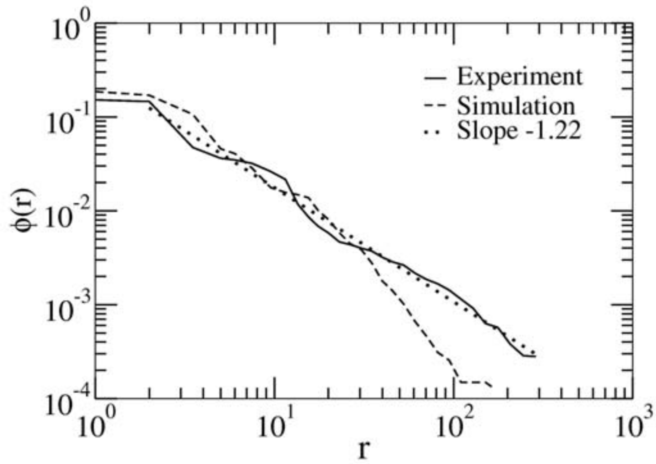

Figure 9. The relative occurrences of braid permutations *Φ(r)* against its rank *r* found in the dynamics of 7 microspheres.

Another characteristic number is the writhe *Wr(t)*. It is equal to the number of over-crossings minus the number of under-crossings, starting with value zero at time zero. Here the time *t* is measured in units of half periods of the external rotating magnetic field. One measure of the fluctuation in the braid pattern is the variation of the writhe around its mean:

$$\delta Wr(t,\tau) = Wr(\tau + t) - Wr(\tau) - t\left\langle \delta Wr(t) \right\rangle, \qquad (4)$$

where $\left\langle \delta Wr(t) \right\rangle = \frac{1}{N}\sum_{t=1}^{N}\left[Wr(t) - Wr(t-1) \right]$. The variance $\sigma^2(t)$ is then:

$$\sigma^2(t) = \left\langle [\delta Wr(t,\tau) - \left\langle \delta Wr(t,\tau) \right\rangle]^2 \right\rangle. \qquad (5)$$

For diffusive processes: $\sigma^2(t) \sim t^{\beta}$, with β= 1 for ordinary diffusion. When β is smaller or larger than 1, the diffusion is anomalous and is denoted as subdiffusion and superdiffusion, respectively.

We have found that the variance of the writhe fluctuations in experiments behave as a power law as shown in Figure 10, with β= 1.66, clearly indicating anomalous diffusion. Simulations based on the simplest model with magnetic and viscous forces showed good agreement with β= 1.82. Theoretical work using generalized Langevin and Fokker-Planck equations has predicted anomalous diffusion with β= 1.66 [25], in good agreement with our results.

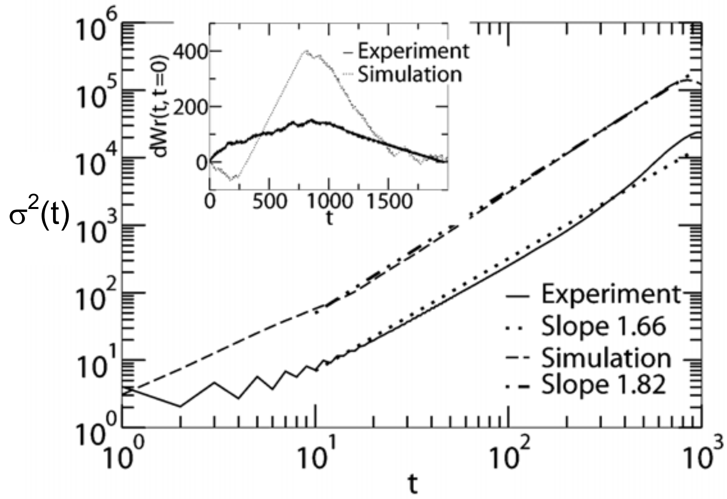

Figure 10. The variances σ^2(t) of the writhe fluctuations (Eq. 5) for the dynamics of 7 microspheres. The inset illustrates how the writhe of the system evolves with time.

5. Interactions of Magnetic Holes in Ferrofluid Layers

So far there has been no satisfactory theoretical description of the effective interactions between magnetic holes in rotating magnetic fields composed of a high frequency rotating inplane component and a constant normal one, and the existence of the observed stable configurations of holes with a finite separation distance [26] has remained unexplained.

Focusing on the boundary conditions of the magnetic fields along the confining plates, we have derived analytically the pair interaction potential in such oscillating fields, and demonstrated for a wide range of conditions the existence of a secondary minimum whose position depends continuously on the ratio β between the out of plane $H_\perp$ and inplane $H_\parallel$ field components [27]. We compare this theory with experiments where the motion of a pair of particles (holes) is followed.

In presence of a far-range field $\vec{H}$ in a ferrofluid of susceptibility χ , each hole generates a dipolar perturbation of dipolar moment equal to the opposite of the displaced ferrofluid, $\vec{\sigma} = -V\chi_{eff}\vec{H}$, where V is the volume of the hole, and $\chi_{eff} = 3\chi/(3+2\chi)$ is an effective susceptibility including a demagnetization factor rendering for the boundary conditions of the magnetic field along the spherical particle boundary [4,28]. The susceptibility contrast between the ferrofluid and the two plane nonmagnetic confining plates leads to a different dipolar field perturbation than the infinite medium expression. According to the image method [29], the boundary conditions for the magnetic field along the plates are fulfilled with an addition of an

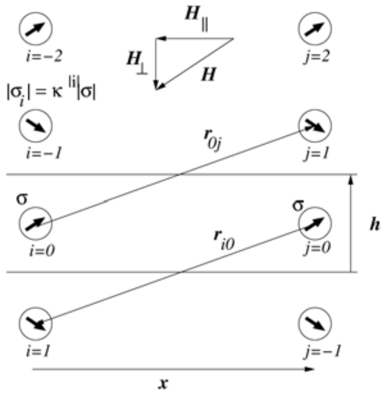

Figure 11. Pair of non magnetic particles in a ferrofluid layer, viewed along the confinement plates, and the series of dipole images accounting for the boundary conditions of the magnetic field along the plates.

infinite series of dipole images to the infinite space expression of the dipolar field emitted in an unbounded medium. The images are constructed as mirror images in the plane boundaries of the initial dipoles or of some previous image, multiplying the magnitude of the dipole at each mirror symmetry operation by an attenuation factor $\kappa = \chi/(\chi+2)$ - see Figure 11.

The instantaneous interaction potential between a pair of confined holes can then, similarly to Eq. (2), be expressed as

$$U = \frac{\mu}{8\pi}\sum_{i\neq j}\left[\frac{\vec{\sigma}_i\cdot\vec{\sigma}_j}{r_{ij}^3} - 3\frac{\left(\vec{\sigma}_i\cdot\vec{r}_{ij}\right)\left(\vec{\sigma}_j\cdot\vec{r}_{ij}\right)}{r_{ij}^5}\right], \qquad (6)$$

where μ is the ferrofluid's permability. The *i*-index runs over both the source and image dipoles, and the *j*-index runs only over the two source dipoles. A detailed analysis of the above shows that the dominant effect for the force components normal to the plates, is the interaction between a particle and its own mirror images, which stabilizes the particles midway between the plates.

Decomposing the instantaneous field in its inplane and normal components $\overrightarrow{H_{\perp}}$ and $\overrightarrow{H_{\|}}$, we define the ratio of their magnitudes $\beta = H_{\perp}/H_{\|}$, the particle diameter and interplate separation respectively as a and h, and the scaled separation as $x = r/h$. At the field rotation frequencies used here, f = 10 – 100 Hz, which exceeds the inverse viscous relaxation time, the motion of the holes can be neglected during a field rotation, and an effective, time-averaged interaction potential can be obtained by averaging over a full rotation of the magnetic field, while the slowly varying separation vector is maintained constant. This leads to the dimensionless effective interaction potential

$$u(x) \equiv \frac{144h^3\overline{U}}{\mu\pi a^6\chi_e^2 H_\parallel^2} = \sum_{l=-\infty}^{+\infty} \kappa^{|l|} \left[\frac{1+(-1)^{|l|}\beta^2}{(x^2+l^2)^{3/2}} - 3\frac{(-1)^{|l|} l^2\beta^2 + y^2/2}{(x^2+l^2)^{5/2}} \right]. \quad (7)$$

The term $l = 0$ corresponds to the source-source interaction term, already used in previous studies [4,26], the others to interactions between a particle and the images of the other one. For all existing ferrofluids, κ is sufficiently smaller than unity so that the prefactor $\kappa^{|l|}$ ensures that the three first images are enough to get a relative precision better than 1% for the potential and its derivatives.

For the micrometer sized particles used here, inertial terms can be neglected, and a characteristic viscous relaxation time can be obtained as the time to separate two particles initially in contact by a distance equal to their size. Balancing a Stokes drag with the magnetic interaction forces derived from the potential above and retaining the main term in Eq.(7), leads to the estimate $T_c = 144\eta / \mu\chi_e^2 H^2 \approx 5s$, for the ferrofluid ($\eta = 9\cdot10^{-3}$ Pa.s, $\mu = \mu_0(1+\chi)$, $\chi = 1.9$, $\mu_0 = 4\pi\cdot10^{-7}$ H.m^{-1}) and a typical field H = 10 Oe.

For a given ferrofluid and field, this central potential can be of four possible types as illustrated in Figure 12. At low normal field $\beta < \beta_m$, the interactions are purely attractive up to contact; at higher ones $\beta_m < \beta < \beta_c$, a secondary minimum at finite distance appears, later on in a regime $\beta_c < \beta < \beta_u$ this minimum becomes the only one, and ultimately interactions are purely repulsive for $\beta_u < \beta$.

From Eq. (7), the separating values of β can be shown to be $\beta_c = 1/\sqrt{2}$, and $\beta_u = \beta_c(1+\kappa)/(1-\kappa)$ which is a growing function of the susceptibility. β_m is a function of the susceptibility which decreases regularly from β_c at zero susceptibility to 0 at an infinite one. For the ferrofluid used in the present experiments $\beta_m \approx 0.55$ and $\beta_u \approx 2.05$. Neglecting the susceptibility contrast along the plates, i.e., terms with $l \neq 0$ in Eq. (7), would correspond to the limiting case $\kappa = 0$, where these three separating values merge, and the interactions are either purely attractive or repulsive. The presence of this susceptibility contrast is thus essential to trap the particles at a given equilibrium distance in this type of field.

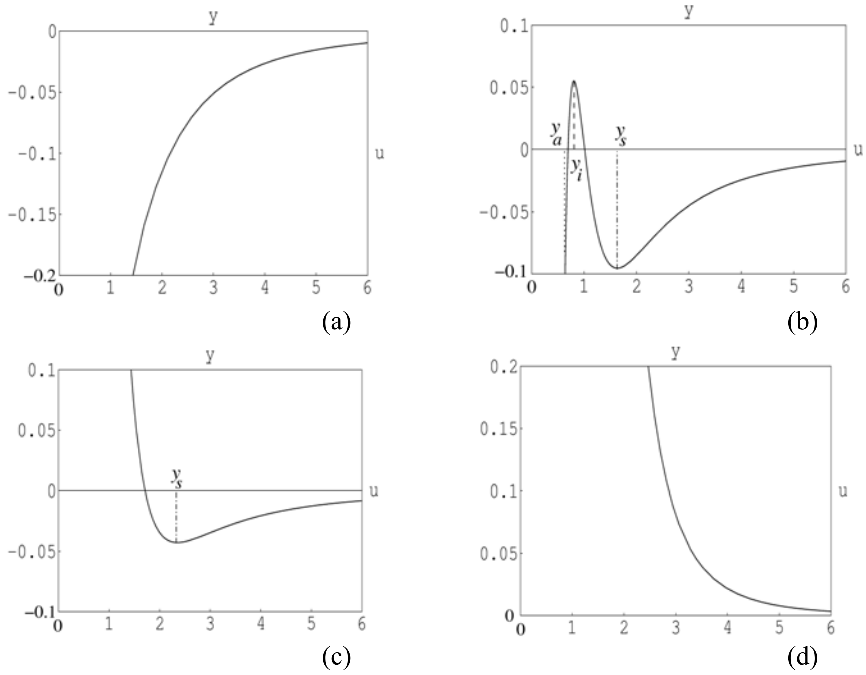

Figure 12. Four possible types of the interaction potential: (a) $\beta<\beta_m$ purely attractive interactions, (b) $\beta_m<\beta<\beta_c$ interactions with secondary minimum, (c) $\beta_c<\beta<\beta_u$ interactions with single equilibrium position at finite distance, (d) $\beta_u<\beta$ purely repulsive interactions.

The motion of pairs of particles initially in contact in a given field was recorded using an optical microscope with an attached video camera. The experiments where carried out using 50 μm diameter nonmagnetic polystyrene particles produced by Ugelstad's technique [15], in a kerozene-based ferrofluid [16]. The confining cell consisted of two glass plates kept at 70 μm separation by using a few 70 μm diameter spheres as spacers. The cell was placed inside three pairs of coils, and the particle motion was recorded and digitized from the microscopy data. The particles were initially brought into contact by applying a fast oscillating, purely inplane field, and at time $t = 0$ the constant normal field component was added. The particle pair observed was separated from any other particle or spacer by more than 20 diameters, in order to avoid unwanted perturbations. A typical record of the scaled distance as function of the scaled time, obtained for a field $H_{\parallel} = 14.2$ Oe at $\beta = 0.8$ is shown in Figure 13.

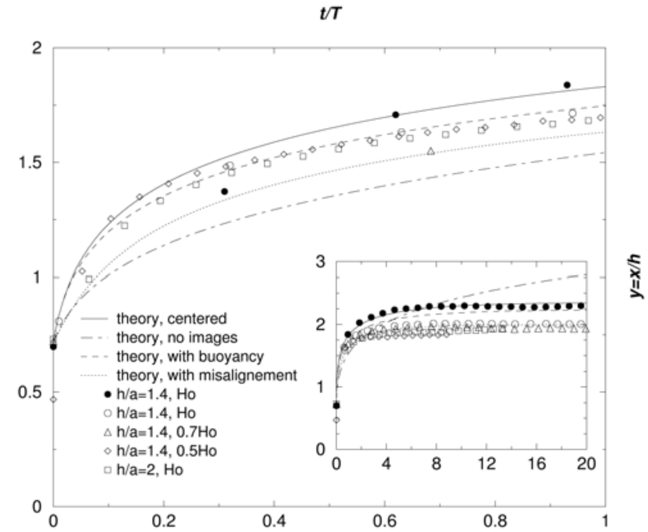

Figure 13. Scaled separation *x/h* between a pair of particles as function of the scaled time *t/T* for theory (continuous line) and an experiment obtained with an oscillating inplane field of magnitude $H_{\parallel} = 14.2$ Oe and a constant normal field $H_{\perp} = 0.8H_{\parallel}$.

In the current case, the time unit is $T = 32$ s, and particles come to the predicted equilibrium distance $r = 2.35h$ after a few minutes. Comparing this data with the present theory (full line) and with the preexisting expression ignoring the effect of the boundary conditions along the nonmagnetic plates [4,26] (dashed line) is clear in showing the importance of the susceptibility contrast for explaining the existence of the secondary potential minimum.

The dynamical equation ruling the particles in this overdamped regime is obtained by balancing the Stokes drag from the embedding fluid with the magnetic interactions, which leads to $\dot{x} = -u'(x)$, where the dot refers to derivation in with respect to the dimensionless time $t' = t/T$, with $T = 3T_c \cdot h^5 / a^5$ being the unit time. The function $t'(x)$ was then numerically evaluated as the integral of $-1/u'$ from the initial a/h to the actual x value of the scaled separation, to obtain the full line of Figure 13.

A range of values of the β parameter was explored in a series of experiments. Some discrepancy between experiments and theory was found at small particle separation and is believed to be due to the effect of the non point-like character of the magnetic holes, which should generate higher order terms in a multipolar expansion at moderate separations r/a. Qualitatively, the dipolar perturbation field of one hole does not fulfill properly the boundary conditions along the surface of another close hole, and a repulsive term corresponding qualitatively to taking into account images of one sphere in the other one, similar to the repulsive effect of images in the plane boundaries on its source particle, becomes sensitive at these short distances.

6. Conclusions

In this review we have shown that nonmagnetic particles in magnetized ferrofluids denoted magnetic holes are in many ways ideal model systems to test various forms of particle self assembly and dynamics.

In particular, chaining of magnetic holes show cluster size scaling behavior and for the first time it has been possible to use braid theory and Zipf Relation to describe the dynamics of magnetic holes in ac magnetic fields. Finally, the precise formulation of interactions of magnetic holes in ferrofluid layers has been presented. We have established the effective pair interactions of magnetic holes, submitted to magnetic fields including constant normal components and high frequency oscillating inplane components. Due to the susceptibility contrast along the glass plates, a family of potentials displaying a secondary minimum at finite separation distance has been proven to exist, which should allow trapping of nonmagnetic bodies at tunable distances via the external field.

A system with interactions such as described here, should be relevant for any colloidal suspension of electrically or magnetically polarizable particles constrained in layers. The realization of the detailed effective interaction potentials of this system makes it also a good candidate as an analog model system to study phase transitions, aggregation phenomena in complex fluids, or fracture phenomena in coupled granular/fluid systems.

Acknowledgements

The Research Council of Norway has in part supported the work described here.

References

1. Linton, D. and Walsh, S.T. (2003) Nature Materials, **2**, 289.
2. Wollny, K., Läuger, J., and Huck, S. (2002) Appl. Rheol. **12**, 25.
3. Clausen, S., Helgesen, G., and Skjeltorp, A.T. (1998) Phys. Rev. E **58**, 4229.
4. Skjeltorp, A.T. (1983) Phys. Rev. Lett. **51**, 2306.
5. Helgesen, G., Skjeltorp, A. T., Mors, P. M., Botet, R., and Jullien, R. (1988) Phys. Rev. Lett. **61**, 1736.
6. Promislow, J. H. E., Gast, A. P., and Fermigier, M. J. (1995) Chem. Phys. **102**, 5492.
7. Cernak, J., Macko, P., and Kasparkova, M. (1991) J. Phys. D **24**, 1609.
8. Cernak, J. (1994) J. Magn. Magn. Mater. **132**, 258.
9. Fraden, S., Hurd, A.J., and Meyer, R.B. (1989) Phys. Rev. Lett. **21**, 2373.
10. Meakin, P. (1983) Phys. Rev. Lett. **51**, 1119.
11. Kolb, M., Botet, R., and Jullien, R. (1983) Phys. Rev. Lett. **51**, 1123.
12. Miyazima, S., Meakin, P., and Family, F. (1987) Phys. Rev. A **36**, 1421.

13. Robinson, D. J. and Earnshaw, J. C. (1992) Phys. Rev. A **46**, 2045; **46**, 2055; **46**, 2065.
14. Vicsek, T. and Family, F. (1984) Phys. Rev. Lett. **52**, 1669.
15. Ugelstad J., et al., (1980) Adv. Colloid Int. Sci. **13**, 101.
16. Types EMG905 and EMG909 from Ferrotec Corporation, 40 Simon St., Nashua, NH 03060-3075, USA.
17. Cernak, J., Helgesen, G., and Skjeltorp, A.T. (2004) unpublished.
18. Kristiansen, K. de L., Helgesen, G., and Skjeltorp, A. T. (2004) Physica A **335**, 413.
19. Moore, C. (1993) Phys. Rev. Lett. **70**, 3675.
20. Pieranski, P., et al. (1996) Phys. Rev. Lett. **77**, 1620.
21. Helgesen, G., Pieranski, P., and Skjeltorp, A. T. (1990) Phys. Rev. A **42**, 7271.
22. Elrifai, E. A. and Morton, H. R. (1994) Quart. J. Math. **45**, 479.
23. Zipf, G. K. (1949) *Human Behavior and The Principle of Least Effort* (Addison-Wesley Press, Massachusetts).
24. Mandelbrot, B. (1954) Word **10**, 1.
25. Wang, K.G. and Tokuyama, M. (1999) Physica A **265**, 341.
26. Helgesen, G, and Skjeltorp, A.T. (1991) J. Magn. Magn. Mater. **97**, 25.
27. Toussaint, R., et al. (2004) Phys. Rev. E **69**, 011407.
28. Bleaney, B. and Bleaney, B. (1978) *Electricity and Magnetism* (Oxford University Press).
29. Weber, E. (1950) *Electromagnetic fields: theory and applications*, vol. 1, (Wiley, New York).

Annexe : publications

I Granulaires, fluides, hydro- et aéro-fractures, failles et avalanches
Ecoulements mixtes, grains et fluides : rôle du fluide dans la mécanique d'interfaces cisaillées, les failles et instabilités gravitaires. 127

I.i Hydrofracturation et aérofracturation ***127***

1. Johnsen, Ø., R. Toussaint, K.J. Måløy and E.G. Flekkøy,
Pattern formation during central air injection into granular materials confined in a circular Hele-Shaw cell, Phys. Rev. E, 74, 011301 (2006). pdf doi:10.1103/PhysRevE.74.011301
P127

2. Johnsen, Ø., R. Toussaint, K.J. Måløy, E.G. Flekkøy and J. Schmittbuhl,
Coupled air/granular flow in a linear Hele-Shaw cell, Phys Rev E, 77, 011301 (2008). doi:10.1103/PhysRevE.77.011301 pdf P141

3. Johnsen, Ø., C. Chevalier, A. Lindner, R. Toussaint, E. Clément, K.J. Måløy, E.G. Flekkøy and J. Schmittbuhl,
Decompaction and fluidization of a saturated and confined granular medium by injection of a viscous liquid or a gas, Phys. Rev. E, 78, 051302 (2008). doi:10.1103/PhysRevE.78.051302 pdf P154

4. Niebling, M., R. Toussaint, E.G. Flekkøy and K.J. Måløy,
Estudios numéricos de Aerofractures en medios poros / Numerical Studies of Aerofractures in Porous Media, Revista Cubana de Fisica, 29, 1E, 1E66, 2012. Open Access P166

5. Niebling, M.J., R. Toussaint, E.G. Flekkøy and K.J. Måløy,
Dynamic aerofracture of dense granular packings, Phys. Rev. E, **86**, 061315, 2012. P171

6. Ghani, I., D. Koehn, R. Toussaint, C. W. Passchier,
Dynamic development of hydrofracture - 2d hybrid numerical modeling of brittle deformation coupled with fluid pressure diffusion, Pure and Applied Geophysics, accepted, 2013. P180

I.ii Instabilités de sédimentations et Rayleigh Taylor granulaire dans les mélanges eau/grains et air/grain ***223***

7. Vinningland, J.L., Ø Johnsen, E.G. Flekkøy, R. Toussaint and K.J. Måløy,
A granular Rayleigh-Taylor instability: experiments and simulations, Phys. Rev. Lett., 99, 048001, (2007). pdf doi:10.1103/PhysRevLett.99.048001 P223

8. Vinningland, J.L., Ø. Johnsen, E.G. Flekkoy, R. Toussaint and K.J. Måløy,
Experiments and Simulations of a gravitational granular flow instability, Phys. Rev. E, 76, 051306 (2007). pdfdoi:10.1103/PhysRevE.76.051306 P227

9. Vinningland, J.L., Ø. Johnsen, E.G. Flekkøy, R. Toussaint and K.J. Måløy,
Influence of particle size in Rayleigh Taylor granular flow instability, Phys. Rev. E 81, 041308 (2010). doi: 10.1103/PhysRevE.81.041308 pdf P240

10. Niebling, M.J., E.G. Flekkøy, K.J. Måløy, R. Toussaint,
Mixing of a granular layer falling through a fluid, Phys. Rev. E 82, 011301 (2010) doi: 10.1103/PhysRevE.82.011301 pdf P248

11. Niebling, M.J., E.G. Flekkøy, K.J. Måløy, R. Toussaint,
Sedimentation instabilities: impact of the fluid compressibility and viscosity, Phys. Rev. E 82, 051302, 2010. doi: 10.1103/PhysRevE.82.051302 pdf P264

12. Vinningland, J.L., Ø. Johnsen, E.G. Flekkøy, R. Toussaint and K.J. Måløy,
Granular Rayleigh Taylor instability, Proc. of the 6th international conference on micromechanics of granular media, Powder and grains 2009, M. Nakagawa and S. Luding, eds, 2009. pdf P272

13. Vinningland, J.L., Ø. Johnsen, E.G. Flekkøy, R. Toussaint and K.J. Måløy,
Granular Rayleigh Taylor instability, Proc. of the Traffic and Granular Flow conference, 2007, Orsay, 2009. pdf P276

14. Vinningland, J.L., R. Toussaint, M. Niebling, E.G. Flekkøy and K.J. Måløy,
Family-Vicsek scaling of detachment fronts in Granular Rayleigh Taylor Instabilities during sedimenting granular/fluid flows, European Physics Journal Special Topics, 204(1):27-40, 2012. doi: 10.1140/epjst/e2012-01550-2 P286

I.iii Mécanique d'interfaces cisaillées et avalanches ***300***

15. Altshuler, E., R. Toussaint, E. Martinez, O. Sotolongo-Costa, K.J. Måløy and J. Schmittbuhl,
Revolving rivers in sandpiles: from continuous to intermittent flows, Phys Rev E, 77, 031305 (2008). doi:org/10.1103/PhysRevE.77.031305 pdf P300

16. Goren, L., E. Aharonov, D. Sparks and R. Toussaint,
The mechanical coupling of fluid-filled granular material under shear, P.A.Geoph., 168, 12, 2011. doi: 10.1007/s00024-011-0320-4 P307

17. Goren, L., E. Aharonov, D. Sparks and R. Toussaint,
Pore pressure evolution in deforming granular material: A general formulation and the infinitely stiff approximation, J. Geophys. Res., 115, B09216, (2010).
doi:10.1029/2009JB007191 pdf P342

18. Travelletti, J., C. Delacourt, P. Allemand, J.-P. Malet, J. Schmittbuhl, R. Toussaint, M. Bastard,
Correlation of multi-temporal ground-based images for landslide monitoring: application, potential and limitations. ISPRS Journal of Photogrammetry and Remote Sensing 70, 39-55, 2012. doi: 10.1016/j.isprsjprs.2012.03.007 P361

19. Travelletti, J., Malet, J.P., Schmittbuhl, J., Toussaint, R., Bastard, M., Delacourt, C., Allemand, P. and van Dam, D.B.,
Multi-temporal terrestrial photogrammetry for landslide monitoring, Proc. of the Florence conference Mountain Risks: Bringing Science to Society, 2010. pdf P378

20. Travelletti, J., C. Delacourt, J.P. Malet, P. Allemand, J. Schmittbuhl, R. Toussaint,
Performance of image correlation techniques for landslide displacement monitoring, Proc. of the 2nd world landslide forum, Rome, 2011. pdf P387

21. Smith, S.A.F., F. Agosta, R. Toussaint, and R.E. Holdsworth,
Foreword to Special Issue: "Fault Zone Structure, Mechanics and Evolution in Nature and Experiment", Journal of Structural Geology, 45, 1-2, 2012. P395

22. Travelletti, J., J.P. Malet, J. Schmittbuhl, R. Toussaint, C. Delacourt, P. Allemand,,

Performance of image correlation techniques for landslide displacement monitoring, Proc. des Journées Aléas Gravitaires 2011, Strasbourg, A. Remaitre et J.P. Malet, eds.

23. Renaud Toussaint, Liran Goren, Einat Aharonov ,David Sparks, Michael Niebling, Eirik Flekkoy, KJ Maloy.,
Role des fluides dans les glissements de terrain, la liquefaction et la lubrification des failles: importance des forces de filtration en conditions drainees. Proceedings des Journees Aleas Gravitaires 2011, Strasbourg, A. Remaitre et J.P. Malet, eds.

24. Toussaint, R., K.J. Måløy, Y. Méheust, G. Løvoll, M. Jankov, G. Schäfer and J. Schmittbuhl,
Two-phase flow: structure and upscaling, consequences on macroscopic transport properties, Vadose Zone Journal, 11, vzj2011.0123, 2012. doi:10.2136/vzj2011.0123 HAL P397

25. Løvoll, G., Y. Méheust, R. Toussaint, J. Schmittbuhl and K.J. Måløy,
Growth activity during fingering in a porous Hele Shaw cell, Phys. Rev. E., 70, 026301 (2004). (cond-mat/0310204) pdf doi:10.1103/PhysRevE.70.026301 P406

26. Toussaint, R., G. Løvoll, Y. Méheust, K.J. Måløy and J. Schmittbuhl
Influence of pore-scale disorder on viscous fingering during drainage, Europhys. Lett., 71, 583 (2005). pdf, ps doi:10.1209/epl/i2005-10136-9 P418

27. Løvoll, G., M. Jankov, K.J. Måløy, R. Toussaint, J. Schmittbuhl, G. Schaefer and Y. Méheust,
Influence of viscous fingering on dynamic saturation-pressure curves in porous media, Transport in Porous Media, 86, 1, 305-324, 2010 DOI: 10.1007/s11242-010-9622-8 pdf P425

28. Jankov, M., G. Løvoll, H.A. Knudsen, K.J. Måløy, R. Planet, R. Toussaint and E.G. Flekkøy,
Effects of pressure perturbations on drainage in an elastic porous medium, Tr. in Porous Media, 84, 3, 569 (2010). doi: 10.1007/s11242-009-9521-z pdf P445

29. Tallakstad, K.T., H.A. Knudsen, T. Ramstad, G. Løvoll, K.J. Måløy, R. Toussaint and E.G. Flekkøy
Steady-state two-phase flow in porous media: statistics and transport properties, Phys. Rev. Lett. 102, 074502 (2009). doi:10.1103/PhysRevLett.102.074502 pdf P462

30. Yan, J., X. Luo, W. Wang, R. Toussaint, J. Schmittbuhl, G. Vasseur, A. Yu, Z. Likuan,
An experimental study of oil secondary migration in a three dimensional tilted porous medium, A.A.P.G. Bulletin, 96(5), 773-788 , 2012. doi: 10.1306/09091110140 P466

31. Yan, J., X. Luo, W. Wang, F. Chen, R. Toussaint, J. Schmittbuhl, G. Vasseur, Z. Likuan
Testing oil saturation distribution in migration paths using NMRI, Journal of Petroleum Science and Petroleum Engineering, 86-87, 237-245, 2012. doi: 10.1016/j.petrol.2012.03.027 P482

32. Nsir, K., G. Schäfer, R. Di Chiara Roupert, O. Razakarisoa, R. Toussaint,
Laboratory experiments on DNAPL gravity fingering in water-saturated porous media, Internat. J. of Multiphase Flow, 40, 83-92, 2012. doi: 10.1016/j.ijmultiphaseflow.2011.12.003 P491

33. K. Nsir, G. Schaefer, O. Razakarisoa, R. Toussaint, J. Schmittbuhl,

44. Toussaint, R. and S.R. Pride,
Fracture localization of disordered solids in compression as a critical phenomenon: I. Statistical Mechanics Formalism., Phys. Rev. E, 66, 036135 (2002). (cond-mat/0209124). pdf doi:10.1103/PhysRevE.66.036135 P582

45. Toussaint, R. and S.R. Pride,
Fracture localization of disordered solids in compression as a critical phenomenon: II: Model hamiltonian for a population of interacting cracks., Phys. Rev. E, 66, 036136 (2002). (cond-mat/0209127). pdf doi:10.1103/PhysRevE.66.036136 P592

46. Toussaint, R. and S.R. Pride,
Fracture localization of disordered solids in compression as a critical phenomenon: III: Analysis of the localization transition, Phys. Rev. E, 66, 036137 (2002). (cond-mat/0209129). pdf doi:10.1103/PhysRevE.66.036137 P601

47. Pride, S.R. and R. Toussaint,
Statistical mechanics of fiber bundles, Physica A, 312, 159 (2002). (condmat/0209131) pdf doi:10.1016/S0378-4371(02)00816-6 P612

48. Toussaint R. and S.R. Pride
Interacting damage models mapped onto Ising and percolation models, Phys. Rev. E, 71, 046127 (2005). (condmat/0403412) pdf doi:10.1103/PhysRevE.71.046127 P625

49. Toussaint, R.
Statistical mechanics of interacting fiber bundles, Proc. of the ICF11, 11th International Conference on Fracture, Torino, 2005. pdf proceedings P640

50. Toussaint R. and A. Hansen
Mean field theory of damage nucleation in the fuse model, Phys. Rev. E, 73, 046103 (2006). (condmat/0403217) pdf, ps doi:10.1103/PhysRevE.73.046103 P646

51. Måløy, K.J., S. Santucci, J. Schmittbuhl and R. Toussaint
Local waiting time fluctuations along a randomly pinned crack front, Phys. Rev. Lett., 96, 045501 (2006). pdf, ps doi:10.1103/PhysRevLett.96.045501 P661

52. Santucci, S., K.J. Måløy, R. Toussaint, and J. Schmittbuhl,
"Self affine scaling during interfacial crack front propagation", in ``Dynamics of Complex Interconnected Systems: Networks and Bioprocesses", NATO ASI series, edited by A.T. Skjeltorp , Kluwer, Dordrecht, 2006. pdf, ps P665

53. Pindra, N., V. Lazarus , J.B. Leblond, J. Schmittbuhl and R. Toussaint,
Deformation of the crack front during propagation in some disordered medium: theoretical and experimental studies, Proc. of the ICF12, 12th International Conference on Fracture, Ottawa, 2009. pdf P676

54. Santucci, S., M. Grob, R. Toussaint, K.J. Måløy, A. Hansen, and J. Schmittbuhl,
Crackling dynamics during the failure of heterogeneous material: Optical and acoustic tracking of slow interfacial crack growth, Proc. of the ICF12, 12th International Conference on Fracture, Ottawa, 2009. pdf P685

55. Grob, M., J. Schmittbuhl, R. Toussaint, L. Rivera, S. Santucci and K.J. Måløy,

Quake catalogs from an optical monitoring of an interfacial crack propagation, P.A.Geoph., 166, 777 (2009).doi:10.1007/s00024-004-0496-z pdf P695

56. Santucci, S., M. Grob, R. Toussaint, J. Schmittbuhl, A. Hansen and K.J. Måløy, Fracture roughness scaling: A case study on planar cracks, Europhys. Lett., 92, 4, 44001, 2010. DOI: 10.1209/0295-5075/92/44001 pdf P718

57. Tallakstad, K.T., R. Toussaint, S. Santucci, J. Schmittbuhl, K.J. Måløy, Local dynamics of a randomly pinned crack front during creep and forced propagation: an experimental study, Phys. Rev. E, 83, 046108, 2011. doi: 10.1103/PhysRevE.83.046108 P723

58. Tallakstad, K.T., R. Toussaint, S. Santucci, and K. J. Måløy, Non Gaussian fluctuations of crack front velocity, Proc. of Soft Matter & Complex Flow congress, Lofoten, Norway, accepted, 2012. P738

59. Tallakstad, K.T., R. Toussaint, S. Santucci, and K. J. Måløy, The non-Gaussian nature of fracture and the survival of fat-tail exponents, Phys. Rev. Lett., 2013. P744

60. Lengline, O., J. Elkhoury, G. Daniel, J. Schmittbuhl, R. Toussaint, J.-P. Ampuero, M. Bouchon Interplay of seismic and aseismic deformations during earthquake swarms: an experimental approach, Earth and Planetary Science Letters, 331-332, 215-223, 2012. doi: 10.1016/j.epsl.2012.03.022 P752

61. Lengliné O., J. Schmittbuhl, J. Elkhoury, J.P. Ampuero, R. Toussaint and K.J. Måløy, Down-scaling of the fracture energy during brittle creep experiments, J. Geoph. Res. B, 116, B0815, 2011. doi: 10.1029/2010JB008059 P760

62. Måløy, K.J., R. Toussaint and J. Schmittbuhl Dynamics and structure of interfacial crack fronts, Proc. of the ICF11, 11th International Conference on Fracture, Torino, 2005. pdf proceedings P774

63. Lengliné, O., R. Toussaint, J. Schmittbuhl, J. Elkhoury, J.P. Ampuero, K.T. Tallakstad, S. Santucci and K.J. Måløy, Average crack front velocity during subcritical fracture propagation in a heterogeneous medium, Phys. Rev. E, 84, 6104, 2011. doi: 10.1103/PhysRevE.84.036104 P780

64. Koehn, D., Ebner, M., Renard, F., Toussaint, R., Passchier, C.W., Modelling of stylolite geometries and stress scaling, Earth and Planetary Science Letters, 341-343, 104-113, 2012. doi: 10.1016/j.epsl.2012.04.046 P793

65. Rolland, A., R. Toussaint, P. Baud, J. Schmittbuhl, N. Conil, D. Koehn, F. Renard and J.P. Gratier, Modeling the growth of stylolites in sedimentary rocks, J. Geoph. Res., 117(6), B06403, 2012. doi: 10.1029/2011JB009065 P803

66. Koehn, D., F. Renard, R. Toussaint, C. Passchier Growth of stylolite teeth patterns depending on normal stress and finite compaction, EPSL, 257, 582 (2007). pdf doi:10.1016/j.epsl.2007.03.015 P821

67. Schmittbuhl, J., F. Renard, J.P. Gratier and R. Toussaint

Ouvrages:

Fracturation des roches: la localisation comme phénomène critique. Editions Universitaires Européennes, 2012. ISBN-13 978-3-8417-9391-1, ISBN-10:3841793916
http://www.morebooks.fr

Articles soumis, en révision :

80. Neuville, A., E.G. Flekkøy, and R. Toussaint,
Influence of asperities on fluid and thermal flow in a fracture: a coupled Lattice Boltzmann study, submitted to JGR B, 2013.

81. A. Spickermann, R. Toussaint, J. Travelletti, J.-P. Malet, Th.W.J. van Asch,
A grain-fluid mixture model to characterize the dynamics of active landslides in fine-grained soils, submitted to J.G.R. E, 2013.

82. Allègre, V., F. Lehmann, L. Jouniaux, P. Sailhac, and R. Toussaint
Modelling the streaming potential dependence on water-content during drainage: Influence of pressure dynamics and fluid flow, submitted to T.I.P.M., 2013.

83. Aochi, H., B. Poisson, R. Toussaint, X. Rachez and J. Schmittbuhl,
The impact of spatial and temporal changes in fault characteristics on induced seismicity due to fluid circulation, submitted to Geoph. J. Int., 2013.

84. Laronne Ben-Itzhak, L., E. Aharonov, Z. Karcz, M. Kaduri and R. Toussaint,
Sedimentary stylolite populations in Limestone: Large-scale field observations and implications for structure evolution, submitted to Journal of Structural Geology, 2013.

85. Rolland, A., R. Toussaint, P. Baud, N. Conil and P. Landrein,
Morphological analysis of stylolites for paleostress estimation in limestones surrounding the Andra Underground Research Laboratory site, submitted to Int. J. Rock Mech. Min. Sci., 2013.

86. Lengliné, O., J. Schmittbuhl, K.J. Måløy, A. Cochard and R. Toussaint,
A brittle creep model of interfacial crack propagation, submitted to Physical Review Letters, 2013.

87. Vasseur, G., Luo, X., Yan, J., Loggia, D., Schmittbuhl, J. and Toussaint, R.
Flow regime associated with secondary migration, submitted to Journal of Marine and Petroleum Geology, 2013.